

Introduction: Batteries and Fuel Cells

This special issue of *Chemical Reviews* covers the electrochemical storage and generation of energy in batteries and fuel cells. This area is gaining tremendous importance for powering high technology devices and for enabling a greener and less energy-intensive transportation industry. Whether the demand is from a cell phone, a computer, or an iPod, consumers are demanding a longer life in a smaller package and at a lower cost with minimal if any wired connection. The consumer generally does not care whether the power source is a battery, a fuel cell, or something else, as long as it works. In the area of greener transportation, there has been a surge of interest in vehicles that are electrically powered, either totally, as planned for the green Beijing Olympic Games, or partially, as in hybrid electric vehicles. The present generation of such vehicles uses a combination of an internal combustion engine and a battery, today nickel metal hydride, as in the Toyota Prius, and tomorrow lithium; a future generation is likely to be a hybrid of a fuel cell and a battery.

Both batteries and fuel cells utilize controlled chemical reactions in which the desired process occurs electrochemically and all other reactions including corrosion are hopefully absent or severely kinetically suppressed. This desired selectivity demands careful selection of the chemical components including their morphology and structure. Nanosize is not necessarily good, and in present commercial lithium batteries, particle sizes are intentionally large. All batteries and fuel cells contain an electro-positive electrode (the anode or fuel) and an electro-negative electrode (the cathode or oxidant) between which resides the electrolyte. To ensure that the anode and cathode do not contact each other and short out the cell, a separator is placed between the two electrodes. Most of these critical components are discussed in this thematic issue.

The issue starts with a general introduction by Brodd and Winter to batteries and fuel cells and the associated electrochemistry. It then continues first with several papers discussing batteries and then with papers discussing fuel cells.

Batteries

Outside of the above introduction, the battery papers describe lithium batteries, where most chemi-

cal and materials research has been focused during the past three decades. The second paper, by Whittingham, begins with a general historical background to lithium batteries and then focuses on the next generation of cathodes. The third, by Xu, gives an in-depth review of the presently used and future electrolytes; this is followed by an extensive review by Arora and Zhang of the separators used in lithium and related batteries. The following paper, by Long, Dunn, Rolison, and White, addresses new three-dimensional concepts for increasing the storage capacity. Critical to the development of new materials are advanced characterization and modeling techniques, and some of these are described by Grey and Dupre and by Reed and Ceder in the last two papers of the battery group. Several papers covering anodes, phosphate and nickel oxide cathodes, and nickel metal hydride batteries did not meet the publication deadline, and it is hoped that they will appear in future issues.

Fuel Cells

Although fuel cells were invented in the middle of the 19th century, they didn't find the first application until space exploration in the 1960s. Since then, the development of fuel cell technology has gone through several cycles of intense activity, each followed by a period of reduced interest. However, during the past two decades, a confluence of driving forces has created a sustained and significant world-wide effort to develop fuel cell materials and fuel cell systems. These driving needs include the demand for efficient energy systems for transportation, the desire to reduce CO₂ emissions and other negative environmental impacts, and the demand for high energy density power sources for portable electronic applications. Due to the high level of interest in fuel cells during the last decade or so, there have been numerous summary articles and symposia focused on the technology state of the art. In this thematic issue, we present a series of summary articles that deal with some of the fundamental scientific issues related to fuel cell development.

A fuel cell that has desirable features for transportation and portable power is the polymer electrolyte membrane (PEM) system. The core of this technology is a polymer membrane that conducts

protons but separates the fuel from the oxidant. The material used historically and most frequently in PEM fuel systems is Nafion, a perfluorocarbon-based polymer carrying sulfonic acid residues. Nafion is a commercial material and has received the most extensive study of any PEM fuel cell membranes. Mauritz and Moore prepared a summary of the current understanding of the large volume of research that has gone into optimizing and understanding this membrane system. Other polymer systems that would have even better performance than Nafion and/or have lower costs are being sought by researchers around the world. Hickner, Ghassemi, Kim, Einsla, and McGrath summarize work on such alternative polymer systems for proton exchange membranes. These types of materials have complex transport properties that involve not just proton movement but also the movement of water. Theoretical treatments of the transport mechanisms and processes in these proton conductors are given by Kreuer, Paddison, Spohr, and Schuster and by Weber and Newman.

In PEM fuel cells, catalyst activity and catalyst efficiency are still significant issues. Russell and Rose summarize fundamental work involving X-ray absorption spectroscopy on catalysts in low temperature fuel cell systems. These types of studies are very useful for developing a detailed understanding of the mechanisms of reactions at catalyst surfaces and could lead to the development of new improved efficient catalysts. Important in the development of fuel cell technology are mathematical models of engineering aspects of a fuel cell system. Wang writes about studies related to this topic.

Finally, in order for PEM fuel cell systems to be affordable for portable power applications, a source

of high energy density fuel must be considered. To this end, Holladay, Wang, and Jones present a review of the developments of using microreactor technology to convert liquid fuels into hydrogen for directly feeding into a PEM fuel cell.

Another fuel cell system undergoing intense research is the solid oxide type. Adler presents the factors that govern the rate limiting oxygen reduction reaction within the solid oxide fuel cell cathodes. McIntosh and Gorte, on the other hand, treat the anode in the solid oxide fuel cell by examining catalytic direct hydrocarbon oxidation. Finally, Calabrese Barton, Gallaway, and Atanossov take a look at the future. In their article, they present a summary of some of the enzymatic biological fuel cells that are being developed as implantable devices and also to power microscale devices.

We hope this collection of papers will provide new researchers in the field with a starting point for advancing research. Furthermore, our hope is to stimulate the next generation of breakthroughs that will lead to the success of fuel cell development.

M. Stanley Whittingham
Chemistry and Materials,
State University of New York at Binghamton

Robert F. Savinell
Chemical Engineering,
Case Western Reserve University

Thomas Zawodzinski
Chemical Engineering,
Case Western Reserve University

CR020705E

X-ray Absorption Spectroscopy of Low Temperature Fuel Cell Catalysts

Andrea E. Russell* and Abigail Rose

School of Chemistry, University of Southampton, Highfield, Southampton SO17 1BJ, U.K.

Received December 16, 2003

Contents

1. Introduction	4613
2. X-ray Absorption Spectroscopy	4614
2.1. XANES	4614
2.2. EXAFS	4615
3. Data Collection and In Situ Cells	4618
4. XAS as a Characterization Method: Pt/C	4620
4.1. Particle Size	4620
4.2. Potential Dependence	4621
4.3. Adsorbates	4624
5. Pt Containing Alloy Catalysts	4626
5.1. PtRu Alloys	4627
5.1.1. Compositional Analysis	4628
5.1.2. Potential Dependence	4628
5.1.3. Adsorbates	4629
5.2. Other Pt Containing Alloy Anode Catalysts	4630
5.3. Pt Containing Alloy Cathode Catalysts	4630
6. Non-Pt Catalysts	4632
7. Conclusion	4633
8. References	4633

1. Introduction

In the last two decades X-ray absorption spectroscopy (XAS) has increasingly been applied to the study of fuel cell catalysts and, in particular, Pt containing catalysts for use in low temperature fuel cells. The increasing use of XAS may be attributed to its unique potential to provide information regarding the oxidation state and local coordination, numbers and identity of neighbors, of the absorbing atom. The advantage of XAS over other characterization methods, such as XPS or SEM/EDAX, lies in the ability to conduct the measurements in situ, in environments that closely mimic those of a working fuel cell.

In the application of XAS to the study of fuel cell catalysts, the limitations of the technique must also be acknowledged; the greatest of which is that XAS provides a bulk average characterization of the sample, on a per-atom basis, and catalyst materials used in low temperature fuel cells are intrinsically nonuniform in nature, characterized by a distribution of particle sizes, compositions, and morphologies. In addition, the electrochemical reactions of interest in fuel cells take place at the surface of catalyst par-

ticles, and XAS is not able to provide a means of directly probing the surface composition or electronic/chemical state of the surface of the catalyst particles. Throughout this review both the advantages and limitations of XAS in the characterization of low temperature fuel cell catalysts will be emphasized.

An XAS experiment measures the change in the absorbance, μx , or fluorescence of the sample as the X-ray energy is scanned through the absorption edge. At the absorption edge the energy of the incident X-ray photon is sufficient to excite a core level electron of the absorbing atom to unoccupied atomic or molecular orbitals. A typical XAS spectrum is shown in Figure 1. The absorption, μx , is defined by the Beer Lambert equation,

$$\mu x = \log(I_0/I_t) \quad (1)$$

where μ is the linear absorption coefficient, x is the sample thickness, I_0 is the intensity of the incident photons, and I_t is that of the transmitted photons. The region closest to the absorption edge has a structure that is characteristic of the local symmetry and electronic structure of the absorbing atom, which is commonly called the XANES, X-ray absorption near edge structure. The position of the absorption edge can provide information regarding the oxidation state of the absorber. The XANES region extends to approximately 50 eV above the absorption edge. At higher energies the energy of the incident X-ray photons is sufficient to excite a core electron of the absorber into the continuum producing a photoelectron with kinetic energy, E_k ,

$$E_k = h\nu - E_{\text{binding}} \quad (2)$$

The ejected photoelectron may be approximated by a spherical wave, which is backscattered by the neighboring atoms. The interference between the outgoing forward scattered, or ejected, photoelectron wave and the backscattered wave gives rise to an oscillation in the absorbance as a function of the energy of the incident photon. These oscillations, which may extend up to 1000 eV above the absorption edge, are called the EXAFS, extended X-ray absorption fine structure. Analysis of the EXAFS provides information regarding the identity of, distance to, and number of near neighboring atoms.

This review will focus on the applications of XAS in the characterization of low temperature fuel cell catalysts, in particular carbon supported Pt electrocatalysts, Pt containing alloys for use as anode and

* To whom correspondence should be addressed. Phone: +44 (0) 2380 593306. Fax: +44 (0) 2380 596805. E-mail: a.e.russell@soton.ac.uk.



Andrea E. Russell was born in California and grew up in Michigan. She obtained her B.S. degree in Chemistry from the University of Michigan, Ann Arbor in 1986 and her Ph.D. in Physical Analytical Chemistry from the University of Utah, Salt Lake City in 1989 working with B. Stanley Pons. She then went to work with William O'Grady at the U.S. Naval Research Laboratory in Washington, DC, where she first started working with synchrotron radiation. In 1991 she moved to the U.K. as a Lecturer at the University of Liverpool, moving in 1994 to the University of Newcastle upon Tyne and in 1997 to the University of Southampton, where she is now a Reader and a Member of the Electrochemistry and Surface Science Group. Her research interests are in the application of spectroscopic methods to further the understanding of structure/property relationships in electrochemistry and electrocatalysis. Full use of the electromagnetic spectrum is made, from the far-infrared through to hard X-rays.



Abigail Rose was raised in Somerset, England. She obtained her B.Sc. degree in Chemistry from the University of Southampton in 1998. She remained at Southampton, obtaining an M.Phil. in 1999 under the supervision of Jeremy Frey and a Ph.D. in Physical Chemistry in 2003 working with Andrea Russell. Her Ph.D. thesis work, funded by the EPSRC at Johnson Matthey, was on the applications of in situ EXAFS to the study of PEM fuel cell catalysts. Presently, she is working as a fuel cell scientist at Dstl, Porton Down, a U.K. Ministry of Defence research laboratory.

cathode catalysts, and, finally, non-Pt containing cathode catalysts. A discussion of the cells that have been used for in situ and gas treatment measurements will be presented. The type of information that can be derived from XAS studies of fuel cell catalysts will be illustrated, and the relevant XAS literature from 1982 to 2003 will be reviewed.

2. X-ray Absorption Spectroscopy

The details of the analysis of the XANES and EXAFS regions of the XAS spectra are beyond the scope of this review. However, as XAS is becoming a more "routine" tool for the study of fuel cell catalysts,

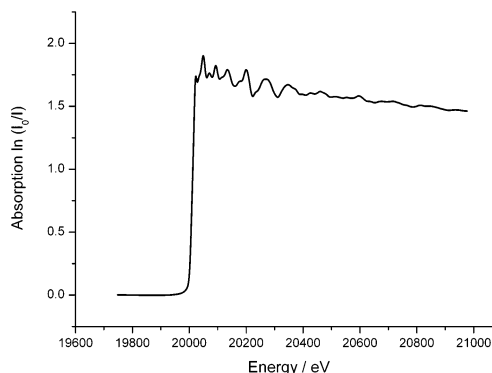


Figure 1. XAS spectrum of a Mo foil collected at the Mo K edge.

we feel that some discussion of the basic aspects of the analysis as applied to fuel cell catalysts is warranted and may assist the nonspecialist in understanding the origins of the information derived from XAS.

2.1. XANES

In the study of fuel cell catalysts, detailed analysis of the XANES region is not common. As mentioned in the Introduction, the position of the absorption edge is related to the oxidation state of the absorbing atom and the detailed features can provide an identification of the neighbors, coordination geometry, and, in the case of clusters of atoms, particle size and morphology. The XANES region of the XAS spectrum is dominated by multiple-scattering and multiphoton absorptions. As such, detailed analysis of this region is less straightforward than that of the EXAFS region, which will be described in section 2.2, and most studies have been limited to a so-called white line analysis, which will be discussed below. However, recent advances in the theoretical models and the availability of computer programs, such as the FEFF8 code developed by Rehr's group,¹ should encourage more detailed analysis of the XANES of supported metal catalysts.

The FEFF8 code is an *ab initio* code that implements a self-consistent, real-space Green's function approach. The recent improvements in the FEFF code are particularly apparent, in the analysis of L_{III} absorption edges, where transitions from the $2p_{3/2}$ level to vacant d-states of the absorbing atom occur. For example, Ankudinov and Rehr² have recently shown that the Pt L_{III} edge of a Pt foil is more reliably reproduced by the FEFF8 code, which is self-consistent, than by the FEFF7 code previously used by Bazin et al.³ The absorption coefficient and, therefore, intensity of the white line for a surface atom are not the same as those for a bulk atom, and this must be taken into account when fitting the XANES of nanoparticles, as demonstrated by Bazin et al. for Pt clusters of 13, 19, 43, and 55 atoms with the fcc structure (O_h symmetry).³ The morphology of the cluster was also shown to be important for Pt clusters⁴ and Cu clusters.⁵ Fitting the XANES data requires comparison of the spectrum to the spectra of a series of relevant reference compounds, which are then simulated using FEFF8. Detailed analysis

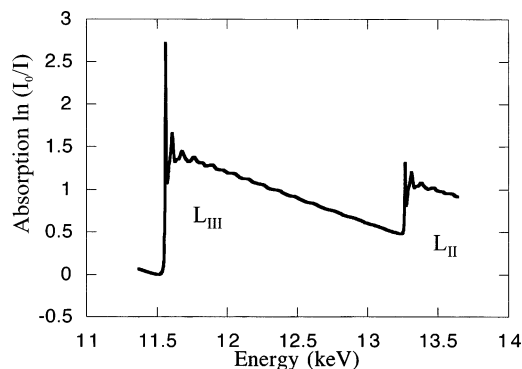


Figure 2. XAS spectrum of $\text{Na}_2\text{Pt}(\text{OH})_6$ powder.

of the XANES of a fuel cell catalyst, with a distribution of particle sizes and morphologies, can then be accomplished using principal component analysis (PCA). However, as noted by Bazin and Rehr,⁵ defining relevant reference compounds and the simulation of a large number of absorption spectra of possible structures, which may only contribute as minor components to the overall spectrum, are major limitations of this technique. However, the PCA-FEFF approach offers a real opportunity to obtain the distribution of the electronic states of catalyst particles.

The XANES region of the Pt L_{III} and L_{II} absorption edges can be used to determine the fractional d-electron occupancy of the Pt atoms in the catalyst sample by a so-called white line analysis. Figure 2 shows the XAS spectrum collected at both Pt L_{III} and L_{II} absorption edges of $\text{Na}_2\text{Pt}(\text{OH})_6$. The sharp features at the absorption edges are called white lines after the white line observed in early photographic film based XAS measurements.⁶ Mansour and co-workers⁷ have shown that comparison of the white line intensities of a sample with those of a reference metal foil provides a measure of the fractional d-electron vacancy, f_{d} , of the absorber atoms in the sample. f_{d} is defined as follows:

$$f_{\text{d}} = (\Delta A_3 + 1.11\Delta A_2)/(A_{3,\text{r}} + 1.11A_{2,\text{r}}) \quad (3)$$

where $A_{3,\text{r}}$ represents the area under the white line at the L_{III} edge and $A_{2,\text{r}}$ represents the area at the L_{II} edge of the reference foil spectrum and

$$\Delta A_x = A_{x,\text{s}} - A_{x,\text{r}} \quad (4)$$

with $x = 2$ or 3 and $A_{x,\text{s}}$ the area under the white line at the L_x edge of the sample spectrum. The areas may be determined by integration of the normalized (defined below) spectra from 10 eV below the absorption edge to 40 eV above the absorption edge or by first subtraction of an arc tangent function fit through the pre- and postabsorption edge regions.

f_{d} can then be used to calculate the total number of unoccupied d-states per Pt atom in the samples as follows:

$$(h_j)_{\text{t,s}} = (1.0 + f_{\text{d}})(h_j)_{\text{t,r}} \quad (5)$$

where $(h_j)_{\text{t,r}}$, t = total, for Pt has been shown to be 0.3.⁸ A large $(h_j)_{\text{t,s}}$ value, thus, indicates a smaller d-electron density and an increased d band vacancy

as compared to those for bulk Pt. Unfortunately, when $(h_j)_{\text{t,s}}$ values have been reported in the fuel cell literature, no estimation of the error in the measurement has been given. Therefore, it is best to treat the determination of $(h_j)_{\text{t,s}}$ as a semiquantitative measurement and to restrict its use to the comparison of relative values and the identification of trends.

2.2. EXAFS

To analyze the EXAFS region of the XAS spectrum, the raw data must first be subjected to background subtraction, determination of the zero point of the energy, and normalization. Background subtraction removes both the variation in the absorbance with energy caused by the other atoms in the sample (the near-linear variation seen before the edge, usually modeled as a modified Victoreen function⁹) and the smooth variation in μ past the absorption edge, corresponding to the absorption of the free atom. The zero point of the energy, E_0 , is usually taken as the inflection point in the absorption edge. This allows the energy of the incident photon, E_{hv} , to be converted to k -space (\AA^{-1}) as follows:

$$k = \left(\frac{2m_e}{\hbar} (E_{\text{hv}} - E_0) \right)^{1/2} \quad (6)$$

Normalization places the measured spectrum on a per-absorber-atom basis, thereby taking into account the concentration of the sample, and is division of the absorption data by the magnitude of the edge step at 50 eV above the absorption edge. The details of XAS data reduction may be found elsewhere.¹⁰

Once the EXAFS spectrum is isolated, the data may then be fitted to the EXAFS equation,

$$\chi(k) = \sum_{j=1}^{\text{shells}} A_j(k) \sin \delta_j(k) \quad (7)$$

with the amplitude function

$$A_j(k) = \frac{N_j}{kR_j^2} S_0^2 F_j(k) e^{-2k^2\sigma_j^2} e^{-2R_j/\lambda(k)} \quad (8)$$

and the phase function

$$\sin \delta(k) = \sin(2kR_j + \varphi_j(k)) \quad (9)$$

where N_j is the number of atoms of type j at the distance R_j from the absorber atom, $F_j(k)$ is the magnitude of the backscattering from atom j , $\delta_j(k)$ is the backscattering phase shift resulting from scattering off atom j , S_0 is the amplitude reduction factor and reflects multielectron effects and central atom shake-up and shake-off due to the relaxation process after photoionization, $e^{-2k^2\sigma_j^2}$ accounts for the finite lifetime of the excited state, σ_j^2 is the relative mean squared disorder along the distance between the absorbing atom and atom j due to thermal and static motions, and λ is the mean free path of the electron.

The backscattering amplitude, $F_j(k)$, and phase shift, $\delta_j(k)$, for the absorber-neighbor pair may be extracted from the EXAFS of reference compounds or calculated theoretically using widely available

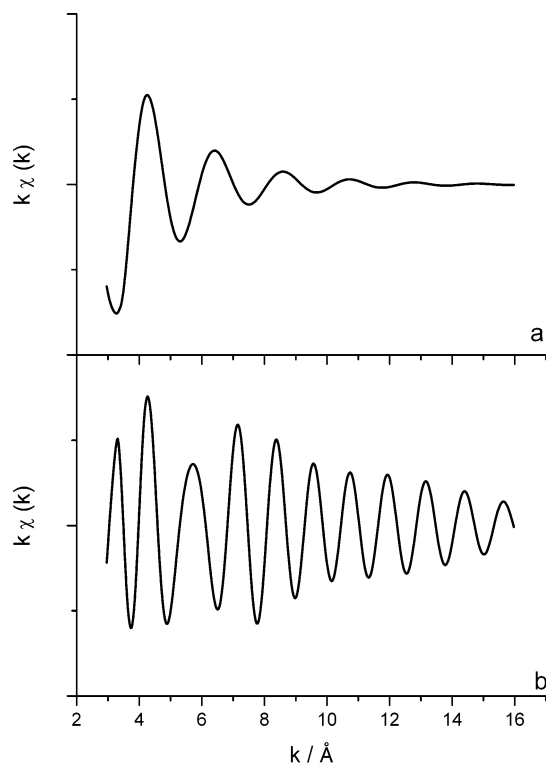


Figure 3. Calculated EXAFS of (a) Pt with six O neighbors at 1.98 Å and (b) Pt with six Pt neighbors at 2.77 Å.

programs such as the FEFF codes developed by John Rehr's group at the University of Washington.^{11–13} These parameters enable the identification of the neighbors surrounding the absorbing atom. In particular, the variation of the backscattering amplitude with energy, or k , provides an indication of the mass of the neighboring atom. The calculated EXAFS for Pt–O and Pt–Pt absorber–neighbor pairs are shown in Figure 3. As can be seen in the figure, the backscattering from a light neighbor, with low Z , is at a maximum at low k values and decays quickly, while that from a heavier neighbor, with high Z , extends to higher values of k . Weighting the EXAFS data from a sample with mixed neighbors by k or k^3 emphasizes the contributions to the EXAFS from the low and high Z neighbors, respectively. The coordination number, N_j , and the distance, R_j , also have easily visualized effects on the EXAFS. Increasing the number of a given type of neighbor increases the amplitude of the EXAFS, as shown in Figure 4 and eq 8. Variation of the near neighbor distance changes the phase of the EXAFS as shown in Figure 5 and eq 9. Attention to the effects of these parameters on the EXAFS can provide a useful starting point in fitting EXAFS data.

Fourier transformation of the EXAFS gives the radial structure function. The EXAFS and corresponding k^3 Fourier transform for a Pt foil standard are shown in Figure 6. As in the case of the raw EXAFS data, k weighting of the Fourier transformation emphasizes the contributions of low Z neighbors, k^1 weighting, or high Z neighbors, k^3 weighting. In the analysis of the EXAFS for a supported fuel cell catalyst, k^2 weighting of the Fourier transform is commonly used, as it provides a compromise, giving weight to the contributions from both low and high

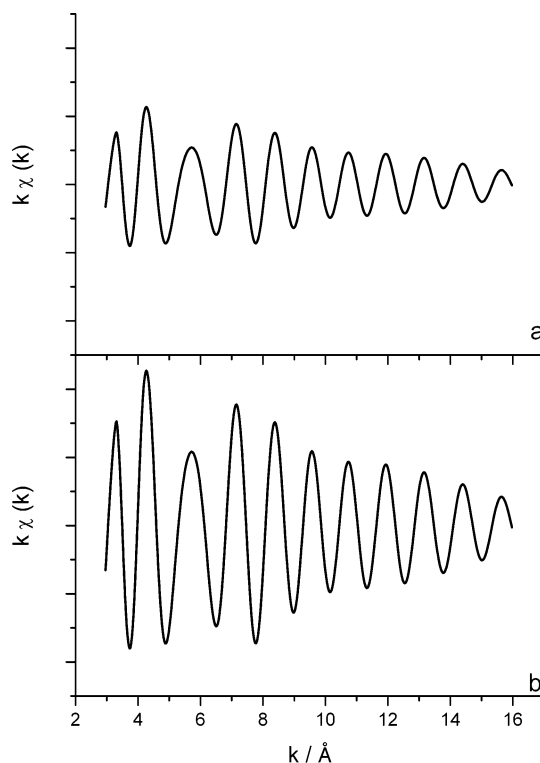


Figure 4. Calculated EXAFS of (a) Pt with six Pt neighbors and (b) Pt with 12 Pt neighbors at 2.77 Å.

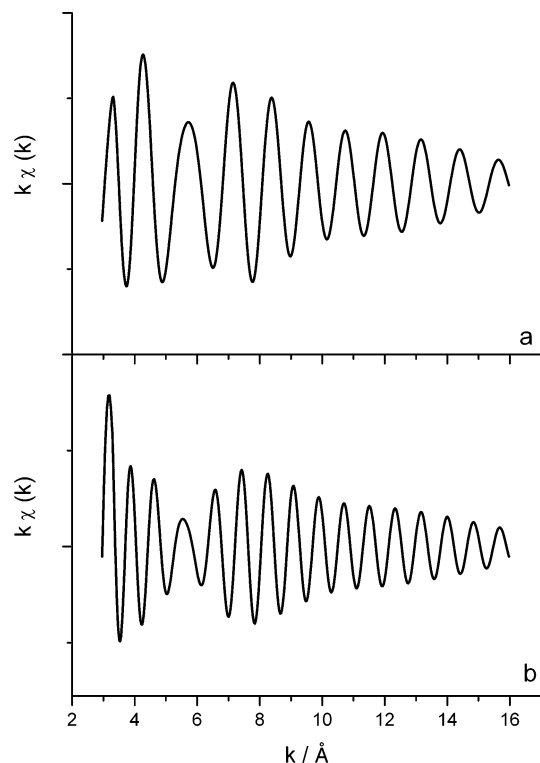


Figure 5. Calculated EXAFS of (a) Pt with six Pt neighbors at 2.77 Å and (b) Pt with six Pt neighbors at 3.42 Å.

Z neighbors. Phase correction of the Fourier transform by the backscattering phase shift of one of the absorber–neighbor pairs is also extensively used. This has the effect of correcting the distances observed in the radial structure function as well as emphasizing the contributions from the chosen ab-

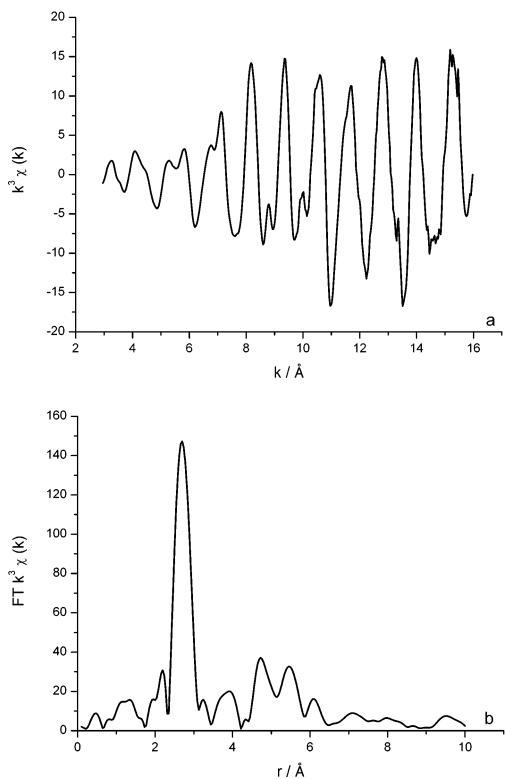


Figure 6. (a) k^3 weighted EXAFS of Pt foil collected at the Pt L_3 edge and (b) the corresponding k^3 weighted Pt phase corrected Fourier transform of the EXAFS data.

sorber–neighbor pair. Without phase correction the positions of the peaks in the radial structure function are all approximately 0.5 Å too short. The Fourier transform shown in Figure 6 corresponds to the radial structure of a Pt atom in the bulk fcc lattice, with 12 neighbors in the first shell, 6 in the second, 12 in the third, and 24 in the fourth. The decreased backscattering contribution from the neighbors at longer distances causes an apparent amplitude reduction of the radial structure function for higher shells, as predicted by eq 8.

EXAFS analysis involves fitting the data to the EXAFS equation to obtain a structural model. Currently, fitting EXAFS data relies on the user to propose candidate neighboring atoms as backscatters. The data are then fitted using the absorber–neighbor pairs. As such, the true applicability of the fits relies on chemical knowledge of the system under investigation obtained using other techniques.

There are many EXAFS analysis programs available, both commercial and free-ware, and the reader is referred to the web site of the International XAS Society for a comprehensive list.¹⁴ In preparing this review article, we found that three of these programs were much more commonly used than the others; the University of Washington UWXAFS package consisting of FEFF^{11–13} and FEFFIT, the Daresbury Laboratory code EXCURVE98 and its predecessor EXCURVE92, and the commercial program XDAP. As described previously, FEFF is a program for the ab initio calculation of phase shifts and effective backscattering amplitudes of single- and multiple-scattering XAFS and XANES spectra for clusters of atoms. There are several versions of FEFF available,

the most recent being FEFF7¹⁵ and FEFF8.¹ Versions of FEFF later than FEFF5, which included multiple-scattering paths, are equally appropriate for the provision of theoretical standards for EXAFS fitting; the improvements in the level of theory in versions 7 and 8 have more impact on the simulation of the XANES as discussed in section 2.1. The FEFFIT program fits the experimental EXAFS data to the theoretical standards calculated using FEFF in r -space and includes an estimate of the errors. EXCURVE98 is a combined theory and fitting program in which the backscattering phase shifts and amplitudes are calculated using rapid curved wave theory¹⁶ and the Rehr Albers theory^{11,12} from the parameters of the radial shells of atoms surrounding the absorber. The EXAFS data are fitted in k -space using least squares refinement, errors are estimated by calculation of the standard deviations of each parameter, and correlations between parameters may be examined. The theoretical standards generated using FEFF and EXCURVE98 can include multiple-scattering pathways. Inclusion of multiple scattering is important if higher coordination shells are to be included in the analysis, particularly those at distances equal to or greater than twice the distance to the first coordination shell. The XDAP program supplied by XSI makes use of both theoretical standards calculated using FEFF and/or experimentally derived backscattering phase shifts and amplitudes extracted from the EXAFS data of reference compounds collected by the user. The use of experimentally derived standards must be treated with caution and relies on the separation of EXAFS contributions from the various neighbors in the reference compound and the quality of the data. The EXAFS data may be fitted in k - or r -space using XDAP, and the program includes a subtraction facility which enables the difference file¹⁷ method to be easily implemented, as will be discussed below in section 4.3.

The errors in the fitting parameters may be obtained from the covariance matrix of the fit if it is available, but they are more commonly estimated by varying one parameter away from its optimal value while optimizing all other parameters until a defined increase in the statistical χ^2 function is obtained.¹⁸ However, the statistical error values obtained do not represent the true accuracies of the parameters. In fact, it is difficult to determine coordination numbers to much better than $\pm 5\%$,^{19,20} and $\pm 20\%$ is more realistic; when the data are collected at room temperature taking into account the strong coupling between the coordination number and Debye Waller terms, the error in the latter may be $\pm 30\%$.

The number of statistically justified free parameters, n , which may be fitted should also be taken into account when fitting the data. This may be estimated from the Nyquist theorem²¹ as follows:

$$n = \frac{2\Delta k \Delta r}{\pi} + 1 \quad (10)$$

where Δk and Δr are the ranges in k - and r -space over which there is useful data. This should not extend to regions where there are no meaningful data above the noise. For a data set with a Δk range of

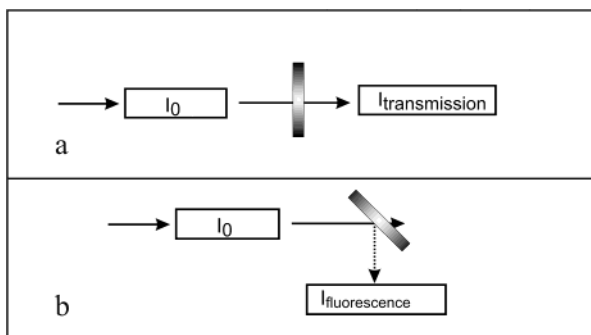


Figure 7. Experimental configuration for (a) transmission measurements and (b) fluorescence measurements. The sample is indicated by the shaded rectangle, I_0 and $I_{\text{transmission}}$ are ionization chamber detectors, and $I_{\text{fluorescence}}$ is a solid-state detector.

10 \AA^{-1} and an r -space interval of 2 \AA , application of the Nyquist theorem limits the free parameters to 14. Finally, the chemical feasibility of the fit should be examined. If the number of free parameters is not limited, it is possible to fit any EXAFS spectrum to a high level of apparent precision, and it is this observation that has given EXAFS a poor reputation in the past.

The IXAS also provides guidelines and standards for the publication of XAS data.^{22,23} In preparing this review, we found that many of the papers included did not adhere to these guidelines and standards, and while this did not invalidate the findings of most of the affected papers, it was occasionally difficult to assess the quality of the data and fits. A common omission was a statistical measure of the goodness of the fit. This may be defined as

$$R_{\text{EXAFS}} = \left\{ \sum_i^N \frac{1}{\sigma_i^{\text{exp}}} (|\chi_i^{\text{exp}} - \chi_i^{\text{th}}|) \right\} \times 100\% \quad (11)$$

where N is the total number of data points, σ^{exp} is the standard deviation for each data point, i , and χ^{exp} and χ^{th} are the experimental and theoretical EXAFS, respectively, although other definitions may be used. It is also expected that at least one representative EXAFS spectrum and the corresponding Fourier transform will be shown with the fit superimposed.

3. Data Collection and in Situ Cells

XAS measurements require a radiation source that is both intense and tunable, and therefore, they are usually conducted using synchrotron radiation. The measurements may be made using either transmission or fluorescence. The former is the more simple but is not suitable for dilute samples where fluorescence is more sensitive. A typical experimental configuration for a transmission measurement is shown in Figure 7. The intensity of the X-rays is monitored before and after the sample, I and I_0 , respectively, using ionization chamber detectors. The thickness or amount of the sample is selected to give an optimal change in the absorbance from one side of the absorption edge to the other in the range 0.3–1.0. The total absorbance of the sample at a given wavelength can be calculated from the X-ray absorp-

tion cross sections of all the elements²⁴ in the sample. The total absorbance of the sample and any other cell components in the X-ray beam path, such as windows or solution layers, should be kept to less than 2.5 to provide the best data quality. A reference metal foil or sample containing the element of interest and a third ionization chamber may be included to provide an internal standard for energy calibration. A full spectrum takes between 20 and 60 min to collect using a conventional scanning monochromator. The data collection time can be reduced to minutes by using a Quick EXAFS monochromator or even seconds if an energy dispersive monochromator is used.^{25–27} The former uses a microstepper to continuously scan the angle of the monochromator crystals, thereby reducing the dead time, and the latter uses a monochromator with a bent crystal to obtain the spectrum in a single exposure on a position sensitive solid-state detector. Unfortunately, a reduction in the quality of the EXAFS data collected usually accompanies any reduction in the collection time.

The experimental configuration for fluorescence measurements is shown in Figure 7. As in the case of transmission measurements, the intensity of the X-rays before the sample is measured using an ionization chamber. The sample is set at 45° to the path of the incident X-rays, so that the maximum solid angle of the fluorescence may be collected at the solid-state detector.

The XAS spectrum provides information regarding the average oxidation state and local coordination of the absorbing element. It is therefore crucially important when designing in situ cells for XAS measurements that complete conversion, electrochemical or chemical, of the material takes place.²⁸ XAS data of fuel cell catalysts may be obtained using samples prepared from the catalyst powders, PTFE or Nafion bound electrodes, or membrane electrode assemblies. Where the catalyst powders are studied, these are often made into pellets diluted with either boron nitride, silica, or polyethylene powder to aid preparation of the pressed pellet, similar to a potassium bromide pellet used in infrared spectroscopy. These particular diluents are chosen because they are composed of low Z elements and, therefore, are transparent at most X-ray energies. A gas treatment cell, such as that shown in Figure 8, has been used to collect the XAS spectra of self-supporting pellets of catalyst powders exposed to gas mixtures at elevated temperatures; the data are collected at either room or liquid nitrogen temperature.^{29,30} The pellet must be permeable to the gas mixture, and therefore, boron nitride was used as the diluent.

A number of designs of transmission in situ XAS cells have been published for the study of bound catalyst electrodes.^{31–33} These cells all utilize a thin-layer geometry to minimize the contribution to the absorbance by electrolyte solution. The cell design reported by McBreen and co-workers³¹ shown in Figure 9 uses three layers of filter paper soaked in the electrolyte as a separator, or later a Nafion membrane³⁴ between the working electrode and a Grafoil counter electrode. Bubbles in the electrolyte, that would result in noise in the XAS data, are

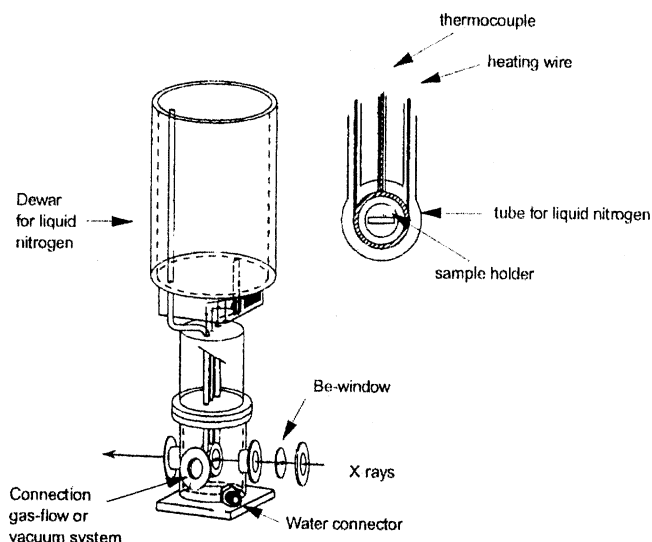


Figure 8. Gas treatment cell for transmission XAS.¹⁵⁴ The sample is prepared as a pressed self-supporting pellet in the sample holder, diluted with BN. The liquid nitrogen dewar enables data collection at 77 K, and the connection to gas-flow or a vacuum system enables control of the sample environment. (Reproduced with permission from ref 154. Copyright 1997 B. L. Mojet).

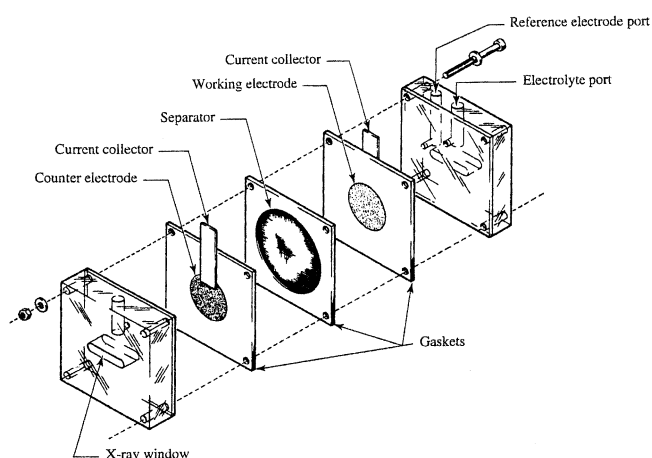


Figure 9. Electrochemical cell for transmission XAS.³¹ (Reproduced with permission from ref 31. Copyright 1987 American Chemical Society.)

prevented by keeping the entire assembly under compression.³⁵ Herron et al.³² also used filter papers as a separator between the working electrode and a gold foil counter electrode (Figure 10) but relied on continuously pumping electrolyte through the cell to sweep out any bubbles, as did the modified design described by Maniguet, Mathew, and Russell,³³ shown in Figure 11. In the former a hole was in the center of the gold foil counter electrode through which the X-rays passed, and in the latter the platinum gauze counter electrode was contained in a concentric electrolyte filled channel outside the path of the X-rays.

Collection of in situ XAS data using a single cell fuel cell avoids problems associated with bubble formation found in liquid electrolytes as well as questions regarding the influence of adsorption of ions from the supporting electrolyte. However, the in situ study of membrane electrode assemblies (MEAs) in a fuel cell environment using transmission

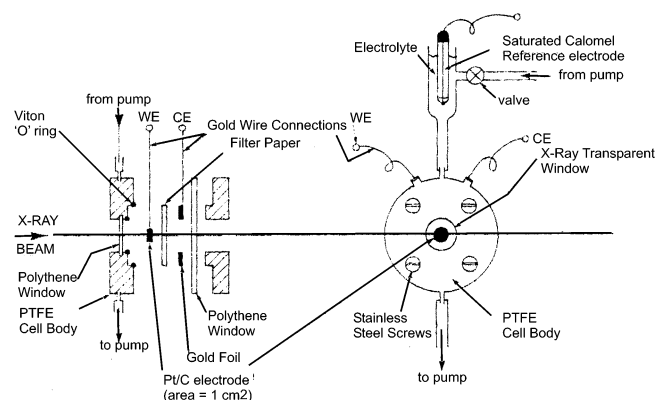


Figure 10. Electrochemical cell for transmission XAS.³² (Reproduced with permission from ref 32. Copyright 1992 Elsevier Sequoia S.A., Lausanne.)

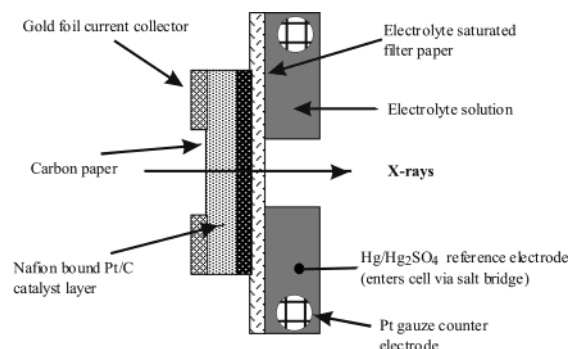


Figure 11. Electrochemical cell for transmission XAS.³³ (Reproduced with permission from ref 33. Copyright 2000 American Chemical Society.)

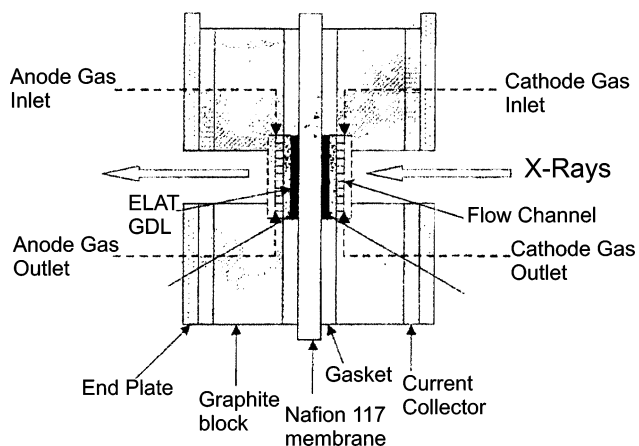


Figure 12. Fuel cell modified for transmission XAS.³⁷ (Reproduced with permission from ref 37. Copyright 2002 American Chemical Society.)

EXAFS requires either removal of the catalyst from the side of the MEA not under investigation³⁶ or exclusion of the absorbing element from this electrode.³⁷ The cell design reported by Viswanathan and co-workers³⁷ shown in Figure 12 is a modification of a single fuel cell. The graphite blocks on each side of the cell containing the flow channels for the gases were thinned to 2 mm to provide a path for the X-ray beam. To avoid problems with sampling the catalysts on both the anode and cathode sides of the MEA, they have replaced the cathode ink with Pd/C. In contrast, the cell design reported by Roth and co-workers³⁶ had a small portion of the Pt/C cathode catalyst removed

to allow investigation of the PtRu/C anode catalyst. This removal of the cathode catalyst in the beam window may modify the current distribution in the region of the anode catalyst probed by the X-rays, and therefore, correlation of the XAS spectra with simultaneously obtained electrochemical measurements may be of limited value.

4. XAS as a Characterization Method: Pt/C

As described above, XAS measurements can provide a wealth of information regarding the local structure and electronic state of the dispersed metal particles that form the active sites in low temperature fuel cell catalysts. The catalysts most widely studied using XAS have been Pt nanoparticles supported on high surface area carbon powders,^{25,27,29,30,32,33,38–52} represented as Pt/C. The XAS literature related to Pt/C has been reviewed previously.^{25,35} In this section of the review presented here, the Pt/C system will be used to illustrate the use of XAS in characterizing fuel cell catalysts.

4.1. Particle Size

The catalysts used in low temperature fuel cells are usually based on small Pt particles dispersed on a carbon support with typical particle sizes in the range 1–10 nm in diameter. The XAS provides a measure of the average electronic state and local coordination of the absorbing atom, for example, Pt, on a per-atom basis, as described above. Thus, the XAS, for both the XANES and EXAFS regions, of such Pt/C catalysts reflects the size of the particles.

The effect of particle size on the XANES region of the XAS spectra for Pt/C catalysts has been investigated by Yoshitake et al.³⁹ and Mukerjee and McBreen.⁴⁶ Figure 13 shows the XANES region as a function of the applied potential at the Pt L₃ edge for 3.7 and ≤1.0 nm diameter particles. The white line intensity increased for both particle sizes as the potential was increased, but the extent of the change was greater for the smaller particles. As described above, the white line intensity at the Pt L₃ and L₂ edges can be used to calculate an average fractional d-electron occupancy, f_d , of the Pt atoms in the particle. The lower white line intensity at negative potentials thus corresponds to a more metallic state. The effect of particle size at the most negative

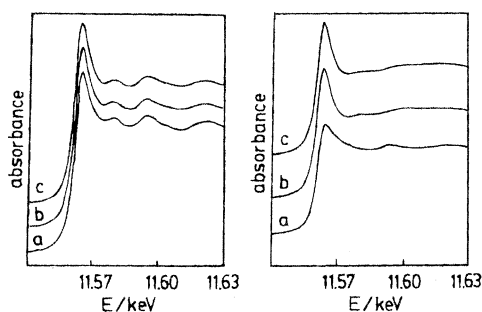


Figure 13. Pt L₃ XANES of 4 wt % Pt/C electrodes (left, 3.7 nm diameter particles; right, <1.0 nm diameter particles) at (a) -0.2 V, (b) 0.5 V, and (c) 1.0 V vs SSCE.³⁹ (Reproduced with permission from ref 39. Copyright 1994 The Electrochemical Society, Inc.)

Table 1. Calculated Values of the Effect of Particle Size on the Fraction of Atoms on the Surface and First Shell Coordination Numbers (CN) for Cuboctahedron (N_{cuboct}) and Icosahedron (N_{icos}) Models for Pt Clusters³¹

Pt loading/ wt %	avg particle size from XRD analysis/Å	surface fraction $N_{\text{surf}}/N_{\text{total}}$	first shell CN	
			N_{cuboct}	N_{icos}
20	30	0.39	10.35	10.62
30	40	0.28	10.87	11.05
40	53	0.24	11.06	11.22
60	90	0.15	11.45	11.54

potential, -0.2 V vs Ag/AgCl, is opposite that found for Pt particles supported on alumina, where a larger f_d value (greater white line intensity) was found for smaller particles. Yoshitake and coauthors attributed this difference to the formation of metal–hydrogen bonds in the electrochemical environment. The smaller particles have a greater fraction of the Pt atoms at the surface that are able to form such bonds. Mukerjee and McBreen⁴⁶ examined this in more detail later and noted that the XANES region for Pt/C catalysts at potentials where hydrogen is adsorbed exhibited widening on the high energy side of the white line peak. Such widening was compared to that previously reported by Mansour et al.^{53,54} and Samant and Boudart⁵⁵ for oxide supported Pt catalyst particles and attributed to the transitions into unoccupied antibonding Pt–H orbitals near the Fermi level.

The effects of particle size on f_d were further investigated by Mukerjee and McBreen.⁴⁶ f_d values were calculated for Pt/C particles with four different diameters at potentials corresponding to the hydrogen adsorption, 0.0 V vs RHE, the double layer, 0.54 V vs RHE, and the oxide formation, 0.84 V vs RHE, regions. Their results are summarized in Table 1. The calculated values show an increased widening of the white line with decreasing particle size at 0.0 V, little effect of particle size at 0.54 V, and an increase in the white line intensity at 0.84 V. The latter was attributed to the adsorption of oxygenated species, and in particular OH. When the change in f_d on going from 0.0 to 0.54 V and then from 0.54 to 0.84 V is normalized by dividing by the fraction of Pt atoms that are at the surface of the particle, as shown in Figure 14, it is apparent that the electronic effects of H and OH adsorption remain greater for the smaller particles. This increased effect was attributed to stronger adsorption of both H and OH on the smaller particles. The intrinsic activity of carbon supported Pt particles for the oxygen reduction reaction, ORR, in acidic solutions has been shown to depend on both the shape and size of the particles,^{56,57} with increased activity observed for larger particles. At the larger particles, the decreased strength of adsorption of OH leaves more of the surface available to take part in the ORR, summarized as the $(1 - \Theta)$ effect in the recent review by Markovic and Ross.⁵⁸

The effects of particle size on the EXAFS region of the XAS spectra are reflected in the coordination numbers obtained in the fits to the EXAFS data. Figure 15 shows the EXAFS or $\chi(k)$ data and corresponding Fourier transforms for a Pt foil, a PtO₂

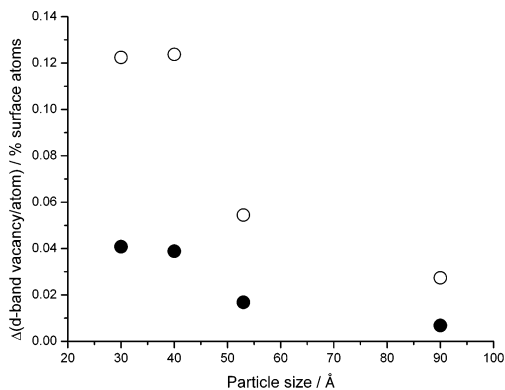


Figure 14. Effect of average particle size on the change in normalized d band vacancies (d band vacancies/% surface atoms) (filled circles) on going from 0.54 to 0.0 V vs RHE and on going from 0.54 to 0.84 V (open circles). (Adapted from ref 31 with permission. Copyright 1998 Elsevier Sequoia S.A., Lausanne.)

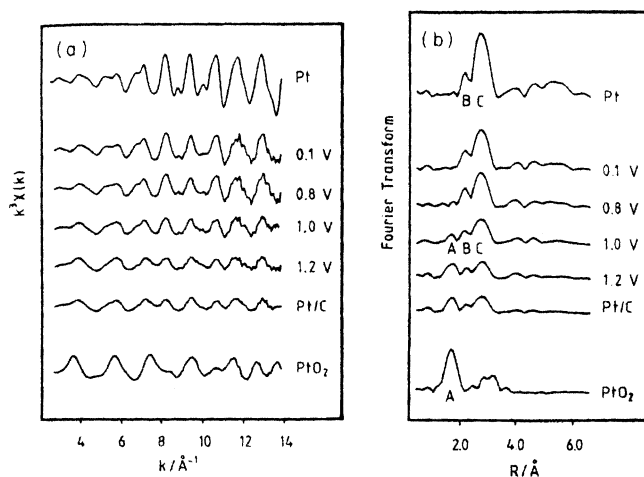


Figure 15. k^3 weighted experimental Pt L_3 EXAFS (a) and corresponding Fourier transforms (b) of Pt foil, a 20 wt % Pt/C electrode at 0.1, 0.8, 1.0, and 1.2 V vs SCE, a dry Pt/C electrode, and a PtO₂ reference sample.³² (Reproduced with permission from ref 32. Copyright 1992 Elsevier Sequoia S.A., Lausanne.)

reference compound, and a Pt/C catalyst electrode. The reduced amplitude of both the EXAFS oscillations and the peak in the Fourier transform at 3.0 Å for the Pt/C electrode compared to that obtained for the Pt foil is a consequence of the smaller number of Pt neighbors at this distance. Bulk Pt metal is fcc, and the first shell coordination number is 12. For small particles, the average first shell coordination number is reduced, as the atoms on the particle surface do not have the full number of neighbors. Benfield⁵⁹ has derived analytical formulas for the number of atoms and average first shell coordination numbers for icosahedron and cuboctahedron clusters with complete shells of atoms. Figure 16 shows the icosahedron and cuboctahedron with 147 atoms formed when four complete shells are present. Benfield's formulas have been used in the interpretation of the EXAFS parameters obtained for supported metal particles to estimate the average particle size. However, these formulas are only valid for icosahedra and cuboctahedra with complete shells. If the outermost shell is incomplete, or can be represented as adatoms on a complete shell, the average particle size

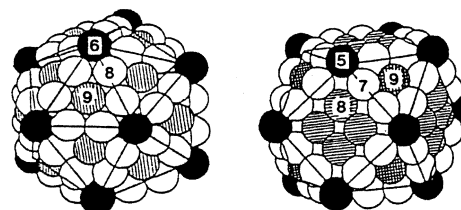


Figure 16. Icosahedron (left) and cuboctahedron (right) with 147 atoms corresponding to four complete shells. The numbers indicate the first shell coordination numbers of the surface atom sites.⁵⁹ (Reproduced with permission from ref 59. Copyright 1992 Royal Society of Chemistry.)

predicted from the first shell coordination number will be smaller than the actual particle size. The presence of incomplete shells and/or deviations from icosahedral or cuboctahedral particle shapes accounts for the observation that the average particle sizes predicted using the first shell coordination numbers obtained from EXAFS are usually smaller than those obtained from TEM measurements of the same catalysts. In addition, the EXAFS measurements represent the per-atom average of all the absorber atoms in the sample and, therefore, include particles too small to be observed using TEM.

4.2. Potential Dependence

The effect of the applied potential on the XANES region of the XAS spectra for Pt/C catalysts has been briefly introduced above and is related to both the adsorption of H at negative potentials and the formation of the oxide at more positive potentials. The adsorption of H and the formation of oxides are also apparent in the EXAFS and corresponding Fourier transforms, as seen in the work by Herron et al.³² shown in Figure 15. As the potential is increased from 0.1 to 1.2 V vs SCE, the amplitude of the peak in the Fourier transform at 2.8 Å decreases and that at 1.8 Å increases. The effect on the EXAFS, $\chi(k)$, data is less easily observed; the amplitude of the oscillations at $k \geq 8 \text{ Å}^{-1}$ decreases as the potential is increased, with the greatest change seen between 0.8 and 1.0 V. The results of fitting these data are shown in Table 2. Note that a value for the inner potential

Table 2. Structural Parameters^a Obtained from Best Least-Squares Fits of the EXAFS for the 20 wt % Pt/C Catalyst Electrode for Various Potentials, E^{17}

E/V vs SCE	atom	N	$r/\text{Å}$	$2\sigma^2/\text{Å}^2$
0.1	Pt	7.5	2.76	0.012
	Pt	2.6	3.90	0.017
	Pt	13.0	4.74	0.026
0.8	O	0.8	2.07	0.012
	Pt	6.4	2.76	0.012
	Pt	3.3	3.90	0.017
1.0	Pt	10.3	4.75	0.026
	O	1.8	2.07	0.013
	Pt	4.7	2.76	0.012
1.2	Pt	2.3	3.89	0.017
	Pt	7.1	4.75	0.026
	O	2.8	2.05	0.013
	Pt	2.9	2.76	0.013
	Pt	1.9	3.91	0.017
	Pt	4.6	4.75	0.026

^a N is the coordination number, r is the neighbor shell distance, and $2\sigma^2$ is the structural disorder term.

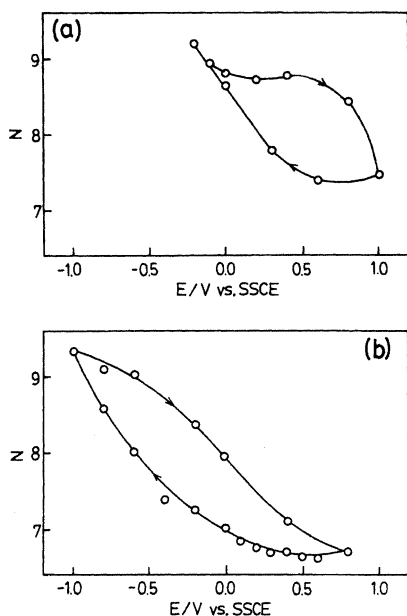


Figure 17. Coordination number of the first Pt–Pt shell for 4 wt % Pt/C electrodes in (a) $0.25 \text{ mol dm}^{-3} \text{ H}_2\text{SO}_4$ and (b) $1 \text{ mol dm}^{-3} \text{ NaOH}$ as a function of the applied potential.⁴⁰ (Reproduced with permission from ref 40. Copyright 1993 Elsevier Sequoia S.A., Lausanne.)

correction, ΔE_0 , was not given in this paper. In the hydrogen adsorption region, at 0.1 V, there are 7.5 first shell Pt neighbors at 2.76 \AA and no O neighbors, corresponding to a well reduced particle. As the potential is increased and the particle becomes oxidized, the first shell Pt neighbors are replaced by O neighbors, eventually reaching 2.8 O neighbors at 2.05 \AA and 2.9 Pt neighbors at 2.75 \AA at 1.2 V. The number of Pt neighbors at longer distances or in higher coordination shells also decreases as the potential is increased. However, the fcc shell structure of bulk Pt is maintained, thereby indicating that only a thin oxide is formed on the particle surface, the thickness of which increases with increasing potential. Yoshitake et al.⁴⁰ have shown that, upon reversing the direction of the potential sweep, a hysteresis in the first shell Pt coordination number is observed. The results can be plotted in a manner similar to a voltammogram and are shown in Figure 17 for a Pt/C electrode in either $0.2 \text{ mol dm}^{-3} \text{ H}_2\text{SO}_4$ or $1 \text{ mol dm}^{-3} \text{ NaOH}$.

Combining the EXAFS results with the potential variation of the white line intensity or f_d , a schematic model of the potential dependent structure of the carbon supported Pt particles has been proposed by Yoshitake et al.⁴⁰ and this model is shown in Figure 18. The effect of increasing the potential in the oxide region is both to grow an oxide film on the surface of the particle and to roughen the particle surface. Upon reversing the potential sweep to remove the oxide, this roughness remains until hydrogen is adsorbed on the particle surface. The influence of adsorbed hydrogen on the first shell Pt coordination number has also been reported by Mukerjee and McBreen,⁶⁰ who compared the EXAFSs of Pt/C catalysts at 0.0 and 0.54 V vs RHE, corresponding to the adsorbed hydrogen and double layer regions, respectively. A decrease in the coordination number was observed

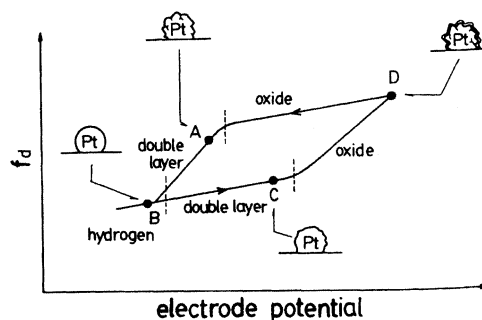


Figure 18. Schematic model of the structure of Pt particles on an f_d voltammogram in relation to the electrode potential. The hydrogen, double layer, and oxide regions are based on cyclic voltammetry. The lattice disorder decreases in the order $D > A > C > B$.⁴⁰ (Reproduced with permission from ref 40. Copyright 1993 Elsevier Sequoia S.A., Lausanne.)

upon increasing the potential, for example, from 10.56 to 8.66 for a 30 \AA particle. They proposed that this change indicated a change in the particle morphology from a sphere at 0.0 V to a flatter raftlike structure at 0.54 V.⁴⁶

The rate of oxide formation and/or removal at Pt/C electrodes has been investigated using energy dispersive EXAFS (EDE) by several authors.^{25,27,40,43,61} In EDE the conventional double crystal, scanning monochromator is replaced by a bent crystal dispersive or Laue monochromator, enabling data over a range of X-ray energies to be collected simultaneously. The transmitted X-rays are monitored using a position sensitive detector, and thus, an entire XAS spectrum can be collected as a single snapshot in as little as 1 s. More recent developments in detector technology may improve the data collection rate to the millisecond time scale,⁶² however, they have not yet been applied to the study of fuel cell electrocatalysts. The rate of oxide formation or removal is measured by monitoring the change in either the first shell Pt or O coordination numbers, N_{Pt} or N_{O} , as a function of time either following a potential step or during a cyclic voltammogram. Figure 19 shows the Fourier transforms as a function of time obtained following a potential step from 0.1 to 1.2 V vs RHE for the oxide formation and back for oxide reduction reported by Allen and co-workers.⁴³ The EXAFS data were fitted and N_{Pt} and N_{O} are shown as a function of time after the potential step in Figure 20. The oxide formation measured as an increase in N_{O} and the absorption peak or white line intensity or a decrease in N_{Pt} was best fit with a logarithmic function with all three indicators changing at the same rate. In contrast, the oxide reduction kinetics were best modeled as a single-exponential function, with different rate constants for the loss of N_{O} and the growth of N_{Pt} . This difference is clearly seen in Figure 20B as a delay between the changes in N_{O} and N_{Pt} . The results highlight an interesting difference between the mechanisms of oxide formation on bulk Pt, which occurs by a place exchange mechanism to form ordered PtO_2 ,^{63–65} and that occurring at small Pt particles. The authors proposed a model of oxide formation at small particles invoking the contrasting driving forces of the formation of Pt–O bonds and

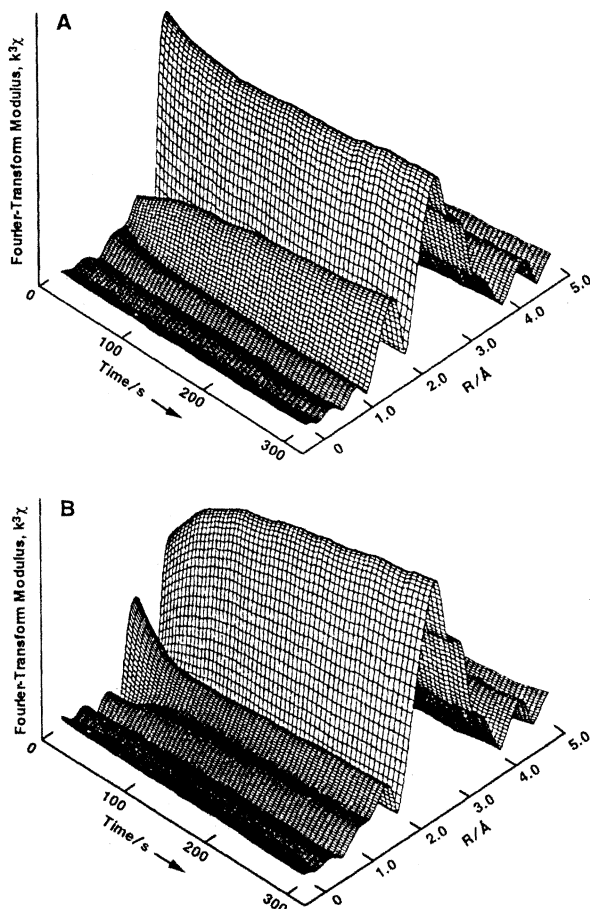


Figure 19. Fourier transform of the Pt L₃ EXAFS acquired during (A) the oxidation and (B) the reduction of a carbon supported Pt catalyst electrode as a function of time. Note that the Fourier transforms have not been phase corrected. The peak at 2.24 Å corresponds to the first shell of Pt near neighbors at 2.76 Å. The peak at 1.50 Å is a combination of the side-lobe from the Pt shell and a shell of O near neighbors at 2.01 Å.⁴³ (Reproduced with permission from ref 43. Copyright 1995 Elsevier Sequoia S.A., Lausanne.)

the minimization of the total surface area of the particle, which has the effect of Pt–Pt restructuring.

O'Grady and co-workers^{47,66} have shown that an additional potential dependent feature may be identified as a low frequency oscillation in the XAS spectrum, which yields peaks in the Fourier transform of the data at values of $r(\text{Å})$ which are too small to be realistically attributed to scattering of the photoelectron off near neighbor atoms.⁶⁷ This phenomenon, termed the atomic X-ray absorption fine structure or AXAFS, is attributed to scattering of the photoelectron by the interstitial charge density around the absorbing atom.⁶⁸ The AXAFS oscillations, $\chi_e(k)$, are superimposed on the background absorption of the free atom, $\mu_a(E)$, giving structure to the atomic absorption, $\mu_0(E)$, as follows.

$$\mu_0(E) = \mu_a(E)[1 + \chi_a(E)] \quad (12)$$

These oscillations are usually removed from the EXAFS, $\chi(k)$, data during the background subtraction process according to eq 12, as previously they were

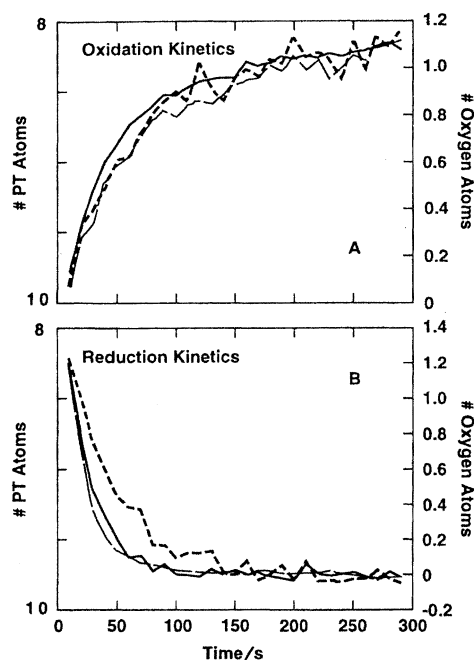


Figure 20. Structural parameters as a function of time extracted by fitting the data shown in Figure 20. (A) Data collected during the oxidation of the Pt/C electrode and (B) during the reduction: long dashes, first shell O coordination number (no. of O atoms); short dashes, first shell Pt coordination number (no. of Pt atoms); solid line, absorption peak intensity (effectively white line intensity).⁴³ (Reproduced with permission from ref 43. Copyright 1995 Elsevier Sequoia S.A., Lausanne.)

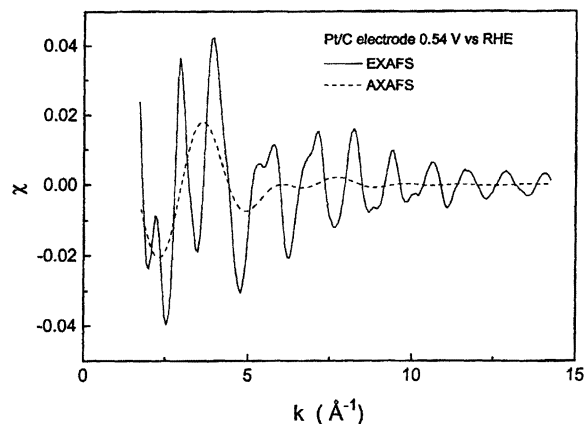


Figure 21. Experimental Pt L₃ EXAFS data for a Pt/C electrode at 0.5 V vs RHE (solid line) and the back transformed Fourier filtered AXAFS signal (dotted line). Fourier filtering parameters: $0.5 \leq k \leq 8.5 \text{ Å}^{-1}$ and $0.15 \leq r \leq 1.7 \text{ Å}$.⁴⁷ (Reproduced with permission from ref 47. Copyright 1998 Elsevier Sequoia S.A., Lausanne.)

not thought to have a fundamental interpretation.

$$\chi(k) = \frac{\mu(k) - \mu_0(k)}{\mu_0(k)} \quad (13)$$

The background removal procedure has been modified by O'Grady et al.⁴⁷ to retain the AXAFS in the EXAFS data. Figure 21 shows the EXAFS of a Pt/C electrode at 0.54 V vs RHE obtained using such a background removal procedure and the isolated AXAFS obtained by applying a Fourier filter in the low $r(\text{Å})$ range. The authors show that the amplitude

of the AXAFS is dependent on the applied electrode potential, increasing as the potential is changed from 0.00 to 0.54 V and then to 0.74 V. Using the FEFF7 code^{69,70} and performing calculations for a Pt₁₃ cluster, they show that the variations in the amplitude of the AXAFS observed can be modeled by including a charge of ± 0.05 e per surface Pt atom. This interpretation is, however, somewhat controversial. The FEFF codes utilize a muffin-tin approximation to the atomic potentials of the absorber and back-scattering atoms. The potentials are assumed to be spherical within the muffin-tin radius and zero outside, which corresponds to the interstitial region. O'Grady and Ramaker⁴⁷ have modified the point of the cutoff between these two potential regions to reproduce the AXAFS features. Such a modification does not overcome any inherent errors in the muffin-tin approximation. It should also be noted that the Fourier filtering range chosen by O'Grady and Ramaker, $0.5 \text{ \AA}^{-1} \leq k \leq 8.5 \text{ \AA}^{-1}$ and $0.15 \text{ \AA} \leq r \leq 1.7 \text{ \AA}$, overlaps with any tail from the peak in the Fourier transform from oxygen neighbors and, therefore, the variations in the AXAFS observed may simply be related to the presence of oxygen neighbors at the higher potentials. Finally, there does not exist a general agreement regarding the physical origins of AXAFS features. Other phenomena such as multi-electron excitations that will influence the shape of the XAS spectrum in the near-edge region must also be considered.⁷¹

4.3. Adsorbates

As described in previous sections, the adsorption of hydrogen and oxide formation at Pt/C electrocatalysts are apparent in both the XANES and EXAFS regions of the spectrum collected at the Pt L₃ edge. XAS spectra are normalized to a per-atom basis, and therefore, the impact of an adsorbate on the spectrum collected at the Pt L₃ edge, or any other Pt edges, will depend on the fraction of the Pt atoms located at the surface of the particle or the dispersion. For typical Pt/C electrocatalyst particles in the 1–5 nm range, the dispersion is 0.6–0.2. The coordination number, N_X , obtained from the EXAFS corresponding to a full monolayer of an adsorbate, X, that did not cause restructuring of the particle, would only be 0.6–0.2. (The larger coordination numbers associated with oxide formation, N_O , therefore, provide evidence of restructuring of the metal particle, as discussed previously.) Such low coordination numbers are smaller than the errors normally associated with fitting the EXAFS data. Collecting the XAS data at an absorption edge associated with the adsorbate and ensuring that any excess of the adsorbate is removed from the sample prior to collection of the XAS data may improve the reliability of the parameters associated with Pt–adsorbate bonds. This method has been used to investigate the underpotential deposition (upd) of Cu,^{72,73} Pb,⁷⁴ and Rb⁷⁵ on Pt/C electrocatalysts. The upd of Cu on Pt/C is described below as an example.

McBreen and co-workers have investigated the upd of Cu from $0.5 \text{ mol dm}^{-3} \text{ H}_2\text{SO}_4 + 4 \times 10^{-4} \text{ mol dm}^{-3} \text{ CuSO}_4$ on to Pt/C, examining both the XANES⁷³ and

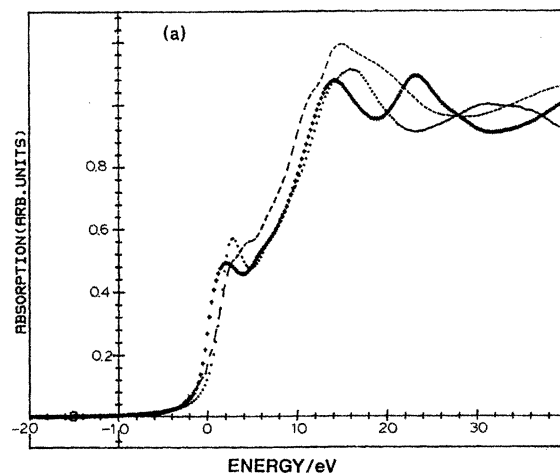


Figure 22. Normalized Cu K XANES for Cu foil (+), Cu₂O (dots), and upd Cu on Pt/C at 0.05 V vs SCE (dashes).⁷³ (Reproduced with permission from ref 73. Copyright 1991 Elsevier Sequoia S.A., Lausanne.)

EXAFS⁷² regions at the Cu K and Pt L₃ absorption edges. To minimize the contributions of Cu species in the electrolyte solution, most of the electrolyte was drained from the cell. Electrochemical control of the Pt/C working electrode was maintained by keeping a small portion of the electrode in contact with the remaining solution. Oxygen was carefully excluded from the drained cell to avoid competing Faradaic processes and to maintain the upd layer. Figure 22 shows the normalized XANES for Cu foil and Cu₂O reference samples as well as that of the Cu upd layer. The edge position for the upd Cu layer was shown to correspond to Cu⁺, and the shape of the edge supported a tetrahedral coordination. At the Pt L₃ edge a slight decrease in the white intensity was observed, corresponding to charge transfer to the Pt upon adsorption of Cu. When the Cu K edge EXAFS data were later examined,⁷² the fitting supported a tetrahedral coordination of the Cu atoms with 1 Pt neighbor at 2.68 Å and 3 O neighbors at 2.06 Å. An additional S neighbor at 2.37 Å was required to reproduce the apparent splitting of the first shell peak in the Fourier transform, as shown in Figure 23. The S neighbor was accounted for by including a coadsorbed SO₄²⁻ anion. The observed splitting of the peak in the Fourier transform was attributed to interference effects between the backscattering from the O and S neighbors. This observation highlights the danger in simply interpreting peaks in the Fourier transforms of EXAFS data as neighbors at the distance indicated by the position of the peaks; in this case neighbors at approximately 1.4, 2.2, and 2.8 Å would have been anticipated. Subsequent surface X-ray scattering measurements of Cu upd on Pt(111) single-crystal surfaces^{76–78} have confirmed the coadsorption of Cu and HSO₄⁺ but disagree with the assignment of the oxidation state of the Cu as +1; rather, the Cu is thought to be uncharged or only slightly positively charged.

In the investigation of adsorbed species using XAS, it is not always possible to probe adsorbate–substrate bonding by changing to the adsorption edge of the adsorbate, for example, the adsorption of carbon monoxide on carbon supported Pt particles. Carbon

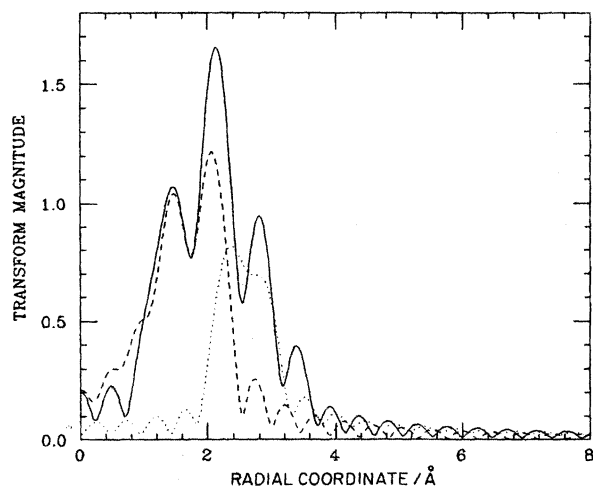


Figure 23. Breakdown of the combined Cu–O and Cu–S contribution (dashed line) and the Cu–Pt contribution (dotted line) to the Fourier transform of the Cu K edge data obtained for an upd layer of Cu on Pt/C at 0.05 V vs SCE.⁷² (Note: Radial coordinate/Å is the same as $R/\text{Å}$.) (Reproduced with permission from ref 72. Copyright 1993 Elsevier Sequoia S.A., Lausanne.)

monoxide adsorption is of particular interest in low temperature fuel cells, as it may be present in the H_2 feed produced by re-forming hydrocarbons and is also a partial oxidation product of methanol, used as the anode feed in the direct methanol fuel cell. The presence of carbon in the support as well as the large background absorption at the C K edge by the other elements present in the fuel cell catalyst and electrolyte preclude investigation at the C K edge. Maniguet et al.³³ have shown that the use of a difference file method¹⁷ to separate the various contributions to the EXAFS obtained at the Pt L_3 edge enables the in situ investigation of the adsorption of CO on Pt/C electrocatalyst electrodes. The difference file method as applied to the CO adsorption on Pt/C may be briefly described as fitting the dominant Pt–Pt contributions to the EXAFS data and then subtracting this fit from the data. The remaining, weaker, Pt–C and/or Pt–O contributions could then be fit. These weaker contributions were then subtracted from the original data and the Pt–Pt contributions refit. The cycle was repeated several times until no further variation in the parameters was observed. Figure 24 shows the Fourier transforms of the isolated Pt–Pt contributions and the

combined Pt–C and Pt–O contributions at 0.05 V vs RHE with adsorbed CO; 1.05 V, where the Pt/C particles are oxidized; and 0.45 V, after the CO has been electrochemically removed from the Pt/C surface. A peak attributed to Pt–C of adsorbed CO is observed at approximately 1.5 Å in Figure 24a and the fit yielded 0.5 C neighbors at a distance of 1.85 Å attributed to linearly adsorbed CO. The other peaks in Figure 24(a) and those in 24(c) were attributed to C neighbors of the support as previously reported by Lampitt et al.³⁰ and O’Grady and Koningsberger.²⁹ These neighbors are present in the EXAFS of all C supported catalyst particles, but are only evident when the dominant contributions from the metal neighbors are removed and are, therefore, not usually included in the fitting. The Fourier transform of the non-Pt contributions at 1.05 V is dominated by O neighbors as anticipated following the onset of oxide formation.

Additional contributions to the EXAFS from the O of the adsorbed CO will have been present in the data presented by Maniguet et al.³³ but were not fitted. For linearly adsorbed CO the collinear or near collinear arrangement of Pt–C≡O enhances the contributions of this multiple-scattering pathway to the EXAFS. Thus, as previously reported for $\text{Os}_3(\text{CO})_{12}$ adsorbed on $\gamma\text{-Al}_2\text{O}_3$ ¹⁷ and $\text{Pt}_2\text{Ru}_4(\text{CO})_{18}$ adsorbed on $\gamma\text{-Al}_2\text{O}_3$,⁷⁹ the O neighbor of the CO ligands could easily be observed in the EXAFS obtained at the Os and Pt and Ru edges, respectively. However, the presence of a large number of Pt neighbors at a similar distance in the case of the Pt/C catalyst dominates the EXAFS data reported by Maniguet et al., masking the contributions of the O neighbors of the adsorbed CO.

The adsorptions of H, O, and SO_4^{2-} on Pt/C electrocatalyst electrodes have been further investigated by O’Grady and Ramaker^{48–51} by comparing the XANES data at the Pt L_2 and L_3 absorption edges. In their analysis, the difference spectrum, which they term AS for antibonding state, is obtained as follows:

$$\text{AS} = \Delta L_3 - \Delta L_2 \quad (14)$$

where ΔL_n is the difference spectrum at the L_n edge between the Pt/C electrode at a reference potential and the potential of interest. The theory behind the subtraction method is that the L_3 edge contains

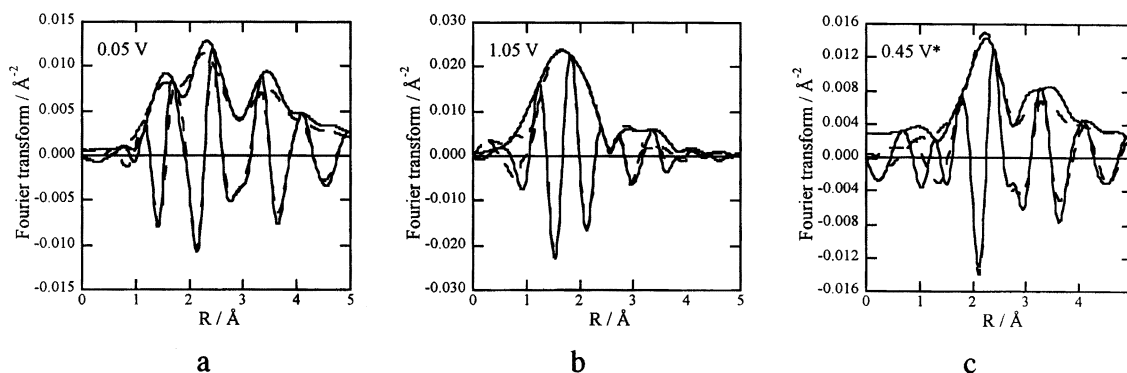


Figure 24. Fourier transforms of the isolated non-Pt contributions to the Pt L_3 EXAFS of a 40 wt % Pt/C electrode at (a) 0.05 V vs RHE, with CO adsorbate present, (b) 1.05 V, with the Pt surface oxidized, and (c) 0.45 V after removal of CO and reduction of oxide.³³ (Reproduced with permission from ref 33. Copyright 2000 American Chemical Society.)

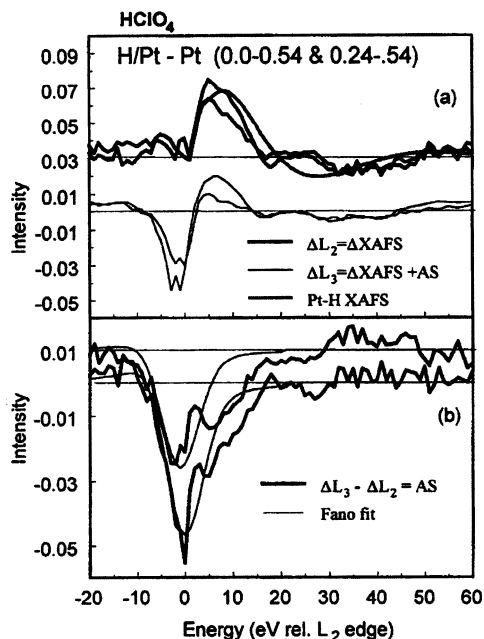


Figure 25. Comparison of the difference spectra for hydrogen adsorbed on Pt/C and Pt/C (0.0–0.54 V and 0.24–0.54 V), for a Pt/C electrode in 1 mol dm⁻³ HClO₄.⁴⁹ (Reproduced with permission from *Journal of Synchrotron Radiation* (<http://journals.iucr.org/>), ref 49. Copyright 1999 International Union of Crystallography.)

contributions from both the 2p_{3/2} to 5d_{3/2} and 5d_{5/2} transitions, while the L₂ edge corresponds to the 2p_{1/2} to 5d_{3/2} transition. Any antibonding orbitals (AS) formed upon adsorption will only contribute to the L₃ spectrum, because at the L₂ edge spin-orbit coupling causes the AS to be nearly filled. Thus, the difference between the XANES data at the L₃ and L₂ edges will represent the valence band density of states probed at the L₃ edge. By first taking the difference between the spectrum at the L_n edge at the potential of interest and a reference potential, and then obtaining the spectrum AS, any observed features should be attributable to changes in the valence band and the formation of any additional antibonding states above the valence band brought about by the change in the applied potential. The antibonding state formed is degenerate with the continuum and, therefore, is a “shape” resonance, which will have a characteristic Fano-resonance line shape.

The Pt L_{2,3} difference spectra for a Pt/C electrode at 0.0 and 0.24 V vs RHE and the reference potential of 0.54 V are shown as an example in Figure 25. In Figure 25a the calculated XAFS for Pt–H is also included and seen to agree with the ΔL₂ spectrum as well as the ΔL₃ spectrum at energies greater than 5 eV relative to the L₂ edge. The remaining features in the ΔL₃ spectrum at lower energies are more clearly seen in the AS spectrum (Figure 25b). The physical origins of the features in the AS spectra are not clear from the papers published thus far, and the detailed interpretation is beyond the scope of this review. The Fano fit shown in Figure 25b is characterized by a resonance energy which is negative for potentials where H is adsorbed, 0.0 and 0.24 V vs RHE, and positive where O is adsorbed, 1.14 V. This

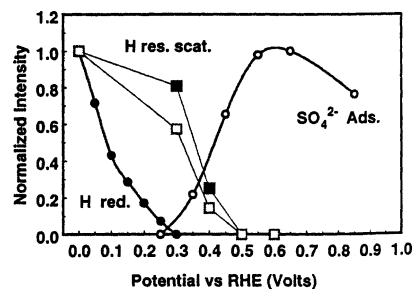


Figure 26. Comparison of the resonance scattering from H atoms or H⁺ obtained by fitting the Fano line shape in HClO₄ (open squares) and H₂SO₄ (closed squares) with the adsorbed hydrogen coverage (closed circles) and sulfate adsorption (open circles) obtained by cyclic voltammetry.⁵⁰ (Reproduced with permission from ref 50. Copyright 2001 The Electrochemical Society, Inc.)

resonance energy has been shown to vary with the size of the metal cluster and becomes more negative as the cluster becomes more metallic.⁸⁰ Thus, the more positive resonance energy at 1.14 V is in agreement with other data showing that the particles are oxidized at this potential.

In Figure 26 the amplitude of the peak in the AS spectrum is plotted as a function of the potential for a Pt/C electrode in 0.5 mol dm⁻³ H₂SO₄ and 1.0 mol dm⁻³ HClO₄. The amplitude of the peak is related to the resonant scattering from H and, therefore, provides a measure of the extent of H adsorption. The offset between the H coverage derived from the electrochemical measurements (filled circles) and that from the AS peak amplitude (squares) has been interpreted as suggesting that hydrogen, as H⁺, does not fully leave the Pt surface until the potential reaches 0.4 V vs RHE and that when the H⁺ leaves the surface, SO₄²⁻ ions are directly adsorbed.⁵⁰ This unexpected result indicates that use of this L_{2,3} difference method may provide new insights regarding adsorption on Pt/C. However, the method cannot be generally applied to other metals of interest as fuel cell catalysts, as it relies on the accessibility of the L₃ and L₂ absorption edges.

5. Pt Containing Alloy Catalysts

XAS is particularly useful in the investigation of alloy electrocatalysts. Unlike XRD measurements, which only reflect the crystalline component of the sample, and TEM, which is limited to particles with diameters greater than 1 nm, XAS provides the average local structure surrounding all of the atoms of the absorbing element in the sample. By collecting the XAS data at the absorption edges corresponding to each element in the alloy under investigation, the extent of intermixing and homogeneity of the alloy may be assessed. It is generally accepted that surface segregation, which is the enrichment of one element in the surface relative to the bulk, is common in bimetallic alloys; see, for example, the review by Campbell⁸¹ and the comments by Markovic and Ross in their recent review.⁵⁸ XAS provides an indirect probe of the surface composition of the catalyst particles, by comparison of the coordination numbers obtained in fitting the data at each absorption edge.

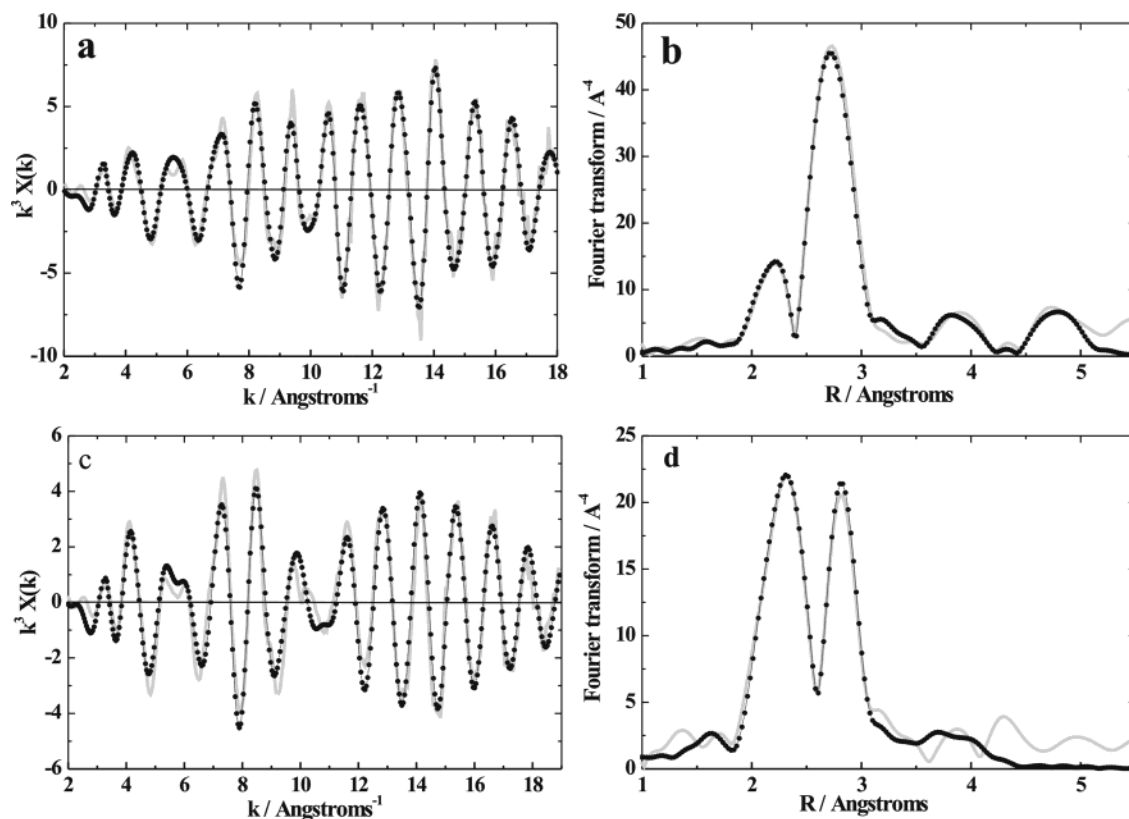


Figure 27. k^3 weighted Pt L_3 EXAFS (a and c) and the corresponding Fourier transforms (b and d) for (a and b) a poorly mixed PtRu/C alloy electrode and (c and d) a well mixed PtRu/C alloy electrode at 0.05 V vs RHE in 1 mol dm^{-3} H_2SO_4 ; experimental data (solid line) and fits (dotted line).⁸⁷ (Reproduced with permission from ref 87. Copyright 2002 S. Maniguet.)

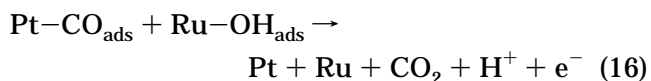
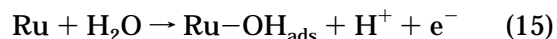
In addition, as described extensively above, the XAS data can be collected in situ and, thereby, enable the investigation of the stability of the alloy system.

The alloy catalysts used in low temperature fuel cells are usually based on Pt. Anode catalysts are sought that have improved tolerance to the presence of carbon monoxide in the reformat derived hydrogen feed for PEM fuel cells or better long term performance for methanol oxidation for direct methanol fuel cells. Cathode alloy catalysts should have enhanced oxygen reduction kinetics and/or tolerance to methanol crossover. Much of our current knowledge regarding the role of secondary, or even ternary, elements in enhancing the electrocatalytic activity of Pt containing electrocatalysts has been derived from studies on well characterized single-crystal electrode surfaces, as summarized in the excellent review by Markovic and Ross.⁵⁸ However, in advancing our understanding of real electrocatalysts, an understanding of the structure of supported nanoparticle catalysts is invaluable. In this section of the review structural investigations of Pt containing alloy catalysts will be presented.

5.1. PtRu Alloys

PtRu alloys are well-known for both their improved CO tolerance^{82–85} and improved methanol oxidation⁸⁶ as compared to the case of Pt. The enhanced behavior of PtRu over Pt has been attributed to a bifunctional

mechanism⁸⁴ (see eqs 14 and 15 below) in which the



Ru provides sites for water activation as well as having an electronic effect on the Pt atoms, such that CO is less strongly adsorbed. In situ XAS measurements have been used to determine the structure of PtRu catalysts, to assess the magnitude of any electronic effect that alloy formation may have on the Pt component of the catalyst, and to provide evidence in support of the bifunctional mechanism.

The analysis of the EXAFS of alloy catalyst particles is inherently more complicated than that of single metals. In the case of PtRu catalysts there is an added complication that the backscattering from Pt and Ru neighbors at similar distances interfere with one another, giving rise to beats in the EXAFS data. This phenomenon was first described by McBreen and Mukerjee⁶⁰ for a poorly alloyed 1:1 atomic ratio PtRu/C catalyst. The presence of beats in the EXAFS data is more apparent in the EXAFS obtained at the Pt L_3 edge for a well mixed 1:1 PtRu/C catalyst than in that of a poorly mixed catalyst of the same composition,⁸⁷ as shown in Figure 27; compare panels a and c. Pandya et al.⁸⁸ showed that the beats occur because the difference in the backscattering phase shifts from Pt and Ru is

approximately π radians in the range $6 \text{ \AA}^{-1} < k < 11 \text{ \AA}^{-1}$, giving rise to destructive interference between the Pt–Pt and Pt–Ru contributions in the EXAFS at the Pt edge. A similar effect is observed at the Ru K edge.⁸⁷ The presence of such beats causes an apparent splitting of the peak corresponding to the first coordination shell in the Fourier transform of the data. In the past, such data were analyzed by constraining some of the analysis parameters, and Fourier filtering to isolate the EXAFS for the first coordination shell was frequently used. Advances in the computer programs used in the fitting and the use of theoretical backscattering phase shifts and amplitudes have meant that such techniques are no longer necessary and the data may be fit as shown in Figure 27, where EXCURVE98^{16,89} was used.

5.1.1. Compositional Analysis

The extent of intermixing of PtRu catalysts has been investigated using EXAFS by a number of authors.^{60,87,90} As shown in Figure 27, the splitting of the first shell peak in the Fourier transform is greater for a well mixed 1:1 PtRu alloy catalyst than for the poorly mixed catalyst. The difference in the extent of intermixing of these two catalysts was confirmed by fitting the data obtained at the Pt L_{III} and Ru K absorption edges. In the case of the well mixed alloy, the coordination environments seen from the Pt and Ru edges were in excellent agreement (same coordination numbers and distances of Pt–Ru and Ru–Pt), while, for the poorly mixed alloy, the Ru edge data showed that much of the Ru was present as an oxide (Ru–O neighbors present and fewer Pt–Ru and Ru–Pt neighbors than predicted by the 1:1 Pt:Ru composition). In fitting the EXAFS data obtained at two edges for such bimetallic particles, it is possible to restrict the number of adjustable parameters by ensuring that the distance between the two metal neighbors and the Debye Waller term for this shell are the same at both edges, as recommended by Meitzner et al.⁹¹ and recently applied by Alexeev and co-workers⁷⁹ in an EXAFS investigation of the structure of Pt–Ru carbonyl clusters on γ -Al₂O₃.

In a similar analysis, comparing the coordination numbers for first shell Pt and Ru neighbors obtained in situ in 1 mol dm⁻³ HClO₄ at the Pt L₃ and Ru K edges at 0.0 V vs RHE, McBreen and Mukerjee were able to estimate that only 10% of the Ru in the commercial catalyst they were investigating was alloyed with the Pt.⁶⁰ Examination of the Ru K edge data showed that the local structure of the Ru corresponded to a Ru oxide, RuO_x, with a Ru–Ru distance of 2.66 Å and a Ru–O distance of 2.02 Å, without any need to include Pt neighbors. Page et al.⁹² have obtained Pt EXAFS for a commercial 1:1 PtRu catalyst and found that the first coordination shell contained only Pt neighbors. They assumed that the structure of the PtRu particles could be best described as an onion, with Pt on the inside and Ru in an outer shell. However, without any evidence of Pt–Ru near neighbor interactions in the EXAFS or Ru K edge data, such an assumption is difficult to justify, and it is more likely that the Ru is present

as a separate oxide phase, as reported by McBreen and Mukerjee.⁶⁰ In addition, these authors report a first shell coordination number of 13.8 for a Pt foil and similar values for the PtRu catalysts when the parameter was allowed to vary, indicating that the analysis package used⁹³ produced suspect results.

Neto and co-workers examined the ex situ Pt L₃ EXAFS for a series of PtRu catalyst powders in air of varying nominal composition from 90:10 through to 60:40 atom %.⁹⁴ The catalysts were prepared using a formic acid reduction method developed by the authors which resulted in very poorly alloyed particles, even after heat treatment to 300 °C under a hydrogen atmosphere. Unfortunately, the authors were not able to obtain Ru K edge data to identify the local structure of the Ru in their catalysts.

Nashner et al.^{95,96} ensured that the average composition of the carbon supported PtRu particles they investigated was PtRu₅ by dispersing a molecular carbonyl cluster, PtRu₅C(CO)₁₆, on to a carbon support followed by reduction with hydrogen. EXAFS analysis of catalyst powders under a H₂ atmosphere at the Pt and Ru edges confirmed that alloy particles were formed and that the local coordination surrounding the Ru atoms contained only Pt and Ru. Comparison of the parameters obtained at the Pt and Ru edges showed that the distribution of the Pt and Ru neighbors in the particles was nonstatistical and could best be described by a segregation of Pt to the surface of the particle.

5.1.2. Potential Dependence

The applied electrode potential has been shown to have an effect on both the XANES and EXAFS of PtRu catalysts. The variations of the Pt d band vacancy per atom, $(h_j)_{t,s}$, with potential over the range 0.0–0.54 V vs RHE for both the poorly mixed 1:1 PtRu/C catalyst investigated by McBreen and Mukerjee⁶⁰ and a well mixed 1:1 PtRu/C catalyst studied by Russell et al.⁹⁷ were less than that for a pure Pt/C catalyst.⁹⁴ McBreen and Mukerjee attributed this difference to a reduction in the adsorption of hydrogen on the Pt sites of the alloy catalyst. The results also provide evidence of an electronic effect upon alloying Pt with Ru. The effects on the Ru XANES were much less significant, but some evidence of a change to a higher oxidation state at potentials above 0.8 V was observed.^{60,98}

For data collected at the Pt L₃ edge, increasing the potential from the hydrogen adsorption region to the double layer region, and subsequently to potentials corresponding to oxide formation at the metal particles, has been shown to be accompanied by a decrease in the total number of first shell metal neighbors, $N_{Pt} + N_{Ru}$.^{60,87,99} McBreen and Mukerjee also reported a slight change in the first shell Pt–Pt bond distance that they claimed provided evidence of a relaxation of the Pt–Ru bonding and subsequent restructuring of the PtRu particle. However, the magnitude of the variation reported, $2.72 \pm 0.01 \text{ \AA}$, was very small and may well be within the experimental error. O'Grady et al.⁹⁹ noted that while no Pt–O neighbors were present in the Pt L₃ data collected at 0.8 V vs RHE, Ru–O neighbors were

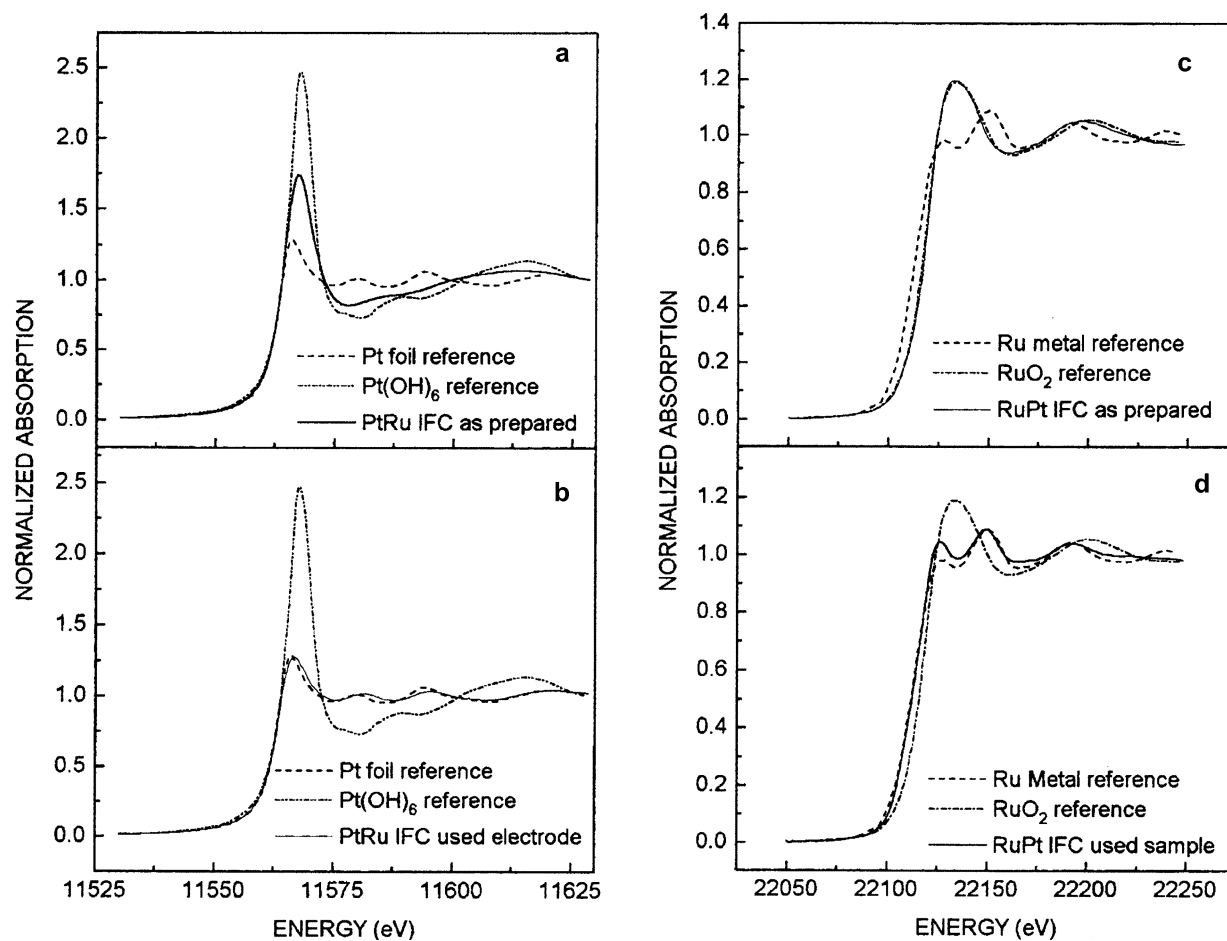


Figure 28. XANES for an unsupported PtRu black catalyst (a and c) as prepared and (b and d) following fuel cell testing as a methanol oxidation catalyst and reference compounds at (a and b) the Pt L_3 edge and (c and d) the Ru K edge.¹⁰² (Reproduced with permission from ref 102. Copyright 2001 American Chemical Society.)

found at approximately 1.8 Å in the Fourier transforms of the Ru K edge data for a 1:1 PtRu/C catalyst. They attributed this difference to removal of Ru from the alloy at such elevated potentials, which has been shown to occur at potentials greater than 0.7 V.¹⁰⁰ Such results may be compared with those of Nashner et al.,⁹⁵ who found that the chemisorption of oxygen on small, 1.6 nm diameter, PtRu₅/C particles was evident as Pt–O neighbors at 1.97 Å and Ru–O neighbors at 2.05 Å in the fitting of the Pt and Ru EXAFS, respectively, but did not result in a change in the metal coordination of the particles greater than the errors associated with the fitting.

The influence of the applied potential on the XAS of PtRu fuel cell catalysts is also apparent in data collected under fuel cell conditions. Viswanathan et al.³⁷ reported XANES data obtained at both the Pt L_3 and Ru K edges for a 1:1 PtRu/C catalyst prepared as a Nafion bound MEA. They found that both the Pt and Ru were metallic in both the freshly prepared MEAs and MEAs under operating conditions.

The importance of collecting such data in situ is illustrated by the work of Lin et al.¹⁰¹ and O'Grady et al.¹⁰² Lin et al. found that a commercial PtRu catalyst consisted of a mixed Pt and Ru oxide, in contrast to the catalyst prepared in their own laboratory. However, the data were collected ex situ in air. O'Grady et al. showed that even a commercial unsupported PtRu catalyst showed heavy oxidation

at both the Pt and Ru edges in the as prepared state but was metallic following treatment in a fuel cell as shown in Figure 28.

5.1.3. Adsorbates

The groups of Mukerjee^{103,104} and O'Grady^{99,105} have both reported the effects of adsorption of methanol on PtRu/C catalysts on the XANES collected at the Pt L_3 edge. Both found that at 0.0 V vs RHE the adsorption of methanol was apparent as a decrease in the broadening of the white line on the high energy side, indicating a decrease in H adsorption. In the absence of methanol, a significant increase in the white line intensity, corresponding to an increased d band vacancy per atom, is observed on increasing the potential from 0.0 to 0.5 V. In the presence of methanol, both groups found that this increase was suppressed. Swider et al.¹⁰⁵ suggested that this indicated that the methanol, or some methanol-derived fragment, donates electrons to the platinum even at such elevated potentials. Mukerjee and Urian¹⁰³ obtained data at an intermediate potential (results shown in Figure 29) and found an initial increase in the d band vacancy per atom at 0.24 V followed by a steady decline at higher potentials. They attributed the initial increase to the formation of C₁ oxide species, CO or CHO, on the surface. The decrease in d band vacancy per atom at the elevated potentials was attributed to formation of oxy-hydrox-

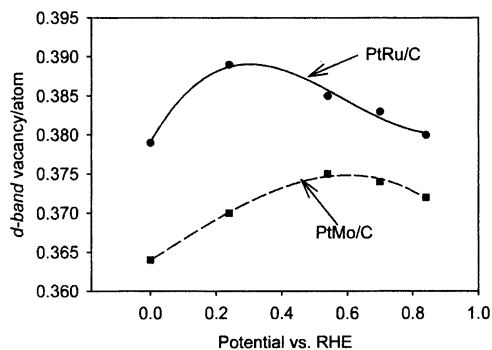


Figure 29. Pt d band vacancy per atom obtained from XANES analysis at the Pt L_3 and L_2 edges for PtRu/C (filled circles) and PtMo/C (filled squares) as a function of the applied potential in $1 \text{ mol dm}^{-3} \text{ HClO}_4 + 0.3 \text{ mol dm}^{-3}$ methanol.¹⁰³ (Reproduced with permission from ref 103. Copyright 2002 Elsevier Sequoia S.A., Lausanne.)

ides of Ru on the surface of the alloy particle that displace the C_1 fragments.

5.2. Other Pt Containing Alloy Anode Catalysts

Mo alloys of Pt have also been shown to enhance the CO tolerance of PEM fuel cell catalysts.^{106–111} Two peaks are often observed in the CO stripping voltammograms for PtMo catalysts: the first at approximately 0.4 V vs RHE and the second at approximately 0.75 V. The first has been attributed to enhanced oxygen transfer from Mo oxy-hydroxide species on the surface of the catalyst particles.^{110–113} XANES at the Mo K and Pt L_3 edges has provided support for the presence of such oxy-hydroxide species. Mukerjee et al.^{103,114} have shown that the position of the Mo K edge shifts to higher energy as the potential is increased from 0.24 to 0.54 V for a 3:1 atomic ratio PtMo/C catalyst. Comparison of the edge position with those of reference compounds indicated that at 0.0 V the oxidation state of the Mo was +V, which they assigned to the hydrated oxide, $\text{MoO}(\text{OH})_2$.¹⁰³ The d band vacancy per Pt atom of PtMo/C catalysts at 0.0 V vs RHE has been shown to be greater than that observed for Pt/C.^{94,97,103,114} Increasing the potential into the double layer region, to 0.5 V, is accompanied by less of an increase in the white line intensity than observed for Pt/C. However, a significant increase is observed at 0.9 V, indicating that the Pt in PtMo catalysts is oxidized at such potentials. Thus, the second CO oxidation peak in the cyclic voltammogram is attributed to CO oxidation facilitated by the formation of oxides on the Pt sites of the catalyst.

PtMo alloys are not as effective as PtRu for methanol, or ethanol, oxidation.^{94,103} As shown in Figure 29, the d band vacancy per Pt atom for the PtMo/C catalyst continues to increase until 0.6 V vs RHE, in contrast to the behavior of PtRu/C.¹⁰³ The authors attribute this difference to the lack of removal of the C_1 fragments from the particle surface by the oxy-hydroxides of Mo. However, the difference in the electrocatalytic activity of PtRu and PtMo catalysts may be attributed to ensemble effects as well as electronic effects. The former are not probed in the white line analysis presented by Mukerjee and co-workers. In the case of methanol oxidation, en-

sembles of three active atoms have been shown to be necessary for dehydrogenation,¹¹⁵ and Mo effectively disrupts such adsorption sites while Ru does not.⁵⁸

The formation of well mixed PtMo alloys is much more difficult than that of PtRu alloys. Pt L_3 EXAFS results have been reported for PtMo/C catalysts with atomic ratios of 3:1 to 4:1 Pt/Mo.^{94,97,103} In all cases the fraction of Mo in the first coordination shell of the Pt atoms is less than that predicted from the atomic ratio. In fact, for the 4:1 catalysts examined by Neto et al.,⁹⁴ the data did not support the inclusion of any Mo neighbors. Combined with the average +V oxidation state of the Mo at 0.0 V reported by Mukerjee,¹⁰³ these results support the view that the PtMo/C catalysts investigated thus far may be described as Pt particles modified by a small amount of Mo and a separate Mo oxide phase. Crabb et al.¹¹⁶ have developed a method that ensures that all of the Mo in the catalyst is associated with the Pt. Using a controlled surface reaction, in which an organometallic precursor of the Mo is reacted with the reduced Pt surface, they prepared Pt/C catalysts modified by submonolayer coverages of Mo. EXAFS collected at the Mo K edge verified that the Mo was in contact with the Pt but was present as an oxide or oxy-hydroxide species in the as prepared catalyst, before application of an applied potential, and at 0.65 V vs RHE. Upon electrochemical reduction at 0.05 V, the number of Pt neighbors in the first coordination shell increased from 0.8 to 4.5, indicating that the Mo was then incorporated into the surface of the metal particle. This catalyst also exhibited improved CO tolerance at low potentials compared to the case of the unmodified Pt/C catalyst, providing added evidence of the role of the oxy-hydroxides of Mo in the enhancement mechanism.

Mukerjee and McBreen have also investigated PtSn/C alloy catalysts and Pt/C catalysts modified by upd layers of Sn,^{117,118} both of which had previously been shown to have enhanced catalytic activity for methanol oxidation.^{115,119,120} They found that the alloy consisted of the Pt_3Sn fcc phase with an increased Pt–Pt bond distance. In contrast to the cases of PtRu and PtMo, the formation of the Sn alloy was accompanied by a decrease in the d band vacancy per Pt atom. Pt XANES results for the upd of Sn on Pt/C showed minimal effects on the d band vacancies of the Pt atoms, and analysis of the EXAFS confirmed that the Pt–Pt distance remained unchanged. EXAFS at the Sn edge for both the upd modified Pt and the $\text{Pt}_3\text{Sn}/\text{C}$ alloy showed Sn–O interactions at all potentials in the range 0.0–0.54 V vs RHE. From these results the authors drew the conclusions that the Sn provides oxygen species to the Pt that enhance methanol oxidation, and that the improved performance of the upd of Sn on Pt/C compared to the alloy was related to the decreased number of sites for dissociative adsorption of methanol on the surface of the Pt_3Sn alloy.

5.3. Pt Containing Alloy Cathode Catalysts

The kinetics of the four electron oxygen reduction reaction at Pt are limited by the very low exchange

current density under the acidic conditions present in both phosphoric acid and low temperature/PEM fuel cells.^{121,122} The electrocatalytic activity of Pt catalyst particles for the oxygen reduction reaction has been shown to improve by alloying with first row transition elements in both phosphoric acid fuel cells^{123–125} and low temperature PEM fuel cells.¹²⁶ Mukerjee et al.^{34,127,128} have shown that XAS studies are uniquely suited to quantifying both the structural and electronic effects of alloying which result from this enhancement.

Mukerjee et al.³⁴ investigated the electrocatalysis of the oxygen reduction reaction at five binary Pt alloys, PtCr/C, PtMn/C, PtFe/C, PtCo/C, and PtNi/C. The kinetics of the oxygen reduction reaction were assessed by measuring the current at 0.9 V vs RHE in a single cell PEM fuel cell at 95 °C and 5 atm pressure of humidified O₂. Enhanced electrocatalysis compared to that of Pt/C was found for all of the alloys investigated, with the best performance reported for the PtCr/C catalyst. XAS data were collected at the Pt L₃ and L₂ edges as well as the K edge of the secondary element for each of the catalysts as a function of the applied potential in 1 mol dm⁻³ HClO₄. To avoid complications in the analysis of the XAS data, the catalysts were subjected to leaching in either 2 mol dm⁻³ KOH, for the PtCr/C, or 1 mol dm⁻³ HClO₄, for all the others, to remove any residual oxides or unalloyed first row transition elements. The catalysts used in the fuel cell measurements were not subjected to such pretreatment.

XANES analysis at the Pt L edges and the K edges of the secondary elements was used to determine the d band occupancy of the Pt atoms in the catalysts and to provide evidence of any redox behavior of the secondary element, respectively. The EXAFS obtained at the Pt L₃ edge verified the presence of the alloy phase as well as a measure of the Pt–Pt bond distance. The results indicated that the electrocatalysis of the oxygen reduction reaction is related to the vacancies of the d band, the Pt–Pt bond distance, and suppression of oxide formation on the surface of the particles. No evidence of redox behavior of the secondary element was found; that is, the position of the absorption edge was not found to be potential dependent. A plot of the electrocatalytic activity versus the electronic (Pt d band vacancies per atom) and geometric (Pt–Pt bond distance) parameters was found to exhibit volcano type behavior, as shown in Figure 30. It should be noted that the order of the d-orbital vacancy points (from left to right, Pt/C, PtMn/C, PtCr/C, PtFe/C, PtCo/C, and PtNi/C) is opposite that for the Pt–Pt bond distance. In both cases the PtCr/C catalyst is found near the top of the volcano curves, indicating that it has the best combination of Pt d band vacancies and contraction of the Pt–Pt bond distance. Such an interplay between d band vacancies, Pt–Pt bond distance, and oxygen reduction activity was also found in studies of the effects of the particle size of binary Pt alloys by Mukerjee et al.¹²⁸ and Min et al.¹²⁹

In a later study of the same series of binary catalysts, Mukerjee and McBreen¹²⁷ showed that the restructuring accompanying the desorption of ad-

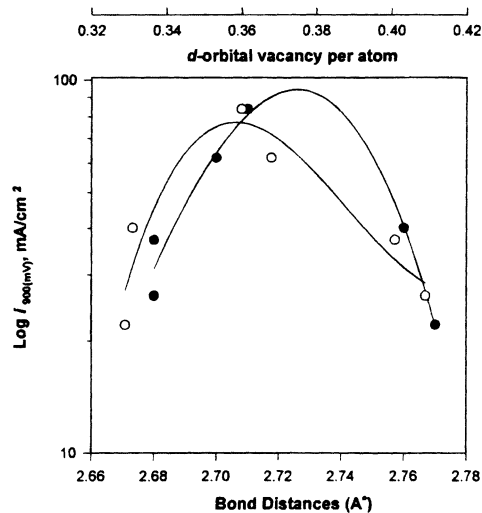


Figure 30. Correlation of the oxygen reduction performance ($\log j_{900 \text{ mV}}$) of Pt and Pt alloy electrocatalysts in a PEM fuel cell with Pt–Pt bond distance (filled circles) and the d band vacancy per atom (open circles) obtained from in situ XAS at the Pt L₃ and L₂ edges.³⁴ (Reproduced with permission from ref 34. Copyright 1995 The Electrochemical Society, Inc.)

sorbed hydrogen previously reported for Pt/C particles⁶⁰ did not occur for these alloys. They also reported that the surfaces of alloy catalysts consist of a Pt skin on the basis of the similarity of the electrochemically determined hydrogen coverages to that of Pt/C. However, EXAFS analysis was not reported for the K edge of the secondary element to support this statement.

Ternary and more complex alloys are now the subjects of investigations that seek further improvements in oxygen reduction activity.^{126,130–136} Structural characterization of such systems using EXAFS methods becomes increasingly complex. XAS data should be collected at absorption edges corresponding to each element in the alloy, but this is not always possible, for example, when the absorption edges of the elements overlap. Kim et al.^{137,138} have reported an XAS study of the ternary alloy, PtCuFe/C. The XAS data were collected at the Pt L₃ edge for powders of PtCuFe/C catalysts of varying Pt content, and Pt₂CuFe and Pt₆CuFe subjected to heat treatments between 500 and 1100 °C. The analysis of the EXAFS data highlights the difficulty in separating the contributions from neighbors that have similar atomic number and, therefore, similar backscattering amplitudes and phase shifts. The contributions of the Cu and Fe could not be reliably separated, and although they were fitted independently, the distances and coordination numbers for the two contributions were found to be the same within the error limit. The ratios of the coordination numbers for the Pt and non-Pt neighbors were in good agreement with their bulk contents, indicating that well ordered alloys were formed. As in the case of the binary alloys, PtCu/C and PtFe/C, a reduced Pt–Pt bond distance, as compared to that for Pt/C, was found. Enhanced mass activities for oxygen reduction were found for the ternary alloys and were attributed to the formation of the ordered alloy phases.

6. Non-Pt Catalysts

Most of the catalysts employed in PEM and direct methanol fuel cells, DMFCs, are based on Pt, as discussed above. However, when used as cathode catalysts in DMFCs, Pt containing catalysts can become poisoned by methanol that crosses over from the anode. Thus, considerable effort has been invested in the search for both methanol resistant membranes and cathode catalysts that are tolerant to methanol. Two classes of catalysts have been shown to exhibit oxygen reduction catalysis and methanol resistance, ruthenium chalcogen based catalysts^{126,139–143} and metal macrocycle complexes, such as porphyrins or phthalocyanines.^{144,145}

EXAFS has been used by Alonso-Vante and co-workers^{146–149} to characterize a series of Ru chalcogenide compounds in situ for catalyst particles deposited onto a conducting SnO₂:F glass support in 0.5 mol dm⁻³ H₂SO₄. The data were collected in reflectance mode with an incident angle of ≤ 1.5 mrad at the Ru K edge. The signal-to-noise ratio of the data collected was very poor, as shown in Figure 31, because it was limited by the thickness of the sample and the collection method. Better results may have been obtained if the data had been collected as fluorescence. Nevertheless, the authors have shown that the catalysts consist of small Ru particles that are stabilized by the presence of the chalcogen, S, Se, or Te, as evidenced by the presence of both chalcogen

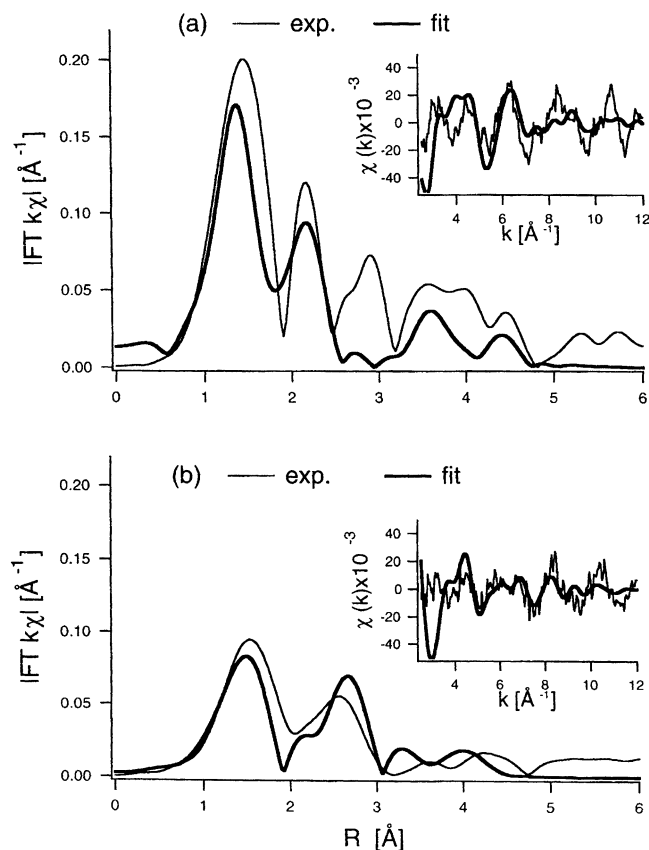


Figure 31. Ru K EXAFS data (insets) and corresponding Fourier transforms for Ru_xSe_y particles on a SnO₂:F support in (a) nitrogen and (b) oxygen saturated 0.5 mol dm⁻³ H₂SO₄: experimental data (thin lines) and fits (thick lines).¹⁴⁹ (Reproduced with permission from ref 149. Copyright 2000 Elsevier Sequoia S.A., Lausanne.)

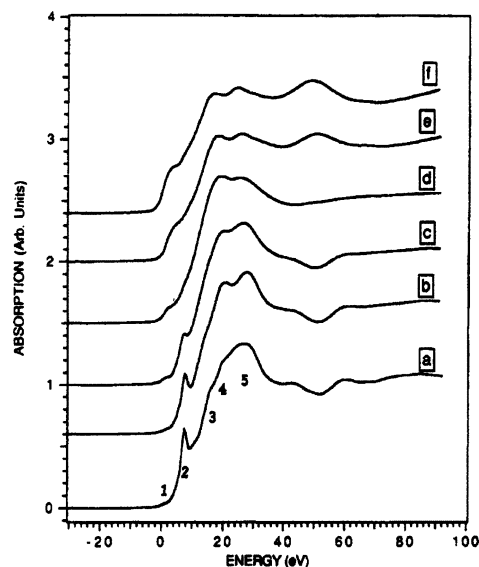


Figure 32. Co K edge XANES for (a) cobalt phthalocyanine (PcCo), (b–e) PcCo on Vulcan XC-72 [(b) untreated sample; (c–e) sample heated to (c) 700 °C, (d) 800 °C, and (e) 1000 °C], and (f) Co metal.¹⁵⁵ (Reproduced with permission from ref 155. Copyright 1992 American Chemical Society.)

and Ru neighbors in the first coordination shell. The local structure surrounding Ru in these catalysts was found to depend on the presence of oxygen in the solution, as also shown in Figure 31, but not on the applied potential. However, the materials are likely to consist of a mixture of phases, and therefore, as EXAFS results reflect the average coordination, the results cannot provide a detailed structural model of these catalysts.

The nature of the catalytic center in oxygen reduction catalysts prepared by the heat treatment of N₄-metal chelates on carbon supports has caused much debate, in particular whether the N₄-metal center is retained in the catalyst. In two early EXAFS studies Joyner et al.¹⁵⁰ and van Wingerden et al.¹⁵¹ showed that the N₄-metal center was retained in carbon supported Co-porphyrin catalysts exposed to temperatures as high as 850 °C. Martins Alves et al. later showed that this center was destroyed at higher temperatures, leaving Co particles on the carbon support. The XANES region for Co phthalocyanine, PcCo, on Vulcan XC-72 subjected to heating to various temperatures under an argon atmosphere is shown in Figure 32. The XANES of the pure PcCo reflects the square planar D_{4h} symmetry of the Co, and the peak labeled 2 provides a fingerprint of the Co–N₄ structure. For temperatures above 700 °C this peak is no longer observed, indicating a loss of the square planar configuration, and the XANES is very similar to that obtained for Co metal. These observations are confirmed by the Fourier transforms of the EXAFS as shown in Figure 33. The Fourier transform of the PcCo exhibits a peak at 1.6 Å for the Co–N distance. As the annealing temperature is increased, the amplitude of this peak decreases and a new peak grows in at 2.2 Å, corresponding to the Co–Co bond, indicating the formation of Co particles. The best oxygen reduction activity was obtained with the catalysts prepared by annealing to 850 °C,

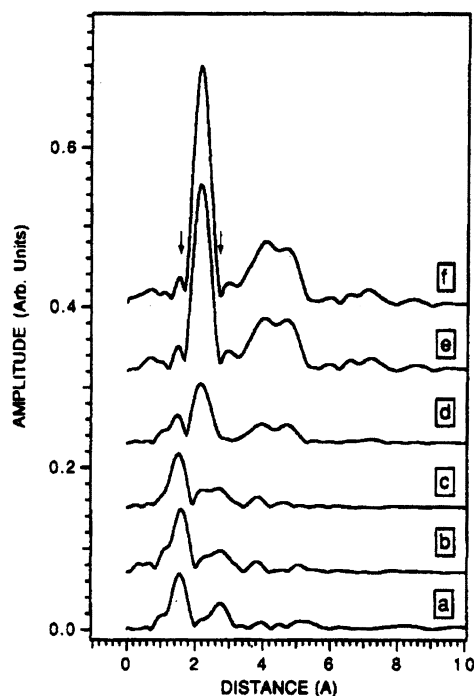


Figure 33. Fourier transforms of the Cu K EXAFS data for the samples described in Figure 32.¹⁵⁵ (Reproduced with permission from ref 155. Copyright 1992 American Chemical Society.)

corresponding to loss of the Co–N₄ center with the smallest Co particles.

The presence of Fe–N₄ was reported by Choi et al. for iron phthalocyanine on carbon,¹⁵² with the formation of an Fe₂O₃-like structure above 900 °C, and by Bron et al. for iron phenanthroline on carbon.¹⁵³ However, it is very difficult to give any weight to the conclusions of Bron et al. based on their EXAFS results, as figures depicting neither the data nor the fit are shown nor is a statistical measure of the goodness of fit reported. The results reported by Choi et al.¹⁵² indicate that the loss of electrocatalytic activity at higher annealing temperatures is more likely to be related to the formation of the inactive Fe₂O₃ phase rather than the loss of the Fe–N₄ center.

7. Conclusion

XAS has been successfully employed in the characterization of a number of catalysts used in low temperature fuel cells. Analysis of the XANES region has enabled determination of the oxidation state of metal atoms in the catalyst or, in the case of Pt, the d band vacancy per atom, while analysis of the EXAFS has proved to be a valuable structural tool. However, the principal advantage of XAS is that it can be used in situ, in a flooded half-cell or true fuel cell environment. While the number of publications has been limited thus far, the increased availability of synchrotron radiation sources, improvements in beam lines brought about by the development of third generation sources, and the development of more readily used analysis software should increase the accessibility of the method. It is hoped that this review will enable the nonexpert to understand both the power and limitations of XAS in characterizing fuel cell electrocatalysts.

8. References

- (1) Ankudinov, A. L.; Ravel, B.; Rehr, J. J.; Conradson, S. D. *Phys. Rev. B* **1998**, *58*, 7565.
- (2) Ankudinov, A. L.; Rehr, J. J.; Low, J. J.; Bare, S. R. *Top. Catal.* **2002**, *18*, 3.
- (3) Bazin, D.; Sayers, D.; Rehr, J. J.; Mottet, C. *J. Phys. Chem. B* **1997**, *101*, 5332.
- (4) Ankudinov, A. L.; Rehr, J. J.; Low, J. J.; Bare, S. R. *J. Chem. Phys.* **2002**, *116*, 1911.
- (5) Bazin, D.; Rehr, J. J. *J. Phys. Chem. B* **2003**, *107*, 12398.
- (6) Cauchois, Y.; Mott, N. F. *Philos. Mag.* **1949**, *40*, 1260.
- (7) Mansour, A. N.; Cook, J. W.; Sayers, D. E. *J. Phys. Chem.* **1984**, *88*, 2330.
- (8) Brown, M.; Peierls, R. E.; Stern, D. E. *Phys. Rev. B* **1977**, *15*, 738.
- (9) Koningsberger, D. C.; Prins, R. *X-ray Absorption*; John Wiley and Sons: New York, 1988.
- (10) Teo, B. K. *EXAFS: Basic principles and data analysis*; Springer-Verlag: Berlin, 1986.
- (11) Rehr, J. J.; Albers, R. C.; Sabinsky, S. I. *Phys. Rev. Lett.* **1992**, *69*, 3397.
- (12) Rehr, J. J.; Albers, R. C. *Phys. Rev. B* **1990**, *41*, 8139.
- (13) Zabinsky, S. I.; Rehr, J. J.; Ankudinov, A.; Albers, R. C.; Eller, M. J. *Phys. Rev. B* **1996**, *52*.
- (14) <http://ixs.csrii.iit.edu/IXS/>.
- (15) Ankudinov, A. L.; Conradson, S. D.; de Leon, J. M.; Rehr, J. J. *Phys. Rev. B* **1998**, *57*, 7518.
- (16) Gurman, S. J.; Binsted, N.; Ross, I. *J. Phys. C* **1984**, *17*, 143.
- (17) Duivenvoorden, F. B. M.; Koningsberger, D. C.; Uh, Y. S.; Gates, B. C. *J. Am. Chem. Soc.* **1986**, *108*, 6254.
- (18) Error reporting recommendations: a report of the standards and criteria committee; IXS Standards and Criteria Committee: 2000.
- (19) Koningsberger, D. C.; Mojet, B. L.; van Dorssen, G. E.; Ramaker, D. E. *Top. Catal.* **2000**, *10*, 143.
- (20) Li, G. G.; Bridges, F.; Booth, C. H. *Phys. Rev. B* **1995**, *52*, 6332.
- (21) Stern, E. A. *Phys. Rev. B* **1993**, *48*, 9825.
- (22) Young, N. A.; Dent, A. J. *J. Synchrotron Radiat.* **1999**, *6*, 799.
- (23) Koningsberger, D. C. *Jpn. J. Appl. Phys., Part 1: Regul. Pap., Short Notes Rev. Pap.* **1993**, *32*, 877.
- (24) McMaster, W. H.; Kerr Del Grande, N.; Mallett, J. H.; Hubbell, J. H. *Compilation of X-ray Cross Sections*; U.S. Department of Commerce: 1969; Vol. UCRL-50174, Section II, Revision I.
- (25) Mathew, R. J.; Russell, A. E. *Top. Catal.* **2000**, *10*, 231.
- (26) Allen, P. G.; Conradson, S. D.; Pennerhahn, J. E. *J. Appl. Crystallogr.* **1993**, *26*, 172.
- (27) Dent, A.; Evans, J.; Newton, M.; Corker, J.; Russell, A.; Abdul Rahman, A. B.; Fiddy, S.; Mathew, R.; Farrow, R.; Salvini, G.; Atkinson, P. *J. Synchrotron Radiat.* **1999**, *6*, 381.
- (28) Sharpe, L. R.; Heineman, W. R.; Elder, R. C. *Chem. Rev.* **1990**, *90*, 705.
- (29) O'Grady, W. E.; Koningsberger, D. C. *Ext. Abstr. Electrochem. Soc.* **1988**, *88-1*, 736.
- (30) Lampitt, R. A.; Carrette, L. P. L.; Hogarth, M. P.; Russell, A. E. *J. Electroanal. Chem.* **1999**, *460*, 80.
- (31) McBreen, J.; O'Grady, W. E.; Pandya, K. I.; Hoffman, R. W.; Sayers, D. E. *Langmuir* **1987**, *3*, 428.
- (32) Herron, M. E.; Doyle, S. E.; Pizzini, S.; Roberts, K. J.; Robinson, J.; Hards, G.; Walsh, F. C. *J. Electroanal. Chem.* **1992**, *324*, 243.
- (33) Maniguet, S.; Mathew, R. J.; Russell, A. E. *J. Phys. Chem. B* **2000**, *104*, 1998.
- (34) Mukerjee, S.; Srinivasan, S.; Soriaga, M. P.; McBreen, J. *J. Electrochem. Soc.* **1995**, *142*, 1409.
- (35) Adzic, R. R.; Wang, J. X.; Ocko, B. M.; McBreen, J. EXAFS, XANES, SXS. In *Handbook of Fuel Cells—Fundamentals, Technology and Applications*; Vielstich, W., Gasteiger, H. A., Lamm, A., Eds.; John Wiley and Sons, Ltd.: New York, 2003; Vol. 2; p 277.
- (36) Roth, C.; Martz, N.; Buhrmester, T.; Scherer, J.; Fuess, H. *Phys. Chem. Chem. Phys.* **2002**, *4*, 3555.
- (37) Viswanathan, R.; Hou, G. Y.; Liu, R. X.; Bare, S. R.; Modica, F.; Mickelson, G.; Segre, C. U.; Leyarovska, N.; Smotkin, E. S. *J. Phys. Chem. B* **2002**, *106*, 3458.
- (38) O'Grady, W. E.; Heald, S. M.; Sayers, D. E.; Budnick, J. I. *Ext. Abstr. Electrochem. Soc.* **1983**, *83-1*, 1071.
- (39) Yoshitake, H.; Yamazaki, O.; Ota, K. *J. Electrochem. Soc.* **1994**, *141*, 2516.
- (40) Yoshitake, H.; Mochizuki, T.; Yamazaki, O.; Ota, K. *J. Electroanal. Chem.* **1993**, *361*, 229.
- (41) Allen, P. G.; Conradson, S. D.; Wilson, M. S.; Gottesfeld, S.; Raistrick, I. D.; Valerio, J.; Lovato, M. *Electrochim. Acta* **1994**, *39*, 2415.
- (42) Yoshitake, H.; Yamazaki, O.; Ota, K. *J. Electroanal. Chem.* **1994**, *371*, 287.
- (43) Allen, P. G.; Conradson, S. D.; Wilson, M. S.; Gottesfeld, S.; Raistrick, I. D.; Valerio, J.; Lovato, M. *J. Electroanal. Chem.* **1995**, *384*, 99.

- (44) Chang, J. R.; Lee, J. F.; Lin, S. D.; Lin, A. S. *J. Phys. Chem.* **1995**, *99*, 14798.
- (45) McBreen, J.; Mukerjee, S. *Ext. Abstr. Electrochem. Soc.* **1996**, *96-2*, 125.
- (46) Mukerjee, S.; McBreen, J. *J. Electroanal. Chem.* **1998**, *448*, 163.
- (47) O'Grady, W. E.; Ramaker, D. E. *Electrochim. Acta* **1998**, *44*, 1283.
- (48) O'Grady, W. E.; Ramaker, D. E. *Ext. Abstr. Electrochem. Soc.* **1999**, *99-1*, 1034.
- (49) O'Grady, W. E.; Ramaker, D. E. *J. Synchrotron Radiat.* **1999**, *6*, 599.
- (50) Ramaker, D. E.; O'Grady, W. E. *Ext. Abstr. Electrochem. Soc.* **2001**, *2001-1*, 1038.
- (51) Teliska, M.; O'Grady, W. E.; Ramaker, D. E. *Ext. Abstr. Electrochem. Soc.* **2002**, *2002-1*, 1330.
- (52) O'Grady, W. E.; Hagans, P. L. *Ext. Abstr. Electrochem. Soc.* **2003**, *2003-1*, 2851.
- (53) Mansour, A. N.; Sayers, D. E.; Cook, J. W.; Short, D. R.; Shannon, R. D.; Katzer, J. R. *J. Phys. Chem.* **1984**, *88*, 1778.
- (54) Mansour, A. N.; Cook, J. W.; Sayers, D. E.; Emrich, R. J.; Katzer, J. R. *J. Catal.* **1984**, *89*, 464.
- (55) Samant, M. G.; Boudart, M. *J. Phys. Chem.* **1991**, *95*, 4070.
- (56) Kinoshita, K. *Electrochemical Oxygen Technology*; Wiley: New York, 1992.
- (57) Markovic, N.; Gasteiger, H.; Ross, P. N. *J. Electrochem. Soc.* **1997**, *144*, 1591.
- (58) Markovic, N. M.; Ross, P. N. *Surf. Sci. Rep.* **2002**, *45*, 121.
- (59) Benfield, R. E. *J. Chem. Soc., Faraday Trans.* **1992**, *88*, 1107.
- (60) McBreen, J.; Mukerjee, S. *J. Electrochem. Soc.* **1995**, *142*, 3399.
- (61) Doyle, S. E.; Roberts, K. J.; Herron, M. E.; Robinson, J.; Walsh, F. C. In *X-ray Absorption Fine Structure*; Hasnain, S. S., Ed.; Ellis Horwood: Chichester, U.K., 1991; p 279.
- (62) Dent, A. J. *Top. Catal.* **2002**, *18*, 27.
- (63) Angerstein-Kozłowska, H.; Conway, B. E. *J. Electroanal. Chem.* **1979**, *95*, 26.
- (64) Angerstein-Kozłowska, H.; Conway, B. E.; Sharp, W. B. A. *J. Electroanal. Chem.* **1973**, *43*, 9.
- (65) Conway, B. E.; Barnett, B.; Angerstein-Kozłowska, H.; Tilak, B. V. *J. Chem. Phys.* **1990**, *93*, 8361.
- (66) O'Grady, W. E.; Qian, X.; Ramaker, D. E. *J. Phys. Chem. B* **1997**, *101*, 5624.
- (67) Holland, B. W.; Pendry, J. B.; Pettifer, R. F.; Bordas, J. J. *J. Phys. C* **1978**, *11*, 633.
- (68) Rehr, J. J.; Booth, C. H.; Bridges, F.; Zabinsky, S. I. *Phys. Rev. B* **1994**, *49*, 12347.
- (69) Ankudinov, A. L.; Rehr, J. J. *Phys. Rev. B* **1997**, *56*, R1712.
- (70) Ankudinov, A. L.; Rehr, J. J. *J. Phys. IV* **1997**, *7*, 121.
- (71) Filipponi, A.; DiCiccio, A. *Phys. Rev. B* **1996**, *53*, 9466.
- (72) McBreen, J. *J. Electroanal. Chem.* **1993**, *357*, 373.
- (73) McBreen, J.; Ogrady, W. E.; Tourillon, G.; Dartyge, E.; Fontaine, A. *J. Electroanal. Chem.* **1991**, *307*, 229.
- (74) McBreen, J.; Sansone, M. *J. Electroanal. Chem.* **1994**, *373*, 227.
- (75) Yoshitake, H.; Yamazaki, O.; Ota, K. I. *J. Electroanal. Chem.* **1995**, *387*, 135.
- (76) Lucas, C. A.; Markovic, N. M.; Ross, P. N. *Phys. Rev. B* **1997**, *56*, 3651.
- (77) Toney, M. F.; Howard, J. N.; Richer, J.; Borges, G. L.; Gordon, J. G.; Melroy, O. R. *Phys. Rev. Lett.* **1995**, *75*, 4472.
- (78) Shi, Z.; Lipkowsky, J. *J. Electroanal. Chem.* **1994**, *364*, 289.
- (79) Alexeev, O. S.; Graham, G. W.; Shelef, M.; Adams, R. D.; Gates, B. C. *J. Phys. Chem. B* **2002**, *106*, 4697.
- (80) Mojte, B. L.; Ramaker, D. E.; Miller, J. T.; Koningsberger, D. C. *Catal. Lett.* **1999**, *62*, 15.
- (81) Campbell, C. T. *Annu. Rev. Phys. Chem.* **1990**, *41*, 775.
- (82) Gasteiger, H. A.; Markovic, N. M.; Ross, P. N. *J. Phys. Chem.* **1995**, *99*, 16757.
- (83) Gasteiger, H. A.; Markovic, N. M.; Ross, P. N. *J. Phys. Chem.* **1995**, *99*, 8290.
- (84) Watanabe, M.; Motoo, S. *J. Electroanal. Chem.* **1975**, *60*, 275.
- (85) Watanabe, M.; Uchida, M.; Motoo, S. *J. Electroanal. Chem.* **1987**, *229*, 395.
- (86) Cameron, D. S.; Hards, G. A.; Thompsett, D. Workshop on direct methanol-air fuel cells, 1992.
- (87) Maniguet, S. EXAFS studies of carbon supported fuel cells electrocatalysts. Ph.D. Thesis, University of Southampton, 2002.
- (88) Pandya, K. I.; Anderson, E. B.; Sayers, D. E.; Ogrady, W. E. *J. Phys. IV* **1997**, *7*, 955.
- (89) Binsted, N. *EXCURVE98*; Daresbury Laboratory: Warrington, U.K., 1998.
- (90) Camara, G. A.; Giz, M. J.; Paganin, V. A.; Ticianelli, E. A. *J. Electroanal. Chem.* **2002**, *537*, 21.
- (91) Meitzner, G.; Via, G. H.; Lytle, F. W.; Sinfelt, J. H. *Physica B* **1989**, *158*, 138.
- (92) Page, T.; Johnson, R.; Hormes, J.; Noding, S.; Rambabu, B. *J. Electroanal. Chem.* **2000**, *485*, 34.
- (93) Ertel, T. S.; Bertagnoli, H.; Huckmann, S.; Kolb, U.; Peter, D. *Appl. Spectrosc.* **1992**, *46*, 690.
- (94) Neto, A. O.; Giz, M. J.; Perez, J.; Ticianelli, E. A.; Gonzalez, E. R. *J. Electrochem. Soc.* **2002**, *149*, A272.
- (95) Nashner, M. S.; Somerville, D. M.; Lane, P. D.; Adler, D. L.; Shapley, J. R.; Nuzzo, R. G. *J. Am. Chem. Soc.* **1996**, *118*, 12964.
- (96) Nashner, M. S.; Frenkel, A. I.; Somerville, D.; Hills, C. W.; Shapley, J. R.; Nuzzo, R. G. *J. Am. Chem. Soc.* **1998**, *120*, 8093.
- (97) Russell, A. E.; Maniguet, S.; Mathew, R. J.; Yao, J.; Roberts, M. A.; Thompsett, D. *J. Power Sources* **2001**, *96*, 226.
- (98) Kabbabi, A.; Durand, R.; Faure, R. *Ext. Abstr. Electrochem. Soc.* **1995**, *95-1*, 750.
- (99) O'Grady, W. E.; Swider, K. E.; Pandya, K. I.; Kowalak, A. D. *Ext. Abstr. Electrochem. Soc.* **1995**, *95-1*, 744.
- (100) Gasteiger, H. A.; Markovic, N.; Ross, P. N.; Cairns, E. J. *J. Phys. Chem.* **1994**, *98*, 617.
- (101) Lin, S. D.; Hsiao, T. C.; Chang, J. R.; Lin, A. S. *J. Phys. Chem. B* **1999**, *103*, 97.
- (102) O'Grady, W. E.; Hagans, P. L.; Pandya, K. I.; Maricle, D. L. *Langmuir* **2001**, *17*, 3047.
- (103) Mukerjee, S.; Urian, R. C. *Electrochim. Acta* **2002**, *47*, 3219.
- (104) Mukerjee, S.; McBreen, J. *Ext. Abstr. Electrochem. Soc.* **1996**, *96-1*, 1130.
- (105) Swider, K. E.; Pandya, K. I.; Kowalak, A. D.; Hagans, P. L.; O'Grady, W. E. *Ext. Abstr. Electrochem. Soc.* **1995**, *95-1*, 742.
- (106) Grgur, B. N.; Markovic, N. M.; Ross, P. N. *J. Serb. Chem. Soc.* **2003**, *68*, 191.
- (107) Ball, S.; Hodgkinson, A.; Hoogers, G.; Maniguet, S.; Thompsett, D.; Wong, B. *Electrochem. Solid State Lett.* **2002**, *5*, A31.
- (108) Grgur, B. N.; Markovic, N. M.; Ross, P. N. *J. Electrochem. Soc.* **1999**, *146*, 1613.
- (109) Mukerjee, S.; Lee, S. J.; Ticianelli, E. A.; McBreen, J.; Grgur, B. N.; Markovic, N. M.; Ross, P. N.; Gialombardo, J. R.; De Castro, E. S. *Electrochem. Solid State Lett.* **1999**, *2*, 12.
- (110) Grgur, B. N.; Markovic, N. M.; Ross, P. N. *J. Phys. Chem. B* **1998**, *102*, 2494.
- (111) Grgur, B. N.; Zhuang, G.; Markovic, N. M.; Ross, P. N. *J. Phys. Chem. B* **1997**, *101*, 3910.
- (112) Grgur, B. N.; Markovic, N. M.; Ross, P. N. *Proton Conducting Membrane Fuel Cells*; 1999.
- (113) Zhang, H. Q.; Wang, Y.; Fachini, E. R.; Cabrera, C. R. *Electrochem. Solid State Lett.* **1999**, *2*, 437.
- (114) Mukerjee, S.; Lee, S. J.; Ticianelli, E. A.; McBreen, J. *Ext. Abstr. Electrochem. Soc.* **1998**, *98-2*, 1087.
- (115) Wang, K.; Gasteiger, H. A.; Markovic, N. M.; Ross, P. N. *Electrochim. Acta* **1996**, *41*, 2587.
- (116) Crabb, E. M.; Ravikumar, M. K.; Qian, Y.; Russell, A. E.; Maniguet, S.; Yao, J.; Thompsett, D.; Hurford, M.; Ball, S. C. *Electrochem. Solid State Lett.* **2002**, *5*, A5.
- (117) Mukerjee, S.; McBreen, J. *J. Electrochem. Soc.* **1999**, *146*, 600.
- (118) Mukerjee, S.; McBreen, J. *Ext. Abstr. Electrochem. Soc.* **1996**, *96-2*, 127.
- (119) Campbell, S. A.; Parsons, R. *J. Chem. Soc., Faraday Trans.* **1992**, *88*, 833.
- (120) Haner, A. N.; Ross, P. N. *J. Phys. Chem.* **1991**, *95*, 3740.
- (121) Srinivasan, S. *J. Electrochem. Soc.* **1989**, *136*, C41.
- (122) Appleby, A. J.; Foulkes, F. R. *Fuel Cell Handbook*; van Norstrand Reinhold: New York, 1989.
- (123) Jalan, V. M. U.S. Patent, 4,202,934, 1980.
- (124) Landsman, D. A.; Laczak, F. J. U.S. Patent, 4,36,944, 1982.
- (125) Mukerjee, S. *J. Appl. Electrochem.* **1990**, *20*, 537.
- (126) Mukerjee, S.; Srinivasan, S. *J. Electroanal. Chem.* **1993**, *357*, 201.
- (127) Mukerjee, S.; McBreen, J. *J. Electrochem. Soc.* **1996**, *143*, 2285.
- (128) Mukerjee, S.; Srinivasan, S.; Soriaga, M. P.; McBreen, J. *J. Phys. Chem.* **1995**, *99*, 4577.
- (129) Min, M. K.; Cho, J. H.; Cho, K. W.; Kim, H. *Electrochim. Acta* **2000**, *45*, 4211.
- (130) Smotkin, E. S.; Diaz-Morales, R. R. *Annu. Rev. Mater. Res.* **2003**, *33*, 557.
- (131) Paulus, U. A.; Wokaun, A.; Scherer, G. G.; Schmidt, T. J.; Stamenkovic, V.; Markovic, N. M.; Ross, P. N. *Electrochim. Acta* **2002**, *47*, 3787.
- (132) Chen, G. Y.; Delafuente, D. A.; Sarangapani, S.; Mallouk, T. E. *Catal. Today* **2001**, *67*, 341.
- (133) Shukla, A. K.; Neergat, M.; Bera, P.; Jayaram, V.; Hegde, M. S. *J. Electroanal. Chem.* **2001**, *504*, 111.
- (134) Neergat, M.; Shukla, A. K.; Gandhi, K. S. *J. Appl. Electrochem.* **2001**, *31*, 373.
- (135) Li, Y. J.; Chang, C. C.; Wen, T. C. *J. Appl. Electrochem.* **1997**, *27*, 227.
- (136) Tamizhmani, G.; Capuano, G. A. *J. Electrochem. Soc.* **1994**, *141*, 968.
- (137) Cho, J. H.; Roh, W. J.; Kim, D. K.; Yoon, J. B.; Choy, J. H.; Kim, H. S. *J. Chem. Soc., Faraday Trans.* **1998**, *94*, 2835.
- (138) Kim, D. K.; Choy, J. H.; Han, K. S.; Hwang, S. J.; Roh, W.; Kim, H. *J. Phys. IV* **1997**, *7*, 953.
- (139) Hilgendorff, M.; Diesner, K.; Schulenburg, H.; Bogdanoff, P.; Bron, M.; Fiechter, S. *J. New Mater. Electrochem. Syst.* **2002**, *5*, 71.
- (140) Tributsch, H.; Bron, M.; Hilgendorff, M.; Schulenburg, H.; Dorbandt, I.; Eyert, V.; Bogdanoff, P.; Fiechter, S. *J. Appl. Electrochem.* **2001**, *31*, 739.

- (141) Bron, M.; Bogdanoff, P.; Fiechter, S.; Dorbandt, I.; Hilgendorff, M.; Schulenburg, H.; Tributsch, H. *J. Electroanal. Chem.* **2001**, *500*, 510.
- (142) Reeve, R. W.; Christensen, P. A.; Dickinson, A. J.; Hamnett, A.; Scott, K. *Electrochim. Acta* **2000**, *45*, 4237.
- (143) Reeve, R. W.; Christensen, P. A.; Hamnett, A.; Haydock, S. A.; Roy, S. C. *J. Electrochem. Soc.* **1998**, *145*, 3463.
- (144) Jasinski, R. *J. Electrochem. Soc.* **1965**, *112*, 526.
- (145) Jahnke, H.; Schönborn, M.; Zimmermann, G. *Top. Curr. Chem.* **1976**, *61*, 133.
- (146) Alonso-Vante, N.; Malakhov, I. V.; Nikitenko, S. G.; Savinova, E. R.; Kochubey, D. I. *Electrochim. Acta* **2002**, *47*, 3807.
- (147) Malakhov, I. V.; Nikitenko, S. G.; Savinova, E. R.; Kochubey, D. I.; Alonso-Vante, N. *J. Phys. Chem. B* **2002**, *106*, 1670.
- (148) Malakhov, I. V.; Nikitenko, S. G.; Savinova, E. R.; Kochubey, D. I.; Alonso-Vante, N. *Nucl. Instrum. Methods Phys. Res., Sect. A: Accel., Spectrom., Dect., Assoc. Equip.* **2000**, *448*, 323.
- (149) Alonso-Vante, N.; Borthen, P.; Fieber-Erdmann, M.; Strehblow, H. H.; Holub-Krappe, E. *Electrochim. Acta* **2000**, *45*, 4227.
- (150) Joyner, R. W.; Vanveen, J. A. R.; Sachtler, W. M. H. *J. Chem. Soc., Faraday Trans. 1* **1982**, *78*, 1021.
- (151) van Wingerden, B.; Vanveen, J. A. R.; Mensch, C. T. J. *J. Chem. Soc., Faraday Trans. 1* **1988**, *84*, 65.
- (152) Choi, H. J.; Kwag, G.; Kim, S. *J. Electroanal. Chem.* **2001**, *508*, 105.
- (153) Bron, M.; Radnik, J.; Fieber-Erdmann, M.; Bogdanoff, P.; Fiechter, S. *J. Electroanal. Chem.* **2002**, *535*, 113.
- (154) Mojet, B. L. Metal-support interactions: a step closer to the origin. Ph.D. Thesis, University of Utrecht, 1997.
- (155) Martins Alves, M. C.; Dodelet, J. P.; Guay, D.; Ladouceur, M.; Tourillon, G. *J. Phys. Chem.* **1992**, *96*, 10898.

CR020708R

Alternative Polymer Systems for Proton Exchange Membranes (PEMs)

Michael A. Hickner,[†] Hossein Ghassemi,[‡] Yu Seung Kim,[§] Brian R. Einsla,^{||} and James E. McGrath^{*||}

Sandia National Laboratory, Albuquerque, New Mexico 87185, Department of Chemical Engineering, Case Western Reserve University, Cleveland, Ohio, Los Alamos National Laboratory, Los Alamos, New Mexico 87545, and Department of Chemistry, Macromolecules and Interfaces Institute, Virginia Polytechnic Institute and State University, Blacksburg, Virginia 24061

Received February 27, 2004

Contents

1. Introduction	4587
2. Nafion and Other Poly(perfluorosulfonic acid) Membranes	4590
3. PEMs Containing Styrene and Its Derivatives	4591
4. Poly(arylene ether)s	4593
4.1. Postsulfonation of Existing Polymers	4593
4.2. Direct Copolymerization of Sulfonated Monomers To Afford Random (Statistical) Copolymers	4595
5. PEMs Based on Poly(imide)s	4597
6. High Performance Polymeric Backbones for Use in PEMs	4600
7. Polyphosphazene PEMs	4603
8. Other Proton Conducting Moieties—Alternatives to Sulfonation	4605
9. Important Considerations in the Design of New PEMs	4607
10. Conclusions	4608
11. Acknowledgements	4609
12. References	4609

1. Introduction

Fuel cells have the potential to become an important energy conversion technology. Research efforts directed toward the widespread commercialization of fuel cells have accelerated in light of ongoing efforts to develop a hydrogen-based energy economy to reduce dependence on foreign oil and decrease pollution. Proton exchange membrane (also termed “polymer electrolyte membrane”) (PEM) fuel cells employing a solid polymer electrolyte to separate the fuel from the oxidant were first deployed in the Gemini space program in the early 1960s using cells that were extremely expensive and had short lifetimes due to the oxidative degradation of their sulfonated polystyrene–divinylbenzene copolymer membranes. These cells were considered too costly and short-lived for real-world applications. The commercialization of Nafion by DuPont in the late 1960s helped to demonstrate the potential interest in ter-

restrial applications for fuel cells, although its major focus was in chloroalkali processes.

PEM fuel cells are being developed for three main applications: automotive, stationary, and portable power. Each of these applications has its unique operating conditions and material requirements. Common themes critical to all high performance proton exchange membranes include (1) high protonic conductivity, (2) low electronic conductivity, (3) low permeability to fuel and oxidant, (4) low water transport through diffusion and electro-osmosis, (5) oxidative and hydrolytic stability, (6) good mechanical properties in both the dry and hydrated states, (7) cost, and (8) capability for fabrication into membrane electrode assemblies (MEAs). Nearly all existing membrane materials for PEM fuel cells rely on absorbed water and its interaction with acid groups to produce protonic conductivity. Due to the large fraction of absorbed water in the membrane, both mechanical properties and water transport become key issues. Devising systems that can conduct protons with little or no water is perhaps the greatest challenge for new membrane materials. Specifically, for automotive applications the U.S. Department of Energy has currently established a guideline of 120 °C and 50% relative humidity as target operating conditions, and a goal of 0.1 S/cm for the protonic conductivity of the membrane.

New membranes that have significantly reduced methanol permeability and water transport (through diffusion and electro-osmotic drag) are required for portable power oriented direct methanol fuel cells (DMFCs), where a liquid methanol fuel highly diluted in water is used at generally <90 °C as the source of protons. Unreacted methanol at the anode can diffuse through the membrane and react at the cathode, lowering the voltage efficiency of the cell and reducing the system’s fuel efficiency. The methanol is usually delivered to the anode as a dilute, for example, 1 M (or less), solution (3.2 wt %), and relatively thick Nafion 117 (1100 EW, 7 mil ~ 178 μm thick) is used to reduce methanol crossover. The dilute methanol feed increases the system’s complexity and reduces the energy density of the fuel, while the thick Nafion membrane increases the resistive losses of the cell, especially when compared to the thinner membranes that are used in hydrogen/air systems. The presence of excessive amounts of water at the cathode through diffusion and electro-osmosis

* To whom correspondence should be addressed. E-mail: jmcgrath@vt.edu.

[†] Sandia National Laboratory.

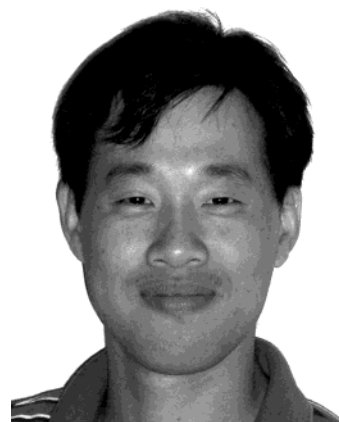
[‡] Case Western Reserve University.

[§] Los Alamos National Laboratory.

^{||} Virginia Polytechnic Institute and State University.



Michael Hickner received his B.S. in Chemical Engineering from Michigan Tech in 1999 and his Ph.D. in Chemical Engineering in 2003 under the direction of James McGrath. Michael's research in Dr. McGrath's lab focused on the transport properties of proton exchange membranes and their structure–property relationships. He has spent time at Los Alamos National Laboratory studying novel membranes in direct methanol fuel cells and is currently a postdoc at Sandia National Laboratories in Albuquerque, NM.



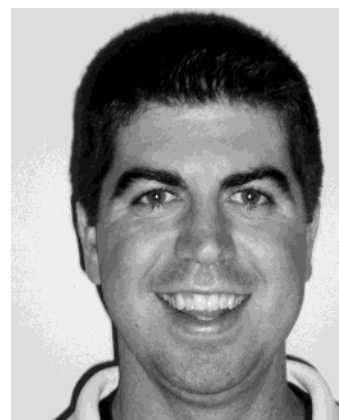
Yu Seung Kim received his Ph.D. at the Korea Advanced Institute of Science and Technology under Prof. Sung Chul Kim (1999). Subsequently, he joined Dr. James E. McGrath's research group at the Virginia Polytechnic Institute and State University (1999–2003), where he began studying polymer electrolyte membranes. His research was focused on the structure–morphology–property relationships of fuel cell membranes. He is currently working at the Los Alamos National Laboratory; his current research includes developing new membranes and electrodes for H₂/air and direct methanol fuel cells.



Hossein Ghassemi is currently a Senior Research Associate in the Department of Chemical Engineering at Case Western Reserve University and is involved in several projects related to fuel cell technology. He received his B.Sc. in Chemistry from Tehran University, in 1984. He then pursued his education toward an M.Sc. in Organic Chemistry at the Institute of Chemistry at Mazandaran, Iran. In May 1990 Dr. Ghassemi moved to Montreal, Canada, to begin his Ph.D. program at the Department of Chemistry at McGill University. He received his Ph.D. under the supervision of Prof. Allan S. Hay, in 1994. He then started his professional career as a Postdoctoral Associate with professor James E. McGrath at the NSF Science and Technology Center for High Performance Polymeric Adhesives and Composites at Virginia Polytechnic Institute and State University. He was involved in several projects sponsored by McDonnell Douglas/ARPA. Among his duties were to perform all aspects of research and development in the area of assignment, adapt and modify standard techniques and procedures, and apply nontraditional approaches and higher levels of problem solving for research. During the past 15 years, Dr. Ghassemi has authored and coauthored more than 20 scientific papers and patents.

results in water management problems both in the catalyst layer and for the system.

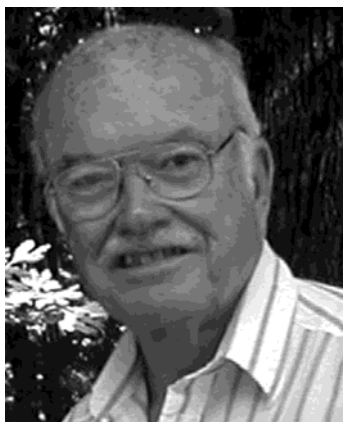
New membrane materials for PEM fuel cells must be fabricated into a well-bonded, robust membrane electrode assembly (MEA) as depicted in Figure 1. In addition to the material requirements of the proton exchange membrane itself as outlined above, the ease of membrane electrode assembly fabrication and the resulting properties of the MEA are also



Brian Einsla was born in Wilkes-Barre, PA, in 1978. He earned his Bachelor of Science degree in 2000 in Chemistry at Virginia Polytechnic Institute and State University. He is currently a fourth-year Ph.D. candidate in the Macromolecular Science and Engineering program at VPI&SU. His research interests have centered around sulfonated heterocyclic copolymers for fuel cell applications, including polyimides, polybenzoxazoles, and polybenzimidazoles.

critical. Current work in the area of fabricating MEAs from novel polymeric membranes has focused on the electrode–membrane interface and the problems of having dissimilar ion conducting copolymers in the membrane and as components of the electrode.¹ Novel membranes must also be adaptable and have the necessary physical strength and ductility in the dry and wet states to survive the stress of electrode attachment. Ion conducting copolymers that are compatible for use in the catalyst layer, in concert with novel polymer membranes, are also an emerging area of research.

Advances in fuel cell technology over the last four decades have come primarily from improved electrocatalysts, membrane electrode assembly fabrication strategies, and cell/stack/system engineering. Apart from Nafion, new ion conducting polymeric materials have played only a minor role in significantly increasing cell performance. However, new materials



James E. McGrath, a member of the prestigious National Academy of Engineering, is currently a University Distinguished Professor of Chemistry at Virginia Tech, as well as the Associate Director of the Macromolecules and Interfaces Institute. He received his B.S. in Chemistry from St. Bernardine of Siena College (1956), his M.S. in Chemistry from the University of Akron (1964), and his Ph.D. in Polymer Science from the University of Akron (1967). After several years in industry at Goodyear Tire and Rubber Company and Union Carbide, Dr. McGrath joined the faculty of Virginia Tech in 1975. He was named Full Professor 5 years later and in 1987 was appointed the Director of the Materials Institute, which later became the National Science Foundation Science & Technology Center for High Performance Polymer Adhesives and Composites (from 1989 to 2000). Since 1979, McGrath has also codirected the Polymer Materials and Interface Laboratory (PMIL). Dr. McGrath's career has included a number of distinguished awards, such as the Herman F. Mark Award (ACS Division of Polymer Chemistry, 1996), "Virginia Scientist of the Year" by the Virginia Museum of Science (1997), the ACS Division of Polymer Chemistry 2002 Applied Polymer Science Award, and, most recently, the P. J. Flory Education Award from the ACS Division of Polymer Chemistry (2004), which he received along with G. L. Wilkes and T. C. Ward. Dr. McGrath's primary research interests include high performance matrix polymers and structural adhesives, high temperature polymer dielectrics for computers, fire-resistant polymers and composites, and synthesis and characterization of new copolymers for proton exchange membranes (fuel cells). He holds 35 patents on a wide variety of topics related to polymer science, and he has coauthored well over 400 publications.

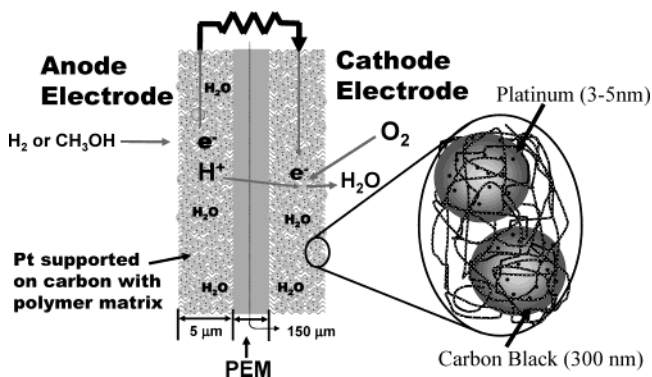


Figure 1. Basic membrane electrode assembly.

are now required to afford successful technology commercialization.

This review will outline the materials requirements for advanced alternative proton exchange membranes for fuel cells, assess recent progress in this area, and provide directions for the development of next-generation materials. The focus will be on the synthesis of polymeric materials that have attached ion conducting groups. State-of-the-art Nafion and its commercially available perfluorosulfonic acid relatives will initially be discussed. Other chain-growth co-

polymers based on styrenic, vinylic, or acrylic monomers will then be reviewed. Next, the large body of recent literature centered on polymeric materials based on step or condensation polymers (poly(ether ether ketone)s, poly(sulfone)s, poly(imide)s, and others) and various strategies for incorporating ionic groups into these materials will be evaluated. Finally, polymeric materials with other acid groups aside from sulfonic acid as the ion conducting moiety will be reviewed and various methodologies for advanced membranes will be presented. This review will highlight the synthetic aspects of ion conducting polymers and the polymer chemical structure considerations for producing useful PEMs. Extensive reviews of polymer-based proton conductors have recently been published.^{2,3,4} Only a brief review of important organic–inorganic composite membranes will be included,^{3b} even though it is predicted that this strategy will be central to future higher temperature systems.

Most of the synthetic methods currently utilized to form ion containing materials result in random or statistical placement of sulfonic acid units along the backbone copolymer chain. It is postulated that the distribution of sulfonic acid groups along the chain, as well as the acid strength and the connecting moiety to the polymer backbone, will have a considerable effect on the resulting morphology and membrane properties. Some block or segmented copolymer systems have been synthesized, but the subtle differences between random and block systems and the advantages/disadvantages of each are not yet well established in the literature for PEMs. This review will also highlight novel strategies for the controlled placement of ionic groups on a polymer or statistical copolymer backbone.

Some definitions are needed to establish a common framework for comparing different polymeric systems. The foremost of these is protonic conductivity. Scientists at Los Alamos National Laboratory (LANL) have devised a facile method for determining the conductivity of proton exchange membranes using electrochemical impedance spectroscopy and a simple cell that allows equilibration in a variety of environments.⁵ This method measures protonic conductivity *in the plane* of the membrane as opposed to *through the plane* (as in a fuel cell), and thus it works well as an initial screening test. Through-plane conductivity measurements⁶ are often more difficult experimentally than in-plane measurements because the measured membrane resistances are small in this geometry and interfacial resistances may play a more significant role.

Water uptake is also important in determining the ultimate performance of proton exchange membrane materials. In essentially all current polymeric materials, water is needed as the mobile phase to facilitate proton conductivity. However, absorbed water also affects the mechanical properties of the membrane by acting as a plasticizer, lowering the T_g and modulus of the membrane. Careful control of water uptake is critical for reducing adverse effects of swelling and degradation of the mechanical properties of the membrane in humid environments, as well as inducing stresses between the membrane and

the electrodes. Water uptake is usually reported as a mass fraction, mass percent, or λ value, where λ equals the number of water molecules absorbed per acid site.

Both conductivity and water uptake rely heavily on the concentration of ion conducting units (most commonly sulfonic acid) in the polymer membrane. The ion content is characterized by the molar equivalents of ion conductor per mass of dry membrane and is expressed as equivalent weight (EW) with units of grams of polymer per equivalent or ion exchange capacity (IEC) with units of milliequivalents per gram (mequiv/g or mmol/g) of polymer (EW = 1000/IEC). Varying the ion content of the membrane can control both its water uptake and conductivity. While it is desirable to maximize the conductivity of the membrane by increasing its ion content (decreasing equivalent weight), other physical properties must be considered. Too many ionic groups will cause the membrane to swell excessively with water, which compromises mechanical integrity and durability.

Meaningful standardized methods for characterizing proton exchange membranes for fuel cells are becoming more established within the fuel cell community and are helping to enhance the identification of promising candidate materials. At the most basic level, the ion exchange capacity, water uptake, and protonic conductivity of the membrane under specific environmental conditions should be measured in comparison to the standard Nafion materials and other systems. Standard important polymer science and engineering parameters such as molecular weight, detailed chemical compositions, morphology, topology, and mechanical behavior are no doubt critical but have only rarely been addressed.

2. Nafion and Other Poly(perfluorosulfonic acid) Membranes

The current state-of-the-art proton exchange membrane is Nafion, a DuPont product that was developed in the late 1960s primarily as a permselective separator in chlor-alkali electrolyzers.^{7,8} Nafion's poly(perfluorosulfonic acid) structure imparts exceptional oxidative and chemical stability, which is also important in fuel cell applications.

Nearly all of the commercially available membranes are based on Nafion. Nafion also has the largest body of literature devoted to its study because of its demonstrated industrial importance and availability. Nafion composite systems also have already become significant in both industrial and academic research. In composite structures, Nafion can be impregnated into an inert Teflon-like matrix (i.e. W. L. Gore membranes⁹), or inorganic additives can be added to a supporting Nafion matrix for improved physical or electrochemical properties (i.e. Ionomem¹⁰). Some critical aspects of Nafion's molecular structure and physical properties will be briefly highlighted to provide a baseline for comparison with the other alternative materials discussed in this review.

Nafion is a free radical initiated copolymer of a crystallizable hydrophobic tetrafluoroethylene (TFE) backbone sequence (~87 mol % at 1100 equivalent

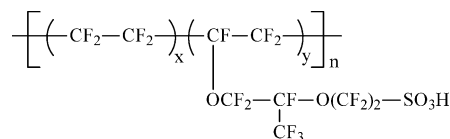


Figure 2. Chemical structure of Nafion. x and y represent molar compositions and do not imply a sequence length.

weight) with a comonomer which ultimately has pendant side chains of perfluorinated vinyl ethers terminated by perfluorosulfonic acid groups. The reported chemical structure of Nafion for PEM membranes is shown in Figure 2.

In theory, ion content can be varied by changing the ratio of the two components (x and y in Figure 2). Nafion has been commercially available in 900, 1100, 1200, and other equivalent weights. However, Nafion 1100 EW in thicknesses of 2, 5, 7, and 10 mil (1 mil equals 25.4 μm) (Nafion 112, 115, 117, and 1110) seems to be the only grades of Nafion that are currently widely available. This equivalent weight provides high protonic conductivity and moderate swelling in water, which seems to suit most current applications and research efforts. Modest retention of a semicrystalline morphology at this composition is no doubt important for mechanical strength. The thinner membranes are generally applied to hydrogen/air applications to minimize Ohmic losses, while thicker membranes are employed for direct methanol fuel cells (DMFCs) to reduce methanol crossover.

Unsaturated perfluoroalkyl sulfonyl fluoride and their derivatives are believed to be the starting comonomers for preparing perfluorosulfonic membranes. Nafion is prepared via the copolymerization of variable amounts of the unsaturated perfluoroalkyl sulfonyl fluoride with tetrafluoroethylene.^{11,12} Unfortunately, there have been no detailed literature reports of Nafion's synthesis and processing, but it is generally thought that the copolymer is then extruded in the melt processable sulfonyl fluoride precursor to form a membrane, which is later converted from the sulfonyl fluoride form by base hydrolysis to the salt or sulfonic acid functionality. It seems unlikely that the sulfonyl fluoride containing precursor unit in the copolymer would self-propagate under free radical conditions. Thus, the length of the comonomer sequence (y) is likely only one unit. Total molecular weight, though obviously important, has not been reported.

Like many other fluoropolymers, Nafion is quite resistant to chemical attack, but the presence of its strong perfluorosulfonic acid groups imparts many of its desirable properties as a proton exchange membrane. Fine dispersions (sometimes incorrectly called solutions) can be generated with alcohol/water treatments.¹³ Such dispersions are often critical for the generation of the catalyst electrode structure and the MEAs. Films prepared by simply drying these dispersions are often called "recast" Nafion, and it is often not realized that its morphology and physical behavior are much different from those of the extruded, more crystalline form.

Other perfluorosulfonate cation exchange membranes with similar structures have also been devel-

oped by the Asahi Chemical Company (Aciplex) and the Asahi Glass Company (Flemion).¹⁴ The Dow Chemical Company also developed a material with a shorter side chain than those of Nafion and the other perfluorosulfonates, which is no longer available.¹⁵ The length of the perfluorosulfonic acid side chain and the values for the equivalent weight may be varied to some extent.

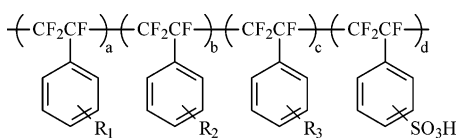
All of these polyperfluorosulfonic acid membranes are expensive and suffer from the same shortcomings as Nafion, namely low conductivity at low water contents, relatively low mechanical strength at higher temperature, and moderate glass transition temperatures.

3. PEMs Containing Styrene and Its Derivatives

As discussed above, the most commonly known and studied PEMs are based on nonaromatic perfluorinated hydrocarbons such as Nafion, Aciplex, Flemion, and what are termed the Dow membranes. However, their chemical synthesis is challenging due to the safety concerns of tetrafluoroethylene and the cost/availability of the perfluoroether comonomers. These issues have relegated detailed synthetic research on polyperfluorosulfonic acid materials to the industrial sector or to a few specialized academic labs.

One alternative to the tetrafluoroethylene-based backbones of the previously discussed materials is the use of styrene and particularly its fluorinated derivatives to form PEMs. As extensively reported in the literature, styrenic monomers are widely available and easy to modify, and their polymers are easily synthesized via conventional free radical and other polymerization techniques.

Presently, two commercial (or semicommercial) PEMs are based on styrene or styrene-like monomers: BAM from Ballard, and Dais Analytic's sulfonated styrene-ethylene-butylene-styrene (SEBS) membrane. Ballard Advanced Materials Corporation introduced a styrenic membrane based on a novel family of sulfonated copolymers incorporating α,β,β -trifluorostyrene and substituted α,β,β -trifluorostyrene comonomers. These are registered as BAM membranes, and their general formula is given in Figure 3.



$R_1, R_2, R_3 =$ alkyls, halogens, OR, $CF=CF_2$, CN, NO_2 , OH

Figure 3. Chemical structure of BAM PEMs.¹⁶

The unsulfonated random copolymers are reportedly synthesized at 50 °C over a period of 48 h using emulsion polymerization with dodecylamine hydrochloride surfactant in water as the reaction system and potassium persulfate as the initiator.¹⁶ The copolymer is then dissolved in an appropriate solvent such as dichloroethane or chloroform and sulfonated using reagents such as chlorosulfonic acid or a sulfur trioxide complex. It has been reported that this generation of BAM membranes exhibited some su-

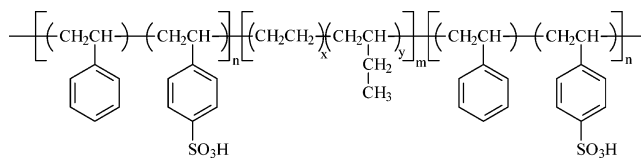


Figure 4. Chemical structure of sulfonated SEBS block copolymer.²¹

perior performance to perfluorinated membranes, such as Nafion 117, at current densities greater than 0.6 A cm⁻².¹⁷ The backbone fluorination was no doubt intended to mitigate hydroperoxide formation, which causes short lifetimes for nonfluorinated partially aliphatic analogues.

There have been few synthetic reports employing these monomers beyond the Ballard work, most likely as a result of presumed high cost and monomer availability. However, the performance and stability demonstrated by these materials in fuel cells may spur further developments in this area. The above-reported copolymers are believed to be random systems both in the chemical composition of the copolymer backbone and with regard to sulfonic acid attachment. Novel methods have been developed for the controlled polymerization of styrene-based monomers to form block copolymers. If one could create block systems with trifluorostyrene monomers, new morphologies and PEM properties with adequate stability in fuel cell systems might be possible, but the mechanical behavior would need to be demonstrated.

Dais Analytic's PEMs (and related materials) are based on well-known commercial block copolymers of the styrene-ethylene/butylene-styrene family, Kraton G1650 being one such system. In one method of forming sulfonated PEMs, the unsulfonated polymer is dissolved in a dichloroethane/cyclohexane solvent mixture. The sulfur trioxide/triethyl phosphate sulfonating complex in solution is then added and allowed to react at temperatures between -5 and 0 °C.¹⁸ The result is a PEM that may be solvent cast (from lower alcohols such as *n*-propanol) to afford an elastomeric hydrogel with conductivities of 0.07–0.1 S/cm when fully hydrated.^{19,20,21} The chemical structure of this type of copolymer is shown in Figure 4. The sulfonated styrene moieties are isolated in blocks, as directed by the anionic polymerization and hydrogenated starting material, but there is not much information on the extent of sulfonation of the styrenic moieties in the blocks. For the process described above, the unsulfonated block copolymer could have a number average molecular weight of about 50 000 g/mol with a styrene content of 20–35 wt % of the triblock copolymer. TEM suggests that the cast films possess cylindrical sulfonated polystyrene domains. The films swell in water, with the extent of swelling being dependent on the sulfonation level.²²

Dais membranes are reported to be much less expensive to produce than Nafion; they are also reported to exhibit a rich array of microphase-separated morphologies because of the ability to tailor the block length and composition of the unsulfonated starting polymer.²³ The main drawback of employing hydrocarbon-based materials is their much

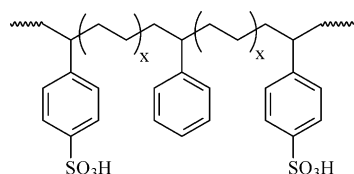


Figure 5. Chemical structure of partially sulfonated styrene–ethylene interpolymer.²¹

poorer oxidative stability compared to perfluorinated or partially perfluorinated membranes due to their partially aliphatic character.²⁴ For this reason, Dais membranes are aimed at portable fuel cell power sources of 1 kW or less, for which operating temperatures are less than 60 °C.

As an extension of the previous work, copolymers based on partially sulfonated ethylene–styrene pseudorandom “interpolymers” have also been employed instead of the block copolymers (Figure 5).^{21,25} Due to the unique nature of the polymerization catalyst, styrene residues are separated by at least one ethylene residue and the acid groups are distributed randomly along the chain. This material provides an economical and unique counterpoint to the sulfonated SEBS PEMs, where the sulfonic acid groups are bunched together in the styrene blocks. Controlling the styrene content in each material provides a route to control the level of sulfonation and resultant ion exchange capacity of the PEM.

Synthetic methods have been developed to incorporate styrene as a graft on to a polymer backbone. Graft polymers, in which ion containing polymer grafts are attached to a hydrophobic backbone, could be suitable structures for studying structure–property relationships in ion conducting membranes, if the length of the graft and the number density of graft chains can be controlled. In principle, the length of the graft would determine the size of ionic domains, whereas the number density of graft chains would determine the number of ionic domains per unit volume. Collectively, the size and number density of ionic aggregates/clusters are expected to control the degree of connectivity between ionic domains.

Recently, several researchers have shown that it is possible to synthesize graft copolymers possessing ionic grafts bound to hydrophobic backbones using macromonomers formed by stable free radical polymerization (SFRP) techniques.²⁶ The detailed synthesis and characterization of this class of copolymer that comprises a styrenic main chain and sodium styrenesulfonate graft chains (PS-*g-macPSSNa*) was reported by Holdcroft et al.²⁷ PS-*g-macPSSNa* was prepared by (1) pseudoliving, tempo-mediated free radical polymerization of sodium styrenesulfonate (SSNa) and (2) termination with divinylbenzene (DVB). The macromonomer, *macPSSNa*, serves as both the comonomer and emulsifier in the emulsion copolymerization with styrene. During polymerization, the DVB terminus is located in the core of micellar particles and is incorporated into growing polystyrene (PS) as graft chains. The synthetic scheme is shown in Figure 6. By adjusting the *macPSSNa*/styrene feed ratio, a series of polymers (PS-*g-macPSSNa*) with uniform graft chain length

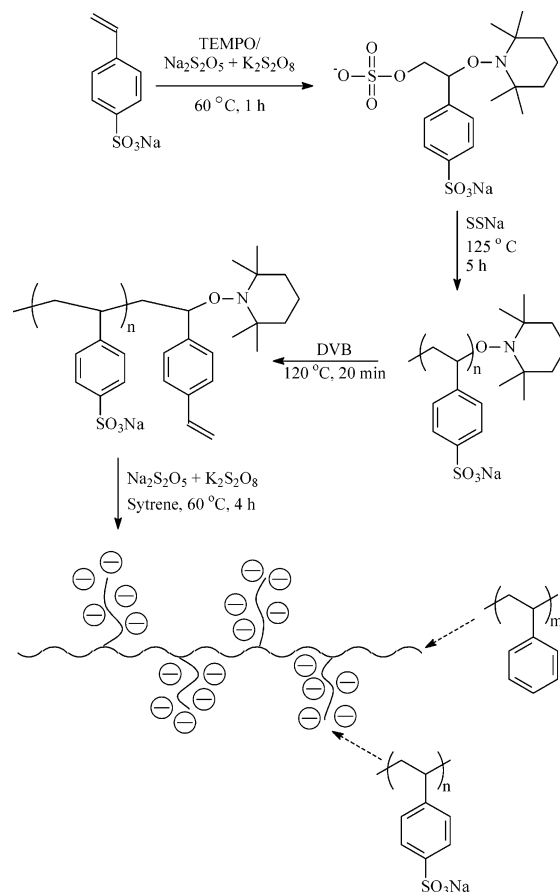


Figure 6. Synthetic scheme of polystyrene-*graft*-poly-styrenesulfonic acid copolymers.^{26,27}

and variable ion content were obtained. For comparison, random copolymers of SSNa and styrene (PS-*r*-SSNa) were prepared by conventional emulsion copolymerization. The two classes of polymer, graft and random, exhibit very different properties of mechanical strength, water uptake, proton conductivity, and thermal behavior as a result of their inherently different morphologies.

Using the same methodology as described above, Holdcroft et al. have also incorporated sodium styrenesulfonate macromonomers as grafts to poly(acrylonitrile) backbone chains.²⁸ The poly(acrylonitrile) backbone is more hydrophilic than the poly(styrene) backbone of the previous study. This allowed the authors to examine the effect that the backbone had on ionic domain morphology, water uptake, conductivity, and oxygen permeability and solubility. Holdcroft’s synthetic methodology for elucidating important PEM properties is excellent, and therefore, this group was able to draw rational conclusions when developing structure–property relationships of ion conducting polymers. These particular materials are probably not suitable PEMs themselves due to the well-known susceptibility of the poly(styrene) backbone or poly(styrene sulfonate) grafts to oxidative degradation in a fuel cell environment.

Poly(styrene sulfonic acid) grafts have also been attached to poly(ethylene-*co*-tetrafluoroethylene) (ETFE)^{28,29} and poly(vinylidene fluoride) (PVDF)³⁰ as shown in Figure 7. These materials were synthesized

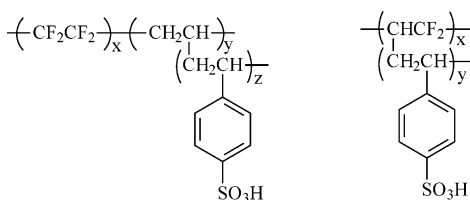


Figure 7. ETFE-*g*-PSSA and PVDF-*g*-PSSA.²⁸

by irradiating ETFE or PVDF preformed membranes with γ radiation and then immersing the irradiated membranes in styrene (usually diluted with toluene) to affect polymerization of poly(styrene) grafts from the backbone. The extent of grafting was reported to be controlled by styrene concentration, choice of diluent, grafting temperature, and grafting time. Once the extent of grafting was characterized by gravimetric means, the membranes were then sulfonated using chlorosulfonic acid.

Gupta et al.^{31,32} and Buchi et al.³³ have investigated the radiation grafting (using a γ radiation source) of tetrafluoroethylene-*co*-hexafluoropropylene (FEP) using styrene and divinylbenzene as monomers in the formation of grafts which are then sulfonated with chlorosulfonic acid. Divinylbenzene was used to create cross-links between grafts and possibly control water swelling of the membranes. Buchi et al. reported that FEP-grafted polystyrene sulfonic acid (FEP-*g*-SSA) systems have physical and electrochemical properties superior to those of Nafion 117 but an inferior fuel cell performance attributed to the gas permeability of the membrane. The excessive gas permeability was proposed to more readily allow HO \cdot attack on the polystyrene grafts and lead to a loss of ion exchange capacity after operating in a fuel cell environment, but no proof was offered. In a study using similar styrene grafted membranes, nearly 10 wt % of the grafts were lost after 100 h of fuel cell operation.³⁴ PEMs may tolerate some degree of backbone degradation during long-term fuel cell operation, but degradation involving a loss of ion exchange capacity (and thus a loss in conductivity) would be obviously undesirable in all situations.

4. Poly(arylene ether)s

Wholly aromatic polymers are thought to be one of the more promising routes to high performance PEMs because of their availability, processability, wide variety of chemical compositions, and anticipated stability in the fuel cell environment. Specifically, poly(arylene ether) materials such as poly(arylene ether ether ketone) (PEEK), poly(arylene ether sulfone), and their derivatives are the focus of many investigations, and the synthesis of these materials has been widely reported.³⁵ This family of copolymers is attractive for use in PEMs because of their well-known oxidative and hydrolytic stability under harsh conditions and because many different chemical structures, including partially fluorinated materials, are possible, as shown in Figure 8. Introduction of active proton exchange sites to poly(arylene ether)s has been accomplished by both a polymer postmodification approach and direct co-

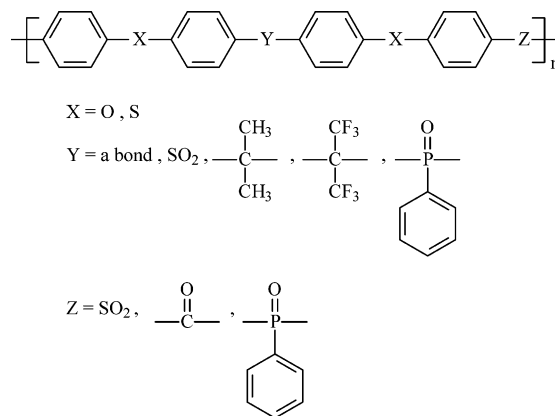


Figure 8. Several possible poly(arylene ether) chemical structures.

polymerization of sulfonated monomers. Both schemes are discussed below.

4.1. Postsulfonation of Existing Polymers

The most common way to modify aromatic polymers for application as a PEM is to employ electrophilic aromatic sulfonation. Aromatic polymers are easily sulfonated using concentrated sulfuric acid, fuming sulfuric acid, chlorosulfonic acid, or sulfur trioxide (or complex thereof). Postmodification reactions are usually restricted due to their lack of precise control over the degree and location of functionalization, the possibility of side reactions, or degradation of the polymer backbone. Regardless, this area of PEM synthesis has received much attention and may be the source of emerging products such as sulfonated Victrex poly(ether ether ketone).^{3a,36}

Sulfonated poly(arylene ether sulfone)s synthesized by attaching sulfonic acid groups in polymer modification reactions have been investigated intensively since the pioneering work of Noshay and Robeson, who developed a mild sulfonation procedure for the commercially available bisphenol A-based poly(ether sulfone).³⁷ Different sulfonating agents have been employed for this polymer modification, such as chlorosulfonic acid^{3a,4} and a sulfur trioxide-triethyl phosphate complex. Sulfonation is an electrophilic substitution reaction; therefore, its application depends on the substituents present on the aromatic ring. Electron-donating substituents will favor reaction, whereas electron-withdrawing substituents will not. Additionally, the sulfonic acid group is usually restricted to the activated position on the aromatic ring. For the case of the bisphenol A-based systems, no more than one sulfonic acid group per repeat unit could be achieved.³⁸

A comparative study of sulfonating agents was undertaken by Genova-Dimitrova et al.³⁹ Their aim was to investigate the characteristics of chlorosulfonic acid (ClSO₃H) and derived trimethylsilylchlorosulfonate ((CH₃)₃SiSO₃Cl) on the sulfonation of bisphenol A-based poly(sulfone). The authors indicated that the strong sulfonating agent, chlorosulfonic acid, yielded an inhomogeneous reaction that could be solubilized with a small amount of dimethylformamide as a cosolvent. Reactions with the mild trimethylsilylchlorosulfonate sulfonating agent were

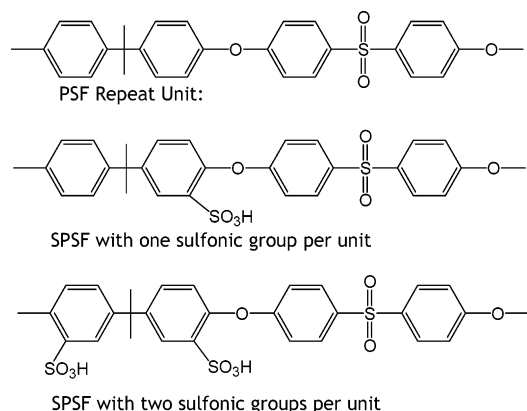


Figure 9. Most likely locations of sulfonic acid attachment in postsulfonated poly(arylene ether sulfone).³⁹

homogeneous reactions. Chlorosulfonic acid also induced chain cleavages during some sulfonations, as indicated by viscometric measurements, whereas no polymer degradation or cross-linking was observed with the milder trimethylsilylchlorosulfonate. Proton nuclear magnetic resonance (¹H NMR) was used to assemble a detailed picture of the kinetics of the sulfonation reaction with trimethylsilylchlorosulfonate. A marked decrease in reaction rate was observed after a degree of sulfonation of 0.74 (74% of the monomer units sulfonated) and 1.35 (68% of the theoretical yield of a degree of sulfonation of 2), as shown in Figure 9. The authors were not able to present a sound explanation for the rate decrease at these two levels of conversion.

Another drawback of the mild sulfonating reagent is that its sulfonation efficiency was low and during short reaction times (4 h) was limited to a degree of sulfonation of 0.85 even when a 3-fold excess of sulfonating agent was employed. Clearly, tradeoffs exist between strong and mild sulfonating agents, but avoiding polymer degradation and side reactions probably outweighs longer reaction times and somewhat lower sulfonation efficiency. The hydrolytic stability of the isopropylidene unit under fuel cell conditions has not been reported.

Poly(ether ether ketone) (PEEK) is an aromatic, high performance, semicrystalline polymer with extremely good thermal stability, chemical resistance, and electrical and mechanical properties. This polymer shows little solubility in organic solvents due to the crystallinity. One of the first ways to characterize PEEK was by sulfonating the polymer. By adding sulfonic acid groups to the backbone, the crystallinity decreased and solubility increased.^{40,41} Commercially available Victrex appears to be one of the more interesting poly(arylene ether)s used for postmodification.

There have been many procedures reported for sulfonating PEEK.^{3a,42,43} General chemical structures for the unsulfonated and sulfonated analogues are given in Figure 10. The sulfonation of PEEK has been reported to be a second-order reaction, which takes place at the aromatic ring flanked by two ether links, due to the higher electron density of the ring.⁴⁴ Since the electron density of the other two aromatic rings in the repeat unit is relatively low due to the electron-attracting nature of the neighboring carbonyl group,

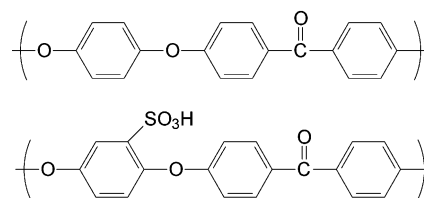


Figure 10. Chemical structures of unsulfonated and sulfonated PEEK.

one sulfonic acid group adds per repeat unit. It has been reported that sulfonation of PEEK with chlorosulfonic acid or fuming sulfuric acid causes a mostly unexplored degradation of the polymer; therefore, concentrated sulfuric acid is typically used.⁴⁵ The sulfonation rate of PEEK in sulfuric acid can be controlled by changing the reaction time, temperature, and acid concentration to provide polymers with a sulfonation range of 30–100% without degradation and cross-linking reactions.⁴⁶ However, it has been shown that the sulfonation of PEEK in sulfuric acid cannot be used to produce truly random copolymers at sulfonation levels less than 30% because dissolution and sulfonation occur in a heterogeneous environment.⁴⁷

Al-Omran and Rose⁴⁸ controlled the location and extent of sulfonation on poly(arylene ether) backbones by copolymerizing 4,4'-dichlorodiphenyl sulfone, durohydroquinone, and hydroquinone to form random copolymers, where only the hydroquinone residue would be expected to be susceptible to sulfonation by sulfuric acid. Although these authors observed sulfonation at positions other than at the desired hydroquinone locations, designing sulfonation sites into a polymer backbone remains an attractive strategy for producing copolymers with known structures. This allows the chemical structure and composition of the material to dictate the extent of sulfonation rather than trying to externally control sensitive and sometimes unpredictable macromolecular sulfonation reactions.

An alternative, but likely expensive, route for derivatizing a commercial polysulfone (Udel) by Kerres et al. was based on a series of steps including metalation, sulfination by SO₂ gas, and oxidation as shown in Figure 11.⁴⁹ One of the key steps in this synthesis is the choice of oxidant to convert the lithium sulfinate to sulfonic acid. Cross-linking reactions during oxidation may reduce the ion exchange capacity of the materials, while polymer chain degradation will result in membranes with quite poor mechanical properties. It was determined that hydrogen peroxide was the best oxidant for low IEC materials because of its ability to access all the ionic groups of the polymer in solution. Higher IEC materials were amenable to oxidation by KMnO₄ without adverse cross-linking or polymer degradation. This synthetic scheme also allows controlled cross-linking of the materials to manipulate swelling and gas permeability.^{50,51} The authors of this study assert the validity of this method for any polymeric species that can be lithiated, and it would be an attractive method for controlled sulfonation if polymer backbone degradation can be avoided.

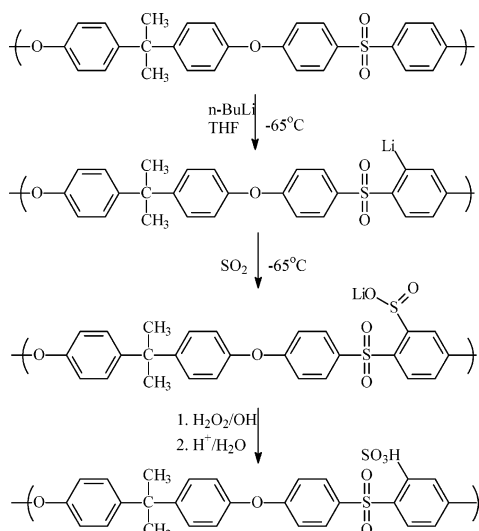


Figure 11. Metalation route to sulfonated polysulfone.⁴⁹

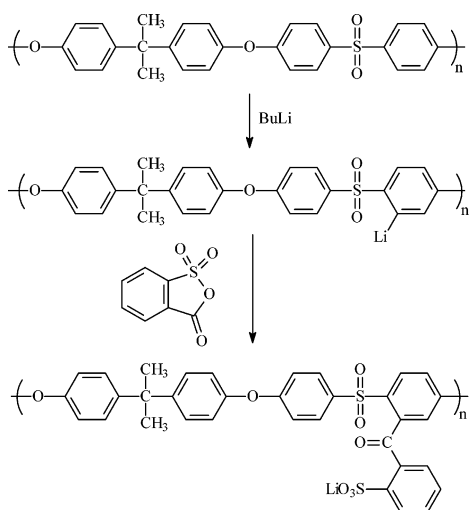


Figure 12. Chemical structure of sulfophenylated polysulfone.⁵²

Similarly, polysulfone has been sulfophenylated by lithiation and anionic reaction with 2-sulfonylbenzoic acid cyclic anhydride (Figure 12).⁵² This provides another method to modify polysulfones by attaching pendant sulfonated phenyl groups via ketone links. It would be interesting to see if the phase separation in these materials was affected by the additional functionality of the ketone or the pendant attachment of the sulfonic acid, as opposed to direct attachment of ionic groups to the aromatic polymer backbone.

4.2. Direct Copolymerization of Sulfonated Monomers To Afford Random (Statistical) Copolymers

There are several major drawbacks of postmodification methods including the lack of control over the degree and location of functionalization, which is usually a problem when dealing with macromolecules. It has been of interest to investigate the effect of sulfonation, for example, on the deactivated sites of the repeat units, since one might expect enhanced stability and higher acidity from two sulfonic acid groups which are attached to an electron-deficient aromatic ring than from one sulfonic acid group

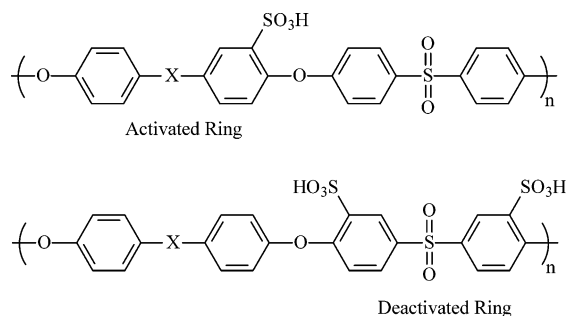


Figure 13. Placement of the sulfonic acid group in postsulfonation (activated ring) versus direct copolymerization (deactivated ring).

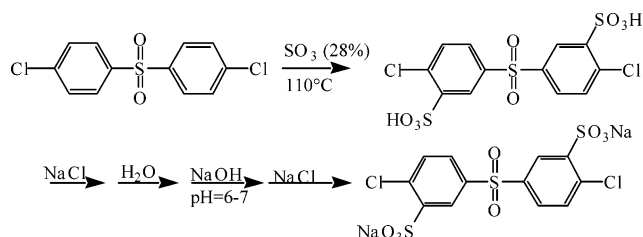


Figure 14. Synthesis of 3,3'-disulfonated 4,4'-dichlorodiphenyl sulfone and its sodium salt.

bonded to an electron-rich aromatic ring.⁵³ Moreover, the opportunity to control and/or increase molecular weight to enhance durability is not feasible if one chooses to conduct a postreaction on an existing commercial product. The difference between sulfonic acid placement in typical examples of postsulfonation and direct copolymerization is shown in Figure 13.

The first report of the required sulfonated monomer was from Robeson and Matzner,⁵⁴ who obtained a composition of matter patent, which primarily was of interest for its flame retarding properties. More recently, Ueda et al.⁵⁵ reported the sulfonation of 4,4'-dichlorodiphenyl sulfone and provided general procedures for its purification and characterization. McGrath's group modified the procedure for disulfonation of the monomer, shown in Figure 14. Sulfonated poly(arylene ether sulfone) copolymers were then synthesized via direct copolymerization in any composition desired as shown in Figure 15.⁵⁶ The directly copolymerized sulfonated materials were produced under very similar reaction conditions employed for many years for the synthesis of unsulfonated poly(arylene ether)s using the weak base route. Only moderately higher reaction temperatures and longer times were needed to obtain high molecular weight copolymers due to the sterically decreased activity of the sulfonated dihalide monomer. Alternatively, increased reactivity can be realized by employing the more expensive disulfonated difluoro dihalide. The copolymerizations were conducted to afford the potassium salt form of the 3,3'-disulfonated 4,4'-dichlorodiphenyl sulfone to take advantage of the enhanced stability of the sulfonic acid salt. These random copolymers displayed a hydrophilic/hydrophobic phase separated morphology that varied depending on the degree of disulfonation (Figure 15). A tapping mode atomic force microscopy (AFM) phase image comparison of the 40% copolymer with Nafion is shown in Figure 16.

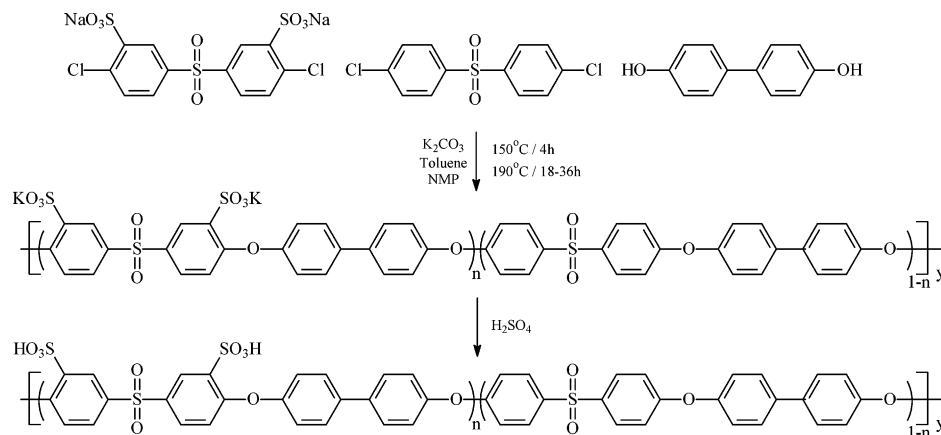
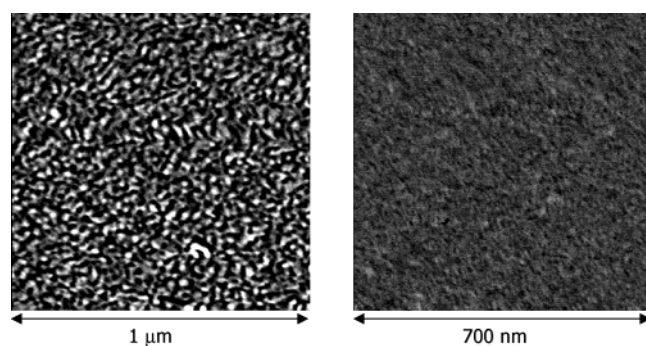


Figure 15. Synthesis of directly copolymerized wholly aromatic sulfonated poly(arylene ether sulfone),⁵⁶ BPSH-*xx*, where *xx* is the ratio of sulfonated/unsulfonated activated halide.



Phase Image of BPSH-40
dark regions are sulfonic acid + water (softer portion)

Phase Image of Nafion 117

Figure 16. Atomic force micrographs of BPSH-40 and Nafion 117.

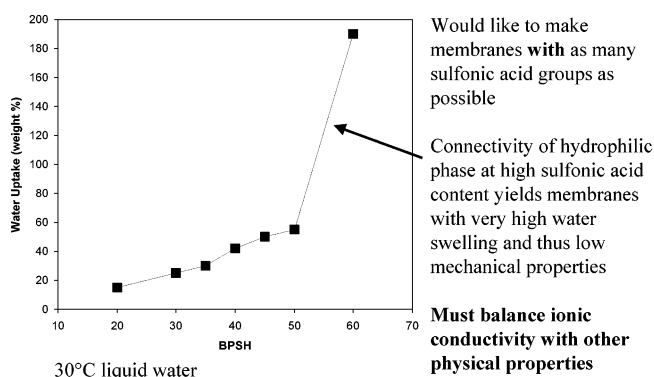


Figure 17. Swelling in 30 °C liquid water for the BPSH series of copolymers.

The conductivity and water uptake of this series of copolymers also increased with disulfonation. However, once the degree of disulfonation reached 60 mol %, a semicontinuous hydrophilic phase was observed and the membranes swelled dramatically, forming a hydrogel that would not be useful as a proton exchange membrane, as illustrated in Figure 17. These results indicate that the protonic conductivity must be balanced with the water swelling and mechanical properties of the membrane in these random copolymers. As with the unsulfonated polymers, many variations are possible in the direct synthesis of sulfonated poly(arylene ether sulfone)s

due to the variety of monomers available, as depicted in Figure 18.

The influence of the bisphenol structure on the direct synthesis of sulfonated poly(arylene ether)s has been studied.⁵⁷ Four bisphenols including bisphenol A, hexafluoroisopropylidene bisphenol (6F), 4,4'-biphenol, and hydroquinone were used for the synthesis of poly(arylene ether)s containing ion conducting units. Generally, the thin film properties of these copolymers scaled with ion exchange capacity. Sulfonated poly(arylene thioether sulfone) copolymers were prepared by direct copolymerization of sulfonated 4,4-difluorodiphenyl sulfone, unsulfonated 4,4-difluorodiphenyl sulfone, and 4,4-thiobisbenzenethiol.⁵⁸ The properties of these copolymers were comparable with those of their poly(ether sulfone) analogue. Copolymers based on hexafluoroisopropylidene bisphenol (6F) have been particularly interesting in initial fuel cell tests.⁵⁹ It is thought that their fluorine content promotes adhesion and electrochemical compatibility with Nafion-based electrodes and reduces swelling. Surface fluorine enrichment of the 6F containing materials may also provide enhanced membrane stability. The degree of sulfonation and method of acidification also influenced the dry dynamic mechanical behavior and T_g values, as presented in Figure 19. The modulus-temperature plot provides further evidence of the short-term thermal stability of the acid form membrane. One also notes broadening of the damping peaks, which may reflect different degrees of association or other phenomena.

Directly copolymerized sulfonated poly(arylene ether ketone) PEMs are also possible by employing a sulfonated dihalide ketone monomer (sodium 5,5'-carbonylbis(2-fluorobenzenesulfonate)), as first reported by Wang.^{60,61} The sulfonated monomer chemical structure is shown in Figure 20.

As described earlier, the choice of bisphenols for the polymerization of poly(arylene ether ketone)s is large.⁶² In particular, the electrochemical properties of the above monomer copolymerized with bisphenol AF were studied. The fundamental PEM characteristics (water uptake and conductivity) were analogous to those of the "BPSH" systems for a given IEC.

Due to the flexibility of incorporating various chemical moieties, sulfonated poly(arylene ether)

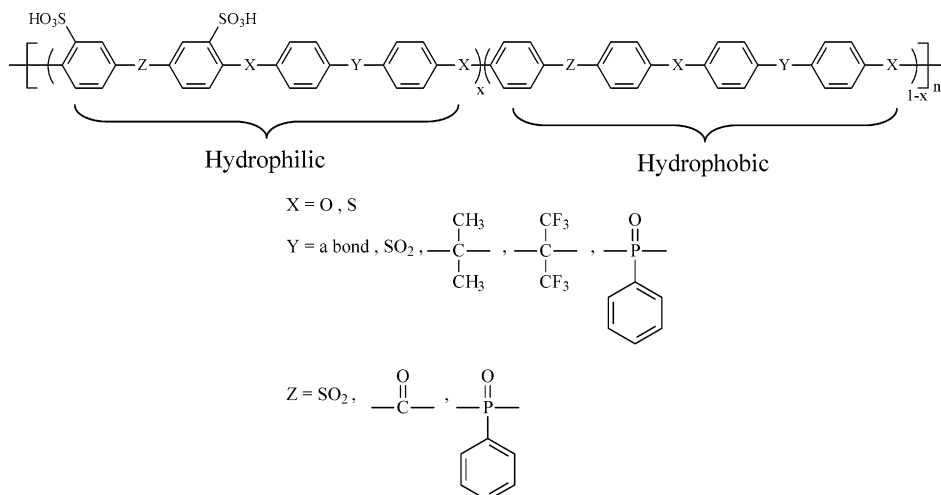
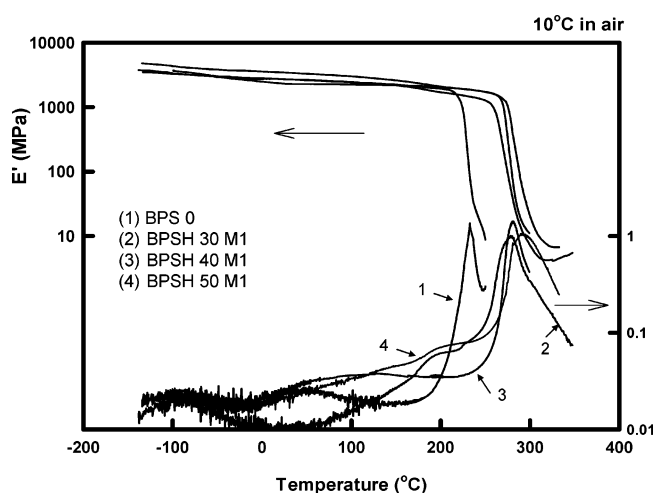


Figure 18. Some possible chemical structures for sulfonated PEMs from poly(arylene ether)s.



Copolymer	T_g	
	M1	M2
BPS-0	223	
BPSH-30	259	270
BPSH-40	268	272
BPSH-50	272	283

Figure 19. Effect of degree of disulfonation and method of acidification on the dynamic mechanical properties of BPSH films.⁵³ M1 and M2 refer to whether acidification was done at 30 or 100 °C, respectively.

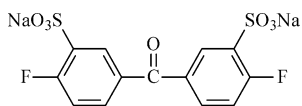


Figure 20. Chemical structure of sodium 5,5'-carbonylbis(2-fluorobenzenesulfonate).

copolymers may serve as ideal hosts for inorganic compounds to form nanocomposite proton exchange membranes.^{3b,63} Additional functionality to increase the compatibilization between the organic and inorganic phases can be imparted to the poly(arylene ether) by the copolymerization of 2,6-dichlorobenzonitrile, hexafluoroisopropylidene bisphenol (6F), and 3,3'-disulfonate-4,4'-dichlorodiphenyl sulfone.⁶⁴

These polymers show lower water uptake than the analogous sulfonated poly(arylene ether sulfone) materials, possibly suggesting some interaction between the aromatic nitrile and sulfonic acid. The phosphine oxide functional moiety could also be used as a compatibilizer with other materials. Sulfonated poly(arylene ether phosphine oxide sulfone) terpolymers have been prepared both with sulfonated triphenyl phosphine oxide⁶⁵ and with triphenyl phosphine oxide with 3,3'-disulfonate-4,4'-dichlorodiphenyl sulfone⁶⁶ as the sulfonic acid bearing monomer. Block copolymers containing phosphine oxide appear to avoid the ether-ether interchange that results when non-phosphine oxide blocks are utilized, and this is being further pursued.⁶⁷

5. PEMs Based on Poly(imide)s

Five-membered ring polyimides are high performance materials and have been investigated for many years. However, when sulfonated phthalic polyimides are used for proton exchange membranes in fuel cells, they quickly degrade, whereas it has been recognized that naphthalenic polyimides are much more stable in fuel cell environments.² It is likely that hydrolysis of the phthalic imide structure leads to chain scission (decrease in molecular weight) and causes the membrane to become brittle. Since the six-membered ring of the naphthalenic polyimide is much more stable to hydrolysis, this chemical structure is somewhat better suited for PEM fuel cell applications but its stability is still questionable.

Genies et al.⁶⁸ used model compounds along with IR and NMR to examine the nature of hydrolysis associated with the sulfonic acid group (needed for proton conduction) in phthalic and naphthalenic polyimides. Model compounds of the sulfonic acid containing phthalic imide (model A) and the sulfonic acid containing naphthalenic imide (model B) were prepared by a one-step high temperature condensation in *m*-cresol. NMR spectroscopy showed that after aging model A in distilled water at 80 °C for 1 h the structure is modified. After aging for 10 h, ¹³C NMR shows that the carbon peaks associated with the starting compound disappear. In addition, ¹³C NMR was used to quantitatively determine the amount of

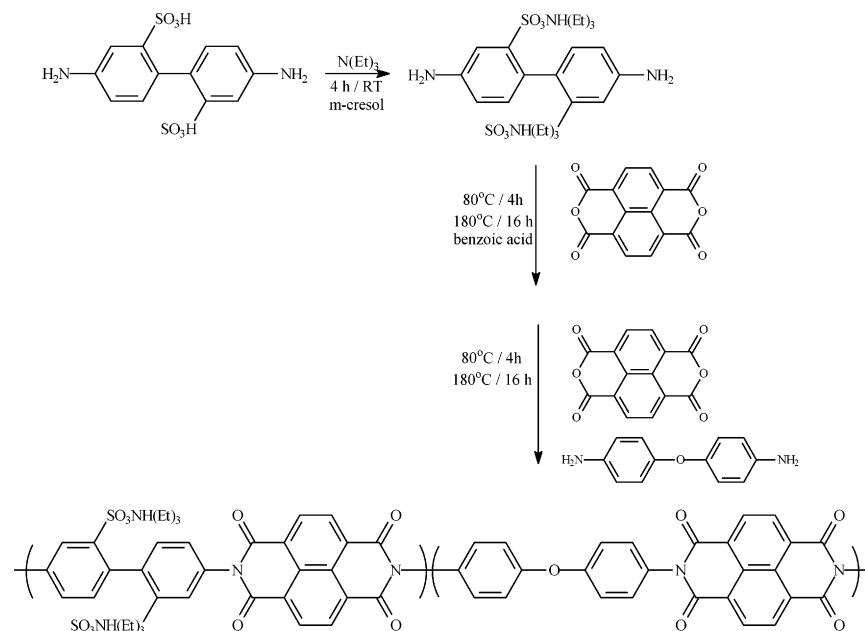


Figure 21. Synthesis of SPI, a sulfonated six-membered ring polyimide based on BDA, ODA, and NDA.⁶⁹

imide, amic acid, and diacid as a function of time during the aging process of model A. From 0 to 2 h of aging, the amic acid is formed preferentially to the diacid. This is interesting because the amic acid should easily hydrolyze to the diacid in water.

In comparison, no structural modification of model B was seen before 120 h of aging (80 °C). However, after 120 h two small doublets appeared in the ¹H NMR spectrum and several additional peaks became noticeable in the ¹³C NMR spectrum. It was determined by NMR and IR spectroscopy that the hydrolysis products were an imide/carboxylic acid and an imide/anhydride. Model B was then aged for 1200 h at 80 °C to quantitatively determine the amount of hydrolysis products as a function of time. The relative intensity of the peaks due to carboxylic acid is constant after some time. The authors suggest that an equilibrium occurs between model B and the products formed during hydrolysis, and therefore, the conversion to hydrolysis products is limited to about 12%. This critical fraction is probably enough to cause some degradation of polymeric materials, but research on six-membered polyimides has remained active.

Genies et al.⁶⁹ designed a synthetic method to produce random and block (segmented) sulfonated copolyimides (SPIs). The synthetic procedure for their most studied copolymer is shown in Figure 21. The first step in the synthesis involves preparation of short sequences of 4,4'-diamino-2,2'-biphenyl disulfonic acid (BDA) condensed with 1,4,5,8-tetracarboxylic dianhydride (NDA). An adjusted ratio of these two monomers allows one to create different block lengths of the sulfonated sequence. In the second polymerization step, the degree of sulfonation can be precisely controlled by regulating the molar ratio of BDA and the unsulfonated diamine, which is 4,4'-oxydianiline (ODA) in SPI. Controlling the degree of sulfonation is important because a high degree of sulfonation generally leads to high swelling or even dissolution of the polyimide membrane. It was found

that a block length of three sulfonated repeat units yields the highest proton conductivity.⁷⁰

Preliminary investigations suggested that six-membered ring polyimides had some promise as PEMs; however, their poor solubility limits membrane formation and subsequent use in fuel cells. For example, the SPI membrane shown above is only soluble in chlorophenol. By introducing a slightly different unsulfonated diamine, 2,2'-diamino-3,4'-biphenyl ether, the resulting polymer is made soluble in *m*-cresol.⁷¹ In Figure 21, the unsulfonated diamine added to the reaction in phase 2 was shown to have a large effect on the solubility, and several novel unsulfonated diamines containing ether linkages and/or bulky substituents were shown to improve solubility.⁶⁹

The preparation of sulfonated polyimides with different ion exchange capacities and sulfonated block lengths was also considered. The solubility of the polyimides was greatly improved by introducing phenyl–ether bonds and bulky groups into the polymer backbones. Random sulfonated copolyimides exhibit better solubility than the sequenced ones in organic solvents. Therefore, improved solubility is a result of the unsulfonated diamine and the microstructure of the polymer chain. For a given polymer structure, the water uptake increases as ionic content increases. However, the number of water molecules per ionic group remains constant, which suggests that water is mainly located in the hydrophilic domains. Both the number of water molecules per ionic group and conductivity are systematically lower for random microstructures than for sequenced copolymers.

By introducing bulky unsulfonated diamines into the polymer backbone, greater interchain spacings can be achieved.^{72,73} It was proposed that the increased spacing could improve conductivity at low relative humidity. Incorporating the larger comonomers prevents regular close parallel packing of the backbones and results in a more open structure, as

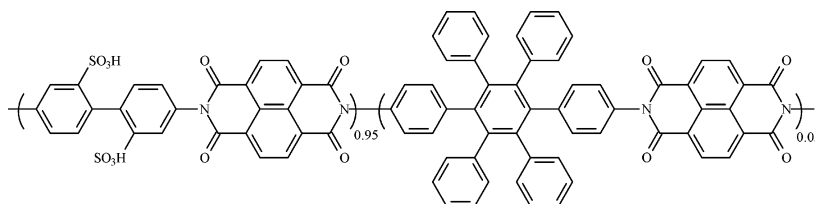


Figure 22. Six-membered ring copolyimide prepared with bulky unsulfonated diamine.

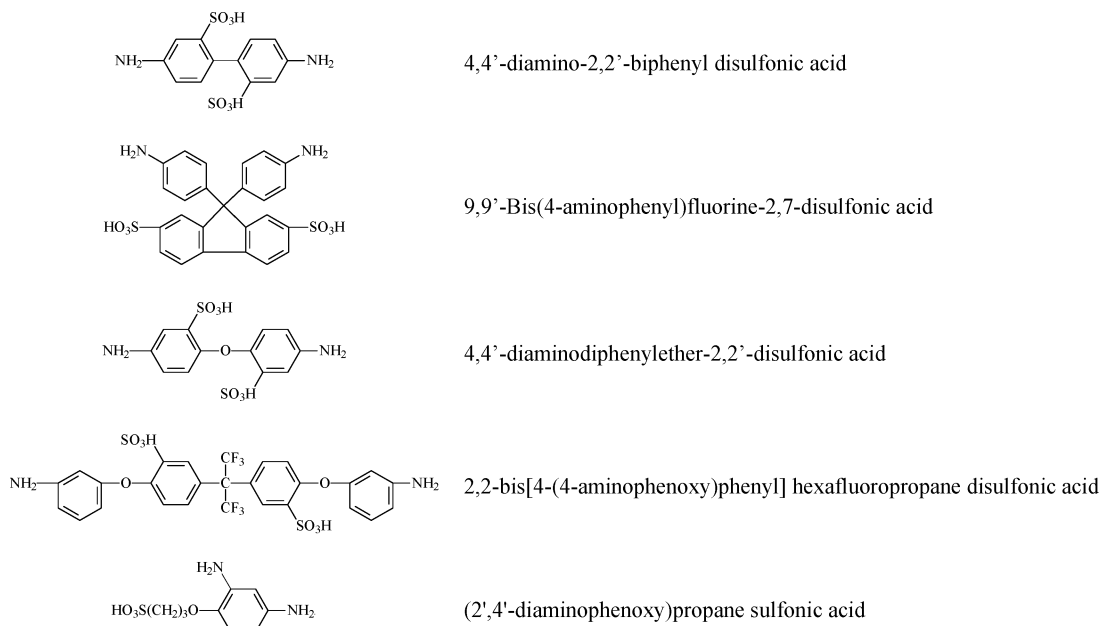


Figure 23. Sulfonated diamines for direct synthesis of sulfonated polyimides.

shown by X-ray diffraction patterns. With greater interchain spacings, more free volume is available for water to occupy. This leads to higher water uptakes and, therefore, higher conductivity, especially at low humidity.

Litt reported that bulky comonomers and sequenced copolymers impart improved water resistance without sacrificing conductivity. However, one sample shown in Figure 22 became brittle after 3 weeks in water above 90 °C. Litt also observed better hydrolytic stability when the unsulfonated diamine with flexible ether linkages was incorporated.^{72,73}

Principally, one commercially available sulfonated diamine (4,4'-diamino-2,2'-biphenyl disulfonic acid) has been used to synthesize sulfonated polyimides. In addition to the commercially available diamine, several novel sulfonated diamines incorporating flexible or kinked structures have been prepared in Okamoto's lab.^{74–77} The chemical structures and names of all five diamines are shown in Figure 23.

A comparison of the hydrolytic stability of several sulfonated six-membered ring polyimides was previously investigated.⁷⁵ Membranes were placed in distilled water at 80 °C until a loss of mechanical properties was observed. Improvements in membrane stability were observed for polymers with lower degrees of sulfonation (lower IEC) and for random copolymers, as opposed to block or sequenced copolymers. Additionally, the flexibility of the sulfonated diamine in the polymer structure was shown to play an important role in stability. By simply changing the sulfonated diamine from the rigid 4,4'-diamino-

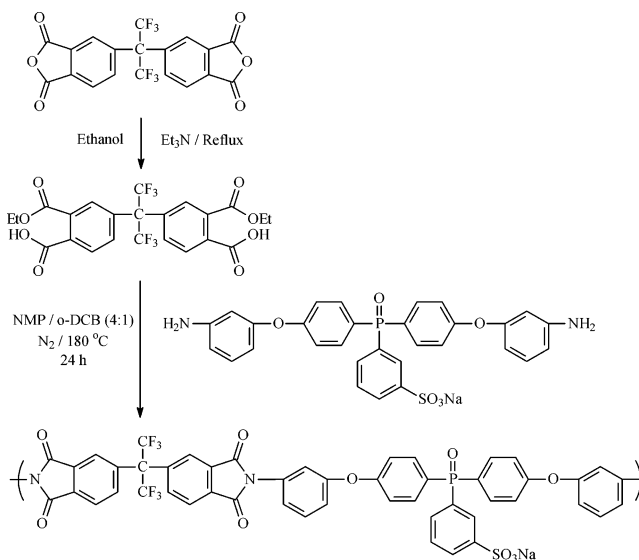


Figure 24. Synthesis of a five-membered ring sulfonated polyimide containing phosphine oxide.⁷⁸

2,2'-biphenyl disulfonic acid (BDA) to the more flexible 4,4'-diaminodiphenyl ether-2,2'-disulfonic acid (ODADS), the stability in water greatly improved. On the other hand, 9,9'-bis(4-aminophenyl)fluorine-2,7-disulfonic acid (BAPFDS), a rigid and bulky sulfonated diamine, showed similar stability to the ODADS series at comparable ion exchange capacities. It is suggested that polyimides derived from BAPFDS should display higher stability due to the highly basic sulfonated diamine.⁷⁶ Aromatic diamines with higher basicity are generally more reactive with dian-

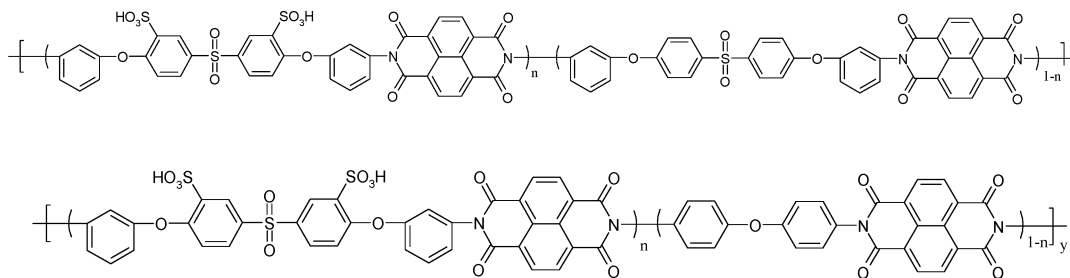


Figure 25. Sulfonated six-membered ring polyimides with novel sulfonated diamines.⁷⁹

hydrides than those with lower basicity. Since hydrolysis is the reverse reaction of polymerization, polyimides derived from more basic diamines should have higher hydrolytic stability. This may be why the more rigid copolymers based on BAPFDS have stabilities similar to the flexible ODADS ones; yet both perform better than BDA-type copolyimides.

Shobha et al.⁷⁸ employed a novel sulfonated diamine containing a phosphine oxide moiety in the synthesis of a five-membered ring sulfonated polyimide. The synthesis is shown in Figure 24.

Since this is a five-membered imide, water stability would be expected to be very poor. To improve stability, Einsla et al.⁷⁹ synthesized two series of six-membered imides (the first with 4,4'-oxydianiline as the unsulfonated diamine and the second with bis-[4-(3-aminophenoxy)phenyl] sulfone) using 3,3'-disulfonic acid-bis[4-(3-aminophenoxy)phenyl] sulfone as the sulfonated diamine, as shown in Figure 25. These polyimides are soluble in *N*-methylpyrrolidone (NMP) and have displayed better, but still limited, stability in water. Their electrochemical properties and fuel cell performance are the subject of an upcoming publication.⁸⁰ For high temperature fuel cell operations requiring a stability of >5000 h, however, the six-membered polyimides have been disappointing candidates, and they are generally being abandoned for use as PEMs. Nonetheless, most of these polyimides have extremely low methanol permeation and low electro-osmotic drag coefficients and might be useful as room temperature DMFC membranes.⁸¹

6. High Performance Polymeric Backbones for Use in PEMs

Other high performance polymer backbones have been explored as PEM materials in addition to poly(arylene ether)s and polyimides. Ductile copolymers with high modulus and glass transition values are desirable PEM candidates. The hydrolytic and oxidative stability of many of these materials remains to be determined. Nevertheless, interesting synthetic methodologies have been employed to investigate these materials, which have been instructive in the search for new PEM candidates.

Poly(phenylquinoxaline) membranes cast from *m*-cresol were sulfonated by reactions in 50% sulfuric acid solution for 2 h followed by drying at 300 °C for 90 min.^{82,83} The attachment site for the sulfonic acid group is believed to be ortho to the ether linkage, as in Figure 26, but even this has yet to be confirmed.

The resulting sulfonation levels varied from roughly 50% to well in excess of 100%, but they typically

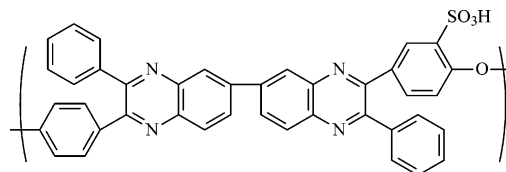


Figure 26. Chemical structure of sulfonated poly(phenylquinoxaline).⁸⁴

ranged between 70 and 100%. The stability of this material in detailed fuel cell performance studies was shown to be <500 h, and this material was subsequently abandoned in favor of materials that showed increased stability under fuel cell conditions.¹⁷

Poly(2,6-dimethyl-1,4-phenylene oxide) (PPO) is an attractive material for the preparation of membranes because it possesses excellent membrane-forming properties, as well as good thermal and chemical stability. PPO was sulfonated with chlorosulfonic acid either in a chloroform solution,⁸⁵ which is a common technique for PPO sulfonation, or in 1,2-dichloroethane.⁸⁶ In both cases, the sulfonated product precipitated after the addition of a certain amount of chlorosulfonic acid and could subsequently be easily isolated. The amount of chlorosulfonic acid needed for the precipitation of SPPO from the 1,2-dichloroethane solution, however, was smaller, and thus the degree of sulfonation of the obtained SPPO was lower (25.4 vs 42.4%) for the sample sulfonated in chloroform. The SPPO has shown good thermal stability and resistance against aqueous solutions of strong acids and bases and oxidation agents.⁸⁷ However, one might expect that the benzylic sites would easily oxidize.

Kobayashi et al. reported sulfonation of poly(4-phenoxybenzoyl-1,4-phenylene) (PPBP) with sulfuric acid and compared the data with those of sulfonated PEEK.⁸⁸ As reported, the authors employed sulfuric acid for the sulfonation reaction to avoid or at least minimize degradation of the polymer by chlorosulfonic acid or fuming sulfuric acid (Figure 27).

Sulfonated poly(4-substituted benzoyl-1,4-phenylene) homopolymers and copolymers using concentrated sulfuric acid or fuming sulfuric acid have been shown to form sulfonated polymers with variable degrees of sulfonation.⁸⁹ To improve film formation of the sulfonated polyphenylenes, multiblock copolymers have been synthesized by reacting a more flexible poly(arylene ether sulfone) with sulfonated polyphenylenes.⁹⁰

1,4-Bis(propylcarbamoyl)-2,3,5,6-tetraphenylbenzene and decafluorobiphenyl were polymerized to form copolymers that could be sulfonated at specific

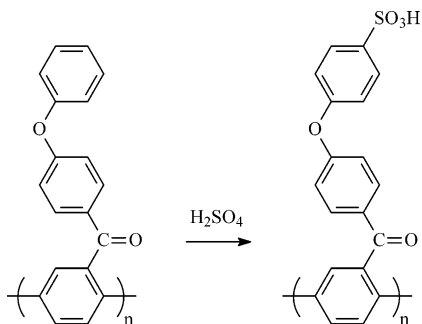


Figure 27. Sulfonation reaction of poly(4-phenoxybenzoyl-1,4-phenylene).⁸⁸

sites by reaction with chlorosulfonic acid in methylene chloride as shown in Figure 28.⁹¹ The reaction of the pendant phenyl rings at the para position with

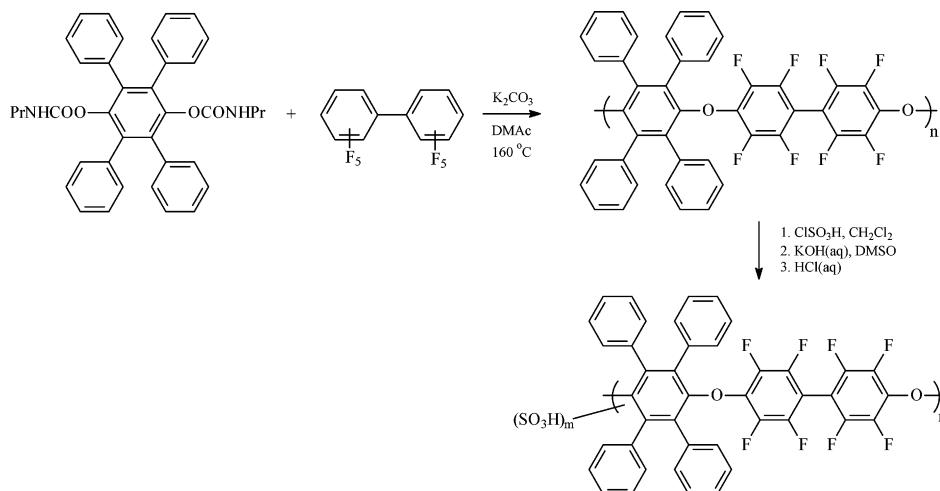


Figure 28. Synthesis and sulfonation of polymers containing tetraphenylphenylene ether and perfluorobiphenylene units.⁹¹

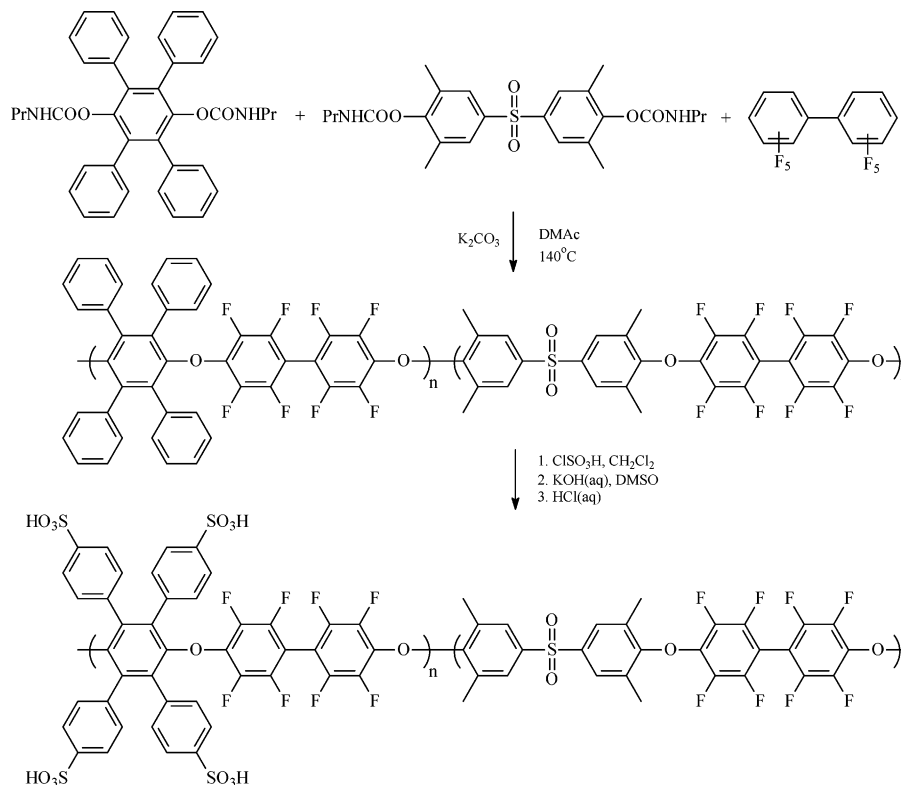


Figure 29. Synthesis of sulfonated copolymers from 1,4-bis(propylcarbamoyl)-2,3,5,6-tetraphenylbenzene, bis(3,5-dimethylphenyl) sulfone, and decafluorobiphenylene.⁹¹

chlorosulfonic acid is quantitative, so the degree of sulfonation can be controlled by the reaction stoichiometry. The above materials were soluble in methanol, which lead to bis(3,5-dimethylphenyl) sulfone being employed as a comonomer, as shown in Figure 29. These copolymers, as well as the synthesis of similar fluoroalkane containing copolymers, highlight the range of materials that can be designed with specific main chain chemical structures to the control resulting properties and sulfonation reactions.⁹²

Poly(phthalazinone ether ketone)s (PPEKs) were synthesized by the reaction of the polymer in mixtures of 95–98% concentrated sulfuric acid and 27–33% fuming sulfuric acid in the absence of other solvents.⁹³ A general reaction scheme is given in Figure 30. The mixed solvent systems of sulfuric acid

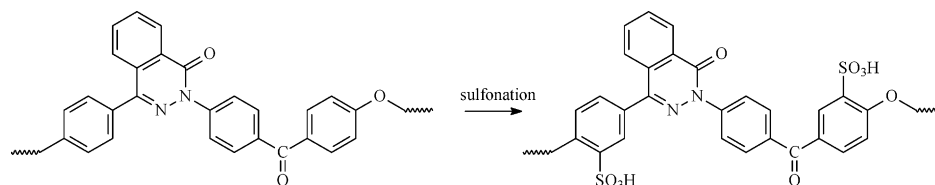


Figure 30. Sulfonation of PPEK.⁹³

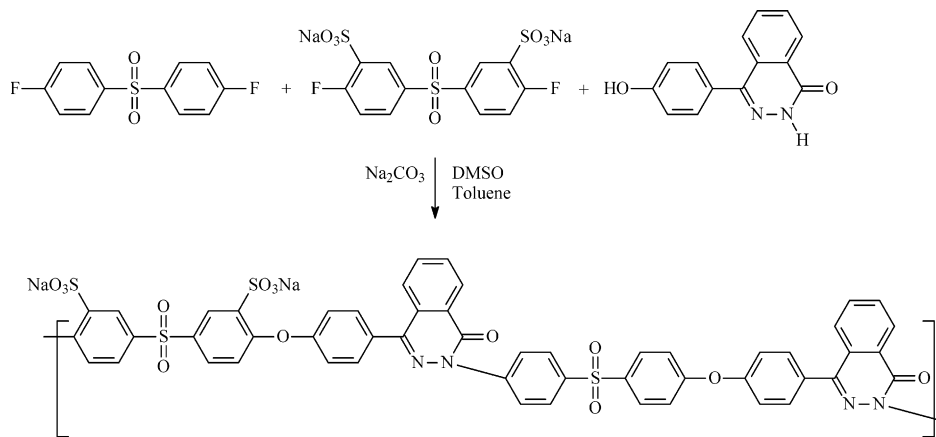


Figure 31. Synthesis of directly polymerized sulfonated poly(phthalazinone ether sulfone).⁹⁴

and fuming sulfuric acid were utilized to limit degradation of the polymer during sulfonation, which occurred in pure fuming sulfuric acid.

As an alternative to the somewhat undesirable postsulfonation approach, Xiao et al. synthesized sulfonated poly(phthalazinone ether sulfone)s utilizing sulfonated 4,4'-difluorodiphenyl sulfone as the sulfonated monomer, as shown in Figure 31.⁹⁴ The authors indicate that the low degree of swelling of these materials may be advantageous in comparison to the case of the directly polymerized sulfonated poly(arylene ether) materials. As they reported, the low swelling is due to hydrogen bonding involving the carbonyl groups of the hydroxyphenyl phthalazinone unit. The proton conductivities of the directly copolymerized materials showed less temperature dependence than those of the corresponding postsulfonated polymers. The hydrolytic stabilities of these copolymers were not reported.

Sulfonation of polybenzimidazole (PBI) can be accomplished by heating the polymer–hydrogen sulfate complex, which can be formed by casting a PBI film from sulfuric acid or immersing a cast PBI film in sulfuric acid and allowing the acid to permeate the membrane, as shown in Figure 32.⁹⁵ This material has received much attention, both as a proton exchange membrane candidate and also as a host for phosphoric acid,^{3d,96} especially given the success of unmodified PBI/phosphoric acid membranes⁹⁷ in high temperature fuel cells, as discussed elsewhere in this review. However, the thermally initiated sulfonation may have induced scission or cross-linking, as evidenced by the sulfonated PBI's insolubility and brittleness.

Sulfonation of polybenzimidazole was also accomplished by proton abstraction with an alkali metal hydride followed by reaction with sodium (4-bromomethyl)benzenesulfonate.^{98,99} The degree of sulfonation in this synthesis can be controlled by the

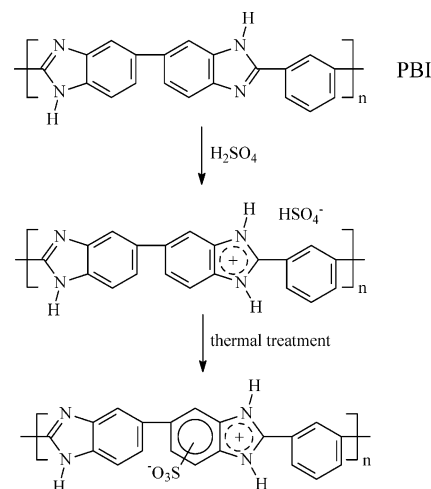


Figure 32. Sulfonation of PBI.⁹⁵

amount of ionized sites with the alkali metal hydride or by controlling the ratio of polybenzimidazole to (4-bromomethyl)benzenesulfonate, as shown in Figure 33. Control of the number and location of ionic groups is critical to a systematic study of the PEM properties and producing consistent material. Complexation phenomena would be expected to be important.

Direct copolymerization of sulfonated monomers has been used to synthesize sulfonated poly(benzimidazoles), poly(benzoxazoles), and poly(benzothiazoles). As an example, Kim et al. synthesized poly(benzthiazole)s from 2,5-diamino-1,4-benzenedithiol dihydrochloride and either 2-sulfoterrephthalic acid sodium salt, 5-sulfoisophthalic acid sodium salt, or 2,4-disulfoisophthalic acid potassium salt in polyphosphoric acid (PPA), as shown in Figure 34.¹⁰⁰ Similar sulfonated poly(benzimidazole)^{96,101} and sulfonated poly(benzoxazole)¹⁰² structures have also been synthesized. A general synthetic scheme for each is shown in Figure 35. The stability of these polymers in aqueous acidic environments appears

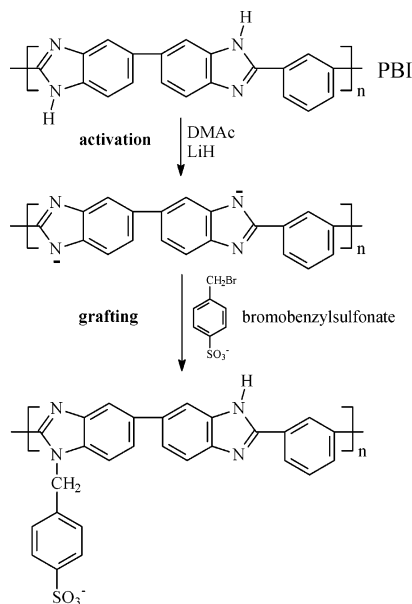


Figure 33. Synthetic scheme for controlled addition of (4-bromomethyl)benzenesulfonate to PBI.^{98,99}

limited and will likely hamper their performance as PEMs.¹⁰³

Mulhaupt et al. synthesized novel soluble copolyarylenes via a Ni(0)-catalyzed coupling reaction of aryl chlorides.¹⁰⁴ Molar ratios of dichlorodiphenyl sulfone (x) to *m*-dichlorobenzene (y) were used to vary the amount of *m*-phenylene in the final copolymer. Then these copolymers were dissolved in chloroform and sulfonated with chlorosulfonic acid. The synthe-

sis and sulfonation are shown in Figure 36. Due to the electron-withdrawing nature of the sulfone group, the copolymers were only susceptible to sulfonation on the *m*-dichlorobenzene residue. The degree of sulfonation could be controlled by the amount of *m*-dichlorobenzene included in the polymerization.

7. Polyphosphazene PEMs

Polyphosphazene-based PEMs are potentially attractive materials for both hydrogen/air and direct methanol fuel cells because of their reported chemical and thermal stability and due to the ease of chemically attaching various side chains for ion exchange sites and polymer cross-linking onto the $-P=N-$ polymer backbone.¹⁰⁵ Polyphosphazenes were explored originally for use as elastomers and later as solvent-free solid polymer electrolytes in lithium batteries, and subsequently for proton exchange membranes.¹⁰⁶

Polyphosphazenes are of great synthetic and technological interest because of the way in which the side groups can be varied over an exceedingly wide range of structures, and this provides access to species with an almost unprecedented variety of tailored properties. They are also particularly suitable for side-group and surface modification chemistry because of the stability of the phosphorus–nitrogen backbone. The surface chemistry of specific polyphosphazenes has been studied by Allcock et al. with respect to the sulfonation process.¹⁰⁵ The target sulfonation reactions were developed initially with

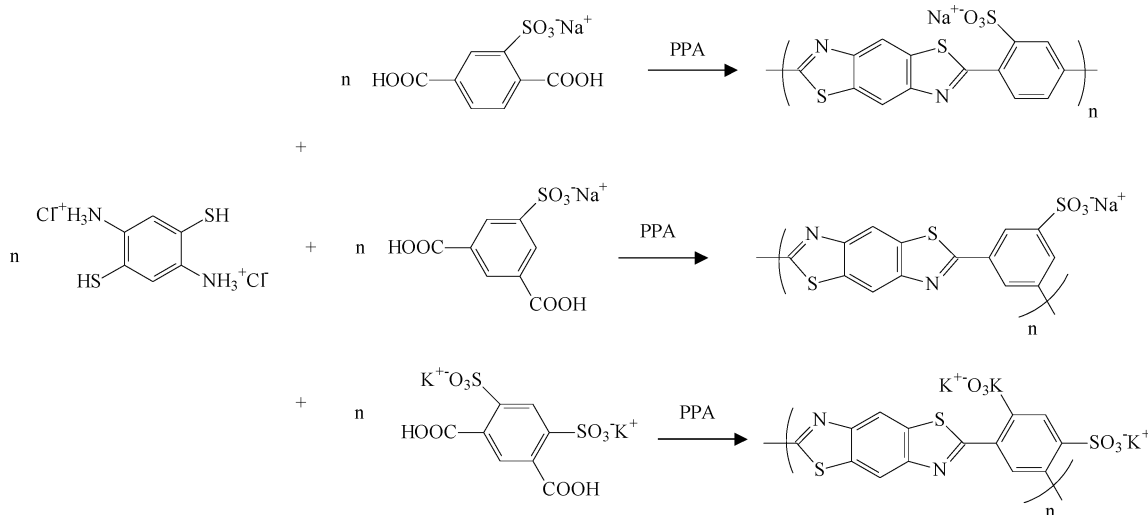


Figure 34. Synthetic scheme for the direct synthesis of sulfonated poly(benzthiazole)s.

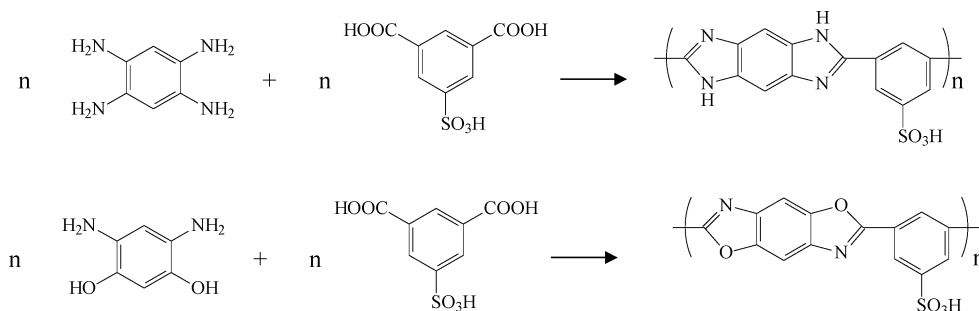


Figure 35. Synthesis of sulfonated poly(benzimidazole) and poly(benzoxazole).

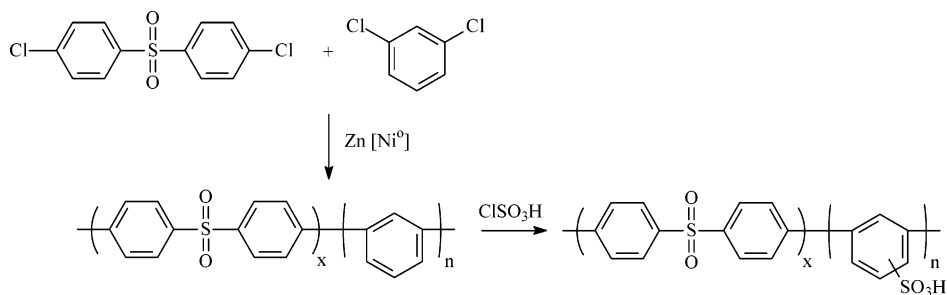


Figure 36. Synthesis and sulfonation of copolyarylenes.¹⁰⁴

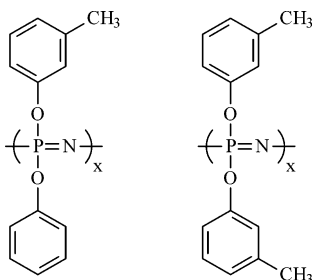


Figure 37. Poly[(3-methylphenoxy)(phenoxy)phosphazene] and poly[bis(3-methylphenoxy)phosphazene].¹¹¹

small-molecule cyclic trimeric phosphazenes to allow careful molecular characterization using the normal range of small-molecule analysis techniques.¹⁰⁷ Once optimized, the same reactions were carried out with the corresponding polymers. Standard polymer solution and materials characterization methods were applied to the product polymers in order to determine the molecular structures and material characteristics. Finally, the same reactions were applied to the surfaces of films prepared from polyphosphazene. The modified surfaces were examined by several surface analysis techniques.

Allcock's research led to the development of polyphosphazene-based PEMs by his small molecule studies of the sulfonation of cyclic trimeric phosphazenes¹⁰⁷ and the surface chemistry of polyphosphazene macromolecules.¹⁰⁵ In a 1993 report, he described the sulfonation of aminophosphazenes with 1,3-propanesultone.¹⁰⁸ While these specific materials are not necessarily ideal as PEMs, this study demonstrated a novel technique for creating sulfonated polyphosphazene materials that may provide more control over the sulfonated polymer product than wholesale sulfonation of a base polymer by a strong sulfonating agent.

Studies by Pintauro and co-workers have shown that poly[(3-methylphenoxy)(phenoxy)phosphazene] and poly[bis(3-methylphenoxy)phosphazene] (Figure 37) can be sulfonated by adding an SO_3 solution in dichloroethane dropwise to a polymer/dichloroethane solution.^{109,110} A high ion exchange capacity (up to 2.0 mequiv/g) material was reported with no detectable polymer degradation.

The sulfonation reaction is controllable, but one report indicates that reaction of the backbone nitrogen occurs before sulfonation on the pendent ring with poly[(3-methylphenoxy)(phenoxy)phosphazene], as shown in Figure 38.¹⁰⁹

Solution-cast membranes (100–200 μm in thickness) from sulfonated polymers with an ion exchange

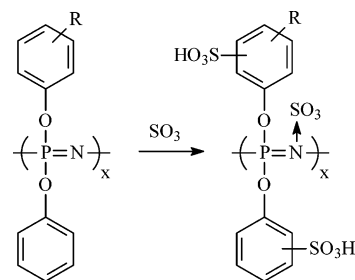


Figure 38. Possible sulfonation sites on poly[(3-methylphenoxy)(phenoxy)phosphazene].¹⁰⁹

capacity ≤ 1.4 mequiv/g exhibited good mechanical properties at room temperature in both the dry and water-swollen states. The reported glass transition temperatures varied from -28 to -10 $^\circ\text{C}$ for unsulfonated poly[bis(3-methylphenoxy)phosphazene] and the sulfonated analogue with an IEC of 2.1 mequiv/g, respectively. These low glass transition temperatures may cause membrane failures under fuel cell conditions and have led researchers to explore sulfonation and cross-linking of these polyphosphazene-based materials.

Pintauro et al. reported that proton exchange membranes with sulfonate fixed charge sites were fabricated from poly[bis(3-methylphenoxy)phosphazene].¹¹¹ The membrane ion exchange capacity was fixed at 1.4 mequiv/g. Membranes with and without cross-linking were examined, where polymer cross-linking was carried out (after sulfonation) by dissolving benzophenone photoinitiator in the membrane casting solution and then exposing the films to UV light after solvent evaporation. It is clear from this work that cross-linking reduced the water uptake and thus many of the membrane's transport properties. However, the protonic conductivity did not seem to differ between the cross-linked and non-cross-linked specimens even though their water uptakes were different. Once a sufficient level of hydration has been reached, it is possible that further addition of water (increases in λ) will have no effect on the protonic conductivity of the membrane due to the counterbalancing forces of increased hydration (higher λ) and increasing the distance between acidic sites (membrane swelling).

In another report polyphosphazene copolymers were synthesized from bis(2-methylphenoxy)phosphazene, which was sulfonated after polymerization.¹¹² Polymers such as polyvinylidene fluoride, polyhexafluoropropylene, and polyacrylonitrile were used to produce a blended membrane system. Polymer blends, cross-linking, and other means of re-enforcement are

generally necessary for polyphosphazene PEMs because of the relatively poor mechanical behavior of pure polyphosphazene films—particularly under hydrated conditions. Rational and controlled cross-linking of membranes could enhance the properties of some currently studied PEMs by decreasing the methanol crossover (with some expense to conductivity, but possibly not) and increasing the maximum working temperature of the membrane by increasing the onset of the hydrated T_g .

8. Other Proton Conducting Moieties—Alternatives to Sulfonation

Interest in new solid polymer electrolytes has driven some research groups to investigate other materials containing proton conducting moieties aside from sulfonic acid. Polymers and copolymers from monomers containing phosphonic-based proton conductors have been reported. Phosphonic and/or phosphinic acid containing polymers have not been well studied because of the rather limited synthetic procedures available for their preparation, compared with sulfonic acid derivatives. Miyatake and Hay

reported the first phosphonic acid containing polymers and copolymers from three phosphine containing aromatic difluorides with moderate molecular weight, as shown in Figure 39.¹¹³

The acid group in this instance is located in the main chain of the copolymer. The majority of acid containing polymers have the sulfonic acid functionality as the proton exchange site. There are a few reports of phosphonic acid containing polymers as membranes for fuel cell applications. They have lower acidity than sulfonic acid; however, their better chemical and thermal stability with respect to the corresponding sulfonic acid-functionalized polymers is believed to offer potential advantages.¹¹⁴ Poly(arylene ether)s containing mono- or dibromotetra-phenylphenylene ether and octafluorobiphenyl units may be used as precursors. The brominated polymers were phosphonated with diethyl phosphite by a palladium-catalyzed reaction. Quantitative phosphonation is reported when high concentrations of catalyst were used. The diethylphosphonated polymers were dealkylated by reaction with bromotrimethylsilane in carbon tetrachloride, followed by hydrolysis

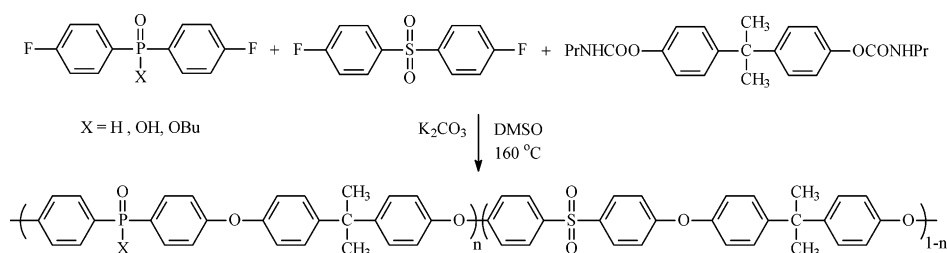


Figure 39. Synthesis of phosphonic acid ($X = OH$) containing poly(arylene ether).¹¹³

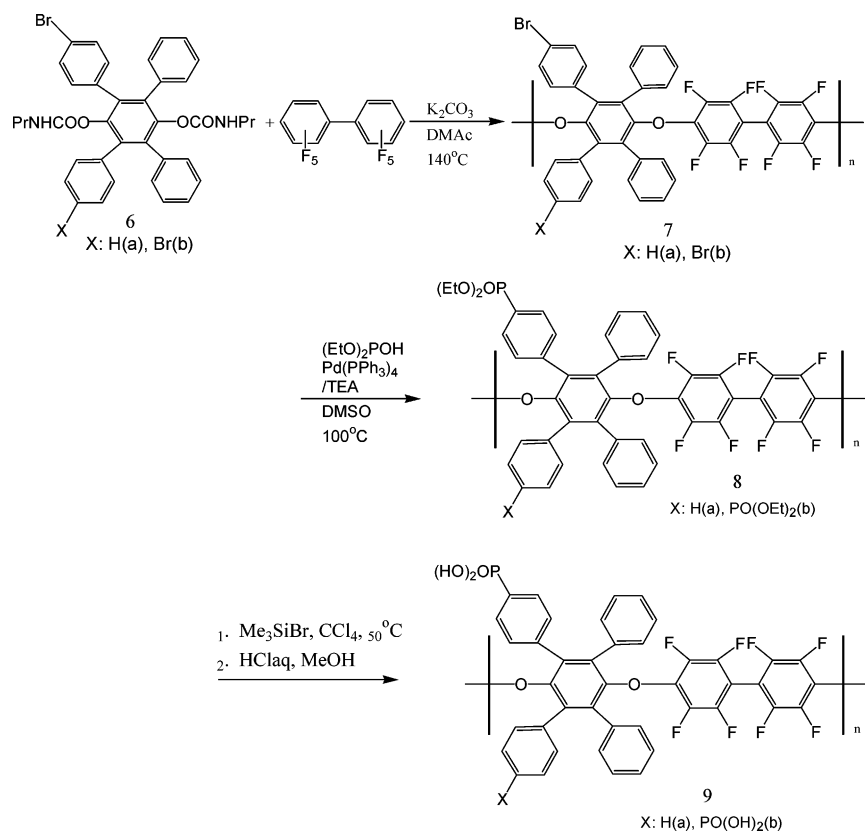


Figure 40. Synthesis of poly(arylene ether)s bearing phosphonic acid groups.¹¹⁴

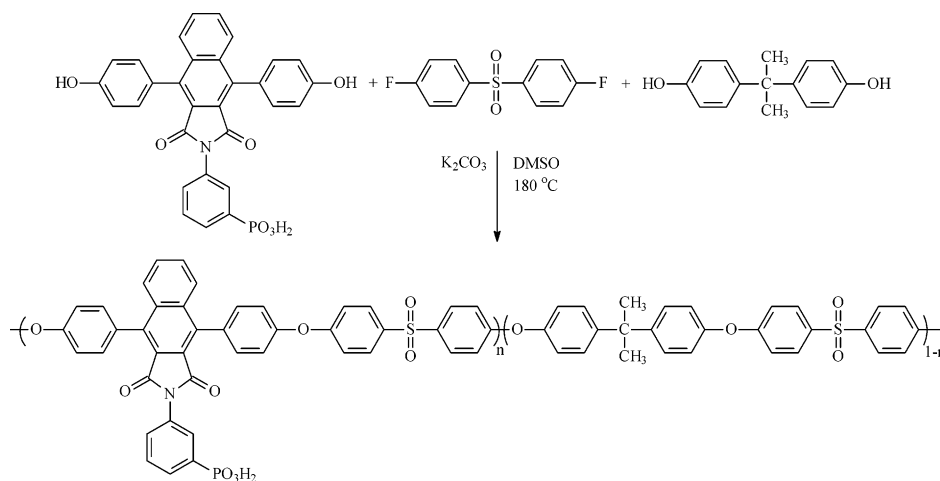


Figure 41. Synthesis of a phosphonic acid containing poly(arylene ether) derived from a phenolphthalein-based bisphenol.¹¹⁵

with hydrochloric acid to form polymers with pendent phosphonic acid groups, as shown in Figure 40.

The authors reported that tough, flexible films were obtained by solution casting from dimethyl sulfoxide (DMSO), which would indicate little or no backbone chain degradation occurred during phosphonation and dealkylation.

Another phosphonic acid containing polymer was also reported by Meng et al. and was based on phenolphthalein chemistry.¹¹⁵ The bisphenol monomer was synthesized from phenolphthalein and *m*-aminophenylphosphonic acid. Poly(arylene ether)s containing phosphonic acid groups were prepared from the bisphenol as shown in Figure 41. This is the first report on the attachment of phenylphosphonic acid groups as side chains to aromatic polyethers. These polyethers had very high glass transition temperatures and high molecular weights. However, their reported conductivities were only 10^{-5} – 10^{-6} S/cm, which is probably too low for these materials to be considered seriously as PEMs.

Allcock et al. also have investigated the use of phosphonated polyphosphazenes as potential membrane materials for use in direct methanol fuel cells (Figure 42).¹¹⁶ Membranes were found to have IEC values between 1.17 and 1.43 mequiv/g and proton conductivities between 10^{-2} and 10^{-1} S/cm. Methanol diffusion coefficients for these membranes were found to be at least 12 times lower than that for Nafion 117 and 6 times lower than that for a cross-linked sulfonated polyphosphazene membrane.

The strength of the acid conducting moiety is thought to play a role in the conductivity of proton exchange membranes. This has encouraged researchers to explore the role of strongly acidic functional groups such as sulfonimide moieties in proton exchange membranes.¹¹⁷ DesMarteau et al. have compared Nafion and a structurally similar bis[(perfluoroalkyl) sulfonyl]imide-based ionomer, as shown in Figure 43.¹¹⁸ There was not a noticeable increase in proton conductivity produced by incorporation of the sulfonimide moiety in their copolymer, in lieu of the perfluorosulfonic acid moiety of Nafion. In fact, their sulfonimide-based copolymer gave similar results in all respects to Nafion. Allcock et al. have also explored sulfonated poly(phosphazene)s with either

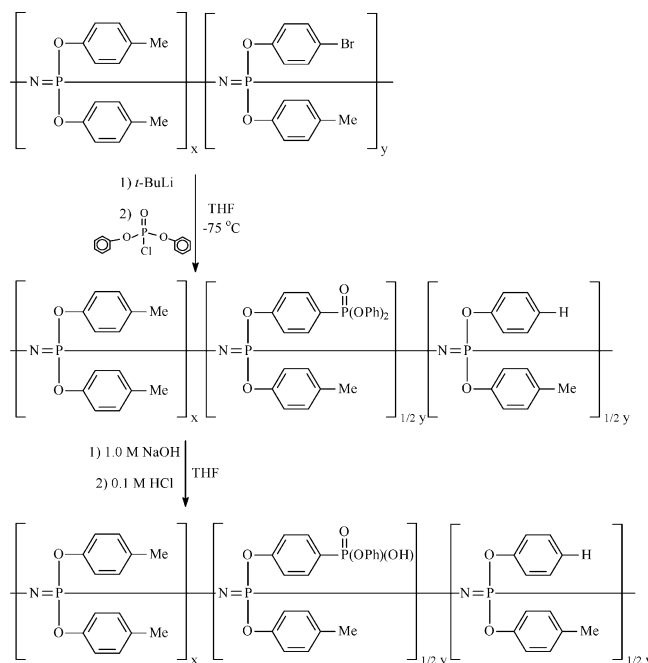


Figure 42. Synthesis of polyphosphazenes bearing phenyl phosphonic acid side groups.¹¹⁶

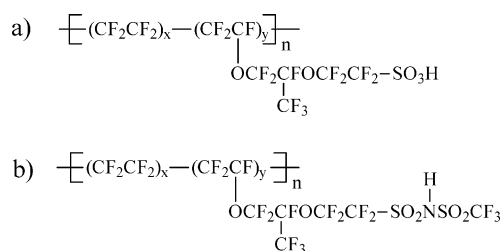


Figure 43. Structure of Nafion and bis[(perfluoroalkyl) sulfonyl]imide.¹¹⁸

sulfonic acid¹⁰⁵ or sulfonimide¹¹⁹ proton conducting substituents.

Cho et al.¹²⁰ have recently described the synthesis of a sulfonimide containing monomer and the resulting poly(arylene ether sulfone) copolymers. In this procedure 3,3'-disulfonate-4,4'-dichlorodiphenyl sulfone was refluxed in thionyl chloride, isolated, and then reacted with trifluoromethanesulfonamide in the presence of triethylamine to form the sulfonamide analogue monomer as shown in Figure 44. This

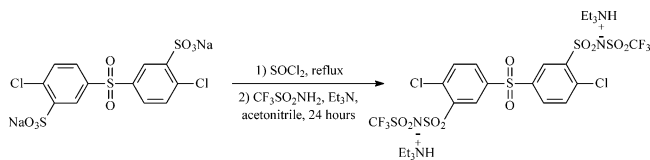


Figure 44. Synthesis of a sulfonimide containing an activated dichloro monomer.¹²⁰

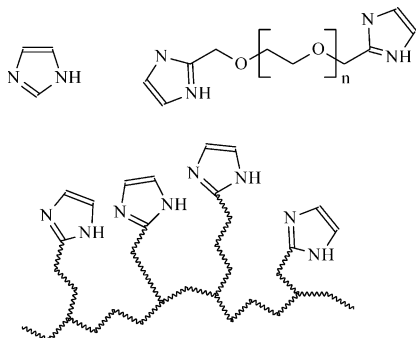


Figure 45. Imidazole proton conductors—both as free molecules and attached to a polymer backbone.¹²³

sulfonimide monomer was then used to form directly polymerized sulfonimide bearing poly(arylene ether sulfone) copolymers in a similar synthesis to that of the sulfonic acid containing copolymer.

All acidic proton conductors discussed so far in this review have relied on the presence of large amounts of water ($\lambda = 10\text{--}30$) as a mobile phase for the conduction of protons. Current targets for automotive use of hydrogen/air fuel cells are 120 °C and 50% or lower relative humidity. Under these conditions, the conductivity of the membrane decreases due to low water uptake at 50% relative humidity and thus creates large resistive losses in the cell. To meet the needs of advanced fuel cell systems, membranes will have to function without large amounts of absorbed water. Organic–inorganic composites are one preferred approach.^{3b,63}

Imidazole proton conductors have been explored as water replacement solvents^{121,122} and have also been attached to polymer backbones¹²³ to replace the acid/water complex in current PEMs (Figure 45).

9. Important Considerations in the Design of New PEMs

As the preceding sections have illustrated, many families of polymers with differing chemical structures and various strategies for incorporation of sulfonic acid groups have been explored as proton exchange membrane materials. Most reports of new materials have included information on ion content (EW or IEC), protonic conductivity, and water uptake. Despite the large body of research on this topic, there are a few basic polymer properties that are still not well-known for common systems or not measured in most reports. Perhaps the most glaring omission in new ion conducting polymer research is the characterization of molecular weight. Molecular weight is one of the most basic properties of polymeric materials and is most commonly measured by gel permeation chromatography ((GPC) or size exclusion chromatography (SEC)) or MALDI-TOF for quantita-

tive determination of the molecular weight distribution or intrinsic viscosity to obtain a relative measure of the molecular weight. Characterization of molecular weight in ion containing systems is complicated by the presence of ionic groups attached to the polymer backbone where ion–ion interactions affect the characteristic size of the macromolecule in a solvent. This ion effect on chain size is often termed as the polyelectrolyte effect. The ionic groups can also cause the polymer chains to associate with the chromatographic column, giving erroneous results. Adding a small amount of lithium bromide or chloride to the chromatographic mobile phase is helpful in suppressing the polyelectrolyte effect in some GPC and intrinsic viscosity experiments to allow characterization of the ion containing materials.

End group analysis by nuclear magnetic resonance (NMR) can also be used to characterize the effects of molecular weight on the properties of proton exchange membranes. In a study by Wang et al., offsetting stoichiometry and endcapping with NMR sensitive *tert*-butyl phenyl groups (18 protons per chain) was used to create a series of sulfonated poly(arylene ether sulfone)s with increasing molecular weight (Figure 46).¹²⁴ It was determined that molecular weight in the range 20 000–40 000 g/mol (20–40K) did not have a large effect on protonic conductivity, but the mechanical properties and water uptake of the material are nevertheless dependent on the molecular weight of the copolymer, possibly related to chain entanglement issues (see Tables 1 and 2).⁸¹ Refinement of these procedures is continuing in our laboratory.

The dependence of mechanical properties on molecular weight brings up another important area of characterization that is often neglected. Proton exchange membranes with good mechanical properties in both the dry and hydrated states are critical to successful MEA fabrication and long-term durability in a fuel cell device. The membrane must be able to withstand the stresses of both electrode processing and attachment and must also be mechanically robust enough to endure startup and shutdown of the fuel cell with the repeated swelling/drying/heating/cooling of the membrane. Nafion acts reasonably well mechanically up to 80 °C as a rubbery material with low modulus but high elongation to break.

These properties are advantageous for MEA fabrication, but Nafion's rubbery behavior is likely detrimental to its long-term performance in high temperature environments. Because of its low glass transition temperature when hydrated (hydrated T_g),¹²⁵ hydrated Nafion undergoes a viscoelastic relaxation causing the membrane to develop pinholes when operated at temperatures near or above 100 °C. A PEM based on a high T_g polymer such as a poly(arylene ether) can increase the membrane's hydrated T_g and potentially limit mechanical degradation of the membrane at increased temperatures.

Molecular weight and mechanical properties are two common but important properties that are measured for a multitude of polymeric systems, but they have thus far been largely neglected in the characterization of PEMs. Often new PEMs will show

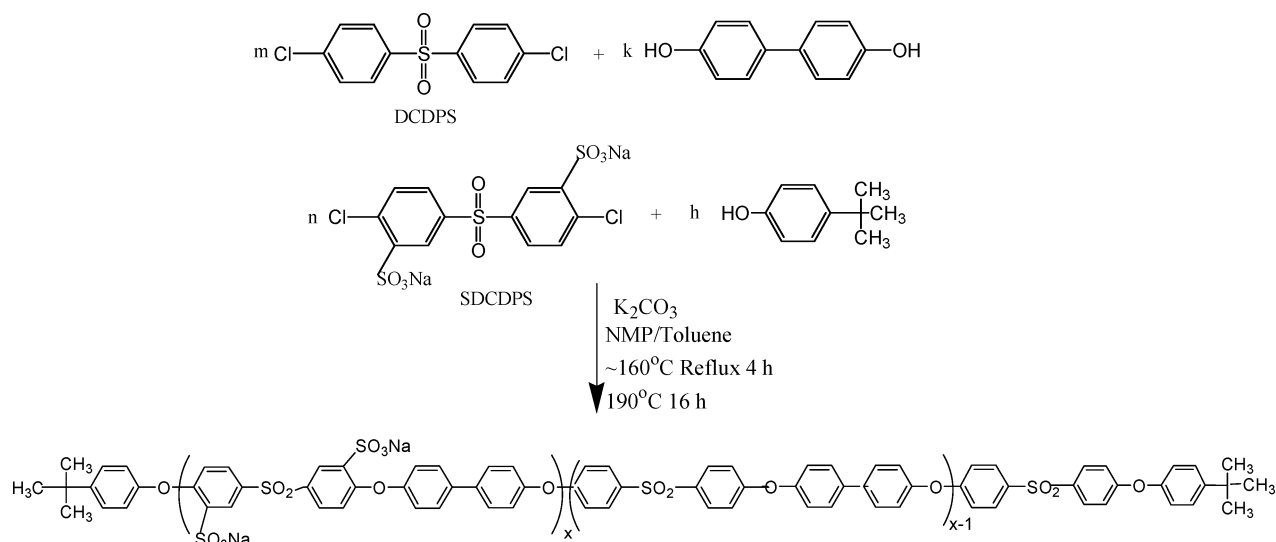


Figure 46. Synthesis of end-capped copolymer (BPS-40): target $M_n = 40\text{K g/mol}$.¹²⁴

Table 1. Characterization of Molecular Weights and Intrinsic Viscosities (no Li salts) for End-Capped BPS-40^a

calc M_n	monomer ratio by mole ^b	$[\eta]^{NMP}$ at 25 °C (dL/g)	$M_n (\times 10^{-3})$ by NMR
20K	43.13/42.13/2	0.54	23.1
30K	64.69/63.69/2	0.61	32.7
40K	86.26/85.26/2	0.87	40.2

^a The IV of noncontrolled BPS-40 is 2.5 dL/g, which is much higher than that of BPS-40–40K. The molecular weight of noncontrolled BPS-40 is much more than 40K. Chemical end-cap techniques could be used to characterize the molecular weight of other sulfonated polymers. ^b [(SDCDPS + DCDPS)/biphenol/*tert*-butylphenol]. SDCDPS/(SDCDPS + DCDPS) = 0.4.

Table 2. Characterization of End-Capped BPS-40 and Stoichiometric Copolymers^a

polymer	IEC (mequiv/g)	SDCDPS (mol %)	water uptake (%)	conductivity (S/cm)
BPS-40–20K	1.60	39.5	51	0.090
BPS-40–30K	1.60	39.8	57	0.092
BPS-40–40K	1.60	39.2	57	0.085
1:1 stoichiometry	1.70	40.1	55	0.100
theory	1.72	40		

^a Membranes acidified by boiling in 0.5 M H₂SO₄. Controlled copolymers have similar chemical compositions, water uptakes, and conductivities, which are independent of molecular weight.

promising protonic conductivity results, but the mechanical properties are not discussed and remain in question, which can hamper efforts to create MEAs.

10. Conclusions

There is a clear need for the synthesis and more complete characterization of new PEM polymeric materials. Polymers bearing functional moieties for proton conduction might also be designed to serve as a host for inorganic compounds to afford a proton conducting component in a blend, as well as a stand-alone PEM. The two current hurdles for polymeric membranes are the high protonic conductivity at low water contents (e.g. under conditions of 120 °C and

50% relative humidity) and long-term durability under fuel cell conditions. Current sulfonic acid-based materials suffer from low conductivity in the absence of water. New proton conducting moieties and morphologies are required to fulfill the requirements of these higher temperature systems. Lower permeability seems to be a good way to address new DMFC systems.

In addition to new ion conducting strategies, basic polymer characterization measurements must be identified and used to more advantage in the development of new PEMs. Issues of molecular weight, mechanical properties, and chemical/physical degradative mechanisms need to be addressed with much more rigor than they have been in the past.

This review has attempted to review the basic research on alternative polymer membranes with attached ionic groups and has tried to highlight examples of materials with a well-defined chemical structure that have been described in the literature. Nafion and similar polyperfluorosulfonic acid membranes still remain the most studied materials due to their commercial applicability and wide availability. However, for all that is known about the properties of these membranes, little is known about their synthesis, chemical composition, or molecular weight. The search for more in depth understanding of the link between the chemical composition of the polymer and its resulting membrane properties has led researchers to synthesize membranes with new, controlled chemical structures. Sulfonated poly(arylene ether)s such as PEEK and poly(sulfone) have shown excellent chemical and thermal stability in fuel cell applications, but their weaker aryl sulfonic acid groups generally cause lower proton conductivity than perfluorosulfonic acid containing membranes. This can be combated by the addition of more sulfonic acid conductors, but it may lead to undesirably large swelling. The weaker acid groups also impede the performance of poly(arylene ether)-based membranes at low relative humidity. These types of membranes are certainly a viable alternative to Nafion in applications where inlet gases with high relative humidity (above 80%) can be used, but their applica-

bility for low relative humidity applications is more challenging.

Postsulfonation of polymers to form PEMs can lead to undesirable side reactions and may be hard to control on a repeatable basis. Synthesis of sulfonated macromolecules for use in PEMs by the direct reaction of sulfonated comonomers has gained attention as a rigorous method of controlling the chemical structure, acid content, and even molecular weight of these materials. While more challenging synthetically than postsulfonation, the control of the chemical nature of the polymer afforded by direct copolymerization of sulfonated monomers and the repeatability of the reactions allows researchers to gain a more systematic understanding of these materials' properties. Sulfonated poly(arylene ether)s, sulfonated poly(imide)s, and sulfonated poly(styrene) derivatives have been the most prevalent of the directly copolymerized materials.

Using the direct synthesis route, the potential of forming well-defined block copolymers with sulfonated and unsulfonated blocks has been realized in poly(styrene) or poly(acrylonitrile)-based materials using styrene sulfonic acid, in poly(imide)s using sulfonated diamines, and in poly(arylene ether sulfone) utilizing phosphine oxide-based comonomers that avoid ether-ether interchange reactions. The synthesis of block materials presents another level of complexity, but studies involving these materials indicate that the blocky nature of the copolymer chemical structure gives rise to increased proton conductivity without massive increases in water swelling. This is an area that shows promise in the rational design of new materials and should be pursued further as a possible route to high temperature membranes.

Sulfonated poly(arylene ether)s have shown promise for durability in fuel cell systems, while poly(styrene)- and poly(imide)-based systems serve as model systems for studying structure-relationship properties in PEMs because their questionable oxidative or hydrolytic stability limits their potential application in real fuel cell systems. Sulfonated high performance polymer backbones, such as poly(phenylquinoxaline), poly(phthalazinone ether ketone)s, polybenzimidazole, and other aromatic or heteroaromatic systems, have many of the advantages of poly(imides) and poly(arylene ether sulfone)s and may offer another route to advanced PEMs. These high performance backbones would increase the hydrated T_g of PEMs while not being as hydrolytically sensitive as poly(imides). The synthetic schemes for these more exotic macromolecules are not as well-known, but the interest in novel PEMs will surely spur developments in this area.

The inorganic poly(phosphazene) backbone has received attention as a PEM candidate. This is an attractive system for study due to its ease of synthesis and subsequent modification by many functional groups. However, these membranes generally show low glass transition temperatures and somewhat poor mechanical properties, and they require cross-linking to enhance their performance in hydrated environments.

Applications of fuel cell technology can be furthered by the use of advanced materials, including organic-inorganic composites.^{3b} Focused programs with clear targets have been developed for fuel cell devices and systems in automotive, stationary, and portable systems. A key component in meeting the goals for each of these systems is the proton exchange membrane. Development efforts have thus far concentrated on the fabrication and design of fuel cell stacks using current materials. New materials must be able to meet the targets for advanced systems, while still remaining somewhat compatible with current hardware and system designs. This can only be accomplished through the directed synthesis of new copolymers with feedback from MEA and fuel cell technology developers.

11. Acknowledgments

The authors appreciate the support of this research by the Department of Energy (Contract No. DE-FC36-01G011086), DARPA-ARO (contract #DAAD19-02-1-0278), NASA Glenn (contract #NCC3-886), UTC Fuel Cells (contract #PO 3651) and the National Science Foundation (No. EHR-0090556, and 9975678). They also thank other members of the McGrath research group and the expert assistance of Ms. Laurie Good.

12. References

- (1) (a) Kim, Y. S.; Pivovar, B. 204th Meeting of the Electrochemical Society, Orlando, FL, Oct 12–16, 2003. (b) Pivovar, B. S.; Hickner, M.; Wang, F.; McGrath, J.; Zelenay, P.; Zawodzinski, T. A., Jr. Pre-Print Archive—American Institute of Chemical Engineers, [Spring National Meeting], New Orleans, LA, United States, Mar 11–14, 2002, p 2433. (c) Hickner, M. A.; Kim, Y. S.; Wang, F.; Harrison, W.; Hill, M.; Dong, L.; Pivovar, B.; Zelenay, P.; McGrath, J. E. *Electrochim. Acta*, in press.
- (2) Savadogo, O. *J. New Mater. Electrochem. Syst.* **1998**, *1*, 47.
- (3) (a) Roziere, J.; Jones, D. *J. Annu. Rev. Mater. Res.* **2003**, *33*, 503. (b) Alberti, G.; Casciola, M. *Annu. Rev. Mater. Res.* **2003**, *33*, 129. (c) Paddison, S. *J. Annu. Rev. Mater. Res.* **2003**, *33*, 289. (d) Schulster, M. F. H.; Meyer, W. H. *Annu. Rev. Mater. Res.* **2003**, *33*, 233.
- (4) Kerres, J. *J. Membr. Sci.* **2001**, *185*, 3.
- (5) Zawodzinski, T. A.; Neeman, M.; Sillerud, L. O.; Gottesfeld, S. *J. Phys. Chem.* **1991**, *95*, 6040.
- (6) (a) Alberti, G.; Casciola, M.; Palombi, R. *J. Membr. Sci.* **2000**, *172*, 233. (b) Alberti, G.; Constantino, U.; Casciola, M.; Ferroni, S.; Massinelli, L.; Staiti, P. *Solid State Ionics* **2001**, *145*, 249. (c) Pivovar, B. S.; Wang, Y.; Cussler, E. L. *J. Membr. Sci.* **1999**, *154*, 155.
- (7) Ibrahim, S. M.; Price, E. H.; Smith, R. A., of E. I. du Pont de Nemours. *Proc. Electrochem. Soc.* **1983**, 83–6.
- (8) Resnick, P. R.; Grot, W. G., of E. I. du Pont de Nemours and Company, Wilmington, DE, Sept 12, 1978; U.S. Patent 4,113, 585.
- (9) Bahar, B.; Cavalca, C.; Cleghorn, S.; Kolde, J.; Lane, D.; Murthy, M.; Rusch, G. *J. New Mater. Electrochem. Syst.* **1999**, *2*, 179.
- (10) (a) Lin, J. C.; Kuntz, H. R.; Cutlip, M. B.; Fenton, J. M. *Proc. 31st Mid-Atl. Ind. Hazard. Waste Conf.* **1999**, *31*, P656. (b) Lin, J. C.; Kuntz, H. R.; Fenton, J. M. *Proc. Electrochem. Soc. Power Sources New Millennium* **2001**, *2000*, 48.
- (11) Beckerbauer, R., of E. I. du Pont de Nemours and Company, Wilmington, DE, Jan 30, 1973; U.S. Patent 3,714,245.
- (12) Grot, W. G., of E. I. du Pont de Nemours and Company, Wilmington, DE, Feb 27, 1973; U.S. Patent 3,718,627.
- (13) Grot, W. G., of E. I. du Pont de Nemours and Company, Wilmington, DE, Feb 21, 1984; U.S. Patent 4,433,082.
- (14) Rikukawa, M.; Sanui, K. *Prog. Polym. Sci.* **2000**, *25*, 1463.
- (15) Tant, M. R.; Darst, K. P.; Lee, K. D.; Martin, C. W. *ACS Symp. Ser.* **1989**, *395*, 370.
- (16) Wei, J.; Stone, C.; Steck, A. E., of Ballard Power Systems, Inc., June 6, 1995; U.S. Patent 5,422,411.
- (17) (a) Steck, A. E. *Proceedings of the first international symposium of new materials for fuel cell systems*; l'Ecole Polytechnique de Montreal: Montreal, 1995; p 74. (b) Steck, A. E.; Stone, C.

- Proceedings of the 2nd International Symposium on New Materials for Fuel Cell and modern battery systems*; l'Ecole Polytechnique de Montreal: Montreal, 1997; p 792.
- (18) Ehrenberg, S. G.; Serpico, J. M.; Wnek, G. E.; Rider, J. N., of Dais Corporation, Oct 21, 1997; U.S. Patent 5,679,482.
- (19) Wnek, G. Abstracts of Papers, 222nd ACS National Meeting, Chicago, IL, United States, August 26–30, 2001.
- (20) Kim, J.; Kim, B.; Jung, B. *J. Membr. Sci.* **2002**, *207*, 129.
- (21) Serpico, J. M.; Ehrenberg, S. G.; Fontanella, J. J.; Jiao, X.; Perahia, D.; McGrady, K. A.; Sanders, E. H.; Kellogg, G. E.; Wnek, G. E. *Macromolecules* **2002**, *35*, 5916.
- (22) Wnek, G. E.; Rider, J. N.; Serpico, J. M.; Einset, A. G.; Ehrenberg, S. G.; Raboin, L. A. *Proc. Electrochem. Soc.* **1995**, *95–23*, 247.
- (23) Wnek, G. E.; Rider, J. N.; Serpico, J. M.; Einset, A. G. *Proceedings of the First International Symposium on Proton Conducting Membrane Fuel Cells*; Electrochemical Society: 1995; p 247.
- (24) Hodgdon, R. B., Jr. *J. Polym. Sci.* **1968**, *6*, 171.
- (25) Serpico, J. M.; Ehrenberg, S. G.; Fontanella, J. J.; McGrady, K. A.; Perahia, D.; Jiao, X.; Sanders, E. H.; Wallen, T. J.; Wnek, G. E. *Polym. Mater. Sci. Eng.* **2002**, *86*, 32.
- (26) Ding, J.; Chuy, C.; Holdcroft, S. *Chem. Mater.* **2001**, *13*, 2231.
- (27) Ding, J.; Chuy, C.; Holdcroft, S. *Macromolecules* **2002**, *35*, 1348.
- (28) Chuy, C.; Ding, J.; Swanson, E.; Holdcroft, S.; Horsfall, J.; Lovell, K. V. *J. Electrochem. Soc.* **2003**, *150*, E271.
- (29) Chuy, C.; Basura, V. I.; Simon, E.; Holdcroft, S.; Horsfall, J.; Lovell, K. V. *J. Electrochem. Soc.* **2000**, *147*, 4453.
- (30) Flint, S. D.; Slade, R. C. T. *Solid State Ionics* **1997**, *97*, 299.
- (31) Gupta, B.; Buchi, F. N.; Scherer, G. G.; Chapiro, A. *Solid State Ionics* **1993**, *61*, 213.
- (32) Gupta, B.; Buchi, F. N.; Scherer, G. G.; Chapiro, A. *Polym. Adv. Technol.* **1994**, *5*, 493.
- (33) Buchi, F. N.; Gupta, B.; Haas, O.; Scherer, G. G. *Electrochim. Acta* **1995**, *40*, 345.
- (34) Becker, W.; Schmidt-Naake, G. *Chem. Eng. Technol.* **2002**, *25*, 373.
- (35) Wang, S.; McGrath, J. E. *Synthesis of Poly(arylene ether)s. Synthetic Methods in Step-Growth Polymers*; Wiley: New York, 2003; p 327.
- (36) Alberti, G.; Casciola, M.; Massinelli, L.; Bauer, B. *J. Membr. Sci.* **2001**, *185*, 73.
- (37) Noshay, A.; Robeson, L. M. *J. Appl. Polym. Sci.* **1976**, *20*, 1885.
- (38) Johnson, B. C.; Yilgor, I.; Tran, C.; Iqbal, M.; Wightman, J. P.; Lloyd, D. R.; McGrath, J. E. *J. Polym. Sci.: Polym. Chem. Ed.* **1984**, *22*, 721.
- (39) Genova-Dimitrova, P.; Baradie, B.; Foscallo, D.; Poinsignon, C.; Sanchez, J. Y. *J. Membr. Sci.* **2001**, *185*, 59.
- (40) Kaliaguine, S.; Mikhailenko, S. D.; Wang, K. P.; Xing, P.; Robertson, G.; Guiver, M. *Catal. Today* **2003**, *82*, 213.
- (41) Robertson, G. P.; Mikhailenko, S. D.; Wang, K.; Xing, P.; Guiver, M. D.; Kaliaguine, S. *J. Membr. Sci.* **2003**, *219*, 113.
- (42) Bauer, B.; Jones, D. J.; Roziere, J.; Tchicaya, L.; Alberti, G.; Casciola, M.; Massinelli, L.; Peraio, A.; Besse, S.; Ramunni, E. *J. New Mater. Electrochem. Syst.* **2000**, *3*, 93.
- (43) Zaidi, S. M. J.; Mikhailenko, S. D.; Robertson, G. P.; Guiver, M. D.; Kaliaguine, S. *J. Membr. Sci.* **2000**, *173*, 17.
- (44) Xing, P.; Robertson, G. P.; Guiver, M. D.; Mikhailenko, S. D.; Wang, K.; Kaliaguine, S. *J. Membr. Sci.* **2004**, *229*, 95.
- (45) Bishop, M. T.; Karasz, F. E.; Russo, P. S.; Langley, K. H. *Macromolecules* **1985**, *18*, 86.
- (46) Huang, R. Y. M.; Shao, P.; Burns, C. M.; Feng, X. *J. Appl. Polym. Sci.* **2001**, *82*, 2651.
- (47) Bailly, C.; Williams, D. J.; Karasz, F. E.; MacKnight, W. J. *Polymer* **1987**, *28*, 1009.
- (48) Al-Omran, A.; Rose, J. B. *Polymer* **1996**, *37*, 1735.
- (49) Kerres, J.; Cui, W.; Richie, S. *J. Polym. Sci., Part A: Polym. Chem.* **1996**, *34*, 2421.
- (50) Kerres, J.; Zhang, W.; Cui, W. *J. Polym. Sci., Part A: Polym. Chem.* **1998**, *36*, 1441.
- (51) Kerres, J.; Cui, W.; Junginger, M. *J. Membr. Sci.* **1998**, *139*, 227.
- (52) Lafitte, B.; Karlsson, L. E.; Jannasch, P. *Macromol. Rapid Commun.* **2002**, *23*, 896.
- (53) Kim, Y. S.; Wang, F.; Hickner, M.; McCartney, S.; Hong, Y. T.; Zawodzinski, T. A.; McGrath, J. E. *J. Polym. Sci., Part B: Polym. Phys.* **2003**, *41*, 2816.
- (54) Robeson, L. M.; Matzner, M., of Union Carbide, Inc., 1983; U.S. Patent 4,380,598.
- (55) Ueda, M.; Toyota, H.; Ochi, T.; Sugiyama, J.; Yonetake, K.; Masuko, T.; Teramoto, T. *J. Polym. Sci., Polym. Chem. Ed.* **1993**, *31*, 853.
- (56) (a) Wang, F.; Hickner, M.; Kim, Y. S.; Zawodzinski, T. A.; McGrath, J. E. *J. Membr. Sci.* **2002**, *197*, 231. (b) Wang, F.; Hickner, M.; Ji, Q.; Harrison, W.; Mecham, J.; Zawodzinski, T. A.; McGrath, J. E. *Macromol. Symp.* **2001**, *175*, 387.
- (57) Harrison, W.; Wang, F.; Mecham, J. B.; Bhanu, V.; Hill, M.; Kim, Y. S.; McGrath, J. E. *J. Polym. Sci., Part A: Polym. Chem.* **2003**, *41*, 2264.
- (58) Wiles, K. B.; Bhanu, V. A.; Wang, F.; McGrath, J. E. *Polym. Prepr.* **2002**, *43*, 993.
- (59) Kim, Y. S.; Sumner, M. J.; Harrison, W. L.; Riffle, J. S.; McGrath, J. E.; Pivovar, B. S. *J. Electrochem. Soc.*, accepted.
- (60) Wang, F.; Chen, T.; Xu, J. *Macromol. Chem. Phys.* **1998**, *199*, 1421.
- (61) Wang, F.; Li, J.; Chen, T.; Xu, J. *Polymer* **1999**, *40*, 795.
- (62) (a) Gao, Y.; Robertson, G. P.; Guiver, M. D.; Jian, X.; Mikhailenko, S. D.; Wang, K.; Kaliaguine, S. *J. Polym. Sci., Part A: Polym. Chem.* **2003**, *41*, 2731. (b) Xing, P.; Robertson, G. P.; Guiver, M. D.; Mikhailenko, S. D.; Kaliaguine, S. *J. Polym. Sci., Part A: Polym. Chem.* **2004**, *42*, 2866.
- (63) Kim, Y. S.; Wang, F.; Hickner, M.; Zawodzinski, T. A.; McGrath, J. E. *J. Membr. Sci.* **2003**, *212*, 263.
- (64) Sumner, M. J.; Harrison, W. L.; Weyers, R. M.; Kim, Y. S.; McGrath, J. E.; Riffle, J. S.; Brink, A.; Brink, H. M. *J. Membr. Sci.* **2004**, *239*, 199.
- (65) Shobha, H. K.; Smalley, G. R.; Sankarapandian, M.; McGrath, J. E. *Polym. Prepr.* **2000**, *41*, 180.
- (66) Wang, F.; Mecham, J.; Harrison, W.; Hickner, M.; Kim, Y. S.; McGrath, J. E. *Polym. Mater. Sci. Eng.* **2001**, *84*, 913.
- (67) Wang, F.; Kim, Y.; Hickner, M.; Zawodzinski, T. A.; McGrath, J. E. *Polym. Mater. Sci. Eng.* **2001**, *85*, 517.
- (68) Genies, C.; Mercier, R.; Sillion, B.; Petiaud, R.; Cornet, N.; Gebel, G.; Pineri, M. *Polymer* **2001**, *42*, 5097.
- (69) Genies, C.; Mercier, R.; Sillion, B.; Cornet, N.; Gebel, G.; Pineri, M. *Polymer* **2001**, *42*, 359.
- (70) Cornet, N.; Diat, O.; Gebel, G.; Jousse, F.; Marsacq, D.; Mercier, R.; Pineri, M. *J. New Mater. Electrochem. Syst.* **2000**, *3*, 33.
- (71) Vallejo, E.; Pourcelly, G.; Gavach, C.; Mercier, R.; Pineri, M. *J. Membr. Sci.* **1999**, *160*, 127.
- (72) Zhang, Y.; Litt, M.; Savinell, R. F.; Wainright, J. S. *Polym. Prepr.* **1999**, *40*, 480.
- (73) Zhang, Y.; Litt, M.; Savinell, R. F.; Wainright, J. S.; Vendramint, J. *Polym. Prepr.* **2000**, *41*, 1561.
- (74) Zhou, W.; Watari, T.; Kita, H.; Okamoto, K.-I. *Chem. Lett.* **2002**, *5*, 534.
- (75) Fang, J.; Guo, X.; Harada, S.; Watari, T.; Tanaka, K.; Kita, H.; Okamoto, K.-I. *Macromolecules* **2002**, *35*, 9022.
- (76) Guo, X.; Fang, J.; Watari, T.; Tanaka, K.; Kita, H.; Okamoto, K.-I. *Macromolecules* **2002**, *35*, 6707.
- (77) Yin, Y.; Fang, J.; Cui, Y.; Tanaka, K.; Kita, H.; Okamoto, K.-I. *Polymer* **2003**, *44*, 4509.
- (78) Shobha, H. K.; Sankarapandian, M.; Glass, T. E.; McGrath, J. E. *Polym. Prepr.* **2000**, *41*, 1298.
- (79) Einsla, B. R.; Hong, Y. T.; Kim, Y. S.; Wang, F.; Gunduz, N.; McGrath, J. E. *J. Polym. Sci., Part A: Polym. Chem.* **2004**, *42*, 862.
- (80) Einsla, B. R.; Kim, Y. S.; Hickner, M.; Hong, Y. T.; Hill, M. L.; Pivovar, B.; McGrath, J. E. *J. Membr. Sci.*, submitted.
- (81) Hickner, M. A. Ph.D. Dissertation, Virginia Polytechnic Institute and State University, September 2003.
- (82) Kopitzke, R. W.; Linkous, C. A.; Nelson, G. L. *J. Polym. Sci., Part A: Polym. Chem.* **1998**, *36*, 1197.
- (83) Kopitzke, R. W.; Linkous, C. A.; Anderson, H. R.; Nelson, G. L. *J. Electrochem. Soc.* **2000**, *147*, 1677.
- (84) Kopitzke, R. W.; Linkous, C. A.; Nelson, G. L. *Polym. Degrad. Stab.* **2000**, *67*, 335.
- (85) Kruczek, B.; Matsuura, T. *J. Membr. Sci.* **1998**, *146*, 263.
- (86) Kosmala, B.; Schauer, J. *J. Appl. Polym. Sci.* **2002**, *85*, 1118.
- (87) Fu, H.; Jia, L.; Xu, J. *J. Appl. Polym. Sci.* **1994**, *51*, 1399.
- (88) Kobayashi, T.; Rikukawa, M.; Sanui, K.; Ogata, N. *Solid State Ionics* **1998**, *106*, 219.
- (89) Ghassemi, H.; McGrath, J. E. *Polymer* **2004**, *45*, 5847.
- (90) Ghassemi, H.; Ndip, G.; McGrath, J. E. *Polymer* **2004**, *45*, 5855.
- (91) Miyatake, K.; Hay, A. S. *J. Polym. Sci., Part A: Polym. Chem.* **2001**, *39*, 3211.
- (92) Miyatake, K.; Oyaizu, K.; Tsuchida, E.; Hay, A. S. *Macromolecules* **2001**, *34*, 2065.
- (93) Gao, Y.; Robertson, G. P.; Guiver, M. D.; Jian, X. *J. Polym. Sci., Part A: Polym. Chem.* **2003**, *41*, 497.
- (94) Xiao, G.; Sun, G.; Yan, D.; Zhu, P.; Tao, P. *Polymer* **2002**, *43*, 5335.
- (95) Powers, E. J.; Serad, G. A. *High Performance Polymers: Their Origin and Development*; Elsevier: Amsterdam, 1986; p 355.
- (96) Asensio, J. A.; Borros, S.; Gomez-Romero, P. *J. Polym. Sci., Part A: Polym. Chem.* **2002**, *40*, 3703.
- (97) (a) Wainright, J. S.; Wang, J. T.; Weng, D.; Savinell, R. F.; Litt, M. *J. Electrochem. Soc.* **1995**, *142*, L121. (b) Xiao, L.; Zhang, H.; Choe, E. W.; Scanlon, E.; Ramanathan, L. S.; Benicewicz, B. C. *Prepr. Symp.—Am. Chem. Soc., Div. Fuel Chem.* **2003**, *48*, 447. (c) Benicewicz, B. ACS Polymer Division Asilomar Conference, February, 2003.
- (98) Glipa, X.; El Haddad, M.; Jones, D. J.; Roziere, J. *Solid State Ionics* **1997**, *97*, 323.
- (99) Gieselman, M. B.; Reynolds, J. R. *Macromolecules* **1992**, *25*, 4832.
- (100) Kim, S.; Cameron, D. A.; Lee, Y.; Reynolds, J. R.; Savage, C. R. *J. Polym. Sci., Part A: Polym. Chem.* **1996**, *34*, 481.
- (101) Dang, T. D.; Bai, S. J.; Heberer, D. P.; Arnold, F. E.; Spry, R. J. *J. Polym. Sci., Part B: Polym. Phys.* **1993**, *31*, 1941.

- (102) Einsla, B. R.; Kim, Y. J.; Tchatchoua, C.; McGrath, J. E. *Polym. Prepr.* **2003**, *44*, 645.
- (103) Sakaguchi, Y. *Functional Condensation Polymers*; Kluwer: New York, 2002.
- (104) Poppe, D.; Frey, H.; Kreuer, K. D.; Heinzel, A.; Mulhaupt, R. *Macromolecules* **2002**, *35*, 7936.
- (105) Allcock, H. R.; Fitzpatrick, R. J.; Salvati, L. *Chem. Mater.* **1991**, *3*, 1120.
- (106) Blonsky, P. M.; Shriver, D. F.; Austin, P.; Allcock, H. R. *J. Am. Chem. Soc.* **1984**, *106*, 6854.
- (107) Allcock, H. R. *Acc. Chem. Res.* **1979**, *12*, 351.
- (108) Allcock, H. R.; Klingenberg, E. H.; Welker, M. F. *Macromolecules* **1993**, *26*, 5512.
- (109) Wycisk, R.; Pintauro, P. N. *J. Membr. Sci.* **1996**, *119*, 155.
- (110) Tang, H.; Pintauro, P. N.; Guo, Q.; O'Connor, S. *J. Appl. Polym. Sci.* **1999**, *71*, 387.
- (111) Guo, Q.; Pintauro, P. N.; Tang, H.; O'Connor, S. *J. Membr. Sci.* **1999**, *154*, 175.
- (112) Carter, R.; Wycisk, R.; Pintauro, P. N. Pre-Print Archive—American Institute of Chemical Engineers, [Spring National Meeting], New Orleans, LA, United States, Mar 11–14, 2002, p 2441.
- (113) Miyatake, K.; Hay, A. S. *J. Polym. Sci., Part A: Polym. Chem.* **2001**, *39*, 1854.
- (114) Miyatake, K.; Hay, A. S. *J. Polym. Sci., Part A: Polym. Chem.* **2001**, *39*, 3770.
- (115) Meng, Y. Z.; Tjong, S. C.; Hay, A. S.; Wang, S. J. *Eur. Polym. J.* **2003**, *39*, 627.
- (116) (a) Allcock, H. R.; Hofmann, M. A.; Ambler, C. M.; Lvov, S. N.; Zhou, X. Y.; Chalkova, E.; Weston, J. *J. Membr. Sci.* **2002**, *201*, 47. (b) Allcock, H. R.; Hofmann, M. A.; Ambler, C. M.; Morford, R. V. *Macromolecules* **2002**, *35*, 3484.
- (117) (a) Koppel, I. A.; Taft, R. W.; Anvia, F.; Zhu, S. Z.; Hu, L. Q.; Sung, K. S.; DesMarteau, D. D.; Yagupolskii, L. M.; Yagupolskii, Y. L.; Ingat'ev, N. V.; Kondratenko, N. V.; Volkonskii, A. Y.; Vlasov, V. M.; Notario, R.; Maria, P. C. *J. Am. Chem. Soc.* **1994**, *116*, 3047. (b) Paddison, S. J.; Pratt, L. R.; Zawodzinski, T.; Reagor, D. W. *Fluid Phase Equilib.* **1998**, *150–151*, 235. (c) Eikerling, M.; Paddison, S. J.; Zawodzinski, T. A. *J. New Mater. Electrochem. Syst.* **2002**, *5*, 15. (d) Hoffman, M. A.; Ambler, C. M.; Maher, A. E.; Chalkova, E.; Zhou, X. Y.; Lvov, S. N.; Allcock, H. R. *Macromolecules* **2002**, *35*, 6490. (e) Ford, L. A.; Smith, D. W., Jr.; DesMarteau, D. D. *Polym. Mater. Sci. Eng.* **2000**, *83*, 10.
- (118) Savett, S. C.; Atkins, J. R.; Sides, C. R.; Harris, J. L.; Thomas, B. H.; Creager, S. E.; Pennington, W. T.; DesMarteau, D. D. *J. Electrochem. Soc.* **2002**, *149*, A1527.
- (119) Hofmann, M. A.; Ambler, C. M.; Maher, A. E.; Chalkova, E.; Zhou, X. Y.; Lvov, S. N.; Allcock, H. R. *Macromolecules* **2002**, *35*, 6490.
- (120) Cho, C. G.; Kim, Y. S.; Hill, M. L.; McGrath, J. E. *Polym. Prepr.* **2003**, *44*, 649.
- (121) Kreuer, K. D.; Fuchs, A.; Ise, M.; Spaeth, M.; Maier, J. *Electrochim. Acta* **1998**, *43*, 1281.
- (122) Schuster, M. F. H.; Meyer, W. H.; Wegner, G.; Herz, H. G.; Ise, M.; Schuster, M.; Kreuer, K. D.; Maier, J. *Solid State Ionics* **2001**, *145*, 85.
- (123) Herz, H. G.; Kreuer, K. D.; Maier, J.; Scharfenberger, G.; Schuster, M. F. H.; Meyer, W. H. *Electrochim. Acta* **2003**, *48*, 2165.
- (124) Wang, F.; Glass, T.; Li, X.; Hickner, M.; Kim, Y. S.; McGrath, J. E. *Polym. Prepr.* **2002**, *43*, 492.
- (125) Kim, Y. S.; Dong, L.; Hickner, M.; Glass, T. E.; Webb, V.; McGrath, J. E. *Macromolecules* **2003**, *36*, 6181.

CR020711A

Transport in Proton Conductors for Fuel-Cell Applications: Simulations, Elementary Reactions, and Phenomenology

Klaus-Dieter Kreuer,^{*‡} Stephen J. Paddison,[§] Eckhard Spohr,[#] and Michael Schuster[‡]

Max-Planck-Institut für Festkörperforschung, Heisenbergstr. 1, D-70569 Stuttgart, Germany, Department of Chemistry, University of Alabama in Huntsville, Huntsville, Alabama 35899, and Forschungszentrum Jülich, D-52425 Jülich, Germany

Received March 4, 2004

Contents

1. Introduction	4637
2. Theoretical Methodologies and Simulation Tools	4640
2.1. Ab Initio Quantum Chemistry	4641
2.2. Molecular Dynamics	4642
2.2.1. Classical Molecular Dynamics and Monte Carlo Simulations	4643
2.2.2. Empirical Valence Bond Models	4644
2.2.3. Ab Initio Molecular Dynamics (AIMD)	4645
2.3. Poisson–Boltzmann Theory	4645
2.4. Nonequilibrium Statistical Mechanical Ion Transport Modeling	4646
2.5. Dielectric Saturation	4647
3. Transport Mechanisms	4648
3.1. Proton Conduction Mechanisms	4648
3.1.1. Homogeneous Media	4648
3.1.2. Heterogeneous Systems (Confinement Effects)	4655
3.2. Mechanisms of Parasitic Transport	4661
3.2.1. Solvated Acidic Polymers	4661
3.2.2. Oxides	4665
4. Phenomenology of Transport in Proton-Conducting Materials for Fuel-Cell Applications	4666
4.1. Hydrated Acidic Polymers	4666
4.2. PBI–H ₃ PO ₄ Adducts	4668
4.3. Heterocycle-Based Systems	4669
4.4. Oxides	4669
5. Recent Approaches toward New Proton-Conducting Materials for Fuel-Cell Applications	4669
6. Acknowledgement	4674
7. References	4675

1. Introduction

The electrolyte is the heart of any fuel cell. Ideally, this component effectively separates the anode and cathode gases and/or liquids and mediates the electrochemical reaction occurring at the electrodes through conducting a specific ion at very high rates during the operation of the fuel cell. In other words,

transport through such electrolytes must be fast and highly selective; these two properties are frequently at odds with each other. Proton-conducting materials are used as the electrolyte for low- and intermediate-temperature fuel cells, which are currently attracting significant interest (i.e., polymer electrolyte membrane or proton exchange membrane fuel cells (PEMFCs)), direct methanol fuel cells (DMFCs), phosphoric acid fuel cells (PAFCs), and alkaline fuel cells (AFCs)). However, these are not true “single ion conductors”, in that the transport phenomena are more complex, involving significant parasitic transport of other species. This review is concerned with the transport properties of presently available and emerging materials that have the potential to be used as the electrolyte for fuel cells soon. Strategies for the development of novel materials with transport properties approaching those of an “ideal separator”, especially in the intermediate temperature range, are also discussed.

The last comprehensive review covering proton conductivity and proton conducting materials was written by one of the authors (dating back to 1996);¹ since then, there have been several other review articles of similar scope (e.g., see Colombari²). There are also many reviews available on separator materials used for fuel cells (see articles in refs 3 and 4 and references therein, recent review-type articles,^{5–8} and a literature survey⁹), which, more or less, address all properties that are relevant for their functioning in a fuel cell. The transport properties are usually described in these articles; however, the treatments are frequently restricted to macroscopic approaches and handwaving arguments about the transport mechanisms. The purpose of the present review is to combine a few recently published results in the context of a discussion of transport phenomena in proton-conducting separator materials, which have some relevance in fuel cell applications (for a more complete list of the comprehensive literature in the field, the interested reader is referred to the aforementioned references).

Hence, the two main foci of this review are (i) the current understanding of the underlying elementary processes and (ii) a phenomenological description of the resulting macroscopic transport phenomena. Because the first aspect comprises proton conduction mechanisms other than the mechanisms of “parasitic transport”, this review may also be considered an

* Author to whom correspondence should be addressed. E-mail address: kreuer@fkf.mpg.de.

[‡] Max-Planck-Institut für Festkörperforschung.

[§] University of Alabama in Huntsville.

[#] Forschungszentrum Jülich.



Klaus-Dieter Kreuer completed his Diploma Thesis on the "Distribution of F^- and OH^- in Hydroxylfluoroapatites" in Mineralogy at the University of Cologne under the supervision of F. Freund in 1979. He received his Ph.D. from the University of Stuttgart (Department of Chemistry) in 1982. His thesis project in the department of A. Rabenau (Max-Planck-Institute for Solid State Research) involved the investigation of inorganic proton-conducting compounds (e.g., layered minerals, zeolites), which showed the correlation of proton mobility and molecular diffusion (vehicle mechanism) for several cases. As a fellow of the "Studienstiftung des Deutschen Volkes", he benefited from the opportunity of a research stay at the California Institute of Technology (with the R. Vaughan group, 1978), and a Max-Planck award (Otto Hahn Medaille) allowed him to join the Massachusetts Institute of Technology (Department of Materials Science) as a visiting scientist (1983–1984). This period was part of his postdoctoral activities at the Max-Planck-Institute for Solid State Research, which were mainly concerned with research on alkaline-ion-conducting framework structures (such as lithium borate glasses and NASICON). From 1986 to 1992, he built up a research group for the development of chemical sensors (pH , O_2) within a Swiss-German company (Endress & Hauser). In 1992, he again joined the Max-Planck-Institute for Solid State Research, where he assisted J. Maier in building up his new department. Since 1990, he has been lecturing at the University of Stuttgart, from which he received his Habilitation Degree in 1999. His research interests are centered around the investigation of the formation and mobility of hydrogen-derived defects in condensed matter. His work comprises materials preparation (inorganic and organic synthesis) and characterization (e.g., by nuclear magnetic resonance (NMR) and simulation techniques). The focus of his research is both a better understanding of fundamental issues and the development of novel materials for specific applications.

update on the corresponding part of ref 1 mentioned previously. The initial application of various simulation techniques to the investigation of fast elementary reactions as being part of proton conduction mechanisms had already summarized in this article. The early molecular dynamics simulation work of Münch et al.¹⁰ on the proton conduction mechanism in $CsHSO_4$ diverse perovskite-type oxides and heterocycles (see Section 3.1.1) provided important insight into the conduction mechanism of model compounds, and some of the recent understanding of proton dynamics in water stems from simulation work (see Section 3.1.1.1). To date, simulation techniques, when appropriately combined with experimental results, establish insight into the path for the development of improved and new proton conductors. The increased availability of computational hardware, along with the improvement and development of new codes, have led to a tremendous dissemination and increased impact of such techniques; hence, we have included a separate section that addresses current "simulation techniques" (Section 2), the results of which are included into the discussion of "transport mechanisms" (Section 3). The latter sec-



Stephen J. Paddison received a B.Sc.(Hon.) in Chemical Physics and a Ph.D. (1996) in Physical/Theoretical Chemistry from the University of Calgary, Canada. He was, subsequently, a postdoctoral fellow and staff member in the Materials Science Division at Los Alamos National Laboratory, where he conducted both experimental and theoretical investigations of sulfonic acid polymer electrolyte membranes. This work was continued while he was part of Motorola's Computational Materials Group in Los Alamos. He is currently an Assistant Professor in the Chemistry and Materials Science Departments at the University of Alabama in Huntsville, AL. Research interests continue to be in the development and application of first-principles and statistical mechanical methods in understanding the molecular mechanisms of proton transport in fuel-cell materials.



Eckhard Spohr received his diploma in Chemistry from the Johannes-Gutenberg-Universität in Mainz, Germany, in 1983. In 1986, he obtained his Ph.D. for computer simulation of water/metal interfaces at the Max-Planck-Institut für Chemie in Mainz. He continued to work for two years as a research associate in the aqueous simulation group of Karl Heinzinger, followed by a two-year visit to the University of California as a Feodor Lynen postdoctoral fellow of the Alexander von Humboldt Foundation, where he studied gas/surface reactions. In 1991, he moved to the Universität Ulm, where he obtained his habilitation degree in 1995 and worked as a University docent until 2000. In 2000, he moved to the Forschungszentrum Jülich, where he currently heads the physical chemistry group in the Institute for Materials and Processes in Energy Systems performing research on low-temperature fuel cells. His research interests center around computer simulations of aqueous electrolytes in confined environments. He teaches courses in theoretical chemistry at the Universität Ulm.

tion is truly cross-disciplinary in nature, because results from outside the fuel cell community are included. This is particularly true for the discussion of the proton mobility in homogeneous media (i.e., Section 3.1.1: water, aqueous solutions, phosphoric acid, imidazole, and simple cubic perovskites), which, in many cases, only constitute a single component of the heterogeneous fuel cell separator material. As a consequence of confinement and interaction of the



Michael Schuster studied chemistry at the Ludwig-Maximilians-Universität in Munich, Germany. He received his Ph.D. in Inorganic Chemistry under the direction of A. Schmidpeter and K. Karaghiosoff for his work on phosphates $P_mX_n^{z-}$ ($X = S, Se, Te$) and their NMR spectroscopic characterization. To continue his research interests in NMR spectroscopy, he moved to the Max-Planck-Institute for Solid State Research in Stuttgart in 2000, where he is working on the development of proton-conducting materials for fuel cells. His studies are focused on the synthesis of imidazole-, sulfonic acid-, and phosphonic acid-based oligomers and polymers and their structural and dynamical properties. Characterization methods particularly include pulsed-field gradient and electrophoretic NMR spectroscopy.

mobile species, e.g., with the corresponding polymer matrixes, the transport properties of these heterogeneous systems are more complex and, therefore, are discussed in the section that follows (i.e., Section 3.1.2). Because most of this work has been done on prototypical materials, this discussion mainly involves readily available and extensively tested materials. However, the property relations may be easily transferred to the transport properties of related materials (Section 4) and may even provide a basis for the understanding of the transport properties of conceptually new proton-conducting separator materials (Section 5).

Apart from mechanistic aspects, we have also summarized the macroscopic transport behavior of some well-studied materials in a way that may contribute to a clearer view on the relevant transport coefficients and driving forces that govern the behavior of such electrolytes under fuel cell operating conditions (Section 4). This also comprises precise definitions of the different transport coefficients and the experimental techniques implemented in their determination; providing a physicochemical rationale behind vague terms such as “cross-over”, which are frequently used by engineers in the fuel cell community. Again, most of the data presented in this section is for the prototypical materials; however, trends for other types of materials are also presented.

Thus, the aim of this review is to give the currently best possible generally applicable understanding of mass and charge transport in fuel-cell-relevant proton conductors, including a description of the fundamental underlying elementary reactions for these transport processes and quantitative phenomenological descriptions of transport in these materials. The first is important for further adaptation of available electrolytes to specific fuel cell conditions or, subsequently, the development of new materials. The latter allows a better understanding of the transient and

steady-state behavior of known materials under the varying conditions of an operating fuel cell. Access to the numerous references providing transport data of proton-conducting fuel cell separators may be found in the corresponding chapters of refs 3 and 4. The referencing of this review is restricted to those papers that are relevant for the more-general picture. Of course, this also comprises extensive cross-referencing to the non-fuel-cell literature.

Before proceeding to this, let us briefly mention a few general directions in recent fuel cell research for which the transport properties of the proton-conducting electrolyte are essential. Much of the current research is on proton exchange membrane (PEM) fuel cells where the electrolyte is DuPont's Nafion or some other sulfonated polymer.⁵ Such polymers naturally combine, in one macromolecule, the high hydrophobicity of the backbone with the high hydrophilicity of the sulfonic acid functional group, which results in a constrained hydrophobic/hydrophilic nanoseparation. The sulfonic acid functional groups aggregate to form a hydrophilic domain that is hydrated upon absorption of water. It is within this continuous domain that ionic conductivity occurs: protons dissociate from their anionic counterion ($-SO_3^-$) and become solvated and mobilized by the hydration water. Water typically must be supplied to the electrolyte through humidification of the feed gases and is also produced by the electrochemical reduction of oxygen at the cathode. This is the reason for two serious problems relevant for the use of such membranes in fuel cells: (i) because high proton conductivity is only obtained at high levels of hydration, the maximum operation temperature is approximately limited to the condensation point of water (i.e., 100 °C for a water pressure of 1 atm (10^5 Pa)); and (ii) any protonic current also leads to transport of water through the membrane (as a result of electroosmotic drag) and, if methanol dissolves in the membrane, this is transported virtually at the same rate. The limited operating temperature and the acidity of the electrolyte makes it necessary to use platinum or platinum alloys (the most active but also the most expensive electrocatalyst) to promote the electrochemical reactions in the anode and cathode structures. However, even with platinum, only rather pure hydrogen can be oxidized at sufficient rates. At the operation temperature of state-of-the-art PEM fuel cells, the rate of direct oxidation of methanol (which is frequently considered an environmentally friendly fuel) is not sufficiently high, and, hence, even trace amounts of CO present in any hydrogen-rich reformat (e.g., produced by steam reforming of methanol or methane) poison platinum-based catalysts through adsorption thus blocking the reaction sites. The humidification requirements, along with the high electro-osmotic drag of water and methanol in conventional membranes, complicate the water and heat management of the fuel cell and lead to a significant chemical short-circuiting, i.e., parasitic chemical oxidation of methanol at the cathode.

Therefore, tremendous engineering effort has been expended to at least control the fluxes of water and methanol in such a way that the resulting transient

and steady-state concentration profiles of these species across the membrane still permit acceptable function of the membrane and the electrode structures. The fact that measured water concentration profiles¹¹ differed substantially from the results of early membrane modeling^{12,13} made it clear that the transport behavior of such membranes were not fully understood. It was the availability of better data and improved phenomenological models concerning the macroscopic transport in such membranes¹⁴ that helped to better describe the behavior of available membranes under fuel cell conditions as a function of the boundary conditions (i.e., current, gas humidification, etc.) and membrane properties (e.g., thickness). In addition, there have been many attempts to modify the transport properties, especially by forming composites with highly dispersed inorganic phases. More radical approaches aim at conceptually different separator material exclusively transporting protons and being able to operate at higher temperatures in a low humidity environment. Such a “dream membrane” is widely considered to be the key to further progress in “low”-temperature fuel cell technology: higher operation temperatures would supersede or simplify gas conditioning and purification, reduce the precious metal loading (along with the problems of heat rejection), while reducing hydration requirements may avoid the need to pressurize the system. Because these aspects are all related to the cost of the fuel cell system, which is increasingly attracting attention, understanding the transport properties as a function of molecular structure and morphology and development of new separator materials are the focal points in current fuel cell research.

Whether future progress will be achieved “within the box” by modifying available materials or by designing conceptually different materials is not yet clear. In any case, a better understanding of the mechanisms governing transport of the various species in the separator materials is useful in the effort of further materials research and development.

2. Theoretical Methodologies and Simulation Tools

This section briefly describes some of the theoretical methods and types of simulations that have recently been applied to understand the structural and dynamical features of transport in proton conductors. Although the transport properties and, hence, mechanisms are strongly correlated to the morphology of the material, theoretical studies of the morphology will not be discussed here.

Quantum chemistry or molecular electronic structure theory is the application of the principles of quantum mechanics to calculate the stationary states of molecules and the transitions between these states. Today, both computational and experimental groups routinely use *ab initio* (meaning “from first principles”) molecular orbital calculations as a means of understanding structure, bonding, reaction paths between intermediates etc. Explicit treatment of the electrons means that, in principle, one does not make assumptions concerning the bonding of a system,

which allows “surprises” to be witnessed. Thus, it is a valuable adjunct to experimental work becoming another powerful tool for the chemist, molecular physicist, and material scientist.

Fundamental information concerning local structure, molecular hydrophilicity, aggregation of ionic groups through the formation of hydrogen bonds, and proton dissociation of acidic groups in the fragments of PEMs has been obtained through the determination of global minimum (i.e., equilibrium) energy structures.^{15–25} Because these techniques explicitly treat all the electrons of the system to obtain the electronic structure, only fragments of polymer have been studied, where the system size has typically been limited to <100 atoms.

The dynamics of particles (i.e., atoms, molecules, ions, etc.) may be investigated through the continuous (i.e., time-evolving) solution of Newton’s equations (i.e., classical molecular dynamics (MD)) or with stochastic methods including Monte Carlo (MC) theory. Classical MD simulations with empirical potentials can handle systems consisting of thousands of particles over time periods of nanoseconds and have been used to study proton transport in materials as a function of parameters such as temperature, water content, and, in polymers, equivalent weight and chemical and physical characteristics of main and side chains.^{26–29} To address continuous changes in valence bond networks during the transport of protons, empirical valence bond (EVB) interaction potentials have been devised.^{30–32} *Ab initio* molecular dynamics (AIMD) simulations have successfully been used to study the proton dynamics in homogeneous systems (e.g., water^{33–36} and imidazole³⁷), and recently even more complex and, therefore, extended “model” systems have been examined (e.g., trifluoromethanesulfonic acid monohydrate^{38,39}). They are computationally very demanding if “meaningful” trajectories of only tens of picoseconds are to be sampled. The payoff in such calculations is the determination of completely new and potentially significant insight into molecular mechanisms. The recent AIMD study of trifluoromethanesulfonic acid monohydrate solid^{38,39} revealed the very first evidence of the possible role of the sulfonate anions and Zundel ion in proton transfer in minimally hydrated PEMs.

Microscopic electrolyte theory (Section 2.4) based on a statistical mechanical framework has recently been applied to study the diffusion of protons in a single hydrated channel or pore in several PEMs.^{40–46} This approach makes several assumptions concerning the pore geometry, distribution of fixed anionic groups, and, primarily, the vehicular mechanism of proton transport through the center of the pore. However, this model has been able to compute the proton self-diffusion coefficient in both Nafion and S-PEEK (sulfonated poly(arylene ether ether ketone)) membranes correctly over a significant range of hydration without resorting to any fitting parameters, requiring only membrane-specific morphology information from small-angle X-ray scattering (SAXS) experiments and structural information from electronic structure calculations.

Confinement of water into regions with dimensions of only a few nanometers, such as typically those found in PEMs, accompanied by a strong electrostatic field due to the anions, will result in a significantly lower dielectric constant for the water than that observed in bulk water. Measurement of this structural ordering of the water has not been accomplished experimentally to date, and this was the motivation to the recent calculation of the dielectric saturation of the water in PEMs with an equilibrium thermodynamical formulation.^{47–51} In addition to information concerning the state of the water this modeling has provided information concerning the distribution of the dissociation protons in sulfonic acid-based PEMs.

The various methodologies are discussed in somewhat more detail in the following sections.

2.1. Ab Initio Quantum Chemistry

Only a very concise description of quantum chemistry is presented in this section; the reader is referred to standard texts for a more complete treatment.^{52–54} The aim of quantum chemistry or ab initio electronic structure theory is the solution of the time-independent Schrödinger equation:

$$H(r; \mathbf{R})\Psi(r; \mathbf{R}) = E(\mathbf{R})\Psi(r; \mathbf{R}) \quad (1)$$

This yields the molecular wave function, $\Psi(r; \mathbf{R})$, which is dependent explicitly on the $3n$ coordinates of all n electrons (denoted collectively as \mathbf{r}) and implicitly on the coordinates of all A nuclei (denoted collectively as \mathbf{R}); and the (total) molecular energy, $E(\mathbf{R})$, which parametrically is dependent only on the nuclear positions. The distinction in functional dependence of these quantities is due to the Born–Oppenheimer (BO) approximation,⁵⁵ which separates (slow) nuclear motion from (fast) electronic motion. It is through determination of $E(\mathbf{R})$ that the potential energy surface is defined. The total energy or molecular electronic Hamiltonian, $H(r; \mathbf{R})$, is an operator consisting of the kinetic energy of all the electrons and the potential energy due to the following forces: electron–nuclear attraction, electron–electron repulsion, and nuclear–nuclear repulsion. Its explicit form in atomic units is

$$H(r; \mathbf{R}) = -\frac{1}{2} \sum_i^n \left(\frac{\partial^2}{\partial \mathbf{x}_i^2} + \frac{\partial^2}{\partial \mathbf{y}_i^2} + \frac{\partial^2}{\partial \mathbf{z}_i^2} \right) - \sum_i^n \sum_{\alpha}^A \frac{Z_{\alpha}}{|\mathbf{r}_i - \mathbf{R}_{\alpha}|} + \frac{1}{2} \sum_i^n \sum_j^n \frac{1}{|\mathbf{r}_i - \mathbf{r}_j|} + \frac{1}{2} \sum_{\alpha}^A \sum_{\beta}^A \frac{Z_{\alpha} Z_{\beta}}{|\mathbf{R}_{\alpha} - \mathbf{R}_{\beta}|} \quad (2)$$

This partial differential equation with $3n$ unknowns is impossible to solve exactly (beyond the hydrogen molecule) and, thus, various approximations are generally made.

In a first class of approximations, the solution is sought of a simpler set of equations rather than the exact equations. Under the Hartree–Fock (i.e., HF) approximation,^{56,57} the function of $3n$ variables is reduced to n functions, which are referenced as

molecular orbitals (MOs), each dependent on only three variables. Each MO describes the probability distribution of a single electron moving in the average field of all other electrons. Because of the requirements of antisymmetry, with respect to the interchange of any two electrons, and indistinguishability of electrons, the trial wave function is a single determinantal wave function of the MOs. The optimum MOs are determined through variationally minimizing $E(\mathbf{R})$. Thus, the HF method is a mean-field method applied to the many-electron problem, the solution of which is commonly referred to as the self-consistent field (SCF). Because HF theory does not include details of the instantaneous electron–electron correlations, several post-HF techniques have been developed, including many-body (or Møller–Plesset) perturbation theory,⁵⁸ and configuration interaction (CISD).⁵⁹ In the former method, a “zero-order” description of the ground-state wave function is assumed to be a determinantal wave function constructed from the HF MOs upon which a perturbation acts that the difference between the sum of Fock operators and the exact Hamiltonian. In CISD, electron-pair correlations are treated self-consistently through the assumption that the wave function is a linear combination of the HF determinant with all determinants formed by single and double orbital substitutions of coefficients determined variationally.

A second approximation that is commonly invoked in all these methods is the expansion of the unknown MOs in terms of a given, fixed, and finite set of functions. These functions are usually referenced as the atomic orbital (AO) basis set, where the atomic orbitals are usually expanded through linear combinations of Gaussians, because of the fact that all required matrix elements may be evaluated analytically.⁶⁰ The basis sets may be “minimal” (i.e., one basis function per atomic orbital), “split valence” (two basis functions per valence atomic orbital, one per core orbital), or higher zeta (where n -zeta means n basis functions per orbital). Multiple basis functions per atomic orbital allow the size of the orbitals to increase (i.e., along a bond axis) or decrease (i.e., perpendicular to a bond axis). The higher-order basis sets may also be augmented with polarization functions (e.g., one or more sets of d functions on first-row atoms) that describe small displacements of the orbitals from atomic centers in the molecular environment, and diffuse functions for anions and Rydberg excited states. The size of the Hamiltonian to be diagonalized is proportional to N^4 (where N is the number of AOs); therefore, the use of large basis sets is very time-consuming.

The majority of the molecular-scale information concerning the effects of structure and local chemistry on proton dissociation and separation in PEM fragments alluded to previously^{15–23} were initially determined using HF theory and split valence local basis sets. Refinements to the equilibrium configurations were made using both Møller–Plesset (MP) perturbation schemes and hybrid density functional theory (described below).

A widely used alternative to the electron correlation treatments mentioned previously is the density

functional theory (DFT),⁶¹ which seeks to determine the exact ground state energy and electron density directly, without computing a many-electron wave function. The electron density is only a function of three variables (unlike the wave function, which is dependent on $3n$ variables); thus, DFT dramatically simplifies the calculations and, therefore, has become the preferred method for treating large molecules. DFT relies on two fundamental theorems.⁶² The first states that the ground-state electron density, $n(\mathbf{r})$, uniquely determines the external potential $v(\mathbf{r})$ and, thus, given the nuclear coordinates, determines the ground-state energy, $E_{v(r)}[n(\mathbf{r})]$, and all properties of the ground state, i.e.,

$$E_{v(r)}[n(\mathbf{r})] \equiv \int v(\mathbf{r})n(\mathbf{r}) \, d\mathbf{r} + F[n(\mathbf{r})]; F[n(\mathbf{r})] \equiv (\Psi[n(\mathbf{r})], (T + U)\Psi[n(\mathbf{r})]) \quad (3)$$

where $F[n(\mathbf{r})]$ is the desired (unknown) functional, and T and U are the kinetic and potential energies, respectively. The second states that, given the functional, it is the one that minimizes the energy, thereby providing a variational principle to determine the density, i.e.,

$$E_{v(r)}[n(\mathbf{r})] \geq E_{v(r)}[n_0(\mathbf{r})] \equiv E \quad (4)$$

$F[n(\mathbf{r})] =$

$$T_s[n(\mathbf{r})] + \frac{1}{2} \int \frac{n(\mathbf{r})n(\mathbf{r}')}{|\mathbf{r} - \mathbf{r}'|} \, d\mathbf{r} \, d\mathbf{r}' + E_{xc}[n(\mathbf{r})] \quad (5)$$

where the first term ($T_s[n(\mathbf{r})]$) is the kinetic energy, the second term the classical Coulombic repulsion energy, and the last term ($E_{xc}[n(\mathbf{r})]$) the exchange correlation energy. The challenge in DFT is the design of accurate functionals, and, specifically, the difficulties lie in determining $T_s[n(\mathbf{r})]$ and $E_{xc}[n(\mathbf{r})]$. Considerable progress in constructing a kinetic energy density functional came through the reformulation of DFT by Kohn and Sham, termed Kohn–Sham (KS) density functional theory.⁶³ In KS-DFT, an artificial reference system is constructed that consists of *noninteracting* electrons, which has exactly the same electron density as the real molecular system of interacting electrons. The kinetic energy is approximated as that of the noninteracting reference system, which can be exactly evaluated in terms of the Kohn–Sham orbitals φ_j . The self-consistent set of KS equations is

$$\left(-\frac{1}{2}\nabla^2 + v(\mathbf{r}) + \int \frac{n(\mathbf{r}')}{|\mathbf{r} - \mathbf{r}'|} \, d\mathbf{r}' + v_{xc}(\mathbf{r}) - \epsilon_j \right) \varphi_j(\mathbf{r}) = 0$$

$$n(\mathbf{r}) = \sum_{j=1}^N |\varphi_j(\mathbf{r})|^2$$

$$v_{xc}(\mathbf{r}) = \delta E_{xc} \frac{[n(\mathbf{r})]}{\delta n(\mathbf{r})}$$

$$E = \sum_1^v \epsilon_j - \int \frac{n(\mathbf{r})n(\mathbf{r}')}{|\mathbf{r} - \mathbf{r}'|} \, d\mathbf{r} \, d\mathbf{r}' - \int v_{xc}(\mathbf{r})n(\mathbf{r}) \, d\mathbf{r} + E_{xc}[n(\mathbf{r})] \quad (6)$$

where the final equation is the expression for the

ground-state energy of the molecular system. These equations differ from the Hartree equations only by the inclusion of the exchange-correlation potential $v_{xc}(\mathbf{r})$. Furthermore, if the exchange correlation energy is partitioned into separate contributions due to correlation and exchange, i.e., $E_{xc}[n(\mathbf{r})] = E_x + E_c$, and only the correlation energy neglected, then the treatment becomes a variant of HF theory. The simplest approximation for $E_{xc}[n(\mathbf{r})]$ is the generally accepted local density approximation (LDA):⁶³

$$E_{xc}^{\text{LDA}}[n(\mathbf{r})] \equiv \int \epsilon_{xc}(n(\mathbf{r}))n(\mathbf{r}) \, d\mathbf{r} \quad (7)$$

where $\epsilon_{xc}(n)$ is the exchange-correlation energy per particle of a uniform interacting electron gas of density n . The KS orbitals in the LDA are surprisingly close to HF orbitals, although DFT–LDA calculations neglect the nonlocal nature of exchange terms that are typical for the HF method. The next level of approximations is the generalized gradient approximation (i.e., GGA):

$$E_{xc}^{\text{GGA}} \equiv \int f(n(\mathbf{r}), |\nabla n(\mathbf{r})|) \, d\mathbf{r} \quad (8)$$

in which $f(n, |\nabla n|)$ is a suitably chosen function of its two variables. Popular correlation GGAs include those of Lee, Yang, and Parr,⁶⁴ Perdew (1986),⁶⁵ and Perdew and Wang (1991).⁶⁶ These gradient-corrected correlation functionals in combination with the Becke exchange functional⁶⁷ (based on considering the exchange energies for rare gases, in addition to the known behavior for the uniform electron gas), typically yield accurate relative energies and good thermochemistry.⁶⁸

As a consequence of the size limitations of the *ab initio* schemes, a large number of more-approximate methods can be found in the literature. Here, we mention only the density functional-based tight binding (DFTB) method,^{69–72} which is a two-center approach to DFT. The method has been successfully applied to the study of proton transport in perovskites⁷³ and imidazole³⁷ (see Section 3.1.1.3). The fundamental constraints of DFT are (i) treatment of excited states and (ii) the ambiguous choice of the exchange correlation function. In many cases, the latter contains several parameters fitted to observable properties, which makes such calculations, in fact, semiempirical.

2.2. Molecular Dynamics

Classical molecular dynamics (MD) implementing predetermined potentials, either empirical or derived from independent electronic structure calculations, has been used extensively to investigate condensed-matter systems.⁷⁴ An important aspect in any MD simulation is how to describe or approximate the interatomic interactions. Usually, the potentials that describe these interactions are determined a priori and the full interaction is partitioned into two-, three-, and many-body contributions, long- and short-range terms, etc., for which suitable analytical functional forms are devised.⁷⁵ Despite the many successes with classical MD, the requirement to devise fixed potentials results in several serious problems

in systems where distinct atoms or molecules cause a myriad of different interatomic interactions that should be parametrized or where the electronic structure or bonding pattern changes qualitatively in the course of the simulation.^{76,77} These drawbacks have been overcome by the various techniques of *ab initio* molecular dynamics (AIMD). An overview of a few of the various MD schemes implemented in the study of proton conduction is presented in the following sections.

2.2.1. Classical Molecular Dynamics and Monte Carlo Simulations

Atomistic computer simulations are a statistical mechanical tool to sample configurations from the phase space of the physical system of interest. The system is uniquely treated by specifying the interactions between the particles (which are usually described as being pointlike), the masses of all the particles, and the boundary conditions. The interactions are calculated either on-the-fly by an electronic structure calculation (see Section 2.2.3) or from potential functions, which have been parametrized before the simulation by fitting to the results of electronic structure calculations or a set of experimental data. In the first case, one frequently speaks of AIMD (see Section 2.2.3), although the motion of the nuclei is still treated classically.

Having specified the interactions (i.e., the model of the system), the actual simulation then constructs a sequence of states (or the system trajectory) in some statistical mechanical ensemble. Simulations can be stochastic (Monte Carlo (MC)) or deterministic (MD), or they can combine elements of both, such as force-biased MC, Brownian dynamics, or generalized Langevin dynamics. It is usually assumed that the laws of classical mechanics (i.e., Newton's second law) may adequately describe the atoms and molecules in the physical system.

The MC scheme was first published by Metropolis et al.⁷⁸ in 1953 and applied to the calculation of the equation of state of a simple hard-sphere liquid. Each configuration in an MC simulation is generated stochastically in such a way that the molecular configuration is dependent only on the previous configuration. The MC method is often performed in the canonical ensemble, i.e., for a fixed number of molecules N placed in a fixed volume V and maintained at a constant temperature T . However, many variants of the method exist (see, e.g., ref 74). During the MC simulation, configurations are generated in such a way that, after many configurations have been obtained, each configuration occurs approximately with the appropriate probability of the canonical ensemble, given by the Boltzmann factor $\exp[-E(\mathbf{R})/(kT)]$, where $E(\mathbf{R})$ is now the interaction potential, and k the Boltzmann constant.

The MD method was first used by Alder and Wainwright.⁷⁹ In the standard MD scheme for equilibrium systems, the positions \mathbf{r}_i of atom i are obtained by solving Newton's equations of motion:

$$m_i \ddot{\mathbf{r}}_i = \mathbf{F}_i = -\nabla_i E(\mathbf{R}) \quad (9)$$

where m_i is its mass and the force \mathbf{F}_i is the negative gradient of the potential energy $E(\mathbf{R})$, with respect to i . The MD scheme leads (contrary to the MC scheme) to a time-correlated sequence of configurations (*trajectory*), which can be analyzed to calculate dynamic properties of the system.

The potential energy is often written as a sum of pairwise additive interactions. Frequently, Coulombic interactions between partially charged atoms and additional interaction functions that describe short-range repulsion due to exchange-correlation effects and long-range disperse attraction are used as ingredients in the interatomic potentials. In most cases, the latter interaction function is of the Lennard-Jones type. Molecular geometry and connectivity is maintained by specifying harmonic or Morse-type stretching interactions along a chemical bond, and angle-bend interactions for valence angles and torsion interactions to maintain molecular conformations. Thus, a typical simple force field is the sum over all pairs of Coulombic and short-range interactions, all bonds, all valence angles, and all dihedral angles in a molecule. More complex force fields can contain more elaborate terms and couplings between them. Many-body induction interactions are often included in the interaction energy $E(\mathbf{R})$ by introducing fluctuating point dipoles or fluctuating point charges, whose value is self-consistently determined through the instantaneous electric field and the atomic or molecular polarizabilities. An alternative is the introduction of extra charged particles in a shell model (SM).⁸⁰

Typical numbers of atoms range over the order of several hundred to several tens of thousands, which are located in a regular cell of volume V . The cell and the particles are replicated infinitely in one, two, or three directions of space, depending on whether a cylindrical or other one-dimensional system, a slab system with two external interfaces, or a bulk system is to be simulated. These periodic boundary conditions avoid undesired surface effects beyond those that one explicitly wishes to study. The cells are open and particles can move freely from one cell to the next. For each particle leaving the cell, one of its replicas enters the cell; therefore, the overall particle number in the cell, and thus the density, remains constant. Because the number of interactions to be calculated in such a system is infinitely large, short-range interactions (such as the Lennard-Jones term) need to be smoothly truncated, and lattice summation methods (such as the Ewald method) are implemented for the treatment of long-range forces.

The theory of statistical mechanics provides the formalism to obtain observables as ensemble averages from the microscopic configurations generated by such a simulation. From both the MC and MD trajectories, ensemble averages can be formed as simple averages of the properties over the set of configurations. From the time-ordered properties of the MD trajectory, additional dynamic information can be calculated via the time correlation function formalism. An autocorrelation function $c_{aa}(t) = \langle a(\tau) \cdot a(t + \tau) \rangle$ is the ensemble average of the product of some function a at time τ and at a later time $t + \tau$.

In an equilibrium system, all times t are equivalent and can thus be averaged over. Transport coefficients can be calculated as integrals over these functions, e.g.,

$$D = \frac{1}{3} \int_0^\infty c_{vv} dt = \lim_{t \rightarrow \infty} \frac{\langle [r(t+\tau) - r(\tau)]^2 \rangle}{6t} \quad (10)$$

The diffusion coefficient D is one-third of the time integral over the velocity autocorrelation function $c_{vv}(t)$. The second identity is the so-called Einstein relation, which relates the self-diffusion coefficient to the particle mean square displacement (i.e., the ensemble-averaged square of the distance between the particle position at time τ and at time $\tau + t$). Similar relationships exist between conductivity and the current autocorrelation function, and between viscosity and the autocorrelation function of elements of the pressure tensor.

2.2.2. Empirical Valence Bond Models

A standard classical force field is able to describe conformational changes of molecules. However, it is generally unable to describe the formation and breaking of chemical bonds. The reason is that the atoms participating in the stretch, bend, and torsion terms of the force field need to be specified initially. Changing this specification during the simulation leads to non-Hamiltonian behavior, which makes the simulation data unusable for analysis. Elegant solutions to this problem are ab initio simulation schemes (see Section 2.2.3), which naturally describe the change of chemical bonding via the instantaneous calculation of the electronic structure. In many situations, this scheme is computationally too expensive to be used. Thus, the need arises to develop empirical potential functions that (i) allow the change of the valence bond network over time and (ii) are simple enough to be used efficiently in an otherwise classical simulation code. For dissociation reactions, one possibility is the use of interaction potential functions with the proper asymptotic behavior. As an example, consider the water molecule. In practically all-empirical water models, O and H atoms carry (fixed) partial charges. Thus, these models are incapable of describing the autodissociation of water. For a model that describes the dissociation into protons and hydroxyl ions, full ionic charges need to be placed on the atoms (i.e., $+e$ for the proton, $-2e$ for oxygen). Such Coulombic interactions are too strong at short and intermediate range; thus, an additional potential function must be constructed.^{81,82} An alternative is the valence bond (VB) method, where the chemical bond in a dissociating molecule is described as the superposition of two states: a less-polar bonded state and an ionic dissociated state. Unlike VB theory in quantum mechanics, the matrix elements of the Hamiltonian are not calculated on an electronic basis (see Section 2.1) but by empirical force fields.

As an example, proton transfer in an H_5O_2^+ complex may be described as a superposition of two states, namely $\text{H}_2\text{O}-\text{H}\cdots\text{OH}_2$ and $\text{H}_2\text{O}\cdots\text{H}-\text{OH}_2$ (where the solid line (—) describes a chemical bond and the dotted line (\cdots) is a hydrogen bond). The

energy of each state is calculated from empirical force field terms for intramolecular hydronium interactions, intramolecular water interactions, and the intermolecular water–hydronium interactions, yielding the energies in state 1 and 2: $H_{11}(\mathbf{R})$ and $H_{22}(\mathbf{R})$, which are generally nonidentical. By further specifying empirical coupling functions $H_{12}(\mathbf{R}) = H_{21}(\mathbf{R})$ as functions of the set of particle coordinates \mathbf{R} , the compound states can be calculated via diagonalization of the 2×2 Hamiltonian matrix. This method is called the empirical valence bond (EVB) method and was first introduced by Warshel and Weiss.^{30–32} $H\mathcal{E}(\mathbf{R})$ can be adjusted to reproduce experimental data or ab initio potential energy surfaces. Approximating the motion of protons as classical on the (time-dependent) ground-state potential energy surface, a viable MD scheme can be developed. The procedure is analogous for larger clusters with more basis states, where a larger matrix must be diagonalized. The ground state of the system is specified by the eigenvector of the lowest-energy eigenvalue.

Simultaneously, Borgis and Vuilleumier^{83–87} and Voth and co-workers^{88–93} developed multistate EVB models for proton transport in aqueous solution. In their models, a protonated cluster involving n water molecules, $\text{H}_{2n+1}\text{O}_n^+$, is described by n zeroth-order VB states. In each of these states, the proton defect is formally located on one of the n O atoms (i.e., one of the n O atoms forms three bonds). At any time t , the ground state is calculated via matrix diagonalization; partial charges (and possibly other parameters of the force field) are reassigned to the complex according to the eigenvector. When the proton defect diffuses structurally through this cluster, the contribution of some states can become negligibly small (because the O atom is too far from the proton defect). It is then possible to remove these water molecules from the cluster and replace them by others, which are closer to the proton defect but do not yet interact with the cluster. Thus, over time, the composition of the proton cluster can change and proton transport is possible. The multistate EVB models were used to investigate the structure of protonated complexes in aqueous solutions, proton transport dynamics, the relaxation of the hydrogen-bonded environment, and the role of the quantum nature of proton motion for structure and dynamics.^{86,89}

Based on these experiences, Walbran and Kornyshev⁹⁴ developed a much simpler two-state EVB model. Their model is designed in such a way that it can be used (i) when treating protons classically and (ii) for systems with high proton concentrations. The rationale behind its development was to eventually investigate proton transport in polymer electrolyte membranes. However, in this initial work, they studied only proton mobility in pure water. The ground-state energy is calculated, as for the other EVB models, from the lowest eigenvalue, in this simple case, according to

$$E = -\frac{1}{2}(H_{11} + H_{22} + \sqrt{H_{11}^2 + H_{22}^2 + 4H_{12}^2}) \quad (11)$$

What distinguishes it from the multistate models is the fact that the partial charges on the atoms are

not determined from the eigenvectors of the ground state but through a charge-switching function, which, in turn, is dependent only on the coordinates of the Zundel complex. Thus, Coulombic interaction (and other time-consuming interactions) can be calculated using the adiabatic (effective) charges. In this way, the calculation of Coulombic interactions is substantially simplified; furthermore, the diagonalization of the individual protonated complexes decouples and can be easily performed, even at water-to-proton ratios on the order of 5–10, for which the use of the multistate EVB models with 10 or more basis states would be impossible when more than one proton is present. The model parameters were fit to reproduce the structure and formation energies of small protonated clusters. Because of the limitation of treating only two VB states and limitations in the parameter choice mandated by the requirement that the model needs to remain Hamiltonian in nature and simultaneously allow proton transport, the model usually underestimates the mobility of excess protonic defects and overestimates the self-diffusion coefficient of water, whereas the temperature dependence is usually close to the experimental values. This two-state EVB model was recently applied to simulations of “model” polymer electrolyte membranes (see Section 3.1.2.).^{26–29}

2.2.3. *Ab Initio* Molecular Dynamics (AIMD)

The basic underlying methodology in AIMD is the computation of the forces acting on the nuclei from electronic structure calculations (see previous discussion) that are performed “on the fly” as the trajectory of the molecules is generated. Thus, the electronic variables are not integrated out beforehand but are active degrees of freedom. This implies that, given a suitable approximate solution of the many-electron problem, “chemically complex” systems may be treated with AIMD. Furthermore, the approximation is shifted from the level of selecting the appropriate potentials to the level of choosing a particular approximation for solution of the Schrödinger equation. Despite these advantages, however, there is a price to be paid in AIMD: the correlation lengths and relaxation times that are accessible are much smaller than what is typically accessible via classical MD. Of the various AIMD techniques, we will restrict our discussion in this review to only two methods: (a) Born–Oppenheimer (BO) molecular dynamics and (2) Car–Parrinello molecular dynamics (CPMD).

In BO AIMD, the static electronic structure is solved at each MD time step, given the set of fixed nuclear positions at that instance in time. Thus, the problem is reduced to solving a time-independent quantum problem concurrently to propagating the nuclei via Newton’s second law. Therefore, the BO method is defined by

$$M_i \ddot{\mathbf{R}}_i(t) = -\nabla_i \min_{\Psi_0} \{ \langle \Psi_0 | H_e | \Psi_0 \rangle \} \quad (12)$$

$$E_0 \Psi_0 = H_e \Psi_0 \quad (13)$$

for the electronic ground state. It is important to realize that the minimum of $\langle H_e \rangle$ must be reached at

each BO MD step, which may be solved (for example) under either the HF approximation or with KS-DFT (see previously given brief method descriptions). A commonly used technique implementing the latter electronic structure approach is the VASP total-energy code.^{95–97}

The Car–Parrinello approach⁹⁸ to AIMD exploits the quantum mechanical adiabatic time-scale separation of fast electronic and slow nuclear motion by transforming that into adiabatic energy scale separation in the framework of dynamical systems theory. This is achieved through mapping the two-component quantum/classical problem onto a two-component purely classical problem with two separate energy scales at the expense of losing the explicit time dependence of the quantum subsystem dynamics. The CPMD method makes use of the following classical Lagrangian:

$$L_{\text{CP}} = \sum_i \frac{1}{2} \mu_i \dot{\langle \psi_i | \psi_i \rangle} + \frac{1}{2} \sum_i M_i \dot{\mathbf{R}}_i^2 - E[\{\psi_i\}, \{\mathbf{R}_i\}] \quad (14)$$

to generate trajectories for the ionic and electronic degrees of freedom via the coupled set of equations of motion:

$$M_i \ddot{\mathbf{R}}_i^\alpha = - \frac{\partial E[\{\psi_i\}, \{\mathbf{R}_i\}]}{\partial \mathbf{R}_i^\alpha} = F_{\text{CP}i}^\alpha \quad (15)$$

$$\mu_i \ddot{\langle \psi_i | \psi_i \rangle} = - \frac{\partial E[\{\psi_i\}, \{\mathbf{R}_i\}]}{\partial \langle \psi_i | \psi_i \rangle} \quad (16)$$

where M_i and \mathbf{R}_i are the mass and position, respectively, of atom i ; $|\psi_i\rangle$ are the KS orbitals, which are allowed to evolve as classical degrees of freedom with inertial parameters μ_i and $\partial E[\{\psi_i\}, \{\mathbf{R}_i\}]$ is the KS energy functional evaluated for the set of ionic positions $\{\mathbf{R}_i\}$ and the set of orbitals $\{\psi_i\}$. The functional derivative of the KS energy is implicitly restricted to variations of $\{\psi_i\}$ that preserve orthonormality. Thus, the electrons are put into their ground state at a fixed set of ionic positions and with the ions moving according to the previously given equation, the electronic orbitals should adiabatically follow the motion of the ions, performing only small oscillations about the electronic ground state. The electronic orbitals will possess a “fictitious” kinetic energy, according to their motion, and, thus, a fictitious mass parameter μ_i . If μ_i is small, then the motion of the orbitals should be fast, relative to the motion of the ions.

2.3. Poisson-Boltzmann Theory

The Poisson–Boltzmann (PB) theory has been used to calculate the influence of the charged groups in PEM pores on the energy barriers for proton jumps and in combination with phenomenological concepts of charge-transfer theory and the temperature dependence of the reaction rate.^{99,100} In the mean-field PB theory, the distribution of mobile charges (here, protons) in a pore is calculated from the boundary conditions and the arrangement of external static charges (here, sulfonate groups), neglecting both

correlations between the mobile charges and a spatially dependent dielectric constant of the water within the pore. Because of such drastic assumptions, the density of the protons near the sulfonate groups is far too high (similar to that predicted by a simple Gouy–Chapman model; see Section 3.1.2.1). Specifying a geometric model and an arrangement of sulfonate groups (slab pores of varying width with a regular lattice of negative point charges on the pore surface⁹⁹), proton distributions and electrostatic potential barriers for proton motion along the pore were calculated. Although the model did not directly yield an absolute value for proton mobility, activation energies of proton transport were estimated, as a function of water content, pore shape, and sulfonate density. A modified PB ansatz, taking into account a more realistic charge distribution for the sulfonate groups, was shown to be qualitatively consistent with MD simulations.²⁷

2.4. Nonequilibrium Statistical Mechanical Ion Transport Modeling

Historically, one of the central research areas in physical chemistry has been the study of transport phenomena in electrolyte solutions. A triumph of nonequilibrium statistical mechanics has been the Debye–Hückel–Onsager–Falkenhagen theory, where ions are treated as Brownian particles in a continuum dielectric solvent interacting through Coulombic forces. Because the ions are under continuous motion, the frictional force on a given ion is proportional to its velocity. The proportionality constant is the friction coefficient and has been intensely studied, both experimentally and theoretically, for almost 100 years.^{101,102} The simple Stokes law, derived from hydrodynamic theory where friction increases with increasing ionic radii, is known to fail for small alkali and halide ions, and, of course, protons.¹⁰³

In an effort to explain the peculiar behavior of small ions in polar solvents, two models have been proposed that attribute different phenomena to solvent response and solute or ion displacement. The first model, which is often called the solventberg model, maintains the classical view of Stokes law but with an “effective” ionic radius originating from solvation.¹⁰⁴ Thus, with solvent molecules regarded as being bound to the ion, the radius of the solvated complex is equivalent to a Stokes radius. The other model is a dielectric friction model, which has been formulated over several decades by Born,¹⁰⁵ Fuoss,¹⁰⁶ Boyd,¹⁰⁷ and Zwanzig,¹⁰⁸ with a complete theoretical framework due to Hubbard and Onsager.^{109,110} This model attempts to describe the dielectric response of the solvent due to perturbation by the motion of an ion. As the ion is displaced from an initial position where the solvent is polarized according to the electrostatic field due to the ion, the solvent polarization is not at equilibrium with the new position of the ion, resulting in a relaxation and consequent energy dissipation of the polarization identified as dielectric (or extra) friction. The dielectric friction is inversely related to the ionic radius. Hence, the ion-size dependence of the friction coefficient has a minimum with increasing ionic radius in both models.

The first microscopic theory for ionic friction in polar solvents was proposed by Wolynes,¹¹¹ in which the ion–solvent interactions were partitioned into short-range repulsive and long-range attractive components. The friction coefficient in the Wolynes model is simplified into the following two terms:

$$\zeta = \zeta_0 + \frac{1}{3k_B T} \langle F_S^2 \rangle \tau_F \quad (17)$$

where ζ_0 is calculated from Stokes law, $\langle F_S^2 \rangle$ is the static mean-square fluctuation in the soft force, and τ_F is its characteristic decay time. Hence, in the case of strong, short-ranged attractive interaction, the drag on an ion reduces to that on a solvated solventberg ion, whereas in the limit of the weak long-ranged attractive ion–solvent interaction case, the dielectric friction picture persists. Subsequent work of Wolynes and co-workers¹¹² attempted to implement this model for monovalent cations (i.e., Li^+ , Na^+ , K^+ , Cs^+) in the model solvents of water, methanol, acetonitrile, and formamide. However, their results were only marginally successful for the case of water; poor agreement with experimental results being obtained for the other solvents. Chen and Adelman¹¹³ generalized the Hubbard–Onsager theory, treating the interplay between the Stokes and dielectric friction contributions within a continuum model, but provided no insight into molecular solvent relaxation due to solute perturbations. Chong and Hirata¹¹⁴ used an interaction-site model and the mode coupling theory to show that the friction coefficient decomposes into hydrodynamic friction, dielectric friction, and a coupling term, according to

$$\zeta = \zeta_{\text{NN}} + \zeta_{\text{ZZ}} + 2\zeta_{\text{NZ}} \quad (18)$$

where ζ_{NN} and ζ_{ZZ} denote the friction from a collective density and dielectric response of the solvent to ionic displacement respectively, and ζ_{NZ} the friction due to their coupling. Their work shows that both the solventberg and dielectric friction mechanisms contribute to the net friction (and thereby diffusion) of small ions and thus there is really no contradiction in the coexistence of these two models. Finally, Bagchi and co-workers^{115–117} have shown that the calculation of the total friction on a moving ion should involve formulation with a mode-coupling-type theory (i.e., used to compute a bare friction) and a calculation of the correlation functions. Their derivation gave the following relation for the friction coefficient:

$$\frac{1}{\zeta} = \frac{1}{\zeta_{\text{bin}} + \zeta_{\rho\rho} + \zeta_{\text{mic},DF}} + \frac{1}{\zeta_{\text{hyd}} + \zeta_{\text{hyd},DF}} \quad (19)$$

where ζ_{bin} and $\zeta_{\rho\rho}$ are the binary and the collective solvent number density (ρ) fluctuation contributions, respectively; $\zeta_{\text{mic},DF}$ is the friction contribution originating from the coupling of the ionic field with the orientational solvent polarization mode; and $\zeta_{\text{hyd},DF}$ and ζ_{hyd} are the hydrodynamic friction contributions with and without polar contribution, respectively.

The first attempt to apply microscopic electrolyte theory to study the mobility of protons in PEMs is due to Paddison and co-workers.^{40–46} Because the

foregoing discussion concerns the mobility of small ions in polar solvents, it would seem that application of this methodology to proton transport is somewhat questionable. However, because their model focuses on the coupled transport of a proton with a water molecule (i.e., an hydronium ion), there is perhaps a more substantial underpinning to the calculation of “a proton friction coefficient” in these membranes. The purpose of their nonequilibrium statistical mechanical transport model is to calculate proton self-diffusion coefficients for hydrated PEMs from molecular and morphological information without resorting to any fitting or adjustable parameters through computation of velocity-independent friction coefficients. Because pulsed-field gradient (PFG) NMR measurements allow for the determination of membrane- and hydration-specific proton self-diffusion coefficients, this kinetic model permits the identification of how molecular chemistry and membrane morphology is connected to a macroscopic quantity that ultimately determines performance of a fuel cell. Their model is based on the methodology of Resibois and others,¹¹⁸ and, because of its surprising success in the calculation of proton self-diffusion coefficients in various PEMs, over a range of hydration levels, a brief description of the model is given here.

Similar to the work described previously,^{111–117} the starting point of the kinetic model is the assumption that, under linear response theory, the ensemble average force is proportional to the velocity of a hydronium ion through the friction coefficient (i.e., $\langle \mathbf{F}_\alpha \rangle = -\zeta \cdot \mathbf{v}_\alpha$). Computation of this average force experienced by a hydronium ion as it transverses the channel, when combined with the Einstein relation, allows for the calculation of the proton self-diffusion coefficient. This pore within a PEM is assumed to possess a cylindrical geometry filled with water molecules, according to the degree of hydration of the membrane. The dissociated acidic functional groups in the pore are modeled as radially symmetric axially periodic arrays of fixed ions (i.e., point charges) and, thus, the average force experienced by the hydronium ion is calculated using the standard methods of statistical mechanics, albeit with a suitably constructed *nonequilibrium* distribution function. This distribution function is obtained from a formal solution of the time evolution or Liouville equation. The Liouville operator is constructed from a Hamiltonian of the system with an inertial reference frame moving at the velocity of the hydronium ion and consists of the kinetic energy of all the water molecules and the net potential energy, because of two-body interactions of the water molecules, hydronium ion, and fixed sites. The respective contributions to the potential energy of the system are due to (i) interactions of the hydronium ion with the water molecules, (ii) interaction of the hydronium ion with the arrays of the fixed sites, (iii) water–water interactions, and (iv) interactions of the water molecules with the fixed sites. Thus, the scalar friction coefficient of the hydronium ion is partitioned into four force–force correlation functions:

$$\zeta_\alpha = \frac{\beta}{3} \int_0^\infty dt (\langle F_{\text{cs}} e^{-iL_0 t} F_{\text{cs}} \rangle_0 + \langle F_{\text{cs}} e^{-iL_0 t} F_{\text{ps}} \rangle_0 + \langle F_{\text{ap}} e^{-iL_0 t} F_{\text{ps}} \rangle_0 + \langle F_{\text{ap}} e^{-iL_0 t} F_{\text{cs}} \rangle_0) \quad (20)$$

where $\beta = 1/(kT)$, and the forces F_{cs} , F_{ps} , and F_{ap} are between the hydronium ion and the water molecules, the fixed sites and the water molecules, and the hydronium ion and the fixed sites, respectively. Only the latter three terms are explicitly evaluated: their sum is taken to be a correction, $\zeta^{(c)}$, to a “zeroth order” friction coefficient. Because this first force-force correlation function involves only the force that the water exerts on the hydronium ion (F_{cs}), it is taken to be either the friction coefficient of a hydronium ion in bulk water calculated with the Stokes relation (this is typically the case for minimally or only partially hydrated membranes), or the friction coefficient of a proton in bulk water derived from experimental diffusion measurements (used for fully hydrated membranes). Structure diffusion of the proton is significant in bulk water (see Section 3.1.1.1.1); thus, their model does account for this contribution to the mobility of the proton in membrane pores through the first term in eq 20, i.e., F_{cs} . The choice of the numerical value of this zeroth-order term is not arbitrary but is dependent on the characteristics (i.e., structure) of the water in the pore; and the latter is assessed using the dielectric saturation model described in the following section.

2.5. Dielectric Saturation

In a typical hydrated PEM, the rigidity of the backbone and the crystallinity of the polymer confine the water (to regions of only nanometers); and with the significant density and distribution of the pendant anionic groups give structural ordering to the water in the membrane. Both experimental^{119–122} and MD simulations^{123–126} have revealed that water confined in systems such as reverse micelles and biological pores possesses a decreased polarity and rate of relaxation, and an increased degree of spatial and orientational order, when compared to bulk water. As such, assumptions of a constant dielectric constant for the water in the pore of a PEM (either that of bulk water or some other values) is clearly incorrect. The water near the polymer backbone and fixed anionic groups is more constrained and ordered than the water located in the center of the pores. This phenomenon resembles that observed for an electrolyte near a charged electrode for which various models have been formulated, including Helmholtz, Gouy–Chapman, Stern, and Grahame (see Section 3.1.2.1).

Structure diffusion (i.e., the Grotthuss mechanism) of protons in bulk water requires formation and cleavage of hydrogen bonds of water molecules in the second hydration shell of the hydrated proton (see Section 3.1); therefore, any constraint to the dynamics of the water molecules will decrease the mobility of the protons. Thus, knowledge of the state or nature of the water in the membrane is critical to understanding the mechanisms of proton transfer and transport in PEMs.

Hence, the recent work of Paul and Paddison,^{47–51} which was alluded to previously, has sought to describe the spatially dependent dielectric constant of the water in PEMs. Their work follows in the spirit of the much earlier pioneering work of Booth¹²⁷ and more recent application of Bontha and Pintauro.¹²⁸ They assume that the field-dependent permittivity of the water, $\epsilon(E)$, may be expressed as the sum of two terms, according to

$$\epsilon(E) = n^2 + \frac{4\pi P(E)}{\epsilon_0 E} \quad (21)$$

where n is the refractive index and E and P are the magnitudes of the electric field and polarization, respectively. The polarization is computed from a realization that it is a functional derivative of the Helmholtz energy, A , i.e.,

$$P(r, E, E_0) = - \frac{\delta A(E, E_0)}{\delta E_0(\mathbf{r})} \quad (22)$$

where the dependence of both the polarization and energy on the electrostatic field due to the fixed anionic groups (E) and an external “probing” electric field (E_0) are explicitly declared. One of the important implications of eq 22 is the inclusion of the electrostatic field as part of the total energy (Hamiltonian) of the system, which removes the nonphysical results of divergence in the dielectric constant.

3. Transport Mechanisms

3.1. Proton Conduction Mechanisms

Despite the variety of proton-conducting separator materials, the inherent protonic charge carriers (*protonic defects*) are solvated by very few types of species. These are essentially water (e.g., in *hydrated acidic polymers*), oxo-acid anions (e.g., in CsHSO_4) or oxo-acids such as phosphoric acid (e.g., in adducts of basic polymers with phosphoric acid), heterocycles (e.g., intercalated into acidic polymers or immobilized via flexible spacers), or oxide ions (forming a hydroxide on the oxygen site of an oxide lattice). These species participate in the formation of protonic charge carriers and the proton conduction mechanism. In a few cases, they are also the protogenic group: i.e., they generate protonic charge carriers by self-dissociation (e.g., in the case of phosphoric acid and to some extent also in heterocycles such as imidazole); in other cases, the protonic charge carriers must be generated extrinsically, by doping with a Brønsted acid or base (i.e., in water containing systems and oxides).

A common and important characteristic of all these species is their involvement in hydrogen bonding. The structural and dynamical nature of this interaction seems to be the key to understanding long-range proton transport in these environments. Strong hydrogen bonding is frequently considered to be a precursor of proton-transfer reactions;¹²⁹ however, long-range proton transport also requires rapid bond breaking and forming processes, which is only ex-

pected to occur in weakly hydrogen bonded systems. Dynamical bond-length variations have long been recognized to be integral for the hydrogen bonding in proton-conducting systems;¹³⁰ however, it is only recently that the appearance of such “dynamical hydrogen bonding” has been explained through a consideration of the chemical interactions of the systems (including hydrogen bonding) in a wide range of configuration space.¹³¹ The interplay of hydrogen bonds with other intermolecular forces is generally examined in refs 132–136.

Proton-conduction mechanisms that occur in the aforementioned proton solvents, when present as a homogeneous phase and as a component of heterogeneous fuel cell separator materials, are described more specifically in the following two sections.

3.1.1. Homogeneous Media

3.1.1.1. Water and Aqueous Solutions. *3.1.1.1.1. Mobility of Excess Protons.* The unusually high mobility (equivalent conductivity) of protons in water and aqueous solutions (under ambient conditions, ~ 9 times higher than that for Li^+ and ~ 5 times higher than that for K^+) has been investigated since the early days of physical chemistry, and the different concepts and approaches have been summarized several times.³⁴ The essential features of the present view dates back to the work of Eigen and De Maeyer.^{137,138} They demonstrated that “structure diffusion”, i.e., the “diffusion” of the structure (hydrogen-bond pattern) in which the excess proton is “tunneling” back and forth, is the rate-limiting step. Ever since, there has been some controversy as to whether the region containing the excess proton may be described as a hydrated hydronium ion (i.e., H_9O_4^+ , later termed the Eigen ion) or a smaller dimer sharing the excess proton (i.e., H_5O_2^+ , the Zundel ion¹³⁹). This debate was largely resolved by the mechanistic details obtained from CPMD simulations (see Section 2.2.3) by Tuckerman et al.^{34,35} and the interpretation of NMR data by Agmon.¹⁴⁰ Independently, they determined a mechanism for the diffusion of excess protons in water, which is illustrated in Figure 1.

The region with an single excess proton within the hydrogen-bond network (protonic defect) corresponds to either a Zundel ion or an Eigen ion. Interestingly, the center of the region of excess charge coincides with the center of symmetry of the hydrogen-bond pattern,¹³¹ i.e., apart from the bonds with the common shared proton, each water molecule of the Zundel ion acts as a proton donor through two hydrogen bonds, and each of the three outer water molecules of the Eigen ion acts as a proton donor in two hydrogen bonds and as an acceptor for the hydronium ion and an additional water molecule (see Figure 1). Changes to these hydrogen-bond patterns through hydrogen-bond breaking and forming processes displaces the center of symmetry in space and, therefore, also the center of the region of excess charge. In this way, a Zundel ion is converted to an Eigen ion, which then transfers into one of three possible Zundel ions (see Figure 1). This type of mechanism may still be termed “structure diffusion”

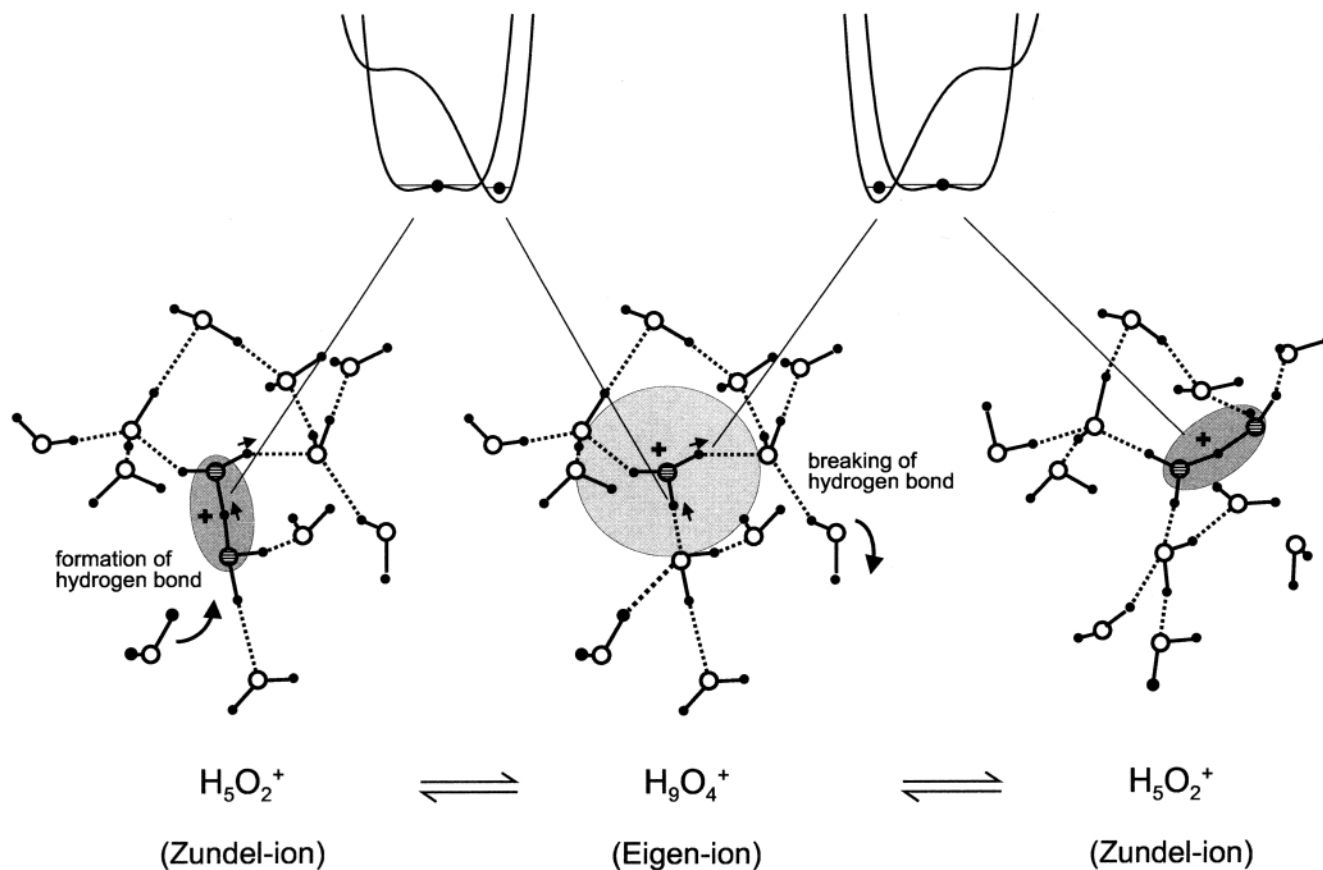


Figure 1. Proton conduction in water. The protonic defect follows the center of symmetry of the hydrogen-bond pattern, which “diffuses” by hydrogen-bond breaking and forming processes; therefore, the mechanism is frequently termed “structure diffusion”. Note that the hydrogen bonds in the region of protonic excess charge are contracted, and the hydrogen-bond breaking and forming processes occur in the outer portion of the complexes (see text). Inserted potentials correspond to nonadiabatic transfer of the central proton in the three configurations (atomic coordinates taken from refs 33 and 34).

(as suggested by Eigen), because the protonic charge follows a propagating hydrogen-bond arrangement or structure.

The sum of all proton displacements involved in the hydrogen-bond breaking and forming processes and the proton displacements within the hydrogen bonds of the Zundel and Eigen ions then corresponds to the net displacement of one unit charge by just a little more than the separation of the two protons in a water molecule (i.e., ~ 200 pm). Although there are no individual, exceptionally fast protons, even on a short time scale, the fast diffusion of protonic defects leads to a slight increase in the physical diffusion of all protons in the system. This is indeed observed for aqueous solutions of hydrochloric acid, for which mean proton diffusion coefficients were observed to be up to 5% higher than the diffusion coefficient of oxygen, as measured by ^1H and ^{17}O PFG NMR,¹⁴¹ reflecting the slightly attenuated correlation of proton and oxygen diffusion in acidic media.

Another interesting feature of this mechanism is that the hydrogen-bond breaking and forming (hydrogen-bond dynamics) and the translocation of protons within the hydrogen bonds occur in different parts of the hydrogen bond network, albeit in a highly concerted fashion. This is the most thermodynamically favorable transport path, because the hydrogen bonds in the center of the two charged complexes are contracted to such an extent that this allows an

almost barrierless proton translocation while the hydrogen-bond breaking and forming processes occur in the weakly bonded outer parts of the complexes. This contraction of the center of the complex is probably a direct consequence of the lower coordination of the involved species (3 instead of ~ 4). The activation enthalpy of the overall transport process is dominated by the hydrogen-bond breaking and forming, which also explains the strong correlation of the proton transport rate and the dielectric relaxation.¹⁴² The Zundel and Eigen complexes are just limiting configurations, and the simulations indeed produce configurations that can hardly be ascribed to one or the other.³⁶ Although simulations find comparable probabilities for the occurrence of both type of complexes,^{34,35} there is experimental evidence for a slight stabilization of the Eigen complex, compared to the Zundel complex, by ~ 2.4 kJ/mol (25 meV).¹⁴³ However, these differences are marginal and do not change the principal features of the mechanism.

One such feature is the potential energy surface for proton transfer in the contracted hydrogen bonds. The time-averaged potential surfaces are almost symmetrical (especially for the Zundel ion) without significant barriers, i.e., the proton is located near the center of the bond. Whether its location is off-center at any time instance is mainly dependent on the surrounding hydrogen-bond pattern, and it is the

change of this pattern that alters the shape (and asymmetry) of this potential and, therefore, the position of the proton within the hydrogen bond (see Figure 1, top). In other words, the proton is transferred almost adiabatically, with respect to the solvent coordinate.¹ This has important consequences on the mechanism when static asymmetric contributions are introduced, i.e., by chemical interactions or the presence of ionic charges (see below). The very low barriers are also the reason for the fact that the mechanism can be well described classically, with respect to the motion of the nuclei (especially the proton); in particular, proton tunneling has only a minor effect on the rate of transfer. Nevertheless, the protonic defect (region of protonic excess charge) may become delocalized through several hydrogen bonds, because of quantum fluctuations.^{36,85}

The mechanism also provides insight into the question as to what extent proton transfer in water is a cooperative phenomenon. In many physical chemistry textbooks, one still finds diagrams showing the concerted transfer of protons within extended hydrogen-bonded water chains (the Grotthuss mechanism) to explain the unusually high equivalent conductivity of protons in this environment. However, the creation of the corresponding dipolar moment in an unrelaxed high dielectric constant environment costs far too much energy to be consistent with a very fast process with low activation energy.^{1,144} As anticipated in ref 1, the propagation mechanism of a protonic defect in a low-dimensional water structure surrounded by a low dielectric environment is obviously between “concerted” and “step-wise”,^{145,146} however, in bulk water, the cooperation is restricted to the dynamics of protons in neighboring hydrogen bonds (also see Figure 1).

One also should keep in mind that water is a liquid with a high self-diffusion coefficient (i.e., $D_{\text{H}_2\text{O}} = 2.25 \times 10^{-5} \text{ cm}^2/\text{s}$ at room temperature) and that the diffusion of protonated water molecules makes some contribution to the total proton conductivity (vehicle mechanism¹⁴⁷). This is $\sim 22\%$ when assuming that the diffusion coefficients of H_2O and H_3O^+ (or H_5O_2^+) are identical. However, as suggested by Agmon,¹⁴⁸ the diffusion of H_3O^+ may be retarded, because of the strong hydrogen bonding in the first hydration shell.

Of course, the relative contributions of “structure diffusion” and “vehicular diffusion” are dependent on temperature, pressure, and the concentrations and types of ions present. With increasing temperature, structure diffusion is attenuated and with increasing pressure the contribution of structure diffusion increases until it reaches a maximum at $\sim 0.6 \text{ GPa}$ (6 kbar).¹ Especially relevant for the later discussion of proton transport in hydrated acidic membranes is the observation that structure diffusion strongly decreases as the acid concentration increases (see Figure 2 and ref 141), which is probably due to changes in the hydrogen-bond pattern (there are progressively more proton donors than corresponding proton acceptor “sites”) and a consequence of the biasing of the hydrogen bonds in the electrostatic field of the ions suppressing the proton-transfer mechanism illustrated in Figure 1.

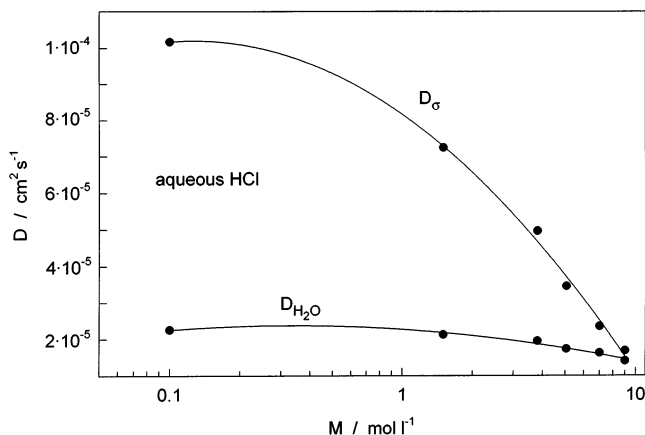


Figure 2. Conductivity diffusion coefficient (mobility) of protons and water self-diffusion coefficient of aqueous solutions of hydrochloric acid (HCl), as a function of acid concentration (molarity, M) (data are taken from ref 141).

3.1.1.1.2. Mobility of Defect Protons. Because basic aqueous solutions also have some relevance for fuel cell applications (e.g., in alkaline fuel cells (AFCs)), the transport mechanism of defect protons (OH^-) is also reviewed here. Although intuition might lead one to assume that the mechanism is reminiscent of that of an excess proton, recent CPMD simulations suggest that this may not be the case.¹⁴⁹ As opposed to Zundel and Eigen complexes, in which the central species are only 3-fold coordinated (under-coordinated, with respect to water in pure water, which is probably the reason for the bond contraction in these complexes; see above) on the average, the hydroxide ion is observed to be coordinated by ~ 4.5 water molecules in an almost-planar configuration with the OH proton pointing out of the plane. This is considered to be a true quantum effect and contradicts the common understanding of a 3-fold coordination.¹⁵⁰ This “hyper-coordination” is suggested to prevent proton transfer from a H_2O to the OH^- , because this would produce an unfavorable H–O–H bond angle of 90° . The proton transfer only occurs when the OH^- coordination is reduced to 3 by breaking one of the 4 hydrogen bonds within the plane and some rearrangement of the remaining bonds occurs, which allows the direct formation of a water molecule with a tetrahedral geometry. Surprisingly, the ground-state coordination of the most favorable configurations around excess protons seem to be similar to the coordination of the transition state for the transport of defect protons. Note, that hyper-coordination of the OH^- is still a matter of controversial debate. The statistical mechanical quasi-chemical theory of solutions suggests that tricoordinated OH^- is the predominant species in the aqueous phase under standard conditions.^{151,152} This finding seems to be in agreement with recent spectroscopic studies on hydroxide water clusters, and it is consistent with the traditional view of OH^- coordination.

It should also be mentioned that OH^- “hyper-coordination” is not observed in concentrated solutions of NaOH and KOH.¹⁵³ In contrast to acidic solutions, where structure diffusion is suppressed with increasing concentration (see above and Figure 2) the transference number of OH^- (e.g., in aqueous

KOH solutions) remains surprisingly high (~ 0.74) for concentrations up to ~ 3 M.

In pure water, excess protons (H_3O^+ , H_5O_2^+) and defect protons (OH^-) are present at identical concentrations; however, because of their low concentration (10^{-7} M under ambient conditions), the diffusion of these defects may be considered to be quasi-independent. Only in small water clusters do zwitterions show a remarkable stability.¹⁵⁴

3.1.1.2. Phosphoric Acid. Although the proton conduction mechanism in phosphoric acid has not been investigated to the same extent, it is evident that the principal features exhibit similarities, along with important differences.

Above its melting point of $T_m = 42$ °C, neat phosphoric acid (H_3PO_4) is a highly viscous liquid with extended intermolecular hydrogen bonding. However, in contrast to the situation in water, there are more possible donor than acceptor sites and the amphoteric character is significantly more pronounced: phosphoric acid may act as both a Brønsted acid and base. In terms of equilibrium constants, both K_a and K_b are reasonably high (K_a of the conjugate base is low). Consequently, phosphoric acid shows a very high degree of self-dissociation (autoprotolysis) of $\sim 7.4\%$,¹⁵⁵ along with some condensation, with H_2PO_4^- , H_4PO_4^+ , H_3O^+ , and $\text{H}_2\text{P}_2\text{O}_7^{2-}$ being the main dissociation products. Because of their high concentration, the separation of the overall conductivity into charge carrier concentration and mobility terms is problematic. Nevertheless, the proton mobility has been calculated from total conductivities by the Nernst–Einstein equation by taking concentrations from ref 155; and the values have been observed to be almost 2 orders of magnitude higher than the values for the diffusion coefficient of the diverse phosphate species obtained directly by ^{31}P PFG NMR¹⁵⁶ and estimated from viscosity measurements via the Stokes–Einstein relation.

Pure phosphoric acid is a liquid with a low diffusion coefficient of phosphate species but an extremely high proton mobility, which must involve proton transfer between phosphate species and some structural rearrangements. The contribution to the total conductivity is $\sim 98\%$; i.e., phosphoric acid is an almost-ideal proton conductor. The total conductivity at the melting point ($T = 42$ °C) is 7.7×10^{-2} S/cm, with an estimated proton mobility of 2×10^{-5} cm²/s.¹⁵⁶ This extremely high proton mobility has also been indirectly determined with ^1H PFG NMR and was observed to be even higher (by a factor of 1.5–2.3). This has been explained by the correlated motion of the oppositely charged defects (H_2PO_4^- , H_4PO_4^+) when they are close to one another (i.e., the case just after their formation (by dissociation of H_3PO_4) and before their neutralization). Correlation effects are actually quite common in proton conductors with high concentrations of charge carriers and they are even more pronounced in other systems (see Section 3.1.1.3 on heterocycles and proton transport in alkaline-metal hydroxides^{157,158}).

Molecular details of the structure diffusion mechanism with the hydrogen-bond breaking and forming and the proton transfer between the different phos-

phate species (essentially H_2PO_4^- , H_3PO_4 , H_4PO_4^+) have not been investigated yet; however, the high degree of self-dissociation suggests that the proton-transfer events are even less-correlated than in water (the system is more tolerant toward protonic charge density fluctuations). The transfer events are probably almost barrierless, as indicated by negligible H/D effects of the diffusion coefficients in mixtures of H_3PO_4 and D_3PO_4 .¹³⁰

The principal proton transport mechanism remains essentially the same with the addition of some water, with a conductivity increase up to 0.25 S/cm under ambient conditions. A ^1H and ^{31}P PFG NMR study also showed that an 85 wt % phosphoric acid system was an almost ideal proton conductor, with 98% of the conductivity originating from the structure diffusion of protons.¹⁵⁹ The combination of high intrinsic charge carrier concentration and mobility renders the possibility of very high conductivities in these systems. In particular, there is no perturbation from extrinsic doping, i.e., there is no suppression of structure diffusion, despite the high concentration of protonic charge carriers. On the other hand, attempts to increase the conductivity of phosphoric acid-based systems by doping have expectedly failed.¹⁶⁰

3.1.1.3. Imidazole. Historically, the interest in hydrogen bonding and proton conductivity in heterocycles has its roots in speculations about the participation of hydrogen bonds in energy and charge transfer in biological systems,¹⁶¹ specifically, concerning the participation of $\text{NH}\cdots\text{N}$ bonds between the imidazole groups of histidine in proton transport in transmembrane proteins.¹⁶² Even Zundel has worked in the field,¹⁶³ and it is not surprising that his view of the proton dynamics in imidazole is closely related to that of water. He suggested a high polarizability of the protons within intermolecular hydrogen bonds and, as a consequence, a very strong coupling between hydrogen bonds, as indicated by the intense IR continuum in the NH stretching regime. Surprisingly, he did not suggest the existence of any complex similar to the Zundel complex in water¹⁶³ (see Section 3.1.1.1), whereas Riehl¹⁶⁴ had already suggested “defect protons” or “proton holes” as requirements to maintain a current in solid imidazole. Early conductivity measurements had their focus on crystalline monoclinic imidazole, which has a structural hydrogen bond length of 281 pm.¹⁶⁵ The measured conductivities were typically low (i.e., $\sim 10^{-8}$ S/cm) with very poor reproducibility.^{161,166,167} Later tracer experiments¹⁶⁸ and a ^{15}N NMR study¹⁶⁹ raised doubts about the existence of proton conductivity in pure crystalline imidazole.

However, the conductivity of liquid imidazole is several orders of magnitude higher ($\sim 10^{-3}$ S/cm at the melting point of $T_m = 90$ °C);¹⁶¹ however, its mechanism was investigated much later. It was the search for chemical environments that were different from water in fuel cell membranes that brought heterocycles back into focus. The potential proton donor and acceptor functions (amphoteric character), the low barrier hydrogen bonding between the highly polarizable N atoms, and the size and shape of the molecule were reasons that Kreuer et al.¹⁷⁰ started

to investigate the usefulness of heterocycles as proton solvents in separator materials for fuel cells. This work also comprises the study of the transport properties of neat and acidified liquid imidazole, pyrazole, and, later, benzimidazole.¹⁷¹ An important finding was that the transport coefficients (i.e., mobility of protonic charge carriers and molecular diffusion coefficients) are similar to those of water at a given temperature, relative to the melting point. This is particularly true for their ratio: i.e., the proton mobility is a factor of ~ 4.5 higher than the molecular diffusion coefficient at the melting point of imidazole.¹⁷⁰ This is a direct indication of fast intermolecular proton transfer and the possibility of structure diffusion in this environment. Subsequently, details were revealed by a CPMD simulation.³⁷ In contrast to earlier suggestions of concerted proton transfer in extended chains of hydrogen bonds^{161,172} (analogous to the proton conduction mechanism in water presented in most textbooks at that time¹⁴⁴), a structure diffusion mechanism similar to that for water (Figure 1) was observed. The region containing the excess proton (intentionally introduced) is an imidazole with both nitrogens protonated and acting as proton donors toward the two next nearest imidazoles in a configuration $\text{Imi}\cdots\text{ImiH}^+\cdots\text{Imi}$ with hydrogen bonds (~ 273 pm) slightly contracted, compared to the average bond length of the system, but still longer than the bonds in the isolated complex (in the gas phase).¹⁷³ The position of the protons within these hydrogen bonds is dependent mainly on the hydrogen bonding between the nearest and next-nearest solvating imidazoles (Figure 3). The hydrogen-bonded structure in imidazole is observed to be chainlike (i.e., low dimensional), with two possible orientations of the hydrogen-bond polarization within segments which are separated by imidazoles with their protonated nitrogen directed out of the chain. This may even form a "cross-linking" hydrogen bond with a nonprotonated nitrogen of a neighboring strand of imidazole. The simulation data revealed the existence of imidazole molecules close to the protonic defect in hydrogen-bond patterns, which rapidly change by bond breaking and forming processes. Similar to water, this shifts the excess proton within the region and may even lead to complete proton transfer, as displayed in Figure 3. There is no indication of the stabilization of a symmetrical complex $(\text{Imi}\cdots\text{H}\cdots\text{Imi})^+$: there always seems to be some remaining barrier in the hydrogen bonds, with the proton being on one side or the other.

As for the CPMD simulation of water, the simulated configuration is artificial, because there is no counter charge compensating for the charge of the excess proton. This is necessary, methodologically, because self-dissociation is unlikely to occur within the simulation box used (i.e., eight imidazole molecules with a single excess proton) and the accessible simulation time (~ 10 ps). The self-dissociation constants for heterocycles (in particular, imidazole) are actually much higher than for water, but degrees of self-dissociation (concentration of protonic charge carriers) of $\sim 10^{-3}$ are still ~ 2 orders of magnitude

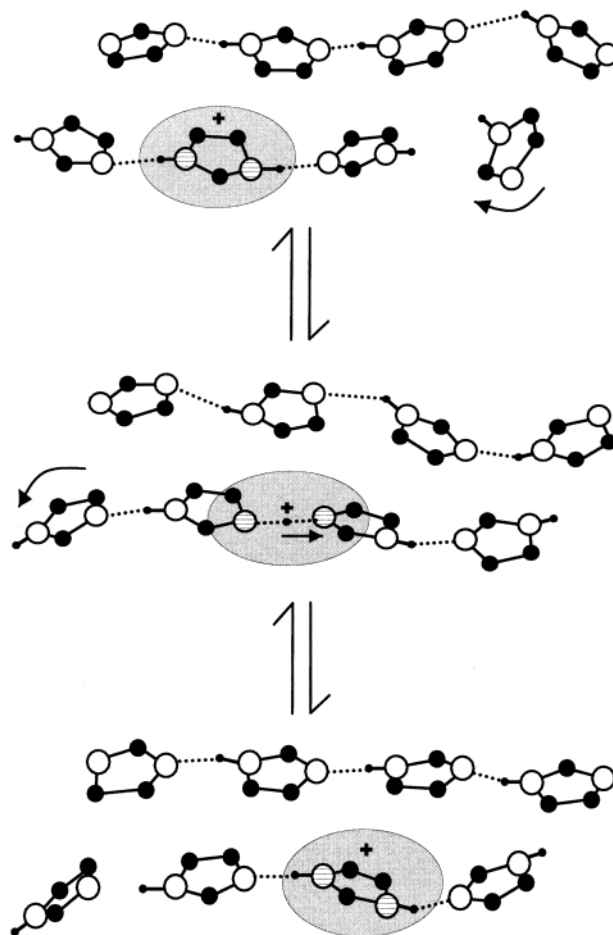


Figure 3. Proton conduction mechanism in liquid imidazole, as revealed by a Car–Parrinello molecular dynamics (CPMD) simulation.³⁷ Note the similarities with the proton conduction mechanism in water (see Figure 1).

lower than that for phosphoric acid (see Section 3.1.1.2). Site-selective proton diffusion coefficients (obtained by ^1H PFG NMR of different imidazole-based systems) show surprisingly high diffusion coefficients for the protons involved in hydrogen bonding between the heteroatoms (nitrogen).¹⁷⁴ Depending on the system, they are significantly higher than calculated from the measured conductivities corresponding to Haven ratios (σ_D/σ) of 3–15. This indicates some correlation in the diffusion of the proton, which may be due to the presence of a counter charge neglected in the simulation.

In pure imidazole, regions containing excess protons must be charge-compensated by proton-deficient regions with electrostatic attraction between these regions (defects) that is dependent on their mutual separation distance and the dielectric constant of the medium. Under thermodynamic equilibrium, such defects are steadily formed and neutralized. Formally, the creation of a protonic defect pair is initiated by a proton transfer from one imidazole to another, with the subsequent separation of the two charged species with a diffusion mechanism as described previously (also see Figure 3). However, this transfer is contrary to the electrostatic field of the counter charge, favoring a reversal of the dissociation process. However, because the two protons of the positively charged imidazolium (ImiH^+) are

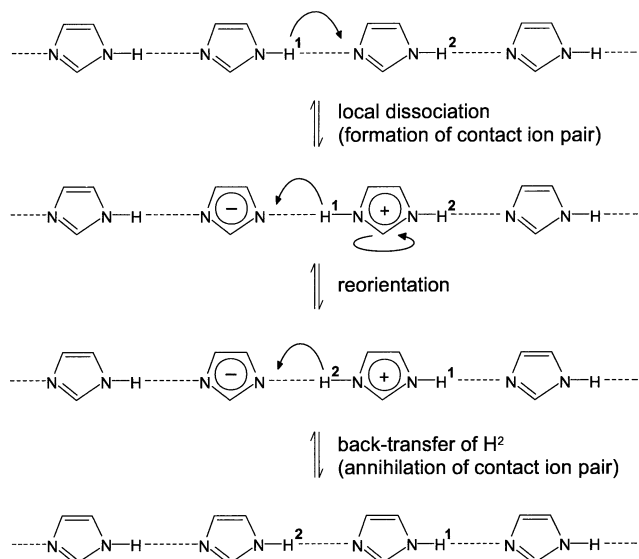


Figure 4. Schematic illustration of correlated proton transfers in pure liquid imidazole leading to proton diffusion but not proton conductivity (see text).

equivalent, there is a 50% chance that another proton is transferred back, provided that the orientational coherence between the dissociating molecules is completely lost. If the same proton is transferred back, the transient formation and neutralization of an ion pair contributes neither to the proton diffusion nor to the proton conductivity. However, if the other proton is transferred back, the protons interchange their positions in the hydrogen bond network, which generates diffusion but no conductivity since the transient charge separation is completely reversed. As illustrated for the most simple mechanism of this type in Figure 4, the sum of all proton translocation vectors form a closed trajectory reminiscent of cyclic intermolecular proton-transfer reactions known to occur in certain organic pyrazole-containing complexes¹⁷⁵ and proton diffusion in hydroxides.^{157,158}

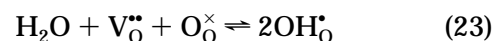
Presently, there is no direct proof for such a mechanism in pure imidazole (e.g., by ¹⁵N NMR); however, the observation that the ratio of the proton diffusion and conduction rates virtually coincide with the Boltzmann factor (i.e., $\exp(-E_{\Phi}(\epsilon)/(kT))$, where E_{Φ} is the electrostatic separation energy of two unit charges in a continuum of dielectric constant ϵ) is a strong indication.

This observation is also indicative of the importance of a high dielectric constant to enable the formation of protonic charge carriers and to allow their mobility being uncorrelated with their conjugated base. Of course, this is also true for the separation of protonic charge carriers from extrinsic dopants such as acids. In addition to the perturbation of the hydrogen bond network (as observed in aqueous solutions), electrostatic effects may also explain the saturation of proton conductivity with increasing acidity of the heterocyclic systems.¹⁷¹ This effect is even more pronounced in polymeric systems with immobilized protogenic groups and will be discussed in Section 3.1.2.3.

3.1.1.4. Simple Cubic Perovskites. Since the work of Stotz and Wagner¹⁷⁶ in 1966, the existence of protonic defects in wide-band-gap oxides at high

temperatures is well-established; and the initial notation OH_0^+ (H_i^+), i.e., the assumption that the defect is a hydroxide ion residing on an oxide ion site carrying a positive relative charge, is still valid. More than a decade later, the systematic investigation of acceptor-doped oxides such as LaAlO_3 , LaYO_3 , or SrZrO_3 , which had already been known for their moderate oxide ion conductivity, provided experimental evidence that these materials may be proton conductors in hydrogen-containing environments.¹⁷⁷ The observed conductivities in these materials were quite low; however, later related compounds based on SrCeO_3 ¹⁷⁸ and BaCeO_3 ¹⁷⁹ with high proton conductivities have been discovered and even tested in different types of electrochemical cells, including fuel cells,^{180–185} but the lack of stability under fuel-cell operating conditions remained an unsolved problem. Almost another two decades passed before oxides were synthesized that combined high proton conductivity with high thermodynamic stability.^{186–188} This brought these materials closer to a realistic alternative for fuel-cell applications and, hence, their transport properties are reviewed here.

The highest conductivities are observed in oxides with perovskite-type structures (ABO_3) with cubic or slightly reduced symmetry.¹⁸⁸ Protonic defects are formed by the dissociative absorption of water, which requires the presence of oxide ion vacancies $\text{V}_\text{O}^{\bullet\bullet}$. The latter may be formed intrinsically by varying the ratio of main constituents or extrinsically to compensate for an acceptor dopant (lower-valent cation). To form protonic defects, water from the gas-phase dissociates into a hydroxide ion and a proton, with the hydroxide ion filling an oxide ion vacancy and the proton forming a covalent bond with a lattice oxygen. In Kröger–Vink notation, this reaction is written



by which two hydroxide ions substituting for oxide ions, i.e., two positively charged protonic defects ($\text{OH}_\text{O}^{\bullet}$), are formed. The crystallographic (time-averaged) structure of such a defect is shown in Figure 5. There are eight orientations of the hydroxide ion stabilized by a hydrogen bond interaction with the eight next-nearest oxygen neighbors in the cubic perovskite structure. As opposed to the cases discussed previously, for which hydrogen bonding is the dominant intermolecular interaction, here, hydrogen bonding is restricted to the defect region. Within this region, hydrogen bonding interferes with other chemical interactions and, together with these, determines the structure and dynamics of the defective region.

As shown by DFTB and CPMD simulations, the principal features of the transport mechanism are rotational diffusion of the protonic defect and proton transfer toward a neighboring oxide ion.^{189–191} That is, only the proton shows long-range diffusion, whereas the oxygens reside in their crystallographic positions. Both experiments^{192–194} and quantum-MD simulations,^{189,190,195,196} have revealed that rotational diffusion is fast with a low activation barrier. This suggests that the proton-transfer reaction is the rate-

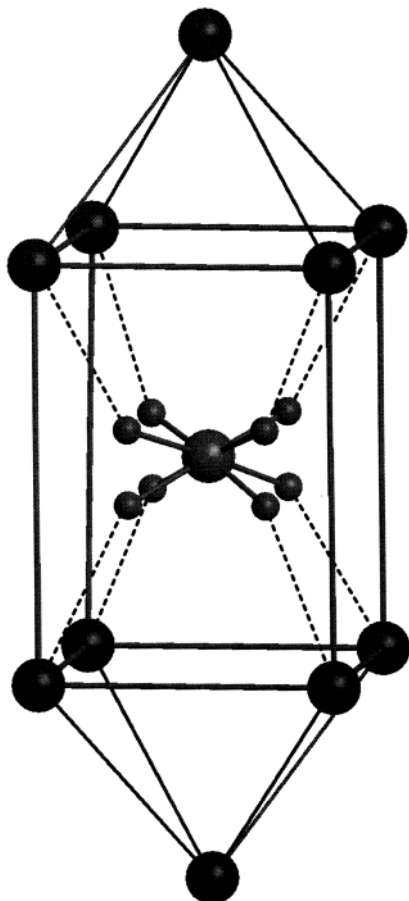


Figure 5. Time-averaged structure of a protonic defect in perovskite-type oxides (cubic case), showing the eight orientations of the central hydroxide ion stabilized by a hydrogen-bond interaction with the eight next-nearest oxygen neighbors.^{186,199}

limiting step in the considered perovskites. On the other hand, the intense red-shifted OH-stretching absorptions in the IR spectra (ref 197 and references therein) and the results of neutron diffraction experiments¹⁹⁸ are indicative of strong hydrogen bond interactions, which favor fast proton-transfer reactions rather than fast reorientation processes, the latter requiring the breaking of such bonds.

Because the structural oxygen separation is larger than 290 pm in most perovskite-type oxides, and strong hydrogen bonds may only be formed at significantly shorter distances, the free energy that the system gains by hydrogen-bond formation is competing with the free energy required for the lattice distortion necessary for hydrogen bonding. A reanalysis of a quantum-MD simulation of a protonic defect in cubic BaCeO_3 ^{131,188,199} demonstrated that these two free-energy contributions almost cancel each other for a wide range of oxygen separation distances (~ 250 – 300 pm). Thus, short oxygen separations, which favor proton transfer, and large oxygen separations, which allow rapid bond breaking, result in similar free energies of the entire system; therefore, these separations have similar probabilities of occurring. Indeed, the simulation found the protonic defect to form short, but transient, hydrogen bonds with all eight nearest oxygen neighbors. In the time-averaged picture observed in the diffraction experiments (see

Figure 5), this leads only to a slight reduction in the structural OH/O separations, in contrast to most instantaneous configurations where one of the eight OH/O separations is reduced to ~ 280 pm, because of hydrogen bonding.^{188,200} Although the hydrogen-bond interaction has a stabilizing effect of ~ 0.5 eV on this configuration, the bond is a “soft”, high-energy hydrogen bond with extended bond-length fluctuations. This also leads to configurations, where the protonic defect acts almost like a free OH with small OH stretching amplitudes, compared to the extended stretching vibrations in the hydrogen bonded state.¹³¹

From the thermodynamics of such “dynamical hydrogen bonds”, one may actually expect an activation enthalpy of long-range proton diffusion of not more than 0.15 eV, provided that the configuration $\text{O}-\text{H}\cdots\text{O}$ is linear, for which the proton-transfer barrier vanishes at O/O distances of less than ~ 250 pm. However, the mobility of protonic defects in cubic perovskite-type oxides has activation enthalpies on the order of 0.4–0.6 eV.¹⁸⁸ This raises the question as to which interactions control the activation enthalpy of proton transfer.

A more-detailed inspection of the MD data showed that, for most configurations with short OH/O separation distances, the proton is not found between the two oxygens on the edge of the octahedron but outside the BO_6 octahedron, as part of a strongly bent hydrogen bond²⁰⁰ that still possesses some barrier for proton transfer. The reason for this is probably the repulsive interaction between the proton and the highly charged B-site cation, which prevents a linear hydrogen bond from forming. The analysis of a few transition-state configurations showed that the B–O bonds are elongated to some extent and that the displacement of the proton being transferred is on the edge of the distorted octahedron.¹³¹ In this way, an almost linear, short configuration of the type $\text{O}-\text{H}\cdots\text{O}$ is formed. The proton transfer in this configuration probably occurs over a remaining barrier, as indicated by the experimentally observed H/D-isotope effects.^{201,202} Although the H/B repulsion is reduced in this configuration, major contributions to the activation enthalpy result from the B–O bond elongation and the proton-transfer barrier. Nevertheless, the H/B repulsion may be used as an estimate of the upper limit for these contributions to the activation enthalpy.

The importance of the H/B repulsion is also witnessed by the observation that the activation enthalpies of proton mobility in cubic perovskites with pentavalent B-site cations (I–V perovskites) are significantly higher than for perovskites with tetravalent B-site cations (II–IV perovskites).^{131,187}

Similar to hydrogen-bonded networks, any reduction in symmetry may decrease the proton conductivity in oxides. This effect has been investigated in detail by comparing structural and dynamical features of protonic defects in yttrium-doped BaCeO_3 and SrCeO_3 ²⁰³ and SrZrO_3 .²⁰⁴ The large orthorhombic distortion of SrCeO_3 has tremendous effects on the arrangement of the lattice oxygen. The cubic oxygen site degenerates into two sites (O1, O2) with different acid/base properties. Although, in SrCeO_3 , the most

basic oxygen is O1, it is O2 in BaCeO₃. Assuming that protons are associated with these sites for the majority of the time, they may show long-range proton transport via the most-frequent O2 sites in BaCeO₃. This is in contrast to SrCeO₃, where long-range proton transport must involve transfer between chemically different O1 and O2 sites. The latter, together with the observed bias in rotational diffusion (defect reorientation), was suggested as the reason behind the higher activation enthalpy and lower conductivity in SrCeO₃, compared to BaCeO₃.²⁰³

The mobility of protonic defects was shown to be very sensitive not only to reduction in the crystallographic symmetry but also to local structural and chemical perturbations induced by the acceptor dopant or by mixed occupancy on the B-site. Traditionally, aliovalent dopants with matching ionic radii are chosen, and, indeed, this simple concept has proven to be successful; e.g., in the development of oxide ion conductors. However, when it comes to proton conductivity in oxides, this approach clearly fails. Although Sc³⁺ and In³⁺ have similar ionic radii to Zr⁴⁺, BaZrO₃ shows much lower proton mobility when doped with scandium or indium, compared to yttrium as an acceptor dopant with a significantly higher ionic radius. For the latter, the proton mobility and corresponding activation enthalpy are virtually independent of the dopant concentration. Electronic structure calculations show a significant effect of the acceptor dopant on the electron density of the neighboring oxygen, including its affinity for the proton (O2). Obviously, the chemical match of the dopant in yttrium-doped BaZrO₃ makes it “invisible” to the diffusing proton.²⁰⁵ However, the most common observation is decreasing proton mobility and increasing activation enthalpy with increasing dopant concentration; e.g., as observed in yttrium-doped BaCeO₃.²⁰⁶ Thus, it is not surprising that mixed occupancy of the B-site in complex perovskites may become unfavorable for proton mobility especially when cation ordering occurs.²⁰⁷

The aforementioned considerations provide a qualitative explanation for the empirical finding that the highest proton conductivities are observed in oxides with a perovskite structure. The framework of corner-sharing octahedral BO₆ shows high coordination numbers for both cation sites (12 for the A-site and 6 for the B-site). There is only one oxygen site in the ideal perovskite structure that has each O atom surrounded by eight nearest and four next-nearest oxygens. Generally the high coordination numbers lead to low bond strengths and smaller angles between the bonds, which is in favor of the above-described dynamics (e.g., the rotational diffusion of the protonic defect corresponds to “dynamical hydrogen bonding” of the OH, with the eight O atoms forming the “reaction cage” (see Figure 5)). If the angles between the possible orientations are small enough, the effective barriers for bond breaking and forming processes are usually <0.2 eV for perovskites with lattice constants that are not too small. In these cases, hydrogen bonding even to the next-nearest oxygen between the vertices of the octahedral become possible, opening another proton-transfer path-

way, as observed in MD simulations of protons in CaTiO₃.¹⁹⁹

3.1.2. Heterogeneous Systems (Confinement Effects)

Homogeneous media have actually been used in commercial (e.g., phosphoric acid fuel cells (PAFCs), AFC) and laboratory fuel cells (e.g., sulfuric acid-based direct methanol fuel cells (DMFCs), hydrogen fuel cells with CsHSO₄ as an electrolyte); however, most modern low-temperature fuel cells rely on the properties of heterogeneous separator materials such as hydrated sulfonic acid functionalized polymers (e.g., Nafion) and the adducts of basic polymers with oxo-acids (e.g., in the system of polybenzimidazole and phosphoric acid (PBI–H₃PO₄)). In these materials, the homogeneous media (discussed previously) are confined within another phase. This geometric situation, which also comprises specific interactions at the usually very large internal interface, not only modifies the transport behavior within the proton-conducting phase, but also leads to the appearance of new transport features, such as electro-osmotic drag (see Section 3.2.1.1). This section reviews the current understanding of proton conduction in these heterogeneous materials.

3.1.2.1. Hydrated Acidic Polymers. Hydrated acidic polymers are, by far, the most commonly used separator materials for low-temperature fuel cells. Their typical nanoseparation (also see Section 1) leads to the formation of interpenetrating hydrophobic and hydrophilic domains; the hydrophobic domain gives the membrane its morphological stability, whereas the hydrated hydrophilic domain facilitates the conduction of protons. Over the past few years, the understanding of the microstructure of these materials has been continuously growing, and this has been crucial for the improved understanding of the mechanism of proton conduction and the observed dependence of the conductivity on solvent (water and methanol) content and temperature.

The microstructure has chiefly been investigated through SAXS and small-angle neutron scattering (SANS) experiments. However, because such experiments on specific samples do not provide sufficient information, diffraction experiments on samples prepared over a wide range of polymer/solvent ratios (even with different types of solvents) have been performed, especially by Gebel and co-workers.^{208–211} Additional information from water transport measurements has been included into the parametrization of the most simple microstructural model, assuming a hydrophobic matrix with a cubic system of cylindrical hydrophilic channels.^{212,213} This approach, although highly simplifying, has the advantage that it allows comparison of the mean numbers for the extensions of the hydrophilic channels and the hydrophobic matrix between for different types of ionomers (also see Section 3.2.1.1). Other constraints such as “maximum entropy” (minimum structure) have also been used to obtain microstructural information from two-dimensional diffraction patterns by direct Fourier synthesis.²¹⁴ In addition, a recent theoretical investigation by Khalatur et al.²¹⁵ that implemented a hybrid Monte Carlo/reference interac-

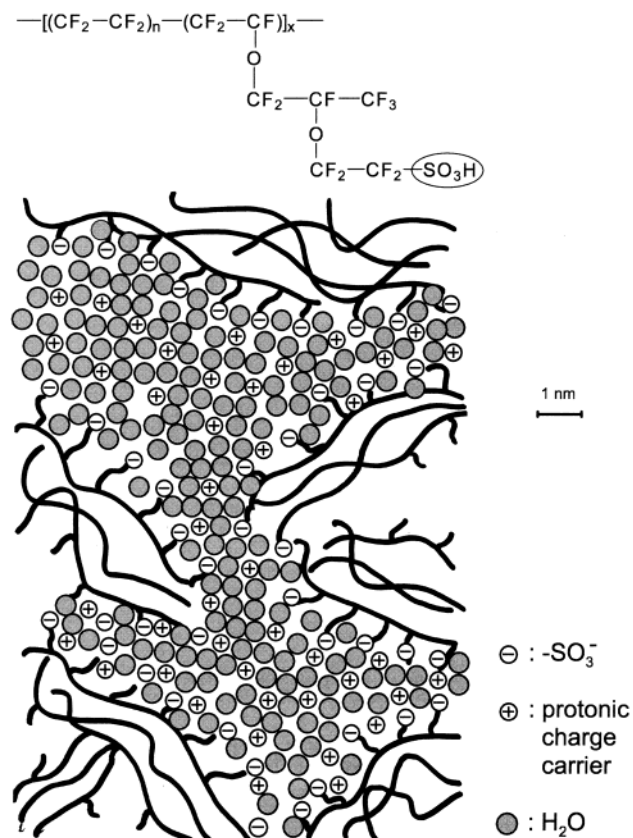


Figure 6. Two-dimensional illustration of some microstructural features of Nafion for an intermediate water content (see text).

tion site model (MC/RISM) technique to probe the morphology of Nafion over a range of hydration levels showed that a continuous network of channels might exist, even at very low water contents. Based on proton conductivity and water diffusion data obtained on diverse membrane materials, Edmondson and Fontanella claimed the existence of a universal percolation threshold at a water volume fraction of $\sim 5\%$.²¹⁶ This conclusion was based on the power-law behavior of the transport coefficients above this water concentration. The observations that the membrane materials continue to conduct below the “threshold” and that the conduction mechanism changes with water content (see below) leave serious doubts about the validity of this interpretation. However, the morphologies resulting from most approaches are in reasonable agreement for the most widely investigated Nafion (1100 g/equiv); the principal microstructural features of this morphology are illustrated in Figure 6 for an intermediate water content. The hydrophobic domain may be described by a framework of low-dimensional objects defining the boundary with the hydrophilic domain. In Nafion, the latter is well-connected, even at low degrees of hydration; i.e., there are almost no dead-end pockets and very good percolation. Because of the side-chain architecture of Nafion, a third transition region between the aqueous domain and the hydrophobic polymer backbone has been introduced. This comprises the hydrated side chains, and a recent SAXS study seems to suggest that this region swells at the expense of the purely aqueous region with increasing degree of

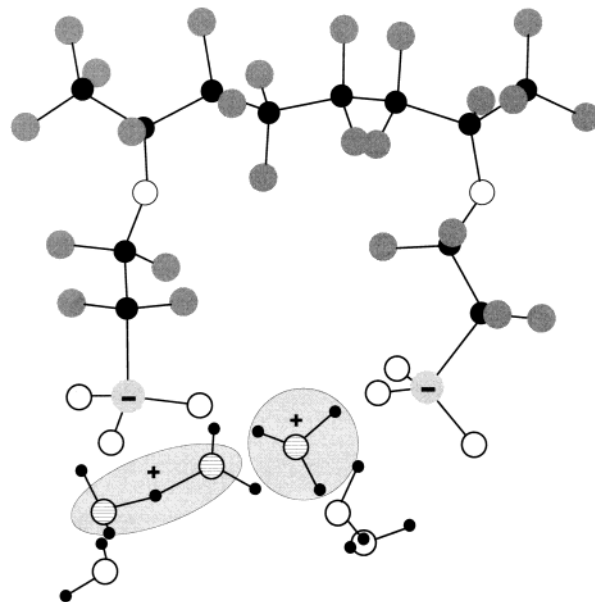


Figure 7. Minimum energy conformation of a two-side-chain fragment of a perfluoro sulfonic acid polymer (Dow) with six water molecules, showing the dissociation of both acidic protons.²³

hydration.²¹⁷ In other words, there is indication for a progressive side-chain unfolding with increasing hydration. This idea is supported by electronic structure calculations (described in Section 2.1) on the entire Nafion side chain,¹⁸ which showed that the unfolding of the chain would require ~ 18 kJ/mol.

Because the hydrophilic sulfonic acid groups are covalently bound to the hydrophobic polymer, they aggregate somewhere in the hydrophobic/hydrophilic transition region, with an average separation of ~ 0.8 nm, compared to ~ 1 nm expected for a totally uniform distribution within the material.²¹²

Electronic structure calculations have shown that only 2–3 water molecules per sulfonic acid group are necessary for dissociation, in accordance with its superacidity when bound to a perfluorinated polymer (Figure 7), and when 6 water molecules are added, separation of the dissociated proton from the sulfonate anion is observed.^{16,20,23} This water (primary hydration of the sulfonic acid group) is actually absorbed at low water partial pressures,¹⁹⁷ indicating the stabilizing effect of water in such systems, as expected from the high energetic stability (at $T = 0$ K) of the H_3O^+ , compared to H_3SO_4^+ ($-\text{SO}_3\text{H}_2^+$).²¹⁸ Apart from water, the hydrophilic domain contains only excess protons as mobile species, while the anionic counter charge is immobilized. This is an inherent advantage of such materials over homogeneous electrolytes with mobile anions (or other conjugated bases), which may interfere with the reactions that occur at the electrocatalysts. Although this situation is reminiscent of the simplest case discussed in Section 3.1.1.1.1 (excess proton in water), it is actually more complex.

If only electrostatics are considered, significant attractive interaction between the excess protons in the aqueous phase and the immobile anionic mirror charge is expected.^{26,27} Recent MD simulations of proton transport in slab pores with sulfonate groups

embedded on the pore walls give the anticipated, essentially constant separation distance of the protons from the fixed anions, despite changes in the amount of water between the slabs. The Debye length (typical electrostatic screening length) of pure water is ~ 800 nm at room temperature and is thus much larger than the typical dimensions of the hydrophilic domain (only a few nanometers). Traditionally, the distribution of charge carriers within the corresponding space charge layer is described by the Gouy–Chapman theory, which has been developed for semi-infinite geometries, or by numerically solving the Poisson–Boltzmann (PB) equation for specific geometries.^{99,100,212,219,220} In either case, one obtains a monotonically decreasing concentration of protonic charge carriers as one moves from the hydrophobic/hydrophilic interface (i.e., where the anion charge resides) toward the center of the hydrated hydrophilic domain. However, this picture is not complete, because these continuum theories neglect any structural inhomogeneity in the vicinity of the electrified interface. In the Gouy–Chapman approach, even a homogeneous distribution of the mirror charge over the interface is assumed; however, the fact that the separation of neighboring sulfonic acid groups (~ 0.8 nm) and the typical extension of the hydrophilic domain (a few nanometers) are of similar order does not justify this assumption. In addition, recent Brownian dynamics simulations of ions in cylindrical nanodimensioned pores have shown that both the PB and Poisson–Nernst–Planck continuum theories substantially overestimate the shielding effects when the radius is less than two Debye lengths.²²¹

The same is true for the assumption of a homogeneous dielectric constant of the aqueous phase: a simplification that is not backed up by dielectric measurements as a function of the water content in the microwave (i.e., gigahertz) range.^{222,223} As known for the near surface region of bulk water or any interface with water on one side, the dielectric constant of the hydrated hydrophilic phase is significantly reduced near the hydrophobic/hydrophilic interface. In addition, the specific interaction of the sulfonic acid group with water (hydration) also decreases the dielectric constant. Therefore, the spatial distribution of the dielectric constant within hydrated domains is strongly dependent on the width of the channels (degree of hydration) and the separation of the dissociated sulfonic acid functional groups. This is an important result from the equilibrium statistical thermodynamic modeling of the dielectric saturation in different types of hydrated polymers described previously (see Section 2.5).^{47–51} As shown in Figure 8 (top), the dielectric constant reaches the bulk value (81) in the center of the channel (pore) for water contents higher than ~ 10 water molecules per sulfonic acid group, whereas, for lower degrees of hydration, even in the center of the channel, the dielectric constant is lower than the bulk value as a consequence of the stronger confinement (Figure 8, bottom). The calculations did not account for specific chemical water–polymer interactions (modeling only the interaction of the sulfonate groups with the water), which are expected to further reduce the

dielectric constant within the hydrated channels. The distribution of the relative permittivity of the water across a hydrated channel has important implications on the distribution of excess protons within the channel. Because the solvation energy of protons becomes more negative with increasing dielectric constant, there is a stabilizing effect for protonic charge carriers in the center of the channels, which heavily modifies the Gouy–Chapman distribution. As illustrated in Figure 8 (top), the decreased dielectric constant in the interfacial region leads to a relative stabilization of the dissociated protons in the central region of the channels. Only at very high water contents (i.e., in the two-phase regime of Nafion with more than 14 water molecules per sulfonic acid group) does one expect a slight relative depletion of charge carriers in the channel center, which is reminiscent of a Gouy–Chapman profile.

The general picture is such that the majority of excess protons are located in the central part of the hydrated hydrophilic nanochannels. In this region, the water is bulklike (for not too low degrees of hydration) with local proton transport properties similar to those described for water in Section 3.1.1.1.1. Therefore, the transport properties are indeed a function of the considered length and time scales,^{224,225} and the activation enthalpies of both proton mobility and water diffusion are similar to those of bulk water and only increase slightly with decreasing degree of hydration for intermediate water contents (Figure 9).^{197,224,226–228}

Apart from the slight retardation of proton mobility (D_p) and water diffusion (D_{H_2O}) within the hydrophilic domain, the decrease in the transport coefficients with decreasing degree of hydration mainly reflects on the decreasing percolation within the waterlike domain. At the highest degrees of hydration, the major proton conduction mechanism is structure diffusion ($D_s > D_{H_2O}$, Figure 9). With decreasing water content, the concentration of excess protons in the aqueous phase is increasing, which, in turn, increasingly suppresses intermolecular proton transfer and, therefore, structural diffusion, as witnessed in aqueous solutions¹⁴¹ (see Figure 2 and Section 3.1.1.1.1). Consequently, proton mobility at intermediate and low degrees of hydration is essentially vehicular in nature. Nonequilibrium statistical mechanics-based calculations (see Section 2.3) of the proton self-diffusion coefficients in Nafion and PEEKK membranes over a range of hydration conditions have addressed this conductivity contribution, and they clearly show that the diffusion of water (vehicle) and hydrated protons (H_3O^+) are retarded, as a result of confinement in an environment where the water and protons are perturbed by the presence of a substantial density of sulfonate (i.e., negative charge) groups.^{45,46} These calculations also showed that structure diffusion contributes to the diffusion of protons at the higher water contents (i.e., > 13 water molecules per sulfonic acid group; see Section 2.4).^{20,22,23} The very high conductivity activation volumes (conductivity decreases with applied pressure ($-kT \partial \ln \sigma / \partial \ln p$)), which are particularly evident in well-separated perfluorosulfonic acid polymers

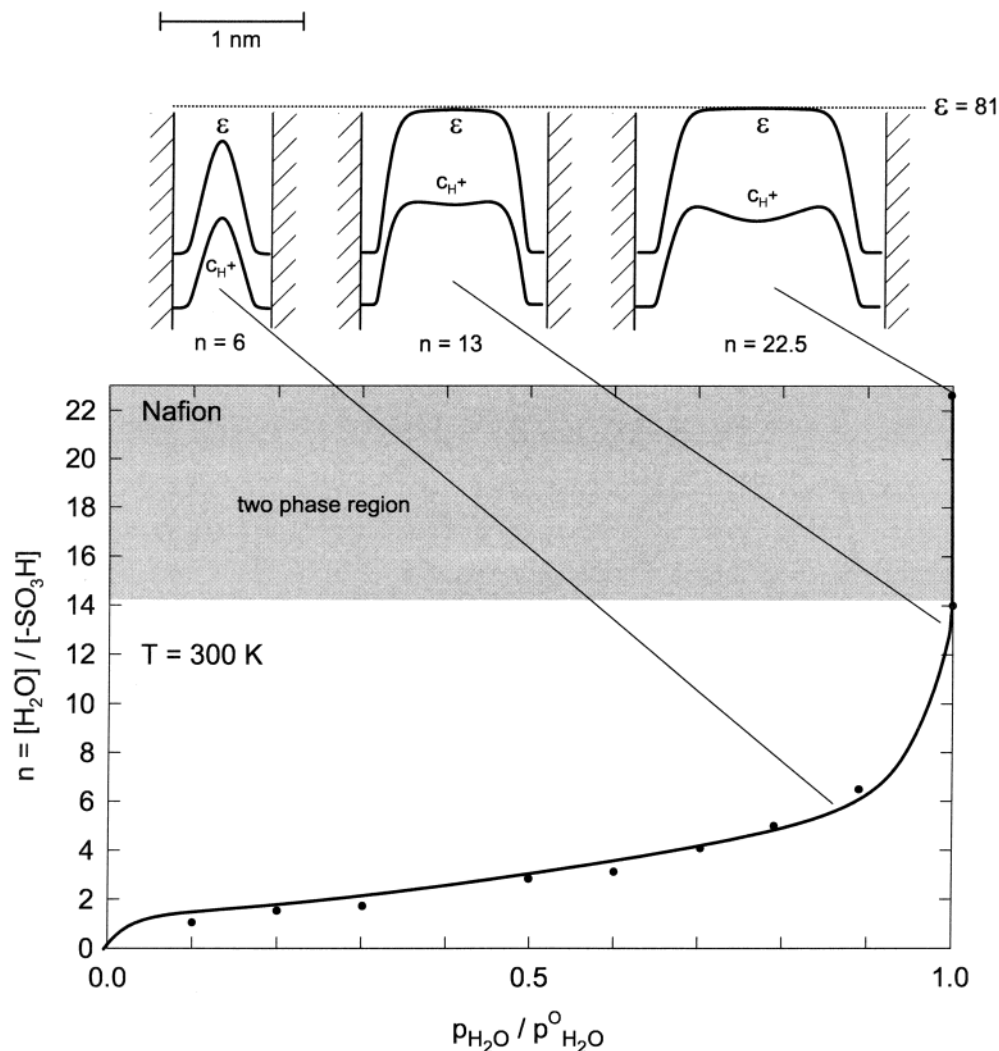


Figure 8. Hydration isotherm for Nafion 117 (equivalent weight (EW) of 1100 g/equiv)¹⁹⁷ and the distribution of the dielectric constant²³ and protonic charge carrier concentration across the hydrated hydrophilic channels (pores) for three different water contents (top).

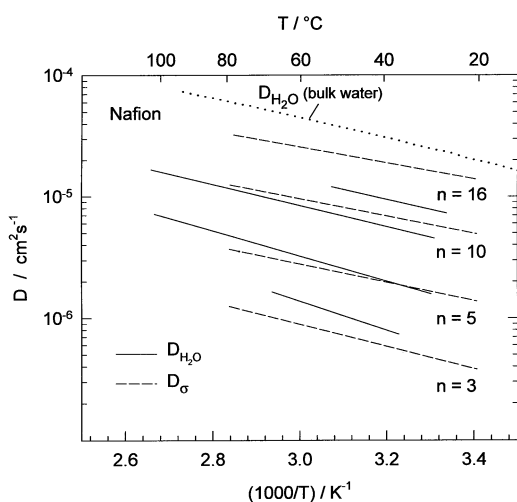


Figure 9. Proton conductivity diffusion coefficient (mobility) and water self-diffusion coefficient of Nafion 117 (EW = 1100 g/equiv), as a function of temperature and the degree of hydration ($n = [H_2O] / [-SO_3H]$).¹⁹⁷

(Nafion, Dow),²¹⁶ may then also be understood as a confinement effect. Pressure probably leads to an increasing dispersion of the water, i.e., the hydro-

phobic and hydrated hydrophobic domains are “squeezed” into each other, forming a more dendritic microstructure with narrower hydrophilic channels. This view explains straightforwardly why conductivity activation volumes in less-separated (better-dispersed) hydrocarbon-based membranes²¹³ are significantly smaller. As long as the confinement does not fall below ~ 1 nm, the water at the center of the channels may still be bulklike (Figure 8), and the diffusion of hydrated protons has a large hydrodynamic component with significant long-range velocity correlations, typical for viscous media. This feature will be addressed later in this article to explain the unusually high electro-osmotic drag coefficients (Section 3.2.1.1).

For very low degrees of hydration (i.e., for Nafion membranes with < 6 water molecules per sulfonic acid group), the decreasing solvent (water) activity leads to a decreasing dissociation of the sulfonic acid group, i.e., an increasing exclusion of protons from the transport in the aqueous phase. Changes in the neighboring chemical group to the sulfonic acid (i.e., changing from a perfluoro methylene to an aromatic carbon: Nafion to S-PEK) will also affect the dissociation and separation of the proton from the acidic group.²⁰ This effect is dependent not only on the

acidity of the sulfonic acid group, but also on the dielectric constant of the water of hydration. With this understanding, the significant decrease of conductivity in the presence of methanol,²¹⁹ which actually exhibits similar self-diffusion coefficients as water (see Section 3.2.1.1) but with a lower dielectric constant, may then be explained by increased ion pairing (decreasing dissociation).

3.1.2.2. Adducts of Basic Polymers with Oxo-acids. To date, the most relevant materials of this type are adducts (complexes) of polybenzimidazole (PBI) and phosphoric acid, as introduced by Wainright et al.²²⁹ In contrast to water, which exhibits a high mobility for protonic defects but a very low intrinsic concentration of protonic charge carriers, phosphoric acid shows both high mobility and a high concentration of intrinsic protonic defects (see Section 3.1.1.2). In other words, phosphoric acid is intrinsically a very good proton conductor with a very small Debye length, and its charge carrier density is hardly affected by the interaction with PBI. Indeed, a strong acid/base reaction occurs between the nonprotonated, basic nitrogen of the PBI repeat unit and the first phosphoric acid absorbed. The transfer of one proton leads to the formation of a benzimidazolium cation and a dihydrogenphosphate anion, forming a stable hydrogen-bonded complex, as shown by infrared spectroscopy.^{230,231} It is a common observation for all systems of this type that their conductivity strongly increases upon further addition of an oxo-acid approaching the conductivity of the pure acid for high acid concentrations (recently free-standing films of PBI·*n*H₃PO₄ with extremely high acid-to-polymer ratios of > 10 have been reported).²³² In particular, there is no indication of participation of the polymer in the conduction process (also see discussion below).

Although no microstructural information is available to date, the macroscopic transport has been investigated in the related system of poly(diallyldimethylammonium-dihydrogenphosphate) and phosphoric acid, (PAMA⁺ H₂PO₄⁻)·*n*H₃PO₄.²³³ The proton mobility (D_o) and the self-diffusion coefficient of phosphorus (D_p), as a measure of the hydrodynamic diffusion of the system, is shown in Figure 10 for a given temperature, as a function of the polymer/acid ratio. Similar to pure phosphoric acid, the mobility of protonic charge carriers is significantly higher than the self-diffusion coefficient of the phosphate species and both transport coefficients decrease with increasing polymer content virtually in the same manner. The main effect, obviously, is just the decreasing percolation within the liquidlike portion of the phosphoric acid domain, which is reminiscent of the situation in hydrated acidic polymers (see Figure 6). At very small acid contents, when all the phosphoric acid is immobilized in the 1:1 complex, only very little conductivity is left.

Similar to that observed for pure phosphoric acid, the transport properties of PBI and phosphoric acid are also dependent on the water activity, i.e., on the degree of condensation (polyphosphate formation) and hydrolysis. There is even indication that these reactions do not necessarily lead to thermodynamic equilibrium, and hydrated orthophosphoric acid may

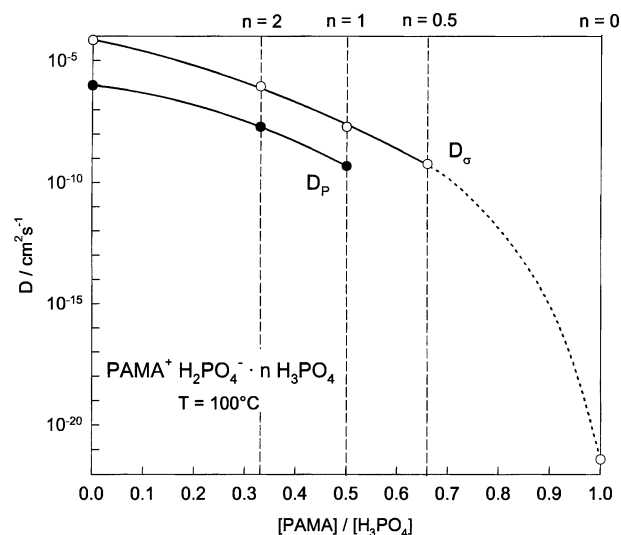


Figure 10. Proton conductivity diffusion coefficient (mobility) and self-diffusion coefficient of phosphorus for poly(diallyldimethylammonium-dihydrogenphosphate)–phosphoric acid ((PAMA⁺H₂PO₄⁻)·*n*H₃PO₄), as a function of the phosphoric acid content.²³³ Note that the ratio D_o/D_p remains almost constant (see text).

coexist with polyphosphates in heterogeneous gel-like microstructures.²³² Not much is known on the mechanism of proton transport in polymer adducts with polyphosphates and/or low hydrates of orthophosphoric acid. The determination of whether the increased conductivity at high water activities is the result of the “plasticizing effect” of the water on the phosphate dynamics and thereby assisting proton transfer from one phosphate to the other, or whether the water is directly involved in the conduction mechanism, has not been elucidated.

3.1.2.3. Separated Systems with Immobilized Proton Solvents. Both types of heterogeneous systems discussed previously are comprised of a polymeric domain and a low-molecular-weight liquidlike domain (e.g., H₂O, H₃PO₄) with weak ionic or hydrogen-bond interaction between the two domains. Apart from other polar solvents, heterocycles such as imidazole, pyrazole, and benzimidazole have been intercalated into sulfonated polymers,^{170,171,234,235} resulting in similar transport properties, as discussed for the hydrated systems in Section 3.1.1.1, although at somewhat higher temperatures. Apart from the proton donor and acceptor sites (N), such solvents contain additional sites (C), which may be used for covalent “grafting” to oligomeric or polymeric structures. If these are hydrophobic (nonpolar), a similar separation as that described in Section 3.1.1.1 may occur, however with covalent bonding bridging the nonpolar/polar “interface”. This approach has been implemented to obtain systems with completely immobilized proton solvents that still exhibit high proton conductivity with structure diffusion as the sole proton conduction mechanism (see Figure 3). Of course, the covalent bonding across the nonpolar/polar interface mediates a significant influence of the nonpolar portion of the structure on the structure and dynamics of the polar proton-conducting domain. This cannot be approximated by simple percolation effects, as discussed for adducts of basic polymers

with oxo-acids (see also Figure 10), but rather in a more complex fashion, involving (i) the position and character of the covalent bonding between the polar solvent and the nonpolar portion of the structure, (ii) the softness of this structure, and (iii) the volume fraction of the polar solvents.

As described in Section 3.1.1.3, the two nitrogens of the heterocycles act equally as proton donors or acceptors. Any covalent immobilization must avoid reduction of this symmetry, which is best achieved using the carbon between the two nitrogens (i.e., C2 in imidazole or C4 in pyrazole) for covalent bonding. Interestingly, this is not the case in histidine, which is an imidazole containing amino acid, which is frequently involved in proton translocation processes. However, the energetic asymmetry is very small (~ 20 meV) in this particular case.²³⁶ The type of bonding seems to be much more important, i.e., only single bonds allow reorientation of the bonded heterocycle, which is a persistent element in the proton conduction mechanism (see Section 3.1.1.3). To minimize the constraints in the dynamical aggregation of the heterocycles, immobilization via flexible spacers, such as alkanes or ethylene oxide (EO) segments, seems to be favored.^{213,237} The optimum spacer length is then given by the optimum balance between heterocycle aggregation and heterocycle density, on one hand, and the dynamics of the hydrogen bond network formed by the heterocycles on the other hand. The compound 2,2'-bis(imidazole), which is a brittle solid with a high melting point, is perfectly aggregated by strong static hydrogen bonding with negligible proton conductivity (according to recent results from the laboratories of one of the authors). Separating the two imidazoles by a soft EO spacer leads to the appearance of significant proton conductivity and a decrease in the melting point and glass-transition temperature (T_g) with increasing spacer length.^{238,239} The conductivity then displays typical VTF behavior and, for a given concentration of excess protons (dopant), it is very similar for all spacer lengths when plotted versus $1/(T - T_0)$, where T_0 is closely related to T_g . For very high spacer lengths, the dilution of the heterocycles by the spacer segments has a tendency to reduce aggregation of the heterocycles and, therefore, once again, reduce proton mobility.

The aggregation of imidazole leading to a continuous hydrogen-bonded structure in crystalline Imi-2 (two imidazole units spaced by two EO repeat units) is shown in Figure 11a.²³⁸ Upon melting, the situation in most parts of the material is more similar to that shown in Figure 11b. This is one result coming from an NMR study²⁴⁰ demonstrating that liquid Imi-2 exhibits ordered domains (similar to the crystalline form), a dynamically disordered but still aggregated domain, and a certain fraction of nonbonded molecules. It is only within the disordered domain (Figure 11b) that fast proton mobility is observed, again demonstrating the delicate balance of aggregation and dynamics in hydrogen-bonded structures with high proton mobility.

Another interesting observation is that heterocycles immobilized in this way may still form dy-

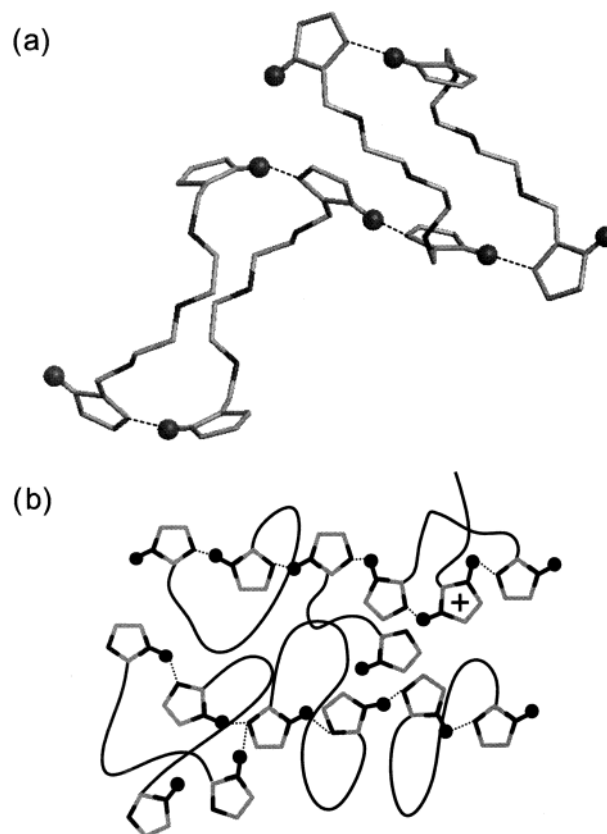


Figure 11. Hydrogen-bonded structure of Imi-2 (two imidazoles spaced by two ethylene oxide (EO) repeat units): (a) in the crystalline state, as revealed by an X-ray structure analysis,²³⁹ and (b) in the liquid state (schematic), as suggested by an NMR study.²⁴⁰ Note that the hydrogen bonds in the solid state are long-lived, whereas the hydrogen bonding in the molten state is highly dynamic (see text).

namical hydrogen-bond networks with very high proton mobility, although the self-diffusion of the heterocycle is significantly retarded. In the systems described previously, D_σ is typically 1 order of magnitude greater than D_{Imi} . Recently, fully polymeric systems with side-chain architectures have been developed that still exhibit high proton mobility, despite complete long-range immobilization of imidazole, i.e., $D_\sigma/D_{\text{Imi}} = \infty$.²⁴¹ This finding is of paramount importance, because it demonstrates that complete decoupling of the long-range transport of protons and heterocycles (the proton solvent) is possible. The reader may recall that complexation of phosphoric acid and a basic polymer does not show any signature of this effect (see Figure 10), which may open the way to the development of true single ion conductors.

One of the problems associated with the use of heterocycles is that the intrinsic concentration of protonic charge carriers can only be moderately increased through acid doping (also see Section 4.3). This is particularly the case when the dynamics within the hydrogen-bonded domain is highly constrained through immobilization (especially in fully polymeric systems), which is probably the direct consequence of a reduced dielectric constant. This also leads to a further increase of the Haven ratio

D_H/D_o , as discussed in Section 3.1.1.3 (also see Figure 4).

Also note that the spacer concept, as verified by several laboratories (e.g., see Perrson and Jannasch²⁴²), has been moved forward to the immobilization of other proton solvents such as phosphonic acid, with very promising results (see Section 5).

3.1.2.4. Composites. Because of the drawbacks in hydrated acidic polymers for application in fuel cells, composites with highly dispersed inorganic phases have also been investigated, and, indeed, certain systems show improved performance in operating fuel cells.^{243,244} The extent that this is due to a modification of the bulk transport properties (in particular, the proton conduction mechanism) or of the membrane/electrode interface has not been conclusively determined. However, the similarities of the bulk transport properties of some modified and unmodified ionomers (see Section 4.1) are indicative of the possible relevance of interfacial effects. In view of the attention such systems are attracting at the moment, some general aspects are summarized here (for a review on the different type of systems, see, e.g., refs 245 and 246). Such composites are usually formed by either dispersing inorganic particles in a solution of the ionomer, followed by film casting and solvent elimination, or by precipitation of inorganic particles within a pre-existing membrane. The latter procedure was first used by Mauritz²⁴⁷ to precipitate SiO₂ particles in Nafion using in situ hydrolysis of tetraethoxysilane (TEOS). Although SiO₂ does not show measurable proton conductivity itself, other inorganic compounds, such as diverse zirconium phosphates and phosphonates or heteropolyacids,^{245,248} have recently been used as fillers. Although these materials possess some intrinsic proton conductivity, it is much lower than that of the ionomeric host (e.g., Nafion) at low temperatures and high humidities. This is also true for the hydrophilicity ("water-retaining properties") of such inorganic particles, which is frequently thought to be responsible for the favorable performance of the corresponding composites in fuel cells.^{234,249} There is actually no experimental evidence for this, and the strong acidity of perfluorosulfonic acid polymers is not expected to be exceeded by any of the aforementioned inorganics. Of course, this does not hold for the water uptake in contact with liquid water, which is sometimes taken as a measure of the water-retaining properties.^{250–252} The higher water uptake under these conditions may be the result of the reduction of the tensile strength of the polymer in the composite, allowing more water to enter as a second phase (which is actually not retained by any specific interaction). The most important effect of filling an ionomer with inorganic particles is probably the modification of the membrane/electrode interface (see above), the microstructure and the elastic properties of the ionomeric component (with a glass transition temperature of $T_g \approx 120$ °C for plain Nafion, the latter may be a specific advantage of the use of composite membranes in this temperature range). These changes may also alter the transport properties in a similar way as discussed for the relationships between microstructure and

transport in plain ionomers (see Sections 3.1.2.1 and 3.2.1). Particularly, in the case of proton-conducting zirconium phosphate prepared via in situ growth within the preformed membrane,²⁵³ the proton conductivity of the highly dispersed filler may have some significance at high temperature and low humidity, where the conductivity of pure Nafion strongly decreases.²⁴⁵

3.2. Mechanisms of Parasitic Transport

The transport of protonic charge carriers is sometimes inherently connected to the transport of other species (e.g., in hydrated acidic polymers, Section 3.1.2.1). Sometimes, there are just indirect mechanistic relationships, or the existence of completely independent transport paths (e.g., protonic charge carriers and electronic holes in oxides). Parasitic transport frequently limits the fuel-cell performance, and a mechanistic understanding is definitely useful in the development of separator materials.

The advantageously low methanol "crossover" of PBI–H₃PO₄ adducts is well-established and the problems related to its low oxygen transport are also well-described.²⁵⁴ However, the fundamentals of these transport phenomena have not been subjected to any systematic investigation. For the recently emerging systems based on heterocycles and other proton solvents (also see Section 5), the investigation of parasitic transport is only just beginning. On the other hand, there is extensive literature on parasitic transport in the widely used hydrated acidic ionomers (especially Nafion). In addition, the transport properties of oxides have also been intensely investigated by groups mainly outside the fuel-cell community.

Therefore, the following discussion of the mechanisms of parasitic transport is restricted to only these two classes of materials.

3.2.1. Solvated Acidic Polymers

As discussed in Section 3.1.2.1, proton transport in acidic polymers occurs within a system of hydrated and connected hydrophilic pores (channels) within the nanoseparated materials. The extension of the channels, which, of course, shows some distribution within a given sample, may range from <1 nm to several nanometers, depending on the type of polymer and the degree of solvation (swelling). This range covers the transition from more solidlike behavior with diffusive transport to a liquidlike regime with additional hydrodynamic transport (viscous flow). Apart from protonic defects, the main species that are confined to the hydrophilic domains are water and methanol (used as the fuel in DMFCs). The transport of these species is highly correlated and therefore discussed together in the following section. The transport mechanisms of fuel-cell relevant gases (O₂, H₂), which may dissolve in the water domains and also in other parts of the nanostructures, are also reviewed in this section.

3.2.1.1. Mechanisms of Solvent (Water, Methanol) Transport. The following types of transport are considered in this section: (i) self-diffusion or tracer diffusion of solvent molecules, which is the unidirec-

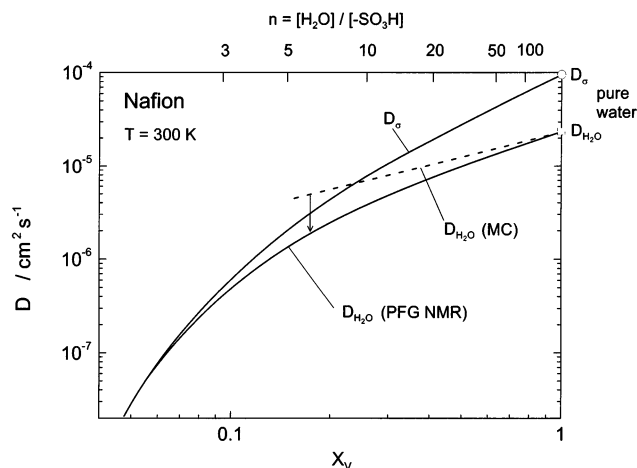


Figure 12. Water self-diffusion coefficient of Nafion 117 (EW = 1100 g/equiv), as a function of the water volume fraction X_V and the water diffusion coefficient obtained from a Monte Carlo (MC) simulation (see text). The proton conductivity diffusion coefficient (mobility) is given for comparison. The corresponding data points are displayed in Figure 14.

tional transport of “marked species” (e.g., this may be an isotopic tracer or the spin-labeled nuclei in PFG NMR experiments) with the thermal energy as the only driving force; (ii) chemical or Fickian diffusion, which is the average drift of a component i in a chemical potential (approximately proportional to $\ln a_i$ or $\ln p_i$) gradient of the particular component related to the concentration gradient via the thermodynamical factor ($d(\ln a_i)/d(\ln c_i)$); and (iii) permeation, which is the flow of a component (frequently solvent) in a total pressure gradient. Following this, the mechanisms of electro-osmotic drag are reviewed. This is the coupled transport of a protonic species and solvent molecules, i.e., the transport of neutral solvent in an electrical field with a vanishing gradient in the chemical potential. This phenomenon is symmetrical to the transport of protons in a chemical potential gradient of solvent in the absence of any electrical field. The coupling of water and methanol transport has not been studied explicitly; however, there is indirect indication of the nature of this coupling, which will also be discussed.

The self-diffusion coefficient of water in Nafion, as measured by PFG NMR,^{197,224,226,255–261} is shown in Figure 12, as a function of the water volume fraction. At high degrees of solvation, this is only slightly lower than the diffusion coefficient obtained from MC simulations of random walk transport within nanostructures parametrized by results of SAXS experiments^{174,212,213} (see Figure 13) assuming the absence of any dead-end channels and a local diffusion coefficient that is identical to the bulk diffusion coefficient of water ($2.25 \times 10^{-5} \text{ cm}^2/\text{s}$) at any position within the well-connected hydrophilic domain. This finding suggests that the major reason for a decrease in the water diffusion coefficient with decreasing water content is the decreasing percolation within the hydrophilic domain, especially at high water contents (also see Section 3.1.2.1). This is also supported by the observation that methanol diffusion follows the same trend (Figure 14a),^{174,262,263} but with somewhat

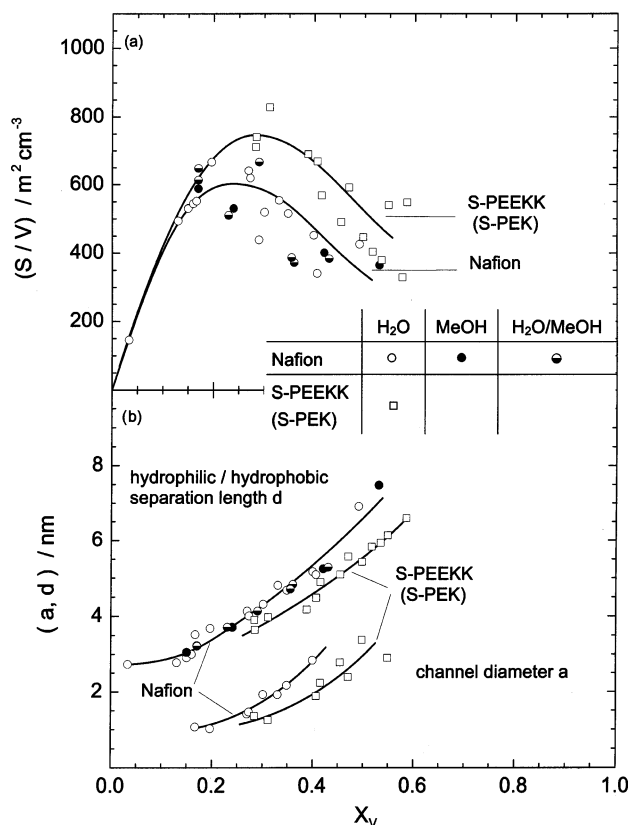


Figure 13. A few microstructural parameters for Nafion and sulfonated poly(arylene ether ketone)s,^{174,208–213} as a function of the solvent (water and/or methanol) volume fraction X_V : (a) the internal hydrophobic/hydrophilic interface, and (b) the average hydrophobic/hydrophilic separation and the diameter of the solvated hydrophilic channels (pores).

lower diffusion coefficients that correspond to the lower self-diffusion coefficient in bulk methanol compared to that in bulk water. At low water contents, however, the experimental diffusion coefficient falls off more rapidly than the simulated one (see Figure 12). One reason is simply the fact that the connectivity within the solvated hydrophilic domains decreases (appearance of dead-end channels, pockets).^{212,213} Another reason is the retardation of water diffusion as a result of increasing confinement, which increases the internal molecular friction within the solvated domain as discussed above (see Sections 3.4 and 3.1.2.1).^{41–46} A comparison of Figures 12 and 13 suggests that this effect becomes particularly evident when the diameter of the channel decreases to $<1 \text{ nm}$.

For comparison purposes, the proton mobility, D_o (for Nafion solvated with water), which is closely related to the self-diffusion coefficient of water, is also plotted. At low degrees of hydration, where only hydrated protons (e.g., H_3O^+) are mobile, it has a tendency to fall below the water diffusion coefficient (this effect is even more pronounced in other polymers), which may be due to the stiffening of the water structure within the regions that contain excess protons, as discussed in Section 3.1.1.1.¹⁴⁸ Interestingly, the proton mobility in Nafion solvated with methanol ($D_o(\text{MeOH})$ in Figure 14a) is even lower than the methanol self-diffusion (D_{MeOH}). This may

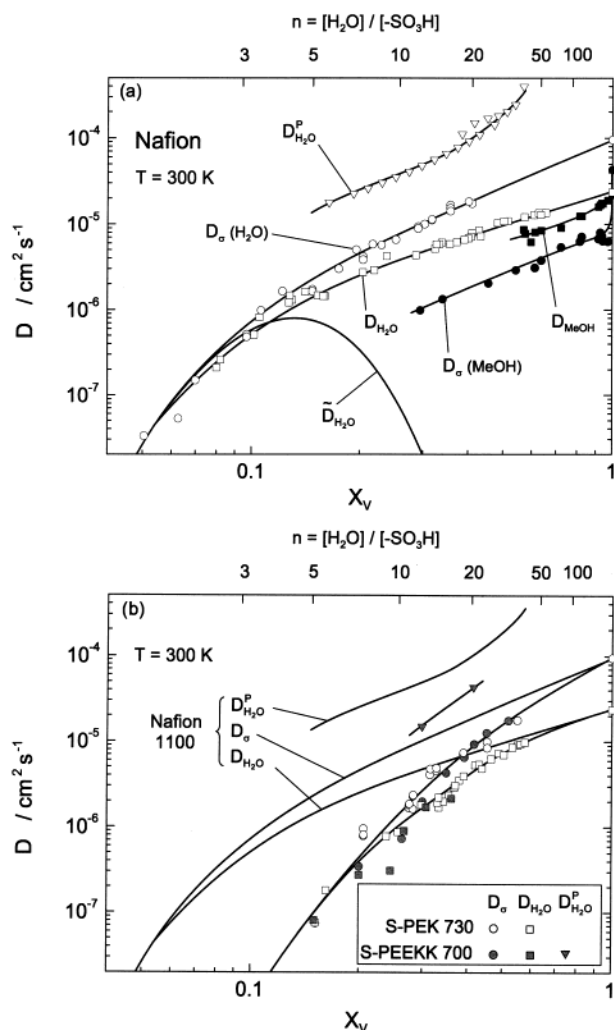


Figure 14. Solvent (water, methanol) diffusion coefficients of (a) Nafion 117 (EW = 1100 g/equiv) and (b) sulfonated poly(arylene ether ketone)s, as a function of the solvent volume fraction. Self-diffusion data ($D_{\text{H}_2\text{O}}$, D_{MeOH}) are taken from refs 197, 224, 226, 255–263 and unpublished data from the laboratory of one of the authors; chemical diffusion coefficients ($\tilde{D}_{\text{H}_2\text{O}}$) are calculated from self-diffusion coefficients (see text), and permeation diffusion coefficients are determined from permeation coefficients.^{212,267,268} Proton conductivity diffusion coefficients for hydrated samples ($D_s(\text{H}_2\text{O})$)^{197,224,226,255–261} and samples solvated with methanol ($D_s(\text{MeOH})$)²⁵⁶ are given for comparison.

be the consequence of the lower dielectric constant of methanol, compared to water, especially under the condition of confinement in a perfluorinated ionomer (see discussion in Section 3.1.2.1 and Figure 8).

When it comes to the equilibration of water concentration gradients, the relevant transport coefficient is the *chemical diffusion coefficient*, $\tilde{D}_{\text{H}_2\text{O}}$. This parameter is related to the self-diffusion coefficient by the thermodynamic factor (see above) if the elementary transport mechanism is assumed to be the same. The hydration isotherm (see Figure 8) directly provides the driving force for chemical water diffusion. Under fuel-cell conditions, i.e., high degrees of hydration, the concentration of water in the membrane may change with only a small variation of the chemical potential of water. In the two-phase region (i.e., water contents of >14 water molecules

per sulfonic acid), any driving force for Fickian water diffusion vanishes, i.e., there is no chemical diffusion. A fitting expression of $\tilde{D}_{\text{H}_2\text{O}}$ is given in ref 264; $\tilde{D}_{\text{H}_2\text{O}}$ data, calculated from $D_{\text{H}_2\text{O}}$ data with thermodynamic factors obtained from the hydration isotherm (Figure 8), are plotted in Figure 14a. There are very few direct measurements of $\tilde{D}_{\text{H}_2\text{O}}$ for water available. Frequently, pervaporation-type experiments are conducted, where the membrane is exposed to liquid water (methanol) on one side and dry flowing nitrogen on the other side.²⁶⁵ A chemical diffusion coefficient may be calculated from the rate of water (methanol) uptake. However, because of the extreme solvent chemical potential difference across the membrane and the thermodynamically poorly defined situation on the gas side, only average, poorly reproducible chemical diffusion coefficients are obtained; i.e., any information on the concentration dependence is lost. Another complication with these experiments is that the total pressure gradient across the membrane induces permeation, which may have contributions from additional transport mechanisms, as will be discussed later. Particularly, in the case of measuring the chemical diffusion of methanol, this problem is elegantly avoided through the use of aqueous solutions of different methanol concentration (activities) on both sides.²⁶⁶ Many other techniques, which are frequently governed by different water (methanol) transport mechanisms (in a complex fashion), have been reviewed by Doyle and Rajendran.²⁶⁴

The driving force for *solvent permeation* is the total pressure gradient across the membrane, which is related to the chemical potential gradient, according to

$$\nabla \bar{\mu}_s = \left(\frac{\partial \mu_s}{\partial p} \right) \nabla \bar{p} = V_s^m \nabla \bar{p} \quad (24)$$

which leads to the following relation between permeation and diffusion:²¹²

$$D_s^p = \frac{RT}{c_s} \left(\frac{P_s}{V_s^m} + \frac{K_{\text{drag}} \sigma}{F^2} \right) \quad (25)$$

where P_s is the permeation coefficient and K_{drag} is the electro-osmotic drag coefficient (discussed below). The most comprehensive water permeation study for Nafion, as a function of water content and temperature, was reported by LaConti et al.²⁶⁷ and Meier et al.²⁶⁸ The diffusion coefficients D_s^p (when adjusted to room temperature) are ~ 1 order of magnitude higher than the diffusion coefficients obtained by NMR techniques (Figure 14a). The “permeation diffusion coefficient” has a tendency to approach the self-diffusion coefficient only at low water contents. This behavior is not expected if the elementary mechanisms of the two types of transport are the same (i.e., quasi-random walk processes exploring the solvent chemical potential distribution in space). Obviously, there is an additional transport component in the permeation mechanism. This is most likely viscous flow far away from local thermodynamic equilibrium, which may also comprise a certain “slip” at the interface with the hydrophobic

domain, which is a well-established phenomenon in hydrodynamics. This Hagen–Poiseuille-type component in the flow is, of course, expected to be strongly dependent on the diameter of the solvated “channels” (see Figure 13). The observation that this component apparently decreases as the water content decreases and virtually disappears in membranes with very narrow channels and strong polymer–solvent interactions (see Figure 14b and Section 4.1) is consistent with this interpretation. Hence, the mechanism of permeation in solvated acidic membranes may be described by a combination of diffusional processes and viscous flow, where the latter contribution increases as the solvent–polymer interaction decreases and the “channel” width (i.e., the degree of hydration and hydrophilic/hydrophobic separation) increases.

The aforementioned view provides a rationale for the distinct differences of the solvent transport coefficients of Nafion and solvated sulfonated polyarylenes (Figure 14b), which are generally less-separated and exhibit stronger polymer–solvent interactions.

Although solvents such as water and methanol are virtually uncharged, the application of an electrical field may induce a drift velocity of such neutral species when solvating an acidic ionomer. This phenomenon, which is known as *electro-osmotic drag*, is the consequence of the interaction of such solvent molecules with ions they solvate, in particular, protons in the case of PEMs. The classical mechanistic theory of electro-osmosis dates back to the time of Helmholtz,²⁶⁹ Lamb,²⁷⁰ Perrin,²⁷¹ and Smoluchowski,²⁷² who assumed that transport occurs only close to the wall in electrical double layers of low charge-carrier concentration and with extensions significantly smaller than the pore (channel) diameter. The corresponding theories qualitatively describe the electro-osmotic drag in wide pore systems, such as clay plugs; however, as discussed in Section 3.1.2.3 (also see Figure 8), both model assumptions are not valid for typical PEM materials such as Nafion. The width of the hydrated (solvated) channels is orders of magnitude smaller than the Debye length of water and the concentration of charge carriers is very high (typically ~ 5 M within the hydrophilic domain). For this type of system, Breslau and Miller developed a model for electro-osmosis from a hydrodynamic point of view.²⁷³ The model treats the ions as spherical particles moving in a continuous viscous medium, with the membrane matrix forming the boundary of the medium. The hydration of the ions is treated by an adequate choice of a hydrated ion radius, stripping off the hydration sphere in narrow channels, and the water structure forming and breaking properties of diverse ions are considered. Channel diameters were not directly accessible by the authors; therefore, the electro-osmotic transport of tetraalkylammonium-exchanged membranes were used to determine an “effective” pore size. Although the assumptions of the model are severe simplifications of the situation in real membranes (heterogeneity of charge and viscosity distribution (also see Figure 8) and channel widths of the extension of only a few molecules), the

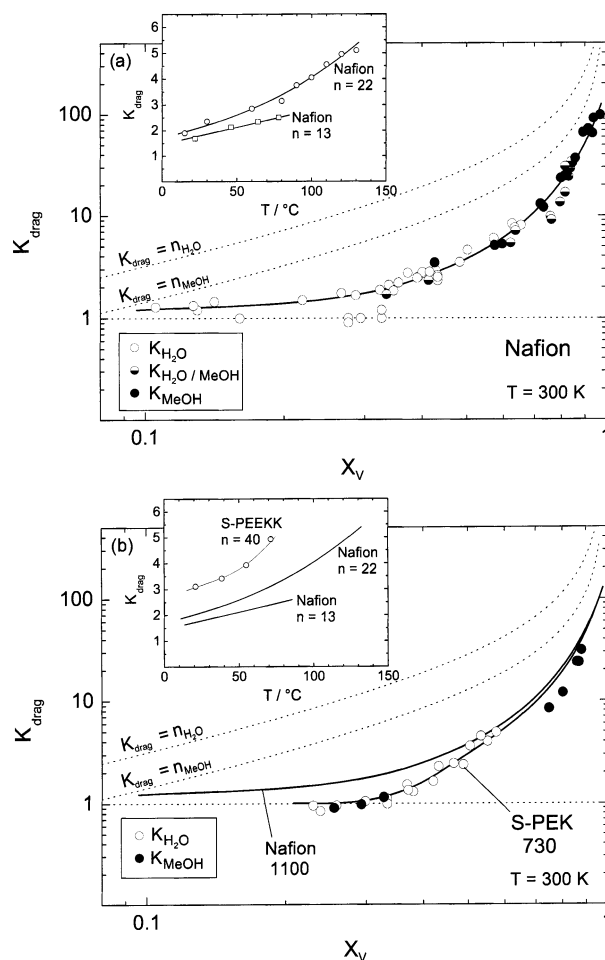


Figure 15. Electro-osmotic drag coefficients K_{drag} of (a) Nafion 117 (EW = 1100 g/equiv) and (b) sulfonated poly(arylene ether ketone)s, as a function of the solvent (water and/or methanol) volume fraction X_V .^{174,212,219,274–281} The normalized drag coefficients for water and methanol are virtually identical; therefore, both are plotted together.

model describes the variation of the electro-osmotic drag within model membranes (polystyrene-based) of different ionic forms surprisingly well.

The data were obtained for given degrees of hydration. Also, for PEM fuel-cell membranes, experimental electro-osmotic drag coefficients are generally reported only over narrow solvation ranges. Typical drag coefficients in the range of 1–2.5 at room temperature (expressed in the number of water molecules per transported protonic charge carrier) were sometimes identified with the number of water molecules solvating the excess proton. Recently, electro-osmotic drag coefficients became accessible by electrophoretic NMR^{174,212,219,274} for a wide range of polymer–solvent volume ratios, and the results clearly confirm the hydrodynamic nature of electro-osmosis, particularly at high degrees of solvation. The data¹⁷⁴ presented in Figure 15, together with data from other authors,^{275–281} essentially show two things: (i) at low degrees of hydration, the electro-osmotic drag coefficient approaches a value of 1 but does not fall below this value; and (ii) with increasing solvent fraction (channel width, Figure 13), the drag coefficient dramatically increases and reaches $\sim 50\%$ of the maximum possible value (dashed line), which corresponds to an identical drift velocity of all solvent

molecules and protonic charge carriers. Considering the fact that, at high degrees of hydration, approximately half of the conductivity is carried by structure diffusion (see Section 3.1.2.1), i.e., the proton mobility (proton self-diffusion coefficient) is about twice the water self-diffusion coefficient, almost all water molecules appear to drift at approximately identical velocity (about half of the drift velocity of protonic charge carriers) in extremely swollen samples. This situation corresponds to minor relative motion of water molecules with respect to each other, i.e., the transport is clearly of a collective nature. The decrease of the drag coefficient with decreasing water content approximately scales with the fourth power of the channel diameter, which is reminiscent of Hagen–Poiseuille-type behavior with continuously increasing “stripping off” of the water molecules. This stripping comes to an end at low degrees of hydration, where the motion of one water molecule remains strongly coupled to the motion of the excess proton ($K_{\text{drag}} \approx 1$; see Figure 15). This is also expected from the high enthalpy of primary hydration (stability of H_3O^+) and the proton conduction mechanism (Section 3.2.1.2), i.e., diffusion of H_3O^+ (vehicle mechanism).

Extremely high degrees of swelling were actually obtained in water/methanol mixtures; and the drag coefficients of water and methanol were determined separately by isotopic labeling (H/D substitution). Interestingly, the normalized drag coefficients (drag coefficient K_i divided by the mole fraction of the corresponding species i) are virtually identical for both species in the mixtures (also see Figure 15). Because water and methanol form almost-ideal solutions with comparable water–water, water–methanol, and methanol–methanol interactions, this behavior provides additional support for a hydrodynamic process. For low degrees of hydration, where electro-osmotic drag becomes diffusional in nature, it is not yet clear, whether there is some preferential solvation of the excess proton by water or methanol (primary hydration). Figure 15b shows that the electro-osmotic drag for sulfonated poly(arylene ether ketone)s is generally lower than that for Nafion, which is partly due to smaller channels. However, even for comparable channel dimensions, the values for electro-osmotic drag are still somewhat lower, which is an indication of the influence of the solvent–polymer interaction on the total electro-osmotic drag. This is also supported by the observation that electro-osmotic drag is generally increasing with increasing temperature (see inserts in Figures 15a and b), whereas the solvent–polymer interaction is decreasing.

There is no quantitative model yet describing the observed electro-osmotic drag coefficients as a function of the degree of hydration and temperature. However, the available data provide strong evidence for a mechanism that is (i) hydrodynamic in the high solvation limit, with the dimensions of the solvated hydrophilic domain and the solvent–polymer interaction as the major parameters; and (ii) diffusive at low degrees of solvation, where the excess proton essentially drags its primary solvation shell (e.g., H_3O^+).

3.2.1.2. Mechanisms of Dissolved Gas Transport. As noted in Section 1, one of the cardinal properties of fuel-cell membrane materials is to be able to effectively separate the reactive masses, in particular, the anode and cathode gases. Accordingly, there have been numerous investigations, especially on oxygen and hydrogen transport across PEMs, and because the current qualitative mechanistic understanding has already existed for some time, only a brief summary is given here.

It already had been recognized by Yeo and McBreen²⁸² that gas (hydrogen and halogens) permeation rates in Nafion are strongly related to water content. The data indicated that most of the gas transport is occurring within the solvated hydrophilic domain at rates only slightly lower than these of water self-diffusion. Ogumi and co-workers^{283,284} later reported that oxygen diffusion in different hydrated membranes are indeed very similar, with the gas solubilities differing significantly. These results made already clear that gases dissolve in both the hydrophobic and the solvated hydrophilic domain, whereas most of the gas transport occurs within the solvated hydrophilic domain. This view is supported by many experimental studies on Nafion^{285–287} and other types of membranes.^{288,289} When hydrated, they all show comparable diffusion and permeation rates for oxygen and hydrogen, and it was not surprising that significantly lower gas transport rates were found for Nafion when water was replaced by phosphoric acid²⁹⁰ or when Nafion was dried.²⁹¹ In the latter case, the gas diffusion rates were reported to be similar to those of plain polytetrafluoroethane (PTFE). Büchi et al.²⁹² actually separated the oxygen solubility and diffusion as a function of temperature for different perfluorinated proton exchange membranes of different equivalent weights. Apart from giving further support to the existing mechanistic understanding, this work showed that the oxygen solubility is decreasing while oxygen permeation is increasing with temperature.

3.2.2. Oxides

From the formation reaction of protonic defects in oxides (eq 23), it is evident that protonic defects coexist with oxide ion vacancies, where the ratio of their concentrations is dependent on temperature and water partial pressure. The formation of protonic defects actually requires the uptake of water from the environment and the transport of water within the oxide lattice. Of course, water does not diffuse as such, but rather, as a result of the ambipolar diffusion of protonic defects (OH'_o) and oxide ion vacancies (V''_o). Assuming ideal behavior of the involved defects (an activity coefficient of unity) the chemical (Fick's) diffusion coefficient of water is

$$\bar{D}_{\text{H}_2\text{O}} = \frac{(2 - X)D_{\text{OH}'_o}D_{V''_o}}{XD_{\text{OH}'_o} + 2(1 - X)D_{V''_o}} \quad (26)$$

where X is the degree of hydration.²⁹³ Under completely dry conditions, i.e., in the absence of proton conductivity, $\bar{D}_{\text{H}_2\text{O}}$ equals the self-diffusion coefficient

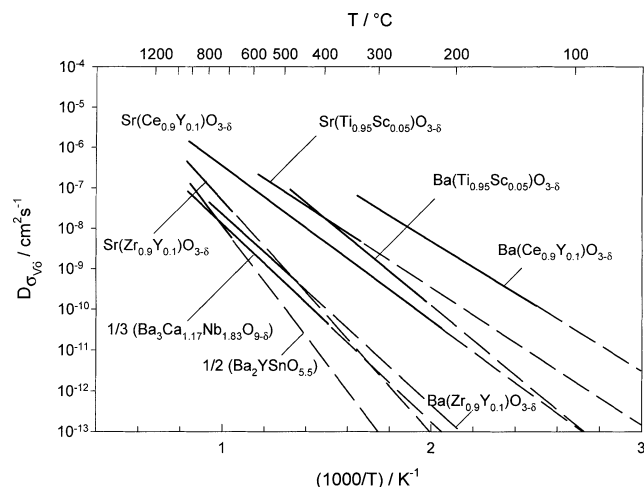


Figure 16. Self-diffusion coefficient of oxide ion vacancies in different perovskite-type oxides,¹⁸⁸ which equals the chemical water diffusion coefficient in the fully hydrated state (see text). (Figure reproduced with the kind permission from Elsevier.)

of protonic defects. However, near the hydration limit (i.e., X close to 1), $\bar{D}_{\text{H}_2\text{O}}$ approaches the self-diffusion coefficient of oxide ion vacancies, which is usually significantly lower than the diffusion coefficient of protonic defects. Because the latter case relates to the conditions in a fuel cell, the self-diffusion coefficient of oxide ion vacancies, which is shown in Figure 16 for a variety of perovskite-type oxides, may be taken as a measure of $\bar{D}_{\text{H}_2\text{O}}$ under these conditions. For a given water partial pressure, $\bar{D}_{\text{H}_2\text{O}}$ increases as temperature increases, because of dehydration and the increasing self-diffusion coefficients for both involved species. Recently, there has been some controversy about the validity of the model;²⁹⁴ however, it is indeed strictly valid in the entire hydration range under the given assumptions.²⁹⁵

It should be mentioned that, apart from oxide ion vacancies existing at low water partial pressures, the appearance of electronic holes (h^\bullet) must be considered at high oxygen activities. In oxides, they are frequently localized on the oxygen ($\text{O}^{2-} + h^\bullet \rightleftharpoons \text{O}^-$) and may be very mobile as large polarons. The ambipolar diffusion, together with protonic defects, then permits chemical diffusion of hydrogen; and the ambipolar diffusion, together with oxide ion vacancies, allows chemical diffusion of oxygen. However, for large-band-gap oxides relevant for fuel-cell applications, this may not be important at temperatures < 750 °C.^{296–298}

4. Phenomenology of Transport in Proton-Conducting Materials for Fuel-Cell Applications

Transport data have been reported for a huge number of proton-conducting materials, some of which are defined rather poorly. They have been recorded by a variety of methods under diverse conditions including ill-defined transient or steady-state situations (e.g., in a running fuel cell). Consequently, reproducibility and comparison of data from different laboratories is problematic. For this reason, we have only compiled the transport data that have

been obtained under thermodynamically defined conditions, preferably those close to thermodynamic equilibrium, i.e., with relatively small perturbations (electrical potential gradients, chemical potential gradients, etc.) applied to the samples. Although far from complete, the diversity of the materials included in this review allow for some general qualitative conclusions (see Section 5). The transport coefficients presented may also allow calculation (or numerical simulation) of fluxes and concentrations for nonequilibrium situations, provided that linear response may be assumed. The purpose of this section is to summarize the transport coefficients of some typical and well-characterized proton conductors without giving any mechanistic explanations, which already have been discussed in Section 3 for prototypical compounds, and also provide rationale for a qualitative understanding of the phenomenological data presented in this section.

4.1. Hydrated Acidic Polymers

For the application of acidic polymers in fuel cells, the most relevant species, for which transport must be considered, are protonic charge carriers, water, methanol, hydrogen, and oxygen. As discussed in Section 3, the transport of all these species predominantly occurs in the same environment, i.e., the solvated hydrophilic domain of the material. In addition to the transport coefficients for each of the five species, one must also consider cross coefficients describing the coupled transport of different species. For a linear description, this already requires a 5×5 matrix with 15 independent coefficients. Together with the publications referenced in Section 3.2.1.2, two more recent studies^{299,300} provide data and further literature on gas (predominately O_2 and H_2) transport in solvated acidic membranes. The reproducibility of these data is somewhat less than that for water transport; however, the general behavior is such that O_2 diffusion is closely related to water diffusion, including its dependence on solvation and temperature, whereas the H_2 diffusion is generally higher (by factors of 2–4). Because the gas solubility within the hydrophilic domain is quite low (i.e., on the order of 10^{-6} mol cm^{-3} for O_2 within the hydrated domain of Nafion at ambient conditions) and decreases with temperature, the gas permeability remains quite low (for O_2 on the order of 10^{-11} mol cm^{-1} s^{-1} in Nafion) and does not increase with temperature to the same degree as the gas and solvent diffusion coefficients.

The following compilation is restricted to the transport coefficients of protonic charge carriers, water, and methanol. These may be represented by a 3×3 matrix with six independent elements if it is assumed that there is just one mechanism for the transport of each species and their couplings. However, as discussed in Sections 3.1.2.1 and 3.2.1, different types of transport occur, i.e., diffusive transport as usually observed in the solid state and additional hydrodynamic transport (viscous flow), especially at high degrees of solvation. Assuming that the total fluxes are simply the sum of diffusive and hydrodynamic components, the transport matrix may

be extended by three more phenomenological elements describing (i) the hydrodynamic components of proton transport coupled to water or methanol permeation, and (ii) the water, and methanol, permeations themselves. Of course, the description of transport with a 3×4 matrix is neither complete nor consistent; however, it is a comfortable way to describe transport in solvated acidic membranes phenomenologically with reasonable precision. The transport equation may then be written

$$\begin{pmatrix} \bar{J}_{\text{H}^+} \\ \bar{J}_{\text{H}_2\text{O}} \\ \bar{J}_{\text{MeOH}} \end{pmatrix} = \begin{pmatrix} L_{11} & L_{12} & L_{13} & L_{14} \\ L_{21} & L_{22} & L_{23} & L_{24} \\ L_{31} & L_{32} & L_{33} & L_{34} \end{pmatrix} \begin{pmatrix} \nabla \tilde{\mu}_{\text{H}^+} \\ \nabla \tilde{\mu}_{\text{H}_2\text{O}} \\ \nabla \tilde{\mu}_{\text{MeOH}} \\ \nabla \bar{P}_{\text{total}} \end{pmatrix}$$

with $L_{ij} = L_{ji}$ (27)

with the driving forces being the gradients of

$$\tilde{\mu}_{\text{H}^+} = \mu_{\text{H}^+}^0 + RT \ln a_{\text{H}^+} + V_{\text{H}^+}^m \rho_{\text{total}} + z_{\text{H}^+} F \Phi \quad (28a)$$

$$\mu_{\text{H}_2\text{O}} = \mu_{\text{H}_2\text{O}}^0 + RT \ln a_{\text{H}_2\text{O}} + V_{\text{H}_2\text{O}}^m \rho_{\text{total}} \quad (28b)$$

$$\mu_{\text{MeOH}} = \mu_{\text{MeOH}}^0 + RT \ln a_{\text{MeOH}} + V_{\text{MeOH}}^m \rho_{\text{total}} \quad (28c)$$

The longitudinal coefficient L_{11} is related to the proton conductivity σ , according to

$$L_{11} = \frac{\sigma}{F^2} \quad (29)$$

L_{22} and L_{33} are related to the self-diffusion and chemical diffusion coefficients of water and methanol:

$$L_{22} = \frac{c_{\text{H}_2\text{O}}^2}{RT} \left(\frac{d(\ln a_{\text{H}_2\text{O}})}{dc_{\text{H}_2\text{O}}} \right) D_{\text{H}_2\text{O}} = \frac{c_{\text{H}_2\text{O}}}{RT} \tilde{D}_{\text{H}_2\text{O}} \quad (30)$$

$$L_{33} = \frac{c_{\text{MeOH}}^2}{RT} \left(\frac{d(\ln a_{\text{MeOH}})}{dc_{\text{MeOH}}} \right) D_{\text{MeOH}} = \frac{c_{\text{MeOH}}}{RT} \tilde{D}_{\text{MeOH}} \quad (31)$$

The cross coefficients are contained in the electro-osmotic drag coefficients:

$$K_{\text{H}_2\text{O}} = \frac{L_{21}}{L_{11}} \quad (32)$$

$$K_{\text{MeOH}} = \frac{L_{31}}{L_{11}} \quad (33)$$

The coefficients L_{14} , L_{24} , and L_{34} describe the viscous flow contributions of the transport of all three species in a total pressure gradient $\nabla \bar{P}_{\text{total}}$. Because a pressure gradient also imposes a chemical potential gradient on each species (eq 24), experimentally, there is always a superposition of diffusive and viscous flow; e.g., for the description of the water flux in a total pressure gradient, all coefficients must be included, i.e.,

$$\bar{J}_{\text{H}_2\text{O}} = L_{21} \nabla \tilde{\mu}_{\text{H}^+} + L_{22} \nabla \tilde{\mu}_{\text{H}_2\text{O}} + L_{23} \nabla \tilde{\mu}_{\text{MeOH}} + L_{24} \nabla \bar{P}_{\text{total}} = P_{\text{H}_2\text{O}} \nabla \bar{P}_{\text{total}} \quad (34)$$

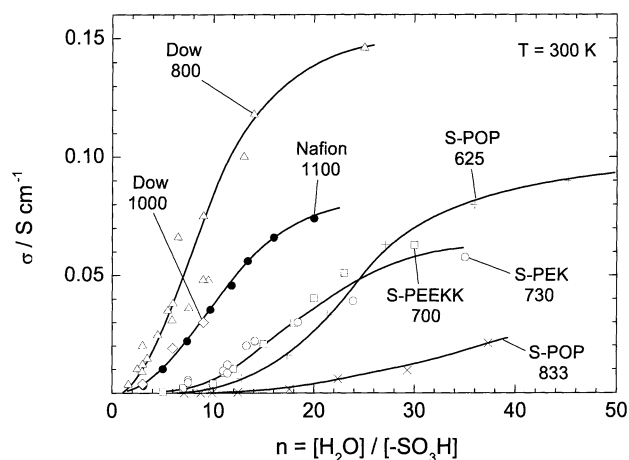


Figure 17. Room-temperature proton conductivity of two Dow membranes^{226,255,260} of different EW values, Nafion, two varieties of sulfonated poly(arylene ether ketone)s (S-PEK and S-PEEK, unpublished data from the laboratory of one of the authors), and sulfonated poly(phenoxyphosphazene)s (S-POPs³⁰¹) of different equivalent weights (685 and 833 g/equiv), as a function of the degree of hydration $n = [\text{H}_2\text{O}]/[-\text{SO}_3\text{H}]$ (number below the compound acronym/name indicates the EW value).

Usually, the total permeation coefficient ($P_{\text{H}_2\text{O}}$) is measured, and this, expressed as a permeation diffusion coefficient $D_{\text{H}_2\text{O}}^p$, is given in the following data compilation.

There are actually no experimental measurements of protonic streaming currents (L_{14}) and coupled water and methanol transport ($L_{23} = L_{32}$); however, the first may be related to the hydrodynamic component of the electro-osmotic drag (L_{12}/L_{11} , L_{13}/L_{11}) (see discussion in Section 3.2.1.1). The second is expected to be qualitatively related to the ratio of the electro-osmotic drag coefficient of water and methanol (L_{12}/L_{13}). In the following, the directly accessible transport coefficients (σ (D_o), $D_{\text{H}_2\text{O}}$, D_{MeOH} , $D_{\text{H}_2\text{O}}^p$, D_{MeOH}^p , $K_{\text{H}_2\text{O}}$, and K_{MeOH}) for different solvated acidic polymers are presented in a way that allows some interesting comparisons and the calculation or estimation of the elements of the transport matrix L_{ij} . In many publications, these transport parameters are reported as a function of the solvent content and are expressed as the number of solvent molecules (i.e., water) per sulfonic acid group. Because of the importance of percolation effects in all considered transport coefficients, we have converted these solvent contents to solvent volume fractions, except for proton conductivities, as shown in Figures 17 and 18.

Figure 17 shows the room-temperature proton conductivity of two sulfonated poly(arylene ether ketone)s, sulfonated poly(phenoxyphosphazene)s (S-POP) of different equivalent weights,^{301–303} Nafion (unpublished data from the laboratory of one of the authors), and two Dow membranes of different equivalent weight.^{226,255,260} Except for one Dow membrane with an equivalent weight of 800 g/equiv, the other membranes have similar (volume) densities of sulfonic acid groups, i.e., similar water volume fractions for a given water content $n = [\text{H}_2\text{O}]/[-\text{SO}_3\text{H}]$. It is a general observation that hydrocarbon membranes require more water to achieve similar conductivities than perfluorosulfonic acid polymers. This effect is

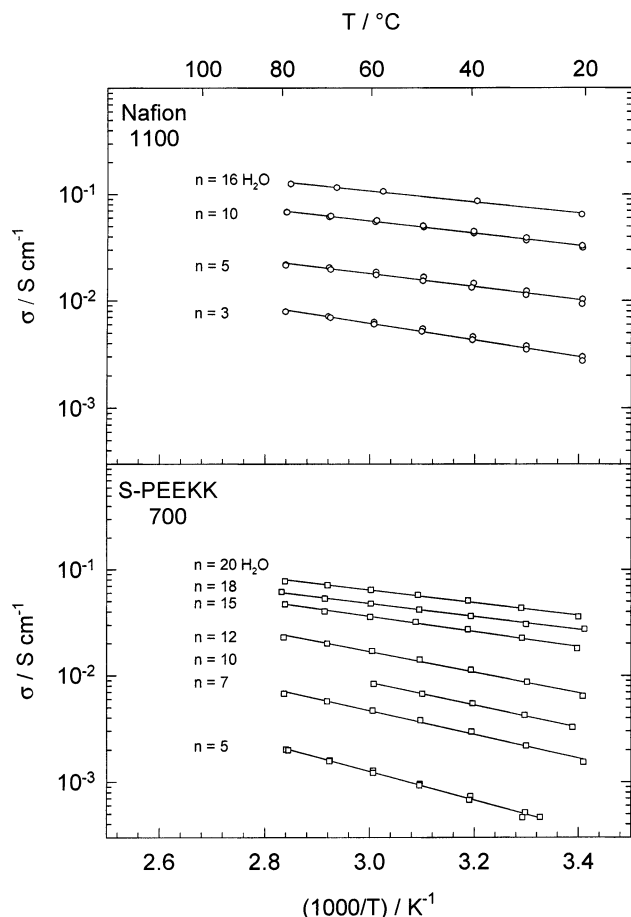


Figure 18. Proton conductivity of (a) Nafion 117 (EW = 1100 g/equiv) and (b) a sulfonated poly(arylene ether ketone), as a function of temperature and degree of hydration ($n = [H_2O]/[-SO_3H]$).¹⁹⁷

most pronounced for the high-equivalent-weight S-POP 833, and, considering the relation between solvent diffusion and proton mobility, this observation is in accordance with the low solvent diffusion coefficients reported for this type of membrane.³⁰² To reach sufficiently high conductivities for fuel-cell applications, such membranes must be in contact with liquid water.²¹⁹

Figure 18 shows the temperature dependence of the proton conductivity of Nafion and one variety of a sulfonated poly(arylene ether ketone) (unpublished data from the laboratory of one of the authors). The transport properties of the two materials are typical for these classes of membrane materials, based on perfluorinated and hydrocarbon polymers. This is clear from a compilation of D_σ , D_{H_2O} , and $D_{H_2O}^p$ data for a variety of membrane materials, including Dow membranes of different equivalent weights,^{226,255,260} Nafion/SiO₂ composites^{243,244,304–306} (including unpublished data from the laboratory of one of the authors), cross-linked polyarylenes,^{307–315} and sulfonated poly(phenoxyphosphazenes)³⁰¹ (Figure 19). The data points all center around the curves for Nafion and S-PEK, indicating essentially universal transport behavior for the two classes of membrane materials (only for S-POP are the transport coefficients somewhat lower, suggesting a more reduced percolation in this particular material). This correlation is also true for the electro-osmotic drag coefficients K_{H_2O} and K_{MeOH}

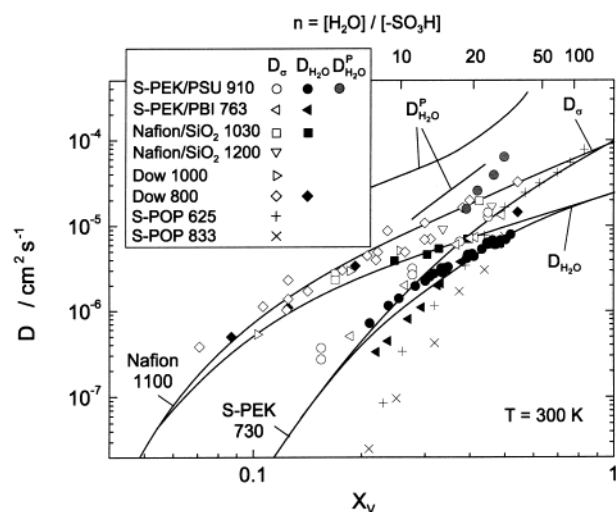


Figure 19. Transport coefficients of diverse membranes based on perfluorinated polymers (Dow^{226,255,260} and Nafion/silica composites^{174,243,244,304–306}), polyarylenes (S-PEK/PSU blends, ionically cross-linked S-PEK/PBI),^{307–315} and sulfonated poly(phenoxyphosphazenes) (S-POPs),³⁰¹ as a function of the water volume fraction X_V . Lines represent data for Nafion and S-PEK (given for comparison); for data points, see Figure 14.

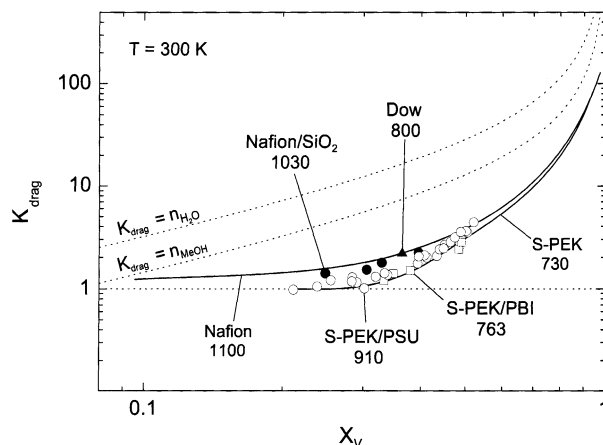


Figure 20. Electro-osmotic drag coefficients of diverse membranes based on perfluorinated polymers (Dow^{226,276} and Nafion/silica composites¹⁷⁴) and polyarylenes (S-PEK/PSU blends, ionically cross-linked S-PEK/PBI¹⁷⁴), as a function of the solvent (water/methanol) volume fraction X_V (see text for references). Lines represent data for Nafion and S-PEK (given for comparison); for data points, see Figure 15. Dashed lines correspond to the maximum possible electro-osmotic drag coefficients for water and methanol, as indicated (see text).

(Figure 20; for this figure, data for the Dow membrane are taken from refs 226 and 276; all other data are from the laboratory of one of the authors), which suggests that the major parameter that controls electro-osmotic transport is simply the degree of swelling and the choice of the type of backbone, particularly for low degrees of swelling (perfluorinated versus hydrocarbon polymer).

4.2. PBI-H₃PO₄ Adducts

The transport data of PBI-H₃PO₄ have extensively been reviewed in two recent papers,^{316,317} and their hybrids with inorganic particles have been characterized in another.³¹⁸ The gas permeability is much

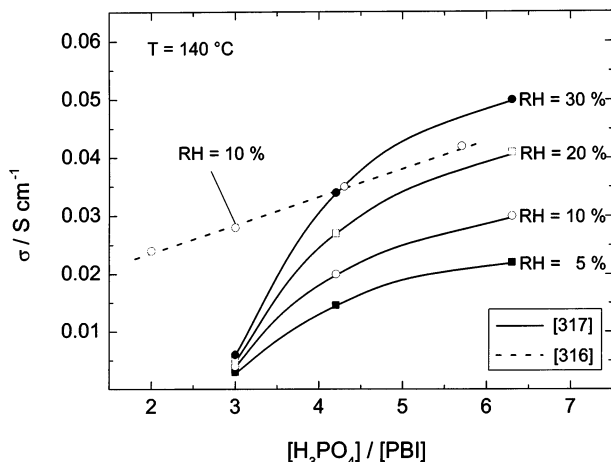


Figure 21. Proton conductivity of $\text{PBI} \cdot n\text{H}_3\text{PO}_4$ adducts, as a function of phosphoric acid concentration and relative humidity (RH).³¹⁷ Data from another source (denoted by the dashed line)³¹⁶ are given for comparison.

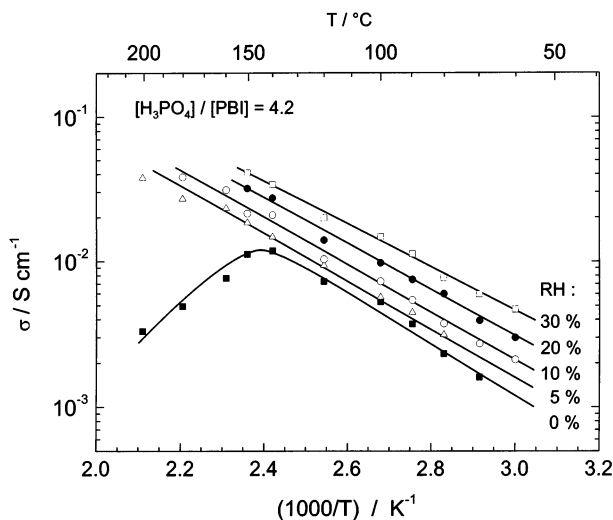


Figure 22. Proton conductivity of $\text{PBI} \cdot n\text{H}_3\text{PO}_4$ adducts, as a function of temperature T and relative humidity RH for a given phosphoric acid concentration.³¹⁷

lower than that in hydrated acidic polymers, and there is almost no water electro-osmotic drag, even at high relative humidities.²⁵⁴ The proton conductivity is mainly dependent on the fraction of phosphoric acid (frequently termed “doping level”), relative humidity (RH), and temperature. The corresponding dependencies are shown in Figures 21 and 22. The data suggest that the presence of water has two effects on the conductivity: (i) a minimum RH value is required to prevent the phosphoric acid from condensing at temperatures above $T \approx 100$ °C; and (ii) excess water leads to a further increase of the conductivity, as observed in pure phosphoric acid (Section 3.1.1.2). The data in Figures 21 and 22 are actually taken from one reference,³¹⁷ except for one curve taken from ref 316, which has been included to demonstrate the only moderate reproducibility.

4.3. Heterocycle-Based Systems

The first heterocycle-based systems that had some relevance in the development of new types of fuel-cell membranes were sulfonated polyarylenes¹⁷⁰ and

Nafion²³⁴ with intercalated heterocycles. Conductivities of $>10^{-2}$ S/cm are easily accessible by such systems; however, the volatility of the heterocycles requires some immobilization. The effect of covalent immobilization on proton conductivity is shown in Figure 23 for imidazole-based systems.^{213,237–239,241,242,319}

It is important to realize that these oligomers have similarly low vapor pressures as ionic liquids. To illustrate the effect of extrinsic charge carrier formation, the evolution of proton conductivity with triflic acid doping is shown for the oligomeric system Imi-2 in Figure 24.²³⁷ For such systems, the mobility of protonic charge carriers is typically 1 order of magnitude higher than the self-diffusion of the oligomers as a whole. Of course, long-range solvent (imidazole, pyrazole, benzimidazole) transport does not occur in fully polymeric systems. Cyclovoltammetry and fuel-cell-type experiments demonstrate that there is at least some transport of oxygen and hydrogen in imidazole-based systems.³²⁰

4.4. Oxides

Apart from protonic defects, the only species that may be transported in proton-conducting wide-band-gap perovskite-type oxides at significant rates are oxide ion vacancies. Although this allows for some chemical water diffusion in the intermediate temperature range (typically 300–700 °C, see Section 3.2.2), hydrogen and oxygen diffusion only occurs under either highly reducing or oxidizing conditions and at significantly higher temperatures, when electrons and holes become relevant as additional defects. Therefore, only proton conductivities for a variety of oxides at a water partial pressure of $p_{\text{H}_2\text{O}} = 30$ hPa are shown in Figure 25 (ref 186 with data from ref 187). Note that the dopant concentration for the examples shown is $\sim 10\%$ and that the proton mobility in such samples may significantly deviate from this in undoped materials (see Section 3.1.1.4).

5. Recent Approaches toward New Proton-Conducting Materials for Fuel-Cell Applications

The suitability of proton-conducting materials as separators in a particular fuel-cell application is essentially dependent on its transport properties, durability, and reactivity. Thus far, this review has focused on the transport properties only, but any approach toward new separator materials must consider all relevant aspects, which makes the development of new competitive materials a complex and challenging task.

Hence, most current strategies are trying to extend the application limits while conserving the specific advantages of well-established sulfonated materials such as Nafion by slightly varying or modifying them. Apart from the maximum operating temperature and the high crossover of water and methanol, long-term stability under fuel-cell conditions is also a severe problem. The first two constraints are related to the humidification requirements (see Section 1), and most materials development processes end up compromising on high proton conductivity on one side

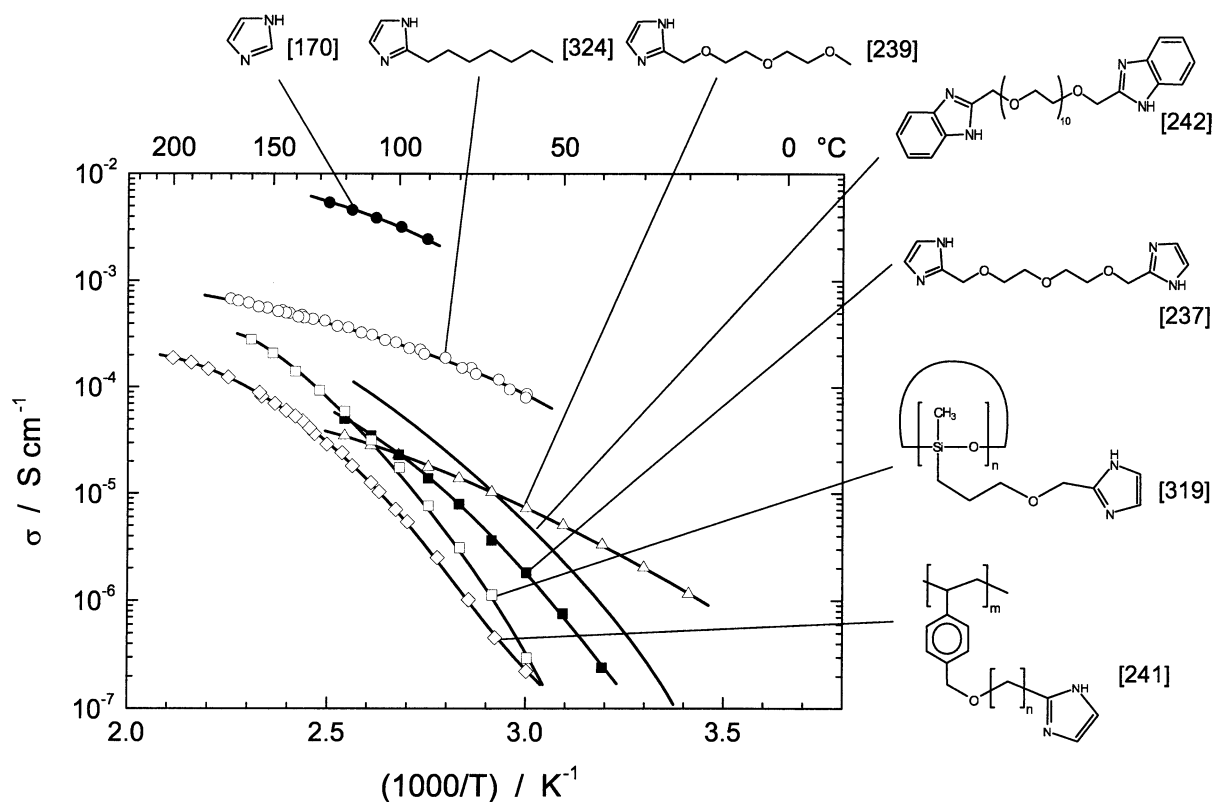


Figure 23. Evolution of proton conductivity of imidazole-based systems with increasing immobilization: from the monomer via oligomers to fully polymeric systems.

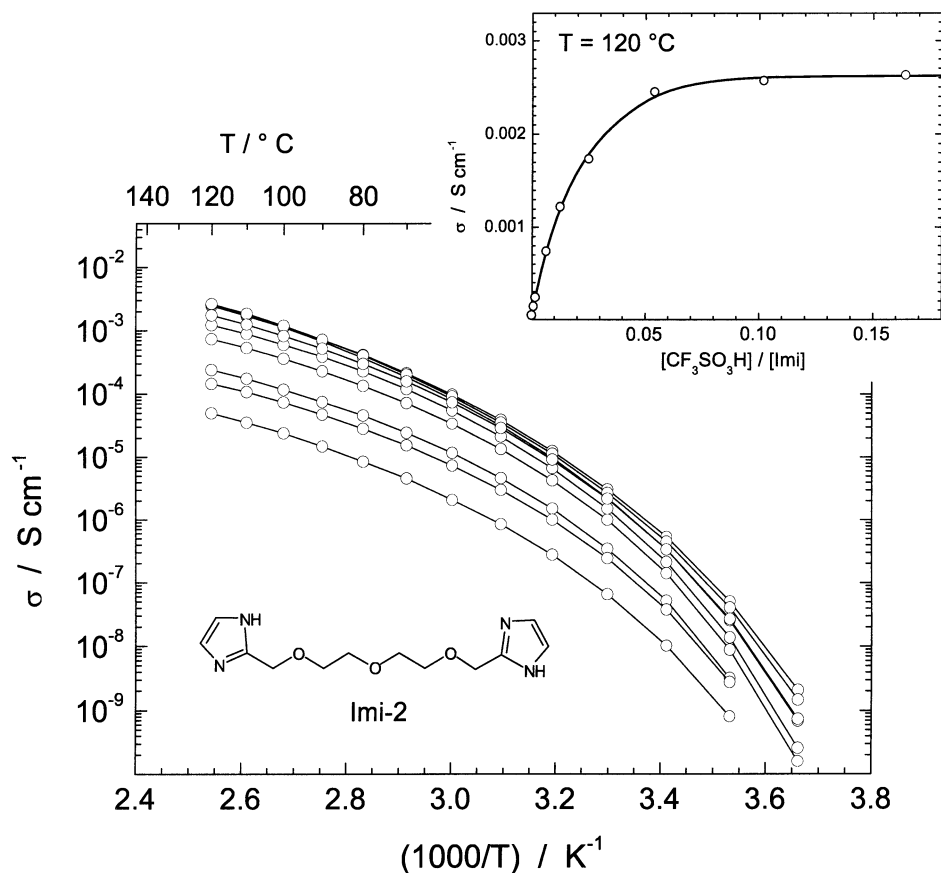


Figure 24. Proton conductivity of Imi-2 (two imidazoles spaced by two ethylene oxide (EO) units), as a function of triflic acid doping.²³⁷ Note that the conductivity has a tendency to level off at high acid concentration (see insert).

and morphological stability (low swelling and insolubility at elevated temperature) and low water and

methanol crossover on the other side. One crucial parameter that allows control of these properties is

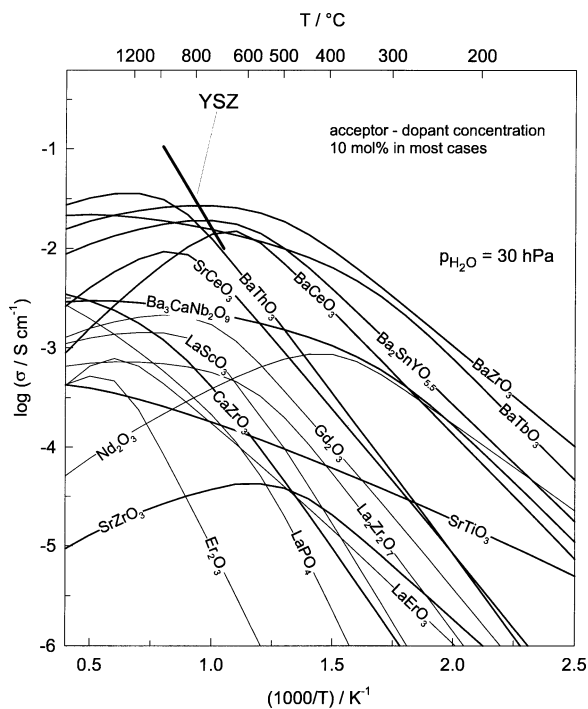


Figure 25. Proton conductivity of various oxides, as calculated from data on proton concentrations and mobilities, according to Norby and Larring (the type of dopant is not indicated; see ref 187 for source data).¹⁸⁶ The conductivity of oxides with a perovskite-type structure are shown by bold lines, and the conductivity of the oxide ion conductor YSZ (yttria-stabilized zirconia) is shown for comparison. (reproduced with the kind permission of *Annual Reviews*, <http://www.AnnualReviews.org>).

the degree of sulfonation (expressed as equivalent weight or ion exchange capacity), and this is usually in the range of 800–1200 g/equiv (0.83–1.25 mequiv/g) for perfluorinated polymers and 600–800 g/equiv (1.25–1.66 mequiv/g) for hydrocarbon separator materials. Despite the diversity of backbones and polymeric architectures, the transport properties are very similar, i.e., the transport coefficients, as a function of the water volume fraction, are similar to those of Nafion (as a representative of perfluorinated membrane materials) and sulfonated poly(arylene ether ketone)s (as a representative for hydrocarbon based membranes) (see Figures 19 and 20). Even the hydration isotherms (absorbed water per sulfonic acid group, as a function of RH) seem to be quite uniform. Only the water uptake in liquid water (or water/methanol mixtures) may differ significantly. Particularly at elevated temperatures, there may be tremendous swelling, and the onset of exaggerated (partially irreversible) swelling is closely related to the mechanical properties of the polymers.

The transport properties that are most significantly affected by changes of the water volume fraction are the water/methanol electro-osmotic drag and permeation, both of which have significant contributions from viscous flow (see Section 3.2.1.1). For DMFC applications (where the membrane is in contact with a liquid water/methanol mixture), this type of transport determines the crossover, which is only acceptably low for solvent volume fractions smaller than ~20 vol % (see Figures 14 and 15). Consequently, recent attempts have been focused on strengthening

the polymer, e.g., by cross-linking^{307–315,321} or forming co-polymers of sulfonated arylenes and polyvinylidene difluoride (PVDF).³²² Initial fuel-cell tests are actually quite promising,³¹³ however, the brittleness of highly cross-linked polymers may cause mechanical failure of the membrane. The formation of composites with isolated inorganic particles usually does not have a positive effect on the swelling properties. In the case of Nafion, it may suppress its crystallinity, which leads to an increased swelling. Nevertheless, improved performance under fuel-cell conditions has been reported in a few cases,^{243,244} and better understanding of the observed effects may guide a more systematic improvement of composites. The design of microstructures with a hydrated sulfonated polymer confined in the pores of a stable well-connected (inorganic) matrix may be another promising approach. The mechanical requirements of such a matrix are actually quite severe, because of the need to compensate for the high pressure due to osmosis and electro-osmotic drag. Some specific interaction between the sulfonated polymer and the confining phase is required to prevent the first from dissolving. Currently, there are several attempts to build such microstructures, some of which are based on controlled precipitation from homogeneous solutions,³²³ and others that rely on sequential formation of the different parts of the microstructure, e.g., by precipitation of inorganic proton conductors in porous PTFE.²⁴⁵ Another degree of freedom that may be exploited is the degree of sulfonation across the membrane. In a DMFC, the anode side of the methanol solution, which is in contact with the methanol solution, may be prevented from swelling by locally reducing the degree of sulfonation (e.g., by laminating layers of different degree of sulfonation³²³ or by surface modification³¹²), whereas an increased degree of sulfonation may prevent drying out on the anode side at high temperatures and low humidity conditions.

As explained in the Introduction, the latter conditions are of paramount importance for PEM fuel-cell technology; however, to date, there are no proton-conducting sulfonated polymer membranes available that satisfy all requirements under these conditions (i.e., $T > 120$ °C, RH < 25%). The most obvious limitation is the low proton conductivity, as a result of low hydration levels under these conditions. Because of their superacidity, which results in high hydrophilicity (see Section 3.1.2.1), the highest equilibrium water contents are observed in perfluorosulfonic acid polymers. However, even for these, a water content of 2.5H₂O/SO₃H (at $T = 144$ °C, RH = 25%; see Figure 26, bottom) is too low to effectively bridge the separation between neighboring sulfonate groups, which is ~0.8 nm in Nafion (1100 g/equiv).²¹² Because of the poor connectivity (percolation) of the possible water structures and the strong local retardation of the water diffusion (see discussion in Section 3.2.1.1), fast proton conduction according to a vehicle mechanism is not possible at such low degrees of hydration. On the other hand, there is theoretical^{38,39} and experimental indication³²⁴ that high proton conductivity may be possible at low hydration levels, pro-

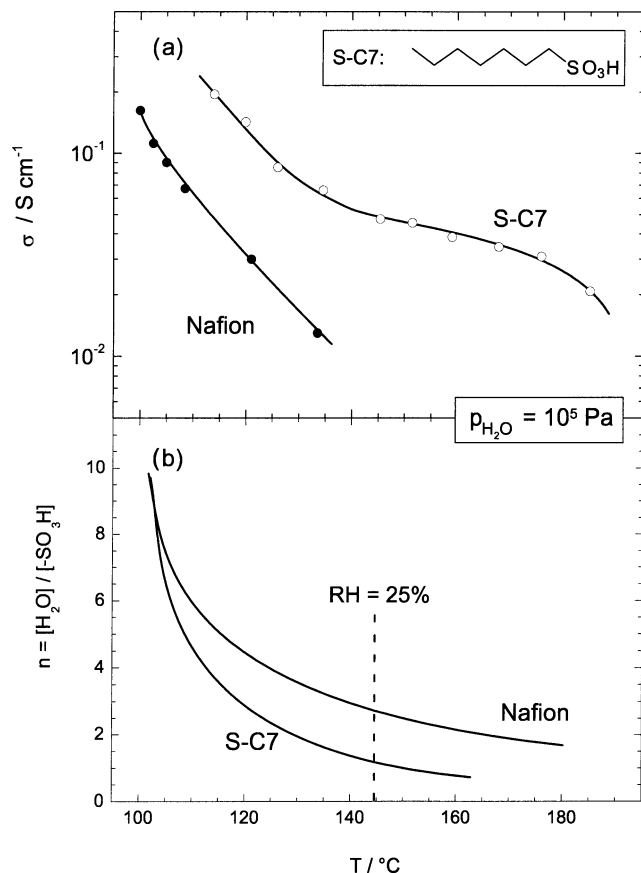


Figure 26. (a) Conductivity and (b) water uptake of S-C7 (heptane terminated by a sulfonic acid functional group) and Nafion 117 (EW = 1100 g/equiv), as a function of temperature at a water partial pressure of $p_{\text{H}_2\text{O}} = 10^5 \text{ Pa}$.³²⁴

vided that the sulfonic acid functional groups are less separated or at least more mobile. The top portion of Figure 26 shows the ionic conductivity of a sulfonated oligomer (heptyl sulfonic acid), which starts to show a decrease in conductivity at a higher temperature than that observed in Nafion, leveling off to a very high conductivity of $\sim 4 \times 10^{-2} \text{ S/cm}$ in the temperature range of 130–170 $^{\circ}\text{C}$ ($p_{\text{H}_2\text{O}} = 10^5 \text{ Pa}$),³²⁴ which is reminiscent of the conductivity behavior of aqueous highly concentrated sulfuric acid.³²⁵ The latter observation indicates that another proton conduction mechanism appears at low humidification levels. Recent electronic structure calculations of a two-side-chain fragment of the Dow membrane demonstrates that a hydration of three water molecules per sulfonic acid leads to dissociation and a configuration in which one of the excess protons is shared between two water molecules (the formation of a Zundel ion) and the other is a hydronium ion between the two sulfonate groups.²³ For somewhat lower water contents, the affinities of the sulfonic acid group and the remaining water structure towards the proton tend to balance. The AIMD (see Section 2.2.3) of triflic acid monohydrate^{38,39} indeed finds excess protons within the water structure, namely, as Zundel and hydronium ions, and shared between neighboring sulfonate groups (Figure 27). Such configurations may have a role in the mechanisms of proton conduction involving the dynamics of both the sulfonate groups and the water

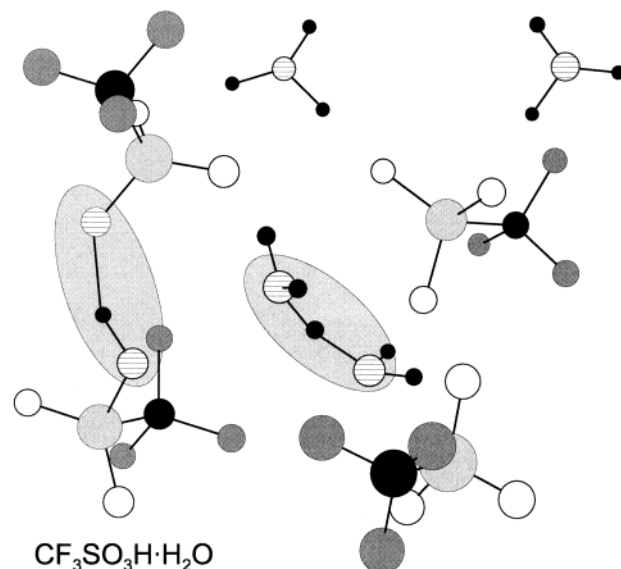


Figure 27. Defective structure of solid trifluoromethane-sulfonic acid hydrate $(\text{CF}_3\text{SO}_3\text{H}\cdot\text{H}_2\text{O})_4$ found using ab initio molecular dynamics (AIMD; see Section 2.2.3 for a description of the technique), showing two hydronium ions hydrogen-bonded to sulfonate groups (as found in the perfect structure) but, more importantly, two "shared protons" (one between two sulfonate groups and the other as part of a Zundel ion; see text). Note that the energy of the defective structure is only $\sim 30 \text{ kJ/mol}$ higher than that of the perfect structure.^{23,38,39}

molecules. Whether this is the case for the high conductivities of lowly hydrated sulfonic acid oligomers (Figure 26) and triflic acid hydrates is not yet clear (the high conductivities may also be the consequence of high self-diffusion coefficients of such ionic, highly fluid systems); however, these observations may justify an inclusion of highly sulfonated systems with significantly smaller $-\text{SO}_3\text{H}$ separations into future work. Polymers with more than one sulfonic acid group per phenyl ring are indeed possible (e.g., for poly(arylene sulfide)s) and interesting conductivities at low humidification have been reported.³²⁶ Of course, the formation of applicable separator materials requires the immobilization of such highly soluble polymers, e.g., in a manner previously described or by making them a constituent of a macromolecular structure with highly sulfonated and unsulfonated components in controlled morphologies (for a current review, see ref 327), which is a strategy pushed forward by several French groups,^{328–331} McGrath et al.,³³² and Miyatake et al.³³³ The latter authors actually reported the highest high-temperature conductivity for a sulfonated polyimide co-polymer that contained fluorenyl moieties, indicating a complex relation between chemistry, microstructure (packing), and proton conductivity for this class of polymers. Note that the typical block separation length for such polymers is on the order of 10–100 nm, i.e., it is well above the scale relevant for the transport mechanisms ($\sim 1 \text{ nm}$), as discussed in Sections 3.1.2.1 and 3.2.1.

Unfortunately, the thermal stability of sulfonated systems is quite limited, particularly when the stabilizing effect of the hydration water is reduced (Section 3.1.2.1). The transport of water not only

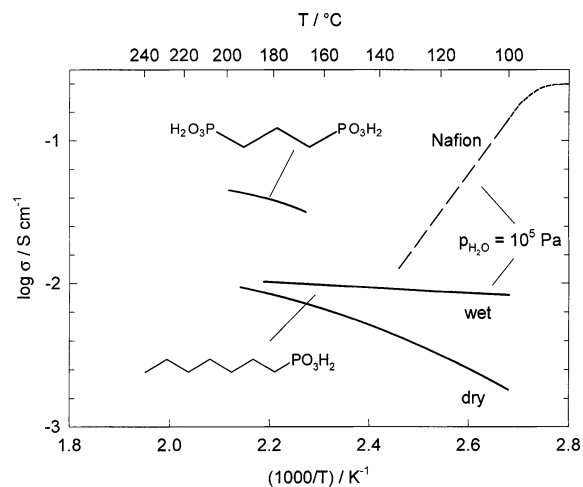


Figure 28. Conductivity of two phosphonic acid-terminated oligomers under dry and wet conditions, compared to the proton conductivity of Nafion at a water partial pressure of $p_{\text{H}_2\text{O}} = 10^5$ Pa.³²⁴

requires water management but also leads to thermodynamic efficiency losses in fuel cells using such membranes as separators. A recent comparative study of oligomers terminated by different protogenic groups (sulfonic acid, imidazole, and phosphonic acid) shows that the more-amphoteric groups show a higher thermal and electrochemical stability in the dry state,³²⁴ where they still show significant proton conductivity. However, as discussed in Section 3.1.2.3, this conductivity seems to be limited to $\sim 10^{-2}$ S/cm for systems based on heterocycles. The other problem with such systems is the high overpotentials for oxygen reduction at platinum cathodes, which already has been observed by Yang et al.²³⁴ For phosphonic acid functionalized systems, however, the conductivities in the dry state are ~ 1 order of magnitude higher, and, as opposed to most heterocycle-based systems, phosphonates have some remaining hydrophilicity. This allows for high proton conductivity at low temperatures (Figure 28) and may help to reduce cathodic overpotentials that are caused by the adsorption of phosphonic groups onto the platinum surface. Of course, this is also an inherent problem of systems that contain free H_3PO_4 , such as the adducts of PBI and phosphoric acid (see Section 3.1.2.2).

Apart from the immobilization of the protogenic group as part of a polymeric architecture (e.g., soft side-chain polymer), ionic immobilization may be another interesting strategy to suppress the volatility of nonaqueous proton solvents. Some molten salts combine low vapor pressure with very high ionic conductivity. However, the latter is usually the consequence of a very high fluidity, resulting in high mobility of all ionic species in the systems. Watanabe et al.³³⁴ have actually reported a few molten salts that contain imidazolium or imidazolium derivatives with very high ionic conductivity. However, the charge carriers are complex ions, which are very mobile as a whole, i.e., the conductivity is not protonic. Nevertheless, when combined with the spacer concept, ionic immobilization may also become relevant for the immobilization of (neutral) proton solvents. Spacer

molecules may be terminated by a proton solvent (e.g., imidazole, phosphonic acid) at one end and by an ionic group at the other end, with the counter charge being just a single ion (this may lead to a liquid (molten) systems with low vapor pressure) or a poly-ion (which may lead to a plastic material).

The use of polymeric constituents becomes progressively critical with increasing temperature; therefore, for durability reasons, partially and even fully inorganic systems have recently attracted interest as proton-conducting separator materials.

Heteropolyacids are frequently used to modify proton-conducting composites,²⁵² or they are just dispersed in inert matrixes.^{335,336} However, because the proton conduction mechanism of such hydrated salts is similar to those of hydrated polymeric systems,³³⁷ these composites show qualitatively similar transport properties. The same is true for organically modified inorganic layered compounds such as titanium phosphate sulfophenylphosphonate, the conductivity of which is dependent on the RH value, in a manner similar to that observed with Nafion.³³⁸

In contrast to this class of materials, acidic salts of oxo-acids may show a proton conduction mechanism, which is more related to that of liquid orthophosphoric acid (see Section 3.1.1.2). The prototypical compound is CsHSO_4 , which shows very high proton conductivity above a first-order phase transition at $T \approx 140$ °C.³³⁹ The conducting phase is still a solid; that is, there is still long-range order but locally, there is a tremendous dynamic reorientational disorder of the sulfate tetrahedral and extended vibrations of both cesium and sulfate characteristic for so-called plastic phases. The hydrogen bonding between the sulfate tetrahedral is highly dynamic in the plastic phase, and almost completely self-dissociated: high proton mobility leading to high proton conductivity.^{1,10,144} Haile et al. tested such type of materials in H_2/O_2 fuel cells³⁴⁰ and recently also in methanol/ O_2 fuel cells.³⁴¹ The current densities obtained were limited by the protonic resistance of the electrolytes (CsHSO_4 and CsH_2PO_4), i.e., no cathodic overpotentials are reported, which is a true advantage, compared to other systems operating under similar conditions. The softness, high solubility in water, sensitivity to reduction, and the very low room-temperature conductivity are still severe disadvantages in these particular compounds; however, there is a plethora of solid acids, some of which may be suitable for fuel-cell applications.

Further increase in the operating temperature of a fuel cell is possible, using proton-conducting oxides as separator materials. Although initial fuel-cell tests (typically in the temperature range of 600–800 °C using pure gases) were quite promising,^{180–184} the combination of high bulk proton conductivity and stability has only recently been achieved.^{186,188,205} Yttrium-doped BaZrO_3 -based oxides actually show the highest bulk conductivity (Figure 25), and they have a high thermodynamic stability, with respect to reactions with acidic gases such as CO_2 .¹⁸⁸ Problems are related to high grain-boundary impedances (which is probably the result of symmetry reduction in the grain-boundary region), current constriction

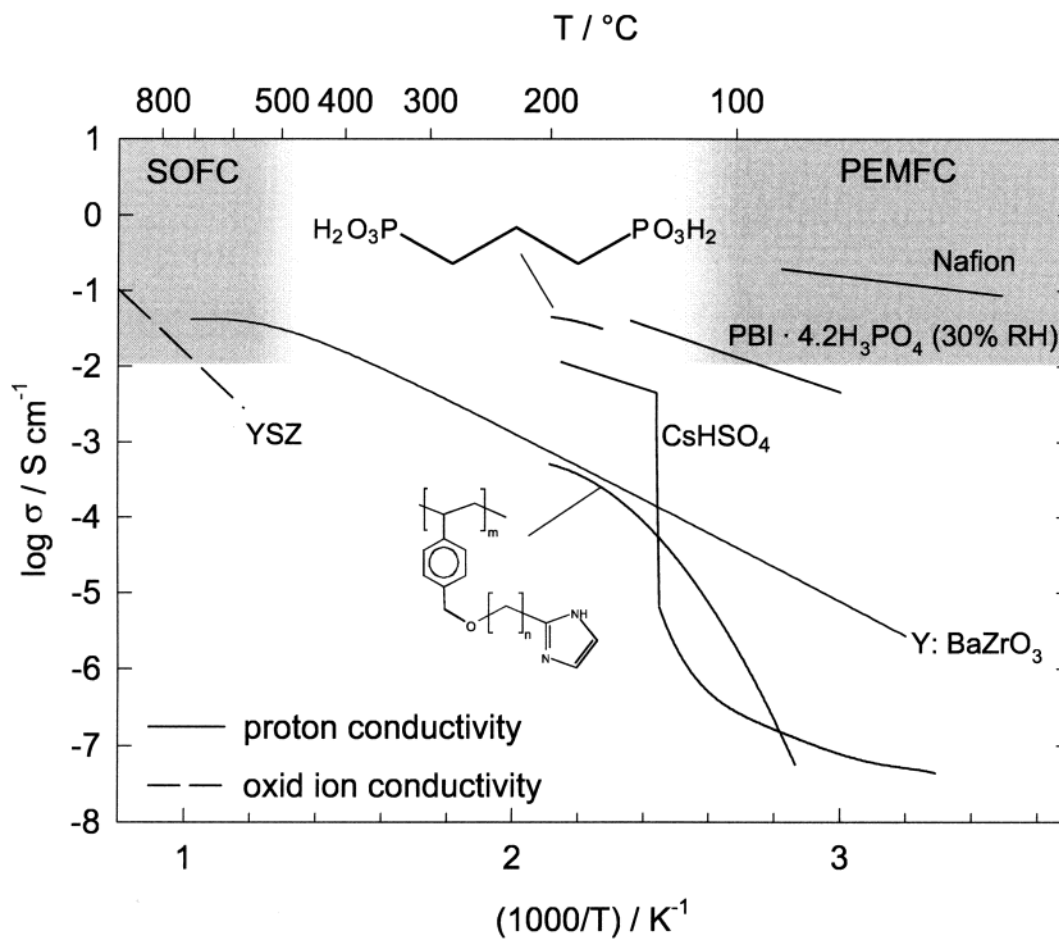


Figure 29. Conductivity of some intermediate-temperature proton conductors, compared to the conductivity of Nafion and the oxide ion conductivity of YSZ (yttria-stabilized zirconia), the standard electrolyte materials for low- and high-temperature fuel cells, proton exchange membrane fuel cells (PEMFCs), and solid oxide fuel cells (SOFCs).

effects, and high cathodic overpotentials at platinum electrodes.¹⁸⁶ More-suitable electrocatalysts have not been developed thus far; therefore, there is probably a huge potential for further improvements. An interesting feature of proton-conducting oxides is, that they may show both proton conductivity and chemical water diffusion under medium dry conditions (Section 3.2.2). This allows the transport of water electrochemically formed at the cathode, to migrate to the anode side, where it may be consumed in fuel-reforming reactions. This approach has been suggested and confirmed by Coors³⁴² and may become the basis for fuel cells operating with dry methane as a fuel.

The key to the development of CO₂-resistant proton-conducting oxides was the maximization of the entropic stabilization of protonic defects.¹⁸⁸ If this approach also led to stable hydroxides with sufficiently high conductivity, AFCs using such electrolytes may operate even with air as the cathode gas. This would be tremendously advantageous, because fuel cells with nonacidic electrolytes may operate with non-noble-metal catalysts such as nickel for the anode and silver for the cathode.

The above-described qualitative considerations hopefully give a flavor for the complexity of the development of novel proton-conducting separator materials for fuel-cell applications. When solely considering proton conductivity, significant progress has been

made over the past few years, and quite a few old and new materials have been reported that show interesting proton conductivities, especially in the intermediate temperature range (see Figure 29).³⁴³ Also, significant progress in the understanding of transport properties has also been made, which is, to a large extent, due to emerging simulation techniques (Section 2) as relatively recent research tools. The level of understanding reached so far has already helped to better control the transport properties of available proton-conducting materials, and surely will be of great help in a more directed search for novel proton-conducting materials for fuel-cell applications. This is indeed necessary, because, presently, Nafion materials, or modified derivatives of its structure with modified pendant chains, lower equivalent weights, or modified processing are still the benchmark PEMs, despite more than twenty years of research into alternatives.

6. Acknowledgement

The authors thank R. Merkle, E. Kotomin, and J. Fleig (all from the Max-Planck-Institut für Festkörperforschung) and the external reviewers for carefully reading the proofs and fruitful discussions. We thank A. Fuchs for assisting in making the figures and the Deutsche Forschungsgemeinschaft (KR 794), the Bundesministerium für Bildung und

Forschung (0329567), and the Energiestiftung Baden-Württemberg (A 19603) for financial support.

7. References

- Kreuer, K. D. *Chem. Mater.* **1996**, *8*, 610.
- Colomban, P. *Ann. Chim.—Sci. Mater.* **1999**, *24*, 1.
- Vielstich, W.; Lamm, A.; Gasteiger, H. A., Eds. *Handbook of Fuel Cells—Fundamentals, Technology and Applications*; Wiley: Chichester, U.K., 2003.
- Annu. Rev. Mater. Res.* **2003**, *33*. (Special issue, Materials for Fuel Cells.)
- Savadogo, O. *J. New Mater. Electrochem. Syst.* **1998**, *1*, 47.
- Li, Q.; He, R.; Jensen, J. O.; Bjerrum, N. J. *Chem. Mater.* **2003**, *15*, 4896.
- Rikukawa, M.; Sanui, K. *Prog. Polym. Sci.* **2000**, *25*, 1463.
- Rozière, J.; Jones, D. J. *Annu. Rev. Mater. Res.* **2003**, *33*, 503.
- Jannasch, P. *Curr. Opin. Colloid Interface Sci.* **2003**, *8*, 96.
- Münch, W.; Kreuer, K. D.; Traub, U.; Maier, J. *J. Mol. Struct. (THEOCHEM)* **1996**, *381*, 1.
- Büchi, F. N.; Huslage, J.; Scherer, G. G. *PSI Annu. Rep.* **1997**, Annex V, 48.
- Springer, T. E.; Zawodzinski, T. A.; Gottesfeld, S. *J. Electrochem. Soc.* **1991**, *138*, 2334.
- Fuller, T. F.; Newman, J. J. *Electrochem. Soc.* **1991**, *140*, 1218.
- Eikerling, M.; Kharkats, Y. I.; Kornyshev, A. A.; Volkovich, Y. M. *J. Electrochem. Soc.* **1998**, *145*, 2677.
- Paddison, S. J.; Pratt, L. R.; Zawodzinski, T.; Reagor, D. W. *Fluid Phase Equilib.* **1998**, *150–151*, 235.
- Paddison, S. J.; Pratt, L. R.; Zawodzinski, T. A., Jr. In *Proton Conducting Membrane Fuel Cells II*; Gottesfeld, S., Fuller, T. F., Eds.; The Electrochemical Society Proceedings Series 98-27; The Electrochemical Society: Pennington, NJ, 1999; p 99.
- Paddison, S. J.; Zawodzinski, T. A., Jr. *Solid State Ionics* **1998**, *113–115*, 333.
- Paddison, S. J.; Pratt, L. R.; Zawodzinski, T. A., Jr. *J. New Mater. Electrochem. Syst.* **1999**, *2*, 183.
- Paddison, S. J.; Pratt, L. R.; Zawodzinski, T. A., Jr. *J. Phys. Chem. A* **2001**, *105*, 6266.
- Paddison, S. J. *J. New Mater. Electrochem. Syst.* **2001**, *4*, 197.
- Eikerling, M.; Paddison, S. J.; Zawodzinski, T. A., Jr. *J. New Mater. Electrochem. Syst.* **2002**, *5*, 15.
- Paddison, S. J. In *Handbook of Fuel Cells Fundamentals Technology and Applications: Volume 3, Fuel Cell Technology and Applications: Part 1*; Vielstich, W., Lamm, A., Gasteiger, H. A., Eds.; Wiley: Chichester, U.K., 2003; p 396.
- Paddison, S. J. *Annu. Rev. Mater. Res.* **2003**, *33*, 289.
- Johansson, P.; Tegenfeldt, J.; Lindgren, J. *Electrochim. Acta* **2000**, *45*, 3055.
- Li, T.; Wlaschin, A.; Balbuena, P. B. *Ind. Eng. Chem. Res.* **2001**, *40*, 4789.
- Spohr, E.; Commer, P.; Kornyshev, A. A. *J. Phys. Chem. B* **2002**, *106*, 10560.
- Commer, P.; Cherstvy, A. G.; Spohr, E.; Kornyshev, A. A. *Fuel Cells* **2002**, *2*, 127.
- Spohr, E. *Mol. Simul.* **2004**, *30*, 107.
- Commer, P.; Hartnig, C.; Seeliger, D.; Spohr, E., submitted to *Mol. Simul.*
- Warshel, A. *Computer Modeling of Chemical Reactions in Enzymes and Solutions*; Wiley: New York, 1991.
- Warshel, A. *J. Phys. Chem.* **1982**, *86*, 2218.
- Warshel, A.; Weiss, R. M. *J. Am. Chem. Soc.* **1980**, *102*, 6218.
- Tuckerman, M.; Laasonen, K.; Sprik, M.; Parrinello, M. *J. Phys. Chem.* **1995**, *99*, 5749.
- Tuckerman, M.; Laasonen, K.; Sprik, M.; Parrinello, M. *J. Chem. Phys.* **1995**, *103*, 150.
- Tuckerman, M. E.; Marx, D.; Klein, M. L.; Parrinello, M. *Science* **1997**, *275*, 817.
- Marx, D.; Tuckerman, M. E.; Hutter, J.; Parrinello, M. *Nature* **1999**, *397*, 601.
- Münch, W.; Kreuer, K.-D.; Silvestri, W.; Maier, J.; Seifert, G. *Solid State Ionics* **2001**, *145*, 437.
- Eikerling, M.; Paddison, S. J.; Pratt, L. R.; Zawodzinski, T. A., Jr. *Chem. Phys. Lett.* **2003**, *368*, 108.
- Paddison, S. J.; Pratt, L. R., submitted to *Mol. Phys.*, 2004.
- Paddison, S. J.; Paul, R.; Zawodzinski, T. A., Jr. In *Proton Conducting Membrane Fuel Cells II*; Gottesfeld, S., Fuller, T. F., Eds.; The Electrochemical Society Proceedings Series 98-27; The Electrochemical Society: Pennington, NJ, 1999; p 106.
- Paddison, S. J.; Paul, R.; Zawodzinski, T. A., Jr. *J. Electrochem. Soc.* **2000**, *147*, 617.
- Paddison, S. J.; Paul, R.; Zawodzinski, T. A., Jr. *J. Chem. Phys.* **2001**, *115*, 7753.
- Paddison, S. J.; Paul, R.; Pivovar, B. S. In *Direct Methanol Fuel Cells*; Narayanan, S., Gottesfeld, S., Zawodzinski, T. A., Eds.; The Electrochemical Society Proceedings Series 01-04; The Electrochemical Society: Pennington, NJ, 2001; p 8.
- Paddison, S. J.; Paul, R.; Kreuer, K. D.; Zawodzinski, T. A., Jr. In *Direct Methanol Fuel Cells*; Narayanan, S., Gottesfeld, S., Zawodzinski, T. A., Eds.; The Electrochemical Society Proceedings Series 01-04; The Electrochemical Society: Pennington, NJ, 2001; p 29.
- Paddison, S. J.; Paul, R.; Kreuer, K. D. *Phys. Chem. Chem. Phys.* **2002**, *4*, 1151.
- Paddison, S. J.; Paul, R. *Phys. Chem. Chem. Phys.* **2002**, *4*, 1158.
- Paul, R.; Paddison, S. J. In *Advances in Materials Theory and Modeling—Bridging Over Multiple-Length and Time Scales*; Bulatov, V., Colombo, L., Cleri, F., Lewis, L. J., Mousseau, N., Eds.; Materials Research Society: Warrendale, PA, 2001; pp AA7.16.1.
- Paul, R.; Paddison, S. J. *J. Chem. Phys.* **2001**, *115*, 7762.
- Paul, R.; Paddison, S. J. *Phys. Rev. E* **2003**, *67*, 016108-1.
- Paul, R.; Paddison, S. J. *Solid State Ionics* **2004**, *168*, 245.
- Paul, R.; Paddison, S. J. *J. Phys. Chem. B* **2004**, *108*, 13231–13241.
- Szabo, A.; Ostlund, N. S. *Modern Quantum Chemistry: Introduction to Advanced Electronic Structure Theory*; McGraw-Hill: New York, 1989.
- McWeeny, R. *Methods of Molecular Quantum Mechanics*; Academic Press: London, 1989.
- Hehre, W. J.; Radom, L.; Schleyer, P. V. R.; Pople, J. A. *Ab Initio Molecular Orbital Theory*; Wiley: New York, 1986.
- Born, M.; Oppenheimer, J. R. *Ann. Phys.* **1927**, *79*, 361.
- Hartree, D. R. *Proc. Cambridge Philos. Soc.* **1928**, *24*, 328.
- Fock, V. A. *Z. Phys.* **1930**, *15*, 126.
- Møller, C.; Plesset, M. S. *Phys. Rev.* **1934**, *46*, 618.
- Shavitt, I. In *Modern Theoretical Chemistry*; Schaefer, H. F., Ed.; Plenum Press: New York, 1977.
- Boys, S. F. *Proc. R. Soc. London A* **1950**, *A200*, 542.
- Parr, R. G.; Yang, W. *Density Functional Theory of Atoms and Molecules*; Oxford: New York, 1989.
- Hohenberg, P.; Kohn, W. *Phys. Rev. B* **1964**, *136*, B864.
- Kohn, W.; Sham, L. J. *Phys. Rev.* **1965**, *140*, A1133.
- Lee, C.; Yang, W.; Parr, R. G. *Phys. Rev. B* **1988**, *37*, 785.
- Perdew, J. P. *Phys. Rev. B* **1986**, *33*, 8822; **1986**, *34*, 7406.
- Perdew, J. P. In *Electronic Structure of Solids*; Ziesche, P., Eschrig, H., Eds.; Akademie Verlag: Berlin, 1991.
- Becke, A. D. *Phys. Rev.* **1988**, *38*, A3098.
- Johnson, B. G.; Gill, P. M. W.; Pople, J. A. *J. Chem. Phys.* **1993**, *98*, 5612.
- Porezag, D.; Frauenheim, T.; Köhler, T.; Seifert, G.; Kaschner, R. *Phys. Rev. B* **1995**, *51*, 12947.
- Seifert, G.; Porezag, D.; Frauenheim, T. *Int. J. Quantum Chem.* **1996**, *58*, 185.
- Frauenheim, T.; Seifert, G.; Elstner, M.; Niehaus, T. A.; Köhler, T.; Amkreutz, M.; Sternberg, M.; Hajnal, Z.; di Carlo, A.; Suhai, S. *J. Phys. C* **2002**, *14*, 3015.
- Seifert, G. In *Encyclopedia of Computational Chemistry*; Wiley: New York, in press.
- Münch, W.; Kreuer, K. D.; Seifert, G.; Maier, J. *Solid State Ionics* **2000**, *136–137*, 183.
- Allen, M. P.; Tildesley, D. J. *Computer Simulation of Liquids*; Clarendon Press: Oxford, U.K., 1987.
- Gray, C. G.; Gubbins, K. E. *Theory of Molecular Fluids*; Clarendon Press: Oxford, U.K., 1984; Vol. 1.
- Remler, D. K.; Madden, P. A. *Mol. Phys.* **1990**, *70*, 921.
- Payne, M. C.; Teter, M. P.; Allan, D. C.; Arias, T. A.; Joannopoulos, J. D. *Rev. Mod. Phys.* **1992**, *64*, 1045.
- Metropolis, N. A.; Rosenbluth, A. W.; Rosenbluth, M. N.; Teller, A. H.; Teller, E. *J. Chem. Phys.* **1953**, *21*, 1087.
- Alder, B. J.; Wainwright, T. E. *J. Chem. Phys.* **1957**, *27*, 1208.
- Dick, B. G.; Overhauser, A. W. *Phys. Rev.* **1958**, *112*, 90.
- Halley, J. W.; Rustad, J. R.; Rahman, A. *J. Chem. Phys.* **1993**, *98*, 4110.
- Hammes-Schiffer, S.; Tully, J. C. *J. Chem. Phys.* **1994**, *101*, 4657.
- Vuilleumier, R.; Borgis, D. *J. Mol. Struct. (THEOCHEM)* **1997**, *436*, 555.
- Vuilleumier, R.; Borgis, D. *J. Phys. Chem. B* **1998**, *102*, 4261.
- Vuilleumier, R.; Borgis, D. *Chem. Phys. Lett.* **1998**, *284*, 71.
- Vuilleumier, R.; Borgis, D. *Isr. J. Chem.* **1999**, *39*, 457.
- Vuilleumier, R.; Borgis, D. *J. Chem. Phys.* **1999**, *111*, 4251.
- Schmitt, U. W.; Voth, G. A. *J. Phys. Chem. B* **1998**, *102*, 5547.
- Schmitt, U. W.; Voth, G. A. *J. Chem. Phys.* **1999**, *111*, 9361.
- Schmitt, U. W.; Voth, G. A. *Isr. J. Chem.* **1999**, *39*, 483.
- Schmitt, U. W.; Voth, G. A. *Chem. Phys. Lett.* **2000**, *329*, 36.
- Kim, J.; Schmitt, U. W.; Gruetzmacher, J. A.; Voth, G. A.; Scherer, N. F. *J. Chem. Phys.* **2000**, *116*, 737.
- Day, T. J. F.; Soudackov, A. V.; Cuma, M.; Schmitt, U. W.; Voth, G. A. *J. Chem. Phys.* **2002**, *117*, 5839.
- Kornyshev, A. A.; Walbran, S. *J. Chem. Phys.* **2001**, *114*, 10039.
- Kresse, G.; Hafner, J. *Phys. Rev. B* **1993**, *47*, 558.
- Kresse, G.; Hafner, J. *Phys. Rev. B* **1994**, *49*, 14251.
- Kresse, G.; Furthmüller, J. *Phys. Rev. B* **1996**, *54*, 11169.
- Car, R.; Parrinello, M. *Phys. Rev. Lett.* **1985**, *55*, 2471.
- Eikerling, M.; Kornyshev, A. A. *J. Electroanal. Chem.* **2001**, *502*, 1.

- (100) Eikerling, M.; Kornyshev, A. A.; Kuznetsov, A. M.; Ulstrup, J.; Walbran, S. *J. Phys. Chem. B* **2001**, *105*, 3646.
- (101) Harned, H. S.; Owen, B. B. *The Physical Chemistry of Electrolyte Solutions*; Reinhold: New York, 1958.
- (102) Wolynes, P. G. *Annu. Rev. Phys. Chem.* **1980**, *31*, 345.
- (103) Kay, R. L. In *Water, A Comprehensive Treatise*; Franks, F., Ed.; Plenum Press: New York, 1973; Vol. 3.
- (104) Robinson, R. A.; Stokes, R. H. *Electrolyte Solutions*, 2nd Edition; Butterworth: London, 1959.
- (105) Born, M. *Z. Phys.* **1920**, *1*, 221.
- (106) Fuoss, R. M. *Proc. Natl. Acad. Sci.* **1959**, *45*, 807.
- (107) Boyd, R. H. *J. Chem. Phys.* **1961**, *35*, 1281.
- (108) Zwanzig, R. *J. Chem. Phys.* **1963**, *38*, 1603; **1970**, *52*, 3625.
- (109) Hubbard, J. B.; Onsager, L. *J. Chem. Phys.* **1977**, *67*, 4850.
- (110) Hubbard, J. B. *J. Chem. Phys.* **1978**, *68*, 1649.
- (111) Wolynes, P. G. *J. Chem. Phys.* **1978**, *68*, 473.
- (112) Colonosmos, P.; Wolynes, P. G. *J. Chem. Phys.* **1979**, *71*, 2644.
- (113) Chen, J. H.; Adelman, S. A. *J. Chem. Phys.* **1980**, *72*, 2819.
- (114) Chong, S.-H.; Hirata, F. *J. Chem. Phys.* **1998**, *108*, 7339.
- (115) Biswas, B.; Roy, S.; Bagchi, B. *Phys. Rev. Lett.* **1995**, *75*, 1098.
- (116) Biswas, B.; Bagchi, B. *J. Chem. Phys.* **1997**, *106*, 5587; *J. Am. Chem. Soc.* **1997**, *119*, 5946.
- (117) Bagchi, B. *J. Chem. Phys.* **1998**, *109*, 3989.
- (118) Resibois, P. M. V. *Electrolyte Theory: An Elementary Introduction to a Microscopic Approach*; Harper and Row: New York, 1968.
- (119) Belletete, M.; Lachapelle, M.; Durocher, G. *J. Phys. Chem.* **1990**, *94*, 5337.
- (120) Guha Ray, J.; Sengupta, P. K. *Chem. Phys. Lett.* **1994**, *230*, 75.
- (121) Das, K.; Sarkar, N.; Das, S.; Datta, A.; Bhattacharyya, K. *Chem. Phys. Lett.* **1996**, *249*, 323.
- (122) Datta, A.; Mandal, D.; Pal, S. K.; Bhattacharyya, K. *J. Phys. Chem. B* **1997**, *101*, 10221.
- (123) Faeder, J.; Ladanyi, B. M. *J. Chem. Phys.* **2000**, *104*, 1033.
- (124) Roux, B.; Karplus, M. *Annu. Rev. Biophys. Biomol. Struct.* **1994**, *23*, 731.
- (125) Breed, J.; Sankaramakrishnan, R.; Kerr, I. D.; Sansom, M. S. P. *Biophys. J.* **1996**, *70*, 1643.
- (126) Senapati, S.; Chandra, A. *J. Phys. Chem. B* **2001**, *105*, 5106.
- (127) Booth, F. *J. Chem. Phys.* **1950**, *19*, 391.
- (128) Bontha, J. R.; Pintauro, P. N. *Chem. Eng. Sci.* **1994**, *49*, 3835.
- (129) Steiner, T. *Angew. Chem.* **2002**, *114*, 50.
- (130) Dippel, T.; Hainovsky, N.; Kreuer, K. D.; Münch, W.; Maier, J. *Ferroelectrics* **1995**, *167*, 59.
- (131) Kreuer, K. D. *Solid State Ionics* **2000**, *136–137*, 149.
- (132) Desiraju, G. R. *Angew. Chem., Int. Ed. Engl.* **1995**, *34*, 2311.
- (133) Desiraju, G. R. *Chem. Commun.* **1997**, (16), 1475.
- (134) Schmidt, G. M. J. *Pure Appl. Chem.* **1971**, *27*, 647.
- (135) Weissbuch, I.; Popovitz-Biro, R.; Lahav, M.; Leiserovitz, L. *Acta Crystallogr. B: Struct. Sci.* **1995**, *51*, 115.
- (136) McDonald, J. C.; Whitesides, G. M. *Chem. Rev.* **1994**, *94*, 2383.
- (137) Eigen, M.; De Maeyer, L. *Proc. R. Soc. (London), Ser. A* **1958**, *247*, 505.
- (138) Eigen, M. *Angew. Chem.* **1963**, *75*, 489.
- (139) Zundel, G.; Metzger, H. *Z. Naturforsch.* **1967**, *22a*, 1412.
- (140) Agmon, N. *Chem. Phys. Lett.* **1995**, *244*, 456.
- (141) Dippel, T.; Kreuer, K. D. *Solid State Ionics* **1991**, *46*, 3.
- (142) Cohen, B.; Huppert, D. *J. Phys. Chem. A* **2003**, *107*, 3598.
- (143) Agmon, N. *Isr. J. Chem.* **1999**, *39*, 493.
- (144) Kreuer, K. D. *Solid State Ionics* **1997**, *94*, 55.
- (145) Sadeghi, R. R.; Cheng, H. P. *J. Chem. Phys.* **1999**, *111*, 2086.
- (146) Cui, Q.; Karplus, M. *J. Phys. Chem. B* **2003**, *107*, 1071.
- (147) Kreuer, K. D.; Rabenau, A.; Weppner, W. *Angew. Chem., Int. Ed. Engl.* **1982**, *21*, 208.
- (148) Agmon, N. *J. Chim. Phys. Phys.-Chim. Biol.* **1996**, *93*, 1714.
- (149) Tuckerman, M. E.; Marx, D.; Parrinello, M. *Nature* **2002**, *417*, 925.
- (150) Trout, B. L.; Parrinello, M. *J. Phys. Chem. B* **1999**, *103*, 7340.
- (151) Asthagiri, D.; Pratt, L. R.; Kress, J. D.; Gomez, M. A. *Chem. Phys. Lett.* **2003**, *380*, 530.
- (152) Asthagiri, D.; Pratt, L. R.; Kress, J. D.; Gomez, M. A. *Proc. Natl. Acad. Sci. (USA)* **2004**, *101*, 7233.
- (153) Chen, B.; Park, J. M.; Ivanov, I.; Tabacchi, G.; Klein, M. L.; Parrinello, M. *J. Am. Chem. Soc.* **2002**, *124*, 8534.
- (154) Kuo, J. L.; Ciobanu, C. V.; Ojamäe, L.; Shavitt, I.; Singer, S. J. *J. Chem. Phys.* **2003**, *118*, 3583.
- (155) Munson, R. A. *J. Phys. Chem.* **1964**, *68*, 3374.
- (156) Dippel, T.; Kreuer, K. D.; Lassègues, J. C.; Rodriguez, D. *Solid State Ionics* **1993**, *61*, 41.
- (157) Spaeth, M.; Kreuer, K. D.; Dippel, T.; Maier, J. *Solid State Ionics* **1997**, *97*, 291.
- (158) Spaeth, M.; Kreuer, K. D.; Maier, J. *J. Solid State Chem.* **1999**, *148*, 169.
- (159) Chung, S. H.; Bajue, S.; Greenbaum, S. G. *J. Chem. Phys.* **2000**, *112*, 8515.
- (160) Schlechter, A.; Savinell, R. F. *Solid State Ionics* **2002**, *147*, 181.
- (161) Kawada, A.; McGhie, A. R.; Labes, M. M. *J. Chem. Phys.* **1970**, *52*, 3121.
- (162) Decoursey, T. E. *Phys. Rev.* **2003**, *83*, 475.
- (163) Zundel, G.; Weidemann, E. G. *Eur. Biophys. Congr., Proc., 1st* **1971**, *6*, 43.
- (164) Riehl, N. *Trans. N.Y. Acad. Sci.* **1965**, *27*, 772.
- (165) Will, G. Z. *Kristallogr.* **1969**, *129*, 211.
- (166) Brown, G. P.; Aftergut, S. *J. Chem. Phys.* **1963**, *38*, 1356.
- (167) Pigon, K.; Chojnacki, H. *Acta Phys. Pol.* **1967**, *31*, 1069.
- (168) McGhie, A. R.; Blum, H.; Labes, M. M. *J. Chem. Phys.* **1970**, *52*, 6141.
- (169) Hickman, B. S.; Mascal, M.; Titman, J. J.; Wood, I. G. *J. Am. Chem. Soc.* **1999**, *121*, 11486.
- (170) Kreuer, K. D.; Fuchs, A.; Ise, M.; Spaeth, M.; Maier, J. *Electrochim. Acta* **1998**, *43*, 1281.
- (171) Kreuer, K. D. *Solid State Ionics: Science & Technology*; Chowdari, B. V. R., Lal, K., Agnihotry, S. A., Khare, N., Sekhon, S. S., Srivastava, P. C., Chandra, S., Eds.; World Scientific: Singapore, 1998, p 263.
- (172) Daycock, J. T.; Jones, G. P.; Evans, J. R. N.; Thomas, J. M. *Nature* **1968**, *218*, 673.
- (173) Tataru, W.; Wojcik, M. J.; Lindgren, J.; Probst, M. *J. Phys. Chem. A* **2003**, *107*, 7827.
- (174) Schuster, M.; Kreuer, K. D.; Maier, J., in preparation.
- (175) Toda, F.; Tanaka, K.; Foces-Foces, C.; Llamas-Saiz, A. L.; Limbach, H. H.; Aguilar-Parrilla, F.; Claramunt, R. M.; López, C.; Elguero, J. *J. Chem. Soc. Chem. Commun.* **1993**, 1139.
- (176) Stotz, S.; Wagner, C. *Ber. Bunsen-Ges. Phys. Chem.* **1966**, *70*, 781.
- (177) Takahashi, T.; Iwahara, H. *1980. Rev. Chim. Minèr.* **1980**, *t17*, 243.
- (178) Iwahara, H.; Uchida, H.; Tanaka, S. *Solid State Ionics* **1983**, *9–10*, 1021.
- (179) Iwahara, H.; Uchida, H.; Ono, K.; Ogaki, K. *J. Electrochem. Soc.* **1988**, *135*, 529.
- (180) Iwahara, H. *Solid State Ionics* **1988**, *28–30*, 573.
- (181) Iwahara, H.; Uchida, H.; Morimoto, K. *J. Electrochem. Soc.* **1990**, *137*, 462.
- (182) Bonanos, N.; Ellis, B.; Mahmood, M. N. *Solid State Ionics* **1991**, *44*, 305.
- (183) Tanigushi, N.; Hatoh, K.; Niikura, J.; Gamo, T. *Solid State Ionics* **1992**, *53–56*, 998.
- (184) Iwahara, H.; Yashima, T.; Hibino, T.; Ushida, H. *J. Electrochem. Soc.* **1993**, *140*, 1687.
- (185) Bonanos, N.; Knight, K. S.; Ellis, B. *Solid State Ionics* **1995**, *79*, 161.
- (186) Kreuer, K. D. *Annu. Rev. Mater. Res.* **2003**, *33*, 333.
- (187) Norby, T.; Larring, Y. *Curr. Opin. Solid State Mater. Sci.* **1997**, *2*, 593.
- (188) Kreuer, K. D. *Solid State Ionics* **1999**, *125*, 285.
- (189) Münch, W.; Seifert, G.; Kreuer, K. D.; Maier, J. *Solid State Ionics* **1996**, *86–88*, 647.
- (190) Shimojo, F.; Hoshino, K.; Okazaki, H.; *J. Phys. Soc. Jpn.* **1997**, *66*, 8.
- (191) Shimojo, F.; Hoshino, K. *Solid State Ionics* **2001**, *145*, 421.
- (192) Pionke, M.; Mono, T.; Schweika, W.; Springer, T.; Schober, T. *Solid State Ionics* **1997**, *97*, 497.
- (193) Matzke, T.; Stimming, U.; Karmonik, C.; Soetramo, M.; Hempelmann, R.; Güthoff, F. *Solid State Ionics* **1996**, *86–88*, 621.
- (194) Hempelmann, R.; Soetramo, M.; Hartmann, O.; Wäppling, R. *Solid State Ionics* **1998**, *107*, 269.
- (195) Münch, W.; Seifert, G.; Kreuer, K. D.; Maier, J. *Solid State Ionics* **1997**, *97*, 39.
- (196) Kreuer, K. D.; Münch, W.; Traub, U.; Maier, J. *Ber. Bunsen-Ges. Phys. Chem.* **1998**, *102*, 552.
- (197) Kreuer, K. D. *Solid State Ionics* **1997**, *97*, 1.
- (198) Sata, N.; Hiramoto, K.; Ishigame, M.; Hosoya, S.; Niimura, N.; Shin, S. *Phys. Rev. B* **1996**, *54*, 15795.
- (199) Münch, W.; Kreuer, K. D.; Seifert, G.; Maier, J. *Solid State Ionics* **2000**, *136–137*, 183.
- (200) Münch, W.; Kreuer, K. D.; Seifert, G.; Maier, J. *Solid State Ionics* **1999**, *125*, 39.
- (201) Nowick, A. S. *Solid State Ionics* **1997**, *97*, 17.
- (202) Kreuer, K. D.; Fuchs, A.; Maier, J. *Solid State Ionics* **1995**, *77*, 157.
- (203) Münch, W.; Kreuer, K. D.; Adams, S.; Seifert, G.; Maier, J. *Phase Transitions* **1999**, *68*, 567.
- (204) Ervine, J. T. S.; Corcoran, D. J. D.; Canales-Vasques, J. *Solid State Ionics* **2002**, *152*, 749.
- (205) Kreuer, K. D.; Adams, S.; Fuchs, A.; Klock, U.; Münch, W.; Maier, J. *Solid State Ionics* **2001**, *145*, 295.
- (206) Kreuer, K. D.; Münch, W.; Ise, M.; He, T.; Fuchs, A.; Traub, U.; Maier, J. *Ber. Bunsen-Ges. Phys. Chem.* **1997**, *101*, 1344.
- (207) Nowick, A. S.; Yang, Du; Liang, K. C. *Solid State Ionics* **1999**, *125*, 303.
- (208) Gebel, G.; Aldebert, P.; Pineri, M. *Polymer* **1993**, *34*, 333.
- (209) Gebel, G.; Lambard, J. *Macromolecules* **1997**, *30*, 7914.
- (210) Gebel, G. *Polymer* **2000**, *41*, 5829.
- (211) Rubalat, L.; Rollet, A. L.; Diat, O.; Gebel, G. *J. Phys. IV* **2002**, *12* (PR6), 197.
- (212) Ise, M. Ph.D. Thesis, University of Stuttgart, Stuttgart, Germany, 2000.

- (213) Kreuer, K. D. *J. Membr. Sci.* **2001**, *185*, 29.
- (214) Elliott, J. A.; Hanna, S.; Elliott, A. M. S.; Cooley, G. E. *Macromolecules* **2000**, *33*, 4161.
- (215) Khalatur, P. G.; Talitskikh, S. K.; Khokhlov, A. R. *Macromol. Theory Simul.* **2002**, *11*, 566.
- (216) Edmondson, C. A.; Fontanella, J. J. *Solid State Ionics* **2002**, *152–153*, 355.
- (217) Haubold, H. G.; Vad, T.; Jungbluth, H.; Hiller, P. *Electrochim. Acta* **2001**, *46*, 1559.
- (218) Kazansky, V.; Solkan, V. *Phys. Chem. Chem. Phys.* **2003**, *5*, 31.
- (219) Kreuer, K. D. in *Handbook of Fuel Cells—Fundamentals, Technology and Applications*; Vielstich, W., Lamm, A., Gasteiger, H. A. Eds.; Wiley: Chichester, U.K., 2003; p 420.
- (220) Eikerling, M.; Kornyshev, A. A.; Stimming, U. *J. Phys. Chem. B* **1997**, *101*, 10807.
- (221) Corry, B.; Kuyucak, S.; Chung, S. H. *Chem. Phys. Lett.* **2000**, *320*, 35.
- (222) Paddison, S. J.; Bender, G.; Kreuer, K. D.; Nicoloso, N.; Zawodzinski, T. A. *J. New Mater. Electrochem. Syst.* **2000**, *3*, 291.
- (223) Paddison, S. J.; Reagor, D. W.; Zawodzinski, T. A. *J. Electroanal. Chem.* **1998**, *459*, 91.
- (224) Kreuer, K. D.; Dippel, T.; Meyer, W.; Maier, J. *Mater. Res. Soc. Symp. Proc.* **1993**, *293*, 273.
- (225) Rollet, A. L.; Simonin, J. P.; Turq, P.; Gebel, G.; Kahn, R.; Vandais, A.; Noël, J. P.; Malveau, C.; Canet, D. *J. Phys. Chem.* **2001**, *105*, 4503.
- (226) Zawodzinski, T. A.; Springer, T. E.; Davey, J.; Jestel, R.; Lopez, C.; Valerio, J.; Gottesfeld, S. *J. Electrochem. Soc.* **1993**, *140*, 1981.
- (227) Kreuer, K. D.; Dippel, T.; Maier, J. *Proc. Electrochem. Soc.* **1995**, *95–23*, 241.
- (228) Cappadonia, M.; Erning, J. W.; Niaki, S. M. S.; Stimming, U. *Solid State Ionics* **1995**, *77*, 65.
- (229) Wainright, J. S.; Wang, J. T.; Weng, D.; Savinell, R. F.; Litt, M. *J. Electrochem. Soc.* **1995**, *142*, L121.
- (230) Glipa, X.; Bonnet, B.; Mula, B.; Jones, D. J.; Rozière, J. J. *Mater. Chem.* **1999**, *9*, 3045.
- (231) Bouchet, R.; Siebert, E. *Solid State Ionics* **1999**, *118*, 287.
- (232) Benicewicz, B. C. Presented as a poster during the 2003 Gordon Research Conference on Fuel Cells, Bristol, RI, July 27–August 1, 2003.
- (233) Bozkurt, A.; Ise, M.; Kreuer, K. D.; Meyer, W. H.; Wegner, G. *Solid State Ionics* **1999**, *125*, 225.
- (234) Yang, C.; Costamagna, P.; Srinivasan, S.; Benziger, J.; Bocarsly, A. B. *J. Power Sources* **2001**, *103*, 1.
- (235) Bozkurt, A.; Meyer, W. H.; Wegner, G. *J. Power Sources* **2003**, *123*, 126.
- (236) Münch, W., unpublished data.
- (237) Schuster, M. F.; Meyer, W. H.; Wegner, G.; Herz, H. G.; Ise, M.; Kreuer, K. D.; Maier, J. *Solid State Ionics* **2001**, *145*, 85.
- (238) Schuster, M. F. H.; Meyer, W. H. *Annu. Rev. Mater. Res.* **2003**, *33*, 233.
- (239) Schuster, M. F. H.; Meyer, W. H.; Schuster, M.; Kreuer, K. D. *Chem. Mater.* **2004**, *16*, 329.
- (240) Goward, G. R.; Schuster, M. F. H.; Sebastiani, D.; Schnell, I.; Spiess, H. W. *J. Phys. Chem. B* **2002**, *106*, 9322.
- (241) Herz, H. G.; Kreuer, K. D.; Maier, J.; Scharfenberger, G.; Schuster, M. F. H.; Meyer, W. H. *Electrochim. Acta* **2003**, *48*, 2165.
- (242) Perrson, J. C.; Jannasch, P. *Chem. Mater.* **2003**, *15*, 3044.
- (243) Miyake, N.; Wainright, J. S.; Savinell, R. F. *J. Electrochem. Soc. A* **2001**, *148*, A898.
- (244) Adjemian, K. T.; Lee, S. J.; Srinivasan, S.; Benziger, J.; Bocarsly, A. B. *J. Electrochem. Soc. A* **2002**, *149*, A256.
- (245) Alberti, G.; Casciola, M. *Annu. Rev. Mater. Res.* **2003**, *33*, 129.
- (246) Kumar, B.; Fellner, J. P. *J. Power Sources* **2003**, *123*, 132.
- (247) Mauritz, K. A.; Warren, R. M. *Macromolecules* **1989**, *22*, 1730.
- (248) Costamagna, P.; Yang, C.; Bocarsly, A. B.; Srinivasan, S. *Electrochim. Acta* **2002**, *47*, 1023.
- (249) Watanabe, M.; Uchida, H.; Seki, Y.; Emori, M. *J. Electrochem. Soc.* **1996**, *143*, 3847.
- (250) Malhotra, S.; Datta, R. *J. Electrochem. Soc.* **1997**, *144*, L23.
- (251) Tazi, B.; Savadogo, O. *Electrochim. Acta* **2000**, *45*, 4329.
- (252) Tazi, B.; Savadogo, O. *J. New Mater. Electrochem. Systems* **2001**, *4*, 187.
- (253) Bonnet, B.; Jones, D. J.; Rozière, J.; Tchicaya, L.; Alberti, G. *J. New Mater. Electrochem. Syst.* **2000**, *3*, 87.
- (254) Weng, D.; Wainright, J. S.; Landau, U.; Savinell, R. F. *J. Electrochem. Soc.* **1996**, *143*, 1260.
- (255) Edmondson, C. A.; Stallworth, P. E.; Chapman, M. E.; Fontanella, J. J.; Wintersgill, M. C.; Chung, S. H.; Greenbaum, S. G. *Solid State Ionics* **2000**, *135*, 419.
- (256) Edmondson, C. A.; Stallworth, P. E.; Wintersgill, M. C.; Fontanella, J. J.; Dai, Y.; Greenbaum, S. G. *Electrochim. Acta* **1998**, *43*, 1295.
- (257) Wintersgill, M. C.; Fontanella, J. J. *Electrochim. Acta* **1998**, *43*, 1533.
- (258) Zawodzinski, T. A.; Neeman, M.; Sillerud, L. O.; Gottesfeld, S. *J. Phys. Chem.* **1991**, *95*, 6040.
- (259) Edmondson, C. A.; Fontanella, J. J.; Chung, S. H.; Greenbaum, S. G.; Wnek, G. E. *Electrochim. Acta* **2001**, *46*, 1623.
- (260) Edmondson, C. A.; Fontanella, J. J. *Solid State Ionics* **2002**, *152–153*, 355.
- (261) Fontanella, J. J.; McLin, M. G.; Wintersgill, M. C.; Calame, J. P.; Greenbaum, S. G. *Solid State Ionics* **1993**, *66*, 1.
- (262) Ren, X.; Springer, T. E.; Zawodzinski, T. A.; Gottesfeld, S. *J. Electrochem. Soc.* **2000**, *147*, 466.
- (263) Hietala, S.; Maunu, S. L.; Sundholm, F. *J. Polym. Sci., Part B: Polym. Phys.* **2000**, *38*, 3277.
- (264) Doyle, M.; Rajendran, G. In *Handbook of Fuel Cells—Fundamentals, Technology and Applications*; Vielstich, W., Lamm, A., Gasteiger, H. A., Eds.; Wiley: Chichester, U.K., 2003; p 351.
- (265) Motupally, S.; Becker, A. J.; Weidner, J. W. *J. Electrochem. Soc.* **2000**, *147*, 3171.
- (266) Verbrugge, M. W. *J. Electrochem. Soc.* **1989**, *136*, 417.
- (267) LaConti, A. B.; Fragala, A. R.; Boyack, J. R. In *Proceedings of the Symposium on Electrode Materials and Processes for Energy Conversion and Storage*; McIntyre, J. D. E., Srinivasan, S., Will, F. G., Eds.; The Electrochemical Society Softbound Proceedings Series, PV 77-6; The Electrochemical Society: Princeton, NJ, 1977; p 354.
- (268) Meier, F.; Kerres, J.; Eigenberger, G. *J. New Mater. Electrochem. Syst.* **2002**, *5*, 91.
- (269) Helmholtz, H. *Weid. Ann.* **1879**, *7*, 337.
- (270) Lamb, H. *Philos. Mag.* **1888**, *5*, 52.
- (271) Perrin, J. *J. Chim. Phys.* **1904**, *2*, 601.
- (272) Smoluchowski, M. *Handbuch der Elektrizität und des Magnetismus*, Vol. II; Barth: Leipzig, 1914.
- (273) Breslau, B. R.; Miller, I. F. *Ind. Eng. Chem. Fundam.* **1971**, *10*, 554.
- (274) Ise, M.; Kreuer, K. D.; Maier, J. *Solid State Ionics* **1999**, *125*, 213.
- (275) Okada, T.; Moller-Holst, S.; Gorseth, O.; Kjelstrup, S. *J. Electroanal. Chem.* **1998**, *442*, 137.
- (276) Ren, X.; Gottesfeld, S. *J. Electrochem. Soc.* **2001**, *148*, A87.
- (277) Zawodzinski, T. A.; Davey, J.; Valerio, J.; Gottesfeld, S. *Electrochim. Acta* **1995**, *40*, 297.
- (278) Zawodzinski, T. A.; Derouin, C.; Radzinski, S.; Sherman, R. J.; Smith, Van T.; Springer, T. E.; Gottesfeld, S. *J. Electrochem. Soc.* **1993**, *140*, 1041.
- (279) Ren, X.; Henderson, W.; Gottesfeld, S. *J. Electrochem. Soc.* **1997**, *144*, L267.
- (280) Xie, G.; Okada, T. *J. Electrochem. Soc.* **1995**, *142*, 3057.
- (281) Fuller, T. F.; Newman, J. *J. Electrochem. Soc.* **1992**, *139*, 1332.
- (282) Yeo, R. S.; McBreen, J. *J. Electrochem. Soc.* **1979**, *126*, 1682.
- (283) Ogumi, Z.; Takehara, Z.; Yoshizawa, S. *J. Electrochem. Soc.* **1984**, *131*, 769.
- (284) Ogumi, Z.; Kuroe, T.; Takehara, Z. *J. Electrochem. Soc.* **1985**, *132*, 2601.
- (285) Sakai, T.; Takenaka, H.; Wakabayashi, N.; Kawami, Y.; Torikai, E. *J. Electrochem. Soc.* **1985**, *132*, 1328.
- (286) Parthasarathy, A.; Martin, C. R.; Srinivasan, S. *J. Electrochem. Soc.* **1992**, *138*, 916.
- (287) Broka, K.; Ekdunge, P. *J. Appl. Electrochem.* **1997**, *27*, 117.
- (288) Hietala, S.; Skou, E.; Sundholm, F. *Polymer* **1999**, *40*, 5567.
- (289) Basura, V. I.; Chuy, C.; Beattie, P. D.; Holdcroft, S. *J. Electroanal. Chem.* **2001**, *501*, 77.
- (290) Savinell, R.; Yeager, E.; Tryk, D.; Landau, U.; Wainright, J.; Weng, D.; Lux, D.; Litt, M.; Rogers, C. *J. Electrochem. Soc.* **1994**, *141*, L46.
- (291) Sakai, T.; Takenaka, H.; Torikai, E. *J. Electrochem. Soc.* **1986**, *133*, 88.
- (292) Büchi, F. N.; Wakizoe, M.; Srinivasan, S. *J. Electrochem. Soc.* **1996**, *143*, 927.
- (293) Kreuer, K. D.; Schönherr, E.; Maier, J. *Solid State Ionics* **1994**, *70/71*, 278.
- (294) Virkar, A. V.; Baek, H.-D. *J. Am. Ceram. Soc.* **2002**, *85*, 3059.
- (295) Kreuer, K. D.; Maier, J. *J. Am. Ceram. Soc.* **2004**, *87*, 1173.
- (296) Bonanos, N. *Solid State Ionics* **1992**, *53–56*, 967.
- (297) He, T.; Kreuer, K. D.; Maier, J. *Solid State Ionics* **1997**, *95*, 301.
- (298) He, T.; Kreuer, K. D.; Baikov, Y. M.; Maier, J. *Proc. Electrochem. Soc.* **1997**, *97*, 1057.
- (299) Gode, P.; Lindbergh, G.; Sundholm, G. *J. Electroanal. Chem.* **2002**, *518*, 115.
- (300) Zang, L.; Ma, C.; Mukerjee, S. *Electrochim. Acta* **2003**, *48*, 1845.
- (301) Tang, H.; Pintauro, P. N. *J. Appl. Polym. Sci.* **2001**, *79*, 49.
- (302) Wycisk, R.; Pintauro, P. N. *J. Membr. Sci.* **1996**, *119*, 155.
- (303) Carter, R.; Evilia, R. F.; Pintauro, P. N. *J. Phys. Chem. B* **2001**, *105*, 2351.
- (304) Young, S. K.; Mauritz, K. A. *J. Polym. Sci., Part B: Polym. Phys.* **2002**, *40*, 2237.
- (305) Dimitrova, P.; Friedrich, K. A.; Stimming, U.; Vogt, B. *Solid State Ionics* **2002**, *150*, 115.
- (306) Antonucci, P. L.; Arico, A. S.; Creti, P.; Ramunni, E.; Antonucci, V. *Solid State Ionics* **1999**, *125*, 431.
- (307) Kerres, J. *J. Membr. Sci.* **2001**, *185*, 3.
- (308) Kerres, J.; Ullrich, A.; Hein, M. *J. Polym. Sci., Part A: Polym. Chem.* **2001**, *39*, 2874.

- (309) Kerres, J.; Van Zyl, A. J. *J. Appl. Polym. Sci.* **1999**, *74*, 428.
- (310) Kerres, J.; Zhang, W.; Cui, W. *J. Polym. Sci., Part A: Polym. Chem.* **1998**, *36*, 1441.
- (311) Kerres, J.; Cui, W.; Reichle, S. *J. Polym. Sci., Part A: Polym. Chem.* **1996**, *34*, 2421.
- (312) Feichtinger, J.; Kerres, J.; Schulz, A.; Walker, M.; Schumacher, J. *J. New Mater. Electrochem. Syst.* **2002**, *5*, 155.
- (313) Kerres, J.; Zhang, W.; Jörissen, L.; Gogel, V. *J. New Mater. Electrochem. Syst.* **2002**, *5*, 97.
- (314) Kerres, J.; Ullrich, A.; Meier, F.; Häring, T. *Solid State Ionics* **1999**, *125*, 243.
- (315) Kerres, J.; Ullrich, A.; Hein, M.; Gogel, V.; Friedrich, K. A.; Jörissen, L. *Fuel Cells* **2004**, *4*, 105.
- (316) He, R.; Li, Q.; Xiao, G.; Bjerrum, N. J. *J. Membr. Sci.* **2003**, *226*, 169.
- (317) Ma, Y.-L.; Wainright, J. S.; Litt, M. H.; Savinell, R. F. *J. Electrochem. Soc.* **2004**, *151*, A8.
- (318) Lassègues, J. C.; Grondin, J.; Hernandez, M.; Marée, B. *Solid State Ionics* **2001**, *145*, 37.
- (319) Scharfenberger, G. Ph.D. Thesis, University Mainz, Germany, 2003.
- (320) Noda, A.; Susan, A. B.; Kudo, K.; Mitsushima, S.; Hayamizu, K.; Watanabe, M. *J. Phys. Chem. B* **2003**, *107*, 4024.
- (321) Guo, Q.; Pintauro, P. N.; Tang, H.; O'Connor, S. *J. Membr. Sci.* **1999**, *154*, 175.
- (322) Yang, Y.; Shi, Z.; Holdcroft, S. *Macromolecules* **2004**, *37*, 1678.
- (323) Jones, D. Presented at EUROMAT 2003, Lausanne, Switzerland.
- (324) Schuster, M.; Rager, T.; Noda, A.; Kreuer, K. D.; Maier, J. *Fuel Cells* **2004**, in press. (Invited paper.)
- (325) Campbell, A. N.; Kartzmark, E. M.; Bisset, D.; Bednas, M. E. *Can. J. Chem.* **1953**, *31*, 303.
- (326) Miyatake, K.; Iyotani, H.; Yamamoto, K.; Tsuchida, E. *Macromolecules* **1996**, *29*, 6969.
- (327) Yang, Y.; Holdcroft, S. *Fuel Cells* **2004**, in press.
- (328) Cornet, N.; Diat, O.; Gebel, G.; Jousse, F.; Marsacq, D.; Mercier, R.; Pineri, M. *J. New Mater. Electrochem. Syst.* **2000**, *3*, 33.
- (329) Genies, C.; Mercier, R.; Sillion, B.; Petiaud, R.; Cornet, N.; Gebel, G.; Pineri, M. *Polymer* **2001**, *42*, 5097.
- (330) Blachot, J. F.; Diat, O.; Putaux, J.-L.; Rollet, A.-L.; Rubatat, L.; Vallois, C.; Müller, M.; Gebel, G. *J. Membr. Sci.* **2003**, *214*, 31.
- (331) Piroux, F.; Espuche, E.; Mercier, R.; Pineri, M. *J. Membr. Sci.* **2003**, *223*, 127.
- (332) Harrison, W. L.; Wang, F.; Mecham, J. B.; Bhanu, V. A.; Hill, M.; Kim, Y. S.; McGrath, J. E. *J. Polym. Sci., Part A: Polym. Chem.* **2003**, *41*, 2264.
- (333) Miyatake, K.; Zhou, H. Y.; Watanabe, M. *Macromolecules* **2004**, *37*, 4956.
- (334) Susan, M. A. B. H.; Noda, A.; Mitsushida, S.; Watanabe, M. *Chem. Commun.* **2003**, *8*, 938.
- (335) Honma, I.; Nakajima, H.; Nishikawa, O.; Sugimoto, T.; Nomura, S. *Solid State Ionics* **2003**, *162–163*, 2003.
- (336) Honma, I.; Nakajima, H.; Nishikawa, O.; Sugimoto, T.; Nomura, S. *J. Electrochem. Soc. A* **2003**, *150*, A616.
- (337) Kreuer, K. D.; Hampele, M.; Dolde, K.; Rabenau, A. *Solid State Ionics* **1988**, *28–30*, 589.
- (338) Alberti, G.; Costantino, U.; Casciola, M.; Ferroni, S.; Massinelli, L.; Staiti, P. *Solid State Ionics* **2001**, *145*, 249.
- (339) Baranov, A. I.; Shuvalov, L. A.; Shchagina, N. M. *JETP Lett.* **1982**, *36*, 459.
- (340) Haile, S. M.; Boysen, D. A.; Chisholm, C. R. I.; Merle, S. M. *Nature* **2001**, *410*, 910.
- (341) Boysen, D. A.; Uda, T.; Chisholm, C. R. I.; Haile, S. M. *Science* **2004**, *303*, 68.
- (342) Coors, W. G. *J. Power Sources* **2003**, *118*, 150.
- (343) Kreuer, K. D. *ChemPhysChem* **2002**, *3*, 771.

CR020715F

Fundamental Models for Fuel Cell Engineering

Chao-Yang Wang*

Departments of Mechanical Engineering and Materials Science and Engineering, Electrochemical Engine Center (ECEC),
The Pennsylvania State University, University Park, Pennsylvania 16802

Received January 23, 2004

Contents

1. Introduction	4727
2. Computational Fuel Cell Dynamics	4727
2.1. CFCF Model Equations	4728
2.2. Computational Aspects	4729
2.2.1. General	4729
2.2.2. Solution Algorithms for Coupled Potential Equations	4729
2.2.3. Mesh Requirement and Parallel Computing	4730
2.3. Material Property Characterization	4730
3. Polymer Electrolyte Fuel Cells	4732
3.1. Single-Phase Conservation Equations	4733
3.2. Water Transport	4736
3.3. Heat Transport	4738
3.4. Electron Transport	4740
3.5. Transient Phenomena	4741
3.6. Large-Scale Simulation	4742
3.7. Liquid Water Transport	4742
3.8. Experimental Diagnostics and Model Validation	4747
3.8.1. Current, Species, and High-Frequency Resistance Distribution Measurements	4747
3.8.2. Temperature Distribution Measurements	4749
3.8.3. Two-Phase Visualization	4750
3.8.4. Experimental Validation	4751
3.9. Modeling the Catalyst Layer at Pore Level	4751
3.10. Summary and Outlook	4752
4. Direct Methanol Fuel Cells	4753
4.1. Technical Challenges	4754
4.1.1. Methanol Oxidation Kinetics	4754
4.1.2. Methanol Crossover	4755
4.1.3. Water Management	4755
4.1.4. Heat Management	4756
4.2. DMFC Modeling	4756
4.2.1. Needs for Modeling	4756
4.2.2. DMFC Models	4756
4.3. Experimental Diagnostics	4757
4.4. Model Validation	4758
4.5. Summary and Outlook	4760
5. Solid Oxide Fuel Cells	4760
5.1. SOFC Models	4761
5.2. Summary and Outlook	4762
6. Closing Remarks	4763

7. Acknowledgments	4763
8. References	4763

1. Introduction

Owing to their high energy efficiency, low pollution, and low noise, fuel cells are widely regarded as 21st century energy-conversion devices for mobile, stationary, and portable power. Through tremendous progress made in the past decade, currently available fuel cell materials appear to be adequate for near-term markets with highest cost entry points. As a result, industries are currently placing their focus on fuel cell design and engineering for better performance, improved durability, cost reduction, and better cold-start characteristics. This new focus has led to an urgent need for identification, understanding, prediction, control, and optimization of various transport and electrochemical processes that occur on disparate length scales in fuel cells.

The purpose of the present review is to summarize the current status of fundamental models for fuel cell engineering and indicate where this burgeoning field is heading. By choice, this review is limited to hydrogen/air polymer electrolyte fuel cells (PEFCs), direct methanol fuel cells (DMFCs), and solid oxide fuel cells (SOFCs). Also, the review does not include microscopic, first-principle modeling of fuel cell materials, such as proton conducting membranes and catalyst surfaces. For good overviews of the latter fields, the reader can turn to Kreuer,¹ Paddison,² and Koper,³ for example.

The review is organized as follows. Section 2 defines a systematic framework for fuel cell modeling research, called computational fuel cell dynamics (CFCF), and outlines its four essential elements. Sections 3–5 review work performed in the past decade on PEFCs, DMFCs, and SOFCs, respectively. Future research needs and directions of the three types of fuel cells are pointed out wherever applicable and summarized separately at the end of each section.

2. Computational Fuel Cell Dynamics

Fuel cell science and technology cuts across multiple disciplines, including materials science, interfacial science, transport phenomena, electrochemistry, and catalysis. Because of the diversity and complexity of electrochemical and transport phenom-

* To whom correspondence should be addressed. E-mail: cwx31@psu.edu.



Chao-Yang Wang received his Ph.D. degree in Mechanical Engineering from the University of Iowa in 1994, and he is currently a Professor of Mechanical Engineering and Materials Science & Engineering at The Pennsylvania State University. He has been the founding director of the Penn State Electrochemical Engine Center (ECEC) since 1997. His research interests include fundamental modeling and experimental diagnostics of various fuel cell/battery systems and their materials.

ena involved in a fuel cell and occurring at disparate length and time scales, fuel cell modeling and simulation requires a systematic framework parallel to computational fluid dynamics (CFD), here termed computational fuel cell dynamics (CFCD). CFCD deals with the coupling of multidimensional transport phenomena with electrochemical kinetics and the transport of charge (electrons and ions) to provide a comprehensive understanding of fuel cell dynamics. CFCD is envisioned to consist of (1) physicochemical model development, (2) advanced numerical algorithms, (3) materials characterization, and (4) model validation at detailed levels.

Section 2.1 gives a generalized summary of fuel cell models, while section 2.2 discusses the need for employing large numerical meshes and hence advanced numerical algorithms for efficient fuel cell simulations. Section 2.3 briefly reviews the efforts, in the literature, to measure basic materials and transport properties as input to fuel cell models.

The need for the fourth element, i.e., model validation against detailed distribution data, has been increasingly acknowledged in the past few years.^{4–6} This is because the global I – V curve is largely inadequate to validate comprehensive CFCD models. This inadequacy can perhaps best be illustrated by a numerical experiment shown in Figure 1. In this experiment, a three-dimensional (3-D) PEFC model (as described in section 3.1) is applied to a single-channel fuel cell using Gore-Select 18 μm membrane with an anode/cathode stoichiometry of 3/2 and anode/cathode inlet relative humidity of 42%/0% at a cell temperature of 80 $^{\circ}\text{C}$. Two cases are simulated using the same model for a cell voltage of 0.75 V. In Case 1, the ionic resistance in two catalyst layers is included, and the kinetic constant of oxygen reduction reaction (ORR) is estimated from the Pt loading. This case yields an average current density of 0.24 A/cm^2 at 0.75 V. In Case 2 (which is hypothetical), however, we neglect the ionic resistance in two catalyst layers (amounting to approximately twice that of the membrane) and then reduce the kinetic

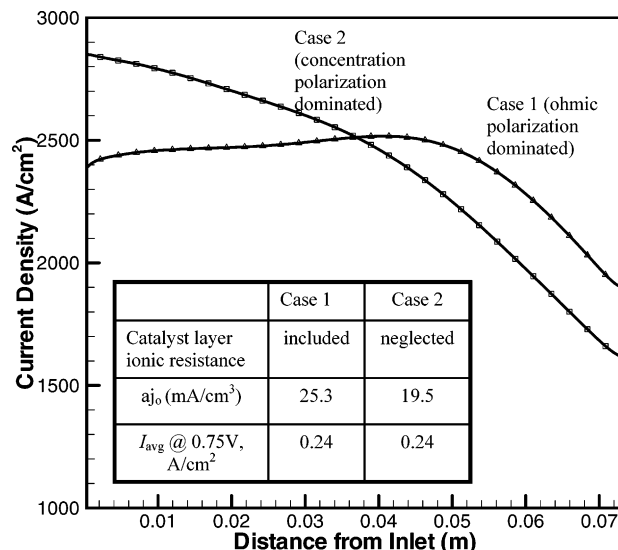


Figure 1. Local current density profiles along a straight-channel fuel cell as predicted by the same computer model for two cases differing only in two model parameters.⁶

constant by 23%. By changing only two parameters (i.e., catalyst layer resistance and kinetic constant of ORR), Case 2 produces exactly the same average current density as Case 1, despite that the two cases fundamentally differ in limiting mechanisms. Case 1 is dominated more by ohmic polarization, thereby exhibiting a slight increase in the local current density near the dry inlet as the membrane becomes more hydrated, and a fall only close to the outlet where oxygen depletion starts to take control. On the other hand, Case 2 is dominated more by concentration polarization with little ohmic loss. As a result, the current distribution in Case 2 closely follows the decline of oxygen concentration due to the stoichiometric effect. Literature efforts involving detailed diagnostics aiming to create benchmark-quality data for CFCD model validation are reviewed in section 3.8 for the PEFC system.

2.1. CFCD Model Equations

A fundamental fuel cell model consists of five principles of conservation: mass, momentum, species, charge, and thermal energy. These transport equations are then coupled with electrochemical processes through source terms to describe reaction kinetics and electro-osmotic drag in the polymer electrolyte. Such convection–diffusion–source equations can be summarized in the following general form

$$\frac{\partial(\rho\phi)}{\partial t} + \nabla(\rho v\phi) = \nabla(\Gamma\nabla\phi) + S \quad (1)$$

where ϕ is a general variable to be solved, ρ the density, v the velocity vector, Γ the diffusion coefficient, and S a source term which includes all terms that cannot be included in the previous terms. For instance, the Darcy's drag exerted on gas flow through porous electrodes of fuel cells is typically accounted for through a source term in the momentum equation. The electro-osmotic drag of water

through a polymer electrolyte can also be formulated as a source term in the water species equation since it differs from conventional mechanisms of transport by diffusion and convection and arises only from an electrochemical system.

Setting $\phi = 1$, the above general transport equation is reduced to

$$\frac{\partial \rho}{\partial t} + \nabla(\rho v) = S_m \quad (2)$$

This equation is usually referred to as the continuity equation or mass conservation equation.⁷ The source term, S_m , in the continuity equation is commonly caused by mass consumption or production from electrochemical reactions as well as mass loss/gain through phase transformation.

Main source terms prevailing in most transport equations for a fuel cell model are due to electrochemical reactions occurring in the electrode comprised of three phases: electronic (*s*), electrolyte (*e*), and gas (*g*). Electrochemical reactions occur at the triple-phase boundary according to the following general formula

$$\sum_k s_k M_k^z = n e^- \quad (3)$$

where the summation is over all species involved in a reaction. M_k is a chemical symbol for species k participating in the electrochemical reaction, z and s are the charge number and stoichiometric coefficient of the species, and n is the number of electrons transferred in the reaction. The values of s_k , z , and n can readily be determined by comparing a specific electrode reaction to this general form. For example, for the oxygen reduction reaction, $2\text{H}_2\text{O} - \text{O}_2 - 4\text{H}^+ = 4e^-$, one has that $s_{\text{H}_2\text{O}} = 2$, $s_{\text{O}_2} = -1$, $s_{\text{H}^+} = -4$, and $n = 4$.

The volumetric production rate of species k due to electrochemical reaction occurring at the triple-phase boundary is given by Faraday's law

$$S_k = -\frac{s_k j}{nF} \quad (4)$$

with

$$j = a i_o \left[\exp\left(\frac{\alpha_a F}{RT} \eta\right) - \exp\left(-\frac{\alpha_c F}{RT} \eta\right) \right] \quad (5)$$

where j is the volumetric transfer current of the reaction, a is the electrochemically active area per unit of electrode volume, i_o is the exchange current density, α_a and α_c are the anodic and cathodic transfer coefficients, respectively, F is Faraday's constant, R is the universal gas constant, and T is the cell temperature. Equation 5, commonly known as the Butler–Volmer equation, describes a large class of electrode reactions.⁸ Under facile and sluggish kinetics, the Butler–Volmer equation is further reduced to linear and Tafel expressions, respectively.

The exchange current density for a reaction, i_o , depends strongly on the compositions and temperature at the reaction interface. The surface over-

potential for an electrochemical reaction, η , is defined as

$$\eta = \Phi_s - \Phi_e - U_o \quad (6)$$

where Φ_s and Φ_e are the electric potentials of the electronic phase and electrolyte, respectively, at the triple-phase interface. The last term in eq 6, U_o , is the thermodynamic equilibrium potential of the reaction, which is, in turn, a function of the reactant and product concentrations at the interface as generally expressed by the Nernst equation. Note that the surface overpotential, η , represents the driving force for an electrochemical reaction.

2.2. Computational Aspects

2.2.1. General

The advection–diffusion equation with a source term can be solved by CFD algorithms in general. Patankar⁹ provided an excellent introduction to numerical fluid flow and heat transfer. Oran and Boris¹⁰ discussed numerical solutions of diffusion–convection problems with chemical reactions. Since fuel cells feature an aspect ratio of the order of 100, $O(100)$, the upwind scheme for the flow-field solution is applicable and proves to be very effective.⁹ Unstructured meshes are commonly employed in commercial CFD codes.

2.2.2. Solution Algorithms for Coupled Potential Equations

A numerical problem unique to the modeling of electrochemical systems in general and fuel cells in particular is the strong coupling between the potentials for the electronic and electrolyte phases. The two potential equations are dependent on each other through the reaction current, where the surface overpotential appears in the exponential terms of Butler–Volmer kinetics. Advanced iterative algorithms are required in order to ensure efficient and converging solutions.^{8,11–13} It appears that the most efficient technique is to solve the two discretized algebraic equations *simultaneously* using Newton's method.^{8,11} For one-dimensional problems, such a direct solution method results in the often-used Band-J subroutine developed by Newman⁸ in the 1960s, in which the Jacobian matrix resulting from Newton's procedure is inverted using LU factorization in each Newton iteration. However, the direct solution is computationally inefficient for a large sparse Jacobian matrix arising from two- and three-dimensional problems. Recently, Wu et al.¹¹ presented a set of modern numerical algorithms to efficiently solve the two strongly coupled potential equations. A Krylov iterative solver, the generalized minimal residual subroutine (GMRES), was used instead of the direct solver (Gauss elimination) to improve solution efficiency of the large, nonsymmetric Jacobian system. In addition, a nonlinear Gauss–Seidel method provided the initial guess for the Newton iteration, and the GMRES solver was preconditioned with a block Gauss–Seidel and multigrid algorithm with a smoother based on the tridiagonal matrix algorithm (TDMA).

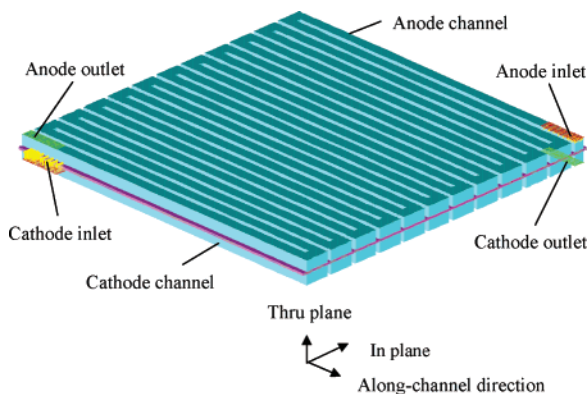


Figure 2. PEFC configuration for numerical modeling.

Within the framework of commercial CFD codes where sequential solution methods are standard, as they need to solve a number of user-specified transport equations, the two potential equations must then be solved through innovative source term linearization.¹⁴

2.2.3. Mesh Requirement and Parallel Computing

Another computational challenge in fuel cell modeling is the need for large meshes for simulation of industrial-scale cells. To fully appreciate the large mesh required, consider a typical geometry of a large-scale PEFC displayed in Figure 2, where the anode flow field (top) and cathode flow field (bottom) sandwich a membrane–electrode assembly (MEA) with two gas diffusion layers (GDL). Let us define the through-plane direction to be perpendicular to the MEA, the along-channel direction to be of gas flow, and the in-plane direction to be across channels through the land area. Suppose that 6–8 grid points are needed to sufficiently resolve each of the five distinctive regions of MEA and two GDLs, with 10 grid points needed in each of the two gas channels, the minimum number of grid points in the through-plane dimension is thus between 50 and 60. In the along-channel direction, 100 grid points are typically required since fuel cell channels are long and exhibit a large aspect ratio (> 100). In the in-plane direction, 10 nodal points are needed for a channel and a land, respectively, thus giving rise to 20 grid points per channel within a flow field. For large-scale fuel cells featuring 20–60-channel flow field, a mesh consisting of 2–6 million grid points is needed.

The majority of numerical work published to date has used no more than a few hundred thousand grid points; that is, there is still 1 order of magnitude gap existing between the current computational capability and that required for high-fidelity PEFC simulation. Meng and Wang¹⁵ made one of the first attempts to bridge this gap by developing a massively parallel computational methodology based on an efficient domain decomposition method. The computational domain is divided into a number of subdomains along the flow direction. Each subdomain is assigned to one processor with proper load balancing. Each processor computes and stores variable solutions within its own subdomain with necessary interactions on subdomain boundaries through communication between proces-

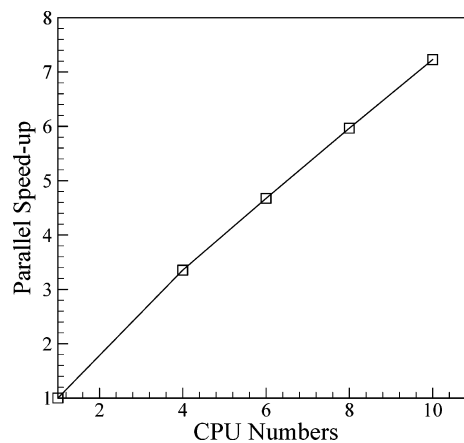


Figure 3. Speedup of a massively parallelized PEFC model.¹⁵

sors. As a fuel cell features a minimal degree of interactions between subdomains along the flow direction, this problem is inherently suited for parallel computing with low communication cost. Benchmark calculations were carried out in a Linux PC cluster comprised of 50 processors of 1.4 GHz AMD Athlon Thunderbird CPU and 512 MB DDR SDRAM. A local 100 Mbps switched Ethernet network was used for message communication. Figure 3 displays the computational performance of the PC cluster, demonstrating greater than 7× speed-up by 10 CPUs running the massively parallelized PEFC model. Roughly 300 iterations are needed for a typical case run, requiring about 1.5 h of computational time using 10 CPUs. This clearly demonstrates the effectiveness of parallel computing in reducing actual computing time for these intensive simulations.

Large-scale calculations using 1–10 million computational cells are presently being carried out in several industrial and academic organizations using the parallel computing method and multiprocessor computers; see section 3.6 for further detail.

2.3. Material Property Characterization

The importance of materials characterization in fuel cell modeling cannot be overemphasized, as model predictions can be only as accurate as their material property input. In general, the material and transport properties for a fuel cell model can be organized in five groups: (1) transport properties of electrolytes, (2) electrokinetic data for catalyst layers or electrodes, (3) properties of diffusion layers or substrates, (4) properties of bipolar plates, and (5) thermodynamic and transport properties of chemical reactants and products.

The most important electrolyte property is ionic conductivity. For the PEFC system, water and proton transport in the polymer electrolyte occurs concurrently. Springer et al.¹⁶ correlated the proton conductivity (in S/cm) in the polymer membrane with its water content as follows

$$\kappa_e = \exp\left[1268\left(\frac{1}{303} - \frac{1}{T}\right)\right](0.005139\lambda - 0.00326) \quad (7)$$

The strong dependence of electrolyte conductivity on

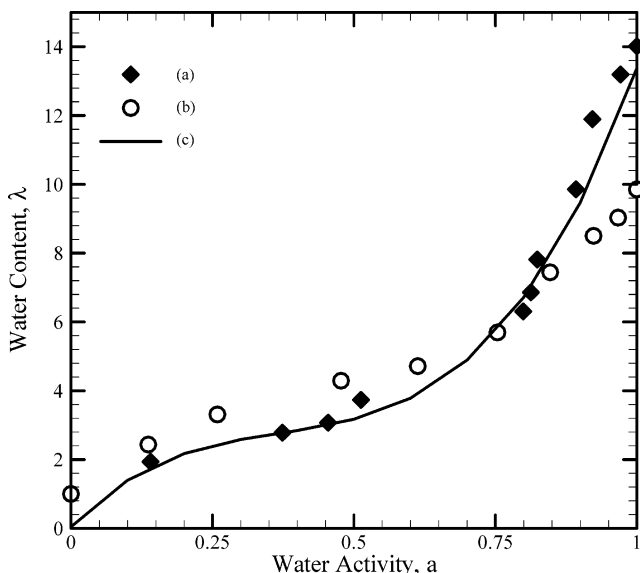


Figure 4. Equilibrium water uptake curve for Nafion membrane: (a) measurement at 30 °C,¹⁸ (b) measurement at 80 °C,¹⁷ (c) Springer's expression, eq 8.

water content is evident from the above correlation. Several studies^{17–22} have been carried out to define the relation between membrane water content and moisture of the surrounding environment, called the water uptake curve as shown in Figure 4. Zawodzinski et al.^{17,18} measured water content of membranes immersed in liquid water and membranes exposed to water vapor at variable activities. It is seen that there is a discontinuity in the membrane water content between equilibration of the membrane with liquid water and with saturated water vapor, both of which correspond to unit water activity. This phenomenon, called “Schröder's paradox”, is observed in a wide variety of polymer/solvent combinations. Water content in the membrane (i.e., the number of H₂O molecules per sulfonic group), λ , depends on the water activity, a , according to the following fit of the experimental data¹⁶

$$\lambda = \begin{cases} 0.043 + 17.81a - 39.85a^2 + 36.0a^3 & \text{for } 0 < a \leq 1 \\ 14 + 1.4(a - 1) & \text{for } 1 \leq a \leq 3 \end{cases} \quad (8)$$

where the water activity is in turn calculated by the ratio of the water partial pressure to the saturated pressure, corresponding to the cell temperature, T . Apparently, the water activity and water content all vary spatially; thus, the proton conductivity κ_e also varies throughout the membrane and catalyst layer. In the catalyst layer, the effective proton conductivity is further modified by Bruggmann factor based on the ionomer content

$$\kappa_e^{\text{eff}} = \epsilon_e^{1.5} \kappa_e \quad (9)$$

where ϵ_e is the ionomer volume fraction.

Two other important electrolyte properties for the PEFC system are the water diffusion coefficient and electro-osmotic drag coefficient. These two param-

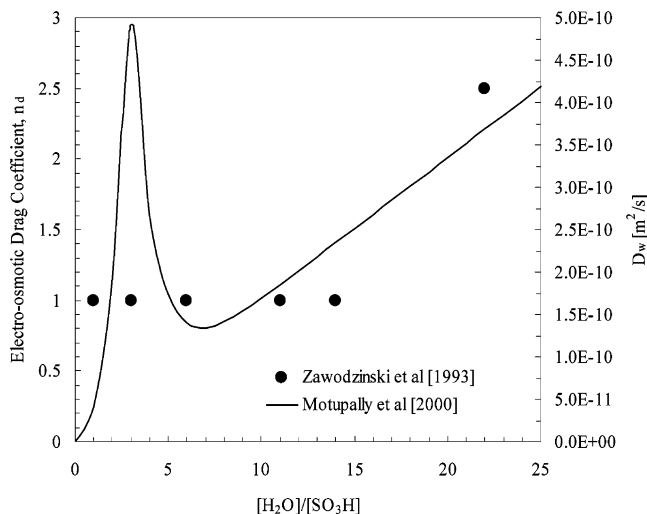


Figure 5. Electro-osmotic drag coefficient and water diffusivity as functions of water content in Nafion membranes.^{23,27}

eters dictate the water content profile within the membrane and thus design of a proper water management scheme for the fuel cell. Water content dependence of diffusion coefficient and electro-osmotic drag coefficient has also been extensively studied.^{23–27} Figure 5 indicates that the electro-osmotic drag coefficient is roughly a constant at unity when $\lambda < 14$ and then linearly increases for water content between 14 and 22. The water diffusion coefficient in the membrane is highly nonlinear and shows a distinctive peak at $\lambda \approx 3$. The nonlinearity in membrane-transport properties excludes analytical solutions and increases the level of difficulty in numerical solutions.

Kreuer¹ presented an excellent discussion of materials and transport properties of proton conducting membranes other than Nafion.

The most important electrokinetic data pertinent to fuel cell models are the specific interfacial area in the catalyst layer, a , the exchange current density of the oxygen reduction reaction (ORR), i_o , and Tafel slope of ORR. The specific interfacial area is proportional to the catalyst loading and inversely proportional to the catalyst layer thickness. It is also a strong function of the catalyst layer fabrication methods and procedures. The exchange current density and Tafel slope of ORR have been well documented in refs 28–31.

Diffusion medium properties for the PEFC system were most recently reviewed by Mathias et al.³² The primary purpose of a diffusion medium or gas diffusion layer (GDL) is to provide lateral current collection from the catalyst layer to the current collecting lands as well as uniform gas distribution to the catalyst layer through diffusion. It must also facilitate the transport of water out of the catalyst layer. The latter function is usually fulfilled by adding a coating of hydrophobic polymer such as poly(tetrafluoroethylene) (PTFE) to the GDL. The hydrophobic polymer allows the excess water in the cathode catalyst layer to be expelled from the cell by gas flow in the channels, thereby alleviating flooding. It is known that the electric conductivity of GDL is

typically an order of magnitude higher in the in-plane direction than the through-plane direction due to the strong anisotropy of GDL fibrous structures. By analogy between electric and heat conduction, it can be expected that the thermal conductivity of GDL exhibits the same degree of anisotropy. Pore size distribution, porosity, and gas permeability were characterized by Mathias et al., albeit without compression, which should add a strong effect on the GDL-transport properties. In addition, the interfacial wetting property, both in the interior and on the surface of porous GDL, was recognized as an important material property of GDL. Mathias et al.³² and Lim and Wang³³ independently performed surface contact angle measurements, based on variants of the capillary rise method. Lim and Wang³³ further reported a strong temperature dependence of water contact angle on GDL, thereby establishing a link to the realistic thermal environment in an operating PEFC. The literature, however, lacks experimental data on the porosity and permeability of GDL under compression or more broadly the quantification of GDL deformation under stress and subsequently GDL structure–flow interactions.

Three properties of the current collector plate are particularly important for CFCD models. One is electric conductivity, the second is thermal conductivity, and the third is surface wettability. These properties for materials such as graphite and metals are well documented in standard textbooks.

The species diffusivity, D_k , varies in different subregions of a PEFC depending on the specific physical phase of component k . In flow channels and porous electrodes, species k exists in the gaseous phase and thus the diffusion coefficient corresponds with that in gas, whereas species k is dissolved in the membrane phase within the catalyst layers and the membrane and thus assumes the value corresponding to dissolved species, usually a few orders of magnitude lower than that in gas. The diffusive transport in gas can be described by molecular diffusion and Knudsen diffusion. The latter mechanism occurs when the pore size becomes comparable to the mean free path of gas, so that molecule-to-wall collision takes place instead of molecule-to-molecule collision in ordinary diffusion. The Knudsen diffusion coefficient can be computed according to the kinetic theory of gases as follows

$$D_{K,k} = \frac{2}{3} \left(\frac{8RT}{\pi M_k} \right)^{1/2} r_p \quad (10)$$

where r_p is the mean pore radius and M_k the molecular weight of the diffusing gas.

The binary diffusion coefficient, $D_{i,k}$, can be either experimentally measured or calculated using the Chapman–Enskog equation.³⁴ The dependence of the diffusion coefficient on temperature and pressure is generally given by⁷

$$D_{i,k}(T,p) = D_{i,k,0} \left(\frac{T}{T_0} \right)^{3/2} \left(\frac{P_0}{p} \right) \quad (11)$$

The combined diffusivity of species k in gas, due to

ordinary and Knudsen diffusion, is then calculated from

$$D_k = \left(\frac{1}{D_{K,k}} + \frac{1}{D_{i,k}} \right)^{-1} \quad (12)$$

In the PEFC system, the mean pore radii of catalyst layers are of the order of 0.1 μm . The Knudsen diffusion coefficients at 80 °C for O₂ and H₂O through the catalyst layer are thus estimated to be 0.32 and 0.43 cm²/s, respectively. These values are comparable to the respective ordinary diffusion coefficients, indicating that Knudsen diffusion further restricts the rates of oxygen and water transport through the cathode catalyst layer in PEFCs and should be taken into account.

Thermodynamic and transport properties of liquids relevant to the DMFC system can be found in Reid et al.³⁵

Key material properties for SOFC, such as the ionic conductivity as a function of temperature, are available in refs 36–39. In addition, Todd and Young⁴⁰ compiled extensive data and presented estimation methods for the calculation of diffusion coefficients, thermal conductivities, and viscosities for both pure components and mixtures of a wide variety of gases commonly encountered in SOFCs. Another excellent source of transport properties for gases and mixtures involved in a SOFC is the CHEMKIN thermodynamic database.⁴¹

3. Polymer Electrolyte Fuel Cells

Polymer electrolyte fuel cells (PEFC) are considered the most promising alternative power plant for transportation because of their high efficiency, low emissions, low operation temperature, and low noise. In the past decade, significant improvements have been achieved in PEFC technology, including improved MEA technology and lowered platinum catalyst loading. Excellent reviews of hydrogen PEFC research up to the mid-1990s were presented by Prater⁴² and Gottesfeld and Zawodzinski,³⁰ and new advances were reported in the most recent compilation of Vielstich et al.⁴³

Much effort has been expended in the last 5 years upon development of numerical models with increasingly less restrictive assumptions and more physical complexities. Current development in PEFC modeling is in the direction of applying computational fluid dynamics (CFD) to solve the complete set of transport equations governing mass, momentum, species, energy, and charge conservation.

Modeling and computer simulation of PEFC began with the pioneering work of Bernardi and Verbrugge^{44,45} and Springer et al.,^{46,47} whose models are essentially one-dimensional. Fuller and Newman,⁴⁸ Nguyen and White,⁴⁹ and Yi and Nguyen^{50,51} subsequently developed pseudo-two-dimensional models accounting for compositional changes along the flow path. While such models are useful for small cells, their applicability to large-scale fuel cells, particularly under high fuel utilization and low humidity conditions, is limited. Nevertheless, the one-dimensional models of Bernardi and Verbrugge^{44,45} and

Springer et al.^{46,47} provided a fundamental framework to build multidimensional, multiphysics models that followed. The pseudo-two-dimensional models developed by Fuller and Newman,⁴⁸ Nguyen and White,⁴⁹ and later Yi and Nguyen^{50,51} further demonstrated the important roles played by water and heat management in maintaining high performance of PEFCs. Effects of anisotropy and inhomogeneity on mass transport through GDL were also numerically investigated.^{52,53}

Gurau et al.⁵⁴ presented a two-dimensional model of transport phenomena in PEFC. This work illustrated the utility of a multidimensional model in the understanding of the internal conditions of a fuel cell, such as the reactant and water distributions. In a separate development, Yi and Nguyen^{50,51} formulated a two-dimensional model to explore hydrodynamics and multicomponent transport in the air cathode of PEFC with an interdigitated flow field. The concept of modeling PEFC within the CFD framework was proposed shortly thereafter.^{55–58} Two-dimensional simulations of coupled electrochemical and transport processes were carried out in using a CFD code,⁵⁵ and the three-dimensional version of the same model was also demonstrated.^{56,59} Independently, Dutta et al.⁵⁷ presented three-dimensional simulation of PEFC using Fluent, a commercial CFD package. Subsequent work was presented in Dutta et al.⁵⁸ and Lee et al.⁶⁰ In the model of Dutta et al.^{57,58} and Lee et al.,⁶⁰ the membrane electrode assembly (MEA) is not included in the computational domain but rather simplified as an interface without thickness. As such, water transport and ohmic potential drop across the membrane are treated using simplified linear relationships as in the early work of Nguyen and White.⁴⁹

Additional work on general-purpose, fully three-dimensional CFCD models was performed by Zhou and Liu⁶¹ using an in-house CFD code, Berning et al.⁶² using the commercial package CFX, and Mazumder and Cole⁶³ using the commercial package CFD-ACE+. Most recently, both STAR-CD and Fluent packages have been applied to large-scale fuel cell modeling through their user-coding capability.^{6,14,15,64–67} Sections 3.1–3.7 will review these works in more detail as well as in the context of various important issues pertinent to the PEFC system.

Efforts have also been made to model two-phase flow and transport in a PEFC, a critical but difficult issue that has repeatedly been emphasized in the literature. To treat liquid water formation in a PEFC, there are two types of models. The simplest approach is a single-phase model in which the gas and liquid are considered a single-fluid mixture and thus share the same velocity field. Also, the interfacial tension effect is completely ignored. In this case, the total amount of water can be obtained by solving a single equation without distinguishing water vapor from liquid water. Once the total water concentration field is obtained, one may allow for the water concentration going beyond the saturation level, essentially assuming supersaturation in the gas phase.^{16,55,59} Alternately, one can truncate the water concentration

at the gas saturation level and account for the extra water in the form of liquid water in a postprocessing manner.^{57,58,60} Sections 3.1–3.6 are devoted to reviewing this class of single-phase models.

The more rigorous approach to liquid water transport is a true two-phase model in which the two phases travel at different velocities. At the same time, the interfacial tension effect and GDL wettability, essential for successful PEFC operation, are fully accounted for. The work of Wang et al.,⁶⁸ Nguyen et al.,^{69–71} You and Liu,⁷² Mazumder and Cole,⁷³ Berning and Djilali,⁷⁴ and Pasaogullari and Wang^{67,75} falls into this category. These two-phase models are reviewed in section 3.7.

Another classification of PEFC models is in terms of volume-averaged (i.e., macrohomogeneous) models or pore-level models. Macroscopic models assume local interfacial equilibrium, namely, electrical, chemical, and thermal equilibrium at the pore level. Conditions of validity of local interfacial equilibrium were carefully defined.⁷⁶ All of the above-cited CFCD models are, strictly speaking, macroscopic models, although theoretical inconsistency may exist in some work. In the two-phase models of Nguyen et al.,^{69–71} Mazumder and Cole,⁶³ and Berning and Djilali,⁶² the water condensation/evaporation rate was expressed according to the local nonequilibrium condition of water vapor in the gas phase, but such a treatment was merely a numerical trick without physical significance. All simulation results in these works virtually corresponded to the local chemical equilibrium condition. Moreover, no dispersion effect arising from the interaction of local fluctuations in velocity and species concentration at the pore level was included in their water vapor transport equation, indicative of an equilibrium macroscopic model. It is interesting to note that a different approach to treating phase change was used for related problems such as drying of porous materials,^{77,78} steam injection for enhanced oil recovery, and groundwater contamination and remediation.⁷⁹

In the following section we will present first a general single-phase model along with detailed discussions on several critical issues in PEFC modeling (i.e., sections 3.1–3.6). This is followed by two-phase modeling of liquid water transport in section 3.7. In section 3.8 we will describe experimental diagnostics which can be used to probe the validity of such models as well as identify future modeling needs. Finally, in section 3.9 we will review work on pore-level modeling of the PEFC catalyst layer.

3.1. Single-Phase Conservation Equations

Various forms of governing equations have been used in PEFC modeling, although all fall under the single-phase assumption. To clarify important subtleties with theoretical rigor, in this subsection we summarize a set of conservation equations and provide detailed comments of various terms that should be used.

The single-phase model described herein considers the total water amount without distinguishing liquid water from water vapor. This approach is valid under the condition that liquid saturation within the gas

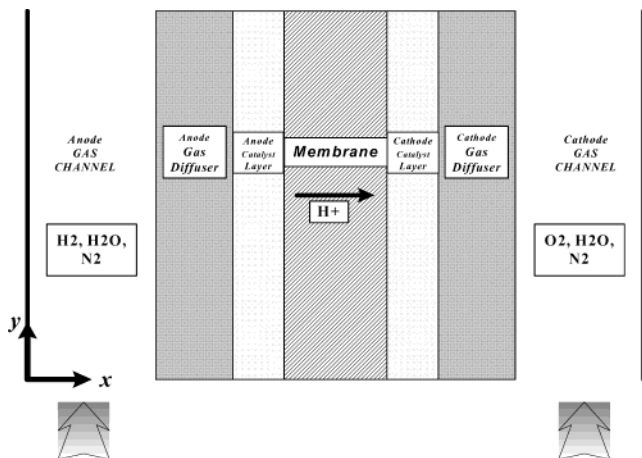


Figure 6. Schematic diagram of a polymer electrolyte fuel cell.

diffusion layer (GDL) is low (e.g., lower than the irreducible liquid saturation S_{ir}) or liquid droplets are small and disperse in gas flow to form a mist flow. This approach is particularly well suited for fuel cell simulations under low humidity operation, a major application of single-phase models.

The fuel cell to be modeled is schematically shown in Figure 6 and divided into seven subregions: the anode gas channel, anode GDL, anode catalyst layer (CL), ionomeric membrane, cathode CL, cathode GDL, and cathode gas channel. The present model considers the anode feed consisting either of hydrogen, water vapor, and nitrogen or hydrogen/water binary gas, whereas humidified air is fed into the cathode channel. Hydrogen oxidation and oxygen reduction reactions are considered to occur only within the active catalyst layers where Pt/C catalysts are intermixed uniformly with recast ionomer.

As explained in section 2, a fundamental PEFC model consists of five principles of conservation: mass, momentum, species, electric charge, and thermal energy. These five balance equations are now summarized in Table 1 with their source terms identified for various regions of a fuel cell. The central idea of this model is to employ a single set of governing equations in all regions throughout a fuel cell. The main assumptions invoked in the model are (1) ideal gas mixtures and (2) incompressible and laminar gas flow due to small pressure gradients and Reynolds numbers. More explanation of each of the five conservation equations follows.

In the mass and momentum equations for both gas channels and GDL, the superficial velocity is used in order to automatically ensure the normal mass

flux continuity at the channel/GDL interface. In addition, the permeability in the membrane is assumed to be very small, say 10^{-30} m², which effectively renders the fluid velocity zero. The momentum source term represents Darcy's drag for flow through a porous medium, which reduces the momentum equation to the Navier–Stokes equation in gas channels, where $K \rightarrow \infty$, and to Darcy's law in GDL and catalyst layers when K is small.

There is a nonzero mass source in the continuity equation, S_m , arising from the summation of all species equations. A general form of this source term is given in Table 1. Use has been made of the assumption that summation of interspecies diffusion within the gas phase is equal to zero. Specifically, one has

$$S_m = \begin{cases} -M_{\text{H}_2} \frac{j}{2F} + M_{\text{H}_2\text{O}} \left[\nabla(D_{w,m} \nabla C_{\text{H}_2\text{O}}) - \nabla(n_d \frac{i_e}{F}) \right] & \text{in anode CL} \\ M_{\text{O}_2} \frac{j}{4F} - M_{\text{H}_2\text{O}} \frac{j}{2F} + M_{\text{H}_2\text{O}} \left[\nabla(D_{w,m} \nabla C_{\text{H}_2\text{O}}) - \nabla(n_d \frac{i_e}{F}) \right] & \text{in cathode CL} \end{cases} \quad (13)$$

In the above, $D_{w,m}$ is the water diffusion coefficient through the membrane phase only. Note also that the water fluxes through the membrane phase, via electro-osmotic drag and molecular diffusion, represent a source/sink term for the gas mixture mass in the anode and cathode, respectively.

The general species equation can be applied to three species, H₂, O₂, and H₂O, with nitrogen being the remaining species of the gas mixture. The species concentration of N₂ can thus be simply calculated from the fact that all species mole fractions sum up to be unity. Species diffusion can be modeled by Fick's law, which is exact for binary gases but a good approximation for multicomponent gases.^{53,80} The electro-osmotic drag coefficient, n_d , is only relevant to the water molecule; thus, its values for other species such as H₂ and O₂ are set to zero.

To close the equation set for mass, momentum, and species conservation, one needs the ideal gas law that describes the gas density varying with its compositions. That is

$$\rho = \sum M_k C_k \quad (14)$$

where the N₂ molar concentration can be calculated

Table 1. Single-Phase PEFC Model: Governing Equations with Source Terms Identified in Various Regions^a

conservation equations	source terms		
	diffusion layers	catalyst layers	membrane
mass		$S_m = \sum_k M_k S_k + M_{\text{H}_2\text{O}} \nabla(D_{w,m} \nabla C_{\text{H}_2\text{O}})$	
momentum	$S_u = (-\mu/K)\bar{u}$	$S_u = (-\mu/K)\bar{u}$	$\bar{u} = 0$
species	$S_k = -\nabla[(n_d/F)i_e] - (s_{kj}/nF)$	$S_k = -\nabla[(n_d/F)i_e] - (s_{kj}/nF)$	$S_k = -\nabla[(n_d/F)i_e]$
charge	$S_\Phi = j$	$S_\Phi = j$	
energy	$S_T = j\eta + T(dU_o/dT) + (i_e^2/\kappa^{\text{eff}})$	$S_T = j\eta + T(dU_o/dT) + (i_e^2/\kappa^{\text{eff}})$	$S_T = i_e^2/\kappa^{\text{eff}}$

^a Electrochemical reaction $\sum_k s_k M_k z = ne^-$, where $M_k \equiv$ chemical formula of species k , $s_k \equiv$ stoichiometry coefficient, and $n \equiv$ number of electrons transferred. In PEM fuel cells there are (anode) $\text{H}_2 - 2\text{H}^+ = 2e^-$ and (cathode) $2\text{H}_2\text{O} - \text{O}_2 - 4\text{H}^+ = 4e^-$.

by $C_{N_2} = p/RT - C_{H_2O} - C_{O_2}$ (or C_{H_2}). In the case of H_2/H_2O binary gas in the anode, the H_2 species transport equation does not need to be solved; instead, its concentration is calculated by $C_{H_2} = p/RT - C_{H_2O}$.

Note that the single-phase model described above fully couples the mass, momentum, and species conservation equations through various source terms. One elegant simplification of this full model is to neglect the mass source term in the continuity equation and assume a constant gas density in the momentum equation. The approximation of constant density is well supported by the study of Dutta et al.,⁵⁸ which predicted a density variation smaller than 5% using a variable-density model, as seen in Figure 7. This simplification thus yields decoupling of the flow field from the species, electric potential, and temperature fields, thereby significantly accelerating the calculations. Possible inaccuracy introduced by this splitting of the problem may occur on the anode side; however, the hydrogen concentration profile is relatively unimportant as the anode overpotential is typically negligible. Therefore, under common operating conditions, this reduced model yields <10% and 14% error in the current distribution for anode stoichiometries of 2.0 and 1.2, respectively.⁸¹ In addition to reducing memory and computational requirements, this splitting of the fuel cell problem has the added advantage of allowing for consideration of different cell voltages/current densities for the same flow field.

The charge-transport equation includes the electrochemical kinetics for both anode and cathode catalyst layers. If we assume an infinitely large electric conductivity of the electronic phase, the electrode becomes an equipotential line, such that

$$\Phi_s = 0 \text{ on the anode}$$

$$\Phi_s = V_{\text{cell}} \text{ on the cathode}$$

If the electric conductivity of electrode matrixes and plates is limited, an additional equation governing charge transport in the electronic phase would have to be solved. This issue is separately addressed in section 3.4.

The source term in the charge equation is used to describe the transfer current between the electronic and electrolyte phases inside of each anode and cathode catalyst layer. The transfer current densities are expressed as follows

$$\text{anode: } j = ai_{o,a} \text{ref} \left(\frac{C_{H_2}}{C_{H_2,\text{ref}}} \right)^{1/2} \left(\frac{\alpha_a + \alpha_c}{RT} F\eta \right) \quad (15)$$

$$\text{cathode: } j = -ai_{o,c} \text{ref} \left(\frac{C_{O_2}}{C_{O_2,\text{ref}}} \right) \exp \left(-\frac{\alpha_c}{RT} F\eta \right) \quad (16)$$

These kinetic expressions represent the hydrogen oxidation reaction (HOR) in the anode catalyst layer and oxygen reduction reaction (ORR) in the cathode catalyst layer, respectively. These are simplified from the general Butler–Volmer kinetics, eq 5. The HOR

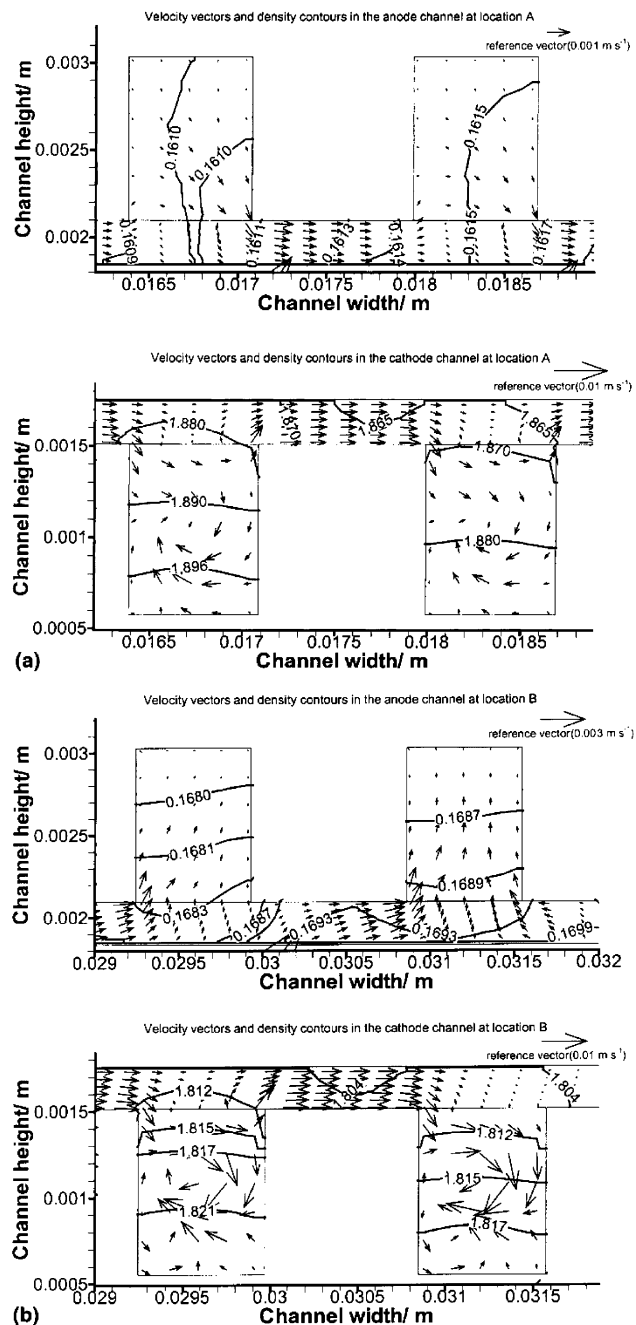


Figure 7. Velocity vectors and gas density contours under very low humidity operation: (a) in the middle and (b) at the exit of a 10 cm² PEFC.⁵⁸

kinetic expression is derived by linearizing the Butler–Volmer equation on the assumption that the HOR reaction is facile and hence the surface overpotential is small. On the other hand, the ORR kinetic reaction is slow, causing high overpotential. Therefore, the ORR kinetic expression is obtained by neglecting the anodic reaction term of the Butler–Volmer equation. It should be noted that the ORR is assumed to be the first-order reaction based on early experimental work of Bernardi and Verbrugge⁴⁵ and Gottesfeld and Zawodzinski.³⁰ The value of $(\alpha_a + \alpha_c)$ in HOR kinetics should be equal to 2, while $\alpha_c = 1$ in ORR corresponds to a Tafel slope of approximately 60 mV/decade. The thermodynamic equilibrium po-

tentials of anode and cathode are assumed to be zero and a function of temperature, respectively, as⁸²

$$U_o = 1.23 - 0.9 \times 10^{-3}(T - 298.15) + \frac{RT}{2F} \left(\ln p_{\text{H}_2} + \frac{1}{2} \ln p_{\text{O}_2} \right) \quad (17)$$

This equilibrium open-circuit potential for a H₂/air fuel cell is calculated from thermodynamic data of reaction enthalpy and entropy changes.

The energy equation entails a detailed account of heat generation due to irreversible heat of the electrochemical reaction, reversible (or entropic) heat, and Joule heating.⁸³ The heat generation term in a CFD model must be unambiguous and location specific. More discussion is deferred to section 3.3. In addition, the heat accumulation in a porous material consisting of the matrix and fluid is given by

$$(\rho c_p)_m = \epsilon(\rho c_p) + (1 - \epsilon)(\rho c_p)_s \quad (18)$$

where the heat capacitance (ρc_p) without subscript refers to the fluid and with subscript “s” refers to the solid matrix.

Six coupled governing equations listed in Table 1 are valid in all regions of a PEFC, and fluxes at an internal boundary between two adjacent regions are automatically continuous. Such a single-domain model is well suited for CFD implementation. In contrast, multidomain models, such as the one developed by Dutta et al.,^{57,58} compute separate solutions for the anode and cathode subdomains, respectively, and then patch the two solutions through the water transport flux across the MEA interface. Numerically, this model is characterized as a solver-in-solver situation.

3.2. Water Transport

Water management is one of the most critical and widely studied issues in PEFC. Water management is referred to as balancing membrane hydration with flooding avoidance. These are two conflicting needs: to hydrate the polymer electrolyte and to avoid flooding in porous electrodes and GDL for reactant/product transport.

Early modeling studies^{16,44,48,49,54,55,57,84,85} have focused on fully humidified fuel/air streams, which ensures a hydrated ionomer membrane, thus yielding a constant proton conductivity and the least ohmic loss. Under those full humidification conditions, however, the gas inside the fuel cell becomes oversaturated and water condensation may occur on the cathode side even at low operating current densities. The ensuing cathode flooding by liquid water subsequently hampers the access of oxygen to the cathode catalyst layer, resulting in a significant concentration polarization. In addition, full humidification of the reactant gases externally requires additional parasitic volume and power in a fuel cell system. Therefore, the recent trend in the industry is to operate PEFC under low humidity conditions while still maintaining an adequately hydrated polymer membrane. Such low humidity operating strategies will

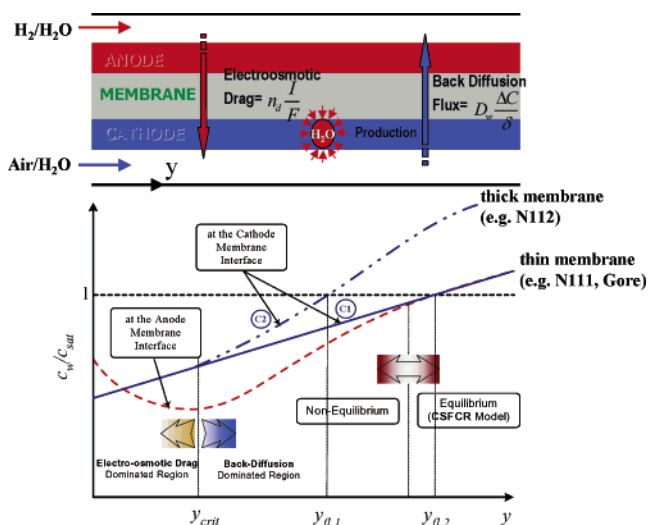


Figure 8. Two-dimensional sketch of water management in a PEM fuel cell whereby the membrane–electrode assembly separates the anode feed channel from the cathode, and a diagram of water uptake profiles in anode and cathode channels.

also reduce cathode flooding and volume as well as cost of the external humidifier. Obviously, this operating regime hinges upon a good understanding of water generation, transport, and distribution within PEFCs.

General features of water transport in a PEFC under low humidity operation is schematically shown in Figure 8. Water is produced in the cathode catalyst layer as a result of ORR or can be brought into the cell by humidified reactant gases represented by anode/cathode inlet relative humidity. Through the electrolyte between the anode and cathode, two modes of water transport are operative: the electro-osmotic drag effect and diffusion driven by the concentration gradient. The water flux due to the electro-osmotic drag is directly proportional to the protonic flux (I_{cell}/F). The diffusion flux of water in the membrane is usually described by a water diffusion coefficient and the gradient in molar concentration of water.

Typical water concentration profiles in the anode and cathode flow channels are also depicted in Figure 8. The water concentration at the anode/membrane interface first decreases along the flow and then reaches the minimal point at which the net water flux across the membrane becomes zero, implying that the electro-osmotic drag is balanced by the back-diffusion of water. Thus, this location also represents a boundary between drag- and diffusion-dominated regimes. The anode water concentration increases after this minimum point due to enhanced back-diffusion driven under a larger cathode water concentration resulting from ORR. On the cathode side, the water concentration profile can take two routes, depending on the membrane thickness. For thin membranes such as Nafion 111 or Gore membranes, water exchange between the anode and cathode via diffusion is so effective that both sides achieve equilibration sufficiently downstream. This is shown as curve C1 in Figure 8. However, thick membranes such as Nafion 112 will make the water concentrations on two sides

of the membrane further diverge, as shown as the curve C2 in Figure 8.

Figure 8 also nicely describes two possible scenarios for electrode flooding. Defining the onset of electrode flooding by the dimensionless water concentration reaching unity (i.e., gas becomes saturated), Figure 8 shows that both anode and cathode will be flooded by liquid water condensed from the gas for thin membranes, while for thick membranes only the cathode is susceptible to flooding.

Water-transport characteristics become quite intricate in low humidity PEFCs. For example, the variation in water concentration down the channel is pronounced as the cell is self-humidifying the inlet dry gases. The in-plane variation from channel to land is also substantial, giving rise to a fully three-dimensional distribution of water concentration. In addition, strong convection effect perpendicularly through the anode GDL, as induced by significant hydrogen consumption under low anode stoichiometry, challenges the conventional model based on diffusive transport. It seems that a comprehensive flow–transport–electrochemical coupled model is necessary to faithfully capture the water-transport characteristics in low humidity PEFCs.

Considerable efforts have been expended in the literature to simulate water management in PEFCs. These studies can be grossly divided into three groups. One group is focused on the physics of water transport and scrutinizes water transport through the polymer membrane. Notable work includes Springer et al.,¹⁶ Fuller and Newman,⁴⁸ Nguyen and White,⁴⁹ Futerko and Hsing,²¹ Hsing and Futerko,⁸⁶ Janssen,⁸⁷ and Kulikovsky.⁸⁰ Springer et al.¹⁶ first introduced a diffusion model for Nafion 117 membrane and included the electro-osmotic drag term as well. They assumed equilibrium between the gas phase and the membrane phase of water in the Nafion membrane and then determined the membrane water content at the interface by the activity of water vapor. Hsing and Futerko⁸⁶ developed a two-dimensional finite element model for a PEFC without external humidification of the inlet gas streams. Flow field was approximated using the potential flow equation with a stream function. The membrane water content at the anode/membrane interface was calculated under the assumption of phase equilibrium between the vapor and membrane phases, and the cathode/membrane interface was assumed to be fully hydrated. More recently, Janssen⁸⁷ demonstrated 1-D and 2-D numerical models to account for water transport through the MEA under various humidification conditions of inlet gases. The computed results were compared with experimental data of Janssen and Overvelde.⁸⁸ In the model of Janssen,⁸⁷ it was assumed that the cell current density is constant everywhere, and the catalyst layers were excluded in the water-transport calculation. Reacting species along the channel and in the through-plane direction were calculated based on the one-dimensional mass-transport assumption. Kulikovsky⁸⁰ presented a multidomain model of water transport in which the diffusion and electro-osmotic drag coefficients through the polymer membrane are taken as

nonlinear functions of water content. It was found that the nonlinearity of the transport properties leads to the dryness on the anode side of the membrane, in accordance with the experimental observations of Buchi and Scherer.⁸⁹ While this group of models is fundamental in nature and reveals rich physics of water distribution through the polymer membrane, it is unable to capture all intricate features of water transport in a low humidity PEFC.

The second group attempted to model water transport throughout an entire fuel cell using the CFD approach.^{62,63,90} These CFD models do not appear to properly model water transport through the polymer membrane. Berning et al.⁶² indicated that no water diffusion in the membrane is included in their model, and thus it is restricted only to conditions with fully hydrated membranes. The single-phase model of Mazumder and Cole⁶³ used neither a water diffusion coefficient nor a drag coefficient in the membrane and therefore is expected to completely ignore any water transport across the membrane. Obviously, this group of models is unable to describe water-transport phenomena through the membrane in the single-phase regime (e.g., low humidity).

The last group of studies^{55,57–59,91} strived to unite different modes of water transport in various parts of a PEFC and develop a comprehensive water-transport model that is both reflective of correct physics, particularly the water transport through the membrane by diffusion and electro-osmotic drag, as well as easy to implement for an entire cell using the CFD approach. This group of models is capable of simulating water management scenario in low humidity cells. Note that the model of Dutta et al.^{57,58} uses an approximate analytical solution for water transport through the membrane by assuming a constant diffusion coefficient and drag coefficient and then embeds it into numerical solutions to the anode and cathode sides separately. This approach eliminates the MEA from the computational domain. However, such a model loses the ability to resolve increasingly important phenomena in MEA. For example, the ionic resistances in the two catalyst layers were treated by ad hoc assumption in this type of models. As PEFC technology moves toward the use of thinner membranes, the ionic resistance in the catalyst layer becomes important and comparable with that in the membrane and therefore must be accurately accounted for. In addition, a PEFC model treating the MEA as an interface without thickness essentially ignores the membrane water storage capacity and therefore cannot be used in simulating transient phenomena (see section 3.5).

In contrast, Wang and co-workers^{55,56,59,91} developed a unified water-transport model applicable throughout a PEFC including the MEA region, thus enabling comprehensive CFCD simulations to be carried out. The model recognizes that there are different phases of water existing in various regions of the PEFC, i.e., water in the gas phase and in the membrane. As a result, phase equilibrium is considered and various modes of water transport, diffusion, convection, and electro-osmotic drag are incorporated in the unified

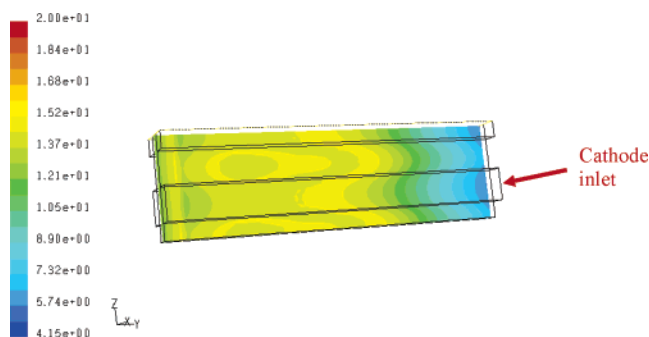


Figure 9. Membrane water content (λ) distribution in a three-straight channel fuel cell (only the half cell is shown due to symmetry) with anode and cathode counter-flow at 0.65 V or average current density of 1.1 A/cm². Anode and cathode feed conditions are humidification temperature = 50 °C, pressure = 2 atm, stoichiometry = 2, and the cell temperature = 80 °C.

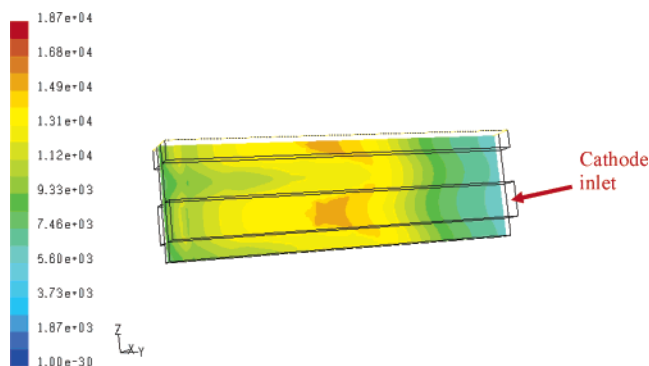


Figure 10. Current distribution (A/m²) in a low humidity fuel cell at 0.65 V or average current density of 1.1 A/cm² with the same operating conditions as in Figure 9.

water-transport equation. A unified water-transport equation within the single-domain CFCD framework is developed with the aid of the equilibrium water uptake curve in the membrane phase. Details were provided by Um.⁹¹ Figure 9 illustrates an example of membrane water content distribution for a low humidity, straight-channel cell with anode and cathode humidification temperatures equal to 50 °C for the 80 °C cell temperature. Figure 10 shows current distribution in the same cell.

Figure 11 displays calculation results of the current and water activity distributions in a 50 cm² fuel cell with serpentine flow field. The cell is operated under rather dry conditions with the anode and cathode relative humidity being 75% and 0, respectively. The line graphs are plotted along the center of the membrane in the cross-section, cutting through the middle of the cell. The simulation shown in Figure 11 exemplifies the present capability of a comprehensive water- and heat-transport model in providing fine details. It is clearly seen that the local current density varies from the channel to rib (or land) areas. Moreover, the current density above the rib is greater than the channel in the inlet portion of the fuel cell because the reactant gases are relatively dry and the ribs protect the membrane from losing water. In contrast, near the outlet portion of the fuel cell where gases become more humidified, the local current density begins to be controlled by oxygen transport,

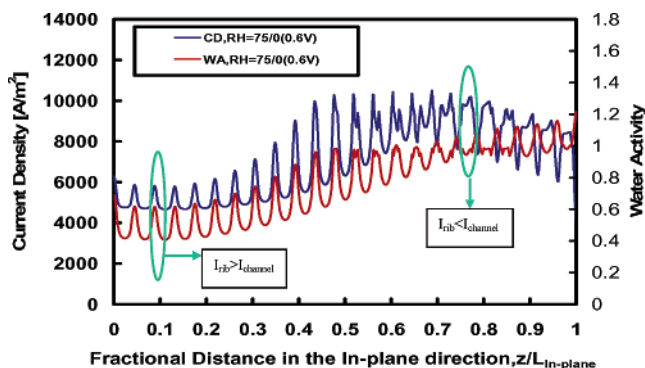


Figure 11. Current and water activity distributions in a low humidity 50 cm² fuel cell with serpentine flow field at 0.6 V or average current density of 0.71 A/cm². The membrane is 18 μ m thick (EW < 1000). The anode/cathode feed conditions are pressure = 3/3 atm, relative humidity = 75%/dry, stoichiometry = 1.2/2, and cell temperature = 80 °C.

thereby showing a higher value in the channel area than the rib.

3.3. Heat Transport

A PEFC produces waste heat in an amount comparable to its electric power output (so that the energy-conversion efficiency is around 50%). Heat generation in PEFC stems from entropic heat of reactions, the irreversibility of the electrochemical reactions, and ohmic resistance (or Joule heating).⁸³ Roughly, the irreversible reaction heat, entropic heat, and Joule heating in a PEFC account for 55%, 35%, and 10% of total heat release, respectively. The last source of heat due to water condensation/evaporation will be discussed in section 3.7 as it is related to two-phase transport. In addition, the polymer membrane has low tolerance for temperature deviation from the operating point. Hydration of polymer membranes also strongly depends on the temperature as the water vapor saturation pressure is an exponential function of temperature. Thus, thermal management in PEFC is inherently coupled with water management and the two factors combine to ensure high performance and durability of a PEFC.

A number of PEFC thermal models have been published in the literature. Early efforts were made by Nguyen and White⁴⁹ and Fuller and Newman.⁴⁸ Nguyen and White⁴⁹ developed a two-dimensional PEFC model with one-dimensional heat transfer in the flow direction. The model considers phase change of water in the flow channel as the only heat source, allowing convective heat transfer between the gas and solid phases. On the other hand, Fuller and Newman⁴⁸ developed a pseudo-two-dimensional thermal PEFC model with one-dimensional mass transfer in the through-membrane direction and one-dimensional heat transfer in the flow direction. On the basis of the known enthalpy change of the overall electrochemical reaction, the model calculated the temperature rise of the flowing gas streams with various external heat transfer coefficients. However, in these early models the temperatures of membrane and electrodes were not differentiated, even though a significant temperature variation in those regions can

be expected in both the through-membrane and flow directions depending on the geometric and operating conditions. Furthermore, the major heat source terms, the entropic and irreversible reaction heats, were not specified in their models. Yi and Nguyen⁵⁰ extended Nguyen and White's⁴⁹ model to include the entropic and irreversible reaction heats along with the phase change heat. However, this model allowed the temperature variation of the solid phase in the flow direction only, assuming uniform temperature in the through-membrane direction.

Wöhr et al.⁹² developed a one-dimensional thermal model for heat and mass transfer in the through-plane direction, particularly for PEFC stacks. Accounting for the entropic and irreversible reaction heats, they computed the temperature profile in the through-membrane direction and predicted the maximum temperature as a function of the number of cells contained in a stack. Rowe and Li⁹³ also developed a one-dimensional model in the through-membrane direction. Including entropic, irreversible, and phase change heats, they further took account of Joule heating in the membrane and anode/cathode catalyst layers. This work predicted the temperature variation in the through-membrane direction under the various current densities and electrode thermal conductivities. A major drawback of this model is the fact that the cathode catalyst layer is assumed to be fully hydrated and the membrane water content is linearly interpolated, indicating inapplicability of the model in low humidity operation.

Multidimensional thermal models were presented by many PEFC modeling groups. Maggio et al.⁹⁴ performed the pseudo-three-dimensional simulations, neglecting the temperature gradient in the flow direction. However they only considered the overall heat source term as $(U_o - V_{\text{cell}})I$. In the three-dimensional models developed by Shimpalee and Dutta⁹⁵ and Costamagna,⁹⁶ the heat source terms were also treated globally and not made location-specific. Berning et al.⁶² presented a three-dimensional PEFC model including irreversible and entropic heat terms in the catalyst layers and Joule heating in the membrane. The main drawback of this model is assuming the membrane to be fully humidified, indicating limited applicability to low humidity operating conditions. Zhou and Liu⁶¹ developed a three-dimensional PEFC model in which the entropic reaction heat ($\sim 35\%$ of total heat) was ignored.

Accurate modeling of the temperature distribution in a PEFC requires accurate information in four areas: heat source, thermal properties of various components, thermal boundary conditions, and experimental temperature-distribution data for model validation. The primary mechanism of heat removal from the catalyst layers is through lateral heat conduction along the in-plane direction to the current collecting land (like a heat sink). Heat removed by gas convection inside the gas channel accounts for less than 5% under typical PEFC operating conditions.

The energy equation in Table 1 contains location-specific heat generation terms, including irreversible heat of the electrochemical reaction, reversible en-

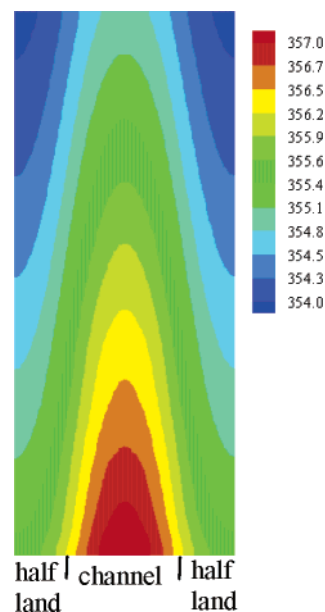


Figure 12. Temperature distribution (in K) in the middle of the membrane ($EW < 1000$) for a straight-channel PEM fuel cell (cell voltage = 0.6 V, average current density = $1.42\text{A}/\text{cm}^2$) with a cell temperature of $80\text{ }^\circ\text{C}$.

tropic heat, and Joule heating.⁸³ The reversible heat related to $T(dU_o/dT)$ was often overlooked in the majority of thermal modeling work in the literature. It represents the entropic heat produced by the cell even under thermodynamic equilibrium and is a significant contributor to overall heat generation.

Solving the energy equation provides prediction of the temperature distribution and its effect on cell performance in a PEFC. Figure 12 presents a temperature distribution in the middle of the membrane for a single-channel PEFC. The maximum temperature rise in this case is $4\text{ }^\circ\text{C}$, which will only affect cell performance slightly. However, the temperature variation depends strongly on the thermal conductivities of the GDL and flow plate as well as thermal boundary conditions.

Among the three heat-generation terms, the irreversible and reversible heat sources of ORR are dominant. For a straight-channel cell shown in Figure 12, the total amount of heat release is 2.57 W, of which the irreversible heat is 55.3%, the reversible heat 35.4%, and the Joule heat only 9.3%! The total heat released from the fuel cell can also be estimated from the overall energy balance, i.e.

$$Q_{\text{heat}} = (U_o - V_{\text{cell}})I_{\text{avg}}A + I_{\text{avg}}AT_{\text{avg}}\left(-\frac{dU_o}{dT}\right) = 2.56\text{ (W)} \quad (19)$$

This is close to the simulated value of 2.57 W, including the irreversible, entropic, and Joule heat. The energy-conversion efficiency of this cell, defined as the ratio of the electric power ($I_{\text{avg}}V_{\text{cell}}A$) to the total energy consumption ($I_{\text{avg}}V_{\text{cell}}A + Q_{\text{heat}}$), is then calculated to be 40%. These simple calculations help demonstrate the validity and accuracy of a nonisothermal PEFC model.

Co-simulation of water and heat management in a 50 cm^2 cell can be seen from Figure 13. The

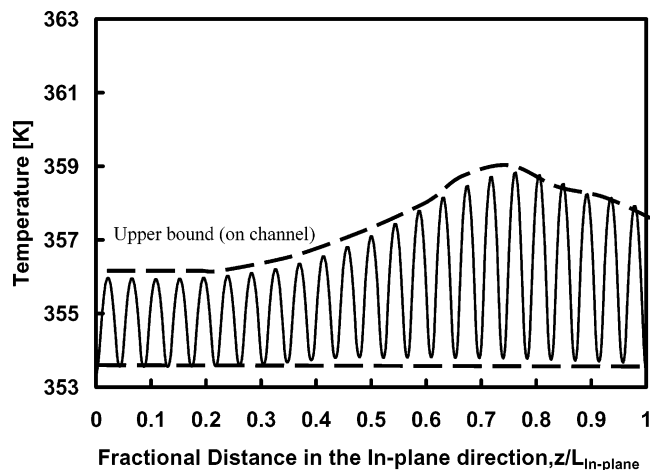


Figure 13. Temperature distribution in a low humidity 50 cm² fuel cell under the same operating conditions as in Figure 11.

membrane temperature fluctuates between channel and land areas. Furthermore, the membrane temperature is higher in the channel area due to lack of effective cooling, increases along the flow path due to higher current density, and then decreases near the outlet due to the current density lowered by oxygen depletion.

An important issue requiring future work is the consideration of anisotropic thermal transport since the thermal conductivity has an order of magnitude difference between the in-plane and through-phase directions as mentioned earlier.

3.4. Electron Transport

An important function of GDL is to provide electron lateral conduction, serving as a bridge between the catalyst layer and the current-collecting land. In nearly all the three-dimensional PEFC models published to date, electron transport in the catalyst layer/GDL as well as in the current collector plate is ignored by assuming a sufficiently large electric conductivity and, consequently, uniform electronic phase potential in these materials. The flow plate has an electric conductivity on the order of 2×10^4 S/m for graphite plates, but the effective electric conductivities of GDL and catalyst layers range only from 300 to 500 S/m (in the through-plane direction). These electronic resistances could significantly change the current distribution, both macroscopically along the flow direction and mesoscopically between the channel and land areas. Although the electron-transport equation was solved in the one-dimensional PEFC models of Bernardi and Verbrugge,^{44,45} the lateral electronic resistance can only be assessed in a three-dimensional geometry. Furthermore, solving the electron-transport equation enables (1) direct incorporation of the contact resistance at interfaces between two mating components in the solution process, (2) direct implementation of the total current as a boundary condition instead of the cell voltage (permitting a true stoichiometry to be employed in PEFC modeling and thus consistency with typical fuel cell experiments), and (3) stack modeling with cells connected in series.

To calculate the electron-transport effect through GDL and flow plate, the charge conservation equation for the electronic phase must be solved additionally, namely

$$\nabla(\sigma^{\text{eff}}\nabla\Phi_s) - j = 0 \quad (20)$$

where σ^{eff} is the conductivity of the electronic phase, Φ_s is the electronic phase potential, and j is the volumetric transfer current density inside the catalyst layer. When applied to the flow plate, eq 20 accounts for the ohmic loss occurring in plates with limited conductivity and small thickness (e.g., graphite plates used in fuel cell stacks).

Meng and Wang¹⁴ performed a three-dimensional study of the effects of electron transport through the gas diffusion layer (GDL). Figure 14 displays the current density distributions in a single-channel fuel cell predicted by including lateral electron transport. As can be seen, without accounting for the lateral electron transport in GDL, the current density is highest in the middle of the channel because the reaction zone there has the easiest access to oxygen. However, once considering the electronic resistivity of GDL in the in-plane direction, the highest current density region is shifted toward the edges of the channel because these locations have the best combination of easy access to oxygen and short path for electron transport onto the current-collecting land. The effective electric conductivity of GDL used in this simulation was assumed to be isotropic and equal to 300 S/m, corresponding to carbon paper from SGL Group. This new finding clearly indicates the necessity to include the lateral electron transport in future CFD models for high-fidelity computer simulations. Physically, this study revealed a new possibility to control the lateral current profile by tailoring the GDL electric property.

The effect of the flow plate electric conductivity on the axial current profile is shown in Figure 15.⁹⁷ It is seen that only with extremely conductive metal plates (i.e., $>2 \times 10^5$ S/m) does the constant current boundary condition also result in an equipotential line in the plate and hence the same current distribution. For graphite plates with an electric conductivity of $\sim 2 \times 10^4$ S/m, the potential drop in the plate between the inlet and outlet locations amounts to 27 mV under the constant current boundary condition, thereby causing a much flatter current density profile within the membrane than that observed when the plate is subject to constant voltage. The example shown in Figure 15 indicates the important impact of bipolar plate electric conductivity on current distribution, a new subject requiring attention in fuel cell engineering. Figure 15 also exemplifies a capability to simulate fuel cell performance under constant total current boundary condition instead of constant cell voltage. This approach is fundamentally different from the common practice in which the cell voltage is iterated until the resulting total current is matched with the prescribed value by running a number of cell simulations.

Meng and Wang¹⁴ found that addition of numerical solution to eq 20 substantially increases computa-

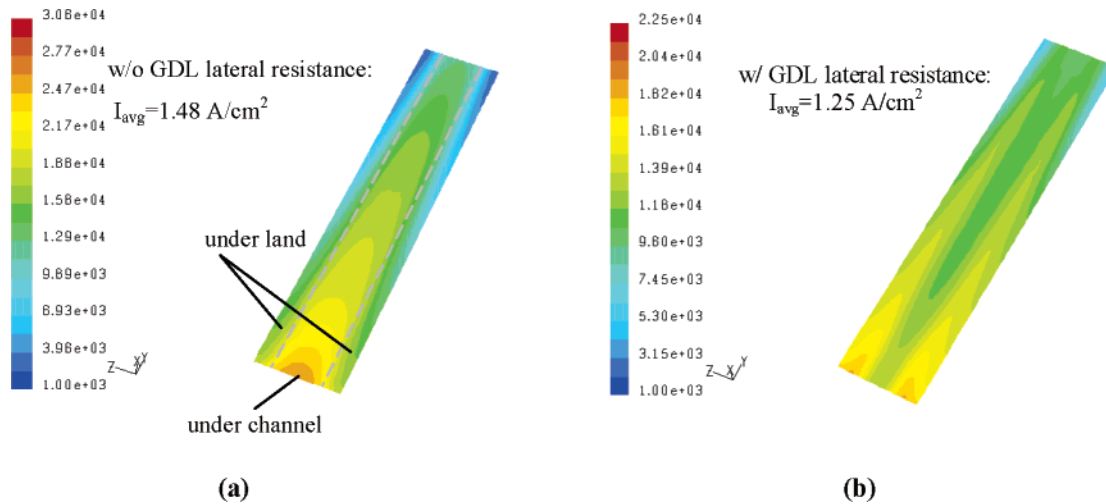


Figure 14. Current distribution in a straight-channel fuel cell at a cell voltage of 0.6 V: (a) without GDL electronic resistance and (b) with GDL electronic resistance.

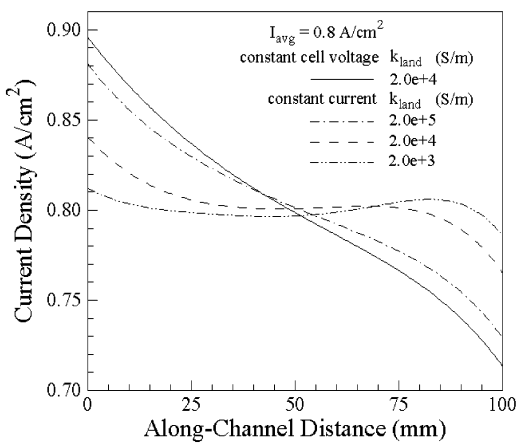


Figure 15. Current density profiles as a function of the flow plate electric conductivity (S/m) in a straight-channel fuel cell with an average current density of 0.8 A/cm².⁹⁷

tional time. In the most recently released commercial CFD code, CD-Adapco Japan apparently has developed a proprietary solution technique for eq 20 and the electrolyte potential equation together which does not incur any increase in computational time.⁹⁸ Moreover, their code, for the first time, accounts for anisotropic electric conductivity in the through-plane and in-plane directions. Future need certainly exists for more efficient numerical algorithms to solve eq 20 in a coupled fashion with the electrolyte potential equation, as described in section 2.2.2.

3.5. Transient Phenomena

Dynamic characteristics of a fuel cell engine are of paramount importance for automotive application. Three primary processes govern the time response of a PEFC. They are (1) electrochemical double-layer discharging, (2) gas transport through channel and GDL, and (3) membrane hydration or dehydration (i.e., between a dry and a hydrated state). The time constant of double-layer discharging is between micro- and milliseconds, sufficiently short to be safely ignored for automotive fuel cells. The time constant for a reactant gas to transport through GDL can be estimated simply by its diffusion time, i.e., $\delta_{\text{GDL}}^2/D_g$.

This gives a time constant between 0.1 and 1 s. The slowest process, however, is membrane hydration, the time constant of which can be estimated by

$$\frac{\rho_m \delta_m \Delta \lambda}{EW} \left(\frac{I}{2F} \right) \quad (21)$$

This is to assume that a dry membrane is hydrated by production water generated at the current density, I . For Nafion 112 and a reference current density of 1 A/cm², this is about 25 s! Therefore, for low humidity cells where the membrane undergoes water content changes, the water accumulation term is essential for transient analyses.

Um et al.⁵⁵ were one of the first to study the transient response of a PEFC to a voltage step change. Due to the fully humidified gas feed on both the anode and cathode, the membrane hydration process no longer contributed to the cell transients; as such, it was sufficient to include gas-transport transients under these fully humidified conditions. For low humidity PEFC, Wang and Wang⁶⁶ further extended the work of Um et al.⁵⁵ to include the membrane hydration transient process. Figure 16 shows a time response of the average current density to a step change in cell voltage in a low humidity fuel cell. Overall, it can be seen that the current density does not simply follow a smooth variation from the steady state at 0.6 V to the steady state at 0.7 V. Instead, there exists significant undershoot and overshoot due, respectively, to the transient phenomena of gas transport and membrane hydration. In addition, with the inclusion of membrane hydration, the fuel cell transients occur over as long as 15 s, a magnitude needing careful attention for automotive application.

Specifically, Figure 16 shows that the current density in a cell with dry cathode gas feed drops nearly instantaneously once the cell voltage is relaxed from 0.6 to 0.7 V due to the fact that the electrochemical double-layer effect has a negligibly small time constant. Further, there exists undershoot in the current density as the oxygen concentration inside the cathode catalyst layer still remains low due to the larger consumption rate under 0.6 V. As the

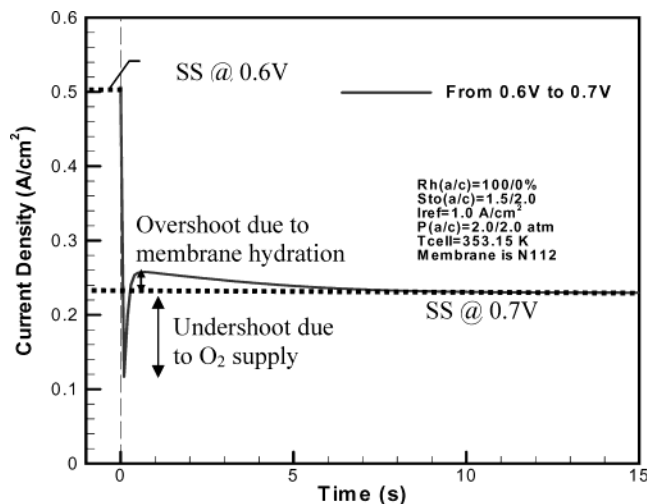


Figure 16. Transient response of current density to a step change of cell voltage from 0.6 to 0.7 V in a fuel cell with a fully humidified anode and dry cathode.⁶⁶

O_2 consumption rate becomes smaller under 0.7 V, the O_2 concentration at the reaction surface recovers, thus leading to an increase in the cell current density. The current rise time corresponds well with the characteristic time scale of gas phase transport as analyzed above. The rise in the cell current, however, experiences an overshoot because the polymer membrane still maintains a higher water content corresponding to 0.6 V. It then takes about 15 s for the membrane to adjust its water content at the steady state corresponding to 0.7 V. This numerical example clearly illustrates the profound impact of water management on transient dynamics of low humidity PEFC engines where the polymer membrane relies on reaction water for hydration or dehydration.

3.6. Large-Scale Simulation

Large-scale simulation of a PEFC is needed in order to consider all three dimensions. The importance of parameter variations in the through-plane direction was first recognized in the earliest 1-D models. Subsequent 2-D models addressed the important facet of changes in reactant and water concentrations along the flow direction, especially when the modern designs of low humidity and low stoichiometry emerged. The third dimension, i.e., the in-plane direction from a channel to a land, has been recognized for its importance of the lateral transport of species and electrons. Here, we are primarily concerned with a mesoscopic scale of approximately 1 mm. On this mesoscale, nonuniform current distribution may result primarily from the low diffusion rate of oxygen in the restricted area covered by the land and GDL resistance to lateral electron motion.

Such a large-scale simulation resolving all three dimensions for industrial-scale fuel cells featuring tens of flow channels is now being made possible by parallel computing on PC clusters using millions of computational cells.⁶⁵ Figure 17 shows the current distribution in a 36-channel fuel cell predicted using 2 560 000 grid points. This 50 cm² fuel cell features a double-pass serpentine flow field on the cathode. To be able to operate under dry air feed, the two

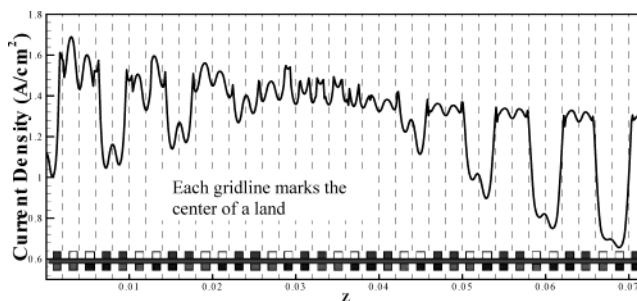


Figure 17. Current density profile in the midchannel cross-section of a 36-channel fuel cell.⁶⁵

passes are made countercurrent with one air inlet on the left and the other air inlet on the right, following a patented idea of Qi and Kaufman.⁹⁹ Such a counterflow serpentine flow field is intended to promote lateral moisture transport between a dry gas channel (near the inlet pass) and its neighboring moist gas channel (near the exit pass) and hence cell internal humidification. Both large-scale variations and channel-to-land local oscillations are visible from the current distribution shown in Figure 17, where the anode feed is fully humidified. Figure 18 displays a profile of the net water-transport coefficient through the membrane in the same cross-section of the cell. This parameter, α , is a combined result of the electro-osmotic drag and molecular diffusion of water through the membrane and is defined as the ratio of the net water flux to the protonic flux; thus, the unit is the number of H_2O/H^+ . As shown in Figure 18, α varies between -0.5 and 1.5 and changes rapidly between closely spaced channels, especially between a dry gas channel and a moist gas channel. The parameter critical to the choice of a suitable water management strategy reflects a complex interplay between the electro-osmotic drag and water diffusion through the membrane. α being positive means the dominance of electro-osmotic drag. Since the drag coefficient is constant at unity in the range of water content in question, α -values greater than unity indicate the electro-osmotic drag aided by the forward diffusion of water from the anode (fully humidified) to the relatively dry cathode. Negative α -values are indicative of the dominance of back diffusion of water from the cathode (high water concentration created by product water) to anode. Figures 17 and 18 clearly illustrate the need for large meshes in order to resolve sharp gradients in the channel-to-land direction in addition to the through-plane and flow directions.

Other work involving large-scale simulation of PEFCs was due to Meng and Wang¹⁵ and Ju and Wang.^{6,100}

3.7. Liquid Water Transport

High current density performance of PEFCs is known to be limited by transport of reactants and products. In addition, at high current densities, excess water is generated and condenses, filling the pores of electrodes with liquid water and hence limiting the reactant transport to catalyst sites. This phenomenon known as "flooding" is an important limiting factor of PEFC performance. A fundamental

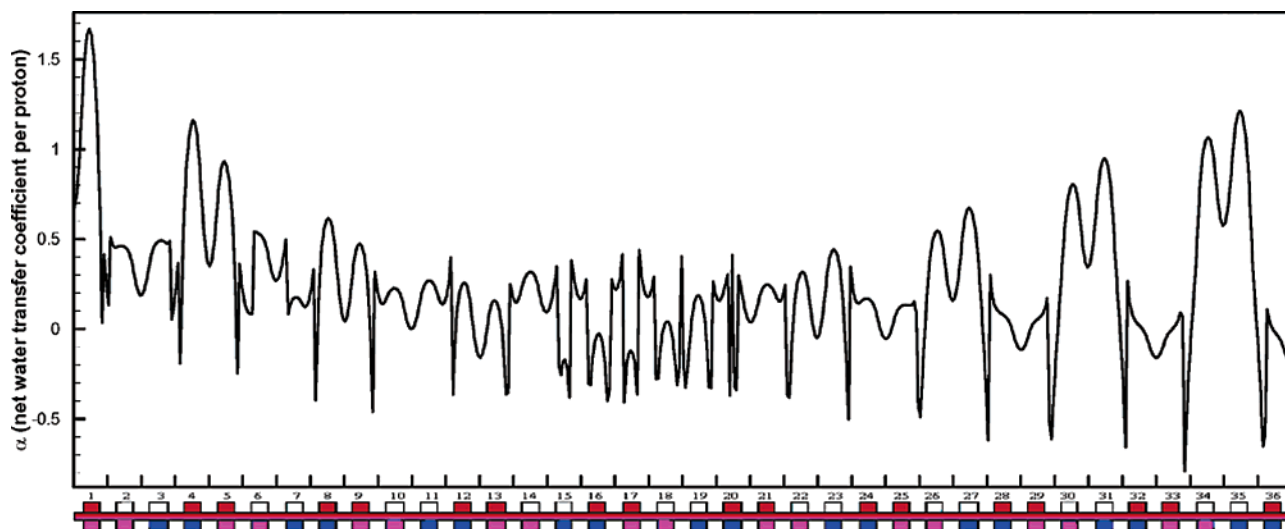


Figure 18. Profile of the net water transport coefficient through the membrane in the midchannel cross-section of a 36-channel fuel cell at $V_{\text{cell}} = 0.65\text{V}$ and $I_{\text{avg}} = 0.91\text{ A/cm}^2$.⁶⁵

understanding of two-phase transport in porous gas diffusion layers (GDL) of PEFC is essential in order to improve performance. Flooding of electrodes is generally linked to high current density operation that results in higher water production rate; yet, flooding can also be seen even at low current densities under certain operating conditions, such as low temperatures and low gas flow rates, due to faster saturation of the gas phase by water vapor. For instance, in automotive fuel cells, cell start-up is performed under ambient conditions in which the temperature is lower than the desired operating temperature, commonly referred as “cold start”. At cold-start temperatures, the saturation vapor pressure of water is extremely low; therefore, saturation of the gas phase with water vapor, hence flooding, may occur even in relatively low current densities, greatly affecting the start-up characteristics and transient dynamics of PEFC operation.

While there exist several studies investigating the two-phase transport in a PEFC,^{46,47,69–72,101,102} none considered the effect of GDL hydrophobicity. Some modeling studies were published in order to predict PEFC performance at given flooding levels without attempting to analyze the transport of liquid water.^{46,47,101,102} He et al.⁶⁹ proposed a two-dimensional two-phase model for PEFC with interdigitated flow field in which they included capillary transport of liquid water in a completely hydrophilic GDL. Wang et al.⁶⁸ developed a two-phase model of the air cathode of PEFC also with a hydrophilic GDL based on the M^2 formulation (multiphase mixture model) of Wang et al.⁷⁹ Subsequently, You et al.⁷² published a similar work investigating the effects of several operating parameters on two-phase transport. Most recently, Mazumder and Cole⁷³ presented a numerical study also based on the M^2 model of Wang and Cheng.⁷⁹ Mazumder and Cole’s model appears to be valid only in the two-phase regime where there is liquid water. Under low humidity inlet conditions where the liquid saturation is zero, this model yielded zero electro-osmotic drag through the polymer membrane. Berning and Djilali⁷⁴ presented a two-phase model for porous GDL and gas channel of a PEFC

while excluding the MEA. Water transport through MEA is thus completely ignored. Berning and Djilali also failed to address the effect of GDL hydrophobicity. None of these above-mentioned studies are intended to investigate and analyze two-phase transport in hydrophobic GDL. A brief review of this subject was given by Wang.⁵

The central question about the physics of liquid water transport through hydrophobic GDL has remained unexplored until recently. Nam and Kaviani¹⁰³ described a one-dimensional model for liquid water transport through hydrophobic GDL. In this model, the gas-phase pressure is assumed to be uniform, thereby rendering the liquid-phase transport governed by the gradient in capillary pressure. The model was used to assess the effects of GDL fiber diameter, porosity, and capillary pressure on the liquid water distribution. Independently, based on extensive experimental observations of liquid water flow in an operating PEFC, Pasaogullari and Wang¹⁰⁴ most recently proposed a systematic theory of liquid water transport through hydrophobic GDL. Condensation results in a tree-like liquid water percolation network in the porous GDL. Liquid water then reaches the interface of the porous GDL with the gas channel, forming liquid droplets. Inside GDL, liquid water is driven by capillary (wicking) action. In hydrophobic GDL, the capillary pressure is negative; hence, the liquid pressure is larger than the gas-phase pressure, whereas in hydrophilic media, the gas-phase pressure is higher than of the liquid phase.

In addition, the liquid pressure increases with liquid saturation; therefore, a liquid pressure gradient is formed from higher to lower liquid saturation regions. This pressure gradient becomes the driving force for liquid water flow, as schematically shown in Figure 19. In PEFC, the liquid saturation is higher at the catalyst layer, due to water generation and electro-osmotic drag, than the GDL–channel interface. Therefore, the liquid pressure gradient formed in the GDL drives liquid water from the reaction sites toward the gas channel. Figure 19 also displays a nearly constant gas pressure profile across the two-phase zone due to much lower gas-phase viscosity.

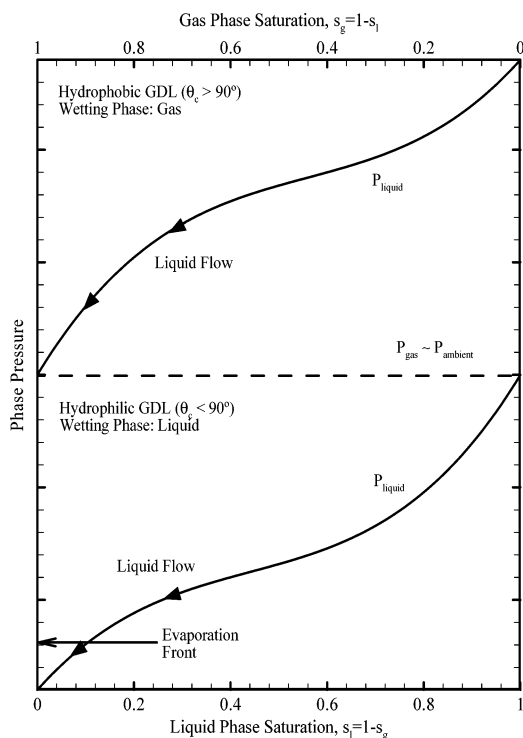


Figure 19. Schematic illustration of liquid- and gas-phase pressure profiles in hydrophilic and hydrophobic porous media.¹⁰⁴

That is, it does not incur much gas pressure drop to drive the gas flow through thin GDL.

It is interesting to note from Figure 19 that although the relative magnitude of the liquid to gas pressure is different in hydrophobic GDL than in hydrophilic GDL, both media provide capillary action to drive liquid water from the inside to the surface. However, the slope of the capillary pressure (i.e., the driving force) is different depending on whether water is the wetting or nonwetting phase. The greater slope of the capillary pressure near the evaporation front (i.e., $s \approx 0$) in hydrophobic GDL is indicative of increased effectiveness of this type of medium for water removal. Furthermore, the liquid pressure buildup in the hydrophobic cathode likely sets up a hydraulic pressure differential to drive water flow back through the membrane into the anode.

The shape of liquid droplets emerging at the GDL/channel interface is governed by the wetting char-

acteristics of the GDL surface. On a hydrophilic surface, which has a contact angle less than 90° , liquid will spread, whereas on a hydrophobic surface, which has a contact angle greater than 90° , the droplet will be of a more spherical shape, covering less pore entry, as depicted in Figure 20.¹⁰⁵

Both theories of liquid water transport through hydrophobic GDL proposed by Nam and Kaviany¹⁰³ and Pasaogullari and Wang¹⁰⁴ require a boundary value of liquid saturation at the GDL/channel interface. This interfacial saturation should not be equal to the immobile saturation (and hence no liquid flow) but depends on the break-off (or detachment) diameter of liquid droplets and population density, both of which are, in turn, strong functions of the GDL surface contact angle and the gas velocity in the flow channel. Nothing has been formally published on this problem, although it is under intensive investigation in industry.

To summarize, to properly model liquid water transport and ensuing flooding effect on cell performance, one must consider four submodels: (1) a model of catalytic surface coverage by liquid water inside the catalyst layer, (2) a model of liquid water transport through hydrophobic microporous layer and GDL, (3) an interfacial droplet model at the GDL surface, and last (4) a two-phase flow model in the gas channel. Both experimental and theoretical works, in academia and industry alike, are ongoing to build models for the four key steps of water generation, transport, and removal from a PEFC.

Pasaogullari and Wang⁶⁷ further developed a 3-D, isothermal, full-cell numerical model for PEFC by integrating the above-described theory of liquid water transport in hydrophobic GDL with other submodels described in sections 3.1–3.3. Figure 21 compares the current density profiles along the flow direction from a two-channel serpentine fuel cell with the anode and cathode in co-flow, as predicted by the single- and two-phase models. The effect of flooding is clearly visible, although the difference in the average current density amounts to only 6% between the two model predictions. It is seen that the current density near the channel inlet is much higher in the single-phase model than the two-phase model, where it suffers from severe flooding of the cathode. Liquid water limits oxygen transport and covers a portion of the active catalyst particles, resulting in lower perfor-

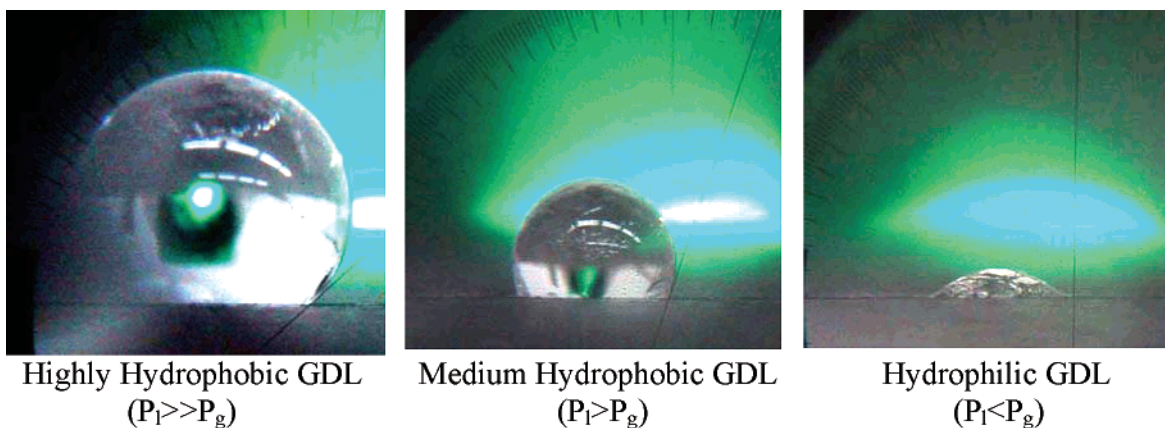


Figure 20. Liquid water droplets on GDL of different wettability at 70°C .¹⁰⁵

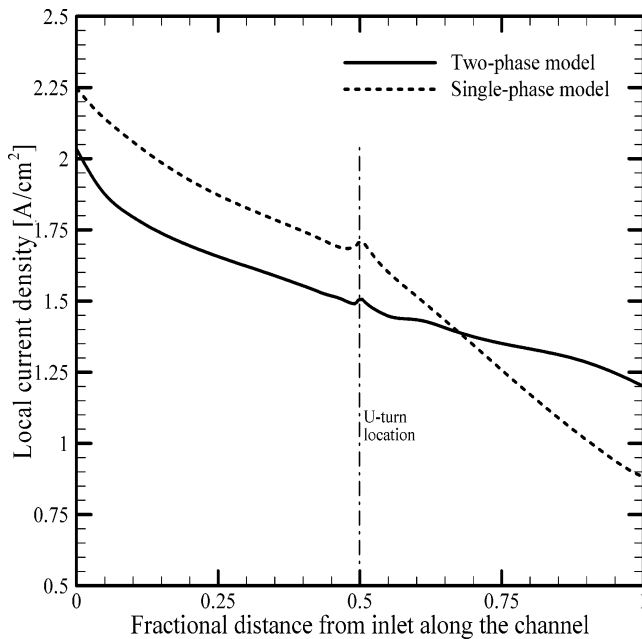


Figure 21. Comparison of local current density distributions in a two-channel serpentine PEFC at $V_{\text{cell}} = 0.4 \text{ V}$.⁶⁷

mance near the inlet. In addition, the current distribution predicted from the two-phase model is more uniform because flooding upstream tends to limit cell performance there as well as oxygen consumption. This leaves a higher oxygen concentration downstream to enhance the current density. Another interesting feature of the current density profiles shown in Figure 21 is seen around the U-turn location, especially with the single-phase model prediction. Due to the mixing effect and secondary flows around the U-turn of serpentine flow channels, the convective transport of oxygen to the catalyst layer is enhanced; hence, a localized spot of higher performance appears in the single-phase results. The same phenomenon is also seen in the two-phase results but at a smaller magnitude, because liquid water in GDL hampers the gas flow and reduces the level of oxygen-transport enhancement under very small gas velocities. In industrial-scale fuel cells, the gas-feed velocities through channels would be much higher, and this phenomenon may also be expected at a larger magnitude even in flooded GDL.

Operating parameters such as humidification and flow rates of inlet reactant streams have a substantial influence on PEFC performance and transport characteristics. A two-dimensional numerical study was performed to investigate these effects.⁶⁷ In Figure 22 the local current density distributions at 0.65 V for different humidification levels are given. It is seen that in the fully humidified case, the local current density monotonically decreases along the flow direction as a result of mass transfer limitations due to both oxygen depletion and flooding. In the case of 70% anode and 20% cathode inlet relative humidity, the membrane stays relatively dry throughout the cell and shows a membrane ionic resistance limited behavior. The current density increases along the flow direction, since the membrane water content is increasing due to ORR. In this case, oxygen depletion is not severe because the current density

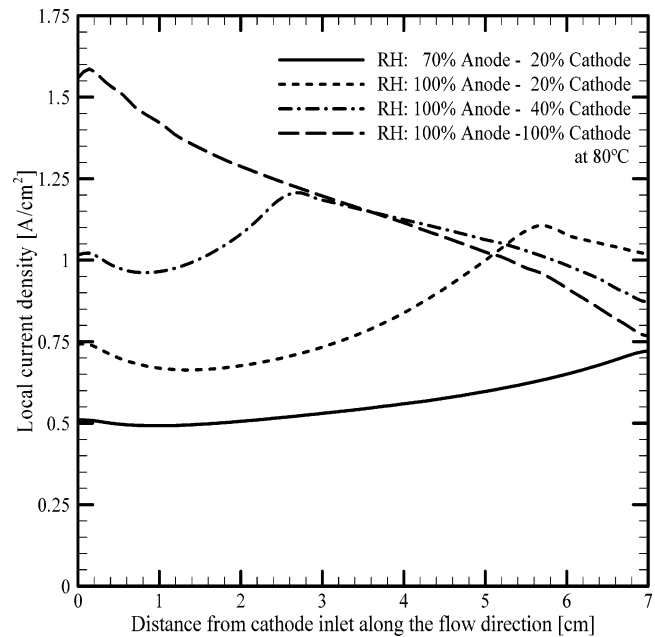


Figure 22. Local current density profiles along the channel direction for different humidification levels at $V_{\text{cell}} = 0.65 \text{ V}$. Anode and cathode stoichiometries are 1.4 at 1.0 A/cm^2 .⁶⁷

overall is small. However, for the lower cathode humidity cases with fully humidified anode inlet (i.e., 20% cathode/100% anode and 40% cathode/100% anode cases), there exist three distinct regimes of the current distribution: (i) the ionic resistance limitation due to membrane dry out in the first part, (ii) a middle section with highest performance where the membrane is fully humidified, and (iii) mass transfer limitations due to flooding and/or oxygen depletion in the last part of the cell. It is seen that even with low cathode inlet humidification levels, i.e., 20% and 40%, the water concentration in porous GDL exceeds the saturation value and flooding takes place in the regions near the channel exit. In these cases the cell suffers from membrane dry out near the inlet, especially on the anode side, due to the electro-osmotic drag of water to the cathode. Near the inlet, the cathode water concentration is lower; therefore, back-diffusion of water from the cathode to anode does not compensate for the electro-osmotic drag, resulting in the anode dry out.

As shown in Figure 23, the fully humidified case shows a maximum liquid saturation around 10% near the inlet and decreases in the flow direction due to decreasing reaction rate in the cathode catalyst layer. The 10% level of liquid saturation results from using a realistic GDL permeability on the order of 10^{-12} m^2 .⁶⁷ Higher liquid saturation values reported in the literature were obtained only by using unrealistically small permeability, i.e., 95% maximum liquid saturation with GDL permeability of $7.3 \times 10^{-15} \text{ m}^2$.⁷⁰

In the low humidity cases, the cell does not produce liquid water immediately but after the water vapor concentration in the gas reaches the saturation value; therefore, the condensation front is pushed downstream, and its location is directly related to cathode inlet relative humidity. In the 20% cathode relative humidity case, it is found that the first two-thirds of

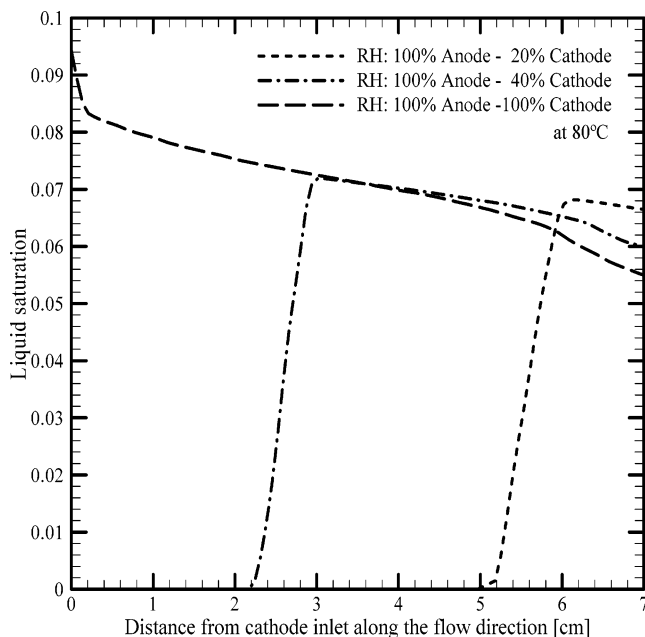


Figure 23. Liquid saturation profiles at cathode GDL–catalyst layer interface along the channel direction for different humidification levels at $V_{\text{cell}} = 0.65$ V. Anode and cathode stoichiometries are 1.4 at 1.0 A/cm^2 .⁶⁷

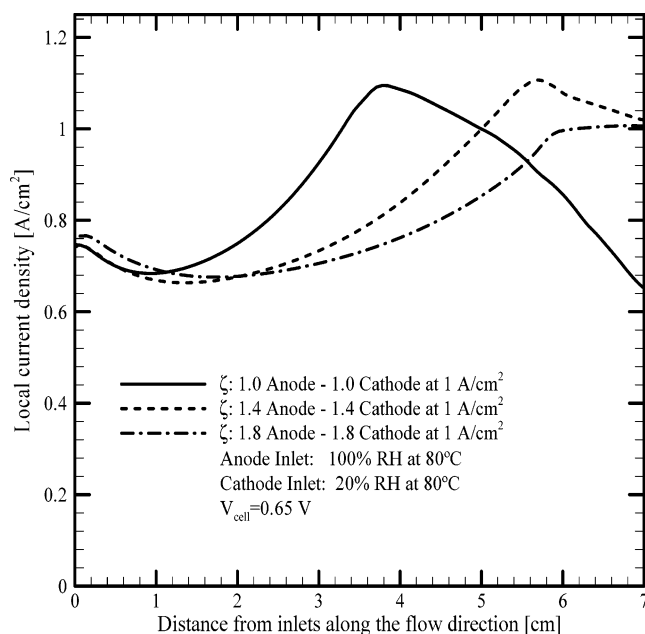


Figure 24. Local current density profiles along the channel direction of single-channel PEFC for different inlet stoichiometric ratios at $V_{\text{cell}} = 0.65$ V at the inlet relative humidity: 20% cathode and 100% anode at 80°C .⁶⁷

the cell is free from liquid water, whereas it is predicted that liquid water starts to appear around one-third of the channel length in the 40% cathode relative humidity case.

The effect of inlet stoichiometry on transport characteristics and performance of PEFC was also investigated by Pasaogullari and Wang.⁶⁷ In Figure 24 the local current density distributions along the flow direction are displayed at a cell voltage of 0.65 V. As explained earlier, the membrane is hydrated much faster in lower flow rates, and therefore, the performance peak is seen earlier in lower stoichio-

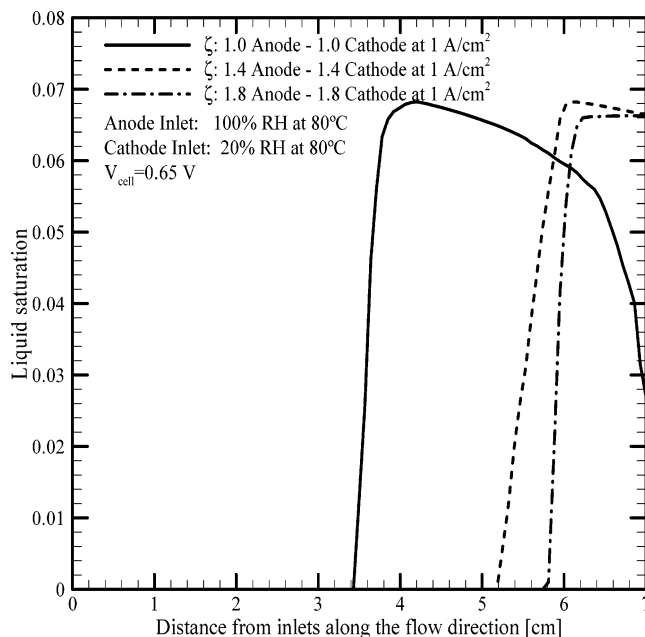


Figure 25. Liquid saturation profiles at cathode GDL–catalyst layer interface along the channel direction of single-channel PEFC for different inlet stoichiometric ratios at $V_{\text{cell}} = 0.65$ V and inlet relative humidity: 20% cathode and 100% anode at 80°C .⁶⁷

metric ratios. However, as the GDL gets saturated with water vapor, water starts to condense and the cell starts to suffer from flooding of GDL as well as oxygen depletion, which result in performance decline. The liquid saturation profiles given in Figure 25 show that with decreasing gas flow rate, the condensation front moves closer to the channel inlet.

Latent heat associated with phase change in two-phase transport has a large impact on the temperature distribution and hence must be included in a nonisothermal model in the two-phase regime. The temperature nonuniformity will in turn affect the saturation pressure, condensation/evaporation rate, and hence the liquid water distribution. Under the local interfacial equilibrium between the two phases, which is an excellent approximation in a PEFC, the mass rate of phase change, \dot{m}_{fg} , is readily calculated from the liquid continuity equation, namely

$$\dot{m}_{fg} = \epsilon \frac{\partial(\rho_f s)}{\partial t} + \nabla(\rho_l \bar{u}) \quad (22)$$

Since the liquid-phase velocity is obtained, for example, from the M^2 model as follows

$$\rho_l \bar{u}_l = \bar{J}_l + \lambda \rho \bar{u} \quad (23)$$

Substituting eq 23 into eq 22 yields

$$\dot{m}_{fg} = \epsilon \frac{\partial(\rho_f s)}{\partial t} + \nabla(\bar{J}_l + \lambda \rho \bar{u}) \quad (24)$$

The heat release or adsorption due to condensation or evaporation is simply given by

$$S_T = h_{fg} \dot{m}_{fg} \quad (25)$$

where h_{fg} is the latent heat of vapor–liquid phase change.

Last, all models describing liquid water transport through GDL can be categorized into two approaches: the M^2 model and unsaturated flow theory (UFT). UFT assumes a constant gas phase pressure, thus effectively decoupling the liquid water transport from gas flow. The models of Nguyen and co-workers,^{69,70} Berning and Djilali,⁷⁴ Nam and Kavinay,¹⁰³ and Pasaogullari and Wang¹⁰⁴ belong to UFT. In contrast, the M^2 model is a more complete two-phase model in which motions of both liquid and gas phases are accounted for. The work of Wang et al.,⁶⁸ You and Liu,⁷² Mazumder and Cole,⁷³ and Pasaogullari and Wang⁶⁷ are based on the M^2 model. Most recently, Pasaogullari and Wang⁷⁵ fully elaborated the differences between the M^2 and UFT models for PEFC GDLs and revealed an interesting new mechanism for oxygen transport that results from the gas counterflow to the liquid water motion. In addition, the roles of a microporous layer played in two-phase transport in a PEFC were elucidated.⁷⁵

3.8. Experimental Diagnostics and Model Validation

Experimental diagnostics not only help develop a fundamental understanding of fuel cell dynamics but also provide benchmark-quality data for CFCD model validation. Motivated by both needs, diagnostic efforts are presently directed toward local distribution measurements (vs global), multiple and simultaneous measurements, in-situ and nonintrusive measurements, as well as simple and well-defined cell configurations rather than experimentation involving various complex configurations of direct interest to the industry. This section reviews work published in the literature on current distribution, high-frequency resistance distribution, mass distribution, temperature distribution, and two-phase visualization for elucidation of the flooding process.

3.8.1. Current, Species, and High-Frequency Resistance Distribution Measurements

Quantification of current, specie, and membrane resistance distributions in a PEFC is critical to understanding key phenomena, such as water management, CO poisoning, and flow-field design effect, and providing valuable data for validation of CFCD models. As indicated by Wang,^{4,5} it is this type of detailed validation that will permit an ultimate understanding of the physicochemical phenomena in PEFC as well as development of computer-aided tools for design and development.

To measure the current distribution in a hydrogen PEFC, Brown et al.¹⁰⁶ and Cleghorn et al.¹⁰⁷ employed the printed circuit board approach using a segmented current collector, anode catalyst, and anode GDL. This approach was further refined by Bender et al.¹⁰⁸ to improve ease of use and quality of information measured. Weiser et al.¹⁰⁹ developed a technique utilizing a magnetic loop array embedded in the current collector plate and showed that cell compression can drastically affect the local current density. Stumper et al.¹¹⁰ demonstrated three methods for the determination of current density distribution of a hydrogen PEFC. First, the partial membrane elec-

trode assembly (MEA) technique involves either masking different areas or partially catalyzing segments of the MEA to determine local current density behavior. Second, the subcell technique involves electrically isolating individual locations of catalyzed anode and opposing cathode from the main cell in order to measure the performance of the desired location. In the passive current mapping technique, an array of shunt resistors normal to an unmodified MEA surface are located between the flow field and a buss plate. Voltage sensors passively determine the potential drop across each resistor, and via Ohm's law, current distribution through the flow plate is determined. While each of the described methods for determination of current distribution has advantages, it is desirable to utilize a nonsegmented MEA in order to preserve true fuel cell operation characteristics and avoid highly individualized specialty membranes. Note also that all predictive models are developed for nonsegmented MEA.

In addition to the use of conventional MEAs and good spatial resolution, the ability to determine transient effects from sudden changes in operating conditions is desired. The nonsegmented passive current mapping technique of Stumper et al.¹¹⁰ allows transient measurement and has good spatial resolution but requires an array of embedded and highly precise shunt resistors. The magnetic loop method of Weiser et al.¹⁰⁹ also allows transient measurements with unaltered MEAs and flow fields but is more difficult to implement than the other methods and cannot be applied to stacks. Recently, Mench and Wang demonstrated an improved technique for accurate current distribution measurements first on a DMFC¹¹¹ and later on a H_2 /air PEFC.¹¹² Independently, Noponen et al.^{113,114} developed and demonstrated a similar technique.

A common problem prevailing in much of the published work on use of the segmented cell is inability to produce a similar level of current density expected from a nonsegmented single cell. Lower performance originates from the difficulty that a segmented cell, if not well designed, fabricated, and assembled, exhibits much higher electric contact resistance between the segmented flow-field plate and GDL. As a result, the measured current distribution is more reflective of the contact resistance distribution than the intrinsic distribution of water and reactants inside the cell. Such an artifact due to intrusiveness of the measurement must be minimized in order for the segmented cell technique to produce truly useful data of current distribution. A future goal for this field is to produce current distribution data representative of automotive operating conditions, such as a temperature level of 80 °C, average current density level of 1 A/cm², and voltage level of 0.6 V. Only then will the segmented cell technique have the potential to become a standard diagnostic tool for fuel cell research and development.

Localized AC impedance and current distributions were measured by Brett et al.¹¹⁵ on a single linear channel with the segmented cathode current collector plate. Figure 26 shows their measured current density and membrane resistance distributions along the

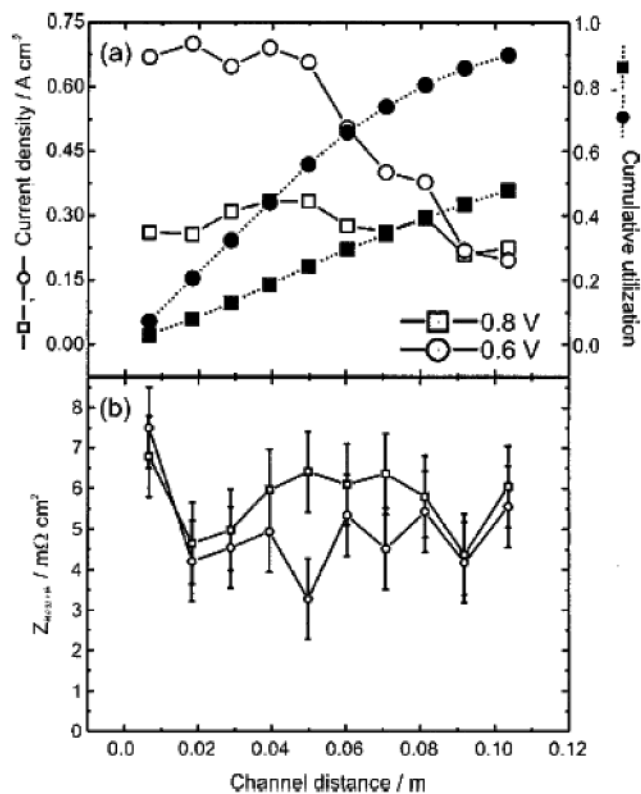


Figure 26. Current (a) and high-frequency resistance (b) distributions at cell potentials of 0.8 and 0.6 V as measured by Brett et al.¹¹⁵

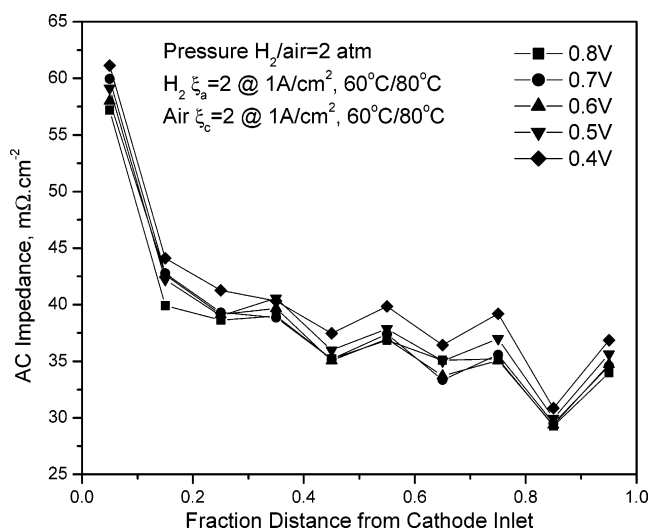


Figure 27. Distribution of high-frequency resistances measured at 1.5 kHz in a low humidity PEFC using 30 μm membrane (EW < 1000).

channel for two cell potentials. Carbon paper along with Nafion 112 was used to construct a MEA in this experimental cell. Interestingly, there is no significant variation between the membrane resistance along the channel length or between the two set potentials, despite a dry cathode feed and the fully humidified anode feed. Figure 27 displays another example of high-frequency resistance (HFR) distributions measured in a low humidity cell with Gore PRIMEA membrane (30 μm, EW < 1000) and carbon cloth as GDL. These measurements also show little variation for different cell potentials. However, the

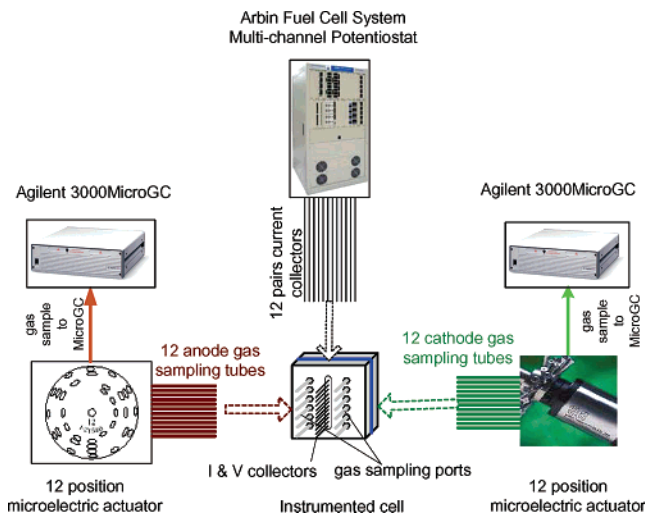


Figure 28. Schematic diagram of the experimental setup for simultaneous measurements of anode/cathode species, current, and high-frequency resistance (HFR) distributions in an operating cell.¹²⁰

higher HFR is clearly seen near the inlet where the membrane is dehydrated by dry inlet gases.

Distributions of water and reactants are of high interest for PEFCs as the membrane conductivity is strongly dependent on water content. The information of water distribution is instrumental for designing innovative water management schemes in a PEFC. A few authors have studied overall water balance by collection of the fuel cell effluent and condensation of the gas-phase water vapor.^{116–118} However, determination of the in situ distribution of water vapor is desirable at various locations within the anode and cathode gas channel flow paths. Mench et al.¹¹⁹ pioneered the use of a gas chromatograph for water distribution measurements. The technique can be used to directly map water distribution in the anode and cathode of an operating fuel cell with a time resolution of approximately 2 min and a spatial resolution limited only by the proximity of sample extraction ports located in gas channels.

More advanced capability exists in an apparatus to simultaneously measure species, current, and high-frequency impedance distributions using segmented fuel cells.¹²⁰ A schematic diagram of the experimental apparatus is shown in Figure 28. Two sets of 12-port electric microactuators and gas chromatographs are used to measure gas concentration distributions on the anode and cathode sides simultaneously. The arrays of multiple scalar distributions obtainable from this apparatus have been the basis for much improvement in CFD modeling in our research program at Penn State. Figure 29 shows the typical current density distributions along the cathode flow path in a PEFC with fully humidified anode and cathode. It is seen that the level of average current density matches well with a realistic fuel cell under similar operating conditions. Moreover, the decline in the local current density along the flow path due to oxygen depletion is evident. This decline is more severe under lower cell voltage or higher average current density. To illustrate the species distribution measurement capability by microGC, Figures 30 and 31 display water mole fraction

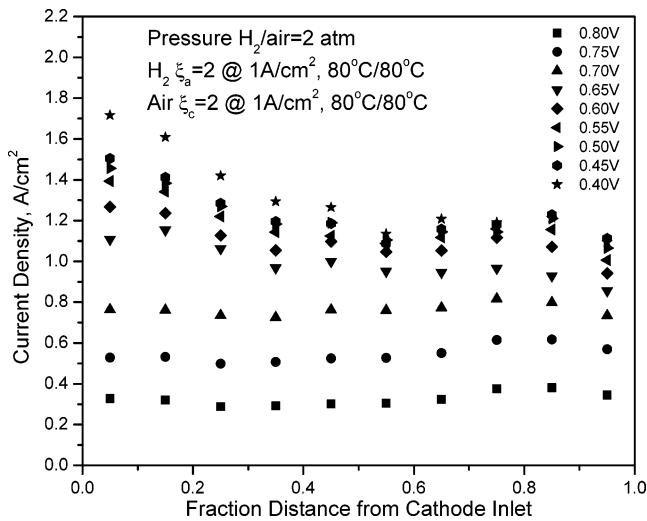


Figure 29. Current density distributions in a fully humidified PEFC using 30 μm membrane ($\text{EW} < 1000$) under various cell voltages.

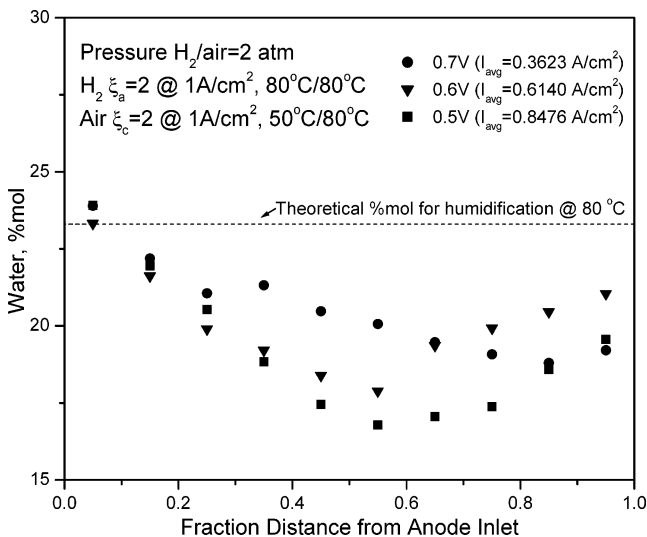


Figure 30. Water mole fraction profiles along the anode gas channel measured by a microGC in a cathode under-humidified PEFC using 30 μm membrane ($\text{EW} < 1000$).

distributions inside the anode and cathode gas channels, respectively, under the conditions that the anode inlet is fully humidified and the cathode humidification temperature is 50 $^{\circ}\text{C}$ relative to the cell temperature of 80 $^{\circ}\text{C}$. It is seen from Figure 30 that the anode water mole fraction shows a decrease-then-increase trend. Beginning from the inlet, the anode gas loses water owing to both electro-osmotic drag and forward diffusion driven by the higher water concentration on the anode side. After a minimum point of water mole fraction at a certain location downstream of the anode channel, the water mole fraction begins to increase again once the water concentration on the cathode side increases and enhances back diffusion from the cathode to anode. It is interesting to note that the location of minimum water mole fraction shifts more downstream when the cell voltage is higher or the amount of water production is lower on the cathode side.

For a relatively dry cathode inlet (i.e., the humidification temperature of 50 $^{\circ}\text{C}$ versus the cell temperature of 80 $^{\circ}\text{C}$), Figure 31 displays how the water

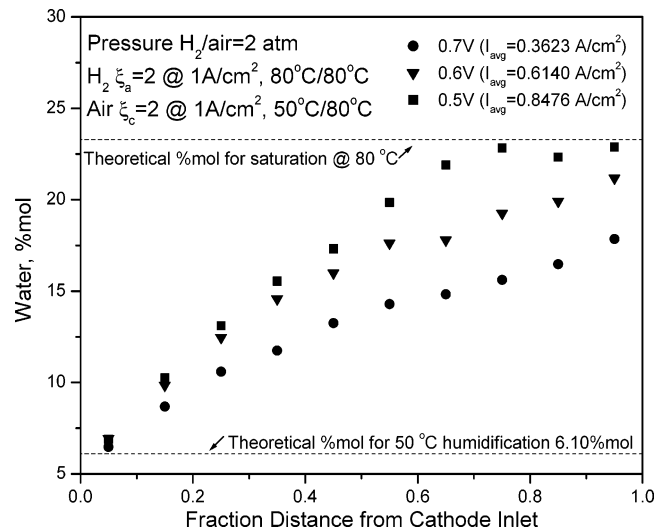


Figure 31. Water mole fraction profiles along the cathode gas channel measured by a microGC in a cathode under-humidified PEFC using 30 μm membrane ($\text{EW} < 1000$).

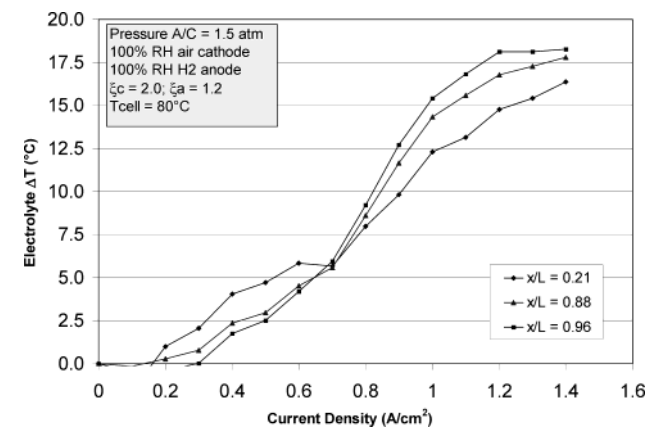
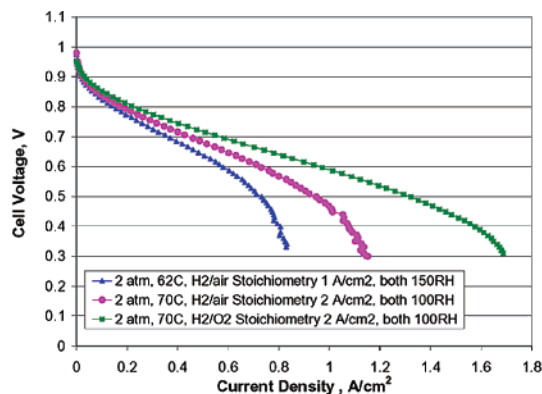


Figure 32. Rise of electrolyte temperature from the initial temperature at open circuit as a function of current density.¹²¹

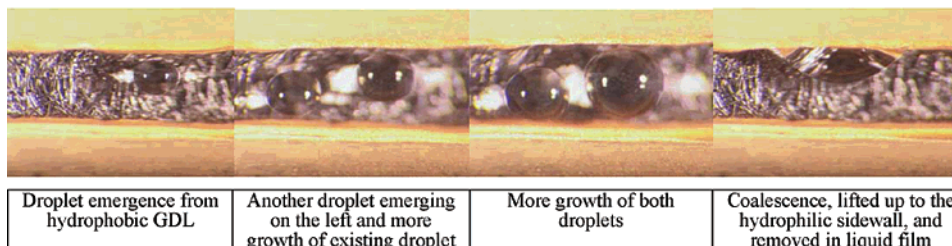
mole fraction increases along the flow path of the cathode gas channel. This increase is nearly linear until approaching the saturation limit. The information from Figures 30 and 31 on water distributions in both the anode and cathode sides yielded the profile of the net water-transport rate through the membrane along the flow direction for the first time.

3.8.2. Temperature Distribution Measurements

Mench et al.¹²¹ developed a technique to embed microthermocouples in a multilayered membrane of an operating PEM fuel cell so that the membrane temperature can be measured in situ. These microthermocouples can be embedded inside two thin layers of the membrane without causing delamination or leakage. An array of up to 10 thermocouples can be instrumented into a single membrane for temperature distribution measurements. Figure 32 shows the deviation of the membrane temperature in an operating fuel cell from its open-circuit state as a function of the current density. This new data in conjunction with a parallel modeling effort of Ju et al.⁶⁴ helped to probe the thermal environment of PEM fuel cells.



(a) Polarization behaviors



(b) Snapshots showing water droplet dynamics from GDL surface

Figure 33. Visualization of liquid water transport in an operating transparent PEFC (45 μm membrane with EW < 1000; GDL, Toray paper TGPH 090 with 20 wt % PTFE loading with a microporous layer).¹²⁵

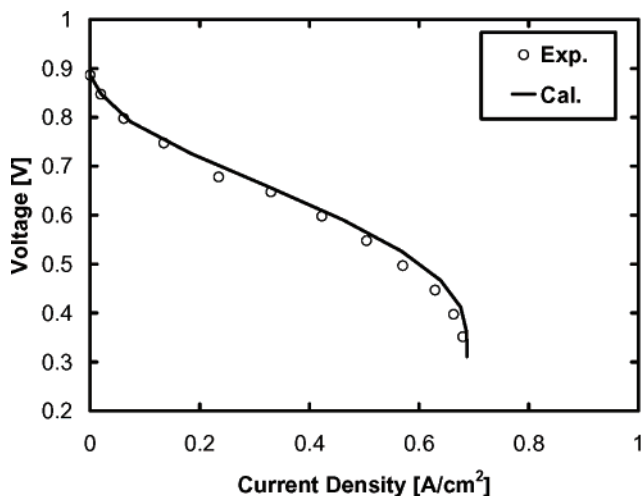
3.8.3. Two-Phase Visualization

To delineate the origin and development of flooding in PEFC, recent research has resorted to two-phase visualization techniques. This can be done either through a transparent cell based on optical diagnostics or a graphite/metal cell visualized by neutron transmission radiography (NR). Bellows et al.¹²² made the first attempt to measure the water content profile within a polymer membrane using NR. Owing to the NR limitation in spatial resolution, a thick membrane of 500 μm was used. Geiger et al.¹²³ reported the two-phase flow patterns observed by NR in the flow field for the first time. Preliminary results of two-phase distributions in both PEFC and DMFC were given; however, the spatial resolution in the presented radiographs appeared inadequate. In addition, Geiger et al. discussed the NR limitation in temporal resolution due to the necessity to use a CCD camera to detect time-dependent processes instead of recording still images to a film with sufficiently long exposure time.

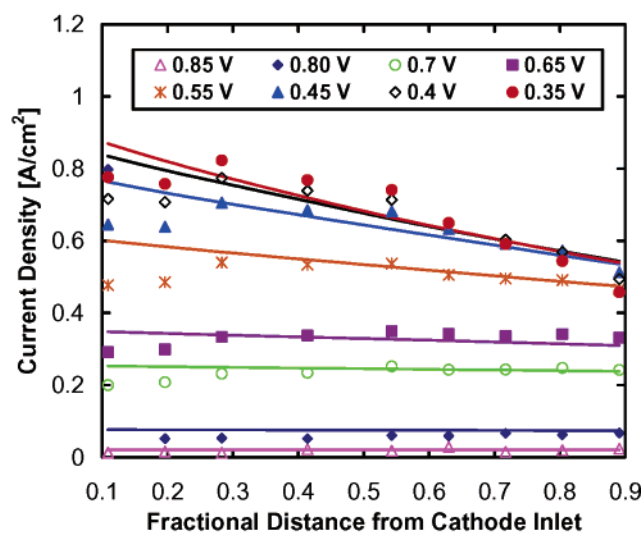
To achieve sufficient spatial and temporal resolution, critical to the capture of two-phase flow phenomena in PEFC that is transient in nature and controlled by surface forces, a parallel effort is currently being made in optical diagnostics. Tuber et al.¹²⁴ attempted to visualize two-phase flow using a transparent test cell made of plexiglass. The cell design and experimental technique are limited to room temperature ($\sim 30^\circ\text{C}$) and low current density ($\sim 300\text{ mA/cm}^2$) conditions. Under these conditions it was observed that clogging of gas channels by liquid water is a major cause for low cell performance. In this operating regime a hydrophilic GDL tends to enhance the cell performance. It should be noted that the same conclusion cannot be extrapolated to auto-

motive fuel cells that feature quite different operating temperature and current density. It is more difficult to visualize two-phase flow and liquid water dynamics in an automotive PEFC operated at higher current densities ($\sim 1\text{ A/cm}^2$) and higher temperatures, due largely to severe fogging.¹²⁵ Figure 33a shows the polarization characteristics of this transparent fuel cell under typical automotive conditions.¹²⁵ Apparently the reasonable electrochemical performance is preserved in this transparent cell. Figure 33b shows a series of normal-view snapshots of water droplet emergence on the GDL surface, growth, coalescence, and removal as liquid film from the sidewall. Observations of the droplet formation on GDL surface reveal a highly transient, cyclic process—water droplets emerge from certain locations from the GDL surface, then grow and sometimes coalesce into a larger drop. When the large drop reaches a size comparable with the channel dimension, it touches the hydrophilic channel wall in the flow field and spreads laterally along it into a thin liquid film. The liquid film becomes continuous and flows toward the exit of the gas channel under the influence of gas shear force. New droplets then form and grow on nearly the same spots of GDL, repeating the cyclic process. However, on the cell scale, a large number of droplets would exist on a sufficiently large surface at any one time, each having its own history of emergence, growth, and removal. Thus, one can anticipate an average current density that is essentially at steady state for a given set of operating conditions.

The visualization study of Yang et al.¹²⁵ further revealed the profound effects of wetting properties of gas channel walls. In a gas channel surrounded by mixed hydrophilic channel surfaces and hydrophobic GDL surface, it was found that water conden-



(a) comparison in average polarization curve



(b) comparison in the current distributions

Figure 34. Comparison of calculation (lines) and experimental (symbols) results for cathode stoichiometry of 2.0 at 0.75 A/cm² and fully humidified anode and cathode: (a) average polarization curve and (b) current distribution. Different colors in panel b represent various cell voltages as defined in the figure legend.⁶

sation occurs preferentially on hydrophilic surfaces, thus giving rise to an opportunity to keep condensation sites away from the GDL by properly tailoring the wetting characteristics of the channel walls and hence alleviate GDL flooding.

3.8.4. Experimental Validation

While highly sophisticated CFD simulations are capable of predicting many details, to date model validation has been conducted mostly against the cell global polarization (or I - V) curve, which is an integral outcome of many interacting phenomena. Ju and Wang⁶ made the first attempt to validate a three-dimensional, single-phase, isothermal PEFC model against current distribution data measured in a 50 cm² fuel cell operated with fully humidified gas feed. Figure 34 shows validation results with a cathode stoichiometry of 2.0 at 0.75 A/cm². An excellent match with the average I - V curve can be seen between the

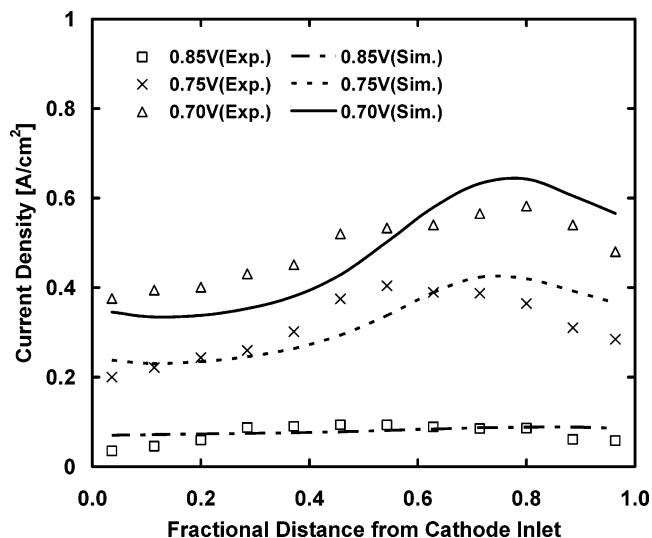


Figure 35. Comparison between simulated and measured current distributions in a PEFC with 15 μm membrane ($\text{EW} < 1000$) and under anode and cathode conditions of 3/3 bar, 1.2/2 stoichiometry, and 75%/0% relative humidity. The cell temperature is 80 °C.¹⁰⁰

simulation and experiment; however, agreement with the current distribution remains unsatisfactory. Reasons for the discrepancy at the current distribution level were then analyzed, leading to improvement in the fundamental understanding of many complex, interacting phenomena occurring in a PEFC. Validation against global I - V curves is insufficient and often misleading.

Detailed validation for low humidity PEFC, where the current distribution is of more interest and likely leads to discovery of optimal water management strategies, was performed most recently.¹⁰⁰ Figure 35 shows a comparison of simulated and measured current density profiles at cell potentials of 0.85, 0.75, and 0.7 V in a 50 cm² cell with anode and cathode RH of 75% and 0%. Both experimental data and simulation results display the characteristics of a low humidity cell: the local current density increases initially as the dry reactants gain moisture from product water, and then it decreases toward the cathode outlet as oxygen depletion becomes severe. The location of the peak current density is seen to move toward the cathode inlet at the lower cell potential (i.e., 0.7 V) due to higher water production within the cell, as expected.

The current state of experimental validation is to validate comprehensive CFD models against distribution data of multiple parameters, such as current and species distributions. This possibility is becoming a reality as a new experimental technique to measure current and species (e.g., water) distributions simultaneously has emerged.¹²⁰ The trend will continue to validate CFD models against multiple arrays of distribution data in order to develop a full understanding of PEFC fundamentals.

3.9. Modeling the Catalyst Layer at Pore Level

The catalyst layer of thickness around 10 μm is a critical component of a PEFC and requires more elaborate treatment. Gottesfeld and Zawodzinski³⁰

provided a good overview of the catalyst layer structure and functions. The oxygen reduction reaction (ORR) occurs in the cathode catalyst layer, and the hydrogen oxidation reaction (HOR) takes place in the anode catalyst layer. Both reactions require active catalyst sites to break the molecular bond in the diatomic gaseous reactant molecules because of the low-temperature environment of a PEFC. HOR has orders of magnitude higher reaction rate than ORR, which leaves ORR as a source of large voltage loss in PEFC. Due to the acid nature of the polymer electrolyte and low-temperature operation, Pt- or Pt-alloys are the best-known catalysts. To enable ORR in the cathode catalyst layer, the layer must provide access for oxygen molecules, protons, and electrons. Therefore, the catalyst layer usually consists of: (1) the ionomer (its amount is also called Nafion content, ϵ_a) to provide a passage for protons to be transported in or out, (2) metal catalysts supported on carbon (the electronic phase volume fraction, ϵ_s) to provide a means for electron conduction, and (3) sufficient porosity (ϵ_g) for the O_2 gas to be transferred to catalyzed sites. The sum of all volume fractions is equal to unity, and individual volume fractions must be optimized to provide the best overall performance of a catalyst layer.

The important processes occurring in a catalyst layer include interfacial ORR at the electrochemically active sites, proton transport in the electrolyte phase, electron conduction in the electronic phase (i.e., Pt/C), and oxygen diffusion through the gas phase, liquid water, and electrolyte phase.

In most of the macroscopic models reported in the literature the active catalyst layer was not the main point of interest but rather treated either as an infinitely thin interface or a macrohomogeneous porous layer. There were a few detailed models specifically developed for PEFC catalyst layers based on the theory of volume averaging. In this field distinction is further made between a homogeneous approach, a film model, and an agglomerate model. The homogeneous model assumes the catalyst layer to be a two-phase system consisting of ionic and electronic phases only, without gas voids. The gaseous reactant transports through the catalyst layer via the electrolyte phase as a dissolved species, and thus the diffusion rate is poor. In the film model gas pores are assumed to exist along with the electronic particles covered by a thin film of polymer electrolyte. On the other hand, the agglomerate model considers gas pores to surround agglomerates consisting of electrolyte films and electronic particles, i.e., a three-phase system. Depending on the pore geometry, agglomerates are planar, cylindrical, and spherical. Nonetheless, all three models belong to the macroscopic theory for multiphase systems in which there is neither resolution to capture pore-level phenomena nor ability to assess the morphological effects.

Springer and Gottesfeld,¹²⁶ Perry et al.,¹²⁷ and Eikerling and Kornyshev¹²⁸ presented several analytical and numerical solutions for the cathode catalyst layer under various conditions. Perry et al. studied the effects of mass-transport limitations on the polarization characteristics of a reaction obeying

Tafel kinetics and predicted a doubling of the Tafel slope as the current density increases or the mass-transport limitations set in. Eikerling and Kornyshev presented analytical expressions in the limiting cases of small currents, fast oxygen diffusion, fast proton transport, and high currents. To verify the theoretical finding regarding the existence of double Tafel slopes, Ihonen et al.¹²⁹ most recently performed an experimental study of mass-transport limitations in the PEFC cathode catalyst layer. A kinetic slope at low current densities and a second Tafel slope at higher current densities were indeed observed on the polarization curves. The experimental evidence appears to suggest that oxygen diffusion is limited in the agglomerates at the pore scale rather than by that in the gas phase across the thickness of the electrode.

However, the above-mentioned macroscopic models do not address localized phenomena on the pore level. To assess the profound effects of the catalyst layer pore structure on polarization performance, Pisani et al.¹³⁰ constructed a pore-level model by volume-averaging microscopic governing equations over an idealized, one-dimensional model geometry of pores. Wang and Wang¹³¹ recently developed a direct numerical simulation (DNS) model to describe the transport of protons, electrons, oxygen, and product water at the pore level (on the order of 100 nm) within a random, microscopically complex catalyst layer. This DNS model is based on a numerical mesh created from either a digitized catalyst layer micrograph or a computer-generated random pore structure according to the prescribed porosity and average pore size. Subsequently, direct simulation of reactant and product transport with reaction is performed on this digital microstructure at the pore level. Such a DNS model can be used as an alternative to experimental trial-and-error for the optimization of compositions and microstructure of a high-performance catalyst layer. Figure 36 shows DNS predictions of the cathode voltage loss as a result of kinetic polarization, ohmic polarization, and mass-transport polarization for a commonly used catalyst layer composition (circles), an optimized design (squares), and a less optimal design (triangles). The three-dimensional contour of O_2 concentration on the right illustrates that the less optimized design exhibits restrictive oxygen transport into the catalyst layer due to a too small porosity.

3.10. Summary and Outlook

Table 2 summarizes and compares the main features of representative CFD models reviewed in this section for PEFCs. It is evident that rapid advances in PEFC modeling over the past 5 years have yielded considerable predictive capabilities. Fully three-dimensional, electrochemical–transport–thermal coupled, and realistic large-scale simulations are possible with today's computing power. A major focus of future research in PEFC modeling will be on liquid water transport and ensuing flooding phenomena. Much remains to be learned about the fundamental physical process of flooding occurrence. Advanced diagnostics, such as visualization by optical diagnostics and 3-D neutron tomography, as well as detailed

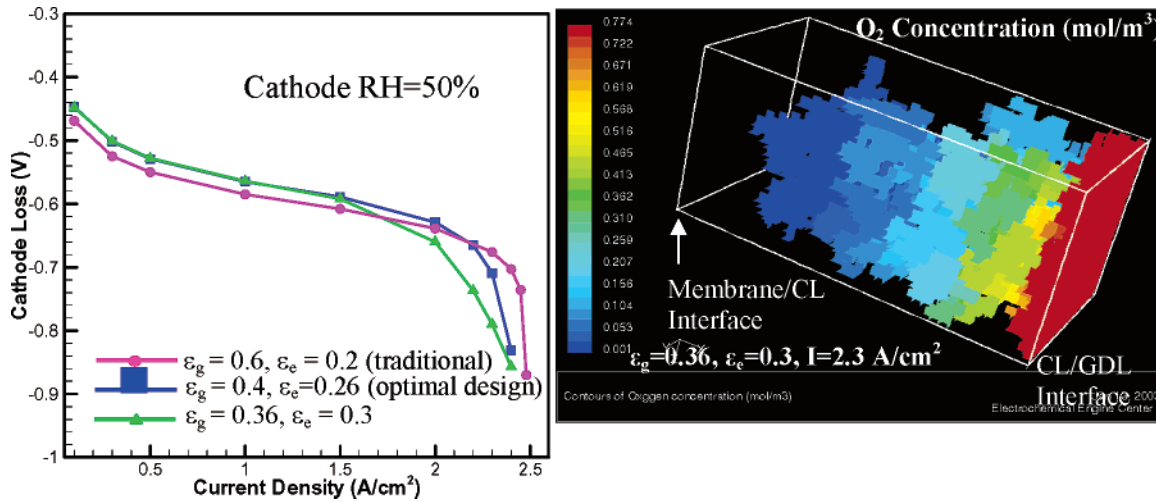


Figure 36. Cathode voltage loss as predicted by direct numerical simulation of proton, oxygen, and water transport in a catalyst layer at the pore level (left), and three-dimensional oxygen concentration contours in a random microstructure of the catalyst layer (right).¹³¹

Table 2. Comparisons of Representative CFD Models for Polymer Electrolyte Fuel Cells (PEFCs)

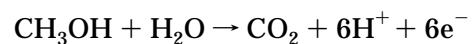
Model Features	CFDRC	Fluent	Penn State U.	STAR-CD Japan	STAR-CD N. America	U. Kansas	U. Miami	U. South Carolina	U. Victoria
Domain Meshed									
Catalyst layers	✓	✓	✓	✓	×	×	✓	×	×
Membrane	✓	✓	✓	✓	×	×	✓	×	✓
Gas diffusion layers	✓	✓	✓	✓	✓	✓	✓	✓	✓
Gas channels	✓	✓	✓	✓	✓	×	✓	✓	✓
Approach/Assumptions									
Species variable	mass fraction	mass fraction	molar conc./ mass fraction	molar conc. /mass fraction	mass fraction	mole fraction	mole/mass fraction	mass fraction	mass fraction
Density	variable	variable	variable/ constant	variable	variable	N/A	constant	variable	variable
Mass source/sink in continuity equation	×	✓	✓	✓	✓	×	×	✓	×
Physics Included									
CL ohmic loss	✓	✓	✓	✓	×	×	✓	×	×
CL transport loss	✓	✓	✓	✓	×	×	✓	×	×
Water transport thru membrane	×	×	✓	✓	✓	×	×	✓	×
					(w/ const. properties)			(w/ const. properties)	
Electron transport	✓	✓	✓	✓	×	×	×	×	×
Contact resistance	×	✓	✓	✓	×	×	×	×	×
Non-isothermal	×	×	✓	✓	✓	×	✓	✓	✓
Two-phase flow in GDL	M ² Model	×	M ² Model	M ² Model	×	UFT Model	M ² Model	×	UFT Model
GDL hydrophobic effects	×	×	✓	✓	×	×	×	×	×
Two-phase flow model in channels	mist flow	×	mist flow & annular film	mist flow	×	×	×	×	un-specified
References/Notes	63, 73	90	55, 59, 14, 64, 67, 81	based on PSU model	based on SC model	69-71	54, 72	57, 58, 60	62, 74

distribution measurements, are critically needed in order to paint a clear picture of how flooding occurs and what are the controlling factors. Once a physical understanding of the flooding process is established, the challenge will turn to how to model and simulate such a complex two-phase flow process with strong interactions with the GDL surface and channel walls.

4. Direct Methanol Fuel Cells

A DMFC is an electrochemical cell that generates electricity based on the oxidation of methanol and reduction of oxygen. Figure 37 illustrates the cell construction and operating principle of a DMFC. An

aqueous methanol solution of low molarity acts as the reducing agent that traverses the anode flow field. Once inside the flow channel, the aqueous solution diffuses through the backing layer, comprised of carbon cloth or carbon paper. The backing layer collects the current generated by the oxidation of aqueous methanol and transports laterally to a land in the current collector plate. The global oxidation reaction occurring at the platinum–ruthenium catalyst of the anode is given by



The carbon dioxide generated from the oxidation

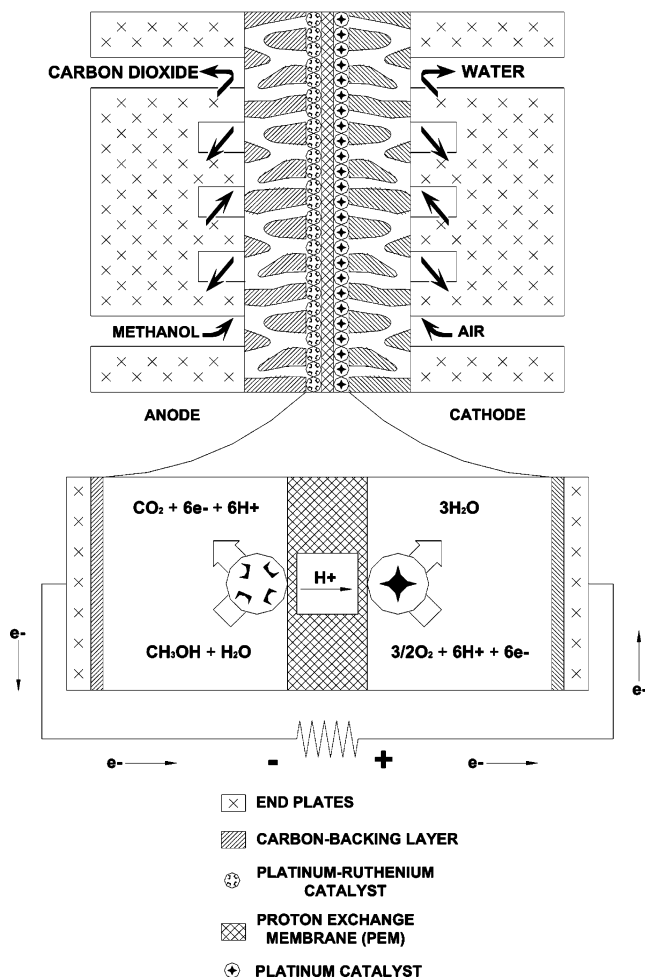
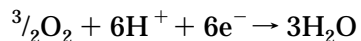


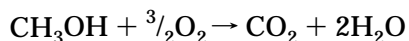
Figure 37. Operating schematic of a direct methanol fuel cell (DMFC).

reaction emerges from the anode backing layer as bubbles and is removed via the flowing aqueous methanol solution.

Air is fed to the flow field on the cathode side. The oxygen in the air combines with the electrons and protons at the platinum catalyst sites to form water. The reduction reaction taking place on the cathode is given by



The two electrochemical reactions are combined to form an overall cell reaction as



Extensive work on DMFC has been conducted by many groups, notably Halpert et al.¹³² of Jet Propulsion Laboratory (JPL) and Giner, Inc., Baldauf and Preidel¹³³ of Siemens, Ren et al.¹³⁴ of Los Alamos National Laboratory (LANL), Scott and co-workers^{135–137} of the University of Newcastle upon Tyne, and Wang and co-workers^{111,138–141} of the Pennsylvania State University. A comparative study of DMFC with hydrogen PEFC was presented by the LANL group.^{134,142} A DMFC requires platinum–ruthenium and platinum loadings roughly five times higher to achieve power densities of 0.05–0.30 W/cm².

A number of extensive reviews have been published as the DMFC research activities has grown nearly exponentially worldwide in recent years. Gottesfeld and Zawodzinski³⁰ briefly summarized research at Los Alamos intended for transportation application and pointed out areas for improvement if DMFC technology is to become a serious power plant candidate for transportation. Among them, reducing catalyst loading to be competitive with reformed/air fuel cells is perhaps a great challenge and a difficult task for the foreseeable future. In a later book chapter, Gottesfeld and Wilson¹⁴² discussed perspectives of DMFC for portable applications. Lamy et al.¹⁴³ provided an in-depth review of DMFC fundamentals, including the reaction mechanisms of methanol oxidation, use of various binary and ternary electrocatalysts, effects of electrode structure and composition on the activity of methanol oxidation, and development of proton conducting membranes with low methanol crossover. It was projected that DMFC will be first commercialized as portable power sources before the year 2010 and that there will be a quantum jump on the technology to be in a position to drive DMFC-powered vehicles 10 years thereafter. Arico et al.¹⁴⁴ reviewed recent advances in DMFC from both fundamental and technological (for portable power) aspects. The fundamental aspects of DMFC reviewed by Arico et al. were concerned with electrocatalysis of methanol oxidation and oxygen reduction in the presence of methanol crossed over from the membrane, and the technological aspects were focused on the proton conducting membranes as well as techniques for fabricating MEA. Neergat et al.¹⁴⁵ provided an excellent review of new materials for DMFC, including novel proton conducting membranes and electrocatalysts. Narayanan et al.¹⁴⁶ and Muller et al.¹⁴⁷ discussed, in detail, the paramount importance of water balance for a portable DMFC system.

4.1. Technical Challenges

As expected, a DMFC exhibits lower power densities than that of a H₂/air PEFC. At present, the H₂/air PEFC requires anode and cathode platinum loadings of less than 1 mg/cm² to achieve power densities of 0.6–0.7 W/cm². However, DMFC has the advantages of easier fuel storage, no need for cooling or humidification, and simpler design. Thus, DMFC is presently considered a leading contender for portable power. To compete with lithium-ion batteries, the first and foremost property of a portable DMFC system is a higher energy density in Wh/L. This requirement entails four key technical challenges to be overcome: (1) low rate of methanol oxidation kinetics on the anode, (2) methanol crossover through the polymer membrane, (3) innovative water management, and (4) heat management.

4.1.1. Methanol Oxidation Kinetics

Combined with methanol crossover, slow anode kinetics lead to a power density of a DMFC that is three to four times lower than that of a hydrogen fuel cell. Much work has been focused on the anodic oxidation of methanol.¹⁴⁸ The mechanism of the

electrocatalytic oxidation of methanol at anode was postulated.^{149,150} Different anode catalyst structures of Pt–Ru were developed,¹⁵¹ and several anode catalysts other than Pt–Ru were explored.^{152–154} Additionally, the effects of the anode electrochemical reaction on cell performance were experimentally studied.^{19,155,156} Lamy et al.¹⁴³ and Arico et al.¹⁴⁴ provided extensive reviews of the most recent work on electrocatalysis. More active catalysts for methanol oxidation enable a certain power density to be realized at higher cell voltage and hence directly impact the energy efficiency of the cell, which translates to the energy density if the amount of fuel carried by a DMFC system is fixed.

4.1.2. Methanol Crossover

Methanol crossover occurs due to the inability of the commonly used perfluorosulfonic acid (PFSA) membrane to prevent methanol from permeating its polymer structure. Diffusion and electro-osmotic drag are the prime driving forces for methanol to transport through the polymer membrane and eventually react with platinum catalyst sites on the cathode, leading to a mixed potential on the cathode. This mixed potential on the cathode causes a decrease in cell voltage. Methanol reaching the cathode also results in decreased fuel efficiency, thus lowering the energy density.

Methanol crossover in DMFC has been extensively studied both experimentally and theoretically. Narayanan et al.¹⁵⁷ and Ren et al.¹⁵⁸ measured the methanol crossover flux with different membrane thickness and showed that the methanol crossover rate is inversely proportional to membrane thickness at a given cell current density, thus indicating that diffusion is dominant. In addition, Ren et al.¹⁵⁹ compared diffusion with electro-osmotic drag processes and demonstrated the importance of electro-osmotic drag in methanol transport through the membrane. In their analysis, methanol electro-osmotic drag is considered a convection effect and the diluted methanol moves with electro-osmotically dragged water molecules. Valdez and Narayanan¹⁶⁰ studied the temperature effects on methanol crossover and showed that the methanol crossover rate increases with cell temperature. Ravikumar and Shukla¹⁵⁶ operated the liquid-feed DMFC at an oxygen pressure of 4 bar and found that cell performance is greatly affected by methanol crossover at methanol feed concentrations greater than 2 M and that this effect aggravates with the operating temperature. Wang et al.¹⁶¹ analyzed the chemical compositions of the cathode effluent of a DMFC with a mass spectrometer. They found that the methanol crossing over the membrane is completely oxidized to CO₂ at the cathode in the presence of Pt catalyst. Additionally, the cathode potential is influenced by the mixed potential phenomenon due to simultaneous methanol oxidation and oxygen reduction as well as poisoning of Pt catalysts by methanol oxidation intermediates. Kauranen and Skou¹⁶² presented a semiempirical model to describe the methanol oxidation and oxygen reduction reactions on the cathode and concluded that the oxygen reduction current is reduced in the presence of methanol oxidation due to surface poisoning.

Developing novel membranes with low methanol crossover would surely increase cell performance and fuel efficiency.^{143,145} Alternatively, Wang and co-workers^{139,140,163} proposed modifying the anode backing structure to mitigate methanol crossover. It was demonstrated that a compact microporous layer can be added in the anode backing to create an additional barrier to methanol transport, thereby reducing the rate of methanol crossing over the polymer membrane. Both practices to control methanol crossover by increasing mass-transfer resistance, either in the anode backing or in the membrane, can be mathematically formulated by a simple relation existing between the crossover current, I_c , and anode mass-transport limiting current, $I_{A,lim}$. That is

$$I_c = I_{c,oc} \left(1 - \frac{I}{I_{A,lim}} \right) \quad (26)$$

where $I_{c,oc}$ is the crossover current at open circuit and I the operating current. In the conventional approach using thick membranes with low methanol crossover, $I_{c,oc}$ is low and $I_{A,lim}$ is set to be high. In contrast, setting up a barrier in the anode backing is essentially reducing the anode limiting current, $I_{A,lim}$, and making the open-circuit crossover current, $I_{c,oc}$, a significant fraction of $I_{A,lim}$, i.e., 50–80%. Two immediate advantages result from this latter cell design principle. One is that more concentrated fuel can be used, thus leading to the much higher energy density of the DMFC system. Lu et al.¹⁴⁰ successfully demonstrated the use of 8 M methanol solution as the anode feed, and Pan¹⁶³ most recently reported a DMFC operated with 10 M (or 30 vol %) methanol fuel solution. Second, this type of DMFC permits use of thin membranes such as Nafion 112, which greatly facilitates water back flow from the cathode to anode,^{140,164} thus addressing another major challenge of portable DMFC to be discussed below.

4.1.3. Water Management

Water management emerges as a new significant challenge for portable DMFC systems. Constrained by the methanol crossover problem, the anode fuel solution has been very dilute, meaning that a large amount of water needs to be carried in the system, therefore reducing the energy content of the fuel mixture. In addition, for each mole of methanol, 1 mol of water is needed for methanol oxidation at the anode and 2.5×6 mol of water is dragged through a thick membrane such as Nafion 117 toward the cathode, assuming that the electro-osmotic drag coefficient of water is equal to 2.5 per proton. This then causes 16 water molecules lost from the anode for every mole of methanol. Water in the anode therefore must be replenished. On the other hand, inside the cathode, there are 15 water molecules transported from the anode and additionally 3 water molecules produced by consuming six protons generated from oxidation of one methanol. The presence of a large amount of water floods the cathode and reduces its performance. The difficult task of removing water from the cathode to avoid severe flooding and supplying water to the anode to make up water

loss due to electro-osmotic drag through the membrane is referred to as innovative water management in a portable DMFC.

Traditionally, a high cathode gas flow rate (high stoichiometry) is employed to prevent flooding. This strategy not only increases parasitic power consumption but also removes excessive water from the fuel cell, making external water recovery more difficult. How to minimize water removal from the cathode and subsequent recovery externally to replenish the anode without causing severe cathode flooding becomes an important engineering issue. A greater understanding and ability to tailor water flow in the cell is of fundamental interest for portable DMFC systems. This is an area where DMFC models play an important role.

4.1.4. Heat Management

Thermal management in a DMFC is intimately tied to water and methanol-transport processes. First, heat generation in a DMFC is much higher than a H₂/air PEFC due to a much lower energy efficiency (it is only 20–25% when the cell is operated between 0.3 and 0.4 V). That is, for a 20 W DMFC system, 60–80 W of waste heat is produced. The waste heat is typically removed from DMFC by liquid fuel on the anode side and water evaporation on the cathode side. The latter also determines the amount of water loss from a DMFC and the load of water recovery by an external condenser. Therefore, while a higher cell temperature promotes the methanol oxidation reaction, it may not be practically feasible from the standpoint of water evaporation loss. Moreover, the higher cell temperature increases the methanol crossover rate, thereby reducing the fuel efficiency and system energy density.

4.2. DMFC Modeling

4.2.1. Needs for Modeling

While attempts continue to elucidate the fundamental electrochemical reaction mechanisms, explore new compositions and structures of catalysts, and develop new membranes and methods to prevent methanol crossover, important system issues relevant to DMFC are emerging, such as water management, gas management, flow-field design and optimization, and cell up-scaling for different applications. A number of physicochemical phenomena take place in a liquid-feed DMFC, including species, charge, and momentum transfer, multiple electrochemical reactions, and gas–liquid two-phase flow in both anode and cathode. Carbon dioxide evolution in the liquid-feed anode results in strongly two-phase flow, making the processes of reactant supply and product removal more complicated. All these processes are intimately coupled, resulting in a need to search for optimal cell design and operating conditions. A good understanding of these complex, interacting phenomena is thus essential and can most likely be achieved through a combined mathematical modeling and detailed experimental approach. It is apparent that three of the four technical challenges discussed in section 4.1 for portable DMFC systems require a basic understand-

ing of methanol, water, and heat-transport processes occurring in a DMFC. This provides a great opportunity to exercise fundamental modeling.

Another good problem for modeling is the micro-DMFC system. Both anode carbon dioxide blockage and cathode flooding are especially acute in micro-systems due to the small channel length scale involved, low operating temperature, dominance of surface tension forces, and requirement for low parasitic power losses in these systems.^{165–169}

In addition, DMFC is a system requiring a high degree of optimization. There are a multitude of operating parameters affecting the performance of a DMFC. These variables include cell temperature, molarity of aqueous methanol solution, cathode pressure, anode and cathode stoichiometry, and flow-field design. Higher cell temperatures improve catalytic activity, but the water loss from the cathode increases. Efficient removal of carbon dioxide gas bubbles and liquid water produced on the anode and cathode, respectively, must be maintained to allow reactants to reach catalyst sites. Removal of carbon dioxide “slugs” and prevention of cathode “flooding” can be attained by increasing flow rates. However, increasing flow rates requires more pumping power. Too high a flow rate on the cathode will dry out the polymer membrane, decreasing proton conductivity and hence cell performance. An understanding of the interdependence of these parameters plays a key role in optimizing the performance of a DMFC.

DMFC modeling thus aims to provide a useful tool for the basic understanding of transport and electrochemical phenomena in DMFC and for the optimization of cell design and operating conditions. This modeling is challenging in that it entails the two-phase treatment for both anode and cathode and that both the exact role of the surface treatment in backing layers and the physical processes which control liquid-phase transport are unknown.

4.2.2. DMFC Models

In the literature, Scott et al.^{170–172} developed several simplified single-phase models to study transport and electrochemical processes in DMFC. Baxter et al.¹⁷³ developed a one-dimensional mathematical model for a liquid-feed DMFC anode. A major assumption of this study was that carbon dioxide is only dissolved in the liquid, and hence, their anode model is a single-phase model. Using a macrohomogeneous model to describe the reaction and transport in the catalyst layer of a vapor-feed anode, Wang and Savinell¹⁷⁴ simulated the effects of the catalyst layer structure on cell performance. Kulikovskiy et al.¹⁷⁵ simulated a vapor-feed DMFC with a two-dimensional model and compared the detailed current density distributions in the backing, catalyst layer, and membrane of a conventional to a new current collector. In another paper, Kulikovskiy¹⁷⁶ numerically studied a liquid-feed DMFC considering methanol transport through the liquid phase and in hydrophilic pores of the anode backing. In both publications of Kulikovskiy the important phenomenon of methanol crossover was ignored. Dohle et al.¹⁷⁷ presented a one-dimensional model for the vapor-feed DMFC and

included the crossover phenomenon. The effects of methanol concentration on the cell performance were studied.

In a three-part paper^{178–180} Meyers and Newman developed a theoretical framework that describes the equilibrium of multicomponent species in the membrane. The transport of species in the membrane based on concentrated-solution theory and membrane swelling were taken into consideration in their model. The transport phenomena in the porous electrodes were also included in their mathematical model. However, the effect of pressure-driven flow was not considered. In addition, the transport of carbon dioxide out of the anode was neglected by assuming that the carbon dioxide is dilute enough to remain fully dissolved in liquid. Nordlund and Lindbergh¹⁸¹ studied the influence of the porous structure on the anode with mathematic modeling and experimental verification. In their model they also assumed that carbon dioxide does not evolve as gas within the electrode. Recently, Wang and Wang¹⁸² presented a two-phase, multicomponent model. Capillary effects in both anode and cathode backings were accounted for. In addition to the anode and cathode electrochemical reactions, the model considered diffusion and convection of both gas and liquid phases in backing layers and flow channels. The model fully accounted for the mixed potential effect of methanol oxidation at the cathode as a result of methanol crossover caused by diffusion, convection, and electroosmosis. The model of Wang and Wang was solved using a finite-volume technique and validated against experimental polarization curves. The model results indicated the vital importance of gas-phase transport in the DMFC anode.

Divisek et al.¹⁸³ presented a similar two-phase, two-dimensional model of DMFC. Two-phase flow and capillary effects in backing layers were considered using a quantitatively different but qualitatively similar function of capillary pressure vs liquid saturation. In practice, this capillary pressure function must be experimentally obtained for realistic DMFC backing materials in a methanol solution. Note that methanol in the anode solution significantly alters the interfacial tension characteristics. In addition, Divisek et al.¹⁸³ developed detailed, multistep reaction models for both ORR and methanol oxidation as well as used the Stefan–Maxwell formulation for gas diffusion. Murgia et al.¹⁸⁴ described a one-dimensional, two-phase, multicomponent steady-state model based on phenomenological transport equations for the catalyst layer, diffusion layer, and polymer membrane for a liquid-feed DMFC.

Despite the fact that much effort has been made to model the DMFC system, considerable work remains, particularly in support of the emerging portable designs and systems. Few have treated the dominating effects of two-phase flow. No model to date has sufficient detail to provide a microfluidic theory for portable systems including effects of channel geometry and wettability characteristics of the GDL on fluid flow in the anode or cathode. Modeling studies are needed to fully elucidate the intricate couplings of methanol, water, and heat-transport

processes. This understanding is key to successful design and operation of portable DMFC systems. Finally, the important role of a microporous layer in DMFC and its tailoring to control the flow of methanol and water remain unknown.

4.3. Experimental Diagnostics

Similarly, experimental diagnostics are an important component of advanced modeling and simulation of DMFCs. Diagnostic techniques for DMFCs have included the following: (1) cyclic voltammetry (CV) to determine the electrochemically active area of the cathode, (2) CO stripping to determine the electrochemically active area of the anode, (3) electrochemical impedance spectroscopy (EIS), (4) anode polarization characterization via a MeOH/H₂ cell as proposed by Ren et al.,¹⁹ (5) methanol crossover rate measurement by CO₂ sensing in the cathode (via FITR, GC, or infrared CO₂ sensors) or measuring the limiting current in a MeOH/N₂ cell (Ren et al.¹⁹), (6) current distribution measurements via a segmented cell in conjunction with a multichannel potentiostat (Mench and Wang¹¹¹), (7) material balance analysis of CH₃OH and H₂O (Narayanan et al.¹⁴⁶ and Muller et al.¹⁴⁷), and (8) two-phase visualization of bubble dynamics^{185–187} on anode and liquid droplet dynamics on cathode.¹⁸⁷ The work in the last three areas is briefly reviewed in this review as they are particularly pertinent to the fundamental modeling of DMFC for cell design and optimization.

Mench and Wang¹¹¹ described an experimental technique to measure current distribution in a 50 cm² instrumented DMFC based on multichannel potentiostat. In this method separate current collector ribs are embedded into an insulating substrate (e.g., Lexan plate) to form a segmented flow-field plate. The resulting flow-field plates for both anode and cathode are then assembled with a regular MEA to form a fuel cell with independently controllable subcells. All subcells are connected to a multichannel potentiostat to undergo potentiostatic experiments simultaneously. The subcell currents measured thus provide information on the current density distribution for the full-scale fuel cell. The spatial and temporal resolution of this method depends on the number of channels available and capabilities of the potentiostat. Current density distribution measurements were made for a wide range of cathode flow rates in order to elucidate the nature of cathode flooding in a DMFC. Figure 38 displays the current density distributions for high and low cathode air flow rates. In the case of high cathode stoichiometry (Figure 38a), it can be seen that the current distributes rather uniformly for all three levels of cell voltage. As expected, the current density increases as the cell voltage decreases. In the case of low cathode stoichiometry (still excessive for the oxygen reduction reaction), Figure 38b clearly shows that a portion of the cathode toward the exit is fully flooded, leading to almost zero current. The information provided in Figure 38 can be used to identify innovative cathode flow-field designs and enables the development of MEA structures with improved water management capabilities.

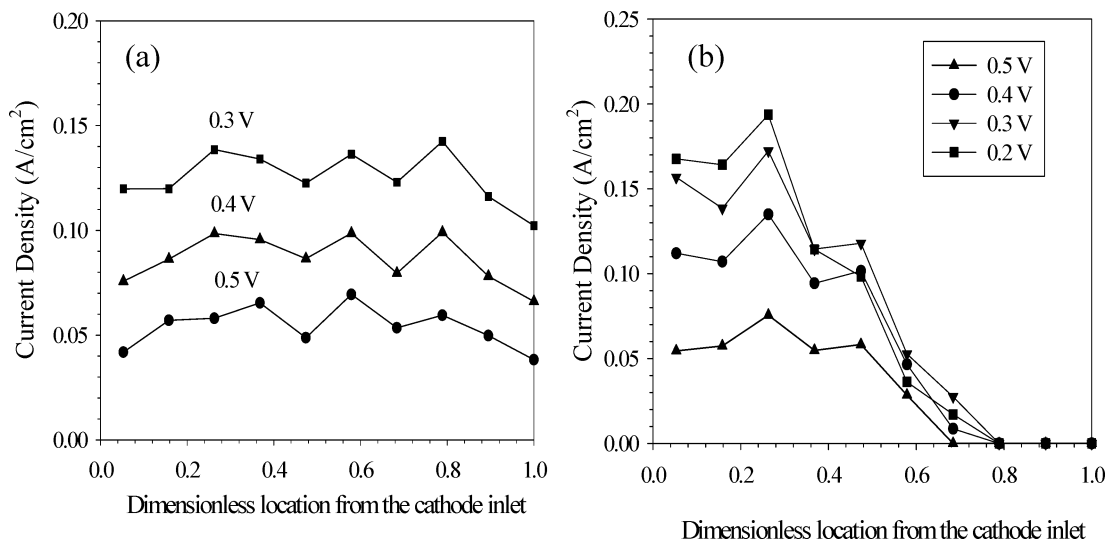


Figure 38. Current density distributions in a 50 cm² DMFC for (a) high cathode air flow rate (stoichiometry of 85 at 0.1 A/cm²) and (b) low cathode air flow rate (stoichiometry of 5 at 0.1 A/cm²).¹¹¹

Material balance analysis proves to be a critical diagnostic tool for the development of portable DMFC systems. In this analysis methanol balance on the anode side along with the methanol crossover rate typically measured by an infrared CO₂ sensor is conducted. In addition, water balance on both anode and cathode sides is performed in which the cathode water amount is carefully collected by a moisture trap and measured.^{146,147} From such analyses Müller et al.¹⁴⁷ revealed that the water balance on the DMFC anode is highly negative, thus calling for membrane development with low water crossover in addition to low methanol crossover.

Gas management on the anode side is an important issue in DMFC design. On the anode side, carbon dioxide is produced as a result of methanol electrochemical oxidation. If CO₂ bubbles cannot be removed efficiently, the anode channels will be blocked, leading to limited mass transport. Argyropoulos et al.^{185,186} were perhaps the first to observe the two-phase flow pattern in the anode channel under various operating conditions. This flow visualization on the anode side yields a valuable understanding of bubble dynamics in DMFC. This study was, however, undertaken under low cell performance. Most recently, Lu and Wang¹⁸⁷ developed a carefully designed transparent DMFC to visualize bubble dynamics on the anode side and liquid droplet (and flooding) dynamics on the cathode. Moreover, Lu and Wang explored the profound effect of backing layer wettability on gas management in DMFC. Figure 39 shows a sequence of images taken at various times at a feed temperature of 85 °C and current density of 100 mA/cm². The images, 1 s apart, were captured from a movie with a time resolution of 1/30 s. The time of the first image was chosen arbitrarily due to the fact that two-phase flow is a regular, periodic event. As shown in Figure 39, the CO₂ bubbles emerge at certain locations and form large and discrete gas slugs in the channel. The bubble motion is governed by the momentum of liquid flow, force of buoyancy on the bubble, and surface tension between the bubble and substrate. It can be seen from Figure 39 that the bubbles are held on the carbon paper by strong surface tension until they

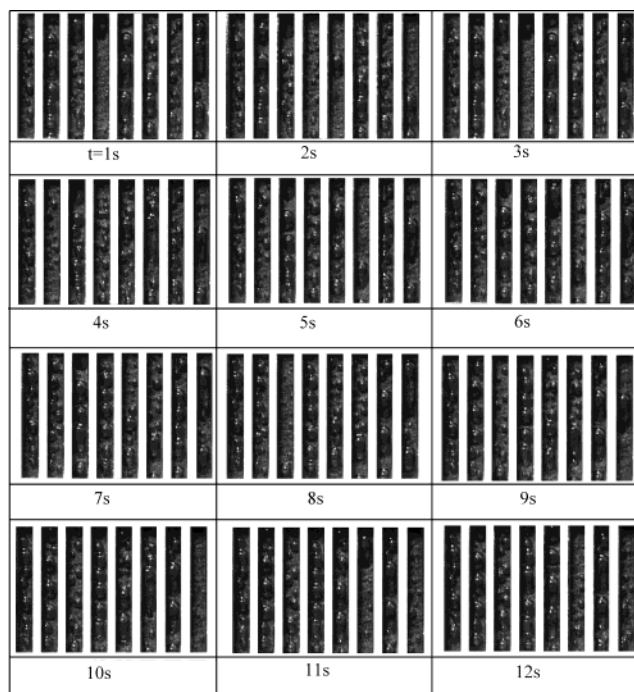


Figure 39. Images of bubble dynamics in the DMFC anode with carbon paper backing layer for 2 M MeOH feed and nonhumidified air at 100 mA/cm² and 85 °C.¹⁸⁷

grow into larger slugs for detachment, clearly indicative of the dominant effect of surface tension in bubble dynamics in DMFC. Once the bubbles grow to a sufficient size, they detach and sweep along the backing surface in the channel. This sweeping process clears all small bubbles preexisting on the backing surface, making new bubbles grow from the smallest size to the full detachment diameter. As a result, the two-phase flow becomes regularly intermittent. The images shown in Figure 39, representative of most DMFC systems under commercial development, indicate the vital importance of considering two-phase flow and transport in a DMFC model.

4.4. Model Validation

Experimental validation of the two-phase DMFC model of Wang and Wang¹⁸² has been carried out for

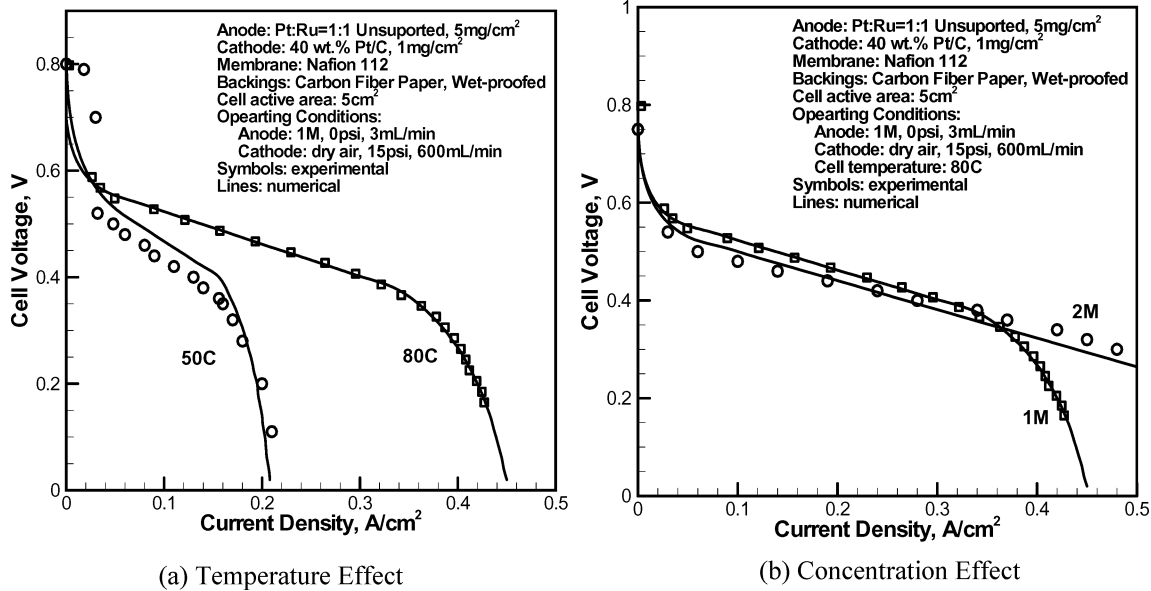


Figure 40. Comparisons of 2-D model predictions with experimental data for a DMFC with (a) temperature effect and (b) concentration effect.¹⁸²

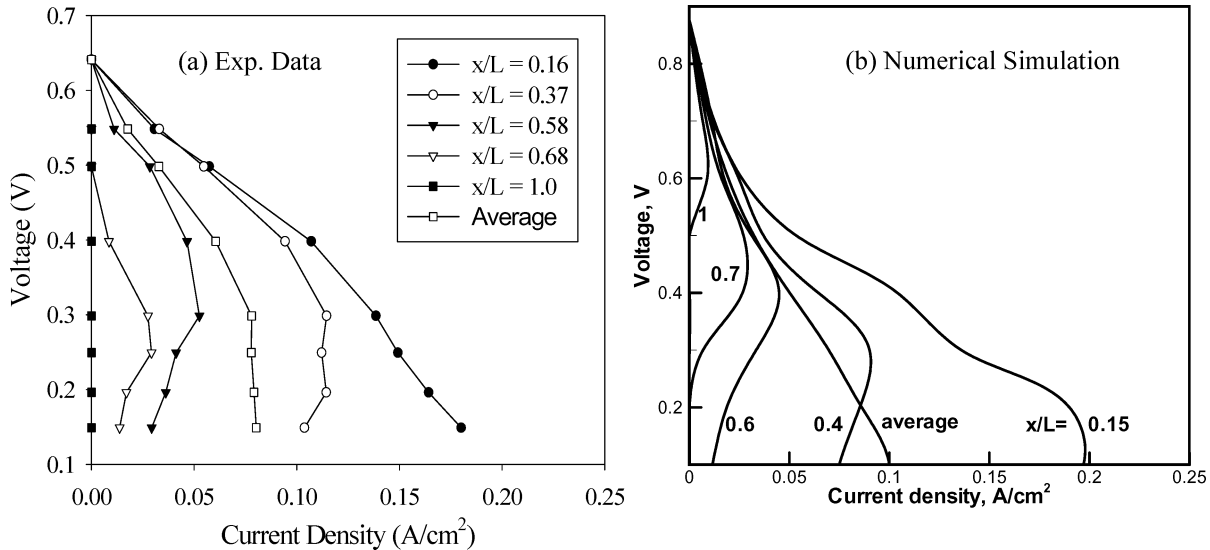


Figure 41. Comparison of localized polarization curves between experiments (a) and model predictions (b) for a 50 cm² DMFC with an anode flow stoichiometry of 2.7 and a cathode air stoichiometry of 5 at 0.1 A/cm².⁵

a 5 cm² graphite cell. A brief description of the cell geometry, MEA compositions, and operating conditions is given in Figure 40. Figure 40a illustrates the capability of the model to predict the polarization curves at two cell temperatures. Excellent agreement is achieved not only in the kinetic- and ohmic-controlled regimes of the polarization curves but also in the mass-transport-controlled regime, where the methanol oxidation kinetics is modeled as a zero-order reaction for molar concentrations above 0.1 M but a first-order reaction for a molarity below 0.1 M. This shift in the reaction order and molarity of transition is consistent with direct kinetics measurements. A lower mass-transport-limiting current density at 50 °C, seen in Figure 40a, is caused by the lower diffusion coefficients in both the liquid and gas phases and the lower saturation methanol vapor concentration in the gas phase at lower temperatures. Using the same model and property data, Figure 40b shows equally satisfactory agreement in

the polarization curves between numerical and experimental results for different methanol feed concentrations. In accordance with these experiments, the model prediction for the 2 M case shows a slightly lower performance (due primarily to higher methanol crossover) and an extended limiting current density. Similar success in validating global $I-V$ curves was also reported by Murgia et al.,¹⁸⁴ among others.

While the model validation against cell overall performance data has been satisfactory and encouraging, as evident from Figure 40, the ultimate test of these highly sophisticated two-phase models is comparison with detailed distribution measurements. Figure 41 presents such an attempt toward developing high-fidelity first-principles models for DMFC. Figure 41a shows a set of localized polarization curves measured using the current distribution measurement technique of Mench and Wang,¹¹¹ and Figure 41b displays the same set of polarization curves predicted from the DMFC two-phase model

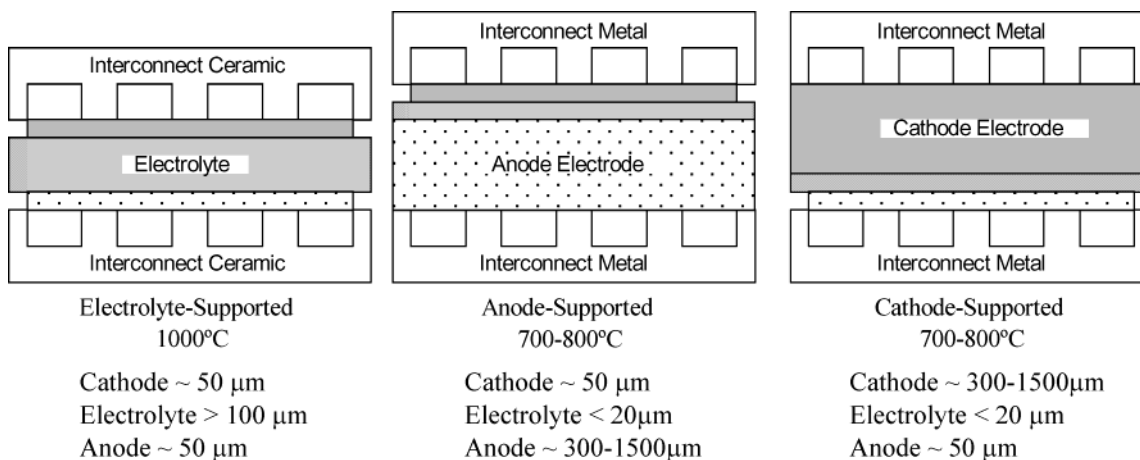


Figure 42. Various planar SOFC configurations (revised from ref 189).

of Wang and Wang.¹⁸² A low air stoichiometry of 5 (although not low for the electrochemical reaction requirement) was deliberately chosen so that cathode GDL flooding may occur and a nonuniform current density distribution results.

The two graphs in Figure 41 share a qualitative similarity. For example, both experiment and model results indicate that the local polarization curves near the dry air inlet exhibit a monotonic function between the voltage and current. Also, the shape of the polarization curves near the exit, from both experiment and simulation, is clearly evidence of flooding in the cathode GDL. Another interesting observation is that the average cell polarization curves, measured and predicted, do not exhibit any sign of cathode flooding, indicating that detailed distribution measurements are absolutely required in order to discern complex physicochemical phenomena occurring inside the cell. Finally, it can be seen from Figure 41 that a satisfactory quantitative comparison between experiment and model is lacking on the detailed level.

Difficulties in obtaining good quantitative agreement between predicted and measured distribution results are indicative that model refinements as well as an improved property database will be needed before accurate quantitative predictions of not only overall polarization curve but also detailed distributions within a DMFC may be obtained.

4.5. Summary and Outlook

Two-phase modeling capabilities for DMFCs have emerged, which unravel the importance of gas-phase transport of methanol as compared to the liquid-phase transport. In addition, much effort is being directed toward developing a coupled model for methanol, water, and heat-transport processes occurring simultaneously in a DMFC. Such models are extremely useful for the discovery of unique design and operation regimes of the DMFC system for portable application, where the high energy density entails using highly concentrated methanol (preferably pure methanol), maintaining healthy water balance, controlling fuel crossover, and improving high-voltage performance. The latter two factors will result in high efficiency of a DMFC. It is expected

that the DMFC model development efforts will be directed less toward refining model accuracy and improving computational speed and more toward applying the models to invent new cell designs and pinpoint areas of improvement.

5. Solid Oxide Fuel Cells

A solid oxide fuel cell (SOFC) consists of two electrodes: anode and cathode, with a ceramic electrolyte between that transfers oxygen ions. A SOFC typically operates at a temperature between 700 and 1000 °C, at which temperature the ceramic electrolyte begins to exhibit sufficient ionic conductivity. This high operating temperature also accelerates electrochemical reactions; therefore, a SOFC does not require precious metal catalysts to promote the reactions. More abundant materials such as nickel have sufficient catalytic activity to be used as SOFC electrodes. In addition, the SOFC is more fuel-flexible than other types of fuel cells, and reforming of hydrocarbon fuels can be performed inside the cell. This allows use of conventional hydrocarbon fuels in a SOFC without an external reformer.

Planar SOFC systems have received much attention lately because of ease of manufacturing and higher performance as compared to tubular types.¹⁸⁸ Planar SOFCs are generally manufactured in three different configurations according to their operating temperatures. For cells operating around 1000 °C, the electrolyte-supported cell configuration is preferred. In this design, anode and cathode are very thin (i.e., 50 μm) and the electrolyte thickness is generally larger than 100 μm. The electrolyte ionic conductivity is a strong function of operating temperature in SOFCs. For SOFCs operating at lower operating temperatures, the ionic conductivity is lower and as such anode- or cathode-supported cell configurations are preferred. In the electrode-supported cell configuration, the electrolyte is usually very thin (i.e., 20 μm) and either anode or cathode is thick enough to serve as the supporting substrate for cell fabrication. The thickness of the supporting electrode varies between 0.3 and 1.5 mm, depending on the design. These three planar SOFC designs are sketched in Figure 42.¹⁸⁹

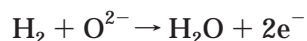
For optimal design and operation of a SOFC, a fundamental and detailed understanding of transport and electrochemical kinetics is indispensable. Efforts are presently underway to understand the multiphysics and obtain the optimal design for SOFCs. For these purposes, a CFD model, similar to those for PEFCs and DMFCs, becomes a valuable tool for design and operation of SOFCs.

5.1. SOFC Models

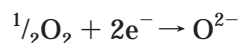
Unlike the comprehensive reviews provided in sections 3 and 4 for PEFC and DMFC, respectively, the present review on SOFC modeling will be brief and is not meant to be exhaustive. Instead, only major trends are indicated by way of representative studies.

For the purpose of modeling, consider a planar SOFC divided into anode gas channel, anode gas diffusion electrode, anode interlayer (active electrode), electrolyte, cathode interlayer (active electrode), cathode gas diffusion electrode, and cathode gas channel. The electrochemical reactions occur in the active regions of the porous electrodes (i.e., interlayers). In an SOFC, oxidant reduction occurs in the active cathode. The oxygen ions are then transported through the electrolyte, after which oxidation of the fuel occurs in the active anode by the following reactions.

Oxidation of fuel at the anode



Reduction of oxidant at the cathode



The anode is generally made of nickel/yttria-stabilized zirconia Cermet. The cathode is an LSM layer chemically expressed as $\text{La}_{1-x}\text{Sr}_x\text{MnO}_3$. The electrolyte is an Y_2O_3 -doped zirconia called YSZ.

The activation overpotentials for both electrodes are high; therefore, the electrochemical kinetics of the both electrodes can be approximated by Tafel kinetics. The concentration dependence of exchange current density was given by Costamagna and Honegger.¹⁹⁰ The open-circuit potential of a SOFC is calculated via the Nernst equation.¹⁹⁰ The conductivity of the electrolyte, i.e., YSZ, is a strong function of temperature and increases with temperature. The temperature dependence of the electrolyte conductivity is expressed by the Arrhenius equation.¹⁹⁰

Earlier modeling studies were aimed at predicting the current and temperature distributions,^{188,190–192} as the nonuniform distributions contribute to stress formation, a major technical challenge associated with the SOFC system. Flow and multicomponent transport were typically simplified in these models that focused on SOFC electrochemistry. Recently, fundamental characteristics of flow and reaction in SOFCs were analyzed using the method of matched asymptotic expansions.^{193–195}

With today's computing power and popular use of CFD codes, SOFC modeling is moving toward multiphysics, electrochemical-transport-coupled, and three-

dimensional descriptions. Prinkey et al.¹⁹⁶ proposed a Fluent-based CFD model to describe reactant flow, transport, and electrochemical reaction in a SOFC. The charge transport was, however, simplified into an algebraic equation accounting for activation polarizations, electrolyte ohmic loss, and concentration polarizations. Moreover, the concentration polarizations were calculated empirically via a prescribed limiting current. This modeling framework is inconsistent in that the limiting current physically is the result of the mass-transport phenomena and thus should be calculated from the solution of species equations instead of being prescribed independently. Recknagle et al.,¹⁹⁷ on the other hand, employed STAR-CD code along with an electrochemistry module to simulate a SOFC with three flow configurations: cross-flow, co-flow, and counter-flow. The effects of cell flow configurations on the distribution of temperature, current, and reactant species were investigated. It was found that for similar fuel utilization and average cell temperature, the co-flow case had the most uniform temperature distribution and the smallest thermal gradients. This study, however, treated the positive electrode–electrolyte–negative electrode (PEN) as a single solid component. Such an approximation is inappropriate to model the latest generation of electrode-supported SOFC where mass diffusion through a thick anode or cathode constitutes a major limitation. Most recently, Ackmann et al.¹⁹⁸ performed a two-dimensional numerical study of mass and heat transport in planar SOFC with focus on elucidating the mass diffusion limitation across the thickness of electrodes as well as in the in-plane direction between the channel and interconnect rib areas. This model of Ackmann et al. also included methane/steam reforming and water–gas shift reaction in addition to the SOFC electrochemical kinetics.

A self-consistent SOFC model was developed based on the same single-domain modeling framework that has been applied to PEFC and DMFC, as elaborated above. This model of Pasaogullari and Wang¹⁹⁹ solves the continuum equations for conservation of mass, momentum, species, thermal energy, and electric charge along with electrochemical kinetics in anode and cathode of a SOFC. The governing equations for the SOFC model of Pasaogullari and Wang¹⁹⁹ were exactly the same as those in Table 1 except that water transport by either electro-osmotic drag or diffusion through the electrolyte becomes irrelevant. The species transport equation was solved for three species: H_2 , O_2 , and H_2O .¹⁹⁹ However, the model is applicable to multiple fuels such as H_2 and CO given that kinetic expressions for co-oxidation of H_2 and CO on Ni catalysts are provided. N_2 was considered as an inert gas in this model.

To illustrate typical simulation results from such multiphysics SOFC models, consider a co-flow and a cross-flow electrolyte-supported cell. The cross-flow geometry is of particular interest because of the complex transport phenomena offered in this cell configuration, a configuration able to provide detailed understanding of mass-transfer limitations. Structured, orthogonal meshes were used for all compu-

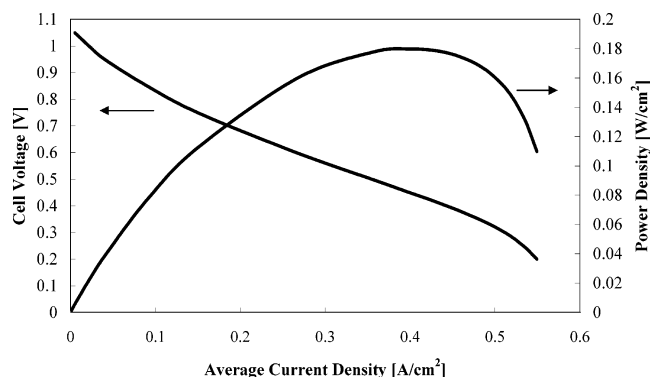


Figure 43. Calculated current–voltage characteristics and power density curve of electrolyte-supported co-flow SOFC at an operating temperature of 1000 °C and anode and cathode stoichiometry of 1.5 and 2.0 at 0.4 A/cm², respectively.¹⁹⁹

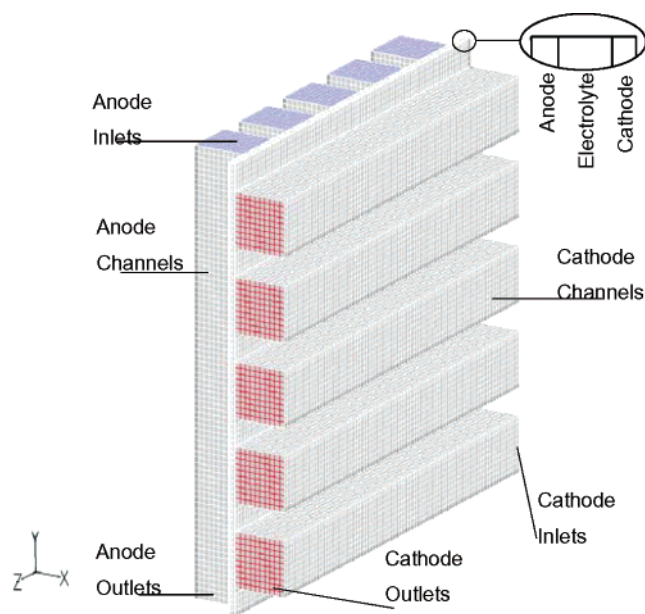


Figure 44. Geometry and mesh of a five-channel cross-flow electrolyte-supported SOFC.

tational meshing. It was found that a $80 \times 80 \times 35$ mesh is sufficient for 3-D, five-channel geometry.¹⁹⁹ It takes ~ 300 iterations to converge a 3-D simulation of the five-channel cross-flow geometry (i.e., 224 000 cells). Figure 43 shows a sample calculation of the polarization behavior of the co-flow cell.

To understand the cross-flow-transport characteristics in a planar SOFC, consider a five-channel cross-flow-type electrolyte-supported SOFC shown in Figure 44 and the simulated current distribution in this cell, shown in Figure 45.¹⁹⁹ It is clearly seen from Figure 45 that the regions facing the channels have much higher current density. This is clearly seen at the zones, where the corresponding anode and cathode gas channels meet. In those regions both of the electrodes receive enough reactant, thereby producing higher current. This 3-D calculation explicitly illustrates the effect of flow-field design on cell performance.

Experimental validation of SOFC models has been quite scarce. Khaleel and Selman²⁰⁰ presented a comparison of 1-D electrochemical model calculations with experimental polarization curves for a range of

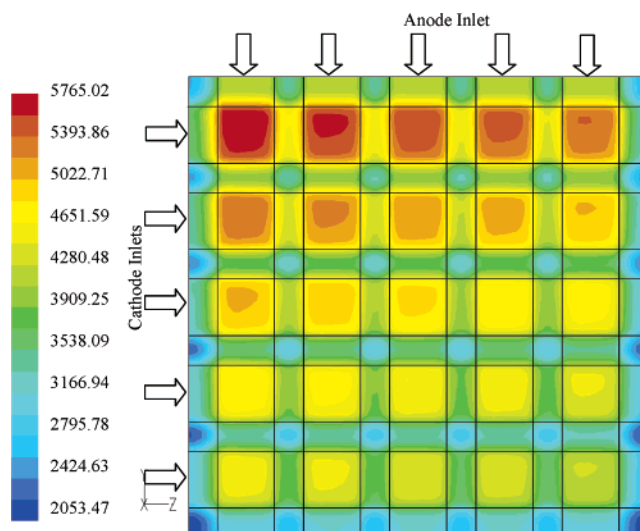


Figure 45. Current distribution (A/m²) at a cell potential of 0.4 V in the five-channel cross-flow electrolyte-supported SOFC (A/m²) under anode and cathode stoichiometries of 1.5 and 2.0, respectively, and a cell temperature of 1000 °C.

hydrogen concentrations in the anode feed. Clearly, this is an area requiring much attention in the future of SOFC modeling, and model validation at a detailed distribution level (e.g., against current and species distribution data) is equally essential.

5.2. Summary and Outlook

A single-domain, self-consistent formulation has been available to describe the electrochemistry, gas dynamics, and multicomponent transport in SOFC. Both Fluent and STAR-CD codes can be adapted for implementation of SOFC models. In addition to predicting the current–voltage characteristics, these CFD models provide valuable insight into the reactant and product distributions, current distribution, and fuel utilization, making it possible to analyze SOFC operation in detail. The latest SOFC models also have the energy equation built in to predict the temperature distribution. The temperature distribution can be coupled to stress analyses, thereby providing a comprehensive computer-aided engineering (CAE) tool for SOFC design and operation. The CFD models are easily extendable to include multiple fuels such as H₂ and CO. In such a case, co-oxidation of H₂ and CO on Ni catalyst must be considered following a similar approach already developed for PEFC in the presence of CO poisoning. Finally, The CFD-based SOFC models can be combined with internal reforming models on the anode. In such a situation, a catalytic chemical reaction is needed as well.

SOFC modeling is the simplest among all three systems reviewed in this paper, since a SOFC does not involve transport phenomena as complex as in a PEFC and DMFC. In addition, SOFC modeling can draw largely upon tremendous existing experiences from combustion and fuel-processing fields. Future directions of SOFC modeling research are toward (1) coupled modeling of SOFC and fuel reforming (whether external or internal), (2) comprehensive

modeling of direct hydrocarbon DOFC systems where spray and evaporation of liquid fuels play important roles, (3) model validation against detailed distribution data, and (4) direct numerical simulation of SOFC electrodes, similar to what is described in section 3.9, to establish a quantitative relationship of electrode microstructure and compositions with cell performance.

6. Closing Remarks

Automotive, stationary, and portable applications place an ever-increasing demand to develop advanced fuel cell technologies with high performance, low cost, and excellent durability. Computer-aided engineering is indispensable in this development process and can dramatically reduce the expensive and time-consuming trial-and-error experimentation currently required. The complexity of fuel cells requires many interacting physicochemical submodels in order for CFD models to be successful. Therefore, a fundamental understanding of the electrochemical and transport processes in fuel cells continues to be necessary. This can be best achieved through a combination of fundamental modeling and detailed diagnostics, as shown in the present review. In addition, further developments in numerical algorithms will eventually allow the use of CFD models in design, optimization, and control of fuel cell systems, thereby significantly accelerating the commercial deployment of fuel cell technologies.

Computational modeling of fuel cells is an important and physically rich subject. Despite emergence of significant experimental and modeling capabilities, much remains to be done before the knowledge of multiscale phenomena occurring in fuel cells can be directly utilized in cell design and product development. Further challenges and research directions have been pointed out at the end of each section for PEFC, DMFC, and SOFC. An upsurge of research activities in this field worldwide is expected in years to come.

7. Acknowledgments

The author acknowledges the contributions of his present and former graduate students, research associates, and industrial/academic collaborators. The writing of this paper was made possible, in part, through the support of the NSF under grant nos. CTS-9733662 and DUE-9979579, DOE under cooperative agreement no. DEFC26-01NT41098, DARPA under grant no. DAAH01-1-R001, Sandia National Laboratories, Argonne National Laboratory, as well as Delphi, General Motors, Toyota, Honda, Nissan, W. L. Gore and Associates, Air Products and Chemicals, and ConocoPhillips.

8. References

- (1) Kreuer, K. D. *J. Membr. Sci.* **2001**, *185*, 29.
- (2) Paddison, S. J. In *Handbook of Fuel Cells*; Vielstich, W., Gasteiger, H. A., Lamm, A., Eds.; John Wiley and Sons Ltd.: England, 2003; Vol. 3, p 397.
- (3) Koper, M. T. M. In *Handbook of Fuel Cells*; Vielstich, W., Gasteiger, H. A., Lamm, A., Eds.; John Wiley and Sons Ltd.: England, 2003; Vol. 2, p 348.
- (4) Wang, C. Y. *Int. J. Transport Phenom.* **2001**, *3*, 131.
- (5) Wang, C. Y. In *Handbook of Fuel Cells*; Vielstich, W., Gasteiger, H. A., Lamm, A., Eds.; John Wiley and Sons Ltd.: England, 2003; Vol. 3, p 337.
- (6) Ju, H.; Wang, C. Y. *J. Electrochem. Soc.*, in press.
- (7) Bird, R. B.; Stewart, W. E.; Lightfoot, E. N. *Transport Phenomena*, 2nd ed.; Wiley: New York, 2002.
- (8) Newman, J. *Electrochemical Systems*, 2nd ed.; Prentice Hall: Englewood Cliffs, NJ, 1991.
- (9) Patankar, S. V. *Numerical Heat Transfer and Fluid Flow*; Hemisphere Publishing Corp.: New York, 1980.
- (10) Oran, E. S.; Boris, J. P. *Numerical Simulation of Reactive Flow*; Cambridge University Press: Cambridge, 2001.
- (11) Wu, J.; Srinivasan, V.; Xu, J.; Wang, C. Y. *J. Electrochem. Soc.* **2002**, *149*, A1342.
- (12) Pisani, L.; Murgia, G.; Valentini, M.; D'Aguanno, B. *J. Electrochem. Soc.* **2002**, *149*, A31.
- (13) Pisani, L.; Murgia, G.; Valentini, M.; D'Aguanno, B. *J. Electrochem. Soc.* **2002**, *149*, A898.
- (14) Meng, H.; Wang, C. Y. *J. Electrochem. Soc.* **2004**, *151*, A358.
- (15) Meng, H.; Wang, C. Y. *Chem. Eng. Sci.* **2004**, *59*, 3331.
- (16) Springer, T. E.; Zawodzinski, T. A.; Gottesfeld, S. *J. Electrochem. Soc.* **1991**, *138*, 2334.
- (17) Zawodzinski, T. A.; Derouin, C.; Radzinski, S.; Sherman, R. J.; Smith, V. T.; Springer, T. E.; Gottesfeld, S. *J. Electrochem. Soc.* **1993**, *140*, 1041.
- (18) Zawodzinski, T. A.; Springer, T. E.; Davey, J.; Jestel, R.; Lopez, C.; Valerio, J.; Gottesfeld, S. *J. Electrochem. Soc.* **1993**, *140*, 1981.
- (19) Ren, X.; Springer, T. E.; Gottesfeld, S. *J. Electrochem. Soc.* **2000**, *147*, 92.
- (20) Walsby, N.; Hietala, S.; Maunu, S. L.; Sundhold, F.; Kallio, T.; Sundholm, G. *J. Appl. Polym. Sci.* **2002**, *86*, 33.
- (21) Feterko, P.; Hsing, I.-M. *J. Electrochem. Soc.* **1999**, *146*, 2049.
- (22) Hinatsu, J. T.; Mizuhata, M.; Takenaka, H. *J. Electrochem. Soc.* **1994**, *141*, 1493.
- (23) Zawodzinski, T. A.; Davey, J.; Valerio, J.; Gottesfeld, S. *Electrochim. Acta* **1995**, *40*, 297.
- (24) Ren, X.; Gottesfeld, S. *J. Electrochem. Soc.* **2001**, *148*, A87.
- (25) Ren, X.; Henderson, W.; Gottesfeld, S. *J. Electrochem. Soc.* **1997**, *144*, L267.
- (26) Ise, M.; Kreuer, K. D.; Maier, J. *Solid State Ionics* **1999**, *125*, 213.
- (27) Motupally, S.; Becker, A. J.; Weidner, J. W. *J. Electrochem. Soc.* **2000**, *147*, 3171.
- (28) Parthasarathy, A.; Srinivasan, S.; Appleby, A. J. *J. Electrochem. Soc.* **1992**, *140*, 2178.
- (29) Lee, S. J.; Mukerjee, J.; McBreen, Y.; Rho, W.; Kho, Y. T.; Lee, T. H. *Electrochim. Acta* **1998**, *43*, 3693.
- (30) Gottesfeld, S.; Zawodzinski, T. A. In *Advances in Electrochemical Science and Engineering*; Tobias, C., Ed.; Wiley and Sons: New York, 1997; Vol. 5.
- (31) Gasteiger, H. A.; Gu, W.; Makharia, R.; Mathias, M. F.; Sompalli, B. In *Handbook of Fuel Cells*; Vielstich, W., Gasteiger, H. A., Lamm, A., Eds.; John Wiley and Sons Ltd.: England, 2003; Vol. 3, p 594.
- (32) Mathias, M. F.; Roth, J.; Flemming, J.; Lehnert, W. In *Handbook of Fuel Cells*; Vielstich, W., Gasteiger, H. A., Lamm, A., Eds.; John Wiley and Sons Ltd.: England, 2003; Vol. 3, p 517.
- (33) Lim, C.; Wang, C. Y. *Electrochim. Acta* **2004**, *49*, 4149.
- (34) Chapman, S.; Cowling, T. G. *Mathematical Theory of Non-Uniform Gases*; Cambridge University Press: Cambridge, 1951.
- (35) Reid, R. C.; Prausnitz, J. M.; Poling, B. E. *The Properties of Gases and Liquids*; McGraw-Hill: New York, 1987.
- (36) Singhal, S. C. *MRS Bull.* **2000**, *16*.
- (37) Minh, N. Q.; Takahashi, T. *Science and Technology of Ceramic Fuel Cells*; Elsevier: Amsterdam, 1995.
- (38) Yokokawa, H. *Key Eng. Mater.* **1998**, *153*, 37.
- (39) Virkar, A. V. *Introduction to Solid Oxide Fuel Cells (SOFC): Science and Technology*; Lecture notes from SOFC Workshop, National Energy Technology Laboratory (NETL), summer 2001.
- (40) Todd, B.; Young, J. B. *J. Power Sources* **2002**, *110*, 186.
- (41) Khee, R. J.; Rupley, F. M.; Miller, J. A. *The Chemkin Thermodynamic Data Base*, SAND87-8215B, UC-4; Sandia National Laboratories, Albuquerque, 1987.
- (42) Prater, K. B. *J. Power Sources* **1994**, *51*, 129.
- (43) *Handbook of Fuel Cells*; Vielstich, W., Gasteiger, H. A., Lamm, A., Eds.; John Wiley and Sons Ltd.: England, 2003; Vol. 3, Part 3.
- (44) Bernardi, D. M.; Verbrugge, M. W. *AIChE J.* **1991**, *37*, 1151.
- (45) Bernardi, D. M.; Verbrugge, M. W. *J. Electrochem. Soc.* **1992**, *139*, 2477.
- (46) Springer, T. E.; Zawodzinski, T. A.; Gottesfeld, S. *J. Electrochem. Soc.* **1991**, *138*, 2334.
- (47) Springer, T. E.; Wilson, M. S.; Gottesfeld, S. *J. Electrochem. Soc.* **1993**, *140*, 3513.
- (48) Fuller, T. F.; Newman, J. *J. Electrochem. Soc.* **1993**, *140*, 1218.
- (49) Nguyen, T.; White, R. E. *J. Electrochem. Soc.* **1993**, *140*, 2178.

- (50) Yi, J. S.; Nguyen, T. V. *J. Electrochem. Soc.* **1999**, *146*, 38.
- (51) Yi, J. S.; Nguyen, T. V. *J. Electrochem. Soc.* **1998**, *145*, 1149.
- (52) Promislow, K.; Stockie, J. M. *SIAM J. Appl. Math.* **2001**, *62*, 180.
- (53) Stockie, J. M.; Promislow, K.; Wetton, B. R. *Int. J. Numer. Methods Fluids* **2003**, *41*, 577.
- (54) Gurau, V.; Liu, H.; Kakac, S. *AIChE J.* **1998**, *44*, 2410.
- (55) Um, S.; Wang, C. Y.; Chen, K. S. *J. Electrochem. Soc.* **2000**, *147*, 4485.
- (56) Um, S.; Wang, C. Y. In *Proceedings of the ASME Heat Transfer Division*; Orlando, FL, 2000; Vol. 1, pp 19–25.
- (57) Dutta, S.; Shimpalee, S.; Van Zee, J. W. *J. Appl. Electrochem.* **2000**, *30*, 135.
- (58) Dutta, S.; Shimpalee, S.; Van Zee, J. W. *Int. J. Heat Mass Transfer* **2001**, *44*, 2029.
- (59) Um, S.; Wang, C. Y. *J. Power Sources* **2004**, *125*, 40.
- (60) Lee, W.-K.; Shimpalee, S.; Van Zee, J. W. *J. Electrochem. Soc.* **2003**, *150*, A341.
- (61) Zhou, T.; Liu, H. *Int. J. Transport Phenom.* **2001**, *3*, 177.
- (62) Berning, T.; Lu, D. M.; Djilali, N. *J. Power Sources* **2002**, *106*, 284.
- (63) Mazumder, S.; Cole, J. V. *J. Electrochem. Soc.* **2003**, *150*, A1503.
- (64) Ju, H.; Meng, H.; Wang, C. Y. *Int. J. Heat Mass Transfer*, submitted for publication.
- (65) Wang, Y.; Wang, C. Y. *Int. J. Heat Mass Transfer*, submitted for publication.
- (66) Wang, Y.; Wang, C. Y. *Electrochim. Acta*, in press.
- (67) Pasaogullari, U.; Wang, C. Y. *203rd Electrochemical Society Meeting*, Paris, May 2003; Abstract 1190. Also *J. Electrochem. Soc.*, in press.
- (68) Wang, Z. H.; Wang, C. Y.; Chen, K. S. *J. Power Sources* **2001**, *94*, 40.
- (69) He, W.; Yi, J. S.; Nguyen, T. V. *AIChE J.* **2000**, *46*, 2053.
- (70) Natarajan, D.; Nguyen, T. V. *J. Electrochem. Soc.* **2001**, *148*, 1324.
- (71) Natarajan, D.; Nguyen, T. V. *J. Power Sources* **2003**, *115*, 66.
- (72) You, L.; Liu, H. *Int. J. Heat Mass Transfer* **2002**, *45*, 2277.
- (73) Mazumder, S.; Cole, J. V. *J. Electrochem. Soc.* **2003**, *150*, A1510.
- (74) Berning, T.; Djilali, N. *J. Electrochem. Soc.* **2003**, *150*, A1598.
- (75) Pasaogullari, U.; Wang, C. Y. *Electrochim. Acta*, in press.
- (76) Wang, C. Y.; Gu, W. B. *J. Electrochem. Soc.* **1998**, *145*, 3407.
- (77) Kaviany, M. *Principles of Heat Transfer in Porous Media*; Springer-Verlag: New York, 1991; p 598.
- (78) Plumb, O. A. In *Handbook of Porous Media*; Vafai, K., Hadim, H. A., Eds.; Marcel Dekker: New York, 2000; p 754.
- (79) Wang, C. Y.; Cheng, P. *Adv. Heat Transfer* **1997**, *30*, 93.
- (80) Kulikovskiy, A. A. *J. Electrochem. Soc.* **2003**, *150*, A1432.
- (81) Wang, Y.; Wang, C. Y. Comparing variable density with constant density models for polymer electrolyte fuel cells. *ECEC Technical Report 2003-02*; Penn State University: University Park, PA, 2003. See also: Modeling polymer electrolyte fuel cells with large density and velocity changes. *J. Electrochem. Soc.*, in press.
- (82) Berger, C. *Handbook of Fuel Cell Technology*; Prentice-Hall: New Jersey, 1968.
- (83) Gu, W. B.; Wang, C. Y. *J. Electrochem. Soc.* **2000**, *147*, 2910.
- (84) Okada, T.; Xie, G.; Gorseth, O.; Kjelstrup, S.; Nakamura, N.; Arimura, T. *Electrochim. Acta* **1998**, *43*, 3741.
- (85) Okada, T.; Xie, G.; Meeg, M. *Electrochim. Acta* **1998**, *43*, 2141.
- (86) Hsing, I.-M.; Futerko, P. *Chem. Eng. Sci.* **2000**, *55*, 4209.
- (87) Janssen, G. J. M. *J. Electrochem. Soc.* **2001**, *148*, A1313.
- (88) Janssen, G. J. M.; Overvelde, M. L. J. *J. Power Sources* **2001**, *101*, 117.
- (89) Buchi, F.; Scherer, G. G. *J. Electrochem. Soc.* **2001**, *148*, A183.
- (90) Prinkey, M. T.; Shahnam, M.; Rogers, W. A.; Gemmen, R. S. In *Proceedings of the 2002 Fuel Cell Seminar*; Palm Springs, CA, 2002; p 913.
- (91) Um, S. Ph.D. Thesis, The Pennsylvania State University, 2002.
- (92) Wohr, M.; Bolwin, K.; Schnurnberger, W.; Fischer, M.; Neubrand, W. *Int. J. Hydrogen Energy* **1998**, *23*, 213.
- (93) Rowe, A.; Li, X. *J. Power Sources* **2001**, *102*, 82.
- (94) Maggio, G.; Recupero, V.; Mantegazza, C. *J. Power Sources* **1996**, *62*, 167.
- (95) Shimpalee, S.; Dutta, S. *Numerical Heat Transfer A* **2000**, *38*, 111.
- (96) Costamagna, P. *Chem. Eng. Sci.* **2001**, *56*, 323.
- (97) Meng, H.; Wang, C. Y. Multidimensional modeling of polymer electrolyte fuel cells under current density boundary condition. Submitted for publication.
- (98) Ishikawa, M. Private communication, 2003.
- (99) Qi, Z.; Kaufman, A. *J. Power Sources* **2002**, *109*, 469.
- (100) Ju, H.; Wang, C. Y.; Cleghorn, S. J.; Beuscher, U. *J. Electrochem. Soc.*, submitted for publication.
- (101) Baschuk, J. J.; Li, X. *J. Power Sources* **2000**, *86*, 181.
- (102) Weisbrod, K. R.; Grot, S. A.; Vanderborgh, N. E. *Electrochem. Soc. Proc.* **1995**, *23*, 153.
- (103) Nam, J. H.; Kaviany, M. *Int. J. Heat Mass Transfer* **2003**, *46*, 4595.
- (104) Pasaogullari, U.; Wang, C. Y. *J. Electrochem. Soc.* **2004**, *151*, A399.
- (105) Lim, C.; Wang, C. Y. Measurement of contact angles of liquid water in PEM fuel cell gas diffusion layer (GDL) by sessile drop and capillary rise methods. *Penn State University Electrochemical Engine Center (ECEC) Technical Report no. 2001-03*; Penn State University: State College, PA, 2001.
- (106) Brown, C. J.; Pletcher, D.; Walsh, F. C.; Hammond, J. K.; Robinson, D. *J. Appl. Electrochem.* **1992**, *22*, 613.
- (107) Cleghorn, S. J. C.; Derouin, C. R.; Wilson, M. S.; Gottesfeld S. *J. Appl. Electrochem.* **1998**, *28*, 663.
- (108) Bender, G.; Wilson, M. S.; Zawodzinski, T. A. *J. Power Sources* **2003**, *123*, 163.
- (109) Wieser, Ch.; Helmbold, A.; Gülzow, E. *J. Appl. Electrochem.* **2000**, *30*, 803.
- (110) Stumper, J.; Campell, S.; Wilkinson, D.; Johnson, M.; Davis, M. *Electrochim. Acta* **1998**, *43*, 3773.
- (111) Mench, M. M.; Wang, C. Y. *J. Electrochem. Soc.* **2003**, *150*, A79.
- (112) Mench, M. M.; Wang, C. Y.; Ishikawa, M. *J. Electrochem. Soc.* **2003**, *150*, A1052.
- (113) Noponen, M.; Mennola, T.; Mikkola, M.; Hottinen, T.; Lund, P. *J. Power Sources* **2002**, *106*, 304.
- (114) Noponen, M.; Hottinen, T.; Mennola, T.; Mikkola, M.; Lund, P. *J. Appl. Electrochem.* **2002**, *32*, 1081.
- (115) Brett, D.; Atkins, S.; Brandon, N. P.; Vesovic, V.; Vasileiadis, N.; Kucernaka, A. *Electrochem. Solid-State Lett.* **2003**, *6*, A63.
- (116) Ren, X.; Gottesfeld, S. *J. Electrochem. Soc.* **2001**, *148*, A87.
- (117) Janssen, G. J.; Overvelde, M. L. *J. Power Sources* **2001**, *101*, 117.
- (118) Lee, W. K.; Van Zee, J. W.; Shimpalee, S.; Dutta, S. *Proc. ASME Heat Transfer Div.* **1999**, *1*, 339.
- (119) Mench, M. M.; Dong, Q. L.; Wang, C. Y. *J. Power Sources* **2003**, *124*, 90.
- (120) Yang, X. G.; Burke, N.; Wang, C. Y.; Tajiri, K.; Shinohara, K. *J. Electrochem. Soc.*, in press.
- (121) Mench, M. M.; Burford, D.; Davis, T. In *Proceedings of the 2003 International Mechanical Engineering Congress and Exposition*; Washington, D.C., ASME, Nov 2003.
- (122) Bellows, R. J.; Lin, M. Y.; Arif, M.; Thompson, A. K.; Jacobsob, D. *J. Electrochem. Soc.* **1999**, *146*, 1099.
- (123) Geiger, A. B.; Tsukada, A.; Lehmann, E.; Vontobel, P.; Wokaun, A.; Scherer, G. G. *Fuel Cells* **2002**, *2*, 92.
- (124) Tuber, K.; Pocza, D.; Hebling, C. *J. Power Sources* **2003**, *124*, 403.
- (125) Yang, X. G.; Zhang, F. Y.; Lubawy, A.; Wang, C. Y. *Electrochem. Solid-State Lett.*, in press.
- (126) Springer, T. E.; Gottesfeld, S. In *Modeling of Batteries and Fuel Cells*; White, R. E., Ed.; 1991; Electrochemical Society Proc. 91–10, p 197.
- (127) Perry, M. L.; Newman, J.; Cairns, E. J. *J. Electrochem. Soc.* **1998**, *145*, 5.
- (128) Eikerling, M.; Kornyshev, A. A. *J. Electroanal. Chem.* **1998**, *453*, 89.
- (129) Jaouen, F.; Lindbergh, G.; Sundholm, G. *J. Electrochem. Soc.* **2002**, *149*, A448.
- (130) Pisani, L.; Valentini, M.; Murgia, G. *J. Electrochem. Soc.* **2003**, *150*, A1558.
- (131) Wang, G. Q.; Wang, C. Y. Presented at 204th Electrochemical Society Meeting, Orlando, FL, Oct 2003.
- (132) Halpert, G.; Narayanan, S. R.; Valdez, T.; Chun, W.; Frank, H.; Kindler, A.; Surampudi, S.; Kosek, J.; Cropley, C.; LaConti, A. In *Proceedings of the 32nd Intersociety Energy Conversion Engineering Conference*; AIChE: New York, 1997; Vol. 2, p 774.
- (133) Baldauf, M.; Preidel, W. *J. Power Sources* **1999**, *84*, 161.
- (134) Ren, X.; Zelenay, P.; Thomas, S.; Davey, J.; Gottesfeld, S. *J. Power Sources* **2000**, *86*, 111.
- (135) Scott, K.; Taama, W. M.; Argyropoulos, P. *Electrochim. Acta* **1999**, *44*, 3575.
- (136) Scott, K. In *Handbook of Fuel Cells*; Vielstich, W., Gasteiger, H. A., Lamm, A., Eds.; John Wiley and Sons Ltd.: England, 2003; Vol. 1, p 70.
- (137) Murgia, G.; Pisani, L.; Shukla, A. K.; Scott, K. *J. Electrochem. Soc.* **2003**, *150*, A1231.
- (138) Mench, M.; Boslet, S.; Thynell, S.; Scott, J.; Wang, C. Y. In *Direct Methanol Fuel Cells*; The Electrochemical Society Proceedings Series; Pennington, NJ, 2001.
- (139) Lim, C.; Wang, C. Y. *J. Power Sources* **2003**, *113*, 145.
- (140) Lu, G. Q.; Wang, C. Y.; Yen, T. J.; Zhang, X. *Electrochim. Acta* **2004**, *49*, 821.
- (141) Yen, T. J.; Fang, N.; Zhang, X.; Lu, G. Q.; Wang, C. Y. *Appl. Phys. Lett.* **2003**, *83*, 4056.
- (142) Gottesfeld, S.; Wilson, M. S. In *Energy Storage Systems for Electronics Devices*; Osaka, T., Datta, M., Eds.; Gordon and Breach Science Publishers: Singapore, 2000; p 487.
- (143) Lamy, C.; Leger, J.-M.; Srinivasan, S. In *Modern Aspects of Electrochemistry*; Bockris, J. O'M., Conway, B. E., White, R. E., Eds.; Kluwer Academic/Plenum Publishers: New York, 2001; p 53.
- (144) Arico, A. S.; Srinivasan, S.; Antonucci, V. *Fuel Cells* **2001**, *1*, 133.

- (145) Neergat, M.; Friedrich, K. A.; Stimming, U. In *Handbook of Fuel Cells*; Vielstich, W., Gasteiger, H. A., Lamm, A., Eds.; John Wiley and Sons Ltd.: England, 2003; Chapter 63, p 856.
- (146) Narayanan, S. R.; Valdez, T. I.; Rohatgi, N. In *Handbook of Fuel Cells*; Vielstich, W., Gasteiger, H. A., Lamm, A., Eds.; John Wiley and Sons Ltd.: England, 2003; Chapter 65, p 894.
- (147) Müller, J.; Frank, G.; Colbow, K.; Wilkinson, D. In *Handbook of Fuel Cells*; Vielstich, W., Gasteiger, H. A., Lamm, A., Eds.; John Wiley and Sons Ltd.: England, 2003; Chapter 62, p 847.
- (148) Wasmus, S.; Kuver, A. *J. Electroanal. Chem.* **1999**, *461*, 14.
- (149) Lin, W. F.; Wang, J. T.; Savinell, R. F. *J. Electrochem. Soc.* **1997**, *144*, 1917.
- (150) Hamnett, A. *Catal. Today* **1997**, *38*, 445.
- (151) Thomas, S. C.; Ren, X.; Gottesfeld, S. *J. Electrochem. Soc.* **1999**, *146*, 4354.
- (152) Liu, L.; Pu, C.; Viswanathan, R.; Fan, Q.; Liu, R.; Smotkin, E. S. *Electrochim. Acta* **1998**, *43*, 3657.
- (153) Hayden, E. *Catal. Today* **1997**, *38*, 473.
- (154) Page, T.; Johnson, R.; Hormes, J.; Noding, S.; Rambabu, B. *J. Electroanal. Chem.* **2000**, *485*, 34.
- (155) Arico, S.; Creti, P.; Modica, E.; Monforte, G.; Baglio, V.; Antonucci, V. *Electrochim. Acta* **2000**, *45*, 4319.
- (156) Ravikumar, M. K.; Shukla, A. K. *J. Electrochem. Soc.* **1996**, *143*, 2601.
- (157) Narayanan, S. R.; Frank, H.; Jeffries-Nakamura, B.; Smart, M.; Chun, W.; Halpert, G.; Kosek, J.; Cropley, C. In *Proton Conducting Membrane Fuel Cells I*; Gottesfeld, S., Halpert, G., Landgrebe, A., Eds.; The Electrochemical Society Proceedings Series: Pennington, NJ, 1995; PV 95–23, p 278.
- (158) Ren, X.; Zawodzinski, T. A.; Uribe, F.; Dai, H.; Gottesfeld, S. In *Proton Conducting Membrane Fuel Cells I*; Gottesfeld, S., Halpert, G., Landgrebe, A., Eds.; The Electrochemical Society Proceedings Series: Pennington, NJ, 1995; PV 95–23, p 284.
- (159) Ren, X.; Springer, T. E.; Zawodzinski, T. A.; Gottesfeld, S. *J. Electrochem. Soc.* **2000**, *147*, 466.
- (160) Valdez, T. I.; Narayanan, S. R. In *Proton Conducting Membrane Fuel Cells II*; Gottesfeld, S., Fuller, T. F., Halpert, G., Eds.; The Electrochemical Society Proceedings Series: Pennington, NJ, 1998; PV 98–27, p 380.
- (161) Wang, J. T.; Wasmus, S.; Savinell, R. F. *J. Electrochem. Soc.* **1996**, *143*, 1233.
- (162) Kauranen, P. S.; Skou, E. *J. Electroanal. Chem.* **1996**, *408*, 189.
- (163) Pan, Y. Ph.D. Thesis, The Pennsylvania State University, 2004.
- (164) Peled, E.; Blum, A.; Aharon, A.; Philosoph, M.; Lavi, Y. *Electrochem. Solid-State Lett.* **2003**, *6*, A268.
- (165) Kelley, S. C.; Deluga, G. A.; Smyrl, W. H. *AIChE J.* **2002**, *48*, 1071.
- (166) Mench, M. M.; Wang, Z. H.; Bhatia, K.; Wang, C. Y. In *Proceedings of IMECE2001*, Vol. 3, ASME, New York, 2001.
- (167) Pavio, J.; Bostaph, J.; Fisher, A.; Hallmark, J.; Mylan, B. J.; Xie, C. G. *Adv. Microelectron.* **2002**, *29*, 1.
- (168) Dyer, C. K. *J. Power Sources* **2002**, *106*, 31.
- (169) Lee, S. J.; Chang-Chien, A.; Cha, S. W.; O'Hayre, R.; Park, Y. I.; Saito, Y.; Prinz, F. B. *J. Power Sources* **2002**, *112*, 410.
- (170) Scott, K.; Argyropoulos, P.; Sundmacher, K. *J. Electroanal. Chem.* **1999**, *477*, 97.
- (171) Sundmacher, K.; Scott, K. *Chem. Eng. Sci.* **1999**, *54*, 2927.
- (172) Argyropoulos, P.; Scott, K.; Taama, W. M. *J. Appl. Electrochem.* **2000**, *30*, 899.
- (173) Baxter, S. F.; Battaglia, V. S.; White, R. E. *J. Electrochem. Soc.* **2000**, *146*, 437.
- (174) Wang, J.; Savinell, R. F. In *Electrode Materials and Processes for Energy Conversion and Storage*; Srinivasan, S., Macdonald, D. D., Khandkar, A. C., Eds.; The Electrochemical Society Proceedings Series: Pennington, NJ, 1994; PV 94–23, p 326.
- (175) Kulikovskiy, A. A.; Divisek, J.; Kornyshev, A. A. *J. Electrochem. Soc.* **2003**, *147*, 953.
- (176) Kulikovskiy, A. A. *J. Appl. Electrochem.* **2000**, *30*, 1005.
- (177) Dohle, H.; Divisek, J.; Jung, R. *J. Power Sources* **2000**, *86*, 469.
- (178) Meyers, J. P.; Newman J. *J. Electrochem. Soc.* **2002**, *149*, A710.
- (179) Meyers, J. P.; Newman J. *J. Electrochem. Soc.* **2002**, *149*, A718.
- (180) Meyers, J. P.; Newman J. *J. Electrochem. Soc.* **2002**, *149*, A729.
- (181) Nordlund J.; Lindbergh G. *J. Electrochem. Soc.* **2002**, *149*, A1107.
- (182) Wang, Z. H.; Wang, C. Y. *J. Electrochem. Soc.* **2003**, *150*, A508.
- (183) Divisek J.; Fuhrmann, J.; Gartner, K.; Jung R. *J. Electrochem. Soc.* **2003**, *150*, A811.
- (184) Murgia, G.; Pisani, L.; Shukla, A. K.; Scott, K. *J. Electrochem. Soc.* **2003**, *150*, A1231.
- (185) Apyropoulos, R.; Scott, K.; Taama, W. M. *Electrochim. Acta* **1999**, *44*, 3575.
- (186) Apyropoulos, R.; Scott, K.; Taama, W. M. *J. Appl. Electrochem.* **1999**, *29*, 661.
- (187) Lu, G. Q.; Wang, C. Y. *J. Power Sources*, **2004**, *134*, 33.
- (188) Yakabe, H.; Ogiwara, T.; Hishinuma, M.; Yasuda, I. *J. Power Sources* **2001**, *102*, 144.
- (189) Singhal, S. C. *Presentation at INDO-US Fuel Cell Workshop*; Washington, D.C., 2002.
- (190) Costamagna, P.; Honegger, K. *J. Electrochem. Soc.* **1998**, *145*, 3995.
- (191) Ahmed, S.; McPheeter, C.; Kumar, R. *J. Electrochem. Soc.* **1991**, *138*, 2712.
- (192) Bessette, N. F., II; Wepfer, W. J.; Winnick, J. *J. Electrochem. Soc.* **1995**, *142*, 3792.
- (193) Billingham, J.; King, A. C.; Copcutt, R. C.; Kendall, K. *SIAM J. Appl. Math.* **1999**, *60*, 574.
- (194) Cooper, R. J.; Billingham, J.; King, A. C. *J. Fluid Mech.* **2000**, *411*, 233.
- (195) King, A. C.; Billingham, J.; Cooper, R. J. *Combust. Theory Model.* **2001**, *5*, 639.
- (196) Prinkey, M.; Gemmen, R. S.; Rogers, W. A. In *Proceedings of IMECE 2001*; ASME: New York, 2001; Vol. 369–4, p 291.
- (197) Recknagle, K. P.; Williford, R. E.; Chick, L. A.; Rector, D. R.; Khaleel, M. A. *J. Power Sources* **2003**, *113*, 109.
- (198) Ackmann, T.; Haart, L. G. J. de; Lehnert, W.; Stolten, D. *J. Electrochem. Soc.* **2003**, *150*, A783.
- (199) Pasaogullari, U.; Wang, C. Y. *Electrochem. Soc. Proc.* **2003**, *2003–07*, 1403.
- (200) Khaleel, M. A.; Selman, J. R. In *High-Temperature Solid Oxide Fuel Cells—Fundamentals, Design and Applications*; Singhal, S. C., Kendall, K., Eds.; Elsevier Ltd.: Oxford, U.K., 2003; p 293.

CR020718S

Enzymatic Biofuel Cells for Implantable and Microscale Devices

Scott Calabrese Barton,^{*,†} Josh Gallaway,[†] and Plamen Atanassov[‡]

Department of Chemical Engineering, Columbia University, New York, New York 10027, and Department of Chemical and Nuclear Engineering, University of New Mexico, Albuquerque, New Mexico 87131

Received July 26, 2004

Contents

1. Introduction	4867
2. Applications	4868
2.1. Implantable Power	4869
2.2. Power from Ambient Fuels	4870
2.3. Conventional Fuel Cells	4870
3. Microbial Biofuel Cells	4871
4. Bioelectrochemistry at the Cathode and Anode of Enzymatic Biofuel Cells	4871
4.1. Enzyme-Catalyzed Direct Electron Transfer	4872
4.2. Biomimetic Electrocatalysts for Fuel Cells	4873
4.3. Mediated Electron Transfer	4873
4.3.1. Diffusional Mediators	4875
4.3.2. Immobilized Mediators	4876
5. Engineering of Enzymatic Biofuel Cell Systems	4881
5.1. Complete Enzymatic Fuel Cells	4881
5.2. Electrode Structures	4882
6. Future Outlook	4883
7. Acknowledgment	4884
8. References	4884

1. Introduction

Biological fuel cells have a long history in the literature,^{1–3} but in recent years, they have come to prominence as more conventional fuel cell technologies have approached mass-market acceptance. Driving the recent ascendance of biofuel cells are the aspects of biocatalysis that are unmatched by conventional low-temperature oxidation–reduction catalysts, namely, activity at near-room temperatures and neutral pH and, more importantly, selective catalytic activity.

Although, until recently, the development of biofuel cell devices has not been extensive, research in biocatalytically modified electrodes, particularly for sensor applications, has provided substantial technological underpinning for current biofuel cell development. There exists significant overlap in technical requirements between sensors and biofuel cells, including chemical and mechanical stability, selectivity, and cost of materials. However, these two technologies diverge in the area of energy supply, in that sensors are generally energy-consuming cells and

biofuel cells must, by definition, be energy producers. This significant difference leads to differing technical requirements, primarily in the areas of current density and cell potential. First, as a driven cell, sensors generally operate at cell potentials greater than open circuit. Second, cell current must be minimized to minimize power consumption. Generally, sensors are designed with currents in the nanoampere to microampere range such that power consumption is very small even for cell potentials near 1 V. Often, cell potential in a sensor must also be minimized to avoid undesired side reactions.

In contrast, as an energy-producing cell, an ideal enzymatic fuel cell generates maximum power, meaning both high current and high potential. Cell materials and structure must be designed such that overpotentials due to kinetics, ohmic resistance, and mass transfer are minimized and current density, particularly in terms of current per unit volume, is maximized. Although challenging in the context of biocatalyzed fuel cells, these issues are common to conventional fuel cell design. Indeed, since William Grove's original experiments in 1839, fuel cells have been stacked, i.e., arranged in series, to achieve higher total system voltage by multiplying individual cell voltage.⁴

A second issue that distinguishes biofuel cells from sensors is stability. Often, biocatalyzed electrochemical sensors are inexpensive enough to be disposable, and therefore, long-term stability is not essential. Should stability be required, one approach is to encapsulate the biocatalytic species in a low-porosity hydrophilic material, such as a silica gel.^{5,6} Hydroxides on the gel surface interact with sugars of the enzyme shell to “cage” the enzyme, restricting translational motion and minimizing enzyme denaturation. Depending on the enzyme, caging of the molecule can result in reduced activity. Such gels also restrict the mobility of reactants and products, leading to mass-transfer limitations in the electrode. This might be a desired result in an amperometric sensor, where mass-transfer-limited signals are often linearly related to reactant concentration.

In contrast, stability is a key aspect of any practical fuel cell, and biofuel cells must have lifetimes ranging from months to years to justify implanted, highly distributed, or consumer portable applications. Such stability is often difficult to achieve in redox enzymes, although introduction of thermophilic species and the use of mutagenic techniques might provide future

* Corresponding author. E-mail: scb@cheme.columbia.edu.

[†] Columbia University.

[‡] University of New Mexico.



Scott Calabrese Barton grew up in Jackson, MI, and earned a B.S. from the University of Notre Dame and a M.S. from the Massachusetts Institute of Technology, both in aerospace engineering. A stint as a noise control engineer at General Motors led to an interest in quiet, efficient electrochemical power, and he returned to earn a Ph.D. in chemical engineering from Columbia University (with Alan West). He was a postdoctoral associate at the University of Texas at Austin (with Adam Heller) and then returned to Columbia as Assistant Professor of Chemical Engineering in 2001. His research focuses on high-rate biocatalytic electrodes for low-temperature fuel cells.



Josh Gallaway was born in Waverly, TN, in 1974 and lived there until attending Case Western Reserve University in 1992, where he earned a B.S. in chemical engineering. Since 2002, he has been a graduate student at Columbia University, studying redox polymer–enzyme systems for use in biofuel cells.

improvements.⁷ The sol–gel caging techniques described above might be applicable to biocatalyzed fuel cell electrodes, but the effects of caging on enzyme activity and species transport are significant concerns. Moreover, supporting materials such as mediators and polymer gels are similarly susceptible to attack by ambient chemical species and mechanical stress imparted by convecting fluids.^{8–10} Thus, although sensor designs can act as starting point for biofuel cell development, the demands of high power and stability ultimately lead the biofuel cell design process down an independent path.

Extensive review literature exists in the area of biological fuel cells. Notably, Palmore and Whitesides summarized biological fuel cell concepts and performance up to 1992.¹¹ More recently, Katz and Willner discussed recent progress in novel electrode chemistries for both microbial and enzymatic fuel cells,¹² and Heller reviewed advances in miniature cells.¹³ This article does not duplicate these valuable contributions. Instead, we focus on the strengths and weak-



Plamen Atanassov grew up in Bulgaria and graduated from the University of Sofia in 1987 specializing in Chemical Physics and Theoretical Chemistry. He joined the Bulgarian Academy of Sciences and became a Member of Technical Staff of its Central Laboratory of Electrochemical Power Sources. During 1988–1989, he was a visiting scientist in the Frumkin's Institute of Electrochemistry, Moscow, Russia, studying bio-electrochemistry of enzymes. He received his doctorate from the Bulgarian Academy of Sciences in Physical Chemistry/Electrochemistry under the guidance of Prof. Ilia Iliev. He moved to the United States in 1992 and later became a research faculty member at the University of New Mexico. In 1999, he joined Superior MicroPowders LLC (now Cabot-SMP), where he was a project leader in fuel cell electrocatalysts development. He returned to the University of New Mexico in 2000 as an Assistant Professor of Chemical and Nuclear Engineering. His research programs include development of non-platinum electrocatalyst for fuel cells, new materials and technologies for micro-power sources, enzymatic biofuel cells, sensor systems design, and integration of microanalytical systems.

nesses of the technology in the context of specific classes of applications and point to areas where additional knowledge is required to properly exploit biological fuel cells. With some exceptions, we focus on contributions made after 1992.

Biofuel cells have traditionally been classified according to whether the catalytic enzymes were located inside or outside of living cells. If living cells are involved, the system is considered to be microbial, and if not, the system is considered enzymatic. Although microbial fuel cells exhibit unique features unmatched by enzymatic cells, such as long-term stability and fuel efficiency, the power densities associated with such devices are typically much lower owing to resistance to mass transfer across cell membranes. Thus, microbial fuel cells are expected to find limited application in small-scale electronic devices. This review focuses on enzymatic biofuel cells. Generally speaking, such cells demonstrate reduced stability because of the limited lifetime of extracellular enzymes and are unable to fully oxidize fuels, but they allow for substantial concentration of catalysts and removal of mass-transfer barriers. Enzymatic biofuel cells therefore produce higher current and power densities, approaching the range of applicability to micro- and miniscale electronics applications.

2. Applications

We begin with a discussion of key applications that can be addressed by biofuel cells and key requirements derived therefrom. The range of possible applications can be broken down into three main

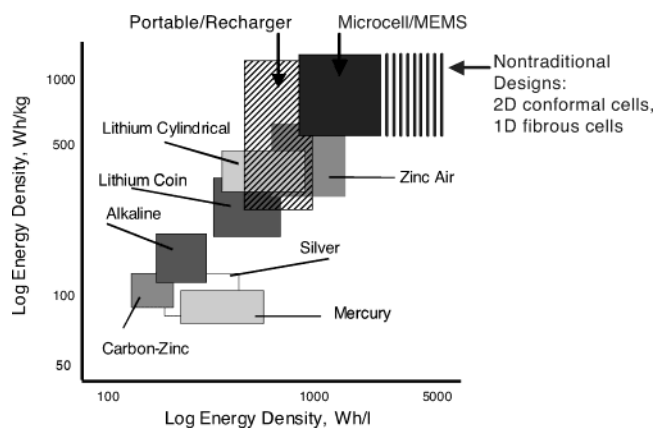


Figure 1. Conceptual product definitions of enzyme-based biofuel cells as they are compared in their specific energy and energy density to the existing primary battery technology. Based on Figure 2 of ref 15. Reproduced with permission. Copyright 1999 The Electrochemical Society, Inc.

subclasses: (1) implantable power, such as microscale cells implanted in human or animal tissue or larger cells implanted in blood vessels; (2) power derived from ambient fuels or oxidants, mainly plant saps or juices, but extendable to sewage and other waste streams; and (3) power derived from conventional fuels, including hydrogen, methanol, and higher alcohols.

Classes 1 and 2 are closely related: The reactants available for implantable power, such as blood-borne glucose, lactate, or oxygen, are ambient in that environment. These two classes are distinct, however, in that an ambient-fueled cell need not be implanted and utilizes plant- or waste-derived fuels, whereas the implantable cell utilizes animal-derived fuels. Class 3 is unique because it competes with well-established conventional fuel cell technology.

All three classes share the fundamental technical requirements of high power density and high stability. Identifying the required energy density and specific energies of biofuel cells depends on their potential product definitions. Microbial fuel cells serve in specific applications where size is not a limitation and the rate of current drain is small: marine power for stationary devices (buoys) or recharging devices based on biological hydrogen gas production.¹⁴ Enzyme-based biofuel cells can be formatted into portable power sources (including portable rechargers) and micro-miniature power sources for independent power-on-chip or microelectromechanical (MEMS) based systems (see Figure 1). The large molecular size of biocatalysts enables implementation of bionanotechnologies in enzyme-based power sources. As a result, one can envision novel design concepts that can substantially deviate from existing power supply form factors: two-dimensional devices for conformal power sources (power-generating coatings) and one-dimensional, fibrous devices leading to "power textiles".

Figure 1 juxtaposes the energy fields of these three potential product definitions with that of conventional primary battery technology. The data on the energy densities for the battery product definitions were adopted from a recent technology review.¹⁵ The expected energy performance figures for biofuel cells

are based on data available in the literature in a variety of formats. It was found that, depending on key technology directions, for example, toward a portable, reserve power or microsystem power application, the results fall into two specific energy ranges. The "shift" toward higher volumetric energy densities in microcell MEMS-based technologies is due to advantages derived from the use of microfabrication techniques in layered structure formation and packaging. As in any fuel cell, critical advantage is derived from the fact that fuel is supplied to the cell, rather than being embedded within it.

2.1. Implantable Power

The most intuitive application of biofuel cells is for implantable power. Biocatalysts are physiological species and have evolved to function in complex physiological environments, efficiently catalyzing reactions at physiological temperature and pH, involving fuels and oxidants present in such environments, and for the most part producing reaction products that are tolerable to the host organism. The selectivity of enzymatic catalysts stands out under such conditions, because no separation of fuel and oxidant is required, as is the case with noble metal catalysts. Additionally, these species generally demonstrate peak activity at physiological temperatures (25–50 °C), and many species have high activity at near-neutral pH. Therefore, the biocatalytic electrodes need not be separated or sealed off from physiological fluids. This allows for simpler cell design and access to high mass-transfer rates because of the presence of ambient convection.

A number of implantable medical devices might benefit from implanted power supplies. The most obvious is the cardiac pacemaker, which has been in use for over 40 years and is currently powered by a lithium-iodine battery with an operating power output of $\sim 1 \mu\text{W}$ and lifetimes exceeding 10 years.^{16,17} The typical energy density of such a battery is 1 W·h/mL; a biofuel cell generating 10 mW/mL, on the high end of what is possible today, would generate equivalent energy in just 4 days. Indeed, the benefit of an implantable biofuel cell compared to a conventional battery is one of high power density and, in some sense, infinite energy density if energy can be derived from physiologically ambient sugars.

A growing field of "functional electrical stimulation" exists wherein artificially applied electrical current is used to control the nervous system, allowing limited control of leg, arm, and finger movement.^{18–20} The power requirements of such systems greatly exceed that of pacemakers, and power for one such device, along with control signals, is provided by radio-frequency induction via a coil implanted in the patient's chest.²¹ Implantable power supplies providing milliwatt-scale power would greatly simplify the design of such systems. Other prosthetic applications such as artificial hearing or vision might also benefit from such a device.^{22–24}

Stability of implanted biofuel cells requires chemical stability in the presence of numerous physiologically active species that attack key electrode components. For example, electrodes exposed to physiological

fluids must be active and stable at neutral pH. This requirement eliminates the majority of fungal laccase species, which are capable of reducing oxygen at high potential but have peak activity in the pH 4–5 range and are essentially inactive at pH 7.^{25,26} Constituent species of blood serum have also been shown to decrease stability of a redox polymer-mediated glucose oxidase electrode.²⁷ Oxidation products of serum-borne urate were found to precipitate in the enzyme-immobilizing hydrogel, interfering with electron transfer, although not inhibiting the activity of the enzyme itself. Zinc and iron cations, however, were shown to reduce both the intrinsic activity of glucose oxidase and the rate of electron transfer, the latter by cross-linking of the polymer gel. High-power devices will likely require ambient convection such as blood flow, raising the issue of mechanical stability as discussed above. Biological stability, associated with the natural immune response to foreign materials, has not yet received significant attention in the context of biofuel cells.

Some of these stability issues can be addressed by the use of protective barrier membranes,^{28,29} at the risk of aggravating another fundamental challenge: reactant mass transfer. Typical reactants present in vivo are available only at low concentrations (glucose, 5 mM; oxygen, 0.1 mM; lactate, 1 mM). Maximum current density is therefore limited by the ability of such reactants to diffuse to and within bioelectrodes. In the case of glucose, flux to cylindrical electrodes embedded in the walls of blood vessels, where mass transfer is enhanced by blood flow of 1–10 cm/s, is expected to be 1–2 mA/cm².³⁰ Mass-transfer rates are even lower in tissues, where such convection is absent. However, microscale electrodes with fiber or microdot geometries benefit from cylindrical or spherical diffusion fields and can achieve current densities up to 1 mA/cm² at the expense of decreased electrode area.³¹

Finally, a complex issue associated with implantable devices is the implantation process itself, involving surgical procedures for inserting, electrically wiring, and stabilizing a device. A biofuel cell implanted in a blood vessel presents significant problems in that it must not act as a clotting agent, must not lead to substantial pressure drop, and must be electrically connected (wired) to the outside of the vessel so that the power produced is accessible. Above all, the host vessel walls must not be damaged by the insertion or ongoing presence of the cell. Indeed, a surgical procedure such as this is worthwhile only if the cell itself is stable and benign enough to last more than a year.

The surgical issues associated with tissue-implanted biofuel cells are less demanding, allowing practical short-term implantation with reduced stability requirements. However, material toxicity is an additional medical issue that does impact tissue-implanted cells. Enzymes such as glucose oxidase (EC 1.1.3.4), laccase (EC 1.10.3.2), and bilirubin oxidase (EC 1.3.3.5) have no known toxicity in the milligram quantities considered for implanted cells, and some synthetic species have received “Generally Recognized as Safe” (GRAS) status from the U.S. Food and

Drug Administration (FDA).^{32,33} Reaction products such as gluconolactone and peroxide are expected to be present in low concentrations.

However, some associated materials might be perceived as toxic. For example, complexes of osmium find frequent use as electron mediators, because of their rich chemistry, stability, and redox activity. Osmium metal and most compounds are considered nontoxic, but the neat tetroxide of osmium is a strong oxidizer and is considered “highly toxic” in the U.S. and “very toxic” by the European Union. On the other hand, the aqueous solution, osmic acid, has been injected at ~1% concentration in several European clinical trials, starting in the 1970s, for treatment of arthritis and hemophilia.^{34,35} No toxic effects were observed. Thus, osmium toxicity might be a question not of in vivo chemistry, but of manufacture, where a concentrated form of the oxide might need to be handled.³⁶

2.2. Power from Ambient Fuels

The exploitation of ambient fuels is attractive in situations where power needs for small electronic devices are distributed, disconnected, and long-term. This might be true for electronic sensor systems for monitoring of plant health, air quality, weather, or the presence of biohazards. In principle, the fuel can be derived from carbohydrates contained in plants or from effluent of human or animal processes.

The monosaccharides glucose and fructose and the disaccharide sucrose, a glucose–fructose dimer, are the primary organic constituents of most plant saps. For example, sugar maple sap is composed of up to 5.4 wt % sucrose (150 mM), with less than 0.2% (11 mM) glucose.³⁷ In contrast, apple juice is typically 12 wt % sugar with a 1:1:2 mass ratio of sucrose/glucose/fructose, and other juices vary in the relative content of these three sugars.^{38–40} Oxidation biocatalysts with activity toward these species are well-known and include glucose oxidase (EC 1.1.3.4), glucose dehydrogenase (EC 1.1.99.17),⁴¹ pyranose oxidase (EC 1.1.3.10),⁴² and oligosaccharide dehydrogenase.^{43–46} Of these, the most active is glucose oxidase, and the most active substrate (reactant species) is glucose.

The issues associated with ambient fuel cells are similar to the implantable issues except that the cell itself need not be implanted and immunoreponse is not as severe. However, utilization of some sugars, such as fructose and sucrose, is not straightforward using well-characterized enzyme systems. This presents a challenge to the utilization of high-fructose and -sucrose species such as maple trees. There are opportunities to “bioreform” such sugars to glucose using enzymes such as invertase (aka sucrase, EC 3.2.1.26).⁴⁷

2.3. Conventional Fuel Cells

Conventional fuel cell systems provide the designer with greater control over operating conditions as compared to the implantable and ambient-fuel categories. For example, the pH of the system can be adjusted well above or below neutral, and the opportunity exists to eradicate all poison species from the system. As previously mentioned, the realm of

conventional fuel cells is crowded with a variety of well-understood technologies that delivers high performance with respect to power density and efficiency. For example, platinum-based hydrogen–air fuel cell electrodes typically operate near 1 A/cm² and 0.65 V, and methanol cells achieve 500 mA/cm² at 0.5 V, orders of magnitude higher than the 1–10 mA/cm² current densities obtainable using the best reported methanol–air biofuel cells to date.^{48,49}

To compete in this arena, biofuel cells must take advantage of inherent biocatalytic properties that cannot be duplicated by conventional technology. Among these key properties are (1) activity at low temperature and near-neutral pH, (2) chemical selectivity, and (3) potentially low-cost production using fermentation and bioseparation technologies. To the extent possible, these properties must be exploited with minimal compromise of power density and stability. This constraint leaves one major class of conventional applications suitable for biofuel cells: small fuel cells for portable power.

Small, direct methanol fuel cells (DMFCs) provide several potential points of entry. First, the current densities of such systems are typically lower, on the order of 100–300 mA/cm², owing to the high kinetic resistance associated with methanol oxidation as compared to hydrogen oxidation. Second, significant material issues are associated with the use of methanol in such cells. One particular issue is methanol crossover. DMFC performance is limited by methanol permeation (crossover) from the anode to the cathode side through commonly used Nafion polymer electrolyte membranes. Methanol crossover reduces fuel efficiency, because the crossover fuel oxidizes catalytically with oxygen at the cathode and depolarizes the cell by lowering the cathode open-circuit potential.⁵⁰ Several approaches to this problem exist, each with its own flaws, but one relevant solution is the use of “selective” oxygen reduction electrocatalysts that do not catalyze the oxidation of methanol, enabling the use of conventional membranes and low temperatures. In the past 30 years, two major classes of transition metal compounds have been proposed as selective oxygen reduction catalysts: macrocyclic complexes such as porphyrins and phthalocyanins^{51–53} and transition metal chalcogenides (e.g., Mo_xRu_ySe_z).^{54,55} Although all of the mentioned catalysts ameliorate losses associated with methanol crossover, they are less active and typically less stable than platinum.

Lastly, cost is a crucial issue in the commercialization of fuel cells, particularly as performance and lifetimes have improved to the threshold of practicability. The major costs associated with these systems are materials-related, with separator and catalyst materials at the top of the list. It is envisioned that the cost of separator materials will decrease with increased production and competition and as alternative materials are perfected. However, the cost of conventional noble metal catalysts, particularly platinum, is expected only to increase with increased production and demand.⁵⁶ Therefore, the cost issue could perhaps be addressed by employing alternative catalysts, including biocatalysts. Enzymes are de-

rived from natural sources and can be manufactured at very low cost using well-established fermentation techniques.

3. Microbial Biofuel Cells

Microbial biofuel cells were the earliest biofuel cell technology to be developed, as an alternative to conventional fuel cell technology. The concept and performance of several microbial biofuel cells have been summarized in recent review chapters.^{11,12} The most fuel-efficient way of utilizing complex fuels, such as carbohydrates, is by using microbial biofuel cells where the oxidation process involves a cascade of enzyme-catalyzed reactions.⁵⁷ The two classical methods of operating the microbial fuel cells are (1) utilization of the electroactive metabolite produced by the fermentation of the fuel substrate^{58–61} and (2) use of redox mediators to shuttle electrons from the metabolic pathway of the microorganism to the electrodes.^{62–65}

Recently, a novel microbial fuel cell harvesting energy from the marine sediment–seawater interface has been reported.¹⁴ Also, a novel photosynthetic biofuel cell that is a hybrid between a microbial and enzymatic biofuel cell has been reported for the very first time.⁶⁶ More recently, reports of an unconventional biomass-fueled ceramic fuel cell can also be found in the literature.⁶⁷ A new concept of “Gastrobots”—hybrid robots that utilize operational power derived from microbial fuel cells—has been introduced.⁶⁸ Finally, the generation of electrical power by direct oxidation of glucose was demonstrated in mediatorless microbial fuel cells, which produced currents up to 3 μA/cm² at unknown cell voltage.⁶⁹

Microbial- and enzyme-based biofuel cells share the characteristic of integrated biocatalytic systems: active enzymes derived from living microorganisms. Technical issues, level of maturity, and practical limitations of the two subdivisions of this technology, however, vary considerably. The two avenues also differ in the level of achieved power densities, although direct comparison is difficult in light of the 10–1000 times smaller size of the enzymatic type. While progress in microbial fuel cell research is expected to continue, we focus our discussion in the following sections on the concepts, challenges, and recent developments in enzymatic biofuel cells.

4. Bioelectrochemistry at the Cathode and Anode of Enzymatic Biofuel Cells

Enzyme biocatalyst assemblies on electrode surfaces usually do not achieve significant electron-transfer communication between the redox center and the conductive support, mostly because of the electrical insulation of the biocatalytic site by the surrounding protein matrixes.⁷⁰ During the past four decades, several methods have been proposed and investigated in the field of bioelectrochemical technology in an effort to establish efficient electrical communication between biocatalysts and electrodes.^{71–81} In general, electron transfer is classified by two different mechanisms (see Figure 2):

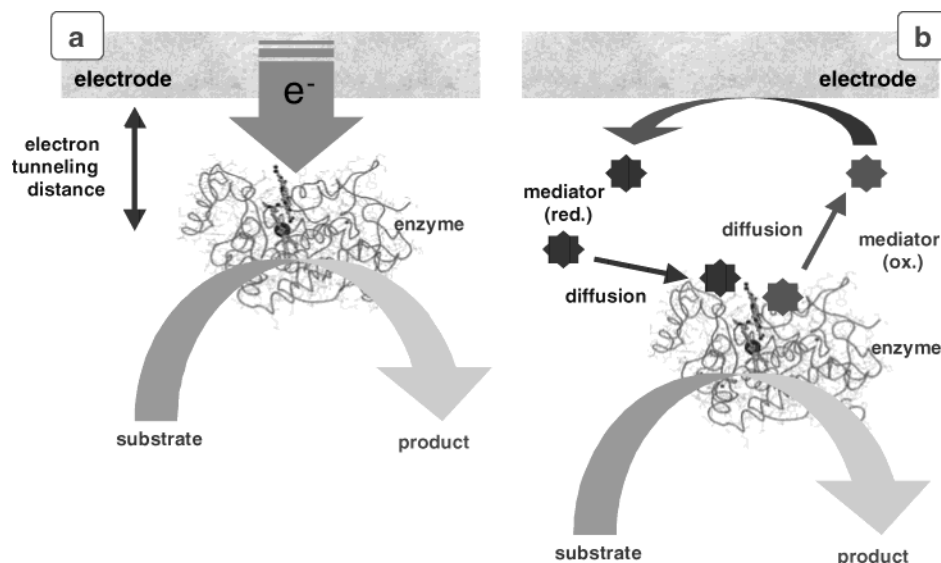


Figure 2. Alternative electron-transfer mechanisms. (a) Direct electron transfer (tunneling mechanism) from electrode surface to the active site of an enzyme. (b) Electron transfer via redox mediator.

mediated electron transfer (MET) and direct electron transfer (DET).

In MET, a low-molecular-weight, redox-active species, referred to as a mediator, is introduced to shuttle electrons between the enzyme active site and the electrode.⁸⁰ In this case, the enzyme catalyzes the oxidation or reduction of the redox mediator. The reverse transformation (regeneration) of the mediator occurs on the electrode surface. The major characteristics of mediator-assisted electron transfer are that (i) the mediator acts as a cosubstrate for the enzymatic reaction and (ii) the electrochemical transformation of the mediator on the electrode has to be reversible. In these systems, the catalytic process involves enzymatic transformations of both the first substrate (fuel or oxidant) and the second substrate (mediator). The mediator is regenerated at the electrode surface, preferably at low overvoltage. The enzymatic reaction and the electrode reaction can be considered as separate yet coupled.

Mediators can exist free in solution; physically entrapped behind a membrane;^{82,83} immobilized in a matrix along with the biocatalyst;^{84,85} or covalently bound to a surface or polymer network,⁷¹ wherein the polymer can be conductive or insulating.^{77,78} Detailed discussion of the various formats is outside scope of this review paper. However, selected immobilization chemistries reported in relation to enzymatic biofuel cells are reviewed in the sections below.

In DET, the enzymatic and electrode reactions are coupled by direct (mediatorless) electron transfer.⁸¹ In this case, the electron is transferred directly from the electrode to the substrate molecule (or vice versa) via the active site of the enzyme. In such a system, the coupled overall process is the redox transformation of the substrate(s), which can be considered as an enzyme-catalyzed electrode process. According to this mechanism, the electrode surface acts as the enzyme cosubstrate, and the enzymatic and electrode reactions cannot be considered as separate, but as formal stages of the bioelectrocatalytic reaction mechanism. The catalytic effect of the enzyme is the

reduction of the overvoltage for reaction of the substrate.

4.1. Enzyme-Catalyzed Direct Electron Transfer

The physicochemical manifestations of bioelectrocatalysis were the focus of intensive investigations during the 1980s. A number of enzymes were found to be capable of direct electron transfer with an electrode, including cytochrome *c*, peroxidase, ferredoxin, plastocyanin, azurin, azotoflavin, and glucose oxidase.^{86–88} Studies of DET with these enzymes led to an electrochemical basis for the investigation of protein structure, mechanisms of redox transformations of protein molecules, and metabolic processes involving redox transformations. Depending on the practical significance of the substrates of these enzymatic reactions, electroanalytical applications of bioelectrocatalysis have begun to appear since the late 1980s.^{43,79,89–91} Recently, the ability of oxidoreductase enzymes to catalyze direct electron transfer has been demonstrated for laccase, lactate dehydrogenase, peroxidase, hydrogenase, *p*-cresolmethylhydroxylase, methylamine dehydrogenase, succinate dehydrogenase, fumarate reductase, D-fructose dehydrogenase, alcohol dehydrogenase, and D-gluconate dehydrogenase.⁷⁹

Application of these bioelectrocatalysts is based on their ability to interact with the electrode surface, forming a "molecular transducer" that converts a chemical signal directly into an electric one.⁷⁹ Among the oxidoreductases, of particular interest are those that catalyze either reduction of oxygen; oxidation of hydrogen, alcohols, and sugars; or transformation of peroxide. These common molecules are of importance for signal generation in biosensors and current generation in biofuel cells. Peroxidase is known to catalyze oxidation of a broad range of polyphenols and aromatic polyamines. Laccase, a copper-containing oxidase, exhibits substrate specificity similar to that of peroxidase.⁹² Laccase catalyzes the oxidation of these substrates by molecular oxygen, forming

water. Peroxidase and laccase were early targets for the investigation of DET reactions.

Direct-electron-transfer (DET) characteristics of laccase on monolayer-modified gold electrodes were studied.⁹³ Three different monolayers were investigated, from which 4-aminothiophenol was found to be optimal for the direct electron transfer to take place. The electrocatalytic reduction of the oxygen at the electrode surface was very much dependent on the orientation of the enzyme and the method of immobilization. Fungal laccase from *Coriolus hirsutus* modified with sodium periodate demonstrated a higher anodic onset potential for oxygen reduction than the tree laccase from *Rhus vernicifera*. Physical immobilization of the enzyme did not give any shifts in anodic potential. A maximum anodic shift in reduction potential of 300 mV was observed for fungal laccase covalently coupled on the electrode surface.

4.2. Biomimetic Electrocatalysts for Fuel Cells

Investigations of enzyme-catalyzed direct electron transfer introduce the basis for a future generation of electrocatalysts based on enzyme mimics. This avenue could offer new methods of synthesis for nonprecious metal electrocatalysts, based on nanostructured (for example, sol-gel-derived) molecular imprints from a biological catalyst (enzyme) with pronounced and, in some cases, unique electrocatalytic properties. Computational approaches to the study of transition state stabilization by biocatalysts has led to the concept of "theozymes".⁹⁴

Understanding the chemistry of the active site during the reaction process is the first step in electrode design and, ultimately, toward biomimetic catalysis. An example are laccases, which are glycosylated multicopper oxidases that oxidize a wide variety of substrates such as diphenols, aryldiamines, and aminophenols. Fungal laccases are less substrate specific than plant laccases.⁹⁵ Spectroscopic and X-ray crystallographic studies have revealed that they contain one blue copper or T1 site and a T2/T3 trinuclear copper cluster site (Figure 3). T2 is the normal copper, and T3 is a bridged copper pair. The cysteine bound to the T1 copper is flanked on either

side by histidines that are ligated to each of the T3 coppers, providing a 1.3-nm pathway for electron transfer from the T1 to the trinuclear cluster.⁹⁶

Electrons acquired by the T1 site from the oxidized cosubstrate are transferred internally by electron tunneling through the cysteine-histidine pathway to the trinuclear site, where oxygen reduces to form water.⁹⁷ The four-electron reduction of dioxygen occurs in two two-electron steps. The fully reduced site first reacts with O₂ to generate a peroxide-level intermediate, which is then further reduced to a hydroxide product by uptake of electrons from T1 and T2, thus bridging the T2 and one of the T3 coppers in the trinuclear copper site. The first step, peroxide formation, is rate limiting, but the overall rate-limiting step is the oxidation of cosubstrate (or reduction of the T1 site), which is strictly outer sphere, involving no binding pocket.⁹²

The redox potential of blue copper oxidases varies from species to species. The high redox potential of around 700 mV in fungal laccase is primarily attributed to nonaxial methionine ligand, a geometry that stabilizes the reduced state. Other factors such as solvent accessibility, dipole orientation, and hydrogen bonding also play an important role.^{98,99}

Different chemical environments surrounding the T1 copper result in different redox potentials. Fungal laccases demonstrate the highest potential, close to the equilibrium potential of oxygen reduction in their respective pH regions (see Table 1). Laccases, however, are anion sensitive, with deactivation involving dissociation of T2 copper from the active site of the enzyme. Alternative copper oxidases such as bilirubin oxidase^{100,101} and ceruloplasmin¹⁰²⁻¹⁰⁵ also have high redox potentials, but their electrochemistry is less well understood and is still being explored.

4.3. Mediated Electron Transfer

The main purpose of redox mediation is to increase the rate of electron transfer between the active site of enzyme biocatalysts and an electrode by eliminating the need for the enzyme to interact directly with the electrode surface. Depending on the enzyme and

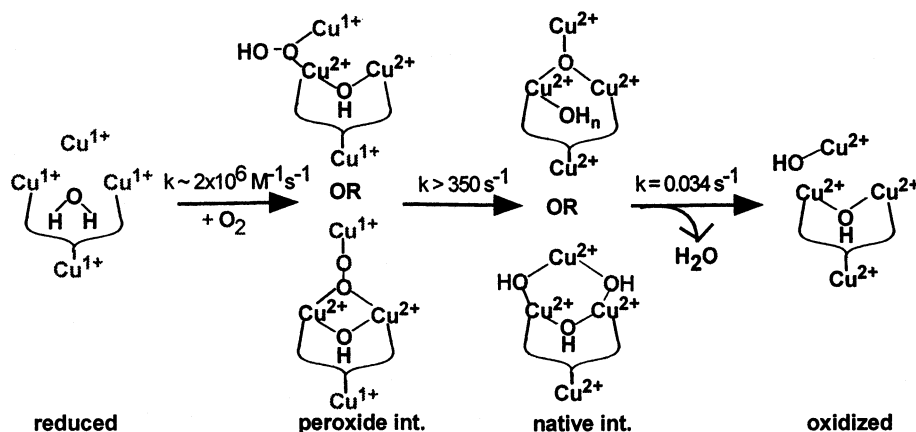
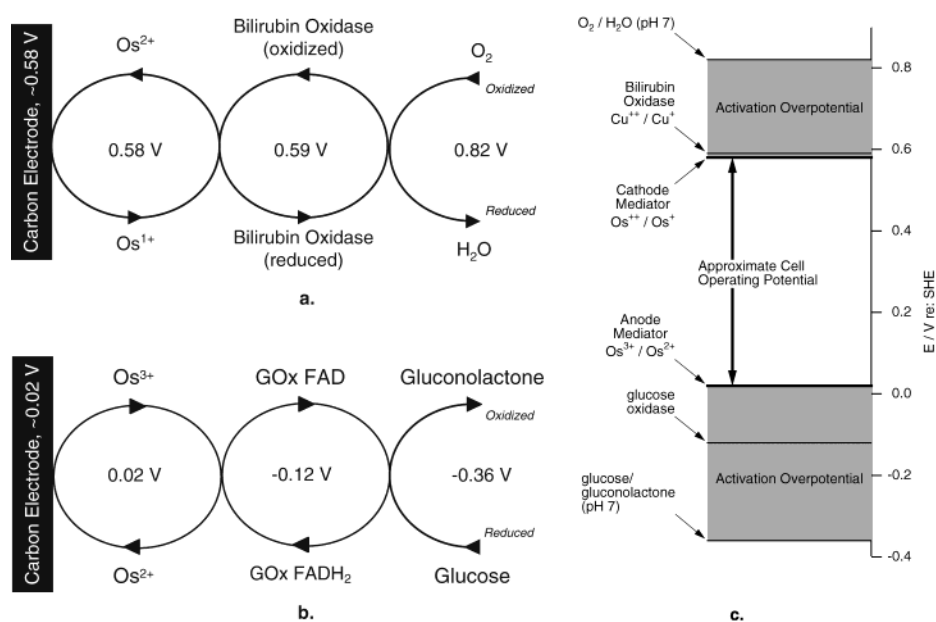


Figure 3. Molecular mechanism for the 4e⁻ reduction of O₂ to H₂O by the multicopper oxidases. Reprinted with permission from ref 99. Copyright 2001 American Chemical Society.

Table 1. Redox Potentials of T1 Copper Site in Some Copper-Containing Enzymes (E^0 in mV vs SHE) and the pH at Which It Was Established⁹²

enzyme	E^0 , mV (pH)	enzyme	E^0 , mV (pH)
Laccases		Ascorbate Oxidase	
<i>Polyporus versicolor</i>	775–785 (pH 4.0)	<i>Cucurbita pepo medullosa</i>	344 (pH 7.4)
<i>Polyporus pinsitus</i>	760–790 (pH 4.0)	<i>Cucumis sativus</i>	350 (pH 7.4)
<i>Coriolus hirsutus</i>	750–850 (pH 4.0)	Ceruloplasmin	
<i>Rhizoctonia solani</i>	680–730 (pH 4.0)	human I	490–580 (pH 7.4)
<i>Trametes versicolor</i>	780–800 (pH 4.0)	bovine	370–390 (pH 7.4)
<i>Pycnoporus cinnabarinus</i>	740–760 (pH 7.0)	Bilirubin Oxidase	
<i>Myrothecium verrucaria</i>	480–490 (pH 7.4)	<i>Myceliophthora thermophila</i>	450–480 (pH 7.0)
<i>Scytalidium thermophilum</i>	480–530 (pH 7.0)		
<i>Rhus Vernicifera</i>	394–434 (pH 7.0)		

**Figure 4.** Potential schematic for a mediated biofuel cell. All potentials specified vs SHE.^{110,126,182}

reaction conditions, rates of mediated electron transfer can exceed by orders of magnitude that of the direct mechanism. However, by introducing an additional transfer step, enzyme–mediator electron transfer is isolated from direct electrode potential control. For typically fast (Nernstian) kinetics between the mediator and electrode surface, the electrode potential merely controls the relative concentrations of oxidized and reduced mediator at the surface. At electrode potentials above its redox potential, mediator species in contact with the surface are primarily oxidized; below the redox potential, such species are primarily reduced. The electrode thus provides a boundary condition for electron flux to and from solution, which can occur either by mediator self-exchange or by bulk mediator diffusion. Both of these mechanisms are diffusional in nature and are therefore the result of gradients in concentration of oxidized and reduced mediator species.

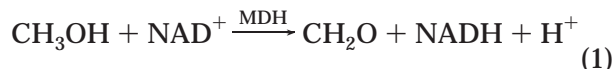
The practical impact of such considerations is that the reversible potential of a mediated biocatalytic electrode is a mixed potential dominated by the mediator couple. By extension, the open-circuit potential of a biofuel cell comprising two such electrodes is primarily determined by the difference in redox potential of the two mediator couples. The difference in redox potential between the mediator and the consumed reactant represents a driving force for electron transfer and therefore must be nonzero. As

shown in Figure 4 for a glucose–oxygen biofuel cell,¹⁰⁶ this difference represents an activation overpotential that reduces the observed open-circuit potential from a theoretical maximum, given by the formal potential difference between the fuel and oxidant. This reduction is in addition to that associated with driving electron transfer between each reactant and its respective biocatalyst.

Therefore, the range of appropriate mediators is limited to those with redox potentials close to that of the chosen enzyme. As previously discussed, mediator selection might also be dictated by other factors such as stability, toxicity, and biocompatibility. Using the format of free diffusion of the redox mediator (benzyl viologen) in solution, a methanol–dioxygen biofuel cell using NAD⁺-dependent dehydrogenases can be found in the literature.⁸² In a similar format, a laccase cathode using the redox mediator ABTS has been designed.¹⁰⁷ Although the format of free diffusion of the redox mediator is the most efficient method of MET, it necessitates semi-permeable membranes or similar technology to retain the mediator near the electrode, limiting its practical application compared to other formats of MET. Despite the vast literature on other formats of MET,^{73–78} the most successful format found in the literature, so far, is the design of miniature enzymatic biofuel cells based on “wired” biocatalysts, using osmium redox polymers.^{26,106,108–110}

4.3.1. Diffusional Mediators

NAD(P)⁺ as Anode Mediator. A majority of redox enzymes require the cation nicotinamide adenine dinucleotide, possibly phosphorylated (NAD(P)⁺) as a cofactor. Of the oxidoreductases listed in *Enzyme Nomenclature*, over 60% have NAD(P)⁺ as a reactant or product.^{111,112} For example, methanol can be oxidized to form formaldehyde by methanol dehydrogenase (MDH, EC 1.1.1.244) according to

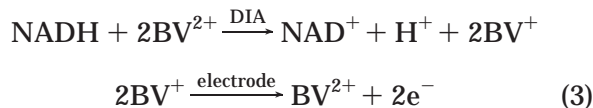


The reduced form, NADH, then releases electrons at an electrode surface, regenerating NAD⁺, by



NAD(P)⁺ can function as a mediator for enzymatic anodes, except that the electrode potential required to reoxidize this molecule electrochemically is typically ~1 V positive of its formal oxidation potential (-320 ± 5 mV), leading to significant activation losses.^{113,114} [Note that all potentials are reported relative to the standard hydrogen electrode (SHE). Potentials relative to Ag|AgCl in original references are adjusted by +0.22 V here.] Moreover, direct oxidation of NAD(P)H at an electrode surface results in fouling and deactivation of the electrode.^{113,115} Thus, in systems utilizing NAD(P)⁺, modified electrodes incorporating either a second biocatalytic cycle or a surface-bound oxidation catalyst are required for efficient oxidation of NAD(P)H. Sensor applications of NAD(P)⁺-dependent enzymes have driven development of a broad range of mechanisms for NAD(P)H regeneration, and several excellent reviews are available in the literature.^{80,116,117}

Palmore et al. applied the biocatalytic approach, utilizing the enzyme diaphorase (EC 1.6.4.3) to catalyze the reoxidation of NADH homogeneously, transferring electrons to a mediator, benzyl viologen.⁸² The mediator was then reoxidized at an electrode surface, with the overall scheme



This approach was coupled to a system of three NAD⁺-dependent enzymes comprised of alcohol dehydrogenase (EC 1.1.1.1), aldehyde dehydrogenase (EC 1.2.1.3), and formate dehydrogenase (EC 1.2.1.2) to create an electrode theoretically capable of complete oxidation of methanol to carbon dioxide, as shown in Figure 5. The anode was, in turn, coupled to a platinum-catalyzed oxygen cathode to produce a complete fuel cell operating at pH 7.5. With no externally applied convection, the cell produced power densities of 0.67 mW/cm² at 0.49 V for periods of less than 1 min, before the onset of concentration polarization.

A carbon felt electrode modified by electropolymerized methylene green has been implemented as the anode in an alcohol–O₂ biofuel cell.⁴⁸ The porous

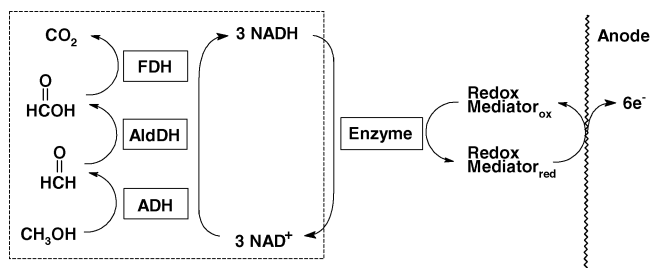


Figure 5. Oxidation of methanol to carbon dioxide by a three-enzyme system consisting of alcohol (ADH), aldehyde (AldDH), and formate (FDH) dehydrogenases. Each enzyme is NAD⁺-dependent, and the NAD⁺ is regenerated by the emission from ref 82. Copyright 1998 Elsevier Science S.A.

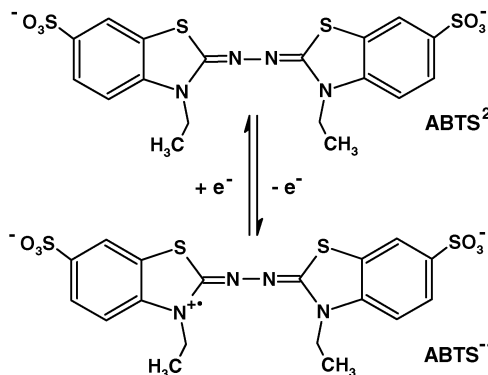


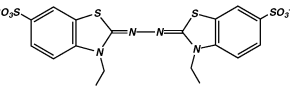
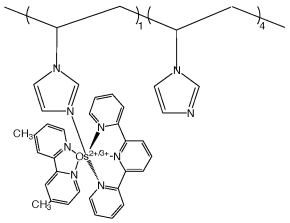
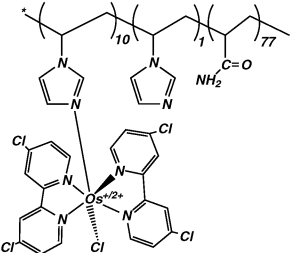
Figure 6. Structure of ABTS in reduced (ABTS²⁻) and oxidized (ABTS^{•-}) forms. Redrawn with permission from ref 107. Copyright 1999 Elsevier Science S.A.

electrode was coated with a Nafion suspension treated with tetrabutylammonium bromide to increase the local pH and the nanoscale pore size of the film, wherein a mixture of alcohol dehydrogenase and aldehyde dehydrogenase was immobilized. Power densities of up to 2 mW/cm² were obtained using an O₂/Pt cathode and ethanol as the fuel; using methanol, a power density of 1.5 mW/cm² was obtained. These bioanodes functioned for more than 30 days with less than 80% loss of activity.

ABTS as Cathode Mediator. Some recent efforts to construct biocatalytic oxygen electrodes have introduced 2,2'-azinobis(3-ethylbenzothiazoline-6-sulfonate), or ABTS, as a diffusional mediator for oxygen-reducing enzymes.¹⁰¹ Having the structure shown in Figure 6 and Table 2 (compound 1), ABTS²⁻ is introduced as a divalent anion that acts as a cosubstrate with oxygen-reducing enzymes having high redox potentials, such as laccase and bilirubin oxidase, oxidizing to a monovalent radical, ABTS^{•-}, at a redox potential of 0.62 V vs SHE.

Palmore et al. first demonstrated the use of ABTS in a biofuel cell cathode, combining it with laccase from *Pyricularia oryzae*.¹⁰⁷ ABTS was dissolved at 2 mM in oxygen-saturated 0.2 M acetate buffer, pH 4, 25 °C. With a glassy carbon working electrode, an open-circuit potential of 0.53 V vs SCE was observed, reflecting the presence of HABTS⁻ in low-pH solution. Protonation of ABTS²⁻ shifts the redox potential to 0.57 V vs SCE.¹¹⁸ With negligible stirring, current densities of 100 μA/cm² were achieved at an electrode potential of 0.4 V vs SCE.

Table 2. Cathode Mediators

Compound	Structure	Redox Potential (V) ^a	O ₂ Reduction Rate (A/cm ²) ^{a,b}	Ref.
1 2,2'-azinobis (3-ethylbenzothiazoline- 6-sulfonate) (ABTS)		0.66, pH 4; 0.72, pH 7	5×10 ⁻⁴ (0.43 V, pH 7 phosphate) ^{c,e}	101,107,118
2 poly{N-vinylimidazole [Os(terpyridine) (4,4'-dimethyl- 2,2'-bipyridine)] ^{2+/3+} }		0.79, pH 5	1×10 ⁻² (0.62 V, pH 5 citrate) ^{d,f}	10,26
3 poly{N-vinylimidazole [Os(4,4'-dichloro- 2,2'-bipyridine) ₂ Cl] ⁺²⁺ -co-acrylamide}		0.58, pH 7.4	9×10 ⁻³ (0.55 V, pH 7 phosphate) ^{c,f}	109,110,166

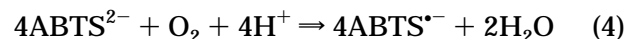
^a Potentials vs SHE. ^b High-surface-area carbon supports in O₂-saturated buffer. ^c Catalyzed by bilirubin oxidase in the presence of chloride. ^d Catalyzed by fungal laccase, chloride absent. ^e Moderate stirring by bubbled gas. ^f Strong stirring by rotating disk electrode at 4 krpm.

At 0.44 V vs SCE, the redox potential of ABTS falls well below that of the Cu²⁺/Cu⁺ couple of laccase (0.54 V vs SCE, pH 4). It is, however, well matched to that of bilirubin oxidase (BOD) another copper-centered, oxygen-reducing enzyme. In contrast to laccase, BOD provides an added benefit of near-peak activity at neutral pH.^{101,109} Tsujimura et al. employed ABTS for mediation of O₂ reduction catalyzed by bilirubin oxidase from *M. verrucaria*.¹⁰¹ Voltammetry was conducted using a glassy carbon electrode in air-saturated pH 7 phosphate buffer, 25 °C, containing 0.25 mM ABTS²⁻ and 0.11 μM BOD. Current densities approaching 40 μA/cm² were observed. Observation of maximum current density for ABTS²⁻ concentrations up to 1.5 mM yielded current densities exceeding 100 μA/cm² and effective Michaelis-Menten parameters of $k_{\text{cat}} = 820/\text{s}$ and $K_{\text{ABTS}} = 11 \mu\text{M}$. A similar study of oxygen concentration yielded $K_{\text{O}_2} = 51 \mu\text{M}$, much less than the air-saturated concentration of oxygen in the buffer (~250 μM). When a high-surface-area carbon felt sheet was used as a working electrode in O₂-saturated buffer containing 0.5 mM ABTS²⁻ and 0.11 μM BOD, current densities of up to 900 μA/cm² were observed, and a similar current density was obtained in air because of the low value of K_{O_2} .

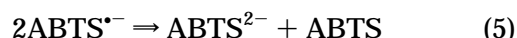
Although the diffusion coefficient ($D_{\text{ABTS}} = 3.2 \times 10^{-6} \text{ cm}^2/\text{s}$) and solubility (>30 mM) of ABTS²⁻ are much higher than those of competing redox polymers, the compound was found to suffer from oxidative degradation at potentials exceeding 0.92 V vs SHE in pH 7 buffer.¹⁰¹ Cyclic voltammetry of ABTS²⁻ detected two oxidation peaks, one at 530 mV that was

reversible and one near 1 V that was reversible at high scan rate (20 V/s) and irreversible at low scan rate (1 V/s). The reversible peak at 530 mV was associated with the one-electron oxidation of ABTS²⁻ to ABTS^{•-}, and the higher-potential, irreversible peak was associated with oxidation of ABTS^{•-} to neutral ABTS. Bulk electrolysis for 20 min at 1.0 V led to the elimination of all peaks, suggesting that ABTS is decomposed at high potential by an unknown mechanism.

Homogeneous, BOD-catalyzed oxygen reduction in the presence of ABTS²⁻, presumably according to the reaction



was monitored using a Clark-type oxygen electrode. The reaction proceeded rapidly up to the limit of depletion of ABTS²⁻ according to eq 4, but thereafter, it continued to consume oxygen, albeit at a lower rate. The authors suggested that ABTS²⁻ might be slowly regenerated by disproportionation of the radical ABTS^{•-}



where the neutral ABTS decomposes as mentioned above. Thus, the redox-active ion is regenerated, but the total ABTS concentration is irreversibly depleted, the process occurring over a time scale of minutes to hours.

4.3.2. Immobilized Mediators

It is desirable to contain enzymes and electron-transfer mediators within an electrode volume to

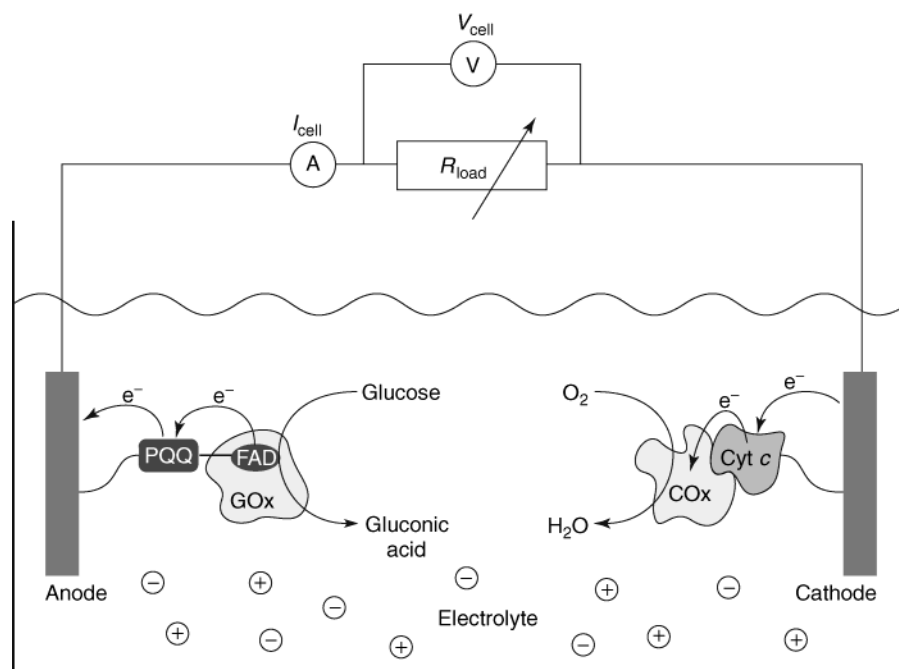


Figure 7. Noncompartmentalized glucose–oxygen biofuel cell. Reprinted with permission from refs 12 and 125. Copyright 2003 John Wiley and Sons Limited. Copyright 1999 Elsevier Science S.A.

maintain concentration and activity. In the case of diffusional mediators, this requires the use of semi-permeable barriers such as polymer membranes, intended to prevent flux of mediator species out of the electrode. However, these membranes also limit the diffusional flux of reactants into and products out of the electrode. Such diffusional limitations might be desirable in the context of an enzymatic sensor, where limiting current can be monitored for amperometric detection of a reactant. In a biofuel cell, however, such limitations lead to performance losses, and diffusional barriers are, in principle, to be avoided.

An alternative containment scheme is immobilization of active species on a surface^{119–125} or within a tethered polymer brush or network.^{10,13,126,127} Surface immobilization can achieve high surface utilization by locating mediators and biocatalysts within nanometers of conducting surfaces. Immobilization on polymer networks allows for dense packing of enzymes within electrode volumes at the expense of long-distance electron mediation between the enzyme active center and a conductive surface. Such mediation often represents the rate-limiting step in the overall electrode reaction.

Examples of surface-immobilized mediators are electropolymerized azines for electro-oxidation of NADH.^{119,120} The extreme form of this approach is formation of biocatalytic monolayer, comprising a surface-bound mediator species that is itself bound to a single enzyme molecule. Katz et al. report a complete cell based on novel architecture at both electrodes (Figure 7).¹²⁵ On the anode side, the FAD center of glucose oxidase is removed from the enzyme shell and covalently attached to a pyrroloquinoline quinone (PQQ) mediator species previously immobilized on a gold surface. The GOx apoenzyme (enzyme with active center removed) is reintroduced in solution and selectively binds to FAD, resulting in a PQQ-

mediated GOx monolayer with physical attachment of its FAD center to the electrode surface.¹²⁸ On the cathode side, a similar approach is taken wherein cytochrome *c* is immobilized on a gold surface by site-specific covalent bonding to a maleimide monolayer.¹²⁹ This monolayer was then exposed to cytochrome oxidase, which complexed with the cytochrome *c* and was subsequently cross-linked with glutaric dialdehyde. A cell combining these two electrodes, operating in 1 mM glucose and air-saturated buffer at pH 7 and 25 °C, generated a maximum current density of 110 $\mu\text{A}/\text{cm}^2$ at 0.04 V cell potential.

More frequently in the literature, labile redox complexes based on osmium or ruthenium are immobilized on water-soluble polymers such as poly(vinyl imidazole) or poly(allylamine), which can, in turn, be immobilized on a surface such as a Langmuir–Blodgett film,^{130,131} chemically cross-linked,^{126,132–135} or electropolymerized¹²⁷ to form a hydrogel. In such structures, the mobility of the polymer backbone provides restricted translational mobility to the redox complex, allowing electron transport via exchange between neighboring centers while preventing their bulk diffusion.^{136,137} Such a scheme leads to electron transport that, in the absence of significant potential gradients (achieved at low current density or by the presence of a supporting electrolyte), can be characterized as a diffusional process and quantified by an apparent diffusion coefficient.¹³⁸ Historically, a major drawback of redox polymer electron mediators has been measured values of apparent diffusion that fall in the 10^{-9} – 10^{-8} range, orders of magnitude lower than those of diffusional species.^{139,140} Recently, an additional degree of translational freedom has been demonstrated in redox polymers wherein the complex is attached to the polymer backbone via a long tether.¹²⁶

Choice of an effective mediator to shuttle electrons between the enzyme active site and the electrode involves several criteria: The mediator must be stable in both oxidized and reduced forms, must engage in rapid electron transfer with the biocatalyst and at the interface with a conducting material, and must have a redox potential allowing the electrode to be poised appropriately to avoid unwanted reactions and minimize overpotential.¹⁴¹ Bipyridine- and terpyridine-based chelates of osmium(II/III) fulfill all of these requirements. In addition, electron-donor characteristics of the ligands effectively tune the redox potential of the metal center,^{142,143} allowing one to engineer the mediator at the molecular level to work in conjunction with a desired enzyme. In general, synthesis can be accomplished by adding the stoichiometric amounts of ligand and osmium chloride salt $(\text{NH}_4)_2\text{OsCl}_6$ and refluxing in ethylene glycol.¹⁴⁴

Osmium generally has a coordination number of six. Complexes of osmium with a chloride remaining in their coordination sphere after addition of the ligands can further be complexed with a pendant group in a polymer, thus producing a *redox polymer*.¹⁴⁵ By choosing a water-soluble polymer backbone that can be cross-linked, one can produce a *redox hydrogel* in an aqueous environment. In this state, the osmium complexes retain their ability to mediate for the enzyme.¹⁴⁶ The polymer binds to the electrode surface by a van der Waals interaction, and the enzyme is immobilized in the redox hydrogel by electrostatic forces or by covalent cross-linking, thus making the system resistant to flow-induced shear.

Redox polymers, defined as polymer molecules that include locally redox-active sites, have been known since at least the 1960s¹⁴⁷ and were incorporated into modified electrodes in the early 1980s.¹⁴⁸ Redox polymers were first employed for immobilization and mediation of redox biocatalysts by the Heller group, in the context of amperometric biosensors.¹⁴⁹ After the external shell of glucose oxidase had first been covalently modified with a variety of redox relays, it was found that approximately 10–20 relay sites could be attached to each protein molecule. This was found to be insufficient for a substantial increase in electron-transfer efficiency, primarily because such a low density of transfer sites did not eliminate the orientation dependence for electron transfer.^{150–152} In contrast, electrostatic complexation of the polyanionic glucose oxidase with a polycationic redox polymer—such as poly(vinylpyridine) partially complexed with $[\text{Os}(\text{2,2}'\text{-bipyridine})_2\text{Cl}]^{+/2+}$ and partially *N*-methylated—led to modified electrodes with a *bulk* enzyme/relay ratio in excess of 10^3 .¹⁵³ Such electrodes produced glucose oxidation current densities of up to $30 \mu\text{A}/\text{cm}^2$ that were proportional to glucose concentration up to 30 mM.

More recently, osmium-based redox polymers of similar structure have been developed as mediators for enzyme-catalyzed reactions relevant to biofuel cells. In this context, the chief development objectives have been tuning the redox potential for both anodes

and cathodes and improving electron-transfer efficiency.

Trudeau et al. reported the earliest redox-polymer-mediated laccase electrode, in the context of an inhibition biosensor.¹⁵⁴ The electrode consisted of laccase from *T. versicolor* coimmobilized with poly(*N*-vinylimidazole), or PVI, complexed with $\text{Os}(\text{bipyridine})_2\text{Cl}_2$.¹⁵⁵ Current densities of $3.5 \mu\text{A}/\text{cm}^2$ were observed at an electrode poised at 0.42 V vs SHE in oxygen-saturated, room-temperature acetate buffer, pH 4.7. Building on this work, a polymer composed of PVI complexed with $\text{Os}(\text{dimethylbipyridine})(\text{terpyridine})$ was synthesized (Table 2, compound **2**).^{10,108} Introducing the terpyridine ligand to eliminate chloride ligands increased the redox potential of 0.77 V vs SHE at pH 5, close to the observed redox potential of fungal laccase. Electrodes composed of laccase and this redox polymer generated current densities of $1.2 \text{ mA}/\text{cm}^2$ on a glassy carbon rotating disk electrode (RDE) in well-stirred, oxygen-saturated citrate buffer, pH 5. The polymer–laccase adduct was then coated on a carbon paper support of $350\text{-}\mu\text{m}$ thickness, mounted on a rotating disk electrode (RDE). When rotated at 4000 rpm to provide substantial stirring, current densities of $7 \text{ mA}/\text{cm}^2$ were obtained. Current decay rates of 40% and 17% per day were observed, respectively, for the glassy carbon and carbon paper electrodes on rotating disk electrodes rotating at 1000 rpm.

A similar polymer, composed of osmium complexed with bis-dichlorobipyridine, chloride, and PVI in a PVI–poly(acrylamide) copolymer (Table 2, compound **3**), demonstrated a lower redox potential, 0.57 V vs SHE, at 37.5°C in a nitrogen-saturated buffer, pH 5.^{109,156} An adduct of this polymer with bilirubin oxidase, an oxygen-reducing enzyme, was immobilized on a carbon paper RDE and generated a current density exceeding $9 \text{ mA}/\text{cm}^2$ at 4000 rpm in an O_2 -saturated PBS buffer, pH 7, 37.5°C . Current decayed at a rate of 10% per day for 6 days on an RDE at 300 rpm. The performance characteristics of electrodes made with this polymer are compared to other reported results in Table 2.

This electrode is unique in that the bilirubin oxidase is active at neutral pH, whereas the laccase cited above is not, even though the redox potential of laccase is somewhat higher. Additionally, the bilirubin oxidase is much less sensitive to high concentrations of other anions such as chloride and bromide, which deactivate laccase.^{25,26} It was shown that mutations of the coordination sphere of bilirubin oxidase led to an increased redox potential of the enzyme, which increased current density and reduced current decay to 5%/day over 6 days at 300 rpm.¹⁵⁷ The latter improvement was attributed to improved electrostatic attraction between the enzyme and the redox polymer. An electrode made with high-purity bilirubin oxidase and this redox polymer has recently been shown to outperform a planar platinum electrode in terms of activation potential and current density of oxygen reduction.¹⁷⁹

A recently reported immobilization approach involved the entrapment of the cyano-metal complexes $[\text{Fe}(\text{CN})_6]^{3-/4-}$, $[\text{W}(\text{CN})_8]^{3-/4-}$, $[\text{Os}(\text{CN})_6]^{3-/4-}$, and

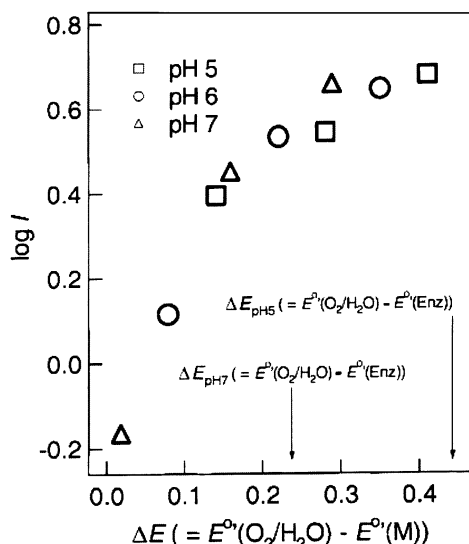


Figure 8. Dependence of the BOD-catalyzed oxygen reduction current density on the difference in formal potentials between the O_2/H_2O couple and a range of cyano-metal complexes (M) for three values of solution pH. Arrows indicate reported values of the BOD formal potential $E^0(\text{Enz})$ relative to that of O_2/H_2O . Reproduced with permission from ref 159. Copyright 2003 Elsevier Science B.V.

$[\text{Mo}(\text{CN})_8]^{3-/4-}$ within a poly(L-lysine) matrix.^{158,159} Similarly to the redox polymer backbones PVI and quaternized poly(vinylpyridine), the poly(L-lysine) is cationic, and immobilization of anionic cyano-metal complex within the polymer matrix was accomplished via electrostatic attraction. Formal redox potentials obtained in room-temperature phosphate buffer at pH 7 were from 0.24, 0.52, 0.69, and 0.78 V for the Fe, W, Os, and Mo cyano complexes, respectively. Cyclic voltammetry of a glassy carbon electrode in an oxygen-saturated solution of the W, Os, and Mo cyano complexes and bilirubin oxidase (BOD) showed a direct correlation between the observed biocatalytic oxygen reduction current and the formal potential difference between the mediator and the O_2/H_2O couple. As shown in Figure 8, this relationship was independent of solution pH. The formal potential of the $\text{Cu}^{+/2+}$ center of BOD was less than that of the Os- and Mo-centered mediators at pH 7. Catalytic oxygen reduction currents were nonetheless observed and were attributed to the overall potential drop. Such an interpretation is consistent with the discussion of Figure 3 above, as the potential difference between the mediator and the reacting species represents the driving force, or activation overpotential, for the electrochemical half-reaction.

When $[\text{W}(\text{CN})_8]^{4-/3-}$ was coimmobilized with BOD and poly(L-lysine) on carbon felt sheet of 1-mm thickness on an RDE, a current density of 17 mA/cm² was observed at 0.4 V and 4000 rpm in oxygen-saturated phosphate buffer, pH 7. The authors partially attribute the high current density to convective penetration of the oxygen-saturated solution within the porous carbon paper electrode. This assertion is justified by calculation of an effective electrode area based on the Levich equation that exceeds the projected area of the experimental electrode by 70%.¹⁶⁰ This conclusion likely applies to any

highly porous electrode that extends from the surface of an RDE into solution to a distance greater than the mass-transfer boundary layer thickness, which, for transport of O_2 from saturated solution at 1000 rpm, is about 20 μm .¹⁶¹

Osmium-based redox polymers designed for glucose anode applications have been developed using a similar approach. Based on polymers designed to mediate glucose oxidase, horseradish peroxidase, and other redox enzymes for sensor applications,^{132,162} attention was focused on reducing the redox potential of the mediator to match that of glucose oxidase (approximately -0.4 V vs SHE for the dissolved enzyme, -0.3 V vs SHE for enzyme adsorbed on carbon)¹⁶³ and improving transport properties while maintaining high activity with respect to the enzyme. Table 3 gives properties and performances of four redox polymers implemented in glucose-oxidizing biofuel cell anodes.

Compounds 4 and 5 of Table 3, implementing methylated^{160,164} and methoxylated^{165,166} bipyridine ligands to the osmium center, were borrowed directly from previous, sensor-targeted chemistries. The redox potentials of these polymers are high, exceeding 0.1 V vs SHE. A high redox potential provides a strong driving force for reoxidation of the GOx enzyme, indicated by current densities exceeding 200 $\mu\text{A}/\text{cm}^2$, yet reduces the overall cell potential.

These redox polymers were modified for reduced redox potential while maintaining activity with GOx. Replacement of the methyl groups (compound 4) with amines (compound 6) resulted in a redox potential decrease of 0.25 V, with only a 15% loss in GOx activity. More recently, further reductions in redox potential were achieved by replacing the bipyridine ligands to osmium by dimethylated bis-imidazole groups (compound 7).¹²⁶

Further, the electron-transport properties of the polymer 7 were enhanced by extending the separation between the redox center and backbone from a single Os- amino linkage to one that extends over 17 bonds. The goal was to provide mobility of the redox center independently of backbone motion, which is necessarily restricted by cross-linking. The mobility of the redox center can be characterized by an apparent diffusion coefficient, D_{app} . According to the relation proposed by Blauch and Saveant^{136,137}

$$D_{\text{app}} = \frac{1}{6} k_{\text{ex}} (\delta^2 + 3\lambda^2) C_T \quad (6)$$

where k_{ex} is a rate constant for electron self-exchange between redox centers, δ is the center-center distance during exchange, λ is the average center displacement from its equilibrium position, and C_T is the total redox center concentration. When a redox center is tethered to a polymer backbone by a short linkage, λ depends primarily on the range of mobility of the backbone itself.

From a basic standpoint, an increased linkage length, N , can increase the value of λ by partially decoupling the motion of the redox center from that of the backbone. In an ideal case, with a well-solvated linkage that does not impair backbone mobility, the value of λ^2 should vary with N . In reality, such

Table 3. Redox Polymer Anode Mediators

Compound	Structure	Redox Potential (V) ^a	Glucose Oxidation Rate, (A/cm ²) ^{a,b}	Ref.
4 Poly{N-vinylimidazole [Os(4,4'-dimethyl-2,2'-bipyridine) ₂ Cl] ⁺²⁺ -co-acrylamide}		0.32, pH 5 0.17, pH 7.2	2×10 ⁻⁴ (0.5 V, pH 5 citrate)	106,164
5 poly{N-vinylpyridine [Os(4,4'-dimethoxy-2,2'-bipyridine) ₂ Cl] ⁺²⁺ }		0.15, pH 7.4	6.5×10 ⁻⁴ (0.37 V, pH 7.4 PBS ^c)	165,166
6 poly{N-vinylimidazole [Os(4,4'-diamino-2,2'-bipyridine) ₂ Cl] ⁺²⁺ }		0.06, pH 7.4	1.7×10 ⁻⁴ (0.22 V, pH 7.4 PBS)	110
7 Poly{N-vinylpyridine [Os(N,N'-dialkylated-2,2'-biimidazole) ₃] ^{2+/3+} }		0.02, pH 7.2	1.1×10 ⁻³ (0.22 V, pH 7.2 PBS); 3.2×10 ⁻⁴ (0.22 V, pH 5 citrate)	126,156,168

^a Potentials vs SHE. ^b Glucose concentration 15 mM, 37 °C. ^c PBS = phosphate buffer solution, typically 20 mM phosphate buffer with 0.1 M NaCl.

changes to polymer structure can have a dramatic impact on backbone dynamics because of increased drag and steric effects and can also impact cross-linking efficiency and solvent interactions. However, such an approach provides an opportunity to increase the low observed values of D_{app} in redox polymers, typically in the 10⁻⁸–10⁻⁹ cm²/s range.

The long linkage in compound **7** led to an apparent diffusion coefficient, D_{app} , that was a factor of 10³ higher than the ~10⁻⁹ cm²/s observed for compound

6, as shown in Figure 9. However, the D_{app} value of the long-linkage polymer was more sensitive to the degree of cross-linking of the backbone, decreasing by 95% as the cross-linker mass fraction was increased from 0 to 25%. Over the same range, the short-linkage redox polymer experienced a 50% decrease in D_{app} . Despite the increased sensitivity to cross-linking, compound **7** still displayed a D_{app} value that was 2 orders of magnitude higher than that of compound **6** under highly cross-linked conditions. As

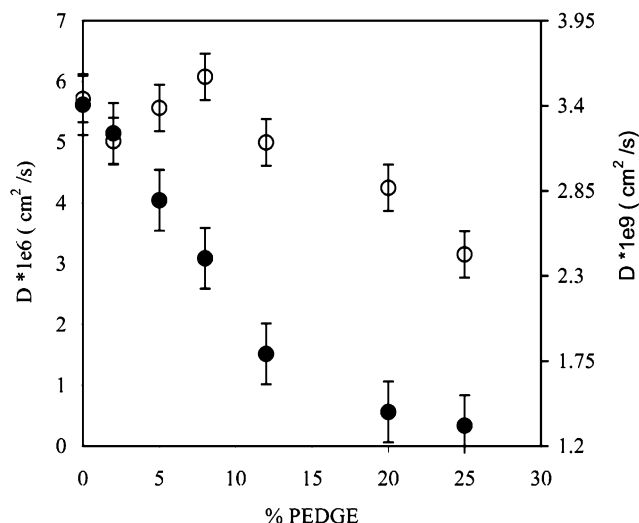


Figure 9. Dependence of D_{app} of compound **6** (○, right axis) and compound **7** (●, left axis) on the weight fraction of the cross-linker. Obtained by cyclic voltammetry and potential-step chronoamperometry on a 3-mm-diameter glassy carbon electrode under argon: 0.1 M NaCl, 20 mM phosphate buffer, pH 7, 37 °C, 20 mV/s. Reprinted with permission from ref 126. Copyright 2003 American Chemical Society.

shown in Table 3, the resulting activity with respect to GOx increased by a factor of 5 to ~ 1 mA/cm².

5. Engineering of Enzymatic Biofuel Cell Systems

The recent literature in bioelectrochemical technology, covering primarily the electrochemical aspects of enzyme immobilization and mediation, includes few reports describing engineering aspects of enzymatic biofuel cells or related devices. Current engineering efforts address issues of catalytic rate and stability by seeking improved kinetic and thermodynamic properties in modified enzymes or synthesized enzyme mimics. Equally important is the development of materials and electrode structures that fully maximize the reaction rates of known biocatalysts within a stable environment. Ultimately, the performance of biocatalysts can be assessed only by their implementation in practical devices.

5.1. Complete Enzymatic Fuel Cells

Several references discussed above^{48,82,107} describe voltaic cells coupling a biocathode or bioanode with a noble metal counter electrode that can be reasonably considered biofuel cells. However, additional levels of difficulty arise when preparing cells containing two bioelectrodes simultaneously^{84,101,121,123,167} and when coupling the two electrodes, composed of differing enzyme systems, in common conditions of pH, temperature, and electrolyte.^{106,110,125,166,168} Three key recent reports where this was achieved are discussed below.

Already mentioned was a complete cell reported by Katz et al. based on monolayer immobilization of mediator and biocatalyst at both anode and cathode (Figure 7).¹²⁵ Operating in 1 mM glucose and air-saturated buffer at pH 7 and 25 °C, the cell generated a maximum current density of 110 μ A/cm² at 0.04 V cell potential, corresponding to a maximum power of

5 μ W/cm². The observed low power is expected because of the monolayer quantity of immobilized enzymes at each electrode, the planarity of the gold substrates, and low redox potential of cytochrome oxidase. However, the significant achievement of active-site-directed binding of biocatalyst at both electrodes in common solvent is notable.

More recently, Tsujimura et al. reported a H₂/O₂ fuel cell operating at pH 7, based on methyl viologen-mediated bacterial cells (*Desulfovibrio vulgaris*) at the anode and ABTS-mediated bilirubin oxidase at the cathode.⁸³ Although beyond the scope of this review in a strict sense, this report is notable as it is the first report of a biocatalyst-based fuel cell operating at pH 7. At both electrodes, carbon felt sheets were immersed in solutions containing pH 7 phosphate buffer and freely diffusing catalysts and mediators, and an anion-exchange membrane separated the two compartments. An open-circuit potential of 1.17 V was reported, which is generally higher than similar observations made of noble-metal-based proton exchange membrane fuel cells operating at much higher temperatures. A limiting current due to transport at the cathode was observed at 0.45 mA/cm², a value that was doubled by doubling the concentration of cathode biocatalyst and mediator. In addition to low current density, the short lifetime (~ 2 h) of this device was noted as an issue.

The authors have also recently reported a compartmentless glucose–oxygen cell relying on pyrroloquinoline quinone (PQQ) mediated soluble glucose dehydrogenase (sGDH) for anodic oxidation of glucose.¹⁶⁹ Although unstable compared to glucose oxidase, sGDH is insensitive to the presence of oxygen and delivers higher activity. A maximum power density of 0.058 mW/cm² was achieved at neutral pH.

Heller and co-workers have published a series of papers based on a miniature membraneless biofuel cell operating on glucose and oxygen.^{106,110,156,166,168} All of the devices consisted of enzymatic electrodes immobilized within and mediated by osmium-based redox hydrogels deposited on 7- μ m-diameter carbon fibers. The fixture for these devices is shown in close-up in Figure 10. The original device consisted of glucose oxidase mediated by a poly(vinylimidazole)–poly(acrylamide) copolymer (PVI–PAM) complexed with Os(dimethylbipyridine)₂Cl at the anode and fungal laccase mediated by PVI complexed with Os(dimethylbipyridine)(terpyridine). These electrodes have been discussed individually in previous sections. The complete cell operated in pH 5 citrate buffer saturated with air and containing 15 mM glucose. At a cell potential of 0.4 V, current densities of 160 and 340 μ A/cm² were obtained at 23 and 37 °C, respectively, limited primarily by anode performance. Current density decreased by $\sim 8\%$ per day over 3 days.

The fuel cell described above exhibited three key flaws. First, the anode redox mediator operates at a redox potential well above that of glucose oxidase, raising the operating potential of the anode and lowering the achievable cell potential. Second, the cell operates at pH 5, near-optimal for the laccase electrode but suboptimal for the current-limiting glucose

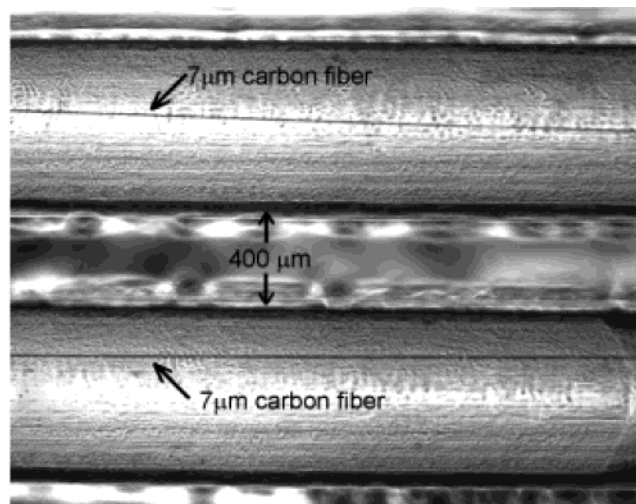


Figure 10. Miniature biofuel cell segment consisting of mediated enzymes immobilized on 7- μm -diameter fibers. Reprinted with permission from ref 106. Copyright 2001 American Chemical Society.

anode. Third, at typical thicknesses of deposited hydrogel films, electron transport via the redox mediator is the rate-limiting step. Later authors have reported improvements on this design by incorporating alternative enzymes and novel redox mediators that overcome these limitations.

For example, the small scale of the device was intended as a demonstration of architecture suitable for implanted applications. Mano et al. demonstrated a miniature fuel cell with bilirubin oxidase at the cathode catalyst that is more active at pH 7 and tolerates higher halide concentrations than does laccase.¹⁵⁶ Additionally, the long-side-chain poly(vinylpyridine)-Os(dialkyl-bis-imidazole)₃ redox polymer discussed above was employed to both lower the anode potential and, via the long side chains, enhance electron transport from the biocatalyst. The cell achieved a current density of 830 $\mu\text{A}/\text{cm}^2$ at 0.52 V and 37 °C in an air-saturated, pH 7 buffer with 15 mM glucose. Thus, power density was more than doubled over the previous design. The stability of the cell was somewhat similar to that of the original cell at 6% current density loss per day over 6 days.

5.2. Electrode Structures

Electrodes for biological fuel cells generating 1 W or greater are expected to be composite structures comprising biocatalysts immobilized on or near the surface of porous conducting solid materials, probably carbon or possibly gold. Therefore, just as in conventional porous fuel cell electrodes, issues of transport to, from, and within these structures are expected to be significant. The challenges go beyond the domain of conventional fuel cells in that enzyme catalysts must generally be maintained within an aqueous phase. Issues of electron transfer within the aqueous phase automatically arise. Additionally, the size, activity, and packing density of biocatalytic active centers can require electrode thicknesses on the order of 100 μm (discussed below), leading to performance limitations associated with transport of reactants and products. The typical diffusion driving force, the

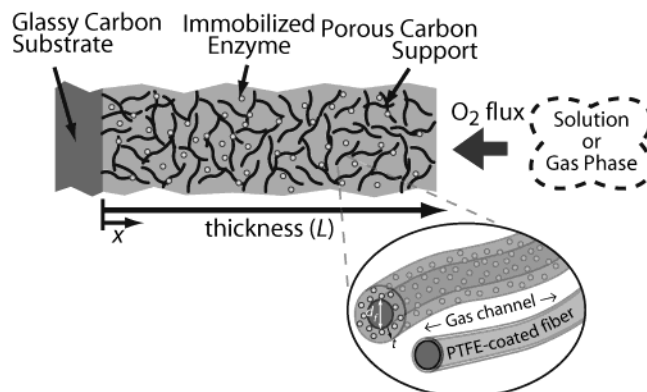


Figure 11. One-dimensional model diagram for supported laccase cathode.¹⁷⁰

diffusion coefficient multiplied by the bulk concentration, is $10^{-11} \text{ mol}\cdot\text{cm}^{-1}\cdot\text{s}^{-1}$ for both glucose and oxygen in water. These values lead to limiting current densities of order 100 $\mu\text{A}/\text{cm}^2$ through such systems, making the engineering of enzyme-immobilizing electrodes for reactant transport crucial to realizing high power density.

A model of such structures has been proposed that captures transport phenomena of both substrates and redox cosubstrate species within a composite biocatalytic electrode.¹⁷⁰ The model is based on macrohomogeneous and thin-film theories for porous electrodes and accounts for Michaelis–Menton enzyme kinetics and one-dimensional diffusion of multiple species through a porous structure defined as a mesh of tubular fibers.^{85,171,172} In addition to the solid and aqueous phases, the model also allows for the presence of a gas phase (of uniformly contiguous morphology), as shown in Figure 11, allowing the treatment of high-rate gas-phase reactant transport into the electrode.

When applied to a laccase-based oxygen-reducing electrode, the model predicted a maximum current density of 9.2 mA/cm^2 at 0.6 V vs SHE for a 300- μm -thick electrode relying on transport of oxygen by diffusion in the liquid phase. However, when either convective transport in the liquid phase or gas-phase diffusive transport was introduced in the electrode, current densities exceeding 50 mA/cm^2 were predicted for air-saturated systems. As is evident in Figure 12, such electrodes will require thicknesses exceeding 100 μm and porosities exceeding 90%, with 25% porosity reserved for the gas phase in a gas diffusion electrode. This work points to enhanced reactant transport as an essential component to high-rate biocatalytic electrodes.

The design of biocatalytic electrodes for activity toward gaseous substrates, such as dioxygen or hydrogen, requires special consideration. An optimal electrode must balance transport in three different phases, namely, the gaseous phase (the source of substrate), the aqueous phase (where the product water is released and ionic transport takes place), and the solid phase (where electronic transport occurs). Whereas the selectivity of biocatalysts facilitates membraneless cells for implementation in biological systems that provide an ambient electrolyte,¹³ gas-diffusion biofuel cells require an electro-

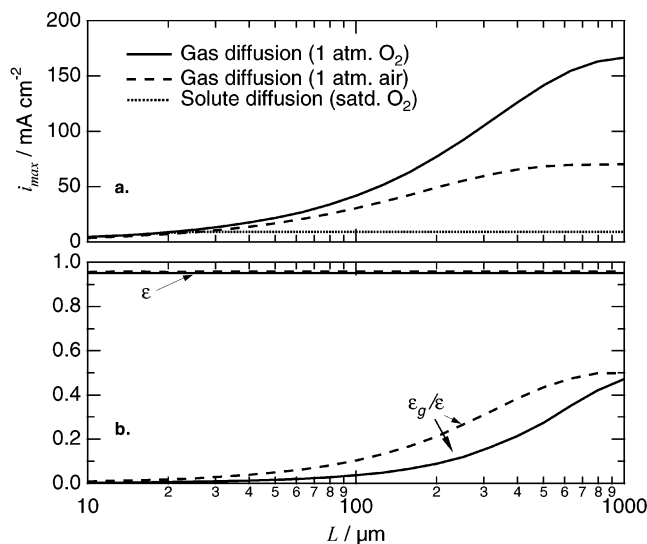


Figure 12. Effect of electrode thickness on performance of an oxygen-reducing laccase electrode: (a) optimum current density, i_{\max} , at 0.5 V vs SHE and (b) optimum support porosity (ϵ) and relative gas-phase porosity (ϵ_g/ϵ) for carbon fiber supported electrodes optimized for (—) gas diffusion in 1 atm O_2 , (---) gas diffusion in 1 atm air, (···) solute diffusion in O_2 -saturated electrolyte. Dissolved oxygen diffusion favors thin electrodes. Gas diffusion favors thick electrodes, particularly in pure O_2 .¹⁷⁰

lytic phase to accomplish ion transfer between electrodes. The electrolyte can be present either as a liquid or more frequently as a liquid-permeable polymer membrane. A liquid phase is also needed to hydrate the biocatalyst, and hydration levels of hydrophilic polymers such as proteins and hydrogels that contact vapor-phase water are significantly lower than when in liquid contact, owing to the well-known Schroeder effect.¹⁷³ Finally, as described above, a hydrophobic phase must be maintained to facilitate gas transport through the electrode. Engineering all of these features into a stable, high-rate gas-phase biocatalytic electrode remains a tremendous challenge.

6. Future Outlook

As Heller and others have stated, the development of successful power sources has always been driven by demand arising from specific applications.¹³ The technological paths to successful biofuel cells will therefore be determined by application specifics: Implanted biofuel cells must exhibit biocompatibility, and cathodes for ex vivo electronics must take advantage of gas-phase oxygen. That being said, a general truth remains: The advantages of biofuel cell technology will compel adoption in any application only if its disadvantages relative to conventional technology are minimal. It is clear that the advantages of biocatalysts are reactant selectivity, activity in physiological conditions, and manufacturability. The weaknesses are equally clear: modest absolute activity and low stability. These two issues are of significance, to a greater or lesser extent, in every conceivable application of this technology.

In our view, there exist two complimentary and overlapping paths toward addressing these issues:

engineering of the protein molecule itself and engineering of the environment in which the molecule is expected to be active. These paths overlap primarily in that they require significant fundamental understanding of the enzyme molecule for progress to be made. Biomimetic techniques are under rapid development as a means to probe mechanistic aspects of biocatalysis.^{174–177} However, the biomimetic approach has not yet produced practical biocatalysts, mainly because, so far, synthesized analogues are more expensive, less active, and more unstable than the natural enzyme. Through such approaches, we have progressed toward understanding transition state stabilization and transport processes at enzyme active sites. However, we generally lack an understanding of how the environment formed by inactive groups impacts the mechanism and stability of activation.

Similarly, efforts to increase enzyme stability by encapsulation in hydrophilic sol–gel matrixes yield the desired stability, generally at the expense of lower absolute activity.^{5,6} The charged surface and small pores of the gel are thought to inhibit denaturation while partially reducing the dynamic motion of entrapped biomolecules and reducing transport and access of substrates to active sites. Engineering of enzyme molecules and immobilization environments will therefore benefit greatly from increased understanding of protein structure–function relationships. Clear understanding of the thermodynamics and dynamics of enzyme molecules such as glucose oxidase, bilirubin oxidase, laccase, and NAD-dependent redox enzymes will lead to new techniques for biomimetics, immobilization, and stabilization of activity. Fortunately, such research is also driven by myriad other potential applications.

As mentioned above, one of the primary challenges at hand is increased biocatalytic power density. Currently available enzymes provide sufficient intrinsic activity. An enzyme of 100-nm² cross section with an activity of 500 electrons per second generates a current density of 80 $\mu\text{A}/\text{cm}^2$ at monolayer loadings, comparable to the results of Katz et al.¹²⁵ For practical biofuel cells operating at current densities above 10 mA/cm^2 , loadings of such an enzyme equivalent to hundreds or thousands of monolayers will be required. Assuming 100 kDa molecular weight, a 1 mg/cm^2 loading—the equivalent of 6000 monolayers or 60- μm thickness—has a theoretical maximum current density of 500 mA/cm^2 . Thus, a key question is how to achieve significant biocatalyst utilization at such loadings, which leads to issues of transport of electrons and substrates within the electrode structure.

A key challenge is electron mediation. Currently, most mediated systems demonstrate high initial activity but introduce an additional source of long-term instability. There is a strong need for improved mediators that can be immobilized for retention, have high chemical and mechanical stability, and maintain high biocatalytic activity at low catalyst–mediator overpotentials. Redox hydrogels have shown great promise in the context of electron transport and redox potential tunability, but still yield electron-transfer

rates lower than the diffusional rates of substrates and have unproven long-term stability.

Conversely, controlled immobilization of enzymes at surfaces to enable high-rate direct electron transfer would eliminate the need for the mediator component and possibly lead to enhanced stability. Novel surface chemistries are required that allow protein immobilization with controlled orientation, such that a majority of active centers are within electron-tunneling distance of the surface. Additionally, spreading of enzymes on the surfaces must be minimized to prevent deactivation due to irreversible changes in secondary structure. Finally, structures of controlled nanoporosity must be developed to achieve such surface immobilization at high volumetric enzyme loadings.

Along with electronic transport improvements must come attention to substrate transport in such porous structures. As discussed above, introduction of gas-phase diffusion or liquid-phase convection of reactants is a feasible approach to enabling high-current-density operation in electrodes of thicknesses exceeding 100 μm . Such a solution is application specific, in the sense that neither gas-phase reactants nor convection can be introduced in a subclass of applications, such as devices implanted in human, animal, or plant tissue. In the context of physiologically implanted devices, the choice becomes either milliwatt to watt scale devices implanted in a blood vessel, where velocities of up to 10 cm/s can be present, or microwatt-scale devices implanted in tissue. Ex vivo applications are more flexible, partially because gas-phase oxygen from ambient air will almost always be utilized on the cathode side, but also because pumps can be used to provide convective flow of any substrate. However, power requirements for pump operation must be minimized to prevent substantial lowering of net power output.¹⁷⁰

Perhaps most importantly, the issue of system lifetime must be addressed. The electrodes and systems described above have demonstrated lifetimes ranging from days to months, depending greatly on the operating conditions and components involved. For a narrow range of applications, specifically week-long hospital stays or military missions, such lifetimes might be acceptable. However, for application in consumer devices or in surgically intensive implanted applications, system lifetime must be extended to the order of years. This is no simple prescription, owing not only to the limited lifetime of redox enzymes themselves but also to the limited chemical and mechanical stability of other electrode components, primarily electron mediators.^{9,10,101,107}

Stabilization of activated oxidoreductases on time scales of months to years has historically been challenging, and the lack of success in this regard has limited the industrial implementation of redox enzymes to applications that do not require long lifetimes. However, as mentioned in the Introduction, some possibility of improved stability has arisen from immobilization of enzymes in hydrophilic cages formed by silica sol-gels and aerogels, primarily for sensor applications.^{178–181} The tradeoff of this approach is expected to be a lowering of current density because

of mass-transfer limitations. Such a tradeoff can be avoided to a certain extent by clever design of high-porosity aerogels with pore sizes ranging from nano-scale to micron scale, but ultimately a balance must be struck between activity and stability.

Having designed the respective cathode and anode with the required power density for a particular application, the final step involves the integration of a biofuel cell with electrical devices. Major integration issues include electrical integration (packaging and voltage matching), fuel delivery, waste removal, and safety. Multicell stacks are desirable to produce the conventional 1–5 V output voltage. Depending on the cell design, whether disposable or rechargeable, a nonambient fuel supply must be either integrated within the cell body or provided as replaceable cartridges. In disposable biofuel cells, environmental constraints and material recycling must be considered. Reaction products must be removed continuously, without any inhibitory or toxic effect on the biocatalyst. Overall safety features of the system, such as leakage or gas buildup, must be thoroughly addressed for both operational and storage conditions.

For biocatalysis to move forward as a viable means of catalyzing fuel cell reactions, the concerted efforts of biologists, chemists, chemical engineers, and materials scientists will be required. Niche applications in microwatt-scale implantable power might be accessible now, and the range of applications is expected to grow as the technology matures and energy demands expand. In the future, improved understanding of biocatalytic function, electron transfer, and substrate interactions will further the effort to put biological catalysts to work for electrical energy production.

7. Acknowledgment

S.C.B. and J.G. gratefully acknowledge the National Science Foundation for support under Award CTS-0239013.

8. References

- (1) Yahiro, A. T.; Lee, S. M.; Kimble, D. O. *Biochim. Biophys. Acta* **1964**, *88*, 375.
- (2) Drake, R. F.; Kusserow, B. K.; Messinger, S.; Matsuda, S. *Trans. Am. Soc. Artif. Intern. Organs* **1970**, *16*, 199.
- (3) Davis, G.; Hill, H. A. O.; Aston, W. J.; Higgins, I. J.; Turner, A. P. F. *Enzyme Microb. Technol.* **1983**, *5*, 383.
- (4) Grove, W. R. *Philos. Mag. J. Sci.* **1842**, *21*, 417.
- (5) Gill, I. *Chem. Mater.* **2001**, *13*, 3404.
- (6) Jin, W.; Brennan, J. D. *Anal. Chim. Acta* **2002**, *461*, 1.
- (7) Gershenson, A.; Arnold, F. H. *Genet. Eng.* **2000**, *22*, 55.
- (8) Binyamin, G.; Heller, A. *J. Electrochem. Soc.* **1999**, *146*, 2965.
- (9) Binyamin, G.; Cole, J.; Heller, A. *J. Electrochem. Soc.* **2000**, *147*, 2780.
- (10) Calabrese Barton, S.; Kim, H.-H.; Binyamin, G.; Zhang, Y.; Heller, A. *J. Phys. Chem. B* **2001**, *105*, 11917.
- (11) Palmore, G. T. R.; Whitesides, G. M. *ACS Symp. Ser.* **1994**, *566*, 271.
- (12) Katz, E.; Shipway, A. N.; Willner, I. In *Handbook of Fuel Cells—Fundamentals, Technology and Applications*; Vielstich, W., Gasteiger, H. A., Lamm, A., Eds.; John Wiley and Sons, Ltd.: London, 2003; Vol. 1, p 355.
- (13) Heller, A. *Phys. Chem. Chem. Phys.* **2004**, *6*, 209.
- (14) Reimers, C. E.; Tender, L. M.; Fertig, S.; Wang, W. *Environ. Sci. Technol.* **2001**, *35*, 192.
- (15) Brodd, R. J. *Electrochem. Soc. Interface* **1999**, *8*, 20.
- (16) Holmes, C. F. *Electrochem. Soc. Interface* **2003**, *12*, 26.

- (17) Linden, D.; Reddy, T. B. *Handbook of Batteries*, 3rd ed.; McGraw-Hill: New York, 2002.
- (18) Bhadra, N.; Kilgore, K. L.; Peckham, P. H. *Med. Eng. Phys.* **2001**, *23*, 19.
- (19) Popovic, M. R.; Curt, A.; Keller, T.; Dietz, V. *Spinal Cord* **2001**, *39*, 403.
- (20) Craelius, W. *Science* **2002**, *295*, 1018.
- (21) Peckham, P. H.; Kilgore, K. L.; Keith, M. W.; Bryden, A. M.; Bhadra, N.; Montague, F. W. *J. Hand Surg.* **2002**, *27*, 265.
- (22) Maynard, E. M. *Annu. Rev. Biomed. Eng.* **2001**, *3*, 145.
- (23) Rauschecker, J. P.; Shannon, R. V. *Science* **2002**, *295*, 1025.
- (24) Zrenner, E. *Science* **2002**, *295*, 1022.
- (25) Tinoco, R.; Pickard, M. A.; Vazquez-Duhalt, R. *Lett. Appl. Microbiol.* **2001**, *32*, 331.
- (26) Calabrese Barton, S.; Pickard, M.; Vazquez-Duhalt, R.; Heller, A. *Biosens. Bioelectron.* **2002**, *17*, 1071.
- (27) Binyamin, G.; Chen, T.; Heller, A. *J. Electroanal. Chem.* **2001**, *500*, 604.
- (28) Quinn, C. P.; Pathak, C. P.; Heller, A.; Hubbell, J. A. *Biomaterials* **1995**, *16*, 389.
- (29) Quinn, C. A. P.; Connor, R. E.; Heller, A. *Biomaterials* **1998**, *18*, 11665.
- (30) For current density, $i = nFDCd^{-1}Sh_{avg}^{-1}$, with $n = 2$, $F =$ Faraday's constant, glucose diffusion coefficient $D = 6.7 \times 10^{-7}$ cm²/s, glucose bulk concentration $C = 5$ mM, and blood vessel diameter $d = 0.4$ cm. The average Sherwood number is given by $Sh_{avg} = 1.6(d^2vL^{-1}D^{-1})^{1/3}$, with average flow velocity v (cm/s) and electrode length $L = 1$ cm assumed.
- (31) For spherical diffusion, $i = 2nFDCd$, with parameters as defined in ref 30 and electrode diameter $d = 10$ μ m.
- (32) Agency Response Letter, GRAS Notice No. GRN 000122; U. S. Food and Drug Administration: Washington, DC, 2003; <http://www.cfsan.fda.gov/~rdb/opa-g122.html> (accessed July 2004).
- (33) Agency Response Letter, GRAS Notice No. GRN 000106; U. S. Food and Drug Administration: Washington, DC, 2002; <http://www.cfsan.fda.gov/~rdb/opa-g106.html> (accessed July 2004).
- (34) Bessant, R.; Steuer, A.; Rigby, S.; Gumpel, M. *Rheumatology* **2003**, *42*, 1036.
- (35) Ayril, X. *Haemophilia* **2001**, *7*, 20.
- (36) Shott, I. *Chem. Eng. News* **2003**, *81*, 146.
- (37) Koelling, M. R.; Heiligmann, R. B. *North American Maple Syrup Producers Manual*; Ohio State University Extension: Columbus, OH, 1996.
- (38) Rodriguez-Saona, L. E.; Fry, F. S.; McLaughlin, M. A.; Calvey, E. M. *Carbohydr. Res.* **2001**, *336*, 63.
- (39) Prodollet, J.; Hischenhuber, C. *Z Lebensm. Unters. Forsch. A: Food Res. Technol.* **1998**, *207*, 1.
- (40) *AIJN Code of Practice for Evaluation of Fruit and Vegetable Juices*; Association of the Industry of Juices and Nectars from Fruits and Vegetables of the European Union: Brussels, Belgium, 1996.
- (41) Markovarga, G. *J. Chromatogr.* **1987**, *408*, 157.
- (42) Liden, H.; Volc, J.; Marko-Varga, G.; Gorton, L. *Electroanalysis* **1998**, *10*, 223.
- (43) Ruzgas, T.; Csoregi, E.; Emneus, J.; Gorton, L.; MarkoVarga, G. *Anal. Chim. Acta* **1996**, *330*, 123.
- (44) Tessema, M.; Csoregi, E.; Ruzgas, T.; Kenausis, G.; Solomon, T.; Gorton, L. *Anal. Chem.* **1997**, *69*, 4039.
- (45) Ikeda, T.; Shibata, T.; Senda, M. *J. Electroanal. Chem.* **1989**, *261*, 351.
- (46) Nilsson, G. S.; Andersson, M.; Ruzgas, T.; Gorton, L. *Anal. Biochem.* **1998**, *265*, 151.
- (47) Volponi, J. V.; Simmons, B. A.; Walker, A.; Ingersoll, D. *The Electrochemical Society Extended Abstracts: The Electrochemical Society: Pennington, NJ, 2004*; p 673.
- (48) Akers, N. L.; Moore, C. M.; Minter, S. D. *Electrochim. Acta* **2004**, in press.
- (49) Akers, N. L.; Minter, S. D. In *Fuel Cell Science, Engineering and Technology*; Shah, R. K., Kandlikar, S. G., Eds.; American Society of Mechanical Engineers: New York, 2004; p 497.
- (50) Ren, X. M.; Zelenay, P.; Thomas, S.; Davey, J.; Gottesfeld, S. *J. Power Sources* **2000**, *86*, 111.
- (51) Bittins-Cattaneo, B.; Wasmus, S.; Lopez-Mishima, B.; Vielstich, W. *J. Appl. Electrochem.* **1993**, *23*, 625.
- (52) Sun, G. Q.; Wang, J. T.; Savinell, R. F. *J. Appl. Electrochem.* **1998**, *28*, 1087.
- (53) Gupta, S.; Tryk, D.; Zecevic, S. K.; Aldred, W.; Guo, D.; Savinell, R. F. *J. Appl. Electrochem.* **1998**, *28*, 673.
- (54) Vante, N. A.; Jaegermann, W.; Tributsch, H.; Hoelne, W.; Yvon, K. *J. Am. Chem. Soc.* **1987**, *109*, 3251.
- (55) Reeve, R. W.; Christensen, P. A.; Hamnett, A.; Haydock, S. A.; Roy, S. C. *J. Electrochem. Soc.* **1998**, *145*, 3463.
- (56) Borgwardt, R. H. *Transp. Res. D* **2001**, *6*, 199.
- (57) Thurston, C. F.; Bennetto, H. P.; Delaney, G. M.; Mason, J. R.; Roller, S. D.; Stirling, J. L. *J. Gen. Microbiol.* **1985**, *131*, 1393.
- (58) Suzuki, S.; Karube, I.; Matsunaga, T.; Kuriyama, S.; Suzuki, N.; Shirogami, T.; Takamura, T. *Biochimie* **1980**, *62*, 353.
- (59) Karube, I.; Matsunaga, T.; Mitsuda, S.; Suzuki, S. *Biotechnol. Bioeng.* **1977**, *19*, 1535.
- (60) Karube, I.; Suzuki, S.; Matsunaga, T.; Kuriyama, S. *Ann. N. Y. Acad. Sci.* **1981**, 91.
- (61) Tanisho, S.; Kamiya, N.; Wakao, N. *Bioelectrochem. Bioenerg.* **1989**, *21*, 25.
- (62) Ardeleanu, I.; Margineanu, D.-G.; Vais, H. *Bioelectrochem. Bioenerg.* **1983**, *11*, 273.
- (63) Park, D. H.; Zeikus, J. G. *Appl. Environ. Microbiol.* **2000**, *66*, 1292.
- (64) Kim, N.; Choi, Y.; Jung, S.; Kim, S. *Biotechnol. Bioeng.* **2000**, *70*, 109.
- (65) Park, D. H.; Kim, S. K.; Shin, I. H.; Jeong, Y. J. *Biotechnol. Lett.* **2000**, *22*, 1301.
- (66) Tsujimura, S.; Wadano, A.; Kano, K.; Ikeda, T. *Enzyme Microb. Technol.* **2001**, *29*, 225.
- (67) Zhu, B.; Bai, X. Y.; Chen, G. X.; Yi, W. M.; Bursell, M. *Int. J. Energy Res.* **2002**, *26*, 57.
- (68) Wilkinson, S. *Auton. Robots* **2000**, *9*, 99.
- (69) Chaudhuri, S. K.; Lovley, D. R. *Nat. Biotechnol.* **2003**, *21*, 1229.
- (70) Armstrong, F. A.; Hill, H. A. O.; Walton, N. J. *Q. Rev. Biophys.* **1985**, *18*, 261.
- (71) Willner, I.; Katz, E. *Angew. Chem., Int. Ed.* **2000**, *39*, 1181.
- (72) Pardo-Yissar, V.; Katz, E.; Willner, I.; Kotlyar, A. B.; Sanders, C.; Lill, H. *Faraday Discuss.* **2000**, 356.
- (73) Willmer, I. *Acta Polym.* **1998**, *49*, 652.
- (74) Kano, K.; Ikeda, T. *Anal. Sci.* **2000**, *16*, 1013.
- (75) Ikeda, T.; Kano, K. *J. Biosci. Bioeng.* **2001**, *92*, 9.
- (76) Willner, I.; Willner, B. *Trends Biotechnol.* **2001**, *19*, 222.
- (77) Habermuller, K.; Mosbach, M.; Schuhmann, W. *Fresenius J. Anal. Chem.* **2000**, *366*, 560.
- (78) Palmisano, F.; Zamboni, P. G.; Centonze, D. *Fresenius J. Anal. Chem.* **2000**, *366*, 586.
- (79) Ghindilis, A. L.; Atanasov, P.; Wilkins, E. *Electroanalysis* **1997**, *9*, 661.
- (80) Bartlett, P. N.; Tebbutt, P.; Whitaker, R. G. *Prog. React. Kinet.* **1991**, *16*, 55.
- (81) Tarasevich, M. R. In *Comprehensive Treatise of Electrochemistry*; Srinivasan, S., Chizmadzhev, Y. A., Bockris, J. O. M., Conway, B. E., Yeager, E., Eds.; Plenum Press: New York, 1985; Vol. 10, p 231.
- (82) Palmore, G. T. R.; Bertschy, H.; Bergens, S. H.; Whitesides, G. M. *J. Electroanal. Chem.* **1998**, *443*, 155.
- (83) Tsujimura, S.; Fujita, M.; Tatsumi, H.; Kano, K.; Ikeda, T. *Phys. Chem. Chem. Phys.* **2001**, *3*, 1331.
- (84) Pizzariello, A.; Stred'ansky, M.; Miertus, S. *Bioelectrochemistry* **2002**, *56*, 99.
- (85) Bartlett, P. N.; Pratt, K. F. E. *J. Electroanal. Chem.* **1995**, *397*, 61.
- (86) Hill, H. A. O. *Pure Appl. Chem.* **1987**, *59*, 743.
- (87) Nakamura, K.; Aizawa, M.; Miyawaki, O. *Electro-enzymology, Coenzyme Regeneration*; Springer-Verlag: Berlin, 1988.
- (88) Guo, L. H.; Hill, H. A. O. *Adv. Inorg. Chem.* **1991**, *36*, 341.
- (89) Lotzbeyer, T.; Schuhmann, W.; Schmidt, H. L. *Sens. Actuators B: Chem.* **1996**, *33*, 50.
- (90) Varfolomeev, S. D.; Kurochkin, I. N.; Yaropolov, A. I. *Biosens. Bioelectron.* **1996**, *11*, 863.
- (91) Gorton, L.; Lindgren, A.; Larsson, T.; Munteanu, F. D.; Ruzgas, T.; Gazaryan, I. *Anal. Chim. Acta* **1999**, *400*, 91.
- (92) Solomon, E. I.; Sundaram, U. M.; Machonkin, T. E. *Chem. Rev.* **1996**, *96*, 2563.
- (93) Gupta, G.; Rajendran, V.; Atanassov, P. *Electroanalysis* **2004**, *16*, 1182.
- (94) Tantillo, D.; Chen, J.; Houk, K. *Curr. Opin. Chem. Biol.* **1998**, *2*, 743.
- (95) Sykes, A. G. *Adv. Inorg. Chem.* **1991**, *36*, 377.
- (96) Cole, J. L.; Avigliano, L.; Morpurgo, L.; Solomon, E. I. *J. Am. Chem. Soc.* **1991**, *113*, 9080.
- (97) Yamanaka, S.; Okawa, H.; Motoda, K.; Yonemura, M.; Fenton, D. E.; Ebadi, M.; Lever, A. B. P. *Inorg. Chem.* **1999**, *38*, 1825.
- (98) Palmer, A. E.; Randall, D. W.; Xu, F.; Solomon, E. I. *J. Am. Chem. Soc.* **1999**, *121*, 7138.
- (99) Palmer, A. E.; Lee, S. K.; Solomon, E. I. *J. Am. Chem. Soc.* **2001**, *123*, 6591.
- (100) Mano, N.; Kim, H.-H.; Heller, A. *J. Phys. Chem. B* **2002**, *106*, 8842.
- (101) Tsujimura, S.; Tatsumi, B.; Ogawa, J.; Shimizu, S.; Kano, K.; Ikeda, T. *J. Electroanal. Chem.* **2001**, *496*, 69.
- (102) Machonkin, T. E.; Solomon, E. I. *J. Am. Chem. Soc.* **2000**, *122*, 12547.
- (103) Calabrese, L. In *Electronics and Biotechnology Advanced (ELBA) Forum Series*; Nicolini, C., Ed.; Plenum Press: New York, 1998; Vol. 3, p 161.
- (104) Musci, G.; Bellonchi, G. C.; Calabrese, L. *Eur. J. Biochem.* **1999**, *265*, 589.
- (105) Farver, O.; Bendahl, L.; Skov, L. K.; Pecht, I. *J. Biol. Chem.* **1999**, *274*, 26135.
- (106) Chen, T.; Calabrese Barton, S.; Binyamin, G.; Gao, Z.; Zhang, Y.; Kim, H.-H.; Heller, A. *J. Am. Chem. Soc.* **2001**, *123*, 8630.
- (107) Palmore, G. T. R.; Kim, H.-H. *J. Electroanal. Chem.* **1999**, *464*, 110.

- (108) Calabrese Barton, S.; Kim, H.-H.; Binyamin, G.; Zhang, Y.; Heller, A. *J. Am. Chem. Soc.* **2001**, *123*, 5802.
- (109) Mano, N.; Kim, H. H.; Zhang, Y. C.; Heller, A. *J. Am. Chem. Soc.* **2002**, *124*, 6480.
- (110) Kim, H. H.; Mano, N.; Zhang, X. C.; Heller, A. *J. Electrochem. Soc.* **2003**, *150*, A209.
- (111) Moss, G. P. *Enzyme Nomenclature*, Nomenclature Committee of the International Union of Biochemistry and Molecular Biology (NC-IUBMB): London, 2003; <http://www.chem.qmul.ac.uk/iubmb/enzyme/> (accessed Jul 2004).
- (112) *Enzyme Nomenclature 1992*; Webb, E. C., Ed.; Academic Press: Orlando, FL, 1992.
- (113) Blaedel, W. J.; Jenkins, R. A. *Anal. Chem.* **1975**, *47*, 1337.
- (114) Fasman, G. D. *Practical Handbook of Biochemistry and Molecular Biology*; CRC Press: Boca Raton, FL, 1989.
- (115) Chenault, H. K.; Whitesides, G. M. *Appl. Biochem. Biotechnol.* **1987**, *14*, 147.
- (116) Gorton, L.; Dominguez, E. In *Encyclopedia of Electrochemistry*; Bard, A. J., Stratmann, M., Wilson, G. S., Eds.; Wiley: New York, 2002; Vol. 9, p 67.
- (117) Simon, E.; Bartlett, P. N. *Surfactant Sci. Ser.* **2003**, *111*, 499.
- (118) Scott, S. L.; Chen, W. J.; Bakac, A.; Espenson, J. H. *J. Phys. Chem.* **1993**, *97*, 6710.
- (119) Karyakin, A. A.; Karyakina, E. E.; Schmidt, H. L. *Electroanalysis* **1999**, *11*, 149.
- (120) Karyakin, A. A.; Karyakina, E. E.; Schuhmann, W.; Schmidt, H. L. *Electroanalysis* **1999**, *11*, 553.
- (121) Willner, I.; Katz, E.; Patolsky, F.; Buckmann, A. F. *J. Chem. Soc., Perkin Trans. 2* **1998**, 1817.
- (122) Willner, I.; Heleg-Shabtai, V.; Blonder, R.; Katz, E.; Tao, G.; Bueckmann, A. F.; Heller, A. *J. Am. Chem. Soc.* **1996**, *118*, 10321.
- (123) Willner, I.; Arad, G.; Katz, E. *Bioelectrochem. Bioenerg.* **1998**, *44*, 209.
- (124) Katz, E.; Riklin, A.; Heleg-Shabtai, V.; Willner, I.; Buckmann, A. F. *Anal. Chim. Acta* **1999**, *385*, 45.
- (125) Katz, E.; Willner, I.; Kotlyar, A. B. *J. Electroanal. Chem.* **1999**, *479*, 64.
- (126) Mao, F.; Mano, N.; Heller, A. *J. Am. Chem. Soc.* **2003**, *125*, 4951.
- (127) Gao, Z.; Binyamin, G.; Kim, H.-H.; Calabrese Barton, S.; Zhang, Y.; Heller, A. *Angew. Chem., Int. Ed. Engl.* **2002**, *41*, 810.
- (128) Riklin, A.; Katz, E.; Willner, I.; Stocker, A.; Buckmann, A. F. *Nature* **1995**, *376*, 672.
- (129) Katz, E.; Heleg-Shabtai, V.; Willner, I.; Rau, H. K.; Haehnel, W. *Angew. Chem., Int. Ed.* **1998**, *37*, 3253.
- (130) Forzani, E. S.; Otero, M.; Perez, M. A.; Tejelo, M. L.; Calvo, E. *J. Langmuir* **2002**, *18*, 4020.
- (131) Pal, P.; Nandi, D.; Misra, T. N. *Thin Solid Films* **1994**, *239*, 138.
- (132) Rajagopalan, R.; Heller, A. In *Molecular Electronics*; Aviram, A., Ratner, M., Eds.; New York Academy of Sciences: New York, 1997; p 241.
- (133) Gregg, B. A.; Heller, A. *J. Phys. Chem.* **1991**, *95*, 5970.
- (134) Daigle, F.; Trudeau, F.; Robinson, G.; Smyth, M. R.; Leech, D. *Biosens. Bioelectron.* **1998**, *13*, 417.
- (135) Danilowicz, C.; Corton, E.; Battaglini, F. *J. Electroanal. Chem.* **1998**, *445*, 89.
- (136) Blauch, D. N.; Saveant, J. M. *J. Am. Chem. Soc.* **1992**, *114*, 3323.
- (137) Blauch, D. N.; Saveant, J. M. *J. Phys. Chem.* **1993**, *97*, 6444.
- (138) Majda, M. In *Molecular Design of Electrode Surfaces*; Murray, R. W., Ed.; Wiley: New York, 1992; Vol. 22, p 159.
- (139) Aoki, A.; Rajagopalan, R.; Heller, A. *J. Phys. Chem.* **1995**, *99*, 5102.
- (140) Aoki, A.; Heller, A. *J. Phys. Chem.* **1993**, *97*, 11014.
- (141) Zakeeruddin, S. M.; Fraser, D. M.; Nazeeruddin, M. K.; Gratzel, M. *J. Electroanal. Chem.* **1992**, *337*, 253.
- (142) Lever, A. B. P. *Inorg. Chem.* **1990**, *29*, 1271.
- (143) Buckingham, D. A.; Dwyer, F. P.; Sargeson, A. M. *Inorg. Chem.* **1966**, *5*, 1243.
- (144) Buckingham, D. A.; Dwyer, F. P.; Sargeson, A. M. *Aust. J. Chem.* **1964**, *17*, 622.
- (145) Forster, R. J.; Vos, J. G. *Macromolecules* **1990**, *23*, 4372.
- (146) Degani, Y.; Heller, A. *J. Am. Chem. Soc.* **1989**, *111*, 2357.
- (147) Cassidy, H. G.; Kun, K. A. *Oxidation-Reduction Polymers; Redox Polymers*; Interscience Publishers: New York, 1965.
- (148) Murray, R. W. *Annu. Rev. Mater. Sci.* **1984**, *14*, 145.
- (149) Heller, A. *Acc. Chem. Res.* **1990**, *23*, 128.
- (150) Degani, Y.; Heller, A. *J. Phys. Chem.* **1987**, *91*, 1285.
- (151) Degani, Y.; Heller, A. *J. Am. Chem. Soc.* **1988**, *110*, 2615.
- (152) Degani, Y.; Heller, A. *J. Am. Chem. Soc.* **1989**, *111*, 2357.
- (153) Pishko, M. V.; Katakis, I.; Lindquist, S. E.; Ye, L.; Gregg, B. A.; Heller, A. *Angew. Chem.* **1990**, *102*, 109.
- (154) Trudeau, F.; Daigle, F.; Leech, D. *Anal. Chem.* **1997**, *69*, 882.
- (155) Ohara, T. J.; Rajagopalan, R.; Heller, A. *Anal. Chem.* **1993**, *65*, 3512.
- (156) Mano, N.; Mao, F.; Heller, A. *J. Am. Chem. Soc.* **2002**, *124*, 12962.
- (157) Mano, N.; Kim, H. H.; Heller, A. *J. Phys. Chem. B* **2002**, *106*, 8842.
- (158) Nakagawa, T.; Tsujimura, S.; Kano, K.; Ikeda, T. *Chem. Lett.* **2003**, *32*, 54.
- (159) Tsujimura, S.; Kawaharada, M.; Nakagawa, T.; Kano, K.; Ikeda, T. *Electrochem. Commun.* **2003**, *5*, 138.
- (160) Bard, A. J.; Faulkner, L. R. *Electrochemical Methods: Fundamentals and Applications*, 2nd ed.; John Wiley: New York, 2001.
- (161) The mass-transfer boundary layer thickness, δ , on a rotating disk electrode can be estimated by $\delta = 1.6D^{1/3}\nu^{1/6}\omega^{-1/2}$, where D is the substrate diffusion coefficient, ν is the solution viscosity, and ω is the disk rotation speed.
- (162) Campbell, C. N.; Heller, A.; Caruana, D. J.; Schmidtke, D. W. In *Electroanalytical Methods for Biological Materials*; Brajter-Toth, A., Chambers, J. Q., Eds.; Marcel Dekker: New York, 2002; p 439.
- (163) Ianniello, R. M.; Lindsay, T. J.; Yacynych, A. M. *Anal. Chem.* **1982**, *54*, 1098.
- (164) de Lumley-Woodyear, T.; Rocca, P.; Lindsay, J.; Dror, Y.; Freeman, A.; Heller, A. *Anal. Chem.* **1995**, *67*, 1332.
- (165) Kenausis, G.; Taylor, C.; Katakis, I.; Heller, A. *J. Chem. Soc., Faraday Trans.* **1996**, *92*, 4131.
- (166) Mano, N.; Heller, A. *J. Electrochem. Soc.* **2003**, *150*, A1136.
- (167) Katz, E.; Filanovsky, B.; Willner, I. *New J. Chem.* **1999**, *23*, 481.
- (168) Mano, N.; Mao, F.; Heller, A. *J. Am. Chem. Soc.* **2003**, *125*, 6588.
- (169) Tsujimura, S.; Kano, K.; Ikeda, T. *Electrochemistry* **2002**, *70*, 940.
- (170) Calabrese Barton, S. *Electrochim. Acta* **2003**, manuscript accepted.
- (171) Newman, J. S. *Electrochemical Systems*, 2nd ed.; Prentice Hall: Englewood Cliffs, NJ, 1991.
- (172) Giner, J.; Hunter, C. *J. Electrochem. Soc.* **1969**, *116*, 1124.
- (173) Schroeder, P. *Z. Phys. Chem.* **1903**, *45*, 75.
- (174) Boulatov, R. *Pure Appl. Chem.* **2004**, *76*, 303.
- (175) Boulatov, R.; Collman, J. P.; Shiryayeva, I. M.; Sunderland, C. J. *J. Am. Chem. Soc.* **2002**, *124*, 11923.
- (176) Bugg, T. D. H. *Tetrahedron* **2003**, *59*, 7075.
- (177) Kim, E.; Chufan, E. E.; Kamaraj, K.; Karlin, K. D. *Chem. Rev.* **2004**, *104*, 1077.
- (178) Chen, Q.; Kenausis, G. L.; Heller, A. *J. Am. Chem. Soc.* **1998**, *120*, 4582.
- (179) Heller, J.; Heller, A. *J. Am. Chem. Soc.* **1998**, *120*, 4586.
- (180) Lev, O.; Wu, Z.; Bharathi, S.; Glezer, V.; Modestov, A.; Gun, J.; Rabinovich, L.; Sampath, S. *Chem. Mater.* **1997**, *9*, 2354.
- (181) Rabinovich, L.; Gun, J.; Tsionsky, M.; Lev, O. *J. Sol-Gel Sci. Technol.* **1997**, *8*, 1077.
- (182) Sober, H. A. *CRC Handbook of Biochemistry: Selected Data for Molecular Biology*, 2nd ed.; CRC Press: Cleveland, OH, 1970.

CR020719K

Review of Developments in Portable Hydrogen Production Using Microreactor Technology

Jamelyn D. Holladay,* Yong Wang, and Evan Jones

Battelle, Pacific Northwest Division, Richland, Washington 99352

Received January 14, 2004

Contents

1. Introduction	4767
2. Reactor Development and Performance Overview	4768
2.1. Fabrication and Design	4769
2.1.1. Materials	4769
2.1.2. Fabrication Techniques	4769
2.1.3. Design Strategies	4770
2.2. Hydrogen Production	4771
2.2.1. Hydrocarbon Reforming	4771
2.2.2. Ammonia Cracking	4773
2.2.3. Other Hydrogen Production Techniques	4773
3. Hydrogen Production from Microreactors	4773
3.1. Subwatt Power	4774
3.1.1. Microreformers (0.01–0.1 W) Developed at Battelle, Pacific Northwest Division	4774
3.1.2. Packed-Bed Microreactor in the Subwatt Power Range	4775
3.1.3. Microscale Preferential Oxidation Reactor	4775
3.2. Power Supplies in the 1–10 W Range	4777
3.2.1. MIT Suspended-Tube Reactor for 1–2 W Power Generation	4777
3.2.2. Lehigh University Methanol Reforming Reactor	4778
3.3. Reactors in the 15–100 W Range	4780
3.3.1. Korea Institute of Energy Research 15 W Power Generation	4780
3.3.2. Battelle, Pacific Northwest Division, 15–100 W Power Generation	4781
3.3.3. MiRTH-e 20–100 W Reactor	4782
3.3.4. Motorola Methanol Fuel Processor	4782
3.3.5. MesoSystems Technology in the 50–100 W Range	4783
3.4. Reactors \leq 500 W	4783
3.4.1. Scalable Methanol Autothermal Reforming Reactor	4783
3.4.2. Portable Power Using a Propane Cracking Reactor System	4783
3.4.3. Methanol Reforming Reactors for a 200 W _e Fuel Cell Power System	4784
3.4.4. Royal Military College of Canada 200–300 W System	4785
3.4.5. Emission-Free Reformer Concept for Portable Power Applications	4785
4. Summary and Outlook	4786
5. Acronyms	4787
6. References	4787

1. Introduction

Technology advancements over time have enabled developments in electronics to move us into a micro-

electronics age. Remarkable achievements have increased functionality while making devices smaller. Each decrease in device size has resulted in greater quality and efficiency. However, as new functionalities are added, power consumption rises alarmingly. Until recently, primary and secondary batteries have been the sole autonomous energy storage solution for these devices, but new and innovative approaches, ranging from microscale rotary engines to thermal electric generators implanted in microscale combustors,^{1–6} are laying the groundwork for alternative technologies that generate electric power from hydrocarbon fuels. One innovative way to utilize the stored energy in hydrocarbon fuels is to strip the hydrogen from its compounds and feed it to a fuel cell, producing electricity.

Fuel cell efficiencies and power densities are increasing, while costs are decreasing, making them a potentially attractive power supply.^{7–9} Polymer electrolyte membrane fuel cells (PEMFCs) have been proposed as battery replacements and for use in hybrid fuel cell battery systems to augment the battery's energy density.^{7–10} However, nontrivial challenges for PEMFCs include hydrogen storage, safety, and water and thermal management.^{7,10} One way to avoid the hydrogen storage problem is to produce hydrogen on demand using miniature reactors. These reactors often have characteristic dimensions, such as channel gaps, which are on the microscale (typically $< 1000 \mu\text{m}$) or mesoscale (1000 μm to a few centimeters) and will be referred to in this article as microreactors. These features are significantly smaller than many conventional reactors (a few inches or more), and they can significantly enhance mass and heat transfer rates. Operating on demand, microreactors liberate the hydrogen from hydrogen containing feedstocks such as hydrocarbons, ammonia, or chemical hydrides, as needed, to power the fuel cell. Over the last 30 years, pioneering and follow-up studies have resulted in new concepts and designs for microreactor applications. This paper reviews the progress in microreactor development focused on fuel cell based power supplies ranging from $< 1 \text{ W}$ to several hundred watts. The discussion first covers reactor types, fabrication and design, and hydrogen production techniques, and then it describes microreactor performance for a wide range of devices.



Jamelyn (Jamie) Holladay received his Master's degree in Chemical Engineering from Brigham Young University in 2000 and has over 4 years of research experience. His work involves microscopic battery design and miniature power supplies using a fuel processor and fuel cell, including microdevice design, heterogeneous catalyst testing, steam reforming, semiconductor processing, PEM fuel cells, and battery fabrication/testing. He is currently contributing to the Sub-Watt Power, Soldier-Portable Power, Soldier-Portable Cooling, and NO_x/SO_x emission reduction projects. In addition to technical advancements, these projects also require frequent communications and interactions with industry, military, and educational institutions. He has three patent applications and over 15 peer reviewed publications.



Yong Wang received his Ph.D. in Chemical Engineering from Washington State University in 1993, and he has 20 years of research and project management experience. His main research interest is in the development of advanced catalysts and novel reactors for hydrogen production, natural gas to liquid fuels, alkane conversion to chemicals, solid acid-catalyzed isomerization/alkylation/dehydration, and upgrading of biomass derived feedstocks, as well as in the elucidation of structural and functional relationship on metal oxide based redox and acid/base catalysis. Dr. Wang has received two R&D 100 Awards, a Presidential Green Chemistry Award, and numerous Battelle and PNNL Key Contributor Awards for his contributions. He was named PNNL Inventor of the Year and Battelle Distinguished Inventor in 2003. He has 87 peer reviewed publications, including 28 issued U.S. patents.

2. Reactor Development and Performance Overview

Microreactors evolved from the process intensification concepts and microfabrication techniques developed for the microelectronics industry. Process intensification was pioneered in the 1970s, arguably by Imperial Chemical Industries (ICI) researcher Colin Ramshaw, who began developing technologies and approaches that considerably reduced the physical size of unit operations while maintaining their



Mr. Jones has a B.S. and M.S. in Chemical Engineering from Washington State University. His current technical interest is in microscale power systems using small-scale reformer reactors. He has been involved in the design and development of both large and laboratory scale test systems and the development of microtechnology for commercial and government clients. Pilot-plant design has ranged from conceptual P&ID's to final engineering, design, and construction as well as installation and operation. He has designed, constructed, and operated several commercial and pilot-scale systems for manufacturing high-purity chemicals for the electronics industry and recovering acid from metal-bearing spent acids. Mr. Jones has received a R&D 100 Award and a Federal Laboratory Consortium Award, and he has over 15 peer reviewed publications.

throughput.^{11,12} Later, the process intensification strategies were combined with microfabrication techniques.¹³ Further size reduction was achieved when multiple unit operations, for example, a combustor, heat exchanger, and catalytic reactor, were integrated into a single device.^{14,15} The field of microreactors has expanded rapidly over the past decade. By the mid 1990s, a handful of organizations were exploring this reaction technology, including IMM, Forschungszentrum Karlsruhe GmbH (Karlsruhe), DuPont, University of Newcastle, MIT, and the Battelle Pacific Northwest National Laboratory. Today there are dozens of research institutes, universities, and companies actively engaged in the development of microreactors. Microreactors are particularly useful for situations where heat and mass transfer are required for good temperature control, to improve yields or selectivity, or where reactions are only mildly endothermic or exothermic.

For hydrogen production, microreactors offer numerous advantages. High heat and mass transfer rates, for example, enable reactions to be performed under more aggressive conditions which favor overall kinetics or space time yields.^{11,13,16} These high rates are due to the high surface-to-volume ratios and short transfer distances in the reactors. For reactions that operate in mass and heat transfer-limited regimes, microreaction devices could be considerably smaller than their conventional counterparts at the same throughput.

There are several challenges that need to be addressed when using the microreactors. Some of these issues include increased sensitivity to fouling, a potentially increased high-pressure drop in the system at high throughput, more difficulty in sealing of the small systems, and increased challenges in system monitoring. Additionally, the high surface area-to-volume ratio allows high heat transfer rates,

Table 1. Microreactor Material Benefits and Drawbacks (Adapted from refs 17 and 18)

substrate	benefits	drawbacks
metal	standard fabrication techniques durable low to modest costs no clean room required	poor compatibility with ceramics and glass
silicon	well characterized silicon fabrication techniques high precision low cost	fragile requires a clean room
LTCC	flexible fabrication refractory and durable low cost no clean room required	nonstandard fabrication sealing
polymers	low cost flexible fabrication	chemical compatibility thermal compatibility sealing

which also create more problems in thermal management. Some of these issues (e.g. pressure drop, heat loss, and sealing) can be minimized through the material selection and reactor design. Other issues, such as system monitoring, require other solutions. For example, thermal couples may be a significant source of heat loss in the system, so a solution is to build them in-situ. Many of the researchers have attempted to address these challenges; unfortunately, oftentimes they do not report their methods for overcoming these challenges.

2.1. Fabrication and Design

To build an efficient and compact microreactor, the fabrication technique must allow for three-dimensional structures and the use of the appropriate materials, and the technique should be low cost.¹³ Since reactants and products must flow in and out of the device, traditional standard thin film techniques are not suitable for the reactor framework. However, thin film techniques are very useful for integration, surface preparation, sensor integration, and finishing or packaging. Fortunately, traditional thin film techniques can be modified for microreactor fabrication; other techniques, which will be discussed below, are also available.

2.1.1. Materials

The fabrication materials chosen must be chemically compatible, have the appropriate thermal properties, and be structurally sound. Table 1 lists the benefits and drawbacks of some common materials used in microreactor fabrication. The materials are divided into four general categories: metals, silicon (which includes materials containing silicon or that are processed with semiconductor fabrication techniques), low-temperature cofired ceramics (LTCC), and plastics.^{17,18} Polymeric materials would be of great interest in microreactors; however, no hydrogen generating microreactors built of polymers were reported in the literature at the time of this review. It would be an interesting area of development, although the thermal and chemical compatibility may be an issue. The material selection process is complicated by the fabrication process; that is, will the fabrication process alter the material properties and,

if so, how? Microreactors have the potential to be manufactured using high-volume, low-cost techniques, but the design, material, and fabrication selections should take cost into account to avoid developing a laboratory curiosity rather than a commercially viable device.¹³

2.1.2. Fabrication Techniques

A number of fabrication techniques meet the general requirements for constructing an efficient and compact microreactor. Popular methods include LIGA, wet and dry etching processes, micromachining, lamination, and soft lithography.

2.1.2.1. LIGA. The LIGA technique was primarily developed by researchers in Germany, with Forschungszentrum Karlsruhe and the Institute for Microtechnology Mainz (IMM) being the primary drivers.¹⁹ This process combines deep lithography, electroplating, and molding (lithographie, galvanoformung, abformtechnik—LIGA)^{13,19} using three general steps. The first step is the pattern transfer using a serial beam writing process or mask into a photoresist or a special photosensitive epoxy, such as SU8, deposited on an electrically conductive substrate.¹³ After any undesirable material is removed (e.g., the mask is developed), a relief structure is formed by electroplating onto the exposed substrate areas. Once the metallic structure is formed, the resist or epoxy is removed. In some instances, this metallic structure may be the final product; however, usually it is used as a master tool for a replication process (such as injection molding, casting, or embossing), which is the final step in the process.^{13,19}

2.1.2.2. Wet and Dry Etching Processes. Wet and dry etching processes have largely been developed for the semiconductor industry. Wet etching uses a liquid etch solution (such as potassium hydroxide to etch silicon) to remove unwanted material from the substrate anisotropically, whereas dry etching tends to use plasmas or reactive plasmas and may be anisotropic or isotropic, depending on the plasma source.¹³ Similar to dry etching is deep reactive ion etching (DRIE), which is often used in the fabrication of microelectromechanical systems (MEMS).¹⁹ Since wet etching is an anisotropic process, it has strong restrictions on the geometries that can be made. Isotropic dry etching enables a wider variety of geometries but is more limited in the materials that can be etched. The initial step in the process is the same as that of LIGA; specifically, a pattern is transferred into a photoresist or other protective layer. The unprotected substrate areas are etched using either technique. Next, the protective layer is removed. To make the final device, several substrates fabricated using this method are stacked on top of each other.¹³

2.1.2.3. Micromachining. In contrast to LIGA and wet/dry etching, the three main processes for micromachining shapes typically do not need the initial deposition of a resist, epoxy, or other protective layers. The equipment also tends to be less expensive for purchasing and maintenance. While not required, these processes are often computer controlled. The first technique involves traditional milling, turning,

and grinding, but with ultraprecision machines that produce small features.^{13,19} The feature sizes are not as small as those constructed from LIGA and other fabrication processes; however, almost any material can be used. The second technique uses laser radiation to remove material or, in some situations, to build up material.¹³ The most common procedure is to remove material by melting, evaporation, decomposition, photoablation, or a combination of these removal techniques. Some development involves building structures by photochemically cross-linking in organic compounds or powder solidification by laser sintering. Both processes can be used to make devices down to critical dimensions of approximately 10 μm ; however, the surfaces tend to be rough, which may cause problems in some cases.¹³ The third technique is electrodischarge machining (EDM), also called micro-electrodischarge machining. This technique is limited to electrically conductive work pieces. Material is removed by small sparks in a dielectric fluid, such as deionized water or oil, between the work piece and an electrode. The main disadvantages of this type of machining are relatively rough surfaces; limitations in miniaturization to the size of the electrodes and spark; and relatively long machining times, which may limit the technology to prototyping and manufacture of mold inserts.¹³

2.1.2.4. Lamination. In a lamination process, several sheets with different patterns are stacked and then brazed or bonded together. In a MEMS-based approach, DRIE is used to make patterns in silicon or other materials. The substrates are then stacked and bonded together using silicon bonding methods developed for MEMS. Another approach, used by researchers at Pacific Northwest National Laboratory (PNNL),¹⁹ is the fabrication of thin metal laminates using stamping, embossing, or processes described previously. These laminates are then stacked and brazed or diffusion bonded into a single device.^{19–21} Lamination is also particularly well suited for fabricating ceramic devices. Ceramic tapes, in the soft, pliable “green state”, are cut, molded, laser cut, and so forth to the desired design and stacked. After curing in high-temperature furnaces, the laminates are bonded into a single structure.¹⁹

2.1.2.5. Soft Lithography. Whitesides and co-workers developed a collection of lithographic techniques referred to as soft lithography.²¹ An elastomer, often poly(dimethylsiloxane), with a pattern embossed on its surface, is used to transfer the pattern onto the substrate (often by stamping). This technique is used in biological applications but can be combined with other polymers, electroplating techniques, or molding of ceramics for low-cost, fast prototyping of devices.^{19,21}

2.1.3. Design Strategies

Various reactor types have been used as the foundation for microreactor designs, including coated wall reactors, packed-bed reactors, structured catalyst reactors, and membrane reactors.

2.1.3.1. Coated Wall Reactors. Techniques for depositing catalyst onto the reactor walls include

wash coating, ink jet printing, aerosol sprays, and thin film deposition by chemical or physical vapor deposition.¹⁹ Wash coating techniques, similar to those used in conventional autoconverter manufacturing, can form a thin layer of catalyst with high surface area on reactor walls which results in more efficient utilization of catalysts compared to their conventional counterparts such as pellets or extrudates. Unfortunately, due to nonuniform surface tension, the wash coating solutions tend to collect in the corners of the reactors.¹⁹ However, in some cases, the surface tension phenomenon can be an advantage, as demonstrated, for example, by the innovative work of Arana et al.,²² who used surface tension to make a stop valve to control catalyst deposition.

With aerosol sprays, the catalyst is deposited directly on the reactor substrate, and the sprays can be used to coat already-formed channels.¹⁹ Ink jet catalyst ink deposition allows precise placement of the catalyst, but at the cost of having to seal the system after deposition, which eliminates some fabrication options such as diffusion bonding. Additionally, the choice of catalyst composition allowed by ink deposition is limited. Physical or chemical vapor deposition techniques place thin catalyst layers with low surface areas. Examples of these techniques include electron beam deposition, radio frequency (RF) sputtering, thermal vaporization, chemical vapor deposition (CVD), and reactive chemical vapor deposition. These resulting smooth surfaces can be roughened by thermal activation to increase their surface area, but surface areas similar to those for wash coating generally cannot be attained. With physical deposition, as with sputtering, it is difficult to achieve uniform coating on nonplanar surfaces. Additionally, both methods are typically limited to metals and simple oxides due to the availability of precursors.

2.1.3.2. Packed-Bed Microreactors. Packed-bed microreactors simply pack conventional catalysts in microreactors. The advantages of using conventional catalysts include decreased cost, increased catalyst availability and reproducibility, and greater understanding of catalyst performance. The high heat and mass transfer rates in microreactors tend to boost the performance of these catalysts.¹⁹ The disadvantages of the packed-bed reactors include a high-pressure drop and potential channeling at high throughput, and the possibility of channel plugging.¹⁹

2.1.3.3. Structured Catalyst Reactors. The powder used in packed-bed reactors can be integrated onto a foam or felt substrate to be used in microreactors.²³ By supporting the catalyst on structured substrates, plugging can be avoided and pressure drop can be reduced due to the large opening pores in the foams or felt (typically 100–300 μm in diameter). Additionally, conventional catalysts typically used in packed-bed reactors can be used, which offers a much wider range of catalyst availability with high reproducibility. This type of reactor often consists of narrow microchannels, where the supported catalysts are placed. Problems associated with “channeling” can be mitigated by designing channel geometries such that the laminar average residence time is

longer than the radial diffusion time. Fast mass transfer rates can be achieved with this design.²⁴

A variation of this technique was developed by Wan et al.²⁵ to grow zeolites in microchannels. The first step was to place seed in the channel(s) where the zeolite was desired. Once the seed was in place, zeolites could be grown using conventional techniques, with the deposition steps repeated a number of times to obtain the desired thickness. These zeolites could be coated or further patterned with photoresist and buffered oxide etch. Once the desired pattern was achieved, the photoresist was stripped using acetone. Free-standing zeolite membranes were also fabricated using this technique with the additional step of silicon etching using tetramethylammonium hydroxide. Wan et al.²⁵ fabricated films of ZSM-5 and titanium silicate-1.

2.1.3.4. Membrane Reactors. Membrane separation techniques are a common way of obtaining high-purity (often $\geq 99.99\%$) hydrogen in industry. For small reactors, it is appealing to combine the hydrogen purification step with the generation reactors to make compact devices.¹⁹ Metal membranes, typically palladium or palladium alloys, are used in these reactors. In conventional systems, high pressures (often greater than 250 psi) and temperatures of 300 °C or more are required for high hydrogen recovery.²⁶ The small feature sizes and complex geometries possible in microreactors have enabled extremely thin metal membranes to be fabricated that allow high hydrogen recovery at relatively low pressures.¹⁹

2.2. Hydrogen Production

Four hydrogen production techniques are reviewed: hydrocarbon reforming; ammonia cracking; and two other, less common, production techniques, pyrolysis and aqueous phase reforming.

2.2.1. Hydrocarbon Reforming

The majority of microreactors currently being developed are designed to produce hydrogen from hydrocarbons. Three basic reforming technologies are steam reforming, partial oxidation, and autothermal reforming. Endothermic steam reforming of hydrocarbons, favored by industry, operates at high temperatures and requires an external heat source. Partial oxidation is an alternative to steam reforming, where the reaction heat is provided by the partial combustion of the hydrocarbon with oxygen. The autothermal reforming process is a thermally neutral hybrid of steam reforming and partial oxidation. All three processes are typically coupled to the shift reactions carried out in the presence of an iron catalyst at about 350 °C and/or a copper catalyst at lower temperatures (210–330 °C) to ensure high yields of hydrogen. Partial oxidation and autothermal processes do not require an external heat source, but an expensive and complex oxygen separation unit is needed (or the hydrogen is diluted with nitrogen, which lowers the fuel cell efficiency). A brief overview of hydrocarbon reforming is given here. Recent articles^{28–30} provide a more in-depth review on hydrocarbon reforming for fuel cells.

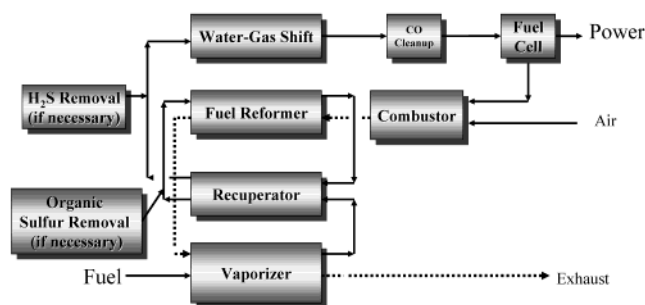


Figure 1. Schematic of fuel reforming process.

Steam reforming is generally the preferred process for hydrogen production.²⁷ Particularly for portable hydrogen production, the requirement of an external heat source can be addressed through the advanced heat and mass transfer provided by microreactors.

Logistic fuels, such as jet and diesel fuels, are readily available, but a compact and effective way to remove sulfur from these fuels is needed for portable hydrogen production. Consequently, for most portable applications, it is likely that sulfur-free fuels, such as methanol, will be used. An additional advantage of methanol is that it is easier to activate at low temperatures than other hydrocarbons. Therefore, a portable hydrogen production unit based on methanol steam reforming would be simpler and less costly than other alternatives. Methanol can also be considered an energy carrier as an alternative to liquefied natural gas.

Methanol steam reforming takes place over Cu or Pd/Zn alloy catalysts^{26,31–38} at low temperatures, typically above 200 °C. Low temperature reduces the equilibrium CO selectivity via the water-gas-shift (WGS) reaction. Therefore, a methane-free hydrogen can be produced at low temperatures and high pressures, while near complete conversion to CO₂ can be achieved. The major disadvantage with Cu-based catalysts is the sintering of metal at temperatures above 330 °C, which is difficult to avoid when part of the methanol is combusted to provide heat for the endothermic methanol steam reforming. Pd/Zn alloy catalysts,^{32,36,39,40} on the other hand, exhibit excellent thermal stability and are nonpyrophoric and, thus, are an advantage for portable hydrogen production.⁴¹ A schematic of the process is shown in Figure 1. For PEM fuel cells, the carbon monoxide levels need to be below 10 ppm; therefore, secondary WGS reactors and a final polishing step (selective partial oxidation or methanation) are typically used.^{26,30,42} In the cases where methanol steam reforming is performed or a metal membrane is used to purify the hydrogen,²⁶ the WGS can be eliminated.

As with the other reactor configurations, vaporizers, heat exchangers, and a heat source are also needed for microreactors.^{26,30,42} Unless the hydrogen is 99.999% pure, the PEM fuel cell typically will utilize 70–80% of the diluted hydrogen fed to it. The unreacted hydrogen from the fuel cell anode, augmented with additional fuel as needed, can be used as fuel for the combustor.²⁶ The use of anode off-gas requires special controls for transient operating conditions; for example, a mechanism is needed to

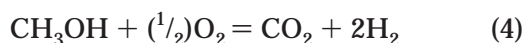
prevent the system from unexpected cooling if the load to the fuel cell is suddenly increased or if the fuel cell hydrogen consumption increases. The system can overheat when the load to the fuel cell is removed, and excess hydrogen is then sent to the combustor.

The reforming, WGS, and oxidation reactions can be generalized as follows for hydrocarbon and methanol fuels:

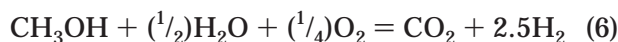
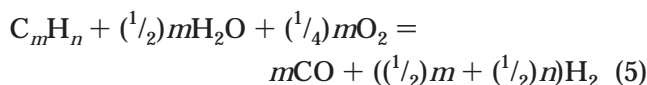
Steam reforming



Partial oxidation



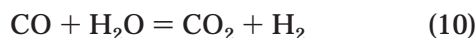
Autothermal reforming



Carbon formation



Water-gas-shift



CO oxidation



Fuel processing reactors are designed to maximize hydrogen production reactions (eqs 1–6 and 10–12) by optimizing the operating conditions and designing the specific catalysts. Under certain conditions, undesirable reactions (eqs 7–9 and 13) will occur.^{26,30,42}

Fuel processing occurs at essentially two different temperature ranges and uses several different types of catalysts.^{26,30,42} Fuel reforming of fuels other than methanol requires temperatures typically greater than 500 °C. The catalysts can be divided into two types: nonprecious metal (typically nickel) and the noble group 8 metals (typically platinum or rhodium based). Conventional steam reformers have severe mass and heat transfer limitations, and the effectiveness factor of the catalyst is typically <5%.⁴³ Therefore, the activity of the catalyst is rarely a limiting factor with conventional reactors,²⁸ and because of their moderate cost, nickel catalysts are used universally in industries. In the case of microreactors

for steam reforming where the intrinsic kinetics of steam reforming can be exploited,²⁴ the noble group 8 metals, particularly Rh,⁴⁴ are preferred, since they exhibit much higher specific activities than nickel catalysts.^{45,46} The high temperatures required for reforming hydrocarbons promote carbon formation; by adding water, the coke formation is decreased. Stoichiometric steam-to-carbon ratios are not sufficient to prevent coke formation. Therefore, ratios higher than the stoichiometry, typically 2.5 or greater, are required to gasify coke and are typically used. Coke formation is much less over the noble group 8 metals. Alkaline components such as magnesia or potassia are added to the catalyst support to minimize the coke formation.⁴⁷

Direct partial oxidation of hydrocarbons and catalytic partial oxidation of hydrocarbons are being used in many of the larger-scale hydrogen production systems for automobile fuel cells.²⁹ The noncatalytic partial oxidation of hydrocarbons in the presence of oxygen and steam typically occurs with flame temperatures of 1300–1500 °C to ensure complete conversion and to reduce soot formation.²⁸ Catalytic partial oxidation is being used to lower the operating temperatures; however, it is proving hard to control because of coke and hot spot formation due to the exothermic nature of the reactions.^{30,42} Krummenacher et al.⁴⁸ have had success using catalytic partial oxidation for decane, hexadecane, and diesel fuel. The high operating temperatures (>800 °C and often >1000 °C)⁴⁸ may make their use for practical portable devices difficult due to thermal management. Autothermal reforming couples steam reforming with catalytic partial oxidation. Partial oxidation or catalytic partial oxidation is used to generate the heat needed to drive the steam reforming reactions in this process. Many of the technical issues of this type of reforming are discussed by Krumpelt and Bellows.^{49–51}

Since carbon monoxide is a poison to PEM fuel cells, it must be reduced to 10 ppm or lower. This can be done by using a metal membrane, as described previously, or catalytically using preferential oxidation or methanation. For fuels other than methanol, the product gas from a reformer contains high amounts of carbon monoxide, often 10% or more.^{26,30,42} A WGS reactor is used to reduce the carbon monoxide and also increase the hydrogen production. A high temperature is desired to achieve fast kinetics but results in high carbon monoxide selectivity due to equilibrium limitations. Therefore, a low-temperature reactor is used to lower the carbon monoxide content to 1% or less. TeGrotenhuis et al.⁵² have demonstrated the potential in using microreactors to build a gradient-temperature WGS reactor that contains the high-temperature WGS and low-temperature WGS in a single unit for >2–3 kW_e units. The most common catalyst for WGS is Cu based,^{26,30,42} although some interesting work is currently being done with molybdenum carbide,⁵³ platinum based catalysts,^{54,55} and Fe–Pa alloy catalysts.⁵⁶

To further reduce the carbon monoxide, a preferential oxidation reactor or a carbon monoxide selective methanation reactor is used.^{26,30} The term “selective oxidation” is also used for preferential oxi-

dation, but more specifically, it refers to cases where carbon monoxide reduction occurs within the fuel cell.²⁶ The preferential oxidation reactor increases the system complexity because carefully measured concentrations of air must be added to the system.^{26,30} However, these reactors are compact, and if excessive air is introduced, some hydrogen is burned. Methanation reactors are simpler in that no air is required; however, for every carbon monoxide reacted, three hydrogen molecules are consumed. Also, the carbon dioxide reacts with the hydrogen, so careful control of the reactor conditions needs to be preserved in order to maintain the selectivity. Therefore, preferential oxidation is currently the primary technique being developed.²⁶ The catalysts for both these systems are typically noble metals such as platinum, ruthenium, or rhodium supported on Al₂O₃.^{26,30}

2.2.2. Ammonia Cracking

Ammonia is an inexpensive and convenient method of storing hydrogen and may be very suitable for portable power applications.⁵⁷ Pure ammonia has a lower heating value (LHV) of 8.9 (kW h)/kg, which is higher than that of methanol (6.2 (kW h)/kg) but less than that of diesel or JP8 (13.2 (kW h)/kg).⁵⁸ Up to about 30 vol % of ammonia can be dissolved in water.⁵⁷ Unfortunately, ammonia is very toxic and its toxicity may make it difficult to establish a suitable infrastructure to distribute it in a concentrated solution. Proponents quickly point out that ammonia's strong odor makes leak detection simple, reducing some of the risk.⁵⁷ The most significant advantage for ammonia is the simplicity of the gas clean up step, since it decomposes into hydrogen and nitrogen. The only gas cleanup required is removal of any unreacted ammonia from the product stream.⁵⁷ Ammonia removal in the stream prior to the PEMFC is essential, since, unlike reversible losses from carbon monoxide exposure, long exposure to ammonia (e.g., >15 h) causes severe and irreversible losses in performance.⁵⁹

Endothermic ammonia cracking is regarded as the reverse of the synthesis reaction, and since it is limited by heat transport, its efficiency can potentially be improved using microreactors. In industry, ammonia synthesis occurs at approximately 500 °C and 250 atm, and it is often represented by the following reaction:⁵⁷

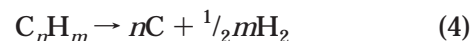


Typical catalysts used in both ammonia synthesis and cracking include iron oxide, molybdenum, ruthenium, and nickel. Unlike synthesis, cracking does not require high pressures, and typically it operates at temperatures around 800–900 °C.⁵⁷

2.2.3. Other Hydrogen Production Techniques

Two other hydrogen production methods, pyrolysis and aqueous reforming, have been explored for use in microreactors. Pyrolysis is the decomposition of hydrocarbons into hydrogen and carbon in water-free and air-free environments.⁶⁰ If no water or air is present, no carbon oxides (e.g., CO or CO₂) are

formed. Consequently, this process offers significant emissions reduction. Since no CO or CO₂ is present, secondary reactors are not necessary. However, if air or water is present, then significant CO₂ and CO emissions will be present. Among the advantages of this process are fuel flexibility, relative simplicity and compactness, a clean carbon byproduct, and reduction in CO₂ and CO emissions.⁶⁰ The reactions can be written in the following form:⁶⁰



Typical unit operations required for this system include vaporizers/preheaters, a pyrolysis reactor, and recuperative heat exchangers. One of the challenges with this approach is the potential for fouling by the carbon formed, which is particularly important in microreactors.

An aqueous phase can also be used to reform or process hydrocarbon fuels or carbohydrates.^{61,62} These reactors often operate at pressures up to 25–30 MPa and temperatures up to 500–750 °C. The advocates of this technology claim that the small characteristic sizes of microreactors more easily accommodate high pressures than larger reactors. The high pressures, in turn, enable the reactors to be even smaller while maintaining the same production rates. However, the balance-of-plant (BOP) components may be difficult to find, depending on the size. In addition, these reactors tend to be large due to low space time yields and in reality do not have a characteristic dimension in the micro or meso range, so they are not reviewed in detail in this paper.

3. Hydrogen Production from Microreactors

Numerous groups using multiple methods have developed microreactors for hydrogen production. These microreactors are discussed, beginning with low-power subwatt production reactors and progressing to the larger units. In general, there are very few references describing the performance of complete micropower systems. Consequently, very few authors report system efficiencies, or if reported, these efficiencies are estimates based on the assumed performance of other components, such as pumps, valves, control systems, and fuel cells. Furthermore, the efficiency of the microscale balance of equipment tends to be lower than that of conventional, larger-scale versions. Fortunately, work is being conducted to improve the microscale balance of equipment, which will in turn improve system efficiencies.

With respect to microscale reactors that produce up to several watts of output, the primary loss of efficiency is from thermal losses. Reformer reactors have areas that reach temperatures above 300 °C, and consequently, loss by conduction can be significant. While microscale systems can have advantages over commercial reactors, one disadvantage is the potential for heat loss by conduction through the relatively large tubing and piping connected to the miniature reactors. The instruments and piping connected to a large-scale reactor represent an insignificant heat loss due to their small size relative to the reactor. However, in a microscale system, the



Figure 2. Battelle subwatt power microreformers. (Reprinted with permission from ref 41. Copyright 2002 Elsevier.)

tubing and instruments connected to the microscale reactor are relatively large and represent a significant potential for heat loss.

3.1. Subwatt Power

3.1.1. Microreformers (0.01–0.1 W) Developed at Battelle, Pacific Northwest Division

Researchers at Battelle, Pacific Northwest Division (Battelle), are developing a methanol reformer for use in subwatt power supplies.^{41,63–69} These reformers were originally designed to operate with high-temperature fuel cells developed and fabricated by Case Western Reserve University.⁶⁹ A complete system incorporates two vaporizers/preheaters, a heat exchanger, a catalytic combustor, and a catalytic methanol reformer in a volume <0.25 cm³ and weighing <1 g.^{41,66,69} These systems, intended for use in micro-sensors and other MEMS devices, were designed to provide <1 W of power. The reformers were fabricated using conventional milling techniques from stainless steel. In addition to the original design, second-generation designs focused on a high-efficiency processor and a low carbon monoxide design that included a selective carbon monoxide methanation reactor for CO cleanup (Figure 2). The initial reactor had a small methanol reformer reactor with a volume of <5 mm³.⁴¹ The second-generation, higher-efficiency design had a larger methanol reforming reactor and smaller heat recuperator heat exchanger, which maintained the original small volume.⁶⁶ The

selective carbon monoxide methanation reactor incorporated into the device to lower the CO levels increased the volume, although it was still <0.25 cm³.⁶⁶ The processor temperature was monitored by a 0.01 in. thermocouple inserted into the catalytic combustion chamber.⁴¹

The reformers were operated without any external heating, even during startup.⁴¹ The combustion fuel was either hydrogen or methanol, depending on the experiments. The startup procedure consisted of feeding a hydrogen–air mixture to the combustor at room temperature. The hydrogen combustion on the catalyst surface would heat the reactor to 70–100 °C. At these temperatures, methanol could be fed to the vaporizers as the combustion fuel. When methanol was to be the only fuel, the amount of hydrogen would be decreased as the combustion of methanol proceeded.⁴¹ The combustor reactor was operated at 250–450 °C, with typical methanol flow rates of 0.2–0.4 cm³/h and air flow rates of 15–25 sccm.^{41,63–70}

The reformer performance is shown in Table 2. The fuel for the original reactor was a 50 wt % mixture of methanol and water. For the higher-efficiency reactor and the system that included carbon monoxide cleanup, the fuel mixture was 60 wt % methanol in water.^{41,66,69} The efficiency was calculated using the following equation:

$$\text{efficiency} = \frac{\Delta H_c(\text{hydrogen produced})}{\Delta H_c(\text{methanol feed}) + \Delta H_c(\text{fuel feed})} \quad (5)$$

where ΔH_c is the lower heating value of the indicated components.⁶⁴

The increase in efficiency between the first- and second-generation reactors was attributed to less water in the feed and lower operating temperatures.⁶⁷ Reactor models indicated that the major source of heat loss was by thermal conduction. The selective methanation reactor lowered the carbon monoxide levels to below 100 ppm, but at the cost of some efficiency. The lower efficiency was attributed to slightly higher operating temperatures and to hydrogen consumption by the methanation process. Typical methane levels in the product stream were 5–6.2%.⁶⁷

Table 2. Battelle Subwatt Power Microscale Fuel Processor Performance^a

feed rate (cm ³ /h)	T (°C)	reformate flow (sccm)	hydrogen (%)	carbon monoxide (%)	carbon dioxide (%)	thermal efficiency (%)
Original Processor ⁶³						
0.05	400	1.1	73–74	1.0–2.0	25–26	9
High-Efficiency Processor ⁶³						
0.05	255	1.2	73–74	0.4–0.6	25–26	15
0.08	263	2.0	73–74	0.5–0.7	24–26	21
0.12	270	3.0	73–74	0.5–0.6	25–26	25
0.15	280	3.8	72–73	0.6–0.7	25–27	28
0.18	313	4.5	72–73	0.8–1.0	25–26	30
0.20	320	4.9	72–73	1.0–1.1	25–26	33
High-Efficiency Processor with Carbon Monoxide Cleanup ⁶³						
0.05	304	1.0	69–70	<0.01	25–25.5	9.5
0.08	323	1.65	69–70	<0.02	25–25.5	14
0.10	330	2.1	69–70	<0.02	25–25.5	17
0.15	345	3.2	68–69	<0.03	25–26	19

^a Methanol conversion > 99%. Data adapted from refs 41 and 63–70.

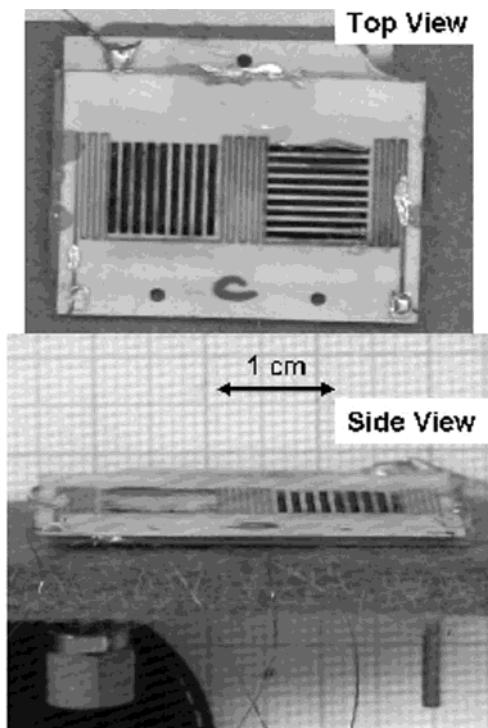


Figure 3. Mesoscale fuel cell fabricated by Case Western Reserve University. (Reprinted with permission from ref 63. Copyright 2001 Elsevier.)

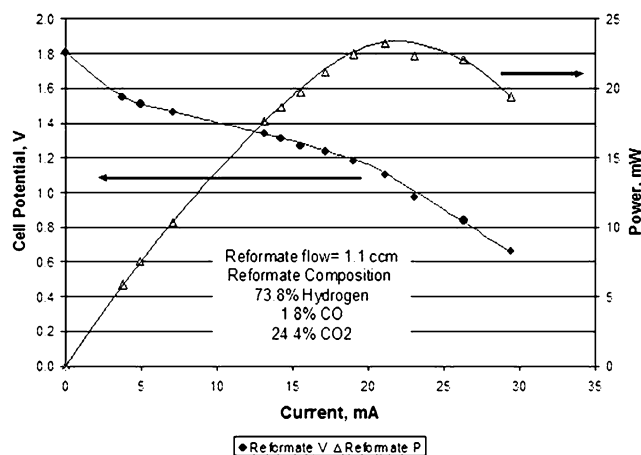


Figure 4. Performance of the mesoscale fuel cell and Battelle's microscale methanol processor. (Reprinted with permission from ref 63. Copyright 2001 Elsevier.)

A mesoscale high-temperature fuel cell was operated using the reformat from the original reactor.⁶⁹ This fuel cell utilized phosphoric acid doped polybenzimidazole (PBI) technology and was fabricated using an amalgamation of conventional and microfabrication techniques (Figure 3). The PBI technology enabled it to operate at temperatures > 125 °C. At these temperatures, the fuel cell can tolerate high levels of carbon monoxide ($\approx 2\%$) while maintaining sufficient ionic conductivity for proper fuel cell operation.⁶⁹ Over 20 mW_e of power was produced from the integrated methanol processor and fuel cell (Figure 4).⁶⁹ Data from fuel cell testing with the other methanol processors have not been reported. In addition, long-term durability and thermal cycling



Figure 5. Miniature reformer showing the evaporator, superheater, reactor, and gas collection insert. The catalyst in the picture is in powder form.³⁷

testing need to be done on both the fuel processor and the fuel cell.

3.1.2. Packed-Bed Microreactor in the Subwatt Power Range

Researchers from the University of Toledo, Case Western Reserve University, the NASA Glenn Research Center, and the National Center for Microgravity Research are collaborating to develop a microreactor consisting of an evaporator, a superheater, a reactor bed, and a "gas collector" within a volume of 1.86 cm³ (Figure 5).³⁷ This cylindrical reactor was built from borosilicate glass. Heat for the processor was provided by Kanthal wire resistance heaters wrapped around the outside of the processor. The reactor was designed for methanol reforming and utilized a commercial (Sud-Chemie C18-07-01) Cu/ZnO on Al₂O₃ support in a powder or pellet form. Figure 5 illustrates the device loaded with a powder catalyst. The device contains 35–50% Cu and 40–55% ZnO with added components to improve its stability. The researchers believe that the Cu/ZnO catalyst not only reforms methanol but also operates as a water-gas-shift (WGS) catalyst. For the experiments, the reactor was loaded with approximately 0.118 g of catalyst powder or 10 catalyst pellets, each with a diameter of 0.48 cm, a thickness of 0.24 cm, and a total mass of 1.14 g.³⁷

The processor was operated at atmospheric pressure and at 117–130 °C or 200 °C. A methanol–water mixture (1:1.5 molar ratio) was fed at 0.1 cm³/h using a syringe pump. The reactors loaded with powder and pellets had comparable results, but the researchers preferred the powder packed bed form for its smaller volume and mass. The best hydrogen production was obtained at low temperatures, providing, on a dry gas basis, 70% hydrogen, 0.5% carbon monoxide, and residual carbon dioxide. Methanol conversion or thermal efficiency was not reported.³⁷

3.1.3. Microscale Preferential Oxidation Reactor

As mentioned earlier, reformat from a fuel processor often needs additional processing to reduce the carbon monoxide levels. Researchers at the Stevens Institute of Technology are developing a microscale preferential oxidation (PrOx) reactor to decrease the carbon monoxide level in the reformat stream to below 100 ppm. As part of their research, they used advanced computational fluid dynamic modeling,

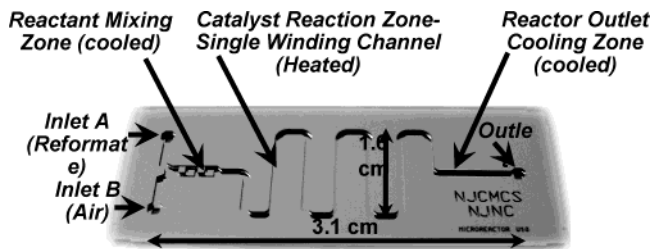


Figure 6. Silicon microreactor for preferential oxidation of CO designed for a 0.25 W_e fuel cell. (The researchers wish to express their gratitude to DARPA for funding Grant N66001-02-1-8942.)

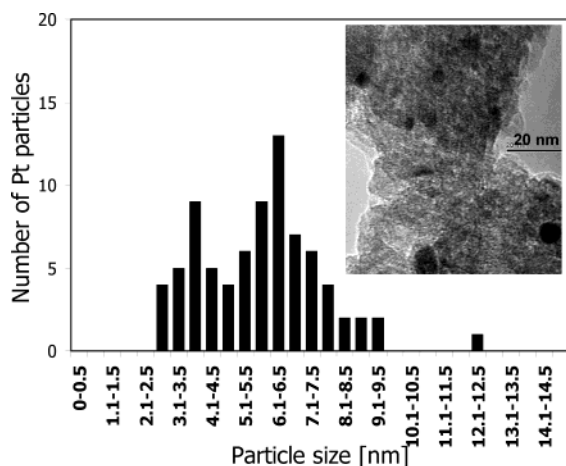


Figure 7. Pt particles' size distribution obtained from TEM on Al_2O_3 support with a TEM image of the catalyst. (The researchers wish to express their gratitude to DARPA for funding Grant N66001-02-1-8942.)

microfabrication to build the reactor, and advanced kinetic modeling to understand their experimental results.^{33,71–78}

Microscale chemical reactors were successfully fabricated on p-type <100> 8 in. silicon wafers by using state-of-the-art silicon bulk micromachining techniques. The microchannels were formed by DRIE.⁷⁶ The reactor consists of dual gas inlets, a mixing region, and a single reaction channel with an outlet (Figure 6).⁷⁴ The microreactor shown in Figure 6 has a channel that is 4.5 cm long, 500 μm wide, and 610 μm deep. The effectiveness of the mixer was confirmed by simulation in FLUENT.

Platinum supported on an alumina catalyst was used in this reactor. The precursor was synthesized using a sol-gel technique.⁷¹ The support, after calcination at 500 $^{\circ}C$, showed a high specific surface area of 400 m^2/g .^{33,72} Transmission electron microscopy (TEM) was used to determine that the platinum particles appeared to have a spherical shape and were evenly distributed on the Al_2O_3 support (Figure 7).^{33,72} The platinum particle size distribution was in the range 2.5–8 nm and showed an indication of a bimodal distribution.^{33,72} The mean Pt particle size was calculated from the X-ray diffraction (XRD) pattern and was found to be 11 nm, while CO chemisorption gave an average particle size of 6 nm, confirming the particle size distribution obtained from TEM.^{33,72}

The general procedure of depositing the catalyst into the reactor is to infiltrate the microchannel with

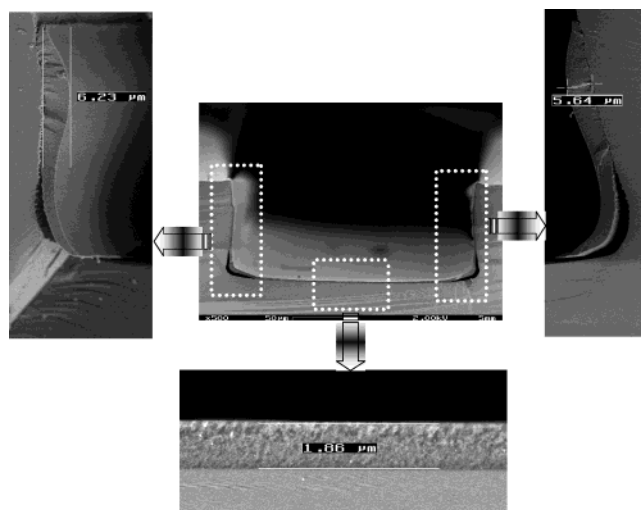


Figure 8. Cross section of a microchannel with detailed left and right sides and bottom of the microchannel with a thin film layer of Pt/ Al_2O_3 catalyst. (The researchers wish to express their gratitude to DARPA for funding Grant N66001-02-1-8942.)

a liquid precursor and then dry and calcine it to make a solid thin film adherent to the walls of the microchannel. Two basic methods were developed to infiltrate the microchannel with the liquid precursor:^{71,72}

Method I was designed for an unbonded microreactor. A micropositioner-controlled pipet tip was used to inject the liquid into the channel from the open top of the channel.

Method II was designed for a bonded microreactor. After the channel was sealed with a Pyrex top plate using the anodic bonding technique, the liquid precursor was infiltrated into the microreactor through the outlet of the reactor under slight pressure and withdrawn. A thin film of solution remained on the walls of the microchannel.

The cross section of a microchannel with the catalyst film was investigated by scanning electron microscopy (SEM) (Figure 8).^{33,71,72} As can be seen from the figure, the thickness of the film in the microchannel was not completely uniform. The thinnest film was on the bottom of the channel, and the thickness increased on the walls and bulged at the top. The thickness of the film catalyst infiltrated in the manner described above was in the range 1–8 μm . The researchers reported that experience with other microchannel geometries showed the shape was connected to the microchannel dimensions, sol density, and capillary forces. The catalyst adhesion to the microreactor walls was satisfactory; however, the thin film can detach in the corners (Figure 8). More exploration must be conducted to optimize film adhesion for robustness.^{33,72}

Microreactors with the thin film catalyst deposited as described were repetitively tested across a wide temperature range. The feed was composed of 1.7% CO, 68% H_2 , and 21% CO_2 with N_2 as the balance. The flow rate was maintained at 5 Ncm^3/min ($\sim 0.6 W_e$) which the researchers believed would be enough for a 0.5 W_e fuel cell. However, using the DOE assumptions (45% for reformer systems), this would translate into approximately 0.27 W_e .⁷⁹ After each

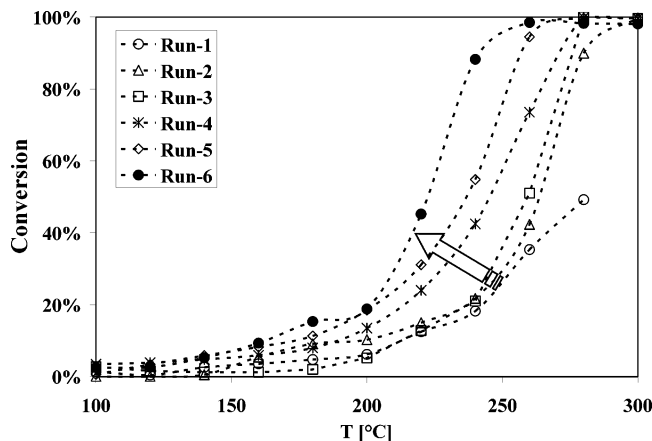


Figure 9. Catalyst activity increase as a function of aging: initial CO conversion with temperature increase for repeated runs [reformat 5 ($\text{N cm}^3/\text{min}$) and dry air 0.5 ($\text{N cm}^3/\text{min}$), $\lambda = 2.57$]. (The researchers wish to express their gratitude to DARPA for funding Grant N66001-02-1-8942.)

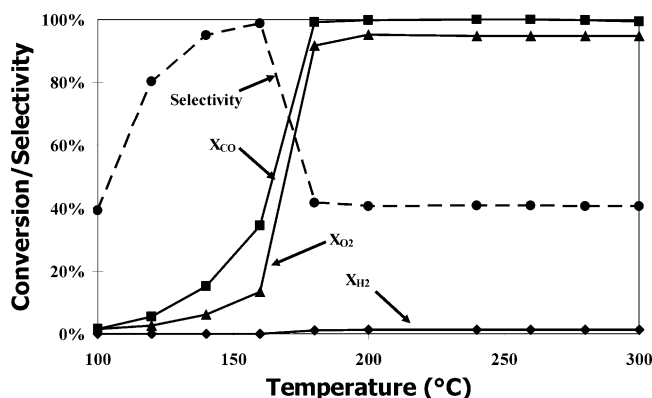


Figure 10. Conversion of CO, O₂, H₂, and CO₂ selectivity as a function of temperature [reformat 5 ($\text{N cm}^3/\text{min}$) and dry air 0.5 ($\text{N cm}^3/\text{min}$), $\lambda = 2.57$, estimated catalyst weight = 1.5 mg].

run, the microreactor was reduced in pure hydrogen.^{73,75,77} Figure 9 shows that the initial conversion was low until the ignition temperature was reached, where a steep increase in conversion was observed and approximately 100% conversion was achieved within about a 60 °C window. Characteristic behavior for CO, H₂, and O₂ conversions and CO₂ selectivity is shown in Figure 10.⁷⁷ The researchers observed that (1) the selectivity consistently increased with an initial conversion increase and topped at approximately 90% at about 10% conversion and (2) the selectivity dropped to approximately 40% at about 100% conversion and 180 °C (Figure 10). Repeated cycles showed that the catalyst continued to improve with initial cycling, and several cycles were necessary to reach its full activity.^{73,75,77}

The catalyst remained active and did not start to deactivate for about 50 h on stream without any regeneration. After that, the catalyst activity started to drop slowly but steadily.⁷³ The deactivation could be caused either by sintering of Pt nanoparticles or by coke deposited on the Pt atoms. If the catalyst deactivation was caused by coking, regeneration may reestablish catalyst activity. However, regeneration in air did not improve catalyst activity, which suggests that the cause of deactivation was not coke.

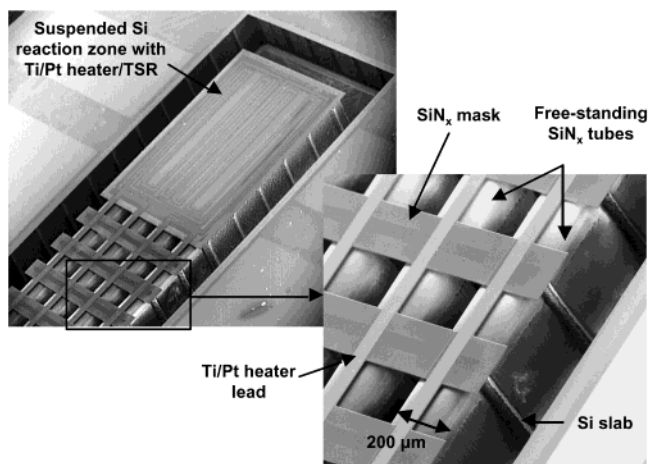


Figure 11. Suspended-tube reactor. (Reprinted with permission from ref 22. Copyright 2003 IEEE.)

More studies are needed to better understand catalyst deactivation and improve stability.

3.2. Power Supplies in the 1–10 W Range

3.2.1. MIT Suspended-Tube Reactor for 1–2 W Power Generation

Researchers at MIT developed an innovative suspended-tube microreactor (Figure 11) to produce up to 9 sccm of hydrogen (1.6 W) by thermally cracking ammonia.⁸⁰ A membrane for hydrogen purification and thermal electric generators was also integrated into the device.^{22,80,81} Other important features of the system included a thin film heater, a temperature-sensing resistor, internal vertical posts within the channels, and passive stop valves. The reactor was designed for thermal isolation, which is considered essential, since “heat loss relative to heat generation is inversely proportional to characteristic length”.⁸¹ The thermal isolation was obtained in two ways:^{22,80} (1) low heat conduction, since the walls were 2 μm thick and 3 mm long and made of SiN, which has a low thermal conductivity, and (2) suspended-tube design, which allows for the vacuum packaging needed to reduce radiation losses at the high operating temperatures.

The reactor was fabricated using a silicon-based molding process. In this process, channels with internal vertical posts were formed initially by DRIE or potassium hydroxide wet etching techniques (Figure 12).^{22,80} Once formed, an ultrathin silicon wafer is bonded to seal the channels. The next step is to coat the inside channel surfaces with low-stress nitrides by low-pressure vapor deposition. The silicon mold is then selectively removed by a process developed at MIT using fluorine gas, leaving the silicon nitride free-standing tubes. Thin film heaters and temperature-sensing resistors are fabricated on the surfaces of the tubes.

Packaging was designed to thermally isolate the device while maintaining electrical and fluid interconnects. The first step was to protect the device from mechanical shock by using spacer chips. Glass-frit bonding techniques were used to bond the chips to the reactor. Low-pressure vacuum packaging and

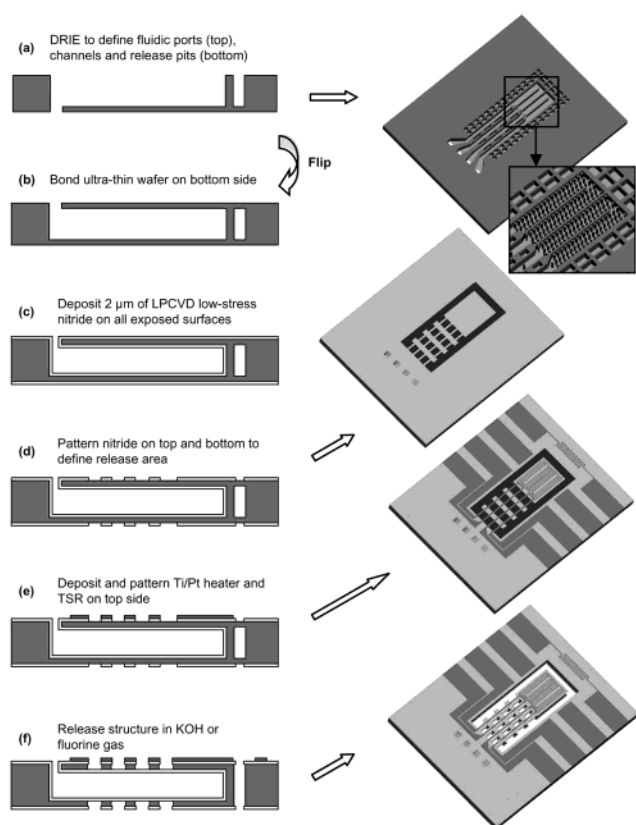


Figure 12. Suspended tube reactor fabrication process. (Reprinted with permission from ref 22. Copyright 2003 IEEE.)

infrared reflective coatings are planned in addition to these chips for further thermal isolation. These packaging strategies must allow for electric and fluidic interconnections. The electric interconnections are necessary for resistive heating for startup and operation when combustion is not used and also for temperature monitoring from temperature-sensitive resistors fabricated on the reactors.^{22,80}

Noble metal catalysts were deposited into the tube reactors using a wash-coat technique.^{22,80} An aqueous solid suspension containing $\text{AlO}(\text{OH})$ and metal salt (e.g., IrCl_4 for iridium catalyst deposition) is wicked into the tubes. The combustion catalyst was required only in the reactor section of the tubes and not in the reactant feed tube to control where the combustion reaction occurred. Therefore, a cleverly designed passive stop valve was built at the junction between the combustor reactor and the inlet tube, which prevented the wash-coat solution from wicking into the inlet tube (Figure 13). After drying, $\text{AlO}(\text{OH})$ was calcined to Al_2O_3 by heating the reactor to 500 °C in nitrogen or air. Finally, the metal catalyst was made by reducing the metal salt in a hydrogen atmosphere at 300 °C for 1 h. Other catalyst materials and deposition techniques are under development.

Arana et al.²² have performed extensive modeling and thermal characterization experiments on their reactor design. They modeled their design consisting of two suspended SiN_x tubes linked with slabs of silicon using two-dimensional computation fluid dynamics and a heat transfer model (Femlab, Comsol Inc.). The heat of reaction of the steam reforming or

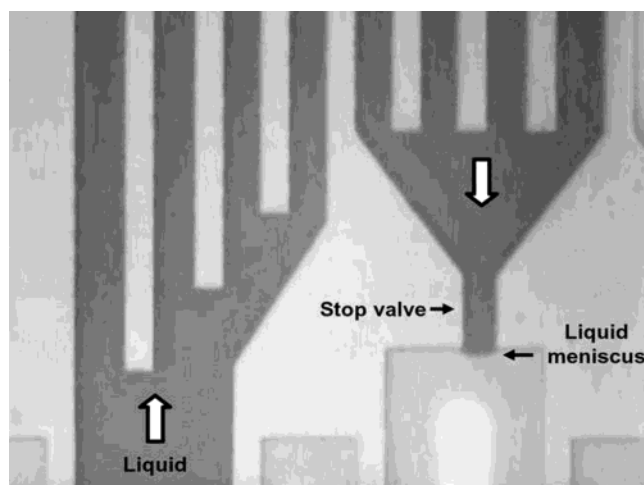


Figure 13. Suspended tube reactor stop valve. (Reprinted with permission from ref 22. Copyright 2003 IEEE.)

ammonia decomposition was not included. The model assumed incompressible fluid flow and close to ideal packaging (negligible losses through the conduction, convection, and radiation). The fluid flows for both the combustion and reforming streams were 10 sccm, and the pressure was atmospheric. The temperature map (Figure 14) shows that the silicon slabs were efficient at transferring thermal energy between the tubes. The model also shows a temperature gradient in the fluids themselves. This temperature gradient may change due to the heat of reaction in the actual system.

The reformer reactor performance as an ammonia cracker was evaluated. The experiments were conducted using a reformer feed composed of 6 sccm ammonia. The reactor was heated with the electric heaters to determine the heater power required to achieve high conversion. In these experiments, approximately 97% of the ammonia feed was converted to hydrogen at ~900 °C (approximately 1.8 W) when operating at atmospheric pressure.^{22,80}

In other experiments, the combustor performance was examined. The combustor was operated with hydrogen or butane in air as the reactant. No reason was given for the selection of butane and not ammonia, which was used for the reformer testing, or methanol, which they also proposed to use. For startup, electrical heaters raised the reactor temperature to the ignition temperature in under 1 s, but once combustion was ignited, no further electrical heating was required. Approximately 1.6 W of thermal power was generated by combusting 0.8 sccm butane in a stoichiometric mixture of air, which should be sufficient power for the ammonia cracking reactions to occur.^{22,80}

3.2.2. Lehigh University Methanol Reforming Reactor

Researchers at Lehigh University are developing a methanol reforming silicon reactor with a palladium membrane for a hydrogen purification system built using semiconductor fabrication techniques.^{82–84} The device is designed to produce hydrogen for fuel cells for portable electronic devices, such as laptop computers and cell phones.

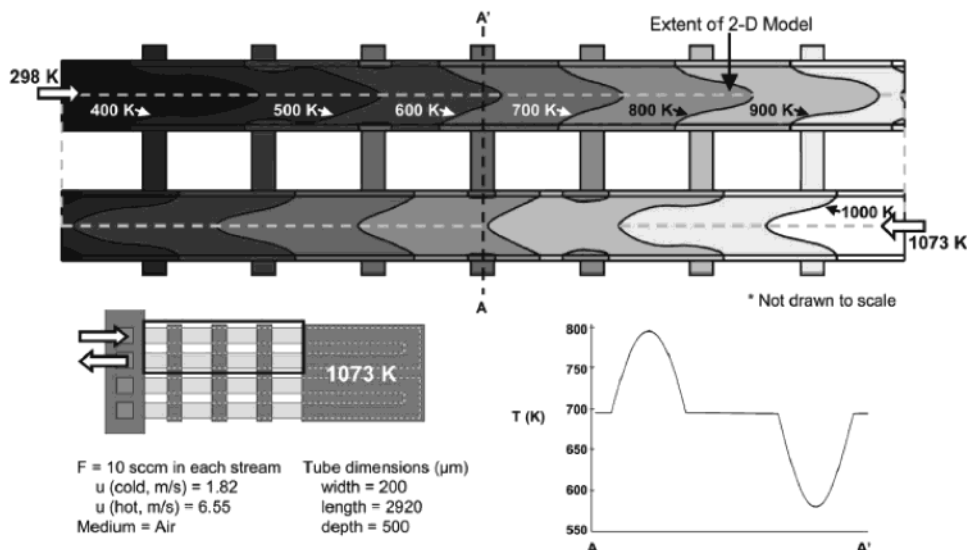


Figure 14. Temperature profile from a 2-D CFD simulation of the suspended-tube reactor (in a vacuum ambient assuming no radiation losses). (Reprinted with permission from ref 22. Copyright 2003 IEEE.)

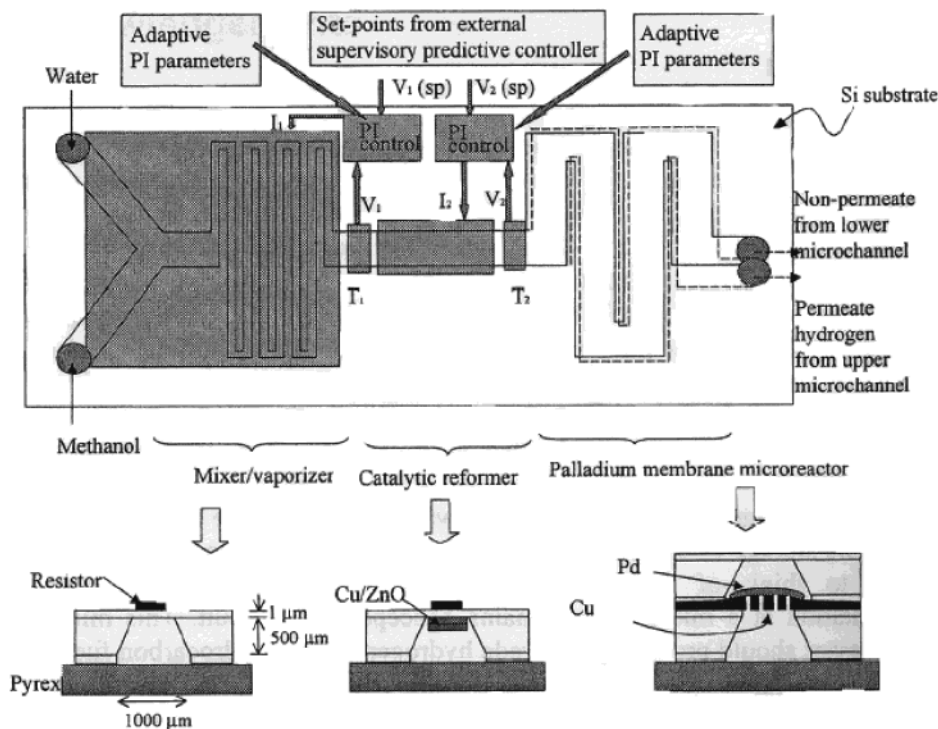


Figure 15. Microreformer illustration. (Reprinted with permission from ref 82. Copyright 2001 Springer.)

The steam reformer is a serpentine channel with a channel width of 1000 μm and depth of 230 μm (Figure 15). Four reformers were fabricated per single 100 mm silicon wafer polished on both sides. In the procedure employed to fabricate the reactors, plasma enhanced chemical vapor deposition (PECVD) was used to deposit silicon nitride, an etch stop for a silicon wet etch later in the process, on both sides of the wafer. Next, the desired pattern was transferred to the back of the wafer using photolithography, and the silicon nitride was plasma etched. Potassium hydroxide was then used to etch the exposed silicon to the desired depth. Copper, approximately 33 nm thick, which was used as the reforming catalyst, was then deposited by sputter deposition. The reactor inlet was made by etching a 1 mm² hole into the end

of one of the channels. First the reactor was covered by black wax, except the end where the hole was desired; then the wafer was etched using potassium hydroxide to form the hole, and the black wax was removed.⁸² The wafer was diced to make four separate reformer reactors.

The reformers were tested in a custom-made stainless steel housing unit.⁸² Graphite pads with appropriate holes for reactant and product interfaces were used as gaskets in the housing. The goal of the tests was to determine if hydrogen could be produced using this configuration. A methanol and water (50:50 by weight) mix was externally vaporized and fed to the reactor, which was maintained at 250 °C. The feed rate was 0.142 g/min. The researchers reported that 0.092 mol of hydrogen per mole of methanol fed

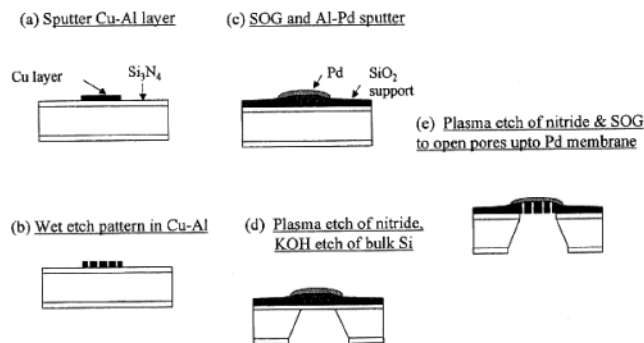


Figure 16. Microscale palladium membrane. (Reprinted with permission from refs 83 and 84. Copyright 2001 and 2002 Springer.)

to the reformer was produced, about 3% of the theoretical maximum of 3 mol of hydrogen per mole of methanol. The next step in the reformer development will be to incorporate a Cu/ZnO catalyst into the reactor.⁸²

The palladium-based membranes were a composite of four layers: copper, aluminum, spin-on-glass (SOG), and palladium. The copper, aluminum, and SOG layers served as a structural support for the thin palladium layer, and the copper was also intended for use as a WGS catalyst in the reactor to increase the yield of hydrogen.^{83,84} The membrane was fabricated in five steps on a 100 mm silicon wafer polished on both sides and with silicon nitride deposited on both sides (Figure 16).^{83,84} First, 66 nm of copper followed by 200 nm of aluminum were sputter deposited on the front of the wafer. The copper was to be used as the catalyst for the WGS reaction, and the aluminum was added to increase the mechanical strength of the free-standing membrane. These metal layers were wet etched into the desired pattern. Next, 500 nm of SOG was deposited and cured for 30 min at 250 °C. The SOG planarized the wafer. A thin layer of aluminum, for adhesion promotion, followed by 200 nm of palladium, was then sputter deposited onto the SOG. The backside of the wafer was patterned by plasma etching the silicon nitride and using a potassium hydroxide solution to etch the bulk silicon, making the reactant flow channels. Pores with a 5.5 μm diameter were opened up to the palladium membrane by plasma etching the silicon nitride and SOG. Two pore arrangements were used: one with pores 14 mm apart and the other with pores 20 mm apart.^{83,84}

Using similar housing as described for the reformer reactor, the membrane's mechanical strength and static hydrogen permeation tests were performed at room temperature. The mechanical strength was tested using pure nitrogen gas. Pressure differentials greater than 15 psi were achieved before the membrane failed.⁸⁴ For the hydrogen permeation tests, one side of the membrane was pressurized to 2 psi with a nitrogen hydrogen mixture (80% nitrogen). At this low temperature and pressure, hydrogen was detected on the other side of the membrane using a quadrupole ion-trap mass spectrometer.⁸⁴ Typical palladium membranes are 25 μm thick or more and are operated at elevated temperatures, >100 °C (usually closer to 300 °C), and elevated pressures,

Table 3. Vaporizer and Reformer Operating Conditions and Performance (Adapted from ref 88)

vaporizer temperature	120 °C
reformer temperature	260 °C
pressure	1 atm
steam-to-carbon molar ratio	1.1:1
reactant flow rate	12 cm ³ /h
conversion	>90%
product gas composition	73.4% hydrogen 25% CO ₂ 1.6% CO
hydrogen production rate	0.498 mol/h = 186 sccm
estimated electric power ^a	15 W

^a Assuming 60% efficient fuel cell utilizing 80% of the hydrogen.

typically >100 psi, and have hydrogen permeation rates such as 1 cm³ H₂ (STP)/(cm² min) (see, for example, refs 85–87). The Lehigh University researchers will need to be able to achieve similar permeation rates.

3.3. Reactors in the 15–100 W Range

3.3.1. Korea Institute of Energy Research 15 W Power Generation

Park et al., who are developing a methanol fuel processor, so far have tested designs for the vaporizer and methanol reformer using electric heating cartridges to provide the thermal energy for the endothermic reaction (Table 3).⁸⁸ A sheet architecture was used to build the units. The microchannels for both the vaporizer and reformer were 500 μm wide and 33 mm long and were patterned onto metal sheets (200 μm thick) using wet chemical etching techniques. Three sheets were stacked to make the total channel depth 600 μm. In addition, manifold sheets with two holes for a flow path and triangular manifolds to enable a more uniform flow distribution were placed on the top and bottom of the stack. The dimensions of the reformer and vaporizer were 70 × 40 × 30 mm³ (excluding fittings).

The catalyst bed was a coated wall reactor using commercial CuZnAl catalyst. An alumina sol was used to enhance the adhesion of the catalyst to the channel walls. After the shims were washed thoroughly, the alumina adhesion layer was deposited using an alumina sol (NYACOL AL20DW colloidal alumina, PQ Corporation) and then dried at 60 °C. To decrease the surface tension of the wash-coat solvent, small amounts of 2-propanol were added to a catalyst slurry of ICI Syntetix 33–5 catalyst, with 20 wt % alumina sol and water. The catalyst was calcined at 350–400 °C for 2 h after air-drying. Before testing, the catalyst was reduced by flowing H₂/N₂ over it at 280 °C.

The reactor was tested using a range of methanol and water concentrations, and researchers found the best results using a water and methanol mixture with a steam-to-carbon ratio (S:C) of 1.1:1.⁸⁸ They were able to achieve 90% conversion at 260 °C with a reactant liquid flow rate of 12 cm³/h. Assuming a fuel cell efficiency of 60% and 80% hydrogen utilization, they estimated the output power to be 15 W. Eventually the complete system will include a cata-

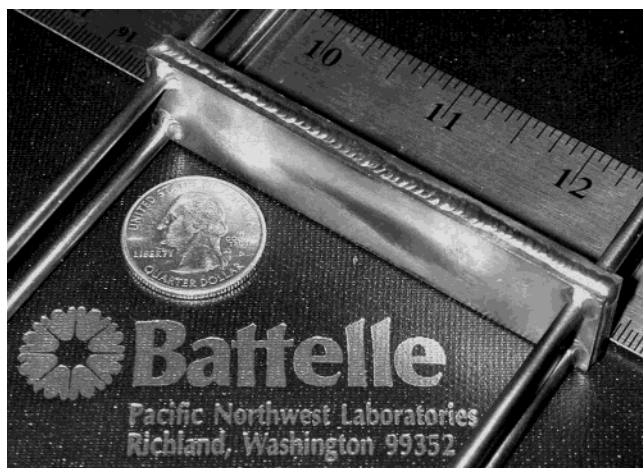


Figure 17. 25–50 W integrated fuel processor.⁶⁴

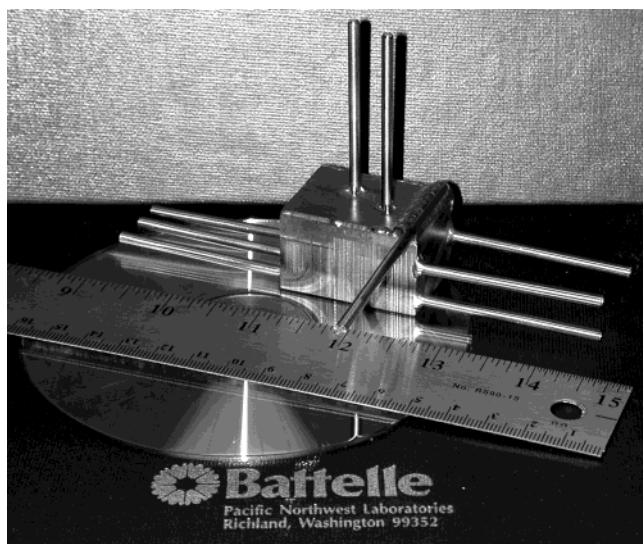


Figure 18. 50 and 100 W integrated fuel processor-cube design.⁸⁹

lytic combustor and carbon monoxide cleanup units.⁸⁸ They will also need to achieve >99% methanol conversion or develop a way to deal with the unconverted methanol.

3.3.2. Battelle, Pacific Northwest Division, 15–100 W Power Generation

Fuel processors being developed at Battelle provide 15 W to over 100 W equivalents of hydrogen from methanol fuel.^{64,89–91} Two architectures based on microchannel technology^{14,15} were used in this work (Figures 17 and 18), which enabled a scalable fabrication over this wide range. The processors consisted of fuel vaporizers and preheaters for both the combustion reactants and steam reforming reactants, a combustor, a steam reformer, heat exchangers, and recuperators.^{64,89–91} The reactors were assembled using a combination of welding, brazing, and diffusion bonding techniques, although the specifics of the techniques and the laminate layer designs are not reported.

In addition to the microchannel technology, Battelle has developed a stable, nonpyrophoric, carbon dioxide selective, methanol reforming catalyst.^{31,32,89–91} The catalyst has been demonstrated to be stable in

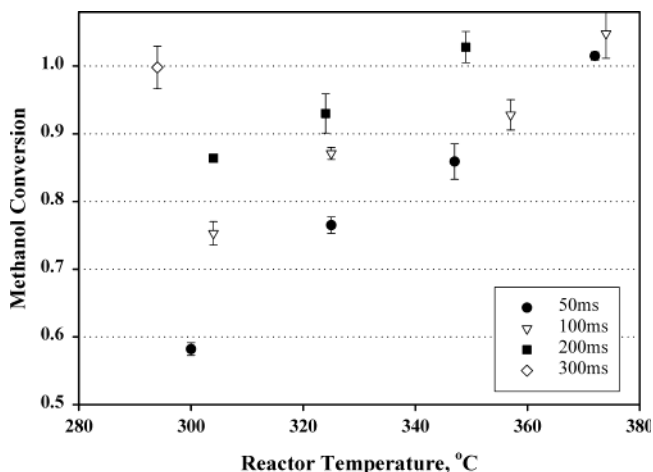


Figure 19. Battelle's methanol specific reforming catalyst. Reactor conditions: atmospheric pressure, reactant feed 50:50 by weight methanol and water mixture, 24 000–50 000 h⁻¹ GHSV. The conversion was reported as moles methanol reacted/moles methanol fed. (Reprinted with permission from ref 91. Copyright 2002 Elsevier.)

Table 4. Battelle Fuel Processor Performance⁷⁰

device design point	20 W	50 W	100 W
demonstrated power, W	6–34	26–54	60–170
volume, cm ³	<20	<25	<30
mass, g	<150	<175	<200
power density, W/L	1800	2100	5600
thermal efficiency, %LHV	28–63	62–84	>80%
energy density, ^a Wh/kg	520–1500 ^b	1032–1732 ^c	1600–2150 ^d

^a Assumes 80% of hydrogen is reacted in the fuel cell, and the fuel cell is 60% efficient. ^b Assumes 1 kg device hardware, 14 day mission, water recycle, anode gas recycle, and parasitic power = 3 W. ^c Assumes 3 kg device hardware, 14 day mission, water recycle, anode gas recycle, and parasitic power = 5 W. ^d Assumes 5 kg device hardware, 14 day mission, water recycle, anode gas recycle, and parasitic power = 10 W.

air, even at elevated temperatures (~200 °C), without loss of activity or carbon dioxide selectivity.^{89–91} No deactivation was observed in a 1000 h lifetime test operating with a water and methanol mixture and at a gas hourly space velocity (GHSV) of 36 000 h⁻¹.^{89–91} The water-to-methanol molar ratio for the mixtures ranged from 3.0:1 to 1.2:1 without any reported difference in lifetime or carbon dioxide selectivity. Typical performance is shown in Figure 19. This catalyst was engineered for operation in low-pressure-drop microchannel reactor configurations.

Recent fuel processor performance is summarized in Table 4. The fuel processors were operated at atmospheric pressure, and the water and methanol feed mixture was about 60 wt % methanol. The typical composition of the reformat stream was 72–74% hydrogen, 24–26% carbon dioxide, and 0.5–1.5% carbon monoxide on a dry gas basis. The carbon monoxide levels were significantly below equilibrium (5.4% at 350 °C), but they still require additional cleanup for use in fuel cells.^{89–91} The fuel processor efficiency was calculated using eq 5 and was reported to be greater than 80%. It is interesting to note that increasing the power 5-fold, from 20 to 100 W, only resulted in a 50% increase in volume and a 33% increase in mass.

Researchers recently began incorporating a catalytic carbon monoxide cleanup system based on

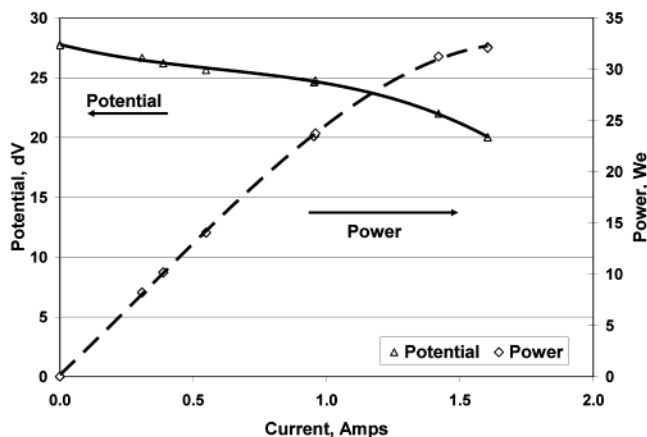


Figure 20. Fuel cell performance demonstration for the Battelle methanol processor and the carbon monoxide removal reactor.⁸⁹

selective carbon monoxide methanation, which decreased the CO to below 100 ppm.⁷⁰ The low carbon monoxide stream from the methanol processor and carbon monoxide removal reactor were used to operate an H-Power fuel cell (Figure 20).⁸⁹

Current efforts are focusing on optimizing the carbon monoxide removal reactor and developing a system prototype using commercially available pumps, blowers, fuel cells, valves, and controllers.⁷⁰ In addition, durability testing along with thermal cycling needs to be done.

3.3.3. MiRTH-e 20–100 W Reactor

The European Union is funding a project to develop microreactor technology for hydrogen and electricity (MiRTH-e) in the 20–100 W size range using methanol steam reforming.^{92,93} Participants include researchers from Shell Global Solutions International (The Netherlands and Great Britain), the Institut für Mikrotechnik Mainz (IMM, Germany), the MESA Research Institute (The Netherlands), the ECN Energy Research Foundation (The Netherlands), The Laboratory of Chemical Reactor Engineering at Eindhoven University of Technology (The Netherlands), and the Laboratoire des Sciences du Génie Chimique of CNRS (France).⁹²

Initially, the reactor was to be built using silicon wafers,⁹² but more recent efforts have focused on a stainless steel reactor.⁹³ The reformer, $7.5 \times 4.5 \times 11.0$ cm³ (371 cm³), houses up to 15 stainless steel plates (0.5 mm thick) with chemically etched microchannels and heating cartridges. Conventional and laser micromachining techniques were used to fabricate the reformer body. The microchannel dimensions are $0.05 \times 0.035 \times 5.0$ cm³. The reactor inlet was carefully designed to allow uniform flow conditions.⁹³

To process the methanol and water mix, a CuZnAl catalyst was wash-coated onto the microchannel walls. The alumina was deposited by dipping the plates into a 20% alumina suspension, which also included a stabilizer and a binder. After any excess was wiped off, the plates were calcined at 600 °C for 1 h in air. Air was removed from the pores by placing the calcined plate in a vacuum. The alumina wash-

coat had a specific area of 72 m²/g, a pore diameter distribution with a maximum of 45 nm, and an average thickness of 10 μm. The copper zinc oxide catalyst (3:1 Cu/Zn ratio) was deposited onto the alumina by impregnating the alumina with a copper zinc nitrate solution and calcining at 300 °C. A loading of 8 wt % was obtained following this preparation technique, although higher loading can be obtained by repeating the impregnation process.⁹³ However, increasing the loading this way may fill in pores, resulting in a net loss of surface area and accessible active catalyst sites hurting performance, so an optimum loading will need to be found.

The reactor performance was evaluated using five wash-coated plates with microchannels. The catalyst was reduced in an atmosphere of 5% hydrogen in nitrogen at 240 °C. Before operation, the catalyst was pretreated at 250 °C for 2 h with a mixture of 30% nitrogen, 47% water, and 23% methanol. This pretreatment brought the catalyst to stable activity before measurements were completed.⁹³ A vaporized mixture of water and methanol (2:1 molar ratio) was fed to the reactor at flow rates from 500 mL/min (STP), and the reactor was operated at atmospheric pressure and 280 °C. Higher-temperature operation was not possible due to limitations of the reactor design. Under these conditions, methanol conversion of 65% was achieved, which translates into approximately 30 W, assuming a fuel cell efficiency of 64%.⁹³ Therefore, increasing the plate number to the 15-plate maximum would result in approximately 90 W.⁹³ Improvements in performance are expected to be achieved by increasing the catalyst loading to 16 wt %. The researchers also reported the need for developing a selective oxidation reactor to decrease the carbon monoxide levels to below 20 ppm.

3.3.4. Motorola Methanol Fuel Processor

A research team from Motorola is developing a methanol fuel processor for use in portable applications. The fuel processor is constructed using ceramic fabrication techniques and includes a fuel vaporizer, a steam reformer, and a catalytic combustor.⁹⁴ The vaporizer is a small chamber loaded with a high-surface-area felt, which allows the high heat transfer rates essential for methanol and water vaporization.⁹⁴ A packed-bed design with alumina-supported CuO/ZnO powder catalyst was selected for the reformer, with the combustor designed to react excess hydrogen from the fuel cell and methanol with air using a platinum catalyst. The catalyst was wash-coated onto the combustor walls.⁹⁴ High methanol conversion rates were achieved at low temperatures (230 °C) using this design. An interesting feature of this development project was the use of PBI-doped with phosphoric acid based fuel cell technology similar to that developed by Case Western Reserve University.⁹⁴ As with the microscale fuel cell using PBI technology described previously, the Motorola fuel cell could operate at high temperatures, enabling the fuel cell to tolerate high levels of carbon monoxide. This CO tolerance negated the need for additional reformat cleanup.⁹⁴

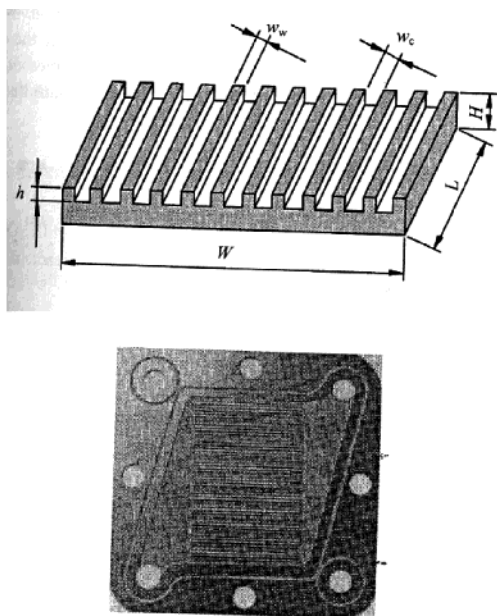


Figure 21. Microchannel reactor chip. (Reprinted with permission from ref 34. Copyright 2003 Elsevier.)

3.3.5. MesoSystems Technology in the 50–100 W Range

MesoSystems is developing a 50 W portable power supply using ammonia as the fuel.^{95,96} The system consists of an ammonia cracking reactor, an ammonia adsorbent, a membrane, heat exchangers, and power controls. They have integrated the system with the necessary pumps, fans, and controls and tested it with fuel cells.

The ammonia cracking reactor is based on what they call mesochannel reactors of stainless steel construction. The reactor operates between 575 and 625 °C at 1 or 4 atm pressure depending on if a membrane is used. Specifics about their membrane and catalysts were not reported. There was an ammonia bypass of 0.2–0.5 wt % of the ammonia feed. Even this small amount of ammonia will irreversibly damage the fuel cell, so they include a proprietary adsorbent. The adsorbent has a capacity of up to 10 wt % ammonia at ppm-level feed stream conditions. Thermal management for the reactor system was accomplished by using compact heat exchangers and innovative high-temperature vacuum insulation panels. The system targets include a 5 min startup and 1000 W h electric power in a 1 L (1 kg) package. This translates into a ~6 wt % hydrogen storage density. They report to have demonstrated this system with H Power Corporation's SSG-50 fuel cell; however, no data were available.⁹⁵ In addition, no lifetime or other durability data were reported.

3.4. Reactors \leq 500 W

3.4.1. Scalable Methanol Autothermal Reforming Reactor

Researchers at the Chinese Academy of Sciences are developing a scalable methanol autothermal reforming (ATR) reactor.³⁴ The microchannel reactor will be composed of multiple "reactor chips" (Figure 21), with each chip able to process enough methanol for approximately 100 W_e hydrogen. Both aluminum and stainless steel were evaluated for use as the chip

substrate. The chips were approximately 7.5 × 7.5 cm². The channels were chemically etched into the metal substrates. The stainless steel chip was 0.34 mm thick and had 48 channels, each channel being 0.17 mm deep, 0.5 mm wide, and 30 mm long. The aluminum chip was 0.8 mm thick and had 38 etched channels, each channel being 0.4 mm deep, 0.8 mm wide, and 30 mm long. The chips were tested in a metal housing that allowed the temperature to be controlled and provided access for the reactant and product streams.

A CeO₂–ZrO₂ supported platinum catalyst was used in this reactor.³⁴ The chips were prepared for the catalyst deposition using the following method. First, the surfaces were cleaned with a Na₂SiO₃ solution to remove any oil and other residues. After the reactor chips were washed with distilled water and dried, CeO₂–ZrO₂ was deposited onto their surfaces, using wash coating techniques. These reactor chips were then dipped into a solution of Pt(NH₃)₄·(OH)₂ (0.1 g/mL) and dried at 120 °C, followed by calcinations at 400 °C in air for 3 h. Before being used, the catalyst was reduced in a 10% hydrogen in nitrogen atmosphere at 400 °C for 2 h.³⁴

After the catalyst was reduced, the microreactor was tested. A water and methanol mixture (1.2:1) was used as the fuel, and the oxygen-to-methanol molar ratio was 0.3:1.³⁴ The oxygen was supplied from air. Using the stainless steel reactor chip with a feed of 186 000 h⁻¹ gas hourly space velocity (GHSV), greater than 99% of the methanol was reacted (reactor conditions = 450 °C and atmospheric pressure). The product gas dry flow was 820 L/h, with 43% being hydrogen (360 L/h). The composition was 43% hydrogen, 0.5% methane, and >15% carbon monoxide, with the rest being nitrogen (from the air feed for ATR operation) and carbon dioxide. The high carbon monoxide levels will require that WGS reactors and preferential oxidation (PrOx) reactors be developed to reduce the carbon monoxide to below 10 ppm.³⁴

3.4.2. Portable Power Using a Propane Cracking Reactor System

Ledjeff-Hey et al. are developing a hydrogen generator able to provide approximately 160 W_e of hydrogen by cracking propane.^{97,98} The overall system consists of two propane cracking batch reactors, a methanation reactor, a combustor, air blowers, eight magnetic valves, a control unit, a fuel cell, an accumulator, and a charge controller (Figure 22). In this system, propane is cracked, producing hydrogen and coke in one reactor while the other is being regenerated.⁹⁸ Initially, some carbon monoxide and carbon dioxide are produced as the residual air from catalyst regeneration is being depleted. The carbon monoxide is removed by the simple methanation reactor in the system. Because the regeneration cycle requires approximately 15 min, the reactor operation is switched every 15 min from cracking to regeneration. During regeneration, coke formed on the catalyst is burned off using air. A key advantage of the propane cracking system is that the product gas has a high hydrogen concentration (>90%) and low

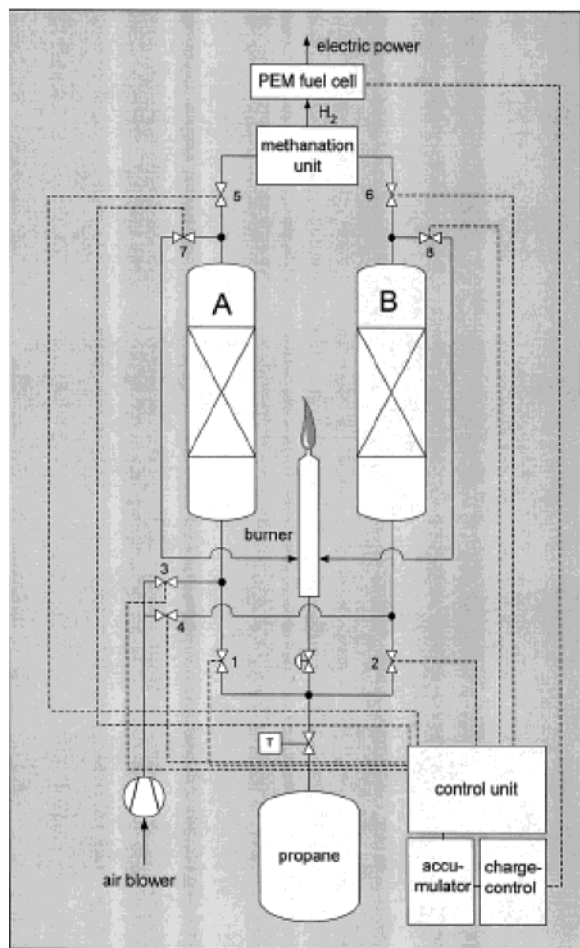


Figure 22. Schematic of a portable fuel cell system with a propane cracker. (Reprinted with permission from ref 98. Copyright 2000 Elsevier.)

carbon monoxide concentration (<1% after the initial 2 min of operation)⁹⁸ However, the authors did not mention the possibility of fouling due to carbon formation. A study on the long-term durability of the system will be interesting.

The catalyst used in this process was a proprietary precious metal catalyst on alumina that was stabilized with a rare earth metal (to prevent sintering).⁹⁸

The researchers reported that this catalyst did not deactivate as quickly as commercially available precious metal catalysts tested.

The complete system with fuel cell is under development. Its projected cost will be \$400–500 (U.S. dollars) for a 130 W_e output.⁹⁸ The system efficiency is estimated to be 9%. This efficiency includes parasitic losses and an assumed fuel cell efficiency of 50%. The parasitic power requirements by the BOP components are about 70 W_e , mostly from the eight magnetic valves, which is one cause for the low system efficiency.⁹⁸ The researchers are looking for lower-power magnetic valves and other solutions to decrease the parasitic power requirements.⁹⁸

3.4.3. Methanol Reforming Reactors for a 200 W_e Fuel Cell Power System

Pfiefer et al. are developing a methanol fuel processor system using steam reforming for a 200 W_e fuel cell based power supply.^{99,100} The researchers are currently working on the methanol reformer reactors, heat exchangers, combustors, and preferential oxidation reactors (Figure 23) for the system.¹⁰⁰ The reactor bodies are either stainless steel or copper.

For the chemical reactor, the researchers used a nanoparticle catalyst deposited on metallic microstructured foils.⁹⁹ They tested Cu/ZnO and Pd/ZnO catalysts deposited on the microstructured foils. The Cu/ZnO catalyst was more active than the Pd/ZnO catalyst and had a lower selectivity to undesired carbon monoxide.¹⁰⁰ However, because the Pd/ZnO catalyst was more stable, it was selected for use in their fuel processor.¹⁰⁰ The Pd/ZnO carbon monoxide selectivity of the powder catalyst pressed into a pellet was lower than that of the nanoparticle catalyst deposited on the microstructured foils. This effect was attributed to contact phases between the catalyst and the metal foils.¹⁰⁰

The reformers were operated at 1.25 bar and up to 310 °C. The feed was composed of 75 g/h of water and 70 g/h of methanol (1.9:1 S/C molar ratio). At 310 °C, over 80% methanol conversion was achieved, with a low amount of carbon monoxide present (<1%). This results in approximately 160 W electric-

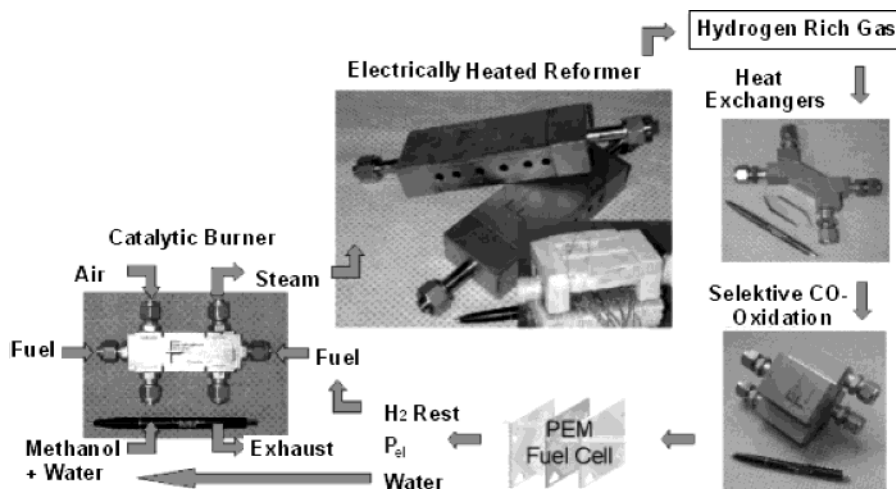


Figure 23. Methanol–steam reformers, heat exchangers, combustor, and selective oxidation reactors; the body material was stainless steel.¹⁰⁰

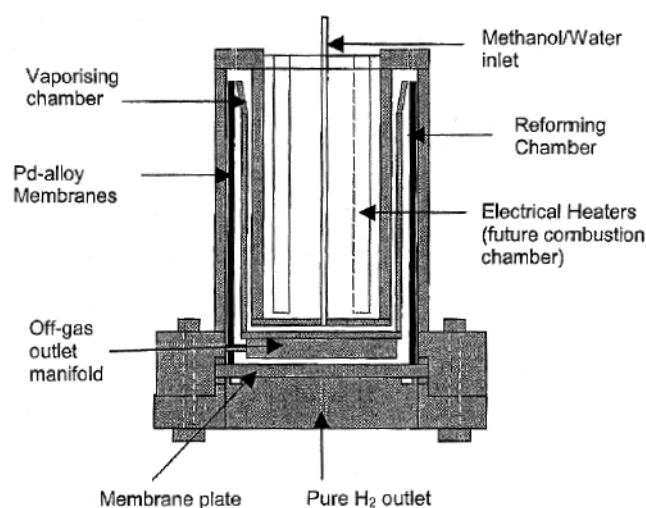


Figure 24. Schematic diagram of the compact steam-methanol processor.¹⁰²

ity production from a 40–45% efficient fuel cell. Therefore, at 100% methanol conversion, the power would be approximately 200 W.¹⁰⁰

3.4.4. Royal Military College of Canada 200–300 W System

Researchers at the Royal Military College of Canada are developing fuel cell hydrogen generation based on methanol reforming technology.^{101–103} They have developed empirical correlations for methanol reforming at 1–4 atm and carbon monoxide yields.¹⁰³ Numerical models for conventional packed-bed methanol reforming reactors have been developed.¹⁰¹ The models included radial heat and mass distributions and also examined deactivation of the Cu/ZnO/Al₂O₃ catalyst in the reactor.¹⁰¹ In addition, the researchers are working on a miniature methanol reformer that will use a membrane for hydrogen purification in the final device.¹⁰²

The fuel processor is sized to provide enough hydrogen for a 200–300 W fuel cell while being the size of a “generous coffee cup”.¹⁰² A measured volume and mass was not reported. It uses a concentric annular design, which will eventually incorporate a combustion chamber (currently electrical heaters) in the middle of the annulus, with a vaporizer, reforming chamber, and palladium alloy hydrogen purifier forming layers (Figure 24). Incorporating a palladium membrane enables pure (>99.999%) hydrogen to be produced but requires elevated pressure operation (>70 psi).¹⁰² The fuel processor contains 259 g of copper-based Sud Chemie G66b methanol steam reforming catalyst (bulk density = 1.4 g/cm³). The reformer and vaporizer components of the device

have been tested using electric heating, and other unit operations will be incorporated in the future.¹⁰²

The reformer was operated for over 554 h, which included 402 h of reforming operation and 152 h of “hot standby.” During hot standby, the catalyst was maintained in the reduced state by flowing 50 cm³ of hydrogen through the catalyst bed, which was kept at a minimum of 260 °C. The reactor was operated over a heater temperature range of 260–300 °C and up to 70 psia. A methanol and water mixture (S/C 1:1 molar) was fed at 1.5–3.5 mL/min. Table 5 summarizes the device performance.¹⁰²

The next step in the processor development will be to integrate the palladium alloy membrane with the methanol steam reformer reactor. The researchers anticipate that the addition of the palladium membrane will improve the reactor performance due to in-situ hydrogen removal.¹⁰²

3.4.5. Emission-Free Reformer Concept for Portable Power Applications

Muradov⁶⁰ proposed using thermal decomposition of hydrocarbons to provide hydrogen for small fuel cells. If the environment is water- and air-free, then the hydrocarbon decomposition products will be coke and hydrogen. Collecting the carbon in a trap and physically removing it is proposed, rather than burning it, as others have done.^{60,98} By collecting the carbon, the process reduces, and may even eliminate, CO and CO₂ emissions.⁶⁰ However, the authors did not address if carbon formed in this system will over time foul the reactor or how this type of system would be made feasible for a portable power supply. The fuel cell and pyrolysis system would consist of a catalytic pyrolytic fuel reformer with a carbon trap and catalytic combustor, a fuel tank, a sulfur trap, a methanator (to remove any residual CO or CO₂), and a fuel cell. Heat for the pyrolysis reactions would be provided by burning the fuel cell anode off-gas. The pyrolytic reforming reactor concept has been demonstrated.

The pyrolytic reforming reactor was a packed bed in a quartz tube reactor. Quartz was selected to reduce the effect of the reactor construction material on the hydrocarbon decomposition rate.⁶⁰ The reactor was packed with 5.0 ± 0.1 g of AC (Darco KB-B) or CB (BP2000) carbon-based catalyst. The reactor was heated electrically and operated at 850–950 °C, and the reactants had a residence time of 20–50 s, depending on the fuel. The reactor was tested with propane, natural gas, and gasoline as the fuels. Experiments showed that a flow of 80% hydrogen, with the remainder being methane, was produced for over 180 min of continuous operation.⁶⁰ The carbon produced was fine particles that could be blown out

Table 5. Methanol Steam Reforming Reactor Performance^a

burner/inlet <i>T</i> (°C)	methanol conversion (%)	methanol/water feed (mL/min)	gas composition, H ₂ /CO/CO ₂	electrical equivalent (W _e)
300/260	97.0	3.5	74.0/2.7/23.3	350
280/240	97.5	2.5	74.0/2.3/23.7	250
260/230	96.0	1.5	74.1/1.8/24.1	150

^a Assumes 12 SLPM hydrogen = 1 kW_e. Adapted from ref 102.

of the reactor into an acceptable container using nitrogen. The estimated energy density, based on the thermal heating value of the hydrogen produced for the reactor system (including tanks), was 1 (kW_{th} h)/kg.⁶⁰ The researchers do not comment on the feasibility of using nitrogen to blow out the fine particles in a real world application. It would be interesting to note if they could use air rather than nitrogen so an additional storage tank is not needed. Nor have they reported lifetime and other durability issues for this system.

4. Summary and Outlook

The development of microreactor technology to produce hydrogen for small, portable, fuel cell based power supplies is progressing at a rapid rate. These small reactors are being designed to provide hydrogen for subwatt power to hundreds of watts of power. Conventional wisdom dictates that, for a fuel cell power system, 1/3 of the volume is for the fuel cell, 1/3 is for the reformer, and 1/3 is for the balance of the plant. With the developments in microreactors reviewed here, the size of the reforming unit is shrinking considerably. Innovative fabrication techniques are being developed and used to manufacture these systems.

The technical success of these palm-sized reactors shows that microfabrication can be used to miniaturize unit operations that traditionally operate at a large scale. Methanol is the dominant fuel in the portable power ranges, but at the higher power levels (>200 W), higher hydrocarbon fuels, such as ethanol and gasoline, are being developed. Commercially available natural gas, propane, gasoline, diesel, or JP8 (for military applications) have not been used as fuels of choice because of their high sulfur content and other impurities. Although ammonia has many attractive characteristics, it has not received the same attention as hydrocarbon fuels.

For these microreactor systems to become viable, several significant technical areas need to be developed: processing system integration, sulfur removal, BOP integration, system durability, and fuel cell integration. The vast majority of microreactors reviewed were composed of the fuel reformer and lacked the other unit operations required for a complete fuel processor system. These additional unit operations include recuperative heat exchangers, vaporizers, a heat source (probably a catalytic combustor or electric heater), secondary conversion reactors (typically a two-stage WGS reactor system), and a final carbon monoxide removal or reduction system (typically a two-stage PrOx or a selective methanation system). Since only parts of the system were developed, efficiencies were often not reported. When efficiencies were reported, they were estimates based on assumed efficiencies of the other components. Although the membrane reactors eliminate the need for the secondary conversion reactors and a final carbon monoxide removal or reduction system, the other unit operations are still required. These unit operations need to be developed and thermally integrated with the fuel reformer. The durability and performance of the individual components and the

complete system will need to be evaluated and proved for a commercially viable product. There have been few lifetime tests, real world tests, or other durability tests done on the microreactors. This should be an area of further work.

For low-power (production of hydrogen for several watts or less power output) reactors, thermal losses caused low efficiencies. Although the reactor size was significantly reduced, in most cases, the piping connecting the reactor to instruments and other components could not be reduced by the same amount. Therefore, the tubing was relatively large and caused a relatively significant heat loss by conduction. In some cases, the thermal losses were reduced by decreasing the connector pipe size, by using advanced insulation, or by using vacuum packaging. The researchers need to continue incorporating these techniques and technologies to improve the system efficiencies, in addition to developing new and innovative ways to prevent heat loss or recapture heat.

Methanol was the fuel of choice for many of the smaller systems due to its low processing temperature and low contaminant (sulfur) level. However, the high energy density of more readily available hydrocarbons, such as propane, natural gas, gasoline, diesel, or JP8 (military logistics fuel), make them attractive candidates for portable power. Several of the reformers reviewed successfully processed sulfur-free versions of these fuels. Thus, obviously, a compact sulfur removal system would be of great interest in this area. Larger-scale systems have been developed that rely on absorbents¹⁰⁴ or selective oxidation of the sulfur compounds;¹⁰⁴ however, they tend to be bulky or have other significant limitations. The development of compact, lightweight, desulfurization systems for portable power is a priority for the use of commercially available fuels.

An often neglected area involves BOP components, especially liquid pumps, air blowers or pumps, controls strategy, valves, water management systems, insulation (for both thermal and noise management), sensors, and power conditioning. Developing of low-cost, efficient, reliable, compact blowers and liquid pumps is particularly important for designs that require elevated pressures, such as membrane reactors. The controls strategy and power conditioning are particularly important in developing a safe robust system. Since the fuel cells produce water, a water management system is crucial, especially when the fuel processor and fuel cell system will be operating close to electronic devices. Of course, the BOP needs to be as compact and efficient as possible. Passive BOP systems are preferred; however, active systems may result in significant savings in size and cost. For example, a fuel cell can be designed to be "air breathing", meaning that the cathode air is supplied by natural convection; however, an active design allows the fuel cell to operate at higher power levels, thus reducing the size of the fuel cell (and its associated platinum and other materials costs) and allowing better water management. The developers will need to optimize these systems for their specific applications.

For the highest efficiency to be achieved, the fuel cell and fuel processor must be closely coupled. Several engineering issues need to be resolved. For example, will the anode off-gas be burned in a combustor for the generation of heat; does it contain a high enough heating value to provide the heat; or can the cathode air be used in the combustor, thus eliminating one air blower? Is flow desired first through the combustor or through the fuel cell? What will this do to the system? The answers to these questions will provide the key to optimal integration and packaging. Nontechnical issues such as cost and regulations will also play a role in the success of commercializing the technology. The micropower system (fuel cell, fuel processor, and BOP components) must be competitively priced with appropriately sized alternative primarily batteries. A customer may be willing to spend more to get a better product, but what is the limit? A report prepared by the Darnell Group, Inc., for the U.S. Fuel Cell Council provides interesting insight into this area.¹⁰⁵ As a comparison scenario, they used the introduction of Li-polymer batteries as an alternative to Li-ion batteries. The Li-polymer batteries offered value-added features such as increased robustness and higher specific energy of 145–190 Wh/kg compared to 120–150 Wh/kg for Li-ion batteries,¹⁰⁶ but at a higher cost. The report recounted that the average original equipment manufacturer (OEM) price for a Li-ion battery pack for mobile phones in 1999 was \$13.59, while for a Li-polymer pack it was \$16.39, a price premium of 21%.¹⁰⁵ For notebook computers, the Li-ion battery pack average price to OEMs was \$60.39, and for Li-polymer, it was \$79.77, a price premium of 32%.¹⁰⁵ In 1999, the Li-polymer battery pack prices were expected to decrease by about 14% per year. However, when this decrease did not occur, the Li-polymer battery “failed” in the marketplace as a significant competitor to Li-ion batteries.¹⁰⁵ However, the Darnell Group also reported that major battery manufacturers, Samsung, SDI, LG Chemicals, and SKC, announced in July 2002 they were planning to make “large investments” in Li-polymer battery technology.¹⁰⁵ This announcement was interpreted to mean lower Li-polymer prices, which will then result in lower Li-ion prices.¹⁰⁵ This report demonstrates that (1) while it may be superior, the fuel cell product needs to be priced competitively with its counterpart batteries and (2) the fuel cell product target price needs to be competitive with future, not current, battery prices, and a sharp decrease in battery prices should be anticipated whenever a fuel cell product is introduced.

Government regulations cover a wide range of subjects pertaining to fuel cell systems, such as the fuel cells themselves, fuel packaging, fuel distribution, carrying fuel cells on airplanes, use and transportation of a flammable fuel on airplanes, and fuel processing for portable devices, particularly indoors and especially important for high-pressure applications. These regulations, which can be viewed on government Web sites and obtained from government resources such as the American National Standards Institute (ANSI), the Code of Federal Regulations

(CFR), the International Code Council (ICC), the National Hydrogen Association, and the International Organization for Standardization (ISO), to name a few, will play a part in dictating the expanded use of fuel cell products.

In this paper, hydrogen generation from microreactors was reviewed, design considerations were discussed, fabrication methods were presented, and examples of reactors over a wide power range were examined. It is clear that a great deal of research is occurring in this relatively new area and that impressive progress has been achieved. With the continuing advancements, the future looks bright for this needed technology.

5. Acronyms

ATR	autothermal reforming
BOP	balance-of-plant
CFD	computational fluid dynamics
CVD	chemical vapor deposition
DRIE	deep reactive ion etching
EDM	electrodischarge machining
GHSV	gas hourly space velocity
LHV	lower heating value
LIGA	lithographie, galvanofornung, abformtechnik
LTCC	low-temperature co-fired ceramics
MEMS	microelectromechanical systems
PBI	polybenzimidazole
PECVD	plasma enhanced chemical vapor deposition
PEMFC	polymer electrolyte membrane fuel cell
PrOx	preferential oxidation
RF	radio frequency
S/C	steam-to-carbon ratio
SEM	scanning electron microscopy
SLPM	standard liters per minute
SOG	spin-on-glass
STP	standard temperature and pressure
SV	space velocity
TEM	transmission electron microscopy
WGS	water-gas-shift
XRD	X-ray diffraction

6. References

- (1) Matta, L. M.; Nan, M.; Davis, S. P.; McAllister, D. V.; Zinn, B. T.; Allen, M. G. American Institute of Aeronautics and Astronautics, Aerospace Sciences Meeting and Exhibit, Reno, NV, 2001; paper 2001-0978.
- (2) Schaevitz, S. B.; Franz, A. J.; Jensen, K. F.; Schmidt, M. A. The 11th International Conference on Solid-State Sensors and Actuators, Munich, Germany, 2001; pp 30–33.
- (3) Fu, K.; Knobloch, A.; Martinez, F.; Walther, D. C.; Fernandez-Pello, C.; Pisano, A. P.; Liepmann, D.; Miyaska, K.; Maruta, K. 2001 International Mechanical Engineering Congress and Exposition, 2001.
- (4) Fu, K.; Knobloch, A. J.; Martinez, F. C.; Walther, D. C.; Fernandez-Pello, C.; Pisano, A. P.; Liepmann, D. 2001 International Mechanical Engineering Congress and Exposition, 2001.
- (5) Maruta, K.; Takeda, K.; Sitzki, L.; Borer, K.; Ronney, P. D.; Wussow, S.; Deutschmann, O. Third Asia-Pacific Conference on Combustion, Seoul, Korea, 2001.
- (6) Richards, C. D.; Bahr, D. F.; Xu, C. G.; Richards, R. F. 36th Intersociety Energy Conversion Engineering Conference, Savannah, GA, 2001.
- (7) Hoogers, G. In *Fuel Cell Technology Handbook*; Hooger, G., Ed.; CRC Press: Boca Raton, FL, 2003.
- (8) Wainright, J. S.; Savinell, R. F. Fall 2000 Meeting of the Electrochemical Society, Phoenix, AZ, 2000.
- (9) Savinell, R. F. Gordon Research Conference on Electrochemistry, CA, 2001.
- (10) Jones, P. B.; Lakeman, J. B.; Mepsted, G. O.; Moore, J. M. *J. Power Sources* **1999**, *80*, 242.
- (11) Oroskar, A. R.; VandenBussche, K. M.; Abdo, S. F. Fifth International Conference on Microreaction Technology, Strasbourg, France, 2001; p 153.

- (12) Henderson, I. R. M. *Process Intensification Topical Session in AICHE Spring 2003*, New Orleans, LA, 2003; p 109.
- (13) Ehrfeld, W.; Ehrfeld, U. *Fifth International Conference on Microreaction Technology*, Strausbourg, France, 2001; p 3.
- (14) Wegeng, R. S.; Drost, M. K.; Call, C. J.; Birmingham, J. G.; McDonald, C. E.; Kurath, D. E.; Friedrich, M. U.S. Patent 5,611,214, 1998.
- (15) Wegeng, R. S.; Drost, M. K.; McDonald, C. E. U.S. Patent 5,811,062, 1997.
- (16) Jensen, K. F. *Chem. Eng. Sci.* **2001**, *56*, 293.
- (17) Thompson, L. T. *Microreaction Technology and Process Intensification Symposium at the 226th American Chemical Society National Meeting*, New York, 2003; abstract 35.
- (18) Johnson, W. L.; Phillips, C. B.; Chen, Z.; Ransom, T. S.; Thompson, L. T. *Microreaction Technology and Process Intensification Symposium at the 226th American Chemical Society National Meeting*, New York, 2003; abstract number 41.
- (19) Tonkovich, A. Y.; Zilka, J. L.; LaMont, M. J.; Wang, Y.; Wegeng, R. S. *Chem. Eng. Sci.* **1999**, *54*, 2947.
- (20) Ameal, T. A.; Papautsky, I.; Warrington, R. O.; Wegeng, R. S.; Drost, M. K. *J. Propul. Power* **2000**, *16*, 577.
- (21) Xia, Y. N.; Whitesides, G. M. *Angew. Chem., Int. Ed. Engl.* **1998**, *37*, 550.
- (22) Arana, L. R.; Schaevitz, S. B.; Franz, A. J.; Schmidt, M. A.; Jensen, K. F. *J. MEMS* **2003**, *12*, 600.
- (23) Tonkovich, A. L. Y.; Wang, Y.; Gao, Y. U.S. Patent 6,440,895B1, 2002.
- (24) Tonkovich, A. Y.; Perry, S.; Wang, Y.; Rogers, W. A.; Qui, D.; Peng, Y. *Chem. Eng. Sci.*, in press.
- (25) Wan, Y. S. S.; Chau, J. L. H.; Gavriilidis, A.; Yeung, K. L. *Fifth International Conference on Microreaction Technology*, Strausbourg, France, 2001; p 94.
- (26) Hoogers, G. In *Fuel Cell Technology Handbook*; Hooger, G., Ed.; CRC Press: Boca Raton, FL, 2003.
- (27) *Catalyst Handbook*, 2nd ed.; Twigg, M. W., Ed.; Wolfe Publishing Ltd.: London, 1989.
- (28) Rostrup-Nielsen, J. In *Encyclopedia of Catalysis*; Horvath, I. T., Ed.; Wiley-Interscience, New York, 2003; Vol. 4.
- (29) Trimm, D. L.; Onsan, Z. I. *Catal. Rev.* **2001**, *43*, 31.
- (30) Song, C. S. *Catal. Today* **2002**, *77*, 17.
- (31) Chin, Y. H.; Dagle, R. A.; Dohnalkova, A.; Hu, J.; Wang, Y. *Catal. Today* **2002**, *77*, 79.
- (32) Chin, Y. H.; Wang, Y.; Dagle, R. A.; Li, X. S. *Fuel Process. Technol.* **2003**, *83*, 193.
- (33) Chen, H.; Ouyang, X.; Shin, W. C.; Park, S. M.; Bednarova, L.; Besser, R. S.; Lee, W. Y. *IMRET 7*, Lausanne, Switzerland, 2003.
- (34) Chen, G.; Yuan, Q.; Li, S.; Pillot, C.; Li, H. *Process Intensification—AICHE Spring 2003*, New Orleans, LA, 2003; p 21.
- (35) Choi, Y.; Stenger, H. G. *Appl. Catal., B: Environ.* **2002**, *38*, 259.
- (36) Cao, C.; Xia, G.; Holladay, J.; Jones, E.; Wang, Y. *Appl. Catal., A: Gen.* **2004**, *262*, 19.
- (37) Gorecki, B. J.; Haylett, D.; Dietrich, D.; Allen, J. *American Institute of Chemical Engineers Topical Proceedings: Fuel Cell Technology: Opportunities and Challenges*, New Orleans, LA, 2002; p 136.
- (38) Takezawa, N.; Kobayashi, H.; Hirose, A.; Shimokawabe, M.; Takahashi, K. *Appl. Catal.* **1982**, *4*, 127.
- (39) Iwasa, N.; Takahashi, K.; Masuda, S.; Takezawa, N. *Catal. Lett.* **1993**, *19*, 211.
- (40) Iwasa, N.; Masuda, S.; Ogawa, N.; Takezawa, N. *Appl. Catal.* **1995**, *125*, 145.
- (41) Holladay, J. D.; Jones, E. O.; Phelps, M.; Hu, J. L. *J. Power Sources* **2002**, *108*, 21.
- (42) Pietrogrande, P.; Bezzeccheri, M. In *Fuel Cell Systems*; Blomen, L. J. M. J., Mugerwa, M. N., Eds.; Plenum Press: New York, 1993.
- (43) Adris, A. M.; Pruden, B. B. *Can. J. Chem. Eng.* **1996**, *74*, 177.
- (44) Wang, Y.; Chin, Y.; Rozmiarek, R. T.; Watson, J.; Tonkovich, A. L. Y. *Catal. Today*, in press.
- (45) Wei, J.; Iglesia, E. *J. Phys. Chem. B* **2004**, *108*, 4094.
- (46) Rostrup-Nielsen, J. R. *J. Catal.* **1973**, *31*, 173.
- (47) Ross, J. R. H. In *Surface and Defect Properties of Solids*; Roberts, M. W., Thomas, J. M., Eds.; Chemical Society: London, 1974; Vol. 4.
- (48) Krummenacher, J. J.; West, K. N.; Schmidt, L. D. *J. Catal.* **2003**, *215*, 332.
- (49) Krumpelt, M. *Joint DOE/ONR Fuel Cell Workshop*, Baltimore, MD, 1999.
- (50) Krumpelt, M.; Krause, T. R.; Carter, J. D.; Kopasz, J. P.; Ahmed, S. *Catal. Today* **2002**, *77*, 3.
- (51) Bellows, R. J. *Joint DOE/ONR Fuel Cell Workshop*, Baltimore, MD, 1999.
- (52) TeGrotenhuis, W. E.; King, D. L.; Brooks, K. P.; Golladay, B. J.; Wegeng, R. S. *6th International Conference on Microreaction Technology*, New Orleans, LA, 2002; p 18.
- (53) Patt, J.; Moon, D. J.; Phillips, C.; Thompson, L. *Catal. Lett.* **2000**, *65*, 193.
- (54) Chandler, B. D.; Schabel, A. B.; Pignolet, L. H. *J. Catal.* **2000**, *193*, 186.
- (55) Hilaire, S.; Wang, X.; Luo, T.; Gorte, R. J.; Wagner, J. *Appl. Catal., A: Gen.* **2001**, *215*, 271.
- (56) Zhao, S.; Gorte, R. J. *Catal. Lett.* **2004**, *92*, 75.
- (57) Wojcik, A.; Middleton, H.; Damopoulos, I.; Van herle, J. *J. Power Sources* **2003**, *118*, 342.
- (58) Gardner, K. *3rd Annual International Symposium on Small Fuel Cells and Battery Technologies for Portable Power Applications*, Washington, DC, 2001.
- (59) Uribe, F. A.; Zawodzinski, T. A. *2001 Joint International Electrochemical Society Meeting*, San Francisco, CA, 2001; p abs. 339.
- (60) Muradov, N. *J. Power Sources* **2003**, *118*, 320.
- (61) Taylor, J. D.; Herdman, C. M.; Wu, B. C.; Wally, K.; Rice, S. F. *Int. J. Hydrogen Energy* **2003**, *28*, 1171.
- (62) Cortright, R. D.; Davda, R. R.; Dumesic, J. A. *Nature* **2002**, *418*, 964.
- (63) Jones, E.; Holladay, J.; Perry, S.; Orth, R.; Rozmiarek, B.; Hu, J.; Phelps, M.; Guzman, C. E. *5th International Conference on Microreaction Technology*, Strausbourg, France, 2001; p 277.
- (64) Holladay, J.; Jones, E.; Palo, D. R.; Phelps, M.; Chin, Y.-H.; Dagle, R.; Hu, J.; Wang, Y.; Baker, E. *Materials Research Society 2002 Fall Meeting*, Boston, MA, 2002; p FF9.2.
- (65) Holladay, J.; Jones, E.; Phelps, M.; Hu, J. *6th International Conference on Microreaction Technology*, New Orleans, LA, 2002; p 107.
- (66) Holladay, J. D.; Jones, E. O.; Phelps, M.; Hu, J. *MEMS Components and Applications for Industry, Automobiles, Aerospace, and Communication*, Oct 22–23, 2001, San Francisco, CA, 2001; p 148.
- (67) Holladay, J. D.; Palo, D. R.; Dagle, R. A.; Phelps, M. R.; Chin, Y. H.; Wang, Y.; Baker, E. G.; Jones, E. O. *J. Power Sources* **2004**, *131*, 69.
- (68) Holladay, J. D.; Phelps, M. R.; Jones, E.; Palo, D. R. *American Institute of Chemical Engineers Topical Conference: Process Intensification*, New Orleans, LA, 2003; p 16.
- (69) Holladay, J. D.; Wainright, J. S.; Jones, E. O.; Gano, S. R. *J. Power Sources*, submitted for publication.
- (70) Holladay, J. D.; Palo, D. R.; Dagle, R. A.; Chin, Y. H.; Cao, J.; Xia, G.; Phelps, M.; Wang, Y.; Jones, E.; Baker, E. G. *Fuel Cell Seminar 2003*, Miami, FL, 2003.
- (71) Bednarova, L.; Chen, H.; Ouyang, X.; Shin, W. C.; Park, S. M.; Besser, R. S.; Lee, W. Y. *3rd International TRI/Princeton Workshop*, Princeton, NJ, 2003.
- (72) Bednarova, L.; Ouyang, X.; Chen, H.; Besser, R. S. *226th ACS National Meeting*, New York City, New York, 2003.
- (73) Bednarova, L.; Ouyang, X.; Chen, H.; Besser, R. S. *226th ACS National Meeting*, New York City, New York, 2003.
- (74) Bednarova, L.; Ouyang, X.; Chen, H.; Lee, W. Y.; Besser, R. S. *ACS Symposium 2003*, 2003; p 846.
- (75) Besser, R. S.; Lee, W. Y.; Ho, P.; Ouyang, X.; Chen, H.; Bednarova, L. *IMRET 7*, Lausanne, Switzerland, 2003.
- (76) Besser, R. S.; Shin, W. C. *J. Vac. Sci. Technol., B* **2003**, *21*, 912.
- (77) Ouyang, X.; Chen, H.; Bednarova, L.; Shin, W.; Besser, R. S. To be published in *CEJ*.
- (78) Ouyang, X.; Ho, P.; Chen, H.; Shin, W. C.; Bednarova, L.; Lee, W. Y.; Besser, R. S.; Pau, S.; Pai, C. S.; Taylor, J. A.; Mansfield, W. M. *AICHE Annual Meeting 2003*, San Francisco, CA, 2003; p Proc. AIChE Annual Meeting.
- (79) Davis, P.; Milliken, J.; Devlin, P.; Gronich, S. *2003 Fuel Cell Seminar*, Miami Beach, FL, 2003; p 760.
- (80) Arana, L. R.; Schaevitz, S. B.; Franz, A. J.; Schmidt, M. A.; Jensen, K. F. *6th International Conference on Microreaction Technology*, New Orleans, LA, 2002; p 147.
- (81) Quiram, D. J.; Hsing, I.-M.; Franz, A. J.; Jensen, K. F.; Schmidt, M. A. *Chem. Eng. Sci.* **2000**, *55*, 3065.
- (82) Pattekar, A. V.; Kothare, M. V.; Karnik, S. V.; Hatalis, M. K. *5th International Conference on Microreaction Technology*, Strausbourg, France, 2001; p 332.
- (83) Karnik, S. V.; Hatalis, M. K.; Kothare, M. V. *5th International Conference on Microreaction Technology*, Strausbourg, France, 2001; p 295.
- (84) Karnik, S. V.; Hatalis, M. K.; Kothare, M. V. *Materials Science of Microelectromechanical Systems (MEMS) Devices IV*, Nov 25–28, 2001, Boston, MA, 2002; p 243.
- (85) Tosti, S.; Bettinali, L.; Violante, V. *Int. J. Hydrogen Energy* **2000**, *25*, 319.
- (86) Li, A.; Liang, W.; Hughes, R. *J. Membr. Sci.* **2000**, *165*, 135.
- (87) Hara, S.; Sakaki, K.; Itoh, N.; Kimura, H.-M.; Asami, K.; Inoue, A. *J. Membr. Sci.* **2000**, *164*, 289.
- (88) Park, G.-G.; Seo, D. J.; Park, S.-H.; Yoon, Y.-G.; Kim, C.-S. *Chem. Eng. J.*, submitted for publication.
- (89) Palo, D. R.; Holladay, J. D.; Dagle, R. A.; Chin, Y. H.; Baker, E. G. *American Institute of Chemical Engineers: 2nd Topical Conference on Fuel Cell Technology*, New Orleans, LA, 2003; p 143.
- (90) Palo, D. R.; Holladay, J. D.; Rozmiarek, R. T.; Guzman-Leong, C. E.; Wang, Y.; Hu, J.; Chin, Y. H.; Dagle, R. A.; Baker, E. G. *5th International Conference on Microreaction Technology*, Strausbourg, France, 2001; p 359.

- (91) Palo, D. R.; Holladay, J. D.; Rozmiarek, R. T.; Guzman-Leong, C. E.; Wang, Y.; Hu, J. L.; Chin, Y. H.; Dagle, R. A.; Baker, E. G. *J. Power Sources* **2002**, *108*, 28.
- (92) Delsman, E. R.; Rebrov, E. V.; de Croon, M. H. J. M.; Schouten, J. C.; Kramer, G. J.; Cominos, V.; Richter, T.; Veenstra, T. T.; van den Berg, A.; Cobden, P. D.; F. A., d. B.; D'Ortona, U.; Falk, L. 5th International Conference on Microreaction Technology, Strasbourg, France, 2001; p 368.
- (93) Cominos, V.; Hardt, S.; Hessel, V.; Kolb, G.; Löwe, H.; Wichert, M.; Zapf, R. 6th International Conference on Microreaction Technology, New Orleans, LA, 2002; p 113.
- (94) Changrani, R.; Gervasio, D.; Koripella, R.; Rogers, S. P.; Samms, S. R.; Tasic, S. 6th International Conference on Microreaction Technology, New Orleans, LA, 2002; p 108.
- (95) Call, C. J.; Powell, M. R.; Fountain, M.; Chellappa, A. S. The Knowledge Foundation's 3rd Annual International Symposium on Small Fuel Cells and Battery Technologies for Portable Power Applications, Washington, DC, 2001.
- (96) Chellappa, A. S.; Powell, M. R.; Fountain, M.; Call, C. J.; Godshall, N. A. *Abstr. Pap. Am. Chem. Soc.* **2002**, *224*, 123-FUEL.
- (97) Ledjeff-Hey, K.; Formanski, V.; Kalk, T.; Roes, J. *J. Power Sources* **1998**, *71*, 199.
- (98) Ledjeff-Hey, K.; Kalk, T.; Mahlendorf, F.; Niemzig, O.; Trautmann, A.; Roes, J. *J. Power Sources* **2000**, *86*, 166.
- (99) Pfeifer, P.; Fichtner, M.; Schubert, K.; Liauw, M. A.; Emig, G. 3rd International Conference on Microreaction Technology, Frankfurt, Germany, 1999.
- (100) Pfeifer, P.; Schubert, K.; Fichtner, M.; Liauw, M. A.; Emig, G. 6th International Conference on Microreaction Technology, New Orleans, LA, 2002; p 125.
- (101) Thurgood, C. P.; Amphlett, J. C.; Mann, R. F.; Peppley, B. A. 2nd Topical Conference on Fuel Cell Technology, 2003 Spring AICHE National Meeting, New Orleans, LA, 2003; p 161.
- (102) Wheeldon, I. R.; Amphlett, J. C.; Mann, R. F.; Peppley, B. A.; Thurgood, C. P. 2nd Topical Conference on Fuel Cell Technology, 2003 Spring AICHE National Meeting, New Orleans, LA, 2003; p 156.
- (103) Amphlett, J. C.; Mann, R. F.; Peppley, B. A.; Stokes, D. M. Proceedings of the 26th Intersociety Energy Conversion Engineering Conference—IECEC '91, Aug 4–9, 1991, Boston, MA, 1991; p 642.
- (104) Lampert, J. Eighth Grove Fuel Cell Symposium, London, England, 2003; p O2B.5.
- (105) *Fuel Cells for Portable Power: Markets, Manufacture and Cost*; Darnell Group Inc.: 2003.
- (106) Ehrlich, G. M. In *Handbook of Batteries*, 3rd ed.; Linden, D., Reddy, T. B., Eds.; McGraw-Hill: New York, 2002.

CR020721B

Factors Governing Oxygen Reduction in Solid Oxide Fuel Cell Cathodes†

Stuart B. Adler

Department of Chemical Engineering, University of Washington, Box 351750, Seattle, Washington 98195-1750

Received March 30, 2004

Contents

1. Introduction	4791	6.1. Sensitivity of Interfacial Electrochemical Kinetics to Secondary Phases and Impurities	4825
2. Understanding the Three-Phase Boundary—A Long History of Inquiry	4793	6.2. Alteration of Material Properties Near the Interface	4828
3. Platinum Electrodes—Interplay of Chemical and Electrochemical Steps	4794	6.3. Ceria as an Alternative Electrolytic Interface	4829
3.1. Two Schools of Thought	4795	6.4. Composite Microstructures	4830
3.2. Chemical Contributions to the Overpotential	4796	6.5. Current Constriction Effects	4832
3.3. Evidence for Diffusion and Adsorption Limitations on Platinum	4797	6.6. Long-Term Degradation	4833
3.4. Important Refinement: Co-limited Reaction Kinetics	4799	6.7. Experimental Artifacts in Electrochemical Measurements	4834
3.5. Unresolved Issues Surrounding Oxygen Reduction on Pt/YSZ	4801	7. Conclusions and Outlook	4837
3.6. Nonstationary Effects	4802	8. Acknowledgements	4838
3.7. Summary: Platinum as a Framework for Understanding Other SOFC Cathodes	4804	9. Nomenclature	4839
4. Perovskite Mixed Conductors and the Role of Bulk Material Properties	4804	10. Glossary of Commonly Used Acronyms	4839
4.1. Perovskite Oxides—Low-Cost Alternative to Platinum	4804	11. Glossary of Some Commonly Used Terms	4839
4.2. Thermodynamic, Kinetic, and Transport Properties of Perovskite Mixed Conductors	4805	12. References	4839
4.3. Defining the Role of the Bulk—Dense Thin-Film Mixed-Conducting Electrodes	4807		
4.4. Chemical Capacitance	4808		
4.5. Porous Mixed Conductors—A More Complex Case	4809		
4.6. One Asymptotic Limit—The Bulk Reaction Path	4810		
4.7. Limitations of Bulk, 1D Transport Models for Porous Mixed Conductors	4813		
4.8. Summary: Importance of the Bulk for Mixed-Conducting SOFC Cathodes	4815		
5. Lanthanum Strontium Manganese Oxide (LSM): Where Surface and Bulk Converge	4816		
5.1. Three-Phase Boundary: Not the Whole Picture	4816		
5.2. Complex Stationary Electrochemical Characteristics and Properties	4817		
5.3. Dense and Patterned Thin Films: Confirming Two Regimes of Operation	4820		
5.4. Nonstationary Behavior in LSM	4823		
5.5. Summary: Uncertainties in Our Understanding of Oxygen Reduction on LSM	4825		
6. Factors Complicating our Understanding of SOFC Cathode Mechanisms	4825		

1. Introduction

Recent worldwide interest in building a decentralized, hydrogen-based energy economy has refocused attention on the solid oxide fuel cell (SOFC) as a potential source of efficient, environmentally friendly, fuel-versatile electric power. Due to its high operating temperature, the SOFC offers several potential advantages over polymer-based fuel cells, including reversible electrode reactions, low internal resistance, high tolerance to typical catalyst poisons, production of high-quality waste heat for (among other uses) reformation of hydrocarbon fuels, as well as the possibility of burning hydrocarbon fuels directly.

Today, SOFCs are much closer to commercial reality than they were 20 years ago, due largely to technological advances in electrode material composition, microstructure control, thin-film ceramic fabrication, and stack and system design. These advances have led to dozens of active SOFC development programs in both stationary and mobile power and contributed to commercialization or development in a number of related technologies, including gas sensors,¹ solid-state electrolysis devices,² and ion-transport membranes for gas separation and partial oxidation.³ Many reviews are available which summarize the technological advances made in SOFCs over the last 15–35 years—readers who are primarily interested in knowing the state-of-the-art in materials, design, and fabrication (including the electrodes) are encouraged to consult these reviews.^{4–12}

This review focuses on the factors governing SOFC cathode performance—advances we have made over

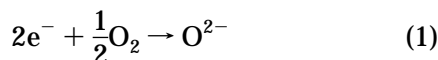
† Dedicated to Brian Steele, 1929–2003. Researcher, Entrepreneur, Consensus Seeker.



Stuart B Adler received his Ph.D. degree in Chemical Engineering in 1993 from the University of California, Berkeley, where he used high-temperature nuclear magnetic resonance (NMR) to probe microstructure, atomic motion, and electronic structure in electrochemical ceramics. His work in ionic materials continued at Imperial College (NATO–NSF fellow), where he developed continuum mechanical theories for high-temperature electrodes. In 1994 he moved to Ceramtec, Inc., where he led research supporting commercialization of ion transport membranes and other oxygen production and removal processes. After rejoining academia in 1999 (CWRU), he moved in 2002 to the University of Washington, Department of Chemical Engineering. There his work in electrochemical ceramics has continued, including advanced measurement and modeling techniques for solid-state electrodes and independent studies of kinetic, transport, and thermodynamic properties of solids. Professor Adler's awards include the NSF–NATO postdoctoral Fellowship (1993), and NSF Career Award (2001), and most recently he is the inaugural recipient of the biennial Charles W. Tobias Young Investigator Award of the Electrochemical Society (2004).

the last 20 years in our scientific understanding of oxygen reduction mechanisms, how these mechanisms vary for different materials and conditions, and remaining questions and challenges that have been generated by this large volume of work.

For the purposes of review, Figure 1 illustrates the basic function of the cathode in a solid oxide fuel cell. Whether acting alone or as part of a stack of cells, each cell consist of a free-standing or supported membrane of an oxygen-ion-conducting electrolyte, often yttria-stabilized zirconia (YSZ). Oxygen, which is fed (usually as air) to one side of the membrane, is reduced by the cathode to oxygen ions via the overall half-cell reaction



Oxygen ions thus created migrate selectively through the membrane to the anode, where they undergo a similar half-cell reaction with a gaseous fuel (either H_2 , syngas, or a hydrocarbon) to produce H_2O and CO_2 . The flow of electrons liberated and consumed at the anode and cathode, respectively, deliver some portion of the reversible work of the reaction to the

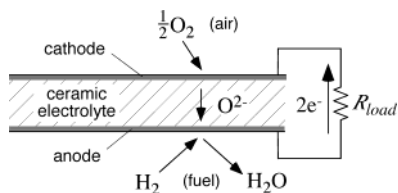


Figure 1. Schematic showing the roles of anode, cathode, and electrolyte in a solid oxide fuel cell (SOFC).

external circuit. The percentage of reversible work converted to electrical work depends on (among other things) the internal losses in the cell, including the ohmic resistance of the electrolyte, as well as the overpotential losses at the anode and cathode.

While ohmic losses in oxide electrolytes are largely understood today, the physics governing the electrode overpotential losses remain an enormous focus of research, with substantial progress being made only in the last 15–20 years. This shift in emphasis from the electrolyte to the electrodes has been driven (in part) by an ability to make increasingly thinner, less resistive, electrolyte films as well as a drive toward lower operating temperatures where the electrodes are a higher percentage of the voltage loss (due to higher activation energy). Much of this work has focused on the cathode, largely because oxygen reduction is generally thought to be the more difficult reaction to activate on SOFCs operating at commercially relevant temperatures. Workers have tried to not only understand electrode mechanisms, but also explore new electrode materials and microstructures, elucidate structure–property–performance relationships, and understand how and why electrode performance changes with time, temperature, thermal cycling, operating conditions, impurities, or other factors that may be pertinent in the design of multicell stacks and systems.

This review attempts to summarize the advances made in our understanding of SOFC cathodes since approximately the early 1980s, when there was a surge in worldwide SOFC research activity. According to the ISI Web-Of-Science *Science Citation Index*, more than 1000 refereed articles pertinent to the topic of SOFC cathodes and cathode materials have been published since 1980. Regrettably, it is not possible to cover this enormous volume of work in uniform detail. Also, new insights regarding SOFC cathodes have not occurred in a vacuum—they have benefited substantially from advances in electrochemical measurement and modeling techniques, improved understanding of cathode materials properties, and new fabrication and characterization techniques which allow control and measurement of electrode microstructure. These enabling developments can only be tangentially reviewed here.

Rather this review focuses on how new approaches have been used by workers to better understand cathode mechanisms and how these mechanisms relate to materials properties and microstructure. This review also attempts to identify ongoing critical questions that will likely be the focus of cathode research and development over the next 10–15 years. In highlighting and discussing in detail the most influential and important work in the field, this review also hopes to summarize the general trends and consensus understanding that has developed in parallel with these key insights. In telling the story of these new developments and challenges, it is the sincere hope of the author to do justice to the many scientists and engineers who have spent their careers contributing to this fascinating and potentially important area of research.

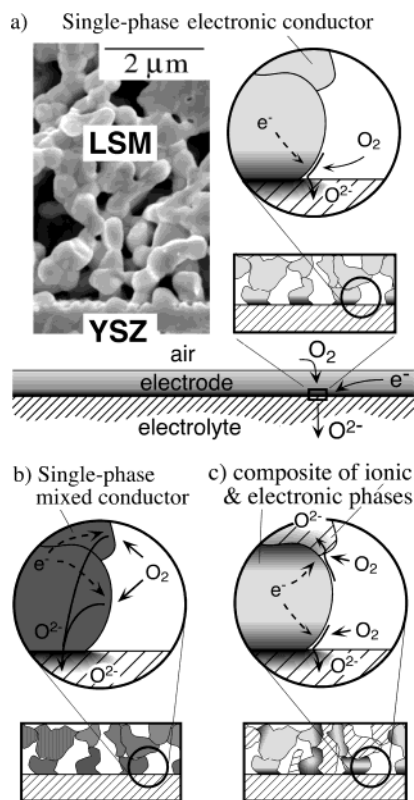


Figure 2. Common strategies for SOFC cathodes: (a) porous single-phase electronically conductive oxide such as (La,Sr)MnO₃ (LSM); (b) porous single-phase mixed conductor; (c) porous two-phase composite. The SEM micrograph of LSM on YSZ in a is adapted from ref 84. (Adapted with permission from ref 84. Copyright 1997 Swiss Federal Institute of Technology.)

2. Understanding the Three-Phase Boundary—A Long History of Inquiry

As illustrated in Figure 2, a SOFC cathode typically consists of a porous single phase or two-phase composite matrix cast onto an oxide ion conducting electrolyte substrate using a low-cost slurry-based process involving powder precursors, such as screen printing. The oxygen, which we wish to reduce to O²⁻, diffuses into the open pores of the electrode and is reduced somewhere within this matrix. For a traditional porous electronic conducting electrode material such as Pt or (La,Sr)MnO₃ (LSM) (Figure 2a), reduction of oxygen is generally thought to be confined close to the electrode/electrolyte interface, where the gas has simultaneous access to both the electronically and ionically conductive phases (illustrated as the shaded active region).

One strategy for trying to improve performance has been to replace LSM with a single-phase *mixed conductor* (material which conducts both oxygen ions and electrons), such as La_{1-x}Sr_xCo_{1-y}Fe_yO_{3-δ} (LSCF) (Figure 2b). By introducing bulk ionic transport, oxygen can be reduced to O²⁻ over a significant portion of the electrode surface, thereby extending the size of the active region and improving the kinetics at temperatures below 800 °C.^{9,13–28} Electronically conductive LSM can also be combined with an ionically conducting oxide (YSZ itself or rare-earth-doped ceria) in a porous composite microstruc-

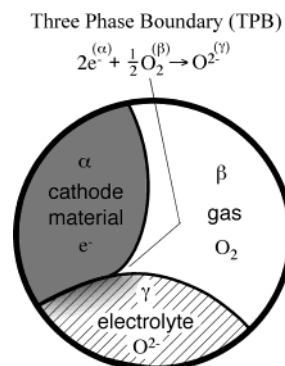


Figure 3. Phenomenological roles of the electronically conducting (electronic) phase (α), gas phase (β), and ionically conducting (ionic) phase (γ) in accomplishing oxygen reduction.

ture (Figure 2c), thereby increasing the contact area between electronically and ionically conductive phases.^{29–34} These strategies can also be combined wherein a composite electrode contains both ionic and mixed conducting phases.^{29,35,36}

While the various strategies described above have proven promising, SOFC electrodes remain largely empirically understood and far from optimized and suffer from numerous short- and long-term degradation problems.^{16,37,38} Reported performances vary tremendously with many unknown variables at work and limited understanding as to how materials properties and microstructure relate to performance and long-term stability.^{39,40}

At the risk of oversimplification, Figure 3 illustrates the phenomenological role of the cathode material, electrolyte material, and gas in accomplishing the reaction in eq 1. Regardless of the microstructure, a common feature of all cathodes is that the cathode material itself (α) (an electronic conductor) makes intimate contact with an electrolyte phase (γ) (an oxygen-ion conductor) along an interface, this interface also being exposed at its edge to the gas phase (β) (where O₂ is available). Phase α is connected at some point away from the interface to a source of electronic current, providing a conduction path for electrons to the interface. Likewise, the electrolyte phase γ is either itself the electrolyte membrane or connected by a continuous ionic path to the electrolyte membrane, providing a sink for the oxygen ions produced in the reaction. The oxygen gas (which diffuses from outside the electrode through interconnected pores or channels) is reduced somewhere in the vicinity of this $\alpha/\beta/\gamma$ interface.

Since this reaction involves ions, electrons, and gas molecules in three separate phases, the edge of the α/γ interface that makes contact with the gas phase β is often described as the three-phase (or triple-phase) boundary (TPB). The concept of the TPB actually dates to the 1920s,⁴¹ when workers studying the oxidation of H₂ on platinum introduced this concept to explain why Pt must be exposed simultaneously to both solution and gas to get significant reaction. This type of electrode, which Schmid called “die diffusionselektrode”⁴¹ or gas-diffusion electrode (GDE), is still called this today by workers studying solution- or polymer-based fuel cells. As

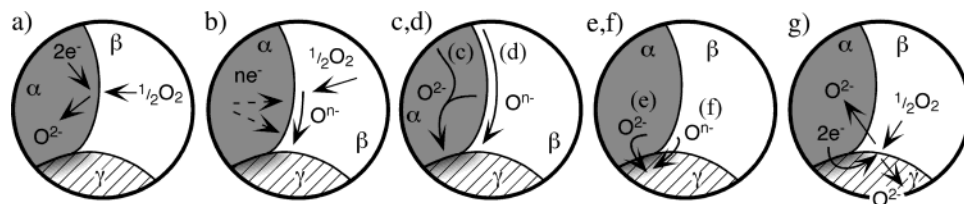


Figure 4. Some mechanisms thought to govern oxygen reduction in SOFC cathodes. Phases α , β , and γ refer to the electronic phase, gas phase, and ionic phase, respectively: (a) Incorporation of oxygen into the bulk of the electronic phase (if mixed conducting); (b) adsorption and/or partial reduction of oxygen on the surface of the electronic phase; (c) bulk or (d) surface transport of O^{2-} or O^{n-} , respectively, to the α/γ interface, (e) Electrochemical charge transfer of O^{2-} or (f) combinations of O^{n-} and e^- , respectively, across the α/γ interface, and (g) rates of one or more of these mechanisms wherein the electrolyte itself is active for generation and transport of electroactive oxygen species.

implied by the name, all GDE reactions share the common feature of involving gas-phase molecules and thus represent a fundamental departure from traditional electrochemical kinetics governing charge transfer across a 2-dimensional interface.⁴²

In the case of SOFCs, a large volume of work shows that for many SOFC electrodes, overall performance scales with the 1D geometric length of this three-phase boundary. As such, the TBP concept and electrode performance models based on it have proven to be some of the most useful phenomenological concepts for guiding design and fabrication of SOFC cathodes, particularly the microstructure.

However, in trying to develop a deeper understanding of the physics and chemistry governing the SOFC cathode reaction, the concept of the three-phase boundary somewhat begs the question as to what specific physical processes actually occur in the vicinity of the three-phase interface and how these processes depend on materials properties, microstructure, etc. Workers studying aqueous gas-diffusion electrodes in the mid-1960s recognized the limitations of the three-phase boundary concept.^{43,44} As an alternative, they began to break down the electrode reaction into individual steps, including the dissolution and diffusion of H_2 in solution and the oxidation of dissolved H_2 at the Pt/solution interface. These and subsequent studies contributed significantly to our fundamental and practical understanding of solution and polymer GDEs, including how molecular diffusion processes contribute to the overall i - V characteristics and how best to arrange the electrolyte inside a flooded electrode. Of particular note is the observation that diffusion processes can often co-limit electrode performance far below limiting current and can mimic activated behavior.⁴⁵ Thus, the phenomenological observation that a GDE obeys Tafel (or Butler-Volmer) kinetics provides no assurance that the electrode is, in fact, activation limited.

Although the SOFC community has generally maintained an empirical approach to the three-phase boundary longer than the aqueous and polymer literature, the last 20 years have seen a similar transformation of our understanding of SOFC cathode kinetics. Few examples remain today of solid-state electrochemical reactions that are not known to be at least partially limited by solid-state or surface diffusion processes or chemical catalytic processes remote from the electrochemical-kinetic interface.

Figure 4 outlines some of the mechanisms either known or theorized in the literature to be important in determining the rate of the oxygen reduction in SOFC cathodes. Oxygen molecules are generally thought to adsorb somewhere onto one or more solid surface(s), where they undergo catalytic and/or electrocatalytic reduction steps to form partially reduced ionic/atomic species (sometimes called "electroactive species"⁴⁶). Before, after, or between partial reduction steps, these species must transport along surfaces, interfaces, or inside the bulk of the electrode material(s) to the electrolyte, where they are fully and formally incorporated as electrolytic O^{2-} . If, how, and where any of these processes happen and what step(s) are rate determining for a particular electrode is often only partially understood.

As evidenced by the cases reviewed below, no single mechanism has been discovered which explains all electrodes. Furthermore, arguments in the literature concerning which theory is correct for a given cathode system usually end in a standoff of equally legitimate interpretations of limited data on dubiously comparable samples. Which step(s) are rate determining, and thus which factors are important for cathode performance, depends strongly on the material(s), microstructure, and processing of the electrode as well as the conditions under which the electrode is tested, including temperature, atmosphere, polarization, time, or other factors, some of which may not be known.

Given these uncertainties, the approach taken here is to review the asymptotic behavior of well-characterized and studied systems, where enough scientific evidence exists to reach a reasonable consensus. Perhaps then it becomes easier to discuss the possible processes governing more complex and less well-characterized systems (and to propose a new set of testable hypotheses about them). To that end, we begin by examining the case of platinum and other noble metals on zirconia, which perhaps enjoys the longest and richest history of research available today.

3. Platinum Electrodes—Interplay of Chemical and Electrochemical Steps

Oxygen reduction on yttria-doped zirconia (YSZ) was first accomplished over 100 years ago (for the purpose of generating light) using a porous platinum electrode.⁴ Since then, oxygen reduction on Pt has been one of the most well-studied electrode reaction

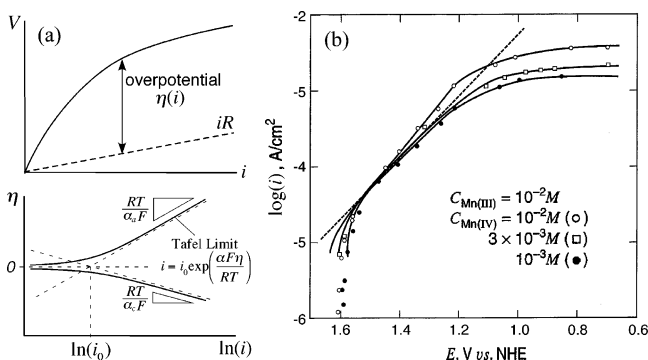


Figure 5. Measurement and analysis of steady-state i - V characteristics. (a) Following subtraction of ohmic losses (determined from impedance or current-interrupt measurements), the electrode overpotential η is plotted vs $\ln(i)$. For systems governed by classic electrochemical kinetics, the slope at high overpotential yields anodic and cathodic transfer coefficients (α_a and α_c) while the intercept yields the exchange current density (i_0). These parameters can be used in an empirical rate expression for the kinetics (Butler–Volmer equation) or related to more specific parameters associated with individual reaction steps.⁴² (b) Example of Mn(IV) reduction to Mn(III) at a Pt electrode in 7.5 M H_2SO_4 solution at 25 °C.³⁶² Below limiting current the system obeys Tafel kinetics with $\alpha_a \approx 1/4$. Data are from ref 363. (Reprinted with permission from ref 362. Copyright 2001 John Wiley & Sons.)

in the history of solid-state ionics. Yet the Pt/solid electrolyte interface is still actively studied today, with many open questions remaining. Many of these questions are relevant to more complex but technologically advanced cathode materials with relevance to today's SOFCs. Thus, platinum constitutes a useful foundation on which to build our understanding of all SOFC cathodes.

3.1. Two Schools of Thought

The field of electrochemical kinetics has traditionally focused on charge-transfer reactions occurring at the surface of a metal electrode in contact with a liquid electrolyte.⁴² As shown in Figure 5, the steady-state i - V characteristics for this type of reaction often obey Tafel kinetics (linear dependence of $\ln(i)$ vs V), which can be analyzed in terms of specific rate-limiting steps occurring at the interface.⁴⁷ As such, measurement and analysis of Tafel parameters have proven to be one of the most useful techniques for understanding electrode reactions, both as a means of isolating the nonlinear electrode response from the linear electrolyte losses as well as providing a theoretical framework for relating these parameters to specific mechanisms.

However, as mentioned previously, gas-diffusion electrodes usually deviate substantially from traditional electrochemical–kinetic behavior, often being limited by multiple rate-determining factors and/or changes in those factors with overpotential or other conditions. In attempting to analyze this type of electrode, one of the most influential experimental techniques to take hold in the solid-state electrochemical literature in the last 35 years is electrochemical impedance spectroscopy (EIS)—also known as a.c. impedance. As illustrated in Figure 6, by measuring the sinusoidal i - V response as a function

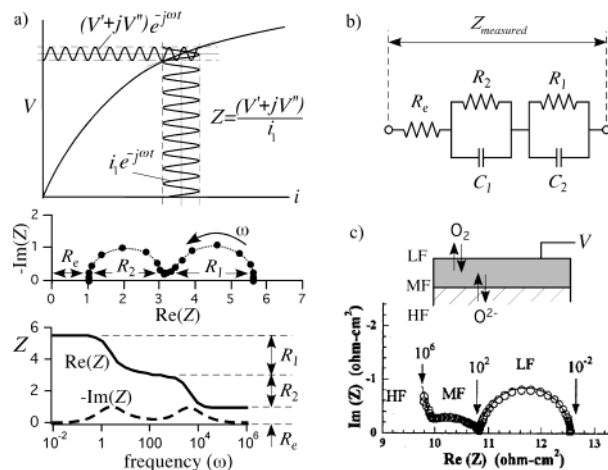


Figure 6. Electrochemical impedance spectroscopy (EIS). (a) The steady-periodic linear response of a cell to a sinusoidal current or voltage perturbation is measured and analyzed in terms of gain and phase shift as a function of frequency (ω). Results are usually expressed in terms of the impedance (Z), the complex ratio of voltage displacement to current displacement (often reported on a Nyquist or Bode plot). Ideally, each charge-transfer-limiting process (electrolyte, electrode process #1, electrode process #2, etc.) is only manifest below a distinct characteristic frequency, resulting in separate features or “arcs” in the impedance diagram of magnitude R_e , R_1 , R_2 , etc. (b) Since EIS is a linear response technique, the time-response of individual processes is often modeled in terms of equivalent circuit elements, with resistance representing charge transfer and capacitance (C_1 , C_2 , etc.) representing charge polarization. This description is often extended to noninterfacial processes by introduction of additional empirically or theoretically derived circuit elements. (c) Example of a dense $\text{La}_{0.5}\text{Sr}_{0.5}\text{CoO}_{3-\delta}$ film on single-crystal YSZ at 750 °C in oxygen.¹⁶² The total impedance in this case is a sum of the electrolyte impedance (high frequency), an interfacial impedance at medium frequency (MF), and a low-frequency (LF) impedance associated with O_2 oxidation/reduction at the surface of the film (see section 4.3). Data are from ref 165. (Adapted with permission ref 165. Copyright 2001 American Institute of Physics.)

of frequency, EIS seeks to separate and identify reaction steps via time scale.^{48,49} Along with current interruption experiments, early measurements of this type on Pt/YSZ or Pt/ceria allowed workers to more specifically isolate the electrode polarization from the electrolyte and begin analyzing this polarization in terms of time-dependent phenomena.

On the basis of the two classes of measurements shown in Figures 5 and 6, workers split into two fundamentally different schools of thought. The first, rooted in the well-established tradition of classical electrochemical kinetics, focused on the observation that these electrodes tend to obey Tafel kinetics at moderate to high overpotential. For example, Figure 7 shows Tafel plots for Pt electrodes on calcia-doped ceria, measured by Wang and Nowick using current interruption techniques over a wide range of T and P_{O_2} .^{50,51} Except for limiting current behavior at high cathodic overpotential, these results fit a Butler–Volmer expression, yielding (at least empirically) an exchange current density and anodic and cathodic transfer coefficients. On the basis of this result, the authors concluded that the electrode reaction must be limited by electrochemical kinetics at the interface.

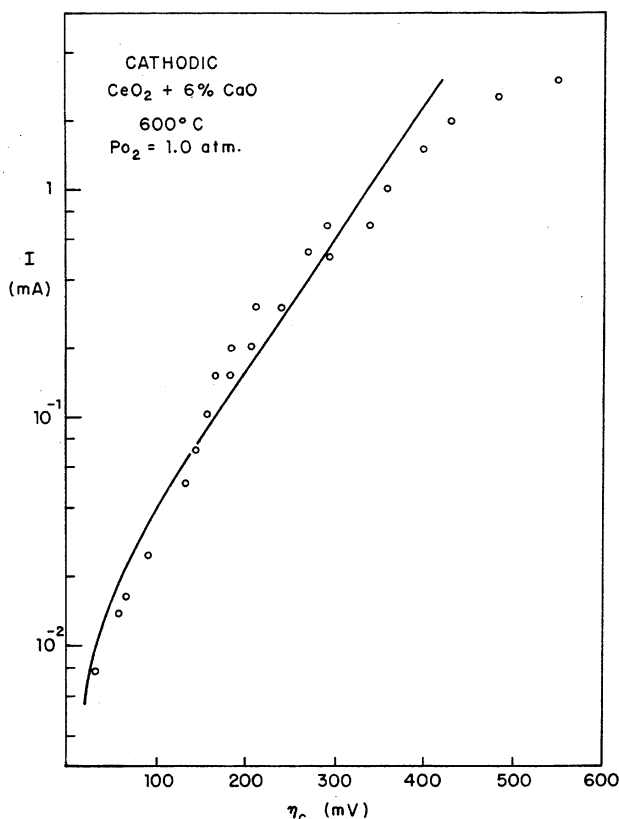


Figure 7. Steady-state cathodic current–overpotential characteristics of porous Pt electrodes on Ca-doped ceria, measured at 600 °C in air using current-interruption. (Reprinted with permission from ref 51. Copyright 1979 Electrochemical Society, Inc.)

The authors modeled the P_{O_2} dependence of the exchange current density in terms of the dissociative adsorption of oxygen on the Pt surface, which influences the exchange current through the equilibrium concentration of adsorbed atomic oxygen. These measurements also showed that the kinetics are independent of electrolyte dopant concentration, leading the authors to suggest that the limiting electrochemical step must occur on the Pt surface. Subsequent publications (as recent as the late 1990s) have continued to reinforce a default viewpoint that SOFC gas-diffusion electrodes are fundamentally limited by electrochemical kinetics.^{17,52,53}

In contrast, the second school of thought focused on the impedance of these electrodes and the fact that when modeled as an equivalent RC circuit, they exhibit a very large capacitance—too large to be explained in terms of traditional double-layer polarization at an interface.⁴⁸ One of the earliest groups to apply impedance for this purpose was Kleitz and co-workers, who studied porous Pt and other noble-metal catalysts on YSZ.⁵⁴ As shown in Figure 8, they generally found that cells respond at frequencies well below 1000 Hz, several orders of magnitude too low to explain in terms of traditional interfacial polarization. Rather, the authors interpreted these low-frequency capacitive effects as changes in concentration of “neutral-O” in the vicinity of the three-phase boundary, concluding that the overpotential must be (at least in part) a concentration overpotential rather than a simple electrochemical–kinetic resistance.

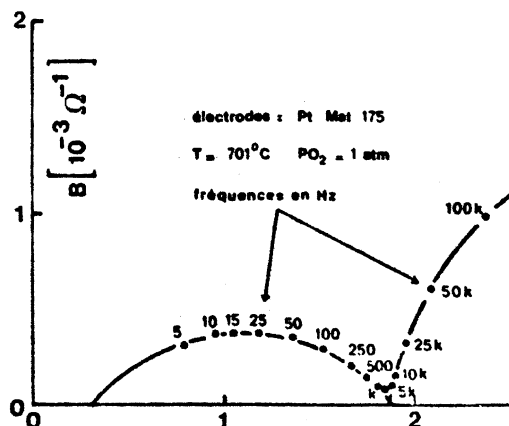


Figure 8. Complex admittance (reciprocal of impedance) or porous Pt on YSZ in air at 700 °C. The largest portion of the impedance (appearing at lowest admittance) exhibits a response frequency of ~ 20 Hz (response time of ~ 0.01 s). (Reprinted with permission from ref 54. Copyright 1973 Laboratoire d'Electrochimie et de Physicochimie des Matériaux et des Interfaces (INPG and CNRS), Saint Martin d'Heres, France.)

As discussed below, the hindsight of the last 30 years suggests that the truth falls in a gray area between these two schools of thought, with chemical adsorption, surface transport, and interfacial electrochemical kinetics all playing a significant role (as well as other factors which are still not fully understood). For this reason, platinum serves as a good starting point since it helps to illustrate how these various factors come into play and how they influence the overall electrode performance and characteristics.

3.2. Chemical Contributions to the Overpotential

To better understand the “diffusion-limited” school of thought mentioned above, it is worth digressing momentarily on another “noble”-metal electrode system: silver on YSZ. Kleitz and co-workers conducted a series of studies of silver point-contact microelectrodes, made by solidifying small (200–2000 μm) silver droplets onto polished YSZ surfaces.⁵⁵ Following in-situ fabrication, the impedance of these silver microelectrodes was measured as a function of T (600–800 °C), P_{O_2} (0.01–1.0 atm), and droplet radius. As an example, Figure 9a shows a Nyquist plot of the impedance under one set of conditions, which the authors resolve into two primary components, the largest (most resistive) occurring at very low frequency (0.01–0.1 Hz) and the second smaller component at moderately low frequency (~ 10 Hz).

Restricting our attention to the more significant, lower-frequency impedance, the authors argue (based on time scale as well as other factors) that a majority of the observed overpotential is associated with absorption and diffusion of atomic oxygen inside the silver droplet. Their proposed mechanism is illustrated in Figure 9b. According to this model, cathodic polarization provides a driving force for atomic oxygen dissolved in the silver to be reduced to oxygen ions and pulled into the electrolyte at the silver/YSZ interface. The resulting depletion of oxygen in the metal near the silver/YSZ interface creates a chemical potential driving force for dissolved oxygen to

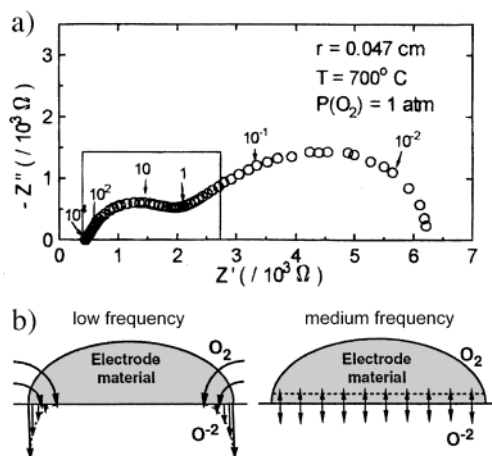


Figure 9. (a) Impedance of a single silver droplet solidified on YSZ, measured at 700 °C in oxygen. (b) Interpretation of the impedance in terms of bulk absorption and transport of oxygen in silver. Explanation for the bifurcation in response frequency: At low frequency, transport occurs everywhere in the droplet, with a higher flux near the droplet edge. At medium frequency transport is confined to a small but uniform region near the silver/YSZ interface, involving little reduction/oxidation of gaseous O_2 . (Adapted with permission from ref 364. Copyright 1997 Electrochemical Society, Inc.)

diffuse to the interface from the bulk of the silver, leading ultimately to depletion of dissolved oxygen near the silver/gas interface. Depletion of oxygen in the silver relative to equilibrium with the gas then provides a driving force for dissociative absorption of gaseous O_2 into the silver. Thus, at steady state, a continuous gradient in oxygen concentration is established that partly limits the overall reaction rate. The authors argue that only this mechanism can explain the very large effective capacitance of the electrode ($\sim 1 \text{ F/cm}^2$). Further evidence for this interpretation includes both the T and P_{O_2} dependence of the resistance and capacitance, which are found to be quantitatively consistent with independently measured oxygen absorption and diffusion properties of silver. Van Herle and McEvoy subsequently confirmed these findings,⁵⁶ concluding further that the kinetics are partially limited by both absorption of gaseous O_2 into the silver as well as diffusion of atomic oxygen through the silver.

Although there are a number of other unresolved issues in interpreting these data (not discussed here), what is clear from their analysis is that a significant portion of the resistance to oxygen reduction in this system is not determined by how fast oxygen is reduced at the Ag/YSZ interface but rather how fast oxygen can get to that interface. On this basis and other examples, Kleitz argued in 1993 that all cathode reactions involve the equivalent of dissolved oxygen in silver—some sort of “electroactive” oxygen species, which must be replenished somehow from the gas phase. This principle, which he titled the “reaction pathway model”, is illustrated in Figure 10. In this model, any charge-transfer (current) pathway A–E–B can be intermediately limited at point E by the availability of a neutral species (or neutral combination of species), whose flow rate (C–E) is not driven directly by electrical-state driving forces.

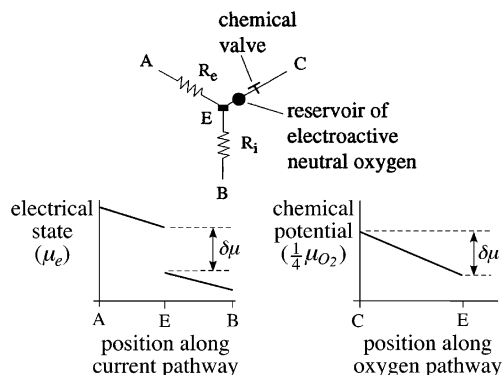


Figure 10. Kleitz's reaction pathway model for solid-state gas-diffusion electrodes. Traditionally, losses in reversible work at an electrochemical interface can be described as a series of contiguous drops in electrical state along a current pathway, for example, A–E–B. However, if charge transfer at point E is limited by the availability of a neutral electroactive intermediate (in this case ad(b)sorbed oxygen at the interface), a thermodynamic (Nernstian) step in electrical state ($\delta\mu$) develops, related to the displacement in concentration of that intermediate from equilibrium. In this way it is possible for irreversibilities along a current-independent pathway (in this case formation and transport of electroactive oxygen) to manifest themselves as electrical “resistance.” This type of “chemical valve”, as Kleitz calls it, may also involve a significant reservoir of intermediates that appears as a “capacitance” in transient measurements such as impedance. Portions of this image are adapted from ref 46. (Adapted with permission from ref 46. Copyright 1993 Risø National Laboratory, Denmark.)

For the purposes of clarity throughout the rest of this review, we hereby define such a neutral flow as a chemical process, since it is driven by chemical potential driving forces and may occur at a rate independent of the faradaic current (except in the limit of steady state).³⁶⁶ Applying this definition, examples of chemical processes include ad(b)sorption and/or dissociation of molecular species, gas-phase diffusion, diffusion of dissolved neutral species, ambipolar (chemical) diffusion of neutral combinations of ions/electrons, or surface diffusion of adsorbed species associated with a mobile mirror charge in the solid phase. Since such species or combinations thereof are net neutral, they can accumulate in large quantity in bulk or on surfaces without violating electroneutrality, acting as a reservoir and leading to slow response times. As we will see for Pt, as well as ensuing examples involving mixed conductors, all electrode reactions are now believed to involve some sort of “chemical valve” of this type which may contribute none, some, or all of the macroscopically observed polarization resistance.

3.3. Evidence for Diffusion and Adsorption Limitations on Platinum

A significant step forward in our understanding of Pt was taken by Verkerk and Burgraff, who in 1983 analyzed the impedance of porous sputtered Pt (and Pt gauze) electrodes on YSZ and gadolinia-doped ceria (GDC).⁵⁷ As shown in Figure 11, they used a Randles circuit to model the interfacial contributions to the impedance, allowing them to subtract from the data the contributions of uncompensated iR and

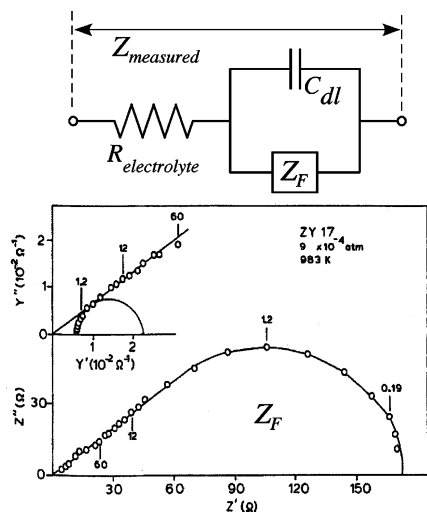


Figure 11. Electrochemical impedance of porous Pt on YSZ at 710 °C and $P_{O_2} = 10^{-3}$ atm. Data has been corrected for double-layer capacitance as described in ref 79. (Reprinted with permission from ref 79. Copyright 1983 The Electrochemical Society, Inc.)

double-layer capacitance at the metal/electrolyte interface. The remaining “faradaic” impedance (Z_F) was found, in the limit of high frequency, to have similar real and imaginary contributions ($\sim 45^\circ$ line on a Nyquist plot), which is a strong indicator that diffusion is an important step in the reaction.⁴⁹ They also showed that the P_{O_2} dependence of the impedance is independent of the electrolyte, suggesting that the diffusion process occurs on the Pt surface (or in the gas phase at lower frequencies and low P_{O_2}). On the basis of independent measurements of oxygen diffusion rates on Pt,⁵⁸ the authors estimated the diffusion distance to be about 50 nm, which supports a commonly held understanding that electrode kinetics should scale with total TPB length (at least for Pt particles larger than $\sim 10^{-5}$ cm). However, an important element left out of this analysis is why the diffusion distance is ~ 50 nm. What establishes this distance? Also, if diffusion is rate limiting, how can one explain the Tafel behavior observed for these electrodes at moderate to high overpotential?

In 1987, Mizusaki and co-workers published two papers that addressed some of these questions.^{59,60} By applying traditional electrochemical kinetics, they argued that the Langmuir isotherm for oxygen adsorption on platinum yields the incorrect P_{O_2} dependence for the exchange current density extracted from the data by fitting to a Butler–Volmer rate expression. They therefore concluded that electrochemical kinetics at the three-phase boundary cannot be the rate-limiting step. Instead, they proposed that the reaction is limited by either (1) dissociative adsorption of oxygen molecules on the Pt surface or (2) surface diffusion of adsorbed oxygen atoms to the three-phase interface. On the basis of the P_{O_2} dependence found in their measurements, they conclude that both situations are possible and that above 600 °C the electrode is diffusion limited while below 500 °C it becomes limited by the rate of dissociative adsorption of O_2 . In either case, however, they derive a logarithmic dependence of current on overpotential, which mimics Tafel kinetics. In this

way they showed that chemical steps (embodying Kleitz’s reaction pathway concept) can still obey “classical” Butler–Volmer kinetics.

How can diffusion or other chemical steps give rise to Tafel behavior? An examination of Mizusaki’s derivation⁵⁹ shows that even when interfacial electrochemical kinetic steps are equilibrated, there remains a Nernstian relationship between the applied potential and the activity of electroactive oxygen on the Pt surface. Thus, as the steady-state potential is varied, the surface concentration at the TPB changes approximately logarithmically. If the rate of adsorption and/or diffusion has a linear or power-law dependence on the surface concentration, it will also depend logarithmically on the potential, leading to a logarithmic dependence of current on potential. Thus, the mere existence of a Tafel slope means very little in terms of proving electrochemical kinetics is limiting or in identifying electrochemical kinetic steps. Rather, the important issue is how the Tafel parameters (empirical though they may be) depend on P_{O_2} and temperature and whether these can be rationalized in terms of specific chemical or electrochemical steps.

During the late 1980s some disagreement appeared in the literature concerning where oxygen concentration gradients exist on the Pt surface. In contrast to Mizusaki, Wang proposed a model in which electroactive oxygen is reduced along the entire interface between Pt and YSZ, with the rate-limiting diffusion process being the diffusion of adsorbed oxygen along the Pt/YSZ interface from the TPB.⁶¹ A similar model was considered by van Hassel for Au on YSZ.⁶² In 1990, however, Robertson and Michaels addressed this question for Pt by modeling steady-state polarization and potential-step chronoamperometry measurements on Pt/YSZ.⁶³ As illustrated in Figure 12a, they considered two cases. Model I: Adsorbed oxygen is reduced along the entire Pt/YSZ interface but must diffuse along this interface from the TPB (where surface coverage is considered to be in equilibrium with the gas). Model II: Adsorbed oxygen is reduced at the three-phase boundary but due to lack of equilibrium with the gas must diffuse along the gas-exposed surface from some other point further away. They found that the qualitative and quantitative features of their data could only be explained using this second model. In particular, as shown in Figure 12b, only diffusion on the gas-exposed Pt surface could explain the $t^{1/2}$ semi-infinite diffusion (Cottrell) behavior of the current at short times. In contrast, the first model predicts constant current until oxygen is depleted at the interface, followed by exponential decay, which was not observed. Subsequent studies of the P_{O_2} dependence of the impedance have reinforced the view that the dominant rate-determining transport step occurs on the gas-exposed Pt surface.^{56,64,65}

Some debate has also appeared concerning the “charge state” of adsorbed oxygen on the Pt surface, whether it is O^{2-} , O^- , uncharged O, etc. This question arises, for example, when one tries to interpret Tafel parameters in terms of a cascade of surface-mediated electrochemical–kinetic steps.⁶⁶ However, as already

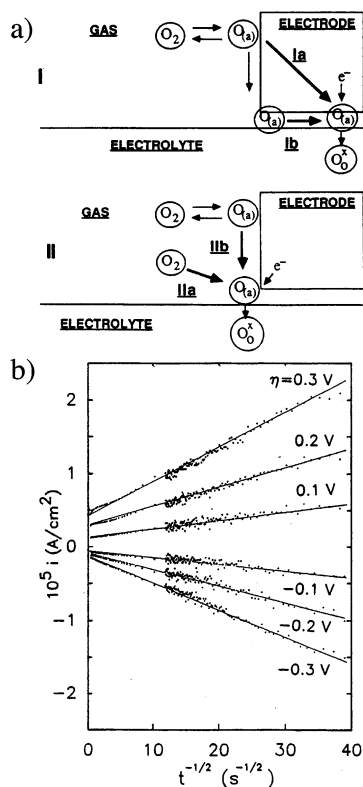


Figure 12. Modeling and measurement of oxygen surface diffusion on Pt. (a) Model I: adsorbed oxygen remains in equilibrium with the gas along the gas-exposed Pt surface but must diffuse along the Pt/YSZ interface to reach an active site for reduction. Model II: adsorbed oxygen is reduced at the TPB but must diffuse there from the gas-exposed Pt surface, which becomes depleted of oxygen near the TPB due to a finite rate of adsorption. (b) Cotrell plot of current at a porous Pt electrode at 600 °C and $P_{O_2} = 10^{-4}$ atm vs time. The linear dependence of current with $t^{-1/2}$ at short times implies semi-infinite diffusion, which is shown by the authors to be consistent only with Model II. (Reprinted with permission from ref 63. Copyright 1990 Electrochemical Society, Inc.)

demonstrated by the work reviewed above, a significant fraction of the overpotential can arise from chemical steps (adsorption and/or diffusion). In analyzing the rates of these chemical processes, one must question whether such partial charge assignments really have any physical meaning from the viewpoint of continuum mechanics. As recently shown by Luerssen et al. (Figure 13),⁶⁷ XPS reveals no difference in electronic structure between oxygen dissociatively adsorbed onto Pt from the gas vs “ionic oxygen species” pumped electrochemically from YSZ onto the Pt surface. Both oxygen sources result in the same change in measurable work function (through the surface dipole concentration). In other words, the “charge” associated with adsorbed oxygen appears to be a unique feature of the surface chemistry of adsorption (e.g., ionic vs covalent) rather than a variable formal valance state subject to electrochemical reduction/oxidation. In this sense, it is somewhat irrelevant what the charge on oxygen is, since (as recently demonstrated by Janek⁶⁸) the driving force for adsorption and transport of adsorbed oxygen is a change or gradient in surface coverage (related to oxygen activity). The rate expressions for

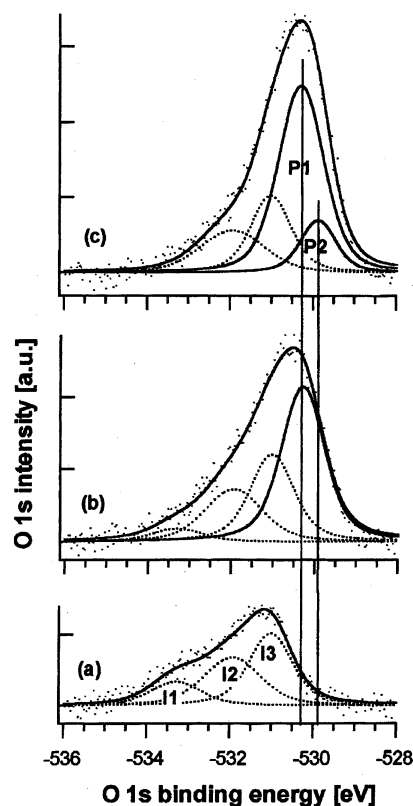


Figure 13. XPS spectra of adsorbed oxygen on a thin-film Pt electrode on single-crystal YSZ: (a) residual O^{1s} spectrum following several “cleaning” cycles at elevated temperature and vacuum ($<10^{-9}$ mbar); (b) O^{1s} spectrum at 350–400 °C under constant $P_{O_2} = 10^{-6}$ mbar; (c) O^{1s} spectrum at 350–400 °C in a vacuum during anodic polarization. The peak “P1”, corresponding to the known spectrum for chemisorbed oxygen at 530.4 eV, appears upon both adsorption of oxygen from the gas (b) and electrochemical pumping of oxygen from YSZ (c). A secondary peak “P2” at lower binding energy also appears upon electrochemical pumping but is too close in energy to P1 to explain in terms of differences in charge state. The authors propose that P2 represents a different adsorption site populated only at high coverage. (Reprinted with permission from ref 67. Copyright 2001 Elsevier.)

these processes are independent of electrical state since they involve neutral combinations of adsorbed oxygen and mirror charges in Pt.

3.4. Important Refinement: Co-limited Reaction Kinetics

As shown by Mizusaki,^{59,60} the faradaic processes occurring on platinum are quite complex, with the possibility that more than one rate-limiting step can dominate under various conditions. A primary piece of evidence that diffusion on Pt plays a role is a 45° straight-line relationship in the Nyquist plot at high frequency, which has led to the widespread use of Warburg elements in equivalent circuit modeling. However, Pt electrodes generally exhibit an impedance considerably different from that predicted by a Warburg element, even when corrected for double-layer capacitance.⁵⁷ Indeed, as recently pointed out by Boukamp, the 45° relationship is not unique to finite-length diffusion, but it is the case for any system that reduces to semi-infinite diffusion in the

limit of high frequency, including systems limited partially (or entirely) by kinetic processes at steady state.⁶⁹

To that end, an important idea contributed by Robertson and Michaels⁶³ was that oxygen reduction on Pt could potentially be *co-limited* by adsorption and diffusion rather than by just one or the other. In modeling the system, they noted that it is not possible for adsorbed oxygen to be in chemical equilibrium with the gas at the gas-exposed Pt surface while at the same time being in electrochemical equilibrium with the applied potential at the three-phase boundary. To resolve this singularity, prior (and several subsequent) models for diffusion introduce an artificial fixed “diffusion length” governing transport from the gas-equilibrated surface to the TPB.^{56,57,59,64,65,70} In contrast, Robertson and Michaels proposed that surface coverage is not in equilibrium with the gas but instead is governed simultaneously by finite rates of adsorption onto and diffusion along the Pt surface. They show that in the limit of short times, this scenario yields semi-infinite diffusion-limited behavior (consistent with potential step and impedance measurements) but at long times enters a co-limited regime, where the rate of both adsorption and diffusion govern the overall kinetics. Since adsorption kinetics are likely to be governed by the same mass-action relationships governing adsorption equilibrium, the co-limited case is similarly supported by the P_{O_2} dependence of the overall kinetics as the case of pure diffusion.

To better understand how a co-limited system can exist, consider the generalized adsorption/diffusion model shown in Figure 14a. A semi-infinite surface, defining a one-dimensional coordinate system (x), is exposed to a gaseous adsorbate (A) at uniform partial pressure. The rate of adsorption of A onto the surface per unit area is given by $r_A = k(c_{A0} - c_A)$, where $c_A(x,t)$ is the local surface concentration of A, c_{A0} is the surface concentration at equilibrium with the gas, and k is a surface exchange coefficient.³⁶⁷ Once adsorbed, A can also diffuse along the surface, with 1-dimensional flux per unit width of $N_A = -D(\partial c_A / \partial x)$, where D is the surface diffusion coefficient. Initially, the entire surface is allowed to equilibrate with the gas at surface concentration c_{A0} . Then at $t \geq 0$, the concentration of species A at $x = 0$ is regulated externally with time-dependent value $c_{A1}(t)$ (established, for example, by equilibrium of an electrochemical reaction such as $A + e^- \leftrightarrow A^-$). This local displacement of the surface concentration provides a driving force for a finite flux of A at $x = 0$ (N_{A1}), which (if electrochemically driven) is related proportionately to current. Conservation of species A leads to

$$\begin{aligned} \frac{\partial c_A}{\partial t} &= D \frac{\partial^2 c_A}{\partial x^2} + k(c_{A0} - c_A) \\ c_A(x, t < 0) &= c_{A0} \\ c_A(x = 0, t) &= c_{A1}(t) \end{aligned} \quad (2)$$

Figure 14b,c shows the time-dependent solution

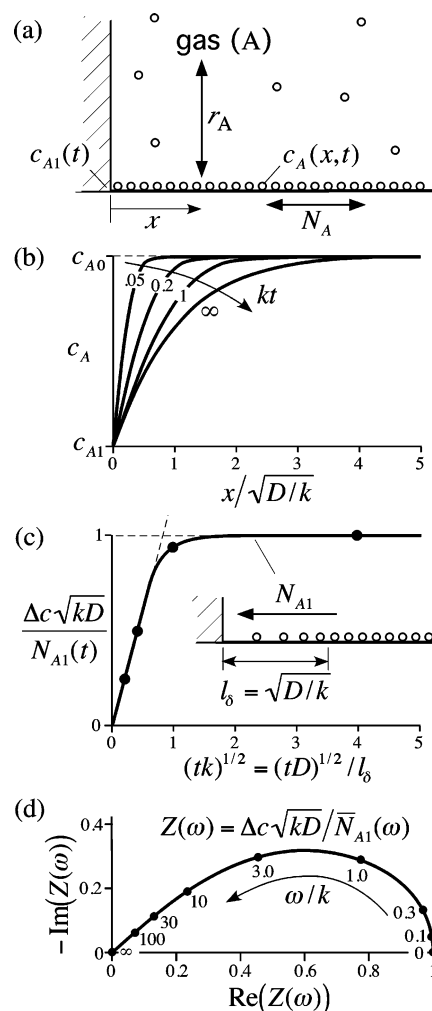


Figure 14. Simple model demonstrating how adsorption and surface diffusion can *co-limit* overall reaction kinetics, as explained in the text. (a) A semi-infinite surface establishes a uniform surface coverage c_{A0} of adsorbate “A” via equilibrium of surface diffusion and adsorption/desorption of A from/to the surrounding gas. (b) Concentration profile of adsorbed species following a step (drop) in surface coverage at the origin. (c) Surface flux of species at the origin ($N_{A1}(t)$) as a function of time. Points marked with a solid circle (●) correspond to the concentration profiles in b. (d) Surface flux of species at the origin ($N_{A1}(\omega)$) resulting from a steady periodic sinusoidal oscillation at frequency ω of the concentration at the origin.

to this system following a step in concentration $c_{A1}(t) = c_{A0} - \Delta c$ at $x = 0$. At short times the diffusion profile expands as $t^{1/2}$, yielding Cottrell behavior for the flux of A at $x = 0$ ($N_{A1}(t)$). This expansion continues until, at steady state, the increasing rate of adsorption (due to increased active area) balances the decreasing rate of diffusion (due to a longer transport path). A utilization length l_0 is established, proportional to $\sqrt{D/k}$, that represents a “compromise” between faster kinetics and slower diffusion. The steady-state flux at $x = 0$ (N_{A1}) is proportional to \sqrt{kD} and thus is governed by both kinetics and diffusion. Similarly, Figure 14d shows the stationary periodic solution to eq 2 for a sinusoidal perturbation $c_{A1}(t) = c_{A0} + \Delta c \cos(\omega t)$ as a function of frequency. The resulting half-tear-drop-shaped impedance (defined here as $\Delta c / \bar{N}_{A1}(\omega)$ at $x = 0$) is somewhat

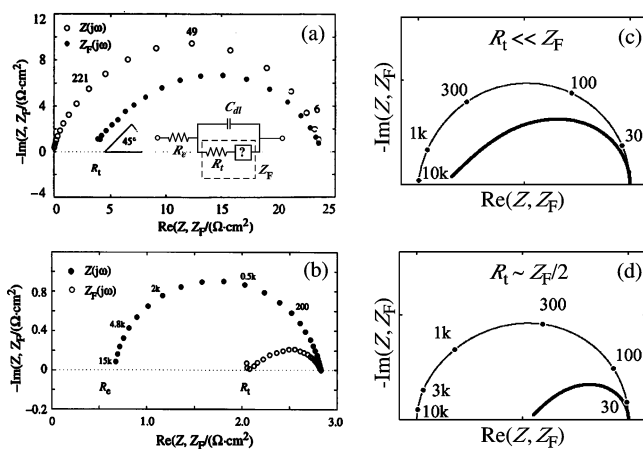


Figure 15. Faradaic impedance (Z_F) of porous Pt electrodes on single-crystal zirconia in oxygen at zero bias, as determined from the total impedance (Z) using the methods of Berthier et al.⁷⁵ (a) $T = 800$ °C and (b) 900 °C. (c) Model assuming the interfacial electrochemical kinetic resistance (R_t) is small compared to chemical resistances. (d) Model assuming R_t is similar to chemical resistances. (Adapted with permission from refs 74 and 84. Copyright 1999 and 1997 Elsevier and Swiss Federal Institute of Technology.)

smoother and more suppressed than a Warburg impedance, with a 45° limit at high frequency and RC-like behavior at low frequency, with a characteristic time constant proportional to $1/k$ and characteristic resistance proportional to $1/\sqrt{kD}$. This response has often been called the “Gerischer impedance” because it was first derived by Gerischer in 1951 for the case of an electrode co-limited by homogeneous reaction and diffusion in the electrolyte.^{69,71}

The co-limited situation illustrated above is quite different than a membrane, for example, where the relative importance of diffusion vs surface kinetics is determined by a geometric length scale (membrane thickness). Rather, by “co-limited” we mean that both k and D are important in establishing the overall rate, regardless of their values, as long as l_δ is small compared to the electrode thickness. If the ratio of D/k changes, it does not change the relative importance of diffusion vs kinetics, merely the size of the active region. This concept of a co-limited reaction rate is not unique to solids; electrochemical engineering is rich with examples of co-limited systems, including examples from classical porous electrode theory⁴⁷ as well as more closely related cases involving gas-diffusion electrodes in polymer-based fuel cells.^{43,44}

Perhaps the strongest recent evidence to date that Pt/YSZ is, in fact, co-limited by adsorption and surface diffusion has been provided by Mitterdorfer and Gauckler.^{72–74} These authors prepared Pt paste electrodes on single-crystal YSZ and measured impedance at $T = 700\text{--}800$ °C and $P_{O_2} = 10^{-4}\text{--}1$ atm in O_2/N_2 mixtures. As shown in Figure 15a,b, the authors used the method of Berthier et al.⁷⁵ to subtract the effect of double-layer capacitance and electrolyte resistance, yielding a true “faradaic impedance” Z_F , which is composed of an interfacial charge-transfer resistance (R_t) plus a chemical impedance not unlike the Gerischer impedance shown

in Figure 14d. The authors constructed a numerical model for oxygen reduction on Pt/YSZ (based on a finite-difference model for the surface) that includes adsorption, diffusion, and electrochemical–kinetics at the TPB. As shown in Figure 15c,d, their model shows similar behavior and when compared to the data allows estimation of physical parameters governing adsorption, surface diffusion, and electrochemical kinetics at the TPB.

Among other things, the authors show that when Langmuir adsorption kinetics are assumed, they find the adsorption and diffusion parameters extracted from their data to depend strongly on surface coverage θ . To explain this, they propose an alternative precursor-mediated adsorption mechanism. With this modification to the model, the kinetic and transport parameters extracted from the data reveal more constant values that are argued to be in reasonable agreement with available independent measurements or calculated estimates.^{73,76–79} The authors conclude that above 800 °C and high P_{O_2} , charge transfer at the TPB competes with adsorption/diffusion, constituting approximately one-half of the total impedance. With decreased temperature or lower P_{O_2} (or increased overpotential), the electrode appears to become limited primarily by chemical processes, with less than 10% attributed to the TPB interface. These results suggest that the system is quite complex and that multiple factors can be important, depending on the specific conditions. Indeed, this may help explain why there has been so much difficulty reaching a consensus on what “the” rate-limiting step really is, i.e., there is no “one” rate-limiting step.

3.5. Unresolved Issues Surrounding Oxygen Reduction on Pt/YSZ

The models proposed by Robertson and Michaels, and later by Mitterdorfer and Gauckler, imply that adsorption and diffusion of oxygen will occur over a finite utilization region, as illustrated in Figure 14b,c, establishing the electrode’s functional zone. Oddly, neither set of authors reported numerical estimates of this size, based on the parameters they extracted from their data. In the case of Mitterdorfer and Gauckler, it is possible to make an estimate using eq 2 and the parameters from their model. This exercise yields values between 50 and 500 nm, depending on T and P_{O_2} (~ 100 nm at 700 °C in air).³⁶⁸ While this range represents a significant extension of the active region beyond the TPB, it is small enough relative to microstructural features to remain consistent with studies of Pt and Pt/YSZ composite electrodes, showing that the active area scales with the geometric length of the three-phase boundary.^{80,81} A more quantitative analysis of the size of the active region has yet to be conducted for Pt on YSZ.

Luerssen and co-workers recently attempted to image the concentration gradients of oxygen on a Pt film electrode near the TPB using PEEM⁶⁷ (see section 3.6). They were able to show that the work function (and thus the surface oxygen coverage) changes following polarization. However, they observed no visible diffusion front emanating (on Pt)

from the TPB. As discussed by the authors, this failure may be a result of the porosity in the Pt film (resulting in changes being seen everywhere). It is also possible that at the very low P_{O_2} 's studied ($<10^{-9}$ mbar) the system becomes entirely adsorption/desorption limited, and thus the oxygen surface coverage changes uniformly over the entire Pt surface. Indeed, an estimate of l_b at this low P_{O_2} based on Mitterdorfer's model (see above) is $\sim 80 \mu\text{m}$ at 700°C , which is on the same order of the size of the Pt surface studied by Luerssen et al. Further studies of this type, if able to be conducted at higher P_{O_2} , may be able to reveal more about the actual size of the utilization region for Pt.

Another open question is the mechanism and electrochemical kinetics governing incorporation of adsorbed oxygen as O^{2-} at the Pt/electrolyte interface (Figure 4f). Mitterdorfer estimated (based on analysis of impedance) that this process can constitute anywhere from 10% to 50% of the electrode overpotential.⁷³ Of particular interest would be to better understand what role the *electrolyte* (or its constituents) plays in this process. For example, Widmer et al.⁸² measured the zero-bias impedance of low-fired (750°C) porous Pt electrodes on various electrolytes including YSZ, gadolinia-doped ceria (GDC), and Ce-implanted YSZ (made by ion implantation of cerium into the surface of YSZ). Their results show that the impedance of Pt on GDC and Ce-implanted YSZ are much lower than for Pt/YSZ. Since electrodes fired at this temperature are likely to be limited by interfacial ionic charge transfer, this result would seem to indicate that the presence of Ce aids the electrochemical kinetics at the TPB, as discussed more fully by McEvoy.⁸³ Unfortunately, isolation and study of this portion of the overpotential is nontrivial. As discussed previously, traditional electrochemical methods (such as steady-state Tafel analysis) are heavily obscured by chemical effects.⁸⁴ Meanwhile, impedance (which we saw can potentially isolate the resistance of the interface via frequency) is limited to linearized response and thus is unable to provide nonlinear information such as the interface-specific exchange current density and anodic/cathodic transfer coefficients. Thus, despite many years of earnest investigation, the electrochemical kinetics governing the actual Pt/YSZ interface (as distinct from adsorption and transport to the TPB) remains largely a mystery.

A related mystery is the wide variability in estimates reported for the true double-layer capacitance of Pt/YSZ interface and how sensitive one's analysis is to this value. The recent work of Mitterdorfer and Gauckler⁷⁴ shown in Figure 15 illustrates the extreme degree to which the double-layer capacitance can obscure the faradaic processes occurring on the electrode at high frequency. In 1991, Robertson and Michaels attempted to measure the double-layer capacitance based on chronoamperometry, showing that the shortest relaxation time scale yields a capacitance of $\sim 10^{-6} \text{ F/cm}^2$ at 700°C , based on the superficial area.⁸⁵ More recently, Kenjo reports a value of $\sim 10^{-5} \text{ F/cm}^2$ using similar measurements.⁸⁶ These values (which are 2–3 orders of magnitude

smaller than the total pseudocapacitance typically ascribed to Pt) compare reasonably with estimates of the charge separation at the Pt/YSZ interface⁸⁵ as well as the capacitance of solution interfaces of similar charge concentration and mobility.⁴⁷ In contrast, the use of equivalent circuit models to extract double-layer capacitance from impedance data typically yields values on the order of $>10^{-4} \text{ F/cm}^2$.^{73,85} While in some cases these values may simply be obscured by faradaic capacitive effects (as originally proposed by Robertson), it remains unclear why the apparent interfacial capacitance appearing in the impedance is so large even *after* faradaic effects have supposedly been accounted for. A likely explanation is that additional transients are occurring at the Pt/YSZ interface at the highest frequencies probed by the impedance, which are neither true interfacial polarization nor faradaic accumulation of reactive intermediates on the gas-exposed Pt surface.

3.6. Nonstationary Effects

Another unresolved issue in our understanding of Pt cathodes is that of nonstationary behavior such as hysteresis or inductive effects, reported under moderate to high polarization. In this context, the term *stationary* refers to behavior exhibiting a well-defined steady state, which is a repeatable function of the materials, processing, and testing conditions. Inherently transient measurements, such as impedance or current-interrupt response, can still be classified as stationary as long as the applied transients involve repeatable deviations from, or relaxations to, a well-defined steady state. In contrast, many workers have observed that electrode characteristics, such as i - V response or the impedance itself, can depend on time and/or operating history. Such dependencies are defined here to be nonstationary since they either are irreversible, involve significant hysteresis, or relax on a time scale so long as to constitute changes in mechanism with respect to processes probed on ordinary time scales.

One of the first specific studies of these effects was reported by Schouler and Kleitz,⁸⁷ who noticed hysteresis in cyclic voltammograms at anodic potentials above about 200 mV. Subsequently a variety of other authors have reported similar findings for Pt at both anodic and cathodic overpotentials.^{88–92} One recent example is provided by Jacobsen and co-workers,⁹⁰ who used linear sweep voltammetry and EIS to quantify the degree and dependence of this hysteresis for Pt ball/YSZ and point YSZ/Pt electrodes. Figure 16 shows some of their results. Unlike a system with a reactive intermediate (in which the return sweep occurs at reduced current due to unfavorable depletion or excess of the reactive intermediate), these voltammograms clearly show that current on the return sweep is enhanced following polarization at a higher potential. The hysteresis loop gets larger with *decreasing* sweep rate until extremely slow sweeps, where a steady state is finally achieved ($\leq 1 \mu\text{V/s}$). This is actually an example of an "apparent" hysteresis (brought on by a large separation in time scales) rather than a true hysteresis in which a

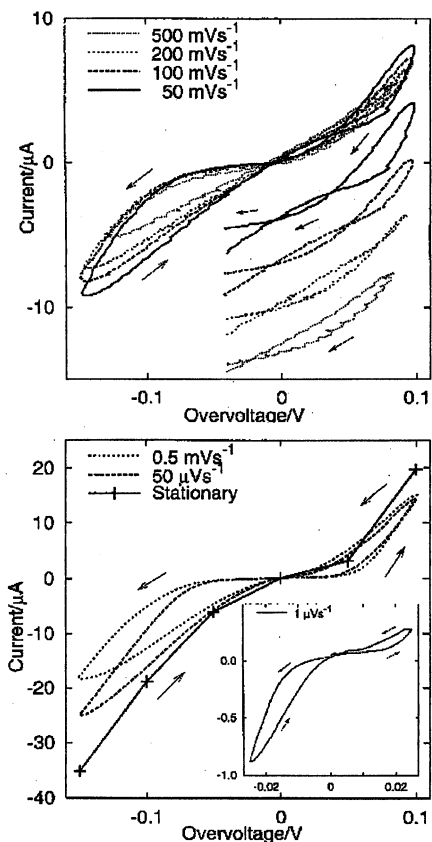


Figure 16. Linear-sweep voltammograms of a YSZ needle electrode in contact with bulk Pt in air at 1000 °C as a function of sweep rate. (Reprinted with permission from ref 90. Copyright 2001 Elsevier.)

history-dependent stable state can be achieved (e.g., magnetic induction of a ferromagnet). As one might expect from this behavior, inductive effects are seen in the impedance, and this effect can also be observed in chronoamperometric measurements, which show a slow rise (~30%) in current over a period of about 3 h following initial polarization. Jacobsen et al. consider, and reject, a number of explanations for this behavior including (1) reactive intermediates on the Pt surface, (2) passivation of the Pt surface by macroscopic layers of platinum oxide, (3) expansion of the reaction zone along the YSZ surface due to reduction and subsequent conduction of YSZ, and (4) Joule heating of the sample. None of these mechanisms, the authors argue, appear to consistently explain the observed transients.

A prominent explanation has been that by cathodically polarizing the cell for a significant period of time, long-lived Pt–O moieties on the surface (or at the TPB) are reduced, opening up catalytic sites for dissociative adsorption, transport, and electrochemical reduction. Perhaps relevant to this idea is a study by von Oertzen and co-workers that challenges the traditional view of Pt as a homogeneous metal surface.⁹³ They used PEEM to show that chemisorbed oxygen on Pt (110) can be incorporated into platinum as a subsurface oxygen “phase” at temperatures as low as 200 °C, provided CO is present to initiate reconstruction of the surface. Perhaps similar alterations of certain portions of a polycrystalline Pt surface (or Pt/YSZ interface), driven by electrochemi-

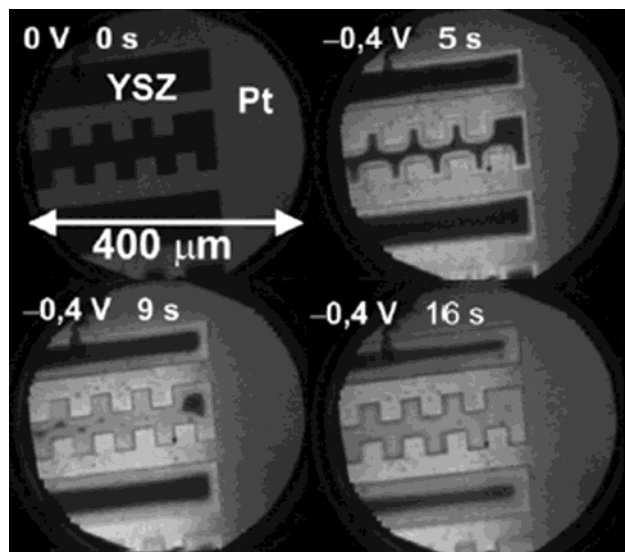


Figure 17. In-situ PEEM images of a cathodically polarized Pt/YSZ/Pt cell as a function of time following cathodic polarization. Dark area in the initial ($t = 0$) image corresponds to the gas-exposed YSZ surface, while the slightly lighter area is Pt. The bright area on Pt following initial polarization corresponds to low work function due to decreased oxygen coverage. In contrast, the bright area that grows slowly outward from the TPB along the YSZ surface corresponds to increased electron concentration. About 1 min is required for the YSZ surface to reach steady state following polarization. (Reprinted with permission from ref 97. Copyright 2002 PCCP Owner Societies.)

cal reduction/oxidation, might account for unexplained inductive (as well as capacitive) effects. Recent measurements of work function transients following polarization⁹⁴ seem to support the idea that Pt undergoes changes in surface structure after establishing a steady-state surface coverage. Similarly, a recent AFM study by Bay and Jacobsen shows that cathodic and anodic polarization can create submicrometer morphological changes at the Pt/YSZ interface, as revealed in postmortem analysis of point-electrode samples.⁹⁵ These observations, which imply a nonstationary Pt/YSZ interface, appear to be consistent with a model by Svensson and Nisancioglu,⁹⁶ which suggests that mobility of oxygen species along the YSZ/Pt interface is an important part (at the atomic level) in determining the interfacial electrochemical kinetics.

Finally, it is worth mentioning recent studies by Luerssen et al.,⁹⁷ who imaged the slow growth of a reduction front along single-crystal YSZ following large cathodic polarization of a Pt film electrode. As shown in Figure 17, this reduction expands the region of reduced oxygen activity well beyond the TPB and appears to alter the work-function distribution on Pt that had been established initially after polarization. Although these measurements were conducted under very low P_{O_2} , they may provide some insight about how hysteretic effects could involve the electrolyte at higher P_{O_2} . Indeed, these images recall earlier suggestions by Kleitz^{55,98} and others⁹⁹ that the electrolyte can play a chemical catalytic role in the absorption and dissociation of oxygen given the right conditions and set of materials.

3.7. Summary: Platinum as a Framework for Understanding Other SOFC Cathodes

The literature reviewed in sections 2–3.6 has shown that oxygen reduction on Pt is quite complex, involving several possible rate-limiting (or co-limiting) steps. As we will see in sections 4 and 5, this complexity is a universal feature of all SOFC cathodes, with many of the same themes and issues reappearing for other materials. We therefore highlight below several general observations about the mechanism of Pt that frame the discussion for other solid-state gas-diffusion electrodes involving O₂. These observations are as follows.

(1) *Chemical reaction steps*: Even if the overall electrochemical reaction involves a molecular species (O₂), it must first be converted to some “electroactive” intermediate form via one or more processes. Although these processes are ultimately driven by depletion or surplus of intermediates relative to equilibrium, the rate at which these processes occur is independent of the current except in the limit of steady state. We therefore label these processes as *chemical processes* in the sense that they are driven by chemical potential driving forces. In the case of Pt, these steps include dissociative adsorption of O₂ onto the gas-exposed Pt surface and surface diffusion of the resulting adsorbates to the Pt/YSZ interface (where formal reduction occurs via electrochemical–kinetic processes occurring at a rate proportional to the current).

(2) *Co-limitation by kinetics and mass transfer*: If an electrode is porous, there is generally no fixed geometric length that defines the importance of diffusion relative to kinetic steps. Rather, reaction and diffusion will occur cooperatively over an active area and at an overall rate that depends on both kinetic and diffusion parameters simultaneously over a wide range of values. We label this situation as a co-limited reaction. In the case of Pt at high P_{O_2} , it would appear that the rates of adsorption and surface diffusion are balanced over a relatively small active region close to the TPB (50–500 nm). This appears to explain why the activity of a Pt electrode generally scales with the length of the geometric three-phase boundary.

(3) *Electrochemical kinetics confined to TPB*: For platinum, the important chemical processes of catalytic reduction and transport occur on the Pt surface, and thus the electroactive species formed are most readily available near the Pt-surface/YSZ interface (TPB). Although it is not entirely clear how these electroactive species are subsequently incorporated into the electrolyte bulk or what role the electrolyte itself plays in this process, there is strong circumstantial evidence that the electrochemical–kinetic step is restricted to an area close to the TPB. Unfortunately very little is known about the nature of this reaction since the details are often obscured by chemical effects involving the Pt surface.

(4) *Nonstationary behavior*: Platinum on YSZ exhibits pronounced hysteretic effects, suggesting that passage of current can alter either the kinetics of the reaction or the dominant reaction pathway itself. As we saw in section 3.6 (and will again in

section 5.4), this type of nonstationary behavior (behavior for which a well-defined steady state does not exist or is subject to relatively long relaxations) remains largely an unsolved mystery for Pt as well as other types of electrodes.

4. Perovskite Mixed Conductors and the Role of Bulk Material Properties

The observations summarized in section 3.7 suggest that if one could extend the transport process of electroactive species from the surface to the *bulk* of the electrode material (as we saw with silver, for example), one could enlarge the active area over which chemical processes occur as well as extend the electrochemical interface to include the entire electrode/electrolyte contact area (not just the TPB). Although silver appears to exhibit sufficient bulk oxygen transport to accomplish these goals, it has not proven to be suitable as an SOFC cathode due to poor catalytic activity toward O₂ as well as mechanical and thermodynamic instability. In contrast, some transition-metal oxides, in addition to being good O₂ catalysts and electronic conductors, exhibit significant ionic conduction while remaining relatively stable at operating conditions. For these mixed conductors (materials which conduct both ions and electrons) the bulk appears to play a significant if not dominant role in determining the electrode kinetics. As such, these materials provide another useful asymptote to consider when extrapolating to more complex materials such as LSM.

4.1. Perovskite Oxides—Low-Cost Alternative to Platinum

Transition-metal oxides were originally investigated as SOFC cathodes due to their good electrical conductivity (most oxides are insulators) and as a relatively low-cost alternative to Pt, which prior to about 1965 was the only SOFC cathode material being considered extensively. One of the first such materials studied was La_{1-x}Sr_xCoO_{3-δ} (LSC) (now one of the most well-studied mixed conductors), reported by Button and Archer in 1966.⁴ This was followed quickly thereafter by a number of other materials having perovskite crystal structure, including La_{1-x}Sr_xMnO_{3±δ} (LSM), which as of ~1973 became the favored material for SOFC cathodes. Since LSM has been so well studied and is also a poor ion conductor (at least at ambient P_{O_2}), we discuss this somewhat more complex material system in its own section (section 5). In the present section we focus on perovskites materials which exhibit significant bulk oxygen ion transport at typical cathodic P_{O_2} and the role this transport plays in the oxygen reduction mechanism.

One of the first such kinetic studies of a perovskite mixed conducting electrode was reported by Ohno and co-workers in 1981, who found La_{1-x}Ca_xCoO_{3-δ} to have better kinetic properties than Pt as an SOFC cathode at 1000–1100 °C.¹⁰⁰ A number of other *περοωσκίτες* of general formula La_{1-x}Sr_xMO_{3-δ} (M = Cr, Mn, Fe, Co) were later studied by Takeda et al.¹⁰¹ To avoid reaction of the perovskites with the YSZ

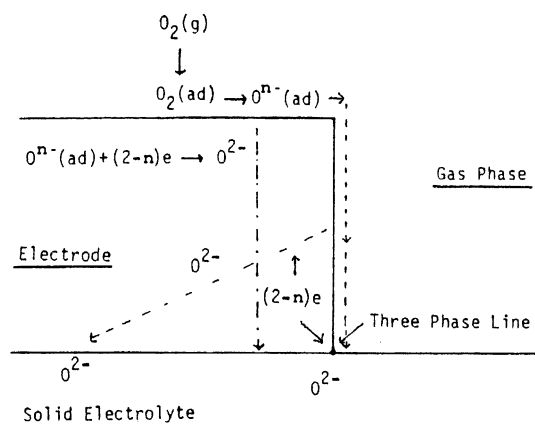


Figure 18. Possible pathways by which oxygen is reduced in a porous mixed conducting electrode. Following dissociative adsorption (which forms a surface-polarizing species O^{n-} , where n represents the unknown partial charge state of adsorbed oxygen), O^{n-} either travels by surface diffusion to the TPB (where it is fully reduced) or is incorporated directly into the mixed conductor as O^{2-} , where it then diffuses to the solid/solid interface. (Adapted with permission from ref 203. Copyright 1987 The Electrochemical Society, Inc.)

electrolyte, these electrodes were fabricated by sputtering porous films of thickness varying from 1 to 3 μm at modest temperatures. They found the best performance with LSC, which initially exhibits significantly lower overpotential than either $\text{La}_{0.7}\text{Sr}_{0.3}\text{FeO}_{3\pm\delta}$ (LSF) or LSM under the conditions studied. The i - V characteristics of LSC were found to be linear at low current density and obey Tafel kinetics at higher current density. The exchange current density obtained by fitting the data to a Butler-Volmer rate expression scales approximately as $P_{\text{O}_2}^{1/4}$ and has an activation energy of ~ 220 kJ/mol. The authors generally found that the overall kinetics improves with increasing Sr content (x), except for LaCoO_3 (which was the best composition they studied). They also noted a thickness dependence—the overall performance improved with thickness until about 2–3 μm , at which point a plateau or slight decline in performance with thickness was observed.

In interpreting their results, Tekada et al. provided the now often-duplicated picture shown in Figure 18, which illustrates the possible paths by which oxygen may become reduced. Citing the high chemical diffusion coefficient for oxygen in LSC, the authors claimed that bulk transport in LSC allows a much larger region of the electrode to be active for oxygen reduction and that this effect is largely responsible for the improved performance over platinum. On the other hand, citing the Tafel behavior, weak P_{O_2} dependence, and high activation energy, the authors argue that the electrode must be limited by interfacial electrochemical kinetics with absorption and transport of oxygen in/on LSC being so fast as to be equilibrated. Although the subsequent 20 years of research have shown that these electrodes are not generally limited by interfacial electrochemical kinetics, this work was foundational in redirecting the SOFC cathode materials effort and in framing the debate for two decades as to what actually limits the rate of oxygen reduction with these materials. Of

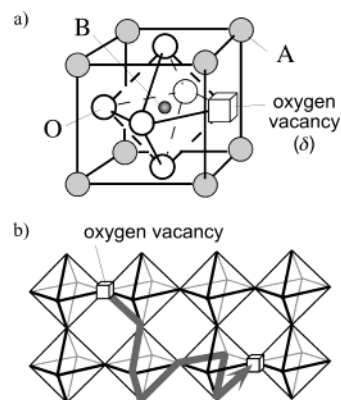


Figure 19. Atomic structure and oxygen transport in mixed conducting perovskites $\text{ABO}_{3-\delta}$. (a) Basic structural element, consisting of a corner-sharing BO_6 octahedron surrounded by charge-compensating A-site cations. (b) Bulk oxygen transport mechanism, involving random hopping of oxygen ion vacancies (δ) on the oxygen sublattice.

particular interest is the suggestion that the *bulk* of the material plays an important role in determining the overall kinetics. As we will see below, this has been proven to be largely correct.

4.2. Thermodynamic, Kinetic, and Transport Properties of Perovskite Mixed Conductors

Figure 19 illustrates the general perovskite crystal structure $\text{ABO}_{3-\delta}$ as it relates to the electronic and ionic transport properties of some transition-metal oxides. In this case, the B-site cation is a reducible transition metal such as Co or Fe (or mixture thereof) and the A-site cation is a mixture of rare and alkaline earths (such as La and Sr). The octahedral symmetry around the transition metal often promotes a metallic or semiconducting band structure at high temperature, leading to high electronic conduction. This structure is also quite stable relative to other crystalline phases, and thus with a judicious choice of A- and B-site cations, it can stably support a large number of oxygen ion vacancies (δ) at SOFC operating conditions, thus facilitating significant bulk ionic oxygen transport. The literature surrounding the properties of transition-metal perovskites extends back more than 50 years and is well beyond the scope of this review; however, the following few paragraphs attempt to summarize some of the salient features.

All materials in the $\text{La}_{1-x}\text{Sr}_x\text{Co}_{1-y}\text{Fe}_y\text{O}_{3-\delta}$ (LSCF) family of materials have electronic transference numbers approaching unity. The electronic structure LSC and LSF has often been described in terms of partially delocalized $\text{O}^{2p}-\text{Co}^{3d}$ band states based on the t_g^2 and e_g levels of crystal-field theory.^{102–104} In the case of LSC (Figure 20a), at high temperature and with 10 mol % Sr or higher, the Fermi energy appears to fall within a half-filled band, comprising a mixture of somewhat localized t^2 states with more delocalized e (σ^*) states.^{105–111} Consistent with this picture, LSC exhibits metallic or semimetallic conduction with a conductivity that decreases with temperature above ca. 500 °C and a Seebeck coefficient approaching zero as the temperature is increased.^{112,113} In contrast, LSF appears to exhibit a weak Hubbard or Hubbard-like band gap arising

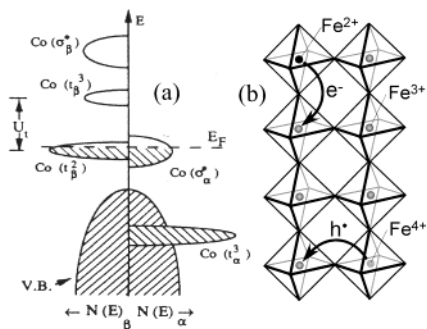


Figure 20. Electronic structure and transport in mixed conducting perovskites. (a) Band picture of electronic structure in the high-temperature metallic phase of $\text{La}_{1-x}\text{Sr}_x\text{CoO}_{3-\delta}$. (Reprinted with permission from ref 109. Copyright 1995 Elsevier.) (b) Localized picture of electron/hole transport in semimetallic $\text{La}_{1-x}\text{Sr}_x\text{FeO}_{3-\delta}$, involving hopping of electrons and/or electron holes (depending on the oxidation state of iron).

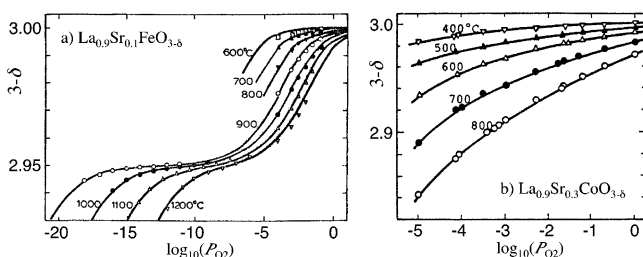


Figure 21. Oxygen stoichiometry in (a) LSF ($x = 0.1$) and (b) LSC ($x = 0.3$) as a function of P_{O_2} and temperature. (Adapted with permission from refs 119 and 121. Copyright 1985 and 1989 Elsevier.)

from electron–electron repulsion on the iron site.^{114,115} This gap results in more localized electronic states, which can be thought of as a spatially localized disproportionation of Fe^{3+} to Fe^{2+} and Fe^{4+} (Figure 20b). As such, LSF has semiconducting or semimetallic properties at high temperature, exhibiting p-type conductivity and Seebeck coefficient at high P_{O_2} (where iron is intermediate between Fe^{3+} and Fe^{4+}) and n-type conductivity and Seebeck coefficient at low P_{O_2} (where iron is intermediate between Fe^{2+} and Fe^{3+}).¹¹⁶ For solid solutions of LSC and LSF having a mixture of iron and cobalt on the B-site, the electronic structure is more complex but generally exhibits more semiconductor-like behavior with high iron content ($y = 0.8$) while being more metallic with high Co content ($y = 0.1$).^{117,118}

Consistent with these differences in electronic structure, LSC and LSF also exhibit very different defect thermodynamics in terms of the dependence of oxygen vacancy concentration (nonstoichiometry δ) as a function of Sr content (x), T , and P_{O_2} . As shown in Figure 21a,¹¹⁹ LSF exhibits a plateau in oxygen nonstoichiometry with P_{O_2} where $\delta = x/2$, corresponding to an average iron oxidation state of Fe^{3+} . At higher P_{O_2} iron becomes oxidized, leading to lower δ , while at lower P_{O_2} more vacancies are formed. As shown by Mizusaki,¹¹⁹ this behavior can be explained quantitatively in terms of point-defect theory,¹²⁰ assuming equilibria among O_2 gas, oxygen vacancies, and localized electrons and holes. In contrast, Figure 21b¹²¹ shows that the oxygen nonstoichiometry in LSC exhibits no such plateau but rather a continuous

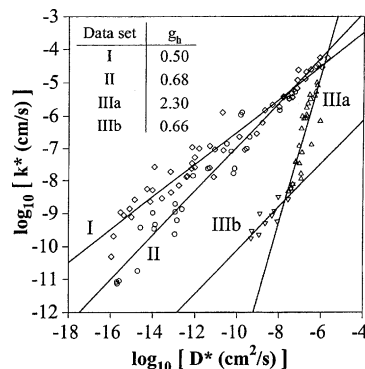


Figure 22. Correlation of the isotope tracer surface exchange coefficient (k^*) vs the oxygen tracer diffusion coefficient (D^*). Data represent a variety of materials under various temperature and P_{O_2} conditions but are classified according to groups. Group I: $\text{La}_{1-x}\text{Sr}_x\text{Mn}_{1-y}\text{Co}_y\text{O}_{3\pm\delta}$, $\text{Sm}_{1-x}\text{CoO}_{3-\delta}$, and $\text{La}_{1-x}\text{Sr}_x\text{Fe}_{1-y}\text{Co}_y\text{O}_{3-\delta}$. Group II: $\text{CaZr}_{0.9}\text{In}_{0.1}\text{O}_{2.95}$, $\text{SrCe}_{0.95}\text{Yb}_{0.05}\text{O}_{2.975}$, and $\text{La}_{1-x}\text{Sr}_x\text{YO}_{3-x/2}$. Group IIIa: oxide fluorites at high temperature plus $\text{La}_{0.9}\text{Sr}_{0.1}\text{Ga}_{0.8}\text{Mn}_{0.2}\text{O}_{2.85}$. Group IIIb: oxide fluorites at low temperature. (Reprinted with permission from ref 141. Copyright 1999 Elsevier.)

increase in vacancy concentration with decreasing P_{O_2} .^{121–124} Mizusaki noted that that this behavior implies that the partial entropy of oxygen incorporation is dominated by the configuration entropy of the vacancies while electron/hole entropy is constant.¹²¹ More recently, Lankhorst et al. modeled this behavior using a point-defect view for oxygen vacancies but treating electrons as delocalized according to a rigid-band model.^{125–127} Nonstoichiometry for mixed iron and cobalt materials has also been investigated^{117,118,128,129} and can be explained to a certain degree by hybrid models invoking both localized and itinerant electronic states.¹³⁰

Although these materials are primarily electronic conductors ($t_{n,p} \approx 1$), the very large concentrations of oxygen vacancies generated in these materials (as shown in Figure 19) has been found to lead to rapid bulk oxygen ionic transport as well as increased rates of exchange of oxygen with the gas. The rates of these processes have been measured by a variety of techniques including electronic blocking methods,^{131–133} $^{18}\text{O}_2$ tracer techniques based on postmortem SIMS analysis,^{134–142} relaxation methods involving the measurement of mass, conductivity, or other properties following a sudden change in P_{O_2} ,^{135,143–148} or direct measurement of permeation through a dense membrane.^{149–153} Although we do not review this literature in detail, some of the highlights relevant to the present discussion are included.

(1) *Higher vacancy concentration leads to faster ion transport and surface exchange.* In general, the more vacancies there are, the faster oxygen can be absorbed by, and move through, the lattice for a given chemical potential driving force. In fact, as shown in Figure 22, many workers have noticed a strong correlation between the equilibrium surface isotope exchange rate (k^*) and the bulk tracer diffusion rate (D^*) that spans 10 orders of magnitude in property values across several classes of materials.¹⁴¹

(2) *Higher electronic conduction is correlated with faster oxygen exchange.* As shown in Figure 22,

materials with high concentrations and/or more mobile electronic carriers tend to have much better surface catalytic properties (k^*) than more purely ionically conductive materials with similar rates of bulk ion transport (D^*). The existence of this universal correlation suggests that there may be a fundamental limit to how active the surface of these materials can be without some type of additional enhancement.

(3) *Available kinetic and transport data are limited to linearized driving force.* The measurement techniques listed above (particularly tracer and relaxation techniques) only probe the rate of oxygen diffusion and surface exchange at or near equilibrium conditions. While transport data can normally be extrapolated to higher driving force (through consideration of the defect structure and appropriate thermodynamic factors), extrapolation of equilibrium surface exchange data to high driving force is impossible without a priori knowledge of the exchange mechanism, which is still an open question. Thus, the nonlinear rate expressions governing absorption or evolution of oxygen at the mixed-conductor surface remain largely unknown today.

4.3. Defining the Role of the Bulk—Dense Thin-Film Mixed-Conducting Electrodes

To better understand the role of bulk oxygen transport in determining the characteristics of mixed-conducting oxide electrodes, workers have focused considerable attention in the last 10–12 years on dense thin-film electrodes having little or no three-phase boundary contact area.^{27,124,154–166} Early attempts struggled with sample preparation, it being difficult to make and verify the existence of uncracked and dense films. Perhaps the first success in this direction was that of Mizusaki and co-workers,¹⁵⁷ who used a pulsed KrF excimer laser to flash evaporate and deposit 1–2 μm thick films of $\text{La}_{0.5}\text{Sr}_{0.5}\text{MnO}_3$ on YSZ. Prior to polarization, these electrodes exhibited a zero-bias impedance much higher than porous LSM electrodes and a performance that *decreased* with increasing P_{O_2} , which is contrary to the normal situation with porous electrodes. They also noticed that the performance scaled inversely with electrode thickness. On the basis of these results, they modeled the electrode as being limited by ambipolar diffusion of oxygen through the bulk of the film and showed that the majority of their observations were consistent with this model, based on the known defect structure of LSM. More recent results appear to confirm this conclusion.^{159,167} It was thus shown that even with a poor ionic conductor such as LSM, a bulk path exists for oxygen reduction and a TPB interface is not strictly necessary for the reaction to occur.

However, as discussed more fully in section 5, it is not entirely clear how significant the bulk path is in the case of LSM, which is almost a pure electronic conductor under typical cathode conditions. In the Mizusaki study cited above, the authors went on to show that following anodic polarization (or strong cathodic polarization), the LSM film becomes severely damaged and cracked and reverts to behavior more

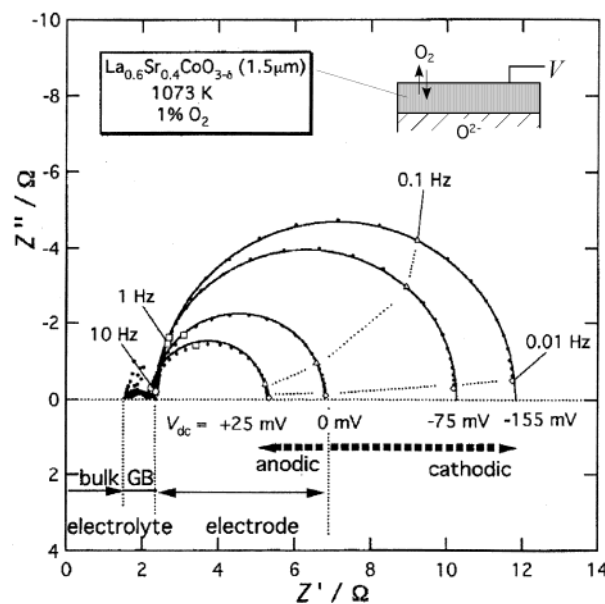


Figure 23. Impedance response of a thin film of LSC ($x = 0.4$) on GDC at 800 °C and $P_{\text{O}_2} = 10^{-2}$ atm as a function of polarization. (Reprinted with permission from ref 124. Copyright 2002 Electrochemical Society Inc.)

consistent with a porous LSM electrode. The authors conclude that this damage results in a creation of TPB contact area and thus changes the relative importance of bulk vs surface transport in allowing electroactive oxygen to reach the electrode/electrolyte interface. In other words, by constraining transport to the bulk artificially using a thin film, one can only prove that bulk transport occurs not that it is the dominant path for transport under all conditions.

In contrast, in a series of collaborative studies, Kawada, Masuda, and co-workers reported excellent success making thin-film electrodes of LSC ($\text{La}_{0.6}\text{Sr}_{0.4}\text{CoO}_{3-x}$) on Ca-doped ceria (CDC) using laser ablation.^{124,158,161} These homogeneous and very-well characterized films were studied by impedance over a range of T , P_{O_2} , and thickness as well as isotope exchange methods to help determine where the resistance to oxygen reduction occurs. As shown in Figure 23, these films exhibit nearly perfect low-frequency semicircular impedances having a resistance and capacitance that can be analyzed quantitatively assuming that absorption/desorption of oxygen at the gas/film interface is rate limiting. The author's isotope-exchange measurements on the same system confirm that the film contributes virtually no resistance to bulk oxygen transport and that there is no resistance for $^{18}\text{O}^{2-}/^{16}\text{O}^{2-}$ exchange across the LSC/CDC interface. Subsequently published studies have consistently confirmed these findings for other perovskite phases having high ionic conductivities.^{27,124,162–166} Both Kawada et al.¹⁶¹ and Yang et al.¹⁶⁵ compared the oxygen surface exchange coefficient for the gas/mixed conductor interface obtained from isotope measurements to that predicted from the impedance and found quantitative agreement over a range of temperatures and P_{O_2} . These results suggest that over length scales of a few micrometers, the bulk will provide little opposition to oxygen transport and thus will be a dominant transport path.

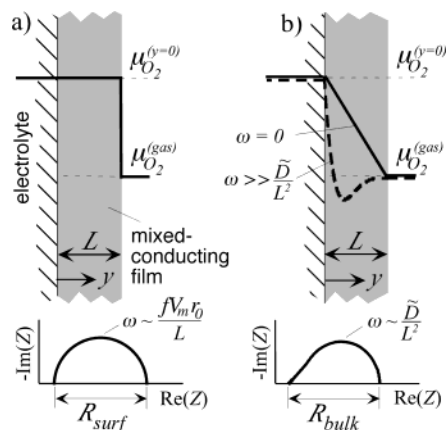


Figure 24. Models illustrating the source of “chemical capacitance” for thin film mixed conducting electrodes. (a) Oxygen reduction/oxidation is limited by absorption/desorption at the gas-exposed surface. (b) Oxygen reduction/oxidation is limited by ambipolar diffusion of O^{2-} through the mixed conducting film. The characteristic time constant for these two physical situations is different (as shown) but involves the same chemical capacitance C_L , as explained in the text.

Results are similar for films deposited on YSZ; however, there appears to be a difference between films deposited on ceria vs YSZ in terms of interfacial electrochemical resistance. As shown previously in Figure 6c, LSC films on YSZ often exhibit a second high-frequency impedance associated with oxygen-ion exchange across the electrode/electrolyte interface.^{27,164–166} That this difference is associated with the solid–solid interface has been confirmed by Mims and co-workers using isotope-exchange methods.¹⁶⁴ As discussed in greater detail in sections 6.1–6.3, this interfacial resistance appears to result from a reaction between the electrode and electrolyte, sometimes detected as a secondary phase at the interface.

As with platinum, these studies reillustrate that oxygen reduction can be separated into chemical steps (in this case absorption of oxygen into and ambipolar transport through the bulk of the mixed conductor film) and electrochemical–kinetic steps (exchange of oxygen ions across the mixed-conductor/electrolyte interface). Besides highlighting the important role of these chemical steps in determining the overall *resistance* of mixed-conducting electrodes, another important consequence of this separation is the concept of chemical capacitance (also known as faradaic or pseudocapacitance) associated with the bulk oxidation/reduction of the material. As discussed below, this chemical capacitance is normally much larger than surface or interfacial capacitances and thus is a useful measure of how much of the bulk is involved, even when we step away from thin films to more complex microstructures.

4.4. Chemical Capacitance

Figure 24 illustrates what gives rise to the measured resistance and capacitance of a mixed-conducting film (as determined by impedance) when the reaction is limited by either (a) chemical reduction of O_2 to O^{2-} at the gas/film interface or (b) transport of oxygen ions in the bulk of the film (where electronic conduction is facile).

If O_2 exchange at the gas-exposed surface is rate limiting (Figure 24a), the relatively fast transport of oxygen ions in the film will cause the film to act as a uniformly concentrated and electrically neutral reservoir for oxygen vacancies and associated electrons/holes. Conservation of vacancies in the film in this case is therefore given by

$$L \frac{\partial [V_O^\cdot]}{\partial t} = N_{V_O^\cdot}|_{y=0} - N_{V_O^\cdot}|_{y=L} \quad (3)$$

where $[V_O^\cdot] = \delta/V_m$ is the vacancy concentration, δ is the oxygen nonstoichiometry in $ABO_{3-\delta}$, V_m is the molar volume of the oxide, and $N_{V_O^\cdot}$ is the vacancy flux in the y direction. In the absence of impedance at the solid–solid interface, a sinusoidal modulation of the current density (i) will cause a proportional faradaic modulation of vacancy flux across the solid–solid interface at $y = 0$

$$N_{V_O^\cdot}|_{y=0} = \frac{-i}{2F} = \frac{-i_1 e^{j\omega t}}{2F} \quad (4)$$

where i_1 is the current modulation amplitude and ω is the frequency in s^{-1} . At the gas/solid interface the absorption/desorption of oxygen results in a vacancy flux related to the displacement of the solid oxygen chemical potential from equilibrium with the gas. Upon linearization, any rate expression for this process can be written in terms of the displacement of δ from equilibrium

$$N_{V_O^\cdot}|_{y=L} = \lim_{N_{V_O^\cdot} \rightarrow 0} \{r_0(1 - e^{(u_{O_2}^{solid} - \mu_{O_2}^{gas})/2RT})\} = r_0 f(\delta - \delta_0) \quad (5)$$

where r_0 is the equilibrium oxygen exchange rate, δ_0 is the value of δ at equilibrium with the gas, and $f = (-\partial \mu_{O_2}/\partial \delta)/RT$ is a thermodynamic factor expressing the ease with which the material changes stoichiometry for a given change in P_{O_2} ($f \approx 1$ means stoichiometry changes easily, $f \gg 1$ means it is hard to change stoichiometry). For a good electronic conductor in the limit of small vacancy concentration, configurational entropy tends to dominate the vacancy free energy such that f scales approximately inversely with vacancy concentration.

Since the solid–solid interface and bulk of the mixed conductor remain in chemical and electrical equilibrium, the measured overpotential η is related directly to the spatially uniform oxidation state of the film through the Nernst equation: $4F\eta = RTf(\delta - \delta_0)$. Solving for $\delta(t)$ and recognizing that the impedance $Z = \eta/i$, one obtains

$$Z = \frac{R_{surf}}{1 + j\omega R_{surf} C_L}$$

$$R_{surf} = \frac{RT}{4F^2} \frac{1}{2r_0}$$

$$C_L = \frac{4F^2}{RT} \frac{2L}{fV_m} \quad (6)$$

where R_{surf} is the area-specific resistance associated with oxygen reduction at the gas-exposed surface and C_L is the effective *chemical* (noninterfacial) capacitance associated with changes in oxygen stoichiometry in the film of thickness L . As shown by the Nyquist plot in Figure 24a, this impedance has a semicircular shape with width R_{surf} and characteristic frequency $1/R_{\text{surf}}C_L$. A similar expression for the chemical capacitance of a surface-limited film was recently derived by Kawada et al. using a transmission line approach.¹²⁴

In the second case (limit of fast kinetics at the gas–solid interface), the film becomes entirely bulk transport limited, corresponding to the limit of Hebb–Wagner polarization. Since electronic conduction is fast, this situation yields a Warburg impedance for finite length diffusion⁴⁹

$$Z = R_{\text{bulk}} \frac{\tanh(\sqrt{j\omega R_{\text{bulk}} C_L})}{\sqrt{j\omega R_{\text{bulk}} C_L}}$$

$$R_{\text{bulk}} = \frac{RT}{4F^2} \frac{FV_m L}{2\tilde{D}} = \frac{L}{\sigma_i} \quad (7)$$

where R_{bulk} is the area-specific resistance associated with ambipolar oxygen diffusion through the bulk of the film (assuming facile electron transport) and \tilde{D} is the chemical diffusion coefficient for oxygen ions. One can also express R_{bulk} in terms of the oxygen ionic conductivity of the film, σ_i , as shown in eq 7. Since oxygen stoichiometry changes occur over the entire thickness of the film, this situation yields the same chemical capacitance (C_L) as the surface-limited case.¹⁶⁸

Thus, in the case of a thin film, when chemical steps (absorption and/or bulk diffusion) are rate limiting, accumulation of electroactive intermediates in the bulk results in a large effective capacitance proportional to the thickness of the film and the ease by which it changes nonstoichiometry. As recently shown by Kawada et al.,¹²⁴ this capacitance is very large (0.1–1 F/cm²) even for relatively thin (1.5 μm) mixed-conducting films. This value is significantly larger than the pseudocapacitance of Pt (~10⁻³ F/cm²), which is dominated by adsorption and transport of oxygen on the Pt surface. If we compare this value to the apparent true interfacial polarization capacitance of the Pt/YSZ interface (10⁻⁶–10⁻⁵ F/cm²), we see an even larger difference. Thus, capacitance is a strong indicator (independent of resistance) as to what degree the interface, surface, and/or bulk are playing in the reaction kinetics for a given material and set of conditions.

Some authors have expressed concerns that bulk accumulation of reactive intermediates (and thus chemical capacitance) violates electroneutrality.^{169,170} However, it should be recalled that reduction (or oxidation) of a material not only involves depletion (or accumulation) of oxygen ions in the bulk but neutral combinations of oxygen ions and compensating electrons/holes which together may accumulate without violating electroneutrality.⁴⁷ Indeed, no other mechanisms have yet been proposed which satisfac-

torily explain such a large capacitance without invoking a bulk reaction pathway. As we will see below, workers have used this concept to understand what is happening in more complex porous systems where the relative roles of kinetics, transport, bulk, and surface are not nearly as clear.

4.5. Porous Mixed Conductors—A More Complex Case

Returning briefly to Figure 4, we see a summary of some of the physical mechanisms postulated in the literature to limit the rate of oxygen reduction in a porous mixed-conducting electrode (some of which we have discussed previously in the context of porous Pt and dense mixed conducting electrodes). These include (a) kinetics of O₂ incorporation into the bulk mixed conductor, (b) kinetics of adsorption and/or partial reduction of oxygen on the mixed-conductor surface, (c) rate of bulk or (d) surface transport of O²⁻ or Oⁿ⁻, respectively, to the mixed-conductor/electrolyte interface, (e) electrochemical–kinetics of charge transfer for O²⁻ or (f) combinations of Oⁿ⁻ and e⁻, respectively, across the mixed-conductor/electrolyte interface, and (g) rates of one or more of these mechanisms wherein the electrolyte itself acts as a mixed conductor due to doping by reaction with the electrode materials.

In the case of a LSM thin film, we noted above that introduction of TPB contact area (via damage of the film) resulted in a fundamental change in the rate-determining step from bulk oxygen transport to some other step (or combination of steps) likely involving the surface. The same fundamental question arises when considering a porous mixed conductor with high ionic conductivity. For a thin film we saw that the mechanism is dominated by the bulk path, a–c–e, with the surface exchange process (a) being rate determining (plus a small contribution from charge transfer (e) when YSZ is the electrolyte). If porosity, and therefore direct TPB contact area, is introduced, does the relative importance of these steps change and/or does a surface path (b–d–f) begin to play a role as it does in the case of Pt?

As discussed in section 4.2, strong interest in mixed-conducting perovskites as gas-separation membranes stimulated a large volume of work in the late 1980s and early 1990s to better understand the properties of mixed-conducting perovskites, including defect thermodynamics, ionic and electronic transport properties, and surface kinetics for absorption/desorption of oxygen. Prompted by the availability of these data, a number of workers in the mid-1990s began a modeling effort to better understand the performance of porous mixed-conducting electrodes^{171,172} and membrane coatings^{173,174} based on these properties. Although these models only consider a limited set of the physics shown in Figure 4, they successfully confirmed the important role of the bulk and (where valid) provided design guidelines relating performance to microstructure and bulk materials properties. Spending some time to understand these models is therefore worth a few pages, both because they help understand the reaction in some limiting cases as well as being a launching platform for

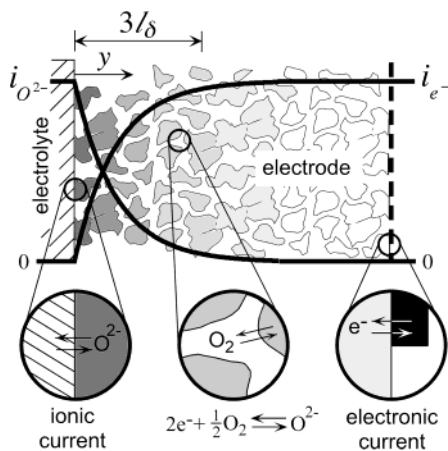


Figure 25. Adler's 1D macrohomogeneous model for the impedance response of a porous mixed conducting electrode. Oxygen reduction is viewed as a homogeneous conversion of electronic to ionic current within the porous electrode matrix, occurring primarily within a distance l_b from the electrode/electrolyte interface (utilization region). (Adapted with permission from ref 28. Copyright 1998 Elsevier.)

understanding more complex cases where the models break down. Where and how these models break down is interesting because it sheds light on what other physical processes may be active.

4.6. One Asymptotic Limit—The Bulk Reaction Path

One limit of behavior considered in the models cited above is an entirely bulk path consisting of steps a–c–e in Figure 4. This asymptote corresponds to a situation where bulk oxygen absorption and solid-state diffusion is so facile that the bulk path dominates the overall electrode performance even when the surface path (b–d–f) is available due to existence of a TPB. Most of these models focus on steady-state behavior at moderate to high driving forces; however, one exception is a model by Adler et al.¹⁷¹ which examines the consequences of the bulk-path assumption for the impedance and chemical capacitance of mixed-conducting electrodes. Because capacitance is such a strong measure of bulk involvement (see above), the results of this model are of particular interest to the present discussion.

As shown schematically in Figure 25, the Adler model takes as its testable hypothesis that mixed conductors with high ionic conductivity function by the same underlying mechanism as a dense film, i.e., path a–c–e in Figure 4. In addition, because ionic transport is relatively fast, the model also assumes that variations in composition within the electrode will occur over distances larger than the size of individual microstructural features (particles) making up the porous electrode. Thus, as is often done in porous electrode theory, transport and reaction in and between the solid and gaseous phases are treated using average structural parameters: surface area (a), porosity (ϵ), and tortuosity (τ). With this assumption, the overall electrode reaction, $2e^- + 1/2 O_2 \rightarrow O^{2-}$, can be viewed as a 1D macrohomogeneous conversion of electronic current to ionic current over the thickness of the electrode, where in this case oxygen

absorption and diffusion act as Kleitz's "chemical valve" (Figure 10), limiting overall charge flow (current) at steady state. This model also considers the effects of gas-phase diffusion and charge-transfer resistance at the electrode/current collector contact.

Because the Adler model is time dependent, it allows prediction of the impedance as well as the corresponding gaseous and solid-state concentration profiles within the electrode as a function of time. Under zero-bias conditions, the model predicts that the measured impedance can be expressed as a sum of electrolyte resistance ($R_{\text{electrolyte}}$), electrochemical kinetic impedances at the current collector and electrolyte interfaces ($Z_{\text{interfaces}}$), and a "chemical" impedance (Z_{chem}) which is a convolution of contributions from chemical processes including oxygen absorption, solid-state diffusion, and gas-phase diffusion inside and outside the electrode.

In the limit of a semi-infinite (thick) porous electrode with no gas-phase diffusion limitations, the chemical term Z_{chem} reduces to an impedance reflecting co-limitation by oxygen absorption and transport.³⁶⁹

$$Z_{\text{chem}} = R_{\text{chem}} \sqrt{\frac{1}{1 + j\omega(R_{\text{chem}} C_b)}} \quad (8)$$

where R_{chem} and C_b are a characteristic resistance and capacitance, respectively, reflecting co-limitation by surface kinetic and transport properties of the mixed conductor

$$R_{\text{chem}} = \frac{RT}{4F^2} \sqrt{\frac{fV_m}{\tilde{D}_{\text{eff}} a r_0}} = \sqrt{\frac{4R_{\text{surf}}}{\sigma_{i,\text{eff}} a}}$$

$$C_b = \frac{4F^2 (1 - \epsilon) l_b}{RT fV_m} \quad (9)$$

where V_m is the molar volume, $\tilde{D}_{\text{eff}} = (1 - \epsilon)\tilde{D}/\tau$ is the effective oxygen-ion chemical diffusion coefficient in the solid (corrected for porosity and path tortuosity), and r_0 and f (as defined previously in eq 5) are the linearized rate of oxygen absorption/desorption and a thermodynamic factor, respectively. As shown in eq 9, one can also express R_{chem} in terms of surface and bulk resistances defined previously in eqs 6 and 7 for a thin film: R_{surf} and $\sigma_{i,\text{eff}} = (1 - \epsilon)\sigma_i/\tau$.

Equation 9 shows that the chemical capacitance in this case is similar to that derived previously in eq 6 for a thin film (C_L); however, in the co-limited situation the important length parameter is not L but rather a characteristic "utilization" length given by

$$l_b = \sqrt{\frac{\tilde{D}_{\text{eff}}}{fV_m a r_0}} = \sqrt{\frac{\sigma_{i,\text{eff}} R_{\text{surf}}}{a}} \quad (10)$$

The significance of this length parameter l_b can be understood by examining the predicted steady-state vacancy concentration profile in the porous electrode as shown in Figure 26a. At steady state, the model predicts that the mixed conductor will be reduced by an amount that decays exponentially with distance

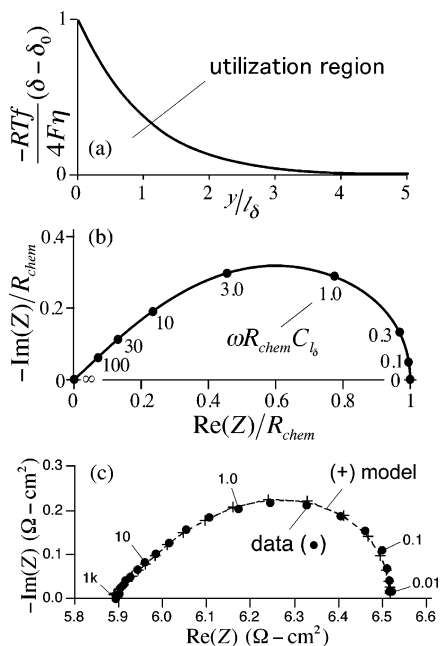


Figure 26. Predictions of the Adler model shown in Figure 25 assuming interfacial electrochemical kinetics are fast. (a) Predicted steady-state profile of the oxygen vacancy concentration (δ) in the mixed conductor as a function of distance from the electrode/electrolyte interface. (b) Predicted impedance. (c) Measured impedance of $\text{La}_{0.6}\text{Ca}_{0.4}\text{Fe}_{0.8}\text{Co}_{0.2}\text{O}_{3-\delta}$ electrodes on SDC at 700 °C in air, fit to the model shown in b using nonlinear complex least squares. Data are from ref 171.

from the electrolyte interface with a characteristic length l_δ describing the size of the active region. Equation 9 shows that the chemical capacitance will be proportional to the size of this region, just as the chemical capacitance of a dense film is proportional to its thickness (eq 6). The difference here is that the amount of material contributing to the capacitance is determined by the kinetic and diffusion parameters rather than a geometric length scale.

Figure 26b shows the impedance predicted by eqs 8 and 9. As previously discussed, this function is known as the Gerischer impedance, derived earlier in section 3.4 for a situation involving co-limited adsorption and surface diffusion (in the context of Pt). As with the surface-mediated case, the present result corresponds to a co-limited reaction regime where both kinetics and transport determine the electrode characteristics (as reflected in the dependency of R_{chem} and C_{lb} on both r_0 and D_{eff}). The essential difference between this and the Pt case is that here the kinetics and diffusion parameters refer to a bulk-mediated rather than surface-mediated process.

As shown in Figure 26c and as discussed more fully elsewhere,¹⁷¹ initial comparisons of this model to impedance data for $\text{La}_{0.6}\text{Sr}_{0.4}\text{Co}_{0.2}\text{Fe}_{0.8}\text{O}_{3-\delta}$ (LSCF) on gadolinia-doped ceria were favorable. A fit of the impedance to eq 8 yielded values of R_{chem} and C_{lb} that were reasonably consistent with those calculated based on the known bulk properties of LSCF. The large chemical capacitance observed (and calculated) in this case corresponds to a significant reduction/oxidation of the bulk, while the Gerischer shape of the impedance (and absence of other impedance

features) suggests that the reaction is co-limited by absorption and transport to the interface.

This result prompted a more complete experimental study by Adler of the impedance of porous $\text{La}_{1-x}\text{Sr}_x\text{CoO}_{3-\delta}$ electrodes on SDC.²⁸ Symmetric LSC/SDC/LSC cells with 2.0 cm² active area were fabricated at three values of strontium content, $x = 0.2, 0.3,$ and $0.4,$ and characterized in terms of surface area (a) and porosity (ϵ) (tortuosity (τ) of the bulk path was also estimated). The impedances of these cells were then studied over a range T and P_{O_2} . Although the resulting impedance data did not match eq 8 as well as shown in Figure 26c, the data did exhibit a single arc with a Gerischer shape and were fit to obtain values of R_{chem} and $t_{\text{chem}} = R_{\text{chem}}C_{lb}$. On the basis of these values (and without other adjustable parameters), the oxygen vacancy diffusion and surface-exchange coefficients were back calculated and compared to independent measurements based on isotope exchange or membrane permeation (see section 4.2). The results suggest the following.

(1) *Preference for the bulk path.* With notable exceptions (see the following section), quantitative comparison of the vacancy diffusion coefficient and surface-exchange coefficient back calculated from the resistance and capacitance are in reasonable agreement with independent measurement both in value as well as dependencies on P_{O_2} and temperature (activation energy). This result suggests that for materials with high ionic conductivity, it is the bulk path (a–c–e in Figure 4) rather than the surface path (b–d–f) that dominates at open circuit. This appears to be the only explanation consistent with the large observed chemical capacitance. Not surprisingly, agreement is best for materials with the highest oxygen vacancy concentration. Application of the model to LSM (which is a poor ionic conductor in air) grossly underpredicts performance, suggesting that porous LSM functions primarily by a surface-mediated mechanism at least near open circuit (see section 5).

(2) *Co-limited kinetics with a significant utilization region.* As with platinum, the model predicts that the chemical portion of the reaction will be co-limited by molecular dissociation and transport. Values of l_δ calculated from the model for the analyzed conditions vary from 0.4 to 20 μm depending on P_{O_2} , temperature, and electrode surface area, with typical values in the 3–5 μm range. This result indicates that a significant portion of the electrode surface is active for oxygen reduction, which explains Takeda's (and other's) observation that the performance of LSC electrodes on YSZ improves with thickness up to a limit of a few micrometers.^{101,175} At around the same time as the Adler model, Zhou and co-workers modeled the effect of porous perfusion layers on mixed-conducting membranes, drawing similar conclusions regarding the co-limited nature of the reaction and estimates of the utilization length.¹⁷⁶ These models further predict that for small surface areas (a) l_δ will exceed the thickness of the porous layer/electrode such that the entire layer becomes active with surface-absorption-limited behavior (semicircular impedance) rather than co-limited. Adler confirmed this

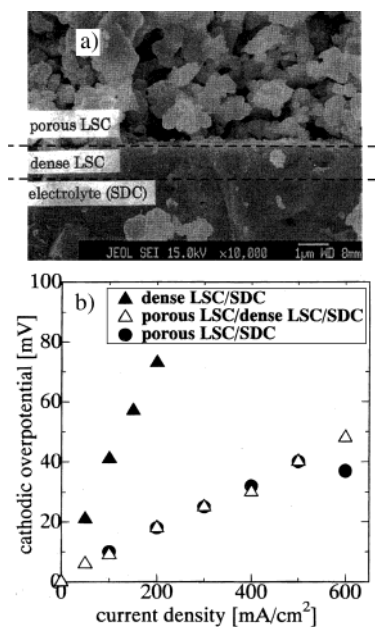


Figure 27. Measured overpotential of a porous LSC electrode on SDC with and without a dense LSC layer in between. (Reprinted with permission from ref 179. Copyright 1998 Electrochemical Society, Inc.)

prediction by oversintering the electrode and showing that the electrode exhibits a surface-limited impedance similar to that predicted by eq 6.²⁸

(3) *Absence of electrochemical-kinetic resistances.* For LSC on SDC at 550 °C and above, additional high-frequency impedance features indicating the presence of an interfacial resistance/capacitance were not observed. This result suggests that the majority of the overpotential is associated with absorption and bulk transport of oxygen, while ion exchange at the LSC/SDC interface remains in electrochemical equilibrium. As we will see in section 6, this conclusion is not universally true of all materials; additional impedance arcs have been observed for perovskites on YSZ and with ceria at lower temperatures or with certain electrolyte dopants. Nonetheless, this result did strongly challenge prior thinking, which had assumed interfacial electrochemical kinetics would be limiting if transport is facile.¹⁰¹

Subsequent studies of porous mixed-conducting electrodes under a variety of conditions have since reinforced the view that the bulk pathway plays an important (if not dominant) role in the electrode kinetics for these materials.^{19,177–184} Of particular note is a study (published the same year as the Adler studies) by Endo and co-workers who used pulsed laser deposition to cast a dense thin ($\sim 1 \mu\text{m}$) film of LSC (40% Sr) onto SDC prior to screen printing and firing a porous LSC electrode of the same composition¹⁷⁹ (Figure 27a). As shown in Figure 27b, they found that the overpotential of the porous electrode is independent of the presence of the film. This result appears to confirm the dominance of the bulk path, since elimination of any possible surface path (including TPB contact area) does nothing to alter the electrode performance. This result also appears to confirm that the active region of the porous LSC layer is large compared to the superficial electrode area, since replacement of the gas-exposed electrolyte with

additional (presumably active) LSC does not significantly enhance performance. Also consistent with a large utilization region is a study by Koyama et al. of porous $\text{Sm}_{0.5}\text{Sr}_{0.5}\text{CoO}_{3-\delta}$ (SSC) on SDC as a function of electrode thickness;¹⁸⁴ they found that the electrode performance improves with thickness up to about 10–15 μm , after which performance saturates.

During the time period that the results described above were published (mid-1990s), workers studying porous mixed conducting electrodes fell into multiple schools of thought regarding the mechanism (not unlike those discussed previously for Pt/YSZ). A number of papers appeared which expressed conflicting (or dissenting) views vis-a-vis the role of the bulk and interface in governing the mechanism and the extent of the utilization region. One of these was work by Gödickemeier et al., who used current-interruption techniques to study the steady-state current-overpotential relationships for LSM and LSC on samaria- and gadolinia-doped ceria.^{14,17} They found that their results fit well to a Butler-Volmer rate expression and thus concluded the electrodes are limited by interfacial electrochemical kinetics rather than transport limited. In this case, by “transport limited” the authors meant simply that a limiting current was not observed at high overpotentials.

However, as we saw in section 3.3 for platinum on YSZ, the fact that $i-\eta$ data fits a Butler-Volmer expression does not necessarily indicate that the electrode is limited by interfacial electrochemical kinetics. Supporting this point is a series of papers published by Svensson et al.,^{172,185,186} who modeled the current-overpotential ($i-\eta$) characteristics of porous mixed-conducting electrodes. As shown in Figure 28a, these models take a similar mechanistic approach as the Adler model but consider additional physics (surface adsorption and transport) and forego time dependence (required to predict impedance) in order to solve for the full nonlinear $i-\eta$ characteristics at steady state.

One significant prediction of the Svensson models is that regardless of whether the reaction path is surface or bulk dominated, the $i-\eta$ characteristics appear Tafelian, even if interfacial electrochemical kinetic steps are equilibrated. As an example, Figure 28b shows the predicted $i-V$ characteristics of a mixed conducting electrode assuming a bulk path as a function of the oxygen vacancy diffusion coefficient. As evidenced by the linear dependence of $\ln(i)$ on V at high currents, the model obeys Tafel kinetics, yet the Tafel parameters (“exchange current density”) depend on a transport parameter. In other words, just as we saw for platinum on YSZ (section 3.3), the mere fact that $i-\eta$ data fits a Butler-Volmer expression does not prove that the electrode is limited by interfacial electrochemical kinetics. The Svensson models show that chemical steps of ad(b)sorption and transport can dominate the observed kinetics well below limiting current, and thus the absence of a measured limiting current does not indicate an absence of transport limitations. On the contrary, diffusion in this case is predicted to produce a variety of finite, Tafel-like, characteristics.

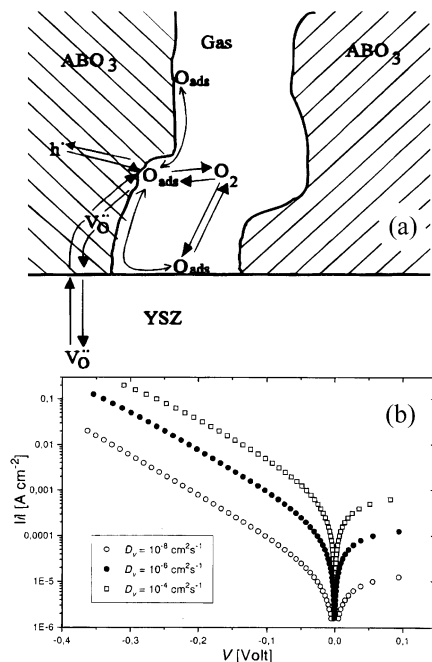


Figure 28. Svensson's macrohomogeneous model for the i - V characteristics of a porous mixed-conducting electrode. (a) The reduction mechanism assuming that both surface and bulk diffusion are active and that direct exchange of oxygen vacancies between the mixed conductor and the electrolyte may occur. (b) Tafel plot of the predicted steady-state i - V characteristics as a function of the bulk oxygen vacancy diffusion coefficient. (Reprinted with permission from ref 186. Copyright 1998 Electrochemical Society, Inc.)

Another set of papers countering the conclusions of the Adler studies (as well as implicitly the Svensson studies) were published by Liu and co-workers, who questioned the validity of the Adler model on several levels.^{169,170,187,188} As discussed elsewhere,¹⁸⁹ many of these questions appear to have arisen primarily from a misunderstanding about the assumptions and terminology of the model (so we will not belabor the points raised again here). However, Liu also raised the more general concern that the model does not consider the "direct" reduction of O_2 at the TPB (traditionally considered the route by which the cathode reaction occurs). While this is certainly true, perhaps the more relevant question is what we mean by the "three-phase boundary"? Certainly from the phenomenological standpoint (Figure 3), one must have three phases involved in the reaction for oxygen reduction to occur. However, when one begins to consider the specific chemical, electrochemical, and transport steps involved, one must abandon the idea of an ideal 1D geometric surface and consider the specific phases, surfaces, and interfaces involved in these steps. A separate consideration of the "direct" TPB reaction is not necessary since it is exactly this reaction that the various models discussed in this review attempt to embody. While a mechanistic approach almost certainly involves oversimplification of the physics, it also allows workers to pose specific hypotheses about the mechanism, predict the consequences of those hypotheses, and test these predictions against measurement. As we will see in the following section, the failure of existing models to predict certain features

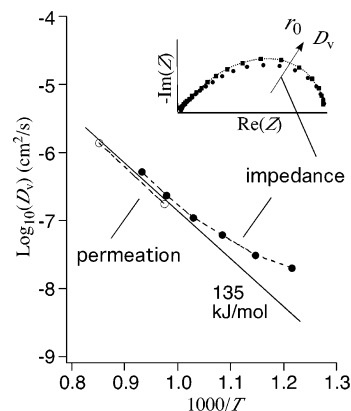


Figure 29. Comparison of the oxygen vacancy diffusion coefficient (D_v) in LSC ($x = 0.2$) determined from permeation measurements vs that extracted from impedance measurements using the model in Figure 26. Data are from refs 190 and 28. (Adapted with permission from ref 28. Copyright 1998 Elsevier.)

of the data and their inconsistency with measurements under certain conditions is actually useful information for understanding how other factors and mechanisms (besides the bulk path) come into play.

4.7. Limitations of Bulk, 1D Transport Models for Porous Mixed Conductors

While subsequent work^{19,177–184} has continued to reinforce the importance of the bulk for porous mixed-conducting electrodes, authors generally debate the degree to which the bulk vs surface paths dominate and under what conditions. In the asymptotic limit of high ionic conductivity, the 1D models discussed above appear to explain i - V characteristics and impedance data well under conditions of facile bulk transport and a reversible interface. However, what happens when the ionic conductivity is not so high and/or the utilization length becomes competitive with microstructural features? Also, what happens when the interface is not reversible?

One clue to this question is provided by where and how the Adler model breaks down in explaining the impedance characteristics of LSC on SDC. For example, Figure 29 compares the apparent vacancy diffusion coefficient of $La_{0.8}Sr_{0.2}CoO_{3-\delta}$ (extracted from the chemical resistance and capacitance²⁸) to the measured value for a bulk membrane (determined from permeation measurements^{190,191}) as a function of temperature in air. At the highest temperatures, agreement is reasonable in both value and activation energy. However, at lower temperatures there is a systematic deviation from activated behavior, with the apparent diffusion coefficient being perhaps 10 times larger than predicted by extrapolation of the permeation data. This deviation also corresponds to a change in the shape of the impedance to being less "Gerischer-like".²⁸ In addition, for $La_{0.8}Sr_{0.2}CoO_{3-\delta}$, the Adler model predicts a utilization length of $l_b = 0.3$ – $0.6 \mu\text{m}$, which is competitive with the microstructural features of the electrode and thus a violation of the formal assumptions of the model.

There are several possible explanations for this behavior, all of which speak to various deficiencies of current models. First, even if the bulk path

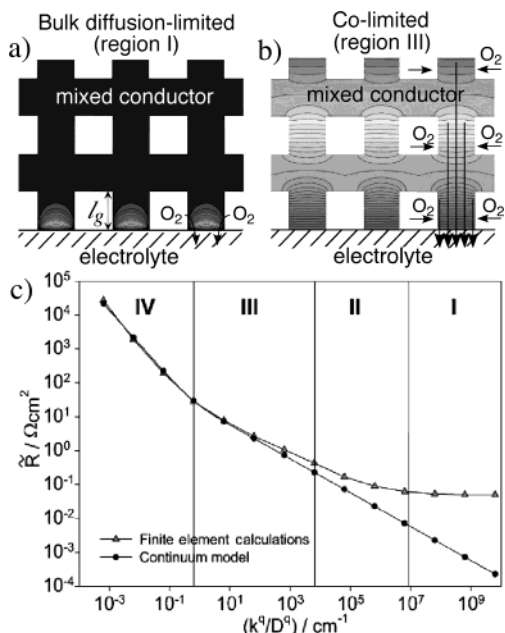


Figure 30. Finite-element calculation of the oxygen vacancy concentration profiles in a porous mixed conducting electrode, assuming a cylinder–block microstructure having a single characteristic dimension l_g . (a) Oxygen reduction is entirely bulk-transport limited. (b) Oxygen is co-limited by absorption and bulk transport as in Figures 25 and 26. (c) Comparison of the predicted resistance to that of a macrohomogeneous model (Figure 26) as a function of absorption kinetics, assuming $l_g = 1.6 \mu\text{m}$. (Adapted with permission from ref 194. Copyright 2003 Annual Reviews.)

dominates, we expect that as the utilization length becomes small, the assumption that reaction/transport can be treated using a 1D macrohomogeneous representation of the microstructure will break down. The most complete studies of this effect has been published by Fleig,^{192–194} who used finite-element analysis (FEA) to compare the predictions of a 1D macrohomogeneous model to that of a full 3D microstructural model. As shown in Figure 30, the 3D model considers bulk absorption and diffusion of oxygen in a hypothetical “cylinder–block” microstructure having characteristic length $l_g = 1.6 \mu\text{m}$. Fleig compared the linearized electrode resistivity predicted by this 3D model to that of a 1D macrohomogeneous representation of the same system as a function of k^q at fixed D^q , where k^q and D^q are linearized constants for surface absorption and bulk diffusion.^{195–197} This comparison shows that as k^q/D^q increases beyond a value of about $0.1–1 \mu\text{m}^{-1}$, the macrohomogeneous assumption breaks down. Indeed, based on the analysis presented in section 4.6, we expect this breakdown to occur when the utilization length $l_b \approx \sqrt{l_g D^q/k^q}$ (approximate translation of eq 10 for Fleig’s variables k^q and D^q) becomes on the same order or smaller than the particle dimensions l_g . This occurs when $k^q/D^q \approx l_g^{-1}$, which in this case is $0.6 \mu\text{m}^{-1}$, in good agreement with Fleig’s results. Furthermore, Fleig shows that when surface absorption becomes fast, the electrode becomes entirely transport limited (with a plateau in performance) vs the macrohomogeneous model (which predicts continued improvement as kinetics get faster). Such

purely transport-limited behavior is not possible with a surface mechanism—this is a unique feature of bulk transport in two or three dimensions.

What Fleig’s results suggest is that even without invoking other mechanisms besides the bulk path, one would have difficulty fitting the characteristics of a porous mixed-conducting electrode accurately using a 1D model (such as the Adler or Svensson models) when l_b is less than a few micrometers. The degree to which these effects are responsible for any lack of agreement with data are unknown. To date, a quantitative modeling of the impedance of LSC or LSF electrodes considering 3D effects has not yet been conducted. This is an ambitious task for several reasons. First, it is not clear that a geometric idealization of the microstructure (such as that used by Fleig) would be sufficient—at the length scale of an individual particle, the details of the actual microstructure (particle size distribution, particle connectivity, contact angle, etc.) might become important. Second, Fleig’s model predicts that under increasingly 3D transport-limited conditions, the ionic oxygen flux will not be uniform across the electrode/electrolyte interface but rather increasingly constricted through an area close to the TPB. This constriction raises the question of whether electrochemical kinetics at the interface might become increasingly important due to reduced area available for charge transfer. Such considerations add considerable complexity to the problem, in terms of both nonlinearity and inhomogeneity at this interface as well as the effect of interfacial resistance on the concentration profiles in the bulk.

However, even if one took 3D effects into consideration, it is unlikely that one could explain all the discrepancies between the Adler model and the measured impedance. For example, Figure 29 shows that the assumption of 1D bulk transport appears to *underpredict* the measured performance. In contrast, Fleig’s modeling studies suggest that ignoring 3D transport effects will generally *overpredict* performance (Figure 30). This forces us to consider a second reason the Adler model may break down: As bulk transport becomes less facile, a parallel mechanism involving the surface path may become increasingly important. Although this widely held belief has not yet been proven definitely, it is nonetheless circumstantially consistent with a variety of observations.

(1) *Inconsistency of performance with a bulk path at low vacancy concentration.* A quantitative comparison between predictions of the Adler model and impedance data for LSC shows the poorest agreement (underprediction of performance) at low temperatures, high P_{O_2} , and/or low Sr content.²⁸ These are the conditions under which the bulk vacancy concentration (and thus also the ionic conductivity and surface exchange rate of oxygen with the bulk) are the lowest. These are exactly the conditions under which we would expect a parallel surface path (if it existed) to manifest itself, raising performance above that predicted for the bulk path alone. Indeed, as discussed more fully in section 5, the Adler model breaks down completely for LSM (a poor ionic conductor at open-circuit conditions), predicting an

electrode impedance many orders of magnitude higher than observed experimentally.¹⁷¹

(2) *Inconsistencies in the chemical capacitance.* As the bulk vacancy concentration is reduced, and hence the predicted chemical capacitance of the bulk (per unit volume) becomes smaller, the portion of chemical capacitance associated with surface species may become increasingly significant. Kuznecov et al. showed that a surface-dominated mechanism should exhibit a similar Gersischer shape as a bulk-dominated mechanism,¹⁹⁸ only with a smaller chemical capacitance. One possible piece of evidence that this occurs is the observation that the apparent utilization length l_b (as extracted from impedance data assuming the Adler model²⁸) generally *decreases* with conditions promoting lower vacancy concentration (lower Sr content, higher P_{O_2}). This observation is somewhat inconsistent with eq 10, which for most mixed conductors predicts that the utilization length will stay approximately *constant* with changes in stoichiometry (as shown previously in Figure 22, the bulk oxygen vacancy concentration tends to influence oxygen exchange and bulk diffusion rates of perovskites similarly,¹⁴¹ leading to a constant ratio of \bar{D}_{eff}/fr_0 in eq 10). One resolution to this apparent inconsistency might be a parallel surface path, which could alternatively explain the measured decrease in chemical capacitance as a confinement of stoichiometry variations to the surface rather than a shrinkage of the bulk utilization region.

(3) *Nonlinear electrode kinetics.* Another possible indicator of a parallel surface path is nonlinearity of the current–overpotential characteristics. In particular, one conclusion of the model by Zhou and co-workers mentioned previously¹⁷⁶ was that the permeation resistance of a porous membrane overlayer is fairly constant with driving force (i.e., linear force–flux relationship) for mixed conductors having high vacancy concentration. This result appears to be consistent with recent measurements of Horita et al.,¹⁸¹ who conducted a study of the impedance of porous LSC electrodes on $\text{La}_{0.8}\text{Sr}_{0.2}\text{Ga}_{0.8}\text{Mg}_{0.2}\text{O}_{2.8}$ (LSGM) electrolyte as a function of cathode overpotential. Among other things, these results show that the electrode kinetics are fairly linear with overpotential for materials with high vacancy concentration but become increasingly nonlinear for materials and conditions promoting the lowest vacancy concentrations. For example, $\text{La}_{0.8}\text{Sr}_{0.2}\text{CoO}_{3-\delta}$ is more nonlinear than $\text{La}_{0.6}\text{Sr}_{0.4}\text{CoO}_{3-\delta}$, and both materials are increasingly nonlinear at lower temperatures. Although the linearity of the bulk path itself has not been well investigated, an increase in nonlinearity with decreasing vacancy concentration might indicate a shift toward a surface-mediated reaction mechanism involving more nonlinear behavior (e.g., increased charge-transfer resistance at the interface due to confinement of the flux near the TPB).

Since the mid-1990's, several models which consider both a bulk *and* surface path have been proposed, including the Svensson models as well as a more recent model by Coffey and co-workers.¹⁹⁹ However, these models have not been definitive in addressing the bulk vs surface question for at least

two fundamental reasons. First, a common feature of these models is that they are limited to nonlinear steady-state behavior and therefore cannot be used to analyze impedance or other measurements with time resolution for various physical processes. As mentioned previously, it is hard to tell what is going on from Tafel parameters since so many things mimic Tafel kinetics. Second and perhaps more fundamentally, there is simply a dearth of independent data for model parameters. Although the mobility of oxygen on the surface of a perovskite is generally thought to be “fast”, its rate relative to bulk transport (as a function of defect concentration) has never been quantitatively determined. Coffey et al. summarize the situation nicely in the concluding paragraph of their paper.¹⁹⁹

“Unfortunately many of these parameters are at best rough approximations if not outright guesses. Consequently our results are not at this time useful in interpreting available electrochemical data; however they are useful in defining what additional experimental measurements need to be made.”

Indeed, in the spirit of this latter comment, the purpose of this review is to consolidate our understanding of SOFC cathodes so that it becomes easier to identify and propose new avenues of research.

4.8. Summary: Importance of the Bulk for Mixed-Conducting SOFC Cathodes

In this section we saw that the active region of a SOFC cathode can be significantly enhanced by incorporating a mixed conductor (a material which conducts both ions and electrons). While electrodes of this type have proven challenging to implement in a SOFC operating environment (see section 6), they nonetheless have taught us a lot about what factors can limit electrode performance and opened the realm of possibilities for future materials development. To summarize, some of the salient points of our current understanding are listed.

(1) *Role of the bulk transport path.* In section 3 we saw that for Pt the dissociation of oxygen and transport of reactive intermediates to the electrode/electrolyte interface is confined to the material surface. With mixed conductors, it is possible for oxygen reduced at the surface to be transported through the bulk of the material to the electrode/electrolyte interface. If bulk transport is facile, this path may dominate, extending both the accessible surface for O_2 reduction as well as broadening the active charge-transfer area from the TPB to include the entire solid–solid contact area.

(2) *Chemical capacitance.* When the mechanism involves significant involvement of the bulk, accumulation of reactive intermediates not only involves surface species but oxidation and reduction of the bulk. This can be detected as an anomalously high effective capacitance, often referred to as a *chemical* (or *pseudo*) *capacitance*. This capacitance can be as large as 0.1–1 F/cm² and thus easily detected by current-interruption or impedance techniques. Thus, capacitance is a strong indicator (independent of resistance) as to what degree the interface, surface, and/or bulk are playing in the

reaction kinetics for a given material and set of conditions.

(3) *Co-limited kinetics*. As with platinum, porous mixed-conducting electrodes are co-limited by molecular dissociation and transport. For mixed conductors with high rates of bulk ionic transport, values of l_b vary from 0.4 to 20 μm depending on P_{O_2} , temperature, and electrode surface area with typical values in the 3–5 μm range. This result indicates that a significant portion of the electrode surface is active for oxygen reduction, not just material in the immediate vicinity of the TPB.

(4) *Sensitivity of interfacial resistance to various factors*. For perovskite mixed conductors on some ceria-based electrolytes, workers have reported virtually zero interfacial resistance such that the electrode overpotential is dominated entirely by dissociation of O_2 and transport of intermediates to the electrode/electrolyte interface. As we will see in section 6, this conclusion is not universally true of all materials; additional impedance arcs have been observed for perovskites on YSZ and with ceria at lower temperatures or with certain electrolyte dopants.

(5) *Relative role of surface vs bulk path not yet known quantitatively*. While it has been clearly established that the bulk transport path plays a role (and may dominate) in the mechanism of mixed-conducting electrodes, our quantitative understanding is currently limited to asymptotic cases (such as thin films or materials with unusually high bulk transport rates). We currently lack general techniques to measure or predict the relative role of the surface vs bulk paths in electrodes of arbitrary composition and processing. Development of such techniques will be an important step in understanding more complex materials and microstructures and in making intelligent materials design choices.

5. Lanthanum Strontium Manganese Oxide (LSM): Where Surface and Bulk Converge

In sections 3 and 4 we examined two asymptotic cases for the mechanism of oxygen reduction. With porous Pt, oxygen reduction appears to occur by a surface-mediated mechanism, where dissociative adsorption and diffusion of oxygen on the gas-exposed Pt surface play a significant (if not dominant) role in determining the overall electrode kinetics. Likewise, for porous mixed conductors with high ionic conductivity, molecular dissociation and transport are equally important; however, with these materials the mechanism appears to proceed by a primarily bulk-mediated path. In both cases it was shown that due to porosity, oxygen dissociation and transport tend to co-limit the reaction (rather than contribute independently). Interfacial electrochemical kinetics can also play a significant role, depending on the exact materials and conditions. Finally, we saw that these two asymptotic limits of behavior begin to merge for materials having some bulk ionic conductivity but not as facile as the best mixed conductors.

Consideration of these asymptotic limits is useful because it potentially helps us to identify, discuss, and study the various physical processes underlying electrode kinetics, even outside those limits. How-

ever, the performances of “real” SOFC cathodes of technological interest generally fall outside these limits for two fundamental reasons. First, SOFC cathodes must satisfy a number of other constraints besides performance, including mechanical and chemical stability, cost, manufacturability, etc.—it is therefore nearly impossible to optimize electrode materials according to only one or two physical properties. Second, as people optimize any system, they will tend to mitigate (knowingly or unknowingly) the most rate-limiting factor until other factors naturally come into play. In other words, if a material’s behavior is asymptotic, it is not likely to be optimized or satisfy more than one design constraint.

One such “more complex” case is $\text{La}_{1-x}\text{Sr}_x\text{MnO}_{3\pm\delta}$ (LSM), which starting in the mid-1970s became (and has remained) one of the most heavily pursued electrode materials for SOFC cathodes. As mentioned earlier, LSM was originally investigated as an SOFC cathode (along with a variety of other transition-metal perovskites) due to its good electrical conductivity and relatively low cost.⁴ However, LSM quickly distinguished itself for a variety of reasons. First, with the right choice of Sr content (x), a nearly exact thermal expansion match between LSM and YSZ can be achieved. This allowed workers to fabricate and explore a wide variety of electrode microstructures and cell geometries with reduced thermal stress generated by thermal cycling. Likewise, Mn is generally less reducible than other transition metals (Co, Fe) in a perovskite matrix, and thus LSM exhibits little or no chemical expansivity,^{200,201} another source of thermal–mechanical stress potentially threatening the integrity of the electrode microstructure. Another advantage of LSM is that it is generally more thermodynamically stable than mixed conductors containing cobalt or iron.²⁰² It is nonetheless reasonably catalytic for O_2 dissociation, unlike materials having similar or higher stability, such as $\text{La}_{1-x}\text{Sr}_x\text{CrO}_3$ for example.²⁰³

As with other SOFC cathode materials (including Pt), early kinetic studies of LSM in the mid-1980s gave rise to multiple schools of thought regarding the reaction mechanism. At that time, LSM was often studied alongside Pt or other perovskites and thus lumped together with these materials in the same debates regarding the rate-limiting step, the role of bulk transport, etc. However, beginning in the early 1990s it became clear that LSM is somewhat different than both Pt or other (more reducible) perovskites in terms of the reaction mechanism, falling somewhat in a gray area among the asymptotic limits described previously. Although the last 10–15 years of work have added significantly to our *qualitative* understanding of LSM, this material has so far continued to elude quantitative descriptions of its performance in terms of underlying mechanisms. For this reason and because LSM is so important technologically, we devote this section to it.

5.1. Three-Phase Boundary: Not the Whole Picture

In the case of Pt, mechanistic considerations suggest that the active region of the electrode is confined

to a region close to the three-phase boundary (TPB), and thus performance has often been reported to scale with the available TPB area. Thus, in addressing the question of how localized the O_2 reduction is in LSM, one approach workers have used is to examine the relationship of performance to microstructure. For example, Mizusaki and co-workers carefully characterized and measured the impedance of $La_{1-x}Ca_xMnO_3$ (LCM) electrodes on YSZ (a very similar material system to LSM/YSZ) as a function of morphology, controlled using various preparation methods and firing conditions.²⁰⁴ They used SEM to estimate the contact area of LCM and YSZ as well as the geometric length of the TPB. While their results showed that the electrode *capacitance* scales with the electrode/electrolyte contact area (as one would expect for interfacial polarization), the resistance and overpotential were found to scale inversely with the length of the TPB, at least at low polarization. A number of other studies of single-phase and composite electrodes have since reinforced the view that the electrode kinetics scale with TPB contact area.^{205–207}

However, there are several equally valid interpretations to this commonly observed result. One possibility is that the reaction is co-limited by adsorption and surface diffusion, where the utilization length is small compared to the average particle size. An alternative (but not mutually exclusive) possibility is that the reaction is limited by electrochemical kinetics at the TPB itself. As with Pt, both situations or a combination thereof would result in the resistance scaling with the reciprocal of the TPB length. A third possibility is that reaction is limited by mechanisms acting farther from the TPB but which scale with electrode geometric factors (such as the electrode surface area) that are strongly *correlated* to the length of the TPB (through the process of sintering, for example). Without the ability to separately control the TPB length while leaving other geometric parameters constant, it is difficult to distinguish these various possibilities. Also, the conditions under which the electrode performance scales with the TPB may not be universal—the electrode may have multiple regimes of operation depending on overpotential and other factors.

One study that tried to address this question was conducted by van Heuveln and co-workers, who attempted to separate the effects of electrode surface area from TPB contact area.^{208,209} Variations in surface area were obtained by using different sintering temperatures, while changes in TPB contact area were accomplished through the use of two powders having different morphologies. Surface area and TPB contact area were determined by image analysis of SEM cross sections; for the surface area the electrode bulk was examined, while for the TPB contact area the electrodes were etched off and the underlying “stain” on YSZ was analyzed. Electrode performance was measured in terms of the overpotential at a fixed current density of 100 mA/cm².

Within the statistical certainty of the data, no general correlation was found between overpotential and TPB length. This could mean that no such

general correlation exists and thus prior studies have been interpreted too narrowly. On the other hand, it is not clear that the comparisons in performance drawn by the authors in this case are fully meaningful. The authors point out that the electrode kinetics are (1) highly nonlinear and (2) very dependent on the polarization history. Thus, it is difficult to say whether two cells operating at the same current density (but different overpotentials) are really at the same operating point vis-à-vis comparison of TPB contact area. Rather, a more significant observation we might draw from such a study is how *difficult* it is to meaningfully correlate the complex (often non-stationary) electrochemical characteristics of LSM to the highly complex microstructure of a porous electrode, at least with today's tools and techniques. As we will see in the sections below, workers have had more success over the last 10–15 years examining electrodes with defined and/or microfabricated geometries, where TPB area and material composition can be more carefully controlled and analyzed.

5.2. Complex Stationary Electrochemical Characteristics and Properties

Like all cathodes, early electrochemical kinetic studies of LSM focused heavily on steady-state d.c. characteristics, attempting to extract mechanistic information from the T and P_{O_2} dependence of linear and Tafel parameters.^{13,203} As recently as 1997, some workers have continued to support a view that LSM is limited entirely by electrochemical kinetics at the LSM/electrolyte interface based on this type of analysis.^{14,17} However, as we have seen for other materials (including Pt), the fact that an electrode obeys Butler–Volmer kinetics means little in terms of identifying rate-limiting phenomena or in determining how close the reaction occurs to the TPB. To understand LSM at a nonempirical level, we must examine other techniques and results.

As we saw with Pt and other perovskites, one such approach is electrochemical impedance spectroscopy (EIS), which attempts to separate various mechanistic steps via time scale. Although quantitative analysis of impedance data in a complex material system like porous LSM involves many uncertainties (see sections 3.1 and 6.7 as well as ref 49), it is usually reliable in terms of separating rough time scales on which various physical processes occur. An example of this approach for understanding LSM is a study by Østergård and Mørgensen,²¹⁰ which examined the impedance of single-phase porous LSM on YSZ as a function of T , P_{O_2} , and polarization. The observed impedance was found to contain at least three distinct features. The highest frequency feature was attributed to interfacial electrochemical kinetic processes at the LSM/YSZ interface. The two lower frequency features were assigned to dissociation and transport, respectively, of oxygen species on the LSM surface.

While such one-to-one assignments of impedance features to specific reaction steps are appealing, it is not clear how definitive they are without further analysis. In particular, based on what we know about

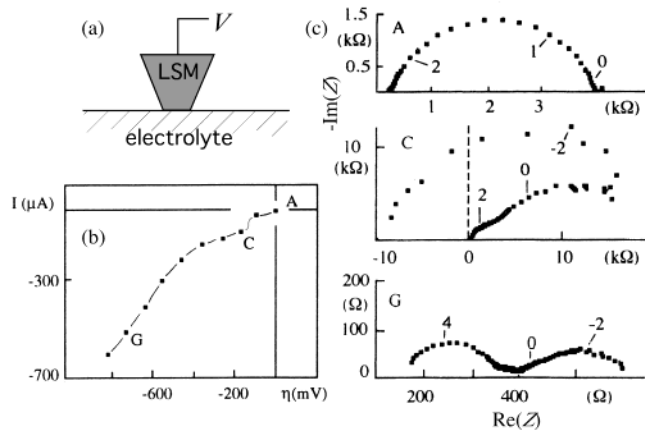


Figure 31. Measurements of polarization and impedance of LSM point-contact electrodes on YSZ. (a) Schematic showing the geometry of the electrode. (b) Steady-state cathodic polarization at 960 °C and $P_{\text{O}_2} = 10^{-3}$ atm. (c) Impedance measured under polarization at the conditions marked in b. (Adapted with permission from ref 211. Copyright 1995 Elsevier.)

Pt and perovskite mixed conductors, we might expect oxygen dissociation and transport on LSM to be co-limiting, resulting in a single “Gerischer-like” impedance feature (as shown in Figures 14 and 15) rather than two independent low-frequency features (as proposed by Østergård and Mørgensen). Also, these particular authors did not attempt to quantitatively analyze the chemical capacitance in terms of a utilization length or bulk vs surface contributions. Without this it is hard to conclude what these various features actually correspond to except perhaps broadly in terms of “chemical” vs “interfacial” time scales.

An important contribution in this regard was a series of studies published by the Laboratoire d’Ionique et d’Electrochimie du Solide (Grenoble), which looked in detail at the i - V characteristics and impedance of LSM point-contact electrodes on YSZ.^{211,212} As shown in Figure 31a, these measurements involved making a single-point contact between a pin-shaped LSM sample and YSZ with known contact area. The i - V characteristics (Figure 31b) show a distinct change in the characteristics of the electrode at cathodic overpotentials greater than a particular critical value, where a relatively discontinuous jump in current is observed. They found this transition occurs anywhere from -150 to -500 mV vs air and is only present in the cathodic direction. The impedance measured at points well below, near, and well above this transition are shown in Figure 31c (A,C,G). Well below the transition (A) the impedance is high with a single arc having resistance $\sim 4000 \Omega$ and capacitance $\sim 10^{-6}$ F. Near the transition (C) the impedance becomes small enough to notice the presence of both a low- and high-frequency feature, but these features are too obscured by inductive effects to resolve completely. Well above the transition (G) both features become well resolved: one at high frequency having resistance $\sim 200 \Omega$ and capacitance 10^{-7} F and the other at low frequency with resistance $\sim 300 \Omega$ and capacitance 10^{-1} F. This low-frequency feature, seen only at high overpotential, is highly reminiscent of the chemical contributions to the

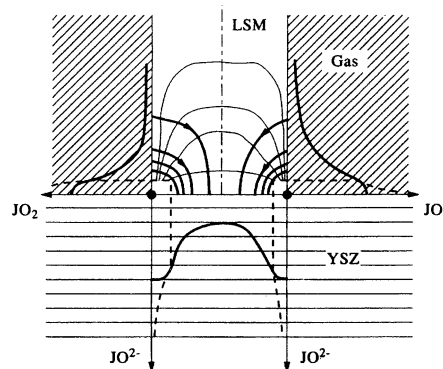


Figure 32. Schematic illustrating the possible location and distribution of bulk oxygen flow in LSM under high polarization conditions. (Reprinted with permission from ref 211. Copyright 1995 Elsevier.)

impedance for mixed conductors having high ionic conductivity, as discussed in section 4.

To explain these results, the workers at Grenoble theorized the existence of two different operating regimes. As shown in Figure 32, the authors proposed that at high overpotential the LSM becomes substantially reduced, creating a large concentration of oxygen ion vacancies near the interface. This non-equilibrium population of vacancies thereby creates a facile transport path through the bulk of the material, leading to a large chemical capacitance (> 1 F/cm² when compared on an area-normalized basis). The presence of an equally sized high-frequency feature likewise suggests a significant contribution to the impedance from oxygen ionic exchange at the solid–solid interface, associated with a much smaller capacitance related to interfacial polarization. The existence of such a “bulk” operating regime at high overpotential appears to be consistent with in-situ X-ray photoelectron spectroscopy (XPS) measurements of porous LSM, which show significant reduction of Mn far beyond the electrode/electrolyte interface upon polarization.²¹³ More recently, as shown in Figure 33, Kuznecov and co-workers showed using field-emission SEM that sustained high cathodic polarization results in the apparent formation of Kirkendall porosity in the bulk of LSM within one particle diameter of the solid–solid interface—a strong indicator of oxygen chemical potential gradients in the bulk.²¹⁴

In contrast, at low overpotential the workers at Grenoble theorized that LSM is primarily an electronic conductor and thus the bulk path is closed off. The observation of finite impedance near open circuit (despite the fact that LSM is a poor bulk ion conductor under these conditions) suggests the existence of a parallel “surface” path that allows transport even when the bulk is not available. Since this surface path involves a much smaller inventory of electroactive species, it is associated with a much smaller chemical capacitance than the bulk path and thus a much higher frequency (Figure 31c (A)). As the overpotential is reduced and the mechanism shifts from bulk to surface, chemical and electrochemical time scales begin to merge, making them difficult to distinguish as separate features in the impedance.

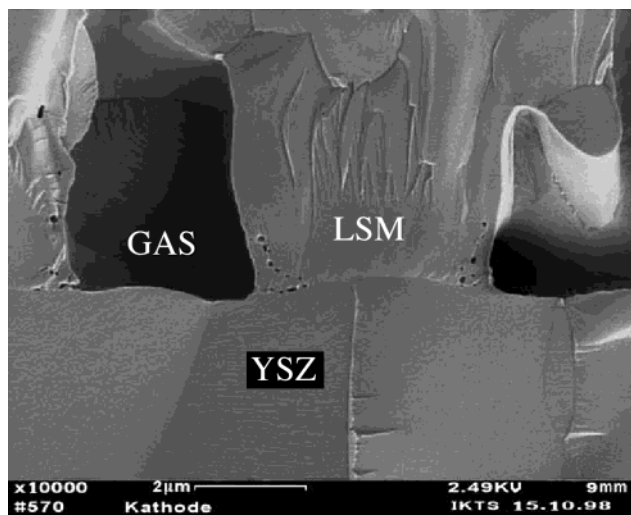


Figure 33. High-resolution field emission SEM of a porous LSM/YSZ interface following polarization for 3 h at -0.8 V at 950 °C in air. The porosity evident at the TPB is not seen in images taken prior to polarization. (Reprinted with permission from ref 214. Copyright 2003 Elsevier.)

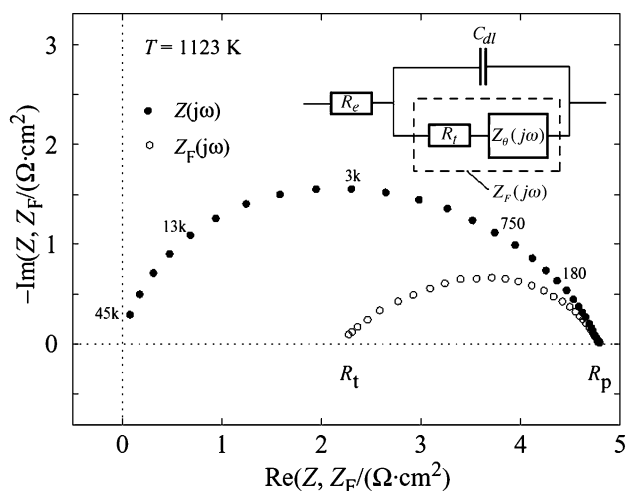


Figure 34. Total impedance (Z) and faradaic impedance (Z_F) of unsintered porous LSM on YSZ measured in air at 850 °C. Electrolyte resistance (R_e) has been subtracted from the total impedance, while both R_e and the double-layer capacitance (C_{dl}) have been subtracted from Z_F . (Reprinted with permission from ref 215. Copyright 1998 Elsevier.)

Hence, a single arc is observed with relatively high characteristic frequency.

More recent impedance studies by Mitterdorfer and Gauckler²¹⁵ of porous LSM on YSZ at low overpotential have shown that this single arc can be separated into electrochemical and chemical contributions by correcting the data for double-layer capacitance using the method of Berthier et al.⁷⁵ As shown in Figure 34, these studies suggest that the electrochemical resistance at the LSM/YSZ interface is generally not zero, even when the LSM/YSZ interface is left unfired. The remaining “faradic” (chemical) impedance has a Gerischer-like shape, consistent with co-limitation by dissociative adsorption and surface diffusion of oxygen. An estimate of the chemical capacitance based on this arc is on the order of 10^{-4} F/cm², which when compared to asymptotic values of LSC and Pt is more consistent with a surface process than a bulk process.

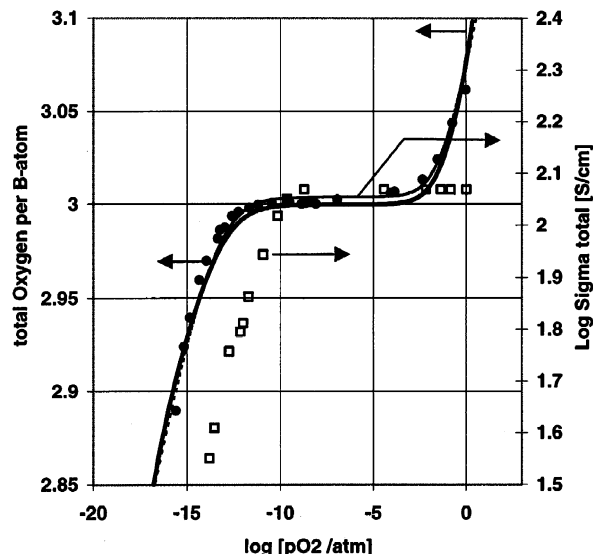


Figure 35. Total conductivity, σ , and oxygen stoichiometry, $3-\delta$, at 1000 °C of $\text{La}_{0.9}\text{Sr}_{0.1}\text{MnO}_{3-\delta}$, from measurements by Kuo et al.³⁶⁵ The model calculations are based on a large polaron model with equilibrium constants as given in ref 216. Thick line: calculated stoichiometry. thin line: calculated conductivity. (Reprinted with permission from ref 216. Copyright 2000 Elsevier.)

A natural question to ask is whether this “two-regime” theory is consistent with the known properties of LSM. As recently reviewed by Poulsen,²¹⁶ the defect structure of LSM has some similarities with other more reducible perovskites such as LSC and LSF. Like these other perovskites, LSM has electrical properties on the border between that of a p-type semiconductor and a metal^{217–219} and becomes oxygen substoichiometric at high temperature and low P_{O_2} ,^{202,220} as shown in Figure 35. However, unlike its more reducible cousins (which may have significant vacancy concentration at atmospheric P_{O_2}), LSM maintains a nearly full perovskite stoichiometry above $\sim 10^{-10}$ atm and in fact becomes superstoichiometric at high P_{O_2} ($>10^{-3}$ atm), containing more oxygen than is consistent with the formal ABO_3 unit cell. Neutron diffraction studies²²¹ as well as numerous defect thermodynamic models^{216,222,223} show that this “superstoichiometric” behavior actually results from the formation of cation vacancies on the A and B sites while the oxygen sublattice remains fully occupied.

One expected consequence of these properties is that LSM will not be a mixed conductor at low polarization under normal cathode conditions. Likewise, at cathode polarizations thermodynamically corresponding to $P_{\text{O}_2} < \sim 10^{-10}$ atm (~ -500 mV) we expect LSM to become reduced, exhibiting ionic transport properties similar to that of LSC or LSF. This transition from a nearly pure electronic conductor at low overpotential to a good mixed conductor at high overpotential is consistent with the Grenoble “two-regime” theory, at least qualitatively. Furthermore, since a transition from superstoichiometric to substoichiometric LSM involves a change in concentration and thus transport of cation vacancies (generally much slower than anions at these temperatures), we might expect significant hysteresis, irreversibility, and/or other nonstationary behavior near the transi-

tion between these two operating regimes. Indeed, as discussed in more detail in section 5.4, work by a variety of authors has shown nonstationary behavior consistent with slow or irreversible transitions under cathodic polarization^{40,213,224–226}. While it is not clear if Mn reduction is the only cause of this behavior, it has certainly been identified as one likely factor.

5.3. Dense and Patterned Thin Films: Confirming Two Regimes of Operation

The previous two sections illustrate the difficulty of understanding the mechanisms governing oxygen reduction on LSM without exact control of the electrode geometry, materials, fabrication, and operating conditions/history. To that end, workers have made significant progress in the last 5–10 years microfabricating dense, patterned electrodes in which geometric lengths such as thickness and TPB length can be specifically controlled. In this way it has been possible to examine various asymptotes of behavior (such as the surface and bulk paths) and probe electrode mechanisms using a variety of techniques including impedance and isotope tracer experiments. These studies have significantly clarified our understanding of LSM and provided a variety of tools that will no doubt be built on extensively in the future.

One asymptote of interest has been the low-overpotential regime, which has been investigated extensively by impedance techniques using thin films. As mentioned previously in section 4.3, one of the first successful attempts to fabricate thin-film perovskites was published by Mizusaki and co-workers,¹⁵⁷ who used a pulsed KrF excimer laser to flash evaporate and deposit 1–2 μm thick films of $\text{La}_{0.5}\text{Sr}_{0.5}\text{MnO}_3$ on YSZ. Near open circuit the initial impedance of these electrodes was found to be controlled by bulk transport of oxygen though the film with a resistance that scales with electrode thickness and performance that *decreases* with increasing P_{O_2} . Indeed, this result appears consistent with what we know of LSM, since in the absence of a parallel surface path the bulk path will be controlled by the very low anionic conductivity of LSM at open-circuit conditions. Following significant anode polarization, the authors found that the LSM film becomes severely damaged and cracked and reverts to impedance behavior more consistent (in shape, time scale, and P_{O_2} dependence) with a porous LSM electrode at low polarization. The authors conclude that this damage results in creation of TPB contact area and thus changes the relative importance of bulk vs surface transport in allowing electroactive oxygen to reach the electrode/electrolyte interface.

More recent studies of dense LSM films appear to confirm these original conclusions as well as fill in some of the details.^{27,159,160,167,227} In particular, Ioroi and co-workers^{159,160} were able to produce very high quality films with clean, well-resolved impedances at 800–1000 °C in air, as shown in Figure 36. Consistent with bulk transport limitations, the impedance of these films was Warburg-like in shape and scaled properly with electrode area and electrode thickness, assuming an entirely bulk path. By extrapolating their results to zero film thickness, the authors also

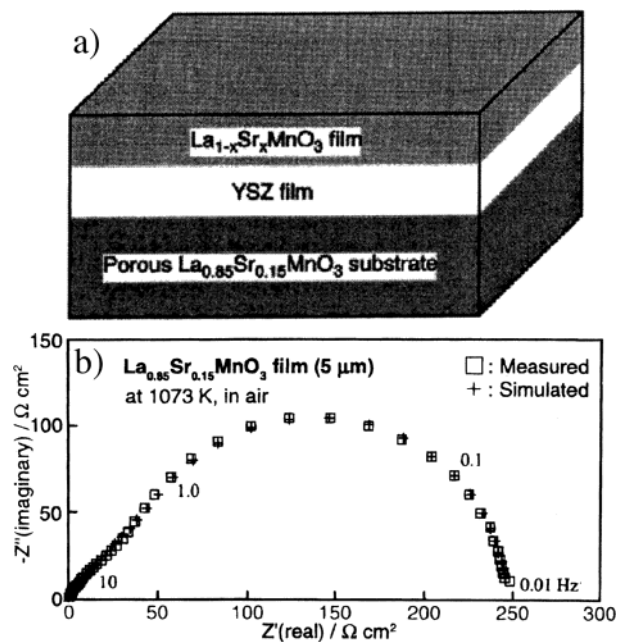


Figure 36. Measured (\square) and simulated ($+$) impedance of a thin (5 μm) dense LSM film on YSZ at 800 °C in air. Simulation is based on a Warburg model for finite length diffusion. (Reprinted with permission from ref 160. Copyright 1998 Electrochemical Society, Inc.)

found evidence of a small finite resistance associated with the gas–solid and/or solid–solid interface(s). This appears to be consistent with the distortion of the impedance from a 45° limit at high frequency, a strong indicator of an electrochemical kinetic contribution and double-layer capacitance associated with the solid–solid interface.²¹⁵

An interesting exercise is to extrapolate Ioroi's values for the bulk transport resistance of a thin film to predict the minimum performance of a porous electrode, assuming bulk transport is rate limiting. In this scenario the interfaces are equilibrated, yielding a 3D bulk transport situation as modeled by Fleig.¹⁸³ By appropriately scaling Fleig's results (Figure 30, region I), one can predict the area-specific resistance of a porous body of block microstructure as a function of σ_i and surface area a . Using the value of L/R_{bulk} from Ioroi's data at 800 °C,¹⁵⁹ eq 7 yields a value of σ_i of ca. $10^{-6} \Omega^{-1} \text{cm}^{-1}$. Applying this value to Figure 30 for a typical electrode area (20 000 cm^2/cm^3), one obtains a minimum resistance of $\sim 0.003 \Omega \text{cm}^2$. By comparison, the actual impedance of a porous LSM electrode of the same composition (made by the same laboratory) at 1000 °C (a much higher temperature) is $\sim 1 (\Omega \text{cm}^2)$.¹⁵⁹

What this calculation shows is that the rate of bulk transport observed in a thin film of LSM is at least 3 orders of magnitude too low to explain the performance of porous LSM at low overpotential, assuming an entirely bulk transport path. This calculation echoes prior estimates of Adler and co-workers, who showed that the zero-bias impedance of porous LSM cannot be explained in terms of a bulk path.¹⁷¹ In addition, estimates of the chemical capacitance based on Ioroi's impedance for porous LSM yield values of 10^{-4} – $10^{-3} \text{F}/\text{cm}^2$, which as mentioned previously in section 5.2 are more consistent with a surface process

than a bulk process. Comparing this capacitance to that of Pt, we might expect a utilization region (l_b) on the LSM surface of perhaps 100–1000 nm; however, no estimates have yet been offered in the literature for this distance.

Stepping beyond the low-overpotential regime, Horita and co-workers examined the degree to which a dense film LSM electrode becomes reduced under moderate to high cathodic polarization using ^{18}O tracer techniques.²²⁷ In these experiments an $^{18}\text{O}_2$ tracer was introduced to the gas atmosphere during steady-state cathodic operation, and then at some later time the tracer was frozen in place via quenching of the sample. The resulting ^{18}O depth profile through the film was then analyzed using secondary-ion mass spectrometry (SIMS). These profiles were found to be consistent with increased vacancy concentration (and thus tracer diffusivity) near the YSZ interface caused by reduction of the film. This result provides perhaps the most direct evidence to date that bulk oxygen transport in LSM is enhanced near the YSZ interface under moderate to high polarization. However, because this film is dense (and thus precludes a parallel surface path), it is difficult to assess the importance of this enhancement vis-à-vis other reaction steps. In particular, the authors observed no difference in tracer ratio across the gas/LSM or LSM/YSZ interfaces, suggesting that the enhancement is not so great in this case as to be faster than interfacial processes.

A more recent study by Brichzin and co-workers²²⁸ examined the impact of enhanced bulk transport at high overpotential on the kinetics when a TPB is present. To accomplish this, the authors took the thin-film technique one step further by examining small circular microelectrode films of varying diameters, contacted individually using a micromanipulator. By varying diameter and thickness and introduction of an alumina-blocking layer at the solid–solid interface, these workers were able to control the ratio of areas available for the surface and bulk paths. Reported were mostly steady-state polarization measurements as a function of geometry factors and anodic or cathodic polarization (± 300 mV). The resolution of the data appears to be quite good, and distinct trends were observed in how the polarization resistance scales with the various geometric factors. The authors analyzed these trends in terms of a qualitative model which estimates the relative importance of the “surface” and “bulk” paths in contributing to the current in the anodic and cathodic regimes.

The results of this analysis are summarized in Figure 37. Like prior workers studying thin films, the authors conclude that dense films without a TPB under small or cathodic polarizations operate primarily by a bulk path since the surface path is blocked. (Interestingly, they found that dense films under *anodic* polarization appear to operate under a mixed regime, although it is not clear how much nucleation and transport of O_2 along the solid–solid interface contributes to the apparent surface path current.) In contrast, as the “porosity” is increased (microelectrode diameter is decreased), the surface path be-

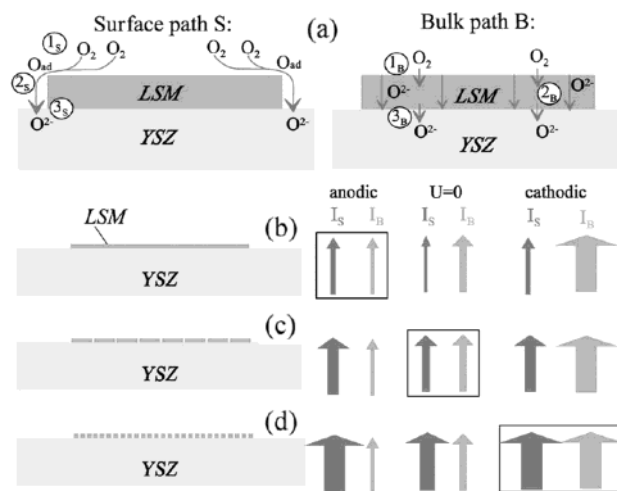


Figure 37. Qualitative summary of current contributions from the surface path (I_S) and the bulk path (I_B) for LSM disk microelectrodes on YSZ based on i - V measurements in air at 800 °C. (Reprinted with permission from ref 228. Copyright 2002 Elsevier.)

comes increasingly important until at high surface areas the surface path dominates at small (and anodic) overpotentials. This appears to be consistent with the calculation discussed above, which shows that the bulk path is insufficient to explain observed current densities at low polarization. Meanwhile, at high cathodic polarization the bulk path appears to remain an important factor even with high TPB area, consistent with the Grenoble and other results (described previously) showing substantial reduction of Mn and an increase in chemical capacitance.

While Brichzin et al.’s results provide further support for a “two-regime” view (at least from a macroscopic viewpoint), it remains unclear exactly where and how the surface-to-bulk transition occurs and to what degree these regimes overlap under a given set of conditions. In particular, Figures 30, 32, and 33 suggest that when surface adsorption/desorption on LSM is fast relative to bulk diffusion, the bulk transport path will be confined primarily to a small region near the TPB interface. In other words, even when a bulk transport path is active, its macroscopic scaling may still obey that of the surface path, making it impossible to separate from true surface processes via geometric scaling alone. Further work of this type involving impedance and other quantitative measurements would undoubtedly help clarify some of these questions.

Also contributing significantly to this “surface vs bulk” debate has been a series of studies by Horita and co-workers employing isotope tracers to track the relative importance of the surface and bulk paths.^{227,229–231} As shown in Figure 38, these authors used *rf*sputtering to deposit a thin-film grid of LSM having thickness 0.5 μm and width 2 μm on the surface of polished polycrystalline YSZ. An $^{18}\text{O}_2$ tracer was then introduced to the atmosphere during cathodic polarization, followed by postmortem analysis of the quenched sample using SIMS (as described previously). By removing the LSM from YSZ in an acid bath, it was also possible to examine the YSZ underneath the LSM grid. The authors also examined

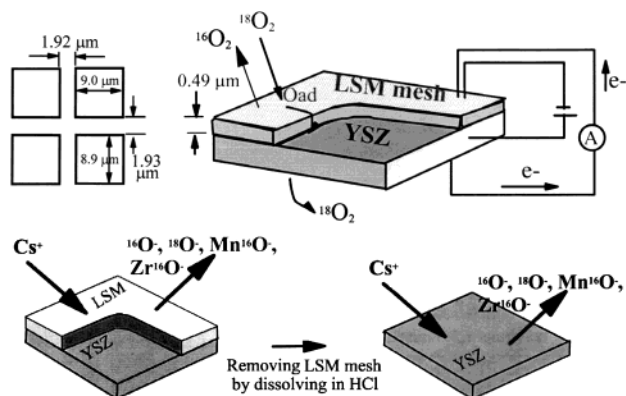


Figure 38. Schematic and geometry of patterned thin-film LSM electrode on YSZ studied by Horita and co-workers. After establishing steady-state cathodic polarization, the atmosphere surrounding the electrode is rapidly switched from $^{16}\text{O}_2$ - to $^{18}\text{O}_2$ -rich for 10 min at fixed total P_{O_2} . The sample is then quenched to room temperature and postmortem analyzed using secondary-ion mass spectrometry (SIMS) imaging. (Reprinted with permission from ref 230. Copyright 2000 Elsevier.)

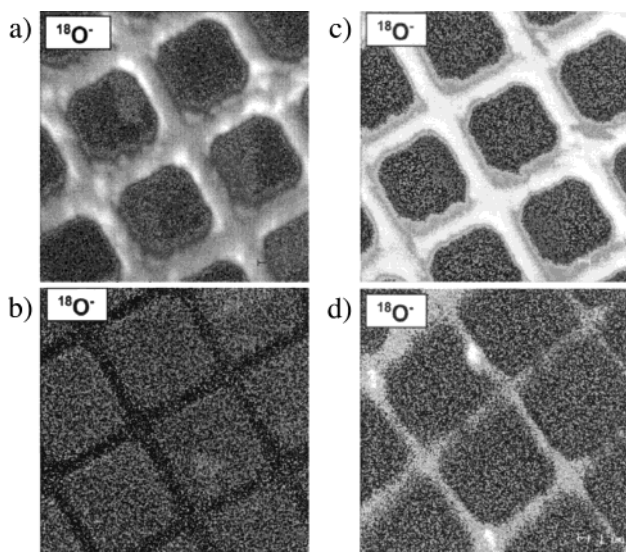


Figure 39. Secondary-ion maps of $^{18}\text{O}^-$ (oxygen tracer) and Mn^{16}O^- (positional reference) of the patterned thin-film electrode shown in Figure 38 following polarization at -0.34 V at 700 °C. (a) Tracer map at the top surface of LSM/YSZ, showing selective incorporation into LSM. (b) Tracer map near the LSM/YSZ interface (acquired after ablation of LSM off the surface with Cs^+), showing deep penetration of tracer into LSM. (Reprinted with permission from ref 230. Copyright 2000 Elsevier.)

the position of various cations (Zr, Mn), both as a spatial reference and as a way to gauge cation interdiffusion.

Figure 39 shows isotope tracer maps for LSM both at the surface and near the interface as a function of polarization. These results indicate that under increasing polarization, isotope tracer is incorporated more deeply into the LSM bulk and that this incorporation occurs everywhere with the LSM near the interface not just at the TPB. This result would seem to corroborate the increased significance of the bulk path with increased overpotential. Consistent with this result, when the LSM is removed and the YSZ underneath is analyzed (Figure 40a), it is found that

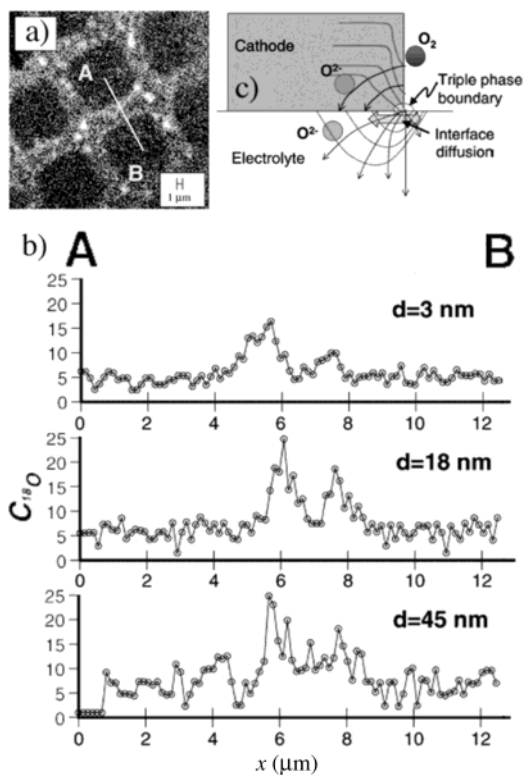


Figure 40. Secondary-ion ratio map ($^{18}\text{O}/^{16}\text{O}$) of YSZ in the cell shown in Figure 39 following removal of LSM by etching in acid. (a) Map at the exposed YSZ surface. (b) Local analysis of the tracer across the region A–B shown in a at various depths, achieved by Cs^+ ion ablation. (c) Qualitative models for oxygen incorporation used to rationalize the results in b. (Reprinted with permission from ref 231. Copyright 2002 Elsevier.)

a significant amount of the tracer is drawn into the YSZ (unlike the gas-exposed YSZ surface, which exhibits no exchange). However, when the isotope profile in the YSZ is carefully analyzed, it is found that a higher-than-average amount of tracer is absorbed in a region beneath the LSM closest to the TPB. Figure 40b shows cross sections of this profile as a function of depth into the YSZ. The region over which the isotope is found to spread is approximately independent of depth.

In interpreting their results Horita et al. considered two possible reasons for increased activity near the TPB (Figure 40c). One possibility is that a parallel surface path exists which produces a high current density and thus tracer incorporation near the TPB. However, this scenario is predicted to result in a narrow distribution of the tracer near the TPB, which increases with depth. In contrast, if the ionic current is generated by a bulk path, a higher-than-average ionic current is also predicted near the TPB (per the results of Fleig shown in Figure 30). However, the spread of the tracer in this case would be approximately independent of depth, which is what Horita et al. observed. If correct, this result suggests that increased current associated with the TPB results from a bulk as well as surface pathway.

What casts some doubt on this interpretation is that the tracer exhibits significant lateral dispersion perpendicular to the TPB, even for gold on YSZ (which the authors also studied). Indeed, the profile

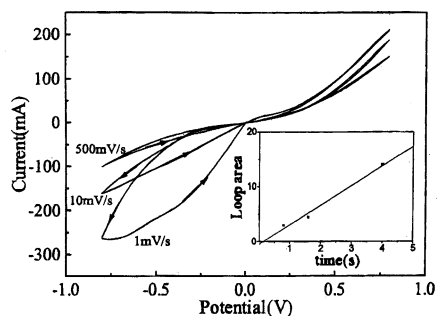


Figure 41. Linear-sweep voltammograms of a porous LSM electrode on YSZ in air at 950 °C as a function of sweep rate. (Reprinted with permission from ref 233. Copyright 1998 The Electrochemical Society, Inc.)

images show evidence of significant defects in the grid film, including spots of enhanced or retarded isotope exchange beneath the LSM. These defects might involve microcracks or interfacial fissures having enhanced tracer mobility relative to the flow of tracer with the applied current. More work is needed (both in measurements and modeling) before this type of study yields a definitive conclusion regarding the relative importance of the surface and bulk paths under an arbitrary set of conditions as well as the size of the active region when the bulk path is engaged.

5.4. Nonstationary Behavior in LSM

In addition to the possibility of multiple transport paths, our understanding of reaction mechanisms on LSM is further complicated (as with platinum) by pronounced nonstationary behavior in the form of hysteresis of inductive effects. These effects are sometimes manifest as the often-mentioned (but little-documented) phenomenon of “burn-in”, a term used in development circles to describe the initial improvement (or sometimes decline) of the cathode kinetics after a few hours or days following initial polarization (after which the performance becomes relatively stable). As recently reported by McIntosh et al., this effect can improve the measured impedance of a composite LSM/YSZ cathode by a factor of 50 relative to an unpolarized cathode at OCV.⁴⁰ Such an effect is important to understand not only because it may lead to insight about the underlying electrode kinetics (and ways to improve them), but also because it challenges the metrics often used to assess and compare relative cell performance.

For perovskite electrodes, the earliest kinetic study of hysteretic effects appears to come from Hammouche and co-workers, who showed that the $i-\eta$ characteristics of porous LSM/YSZ in air at 960 °C exhibit a potentiodynamic hysteresis when scanned slowly (1 mV/s) between 0 and -1200 mV cathodic polarization.²²⁴ A clearer demonstration of this effect, more recently provided by Jiang and co-workers, is shown in Figure 41.^{232,233} Hammouche and co-workers attributed this hysteresis to the formation of oxygen vacancies in LSM at high overpotential, which (as discussed in sections 5.2 and 5.3) appears to open a parallel bulk-transport-mediated reaction pathway. However, if this was the only explanation,

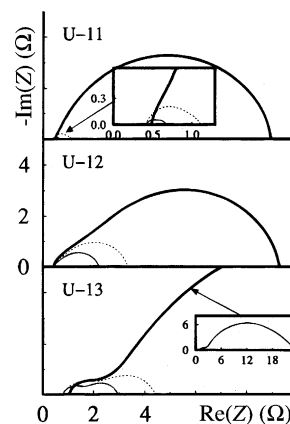


Figure 42. Impedance characteristics of porous LSM electrodes on YSZ, measured at zero bias and 945 °C in air, as a function of polarization history and processing conditions. U-11, U-12, and U-13 correspond to firing temperatures of 1100, 1200, and 1300 °C, respectively. Bold line: initial impedance. Thin line: impedance measured 2 min following cathodic polarization at 100 mA/cm² for 30–90 min. Dashed line: impedance measured 30 min following cathodic polarization. (Reprinted with permission from ref 209. Copyright 1997 The Electrochemical Society, Inc.)

one would expect this hysteresis to close with decreasing scan rate, not open. Indeed, the relaxation time for bulk oxygen vacancy disturbances (based on the impedance under the same conditions²¹¹) is about 16 s, much faster than implied by the voltammograms (20+ min).

Perhaps further insight can be gained by examining the impedance as a function of polarization history, which has been documented by a number of workers.^{40,208,209,226,234,235} As shown by van Heuveln et al.,²⁰⁹ reproduced in Figure 42, the zero-bias impedance of porous LSM electrodes on YSZ at 945 °C in air decreases following 30–90 min of cathodic polarization and then relaxes back toward its original characteristics over a similar period of time. This return to original behavior, consistent with the reversal of the hysteresis in the voltammograms in Figure 41, eliminates irreversible microstructural evolution as a primary cause of this effect, as proposed earlier by Tsukuda.²³⁶ Although the authors failed to mark frequencies on their impedance diagrams, they fit the impedance to an equivalent circuit exhibiting two time scales and reported the capacitances. From this it can be determined that the higher frequency feature of the impedance (with a time scale of ~100 kHz, capacitance $\approx 10^{-5}$ F/cm²) is independent of polarization history, while the lower frequency feature (100–1000 Hz, capacitance $\approx 10^{-3}$ F/cm²) shrinks following polarization by up to a factor of 50, depending on electrode firing temperature. Jiang and co-workers reported similar behavior for A-site-deficient LSM on YSZ at 800 °C (where all time scales get longer), showing that it takes ~4 h for polarization to have its full effect. More recently, McIntosh et al.⁴⁰ witnessed similar effects for composite LSM/YSZ electrode in an operating fuel cell; both the impedance and steady-state overpotential at low polarization drop by a factor of 50 following high polarization, and these changes primarily effect

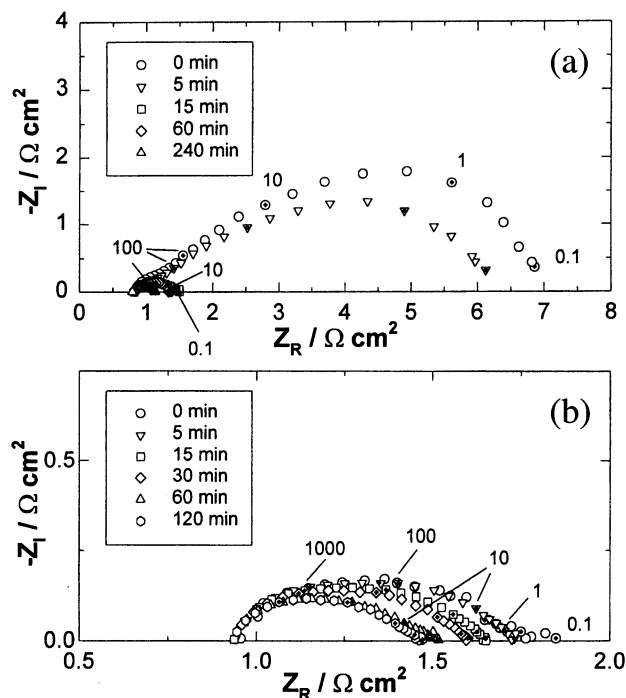


Figure 43. Impedance characteristics of porous LSM electrodes on YSZ, measured at zero bias and 900 °C in air, following various amounts of time under cathodic polarization at 200 mA/cm²: (a) normal sample, (b) sample etched in 1 M HCl solution for ~15 min. (Reprinted with permission from ref 226. Copyright 2001 Elsevier.)

the low-frequency portion of the impedance. The initial characteristics of the cell are largely recovered after several hours sitting at zero polarization.

As discussed in sections 5.2 and 5.3 (and elaborated on more fully in section 6), the higher frequency feature is likely related to the interface while the low-frequency feature is more consistent with chemical processes on the LSM surface. Thus, van Heuveln's result above suggests it is surface diffusion (as proposed van Heuveln²⁰⁹) and/or oxygen adsorption/dissociation that temporarily improves with polarization. Hammouche's suggestion (above) that this hysteresis corresponds to the opening and closing of a parallel bulk oxygen transport path seems unlikely, since the lowest frequencies in the impedance (~0.01 Hz at 950 °C²¹¹) come nowhere close to the 1–10 h time scales exhibited by the hysteresis.

A result of significant interest in this discussion is that of Jiang and Love,²²⁶ who examined the effects of acid treatment (as well as polarization) on the performance of A-site-deficient porous LSM on YSZ at 900 °C in air (Figure 43). Consistent with prior studies, they showed that cathodic polarization substantially reduces the low-frequency portion of the impedance response at zero bias. They then studied an identical electrode that had been etched in 1 M HCl for ~15 min at room temperature prior to testing. The acid-etched cell had a much smaller impedance to start with, nearly identical to that of an unetched cell that had been polarized for several hours. Cathodic polarization of the etched cell yielded little additional benefit. Again, it was only the low-frequency portion of the impedance that was reduced by acid etching.

One explanation offered by the authors is that MnOx- and/or SrO-like phases or moieties naturally exist on the LSM surface, which initially retard O₂ adsorption; upon etching (and presumably upon polarization somehow), these obstructing phases are removed, facilitating dissociative adsorption and/or surface transport. One piece of evidence that the LSM surface composition is altered significantly comes from the observation that following the etching the acid was found by ICP analysis to contain amounts of Sr, Mn, and La inconsistent with the bulk cation stoichiometry, suggesting selective etching of Sr > Mn ≫ La. Thus, either LSM started with excess Mn and Sr on the surface or ended up depleted in Mn and Sr. One appeal of this theory is that the time required for similar changes to occur to the electrode surface under polarization would be dictated by diffusion of the cations involved (La, Sr, Mn), which might reasonably require many hours even at 973 K. Such a slow change appears to be more consistent with the relaxation time of the electrode performance (hours) than other processes such as anion diffusion (minutes).

It has been noted (mostly in the context of perovskite membranes) that a large gradient in oxygen chemical potential can cause kinetic demixing of the cation constituents in a transition-metal oxide.^{237–242} While we do not review this literature in any detail, a common observation is that for a binary or ternary oxide, segregation of different cations along the μ_{O₂} gradient are expected, depending on their mobility and transport coupling. This is particularly true for LSM, which is cation nonstoichiometric under ambient P_{O₂},²¹⁶ thus, cation motion and crystal convection is expected under P_{O₂} gradients. We saw strong evidence in section 5 that under high polarization, LSM operates (at least in part) via a bulk oxygen transport path, which similarly corresponds to a μ_{O₂} gradient across the material between the gas-exposed surface and the solid–solid interface. Thus, any sustained bulk oxygen transport might easily explain cation segregation to/from the surface. Some evidence for cation movement is apparent Kirkendall porosity formed in the corner region of LSM near the TPB under sustained cathodic polarization (Figure 33). Thus, while the hysteresis may not correspond *directly* to a change from surface to bulk path (and back), it may nonetheless be caused by this transition given sufficient time under load.

As discussed in section 6.1, a relatively exhaustive HRTEM and AFM study was conducted by Mitterdorfer and Gauckler of how secondary phases form at the LSM/YSZ boundary and how these phases effect electrode kinetics.²¹⁵ This study placed the time scale for cation-transport processes in the correct range to be consistent with the theory described above. However, while all this may be interesting and useful speculation, to date no in-depth studies of the LSM surface as a function of A/B ratio, polarization history, or other factors have been performed which would corroborate any of these hypotheses. Such a study would require combining detailed materials characterization with careful electrochemical measurements on well-defined model systems. Given the

fact that polarization has such a profound (and generally underappreciated) influence on performance, it seems likely this would be an important subject for investigation in the future.

5.5. Summary: Uncertainties in Our Understanding of Oxygen Reduction on LSM

The work reviewed in sections 5.1–5.4 represents a significant improvement over the last 10–15 years in our understanding of oxygen reduction mechanisms on LSM. However, significant uncertainties remain due in part to the complexity of the reaction mechanism itself but also the extreme sensitivity of the limiting factors to the exact structure, processing history, operating conditions, and operation history of the electrode. To summarize, some of the relevant highlights (and remaining challenges) are given below.

(1) *Surface path at low overpotential.* Qualitative and quantitative analysis of impedance data, tracer studies, as well as various studies of thin-film electrodes suggest that under low-overpotential LSM operates primarily via a surface-mediated mechanism (like Pt). This conclusion appears to be consistent with the properties of LSM, which is fully oxygen stoichiometric under ambient P_{O_2} . However, little is known about how far the active region of reduction extends beyond the solid/solid interface (via surface diffusion) or the relative importance of chemical steps (on the LSM surface) vs electrochemical kinetics at the solid/solid interface.

(2) *Bulk path at moderate to high overpotential.* Studies of impedance time scales, tracer diffusion profiles, and electrode microstructure suggest that at moderate to high cathodic overpotential, LSM becomes sufficiently reduced to open up a parallel bulk transport path near the three-phase boundary (like the perovskite mixed conductors). This effect may explain the complex dependence of electrode performance on electrode geometry and length scale. To date, no quantitative measurements or models have provided a means to determine the degree to which surface and bulk paths contribute under an arbitrary set of conditions.

(3) *Pronounced nonstationary behavior.* Numerous workers have reported significant hysteresis and/or irreversibility in the behavior of LSM. This factor is important to be aware of since it is possible for two labs studying the same types of electrodes under similar conditions to arrive at completely different conclusions, depending on the exact history of fabrication and testing. Hopefully as workers move forward, these effects will provide additional clues as to the reaction mechanism dominating under specific conditions.

(4) *Extreme sensitivity to processing and operating history.* It has proven difficult to arrive at a consensus understanding of oxygen reduction on LSM, in part because electrode performance/characteristics depend so strongly on the exact details of processing and operating history. Many of the outstanding issues are tied so strongly to the subtleties of processing that they warrant their own section (section 6). For example, as discussed in sections 6.1–6.3, the resis-

tance of the solid/solid interface may depend significantly on the formation of insulating reaction products between LSM and the electrolyte. In addition, the composite microstructure of a commercially relevant fuel-cell electrode is significantly more complex than the ideal structures discussed so far—a significant remaining issue is the relationship of performance to microstructure in light of our understanding of the reaction mechanism itself (section 6.4).

6. Factors Complicating our Understanding of SOFC Cathode Mechanisms

The results reviewed in sections 3–5 represent significant progress over the last ~20 years in understanding basic mechanisms governing oxygen reduction in SOFC cathodes. However, it should be emphasized that this knowledge has been built by studying a large number of materials and cases over a long period of time, often by examining model systems or asymptotic cases. This is not the same thing as being able to diagnose the mechanism of a particular electrode under a specific set of conditions or knowing all the factors that govern the rates of the various physical processes comprising that mechanism. In particular, workers have found that the rates of these processes as well as their relative importance in the mechanism depend significantly on a number of “outside” factors not determined by the mechanism itself. Some examples include secondary phases and impurities influencing electrochemical kinetics at the interface, the macroscopic geometry and microstructure of the electrode, or changes in the properties of the materials due to fabrication conditions or degradation. An enormous amount of work has been conducted in the last 15–20 years to understand these various factors; the purpose of this section is to review those factors that have been the most well studied and/or appear to have the greatest significance in determining the rate of oxygen reduction within SOFC cathodes.

6.1. Sensitivity of Interfacial Electrochemical Kinetics to Secondary Phases and Impurities

One of the most heavily studied factors thought to influence cathode performance has been the issue of *reactivity* between the electrode material and the electrolyte (usually YSZ) to form insulating secondary phases. This subject is sufficiently broad and complex to warrant its own review, and readers having a detailed interest in this topic are encouraged to read previous literature reviews in papers by Kawada²⁴³ and Mitterdorfer.²¹⁵ Our main focus here is on how these secondary phases (or other impurities) appear to retard the reaction, particularly electrochemical kinetic processes occurring at the interface.

As early as 1969, studies of perovskites on YSZ suggested the formation of insulating reaction products at the interface during processing and/or cell operation.²⁴⁴ This was confirmed in 1985 by Lau and Singhal, who showed that $La_2Zr_2O_7$ forms at the interface between dense LSM and single-crystal YSZ at typical electrode processing temperatures.²⁴⁵ Soon after, Yamamoto and co-workers published a study

of sputtered $\text{La}_{1-x}\text{Sr}_x\text{MO}_{3-\delta}$ electrodes on YSZ ($M = \text{Co, Fe, Mn, Cr}$), annealed at various temperatures from 900 to 1100 °C and examined using SEM and X-ray diffraction (XRD). These studies identified multiple secondary phases which were identified as $\text{La}_2\text{Zr}_2\text{O}_7$ (LZ) and Sr_2ZrO_4 (SZ). The amount of these secondary phases depended on the exact composition of the materials involved but generally increased with annealing temperature and time. They likewise found that electrode resistance increases with annealing time, suggesting that these phases play a significant role in retarding electrode/electrolyte interfacial processes. A variety of other perovskite electrode materials have since been shown to react with YSZ, including $\text{La}_{1-x}\text{Ca}_x\text{MnO}_{3\pm\delta}$ (LCM),^{246,247} $\text{Gd}_{1-x}\text{Sr}_x\text{CoO}_{3-\delta}$,²⁴⁸ $\text{La}_{1-x}\text{Sr}_x\text{Co}_{1-y}\text{Fe}_y\text{O}_{3-\delta}$ (LSCF),^{249,250} and LSC and LSF.²⁵¹ Yokokawa and co-workers examined the relative thermodynamic stability of various perovskite phases with respect to reaction products in the presence of zirconia, providing a framework for understanding the thermodynamic driving force behind the formation of these phases.^{252,253}

Exactly how these secondary phases influence cathode performance remains somewhat circumstantial. Labrincha et al.²⁵⁴ studied the electrical properties of LZ over a range of temperature and P_{O_2} and found it to have low conductivity under typical SOFC cathode operating conditions ($\sim 10^{-4} \Omega \text{ cm}^2$ at 1000 °C). This suggests that even a small layer of this material is likely to significantly interfere with charge transfer at the perovskite/YSZ interface. Poulsen and Vanderpuij²⁵⁵ have likewise shown that a variety of possible lanthanum zirconate and strontium zirconate reaction products are possible, which have electrical properties likely to interfere with interfacial charge transfer. Consistent with this hypothesis, numerous workers have reported perovskites on YSZ to exhibit a high-frequency impedance feature suggestive of interfacial resistance.^{27,164–166,187,210,211,215} Workers have also made significant progress in understanding how and where these phases form, leading to a variety of logical suppositions about why they may influence interfacial electrochemical kinetics or other processes governing performance.

One of the first studies of how these secondary phases form was performed by van Roosmalen and Cordfunke.²⁵⁶ These authors used SEM/EDS and XRD to study postannealed diffusion couples of LSM and YSZ as well as pressed and fired powder mixtures of LSM and YSZ. These experiments showed that reaction products in sufficient quantity to detect by XRD (1–3%) form at temperatures as low as 1170 °C. The two principle reaction products observed were $\text{La}_2\text{Zr}_2\text{O}_7$ (LZ) and SrZrO_3 (SZ), with the relative amount of LZ and SZ depending on the La/Sr ratio in the LSM. Calcia- and baria-doped LaMnO_3 were found to be similarly reactive with YSZ, and reactivity of LSM with YSZ having 3% or 8% yttria was found to be similar. In the case of the diffusion couples, the layer of reaction products formed at the interface was found (using SEM) to be on the order of 1 μm after 600 h at 1280 °C and 10–15 μm after 600 h at 1480 °C. By employing Pt diffusion markers

at the diffusion couple interface, the authors concluded that the reaction proceeds by cationic diffusion of La and Sr through the interfacial LZ and/or SZ layer, resulting in the formation of cation vacancies in LSM and the continued precipitation of LZ and/or SZ on the YSZ side of the interfacial layer. Consistent with this hypothesis was the observation of Kirkendall porosity in the LSM phase near the interface, which would be expected to form upon sufficient depletion of A-site cations in the LSM phase.

Since the formation of secondary phases at the interface appears to be associated with activity and mobility of the A-site cations, a variety of workers have investigated perovskites with A/B cation ratio < 1 in an attempt to mitigate the formation of reaction products. An early example is a study by Yamamoto et al.,²⁵⁷ who showed using XRD that no reaction products form between $\text{La}_{0.8}\text{MnO}_3$ and YSZ after sintering at 1200 °C for 200 h. Such prevention (or at least delay/retardation) of reaction products for perovskites with A/B ratio < 1 has since been reported by a variety of workers.^{235,243,249,258–261} Unfortunately there are generally few results that really tie the reduction of these phases to improvements in electrode performance (let alone particular aspects of that performance such as the interfacial electrochemical kinetics). Indeed, even with materials having A/B ratios < 1 , reaction products often still appear at higher temperatures and/or longer annealing times. Thus, given that these phases are often detected using XRD (which has a detection limit of 1–3%), it is not entirely clear that secondary phases are not still present in undetectable quantities. Also, depending on the mechanism of secondary phase formation, the low A/B ratio may only serve to delay rather than prevent secondary phases. For example, one prominent idea has been that dissolution of relatively small and mobile B-site cations from the electrode material into YSZ leads to a local increase in A-site activity at the interface.²⁴³ Given enough time and temperature, this may occur even when the A/B ratio is initially low enough to be thermodynamically stable with respect to reaction products. In support of this idea are thermodynamic calculations by Yokokawa et al.,^{252,253,262} who showed that Mn is highly soluble in YSZ and that this solubility is P_{O_2} dependent, suggesting that the formation of these various phases may be very sensitive to how easily oxygen can transport to/from the interface during electrode processing.

Of interest to this discussion is a paper by Simner et al.,²⁵¹ which challenges whether one can always detect deleterious materials at the interface as explicit phases. Motivated by the observation that perovskites LSC and LSF exhibit better performance on ceria (see section 6.3), they did a careful examination of the reactivity of LSC and LSF with 8 mol % YSZ, fired as mixed and pressed powders up to 1400 °C. Not surprisingly, LSC was found to be very reactive, forming large amounts of LZ, SZ, and Co_3O_4 . In contrast, LSF was generally less reactive, and in the case of A-site-deficient LSF, $(\text{La}_{0.8}\text{Sr}_{0.2})_{0.95}\text{FeO}_{3-\delta}$, the authors could not find evidence of secondary phases using SEM or XRD. Nonetheless, measurable

angle shifts ($\sim 2^\circ$ in 2Θ) were observed for the primary LSF diffraction lines, indicating a significant change in average unit cell size. The authors interpreted this change in terms of Zr^{4+} dissolution into the perovskite, which they show to reduce substantially the electrical conductivity of LSF. While it is not clear how deeply Zr would dissolve into an LSF electrode, it is also not clear how much would be needed to degrade performance. In other words, it is entirely possible that even when secondary phases are not detected in large enough quantities to see by SEM and XRD, a thin (1–10 nm) insulating layer of a secondary phase (or simply a compositionally modified primary phase) could still exist that introduces an interfacial resistance.

We should also point out that annealing of the interface, though ultimately responsible for the formation of secondary phases, may be a very important part of establishing ionic contact. For example, Horita et al.²⁶³ recently conducted $^{18}O_2$ tracer experiments on sputtered films of LSM on YSZ and showed that the “as-sputtered” interface (fabricated at 700 °C) has significantly higher resistance to ion exchange, which they attribute (based on SEM images) to a lack of bonding at a local level. With increased annealing time and temperature, the LSM and YSZ bond more completely, corresponding to facile ion exchange across the LSM/YSZ interface.

To better understand the structure and composition of the interface and its impact on interfacial electrochemical kinetics, a number of workers have conducted more detailed characterization studies of the perovskite/electrolyte interface using high-resolution transmission electron microscopy (HRTEM), electron diffraction, X-ray photoelectron spectroscopy (XPS), and atomic force microscopy (AFM).^{215,264–268} Of particular interest is a paper by Mitterdorfer and Gauckler,²¹⁵ who studied nucleation and growth of LZ between porous $La_{0.85}Sr_{0.15}Mn_yO_{3\pm\delta}$ with (001)-oriented 9.5 mol % doped YSZ single crystals using HRTEM, AFM, and XPS, as well as the impact of these phases in terms of electrode impedance. As illustrated in Figure 44, their results suggest that when LSM is A-site rich ($y = 0.98$), nucleation of LZ occurs at the TPB, where oxygen exchange is facile and La^{3+} and Zr^{4+} are available via surface diffusion. Once an island of LZ forms, it can then grow along the LSM/YSZ interface. In contrast, when LSM is A-site deficient ($y = 1.02$), initial nucleation of LZ is retarded; epitaxial growth of a Mn-rich YSZ phase occurs first, drawing Mn out of LSM and Zr^{4+} and Y^{3+} from the surrounding YSZ surface. Once sufficient Mn has been extracted from LSM, LZ then precipitates at the TPB.

What these results show is that regardless of A-site deficiency, eventual nucleation of the undesirable phase occurs exactly where it is least desired: at the TPB, where it results in an insulating gap between the LSM and YSZ surfaces. Restricting our attention to the low-overpotential regime, we might expect this gap to interfere with two processes: (1) surface diffusion of electroactive oxygen along the LSM surface to the TPB and (2) the electrochemical formation of O^{2-} at the TPB due to limited avail-

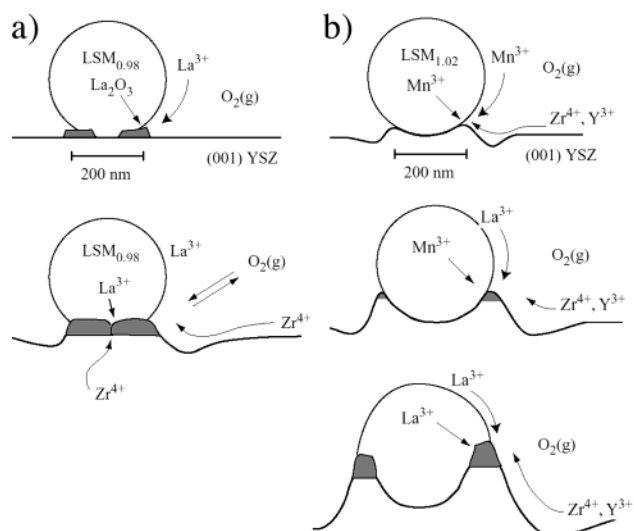


Figure 44. Qualitative description of $La_2Zr_2O_7$ (LZ) formation at the LSM/YSZ single-crystal interface based on HRTEM and AFM measurements, as explained in the text. Shaded region corresponds to LZ. (Adapted with permission from ref 215. Copyright 1998 Elsevier.)

ability of electronic charge carriers. Consistent with this hypothesis, Mitterdorfer and Gauckler observed apparent increases in both electrochemical and chemical contributions to the impedance upon annealing of the electrode.²¹⁵

However, beyond this, it is difficult to draw a more specific conclusion. In particular, it is now known how the electrochemical and chemical contributions to the impedance evolve through the different stages of development of these phases. Also, at higher overpotential (or with perovskite mixed conductors) we might expect the impact of these secondary phases to depend significantly on the relative roles of the surface and bulk paths as well as how far these phases spread along the LSM/YSZ interface (where they may also block ionic exchange across the solid/solid interface). Unfortunately, besides the general observation that performance gets worse with the formation of these phases, little is known. A more direct linkage of these phases to the exact changes seen in resistance and frequency response (as a function of overpotential and time) remains elusive.

Finally, it would be remiss not to mention the potential impact of *impurities* in influencing various electrode rate processes, particularly at the electrode/electrolyte interface. For example, Kuscer and co-workers²⁶⁹ showed that during accelerated aging of LSM electrodes on YSZ, small amounts of silica in the electrolyte tended to migrate to the interface, forming an amorphous La–silicate phase between the electrode and electrolyte. Besides the potential impact on interfacial electrochemical kinetics, formation of this phase was implicated in the observed delamination of the electrode from the electrolyte over time (see section 6.6). Similarly, concurrent preliminary work at Imperial College has shown that small amounts of silica introduced during processing of perovskite/ceria electrodes had a deleterious influence on performance.^{270,271} Given the propensity of silica to form low-melting eutectics and move along ceramic grain boundaries, one would also suspect

sensitivity to the presence of alkaline or alkaline-earth materials (common components of furnace insulation!). However, while the impact of certain impurities (particularly silica) on the properties of ion conductors is well known,^{272–275} there have only been a few studies to date that really investigate the impact of these impurities on electrode performance.

6.2. Alteration of Material Properties Near the Interface

Further complicating our understanding of interfacial electrochemical kinetics (as well as electrode kinetics as a whole) is the observation that bonding of the electrode material with the electrolyte may result in changes to the electrode and/or electrolyte materials in the general vicinity of the interface. In section 6.1 we already saw some examples of this, for example, the dissolution on Mn in YSZ, altering its ionic conductivity,^{243,276} or the dissolution of Zr into LSF, potentially reducing its electronic conductivity.²⁵¹ Thus, it is possible that effects that appear to be associated with the interface (due to their geometric scaling or impedance time scale) may in fact be local variations of chemical processes in the near-interfacial region.

One notable possibility is that interdiffusion of the electrode and electrolyte during bonding may result in changes in cation composition (and therefore properties) of the electrode. Recent results supporting this possibility were published by Horita et al.,²⁶³ who examined $^{18}\text{O}_2$ tracer diffusion in a sputtered thin film of A-site-deficient LSM on YSZ. As discussed previously, this result showed enhancement of ionic exchange across the LSM/YSZ interface with annealing, due to improved bonding. What is also of interest is that the authors observed an approximately 3-fold decrease in the apparent ^{18}O tracer diffusion coefficient of the film upon annealing above ~ 1000 °C. This was explained by the authors in terms of changes in cation composition of the film due to diffusion of Y and Zr into LSM, which according to their SIMS depth profiles penetrate ~ 1 μm at 1300 °C. Although SIMS intensities are not considered a quantitative measure of concentration, the Y and Zr intensities 800 nm deep into the LSM region were on the order of 10% of that in YSZ itself. Unfortunately, since no XRD or TEM cross-sections were performed, it is difficult to entirely eliminate the possibility that secondary phases contribute to these cation intensities. However, this study does serve to illustrate that significant changes in bulk transport properties may occur simply due to interdiffusive bonding.

A related finding was reported by Kawada et al.,¹²⁴ who studied the impedance of thin laser-deposited films of LSC on SDC. As discussed in section 4.3, they analyzed the apparent chemical capacitance of the films in terms of changes in bulk oxygen stoichiometry. In so doing they discovered a very surprising result: the apparent oxygen vacancy concentration in the film in air is approximately 4 times smaller than for bulk LSC having the same cation composition (60/40 La/Sr). Further analysis suggested that

the *enthalpy* of oxygen incorporation into LSC is different for the film than for the bulk material. ICP analysis of the film following dissolution in acid confirmed that it had a 60/40 La/Sr ratio, although somewhat depleted in Co (6%). This level of B-site deficiency does not seem to explain such a significant departure from bulk properties. After considering and rejecting several other possibilities, the authors proposed that *stress* in the film due to a forced match with the underlying ceria might explain the apparent additional contribution to the oxygen exchange enthalpy. This as yet unproven hypothesis is intriguing since it implies that material properties may be subject to modification at an interface even when reaction and/or interdiffusion does not occur.

Finally, another possibility often discussed in the literature is that cation “dopants” from the electrode may enhance the electronic conductivity of the gas-exposed surface of the electrolyte in the vicinity of the TPB, thereby extending the reduction zone along the electrolyte surface via mixed conduction. The surface exchange rate of oxygen on both YSZ- and rare-earth-doped ceria (as measured by isotope methods) is only about 1 order of magnitude lower than on LSM at 700 °C.^{277–279} Thus, if there were sufficient electronic conduction at the surface or in the bulk of the electrolyte, it might be possible for net reduction to O^{2-} to occur on the gas-exposed electrolyte surface. There is precedence in the catalysis literature that this can happen; for example, workers studying CO or CH_4 oxidation on $\text{CeO}_2/\text{ZrO}_2$ -supported Pt and Pd catalysts at high temperature^{280,281} have generally shown that the support enhances performance via reduction and mixed conduction of oxygen in the fluorite phase. Workers have also suggested that mixed conduction in ceria can play a role in SOFC anodes.²⁸² Various workers have provided circumstantial evidence that this might occur under oxidizing conditions at an SOFC cathode. For example, Kleitz and co-workers⁵⁵ noted that the high-frequency (presumably interfacial) impedance of small silver droplet electrode scales as $r^{-0.6}$, where r is the droplet radius. They explained this weak geometry dependence as an outward expansion of the charge-transfer zone away from the TPB along the electrolyte surface. Another example is work by van Hassel and co-workers, who, as shown in Figure 45, found that the performance of porous gold cathodes on YSZ (normally a very poor oxygen catalyst) is significantly enhanced at all overpotentials by prior coating with Fe_2O_3 and/or implantation of iron into the electrolyte surface.^{99,283} Widmar and co-workers reported similar enhancements for low-fired (750 °C) Pt electrode on YSZ implanted with Ce or Mn at low overpotential.⁸²

However, to date there does not appear to be much evidence that *mixed conduction* in the electrolyte plays the dominant role in the enhancements mentioned above. First, it should be emphasized that a finite rate of oxygen exchange at the electrolyte surface (as measured at equilibrium by isotope methods) is a necessary but insufficient criterion for finite rates of oxygen reduction; for there to be a *net* production of O^{2-} at the electrolyte surface, electrons

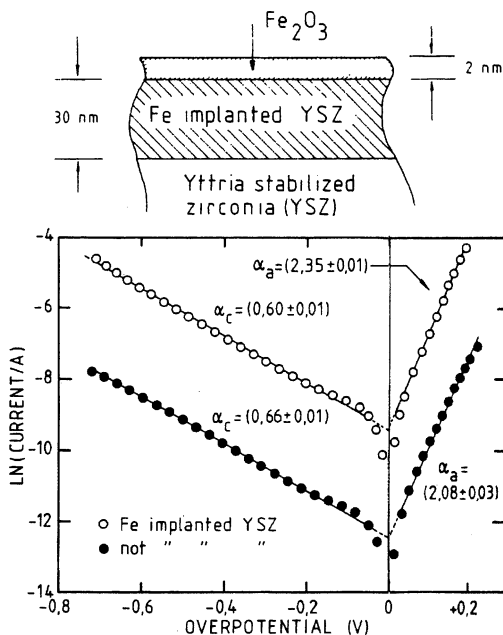


Figure 45. Current–overpotential characteristics of porous gold electrodes on YSZ at 770 °C and $P_{O_2} = 1$ atm, comparing YSZ that has, and has not, been implanted with 8×10^{16} atoms/cm² of ⁵⁶Fe at 15 kV. (Reprinted with permission from ref 99. Copyright 1992 Elsevier.)

must also be able to gain access to the surface. Workers have generally shown that when YSZ is implanted or alloyed homogeneously with Fe or Mn, its electrical conductivity is not significantly enhanced, even under moderately reducing conditions.^{82,243,284–286} Second, in isotope studies of low-temperature bifunctional CO oxidation catalysts, such as Au/Fe₂O₃, workers have shown that the role of the transition metal in the support is essentially *catalytic*, i.e., stabilization of physisorbed O₂ at the Au/oxide interface, leading to enhanced oxidation rates.^{287–289} It is likewise possible that enhanced performance of metal cathodes on YSZ incorporating transition metals or (other d-orbital cations) is an electrochemical–kinetic effect localized to the TPB where by “localized” we mean simply “within a distance accessible by electrons from the electrode material”. Indeed, as shown in Figure 45, the enhancements observed by van Hassel and co-workers upon implantation of Fe into YSZ correspond to an increase in the apparent exchange current density while the Tafel slope remains constant over several orders of magnitude. This observation suggests that iron acts to promote the existing rate processes (either on the Au surface or at the TPB) rather than by changing the mechanism toward an alternative chemical pathway involving the electrolyte. Finally, we should point out that gold is a poor oxygen catalyst at high temperature. In the case of a highly catalytic perovskite, it is not clear that incorporation of transition metals from the electrode into the electrolyte surface is going to provide any significant catalytic benefit not already provided by the electrode itself, particularly in cases where the utilization region is large and thus the exposed electrolyte surface makes up such a small percentage of the area available for dissociative adsorption.

6.3. Ceria as an Alternative Electrolytic Interface

In attempting to develop fuel cells based on ceria-based electrolytes, workers have also examined the reactivity of various perovskite electrode materials with doped ceria. An early example is a study by Chen and co-workers,²⁵⁰ who used a spin-coating technique to deposit LSCF electrodes on YSZ as well as 20 mol % samaria-doped ceria (CeO₂)_{0.8}(SmO_{1.5})_{0.2} (SDC). Consistent with previous findings, LSCF was observed to react with YSZ to form LZ and SZ byproducts. In contrast, analogous Ce-based compounds resulting from a reaction between LSCF and SDC were not observed. Consistent with this observation were Chen et al.’s measurements of electrode impedance, which suggest LSCF exhibits less interfacial resistance when processed and tested under the same conditions on the same substrate. On the basis of this result, the authors suggested addition of a ceria-based “protection layer” between the perovskite electrode and YSZ, an idea which is now actively being developed for intermediate temperature fuel cells.²⁵¹

Consistent with Chen et al.’s observations was a study by Adler and co-workers (described previously in section 4), who measured the impedance of LSCF on SDC at intermediate temperatures. Their measurements showed that above about 700 °C in air the impedance is dominated by a single Gerischer-like impedance found to be consistent with a bulk-mediated reaction pathway. Although the possible role of the surface path cannot be entirely excluded in this case, what is clear is that the impedance is dominated by chemical dissociation and transport steps while electrochemical incorporation at the interface remains largely equilibrated at least above ~650 °C. Adler et al. mention in passing that at lower temperatures (450–550 °C) a small high-frequency arc with a high activation energy appears, indicating the onset of interfacial electrochemical kinetic resistance. However, it is unclear if this additional resistance is associated with secondary phases or simply an inherent resistance to ionic exchange between two dissimilar ionic phases (as has been observed, for example, at the physical interface between two pieces of YSZ²⁹⁰). This apparent lack of an interfacial resistance (as evidenced by the absence of a distinct high-frequency impedance arc) appears to be a general feature of perovskite mixed conductors on rare-earth-doped ceria or (La,Sr)(Ga,Mn)O₃ electrolytes.^{18,19,22,28,177,179–181,184,250,291,292}

A notable exception may be Sr-doped ceria. As reported by Liu and Wu,¹⁸⁷ LSCF electrodes on 10 mol % Sr-doped ceria exhibit a significant high-frequency impedance arc in air at 650–750 °C, which is comparable in frequency (but somewhat smaller) to that observed for identically processed and tested LSCF electrodes on 8 mol % YSZ. One explanation may be found in the thermodynamic data for the Sr–Ce–O system, which shows that the solubility of SrO in CeO₂ is less than 10 mol % at these temperatures.^{293–295} Thus, precipitation of SrCeO₃ at the LSCF/ceria interface is favored, depending on the exact firing conditions and A/B ratio of the perovskite. Oddly, the authors did not consider this possibility,

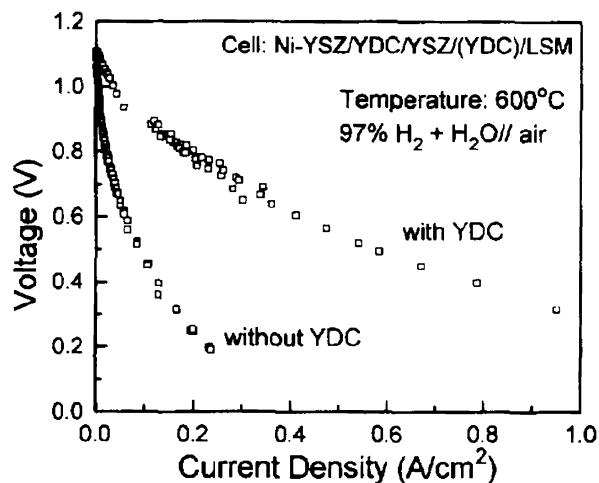


Figure 46. Performance characteristics of a cathode-supported thin film Ni-YSZ/YSZ/LSM fuel cell at 600 °C in humidified H₂ and air with and without a dense protective yttria-doped ceria (YDC) protection layer introduced between the porous LSM cathode and the thin-film electrolyte. (Reprinted with permission from ref 296. Copyright 1997 Elsevier.)

citing the variations in impedance with different electrolytes as proof that oxygen reduction is limited by electrochemical kinetics at the TPB. On the contrary, the very large apparent chemical capacitance ($\sim 1 \text{ F/cm}^2$) associated with the low-frequency impedance feature (which is similar in shape, size, and frequency for both YSZ- and Sr-doped ceria) suggests a bulk-mediated path involving absorption and transport in LSCF. Meanwhile, the differences seen at high frequency between YSZ- and Sr-doped ceria might easily be explained in terms of different secondary phases formed, whose likely effect is to interfere with ion-transfer across the entire solid–solid interface (not just at the TPB).

Given the apparent reversibility of the perovskite/rare-earth-doped ceria interface, Various workers have more recently investigated Chen's original suggestion of a ceria-based protection layer between YSZ and perovskite cathodes.^{296–299} As shown in Figure 46, Tsai and co-workers found that by introducing a 0.4 μm thick sputtered layer of yttria-doped ceria between YSZ and porous LSM, overall current density of their cathode-supported fuel cell could be improved by a factor of approximately 5 \times . More recently, anode-supported YSZ fuel cells using a single-phase porous LSF cathode with a Sm-doped ceria protection layer have been reported to exceed operating voltages of 900 mV at current densities of 100 mA/cm².²²⁹⁸ This performance is competitive with some of the best composite LSM/YSZ cathodes available today (see section 6.4). While these results are exciting, more work is needed to confirm/reject current hypotheses about how these layers actually work to improve performance and compare performances meaningfully among various development groups.

6.4. Composite Microstructures

Figure 2 illustrated two dominant strategies that have been used to enhance the performance of SOFC cathodes. One has been the introduction of ionic

conduction into the electrode material so as to extend the active region beyond the electrode/electrolyte interface. Along with ionic conduction, however, comes potential problems including increased chemical and thermal expansion and higher apparent reactivity between electrode and electrolyte (section 6.1). An alternative strategy has been to combine a YSZ-compatible electrode material such as LSM with an ionically conducting second phase (e.g., YSZ itself) in a composite matrix. While the active region of an LSM electrode may generally be more confined to the LSM/YSZ interface than a mixed conductor, the composite matrix makes up for this deficiency by extending the LSM/YSZ interface. This strategy has proven to be very promising but adds some complexity to our diagnosis and understanding of which processes dominate the overall observed overpotential.

One of the first attempts to implement this strategy was reported by Kenjo and co-workers,^{300,301} who fabricated and tested the performance of porous Pt composite electrodes containing YSZ, SDC, and erbia-stabilized bismuth oxide (ESB) as well as composites of A-site-deficient La_{0.85}MnO₃ (LM) and YSZ. The electrode polarization losses of these electrodes were measured using current-interruption techniques as a function of electrode thickness. For Pt/ESB and LM/YSZ, the presence of the electrolyte was found to enhance performance significantly (5–10 times) depending on processing conditions and the volume fraction of the electrolyte. As shown in Figure 47, performance was also found to increase with electrode thickness, saturating at a thickness of $\sim 10 \mu\text{m}$ (30 or 40 μm for Pt/ESB). In the case of Pt/YSZ and Pt/SDC, no enhancement was observed; however, the authors proved using electrical conductivity measurements that with their particular preparation method any significant fraction of YSZ and SDC particles interferes with the electrical connectivity among Pt particles, making the electrode too resistive to function in these cases.

As shown in Figure 48, the authors explained their results in terms of a macrohomogeneous model similar to that used previously for aqueous gas-diffusion electrodes.³⁰² With this approach the electronic and ionic conductors (Figure 48a) are viewed as homogeneously interpenetrating subphases, the electronic conductor having relatively high electrical conductivity, while the ionic conductor has finite ionic resistivity $\rho = 1/\sigma_i$. At the interface between these phases, oxygen reduction occurs at a rate proportional to the local overpotential, resulting in passage of current from the ionic to the electronic phase, $i_v = \eta(x)/k$, where $\eta(x)$ is the local overpotential and k in this case is the interfacial resistance per unit volume ($\Omega \text{ cm}^3$). Consideration of charge conservation a la classic porous electrode theory³⁰³ leads to the solutions shown in Figure 48c,d. In analogy to the situation shown in Figures 14b and 26a, the composite electrode is found to be co-limited by interfacial resistance and ionic transport in the ionic subphase, exhibiting a maximum utilization region of size $\sim \sqrt{k/\rho}$ and overall resistance proportional to $\sqrt{\rho/k}$ for

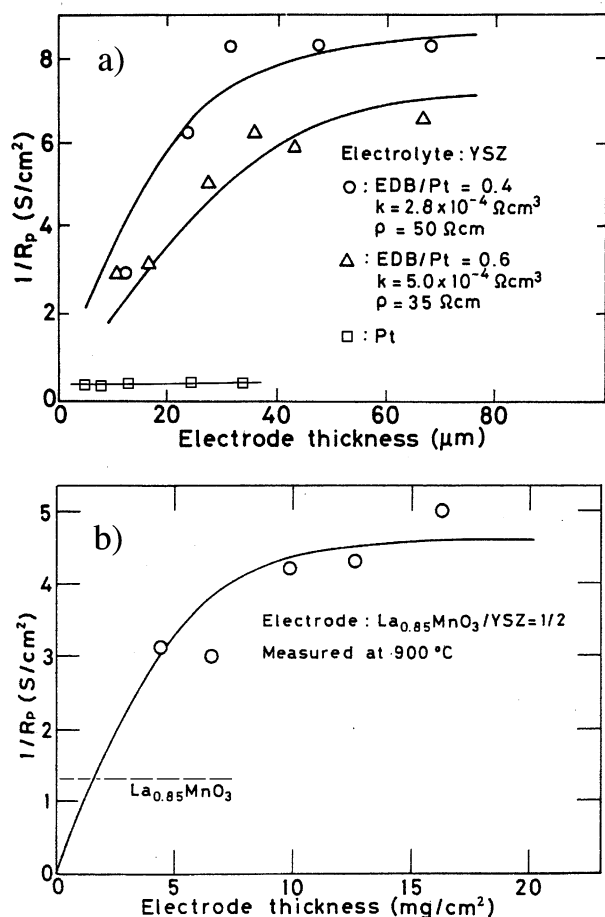


Figure 47. Measured area-specific admittance (reciprocal of the polarization resistance R_p) as a function of electrode thickness for Pt/ESB and LSM/YSZ composite electrodes. Performance of the same electrode materials without an ionic subphase are also shown for comparison. Lines indicate fits to the model shown in Figure 48, as discussed in the text. (Reprinted with permission from refs 300 and 301. Copyright 1991 and 1992 The Electrochemical Society, Inc. and Elsevier, respectively.)

an infinitely thick electrode. As shown in Figure 47, fitting of this model yields values of ρ and k found to be in reasonable agreement with the properties of ESB and YSZ given the uncertainties in the details of the microstructure (interparticle contact, ionic tortuosity, interphase contact area).

What this result shows is that for materials having a small natural active region as a single porous phase (50–500 nm for Pt, perhaps somewhat larger for LM), the use of a composite microstructure can significantly enhance performance, extending the active region to include a much larger fraction of the electrode material ($\sim 10 \mu m$). A number of workers have since demonstrated the benefits of this approach for LSM/YSZ, some reporting active regions of similar size (5–10 μm) as single-phase mixed conductors.^{304,305} Besides establishing a new paradigm in how to design SOFC cathodes, this approach has also introduced a new set of issues to be considered, including the efficiency of the ionic and electronic transport paths,^{24,306–309} quality and quantity of internal interfacial contact between the ionic and electronic subphases,^{30,310} functional grading of the materials for structural or other purposes,^{36,311–313}

and tuning of the microstructure to match the local natural extension region of the electrode material.

As one might expect, interpreting the electrochemical characteristics of composite electrodes is considerably more challenging than understanding their single-phase counterparts. Since work in this area is sparse, we confine this discussion to a few of the salient differences. First, the various physical processes contributing to the overpotential are more difficult to separate. With a single-phase electrode, ohmic losses associated with the electrolyte (and in some cases also interfacial electrochemical kinetics) can be isolated or treated using equivalent circuit analogies independent of how complex the processes occurring in the electrode itself may be. In contrast, as implied by Figure 48, the characteristics of a composite electrode involve an inherent convolution of the ohmic loss in the electrolytic subphase with the electrochemical and chemical losses at the junction between the ionic and electronic (or mixed conducting) subphases. This leads to wide dispersion and overlap among the time scales for these processes, making interpretation of impedance extremely challenging, as recently reviewed by Jørgensen and Mogenssen.³¹

Second, the electrochemical characteristics of composite electrodes are generally much more sensitive to the details of the microstructure than single-phase materials.^{30,35} Indeed, embedded in the parameter k in Figure 48 are literally *all* the physical processes reviewed in sections 3–5 plus the details of how the two subphases are interconnected. While various authors have attempted to relate τ in more detail to the microstructure, modeling is often limited to idealized hypothetical microstructures that may or may not be relatable in a quantitative way to the real system.^{307,314} In addition, since composite electrodes work by maximizing surface area and interfacial contact, they are often fired at much lower temperatures than their single-phase counterparts, leading to additional uncertainty as to the geometry and quality of interparticle contact. These details of the microstructure and interfaces, which may be critical to performance, are extremely difficult to quantify using current cross-sectional sampling techniques (SEM, HRTEM, SIMS, AFM).

Finally, due to their high surface area, composite electrodes often incorporate microstructural features competitive or smaller than the active region of a single-phase electrode of the same material. In this situation, we expect chemical transport processes to be largely equilibrated on a local (submicrometer) length scale, leaving dissociative oxygen ab(s)orption as the only significant chemical resistance. One consequence of this situation is that the electrochemical kinetics contributing to k in Figure 48 may not be the same as those governing the kinetics of a single-phase electrode, even when TPB area is known and properly accounted for. Rather, the mechanism itself may shift toward a different set of co-limiting steps, in particular catalytic reduction, interfacial electrochemical kinetics, and ionic transport in the ionic subphase.

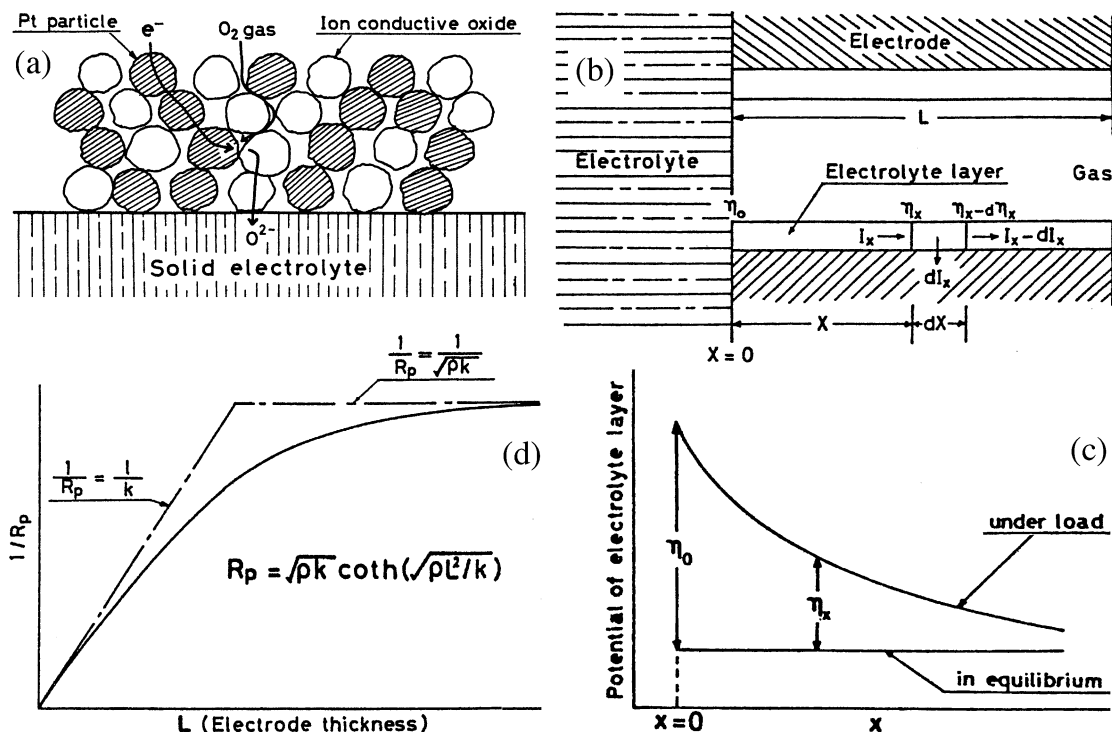


Figure 48. Kenjo's 1D macrohomogeneous model for polarization and ohmic losses in a composite electrode. (a) Sketch of the composite microstructure. (b) Description of ionic conduction in the ionic subphase and reaction at the TPB's in terms of interpenetrating thin films following the approach of ref 302. (c) Predicted overpotential profile in the electrode near the electrode/electrolyte interface. (d) Predicted admittance as a function of the electrode thickness as used to fit the data in Figure 47. (Reprinted with permission from refs 300 and 301. Copyright 1991 and 1992 Electrochemical Society, Inc. and Elsevier, respectively.)

Despite these uncertainties, however, workers have made impressive advances in cathode performance over the last 5–7 years using composite microstructures. A recent paper by McIntosh et al. reports the area-specific resistance of a 50–50 LSM–YSZ composite (fabricated from powders at 1250 °C) to be about $\sim 0.2 \Omega \text{ cm}^2$, both in a half cell and fuel-cell configurations following polarization.⁴⁰ Barnett and co-workers report somewhat higher resistances for LSM/GDC composites ($\sim 1.0 \Omega \text{ cm}^2$ at 700 °C³³); however, it should be noted that these electrodes had never seen a bias and thus may have much higher performance under load (see section 5.4). Electrodes incorporating mixed conductors as the electronic subphase generally have even higher performance. As an example, Figure 49 shows the impedance (as a function of temperature in air) of a low-fired (900 °C) LSCF/GDC composite electrode on YSZ made by Murray and co-workers.³⁵ This electrode has an ASR of $\sim 0.03 \Omega \text{ cm}^2$ at 700 °C with no polarization history. Huang and co-workers reported cathode resistances of $\sim 0.1 \Omega \text{ cm}^2$ at 700 °C for LSC/YSZ and LSF/YSZ composites made by impregnation techniques.^{315,316}

6.5. Current Constriction Effects

In passing, we should also mention one additional microstructural factor potentially impacting the overall electrode performance: constriction of the ionic current in the electrolyte near the electrode/electrolyte interface. To better understand this effect, consider a circular disk electrode of diameter d immersed in a semi-infinite electrolyte of conductivity

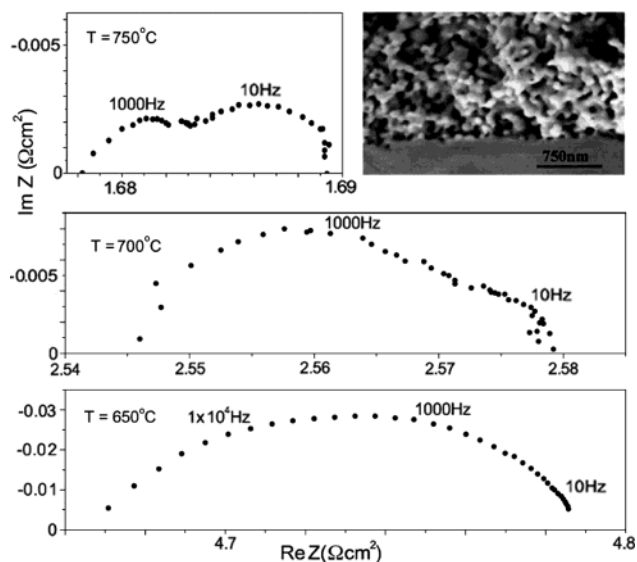


Figure 49. Impedance of a low-fired composite LSCF/GDC electrode on YSZ in air as a function of temperature. (Inset) SEM of the microstructure of the electrode showing very fine porosity but effective interparticle contact. (Reprinted with permission from ref 35. Copyright 2002 Elsevier.)

σ_i (Figure 50a). It can be shown that the measured IR drop occurs primarily within a distance d of the electrode with a value given by⁴⁷

$$V_{IR} = \frac{I}{2d\sigma_i} \quad (11)$$

where I is the total current. If one views the interface between a solid electrolyte and a porous electrode as

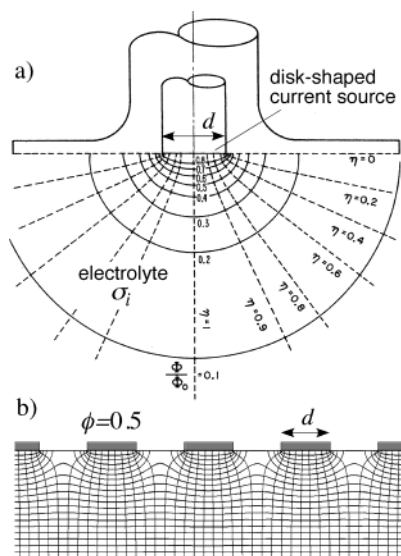


Figure 50. (a) Primary potential distribution surrounding a disk-shaped electrode. (Reprinted with permission from ref 47. Copyright 2004 John Wiley & Sons.) (b) Finite-element calculation of the 2D primary potential profile near an electrode with regular periodic contact to the electrolyte ($\phi = 0.5$). Horizontal lines on the contour plot are lines of constant potential; vertical lines follow the current path.

an array of such small current sources, one expects that as the size of these sources get very small, the IR resistance will become increasingly dominated by the constriction of the current near each source rather than the superficial current density of the cell.

Workers have shown theoretically that this effect can be caused both at the microstructural level (due to funneling of the current near the TPB) as well as on a macroscopic level when the electrode is not perfectly electronically conductive and the current collector makes only intermittent contact.^{206,244,317} Fleig and Maier further showed that current constriction can have a distortional effect on the frequency response (impedance), which is sensitive to the relative importance of the surface vs bulk path.³¹⁸ In particular, they showed that unlike the bulk electrolyte resistance, the constriction resistance can appear at frequencies overlapping the interfacial impedance. Thus, the effect can be hard to separate experimentally from interfacial electrochemical-kinetic resistances, particularly when one considers that many of the same microstructural parameters influencing the electrochemical kinetics (TPB area, contact area) also influence the current constriction.

To facilitate estimates of this effect on the microstructural level, we point out the existence of an important dimensionless group, J , that describes the ratio of the current constriction resistance to the electrode resistance.^{47,319} If $J \ll 1$, then we expect the constriction effect will be small compared to the electrode resistance, while if $J \geq 1$, the constriction effect is expected to be significant. For example, in the case shown in Figure 50a, J is derived by dividing V_{IR} (given by eq 11) by the electrode overpotential $\eta = IR_{\text{electrode}}$, where $R_{\text{electrode}}$ is the total effective resistance of the disk (in Ω). If we consider a large number of well-separated disks (Figure 50b) and re-

express $R_{\text{electrode}}$ on a superficial-area-normalized basis, J is given approximately by

$$J \approx 0.4 \frac{d}{\phi R_{\text{ASR}} \sigma_i} \quad (12)$$

where R_{ASR} is the area-specific resistance of the electrode and ϕ is the fraction of the area through which current must flow at the interface. Applying eq 12 to a bulk-path-dominated electrode (Figure 50b), we can estimate J by taking d to be the average diameter of the solid–solid contact points while ϕ is the fraction of the electrolyte surface covered by the electrode. For 2D rather than 3D constriction, the situation is similar;³¹⁹ thus, for a surface-dominated mechanism, we would take d to be the effective width of the TPB while ϕ would correspond the fraction of the electrolyte surface within one-half TPB width of the TPB line.

As an example, consider a porous LSC electrode with an average particle diameter of $0.2 \mu\text{m}$ operating via a bulk path. If the porosity is 30%, then ϕ will be approximately 0.7. Assuming a superficial electrode resistance of $0.05 \Omega \text{ cm}^2$ at 750°C and an electrolyte conductivity of $0.03 \Omega \text{ cm}^{-1}$, then $J \approx 0.01$. Thus, current constriction is probably not an issue in this case. Alternatively, consider a porous LSM electrode of similar morphology and performance, assuming a TPB width of $\sim 1 \text{ nm}$. In this case ϕ will be approximately 1.4% of the superficial area. Thus, J would be ~ 0.002 . Again, this is a number much smaller than 1. These back-of-the-envelope calculations suggest that microscopic current constriction is not a large effect under most practical situations, and thus most excess ohmic losses reported in the literature arise from more macroscopic current constriction effects (such as insufficient current collection).^{206,320} However, it is probably wise for investigators to make estimates of J to ensure further analysis is not required for their system.

6.6. Long-Term Degradation

A second form of nonstationary behavior is irreversible long-term degradation of the electrodes, explicitly with either time or time under operation in a given environment. Unfortunately, the literature in this area is neither plentiful nor consistent. In particular, there is a dearth of publications reporting test data past about 100 h due (no doubt) to the extreme cost of conducting long-term testing. As a result, degradation has remained primarily a subject of concern for industrial developers who have the resources needed to tackle this issue but by the same token are generally loath to publish important, hard-fought trade secrets. Furthermore, of the few reports that have been published, results often vary wildly for seemingly similar material systems. For example, workers have reported fuel cells based on porous LSM cathodes lasting $> 50\,000 \text{ h}$ with less than 5% degradation,³²¹ while others have reported cathode degradation of 1000% in less than 50 h.³²² Given this general lack of consensus as to rates and causes of long-term degradation, we only briefly mention a few of the factors reported to cause acute short-term degradation (100–1000 h).

(1) *Morphological evolution.* Driven in part by parallel studies on nickel sintering and degradation in SOFC anodes,^{323–326} one concern has been that LSM (or other ceramic cathode materials) can sinter over time, losing active surface area and thus activity. Several workers have reported morphological changes in LSM electrodes with time or with time under current load, which has been correlated with degradation.^{157,214,322,327–329} Why the changes occur and how they effect performance is not very clear. It is also not clear that these changes are all caused by the same thing or that all electrodes are likely to experience these changes.

(2) *Chromium contamination.* As discussed previously, one must always be aware of the possible presence of impurities which could have a variety of effects, including enhancing sintering at operating temperatures. An impurity of particular concern has been chromium, which is often part of the interconnect (bipolar plate) in an SOFC stack either as a LaCrO₃ (ceramic interconnect) or as part of an alloy in the case of a metal interconnect. Workers have shown that Cr can be quite mobile in an SOFC environment^{330,331} and linked it clearly to degradation.³³² There has also been a considerable amount of recent work that has probed the mechanism by which Cr degrades performance.^{182,333–335} It appears that perovskite mixed conductors are less susceptible to the effects of chrome than LSM, possibly because they function by a bulk mechanism, which is less influenced by the contamination of the surface by Cr-containing species.

(3) *Evolution of secondary phases.* Another concern has been continued formation of LZ and SZ secondary phases at the perovskite/YSZ interface as a function of time or current density.^{336,337} Accelerated testing, achieved by sustained heat treatments of the electrode, suggests that degradation can occur by this mechanism.^{338,339} However, whether such thermal treatments can be meaningfully extrapolated to predict natural degradation processes is unclear.

(4) *Thermal cycling.* Finally, we should also mention the issue of thermal cycling, which is a likely source of stress on cells in a commercial SOFC device due to thermal and chemical mismatches among the various materials.^{340,341} Hsiao and Selman have shown that this effect has a primary influence on the interface, causing literal separation of the electrode from the electrolyte.

6.7. Experimental Artifacts in Electrochemical Measurements

As we have seen in the previous sections, our understanding of SOFC cathode mechanisms often hinges on interpretation on the magnitude and time scale of electrochemical characteristics. However, these characteristics are often strongly influenced by factors that have nothing to do with the electrode reaction itself but rather the setup of the experiment. In this section we point out two commonly observed effects that can potentially lead to experimental artifacts in electrochemical measurements: (1) polarization resistance caused gas-phase diffusion and (2) artifacts related to the cell geometry. As we will

see below, these effects commonly influence the polarization, leading to experimental errors, or appear as “features” in the impedance or other electrochemical measurements that workers misinterpret as part of the electrode reaction mechanism.

(1) *Gas-phase effects.* In aqueous electrochemistry, a rotating disk electrode is often employed to ensure that mass-transfer effects do not obscure the measurement of electrochemical kinetics except at very high polarization (limiting current). In contrast, the gas inside the pore network of a GDE is *stagnant* and may be so for some distance outside the electrode due to the presence of additional materials required for current collection and/or mechanical support (mass-transfer distances of 30–1000 μm are not uncommon). In addition, the molar concentration of a gas is $\sim 10^3$ times lower than a liquid. Partially compensating for these factors is the fact that gas-phase diffusion is typically 5 orders of magnitude faster than diffusion in aqueous solution. For example, the binary diffusion coefficient of oxygen in air at 700 °C is $\sim 1 \text{ cm}^2/\text{s}$ compared to the diffusion coefficient of dissolved O₂ in H₂O at 25 °C ($\sim 2 \times 10^{-5} \text{ cm}^2/\text{s}$). However, these estimates also suggest that at O₂ concentrations of $\sim 10^{-2}$ atm or below we might expect gas-phase diffusion to become significant.

One can roughly estimate the effects of gas-phase diffusion at steady state using a simple 1D diffusion model, which has been employed (in some form) by numerous workers.^{171,342,343} This approach yields the following expression for the linearized steady-state chemical resistance due to binary diffusion of O₂ in a stagnant film of thickness L ¹⁷¹

$$R_{\text{gas}} = \frac{RT}{4F^2} \frac{LV_m}{2x_{\text{O}_2}^\infty D_{\text{AB}}^{\text{eff}}} \quad (13)$$

where $x_{\text{O}_2}^\infty$ (assumed $\ll 1$) is the mole fraction of oxygen in the well-mixed region outside the film layer, $V_m = RT/P$ is the molar volume of the gas, and $D_{\text{AB}}^{\text{eff}}$ is the effective diffusion coefficient which may depend on porosity and tortuosity of the electrode as well as the effects of Knudsen diffusion (note the similarity to eq 7). As an example, for a diffusion layer of 100 μm , an effective diffusion coefficient of 0.1 cm^2/s , a gas concentration of 10^{-3} (total pressure 1 atm), and a temperature of 1000 K, this equation predicts a resistance of $\sim 1 \Omega \text{ cm}^2$.

Thus, not surprisingly, numerous workers have knowingly (or unknowingly) observed this effect in polarization and impedance measurements.^{28,70,79,171,184,291,342–347} For materials having a small apparent utilization region l_0 compared to the electrode thickness (e.g., porous Pt or LSM at low polarization), gas-phase effects normally appear as a separate arc in the impedance at low frequency.^{70,79,345–347} As an example, Figure 51 shows the impedance of porous LSM/YSZ composite electrodes on YSZ at 950 °C, measured as a function of P_{O_2} using blended gases of O₂ in N₂. An arc with frequency ~ 1 Hz appears below $P_{\text{O}_2} = 5\%$ and grows dramatically with decreasing P_{O_2} .³⁴⁶ Telltale signs that this arc is related to gas-phase diffusion are (1) the admittance associated with this arc is first order in P_{O_2} , (2) when

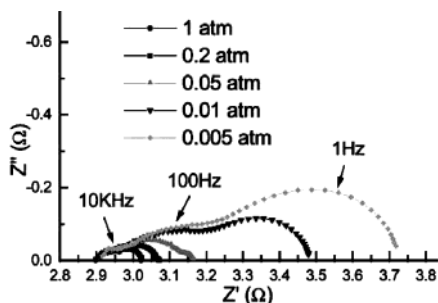


Figure 51. Zero-bias impedance of a 60%/40% LSM/YSZ composite cathode, measured at 950 °C as a function of P_{O_2} .³⁴⁶ The magnitude of the lowest-frequency arc (~ 1 Hz) was quantified using equivalent circuit analysis and found to scale inversely with P_{O_2} and only weakly with temperature. (Reprinted with permission from ref 346. Copyright 2001 Elsevier.)

measured as a function of temperature, the polarization associated with this arc is found to have a very small activation energy, and (3) the very low frequency of the arc, which can generally be understood in terms of the relative chemical capacitances involved, as follows. As discussed in sections 3–5, the chemical capacitance associated with the faradaic impedance is proportional to the linearized storage capacity of adsorbed oxygen on the electrode surface within a distance l_0 of the interface. However, when gas-phase diffusion resistance is present, the relevant oxygen storage capacity involves the entire electrode surface (thickness L) as well as the storage capacity of the gas itself (which may be particularly significant if there is a large stagnant layer outside the electrode). Yoon et al. showed that gas-phase diffusion in the electrode itself and mass-transfer limitations outside the electrode (caused by a flow-rate-dependent boundary layer) appear as separate impedance features due to the relatively large storage capacity of the gas above the cell.³⁴⁷

In cases where the utilization region approaches the electrode thickness (e.g., perovskite mixed conductors), it can be harder to discern gas-phase effects as a separate feature since the time scales begin to merge. Some techniques workers have used in this situation include varying the total pressure while keeping P_{O_2} constant¹⁸⁴ (since binary diffusion coefficients scale inversely with P_{total} at low pressure³⁴⁸) or replacing the diluent gas (usually N_2 or Ar) with He^{28,346,347} (since the binary diffusion coefficient for O_2 in He is about 4–5 times smaller than for O_2 in N_2 ³⁴⁹). As an example, Figure 52a shows the impedance of LSC electrodes on rare-earth-doped ceria at 750 °C as a function of P_{O_2} when a relatively thick ($\sim 20 \mu m$) porous silver current collector is used. Replacement of air with 20.9% O_2 in He has little effect on the impedance at zero bias. However, there is measurable difference between 4.0% O_2 in N_2 vs 4.0% O_2 in He. The higher resistance in N_2 is accompanied by a proportionate decrease in characteristic frequency rather than the appearance of a second feature in the impedance. As shown in Figure 52b, Koyama et al. showed similar findings for SSC on SDC at 800 °C and $P_{O_2} = 0.01$ atm by varying total pressure.¹⁸⁴ The similarity in time scale for the chemical vs gas-transport impedances in these cases

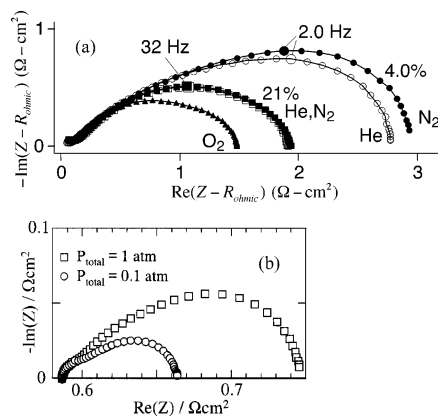


Figure 52. Effect of binary gas-phase diffusion on the impedance characteristics of porous mixed-conducting electrodes at low P_{O_2} : (a) zero-bias impedance of LSC on rare-earth-doped ceria at 1 atm and 750 °C as a function of P_{O_2} using concentrations and balance gases as indicated. (Reprinted with permission from ref 350. Copyright 2000 Elsevier B.V.) (b) Zero-bias impedance of SSC ($x = 0.5$) on SDC at 800 °C and $P_{O_2} = 0.01$ atm as a function of total pressure. (Reprinted with permission from ref 184. Copyright 2001 Electrochemical Society, Inc.)

likely reflects a large utilization length since if the active region is already a significant fraction of the electrode bulk, any fluctuations in solid and gas composition resulting from gradients in gas concentration add little to the already large chemical capacitance.

The results reviewed above suggest that gas-phase diffusion can contribute significantly to polarization as O_2 concentrations as high as a few percent and are not necessarily identifiable as a separate feature in the impedance. Workers studying the P_{O_2} -dependence of the electrode kinetics are therefore urged to eliminate as much external mass-transfer resistance in their experiments as possible and verify experimentally (using variations in balance gas or total pressure) that gas-phase effects are not obscuring their results.

(2) *Cell geometry effects.* Figure 53a illustrates a typical cell configuration used by workers wishing to isolate the polarization losses of a specific SOFC electrode. In this case, the cell consists of a thin (10–500 μm) electrolyte with active (current bearing) electrodes on each side. The reference electrode is placed on the surface of the inactive (unelectroded) portion of the electrolyte, on one or both sides of the cell, some distance away from the edge of the active electrodes. Ideally, the purpose of this configuration is to measure the electrolyte potential along an equipotential surface “somewhere between the two active electrodes”. If two reference electrodes are used, they will yield redundant information (differing only in Nernst potential), provided they are placed a distance greater than ~ 3 electrolyte thicknesses from the edge of the active electrodes and the gas on each side of the cell is well mixed.³⁵⁰ Assuming this idealization, the total cell voltage losses (V_{total}) can be divided into two parts as shown in Figure 53b: V_A , which contains the overpotential of the first electrode plus some fraction of the electrolyte potential drop, and V_B , which contains the overpotential of the second electrode plus the remaining fraction

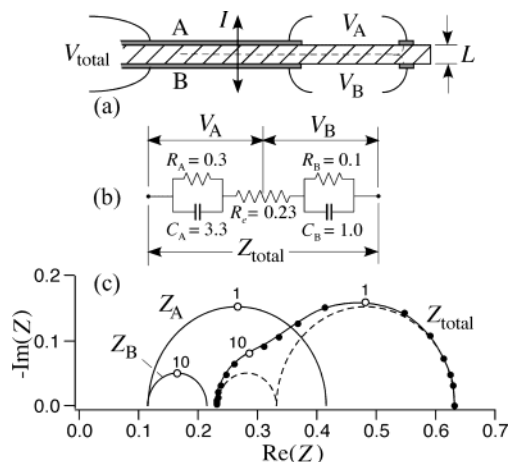


Figure 53. Idealized half-cell response of a thin solid electrolyte cell. (a) Cell geometry including working electrodes A and B and reference electrode(s). (b) Equivalent circuit model for the cell in a, where the electrolyte and two electrodes have area-specific resistances and capacitances as indicated. (c) Total cell and half-cell impedance responses, calculated assuming the reference electrode remains equipotential with a planar surface located somewhere in the middle of the active region, halfway between the two working electrodes, as shown in a.

of the electrolyte potential losses. Assuming this division can be achieved, Figure 53c illustrates the resulting separation of the total cell impedance into two ideal half-cell impedances, supposing (for the purposes of example) electrodes with simple linear RC behavior.

Although experimentalists often assume validity of the idealization shown in Figure 53, numerous studies have illustrated the difficulty of making accurate polarization measurements with this type of configuration.^{319,350–358} Nagata et al.³⁵¹ and Hsieh et al.³⁵² have shown experimentally that electrode geometries similar to Figure 53 can yield large inaccuracies in the measured steady-state electrode overpotential and impedance. A number of workers have since attempted to simulate these effects.^{319,350,353–355} In particular, Winkler et al.³⁵³ used the finite-element method to calculate the primary (infinite frequency) and secondary (zero frequency) d.c. potential distributions for various electrode geometries and reference electrode locations. These calculations showed that a slight *misalignment* of the active electrodes on a thin cell can cause a frequency-dependent displacement of the reference potential, leading to significant inaccuracies in the electrode resistance extracted from a.c. impedance measurements. Adler et al. corroborated these findings³⁵⁰ and more recently extended FEA analysis to include both the real and imaginary response, allowing determination of distortional effects on the impedance in arbitrary geometries over the entire frequency spectrum.³¹⁹

As an example, Figure 54a shows the zero-bias impedance of LSC electrodes on rare-earth-doped ceria in air at 750 °C measured using a symmetric cell incorporating a traditional reference electrode.³⁵⁰ Although the two screen-printed electrodes (1 and 2) were processed identically and aligned to an accuracy of ~ 0.1 mm, the cell response is highly asymmetric

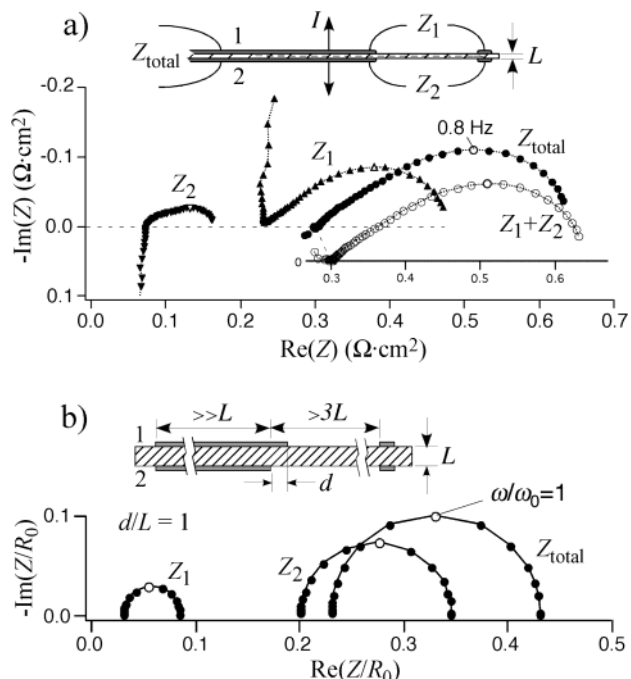


Figure 54. Measured (a) and simulated (b) effect of electrode misalignment. (a) Total-cell and half-cell impedances of a symmetric LSC/rare-earth-doped ceria/LSC cell with nominally identical porous LSC ($x = 0.4$) electrodes, measured at 750 °C in air based on the cell geometry shown.³⁵⁰ (b) Finite-element calculation of the total-cell and half-cell impedances of a symmetric cell with identical R–C electrodes, assuming a misalignment of the two working electrodes (d) equal to the thickness of the electrolyte (L).³¹⁹

with nearly 80% of the iR resistance being apportioned to electrode 2. The two half-cell impedances differ in both shape and magnitude and exhibit anomalous “capacitive” and “inductive” effects at high frequency (that sum to zero in the total impedance). In addition, despite high reproducibility of the total cell impedance from sample to sample, the scatter in the half-cell response among samples is substantial.³⁵⁰ One explanation for these effects is illustrated in Figure 54b, which shows a finite-element simulation of the half-cell impedance for identical “RC” electrodes, misaligned by a distance d equal to the thickness of the electrolyte ($d/L = 1$). This calculation suggests that the observations in Figure 54a may simply be caused by statistical variation in the alignment of the electrodes (which was subject to the limitations of a manually aligned screen printer in this case).

Furthermore, Boukamp³⁵⁸ and Adler³¹⁹ showed that when the electrodes on opposite sides of a cell are different from each other (as they are in a fuel cell), errors may not only involve a numerical scaling factor but also cross-contamination of anode and cathode frequency response in the measured half-cell impedances. For example, Figure 55a shows the calculated half-cell impedance of the cell idealized in Figure 53a, assuming alignment errors of ± 1 electrolyte thickness. Significant distortion of the half-cell impedances (Z_A and Z_B) from the actual impedance of the electrodes are apparent,³¹⁹ including “cross-talk”³⁵⁸ of anode and cathode frequency response (1 and 10 Hz, respectively), as well as a

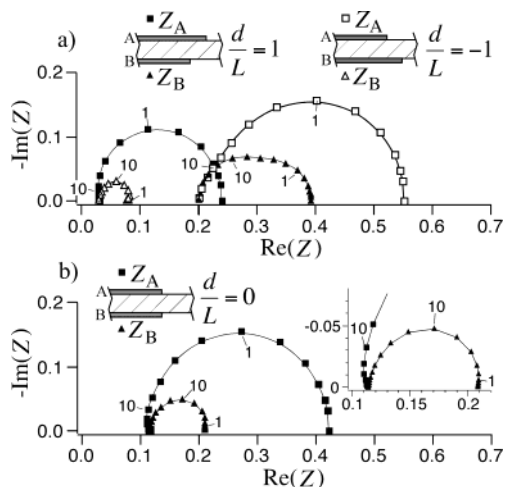


Figure 55. Simulated half-cell impedances of the cell shown in Figure 53, calculated using finite-element analysis.³¹⁹ (a) Half-cell responses assuming an electrode misalignment d/L equal to ± 1 , as defined in Figure 54c. (b) Half-cell responses assuming perfect electrode alignment ($d/L = 0$).

number of possible inductive artifacts. Figure 55b further shows that distortions of the impedance will occur even when alignment is perfect due to the inherent asymmetry of the potential distribution at intermediate frequency.³¹⁹ These results potentially call into question the interpretation of half-cell measurements on all thin electrolytes (particularly very thin, supported electrolytes), not only in terms of measurement error, but also possible misinterpretation of frequency artifacts as “steps” in the reaction mechanism.

A number of different approaches have been developed by workers to combat these problems. One has simply been to avoid half-cell measurements altogether, focusing instead on the response of symmetric cells at zero bias²⁸ or fuel cells under load where the anode impedance is either small or identifiable by frequency in the impedance spectrum.⁴⁰ Another approach has been to use a very thick electrolyte⁴⁰ (where alignment is less of an issue), ideally incorporating a reference electrode near the working electrode via a hole in the electrolyte.³⁵³ According to FEA simulations, the thick pellet approach appears to provide good accuracy³⁵³ as well as frequency isolation³¹⁹ but is generally limited to lower current densities due to finite compliance voltage and Joule heating of the sample. Workers have also proposed various microelectrode geometries that (in principle) should exhibit excellent frequency isolation.^{319,359,360} Early experimental results with this approach appear to be favorable,³⁶¹ but more work is needed to develop a truly robust and reliable way of doing half-cell measurements at arbitrary current densities and frequencies.

7. Conclusions and Outlook

The literature reviewed in sections 2–6 represents significant advances made in the last 20 years in our understanding of solid oxide fuel-cell cathodes. At the same time, however, this work has also underscored how *complex* the oxygen reduction reaction is, mak-

ing it difficult to provide a step-by-step prescription to developers or researchers for the way forward. Rather, here we simply attempt to summarize some of the general conclusions that have emerged from this large volume of work and also highlight areas where future work is likely to make an impact.

One theme that appears to emerge repeatedly in the literature reviewed above is that there is generally no one rate-determining step (RDS) on which to focus our attention. This absence of a RDS appears to arise from two fundamental factors. First, we saw that for oxygen to be incorporated as ionic current (O^{2-}) at the electrode/electrolyte interface, O_2 gas must first be converted to some “electroactive” intermediate form via one or more reaction steps, which we labeled as *chemical* processes (as defined in section 3.2). Since O_2 is a relatively stable molecule even at high temperature, it is perhaps not surprising that these chemical steps are often found to dominate the electrode polarization, even when interfacial electrochemical kinetic resistances are significant. Given that the microstructure is usually a compromise between improved surface area (lower firing temperature) vs improved interfacial contact (higher firing temperature), we are often likely to find optimized electrodes in a mixed regime where electrochemical and chemical contributions to the overpotential are somewhat balanced.

Second, we observed generically that the chemical portion of the reaction mechanism involves an ad(b)sorption step onto (or into) the electrode material, followed by an ambipolar transport step on (or within) the material to the interface (paths a–c–e or b–d–f in Figure 4). As shown in section 3.4, these ad(b)sorption and transport steps tend to be *co-limiting* in a porous microstructure, meaning that both determine the overall rate over a wide range of values of the relevant rate parameters. In section 6.4 we further saw that for composite microstructures (which most state-of-the-art cathodes are) the electrode kinetics also become co-limited by ohmic losses in the ionic subphase. Combining this observation with those in the preceding paragraph, we might expect an optimized composite electrode to be simultaneously limited by at least four physical processes: ad(b)sorption of oxygen, ambipolar transport to the solid–solid interface, interfacial electrochemical kinetics, and ionic transport in the ionic subphase. Conceivably, improvements to *any* of these processes will help overall performance to some degree.

However, as mentioned in section 6, our awareness of this situation is not the same as being able to quantify the contributions of these various physical processes to the performance of a particular electrode under a specific set of conditions or in understanding all the factors that govern the rates of these processes. Unfortunately, due to the inherently convoluted nature of electrochemical and chemical processes, it has proven extremely difficult to isolate and study these processes individually in a complex system. We saw in sections 3–5 that impedance techniques can in some cases be used to isolate the *linearized* resistance of the interface from that of slower chemical steps via time scale. Various workers

have also shown that by accounting for the interfacial double-layer capacitance, one can often quantify the interfacial resistance even when electrochemical and chemical time scales begin to merge. As with all impedance studies, however, these analyses are limited to linearized conditions and subject to the vagaries of modeling the interface as an equivalent circuit. New techniques are needed that have an ability to more unambiguously separate overlapping physical effects in both simple and complex microstructures.

Moreover, despite the many advances in electrochemical measurement and modeling, our understanding of SOFC cathode mechanisms remains largely circumstantial today. Our understanding often relies on having limited explanations for an observed phenomenon (e.g., chemical capacitance as evidence for bulk transport) rather than direct independent measures of the mechanism (e.g., spectroscopic evidence of oxidation/reduction of the electrode material). At various points in this review we saw that high-vacuum techniques commonly employed in electrocatalysis can be used in some limited cases for SOFC materials and conditions (PEEM, for example). New in-situ analytical techniques are needed, particularly which can be applied at ambient pressures, that can probe what is happening in an electrode as a function of temperature, P_{O_2} , polarization, local position, and time.

Throughout the review, we also saw that authors have made substantial progress (particularly in the last 5–7 years) deconvoluting overlapping effects by studying systems of controlled geometry or fabricated microstructures. Hopefully this work will continue and employ new analytical techniques (such as tracer incorporation or local probes of composition and/or thermodynamic potentials) in order to make quantitative measurements of the rate-limiting steps involved. At the same time, it remains important to extend these techniques to commercially relevant microstructures both experimentally and theoretically. Advanced characterization methods such as FIB–SEM, SIMS, and AFM, combined with the many advances made in finite-element modeling, may make it increasingly possible to treat these more complex cases.

One particularly neglected issue appears to be the matching of the microstructure to the important length scales governing the mechanism. Composite electrodes are normally optimized according to the simple paradigm that increased TPB area is a good thing. However, is this always the case? For example, consider a composite electrode consisting of doped ceria and a perovskite mixed conductor. As mentioned in section 6.4, we might expect the mixed conductor, even within the composite, to exhibit a “local” utilization length (l_b^{local}) determining the extension of the TPB beyond each interparticle contact. If all particles are smaller than this distance, then the perovskite particles will be diffusionally equilibrated locally. In this situation we might not want a high TPB area but rather a very high surface area mixed conductor with more moderately sized ceria particles offering a very efficient ionic transport

path. While this is just a hypothetical example, it illustrates how understanding of the mechanism, combined with appropriate new fabrication techniques, might allow a more directed approach to electrode microstructural design.

Another neglected issue, from both a practical and fundamental perspective, is nonstationary behavior, including degradation. Why electrode performances change with time, polarization history, or other factors is very poorly understood but of significant concern to developers. SOFC stack design is very sensitive to the exact performance of the cell, and these stacks are expected to have a service life of at least 5–10 years. Yet the reported performances and degradation rates of SOFC cathodes vary so tremendously from lab to lab that it is difficult to compare, let alone choose, a material system without a substantial independent development effort. If some of these seemingly “random” variables were better identified, it would not only accelerate development but also likely aid fundamental research (by eliminating factors that otherwise obscure what workers are trying to study).

Finally, we have also seen substantial advances in electrode modeling in the last 5–10 years, including new techniques for nonlinear and time-dependent phenomena. These efforts must continue in order to achieve improved *quantitative* linkages among performance, microstructure, and materials properties. However, as mentioned in section 4.7, there is generally a dearth of independent property data for many of the physical processes entering these models. New techniques are needed that can isolate select physical processes, particularly involving the surface of electrode materials. For example, while bulk diffusion in mixed conductors is relatively well understood, it has proven difficult to isolate the rate of surface diffusion independent of the bulk. Also, tracer techniques have allowed us to measure the linearized exchange rate of oxygen on a mixed conductor surface, but it remains largely unknown how the rates of absorption/desorption depend on driving force when substantial displacements from equilibrium are involved.

8. Acknowledgments

The author would first like to acknowledge the many workers who have contributed to this line of research over the last 20 years, whose work has been cited herein. He would also like to thank several individuals for helpful discussions and/or careful readings of the manuscript: Scott Barnett, Roger deSouza, Raymond Gorte, Ronald Imbuhl, Allan Jacobson, Juergen Janek, Tatsuya Kawada, Joachim Maier, Augustin McEvoy, Steve McIntosh, Ian Metcalfe, Andreas Mitterdorfer, John Newman, Steven Russek, Brian Steele, Eric Stuve, and Harry Tuller. Preparation of the manuscript was also aided substantially on a logistic level by Ladonna Kennedy, Lai Lu, and Ryan Reed. Finally, the author would also like to thank his department, students, and family for their patience during the preparation and revision of the manuscript.

9. Nomenclature

a (cm ² /cm ³)	surface area per unit volume
α_a, α_c (dimensionless)	anodic and cathodic transfer coefficients
C_i (F/cm ²)	capacitance associated with process or lengthscale i
c_i (mol/cm ³ or mol/cm ²)	bulk or surface concentration of species i
d (cm)	diameter or other characteristic length
δ (dimensionless)	oxygen nonstoichiometry in ABO _{3-δ}
D^* (cm ² /s)	oxygen tracer diffusion coefficient
D_i (cm ² /s)	single component diffusion coefficient for species i
\bar{D} (cm ² /s)	chemical (ambipolar) diffusion coefficient
ϵ (dimensionless)	porosity
ϕ (dimensionless)	fraction of interface permitting passage of current
f (dimensionless)	a thermodynamic factor ($-\partial\mu_{O_2}/\partial\delta$)/ RT
F (C/mol)	Faraday's constant (96,487 C/mol)
η (V)	overpotential
I (A)	total current
i (A/cm ²)	current density
i_0 (A/cm ²)	exchange current density
J (dimensionless)	ratio of ohmic constriction to interfacial resistance
k, k^* (cm/s or s ⁻¹)	surface exchange coefficient
" k " (Ω -cm ³)	volume-specific interfacial resistance in a composite
L (cm)	thickness
l_δ (cm)	utilization length
l_g (cm)	characteristic length of a porous microstructure
μ_i (J/mol)	chemical or electrochemical potential of species i
N_i (mol/area/s)	flux of species " i "
P_{O_2} (bar)	partial pressure of oxygen
ρ (Ω -cm)	resistivity
r_0 (mol/cm ² /s)	equilibrium gas-surface exchange rate
r_i (mol/cm ² /s)	area-specific reaction rate involving species i
R (J/mol/K)	ideal gas constant (8.314 J/mol/K)
R_i (Ω -cm ²)	area-specific resistance associated with process i
σ_i (Ω^{-1} cm ⁻¹)	ionic conductivity
T (K or °C)	temperature
t (s)	time
τ (dimensionless)	tortuosity
t_i (dimensionless)	transference number for species i
V (V)	voltage
V_m (cm ³ /mol)	molar volume (on a formula-unit basis)
ω (s ⁻¹)	frequency in radians
x, y (position) (cm)	position
x, y (stoich) (dimensionless)	A-site or B-site stoichiometry parameters
Z (Ω or Ω -cm ²)	impedance

10. Glossary of Commonly Used Acronyms

AFM	atomic force microscopy
CDC	Ca-doped ceria (Ce _{1-x} Ca _x O _{2-x/2})
ESB	erbium-doped bismuth oxide
EIS	electrochemical impedance spectroscopy
FEA	finite-element analysis
FIB-SEM	SEM cross-sectional imaging using focused ion beams

GDC	gadolinia-doped ceria (Ce _{1-x} Gd _x O _{2-x/2})
GDE	gas-diffusion electrode
HRTEM	high-resolution transmission electron microscopy
LCM	La _{1-x} Ca _x MnO ₃
LM	La _x MnO ₃
LSC	La _{1-x} Sr _x CoO _{3-δ}
LSCF	La _{1-x} Sr _x Co _{1-y} Fe _y O _{3-δ}
LSF	La _{1-x} Sr _x FeO _{3-δ}
LSGM	La _{0.8} Sr _{0.2} Ga _{0.8} Mg _{0.2} O _{2.8}
LSM	La _{1-x} Sr _x MnO _{3$\pm$$\delta$}
LZ	lanthanum zirconate (La ₂ Zr ₂ O ₇)
PEEM	photoelectron emission microscopy
SEM	scanning electron microscopy
SIMS	secondary-ion mass spectrometry
SOFC	solid oxide fuel cell
SDC	samarium-doped ceria (Ce _{1-x} Sm _x O _{2-x/2})
SSC	Sm _{0.5} Sr _{0.5} CoO _{3-δ}
SZ	strontium zirconate
TPB	three-phase (or triple-phase) boundary
XPS	X-ray photoelectron spectroscopy
XRD	X-ray diffraction (powder)
YSZ	yttria-stabilized zirconia (Zr _{1-x} Y _x O _{2-x/2})

11. Glossary of Some Commonly Used Terms

chemical (or "pseudo") capacitance	a macroscopically observed capacitive relationship between current and voltage arising from chemical oxidation/reduction of a material or other charge-compensated accumulation of species
chemical (or "ambipolar") diffusion	diffusion of neutral combinations of ionic and/or electronic species under a chemical potential (concentration) driving force
chemical process	a physical or chemical rate process that may occur at a rate independent of current and is driven by a chemical-potential driving force
co-limited reaction	Situation in a porous gas-diffusion electrode wherein the utilization length and steady-state flow of current depends on both kinetic and transport properties
electrochemical kinetic process	a kinetic process involving a net faradaic current across an interface and is driven by an electrochemical potential driving force
mixed conductor	a material containing both mobile ions and mobile electrons (including holes and/or small polarons)
three-phase (or "triple-phase") boundary (TPB)	the one-dimensional interface within an electrode microstructure where gaseous, electronic, and ionic subphases meet
utilization length (l_δ)	size of the active region within a porous electrode, established by a balance of reaction and transport rates at steady state (see co-limited reaction)

12. References

- (1) Alcock, C. B. *Solid State Ionics* **1992**, 53-56, 3.
- (2) Kilner, J.; Benson, S.; Lane, J.; Waller, D. *Chem. Ind.* **1997**, 907.
- (3) Mazanec, T. J. *Solid State Ionics* **1994**, 70/71, 11.
- (4) Mobius, H. H. *J. Solid State Electrochem.* **1997**, 1, 2.

- (5) Singhal, S. C. *Proc. Electrochem. Soc.* **1998**, 97–24, 125.
- (6) Badwal, S. P. S.; Foger, K. *Mater. Forum* **1997**, 21, 187.
- (7) Yamamoto, O. *Electrochim. Acta* **2000**, 45, 2423.
- (8) Steele, B. C. H. *Solid State Ionics* **2000**, 134, 3.
- (9) Skinner, S. J. *Int. J. Inorg. Mater.* **2001**, 3, 113.
- (10) Will, J.; Mitterdorfer, A.; Kleinlogel, C.; Perednis, D.; Gauckler, L. J. *Solid State Ionics* **2000**, 131, 79.
- (11) McEvoy, A. J. *J. Mater. Sci.* **2001**, 36, 1087.
- (12) Ormerod, R. M. *Chem. Soc. Rev.* **2003**, 32, 17.
- (13) Yamamoto, O.; Takeda, Y.; Kanno, R.; Tomida, Y. *Nippon Kagaku Kaishi* **1988**, 1324.
- (14) Godickemeier, M.; Sasaki, K.; Gauckler, L. J.; Riess, I. *Solid State Ionics* **1996**, 86–88, 691.
- (15) Kilner, J. A. *Bol. Soc. Esp. Ceram. Vidrio* **1998**, 37, 247.
- (16) Steele, B. C. H.; Hori, K. M.; Uchino, S. *Solid State Ionics* **2000**, 135, 445.
- (17) Godickemeier, M.; Sasaki, K.; Gauckler, L. J.; Riess, I. *J. Electrochem. Soc.* **1997**, 144, 1635.
- (18) Lane, J. A.; Adler, S.; Middleton, P. H.; Steele, B. C. H. *Solid Oxide Fuel Cells (SOFC-IV)*; 1995; pp 584–96.
- (19) Maguire, E.; Gharbage, B.; Marques, F. M. B.; Labrincha, J. A. *Solid State Ionics* **2000**, 127, 329.
- (20) Rohland, B. *Mater. Sci. Forum* **1991**, 76, 149.
- (21) Takahashi, T.; Ihara, M.; Yamada, K. *Proc. Electrochem. Soc.* **1995**, 95–1, 1009.
- (22) Colomer, M. T.; Steele, B. C. H.; Kilner, J. A. *Solid State Ionics* **2002**, 147, 41.
- (23) Steele, B. C. H. *Solid State Ionics* **1997**, 94, 239.
- (24) Dusastre, V.; Kilner, J. A. *Solid State Ionics* **1999**, 126, 163.
- (25) Schafer, W.; Koch, A.; HeroldSchmidt, U.; Stolten, D. *Solid State Ionics* **1996**, 86–8, 1235.
- (26) Liu, W.; Zhang, Z. P.; Xia, C. R.; Xie, J. Q.; Chen, C. S. *J. Inorg. Mater.* **2000**, 15, 849.
- (27) Endo, A.; Fukunaga, H.; Wen, C.; Yamada, K. *Solid State Ionics* **2000**, 135, 353.
- (28) Adler, S. B. *Solid State Ionics* **1998**, 111, 125.
- (29) Murray, E. P.; Barnett, S. A. *Proc. Electrochem. Soc.* **1999**, 99–19, 369.
- (30) Jorgensen, M. J.; Primdahl, S.; Bagger, C.; Mogensen, M. *Solid State Ionics* **2001**, 139, 1.
- (31) Jorgensen, M. J.; Mogensen, M. *J. Electrochem. Soc.* **2001**, 148, A433.
- (32) Lu, Z.-G.; Jiang, Y.; Dong, Y.-L.; Zhang, Y.-H.; Yan, J.-W. *Gaodeng Xuexiao Huaxue Xuebao* **2001**, 22, 791.
- (33) Murray, E. P.; Barnett, S. A. *Solid State Ionics* **2001**, 143, 265.
- (34) Barbucci, A.; Bozzo, R.; Cerisola, G.; Costamagna, P. *Electrochim. Acta* **2002**, 47, 2183.
- (35) Murray, E. P.; Sever, M. J.; Barnett, S. A. *Solid State Ionics* **2002**, 148, 27.
- (36) Hart, N. T.; Brandon, N. P.; Day, M. J.; Lapena-Rey, N. *J. Power Sources* **2002**, 106, 42.
- (37) Steele, B. C. R. *Acad. Sci. Serie II Fascicule C: Chim.* **1998**, 1, 533.
- (38) Kleitz, M.; Petitbon, F. *Solid State Ionics* **1996**, 92, 65.
- (39) Jorgensen, M. J.; Holtappels, P.; Appel, C. C. *J. Appl. Electrochem.* **2000**, 30, 411.
- (40) McIntosh, S.; Adler, S. B.; M, V. J.; Gorte, R. A. *Electrochem. Solid State Lett.* **2004**, 7, A111.
- (41) Schmid, A.; Enke, F., Eds.; Stuttgart, 1923.
- (42) Vetter, K. J. *Electrochemical Kinetics, Theoretical and Experimental Aspects*; Academic Press: New York, 1967.
- (43) Srinivasan, S.; Hurwitz, H. D.; Bockris, J. O. M. *J. Phys. Chem.* **1967**, 46, 3108.
- (44) Giner, J.; Hunter, C. *J. Electrochem. Soc.* **1969**, 116, 1125.
- (45) Perry, M. L.; Newman, J.; Cairns, E. J. *J. Electrochem. Soc.* **1998**, 145, 5.
- (46) Kleitz, M.; Kloidt, T.; Dessemond, L. *High-Temperature Electrochemical Behavior of Fast Ion and Mixed Conductors*; Roskilde: Denmark, 1993; p 89.
- (47) Newman, J. S. *Electrochemical Systems*, 2nd ed.; Prentice Hall: New York, 1991.
- (48) Bauerle, J. E. *J. Phys. Chem.: Solids* **1969**, 30, 2657.
- (49) MacDonald, J. R. *Impedance Spectroscopy; Emphasizing Solid Materials and Systems*; John Wiley and Sons: New York, 1987.
- (50) Wang, D. Y.; Nowick, A. S. *J. Electrochem. Soc.* **1979**, 126, 1166.
- (51) Wang, D. Y.; Nowick, A. S. *J. Electrochem. Soc.* **1979**, 126, 1155.
- (52) Okamoto, H.; Kawamura, G.; Kudo, T. *Electrochim. Acta* **1983**, 28, 379.
- (53) Hu, H.; Liu, M. *J. Electrochem. Soc.* **1997**, 144, 3561.
- (54) Schouler, E.; Giroud, G.; Kleitz, M. *J. Chim. Phys.* **1973**, 70, 1309.
- (55) Kleitz, M.; Dessemond, L.; Kloidt, T.; Steil, M. C. *Solid Oxide Fuel Cells IV*; 1995; pp 527–536.
- (56) van Herle, J.; McEvoy, A. J. *J. Phys. Chem. Solids* **1994**, 55, 339.
- (57) Verkerk, M. J.; Burggraaf, A. J. *J. Electrochem. Soc.* **1983**, 130, 78.
- (58) Lewis, R.; Gomer, R. *Surf. Sci.* **1968**, 12, 157.
- (59) Mizusaki, J.; Amano, K.; Yamauchi, S.; Fueki, K. *Solid State Ionics* **1987**, 22, 313.
- (60) Mizusaki, J.; Amano, K.; Yamauchi, S.; Fueki, K. *Solid State Ionics* **1987**, 22, 323.
- (61) Wang, D. Y. *J. Electrochem. Soc.* **1990**, 137, 3660.
- (62) van Hassel, B. A.; Boukamp, B. A.; Burggraaf, A. J. *Solid State Ionics* **1991**, 48, 139.
- (63) Robertson, N. L.; Michaels, J. N. *J. Electrochem. Soc.* **1990**, 137, 129.
- (64) van Herle, J.; McEvoy, A. J. *Ber. Bunsen-Ges.-Phys. Chem. Chem. Phys.* **1993**, 97, 470.
- (65) Schwandt, C.; Weppner, W. *J. Electrochem. Soc.* **1997**, 144, 3728.
- (66) Kenjo, T.; Shiroichi, N. *Electrochim. Acta* **1997**, 42, 3461.
- (67) Luerssen, B.; Janek, J.; Imbihl, R. *Solid State Ionics* **2001**, 141, 701.
- (68) Janek, J.; Rohnke, M.; Luerssen, B.; Imbihl, R. *Phys. Chem. Chem. Phys.* **2000**, 2, 1935.
- (69) Boukamp, B. A.; Bouwmeester, H. J. M. *Solid State Ionics* **2003**, 157, 29.
- (70) Kamata, H.; Hosaka, A.; Mizusaki, J.; Tagawa, H. *Solid State Ionics* **1998**, 106, 237.
- (71) Gerischer, H. *Z. Phys. Chem.* **1951**, 198, 216.
- (72) Mitterdorfer, A.; Gauckler, L. J. *Solid State Ionics* **1999**, 117, 187.
- (73) Mitterdorfer, A.; Gauckler, L. J. *Solid State Ionics* **1999**, 117, 203.
- (74) Mitterdorfer, A.; Gauckler, L. J. *Solid State Ionics* **1999**, 120, 211.
- (75) Berthier, F.; Diard, J.-P.; Le Gorrec, B.; Montella, C. *Corrosion* **1995**, 51, 105.
- (76) Gland, J. L.; Sexton, B. A.; Fisher, G. B. *Surf. Sci.* **1980**, 95, 587.
- (77) Gorte, R.; Schmidt, L. D. *Surf. Sci.* **1978**, 76, 559.
- (78) Lewis, R.; Gomer, R. *Surf. Sci.* **1968**, 12, 157.
- (79) Verkerk, M. J.; Hammink, M. W. J.; Burggraaf, A. J. *J. Electrochem. Soc.* **1983**, 130.
- (80) Kenjo, T.; Yamakoshi, Y.; Wada, K. *J. Electrochem. Soc.* **1993**, 140, 2151.
- (81) Sasaki, K.; Tamura, J.; Dokiya, M. *Solid State Ionics* **2001**, 144, 223.
- (82) Widmer, S.; Tate, T. J.; Thampi, K. R.; McEvoy, A. J. *Solid Oxide Fuel Cells V; Aachen: Germany*, 1997; pp 451–461.
- (83) McEvoy, A. J. *Solid State Ionics* **2000**, 132, 159.
- (84) Mitterdorfer, A. Ph.D., Swiss Federal Institute of Technology, 1997.
- (85) Robertson, N. L.; Michaels, J. N. *J. Electrochem. Soc.* **1991**, 138, 1494.
- (86) Kenjo, T.; Tsukamoto, K. *Solid Oxide Fuel Cells V; Aachen: Germany*, 1997; pp 431–440.
- (87) Schouler, E. J. L.; Kleitz, M. *J. Electrochem. Soc.* **1987**, 134, 1045.
- (88) Chao, T.; Walsh, K. J.; Fedkiw, P. S. *Solid State Ionics* **1991**, 47, 277.
- (89) Sridhar, S.; Stancovski, V.; Pal, U. B. *J. Electrochem. Soc.* **1997**, 144, 2479.
- (90) Jacobsen, T.; Zachau-Christiansen, B.; Bay, L.; Jorgensen, M. *J. Electrochim. Acta* **2001**, 46, 1019.
- (91) Shkerin, S. N.; Perfilov, M. V. *Elektrokhimiya* **1990**, 26, 1468.
- (92) Shkerin, S. N.; Perfilov, M. V. *Soviet Electrochem.* **1992**, 28, 1106.
- (93) von Oertzen, A.; Mikhailov, A.; Rotermund, H. H.; Ertl, G. *Surf. Sci.* **1996**, 350, 259.
- (94) Emery, D. A.; Middleton, P. H.; Metcalfe, I. S. *Surf. Sci.* **1998**, 405, 308.
- (95) Bay, L.; Jacobsen, T. *Solid State Ionics* **1997**, 93, 201.
- (96) Svensson, A. M.; Nisancioglu, K. *J. Electrochem. Soc.* **1998**, 145, 3130.
- (97) Luerssen, B.; Janek, J.; Günther, S.; Kiskinova, M.; Imbihl, R. *Phys. Chem. Chem. Phys.* **2002**, 4, 2673.
- (98) Kleitz, M.; Dessemond, L.; Kloidt, T. *Solid Oxide Fuel Cells IV*; 1995; pp 35–44.
- (99) van Hassel, B. A.; Boukamp, B. A.; Burggraaf, A. J. *Solid State Ionics* **1992**, 51, 161.
- (100) Ohno, Y.; Nagata, S.; Sato, H. *Solid State Ionics* **1981**, 3/4, 439.
- (101) Takeda, Y.; Kanno, R.; Noda, M.; Yamamoto, O. *Bull. Inst. Chem. Res.* **1986**, 64, 157.
- (102) Raccach, P. M.; Goodenough, J. B. *Phys. Rev.* **1967**, 155, 932.
- (103) Jaya, S. M.; Jagadish, R.; Rao, R. S.; Asokamani, R. *Phys. Rev. B* **1991**, 43, 13274.
- (104) Ishikawa, T.; Park, S. K.; Katsufuji, T.; Arima, T.; Tokura, Y. *Phys. Rev. B* **1998**, 58, 13326.
- (105) Raccach, P. M.; Goodenough, J. B. *J. Appl. Phys.* **1968**, 39, 1209.
- (106) Bhide, V. G.; Rajoria, D. S.; Reddy, Y. S.; Rao, G. R.; Rao, G. V. S.; Rao, C. N. R. *Phys. Rev. Lett.* **1972**, 27, 1133.
- (107) Bhide, V. G.; Rajoria, D. S.; Rao, C. N. R.; Rao, G. R.; Jadhao, V. G. *Phys. Rev. B* **1975**, 12, 2832.
- (108) Ganguly, P.; Kumar, P. S. A.; Santhosh, P. N.; Mulla, I. S. *J. Phys.: Condens. Matter* **1994**, 6, 533.
- (109) Senaris-Rodríguez, M. A.; Goodenough, J. B. *J. Solid State Chem.* **1995**, 118, 323.

- (110) Takahashi, H.; Munakata, F.; Yamanaka, M. *Phys. Rev. B* **1998**, *57*, 15211.
- (111) Caciuffo, R.; Mira, J.; Rivas, J.; Seneris-Rodriguez, M. A.; Radaelli, P. G.; Carsughi, F.; Fiorani, D.; Goodenough, J. B. *Europhys. Lett.* **1999**, *45*, 399.
- (112) Mizusaki, J.; Tabuchi, J.; Matsuura, T.; Yamauchi, S.; Fueki, K. *J. Electrochem. Soc.* **1987**, *136*, 2082.
- (113) Petrov, A. N.; Kononchuk, O. F.; Andreev, A. V.; Cherepanov, V. A.; Kofstad, P. *Solid State Ionics* **1995**, *80*, 189.
- (114) Chainani, A.; Mathew, M.; Sarma, D. D. *Phys. Rev. B* **1993**, *48*, 14818.
- (115) Torrance, J. B.; Lacorre, P.; Asavaroengchai, C.; Metzger, R. M. *Physica C* **1991**, *182*, 351.
- (116) Mizusaki, J.; Sasamoto, T.; Cannon, W. R.; Bowen, H. K. *J. Am. Ceram. Soc.* **1983**, *66*, 247.
- (117) Tai, L.-W.; Nasrallah, M. M.; Anderson, H. U.; Sparlin, D. M.; Sehlin, S. R. *Solid State Ionics* **1995**, *76*, 259.
- (118) Stevenson, J. W.; Armstrong, T. R.; Carneim, R. D.; Pederson, L. R.; Weber, W. J. *J. Electrochem. Soc.* **1996**, *143*, 2722.
- (119) Mizusaki, J.; Yoshihiro, M.; Yamauchi, S.; Fueki, K. *J. Solid State Chem.* **1985**, *58*, 257.
- (120) Allnatt, A. R.; Lidiard, A. B. *Atomic Transport in Solids*; Cambridge University Press: New York, 1993.
- (121) Mizusaki, J.; Mima, Y.; Yamauchi, S.; Fueki, K.; Tagawa, H. *J. Solid State Chem.* **1989**, *80*, 102.
- (122) Petrov, A. N.; Cherepanov, V. A.; Kononchuk, O. F.; Gavrilo, L. Y. *J. Solid State Chem.* **1990**, *87*, 69.
- (123) Lankhorst, M. H. R.; Bouwmeester, H. J. M. *J. Electrochem. Soc.* **1997**, *144*, 1268.
- (124) Kawada, T.; Suzuki, J.; Sase, M.; Kaimai, A.; Yashiro, K.; Nigara, Y.; Mizusaki, J.; Kawamura, K.; Yugami, H. *J. Electrochem. Soc.* **2002**, *149*, E252.
- (125) Lankhorst, M. H. R.; Bouwmeester, H. J. M.; Verweij, H. *Phys. Rev. Lett.* **1996**, *77*, 2989.
- (126) Lankhorst, M. H. R.; Bouwmeester, H. J. M.; Verweij, H. *J. Solid State Chem.* **1997**, *133*, 555.
- (127) Lankhorst, M. H. R.; Bouwmeester, H. J. M.; Verweij, H. *Solid State Ionics* **1997**, *96*, 21.
- (128) Tai, L.-W.; Nasrallah, M. M.; Anderson, H. U.; Sparlin, D. M.; Sehlin, S. R. *Solid State Ionics* **1995**, *76*, 273.
- (129) Lankhorst, M. University of Twente, 1997.
- (130) Lankhorst, M. H. R.; ten Elshof, J. E. *J. Solid State Chem.* **1997**, *130*, 302.
- (131) Teraoka, Y.; Zhang, H. M.; Okamoto, K.; Yamazoe, N. *Mater. Res. Bull.* **1988**, *23*, 51.
- (132) Teraoka, Y.; Nobunaga, T.; Okamoto, K.; Miura, N.; Yamazoe, N. *Solid State Ionics* **1991**, *48*, 207.
- (133) Diethelm, S.; Closset, A.; Nisancioglu, K.; Van herle, J.; McEvoy, A. J.; Gur, T. M. *J. Electrochem. Soc.* **1999**, *146*, 2606.
- (134) Kilner, J. A.; Steele, B. C. H.; Ilkov, L. *Solid State Ionics* **1984**, *12*, 89.
- (135) Ishigaki, T.; Yamauchi, S.; Kishio, K.; Mizusaki, J.; Fueki, K. *J. Solid State Chem.* **1988**, *73*, 179.
- (136) Bouwmeester, H. J. M.; Kruidhof, H.; Burggraaf, A. J. *Solid State Ionics* **1994**, *72*, 185.
- (137) Kilner, J. A.; Souza, R. A. D.; Fullarton, I. C. *Solid State Ionics* **1996**, *86–88*, 703.
- (138) Routbort, J. L.; Doshi, R.; Krumpelt, M. *Solid State Ionics* **1996**, *90*, 21.
- (139) van Doorn, R. H. E.; Fullarton, I. C.; de Souza, R. A.; Kilner, J. A.; Bouwmeester, H. J. M.; Burggraaf, A. J. *Solid State Ionics* **1997**, *96*, 1.
- (140) De Souza, R. A.; Kilner, J. A. *Solid State Ionics* **1998**, *106*, 175.
- (141) De Souza, R. A.; Kilner, J. A. *Solid State Ionics* **1999**, *126*, 153.
- (142) Bredesen, R.; Mertins, F.; Norby, T. *Catal. Today* **2000**, *56*, 315.
- (143) Ma, B.; Balachandran, U.; Park, J. H.; Segre, C. U. *Solid State Ionics* **1996**, *83*, 65.
- (144) ten Elshof, J. E.; Lankhorst, M. H. R.; Bouwmeester, H. J. M. *Solid State Ionics* **1997**, *99*, 15.
- (145) ten Elshof, J. E.; Lankhorst, M. H. R.; Bouwmeester, H. J. M. *J. Electrochem. Soc.* **1997**, *144*, 1060.
- (146) Lane, J. A.; Benson, S. J.; Waller, D.; Kilner, J. A. *Solid State Ionics* **1999**, *121*, 201.
- (147) Kriegel, R.; Pippardt, U.; Voigt, I. *Sep. Purif. Technol.* **2001**, *25*, 127.
- (148) Chen, X.; Adler, S. B. Manuscript in preparation.
- (149) Fueki, K.; Mizusaki, J.; Yamauchi, S.; Ishigaki, T.; Mima, Y. 10th International Symposium on the Reactivity of Solids; pp 339–343.
- (150) ten Elshof, J. E.; Bouwmeester, H. J. M.; Verweij, H. *Solid State Ionics* **1995**, *81*, 97.
- (151) ten Elshof, J. E.; Bouwmeester, H. J. M.; Verweij, H. *Solid State Ionics* **1996**, *89*, 81.
- (152) Figueiredo, F. M.; Marques, F. M. B.; Frade, J. R. *Solid State Ionics* **1998**, *111*, 273.
- (153) Kim, S.; Yang, Y. L.; Jacobson, A. J.; Abeles, B. *Solid State Ionics* **1998**, *106*, 189.
- (154) Zhang, C.; Deng, H.; Varon, J.; Abeles, B.; Yang, Y.; Pham, A. Q.; Jacobson, A. J. *MRS* **1994**, *1*.
- (155) Garbage, B.; Pagnier, T.; Hammou, A. *J. Electrochem. Soc.* **1994**, *141*, 2118.
- (156) Van Herle, J.; McEvoy, A. J.; Thampi, K. R. *Electrochim. Acta* **1994**, *39*, 1675.
- (157) Mizusaki, J.; Saito, T.; Tagawa, H. *J. Electrochem. Soc.* **1996**, *143*, 3065.
- (158) Masuda, K.; Kawada, T.; Kaimai, A.; Kawamura, K.; Nigara, Y.; Mizusaki, J.; Yugami, H.; Arashi, H. *5th International Symposium on Solid Oxide Fuel Cells*; Aachen: Germany, 1997; p 473.
- (159) Ioroi, T.; Hara, T.; Uchimoto, Y.; Ogumi, Z.; Takehara, Z. *J. Electrochem. Soc.* **1997**, *144*, 1362.
- (160) Ioroi, T.; Hara, T.; Uchimoto, Y.; Ogumi, Z.; Takehara, Z. *J. Electrochem. Soc.* **1998**, *145*, 1999.
- (161) Kawada, T.; Masuda, K.; Suzuki, J.; Kaimai, A.; Kawamura, K.; Nigara, Y.; Mizusaki, J.; Yugami, H.; Arashi, H.; Sakai, N.; Yokokawa, H. *Solid State Ionics* **1999**, *121*, 271.
- (162) Yang, Y. L.; Chen, C. L.; Chen, S. Y.; Chu, C. W.; Jacobson, A. J. *J. Electrochem. Soc.* **2000**, *147*, 4001.
- (163) Fukunaga, H.; Koyama, M.; Takahashi, N.; Wen, C.; Yamada, K. *Solid State Ionics* **2000**, *132*, 279.
- (164) Mims, C. A.; Joos, N. I.; van der Heide, P. A. W.; Jacobson, A. J.; Chen, C.; Chiu, C. W.; Kim, B. I.; Perry, S. S. *Electrochem. Solid State Lett.* **2000**, *3*, 59.
- (165) Yang, Y.; Jacobson, A. J.; Chen, C. L.; Luo, G. P.; Ross, K. D.; Chu, C. W. *Appl. Phys. Lett.* **2001**, *79*, 776.
- (166) Ringuede, A.; Fouletier, J. *Solid State Ionics* **2001**, *139*, 167.
- (167) Endo, A.; Ihara, M.; Komiya, H.; Yamada, K. *Solid State Ionics* **1996**, *86–88*, 1191.
- (168) Adler, S. B. *Solid State Ionics* **2000**, *135*, 603.
- (169) Liu, M.; Winnick, J. *J. Electrochem. Soc.* **1997**, *144*, 1881.
- (170) Liu, M.; Winnick, J. *Solid State Ionics* **1999**, *118*, 11.
- (171) Adler, S. B.; Lane, J. A.; Steele, B. C. H. *J. Electrochem. Soc.* **1996**, *143*, 3554.
- (172) Svensson, A. M.; Sunde, S.; Nisancioglu, K. *Solid State Ionics* **1996**, *86–88*, 1211.
- (173) Abeles, B. *Proc. Electrochem. Soc.* **1997**, *96–27*, 1.
- (174) Deng, H.; Zhou, M.; Abeles, B. *Solid State Ionics* **1994**, *74*, 75.
- (175) Bae, J. M.; Steele, B. C. H. *Solid State Ionics* **1998**, *106*, 255.
- (176) Zhou, M.; Deng, H.; Abeles, B. *Solid State Ionics* **1996**, *93*, 133.
- (177) Shirman, J.; Lane, J.; Kilner, J. A. Electrochemical Society Meeting, 1997; p 2129.
- (178) Steele, B. C. H.; Bae, J.-M. *Solid State Ionics* **1998**, *106*, 255.
- (179) Endo, A.; Wada, S.; Wen, C.-J.; Komiya, H.; Yamada, K. *J. Electrochem. Soc.* **1998**, *145*, L35.
- (180) Horita, T.; Yamaji, K.; Sakai, N.; Yokokawa, H.; Weber, A.; Ivers-Tiffée, E. *J. Electrochem. Soc.* **2001**, *148*, A456.
- (181) Horita, T.; Yamaji, K.; Sakai, N.; Yokokawa, H.; Weber, A.; Ivers-Tiffée, E. *Electrochim. Acta* **2001**, *46*, 1837.
- (182) Jiang, S. P. *Solid State Ionics* **2002**, *146*, 1.
- (183) Fleig, J. *Ann. Rev. Mater. Res.* **2003**, *33*, 361.
- (184) Koyama, M.; Wen, C. J.; Masuyama, T.; Otomo, J.; Fukunaga, H.; Yamada, K.; Eguchi, K.; Takahashi, H. *J. Electrochem. Soc.* **2001**, *148*, A795.
- (185) Svensson, A. M.; Sunde, S.; Nisancioglu, K. *J. Electrochem. Soc.* **1997**, *144*, 2719.
- (186) Svensson, A. M.; Sunde, S.; Nisancioglu, K. *J. Electrochem. Soc.* **1998**, *145*, 1390.
- (187) Liu, M.; Wu, Z. *Solid State Ionics* **1998**, *107*, 105.
- (188) Liu, M. L. *J. Electrochem. Soc.* **1998**, *145*, 142.
- (189) Adler, S. B.; Lane, J. A.; Steele, B. C. H. *J. Electrochem. Soc.* **1997**, *144*, 1884.
- (190) van Doorn, R. H. E. University of Twente, 1996.
- (191) van Doorn, R. H. E.; Burggraaf, A. J. *Solid State Ionics* **2000**, *128*, 65.
- (192) Fleig, J. *J. Power Sources* **2002**, *105*, 228.
- (193) Fleig, J.; Maier, J. 203 Meeting of the Electrochemical Society, Paris, 2003; p 509.
- (194) Fleig, J. *Annu. Rev. Mater. Sci.* **2003**.
- (195) Maier, J. *Solid State Ionics* **1998**, *112*, 197.
- (196) Maier, J. *preprint* **1999**, *1*.
- (197) Maier, J.; Jamnik, J.; Leonhardt, M. *Solid State Ionics* **2000**, *129*, 25.
- (198) Kuznecov, M.; Otschik, P.; Eichler, K.; Schaffrath, W. *Ber. Bunsen-Ges.-Phys. Chem. Chem. Phys.* **1998**, *102*, 1410.
- (199) Coffey, G. W.; Pederson, L. R.; Rieke, P. C. *J. Electrochem. Soc.* **2003**, *150*, A1139.
- (200) Atkinson, A.; Ramos, T. *Solid State Ionics* **2000**, *129*, 259.
- (201) Adler, S. B. *J. Am. Ceram. Soc.* **2001**, *84*, 2117.
- (202) Mizusaki, J.; Tagawa, H.; Naraya, K.; Sasamoto, T. *Solid State Ionics* **1991**, *49*, 111.
- (203) Takeda, Y.; Kanno, R.; Noda, M.; Tomida, Y.; Yamamoto, O. *J. Electrochem. Soc.: Electrochem. Sci. Technol.* **1987**, *134*, 2656.
- (204) Mizusaki, J.; Tagawa, H.; Tsuneyoshi, K.; Sawata, A. *J. Electrochem. Soc.* **1991**, *138*, 1867.
- (205) Nagata, M.; Hotta, H.; Iwahara, H. *J. Appl. Electrochem.* **1994**, *24*, 411.
- (206) Sasaki, K.; Wurth, J. P.; Gschwend, R.; Godickemeier, M.; Gauckler, L. J. *J. Electrochem. Soc.* **1996**, *143*, 530.

- (207) Fukunaga, H.; Ihara, M.; Sakaki, K.; Yamada, K. *Solid State Ionics* **1996**, *86–88*, 1179.
- (208) van Heuveln, F. H.; Bouwmeester, H. J. M.; vanBerkel, F. P. F. *J. Electrochem. Soc.* **1997**, *144*, 126.
- (209) van Heuveln, F. H.; Bouwmeester, H. J. M. *J. Electrochem. Soc.* **1997**, *144*, 134.
- (210) Ostergard, M. J. L.; Mogensen, M. *Electrochim. Acta* **1993**, *38*, 2015.
- (211) Siebert, E.; Hammouche, A.; Kleitz, M. *Electrochim. Acta* **1995**, *40*, 1741.
- (212) Lauret, H.; Hammou, A. *J. Eur. Ceram. Soc.* **1996**, *16*, 447.
- (213) Lee, H. Y.; Cho, W. S.; Oh, S. M.; Wiemhofer, H. D.; Gopel, W. *J. Electrochem. Soc.* **1995**, *142*, 2659.
- (214) Kuznecov, M.; Otschik, P.; Obenaus, P.; Eichler, K.; Schaffrath, W. *Solid State Ionics* **2003**, *157*, 371.
- (215) Mitterdorfer, A.; Gauckler, L. J. *Solid State Ionics* **1998**, *111*, 185.
- (216) Poulsen, F. W. *Solid State Ionics* **2000**, *129*, 145.
- (217) Chakraborty, A.; Choudhury, P.; Maiti, H. S. *Proc. Electrochem. Soc.* **1995**, *95–1*, 612.
- (218) Kim, M. C.; Park, S. J. *Yoop Hakhoechi* **1992**, *29*, 900.
- (219) Li, Z.; Behruzi, M.; Fuerst, L.; Stoeber, D. *Proc. Electrochem. Soc.* **1993**, *93–4*, 171.
- (220) Hammouche, A.; Siebert, E.; Hammou, A.; Kleitz, M.; Caneiro, A. *J. Electrochem. Soc.* **1991**, *138*, 1212.
- (221) Tofield, B. C.; Scott, W. R. J. *Solid State Chem.* **1974**, *10*, 183.
- (222) Yokokawa, H.; Horita, T.; Sakai, N.; Dokiya, M.; Kawada, T. *Solid State Ionics* **1996**, *86–88*, 1161.
- (223) Tanasescu, S.; Totir, N. D.; Marchidan, D. I. *Electrochim. Acta* **1998**, *43*, 1675.
- (224) Hammouche, A.; Siebert, E.; Kleitz, M.; Hammou, A. *Proc. Electrochem. Soc.* **1989**, *89–11*, 265.
- (225) Hammouche, A.; Siebert, E.; Hammou, A.; Kleitz, M.; Caneiro, A. *J. Electrochem. Soc.* **1991**, *138*, 1212.
- (226) Jiang, S. P.; Love, J. G. *Solid State Ionics* **2001**, *138*, 183.
- (227) Horita, T.; Yamaji, K.; Sakai, N.; Yokokawa, H.; Kato, T. *J. Electrochem. Soc.* **2001**, *148*, J25.
- (228) Brichzin, V.; Fleig, J.; Habermeier, H. U.; Cristiani, G.; Maier, J. *Solid State Ionics* **2002**, *152–153*, 499.
- (229) Horita, T.; Yamaji, K.; Ishikawa, M.; Sakai, N.; Yokokawa, H.; Kawada, T.; Kato, T. *J. Electrochem. Soc.* **1998**, *145*, 3196.
- (230) Horita, T.; Yamaji, K.; Sakai, N.; Yokokawa, H.; Kawada, T.; Kato, T. *Solid State Ionics* **2000**, *127*, 55.
- (231) Horita, T.; Yamaji, K.; Sakai, N.; Xiong, X. P.; Kato, T.; Yokokawa, H.; Kawada, T. *J. Power Sources* **2002**, *106*, 224.
- (232) Jiang, Y.; Wang, S.; Zhang, Y.; Yan, J.; Li, W. *Solid State Ionics* **1998**, *110*, 111.
- (233) Jiang, Y.; Wang, S.; Zhang, Y.; Yan, J.; Li, W. *J. Electrochem. Soc.* **1998**, *145*, 373.
- (234) Jorgensen, M. J.; Primdahl, S.; Mogensen, M. *Electrochim. Acta* **1999**, *44*, 4195.
- (235) Jiang, S. P.; Love, J. G.; Zhang, J. P.; Hoang, M.; Ramprakash, Y.; Hughes, A. E.; Badwal, S. P. S. *Solid State Ionics* **1999**, *121*, 1.
- (236) Tsukuda, H.; Yamashita, A. 1st European Solid Oxide Fuel Cells Forum, Oct 3–7, 1994, Baden, Switzerland, 1994.
- (237) Monceau, D.; Petot, C.; Petotervas, G. *Solid State Ionics* **1991**, *45*, 231.
- (238) Petot, C.; Armanet, F.; Klimczyk, H.; Petotervas, G. *Solid State Ionics* **1992**, *50*, 87.
- (239) Petotervas, G.; Petot, C.; Monceau, D.; Loudjani, M. *Solid State Ionics* **1992**, *53–6*, 270.
- (240) Belova, I. V.; Brown, M. J.; Murch, G. E. *Acta Mater.* **2003**, *51*, 1821.
- (241) Brown, M. J.; Belova, I. V.; Murch, G. E. *Phil. Mag.* **2003**, *83*, 1855.
- (242) Martin, M. *J. Chem. Thermodyn.* **2003**, *35*, 1291.
- (243) Kawada, T.; Sakai, N.; Yokokawa, H.; Dokiya, M.; Anzai, I. *Solid State Ionics* **1992**, *50*, 189.
- (244) Tedmon, C. S., Jr.; Spacil, H. S.; Mitoff, S. P. *J. Electrochem. Soc.: Electrochem. Sci.* **1969**, *1969*, 1170.
- (245) Lau, S. K.; Singhal, S. C. *Proc. Corrosion* **1985**, *85*, 79.
- (246) Takeda, Y.; Hoshino, Y.; Sakaki, Y.; Kawahara, T.; Imanishi, N.; Yamamoto, O. *J. Mater. Sci. Lett.* **1992**, *11*, 1113.
- (247) Takeda, Y.; Sakaki, Y.; Ichikawa, T.; Imanishi, N.; Yamamoto, O.; Mori, M.; Abe, T. *Solid State Ionics* **1994**, *72*, 257.
- (248) Takeda, Y.; Ueno, H.; Imanishi, N.; Yamamoto, O.; Sammes, N.; Philipps, M. B. *Solid State Ionics* **1996**, *86–8*, 1187.
- (249) Kostogloudis, G. C.; Tsiniarakis, G.; Ftikos, C. Personal communication, 1999.
- (250) Chen, C. C.; Nasrallah, M. M.; Anderson, H. U. *Proc. Electrochem. Soc.* **1993**, *93–4*, 598.
- (251) Simner, S. P.; Shelton, J. P.; Anderson, M. D.; Stevenson, J. W. *Solid State Ionics* **2003**, *161*, 11.
- (252) Yokokawa, H.; Sakai, N.; Kawada, T.; Dokiya, M. *J. Electrochem. Soc.* **1991**, *138*, 2719.
- (253) Yokokawa, H.; Sakai, N.; Kawada, T.; Dokiya, M. *Solid State Ionics* **1992**, *52*, 43.
- (254) Labrincha, J. A.; Frade, J. R.; Marques, F. M. B. *J. Mater. Sci.* **1993**, *28*, 3809.
- (255) Poulsen, F. W.; Vanderpuil, N. *Solid State Ionics* **1992**, *53–6*, 777.
- (256) Vanroosmalen, J. A. M.; Cordfunke, E. H. P. *Solid State Ionics* **1992**, *52*, 303.
- (257) Yamamoto, O.; Takeda, Y.; Kanno, R.; Kojima, T. First International Symposium on Solid Oxide Fuel Cells, 1989; p 242.
- (258) Ostergard, M. J. L.; Clausen, C.; Bagger, C.; Mogensen, M. *Electrochim. Acta* **1995**, *40*, 1971.
- (259) Stochniol, G.; Syskakis, E.; Naoumidis, A. *J. Am. Ceram. Soc.* **1995**, *78*, 929.
- (260) Stochniol, G.; Broel, S.; Naoumidis, A.; Nickel, H. *Fresenius J. Anal. Chem.* **1996**, *355*, 697.
- (261) Anastogloudis, G. C.; Ftikos, C. *Solid State Ionics* **1999**, *126*, 143.
- (262) Yokokawa, H.; Horita, T.; Sakai, N.; Kawada, T.; Dokiya, M. First European Solid Oxide Fuel Cell Forum, Baden-Baden, 1994; p 425.
- (263) Horita, T.; Yamaji, K.; Negishi, H.; Sakai, N.; Yokokawa, H.; Kato, T. *Solid State Ionics* **2000**, *136–137*, 897.
- (264) Clausen, C.; Bagger, C.; Bildesorensen, J. B.; Horsewell, A. *Solid State Ionics* **1994**, *70*, 59.
- (265) Mitsuyasu, H.; Eguchi, K.; Arai, H. *Solid State Ionics* **1997**, *100*, 11.
- (266) Wiik, K.; Schmidt, C. R.; Shamsili, S.; Einarsrud, M. A.; Grande, T. *High Temp. Electrochem.: Ceram. Met., Proc. Risoe Int. Symp. Mater. Sci.*, *17th* **1996**, 491–496.
- (267) Wiik, K.; Schmidt, C. R.; Faaland, S.; Shamsili, S.; Einarsrud, M. A.; Grande, T. *J. Am. Ceram. Soc.* **1999**, *82*, 721.
- (268) Bertrand, G. L.; Caboche, G.; Domenichini, B.; Dufour, L. C. *Surf. Interface Anal.* **2000**, *30*, 561.
- (269) Kuscer, D.; Holc, J.; Hrovat, M.; Bernik, S.; Samardzija, Z.; Kolar, D. *Solid State Ionics* **1995**, *78*, 79.
- (270) Bae, J. M.; Steele, B. C. H. *Solid State Ionics* **1998**, *106*, 247.
- (271) Dusastre, V.; Steele, B. C. H. Personal communication, 1997.
- (272) Appel, C. C.; Bonanos, N. *J. Eur. Ceram. Soc.* **1999**, *19*, 847.
- (273) Uchikoshi, T.; Sakka, Y.; Hiraga, K. *J. Electrocer.* **1999**, *4*, 113.
- (274) De Souza, M. F.; De Souza, D. P. F. *J. Mater. Sci.* **1999**, *34*, 6107.
- (275) Steele, B. C. H. *Solid State Ionics* **2000**, *129*, 95.
- (276) Kawada, T.; Sakai, N.; Yokokawa, H.; Dokiya, M. *Solid State Ionics* **1992**, *53–6*, 418.
- (277) Manning, P. S.; Sirman, J. D.; Kilner, J. A. *Solid State Ionics* **1996**, *93*, 125.
- (278) Manning, P. S.; Sirman, J. D.; De Souza, R. A.; Kilner, J. A. *Solid State Ionics* **1997**, *100*, 1.
- (279) Horita, T.; Yamaji, K.; Sakai, N.; Ishikawa, M.; Yokokawa, H.; Kawada, T.; Dokiya, M. *Electrochem. Solid State Lett.* **1998**, *1*, 4.
- (280) Bozo, C.; Guilhaume, N.; Herrmann, J. M. *J. Catal.* **2001**, *203*, 393.
- (281) Putna, E. S.; Bunluesin, T.; Fan, X. L.; Gorte, R. J.; Vohs, J. M.; Lakis, R. E.; Egami, T. *Catal. Today* **1999**, *50*, 343.
- (282) Lu, C.; Worrell, W. L.; Vohs, J. M.; Gorte, R. J. *J. Electrochem. Soc.* **2003**, *150*, A1357.
- (283) van Hassel, B. A.; Boukamp, B. A.; Burggraaf, A. J. *Solid State Ionics* **1992**, *53–6*, 890.
- (284) van Hassel, B. A.; Burggraaf, A. J. *Solid State Ionics* **1992**, *57*, 193.
- (285) Kim, J. H.; Choi, G. M. *Solid State Ionics* **2000**, *130*, 157.
- (286) Boukamp, B. A.; Raming, T. P.; Winnubst, A. J. A.; Verweij, H. *Solid State Ionics* **2003**, *158*, 381.
- (287) Kahlich, M. J.; Gasteiger, H. A.; Behm, R. J. *J. Catal.* **1999**, *182*, 430.
- (288) Liu, H. C.; Kozlov, A. I.; Kozlova, A. P.; Shido, T.; Iwasawa, Y. *Phys. Chem. Chem. Phys.* **1999**, *1*, 2851.
- (289) Schubert, M. M.; Hackenberg, S.; van Veen, A. C.; Muhler, M.; Plzak, V.; Behm, R. J. *J. Catal.* **2001**, *197*, 113.
- (290) Fabry, P.; Schouler, E.; Kleitz, M. *Electrochim. Acta* **1978**, *23*, 539.
- (291) Lane, J. A.; Middleton, P. H.; Fox, H.; Steele, B. C. H.; Kilner, J. A. 2nd International Symposium on Ionic and Mixed Conducting Ceramics, 1994; pp 489–504.
- (292) Sahibzada, M.; Benson, S. J.; Rüdken, R. A.; Kilner, J. A. *Solid State Ionics* **1998**, *115*, 285.
- (293) Chavan, S. V.; Tyagi, A. K. *Thermochim. Acta* **2002**, *390*, 79.
- (294) Longo, V.; Meriani, S.; Ricciardiello, F. *J. Am. Ceram. Soc.* **1981**, *64*, C38.
- (295) Sorokina, S. L.; Skolis, Y. Y.; Kovba, M. L.; Levitskii, V. A. *Zh. Fiz. Khim.* **1986**, *60*, 310.
- (296) Tsai, T.; Barnett, S. A. *Solid State Ionics* **1997**, *98*, 191.
- (297) Tsai, T.; Perry, E.; Barnett, S. *J. Electrochem. Soc.* **1997**, *144*, L130.
- (298) Simner, S. P.; Bonnett, J. F.; Canfield, N. L.; Meinhardt, K. D.; Sprenkle, V. L.; Stevenson, J. W. *Electrochem. Solid State Lett.* **2002**, *5*, A173.
- (299) Simner, S. P.; Bonnett, J. R.; Canfield, N. L.; Meinhardt, K. D.; Shelton, J. P.; Sprenkle, V. L.; Stevenson, J. W. *J. Power Sources* **2003**, *113*, 1.

- (300) Kenjo, T.; Osawa, S.; Fujikawa, K. *J. Electrochem. Soc.* **1991**, *138*, 349.
- (301) Kenjo, T.; Nishiya, M. *Solid State Ionics* **1992**, *57*, 295.
- (302) Austin, L. G.; Ariet, M.; Walker, R. D.; Wood, G. B.; Comyn, R. H. *Ind. Eng. Chem. Fundam.* **1965**, *4*, 321.
- (303) Newman, J.; Tiedemann, W. *AIChE J.* **1975**, *21*, 25.
- (304) Juhl, M.; Primdahl, S.; Manon, C.; Mogensen, M. *J. Power Sources* **1996**, *61*, 173.
- (305) Mogensen, M.; Skaarup, S. *Solid State Ionics* **1996**, *86–88*, 1151.
- (306) Tanner, C. W.; Fung, K. Z.; Virkar, A. V. *J. Electrochem. Soc.* **1997**, *144*, 21.
- (307) Virkar, A. V.; Chen, J.; Tanner, C. W.; Kim, J. W. *Solid State Ionics* **2000**, *131*, 189.
- (308) Kim, J. D.; Kim, G. D.; Moon, J. W.; Lee, H. W.; Lee, K. T.; Kim, C. E. *Solid State Ionics* **2000**, *133*, 67.
- (309) Kim, J.-D.; Kim, G.-D.; Park, J.-A. *Han'guk Seramik Hakhoehchi* **2000**, *37*, 227.
- (310) Mogensen, M.; Primdahl, S.; Jorgensen, M. J.; Bagger, C. J. *Electroceram.* **2000**, *5*, 141.
- (311) Figueiredo, F. M.; Frade, J. R.; Marques, F. M. B. *Solid State Ionics* **2000**, *135*, 463.
- (312) Figueiredo, F. M.; Marques, F. M. B.; Frade, J. R. *J. Electroceram.* **2001**, *7*, 47.
- (313) Xia, C.; Rauch, W.; Wellborn, W.; Liu, M. *Electrochem. Solid State Lett.* **2002**, *5*, A217.
- (314) Sunde, S. *J. Electroceramics* **2000**, *5*, 153.
- (315) Huang, Y.; Vohs, J. M.; Gorte, R. J. Submitted for publication.
- (316) Huang, Y.; Ahn, K.; Vohs, J. M.; Gorte, R. J. Submitted for publication.
- (317) van Heuveln, F. H.; van Berkel, F. P. F.; Huijsmans, J. P. P. *High-Temperature Electrochemical Behavior of Fast Ion and Mixed Conductors*; Roskilde: Denmark, 1993; p 53.
- (318) Fleig, J.; Pham, P.; Sztulzaft, P.; Maier, J. *Solid State Ionics* **1998**, *113–115*, 739.
- (319) Adler, S. B. *J. Electrochem. Soc.* **2002**, *149*, E166.
- (320) McIntosh, S.; Vohs, J. M.; Gorte, R. J. *J. Electrochem. Soc.* **2003**, *150*, A470.
- (321) Singhal, S. C. *Solid Oxide Fuel Cells V*; Aachen: Germany, 1997; pp 37–50.
- (322) Choi, J. H.; Jang, J. H.; Ryu, J. H.; Oh, S. M. *J. Power Sources* **2000**, *87*, 92.
- (323) Minh, N. Q. *J. Am. Ceram. Soc.* **1993**, *76*, 563.
- (324) Iwata, T. *J. Electrochem. Soc.* **1996**, *143*, 1521.
- (325) Murata, K.; Shimotsu, M. *Electrochem.* **1999**, *67*, 789.
- (326) Primdahl, S.; Mogensen, M. *J. Appl. Electrochem.* **2000**, *30*, 247.
- (327) Umemura, F.; Amano, K.; Michibata, H.; Kimura, A. *Denki Kagaku* **1995**, *63*, 128.
- (328) Choi, J. H.; Jang, J. H.; Oh, S. M. *Electrochim. Acta* **2001**, *46*, 867874.
- (329) Jiang, S. P.; Love, J. G. *Solid State Ionics* **2003**, *158*, 45.
- (330) Hilpert, K.; Das, D.; Miller, M.; Peck, D. H.; Weiss, R. J. *Electrochem. Soc.* **1996**, *143*, 3642.
- (331) Quadakkers, W. J.; Greiner, H.; Hansel, M.; Pattanaik, A.; Khanna, A. S.; Mallener, W. *Solid State Ionics* **1996**, *91*, 55.
- (332) Badwal, S. P. S.; Deller, R.; Foger, K.; Ramprakash, Y.; Zhang, J. P. *Solid State Ionics* **1997**, *99*, 297.
- (333) Matsuzaki, Y.; Yasuda, I. *Solid State Ionics* **2000**, *132*, 271.
- (334) Matsuzaki, Y.; Yasuda, I. *J. Electrochem. Soc.* **2001**, *148*, A126.
- (335) Jiang, S. P.; Zhang, J. P.; Zheng, X. G. *J. Eur. Ceram. Soc.* **2002**, *22*, 361.
- (336) Lee, H. Y.; Oh, S. M. *Solid State Ionics* **1996**, *90*, 133.
- (337) Tu, H. Y.; Takeda, Y.; Imanishi, N.; Yamamoto, O. *Solid State Ionics* **1997**, *100*, 283.
- (338) Brant, M. C.; Dessemond, L. *Solid State Ionics* **2000**, *138*, 1.
- (339) Brant, M. C.; Matencio, T.; Dessemond, L.; Domingues, R. Z. *Chem. Mater.* **2001**, *13*, 3954.
- (340) Khandkar, A. C.; Elangovan, S.; Liu, M.; Timper, M. *Thermal Cycle Fatigue Behavior of High-Temperature Electrodes*; Ceramtec, Inc.: 1994.
- (341) Hsiao, Y. C.; Selman, J. R. *Solid State Ionics* **1997**, *98*, 33.
- (342) Primdahl, S.; Mogensen, M. *J. Electrochem. Soc.* **1998**, *145*, 2431.
- (343) Primdahl, S.; Mogensen, M. *J. Electrochem. Soc.* **1999**, *146*, 2827.
- (344) Deng, H.; Zhou, M.; Abeles, B. *Solid State Ionics* **1994**, *1*.
- (345) van Herle, J.; McEnvoy, A. J.; Thampi, K. R. *Electrochim. Acta* **1996**, *41*, 1447.
- (346) Kim, J. D.; Kim, G. D.; Moon, J. W.; Park, Y. I.; Lee, W. H.; Kobayashi, K.; Nagai, M.; Kim, C. E. *Solid State Ionics* **2001**, *143*, 379.
- (347) Yoon, S. P.; Nam, S. W.; Kim, S.-G.; Hong, S.-A.; Hyun, S.-H. *J. Power Sources* **2003**, *115*, 27.
- (348) Bird, R. B.; Stewart, W. E.; Lightfoot, E. N. *Transport Phenomena*, 2nd ed.; John Wiley and Sons: New York, 2002.
- (349) *Perry's Chemical Engineers' Handbook*, 50th ed.; Perry, R. H., Green, D. W., Maloney, J. O., Eds.; McGraw-Hill: New York, 1984.
- (350) Adler, S. B.; Henderson, B. T.; Wilson, M. A.; Taylor, D. M.; Richards, R. E. *Solid State Ionics* **2000**, *134*, 35.
- (351) Nagata, M.; Itoh, Y.; Iwahara, H. *Solid State Ionics* **1994**, *67*, 215.
- (352) Hsieh, G.; Mason, T. O.; Garboczi, E. J.; Pederson, L. R. *Solid State Ionics* **1997**, *96*, 153.
- (353) Winkler, J.; Hendriksen, P. V.; Bonanos, N.; Mogensen, M. *J. Electrochem. Soc.* **1998**, *145*, 1184.
- (354) Figueiredo, F. M.; Frade, J.; Marques, F. M. B. *Boletín De La Sociedad Espanola De Ceramica Y Vidrio* **1999**, *38*, 639.
- (355) Kato, T.; Momma, A.; Kaga, Y.; Nagata, S.; Kasuga, Y.; Kitase, M. *Solid State Ionics* **2000**, *132*, 287.
- (356) Myland, J. C.; Oldham, K. B. *Anal. Chem.* **2000**, *72*, 3972.
- (357) Oldham, K. B.; Stevens, N. P. C. *Anal. Chem.* **2000**, *72*, 3981.
- (358) Boukamp, B. A. *Solid State Ionics* **2001**, *143*, 47.
- (359) Hashibon, A.; Raz, S.; Riess, I. *Solid State Ionics* **2002**, *149*, 167.
- (360) Fleig, J. *Solid State Ionics* **2003**, *161*, 279.
- (361) Adler, S. B. Manuscript in preparation.
- (362) Bard, A. J.; Faulkner, L. R. *Electrochemical Methods*, 2nd ed.; John Wiley and Sons: 2001.
- (363) Vetter, K. J.; Manecke, G. *Z. Phys. Chem.* **1950**, *195*, 337.
- (364) Jimenez, R.; Kloidt, T.; Kleitz, M. *J. Electrochem. Soc.* **1997**, *144*, 582.
- (365) Kuo, J. H.; Anderson, H. U.; Sparlin, D. M. *J. Solid State Chem.* **1989**, *83*, 52.
- (366) In prior publications (refs 28 and 168) the term “non-charge-transfer” has been used to describe such neutral flows. However, this terminology has sometimes generated unintended confusion and/or controversy, since many chemical processes not resulting in a net flow of current do involve charge transfer at the atomic/molecular level (e.g., chemisorption). To avoid this confusion, the term “chemical” is hereby instated in this review to describe processes that are driven by chemical potential driving forces and may occur at a rate decoupled from the faradaic current while the term “electrochemical” is restricted to processes involving net passage of faradaic (noninterfacially polarizing) current due to an electrochemical potential driving force.
- (367) In this case the exchange coefficient k has units of s^{-1} (rather than the usual cm/s) because of the reduced dimensionality of the system, i.e., fluxes are written in terms of surface concentrations rather than volumetric concentration.
- (368) For this estimate, values for the surface diffusion coefficient (D) and the surface exchange coefficient (k) in eq 2 were obtained by linearizing Mitterdorfer's rate expressions for surface transport and adsorption/desorption (ref 84) and re-expressing in terms of the driving forces in eq 2.
- (369) These expressions for R_{chem} , C_{δ} , and l_{δ} have the same meaning as R_{chem} , $C_{chem} = (l_{chem}/R_{chem})$, and δ , respectively, as defined in the original cited articles (refs 171 and 28). However, the nomenclature and parameters used here have been updated both to aid clarity and improve consistency with eqs 3–7. In particular, the length parameter previously symbolized as “ δ ” in the cited papers has been renamed “ l_{δ} ” to avoid confusion with the oxygen nonstoichiometry δ in $ABO_{3-\delta}$. The subscript on the chemical capacitance has also been made more specific to indicate the size of the region disturbed by concentration gradients.

Direct Hydrocarbon Solid Oxide Fuel Cells

Steven McIntosh and Raymond J. Gorte*

Department of Chemical and Biomolecular Engineering, University of Pennsylvania, Philadelphia, Pennsylvania 19104

Received October 31, 2003

Contents

1. Introduction	4845
2. SOFC Fundamentals	4846
2.1. Definition of Direct Utilization SOFC	4846
2.2. Basic Operating Principles of SOFC	4846
2.3. Anode Three-Phase Boundary	4847
2.4. SOFC Thermodynamics	4848
2.5. SOFC Electrode Losses	4849
2.6. Electrode Characterization	4850
3. Carbon Formation	4851
4. Operation of SOFC on Hydrocarbon Fuels	4852
4.1. SOFC with Ni-Based Anodes	4853
4.2. Ceramic Anodes	4854
5. Copper-Based Anodes	4856
5.1. Preparation Methods	4856
5.2. Catalysis	4858
5.3. Fuel Dependences and Sulfur Tolerance	4860
5.4. Impact of Fuel Utilization	4861
5.5. Anodes Based on Alloys	4861
5.6. Carbon-Based Anodes	4862
6. Conclusions	4863
7. Acknowledgments	4863
8. References	4863

1. Introduction

The promise of direct and efficient conversion of chemical to electrical energy makes fuel cell development an area of great technological interest. The advantages over traditional power generation systems are numerous. Most prominent is the increased efficiency associated with directly converting chemical energy to electrical energy. Fuel cells are not subject to the Carnot-cycle limitations, and unlike high-efficiency turbines, exhibit their highest efficiency at low loads. Fuel cells do not produce significant quantities of NO_x , SO_x , or particulate pollutants. Compared to normal batteries, fuel cells can have much higher energy densities and can be recharged more quickly and easily. Finally, fuel cells can be applied in applications that require both low and high power outputs, and they can be modular and portable.

One of the main limitations of current fuel cell technologies is the requirement that the fuel be



Steven McIntosh was born in Dundee, Scotland in 1977. He received his Bachelor of Engineering in Chemical Engineering from the University of Edinburgh in 1999. He is currently completing his Ph.D. degree at the University of Pennsylvania. The focus of his thesis is the development and characterization of direct-hydrocarbon solid oxide fuel cells. After a postdoctoral year, he will start as an Assistant Professor in Chemical Engineering at the University of Virginia in 2005.



Dr. R. J. Gorte joined the faculty at the University of Pennsylvania in 1981 after receiving his Ph.D. from the University of Minnesota. He is currently the Russell Pearce and Elizabeth Crimian Heuer Professor of Chemical Engineering. Since joining Penn, Dr. Gorte has served as Chairman of Chemical Engineering from 1995 to 2000 and was the Carl V. S. Patterson Professor of Chemical Engineering from 1996 through 2001. He has received a number of awards, including the 1997 Parravano Award of the Michigan Catalysis Society, the 1998 Philadelphia Catalysis Club Award, the 1999 Paul Emmett Award of the North American Catalysis Society, and the 2001 Penn Engineering Distinguished Research Award. He is on the Board of Editors of *Journal of Molecular Catalysis A* and the *Journal of Catalysis*.

hydrogen. Although hydrogen is often referred to as being the ideal fuel of the future, there are a number of problems relating to hydrogen generation and storage that must be overcome before it can be

* Author to whom correspondence should be addressed. E-mail: gorte@seas.upenn.edu. Tel: (215) 898-4439. Fax: (215) 573-2093.

implemented on a wide scale. One of the biggest problems is that, at the present time, an estimated 96% of hydrogen is produced by reforming hydrocarbons,¹ and even with highly optimized large-scale production, between 20 and 30% of the fuel value of the hydrocarbons is lost during this process.¹ A second major problem for portable applications is fuel storage since it is difficult and expensive to store hydrogen in a form that has an energy density comparable to that of hydrocarbon liquids. Until other sources of hydrogen become available and hydrogen-storage problems are resolved, it is difficult to see how hydrogen can make major inroads as a fuel supply.

A major advantage of solid oxide fuel cells (SOFC) is that they have much greater fuel flexibility due to the fact that O^{2-} anions are the species transported through the membrane. This allows SOFC to operate, in principle, on any combustible fuel. A second advantage of SOFC is that they operate at high temperatures where the waste heat can be used either for running steam turbines or for running the endothermic, steam-reforming reactions. Indeed, both of these concepts are used in prototype SOFC units. The high operating temperatures of SOFC, required for sufficient oxygen-ion conductivity, are an advantage for utilizing waste heat. While the high operating temperatures have caused early work on SOFC to be focused on large-scale applications, a number of groups are currently working on small to medium sized systems for battery replacement and auxiliary power units.²⁻¹¹

There have already been a number of excellent reviews describing many aspects of SOFC,¹²⁻²³ and we will not try to duplicate that literature. For information on stack designs and cells operating on H_2 or on synthesis gas (a mixture of H_2 and CO) produced by reforming, we refer the reader to those other reviews. In this review, we will focus on recent work aimed at operating SOFC directly on hydrocarbon fuels and on anode materials that are compatible with direct hydrocarbon utilization. We have further restricted the scope to the performance and analysis of single-cell systems. While stacks that operate directly on hydrocarbons will likely need to be different from more traditional stacks, the development of direct-utilization SOFC is still in its infancy, with only one report of preliminary data on the stack level.²⁴

We will begin this paper with a very brief tutorial covering the fundamental principles of SOFC operation before examining the important issues and current status of research relating to direct-utilization SOFC. The most critical issue for SOFC operating on hydrocarbon fuels without reforming is the need for anodes that do not catalyze carbon formation at the high SOFC operating temperatures. Because Ni-based anodes do not appear to be suitable for direct utilization, we will only briefly review work on these anodes. Finally, because relatively few groups have worked on direct utilization, this review will have a heavy emphasis on our own work at the University of Pennsylvania.

2. SOFC Fundamentals

2.1. Definition of Direct Utilization SOFC

There has been some controversy in the literature over precisely what should be called direct oxidation or direct utilization of hydrocarbons in an SOFC.²⁵ As pointed out by Marina and Mogensen²⁶ and Park et al.,²⁷ direct, electrochemical oxidation of complex hydrocarbons is unlikely to occur in one step. Even in the case of methane, the reaction produces eight electrons and must almost certainly occur in multiple steps.

It has been argued that all steps in the reaction must be electrochemical in nature for the process to be called direct oxidation.²⁵ According to this definition, any process that involves cracking of the hydrocarbon on the anode material, followed by electrochemical oxidation of the cracking products, should not be considered to be direct oxidation. The primary reason for using this narrow definition for direct oxidation is that the open-circuit voltage (OCV) of the cell will be equal to the theoretical, Nernst potential if there are no other losses and if all steps in the oxidation mechanism are electrochemical.

However, applying a similar definition to heterogeneous catalysts, one would probably conclude that there is no such thing as a hydrocarbon oxidation catalyst. For example, considering methane oxidation by O_2 over a heterogeneous Pd catalyst, the first step almost certainly involves C–H bond scission to form carbon-containing surface species on the Pd.²⁸ These surface species are then oxidized in subsequent steps. Using the same definition for heterogeneous oxidation as has been used for direct oxidation in SOFC, Pd should probably be considered a cracking catalyst that is also capable of oxidizing the cracking products. Similarly, it seems unlikely that electrochemical oxidation of hydrocarbons could ever occur without catalytic components in the anode promoting C–H and C–C bond scissions. Such a strict definition of direct oxidation based on mechanistic steps does not seem either practical or useful to us.

First, we will refer to the direct use of hydrocarbon fuels in an SOFC as direct utilization rather than direct oxidation. Second, we recognize that the broadest definition of direct utilization, exclusive from mechanistic considerations, should include rather conventional use of fuel by internal reforming, with steam being cofed to the fuel cell with the hydrocarbon. Indeed, this nomenclature has been used for many years with molten-carbonate fuel cells.^{29,30} However, because internal reforming is essentially limited to methane and because the addition of steam with the fuel adds significant system complexity, we will focus primarily on systems and materials in which the hydrocarbons are fed to the fuel cell directly without significant amounts of water or oxygen.

2.2. Basic Operating Principles of SOFC

The operating principles behind an SOFC are shown schematically in Figure 1. Like all fuel cells, the SOFC consists of three main components: a

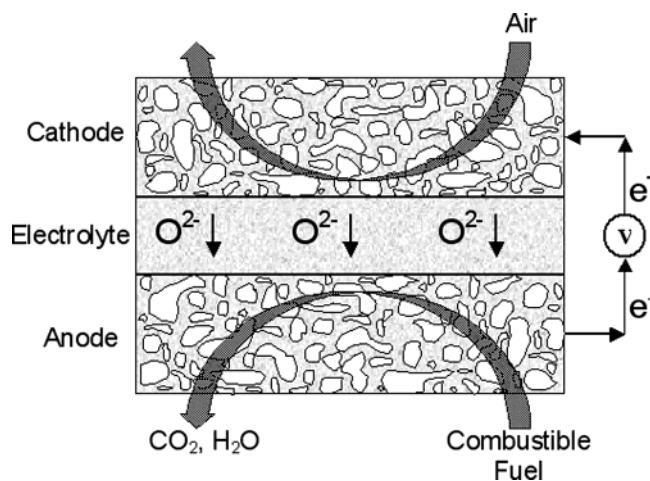
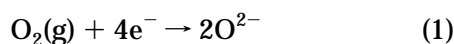


Figure 1. Schematic of SOFC operating principle. (Reproduced with permission from ref 171. Copyright 2003 Elsevier.)

cathode (or air electrode), an anode (or fuel electrode), and an electrolyte. The distinguishing feature of an SOFC is that the electrolyte is an ion-conducting ceramic and an electronic insulator. While proton-conducting ceramics are known,^{31–36} the vast majority of work on SOFC has been performed with ceramics that are oxygen–anion conductors.

Under operation, molecular oxygen is reduced to oxygen anions using electrons supplied from an external circuit at the cathode, according to the following reaction:

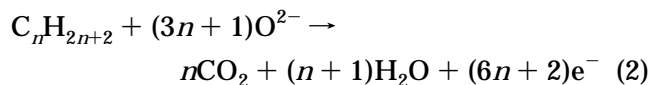


In addition to being able to catalyze the dissociation of O_2 , the material used for the cathode must be electronically conductive in the presence of air at high temperature, a property found primarily in noble metals and electronically conductive oxides. Ionic conductivity is also desirable for extending the reaction zone well into the electrode since the ions must ultimately be transferred to the electrolyte. Since precious metals are prohibitively expensive when used in quantities sufficient for providing electronic conductivity, essentially all SOFC prototypes use perovskite-based cathodes, with the most common material being a Sr-doped LaMnO_3 (LSM).¹⁵ In most cases, the cathode is a composite of the electronically conductive ceramic and an ionically conductive oxide, often the same material used in the electrolyte.

The electrolyte is probably the most crucial component of SOFC. It must be dense to separate the fuel and air compartments of the cell, and retain its high ion conductivity and low electronic conductivity over a very wide range of oxygen fugacities (referred to here as oxygen pressures, $P(\text{O}_2)$), from values close to 1 atm on the cathode side to values that could be below 10^{-20} atm at the anode. The operating temperature of the SOFC is set by the requirement for high ionic conductivity in the electrolyte and must be greater than approximately 973 K with yttria-stabilized zirconia (YSZ), the current material of choice.¹⁵ While other materials having higher ionic conductivities at lower temperatures are being considered, most of these materials do not have the same

high stability and low electronic conductivity at low $P(\text{O}_2)$. Since decreased operating temperatures simplify the materials requirements in other parts of the SOFC, there is a trend toward using very thin electrolytes supported on one of the electrodes.

Driven by the difference in oxygen chemical potential between fuel and air compartments of the cell, oxygen anions migrate through the electrolyte to the anode where they are consumed by oxidation of the fuel according to eq 2.



The electrons released by this reaction flow through an external circuit to the cathode to complete the circuit. Analogous to the cathode, the anode must be catalytically active for the oxidation reaction and retain sufficient electronic and ionic conductivities. For example, with the current state-of-the-art anode materials, which are Ni–YSZ, ceramic–metallic (cermet) composites, Ni provides the catalytic activity and electronic conductivity, while the YSZ component provides ionic conductivity and a thermal expansion match with the YSZ electrolyte. While metals other than Ni can be used in the anode, Ni is almost universally used because it is inexpensive, has excellent mechanical and electrical properties, and is a good steam-reforming catalyst. Typical cermets contain at least 30 vol % Ni to ensure high electronic conductivity through a fully percolated matrix.³⁷ However, a major limitation to Ni-based anodes is that Ni catalyzes the formation of graphitic carbon at low $\text{H}_2\text{O}/\text{C}$ ratios, as we will discuss in more detail later in this review. Alternative materials have been suggested, including electronically conductive perovskites and Cu-based cermets.

Any one of the three components in SOFC, the cathode, anode, or electrolyte, can provide the structural support for the cells. Traditionally, the electrolyte has been used as the support; however, this approach requires the use of thick electrolytes, which in turn requires high operating temperatures. Electrode-supported cells allow the use of thin electrolytes. The Siemens–Westinghouse Corporation has developed a cathode-supported design,^{38–40} although this has required electrochemical vapor deposition of the YSZ electrolyte. Most other groups have focused on anode-supported cells. In all cases, it is important to maintain chemical compatibility of those parts that come in contact and to match the thermal expansion coefficients of the various components. A large amount of research has been devoted to these important issues, and we refer the interested reader to other reviews.^{15,16,18,19,41}

2.3. Anode Three-Phase Boundary

Because the performance of an SOFC depends strongly on the anode structure, it is useful to consider how the anode works on a microscopic scale.^{42,43} The electrochemical reaction can only occur at the three-phase boundary (TPB), which is defined as the line at which the electrolyte, the electron-

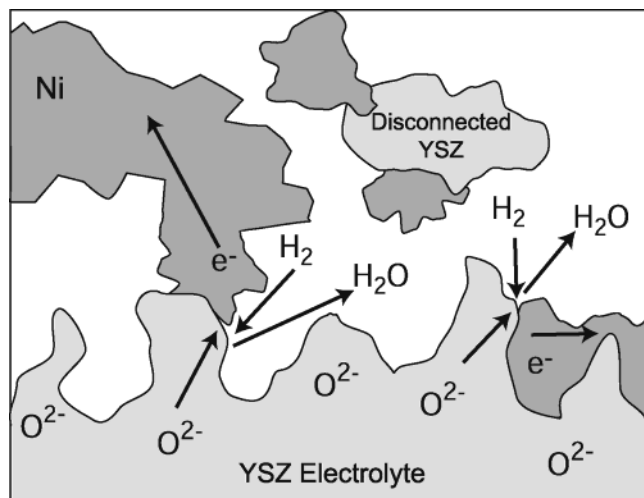


Figure 2. Schematic of Ni/YSZ anode three-phase boundary.

conducting metal phase, and the gas phase all come together. A cartoon of the region between the electrolyte and the anode where the TPB exists is shown in Figure 2. If there is a breakdown in connectivity in any one of the three phases, the reaction cannot occur. If ions from the electrolyte cannot reach the reaction site, if gas-phase fuel molecules cannot reach the site, or if electrons cannot be removed from the site, then that site cannot contribute to the performance of the cell. While the structure and composition clearly affect the size of the TPB, various theoretical and experimental methods have been used to estimate that, under normal conditions, the region in which the TPB exists extends no more than approximately 10 μm from the electrolyte into the electrode.^{42,44–49} Essentially, so long as the diffusion of ions through the electrolyte partially limits the performance, the concentration of excess ions in the oxide phase of the anode will be insignificant beyond this distance.

The TPB concept has important implications for optimization of both anodes and cathodes. To facilitate transfer of O^{2-} to or from the electrolyte, it is necessary to have fingers of the electrolyte material extending from the electrolyte, into the electrode. A detailed analysis of the role of these fingers has been carried out for cathodes,^{48,50–52} and similar concepts are almost certainly applicable to the anode. It is important to note that the electrolyte material within the electrode is only effective if it is sintered to the electrolyte itself. When oxide particles are simply pressed together at low temperatures, there will be large grain-boundary resistances that will prevent the free flow of oxygen anions. Removing the grain-boundary resistance between YSZ particles typically requires a sintering temperature of at least 1500 K.

While high temperatures do not severely limit fabrication of Ni–YSZ cermets, they can impact the way in which other composite electrodes are made. This is well-known for cathodes, where the most commonly used material is a composite of YSZ and Sr-doped LaMnO_3 (LSM). The primary reason for using LSM, rather than materials such as Sr-doped LaFeO_3 (LSF) or LaCoO_3 (LSC) that exhibit a better performance, is that LSM–YSZ mixtures can be

Table 1. Standard Cell Potential, E° , for Various Fuels at 973 and 1073 K (Reprinted with permission from ref 164. Copyright 2004 The Electrochemical Society, Inc.)

fuel	E° , 973 K (V)	E° , 1073 K (V)
hydrogen	1.01	0.98
carbon monoxide	0.99	0.98
methane	1.05	1.04
<i>n</i> -butane	1.13	1.12
toluene	1.13	1.12
<i>n</i> -decane	1.14	1.13

heated to higher temperatures before undergoing a solid-state reaction with YSZ.^{41,53–55} When Ni is replaced by other metals or by electronically conductive ceramics, the issue of reaction with YSZ at the anode sintering temperatures must be revisited.

2.4. SOFC Thermodynamics

The maximum electrical energy available from a fuel cell is determined by the Gibbs free energy difference across the electrolyte membrane, ΔG . This determines the equilibrium voltage of the cell, E , through the Nernst equation, which is nothing more than a restatement in electrical units of how ΔG ($= 2FE$) changes with pressure.

$$E = (RT/2F) \ln\{P(\text{O}_2 \text{ cathode})^{1/2}/P(\text{O}_2 \text{ anode})^{1/2}\} \quad (3)$$

In this equation, F is Faraday's constant, the product of Avogadro's constant and the charge on an electron. Since fuel, not a mixture of O_2 , is fed to the anode, $P(\text{O}_2 \text{ anode})$ is assumed to be fixed by the equilibrium relationship. For example, with H_2 as the fuel

$$P(\text{O}_2 \text{ anode})^{1/2} = \exp\{-\Delta G^\circ/RT\}P(\text{H}_2\text{O}_{\text{anode}})/P(\text{H}_2 \text{ anode}) \quad (4)$$

and eq 3 becomes

$$E = E^\circ + (RT/2F) \ln\{P(\text{H}_2 \text{ anode})P(\text{O}_2 \text{ cathode})^{1/2}/P(\text{H}_2\text{O}_{\text{anode}})\} \quad (5)$$

Here, we have substituted E° , the standard potential for oxidation of H_2 , for $-2F\Delta G^\circ$, where ΔG° is the free energy change for reaction under standard conditions. Obviously, similar relationships can be written to calculate the equilibrium potentials for other fuels. For example, for alkanes, $\text{C}_n\text{H}_{2n+2}$, the analogous relationship between partial pressures and the equilibrium cell potential is the following

$$E = E^\circ + (RT/2(3n+1)F) \times \ln\{P(\text{C}_n\text{H}_{2n+2} \text{ anode})P(\text{O}_2 \text{ cathode})^{(3n+1)/2}/P(\text{H}_2\text{O}_{\text{anode}})^{n+1}P(\text{CO}_2 \text{ anode})^n\} \quad (6)$$

At the temperatures of interest for SOFC applications, the standard potentials for oxidation, E° , are similar for hydrocarbon fuels and for H_2 and CO , as shown in Table 1. Since E° for H_2 is more temperature dependent than the E° for hydrocarbons, the thermodynamic advantage for hydrocarbon fuels is more apparent at higher temperatures. However, the

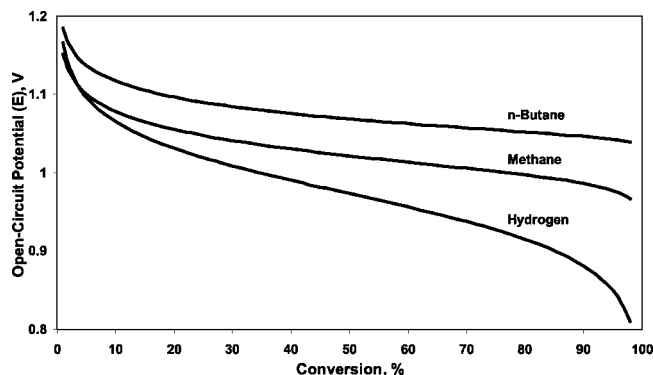


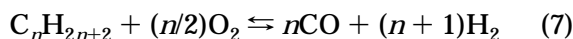
Figure 3. Theoretical open-circuit potential as a function of conversion to total oxidation of hydrogen, methane, and *n*-butane at 973 K.

standard potentials tell only part of the story since the theoretical Nernst potentials for hydrocarbons are not as dependent on fuel conversion. This is shown in Figure 3, where the Nernst potentials for H₂, CH₄, and *n*-butane, calculated from eqs 5 and 6, are shown as a function of conversion at 973 K. For these calculations, the hydrocarbons were assumed to react directly to CO₂ and H₂O, with no intermediate products, so that P(H₂O_{anode}) and P(CO₂ anode) were determined from the stoichiometry of the reaction. The effect of conversion on the equilibrium potential is quite pronounced for H₂ in that the potential drops by 15% between 10 and 80% conversion. However, for the hydrocarbon fuels, the effect of conversion is much less, with a decline of only 1% over the same range for *n*-butane. Essentially, the hydrocarbons act as a buffer to prevent changes in P(O₂); this buffering of P(O₂) increases with the size of the hydrocarbon. The implication of this result is that the thermodynamic efficiency of a fuel cell operating directly on hydrocarbon fuels can be significantly higher.

2.5. SOFC Electrode Losses

In an ideal fuel cell, the efficiency is $\Delta G/\Delta H$.⁵⁶ Since this ratio can be close to unity, the losses could be negligible. In practice, the energy losses in the fuel cell are significantly higher. To calculate the electrical energy derived from a given amount of fuel using a fuel cell, one can simply take the product of the number of electrons produced times the potential of those electrons. Therefore, for a fixed amount of fuel, energy losses occur if either the number of electrons that are produced decreases or if the cell potential decreases.

The number of electrons produced per molecule is an important issue for hydrocarbons. While the addition of H₂O to the fuel for steam reforming has no effect on electron production, reforming of hydrocarbons larger than methane is usually accomplished through partial oxidation, with the ideal reaction shown in eq 7



Whereas a mole of C_{*n*}H_{2*n*+2} is capable of producing 6*n* + 2 electrons, the ideal products from the partial oxidation can produce only 4*n* + 2 electrons. If the electrons are produced with the same potential in

both cases, the partial oxidation of the alkanes results in the loss of approximately 30% of the total energy available in the fuel. In other words, while the conventional calculation of the efficiency of the reforming process is based on the enthalpy difference between the initial hydrocarbon fuel and the CO and H₂ produced from that fuel, the efficiency is more properly calculated from the change in the Gibbs free energies of the alkane reactant and the CO and H₂ products. The free energies are reflected in the standard potentials, and since the standard potentials at the normal SOFC operating temperatures are essentially the same for hydrocarbon fuels as for H₂ and CO (see Table 1), the electron counting we have performed here accurately reflects the true loss in the energy of the fuel.

The cell potential is simply the work that can be accomplished by the electrons produced in the SOFC, and this potential decreases from the equilibrium value due to losses in the electrodes and the electrolyte. For YSZ electrolytes, the losses are purely ohmic and are equal to the product of the current and the electrolyte resistance. Within the electrodes, the losses are more complex. While there can be an ohmic component, most of the losses are associated with diffusion (both of gas-phase molecules to the TPB and of ions within the electrode) and slow surface kinetics. For example, concentration gradients for either O₂ (in the cathode) or H₂ (in the anode) can change the concentrations at the electrolyte interface,^{57–59} which in turn establish the cell potential. Similarly, slow surface kinetics could result in the surface at the electrolyte interface not being in equilibrium with the gas phase.

An interesting point in this regard is that the complexity of hydrocarbon oxidation reactions allows for the possibility that equilibrium may be established with partial oxidation reactions, which may or may not be observable in the gas phase. For example, for cells with Cu/CeO₂/YSZ anodes, we have found the measured OCV in humidified methane to be ~250 mV lower than that predicted by equilibrium with total oxidation products, even though the same cell gave good agreement between measured and predicted OCVs in H₂.⁶⁰ Furthermore, in that same study, the addition to the anode of a precious metal catalyst increased the measured OCV for methane and had no effect on the OCV for H₂. This observation could be explained by an equilibrium between methane and partial oxidation products, such as formaldehyde; however, measurements of the gas-phase products showed that the total oxidation products, CO₂ and water, were produced in amounts consistent with methane consumption.⁶¹ Therefore, the lower OCV with methane is likely due to the establishment of partial oxidation products that remain on the surface of the anode, or nonelectrochemical surface reactions, as discussed in Section 1.2. These losses are not observed with oxidation of H₂ because only one stable product, water, can be formed with this fuel. In the case of methane, it is noteworthy that the addition of precious metal catalysts to the anode could significantly increase the measured OCV.⁶⁰

2.6. Electrode Characterization

A more complete discussion of characterization techniques is given elsewhere;¹⁴ however, we wish to make a few important points here before discussing specific electrode materials. Prior to discussing techniques, it is important to recognize that electrode characterization is difficult and that there are large discrepancies in the values that have been reported in the literature for common electrode materials. For example, a brief survey of the recent literature on LSM–YSZ composite electrodes indicates a cathode ASR (area specific resistance; the losses can be calculated by multiplying this value with the current density) between 27⁶² and 2.49⁶³ ohm cm² for cathodes operating at 973 K in air. On the other hand, Kim et al.⁵⁸ reported a total cell ASR of 0.28 ohm cm² at 0.7 V using a cell with an LSM–YSZ cathode. While part of the variability in reported ASR for LSM–YSZ cathodes is due to differences in the materials used in the various studies, at least some of the differences appear to be due to issues surrounding the measurement of electrode losses.⁶⁴ We suggest that the inherent difficulties associated with measuring LSM–YSZ losses will also manifest themselves in the characterization of other cathode and anode materials.

The two main techniques for measuring electrode losses are current interrupt and impedance spectroscopy. When applied between cathode and anode, these techniques allow one to separate the electrode losses from the electrolyte losses due to the fact that most of the electrode losses are time dependent, while the electrolyte loss is purely ohmic. The instantaneous change in cell potential when the load is removed, measured using current interrupt, can therefore be associated with the electrolyte. Alternatively, the electrolyte resistance is essentially equal to the impedance at high frequency, measured in impedance spectroscopy. Because current-interrupt is simply the pulse analogue to impedance spectroscopy,¹⁴ the two techniques, in theory, provide exactly the same information. However, because it is difficult to make a perfect step change in the load, we have found impedance spectroscopy much easier to use and interpret.

To illustrate the use of impedance spectroscopy in analyzing cell performance, we consider data obtained on a cell with a Cu–ceria–YSZ anode, operating in H₂ and *n*-butane at 983 K. Figure 4 shows the V–I curves for H₂ and *n*-butane on an electrolyte-supported cell with a 550 μm electrolyte.⁶⁵ For H₂, the curve is essentially linear for current densities ranging from 0 to 400 mA/cm², while the V–I curve for *n*-butane is highly nonlinear over this range of current densities. The impedance spectra for H₂ and *n*-butane, taken as a function of current density, are shown in Figure 5. For H₂, the spectra are essentially independent of current density. The ohmic resistance that we associate primarily with the electrolyte, R_{Ω} , is obtained from the high-frequency intercept of the Cole–Cole plot with the real axis, 2.5 Ω cm², while the total cell impedance, 4.0 Ω cm², is obtained from either the low-frequency intercept in the Cole–Cole plot or from the slope of the V–I curve. The total

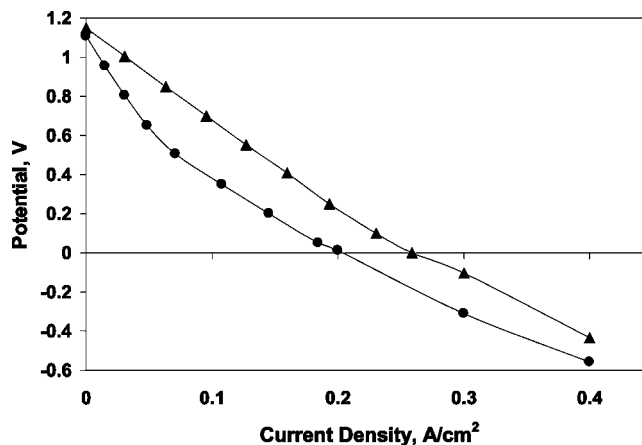


Figure 4. Cell potential as a function of current density for a 550- μm electrolyte-supported cell at 973 K in H₂ (\blacktriangle) and *n*-butane (\bullet) fuels. (Reprinted with permission from ref 65. Copyright 2003 The Electrochemical Society, Inc.)

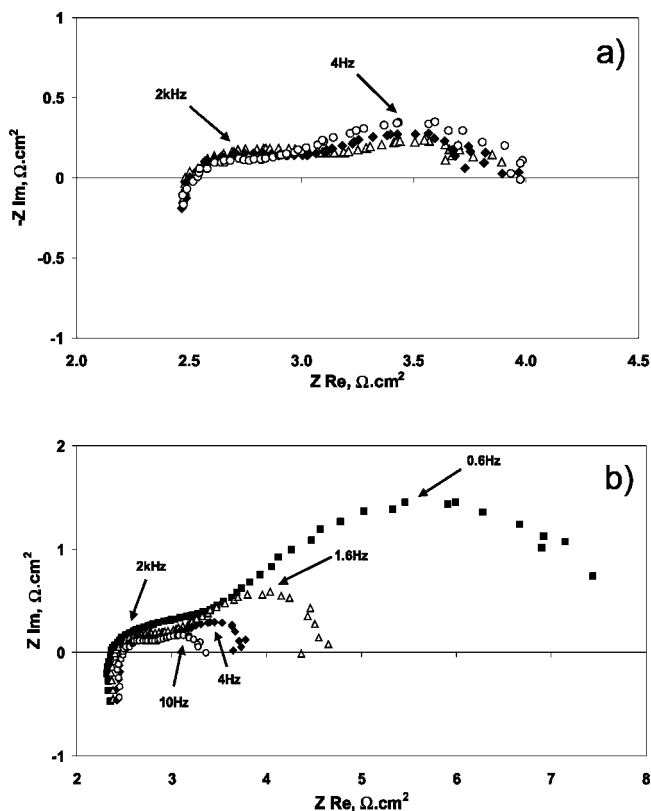


Figure 5. Two-probe impedance spectra measured at (\blacksquare) 50, (\triangle) 100, (\blacklozenge) 200, and (\circ) 400 mA/cm² for (a) H₂ and (b) *n*-butane fuel at 973 K. (Reprinted with permission from ref 65. Copyright 2003 The Electrochemical Society, Inc.)

electrode impedance, R_E , is the difference between the total cell impedance and R_{Ω} . For *n*-butane, the curvature in the V–I curve is manifested in the fact that R_E changes with current density, as shown in Figure 5b. Since the cathode and electrolyte were the same for H₂ and *n*-butane, the differences between the two sets of data must be associated with additional anode losses with *n*-butane as fuel.

In general, it is necessary to have a reference electrode to separate anode and cathode losses. In this case, the impedance spectrum between reference and either anode or cathode allows one to determine the electrode loss from the nonohmic part of the

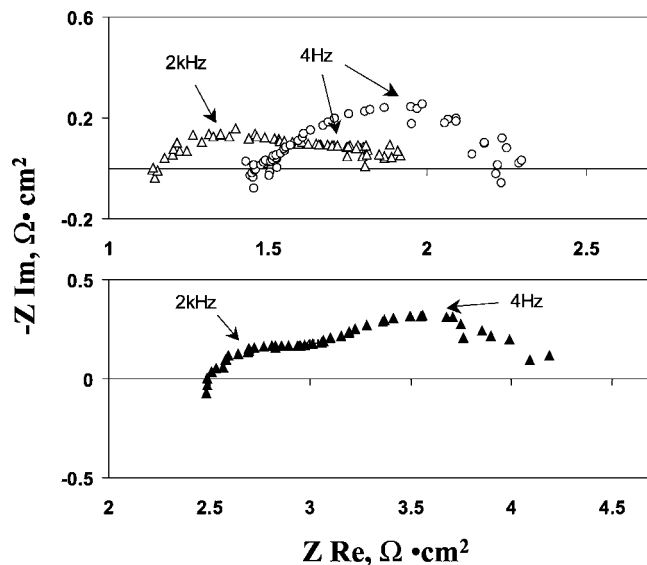


Figure 6. Impedance spectra for a 550- μm electrolyte-supported cell at 983 K and 350 mA/cm² using H₂. Ref \rightarrow cathode (Δ) and ref \rightarrow anode (\circ) and anode \rightarrow cathode (\blacktriangle). (Reprinted with permission from ref 65. Copyright 2003 The Electrochemical Society, Inc.)

spectrum. This is illustrated in Figure 6, where the reference-to-cathode and reference-to-anode spectra are shown for the same cell as that discussed in the previous paragraph, using H₂ as the fuel. It is noteworthy that the ohmic resistances in both spectra are almost the same, and almost exactly one-half of the total ohmic resistance of the cell, showing that the reference electrode is sampling the potential at the center of the electrolyte. Furthermore, the characteristic frequencies for the anode and cathode spectra, 4 and 2 kHz, are also different. For this cell, the anode and cathode impedances are 1.1 and 0.4 $\Omega \text{ cm}^2$, respectively.

However, it should be recognized that improper placement of the reference and working electrodes will give erroneous results,^{65–71} and even a small overlap of the working electrodes can lead to serious errors. For example, it is common practice to attach a reference electrode on the electrolyte, next to the cathode, on anode-supported cells. For this configuration, it is easily shown that all of the anode losses appear as cathode losses.⁶⁵ This error may, in some cases, lead to the belief that anode losses are negligible as compared to cathode losses, when the opposite may in fact be true. Furthermore, even with perfect alignment of the working electrodes, differences in the characteristic frequencies of the two electrodes can lead to losses in one of the electrodes appearing in the other electrode.^{65,69} Indeed, it is for this reason that we avoid current-interrupt methods since they do not allow one to determine the characteristic frequencies associated with the electrode losses and therefore to observe this type of measurement error.

3. Carbon Formation

A primary issue in the operation of any fuel cell using hydrocarbon fuels, whether or not steam is present with the hydrocarbon fuel, is the requirement

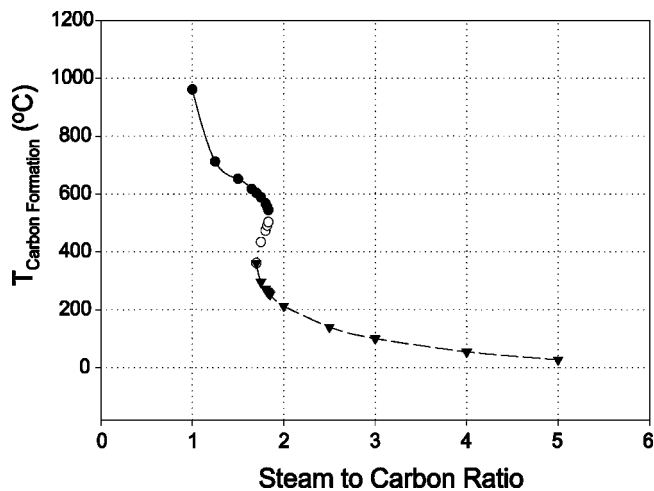


Figure 7. Carbon formation temperature for *n*-octane fuel as a function of steam-to-carbon ratio.⁷⁶

that the fuel cell not be fouled by deposition of carbon-containing residues. At the high operating temperatures of an SOFC, hydrocarbons can react on the surfaces of the anode, on the interconnect plates, and on the tubing leading into the anode. Hydrocarbons can also react in the gas phase via free-radical cracking and polymerization, forming tars that can then deposit on the anode surfaces. Because of this issue, it is common to map the region of stability for hydrocarbon fuels based on thermodynamic calculations of carbon stability.^{72–75} For example, Figure 7 shows a stability diagram for steam reforming of *n*-octane as a function of H₂O/C ratio and temperature.⁷⁶ According to this calculation, regions to the right side of the curve should allow stable operation.

Stability maps such as that shown in Figure 7 must be viewed with great caution since kinetics, not thermodynamics, are primarily responsible for stability. For example, the thermodynamic calculations imply that one could steam reform *n*-octane over a traditional Ni catalyst using an H₂O/C ratio of 2 so long as the temperature is above 473 K. However, in our experience, attempts to perform steam reforming using an H₂O/C ratio of 2 on Ni catalysts will result in catastrophic formation of carbon for hydrocarbons other than methane.⁷⁷ Furthermore, the choice of catalytic materials used for steam reforming strongly affects the parameter space over which materials are stable,⁷⁸ showing that one must look more carefully at the mechanism that is responsible for carbon formation in a given system. Finally, the chemical nature of the carbonaceous deposits differs with the catalysts present in the systems.

The formation of carbon over Ni, Fe, and Co has been extensively studied, both for catalytic applications^{79–86} and for dusting or dry corrosion, the problem of pitting when steels are exposed to hydrocarbons at high temperatures.^{87,88} Recently, the properties of Ni for forming carbon have even been proposed for use in the manufacture of carbon nanofibers.^{89,90} The mechanism on each of these metals, shown diagrammatically in Figure 8a, involves deposition of a carbon source onto the metal surface, dissolution of the carbon into the bulk of the metal, and finally precipitation of carbon as a fiber

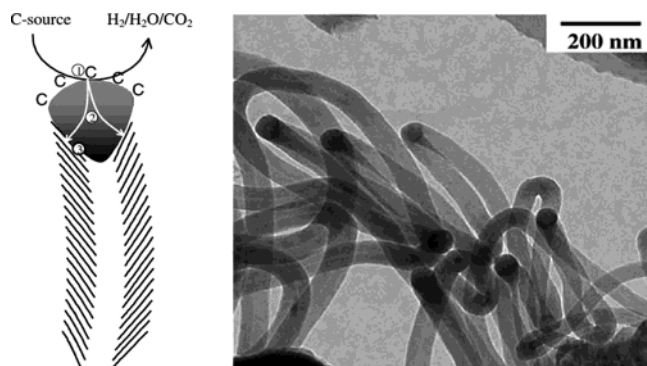


Figure 8. (a) Diagram and (b) microscopy image of carbon formation mechanism from unsupported Ni exposed to 20% $C_2H_4/7\% H_2$ at 823 K. (Reprinted with permission from ref 90. Copyright 2002 Elsevier.)

at some surface of the metal particle. Figure 8b shows a micrograph of a Ni catalyst that had been exposed to a mixture of C_2H_4 and H_2 ; the Ni particles are clearly seen at the tips of the carbon filaments. Furthermore, similar filaments were formed from exposure to an Ar-diluted syn-gas feed with a composition of 20% CO and 7% H_2 at 823 K.⁹⁰ It is important to recognize that the Ni in Figure 8b is physically lifted from its initial surface and is not merely covered by carbon; this explains the pitting that is observed in dry corrosion. The mechanism also explains why it is necessary to use very high H_2O/C ratios for steam reforming of hydrocarbons larger than methane on Ni catalysts.⁹¹ Filament formation on Ni occurs when carbon deposition onto the Ni surface occurs more rapidly than carbon removal by steam, even if thermodynamic calculations show that carbon will not be stable at equilibrium.

Carbonaceous compounds can also form in the absence of a catalyst by free-radical, gas-phase condensation reactions. The formation of this pyrolytic carbon is known in steam-reforming reactors where it can be controlled to some extent by minimizing the free volume within the reactor chamber.⁹¹ This type of carbon does not form readily with methane but can be severe with larger hydrocarbons. The compounds formed by free-radical reactions tend to be quite different from the graphitic carbon formed by metal catalysts. For example, Lee et al. showed that the compounds formed by passing pure, undi-

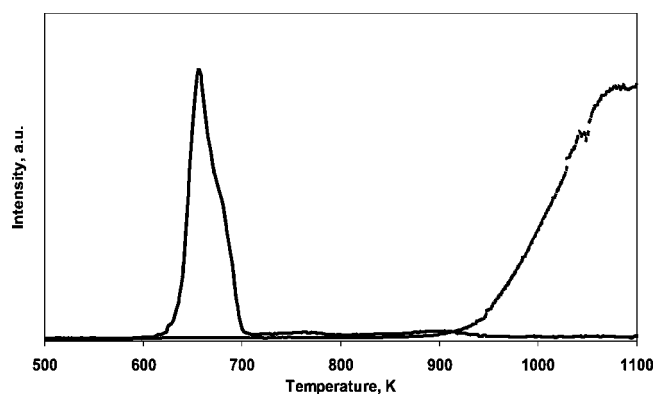


Figure 9. Temperature programmed oxidation (TPO) data showing CO_2 evolution ($m/e = 44$) of thermally deposited carbon from a Cu- CeO_2 -YSZ SOFC anode material after exposure to *n*-butane for 30 min (solid line) and a graphite powder sample (dashed line). (Reprinted with permission from ref 172. Copyright 2003 The Electrochemical Society, Inc.)

luted *n*-butane over a Cu plate for 24 h at 973 K were soluble in toluene and were primarily polyaromatic,⁹² as shown in Table 2. Temperature-programmed oxidation (TPO) measurements performed on Cu-ceria-YSZ composites after exposure to pure *n*-butane at 973 K for 30 min also indicated that these compounds were easily oxidized as compared to graphite powders. This is shown in Figure 9, where TPO results for the deposits are compared to TPO for graphite.

In addition to the fact that carbon formed by gas-phase pyrolysis is chemically different from that which forms catalytically on Ni, it is important to recognize that carbon formed by pyrolysis forms on the surface rather than in the bulk of the material. Because of this, pyrolysis does not result in pitting of the surfaces to which the hydrocarbon is exposed. Furthermore, on porous Ni cermets, carbon fiber formation can lead to fracture of the electrode caused by the stresses induced by the carbon fibers. Such stresses do not occur upon deposition of pyrolytic carbon.

4. Operation of SOFC on Hydrocarbon Fuels

There are two basic strategies for directly converting hydrocarbons to electrical energy in an SOFC.

Table 2. Chemical Composition of the Carbon Deposit Formed on a Cu Plate after 24 h Exposure to *n*-Butane at 973 K^a

name	<i>m/e</i>	no. of aromatic rings
styrene, bicyclo [4,2,0]octa-1.3.5-triene	104	1
ethyl methyl benzene, propenyl benzene etc.	118	1
1,4-dihydronaphthalene	130	1
naphthalene: $C_{10}H_8$	128	2
acenaphthene: $C_{12}H_{10}$	154	2
acenaphthylene: $C_{12}H_8$	152	2
phenanthrene, anthracene: $C_{14}H_{10}$	178	3
2-methy-phenanthrene, 1-methyl-anthracene: $C_{15}H_{12}$	192	3
2-phenylnaphthalene: $C_{16}H_{12}$	204	3
pyrene: $C_{16}H_{10}$	202	4
benzo[<i>a</i>]fluorine, benzo[<i>b</i>]fluorine: $C_{17}H_{12}$	216	3
benzo[<i>a</i>]anthracene, chrysene, triphenylene: $C_{18}H_{12}$	228	4
benzo-pyrene, perylene: $C_{20}H_{12}$	252	5
benzo[ghi]perylene, anthanthrene: $C_{22}H_{12}$	276	6

^a Reprinted with permission from ref 164. Copyright 2004 The Electrochemical Society, Inc.

The first involves using conventional, Ni-based anodes under conditions in which carbon does not form. This approach necessitates operation in a thermodynamically stable composition and temperature regime but still requires the exercise of caution, given that carbon can form catalytically on Ni surfaces. The second strategy involves using alternative anode materials that do not catalyze carbon formation. Again, caution must be exercised since the cell could be operating under thermodynamically unstable conditions. While most processes of interest do not proceed to thermodynamic equilibrium (or else life itself would be impossible), the high operating temperatures of an SOFC do tend to promote an approach to equilibrium. Furthermore, this second strategy of using alternative materials requires that one avoid catalytic materials on any surface to which the fuel could come into contact, including the bipolar plates and the tubes used to feed the fuel to the anode, not just the anode.

4.1. SOFC with Ni-Based Anodes

At the present time, the most advanced SOFCs are clearly those based on Ni-YSZ, composite anodes. The Ni in these cermet anodes provides electronic conductivity and catalytic activity, both for direct oxidation and for steam reforming of methane. The YSZ provides both ionic conductivity to allow O^{2-} to diffuse farther into the anode and a structural support for the anode that prevents Ni sintering. In some cases, doped ceria is substituted for the YSZ to increase the ionic conductivity.⁹³⁻⁹⁵ In addition to exhibiting excellent electrochemical performance in H_2 , Ni cermets are relatively simple to fabricate. For example, tape-calandring and -casting methods have been developed in which the initial green body is a mixture of NiO and YSZ.¹² Because NiO and YSZ do not form solid solutions, even at high temperatures, this green body can be sintered to form a NiO-YSZ composite and then reduced to form a porous Ni-YSZ cermet. So long as the cermet is approximately 30 vol % Ni,¹² there is sufficient electronic conductivity.

In conventional operation with methane fuels, steam is fed together with the hydrocarbon to promote the steam-reforming reaction and to avoid carbon formation. Because the surface area of Ni in the anode is low, additional catalyst beds are usually included in the anode compartment. In general, only methane can be internally reformed due to the fact that much higher H_2O/C ratios are required for stability with larger hydrocarbons. An important issue with reforming methane in the anode compartment is the fact that steam reforming is strongly endothermic. This can help to remove some of the heat generated by cell inefficiencies, but it can also make it difficult to control the system because of cold spots in the cell, which in turn lead to lower performance on certain parts of the anode. Therefore, some of the reforming is carried out before sending the fuel into the anode compartment. Because operation of conventional SOFC with methane has been discussed in detail elsewhere, we refer the interested reader to several other reviews to learn more about the subject.⁹⁶⁻⁹⁸

Barnett and co-workers recently reported that it might be possible to utilize hydrocarbons directly in SOFC with Ni-based anodes.^{94,99-102} First, with methane, they observed that there is a narrow temperature window, between ~ 550 and 650 °C, in which carbon is not as stable. The equilibrium constant for methane dissociation to carbon and H_2 is strongly shifted to methane below 650 °C, and the equilibrium constant for the Boudouard reaction, the disproportionation of CO to carbon and CO_2 , is shifted to CO above 550 °C.⁹⁹ Therefore, in this temperature range, they reported that it is possible to operate the cell in a stable manner. (However, a subsequent report by this group showed that there is no stable operating window for ethane due to the fact that carbon formation from ethane is shifted to lower temperatures.¹⁰⁰) In more recent work, this group has suggested that, even when carbon does form on Ni-based anodes, it may be possible to remove this carbon as fast as it forms if the O^{2-} flux from the electrolyte is sufficient to remove carbon faster than it is formed.^{94,100,101} Observations by Weber et al. have confirmed the possibility of stable operation in methane.¹⁰³ Similarly, Kendall et al.¹⁰⁴ showed that dilution of methane with CO_2 caused a shift in the reaction mechanism that allowed for more stable operation.

While we acknowledge that the results with methane on Ni cermets are scientifically interesting and that it may be possible to operate a fuel cell with hydrocarbon fuels using Ni-based anodes and low steam contents in a laboratory environment, we do not believe this approach is practical. First, the problem of carbon fiber formation is catastrophic if control of the system is lost. In experiments performed in our laboratory, the effect of exposing a Ni-YSZ cermet to dry methane at 1073 K for 1.5 h resulted in complete destruction of the cermet, with carbon formation equal to several times the weight of the Ni cermet and fracture of the cermet and attached electrolyte layer.¹⁰⁵ Therefore, if it were necessary to operate in a very narrow temperature window to maintain stability, any temperature excursions in the stack, such as might occur during increased loading, would be unacceptable.

Second, it is not possible to prevent carbon formation by a high O^{2-} flux through the electrolyte. O^{2-} can only be responsible for carbon removal in the region near the three-phase boundary, a region that extends no more than approximately 10 μm from the electrolyte interface. This implies that the O^{2-} flux can have no influence on the majority of the Ni cermet, so that the protection afforded the anode through high cell performance is strictly due to the generation of steam or CO_2 . While it may be possible to maintain reasonable conversions and high steam concentrations over small-scale, laboratory cells, this will be much harder to do with larger cells, where the conversion at the fuel entrance to the cell will be low. Indeed, the published work with dry methane on Ni cermets has observed significant carbon formation for cells operated at open circuit¹⁰¹ and anode delamination near the entrance of larger cells.¹⁰³

Finally, an additional approach to using hydrocarbon fuels with Ni-based anodes involves using methanol and ethanol, molecules that carry sufficient oxygen to avoid carbon formation.¹⁰⁶ Unlike the case with low-temperature fuel cells, methanol crossover is not an issue with ceramic membranes. Since methanol decomposes very readily to CO and H₂, SOFC can operate with a very high performance using this fuel.^{106,107} In addition, recent work has shown promising performance levels with limited carbon deposition using dimethyl ether as fuel.^{108,109}

4.2. Ceramic Anodes

The usual approach to choosing materials for SOFC anodes that will be operated with hydrocarbon fuels is to look first at materials that are good reforming catalysts. Indeed, Ni is one of the best steam-reforming catalysts and is used commercially for that application.¹¹⁰ Fe and Co have been considered as replacements for Ni since these metals, too, are excellent reforming catalysts. Unfortunately, the same properties that make these metals good reforming catalysts also make them excellent catalysts for the formation of carbon. Therefore, to avoid this problem and operate in hydrocarbon fuels without extensive reforming, it is probably necessary to take a different approach and look at electronically conductive materials that are not good reforming catalysts.

Electronically conductive metal oxides are particularly attractive for this application. Metal oxides tend to be poor reforming catalysts; and, unless reduced to their respective metals, unlikely to form carbon fibers by the mechanism discussed in Section 3. Because they can have very high melting temperatures and relatively low surface energies, oxides tend to be resistant to sintering as compared to metals and could retain anode porosity under extreme conditions. Some oxides exhibit both electronic and ionic conductivity. High ionic conductivity can improve electrode performance by enhancing the size of the TPB, as clearly demonstrated by work on cathode materials.^{111–116} Finally, with conductive oxides, it is feasible that the electrode could be a single material, rather than a composite of two or more materials.¹¹⁷ The potential for solid-state reactions and thermal mismatch problems makes the single component electrode attractive.

Ceria, particularly when doped with Gd₂O₃ or Sm₂O₃,^{118–122} has received some attention for direct hydrocarbon conversion in SOFC. Dating back to Steele and co-workers,¹²³ interesting properties have been demonstrated for ceria-based anodes in direct utilization of methane. Later work suggested that the performance of ceria-based anodes in hydrocarbons could be improved by the addition of precious-metal catalysts, at dopant levels,¹²⁴ but the performance of these cells was still too low for practical considerations. The problem with doped ceria is likely that its electronic conductivity is not sufficient. In general, the electrode material should have a conductivity greater than 1 S/cm in order to be practical since a conductivity of 1 S/cm would lead to a cell resistance of 0.1 Ω cm² for an electrode thickness of 1 mm, even

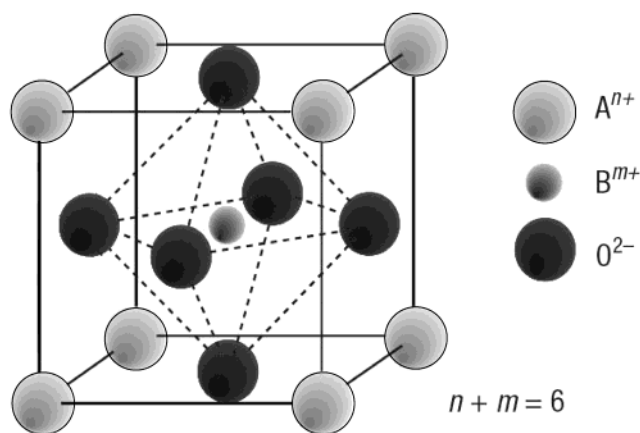


Figure 10. Unit cell of ABO₃ perovskite structure. (Reprinted with permission from *Nature Materials* (<http://www.nature.com/nmat>), ref 128. Copyright 2003 Nature Publishing Group.)

if the electrode were not porous but dense and no other loss mechanisms were operative within the electrode. At 1073 K, the conductivity of Gd-doped ceria is only 0.08 S/cm.¹¹⁸

It is interesting to notice that Marina and co-workers reported excellent performance using a Gd-doped ceria (GDC) anode.¹²⁵ At 1000 °C, these investigators reported an anode ASR of 0.39 Ω cm² and indicated that they found no carbon deposition with methane using an H₂O/C ratio as low as 0.3 after 1000 h. (The lack of carbon formation is noteworthy since thermodynamic calculations indicate that carbon should be stable under these conditions,^{74,75} another indication that carbon formation is related more to kinetic than to thermodynamic considerations.) However, the high performance achieved in this study was almost certainly due to the fact that the GDC anode thickness was between 10 and 15 μm. This implies that the current collector in the cell, a mixture of Au and GDC in this case, becomes even more crucial than usual. One could also argue that this anode is essentially an Au-GDC composite, with Au providing the electronic conduction. Higher electronic conductivities can be obtained in metal oxides having the perovskite structure; the standard materials used for SOFC cathodes, such as LSM, are of this class. For cathode applications, the electrode material must have high electronic conductivity under oxidizing atmospheres, quite different from that experienced in the anode chamber. However, oxides with the perovskite structure can be tailored considerably to achieve the desired properties.^{126–128} Perovskites with the general formula ABO₃, where A and B are cations with a total charge of +6, have the unit cell shown in Figure 10. The lower valence A cations are larger and reside on the 6-fold coordinated corners of a simple cubic lattice, with the B cations occupying the 12-fold coordinated center site. The oxygen atoms are found in a face-centered structure around the central B cation.

The perovskite structure is stable to relatively large amounts of dopant ions on either A or B sites. Oxygen vacancies are introduced into the lattice, either through transition-metal redox processes or by doping on the A or B sites with lower valence cations.

Doping of the lattice can alter the structural stability, catalytic activity, and ionic and electronic conductivities of the perovskite. For example, at oxygen contents just below stoichiometry, A-site doped perovskites of the form $\text{La}_{1-x}\text{Sr}_x\text{FeO}_3$ show *p*-type conductivity. This is due to the Sr-induced charge deficiency being balanced by oxygen vacancies, and relative to the neutral lattice, positively charged Fe ions. At low oxygen activity, the mechanism is *n*-type as the Fe ions are reduced. There are numerous reviews in the literature presenting a more detailed discussion of perovskite material properties.^{129–131}

For application as SOFC anodes, the perovskite must be capable of catalyzing the hydrocarbon oxidation reactions while maintaining high electronic conductivity and structural stability in the highly reducing environment. There have been a number of studies to investigate the stability of various perovskites for this application.^{132,133} For example, materials based on doped LaCrO_3 were reported to be quite stable.¹³⁴ Depending on the dopant, degradation can occur due to reaction with YSZ, due to reduction of the oxide, or due to electrochemical demixing;¹³⁵ however, it was reported that, for this material, degradation can be slow even when the oxide is thermodynamically unstable. Furthermore, while many perovskite oxides would not be stable in the anode environment, there are certainly other materials that would be.

The catalytic activities of some perovskites for methane oxidation and steam reforming have also been studied, and it appears that the activity of some materials can be reasonably attractive.^{136–143} Considering again materials based on LaCrO_3 , steam-reforming and methane oxidative-coupling activities have been shown to depend strongly on the dopant ion.¹⁴¹ Materials doped with Ni gave particularly high steam-reforming activities with lower propensity for carbon formation as compared to a normal Ni catalyst. However, it should be noted that the steam-reforming activity of these materials was reported to be due to reduction and removal of the Ni from the perovskite lattice, a potential source of carbon formation for SOFC anodes operating with dry hydrocarbons. The catalytic properties are also dependent on the oxidation state of the perovskite. For example, Baker et al.¹³⁶ and Metcalfe and Baker¹³⁷ showed that methane oxidation activities over $\text{La}_{0.8}\text{Ca}_{0.2}\text{CrO}_3$ depended on whether the perovskite had been oxidized or reduced. Methane oxidation to CO_2 was the dominant reaction over a preoxidized sample, but dissociation to carbon and hydrogen occurred once the sample was sufficiently reduced. The presence of easily accessible surface oxygen was suggested as the reason for the change in reaction mechanism.

As with doped ceria, low electronic conductivity is an issue with perovskite anodes as well. Some perovskites show very high electronic conductivities under oxidizing environments, but most of these materials are much less conductive under the reducing environments to which they will be exposed at the anode. For example, the conductivity of $\text{La}_{0.75}\text{Sr}_{0.25}\text{Cr}_{0.5}\text{Mn}_{0.5}\text{O}_3$, a promising material developed by Tao and Irvine,¹¹⁷ decreases by almost 2 orders of

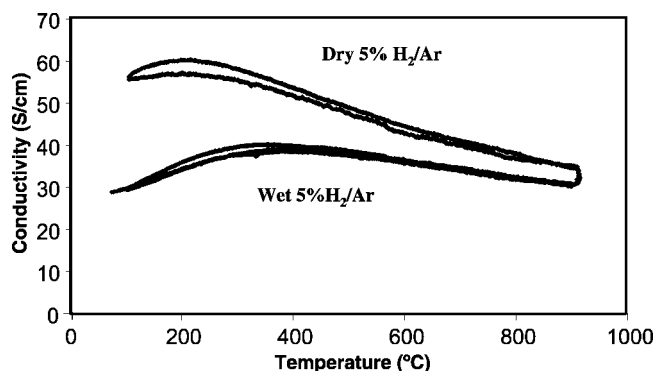


Figure 11. Plot of conductivity vs temperature for $\text{La}_2\text{Sr}_4\text{Ti}_6\text{O}_{19-\delta}$ in dry and wet 5% H_2/Ar . (Reprinted with permission from ref 145. Copyright 2003 Elsevier.)

magnitude at 1000 K when the environment changes from air to 5% H_2 . An intriguing exception to this is La-doped SrTiO_3 .¹⁴⁴ Recent reports indicate that this material can exhibit conductivities as high as 500 S/cm at 1273 K when it has been reduced at very high temperatures.¹⁴⁴ Unfortunately, these high conductivities appear to be unstable, decreasing irreversibly after exposure to $\text{P}(\text{O}_2)$ levels that are typical of those found in the SOFC anode compartment.^{144,145} Figure 11, which shows the conductivity of $\text{La}_2\text{Sr}_4\text{Ti}_6\text{O}_{19-\delta}$ as a function of temperature in dry and humidified (3% H_2O) 5% H_2/Ar , demonstrates this loss in conductivity with even very low water contents.

Even when exposed to water, the conductivity of the doped SrTiO_3 at 973 K, 35 S/cm, would seem to be adequate for achieving good anode performance. However, it should be recognized that a high-performance anode will need to be porous and likely be in the form of a composite with an ionic-conducting oxide to enhance the TPB. For example, with cathodes based on Sr-doped LaMnO_3 (LSM) and YSZ, the conductivity of the composite can be more than a factor of 10 lower than that of dense LSM.¹⁴⁶ Furthermore, the intrinsic conductivity of these oxides that are used for cathodes is well over 100 S/cm.

The previous discussion has focused on the properties of perovskite materials rather than on their performance as anodes. The number of actual fuel-cell studies is more limited, but this literature has been reviewed recently by Irvine.¹⁴⁷ Various perovskites have been investigated as potential SOFC anode materials; however, these early efforts were hampered by low electrochemical activity toward methane oxidation,^{143,148} poor anode structure,¹⁴⁴ or insufficient electrode conductivity.⁴⁵ Most recently, Tao and Irvine¹¹⁷ demonstrated that an anode based on $(\text{La}_{0.75}\text{Sr}_{0.25})_{0.9}\text{Cr}_{0.5}\text{Mn}_{0.5}\text{O}_3$ can provide reasonable power densities at 1173 K in 3% humidified CH_4 . Barnett and co-workers also reported stable power generation with methane and propane fuels on an anode based on LaCrO_3 ,⁹⁴ however, they reported that the addition of Ni, in levels too small to affect the conductivity, was crucial in providing activity for the electrochemical oxidation reactions.

Finally, a number of other mixed oxides that do not have the perovskite structure have also been examined. For example, niobium titanates with the rutile structure,¹⁵⁰ tetragonal tungsten bronze

($\text{Sr}_{1-x}\text{Ba}_x$) $_{0.6}\text{Ti}_{0.2}\text{Nb}_{0.8}\text{O}_{3-}$ phases,^{151,152} and yttria-titania zirconates^{153,154} have been investigated. All of these materials are likely to be stable for direct hydrocarbon utilization, but none has shown adequate performance for reasons similar to those outlined for the other oxides.

5. Copper-Based Anodes

Another solution to avoiding the coking problems associated with Ni-based anodes is to simply replace the Ni with a metal that is not a catalyst for carbon formation. Metals generally have much higher electronic conductivities than do oxides, so that this problem with ceramic anodes can be circumvented. Unfortunately, there is no metal replacement for Ni that has perfect properties, so that it is necessary to make compromises based on the other performance requirements to select the replacement for Ni. First, the metal must be stable, both to the high operating temperatures and to the range of $P(\text{O}_2)$ experienced in the anode. Metals with low melting temperatures are excluded, as are metals such as Mo that would be oxidized by water in the anode compartment. Second, because the metals must be present in quantities sufficient to provide electronic conductivity, precious metals are excluded because of cost.

In our laboratory, we have focused on replacing Ni with Cu. Cu does not catalyze carbon formation and is stable to higher $P(\text{O}_2)$ than is Ni. The disadvantages of Cu are that Cu and its oxides have relatively low melting temperatures: 1356 K for Cu, 1508 K for Cu_2O , and 1600 K for CuO. The low melting temperatures for the oxides, in particular, make the fabrication procedures typically used for Ni-cermet inapplicable. Finally, because Cu is not a good oxidation catalyst, we have found that it is necessary to incorporate a separate oxidation catalyst into the anode to achieve a reasonable performance. Because we believe that the problems associated with Cu-based anodes can be overcome and that Cu cermet show great promise for direct-utilization SOFC, the remainder of this review will focus on these materials.

5.1. Preparation Methods

The most commonly used method for producing Ni-cermet anodes starts by simply mixing NiO and the electrolyte (e.g., YSZ) powders. These mixtures can be screen printed onto the electrolyte for electrolyte-supported cells, or for anode-supported cells, the mixtures can be made into plates by pressing, tape-casting, or tape-calendering.¹² The oxide composites are then heated to a temperature that is sufficient to allow the electrolyte powder in the electrode to become sintered together with the electrolyte. After this high-temperature sintering, the NiO is reduced to Ni by heating in H_2 .

Unfortunately, it appears that this method cannot be applied to the fabrication of Cu cermet due to the low melting temperatures of CuO and Cu_2O . For lower sintering temperatures, it is likely that the electrolyte powder within the electrode does not become connected, either to itself or to the electrolyte.

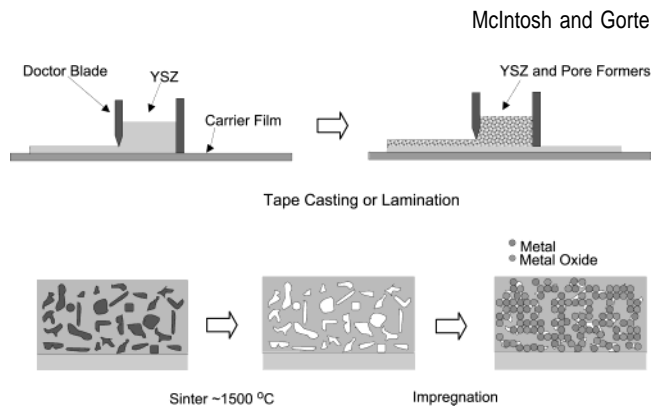


Figure 12. Schematic of SOFC manufacture by tape-casting. (Reprinted with permission from ref 159. Copyright 2000 Wiley-VCH.)

There are indications that these poorly sintered materials are unstable upon reduction of the copper oxides. Two separate studies, one with Cu–YZT¹⁵⁵ and the other with Cu–GDC,¹⁵⁶ have found that the Cu migrates out of the porous electrolyte matrix during reduction.

To avoid these problems, we developed several novel fabrication methods in which the porous oxide component of the cermet is prepared first with additional components added in separate steps that do not require high-temperature processing. In our early work, the porous oxide was prepared from YSZ fibers, stabilized with a zircon coating, supported on relatively thick YSZ electrolyte plates.^{157,158} A glycerol slurry of the fibers and normal YSZ powder was applied to the YSZ electrolyte and calcined to high temperatures to form a porous matrix. The matrix was then impregnated with aqueous solutions of nitrate salts, heated to 723 K to decompose the nitrate, and finally reduced in H_2 at the operating conditions to form the anode composite. However, this method does not allow for the fabrication of anode-supported, thin electrolytes, which are required to achieve high performance.

A second method for establishing a porous oxide matrix into which a wide variety of materials can be impregnated involves dual tape-casting, as shown schematically in Figure 12.¹⁵⁹ In tape-casting, oxide powders are mixed together with binders and surfactants and then spread into a film over a carrier such as Mylar.¹⁶⁰ Upon calcination, the binders are burned out, and the oxide particles are sintered to form dense structures. Pore formers, such as graphite or cellulose, can be added to the green tape to introduce a controlled level of porosity. In dual tape casting, a second layer, which could have a different composition, is spread onto the first green layer. In the case shown in Figure 12, graphite pore formers were added to the second layer to achieve porosity after calcination but not to the first. Since the porous layer can be thick and mechanically strong, the dense electrolyte layer can be very thin. Also, pore formers can be added equally well to pressed powders as to tapes. Notice that this methodology can be applied to other electrolyte materials, such as Sm-doped ceria (SDC).¹⁶¹

The shape of the pores in the porous oxide matrix can be controlled quite effectively through the shape of the pore formers that are used.¹⁶² Figure 13 shows

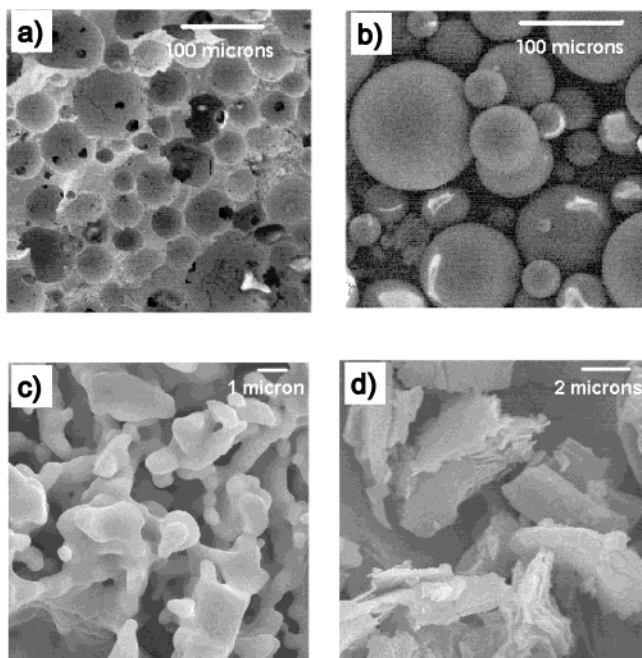


Figure 13. SEM of (a) YSZ ceramic made with 36 wt % PMMA and (b) the PMMA spheres used. (c) YSZ ceramic made with 36 wt % graphite and (d) the graphite particles used. (Reprinted with permission from ref 162. Copyright 2003 The American Ceramic Society (<http://www.ceramics.org>.)

scanning electron micrographs (SEM) of two ceramic pieces made from YSZ with polymethyl methacrylate (PMMA) or graphite pore formers, along with images of the pore formers themselves. The data are especially clear for PMMA, where the spherical pore formers lead to spherical cavities in the ceramic. The correspondence between cavity and pore-former shape is less clear with graphite, but the size of the pores in the resulting ceramic is certainly similar to the size of the graphite particles. It is interesting to notice that the pore formers leave the ceramic piece at a temperature well below the temperature at which the tape begins to shrink.¹⁶² For example, with PMMA, the pore former had been completely removed by 700 K, while the tape began to shrink only above 1300 K. This helps to explain why the sizes of the cavities in the ceramic piece are somewhat smaller than the size of the pore formers. Obviously, the structure of the pore formers is built into the ceramic at low temperatures, well before most densification occurs, and the pores then shrink at the higher temperatures.

A variation on this dual-tape-casting method involves making a NiO–YSZ composite with a thin YSZ electrolyte in the same manner that is used to make a normal, anode-supported electrolyte with Ni–YSZ cermets.^{162,163} After reduction of NiO, the Ni can be leached out of the YSZ using boiling nitric acid, leaving a dense YSZ layer supported on the porous YSZ substrate. SEM pictures of porous YSZ prepared by leaching Ni from Ni–YSZ cermets are shown in Figure 14. In a manner similar to that for PMMA and graphite pore formers (Figure 13) the pore structure of these materials may be controlled by the size and shape of the NiO powder used. The porosity of a typical sample was estimated to be 77% by Hg

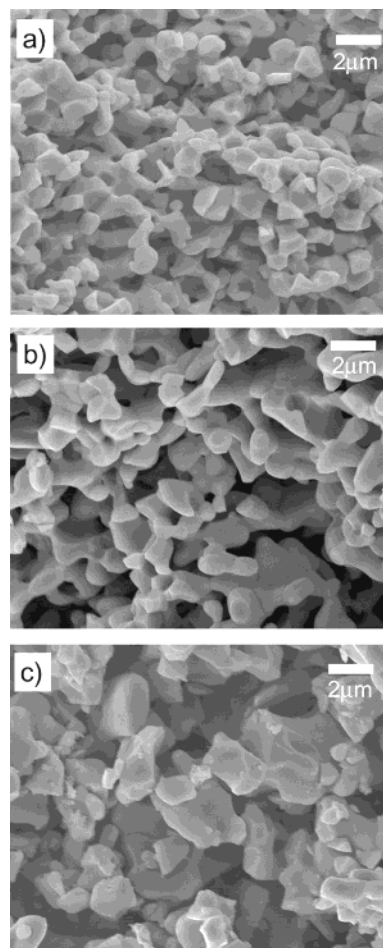


Figure 14. SEM micrographs of porous YSZ produced by acid leaching NiO/YSZ composites. The YSZ had an average particle size of $0.58 \mu\text{m}$ and the NiO average particle size of (a) 1.2 , (b) 4.3 , and (c) $17 \mu\text{m}$. (Reprinted with permission from ref 162. Copyright 2003 The American Ceramic Society (<http://www.ceramics.org>.)

porosimetry, and a fairly narrow pore-size distribution between 2 and $4 \mu\text{m}$ can be achieved.

While it is likely that other methods for preparing Cu cermets will be devised, the materials prepared by dual-tape-casting have some very attractive features. Obviously, the oxide component is very well-connected because it has been sintered at high temperatures. Furthermore, the anode pore structure can be easily tailored by varying the pore former type and quantity. Perhaps of greater significance is the flexibility in anode composition that this high-temperature sintering/low-temperature processing methodology provides. Low-temperature processing allows incorporation of a wide range of catalytic and metallic components by avoiding solid-state reactions. In addition, the surface area and activity of the catalytic material may be preserved. This ability to add a wide variety of materials will be shown to be very important in subsequent sections.

Furthermore, because the Cu is added after the oxide matrix has been established, the structure of the composite is clearly not random; therefore, less metal should be necessary for achieving high electronic conductivities.¹⁶⁴ Figure 15 shows the conductivity of porous YSZ slabs as a function of Cu content in H_2 at 973 K. The porous YSZ was formed using

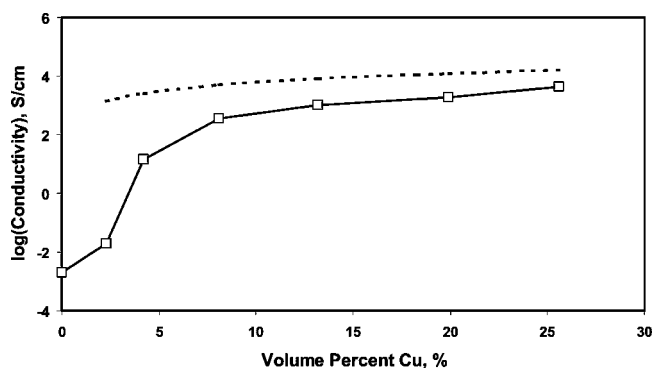


Figure 15. Conductivity as a function of copper content in a porous YSZ slab at 973 K in H_2 . The dashed line shows the conductivity predicted for the formation of a thin copper film. (Reprinted with permission from ref 164. Copyright 2004 The Electrochemical Society, Inc.)

graphite pore formers, and the Cu was added by impregnation with aqueous solutions of $Cu(NO_3)_2$, followed by calcination in air at 723 K and reduction in H_2 at 973 K. The conductivity was measured by the four-probe technique. As shown in the figure, the effective conductivity increases dramatically with the addition of relatively small amounts of Cu. The conductivity is 14 S/cm at 4 vol % (11 wt %) Cu and reaches a value of almost 4000 S/cm for 26 vol % (43 wt %). These values are lower than one would predict assuming Cu formed a continuous thin film over the surface of the YSZ; the dashed line in Figure 15 was calculated from the bulk conductivity of Cu, assuming that Cu simply coats the YSZ pores. Obviously, the difference between the measured and calculated values is due to the fact that Cu forms particles that are not necessarily connected. The relationship between conductivity and Cu content for the cermet in this study is very different from that found in earlier studies of more conventional Ni-YSZ¹² and Cu-YZT¹⁵⁵ cermets, where a sharp jump in conductivity is observed at a percolation threshold, near 30 vol % metal.

5.2. Catalysis

The catalytic activity of the anode toward oxidation reactions is a dominant factor in determining SOFC performance, particularly with hydrocarbon fuels. In Cu-cermet anodes, the only role played by Cu is that of electronic conductor. The Cu does not appear to have any catalytic function, and the oxidation reaction in the TPB relies on the addition of other components, primarily ceria.^{157–159,165} The evidence for this is as follows. First, Cu-YSZ anodes that do not contain ceria exhibit very low performance, even though they are stable in hydrocarbon fuels.^{157–159} Second, substitution of Cu with Au has essentially no effect on anode performance.¹⁶⁶ Since Au is usually thought to be catalytically inert, it seems unlikely that Cu and Au would perform in a similar manner if Cu had a catalytic function.

Other evidence for the importance of catalysis in anode performance came from an examination of the products formed by Cu-ceria-YSZ and Cu-molybdena-YSZ anodes in membrane-reactor measurements.¹⁶⁵ The anodes in these experiments both had

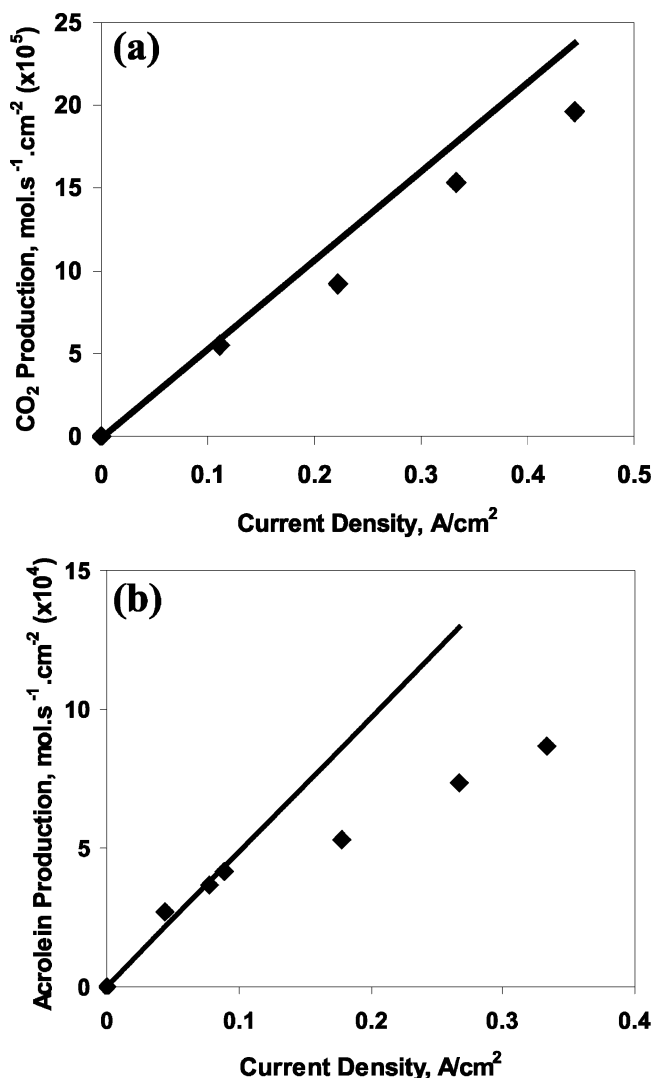
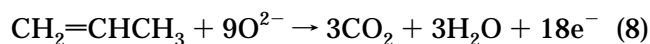


Figure 16. Propylene conversion and product-selectivity results for the membrane-reactor measurements performed at 723 K with pure propylene as the feed. The results in panel a were for the SOFC with a Cu-ceria-YSZ anode, and the results in panel b were for the Cu-molybdena-YSZ anode. In panel a, the points are the rate of CO_2 production, and the line was calculated from the current density and eq 8. In panel b, the points show the production of acrolein, and the line was calculated from eq 9. (Reprinted with permission from ref 165. Copyright 2002 Elsevier.)

20 wt % Cu and 10 wt % added oxide and were identical except for the composition of the added oxide. A power supply was used to fix the potential across the electrodes, while pure propylene was fed to the cells at a temperature of 723 K. The products leaving the anodes were then analyzed as a function of the current density using a gas chromatograph. Results for the Cu-ceria-YSZ anode are shown in Figure 16a. The conversion of propylene at open circuit was negligible but increased almost linearly with the current density. The points shown in the figure are the CO_2 production rates calculated from the chromatographic analysis, while the line is the predicted CO_2 production rate based on Faraday's equation and the measured current



Since only traces of CO were observed and CO_2 and

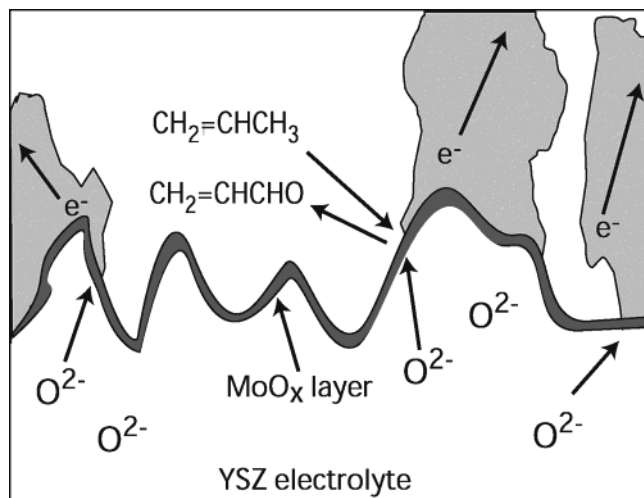
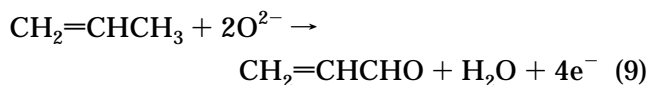


Figure 17. Schematic of anode TPB region during the partial oxidation of propylene. (Reprinted with permission from ref 165. Copyright 2002 Elsevier.)

water were the primary products, the deviation between the line and the points represents a failure to close the mass balance, probably due to an uncertainty in the total flow rate.

Results for the cell with a Cu–molybdena–YSZ anode, shown in Figure 16b, were very different. Unlike ceria, which is a nonselective oxidation catalyst, molybdena is a selective catalyst for the partial oxidation of propylene to acrolein ($\text{CH}_2=\text{CHCHO}$) and is used commercially for this process.¹⁶⁷ The primary product at low conversion over the Cu–molybdena–YSZ electrode was acrolein, produced according to the reaction



Again, points on the curve were the measured acrolein production rates, and the line is the predicted production rate based on the current and the stoichiometry according to eq 9. At higher conversions, we observed significant amounts of CO_2 and water, sufficient to explain the difference between the acrolein production and the current. It should be noted that others have also observed the electrochemical production of acrolein in a membrane reactor with molybdena in the anode.¹⁶⁶ The selective oxidation of propylene to acrolein with the Cu–molybdena–YSZ anode can only be explained if molybdena is undergoing a redox reaction, presumably being oxidized by the electrolyte and reduced by the fuel. By inference, ceria is also likely acting as a catalyst, but for total oxidation.

The simplest interpretation of these results is that ceria and molybdena act as catalysts in the TPB region, as shown in Figure 17. Either molybdena or ceria are oxidized by O^{2-} coming through the electrolyte and then subsequently reduced by the fuel. According to this picture, reaction at the TPB is a simple redox process with a nonconventional oxygen source. Because molybdena is selective for the oxidation of propylene to acrolein, while ceria is nonselective, the products formed in cells with these two catalysts are different.

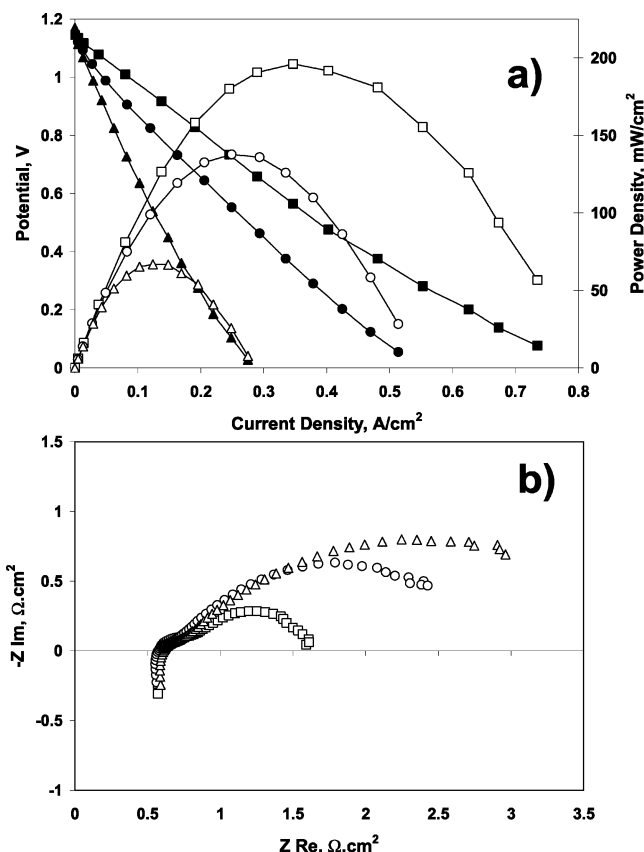


Figure 18. (a) Cell potential (closed symbols) and power density (open symbols) as a function of current density and (b) impedance spectra measured at 330 mA/cm^2 . The cells were calcined for 2 h in air at (\square) 723 K, (\circ) 1273 K, and (\triangle) 1523 K before testing. Measurements were made at 973 K in pure H_2 . (Reprinted with permission from ref 169. Copyright 2003 The Electrochemical Society, Inc.)

The anode performance was also found to depend strongly on ceria particle size and morphology, as expected since catalytic properties are crucial.¹⁶⁹ This is demonstrated by the results in Figure 18, which show data for three otherwise identical cells except for the fact that the ceria deposits were calcined in air to either 723, 1273, or 1523 K before the Cu phase was added. While the open-circuit voltage (OCV) on all three cells was in good agreement with the Nernst equation, the maximum power densities decreased with calcination temperature, going from greater than 200 mW/cm^2 to less than 70 mW/cm^2 after calcination to 1523 K. Impedance spectra, shown in Figure 18b, demonstrated that the performance changes were due to changes in the anode. In all three cells, the electrolyte resistance was in good agreement with the expected resistance of the YSZ electrolyte. However, the low-frequency ($\sim 4 \text{ Hz}$) arc that can be assigned to the anode increased from $0.8 \Omega \text{ cm}^2$ following calcination at 723 K, to $>1.8 \Omega \text{ cm}^2$ at 1273 K and $>2.6 \Omega \text{ cm}^2$ at 1523 K. XRD results showed that increasing sintering temperature increased the ceria crystallite size but did not form any new phases within the anode. It is noteworthy that high-temperature calcination of the ceria would have been expected to improve ionic conductivity within the ceria by growth of the ceria crystallites, so that the decreased performance is more likely associated with catalytic properties.

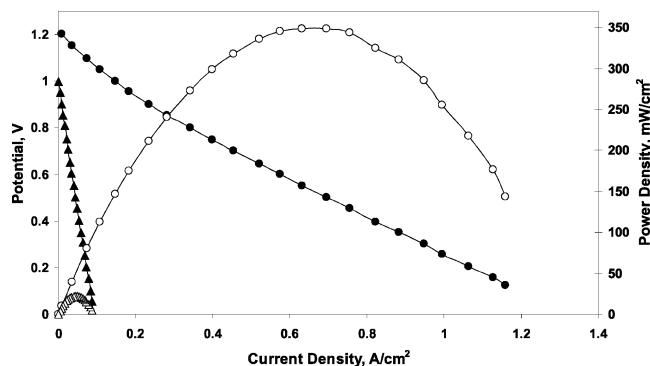


Figure 19. Cell potential (closed symbols) and power density (open symbols) as a function of current density at 973 K in CH₄ for cells with anodes containing (▲) 10% CeO₂ and (●) 10% CeO₂ 1% Pd. (Reprinted with permission from ref 60. Copyright 2003 The Electrochemical Society, Inc.)

While ceria is a good hydrocarbon oxidation catalyst, its catalytic activity can be significantly enhanced by the addition of precious metals such as Pt, Pd, and Rh.⁶⁰ Unfortunately, cells that contain both Cu and precious metals result in the formation of a catalytically inactive alloy, so that the performance of these cells is essentially indistinguishable from cells made without the addition of precious metals. However, as we will discuss in a subsequent section, electronic conductivity can be obtained in the anode by forming a carbonaceous layer. When electronic conductivity is achieved through carbon deposits, the addition of precious metals at dopant levels into the ceria has a large impact on performance. Figure 19 shows the performance curves in dry methane at 973 K for cells in which the anodes contained 10 wt % CeO₂, with and without the addition of 1 wt % Pd. The addition of Pd increased the power density by greater than 1 order of magnitude, from 22 to 350 mW/cm². The large increase in anode performance is almost certainly associated with enhanced catalytic activity for C–H bond breaking in CH₄.

5.3. Fuel Dependences and Sulfur Tolerance

The performance of SOFCs with Cu–ceria–YSZ anodes has been tested with a wide variety of hydrocarbon fuels, and this has been documented elsewhere.^{105,170–171} With the exception of methane, which is known to be relatively unreactive in normal heterogeneous reactions as well, all of the hydrocarbons we examined appear to give similar performance characteristics. The fuels that were tested include *n*-butane, *n*-decane, toluene, and a synthetic diesel. The main difference observed between the various fuels is that some fuels tend to form tars more readily via gas-phase free-radical chemistry. Otherwise, with the exception of CH₄, all hydrocarbons that were investigated showed similar power densities. This is shown in Figure 20, which displays the voltage and current densities for *n*-decane, toluene, and synthetic diesel as a function of time. In this case, the hydrocarbon fuels were diluted in dry N₂ to a concentration of 40 wt % hydrocarbon to prevent condensation of unreacted fuels that leave the cell. (In our studies, the active area for the fuel cell is typically 0.5 cm², and a current density of 1 A/cm² would require a flow

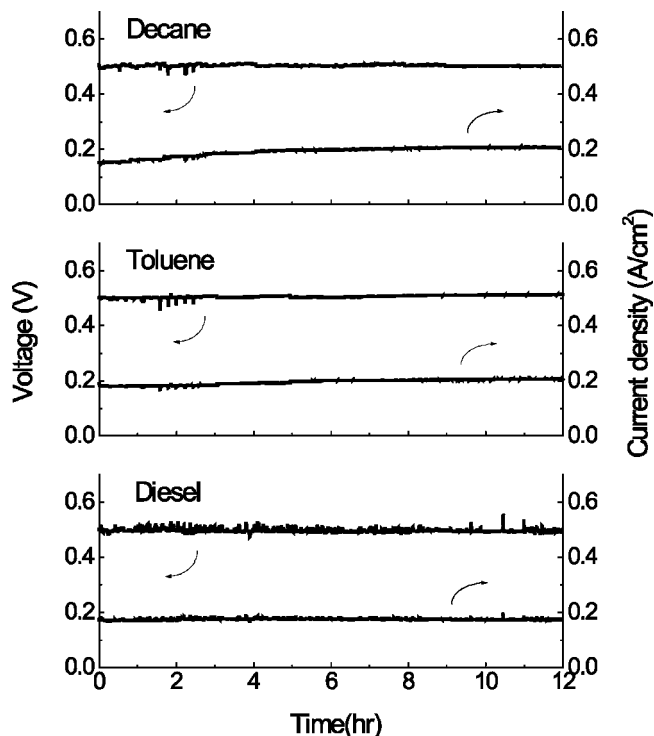


Figure 20. Cell potential and current density as a function of time for *n*-decane, toluene, and the diesel fuel. Each of the fuels was fed to the cell with N₂ at a concentration of 40 wt % hydrocarbon. (Reprinted with permission from ref 105. Copyright 2001 The Electrochemical Society, Inc.)

rate of only ~0.1 g/h of *n*-decane at 100% fuel conversion; therefore, the conversions are usually quite low.)

The issue of tar formation is an important one since the anode will obviously cease to function if it becomes filled with tar. In measurements of tar formation rates with *n*-butane at 973 K, we have recently found that identical amounts of tar are formed on porous YSZ and YSZ with Cu and ceria after 24 h.¹⁷² The fact that the rate of tar deposition is the same whether Cu and ceria are present or not strongly implies that the tar is formed in the gas phase and then deposits onto the anode under operating conditions. Further evidence for gas-phase formation of the tars comes from analysis of the tar by gas chromatography, which showed that the tar consists primarily of polyaromatics with a range of molecular weights⁹² since these are the expected products from the gas-phase reaction. Indeed, since many of the gas-phase pyrolysis reactions have been characterized, Walters et al.¹⁷³ recently modeled these reactions for light hydrocarbons under SOFC conditions to understand when polyaromatic compounds will likely form and showed that it is only likely to be a problem at the entrance to the fuel cell. However, it is important to notice that gas-phase free-radical reactions are strongly affected by wall effects and that free-radical pyrolysis is routinely minimized in steam-reforming reactors by removing dead volume.¹⁷⁴ Therefore, proper engineering of the flow channels will likely eliminate or at least minimize this problem.

Another issue with hydrocarbon fuels is that essentially all contain some sulfur, and fuel cells can

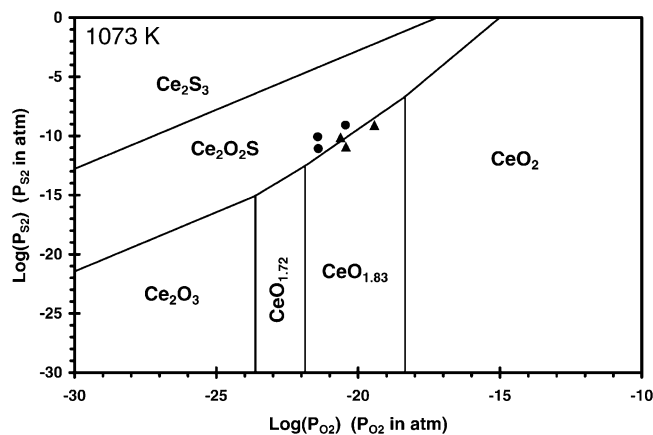


Figure 21. Calculated Ce–O–S phase diagram at 1073 K. The circles and triangles correspond to conditions for which $\text{Ce}_2\text{O}_2\text{S}$ and cerium oxide were experimentally determined stable. (Reprinted with permission from ref 175. Copyright 2000 Elsevier.)

be very sensitive to even small amounts of sulfur. For example, Ni is used as a getter for H_2S in automotive, emissions-control catalysis, and problems of NiS formation occur in SOFCs. Indeed, the sensitivity of SOFC anodes to sulfur impurities appears to be related to the stability of sulfur compounds that can be formed by the materials in the anodes. In the case of Cu–ceria–YSZ anodes, the component most sensitive to sulfur is ceria. A phase diagram for the formation of ceria–sulfur compounds under reducing conditions is presented in Figure 21. Experimental studies on the formation of Ce–O–S compounds have shown good agreement with these thermodynamic predictions.¹⁷⁵ Furthermore, conditions that lead to SOFC performance degradation match well with the thermodynamic regime where $\text{Ce}_2\text{O}_2\text{S}$ is predicted to be stable.¹⁷⁶ It is fortunate that reasonably high sulfur concentrations can be used with the Cu–ceria–YSZ anodes; however, the issue of sulfur sensitivity must be evaluated for any additives that are incorporated in the anode.

5.4. Impact of Fuel Utilization

As discussed in Section 2.4, the Nernst potentials for SOFC operating on hydrocarbons are not as strongly affected by fuel utilization as they are with H_2 . However, this advantage is likely to be offset at least somewhat by potential diffusion problems as a result of the dilution that will occur with hydrocarbons. For example, at 50% utilization of *n*-butane, the fuel concentration will be only 10% due to the fact that 4 mol of CO_2 and 5 mol of H_2O are formed for the oxidation of each mol of *n*-butane. While we are not aware of any studies with SOFC operating with hydrocarbons at high fuel utilizations, Costas-Nunes et al. simulated the effect of high fuel conversions with *n*-butane by oxidizing the fuel in pure O_2 , either over pure ceria or a Pd/ceria catalyst at 973 K, before admitting it to the anode compartment of the cell.¹⁷⁷ A summary of their results is provided in Figure 22, where the maximum power densities are plotted as a function of fuel conversion using both the ceria and the Pd/ceria catalysts. Figure 22 also shows the maximum power density obtained for

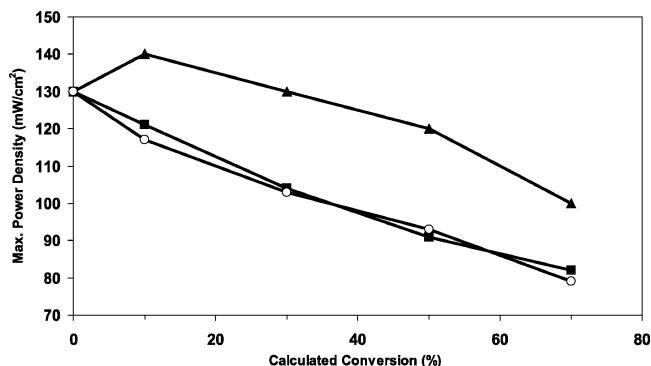


Figure 22. Maximum power density for a Cu– CeO_2 –YSZ anode SOFC as a function of the conversion of fuel entering the anode compartment. The data for preoxidation of *n*-butane by ceria (■) and 1 wt % Pd–ceria (▲) are shown. The maximum power densities obtained when *n*-butane was diluted with He to a concentration equivalent to that obtained by total oxidation are shown by (○). (Reprinted with permission from ref 177. Copyright 2003 The Electrochemical Society, Inc.)

n-butane that had diluted in He to the same extent as that expected for dilution by CO_2 and H_2O at a particular conversion. It should be noted that the behavior was not diffusion-limited under any of the conditions studied in these cells.

First, it is noteworthy that the maximum power densities obtained with *n*-butane diluted in He are very similar to those obtained with the cell operating on *n*-butane preoxidized over a ceria catalyst. Given that chromatographic analysis of the products formed by oxidation over the ceria catalyst showed primarily that CO_2 and H_2O were the products, it appears that CO_2 and H_2O act primarily as diluents for the Cu-based anodes in this study. Obviously, the dilution has a serious impact on performance. However, when *n*-butane oxidation was carried out over a Pd–ceria catalyst, which is known to be very active for steam reforming,⁷⁷ the cell performance was much higher for a given fuel utilization. Chromatographic analysis showed that the increased performance was due to the formation of significant amounts of H_2 generated by steam reforming of *n*-butane with the steam generated by hydrocarbon oxidation. The maximum power density generated by the cell was as much as 30% with the addition of a reforming component within the oxidation catalyst. On the basis of these results, it is suggested that the inclusion of a steam-reforming catalyst within the anode compartment of direct-conversion SOFC should improve their performance at high fuel utilization.

5.5. Anodes Based on Alloys

As discussed in previous sections, Cu acts primarily as an electronic conductor within the Cu-based anodes. Because it is a poor catalyst for C–H and C–C bond scission, it is essential to incorporate an oxidation catalyst, ceria, within the anode. While Ni has many attractive properties, its propensity for catalyzing carbon formation prevents its use in dry hydrocarbons at high temperatures. One approach for enhancing the catalytic properties of Cu and stabilizing the tendency of Ni for forming carbon is to use Cu–Ni alloys. Cu–Ni alloys have been used

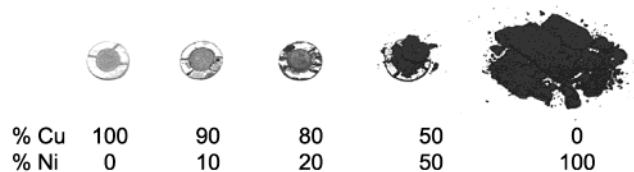


Figure 23. Photographs of cell anodes containing Cu and Ni alloys of varying composition after exposure to dry CH_4 at 1073 K for 1.5 h. (Reprinted with permission from ref 163. Copyright 2002 The Electrochemical Society, Inc.)

for the anodes in molten-carbonate fuel cells in an application where the alloys were found to be more sulfur tolerant as compared to pure Ni.¹⁷⁸

Using similar methods to make anodes based on Cu–Ni alloys as were used to make the Cu-based cermets, Kim et al.¹⁷⁹ showed that carbon formation on the alloy cermets was significantly suppressed as compared to carbon formation on the pure Ni. This is shown by the picture in Figure 23, in which cermets having various Cu–Ni contents were exposed to dry methane at 1073 K for 1.5 h. The photograph graphically shows that only small amounts of carbon formed on the alloys as compared to what formed on the purely Ni cermet. Using an anode made from $\text{Cu}_{0.8}\text{Ni}_{0.2}$, they were able to operate the cell for 500 h in dry methane at 1073 K. During that time, the power density continued to rise, up to a value of more than 320 mW/cm^2 . The initial poor performance on these alloy anodes appears to have been associated with poor connectivity within the metal phase, with carbon deposits providing that increased conductivity over time. On the basis of this mechanism, one should expect that the initial performance would have been high if more metal had been incorporated within the anode.

The fact that carbon deposited over time on the Cu–Ni alloys is obviously a concern. A later study of anodes based on Cu–Ni alloys found that increasing the reduction temperature from 973 to 1073 K changed the stability of $\text{Cu}_{0.8}\text{Ni}_{0.2}$ alloys toward carbon formation in the presence of *n*-butane at 973 K.¹⁸⁰ Cells reduced at 973 K fractured immediately upon exposure to *n*-butane at this temperature due to the catalytic formation of graphitic carbon, while cells reduced at 1073 K were stable for at least 3 h when exposed to *n*-butane at 973 K. This indicates that there must be mobility of the two metals at the typical operating temperatures used in the cell. Indeed, previous work on Cu–Ni alloy catalysts has shown that the tendency of the catalyst to form coke is strongly affected if the catalyst is reduced at a temperature greater than 1013 K.¹⁸¹ While Cu and Ni form solid solutions, it has been found that Ni ensemble size on the surface can be decreased to a minimum size for carbon formation activity with the proper pretreatments.¹⁸² The surface segregation of Cu–Ni alloys is due to Cu having a lower surface energy than Ni,¹⁸³ so that the surfaces of Cu–Ni alloys tend to be Cu rich phase. At higher temperatures, the surface concentration of Ni should increase due to entropic effects. However, Ni ensemble size will also decrease for the same reason, which is probably the explanation for the higher stability of Cu–Ni alloys following high-temperature reduction.

Cu–Co mixtures were also investigated for anode cermets and shown to have interesting properties.¹⁸⁰ Cu and Co have a very limited range of compositions where alloys are formed, and diffraction measurements showed that anodes made from mixtures of these two materials had two metal phases. However, mixtures of these metals with Co contents as high as 50 wt % of the metal were stable in *n*-butane at 973 K for at least 3 h. Since cermets made with 100% Co were not stable to carbon formation under these conditions, it appears that the Co-rich phase must be covered by Cu. There is evidence for surface alloys of Cu and Co, formed because the surface free energy of Cu (1.96 J/m^2) is lower than that of Co (3.23 J/m^2), providing a driving force for Cu to segregate to a Cu–Co surface.¹⁸⁴

While only a limited amount of testing has been performed on cells made with Cu–Co mixtures, the initial results were intriguing. The addition of even 5% Co to Cu significantly increased the performance of the cells for operation in H_2 at 973 K, from 220 mW/cm^2 on the Cu-based anode to more than 310 mW/cm^2 on the $\text{Cu}_{0.95}\text{Co}_{0.05}$ anode. A Cu–Co cell also exhibited a power density of 360 mW/cm^2 in pure *n*-butane at 1073 K, suggesting that bimetallic anodes are worth considering for fuel cells that operate on hydrocarbons.

5.6. Carbon-Based Anodes

Depending on its form, carbon can exhibit reasonably high electronic conductivity. Therefore, one possibility for operating a fuel cell on hydrocarbons is to use carbon itself as the conductor. While relatively little information on this approach is available in the scientific literature, there are indications in the patent literature that this approach has found some success.¹⁸⁵

At Penn, we have also observed that reasonably high conductivities can be achieved by depositing carbon into a porous YSZ matrix.^{164,172} After exposing a porous YSZ matrix to *n*-butane for 20 h at 973 K, the conductivity was found to increase from 0.002 to 6 S/cm . As discussed in an earlier section, carbon deposits formed by exposure to small hydrocarbons appear to be due to gas-phase, free-radical reactions, with the condensation products depositing only later onto the anode. This is shown by the fact that identical amounts of tar are formed on YSZ substrates, whether Cu or ceria are present. The chemical nature of the carbon deposits has been analyzed using a GC–mass spectrometer, with the results shown in Table 2.⁹² These deposits were formed by flowing *n*-butane over a Cu plate at 973 K. They were then dissolved in toluene before analysis. What the results show is that the molecules are largely polycyclic aromatic compounds that are conductive due to the aromatic ring structure. However, they are clearly not graphitic in nature and can be oxidized at relatively low temperatures as compared to graphite powders.¹⁷²

Anodes using carbon deposits as the conductor can exhibit reasonably high performance. This was shown earlier, in Figure 19, where carbon formed by decomposition of *n*-butane provided the conductivity

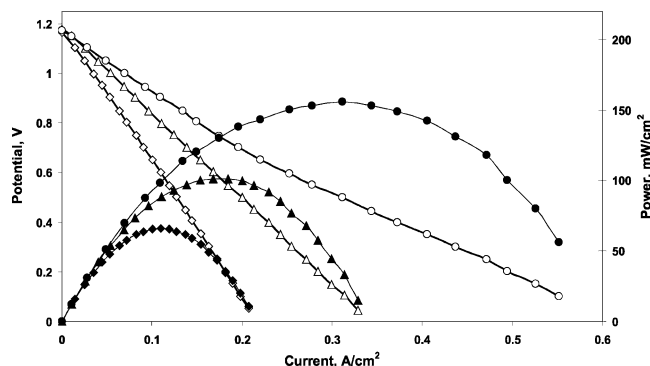


Figure 24. Cell potential (open symbols) and power density (closed symbols) as a function of current for an anode containing 10 wt-% CeO_2 utilizing H_2 fuel at 973 K following 10 min (\blacklozenge), 1 h (\blacktriangle), and 24 h (\bullet) exposure to n -butane. (Reprinted with permission from ref 164. Copyright 2004 The Electrochemical Society, Inc.)

and Pd and ceria provided the catalytic activity. Figure 24 shows how the conductivity due to carbon evolves with time.¹⁶⁴ In this experiment, the anode was initially a porous, YSZ matrix containing only 10 wt-% CeO_2 . Prior to n -butane exposure, there was enough conductivity in the anode to achieve an open-circuit voltage (OCV) of 1.16 V, but the maximum power density was a negligible 7 mW/cm². Exposing the anode to n -butane for 10 min, 1 h, or 24 h led to increasingly better performance, with the maximum power densities in H_2 at 973 K of 65, 100, and 155 mW/cm², respectively. The primary change in the cell impedance spectra with n -butane exposure time was a decrease in the ohmic resistance from 3.86 cm² after 10 min, to 2.20 cm² after 1 h, and 0.71 cm² after 24 h. The nonohmic impedance decreased only slightly with n -butane exposure time.

While carbon-containing anodes are scientifically intriguing, it is difficult to see how one could achieve stable performance with these under practical operating conditions. For operation of cells at higher fuel utilization, parts of the anode will be exposed to high steam contents, conditions under which the carbon phases will not be stable.

6. Conclusions

We believe the development of fuel cells that directly utilize hydrocarbon fuels, without the addition of large amounts of steam or air together with the fuel, is a worthwhile and realizable goal. The advantages for using readily available fuels, together with the high intrinsic efficiencies that are possible with fuel cells, are potentially enormous. Admittedly, while great progress has been made toward this development goal, there still are issues that need to be resolved. The reason for our optimism is that, in contrast to the vast literature describing methods for optimizing Ni-cermet anodes, only a very small amount of work has been performed on alternative materials that do not catalyze carbon formation in the way that Ni does. Even so, the performance of cells made with some of these alternative materials is approaching the performance levels achieved by cells with Ni-cermet anodes. While the stability of some of these alternative anodes, especially the Cu-

based systems, toward high temperatures and long operating times has not yet been demonstrated, one should recognize that it is still very early in the development of these materials. As with any new system, novel fabrication methods and the inclusion of promoters and stabilizers should lead to significant improvements. This work is continuing to advance rapidly.

7. Acknowledgments

Prof. John M. Vohs has been a key collaborator on the Cu-based anodes from the beginning. The actual development of Cu-based anodes started with the work of Drs. Radu Craciun and Seungdoo Park. Others who contributed to this project are as follows: Kipyung Ahn, Shengli An, Marta Boaro, Robert Ferrizz, Hongpeng He, Diana Hou, Yingyi Huang, Sukwon Jung, Hyuk Kim, Venkat V. Krishnan, Shung-Ik Lee, Gang Liu, Chun Lu, Olga Costa-Nunes, Juliega Regal, Calvin da Rosa, Joyce W. Tam, Conghua Wang, Zachary Zisman, and Prof. Wayne Worrell. None of this would have been possible without financial support, initially from the Gas Research Institute, and later from the Office of Naval Research and DARPA through the Palm Power Program.

8. References

- (1) Armor, J. N. *Appl. Catal. A* **1999**, *176*, 159.
- (2) Dokiya, M. *Solid State Ionics* **2002**, *152*, 383.
- (3) Bernay, C.; Marchand, M.; Cassir, M. *J. Power Sources* **2002**, *108*, 139.
- (4) Yamada, K.; Takahashi, N.; Wen, C. J. *J. Chem. Eng. Jpn.* **2002**, *35*, 1290.
- (5) Williams, M. C.; Strakey, J. P. In *SOFC VIII*; Singhal, S. C., Dokiya, M., Eds.; The Electrochemical Society Proceedings Series PV 2003-07; The Electrochemical Society: Pennington, NJ, 2003; p 3.
- (6) Botti, J. J. In *SOFC VIII*; Singhal, S. C., Dokiya, M., Eds.; The Electrochemical Society Proceedings Series PV 2003-07; The Electrochemical Society: Pennington, NJ, 2003; p 16.
- (7) Minh, N. In *SOFC VIII*; Singhal, S. C., Dokiya, M., Eds.; The Electrochemical Society Proceedings Series PV 2003-07; The Electrochemical Society: Pennington, NJ, 2003; p 43.
- (8) Mukerjee, S.; Shaffer, S.; Zizelman, J. In *SOFC VIII*; Singhal, S. C., Dokiya, M., Eds.; The Electrochemical Society Proceedings Series PV 2003-07; The Electrochemical Society: Pennington, NJ, 2003; p 88.
- (9) Petruzzi, L.; Cocchi, S.; Fineschi, F. *J. Power Sources* **2003**, *118*, 96.
- (10) Schiller, G.; Henne, R.; Lang, M.; Muller, M. *Mater. Sci. Forum* **2003**, *426-4*, 2539.
- (11) Winkler, W.; Lorenz, H. *J. Power Sources* **2002**, *105*, 222.
- (12) Minh, N. Q. *J. Am. Ceram. Soc.* **1993**, *76*, 563.
- (13) Steele, B. C. H. *Solid State Ionics* **1996**, *86-88*, 1223.
- (14) Badwal, S. P. S.; Fogger, K. *Ceram. Int.* **1996**, *22*, 257.
- (15) Steele, B. C. H. *Philos. Trans. R. Soc. London A* **1996**, *354*, 1695.
- (16) Kawada, T.; Yokokawa, H. *Key Eng. Mater.* **1997**, *125-126*, 187.
- (17) McEvoy, A. J. *Mater.-wiss. u. Werkstofftech.* **2002**, *33*, 331.
- (18) Tietz, F.; Buchkremer, H.-P.; Stöver, D. *Solid State Ionics* **2002**, *152-153*, 373.
- (19) Tietz, F. *Mater. Sci. Forum* **2003**, *426-432*, 4465.
- (20) Ormerod, R. M. *Chem. Soc. Rev.* **2003**, *32*, 17.
- (21) Quadakkers, W. J.; Piron-Abellan, J.; Shemet, V.; Singheiser, L. *Mater. High Temp.* **2003**, *20*, 115.
- (22) Brandon, N. P.; Skinner, S.; Steele, B. C. H. *Annu. Rev. Mater. Sci.* **2003**, *33*, 183.
- (23) Metcalfe, I. S. *Chem. Eng. Technol.* **2003**, *26*, 857.
- (24) Paz, E. E.; Wang, C.; Palanisamy, C.; Gorte, R. J.; Vohs, J. M. In *SOFC VIII*; Singhal, S. C., Dokiya, M., Eds.; The Electrochemical Society Proceedings Series PV 2003-07; The Electrochemical Society: Pennington, NJ, 2003; p 787.
- (25) Mogensen, M.; Kammer, K. *Annu. Rev. Mater. Res.* **2003**, *33*, 321.
- (26) Marina, O. A.; Mogensen, M. *Appl. Catal. A* **1999**, *189*, 117.
- (27) Park, S.; Vohs, J. M.; Gorte, R. J. *Nature* **2000**, *404*, 265.

- (28) Craciun, R.; Shereck, B.; Gorte, R. J. *Catal. Lett.* **1998**, *51*, 149.
- (29) Fellows, R. J. *Power Sources* **1998**, *71*, 281.
- (30) Kortbeek, P. J.; Ottervanger, R. J. *Power Sources* **1998**, *71*, 223.
- (31) Stevenson, D. A.; Jiang, N.; Buchanan, R. M.; Henn, F. E. G. *Solid State Ionics* **1993**, *62*, 279.
- (32) Nowick, A. S.; Du, Y. *Solid State Ionics* **1995**, *77*, 137.
- (33) Zhu, B.; Rundgren, K.; Mellander, B.-K. *Solid State Ionics* **1997**, *97*, 385.
- (34) Iwahara, H. *Solid State Ionics* **1999**, *125*, 271.
- (35) Corcoran, D. J. D.; Tunstall, D. P.; Irvine, J. T. S. *Solid State Ionics* **2000**, *136*, 297.
- (36) Kreuer, K. D. *Annu. Rev. Mater. Res.* **2003**, *33*, 333.
- (37) Dees, D. W.; Claar, T. D.; Easler, T. E.; Fee, D. C.; Mrazek, F. C. *J. Electrochem. Soc.* **1987**, *134*, 2141.
- (38) George, R. A.; Bessette, N. F. *J. Power Sources* **1998**, *71*, 131.
- (39) Casanova, A. J. *Power Sources* **1998**, *71*, 65.
- (40) Singhal, S. C. *Solid State Ionics* **2000**, *135*, 305.
- (41) Yokokawa, H. *Annu. Rev. Mater. Res.* **2003**, *33*, 581.
- (42) Wang, X.; Nakagawa, N.; Kato, K. *J. Electrochem. Soc.* **2001**, *148*, A565.
- (43) Horita, T.; Yamaji, K.; Sakai, N.; Xiong, Y.; Kato, T.; Yokokawa, H.; Kawada, T. *J. Power Sources* **2002**, *106*, 224.
- (44) Mizusaki, J.; Tagawa, H.; Tsuneyoshi, K.; Sawata, A. *J. Electrochem. Soc.* **1991**, *138*, 1867.
- (45) de Haart, L. G. J.; Kuipers, R. A.; de Vries, K. J.; Burggraaf, A. J. *J. Electrochem. Soc.* **1991**, *138*, 1970.
- (46) Østergård, M. J. L.; Mogensen, M. *Electrochim. Acta* **1993**, *38*, 2015.
- (47) Fukunaga, H.; Ihara, M.; Sakaki, K.; Yamada, K. *Solid State Ionics* **1996**, *86–88*, 1179.
- (48) Tanner, C. W.; Fung, K.-Z.; Virkar, A. V. *J. Electrochem. Soc.* **1997**, *22*, 144.
- (49) Brown, M.; Primdahl, S.; Mogensen, M. *J. Electrochem. Soc.* **2000**, *475*, 147.
- (50) Virkar, A. V.; Fung, K. Z.; Tanner, C. W. U.S. Patent No. 5,543,239, 1996.
- (51) Fleig, J. *J. Power Sources* **2002**, *105*, 228.
- (52) Herbstritt, D.; Müller, A. C.; Weber, A.; Ivers-Tiffée, E. In *SOFC VIII*; Singhal, S. C., Dokiya, M., Eds.; The Electrochemical Society Proceedings Series PV 2003–07; The Electrochemical Society: Pennington, NJ, 2003; p 1330.
- (53) Kleveland, K.; Einarsrud, M.-A.; Schmidt, C. R.; Shamsili, S.; Faaland, S.; Wiik, K.; Grande, T. *J. Am. Ceram. Soc.* **1999**, *82*, 729.
- (54) Colomer, M. T.; Steele, B. C. H.; Kilner, J. A. *Solid State Ionics* **2002**, *147*, 41.
- (55) Simmer, S. P.; Bonnett, J. F.; Canfield, K. D.; Shelton, J. P.; Sprenkle, V. L.; Stevenson, J. W. *J. Power Sources* **2003**, *113*, 1.
- (56) EG&G Technical Services, Inc. *Fuel Cell Handbook 6th Edition*; DOE/NETL-2002/1179; U.S. Department of Energy, Office of Fossil Energy, National Energy Technology Laboratory: Morgantown, WV; p 2.1–2.26.
- (57) Svensson, A. M.; Sunde, S.; Nisancioglu, K. *Solid State Ionics* **1996**, *86–88*, 1211.
- (58) Kim, J.-H.; Virkar, A. V.; Fung, K.-Z.; Mehta, K.; Singhal, S. C. *J. Electrochem. Soc.* **1999**, *146*, 69.
- (59) Williford, R. E.; Chick, L. A.; Maupin, G. D.; Simmer, S. P.; Stevenson, J. W. *J. Electrochem. Soc.* **2003**, *150*, A1067.
- (60) McIntosh, S.; Vohs, J. M.; Gorte, R. J. *Electrochem. Solid-State Lett.* **2003**, *6*, A240.
- (61) Park, S.; Craciun, R.; Vohs, J. M.; Gorte, R. J. *J. Electrochem. Soc.* **1999**, *146*, 3603.
- (62) Juhl, M.; Primdahl, S.; Manon, C.; Mogensen M. *J. Power Sources* **1996**, *61*, 173.
- (63) Murray, E. P.; Barnett, S. A. *Solid State Ionics* **2001**, *143*, 265.
- (64) McIntosh, S.; Adler, S. B.; Vohs, J. M.; Gorte, R. J. *Electrochem. Solid-State Lett.* **2004**, *7*, A111.
- (65) McIntosh, S.; Vohs, J. M.; Gorte, R. J. *J. Electrochem. Soc.* **2003**, *150*, A1305.
- (66) Jiang, S. P.; Love, J. G.; Badwal, S. P. S. *Key Eng. Mater.* **1997**, *125–126*, 81.
- (67) Winkler, J.; Hendriksen, P. V.; Bonanos, N.; Moegensen, M. *J. Electrochem. Soc.* **1998**, *145*, 1184.
- (68) Figueiredo, F. M.; Frade, J.; Marques, F. M. B. *Bol. Soc. Esp. Ceram. Vidrio* **1999**, *38*, 369.
- (69) Adler, S. B.; Henderson, B. T.; Wilson, M. A.; Taylor, D. M.; Richards, R. E. *Solid State Ionics* **2000**, *134*, 35.
- (70) Kato, T.; Momma, A.; Kaga, Y.; Nagata, S.; Kasuga, Y.; Kitase, M. *Solid State Ionics* **2000**, *132*, 287.
- (71) Chan, S. H.; Chen, X. J.; Khor, K. A. *J. Appl. Electrochem.* **2001**, *31*, 1163.
- (72) Takeguchi, T.; Kani, Y.; Yano, T.; Kikuchi, R.; Eguchi, K.; Tsujimoto, K.; Uchida, Y.; Ueno, A.; Omoshiki, K.; Aizawa, M. *J. Power Sources* **2002**, *112*, 588.
- (73) Eguchi, K.; Kojo, H.; Takeguchi, T.; Kikuchi, R.; Sasaki, K. *Solid State Ionics* **2002**, *152–153*, 411.
- (74) Sasaki, K.; Teraoka, Y. *J. Electrochem. Soc.* **2003**, *150*, A878.
- (75) Sasaki, K.; Teraoka, Y. *J. Electrochem. Soc.* **2003**, *150*, A885.
- (76) EG&G Technical Services, Inc. *Fuel Cell Handbook 6th Edition*; DOE/NETL-2002/1179; U.S. Department of Energy, Office of Fossil Energy, National Energy Technology Laboratory: Morgantown, WV; p 8–24.
- (77) Wang, X.; Gorte, R. J. *Catal. Lett.* **2001**, *73*, 15.
- (78) Wang, X.; Gorte, R. J. *App. Catal. A* **2002**, *224*.
- (79) Baker, R. T. K.; Barber, M. A.; Harris, P. S.; Feates, F. D.; Waite, R. J. *J. Catal.* **1972**, *26*, 51.
- (80) Baker, R. T. K.; Harris, P. S.; Henderson, J.; Thomas, R. B. *Carbon* **1975**, *13*, 17.
- (81) Baker, R. T. K.; Harris, P. S.; Terry, S. *Nature* **1975**, *253*, 37.
- (82) Keep, C. W.; Baker, R. T. K.; France, J. A. *J. Catal.* **1977**, *47*, 232.
- (83) Bartholomew, C. H. *Catal. Rev.—Sci. Eng.* **1982**, *24*, 67.
- (84) Baker, R. T. K. *Carbon* **1989**, *27*, 315.
- (85) Zhang, T.; Amiridis, M. D. *Appl. Catal. A* **1998**, *167*, 161.
- (86) Monnerat, B.; Kiwi-Minsker, L.; Renken, A. *Chem. Eng. Sci.* **2001**, *56*, 633.
- (87) Chun, C. M.; Mumford, J. D.; Ramanarayanan, T. A. In *SOFC VI*; Singhal, S. C., Dokiya, M., Eds.; The Electrochemical Society Proceedings Series PV 1999–19; The Electrochemical Society: Pennington, NJ, 1999; p 621.
- (88) Toh, C. H.; Munroe, P. R.; Young, D. J.; Foger, K. *Mater. High Temp.* **2003**, *20*, 129.
- (89) Chen, P.; Zhang, H.-B.; Lin, G.-D.; Hong, Q.; Tsai, K. R. *Carbon* **1997**, *100–11*, 1495.
- (90) Toebes, M. L.; Bitter, J. H.; van Dillen, A. J.; de Jong, K. P. *Catal. Today* **2002**, *76*, 33.
- (91) Farrauto, R. J.; Bartholomew, C. H. *Fundamentals of Industrial Catalytic Processes*, 1st ed.; Blackie Academic and Professional: London, 1997; p 351.
- (92) Lee, S.-I.; McIntosh, S.; Vohs, J. M.; Gorte, R. J. In *SOFC VIII*; Singhal, S. C., Dokiya, M., Eds.; The Electrochemical Society Proceedings Series PV 2003–07; The Electrochemical Society: Pennington, NJ, 2003; p 865.
- (93) Wang, J. B.; Jang, J.-C.; Huang, T.-J. *J. Power Sources* **2003**, *122*, 122.
- (94) Liu, J.; Madsen, B. D.; Ji, Z.; Barnett, S. A. *Electrochem. Solid-State Lett.* **2002**, *5*, A122.
- (95) Livermore, A. J. A.; Cotton, J. W.; Ormerod, R. M. *J. Power Sources* **2000**, *86*, 411.
- (96) Dicks, A. L. *J. Power Sources* **1996**, *61*, 113.
- (97) Clarke, A. H.; Dicks, A. L.; Pointon, K.; Smith, T. A.; Swann, A. *Catal. Today* **1997**, *38*, 411.
- (98) Dicks, A. L. *J. Power Sources* **1998**, *71*, 111.
- (99) Murray, E. P.; Tsai, T.; Barnett, S. A. *Nature* **1999**, *400*, 649.
- (100) Murray, E. P.; Barnett, S. A. In *SOFC VI*; Singhal, S. C., Dokiya, M., Eds.; The Electrochemical Society Proceedings Series PV 1999–19; The Electrochemical Society: Pennington, NJ, 1999; p 1001.
- (101) Liu, J.; Barnett, S. A. *Solid State Ionics* **2003**, *158*, 11.
- (102) Zhan, Z.; Madsen, B. D.; Liu, J.; Barnett, S. A. In *SOFC VIII*; Singhal, S. C., Dokiya, M., Eds.; The Electrochemical Society Proceedings Series PV 2003–07; The Electrochemical Society: Pennington, NJ, 2003; p 1286.
- (103) Weber, A.; Sauer, B.; Müller, A. C.; Herbstritt, D.; Ivers-Tiffée, E. *Solid State Ionics* **2002**, *152–153*, 543.
- (104) Kendall, K.; Finnerty, C. M.; Saunders, G.; Chung, J. T. *J. Power Sources* **2002**, *106*, 323.
- (105) Kim, H.; Park, S.; Vohs, J. M.; Gorte, R. J. *J. Electrochem. Soc.* **2001**, *148*, A693.
- (106) Jiang, Y.; Virkar, A. V. *J. Electrochem. Soc.* **2001**, *148*, A706.
- (107) Saunders, G. J.; Kendall, K. *J. Power Sources* **2002**, *106*, 258.
- (108) Wang, S.; Isihara, T.; Takita, Y. *Electrochem. Solid-State Lett.* **2002**, *5*, A177.
- (109) Murray, E. P.; Harris, S. J.; Jen, H. *J. Electrochem. Soc.* **2002**, *149*, A1127.
- (110) Farrauto, R. J.; Bartholomew, C. H. *Fundamentals of Industrial Catalytic Processes*, 1st ed.; Blackie Academic and Professional: London, 1997; p 349.
- (111) Murray, E. P.; Barnett, S. A. *Solid State Ionics* **2001**, *143*, 265.
- (112) Ralph, J. M.; Schoeler, A. C.; Krumpelt, M. *J. Mater. Sci.* **2001**, *36*, 1161.
- (113) Hart, N. T.; Brandon, N. P.; Day, M. J.; Lapeña-Rey, N. *J. Power Sources* **2002**, *106*, 42.
- (114) Colomer, M. T.; Steele, B. C. H.; Kilner, J. A. *Solid State Ionics* **2002**, *147*, 41.
- (115) Simmer, S. P.; Bonnett, J. F.; Canfield, N. L.; Meinhardt, K. D.; Shelton, J. P.; Sprenkle, V. L.; Stevenson, J. W. *J. Power Sources* **2003**, *113*, 1.
- (116) Huang, Y.; Vohs, J. M.; Gorte, R. J. *J. Electrochem. Soc.* **2004**, *151*, A646.
- (117) Tao, S.; Irvine, J. T. S. *Nat. Mat.* **2003**, *2*, 320.
- (118) Eguchi, K.; Setoguchi, T.; Inoue, T.; Arai, H. *Solid State Ionics* **1992**, *52*, 165.
- (119) Mogensen, M.; Lindegaard, T.; Hansen, U. R.; Mogensen, G. *J. Electrochem. Soc.* **1994**, *141*, 2122.
- (120) Eguchi, K. *J. Alloys Compd.* **1997**, *250*, 486.

- (121) Mogensen, M.; Sammes, N. M.; Tompsett, G. A. *Solid State Ionics* **2000**, *129*, 63.
- (122) Ramírez-Cabrera, E.; Laosiripojana, N.; Atkinson, A.; Chadwick, D. *Catal. Today* **2003**, *78*, 433.
- (123) Steele, B. C. H.; Middleton, P. H.; Rudkin, R. A. *Solid State Ionics* **1990**, *40–41*, 388.
- (124) Putna, E. S.; Stubenrauch, J.; Vohs, J. M.; Gorte, R. J. *Langmuir* **1995**, *11*, 4832.
- (125) Marina, O. A.; Bagger, C.; Primdahl, S.; Mogensen, M. *Solid State Ionics* **1999**, *123*, 199.
- (126) Bouwmeester, H. J. M.; Burggraaf, A. J. In *The CRC Handbook of Solid State Electrochemistry*; Gellings, P. J., Bouwmeester, H. J. M., Eds.; CRC Press: Boca Raton, FL, 1997; p 481.
- (127) Sauvet, A.; Irvine, J. T. S. *Fuel Cells* **2001**, *1*, 205.
- (128) Boukamp, B. A. *Nat. Mat.* **2003**, *2*, 294.
- (129) Andersen, H. U. *Solid State Ionics* **1992**, *52*, 33.
- (130) Mizusaki, J. *Solid State Ionics* **1992**, *52*, 79.
- (131) van Hassel, B. A.; Kawada, T.; Sakai, N.; Yokokawa, H.; Dokiya, M.; Bouwmeester, H. J. M. *Solid State Ionics* **1993**, *66*, 295.
- (132) Yokokawa, H.; Sakai, N.; Kawada, T.; Dokiya, M. *Solid State Ionics* **1992**, *52*, 43.
- (133) Xu, S. J.; Thomson, W. J. *Ind. Eng. Chem. Res.* **1998**, *37*, 1290.
- (134) Sfeir, J. *J. Power Sources* **2003**, *118*, 276.
- (135) Sfeir, J.; van Herle, J.; McEvoy, A. J. *J. Eur. Ceram. Soc.* **1999**, *19*, 897.
- (136) Baker, R. T.; Metcalfe, I. S.; Middleton, P. H.; Steele, B. C. H. *Solid State Ionics* **1994**, *72*, 328.
- (137) Metcalfe, I. S.; Baker, R. T. *Catal. Today* **1996**, *27*, 285.
- (138) Stojanović, M.; Mims, C. A.; Modallal, H.; Yang, Y. L.; Jacobson, A. J. *J. Catal.* **1997**, *166*, 324.
- (139) Weston, M.; Metcalfe, I. S. *Solid State Ionics* **1998**, *113–115*, 247.
- (140) Hartley, A.; Sahibzada, M.; Weston, M.; Metcalfe, M.; Mantzavinos, D. *Catal. Today* **2000**, *55*, 197.
- (141) Sfeir, J.; Buffat, P. A.; Möckli, P.; Xanthopoulos, N.; Vasquez, R.; Mathieu, H. J.; van Herle, J.; Thampi, K. R. *J. Catal.* **2001**, *202*, 229.
- (142) Kirchnerova, J.; Alifanti, M.; Delmon, B. *Appl. Catal., A* **2002**, *231*, 65.
- (143) Alifanti, M.; Auer, R.; Kirchnerova, J.; Thyrion, F.; Grange, P.; Delmon, B. *Appl. Catal. B* **2003**, *41*, 71.
- (144) Marina, O. A.; Canfield, N. L.; Stevenson, J. W. *Solid State Ionics* **2002**, *149*, 21.
- (145) Canales-Vázquez, J.; Tao, S. W.; Irvine, J. T. S. *Solid State Ionics* **2003**, *159*, 159.
- (146) He, H.; Huang, Y.; Regal, J.; Boaro, M.; Vohs, J. M.; Gorte, R. J. *J. Am. Ceram. Soc.* **2004**, *87*, 331.
- (147) Irvine, J. T. S.; Sauvet, A. *Fuel Cells* **2001**, *1*, 205.
- (148) Primdahl, S.; Hansen, J. R.; Grahl-Madsen, L.; Larsen, P. H. *J. Electrochem. Soc.* **2001**, *148*, A74.
- (149) He, H.; Huang, Y.; Vohs, J. M.; Gorte, R. J. *Solid State Ionics*, in press.
- (150) Reich, C. M.; Kaiser, A.; Irvine, J. T. S. *Fuel Cells* **2001**, *1*, 249.
- (151) Slater, P. R.; Irvine, J. T. S. *Solid State Ionics* **1999**, *120*, 125.
- (152) Kaiser, A.; Bradley, J. L.; Slater, P. R.; Irvine, J. T. S. *Solid State Ionics* **2000**, *135*, 519.
- (153) Kelaidopoulou, A.; Siddle, A.; Dicks, A. L.; Kaiser, A.; Irvine, J. T. S. *Fuel Cells* **2001**, *1*, 219.
- (154) Kelaidopoulou, A.; Siddle, A.; Dicks, A. L.; Kaiser, A.; Irvine, J. T. S. *Fuel Cells* **2001**, *1*, 226.
- (155) Kiratzis, N.; Holtappels, P.; Hatchwell, C. E.; Mogensen, M.; Irvine, J. T. S. *Fuel Cells* **2001**, *1*, 211.
- (156) Joerger, M. B.; Baeurle, L. M.; Gauckler, L. J. In *Proceedings of the 5th European Solid Oxide Fuel Cell Forum*; Huijsmans, J., Ed.; The European Fuel Cell Forum: Oberrohrdorf, Switzerland, 2002; p 475.
- (157) Craciun, R.; Park, S.; Gorte, R. J.; Vohs, J. M.; Wang, C.; Worrell, W. L. *J. Electrochem. Soc.* **1999**, *146*, 4019.
- (158) Park, S.; Craciun, R.; Vohs, J. M.; Gorte, R. J. *J. Electrochem. Soc.* **1999**, *146*, 3603.
- (159) Gorte, R. J.; Park, S.; Vohs, J. M.; Wang, C. *Adv. Mater.* **2000**, *12*, 1465.
- (160) Mistler, R. E.; Twiname, E. R. *Tape Casting: Theory and Practice*; The American Ceramic Society: Westerville, OH, 2002.
- (161) Lu, C.; Worrell, W. L.; Gorte, R. J.; Vohs, J. M. *J. Electrochem. Soc.* **2003**, *150*, A354.
- (162) Boaro, M.; Vohs, J. M.; Gorte, R. J. *J. Am. Ceram. Soc.* **2003**, *86*, 395.
- (163) Kim, H.; da Rosa, C.; Boaro, M.; Vohs, J. M.; Gorte, R. J. *J. Am. Ceram. Soc.* **2002**, *85*, 1473.
- (164) McIntosh, S.; He, H.; Lee, S.-I.; Costa-Nunes, O.; Krishnan, V. V.; Vohs, J. M.; Gorte, R. J. *J. Electrochem. Soc.* **2004**, *151*, A604.
- (165) McIntosh, S.; Vohs, J. M.; Gorte, R. J. *Electrochim. Acta* **2002**, *47*, 3815.
- (166) Lu, C.; Worrell, W. L.; Vohs, J. M.; Gorte, R. J. *J. Electrochem. Soc.* **2003**, *150*, A1357.
- (167) Farrauto, R. J.; Bartholomew, C. H. *Fundamentals of Industrial Catalytic Processes*, 1st ed.; Blackie Academic and Professional: London, 1997; p 489.
- (168) Stoukides, M. *Catal. Rev. Sci. Eng.* **2000**, *42*, 1.
- (169) He, H.; Vohs, J. M.; Gorte, R. J. *J. Electrochem. Soc.* **2003**, *150*, A1470.
- (170) Gorte, R. J.; Vohs, J. M. *J. Power Sources* **2002**, *106*, 10.
- (171) Gorte, R. J.; Vohs, J. M. *J. Catal.* **2003**, *216*, 477.
- (172) McIntosh, S.; Vohs, J. M.; Gorte, R. J. *J. Electrochem. Soc.* **2003**, *150*, A470.
- (173) Walters, K. M.; Dean, A. M.; Zhu, H.; Kee, R. J. *J. Power Sources* **2003**, *123*, 182.
- (174) Farrauto, R. J.; Bartholomew, C. H. *Fundamentals of Industrial Catalytic Processes*, 1st ed.; Blackie Academic and Professional: London, 1997; p 355.
- (175) Ferrizz, R. M.; Gorte, R. J.; Vohs, J. M. *Appl. Catal. B* **2003**, *43*, 273.
- (176) Kim, H.; Vohs, J. M.; Gorte, R. J. *Chem. Commun.* **2001**, 2334.
- (177) Costa-Nunes, O.; Vohs, J. M.; Gorte, R. J. *J. Electrochem. Soc.* **2003**, *150*, A858.
- (178) EG&G Technical Services, Inc. *Fuel Cell Handbook*, 5th ed.; DOE/NETL-2000; U.S. Department of Energy, Office of Fossil Energy, National Energy Technology Laboratory: Morgantown, WV, 2000, p 138.
- (179) Kim, H.; Lu, C.; Worrell, W. L.; Vohs, J. M.; Gorte, R. J. *J. Electrochem. Soc.* **2002**, *149*, A247.
- (180) Lee, S.-I.; Vohs, J. M.; Gorte, R. J. *J. Electrochem. Soc.*, submitted.
- (181) Rodriguez, N. M.; Kim, M. S.; Baker, T. K. *J. Catal.* **1993**, *140*, 16.
- (182) Sinfelt, J. H.; Carter, J. L.; Yates, D. J. C. *J. Catal.* **1972**, *24*, 283.
- (183) Zhu, L.; Depristo, A. E. *J. Catal.* **1997**, *167*, 400.
- (184) Kim, S.-K.; Kim, J.-S.; Han, J. Y.; Seo, J. M.; Lee, C. K.; Hong, S. C. *Surf. Sci.* **2000**, *453*, 47.
- (185) Tao, T. T., U.S. Patent Application 20020015877, 2002.

CR020725G

Modeling Transport in Polymer-Electrolyte Fuel Cells

Adam Z. Weber* and John Newman

Department of Chemical Engineering, University of California, Berkeley, California 94720-1462

Received December 5, 2003

Contents

1. Introduction	4679	6. Other Effects	4715
2. Overview of Models	4680	6.1. Nonisothermal Models	4716
2.1. Historical	4681	6.2. Transient Models	4719
2.2. Detailed by Affiliation	4682	7. Other Models	4720
2.2.1. Springer et al. Model and Derivatives	4682	8. Summary	4721
2.2.2. Bernardi and Verbrugge Model and Derivatives	4683	9. Acknowledgments	4722
2.2.3. Computational-Fluid-Dynamics Models	4683	10. Nomenclature	4722
2.2.4. Other Macrohomogeneous Models	4684	11. References	4723
3. General Aspects and Equations	4685		
3.1. Modeling Methodologies	4685		
3.2. General Equations	4685		
3.2.1. Thermodynamics	4685		
3.2.2. Kinetics	4686		
3.2.3. Ohmic Losses	4687		
3.2.4. Mass-Transfer Limitations	4687		
3.3. Zero-Dimensional Models	4688		
4. Fuel-Cell Sandwich Modeling	4689		
4.1. Conservation Equations	4689		
4.2. Membrane Modeling	4690		
4.2.1. Microscopic and Physical Models	4691		
4.2.2. Diffusive Models	4692		
4.2.3. Hydraulic Models	4694		
4.2.4. Hydraulic–Diffusive Models	4694		
4.2.5. Combination Models	4695		
4.3. Diffusion-Media Modeling	4695		
4.3.1. Gas-Phase Transport	4696		
4.3.2. Treatment of Liquid Water	4697		
4.4. Catalyst-Layer Modeling	4700		
4.4.1. General Governing Equations	4701		
4.4.2. Interface Models	4702		
4.4.3. Microscopic and Single-Pore Models	4703		
4.4.4. Simple Macrohomogeneous Models	4704		
4.4.5. Embedded Macrohomogeneous Models	4707		
4.4.6. Catalyst-Layer Flooding	4708		
4.5. Multilayer Simulations	4709		
4.5.1. Numerical Solution and Boundary Conditions	4709		
4.5.2. General Multilayer Simulation Results	4710		
5. Multidimensional Effects	4711		
5.1. Two-Dimensional Models	4711		
5.1.1. Along-the-Channel Models	4711		
5.1.2. Under-the-Rib Models	4713		
5.2. Three-Dimensional Models	4714		

1. Introduction

Fuel cells may become the energy-delivery devices of the 21st century. Although there are many types of fuel cells, polymer-electrolyte fuel cells are receiving the most attention for automotive and small stationary applications. In a polymer-electrolyte fuel cell, hydrogen and oxygen are combined electrochemically to produce water, electricity, and some waste heat.

During the operation of a polymer-electrolyte fuel cell, many interrelated and complex phenomena occur. These processes include mass and heat transfer, electrochemical reactions, and ionic and electronic transport. Only through fundamental modeling, based on physical models developed from experimental observations, can the processes and operation of a fuel cell be truly understood. This review examines and discusses the various regions in a fuel cell and how they have been modeled.

The focus of this review is to discuss the different fuel-cell models with the overall goal of presenting a picture of the various types of transport in fuel cells. Although the majority of the literature fuel-cell models have been examined, there are undoubtedly some that were left out. In terms of time frame, this review focuses mainly on models that have been published through the end of 2003.

In discussing the various models, this review starts with a historical background where the models are presented and their advantages and disadvantages are briefly discussed. However, direct comparisons of the different models to each other are hard to make because they vary in their approach and complexity, and one model may do a good job in one region (e.g., the membrane) but not in another (e.g., the electrode). Furthermore, almost all of them agree with some sort of experimental data. Therefore, the majority of this review delves into how the various regions and effects are modeled independently of each other. It is our feeling that the reader will get more by

* Corresponding author. E-mail: aweber@uclink.berkeley.edu. Telephone: 510-643-1972. Fax: 510-642-4778.



Adam Weber was born in 1976 in Fort Lauderdale, FL. He studied chemical engineering at Tufts University, where he earned B.S. and M.S. degrees in 1999. His thesis topic was on low-temperature carbon-monoxide oxidation using gold supported on ceria catalysts under the guidance of Maria Flytzani-Stephanopoulos. His work was supported by the EPA through a STAR graduate fellowship and through the Astronaut Scholarship Foundation. After spending a year on a Fulbright scholarship in Australia, he entered the Ph.D. program at University of California—Berkeley in chemical engineering under the guidance of John Newman. He once again earned an EPA STAR graduate fellowship for his dissertation work on the mathematical modeling of transport inside polymer-electrolyte fuel cells.



John Newman received his B.S. in chemical engineering from Northwestern in 1960 and his M.S. and Ph.D. from University of California—Berkeley in 1962 and 1963, respectively. Then he joined the faculty at U. C. Berkeley, where he has remained for the past 41 years. He also holds an appointment as a faculty senior scientist at Lawrence Berkeley National Laboratory. Recently, he spent a semester in 2002 as the Onsager Professor at the Norwegian University of Science and Technology in Trondheim, Norway. His interests lie in understanding the fundamental processes in electrochemical engineering and other coupled phenomena. He is a member of the National Academy of Engineering and a Fellow of The Electrochemical Society as well as being a highly cited author of over 300 publications in the field of electrochemistry.

examining the modeling equations and approaches per region than through just an encyclopedic list and discussion of the various models. In this context, if the reader is just interested in a single region or effect, all of the relevant models, approaches, phenomena, and equations can easily be found. Finally, although the majority of the models discussed are for hydrogen polymer-electrolyte fuel cells, the underlying phenomena and many of the regions are applicable to other types of polymer-electrolyte fuel cells, such as direct-methanol fuel cells.

In this review, the discussion and models are classified by their geometric dimensionality. The zero-dimensional (0-D) models are mainly empirical

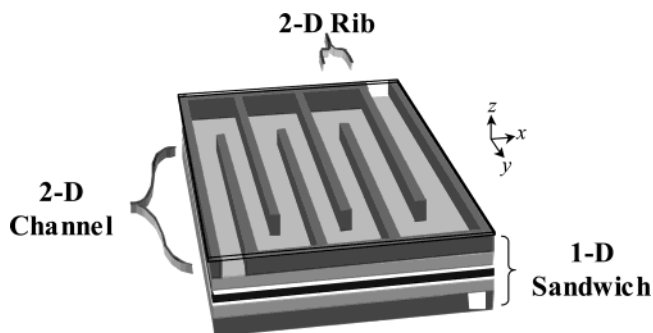


Figure 1. Fuel-cell schematic showing the different model dimensionalities. 0-D models are simple equations and are not shown, the 1-D models comprise the sandwich (z direction), the 2-D models comprise the 1-D sandwich and either of the two other coordinate directions (x or y), and the 3-D models comprise all three coordinate directions.

and model the fuel cell with a simple equation. The 1-D models treat the fuel-cell sandwich in varying degrees of complexity. These are the majority of the models, and they model the different regions of the fuel-cell sandwich with everything from simple equations to complex expressions derived from physical models. Furthermore, they can incorporate other (nongeometric) dimensional effects in terms of size, that is, microscopic and macroscopic effects (e.g., consumption of reactant in a pore of a particle which is within a porous electrode). The 1-D models are the major focus of this review. What we term the 2-D models deal with effects in the fuel cell that occur in the sandwich as well as in another direction, either across or along the gas channel. Finally, the 3-D models include the 1-D sandwich and consider effects in both directions in the flow field. Figure 1 shows a schematic of a fuel cell, showing the different (non-zero) modeling dimensions as defined in this article.

The outline of this review is as follows. First, the general overview of the models is presented in both a historical and research-group context. Next, the general modeling methodologies and overall phenomena are looked at, including the 0-D models. In the following section, the 1-D fuel-cell sandwich is discussed in detail by layer (catalyst layers, diffusion media, membrane, and multilayer). This section is the longest of the review because the sandwich has the most complex phenomena and is the heart of the fuel cell; it also is the most often modeled. Following this discussion, the multidimensional effects and models are considered. Next, nonisothermal and transient effects and models are examined. Finally, some related fuel-cell models are noted, and this is followed by a summary.

2. Overview of Models

The number of published fuel-cell-related models has increased dramatically in the past few years, as seen in Figure 2. Not only are there more models being published, but they are also increasing in complexity and scope. With the emergence of faster computers, the details of the models are no longer constrained to a lot of simplifying assumptions and analytic expressions. Full, 3-D fuel-cell models and the treatment of such complex phenomena as two-

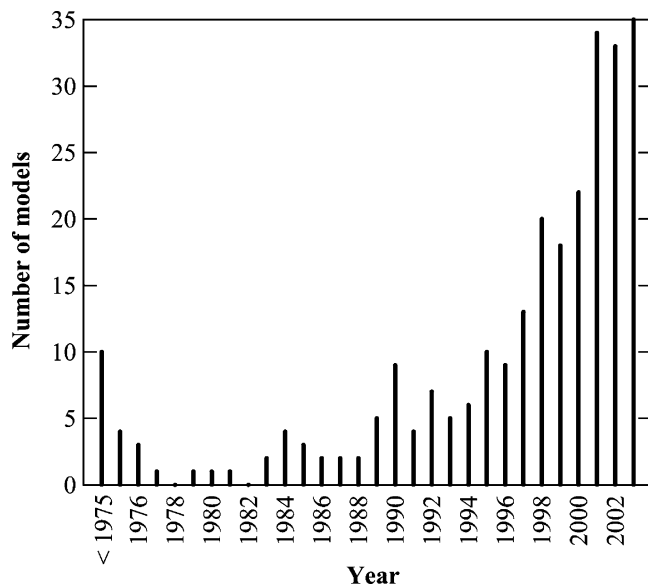


Figure 2. Bar graph showing the number of polymer-electrolyte related fuel-cell models published per year.

phase flow are becoming more common. In this section, an overview of the various fuel-cell models is presented with brief comments about their strengths and weaknesses. First, a short chronology of the major features and trends is outlined. This is followed by a description of the various models by research group. In both of these overviews, only select models are presented with a focus on macroscopic models that have a complete description of at least two layers of the 1-D fuel-cell sandwich. Other models, in addition to the ones below, are discussed in the appropriate sections of this review.

2.1. Historical

The beginning of modeling of polymer-electrolyte fuel cells can actually be traced back to phosphoric-acid fuel cells. These systems are very similar in terms of their porous-electrode nature, with only the electrolyte being different, namely, a liquid. Giner and Hunter¹ and Cutlip and co-workers^{2–5} proposed the first such models. These models account for diffusion and reaction in the gas-diffusion electrodes. These processes were also examined later with porous-electrode theory.^{6,7} While the phosphoric-acid fuel-cell models became more refined, polymer-electrolyte-membrane fuel cells began getting much more attention, especially experimentally.

Out of these experiments, simple 0-D models were used to analyze the data (for examples, see refs 8–12). These models normally fit the experimental data with a single equation, and although they demonstrate good fits and are quick and easy to implement, they are less reliable in predicting and explaining behavior. As the experiments and viability of polymer-electrolyte fuel cells became more widespread, models were designed to simulate their performance and gain understanding of the underlying fundamental transport processes. From these early models, the two main fundamental ones were those of Bernardi and Verbrugge¹³ and Springer et al.¹⁴ Both of them treat the fuel-cell sandwich,

composed of membrane, diffusion media, and catalyst layers, and are isothermal and 1-D. The Bernardi and Verbrugge model assumes a fully hydrated membrane and incorporates porous-electrode equations and Stefan–Maxwell diffusion in the diffusion media and catalyst layers. The model of Springer et al. does not use porous-electrode equations but does consider a changing water content in the membrane. This allows for variable properties in the membrane such as conductivity and the water diffusion coefficient. Most models today can trace their roots back to these models, and some are direct descendants, as discussed in the next section.

The next two major models were those by Fuller and Newman¹⁵ and Nguyen and White,¹⁶ who both examined flow effects along the channel. These models allowed for a more detailed description of water management and the effect of dry gas feeds and temperature gradients. Throughout the next few years, several more 0-D models and 1-D models were generated.^{12,17–23} Also, some simulations examined more detailed 2-D effects, such as rib spacing.^{24,25}

As interest grew in fuel cells in the late 1990s, more and more models were generated. Many of these models tried to understand and describe the cathode.^{26–37} The interest was to optimize the catalyst layer and increase its efficiency, thereby reducing the precious-metal loading and increasing performance. Out of these models, those of Durand and co-workers^{30–34} advocated strongly for the use of agglomerate models, where the microstructure of the cathode is considered explicitly. Another important model was that of Perry et al.,³⁶ which examined limiting behavior in the cathode and its possible diagnosis. Around this time as well, interest grew in membrane modeling,^{38–43} as well as incorporating transient, nonisothermal, and multidimensional effects in complete fuel-cell models.^{44–50}

In 2000 and 2001, fuel-cell models were produced by the dozens. These models were typically more complex and focused on such effects as two-phase flow^{50–56} where liquid-water transport was incorporated. The work of Wang and co-workers^{57–59} was at the forefront of those models treating two-phase flow comprehensively. The liquid-water flow was shown to be important in describing the overall transport in fuel cells. Other models in this time frame focused on multidimensional, transient, and more microscopic effects.^{60–73} The microscopic effects again focused on using an agglomerate approach in the fuel cell as well as how to model the membrane appropriately.

In the last couple of years, the same trend toward more complex and complete models has continued, aided by the increases in computer processing speed. One way to address issues in more detail is through incorporating and examining complex effects such as flow-field design and two-phase flow.^{74–88} The other way is to step back and examine a specific region of the fuel cell, such as the membrane or catalyst layer, and model that rigorously.^{89–100} Whichever the case, the models today tend to be more complex, with detailed consideration of the important aspects of fuel cells, such as water management.

2.2. Detailed by Affiliation

Although the number of models is large, the number of modeling groups and approaches is significantly fewer. The obvious reason is that as a group becomes more familiar with a model, they continually upgrade it in terms of complexity to make it more physically realistic. For an approach, if it is general, then the community adopts and alters it. For this reason, it makes sense to give an overview of the models by these criteria. In this section, the models are discussed in terms of the research groups, where the progress of each group is highlighted and easily ascertained. These groups are loosely categorized by modeling approach. To save space, a research group is located only under the most appropriate heading, even if all of their models do not conform to that heading. Once again, the models discussed here are primarily those that model at least two layers of the 1-D sandwich of a single polymer-electrolyte fuel cell. Other models such as membrane, stack, impedance, electrode, empirical 0-D, and direct-methanol fuel-cell models and specific treatments of each layer can be found in later sections of this review and are not discussed below.

2.2.1. Springer et al. Model and Derivatives

As mentioned above, one of the first 1-D fuel-cell models was by Springer et al.¹⁴ at Los Alamos National Laboratory (LANL). The model is isothermal and considers polarization and electrode effects only through a simple 0-D type of polarization equation. However, the membrane does have variable water content, although liquid water was not considered explicitly. The modeling results showed the importance of keeping the membrane well hydrated, and discussed the importance of water management. Springer et al.¹⁰¹ took the original model and added a detailed cathode model to it. They examined utilization of the catalyst and the effects of performance on various parameters such as the diffusion-medium porosity and the inlet-gas composition. The cathode is treated as a uniformly distributed layer, and the model does not treat flooding. Springer et al.^{102,103} also added impedance to their original model to explore other effects and compare to another set of data. They were one of the first to do this. Finally, recently, they have come up with a sophisticated anode model to go along with the overall model that includes the effects of carbon monoxide poisoning.¹⁰⁴

Several groups were influenced by the work of the group at LANL. Models by these groups treat the membrane and fuel cell in a similar fashion, while adding various complexities. While not necessarily truly a derivative of Springer, the model of Wang and Savinell¹⁷ has a very similar approach, except that they incorporate an agglomerate model of the catalyst layer. They examine the effects of feed concentration and humidity, although they do not consider changes down the gas channel. They also examine carbon monoxide poisoning and discuss the structure of the anode.

Similar to the above model, that of Ridge et al.¹⁰⁵ examines the microstructure of the cathode catalyst layer in more detail. Their analysis is thorough and

shows the effect of such factors as Teflon loading and proton conductivity. Their implementation of an agglomerate model is perhaps the first application of this to polymer-electrolyte fuel-cell catalyst layers. Similar to this model, that of Rho and Srinivasan¹⁹ looks at effects in the cathode in terms of operating conditions using a detailed agglomerate model. Their model was also relatively early and does a good job in describing observations in terms of interactions at the agglomerate scale. Finally, Weisbrod et al.¹⁰⁶ incorporated a porous-electrode model into the Springer et al. model to examine both kinetic and mass-transfer losses in more detail.

Perhaps the most renowned researcher to follow the Springer modeling concept is Trung Van Nguyen. His first model examined 2-D effects along the gas channel.¹⁶ It is a pseudo-2-D model and has a very similar basis to that of the Springer et al. model. Although its membrane model assumes only a linear gradient in water concentration, it accounts for liquid-water flow and is nonisothermal. The model clearly showed that water and heat management are interrelated and very important for optimal fuel-cell operation. The model also examined the effects of having a nonuniform current-density distribution down the flow channel. Finally, although liquid water was considered in terms of energy, it had a negligible volume, and the electrodes were treated as interfaces.

Nguyen's group at the University of Kansas continued to upgrade this model. They also examined other effects in the fuel cell. Yi and Nguyen¹⁰⁷ took essentially the same model as that of Nguyen and White¹⁶ above and added coolant-plate and heat-exchange equations. They also examined further the effects of differential pressures and humidification conditions of the anode. The research group reduced some of the limitations of the model and made it two-phase and a true two-dimensional model, where the flow-field structure of ribs and channels was examined.^{48,52,108} The models that first did this were for interdigitated flow fields and, along with the model of Kazim et al.,⁴⁶ were some of the very first models to address this type of flow field.^{48,52} Nguyen and co-workers were also some of the first researchers to examine two-phase flow, and they clearly showed how important saturation effects are at the cathode. The two-phase flow models use empirical expressions for the saturation functions taken from matching experimental data. However, these models assume a net water flux through the membrane and infinitely thin catalyst layers, which somewhat limits their applicability. The recent models of Natarajan and Nguyen^{56,87} examined transient and 3-D effects, as well as limitations due to flooding in the catalyst-layer interfacial regions. Overall, the work of this group has pioneered examining two-phase flow effects.

Other Springer model derivatives include those of Ge and Yi,¹⁰⁹ van Bussel et al.,⁴⁴ Wöhr and co-workers,^{26,45} and Hertwig et al.⁹⁹ Here, the models described above are slightly modified. The model of Hertwig et al. includes both diffusive and convective transport in the membrane. It also uses a simplified two-phase flow model and shows 3-D distributions

of various properties in the fuel cell. The model of van Bussel et al. mainly focused on 2-D and dynamic water transport in the membrane by diffusion and electroosmotic flow. They showed agreement with polarization curves and explained the experimental results for counterflow and coflow operation and stability with dry gases based on the water-content distribution of the membrane. This is one of the first transient models. Another early transient model is that of Woehr et al.⁴⁵ Similar to the model of van Bussel et al., the membrane is accounted for by diffusion, but Woehr et al. also include liquid saturation and nonisothermal effects. The model does a good job in showing temperature spikes in single cells as well as in stacks. The catalyst-layer and diffusion-media models for this model were based on the earlier work by Bevers et al.²⁶ Here, the cathode side of a membrane was simulated including liquid-water and energy effects. The simulation results demonstrate good agreement with experimental data and allow for an increased understanding and calculation of meaningful physical parameters. Finally, the model of Ge and Yi is 2-D and uses the same kind of membrane model as van Bussel et al. They examine the effect of differential pressures, flow arrangement, and temperature.

2.2.2. Bernardi and Verbrugge Model and Derivatives

Around the same time as the model of Springer et al., Bernardi and Verbrugge¹³ published their fuel-cell model. This model was based on their gas-diffusion electrode model¹¹⁰ and that of Verbrugge and Hill.¹¹¹ Prior to their fuel-cell model, Bernardi¹¹² published a relatively simple study of the water balance in a fuel cell, highlighting the importance of water management and the sensitivity of the water balance to changes in operating conditions such as humidity, temperature, and pressure. The Bernardi article was a seminal paper and the first to stress water management. The fuel-cell model of Bernardi and Verbrugge includes transport of both gas and liquid in the diffusion media, detailed porous-electrode models for both electrodes, and a membrane model based on Schlögl's equation (see eq 34) with gas crossover. The model is 1-D and isothermal, and the main limitation of the model is that the membrane is assumed to be fully hydrated. This limits the applicability of the model to humidified feeds and/or thin membranes. Another limitation of the model is the neglect of true two-phase flow; the model only uses constant volume fractions for the various phases. Notwithstanding these limitations, the model allows for a detailed examination of liquid water pressure profiles and how many different operating and structural parameters affect overall fuel-cell performance.

Not surprisingly, the Bernardi and Verbrugge model forms the basis for many other models that came after it, most notably the computational-fluid-dynamics (CFD) models, as discussed in the next section. In terms of direct descendants of this model, the model of Chan et al.¹¹³ takes the Bernardi and Verbrugge model and incorporates carbon monoxide effects at the anode as per the Springer et al.¹⁰⁴ description. The models of Li and co-workers^{50,71,114–116}

start with the Bernardi and Verbrugge framework and include additional effects. The model of Marr and Li¹¹⁴ uses an agglomerate catalyst-layer model in order to ascertain more easily the effects of changing various layer properties such as porosity and membrane loading. Baschuk and Li⁵⁰ took the Marr and Li model further by incorporating mass-transfer limitations in the cathode due to water flooding. They did this using an additional liquid-film resistance as an unknown parameter and were able to predict different levels of flooding as a function of cell polarization. The model of Rowe and Li⁷¹ built on the other models and includes nonisothermal operation, which allows for a better study of water management in the 1-D fuel-cell sandwich. Finally, some of the models of Li and co-workers focus on carbon monoxide poisoning of the anode electrocatalysts.^{115,116}

The last main group of models that directly follow the Bernardi and Verbrugge model are those from Italy by Murgia et al.^{95,117} and Pisani et al.^{78,91,118} In the first of these models, the original Bernardi and Verbrugge model is simplified to help its convergence.⁹⁵ This was done by integrating over the catalyst layers and using that result in the 1-D simulation. They argued that numerical accuracy was not compromised and computational cost and numerical instability were greatly reduced. The next of the models added two-phase flow effects and an agglomerate model for the catalyst layer, which addressed the need for a changing water content. A recent model from this group⁹¹ examines analytic expressions for the catalyst layer. It does a good job in examining effects on the agglomerate scale and looks at how the shape and distribution of electrocatalyst agglomerates affect polarization behavior. They also use their models to understand direct-methanol fuel-cell electrodes.

2.2.3. Computational-Fluid-Dynamics Models

With the increased computational power of today's computers, more detailed simulations are possible. Thus, complex equations such as the Navier–Stokes equation can be solved in multiple dimensions, yielding accurate descriptions of such phenomena as heat and mass transfer and fluid and two-phase flow throughout the fuel cell. The type of models that do this analysis are based on a finite-element framework and are termed CFD models. CFD models are widely available through commercial packages, some of which include an electrochemistry module. As mentioned above, almost all of the CFD models are based on the Bernardi and Verbrugge model. That is to say that the incorporated electrochemical effects stem from their equations, such as their kinetic source terms in the catalyst layers and the use of Schlögl's equation for water transport in the membrane.

The first major CFD models were those by Liu and co-workers^{25,119} at the University of Miami. They are nonisothermal and the first multidimensional models. They allowed for a more in-depth study of the effects along the channels than the models described above. While the original model by Gurau et al.²⁵ did not include liquid-water transport, it did have a variable water content in the membrane. To study

flooding effects, Gurau et al.¹²⁰ modeled the cathode region of the fuel cell by a simple approach where the cathode diffusion medium is broken down into regions of different gas-phase volume fractions. They developed analytic expressions and showed how flooding can limit fuel-cell performance. Later models by Liu and co-workers^{79,121} incorporated the multiphase mixture model of Wang and co-workers^{57–59} to study the effect of liquid water in their CFD simulations.

As mentioned, almost all of the CFD models use the Bernardi and Verbrugge approach of Schlogl's equation. The exceptions to these are the models from the University of South Carolina.^{51,54,60,73,82} These models use an approach similar to that of Springer et al. in that water transport in the membrane is due to diffusion and the diffusion coefficient is a function of water content; they assume a linear concentration profile of water in the membrane. Out of these models, Shimpalee and Dutta⁶⁰ generated one of the first with CFD. It examined primarily the 3-D temperature profile. Later models by Dutta et al.^{51,54} also examined mass-transfer and complete 3-D effects. While these examined the fuel cell in more depth, liquid water was not really treated in these models. It was assumed to be part of the gas phase in thin film or droplet form and for the most part ignored. A recent model by Lee et al.⁸² demonstrated good agreement with experiment and allowed for an understanding of the nonuniform current-density and membrane-conductivity distributions.

The next step forward in CFD models came from the work of Wang and co-workers.^{57,64,76,122–124} Their first model⁶⁴ was similar to Garua et al.²⁵ except that it was transient. Their next model incorporated liquid effects rigorously using the multiphase mixture model of Wang and Cheng.^{58,59} Their approach is similar to the South Carolina one above, but by considering mixture parameters and the appropriate saturation equations, the liquid-phase flow was calculated. The modeling domain for this model was basically the cathode side of the fuel cell, where a net water flux through the membrane was assumed. Very recent models examine the effects of solid-phase properties such as electronic conductivity¹²⁴ and wettability,¹²³ as well as interdigitated flow fields.⁷⁶

Around the same time as the other models were the models of Djilali and co-workers.^{47,80,125} The first of these⁴⁷ was 2-D, and while it accounted for liquid-water flow, saturation effects were neglected, since they assumed two independent networks for liquid and gas. Their next model used the same approach but was 3-D.¹²⁵ Their most recent model accounted for saturation effects and coupled the liquid and vapor flows.⁸⁰ It was able to show temperature, concentration, and water distributions in the 3-D flow field.

Recently, other CFD models have been published. The model of Siegel et al.⁹⁰ used an agglomerate approach instead of the porous-electrode approach of the other CFD models. They showed that the agglomerate approach enables good comparisons to experimental data and showed the effects of agglomerate radius and membrane loading on perfor-

mance. However, they did not include liquid flow in their model. The two models by Mazumder and Cole^{84,85} considered simulations with and without liquid-water flow. They showed better agreement when liquid-water flow and flooding were considered, and this was done with the multiphase mixture model. Furthermore, both models were 3-D and utilized complete porous-electrode descriptions of the catalyst layers with simple membrane models. The final CFD models are those of Costamagna⁶⁵ and Bradean et al.¹²⁶ Both of these models considered the same types of effects as the other CFD ones. The model of Costamagna is notable in that it considered both convective and diffusive flow in the membrane.

2.2.4. Other Macrohomogeneous Models

There are some modeling methodologies and research groups that do not fit exclusively into the above categories but should be mentioned. The foremost among these are the models by Newman and co-workers. Their models focus on fundamental phenomena and are usually simple in their dimensionality. In terms of fuel cells, Newman¹²⁷ used a simple pseudo-2-D model to look at optimization of hydrogen utilization in a phosphoric-acid fuel cell. Polymer-electrolyte fuel-cell modeling started with the models of Fuller¹²⁸ and Fuller and Newman.¹⁵ In these models, concentrated solution theory was used to describe diffusive transport in the membrane, which was a slight improvement to the Springer et al. framework. The Fuller and Newman model was one of the first to examine water and thermal management simultaneously and along the gas channel, although it did not contain a description of liquid-water flow. West and Fuller²⁴ took a similar model and used it to model the 2-D effects of ribs and channels. Dannenberg et al.¹²⁹ basically used the same model as Fuller and Newman, but they incorporated agglomerate effects in the catalyst layer and a different water uptake isotherm in order to examine the effect of changing operating conditions. Finally, the models by Meyers and Newman^{130–132} also improved upon the Springer et al. framework by using a thermodynamically rigorous treatment of transport in the membrane for the optimization of direct-methanol fuel cells.

The next set of Newman group models were aimed at demonstrating the applicability of models to diagnostic techniques. Perry et al.³⁶ examined the changes in the Tafel slope due to changes in the controlling phenomena in the cathode side of the fuel cell. This model was updated by Weber et al.,¹³³ who added explicit oxygen mass-transfer limitations in the diffusion media, and again later by Jaouen et al.,⁹⁸ who treated the catalyst layers as agglomerates.

Recently, Weber and Newman^{89,93,94,134} introduced a framework for bridging the gap between the Bernardi and Verbrugge and the Springer et al. membrane approaches. The membrane model was used in a simple fuel-cell model, and it showed good agreement with experimentally measured water-balance data under a variety of conditions.¹³⁴ The fuel-cell model was similar to the model of Janssen,⁵⁵ who used chemical potential as a driving force in the

membrane, but Weber and Newman also accounted for such effects as Schroeder's paradox. Other membrane-modeling approaches in fuel-cell models besides those mentioned above include those by Datta and co-workers,^{63,72,92} who use a dusty-gas approach, and Hsing and co-workers,^{41,61,62} who use Flory-Huggins theory. Finally, Weber et al.⁷⁴ and Weber and Newman⁸⁸ have recently developed models to account for saturation effects and flooding phenomena. Along with the model of Nam and Kaviani,⁸⁶ they are some of the first to account for composite and hydrophobic diffusion media.

Within the last five years, many fuel-cell models have come out of the Research Center in Julich, Germany. These models have different degrees of complexity and seek to identify the limiting factors in fuel-cell operation. The model of Kulikovsky et al.³⁷ examined a 2-D structure of rib and channel on the cathode side of the fuel cell, and is similar to that of Springer et al. Other models by Kulikovsky included examination of depletion along long feed channels^{67,83} and effects in the catalyst layers.^{69,96,135} The most recent model by Kulikovsky⁸¹ relaxed the assumption of constant water content in the membrane and examined quasi 3-D profiles of it. Also at the research center, Eikerling et al.^{28,40,70,136-138} developed many different models. Most of these were concerned with modeling the membrane^{40,70,136,138} and cathode side of the fuel cell.^{28,137} These models were complex and focused on statistically relating macroscopic phenomena to structural properties. In both systems, they developed fundamental equations for the transport processes and examined different limiting cases, leading toward optimization analysis.

3. General Aspects and Equations

The performance of a fuel cell is most often reported in the form of a polarization curve. Such a curve is shown in Figure 3. Roughly speaking, the polarization curve can be broken down into three main regions. At low currents, the behavior of a fuel cell is dominated by kinetic losses. These losses

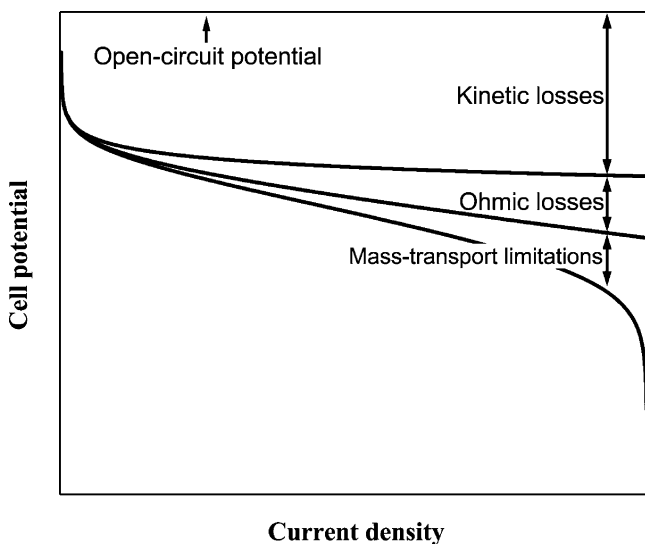


Figure 3. Example of a polarization curve showing the typical losses in a polymer-electrolyte fuel cell.

mainly stem from the high overpotential of the oxygen-reduction reaction (ORR), although the presence of carbon monoxide will produce a similar effect at the anode. As the current is increased, ohmic losses become a factor in lowering the overall cell potential. These ohmic losses are mainly from ionic losses in the electrodes and separator, although contact and electronic resistances can be important under certain operating conditions and cell configurations. At high currents, mass-transport limitations become increasingly important. These losses are due to reactants not being able to reach the electrocatalytic sites. Typically, oxygen is the problem due to flooding of the cathode by liquid water, but protons and electrons can also result in mass-transfer limitations. Before examining general polarization-curve models, some discussion should be made of the approach used for modeling and the equations used for the general regions of the polarization curve.

3.1. Modeling Methodologies

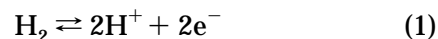
There are different global methodologies for modeling fuel cells and, in particular, the fuel-cell sandwich. The easiest division to make is between macroscopic and microscopic models. The microscopic models seek to model transport on an individual pore level, whereas the macroscopic ones are continuum and average over this level. Although the microscopic models may provide more realistic conditions and factors, they require a lot more knowledge of the microstructure and are much more expensive in terms of computation time. Macroscopic models are more common for fuel cells, although some microscopic details should be incorporated into them. An example of this is the agglomerate model for fuel-cell catalyst layers, as discussed below. This review focuses mainly on macroscopic models.

In a macrohomogeneous approach, the exact geometric details of the modeling domain are neglected. Instead, the domain is treated as a randomly arranged porous structure that can be described by a small number of variables such as porosity and surface area per unit volume. Furthermore, transport properties within the domain are averaged over the electrode volume. Thus, all variables are defined at all positions within the domain. Averaging is performed over a region that is small compared to the size of the electrode but large compared to the microstructure.

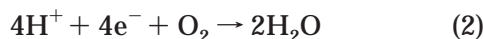
3.2. General Equations

3.2.1. Thermodynamics

As shown in Figure 3, the open-circuit potential represents the highest voltage obtainable for a single cell. This potential is derived from thermodynamics. The overall fuel-cell reaction can be broken down into the two global electrode reactions. If hydrogen is the primary fuel, it oxidizes at the anode according to the reaction



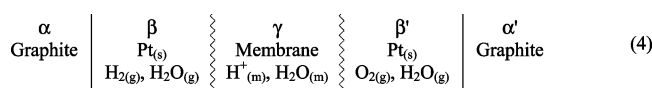
At the cathode, oxygen is reduced



Although the above reactions are written in terms of the global species, no specific mention has been made about how the reaction proceeds. For example, each reaction can be broken down into single electron-transfer reactions, and the gas probably dissolves into the membrane that is covering the electrocatalyst sites (e.g., platinum on carbon). Some more comments about this can be found in section 4.4. Adding eqs 1 and 2 yields the overall reaction



A typical polymer–electrolyte fuel cell can be represented as



where each Greek letter identifies a distinct phase and the wavy lines imply that the membrane phase boundary is not sharp; rather, the membrane extends into adjacent regions and may include water activity gradients. The potential of this cell is¹³⁹

$$FU = -F(\Phi^\alpha - \Phi^{\alpha'}) = \mu_{\text{e}^-}^\alpha - \mu_{\text{e}^-}^{\alpha'} \quad (5)$$

where F is Faraday's constant, U is the thermodynamically defined reversible cell potential, Φ^α is the electrical potential of phase α , and $\mu_{\text{e}^-}^\alpha$ is the electrochemical potential of electrons in phase α . After introducing expressions for the activities of the various components,¹³⁹ this becomes

$$FU = FU^\theta + \frac{RT}{2} \ln a_{\text{H}_2}^\beta + \frac{RT}{4} \ln a_{\text{O}_2}^{\beta'} - \frac{RT}{2} \ln a_{\text{w}}^{\beta'} + (\mu_{\text{H}^+}^\beta - \mu_{\text{H}^+}^{\beta'}) \quad (6)$$

where a_i^β is the activity of species i in phase β and the subscript w stands for water, R is the ideal-gas constant, T is the absolute temperature, and U^θ is the standard cell potential, a combination of appropriately chosen reference states that is a function of temperature and can be unit dependent. This equation reduces to a Nernst equation^{139,140}

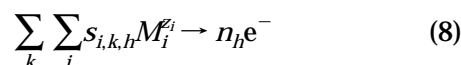
$$U = U^\theta + \frac{RT}{2F} \ln \left(\frac{P_{\text{H}_2} \sqrt{P_{\text{O}_2}}}{P_{\text{w}}} \right) \quad (7)$$

when the gases are assumed to be ideal and gradients in the electrolyte are zero or neglected. Values and expressions for the parameters in the above equation, as well as further thermodynamic discussions, can be found in various books.^{139–144}

3.2.2. Kinetics

The initial drop in the polarization curve is due to the sluggish kinetics of the ORR at the temperatures normally used for current polymer-electrolyte fuel-cell operation (<100 °C). A typical electrochemical

reaction can be expressed as



where $s_{i,k,h}$ is the stoichiometric coefficient of species i residing in phase k and participating in electron-transfer reaction h , n_h is the number of electrons transferred in reaction h , and $M_i^{z_i}$ represents the chemical formula of i having valence z_i .

The rate of an electrochemical reaction depends on the concentrations of the various species and the potential drop across the reaction interface between phases k and p , which are normally the electrode and electrolyte, respectively. In general, a Butler–Volmer expression can be used to describe the kinetics

$$i_{h,k-p} = i_{0,h} \left[\prod_i^a \frac{p_i}{p_i^{\text{ref}}} \exp \left(\frac{\alpha_a F}{RT} (\Phi_k - \Phi_p - U_h^{\text{ref}}) \right) - \prod_i^c \frac{p_i}{p_i^{\text{ref}}} \exp \left(\frac{-\alpha_c F}{RT} (\Phi_k - \Phi_p - U_h^{\text{ref}}) \right) \right] \quad (9)$$

where $i_{h,k-p}$ is the transfer current between phases k and p due to electron-transfer reaction h , the products are over the anodic and cathodic reaction species, respectively, α_a and α_c are the anodic and cathodic transfer coefficients, respectively, p_i and p_i^{ref} are the partial pressure and reference partial pressure for species i , respectively, and $i_{0,h}$ and U_h^{ref} are the exchange current density per unit catalyst area and the potential of reaction h evaluated at the reference conditions and the operating temperature, respectively. The reference potential can be determined using a Nernst equation (e.g., see eq 7); if the reference conditions are the same as the standard conditions (i.e., 100 kPa pressure for the different gas species), then U_h^{ref} has the same numerical value as U_h^θ .

The term in parentheses in eq 9 can be written in terms of an electrode overpotential

$$\eta_{h,k-p} = \Phi_k - \Phi_p - U_h^{\text{ref}} \quad (10)$$

In this review, the reference electrode used is defined as a platinum metal electrode exposed to hydrogen at the same temperature and electrolyte (e.g., Nafion) as the solution of interest. With this reference electrode, the electrode overpotential defined in eq 10 is the same as having the reference electrode located next to the reaction site but exposed to the reference conditions (i.e., it carries its own extraneous phases with it). Typical values for the reference conditions are those in the gas channels. If the reference electrode is exposed to the conditions at the reaction site, then a surface overpotential can be defined

$$\eta_{s,h,k-p} = \Phi_k - \Phi_p - U_h \quad (11)$$

where U_h is the reversible potential of reaction h (e.g., see eq 7). The surface overpotential is the overpotential that directly influences the reaction rate

across the interface. Comparing eqs 10 and 11, one can see that the electrode overpotential contains both a concentration and a surface overpotential for the reaction.

For the hydrogen-oxidation reaction (HOR) at the anode, eq 9 becomes, in the absence of poisons,

$$i_{\text{HOR},1-2} = i_{0,\text{HOR}} \left[\frac{p_{\text{H}_2}}{p_{\text{H}_2}^{\text{ref}}} \exp\left(\frac{\alpha_a F}{RT}(\eta_{\text{HOR},1-2})\right) - \exp\left(\frac{-\alpha_c F}{RT}(\eta_{\text{HOR},1-2})\right) \right] \quad (12)$$

where 1 and 2 denote the electron- and proton-conducting phases, respectively. Because the electrolyte is a polymer of defined acid concentration, the proton concentration does not enter directly into eq 12. Furthermore, due to the reference electrode used, the reference potential and reversible potential are both equal to zero. Equation 12 reduces to a Nernst relationship when the ratio i/i_0 becomes small, which is normally the case for the HOR.^{13,17,145-149}

The oxygen-reduction reaction (ORR), on the other hand, is slow and represents the principal inefficiency in many fuel cells. Due to its sluggishness, the ORR is modeled reasonably well with Tafel kinetics with a first-order dependence on oxygen partial pressure^{10,150,151}

$$i_{\text{ORR},1-2} = -i_{0,\text{ORR}} \left(\frac{p_{\text{O}_2}}{p_{\text{O}_2}^{\text{ref}}} \right) \exp\left(\frac{-\alpha_c F}{RT}(\eta_{\text{ORR},1-2})\right) \quad (13)$$

A linear fit on a Tafel plot of overpotential versus the log of the current density yields the commonly reported Tafel slope

$$b = 2.303 \frac{RT}{\alpha_c F} \quad (14)$$

For the kinetic region, the values of the theoretical and experimental Tafel slopes have been shown to agree with α_c equal to 1.^{9,10,150,152-157}

If eq 13 were to be written with respect to the surface overpotential, as defined by eq 11, instead of the electrode overpotential, then it would read

$$i_{\text{ORR},1-2} = -i_{0,\text{ORR}} \left(\frac{p_{\text{O}_2}}{p_{\text{O}_2}^{\text{ref}}} \right)^{3/4} \exp\left(\frac{-\alpha_c F}{RT} \eta_{s,\text{ORR},1-2}\right) \quad (15)$$

The power or the exponent with respect to oxygen is different because of the overpotential being used. As discussed by Newman,¹³⁹ the difference is due to how the exchange current density is defined and its dependence written, and both equations are consistent with a reaction order of 1. Mathematically, one can show that the exponent on oxygen changes from 1 to $3/4$ if α_c is equal to 1.¹⁵⁸ While eq 15 has perhaps a better defined overpotential and contains only a kinetic term and not also a thermodynamic term, eq 13 is often easier to use in simulations and in conceptualizing the dependence of the kinetics on gas concentration. Either equation is correct, and one must recognize which one is being used when analyz-

ing or comparing data and modeling results, as pointed out by Gasteiger et al.¹⁵⁸ Furthermore, the exchange current densities in the two equations are not necessarily equal because they are (perhaps different) functions of the reference pressures.

As noted, the equations above are a general starting point for describing the ORR, the HOR, and the kinetic regime. More detailed models, which examine such effects as the nature of the reaction interface, are discussed in later sections.

3.2.3. Ohmic Losses

The second part of the polarization curve is the ohmic regime. In this region, the potential varies linearly with the current density. This allows for Ohm's law to be used for modeling purposes

$$\Delta\Phi = iR' \quad (16)$$

where R' is the overall resistance in the fuel cell. For the ohmic region, this resistance is essentially constant; that is, it is not a strong function of the current density or potential. The resistance can either be measured experimentally by fitting polarization curves or be determined through modeling. It is a composite of the general electronic and ionic resistances through the fuel cell and is similar to a contact resistance. It does not include those resistances resulting from mass-transfer effects such as membrane dehydration, which are discussed below. In later sections, models that calculate R' are discussed in detail.

3.2.4. Mass-Transfer Limitations

The last part of the polarization curve is dominated by mass-transfer limitations (i.e., concentration overpotential). These limitations arise from conditions wherein the necessary reactants (products) cannot reach (leave) the electrocatalytic site. Thus, for fuel cells, these limitations arise either from diffusive resistances that do not allow hydrogen and oxygen to reach the sites or from conductive resistances that do not allow protons or electrons to reach or leave the sites. For general models, a limiting current density can be used to describe the mass-transport limitations. For this review, the limiting current density is defined as the current density at which a reactant concentration becomes zero at the diffusion medium/catalyst layer interface.

As mentioned, membrane dehydration can result in a problem where the membrane conductivity decreases to the point that it no longer conducts protons away from the reaction sites. Also, the distributed ohmic effects coupled with mass transfer in the porous electrode can result in a concentration overpotential that limits performance. In addition, if the diffusion media are composed mainly of insulating solids such as Teflon, electron conduction can become limiting. However, the most common cause for mass-transfer limitations is due to oxygen being inhibited from reaching the cathode reaction sites. This is normally due to flooding in either the catalyst layer or the diffusion medium because air and hydrogen are normally fed into a fuel cell, water is

produced at the cathode, and the diffusion coefficient of hydrogen is greater than that of oxygen.^{142,149}

For typical fuel-cell designs, mass transport through the fuel-cell sandwich occurs mainly by diffusion. The simplest way to describe diffusion is by Fick's law¹⁴⁹

$$\mathbf{N}_i = -\frac{D_i}{RT}\nabla p_i \quad (17)$$

where \mathbf{N}_i is the superficial flux density of species i and D_i is the diffusion coefficient of species i in the mixture. As discussed later, many models use more complex expressions and effective diffusion coefficients. These complexities allow the nature of the fuel-cell porous media to be accounted for, as well as counterdiffusion of water vapor and flooding of the porous media by liquid water.

An expression for the limiting current density due to oxygen transport can be derived by the following procedure. With Faraday's law for the oxygen flux in the ORR and rearrangement of Fick's law, the oxygen partial pressure at the catalyst layer, $p_{\text{O}_2}^{\text{CL}}$, can be related to the limiting current density, i_{lim} , and the oxygen partial pressure in the bulk, $p_{\text{O}_2}^{\text{bulk}}$,¹²⁷

$$p_{\text{O}_2}^{\text{CL}} = p_{\text{O}_2}^{\text{bulk}}\left(1 - \frac{i}{i_{\text{lim}}}\right) \quad (18)$$

Equation 18 can be used to write the ORR rate in eq 13 or 15 in terms of the limiting current density, an experimentally measurable quantity, rather than the oxygen partial pressure.

3.3. Zero-Dimensional Models

The simplest fuel-cell models describe the polarization behavior by a single equation; hence, they are 0-D. Even though these models are relatively simple and usually empirical, they are valuable for determining kinetic parameters as well as comparing the various losses in the system to one another. The 0-D modeling equations can be derived by combination of the above governing equations for each regime. The drawbacks of these models are that they do not yield true mechanistic behavior and fundamental understanding and that they are not good for predicting performance or optimization.

0-D models are very helpful in determining kinetic parameters and general ohmic resistance from data.^{9,10,21,23,152,159–161} A typical expression for this type of analysis is

$$V = U + b \log(i_0) - b \log(i) - R'i \quad (19)$$

where V is the cell potential and i is the superficial current density through the membrane. The first and second terms may be combined to form a potential intercept, U ; this quantity is a convenient way to group terms pertaining to (possibly unknown) thermodynamic and kinetic constants.

Upon comparison to data, the models demonstrate the aforementioned value of α_c being equal to 1. Not only are exchange current densities measured, but the effect of temperature can be studied in more detail, as well as the type and thickness of mem-

brane. For example, the model of Amphlett et al.²¹ accounts for all of the temperature dependences through empirical fitting parameters. 0-D models also allow for deviations from the theoretical expression presented above to be investigated. For example, fitting eq 19 to some experimental data yields a double Tafel slope at higher current densities. This change in the Tafel slope is caused by transport limitations, something not explicitly taken into account in the above equation. In other words, the equation cannot fit the whole polarization curve with just one set of parameter values.

To make the model less empirical, gas-phase mass-transport limitations can be incorporated into the modeling equation explicitly¹²

$$V = U - b \log(i) - R'i - m \exp(ni) \quad (20)$$

where m and n are fitting parameters. Although the above expression yields good fits with the data, it is more empirical than if the limiting current density is used^{97,139,161}

$$V = U - b \log(i) - R'i + b \log\left(1 - \frac{i}{i_{\text{lim}}}\right) \quad (21)$$

Other modifications to include mass-transport limitations deal with changing the last term to be a more complicated function of current with more fitting parameters.^{118,162,163}

The final 0-D equation presented here stems from incorporating the gas-pressure dependences directly instead of through a limiting current density, which normally only considers oxygen effects. This equation was proposed by Newman¹²⁷ for phosphoric-acid fuel cells and predates the above polymer–electrolyte fuel-cell expressions. It has the form

$$V = U^0 + \frac{RT}{F} \ln(a_{1,2}i_0L) - \frac{RT}{F} \ln\left(\frac{i}{p_{\text{O}_2}}\right) + \frac{RT}{2F} \ln(p_{\text{H}_2}) - R'i \quad (22)$$

where $a_{1,2}$ is the interfacial area of the catalyst per unit volume of electrode and L is the thickness of the cathode catalyst layer. Thus, the quantity $a_{1,2}L$ is a roughness factor, a ratio of catalyst area to superficial electrode area. Out of all the approaches to include mass transport, eqs 21 and 22 are the most phenomenological, but with the fewest fitting parameters, they do not fit the data the best.

To examine how well the models agree with the data, Figure 4 shows model fits using eq 20. As can be seen, the model fits the data very well even with different operating conditions of oxygen mole fraction and gas pressure. Of course, the model parameters are adjusted for the conditions. As mentioned, such polarization-equation fits are useful for getting parameter values and perhaps some gross understanding, but they cannot really be used for optimization, prediction, or in-depth examination of the underlying phenomena. In essence, they are curve fits. It is difficult for them to treat interacting phenomena in

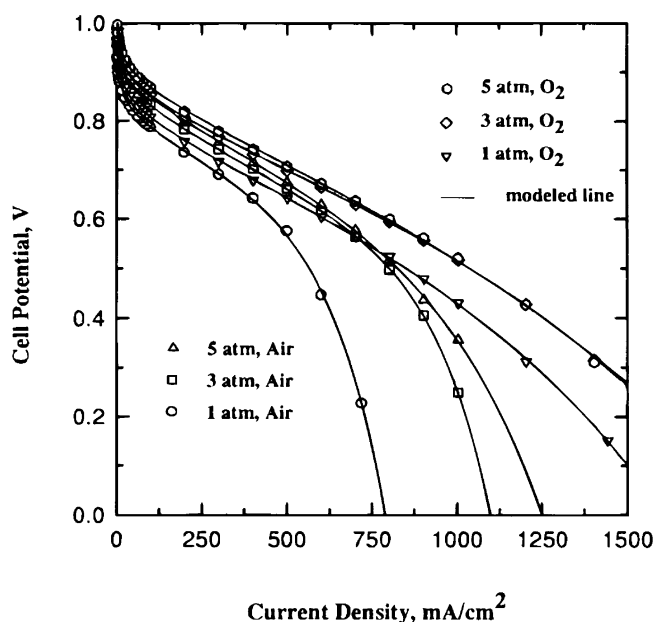


Figure 4. Model and experiment comparison of polarization curves for air or oxygen at different gas pressures and at 70 °C using eq 20. (Reproduced with permission from ref 12. Copyright 1995 The Electrochemical Society, Inc.)

a clear way, such as drying of a membrane with current density or temperature or flooding with liquid water.

More complicated expressions than those above can be used in the 0-D models, but these usually stem from a more complicated analysis. For example, the equation used by Ticianelli and co-workers^{29,156} comes from analysis of the catalyst layer as a flooded agglomerate. In the same fashion, eq 21 can be embedded and used to describe the polarization behavior within a much more complicated model. For example, the models of Springer et al.¹⁴ and Weber and Newman⁷⁴ use a similar expression to eq 21, but they use a complicated 1-D model to determine the parameters such as i_{lim} and R . Another example is the model of Newman,¹²⁷ who uses eq 22 and takes into account reactant-gas depletion down the gas channels by, in essence, having a limiting current density that depends on the hydrogen utilization. All of these types of models, which use a single equation to describe the polarization behavior within a more complicated model, are discussed in the context of the more complicated model.

4. Fuel-Cell Sandwich Modeling

The fuel-cell sandwich describes the 1-D cross section of the fuel cell (see Figure 1) and is shown in Figure 5. For the single dimension, flow is taken to be normal to the various layers. Flow in the other directions is discussed in section 5. The fuel-cell sandwich contains the gas channels or flow fields, diffusion media, catalyst layers, and membrane. Additional layers are sometimes incorporated into the sandwich, such as separating the diffusion media into microporous and gas-diffusion layers. Fuel cells operate in the following manner.

The fuel is fed into the anode flow field, moves through the diffusion medium, and reacts electro-

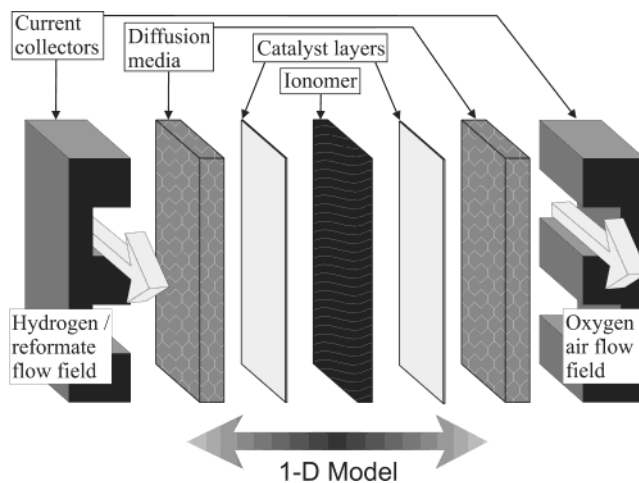


Figure 5. 3-D schematic showing the various layers of the fuel-cell sandwich.

chemically at the anode catalyst layer to form hydrogen ions and electrons. The diffusion medium is typically a carbon cloth or carbon paper, possibly treated with Teflon. The catalyst layer usually contains platinum or a platinum alloy supported on carbon and an ionomeric membrane material such as Nafion. The oxidant, usually oxygen in air, is fed into the cathode flow field, moves through the diffusion medium, and is electrochemically reduced at the cathode by combination with the generated protons and electrons. The water, either liquid or vapor, produced by the reduction of oxygen at the cathode exits the fuel cell through either the cathode or anode flow field. The electrons generated at the anode pass through an external circuit and may be used to perform work before they are consumed at the cathode.

Mass and energy transport occur throughout all of the various sandwich layers. These processes, along with electrochemical kinetics, are key in describing how fuel cells function. In this section, thermal transport is not considered, and all of the models discussed are isothermal and at steady state. Some other assumptions include local equilibrium, well-mixed gas channels, and ideal-gas behavior. The section is outlined as follows. First, the general fundamental equations are presented. This is followed by an examination of the various models for the fuel-cell sandwich in terms of the layers shown in Figure 5. Finally, the interplay between the various layers and the results of sandwich models are discussed.

4.1. Conservation Equations

The number of equations and unknowns must balance. Thus, one can calculate the appropriate number of needed relationships from the degrees of freedom of a system, as shown for various systems by Newman.¹⁶⁴ In terms of the relations, the equations can be broken down into five main types. The first are the conservation equations, the second are the transport relations, the third are the reactions, the fourth are equilibrium relationships, and the fifth are the auxiliary or supporting relations, which include variable definitions and such relations as Faraday's law.

As noted in the Introduction, one of the defining characteristics of any fuel-cell model is how it treats transport. Thus, these equations vary depending on the model and are discussed in the appropriate subsections below. Similarly, the auxiliary equations and equilibrium relationships depend on the modeling approach and equations and are introduced and discussed where appropriate. The reactions for a fuel cell are well-known and were introduced in section 3.2.2. Of course, models modify the reaction expressions by including such effects as mass transfer and porous electrodes, as discussed later. Finally, unlike the other equations, the conservation equations are uniformly valid for all models. These equations are summarized below and not really discussed further.

It is necessary to write a material balance for each independent component in each phase. The differential form of the material balance for species i in phase k is¹³³

$$\frac{\partial c_k c_{i,k}}{\partial t} = -\nabla \cdot \mathbf{N}_{i,k} - \sum_h a_{1,k} s_{i,k,h} \frac{i_{h,1-k}}{n_h F} + \sum_l s_{i,k,l} \sum_{p \neq k} a_{k,p} r_{l,k-p} + \sum_g s_{i,k,g} \epsilon_k R_{g,k} \quad (23)$$

The term on the left side of the equation is the accumulation term, which accounts for the change in the total amount of species i held in phase k within a differential control volume. This term is assumed to be zero for all of the sandwich models discussed in this section because they are at steady state. The first term on the right side of the equation keeps track of the material that enters or leaves the control volume by mass transport. The remaining three terms account for material that is gained or lost due to chemical reactions. The first summation includes all electron-transfer reactions that occur at the interface between phase k and the electronically conducting phase (denoted as phase 1). The second summation accounts for all other interfacial reactions that do not include electron transfer, and the final term accounts for homogeneous reactions in phase k .

In the above expression, $c_{i,k}$ is the concentration of species i in phase k , and $s_{i,k,l}$ is the stoichiometric coefficient of species i in phase k participating in heterogeneous reaction l (see eq 8). $a_{k,p}$ is the specific surface area (surface area per unit total volume) of the interface between phases k and p . $i_{h,k-1}$ is the normal interfacial current transferred per unit interfacial area across the interface between the electronically conducting phase and phase k due to electron-transfer reaction h , and it is positive in the anodic direction. In the above expression, Faraday's law

$$N_{i,k} = \sum_h s_{i,k,h} \frac{i_{h,1-k}}{n_h F} \quad (24)$$

was used to change the interfacial current density into an interfacial flux quantity. Furthermore, a current $i_{h,1-k}$, written with two subscripts, implies an interfacial, or transfer, current density. Conversely,

a current \mathbf{i}_k , written in boldface and with a single subscript, indicates the total current density carried within phase k

$$\mathbf{i}_k = F \sum_i z_i \mathbf{N}_{i,k} \quad (25)$$

where z_i is the valence or charge number of species i . Finally, $r_{l,k-p}$ is the rate of the heterogeneous reaction l per unit of interfacial area between phases k and p . $R_{g,k}$ is the rate of a strictly homogeneous reaction g in phase k per unit volume of phase k .

Because a large electrical force is required to separate charge over an appreciable distance, a volume element in the electrode will, to a good approximation, be electrically neutral. For fuel-cell models, electroneutrality is often assumed for each phase

$$\sum_i z_i c_{i,k} = 0 \quad (26)$$

The assumption of electroneutrality implies that the diffuse double layer, where there is significant charge separation, is small compared to the volume of the domain, which is normally the case. Because there is no accumulation of charge and electroneutrality has been assumed, the divergence of the total current density is zero

$$\sum_k \nabla \cdot \mathbf{i}_k = 0 \quad (27)$$

Equations 23 and 27 represent the mass and current conservation equations, respectively. These apply for all of the models discussed.

4.2. Membrane Modeling

One of the most important parts of the fuel cell is the electrolyte. For polymer-electrolyte fuel cells this electrolyte is a single-ion-conducting membrane. Specifically, it is a proton-conducting membrane. Although various membranes have been examined experimentally, most models focus on Nafion. Furthermore, it is usually necessary only to modify property values and not governing equations if one desires to model other membranes. The models presented and the discussion below focus on Nafion.

Nafion is a copolymer of poly(tetrafluoroethylene) and polysulfonyl fluoride vinyl ether. It has fixed anions, which are sulfonic acid sites, and consequently, by electroneutrality, the concentration of positive ions is fixed. Furthermore, the transference number of protons in this system is 1, which greatly simplifies the governing transport equations, as seen below. There can be different forms of Nafion in terms of the positive counterion (e.g., proton, sodium, etc.). Most models deal only with the proton or acid form of Nafion, which is the most common form used in polymer-electrolyte fuel cells due to its high proton conductivity.

Since the membrane is such a key element in the fuel cell, it has had a lot of attention in terms of modeling. There have been many microscopic and

physical models in addition to the macroscopic ones. The microscopic models focus solely on the membrane and examine single ions and pore-level effects. The macroscopic models are often more empirical and focus on describing the transport and relevant parameters of the membrane in a macrohomogeneous fashion. As per the overall approach of this review, discussion is mainly on the macroscopic models.

The macroscopic models can be sorted into two main categories, those that assume the membrane system is a single phase, and those that assume it is two phases. Each is discussed separately below. In either of these models, the membrane system is assumed to have three main components: membrane, protons, and water. For the three-species system, there should be $\frac{1}{2}N(N-1) = 3$ transport properties.¹³³ The above set of properties neglects any other kind of ions in the membrane, which is an assumption that almost all of the models make. Furthermore, the above property count does not consider hydrogen or oxygen crossover in the membrane. Such crossover results in only a small inefficiency and does not significantly influence proton or water transport. There are some models that take this into account, the most notable being by Bernardi and Verbrugge.¹¹⁰ If desired, crossover can easily be added to any model.⁹⁴

Before discussing the models and their approaches in more detail, some mention should be made on the microscopic models and the overall physical picture of Nafion. Since membrane-only models, especially the microscopic ones, are covered in another review,¹⁶⁵ the discussion below is shortened.

4.2.1. Microscopic and Physical Models

There have been many microscopic models based on statistical mechanics,^{38,136,166–172} molecular dynamics,^{173–180} and macroscopic phenomena applied to the microscopic structure of the membrane.^{63,111,138,181–201} These models provide the fundamental understanding of processes such as diffusion and conduction in the membrane on a single-pore level. They allow for the evaluation of how small perturbations like heterogeneity of pores and electric fields affect transport, as well as the incorporation of small-scale effects. These models are also the only ones to look at different forms of Nafion as well as the effect of other ions in the membrane (e.g., those from a salt solution).^{42,43,111,192–201} They also divide the membrane into more than just the three species of the macroscopic models; as examples, the membrane may be broken down into ionic and backbone moieties, and proton conduction may be by different proton–water complexes. Finally, almost all of the microscopic models treat the membrane as a two-phase system. While the microscopic models yield valuable information about what goes on inside the membrane, in general, they are too complex to use in an overall fuel-cell model.

Many of today's models are based on the early physical models of Hsu and Gierke¹⁸² and Yeager and Steck.¹⁸⁴ These models, along with the relevant experimental data, were reviewed recently by Weber and Newman.^{89,93} Out of their analysis came a

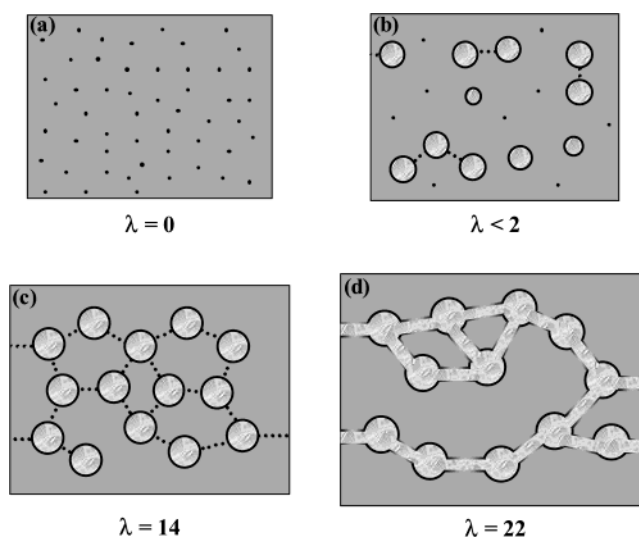


Figure 6. Evolution of the membrane structure as a function of water content, λ (moles of water per mole of sulfonic acid sites). The pictures are cross-sectional representations of the membrane where the gray area is the fluorocarbon matrix, the black is the polymer side chain, the light gray is the liquid water, and the dotted line is a collapsed channel. (Reproduced with permission from ref 89. Copyright 2003 The Electrochemical Society, Inc.)

physical model of transport in Nafion, which could be used as a foundation for a macrohomogeneous model. Figure 6 shows a schematic summary of the Weber and Newman model. The main focus of the model is how the membrane structure changes as a function of water content, where λ is the moles of water per mole of sulfonic acid sites and is measured by examining the weight gain of an equilibrated membrane.

In panel a, the dry membrane absorbs water in order to solvate the acid groups. This initial water is associated strongly with the sites. Additional water causes the water to become less bound, and inverted micelles form in the polymer matrix, panel b. With more water uptake, these clusters grow and form interconnections with each other. The connections, or collapsed channels, are transitory and have hydrophobicities comparable to that of the matrix. The cluster–channel network forms on the basis of a percolation-type phenomenon of the clusters; therefore, to form a transport pathway, the clusters must grow and be close enough together to be linked by the collapsed channels. From conductivity data, this percolation threshold is shown practically to occur around $\lambda = 2$.⁹⁴ Panel c corresponds to a membrane that is in contact with saturated water vapor, where a complete cluster–channel network has formed. When there is liquid water at the boundary of the membrane, structural reorganization occurs because the aqueous environment repels the fluorocarbon-rich skin of the ionomer. This inversion allows for the liquid water to infiltrate and expand the channels, causing them to stabilize and the various clusters to agglomerate along them; as a result, a porelike structure forms, panel d. In this structure, the channels are still hydrophobic on average. Because the channels are now filled with liquid, the uptake of the membrane has increased without a change in

the chemical potential of the water (i.e., Schroeder's paradox²⁰²).

In the physical model, there are two separate structures for the membrane depending on whether the water at the boundary is vapor or liquid; these are termed the vapor- or liquid-equilibrated membrane, respectively. The main difference between the two is that, in the vapor-equilibrated membrane, panel c, the channels are collapsed, while, in the liquid-equilibrated case, panel d, they are expanded and filled with water. These two structures form the basis for the two types of macroscopic models of the membrane.

4.2.2. Diffusive Models

The diffusive models treat the membrane system as a single phase. They correspond more-or-less to the vapor-equilibrated membrane (panel c of Figure 6). Because the collapsed channels fluctuate and there are no true pores, it is easiest to treat the system as a single, homogeneous phase in which water and protons dissolve and move by diffusion. Many membrane models, including some of the earliest ones, treat the system in such a manner.

Since the membrane is stationary, only the water and protons move in the membrane system. The simplest membrane models either neglect the water movement or treat it as a known constant. For the proton movement, the simplest treatment is to use Ohm's law (eq 16 in differential form)

$$\mathbf{i}_2 = -\kappa \nabla \Phi_2 \quad (28)$$

where κ is the ionic conductivity of the membrane. This can easily be integrated to yield a resistance for use in a polarization equation (see the 0-D models above). The above water and proton treatments are relatively trivial and are often used when the purpose of the model is to examine effects outside the membrane (e.g., cathode flooding)^{26,48,52,56,57,69,80,85–87,101,105,120} or when only general trends are desired.^{19,20,75,114,203,204} Below, more rigorous treatments are examined.

4.2.2.1. Dilute Solution Theory. Equation 28 is the result of using dilute solution theory.¹³⁹ Such an analysis yields the Nernst–Planck equation

$$\mathbf{N}_{i,2} = -z_i u_i F c_{i,2} \nabla \Phi_2 - D_i \nabla c_{i,2} + c_{i,2} \mathbf{v}_2 \quad (29)$$

The first term in the expression is a migration term, representing the motion of charged species that results from a potential gradient. The migration flux is related to the potential gradient ($-\nabla \Phi_2$) by a charge number, z_i , concentration, c_i , and mobility, u_i . The second term relates the diffusive flux to the concentration gradient. The final term is a convective term and represents the motion of the species as the bulk motion of the solvent carries it along. For the analysis of the one-phase systems, the solvent is the membrane, and thus, $\mathbf{v}_2 = 0$.

Dilute solution theory considers only the interactions between each dissolved species and the solvent. The motion of each charged species is described by its transport properties, namely, the mobility and the diffusion coefficient. These transport properties can

be related to one another at infinite dilution via the Nernst–Einstein equation^{139,205,206}

$$D_i = RTu_i \quad (30)$$

So long as the solute species are sufficiently dilute that the interactions among them can be neglected, material balances can be written upon the basis of the above expression for the flux.

If water movement in the membrane is also to be considered, then one way to do this is to again use the Nernst–Planck equation. Because water has a zero valence, eq 29 reduces to Fick's law, eq 17. However, it is also well documented that, as the protons move across the membrane, they induce a flow of water in the same direction. Technically, this electroosmotic flow is a result of the proton–water interaction and is not a dilute solution effect, since the membrane is taken to be the solvent. As shown in the next section, the electroosmotic flux is proportional to the current density and can be added to the diffusive flux to get the overall flux of water

$$\mathbf{N}_{w,2} = \frac{\xi \mathbf{i}_2}{F} - D_w \nabla c_{w,2} \quad (31)$$

where ξ is the electroosmotic coefficient. The above equation, along with Ohm's law, has been used successfully for most of the models that treat the membrane as a single phase.^{14,16,17,39,44,51,54,60,81,82,90,129,159,207} The deviations and complications in the models arise from what function to use for the transport properties, κ , ξ , and D_w , as well as the concentration of water in the membrane, $c_{w,2}$. To understand the differences in the models, a closer look at these functions is required, but first the models that use concentrated solution theory will be presented.

4.2.2.2. Concentrated Solution Theory. For an electrolyte with three species, it is as simple and more rigorous to use concentrated solution theory. Concentrated solution theory takes into account all binary interactions between all of the species. For membranes, this was initially done by Bennion²⁰⁸ and Pintauro and Bennion.²⁰⁹ They wrote out force balances for the three species, equating a thermodynamic driving force to a sum of frictional interactions for each species. As discussed by Fuller,¹²⁸ Pintauro and Bennion also showed how to relate the interaction parameters to the transport parameters mentioned above. The resulting equations for the three-species system are

$$\mathbf{i}_2 = -\frac{\kappa \xi}{F} \nabla \mu_{w,2} - \kappa \nabla \Phi_2 \quad \text{and} \quad (32)$$

$$\mathbf{N}_{w,2} = \frac{\xi \mathbf{i}_2}{F} - \alpha_w \nabla \mu_{w,2} \quad (33)$$

where μ_w represents the chemical potential of water and α_w is the transport coefficient of water. The equation for the membrane is ignored, since it is dependent on the other two equations by the Gibbs–Duhem equation. The above equations have also been arrived at using an irreversible thermodynamics approach.^{210,211} Similar equations to those above were

used by Wöhr et al.,⁴⁵ who put them in a Stefan–Maxwell framework.¹⁴⁹

Upon comparison of eq 32 to 28, it is seen that the proton–water interaction is now taken into account. This interaction is usually not too significant, but it should be taken into account when there is a large gradient in the water (e.g., low humidity or high-current-density conditions). Upon comparison of eq 33 to 31, it is seen that the equations are basically identical where the concentration and diffusion coefficient of water have been substituted for the chemical potential and transport coefficient of water, respectively. Almost all of the models using the above equations make similar substitutions for these variables.^{15,24,61,62,128}

The models by Janssen⁵⁵ and Weber and Newman⁹⁴ do not substitute for the chemical potential. Janssen took the transport coefficient as a fitting parameter. His model showed good agreement with water balance data under different conditions. Weber and Newman utilize the chemical-potential driving force directly and use a diffusion coefficient relative to that driving force for their vapor-equilibrated transport mode. Janssen states that using a chemical-potential driving force does not necessitate making the distinction between diffusive or convective flow in the membrane. However, as Meyers²¹² points out, by assuming the membrane system is a single phase, it cannot support a pressure difference inside it. The only way that a single-phase membrane model can have a pressure difference across it is if the chemical potential or water concentration is being altered at the boundaries. This problem is why single-phase membrane models cannot adequately describe transport for fully hydrated membranes where the driving force is the liquid pressure. This point is discussed further in section 4.2.4.

4.2.2.3. Membrane Water Content. Whether the dilute solution or concentrated solution theory equations are used to model the membrane system, functional forms for the transport parameters and the concentration of water are needed. The properties are functions of temperature and the water content, λ .⁹⁴ In the models, empirical fits are used^{14–17,24,44,51,54,60–62,82,128} or the properties are assumed constant.^{39,81,90,159} A review of these properties and how each model implements them is beyond the scope of this paper. Weber and Newman⁹⁴ review many of the data and discuss the functional forms for the properties from a physical standpoint.

Different models determine λ in different ways. Nafion exhibits a water-uptake isotherm as shown in Figure 7. The dashed line in the figure shows the effects of Schroeder's paradox, where there is a discontinuous jump in the value of λ . Furthermore, the transport properties have different values and functional forms at that point. Most models used correlate λ with the water-vapor activity, a_w^G , since it is an easily calculated quantity. An exception to this is the model of Siegel et al.,⁹⁰ which assumes a simple mass-transfer relationship. There are also models that model the isotherm either by Flory–Huggins theory^{41,61,62} or equilibrium between water and hydrated protons in the membrane and water vapor

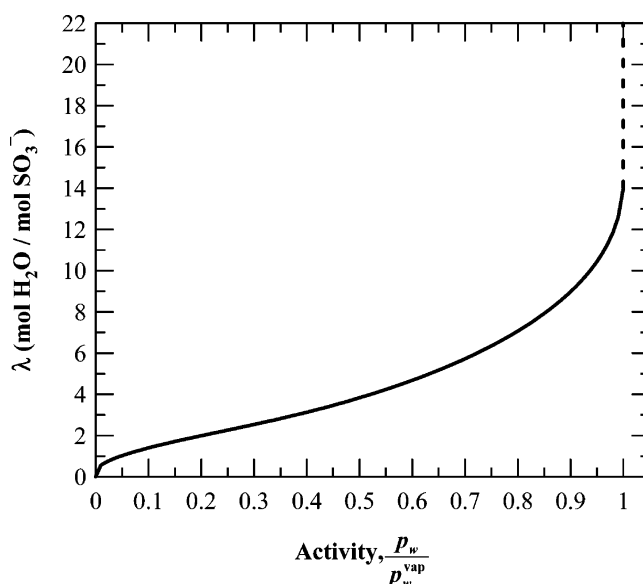


Figure 7. Equilibrium water-uptake or isotherm curve at 30 °C. The dashed line signifies the effect of Schroeder's paradox, a change in water uptake at the same chemical potential depending on the phase of water next to the membrane; liquid is at $\lambda = 22$.

next to it.^{63,92,94,130} Finally, although it is known that the isotherm is a function of temperature, only a few models include this feature.^{61–63,72,94,129} Most models just use an isotherm at a given temperature, usually 30 °C.

Schroeder's paradox is an observed phenomenon that needs to be considered in any model where the membrane is not either fully hydrated or dehydrated. There are various methods to account for Schroeder's paradox. The easiest way is to ignore it (i.e., either only vapor filled or fully hydrated), which a majority of the models do. Next, it can be treated as a discontinuity or by assuming a functional form of the water content such that λ and a_w^G continue to increase.^{16,51,54,60,64,71,81,82,109,129} Hence, supersaturated conditions exist, which are only physically realistic if water is assumed to be a mist or suspended in the gas. More physical and rigorous models have also been generated.

Eikerling et al.¹³⁸ have a random network of pores that are filled with either bulklike water or bound water, and impregnation by liquid water is easier than condensation. They use effective medium theory to predict conductivity results from impedance data. Their model is more of a microscopic one in which λ is calculated by changing the number of pores that are filled and examining the types of liquid-film bonds between pores. Similarly, Weber and Newman⁹⁴ use capillary arguments where the liquid pressure expands the collapsed channels within the membrane. Thus, there is a continuous transition between the vapor- and liquid-equilibrated membranes that can occur within the membrane. The transition itself can be relatively sharp, which is not unexpected for a phase-change-type behavior. Finally, Choi and Datta⁹² recently came up with an explanation of Schroeder's paradox that involves having evaporation at the liquid-filled pore mouth for a vapor-equilibrated membrane. The resulting me-

niscus causes a higher energy that the membrane must equilibrate with, thus lowering its water content. Out of the above three models, only that of Weber and Newman has been used in a fuel-cell sandwich model.

Those models that use an empirical expression for the isotherm often have different driving forces. One of the first models to use an isotherm was that by Springer et al.¹⁴ In that model, λ was used as the driving force for water flow in the membrane, and an activity coefficient was used to account for the isotherm behavior. This same approach was used by van Bussel et al.⁴⁴ and Wang and Savinell.¹⁷ The latter case examined the anode and assumed a flux of water through the membrane to help determine the membrane water concentration. Similar approaches to that of Springer et al. were used by Kulikovsky,⁸¹ Fuller and Newman,¹⁵ Dannenberg et al.,¹²⁹ and West and Fuller.²⁴ The models of Nguyen and White¹⁶ and Shimpalee and co-workers^{51,54,60,82} assume a linear change in water concentration in the membrane. Finally, Okada and co-workers^{39,207} use analytic and perturbation expressions for how the concentration of water changes. They start with vapor-equilibrated membranes and treat them with either semi-infinite or finite boundary conditions.

4.2.3. Hydraulic Models

In opposition to the single-phase treatment of the membrane system mentioned above are the models that assume the membrane system is two phases. This type of model corresponds to the liquid-equilibrated membrane shown in panel d of Figure 6. In this structure, the membrane is treated as having pores that are filled with liquid water. Thus, the two phases are water and membrane.

The addition of a second phase means that there is also an additional degree of freedom. This results in the ability of the membrane system to sustain a pressure gradient in the water because of a possibly unknown stress relation between the membrane and fluid at every point in the membrane. However, diffusion of water becomes meaningless, since the water is assumed to be pure in the models discussed here. Furthermore, unlike the cases of the models discussed above, the water content of the membrane is assumed to remain constant ($\lambda = 22$) as long as the pores are filled and the membrane has been pretreated appropriately. For cases where the pores do not remain filled, see sections 4.2.4 and 4.2.5.

The first model to describe the membrane in the above fashion was that of Bernardi and Verbrugge,^{13,110} which was based on earlier work by Verbrugge and Hill.^{111,213,214} This model utilized a dilute solution approach that used the Nernst-Planck equation (eq 29) to describe the movement of protons, except that now \mathbf{v} is not equal to zero. The reason is that, because there are two phases, the protons are in the water and the velocity of the water is given by Schlogl's equation^{213,215}

$$\mathbf{v}_{w,2} = -\left(\frac{k}{\mu}\right)\nabla p_L - \left(\frac{k_\Phi}{\mu}\right)z_f c_f F \nabla \Phi_2 \quad (34)$$

where k and k_Φ are the effective hydraulic and electrokinetic permeability, respectively, p_L is the hydraulic or liquid pressure, μ is the water viscosity, and z_f and c_f refer to the charge and concentration of fixed ionic sites, respectively.

In the above system, the movement of water can be attributed to a potential gradient and a pressure gradient. The movement of water by a pressure gradient is determined primarily by an effective permeability of water moving through the pore network. This approach is quite useful for describing fuel-cell systems where the membrane is well hydrated, but it requires that the water content be uniform across the membrane, with only a pressure gradient as a driving force for water movement. Such a treatment does not necessarily lend itself to describing the flux of water resulting when there is a water-activity gradient across the membrane (i.e., when the membrane is not fully hydrated).

The Bernardi and Verbrugge model also assumes that there is a gas volume fraction in the membrane that remains constant. This does not necessarily agree with the physical picture presented and experimental evidence. The reason for including the gas volume fraction was to allow for gas crossover through the membrane. Such a process though can be included using Fick's law for the gases in the membrane, since the diffusion coefficients of oxygen and hydrogen in Nafion are known. Many other models use the same approach and equations as Bernardi and Verbrugge, especially systems wherein the membrane is expected to be well hydrated (e.g., saturated gas feeds).^{25,47,50,64,78,95,125}

Unlike the cases of the single-phase models above, the transport properties are constant because the water content does not vary, and thus, one can expect a linear gradient in pressure. However, due to Schroeder's paradox, different functional forms might be expected for the vapor- and liquid-equilibrated membranes.

Instead of the dilute solution approach above, concentrated solution theory can also be used to model liquid-equilibrated membranes. As done by Weber and Newman,⁹⁴ the equations for concentrated solution theory are the same for both the one-phase and two-phase cases (eqs 32 and 33) except that chemical potential is replaced by hydraulic pressure and the transport coefficient is related to the permeability through comparison to Darcy's law. Thus, eq 33 becomes

$$\mathbf{N}_{w,2} = \xi \frac{\mathbf{i}_2}{F} - \frac{k}{\mu \bar{V}_w} \nabla p_L \quad (35)$$

where \bar{V}_w is the molar volume of water.

4.2.4. Hydraulic-Diffusive Models

The two approaches above can be contrasted to one another. In the first approach, section 4.2.2, water moves by diffusion, and pressure-driven flow is excluded as a separate driving force. In the second approach, section 4.2.3, only pressure-driven flow is used, and there is no diffusive flow because the liquid

water in the pores is pure. To describe both effects, some other kind of model is needed.

As mentioned at the end of section 4.2.2.2, a one-phase open system cannot support a pressure gradient without experiencing bulk flow. One way around this restriction is to use the chemical potential as the overall driving force.^{55,94} In essence, this driving force combines those of pressure and activity

$$\nabla\mu_{w,k} = RT\nabla \ln a_{w,k} + \bar{V}_w \nabla p_k \quad (36)$$

where p_k is the total pressure of phase k . For the single-phase system, there is not an additional degree of freedom to have both types of gradients. Thus, the above equation and approach requires that an additional relation is needed to specify both variables, and this is given by assuming local equilibrium (i.e., there is only one overall gradient, that of chemical potential).

Another way around the problem of pressure-driven flow in the single-phase membrane was presented by Meyers.²¹² He worked around the problem by allowing for a discontinuity in pressure at the membrane/solution interface, even though the electrochemical potential of all soluble species is continuous. He argued that additional mechanical stresses compressing the membrane should be indistinguishable from the thermodynamic pressure, and thus, the thermodynamic pressure might be discontinuous at the interface.

There have been various models that try to incorporate both diffusive flow and convective flow in one type of membrane and using one governing transport equation.^{63,65,71,72,79,99,107} They are based somewhat on concentrated solution theory where the concentration and total gas-phase pressure driving forces are used

$$\mathbf{N}_{w,2} = \frac{i_2}{F} - D_w \nabla c_{w,2} - c_{w,2} \frac{k}{\mu} \nabla p_G \quad (37)$$

A dusty-fluid model²¹⁶ has also been used to combine the effects, which adds convection to the Stefan–Maxwell framework, as discussed in a later section.^{63,72} This approach is akin to eq 37. As discussed above, the concentration of water may be replaced by a function of λ .

The problem with the above approach lies in the meaning of the two different gradients. As noted above, the pressure driving force does not make sense for a one-phase system. Thus, the model implicitly assumes a two-phase system. In a two-phase system, the interstitial concentration of water never varies, and the superficial concentration varies only if the volume fraction of water changes in the membrane. Furthermore, the use of a gas pressure means that a gas-phase is assumed to exist in the membrane, something that does not agree with experimental data. Overall, treatment in this manner is the same as that for the diffusive models except for an additional parameter to account for results that show a greater flux of water from cathode to anode when the fuel cell is operated with a pressure differential. This addition helps to fit some of the data, but it is not rigorous or consistent.

4.2.5. Combination Models

There is a need to be able to describe both types of behavior, diffusive and hydraulic, in a consistent manner, which also agrees with experimental data. For example, a membrane with a low water content is expected to be controlled by diffusion, and an uptake isotherm needs to be used (see Figure 7). The reasons for this are that there is not a continuous liquid pathway across the medium and that the membrane matrix interacts significantly with the water due to binding and solvating the sulfonic acid sites. A hydraulic pressure in this system may not be defined.

On the other hand, when the membrane is saturated, transport still occurs. This transport must be due to a hydraulic-pressure gradient because oversaturated activities are nonphysical. In addition, Buechi and Scherer²¹⁷ found that only a hydraulic model can explain the experimentally observed sharp drying front in the membrane. Overall, both types of macroscopic models describe part of the transport that is occurring, but the correct model is some kind of superposition between them.^{94,218} The two types of models are seen as operating fully at the limits of water concentration and must somehow be averaged between those limits. As mentioned, the hydraulic–diffusive models try to do this, but from a nonphysical and inconsistent standpoint that ignores Schroeder's paradox and its effects on the transport properties.

Weber and Newman⁹⁴ do the averaging by using a capillary framework. They assume that the two transport modes (diffusive for a vapor-equilibrated membrane and hydraulic for a liquid-equilibrated one) are assumed to occur in parallel and are switched between in a continuous fashion using the fraction of channels that are expanded by the liquid water. Their model is macroscopic but takes into account microscopic effects such as the channel-size distribution and the surface energy of the pores. Furthermore, they showed excellent agreement with experimental data from various sources and different operating conditions for values of the net water flux per proton flux through the membrane.¹³⁴

Eikerling et al.^{40,138} used a similar approach except that they focus mainly on convective transport. As mentioned above, they use a pore-size distribution for Nafion and percolation phenomena to describe water flow through two different pore types in the membrane. Their model is also more microscopic and statistically rigorous than that of Weber and Newman. Overall, only through combination models can a physically based description of transport in membranes be accomplished that takes into account all of the experimental findings.

4.3. Diffusion-Media Modeling

As shown in Figure 5, the diffusion media are the porous backings between the catalyst layers and the gas channels. They provide structural support, distribute the reactant gases, and provide a pathway for electrons, gases, and liquid water to move to or from the catalyst layers. The diffusion media are

often composed of either a single gas-diffusion layer or a composite structure of a gas-diffusion layer and a microporous layer. It should be noted that there are only a few models that treat composite diffusion media in a rigorous fashion.^{86,88,122} Most models treat only gas-diffusion layers.

Besides gas and liquid transport in the diffusion media, there is also electronic conduction. Most models neglect this due to the high conductivity of the carbon in the diffusion media, although it can become a limiting factor due to geometry¹²⁴ or diffusion-media composition.⁸⁸ For those that take it into account, Ohm's law is used

$$\mathbf{i}_1 = -\sigma_0 \epsilon_1^{1.5} \nabla \Phi_1 \quad (38)$$

where ϵ_1 and σ_0 are the volume fraction and electrical conductivity of the electronically conducting phase, respectively. The above equation has been adjusted for porosity and tortuosity using a Bruggeman correction.^{219–222} In the diffusion media, carbon is the conducting phase and the other solid component, Teflon, is insulating.

The mass balances of the species in the diffusion media can be deduced from eq 23. Furthermore, the fluxes of the various species are often already known at steady state. For example, any inert gases (e.g., nitrogen) have a zero flux, and the fluxes of reactant gases are related to the current density by Faraday's law (eq 24). Although water generation is given by Faraday's law, water can evaporate or condense in the diffusion media. These reactions are often modeled by an expression similar to

$$r_{\text{evap}} = k_m a_{\text{G,L}} (p_w - p_w^{\text{vap}}) \quad (39)$$

where r_{evap} is the molar rate of evaporation per unit volume, k_m is a mass-transfer coefficient per unit interfacial surface area, $a_{\text{G,L}}$ is the interfacial gas–liquid surface area per unit volume, p_w is the partial pressure of water in the gas phase, and p_w^{vap} is the vapor pressure of water, which can be corrected for pore effects by the Kelvin equation.²²³ Although different models may write eq 39 in slightly different forms (e.g., with a switching function), the underlying equation and principles are the same. Finally, the two-phase models may also have an interfacial area that depends on the water content of the media (for example, see ref 86). Overall, the value of $k_m a_{\text{G,L}}$ is typically high enough that the gas is saturated if liquid water exists; that is, $p_w = p_w^{\text{vap}}$ (using this last expression means that a special treatment is needed to combine the vapor and liquid material balances for water so as to eliminate the net evaporation rate).

In terms of transport, both gas- and liquid-phase transport should be described. Below, approaches for both types of transport are examined, with the gas-phase transport being treated first.

4.3.1. Gas-Phase Transport

Almost every model treats gas-phase transport in the fuel-cell sandwich identically. The Stefan–Maxwell equations are used (one of which is depend-

ent on the others, since the partial pressures sum to unity)

$$\nabla x_i = \sum_{j \neq i} \frac{x_j \mathbf{N}_j - x_i \mathbf{N}_i}{c_T D_{ij}^{\text{eff}}} \quad (40)$$

where c_T is the total concentration or molar density of all of the gas species, x_i is the mole fraction of species i , and D_{ij}^{eff} is the effective binary interaction parameter between i and j , by the Onsager reciprocal relationships, $D_{ij}^{\text{eff}} = D_{ji}^{\text{eff}}$ for ideal gases. The effective diffusion coefficient is defined as

$$D_{ij}^{\text{eff}} = \frac{\epsilon_G}{\tau_G} D_{ij} \quad (41)$$

where ϵ_G and τ_G are the volume fraction and tortuosity of the gas phase, respectively. If liquid water is ignored, then ϵ_G is set to the value of the bulk porosity of the medium, ϵ_0 . If liquid water is not ignored, then another treatment is required, as discussed in the next section. Typically, a Bruggeman expression is used for the tortuosity^{219–222}

$$\tau_G = \epsilon_G^{-0.5} \quad (42)$$

However, the above expression can underpredict the tortuosity at low porosities.^{86,102} Nam and Kaviani⁸⁶ have a very good discussion of the appropriate function to use for the tortuosity, in which changing values due to liquid saturation are also accounted for.

The gases in a fuel cell are typically hydrogen and water on the fuel side, and air and water on the oxidant side. Since there are not many components to the gases and one of the equations in eq 40 can be replaced by the summation of mole fractions equals 1, many models simplify the Stefan–Maxwell equations. In fact, eq 40 reduces to Fick's law for a two-component system. Such simplifications are trivial and are not discussed here.

As the pore size decreases, molecules collide more often with the pore walls than with each other. This movement, intermediated by these molecule–pore–wall interactions, is known as Knudsen diffusion.²²⁴ Some models have begun to take this form of diffusion into account.^{26,37,45,49,69,72,74,81} In this type of diffusion, the diffusion coefficient is a direct function of the pore radius.¹⁴⁹ In the models, Knudsen diffusion and Stefan–Maxwell diffusion are treated as mass-transport resistances in series^{149,225} and are combined to yield

$$\nabla x_i = -\frac{\mathbf{N}_i}{c_T D_{K_i}^{\text{eff}}} + \sum_{j \neq i} \frac{x_j \mathbf{N}_j - x_i \mathbf{N}_i}{c_T D_{ij}^{\text{eff}}} \quad (43)$$

where the $D_{K_i}^{\text{eff}}$ is the effective Knudsen diffusion coefficient. In effect, the pore wall, with zero velocity, constitutes another species with which the diffusing species interact, and it determines the reference velocity used for diffusion.²²⁶ The above equation also can be derived from a dusty-gas analysis.²¹⁶

From an order-of-magnitude analysis, when the mean-free path of a molecule is less than 0.01 times the pore radius, bulk diffusion dominates, and when it is greater than 10 times the pore radius, Knudsen diffusion dominates. This means that Knudsen diffusion is significant when the pore radius is less than about 0.5 μm . For reference, a typical carbon gas-diffusion layer has pores between 0.5 and 20 μm ^{227–229} in radius, and a microporous layer contains pores between 0.05 and 2 μm .^{230,231} Thus, while Knudsen diffusion may not have to be considered for gas-diffusion layers, it should be accounted for in microporous and catalyst layers.

While most models treat gas-phase flow as purely due to diffusion (i.e., the total gas pressure or concentration remains uniform), some models take into account convection in the gas-phase.^{25,45,48,51,52,54,60–64,72,80,82,90,122,125,126,216} This is usually done by the addition of Darcy's law for the gas phase

$$\mathbf{v}_G = -\frac{k_G}{\mu_G} \nabla p_G \quad (44)$$

where k is the effective permeability. The above relation can be made into a flux by multiplying it by the total concentration of the gas species.

One way to include the effect of gas-phase pressure-driven flow is to use eq 44 as a separate momentum equation.^{51,54,60–62,64,80,82,125} The models that do this are primarily CFD ones. Another way to include pressure-driven flow is to incorporate eq 44 into the Stefan–Maxwell equations, as per the dusty-gas model^{45,63,90,126,216}

$$\nabla x_i = -\frac{x_i k_G}{D_{K_i}^{\text{eff}} \mu_G} \nabla p_G + \sum_{j \neq i} \frac{x_j \mathbf{N}_j - x_i \mathbf{N}_i}{c_T D_{i,j}^{\text{eff}}} - \frac{\mathbf{N}_i}{c_T D_{K_i}^{\text{eff}}} \quad (45)$$

However, this is not necessarily a rigorously correct treatment, since the bulk-fluid velocity should not just be linearly combined with the transport equations. Instead, one of the Stefan–Maxwell equations should be replaced by eq 44, since it is in essence the summation of the mass velocities of the gas species.²²⁶

Although there are models that incorporate gas-phase pressure-driven flow in the diffusion media, the question can arise as to whether this is a significant effect. The results of almost all of the models show that the pressure difference through the sandwich is minimal, and the assumption of uniform gas pressure is probably fine for most conditions (for examples, see refs 13, 56, 57, and 134). This is as expected, since the gases flow parallel to the sandwich and, due to a no-slip condition, move through the diffusion media primarily by diffusion. There is a caveat to the above conclusion in that some models do show that even a small pressure difference hinders mass transfer if it is in the direction out of the sandwich; however, this effect depends greatly on the permeability of the diffusion media and is somewhat debatable. In addition, small pressure gradients when coupled with thermal gradients might affect water transport significantly, as discussed in later sections.

The main reason there are models that account for gas-phase pressure-driven flow is that these models are often multidimensional and are considering effects besides just through the 1-D fuel-cell sandwich. As discussed in a later section, the pressure difference down a gas channel is much more significant than that through the sandwich. The only type of fuel cell where gas-phase pressure-driven flow needs to be accounted for in the fuel-cell sandwich is one using an interdigitated flow field.^{48,52,232} In these types of fuel cells, the gas channels are not continuous through the fuel cell, and thus, gas is forced by both convection and diffusion through the diffusion media to reach the next gas channel.

4.3.2. Treatment of Liquid Water

Liquid water has been modeled to various degrees in fuel cells, and the different approaches are discussed in terms of their complexity. The simplest way to account for liquid water, besides ignoring it, is to treat it essentially as a solid species that occupies a certain volume fraction. Its transport is not considered, and the only effect it has is to decrease the gas-phase volume. This decreases the effective diffusion coefficients of the gas species (see eq 41) and somewhat takes into account flooding. The models that do this approach usually use the volume fraction of water as a fitting parameter.^{14,50,72,75,101,120} Out of these models, those of Chu et al.,⁷⁵ Gurau et al.,¹²⁰ and Baschuck and Li⁵⁰ use a liquid volume fraction that is a function of position to mimic flooding effects. Chu et al. showed the effect of different variations in the liquid volume fraction on various fuel-cell parameters including potential, oxygen mass fraction, and current density. Gurau et al. came up with an analytic solution for the cathode side of the fuel cell and showed how the limiting current density and polarization effects depended on the different liquid volume fractions. Baschuck and Li fit polarization curves by having different liquid volume fractions at each point. The resultant volume-fraction profile gives an idea about how flooding occurs and progresses.

The next more complicated treatment of liquid water is to have a way in which to model also its transport without going to a two-phase model. The models of this sort assume that the liquid water exists as droplets that are carried along in the gas stream.^{16,25,65} Thus, while evaporation and condensation occur, a separate liquid phase does not have to be modeled. Instead, the liquid is assumed to be a component of the gas, and usually one that has a negligible effect on the gas-phase flow and velocity. There is a change in the gas-phase volume fraction due to the water, however. This type of model allows for the existence and location of liquid water to be noted, and to a limited extent the change in the water pressure or concentration.

The above two types of models are essentially one phase. To model liquid-water flow accurately, two-phase models are required. Liquid-phase transport is similar to the gas-phase pressure-driven flow described above. There is no diffusion component to water movement because the liquid water is assumed

to be pure. Thus, the flux form of Darcy's law models the flow of liquid water

$$\mathbf{N}_{w,L} = - \frac{k}{\bar{V}_w \mu} \nabla p_L \quad (46)$$

where \bar{V}_w is the molar volume of water and all of the properties are valid for pure water. Many models use the above equation with a set value of the liquid-phase volume fraction.^{13,47,52,71,78,95,99,107,110,125} In essence, such a picture assumes that there are isolated gas and liquid pores in the medium. This makes some sense, since the medium contains hydrophilic and hydrophobic materials and pores, but in reality there should be some transfer between them as well as a changing volume fraction. Another way to look at it is that it is describing a thin film of liquid that coats a hydrophilic surface.

In the same fashion as that of the above models, those of Wöhr et al.⁴⁵ and Bevers et al.^{26,129} use a similar expression to eq 46 but instead use a surface diffusion coefficient instead of the effective permeability divided by the viscosity. Also, they use a water-loading gradient that one could relate to a water pressure. Bevers et al. also have a volume fraction that changes with respect to time. The model of Janssen⁵⁵ also has a similar equation to those of the other models but instead uses a driving force of chemical potential and a fitting parameter for the permeability. Weber and Newman¹³⁴ use a similar approach to that of Janssen but use a liquid-pressure-gradient driving force. They basically use the permeability as a fitting parameter that is set under only one set of operating conditions for each laboratory setup.

Finally, there are the models that use a phase mixture approach.^{51,54,60,82} In this approach, the two phases are treated as a single-phase mixture. Thus, all parameters are mixture parameters for the two phases. However, unlike the cases of the single-phase models, eq 46 is used for the liquid, which effectively determines its mass flux. A problem with this approach is that the mixture moves with a single velocity (i.e., the gas and liquid move with the same velocity). Thus, the liquid pressure is a result of this velocity; it does not really have a separate driving force. Although these simplifications are made, usually to help in numerical stability and computation time, the models do a reasonable job in predicting the water balance of the fuel cell. This approach can be seen as a simplified version of the multiphase mixture model by Wang and Cheng,^{58,59} as discussed below. While the above models describe liquid-water transport to some extent, the existence of partially saturated media requires the use of capillary equations and a rigorous two-phase description of two-phase flow.

4.3.2.1. Rigorous Two-Phase Flow Models. It is well-known that gas and liquid interact to a certain extent in a porous medium. Over the decades, many different modeling approaches have been developed for two-phase flow in porous media. These approaches range from a simple bundle-of-capillaries model to very complex 3-D network models incorpo-

rating a detailed description of a medium's microstructure. A complete description of the various modeling approaches is beyond the scope of this article, and the reader is referred to reviews and books on the subject.^{223,233,234} In this section, only those models that are used for modeling the diffusion media in fuel cells are discussed.^{56,57,74,78–80,85–87} These models are macroscopic and on the simpler end of the porous-media-model scale, which makes them easier to use although less accurate.

The interaction between liquid and gas is characterized by a capillary pressure, contact angle, surface tension, and pore radius^{223,234–236}

$$p_C = p_L - p_G = - \frac{2\gamma \cos \theta}{r} \quad (47)$$

where γ is the surface tension of water, r is the pore radius, and θ is the internal contact angle that a drop of water forms with a solid. Equation 47 is based on how liquid water wets the material; hence, for a hydrophilic pore, the contact angle is $0^\circ \leq \theta < 90^\circ$, and for a hydrophobic one, it is $90^\circ < \theta \leq 180^\circ$ (for examples, see refs 86 and 123).

One of the most important aspects of the two-phase models is their ability to predict the liquid saturation as a function of position. The saturation, S , is defined as the amount of pore volume that is filled with liquid; thus

$$\epsilon_C = \epsilon_0(1 - S) \quad (48)$$

This equation shows that the saturation greatly affects the effective gas-phase diffusion coefficients. Hence, flooding effects are characterized by the saturation.

In the models, the saturation is normally calculated using an empirical function to relate the capillary pressure to the saturation. Nguyen and co-workers^{56,87} use a function they developed from fitting data, and Pisani et al.⁷⁸ use a function with an unknown fitting parameter, while the other models use the empirically determined Leverett J -function.^{57,79,80,85,86,123} A different approach than that using a functional form for the capillary pressure–saturation relationship is to calculate the saturation using a model. Weber and Newman⁷⁴ do this using a random cut-and-rejoin bundle-of-capillaries model²²³ in order to integrate analytically the pore-size distribution of the diffusion media to get the saturation. In their analysis, they also explicitly account for the mixed wettability of the diffusion media (i.e., eq 47 is an integration limit, and there are separate hydrophobic and hydrophilic pore-size distributions). Along with Nam and Kaviani,⁸⁶ they have the only model to account for such effects. The use of a bundle-of-capillaries type of model is not necessarily rigorous because it idealizes the actual porous network.

Only a handful of models treat the diffusion media as at least partially hydrophobic;^{74,78,86,123} the others treat the medium as entirely hydrophilic. Although in principle it does not change the approach, the physical picture and boundary conditions must change. An entirely hydrophilic medium means that the liquid pressure must always be below the gas pres-

sure or the medium is flooded. This is taken into account in the models by assuming that the saturation equals zero at the interface of a diffusion medium with a gas channel. In principle, this seems fine, yet it also means that the liquid pressure is much lower than the gas pressure (and can even approach a value of zero) at this interface. The hydrophobic models assume that at this interface the capillary pressure is equal to zero, or in other words the liquid pressure equals the gas pressure. This assumption is not necessarily true due to menisci formation in the diffusion media, but it seems to be a more valid assumption, especially since the diffusion media have added Teflon to keep them from flooding (i.e., there is a need to have hydrophobic pores). The true boundary condition is probably a thermodynamic balance that also considers multidimensional flow effects.

To determine the saturation for any of the models, the capillary pressure must be known at every position within a diffusion medium. Hence, the two-phase models must determine the gas and liquid pressure profiles. In typical two-phase flow in porous media, the movement of both liquid and gas is determined by Darcy's law for each phase and eq 47 relates the two pressures to each other. Many models utilize the capillary pressure functionality as the driving force for the liquid-water flow

$$\mathbf{N}_{w,L} = -\frac{k}{V_w \mu} \nabla p_L = -\frac{k}{V_w \mu} (\nabla p_C + \nabla p_G) = -\frac{k}{V_w \mu} \nabla p_C \quad (49)$$

where the last equality is justified by the assumption of a uniform gas pressure in the fuel-cell sandwich. A useful relation in calculating the effective permeability, k , is to define a relative permeability, k_r ,

$$k = k_r k_{\text{sat}} \quad (50)$$

where k_{sat} is the saturated permeability, or the permeability at complete saturation, of the medium. k_{sat} depends only on the structure of the medium and has either been assumed,^{57,80,85} used as a fitting parameter,^{56,74,87} or estimated using a Carman-Kozeny equation.⁸⁶

If the dependence of k_r on saturation is known, then it can be used in eq 49 (via eq 50) directly. Nguyen and co-workers^{56,87} and Berning and Djilali⁸⁰ assume a linear dependence of k_r on saturation, and most of the other models use a cubic dependence;^{57,78,79,85,86} the model of Weber and Newman⁷⁴ yields close to a cubic dependence. This last model differs from the others because it obtains an analytic expression for k_r as a function of the capillary pressure (the independent variable). Furthermore, they also calculated and used residual or irreducible saturations, which are known to exist^{59,223,234,235} but have only been incorporated into a few other models.^{78,86} In accordance with typical data, a cubic dependence is the most often observed, although the other dependences help in the mathematical convergence of the models

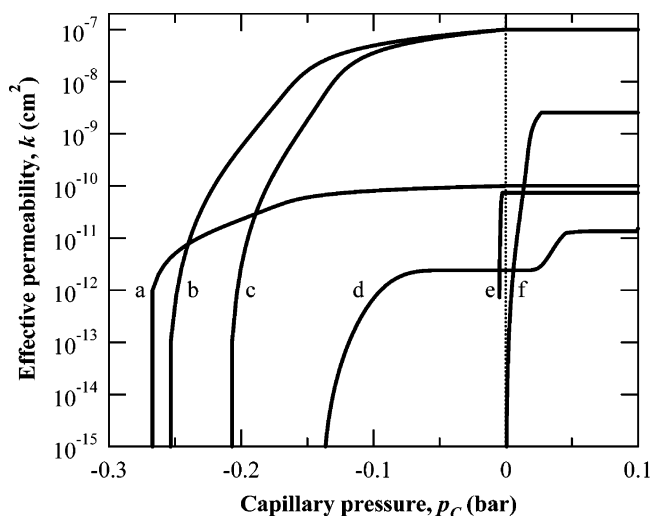


Figure 8. Effective permeability as a function of capillary pressure for the different two-phase models for the gas-diffusion layer. The lines correspond to the models of (a) Berning and Djilali,⁸⁰ (b) You and Liu⁷⁹ and Mazumder and Cole,⁸⁵ (c) Wang et al.,⁵⁷ (d) Weber and Newman,⁷⁴ (e) Natarajan and Nguyen,⁵⁶ and (f) Nam and Kaviany.⁸⁶

without increasing the overall error of the simulations too much.

The different capillary pressure, saturation, and permeability relationships of the different models can be compared. To do this, the effective permeabilities from some of the different models are plotted as a function of the capillary pressure in Figure 8. In the figure, the capillary pressure at which the effective permeability no longer changes is where the medium is fully saturated. Also, the values of the effective permeability are dependent on the diffusion media being tested. Furthermore, the value of the effective permeability at the right end of the curves corresponds to the saturated permeability, except for the model of Weber and Newman, who use a gas-phase residual saturation.

The values of the effective permeabilities vary over orders of magnitude, and this corresponds to the different results of the models. Furthermore, as discussed in various papers,^{56,80,85} the effective permeability of Natarajan and Nguyen (curve e) varies significantly over a very small pressure range, although they state that their capillary-pressure equation mimics data well. With respect to the various equations, the models that use the Leverett J -function^{57,79,80,85,86} all have a similar shape except for that of Berning and Djilali (curve a), who used a linear variation in the permeability with respect to the saturation. The differences in the other curves are due mainly to different values of porosity and saturated permeability. As mentioned above, only the models of Weber and Newman (curve d) and Nam and Kaviany (curve f) have hydrophobic pores, which is why they increase for positive capillary pressures. For the case of Weber and Newman, the curve has a stepped shape due to the integration of both a hydrophilic and a hydrophobic pore-size distribution.

The addition of the gas and water mass balances (eq 39 with eq 23) along with the above transport equation (eq 46) and constitutive relationships com-

pletely specifies the system of equations. In making these equations, some of the models include the effect of gravity and an additional advection or convection term. These other terms are secondary effects and, in a fashion similar to that of the full Navier–Stokes equations, are not as important as the Darcy effects due to the small pore sizes and low permeability. Even though there is a closed set of equations, it is often hard to get the simulations to converge, especially if they are multidimensional. Thus, the computational-fluid-dynamics models^{57,79,80,85} use the multiphase mixture model.^{58,59}

As mentioned above, this approach treats each phase as a constituent to a mixture. Thus, all parameters are mixture parameters and must be averaged, usually by the saturation. Unlike the models mentioned at the end of the previous section, the models here use capillary phenomena. Furthermore, although the mixture moves at a mass-average velocity, interfacial drag between the phases and other conditions allow each separate phase velocity to be determined. The liquid-phase velocity is found by^{57,59}

$$\mathbf{v}_L = \lambda_L \frac{\rho_m}{\rho_L} \mathbf{v}_m + \frac{k\lambda_L(1 - \lambda_L)}{\epsilon_0 \rho_L \nu_m} [\nabla p_C + (\rho_L - \rho_G) \mathbf{g}] \quad (51)$$

where the subscript m stands for the mixture, ρ_k and ν_k are the density and kinematic viscosity of phase k , respectively, and λ_L is the relative mobility of the liquid phase

$$\lambda_L = \frac{k_{r,L}/\nu_L}{k_{r,L}/\nu_L + k_{r,G}/\nu_G} \quad (52)$$

In eq 51, the first term represents a convection term, and the second comes from a mass flux of water that can be broken down as flow due to capillary phenomena and flow due to interfacial drag between the phases. The velocity of the mixture is basically determined from Darcy's law using the properties of the mixture. The appearance of the mixture velocity is a big difference between this approach and the others, and it could be a reason the permeability is higher for simulations based on the multiphase mixture model.

The overall gain of the multiphase mixture model approach above is that the two-phase flow is still considered, but the simulations have only to solve pseudo-one-phase equations. Problems can arise if the equations are not averaged correctly. Also, the pseudo-one-phase treatment may not allow for pore-size distribution and mixed wettability effects to be considered. Furthermore, the multiphase mixture model predicts much lower saturations than those of Natarajan and Nguyen^{56,87} and Weber and Newman⁷⁴ even though the limiting current densities are comparable. However, without good experimental data on relative permeabilities and the like, one cannot say which approach is more valid.

Finally, some of the models use an equation of the type^{52,80,85}

$$\mathbf{N}_{w,L} = -D_S \nabla S \quad (53)$$

where D_S is a so-called capillary diffusivity

$$D_S = \frac{k}{\mu \bar{V}_w} \frac{dp_C}{dS} \quad (54)$$

Although the above equation is valid, it gives the false impression that the saturation is the driving force for fluid flow and that a saturation condition should be used as a boundary condition. Furthermore, care must be taken in the interpretation of the capillary diffusivity.

4.4. Catalyst-Layer Modeling

Electrochemical reactions take place at the catalyst layers of the fuel cell. At the anode and cathode, hydrogen is oxidized (eq 1) and oxygen is reduced (eq 2), respectively. These layers are often the thinnest in the fuel-cell sandwich but are perhaps the most complex because this is where electrochemical reactions take place and where all of the different types of phases exist. Thus, the membrane and diffusion media models must be used in the catalyst layer along with additional expressions related to the electrochemical kinetics on the supported electrocatalyst particles.

A schematic of a typical fuel-cell catalyst layer is shown in Figure 9, where the electrochemical reactions occur at the two-phase interface between the electrocatalyst (in the electronically conducting phase) and the electrolyte (i.e., membrane). Although a three-phase interface between gas, electrolyte, and electrocatalyst has been proposed as the reaction site, it is now not believed to be as plausible as the two-phase interface, with the gas species dissolved in the electrolyte. This idea is backed up by various experimental evidence, such as microscopy, and a detailed description is beyond the scope of this review. Experimental evidence also supports the picture in Figure 9 of an agglomerate-type structure where the electrocatalyst is supported on a carbon clump and is covered by a thin layer of membrane.^{162,237–240} Sometimes a layer of liquid water is assumed to exist on top of the membrane layer, and this is discussed in section 4.4.6. Figure 9 is an idealized picture, and

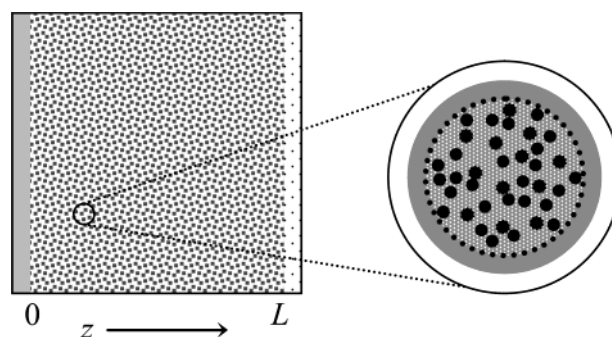


Figure 9. Idealized schematic of the cathode catalyst layer (going from $z = 0$ to $z = L$) between the membrane and cathode diffusion medium showing the two main length scales: the agglomerate and the entire porous electrode. Gray, white, and black indicate membrane, gas, and electrocatalyst, respectively, and the gray region outside of the dotted line in the agglomerate represents an external film of membrane or water on top of the agglomerate.

the actual structure is probably more of a “spaghetti and meatball” structure, where the carbon agglomerates are connected to each other and covered by thin tendrils of membrane.

Various modeling approaches have been used for the catalyst layers, with different degrees of success. The approach taken usually depends on how the other parts of the fuel cell are being modeled and what the overall goal of the model is. Just as with membrane modeling, there are two main classes of models. There are the microscopic models, which include pore-level models as well as more detailed quantum models. The quantum models deal with detailed reaction mechanisms and elementary transfer reactions and transition states. They are beyond the scope of this review and are discussed elsewhere, along with the issues of the nature of the electrocatalysts.^{151,241–243}

The other type of model is the macrohomogeneous model. These models are macroscopic in nature and, as described above, have every phase defined in each volume element. Almost all of the models used for fuel-cell electrodes are macrohomogeneous. In the literature, the classification of macrohomogeneous models is confusing and sometimes contradictory. To sort this out, we propose that the macrohomogeneous models be subdivided on the basis of the length scale of the model. This is analogous to dimensionality for the overall fuel-cell models.

In this scheme, the first type of model is the 0-D-type models or interface models, where a single equation is used without regard to the structure of the catalyst layers. Next are the 1-D-type models, which either account for changes across the layer or account for only local effects in the agglomerate. Typically, those that account for changes across the layer are called porous-electrode, macrohomogeneous, or thin-film models, and those that account for changes in the agglomerate are called agglomerate models. However, the agglomerate models are still macrohomogeneous models, and they may include effects across the layer as well. In the same fashion, some porous-electrode models include agglomerate-scale interactions. The models that include effects on only one length scale are termed simple. They are further subdivided on the basis of the length scale modeled, such that porous-electrode and agglomerate correspond to the length scales of the layer and agglomerate, respectively. Those models that include effects on both length scales (i.e., 2-D-type models) are known as embedded macrohomogeneous models. Finally, there are no 3-D-type models because there are only two primary length scales (the catalyst layer and the agglomerate) in these regions.

An examination of the catalyst-layer models reveals the fact that there are many more cathode models than anode ones. In fact, basically every electrode-only model is for the cathode. This arises because the cathode has the slower reaction; it is where water is produced, and hence, mass-transfer effects are much more significant; and it represents the principal inefficiency of the fuel cell. In other words, while the cathode model can be separate from the anode model, the converse is not true due to the

above reasons. Finally, the anode can almost always be modeled as a simplified cathode model, with the exception of poisoning of the electrocatalyst. For these reasons, the discussion below focuses mainly on the cathode models; the anode models require only a switch in the kinetic expression and various property values.

In this section, the reactions and general equations for the catalyst layers are presented first. Next, the models are examined starting with the interface models, then the microscopic ones, and finally the simple and embedded macrohomogeneous ones. Finally, at the end of this section, a discussion about the treatment of flooding is presented.

4.4.1. General Governing Equations

Although the various models contain their own equations, they are derived from basically the same set of governing expressions, regardless of the effects being modeled. As mentioned, the reactions at the anode and cathode are termed the HOR and ORR, respectively. For the HOR, the reaction is fast and can be described by a Butler–Volmer kinetic expression, eq 12. However, if the feed stream is reformat or contains poisons such as carbon monoxide, the reaction rate is quite different. In this situation, the carbon monoxide adsorbs to the electrocatalyst sites and effectively decreases the reaction rate. There have been various models that account for this by doing a carbon monoxide site balance and examining the reaction steps involved.^{17,104,113,115,244–248} Of these models, the one by Springer et al.¹⁰⁴ is probably the most comprehensive and does the best job in terms of agreement with experimental data. The treatment of the effect of poisons on kinetics is beyond the scope of this review and is not discussed further. For the ORR, a Tafel expression, eq 13, is normally used due to the slow kinetics of the four-electron-transfer reaction. As discussed in section 3.2.2, either eq 13 or eq 15 can be used, with the difference being in the overpotential used (i.e., whether the surface and concentration or just the surface overpotential is used, respectively). As discussed, this difference basically corresponds to the placement of the, perhaps imaginary, reference electrode.

In general, catalyst layers contain many phases: liquid, gas, different solids, and membrane. Because the layers have multiple phases, effective values must be used for the transport properties such as membrane conductivity; this is typically done using a Bruggeman expression (see eqs 41 and 42). Because of the complexity of the layers, it is worthwhile to do a variable and equation count. In the most general case, the membrane, diffusion medium, and kinetic equations are used. This gives the set of variables and equations as listed in Table 1. It should be noted that since there are multiple phases in the catalyst layer, appropriate volume fractions and Bruggeman expressions are required for such equations as Ohm's law in the membrane phase. Another point is that the complete set of equations is seldom used in modeling. Often, simplifying assumptions are used. For example, the ohmic drop in the matrix or solid is often ignored due to its high conductivity. Also,

Table 1. List of Important Variables and Their Governing Equations or Conditions for the Catalyst Layer

variable		equation
overall liquid water flux	\mathbf{N}_L	23
overall membrane water flux	\mathbf{N}_w	23
gas-phase component flux	$\mathbf{N}_{G,i}$	23
gas-phase component partial pressure	$p_{G,i}$	43
liquid pressure	p_L	49
membrane water chemical potential ^a	μ_w	33 or 34
electronic-phase current density	\mathbf{i}_1	38
membrane current density	\mathbf{i}_2	32 or 28
electronic-phase potential	Φ_1	27
membrane potential	Φ_2	55 or 64
temperature	T	set or 76 or 78
total gas pressure	p_G	set or 44
liquid saturation	S	see section 4.3.2.1

^a This can be directly related to the liquid pressure depending on what equation or approach is used.

treatment of the membrane phase is usually done using Ohm's law and ignoring the water flux through the membrane. While Table 1 lists all of the governing variables and equations, it does not necessarily say how to relate the variables to each other, since more than one variable may occur in a given equation.

The membrane and diffusion-media modeling equations apply to the same variables in the same phase in the catalyst layer. The rate of evaporation or condensation, eq 39, relates the water concentration in the gas and liquid phases. For the water content and chemical potential in the membrane, various approaches can be used, as discussed in section 4.2. If liquid water exists, a supersaturated isotherm can be used, or the liquid pressure can be assumed to be either continuous or related through a mass-transfer coefficient. If there is only water vapor, an isotherm is used. To relate the reactant and product concentrations, potentials, and currents in the phases within the catalyst layer, kinetic expressions (eqs 12 and 13) are used along with zero values for the divergence of the total current (eq 27).

The kinetic expressions result in transfer currents that relate the potentials and currents in the electrode (platinum on carbon) and electrolyte (membrane) phases as well as govern the consumption and production of reactants and products. To simplify the equations and approaches for the case of one ionically and one electronically conducting phase, it is useful to use the relation

$$\nabla \cdot \mathbf{i}_2 = -\nabla \cdot \mathbf{i}_1 = a_{1,2} i_{h,1-2} \quad (55)$$

where $-\nabla \cdot \mathbf{i}_1$ represents the total anodic rate of electrochemical reactions per unit volume of electrode and $i_{h,1-2}$ is the transfer current for reaction h between the membrane and the electronically conducting solid (i.e., eqs 12 and 13 for the HOR and ORR, respectively). The above charge balance assumes that faradaic reactions are the only electrode processes; double-layer charging is neglected (as is appropriate under steady-state conditions). This equation can be used in the conservation-of-mass equation

(eq 23) to simplify it. For example, if the ORR is the only reaction that occurs at the cathode, the following mass balance results

$$\begin{aligned} \nabla \cdot \mathbf{N}_{O_2,G} = \\ -\frac{1}{4F} a_{1,2} i_{0,ORR} \left(\frac{p_{O_2}}{p_{O_2}^{ref}} \right) \exp \left(-\frac{\alpha_c F}{RT} (\eta_{ORR,1-2}) \right) = \frac{1}{4F} \nabla \cdot \mathbf{i}_1 \end{aligned} \quad (56)$$

This equation is often used in the various cathode models.

Before discussing the models, a note should be made concerning catalyst loading. Many models use platinum loading in their equations, especially for optimizing designs and in normalizing the current produced (equivalent to a turnover frequency in catalysis). In this respect, the catalyst loading, m_{Pt} , is the amount of catalyst in grams per geometric area of the fuel-cell face (x, y in Figure 1). If a turnover frequency is desired, the reactive surface area of platinum, A_{Pt} , can be used (usually given in m^2/g). This area can be related to the radius of a platinum particle, assuming perhaps a certain roughness factor, but more often it is experimentally inferred using cyclic voltammetry measuring the hydrogen adsorption. These variables can usually be determined and then used to calculate the specific interfacial area between the electrocatalyst and electrolyte,

$$a_{1,2} = \frac{m_{Pt} A_{Pt}}{L} \quad (57)$$

where L is the thickness of the catalyst layer. This assumes a homogeneous distribution of electrocatalyst in the catalyst layer.

A factor closely related to the catalyst loading is the efficiency or utilization of the electrode. This tells how much of the electrode is actually being used for electrochemical reaction and can also be seen as a kind of penetration depth. To examine ohmic and mass-transfer effects, sometimes an effectiveness factor, E , is used. This is defined as the actual rate of reaction divided by the rate of reaction without any transport (ionic or reactant) losses. With this introduction of the parameters and equations, the various modeling approaches can be discussed.

4.4.2. Interface Models

The simplest way to treat the catalyst layers is to assume that they exist only at the interface of the diffusion media with the membrane. Thus, they are infinitely thin, and their structure can be ignored. This approach is used in complete fuel-cell models where the emphasis of the model is not on the catalyst-layer effects but on perhaps the membrane, the water balance, or multidimensional effects. There are different ways to treat the catalyst layer as an interface.

If a detailed potential is not required in the model, then the catalyst layer can be treated as simply the location where oxygen and hydrogen are consumed and water is produced. Hence, Faraday's law (eq 24) is used as a generation/consumption term in the

boundary condition for the mass balance between the membrane and the diffusion medium. The models that focus mainly on water management, a quantity tied to the current density, use this type of treatment of the catalyst layers.^{55,81,112,126,134} A slightly more sophisticated treatment is to model the catalyst layers as described above but then use an overall polarization equation (e.g., eq 21) with the simulation results to yield a potential for the cell at the specific current density.^{14,65,74,86,127,203}

A more sophisticated and more common treatment of the catalyst layers still models them as interfaces but incorporates kinetic expressions at the interfaces. Hence, it differs from the above approach in not using an overall polarization equation with the results, but using kinetic expressions directly in the simulations at the membrane/diffusion medium interfaces. This allows for the models to account for multidimensional effects, where the current density or potential changes,^{16,24,46–48,51,52,54,56,60–62,66,80,82,87,107,125} although some of the earlier and water-management models are 1-D and treat the catalyst layer in this manner.^{20,57,75,109} This treatment means that both Faraday's law and the kinetic expressions are used as boundary conditions at the diffusion media and membrane interfaces. This type of treatment also allows for nonuniform current density distributions to exist, because the potential is constant in a cell due to the equipotential surfaces of the bipolar plates. Another way to look at these models is that the surface overpotential and reactant gas concentrations are assumed uniform throughout the catalyst layers, and this is used in the kinetic expressions to calculate the current density. In fact, it is common for these models to use the overpotential as a fitting parameter.

Overall, the interface models are basically 0-D. They assume that all of the relevant variables in the catalyst layers are uniform in their values across the layer. This has some justification in that the catalyst layers are very thin, and it is adequate if other effects that are modeled are more significant; however, the catalyst layers should be modeled in more detail to ensure that all the relevant interactions are accounted for and to permit optimization of such parameters as catalyst loading.

4.4.3. Microscopic and Single-Pore Models

The earliest models of fuel-cell catalyst layers are microscopic, single-pore models, because these models are amenable to analytic solutions. The original models were done for phosphoric-acid fuel cells. In these systems, the catalyst layer contains Teflon-coated pores for gas diffusion, with the rest of the electrode being flooded with the liquid electrolyte. The single-pore models, like all microscopic models, require a somewhat detailed microstructure of the layers. Hence, effective values for such parameters as diffusivity and conductivity are not used, since they involve averaging over the microstructure.

There are two main types of single-pore models. In the first, the approach of Giner and Hunter¹ is taken in which there are straight, cylindrical gas pores of a defined radius. These pores extend the

length of the catalyst layer, and reaction takes place at their surface. These models are termed the gas-pore models.^{249–252} The second type of model follows the scheme of Grens²⁵³ and Cutlip.² In this approach, there are still gas pores, but there are also pores filled with electrolyte and catalyst. It is in these other pores that reaction, diffusion, and migration occur. These models are termed the flooded-agglomerate models.^{3–5,254–257} Although there are the two approaches, the distinction between them is often blurred.

The equations used in these models are primarily those described above. Mainly, the diffusion equation with reaction is used (e.g., eq 56). For the flooded-agglomerate models, diffusion across the electrolyte film is included, along with the use of equilibrium for the dissolved gas concentration in the electrolyte. These models were able to match the experimental findings such as the doubling of the Tafel slope due to mass-transport limitations. The equations are amenable to analytic solution mainly because of the assumption of first-order reaction with Tafel kinetics, which means that eq 13 and not eq 15 must be used for the kinetic expression. The different equations and limiting cases are described in the literature models as well as elsewhere.^{258,259}

Of these models, the flooded-agglomerate one shows better agreement with experimental data. This is not unexpected, since it probably models the actual microstructure better and also has more parameters. A problem with the single-pore models is that in reality there are multiple pores that are tortuous. Furthermore, the driver of having analytic expressions becomes less important, as computer power has progressed. Overall, the single-pore models represent a good first start in simulating fuel-cell electrodes and form the core of many more complicated models as discussed below. However, macrohomogeneous and more sophisticated models provide for more physically realistic simulations. Finally, while these models do a good job for phosphoric-acid fuel cells, it is unknown how well they work for polymer-electrolyte fuel cells where, since the electrolyte is a solid, it does not necessarily penetrate the pore space.

The only other truly microscopic models for the catalyst layers are those by Durand and co-workers.^{30–33,260} In these models, spherical agglomerate structures are assumed to exist in regular 3-D hexagonal arrays. Between the agglomerates, either there are gas pores or the region is flooded with electrolyte. The reason these models are microscopic and not macrohomogeneous is that they examine interactions in such a way that there is a dependence on the exact way in which the agglomerates are placed. Furthermore, not all of the phases are defined in every volume element. The equations solved are mainly Ohm's law and Fick's law with kinetic expressions. The results of the models show the concentration contours around a particle and agree with experimental current densities and trends. Such a model also allows for the detailed placement of the electrocatalyst particles to be studied, even though it may not be possible to make such an arrangement experimentally. To expand on the last comment, the

benefit of these microscopic models is that they clearly show how the HOR occurs next to the membrane and how the packing and structure of the agglomerate particles help to enhance or reduce the overall efficiency of the anode, something that the classical models above could not demonstrate.

4.4.4. Simple Macrohomogeneous Models

There are many models that use essentially only one length scale but average over the microscopic details of a region. These models are termed simple macrohomogeneous models. As described in section 3.1, the macrohomogeneous approach assumes that all phases exist at all points in the volume and that properties and phases can be categorized by a handful of parameters including the volume fraction and surface area per volume. Although these models do not include microstructural details, they do use many of the same equations and physical ideas of the single-pore models. The two main length scales studied are over the whole catalyst layer or over the agglomerate (see Figure 9), and each are discussed below.

4.4.4.1. Porous-Electrode Models. The porous-electrode models are based on the single-pore models above, except that, instead of a single pore, the exact geometric details are not considered. Euler and Nonnenmacher²⁶¹ and Newman and Tobias⁷ were some of the first to describe porous-electrode theory. Newman and Tiedemann⁶ review porous-electrode theory for battery applications, wherein they had only solid and solution phases. The equations for when a gas phase also exists have been reviewed by Bockris and Srinivasan²⁶² and DeVidts and White.²⁶³ and porous-electrode theory is also discussed by Newman¹³⁹ in more detail.

Porous-electrode theory is concerned about the overall reaction distribution in the catalyst layer. Thus, it is assumed that the main effects do not occur within the agglomerates. In other words, the agglomerates all have a uniform concentration and potential. Conceptually, porous-electrode theory can be visualized as a resistor network, as shown Figure 10. Physically, the figure is showing that electron, proton, and kinetic resistances govern the reaction distribution. Thus, the overpotential and transfer current in the electrode are functions of position because the current travels along the path of least resistance. The effect of concentration is accounted for in the calculation of the charge-transfer resistance, which is derived directly from the kinetic expressions and likely to be nonlinear. Finally, to be

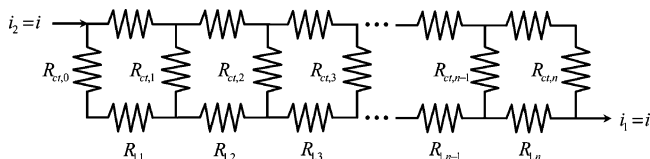


Figure 10. Resistor-network representation of porous-electrode theory. The total current density, i , flows through the electrolyte phase (2) and the solid phase (1) at each respective end. Between, the current is apportioned on the basis of the resistances in each phase and the charge-transfer resistances. The charge-transfer resistances can be nonlinear because they are based on kinetic expressions.

rigorous, the charge-transfer resistances in Figure 10 should be in parallel with a capacitor representing double-layer charging. However, this can be neglected for the steady-state operation of fuel cells and introduced if transients or impedance is studied.

The governing equations for the simple porous-electrode models are as referenced in Table 1. The characteristic length scale is the thickness of the catalyst layers. There are also some variations in the treatment of the simple porous-electrode models. In the first set of models, the catalyst layers are integrated over, and the expression is included as a boundary condition in calculating the cell potential or current density.^{37,95,99} This treatment is very similar to that of the interface models, except that potential drops for the matrix and solution phases are accounted for. The reason for doing the integration is that, if the reaction distribution is mainly uniform, then there is no loss in numerical accuracy and there is a gain in numerical stability and easier convergence.

The next set of models treats the catalyst layers using the complete simple porous-electrode modeling approach described above. Thus, the catalyst layers have a finite thickness, and all of the variables are determined as per Table 1 with a length scale of the catalyst layer. While some of these models assume that the gas-phase reactant concentration is uniform in the catalyst layers,^{15,67,69} most allow for diffusion to occur in the gas phase.^{13,25,26,28,45,71,72,110,121,133,204} These models are essentially macrohomogeneous versions of the single-gas-pore models.

The final simple macrohomogeneous porous-electrode models are the ones that are more akin to thin-film models. In these models, the same approach is taken, but instead of gas diffusion in the catalyst layer, the reactant gas dissolves in the electrolyte and moves by diffusion and reaction.^{17,36,50,64,101,114,264} The governing equations are more-or-less the same as above, except that now a concentration instead of a partial pressure appears in the kinetic expressions and the governing equations for mass transport of the reactant and product gas species become ones of diffusion in the membrane or water (if a water layer is assumed to exist). The reason these models are still simple models is that only the length scale of the catalyst layer is considered, and the concentrations of the species are assumed to be in equilibrium with their respective gas-phase partial pressures (i.e., Henry's law applies).

As mentioned, the reaction distribution is the main effect on the catalyst-layer scale. Because of the facile kinetics (i.e., low charge-transfer resistance) compared to the ionic resistance of proton movement for the HOR, the reaction distribution in the anode is a relatively sharp front next to the membrane. This can be seen in analyzing Figure 10, and it means that the catalyst layer should be relatively thin in order to utilize the most catalyst and increase the efficiency of the electrode. It also means that treating the anode catalyst layer as an interface is valid. On the other hand, the charge-transfer resistance for the ORR is relatively high, and thus, the reaction distribution is basically uniform across the cathode. This means

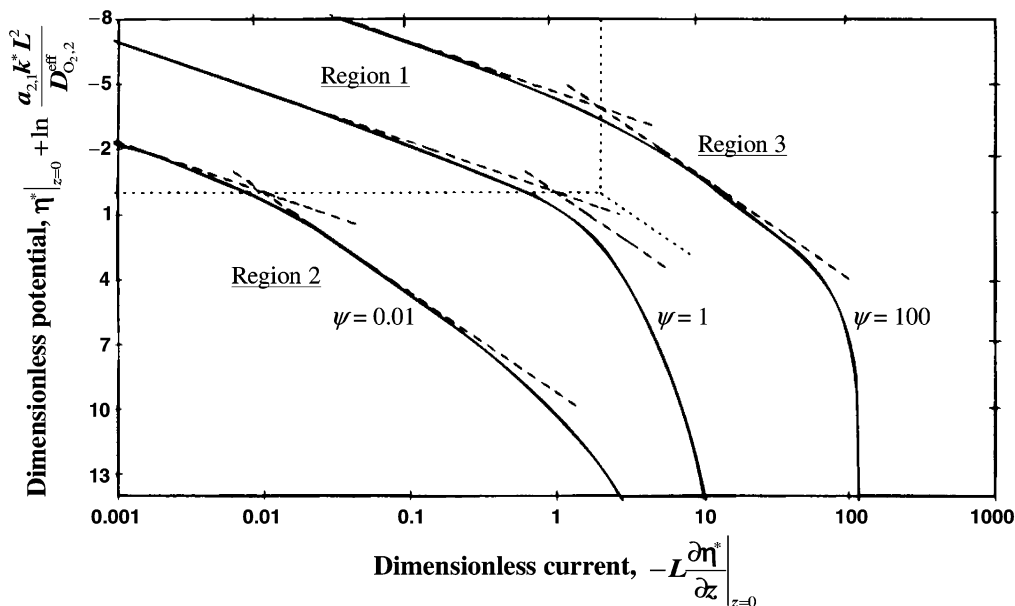


Figure 11. Tafel plot of flooded porous-electrode simulation results for the cathode at three different values of $\psi = 2.3nFD_{O_2,2}^{eff}c_{O_2,2}|_{z=L}/bk^{eff}$. The z coordinate ranges from 0 (catalyst layer/membrane interface) to L (catalyst layer/diffusion medium interface), the dimensionless overpotential is defined as $\eta^* = -\alpha_c F/RT(\eta_{ORR,1-2})$, and the ORR rate constant is defined as $k^* = i_{0ORR}/nF C_{O_2,2}^{ref}$. (Reproduced with permission from ref 36. Copyright 1998 The Electrochemical Society, Inc.)

that simplifying assumptions such as a uniform surface overpotential ($\eta_{SRR,1-2}$) can be justified, and basically all of the catalyst is being utilized in the layer as long as the mass-transfer of oxygen does not become limiting. In this case, the charge-transfer resistance next to the membrane becomes much higher than the other ones, and the catalyst is less utilized in that region, since there is less oxygen. One should note that with Tafel kinetics, which prevail for the ORR, the nonuniformity of the reaction distribution is governed by the current density and electrode thickness and not by the exchange current density.

The above effects can also be seen in the different regimes of the polarization curve. To study these effects, Perry et al.³⁶ made Tafel plots of their simulation results, which used a flooded porous-electrode model of the cathode catalyst layer. These plots are shown in Figure 11, where they are a function of a dimensionless parameter that is essentially a ratio of oxygen mass transfer to ionic conduction. The Tafel plots show a doubling of the Tafel slope when either the mass-transfer or ionic limitations are controlling, regions 2 and 3, respectively. In region 1, kinetics is controlling. Figure 11 allows one to understand and visualize how the interplay between the different phenomena and variables, such as current, gas diffusion both inside and outside the catalyst layer, and proton conduction inside the catalyst layer, affects polarization behavior. Although the model is for the cathode, it is equally valid for the anode, where the parameter values normally result in kinetic control (region 1).

The results of Perry et al. allow for the development of a diagnostic method that determines the limiting behavior from simple experimental data. In a similar analysis, Weber et al.¹³³ added mass transport in the diffusion media explicitly and analyzed

their results in terms of ohmic, kinetic, or mass-transfer control situations. Like Perry et al., they discuss how simple experiments such as oxygen gain, the gain in performance with oxygen instead of air, can help determine a given fuel cell's controlling phenomena. Eikerling and Kornyshev²⁸ also show the same behavior, and they analyze the resistances with analytic expressions for the various limiting cases. Finally, Jaouen et al.⁹⁸ examine similar cases to those above but include agglomerate effects, as discussed in detail in section 4.4.5.

4.4.4.2. Agglomerate Models. The simple macro-homogeneous agglomerate models consider only effects that occur on the agglomerate length scale. In essence, they assume a uniform reaction-rate distribution, that is, a uniform gas concentration and surface overpotential through the thickness of the catalyst layer. As mentioned above, the simple agglomerate models more accurately represent the structure of the catalyst layers than the simple porous-electrode models. These models are very similar to the microscopic models of Durand and co-workers discussed above, except that the geometric arrangement is averaged over and each phase exists in each volume element.

For the agglomerate model, the characteristic length scale is the radius of the agglomerate, R_{agg} , and all of the agglomerates are assumed to be the same shape and size. In the model, the reactant or product diffuses through the electrolyte film surrounding the particle and into the agglomerate, where it diffuses and reacts. Hence, there is a concentration and possibly a potential distribution within the agglomerate. The equations for modeling the agglomerate are similar to those listed in Table 1, except that either spherical or cylindrical coordinates are used for the gradients. The reason they are not identical is that the agglomerate scale is es-

essentially a subscale or microscopic scale in the catalyst layer. This is the same as examining a bed of sand, where the normal resolution looks at changes across the box and the agglomerate scale looks at changes within individual grains (see Figure 9). In a macrohomogeneous model, it is necessary to average over the agglomerate scale, and hence, effectiveness factors, both internal and overall,²⁶⁵ are often used.

The analysis below is given for the ORR, since the agglomerate and embedded models mainly examine the cathode; reaction at the anode can be derived in a similar manner. The analysis is basically the same as that of reaction and diffusion in a catalyst pellet. For the analysis, an effectiveness factor is used, which allows for the actual rate of reaction to be written as (see eq 55)

$$\nabla \cdot \mathbf{i}_2 = a_{1,2} i_{h,1-2} E \quad (58)$$

Since the ORR is a first-order reaction following Tafel kinetics, the solution of the mass conservation equation (eq 23) in a spherical agglomerate yields an analytic expression for the effectiveness factor of^{149,265}

$$E = \frac{1}{3\phi^2} (3\phi \coth(3\phi) - 1) \quad (59)$$

where ϕ is the Thiele modulus for the system²⁶⁶

$$\phi = \zeta \sqrt{\frac{K}{D_{O_2,agg}^{eff}}} \quad (60)$$

where ζ is the characteristic length of the agglomerate (volume per surface area), $R_{agg}/3$ for spheres, $R_{agg}/2$ for cylinders, and δ_{agg} for slabs, and K is a rate constant given by

$$K = \frac{a_{1,2} i_{0,ORR}}{4F c_{O_2}^{ref}} \exp\left(-\frac{\alpha_c F}{RT} (\eta_{ORR,1-2})\right) \quad (61)$$

where the reference concentration is that concentration in the agglomerate that is in equilibrium with the reference pressure

$$c_{O_2}^{ref} = P_{O_2}^{ref} H_{O_2,agg} \quad (62)$$

where $H_{O_2,agg}$ is Henry's constant for oxygen in the agglomerate. Similar expressions to eq 59 have also been derived for other types of reactions and geometries,^{149,265} and while eq 59 is derived for spheres, with the appropriate Thiele modulus, it results in deviations less than 10% in the value of the effectiveness factor for other geometries. The above rate constant can be related to the transfer current density, $i_{ORR,1-2}$ (see eq 13). Also, one notices that the Thiele modulus is independent of the surface concentration for a first-order reaction.

If external mass-transfer limitations can be neglected, then the surface concentration in eq 58 (via eq 13) can be set equal to the bulk concentration, which is assumed uniform throughout the catalyst layer in the simple agglomerate models. Otherwise, the surface concentration is unknown and must be

calculated. To do this, an expression for the diffusion of oxygen to the surface of the agglomerate is written

$$W_{O_2}^{diff} = A_{agg} D_{O_2, film} \frac{c_{O_2}^{bulk} - c_{O_2}^{surf}}{\delta_{film}} \quad (63)$$

where $W_{O_2}^{diff}$ is the molar flow rate of oxygen to the agglomerate, A_{agg} is the specific external surface area of the agglomerate, and the film can be either membrane or water (if two or more films are desired, similar expressions can be written for each film). The above expression uses Fick's law and a linear gradient, which should be valid due to the low solubility of oxygen, steady-state conditions, and thinness of the film. At steady state, the above flux is equal to the flux due to reaction and diffusion in the agglomerate (as well as the flux through any other films), and thus, the unknown surface concentration(s) can be replaced. Doing this and using the resultant expression in the conservation equation (eq 56) yields

$$\nabla \cdot \mathbf{i}_1 = 4F c_{O_2}^{bulk} \left(\frac{1}{\frac{\delta_{film}}{A_{agg} D_{O_2, film}} + \frac{1}{KE}} \right) \quad (64)$$

This equation is the governing equation for the agglomerate models for the cathode, and without external mass-transfer limitations, it results in eq 58. For the anode, a similar analysis can be done.

There is only a handful of models that simulate the catalyst layers using the simple agglomerate model,^{44,90,105,120,160,267,268} because most agglomerate models are developed for comparison purposes (discussed in the following section) or are macrohomogeneous embedded models (i.e., take into account the catalyst-layer length scale as well) and are discussed in section 4.4.5. The results of the simple agglomerate models are helpful in trying to understand and optimize catalyst-layer parameters such as loading and agglomerate size. For example, it has been shown that fuel-cell performance increases with a decrease in agglomerate radius until a maximum plateau is reached.^{90,105} This limit results because the effectiveness factor plateaus at a value of 1 at a finite radius. However, this result does not necessarily hold if the agglomerate is not at a uniform temperature throughout.

4.4.4.3. Model Comparison. The distinction between the two simple macrohomogeneous models deals with the length scales of the effects being studied. While both show similar effects such as doubling of the Tafel slope due to mass-transport limitations, the question arises as to where the limitations are occurring. To get a better grasp on the two different approaches, several researchers have compared them to each other and experimental data.^{27,34,35,49,53} Of particular note is the analysis of Boyer et al.,⁴⁹ who examined the characteristic length scales for the various processes such as diffusion in the gas phase, diffusion in the agglomerate, proton migration in the catalyst layer, and so forth. These length scales are simple expressions and can let one

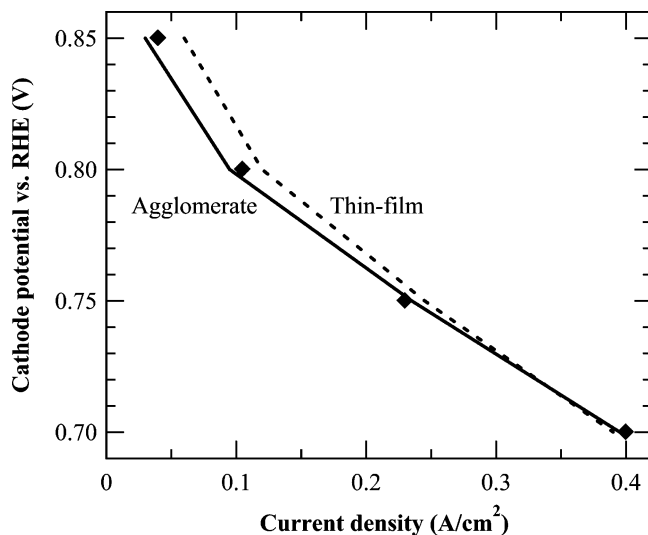


Figure 12. Comparison of simple macrohomogeneous agglomerate (solid line) and thin-film (dashed line) cathode models to experimental data (diamonds). Data are adapted from ref 34.

easily identify which scale is more important for the conditions being studied. Hence, one will know which model is the best to use. In general, they arrived at the conclusions that the simple agglomerate model is accurate for the cathode but that a porous-electrode approach is better in the anode due to the highly nonuniform reaction distribution. They also showed how to optimize various parameters such as Nafion loading.

The rest of the comparisons were done for the cathode. The results all showed that the agglomerate model fits the data better than the porous-electrode model. However, it should be noted that the porous-electrode model used was usually a thin-film model and so was not very robust. Furthermore, the agglomerate model has more parameters that can be used to fit experimental data. Finally, some of the agglomerate models compared were actually embedded models that account for both length scales, and therefore, they normally agree better with the experimental data.

The main problem with the porous-electrode models according to Gloaguen et al.^{34,35} is that they overestimate oxygen transport limitations, but that is because they used thin-film models that did not contain gas pores. Chan and Tun⁵³ compared much more similar agglomerate and porous-electrode models and noted the effects of changing different parameters on performance. They showed that the agglomerate model is more sensitive to changes in mass-transport resistances caused by flooding than the porous-electrode models. A final comparison was done by Broka and Ekdunge.²⁷ They compared the models to experimental data and microscopy and arrived at the conclusion that the agglomerate model is a more accurate representation, although they also showed that with the addition of a mass-transfer coefficient in the porous-electrode model it can agree with the data as well as the agglomerate model.

A comparison of the two models with experimental data is given in Figure 12. In the figure, simulations were run with a simple agglomerate model and a

simple thin-film model. As can be seen, the agglomerate model fits the data much better than the thin-film model, although the lack of a gas phase in the thin-film model makes it less rigorous than the simple porous-electrode model described above. The difference between the models declines at higher current densities where the reaction distribution is becoming nonuniform. In fact, for anode simulations the porous-electrode model should be better due to the much more nonuniform reaction distribution. At low current densities, the reaction distribution is uniform, and the most important effects happen at the agglomerate scale; that is why the agglomerate model fits the data better in that regime. While these simple models are acceptable, a more complex embedded model where both are used should be the best in terms of accuracy.

4.4.5. Embedded Macrohomogeneous Models

The above simple models account for only one length scale. To account for both the local agglomerate level and effects across the porous electrode, embedded macrohomogeneous models are used. Even though the simple agglomerate models account for many effects, they cannot truly consider reaction distributions and proton migration across the catalyst layer. As noted above, these effects are important in certain circumstances (e.g., within the anode catalyst layer, within a flooded catalyst layer, and within a catalyst layer with a dehydrated membrane). The application of embedded models is very straightforward. Finally, the original model of Iczkowski and Cutlip⁵ was really a precursor of the embedded models, and agglomerate models rather than porous-electrode ones are more likely to become embedded models.

There are two ways in which the embedded model can be used. In the first, the porous-electrode modeling equations are used as discussed above and in Table 1. Next, a mass-transfer term is added to account for the flux to the agglomerate. In this situation, there is basically a film between the reaction site and the gas pore, although this exact structure is averaged over in the macrohomogeneous approach. Thus, in a single volume element, the diffusive and reaction fluxes are related at the boundary of the agglomerate film. This approach is basically the same as accounting for external mass-transfer limitations within each volume element. Because this approach adds only an additional resistance to charge transfer due to diffusion, it is not more computationally costly than the porous-electrode model and yields an extra fitting parameter if desired (the thickness of the film or the mass-transfer coefficient) and more realistic behavior, especially for incorporating flooding effects. There are a few models that use this approach.^{19,84,85}

The other approach is more complicated and requires a deeper knowledge of the agglomerate structure or yields more fitting parameters. In this approach, the porous-electrode equations are used, but now the effectiveness factor and the agglomerate model equations are incorporated. Hence, eq 64 is used to get the transfer current in each volume element. The gas composition and the overpotential

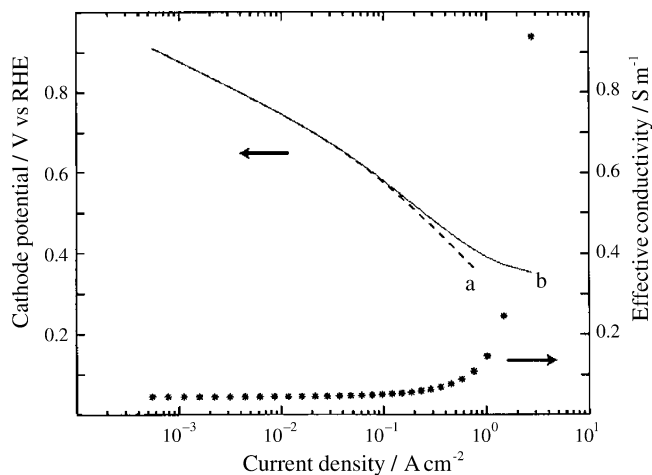


Figure 13. Plot of cathode potential as a function of current density for a macrohomogeneous embedded model where the proton conductivity is assumed to be uniform (0.044 S/m), curve a, or varies with water production (changing humidity) across the catalyst layer, curve b. (Reproduced with permission from ref 98. Copyright 2002 The Electrochemical Society, Inc.)

change across the catalyst layer due to ohmic, mass-transfer, and reaction effects. While this approach is slightly more complicated and requires knowing values for more parameters, the payoffs are greater in that it does the best job in representing the physical reality of the catalyst layer and includes all of the relevant effects. This is in agreement with the analysis of Pisani et al.,⁹¹ who compared different agglomerate structures with each other and the porous-electrode model. Other models also use this approach.^{36,78,98,129,269} Finally, it should be noted that an overall effectiveness factor that considers both external and internal mass transfer to and through the agglomerate can be used as a fitting parameter, thereby avoiding the necessity of detailed calculations and perhaps multiple fitting parameters on the agglomerate scale.

In terms of the cathode models, that of Maja et al.²⁶⁹ in essence examined the effect of having two different agglomerate radii. They showed that this is important for being able to predict the correct limiting current density. Pisani et al.⁷⁸ used analytic expressions for cylindrical agglomerates that are basically flooded pores. They then integrated over the catalyst layer to get an overpotential and current density for use as a boundary condition in the overall 1-D fuel-cell model. As mentioned above, Jaouen et al.⁹⁸ examined the cathode polarization curve in a manner similar to those of Perry et al.³⁶ and Weber et al.¹³³ However, the addition of the agglomerate length scale allowed them to examine more complex behavior. This can be seen in Figure 13, where the embedded model shows a more complex cathode-potential curve due to tradeoffs between the two length scales. In the figure, consideration of a changing ionic conductivity due to water production hydrating the membrane causes the potential curve to move from a double Tafel slope back toward a single Tafel slope.

While it is evident that the embedded model is the best one to use, it requires additional complexity and

more parameters, not all of which may be known. If the controlling phenomena are known, which seldom are a priori, then the appropriate simple model can be used. Diagnostic techniques aimed at determining the controlling phenomena and perhaps parameter values are discussed by Perry et al.,³⁶ Weber et al.,¹³³ and Jaouen et al.⁹⁸ They advocate conducting simple experiments, such as oxygen gain and varying layer thickness, and analyzing the results. The analysis and results of their models can be summarized as follows for the different operating regimes. Control by oxygen diffusion in the agglomerate results in a double Tafel slope, and the total current density is proportional to the active layer thickness, is first-order in oxygen, and has a low sensitivity to gas humidity. Control by proton transport in the catalyst layer results in a double Tafel slope, and the current density is independent of the layer thickness, is half-order in oxygen, and increases with relative humidity. Control by both of the above results in a quadruple Tafel slope. Control by oxygen diffusion in both the agglomerate and covering film results in the progressive disappearance of quadruple and double Tafel slopes with increasing film thickness. Control by oxygen diffusion in the layer and either proton diffusion in the layer or oxygen diffusion in the agglomerate yields a double Tafel slope that also progressively disappears.

4.4.6. Catalyst-Layer Flooding

Flooding of the catalyst layer is treated in a separate section because various models with different approaches have addressed it and it is important, especially in the cathode. There are two main ways in which flooding is considered, and they depend on how the catalyst layer is modeled. If an agglomerate model is used and if liquid water exists in the fuel cell, a liquid film covering the membrane film of the agglomerates can be assumed. Thus, the flooding of the catalyst layer is easily incorporated into the external mass-transfer limitation (eqs 63 and 64) where the reactant gases have to diffuse through a water film as well as the membrane layer.^{50,114} Due to the low diffusivity and solubility of oxygen in water, only a very thin liquid film is needed to inhibit reaction. All of the agglomerate models can easily incorporate flooding in this manner, with perhaps the thickness of the film used as a fitting parameter.

The other way to incorporate flooding in the catalyst layers is to use the two-phase modeling approach described in section 4.3.2.1. This involves calculating the liquid saturation in the catalyst layer and then adjusting the interfacial area accordingly. This is done by a linear expression

$$a_{1,2} = a_{1,2}^0(1 - S) \quad (65)$$

where $a_{1,2}^0$ is the maximum or dry specific interfacial area. There are a few models that use this approach.^{52,56,57,87,109} Equation 64 assumes a homogeneous distribution of electrocatalyst through the catalyst layers, which is a fine first approximation, although accounting for the electrocatalyst location (e.g., hydrophilic versus hydrophobic pores) would be more rigorous.

In comparing the two approaches, it seems that the saturation approach allows for greater reaction rates (higher current densities). The reason is that the catalyst layers have small pores and are hydrophobic, and thus, it takes a high liquid pressure to flood them, whereas even a thin film can effectively shut down the reaction. Of course, the film is spread over a much larger surface area and depends on the agglomerate radius. It is tough to say which approach is better, but because the saturation equations for the diffusion media are well developed compared to having an unknown water film thickness that may vary with position, it is our belief that eq 65 should be incorporated into an embedded catalyst-layer model.

It is known that flooding is important at high current densities, especially at the cathode. However, one may wonder if the performance loss is due to blockage of the catalyst sites by water or by flooding of the diffusion media. In the literature models, flooding of the diffusion media has garnered more attention. Flooding of the diffusion media seems also to agree with the fact that the diffusion media are much thicker and more hydrophilic with larger hydrophobic pores than the catalyst layers, but they also have a higher porosity. Furthermore, due to the normally high surface area of active material in the catalyst layers, some flooding can occur without a significant detriment to performance.¹²³ Experimental data with microporous layers between the catalyst layer and diffusion media (for examples, see refs 270–272) are inconclusive. Some indicate that, due to their often hydrophobic nature, they keep water out of the diffusion media. However, other microporous layers are thought to wick water out of the catalyst layers due to their small pores. In reality, the physical situation is that flooding should be considered in both regions. Overall, the catalyst layers are complex and have been treated by various means, with macrohomogeneous embedded models agreeing the best with the physical picture, while also not being too complicated to use in fuel-cell simulations.

4.5. Multilayer Simulations

The purpose of this section is to describe the general results of models that contain more than one of the layers described above. It is beyond the scope of this article to analyze every model and its results in detail, especially since they have already been discussed to a certain extent in section 2. Many of the models make tradeoffs between complexity, dimensionality, and what effects are emphasized and modeled in detail. It is worth noting that those models that employ a CFD approach seem to be the best suited for considering multidimensional effects. In this section, the ways in which the multilayer models are solved and connected are discussed first. Next, some general trends and results are presented.

4.5.1. Numerical Solution and Boundary Conditions

Due to the complexity and interconnectivity of the governing equations and constitutive relationships, most fuel-cell models are solved numerically. Al-

though analytic solutions are obtainable in certain instances, these usually involve assumptions that make the solution of limited significance. Furthermore, the power of digital computers is continually progressing such that the computational cost of running simulations becomes manageable.

For most numerically solved models, a control-volume approach is used. This approach is based on dividing the modeling domain into a mesh. Between mesh points, there are finite elements or boxes. Using Taylor series expansions, the governing equations are cast in finite-difference form. Next, the equations for the two half-boxes on either side of a mesh point are set equal to each other; hence, mass is rigorously conserved. This approach requires that all vectors be defined at half-mesh points, all scalars at full-mesh points, and all reaction rates at quarter-mesh points. The exact details of the numerical methods can be found elsewhere (for example, see ref 273) and are not the purview of this review article. The above approach is essentially the same as that used in CFD packages (e.g., Fluent) or discussed in Appendix C of ref 139 and is related to other numerical methods applied to fuel-cell modeling.^{274,275}

The various layers of the fuel-cell sandwich described above are linked to each other through boundary conditions, which apply at the mesh point between two regions. There are two main types of boundary conditions, those that are internal and those that are external. The internal boundary conditions occur between layers inside the modeling domain, and the external ones are the conditions at the boundary of the entire modeling domain.

Typically, coupled conditions are used for internal boundaries wherein the superficial flux and interstitial concentration of a species are made continuous. However, as mentioned above, boundary conditions between the membrane and electrode can involve the fact that there is only ionic current in the membrane and that the uptake isotherms mean that water content changes from λ in the membrane to partial pressure in the electrode. On the other side of the electrode, the boundary condition should state that all of the current is electronic. Another common boundary condition is to have a change in concentration because a species dissolves. This is similar to the internal boundary condition in the membrane and is used sometimes for electrodes where phases are not continuous across the boundary. Finally, internal boundary conditions can represent modeling regions that are not modeled in depth. For example, a water flux and kinetic equation can be used at the boundary between the cathode diffusion medium and the membrane if the catalyst layer is not modeled rigorously. Another example is setting the flux of water through the membrane and its ohmic resistance at a single boundary point.

Depending on the modeling domain, the last boundary condition is sometimes also used as an external boundary condition (e.g., half-cell models). The external boundary conditions specify the concentrations and values for all of the species and variables at the boundary. Examples include specifying the inlet conditions, such as gas feed rates, composition,

temperature, and humidity, or specifying the current density or potential. The external boundary conditions are often the same as the operating conditions and, therefore, are very similar for most simulations, although there can be differences such as what condition is used for two-phase flow (i.e., zero saturation or zero capillary pressure).

4.5.2. General Multilayer Simulation Results

In terms of sandwich models, there are four main varieties. The first are those that treat only one layer in the sandwich, and they were discussed above. The second are those that treat multiple layers of the sandwich but not all of them.^{26,37,50,56,57,75,86,105,110,120,153,252}

These are typically cathode models that include the diffusion medium and perhaps a membrane water flux. Next are the models that treat all of the layers of the sandwich and are only 1-D.^{13,14,17,20,45,71,72,74,78,95,98,99,101,112,203} Finally, there are those that are multidimensional and treat all of the layers; these are discussed in detail in section 5.

The models should duplicate the effects seen by experiment. Thus, as the temperature is raised, better performance is obtained up to a point. An optimum is reached because, even though property values are usually increasing, so does the water vapor pressure. Consequently, if the feeds are saturated, the reactant gas partial pressure is lower, which affects the kinetics, and if the feeds are dry, it is harder to hydrate the membrane and there are higher ohmic losses. These issues can become important during operation of high-temperature fuel cells. As discussed in section 5.1.1, water concentration effects down the gas channels need to be considered for dry feeds, and therefore, a 1-D model does not suffice. Gains in performance are also seen in fuel cells operating with pure oxygen or under elevated pressure. In these cases, fuel cells perform better not only because of higher reactant gas pressures but also because flooding is not as critical (i.e., the limiting current density increases due to lower mass-transport limitations).

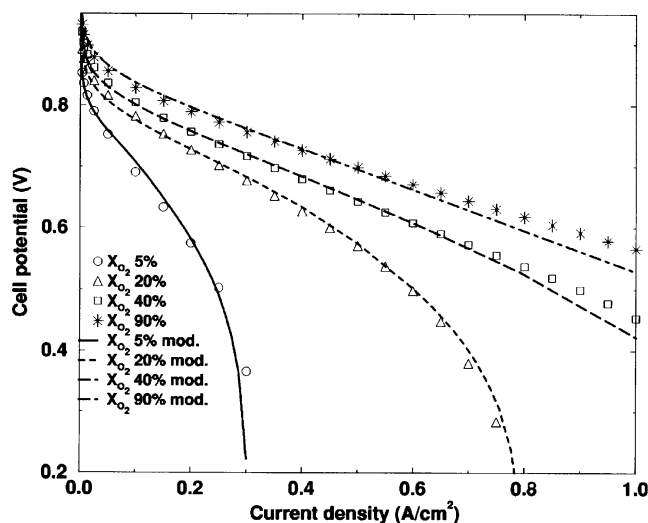


Figure 14. Comparison between experiment and simulation for different humidified oxygen feeds. (Reproduced with permission from ref 78. Copyright 2002 The Electrochemical Society, Inc.)

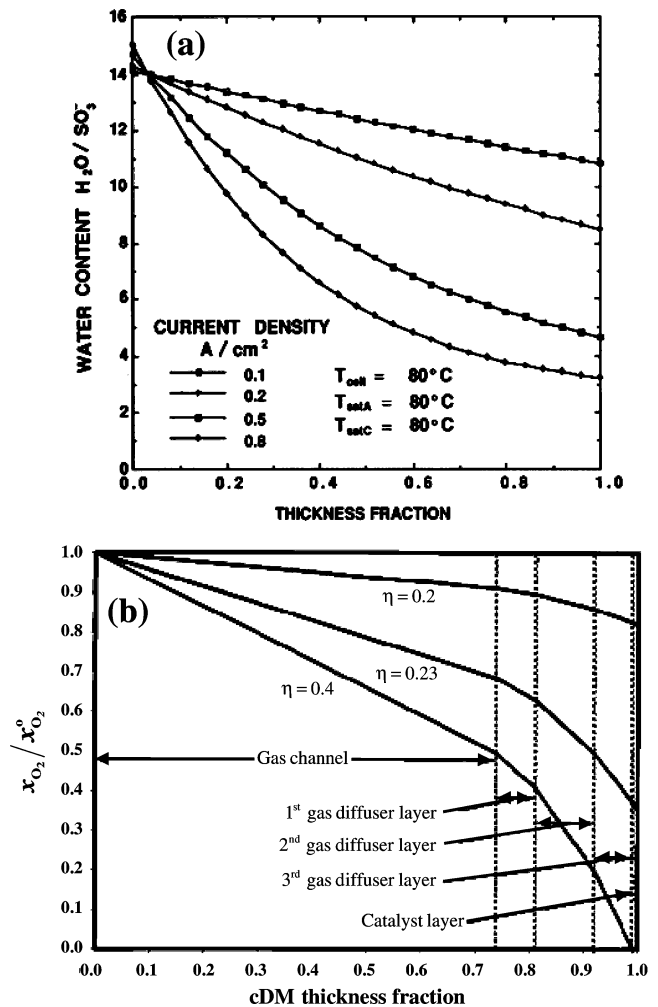


Figure 15. Simulation results showing membrane dehydration (a) and cathode flooding (b). (a) λ as a function of membrane position (cathode on the left) for different current densities. (Reproduced with permission from ref 14. Copyright 1991 The Electrochemical Society, Inc.) (b) Dimensionless oxygen mole fraction as a function of cathode-diffusion-medium position and cathode overpotential. (Reproduced with permission from ref 120. Copyright 2000 The Electrochemical Society, Inc.)

This last point is shown very well in Figure 14, where model and experimental data are compared for different oxygen concentrations. In some sense, this is an analogue to Figure 4, where a 1-D and not a 0-D model is used. Figure 14 demonstrates good fits between experiments and 1-D model simulations. In this model, flooding was accounted for in the diffusion media and the simple agglomerate model was used for the catalyst layers. The membrane model considered only the liquid-equilibrated transport mode, which is why the ohmic region in some of the curves deviates from the experimental data. Overall though, the 1-D sandwich model does a good job in fitting the data for humidified feeds and in predicting the full polarization curve, especially at low oxygen concentrations.

Most of the models show that fuel-cell performance is a balance among the various losses shown in Figure 3, in particular, ohmic losses and mass-transport limitations, which both increase with current. The reason for this is that the kinetic losses are hard to mitigate without significantly changing op-

erating conditions or using better catalysts, as discussed above. Models show that ohmic losses mainly result from the membrane drying out at the anode side of the membrane-electrode assembly. This is shown in Figure 15a. This is not to say that ohmic losses do not occur in other parts of the fuel cell, just that they are not as dominant. The mass-transport limitations are due mainly to flooding of the cathode side of the fuel cell, as shown in Figure 15b. The answers that models predict to the above tradeoffs focus mainly on increasing the flux of water in the membrane from cathode to anode and increasing the oxygen partial pressure in the cathode. To these extents, models agree with experiment in showing that thinner membranes, higher-oxygen-content feeds and pressures, and the use of a microporous layer between the catalyst layer and a gas-diffusion layer all yield better performing fuel cells.

Finally, fuel-cell models allow for optimization studies. For example, understanding the current distribution in the electrode allows one to understand the effect of changing its thickness and how to decrease catalyst loading by proper platinum placement. Such modeling results can be credited for the manufacturing of fuel cells that have thinner anodes than cathodes due to more of a nonuniform reaction distribution in the anode. Other optimization studies include looking at different structural and physical properties such as thicknesses, porosities, and so forth. However, optimization studies should be confined to those models that are more physical and complex. Overall, the best fuel-cell sandwich models have a physical basis; take into account all of the sandwich layers; have a minimum of fitting parameters; agree with experimental data trends; and adequately model the dominant transport phenomena.

5. Multidimensional Effects

Although the fuel-cell sandwich is the heart of a fuel cell, there are important effects that are not found when only a 1-D model is used. These effects basically arise from the fact that a fuel cell is in reality a 3-D structure, as shown in Figures 1 and 5. Many models explore these effects and are discussed in this section. These models always include the fuel-cell sandwich as one of the dimensions. First, the 2-D models are examined and then the 3-D ones. Because there is another review in this issue that focuses on these models in more depth, the discussion below is shortened.²⁷⁶

5.1. Two-Dimensional Models

As shown in Figures 1 and 5, there are two possible ways that 2-D effects can be incorporated, either along the channel (y,z) or under the rib (x,z). The modeling domains of these two effects are shown parts a and b, respectively, of Figure 16. The rib effects take into account the fact that there is a solid rib between two channels, which affects transport in the sandwich. This latter effect is germane to interdigitated flow fields. Both of the 2-D effects are discussed below, starting with the along-the-channel models.

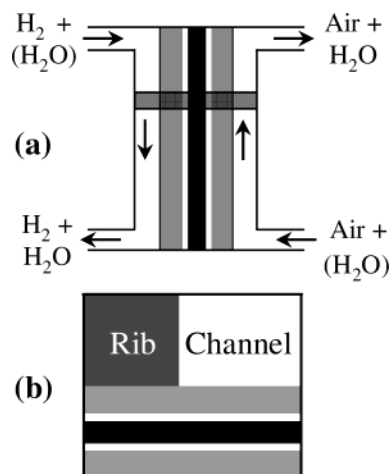


Figure 16. Schematic showing the modeling domain for the 2-D models. (a) Along-the-channel domain where the 1-D sandwich is highlighted for the pseudo-2-D case. (b) Rib domain showing only the cathode side rib and channel.

5.1.1. Along-the-Channel Models

There are two main ways that transport along the channel can be treated. The first is to assume that changes within the fuel-cell sandwich occur only in the direction perpendicular to it (z axis).^{15,16,44,55,107,109,127,129,134} This assumption effectively means that the models have only to account for a change in the boundary conditions or values along the channel. This kind of treatment is termed pseudo-2-D. A limiting case of the pseudo-2-D model may be seen as those models that are 1-D but use an average concentration for each species in the gas channels.^{14,74,88,101} The other kind of treatment is to use a full 2-D simulation in which equations and parameters change in both directions in the sandwich and gas channels.^{25,47,61,62,64,66,79,90} With proper discretization, the pseudo-2-D models can accurately reflect the results of the full 2-D models.

For a full 2-D model, the only change in the equations is that the vector components now occur in two directions. The various regions are normally assumed to be isotropic so that the property-value expressions are the same for each direction. If data are known, then the expressions can be altered accordingly. The gas channels are the only new modeling domains introduced.

The gas channels contain various gas species including reactants (i.e., oxygen and hydrogen), products (i.e., water), and possibly inerts (e.g., nitrogen and carbon dioxide). Almost every model assumes that, if liquid water exists in the gas channels, then it is either as droplets suspended in the gas flow or as a water film. In either case, the liquid water has no effect on the transport of the gases. The only way it may affect the gas species is through evaporation or condensation. The mass balance of each species is obtained from a mass conservation equation, eq 23, where evaporation/condensation are the only reactions considered.

For movement of the gases, various treatments can be used. The simplest is to use mass balances down the flow channel. This is the same as saying that there is plug flow and the pressure remains uniform,

something that is not valid under certain operating conditions or with long or interdigitated flow fields. A robust treatment would be to use the Navier–Stokes equation

$$\mathbf{v}_G \cdot \nabla (\rho_G \mathbf{v}_G) = -\nabla p_G + \mu_G \nabla^2 \mathbf{v}_G \quad (66)$$

where \mathbf{v}_G is the mass-average velocity of the gas phase. For the gas channels, Darcy's law is not valid because they are not porous. If desired, diffusion terms (e.g., Stefan–Maxwell equations) can be used in conjunction with the above equation to result in convective-diffusion equations. However, axial dispersion is normally negligible compared to pressure-driven flow. Finally, simpler flow equations are also often used such as assuming plug flow or Poiseuille flow. If only a pressure drop down the channel is required, correlations from fluid dynamics can be used to determine it (e.g., Ergun equation).^{149,277}

In terms of boundary conditions, the following apply. The gas-channel plates represent equipotential surfaces, which serve to set the overall cell potential. In terms of flows, the gases are usually assumed to be either in a coflow or counterflow arrangement, although the physical system may be in cross-flow. The inlet flow rates and concentrations must be specified; setting the stoichiometry of the inlet gases and the humidity serves to do this. The stoichiometries are normally based on the total current of the cell, and when they are time independent, the results are independent of the active area or the channel length. The reason for this is that all the fluxes become proportional to the active area, which can be canceled out. Setting the outlet pressure and the inlet temperature also serves as boundary conditions. A no-slip condition at the gas channel wall is also valid. The conditions needed at the interfaces of the gas channels and the diffusion media are now coupled, internal boundary conditions, which were discussed previously.

Now that the methodology and equations have been introduced, one may wonder what the effects along the channel are. The most significant effects deal with the changing gas composition. As the feed gases react, their concentration goes down unless the feed stoichiometries are very high. This means that the reaction rate decreases and a nonuniform current distribution is generated. In fact, with very long channels, the decrease in concentration of the feed gases might result in a type of limiting current density.⁶⁶ Such a distribution can have a variety of effects including nonuniform temperature distributions, places where the membrane dries out, and poorly utilized catalytic areas.

To expand on the last remark, the simulation results from Fuller and Newman¹⁵ are shown in Figure 17. The curves clearly show a nonuniform current distribution that is mainly due to the change in the gas concentrations and the membrane hydration. In the simulation, the initial decrease in the current density is due to the change in the oxygen concentration. However, once enough water is generated to hydrate the membrane, the increased conductivity yields higher local current densities. What

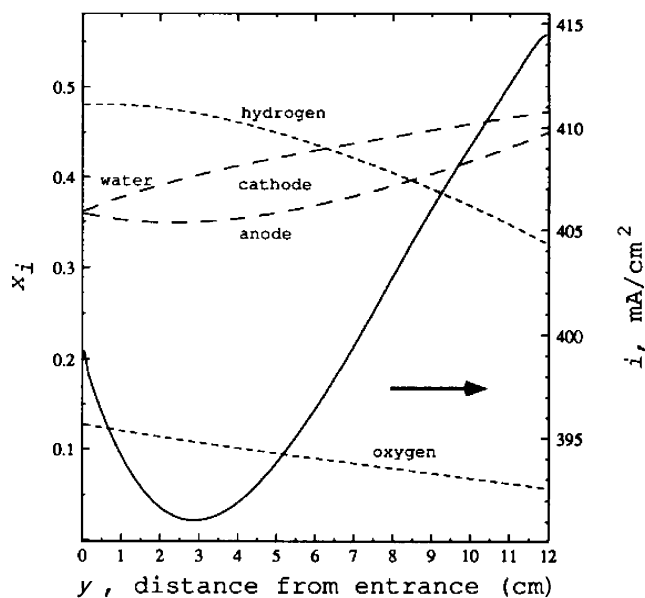


Figure 17. Mole fraction of water vapor, hydrogen, and oxygen in the gas channels at a cell potential of 0.72 V, at a temperature of 80 °C, and in a coflow arrangement. The local current density is shown by the solid line. (Reproduced with permission from ref 15. Copyright 1993 The Electrochemical Society, Inc.)

the figure shows is that these effects are significant, and if one were to use a 1-D model, these effects would be lost. Fuller and Newman also show that the membrane can dehydrate along the channel due to nonisothermal effects.

Because of gas composition changes along the channel, a 2-D model is necessary to describe dry feeds. This is true since not only does the oxygen concentration vary, but, perhaps more importantly, the water does as well. This is seen in Figure 17, where the increase in current density is due to the increase in water in the system. To study this further, Janssen⁵⁵ and Weber and Newman¹³⁴ ran simulations where the inlet gases were dry and the flow was countercurrent. They studied the water balance of the fuel cell, and some of their results are given in Figure 18. Figure 18a clearly shows that, with countercurrent operation, the water is recycled in that the water produced near the air inlet helps to keep the membrane hydrated near the dry hydrogen inlet. It is noted that Figure 18a is basically a composite of the cases where one gas is fed dry and the other humidified. The 2-D membrane hydration is shown in Figure 18b. This figure clearly shows Schroeder's paradox in the sharp drop off in the water content, where the drop signifies the point where liquid water and the liquid-equilibrated transport mode cease to exist in the membrane. It also shows that the highest water content is near the cathode inlet and that, although the water is recycled, dehydration problems can arise near the hydrogen inlet. However, these simulations assumed uniform current distributions, which is not valid but affects the potential of the cell more than the water balance. Figure 18 also shows that, due to the slower diffusion of water vapor in air than in hydrogen, it is more important for the anode to be humidified. Other models have also reached this conclusion.^{16,25,44,47,129}

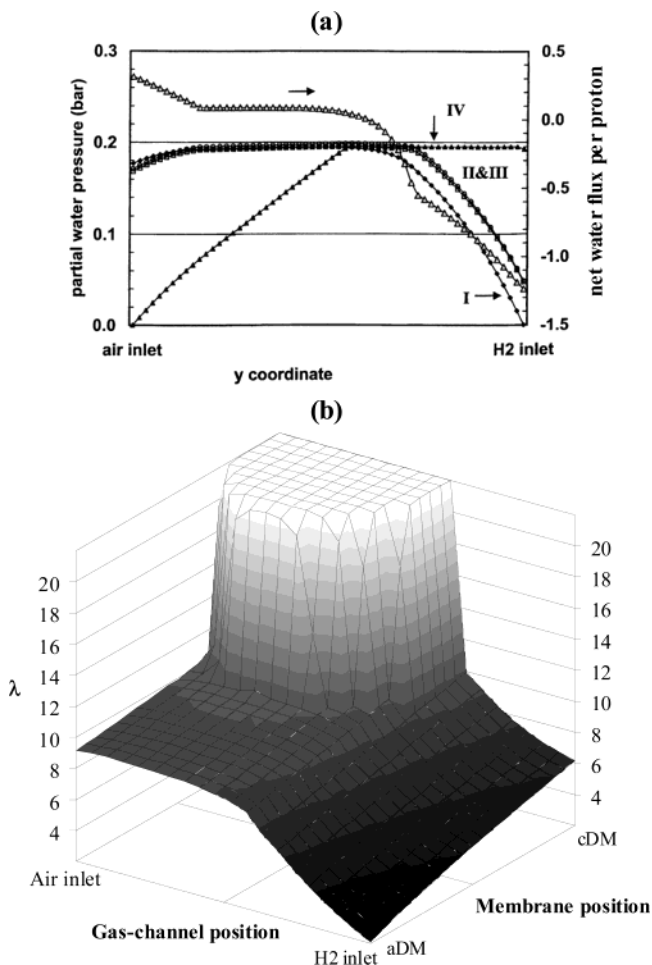


Figure 18. Pseudo-2-D simulation results at 0.4 A/cm^2 where the feed gases are dry and countercurrent. (a) Water partial pressure profiles at four positions in the fuel-cell sandwich as a function of distance along the channel; the positions are at the anode and cathode gas channels (I and IV) and catalyst layers (II and III), respectively. Also plotted is the value of β , the net flux of water per proton flux, as a function of position. The data are from Janssen.⁵⁵ (Reproduced with permission from ref 55. Copyright 2001 The Electrochemical Society, Inc.) (b) Membrane water content as a function of position both along the gas channel and through the thickness of the membrane for the same simulation conditions as above. The data are from Weber and Newman.¹³⁴ (Reproduced with permission from ref 55 and 134. Copyright 2004 The Electrochemical Society, Inc.)

The 2-D models also allow for different effects to be studied in depth. For example, the simulations show that, as mentioned above, countercurrent flow yields better performance than coflow due to water recycling.^{16,25,44,47,109} This is something that a 1-D model cannot address. The 2-D models also have studied pressure differentials and design strategies to help boost performance.^{64,107,109} Finally, the 2-D models allow for optimization studies to be conducted, such as minimizing cost and examining the effects of fuel utilization,¹²⁷ and seeing how structural variables change the performance.^{16,25,44,47,79} This last is perhaps better addressed with a complex 1-D model rather than a simpler 2-D one.

Overall, effects along the channel are significant and need to be considered. This is especially true in cases where the composition in the gas channel is expected to vary significantly. Some examples of

these conditions include low stoichiometry feeds, low humidity feeds, and temperature effects at high current densities. Furthermore, for the cases outlined above, such flow is the most important multidimensional effect. Although full 2-D models do not necessarily have to be done, flow along the channels needs to be accounted for in some fashion.

5.1.2. Under-the-Rib Models

As shown in Figure 16b, the 2-D rib models deal with how the existence of a solid rib affects fuel-cell performance.^{24,37,46,56,57,126,278} They do not examine the along-the-channel effects discussed above. Instead, the relevant dimensions deal with the physical reality that the gas channel/diffusion media interfaces are not continuous. Instead, the ribs of the flow-channel plates break them. These 2-D models focus on the cathode side of the fuel-cell sandwich because oxygen and water transport there have a much more significant impact on performance. This is in contrast to the along-the-channel models that show that the underhumidification of and water transport to the anode are more important than those for the cathode.

As mentioned, the 2-D rib effects are crucial in understanding transport in interdigitated flow fields.^{108,232} In these flow fields, the gas channels are not continuous, and thus, the gases must pass through the diffusion media. The benefit of such a configuration is that water removal and reactant gas distribution are better because of the convective flow of gases through the diffusion media. However, such flow also means that there is a much higher pressure drop. Some models, of note those of Nguyen and co-workers,^{48,52} Um and Wang,⁷⁶ Zhukovsky,⁷⁷ and Kazim et al.,⁴⁶ have specifically looked at interdigitated flow fields. Their results show the importance of having more gas channels with smaller widths, among other things. Interdigitated flow fields are not discussed further in this review.

The equations for modeling the 2-D rib effects require a domain where the boundary conditions in terms of gas flow and composition are specified only at the channel. At the solid rib, there is no flux of gas and liquid, but all of the electronic current must pass through it. Furthermore, the modeling domain is usually as shown in Figure 16b; thus, only a half channel and rib is modeled, and symmetry conditions can be used to model the other half. Besides those noted above, the boundary conditions and equations are more-or-less the same as those discussed in section 4.

As can be seen in the different boundary conditions, the main effects of having ribs are electronic conductivity and transport of oxygen and water, especially in the liquid phase. In terms of electronic conductivity, the diffusion media are mainly carbon, a material that is fairly conductive. However, for very hydrophobic or porous gas-diffusion layers that have a small volume fraction of carbon, electronic conductivity can become important. Because the electrons leave the fuel cell through the ribs, hot spots can develop with large gradients in electron flux density next to the channel.^{37,124} Furthermore, if the conductivity of the gas-diffusion layer becomes too small, a

nonuniform reaction distribution can be generated with the highest rate occurring across from the ribs.^{37,124}

Although usually the transport of electrons is not limiting, the transport of oxygen can be. For example, at high overpotentials or low oxygen concentrations, the oxygen has a much higher concentration across from the channels and not the ribs.^{37,56,278} What this means is that once again a nonuniform reaction distribution is generated, which results in a nonuniform current distribution and all of the associated effects with it (e.g., hot spots, flooding, membrane dehydration, etc.). Under these circumstances, mass transport is an important consideration. Oxygen diffusion is expected to cause the above problems, which are exacerbated by the presence of liquid water.

Figure 18 shows that, even when the cathode is relatively dry, liquid water exists in the cathode. What the 2-D rib models show is that this liquid water cannot be effectively removed if it is next to the rib because it has no way to get out of the cell.^{24,56,126} In fact, this effect is perhaps more important in generating nonuniform reaction-rate distributions. Simulation results from Natarajan and Nguyen,⁵⁶ shown in Figure 19, clearly demonstrate the entrainment of liquid water in the gas-diffusion layer next to the rib. In fact, Figure 19a shows that the diffusion medium next to the rib is fully flooded. They correlated a more uniform reaction-rate distribution with a decrease in the extent of flooding. Furthermore, they showed that these effects become less important at higher cell potentials because the fuel cell operates in the kinetic regime in which mass-transport limitations are only minor (see Figure 3).

It is clear that the ribs can have a detrimental effect on fuel-cell performance by creating a nonuniform current distribution due to poor mass transfer of oxygen. This is shown in detail in Figure 19b, where the current distribution is shown for different rib and channels sizes. Clearly, the smaller channels and ribs provide more uniform current distributions. This is because there are smaller regions of flooding, since the water has more pathways to leave the gas-diffusion layer and enter the channel. This effect has also been modeled by others.^{24,126} It is also interesting that, although the gas-diffusion layer is flooding, the ribs also are making sure the membrane is better hydrated due to the increased liquid pressure throughout the gas-diffusion layer. Consequently, there is a tradeoff between decreased ohmic losses in the membrane and mass-transfer limitations in the cathode diffusion medium. For dry systems, ribs might actually help performance, while, for saturated systems, they only hinder it.

Overall, the rib effects are important when examining the water and local current distributions in a fuel cell. They also clearly show that diffusion media are necessary from a transport perspective. The effect of flooding of the gas-diffusion layer and water transport is more dominant than the oxygen and electron transport. These effects all result in nonuniform reaction-rate distributions with higher current densities across from the channels. Such analysis can lead to optimized flow fields as well as

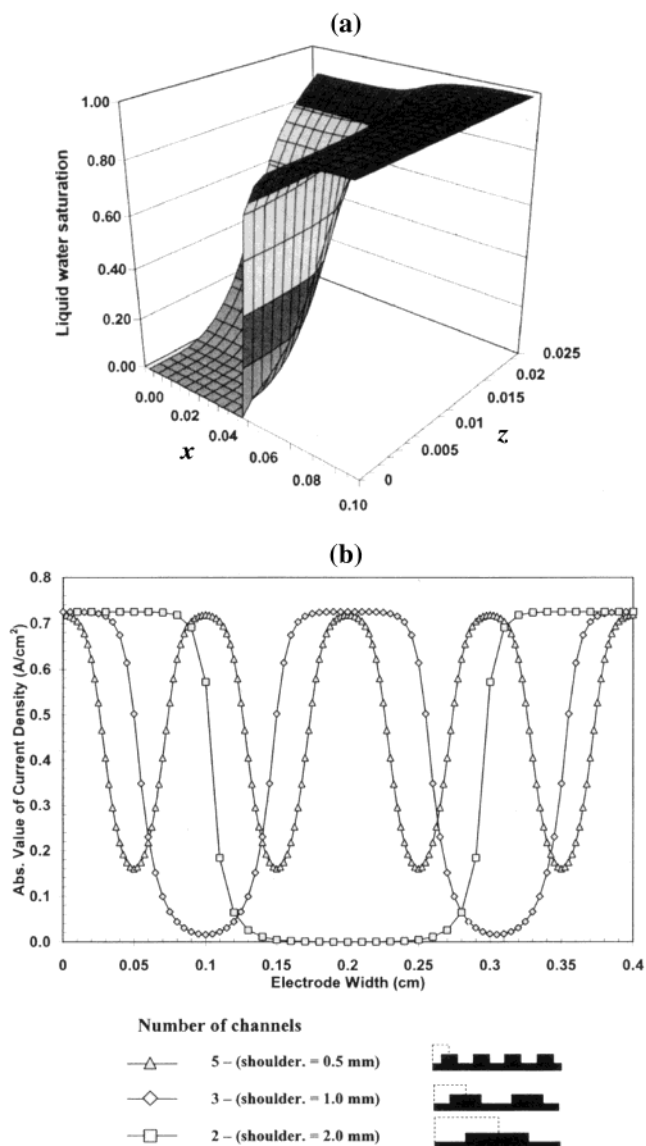


Figure 19. Liquid saturation and current density of the cathode as a function of position for the case of dry air fed at 60 °C. (a) Liquid saturation in the gas-diffusion layer where the channel goes from $x = 0$ to 0.05 cm and the rib is the rest; the total cathode overpotential is -0.5 V. (b) Current-density distributions for different channel/rib arrangements. (Reproduced with permission from ref 56. Copyright 2001 The Electrochemical Society, Inc.)

perhaps catalyst layers in terms of placing catalyst only where higher reaction rates are expected (i.e., minimize catalyst loading).

5.2. Three-Dimensional Models

The 3-D models try to capture all of the effects mentioned above, in both 2-D directions as well as in the 1-D sandwich.^{51,54,60,76,77,80,82,87,119,124,125,279–281} The domain is as shown in Figure 1. 3-D models have the potential to accurately represent the true operation of a fuel cell. In principle, these models are the ones that should be used to obtain the best designs and optimization of various properties and operating conditions. However, while the current published models are complex on an overall global scale, they are usually not very detailed on the 1-D sandwich scale. For example, almost all of these models have

neither a robust membrane model nor a rigorous two-phase model. In addition, validation of these models is usually done by comparing only one polarization curve (normally because of the computational costs of the models), which may or may not be representative of the regimes in which the models are run.⁸⁴

In terms of modeling, the equations are the same as those in section 4, with perhaps some simplifications. Additional boundary conditions are required due to the higher dimensionality of the equations, but these are relatively straightforward, such as no fluxes of gas species across the external boundary of the gas channels.

The general results of the 3-D models are more-or-less a superposition of the 2-D models discussed above. Furthermore, most of the 3-D models do not show significant changes in the 1-D sandwich in a local region. In other words, a pseudo-3-D approach would be valid in which the 1-D model is run at points in a 2-D mesh wherein both the channel and rib effects can easily be incorporated. Another pseudo-3-D approach is where the 2-D rib models are used and then moved along the channel, similar to the cases of the pseudo-2-D models described above.⁸⁷ This latter approach is similar to that by Baker and Darling.²⁸¹ In their model, they uncouple the different directions such that there is a 1-D model in the gas channel and multiple 2-D rib models. However, they neither treat the membrane nor have liquid water. In all, the use of CFD means that it is not significantly more complicated to run a complete 3-D model in all domains.

The 3-D models show that the flooding problems associated with the ribs and the oxygen depletion along the channel compound each other.^{69,82,87} Thus, flooding is worse across from the ribs, and the reaction rate distribution is more nonuniform. However, as mentioned above, for nonhumidified feeds, the effects down the channel are more significant. This is seen in Figure 20, where the local current density can be associated with the oxygen concentration. Although the rib scale is a little hard to discern, there is a definite change in the current density along the length scale. The highest current density is obtained at the inlet because the cathode is less flooded and the oxygen concentration is highest. The current density drops and then increases near the exit due to the increase in the back flux of water from cathode to anode and a fully hydrated membrane. The figure clearly shows that there is an entrance region with large nonuniformities. The compounding of the 2-D effects shown by the 3-D models also results in the 2-D models underpredicting the water removal rate. This means that saturations are higher than expected in the diffusion media.⁸⁵

In addition, the models demonstrated that the water balance is important and can alter potential and reactant location.^{51,54,60} For example, the reaction distribution is closer to the channel than the rib near the inlet regions for humidified feeds. The reason is that, as the water moves from anode to cathode, there is more flooding, but the movement of water in this direction decreases along the channel because of lower current densities associated with lower oxygen

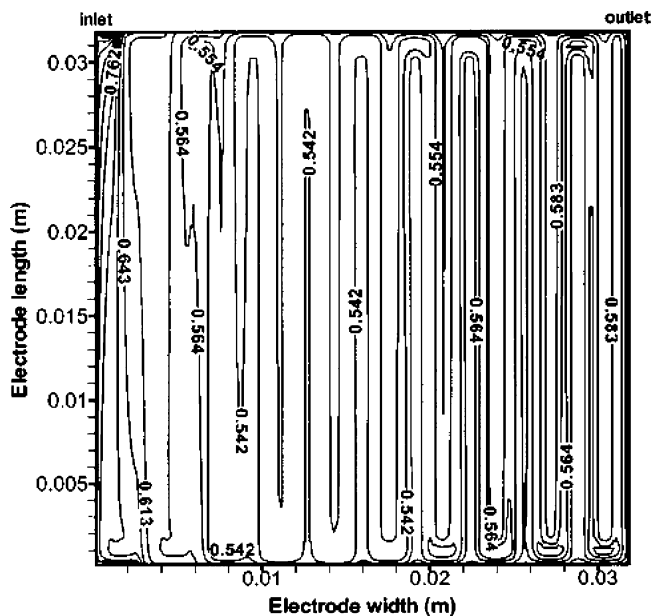


Figure 20. Local current density contours at a cell potential of 0.6 V for cocurrent flow of dry air and humidified hydrogen at 65 °C. (Reproduced with permission from ref 82. Copyright 2003 The Electrochemical Society, Inc.)

concentrations. In the same fashion, the 3-D models also show that ribs are beneficial if the anode is fed dry because of better membrane hydration, and again, this mainly occurs in an entrance region.⁸¹ 3-D simulations with and without liquid water clearly show that, for humidified feeds, liquid water must be accounted for, especially if operating in the mass-transfer regime of the polarization curve.^{84,85}

One of the benefits of a 3-D model is the ability to examine the effect of flow-field design. For example, Kumar et al.^{279,280} showed that having hemispherical channels provides more convective flow through the gas-diffusion layers and better overall fuel-cell performance. Furthermore, they showed that there are benefits to having flow channels that have a saturated permeability comparable to that of the diffusion media. Once again, in these cases there is more convective-type flow through the diffusion media. Both of the above designs try to mimic interdigitated flow channels to a certain extent. Baker and Darling²⁸¹ showed that there is more convective flow through the diffusion media farther away from the U-turns in serpentine flow fields. They also demonstrated that at high current densities the flow field acts more as a single pass than at low current densities where the concentration is more uniform due to higher transport through the diffusion media between adjacent channels.

The inclusion of multidimensional effects is important to realistically mimic transport in the fuel cell. This is not to say that certain cases and factors cannot be collapsed to lower dimensionality, but one must be aware of higher dimensional effects, lest they become important.

6. Other Effects

To complete the discussion of the macroscopic fuel-cell models, two other effects should be examined. These effects can be important, have not really been

discussed so far, and alter the system of governing equations. The first effect is taking into account transport and generation of heat in the fuel cell. The reaction is an oxidation process that generates heat, mainly because of irreversibilities. Water condensation and evaporation are also important heat sources and sinks. The second effect is transient operation of a fuel cell. This is important in many instances such as automotive applications, where fuel cells are expected to undergo transients, especially during acceleration, start up, and shut down.

6.1. Nonisothermal Models

The discussion of nonisothermal effects has been delayed until this section because the models that account for such effects constitute a relatively small subset of the total number of models and have already been discussed above in other contexts.^{15,16,25,26,45,60,71,80,82,84–86,90,107,125,126} Furthermore, the complex (i.e., multidimensional) models are the ones that usually take into account temperature effects. One result of the nonisothermal models is that the temperature distribution in the 1-D fuel-cell sandwich is basically uniform (around 1 °C or so), and thus, the isothermal assumption is usually valid for the sandwich. The cases where larger deviations from a uniform temperature distribution occur are in the inlets and outlets of the fuel cell and also depend on operating conditions, such as feed-gas humidity.

When discussing nonisothermal models, the focus is on those models that account for heat generation, consumption, and transfer. A distinction is made between this type of model and those that have properties and parameters that depend on temperature but assume a uniform temperature distribution. Many of the models discussed above fall into this latter category and allow for the effects of operating temperature changes but not a temperature gradient. For most conditions, the change in parameter values with temperature has a more significant impact than accounting for temperature gradients, although the two are coupled to a certain extent.

There are various changes that must be done to include nonisothermal effects. The most important is the addition of an energy conservation equation instead of setting the temperature to a constant; it is discussed below. The other changes are the inclusions of the appropriate thermal effects to the equations described above. To be rigorous, these effects need to be included, but they are usually negligible or are already accounted for. For example, a temperature distribution within an agglomerate can give different values of the effectiveness factor, but due to the size and properties of the agglomerate, it is sufficient to assume that it is at a uniform temperature. Another consideration is that, because the chemical potential is undefined in a nonuniform temperature field, a term must be added to account for this. Thus, a thermodynamically rigorous expression for the driving forces for transport must be used,

$$\mathbf{d}_{i,k} = c_{i,k}[\nabla\mu_{i,k} + \bar{S}_{i,k}\nabla T_k] \quad (67)$$

where $\bar{S}_{i,k}$ is the partial molar entropy of species i .

The addition of the temperature component comes from analysis leading to the Gibbs–Duhem equation.²⁸² In addition to the above driving force, expressions must be added that result in thermal diffusion.¹³⁹ However, because thermal diffusion is small relative to other effects such as conduction, and there are small gradients in temperature in fuel cells, this type of transport can be neglected. Similarly, the effect of diffusion on heat flux, the Dufour effect, is likewise neglected.¹³⁹ In addition, heats of mixing for ideal gases are zero, and for the other components they are assumed negligible.²⁸³ Overall, because the above effects are neglected, if one follows the derivations given in section 4, then one obtains the same set of governing equations. Thus, the equations reviewed above remain valid for use in nonisothermal systems, as long as the above assumptions are accepted.

As mentioned, to include nonisothermal effects, an overall thermal energy balance needs to be added to the set of governing equations. The energy conservation equation can be written for phase k in the form^{139,149}

$$\rho_k \hat{C}_{p,k} \left(\frac{\partial T_k}{\partial t} + \mathbf{v}_k \cdot \nabla T_k \right) + \left(\frac{\partial \ln \rho_k}{\partial \ln T_k} \right)_{p_k, x_{i,k}} \left(\frac{\partial p_k}{\partial t} + \mathbf{v}_k \cdot \nabla p_k \right) = Q_{k,p} - \nabla \cdot \mathbf{q}_k - \tau : \nabla \mathbf{v}_k + \sum_i \bar{H}_{i,k} \nabla \cdot \mathbf{J}_{i,k} - \sum_i \bar{H}_{i,k} \mathcal{R}_{i,k} \quad (68)$$

In the above expression, the first term represents the accumulation and convective transport of enthalpy, where $\hat{C}_{p,k}$ is the heat capacity of phase k . The second term is energy due to reversible work. For condensed phases this term is negligible, and an order-of-magnitude analysis for ideal gases with the expected pressure drop in a fuel cell demonstrates that this term is negligible compared to the others; therefore, it is ignored in all of the models.

The first two terms on the right side of eq 68 represent the net heat input by conduction and interphase transfer. The first is due to heat transfer between two phases

$$Q_{k,p} = h_{k,p} a_{k,p} (T_p - T_k) \quad (69)$$

where $h_{k,p}$ is the heat-transfer coefficient between phases k and p per interfacial area. Most often this term is used as a boundary condition, since it occurs only at the edges. However, in some modeling domains (e.g., along the channel) it may need to be incorporated as above. The second term is due to the heat flux in phase k

$$\mathbf{q}_k = - \sum_i \bar{H}_{i,k} \mathbf{J}_{i,k} - k_{T_k}^{\text{eff}} \nabla T_k \quad (70)$$

where $\bar{H}_{i,k}$ is the partial molar enthalpy of species i in phase k , $\mathbf{J}_{i,k}$ is the flux density of species i relative to the mass-average velocity of phase k

$$\mathbf{J}_{i,k} = \mathbf{N}_{i,k} - c_{i,k} \mathbf{v}_k \quad (71)$$

and $k_{T_k}^{\text{eff}}$ is the effective thermal conductivity of phase k . This means that it was corrected for the volume fraction of the phase by perhaps a Bruggeman equation (eq 42).

The third term on the right side of eq 68 represents viscous dissipation, the heat generated by viscous forces, where τ is the stress tensor. This term is also small, and all of the models except those of Mazumder and Cole^{84,85} neglect it. The fourth term on the right side comes from enthalpy changes due to diffusion. Finally, the last term represents the change in enthalpy due to reaction

$$\sum_i \bar{H}_{i,k} \mathcal{R}_{i,k} = - \sum_h a_{1,k} i_{h,1-k} (\eta_{s_{h,1-k}} + \Pi_h) - \sum_{p \neq k} \Delta H_p a_{k,p} r_{l,k-p} - \sum_g \Delta H_g R_{g,k} \quad (72)$$

where the expressions can be compared to those in the conservation-of-mass equation (eq 23). The above reaction terms include homogeneous reactions, interfacial reactions (e.g., evaporation), and interfacial electron-transfer reactions. The latter contains expressions for both the reversible and irreversible heat generation due to electrochemical reaction, as derived by Newman and Thomas-Alyea.²⁸⁴ The irreversible heat generation is represented by the surface overpotential. The reason the electrode overpotential, which contains a surface overpotential, is not used is that the generation of heat is due to the reaction at the interface; thus, a reference electrode next to the interface is used. This point is discussed further below. The reversible heat generation is represented by the second term, Π_h , which is the Peltier coefficient for charge-transfer reaction h ²⁸⁵ and can be expressed as²⁸⁴

$$\Pi_h \approx \frac{T}{n_h F} \sum_i S_{i,k,h} \bar{S}_{i,k} = T \frac{\Delta S_h}{n_h F} \quad (73)$$

where ΔS_h is the entropy of reaction h . The above equation neglects transported entropy (hence, the approximate sign), and the summation includes all species that participate in the reaction (e.g., electrons, protons, oxygen, hydrogen, water). The models that take into account reversible heating either use values for ΔS_h for the two fuel-cell half reactions^{26,45,71,80,90,125} or just do an overall energy balance where the total fuel-cell reaction entropy is used.^{15,16,65,107}

Almost all of the models assume local thermal equilibrium between the various phases. The exceptions are the models of Berning et al.,^{80,125} who use a heat-transfer coefficient to relate the gas temperature to the solid temperature. While this approach may be slightly more accurate, assuming a valid heat-transfer coefficient is known, it is not necessarily needed. Because of the intimate contact between the gas, liquid, and solid phases within the small pores of the various fuel-cell sandwich layers, assuming that all of the phases have the same temperature as each other at each point in the fuel cell is valid. Doing this eliminates the phase dependences in the above equations and allows for a single thermal energy equation to be written.

The assumption of local thermal equilibrium also means that an overall effective thermal conductivity is needed, because there is only a single energy equation. One way to calculate this thermal conductivity is to use Bruggeman factors,

$$k_T^{\text{eff}} = \sum_k \epsilon_k^{1.5} k_{T_k} \quad (74)$$

an expression that assumes that thermal conduction in the phases is in parallel. Some other models take the average as^{25,80,84,85,125}

$$k_T^{\text{eff}} = -2k_s + \frac{1}{\frac{\epsilon_0}{2k_s + k_G} + \frac{1 - \epsilon_0}{3k_G}} \quad (75)$$

where k_G and k_s are the thermal conductivities of the gas and solid (both conductive and nonconductive components) phases, respectively. A final way to calculate an effective thermal conductivity is to realize that the thermal conductivity of the solid is the larger and use that value,^{26,45,65} although the porosity and tortuosity should be considered for the different solid phases.

Most of the models use a simplified analogue of eq 68 where eqs 69, 70, and 72 have been substituted into it and local thermal equilibrium is assumed and the equation is summed over phases. The resultant equation is then further simplified for fuel cells

$$\sum_k \rho_k \hat{C}_{p_k} \left(\frac{\partial T}{\partial t} + \mathbf{v}_k \cdot \nabla T \right) = \sum_k h_{k,\text{ext}} a_{k,\text{ext}} (T_{\text{ext}} - T) + \nabla \cdot (k_T^{\text{eff}} \nabla T) - \sum_k \sum_i \mathbf{J}_{i,k} \cdot \nabla \bar{H}_{i,k} + \sum_{1-k} \sum_h a_{1,k} i_{h,1-k} (\eta_{s_{\text{ORR},1-k}} + \Pi_h) + \Delta H_{\text{evap}} r_{\text{evap}} \quad (76)$$

where the evaporation rate is given by eq 39. In the above equation, the summation over species i includes all reacting species including electrons and protons, the summation over $1 - k$ denotes summation over all reaction interfaces between phase k and the electronically conducting solid, and the subscript ext denotes heat transfer that is external to the control volume and is normally found only in the gas channels where there may be a heat-transfer plate, fluid, or reservoir. For boundary conditions, continuity in temperature and thermal flux serve as the internal boundary conditions. For the external boundary conditions, the inlet temperature is specified, and at the edges, either an external heat-transfer relation is used (if not already added into eq 76) or the wall is assumed to be adiabatic. The latter corresponds to a cell inside a stack, and the former to cells in contact with perhaps coolant plates.

In the gas channels, the models have convection of enthalpy, conduction through the graphite plates, and heat transfer to the ambient environment or cooling fluid if that case is being studied.^{15,16,65,80,90,107,125,126} In the diffusion layers, there is conduction of heat but no convective motion. There is also no external heat transfer. However, there is Joule heating,^{139,164,286} as discussed below. The cata-

lyst layers have the same thermal effects as the diffusion media, except that there is also heat generation, as discussed above. In the membrane, there is conduction, Joule heating, and some enthalpy that is carried by diffusion or convection. While most models account for this, some do not,^{60,80,84,85,90,125} and some are only cathode models.^{26,86,126} Also, some of the models assume that all of the water from the membrane vaporizes,^{60,82,86,90} which consumes a lot of heat and is not necessarily correct; it depends on the membrane model being used and the conditions in the catalyst layer.

Joule heating is due to the passage of current. It can be derived from the third term on the right side of eq 76

$$-\sum_i \mathbf{J}_{i,1} \cdot \nabla \bar{H}_{i,1} = -\mathbf{i}_1 \cdot \nabla \Phi_1 = \frac{\mathbf{i}_1 \cdot \mathbf{i}_1}{\sigma^{\text{eff}}} \quad (77)$$

The above is derived by using the definition of current density and relating the gradients of enthalpy and electrochemical potential for a system of uniform temperature. This type of heating can similarly be calculated for the ionically conducting phase where the ionic conductivity is used instead of the electronic conductivity. Joule heating is important in the membrane because a temperature change can cause an appreciable change in water content if the membrane is close to saturation.^{41,63,94} Even though it can be important, not all of the models include it.^{26,60,82,86,126}

Equation 76 is valid for local heat generation and analysis. However, there are some models that treat only heat transfer in the gas channels and assume that the fuel-cell sandwich remains isothermal,^{15,16,107,129} an assumption that is arguably valid from other simulation results. In this approach, only thermal convection and external heat transfer in the gas channels are used, and an energy balance yields the total energy produced in the fuel-cell sandwich.^{164,286,287} This energy balance has the form

$$Q = \sum_{k-p} \sum_h a_{k,p} j_{h,k-p} (U_{H_h} - V) \quad (78)$$

where Q is the total heat generated per unit volume, V is the (observed) cell potential, the summations are over all the electron-transfer reactions and interfaces, and U_{H_h} is the enthalpy potential for reaction h ,

$$U_{H_h} = \frac{\Delta H_h}{n_h F} = U_h - T \frac{\partial U_h}{\partial T} \quad (79)$$

and is a function of temperature. Equation 78 is simple to use, since the necessary quantities are relatively easy to obtain. This is especially true if only a single fuel-cell reaction occurs, wherein the enthalpy of the overall reaction can be used directly with the observed current density per unit volume to yield Q . Equation 78 is good if just the amount, and not the precise location of heat generation, is required. An example is a pseudo-2-D model where

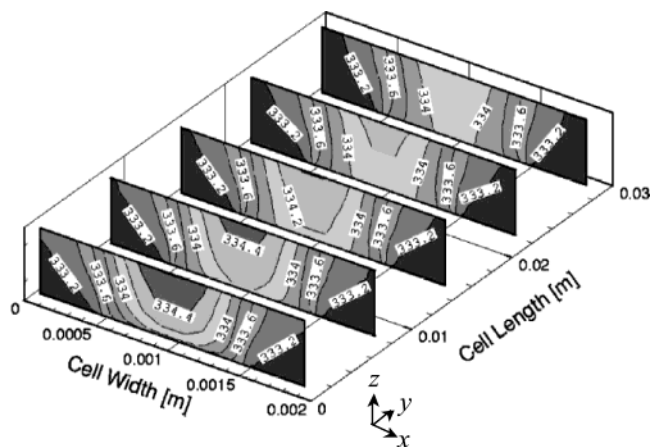


Figure 21. Temperature distribution in kelvin inside the cathode diffusion medium at a current density of 1.2 A/cm² and with saturated feeds. (Reproduced with permission from ref 80. Copyright 2003 The Electrochemical Society, Inc.)

the 1-D sandwich is taken to be isothermal and only the total heat generated in each sandwich layer is required.

Equation 78 can be used to show that the concentration overpotential due to gas diffusion does not generate heat. To do this, a virtual experiment is setup. First, the total amount of heat generation of a complete fuel cell is calculated. Next, one imagines that diffusion media are added to the fuel cell in such a way that the partial pressure of the reactant gases and all ohmic effects remain the same within the catalyst layers and fuel cell. Hence, only the partial pressures of the gases in the gas channels increase. According to eq 78, since the conditions are identical in the fuel cell, the heat generation is the same (i.e., no terms change). In other words, there is no heat generation due to this concentration overpotential. This can also be seen if the cell potential is divided into a summation of various overpotentials, where the effect of changing gas concentration in the diffusion media cancels. However, if the gases are not ideal, then some heat will be generated through the $\mathbf{J}_{i,1} \cdot \nabla \bar{H}_{i,1}$ term in eq 76.

The nonisothermal models allow for detailed temperature distributions to be generated, as shown in Figure 21. In the figure, the temperature is highest in the channel and decreases along the channel, because the rib has a higher thermal conductivity and the reaction rate is higher closer to the channel inlet. These effects have been seen with other models.^{60,65,80} Although the temperature gradient is not large, it is greater in the cell sandwich than along the gas channel. The main reason is that condensation is occurring in the diffusion medium, which releases heat in addition to that released at the reaction sites. Whether the temperature is largest along the channel or in the sandwich depends on the length of the channels, the boundary conditions set at the channels (i.e., insulating or conductive), and the operating conditions. For example, with dry-gas feeds, the temperature gradients along the channel become larger, and the inlet region becomes susceptible to membrane dehydration, as seen with some

of the other models (for examples, see refs 15 and 60).

Overall, the models show that nonisothermal effects mainly influence the water balance and current distribution. The water balance affects the competition between membrane dehydration and mass-transfer limitations, both of which are functions of temperature. Because water vaporization has a high enthalpy change, the models that do not take into account liquid water and evaporation/condensation reactions^{15,84,90,126} cannot explore many significant heat effects. On the other hand, models that always have a fully hydrated membrane are valid for only specific circumstances where there is always liquid water.^{25,80,84,85,125} As discussed in the previous sections, this does not occur often, especially at the anode. Thus, a full membrane model is required, especially since membrane dehydration and temperature rise exacerbate each other.^{65,128} In addition, pressure and temperature gradients can combine to produce significant effects on water management through evaporation and condensation of water (i.e., changing the partial pressure and vapor pressure of water).

To be complete in understanding and modeling water management, especially on a multidimensional or stack level, nonisothermal effects should be included. However, it is an adequate first approximation to assume that a sandwich and perhaps even a single cell are isothermal, as long as the dependence of the various parameters on temperature is included in the model. Finally, to be rigorous, some of the thermal effects assumed to be negligible could be added, such as heats of mixing of species into the membrane, temperature effects in the catalyst agglomerates, and thermal diffusion.

6.2. Transient Models

The other effect considered in this section deals with transients in a single fuel cell. The transient models examine step changes in potential and related phenomena (e.g., gas flow rates, water production, and current density). Hence, they are aimed at examining how a fuel-cell system handles different load requirements, which may occur during automotive operation or start up and shut down. They are not trying to model slow degradation processes that lead to failure or the transients associated with impedance experiments (i.e., potential or current oscillations). These types of models are discussed in section 7.

There are not many models that do transients, mainly because of the computational cost and complexity. The models that do have mainly been discussed above. In terms of modeling, the equations use the time derivatives in the conservation equations (eqs 23 and 68) and there is still no accumulation of current or charging of the double layer; that is, eq 27 still holds. The mass balance for liquid water requires that the saturation enter into the time derivative because it is the change in the water loading per unit time. However, this treatment is not necessarily rigorous because a water capacitance term should also be included,²³⁴ although it can be neglected as a first approximation.

One of the first models to examine transients in polymer-electrolyte fuel cells was a stack-level model by Amphlett et al.²⁸⁸ Their model is mainly empirical and examines temperature and gas flow rates. They showed that transient behavior lasts for a few minutes in a stack before a new steady state is reached. In a similar stack-level analysis, Yerramalla et al.²⁸⁹ used a slightly more complicated single-cell model and examined the shape of the transients. They noticed voltage behavior that had oscillations in it and some leakage current. Their overall analysis was geared to the development of a controller for the stack.

In terms of the more complicated single-cell models, which have been discussed in various contexts above, van Bussel et al.⁴⁴ mainly examined the transient behavior of the water content of the membrane with their model. They clearly showed that coflow operation with dry gases as well as counterflow with dry gases and high stoichiometries all lead to cases where the membrane dries out and the fuel cell cannot operate for more than a few minutes. This analysis shows that the drying out of the membrane is a much faster process in an operating fuel cell than with a naked membrane, where dehydration occurs over a much longer time scale.²⁹⁰ The modeling results also agreed with the transient uptake model of Nguyen and Vanderborgh,²⁹¹ which also showed that the initial development of the membrane water profile required a few minutes.

Um et al.⁶⁴ also examined a transient using their complex model. They saw that in a matter of tens of seconds the current density response reached steady state after a change in potential. However, their model did not include liquid water. The most complex model to examine transients is that of Natarajan and Nguyen.⁵⁶ It should be noted that although the model of Bevers et al.²⁶ has transient equations, they do not report any transient results. Natarajan and Nguyen included liquid saturation effects and water transport in their model. They clearly showed the flooding of the diffusion media and that it takes on the order of a couple of minutes for the profiles to develop.

The above models clearly demonstrated that the transient response of the electrical phenomena in a fuel cell is fast. The limiting time constant in the fuel cell is the liquid-water transport and its associated effects, which agree with experimental findings.^{292,293} This time constant causes a slow approach to steady state that can be on the order of tens of minutes in certain circumstances.²⁹² However, the majority of the change in the parameters of interest (power, current density, etc.) occurs within a much shorter time, and although the approach due to liquid water is long, the overall change in the parameter values is minor. For example, with a change in potential, the current density will reach a significant fraction of its steady-state value in a short time and then slowly decay toward it.

Some other general comments can also be made. For a stack, the interconnectivity of the cells means that the overall response will exhibit slower time constants than those for a single cell. However, the stack response (at least in terms of electrical vari-

ables) is still probably faster than the responses of the other components in the fuel-cell system such as compressors and so forth (for example, see ref 294). In the final analysis, as a first try, transient behavior of a fuel cell can be adequately modeled using a pseudo-steady-state model. This type of approach would involve stepping the single-cell model through various steady states, where the operating conditions such as potential, current, or flow rates change. Of course, the stepping rate would have to be determined. The approach is the same as assuming instantaneous achievement of steady state, or in other words infinitesimal time constants. If more specific phenomena need to be described such as liquid-water transport, then a full transient model should be used. Finally, due to load-leveling devices and possible hybridization of a fuel-cell system, transient models should be explored only after the relevant effects described in the preceding sections (e.g., flooding) are examined, or if specific phenomena such as start up from freeze are being considered.

7. Other Models

Other types and aspects of polymer-electrolyte fuel cells have also been modeled. In this section, those models are quickly reviewed. This section is written more to inform than to analyze the various models. The outline of this section in terms of models is stack models, impedance models, direct-methanol fuel-cell models, and miscellaneous models.

As mentioned above, stack models are useful for analyzing full system performance including perhaps auxiliary components in the system such as compressors. In terms of equations, almost all of the models use simple global balances and equations because single cells are not the focus of the models; thus, they use equations similar to eqs 21 and 78. In terms of other equations, normally they use typical flow and heat balances as well as the appropriate current and voltage relations, which take into account how the cells are connected together. The stack models can be separated into two categories, those that consider the stack only^{45,288,289,295–299} and those that consider a whole power system.^{100,294,300,301}

The models that examine only stacks focus mainly on the temperature distribution within the stack. As mentioned, there is a much higher temperature gradient in the stack than in a single cell, and it provides design information in terms of coolant flow rate, among other things.^{45,296,298} Also, as mentioned above, transient effects have also been examined.^{288,289} Lee et al.^{298,299} examined many different profiles in the stack including temperature, relative humidity, pressure, and current density, and their models can be used to predict flooding and various gradients in the stack. Similarly, the model of Thirumalai and White²⁹⁷ examined reactant distribution and design of the flow field and manifold.

As mentioned, there are also models of complete fuel-cell power systems in which the stack is but one component. These models have the benefit of examining true designs and the interconnections between components, but they usually require an even weaker model of an individual fuel cell. In fact, the entire

fuel-cell stack may be modeled with only single equations in the form of eqs 21 and 78.^{100,300} The models show such tradeoffs as compressor power required and performance gain due to pressurized and humidified feeds. In terms of the models, Ahmed et al.^{100,300} considered the total water requirements needed both for the fuel cell and for the reformer reactors. Cownden et al.³⁰⁰ looked mainly at the total system power and saw the effects of compressors, pressure drops, coolant flows, and the efficiencies of the various components in the system. Ahluwalia et al.³⁰¹ studied the gain in overall stack performance and design when high-temperature polymer-electrolyte systems are considered. Finally, the model of De Francesco and Arato²⁹⁴ looks at transients and start-up conditions and procedures. Overall, while the stack models use simplified and usually empirical equations for a single cell, they provide benefits in actually designing operating systems. In these cases, the data for the empirical expressions are known, and complex modeling may not be required.

The next set of models examined in this section is impedance models. Impedance is often used to determine parameters and understand how the fuel cell is operating. By applying only a small perturbation during operation, the system can be studied in situ. There are many types of impedance models. They range from very simple analyses to taking a complete fuel-cell model and shifting it to the frequency domain. The very simple models use a simple equivalent circuit just to understand some general aspects (for examples, see refs 302–304).

The next more complicated models focus on analyzing the impedance spectra using complex equivalent circuits.^{103,137,221,305–312} Most of these models use a series of resistors to represent transport in the membrane and diffusion media. The porous electrodes are modeled similarly to Figure 10, with the addition of a double-layer capacitance term in parallel with each charge-transfer resistance. Most of the models show such effects as increased high-frequency resistance as the membrane dehydrates and an increased low-frequency loop as flooding occurs. The model of Wang et al.³⁰⁶ also considers how carbon monoxide affects performance in the anode. Out of these models, the one of Eikerling and Kornyshev¹³⁷ is the most sophisticated. It shows specifically how ohmic and oxygen limitations affect the impedance of the cathode. With such a model, meaningful analysis of experimental impedance plots can be made and governing phenomena noted, as well as the determination of general transport parameters such as the resistance of the membrane.

While a good equivalent-circuit representation of the transport processes in a fuel cell can lead to an increased understanding, it is not as good as taking a 1-D sandwich model and taking it into the frequency domain. These models typically analyze the cathode side of the fuel cell.^{102,313,314} The most comprehensive is probably that of Springer et al.¹⁰² The use of impedance models allows for the calculation of parameters, like gas-phase tortuosity, which cannot be determined easily by other means, and can also allow for the separation of diffusion and migra-

tion effects. Overall, impedance is a very powerful experimental tool, but its results are only as good as the model used to analyze it.

The next models that should be mentioned are those for direct-methanol fuel cells.^{68,117,130–132,295,315–325} A direct-methanol fuel cell is very similar to the hydrogen fuel cells in this review, with the exception of the fuel. In a direct-methanol fuel cell, methanol is fed instead of hydrogen and reacts according to the reaction



and the cathode ORR (eq 2) is the same. The design of the fuel cell is the same as the polymer-electrolyte models described above. The methanol reaction is much slower than hydrogen oxidation and is a significant source of performance loss for the direct-methanol fuel cells. However, because methanol is a liquid, the membrane is always fully hydrated. Even though the membrane has better conductivity, a fully hydrated membrane also means that there is a significant amount of methanol crossover. This crossover is one reason that thicker membranes are used in methanol fuel cells than in hydrogen ones. Treatment of the transport phenomena becomes much more complex due to the presence of methanol^{130,131} and also because there is liquid on both sides of the fuel cell.

In terms of modeling, all of the different types of models discussed above have been used. The major problems are methanol crossover, flooding, the kinetics of the cathode, and predominately mass-transfer and reaction of methanol at the anode. It is beyond the scope of this review to discuss all of the models for direct-methanol fuel cells. The major ones are listed in the references and have been mentioned here only because of their similarity to those discussed in this article. The governing phenomena and equations are basically the same with only slight variations to take into account methanol in the membrane, different anode kinetics, and diffusion of methanol in water instead of hydrogen in water vapor. It should be noted that direct-methanol fuel cells are being considered for portable applications due to their more energy-dense fuel and simple liquid-injection systems, among other things.

Finally, there are some miscellaneous polymer-electrolyte fuel cell models that should be mentioned. The models of Okada and co-workers^{42,43,326} have examined how impurities in the water affect fuel-cell performance. They have focused mainly on ionic species such as chlorine and sodium and show that even a small concentration, especially next to the membrane at the cathode, impacts the overall fuel-cell performance significantly. There are also some models that examine having free convection for gas transfer into the fuel cell.^{327–329} These models are also for very miniaturized fuel cells, so that free convection can provide enough oxygen. The models are basically the same as the ones above, but because the cell area is much smaller, the results and effects can be different. For example, free convection is used for both heat transfer and mass transfer, and the small

length scale means that such effects as Knudsen diffusion and water droplet formation and flooding can be more important. These models are normally 3-D and focus more on the flow-field design and the gas channels than on the complex relationships within the fuel-cell sandwich.

The final group of models is those that incorporate possible failure mechanisms.^{330–333} These failure mechanisms are time or condition dependent and are not the same as the effects examined in earlier sections, such as carbon monoxide poisoning, that was also valid for steady-state operation. The model by Darling and Meyers³³⁰ examined platinum catalyst loss as the potential is cycled. This is something that has also been observed in phosphoric-acid fuel cells^{334,335} and can occur during start up and shut down. Similar to the case of the Darling and Meyers model, Wendt et al.³³¹ examined catalyst aging due to changing catalyst morphology and, to a lesser extent, accumulation of impurities. The models of Jiang and Chu³³² and Fowler et al.³³³ examined slow voltage degradation over time for a cell stack and a single cell, respectively. They do this by including time-dependent rate constants for the kinetic reactions as well as a membrane deterioration term that limits the maximum water content of the membrane. Both use semiempirical equations to model the fuel-cell behavior, but they are some of the first to model fuel-cell failure. The above models are notable because durability issues are becoming increasingly significant and have not received much attention in the literature either theoretically or experimentally (for examples, see refs 336–338).

8. Summary

In this review, we have examined the different models for polymer-electrolyte fuel cells operating with hydrogen. The major focus has been on transport of the various species within the fuel cell. The different regions of the fuel cell were examined, and their modeling methodologies and equations were elucidated. In particular, the 1-D fuel-cell sandwich was discussed thoroughly because it is the most important part of the fuel-cell assembly. Models that included other effects such as temperature gradients and transport in other directions besides through the fuel-cell sandwich were also discussed.

Models were not directly compared to each other; instead they were broken down into their constitutive parts. The reason for this is that validation of the models is usually accomplished by comparison of simulation to experimental polarization data (e.g., Figure 3). However, other data can also be used such as the net flux of water through the membrane. In fitting these data, the models vary not only in their complexity and treatments but also in their number and kind of fitting parameters. This is one reason it is hard to justify one approach over another by just looking at the modeling results. In general, it seems reasonable that the more complex models, which are based on physical arguments and do not contain many fitting parameters, are perhaps closest to reality. Of course, this assumes that they fit the experimental data and observations. This last point

has been overlooked in the validation of many models. For example, a model may fit the data very well for certain operating conditions, but if it does not at least predict the correct trend when one of those conditions is changed, then the model is shown to be valid only within a certain operating range.

This review has highlighted the important effects that should be modeled. These include two-phase flow of liquid water and gas in the fuel-cell sandwich, a robust membrane model that accounts for the different membrane transport modes, nonisothermal effects, especially in the directions perpendicular to the sandwich, and multidimensional effects such as changing gas composition along the channel, among others. For any model, a balance must be struck between the complexity required to describe the physical reality and the additional costs of such complexity. In other words, while more complex models more accurately describe the physics of the transport processes, they are more computationally costly and may have so many unknown parameters that their results are not as meaningful. Hopefully, this review has shown and broken down for the reader the vast complexities of transport within polymer-electrolyte fuel cells and the various ways they have been and can be modeled.

9. Acknowledgments

The authors would like to thank the following people for their input in helping write and proof this manuscript: Robert Darling, Jeremy Meyers, and Karen Thomas-Alyea. The authors would also like to thank Bob Savinell and Tom Zawodzinski for the opportunity to write this review.

10. Nomenclature

a_i^α	activity of species i in phase α
$a_{k,p}$	interfacial surface area between phases k and p per unit volume, $1/\text{cm}$
$a_{1,2}^\circ$	interfacial area between the electronically conducting and membrane phases with no flooding, $1/\text{cm}$
A_{agg}	specific external surface area of the agglomerate, $1/\text{cm}$
A_{Pt}	reactive surface area of platinum, cm^2/g
b	Tafel slope, defined by eq 14 for the ORR, V
$c_{i,k}$	interstitial concentration of species i in phase k , mol/cm^3
c_T	total solution concentration or molar density, mol/cm^3
\hat{C}_{pk}	heat capacity of phase k , $\text{J}/\text{g}\cdot\text{K}$
\mathbf{d}_i	driving force per unit volume acting on species i in phase k , J/cm^4
D_i	Fickian diffusion coefficient of species i in a mixture, cm^2/s
D_S	capillary diffusivity, cm^2/s
$D_{i,j}$	diffusion coefficient of i in j , cm^2/s
D_{K_i}	Knudsen diffusion coefficient of species i , cm^2/s
E	effectiveness factor
F	Faraday's constant, $96\,487\text{ C}/\text{equiv}$
g	acceleration due to gravity, cm/s^2
$h_{k,p}$	heat-transfer coefficient between phases k and p , $\text{J}/\text{cm}^2\cdot\text{s}\cdot\text{K}$
$\bar{H}_{i,k}$	partial molar enthalpy of species i in phase k , J/mol
$H_{i,j}$	Henry's constant for species i in component j , $\text{mol}/\text{cm}^3\cdot\text{kPa}$

ΔH_l	heat or enthalpy of reaction l , J/mol
i	superficial current density through the membrane, A/cm^2
\mathbf{i}_k	current density in phase k , A/cm^2
$i_{0,h}$	exchange current density for reaction h , A/cm^2
$i_{h,k-p}$	transfer current density of reaction h per interfacial area between phases k and p , A/cm^2
i_{lim}	limiting current density, A/cm^2
$\mathbf{J}_{i,k}$	flux density of species i in phase k relative to the mass-average velocity of phase k , $\text{mol}/\text{cm}^2\cdot\text{s}$
k	effective hydraulic permeability, cm^2
K	ORR rate constant as defined by eq 61, $1/\text{s}$
k^*	ORR rate constant in Figure 11, cm/s
$k_{T,k}$	thermal conductivity of phase k , $\text{J}/\text{cm}^2\cdot\text{K}$
k_r	relative hydraulic permeability
k_{sat}	saturated hydraulic permeability, cm^2
k_ϕ	electrokinetic permeability, cm^2
L	catalyst layer thickness, cm
m	parameter in the polarization equation (eq 20)
m_{Pt}	loading of platinum, g/cm^2
M_i	molecular weight of species i , g/mol
M_i^z	symbol for the chemical formula of species i in phase k having charge z_i
n	parameter in the polarization equation (eq 20)
n_h	number of electrons transferred in electrode reaction h
$\mathbf{N}_{i,k}$	superficial flux density of species i in phase k , $\text{mol}/\text{cm}^2\cdot\text{s}$
p_i	partial pressure of species i , kPa
p_C	capillary pressure, kPa
p_k	total pressure of phase k , kPa
p_w^{vap}	vapor pressure of water, kPa
\mathbf{q}_k	superficial heat flux through phase k , $\text{J}/\text{cm}^2\cdot\text{s}$
Q	total amount of heat generated, $\text{J}/\text{cm}^2\cdot\text{s}$
$Q_{k,p}$	heat flux transferred between phases k and p , $\text{J}/\text{cm}^3\cdot\text{s}$
r	pore radius, cm
r_{evap}	rate of evaporation, $\text{mol}/\text{cm}^3\cdot\text{s}$
$r_{l,k-p}$	rate of reaction l per unit of interfacial area between phases k and p , $\text{mol}/\text{cm}^2\cdot\text{s}$
R	ideal-gas constant, $8.3143\text{ J}/\text{mol}\cdot\text{K}$
R_{agg}	agglomerate radius, cm
$R_{g,k}$	rate of homogeneous reaction g in phase k , $\text{mol}/\text{cm}^3\cdot\text{s}$
$R_{i,j}$	resistance of resistor i,j in Figure 10 where ct stands for charge-transfer, $\Omega\cdot\text{cm}^2$
\mathcal{R}	total ohmic resistance, $\Omega\cdot\text{cm}^2$
$\mathcal{R}_{i,k}$	total rate of reaction of species i in phase k , $\text{mol}/\text{cm}^3\cdot\text{s}$
$S_{i,k,l}$	stoichiometric coefficient of species i in phase k participating in reaction l
S	liquid saturation
$\bar{S}_{i,k}$	molar entropy of species i in phase k , $\text{J}/\text{mol}\cdot\text{K}$
ΔS_h	entropy of reaction h , $\text{J}/\text{mol}\cdot\text{K}$
t	time, s
T	absolute temperature, K
T_k	absolute temperature of phase k , K
u_i	mobility of species i , $\text{cm}^2\cdot\text{mol}/\text{J}\cdot\text{s}$
U_h	reversible cell potential of reaction h , V
U	potential intercept for a polarization equation, V
U_h^θ	standard potential of reaction h , for oxygen reduction, 1.229 V at $25\text{ }^\circ\text{C}$
U_{H_h}	enthalpy potential, V
\mathbf{v}_k	superficial velocity of phase k , cm/s
V	cell potential, V
\bar{V}_i	(partial) molar volume of species i , cm^3/mol
$W_{\text{O}_2}^{\text{diff}}$	molar flow rate of oxygen to the agglomerate, $\text{mol}/\text{cm}^3\cdot\text{s}$
x	distance across the flow field, cm
$x_{i,k}$	mole fraction of species i in phase k

y	distance along the flow-field channel, cm
z	distance across the cell sandwich, cm
z_i	valence or charge number of species i
<i>Greek Letters</i>	
α_a	anodic transfer coefficient
α_c	cathodic transfer coefficient
α_w	water transport coefficient, mol ² /J·cm·s
β	net water flux per proton flux through the membrane
γ	surface tension, N/cm
δ_n	diffusion length or thickness of region n , cm
ζ	characteristic length, cm
ϵ_k	volume fraction of phase k
ϵ_0	bulk porosity
ν_k	kinematic viscosity of phase k , cm ² /s
ξ	electroosmotic coefficient
Π_h	Peltier coefficient for charge-transfer reaction h , V
ρ_k	density of phase k , g/cm ³
σ_0	standard conductivity in the electronically conducting phase, S/cm
$\eta_{h,k-p}$	electrode overpotential of reaction h between phases k and p (see eq 10), V
$\eta_{sh,k-p}$	surface overpotential of reaction h between phases k and p (see eq 11), V
η^*	dimensionless overpotential in Figure 11
θ	contact angle, deg
κ	conductivity of the ionically conducting phase, S/cm
λ	moles of water per mole of sulfonic acid sites
λ_L	relative mobility of the liquid phase
μ	viscosity, Pa·s
μ_i	(electro)chemical potential of species i , J/mol
μ_i^α	electrochemical potential of species i in phase α , J/mol
τ	stress tensor, kPa
τ_k	tortuosity of phase k
ϕ	Thiele modulus, defined by eq 60 for the ORR
Φ_k	potential in phase k , V
ψ	dimensionless parameter in Figure 11

Subscripts/Superscripts

1	electronically conducting phase
2	ionically conducting phase
agg	agglomerate
CL	catalyst layer
eff	effective value, corrected for tortuosity and porosity
ext	external to the control volume
f	fixed ionic site in the membrane
film	film covering the agglomerate
g	homogeneous reaction number
G	gas phase
h	electron-transfer reaction number
HOR	hydrogen-oxidation reaction
i	generic species
j	generic species
k	generic phase
l	heterogeneous reaction number
L	liquid phase
m	mixture
ORR	oxygen-reduction reaction
p	generic phase
ref	parameter evaluated at the reference conditions
s	solid phase
w	water

11. References

- Giner, J.; Hunter, C. *J. Electrochem. Soc.* **1969**, *116*, 1124.
- Cutlip, M. B. *Electrochim. Acta* **1975**, *20*, 767.
- Cutlip, M. B.; Yang, S. C.; Stonehart, P. *J. Electrochem. Soc.* **1986**, *133*, C299.
- Cutlip, M. B.; Yang, S. C.; Stonehart, P. *Electrochim. Acta* **1991**, *36*, 547.
- Iczkowski, R. P.; Cutlip, M. B. *J. Electrochem. Soc.* **1980**, *127*, 1433.
- Newman, J.; Tiedemann, W. *AIChE J.* **1975**, *21*, 25.
- Newman, J. S.; Tobias, C. W. *J. Electrochem. Soc.* **1962**, *109*, 1183.
- Paganin, V. A.; Ticianelli, E. A.; Gonzalez, E. R. *J. Appl. Electrochem.* **1996**, *26*, 297.
- Parthasarathy, A.; Srinivasan, S.; Appleby, A. J.; Martin, C. R. *J. Electrochem. Soc.* **1992**, *139*, 2530.
- Parthasarathy, A.; Srinivasan, S.; Appleby, A. J.; Martin, C. R. *J. Electrochem. Soc.* **1992**, *139*, 2856.
- Ticianelli, E. A.; Derouin, C. R.; Redondo, A.; Srinivasan, S. *J. Electrochem. Soc.* **1988**, *135*, 2209.
- Kim, J.; Lee, S. M.; Srinivasan, S.; Chamberlin, C. E. *J. Electrochem. Soc.* **1995**, *142*, 2670.
- Bernardi, D. M.; Verbrugge, M. W. *J. Electrochem. Soc.* **1992**, *139*, 2477.
- Springer, T. E.; Zawodzinski, T. A.; Gottesfeld, S. *J. Electrochem. Soc.* **1991**, *138*, 2334.
- Fuller, T. F.; Newman, J. *J. Electrochem. Soc.* **1993**, *140*, 1218.
- Nguyen, T. V.; White, R. E. *J. Electrochem. Soc.* **1993**, *140*, 2178.
- Wang, J.-T.; Savinell, R. F. *Electrochim. Acta* **1992**, *37*, 2737.
- Chan, D. S.; Wan, C. C. *J. Power Sources* **1994**, *50*, 261.
- Rho, Y. W.; Srinivasan, S.; Kho, Y. T. *J. Electrochem. Soc.* **1994**, *141*, 2089.
- Amphlett, J. C.; Baumert, R. M.; Mann, R. F.; Peppley, B. A.; Roberge, P. R.; Harris, T. J. *J. Electrochem. Soc.* **1995**, *142*, 1.
- Amphlett, J. C.; Baumert, R. M.; Mann, R. F.; Peppley, B. A.; Roberge, P. R.; Harris, T. J. *J. Electrochem. Soc.* **1995**, *142*, 9.
- Ticianelli, E. A. *J. Electroanal. Chem.* **1995**, *387*, 1.
- Mosdale, R.; Srinivasan, S. *Electrochim. Acta* **1995**, *40*, 413.
- West, A. C.; Fuller, T. F. *J. Appl. Electrochem.* **1996**, *26*, 557.
- Gurau, V.; Liu, H.; Kakac, S. *AIChE J.* **1998**, *44*, 2414.
- Bevens, D.; Wöhr, M.; Yasuda, K.; Oguro, K. *J. Appl. Electrochem.* **1997**, *27*, 1254.
- Broka, K.; Ekdunge, P. *J. Appl. Electrochem.* **1997**, *27*, 281.
- Eikerling, M.; Kornyshev, A. A. *J. Electroanal. Chem.* **1998**, *453*, 89.
- de Sena, D. R.; Ticianelli, E. A.; Gonzalez, E. R. *Electrochim. Acta* **1998**, *43*, 3755.
- Antoine, O.; Bultel, Y.; Durand, R.; Ozil, P. *Electrochim. Acta* **1998**, *43*, 3681.
- Bultel, Y.; Ozil, P.; Durand, R. *J. Appl. Electrochem.* **1998**, *28*, 269.
- Bultel, Y.; Ozil, P.; Durand, R. *Electrochim. Acta* **1998**, *43*, 1077.
- Bultel, Y.; Ozil, P.; Durand, R. *J. Appl. Electrochem.* **1999**, *29*, 1025.
- Gloaguen, F.; Durand, R. *J. Appl. Electrochem.* **1997**, *27*, 1029.
- Gloaguen, F.; Convert, P.; Gamburzev, S.; Velev, O. A.; Srinivasan, S. *Electrochim. Acta* **1998**, *43*, 3767.
- Perry, M. L.; Newman, J.; Cairns, E. J. *J. Electrochem. Soc.* **1998**, *145*, 5.
- Kulikovskiy, A. A.; Divisek, J.; Kornyshev, A. A. *J. Electrochem. Soc.* **1999**, *146*, 3981.
- Paddison, S. J.; Zawodzinski, T. A. *Solid State Ionics* **1998**, *115*, 333.
- Okada, T.; Xie, G.; Meeg, M. *Electrochim. Acta* **1998**, *43*, 2141.
- Eikerling, M.; Kharkats, Y. I.; Kornyshev, A. A.; Volkovich, Y. M. *J. Electrochem. Soc.* **1998**, *145*, 2684.
- Futerko, P.; Hsing, I. M. *J. Electrochem. Soc.* **1999**, *146*, 2049.
- Okada, T. *J. Electroanal. Chem.* **1999**, *465*, 1.
- Okada, T. *J. Electroanal. Chem.* **1999**, *465*, 18.
- van Bussel, H.; Koene, F. G. H.; Mallant, R. *J. Power Sources* **1998**, *71*, 218.
- Wöhr, M.; Bolwin, K.; Schnurmberger, W.; Fischer, M.; Neubrand, W.; Eigenberger, G. *Int. J. Hydrogen Energy* **1998**, *23*, 213.
- Kazim, A.; Liu, H. T.; Forges, P. *J. Appl. Electrochem.* **1999**, *29*, 1409.
- Singh, D.; Lu, D. M.; Djilali, N. *Int. J. Eng. Sci.* **1999**, *37*, 431.
- Yi, J. S.; Nguyen, T. V. *J. Electrochem. Soc.* **1999**, *146*, 38.
- Boyer, C. C.; Anthony, R. G.; Appleby, A. J. *J. Appl. Electrochem.* **2000**, *30*, 777.
- Baschuk, J. J.; Li, X. *J. Power Sources* **2000**, *86*, 181.
- Dutta, S.; Shimpalee, S.; Van Zee, J. W. *J. Appl. Electrochem.* **2000**, *30*, 135.
- He, W.; Yi, J. S.; Nguyen, T. V. *AIChE J.* **2000**, *46*, 2053.
- Chan, S. H.; Tun, W. A. *Chem. Eng. Technol.* **2001**, *24*, 51.
- Dutta, S.; Shimpalee, S.; Van Zee, J. W. *Int. J. Heat Mass Transfer* **2001**, *44*, 2029.
- Janssen, G. J. M. *J. Electrochem. Soc.* **2001**, *148*, A1313.
- Natarajan, D.; Nguyen, T. V. *J. Electrochem. Soc.* **2001**, *148*, A1324.
- Wang, Z. H.; Wang, C. Y.; Chen, K. S. *J. Power Sources* **2001**, *94*, 40.
- Wang, C. Y.; Cheng, P. *Int. J. Heat Mass Transfer* **1996**, *39*, 3607.
- Wang, C. Y.; Cheng, P. *Adv. Heat Transfer* **1997**, *30*, 93.

- (60) Shimpalee, S.; Dutta, S. *Numer. Heat Transfer, Part A* **2000**, *38*, 111.
- (61) Hsing, I. M.; Futerko, P. *Chem. Eng. Sci.* **2000**, *55*, 4209.
- (62) Futerko, P.; Hsing, I. M. *Electrochim. Acta* **2000**, *45*, 1741.
- (63) Thampan, T.; Malhotra, S.; Tang, H.; Datta, R. *J. Electrochem. Soc.* **2000**, *147*, 3242.
- (64) Um, S.; Wang, C.-Y.; Chen, K. S. *J. Electrochem. Soc.* **2000**, *147*, 4485.
- (65) Costamagna, P. *Chem. Eng. Sci.* **2001**, *56*, 323.
- (66) Dohle, H.; Kornyshev, A. A.; Kulikovskiy, A. A.; Mergel, J.; Stolten, D. *Electrochem. Commun.* **2001**, *3*, 73.
- (67) Kornyshev, A. A.; Kulikovskiy, A. A. *Electrochim. Acta* **2001**, *46*, 4389.
- (68) Kulikovskiy, A. A. *Electrochem. Commun.* **2001**, *3*, 572.
- (69) Kulikovskiy, A. A. *Fuel Cells* **2001**, *1*, 162.
- (70) Eikerling, M.; Kornyshev, A. A.; Kuznetsov, A. M.; Ulstrup, J.; Walbran, S. *J. Phys. Chem. B* **2001**, *105*, 3646.
- (71) Rowe, A.; Li, X. G. *J. Power Sources* **2001**, *102*, 82.
- (72) Thampan, T.; Malhotra, S.; Zhang, J. X.; Datta, R. *Catal. Today* **2001**, *67*, 15.
- (73) Shimpalee, S.; Lee, W. K.; Van Zee, J. W. The Electrochemical Society Extended Abstracts, September 2–7, 2001; Abstract 458.
- (74) Weber, A. Z.; Darling, R. M.; Newman, J. *J. Electrochem. Soc.*, in press.
- (75) Chu, H.-S.; Yeh, C.; Chen, F. *J. Power Sources* **2002**, *123*, 1.
- (76) Um, S.; Wang, C. Y. *J. Power Sources* **2004**, *125*, 40.
- (77) Zhukovskiy, K. V. *AIChE J.* **2003**, *49*, 3029.
- (78) Pisani, L.; Murgia, G.; Valentini, M.; D'Aguanno, B. *J. Electrochem. Soc.* **2002**, *149*, A898.
- (79) You, L. X.; Liu, H. T. *Int. J. Heat Mass Transfer* **2002**, *45*, 2277.
- (80) Berning, T.; Djilali, N. *J. Electrochem. Soc.* **2003**, *150*, A1598.
- (81) Kulikovskiy, A. A. *J. Electrochem. Soc.* **2003**, *150*, A1432.
- (82) Lee, W. K.; Shimpalee, S.; Van Zee, J. W. *J. Electrochem. Soc.* **2003**, *150*, A341.
- (83) Kulikovskiy, A. A. *Electrochem. Commun.* **2002**, *4*, 527.
- (84) Mazumder, S.; Cole, J. V. *J. Electrochem. Soc.* **2003**, *150*, A1503.
- (85) Mazumder, S.; Cole, J. V. *J. Electrochem. Soc.* **2003**, *150*, A1510.
- (86) Nam, J. H.; Kaviany, M. *Int. J. Heat Mass Transfer* **2003**, *46*, 4595.
- (87) Natarajan, D.; Nguyen, T. V. *J. Power Sources* **2003**, *115*, 66.
- (88) Weber, A. Z.; Newman, J. In *Advanced Materials for Fuel Cells and Batteries*; Ehrlich, G., Arora, P., Ofer, D., Savinell, R. F., Zawodzinski, T., D'Souza, F., Eds.; The Electrochemical Society Proceeding Series: Pennington, NJ, 2003.
- (89) Weber, A. Z.; Newman, J. *J. Electrochem. Soc.* **2003**, *150*, A1008.
- (90) Siegel, N. P.; Ellis, M. W.; Nelson, D. J.; von Spakovsky, M. R. *J. Power Sources* **2003**, *115*, 81.
- (91) Pisani, L.; Valentini, M.; Murgia, G. *J. Electrochem. Soc.* **2003**, *150*, A1558.
- (92) Choi, P.; Datta, R. *J. Electrochem. Soc.* **2003**, *150*, E601.
- (93) Weber, A. Z.; Newman, J. In *Proton Conducting Membrane Fuel Cells III*; Van Zee, J. W., Fuller, T. F., Gottesfeld, S., Murthy, M., Eds.; The Electrochemical Society Proceeding Series: Pennington, NJ, 2002.
- (94) Weber, A. Z.; Newman, J. *J. Electrochem. Soc.* **2004**, *151*, A311.
- (95) Murgia, G.; Pisani, L.; Valentini, M.; D'Aguanno, B. *J. Electrochem. Soc.* **2002**, *149*, A31.
- (96) Kulikovskiy, A. A. *Electrochem. Commun.* **2002**, *4*, 318.
- (97) Kulikovskiy, A. A. *Electrochem. Commun.* **2002**, *4*, 845.
- (98) Jaouen, F.; Lindbergh, G.; Sundholm, G. *J. Electrochem. Soc.* **2002**, *149*, A437.
- (99) Hertwig, K.; Martens, L.; Karwoth, R. *Fuel Cells* **2002**, *2*, 61.
- (100) Ahmed, S.; Kopasz, J.; Kumar, R.; Krumpelt, M. *J. Power Sources* **2002**, *112*, 519.
- (101) Springer, T. E.; Wilson, M. S.; Gottesfeld, S. *J. Electrochem. Soc.* **1993**, *140*, 3513.
- (102) Springer, T. E.; Zawodzinski, T. A.; Wilson, M. S.; Gottesfeld, S. *J. Electrochem. Soc.* **1996**, *143*, 587.
- (103) Springer, T. E.; Raistrick, I. D. *J. Electrochem. Soc.* **1989**, *136*, 1594.
- (104) Springer, T. E.; Rockward, T.; Zawodzinski, T. A.; Gottesfeld, S. *J. Electrochem. Soc.* **2001**, *148*, A11.
- (105) Ridge, S. J.; White, R. E.; Tsou, Y.; Beaver, R. N.; Eisman, G. A. *J. Electrochem. Soc.* **1992**, *139*, 1902.
- (106) Weisbrod, K. R.; Grot, S. A.; Vanderborgh, N. E. In *First International Symposium on Proton Conducting Membrane Fuel Cells*; Landgrebe, A. R., Gottesfeld, S., Halpert, G., Eds.; The Electrochemical Society Proceeding Series; Pennington, NJ, 1995; Vol. PV 95–23.
- (107) Yi, J. S.; Nguyen, T. V. *J. Electrochem. Soc.* **1998**, *145*, 1149.
- (108) Wood, D. L.; Yi, Y. S.; Nguyen, T. V. *Electrochim. Acta* **1998**, *43*, 3795.
- (109) Ge, S.-H.; Yi, B.-L. *J. Power Sources* **2003**, *124*, 1.
- (110) Bernardi, D. M.; Verbrugge, M. W. *AIChE J.* **1991**, *37*, 1151.
- (111) Verbrugge, M. W.; Hill, R. F. *J. Electrochem. Soc.* **1990**, *137*, 886.
- (112) Bernardi, D. M. *J. Electrochem. Soc.* **1990**, *137*, 3344.
- (113) Chan, S. H.; Goh, S. K.; Jiang, S. P. *Electrochim. Acta* **2003**, *48*, 1905.
- (114) Marr, C.; Li, X. G. *J. Power Sources* **1999**, *77*, 17.
- (115) Baschuk, J. J.; Li, X. G. *Int. J. Energy Res.* **2003**, *27*, 1095.
- (116) Baschuk, J. J.; Rowe, A. M.; Li, X. G. *J. Energy Resour. Technol.* **2003**, *125*, 94.
- (117) Murgia, G.; Pisani, L.; Shukla, A. K.; Scott, K. *J. Electrochem. Soc.* **2003**, *150*, A1231.
- (118) Pisani, L.; Murgia, G.; Valentini, M.; D'Aguanno, B. *J. Power Sources* **2002**, *108*, 192.
- (119) Zhou, T.; Liu, H. *Int. J. Trans. Phenom.* **2001**, *3*, 177.
- (120) Gurau, V.; Barbir, F.; Liu, H. *J. Electrochem. Soc.* **2000**, *147*, 2468.
- (121) You, L. X.; Liu, H. T. *Int. J. Hydrogen Energy* **2001**, *26*, 991.
- (122) Pasaogullari, U.; Wang, C. Y. 204th Meeting of the Electrochemical Society, Orlando, FL, 2003; Abstract 1103.
- (123) Pasaogullari, U.; Wang, C. Y. *J. Electrochem. Soc.* **2004**, *151*, A399.
- (124) Meng, H.; Wang, C. Y. *J. Electrochem. Soc.* **2004**, *151*, A358.
- (125) Berning, T.; Lu, D. M.; Djilali, N. *J. Power Sources* **2002**, *106*, 284.
- (126) Bradean, R.; Promislow, K.; Wetton, B. *Numer. Heat Transfer, Part A* **2002**, *42*, 121.
- (127) Newman, J. *Electrochim. Acta* **1979**, *24*, 223.
- (128) Fuller, T. F. Ph.D. Dissertation, University of California—Berkeley, 1992.
- (129) Dannenberg, K.; Ekdunge, P.; Lindbergh, G. *J. Appl. Electrochem.* **2000**, *30*, 1377.
- (130) Meyers, J. P.; Newman, J. *J. Electrochem. Soc.* **2002**, *149*, A710.
- (131) Meyers, J. P.; Newman, J. *J. Electrochem. Soc.* **2002**, *149*, A718.
- (132) Meyers, J. P.; Newman, J. *J. Electrochem. Soc.* **2002**, *149*, A729.
- (133) Weber, A.; Darling, R.; Meyers, J.; Newman, J. In *Handbook of Fuel Cells: Fundamentals, Technology, and Applications*; Vielstich, W., Lamm, A., Gasteiger, H. A., Eds.; John Wiley & Sons: New York, 2003; Vol. 1.
- (134) Weber, A. Z.; Newman, J. *J. Electrochem. Soc.* **2004**, *151*, A326.
- (135) Kulikovskiy, A. A. *Electrochem. Commun.* **2003**, *5*, 530.
- (136) Eikerling, M.; Paddison, S. J.; Zawodzinski, T. A. *J. New Mater. Electrochem. Syst.* **2002**, *5*, 15.
- (137) Eikerling, M.; Kornyshev, A. A. *J. Electronanal. Chem.* **1999**, *475*, 107.
- (138) Eikerling, M.; Kornyshev, A. A.; Stimming, U. *J. Phys. Chem. B* **1997**, *101*, 10807.
- (139) Newman, J. S. *Electrochemical Systems*, 2nd ed.; Prentice Hall: Englewood Cliffs, NJ, 1991.
- (140) Bard, A. J.; Faulkner, L. R. *Electrochemical Methods: Fundamentals and Applications*, 2nd ed.; John Wiley & Sons: New York, 2001.
- (141) Bockris, J. O'M.; Reddy, A. K. N. *Modern Electrochemistry*; Plenum Press: New York, 1973.
- (142) Perry, R. H.; Green, D. W. *Perry's Chemical Engineers' Handbook*, 7th ed.; McGraw-Hill: New York, 1997.
- (143) Latimer, W. *Oxidation Potentials*, 2nd ed.; Prentice-Hall: Englewood Cliffs, NJ, 1952.
- (144) Lewis, G.; Randall, M. *International Critical Tables*; McGraw-Hill: New York, 1930.
- (145) Vetter, K. J. *Electrochemical Kinetics*; Academic Press: New York, 1967.
- (146) Wang, J. X.; Brankovic, S. R.; Zhu, Y.; Hanson, J. C.; Adzic, R. R. *J. Electrochem. Soc.* **2003**, *150*, A1108.
- (147) Maruyama, J.; Inaba, M.; Katakura, K.; Ogumi, Z.; Takehara, Z. *J. Electronanal. Chem.* **1998**, *447*, 201.
- (148) Mello, R. M. Q.; Ticianelli, E. A. *Electrochim. Acta* **1997**, *42*, 1031.
- (149) Bird, R. B.; Stewart, W. E.; Lightfoot, E. N. *Transport Phenomena*, 2nd ed.; John Wiley & Sons: New York, 2002.
- (150) Appleby, A. J. *J. Electrochem. Soc.* **1970**, *117*, 328.
- (151) Kinoshita, K. *Electrochemical Oxygen Technology*; John Wiley & Sons: New York, 1992.
- (152) Beattie, P. D.; Basura, V. I.; Holdcroft, S. *J. Electronanal. Chem.* **1999**, *468*, 180.
- (153) Rho, Y. W.; Velev, O. A.; Srinivasan, S. *J. Electrochem. Soc.* **1994**, *141*, 2084.
- (154) Parthasarathy, A.; Dave, B.; Srinivasan, S.; Appleby, A. J.; Martin, C. R. *J. Electrochem. Soc.* **1992**, *139*, 1634.
- (155) Parthasarathy, A.; Srinivasan, S.; Appleby, A. J.; Martin, C. R. *J. Electronanal. Chem.* **1992**, *339*, 101.
- (156) Perez, J.; Gonzalez, E. R.; Ticianelli, E. A. *J. Electrochem. Soc.* **1998**, *145*, 2307.
- (157) Uribe, F. A.; Springer, T. E.; Gottesfeld, S. *J. Electrochem. Soc.* **1992**, *139*, 765.
- (158) Gasteiger, H. A.; Gu, W.; Makharia, R.; Mathias, M. F.; Sompalli, B. In *Handbook of Fuel Cells: Fundamentals, Technology, and Applications*; Vielstich, W., Lamm, A., Gasteiger, H. A., Eds.; John Wiley & Sons: New York, 2003; Vol. 3.
- (159) Sena, D. R.; Ticianelli, E. A.; Paganin, V. A.; Gonzalez, E. R. *J. Electronanal. Chem.* **1999**, *477*, 164.
- (160) Lee, S. J.; Mukerjee, S.; McBreen, J.; Rho, Y. W.; Kho, Y. T.; Lee, T. H. *Electrochim. Acta* **1998**, *43*, 3693.
- (161) Liebhafsky, H. A.; Cairns, E. J.; Grubb, W. T.; Niedrach, L. W. In *Fuel Cell Systems*; Young, G. J., Linden, H. R., Eds.; American Chemical Society: Washington, DC, 1965; Vol. 47.

- (162) Passalacqua, E.; Lufrano, F.; Squadrito, G.; Patti, A.; Giorgi, L. *Electrochim. Acta* **2001**, *46*, 799.
- (163) Squadrito, G.; Maggio, G.; Passalacqua, E.; Lufrano, F.; Patti, A. *J. Appl. Electrochem.* **1999**, *29*, 1449.
- (164) Newman, J. *Ind. Eng. Chem. Res.* **1995**, *34*, 3208.
- (165) Kreuer, K. D. *Chem. Rev.* **2004**, *104*, 4637.
- (166) Paddison, S. J.; Paul, R.; Zawodzinski, T. A. *J. Electrochem. Soc.* **2000**, *147*, 617.
- (167) Khalatur, P. G.; Talitskikh, S. K.; Khokhlov, A. R. *Macromol. Theory Simul.* **2002**, *11*, 566.
- (168) Krueger, J. J.; Simon, P. P.; Ploehn, H. J. *Macromolecules* **2002**, *35*, 5630.
- (169) Li, T.; Wlaschin, A.; Balbuena, P. B. *Ind. Eng. Chem. Res.* **2001**, *40*, 4789.
- (170) Paddison, S. J.; Paul, R.; Zawodzinski, T. A. *J. Chem. Phys.* **2001**, *115*, 7753.
- (171) Paul, R.; Paddison, S. J. *J. Chem. Phys.* **2001**, *115*, 7762.
- (172) Paddison, S. J. *J. New Mater. Electrochem. Syst.* **2001**, *4*, 197.
- (173) Vishnyakov, A.; Neimark, A. V. *J. Phys. Chem. B* **2001**, *105*, 7830.
- (174) Mologin, D. A.; Khalatur, P. G.; Kholhlov, A. R. *Macromol. Theory Simul.* **2002**, *11*, 587.
- (175) Spohr, E.; Commer, P.; Kornyshev, A. A. *J. Phys. Chem. B* **2002**, *106*, 10560.
- (176) Vishnyakov, A.; Neimark, A. V. *J. Phys. Chem. B* **2000**, *104*, 4471.
- (177) Vishnyakov, A.; Neimark, A. V. *J. Phys. Chem. B* **2001**, *105*, 9586.
- (178) Din, X. D.; Michaelides, E. E. *AIChE J.* **1998**, *44*, 35.
- (179) Commer, P.; Cherstvy, A. G.; Spohr, E.; Kornyshev, A. A. *Fuel Cells* **2002**, *2*, 127.
- (180) Jinnouchi, R.; Okazaki, K. *Microscale Thermophys. Eng.* **2003**, *7*, 15.
- (181) Yeo, S. C.; Eisenberg, J. *J. Appl. Polym. Sci.* **1977**, *21*, 875.
- (182) Hsu, W. Y.; Gierke, T. D. *J. Membr. Sci.* **1983**, *13*, 307.
- (183) Eisenberg, A. *Macromolecules* **1970**, *3*, 147.
- (184) Yeager, H. L.; Steck, A. J. *Electrochem. Soc.* **1981**, *128*, 1880.
- (185) Eisenberg, A. *Bull. Am. Phys. Soc.* **1969**, *14*, 382.
- (186) Dreyfus, B. *J. Polym. Sci., Part B: Polym. Phys.* **1983**, *21*, 2337.
- (187) Koter, S. *J. Membr. Sci.* **2000**, *166*, 127.
- (188) Datye, V. K.; Taylor, P. L.; Hopfinger, A. J. *Macromolecules* **1984**, *17*, 1704.
- (189) Mauritz, K. A.; Rogers, C. E. *Macromolecules* **1985**, *18*, 483.
- (190) Pintauro, P. N.; Verbrugge, M. W. *J. Membr. Sci.* **1989**, *44*, 197.
- (191) Uitto, O. D.; White, H. S.; Aoki, K. *Anal. Chem.* **2002**, *74*, 4577.
- (192) Guzmangarcia, A. G.; Pintauro, P. N.; Verbrugge, M. W.; Hill, R. F. *AIChE J.* **1990**, *36*, 1061.
- (193) Tandon, R.; Pintauro, P. N. *J. Membr. Sci.* **1997**, *136*, 207.
- (194) Wendt, R. P.; Klein, E.; Lynch, S. *J. Membr. Sci.* **1976**, *1*, 165.
- (195) Cwirko, E. H.; Carbonell, R. G. *J. Membr. Sci.* **1992**, *67*, 227.
- (196) Bontha, J. R.; Pintauro, P. N. *Chem. Eng. Sci.* **1994**, *49*, 3835.
- (197) Koter, S. *J. Membr. Sci.* **2002**, *206*, 201.
- (198) Narebska, A.; Koter, S.; Kujawski, W. *Desalination* **1984**, *51*, 3.
- (199) Yang, Y. H.; Pintauro, P. N. *AIChE J.* **2000**, *46*, 1177.
- (200) Pintauro, P. N.; Bennion, D. N. *Ind. Eng. Chem. Fundam.* **1984**, *23*, 234.
- (201) Capecci, S. W.; Pintauro, P. N.; Bennion, D. N. *J. Electrochem. Soc.* **1989**, *136*, 2876.
- (202) Schroeder, P. *Z. Phys. Chem.* **1903**, *45*, 57.
- (203) Mann, R. F.; Amphlett, J. C.; Hooper, M. A. I.; Jensen, H. M.; Peppley, B. A.; Roberge, P. R. *J. Power Sources* **2000**, *86*, 173.
- (204) Leddy, J.; Iverson, A. E.; Vanderborgh, N. E. In *Electrochemical and Thermal Modeling of Battery, Fuel Cell, and Photoenergy Conversion Systems*; Selman, J. R., Maru, H. C., Eds.; The Electrochemical Society Proceeding Series; Pennington, NJ, 1986; Vol. PV 86–12.
- (205) Einstein, A. *Ann. Phys.* **1905**, *17*, 549.
- (206) Nernst, W. *Z. Phys. Chem.* **1888**, *2*, 613.
- (207) Okada, T.; Xie, G.; Tanabe, Y. *J. Electronanal. Chem.* **1996**, *413*, 49.
- (208) Bennion, D. N. *Mass Transport of Binary Electrolyte Solutions in Membranes*; Water Resources Center Desalination Report No. 4; Department of Engineering, University of California—Los Angeles: 1966.
- (209) Pintauro, P. N.; Bennion, D. N. *Ind. Eng. Chem. Fundam.* **1984**, *23*, 230.
- (210) Auclair, B.; Nikonenko, V.; Larchet, C.; Metayer, M.; Dammak, L. *J. Membr. Sci.* **2002**, *195*, 89.
- (211) Koter, S.; Hamann, C. H. *J. Non-Equilib. Thermodyn.* **1990**, *15*, 315.
- (212) Meyers, J. P. Ph.D. Dissertation, University of California—Berkeley, 1998.
- (213) Verbrugge, M. W.; Hill, R. F. *J. Electrochem. Soc.* **1990**, *137*, 3770.
- (214) Verbrugge, M. W.; Hill, R. F. *J. Electrochem. Soc.* **1990**, *137*, 1131.
- (215) Schlogl, R. *Z. Phys. Chem.* **1955**, *3*, 73.
- (216) Mason, E. A.; Malinauskas, A. P. *Gas Transport in Porous Media: The Dusty-Gas Model*; Elsevier: Amsterdam, 1983.
- (217) Buchi, F. N.; Scherer, G. G. *J. Electrochem. Soc.* **2001**, *148*, A183.
- (218) Kreuer, K. D. *Solid State Ionics* **1997**, *97*, 1.
- (219) De La Rue, R. E.; Tobias, C. W. *J. Electrochem. Soc.* **1959**, *106*, 827.
- (220) Bruggeman, D. A. G. *Ann. Phys.* **1935**, *24*, 636.
- (221) Li, G.; Pickup, P. P. *J. Electrochem. Soc.* **2003**, *150*, C745.
- (222) Bernardi, D. M. Ph.D. Dissertation, University of California, 1986.
- (223) Dullien, F. A. L. *Porous Media: Fluid Transport and Pore Structure*, 2nd ed.; Academic Press: New York, 1992.
- (224) Knudsen, M. *The Kinetic Theory of Gases*; Methuen: London, 1934.
- (225) Rothfeld, L. B. *AIChE J.* **1963**, *9*, 19.
- (226) Weber, A. Z.; Newman, J. *Int. Commun. Heat Mass Transfer*, in press.
- (227) Passalacqua, E.; Squadrito, G.; Lufrano, F.; Patti, A.; Giorgi, L. *J. Appl. Electrochem.* **2001**, *31*, 449.
- (228) Tucker, M. C.; Odgaard, M.; Yde-Anderson, S.; Thomas, J. O. 203rd Meeting of the Electrochemical Society, Paris, 2003; Abstract 1235.
- (229) Jordan, L. R.; Shukla, A. K.; Behrsing, T.; Avery, N. R.; Muddle, B. C.; Forsyth, M. *J. Power Sources* **2000**, *86*, 250.
- (230) Jordan, L. R.; Shukla, A. K.; Behrsing, T.; Avery, N. R.; Muddle, B. C.; Forsyth, M. *J. Appl. Electrochem.* **2000**, *30*, 641.
- (231) Kong, C. S.; Kim, D.-Y.; Lee, H.-K.; Shul, Y.-G.; Lee, T.-H. *J. Power Sources* **2002**, *108*, 185.
- (232) Wilson, M. S. U.S. Patent 5,641,586, 1995.
- (233) Miller, C. T.; Christakos, G.; Imhoff, P. T.; McBride, J. F.; Pedit, J. A.; Trangenstein, J. A. *Adv. Water Resources* **1998**, *21*, 77.
- (234) Bear, J. *Dynamics of Fluids in Porous Media*; Dover Publications: New York, 1988.
- (235) Smith, W. O. *Physics* **1933**, *4*, 425.
- (236) Leverett, M. C. *Trans. Am. Inst. Min., Metall. Pet. Eng.* **1941**, *142*, 152.
- (237) Fischer, A.; Jindra, J.; Wendt, H. *J. Appl. Electrochem.* **1998**, *28*, 277.
- (238) Ticianelli, E. A.; Beery, J. G.; Srinivasan, S. *J. Appl. Electrochem.* **1991**, *21*, 597.
- (239) Cheng, X.; Yi, B.; Han, M.; Zhang, J.; Qiao, Y.; Yu, J. *J. Power Sources* **1999**, *79*, 75.
- (240) Uchida, M.; Aoyama, Y.; Eda, N.; Ohta, A. *J. Electrochem. Soc.* **1995**, *142*, 4143.
- (241) *Handbook of Fuel Cells: Fundamentals, Technology, and Applications, Vol. 2—Electrocatalysis*; Vielstich, W., Lamm, A., Gasteiger, H. A., Eds.; John Wiley & Sons: New York, 2003.
- (242) Mukerjee, S. *J. Appl. Electrochem.* **1990**, *20*, 537.
- (243) Markovic, N. M.; Schmidt, T. J.; Stamenkovic, V.; Ross, P. N. *Fuel Cells* **2001**, *1*, 105.
- (244) Vogel, W.; Lundquist, J.; Ross, P.; Stonehart, P. *Electrochim. Acta* **1975**, *20*, 79.
- (245) Zhang, J. X.; Thampan, T.; Datta, R. *J. Electrochem. Soc.* **2002**, *149*, A765.
- (246) Bellows, R. J.; MarucchiSoos, E. P.; Buckley, D. T. *Ind. Eng. Chem. Res.* **1996**, *35*, 1235.
- (247) Stonehar, P. *Electrochim. Acta* **1967**, *12*, 1185.
- (248) Bhatia, K. K.; Wang, C.-Y. *Electrochim. Acta* **2004**, *49*, 2333.
- (249) Grens, E. A.; Turner, R. M.; Katan, T. *Adv. Energy Convers.* **1964**, *4*, 109.
- (250) Chirkov, Y. G. *Elektrokhimiya* **1975**, *11*, 36.
- (251) Chirkov, Y. G. *Elektrokhimiya* **1972**, *7*, 1826.
- (252) Viitanen, M.; Lampinen, M. *J. Power Sources* **1990**, *32*, 207.
- (253) Grens, E. A. *Ind. Eng. Chem. Fundam.* **1966**, *5*, 542.
- (254) Yang, S. C.; Cutlip, M. B.; Stonehart, P. *Electrochim. Acta* **1990**, *35*, 869.
- (255) Yang, S. C.; Cutlip, M. B.; Stonehart, P. *Electrochim. Acta* **1989**, *34*, 703.
- (256) Vogel, W.; Bradford, A.; Lundquist, J. *Electrochim. Acta* **1972**, *17*, 1735.
- (257) Bjornbom, P. *Electrochim. Acta* **1987**, *32*, 115.
- (258) Srinivasan, S.; Hurwitz, H. D. *Electrochim. Acta* **1967**, *12*, 495.
- (259) Srinivasan, S.; Hurwitz, H. D.; Bockris, J. O'M. *J. Chem. Phys.* **1967**, *46*, 3108.
- (260) Bultel, Y.; Ozil, P.; Durand, R. *J. Appl. Electrochem.* **2000**, *30*, 1369.
- (261) Euler, J.; Nonnenmacher, W. *Electrochim. Acta* **1960**, *2*, 268.
- (262) Bockris, J. O'M.; Srinivasan, S. *Fuel Cells: Their Electrochemistry*; McGraw-Hill: New York, 1969.
- (263) DeVidts, P.; White, R. E. *J. Electrochem. Soc.* **1997**, *144*, 1343.
- (264) Gloaguen, F.; Andolfatto, F.; Durand, R.; Ozil, P. *J. Appl. Electrochem.* **1994**, *24*, 863.
- (265) Fogler, H. S. *Elements of Chemical Reaction Engineering*, 2nd ed.; Prentice Hall: Upper Saddle River, NJ, 1992.
- (266) Thiele, E. W. *Ind. Eng. Chem.* **1939**, *31*, 916.
- (267) Fuller, T. F.; Luczak, F. J.; Wheeler, D. J. *J. Electrochem. Soc.* **1995**, *142*, 1752.
- (268) Stonehart, P.; Ross, P. N. *Electrochim. Acta* **1976**, *21*, 441.
- (269) Maja, M.; Tosco, P.; Vanni, M. *J. Electrochem. Soc.* **2003**, *148*, A1368.
- (270) Qi, Z. G.; Kaufman, A. *J. Power Sources* **2002**, *109*, 38.

- (271) Wilson, M. S.; Valerio, J. A.; Gottesfeld, S. *Electrochim. Acta* **1995**, *40*, 355.
- (272) Janssen, G. J. M.; Overvelde, M. L. J. *J. Power Sources* **2001**, *101*, 117.
- (273) Patankar, S. *Numerical Heat Transfer and Fluid Flow*; Hemisphere Publishing Corporation: Bristol, PA, 1980.
- (274) Soares, G. E.; Kosanovich, K. A. *Ind. Eng. Chem. Res.* **1997**, *36*, 4264.
- (275) Duan, T.; Weidner, J. W.; White, R. E. *J. Power Sources* **2002**, *107*, 24.
- (276) Wang, C. Y. *Chem. Rev.* **2004**, *104*, 4727.
- (277) McCabe, W. L.; Smith, J. C.; Harriott, P. *Unit Operations of Chemical Engineering*, 5th ed.; McGraw-Hill, Inc.: New York, 1993.
- (278) Meyers, J. P.; Villwock, R. D.; Darling, R. M.; Newman, J. In *Advances in Mathematical Modeling and Simulation of Electrochemical Processes and Oxygen Depolarized Cathodes and Activated Cathodes for Chlor-Alkali Processes*; Van Zee, J. W., Fuller, T. F., Foller, P. C., Hine, F., Eds.; The Electrochemical Society Proceedings Series; Pennington, NJ, 1998; Vol. PV 98-10.
- (279) Kumar, A.; Reddy, R. G. *J. Power Sources* **2003**, *114*, 54.
- (280) Kumar, A.; Reddy, R. G. *J. Power Sources* **2003**, *113*, 11.
- (281) Baker, D. R.; Darling, R. M. *Int. J. Trans. Phenom.* **2001**, *3*, 177.
- (282) Hirschfelder, J. O.; Curtiss, C. F.; Bird, R. B. *Molecular Theory of Gases and Liquids*; John Wiley & Sons: New York, 1954.
- (283) Thomas, K. E.; Newman, J. *J. Electrochem. Soc.* **2003**, *150*, A176.
- (284) Newman, J.; Thomas-Alyea, K. E. *Electrochemical Systems*, 3rd ed.; John Wiley & Sons: New York, 2004.
- (285) Agar, J. N. In *Advances in Electrochemistry and Electrochemical Engineering*; Delahay, P., Ed.; John Wiley & Sons: New York, 1963; Vol. 3.
- (286) Rao, L.; Newman, J. *J. Electrochem. Soc.* **1997**, *144*, 2697.
- (287) Bernardi, D. M.; Pawlikowski, E.; Newman, J. *J. Electrochem. Soc.* **1985**, *132*, 5.
- (288) Amphlett, J. C.; Mann, R. F.; Peppley, B. A.; Roberge, P. R.; Rodrigues, A. *J. Power Sources* **1996**, *61*, 183.
- (289) Yerramalla, S.; Davari, A.; Feliachi, A.; Biswas, T. *J. Power Sources* **2003**, *124*, 104.
- (290) Zawodzinski, T. A.; Derouin, C. R.; Radzinski, S.; Sherman, R.; Smith, V. T.; Springer, T. E.; Gottesfeld, S. *J. Electrochem. Soc.* **1993**, *140*, 1041.
- (291) Nguyen, T. V.; Vanderborgh, N. E. *J. Membr. Sci.* **1998**, *143*, 235.
- (292) He, W. S.; Lin, G. Y.; Van Nguyen, T. *AIChE J.* **2003**, *49*, 3221.
- (293) Mosdale, R.; Gebel, G.; Pineri, M. *J. Membr. Sci.* **1996**, *118*, 269.
- (294) De Francesco, M.; Arato, E. *J. Power Sources* **2002**, *108*, 41.
- (295) Scott, K.; Argyropoulos, P.; Taama, W. M. *Chem. Eng. Res. Des.* **2000**, *78*, 881.
- (296) Maggio, G.; Recupero, V.; Mantegazza, C. *J. Power Sources* **1996**, *62*, 167.
- (297) Thirumalai, D.; White, R. E. *J. Electrochem. Soc.* **1997**, *144*, 1717.
- (298) Lee, J. H.; Lalk, T. R.; Appleby, A. J. *J. Power Sources* **1998**, *70*, 258.
- (299) Lee, J. H.; Lalk, T. R. *J. Power Sources* **1998**, *73*, 229.
- (300) Cownden, R.; Nahon, M.; Rosen, M. *Int. J. Hydrogen Energy* **2001**, *26*, 615.
- (301) Ahluwalia, R. K.; Doss, E. D.; Kumar, R. *J. Power Sources* **2003**, *117*, 45.
- (302) Paganin, V. A.; Oliveira, C. L. F.; Ticianelli, E. A.; Springer, T. E.; Gonzalez, E. R. *Electrochim. Acta* **1998**, *43*, 3761.
- (303) Brett, D. J. L.; Atkins, S.; Brandon, N. P.; Vesovic, V.; Vasileiadis, N.; Kucernak, A. *Electrochem. Solid-State Lett.* **2003**, *6*, A63.
- (304) Andraeus, B.; McEvoy, A. J.; Scherer, G. G. *Electrochim. Acta* **2002**, *47*, 2223.
- (305) Wagner, N. *J. Appl. Electrochem.* **2002**, *32*, 859.
- (306) Wang, X.; Hsing, I. M.; Leng, Y. J.; Yue, P. L. *Electrochim. Acta* **2001**, *46*, 4397.
- (307) Ciureanu, M.; Roberge, R. *J. Phys. Chem. B* **2001**, *105*, 3531.
- (308) Sorensen, T. S.; Kjelstrup, S. *J. Colloid Interface Sci.* **2002**, *248*, 355.
- (309) Bultel, Y.; Genies, L.; Antoine, O.; Ozil, P.; Durand, R. *J. Electronanal. Chem.* **2002**, *527*, 143.
- (310) Yuh, C. Y.; Selman, J. R. *AIChE J.* **1988**, *34*, 1949.
- (311) Raistrick, I. D. *Electrochim. Acta* **1990**, *35*, 1579.
- (312) Fritts, S. D.; Savinell, R. F. *J. Power Sources* **1989**, *28*, 301.
- (313) Guo, Q.; Cayetano, M.; Tsou, Y.-M.; De Castro, E. S.; White, R. E. *J. Electrochem. Soc.* **2003**, *150*, A1440.
- (314) Jaouen, F.; Lindbergh, G. *J. Electrochem. Soc.* **2003**, *150*, A1699.
- (315) Scott, K.; Argyropoulos, P.; Sundmacher, K. *J. Electronanal. Chem.* **1999**, *477*, 97.
- (316) Scott, K.; Taama, W. M.; Argyropoulos, P.; Sundmacher, K. *J. Power Sources* **1999**, *83*, 204.
- (317) Scott, K.; Taama, W. M.; Kramer, S.; Argyropoulos, P.; Sundmacher, K. *Electrochim. Acta* **1999**, *45*, 945.
- (318) Baxter, S. F.; Battaglia, V. S.; White, R. E. *J. Electrochem. Soc.* **1999**, *146*, 437.
- (319) Fan, J. R.; Hu, G. L.; Yao, J.; Cen, K. F. *Energy Fuels* **2002**, *16*, 1591.
- (320) Argyropoulos, P.; Scott, K.; Shukla, A. K.; Jackson, C. *Fuel Cells* **2002**, *2*, 78.
- (321) Argyropoulos, P.; Scott, K.; Taama, W. M. *Chem. Eng. J.* **1999**, *73*, 217.
- (322) Argyropoulos, P.; Scott, K.; Taama, W. M. *J. Power Sources* **1999**, *79*, 169.
- (323) Argyropoulos, P.; Scott, K.; Taama, W. M. *J. Appl. Electrochem.* **2000**, *30*, 899.
- (324) Birgersson, E.; Nordlund, J.; Ekstrom, H.; Vynnycky, M.; Lindbergh, G. *J. Electrochem. Soc.* **2003**, *150*, A1368.
- (325) Andrian, S. V.; Meusinger, J. *J. Power Sources* **2000**, *91*, 193.
- (326) Okada, T. *J. New Mater. Electrochem. Syst.* **2001**, *4*, 209.
- (327) Li, P. W.; Schaefer, L.; Wang, Q. M.; Zhang, T.; Chyu, M. K. *J. Power Sources* **2003**, *115*, 90.
- (328) Li, P. W.; Zhang, T.; Wang, Q. M.; Schaefer, L.; Chyu, M. K. *J. Power Sources* **2003**, *114*, 63.
- (329) Chu, D.; Jiang, R. Z. *J. Power Sources* **1999**, *83*, 128.
- (330) Darling, R. M.; Meyers, J. P. *J. Electrochem. Soc.* **2003**, *150*, A1523.
- (331) Wendt, H.; Brenscheidt, T.; Fischer, A. *Philos. Trans. R. Soc. London, Ser. A* **1996**, *354*, 1627.
- (332) Jiang, R. Z.; Chu, D. *J. Power Sources* **2001**, *92*, 193.
- (333) Fowler, M. W.; Mann, R. F.; Amphlett, J. C.; Peppley, B. A.; Roberge, P. R. *J. Power Sources* **2002**, *106*, 274.
- (334) Aragane, J.; Murahashi, T.; Odaka, T. *J. Electrochem. Soc.* **1988**, *135*, 844.
- (335) Honji, A.; Mori, T.; Tamura, K.; Hishinuma, Y. *J. Electrochem. Soc.* **1988**, *135*, 355.
- (336) Liu, W.; Ruth, K.; Rusch, G. *J. New Mater. Electrochem. Syst.* **2001**, *4*, 227.
- (337) Pozio, A.; Silva, R. F.; De Francesco, M.; Giorgi, L. *Electrochim. Acta* **2003**, *48*, 1543.
- (338) Kiwi, J.; Denisov, N.; Gak, Y.; Ovanesyan, N.; Buffat, P. A.; Suvorova, E.; Gostev, F.; Titov, A.; Sarkison, O.; Albers, P.; Nadtchenko, V. *Langmuir* **2002**, *18*, 9054.

CR020729L

What Are Batteries, Fuel Cells, and Supercapacitors?

Contents

1. Introduction	4245
1.1. Batteries versus Fuel Cells versus Electrochemical Capacitors	4245
1.2. Definitions	4247
1.3. Thermodynamics	4248
1.4. Kinetics	4249
1.5. Experimental Techniques	4250
1.6. Current Distribution and Porous Electrodes	4251
2. Batteries	4252
2.1. Introduction and Market Aspects	4252
2.2. Battery Operations	4253
2.3. Characteristics of Common Battery Systems	4254
2.4. Primary Batteries	4254
2.5. Rechargeable Batteries	4257
2.6. Selection Criteria for Commercial Battery Systems	4258
3. Fuel Cells	4259
3.1. Introduction and Market Aspects	4259
3.2. Fuel Cell Operation	4261
3.3. Characteristics of Various Types of Fuel Cells	4264
4. Electrochemical Capacitors (ECs)	4266
4.1. Introduction and Market Aspects	4266
4.2. Characteristics of the Electrical Double Layer	4267
4.3. EC Operation	4267
5. Summary	4269

1. Introduction

1.1. Batteries versus Fuel Cells versus Electrochemical Capacitors

Energy consumption/production that rely on the combustion of fossil fuels is forecast to have a severe future impact on world economics and ecology. Electrochemical energy production is under serious consideration as an alternative energy/power source, as long as this energy consumption is designed to be more sustainable and more environmentally friendly. Systems for electrochemical energy storage and conversion include batteries, fuel cells, and electrochemical capacitors (ECs). Although the energy storage and conversion mechanisms are different, there are “electrochemical similarities” of these three systems. Common features are that the energy-providing processes take place at the phase boundary of the electrode/electrolyte interface and that electron and ion transport are separated. Figures 1 and 2 show the basic operation mechanisms of the three systems. Note that batteries, fuel cells, and supercapacitors all consist of two electrodes in contact with an electrolyte solution. The requirements on electron and ion conduction in electrodes and the electrolyte are given in Figure 1 and are valid for all three systems.



Dr. Martin Winter is currently University Professor for Applied Inorganic Chemistry and Electrochemistry at the Institute for Chemistry and Technology of Inorganic Materials, Graz University of Technology (Austria). His fields of specialization are applied electrochemistry, chemical technology and solid state electrochemistry with special emphasis on the development and characterization of novel materials for rechargeable lithium batteries.



Dr. Ralph J. Brodd is President of Broddarp of Nevada. He has over 40 years of experience in the technology and market aspects of the electrochemical energy conversion business. His experience includes all major battery systems, fuel cells, and electrochemical capacitors. He is a Past President of the Electrochemical Society and was elected Honorary Member in 1987. He served as Vice President and National Secretary of the International Society of Electrochemistry as well as on technical advisory committees for the National Research Council, the International Electrochemic Commission, and NEMA and on program review committees for the Department of Energy and NASA.

In batteries and fuel cells, electrical energy is generated by conversion of chemical energy via redox reactions at the anode and cathode. As reactions at the anode usually take place at lower electrode potentials than at the cathode, the terms negative and positive electrode (indicated as minus and plus poles) are used. The more negative electrode is designated the anode, whereas the cathode is the more positive one. The difference between batteries and fuel cells is related to the locations of energy storage and conversion. Batteries are closed systems, with the anode and cathode being the charge-transfer medium and taking an active role in the redox

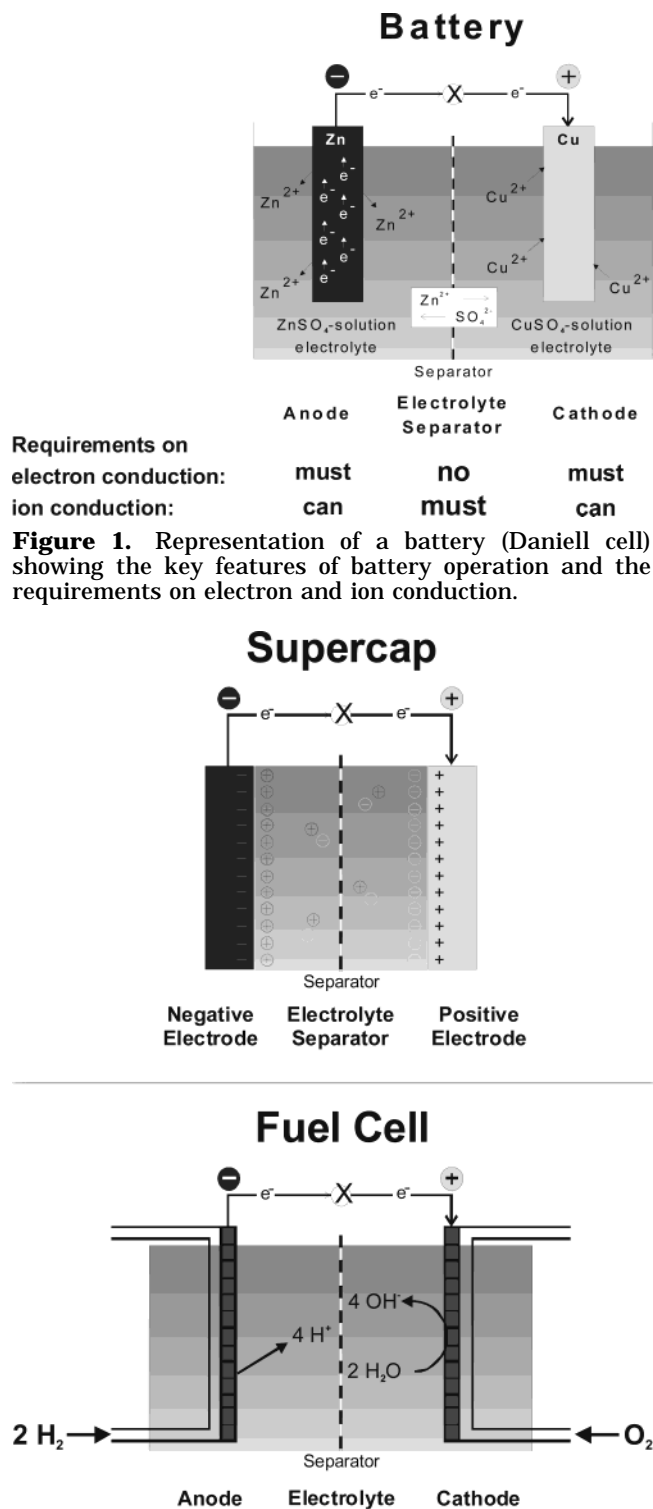


Figure 1. Representation of a battery (Daniell cell) showing the key features of battery operation and the requirements on electron and ion conduction.

reaction as “active masses”. In other words, energy storage and conversion occur in the same compartment. Fuel cells are open systems where the anode and cathode are just charge-transfer media and the active masses undergoing the redox reaction are delivered from outside the cell, either from the environment, for example, oxygen from air, or from

a tank, for example, fuels such as hydrogen and hydrocarbons. Energy storage (in the tank) and energy conversion (in the fuel cell) are thus locally separated.¹

In electrochemical capacitors (or supercapacitors), energy may not be delivered via redox reactions and, thus the use of the terms anode and cathode may not be appropriate but are in common usage. By orientation of electrolyte ions at the electrolyte/electrolyte interface, so-called electrical double layers (EDLs) are formed and released, which results in a parallel movement of electrons in the external wire, that is, in the energy-delivering process.

In comparison to supercapacitors and fuel cells, batteries have found by far the most application markets and have an established market position. Whereas supercapacitors have found niche markets as memory protection in several electronic devices, fuel cells are basically still in the development stage and are searching to find a “killer application” that allows their penetration into the market. Fuel cells established their usefulness in space applications with the advent of the Gemini and Apollo space programs. The most promising future markets for fuel cells and supercapacitors are in the same application sector as batteries. In other words, supercapacitor and fuel cell development aim to compete with, or even to replace, batteries in several application areas. Thus, fuel cells, which originally were intended to replace combustion engines and combustion power sources due to possible higher energy conversion efficiencies and lower environmental impacts, are now under development to replace batteries to power cellular telephones and notebook computers and for stationary energy storage. The motivation for fuel cells to enter the battery market is simple. Fuel cells cannot compete today with combustion engines and gas/steam turbines because of much higher costs, inferior power and energy performance, and insufficient durability and lifetime. With operation times of typically <3000 h and, at least to an order of magnitude, similar costs, batteries are less strong competitors for fuel cells.

The terms “specific energy” [expressed in watt-hours per kilogram (Wh/kg)] and “energy density” [in watt-hours per liter (Wh/L)] are used to compare the energy contents of a system, whereas the rate capability is expressed as “specific power” (in W/kg) and “power density” (in W/L). Alternatively, the attributes “gravimetric” (per kilogram) and “volumetric” (per liter) are used. To compare the power and energy capabilities, a representation known as the Ragone plot or diagram has been developed. A simplified Ragone plot (Figure 3) discloses that fuel cells can be considered to be high-energy systems, whereas supercapacitors are considered to be high-power systems. Batteries have intermediate power and energy characteristics. There is some overlap in energy and power of supercapacitors, or fuel cells, with batteries. Indeed, batteries with thin film

¹ Strictly speaking, a single electrochemical power system is denoted a cell or element, whereas a series or parallel connection of cells is named a battery. The literature is confusing, as the terms fuel CELL and BATTERY are used independent of the number of cells described.

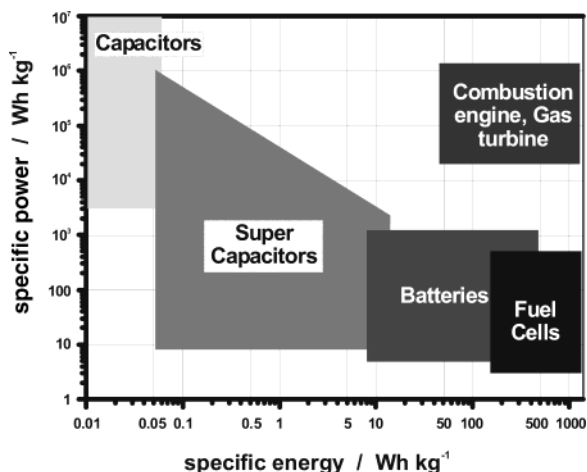


Figure 3. Simplified Ragone plot of the energy storage domains for the various electrochemical energy conversion systems compared to an internal combustion engine and turbines and conventional capacitors.

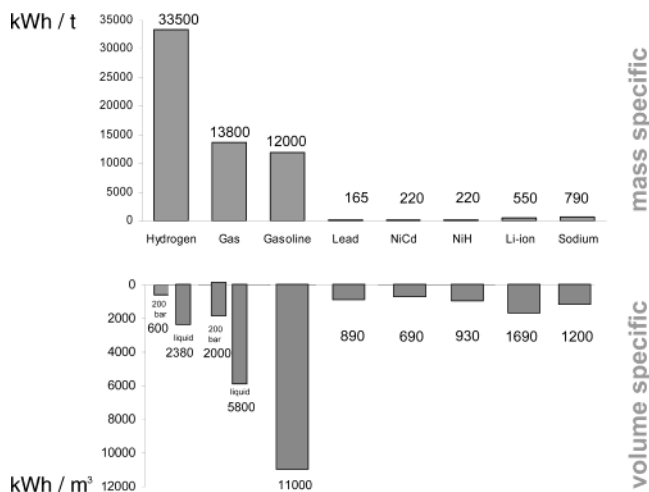


Figure 4. Theoretical specific energies [(kWh)/tonne] and energy densities [(kWh)/m³] of various rechargeable battery systems compared to fuels, such as gasoline, natural gas, and hydrogen.

electrodes exhibit power characteristics similar to those of supercapacitors. Moreover, there are also hybrids such as metal/air batteries (or, in other words, metal/air fuel cells), which contain a battery electrode (metal anode) and a fuel cell electrode (air cathode). Finally, Figure 3 also shows that no single electrochemical power source can match the characteristics of the internal combustion engine. High power and high energy (and thus a competitive behavior in comparison to combustion engines and turbines) can best be achieved when the available electrochemical power systems are combined. In such hybrid electrochemical power schemes, batteries and/or supercapacitors would provide high power and the fuel cells would deliver high energy.

Figure 4 shows the theoretical specific energies [(kWh)/t] and energy densities [(kWh)/m³] of various rechargeable battery systems in comparison to fuels, such as gasoline, natural gas, and hydrogen. The inferiority of batteries is evident. Figure 5, showing driving ranges of battery-powered cars in comparison to a car powered by a modern combustion engine, gives an impressive example of why fuel

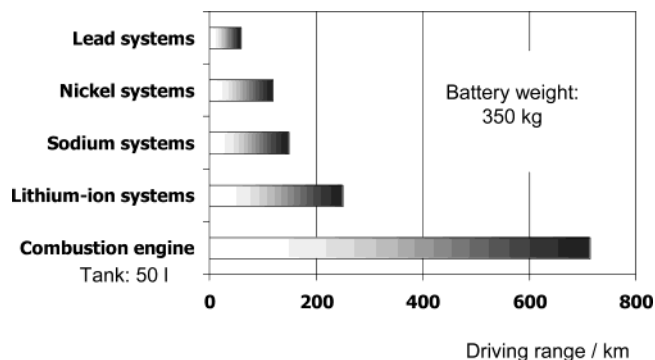


Figure 5. Comparison of the driving ranges for a vehicle powered by various battery systems or a gasoline-powered combustion engine.

cells, and not batteries, are considered for replacement of combustion engines. The theoretical values in Figure 4 are an indication for the maximum energy content of certain chemistries. However, the practical values differ and are significantly lower than the theoretical values. As a rule of thumb, the practical energy content of a rechargeable battery is 25% of its theoretical value, whereas a primary battery system can yield >50% of its theoretical value in delivered energy. In the future, fuel cells might be able to convert the used fuels into electrical energy with efficiencies of >70%. The difference between the theoretical and practical energy storage capabilities is related to several factors, including (1) inert parts of the system such as conductive diluents, current collectors, containers, etc., that are necessary for its operation, (2) internal resistances within the electrodes and electrolyte and between other cell/battery components, resulting in internal losses, and (3) limited utilization of the active masses, as, for example, parts of the fuel in a fuel cell leave the cell without reaction or as, for example, passivation of electrodes makes them (partially) electrochemically inactive. However, as batteries and fuel cells are not subject to the Carnot cycle limitations, they may operate with much higher efficiencies than combustion engines and related devices.

1.2. Definitions

The following definitions are used during the course of discussions on batteries, fuel cells, and electrochemical capacitors.

A *battery* is one or more electrically connected electrochemical cells having terminals/contacts to supply electrical energy.

A *primary battery* is a cell, or group of cells, for the generation of electrical energy intended to be used until exhausted and then discarded. Primary batteries are assembled in the charged state; discharge is the primary process during operation.

A *secondary battery* is a cell or group of cells for the generation of electrical energy in which the cell, after being discharged, may be restored to its original charged condition by an electric current flowing in the direction opposite to the flow of current when the cell was discharged. Other terms for this type of battery are rechargeable battery or accumulator. As secondary batteries are usually assembled in the

discharged state, they have to be charged first before they can undergo discharge in a secondary process.

A *specialty battery* is a primary battery that is in limited production for a specific end-use. In this paper specialty batteries will not be particularly addressed.

The *anode* is the negative electrode of a cell associated with oxidative chemical reactions that release electrons into the external circuit.

The *cathode* is the positive electrode of a cell associated with reductive chemical reactions that gain electrons from the external circuit.

Active mass is the material that generates electrical current by means of a chemical reaction within the battery.

An *electrolyte* is a material that provides pure ionic conductivity between the positive and negative electrodes of a cell.

A *separator* is a physical barrier between the positive and negative electrodes incorporated into most cell designs to prevent electrical shorting. The separator can be a gelled electrolyte or a microporous plastic film or other porous inert material filled with electrolyte. Separators must be permeable to the ions and inert in the battery environment.

A *fuel cell* is an electrochemical conversion device that has a continuous supply of fuel such as hydrogen, natural gas, or methanol and an oxidant such as oxygen, air, or hydrogen peroxide. It can have auxiliary parts to feed the device with reactants as well as a battery to supply energy for start-up.

An *electrochemical capacitor* is a device that stores electrical energy in the electrical double layer that forms at the interface between an electrolytic solution and an electronic conductor. The term applies to charged carbon-carbon systems as well as carbon-battery electrode and conducting polymer electrode combinations sometimes called ultracapacitors, supercapacitors, or hybrid capacitors.

Open-circuit voltage is the voltage across the terminals of a cell or battery when no external current flows. It is usually close to the thermodynamic voltage for the system.

Closed-circuit voltage is the voltage of a cell or battery when the battery is producing current into the external circuit.

Discharge is an operation in which a battery delivers electrical energy to an external load.

Charge is an operation in which the battery is restored to its original charged condition by reversal of the current flow.

Internal resistance or impedance is the resistance or impedance that a battery or cell offers to current flow.

The *Faraday constant*, F , is the amount of charge that transfers when one equivalent weight of active mass reacts, 96 485.3 C/g-equiv, 26.8015 Ah/g-equiv.

Thermal runaway is an event that occurs when the battery electrode's reaction with the electrolyte becomes self-sustaining and the reactions enter an autocatalytic mode. This situation is responsible for many safety incidents and fires associated with battery operations.

1.3. Thermodynamics

The energy storage and power characteristics of electrochemical energy conversion systems follow directly from the thermodynamic and kinetic formulations for chemical reactions as adapted to electrochemical reactions. First, the basic thermodynamic considerations are treated. The basic thermodynamic equations for a reversible electrochemical transformation are given as

$$\Delta G = \Delta H - T\Delta S \quad (1)$$

and

$$\Delta G^\circ = \Delta H^\circ - T\Delta S^\circ \quad (2)$$

where ΔG is the Gibbs free energy, or the energy of a reaction available (= free) for useful work, ΔH is the enthalpy, or the energy released by the reaction, ΔS is the entropy, and T is the absolute temperature, with $T\Delta S$ being the heat associated with the organization/disorganization of materials. The terms ΔG , ΔH , and ΔS are state functions and depend only on the identity of the materials and the initial and final states of the reaction. The degree symbol is used to indicate that the value of the function is for the material in the standard state at 25 °C and unit activity.

Because ΔG represents the net useful energy available from a given reaction, in electrical terms, the net available electrical energy from a reaction in a cell is given by

$$\Delta G = -nFE \quad (3)$$

and

$$\Delta G^\circ = -nFE^\circ \quad (4)$$

where n is the number of electrons transferred per mole of reactants, F is the Faraday constant, being equal to the charge of 1 equiv of electrons, and E is the voltage of the cell with the specific chemical reaction; in other words, E is the electromotive force (emf) of the cell reaction. The voltage of the cell is unique for each reaction couple. The amount of electricity produced, nF , is determined by the total amount of materials available for reaction and can be thought of as a capacity factor; the cell voltage can be considered to be an intensity factor. The usual thermodynamic calculations on the effect of temperature, pressure, etc., apply directly to electrochemical reactions. Spontaneous processes have a negative free energy and a positive emf with the reaction written in a reversible fashion, which goes in the forward direction. The van't Hoff isotherm identifies the free energy relationship for bulk chemical reactions as

$$\Delta G = \Delta G^\circ + RT \ln(A_P/A_R) \quad (5)$$

where R is the gas constant, T the absolute temperature, A_P the activity product of the products and A_R the activity product of the reactants. Combining eqs 4 and 5 with the van't Hoff isotherm, we have the

Nernst equation for electrochemical reactions:

$$E = E^\circ + (RT/nF) \ln(A_P/A_R) \quad (6)$$

Faraday's laws, as summarized in eq 7, give the direct relationship between the amount of reaction and the current flow. There are no known exceptions to Faraday's laws.

$$g = \frac{It(\text{MW})}{nF} \quad (7)$$

g is the grams of material transformed, I is the current flow (amps), t is the time of current flow (seconds, hours), MW is the molecular or atomic weight of the material being transformed, and n is the number of electrons in the reaction.

Assuming thermodynamic reversibility² of the cell reaction and with the help of eqs 1 and 3, we can obtain the reversible heat effect.

$$\Delta G = -nFE = \Delta H - T\Delta S \quad (8)$$

$$= \Delta H - nFT(dE/dT) \quad (9)$$

By measuring the cell voltage as a function of temperature, the various thermodynamic quantities for the materials in an electrode reaction can be determined experimentally. If dE/dT is positive, the cells will heat on charge and cool on discharge. Lead acid is an example of a negative dE/dT , where the cells cool on charge and heat on discharge. Ni–Cd is an example of a positive dE/dT , where the cells heat on charge and cool on discharge. Heating and cooling of the cell can proceed with heat exchange with the environment. In general, the entropic heat is negligibly small compared to the irreversible heat released, q , when a cell is in operation. Equation 10 describes total heat release, including the reversible thermodynamic heat release along with the irreversible joule heat from operation of the cell in an irreversible manner, during charge or discharge at finite current/rate. Irreversible behavior manifests itself as a departure from the equilibrium or thermodynamic voltage. In this situation, the heat, q , given off by the system is expressed by an equation in which E_T is the practical cell terminal voltage and E_{OCV} is the voltage of the cell on open circuit.

$$q = T\Delta S + I(E_{\text{OCV}} - E_T) \quad (10)$$

$$q = \text{heat given off by the system} \quad (11)$$

The total heat released during cell discharge is the sum of the thermodynamic entropy contribution plus the irreversible contribution. This heat is released inside the battery at the reaction site on the surface of the electrode structures. Heat release is not a

² A process is thermodynamically reversible when an infinitesimal reversal in a driving force causes the process to reverse its direction. Since all actual processes occur at finite rates, they cannot proceed with strict thermodynamic reversibility and thus additional nonreversible effects have to be regarded. In this case, under practical operation conditions, voltage losses at internal resistances in the cell (these kinetic effects are discussed below) lead to the irreversible heat production (so-called Joule heat) in addition to the thermodynamic reversible heat effect.

problem for low-rate applications; however, high-rate batteries must make provisions for heat dissipation. Failure to accommodate/dissipate heat properly can lead to thermal runaway and other catastrophic situations.

1.4. Kinetics

Thermodynamics describe reactions at equilibrium and the maximum energy release for a given reaction. Compared to the equilibrium voltage (= open circuit voltage, E_{OCV}), the voltage drops off (= "electrode polarization" or "overvoltage") when current is drawn from the battery because of kinetic limitations of reactions and of other processes must occur to produce current flow during operation. Electrochemical reaction kinetics follow the same general considerations as those for bulk chemical reactions. However, electrode kinetics differs from chemical kinetics in two important aspects: (1) the influence of the potential drop in the electrical double layer at an electrode interface as it directly affects the activated complex and (2) the fact that reactions at electrode interfaces proceed in a two-dimensional, not three-dimensional, manner. The detailed mechanism of battery electrode reactions often involves a series of physical, chemical, and electrochemical steps, including charge-transfer and charge transport reactions. The rates of these individual steps determine the kinetics of the electrode and, thus, of the cell/battery. Basically, three different kinetics effects for polarization have to be considered: (1) *activation* polarization is related to the kinetics of the electrochemical redox (or charge-transfer) reactions taking place at the electrode/electrolyte interfaces of anode and cathode; (2) *ohmic* polarization is interconnected to the resistance of individual cell components and to the resistance due to contact problems between the cell components; (3) *concentration* polarization is due to mass transport limitations during cell operation. The polarization, η , is given by

$$\eta = E_{\text{OCV}} - E_T \quad (12)$$

where E_{OCV} is the voltage of the cell at open circuit and E_T is the terminal cell voltage with current, I , flowing.

Activation polarization arises from kinetics hindrances of the charge-transfer reaction taking place at the electrode/electrolyte interface. This type of kinetics is best understood using the absolute reaction rate theory or the transition state theory. In these treatments, the path followed by the reaction proceeds by a route involving an activated complex, where the rate-limiting step is the dissociation of the activated complex. The rate, current flow, i ($I = iA$ and $I_0 = I_0/A$, where A is the electrode surface area), of a charge-transfer-controlled battery reaction can be given by the Butler–Volmer equation as

$$i = i_0 \exp(\alpha F\eta/RT) - \exp((1 - \alpha)F\eta)/RT \quad (13)$$

where the exchange current density, $i_0 = k_0FA$ is the exchange current density (k_0 is the reaction rate

constant for the electrode reaction, and A is the activity product of the reactants), η is the polarization or departure (overpotential) from equilibrium ($\eta = E_{\text{OCV}} - E_T$), and α is the transfer coefficient, which is best considered as the fraction of the change of overpotential that leads to a change in the rate constant for charge-transfer reaction. The exchange current density is directly related to the reaction rate constant, to the activities of reactants and products, and to the potential drop across the double layer. Reactions with larger i_0 are more reversible and have lower polarization for a given current flow. Electrode reactions having high exchange currents (i_0 in the range of 10^{-2} A/cm²) at room temperature are favored for use in battery applications. The buildup and decay of the activation polarization are fast and can be identified by the voltage change on current interruption in a time frame of 10^{-2} – 10^{-4} s.

The activation polarization follows the Tafel equation derived from eq 13

$$\eta = a - b \log(II_0) \quad (14)$$

where a and b are constants.

Ohmic polarization arises from the resistance of the electrolyte, the conductive diluent, and materials of construction of the electrodes, current collectors, terminals, and contact between particles of the active mass and conductive diluent or from a resistive film on the surface of the electrode. Ohmic polarization appears and disappears instantaneously ($\leq 10^{-6}$ s) when current flows and ceases. Under the effect of ohmic resistance, R , there is a linear Ohm's Law relationship between I and η .

$$\eta = IR \quad (15)$$

As the redox reactions proceed, the availability of the active species at the electrode/electrolyte interface changes. Concentration polarization arises from limited mass transport capabilities, for example, limited diffusion of active species to and from the electrode surface to replace the reacted material to sustain the reaction. Diffusion limitations are relatively slow, and the buildup and decay take $\geq 10^{-2}$ s to appear. For limited diffusion the electrolyte solution, the concentration polarization, can be expressed as

$$\eta = (RT/n) \ln(C/C_0) \quad (16)$$

where C is the concentration at the electrode surface and C_0 is the concentration in the bulk of the solution. The movement or transport of reactants from the bulk solution to the reaction site at the electrode interface and vice versa is a common feature of all electrode reactions. Most battery electrodes are porous structures in which an interconnected matrix of small solid particles, consisting of both nonconductive and electronically conductive materials, is filled with electrolyte. Porous electrode structures are used to extend the available surface area and lower the current density for more efficient operation.

1.5. Experimental Techniques

In practical batteries and fuel cells, the influence of the current rate on the cell voltage is controlled

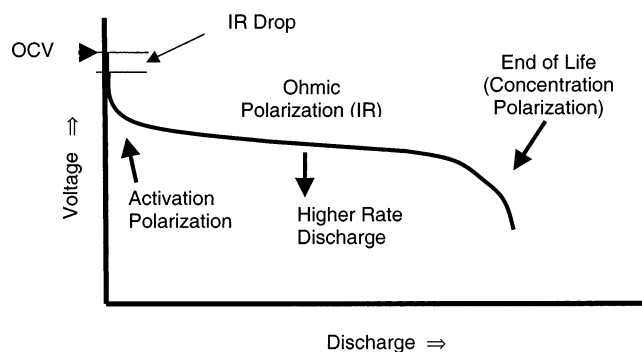


Figure 6. Typical discharge curve of a battery, showing the influence of the various types of polarization.

by all three types of polarization. A variety of experimental techniques are used to study electrochemical and battery reactions. The most common are the direct measurement of the instantaneous current–voltage characteristics on discharge curve shown in Figure 6. This curve can be used to determine the cell capacity, the effect of the discharge–charge rate, and temperature and information on the state of health of the battery.

The impedance behavior of a battery is another common technique that can reveal a significant amount of information about battery operation characteristics. The impedance of an electrode or battery is given by

$$Z = R + j\omega X \quad (17)$$

where $X = \omega L - 1/(\omega C)$, $j = \sqrt{-1}$, and ω is the angular frequency ($2\pi f$); L is the inductance, and C is the capacitance. A schematic of a battery circuit and the corresponding Argand diagram, illustrating the behavior of the simple electrode processes, are shown in Figure 7a. Activation processes exhibit a semicircular behavior with frequency that is characteristic of relaxation processes; concentration processes exhibit a 45° behavior characteristic of diffusion processes often referred to as Warburg behavior; ohmic components are independent of frequency.

Each electrode reaction has a distinctive, characteristic impedance signature. A schematic of a battery circuit and the corresponding Argand diagram, illustrating the behavior of the simple processes, are shown in Figure 7b. In ideal behavior, activation processes exhibit a semicircular behavior with frequency that is characteristic of relaxation processes; concentration processes exhibit a 45° behavior characteristic of diffusion processes, and ohmic polarizations have no capacitive character and are independent of frequency. The frequency of the maximum, f_m , of the semicircle gives the relaxation time, where $\tau = 1/f_m = RC$. Here R is related to the exchange current for the reaction and C is called the polarization capacitance, C_p . Typically, the C_p is of the order of 200 $\mu\text{F}/\text{cm}^2$, ~ 10 times larger than the capacitance of the EDL. Some electrochemical capacitors take advantage of this capacitance to improve their performance of the supercapacitors. Battery electrodes have large surface areas and, therefore, exhibit large

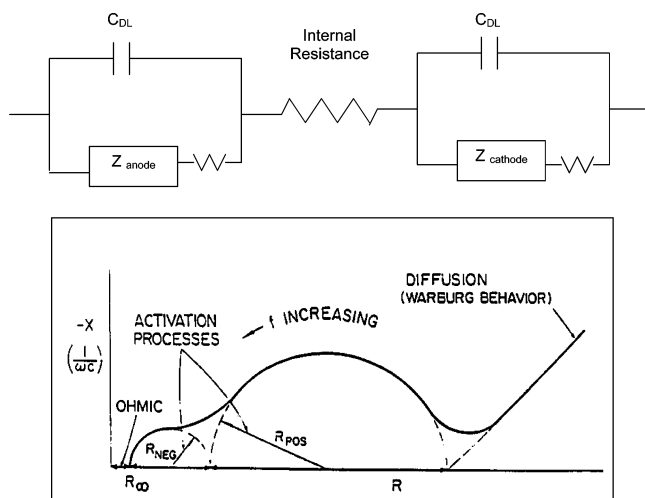


Figure 7. (A, top) Simple battery circuit diagram, where C_{DL} represents the capacitance of the electrical double layer at the electrode–solution interface (cf. discussion of supercapacitors below), W depicts the Warburg impedance for diffusion processes, R_i is the internal resistance, and Z_{anode} and $Z_{cathode}$ are the impedances of the electrode reactions. These are sometimes represented as a series resistance capacitance network with values derived from the Argand diagram. This reaction capacitance can be 10 times the size of the double-layer capacitance. The reaction resistance component of Z is related to the exchange current for the kinetics of the reaction. (B, bottom) Corresponding Argand diagram of the behavior of impedance with frequency, f , for an idealized battery system, where the characteristic behaviors of ohmic, activation, and diffusion or concentration polarizations are depicted.

capacitances. It is common for cells to have a capacitance of farads and a resistance of milliohms.

The experimental techniques described above of charge–discharge and impedance are nondestructive. “Tear-down” analysis or disassembly of spent cells and an examination of the various components using experimental techniques such as Raman microscopy, atomic force microscopy, NMR spectroscopy, transmission electron microscopy, XAS, and the like can be carried out on materials-spent battery electrodes to better understand the phenomena that lead to degradation during use. These techniques provide diagnostic techniques that identify materials properties and materials interactions that limit lifetime, performance, and thermal stability. The accelerated rate calorimeter finds use in identifying safety-related situations that lead to thermal runaway and destruction of the battery.

1.6. Current Distribution and Porous Electrodes

Most practical electrodes are a complex composite of powders composed of particles of the active material, a conductive diluent (usually carbon or metal powder), and a polymer binder to hold the mix together and bond the mix to a conductive current collector. Typically, a composite battery electrode has ~30% porosity with a complex surface extending throughout the volume of the porous electrode. This yields a much greater surface area for reaction than the geometric area and lowers polarization. The pores of the electrode structures are filled with electrolyte.

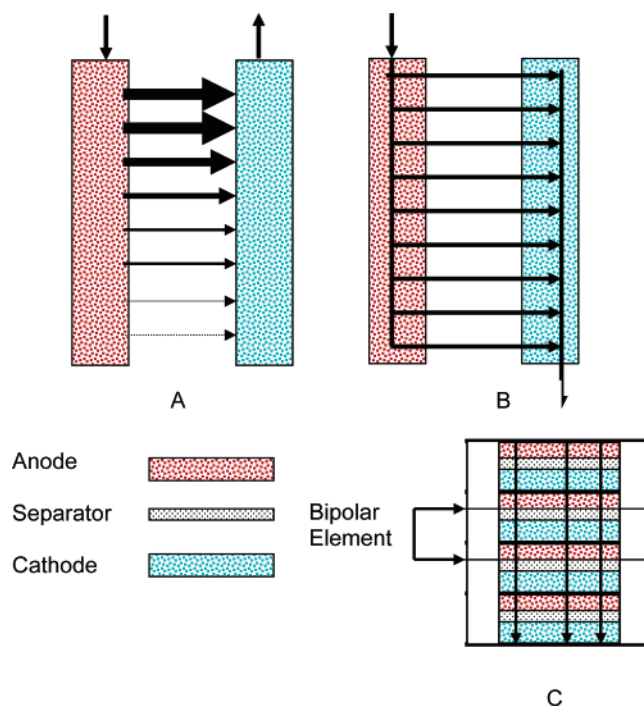


Figure 8. Primary current distribution on the front surface of the electrodes based on Kirkhof’s law calculation for three different cell constructions: (A) Both connections to the cell are at the top. The higher resistance path at the bottom sections of the electrode reduces the current flow and results in a nonuniform current distribution. (B) All paths have equal resistance, and a uniform current distribution results. (C) The bipolar construction has equal resistance from one end to the other.

Although the matrix may have a well-defined planar surface, there is a complex reaction surface extending throughout the volume of the porous electrode, and the effective active surface may be many times the geometric surface area. Ideally, when a battery produces current, the sites of current production extend uniformly throughout the electrode structure. A nonuniform current distribution introduces an inefficiency and lowers the expected performance from a battery system. In some cases the negative electrode is a metallic element, such as zinc or lithium metal, of sufficient conductivity to require only minimal supporting conductive structures.

Two types of current distribution, primary and secondary, can be distinguished. The primary distribution is controlled by cell geometry. The placing of the current collectors strongly influences primary current distribution on the geometric surface area of the electrodes. The monopolar construction is most common. The differences in current distribution for top connections and opposite end current collection are shown in Figure 8A,B. With opposite end connections the current distribution is more uniform and results in a more efficient use of the active material. The bipolar construction depicted in Figure 8C gives uniform current distribution wherein the anode terminal or collector of one cell serves as the current collector and cathode of the next cell in pile configuration.

Secondary current distribution is related to current production sites inside the porous electrode itself. The

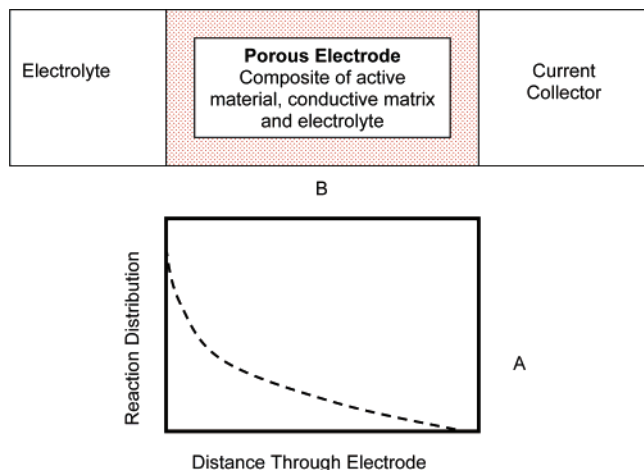


Figure 9. Schematic porous electrode structure: (A) Electrons from the external circuit flow in the current collector which has contact to the conductive matrix in the electrode structure. The redox reaction at the electrode produces electrons that enter the external circuit and flow through the load to the cathode, where the reduction reaction at the cathode accepts the electron from the external circuit and the reduction reaction. The ions in the electrolyte carry the current through the device. (B) The reaction distribution in the porous electrode is shown for the case where the conductivity of the electrode matrix is higher than the conductivity of the electrolyte.

incorporation of porous electrode structures increases the surface area and shortens diffusion path lengths to the reaction site. Current-producing reactions can penetrate into a porous electrode structure to considerable depth below the surface of the electrodes as noted in Figure 9. The location of the reaction site inside a porous electrode is strongly dependent on the characteristics of the electrode structure and reactions themselves. The key parameters include the conductivity of the electrode matrix, electrolyte conductivity, the exchange current, the diffusion characteristics of reactants and products, and the total current flow. In addition, the porosity, pore size, and tortuosity of the electrode play a role. The effectiveness of a porous electrode can be estimated from the active surface area, S , in cm^2/cm^3 , and the penetration depth L_p of the reaction process into the porous electrode. Factors that influence the secondary current distribution are the conductivity of the electrolyte and electrode matrix, the exchange current of the reactions, and the thickness of the porous layer. Sophisticated mathematical models to describe and predict porous electrode performance of practical systems have been developed. These formulations based on models of primary and secondary battery systems permit rapid optimization in the design of new battery configurations. The high-rate performance of the present SLI automotive batteries has evolved directly from coupling current collector designs with the porous electrode compositions identified from modeling studies.

Modeling has become an important tool in developing new battery technology as well as for improving the performance of existing commercial systems. Models based on engineering principles of current distribution and fundamental electrochemical reaction parameters can predict the behavior of porous

electrode structures from the older lead acid automotive technology to the newest lithium ion (Li ion) technology.

2. Batteries

2.1. Introduction and Market Aspects

Batteries are self-contained units that store chemical energy and, on demand, convert it directly into electrical energy to power a variety of applications. Batteries are divided into three general classes: primary batteries that are discharged once and discarded; secondary, rechargeable batteries that can be discharged and then restored to their original condition by reversing the current flow through the cell; and specialty batteries that are designed to fulfill a specific purpose. The latter are mainly military and medical batteries that do not find wide commercial use for various reasons of cost, environmental issues, and limited market application. They generally do not require time to start-up. At low drains, up to 95% of the energy is available to do useful work.

advantages	disadvantages
<ul style="list-style-type: none"> operate over a wide temperature range choice of chemical system and voltage operate in any orientation do not require pumps, filters, etc. variable in size commonality of cell sizes, worldwide can deliver high current pulses can choose best battery for a specific purpose (portable, mobile, and stationary applications) 	<ul style="list-style-type: none"> low energy content compared to gasoline and other fuels expensive compared to coal and gasoline no single general purpose system

Success in the battery market depends largely on four factors, noted in Figure 10. The market for batteries in Table 1 is directly related to the applications they serve, such as automobiles, cellular phones, notebook computers, and other portable electronic devices. The growth in any particular segment follows closely the introduction of new devices powered by batteries. The introduction of new materials with higher performance parameters gives the various designers freedom to incorporate new functionality in present products or to create new products to

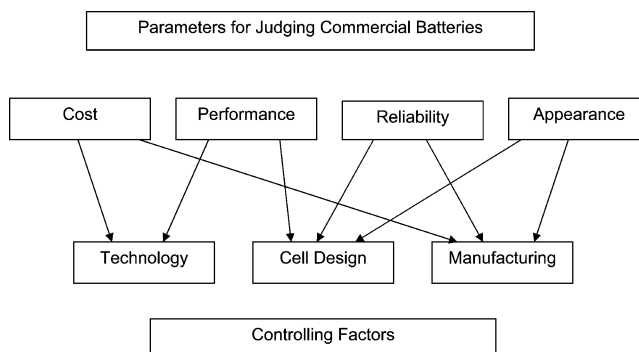


Figure 10. How batteries are judged by users and the factors that control these criteria.

Table 1. Estimated Battery Market in 2003 (\$ Millions of Dollars)

system	market size
primary	
carbon–zinc	6500
alkaline	10000
lithium, military, medical, etc.	3400
subtotal	19900
secondary	
lead acid	18400
small sealed rechargeable cells	
lithium ion	3500
nickel metal hydride	1800
nickel cadmium	1500
other ^a	3100
subtotal	28300
total battery market	48200

^a Large vented and sealed Ni–Cd, Ni–Fe, Ag–Zn, etc.

expand the market scope. Batteries for notebook computers have experienced double-digit growth, whereas the automobile SLI market segment has grown with the gross national product. Batteries can range in size from aspirin tablet (and even smaller) with a few tens of mAh, for in-the-ear hearing aids, to a building with 40 MWh for energy storage and emergency power.

2.2. Battery Operations

Figure 11 depicts the basic elements of a battery. Figure 12 illustrates the operation of a battery, showing the energy levels at the anode (negative) and cathode (positive) poles and the electrolyte expressed in electronvolts. The negative electrode is a good reducing agent (electron donor) such as lithium, zinc, or lead. The positive electrode is an electron acceptor such as lithium cobalt oxide, manganese dioxide, or lead oxide. The electrolyte is a pure ionic conductor that physically separates the anode from the cathode.

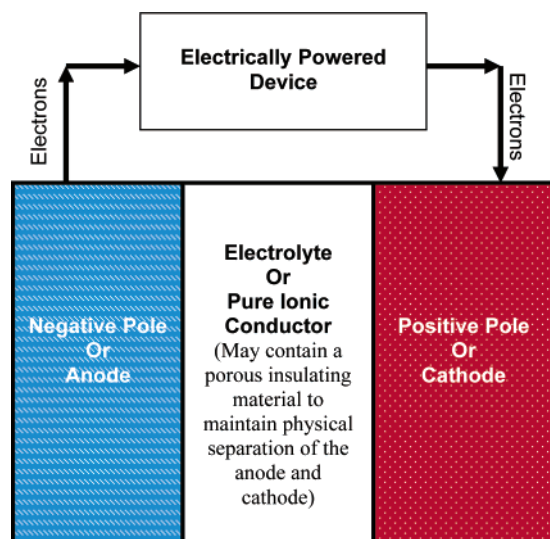


Figure 11. Block diagram of a cell or battery powering a device. If a battery is recharged, the load is replaced with an energy source that imposes a reverse voltage that is larger than the battery voltage and the flow of electrons is reversed.

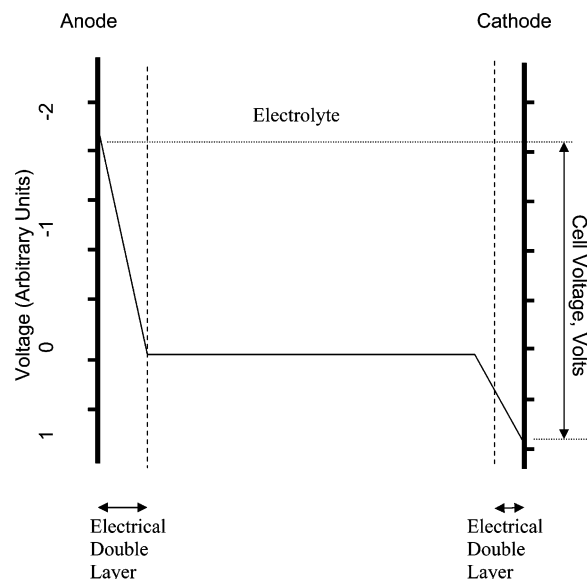


Figure 12. Voltage levels in the various sections of the unit cell of a battery, fuel cell, or electrochemical capacitor. The structure and composition of the electrical double layer differ at the anode and cathode.

In practice, a porous electrically insulating material containing the electrolyte is often placed between the anode and cathode to prevent the anode from directly contacting the cathode. Should the anode and cathode physically touch, the battery will be shorted and its full energy released as heat inside the battery. Electrical conduction in electrolytic solutions follows Ohm's law: $E = IR$.

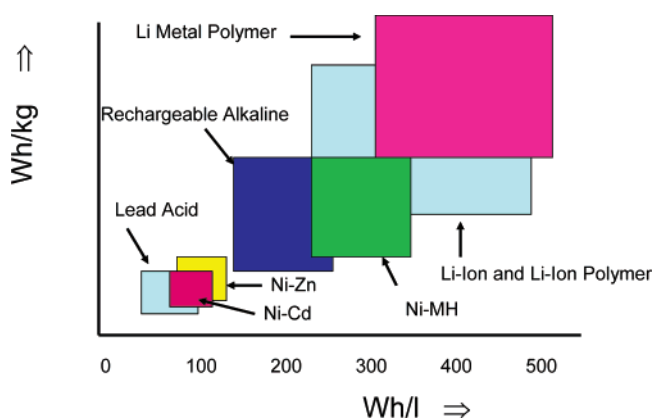
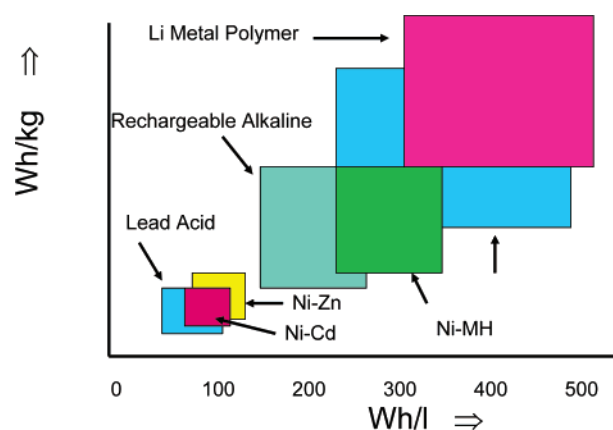
Battery electrolytes are usually liquid solvent-based and can be subdivided into aqueous, nonaqueous, and solid electrolytes. Aqueous electrolytes are generally salts of strong acids and bases and are completely dissociated in solution into positive and negative ions. The electrolyte provides an ionic conduction path as well as a physical separation of the positive and negative electrodes needed for electrochemical cell operation. Each electrolyte is stable only within certain voltage ranges. Exceeding the electrochemical stability window results in its decomposition. The voltage stability range depends on the electrolyte composition and its purity level. In aqueous systems, conductivities of the order of 1 S/cm are common. The high conductivity of aqueous solvent-based electrolytes is due to their dielectric constants, which favor stable ionic species, and the high solvating power, which favors formation of hydrogen bridge bonds and allows the unique Grotthuss conductivity mechanism for protons. Thermodynamically, aqueous electrolytes show an electrochemical stability window of 1.23 V. Kinetic effects may expand the stability limit to ~ 2 V.

In the nonaqueous organic solvent-based systems used for lithium batteries, the conductivities are of the order of 10^{-2} – 10^{-3} S/cm⁻¹. Compared to water, most organic solvents have a lower solvating power and a lower dielectric constant. This favors ion pair formation, even at low salt concentration. Ion pair formation lowers the conductivity as the ions are no longer free and bound to each other. Organic electrolytes show lower conductivities and much higher

Table 2. Common Commercial Battery Systems

common name	nominal voltage	anode	cathode	electrolyte
primary				
Leclanché (carbon–zinc)	1.5	zinc foil	MnO ₂ (natural)	aq ZnCl ₂ –NH ₄ Cl
zinc chloride (carbon–zinc)	1.5	zinc foil	electrolytic MnO ₂	aq ZnCl ₂
alkaline	1.5	zinc powder	electrolytic MnO ₂	aq KOH
zinc–air	1.2	zinc powder	carbon (air)	aq KOH
silver–zinc	1.6	zinc powder	Ag ₂ O	aq KOH
lithium–manganese dioxide	3.0	lithium foil	treated MnO ₂	LiCF ₃ SO ₃ or LiClO ₄ ^a
lithium–carbon monofluoride	3.0	lithium foil	CFx	LiCF ₃ SO ₃ or LiClO ₄ ^a
lithium–iron sulfide	1.6	lithium foil	FeS ₂	LiCF ₃ SO ₃ and/or LiClO ₄ ^a
rechargeable				
lead acid	2.0	lead	PbO ₂	aq H ₂ SO ₄
nickel–cadmium	1.2	cadmium	NiOOH	aq KOH
nickel–metal hydride	1.2	MH	NiOOH	aq KOH
lithium ion	4.0	Li(C)	LiCoO ₂	LiPF ₆ in nonaqueous solvents ^a
specialty				
nickel–hydrogen	1.2	H ₂ (Pt)	NiOOH	aq KOH
lithium–iodine	2.7	Li	I ₂	LiI
lithium–silver–vanadium oxide	3.2	Li	Ag ₂ V ₄ O ₁₁	LiAsF ₆ ^a
lithium–sulfur dioxide	2.8	Li	SO ₂ (C)	SO ₂ –LiBr
lithium–thionyl chloride	3.6	Li	SOCl ₂ (C)	SOCl ₂ –LiAlCl ₄
lithium–iron sulfide (thermal)	1.6	Li	FeS ₂	LiCl–LiBr–LiF
magnesium–silver chloride	1.6	Mg	AgCl	seawater

^a In nonaqueous solvents. Exact composition depends on the manufacturer, usually propylene carbonate–dimethyl ether for primary lithium batteries and ethylene carbonate with linear organic carbonates such as dimethyl carbonate, diethyl carbonate, and ethylmethyl carbonate for lithium ion cells.

**Figure 13.** Energy storage capability of common commercial primary battery systems.**Figure 14.** Energy storage capability of common rechargeable battery systems.

viscosities than aqueous electrolytes. Organic solvent-based electrolytes (again with the help of kinetics) are limited to ~ 4.6 V. Exceeding the voltage limit in the organic electrolytes results in polymerization or decomposition of the solvent system. Solid electrolyte batteries have found limited use as the power source for heart pacemakers and for use in military applications. The basic principles described above apply to fuel cells and electrochemical capacitors as well as to batteries.

2.3. Characteristics of Common Battery Systems

A list of common commercial systems is found in Table 2. A graphical representation of the energy storage capability of common types of primary and secondary batteries is shown in Figures 13 and 14. It is beyond the scope of this paper to discuss all systems in detail. Instead, we want to review the most common electrode mechanisms for discharge and charge depicted in Figure 15.

2.4. Primary Batteries

Figure 15A shows the discharge reaction of a CuS electrode in a Li–CuS cell. During the cell reaction, Cu is displaced by Li and segregates into a distinct solid phase in the cathode. The products of this displacement type of reaction, Li₂S and Cu, are stable, and the reaction cannot be easily reversed. Hence, the electrode reactions cannot be recharged and the cell is considered to be a primary cell, as the discharge reaction is not reversible. The Li electrode in Figure 15B is discharged by oxidation. The formed Li⁺ cation is going into solution. The reaction is reversible by redeposition of the lithium. However, like many other metals in batteries, the redeposition of the Li is not smooth, but rough, mossy, and dendritic, which may result in serious safety problems. This is in contrast to the situation with a lead electrode in Figure 15C, which shows a similar solution electrode. Here, the formed Pb²⁺ cation is only slightly soluble in sulfuric acid solution, and PbSO₄ precipitates at the reaction site on the elec-

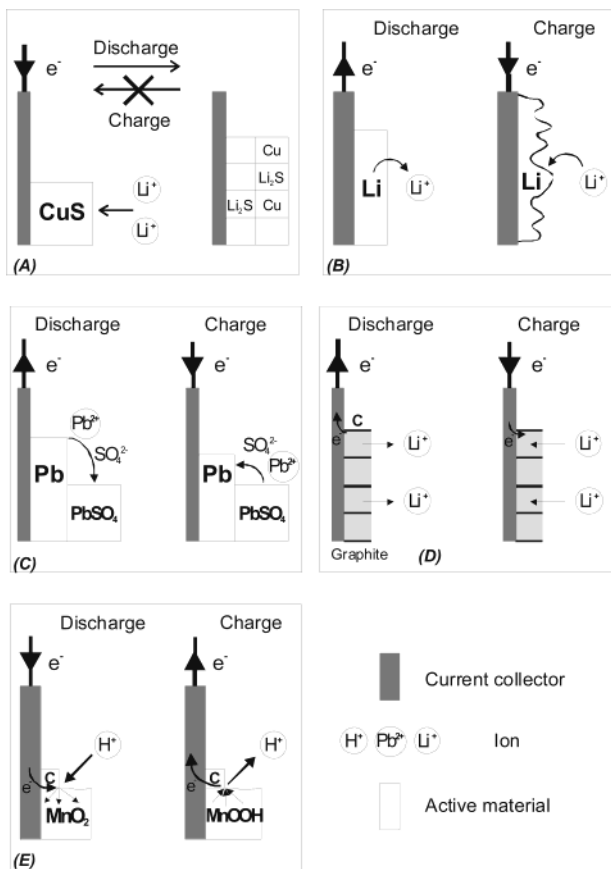


Figure 15. Schematics showing various discharge and charge mechanisms of battery electrodes, which serve as examples of the battery electrode charge/discharge mechanisms discussed in the text.

trode surface. This solution–precipitation mechanism is also working during the charge reaction, when PbSO₄ dissolves and is retransformed into metallic Pb. Figure 15D shows a typical electrochemical insertion reaction. The term “electrochemical insertion” refers to a solid-state redox reaction involving electrochemical charge transfer, coupled with insertion of mobile guest ions (in this case Li⁺ cations) from an electrolyte into the structure of a solid host, which is a mixed, that is, electronic and ionic, conductor (in this case graphite). Unlike displacement type electrodes (Figure 15A) and solution type electrodes (Figure 15B), the insertion electrodes (Figure 15D) have the capability for high reversibility, due to a beneficial combination of structure and shape stability. Many secondary batteries rely on insertion electrodes for the anode and cathode. A prerequisite for a good insertion electrode is electronic and ionic conductivity. However, in those materials with poor electronic conductivity, such as MnO₂, good battery operation is possible. In this case, highly conductive additives such as carbon are incorporated in the electrode matrix, as in Figure 15E. The utilization of the MnO₂ starts at the surface, which is in contact with the conductive additive and continues from this site throughout the bulk of the MnO₂ particle. Most electrodes in batteries follow one of the basic mechanisms discussed in Figure 15.

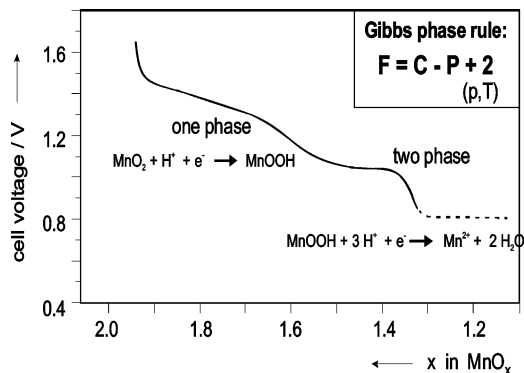


Figure 16. Two-step discharge curve of a MnO₂ electrode in aqueous solution showing the influence of one- and two-phase discharge reaction mechanisms on the shape of the discharge curve. The different shapes of the discharge curves can be explained with the help of the Gibbs phase rule.

Zinc manganese batteries consist of MnO₂, a proton insertion cathode (cf. Figure 15E), and a Zn anode of the solution type. Depending on the pH of the electrolyte solution, the Zn²⁺ cations dissolve in the electrolyte (similar to the mechanism shown in Figure 15B) or precipitate as Zn(OH)₂ (cf. mechanism in Figure 15C).

The discharge reaction of the MnO₂ electrode proceeds in two one-electron reduction steps as shown in the discharge curve (Figure 16). Starting at cell voltages of 1.5 V, a coupled one-electron transfer and proton insertion reaction takes place. The transformation of MnO₂ into MnOOH is a one-phase reaction. Further reduction leads to a phase change as the solid MnOOH turns into Mn²⁺ soluble in the solution, that is, a two-phase reaction. This is consistent with the Gibbs phase rule that predicts the shape of the discharge curve for one- and two-phase reactions (Figure 16). When the number of phases, P , is equal to the number of components, C , taking part in the reaction as in the case of a two-phase reaction, the number of degrees of freedom \mathcal{F} (= number of thermodynamic parameters that have to be specified to define the system) is 2. If the values of two parameters, usually pressure, p , and temperature, T , are specified, there is no degree of freedom left and other parameters of the system such as voltage have to be constant. Hence, the cell voltage stays constant for a two-phase discharge reaction. If there is a degree of freedom left, as in the case of a one-phase reaction, the cell voltage can be a variable and changes (slopes-off) during discharge.

Zinc–manganese batteries dominate the primary battery market segment. Leclanché invented the original carbon–zinc cell in 1860. He used a natural manganese dioxide–carbon black core cathode with aqueous zinc chloride–ammonium chloride electrolyte, contained in a zinc can. An alternative version employs a zinc chloride electrolyte and a synthetic electrolytic manganese dioxide and has better performance than the original Leclanché cell. The carbon–zinc with zinc chloride electrolyte gives about the same performance, on lower radio-type drains, as the alkaline cell and is strong in the Japanese and European markets. The carbon–zinc cell still finds

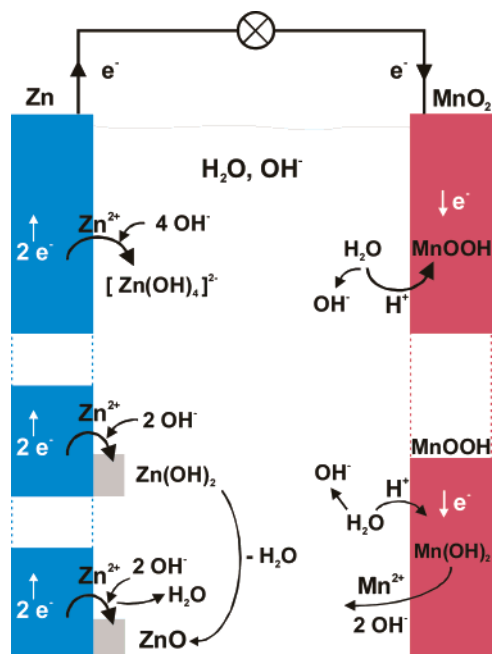


Figure 17. Discharge mechanism of a Zn–MnO₂ cell. From top to bottom, various stages of the discharge reaction are depicted. On the Zn side, the local change of the pH alters the composition of the discharge product.

wide use, and in 2003, worldwide it outsold the alkaline cell about 30 billion to 12 billion cells.

In the United States, the alkaline electrolyte (KOH) version accounts for ~80% of sales. The detailed discharge reaction mechanism is shown in Figure 17. The influence of the pH and the change of the pH of the electrolyte solution during discharge on the formation/solubility of various zincate compounds [e.g., Zn(OH)₄²⁺, etc.] to a change from a one phase to a two phase reaction at the point where Zn(OH)₂ begins to precipitate. It should be noted that local pH changes occur also during discharge of the MnO₂ electrode (Figure 15E).

Compared to the carbon–zinc cell, the alkaline cell is more reliable, has better performance, and is best for higher rate applications required for advanced portable electronic devices. The current version of the alkaline cell is mercury free. Instead, it uses a combination of alloying agents and corrosion inhibitors to lower the hydrogen gas generation from corrosion of the zinc anode and to compensate for the corrosion protection originally provided by the mercury. A synthetic gel holds the zinc powder anode together. The cathode is composed of an electrolytic manganese dioxide–graphite mixture with critical impurities controlled to a ≤1 ppm level.

The zinc–air battery system has the highest energy density of all aqueous batteries and equals that of the lithium thionyl chloride battery (which is the highest energy density lithium battery). The high energy density results from the cell design, as only the zinc powder anode is contained in the cell. The other reactant, oxygen, is available from the surrounding air. The air electrode is a polymer-bonded carbon, sometimes catalyzed with manganese dioxide. The electrode has a construction similar to that of fuel cell electrodes (see section 3). The zinc–air

system has captured the hearing aid market. Cells are available in sizes smaller than an aspirin tablet that fit into the ear to power the hearing aid.

The main applications of Zn–Ag₂O cells are button cells for watches, pocket calculators, and similar devices. The cell operates with an alkaline electrolyte. The Zn electrode operates as discussed, whereas the Ag₂O electrode follows a displacement reaction path (cf. Figure 15A).

Primary lithium cells use a lithium metal anode, the discharge reaction of which is depicted in Figure 15B. Due to the strong negative potential of metallic lithium, cell voltages of 3.7 V or higher are possible. As the lithium metal is very reactive, the key to battery chemistry is the identification of a solvent system that spontaneously forms a very thin protective layer on the surface of metallic lithium, called the solid electrolyte interphase (SEI) layer. This electronically insulating film selectively allows lithium ion transport. Lithium batteries show higher energy density than the alkaline cells but have a lower rate capability because of the lower conductivity of the nonaqueous electrolyte and the low lithium cation transport rate through the SEI.

Commercial lithium primary batteries use solid and liquid cathodes. Solid cathodes include carbon monofluoride, CF_x, manganese dioxide (MnO₂), FeS₂, and CuS. Chemical (CMD) or electrolytic manganese dioxide (EMD) is used as the cathode with high-temperature treatment to form a water-free active material. The CF_x is made from the elements, and its cost is somewhat higher than that of the manganese dioxide cathode material. These cells are designed for relatively low-rate applications. Both chemistries are very stable, and cells can deliver ≥80% of their rated capacity after 10 years of storage. The lithium iron sulfide (FeS₂) system has been developed for high-rate applications and gives superior high-rate performance compared to the alkaline zinc–manganese cells. Typically, the electrolyte is propylene carbonate–dimethyl ether (PC–DME) with lithium triflate (LiSO₃CF₃) or lithium perchlorate (LiClO₄) salt.

The lithium thionyl chloride system employs a soluble cathode construction. The thionyl chloride acts as the solvent for the electrolyte and the cathode active material. It has the highest energy density of any lithium cell and is equal to that of the zinc–air aqueous cell. The reaction mechanism of the cell is explained in Figure 18. In the inorganic electrolyte (LiAlCl₄ dissolved in SOCl₂) the lithium metal and the electrolyte react chemically and form a SEI mainly consisting of LiCl and S. LiCl and S are also the products of the electrochemical discharge reaction at the carbon positive electrode, where the liquid cathode SOCl₂ is reduced. The cell discharge stops when the electronically insulating discharge products block the carbon electrode.

Lithium–sulfur dioxide cells also use a liquid cathode construction. The SO₂ is dissolved in an organic solvent such as PC or acetonitrile. Alternatively, SO₂ is pressurized at several bars to use it in the liquid state. The cell reaction is similar to that depicted in Figure 18, with electronically insulating

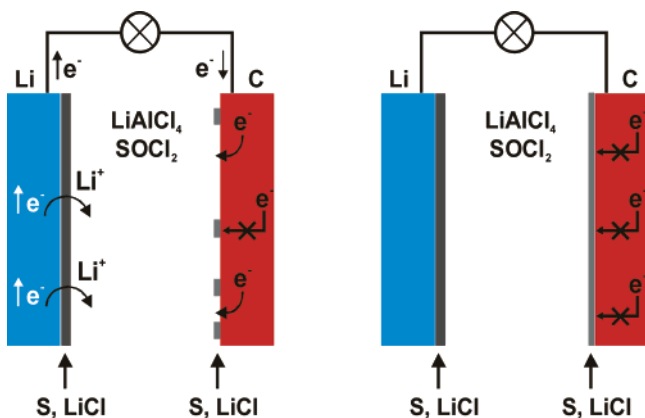


Figure 18. Discharge mechanism of a Li–SOCl₂ cell. The cell can operate until the surface of the carbon cathode is fully covered by electronically insulating LiCl and S discharge products. The Li–SO₂ cell is also a soluble cathode system with a cell construction similar to that of the Li–SOCl₂ cell. It follows a similar discharge reaction where the reaction product is LiS₂O₄.

Li₂S₂O₄ being the SEI component at the Li anode and the solid discharge product at the carbon cathode. The Li–SOCl₂ and Li–SO₂ systems have excellent operational characteristics in a temperature range from –40 to 60 °C (SOCl₂) or 80 °C (SO₂). Typical applications are military, security, transponder, and car electronics. Primary lithium cells have also various medical uses. The lithium–silver–vanadium oxide system finds application in heart defibrillators. The lithium–iodine system with a lithium iodide solid electrolyte is the preferred pacemaker cell.

2.5. Rechargeable Batteries

Rechargeable cells generally have lower energy storage capability than primary cells. The additional requirements for rechargeability and long operation limit the choice of chemical systems and constructions to those that are more robust than for primary batteries. The lead acid battery dominates the rechargeable market. Both the Pb and PbO₂ electrode reaction mechanisms follow the solution–precipitation mechanism as depicted in Figure 15C and the cell reaction shown in Figure 19. In addition to the lead and lead oxide electrodes, sufficient amounts of

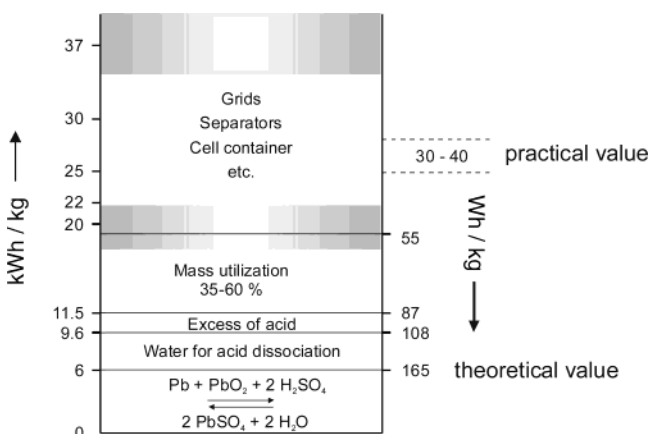


Figure 19. Depiction of the components of a lead acid battery showing the differences between theoretical and practical energy density of a lead acid battery and source of the differences.

sulfuric acid and water have to be provided for the cell reaction and formation of the battery electrolyte. For ionic conductivity in the charged and discharged states, an excess of acid is necessary. Considering the limited mass utilization and the necessity of inactive components such as grids, separators, cell containers, etc., the practical value of specific energy (Wh/kg) is only ~25% of the theoretical one (Figure 19) for rechargeable batteries. Due to the heavy electrode and electrolyte components used, the specific energy is low.³ Nevertheless, the lead acid system serves a variety of applications from automotive SLI and motive power for forklift trucks and the like to stationary energy storage for uninterruptible power supplies. Its low cost and established recycling processes make it one of the “greenest” battery systems. According to Battery Council International, Inc., ~98% of the lead acid batteries in the United States are recycled.

Nickel–cadmium (Ni–Cd) was the first small sealed rechargeable cell. In alkaline (KOH) electrolyte, the Cd negative electrode functions reversibly, according to a solution–precipitation mechanism (cf. Figure 15C) with Cd(OH)₂ being the discharge product. The Ni positive electrode is actually a Ni(OH)₂ electrode, which is able to reversibly de-insert/insert protons during discharge/charge. It has excellent low-temperature and high-rate capabilities. For a long time, it was the only battery available for power tools. It powered the early cellular phones and portable computers. The availability of stable hydrogen storage alloys provided the impetus for the creation of the nickel–metal hydride (Ni–MH) cell. The hydrogen storage alloy is a proton-inserting negative electrode material that replaced the environmentally threatened cadmium negative electrode in the Ni–Cd. The positive electrode and the electrolyte stayed the same. Ni–MH quickly replaced the Ni–Cd for electronic applications because of its significantly higher energy storage capability and somewhat lighter weight. The Ni–MH has poor low-temperature capability and limited high-rate capability, but its higher energy density served to spur the development of the portable electronic device market. Today, it is the battery of choice for hybrid gasoline–electric vehicles and is beginning to challenge the Ni–Cd for power tool applications.

The Li ion battery, with significantly higher energy density and lighter weight, replaced the Ni–MH as soon as production capability was available. It is now the battery of choice for portable electronic devices and is challenging the Ni–MH for the hybrid vehicle application. The Li ion cell has a carbon/graphite anode, a lithium–cobalt oxide cathode, and an organic electrolyte of lithium hexafluorophosphate (LiPF₆) salt with ethylene carbonate–organic solvent mixture. As in the Ni–MH battery, both the anode and cathode in the Li ion cell follow an insertion mechanism; however, instead of protons, lithium cations are inserted and de-inserted (cf. Figure 15D).⁴

³ A specific energy of 30 Wh/kg literally means that 1 kg of a lead acid battery is able to power a 60 W lamp for only 0.5 h.

⁴ For layered host materials as used in the lithium ion cell, the term “intercalation” is used for the insertion of guests into the host structure.

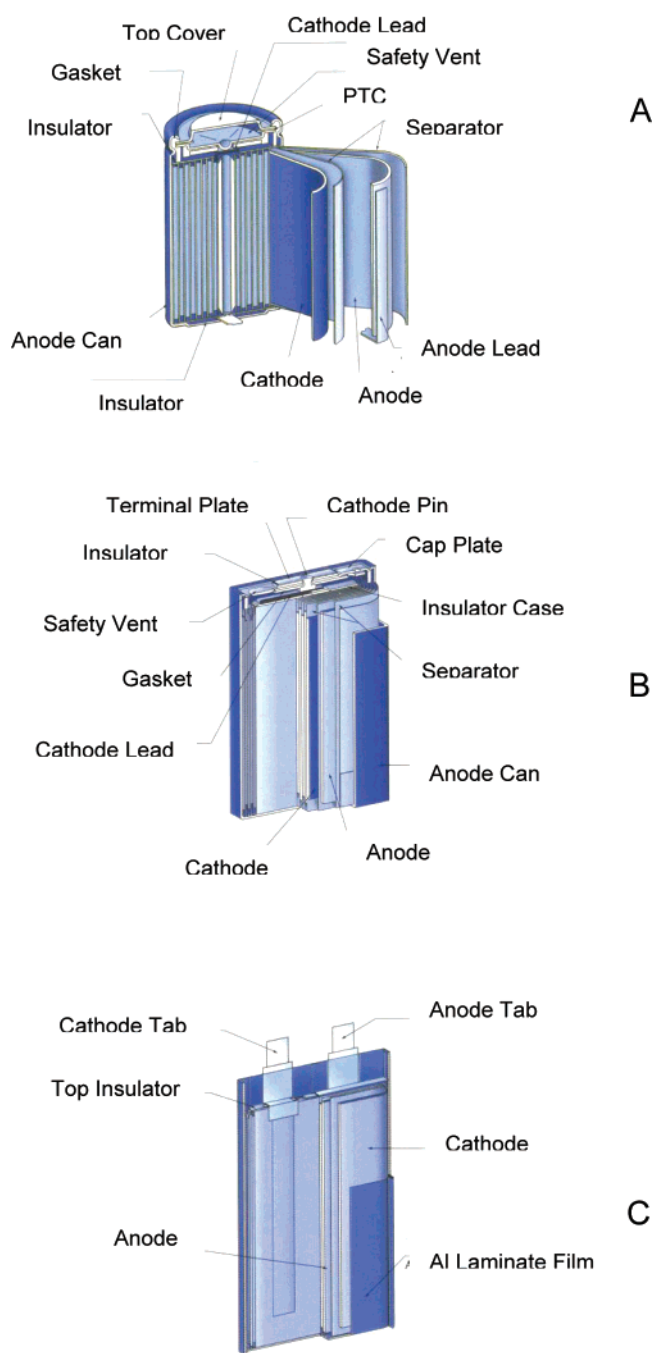


Figure 20. Construction of (A) cylindrical, (B) prismatic, and (C) polymer Li ion cells. (Reprinted with permission from a brochure by Sony Corporation).

Sony introduced the Li ion in 1991. Since its introduction, it has more than doubled in capacity in response to the demand for higher performance portable electronic devices, such as cellular phones and notebook computers. The construction of the Li ion cells is shown in Figure 20. Cells are available in both liquid electrolyte and plasticized polymer electrolyte configurations. New anode and cathode materials hold promise to double the present performance over the next 10 years. The Li ion market is poised to segment into the higher performance, higher cost segment, which continues the increase in energy density, and a segment with lower cost

materials but with high-rate performance for hybrid electric vehicle and power tool applications. The new materials that make possible this improvement in performance are discussed elsewhere and are beyond the scope of this overview.

Lithium metal rechargeable cells would have the highest energy of all battery systems. Unfortunately, on recharge, the lithium has a strong tendency to form mossy deposits and dendrites in the usual liquid organic solvents (cf. Figure 15B). This limits the cycle life to ~ 100 – 150 cycles (considerably lower than the 300 cycles required for a commercial cell), as well as increasing the risk of a safety incident. Rechargeable lithium metal–vanadium oxide cells (Li-VO_x) with poly(ethylene oxide) polymer electrolytes have been developed for stationary energy storage applications.

Only a few of the thousands of proposed battery systems have been commercialized. A set of criteria can be established to characterize reactions suitable for use in selecting chemical systems for commercial battery development. Very few combinations can meet all of the criteria for a general purpose power supply. The fact that two of the major battery systems introduced more than 100 years ago, lead acid (rechargeable) and zinc–manganese dioxide (primary), are still the major systems in their category is indicative of the selection process for chemical reactions that can serve the battery marketplace.

2.6. Selection Criteria for Commercial Battery Systems

A set of criteria that illustrate the characteristics of the materials and reactions for a commercial battery system follow.

1. *Mechanical and Chemical Stability.* The materials must maintain their mechanical properties and their chemical structure, composition, and surface over the course of time and temperature as much as possible. This characteristic relates to the essential reliability characteristic of energy on demand. Initially, commercial systems were derived from materials as they are found in nature. Today, synthetic materials can be produced with long life and excellent stability. When placed in a battery, the reactants or active masses and cell components must be stable over time in the operating environment. In this respect it should be noted that, typically, batteries reach the consumer ~ 9 months after their original assembly. Mechanical and chemical stability limitations arise from reaction with the electrolyte, irreversible phase changes and corrosion, isolation of active materials, and local, poor conductivity of materials in the discharged state, etc.

2. *Energy Storage Capability.* The reactants must have sufficient energy content to provide a useful voltage and current level, measured in Wh/L or Wh/kg. In addition, the reactants must be capable of delivering useful rates of electricity, measured in terms of W/L or W/kg. This implies that the kinetics of the cell reaction are fast and without significant kinetics hindrances. The carbon–zinc and Ni–Cd systems set the lower limit of storage and release capability for primary and rechargeable batteries, respectively.

3. *Temperature Range of Operation.* For military applications, the operational temperature range is from -50 to 85 °C. Essentially the same temperature range applies to automotive applications. For a general purpose consumer battery, the operating temperature range is ~ 0 – 40 °C, and the storage temperatures range from -20 to 85 °C. These temperatures are encountered when using automobiles and hand-held devices in the winter in northern areas and in the hot summer sun in southern areas.

4. *Self-Discharge.* Self-discharge is the loss of performance when a battery is not in use. An acceptable rate of loss of energy in a battery depends somewhat on the application and the chemistry of the system. People expect a battery to perform its intended task on demand. Li–MnO₂ primary cells will deliver 90% of their energy even after 8 years on the shelf; that is, their self-discharge is low. Some military batteries have a 20-year storage life and still deliver their rated capacity. On the other hand, rechargeable batteries can be electrically restored to their operating condition and generally have more rapid loss of capacity on storage. The rechargeable Ni–MH cell, for instance, will lose up to 30% of its capacity in a month. Usually, self-discharge increases with temperature.

5. *Shape of the Discharge Curve.* The issue of a sloping versus a flat discharge depends on the intended use. For operation of an electronic device, a flat, unchanging, discharge voltage is preferred. A sloping discharge is preferred for applications when determining the state-of-charge is important. This may be modified somewhat by the impact of cost. Although a constant brightness is preferred in a flashlight, the user may select carbon–zinc with a sloping discharge for its lower cost. The influence of one- or two-phase reactions on the shape of the discharge curve was discussed previously (cf. Figure 16).

6. *Cost.* The cost of the battery is determined by the materials used in its fabrication and the manufacturing process. The manufacturer must be able to make a profit on the sale to the customer. The selling price must be in keeping with its perceived value (tradeoff of the ability of the user to pay the price and the performance of the battery). Alkaline primary Zn–MnO₂ is perceived to be the best value in the United States. However, in Europe and Japan the zinc chloride battery still has a significant market share. In developing countries, the lower cost Leclanché carbon–zinc is preferred. Likewise, lead acid batteries are preferred for automobile SLI over Ni–Cd with superior low-temperature performance but with a 10 times higher cost.

7. *Safety.* All consumer and commercial batteries must be safe in the normal operating environment and not present any hazard under mild abuse conditions. The cell or battery should not leak, vent hazardous materials, or explode.

Added criteria for rechargeable batteries are as follows:

8. *Ability To Recharge and Deliver Power.* The rechargeable battery systems place a severe added requirement. The active materials must be capable

of being restored exactly to their original condition (crystal structure, chemical composition, etc.) on reversal of the current flow (charging). After being recharged by current reversal, the electrode materials must be able to deliver the same rate of discharge while maintaining their voltage level. Very few chemical systems exhibit this characteristic.

9. *Cycle Life.* It is not enough for a chemical system to be recharged and deliver power to qualify as a commercial rechargeable system. A commercial cell must be capable of completely discharging its energy and then fully recharging a minimum of 300 times and not lose $>20\%$ of its capacity. This requires a very robust system and reversible electrode reactions. There can be no side reactions that result in the loss of the active materials during the charge–discharge cycle.

10. *Charge Time.* The time it takes to recharge a battery completely relates to the use. For convenience, recharging in 15 min is accepted for many consumer applications. However, fast charging places a stress on the robustness of the electrode reactions and may result in shortened cycle life. Most batteries require 3–8 h to recharge completely and maintain their required cycle life. This slower charge rate allows time for the atoms and molecules to find their correct positions in the charged material.

11. *Overcharge/Overdischarge Protection.* When a battery is forced outside its thermodynamic voltage levels, the reaction path becomes unstable; irreversible new reactions can occur, and new compounds can form. These events harm the active material and either reduce the capacity or render the system inoperable. In addition, unsafe battery conditions may occur under overcharge/overdischarge conditions. The Ni–Cd, Ni–MH, and lead acid have a built-in overcharge and overdischarge characteristic based on an oxygen recombination mechanism. Cell designs often use the ratio of the capacities of each electrode (cell balance) to accomplish protection of the battery system. It is also possible to use electronic controls to control the charge and discharge voltage limits within safe limits. The lithium–cobalt oxide cathode in the Li ion system is protected from overvoltage and overdischarge by electronic means. Voltage excursions outside its operating range can cause irreversible changes in its crystal structure and damage cell operations.

3. Fuel Cells

3.1. Introduction and Market Aspects

The chemical energy stored in hydrogen and several hydrocarbon fuels is significantly higher than that found in common battery materials. This fact provides the impetus to develop fuel cells for a variety of applications. Fuel cells are an ideal primary energy conversion device for remote site locations and find application where an assured electrical supply is required for power generation, distributed power, remote, and uninterruptible power. Figure 21 depicts the operation of typical fuel cells. The various components of a functioning fuel cell are shown in Figures 22 and 23. Operating fuel cells are complex

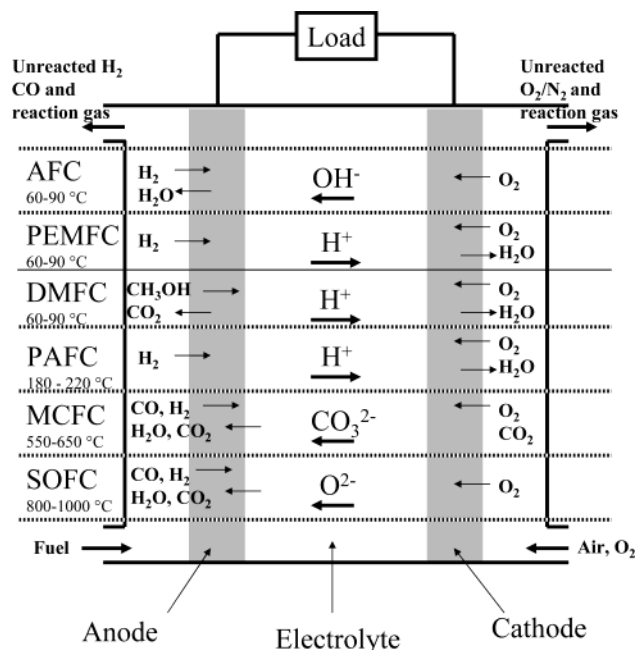


Figure 21. Summary of the reactions and processes that occur in the various fuel cell systems.

chemical plants that require sophisticated manufacturing techniques and control circuitry.

Some companies, hospitals, and buildings are choosing to install fuel cell power in order to be free from the outages experienced in utility supply lines. Previously, emphasis had been placed on the development of large fuel cells in the 200–300 kW range for these applications. Several demonstration projects of 1 MW and larger fuel cells have been undertaken, usually composed of units of 250 kW output. Smaller fuel cells in the range of 50–75 kW are now under intense development for use in automobile and bus propulsion, where their low emission characteristic finds favor. The direct conversion methanol fuel cells in the range of 5–25 W are proposed for portable electronics as a replacement for Li ion and Ni–MH batteries. The more promising commercial applications of fuel cells appear to be as a stationary power source for central and dispersed power stations (megawatts) and as mobile power for portable electronic devices and automobiles.

advantages	disadvantages
efficient energy conversion	complex to operate
modular construction	best as primary energy source
nonpolluting	impurities in gas stream shorten life
low maintenance	pulse demands shorten cell life
silent	expensive
safe	limited availability
high energy density	low durability
	low power density per volume

Although several fuel cell technologies are reaching technical maturity, the economics of a fuel cell are not clear. The commercial potential of fuel cells will depend on the ability to reduce catalyst and other expensive materials costs and to manufacture the units at a competitive cost. Many uses of fuel cells place a premium on specific performance characteristics. The relatively simple alkaline fuel cells (AFC)

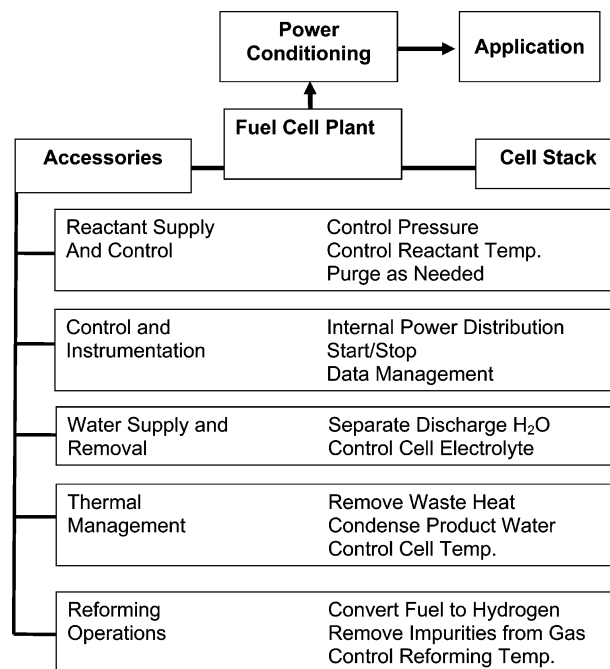


Figure 22. Block diagram of the component parts of a functioning fuel cell.

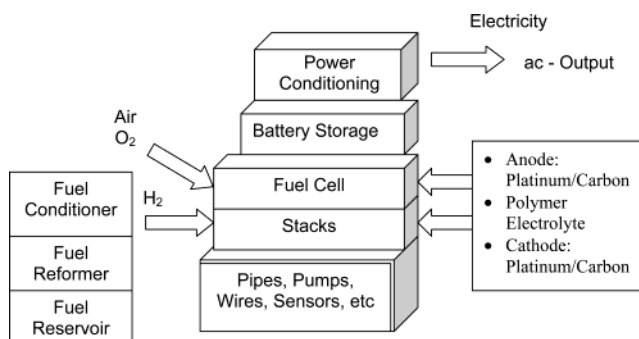


Figure 23. Depiction of the components of a complete fuel cell system including the re-former and power conditioning unit.

will continue to be used in space applications, where high energy densities and cryogenic storage of hydrogen and oxygen represent a cost savings by lowering the weight of the launch vehicle. They are also used for longer space missions, when the high reliability and the production of drinking water are important considerations. The high cost of qualifying a new technology is a strong impediment for replacing the AFC in space applications.

Fuel cells offer the cleanest power generation possible. They are quiet in operation and can be located close to the application. They produce much less greenhouse emissions and can be more efficient in conversion of the energy in a fuel into power than gasoline engines or utility thermal power plants. Fuel cells are best utilized as a steady energy source and not as a power source to supply dynamic demands. For applications that require varying power demands, such as automotive propulsion, the use of the fuel cell in a hybrid configuration with a battery or EC will be required. The fuel cell provides steady power demand while the battery or EC handles the surge for regenerative braking and acceleration as well as initial start-up.

Table 3. Types of Fuel Cells

advantages	disadvantages	comments
	Alkaline (AFC) ^a	
mechanically rechargeable low-cost KOH electrolyte	limited activated life intolerant of impurities in gas streams CO ₂ and CO pure H ₂ only suitable fuel	original development >30 years ago Apollo fuel cell operates at room temp to 80 °C demo in vehicles in the 1970s
	Polymer Electrolyte Membrane Fuel Cell (PEMFC)	
nonvolatile electrolyte few materials problems CO ₂ rejecting electrolyte pressure differential between anode and cathode polymer electrolyte	expensive catalysts required CO a strong poison H ₂ O management essential high-cost electrolyte pure H ₂ only suitable fuel oxygen kinetics are slow intolerant of impurities limited life water management essential	operates best at 60–90 °C originally developed for space by GE hydrogen fuel (re-formed hydrocarbons, pure H ₂ , MH storage) main development efforts for automotive and stationary applications
	Direct Methanol Fuel Cell (DMFC)	
direct fuel conversion slow electrode kinetics improved wt and vol polymer electrolyte	stable reaction intermediates high catalyst loadings water management essential low overall efficiency methanol hazardous	operates best at 60 to 90 °C) same construction as PEMFC methanol fuel eliminates reformer lower current capability methanol crossover reduces efficiency needs new membrane, higher efficiency high catalyst loadings main effort for portable electronic devices
	Phosphoric Acid Fuel Cell (PAFC)	
CO ₂ rejecting electrolyte high fuel efficiency	H ₂ only suitable fuel anode CO catalyst poison O ₂ kinetics hindered low conductivity electrolyte high-cost catalysts limited life	operates best at ~200 °C stationary energy storage (nominal units, 250 kW) available commercially
	Molten Carbonate Fuel Cell (MCFC)	
fast electrode kinetics high efficiency CO/CH ₄ usable fuel direct reforming feasible high-grade heat available	materials problems and life low sulfur tolerance high ohmic electrolyte low tolerance to sulfur need to recycle CO ₂ limited life	operates best at 550 °C nickel catalysts, ceramic separator membrane hydrocarbon fuels re-formed in situ several large demonstration units significant government support
	Solid Oxide Fuel Cell (SOFC)	
high grade heat available fast electrode kinetics in situ reforming feasible no electrolyte management high system efficiency tolerant of impurities	high fabrication costs severe materials constraints high electrolyte conductivity	operates at 900 °C conducting ceramic oxide electrodes hydrocarbon fuels re-formed in situ least sensitive to sulfur, etc.

^a Metal air batteries with replaceable anodes are often considered to be a fuel cell but are not considered here.

Fuel cells have been identified as a nearly ideal solution to power the requirements for motor vehicle manufacturers, utility and nonutility generators, and portable electronic devices. Each segment has significant incentives to develop alternate power sources. For automakers, the incentive is environmentally related, coupled with strong support from government programs designed to move away from fossil hydrocarbon fuels. For the utilities, increasing environmental pressure and power demand, coupled with limited generation capability, have created a need for distributed power generation and storage. In a similar vein, those who need an uninterrupted power supply, or freedom from the utility grid, find fuel cells to be an attractive option. Direct methanol fuel cells for portable electronic devices such as notebook computers seem close to commercial reality and will compete with batteries for this market. The key challenge for each will be to meet the cost-perfor-

mance barrier in a small size as well as governmental regulations.

It is estimated that the fuel cell market for distributed power and demonstration projects and contracts amounted to about \$100 million for 2003. Research and development contracts to develop fuel cells for automotive propulsion and stationary energy storage are an order of magnitude larger.

3.2. Fuel Cell Operation

Fuel cells, like batteries, convert the chemical energy residing in a fuel into electrical energy on demand. As in batteries and other electrochemical cells, fuel cells consist of an anode, where oxidation occurs, a cathode, where reduction occurs, and an electrolyte, where ions carry the current between the electrodes. Fuel cells differ from batteries in that the fuel and oxidant are not contained within the fuel

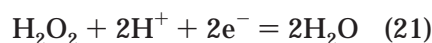
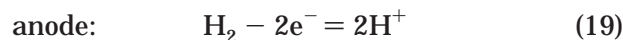
cell compartment but supplied continuously from an external source. In a real sense, fuel cells are like internal combustion engines, as they operate only so long as the fuel is supplied. Fuel cells are not electrically recharged, but after use, the tank is refilled with fuel. From an operational point of view, the fuel of choice is hydrogen gas, with the exhaust gas being water. Other fuels and hydrocarbons must be converted to hydrogen for use in a fuel cell. The direct conversion of fuels such as CH₃OH and CH₄ is possible under certain conditions. Each type of fuel cell has a unique set of processes and reactions to describe its operation. A summary of the characteristics for the various fuel cell systems is given in Tables 3 and 4.

The basic reaction of a H₂-O₂ fuel cell is



For this reaction $\Delta G^\circ = -235.76 \text{ kJ/mol}$ and $\Delta H^\circ = -285.15 \text{ kJ/mol}$. Fuel cells follow the thermodynamics, kinetics, and operational characteristics for electrochemical systems outlined in sections 1 and 2. The chemical energy present in the combination of hydrogen and oxygen is converted into electrical energy by controlled electrochemical reactions at each of the electrodes in the cell.

Fuel cells can be roughly divided into low-temperature (ca. <200 °C) and high-temperature (ca. >450 °C) fuel cells. Low-temperature fuel cells typically use alkaline or acidic electrolytes. In acidic electrolytes the electrode reactions are



Oxygen undergoes a two-step indirect reduction reaction. The stable H₂O₂ intermediate is undesirable, as it lowers the cell voltage and H₂O₂ attacks and corrodes the carbonaceous electrode material commonly used. Better catalysts are needed to speed the decomposition of H₂O₂ to reduce its impact on the overall reaction. Similarly, a catalyst can enhance the H₂ dissociation rate at the anode. Platinum or platinum alloys are usually employed as catalysts to speed the reactions on both electrodes in low-temperature fuel cells. The hydrogen reaction kinetics are fairly fast and do not require as high platinum loading to deliver high currents. To suppress the two-step oxygen reduction, significantly more catalyst is required. Due to the very high price of nanostructured Pt, the Pt may be distributed on a porous high surface area carbon. Typical catalyst loadings are ~0.1 mg/cm² of platinum or platinum alloy catalyst on the anode and ~0.5 mg/cm² catalyst on the cathode. However, the catalyst loading varies, depending on the type of fuel cell and its application. A major thrust in research on low-temperature fuel cells is to reduce the catalyst loading, to improve CO tolerance, and to identify lower cost catalysts. As the

Table 4. Typical Characteristics of Various Fuel Cell Systems

type	anode feed	anode composition	cathode feed	cathode composition and alternatives	electrolyte	operating temp, °C
alkaline (AFC)	pure hydrogen	carbon/platinum catalyst	oxygen (or air)	carbon/platinum catalyst	aq KOH	ambient-90
PEM (PEMFC)	pure hydrogen	carbon/platinum catalyst	oxygen or air	carbon/platinum catalyst	acidic polymer	ambient-90
direct methanol (DMFC)	methanol or methanol-water	carbon/platinum catalyst	oxygen or air	carbon/platinum catalyst	acidic polymer	60-90
phosphoric acid (PAFC)	pure hydrogen	carbon/platinum catalyst	oxygen or air	carbon/platinum catalyst	phosphoric acid in SiC matrix	200
molten carbonate (MCFC)	hydrogen or natural gas	porous Ni	oxygen or air	porous NiO	molten Li ₂ CO ₃ in LiAlO ₂ ⁻	550
solid oxide (SOFC)	gasoline or natural gas	porous cermet of Ni or Co and yttria-zirconia	oxygen or air	strontia-doped lanthanum-manganite Perovskite	yttria-stabilized or yttria/calcia-stabilized zirconia support	900 ^a

^a Mg- or Sr-doped lanthanum chromate as cell interconnects.

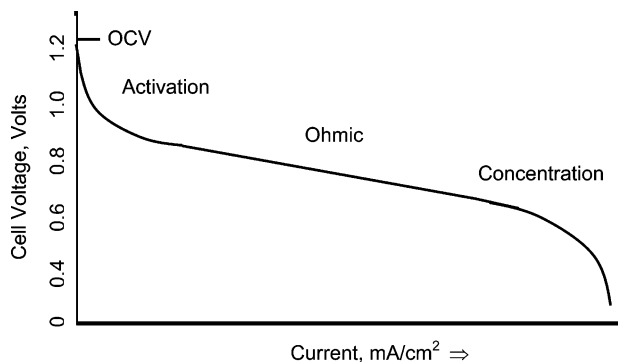


Figure 24. Typical power curve for a fuel cell. The voltage drops quickly from the OCV due to the formation of the peroxide intermediate. Operation of the fuel cell at the knee of the curve where concentration is limiting performance can damage the electrodes and lead to rapid deterioration of cell operation.

O_2 and H_2 dissociation kinetics are better at higher temperatures ($> 400\text{ }^\circ\text{C}$), low-cost electrode structures of high surface area Ni and oxides such as spinels or perovskites to replace the very effective, but costly, Pt catalysts have been sought.

Fuel cell electrodes are more complex structures than battery electrodes. They serve three functions: (1) to ensure a stable interface between the reactant gas and the electrolyte, (2) to catalyze the electrode reactions, and (3) to conduct the electrons from or to the reaction sites. A significant problem is the control of the interface at the juncture of the reactant (gas) phase, the electrolyte medium, and the catalyzed conducting electrode, the so-called “three-phase boundary”, where the electrolyte, electrode, and gas all come together. A stable three-phase boundary is critical to good performance and long operation. Therefore, the porosity and the wetting behavior with electrolyte and the electrode surface must be precisely adjusted.

Fuel cells can operate with very high electrical efficiencies approaching 60–70%. If the waste heat of the fuel cell is also used, fuel efficiencies of 90% are possible. The performance of the fuel cell is judged by the voltage–current curve depicted in Figure 24. The operating voltage is significantly less than the theoretical 1.23 V as the actual cell reaction involves H_2 , O_2 , and H_2O and also the peroxide intermediate (cf. above), the latter influencing the Nernst voltage and the OCV. The activation, ohmic, and diffusion polarization characteristics determine the shape of the fuel cell discharge curve as they do for batteries (cf. Figure 7).

As for the other electrochemical storage/conversion devices, the fuel cell electrolyte must be a pure ionic conductor to prevent an internal short circuit of the cell. It may have an inert matrix that serves to physically separate the two electrodes. Fuel cells may contain all kinds of electrolytes including liquid, polymer, molten salt, or ceramic.

Hydrogen gas is the preferred fuel for low-temperature fuel cells. The main obstacle in the use of hydrogen as energy carrier is that hydrogen is not a readily available fuel. In high-temperature fuel cells, a hydrocarbon fuel, for example, methane or gasoline, can be fed directly into the cell. To use hydrocarbons

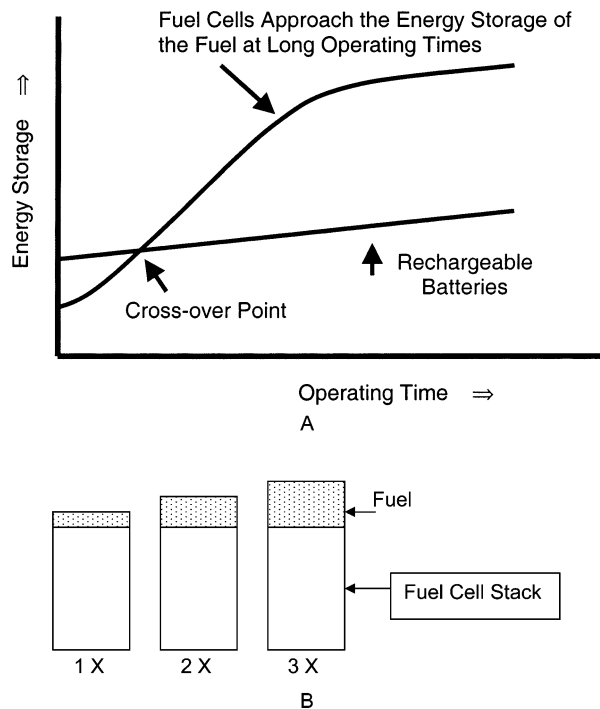


Figure 25. (A) Comparison of the energy storage capability of fuel cells and batteries. Only after several refueling operations are fuel cells more efficient energy storage devices on a Wh/L and Wh/kg basis. (B) Fuel cells have a set volume and weight for the fuel cell stack and peripherals to supply the reactants to the stack. The small incremental fuel volume to continue operation supplying energy makes them more efficient for longer operations.

in low-temperature fuel cells, the hydrocarbon fuels must be converted into hydrogen through a separate re-forming step placed between the tank and the fuel cell. Any trace amounts of CO, CO_2 , and H_2S found in the hydrogen-rich re-formate gas must be removed before using the gas, as they irreversibly block the Pt catalyst and thus “poison” the electrode. To reduce dependence on hydrocarbon fuels, the use of off-peak electricity from a series of new nuclear plants has been proposed, to produce the hydrogen for use in automotive applications.

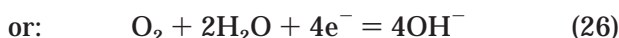
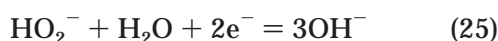
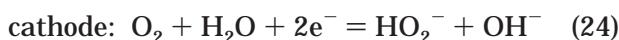
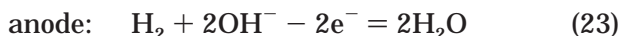
Apart from hydrocarbons and gasoline, other possible fuels include hydrazine, ammonia, and methanol, to mention just a few. Fuel cells powered by direct conversion of liquid methanol have promise as a possible alternative to batteries for portable electronic devices (cf. below). These considerations already indicate that fuel cells are not stand-alone devices, but need many supporting accessories, which consume current produced by the cell and thus lower the overall electrical efficiencies. The schematic of the major components of a so-called “fuel cell system” is shown in Figure 22. Fuel cell systems require sophisticated control systems to provide accurate metering of the fuel and air and to exhaust the reaction products. Important operational factors include stoichiometry of the reactants, pressure balance across the separator membrane, and freedom from impurities that shorten life (i.e., poison the catalysts). Depending on the application, a power-conditioning unit may be added to convert the direct current from the fuel cell into alternating current.

Fuel cell systems are not very volume efficient. The ancillary equipment to operate the device can be two to three times larger than the fuel cells themselves, where energy conversion actually occurs. Everything considered, the fuel cell stack⁵ is much less than 50% of the total volume of the unit. In addition, fuel cell stacks themselves have a low energy density in Wh/L and Wh/kg compared to batteries as the gas distribution system requires significant extra volume and weight. Only by taking into account the continuous supply of fuel to the system during long-term operation is the energy density of the fuel cell greater than that of advanced battery systems, as shown in Figure 25. However, due to the slow kinetics, especially at the oxygen cathode side, the power capability of fuel cells is lower than that of most batteries and inferior to combustion engines and gas turbines (cf. Figure 3). The detrimental impact of the weight and volume of the fuel cell may be hidden by giving the "power capability" in A/cm² and not in W/L or W/kg.

3.3. Characteristics of Various Types of Fuel Cells

Fuel cells are typically classified by the type of electrolyte. Apart from certain specialty types, the five major types of fuel cells are alkaline fuel cell (AFC), polymer electrolyte fuel cell (PEMFC), phosphoric acid fuel cell (PAFC), molten carbonate fuel cell (MCFC), and solid oxide fuel cell (SOFC).

The AFC is one of the oldest fuel cell types. The cell reactions are as follows (the existence of the peroxide intermediate HO₂⁻ has been already discussed):



The AFC was first developed for the Apollo missions. An updated version has been developed and is still in use to provide electrical power for shuttle missions. These power plants reach efficiencies of 60% in space applications. The electrolyte is potassium hydroxide based. Noble metal catalysts are very active in the AFC for both the hydrogen and oxygen electrodes. The hydrogen and oxygen kinetics are more facile in alkaline than acid electrolytes, thus resulting in higher cell voltages.⁶ This permits the use of non-noble metal catalysts, such as Raney nickel, for the fuel electrode. Silver and spinel-type oxides along with iron phthalocyanines and other porphyrins are good catalysts for the oxygen (air) electrodes. These catalysts cannot be used in acidic

⁵ A fuel stack is a series connection of fuel cells. Strictly speaking, it is fuel cell battery (cf. footnote 1). The composition and design of the fuel cell stack differ for the implementation of each type of cell.

⁶ The higher voltage is not only due to better kinetics but also due to the fact that oxygen reaction via the intermediate peroxide (HO₂⁻ in alkaline electrolytes) is more facile.

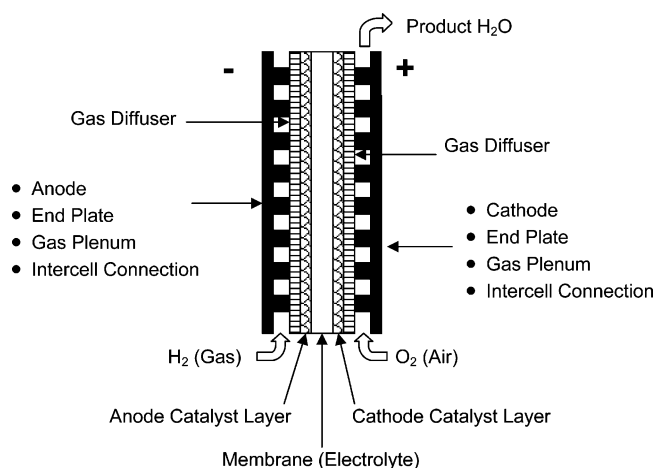


Figure 26. Schematic of a polymer electrolyte membrane (PEM) fuel cell. The fuel cell stacks operate at 30–180 °C with 30–60% efficiency. Fuel options include pure hydrogen, methanol, natural gas, and gasoline.

electrolytes, as they are soluble in acidic media. The AFC is susceptible to CO₂ contamination of the electrolyte (clogs the pores) when air is used as well as to poisoning of the Pt and Ni catalyst by sulfide and CO impurities in the feedstock. In other words, the AFC requires pure hydrogen and oxygen as reactants. Because of the requirement of pure fuels and elimination of CO₂ for long life, terrestrial applications are limited. Both electrodes are fabricated with an active layer of platinum catalyst on carbon support and binder that is backed by a wet-proofed Teflon [PTFE, poly(tetrafluoroethylene)] bonded carbon layer to control the wetting of the electrodes by the electrolyte and thus the location of the three-phase boundary. The carbons are generally treated to remove active entities on the surface before being catalyzed. Graphite bipolar endplates contain the gas flow channels and serve to provide waste heat removal. On shutdown, it is common to have the electrolyte empty into a sump on earthbound applications, as the cathode needs to be protected from both absorption of CO₂ by the electrolyte and corrosion by wet O₂. The AFC operates at up to 1 A/cm² at 0.7 V.

The PEMFC was first developed for the Gemini space vehicle. The electrodes are formed on a thin layer on each side of a proton-conducting polymer membrane, used as electrolyte. In a sense, the electrolyte is composed similarly to plasticized electrolyte in a Li ion cell, where a liquid electrolyte component is immobilized in a polymer matrix. It consists of a solid polymer PTFE backbone with a perfluorinated side chain that is terminated with a sulfonic acid group. Hydration of the membrane yields dissociation and solvation of the proton of the acid group. The solvated protons are mobile within the polymer and provide electrolyte conductivity. The membrane has low permeability to oxygen and hydrogen (crossover) for high coulombic efficiency. A typical PEMFC is depicted in Figure 26.

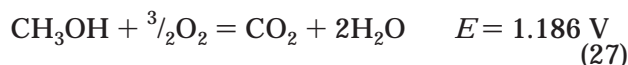
A graphite (or metal) plate serves as the plenum for the gas supply and for heat removal. A catalyzed carbon layer is applied to the membrane surface. A thicker gas diffusion layer or porous carbon paper

provides gas transport to the reaction zone. The composition and amount of catalyst differ for each electrode. The anode has a lower catalyst loading than the cathode. The platinum-based catalysts are sensitive to H₂S and CO impurities among others so they must be eliminated from the feedstock for long operation. The catalyst content of the anode is ~0.1 mg/cm², and that of the cathode is ~0.5 mg/cm².

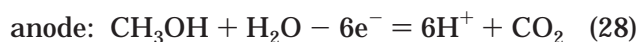
Water management in the membrane is critical to long-term performance. The proton transport carries water along (water drag) while carrying the current. The water concentration gradient results in back-diffusion. However, for operation at high current, the anode side of the membrane must be humidified or it will dehydrate. By the same token, product water is removed from the cathode side in the air stream to prevent flooding of the active layer. For reliable operation, a water content of 30–60% in the membrane is preferred for reliable operation.

For higher temperature operation, a polybenzimidazole-based polymer electrolyte may be preferred. The PEMFC structures have good mechanical integrity under compression and expansion from differential temperature and pressure gradients that occur during operation. This system has minimal materials problems, except for the cost and operation characteristics of the membrane. The PEMFC operates at ~1 A/cm² at 0.7 V. The electrode reactions in acidic media have been discussed above.

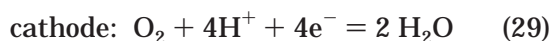
The DMFC uses the same basic cell construction as for the PEMFC. It has the advantage of a liquid fuel in that is easy to store and transport. There is no need for the re-former to convert the hydrocarbon fuel into hydrogen gas. The anode feedstock is a methanol and water mixture or neat methanol, depending on cell configuration. The DMFC is under development as a power source for portable electronic devices such as notebook computers and cellular phones. The pure methanol or a methanol–water mixture would be stored in a cartridge similar to that used for fountain pens. Refueling would involve the quick replacement of the cartridge. The platinum–ruthenium catalyst loadings for the anode are higher than for the PEMFC and are in the range of 1–3 mg/cm². Without the ruthenium, that is, with neat Pt, the anode reaction produces a stable formic acid intermediate. The reaction for the direct conversion of methanol has a similar voltage as for hydrogen. The overall cell reaction is



The reaction at the anode is



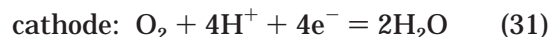
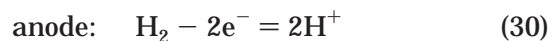
and



Due to the chemical similarity of water and methanol, the methanol has considerable solubility in the polymer membrane, leading to significant crossover

from the anode side to the cathode side of the cell. On reaching the cathode, the methanol is oxidized. This significantly lowers the cathode voltage and the overall efficiency of cell operation. The typical DMFC yields ~0.5 V at 400 mA/cm² at 60 °C.

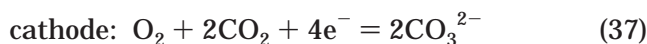
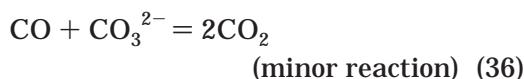
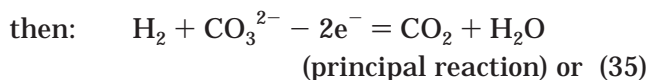
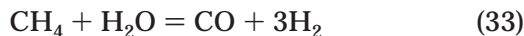
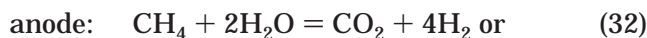
The PAFC is another fuel cell operating in acidic media. It has been frequently used in energy storage applications. The cell operates at ~200 °C. Below 150 °C, its conductivity is reduced, and above 220 °C, the phosphoric acid is too volatile and tends to decompose. A SiC matrix separator holds the acid. The acid rejects the water reaction product. Above 150 °C, some CO can be tolerated in the anode feedstock. The kinetic hindrance at the oxygen cathode is the major source of losses. The active layer of platinum catalyst on carbon black support and polymer binder is backed by a carbon paper with 90% porosity, reduced somewhat by PTFE binder. The active layer consists of pores in the range of 3–50 μm with micropores in the range of 0.0035 μm. The anode operates at nearly reversible voltage with ~0.1 mg/cm² catalyst loading. The cathode requires a higher catalyst loading of ~1 mg/cm² of catalyst. Graphite bipolar endplates contain the gas flow channels and serve to provide heat removal by liquid flow. On shutdown, the cathode needs to be protected from corrosion by wet O₂. The electrode reactions are



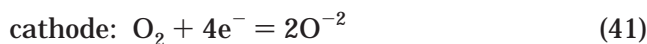
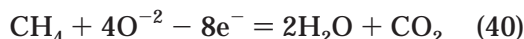
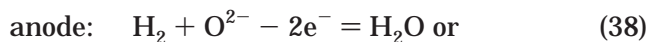
The hot H₃PO₄ electrolyte rejects water, the reaction product. The high temperature favors H₂O₂ decomposition, and peroxide buildup is less pronounced than for the aqueous electrolyte systems.

The MCFC finds application in energy storage applications. It operates best at ~560 °C, and the waste heat can be used in cogeneration. The system does not use any noble metal catalysts and has a higher efficiency than the PEMFC and the PAFC. The separator is a LiAlO₂ ceramic tile separator filled with molten carbonates to prevent crossover of the reactants and aid in CO₃²⁻ transport. Lithium-rich carbonate electrolytes have higher conductivity but lower gas solubility and higher corrosion rates. At the operating temperature, problem areas include NiO dissolution and structural stability of the anodes and cathodes, changes in pore size distribution, and distortion of the electrode structures. Alternate LiFeO₂ cathode materials have low conductivity, and Ni–Cr anode materials have creep and stability issues. Control of the pore diameter is critical in the separator tiles. Increased pressure raises voltage but increases gas solubility and cathode dissolution and lowers operating life. The performance is limited by the electrolyte resistivity and the removal of the heat generated by the losses in electrode polarization. The cells are sensitive to sulfur contamination because of its effect on the nickel electrode materials and catalyst. Other problem areas include seal stability during thermal cycling and electrolyte creep. Typical operating parameters are 150 mA/cm² at 0.8 V at 600 °C. The anode reactions using the fuel methane (or

CO and H₂ stemming from CH₄ conversion) are



The SOFC operates at ~800–1000 °C with O²⁻ conduction in the solid phase. Limitations and problems arise from the high operating temperatures and place severe restrictions on the choice of materials. The materials must have very similar coefficients of expansion and be chemically stable in oxidizing and reducing conditions. At the operating temperatures, the hydrocarbon fuels (plus water, if needed) are quickly and completely re-formed in situ. The system operates at close to 96% thermodynamic efficiency and is tolerant to most impurities. It can deliver high-quality heat for cogeneration applications. The SOFC can operate on most any hydrocarbon or hydrogen fuel and is tolerant of short circuiting and to overloads. No noble metal catalysts are required. The anode consists of a porous cermet of Ni or Co catalyst on yttria-stabilized zirconia. The zirconia acts to inhibit grain growth of the catalyst particles of nickel or cobalt and protects against thermal expansion. The electrolyte itself consists of yttria-stabilized zirconia, which can be additionally deposited onto a calcia-stabilized zirconia. Yttria and calcia doping provide oxygen defects for better conductivity. The cathode is generally a strontia-doped lanthanum–manganite perovskite. The Sr dopant provides for oxygen transfer to the cathode–electrolyte interface. A Mg- or Sr-doped lanthanum chromate is used for the current collector and the intercell connection. It is impervious to the fuel and oxygen gases and is chemically and structurally stable in thin, dense, layered configurations. The cells operate at ~1 A/cm² at 0.7 V. Cells are constructed in cylindrical form or in the flat plate format shown in Figure 27. The cell reactions are



4. Electrochemical Capacitors (ECs)

4.1. Introduction and Market Aspects

ECs are sometimes called supercapacitors, ultracapacitors, or hybrid capacitors. The term ultracapacitor or supercapacitor is usually used to describe

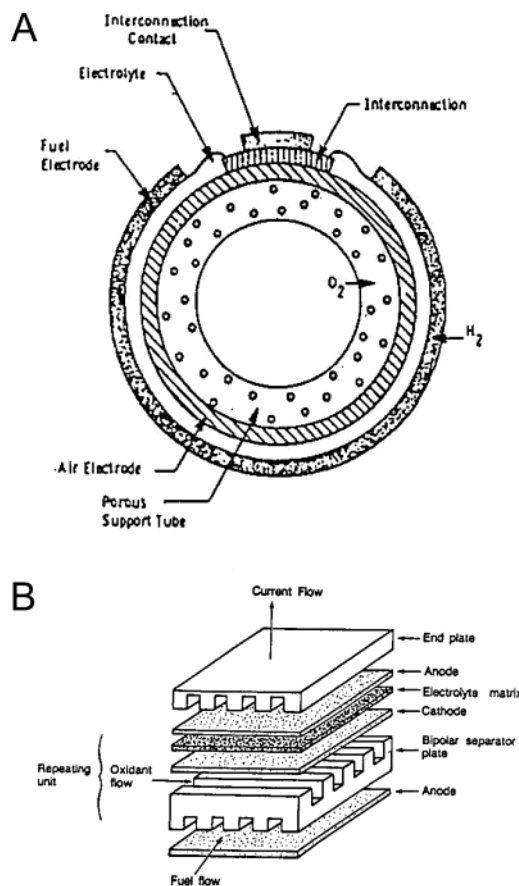


Figure 27. Schematic view of SOFC cylindrical and flat plate cell constructions.

an energy storage device based on the charge storage in the electrical double layer (EDL) of a high-surface-area carbon in aqueous electrolytes. The market for these devices used for memory protection in electronic circuitry is about \$150–\$200 million annually. New potential applications for ECs include the portable electronic device market, the power quality market, due particularly to distributed generation, and low-emission hybrid cars, buses, and trucks.

There is no commonly accepted nomenclature for ECs except that the definitions of anode, cathode, etc., carry over from battery and fuel cell usage, such as the anode as the negative terminal and cathode as the positive terminal. In general, ultracapacitors have referred to capacitors with two high-surface-area carbon electrodes for the anode and cathode. This arrangement where both electrodes have the same configuration will be referred to as a symmetric capacitor. The term supercapacitor has also been used to refer to the symmetric combination of two carbon electrodes that are catalyzed with ruthenium dioxide (RuO₂). The RuO₂ introduces a redox couple between two valence states of ruthenium, to result in higher capacitance for the carbon electrodes, but with a penalty in slower time constant for reacting to a pulse demand. A second type of EC combines a battery or redox electrode with a carbon electrode, such as nickel hydroxide cathode with a carbon anode. These supercapacitor or hybrid capacitors will be referred to as an asymmetric EC.

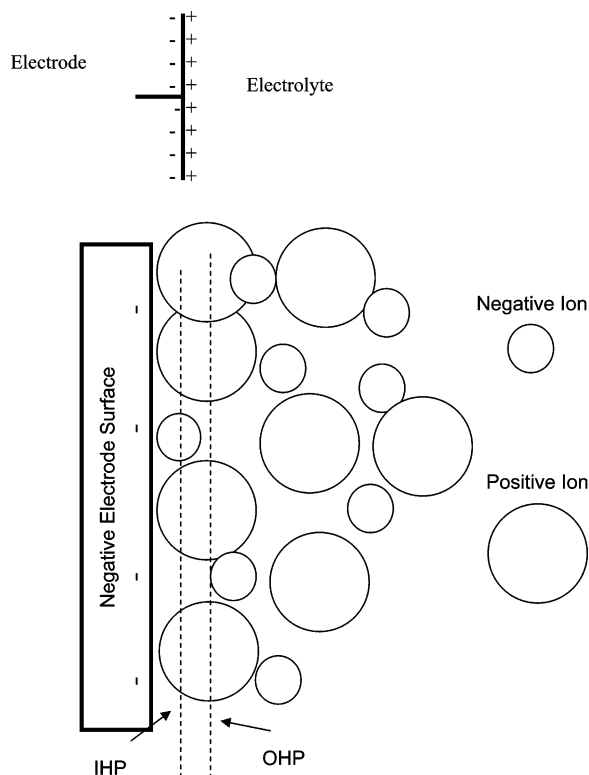


Figure 28. (A, top) Simple Helmholtz model of the electrical double layer. It is essentially a picture of a conventional capacitor. (B, bottom) Depiction of the electrical double layer at the surface of the negative electrode showing the outer Helmholtz plane (OHP) and the inner Helmholtz plane (IHP). The inner Helmholtz plane (IHP) refers to the distance of closest approach of specifically adsorbed ions and solvent molecules to the electrode surface. The outer Helmholtz plane (OHP) refers to the distance of ions, which are oriented at the interface by coulomb forces.

4.2. Characteristics of the Electrical Double Layer

When an electrode, that is, an electronic conductor, is immersed into an electrolyte solution, that is, an ionic conductor, there is a spontaneous organization of charges at the surface of the electrode and in the electrolyte facing the electrode. This EDL forms at the electrode–electrolyte interface with one layer at the surface inside the conductor and the other layer in the electrolyte as depicted in Figure 28. The two charged layers are considered to behave as a physical capacitor, with the charges in the solution and in the conductor separated by a distance of the order of molecular dimensions. The characteristics of the EDL depend on the electrode surface structure, the composition of the electrolyte, and the potential field between the charges at the interface. Depending on the surface charge of the electrode materials, positive or negative ions from the electrolyte form the solution part of the EDL at the interface between the electrode and the electrolyte. A simplified structure is shown in Figure 28A for the case of a negatively charged electrode surface. According to this simple Helmholtz model, the charges are concentrated on each side of the electrode surface. A more complex model of the EDL structure in Figure 28B takes into account the different sizes of the ions and their

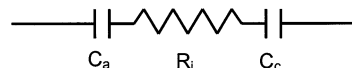
reactivity with the surface. The outer Helmholtz plane (OHP) refers to the distance of closest approach of nonspecifically adsorbed ions (generally cations) in solution. Cations that populate the OHP are usually solvated and thus are generally larger than the less solvated anions. The interactions of the ions of the OHP with the surface charge have the character of coulombic interactions. The inner Helmholtz plane (IHP) refers to the distance of closest approach of specifically adsorbed ions (generally anions) and/or adsorbed solvent molecules to the electrode surface. These adsorption processes are determined by chemical affinities of the ions to the electrode surface and the field strength in the EDL. In practice, the structure of the EDL is much more complex than the models discussed above.

The double layer at the electrode surface forms and relaxes almost instantaneously. It has a time constant, or time of formation, of $\sim 10^{-8}$ s. Therefore, the structure of the double layer has the capability to respond rapidly to potential changes in the same time frame. The process involves only a charge rearrangement, not a chemical reaction. This rapid response to change is in contrast to the situation with the redox electrode reactions in batteries and fuel cells. The time constant for the redox reactions is much slower and in the range of 10^{-2} – 10^{-4} s related to the impedance of the reaction. The redox reactions contribute to “polarization capacitance” associated with the electrode reactions. The other main difference between supercapacitors and batteries and fuel cells is the reversibility (short time constant) of the EDL process compared to the longer time constant of the redox reactions and the stress from detrimental side reactions, which reduce the cycle life and long-term stability of the device. Whereas cycle life and stability of the double layer electrochemical capacitor can easily exceed 1 million cycles, battery electrodes can reach this level only if charged and discharged at a low depth of discharge.

When carbons are placed in an electrolyte, they generally assume a voltage near the zero point of charge of the EDL. In aqueous solutions, this is near 0 V versus hydrogen. By applying an external voltage, many more additional ions and electrons can be moved to the double layer, increasing the capacitance C (= charge per applied voltage, $C = Q/U$). As a rule of thumb, carbons and metals typically have a double-layer capacitance in the range of 10 – $40 \mu\text{F}/\text{cm}^2$. The exact values depend mainly on the voltage and the extent of participation of the IHP in the electrical double layer. A high-surface-area carbon electrode can yield a capacitance of ~ 4 F/g.

4.3. EC Operation

As noted above, electrochemical capacitors are close cousins to batteries. The simple circuit shown illustrates their basic operation.



Here, C_a and C_c are the double-layer capacitances of the anode and cathode, respectively. R_i is the internal

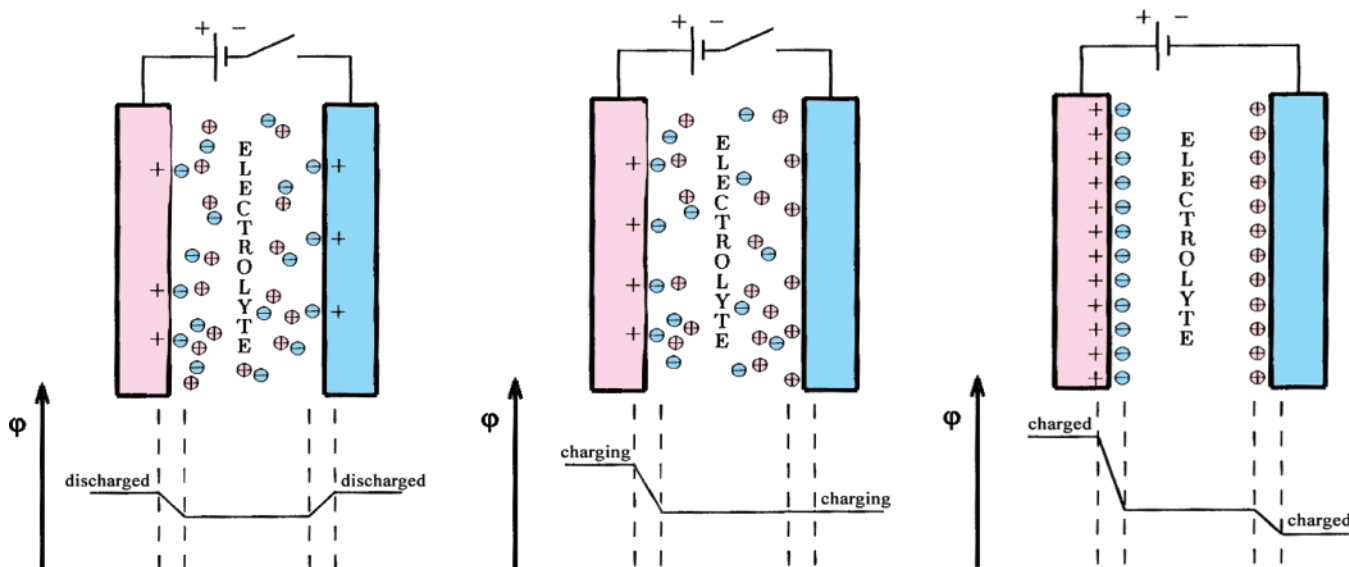


Figure 29. Depiction of the charging process of a symmetric capacitor.

resistance of the cell. For capacitors in series

$$1/C = 1/C_a + 1/C_c \quad (42)$$

If $C_a = C_c$, as would be expected for an ultracapacitor, then

$$C = 1/2 C_a \quad (43)$$

High-surface-area carbon is the material of choice, as it combines a large surface area wetted by the electrolyte, high electronic conductivity, and chemical and electrochemical stabilities with low cost. The capacitance of these devices can be orders of magnitude larger than those of conventional dry and electrolytic capacitors. The voltage for electrochemical capacitors with aqueous electrolytes is ~ 1 V, limited by the voltage stability of the electrolyte. By switching to an organic-based electrolyte, voltages of up to 2.7 V can be found in practice. However, the organic electrolytes have lower double-layer capacitance and poorer conductivity. Because the energy storage is given by energy = $1/2 QV^2$, the higher voltage permitted by an organic electrolyte significantly increases the energy storage capability of the EC. Because the resistivity is ~ 100 times larger than for aqueous electrolytes, the time constant for response to a large pulse is slower for the nonaqueous electrolyte-based ECs.

The charge–discharge of a symmetric EC composed of two carbon electrodes with approximately the same mass immersed in an aqueous or nonaqueous electrolyte is shown in Figure 29. With zero applied charge Q , both electrodes of a cell are at the same voltage. The potential of the electrodes increases in opposite directions during charge, as each has approximately the same capacitance. Maximum cell operating voltage is reached when one of the electrodes reaches the stability limit of the electrolyte.

The asymmetric type of EC incorporates a battery electrode as one of the electrodes. The battery electrode has a capacitance associated with the redox

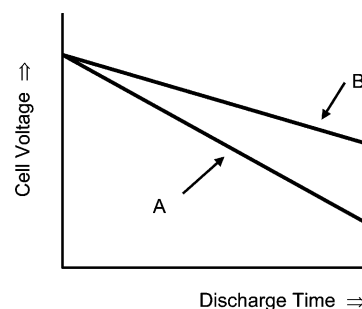


Figure 30. Operation principle of an EC in the discharged state, during charging, and in the charged state: (A) for a symmetric construction and (B) for an asymmetric construction.

battery reaction of ~ 10 times the capacitance of the electrical double layer. For instance, if the nickel battery cathode is substituted for the cathode in a symmetric capacitor, for example, NiOOH for carbon, then substituting $C_c = 10C_a$ in eq 42, the capacitance of the EC is essentially doubled.

$$1/C = 1/C_a + 1/10C_a \quad (44)$$

$$C \approx C_a \quad (45)$$

This asymmetric type of EC is often termed a “hybrid” capacitor. The typical discharge curve for this hybrid EC is shown in Figure 30. Because the battery electrode has a capacity of 3–10 times that of the double-layer electrode, it remains at an invariant voltage during charge and discharge. As a result, the discharge voltage of the hybrid capacitor falls more slowly than that of the carbon–carbon EDL capacitor.

In some cases, the kinetics of the redox charge–discharge reactions can proceed almost as quickly and reversibly as EDL charging. Thin film redox electrodes, based on the lithium intercalation/insertion principle such as $\text{Li}_4\text{Ti}_5\text{O}_{12}$, exhibit high reversibility and fast kinetics. The RuO_2 materials deposited on carbon show “pseudo-capacitive” charge–

discharge behavior as do polymeric materials such as polyaniline, polypyrrole, and polydiaminoanthraquinone (DAAQ). These have facile kinetics and have shown high capacitance and long life. The insertion of anions and cations into their structure can yield capacitances of up to 200 $\mu\text{F}/\text{cm}^2$ and, moreover, they can be easily fabricated as thin films.

5. Summary

Electrochemical energy conversion devices are pervasive in our daily lives. Batteries, fuel cells and supercapacitors belong to the same family of energy conversion devices. They are all based on the fundamentals of electrochemical thermodynamics and kinetics. All three are needed to service the wide energy requirements of various devices and systems. Neither

batteries, fuel cells nor electrochemical capacitors, by themselves, can serve all applications.

Martin Winter
Institute for Chemistry and Technology of
Inorganic Materials, Graz University of
Technology, Stremayrgasse 16,
A-8010 Graz, Austria

Ralph J. Brodd*
Broddarp of Nevada, Inc.,
2161 Fountain Springs Drive,
Henderson, Nevada 89074

CR020730K

Lithium Batteries and Cathode Materials

M. Stanley Whittingham*

Department of Chemistry and Materials Science, State University of New York, Binghamton, New York 13902-6000

Received June 16, 2004

Contents

1. Introduction	4271	6. Conclusions and What Does the Future Hold	4297
2. Origins of the Lithium Battery	4273	7. Abbreviations and Specialized Terms	4297
2.1. Early Concepts	4273	8. Acknowledgments	4297
2.2. Molten Salt Systems at Argonne National Laboratory and General Motors	4273	9. References	4297
2.3. Concept of Mixed Conductors	4273		
2.4. Early Intercalation Concept	4274		
3. 1972–1980: Birth of the Rechargeable Lithium Battery	4274		
3.1. Intercalation in the Layered Dichalcogenides	4274		
3.2. Trichalcogenides and Related Materials	4277		
3.3. Movement into Oxides	4277		
3.3.1. Layered Oxides	4277		
3.3.2. High-Valent Oxides of Vanadium and Molybdenum	4277		
3.3.3. Mixed-Valent Oxides of Vanadium— V_6O_{13} and LiV_3O_8	4278		
3.3.4. Double-Sheet Structures: Xerogels, δ -Vanadium Oxides, and Nanotubes	4278		
4. 1980–1990: Era of Layered Oxides and First Large Commercialization	4279		
4.1. Early Studies of Layered Oxides	4279		
4.2. Lithium Cobalt Oxide, $LiCoO_2$	4280		
4.3. Lithium Nickel Oxide, $LiNiO_2$	4281		
5. 1990–Present: Second-Generation Lithium Batteries	4282		
5.1. Spinels	4282		
5.2. Other Layered Oxides	4283		
5.2.1. Mixed Nickel–Cobalt Dioxide, $LiNi_{1-y}Co_yO_2$	4283		
5.2.2. Lithium Manganese Dioxide, $LiMnO_2$	4283		
5.2.3. Mixed Manganese–Cobalt Dioxide, $LiMn_{1-y}Co_yO_2$	4284		
5.2.4. Mixed Nickel–Manganese Dioxide, $LiNi_{1-y}Mn_yO_2$ —Multielectron Redox Systems	4285		
5.2.5. Mixed Nickel–Manganese–Cobalt Dioxide, $LiNi_{1-y-z}Mn_yCo_zO_2$	4287		
5.2.6. Lithium-Rich Mixed-Metal Dioxides, $Li_{1+x}M_{1-x}O_2$	4292		
5.3. Iron Compounds Including Oxides and Phosphates	4293		
5.3.1. Olivine Phase	4293		
5.3.2. Other Iron Phosphate Phases	4295		
5.3.3. Vanadium Phosphate Phases	4296		

1. Introduction

In the previous paper Ralph Brodd and Martin Winter described the different kinds of batteries and fuel cells. In this paper I will describe lithium batteries in more detail, building an overall foundation for the papers that follow which describe specific components in some depth and usually with an emphasis on the materials behavior. The lithium battery industry is undergoing rapid expansion, now representing the largest segment of the portable battery industry and dominating the computer, cell phone, and camera power source industry. However, the present secondary batteries use expensive components, which are not in sufficient supply to allow the industry to grow at the same rate in the next decade. Moreover, the safety of the system is questionable for the large-scale batteries needed for hybrid electric vehicles (HEV). Another battery need is for a high-power system that can be used for power tools, where only the environmentally hazardous Ni/Cd battery presently meets the requirements.

A battery is a transducer that converts chemical energy into electrical energy and vice versa. It contains an anode, a cathode, and an electrolyte. The anode, in the case of a lithium battery, is the source of lithium ions. The cathode is the sink for the lithium ions and is chosen to optimize a number of parameters, discussed below. The electrolyte provides for the separation of ionic transport and electronic transport, and in a perfect battery the lithium ion transport number will be unity in the electrolyte. The cell potential is determined by the difference between the chemical potential of the lithium in the anode and cathode, $\Delta G = -EF$.

As noted above, the lithium ions flow through the electrolyte whereas the electrons generated from the reaction, $Li = Li^+ + e^-$, go through the external circuit to do work. Thus, the electrode system must allow for the flow of both lithium ions and electrons. That is, it must be both a good ionic conductor and an electronic conductor. As discussed below, many electrochemically active materials are not good electronic conductors, so it is necessary to add an electronically conductive material such as carbon

* To whom correspondence should be addressed. Phone and fax: (607) 777-4623. E-mail: stanwhit@binghamton.edu.



M. Stanley Whittingham was born in Nottingham, England, and received his B.A. and D.Phil. degrees in Chemistry from Oxford University working with Peter Dickens. In 1968 he went to Professor Robert A. Huggins research group in the Materials Science Department at Stanford University as a Postdoctoral Research Associate to study fast-ion transport in solids. In 1972 he joined Exxon Research and Engineering Company to initiate a program in alternative energy production and storage. After 16 years in industry he joined the Binghamton campus of the State University of New York as Professor of Chemistry to initiate an academic program in Materials Chemistry. Presently he is also Professor of Materials Science and Director of the Materials Science Program and Institute for Materials Research. He was awarded the Young Author Award of the Electrochemical Society in 1971, a JSPS Fellowship in the Physics Department of the University of Tokyo in 1993, and the Battery Research Award of the Electrochemical Society in 2002 and was elected a Fellow of the Electrochemical Society in 2004. He was Principal Editor of the journal *Solid State Ionics* for 20 years. His recent work focuses on the synthesis and characterization of novel microporous and nano-oxides and phosphates for possible electrochemical and sensor applications.

black. To physically hold the electrode together, a binder is also added. In these cases the electrochemical reaction can only occur at those points where the active material, the conductive diluent, and electrolyte meet. Thus, most electrodes are complex porous composites.

This review will be mainly concerned with the cathode. The anode, the source of lithium, is normally a graphitic carbon and will be discussed in detail by Rachid Yazami in a future issue. The electrolyte solution commonly comprises a lithium salt dissolved in a mixture of organic solvents, examples include LiPF_6 or LiBOB (the BOB is the anion with the boron coordinated by two oxalate groups) in an ethylene carbonate/dimethyl carbonate solvent; Kang Xu discusses electrolytes later in this issue. Although organic polymers containing lithium ions have been studied for several decades as possible electrolytes, their conductivity is still too low, and so they are only used when a liquid is added to give a plasticized state. In a few cases, solid electrolytes have been used for a few specialized applications such as for oil well logging where elevated temperatures are found. Though the ions flow through the electrolyte, the anode and cathode must be physically separated to prevent an electrical short. This is accomplished by using a porous separator material, which allows wetting by the electrolyte and the flow of lithium ions through it. P. Aurora discusses these materials in detail.

For most consumer devices, energy storage is key; operating time is key, so the more the better, as, for

example, in cell phones, laptop computers, and MP3 players such as the iPod. For some larger applications, such as the battery in hybrid electric vehicles (HEV), power is most important as the materials must be able to charge sufficiently fast to take advantage of regenerative braking; otherwise, much of the gas savings are lost. The all-electric consumer electric vehicle is probably dead, at least in the United States, because of its limited range and the user's desire for instant heating and air-conditioning among other high-power consumption devices. However, there is still much interest in Asia, particularly for scooters as well as for all electric vehicles.

The key requirements for a material to be successfully used as a cathode in a rechargeable lithium battery are as follows.

- (1) The material contain a readily reducible/oxidizable ion, for example a transition metal.
- (2) The material react with lithium in a reversible manner.
 - (a) This dictates an intercalation-type reaction in which the host structure essentially does not change as lithium is added.
- (3) The material react with lithium with a high free energy of reaction.
 - (a) High capacity, preferably at least one lithium per transition metal.
 - (b) High voltage, preferably around 4 V (as limited by stability of electrolyte).
 - (c) This leads to a high-energy storage.
- (4) The material react with lithium very rapidly both on insertion and removal.
 - (a) This leads to high power density, which is needed to replace the Ni/Cd battery or for batteries that can be recharged using HEV regenerative braking.
- (5) The material be a good electronic conductor, preferably a metal.
 - (a) This allows for the easy addition or removal of electrons during the electrochemical reaction.
 - (b) This allows for reaction at all contact points between the cathode active material and the electrolyte rather than at ternary contact points between the cathode active material, the electrolyte, and the electronic conductor (such as carbon black).
 - (c) This minimizes the need for inactive conductive diluents, which take away from the overall energy density.
- (6) The material be stable, i.e., not change structure or otherwise degrade, to overdischarge and overcharge.
- (7) The material be low cost.
- (8) The material be environmentally benign.

Almost all of the research and commercialization of cathode materials has centered on two classes of materials. The first contains layered compounds with an anion close-packed or almost close-packed lattice in which alternate layers between the anion sheets are occupied by a redox-active transition metal and lithium then inserts itself into the essentially empty remaining layers. This structure is depicted in Figure 1. This group is exemplified by first LiTiS_2 , followed

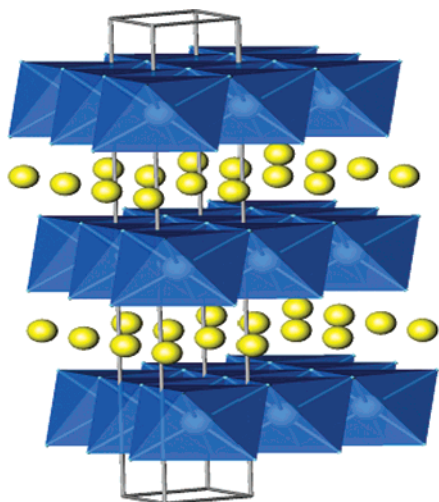


Figure 1. Layered structure of LiTiS_2 , LiVSe_2 , LiCoO_2 , LiNiO_2 , and $\text{LiNi}_y\text{Mn}_y\text{Co}_{1-2y}\text{O}_2$, showing the lithium ions between the transition-metal oxide/sulfide sheets. The actual stacking of the metal oxide sheets depends on the transition metal and the anion.

by LiCoO_2 , $\text{LiNi}_{1-y}\text{Co}_y\text{O}_2$, and today $\text{LiNi}_y\text{Mn}_y\text{Co}_{1-2y}\text{O}_2$. The spinels may be considered as a special case where the transition-metal cations are ordered in all the layers. The materials in the second group have more open structures, like many of the vanadium oxides, the tunnel compounds of manganese dioxide, and most recently the transition-metal phosphates, such as the olivine LiFePO_4 . The first group, because of their more compact lattices, will have an inherent advantage in energy stored per unit of volume, but some in the second group, such as LiFePO_4 , are potentially much lower cost. The following discussion will center predominantly on these two classes of materials.

2. Origins of the Lithium Battery

2.1. Early Concepts

Some of the earliest concepts came from Japan, where Matsuchita developed¹ the $\text{Li}/(\text{CF})_n$ battery that was used, for example, in fishing floats. Lithium fluoride and carbon are the final reaction products, but the cell potential of 2.8–3.0 V suggests a different electrochemical reaction. It was proposed that lithium initially intercalates the carbon monofluoride lattice and subsequently the lithium fluoride is formed:² $\text{Li} + (\text{CF})_n \rightarrow \text{Li}_x(\text{CF})_n \rightarrow \text{C} + \text{LiF}$. Although much work has continued sporadically on the carbon fluorides, by Exxon and others, the major challenge has been to make this reaction reversible even when lower fluoride levels were used. Sanyo, the largest manufacturer today of both lithium rechargeable and nickel metal hydride batteries, developed^{3,4} one of the earliest lithium batteries with the Li/MnO_2 system that they initially sold in solar rechargeable calculators.⁵ Some early work on ambient systems was also underway in the United States by 1970, for example, by Dey et al.⁶ on the lithium reactivity with a range of metals, such as aluminum.

Many primary lithium batteries have been developed for use in the medical field starting with the

lithium iodine cell. The majority of the implantable cardiac defibrillators use in the last 20 years have used, as active cathode material, silver vanadium oxide, $\text{Ag}_2\text{V}_4\text{O}_{11}$.^{7–9} During discharge the silver is reduced to silver metal, and in addition, more than one lithium per vanadium can be reacted, giving it a capacity over 300 mAh/g. The presence of metallic silver greatly improves the electronic conductivity and thus the rate capability. Future medical devices, such as heart-assist devices, will require rechargeable systems because the capacity of primary cells cannot provide the power needed for active medical devices. The copper analogue also reacts by exuding the metal.

2.2. Molten Salt Systems at Argonne National Laboratory and General Motors

Most of the early work^{10–12} on lithium rechargeable batteries used a molten salt as electrolyte and operated at around 450 °C. The earliest cells used molten lithium and molten sulfur as the two electrodes, but the problems with electrode containment proved insurmountable. The anode used in the final versions was the lithium aluminum alloy, LiAl , and iron sulfides, such as FeS and FeS_2 , which replaced the molten sulfur of the early designs. Development ceased around 1990 when corrosion, temperature, and other issues overwhelmed the advantages of the system, the sodium sulfur system appeared more promising, and early results on ambient lithium rechargeable systems began to show promise. These low-cost iron sulfides were also considered in the 1970s in ambient temperature cells. Iron pyrite was found¹³ to react with an initial constant potential of 1.5 V, allowing it to replace the more expensive Ag-Zn button cells and later making it a drop-in replacement for the Zn/MnO_2 alkaline cell. It is presently marketed by Eveready as a primary high-energy cell. On recharge the structure changes and the subsequent discharge has a two-step profile with an initial discharge of around 2 V.¹³

It is still the dream of battery researchers to develop a cell based on the lithium/sulfur couple which on paper has a simple chemistry, has a much higher energy density than most of the cathode materials to be discussed below, and should be capable of high rates if the sulfur is in solution. Recent work¹⁴ has achieved high capacities at 2 V even at as low temperatures as –40 °C in electrolyte solvents of dioxolane and dimethoxyethane. These cells with their liquid polysulfide cathode have generated specific power exceeding 750 W/kg at 25 °C. However, such cells still have significant issues with self-discharge on standing, lithium recharging, and the highly resistive nature of the cathode. Whether all these issues will be overcome is still much debated. A recent concept¹⁵ to protect the lithium anode from the reactive polysulfide medium is to coat it with a single-ion conducting glass.

2.3. Concept of Mixed Conductors

In 1967 Yao and Kummer reported¹⁶ the remarkable electrolytic behavior of the β -alumina class of

materials, $\text{Na}_{1+x}\text{Al}_{11}\text{O}_{17}$, which was proposed as the electrolyte for a battery having a molten sodium anode and a molten sulfur cathode operating around 300 °C. The measurement of the ionic conductivity of these materials required a new approach, as their high ionic conductivity required the use of ionically reversible electrodes and the obvious electrode sodium was too difficult to handle. To overcome this problem, the nonstoichiometric oxide bronzes of tungsten and vanadium were used,^{17–19} for example, Na_xWO_3 and $\text{Li}_x\text{V}_2\text{O}_5$; these bronzes have a wide range of composition, are metallic conductors, and thus could readily serve as electrodes reversible to both alkali ions and electrons. Their mixed conductivity also led to the proposed use of the vanadium oxide as electrodes for sodium or lithium batteries: $\text{Li-Li}_x\text{V}_2\text{O}_5$.

2.4. Early Intercalation Concept

Around 1970 two groups began studying the idea of placing electrochemically active species inside an electrically conductive host. At Bell Laboratories, Broadhead et al.^{20,21} conceived of intercalating iodine or sulfur between the layers of a dichalcogenide host material such as niobium diselenide. They believed that the dichalcogenide host material itself was electrochemically inert.²² Such materials showed good cyclability at low depths of discharge. Subsequently, they found that when selenium reacted with NbSe_2 , it formed the triselenide NbSe_3 which exhibited very good electrochemical behavior.²³ At Stanford, Armand et al.^{24–26} tried to incorporate oxides such as CrO_3 , and subsequently halides, between the layers of graphite. Again, electrochemical activity was found. However, subsequent work showed that in both these cases no intercalation had occurred and that the electrodes were mixtures of the guest and host materials. The large amount of host material required also made this concept infeasible due to the resulting poor energy density. A similar concept,²⁷ still not tested, was to use as electrodes two known graphite materials C_8K and C_8Br where on discharge the potassium and bromine would react in a suitable solvent and on charge would be intercalated into their respective graphite electrodes.

3. 1972–1980: Birth of the Rechargeable Lithium Battery

3.1. Intercalation in the Layered Dichalcogenides

Around 1970 researchers at Stanford²⁸ discovered that a range of electron-donating molecules and ions could be intercalated into the layered dichalcogenides, in particular, tantalum disulfide, TaS_2 . These guest–host intercalation reactions modified the physical properties and, in particular, were found to enhance the superconducting transition temperature from 0.8 to over 3 K. It was also discovered that such compounds remained superconducting even when the guest molecules were paramagnetic.²⁹ These studies continued at Exxon, where an investigation of the formation of the hydrated alkali-metal intercalates of tantalum disulfide, which showed the

highest superconducting transition temperature, resulted in the discovery of the very high free energy of reaction of the alkali ions with these layered materials. Thus, the stability of the hydrates, $\text{K}_x(\text{H}_2\text{O})\text{-TaS}_2$, could be explained³⁰ as being due to their salt-like behavior, in contrast to the metallic-like behavior of the corresponding compounds of graphite, C_8K . It was also found that such intercalation reactions could also be accomplished in an electrochemical cell either by electrolyzing dissolved salts or by inserting ions from the anode.^{31–33}

Of all the layered dichalcogenides, titanium disulfide was the most appealing for consideration as an energy storage electrode:^{34–38} it was the lightest. It was subsequently discovered that it was a semi-metal,³⁹ so no conductive diluent was needed in the cathode structure, and any such addition was found to be detrimental to the electrochemical behavior. It was also found to form a single phase with lithium over the entire composition range of Li_xTiS_2 for $0 \leq x \leq 1$.⁴⁰ This lack of phase change enables all the lithium to be removed reversibly, without the need for energy wastage associated with the nucleation of new phases or the sluggish reactions when massive rearrangement of the host must occur as the lithium content is changed. This behavior may be contrasted with that observed in LiCoO_2 , to be discussed below, where phase changes result in only about one-half of the lithium being readily cycled in to and out of the compound; today the capacity has been improved but is still well below the goal of one lithium per transition-metal ion. Some specifics of the lithium titanium disulfide cell will now be described, as they are typical of what is desired in advanced lithium batteries. Although they will not be discussed here, there was also interest^{41–44} in using the disulfides as the cathodes of sodium batteries; such systems are seriously complicated by phase changes as the sodium content changes in Na_xTiS_2 or Na_xTaS_2 due to the sodium favoring trigonal prismatic coordination at intermediate x values and octahedral coordination as x approaches one.

Titanium disulfide has a hexagonal close-packed sulfur lattice with the titanium ions in octahedral sites between alternating sulfur sheets, as shown in Figure 1. The TiS_2 sheets are stacked directly on top of one another, giving the sulfur anion stacking sequence ABAB. For nonstoichiometric sulfide $\text{Ti}_{1+y}\text{S}_2$ or for TiS_2 prepared at high temperatures, some of the titanium is found in the empty van der Waals layer. These disordered titanium ions prevent the intercalation of large molecular ions and impede the intercalation of even small ions such as lithium by pinning the TiS_2 sheets together,⁴⁵ thus reducing their diffusion coefficients. Thus, material with the highest reactivity for lithium should have an ordered structure, which dictates that it be prepared at temperatures below around 600 °C.^{46–48} We will see that this is also important for the similarly structured layered oxides, discussed below, and even for tunnel structures such as LiFePO_4 , where errant Fe ions in the Li sites can reduce reactivity^{49,50} and diffusion of lithium.⁵¹

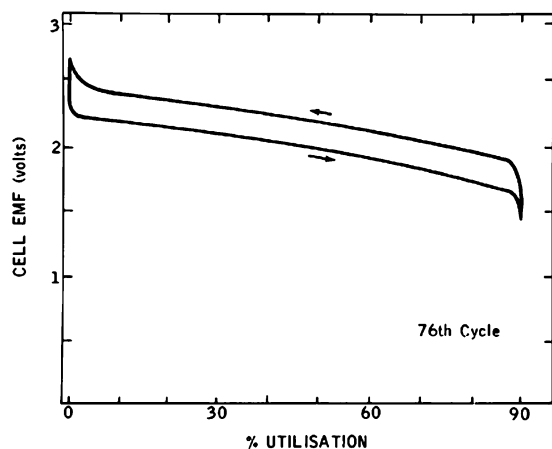


Figure 2. Discharge/charge curve of Li/TiS_2 at $10 \text{ mA}/\text{cm}^2$ (reprinted with permission from ref 13, copyright 1978 Elsevier).

A typical insertion/removal galvanostatic cycle for lithium in titanium disulfide is shown in Figure 2, where the current used is $10 \text{ mA}/\text{cm}^2$. This curve shows the behavior typical of a single phase all the way from TiS_2 to LiTiS_2 , so that no energy is expended in nucleating a new phase. However, closer examination of the intercalation potential curve, using the incremental capacity method for the first time, showed localized ordering of the lithium ions.⁵² The electrolyte used was 2.5 M lithium perchlorate in dioxolane, which was found to be an exceptional electrolyte for effective lithium plating; this solvent also does not co-intercalate with the lithium into the sulfide. In contrast, when propylene carbonate was used as the solvent, any trace amount of moisture resulted in the co-intercalation of the propylene carbonate with a concomitant large expansion of the lattice.⁴⁵ Such co-intercalation of solvent also prevented the use of graphite as an anode for lithium for many years, until appropriate nonintercalating solvents were found,^{53,54} initially dioxolane and then a mixture of carbonate solvents. Dioxolane was also found to be an effective electrolyte solvent for cells using niobium triselenide.^{55,56} However, the electrolyte of LiClO_4 in dioxolane is inherently unsafe.⁵⁷ This clean electrolyte system allows these intercalation reactions to be readily followed by in-situ X-ray diffraction⁵⁸ and in the optical microscope, which show the microscopic details of the intercalation process.⁵⁹

The ready reversibility of lithium in titanium disulfide has permitted deep cycling for close to 1000 cycles with minimal capacity loss, less than 0.05% per cycle, with excess lithium anodes. Exxon marketed button cells with LiAl anodes⁶⁰ and TiS_2 cathodes for watches and other small devices in 1977–1979; the LiAl anode improved the safety of the cells. Some of the largest lithium single cells built to date are those exhibited by Exxon at the Electric Vehicle Show in Chicago in 1977, shown in Figure 3.

Most of the other dichalcogenides are also electrochemically active,¹³ and many show a similar single-phase behavior with lithium intercalation. Vanadium diselenide is an exception,⁶¹ showing two-phase be-

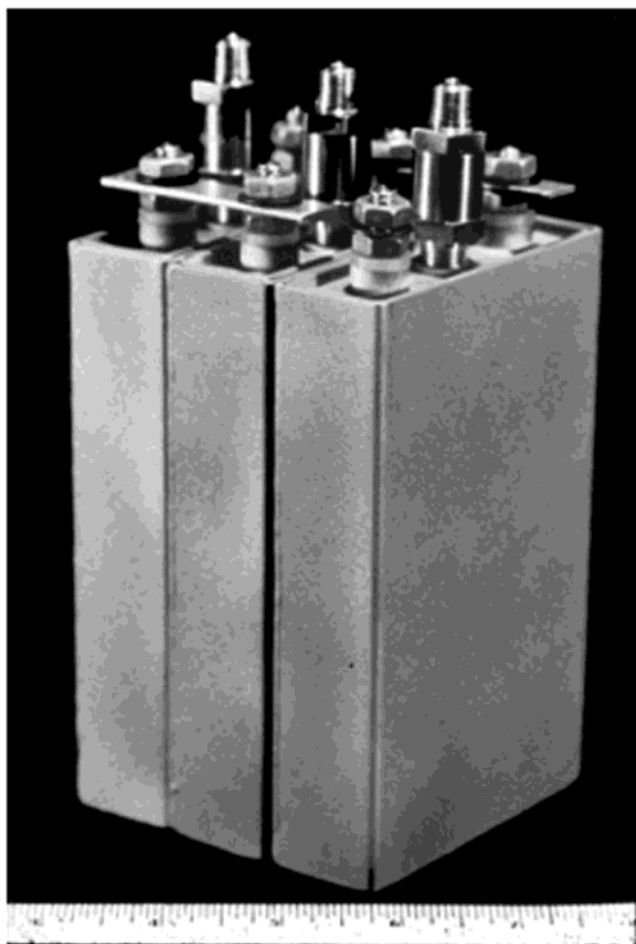


Figure 3. Large cells of LiTiS_2 constructed for the Chicago automotive show in 1977; vents were used for the $\text{LiB}(\text{CH}_3)_4$ salt in dioxolane.

havior as shown in Figure 4. Initially, VSe_2 is in equilibrium with Li_xVSe_2 , where $x \approx 0.25$, then Li_xVSe_2 is in equilibrium with LiVSe_2 , and finally LiVSe_2 is in equilibrium with Li_2VSe_2 . The initial two-phase behavior may be associated with the unusual d/a ratio, which is presumably caused by the desire of group VB elements to have trigonal prismatic coordination with sulfur and selenium, but in VSe_2 the vanadium is octahedral (this d/a is almost that of TP coordination). When lithium is intercalated, the structure becomes typically octahedral with a standard d/a ratio. The ready reversibility of lithium in VSe_2 , even at $10 \text{ mA}/\text{cm}^2$, shows that single-phase behavior is not critical to effective use as a battery cathode; however, the phases formed only differ by slight deformations of the octahedra, not wholesale movement of anion sheets as in the conversion of Li_xCoO_2 to CoO_2 .

Vanadium diselenide also showed the feasibility of intercalating a second lithium into the lattice. The $\text{LiVSe}_2/\text{Li}_2\text{VSe}_2$ system must be two phase, as the lithium in LiVSe_2 is in octahedral coordination whereas in Li_2VSe_2 the lithium must move to tetrahedral coordination and both sites cannot be occupied at the same time. This two-lithium intercalation^{61,62} can be accomplished either electrochemically or chemically, for example, by using butyllithium. Other dilithium layered materials such as Li_2NiO_2 have also been formed⁶³ both electrochemically and chemically

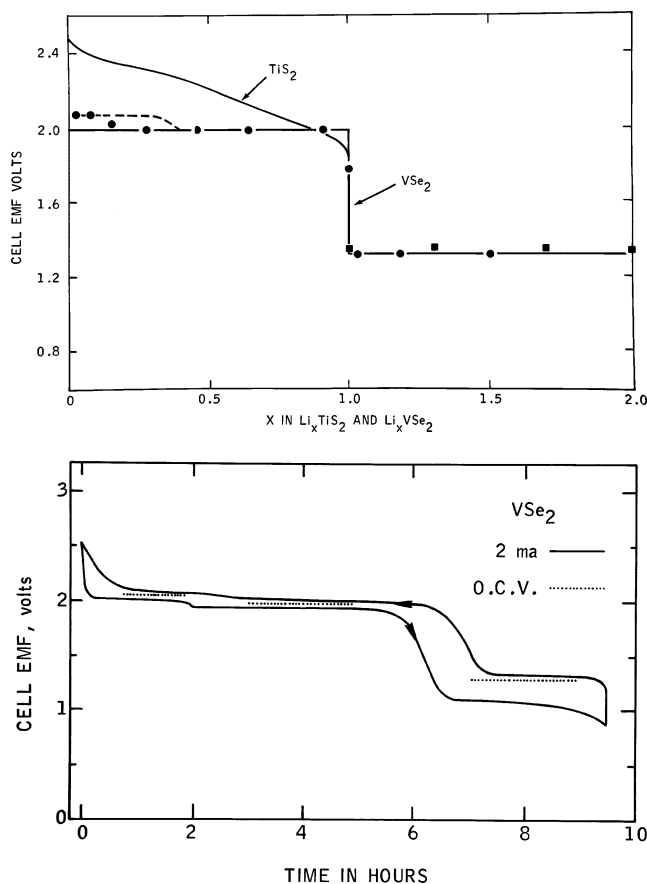


Figure 4. Electrochemical insertion of lithium into vanadium diselenide, showing reaction of two lithium (reprinted with permission from ref 61, copyright 1978 Elsevier):⁶¹ (top) open-circuit potentials, (bottom) behavior on cycling at 2 mA/cm².

using lithium benzophenone in tetrahydrofuran; its structure switches from the 3R-LiNiO₂ phase to one identical to those of Li₂TiS₂ and Li₂VSe₂, where the lithium ions sit in all the tetrahedral sites between the NiO₂ sheets forming a 1T structure. In a similar manner, Li₂Mn_{0.5}Ni_{0.5}O₂ has also been synthesized in electrochemical cells, and both lithium ions can be cycled when part of the Mn is substituted by titanium.⁶⁴

The group VI layered disulfides were originally not thought to be of much interest because of poor rechargeability. However, Haering et al.⁶⁵ showed that in MoS₂, which occurs naturally as molybdenite, if the molybdenum coordination could be changed from trigonal prismatic to octahedral, then the MoS₂ so formed could be effectively used as a cathode. They accomplished this transformation by inserting one lithium per MoS₂ into the lattice and then letting it convert to the new phase. This system formed the foundation of a commercial battery developed by MoliEnergy in British Columbia.⁶⁵

Although the Li/TiS₂ batteries were usually constructed in the charged state with pure lithium or LiAl anodes,⁶⁰ they were also built³⁴ in the discharged state with LiTiS₂ cathodes as now used in all LiCoO₂ cells. In this scenario the cells must first be charged by the deintercalation of the lithium ions. Whereas LiVS₂ and LiCrS₂ were well known in the literature, the lithium-free compounds had not been successfully

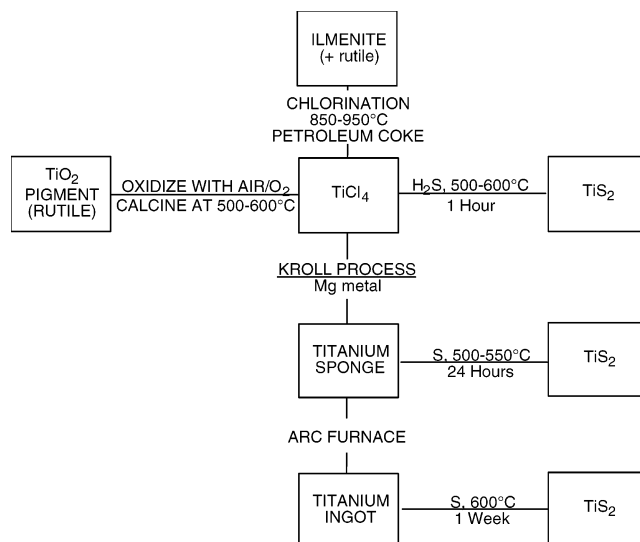


Figure 5. Synthesis approaches for titanium disulfide, after ref 46.

synthesized because the sulfides VS₂ and CrS₂ are thermodynamically unstable at the usual temperatures used for synthesis. Murphy et al.^{66,67} showed that these compounds could be formed by the deintercalation of the lithium at ambient temperatures; this work has led to a new route for the synthesis of metastable compounds—the deintercalation of stable phases.

The metastable spinel form of TiS₂, which has cubic close-packing of the sulfide ions, was similarly formed by the deintercalation of copper from CuTi₂S₄.^{68–70} This cubic structure can also be reversibly intercalated with lithium, although the diffusion coefficient is not as high as in the layered form.

When a battery is being commercialized, the synthesis process used in the laboratory often cannot be used because of the processing costs or cost of the starting materials. As an example, titanium disulfide will be considered where in the laboratory bulk titanium was used to provide electronic-grade titanium disulfide and sponge titanium provided research battery-grade material. The latter could be produced 1 lb at a time in silica tubes, had a surface area of 5 m²/g, and allowed current densities of 10 mA/cm² to be achieved. However, both involved reaction with sulfur, which took from hours for the sponge to days for the bulk metal. Such material would cost more than \$100/lb. An inspection of the commercial process, shown in Figure 5, for sponge manufacture revealed that the precursor was titanium tetrachloride, a liquid at room temperature. This tetrachloride is available in tonnage quantities as it is used in the manufacture of titanium dioxide paint pigment. Therefore, a manufacturing process was devised by two European companies that involved the formation of stoichiometric TiS₂ by deposition from the gas-phase reaction of TiCl₄ with H₂S. This produced a sulfide with a morphology with many plates growing in three dimensions from a single central point, which shows excellent electrochemical behavior.

The stoichiometry and ordering of the titanium is critical to the electrochemical behavior of TiS₂. Stoi-

chiometric and ordered TiS_2 has been shown to exist⁷¹ if the temperature is kept below 600 °C and to have metallic conductivity.³⁹ The titanium disorder can be readily measured by attempting to intercalate weakly bonding species such as ammonia or pyridine. In practice, a slight excess of titanium, $\leq 1\%$, is beneficial in that it reduces the corrosiveness of the sulfur without significantly impacting the cell potential or the lithium diffusion coefficient. It is preferable to add this extra metal to the initial reaction medium.

3.2. Trichalcogenides and Related Materials

As noted above, Trumbore et al. at Bell Labs discovered the electrochemical behavior of the triselenide of niobium. NbSe_3 was found^{23,72,73} to react reversibly with three lithium ions to form Li_3NbSe_3 in a single phase. The other trichalcogenides also readily react with lithium but not in such a reversible manner. Thus, in TiS_3 , which is best represented as $\text{TiS}(\text{S}-\text{S})$, the polysulfide group reacts first with two lithium, breaking the S-S bond to form Li_2TiS_3 in a two-phase reaction; this is followed by the reduction of the titanium from Ti^{4+} to Ti^{3+} in a single-phase reaction similar to TiS_2 itself.⁴⁰ Only this second step is readily reversible, unlike Li_3NbSe_3 , where all three lithium ions are reversible.

A number of other chalcogenide-rich materials have been studied, but although many of them have a high capacity, their rates of reaction or conductivity are low. This can be ameliorated to some extent by admixing them with a high rate high-conductivity material such as TiS_2 or VSe_2 .^{74,75} At high rates of lithium insertion the latter undergo reaction first, and then when the rate is reduced they are recharged by the other component, making them available for the next high-current pulse. This mixed-cathode approach might reemerge as batteries must meet both high-power and high-energy demands.

In this time period a range of chemical reagents was devised to mimic the electrochemical reaction, either lithium reaction or lithium removal, so as to speed-up the evaluation of new materials and get an idea of ease and depth of reaction. The most common lithiating agent is *n*-butyllithium in hexane, a straw-colored liquid, with clean clear easily identified reaction products such as octane, butane, and butene.^{62,76,77} Although highly reactive with a potential of around 1 V versus lithium metal, this reactant gave much purer products than prior methods using naphthalene or liquid ammonia solvent. A series of other chemical reagents with known redox potentials can be used to control the reductive or oxidative intercalation of materials.⁷⁸

3.3. Movement into Oxides

3.3.1. Layered Oxides

Surprisingly the layered oxides with the same structures as the layered dichalcogenides were not studied in that time period. The thought was presumably that oxides toward the right of the periodic table would be of little interest, and it was not considered that lithium could be readily removed

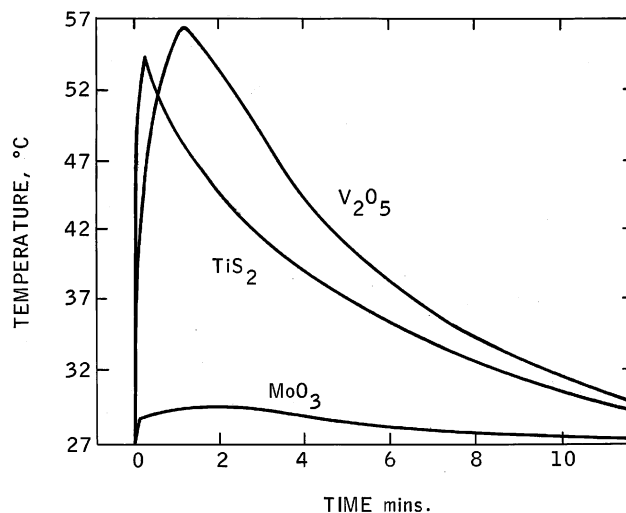


Figure 6. Reaction of *n*-butyllithium with titanium disulfide, vanadium pentoxide, and molybdenum trioxide (reprinted with permission from ref 77, copyright 1977 The Electrochemical Society).

from the layered materials such as LiCoO_2 , which were of more interest for their magnetic properties.

3.3.2. High-Valent Oxides of Vanadium and Molybdenum

Vanadium pentoxide, V_2O_5 , and molybdenum trioxide, MoO_3 , were two of the earliest studied oxides. Molybdenum oxide reacts readily with around 1.5 lithium/molybdenum,^{40,79} but is of little interest because of its low rate of reaction which is readily determined by the rate of temperature rise when the solid is added to the chemical lithiating agent *n*-butyllithium.⁷⁷ Figure 6 shows the heat of reaction for three cathode materials, TiS_2 , V_2O_5 , and MoO_3 ; the higher the temperature increase, the greater the power capability of the material. A high-power material should be able to boil the hexane solution.

Vanadium pentoxide has been investigated for 30 years;^{40,80–84} it has a layered structure with weak vanadium–oxygen bonds between the layers and is now known to react by an intercalation mechanism:^{40,85} $x\text{Li} + \text{V}_2\text{O}_5 = \text{Li}_x\text{V}_2\text{O}_5$.

The structural behavior on lithium insertion is fairly complex with the initial lithium merely intercalating the structure, first forming the α -phase ($x < 0.01$) and then the ϵ -phase ($0.35 < x < 0.7$), where the layers are more puckered. At $x = 1$, shifting of one layer out of the two leads to the δ -phase. However, if more than one lithium is discharged, then significant permanent structural changes occur, giving the γ -phase, which can be cycled in the range $0 \leq x \leq 2$. In the α -, ϵ -, and δ -phases the VO_5 square pyramids that make up the structure of V_2O_5 are arranged in rows which have the apexes ordered up, up, down as shown schematically in Figure 7. In contrast, in the highly puckered γ -phase, these are organized up, down, up, down. A rock-salt structure is formed when still more lithium is added; this compound is called the ω - $\text{Li}_3\text{V}_2\text{O}_5$ phase. This ω -phase cycles in a single solid–solution phase with the last lithium coming out at over 4 V, clearly showing the difference between this phase and the initial vanadium pentoxide phase, which has an open-circuit

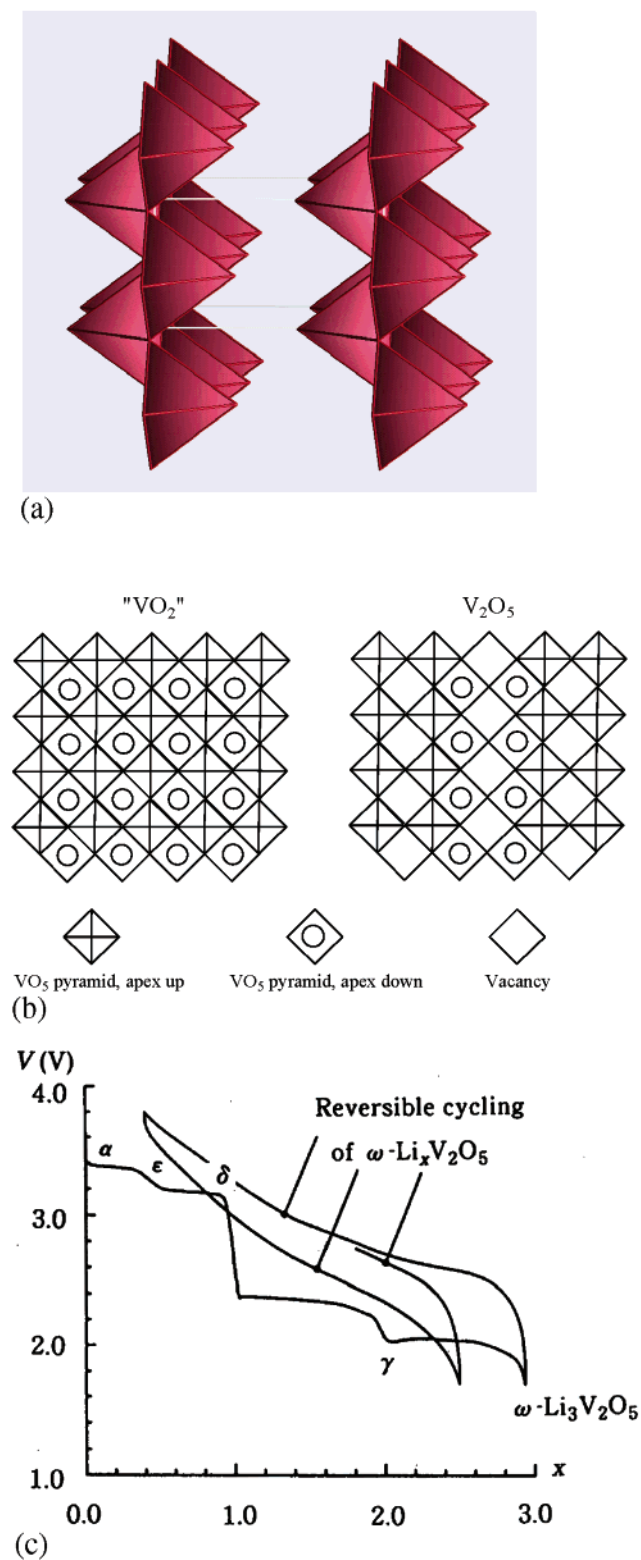


Figure 7. Structure and discharge of vanadium pentoxide: (a) structure of V₂O₅ showing the square pyramids sharing edges of the basal planes; (b) schematic showing basal planes sharing edges and the orientation of the apices of the pyramids comparing the structure in the perfect lattice of VO₂ compared with the ordered defect lattice of V₂O₅ (reprinted with permission from ref 364, copyright 1996 The Electrochemical Society); and (c) electrochemical lithium intercalation into V₂O₅ showing the evolution of phases with degree of lithium intercalation and the cycling of ω -phase (reprinted with permission from ref 82, copyright 1994 Elsevier).

potential of 3.5 V. This behavior is shown in Figure 7. The ω -material has a tetragonal structure, which on extended cycling becomes a simple rock-salt structure with $a = 4.1 \text{ \AA}$ with the formula Li_{0.6}V_{0.4}O. Delmas⁸² reviewed these structural modifications and attributes the high OCV at low lithium content to the metastability of the defective rock-salt lattice which can contain up to 60% vacancies on the cation sublattice. The single sloping discharge plateau from almost 4 to under 2 V makes it uninteresting for practical applications where the change in potential should preferably be under 0.5 V; moreover, this phase also rapidly loses capacity on cycling.

3.3.3. Mixed-Valent Oxides of Vanadium—V₆O₁₃ and LiV₃O₈

Murphy et al.⁸⁶ made an extensive study of a number of vanadium oxides and discovered the excellent electrochemical behavior of the partially reduced vanadium oxide, V₆O₁₃, which reacts with up to 1 Li/V. They also recognized that the method of preparation, which determines the V:O ratio, critically controls the capacity for reaction with lithium. The structure consists of alternating double and single sheets of vanadium oxide sheets made up of distorted VO₆ octahedra. A variety of sites are available for lithium intercalation, which if filled sequentially would lead to the various steps seen in the discharge curve. The lattice first expands along the c -axis and then along the b -axis. Thomas et al.^{87–91} made an in-depth study of the complex intercalation process in single crystals of V₆O₁₃. This phase was one of the leading candidates for polymer electrolyte batteries, which require a lower voltage system because of the limited thermodynamic stability of the polymer.

Another vanadium oxide that has received much attention is LiV₃O₈, which has a layer structure composed of octahedral and trigonal bipyramidal ribbons that can be swelled just like other layered compounds and can intercalate lithium.^{92,93} Here again, the method of preparation is important to its electrochemical characteristics.⁹⁴ West et al.⁹⁵ made a systematic study of the impact of synthesis technique on capacity and cycling and showed that amorphous material increased the capacity above 2 V from 3–4 lithium per mole of LiV₃O₈ at low current drains, 6–200 $\mu\text{A}/\text{cm}^2$.

3.3.4. Double-Sheet Structures: Xerogels, δ -Vanadium Oxides, and Nanotubes

There has been much interest in vanadium oxides formed by sol–gel processes.^{96–98} These can be formed by acidification of a sodium vanadate solution, for example, by passing it down an acidified ion-exchange column. The resulting orange gel on drying has the formula H_xV₂O₅· n H₂O. About 1.1 mol of water may be removed under vacuum or on mild heating, leading to H_{0.3}V₂O₅·0.5H₂O, based on its high cation-exchange capability. The interlayer spacing is around 8.8 \AA , which swells to 11.5 \AA for the more hydrated form with 1.8H₂O. The protons and water can be readily exchanged for lithium and polar solvents. These vanadium oxide gels can be also

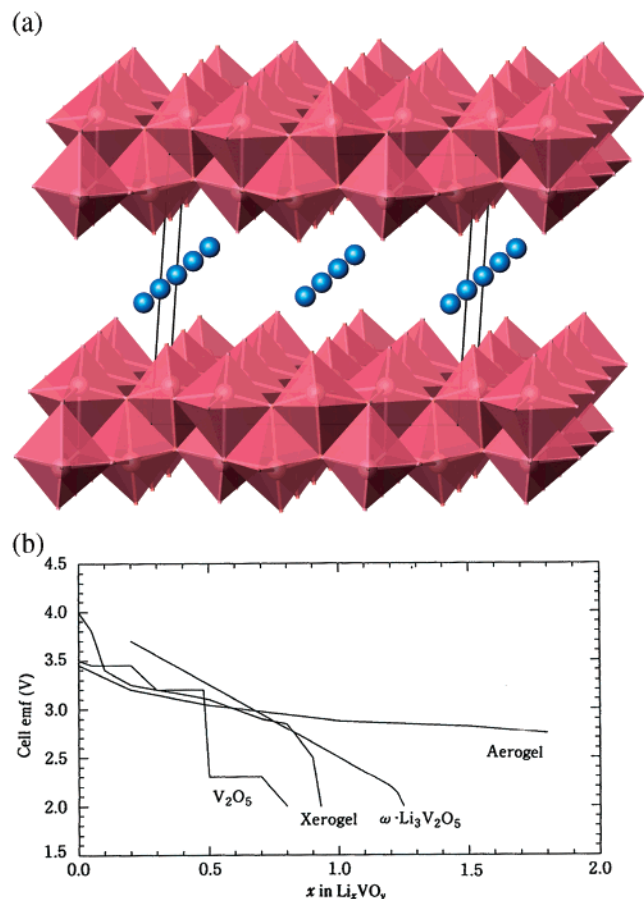


Figure 8. (a) Structure of the two-layer structure found in xerogel, and (b) comparison of the electrochemical behavior of the crystalline,⁸² xerogel,³⁶² ω -phase,⁸³ and aerogel¹⁰⁰ forms of vanadium pentoxide.

made⁹⁹ by the hydrogen peroxide treatment of V₂O₅. These xerogel vanadium pentoxides contain sheets comprised of two vanadium oxide layers, with all the vanadyl bonds on the outside leading to a distorted octahedral coordination around the lithium instead of the square pyramidal coordination found in crystalline V₂O₅. Recently, it was reported¹⁰⁰ that making V₂O₅ through an aerogel process with supercritical drying in CO₂/acetone gives a much more electrochemically active product, H_yV₂O₅·0.4H₂O·carbon; the amount of carbon was 3.9 wt %. The dried material, which had a 12.5 Å lattice spacing, reacts with lithium in a single continuous discharge curve with a midpoint emf of around 3.1 V and a total lithium uptake of 4.1 Li by 2.8 V, thus giving a much higher capacity than crystalline V₂O₅ as shown in Figure 8.

The double layers of vanadium oxide found in the xerogel have been described in a number of other vanadium oxides by Galy¹⁰¹ and Oka;¹⁰² they also form the double sheets described above for V₆O₁₃. These oxides, in which the vanadium is found in distorted VO₆ octahedra, show particularly attractive electrochemical capacities^{103–107} exceeding 200 mAh/g in some cases, as shown in Figure 9. However, at the present time their rate capability appears somewhat limited. More recently vanadium oxide nanotubes have been synthesized, first by Spahr et al.;^{108,109} these compounds also contain double sheets of vanadium oxide and again have interesting but complex

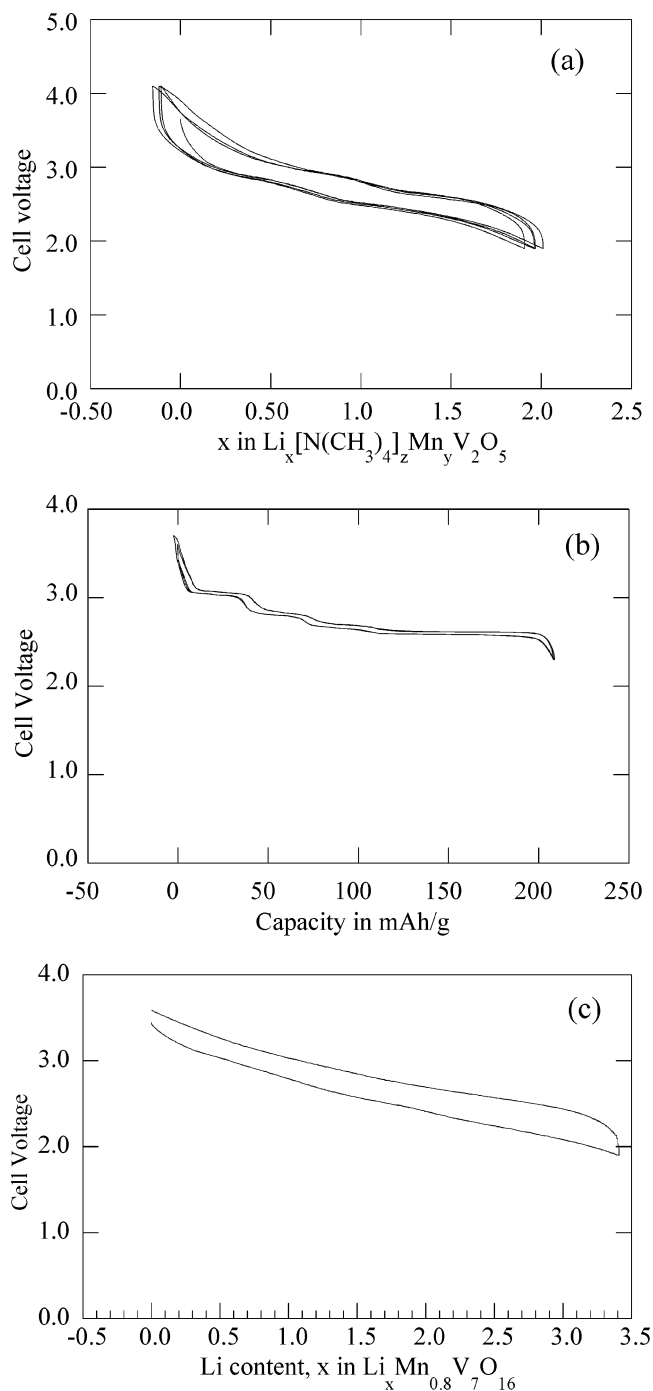


Figure 9. Electrochemical behavior of (a) δ -Mn_yV₂O₅ (reprinted with permission from ref 105, copyright 2000 Elsevier), (b) δ -NH₄V₄O₁₀, and (c) Mn vanadium oxide nanotubes.¹¹²

electrochemical behavior.¹¹⁰ In some cases the capacity increases on cycling;¹¹¹ the electrochemical behavior of the manganese ion-exchanged compound is also shown¹¹² in Figure 9.

4. 1980–1990: Era of Layered Oxides and First Large Commercialization

4.1. Early Studies of Layered Oxides

Although the heavier alkali-metal compounds of the oxides of manganese, cobalt, chromium, and

others had been extensively studied by a number of groups, in particular, at Bordeaux by Hagemmuller and Delmas^{113–119} in the 1970s, there was essentially no in-depth study of the corresponding lithium compounds. This was not dissimilar to the situation in Nantes, where Rouxel et al.^{119–122} were researching the layered dichalcogenides at the same time. This can be in part associated with the lack of a good lithiating agent, which was solved with the discovery of the synthetic prowess of *n*-butyllithium and electrochemical synthesis.

In the studies in the 1970s the structures of these layered oxides and chalcogenides were extensively studied. Whereas lithium only occupies octahedral sites in the strictly layered materials when the Li/transition-metal ratio is unity or less, the larger alkali ions often occupy trigonal prismatic sites. Which site is occupied depends on the alkali cation size and their concentration, with some ions such as sodium exhibiting a range of structures. The stacking of the MO₂ slabs in the overall structure depends on the alkali site occupancy. As significant reorganization of the lattice must occur in switching from one structure to another, such changes will impede electrochemical reactions. Thus, it is important to know the phases formed as the alkali concentration changes. In the case of the small lithium ion, one needs only be concerned with the stacking sequence and whether it changes as the lithium concentration changes as the lithium ion normally occupies only the octahedral sites for $x \leq 1$ in Li_{*x*}MO₂. For most layered oxides the transition metal also only occupies octahedral sites. There are at least three different stacking sequences of the MO₂ slabs (building blocks) that can form the unit cell; the lithium ions reside between the slabs. These three stacking arrangements are as follows.

- Single blocks stacked upon one another, as in, for example, LiTiS₂, CoO₂, and TiS₂. This is the CdI₂ structure. This is a hexagonal close-packed lattice. A special case of the single block structure is given by the dilithium compounds, such as Li₂VSe₂, where the lithium resides on all the tetrahedral sites.
- Double blocks stacked upon one another, normally formed by ion exchange from a sodium-containing compound.
- Triple blocks, each block displaced by one-third in the basal plane, stacked on top of one another. This sequence is very common in the lithiated oxides, such as LiCoO₂ (the α -NaFeO₂ structure). This is a cubic close-packed lattice.

In addition, at very low lithium contents not every layer between the slabs need be occupied by lithium ions but, for example, just every other layer. This is known as a second-stage compound. The above three stacking arrangements can also be described in terms of the positions of the atoms. Thus, if a slab is described by the designation AcB, where A, B, and C represent the three possible positions of the anions in the hexagonal lattice and a, b, and c represent the cation positions, then the three stacking sequences

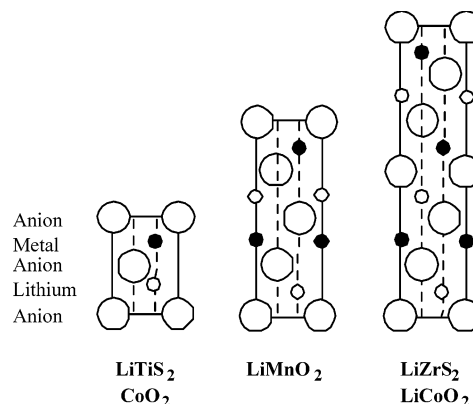


Figure 10. Schematic of stacking of building blocks for one-block, two-block, and three-block structures.

described above may be represented for the dioxide MO₂ and lithiated LiMO₂ as follows.

slab stacking	MO ₂	LiMO ₂
single block	..(AcB)(AcB)..	..(AcB)c(AcB)..
double block	..(AcBCaB)(AcBCaB)..	..(AcBaCaB)c(AcBaCaB)..
triple block	..(AcBCbABaC)- (AcBCbABaC)..	..(AcBaCbAcBaC)b- (AcBaCbAcBaC)..

It can thus be seen that long-range atomic motion (slab-sliding) is required to convert one of these structures into another one. These arrangements are shown schematically in Figure 10. It can also be noted that in the single block structures all the cations are stacked directly above each other, while in the triple block structure all the cations are staggered to minimize any ionic interactions. Thus, the former tends to be formed by more covalent lattices and the latter by the more ionic lattices. In addition to these idealized hexagonal lattices, there are a number of instances in which the lattice is distorted and where cations migrate between the slabs and the interslab region. This, often unintended migration, can play a significant role in the reactivity and electrochemical behavior of the material. The special case of the dilithium compounds, Li₂MO₂, where the lithiums are in tetrahedral sites, can be represented by the slab-stacking sequence ..(AcB)-ba(AcB)... There is only one realistic stacking sequence because an octahedral site in the transition-metal layer cannot be occupied directly opposite a tetrahedral site. Where some octahedral sites are occupied in the lithium layer, the total lithium content will be less than two and/or the lattice will become distorted or even amorphous.

4.2. Lithium Cobalt Oxide, LiCoO₂

Goodenough recognized that LiCoO₂ had a structure similar to the layered structures of the dichalcogenides and showed that the lithium could be removed electrochemically, thus making it a viable cathode material.¹²³ LiCoO₂ has the α -NaFeO₂ structure with the oxygens in a cubic close-packed arrangement. On complete removal of the lithium, the oxygen layers rearrange themselves to give hexagonal close packing of the oxygen in CoO₂.¹²⁴ Between these composition limits several phases are

formed with varying degrees of distortion of the ccp oxygen lattice. The composition $\text{Li}_{0.5}\text{CoO}_2$ can also be formed in the spinel form,¹²⁵ though it appears to be metastable and is not normally formed during the cycling of the Li_xCoO_2 electrode. However, a recent TEM study¹²⁶ has identified the spinel phase originating on the surface of heavily cycled LiCoO_2 cathodes.

SONY combined the LiCoO_2 cathode with a carbon anode to make the first successful Li-ION battery,^{127,128} which now dominates the lithium battery market. The carbon anode, which forms the compound LiC_6 on reaction with lithium, makes a much safer battery than if pure lithium is used as there is much less chance of the formation of dendritic lithium, which can lead to cell shorting. The use of graphitic carbon can result in the loss of 100–300 mV in cell potential, which is feasible with the higher potential LiCoO_2 cathode but not with the lower potential of the TiS_2 cathode. The commercial cell is built in the discharged state: C- LiCoO_2 . It thus must be charged before use. The theoretical capacity of the LiCoO_2 cell is relatively low at around 130 mAh/g because only around 0.5 Li/Co can be reversibly cycled without causing cell capacity loss due to changes in the LiCoO_2 structure. This can be associated with two factors: phase changes that cause low reaction rates and the poor stability of the electrode at low lithium contents. The message here may be that reactive nanosize materials/components may not be viable for commercial batteries because of safety and life considerations.

The diffusion of lithium in LiCoO_2 is $5 \times 10^{-9} \text{ cm}^2/\text{s}$, which compares with $10^{-8} \text{ cm}^2/\text{s}$ for LiTiS_2 .¹²⁹ These high diffusivity values are consistent with the ability to cycle these two cathodes at 4¹²⁹ and 10 mA/cm²,¹³ respectively. However, the conductivity of Li_xCoO_2 remains a challenge as it is reported¹³⁰ to change dramatically with composition, behaving like a metal at $x = 0.6$ and a typical semiconductor at $x = 1.1$ (the typical lithium-rich material used in commercial cells), changing by 2¹³¹ (for the $x = 1.1$ compound) to 4¹³⁰ (for the $x = 1.0$ compound) orders of magnitude at ambient temperatures and up to 6 orders of magnitude at lower temperatures.¹³¹

The energy density of commercial cells has almost doubled since their introduction in 1991; since 1999 the volumetric energy density has increased from 250 to over 400 Wh/l.¹³² Details of the original commercial cells have been reviewed by Nishi,¹³³ where key aspects are discussed concerning the need for large particle size, 15–20 μm , to increase safety and the intentional incorporation of lithium carbonate into the cathode to provide a safety valve. The lithium carbonate decomposes, releasing carbon dioxide when the charging exceeds 4.8 V, which breaks electrical flow in the cell. These lithium cobalt oxides also contain excess lithium and can be best represented by the formula $\text{Li}_{1+x}\text{Co}_{1-x}\text{O}_2$.

In 1999 Cho et al. reported^{134–138} in a pioneering series of papers that the capacity could be improved by coating a metal oxide or phosphate on the surface of the LiCoO_2 particles. They found that the capacity could be increased to 170 mAh/g when cycled between

2.75 and 4.4 V without capacity fade over 70 cycles. Other researchers^{139–141} quickly confirmed the positive results of surface coatings. The mechanism of protection is related to minimizing the reactivity of Co^{4+} on charge with the acidic HF in the electrolyte coming from the interaction of moisture with the electrolyte salt LiPF_6 .¹⁴² Removing the source of the HF should eliminate the capacity loss as found^{143,144} for the spinel LiMn_2O_4 , where switching to the LiBOB salt essentially eliminated manganese dissolution and capacity loss. This was also the case for LiCoO_2 ,¹⁴⁵ where replacing the LiPF_6 salt by LiBOB or by completely drying the LiCoO_2 by heating to over 550 °C, improved the capacity retention at 180 mAh/g at a 4.5 V cutoff. Above this 4.5 V level, the three-block cubic close-packed Li_xCoO_2 converts to the 1T one-block hexagonal close-packed structure of CoO_2 ; this requires substantial movement of the oxygen layers in going from ABCA to ABA stacking sequence which will eventually significantly disrupt/disorder the structure. Thus, one cannot expect capacities for LiCoO_2 much above 180 mAh/g to be attainable over hundreds of cycles. A more recent study¹⁴⁶ suggests that CoO_2 has a monoclinically distorted CdCl_2 structure, whereas NiO_2 has a monoclinically distorted CdI_2 structure, but little detail is given and no mention is made of the nickel content or distribution.

Although the LiCoO_2 cathode dominates the rechargeable lithium battery market, there is a limited availability of cobalt, which causes it to have a high price. This price limits its use to small cells, such as those used in computers, cell phones, and cameras. An alternative cathode will be needed for large-scale applications, as envisioned in HEV or for load leveling. The LiCoO_2 patent¹⁴⁷ covered more than this one cathode, describing all layered transition-metal oxides with the $\alpha\text{-NaFeO}_2$ structure where the transition metal is vanadium through nickel. In addition, combinations of the transition metals were described, such as $\text{LiCo}_{1-y}\text{Ni}_y\text{O}_2$. In addition, another patent¹⁴⁸ covers the electrode intercalation process for forming the alkali-metal compounds A_xMO_2 with the $\alpha\text{-NaFeO}_2$ structure where A is Li, Na, or K and $x < 1$.

4.3. Lithium Nickel Oxide, LiNiO_2

Lithium nickel oxide, LiNiO_2 , is isostructural with lithium cobalt oxide but has not been pursued in the pure state as a battery cathode for a variety of reasons, even though nickel is more readily available than cobalt. First, it is not clear that stoichiometric LiNiO_2 exists. Most reports suggest excess nickel as in $\text{Li}_{1-y}\text{Ni}_{1+y}\text{O}_2$; thus, nickel is always found in the lithium layer, which pins the NiO_2 layers together, thereby reducing the lithium diffusion coefficient and the power capability of the electrode. Second, compounds with low lithium contents appear to be unstable due to the high effective equilibrium oxygen partial pressure, so that such cells are inherently unstable and therefore dangerous in contact with organic solvents. A second lithium can be inserted either chemically or electrochemically, as in $\text{Li}_{1.8}\text{Ni}_{1+y}\text{O}_2$, which is a mixture as expected of “ LiNiO_2 ” and “ Li_2NiO_2 ”.⁶³

We will discuss in section 5.2.1 of this review the modification of this material by replacing a part of the nickel by other elements such as cobalt and aluminum. The former assists in ordering the structure, that is keeping the nickel in the nickel layer, and the latter, being redox inactive, prevents the complete removal of all the lithium, thus additionally stabilizing the structure and preventing any phase changes that might occur at very low or zero lithium content. Unlike cobalt and nickel, manganese does not form a stable LiMnO_2 phase with the LiCoO_2 structure, with the spinel structure being the stable phase at the composition $\text{Li}_{0.5}\text{MnO}_2$. As there are a myriad of structures¹⁴⁹ with the 1:2 Mn:O ratio, other structures may be stable at different lithium contents.

5. 1990–Present: Second-Generation Lithium Batteries

5.1. Spinel

The spinel cathode LiMn_2O_4 , originally proposed by Thackeray et al.,¹⁵⁰ has been extensively developed by the Bellcore labs,^{151–153} and has recently been reviewed by Thackeray¹⁵⁴ with the key structural aspects by Yonemura et al.¹⁵⁵ The anion lattice again contains cubic close-packed oxygen ions and is closely related to the $\alpha\text{-NaFeO}_2$ layer structure, differing only in the distribution of the cations among the available octahedral and tetrahedral sites. The discharge proceeds in predominantly two steps, one around 4 V and the other around 3 V as shown in Figure 11. Usually only the 4 V plateau is used, so that the cell is constructed in the discharged state and must be charged before use just as for LiCoO_2 .

charging: $\text{LiMn}_2\text{O}_4 \rightarrow \text{Mn}_2\text{O}_4 + \text{Li}$ (inserted into anode host, such as graphitic carbon)

It has been reported^{153,156} that the value of the cubic lattice parameter, which is directly related to the average oxidation state of the manganese, is critical to obtain effective cycling. The lattice parameter should preferably be 8.23 Å or less, and such values are associated with lithium-rich materials, $\text{Li}_{1+x}\text{Mn}_{2-x}\text{O}_4$, where the average manganese oxidation state is 3.58 or higher; this value minimizes dissolution of manganese and also the impact of the

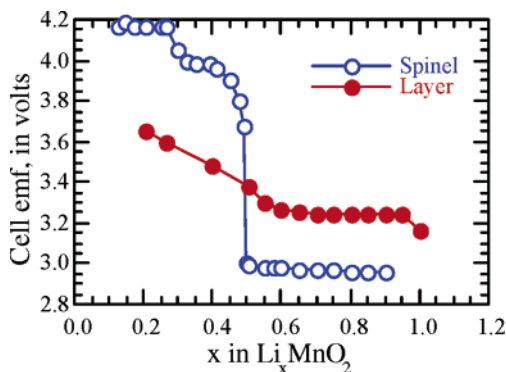


Figure 11. Potential profile of LiMnO_2 and spinel LiMn_2O_4 (data from Bruce and Whittingham).

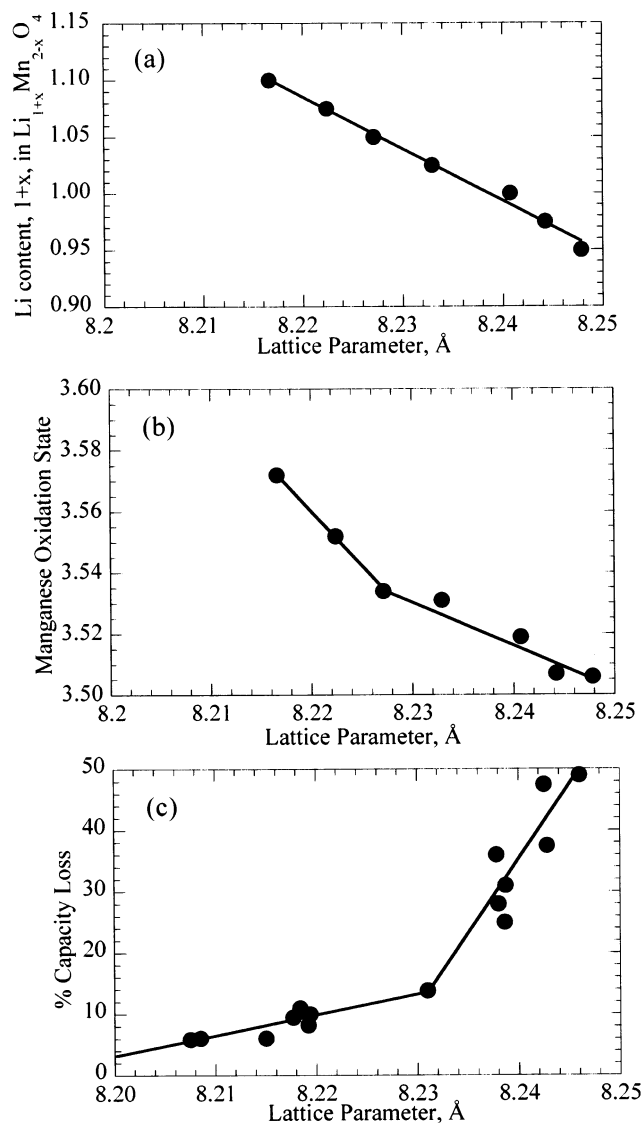


Figure 12. Correlation of the lattice parameter of the spinel $\text{Li}_{1+x}\text{Mn}_{2-x}\text{O}_4$ with (a) the lithium content, (b) manganese oxidation state, and (c) capacity loss of the cell over the first 120 cycles, after ref 157.

Jahn–Teller distortion associated with the Mn^{3+} ion. The variation in lattice parameter, a_0 , with chemical composition in $\text{Li}_{1+x}\text{Mn}_{2-x}\text{O}_2$ is shown in Figure 12a (after ref 157); its variation is given by $a_0 = 8.4560 - 0.21746x$.

The lattice parameter may also be used as an indirect measurement of the manganese oxidation state, shown in Figure 12b. Figure 12c, in addition, shows clearly the impact of lattice parameter on the percent capacity loss over the first 120 cycles. The retention of cycling capacity at elevated temperatures can be helped by the simultaneous doping with aluminum and fluoride ions, as in $\text{Li}_{1+x}\text{Mn}_{1-x-y}\text{Al}_y\text{O}_{4-z}\text{F}_z$, where y and z are around 0.2.¹⁵⁷ Moreover, if the potential on the surface of the spinel is kept above that for the formation of the $\text{Li}_2\text{Mn}_2\text{O}_4$ phase, then the formation of Mn^{2+} by the disproportionation of surface Mn^{3+} ions is minimized: $2\text{Mn}^{3+} = \text{Mn}^{2+} + \text{Mn}^{4+}$. It is the divalent manganese ions that are soluble in the acidic electrolyte, and so every attempt must be made to minimize their formation. Once dissolved into the electrolyte, the manganese ions can

diffuse across to the anode and be reduced there to manganese metal, thereby using up the lithium and reducing the electrochemical capacity of the cell.

This spinel is presently the center of much interest as the cathode of a high-power lithium battery for hybrid electric vehicles, even though under high drain rates its capacity is only around 80 mA/g. This material has been plagued by self-discharge when left under full charge, particularly at elevated temperatures; however, this problem may have been solved by switching from the fluoride-containing LiPF_6 salt, which in the presence of traces of moisture can generate HF, to salts such as LiBOB.^{143,144} The spinel used is in a stabilized form in which a part of the manganese has been substituted as in $\text{Li}_{1.06}\text{Mn}_{1.95}\text{Al}_{0.05}\text{O}_4$, and there have been several hundred studies on the impact of this substitution.^{157–159} These studies will not be discussed here. An alternate solution pioneered by the Korean school is to coat the surface of the spinel particles with materials such as zirconium dioxide or AlPO_4 , which are believed to act as getters for any HF.

One spinel, $\text{Li}_4\text{Ti}_5\text{O}_{12}$, is under serious consideration as an anode in high-power cells as its charging potential (lithium insertion) is around 1.55 V,^{160–162} so there is no danger of lithium metal deposition as might occur on graphitic carbon at high rates. Rates as high as 12C have been claimed (total reaction in 60/12 = 5 min), both with nano- and microstructured materials at 60 °C.¹⁶³ This electrode is being considered in combination with a high-rate cathode such as a mixed layered oxide or with the spinel LiMn_2O_4 to give a lower cost and safe 2.5 V cell. It has also been coupled with the olivine LiFePO_4 (see later in this paper) and cycles well at a potential of 1.8 V with no capacity loss over a 100 cycles.¹⁶⁴ If coupled with a high-voltage spinel, then the cell potential might attain 3.5–4 V.¹⁶⁵

5.2. Other Layered Oxides

5.2.1. Mixed Nickel–Cobalt Dioxide, $\text{LiNi}_{1-y}\text{Co}_y\text{O}_2$

Many different elements can be substituted into the $\alpha\text{-NaFeO}_2$ -type structure, and they impact the layeredness of the structure, its stability on lithium removal, and the retention of capacity on cycling. In a series of papers the Delmas group^{166–169} and Zhecheva et al.¹⁷⁰ determined the structural details and physical properties of the $\text{LiNi}_{1-y}\text{Co}_y\text{O}_2$ system and showed that there is an increased ordering as the cobalt concentration increases; they found that the $d/3a$ ratio increases monotonically from 1.643 to 1.652 as y increases from 0 to 0.4 and that there is no nickel content on the lithium sites for $y \geq 0.3$. Thus, cobalt suppresses the migration of nickel to the lithium site in the mixed Li nickel/cobalt compounds and one would expect and finds the same behavior in the Li nickel/manganese/cobalt oxides. Cobalt is also reported to facilitate the oxidation of iron atoms in the structure.¹⁷¹ Other ions, such as iron, do not have the same positive effect as cobalt; thus, in the compound $\text{LiNi}_{1-y}\text{Fe}_y\text{O}_2$ the capacity is reduced with increasing iron content and the iron has no positive

effects on the layeredness of the structure.¹⁷² Thus, for $y = 0.10, 0.20,$ and 0.30 the amount of 3d metal in the lithium layer is 6.1%, 8.4%, and 7.4%, respectively, for samples formed at 750 °C. Although a LiFeO_2 compound would be ideal for a low-cost battery, it has been reported¹⁷³ that the lithium cannot be deintercalated within the normal potential ranges used in lithium batteries; this is explained¹⁷⁴ by the lack of compression of the FeO_6 octahedra which makes the reduction of one electron from Fe^{3+} very difficult.

An issue with all these layered oxides is their electronic conductivity, which is not uniformly high across the lithium composition range, or nickel substitution. Thus, cobalt substitution in LiNiO_2 , as in $\text{LiNi}_{0.8}\text{Co}_{0.2}\text{O}_2$, reduces the conductivity.¹⁶⁹ In addition, as lithium is removed from the phase $\text{Li}_x\text{Ni}_{0.1}\text{Co}_{0.9}\text{O}_2$ ¹⁶⁸ or from Li_xCoO_2 ¹³⁰ the conductivity was found to increase dramatically by some 6 orders of magnitude to around 1 S/cm from $x = 1$ to 0.6. These dramatic changes demand that a conductive diluent be added to the cathode-active material, which reduces both the energy storage and the power capabilities.

Studies have shown that the cobalt-substituted nickel oxides are more stable and thus are less likely to lose oxygen than the pure nickel oxide. The addition of a little of a redox-inactive element such as magnesium reduces the capacity fading on cycling,¹⁷⁵ as in $\text{LiNi}_{1-y}\text{Mg}_y\text{O}_2$;¹⁷⁶ this inert element prevents the complete removal of all the lithium and thus minimizes possibly structural collapse and reaching such a high level of oxygen partial pressure— NiO_2 itself is thermodynamically unstable at 25 °C, as the equilibrium oxygen partial pressure exceeds 1 atm.

Substituted nickel oxides, such as $\text{LiNi}_{1-y-z}\text{Co}_y\text{Al}_z\text{O}_2$, are prime candidates for the cathode of advanced lithium batteries for use in large-scale systems as required for hybrid electric vehicles. On charging these mixed oxides the nickel is oxidized first to Ni^{4+} then the cobalt to Co^{4+} .¹⁷⁷ SAFT has constructed cells with these substituted nickel oxides that have been cycled 1000 times at 80% depth of discharge with an energy density of 120–130 Wh/kg.¹⁷⁸

5.2.2. Lithium Manganese Dioxide, LiMnO_2

Much interest has been placed on the layered LiMnO_2 compound for its prospects of providing not only a low-cost but also an environmentally benign cathode material.^{179–181} However, it is not thermodynamically stable at elevated temperature and thus cannot be synthesized by the same methods as used for materials like NaMnO_2 . Instead, other approaches must be used. One approach is to ion exchange the sodium compound, giving LiMnO_2 , which was accomplished independently by Bruce¹⁸¹ and Delmas;¹⁸² starting with different layered structures maintains the stacking order of the parent manganese oxide, thus allowing study of the impact of stacking sequence on electrochemical performance. An alternative preparative approach is to synthesize the structure at low temperatures, as, for example, by hydrothermal synthesis/decomposition of alkali

permanganates,^{180,183–185} which in the case of lithium results in the composition $\text{Li}_{0.5}\text{MnO}_2 \cdot n\text{H}_2\text{O}$. Mild warming causes the loss of water to give the desired layered Li_xMnO_2 ; overheating to 150 °C results in the formation of the spinel LiMn_2O_4 . Birnessite-type phases have also been made by acid treatment of manganese oxides.^{186–189}

However, Li_xMnO_2 easily converts to the thermodynamically stable spinel structure upon cycling lithium in and out but apparently not on acid delithiation;¹⁹⁰ this conversion requires no oxygen diffusion as both structures have ccp oxygen lattices. This ccp lattice has oxygen layers in the sequence AcB|aCbA|cBaC|bA , i.e., there are three building blocks— MnO_2 blocks (upper case is oxygen, lower case is manganese, italic lower case is lithium). Two approaches to stabilize the layered LiMnO_2 have been taken. In the geometric stabilization approach, non-ccp structures are proposed such as tunnel structures,^{191–195} two-block (see Figure 10) or other non CCP close-packed structures,¹⁹⁶ or “pillars” are placed between the layers to provide the stabilization. We reported on compounds KMnO_2 ^{180,184} and $(\text{VO})_y\text{MnO}_2$,^{197,198} which are examples of such pillared structures. The former is stable to spinel formation at low current densities, and the latter shows excellent stability but poor rate capability. The groups of Dahn and Doeff among others have pursued non-ccp structures by looking at tunnel structures such as $\text{Li}_{0.44}\text{MnO}_2$ ^{191,193,194} and also by ion-exchanging layered sodium manganese oxide compounds with non-ccp stacking of the oxygen sheets;^{199–205} these sheets cannot readily reorganize after ion exchange to give ccp stacking. This results in, for example, the two-block rather than the three-block structures such as O3, which is that of ccp LiMnO_2 . Such compounds have also been studied with partial substitution of the manganese by, for example, Co.²⁰⁵ This ion-exchange process also results in much faulting in the stacking of the layers, which impedes the layers from reordering into the thermodynamically stable O3 phase. However, these phases intercalate lithium over a rather wide range of potential and in some cases over two potential steps.²⁰¹

In the electronic stabilization approach the goal is to make the electronic properties of Mn to be more cobalt-like by substitution of the Mn with more electron rich elements such as Ni.¹⁹⁶ The successful substitution of Mn by Co^{190,206,207} and Ni^{208–214} has been reported. The first studies on $\text{LiNi}_{1-y}\text{Mn}_y\text{O}_2$, for $0 < y \leq 0.5$, indicated low capacities and poor reversibility.²¹² However, Spahr et al. later demonstrated a high capacity and reversibility for $\text{LiNi}_{0.5}\text{Mn}_{0.5}\text{O}_2$ ²¹³ with a discharge curve typical of that of LiNiO_2 . More recently, the compounds $\text{LiNi}_{1-y-z}\text{Mn}_y\text{Co}_z\text{O}_2$ have been extensively investigated in the last 3 years and found to have properties that qualify them as possible candidates for the replacement of LiCoO_2 .^{198,215–237} In addition to their high lithiation capacities and reversibility, these compounds show higher thermal stabilities compared to the Co-free compounds. These compounds are discussed in the next sections. The layered-to-spinel phase transition in Li_xMnO_2 has also been considered

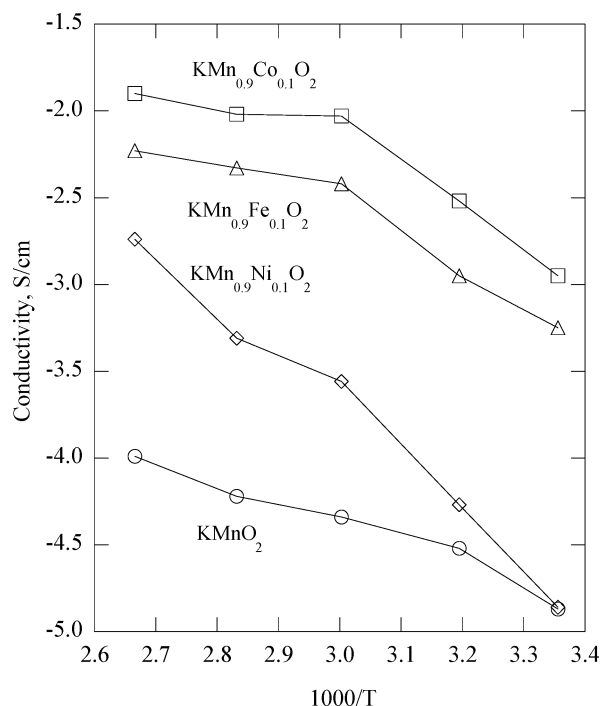


Figure 13. Electronic conductivity of pillared KMnO_2 with 10% Co, Ni, and Fe substitution of the Mn.

theoretically²³⁸ and found to go in a two-step process; in the first step a fraction of the lithium and manganese ions move rapidly into tetrahedral sites, and in the second stage these order into the spinel arrangement of cations.

5.2.3. Mixed Manganese–Cobalt Dioxide, $\text{LiMn}_{1-y}\text{Co}_y\text{O}_2$

Bruce et al.^{206,239,240} investigated the synthesis and electrochemical behavior of cobalt-substituted $\text{LiMn}_{1-y}\text{Co}_y\text{O}_2$. They synthesized this material from the sodium analogue by ion exchange and achieved values of y up to 0.5. These substituted materials have the $\alpha\text{-NaFeO}_2$ structure. These materials, just like the unsubstituted LiMnO_2 , convert to the spinel structure on cycling even at the low cycling rate of 0.1 mA/cm^2 ; for $y = 0.1$, this begins to occur on the first cycle and is not apparent until the thirtieth cycle for $y = 0.3$. However, they cycle over the 3 V spinel plateau very well. The conversion to spinel is expected to occur very rapidly at elevated temperatures.

The partial substitution of the manganese ions by cobalt, iron, or nickel was found to significantly increase the electronic conductivity of the manganese oxide, which in the pure state as in LiMnO_2 or KMnO_2 is around 10^{-5} S/cm, too low to allow rapid reaction without addition of a conductive diluent. To obtain sufficiently dense material for conductivity measurement, the potassium analogues were synthesized at elevated temperatures with 10% of the manganese substituted. The data,²⁴¹ shown in Figure 13, clearly show the advantage of adding cobalt, which enhanced the conductivity by almost 2 orders of magnitude. Nickel had the least effect, and we will discuss the impact of joint additions of cobalt and nickel as in $\text{LiNi}_{0.4}\text{Mn}_{0.4}\text{Co}_{0.2}\text{O}_2$.²¹⁹

These cobalt-substituted materials can also be prepared hydrothermally, and their cycling behavior

is much improved over the cobalt-free compounds.²⁴² Conversion to spinel is observed on the first charge cycle at rates of 1 mA/cm², even when larger cations such as potassium are incorporated into the structure as pillaring agents. The layered-to-spinel phase transition in Li_xMnO₂ has subsequently been explained through modeling.²³⁸

Work on these cobalt-substituted α -NaFeO₂ structure materials, where manganese is the redox-active ion, has essentially ceased because of the inability to maintain the structure relative to conversion to the spinel structure under realistic cycling conditions. Doping elements other than cobalt have also been investigated, but substitution by nickel leads to a system where the manganese becomes the structure stabilizer and nickel the electrochemically active ion. These compounds are thus best described as substituted nickel oxides in which the manganese remains in the tetravalent state and the nickel is redox active between the +2 and +4 oxidation states; the manganese helps in reducing the cost and stabilizing the lattice. Cobalt, as will be discussed below, plays a critical role in controlling the ordering of the 3d ions in the structure.

5.2.4. Mixed Nickel–Manganese Dioxide, LiNi_{1-y}Mn_yO₂—Multielectron Redox Systems

The groups of Amundsen and Davidson announced results on the Li–Mn–Cr–O₂ system^{243,244} at the 2000 Lithium Battery meeting in Como. They found^{245–250} that these mixed-metal compounds had the NaFeO₂ structure and cycled well when a substantial part of the transition metals were substituted by lithium as in Li₃CrMnO₅ or described in the layered form as Li[Li_{0.2}Mn_{0.4}Cr_{0.4}]O₂. The discharge curve showed the typical behavior of a single phase rather than the two-phase, two-step behavior of the spinel. The manganese has the 4+ oxidation state, and all the lithium can be removed giving Cr(VI). What was surprising was the high mobility of the chromium, which during the redox process must move from an octahedral to a tetrahedral site; increasing the temperature from 20 to 55 °C increased the cell capacity from around 125 to 165 mAh/g, consistent with having to move the highly charged chromium ion as well as the lithium ion. Capacities as high as 220 and 200 mAh/g were obtained at low rates, 3²⁴⁸ and 10 mA/g,²⁴⁷ respectively, from 2.5 to 4.5 V. The lithium ions in the transition-metal layer were found clustered around the manganese ions as in Li₂MnO₃, and the system can be considered as a solid solution of Li₂MnO₃ and LiCrO₂. Although of little commercial interest, because of the toxicity of Cr(VI), this pioneering research provoked much thinking about other multielectron redox reactions which are discussed below. The corresponding solution between Li₂MnO₃ and LiCoO₂ did not show similar behavior, with the capacity decreasing with increasing manganese content when cycled between 3.0 and 4.2 or 4.3 V.^{207,251}

The LiNi_{1-y}Mn_yO₂ phase system was studied by the Dahn group²¹² in 1992. They reported a solid solution for $y \leq 0.5$ but a deterioration of the electrochemical behavior with increasing manganese content. Spahr

et al.²¹³ repeated the work, also showing a maximum solubility of 0.5 Mn. They however found optimum electrochemical behavior for the composition LiNi_{0.5}Mn_{0.5}O₂. They reported XPS and magnetic data that are consistent with the present interpretation of Ni²⁺ and Mn⁴⁺ ions rather than Ni³⁺ and Mn³⁺ and showed electrochemical cycling curves very reminiscent of LiNiO₂. This compound, which we will call the 550 material (0.5 Ni, 0.5 Mn, 0.0 Co) was rediscovered by Ohzuku²¹⁴ in 2001, who reported very good electrochemical data, and this was reconfirmed almost immediately by the Dahn group.²⁵² These papers ignited a substantial amount of work on this composition and on the cobalt-substituted compounds, in particular those with the formula LiNi_yMn_yCo_{1-2y}O₂, where $0.5 \leq y \leq 0.33$, which can be considered as a solid solution of LiNi_{0.5}Mn_{0.5}O₂ and LiCoO₂.

Manganese shows no significant layer stabilization capability as up to 10% nickel is found on the lithium sites, 9.3%²⁵³ for a sample formed at 1000 °C, and 11.2% for a sample formed at 900 °C;²⁵⁴ this nickel is expected to reduce the rate capability of the electrode. The phase LiNi_{0.5}Mn_{0.5}O₂ has the expected hexagonal lattice with $a = 2.894 \text{ \AA}$ and $c = 14.277 \text{ \AA}$,²¹³ $a = 2.892 \text{ \AA}$ and $c = 14.301 \text{ \AA}$,²¹⁴ $a = 2.891 \text{ \AA}$ and $c = 14.297 \text{ \AA}$,²⁵³ $a = 2.888 \text{ \AA}$ and $c = 14.269 \text{ \AA}$,²⁵⁴ $a = 2.887 \text{ \AA}$ and $c = 14.262 \text{ \AA}$,²⁵⁵ $a = 2.895 \text{ \AA}$ and $c = 14.311 \text{ \AA}$,²⁵⁶ and mean $c/3a = 1.647$. There is some disagreement about the structure formed on lithium removal. Venkatraman et al. reported²⁵⁴ a single phase for $0 \leq \text{Li} \leq 1$ with continuously varying lattice parameters; the data reported for Li_{0.2}Ni_{0.5}Mn_{0.5}O₂ is consistent with single-phase behavior. However, Yang et al.²⁵⁶ reported that on delithiation a second hexagonal phase with $a = 2.839 \text{ \AA}$, $c = 14.428 \text{ \AA}$ was formed; this is in contrast to the pure LiNiO₂, where a third hexagonal phase is also found. Arachi et al. reported²⁵³ the formation of a monoclinic phase for Li_{0.5}Ni_{0.5}Mn_{0.5}O₂ with $a = 4.924 \text{ \AA}$, $b = 2.852 \text{ \AA}$, $c = 5.0875 \text{ \AA}$, $\beta = 108.81^\circ$. Yang et al.²⁵⁶ also reported that excess lithium could be intercalated with a slight expansion of the hexagonal cell to $a = 2.908 \text{ \AA}$ and $c = 14.368 \text{ \AA}$; this is possibly the phase Li₂Ni_{0.5}Mn_{0.5}O₂ and if so raises the question of which site the nickel in the lithium layer occupies if the lithium takes up the tetrahedral sites. One would not expect the rhombohedral structure reported but rather a single block structure with c around 4.8 Å if the lithiums are in the tetrahedral sites; the lithium ions in tetrahedral sites would be much too close to the transition-metal ions in the transition-metal layer. There is no data reported on the stability of this phase, which might be expected to be metastable like Li₂NiO₂, which converts⁶³ at 400 °C to the orthorhombic form of Li₂NiO₂.²⁵⁷

Spahr et al. reported²¹³ in 1998 a capacity of 150 mAh/g falling to 125 mAh/g after 25 cycles and to 75 mAh/g after 50 cycles for a 550 sample prepared at 700 °C; they also showed that the capacity and capacity retention increased as the synthesis temperature was increased from 450 to 700 °C, which we now know to be too low a temperature for optimum electrochemical behavior. Ohzuku et al.²¹⁴

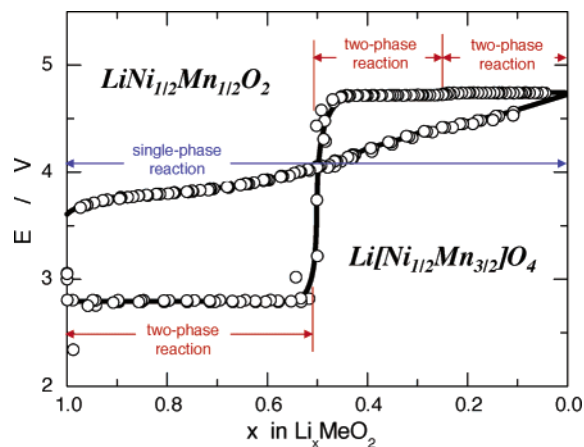


Figure 14. Lithium cell potentials of the two lithium nickel manganese dioxides with layered and spinel structures.²⁶⁰

prepared the 550 material at 1000 °C and reported a constant capacity of 150 mAh/g at 0.1 mA/cm² for 30 cycles using top-up charging at 4.3 V. The cell potential^{214,258,259} varies from around 4.6 to 3.6 V as shown in Figure 14;²⁶⁰ it shows a single phase for all x values in $\text{Li}_x\text{Ni}_{0.5}\text{Mn}_{0.5}\text{O}_2$. The composition $\text{LiNi}_{0.25}\text{Mn}_{0.75}\text{O}_4$, which has the spinel rather than the layered structure, shows the typical two-phase, two-step spinel discharge potential and is very similar to that of LiMnO_2 shown in Figure 11 except for the higher potentials in this case. The 550 material, synthesized at 900 °C and quenched to room temperature, also showed a capacity exceeding 150 mAh/g for over 50 cycles in thin film configuration.²⁵² Material cycled²⁶¹ with a 4.4 V top-up constant potential charge after a constant current charge to 4.4 V showed an initial capacity exceeding 170 mAh/g but decayed over 20 cycles to less than 150 mAh/g, whereas a sample charged to just 4.2 V only had a capacity of 130 mAh/g but maintained this capacity much better; increasing the temperature to 50 °C increased the fade rate except where the maximum charge potential was limited to 4.2 V. The 550 composition showed a lithium diffusion coefficient of around 3×10^{-10} cm²/s for most of the lithium composition range. A contradictory report²⁵⁵ shows good cycling stability at 0.1 mA/cm² (10 mA/g) even when charged to 4.6 V, with the capacity increasing from 150 to 190 mAh/g as the charging cutoff potential is raised from 4.3 to 4.6 V. A material formed at 1000 °C showed a lower capacity of around 120 mAh/g at 0.1 mA/cm²; the capacity was increased to about 140 mAh/g by addition of 5% cobalt, aluminum, or titanium.²⁶² This suggests that the synthesis temperature of 1000 °C may be too high, leading possibly to excess nickel in the lithium layer. This 550 compound can intercalate a second lithium, particularly when some titanium is added, $y\text{LiNi}_{0.5}\text{Mn}_{0.5}\text{O}_2 \cdot (1-y)\text{Li}_2\text{TiO}_3$, which results from reduction of Mn(IV) to Mn(II);⁶⁴ no structural data was given for this new phase. Lu et al.²⁵² showed that the capacity could be increased from around 160 to 200 mAh/g at 30 °C by substituting a part of the transition metals by lithium, $\text{Li}[\text{Ni}_{1/3}\text{Mn}_{5/9}\text{Li}_{1/9}]\text{O}_2$. There is one report²⁶³ of conductive carbon coatings raising the capacity, but even then the capacity was lower than

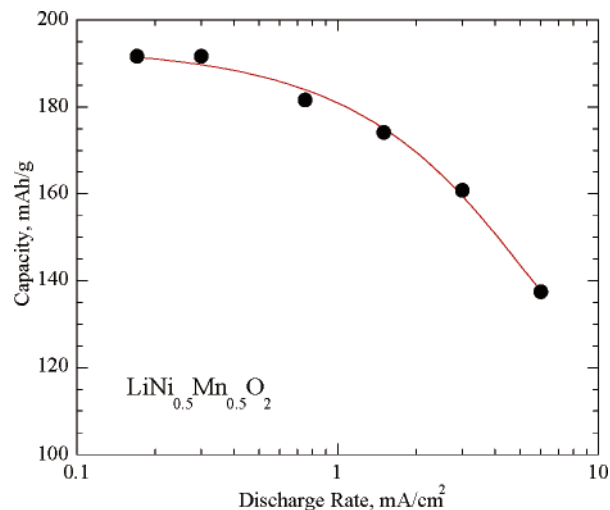


Figure 15. Ragone plot for $\text{LiNi}_{0.5}\text{Mn}_{0.5}\text{O}_2$ showing the capacity of the cathode as a function of the discharge current density (data from ref 258).

those reported above. The rate capability has been determined in another study,²⁵⁸ where the capacity approaches 200 mAh/g at 0.17 mA/cm², falling off to 130 mAh/g at 6 mA/cm²; all cells were charged at 0.17 mA/cm² and then held at 4.5 V for 19 h; cathode loading was around 15 mg/cm². These data are shown in Figure 15 as a Ragone plot and strongly suggest that pulse discharge rates in excess of 10 mA/cm² should be achievable. Rate data will also be needed on charging if such cells are to be considered for HEV applications.

The electrochemically active element in this compound is nickel, which cycles between the +2 and +4 valence states, while the manganese remains as +4 throughout independent of the lithium content. First-principal quantum mechanical calculations²⁶⁴ as well as structural measurements confirm this redox assignment. As the manganese is always 4+, there is no concern with the Jahn–Teller distortion associated with the Mn³⁺ ion. Consistent with this model it should be possible to replace the manganese by an element such as titanium; Kang et al.²⁶⁵ synthesized the compound $\text{Li}_{0.9}\text{Ni}_{0.45}\text{Ti}_{0.55}\text{O}_2$ with the $\alpha\text{-NaFeO}_2$ structure by ion exchange of the sodium analogue, as high temperatures lead to complete cation disorder and a rock-salt structure. About one-half of the lithium could be removed in an electrochemical cell, with only about one-half of that being re-intercalated on discharge; this is believed to be due to cation, probably titanium, migration into the lithium layer. Clearly, the manganese ion plays a key stabilizing influence on the $\alpha\text{-NaFeO}_2$ structure.

Little is known about the electrical conductivity of the 550 material. One measurement shows a conductivity of 6×10^{-5} S/cm at 25 °C²¹⁹ for the fully lithiated $\text{LiNi}_{0.5}\text{Mn}_{0.5}\text{O}_2$. The magnetic susceptibility exhibits Curie–Weiss behavior at elevated temperatures.²⁶²

The precise details of the structure of $\text{Li}_x\text{Ni}_{0.5}\text{Mn}_{0.5}\text{O}_2$ are complex, with a superstructure being observed in the X-ray diffraction pattern.^{252,266} Long-range order has been detected by transmission electron microscopy,²⁶⁷ and the domain size of this

ordering increases with the lithium content from 1 to 2 nm in the 550 compound to complete ordering in Li_2MnO_3 . As noted above, there is apparently always 8–10% nickel in the lithium layer and a corresponding amount of lithium in the transition-metal layer. Grey et al.,²⁶⁸ using NMR studies, have shown that the lithium in the transition-metal layer is surrounded by six manganese ions, as in Li_2MnO_3 . Ceder and Grey thus propose,²⁶⁹ supported by experiments and calculations, that the composition of the transition-metal layer requires 0.5/6 lithium (~8%); the manganese ions in turn are surrounded by nickel ions on the hexagonal lattice, leading to a $2\sqrt{3} \times 2\sqrt{3}$ superlattice. On charging, the lithium is initially removed from the lithium layer, but when two adjacent lithium sites become vacant in that layer, then the lithium ion in the transition-metal layer can drop down from its octahedral site into the vacant tetrahedral site. This is consistent with the NMR observation of the reversible removal of the lithium ion from the transition-metal layer on charging the material. This tetrahedral lithium is only removed at the highest potential, i.e., only after all the octahedral lithium is removed. This model is consistent with the presence of the tetrahedral lithium in $\text{Li}_{0.5}\text{Ni}_{0.5}\text{Ni}_{0.5}\text{O}_2$ proposed by Kobayashi et al.^{270,271}

In conclusion, the 550 material has the following cathode characteristics.

- (1) It has a capacity of around 180 mAh/g for at least 50 cycles under mild cycling conditions.
 - (a) Overcharging increases capacity fade, but a protective coating might help.
 - (b) The synthesis temperature should be in excess of 700 °C and less than 1000 °C, probably optimally around 900 °C.
- (2) There are always nickel ions in the lithium layer, up to 10%, which will restrict the rate capability and compromise the energy density.
 - (a) Cobalt additions can reduce the level of nickel in the lithium layer, as in $\text{LiNi}_{1-y}\text{Co}_y\text{O}_2$.
 - (b) The lithium in the transition-metal layer may be a necessary structural component.
- (3) The structure of the lithium poor phase is unclear.
- (4) Nickel is the electrochemically active ion.
- (5) The electronic conductivity needs increasing.

5.2.5. Mixed Nickel–Manganese–Cobalt Dioxide, $\text{LiNi}_{1-y-z}\text{Mn}_y\text{Co}_z\text{O}_2$

Consideration of the above leads logically to a mixing of the three transition metals, and the reports of such compounds were first published in 1999 by Liu et al.²⁷² and in 2000 by Yoshio et al.,²²⁸ and the latter hypothesized that the addition of cobalt to $\text{LiMn}_{1-y}\text{Ni}_y\text{O}_2$ would stabilize the structure in a strictly two-dimensional fashion. They found that the transition-metal content in the lithium layer fell from 7.2% for $\text{LiMn}_{0.2}\text{Ni}_{0.8}\text{O}_2$ to 2.4% for $\text{LiMn}_{0.2}\text{Ni}_{0.5}\text{Co}_{0.3}\text{O}_2$ and that the lithium insertion capacities exceeded 150 mAh/g for the cobalt-substituted compounds. Ohzuku et al.,²¹⁵ studying the symmetric compound $\text{LiNi}_{0.33}\text{Mn}_{0.33}\text{Co}_{0.33}\text{O}_2$, synthesized at 1000 °C, also found a capacity of around 150 mAh/g cycling be-

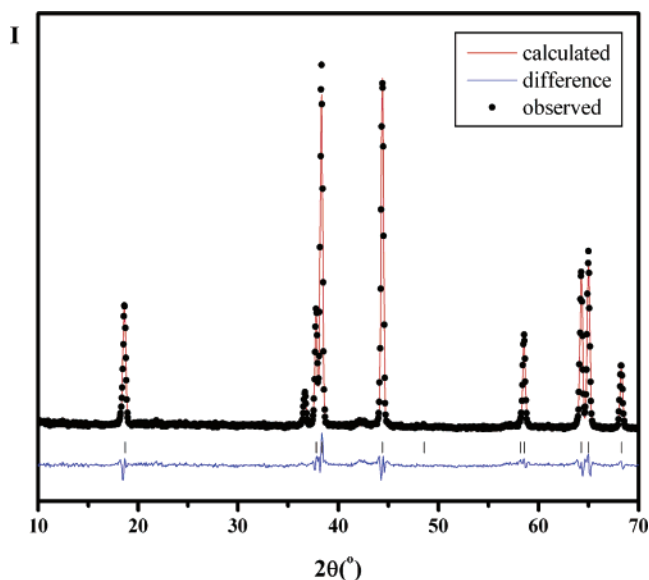


Figure 16. Neutron powder diffraction pattern of a layered substituted nickelate, $\text{LiNi}_{0.4}\text{Mn}_{0.4}\text{Co}_{0.2}\text{O}_2$.

tween 2.5 and 4.2 V at 0.17 mA/cm² at 30 °C; raising the charge cutoff potential to 5.0 V increased the capacity to over 220 mAh/g, but capacity fade was evident. This compound will be referred to as the 333 material.

The synthesis of these $\text{LiNi}_{1-y-z}\text{Mn}_y\text{Co}_z\text{O}_2$ compounds is typically accomplished using a modified mixed-hydroxide approach by reacting $\text{Ni}_{1-y-z}\text{Mn}_y\text{Co}_z(\text{OH})_2$ with a lithium salt in air or oxygen as described in Liu's first synthesis²⁷² at 750 °C, which is now known to be below the optimum temperature of 800–900 °C.²¹⁹ These conditions result in a single phase with the layered O3 structure. A typical diffraction pattern, as given in Figure 16, conforms to the R3m symmetry of the $\alpha\text{-NaFeO}_2$ structure. The structure consists of a cubic close-packed arrangement of the oxide ions. The transition-metal ions in the structure occupy alternating layers in octahedral sites. The structure and properties of the precursor hydroxide compound have been studied;²⁷³ it has the CdI_2 structure like TiS_2 but with some turbostratic disorder and on heating can convert to a spinel phase.

The cell parameters^{219,228,233,236} of this tri-transition-metal compound are slightly dependent on the transition metals as shown in Figure 17. Both the in-plane *a* parameter and the interlayer spacing *c* increases with the Ni content and decreases with the Co content for constant Mn content.^{219,228} For compositions $\text{LiNi}_y\text{Mn}_y\text{Co}_{1-2y}\text{O}_2$, the *a* and *c* parameters obey Vegard's law, decreasing linearly with increasing cobalt content.²³³ For constant nickel content, the *a* parameter is directly proportional to [Mn] and inversely proportional to [Co], which is indicative of a larger Mn ion compared to the Co ion. This observation is contrary to the suggestion²³⁶ that Mn does not have any effect on the parameters.

The ratio *c*/3*a* of the lattice constants is a direct measure of the deviation of the lattice from a perfect cubic close-packed lattice, which is it measures the layeredness of the lattice. An ideal ccp lattice has a *c*/3*a* ratio of 1.633, whereas a pure layered lattice with no transition metal in the lithium layer has a

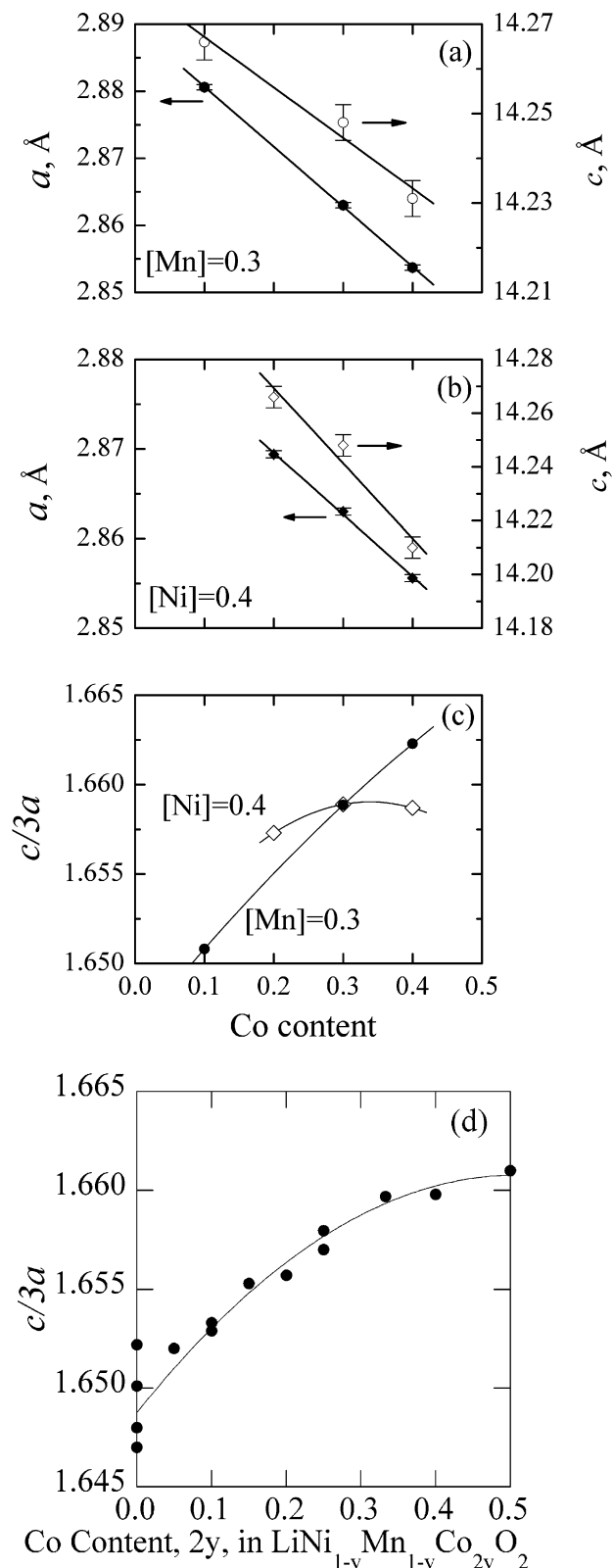


Figure 17. Cell parameters and $d/3a$ ratio of layered $\text{LiNi}_y\text{Mn}_z\text{Co}_{1-y-z}\text{O}_2$, and $c/3a$ ratio of the symmetric $\text{LiNi}_{1-y}\text{Mn}_{1-y}\text{Co}_{2y}\text{O}_2$. (Parts a–c are reproduced with permission from ref 219, copyright 2004 The Royal Society of Chemistry.)

$d/3a$ ratio of 1.672 for TiS_2 and when intercalated increases to 1.793 for LiTiS_2 .⁴⁵ The unusually low value for CoO_2 of 1.52¹²⁴ increases to 1.664 for LiCoO_2 . ZrS_2 also has an anomalously low value of 1.592, which increases to 1.734 in LiZrS_2 . The closer

the value is to 1.633, the greater the transition-metal content in the lithium layer; thus, LiNiO_2 has a $d/3a$ ratio of 1.639,²¹³ almost the same as in the spinel LiNi_2O_4 ,²⁷⁴ and that for $\text{LiNi}_{0.5}\text{Mn}_{0.5}\text{O}_2$ is 1.644–1.649 depending on the investigator,^{213,252,270} addition of a second lithium as in Li_2NiO_2 ⁶³ and $\text{Li}_2\text{Ni}_{0.5}\text{Mn}_{0.5}\text{O}_2$ ²⁵⁶ changes the d/a ratio very little, 1.648 and 1.647, respectively. Figure 17 shows that this ratio becomes much larger as soon as any cobalt is added to the structure, indicating that cobalt confers layer-like behavior to the lattice. Whereas the plot for $[Mn] = 0.3$ shows a closer approach to the cubic ideal value of 1.633, as the Co content decreases (that is as the Ni content increases), that for $[Ni] = 0.4$ shows little change. Thus, the $d/3a$ ratio is strongly determined by the nickel concentration, with the cobalt presence lessening the amount of nickel in the lithium layer. Figure 17d shows that the $d/3a$ ratio increases continuously with the cobalt content when $[Ni] = [Mn]$. An analysis of the published data^{213,270} on $\text{LiNi}_{1-y}\text{Mn}_y\text{O}_2$ indicates essentially no change of the $d/3a$ ratio of 1.644 ± 0.005 with manganese content for $0.1 \leq y \leq 0.5$. The mean of all the data for the composition $\text{LiNi}_{0.33}\text{Mn}_{0.33}\text{Co}_{0.33}\text{O}_2$ is 1.657, which is more layered than the mean 1.647 for the cobalt-free $\text{LiNi}_{0.5}\text{Mn}_{0.5}\text{O}_2$. For the 333 composition, the $d/3a$ ratio decreases with increase of formation temperature from 900 to 1100 °C according to the equation $d/3a = 1.680 - 2.35 \times 10^{-5} T$, indicating an increasing nickel content in the lithium layer with increasing temperature.

Rietveld refinement was used²⁷⁶ to determine the distribution of the transition-metal ions in the layered structure between the 3b and 3a sites; in a fully ordered layered structure, these sites should be fully occupied by transition metal and lithium, respectively. The average scattering factor of the transition-metal ions in the metal layer, 3b sites, was taken to be equal to that of Co, whereas that in the lithium layer occupying the interlayer site, 3a, was taken to be equal to that of Ni. Figure 16 shows the neutron diffraction pattern of the 442 material, and Rietveld comparison with the X-ray powder diffraction clearly showed that the transition metal in the lithium layer is nickel, not cobalt or manganese. A similar conclusion²³⁴ was reached in a recent neutron study on the 333 composition. Figure 18 shows the occupancy on the Li site (3a site) as a function of overall composition and synthesis temperature. The data clearly indicates that the transition-metal disorder is suppressed by increasing cobalt content but not to the same degree as in $\text{LiNi}_{1-y}\text{Co}_y\text{O}_2$, where nickel disorder is only observed for $y \leq 0.3$, and increased by increasing the nickel content. However, the synthesis temperature has as profound an effect as composition, as also indicated in Figure 18 for the composition $\text{LiNi}_{0.4}\text{Mn}_{0.4}\text{Co}_{0.2}\text{O}_2$, where the sample prepared at 1000 °C then rapidly cooled to ambient temperatures has almost 10% Ni occupancy in the lithium layer. Kim et al. also reported²³⁴ a high Ni content of 5.9% on the Li site for samples of the 333 composition prepared at 950 °C. Only at 800 °C does the nickel disorder drop to zero with increasing cobalt content. At 900 °C even with more cobalt than nickel

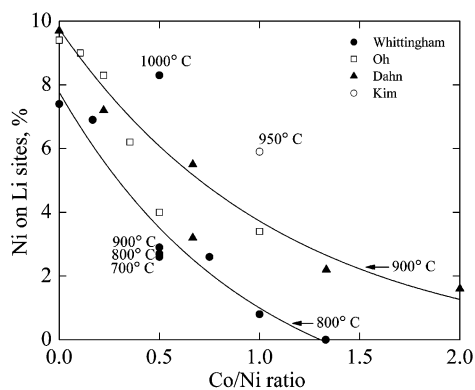


Figure 18. Lattice disorder, percent of lithium sites occupied by nickel ions in $\text{LiNi}_y\text{Mn}_z\text{Co}_{1-y-z}\text{O}_2$. Materials synthesized at 800 °C for Whittingham²¹⁹ and 900 °C for Oh,²⁷⁸ Dahn,^{216,236} and Kim²³⁴ unless otherwise stated.

in the material there is still considerable nickel disorder, almost 2% more Ni in the lithium layer at 900 °C than at 800 °C for all compositions. Clearly high temperature increases the disorder of the nickel ions just as earlier observed for TiS_2 ; this effect may be reduced by a slow cooling of the sample in an oxidizing environment or a hold at 800 °C or slightly lower if the original synthesis is carried out at higher temperatures. This will allow the partial reordering of the ions.²³⁵

Although these materials show good electrochemical behavior, their electronic conductivity is still low for a high-rate cathode, and a means needs to be found to increase the conductivity without the addition of excessive amounts of a conductor such as carbon black, which will reduce the volumetric energy storage capacity. There has also been a report²³⁷ of the low packing density of powders which will also severely reduce the volumetric energy density. The conductivity of $\text{LiNi}_{0.5}\text{Mn}_{0.5}\text{O}_2$ was 6.2×10^{-5} S/cm; this increased on cobalt addition to 1.4×10^{-4} S/cm for $\text{LiNi}_{0.4}\text{Mn}_{0.4}\text{Co}_{0.2}\text{O}_2$ at 21 °C and 6.8×10^{-4} S/cm at 100 °C.²¹⁹ The value of the cobalt-free compound is similar to that observed previously²⁴¹ for KMnO_2 and LiMnO_2 , but in that case 2–10% Co substitution led to a 100-fold increase in the conductivity to around 10^{-3} S/cm. This rather low effect of cobalt substitution is not totally unexpected as cobalt substitution in LiNiO_2 , as in $\text{LiNi}_{0.8}\text{Co}_{0.2}\text{O}_2$, reduces the conductivity.¹⁶⁹ Sun et al.²³³ reported conductivity values of $2\text{--}5 \times 10^{-4}$ S/cm essentially independent of composition for cobalt contents up to 0.5, which suggests that changes in the electrochemical behavior with composition is not a function of changes in conductivity. However, they found²³³ that increasing the cobalt content increased the rate capability, which might be associated with the lack of pinning Ni^{2+} ions in the lithium layers, which would reduce the diffusivity of the lithium.

There have been a number of studies of the physical and bonding behavior of these mixed transition-metal oxides, which conclude that in the fully lithiated compounds the cobalt is trivalent, the nickel predominantly divalent, and the manganese tetravalent. Thus, the electrochemically active species is predominantly nickel with the cobalt playing an

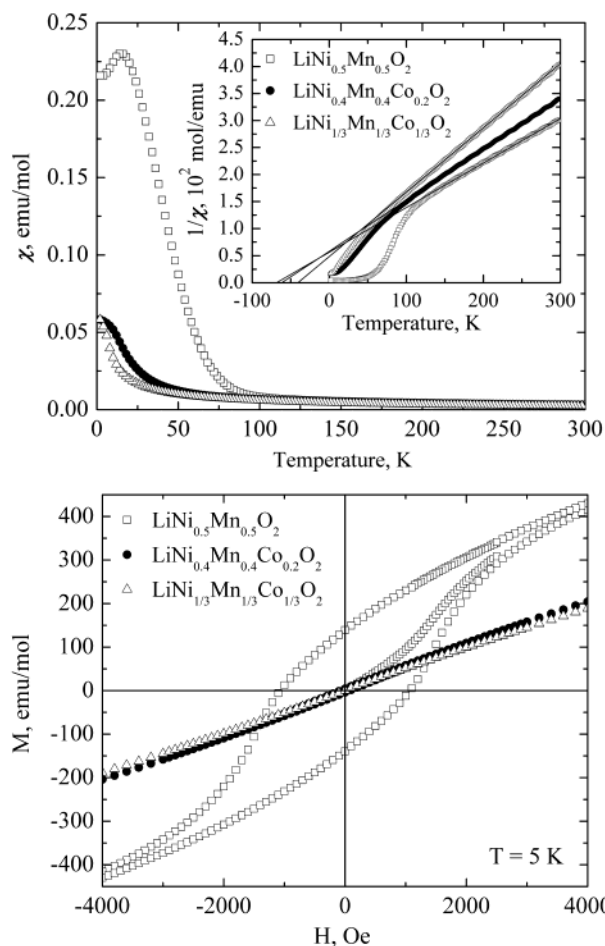


Figure 19. Magnetic behavior of $\text{LiNi}_{0.5}\text{Mn}_{0.5}\text{O}_2$, $\text{LiNi}_{0.4}\text{Mn}_{0.4}\text{Co}_{0.2}\text{O}_2$, and $\text{LiNi}_{0.33}\text{Mn}_{0.33}\text{Co}_{0.33}\text{O}_2$: (a) susceptibility and (b) field effect (after Ma et al.).²⁷⁶

active redox role only in the later stages of lithium removal. The manganese is merely a spectator ion but a critical one as at a minimum it reduces the cost of the cathode. Studies of the magnetic behavior of the compounds gives information about the location of the nickel ions, but studies of the magnetic moment from Curie–Weiss behavior do not give much key information as the combination $\text{Ni}^{3+} + \text{Mn}^{3+} + \text{Co}^{3+}$ gives an almost identical moment to the combination $\text{Ni}^{2+} + \text{Mn}^{4+} + \text{Co}^{3+}$.²¹⁹ However, the presence of nickel ions in the lithium layer results in a hysteresis loop in the magnetic moment both for the mixed material $\text{Li}(\text{NiMnCo})\text{O}_2$ and in $\text{LiNi}_{1-y}\text{Al}_y\text{O}_2$.²⁷⁵ The magnetic behavior of several of these phases is shown in Figure 19 and shows that at the higher temperatures they obey the Curie–Weiss law; as the addition of cobalt increases from 0.0 to 0.2 to 0.33, the hysteresis loop decreases, indicating a reduction in the Ni^{2+} content in the lithium layer.²⁷⁶

XPS studies have been made on a number of compositions of these transition-metal oxides, and all indicate predominantly divalent nickel. Thus, for the 442 compound the Co spectrum is clearly Co^{3+} , and the Mn spectrum can be assigned to 80% Mn^{4+} with 20% Mn^{3+} . The Ni spectrum is characterized by an intense and complicated satellite structure and consistent with 80% Ni^{2+} and 20% Ni^{3+} . Studies on $\text{LiNi}_{0.33}\text{Mn}_{0.33}\text{Co}_{0.33}\text{O}_2$,²²⁴ $\text{LiNi}_{0.5}\text{Mn}_{0.5}\text{O}_2$,²⁷⁷ and

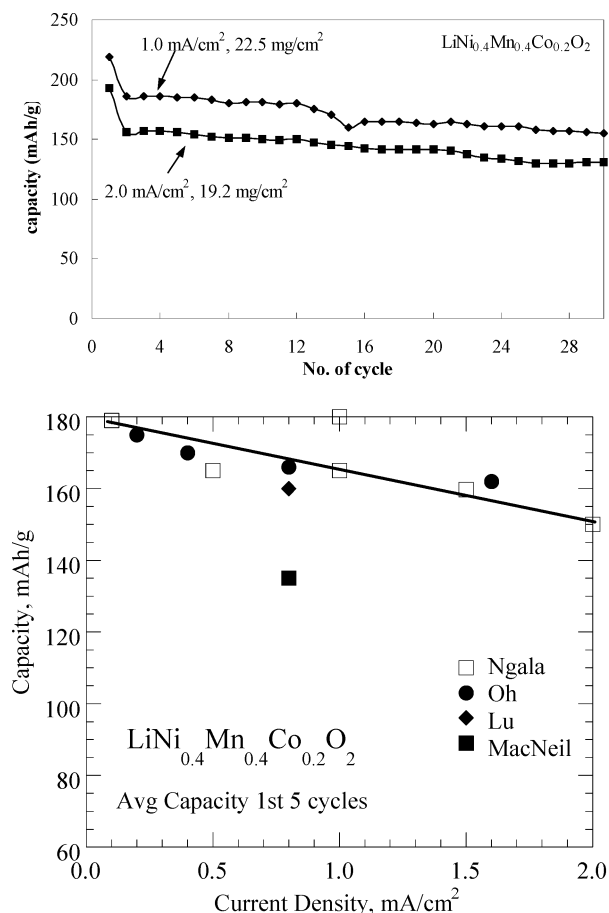


Figure 20. Electrochemical behavior of $\text{LiNi}_{0.4}\text{Mn}_{0.4}\text{Co}_{0.2}\text{O}_2$: (a) capacity as a function of a cycle at 1 and 2 mA/cm^2 (reproduced with permission from ref 219, copyright 2004 The Royal Society of Chemistry) and (b) capacity as a function of discharge rate, average capacity of first five cycles. Cutoff on charge, 4.3 V at 22 °C Ngala,²¹⁹ 4.4 V at 30 °C Oh,²⁷⁸ 4.4 V at 30 °C Lu,²¹⁶ and 4.2 V at 30 °C MacNeil.²³⁶

$\text{LiNi}_y\text{Co}_{1-2y}\text{Mn}_y\text{O}_2$,²¹⁶ with $y = 1/4$ and $3/8$, also suggested $2+$ and $4+$ as the predominant oxidation states for nickel and manganese, respectively, which then designates the nickel as the key electrochemically active species.

The electrochemical behavior of a number of different compositions over a range of current densities have been studied, and two of these studies identified^{198,219,220,278} the 442 material as having the highest capacity and maintaining its capacity on cycling. Pure $\text{Li}_{1-y}\text{Ni}_{1+y}\text{O}_2$ had the lowest capacity. The electrochemical behavior of a sample of the 442 composition,²²⁰ synthesized at 900 °C, at 22 °C is shown in Figure 20, for current densities of 1 and 2 mA/cm^2 within the potential window 2.5–4.3 V; these are equivalent to rates of 44 and 104 mA/g. All the samples had an initial potential around 3.8 V. The temperature of synthesis was found to be important with the optimum capacity and capacity retention being found at 800–900 °C, with a much lower capacity being found for samples prepared at 1000 °C.²²⁰ The rate capability of the 442 composition is also shown in Figure 20 and shows the excellent reproducibility between the different research groups. Oh et al.²⁷⁸ found a constant capacity for 442 of 175 mAh/g at 0.2 mA/cm^2 (20 mA/g or C/8) for 30 cycles

within the potential window of 2.8–4.4 V; this capacity dropped slightly to 170, 165, and 162 mAh/g as the current density increased to 40, 80, and 160 mA/g (1.6 mA/cm^2 or C rate). The Dahn group has found similar good cycling ability for the close composition $\text{LiNi}_{0.375}\text{Mn}_{0.375}\text{Co}_{0.25}\text{O}_2$, where one sample²¹⁶ with 5.5% Ni on the lithium sites showed at 30 °C a capacity of 160 mAh/g dropping to 140 mAh/g after 50 cycles at a rate of 40 mA/g; raising the temperature to 55 °C increased the capacity to 170 mAh/g, and it dropped only to 160 mAh/g after 50 cycles. A second sample²³⁶ which had only 3.2% Ni on the Li site had a lower capacity of 135–130 mAh/g over 50 cycles at 30 mA/g due to only being charged to 4.2 V; increasing the charging to 4.4 V increases the capacity by 20–30 mAh/g. This shows the critical effect of charging potential. As noted for the LiCoO_2 cathode above, without doubt an appropriate coating would allow the charging potential and hence the capacity to be increased. It is not clear yet how critical the nickel level in the lithium layer is as most studies have been made on compounds with 2–5% nickel levels with no obvious difference in behavior. This is an area that merits further evaluation and understanding.

There have been the largest number of studies on the 333 composition, which have been made by a number of synthetic techniques over a wide range of temperatures. Most of these studies show similar behavior with the capacity increasing with increasing charging potential. Increase of synthesis temperature from 800 to 900 °C increases the initial capacity from 173 to 190 mAh/g and the capacity after 16 cycles to 180 from 160 at the 0.3C rate in the potential window 3.0–4.5 V.²²⁶ Ohzuku similarly reported^{215,231} capacities of 150 mAh/g for a 4.2 V cutoff and 200 mAh/g for 4.6 and 5.0 V charging; others have reported^{224,225} similar increases in capacity on increasing the charging potential, but in some cases there is marked capacity fade.²³⁴ Spray drying the powder has been reported²⁷⁹ to increase the capacity, 195 mAh/g at 0.2 mA/cm^2 (20 mA/g) within the potential window of 3–4.5 V. Replacing one-half of the cobalt ions by iron in the 333 composition with the goal of increasing the cell capacity below 4.5 V resulted in a higher cell polarization, lower capacity, and increased capacity fade.²⁸⁰

The structural changes accompanying the removal of Li from a number of these materials have been investigated. In the case of $\text{LiNi}_{0.4}\text{Mn}_{0.4}\text{Co}_{0.2}\text{O}_2$, the change in cell volume is less than 2%, much less than the 5% reported for $\text{Li}_x\text{Ni}_{0.75}\text{Co}_{0.25}\text{O}_2$ ²⁸¹ and Li_xTiS_2 ,⁴⁰ making this compound much less liable to mechanically fracture on cycling. The 333 compound also shows a volume change of less than 2% as the lithium is removed.²³⁴ This small change of volume is associated with compensating changes in the a and c parameters. When the c parameter increases, the a parameter contracts and vice versa. These results are shown in Figure 21 for the 442 compound,²⁷⁶ where the X-ray pattern was forced to fit the simple hexagonal lattice of the LiMO_2 . In reality the situation is probably more complex when x is less than around 0.3, and a more in-depth interpretation is

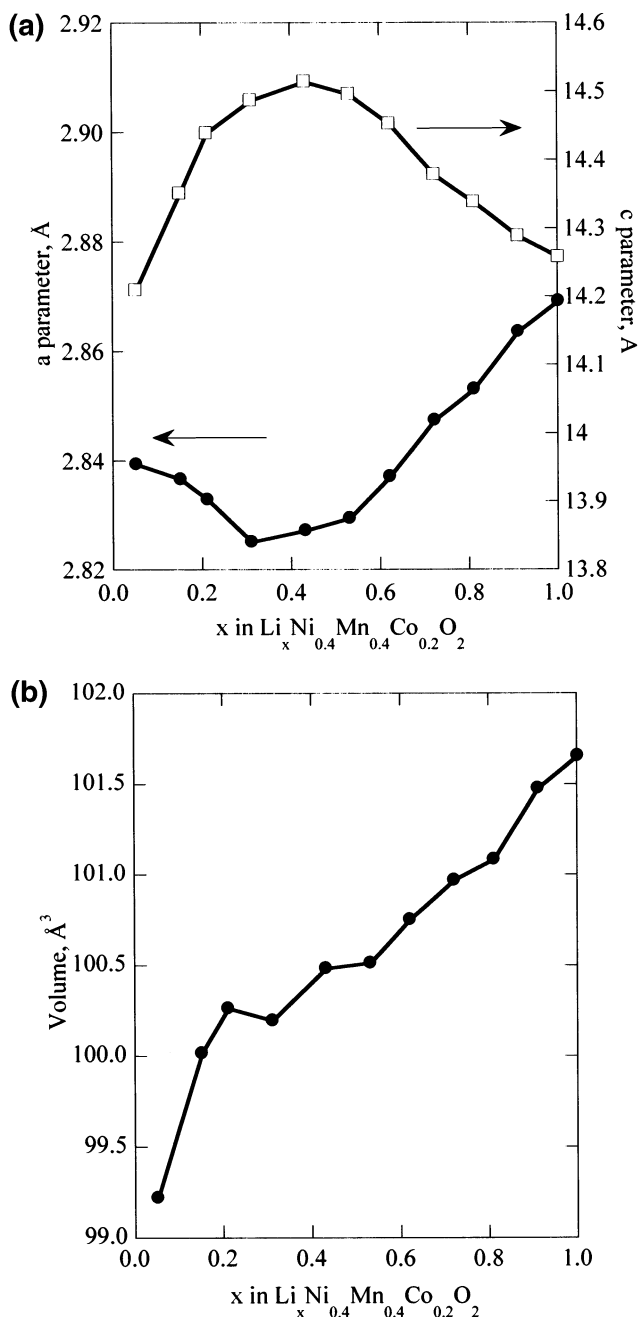


Figure 21. Lattice parameters of $\text{Li}_x\text{Ni}_{0.4}\text{Mn}_{0.4}\text{Co}_{0.2}\text{O}_2$: (a) a and c in Å and (b) volume in Å^3 (after Ma et al.).²⁷⁶

underway. At the lowest lithium content $\text{Li}_{0.05}\text{Ni}_{0.4}\text{Mn}_{0.4}\text{Co}_{0.2}\text{O}_2$ there is a trace amount of the one-block structure (1T) of TiS_2 or CoO_2 , in contrast to LiCoO_2 itself where large amounts of this structure would be seen. Thus, it appears that the 2–3% Ni on the Li sites is impeding the structural reorganization; this might be very advantageous for capacity retention on deep cycling of the material and speaks toward leaving some nickel disorder in the structure. This is consistent with an earlier study²⁸² on the NiO_2 phases, which found that the 1T phase is formed for $\text{Ni}_{1.02}\text{O}_2$ but not for nickel contents above 1.07, suggesting that the NiO_2 slabs are pinned by the extra nickel and thus cannot slide to form the 1T form. That study also found that the 1T phase slowly and irreversibly transformed at high potentials into a rhombohedral phase due to the migration of ad-

ditional nickel ions into the interslab region. Thus, every effort should be made to prevent formation of the 1T structure in nickel-rich compounds to avoid capacity fade on deep charging. In the case of MnO_2 itself, the manganese ions migrate at high potentials to form a spinel-like phase²⁴² and do not migrate back when lithium is re-intercalated.

Inspecting Figure 21 shows that as the electron density on the oxygen ions decreases, their effective size also decreases, leading to the smaller a parameter (oxygen diameter). Reducing the lithium content causes the c parameter to increase, presumably as the electrostatic attractive forces between the negative layers and the positive lithium ions decrease. Although a cursory study of the X-ray diffraction patterns suggests a continuous change in the structure as the lithium is removed, more in-depth studies suggest otherwise. Thus, one report²¹⁷ proposes that four hexagonal phases are formed as the lithium is removed from the 333 compound, and another²²⁹ suggests that a monoclinic phase is formed. Clearly additional studies are required ideally on single crystals if they can be synthesized, much as was accomplished with V_6O_{13} .

Are these cathodes ready and able to replace the stabilized LiCoO_2 used in most Li-Ion batteries today? A recent joint academic/industrial study²⁸³ suggests that the 333 compound is at least equal to or superior to the LiCoO_2 cathode. In a prismatic cell configuration, it showed a constant capacity of 600 mAh over 30 cycles at C rate. The cell can also be charged to a higher potential cutoff without the capacity loss associated with CoO_2 structure changes (O3 to 1T—ccp to hcp) in LiCoO_2 , which results in a 10–20 mAh/g higher storage capability. An issue with all these layered oxides is their inherent thermodynamic instability upon lithium removal. Although MnO_2 is stable in air at room temperature, neither CoO_2 or NiO_2 is, both having effective oxygen partial pressures in excess of 1 atm. The stable oxidation states of Mn, Co, and Ni in their simple binary oxides are 4, 2, and 2, respectively; on heating to over 500 °C, Mn_2O_3 becomes the stable oxide followed by Mn_3O_4 at still higher temperatures. Thus, their kinetic stability can create problems if there is any thermal excursion in the cell. For the four oxides $\text{Li}_x\text{Ni}_{1.02}\text{O}_2$, $\text{Li}_x\text{Ni}_{0.89}\text{Al}_{0.16}\text{O}_2$, $\text{Li}_x\text{Ni}_{0.70}\text{Co}_{0.15}\text{O}_2$, and $\text{Li}_x\text{Ni}_{0.90}\text{Mn}_{0.10}\text{O}_2$, a structural transformation first to a spinel phase and then to a rock-salt phase was found^{284,285} for lithium x values of 0.5 or less. The second transformation is accompanied by a loss of oxygen, and the first may be depending on the composition but usually when x is less than 0.5; the latter oxygen release occurs at lower temperature as the lithium content decreases and as low as 190 °C for $\text{Li}_{0.3}\text{Ni}_{1.02}\text{O}_2$. The stability is improved on aluminum or cobalt substitution. The compound $\text{Li}_{0.1}\text{NiO}_2$ is reported²⁸⁶ to lose weight at 200 °C forming a rock-salt structure. The substitution of manganese for nickel appears to move the transition to the spinel to higher temperatures; thus, $\text{Li}_{0.5}\text{Ni}_{0.5}\text{Mn}_{0.5}\text{O}_2$ even after 3 days at 200 °C is still layered,²⁸⁷ but a spinel phase is formed above 400 °C and is stable to much higher temperatures for the 1:1 Ni:Mn lithium-free

compound, eventually giving a mixture of spinel and nickel oxide in air and NiO + Mn₃O₄ in nitrogen.²⁸⁸ The compounds Li_{0.5}Ni_{0.4}Mn_{0.4}Co_{0.2}O₂ and Li_{0.5}Ni_{0.33}-Mn_{0.33}Co_{0.33}O₂ both begin to lose weight above 300 °C with major weight loss, 7–8%, only above 450 °C,²⁷⁶ which corresponds to reduction of Co(III) to Co(II) and any Ni(IV) to (Ni(II)); the manganese remains Mn(IV), and the structure begins to change to spinel by 350 °C, and the spinel phase is still present at 600 °C.

In conclusion the solid solutions of the 550 material and LiCoO₂ have the following cathode characteristics.

- (1) They have a capacity of around 170 mAh/g for at least 50 cycles under mild cycling conditions to 4.4 V and over 150 mAh/g at 2 mA/cm².
 - (a) A higher charge potential cutoff increases capacity.
 - (b) The synthesis temperature should be in excess of 700 °C and less than 1000 °C, probably optimally around 900 °C.
- (2) The cobalt reduces the number of nickel ions in the lithium layer.
 - (a) The final heating temperature needs to be no higher than 800 °C.
 - (i) The ratio of Co/Ni needs to be greater than 1 to eliminate all Ni in the lithium layer.
 - (b) For a final anneal temperature of 900 °C, there will always be nickel ions in the lithium layer.
 - (c) A certain level of nickel ions will deter the formation of the one-block structure at low lithium concentrations.
 - (i) Minimization of formation of the one-block structure on charging will help maintain capacity on cycling.
 - (ii) There is a need for a determination of the acceptable or desirable level of nickel in the lithium layer, as it may well not be zero.
- (3) There is probably not a single phase for all lithium values from 0 to 1 in Li_x(NiMnCo)O₂.
 - (a) The structure needs determining at low *x* values.
 - (i) The 442 compound only forms small amounts of the one-block structure by *x* = 0.05.
- (4) Nickel is the electrochemically active ion at low potentials.
 - (a) Cobalt is only active at the higher potentials.
- (5) The electronic conductivity needs increasing.
- (6) The optimum composition is still to be determined for energy storage, power capability, lifetime, and cost considerations.

5.2.6. Lithium-Rich Mixed-Metal Dioxides, Li_{1+x}M_{1-x}O₂

As discussed earlier in the case of the chromium^{243,244} and cobalt²⁵¹ systems, excess lithium can be incorporated into the layered structure through a solid solution of Li₂MnO₃ and LMO₂, where M = Cr

or Co. The transition-metal cation can also be nickel or manganese including mixtures such as LiNi_{1-y}Co_yO₂ as pointed out by Yoshio,²²⁸ Thackeray,^{289,290} and Dahn,²⁵² and the Li₂MnO₃ can be replaced by related materials such as Li₂TiO₃ and Li₂ZrO₃. Li₂MnO₃ can be represented in the normal layered notation as Li[Li_{1/3}Mn_{2/3}]O₂. These solid solutions can thus be represented as LiM_{1-y}[Li_{1/3}Mn_{2/3}]_yO₂, where M can be, for example, Cr, Mn, Fe, Co, Ni, or mixtures thereof. Addition of extra lithium will tend to push the manganese away from trivalent to tetravalent, thus minimizing the impact of any Jahn–Teller distortion coming from Mn³⁺.

Of particular curiosity is the end-member Li₂MnO₃ which has been shown^{291,292} to exhibit unexpected electrochemical activity on charging as the manganese is already in the 4+ oxidation state. This “overcharging” can be associated with two phenomena, removal of lithium with the concomitant loss of oxygen giving a defective oxygen lattice and the removal of lithium by decomposition of the electrolyte giving protons which can ion exchange for the lithium. Which mechanism predominates depends on the temperature and chemical composition of the oxide lattice.²⁹³ In both cases the manganese oxidation state remains unchanged. When significant amounts of hydrogen are ion exchanged, the MO₂ slabs slide to give prismatic coordination between the layers as this, combined with a contraction in the interlayer spacing of around 0.3 Å, leads to optimum hydrogen bonding.²⁹² These protons are lost as water on heating the oxide to around 150 °C.²⁹² Acid leaching of Li₂MnO₃ also results in the removal of lithium, and here again both mechanisms of Li₂O removal^{294,295} and proton exchange²⁹⁶ are believed to be operative. Acid leaching of the lithium stoichiometric compounds, such as LiNi_{0.4}Mn_{0.4}Co_{0.2}O₂, also results in removal of lithium and a small amount of proton exchange.²⁷⁶

The ease of oxygen removal from the close-packed lattice when lithium rich had been demonstrated²⁹⁷ by its ready reduction by ammonia gas at 200 °C in the case of the spinel Li[Li_{1/3}Mn_{5/3}]O₄. It was also shown²⁹⁷ that this oxygen could be removed by electrochemically charging above around 4.3 V; the material then showed the 4 V discharge behavior typical of a spinel. These reduced materials can best be represented as Li[Li_{1/3}Mn_{5/3}]O_{4-δ}.

Dahn et al. studied²⁵² the solid solution Li₂MnO₃–LiNiO₂, which can be written as Li[Ni_yLi_(1/3-2y/3)Mn_(2/3-y/3)]O₂ = *y*LiNiO₂ + (1–*y*)Li[Li_{1/3}Mn_{2/3}]O₂. The *a* and *c* hexagonal lattice parameters increased linearly with the nickel content, *y*, from 0.08 to 0.5 with the *d*3*a* ratio decreasing linearly, showing that the layeredness decreased with increasing nickel content as expected. Cells of these materials showed an irreversible charging plateau around 4.5 V, which is believed to be due to loss of oxygen as described above. Before the plateau all the nickel is oxidized to Ni⁴⁺. After this “overcharging” the electrodes were found to cycle well at 30 °C between 2.0 and 4.6 V with the capacity increasing inversely with the value of *y*: 160, 180, and 200 mAh/g, respectively, for *y* = 1/2, 5/12, and 1/3 (this trend has been confirmed²⁹⁸).

The first has no excess lithium and the lowest capacity, showing the advantage of excess lithium. The capacity of the $y = 1/3$ material increased to 220 mAh/g when the cycling temperature was increased to 55 °C. However, this high charging level results in a lower thermal stability of the material.²⁵² The addition of excess lithium to the 550 composition, $\text{Li}_{1+x}(\text{Ni}_{0.5}\text{Mn}_{0.5})_{1-x}\text{O}_2$ was reported²⁹⁹ to increase the stability of the material. The system Li_2MnO_3 – LiNiO_2 – LiMnO_2 has been studied,³⁰⁰ and it shows complete solubility along the Li_2MnO_3 – LiNiO_2 line; the electrochemical capacity was found to fall rapidly as the nickel content decreased when the charging potential was limited to 4.3 V.

Thackeray et al.³⁰¹ showed that Li_2TiO_3 forms a solid solution with $\text{LiNi}_{0.5}\text{Mn}_{0.5}\text{O}_2$ and that the titanium helped allow the intercalation of a second lithium into the structure.⁶⁴ The advantages of adding Li_2MnO_3 to the layered cathode material have even been reported for manganese-rich materials, which would be unstable otherwise relative to spinel formation. Thus, $\text{Li}[\text{Li}_{0.2}\text{Ni}_{0.2}\text{Mn}_{0.6}]\text{O}_2$ showed a steady-state capacity of around 200 mAh/g between 2.0 and 4.6 V at 0.1 mA/cm², after gaining capacity for the first 10 cycles.³⁰² The behavior and stability of this material at higher rates was not reported. Addition of some cobalt to these manganese-rich compounds was reported to help retain the capacity at higher discharge rates.²²² Magnesium has also been proposed as a stabilizing agent for manganese-rich materials.³⁰³

Thus, there is one more parameter, the lithium excess content, to be considered in addition to the nickel, cobalt, and manganese ratios in designing the optimum composition for the ideal cathode. Each of these elements has its own role to play, whether it is stabilizing the lattice (the manganese), being the electrochemically active member (the nickel), ordering the transition metals and perhaps increasing the rate capability and the conductivity (the cobalt), or increasing the capacity (the lithium). Whether other elements will play a critical role is yet to be determined, but some elements such as titanium have been found to decrease the rate capability and migrate to the lithium layer.

5.3. Iron Compounds Including Oxides and Phosphates

A number of researchers,^{173,304,305} particularly in Japan, have been pursuing the oxides of iron as potential cathode materials for lithium cells. However, materials of the type LiFeO_2 have shown little ability for lithium removal. A number of other iron compounds have been studied over the years, including FeOCl ,³⁰⁶ FePS_3 ,³⁰⁷ KFeS_2 ,³⁰⁸ and FeS_2 ,¹³ but none showed much reversibility. Although metal phosphates have been studied for more than 20 years since the discovery of fast ion transport in NASICON, it is only recently that they have been considered as cathodes^{309–312} or anodes^{312–314} of lithium batteries.

5.3.1. Olivine Phase

Emphasis changed radically in 1997 with the discovery of the electrochemical properties of the

olivine phase, in particular LiFePO_4 , by Padhi et al.³⁰⁹ This is the first cathode material with potentially low cost and plentiful elements and also environmentally benign that could have a major impact in electrochemical energy storage. For LiFePO_4 , the discharge potential is about 3.4 V vs lithium and no obvious capacity fading was observed even after several hundred cycles. Its capacity approaches 170 Ah/kg, higher than that obtained by LiCoO_2 and comparable to stabilized LiNiO_2 , and moreover, it is very stable during discharge/recharge. Since its discovery, many research groups have tried to improve the performance of this material.^{49,50,198,315–326}

LiFePO_4 can be synthesized by high-temperature reactions,³⁰⁹ under hydrothermal conditions,⁵⁰ or by sol–gel methods.³²⁷ Although the olivine phase can be very easily synthesized hydrothermally within just a few minutes and its X-ray pattern looks good, it gives poor electrochemical properties; a close examination of the structure showed that there are about 7% iron atoms in the lithium site, and this is reflected in the lattice parameters of $a = 10.381$ Å, $b = 6.013$ Å, and $c = 4.716$ Å compared with those for ordered LiFePO_4 of $a = 10.333$ Å, $b = 6.011$ Å, and $c = 4.696$ Å.¹⁹⁸ These iron atoms essentially block diffusion of the lithium ions, as the diffusion is fast only along the tunnel and not between them;⁵¹ thus, it will be critical in the use of this material to ensure ordering of the lithium and iron atoms. Firing the hydrothermal material to 700 °C resolved the disorder. Recent studies suggest that the hydrothermal approach can be improved by modifying the synthesis conditions, for example, by adding a reducing agent such as ascorbic acid³²⁸ to prevent surface ferric films; the hydrothermal method can also produce material with excellent electrochemical behavior even without a carbon coating,³²⁹ as is necessary in most instances as discussed below.

As this material has a very low conductivity at room temperature, it could achieve the theoretical capacity only at a very low current density³¹⁵ or at elevated temperatures,³¹⁷ as suggested by Padhi³⁰⁹ due to the low lithium diffusion at the interface. Ravet et al.³¹⁸ showed that a carbon coating significantly improves the electrochemical performance of this material; sucrose was proposed³¹⁹ as one carbon precursor, and it was used on the initial hydrothermal samples.⁵⁰ Many other studies have been made on finding means to improve the electronic conductivity of the LiFePO_4 particles.^{49,198,320,321,323–326} Very pure LiFePO_4 samples are reported to have an electronic conductivity of 10^{-9} S/cm,³²⁴ whereas samples made from reagent-grade carbon-containing materials have a conductivity of around 10^{-5} – 10^{-6} S/cm.¹⁹⁸ Huang et al.³²⁰ proposed coating the material with carbon-gel during the synthesis step and found capacities approaching 100% at very low cathode loadings, 5 mg/cm², and rather high carbon contents, 20%. They obtained 800 cycles at around 120 mAh/g at high rates. Masquelier proposed³²¹ extensive milling of the material with carbon and then found high capacities at elevated temperatures. A 2002 paper by Chang et al.³²⁴ showed excellent electrochemical behavior when the LiFePO_4 was “doped” with parts

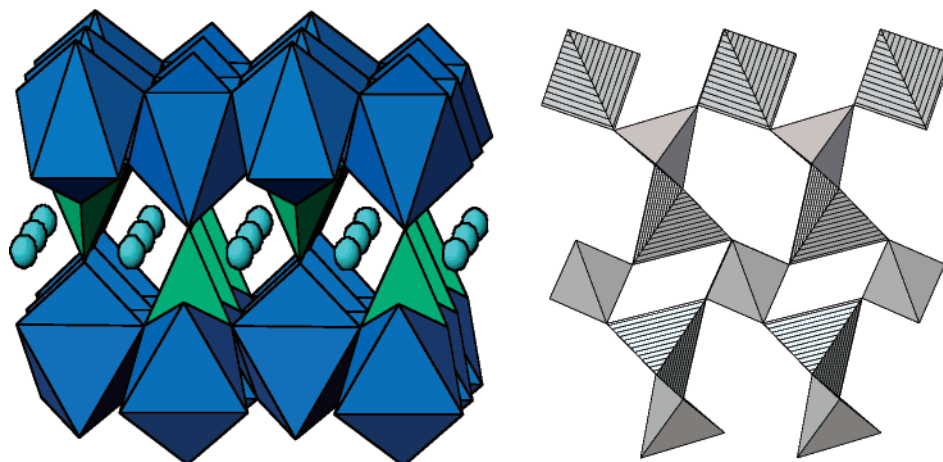


Figure 22. Structures of orthorhombic LiFePO_4 and trigonal quartz-like FePO_4 .

per million of elements such as niobium, which increased the conductivity by 8 orders of magnitude. This paper caused a surge of interest in this compound and in an understanding of what causes the conductivity changes; a recent paper by Nazar et al.³²⁵ has shown that the conductivity increase is related to the formation of a highly conductive iron phosphide, Fe_2P , surface film; this film is formed at high temperature, particularly in the presence of a reducing agent such as carbon.

The olivine structure is shown in Figure 22, and on lithium removal the phase FePO_4 is formed; LiFePO_4 and FePO_4 have essentially the same structure. This FePO_4 is isostructural with heterosite, $\text{Fe}_{0.65}\text{Mn}_{0.35}\text{PO}_4$. This is a two-phase system with LiFePO_4 being in equilibrium with FePO_4 as shown in the cycling plot in Figure 23a.¹⁹⁸ This figure shows that 100% capacity of the lithium is cyclable at 1 mA/cm^2 at 60 °C even at electrode loadings of 80 mg/cm^2 ; at room temperature, around 70% can be cycled at 1 mA/cm^2 and 100% at 0.1 mA/cm^2 . Even at 10 mA/cm^2 , almost 70% of the capacity is obtained at low loadings, as shown in Figure 23b.

Critical to the use of LiFePO_4 is its reactivity and thermal stability and that of its charged product, FePO_4 . Thomas reported³¹⁷ that there were no thermal excursions observed in cells or in a DSC experiment in the range 25–85 °C. However, the olivine structure is inherently unstable because of the edge sharing between octahedra and tetrahedra, and under pressure it converts to the spinel phase as observed in the earth's mantle. Recently, the transformation of orthorhombic LiFePO_4 to an olivine-like LiFePO_4 with the lithium in tetrahedral sites has been reported;³³⁰ this form is electrochemically inactive. In addition, more than two crystalline forms of FePO_4 are known: the orthorhombic form isostructural with LiFePO_4 where the iron is found in FeO_6 octahedra and the trigonal form in which the iron is found in FeO_4 tetrahedra. These are shown in Figure 22. The orthorhombic structure has been discussed extensively.³⁰⁹ The trigonal form is composed of FeO_4 and PO_4 tetrahedra, each FeO_4 tetrahedron shares its four corners with four PO_4 tetrahedra and vice versa, giving a quartz-like structure. The all-tetrahedral form is electrochemically unreactive as Fe(II) is not stable in tetrahedral configuration, and more-

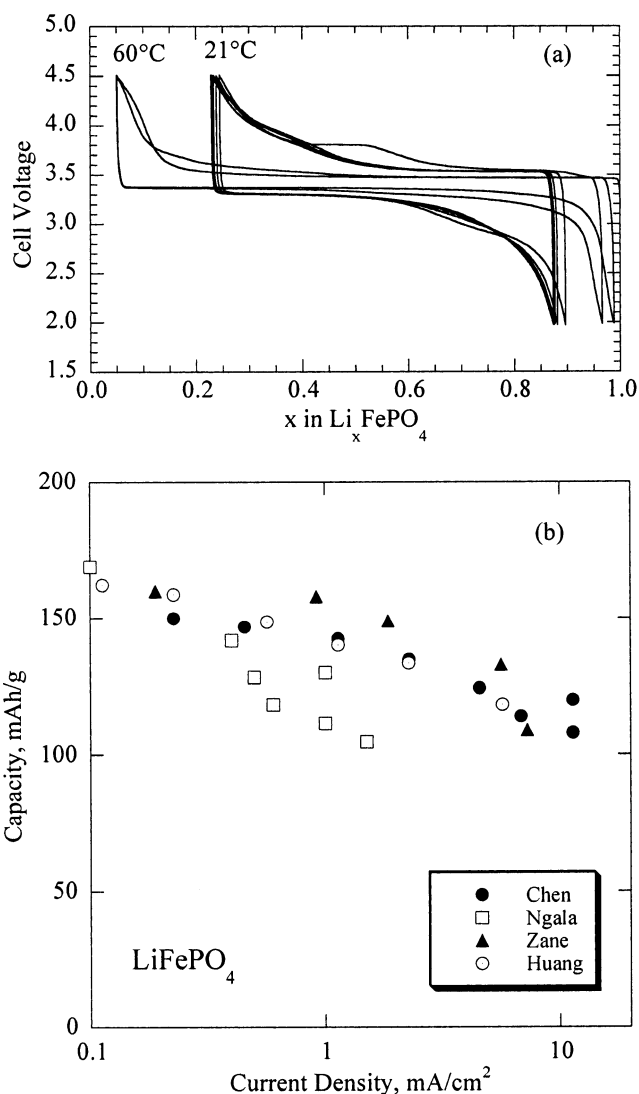


Figure 23. Electrochemical behavior of LiFePO_4 : (a) cycling at 1 mA/cm^2 at 21 and 60 °C (reprinted with permission from ref 198, copyright 2003 Elsevier) and (b) Ragone plot for LiFePO_4 from four groups, Chen³³² (8 mg/cm^2 loading and about 10 wt % carbon), Ngala²¹⁹ (20–80 mg/cm^2 and 10% carbon), Zane³⁶³ (10 mg/cm^2 and 20% carbon), and Huang³²⁰ (5 mg/cm^2 and 20% carbon).

over, surface glassy films tend to form at high temperatures.⁴⁹ Thus, care must be taken to ensure that it is not formed during the synthesis of LiFePO_4

Table 1. Chemical Reactivity of Iron Phosphates⁴⁹

compound	synthesis method	BuLi reactivity (mol/Fe)
LiFePO ₄	high temperature	1.85
LiFePO ₄	hydrothermal	0.29
FePO ₄	orthorhombic	3.25
FePO ₄	trigonal (700 °C-tetrahedral iron)	2.90
FePO ₄ ·2H ₂ O	amorphous phase	7.20
LiFePO ₄ (OH)	hydrothermal	3.24

or its precursors. At low temperatures, when lithium ions are absent, amorphous FePO₄·2H₂O can be formed (see below); although it is electrochemically active, dehydration at high temperatures leads to the tetrahedral form of FePO₄, which is electrochemically inactive.³³¹

It is essential to understand the long-term stability of electrode materials to ensure the extended life of any battery. Thus, it is important to better understand the reactivity of both the LiFePO₄ and the FePO₄ orthorhombic phases. For example, what happens when LiFePO₄ is over discharged or does the orthorhombic FePO₄ slowly switch to the quartz form over time? When iron phosphates are reacted with an excess of *n*-butyllithium it was reported⁴⁹ that all but one reacted with sufficient butyllithium to form lithium phosphate and iron as shown in Table 1. Thus, it appears that these phosphate lattices are destroyed at low lithium potentials; *n*-butyllithium is about 1 V versus pure lithium. An electrochemical study⁴⁹ where the LiFePO₄ cathode was subjected to a discharge down to 1.0 V at 0.4 mA/cm² confirmed that lithium reacts with destruction of the LiFePO₄ lattice and considerable loss of capacity. After five cycles the capacity had dropped by 80%. Thus, lithium iron phosphate cells will require overdischarge protection in commercial applications. On the other hand, no evidence has been found for the conversion of the metastable orthorhombic FePO₄ phase to the quartz-like trigonal phase under normal electrochemical conditions. Moreover, unlike the layered oxides described earlier, there is no tendency to lose oxygen on lithium removal from the lattice.

The low density of LiFePO₄ results in a low volumetric density, and so it is critical that the minimum volume of carbon and organic binder be used in the electrode. Taking the density of LiFePO₄, Teflon, and carbon black as 3.6, 2.2, and 1.8 g/cm³, respectively, then an electrode containing 10 wt % carbon and 5 wt % Teflon will have a volumetric energy density 25% less than the theoretical value. This assumes that all the particles pack equally efficiently, which is unlikely to be the case with the poor packing associated with carbon, particularly with decomposed sugar. A tap density study suggested that this carbon packs poorly, so the volumetric density penalty may be very significant.³³² A number of carbons have been studied to determine how much carbon is needed for optimum electrochemical behavior. For carbon black little difference was observed for carbon loadings from 6 to 15 wt %, except that the polarization observed was slightly higher at 6 wt %; the method of carbon addition, whether carbon black, carbon gel, sugar, or aqueous

gelatin,³³³ did not appear to be important. However, the temperature of firing the reaction mixture appears to be much more important as that determines the amount of graphitic compound on the LiFePO₄ surface; sp² carbon was found to be much more effective than sp³ carbon.³³⁴ The particle size is almost certainly controlled by the carbon in the reaction mixture, even when only coming from carbon in the reagent materials, leading to the positive behavior of several samples.³²⁴ The temperature of preparation was found to be important, with that prepared at 675 °C showing the best behavior in one study.³³⁵

Much of the above discussion has centered on the iron phase of the LiMPO₄ olivine structure, but the transition metal may also be manganese, nickel, and cobalt. The naturally occurring form contains both iron and manganese. None of these other forms has yet showed superior electrochemical behavior to the iron compound, even though they have higher discharge potentials.³³⁶ The mixed Fe–Mn compound discharges in two distinct steps, which can be associated, respectively, with the iron and manganese redox reactions. Several research groups have studied the cycling behavior of the pure LiMnPO₄ compound.^{337,338} The results are controversial: Yamada et al.³³⁷ related the inability to extract lithium from LiMnPO₄ electrochemically to the thermodynamic instability of olivine-type MnPO₄ due to the Jahn–Teller effect of Mn³⁺; Li et al.³³⁸ reported a reversible capacity of about 140 mAh/g for the reaction between LiMnPO₄ and MnPO₄. Recently, Delacourt et al.³³⁹ studied the LiMnPO₄ formed by direct precipitation and obtained a reversible capacity of 70 mAh/g after carbon coating by ball milling the materials with carbon black. This suggests that MnPO₄ is thermodynamically stable. Song et al.³⁴⁰ studied LiMnPO₄, formed from the thermal decomposition of LiMnPO₄(OH), and found the Mn³⁺/Mn²⁺ transformation at about 4.1 V with a high polarization and low capacity; heating with carbon black did not result in any dramatic enhancement of the capacity. Ceder et al.,³⁴¹ using an advanced theoretical treatment, have calculated the open-circuit voltages and the band gap in these phosphates, and found that as expected they are very high. The open-circuit voltages are 3.5 V for LiFePO₄, 4.1 V for LiMnPO₄, 4.8 V for LiCoPO₄, and 5.1 V for LiNiPO₄, thus explaining the lack of electrochemical activity for LiNiPO₄ within the normal cycling potential range. The very high calculated band gaps of 3.7 and 3.8 eV for LiFePO₄ and LiMnPO₄ are consistent with their color and diffuse reflectance spectra and suggest that band-gap differences do not explain the different electrochemical behavior; the electronic conductivity is likely due to a polaron mechanism.³⁴² Some other recent theoretical calculations^{343,344} suggesting that these materials are semi-metals are inconsistent with their white color and are almost certainly in error due to problems with the theory used.

5.3.2. Other Iron Phosphate Phases

Several other iron phosphate structures have been described. The phase Li₃Fe₂(PO₄)₃ has been stud-

ied,^{50,311,312} and it discharges below 3 V and carries more phosphate deadweight than LiFePO_4 , so has been of less interest since the discovery of LiFePO_4 . Three groups^{345–347} have studied the electrochemical behavior of the hydrated and anhydrous phase $\text{FePO}_4 \cdot n\text{H}_2\text{O}$ and found essentially identical results. Amorphous and crystalline $\text{FePO}_4 \cdot n\text{H}_2\text{O}$ were prepared hydrothermally and then heat-treated over a range of temperatures. The material obtained from the amorphous dihydrate shows more than double the capacity of the material obtained from the crystalline dihydrate, 0.75 vs 0.3 Li/FePO_4 , respectively. This might be associated with the amorphous nature of the former relative to the more crystalline structure of the latter; also, the latter has iron in an essentially tetrahedral environment. The capacity of the former is similar to that reported by Prosini et al.³⁴⁸ for a biphasic mixture of phosphate and iron oxide. Both the amorphous and crystalline materials show behavior more typical of a single-phase reaction, Li_xFePO_4 , as opposed to the two-phase behavior of the LiFePO_4 – FePO_4 system. The discharge curves of amorphous FePO_4 obtained at different temperatures at 0.2 mA/cm^2 , between 4 and 2 V, are shown in Figure 24 as are also the cycling curves and the rate capability of the amorphous FePO_4 sample heated at 350 °C at different current densities, $I_c = I_d$.

Another class of iron phosphates is that related to the minerals Giniite and Lipscombite. The structure in this case consists of rods containing face-sharing FeO_6 octahedra, stacked orthogonally to one another, giving nonintersecting tunnels through which lithium ions can diffuse. The discharge potentials in this case are sloping and lower than those of the $\text{LiFePO}_4/\text{FePO}_4$ system.^{349,350}

5.3.3. Vanadium Phosphate Phases

A number of vanadium phosphates have also been studied as potential cathodes, including those of general formula $\text{Li}_3\text{V}_2(\text{PO}_4)_3$ ^{351–356} and VOPO_4 .³⁵⁷ $\text{Li}_3\text{V}_2(\text{PO}_4)_3$ exists in two forms: the thermodynamically stable monoclinic form and a rhombohedral form that can be formed by ion exchange from the stable sodium analogue with the NASICON structure. Two lithium ions can be removed from the rhombohedral form at 3.77 V, and only 1.3 can be reinserted.³⁵³ The monoclinic form is of more interest as a cathode as all three lithium ions can be readily removed and reversibly intercalated at high rate.^{351,352} However, the electrochemistry of this cathode is complex, showing a series of steps on charging but a solid solution on lithium insertion from 0 to 2 lithium followed by two-phase behavior.³⁵⁵ This cathode is being commercialized by Valence Technology.

The ϵ - VOPO_4 compound has particularly interesting properties,³⁵⁸ with an approximately 4 V flat discharge potential some 0.5 V higher than LiFePO_4 and with higher electronic conductivity, leading to the possibility of attaining higher power systems than for LiFePO_4 but at the expense of higher cost. The ϵ - VOPO_4 can be synthesized by removal of the hydrogen atoms from $\text{VPO}_4 \cdot 2\text{H}_2\text{O} (= \text{H}_2\text{VOPO}_4)$ either thermally³⁵⁹ or by electrochemical deintercalation.³⁴⁰

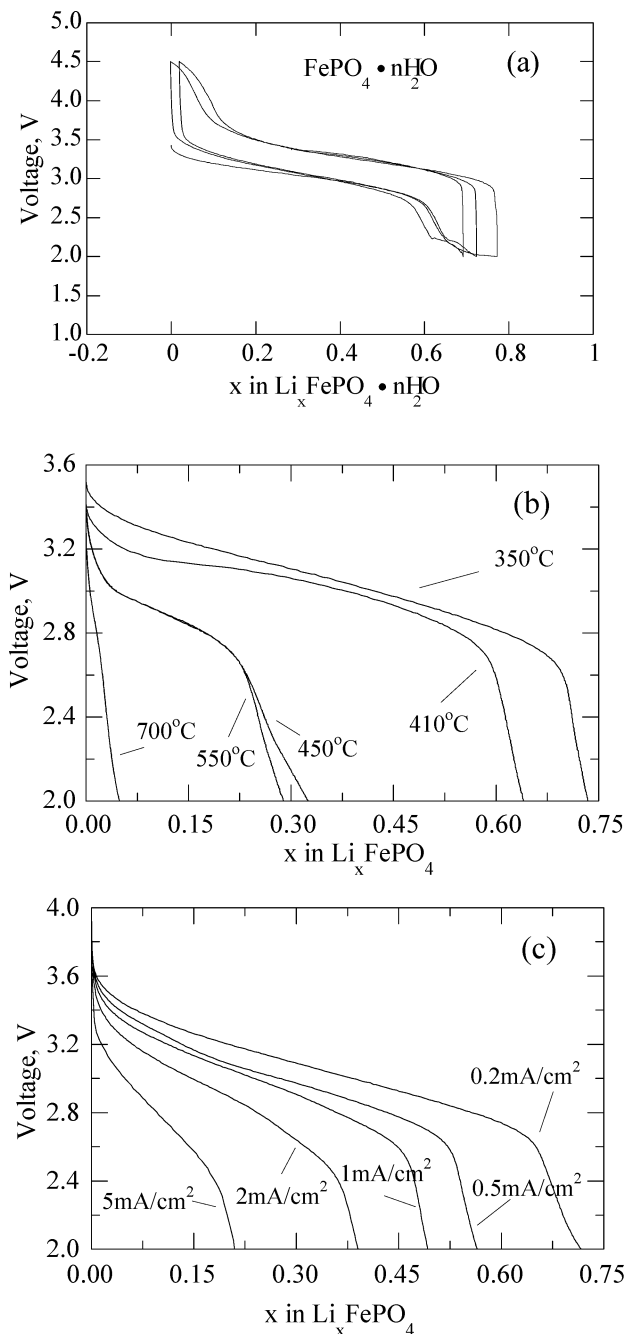


Figure 24. Electrochemical behavior of $\text{FePO}_4 \cdot n\text{H}_2\text{O}$ formed by the thermal decomposition of $\text{FePO}_4 \cdot n\text{H}_2\text{O}$: (a) discharge of FePO_4 as a function of annealing temperature, (b) cycling of FePO_4 annealed at 350 °C, and (c) rate capability of FePO_4 annealed at 350 °C (reprinted with permission from refs 49 and 345, copyright 2002 Elsevier).

In the latter, after the H_2VOPO_4 is electrochemically oxidized in a $\text{LiPF}_6/\text{EC-DMC}$ solution to give ϵ - VOPO_4 , the ϵ - VOPO_4 can be reduced by reversing the current flow to give first LiVOPO_4 and then Li_2VOPO_4 , as shown in Figure 25a.³⁴⁰ As expected from the ease of these reactions, the structures of all four compounds are closely related, as shown in Figure 25b;³⁶⁰ the building block for all these structures, which consists of VO_6 octahedra and PO_4 tetrahedra, is shown at the lower right.

If a still higher redox potential is desired, then heating ϵ - VOPO_4 with LiF and carbon black at 550

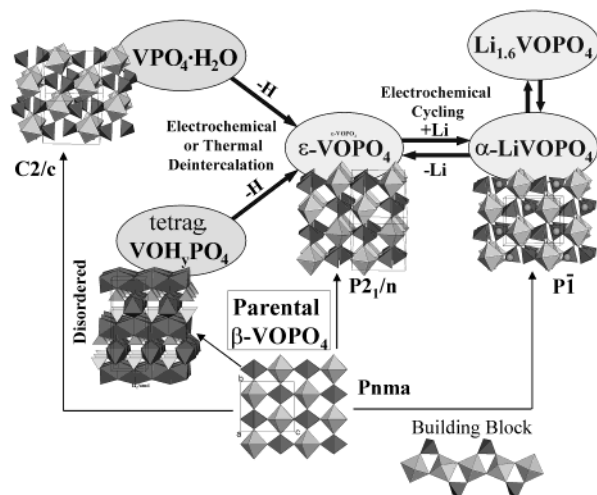
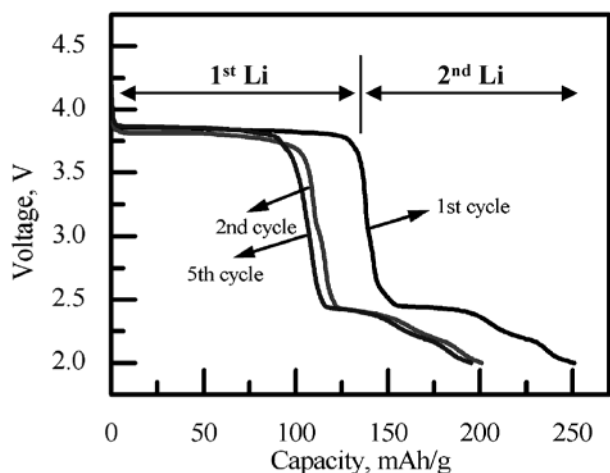


Figure 25. (top) Electrochemical intercalation of lithium into ϵ -VOPO₄,³⁴⁰ and (bottom) relationship between the various structures in the VOPO₄ system; the building block for all these structures is shown at the lower right.

°C for 15 min and then rapidly cooling to room temperature leads to the formation of LiVPO₄F.³⁶¹ This compound is isostructural with LiMPO₄(OH) (M = Fe, Mn). It has a potential of 4.2 V and a capacity of 0.55 Li per formula unit or 156 mAh/g.³⁴⁰

6. Conclusions and What Does the Future Hold

Lithium batteries have made substantial and significant gains in the last 30 years from becoming a curiosity to becoming the dominant rechargeable battery for consumer portable applications. However, the next market opportunities will be much tougher to conquer as they mostly demand higher power capabilities at lower costs and often in larger systems with enhanced safety. The prime markets are the high-power segment presently dominated by the environmentally unfriendly Ni/Cd battery and the HEV segment presently occupied by the Ni/metal hydride battery. The layered oxides will, without doubt, continue their ongoing improvement with mixed transition metals slowly displacing the pure cobalt system; they appear to offer enhanced safety with enhanced capacity at a lower cost and are drop-in technology. The lithium iron phosphate cathode offers the first potentially low-cost cathode, but this

will only be achieved if the costs of the other cell components are also reduced. These include the electrolyte, a lower cost anode with added safety features including the use of natural graphite, and probably the use of thicker cathodes to reduce the cost of electrode support materials, separators, etc. It can be anticipated that totally new materials with unexpected properties will be discovered, so that the goal of at least one lithium cycling per transition metal at a rate of 10 mA/cm² can be achieved with pulse charging and discharging at still higher rates.

7. Abbreviations and Specialized Terms

anode	electropositive electrode
cathode	electronegative electrode
<i>C</i> rate	measure of the time for cell discharge in reciprocal hours, time of discharge = 1/ <i>C</i> in hours
HEV	hybrid electric vehicle
LiBOB	lithium bis(oxalato)borate LiB(C ₂ O ₄) ₂
LiPF ₆	lithium hexafluorophosphate, LiPF ₆
NASICON	sodium superionic conductor
Ragone plot	a plot of the electrochemical cell capacity as a function of the magnitude of the discharge or charge current
Vegard's Law	for a solid solution the lattice parameter varies linearly with composition

8. Acknowledgments

This work was supported by the US Department of Energy, Office of FreedomCAR and Vehicle Technologies, through the BATT program at Lawrence Berkeley National Laboratory and by the National Science Foundation through grant DMR0313963. I thank Drs. Marca Doeff, Kang Xu, and Michael Thackeray for many constructive suggestions for improving the first draft of this manuscript. I also thank Professor T. Ohzuku for providing Figure 14 and Miaomiao Ma, Natasha Chernova and Peter Zavalij for help and much data.

9. References

- (1) Watanabe, N.; Fukuba, M. U.S. Patent 3,536,532, 1970.
- (2) Whittingham, M. S. *J. Electrochem. Soc.* **1975**, *122*, 526.
- (3) Ikeda, H.; Saito, T.; Tamaru, H. *Denki Kagaku* **1977**, *45*, 314.
- (4) Ikeda, H.; Uena, S.; Saito, T.; Nakaido, S.; Tamaru, H. *Denki Kagaku* **1977**, *45*, 391.
- (5) Sanyo, Lithium Battery Calculator, Model CS-8176L.
- (6) Dey, A. N. *J. Electrochem. Soc.* **1971**, *118*, 1547.
- (7) Liang, C. C.; Bolster, M. E.; Murphy, R. M. U.S. Patents 4,310,609 and 4,391,729, 1982.
- (8) Takeuchi, E. S.; Thiebolt, W. C. *J. Electrochem. Soc.* **1988**, *135*, 2691.
- (9) Crespi, A.; Schmidt, C.; Norton, J.; Chen, K.; Skarstad, P. *J. Electrochem. Soc.* **2001**, A30.
- (10) Vissers, D. R.; Tomczuk, Z.; Steunenberg, R. K. *J. Electrochem. Soc.* **1974**, *121*, 665.
- (11) Gay, E. C.; Vissers, D. R.; Martino, F. J.; Anderson, K. E. *J. Electrochem. Soc.* **1976**, *123*, 1591.
- (12) Kaun, T. D.; Nelson, P. A.; Redey, L.; Vissers, D. R.; Henriksen, G. L. *Electrochim. Acta* **1993**, *38*, 1269.
- (13) Whittingham, M. S. *Prog. Solid State Chem.* **1978**, *12*, 41.
- (14) Mikhaylik, Y. V.; Akridge, J. R. *J. Electrochem. Soc.* **2003**, *150*, A306.
- (15) Visco, S. J. (PolyPlus-Battery) U.S. Patent 6,214,061, 2004.
- (16) Yao, Y. Y.; Kummer, J. T. *J. Inorg. Nucl. Chem.* **1967**, *29*, 2453.
- (17) Whittingham, M. S.; Huggins, R. A. *J. Chem. Phys.* **1971**, *54*, 414.
- (18) Whittingham, M. S.; Huggins, R. A. *NBS Spec. Pub.* **1972**, *364*, 139.
- (19) Whittingham, M. S. In *Fast Ion Transport in Solids*; van Gool, W., Ed.; North-Holland: Amsterdam, 1973.

- (20) Trumbore, F. A.; Broadhead, J.; Putvinski, T. M. *Electrochem. Soc. Abstr.* **1973**, 1973-2, 61.
- (21) Broadhead, J.; Trumbore, F. A. *Electrochem. Soc. Abstr.* **1973**, 1977-1, 178/179.
- (22) Broadhead, J. U.S. Patent 3,791,867, 1973.
- (23) Murphy, D. W.; Trumbore, F. A. *J. Electrochem. Soc.* **1976**, 123, 960.
- (24) Armand, M. B. In *Fast Ion Transport in Solids*; van Gool, W., Ed.; North-Holland: Amsterdam, 1973.
- (25) Armand, M. B.; Touzan, P. *Mater. Sci. Eng.* **1977**, 31, 319.
- (26) Armand, M. B. U.S. Patent 4,041,220, 1977.
- (27) Whittingham, M. S. *Layered Compounds*; Asilomar: Monterey, CA, 1972.
- (28) Gamble, F. R.; Osiecki, J. H.; Cais, M.; Pishardy, R.; Disalvo, F. J.; Geballe, T. H. *Science* **1971**, 174, 493.
- (29) Gamble, F. R.; Thompson, A. H. *Solid State Commun.* **1978**, 27, 379.
- (30) Whittingham, M. S. *Mater. Res. Bull.* **1974**, 9, 1681.
- (31) Whittingham, M. S. *J. Chem. Soc., Chem. Commun.* **1974**, 328.
- (32) Whittingham, M. S. U.S. Patent 4040017 and U.K. Patent 1468244, 1973.
- (33) SubbaRao, G. V.; Tsang, J. C. *Mater. Res. Bull.* **1974**, 9, 921.
- (34) Whittingham, M. S. U.S. Patent 4009052 and U.K. Patent 1468416, 1973.
- (35) Whittingham, M. S. *Science* **1976**, 192, 1126.
- (36) Whittingham, M. S. *Chemtech* **1979**, 9, 766.
- (37) Whittingham, M. S.; Chianelli, R. R. *J. Chem. Educ.* **1980**, 57, 569.
- (38) Holleck, G. L.; Driscoll, J. P. *Electrochim. Acta* **1977**, 22, 647.
- (39) Thompson, A. H. *Phys. Rev. Lett.* **1975**, 35, 1786.
- (40) Whittingham, M. S. *J. Electrochem. Soc.* **1976**, 123, 315.
- (41) Steele, B. C. H. In *Fast Ion Transport in Solids*; van Gool, W., Ed.; North-Holland: Amsterdam, 1973.
- (42) Basu, S.; Worrell, W. In *Fast Ion Transport in Solids*; Vashishta, P., Mundy, J. N., Shenoy, G. K., Eds.; Elsevier-North-Holland: New York, 1979.
- (43) Newman, G. H.; Klemann, L. P. *J. Electrochem. Soc.* **1980**, 127, 2097.
- (44) Winn, D. A.; Shemilt, J. M.; Steele, B. C. H. *Mater. Res. Bull.* **1976**, 11, 559.
- (45) Whittingham, M. S.; Gamble, F. R. *Mater. Res. Bull.* **1975**, 10, 363.
- (46) Whittingham, M. S.; Panella, J. A. *Mater. Res. Bull.* **1981**, 16, 37.
- (47) Whittingham, M. S. U.S. Patent 4,007,055, 1975.
- (48) Whittingham, M. S. U.S. Patent 4,084,046, 1975.
- (49) Yang, S.; Song, Y.; Zavalij, P. Y.; Whittingham, M. S. *Electrochem. Commun.* **2002**, 4, 239.
- (50) Yang, S.; Zavalij, P. Y.; Whittingham, M. S. *Electrochem. Commun.* **2001**, 3, 505.
- (51) Morgan, D.; VanderVen, A.; Ceder, G. *Electrochem. Solid State Lett.* **2004**, 7, A30.
- (52) Thompson, A. H. *Phys. Rev. Lett.* **1978**, 40, 489.
- (53) Yazami, R.; Touzain, P. *J. Power Sources* **1983**, 9, 365.
- (54) Basu, S. U.S. Patent 4,423,125, 1982.
- (55) Whittingham, M. S.; Newman, G. H. *J. Electrochem. Soc.* **1981**, 128, 706.
- (56) Whittingham, M. S.; Newman, G. H. U.S. Patent 4,086,403, 1976.
- (57) Newman, G. H.; Francis, R. W.; Gaines, L. H.; Rao, B. M. L. *J. Electrochem. Soc.* **1980**, 127, 2025.
- (58) Chianelli, R. R.; Scanlon, J. C.; Rao, B. M. L. *J. Electrochem. Soc.* **1978**, 125, 409.
- (59) Chianelli, R. R. *J. Cryst. Growth* **1976**, 34, 239.
- (60) Rao, B. M. L.; Francis, R. W.; Christopher, H. A. *J. Electrochem. Soc.* **1977**, 124, 1490.
- (61) Whittingham, M. S. *Mater. Res. Bull.* **1978**, 13, 959.
- (62) Murphy, D. W.; DiSalvo, F. J.; Hull, G. W.; Waszczak, J. V. *Inorg. Chem.* **1976**, 15, 17.
- (63) Dahn, J. R.; Sacken, U. v.; Michal, C. A. *Solid State Ionics* **1990**, 44, 87.
- (64) Johnson, C. S.; Kim, J.-S.; Kropf, A. J.; Kahaian, A. J.; Vaughey, J. T.; Thackeray, M. M. *Electrochem. Commun.* **2002**, 4, 492.
- (65) Haering, R. R.; Stiles, J. A. R.; Brandt, K. U.S. Patent 4,224,390, 1980.
- (66) Murphy, D. W.; Carides, J. N.; DiSalvo, F. J.; Cros, C.; Waszczak, J. V. *Mater. Res. Bull.* **1977**, 12, 825.
- (67) Murphy, D. W.; Cros, C.; DiSalvo, F. J.; Waszczak, J. V. *Inorg. Chem.* **1977**.
- (68) Schöllhorn, R.; Payer, A. *Angew. Chem., Int. Ed. Engl.* **1985**, 24, 67.
- (69) Sinha, S.; Murphy, D. W. *Solid State Ionics* **1986**, 20, 81.
- (70) Goodenough, J. B.; Manthiram, A.; Wnetrzewski, B. *J. Power Sources* **1993**, 43-44, 269.
- (71) Thompson, A. H.; Gamble, F. R.; Symon, C. R. *Mater. Res. Bull.* **1975**, 10, 915.
- (72) Trumbore, F. *J. Power Sources* **1989**, 26, 65.
- (73) Murphy, D. J.; Trumbore, F. A. *J. Cryst. Growth* **1977**, 39, 185.
- (74) Whittingham, M. S.; Jacobson, A. J. U.S. Patent 4,233,375, 1979.
- (75) Whittingham, M. S.; Jacobson, A. J. *J. Electrochem. Soc.* **1981**, 128, 485.
- (76) Dines, M. B. *Mater. Res. Bull.* **1975**, 10, 287.
- (77) Whittingham, M. S.; Dines, M. B. *J. Electrochem. Soc.* **1977**, 124, 1387.
- (78) Murphy, D. W.; Christian, P. A. *Science* **1979**, 205, 651.
- (79) Dampier, F. W. *J. Electrochem. Soc.* **1974**, 121, 656.
- (80) Walk, C. R.; Gore, J. S. *J. Electrochem. Soc.* **1975**, 122, 68C.
- (81) Walk, C. R.; Margalit, N. *J. Power Sources* **1997**, 68, 723.
- (82) Delmas, C.; Cognac-Auradou, H.; Cocciantelli, J. M.; Ménétrier, M.; Doumerc, J. P. *Solid State Ionics* **1994**, 69, 257.
- (83) Delmas, C.; Cognac-Auradou, H.; Cocciantelli, J. M.; Ménétrier, M.; Doumerc, J. P. *Solid State Ionics* **1994**, 69, 257.
- (84) Dickens, P. G.; French, S. J.; Hight, A. T.; Pye, M. F. *Mater. Res. Bull.* **1979**, 14, 1295.
- (85) Whittingham, M. S. *Electrochem. Soc. Abstr.* **1975**, 1975-1, 40.
- (86) Murphy, D. W.; Christian, P. A.; Disalvo, F. J.; Carides, J. N. *J. Electrochem. Soc.* **1979**, 126, 497.
- (87) Bergström, Ö.; Gustafsson, T.; Thomas, J. Abstracts of the XVII International Union of Crystallography Congress, Seattle, WA; International Union of Crystallography (<http://www.iucr.ac.uk/>): Cambridge, U.K., 1996.
- (88) Bergström, Ö.; Gustafsson, T.; Thomas, J. O. *Acta Crystallogr.* **1997**, C53, 528.
- (89) Bergström, Ö.; Gustafsson, T.; Thomas, J. O. *Acta Crystallogr.* **1998**, C54, 1204.
- (90) Howing, J.; Gustafsson, T.; Thomas, J. O. *Acta Crystallogr.* **2003**, B59, 747.
- (91) Bjork, H.; Lidin, S.; Gustafsson, T.; Thomas, J. O. *Acta Crystallogr.* **2001**, B57, 759.
- (92) Besenhard, J. O.; Schöllhorn, R. *J. Power Sources* **1976**, 1, 267.
- (93) Schöllhorn, R.; Klein-Reesink, F.; Reimold, R. *J. Chem. Soc., Chem. Commun.* **1979**, 398.
- (94) Nassau, K.; Murphy, D. W. *J. Non-Cryst. Solids* **1981**, 44, 297.
- (95) West, K.; Zachau-Christiansen, B.; Skaarup, S.; Saidi, Y.; Barker, J.; Olsen, I. I.; Pynenburg, R.; Koksbang, R. *J. Electrochem. Soc.* **1996**, 143, 820.
- (96) Livage, J. *Mater. Res. Bull.* **1991**, 26, 1173.
- (97) Livage, J. *Chem. Mater.* **1991**, 3, 578.
- (98) Livage, J.; Baffier, N.; Pereira-Ramos, J. P.; Davidson, P. *Mater. Res. Soc. Proc.* **1995**, 369, 179.
- (99) Chandrappa, G. T.; Steunou, N.; Livage, J. *Nature* **2002**, 416, 702.
- (100) Le, D. B.; Passerini, S.; Guo, J.; Ressler, J.; Owens, B. B.; Smyrl, W. H. *J. Electrochem. Soc.* **1996**, 143, 2099.
- (101) Galy, J. *J. Solid State Chem.* **1992**, 100, 229.
- (102) Oka, Y.; Yao, T.; Yamamoto, N. *J. Solid State Chem.* **1997**, 132, 323.
- (103) Zhang, F.; Zavalij, P. Y.; Whittingham, M. S. *Mater. Res. Bull.* **1997**, 32, 701.
- (104) Zhang, F.; Zavalij, P. Y.; Whittingham, M. S. *Mater. Res. Soc. Proc.* **1998**, 496, 367.
- (105) Zhang, F.; Whittingham, M. S. *Electrochem. Commun.* **2000**, 2, 69.
- (106) Torardi, C. C.; Miao, C. R.; Lewittes, M. E.; Li, Z. *Electrochem. Soc. Proc.* **2000**, 2000-21, 68.
- (107) Torardi, C. C.; Miao, C. R.; Lewittes, M. E.; Li, Z. *J. Solid State Chem.* **2002**, 163, 93.
- (108) Spahr, M. E.; Stoschitzki-Bitterli, P.; Nesper, R.; Müller, M.; Krumeich, F.; Nissen, H. U. *Angew. Chem., Int. Ed. Engl.* **1998**, 37, 1263.
- (109) Spahr, M. E.; Stoschitzki-Bitterli, P.; Nesper, R.; Haas, O.; Novak, P. *J. Electrochem. Soc.* **1999**, 146, 2780.
- (110) Edström, K.; Gustafsson, T.; Nordlinder, S. *Electrochem. Solid State Lett.* **2001**, 4, A129.
- (111) Nordlinder, S.; Edström, K.; Gustafsson, T. *Electrochem. Solid State Lett.* **2001**, 4, A129.
- (112) Doble, A.; Ngala, K.; Yang, S.; Zavalij, P. Y.; Whittingham, M. S. *Chem. Mater.* **2001**, 13, 4382.
- (113) Delmas, C.; Devalette, M.; Fouassier, C.; Hagenmuller, P. *Mater. Res. Bull.* **1975**, 10, 393.
- (114) Delmas, C.; Fouassier, C.; Hagenmuller, P. *J. Solid State Chem.* **1975**, 13, 165.
- (115) Delmas, C.; Fouassier, C.; Réau, J.-M.; Hagenmuller, P. *Mater. Res. Bull.* **1976**, 11, 1081.
- (116) Delmas, C.; Fouassier, C. *Z. Anorg. Allg. Chem.* **1976**, 420, 184.
- (117) Delmas, C.; Fouassier, C.; Hagenmuller, P. *Physica* **1980**, 99B, 81.
- (118) Delmas, C.; Braconnier, J.-J.; Fouassier, C.; Hagenmuller, P. *Solid State Ionics* **1981**, 3/4, 165.
- (119) LeBlanc, A.; Danot, M.; Trichet, L.; Rouxel, J. *Mater. Res. Bull.* **1974**, 9, 191.
- (120) Rouxel, J.; Danot, M.; Bichon, J. *Bull. Soc. Chim. Fr.* **1971**, 3930.
- (121) Danot, M.; Blanc, A. L.; Rouxel, J. *Bull. Soc. Chim. Fr.* **1969**, 2670.
- (122) Danot, M.; Rouxel, J. *C. R. Acad. Sci. Paris* **1973**, C276, 1283.
- (123) Mitushima, K.; Jones, P. C.; Wiseman, P. J.; Goodenough, J. B. *Mater. Res. Bull.* **1980**, 15, 783.

- (124) Amatucci, G. G.; Tarascon, J. M.; Klein, L. C. *J. Electrochem. Soc.* **1996**, *143*, 1114.
- (125) Rossen, E.; Reimers, J. N.; Dahn, J. R. *Solid State Ionics* **1993**, *62*, 53.
- (126) Gabrisch, H.; Yazimi, R.; Fultz, B. *J. Electrochem. Soc.* **2004**, *151*, A891.
- (127) Nagaura, T.; Tozawa, K. *Prog. Batteries Solar Cells* **1990**, *9*, 209.
- (128) Ozawa, K. *Solid State Ionics* **1994**, *69*, 212.
- (129) Goodenough, J. B.; Mizushima, K. U.S. Patent 4,302,518, 1981.
- (130) Imanishi, N.; Fujiyoshi, M.; Takeda, Y.; Yamamoto, O.; Tabuchi, M. *Solid State Ionics* **1999**, *118*, 121.
- (131) Levasseur, S.; Menetrier, M.; Suard, E.; Delmas, C. *Solid State Ionics* **2000**, *128*, 11.
- (132) Yonezu, I.; Tarui, H.; Yoshimura, S.; Fujitani, S.; Nohma, T. Abstracts of the International Meeting On Lithium Batteries; Electrochemical Society: Pennington, NJ, 2004; Vol. 12, abstract 58.
- (133) Nishi, Y. In *Lithium Ion Batteries*; Wakihara, M., Yamamoto, O., Eds.; Kodansha: Tokyo, 1998.
- (134) Cho, J.; Kim, G. *Electrochem. Solid State Lett.* **1999**, *2*, 253.
- (135) Cho, J.; Kim, C.; Yoo, S. I. *Electrochem. Solid State Lett.* **2000**, *3*, 362.
- (136) Cho, J.; Kim, Y. J.; Park, B. *Chem. Mater.* **2000**, *12*, 3788.
- (137) Cho, J.; Kim, Y. J.; Park, B. *J. Electrochem. Soc.* **2001**, *148*, A1110.
- (138) Cho, J.; Kim, Y. J.; Kim, J. T.; Park, B. *Angew. Chem., Int. Ed.* **2001**, *40*, 3367.
- (139) Wang, Z.; Wu, C.; Liu, L.; Chen, L.; Huang, X. *Solid State Ionics* **2002**, *148*, 335.
- (140) Wang, Z.; Wu, C.; Liu, L.; Wu, F.; Chen, L.; Huang, X. *J. Electrochem. Soc.* **2002**, *149*, A466.
- (141) Liu, L.; Wang, Z.; Li, H.; Chen, L.; Huang, X. *Solid State Ionics* **2002**, *152*, 341.
- (142) Cho, J.; Park, B. *Lithium Battery Discussion Electrode Materials*, Bordeaux, 2003; Abstract 1.
- (143) Liu, J.; Xu, K.; Jow, T. R.; Amine, K. *Electrochem. Soc. Abstr.* **2002**, *2002-2*, 135.
- (144) Amine, K.; Liu, J.; Kang, S.; Belharouak, I.; Hyung, Y.; Vissers, D.; Henriksen, G. *J. Power Sources* **2004**, *129*, 14.
- (145) Chen, Z.; Dahn, J. R. *Electrochim. Acta* **2004**, *49*, 1079.
- (146) Seguin, L.; Amatucci, G.; Anne, M.; Chabre, Y.; Strobel, P.; Tarascon, J. M.; Vaughan, G. *J. Power Sources* **1999**, *81-82*, 604.
- (147) Goodenough, J. B.; Mizushima, K. U.S. Patent 4,302,518, 1980.
- (148) Goodenough, J. B.; Mizushima, K. U.S. Patent 4,357,215, 1981.
- (149) Whittingham, M. S.; Zavalij, P. Y. *Solid State Ionics* **2000**, *131*, 109.
- (150) Thackeray, M. M.; David, W. I. F.; Bruce, P. G.; Goodenough, J. B. *Mater. Res. Bull.* **1983**, *18*, 461.
- (151) Tarascon, J. M.; Guyomard, D. *Solid State Ionics* **1994**, *69*, 222.
- (152) Tarascon, J. M.; McKinnon, W. R.; Coowar, F.; Bowmer, T. N.; Amatucci, G.; Guyomard, D. *J. Electrochem. Soc.* **1994**, *141*, 1421.
- (153) Tarascon, J. M.; Wang, E.; Shokoohi, F. K.; McKinnon, W. R.; Colson, S. *J. Electrochem. Soc.* **1991**, *138*, 2859.
- (154) Thackeray, M. M. *Prog. Solid State Chem* **1997**, *25*, 1.
- (155) Yonemura, M.; Yamada, A.; Kobayashi, H.; Tabuchi, M.; Kamiyama, T.; Kawamoto, Y.; Kanno, R. *J. Mater. Chem.* **2004**, *14*, 1948.
- (156) Tarascon, J. M. U.S. Patent 5,135,732, 1992.
- (157) Amatucci, G. G.; Pereira, N.; Zheng, T.; Tarascon, J.-M. *J. Electrochem. Soc.* **2001**, *148*, A171.
- (158) Amatucci, G. G.; Pereira, N.; Zheng, T.; Plitz, I.; Tarascon, J.-M. *J. Power Sources* **1999**, *81-82*, 39.
- (159) Shin, Y.; Manthiram, A. *J. Electrochem. Soc.* **2004**, *151*, A204.
- (160) Ferg, E.; Gummow, R. J.; Kock, A. D.; Thackeray, M. M. *J. Electrochem. Soc.* **1994**, *141*, L147.
- (161) Ohzuku, T.; Ueda, A.; Yamamoto, N. *J. Electrochem. Soc.* **1995**, *142*, 1431.
- (162) Zaghbi, K.; Simoneau, M.; Armand, M.; Gauthier, M. *J. Power Sources* **1999**, *81-82*, 300.
- (163) Tessier, C.; Fachetti, O.; Siret, C.; Castaing, F.; Jordy, C.; Boeue, J. P.; Biensan, P. *Lithium Battery Discussion Electrode Materials*, Bordeaux, 2003; Abstract 29.
- (164) Franger, S.; Bourbon, C.; LeCras, F. *J. Electrochem. Soc.* **2004**, *151*, A1024.
- (165) Panero, S.; Satolli, D.; Salamon, M.; Scrosati, B. *Electrochem. Commun.* **2000**, *2*, 810.
- (166) Rougier, A.; Saadouane, I.; Gravereau, P.; Willmann, P.; Delmas, C. *Solid State Ionics* **1996**, *90*, 83.
- (167) Saadoune, I.; Delmas, C. *J. Solid State Chem.* **1998**, *136*, 8.
- (168) Saadoune, I.; Menetrier, M.; Delmas, C. *J. Mater. Chem.* **1997**, *7*, 2505.
- (169) Saadoune, I.; Delmas, C. *J. Mater. Chem.* **1996**, *6*, 193.
- (170) Zhecheva, E.; Stoyanova, R. *Solid State Ionics* **1993**, *66*, 143.
- (171) Prado, G.; Fournes, L.; Delmas, C. *J. Solid State Chem.* **2001**, *159*, 103.
- (172) Prado, G.; Rougier, A.; Fournes, L.; Delmas, C. *J. Electrochem. Soc.* **2000**, *147*, 2880.
- (173) Kanno, R.; Shirane, T.; Inaba, Y.; Kawamoto, Y. *J. Power Sources* **1997**, *68*, 145.
- (174) Delmas, C.; Menetrier, M.; Croguennec, L.; Levasseur, S.; Peres, J. P.; Poullierie, C.; Prado, G.; Fournes, L.; Weill, F. *Int. J. Inorg. Mater.* **1999**, *1*, 11.
- (175) Poullierie, C.; Pertont, F.; Biensan, P.; Peres, J. P.; Broussely, M.; Delmas, C. *J. Power Sources* **2001**, *96*, 293.
- (176) Poullierie, C.; Croguennec, L.; Delmas, C. *Solid State Ionics* **2000**, *132*, 15.
- (177) Nakai, I.; Nakagome, T. *Electrochem. Solid State Lett.* **1998**, *1*, 259.
- (178) Broussely, M. *Lithium Battery Discussion*, Bordeaux-Arcachon 2001.
- (179) Delmas, C.; Capitaine, F. Abstracts of the 8th International Meeting Lithium Batteries; Electrochemical Society: Pennington, NJ, 1996; Vol. 8, abstract 470.
- (180) Chen, R.; Whittingham, M. S. *J. Electrochem. Soc.* **1997**, *144*, L64.
- (181) Armstrong, A. R.; Bruce, P. G. *Nature* **1996**, *381*, 499.
- (182) Capitaine, F.; Gravereau, P.; Delmas, C. *Solid State Ionics* **1996**, *89*, 197.
- (183) Chen, R.; Zavalij, P. Y.; Whittingham, M. S. *Mater. Res. Soc. Proc.* **1997**, *453*, 653.
- (184) Chen, R.; Zavalij, P.; Whittingham, M. S. *Chem. Mater.* **1996**, *8*, 1275.
- (185) Chen, R.; Chirayil, T.; Whittingham, M. S. *Solid State Ionics* **1996**, *86-88*, 1.
- (186) Bach, S.; Henry, M.; Baffier, N.; Livage, J. *J. Solid State Chem.* **1990**, *88*, 325.
- (187) Bach, S.; Pereiramos, J. P.; Cachet, C.; Bode, M.; Yu, L. T. *Electrochim. Acta* **1995**, *40*, 785.
- (188) Bach, S.; Pereira-Ramos, J. P.; Baffier, N. *J. Solid State Chem.* **1995**, *120*, 70.
- (189) Pereira-Ramos, J. P.; Baddour, R.; Bach, S.; Baffier, N. *Solid State Ionics* **1992**, *53-56*, 701.
- (190) Stoyanova, R.; Zhecheva, E.; Zarkova, L. *Solid State Ionics* **1994**, *73*, 233.
- (191) Doeff, M. M.; Richardson, T. J.; Kopley, L. *J. Electrochem. Soc.* **1996**, *143*, 2507.
- (192) Whittingham, M. S. *1996 USDOE BATT Annual Report*; USDOE: Washington, D.C., 1997.
- (193) Doeff, M. M.; Peng, M. Y.; Ma, Y.; Visco, S. J.; DeJonghe, L. C. U.S. Patent 5,558,961, 1996.
- (194) Doeff, M. M.; Richardson, T. J.; Hwang, K.-T.; Anapolsky, A. *ITE Battery Lett.* **2001**, *2*, B.
- (195) Armstrong, A. R.; Huang, H.; Jennings, R. A.; Bruce, P. G. *J. Mater. Chem.* **1998**, *8*, 255.
- (196) Chen, R.; Whittingham, M. S. Proceedings of the Annual Automotive Technology Development Customers Coordination Meeting, Dearborn, MI, Oct. 27-30, 1997; USDOE: Washington, DC, 1997; Vol. III, p 301.
- (197) Zhang, F.; Ngala, K.; Whittingham, M. S. *Electrochem. Commun.* **2000**, *2*, 445.
- (198) Yang, S.; Song, Y.; Ngala, K.; Zavalij, P. Y.; Whittingham, M. S. *J. Power Sources* **2003**, *119*, 239.
- (199) Lu, Z.; Dahn, J. R. *Chem. Mater.* **2001**, *13*, 1252.
- (200) Lu, Z.; Dahn, J. R. *Chem. Mater.* **2001**, *13*, 2078.
- (201) Lu, Z.; Dahn, J. R. *J. Electrochem. Soc.* **2001**, *148*, A237.
- (202) Lu, Z.; Dahn, J. R. *Chem. Mater.* **2000**, *12*, 3583.
- (203) Eriksson, T. A.; Lee, Y. J.; Hollingsworth, J.; Reimer, J. A.; Cairns, E. J.; Zhang, X.-f.; Doeff, M. M. *Chem. Mater.* **2003**, *15*, 4456.
- (204) Dolle, M.; Hollingsworth, J.; Richardson, T. J.; Doeff, M. M. *Solid State Ionics* **2004**, in press.
- (205) Shaju, K. M.; SubbaRao, G. V.; Chowdari, B. V. R. *Electrochim. Acta* **2003**, *48*, 2691.
- (206) Armstrong, A. R.; Gitzendanner, R.; Robertson, A. D.; Bruce, P. G. *Chem. Commun.* **1998**, 1833.
- (207) Numata, K.; Yamanaka, S. *Solid State Ionics* **1999**, *118*, 117.
- (208) Fujiwara, M.; Yamada, S.; Kanda, M. Extended Abstracts of 34th Battery Symposium. Nagoya, Japan; The Electrochemical Society of Japan: Tokyo, Japan, 1993; Vol. 34, p 135.
- (209) Yoshio, M.; Yamato, K.; Itoh, J.; Noguchi, H.; Okada, M.; Mouri, T. *Electrochem. Soc. Proc.* **1994**, *94-28*, 251.
- (210) Nitta, Y.; Okamura, K.; Haraguchi, K.; Kobayashi, S.; Ohta, A. *J. Power Sources* **1995**, *54*, 511.
- (211) Caurant, D.; Baffier, N.; Bianchi, V.; Grégoire, G.; Bach, S. *J. Mater. Chem.* **1996**, *6*, 1149.
- (212) Rossen, E.; Jones, C. D. W.; Dahn, J. R. *Solid State Ionics* **1992**, *57*, 311.
- (213) Spahr, M. E.; Novák, P.; Schnyder, B.; Haas, O.; Nesper, R. *J. Electrochem. Soc.* **1998**, *145*, 1113.
- (214) Ohzuku, T.; Makimura, Y. *Chem. Lett.* **2001**, 744.
- (215) Ohzuku, T.; Makimura, Y. *Chem. Lett.* **2001**, 642.
- (216) Lu, Z.; MacNeil, D. D.; Dahn, J. R. *Electrochem. Solid State Lett.* **2001**, *4*, A200.
- (217) Wang, Z.; Sun, Y.; Chen, L.; Huang, X. *J. Electrochem. Soc.* **2004**, *151*, A914.

- (218) Tsai, Y. W.; Lee, J. F.; Liu, D. G.; Hwang, B. J. *J. Mater. Chem.* **2004**, *14*, 958.
- (219) Ngala, J. K.; Chernova, N. A.; Ma, M.; Mamak, M.; Zavalij, P. Y.; Whittingham, M. S. *J. Mater. Chem.* **2004**, *14*, 214.
- (220) Ngala, J. K.; Chernova, N.; Matienzo, L.; Zavalij, P. Y.; Whittingham, M. S. *Mater. Res. Soc. Symp.* **2003**, *756*, 231.
- (221) Hwang, B. J.; Tsai, Y. W.; Chen, C. H.; Santhanam, R. *J. Mater. Chem.* **2003**, *13*, 1962.
- (222) Kim, J.-H.; Park, C. W.; Sun, Y.-K. *Solid State Ionics* **2003**, *164*, 43.
- (223) Jiang, J.; Dahn, J. R. *Electrochem. Commun.* **2004**, *6*, 39.
- (224) Shaju, K. M.; Rao, G. V. S.; Chowdari, B. V. R. *Electrochim. Acta* **2002**, *48*, 145.
- (225) Park, S. H.; Yoon, C. S.; Kang, S. G.; Kim, H.-S.; Moon, S.-I.; Sun, Y.-K. *Electrochim. Acta* **2004**, *49*, 557.
- (226) Hwang, B. J.; Tsai, Y. W.; Carlier, D.; Ceder, G. *Chem. Mater.* **2003**, *15*, 3676.
- (227) Koyama, Y.; Tanaka, I.; Adachi, H.; Makimura, Y.; Ohzuku, T. *J. Power Sources* **2003**, *119–121*, 644.
- (228) Yoshio, M.; Noguchi, H.; Itoh, J.-i.; Okada, M.; Mouri, T. *J. Power Sources* **2000**, *90*, 176.
- (229) Belharouak, I.; Sun, Y.-K.; Liu, J.; Amine, K. *J. Power Sources* **2003**, *123*, 247.
- (230) Chen, Y.; Wang, G. X.; Konstantinov, K.; Liu, H. K.; Dou, S. X. *J. Power Sources* **2003**, *119–121*, 184.
- (231) Yabuuchi, N.; Ohzuku, T. *J. Power Sources* **2003**, *119–121*, 171.
- (232) Yoon, W.-S.; Grey, C. P.; Balasubramanian, M.; Yang, X.-Q.; Fischer, D. A.; McBreen, J. *Electrochem. Solid State Lett.* **2004**, *7*, A53.
- (233) Sun, Y.; Ouyang, C.; Wang, Z.; Huang, X.; Chen, L. *J. Electrochem. Soc.* **2004**, *151*, A504.
- (234) Kim, J.-M.; Chung, H.-T. *Electrochim. Acta* **2004**, *49*, 937.
- (235) Jouanneau, S.; Eberman, K. W.; Krause, L. J.; Dahn, J. R. *J. Electrochem. Soc.* **2003**, *150*, A1637.
- (236) MacNeil, D. D.; Lu, Z.; Dahn, J. R. *J. Electrochem. Soc.* **2002**, *149*, A1332.
- (237) Jouanneau, S.; Macneil, D. D.; Lu, Z.; Beattie, S. D.; Murphy, G.; Dahn, J. R. *J. Electrochem. Soc.* **2003**, *150*, A1299.
- (238) Reed, J.; Ceder, G.; VanDerVen, A. *Electrochem. Solid State Lett.* **2001**, *4*, A78.
- (239) Armstrong, A. R.; Paterson, A. J.; Robertson, A. D.; Bruce, P. G. *Chem. Mater.* **2002**, *14*, 710.
- (240) Armstrong, A. R.; Robertson, A. D.; Bruce, P. G. *Electrochim. Acta* **1999**, *45*, 285.
- (241) Sharma, P.; Moore, G.; Zhang, F.; Zavalij, P. Y.; Whittingham, M. S. *Electrochem. Solid-State Lett.* **1999**, *2*, 494.
- (242) Zhang, F.; Whittingham, M. S. *Electrochem. Solid State Lett.* **2000**, *3*, 309.
- (243) Ammundsen, B.; Desilvestro, H.; Paulson, J. M.; Steiner, R.; Pickering, P. J. 10th International Meeting on Lithium Batteries, Como, Italy, May 28–June 2, 2000; Electrochemical Society: Pennington, NJ, 2000.
- (244) Storey, C.; Kargina, I.; Grincourt, Y.; Davidson, I. J.; Yoo, Y.; Seung, D. Y. 10th International Meeting on Lithium Batteries, Como, Italy, May 28–June 2, 2000; Electrochemical Society: Pennington, NJ, 2000; Vol. 10, abstract 234.
- (245) Paulsen, J. M.; Ammundsen, B.; Desilvestro, H.; Steiner, R.; Hassell, D. *Electrochem. Soc. Abstr.* **2000**, *2002–2*, 71.
- (246) Whitfield, P. S.; Davidson, I. J.; Kargina, I.; Grincourt, Y.; Ammundsen, B.; Steiner, R.; Suprun, A. *Electrochem. Soc. Abstr.* **2000**, *2000–2*, 90.
- (247) Grincourt, Y.; Storey, C.; Davidson, I. J. *J. Power Sources* **2001**, *97–98*, 711.
- (248) Storey, C.; Kargina, I.; Grincourt, Y.; Davidson, I. J.; Yoo, Y. C.; Seung, D. Y. *J. Power Sources* **2001**, *97–98*, 541.
- (249) Balasubramanian, M.; McBreen, J.; Davidson, I. J.; Whitfield, P. S.; Kargina, I. *Electrochem. Soc.* **2002**, *149*, A176.
- (250) Ammundsen, B.; Paulsen, J.; Davidson, I.; Liu, R.-S.; Shen, C.-H.; Chen, J.-M.; Jang, L.-Y.; Lee, J.-F. *J. Electrochem. Soc.* **2002**, *149*, A431.
- (251) Numata, K.; Sakaki, C.; Yamanaka, S. *Solid State Ionics* **1999**, *117*, 257.
- (252) Lu, Z.; MacNeil, D. D.; Dahn, J. R. *Electrochem. Solid State Lett.* **2001**, *4*, A191.
- (253) Arachi, Y.; Kobayashi, H.; Emura, S.; Nakata, Y.; Tanaka, M.; Asai, T. *Chem. Lett.* **2003**, *32*, 60.
- (254) Venkatraman, S.; Manthiram, A. *Chem. Mater.* **2003**, *15*, 5003.
- (255) Sun, Y.-K.; Yoon, C. S.; Lee, Y. S. *Electrochim. Acta* **2003**, *48*, 2589.
- (256) Yang, X.-Q.; McBreen, J.; Yoon, W.-S.; Grey, C. P. *Electrochem. Commun.* **2002**, *4*, 649.
- (257) Rieck, H.; Hoppe, R. Z. *Anorg. Allg. Chem.* **1972**, *392*, 193.
- (258) Makimura, Y.; Ohzuku, T. *J. Power Sources* **2003**, *119–121*, 156.
- (259) Ariyoshi, K.; Iwakoshi, Y.; Nakayama, N.; Ohzuku, T. *J. Electrochem. Soc.* **2004**, *151*, A296.
- (260) Ohzuku, T. Personal Communication, 2004.
- (261) Shaju, K. M.; SubbaRao, G. V.; Chowdari, B. V. R. *Electrochim. Acta* **2004**, *49*, 1565.
- (262) Kang, S.-H.; Kim, J.; Stoll, M. E.; Abraham, D.; Sun, Y. K.; Amine, K. *J. Power Sources* **2002**, *112*, 41.
- (263) Cushing, B. L.; Goodenough, J. B. *Solid State Sci.* **2002**, *4*, 1487.
- (264) Reed, J.; Ceder, G. *Electrochem. Solid State Lett.* **2002**, *5*, A145.
- (265) Kang, K.; Carlier, D.; Reed, J.; Arroyo, E. M.; Ceder, G.; Croguennec, L.; Delmas, C. *Chem. Mater.* **2003**, *15*, 4503.
- (266) Ohzuku, T.; Makimura, Y. *Electrochem. Soc. Abstr.* **2003**, *2003–1*, 1079.
- (267) Meng, Y. S.; Ceder, G.; Grey, C. P.; Yoon, W.-S.; Shao-Horn, Y. *Electrochem. Solid State Lett.* **2004**, *7*, A155.
- (268) Yoon, W.-S.; Iannopollo, S.; Grey, C. P.; Carlier, D.; Gorman, J.; Reed, J.; Ceder, G. *Electrochem. Solid State Lett.* **2004**, *7*, A167.
- (269) Ceder, G.; Meng, Y.-S.; Shao-Horn, Y.; Grey, C. P. 12th International Meeting on Lithium Batteries; Electrochemical Society: Pennington, NJ, 2004; Vol. 12, abstract 22.
- (270) Kobayashi, H.; Sakaebe, H.; Kageyama, H.; Tatsumi, K.; Arachi, Y.; Kamiyama, T. *J. Mater. Chem.* **2003**, *13*, 590.
- (271) Kobayashi, H.; Arachi, Y.; Kageyama, H.; Tatsumi, K. *J. Mater. Chem.* **2004**, *14*, 40.
- (272) Liu, Z.; Yu, A.; Lee, J. Y. *J. Power Sources* **1999**, *81–82*, 416.
- (273) Jouanneau, S.; Dahn, J. R. *Chem. Mater.* **2003**, *15*, 495.
- (274) Thomas, M. G. S. R.; David, W. I. F.; Goodenough, J. B. *Mater. Res. Bull.* **1985**, *20*, 1137.
- (275) Guilmard, M.; Poullerie, C.; Croguennec, L.; Delmas, C. *Solid State Ionics* **2003**, *160*, 39.
- (276) Ma, M.; Chernova, N. A.; Zavalij, P. Y.; Whittingham, M. S. *J. Power Sources* **2004**, in press.
- (277) Cushing, B. L.; Goodenough, J. B. *Solid State Sci.* **2002**, *4*, 1487.
- (278) Oh, S. W.; Park, S. H.; Park, C.-W.; Sun, Y.-K. *Solid State Ionics* **2004**, *171*, 167.
- (279) Li, D.-C.; Muta, T.; Zhang, L.-Q.; Yoshio, M.; Noguchi, H. *J. Power Sources* **2004**, *132*, 150.
- (280) Meng, Y. S.; Wu, Y. W.; Hwang, B. J.; Li, Y.; Ceder, G. *J. Electrochem. Soc.* **2004**, *151*, A1134.
- (281) Ohzuku, T.; Nakura, K.; Aoki, T. *Electrochim. Acta* **1999**, *45*, 151.
- (282) Croguennec, L.; Poullerie, C.; Delmas, C. *Solid State Ionics* **2000**, *135*, 259.
- (283) Yoshizawa, H.; Ohzuku, T. *Denki Kagaku* **2003**, *71*, 1177.
- (284) Guilmard, M.; Croguennec, L.; Delmas, C. *Chem. Mater.* **2003**, *15*, 4476.
- (285) Guilmard, M.; Croguennec, L.; Delmas, C. *Chem. Mater.* **2003**, *15*, 4484.
- (286) Arai, H.; Sakurai, Y. *J. Power Sources* **1999**, *80–81*, 401.
- (287) Manthiram, A.; Chu, S. *Electrochem. Soc. Abstr.* **2000**, *2000–2*, 72.
- (288) Chen, R.; Zavalij, P. Y.; Whittingham, M. S.; Greedan, J. E.; Raju, N. P.; Bieringer, M. *J. Mater. Chem.* **1999**, *9*, 93.
- (289) Thackeray, M. M.; Johnson, C. S.; Amine, K.; Kim, J. U.S. Patent 6,677,082, 2004.
- (290) Thackeray, M. M.; Johnson, C. S.; Amine, K.; Kim, J. U.S. Patent 6,680,143, 2004.
- (291) Robertson, A. D.; Bruce, P. G. *Chem. Commun.* **2002**, 2790.
- (292) Robertson, A. D.; Bruce, P. G. *Chem. Mater.* **2003**, *15*, 1984.
- (293) Armstrong, A. R.; Bruce, P. G. *Electrochem. Solid State Lett.* **2004**, *7*, A1.
- (294) Russouw, M. H.; Thackeray, M. M. *Mater. Res. Bull.* **1991**, *26*, 463.
- (295) Russouw, M. H.; Liles, D. C.; Thackeray, M. M. *J. Solid State Chem.* **1993**, *104*, 464.
- (296) Paik, Y.; Grey, C. P.; Johnson, C. S.; Kim, J.-S.; Thackeray, M. M. *Chem. Mater.* **2002**, *14*, 5106.
- (297) Richard, M. N.; Fuller, E. W.; Dahn, J. R. *Solid State Ionics* **1994**, *73*, 81.
- (298) Shin, S.-S.; Sun, Y.-K.; Amine, K. *J. Power Sources* **2002**, *112*, 634.
- (299) Myung, S.-T.; Komaba, S.; Kumagai, N. *Solid State Ionics* **2004**, *170*, 139.
- (300) Zhang, L.; Noguchi, H.; Yoshio, M. *J. Power Sources* **2002**, *110*, 57.
- (301) Kim, J.-S.; Johnson, C. S.; Thackeray, M. M. *Electrochem. Commun.* **2002**, *4*, 205.
- (302) Kang, S.-H.; Sun, Y. K.; Amine, K. *Electrochem. Solid State Lett.* **2003**, *6*, A183.
- (303) Lee, C. W.; Sun, Y.-K.; Prakash, J. *Electrochim. Acta* **2004**, *49*, 4425.
- (304) Kanno, R.; Shirane, T.; Kawamoto, Y.; Takeda, Y.; Takano, M.; Ohashi, M.; Yamaguchi, Y. *J. Electrochem. Soc.* **1996**, *143*, 2435.
- (305) Kanno, R.; Shirane, T.; Kawamoto, Y. Abstracts of the 8th International Meeting on Lithium Batteries; Electrochemical Society: Pennington, NJ, 1996; Vol. 8, abstract 133.
- (306) Whittingham, M. S. U.S. Patent 4,049,887, 1996.
- (307) Thompson, A. H.; Whittingham, M. S. *Mater. Res. Bull.* **1977**, *12*, 741.
- (308) Jacobson, A. J.; Whittingham, M. S. U.S. Patent 4,143,213, 1978.
- (309) Padhi, A. K.; Nanjundaswamy, K. S.; Goodenough, J. B. *J. Electrochem. Soc.* **1997**, *144*, 1188.
- (310) Masquelier, C.; Padhi, A. K.; Nanjundaswamy, K. S.; Goodenough, J. B. *J. Solid State Chem.* **1998**, *135*, 228.

- (311) Morcrette, M.; Wurm, C.; Masquelier, C. *Solid State Sci.* **2002**, *4*, 239.
- (312) Masquelier, C.; Padhi, A. K.; Nanjundaswamy, K. S.; Goodenough, J. B. *J. Solid State Chem.* **1998**, *135*, 228.
- (313) Chen, J.-M.; Li, Y. J.; Hurg, W.-M.; Whittingham, M. S. (Industrial Technology Research Institute, Chutung, Taiwan) U.S. Patent 5,514,490, 1996.
- (314) Li, Y. J.; Whittingham, M. S. *Solid State Ionics* **1993**, *63*, 391.
- (315) Yamada, A.; Chung, S. C.; Hinokuma, K. *J. Electrochem. Soc.* **2001**, *148*, A224.
- (316) Andersson, A. S.; Kalska, B.; Häggström, L.; Thomas, J. O. *Solid State Ionics* **2000**, *130*, 41.
- (317) Andersson, A. S.; Thomas, J. O.; Kalska, B.; Häggström, L. *Electrochem. Solid-State Lett.* **2000**, *3*, 66.
- (318) Ravet, N.; Goodenough, J. B.; Besner, S.; Simoneau, M.; Hovington, P.; Armand, M. *Electrochem. Soc. Abstr.* **1999**, 99–2, 127.
- (319) Ravet, N.; Besner, S.; Simoneau, M.; Vallée, A.; Armand, M.; Magnan, J.-F. (Hydro-Quebec) European Patent 1049182A2, 2000.
- (320) Huang, H.; Yin, S.-C.; Nazar, L. F. *Electrochem. Solid State Lett.* **2001**, *4*, A170.
- (321) Masquelier, C.; Wurm, C.; Morcrette, M.; Gaubicher, J. International Meeting on Solid State Ionics, Cairns, Australia, July 9–13, 2001; The International Society of Solid State Ionics: 2001; paper A-IN-06.
- (322) Prosini, P. P.; Zane, D.; Pasquali, M. *Electrochim. Acta* **2001**, *46*, 3517.
- (323) Yang, S.; Song, Y.; Zavalij, P. Y.; Whittingham, M. S. *Mater. Res. Soc. Proc.* **2002**, *703*, V7.9.
- (324) Chung, S.-Y.; Bloking, J. T.; Chiang, Y.-M. *Nat. Mater.* **2002**, *1*, 123.
- (325) Herle, P. S.; Ellis, B.; Coombs, N.; Nazar, L. F. *Nat. Mater.* **2004**, *3*, 147.
- (326) Croce, F.; Epifanio, A. D.; Hassoun, J.; Deptula, A.; Olczac, T.; Scrosati, B. *Electrochem. Solid State Lett.* **2002**, *5*, A47.
- (327) Hu, Y.; Doeff, M. M.; Kostecky, R.; Fiñones, R. *J. Electrochem. Soc.* **2004**, *151*, A1279.
- (328) Shiraishi, K.; Dokko, K.; Kanamura, K. 12th International Meeting on Lithium Batteries; Electrochemical Society: Pennington, NJ, 2004; Vol. 12, abstract 297.
- (329) Nuspi, G.; Vogler, C.; Eisgruber, M.; Wimmer, L.; Schall, N.; Fietzek, C.; Weydanz, W. 12th International Meeting on Lithium Batteries; Electrochemical Society: Pennington, NJ, 2004; Vol. 12, abstract 293.
- (330) Garcia-Martin, O.; Alvarez-Vega, M.; Garcia-Alvarado, F.; Garcia-Jaca, J.; Gallardo-Amores, J. M.; Sanjuán, M. L.; Amador, U. *Chem. Mater.* **2001**, *13*, 1570.
- (331) Whittingham, M. S.; Yang, S.; Ngala, K.; Doble, A.; Zavalij, P. Y. International Meeting on Solid State Ionics, Cairns, Australia, July 9–13, 2001; The International Society of Solid State Ionics: 2001; paper A-KN-06.
- (332) Chen, Z.; Dahn, J. R. *J. Electrochem. Soc.* **2002**, *149*, A1184.
- (333) Dominko, R.; Gaberscek, M.; Drogenik, J.; Bele, M.; Pejovnik, S. *Electrochem. Solid State Lett.* **2001**, *4*, A187.
- (334) Doeff, M. M.; Hu, Y.; McLarnon, F.; Kostecky, R. *Electrochem. Solid State Lett.* **2003**, *6*, A207.
- (335) Takahashi, M.; Tobishima, S.; Takei, K.; Sakurai, Y. *J. Power Sources* **2001**, *97–98*, 508.
- (336) Okada, S.; Sawa, S.; Egashira, M.; Yamaki, J.-i.; Tabuchi, M.; Kageyama, H.; Konishi, T.; Yoshino, A. *J. Power Sources* **2001**, *97–98*, 430.
- (337) Yamada, A.; Chung, S.-C. *J. Electrochem. Soc.* **2001**, *148*, A960.
- (338) Li, G.; Azuma, H.; Tohda, M. *Electrochem. Solid State Lett.* **2002**, *5*, A135.
- (339) Delacourt, C.; Poizot, P.; Morcrette, M.; Tarascon, J.-M.; Masquelier, C. *Chem. Mater.* **2004**, *16*, 93.
- (340) Song, Y.; Zavalij, P. Y.; Chernova, N. A.; Whittingham, M. S. *J. Electrochem. Soc.*, in press.
- (341) Zhou, F.; Cococcioni, M.; Marianetti, C.; Morgan, D.; Chen, M.; Ceder, G. 12th International Meeting on Lithium Batteries; Electrochemical Society: Pennington, NJ, 2004; Vol. 12, abstract 283.
- (342) Morgan, D.; Maxisch, T.; Zhou, F.; Cococcioni, M.; Kang, K.; Ceder, G. 12th International Meeting on Lithium Batteries; Electrochemical Society: Pennington, NJ, 2004; Vol. 12, abstract 282.
- (343) Osorio-Guillen, J. M.; Holm, B.; Ahuja, R.; Johansson, B. *Solid State Ionics* **2004**, *167*, 221.
- (344) Xu, Y.-N.; Chung, S.-Y.; Bloking, J. T.; Chiang, Y.-M.; Ching, W. Y. *Electrochem. Solid State Lett.* **2004**, *7*, A131.
- (345) Song, Y.; Yang, S.; Zavalij, P. Y.; Whittingham, M. S. *Mater. Res. Bull.* **2002**, *37*, 1249.
- (346) Masquelier, C.; Reale, P.; Wurm, C.; Morcrette, M.; Dupont, L.; Larchera, D. *J. Electrochem. Soc.* **2002**, *149*, A1037.
- (347) Hong, Y.-S.; Ryu, K. S.; Park, Y. J.; Kim, M. G.; Leeb, J. M.; Chang, S. H. *J. Mater. Chem.* **2002**, *12*, 1870.
- (348) Prosini, P. P.; Cianchi, L.; Spina, G.; Lisi, M.; Scaccia, S.; Carewska, M.; Minarini, C.; Pasquali, M. *J. Electrochem. Soc.* **2001**, *148*, A1125.
- (349) Song, Y.; Zavalij, P.; Whittingham, M. S. *Mater. Res. Soc. Proc.* **2003**, *756*, 249.
- (350) Song, Y.; Zavalij, P. Y.; Chernova, N. A.; Whittingham, M. S. *Chem. Mater.* **2004**, in press.
- (351) Barker, J.; Saidi, M. Y. U.S. Patent 5,871,866, 1999.
- (352) Saidi, M. Y.; Barker, J.; Huang, H.; Adamson, G. *Electrochem. Solid State Lett.* **2002**, *5*, A149.
- (353) Gaubicher, J.; Goward, G.; Wurm, C.; Masquelier, C.; Nazar, L. F. *Chem. Mater.* **2000**, *12*.
- (354) Yin, S. C.; Grondley, H.; Strobel, P.; Nazar, L. F. *J. Am. Chem. Soc.* **2003**, *125*, 326.
- (355) Yin, S. C.; Strobel, P.; Anne, M.; Nazar, L. F. *J. Am. Chem. Soc.* **2003**, *125*, 10402.
- (356) Huang, H.; Yin, S.-C.; Kerr, T.; Nazar, L. F. *Adv. Mater.* **2002**, *14*, 1525.
- (357) Azmi, B. M.; Ishihara, T.; Nishiguchi, H.; Takita, Y. *J. Power Sources* **2003**, *119–121*, 273.
- (358) Kerr, T. A.; Gaubischer, J.; Nazar, L. F. *Electrochem. Solid State Lett.* **2000**, *3*, 460.
- (359) Lim, S. C.; Vaughey, J. T.; Harrison, W. T. A.; Dussak, L. L.; Jacobson, A. J.; Johnson, J. W. *Solid State Ionics* **1996**, *84*, 219.
- (360) Zavalij, P. Y.; Whittingham, M. S. *Rigaku J.* **2004**, *21*, 2.
- (361) Barker, J.; Saidi, M. Y.; Swoyer, J. L. *J. Electrochem. Soc.* **2003**, *150*, A1394.
- (362) Pereira-Ramos, J. P.; Baffier, N.; Pistoia, G. In *Lithium Batteries*; Pistoia, G., Ed.; Elsevier: Amsterdam, 1994; Vol. 5.
- (363) Zane, D.; Carewska, M.; Scaccia, S.; Cardellini, F.; Prosini, P. *Electrochim. Acta* **2004**, *49*, 4259.
- (364) Chirayil, T. A.; Zavalij, P. Y.; Whittingham, M. S. *J. Electrochem. Soc.* **1996**, *143*, L193.

CR020731C

Role of Electronic Structure in the Susceptibility of Metastable Transition-Metal Oxide Structures to Transformation

John Reed and Gerbrand Ceder*

Department of Materials Science and Engineering, Massachusetts Institute of Technology, Building 13-5056, 77 Massachusetts Avenue, Cambridge, Massachusetts 02139

Received March 1, 2004

Contents

1. Introduction	4513
2. Transformation Mechanisms	4514
3. Density Functional Theory	4516
4. Comparison between the Activation Barriers for Co and Mn Migration	4516
5. Valence of Co and Mn during Migration	4517
6. Ligand-Field Effects on the Energetics of Migrating Co and Mn	4518
7. Summary of Important Factors Influencing Co and Mn Site Preference in ccp Oxides	4520
8. Effect of Chemical Substitutions on Mn Site Preference	4521
8.1. Electronic Structure Model for the Energetics of Mn Oxides	4524
9. Qualitative Ionization Scale	4526
10. Effect of Valence on Site Preference of Other 3d Transition Metals	4527
10.1. Ti	4528
10.2. V	4528
10.3. Cr	4529
10.4. Mn	4529
10.5. Fe	4529
10.6. Co	4530
10.7. Ni	4530
10.8. Cu	4530
10.11. Overall Trends for 3d Metals	4530
11. Conclusions	4531
12. Acknowledgments	4532
13. References	4532

1. Introduction

Kinetic stability is a key aspect of Li-insertion compounds used in rechargeable Li batteries. To obtain high capacity, the Li ions need to be cycled over a wide range of concentrations within the host structure of the insertion compound. This almost invariably brings the host structure outside its range of thermodynamic stability at some stage of the electrochemical cycle. Maintaining a desirable host structure over repeated electrochemical cycles often hinges upon the host structures resistance against

transforming into more stable phases when it becomes thermodynamically metastable. The ability to resist phase transformation can have an important impact on the overall performance of a Li-insertion compound used as an electrode material in a Li rechargeable battery.

The focus of this paper is on the role electronic structure plays in determining the site preference and mobility of 3d transition-metal ions in an oxide and how these factors in turn affect the resistance of metastable 3d transition-metal oxides against transformation. This is a relevant topic to the Li rechargeable battery field because 3d transition-metal oxides are often used as positive electrode materials.

Lithium manganese oxide structures serve as the main prototype of a 3d transition-metal oxide system used in this investigation. Lithium manganese oxides have been intensely researched as candidate positive electrode materials for use in Li rechargeable batteries because they offer the possibility of high capacity combined with good safety. This desirable combination is a consequence of the relative stability of the fully charged MnO_2 structures. Mn is also less expensive than Co, the transition metal commonly used today in positive electrode materials for rechargeable Li batteries.¹

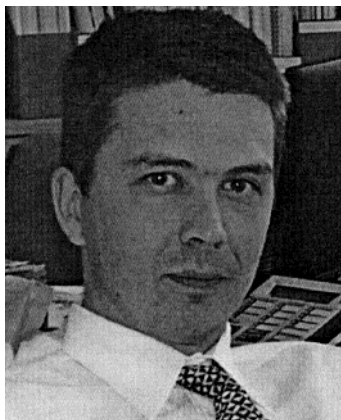
The Mn oxide structures that have received the most attention as possible positive electrode materials are spinel,^{2–4} α - NaFeO_2 -type layered,^{5–9} and orthorhombic ($Pmnm$).^{2,3} All three of these structures have a close-packed (sometimes slightly distorted) oxygen array in a fcc-like stacking with Mn occupying octahedral sites and Li occupying either octahedral or tetrahedral sites. Unfortunately, each of these structures has problems that have hindered their practical use in Li rechargeable batteries thus far.^{2,3,5,10,11} For the α - NaFeO_2 -type layered and orthorhombic ($Pmnm$) structures the primary problem is that they undergo structural transformation with electrochemical cycling. As such the Mn oxides are a good prototype for investigating the relationship between transformation kinetics and electronic structure.

One advantage that spinel-like $\text{Li}_x\text{Mn}_2\text{O}_4$ (s - $\text{Li}_x\text{Mn}_2\text{O}_4$) has over the other candidates is that it is not susceptible to any major structural transformation upon electrochemical cycling over the $0 \leq X_{\text{Li}} \leq 2$ range.² This is due in part to s - $\text{Li}_x\text{Mn}_2\text{O}_4$ being

* To whom correspondence should be addressed. Phone: (617) 253-1581. Fax: (617) 258 6534. E-mail gceder@mit.edu.



John Reed received his Ph.D. degree in Materials Science and Engineering from the Massachusetts Institute of Technology in 2003. Currently he is doing postdoctoral work for the Massachusetts Institute of Technology in addition to being a visiting scientist at Lawrence Berkeley National Laboratory. His current interests are energy technologies and utilization of computational methods to analyze materials used in these technologies, as well as identification of new candidate materials. His primary research focus to date has been on transition-metal oxide materials used in the positive electrodes of Li rechargeable batteries and the physics and chemistry that govern their properties.



Gerbrand Ceder is the R. P. Simmons Professor of Materials Science and Engineering at the Massachusetts Institute of Technology. He received his engineering degree in Metallurgy and Applied Materials Science from the University of Leuven, Belgium, in 1988, and his Ph.D. degree in Materials Science from the University of California at Berkeley in 1991, at which time he joined the MIT faculty. Ceder's research interests lie in computational modeling of material properties and design of novel materials. He has published over 160 scientific papers in the fields of alloy theory, oxide phase stability, high-temperature superconductors, and Li-battery materials, and holds three current or pending U.S. patents. He has received numerous awards among which a Career Award from the National Science Foundation, the Robert Lansing Hardy Award from The Metals, Minerals and Materials Society for "exceptional promise for a successful career", the 2004 Battery Research Award from the Electrochemical Society, and an award from the graduate students at MIT for best teaching. He has worked with several U.S. and international materials companies to use modeling to design and optimize materials for high-performance applications. He is also a co-founder of Computational Modeling Consultants, which provides first-principles materials modeling services to industry. He is currently head of the Theory and Modeling Division of the Institute for Soldier Nano Technology at MIT and a group leader for the Research Program on High Performance Power Sources in the Center for Materials Science and Engineering.

thermodynamically stable at $X_{\text{Li}} = 1$. Additionally $s\text{-Li}_x\text{Mn}_2\text{O}_4$ retains its structural integrity at high and low lithiation even though it becomes energetically metastable at those compositions.²

The low energy of the spinel structure at the LiMn_2O_4 composition is not unique to Mn. For the 3d transition metals from Ti to Cu, the energy of the spinel structure is lower than the energy of the layered structure.^{12,13} This is not too surprising since there is a greater separation between neighboring positively charged Li and M cations ($M \equiv 3d$ transition-metal ion) in the spinel structure—where the Li occupy tetrahedral sites and the M octahedral sites—than in the layered structure—where both Li and M occupy octahedral sites.²

As mentioned previously, both $\alpha\text{-NaFeO}_2$ -type layered ($I\text{-Li}_x\text{MnO}_2$) and orthorhombic ($o\text{-Li}_x\text{MnO}_2$) lose their structural integrity with electrochemical cycling, in contrast to $s\text{-Li}_x\text{Mn}_2\text{O}_4$, and rapidly transform to a spinel-like material at partial lithiation.^{9,14–17} This results in a substantial drop in capacity over the first few charge/discharge cycles.⁸ However, capacity is recovered with additional cycling as the transformation to spinel moves toward completion.¹⁸ The transformed spinel-like material is reported to have properties such as reduced Jahn–Teller distortion and greater durability that are actually superior to conventionally synthesized $s\text{-Li}_x\text{Mn}_2\text{O}_4$ spinel.^{15,18,19} Nonetheless, there remains an interest in making layered manganates that can resist transforming into spinel.

Although spinel is energetically favored at the $\text{Li}_{1/2}\text{MO}_2$ composition for all of the 3d transition metals from Ti to Cu, the rate at which the layered structure transforms to spinel varies substantially for each 3d metal. For Li_xMnO_2 the transformation from layered to spinel occurs rapidly at room temperature. In the case of Li_xNiO_2 , heating is required in order for layered to rapidly transform to spinel.²⁰ While for Li_xCoO_2 the transformation of layered to spinel appears to be even more difficult, with the conversion only detected by TEM in the surface layers of highly cycled $I\text{-Li}_x\text{CoO}_2$.^{21,22} In the following sections the transformation of the layered $\alpha\text{-NaFeO}_2$ structure to spinel will be focused upon as an example (with significant relevance to the battery field) that illustrates the influence of electronic structure on the transformation kinetics of 3d transition-metal oxides.

2. Transformation Mechanisms

The transformation of $I\text{-Li}_x\text{MO}_2$ or $o\text{-Li}_x\text{MO}_2$ into $s\text{-Li}_x\text{M}_2\text{O}_4$ ($M \equiv 3d$ transition-metal ions) does not require oxygen rearrangement since all the structures share a cubic closed-packed (ccp) oxygen anion sublattice. In all three structures M ions occupy octahedral interstitial positions while the Li occupy either octahedral or tetrahedral interstices.² Hence, the transformation of $I\text{-Li}_x\text{MnO}_2$ or $o\text{-Li}_x\text{MnO}_2$ to $s\text{-Li}_x\text{Mn}_2\text{O}_4$ involves a rearrangement of Mn from the set of octahedral sites characterizing $I\text{-LiMnO}_2$ or $o\text{-LiMnO}_2$ to the set of octahedral sites characterizing $s\text{-LiMnO}_2$ (as well as rearrangement of the Li ions).

Formation of spinel from $I\text{-Li}_x\text{MnO}_2$ requires the movement of one-fourth of the Mn ions from the Mn (111) plane into the Li (111) plane as can be seen by examining Figure 1.

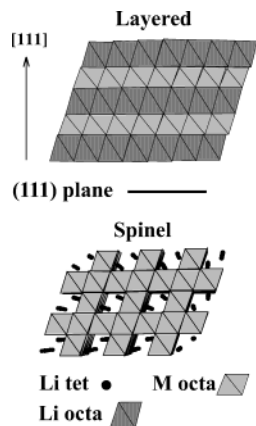


Figure 1. I - Li_xMO_2 (layered) and s - $\text{Li}_2\text{M}_2\text{O}_4$ (spinel) structures ($M \equiv 3d$ transition metal). M occupy octahedral sites in both structures. In I - Li_xMO_2 , M and Li (and/or vacancies) alternately occupy (111) planes of the ccp oxygen sublattice. The (111) plane parallel to the M layers is indicated by the black line between the layered and spinel structures. The [111] direction is shown as well. In s - $\text{Li}_{1/2}\text{MnO}_2$, (111) planes with three-fourths of the Mn alternate with (111) planes with one-fourth of the Mn . Li ions occupy tetrahedral sites in the planes with one-fourth of the Mn . The planes with three-fourths of the Mn are free of Li . In fully lithiated spinel-like s - $\text{Li}_2\text{Mn}_2\text{O}_4$, the Li move into octahedral sites. Three-fourths of the Li are in the (111) plane with one-fourth of the Mn , and one-fourth of the Li are in the plane with three-fourths of the Mn .

For o - Li_xMnO_2 , 50% of the Mn ions need to change position in order to form spinel.² The characteristics of the orthorhombic, α - NaFeO_2 -type layered, and spinel structures as well as many other ordered rock-salt structures have been covered in detail by Thackeray.²

Given that the structural transformation of the α - NaFeO_2 -type layered and orthorhombic structures to spinel only requires cation migration, the varying resistance of transition-metal compositions against the transformation (i.e., low resistance for Mn , high for Co) is most likely connected to the diffusion kinetics of the respective 3d transition-metal ions.

An ion can take two extreme paths in migrating between octahedral sites of a ccp oxygen framework, as occurs during the transformation of I - Li_xMnO_2 or o - Li_xMnO_2 to s - $\text{Li}_x\text{Mn}_2\text{O}_4$. These two paths are shown in Figure 2. The most direct path travels straight through the edge shared by neighboring octahedra, i.e., the $O_h \rightarrow O_h$ path through E shown in Figure 2. This path, while short, brings the cation in close proximity to the coordinating oxygen anions. A more open but longer path is through a nearest neighbor (n.n.) tetrahedral site via the faces (F) it shares with the neighboring octahedra (i.e., path $O_h \rightarrow T_d \rightarrow O_h$ in Figure 2).

While the octahedra shown in Figure 2 are undistorted, this is generally not the case in structures such as I - Li_xMnO_2 and o - Li_xMnO_2 . In these cases the octahedra are distorted by both the cationic ordering which breaks the cubic symmetry of the underlying oxygen sublattice and the Jahn–Teller distortion when Mn^{3+} is present. Consequently, not all of the octahedral edges (E) or faces (F) that Mn can pass through are equivalent in I - Li_xMnO_2 and o - Li_xMnO_2 .

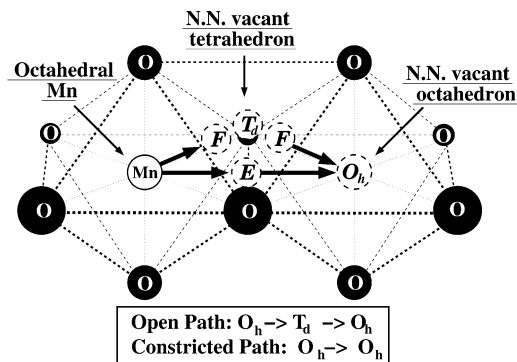


Figure 2. The most direct path an octahedral Mn can follow to a vacant nearest neighbor octahedral site (O_h) is through the edge (E) shared by the two sites. This path ($O_h \rightarrow O_h$) is also the most constricted in terms of separation between the migrating Mn and the surrounding oxygen anions. The minimum separation occurs as Mn passes through the center of the octahedral edge labeled E . A more open path between octahedral sites is via a nearest neighbor (n.n.) tetrahedral site (T_d). Along this path ($O_h \rightarrow T_d \rightarrow O_h$) the minimum separation between a migrating Mn and surrounding oxygens occurs as Mn passes through the center of the shared triangular face between the n.n. octahedron and tetrahedron (F). In a perfect octahedron the distance between the corner oxygens and the center of the triangular face (i.e., distance from O to F) is 1.155 times the distance from corner oxygens to the center of the edge (i.e., distance from O to E in Figure 2).

Generally, the activation barrier for a transition-metal ion passing through the triangular oxygen face (F) along a $O_h \rightarrow T_d \rightarrow O_h$ type path is expected to be less than the barrier to pass through the oxygen edge (E) along a $O_h \rightarrow O_h$ type path. The separation between cation and oxygen is about 15% greater at F than at E (assuming an undistorted octahedron). Hence, there should be less Pauli repulsion from the electron clouds of the oxygen when the cation passes through the octahedral face (F) than when passing through the octahedral edge (E). Previous work has shown that Li favors a $O_h \rightarrow T_d \rightarrow O_h$ type path when diffusing in the Li layer of I - Li_xCoO_2 .²³ It is expected that 3d metal ions will typically take $O_h \rightarrow T_d \rightarrow O_h$ type paths (Figure 2) as well when diffusing through a ccp oxygen framework, such as during the transformation of I - Li_xMnO_2 or o - Li_xMnO_2 to s - $\text{Li}_x\text{Mn}_2\text{O}_4$. The results of first-principles calculations discussed in the following sections support this view.

A notable exception to the general favorability of $O_h \rightarrow T_d \rightarrow O_h$ type paths for cation migration is cases where the intermediate tetrahedral site (T_d) shares a face with an octahedral site occupied by another cation. The passage of a 3d metal ion through such tetrahedral sites is typically calculated to be high in energy, in some cases higher than the energy for passing through the octahedral edge (i.e., the $O_h \rightarrow O_h$ path).²⁴ This is due to the small separation and hence strong repulsion between face-sharing cations in a ccp oxygen framework.

In the following sections it will be shown that first-principles calculations and ligand-field theory indicate that the energetics for the passage of a 3d ion like Mn through intermediate triangular (F) and tetrahedral (T_d) sites is highly effected by its oxidation state.⁷⁶ This suggests that the kinetics of phase

transformations involving 3d ion rearrangements in a ccp oxygen framework will depend strongly upon oxidation state. Since the maintenance of structural integrity is a desirable feature for an electrode material, the effect of valence on ionic mobility is an important consideration when designing electrodes. For multivalent TM ions it is possible that the TM ion could have a low mobility in one valence,- but a high mobility in another, which could make the host structure vulnerable to transformation during electrochemical cycling.

3. Density Functional Theory

Much of the quantitative information in this paper is derived from first-principles calculations based on density functional theory (DFT).^{25–27} Experimentally it is difficult to determine ion migration paths and energy barriers along migration paths in structural transformations such as from *I*-Li_xMnO₂ to *s*-LiMn₂O₄. Examining the atomic-scale ionic movements that could occur in such a transformation using first-principles calculations can therefore be informative.

For characteristics of TM oxides such as Li_xMnO₂ or Li_xCoO₂ that can be experimentally determined, it is found that the calculated results presented in this paper are in good agreement with experiment.⁷⁷ Additionally, previous studies have found that various properties of 3d TM oxides can be determined with good accuracy using DFT-based methods.^{13,28,29} This gives credibility to the findings of this paper which rely upon the rich and precise atomic-scale detail provided by first-principles calculations.

The density functional calculations were performed using the Vienna Ab Initio Simulation Package (VASP).³⁰ The spin-polarized generalized gradient approximation,^{31,32} Perdue–Wang exchange correlation function, and ultrasoft pseudopotentials were used.³³

Defects can be calculated in supercells that are multiples of the unit cell for the underlying undefected structure (e.g., *I*-Li_{1/2}MnO₂). If the supercell is large enough, the periodic images of the defect will have negligible interaction, giving an approximation of an isolated lone defect.

Such an approximation of periodicity was made for the calculations discussed in the next section (section 4). The supercells for these calculations were composed of either 12 or 32 primitive Li_xMO₂ unit cells (M ≡ 3d TM ion; 0 ≤ *x* ≤ 1) that contained various M defects. The lattice parameters of the supercells were kept constant at the parameters for the undefected structure, while the ionic coordinates were allowed to relax. A 2 × 2 × 2 *k*-point mesh was used for the calculations on the 12-unit supercells and a 1 × 1 × 1 *k*-point mesh for the 32-unit supercells. The primitive Li_xMO₂ unit cells used to construct the super cells had previously been calculated with full relaxation of lattice parameters as well as ionic coordinates.

Later sections will draw upon the results of calculations on *I*-Li_xMO₂, *s*-Li_xM₂O₄, and related metastable crystalline structures. For these calculations a Li_xM₄O₈ (0 ≤ *x* ≤ 4) unit cell and a 4 × 4 × 4 *k*-point

mesh were used. Both the lattice parameters and the ionic coordinates were allowed to fully relax.

The bulk of the calculations in this study were performed on Mn oxide structures; however, as a reference, many equivalent calculations were also carried out for Li_xCoO₂ (0 ≤ *x* ≤ 1). This system was chosen for comparison with Li_xMnO₂ because in the layered form it is does not undergo significant phase transformations with electrochemical cycling despite becoming energetically metastable relative to spinel at partial lithiation.^{34–37} This resistance to transformation has allowed layered Li_xCoO₂ to become the standard positive electrode material for use in commercial Li rechargeable batteries.

Finally, some calculations equivalent to those performed with Mn and Co were carried out for oxides of the other 3d transition metals, from Ti to Cu, to demonstrate some general principles governing this class of materials.

4. Comparison between the Activation Barriers for Co and Mn Migration

Figures 3 and 4 show the energy barriers calculated for Mn and Co movements out of a TM layer octahedron and into the Li/vacancy layer of the layered α-NaFeO₂-type structure (recall that the TM cations have to migrate into the Li/vacancy layer for the transformation to spinel). The cation positions used in these calculations follow the *O_h* → *O_h* (Figure 3) and *O_h* → *T_d* → *O_h* (Figure 4) type paths shown in Figure 2.

Figure 3 shows the calculated energy barrier for Mn and Co hopping directly through an octahedral edge (*E*) into a Li/vacancy layer octahedron. The barrier illustrated at the top of Figure 3 is the calculated result when the Li content is *X*_{Li} = 0 (i.e., MO₂, M ≡ Mn or Co); the bottom plot corresponds to

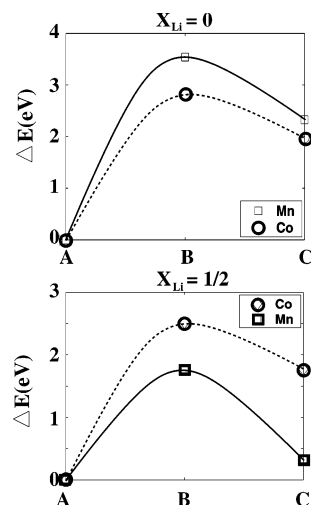


Figure 3. Energy of Co/Mn ion along the *O_h* → *O_h* transition path from an octahedral site in the TM layer, through a shared edge, to an octahedral site in the vacancy/Li layer: (top) delithiated *X*_{Li} = 0 (M⁴⁺), (bottom) half-lithiated *X*_{Li} = 1/2 (average M^{3.5+}). (A) (on *x* axis) Layered structure with no transition metal in the empty/lithium layer (i.e., no defects). (B) A single TM atom located in the shared edge between neighboring octahedra (i.e., *E* in Figure 2). (C) A single TM atom defect in an empty/lithium layer octahedron.

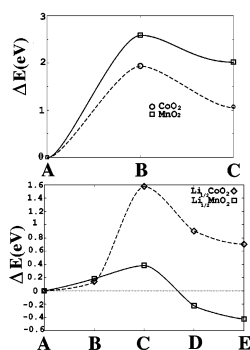


Figure 4. Energy for a Mn/Co ion along the path from an octahedral site in the TM ion layer to a tetrahedral site in the Li/vacancy layer. (top) Delithiated MO_2 ($M \equiv \text{Mn}$ or Co): (A) layered structure, (B) single TM ion located in triangular face between TM layer and empty layer (i.e., F in Figure 2), (C) single tetrahedral TM defect in empty layer. (bottom) Half-lithiated, i.e., $\text{Li}_{1/2}\text{MO}_2$: (A) layered structure, (B) Li disorder to create a trivacancy around a tetrahedron in the Li layer (prevents high-energy face-sharing cations for tetrahedral defect), (C) single TM ion located in triangular face between TM layer and Li layer, (D) single tetrahedral TM defect in Li layer, (E) both Li and TM ion in tetrahedral sites (tetrahedral site available to Li due to vacancy created by TM defect).

a Li content of $X_{\text{Li}} = 1/2$. The TM ion hop in both cases is along the “constricted” $O_h \rightarrow O_h$ path shown in Figure 2 and results in the formation of an octahedral Mn or Co defect in the Li/vacancy layer.

Figure 4 shows the calculated energy barrier for Mn and Co hopping through an octahedral face (F) into a nearest neighbor tetrahedron in the Li/vacancy layer at $X_{\text{Li}} = 0$ and $1/2$. This path is the first half ($O_h \rightarrow T_d$) of the “open” $O_h \rightarrow T_d \rightarrow O_h$ path pictured in Figure 2.

Figures 3 and 4 catalog the plausible initial steps in the transformation of the layered structure to spinel. Other $O_h \rightarrow O_h$ and $O_h \rightarrow T_d \rightarrow O_h$ cation hops within the transition-metal layer have also been calculated, but they were found to be particularly high in energy due to cationic repulsion and hence are ruled out.²⁴

As expected, the barrier is calculated to be lower (at a given lithium content) for hops from octahedra to n.n. tetrahedra through a shared face ($O_h \rightarrow T_d$) than hops directly between octahedra through an octahedral edge ($O_h \rightarrow O_h$). This is consistent with experimental results that indicate Mn migrates through tetrahedral sites during the transformation of orthorhombic or layered Li_xMnO_2 into spinel.^{17,38}

Some additional noteworthy features of the calculated results shown in Figures 3 and 4 are as follows.

(i) The barrier for the TM ion to leave its site in the TM layer is high for both Co and Mn at MO_2 composition.

(ii) The formation energy of a tetrahedral Mn defect in the layered structure at $X_{\text{Li}} = 1/2$ is negative, while it is positive for Co.

(iii) The activation barriers for Mn migration are higher than those for Co at $X_{\text{Li}} = 0$, but they are much lower at $X_{\text{Li}} = 1/2$.

The relatively low energy for Mn migration out of the TM layer and into n.n. tetrahedra in the Li/vacancy layer at $X_{\text{Li}} = 1/2$ is probably the Achilles

heel of the Li_xMnO_2 material. It suggests that Mn can easily move out of the layered configuration into the Li/vacancy layer at this composition. This should facilitate the rapid transformation of $\text{Li}_{1/2}\text{MnO}_2$ to $s\text{-LiMn}_2\text{O}_4$ since Mn ions need to move from the TM layer to the Li/vacancy layer during the transformation. The results of additional calculations, for example, on the second half of the $O_h \rightarrow T_d \rightarrow O_h$ path, reported elsewhere further attest to the relative ease for Mn to move between octahedral and tetrahedral sites along the reaction path toward spinel at $X_{\text{Li}} = 1/2$ in Li_xMnO_2 .²⁴

Co by contrast is seen in Figures 3 and 4 to have high-energy barriers at both delithiated and partially lithiated compositions along either type of pathway ($O_h \rightarrow T_d \rightarrow O_h$ or $O_h \rightarrow O_h$) into the Li/vacancy layer. Results of TM ion defect calculations at full lithiation, i.e., $X_{\text{Li}} = 1$, which are not shown,⁷⁶ indicate that both Co and Mn are prevented from entering the Li layer by the lack of octahedral lithium vacancies.

The calculated low activation barrier and defect energy for Mn going $O_h \rightarrow T_d$ at partial lithiation is consistent with the lack of stability of Li_xMnO_2 against transformation into spinel observed experimentally. Likewise, the high activation barriers for all possible Co hops out of the TM layer are consistent with the relative stability observed experimentally for layered Li_xCoO_2 .

Figures 3 and 4 illustrate that TM ion defect energies and activation barriers to forming defects appear to be highly sensitive to the Li concentration in the layered structure. The relative stability of Mn and Co in the TM layer octahedra changes dramatically with increasing Li content, with Mn calculated to be more stable than Co at $X_{\text{Li}} = 0$ and far less stable at $X_{\text{Li}} = 0.5$. The next section will show that as the average oxidation state of the TM ions changes from +4 to +3.5, due to the Li content changing from $X_{\text{Li}} = 0$ to 0.5, different charge-transfer reactions accompany tetrahedral defect formation for Mn as well as for Co. This provides an explanation for the qualitative change in Mn behavior compared to Co and highlights the important role that electronic structure plays in the mobility of these ions.

5. Valence of Co and Mn during Migration

Figures 3 and 4 indicate a significant variation in the Mn and Co migration barrier along the $O_h \rightarrow T_d \rightarrow O_h$ and $O_h \rightarrow O_h$ paths as the oxidation state changes.

Using the calculated electron spin density, the ionic valences can be determined by integrating the electron spin density in a sphere about the ionic centers. Integrating spin density provides the net spin associated with a given TM ion. This captures the formal valence of the cation better than integrating the charge density because it distinguishes the partially filled 3d orbitals of the transition-metal cation from the filled p orbitals of the coordinating oxygens. With this method it is possible to detect the charge-transfer and/or bonding changes that occur for a TM ion as it moves along its migration path.^{39,40}

The results of such spin integrations are shown in Figure 5 for Co (top) and Mn (bottom) in various

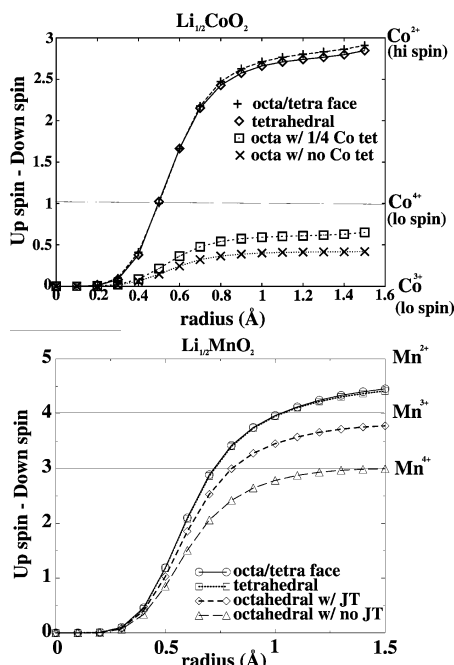


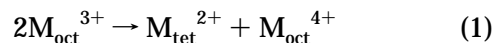
Figure 5. Integrated net spin for Co and Mn cations along the $O_h \rightarrow T_d$ path into the Li/vacancy layer at $X_{\text{Li}} = 1/2$. (top) $\text{Li}_{1/2}\text{CoO}_2$ layered O_h Co ions (labeled octa w/no Co tet) have an oxidation state of $\sim +3.5$ ($t_{2g}^{5.5}$). The migrating Co in triangular (octa/tetra face) or tetrahedral coordination takes on nearly 3 units of electron spin ($1/2\mu_B$), giving an oxidation state approaching +2 ($e^4t_2^3$). When one-fourth of the Co are in T_d sites with +2 charge, the other three-fourths of the Co in O_h sites (octa w/1/4 Co tet) have a raised oxidation state from $\sim +3.6$ to +3.7. (bottom) $\text{Li}_{1/2}\text{MnO}_2$: The migrating Mn (octa/tetra face and tetrahedral) has about 4.5 units of electron spin, giving an oxidation state of $\sim +2.5$ ($e^2t_2^{2.5}$). Mn in Jahn–Teller-distorted octahedra (octahedral w/JT) are $\sim +3$ ($t_{2g}^3e_g^1$); in non-Jahn–Teller-distorted octahedra (octahedral w/no JT) they are +4 (t_{2g}^3).

positions along the $O_h \rightarrow T_d \rightarrow O_h$ path at $t_{\text{Li}} = 1/2$. Figure 5 shows the amount of electron spin (in units of $1/2\mu_B$) as a function of integration radius. The total spin initially rises rapidly with radius as the d orbitals are integrated over. However, then the spin levels off as the nonpolarized oxygen states are reached. The value at this plateau is used in determining the formal valence of the TM cations. For example, the bottom of Figure 5 shows Mn^{4+} which plateaus at a total electron spin of 3, reflecting the $t_{2g}^3e_g^0$ d-orbital filling of Mn^{4+} .

Even though the average formal valence state of the TM is +3.5 at $X_{\text{Li}} = 1/2$, Figure 5 shows that the migrating Mn (Co) ion in triangular or tetrahedral coordination takes on quite a different valence from the surrounding octahedral Mn (Co) ions. The migrating Mn (Co) ion gains d electrons when it passes through the triangular octahedron face and keeps them as it continues into the neighboring tetrahedral site in the Li/vacancy layer.

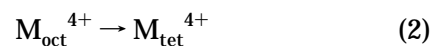
The spin integration results of Figure 5 indicate that when forming a tetrahedral Mn (Co) defect at $X_{\text{Li}} = 1/2$, the migrating Mn (Co) approaches a +2 valence state while a neighboring octahedral Mn (Co) is oxidized toward +4. This constitutes a charge-disproportionation reaction which can be approxi-

mately expressed by the following equation (where M_{tet}^{2+} is the migrating TM ion)



A similar charge disproportionation reaction is reported to occur during the degradation of $s\text{-Li}_x\text{Mn}_2\text{O}_4$ with electrochemical cycling whereby the Mn^{2+} dissolves into the electrolyte.²

Using the spin integration method described above, it was also determined that at an average formal valence of +4 ($X_{\text{Li}} = 0$) both Mn and Co undergo a simple tetrahedral defect reaction



6. Ligand-Field Effects on the Energetics of Migrating Co and Mn

Size effects are often an important contribution to the energy of ionic systems. However, surprisingly cation size appears to have little if any effect on the propensity of Mn or Co to enter tetrahedral coordination in the Li_xMO_2 ccp oxide system. According to Pauling's first rule, a smaller cation should be more energetically favorable in a small interstitial site than a larger cation.⁴¹ The tetrahedral sites formed by oxygen anions in a ccp structure are smaller than the octahedral sites, so by Pauling's first rule smaller cations should have a greater propensity to enter tetrahedral coordination than larger cations. However, the behavior of the Li_xMnO_2 and Li_xCoO_2 systems is very different than what is expected according to Pauling's first rule.

On the basis of cationic radii reported in the scientific literature (53 pm for $\text{Co}_{\text{oct}}^{4+}$ and 40 pm for $\text{Co}_{\text{tet}}^{4+}$; 53 pm for $\text{Mn}_{\text{oct}}^{4+}$ and 39 pm for $\text{Mn}_{\text{tet}}^{4+}$),⁴² one would expect the tetrahedral defect energies and activation barriers for MnO_2 and CoO_2 to be roughly the same. However, as seen previously, the calculated energy for the tetrahedral Mn^{4+} defect is almost twice as high as that of Co^{4+} . The activation barrier for the octahedron–tetrahedron hop is also significantly higher for Mn^{4+} (Figure 4 top).

For the composition $\text{Li}_{1/2}\text{MO}_2$ ($M \equiv \text{Co}, \text{Mn}$), the relevant cations to consider are M^{2+} in tetrahedral coordination, M^{3+} in octahedral coordination, and M^{4+} (given above) in octahedral coordination (58 pm for $\text{Co}_{\text{tet}}^{2+}$ and 54.5 pm for $\text{Co}_{\text{oct}}^{3+}$; 66 pm for $\text{Mn}_{\text{tet}}^{2+}$ and 64.5 pm for $\text{Mn}_{\text{oct}}^{3+}$).⁴²

The radius of Co is less than or equal to the radius of Mn at all oxidation states and coordinations relevant to the $\text{Li}_{1/2}\text{MO}_2$ composition. However, as discussed in the previous section, Mn^{2+} is calculated to be more energetically favored in tetrahedral coordination and have a lower activation barrier for the $O_h \rightarrow T_d$ hop than Co^{2+} , despite being the larger cation.

Finally, according to Pauling's first rule one would expect lower tetrahedral defect and activation barrier energies in MO_2 than in $\text{Li}_{1/2}\text{MO}_2$ for both Co and Mn since the +4 cations have smaller radii than the +2 cations. Again, site-occupancy predictions based on Pauling's first rule run contrary to the results calculated from first principles.

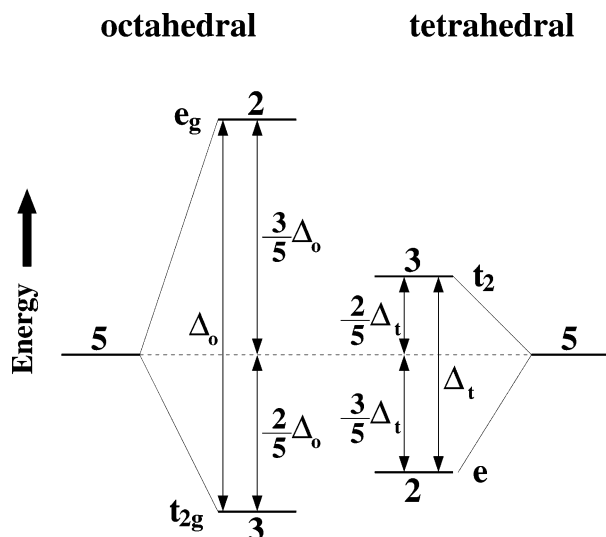


Figure 6. Energy splitting of the d orbitals in octahedral and tetrahedral coordination. The numbers at each level indicate the energy degeneracy that still remains after ligand-field splitting. Note that the energy barycenter (i.e., “center of energy”) need not be the same in octahedral and tetrahedral coordination as pictured.

It appears that for the layered Mn and Co oxides considered, ionic size effects do not play a significant role in the preference for octahedral or tetrahedral sites nor in the activation barrier to hops between the two. Consequently, size effects probably do not play a significant role in determining the mobility of Mn or Co through a ccp oxide framework. In contrast, the results indicate that valence and electronic structure are more decisive factors in the site preference of Mn or Co and hence in their propensity to migrate through a ccp oxide framework. This is consistent with the work of Goodenough that found valence to be an important determinant of the site preference of 3d TM ions in oxides.⁴³

The role of electronic structure in Mn and Co site preference and mobility can to some extent be understood through ligand-field theory (LFT).^{44,45} LFT qualitatively explains how the degeneracy of the 3d orbitals is broken when a free TM ion is surrounded by coordinating anions. The ligand-field splitting of d orbitals in octahedral and tetrahedral coordination is pictured in Figure 6.⁴⁵

In octahedral coordination, the d level splits into the e_g level, which is 2-fold degenerate, and the t_{2g} level, which is 3-fold degenerate. The energy separation between the t_{2g} and e_g levels is called the ligand-field splitting ($\equiv \Delta_o$). The t_{2g} level, composed of the d_{yz} , d_{xy} , and d_{xz} orbitals modified by the octahedral ligand field, is lowered $(2/5)\Delta_o$ relative to the energy barycenter, i.e., “center of energy”, of the d orbitals. The e_g level, composed of the d_{z^2} and $d_{x^2-y^2}$ orbitals, is raised $(3/5)\Delta_o$.⁴⁵

For d orbitals placed in tetrahedral coordination, the t_2 level contains the d_{yz} , d_{xy} , and d_{xz} orbitals modified by the tetrahedral ligand field and the e level contains the d_{z^2} and $d_{x^2-y^2}$ orbitals. Figure 6 illustrates how the energy levels in tetrahedral coordination are inverted relative to those in octahedral coordination (Figure 6).

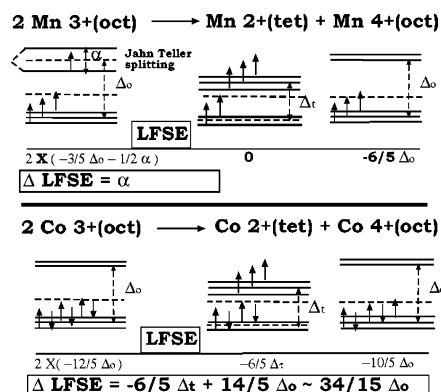


Figure 7. Change in LFSE associated with the charge disproportionation reaction in both $\text{Li}_{1/2}\text{MnO}_2$ (high-spin Mn^{3+}) and $\text{Li}_{1/2}\text{CoO}_2$ (low-spin octahedral Co). Δ_o and Δ_t equal the octahedral and tetrahedral ligand-field energy splittings, respectively. The Jahn–Teller splitting equals α . The proportionality between Δ_o and Δ_t is taken from crystal-field theory to be $-4/9\Delta_o = \Delta_t$.⁴⁶ Note that the energy barycenter (dashed line) is drawn as a constant, but this is not generally the case nor does it affect the change in LFSE (although it certainly affects the change in total energy).

Using LFT, the change in the ligand-field stabilization energy (LFSE) for the charge disproportionation reaction (eq 1) can be estimated for Mn and Co as shown in Figure 7.

The change in LFSE for the charge disproportionation reaction that produces tetrahedral Mn at $X_{\text{Li}} = 1/2$ is projected to be equal to the energy of the Jahn–Teller splitting (α). For Co, on the other hand, the change in LFSE is projected to be more than twice the energy of the octahedral ligand-field splitting ($34/15\Delta_o$), which should be much larger than the Mn Jahn–Teller splitting α .^{47,48} Hence, LFT indicates that charge disproportionation is much more costly in ligand-field stabilization for Co than for Mn at $X_{\text{Li}} = 1/2$. This is consistent with a much lower mobility for $\text{Co}^{3.5+}$ than Mn^{3+} in a ccp oxide and therefore a greater resistance of metastable Co oxides such as $\text{Li}_{1/2}\text{CoO}_2$ against transformation. Experimental evidence supporting the decisive role LFSE plays in the differing stability of the layered structures incorporating Mn, Co, as well as Ni has been reported by Choi, Manthiram et al.⁴⁹

It should be kept in mind that while LFSE is important, it is one of many contributions to the energy in the Li_xMnO_2 and Li_xCoO_2 systems. For example, the d levels in Figure 7 are drawn with a constant center of energy, or barycenter (indicated by the dashed line), but this is not generally the case. Hence, in addition to a change in the splitting of the d levels with changing coordination, there can be a shift in their average energy.

Also, the change in LFSE does not account for the energy cost of spin pairing (two electrons with opposing spin occupying the same orbital).^{50,51} This is not relevant for Mn in this case, but for Co the change in LFSE of the charge disproportionation reaction is probably somewhat counteracted by the change in spin pairing energy (SPE), since a high-spin ion is formed from low-spin ions. The products of Co^{3+} charge disproportionation have four unpaired d elec-

trons while the reactants have none, making the products more favorable in terms of SPE (Figure 7).

7. Summary of Important Factors Influencing Co and Mn Site Preference in ccp Oxides

The association shown in sections 4 and 5 between the +2 oxidation state and a relatively low energy for tetrahedral Mn defects in the layered structure is found to carry over to the site preference of Mn in periodic crystalline structures (likewise the high energy for Co occupancy of tetrahedral sites). Table 1 gives the calculated energy difference between layered $\text{Li}_{1/2}\text{MO}_2$ and other crystal structures with varying amounts of tetrahedral TM cations. Note that the $X_{\text{Li}} = 0.5$ structures with tetrahedral Mn in Table 1 are markedly lower in energy relative to the layered structure ($\text{Li}_{1/2}\text{MO}_2$) than are those with tetrahedral Co.

For the partially inverse spinel structure ($ps\text{-}(\text{LiM})_{\text{tet}}(\text{LiM}_3)_{\text{oct}}\text{O}_8$) shown in Table 1, one-fourth of the Co or Mn in tetrahedral sites are calculated to have a +2 formal valence while three-quarters in octahedral sites adopt a +4 formal valence (giving the overall average valence of +3.5 required by charge balance). Similar to the tetrahedral defect calculations for Mn and Co at $X_{\text{Li}} = 1/2$ (Figure 4, bottom), the $ps\text{-}(\text{LiMn})_{\text{tet}}(\text{LiMn}_3)_{\text{oct}}\text{O}_8$ is calculated to be lower in energy than $\text{Li}_{1/2}\text{MnO}_2$ while $ps\text{-}(\text{LiCo})_{\text{tet}}(\text{LiCo}_3)_{\text{oct}}\text{O}_8$ is calculated higher in energy than $\text{Li}_{1/2}\text{CoO}_2$. The generally low energy associated with the charge disproportionation of Mn^{3+} to produce $\text{Mn}_{\text{tet}}^{2+}$ (eq 1) indicated by the calculations of this section, as well as in sections 4 and 5, is consistent with the experimental observation that Mn^{3+} in many environments favors charge disproportionation.⁵²

The importance of electron supply in the energetics of tetrahedral Mn is demonstrated by the inverse spinel ($is\text{-}(\text{Mn}_2)_{\text{tet}}(\text{Li}_2\text{Mn}_2)_{\text{oct}}\text{O}_8$) result in Table 1. In $is\text{-}(\text{Mn}_2)_{\text{tet}}(\text{Li}_2\text{Mn}_2)_{\text{oct}}\text{O}_8$ one-half of all the Mn are in tetrahedral coordination but there are not enough electrons available for these Mn to take on a +2 oxidation state without the other Mn being oxidized above +4. Instead, the valences for Mn are calculated to be +3 in tetrahedral coordination and +4 in octahedral coordination (giving the required average valence of +3.5). The relatively high energy of $is\text{-}$

Table 1. Energy of Mn and Co Oxides with Varying Amounts of Tetrahedral TM Ions (Comparison of Co and Mn oxides at $X_{\text{Li}} = 0.5$)^a

structure	fraction of M tet	energy (eV)/M cation	
		$\text{Li}_{1/2}\text{-MnO}_2$	$\text{Li}_{1/2}\text{-CoO}_2$
$\text{Li}_{1/2}\text{MO}_2$ (layered)	0	0.0	0.0
$s\text{-LiM}_2\text{O}_4$ (spinel)	0	-0.2489	-0.1791
$(\text{LiM})_{\text{tet}}(\text{LiM}_3)_{\text{oct}}\text{O}_8$ (part. inv. spin.)	1/4	-0.0829	0.1448
$(\text{M}_2)_{\text{tet}}(\text{Li}_2\text{M}_2)_{\text{oct}}\text{O}_8$ (inv. spin.)	1/2	0.2447	0.3627

^a Energies are relative to the $\text{Li}_{1/2}\text{MO}_2$ structure for $\text{M} \equiv \text{Mn}$ and $\text{M} \equiv \text{Co}$, respectively. The second column lists the fraction of TM cations in tetrahedral coordination for a given structure. The structure labeled $(\text{LiM})_{\text{tet}}(\text{LiM}_3)_{\text{oct}}\text{O}_8$ (part. inv. spin.) corresponds to a partially inverse spinel and $(\text{M}_2)_{\text{tet}}(\text{Li}_2\text{M}_2)_{\text{oct}}\text{O}_8$ (inv. spin.) to a fully inverse spinel (i.e., antispinel).

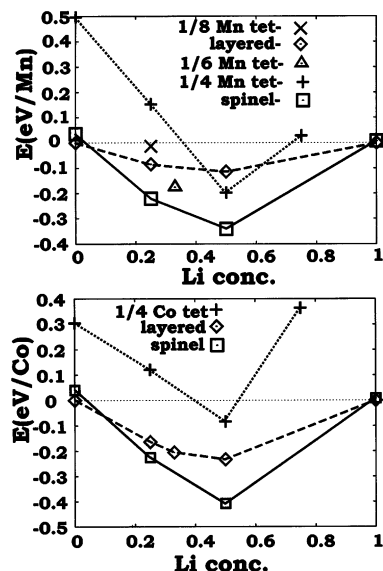


Figure 8. Formation energy versus Li concentration for three structures of Mn oxide (top) and Co oxide (bottom): (\square) $s\text{-Li}_x\text{M}_2\text{O}_4$ -labeled spinel, (\diamond) Li_xMnO_2 -labeled layered, and (+) partially inverse spinel structure with 1/4 Mn tetrahedral ($ps\text{-}(\text{Li}_x\text{M})_{\text{tet}}(\text{Li}_y\text{M}_3)_{\text{oct}}\text{O}_8$; $0 \leq x \leq 1$ and $0 \leq y \leq 2$) labeled 1/4 Mn tet. As the Li content is increased, the Li is added to the tetrahedral site first of $ps\text{-}(\text{Li}_x\text{M})_{\text{tet}}(\text{Li}_y\text{M}_3)_{\text{oct}}\text{O}_8$, and then to the octahedral sites. For Mn, there also is the energy of (Δ) a structure with one-sixth of the Mn in tetrahedral sites at $X_{\text{Li}} = 1/3$ labeled 1/6 Mn tet with a triangle data point and (\times) a structure with one-eighth of the Mn in tetrahedral sites at $X_{\text{Li}} = 1/4$ labeled 1/8 Mn tet.

(Mn_2)_{tet}(Li_2Mn_2)_{oct}O₈ compared to $\text{Li}_{1/2}\text{MnO}_2$ further demonstrates that only the +2 oxidation state (out of the oxidation states +2 through +4) seems to be correlated with the low-energy occupation of tetrahedral sites by Mn.

Hence, the passage of Mn between octahedral sites via an intermediate tetrahedral site (i.e., the “open” $O_h \rightarrow T_d \rightarrow O_h$ path of Figure 2) is expected to be greatly facilitated when the Mn can take on a +2 valence in the tetrahedral site. The amount of Mn ions that can become +2 is determined by the average degree of Mn oxidation which is determined by the Li content.

The average Li content also determines the number of available tetrahedral sites that Mn can enter without sharing faces with Li ions in n.n. octahedral sites. Therefore, while LiMnO_2 has sufficient electrons available for one-half of the Mn to take on a +2 valence through charge disproportionation of Mn^{3+} (eq 1), Mn movement into tetrahedral sites in LiMnO_2 is still expected to be highly unfavorable due to electrostatic interactions with Li in face-sharing n.n. octahedra.

This interplay between electron supply and cation repulsion on the energetics of structures with tetrahedral Mn or Co is illustrated by Figure 8, which gives the calculated energies per TM ion for various structures over a range of Li contents. The results for the $ps\text{-}(\text{Li}_x\text{M})_{\text{tet}}(\text{Li}_y\text{M}_3)_{\text{oct}}\text{O}_8$ structure ($0 \leq x \leq 1$ and $0 \leq y \leq 2$) are shown for both $\text{M} \equiv \text{Co}$ and Mn (with increasing lithiation the Li was added to the tetrahedral sites first, then octahedral). These ener-

gies, labeled 1/4 M tet with + data points in Figure 8, are compared with the energies of the l - Li_xMO_2 and s - LiM_2O_4 structures (labeled layered with diamond data points and spinel with square data points, respectively). Additionally, for Mn the results are shown for a structure with one-sixth of the Mn in tetrahedral sites at $X_{\text{Li}} = 1/3$ (labeled 1/6 Mn tet with a triangle data point) and a structure with one-eighth of the Mn in tetrahedral sites at $X_{\text{Li}} = 1/4$ (1/8 Mn tet with a \times data point). These respective Li contents were chosen because they allow the Mn to disproportionate so that all of the tetrahedral Mn are +2 and all of the octahedral Mn are +4.

When the average formal valence is +4, the calculated energy difference between ps -(Mn) $_{\text{tet}}$ (Mn) $_{\text{3oct}}$ O $_8$ and l -MnO $_2$ is larger than that between ps -(Co) $_{\text{tet}}$ -(Co) $_{\text{3oct}}$ O $_8$ and l -CoO $_2$. This resembles the results of the tetrahedral defect calculations in l -MO $_2$ (Figure 4, top) where the energy of the tetrahedral Mn $^{4+}$ defect is calculated to be higher than the energy of the Co $_{\text{tet}}$ $^{4+}$ defect.

Figure 8 shows that with the addition of Li the energy of ps -(Li $_x$ M) $_{\text{tet}}$ (Li $_y$ M) $_{\text{3oct}}$ O $_8$ drops much more rapidly relative to the layered structure for Mn than for Co. Around the Li $_{1/2}$ MnO $_2$ composition (i.e., ps -(LiM) $_{\text{tet}}$ (LiM) $_{\text{3oct}}$ O $_8$), when all of the tetrahedral Mn have a +2 valence and all of the octahedral Mn are +4 (i.e., total charge disproportionation), ps -(Li $_x$ Mn) $_{\text{tet}}$ (Li $_y$ Mn) $_{\text{3oct}}$ O $_8$ drops below l -Li $_{1/2}$ MnO $_2$ in energy. The particularly steep drop in energy of ps -(Li $_x$ Mn) $_{\text{tet}}$ -(Li $_y$ Mn) $_{\text{3oct}}$ O $_8$ compared to l -Li $_x$ MnO $_2$ with increasing Li concentration is due to the increase in electron supply, making more Mn $_{\text{tet}}$ $^{2+}$ possible.

For Co, the energy of ps -(Li $_x$ Co) $_{\text{tet}}$ (Li $_y$ Co) $_{\text{3oct}}$ O $_8$ by contrast never drops below that of l -Li $_x$ CoO $_2$. The results of Figure 8 for crystalline structures, like those in Table 1, mimic the results of the tetrahedral defect calculations (Figure 4). In each case tetrahedral Co is found to be unfavorable at all lithium concentrations and oxidation states considered, while tetrahedral Mn is found to be favorable at the Li $_{1/2}$ MnO $_2$ composition when it has a +2 valence.

Further bolstering the association of +2 valence with low-energy tetrahedral site occupancy by Mn is the relatively low energy of Li $_x$ MnO $_2$ structures with one-sixth and one-eighth of the Mn in tetrahedral coordination (marked with an \times and a triangle in Figure 8) at lithium concentrations giving the tetrahedral Mn a +2 valence and the octahedral Mn a +4 valence (Li $_{1/3}$ MnO $_2$ and Li $_{1/4}$ MnO $_2$ compositions, respectively).

For Li concentration higher than Li $_{1/2}$ MO $_2$ there is a rapid rise in energy for both ps -(Li $_x$ Mn) $_{\text{tet}}$ (Li $_y$ Mn) $_{\text{3oct}}$ O $_8$ and ps -(Li $_x$ Co) $_{\text{tet}}$ (Li $_y$ Co) $_{\text{3oct}}$ O $_8$ even though the tetrahedral TM ions maintain a +2 valence. The cause of this energy rise is the strong repulsion between Li $_{\text{oct}}^+$ and Mn $_{\text{tet}}$ $^{2+}$ or Co $_{\text{tet}}$ $^{2+}$ that share a polyhedral face. Above a Li content of one-half Li per TM ion, the ps -(Li $_x$ M) $_{\text{tet}}$ (Li $_y$ M) $_{\text{3oct}}$ O $_8$ structure can only accommodate Li in sites that share at least one face with another cation. At the LiMO $_2$ composition both ps -(LiMn) $_{\text{tet}}$ (Li $_3$ Mn) $_{\text{3oct}}$ O $_8$ and ps -(LiCo) $_{\text{tet}}$ (Li $_3$ Co) $_{\text{3oct}}$ O $_8$ are unstable with the tetrahedral Mn and Co being forced back into the TM layer octahedra by repulsive

interactions with face-sharing Li ions (hence the lack of a + data point at $X_{\text{Li}} = 1$ in Figure 8).

Figure 8 exemplifies the conflicting requirements for low-energy occupancy and passage through tetrahedral sites by Mn in Li $_x$ MnO $_2$ with a ccp oxide framework. It requires the coexistence of both Li vacancies to provide tetrahedral sites without face-sharing cations and Mn $^{3+}$ that can form Mn $_{\text{tet}}$ $^{2+}$ through charge disproportionation (eq 1). However, an increase in the concentration of Li vacancies decreases the amount of Mn $^{3+}$ that can undergo charge disproportionation (eq 1) and vice versa. This suggests that the bulk of the Mn migration out of the transition-metal layer during the transformation of l -Li $_x$ MnO $_2$ occurs at partial lithiation when Mn $^{3+}$ and Li vacancies coexist.³⁹

The required coexistence of Mn $_{\text{oct}}$ $^{3+}$ and Li vacancies for the easy migration of Mn between octahedral sites via a tetrahedral intermediate also explains the ability of s -Li $_x$ Mn $_2$ O $_4$ to withstand electrochemical cycling over the $0 \leq X_{\text{Li}} \leq 2$ range without significant cation rearrangement, even though the spinel ordering is thermodynamically unstable near $x = 0$ and 2.

When the spinel-like structure becomes metastable near $X_{\text{Li}} = 0$, most of the Mn are +4 and there are little or no Mn $^{3+}$ that can charge disproportionate. Hence, Mn passage through tetrahedral sites is probably very unfavorable energetically. This cuts off the "open" $O_h \rightarrow T_d \rightarrow O_h$ path of Figure 2. As a result, the Mn are "trapped" in the metastable spinel-like configuration (l -MnO $_2$) at high charge. When the spinel structure becomes metastable near $X_{\text{Li}} = 2$ there is a lack of Li vacancies. This also prevents Mn rearrangement even though Mn $_{\text{oct}}$ $^{3+}$, which can undergo charge disproportionation, are in abundance. Consequently, the metastable s -Li $_2$ Mn $_2$ O $_4$ is preserved at deep discharge as well. When Mn $_{\text{oct}}$ $^{3+}$, which can charge disproportionate, and Li vacancies coexist at one-half lithiation, the spinel structure is thermodynamically stable. Therefore, when the Mn are most prone to migration, there is no thermodynamic driving force to do so and the spinel host structure is retained (although Mn can still dissolve into the electrolyte through charge disproportionation).

This discussion has focused on stoichiometric spinel structure, but nonstoichiometric spinels can exist as well. In the case of spinels that are oxygen deficient there could be significant concentrations of Mn $^{3+}$ remaining at full charge. The results of this study suggest that such spinels may be susceptible to cation rearrangement if they are energetically metastable.

8. Effect of Chemical Substitutions on Mn Site Preference

In sections 4, 5, and 7 it was shown how low-energy occupation and passage through tetrahedral sites by Mn is associated with the +2 oxidation state. It was also shown that Mn $_{\text{oct}}$ $^{3+}$ can readily produce Mn $_{\text{tet}}$ $^{2+}$ through charge disproportionation (eq 1). On the other hand, tetrahedral Mn with a +3 or +4 oxidation state was found to be less favorable.

Chemical substitutions that oxidize Mn $_{\text{oct}}$ $^{3+}$, which might otherwise produce Mn $_{\text{tet}}$ $^{2+}$ through charge

disproportionation, are a promising approach for hindering the transformation of metastable host structures such as $I\text{-Li}_x\text{MnO}_2$. Such chemical substitutions would be expected to hinder Mn passage along $O_h \rightarrow T_d \rightarrow O_h$ (Figure 2) type paths.

There are two categories of elements that will likely produce the desired effect: fixed low-valence cations and electronegative (relative to $\text{Mn}_{\text{oct}}^{3+}$) multivalent cations. It should be noted that fixed low-valence cations have the drawback of reducing the capacity since it is extremely difficult to oxidize Mn above +4. Some cations in these categories that have already been shown experimentally to improve the electrochemical performance of $I\text{-Li}_x\text{MnO}_2$ and/or $o\text{-Li}_x\text{MnO}_2$ include Al^{3+} ,¹⁸ Co^{3+} ,⁷ Cr^{3+} ,⁵³ Ni^{2+} ,⁵⁴ Li^+ , and Cr^{3+} .⁵⁵

A series of first-principles results will now be shown that demonstrate the effect of a variety of chemical substitutions on the valence of Mn and how this in turn affects the site preference of Mn.

As discussed previously, a strong preference by Mn for octahedral over tetrahedral coordination should result in reduced mobility for Mn through a ccp oxygen framework. A reduced mobility for Mn in turn could increase the resistance of metastable chemically substituted Mn oxide structures against structural transformation.

The results of sections 4, 5, and 7 indicate that there is a good correlation between the energetics of a tetrahedral Mn defect in $I\text{-Li}_x\text{MnO}_2$ and the energy difference between $I\text{-Li}_x\text{MnO}_2$ and a periodic small unit cell structure with tetrahedral Mn like $ps\text{-}(\text{Li}_x\text{Mn})_{\text{tet}}(\text{Li}_y\text{Mn}_3)_{\text{oct}}\text{O}_8$ provided the Li contents and tetrahedral Mn oxidation states are the same in both the periodic structure and the tetrahedral Mn defect calculation. Specifically, $\text{Mn}_{\text{tet}}^{4+}$ is found to be relatively unfavorable whether it occurs as a defect in layered $I\text{-MnO}_2$ or within a periodic structure like $ps\text{-}(\text{Mn})_{\text{tet}}(\text{Mn}_3)_{\text{oct}}\text{O}_8$. Likewise, $\text{Mn}_{\text{tet}}^{2+}$ is found to be relatively favorable whether it occurs as a defect in layered $I\text{-Li}_{1/2}\text{MnO}_2$ or within $ps\text{-}(\text{LiMn})_{\text{tet}}(\text{LiMn}_3)_{\text{oct}}\text{O}_8$.

To gauge the favorability of Mn entering tetrahedral sites in the presence of chemical substitutions that alter the Mn oxidation state, the energy difference between structures such as $ps\text{-}(\text{LiMn})_{\text{tet}}(\text{LiSub}_3)_{\text{oct}}\text{O}_8$ ($Sub \equiv \text{Mn}$ and/or substitutional elements) with tetrahedral Mn and $I\text{-Li}_{1/2}\text{Mn}_{1/4}\text{Sub}_{3/4}\text{O}_2$ ($Sub \equiv \text{Mn}$ and/or substitutional elements) without tetrahedral Mn have been evaluated over a large range of chemical substitutions.

It is assumed that as with pure Mn oxides, the site preference for Mn at a given valence will be reflected by the energy difference between the chemically substituted compounds with and without tetrahedral Mn. The use of simple structures such as $ps\text{-}(\text{LiMn})_{\text{tet}}(\text{LiSub}_3)_{\text{oct}}\text{O}_8$ with tetrahedral Mn instead of large supercells with tetrahedral Mn defects, like those used in section 4, greatly reduces the calculation time.

Obviously it is an approximation to use the energy difference between a structure with tetrahedral Mn and a structure with only octahedral Mn as an indication of Mn mobility in a ccp oxide. To precisely determine Mn mobility along the “open” $O_h \rightarrow T_d \rightarrow O_h$ path, the activation barrier is the required quan-

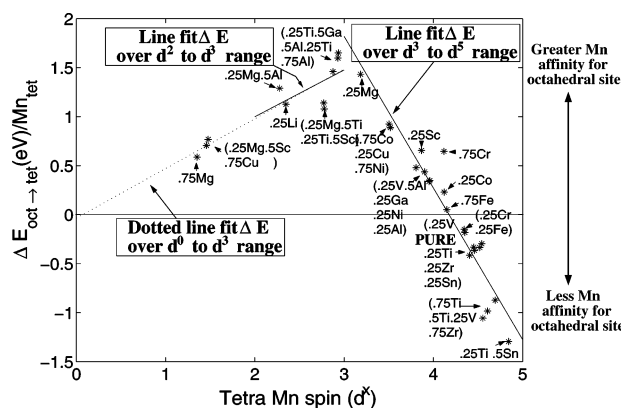


Figure 9. Energy difference between $ps\text{-}(\text{LiMn})_{\text{tet}}(\text{LiSub}_3)_{\text{oct}}\text{O}_8$ with tetrahedral Mn and $I\text{-Li}_{1/2}\text{Mn}_{1/4}\text{Sub}_{3/4}\text{O}_2$ without tetrahedral Mn as a function of the spin on the tetrahedral Mn (Tetra Mn spin d^x). $Sub \equiv$ elements substituted for Mn and/or Mn. Pure $\text{Li}_{1/2}\text{MnO}_2$ is labeled “pure”. Each data point (*) has been labeled according to the element substituted (e.g., Co) and the fraction of Mn in the “pure” structural counterpart they have replaced (e.g., 0.25). The substituted elements occupy only O_h sites in both $ps\text{-}(\text{LiMn})_{\text{tet}}(\text{LiSub}_3)_{\text{oct}}\text{O}_8$ and $I\text{-Li}_{1/2}\text{Mn}_{1/4}\text{Sub}_{3/4}\text{O}_2$. Mn occupies T_d sites and any available O_h sites in $ps\text{-}(\text{LiMn})_{\text{tet}}(\text{LiSub}_3)_{\text{oct}}\text{O}_8$ and only O_h sites in $I\text{-Li}_{1/2}\text{Mn}_{1/4}\text{Sub}_{3/4}\text{O}_2$. For data points that are clumped together, a single label containing all the chemical substitutions contained in the cluster of points is enclosed in parentheses (e.g., 0.25Cr, 0.25Fe). The chemical substitutions listed in these labels are ordered (going from top to bottom in the label) from lowest Mn_{tet} d spin to highest, i.e., from left-most data point to right-most in the cluster. The data points for 0.25 Cu and 0.75 Ni cannot be resolved because they have nearly the same coordinates: (0.25 Cu, 3.517, 0.887 eV); (0.75 Ni, 3.519, 0.886 eV).

tity not the energy in tetrahedral coordination. However, if the energy of tetrahedral site occupancy for Mn is high, the activation barrier for the $O_h \rightarrow T_d \rightarrow O_h$ path can only be equal or higher. Therefore, the energetics of Mn in tetrahedral coordination can provide an upper bound on the mobility of Mn along the $O_h \rightarrow T_d \rightarrow O_h$ path.

Figure 9 shows the energy difference between $ps\text{-}(\text{LiMn})_{\text{tet}}(\text{LiSub}_3)_{\text{oct}}\text{O}_8$ ($Sub \equiv \text{Mn}$ and/or elements substituted for Mn) and $I\text{-Li}_{1/2}\text{Mn}_{1/4}\text{Sub}_{3/4}\text{O}_2$, which is believed to be a particularly good gauge for the stability of the layered structure. The reason for this is that $ps\text{-}(\text{LiMn})_{\text{tet}}(\text{LiSub}_3)_{\text{oct}}\text{O}_8$ is equivalent to a tetrahedral Mn and Li defect placed in a small supercell of layered structure (four MnO_2 units as opposed to the 12 and 32 MnO_2 unit supercells used in section 4). Hence, its energy should be related to the Mn tetrahedral defect energy in layered at a given composition. Furthermore, the partially inverse spinel ($ps\text{-}(\text{LiMn})_{\text{tet}}(\text{LiSub}_3)_{\text{oct}}\text{O}_8$) can be easily formed from $I\text{-Li}_{1/2}\text{Mn}_{1/4}\text{Sub}_{3/4}\text{O}_2$ by moving one-fourth of the Mn into nearest neighbor tetrahedra in the Li layer, which equals the fraction of Mn that move from the TM layer to the Li layer during the transformation of layered to spinel (i.e., one Mn per eight oxygen).^{78,79} Therefore, $ps\text{-}(\text{LiMn})_{\text{tet}}(\text{LiSub}_3)_{\text{oct}}\text{O}_8$ could resemble intermediate structures that arise during the transformation.

Consistent with the proposed importance of Mn valence and LFSE, low fixed valence cations (e.g., Al^{3+} , Mg^{2+} , Li^+) and electronegative multivalent

cations (e.g., Co^{3+} , Ni^{2+} , Cu^{2+}) that oxidize Mn^{3+} are calculated to stabilize Mn in the octahedral sites of $I\text{-Li}_{1/2}\text{Mn}_{1/4}\text{Sub}_{3/4}\text{O}_2$. This is indicated in Figure 9 by the $ps\text{-}(\text{LiMn})_{\text{tet}}(\text{LiSub})_{\text{oct}}\text{O}_8$ with these chemical substitutions (i.e., $\text{Sub} \equiv \text{Al, Mg, Li, Co, Ni, or Cu}$) being higher in energy than $I\text{-Li}_{1/2}\text{Mn}_{1/4}\text{Sub}_{3/4}\text{O}_2$ rather than lower as is the case for pure $\text{Li}_{1/2}\text{MnO}_2$ (labeled “pure” in Figure 9).

The correspondence between chemical substitutions that have been reported to experimentally stabilize layered $I\text{-Li}_x\text{MnO}_2$ material and/or improve its capacity (e.g., Al^{3+} , Co^{3+} , Cr^{3+} , Ni^{2+} , Li^+) and the chemical substitutions that are calculated to stabilize Mn in the layered octahedral sites according to Figure 9 is reassuring.^{7,18,53–55} Another encouraging feature of Figure 9 is that none of the elements that are found in compositions calculated to destabilize the layered structure (e.g., Ti^{4+} , Zr^{4+} , Sn^{4+} , V^{5+}) have been reported experimentally to be successful in stabilizing $I\text{-Li}_x\text{MnO}_2$ material.

Cr substitution provides a particular example that supports interpreting the results of Figure 9 as a measure of the layered structures stability against transformation. Experiments have shown that reducing the Mn/Cr ratio in Cr-substituted $I\text{-Li}_x\text{MnO}_2$ reduces in size or eliminates the spinel-type step in the voltage curve that arises during electrochemical cycling of pure $I\text{-Li}_x\text{MnO}_2$.^{53,56} This implies that Cr substitution can hinder or prevent the transformation of the layered structure to spinel.

Davidson et al. found that replacing one-fourth of the Mn in $I\text{-Li}_x\text{MnO}_2$ with Cr fails to prevent a step in the voltage curve from developing with electrochemical cycling.⁵³ The calculated energy of the partially inverse spinel $ps\text{-}(\text{LiMn})_{\text{tet}}(\text{LiCrMn}_2)_{\text{oct}}\text{O}_8$ with one-fourth of the Mn substituted with Cr is -0.1494 eV/(Mn_{tet}) lower in energy than $I\text{-Li}_{1/2}(\text{Cr}_{1/4}\text{Mn}_{3/4})\text{O}_2$. Using this result as a gauge of stability suggests that the layered structure with one-fourth Cr should still be susceptible to forming tetrahedral Mn and hence should still be susceptible to transforming into spinel, consistent with experimental observation.

A compound with one-half of the Mn ions substituted by Cr was found to have no spinel step in its voltage curve.⁵³ The energy of $(\text{LiMn})_{\text{tet}}(\text{LiCr}_2\text{Mn})_{\text{oct}}\text{O}_8$ for this case is calculated to be 0.2806 eV/(Mn_{tet}) higher in energy than $I\text{-Li}_{1/2}(\text{Cr}_{1/2}\text{Mn}_{1/2})\text{O}_2$.²⁴ This result suggests that forming tetrahedral Mn in the layered structure with one-half Cr should be unfavorable, and hence the structure should resist transforming into spinel, again consistent with observation. While Figure 9 may give a measure of the stability of chemically substituted layered compounds against Mn migration into the Li/vacancy layer, it should be kept in mind that the elements substituted for Mn may themselves be prone to migration into the Li/vacancy layer. However, in the Davidson experiment it appears that both the Cr and Mn resist migrating into the Li/vacancy layer when the Mn is sufficiently oxidized.

In addition to revealing which chemical substitutions could prevent the transformation of the layer structure, Figure 9 also illustrates the relation

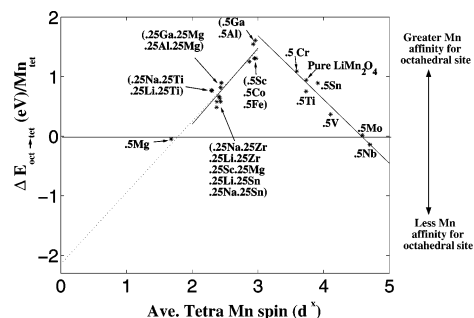


Figure 10. Equivalent plot to Figure 9 except ΔE gives the energy difference between fully inverse spinel, i.e., antispinel ($is\text{-Mn}_{\text{tet}}(\text{LiSub})_{\text{oct}}\text{O}_4$; $\text{Sub} \equiv$ substitutional elements or Mn) and spinel ($s\text{-Li}_{\text{tet}}(\text{MnSub})_{\text{oct}}\text{O}_4$). Also, the x axis is now the average spin on the tetrahedral Mn since there are two tetrahedral Mn per inverse spinel unit cell. All of the chemical substitutions replace 50% of the Mn ions. In the anti-spinel, all of the octahedral Mn are chemically substituted. In the spinel half of the octahedral Mn are chemically substituted.

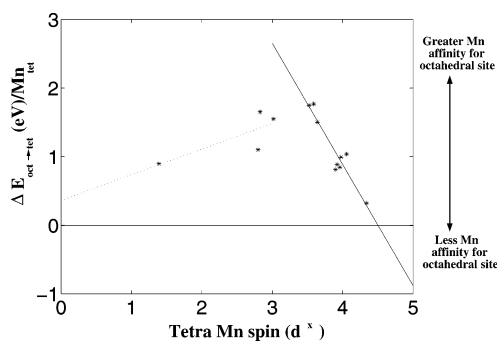


Figure 11. Equivalent plot to Figure 9 at $X_{\text{Li}} = 0.25$.

between the valence of Mn and its energy in tetrahedral coordination. Starting at $\text{Mn}_{\text{tet}}^{2+}$ (i.e., d^5 filling), the relative energy of $ps\text{-}(\text{LiMn})_{\text{tet}}(\text{LiSub})_{\text{oct}}\text{O}_8$ rises roughly linearly with increasing valence (i.e., decreasing d filling) to a maximum peak at around +4 valence (i.e., d^3 filling) for the tetrahedral Mn.

This is consistent with calculations shown in sections 4, 5, and 7 that found the tetrahedral Mn^{4+} defect (Figure 4) as well as the delithiated $ps\text{-}(\text{Mn})_{\text{tet}}(\text{Mn}_3)_{\text{oct}}\text{O}_8$ (Figure 8) to be particularly high in energy. It is also consistent with experimental results that show chemical substitutions which oxidize Mn to +4 such as Ni^{40} increase the stability of the layered structure.⁵⁴ When Mn is oxidized to +4 it becomes, practically speaking, electrochemically inactive in $I\text{-Li}_x\text{MO}_2$ materials due to the great difficulty in oxidizing Mn above +4.

Figure 9 indicates that chemical substitutions which oxidize Mn stabilize the layered structure against transformation only up to a point. At valences higher than +4, i.e., tetrahedral Mn orbital fillings less than d^3 , the trend abruptly shifts (Figure 9). Although in reality such valences are rare for Mn in ccp oxides, Mn is predicted to become less stable in the layered octahedral sites with valences increasing above +4.

Figures 10–13 give further confirmation that the maximum energy for Mn occupation of tetrahedral sites in a ccp oxide occurs when the Mn valence is +4 (i.e., d^3 filling), independent of cation ordering. Figures

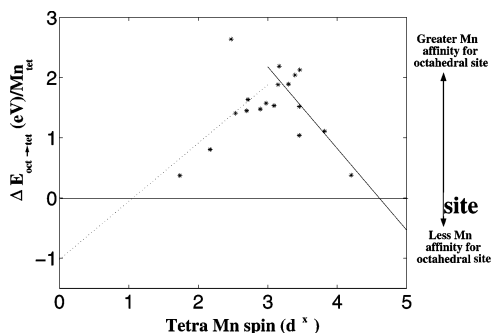


Figure 12. Equivalent plot to Figure 9 at $X_{\text{Li}} = 0$.

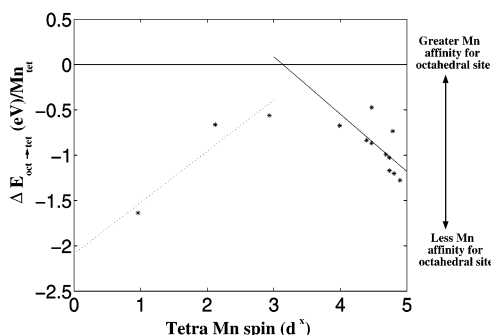


Figure 13. Energy difference between the $s\text{-(Mn)}_{\text{tet}}\text{-(Sub}_2\text{)}_{\text{oct}}\text{O}_4$ spinel and $rs\text{-(MnSub}_2\text{)}_{\text{oct}}\text{O}_4$ cation-deficient rock-salt structures.

10–13 contain energy plots equivalent to Figure 9 that were generated from comparisons between fully inverse spinel ($is\text{-(Mn)}_{\text{tet}}\text{(LiSub)}_{\text{oct}}\text{O}_4$) and spinel ($s\text{-(Li(MnSub))O}_4$), $ps\text{-(LiMn)}_{\text{tet}}\text{(Sub}_3\text{)}_{\text{oct}}\text{O}_8$ and $I\text{-Li}_{1/4}\text{-Mn}_{1/4}\text{Sub}_{3/4}\text{O}_2$, $ps\text{-(Mn)}_{\text{tet}}\text{(Sub}_3\text{)}_{\text{oct}}\text{O}_8$ and $I\text{-Mn}_{1/4}\text{Sub}_{3/4}\text{O}_2$, spinel $s\text{-(Mn)}_{\text{tet}}\text{(Sub}_2\text{)}_{\text{oct}}\text{O}_4$ and cation-deficient rock-salt $rs\text{-(MnSub}_2\text{)}_{\text{oct}}\text{O}_4$. Figure 10 is particularly notable because it illustrates how chemical substitutions which reduce Mn_{tet} toward an ideal +2 d-orbital filling (e.g., 0.5 Nb), or that oxidize Mn_{tet} well above +4 (e.g., 0.5 Mg) are calculated to actually make the fully inverse spinel with tetrahedral Mn more stable than spinel at one-half lithiation.

8.1. Electronic Structure Model for the Energetics of Mn Oxides

Figures 9–13 show that the energy difference between structures with and without tetrahedral Mn is approximately a linear function of d-orbital filling on the tetrahedral Mn within certain ranges.

One can intuitively understand the piecewise linear structure of the plots in Figures 9–13 using a simple model based on the change in electronic structure when Mn moves from an octahedral to a tetrahedral site. In this model it is assumed that the slopes of the lines in Figures 9–13 are equal to the energy difference between the energetically highest occupied d orbital (HODO) of the tetrahedral Mn and the HODO of the octahedral Mn. This assumption is consistent with electrons being transferred between octahedral d levels and tetrahedral d levels that are fixed with respect to each other independent of oxidation state.

Given the typical d-orbital splitting for tetrahedral and octahedral environments this leads to three different regimes for the energy change when Mn

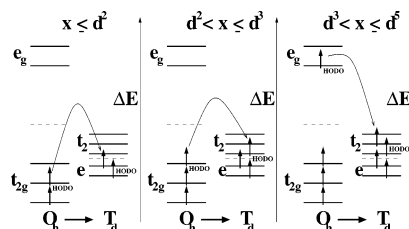


Figure 14. In tetrahedral coordination (T_d) the d-orbital splitting is opposite and smaller in magnitude than the d-orbital splitting in octahedral coordination (O_h). Consequently, the transfer of electrons from d orbitals in an O_h ligand field to d orbitals in a T_d field as Mn moves from an octahedral to a tetrahedral site falls into three different regimes: $x \leq 2$, $2 < x \leq 3$, and $3 < x \leq 5$. These regimes are distinguished by the highest occupied d orbital (HODO) in the O_h and T_d fields. Only integer fillings of the d shell are pictured, but fractional fillings can occur as well.

moves from octahedral to tetrahedral coordination as illustrated in Figure 14 (this model neglects the splitting of the e_g level by Jahn–Teller distortion). Figure 14 schematically pictures how the d orbitals change for a Mn that moves from octahedral (O_h) coordination (e.g., in the layered structure) to tetrahedral (T_d) coordination (e.g., tetrahedral site in $ps\text{-(LiMn)}_{\text{tet}}\text{(LiSub}_3\text{)}_{\text{oct}}\text{O}_8$).

The different regimes that occur as a function of the tetrahedral Mn d-orbital filling (d^x) are as follows.

(1) $x \leq 2$. In this regime as Mn moves from octahedral to tetrahedral coordination the d electrons move from t_{2g} (lowered octahedral d) to e (lowered tetrahedral d) orbitals. The energy difference between tetrahedral and octahedral Mn is given by the energy difference between the filled e and t_{2g} orbitals plus a constant ($\Delta E_{\text{Mn}^{7+}}$) that accounts for other energy contributions independent of d-orbital filling ($\Delta E_{\text{Mn}^{7+}}$ is the ΔE intercept at d^0 of Figures 9–13).

$$\Delta E_{\text{oct} \rightarrow \text{tet}} = (E_e - E_{t_{2g}})x + \Delta E_{\text{Mn}^{7+}} \quad (3)$$

(2) $2 < x \leq 3$. The energy difference in this regime includes the contribution from the $x \leq 2$ regime plus the energy difference between the filled t_2 (raised tetrahedral d) and the t_{2g} (lowered octahedral d) orbitals giving

$$\Delta E_{\text{oct} \rightarrow \text{tet}} = (E_{t_2} - E_{t_{2g}})(x - 2) + 2(E_e - E_{t_{2g}}) + \Delta E_{\text{Mn}^{7+}} \quad (4)$$

(3) $3 < x \leq 5$. The energy difference in this regime includes the contribution from the $x \leq 2$ and $2 < x \leq 3$ regimes plus the energy difference between the filled t_2 (raised tetrahedral d) and e_g (raised octahedral d) orbitals giving

$$\Delta E_{\text{oct} \rightarrow \text{tet}} = (E_{t_2} - E_{e_g})(x - 3) + (E_{t_2} - E_{t_{2g}}) + 2(E_e - E_{t_{2g}}) + \Delta E_{\text{Mn}^{7+}} \quad (5)$$

This simple model, which gives a piecewise linear relationship between the energy of tetrahedral Mn and its valence, fits the results of Figures 9–13 surprisingly well, considering the wide variety of single and multivalent cation substitutions used in generating these plots. This again indicates the

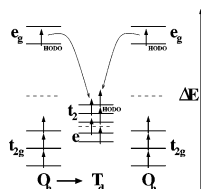


Figure 15. Schematic of the charge disproportionation reaction which involves two Mn as opposed to the single Mn reactions shown in Figure 14. Charge disproportionation can occur over the $3 < x \leq 5$ filling range. The set of orbitals O_h and T_d linked by a right arrow (\rightarrow) correspond to the Mn moving from octahedral to tetrahedral coordination. The other set of orbitals labeled O_h correspond to a Mn that remains in octahedral coordination. Integer fillings of the d shell are pictured, but fractional fillings can occur as well.

substantial role Mn valence plays in determining its site energy.

The model of eqs 3–5 suggests that the energy of a manganese oxide can be conveniently separated into two contributions. One contribution is from the interactions involving Li cations, O anions, Mn^{7+} (i.e., d^0) ionic cores, and elements substituting for Mn (d^0 ionic cores if the d orbitals of these elements are filled). The difference in this energy term between the structures with and without tetrahedral Mn equals the y intercept ($\Delta E_{Mn^{7+}}$) of $\Delta E_{oct-tet}$ given by eqs 3–5. The other energy contribution is from the energy of the filled Mn d orbitals (and in some instances the substitutional element d orbitals) which gives the piecewise linear valence dependent terms of $\Delta E_{oct-tet}$ in eqs 3–5.

The simple d-level splitting model of eqs 3–5 explains well the abrupt change in slope as the orbital filling moves from the $2 < x \leq 3$ regime to the $3 < x \leq 5$ regime (Figures 9–12). When the filling of the Mn d orbitals exceeds d^3 , the HODO of the octahedral Mn goes from being lower in energy (t_{2g}) to higher in energy (e_g) than the HODO of the tetrahedral Mn (t_2). Therefore, at d^3 the slope of $\Delta E_{oct-tet}$ as a function of Mn_{tet} d filling abruptly changes sign from positive to negative. The $x \leq 2$ regime cannot be resolved from the $2 < x \leq 3$ regime in Figures 9–13, which suggests that there is little splitting between the Mn d orbitals in tetrahedral coordination (i.e., t_2 and e).

While Figure 14 only illustrates a single Mn^{7+} ion core and its associated d electrons moving from O_h to T_d coordination, the proposed model of eqs 3–5 can also be used to account for charge disproportionation (eq 1). When charge disproportionation occurs an additional electron is transferred to the tetrahedral Mn t_2 orbital from a Mn e_g orbital (or perhaps another multivalent cation d orbital) that remains in octahedral coordination. The HODOs over the $3 < x \leq 5$ d-filling regime (i.e., t_2 tetrahedral, e_g octahedral) remain the same whether charge disproportionation occurs or not. Therefore, the presence of charge disproportionation should not change the slope of the plot over the $3 < x \leq 5$ regime according to eq 5. This can be seen by comparing the $3 < x \leq 5$ regime of Figure 14 with the disproportionation reaction diagrammed in Figure 15.

Equations 3–5 can be used to estimate the octahedral ligand-field splitting (Δ_o) from the slopes of

the lines fit to Figures 9–13. The octahedral ligand-field splitting is found to be roughly the same for all of the MnO_2 host structures and Li contents considered (i.e., Figures 9–12), ranging from $\Delta_o = 2.1$ to 2.3 eV. These values resemble the ligand-field splitting reported experimentally for MnO_2 of 2.5 eV.⁵⁷ The estimated octahedral ligand-field splitting for the Mn_3O_4 structures on the other hand (Figure 13) is found to be much lower at $\Delta_o = 1.2$ eV. This is close to the ligand-field splitting reported experimentally for MnO of 1.3 eV.⁵⁷

In addition to having a lower estimated Δ_o , the calculations on Mn_3O_4 (Figure 13) differ from the MnO_2 host structures in having the y intercept $\Delta E_{Mn^{7+}}$ shifted to such a negative value that the tetrahedral Mn structure ($s\text{-}(Mn)_{tet}(Sub_2)_{oct}O_4$) is always lower in energy than the structure with only octahedral Mn ($rs\text{-}(Mn)_{oct}O_4$), although a maximum in energy at Mn_{tet}^{4+} is maintained.

While the piecewise linear regions and energy maximum around +4 valence of Figures 9–13 are consistent with ligand-field effects, it is important to bear in mind that LFSE cannot by itself predict the energy difference between octahedral and tetrahedral Mn.

For example, in section 6 the change in LFSE associated with the charge disproportionation reaction creating tetrahedral Mn^{2+} (eq 1) is projected to be equal to the Jahn–Teller splitting α , i.e., a positive energy (see Figure 7). However, first-principles calculations show that the energy of producing tetrahedral Mn^{2+} through charge disproportionation (eq 1) in $I\text{-}Li_{1/2}MnO_2$ is negative (Figures 4, 8, and 9).

The possibility that Mn generally favors tetrahedral coordination as its valence approaches +2 (i.e., d^5) is unlikely given that MnO has a rock-salt structure not zinc blende or some other structure with Mn_{tet}^{2+} . Instead, the driving force for Mn movement out of the octahedral sites of $I\text{-}Li_{1/2}MnO_2$ into neighboring Li layer tetrahedral sites appears to be due to the unique cationic ordering and associated cationic interactions that are present in $I\text{-}Li_{1/2}MnO_2$.

In the case of $I\text{-}Li_{1/2}MnO_2$, the positive change in LFSE for charge disproportionation (i.e., α) is insufficient to counter the cationic interactions that favor Mn movement into Li layer tetrahedra. Conversely, in chemically substituted compounds such as $I\text{-}Li_{1/2}\text{-}Mn_{3/4}Mg_{1/4}O_2$, the much higher change in LFSE associated with Mn^{4+} movement from octahedral to tetrahedral coordination ($38/45 \Delta_o$ assuming $-4/9 \Delta_o = \Delta_t$) overwhelms the interactions favoring the formation of tetrahedral Mn^{4+} so that it becomes highly unfavorable energetically.

While LFSE can be useful for explaining the trends of Mn site preference with valence, it does not capture important energy contributions that are more sensitive to cationic ordering. These energy contributions, for example, make the formation of tetrahedral Mn^{2+} favorable in $I\text{-}Li_{1/2}MnO_2$ but unfavorable in $s\text{-}LiMn_2O_4$. A more clear picture of these energy contributions can be gained from the model of eqs 3–5.

One energy contribution that is sensitive to cationic ordering given explicitly in eqs 3–5 is the y intercept $\Delta E_{Mn^{7+}}$. According to the proposed model $\Delta E_{Mn^{7+}}$

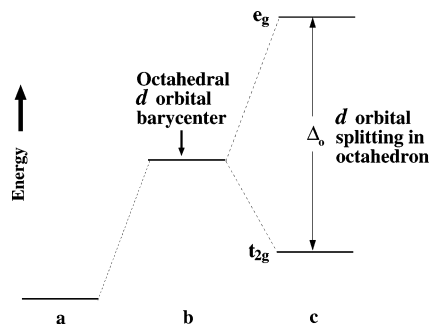


Figure 16. Effect of octahedral coordination on the energy of TM 3d orbitals: (a) 3d level of free TM ion. 3d orbitals are degenerate. (b) Average interactions between anions, neighboring cations, and 3d electrons shift the average energy of the 3d orbitals. (c) Splitting of 3d energy levels in an octahedral ligand field. Note that while the energy of the 3d orbitals may be increasing due to the negatively charged ligands, the overall energy of the system is decreasing in going from a free ion to bound one.

accounts for the interactions involving Li cations, O anions, Mn^{7+} (i.e., d^0) ionic cores, and elements substituting for Mn (d^0 ionic cores if the d orbitals of these elements are filled). It is assumed that these interactions are primarily electrostatic. $\Delta E_{\text{Mn}^{7+}}$ can have a substantial effect on site energetics as the difference in y -intercepts of Figures 9–13 show.

The other energy contribution that is sensitive to cationic ordering is implicitly part of d-orbital terms such as $(E_{t_2} - E_{e_g})(x - 3)$ in eqs 3–5. A coefficient such as $(E_{t_2} - E_{e_g})$, which gives the energy difference between the tetrahedral t_2 and octahedral e_g orbitals, can be broken down into two parts.

One part depends on the ligand-field splitting in a given coordination (i.e., Δ_o and Δ_t). This part is the change in LFSE is represented in Figure 7 (e.g., α for Mn charge disproportionation; eq 1, $38/45 \Delta_o$ for $\text{Mn}^{4+} \text{O}_h \rightarrow T_d$).

The other part depends on the average energy of the d orbitals, i.e., the energy barycenter, in a given site. The energy barycenter of d orbitals in octahedral coordination is represented by the level above b in Figure 16.⁴⁵ In moving Mn between octahedral and tetrahedral sites there is a change in LFSE caused by the change in the splitting of the d orbitals (e.g., from t_{2g} and e_g to e and t_2) and a change in energy barycenter caused by the change in the average interactions experienced by electrons in the d orbitals.

Taking into account the change in barycenter of the d levels and the interactions involving the Mn^{7+} ionic cores, a more complete expression for the energy change (ΔE_{cd}) associated with the Mn charge disproportionation reaction (eq 1) than that given in Figure 7 can be obtained

$$\begin{aligned} \Delta E_{\text{cd}} &= (5E_{\text{tb}} + E_{\text{Mn}_{\text{tet}}^{7+}}) + \left(3E_{\text{ob}} - \frac{6}{5}\Delta_o + E_{\text{Mn}_{\text{oct}}^{7+}}\right) - \\ &\quad 2\left(4E_{\text{ob}} - \frac{3}{5}\Delta_o - \frac{\alpha}{2} + E_{\text{Mn}_{\text{oct}}^{7+}}\right) \\ \Delta E_{\text{cd}} &= 5(E_{\text{tb}} - E_{\text{ob}}) + \alpha + (E_{\text{Mn}_{\text{tet}}^{7+}} - E_{\text{Mn}_{\text{oct}}^{7+}}) \\ \Delta E_{\text{cd}} &= 5\Delta E_{\text{b}} + \alpha + \Delta E_{\text{Mn}^{7+}} \end{aligned} \quad (6)$$

The change in LFSE of α associated with the charge disproportionation reaction of Mn (Figure 7) is now augmented with two other terms to give a more complete expression for the total energy change: ΔE_{b} , which equals the change in the d barycenter ($E_{\text{tb}} - E_{\text{ob}}$), and $\Delta E_{\text{Mn}^{7+}}$, which equals the change in Mn core interaction energies when Mn moves from an octahedral to a tetrahedral site ($E_{\text{Mn}_{\text{tet}}^{7+}} - E_{\text{Mn}_{\text{oct}}^{7+}}$).

Equation 6 helps clarify why the energy of the charge disproportionation reaction producing tetrahedral Mn in $l\text{-Li}_{1/2}\text{MnO}_2$ is negative. The y intercept of Figure 9 is close to zero, which indicates that $\Delta E_{\text{Mn}^{7+}} \approx 0$ when changing from $l\text{-Li}_{1/2}\text{MnO}_2$ to $(ps\text{-}(\text{LiMn})_{\text{tet}}(\text{LiMn}_3)_{\text{oct}}\text{O}_8)$. Therefore, in this case the energy of charge disproportionation is approximately $\Delta E_{\text{cd}} = 5\Delta E_{\text{b}} + \alpha$. Since α is positive, ΔE_{b} must be negative for the formation of tetrahedral Mn in $l\text{-Li}_{1/2}\text{MnO}_2$ to be energetically favored. In other words, the d-orbital energy barycenter in $ps\text{-}(\text{LiMn})_{\text{tet}}(\text{LiMn}_3)_{\text{oct}}\text{O}_8$ is lower than the barycenter in $l\text{-Li}_{1/2}\text{MnO}_2$ according to this model.

Just as values for Δ_o can be estimated from Figures 9–13 using eqs 3–5, so to can values for ΔE_{b} and $\Delta E_{\text{Mn}^{7+}}$. Whereas Δ_o is estimated to be roughly constant (2.1–2.3 eV) for the MnO_2 host structures (Figures 9–12), the values of ΔE_{b} and $\Delta E_{\text{Mn}^{7+}}$ are estimated to vary much more widely (−0.48 to 0.29 eV and −2.1 to 0.36 eV, respectively). This is consistent with the d-orbital barycenter and the Mn^{7+} core interactions being more sensitive to cationic ordering than the ligand-field splitting, as previously suggested.

Since the LFSE term is determined by Mn valence and appears to be relatively insensitive to cation ordering in the MnO_2 host structures, it would seem to be the easiest energy term to manipulate through chemical substitutions. This is because the exact placement of the chemical substitutions in the Mn sublattice would presumably be less important for the LFSE term than for the terms that are more sensitive to cationic ordering (i.e., ΔE_{b} and $\Delta E_{\text{Mn}^{7+}}$).

9. Qualitative Ionization Scale

The previous sections highlighted the role valence plays in determining Mn site preference and mobility through a ccp oxide framework and consequently in the susceptibility of metastable structures such as $l\text{-Li}_x\text{MnO}_2$ to structural transformation. Since chemical substitutions are one way of manipulating the valence of Mn, it is useful to be able to predict the effect substituted cations will have on the valence of Mn in either tetrahedral or octahedral sites. The large number of calculations used to produce Figures 9–13 can be used to provide a qualitative oxidation/reduction strength of the substituted TM ions that Mn coexists with in Figures 9–13 can be obtained by determining the valence of each cation using the spin integration method described in section 5.

Figure 17 holds in a compact form all of the valence information on crystalline TM oxides produced by the first-principles calculations of this study. The position of a given ion pair (e.g., $\text{Ni}_{\text{oct}}^{3+-4+}$) on the chart

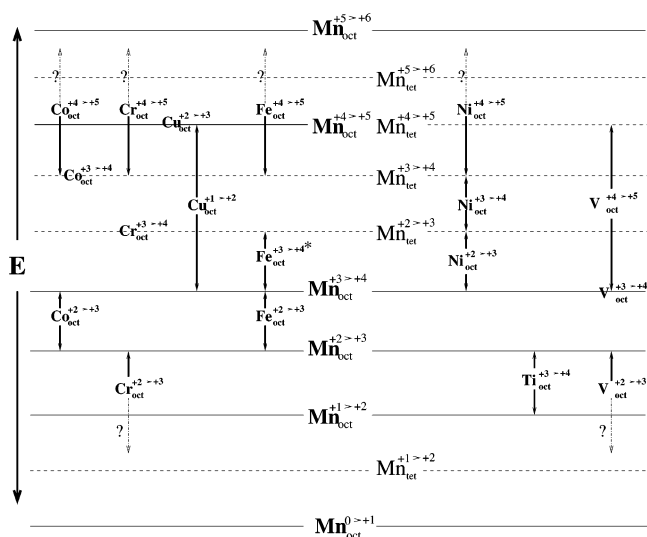


Figure 17. Qualitative ionization energies for 3d ions at various valences in an oxide framework. The position of a given ion pair indicates the energy ranking of that ionization reaction. Comparisons are relative to Mn ionization energies in O_h and T_d coordination labeled prominently in the center of the figure. Solid black arrows indicate well-determined upper and/or lower energy limits for a given ionization energy. Dashed lines with a question mark indicate that in that direction the energy limit was not determined. For example, the ionization energy $\text{Cr}_{\text{oct}}^{2+ \rightarrow 3+}$ is calculated to be lower in energy than $\text{Mn}_{\text{oct}}^{2+ \rightarrow 3+}$ but it is uncertain which Mn ionization energy it lies above. If an ionization energy lies at the same level as one of the Mn energies and does not have an arrow on either side (e.g., $\text{Co}_{\text{oct}}^{3+ \rightarrow 4+}$), that ionization energy and the Mn energy which it is level with were found to be approximately equal in energy (i.e., $\text{Co}_{\text{oct}}^{3+ \rightarrow 4+} \approx \text{Mn}_{\text{tet}}^{3+ \rightarrow 4+}$). The chart entry $\text{Fe}_{\text{oct}}^{3+ \rightarrow 4+}$ marked with an asterisk (*) contradicts the result calculated for anti-spinel $(\text{Mn})_2(\text{Li}_2\text{Fe}_2)\text{O}_8$ but it is consistent with all other calculations performed on $\text{Li}_x(\text{MnFe})\text{O}_2$ structures.

indicates the relative energy ranking of that ionization reaction (e.g., the ionization energy of $\text{Ni}_{\text{oct}}^{3+}$ to $\text{Ni}_{\text{oct}}^{4+}$) compared to the various ionization energies of Mn in octahedral and tetrahedral coordination. The qualitative ranking of the Mn ionization energies in octahedral and tetrahedral coordination is labeled prominently along the center of Figure 17.

The purpose of this scale is to aid in qualitatively predicting the effect of 3d TM ion chemical substitutions on the valence of Mn in octahedral or tetrahedral sites of a ccp oxide. This scale can be useful for choosing chemical substitutions that will keep octahedral Mn in a relatively immobile valence state (i.e., near +4) over the range of an electrochemical cycle where the coexistence of Mn^{3+} and Li vacancies would allow the rapid transformation of a metastable ccp oxide (e.g., as with $I\text{-Li}_x\text{MnO}_2$ or $o\text{-Li}_x\text{MnO}_2$).

To illustrate the use of the qualitative ionization scale given in Figure 17, consider the case of layered $\text{Li}(\text{Ni}_{1/2}\text{Mn}_{1/2})\text{O}_2$.⁵⁸ Assuming that the oxidation states of Li and O are +1 and -2, respectively (calculated to be true except in extremely electron-deficient cases), Ni and Mn must hold an average valence of +3. Moving up from the bottom of the scale one notes $\text{Mn}_{\text{oct}}^{3+ \rightarrow 4+}$ is ranked lower than $\text{Ni}_{\text{oct}}^{2+ \rightarrow 3+}$. This means Mn^{3+} is favored to be oxidized to +4 over Ni^{2+} being oxidized to +3. Since one-half Mn^{4+} and one-

half Ni^{2+} gives an average valence of +3 required by the Li content, the predicted valences are Mn^{4+} and Ni^{2+} . This matches calculated⁴⁰ and experimental results.⁵⁹

Since Figure 17 is constructed only with calculations on Mn oxides substituted with *one* other 3d metal, it is not clear whether using Figure 17 to predict the valence of two or more non-Mn 3d TM ions coexisting in an oxide would be valid. However, with additional calculations on non-Mn TM oxide compositions perhaps Figure 17 can be expanded to address combinations of non-Mn TM ions.

10. Effect of Valence on Site Preference of Other 3d Transition Metals

Since the results of the previous sections indicate that the site preference and tendency toward migration of Mn or Co is strongly affected by the electron occupancy of the d levels split by ligand-field effects, it is possible that this may be the case for all of the 3d TM ions.

The 3d orbitals of Mn and Co and those of the other first-row transition metals should have a qualitatively similar ligand-field splitting in octahedral or tetrahedral sites of an oxide.^{44,45} The magnitude of the splitting may vary as it depends on the extent of overlap between the TM d and oxygen p states.^{46,60} However, as a first approximation it is instructive to neglect this variation in ligand-field splitting across the 3d series and simply characterize a TM ion at a given valence by the number and configuration (e.g., high or low spin) of its d electrons. For example, Fe^{3+} would be expected to behave somewhat similar to Mn^{2+} when both have a high-spin d^5 configuration (e.g., $t_{2g}^3e_g^2$ in octahedral coordination).

The relative energetics of tetrahedral and octahedral occupancy for Mn and Co in a ccp oxide with $\text{Li}_{1/2}\text{MO}_2$ composition was observed to be consistent with the projected change in LFSE for Mn and Co when they are moved from octahedral to tetrahedral coordination (Figure 7; section 6). To test how well this trend holds for other 3d transition metals, calculations equivalent to those done with Mn and Co in section 7 were performed for the transition metals Ti through Cu on the $ps\text{-}(\text{LiM})_{\text{tet}}(\text{LiM}_3)_{\text{oct}}\text{O}_8$ and $I\text{-Li}_{1/2}\text{MO}_2$ ($M \equiv 3d$ TM) structures as well their delithiated counterparts $ps\text{-}(\text{M})_{\text{tet}}(\text{M}_3)_{\text{oct}}\text{O}_8$ and $I\text{-MO}_2$.

Table 2 gives the calculated energy difference ($\Delta E_{\text{oct} \rightarrow \text{tet}}$) between $ps\text{-}(\text{LiM})_{\text{tet}}(\text{LiM}_3)_{\text{oct}}\text{O}_8$ and $I\text{-Li}_{1/2}\text{MO}_2$ for the 3d transition metals from Ti to Cu (ordered lowest $\Delta E_{\text{oct} \rightarrow \text{tet}}$ to highest). It also lists the change in valence and d-orbital filling that accompanies the structural change from $I\text{-Li}_{1/2}\text{MO}_2$ to $ps\text{-}(\text{LiM})_{\text{tet}}(\text{LiM}_3)_{\text{oct}}\text{O}_8$. The valence and d-orbital filling have been determined using spin integration as described in section 5. For each respective change in d-orbital filling that accompanies the formation of tetrahedral M, the projected change in LFSE and spin-pairing energy (SPE) is given. The SPE is important to consider because the splitting from spin pairing (Δ_s) can be of comparable magnitude to the splitting from the ligand field in 3d transition metals (hence the existence of high-spin octahedral cations when $\Delta_s > \Delta_o$).^{50,51} Δ_s is the additional repulsive

Table 2. Energy Differences between $ps\text{-(LiM)}_{\text{tet}}(\text{LiM}_3)_{\text{oct}}\text{O}_8$ and $I\text{-Li}_2\text{M}_4\text{O}_8$ ($M \equiv 3d$ TM) for Each 3d TM from Ti to Cu Listed from Lowest ΔE to Highest^a

reaction	$\Delta E_{\text{oct} \rightarrow \text{tet}}$ (eV)	d filling	Δ LFSE and SPE
$2\text{Mn}_{\text{oct}}^{3+} \rightarrow \text{Mn}_{\text{oct}}^{4+} + \text{Mn}_{\text{tet}}^{2+}$	-0.33	$2t_{2g}^3 e_g^1 \rightarrow t_{2g}^3 + e^2 t_2^3$	α
$4\text{Fe}_{\text{oct}}^{3.5+} \rightarrow \text{Fe}_{\text{tet}}^{3+} + 3\text{Fe}_{\text{oct}}^{3.67+}$	-0.17	$4t_{2g}^{4\frac{1}{2}} \rightarrow e^2 t_2^3 + 3t_{2g}^{4\frac{1}{3}}$	$2\Delta_o - 2\Delta_s$
$\text{Cu}_{\text{oct}} \rightarrow \text{Cu}_{\text{tet}}^b$	-0.15	NA	NA
$4\text{Ti}_{\text{oct}}^{3.5+} \rightarrow \text{Ti}_{\text{tet}}^{4+} + 3\text{Ti}_{\text{oct}}^{3.33+}$	-0.12	$4t_{2g}^{1\frac{1}{2}} \rightarrow e^0 t_2^0 + 3t_{2g}^{2\frac{3}{3}}$	0
$\text{V}_{\text{oct}}^{3.5+} \rightarrow \text{V}_{\text{tet}}^{3.5+}$	0.039	$t_{2g}^{1\frac{1}{2}} \rightarrow e^{1\frac{1}{2}}$	$(3/5)\Delta_o - (9/10)\Delta_t$
$\text{Cr}_{\text{oct}}^{3.5+} \rightarrow \text{Cr}_{\text{tet}}^{3.5+}$	0.30	$t_{2g}^{2\frac{1}{2}} \rightarrow e^2 t_2^{1\frac{1}{2}}$	$\Delta_o - \Delta_t$
$2\text{Ni}_{\text{oct}}^{3+} \rightarrow \text{Ni}_{\text{oct}}^{4+} + \text{Ni}_{\text{tet}}^{2+}$	0.43	$2t_{2g}^6 e_g^1 \rightarrow t_{2g}^6 + e^4 t_2^4$	$(6/5)\Delta_o - (4/5)\Delta_t + \alpha$
$4\text{Co}_{\text{oct}}^{3.5+} \rightarrow 3\text{Co}_{\text{oct}}^{4+} + \text{Co}_{\text{tet}}^{2+}$	0.58	$4t_{2g}^{5\frac{1}{2}} \rightarrow 3t_{2g}^5 + e^4 t_2^3$	$(14/5)\Delta_o - (6/5)\Delta_t - 2\Delta_s$

^a Column 1 gives the valence states accompanying the movement of the TM ion from octahedral to tetrahedral coordination. Column 2 gives the energy difference between $ps\text{-(LiM)}_{\text{tet}}(\text{LiM}_3)_{\text{oct}}\text{O}_8$ and $I\text{-Li}_2\text{M}_4\text{O}_8$ per tetrahedral M. Column 3 holds the change in d -orbital filling that results from moving the TM ion from octahedral to tetrahedral coordination. The projected change in LFSE and spin pairing energy (SPE) that results from the change in d -orbital filling is listed in column 4. This energy is expressed in terms of the octahedral splitting (Δ_o), the tetrahedral splitting (Δ_t), the Jahn–Teller splitting (α), and the spin-pairing splitting (Δ_s). Δ_s is the additional repulsive energy from two electrons of opposing spin occupying the same d orbital. ^b The change in valence/ d filling for Cu could not be determined using the method of section 5.

Table 3. Energy Differences between $ps\text{-(M)}_{\text{tet}}(\text{M}_3)_{\text{oct}}\text{O}_8$ and $I\text{-M}_4\text{O}_8$ ($M \equiv 3d$ TM) for Each 3d TM from Ti to Cu Listed from Lowest ΔE to Highest^a

reaction	$\Delta E_{\text{oct} \rightarrow \text{tet}}$ (eV)	d filling	Δ LFSE and SPE
$\text{Cr}_{\text{oct}}^{4+} \rightarrow \text{Cr}_{\text{tet}}^{4+}$	0.54	$t_{2g}^2 \rightarrow e^2$	$(4/5)\Delta_o - (6/5)\Delta_t$
$\text{V}_{\text{oct}} \rightarrow \text{V}_{\text{tet}}^b$	0.57	NA	NA
$\text{Ti}_{\text{oct}}^{4+} \rightarrow \text{Ti}_{\text{tet}}^{4+}$	0.64	$t_{2g}^0 \rightarrow e^0$	0
$\text{Fe}_{\text{oct}} \rightarrow \text{Fe}_{\text{tet}}^b$	0.76	NA	NA
$\text{Cu}_{\text{oct}} \rightarrow \text{Cu}_{\text{tet}}^b$	1.0	NA	NA
$\text{Co}_{\text{oct}}^{4+} \rightarrow \text{Co}_{\text{tet}}^{4+}$	1.3	$t_{2g}^5 \rightarrow e^2 t_2^3$	$2\Delta_o - 2\Delta_s$
$\text{Mn}_{\text{oct}}^{4+} \rightarrow \text{Mn}_{\text{tet}}^{4+}$	2.1	$t_{2g}^3 \rightarrow e^2 t_2^1$	$(6/5)\Delta_o - (4/5)\Delta_t$
$\text{Ni}_{\text{oct}}^{4+} \rightarrow \text{Ni}_{\text{tet}}^{4+}$	2.6	$t_{2g}^6 \rightarrow e^3 t_2^3$	$(12/5)\Delta_o - (3/5)\Delta_t - 2\Delta_s$

^a Column 1 gives the valence states accompanying the movement of the TM ion from octahedral to tetrahedral coordination. Column 2 gives the energy difference between $ps\text{-(M)}_{\text{tet}}(\text{M}_3)_{\text{oct}}\text{O}_8$ and $I\text{-M}_4\text{O}_8$ per tetrahedral M. Column 3 holds the change in d -orbital filling that results from moving the TM ion from octahedral to tetrahedral coordination. The projected change in LFSE and spin-pairing energy (SPE) that results from the change in d -orbital filling is listed in column 4. This energy is expressed in terms of the octahedral splitting (Δ_o), the tetrahedral splitting (Δ_t), and the spin-pairing splitting (Δ_s). ^b The change in valence/ d filling for Cu, Fe, and V could not be determined using the method of section 5.

energy caused by two electrons of opposing spin occupying the same d orbital. For finding the change in SPE of Tables 2 and 3, Δ_s is assumed to be roughly equal for both octahedrally and tetrahedrally coordinated d orbitals. Table 3 contains the results from calculations on $ps\text{-(M)}_{\text{tet}}(\text{M}_3)_{\text{oct}}\text{O}_8$ and $I\text{-MO}_2$ for the 3d transition metals from Ti to Cu (ordered lowest $\Delta E_{\text{oct} \rightarrow \text{tet}}$ to highest).

Each 3d metal from Ti to Cu in Table 2 and 3 will now be discussed.

10.1. Ti

Ti is calculated to have a delocalized d band in $I\text{-Li}_{1/2}\text{TiO}_2$. This is reflected by each Ti holding a +3.5 charge. In $I\text{-TiO}_2$, Ti is calculated to have an empty d band and a +4 valence. At both Li concentrations the tetrahedral Ti is +4 and the projected change in LFSE and SPE for Ti moving from octahedral to tetrahedral coordination is zero. This is consistent with Ti having a relatively low calculated value for $\Delta E_{\text{oct} \rightarrow \text{tet}}$ (fourth lowest in Table 2 and third lowest in Table 3).

However, the fact that $\Delta E_{\text{oct} \rightarrow \text{tet}}$ for Ti is higher than Mn and Fe in Table 2 and higher than Cr in Table 3 runs contrary to expectations based solely on LFSE and SPE since Mn and Fe at $X_{\text{Li}} = 1/2$ and Cr at $X_{\text{Li}} = 0$ have a projected change in LFSE and SPE that is greater than zero.

If $I\text{-Li}_x\text{TiO}_2$ could be synthesized, the negative value of $\Delta E_{\text{oct} \rightarrow \text{tet}}$ for $\text{Li}_{1/2}\text{TiO}_2$ (-0.12 eV) suggests that Ti

in a layered structure could be susceptible to migration into the Li layer at partial lithiation. Experimentally layered LiTiO_2 has not been synthesized as the similar ionic size between Li and Ti leads to a disordered rock-salt structure.⁶¹ Layered $\text{Li}(\text{Ni}_{0.45}\text{Ti}_{0.55})\text{O}_2$ has been synthesized; however, it suffers from poor cyclability which is blamed on Ti migration into the Li/vacancy layer.⁶² Additionally, Ti has been reported to migrate into the Na layer of layered NaTiO_2 .⁶³ These experimental observations are consistent with the relative ease Ti^{4+} is expected to have in moving between octahedral and tetrahedral coordination due to a lack of ligand-field stabilization.

10.2. V

At $X_{\text{Li}} = 1/2$, V is calculated to maintain the same valence (+3.5) in octahedral and tetrahedral coordination, i.e., there is no charge disproportionation in forming tetrahedral V at this Li composition (Table 2). The projected change in LFSE and SPE at $X_{\text{Li}} = 1/2$ is $(3/5)\Delta_o - (9/10)\Delta_t$, which is positive whether the proportionality given by crystal-field theory $|4/9\Delta_o| = |\Delta_t|$ is assumed⁴⁶ or if $\Delta_t \approx 0$ is assumed as the results in section 8 suggest for Mn. The greater change in LFSE and SPE for $\text{Li}_{1/2}\text{VO}_2$ than for $\text{Li}_{1/2}\text{TiO}_2$ is consistent with a greater value of $\Delta E_{\text{oct} \rightarrow \text{tet}}$ in Table 2. This suggests that V should be less prone than Ti to enter tetrahedral sites at this average valence, and hence $I\text{-Li}_{1/2}\text{VO}_2$ should be more resistant against transformation than $I\text{-Li}_{1/2}\text{TiO}_2$. How-

ever, $\Delta E_{\text{oct} \rightarrow \text{tet}}$ is still relatively small (0.039 eV/ V_{tet}), suggesting that V might still easily migrate out of metastable octahedral sites at this composition.

The value of $\Delta E_{\text{oct} \rightarrow \text{tet}}$ for VO_2 was calculated to be the second lowest in Table 3. Unfortunately the valences of V in $ps\text{-(M)}_{\text{tet}}(\text{M}_3)_{\text{oct}}\text{O}_8$ could not be clearly determined using the spin integration method of section 5 because the net spin on the V did not match a spin-polarized configuration consistent with the average formal oxidation state. Instead, the V took on a non-spin-polarized state.

10.3. Cr

Like V, Cr is calculated to maintain a +3.5 oxidation state in both octahedral and tetrahedral coordination at $X_{\text{Li}} = 1/2$ (Table 2). At this lithium concentration the projected change in LFSE and SPE is higher for Cr than for V, which is consistent with the greater value of $\Delta E_{\text{oct} \rightarrow \text{tet}}$ calculated for Cr in Table 2. This supports Cr having a stronger preference for octahedral sites at the +3.5 valence than V. At +4 valence Cr was calculated to have the lowest $\Delta E_{\text{oct} \rightarrow \text{tet}}$ in Table 3. This is consistent with the relatively low projected change in LFSE and SPE for Cr^{4+} moving from octahedral to tetrahedral coordination ($(4/5)\Delta_o - (6/5)\Delta_t$).

The enhanced stability of $I\text{-Li}_x(\text{Cr}_{1/2}\text{Mn}_{1/2})\text{O}_2$ reported experimentally can be explained by these results.⁵³ As $I\text{-Li}(\text{Cr}_{1/2}\text{Mn}_{1/2})\text{O}_2$ is delithiated, the Mn is oxidized to +4 first according to section 9 and experiment.⁵⁵ As already discussed, Mn^{4+} is highly stable in octahedral coordination. Cr is oxidized to +4 later in the charge, when Li vacancies that can facilitate TM ion migration are more plentiful. The relatively high value of $\Delta E_{\text{oct} \rightarrow \text{tet}}$ calculated for $\text{Cr}^{3.5+}$ in Table 2 probably reflects a strong preference for octahedral coordination at this valence. One would expect Cr to have an even stronger preference for octahedral coordination in $I\text{-Li}_{1/2}(\text{Cr}_{1/2}\text{Mn}_{1/2})\text{O}_2$ since its valence is +3 which has a t_{2g}^3 orbital filling—the same orbital filling as Mn^{4+} .

While Cr^{4+} has the lowest $\Delta E_{\text{oct} \rightarrow \text{tet}}$ in Table 3 and relatively weak ligand-field stabilization, the absolute value of $\Delta E_{\text{oct} \rightarrow \text{tet}}$ (0.54 eV) for CrO_2 is still higher than that for $\text{Li}_{1/2}\text{CrO}_2$ (0.3 eV). Furthermore, there probably is no longer a driving force to convert to spinel in highly delithiated $I\text{-Li}_x(\text{Cr}_{1/2}\text{Mn}_{1/2})\text{O}_2$. The fact that the structural integrity of $I\text{-Li}_x(\text{Cr}_{1/2}\text{Mn}_{1/2})\text{O}_2$ is maintained over delithiation attests to a relatively strong octahedral site preference exhibited by Cr at partial lithiation.

It has been observed that when Cr^{6+} is formed in delithiated $I\text{-Li}(\text{Li}_{1/5}\text{Mn}_{2/5}\text{Cr}_{2/5})\text{O}_2$, it spontaneously moves into tetrahedral coordination.⁵⁵ This is consistent with the lack of d electrons for Cr^{6+} and hence the lack of ligand-field stabilization.

10.4. Mn

Mn goes from having the lowest $\Delta E_{\text{oct} \rightarrow \text{tet}}$ at $X_{\text{Li}} = 0.5$ (Table 2) to the second highest $\Delta E_{\text{oct} \rightarrow \text{tet}}$ at $X_{\text{Li}} = 0$ (Table 3). The low value of $\Delta E_{\text{oct} \rightarrow \text{tet}}$ for Mn at $X_{\text{Li}} = 0.5$ is consistent with a relatively small projected

change in LFSE and SPE equal to the Jahn–Teller splitting (α).^{47,48}

As mentioned before, the fact that $\Delta E_{\text{oct} \rightarrow \text{tet}}$ is lower for Mn than for Ti despite α being greater than zero runs contrary to expectations based solely on LFSE. According to the simple model of eqs 3–5 in section 8.1, the low energy of $ps\text{-(LiMn)}_{\text{tet}}(\text{LiMn}_3)_{\text{oct}}\text{O}_8$ compared to $I\text{-Li}_{1/2}\text{MnO}_2$ can be explained by a lower d barycenter in $ps\text{-(LiMn)}_{\text{tet}}(\text{LiMn}_3)_{\text{oct}}\text{O}_8$ (eq 6). The d electrons of the tetrahedral Mn^{2+} enter d orbitals that are shifted lower in energy, probably because they are surrounded by less negative charge in a tetrahedral site than in an octahedral one. Ti^{4+} , on the other hand does not have any d electrons, so there is no energy reduction resulting from a lower tetrahedral d barycenter.

Another factor that could make $\Delta E_{\text{oct} \rightarrow \text{tet}}$ particularly low for Mn in Table 2 is the half-full orbital shells of Mn^{2+} and Mn^{4+} (the products of Mn^{3+} charge disproportionation). In general, half-full or full orbital shells have lower energy than other fillings because the electron–electron repulsion is decreased⁶⁴ (this is why in the chemistry of low atomic number elements the electrons arrange so often to produce full “octets”). On this basis one expects Mn^{2+} to have a lower electron–electron repulsion energy due to its half-full d shell⁶⁴ ($e^2t_2^3$ in tetrahedral coordination). It is also favorable for the levels that result from ligand-field splitting to be half-full or full.⁵⁰ Therefore, the half-full t_{2g} level (t_{2g}^3) of Mn^{4+} is favorable in this regard as well. The energetic favorability of half-filled levels is another reason Mn^{3+} in many environments is observed to be unstable to both reduction to Mn^{2+} and oxidation to Mn^{4+} .⁵²

10.5. Fe

At $X_{\text{Li}} = 0.5$ there is a large positive change in LFSE ($2\Delta_o$) for the formation of tetrahedral Fe. However, this is counteracted by a large negative change in spin-pairing energy ($-2\Delta_s$). The decrease in spin-pairing energy is caused by one of the low-spin $\text{Fe}_{\text{oct}}^{2/3+}$ becoming high-spin $\text{Fe}_{\text{tet}}^{3+}$. Recalling that Δ_s can be comparable in magnitude to Δ_o in 3d metal oxides,^{50,51} the net change in LFSE and SPE given for Fe in Table 2 is probably small. This is consistent with the negative value calculated for $\Delta E_{\text{oct} \rightarrow \text{tet}}$ (-0.17 eV/Fe tet). However, the net change in LFSE and SPE should still have a positive value since Fe is calculated to be low spin in octahedral coordination ($t_{2g}^{4.5}$ or $t_{2g}^{4.33}$), indicating that $|\Delta_s| < |\Delta_o|$.

$I\text{-LiFeO}_2$ has been synthesized by ion exchange from NaFeO_2 , but it shows little or no electrochemical activity.⁶⁵ It was not reported whether this is a result of Fe^{3+} migration; however, the results of Table 2 suggest that Fe should be susceptible to migration out of the TM layer at partial lithiation in $I\text{-Li}_x\text{FeO}_2$.

At $X_{\text{Li}} = 0$ Fe was found to be of intermediate stability in octahedral coordination. Unfortunately the valences of the Fe ions could not be clearly determined using the spin integration method of section 5 because the net spin on the Fe did not match a high-spin or low-spin configuration consistent with the average formal oxidation state (+4). This suggests that the d-orbital filling takes on an

intermediate spin configuration for Fe and/or the assumed oxygen formal oxidation state of -2 is no longer justified due to strong covalency between the Fe and O.

10.6. Co

Co has the highest value of $\Delta E_{\text{oct} \rightarrow \text{tet}}$ in Table 2. This is consistent with it having the largest projected change in LFSE ($(14/5)\Delta_o - (6/5)\Delta_t$). However, the change in LFSE is somewhat counteracted by a negative change in spin-pairing energy ($-2\Delta_s$). The spin-pairing energy is reduced in the charge disproportionation of Co where four d fillings of $t_{2g}^{5.5}$ change to three t_{2g}^5 and $e_g^4 t_{2g}^3$. This helps explain why $\Delta E_{\text{oct} \rightarrow \text{tet}}$ calculated for Co is not as high compared to the other 3d metals as one would expect on the basis of LFSE alone.

At $X_{\text{Li}} = 0$ Co has the third highest $\Delta E_{\text{oct} \rightarrow \text{tet}}$. Its change in LFSE and SPE is $2\Delta_o - 2\Delta_s$ and the same as Fe at $X_{\text{Li}} = 0.5$, which has a low $\Delta E_{\text{oct} \rightarrow \text{tet}}$. A possible explanation for this is that the magnitude of Δ_o is higher and/or the magnitude of Δ_s is lower for Co^{4+} than for $\text{Fe}^{3.5+}$.

The remarkable success of LiCoO_2 as an electrode material is likely related to the strong intrinsic preference of Co for octahedral sites over the $+3$ to $+4$ valences as indicated by the high calculated value of $\Delta E_{\text{oct} \rightarrow \text{tet}}$ in Tables 2 and 3. This strong preference of Co for octahedral sites clearly suggests that Co will not easily migrate through an close-packed oxygen framework at these oxidation states.

10.7. Ni

Ni is calculated to have the second highest $\Delta E_{\text{oct} \rightarrow \text{tet}}$ at $X_{\text{Li}} = 0.5$ and the highest $\Delta E_{\text{oct} \rightarrow \text{tet}}$ at $X_{\text{Li}} = 0$. At $X_{\text{Li}} = 0.5$, Ni is calculated to undergo a charge disproportionation reaction (eq 1) similar to Mn and Co. The projected change in LFSE and SPE is higher for Ni than Cr, which is consistent with the higher value of $\Delta E_{\text{oct} \rightarrow \text{tet}}$ calculated for Ni than Cr in Table 2. On the basis of these calculations, Ni is expected to be the second most stable in octahedral sites at an average valence of $+3.5$ of the 3d metals from Ti to Cu.

The high value of $\Delta E_{\text{oct} \rightarrow \text{tet}}$ calculated for Ni at $X_{\text{Li}} = 0$ is consistent with the large projected change in LFSE ($12/5\Delta_o - 3/5\Delta_t$). However, as with $\text{Co}^{3.5+}$, the change in LFSE is somewhat counteracted by a negative change in spin-pairing energy ($-2\Delta_s$), which helps explain why $\Delta E_{\text{oct} \rightarrow \text{tet}}$ calculated for Ni^{4+} is not as high compared to the other 3d metals as one would expect on the basis of LFSE alone.

The calculated stability of Ni in octahedral coordination is consistent with the good electrochemical performance observed experimentally for $\text{Li}(\text{MnNi})\text{O}_2$ compounds. The Ni^{2+} oxidizes Mn to $+4$, which as already discussed has a strong preference for octahedral sites. When the average valence of Ni is between $+3$ and $+4$, there is a high concentration of Li vacancies that would facilitate ion migration, except for the strong preference of Ni for octahedral sites over this valence range. Ni^{2+} also most likely has a strong preference for octahedral coordination

due to ligand-field effects, although probably not as strong as Ni^{3+} since there is an additional electron in the e_g level.

10.8. Cu

At an average formal valence of $+3.5$, Cu is calculated to have the third lowest $\Delta E_{\text{oct} \rightarrow \text{tet}}$ equal to -0.15 eV per tetrahedral Cu. This suggests that Cu at this average valence does not have a strong preference for octahedral sites. At an average formal valence of $+4$, $\Delta E_{\text{oct} \rightarrow \text{tet}}$ for Cu (1 eV) is ranked fourth highest in Table 3. In practice, such high oxidation states for Cu are probably difficult to achieve. However, if it were to occur, a metastable structure like Li_xCuO_2 should be prone to transformation at partial lithiation according to these results. Unfortunately, the valence of Cu in both cases could not be clearly determined using the spin integration method of section 5.

10.11. Overall Trends for 3d Metals

The energy of all the 3d metals entering tetrahedral coordination from the Li_xMO_2 structure decreases as X_{Li} goes from 0 to $1/2$. This is similar to the defect calculations on Co and Mn in section 4 that found tetrahedral defect energies in the layered structure to decrease for both as Li content increases from 0 to $1/2$.

At $X_{\text{Li}} = 0.5$, three of the eight TM ions (Mn, Co, and Ni) were found to undergo a major charge disproportionation reaction (eq 1) when moved from octahedral to tetrahedral coordination. In contrast, at $X_{\text{Li}} = 0$ none were found to undergo charge disproportionation.

Table 2 shows a good correlation between the relative energetics of octahedral and tetrahedral site occupancy by a 3d metal ion and the projected change in LFSE for moving a 3d metal ion from octahedral to tetrahedral coordination. From rows 4 (Ti) to 8 (Co) in Table 2 the correlation is perfect; the value calculated for $\Delta E_{\text{oct} \rightarrow \text{tet}}$ increases along with the projected change in LFSE (from 0 for Ti to $(14/5)\Delta_o - (6/5)\Delta_t$ for Co).

The two deviations from this trend are Mn and Fe, which have the two most negative values for $\Delta E_{\text{oct} \rightarrow \text{tet}}$. Both of these cases probably have relatively small net changes in LFSE and SPE, which is consistent with a more general association between low values of $\Delta E_{\text{oct} \rightarrow \text{tet}}$ and low projected changes in LFSE and SPE. The case of Fe illustrates that focusing exclusively on LFSE can be misleading when spin pairing is present, especially in low-spin cations.

Table 3 also shows a good correlation between $\Delta E_{\text{oct} \rightarrow \text{tet}}$ and the projected change in LFSE, with the largest changes in LFSE being associated with the highest values of $\Delta E_{\text{oct} \rightarrow \text{tet}}$.

The results given in Tables 2 and 3 support the decisive role of LFSE in the site preference and most likely the mobility of 3d metal ions in a ccp lattice. For Mn, Ni, and Co the results in Table 2 are consistent with the experimental work of Choi, Manthiram et al. who found increasing resistance of Li_xMO_2 against transformation into spinel as M is

changed from Mn to Ni to Co.⁴⁹ Table 2 shows that $\Delta E_{\text{oct} \rightarrow \text{tet}}$ and the projected change in LFSE and SPE for Ni fall between those values for Mn and Co; this agrees with the observed intermediate stability of $I\text{-Li}_x\text{NiO}_2$ compared to $I\text{-Li}_x\text{MnO}_2$ and $I\text{-Li}_x\text{CoO}_2$.

11. Conclusions

For phase transformations involving rearrangement of transition-metal cations over octahedral sites within a fixed ccp oxide framework, such as the transformation of layered Li_xMnO_2 to spinel, the results of this study indicate that the low-energy pathway for transition-metal migration between octahedral sites is through a shared nearest neighbor tetrahedral site (i.e., $O_h \rightarrow T_d \rightarrow O_h$) rather than directly between octahedral sites ($O_h \rightarrow O_h$). This suggests that the smaller the energy change is for transition-metal ion movement between octahedral and tetrahedral coordination, the more easily the TM ions should be able to rearrange in a ccp oxide when transforming from a metastable structure to a stable one. As a result, the resistance against transformation of metastable transition-metal oxides with a ccp oxygen sublattice (e.g., Li_xMnO_2 with $\alpha\text{-NaFeO}_2$ structure) will depend on the relative stability of the transition metal in octahedral coordination compared to tetrahedral coordination. The availability of empty tetrahedra without any cations occupying nearest neighbor face-sharing octahedra is also an important factor in the ability of TM ions to migrate through a ccp oxide. Such tetrahedra provide a relatively low-energy pathway by avoiding the highly repulsive interaction between face-sharing cations.

The energetics of Mn movement between octahedral and tetrahedral sites is found to be particularly sensitive to valence. Of the 3d transition metals from Ti to Cu, Mn is calculated to be the second most stable in octahedral coordination at +4 valence and the least stable at +3 valence. This appears to result from a large difference in ligand-field stabilization between the +4 to +3 states of charge for Mn. The most unfavorable change in LFSE associated with Mn movement from octahedral to tetrahedral coordination occurs when Mn is +4 with three spin-polarized d electrons occupying a half-filled t_{2g} shell in octahedral coordination. In contrast, $\text{Mn}_{\text{oct}}^{3+}$ ($t_{2g}^3 e_g^1$) is calculated to undergo a charge disproportionation reaction (eq 1), forming $\text{Mn}_{\text{tet}}^{2+}$ ($e^2 t_2^3$) and $\text{Mn}_{\text{oct}}^{4+}$ (t_{2g}^3), which allows Mn^{2+} movement into tetrahedral coordination with a relatively low change in LFSE.

The low-energy passage of Mn through tetrahedral sites enabled by $\text{Mn}_{\text{oct}}^{3+}$ charge disproportionation appears to underlie the instability of metastable ccp Mn oxides such as the layered $\alpha\text{-NaFeO}_2$ and orthorhombic structures with electrochemical cycling. In both of these structures $\text{Mn}_{\text{oct}}^{3+}$, which can charge disproportionate, and Li vacancies, which facilitate Mn migration by providing empty tetrahedral sites without face-sharing cations, coexist over the Li concentration range where these structures are not thermodynamically stable.

Spinel-like $\text{Li}_x\text{Mn}_2\text{O}_4$, on the other hand, maintains its structural integrity, even when it is not thermodynamically stable at high and low lithium content.

This is probably because significant amounts of Mn^{3+} and Li vacancies do not coexist over ranges of Li concentration where the spinel-like structure is metastable. At low lithium concentrations the Mn are primarily in the +4 oxidation state and consequently have relatively low mobility. At high Li content ($x \approx 2$ in $\text{Li}_x\text{Mn}_2\text{O}_4$) there are insufficient Li vacancies to allow easy Mn rearrangement. When substantial concentrations of Mn^{3+} and Li vacancies coexist in $s\text{-LiMn}_2\text{O}_4$, the spinel structure is thermodynamically stable and hence not adversely effected by the increased mobility of Mn. However, there still is the problem of Mn dissolution into the electrolyte through Mn^{3+} charge disproportionation.

LFSE also appears to be a decisive factor in the site preference of other 3d TM ions in a ccp oxide. As with Mn, this should impact the resistance of other metastable 3d TM oxides against transformation. The resistance against transformation imparted by ligand-field effects appears to be epitomized in the case of layered Li_xCoO_2 . Contrary to the case with Mn, the change in LFSE associated with Co movement from octahedral to tetrahedral coordination is highly unfavorable in $\text{Li}_{1/2}\text{CoO}_2$. This provides impressive stability for layered Li_xCoO_2 with electrochemical cycling over Li concentrations where the spinel structure is thermodynamically stable (e.g., $\text{Li}_{1/2}\text{CoO}_2$).

The results of this investigation lead to the prediction that, in general, metastable Mn oxide structures with a ccp oxygen sublattice will rapidly transform to stable ccp structures if Mn^{3+} and/or Mn^{2+} coexist with sufficient vacant interstitial sites. This is due to the lack of ligand-field stabilization for $\text{Mn}_{\text{oct}}^{2+}$ and the susceptibility of $\text{Mn}_{\text{oct}}^{3+}$ to charge disproportionation, which results in low ligand-field stabilization. This in turn makes tetrahedral sites relatively accessible to Mn, which facilitates cationic rearrangement.

The energy difference between oxide structures with and without Mn in tetrahedral coordination can be fitted reasonably well to a simple model in which the energy difference is broken down into two contributions. One contribution is independent of Mn d-orbital filling and hence Mn valence. It accounts for the change in interaction energy between a Mn^{7+} (i.e., d^0) ionic core and the surrounding cations as a Mn moves from an octahedral to a tetrahedral site. The other energy contribution is from the changing energy of the filled d orbitals as Mn is moved from octahedral to tetrahedral coordination. The latter energy contribution varies in a piecewise linear fashion with Mn valence and has a peak at Mn^{4+} , reflecting the ligand-field splitting of octahedrally and tetrahedrally coordinated d orbitals.

The energy contribution from the changing Mn d orbitals as Mn moves from octahedral to tetrahedral coordination can in turn be separated into the change of the Mn d-orbital energy barycenter and the change in ligand-field stabilization energy. While the change in LFSE is determined by the Mn valence, the d-orbital barycenter and the energy of interactions involving the Mn^{7+} ionic cores are found to be much more sensitive to cationic ordering.

Using ionic valences found through a large series of calculations on substituted Mn oxides, a qualitative ionization scale between Mn and other 3d metals has been constructed. This scale allows one to predict the valences for Mn (in octahedral and/or tetrahedral coordination) coexisting with another 3d TM cation (in octahedral coordination) in a ccp oxide. This could be useful for designing TM oxide materials with improved kinetic stability over the range of Li concentrations covered by electrochemical cycling.

The findings of this study point to a number of different strategies for producing lithium manganese oxide structures, other than spinel, that resist transformation with electrochemical cycling. If a metastable ccp oxide structure such as β - Li_xMnO_2 or α - Li_xMnO_2 ($X_{\text{Li}} < 1$) is used, high concentrations of $\text{Mn}_{\text{oct}}^{3+}$ and Li vacancies should be prevented from coexisting over regions of metastability. This can be accomplished by chemically substituting for Mn with low fixed valence and/or electronegative multivalent cations that can oxidize the Mn e_g orbital. There are many different examples of this approach that have had some success experimentally.^{7,18,53–55} Another way of oxidizing the Mn e_g orbital is to introduce vacancies into the Mn sublattice.⁶⁶

Given that Mn^{4+} is the most stable valence in octahedral coordination, it might be desirable for Mn to be electrochemically cycled between elevated oxidation states centered closer to +4 rather than over the +3/+4 redox range characteristic of Li_xMnO_2 structures. Unfortunately at this time there probably are not any electrolytes that can withstand the oxidative strength of Mn at valences higher than +4.⁶⁷ An additional problem with Mn charged above +4 in ccp oxides is the possibility of decomposition reactions producing O_2 .^{58,68}

Another strategy is to use a structure with an oxygen sublattice that is different from that of spinel (i.e., non-ccp). For such a structure to transform into spinel the oxygen needs to rearrange, which should make the transformation much more difficult.

One way this has been accomplished experimentally is by using a close-packed oxide structure that is not cubic-close packed.^{69,70} Such structures may be more resistant against transformation to spinel, but there still is a network of octahedral and tetrahedral sites that could possibly allow undesirable Mn movement during electrochemical cycling. The phospholivine structure is an example of a non-ccp oxide that has shown good reversible capacity with iron (LiFePO_4) however not with Mn (although Mn combined with Fe is reported to perform well).⁷¹ Oxides containing polyanions such as PO_4^{-3} offer a rich diversity of structures that might be suitable for use in a positive electrode.⁷²

Another option is to use a non-close-packed structure. A more open structure can constrain Mn by eliminating energetically favorable sites it can migrate through (e.g., tetrahedral sites). A layered structure can be made less close packed by pillaring open the Li/vacancy layer with a large cation like K^+ or with a cluster of atoms.⁷³ The tunneled Mn oxides are another example of non-close-packed structures. Good cyclability and resistance against transforma-

tion to spinel has been achieved by Doeff et al. using such a structure.^{74,75}

12. Acknowledgments

This research was supported in part by the MRSEC Program of the National Science Foundation under award number DMR-02-13282 and by the Assistant Secretary for Energy Efficiency and Renewable Energy, Office of Freedom CAR and Vehicle Technologies, of the U.S. Department of Energy under Contract No. DE-AC03-76SF00098, Subcontract No. 6517748 with the Lawrence Berkeley National Laboratory. Methodological developments that made this work possible have been supported by the Department of Energy under contract number DE-FG02-96ER45571. NPACI is acknowledged for providing substantial computing resources for this work. G.C. acknowledges a faculty development chair from R. P. Simmons.

13. References

- (1) Mizushima, K.; Jones, P. C.; Wiseman, P. J. *Solid State Ionics* **1981**, 3–4 (Aug), 171.
- (2) Thackeray, M. *Prog. Solid State Chem.* **1997**, 25, 1.
- (3) Winter, M.; Besenhard, J.; Spahr, M.; Novak, P. *Adv. Mater.* **1998**, 10, 725.
- (4) Bruce, P. *Chem. Commun.* **1997**, 1817.
- (5) Armstrong, A. R.; Bruce, P. G. *Nature* **1996**, 381, 499.
- (6) Capitaine, F.; Gravereau, P.; Delmas, C. *Solid State Ionics Diffusion React.* **1996**, 89, 197.
- (7) Armstrong, A.; Robertson, A.; Bruce, P. *Electrochem. Acta* **1999**, 45, 285.
- (8) Bruce, P.; Armstrong, A.; Gitzendanner, R. *J. Mater. Chem.* **1999**, 193.
- (9) Shao-Horn, Y.; Hackney, S. A.; Armstrong, A. R.; Bruce, P. G.; Gitzendanner, R.; Johnson, C. S.; Thackeray, M. M. *J. Electrochem. Soc.* **1999**, 146, 2404.
- (10) Armstrong, A.; Robertson, A.; Gitzendanner, R.; Bruce, P. *J. Solid State Chem.* **1999**, 145, 549.
- (11) Broussely, M.; Biensan, P.; Simon, B. *Electrochem. Acta* **1999**, 45, 3.
- (12) Van der Ven, A.; Ceder, G. *Phys. Rev. B* **1999**, 59 (2), 742.
- (13) Ceder, G.; Van der Ven, A. *Electrochem. Acta* **1999**, 45 (1–2), 13150.
- (14) Blyr, A.; Sigala, C.; Amatucci, G.; Guyomard, D.; Chabre, Y. *J. Electrochem. Soc.* **1998**, 145, 194.
- (15) Chiang, Y.-M.; Sadoway, D. R.; Jang, Y. I.; Huang, B.; Wang, H. *Electrochem. Solid State Lett.* **2** **1999**, 3, 107.
- (16) Vitins, G.; West, K. *J. Electrochem. Soc.* **1997**, 144, 2587.
- (17) Chiang, Y.-M.; Wang, H.; Jang, Y. *Chem. Mater.* **2001**, 13, 53.
- (18) Wang, H.; Jang, Y.; Chiang, Y.-M. *Electrochem. Solid State Lett.* **1999**, 2 (10), 490.
- (19) Hunter, J. C. *J. Solid State Chem.* **1981**, 39, 142.
- (20) David, W. I. F.; Thackeray, M. M.; Bruce, P. G.; Goodenough, J. B. *Mater. Res. Bull.* **1984**, 19, 99.
- (21) Wang, H.; Jang, Y.-I.; Huang, B.; Sadoway, D. R.; Chiang, Y.-M. *J. Electrochem. Soc.* **1999**, 146, 473.
- (22) Gabrisch, H.; Yazami, R.; Fultz, B. *J. Power Sources* **2003**, 119, 674.
- (23) Van der Ven, A.; Ceder, G. *Electrochem. Solid State Lett.* **2000**, 3 (7).
- (24) Reed, J. Ab Initio Study of Cathode Materials for Lithium Batteries. Ph.D. Thesis, M.I.T., 2003; p 65.
- (25) Parr, R. G.; Yang, W. *Density-Functional Theory of Atoms and Molecules*; Oxford University Press: New York, 1989; pp 51–52.
- (26) Parr, R. G.; Yang, W. *Density-Functional Theory of Atoms and Molecules*; Oxford University Press: New York, 1989; pp 142–145.
- (27) Ohno, K.; Esfarjani, K.; Kawazoe, Y. *Computational Materials Science*; Springer-Verlag: Berlin, Heidelberg, 1999; pp 21–25.
- (28) Mishra, S. K.; Ceder, G. *Phys. Rev. B* **1999**, 59, 6120.
- (29) Van der Ven, A.; Aydinol, M. K.; Ceder, G. *J. Electrochem. Soc.* **1998**, 145 (6), 2149.
- (30) Kresse, G.; Furthmüller, J. *Phys. Rev. B* **1996**, 54 (11), 169.
- (31) Parr, R. G.; Yang, W. *Density-Functional Theory of Atoms and Molecules*; Oxford University Press: New York, 1989; pp 153 and 154.

- (32) Ohno, K.; Esfarjani, K.; Kawazoe, Y.; *Computational Materials Science*; Springer-Verlag: Berlin, Heidelberg, 1999; pp 106 and 107.
- (33) Vanderbilt, D. *Phys. Rev. B* **1990**, *41*, 7892.
- (34) Mizushima, K.; Jones, P. C.; Wiseman, P. J.; Goodenough, J. B. *Mater. Res. Bull.* **1980**, *15*, 783.
- (35) Orman, H. J.; Wiseman, P. J. *Acta Crystallogr., Sect. C* **1984**, *139*, 12.
- (36) Ceder, G.; Van der Ven, A. *Electrochim. Acta* **1999**, *45*, 131.
- (37) Wolverton, C.; Zunger, A. *J. Electrochem. Soc.* **1998**, *145*, 2424.
- (38) Gummow, R.; Liles, D. C.; Thackeray, M. M. *Mater. Res. Bull.* **1993**, *28*, 1249.
- (39) Reed, J.; Ceder, G.; Van der Ven, A. *Electrochem. Solid State Lett.* **2001**, *4* (6), A78.
- (40) Reed, J.; Ceder, G. *Electrochem. Solid State Lett.* **2002**, *5* (7), A145.
- (41) Borg, R. J.; Dienes, G. J. *The Physical Chemistry of Solids*; Academic Press: New York, 1992; pp 148–152.
- (42) Burns, R. G. *Mineralogical Applications of Crystal Field Theory*; Cambridge University Press: New York, 1970, 1993; p 464.
- (43) Goodenough, J. B.; Loeb, A. L. *Phys. Rev.* **1955**, *198*, 391.
- (44) Figgis, B. N.; Hitchman, M. A. *Mineralogical Applications of Crystal Field Theory*; Wiley-VCH: New York, 2000; p 116.
- (45) Burns, R. G. *Mineralogical Applications of Crystal Field Theory*; Cambridge University Press: New York, 1970, 1993; p 17.
- (46) Burns, R. G. *Mineralogical Applications of Crystal Field Theory*; Cambridge University Press: New York, 1970, 1993; p 22.
- (47) Burns, R. G. *Mineralogical Applications of Crystal Field Theory*; Cambridge University Press: New York, 1970, 1993; p 231.
- (48) Burns, R. G. *Mineralogical Applications of Crystal Field Theory*; Cambridge University Press: New York, 1970, 1993; p 231.
- (49) Choi, S.; Manthiram, S. *J. Electrochem. Soc.* **2002**, *149* (9), A1157.
- (50) Figgis, B. N.; Hitchman, M. A. *Mineralogical Applications of Crystal Field Theory*; Wiley-VCH: New York, 2000; pp 166–177.
- (51) Burns, R. G. *Mineralogical Applications of Crystal Field Theory*; Cambridge University Press: New York, 1970, 1993; p 433.
- (52) Burns, R. G. *Mineralogical Applications of Crystal Field Theory*; Cambridge University Press: New York, 1970, 1993; p 18.
- (53) Davidson, I. J.; McMillan, R. S.; Slego, J.; Luan, B.; Kargina, I.; Murray, J. J.; Swinson, I. P. *J. Power Sources* **1999**, *81–82*, 406.
- (54) Rossen; Jones, C. D. W.; Dahn, J. R. *Solid State Ionics* **1992**, *57*, 311.
- (55) Ammundsen, B.; Paulsen, J. *Adv. Mater.* **2001**, *13*, 943.
- (56) Ammundsen, B.; Desilvestro, J.; Groutso, T.; Hassell, D.; Metson, J. B.; Regan, E.; Steiner, R.; Pickering, P. J. *J. Electrochem. Soc.* **2000**, *147*, 4078.
- (57) de Groot, F. M. F.; Grioni, M.; Fuggle, J. C.; Ghislen, J.; Sawatzky, G. A.; Petersen, H. *Phys. Rev. B* **1989**, *40*, 5715.
- (58) Lu, Z.; Dahn, J. R. *J. Electrochem. Soc.* **2002**, *149* (7) A815.
- (59) Park, H.-S.; Hwang, S.-J.; Choy, J.-H. *J. Phys. Chem. B* **2001**, *105*, 4860.
- (60) Burns, R. G. *Mineralogical Applications of Crystal Field Theory*; Cambridge University Press: New York, 1970, 1993; p 436.
- (61) Chang, S. H.; Kang, S. G.; Song, S. W.; Yoon, J. B.; Choy, J. H. *Solid State Ionics* **1996**, *86–88*, 171.
- (62) Kang, K.; Carlier, D.; Reed, J.; Arroyo, E.; Ceder, G.; Croguennec, L.; Delmas, C. *Chem. Mater.* **2003**, *15*, 4503.
- (63) Maazaz, A.; Delmas, C.; Hagenmuller, P. *J. Inclusion Phenom.* **1983**, *1*, 45.
- (64) Bethe, H.; Jackiw, R. *Intermediate Quantum Mechanics*; Addison-Wesley Longman, Inc.: New York, 1986, 1997; pp 80 and 81.
- (65) Kanno, R.; Shirane, T.; Inaba, Y.; Kawamoto, Y. *J. Power Sources* **1997**, *68* (1), 145.
- (66) Raekelboom, E. A.; Hector, A. L.; Owen, J.; Vitins, G.; Weller, M. T. *Chem. Mater.* **2001**, *13* (12), 4618.
- (67) Robertson, A. D.; Bruce, P. G. *Chem. Commun.* **2002**, *23*, 2790.
- (68) Lu, Z.; Beaulieu, L. Y.; Donabarger, R. A.; Thomas, C. L.; Dahn, J. R. *J. Electrochem. Soc.* **2002**, *149* (7) A815.
- (69) Paulsen, J. M.; Larcher, D.; Dahn, J. R. *J. Electrochem. Soc.* **2000**, *147* (8), 2862.
- (70) Eriksson, T. A.; Lee, Y. J.; Hollingsworth, J.; Reimer, J. A.; Cairns, E. J.; Zhang, X.-F.; Doeff, M. M. *Chem. Mater.* **2003**, *15*, 4456.
- (71) Padhi, A. K.; Nanjundaswamy, K. S.; Goodenough, J. B. *J. Electrochem. Soc.* **1997**, *144* (4), 1188.
- (72) Patoux, S. Matériaux d'électrode positive à charpente polyanionique pour batteries au lithium: Approches cristallographiques et électrochimiques. Thèse de Doctorat, L'Université de Picardie Jules Verne, 2003.
- (73) Zhang, F.; Ngala, K.; Whittingham, M. S. *Electrochem. Commun.* **2000**, *2*(6) 445.
- (74) Doeff, M. M.; Richardson, T. J.; Kepley, L. *J. Electrochem. Soc.* **1996**, *143*(8), 2507.
- (75) Doeff, M. M.; Anapolsky, A.; Edman, L.; Richardson, T. J.; De Jonghe, L. C. *J. Electrochem. Soc.* **2001**, *148* (3), A230.
- (76) Reed, J. Ab Initio Study of Cathode Materials for Lithium Batteries. Ph.D. Thesis, M.I.T., 2003; pp 78–85.
- (77) Reed, J. Ab Initio Study of Lithium Manganese Oxides. M.S. Thesis, M.I.T., 2001; pp 49–57.
- (78) Reed, J. Ab Initio Study of Cathode Materials for Lithium Batteries. Ph.D. Thesis, M.I.T., 2003; pp 152–161.
- (79) Reed, J. Ab Initio Study of Cathode Materials for Lithium Batteries. Ph.D. Thesis, M.I.T., 2003; pp 235–236.

CR020733X

NMR Studies of Cathode Materials for Lithium-Ion Rechargeable Batteries

Clare P. Grey* and Nicolas Dupré

Department of Chemistry, State University of New York at Stony Brook, Stony Brook, New York 11794-3400

Received February 24, 2004

Contents

1. Introduction	4493
2. NMR Background	4494
2.1. Lithium NMR Spectra of Cathode Materials: Introduction	4494
2.2. NMR Spectra of Paramagnetic Materials	4494
2.2.1. Fermi-Contact Interaction	4496
2.2.2. Dipolar Coupling	4496
3. Extracting Chemical Information from the Spectra of Paramagnetic Materials	4497
3.1. Fermi-Contact Interaction	4497
3.2. Dipolar Interaction	4500
4. Applications of NMR Spectroscopy to the Study of Cathode Materials	4501
4.1. Spinel	4501
4.1.1. Cation-Doped Spinel	4502
4.2. Cr ³⁺ - and Ni ²⁺ -Substituted Layered Lithium Manganates	4504
4.3. LiCoO ₂ and Related Materials	4505
4.4. Lithium Phosphates	4506
4.5. Vanadates	4507
4.5.1. ⁵¹ V NMR	4507
4.5.2. NMR Studies of Vanadium Oxides	4507
4.5.3. Vanadium Phosphates	4509
5. Conclusions	4510
6. Acknowledgments	4510
7. References	4510



Clare P. Grey received her B.A. (1987) and D. Phil. (1990) degrees in Chemistry from the University of Oxford. At Oxford she worked with Professors Tony Cheetham and Christopher Dobson on the application of solid-state NMR to problems in solid-state chemistry. She then spent a year as a postdoctoral fellow at the University of Nijmegen in The Netherlands with Professor Wiebren Veeman, where she developed new NMR methods for measuring internuclear distances in systems with quadrupolar nuclei. She was a visiting scientist at the DuPont Experimental Station in Wilmington (1992–1994), where she worked with Dr. Alexander Vega on NMR theory and on the application of NMR to molecular sieves and inorganic–organic composites. She joined the faculty at SUNY Stony Brook in 1994 as Assistant Professor and was promoted to Full Professor in 2001. She uses solid-state NMR spectroscopy, in combination with other characterization techniques such as diffraction, to understand the role that local structure plays in controlling the physical properties of a wide range of materials. Current studies include the investigation of electrode materials for lithium-ion rechargeable batteries, anionic conductors, and ion-exchange and sorption properties of soil minerals, molecular sieves, and layered materials.

1. Introduction

Lithium intercalation or insertion materials have been widely investigated in the search for new electrode materials for use in high-voltage rechargeable batteries.^{1–6} The first commercial Li-ion rechargeable battery contains the layered materials LiCoO₂ (Figure 1) and graphite as the cathode (or positive electrode) and anode (or negative electrode), respectively.⁷ Although this battery is the current standard in many applications including cell phones and laptops, its slow charge and discharge rates and cost have prevented its use in applications that require cheap high power and capacity, such as hybrid electric vehicles and electric vehicles. The toxicity of Co is also an issue. A wide variety of materials have been studied,^{5,6} which include doped LiCoO₂ phases, layered compounds based on the LiCoO₂ structure (e.g., LiNiO₂⁸ and LiNi_{0.5}Mn_{0.5}O₂^{9,10}),



Nicolas Dupré was born in Chatillon-sous-Bagneux, France, in 1975. He received his Ph.D. (2001) degree from Université Pierre et Marie Curie–Paris VI working under the direction of Professor Michel Querton. He was appointed as a postdoctoral associate at SUNY Stony Brook in 2002, where he works with Professor Clare P. Grey. His current research interests are focused on the study of the behavior of materials for lithium batteries using solid-state NMR.

* To whom correspondence should be addressed. E-mail: cgrey@notes.cc.sunysb.edu.

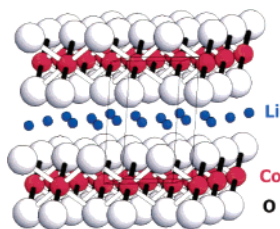


Figure 1. Structure of the cathode material LiCoO_2 , showing the alternating layers formed by edge-sharing CoO_6 octahedra and Li^+ .

and a series of materials with two- and three-dimensional hosts for Li (e.g., $\text{Li}_{1+x}\text{Mn}_{2-x}\text{O}_4$ ¹¹ and LiFePO_4 ¹²). While long-range structural information is typically available from diffraction methods, solid-state NMR is an extremely useful tool for characterizing local structure in these materials, even in highly disordered systems. The lithium nuclei (^7Li and ^6Li) are typically (but by no means exclusively) used as probes because it is the lithium ions that are directly involved in the electrochemical processes. The NMR spectra are strongly influenced by the electronic structure of the materials, and it is often possible to distinguish between insulators and conductors and between diamagnets and paramagnets. The method is quantitative and can be used to determine which species are removed on charging the battery and how the local structures change on extended cycling. NMR is also sensitive to dynamics that occur on the NMR time scale, and one-dimensional (1D) and two-dimensional (2D) NMR have, for example, been used to investigate Li-ion motion in vanadates (1D)¹³ and between two different nanosized domains in anatase, Li_yTiO_2 .¹⁴

This paper describes the approaches taken by us and other researchers over the past few years to interpret and extract chemical information from this class of materials. We focus on ex-situ analysis of electrode materials (i.e., samples that have been extracted from cycled batteries) since these approaches allow higher resolution spectra to be obtained. Use of a toroid detector (to obtain the NMR signal) has allowed working batteries to be studied in situ by spectroscopy and imaging methods,¹⁵ and more recent studies have shown that NMR signals may be obtained from plastic bag batteries.¹⁶ In-situ methods have not, to date, been combined with the high-resolution method magic angle spinning (MAS) due to a number of experimental difficulties that still need to be surmounted and are, therefore, not discussed here. The theory required to interpret the NMR spectra is first presented (section 2); the use of this theory to extract chemical information is then described (section 3). This is followed by illustrative recent examples from the field. In so far as this is possible, section 4 has been written so that it does not require a detailed understanding of NMR theory (beyond that discussed in section 2.1) and should be accessible to the non-NMR audience. A more comprehensive discussion of some of the technical aspects associated with obtaining NMR spectra of cathode materials can be found in an earlier review article.¹⁷

2. NMR Background

2.1. Lithium NMR Spectra of Cathode Materials: Introduction

The chemical shift range for lithium NMR spectra is very small, and it is not always possible to resolve resonances due to different local environments in the NMR spectra of diamagnetic materials based solely on the chemical shift interaction. Sometimes improved resolution can be obtained at higher field strengths, allowing chemical information to be extracted from the spectra.^{18,19} Fortunately, the lithium NMR spectra of most battery samples are strongly affected by a series of larger interactions which include quadrupole coupling (^6Li , $I = 1$; ^7Li , $I = 3/2$) and interactions with unpaired electrons for paramagnetic samples (hyperfine interactions) and with the conduction electrons in metals (the Knight shift). ^7Li has the much higher natural abundance (93%) and larger quadrupolar and gyromagnetic moments. In contrast, ^6Li is only 7% abundant, but its smaller quadrupole and gyromagnetic moments can result in higher resolution spectra that are often easier to interpret. The quadrupolar interaction, which results from the interaction of the quadrupolar nucleus with the electric field gradient (EFG) at the nucleus, is typically very small for ^6Li but can result in characteristic broadening in static and a series of spinning sidebands in magic angle spinning (MAS) ^7Li NMR spectra due to the satellite ($|+3/2\rangle - |1/2\rangle$ and $|-1/2\rangle - |-3/2\rangle$) transitions. This (anisotropic) interaction contains information concerning the local environments at the lithium nucleus and can be used to distinguish between ions in distorted and more symmetric environments. Many battery materials are paramagnetic in the discharged or charged state. For example, the cathode material LiMn_2O_4 is a mixed-valence compound containing Mn^{3+} (d^4) and Mn^{4+} (d^3) ions. Although the Co^{3+} d electrons in Li_xCoO_2 are paired in the fully discharged state, Li_xCoO_2 contains Co^{4+} d^5 ions when charged. The NMR spectra of paramagnetic materials are dominated by the interactions between the nuclear and electronic spins (Figures 2 and 3). These interactions may be much larger than any of the other interactions and can dominate the spectra of these materials, but they can also contain valuable information concerning both local crystallographic and electronic structure. Hence, we will now consider these interactions in some detail.

2.2. NMR Spectra of Paramagnetic Materials

Paramagnetic ions with electronic spin, S (e.g., $S = 3/2$ for d^3 ions Mn^{4+} and Cr^{3+}), are associated with magnetic moments, μ_e , that align in the presence of a static magnetic field, B_0 (Figure 2), typically defined to be the z -direction. S_z represents the component of the spin along this direction. Electron spin resonance (ESR) probes the transitions between the different spin (or Zeeman) states $|m_s\rangle$. Often the lifetime of an ion in a particular electronic state (T_{1e}) is very short on the relatively long time scale probed by NMR (from many seconds to 10^{-8} s, depending on the size

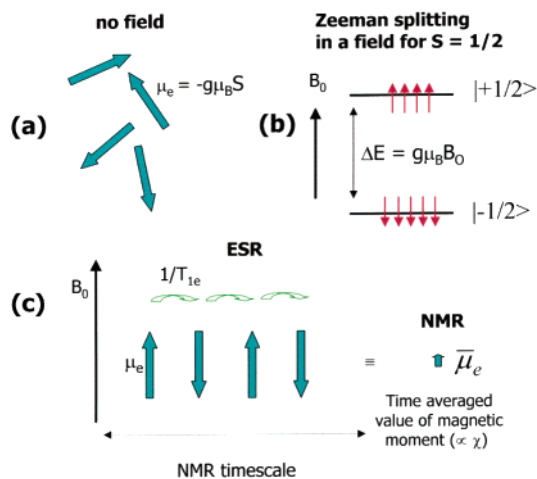


Figure 2. (a, b) Effect of a static magnetic field on a paramagnet with magnetic moment μ_e and electronic spin $S = 1/2$. Note that the lowest energy level for $S = 1/2$ in the magnetic field is the $| -1/2 \rangle$ state due to negative charge of the electron. (The magnetic moment of the electron μ_e associated with this state is still aligned along the direction of the static magnetic field; in many of the subsequent drawings, we will use arrows to represent directions of the net magnetic moments on the electrons/paramagnets.) (c) ESR probes the transitions between the spins states $| +1/2 \rangle \leftrightarrow | -1/2 \rangle$. Spins in these states relax with a rate $1/T_{1e}$, which is typically much faster than the size of many of the interactions probed by NMR (i.e., T_{1e} is shorter than the NMR time scale). Thus, NMR experiments are generally only sensitive to the time-averaged value of the magnetic moment, $\bar{\mu}_e (-g\mu_B \langle S_z \rangle)$.

of the electron–nuclear interaction). In this situation, the NMR spins cannot couple to S_z (i.e., the different spin states $|m_s\rangle$) and instead couple with the time average of the local field, $\langle S_z \rangle$. This is nonzero due to the differences in populations of the different $|m_s\rangle$ states in a magnetic field. The time average of S_z is proportional to the net magnetic moment of an ensemble, which is the quantity measured in a magnetic susceptibility measurement

$$\langle S_z \rangle = - \frac{B_0}{\mu_0 g N_0 \mu_B} \chi_M \quad (1)$$

where μ_0 is the permeability, g the electron g -factor, μ_B the Bohr magneton, N_0 Avogadro's number, and χ_M the magnetic molar susceptibility in $\text{m}^3 \text{mol}^{-1}$.²⁰

The size of the electron–nuclear interaction can be quantified via a hyperfine coupling constant, A/h (in Hz) (see below), and NMR experiments are feasible for ions with short T_{1e} s, such that²¹

$$|A/h| \ll 1/T_{1e} \quad (2)$$

As the T_{1e} s lengthen and $1/T_{1e}$ (s^{-1}) approaches the size of the electron–nuclear interaction, considerable NMR line broadening can occur, and it may not be possible to acquire high-resolution NMR spectra under these conditions. The effect of T_{1e} on the nuclear relaxation times is discussed in more detail in ref 22. Large hyperfine constants are observed (of many MHz) when the nuclear and electronic spins are on the same atom. For example, a hyperfine constant A/h of -324 MHz was measured by electron

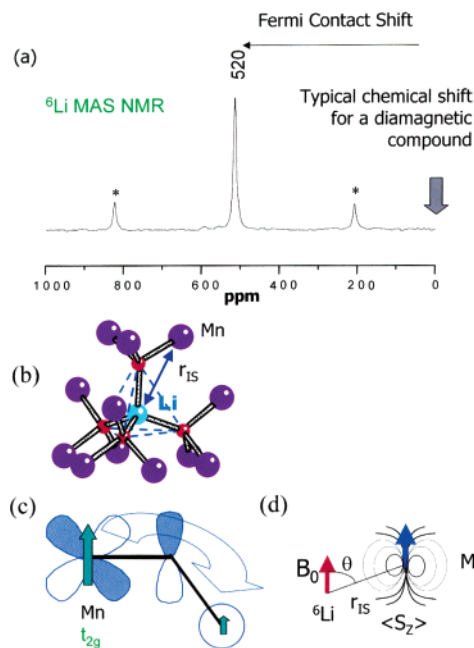


Figure 3. (a) ${}^6\text{Li}$ MAS NMR spectrum of the spinel LiMn_2O_4 synthesized at 850°C acquired with a spinning speed of 10 kHz at a field strength of 4.7 T. The spinning sidebands and the isotropic shift are marked with asterisks and its shift value (520 ppm), respectively. (b) Li local environment in LiMn_2O_4 showing a tetrahedrally coordinated Li ion and the 12 nearest Mn ions (in the octahedral sites of the spinel structure). Schematics illustrating (c) the transfer of unpaired electron spin density from the unpaired electrons in the t_{2g} d electrons (on one of the 12 nearby Mn ions) via the $2p$ orbitals on the intervening oxygen atom to the $2s$ orbital on Li, which causes the large shift seen for the LiMn_2O_4 isotropic resonance and (d) the dipolar coupling between a ${}^6\text{Li}$ nuclear spin and net magnetic moment due to a nearby Mn ion. The spinning sidebands shown in (a) primarily result from this interaction, which is not completely removed by MAS.³⁴

spin resonance (ESR) for the $S = 1/2$ ${}^{51}\text{V}^{4+}$ vanadyl ions in $\text{VO}(\text{H}_2\text{O})_5^{2+}$,²³ and the T_{1e} 's for these ions are 10^{-8} – 10^{-9} s.²² $1/T_{1e}$ is similar in magnitude to A/h , and high-resolution NMR spectra are not observed. When the nuclei under observation are further from the paramagnet, A is much smaller (the proton–electron hyperfine coupling constants are only 2.1 – 0.01 MHz for water molecules in the same vanadyl complex^{24–26}) and the condition in eq 2 is more readily achieved. This is the case for lithium spins, which are generally separated by two or more bonds from the paramagnet. In addition, bonding involving Li^+ is largely ionic, again reducing the size of A . Shorter T_{1e} s are generally observed for ions with $S > 1/2$ ($S \neq 5/2$), such as Mn^{3+} , Ni^{2+} , and Co^{2+} , and higher resolution spectra are more readily achieved.²² Broader ${}^6\text{Li}/{}^7\text{Li}$ resonances have been observed for local environments containing the paramagnetic $S = 1/2$ ion Ni^{3+} (e.g., for LiNiO_2 ²⁷ and $\text{LiCo}_{1-x}\text{Ni}_x\text{O}_2$ ²⁸), but the resonances are not sufficiently broad to prevent detailed analysis of the local environments in these compounds.^{28,29}

The nuclear spins can interact with the time-averaged magnetic moments via either through-space (dipolar) or through-bond (Fermi-contact) interactions. The ${}^6\text{Li}$ MAS NMR spectrum of LiMn_2O_4 is

presented in Figure 3a to illustrate the effect of the different interactions on the NMR spectrum of this paramagnetic material.

2.2.1. Fermi-Contact Interaction

This is a measure of the unpaired electron spin density that is transferred from the paramagnet to the nucleus of the spin under observation. In the regime defined by eq 2, the NMR shift ($\delta = (\Delta\omega/\omega_0)$) induced by the Fermi-contact interaction is directly proportional to $\langle S_z \rangle$ ^{30,31}

$$\frac{\Delta\omega}{\omega_0} = -\frac{A_c}{\omega_0 h} \langle S_z \rangle \quad (3)$$

The sign (and size) of the hyperfine constant A_c/h (Hz) determines the direction (and size) of the shift

$$A_c/h = g\mu_B\gamma_N\rho(r=0)\mu_0/3S \quad (4)$$

and depends on the electron spin (i.e., unpaired electron) density at the nucleus, $\rho(r=0)$. γ_N is the gyromagnetic ratio for the isotope studied by NMR, and ω_0 is its Larmor frequency (in radians). The ⁶Li/⁷Li hyperfine shift can be very large for many transition-metal oxides and shift the Li resonances well out of the typical range observed in the Li NMR of diamagnetic materials (0 ± 5 ppm) (Figure 3a).

$\rho(0)$ depends on the connectivity between the orbitals on the paramagnet and the orbitals on the NMR-active atom (Figure 3c). Only the electrons in s orbitals are associated with a finite probability of being found at the nucleus, and only the electron density transferred to the s orbitals needs to be considered. Electron density may be transferred either directly from the paramagnet or indirectly via a transferred hyperfine interaction to the s orbitals, and thus, the interaction contains chemical information about the bonding involving the paramagnets, Li, and the intervening oxygen atoms. For example, in LiMn₂O₄, the transferred hyperfine interaction will primarily involve the manganese t_{2g}, oxygen 2p, and Li 2s orbitals (Figure 3c). The Fermi contact shift is generally considered to be additive, so that the shift due to many magnetic ions may be obtained from a sum of the shifts induced by each magnetic ion, although exceptions occur in systems with very delocalized spin states. One challenge in this field has been to relate shift to local environment to extract chemical information from these often-complex systems. The correlation between shift and local environment will be explored in some detail in section 3.

The Knight shift, which dominates the spectra of metallic samples, is analogous to the Fermi-contact shift, except that now the shift is a measure of the density of states at the Fermi level, $N(E_f)$. This relationship arises because the Pauli paramagnetism χ_p of a metal is proportional to $N(E_f)$,³² and thus, since the electron–nucleus interaction is dependent on $\langle S_z \rangle$ and hence χ (eqs 1 and 3), the Knight shift is dependent on $N(E_f)$. Again, since hyperfine coupling requires that unpaired electron density is present at the nucleus under investigation, the Knight shift

depends, to a first approximation, on the contribution of the s orbitals of the NMR-active atom (lithium) to the crystal orbitals with energies at or very close to E_f (i.e., $N(E_f)_{\text{Li},2s}$ the Li 2s partial density of states at the Fermi level; this can be quite different than the value of $N(E_f)$ that is important in controlling the bulk conductivity of the sample). Often the d or p orbitals at the atom under investigation may have larger contributions to $N(E_f)$. This will be the case for some metals and the ⁵¹V Knight shifts of vanadates. Here, spin density can also be transferred to the s orbitals via a polarization mechanism and both positive and negative Knight shifts can result, depending on the nature, populations, and locations of the orbitals involved in the process. Polarization mechanisms are discussed in more detail in section 3.1.

2.2.2. Dipolar Coupling

The dipolar interaction is the same interaction that occurs between two or more nuclear moments and is caused by the local magnetic fields of the nuclear or electronic (S) spins that are felt at the nearby nuclear (I) spin (Figure 3d). When the dipolar interaction involves coupling to $S = 1/2$ nuclear spins, coupling to both the $|1/2\rangle$ and $|-1/2\rangle$ eigenstates will occur, resulting in the classic Pake doublet pattern for a powder. In contrast, when the second set of coupled spins are electrons (or paramagnetic ions), the nuclear spins can only couple to the time-averaged magnetic moment (again because the electronic relaxation time T_{1e} is extremely fast on the NMR time scale). The line shape in this case resembles that of the chemical shift anisotropy (CSA), and like the CSA, it scales linearly with the field.³³ The Hamiltonian for this interaction, H_{en} , can be represented by^{33,34}

$$H_{\text{en}} = \frac{\mu_0}{4\pi} \bar{\mu}_e \tilde{D}_{\text{en}} \mu_N \quad (5)$$

where $\bar{\mu}_e$ is the time (or thermally) averaged magnetic moment of the electrons (i.e., $-g\mu_B\langle S_z \rangle$) and \tilde{D}_{en} is the dipolar coupling tensor between the unpaired electron and nucleus, which is defined by its matrix elements as follows^{35,36}

$$D_{ij} = \frac{1}{r^3} (\delta_{ij} - 3e_i e_j) \quad (6)$$

and depends on both the distance between the nuclear and electronic spins, r (e.g., the Li and Mn atoms in Figure 3b), and the orientation of the interatomic (Li–Mn) vector with respect to the static magnetic field, B_0 . δ_{ij} is the Kronecker delta ($\delta_{ij} = 1$ for $i = j$ and 0 for $i \neq j$), e_i and e_j are the x , y , z components of a unit vector pointing from the nuclear spin to the electron spin in a chosen coordinate system. These interactions (and the CSA) are second-rank tensors and therefore averaged by MAS. Since the size of the dipolar interaction is generally larger than the MAS frequency, a series of spinning sidebands result (Figure 3a) that contains information concerning the size of the interaction and the relative orientation of the spins.³⁷

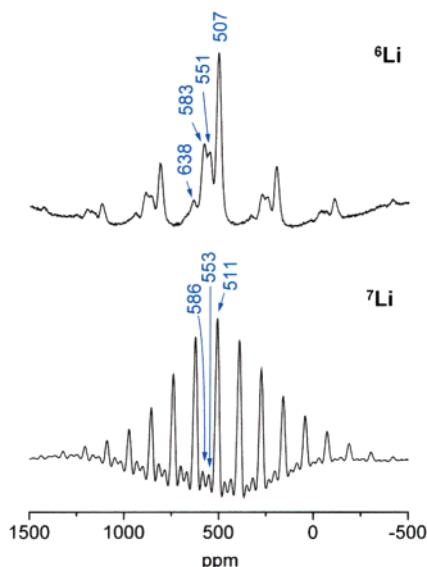


Figure 4. Comparison of the spectra of LiMn_2O_4 synthesized at $600\text{ }^\circ\text{C}$ obtained with ^6Li and ^7Li MAS NMR at a MAS spinning speed of $\sim 10.5\text{ kHz}$ and a magnetic field strength of 4.7 T (200 MHz for ^1H). (Reprinted with permission from ref 17. Copyright 2003 Elsevier.)

For isotropic magnetic moments, $\bar{\mu}_e$, the interaction results in a line broadening of the resonance only but no overall shift.³⁸ This will not be the case for an anisotropic magnetic moment. Here, both line broadening and a “pseudo-contact” shift will occur. This is an important mechanism for “shift reagents” in solution NMR and has also been shown to be necessary to explain the ^{89}Y shifts that arise due to lanthanide ions in the solid state.³⁹ The pseudo-contact shift arises from a similar mechanism as the broadening and line splitting due to a coupling to a quadrupolar nucleus (the interaction involves a fourth-rank tensor). Thus, the line broadening is no longer completely removed by MAS. In many of the batteries studied to date, the size of the shift and line broadening are small and the interaction can often be ignored to a first approximation. More detailed studies are still, however, required to correlate this interaction with line broadening.

The size of the dipolar interaction is often straightforward to calculate as $\langle S_z \rangle$ can be readily estimated from expressions for the susceptibility. For example, assuming spin-only paramagnetism, which is a good approximation for d^3 ions such as Mn^{4+} and Cr^{3+} ,^{40,41}

$$\chi = (\mu_0/4\pi)N_0g^2\mu_B^2S(S+1)/3kT \quad (7)$$

and thus $\bar{\mu}_e$ is given by⁴²

$$\bar{\mu}_e = g^2\mu_B^2S(S+1)B_0/3kT \quad (8)$$

where k is the Boltzmann constant. In an extended solid, the nuclear spins are typically surrounded by more than one paramagnet and the total Hamiltonian for the dipolar coupling, H_{en} , is obtained by summing the individual coupling tensors for coupling to each individual paramagnetic ions in successive coordination spheres.^{34,43}

Since μ_N , the magnetic moment ($=\gamma_N(h/2\pi)I_Z$), depends on the gyromagnetic ratio, γ_N , larger dipolar

couplings are seen for nuclei with larger values of γ_N . Thus, ^7Li with its much larger gyromagnetic ratio than ^6Li ($\gamma_{^7\text{Li}}/\gamma_{^6\text{Li}} = 2.6$) results in MAS spectra with much larger spinning sideband manifolds. Furthermore, unlike the dipolar coupling between nuclear spins, the size of the interaction depends on the magnetic field strength (eq 8). Consequently, the effect of this interaction can be minimized and spectra simplified by using low fields, fast MAS, and nuclei with low γ_N s. The effect of γ_N is illustrated in Figure 4, which compares the ^6Li and ^7Li spectra of the spinel LiMn_2O_4 prepared at $600\text{ }^\circ\text{C}$ obtained at an identical spinning speed and magnetic field strength. The sidebands in this system result primarily from the dipolar interactions. Clearly, it is difficult to see all the resonances in the ^7Li spectrum at this spinning speed, and some of the weaker peaks are obscured by the sidebands originating from the more intense resonance at ca. 511 ppm .

3. Extracting Chemical Information from the Spectra of Paramagnetic Materials

3.1. Fermi-Contact Interaction

To extract chemical information from the NMR spectra of paramagnetic battery samples (e.g., Figure 3a), we need to be able to assign a particular value of the hyperfine shift to a specific local environment. To achieve this goal, we^{44–47} and other workers^{28,48,49} have now studied a series of lithium compounds containing transition metals with electronic configurations from d^1 to d^8 . This has allowed us to rationalize the differences in the shift mechanisms that result from the presence of unpaired electrons in the t_{2g} and e_g orbitals of the transition-metal ions. Since the interaction is analogous to the J -coupling that occurs between nuclei and to magnetic interactions between paramagnets, approaches similar to those used in these fields may be used to predict the sign and magnitude of the hyperfine interaction. The correlations developed between the shift and local environment in these lithium NMR studies will now be explored.

To rationalize the large hyperfine shifts observed for lithium manganates such as the spinel LiMn_2O_4 (Figure 3a), we synthesized a whole series of compounds within the $\text{MnO}_2\text{--LiMnO}_2\text{--Li}_2\text{MnO}_3$ phase diagram. The NMR spectra of these compounds were then acquired to obtain typical hyperfine shift ranges for these materials (Figure 5). Even without a complete understanding of the causes of these large shifts, it then became possible to assign different shift ranges to different lithium local environments. For example, lithium spins in the octahedral site of a Mn^{4+} spinel typically give rise to a resonance at $1800\text{--}2300\text{ ppm}$, while lithium spins in the tetrahedral site of the spinel resonate at ca. 800 ppm . This is illustrated in Figure 5 for the ordered spinel $(\text{Li}_{0.5}\text{Zn}_{0.5})_{\text{tet}}(\text{Li}_{0.5}\text{Mn}_{1.5})\text{O}_4$, which contains Li ions on both the octahedral and tetrahedral sites of the spinel structure. Two resonances are clearly visible, which can be assigned using our hyperfine shift scale to the two different sites in this structure.⁵⁰ Similar approaches have been used by us and others to deter-

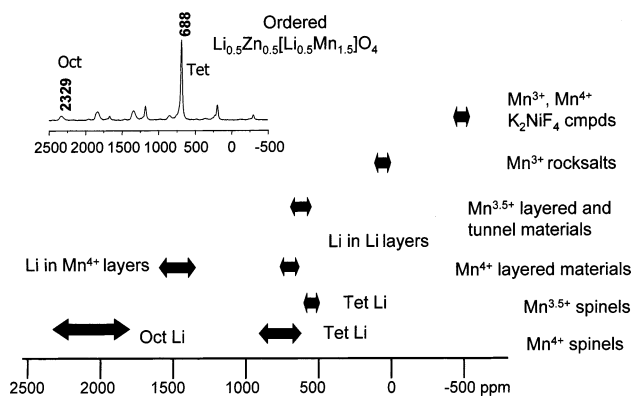


Figure 5. ${}^6\text{Li}$ MAS NMR spectrum of the Mn(IV) spinel $(\text{Li}_{0.5}\text{Zn}_{0.5})_{\text{tet}}(\text{Li}_{0.5}\text{Mn}_{1.5})_{\text{Oct}}\text{O}_4$ and the typical hyperfine shifts observed for lithium in a series of local environments. Hyperfine shifts are given next to the two isotropic resonances in the ${}^6\text{Li}$ spectrum; all other peaks are spinning sidebands, which are predominantly caused by the electron–nuclear dipolar coupling.

mine the locations of lithium ions in a series of transition-metal-doped spinels, $\text{LiMn}_{2-x}\text{M}_x\text{O}_4$ ($\text{M} = \text{Cu}, \text{Co}, \text{Li}, \text{Ni}, \text{Cr}$).^{17,51}

We examined the local environments around lithium in a series of Mn(IV) compounds to explain the different hyperfine shifts in these materials. By breaking up the local environments according to the numbers of manganese ions in the first cation coordination sphere around lithium and the Li–O–Mn bond angles, we determined the contribution of each Li–O–Mn interaction to the overall lithium shift.^{17,44} This analysis involves two assumptions: (1) that the major shift contribution arises from the hyperfine shift due to manganese ions in the first cation coordination sphere and (2) that there are no significant interactions between paramagnets at the temperatures at which the NMR spectra were acquired (close to room temperature). This latter assumption allows the shifts between different compounds to be compared. (The validity of this assumption can be tested by studying the temperature dependence of the shifts to determine whether there is any evidence for large deviations from Curie–Weiss behavior.^{45,46}) For example, one local environment for Li in Li_2MnO_3 contains 12 sets of Li–O–Mn⁴⁺ bonds, each with a bond angle of close to 90° (Figure 6a). This environment is associated with a hyperfine shift of 1500 ppm or a shift of 125 ppm per Li–O–Mn⁴⁺ interaction. More generally, Li⁺–O–Mn⁴⁺ bonds with bond angles of 90° were found to result in large positive shifts of ca. 120–150 ppm, while linear Li–O–Mn⁴⁺ bonds resulted in smaller negative shifts from –60 to –125 ppm, the exact value depending largely on the coordination number of oxygen (Table 1).⁴⁷

The size and direction of the shifts was then rationalized by using the Goodenough–Kanamori rules, originally designed to predict the sign of the coupling between d electrons in transition-metal oxides. For example, overlap between a half-filled t_{2g} orbital of a manganese ion and an empty 2s lithium orbital in a Li–O–Mn 90° arrangement may occur either directly or via an intervening p orbital on an oxygen atom. In the case of the transferred hyperfine interaction, an interaction with the t_{2g} electron and

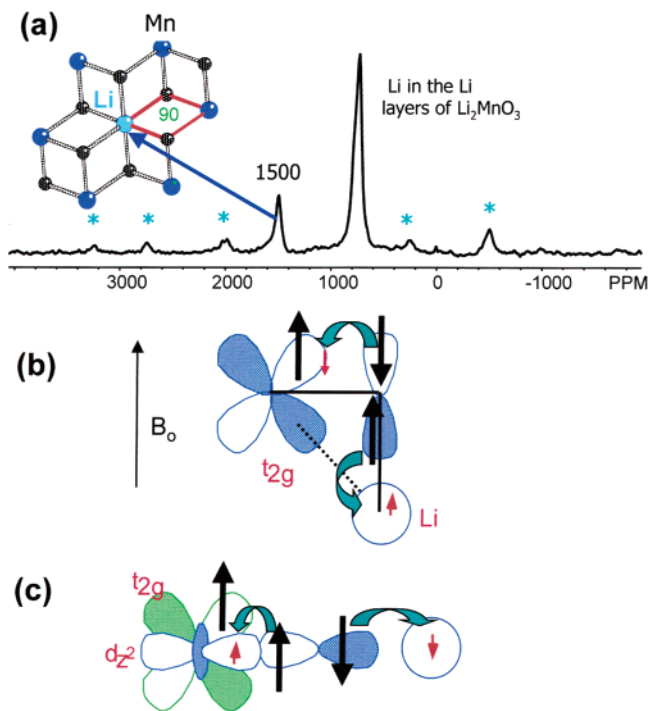


Figure 6. ${}^6\text{Li}$ MAS NMR spectrum of the layered compound Li_2MnO_3 acquired at a MAS frequency, ν_r , of 35 kHz. Spinning sidebands are marked with asterisks. The local environment in the Mn⁴⁺/Li⁺ layers that gives rise to the isotropic resonance at 1500 ppm is shown. Spin density may be transferred to the 2s orbital of Li via the interaction with (b) a half-filled t_{2g} orbital and (c) an empty d_{z^2} Mn orbital to produce the hyperfine shifts seen in the spectrum of Li_2MnO_3 . The large arrows represent the magnetic moments of the electrons in the t_{2g} and p orbitals, while the smaller arrows indicate the sign of the spin density that is transferred to the Li 2s and transition-metal d orbitals.

Table 1. Comparison of the Hyperfine Shifts (in ppm) Observed for Lithium Coordinated to a Single Mn⁴⁺ Ion via an Intervening Oxygen Ion for a Series of Local Environments^a

Li–O–M bond angle (deg)	O _{oct} ^b	O _{tet} ^c	O _{linear} ^d
90	122	163	
122		76	
180	–60	–75	–125

^a Shifts are classified according to the coordination number or environment of the intervening oxygen atom in each Li–O–Mn⁴⁺ interaction. ^b Li_2MnO_3 .⁴⁷ ^c Spinel compounds such as $(\text{Li}_{0.5}\text{Zn}_{0.5})(\text{Li}_{0.5}\text{Mn}_{1.5})\text{O}_4$.⁵⁰ ^d Perovskite and K_2NiF_4 -related compounds such as $\text{La}_2(\text{LiMn})_{0.5}\text{O}_4$.⁵³

the filled oxygen p orbital can only occur via transfer of spin density of the opposite sign to that already present in the half-filled t_{2g} orbital since the t_{2g} orbital is half-filled (Figure 6b). This then results in transfer of positive spin density to the empty Li 2s orbital and shifts of ca. 120–150 ppm per Li–O–Mn interaction. In the case of a 180° interaction, no direct overlap mechanism is possible involving the t_{2g} orbitals. In this case, the interaction occurs via the empty e_g orbitals (Figure 6c). Here, the exchange coupling between the e_g and t_{2g} orbitals on the same atom favors the transfer of spin density with the same sign of spin polarization as that in the t_{2g} orbitals to the e_g orbitals. This results in a net transfer of negative spin polarization from manganese to the empty 2s

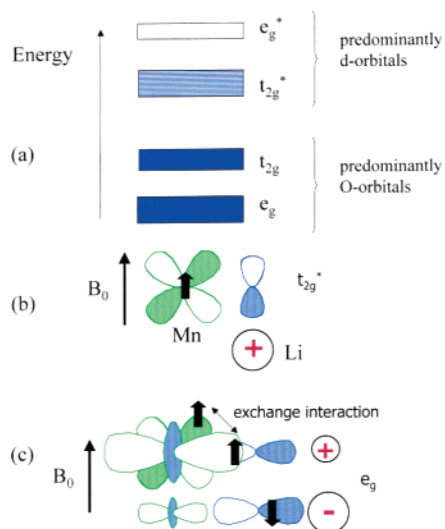


Figure 7. (a) (Partial) band diagram for a transition-metal oxide, with transition-metal ions located in sites with octahedral symmetry. (The t_{2g} and t_{2g}^* crystal orbitals are formed from an overlap of the t_{2g} d orbitals and oxygen 2p atomic orbitals, while the e_g and e_g^* crystal orbitals are formed from the e_g d orbitals and oxygen 2p and 2s atomic orbitals. The t_{2g}^* bands are partially occupied for Mn^{4+} and Cr^{3+} d^3 ions.) (b) Delocalization mechanism involving the half-filled t_{2g}^* crystal orbital, and (c) polarization mechanism involving the two one-electron orbitals that make up the “filled e_g orbital”. The sizes of orbitals in c represent the relative contributions of these orbitals to the crystal (or molecular) orbital; the sign of the spin-density transferred to the Li 2s orbital is indicated with a “+” or “-” sign.

Li orbital and, consequently, a negative shift. The lithium (tetrahedral) environment in the spinel structure contains 12 Li–O–Mn bond angles of ca. 122° (Figure 3b), and a shift intermediate between that observed for linear and 90° interactions is observed of ca. 76 ppm, as expected, based on orbital overlap arguments. The tetrahedral site in the ordered spinel $(Li_{0.5}Zn_{0.5})(Li_{0.5}Mn_{1.5})O_4$, whose spectrum was shown in Figure 5, contains nine sets of Li–O–Mn bonds with 122° bond angles (the remaining three are Li–O–Li bonds), consistent with the shift for this environment of 688 ppm.

The different shift mechanisms may be understood in more detail by considering the effect of the magnetic field on the populations and energies of the different crystal orbitals (Figure 7a). Transfer of electron density via the 90° interaction arises due to a direct delocalization of spin density due to overlap between the half-filled t_{2g}^* , oxygen π^* , and empty Li 2s atomic orbitals (the delocalization mechanism, Figure 7b).⁵² This overlap is responsible for the formation of the t_{2g}^* (antibonding) molecular orbital in a molecule or the t_{2g}^* crystal orbital (or band) in a solid. No shift occurs for the 180° interaction from this mechanism as the e_g^* orbitals are empty.

A second mechanism (the polarization mechanism) arises due to the polarization of the fully occupied (bonding) crystal orbitals formed by the e_g , oxygen 2p, and Li 2s atomic orbitals in the presence of a magnetic field. A fully occupied crystal (or molecular) orbital in reality comprises one one-electron orbital occupied by a “spin-up” electron and a second one-

electron orbital occupied by a “spin-down” electron. This results in the so-called “fully occupied” crystal orbital that contains two paired electrons. In the presence of a field, the energies of the two orbitals are no longer necessarily identical, the one-electron orbital with a magnetic moment aligned with the field being lower in energy. In the case of a “half-filled” orbital, this is the source of the hyperfine shift, as only one out of the two one-electron orbitals is occupied. However, when both of these one-electron orbitals are occupied this does not directly result in a shift. Instead, the shift arises from the effect of the field on the contributions of the different orbitals to the crystal orbitals. In the absence of a magnetic field, the individual one-electron orbitals are identical (i.e., the contributions of the different atomic orbital to the crystal orbital are the same), but this need not be the case when a field is applied. Exchange coupling between electrons in different orbitals lowers the energy of electronic configurations containing parallel electrons. Thus, the presence of “spin-up” electrons in the t_{2g}^* orbitals will stabilize the “spin-up” one-electron orbital formed from the e_g orbitals. This results in a polarization of the e_g crystal orbitals, so that the contribution of e_g atomic orbital to the crystal orbital will be larger for the “spin-up” one-electron orbital and smaller for the “spin-down” orbital. This is illustrated schematically in Figure 7c. Since the “spin-down” orbital is still a one-electron orbital, the contribution to this orbital from the oxygen 2p and Li 2s atomic orbitals must be larger, and thus the concentration of “spin-down” electrons on the Li 2s orbitals is higher than the concentration of “spin-up” electrons, resulting in a net transfer of negative spin density. This picture is entirely equivalent to one where the presence of the magnetic field is considered to mix the e_g and e_g^* orbitals—the extent of mixing is different for the “spin-up” and “spin-down” orbitals, leading to differences in the contributions of the metal d, 2p O, and 2s Li atomic orbitals to the crystal orbitals. A similar phenomenon can occur, for example, in a ferromagnetic solid, the presence of ordered electronic spins acting as the source of the local magnetic field.

The relative sizes of the polarization and delocalization mechanisms will depend on the orbitals involved in the overlap and the occupancies of the metal orbitals. For example, the polarization mechanism appears to be relatively weak for Ni^{3+} , in contrast to Mn^{4+} and Cr^{3+} , even when both mechanisms involve e_g orbitals.⁵² This is most likely due to the smaller exchange interaction expected for the Ni^{3+} system, which contains fewer unpaired electrons. Some earlier studies neglected the polarization mechanism, assuming that it was much weaker than the other possible shift mechanisms, which lead to incorrect assignments.²⁸

Recent density functional theory (DFT) calculations have been used to calculate the transfer of unpaired electron spin densities to the nearby atoms and analyze the orbitals involved in these mechanisms.⁵² For example, Figure 8 shows the spin densities obtained for Cr^{3+} -doped $LiCoO_2$. The spin densities can be calculated by subtracting the “spin-up” elec-

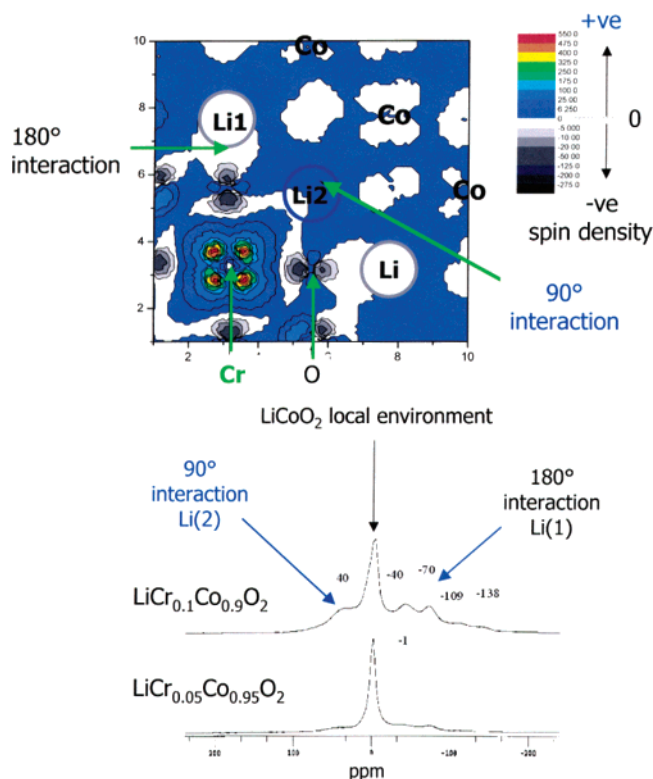


Figure 8. Calculated spin polarization density map in a Co/Cr–O–Li plane in $\text{LiCr}_{1/8}\text{Co}_{7/8}\text{O}_2$ from DFT calculations.⁵² The positions of the Cr, Co, Li, and O ions are indicated. Li(1) has a Cr^{3+} ion as its second cation coordination shell, while Li(2) has a Cr^{3+} ion in its first cation coordination shell. The ^6Li spectra of $\text{LiCr}_x\text{Co}_{1-x}\text{O}_2$ ($x = 0.05$ and 0.1)⁴⁷ are shown along with the assignments of resonances corresponding to Li(1) and Li(2) local environments.

tron density from the “spin-down” electron density at a particular location in space. The unpaired electron density in the Cr^{3+} (d^3) t_{2g} atomic orbital is clearly visible. Direct overlap of this orbital with a nearby $2p$ O orbital results in positive spin density in this orbital and positive spin density at the site of the Li nucleus, connected via the 90° interaction. This is consistent with the resonance at 40 ppm seen in the ^6Li NMR spectrum of $\text{LiCo}_{1-x}\text{Cr}_x\text{O}_2$ ($x = 0.1$ and 0.05), which was also assigned to the presence of one Cr^{3+} in the local coordination sphere of a lithium ion. Negative spin density is present in the $2p$ O orbital that points directly to the Cr^{3+} ion and the Li ion connected via this 180° interaction, consistent with the observation of a resonance at -70 ppm in the NMR spectrum.

Analysis of the spectra of Mn(III) compounds is more complicated as (i) the e_g orbitals are partially filled, (ii) Jahn–Teller distortions typically occur resulting in one half-filled and one empty e_g^* orbital, (iii) many of these compounds contain sizable anti-ferromagnetic interactions between manganese ions, which result in strong deviations from Curie–Weiss behavior, even at around room temperature. We have analyzed the Mn(III) compounds by examining the Mn–O bond lengths, the longer Mn–O bond lengths (of greater than 2 Å) in the MnO_6 octahedra being indicative of electron occupancy of the (antibonding) e_g^* orbitals. The Mn(III) compound, $\text{La}_2(\text{LiMn})_{0.5}\text{O}_4$

will be considered initially since this contains isolated manganese ions within the Li/Mn/O planes that are only weakly coupled.⁵³ $\text{La}_2(\text{LiMn})_{0.5}\text{O}_4$ is isostructural with K_2NiF_4 , and the lithium is coordinated to four manganese ions via linear Li–O–Mn bonds. A shift of -480 ppm was observed for this compound. This is consistent with a Jahn–Teller distortion of the d^4 Mn ions and the population of the e_g^* (d_z^2) orbital perpendicular to the Li–O–Mn axes (i.e., perpendicular to the Li/Mn/O planes), so that the Li shift is dominated by the four interactions involving empty $d_{x^2-y^2}$ orbitals. The shift mechanism is similar to that observed for interactions involving empty d_{z^2} orbitals (Figures 6c and 7c).⁵³

The three Mn^{3+} rock-salt related compounds with stoichiometry LiMnO_2 show much smaller shifts of between 40 and 143 ppm in comparison to the shifts observed for $\text{La}_2(\text{LiMn})_{0.5}\text{O}_4$ and the Mn(IV) compounds.⁴⁵ All the lithium atoms in these compounds have similar numbers of manganese ions in their local coordination sphere, resulting in 12 Li–O–Mn 90° interactions, but differ in the number of types of Li–O–Mn 180° interactions. The slightly larger shifts seen for the tetragonal- $\text{Li}_2\text{Mn}_2\text{O}_4$ and monoclinic- LiMnO_2 compounds (99–143 ppm) in comparison to the shift seen for orthorhombic- LiMnO_2 (40 ppm) may be rationalized by the presence of additional interactions involving half-filled e_g orbitals, which, for the same reason discussed for the 90° interactions involving t_{2g} orbitals, should result in a positive shift. However, by using arguments outlined above for the Mn(IV) compounds, we would predict a very large shift for these Mn(III) compounds of greater than 1400 ppm. One cause of the large differences is the strong anti-ferromagnetic interactions between Mn^{3+} ions, which are responsible for non-Curie–Weiss behavior and in the case of o- LiMnO_2 for a Néel transition temperature of -11 °C.⁵⁴ This suggestion was tested by following the ^6Li shifts of these compounds as a function of temperature.⁴⁵ These results demonstrate significant deviation from Curie–Weiss temperature dependence, the shifts being essentially independent of temperature between 0 and 250 °C. Recent density functional theory (DFT) calculations for m- LiMnO_2 suggest that changes in bond lengths caused by the Jahn–Teller distortion also strongly affect the relative magnitudes of the different shift mechanisms, resulting in smaller than predicted shifts for these compounds.⁵²

These findings are not unique to the manganese systems, and other materials showing strong anti-ferromagnetic interactions between paramagnets show smaller than predicted shifts. Examples include the NMR spectra of α and β LiFeO_2 where shifts of ca. 500 ppm were observed,²⁷ even though the d^5 Fe^{3+} ions in these compounds contain both partially filled t_{2g} and e_g atomic orbitals. Again, strong deviations from Curie–Weiss behavior are seen for these compounds.

3.2. Dipolar Interaction

Although the sidebands that result from the dipolar interaction can often complicate analysis of the

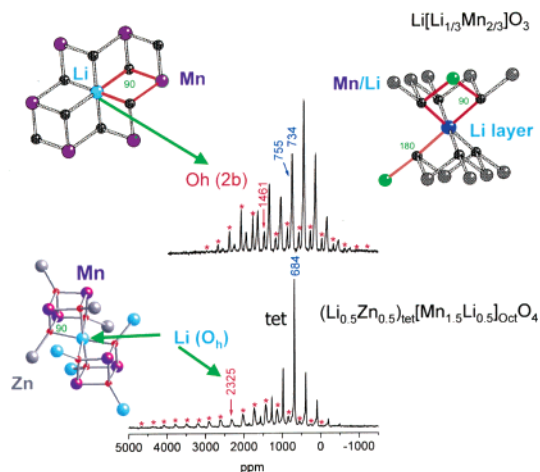


Figure 9. ${}^6\text{Li}$ MAS NMR spectra of the ordered spinel $[\text{Li}_{0.5}\text{Zn}_{0.5}]_{\text{tet}}[\text{Li}_{0.5}\text{Mn}_{1.5}]_{\text{Oct}}\text{O}_4$ and Li_2MnO_3 .³⁴ The asterisks indicate the spinning sidebands of the resonances from Li in the octahedral site in the spinel and the 2b site of Li_2MnO_3 (i.e., the site due to Li in the Mn layers). The local environments for Li in these sites and the Li in the Li layers of Li_2MnO_3 are shown. These spectra were acquired at a moderately slow spinning speed of 8.7–8.8 kHz (cf. Figure 6) to increase the intensity seen in the spinning sidebands (relative to the isotropic resonance), improving the accuracy of the analysis of the sideband manifolds.

spectrum (Figure 3), this interaction does contain extremely useful structural information that can be relatively straightforward to extract. The effect of different arrangements of paramagnetic ions on the NMR spectra has been explored, and different arrangements can result in characteristic line shapes. This is illustrated in Figure 9 for the two Mn^{4+} compounds Li_2MnO_3 and the spinel $(\text{Li}_{0.5}\text{Zn}_{0.5})_{\text{tet}}(\text{Mn}_{1.5}\text{Li}_{0.5})_{\text{Oct}}\text{O}_4$. The Li ions in the transition-metal layers of Li_2MnO_3 and in the octahedral site of the spinel are coordinated to the same number of Mn ions (six), but the arrangements of these ions are very different. For Li_2MnO_3 , these ions are located in the same plane as the central Li ion (an oblate arrangement), while in the spinel, they lie above and below an imaginary plane running through Li (a prolate arrangement). As discussed above, the total dipolar coupling interaction is a sum of all the individual Li– Mn^{4+} dipolar interactions. The total interaction will be very sensitive to the relative orientations of the Li–Mn interatomic vectors. For the sites in the two compounds discussed here, although the magnitude of the interaction is similar, the sign of the interaction is opposite in sign. Differences in the signs of the interaction result in characteristic changes in the line shapes of the two compounds. The shapes of the sideband manifolds for the two groups of resonances in Li_2MnO_3 ($= \text{Li}[\text{Li}_{1/3}\text{Mn}_{2/3}]_2\text{O}_2$ in the notation used to describe layered compounds) are also very different. Li located in the Li layers is nearby manganese ions arranged above and below the plane of Li ions, and thus the shape of the sideband manifolds of the resonance due to this site is similar to that seen for the octahedral sites in the spinel. The shape is characteristic for Li ions between layers of paramagnetic ions and may be used as a signature for this environment. Much smaller sideband manifolds are seen for the tetrahedral sites, in part because the Li–

Mn distances are larger and also because the ions are arranged more symmetrically around the tetrahedral Li ions so that individual dipolar couplings partially cancel, resulting in a smaller overall dipolar coupling. Again, this smaller dipolar coupling can be used as a signature for the tetrahedral site in these compounds.

4. Applications of NMR Spectroscopy to the Study of Cathode Materials

MAS NMR has now been used to study LiCoO_2 -derived layered materials^{28,29,55} as well as a wide range of alternative cathode materials including manganates,^{44,48,49,56–58} vanadates,^{13,59–61} and iron and vanadium phosphates.^{62–64} We will now discuss the application of NMR to some of these materials to illustrate the type of information that has been (and can be) obtained by using this method.

4.1. Spinel

The spinel materials, $\text{LiMn}_{2-x}\text{M}'_x\text{O}_4$, have been the most extensively investigated of all the lithium manganates.^{65,66} These materials can be cycled at ca. 4 V (vs Li) from LiMn_2O_4 to MnO_2 , the manganese ions retaining the spinel host framework throughout.^{1,67} Capacities of 148 mAg^{-1} are, in theory, possible for the stoichiometric spinel, but in practice no more than $100\text{--}120 \text{ mAg}^{-1}$ has been achieved over multiple charge–discharge cycles.⁶⁸ The spinels represent cheap alternative cathode materials which can be charged and discharged sufficiently rapidly to meet the power requirements for use in electric vehicles. Unfortunately, many of the spinels suffer from rapid capacity fade following extended storage or on cycling, particularly at high temperatures.⁵ This has prompted much research on these materials to identify the source and then prevent this fade.^{69–71} Surface treatment methods have also been developed to help prevent manganese dissolution,⁶⁹ and Li-excess spinels $\text{Li}_{1+x}\text{Mn}_{2-x}\text{O}_4$, $x = 0.05\text{--}0.1$, are now being produced as cheap cathode materials particularly for use in high-power applications. Figure 10 shows a typical potential profile (obtained in a galvanostatic mode, i.e., by using constant current) for the spinel $\text{Li}_{1.05}\text{Mn}_{1.95}\text{O}_4$.⁵⁶ Initial capacities of 125/115 (charging/discharging) mAh/g were obtained (theoretical capacity = 126 mAh/g). Good capacity retention was observed for this material, with 96% of the initial discharge capacity being retained after 30 cycles.

NMR spectroscopy has been performed on these systems to investigate structure before and after electrochemical cycling. A large hyperfine shift of more than 500 ppm from the chemical shift range of typical diamagnetic compounds containing lithium is typically observed in the ${}^6\text{Li}$ or ${}^7\text{Li}$ MAS NMR spectrum of the stoichiometric spinel LiMn_2O_4 (Figure 2) synthesized in air at a temperature of between 700 and 850 °C.^{44,48,58,72} LiMn_2O_4 is a mixed-valent compound containing both Mn^{3+} and Mn^{4+} ions; it is also a hopping semiconductor, hopping occurring between the e_g orbitals of the manganese ions. Since this hopping time scale is fast in comparison to the

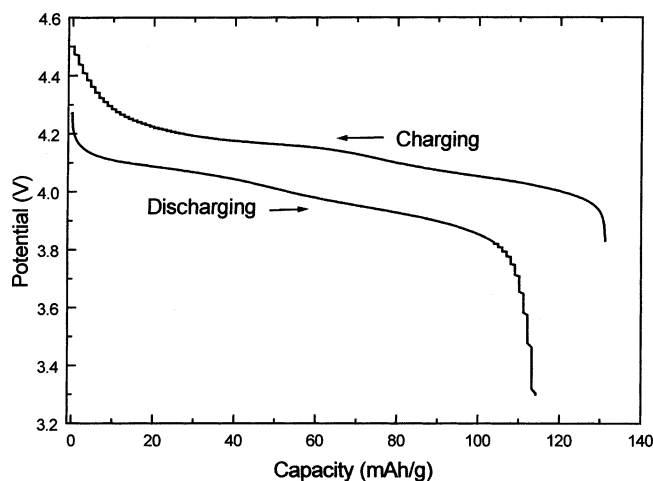


Figure 10. Potential profile of $\text{Li}_{1.05}\text{Mn}_{1.95}\text{O}_4$ during the first charge and discharge in the voltage range of 3.3–4.5 V. The cell (comprising $\text{Li}_{1.05}\text{Mn}_{1.95}\text{O}_4$ as the positive electrode (cathode) and Li as the negative electrode (anode)) was charged/discharged with a constant current corresponding to a charge rate of $C/10$ (~ 10 mA per gram of active material; $C/10$ indicates that the cell was fully charged in 10 h; a charge rate of 1C corresponds to 1 h). [Similar cells and cycling conditions were used to prepare the samples for the NMR experiments described in section 4.1.1 and in ref 56. Here, cycling was arrested at different potentials, the cells disassembled in a glovebox, and the cathode mixtures packed in NMR rotors.]

NMR time scale (ca. 10^{-5} s), the lithium spins “see” an average manganese oxidation state of 3.5 (i.e., “ $\text{Mn}^{3.5+}$ ” ions), and thus there is only one magnetically inequivalent lithium site (the 8a site). The NMR spectra are clearly sensitive to this hopping mechanism, and NMR spectroscopy may be used to follow the partial charge-ordering process that occurs just below room temperature in the stoichiometric material.⁴⁴

In our initial study of these systems⁴⁴ we investigated the effect of synthesis temperature on the local structure in the nominally stoichiometric spinel LiMn_2O_4 , since its stoichiometry and manganese oxidation state depend on the preparation conditions: $\text{Li}_2\text{Mn}_4\text{O}_9$ (Mn^{4+}) may be synthesized at 400 °C,⁷³ while an increase of temperature results in the formation of defect spinels with a progressive reduction of the manganese oxidation state. Eventually an average oxidation state for manganese of 3.5 is achieved in the stoichiometric material LiMn_2O_4 synthesized at ~ 850 °C.⁷⁴ Figure 11 shows that the ^6Li MAS NMR spectra of this compound vary dramatically with synthesis temperature. Despite the fact that the structure of the stoichiometric spinel contains only *one* crystallographic site for lithium (the 8a site; see Figure 3b), a large number of different *local* environments are observed for the compounds synthesized at lower temperatures. The spectrum of the material synthesized at a temperature of 600 °C resembles the spectrum of samples with excess lithium (e.g., $\text{Li}_{1.05}\text{Mn}_{1.95}\text{O}_4$),⁵⁶ which typically show improved cycling behavior.^{75–77} Furthermore, a weak resonance at 2300 ppm can be detected in the ^7Li MAS NMR spectra of the materials synthesized at both 550 and 600 °C, collected using an extremely fast MAS spinning speed of 40 kHz.¹⁷

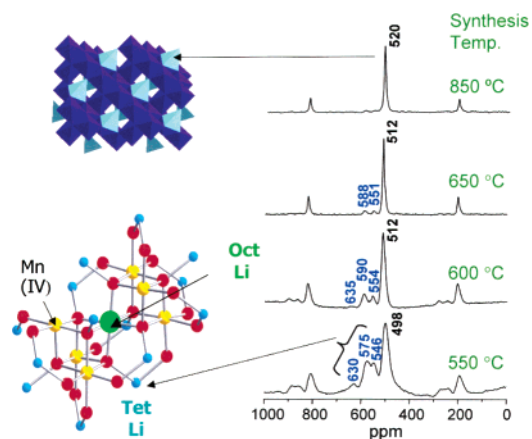


Figure 11. ^6Li MAS NMR spectra of the spinel LiMn_2O_4 (structure shown on the left) as a function of synthesis temperature (adapted from ref 44). The cluster of Mn^{4+} ions formed as a result of Li substitution on the octahedral site is shown, and the resonances due to Li ions near this cluster are assigned.

The spinning sideband pattern seen for this resonance is similar to that found for the octahedral site in the spinel $\text{Li}_{0.5}\text{Zn}_{0.5}[\text{Mn}_{0.5}\text{Li}_{0.5}]\text{O}_4$, confirming that this resonance is due to Li substitution (for Mn) on the octahedral (16d) site of the spinel structure. Thus, the spectra provided clear evidence that the samples prepared at lower temperature contain excess Li, despite their stoichiometry. The residual Mn is presumably present as Mn_2O_3 , as shown by Paulsen et al.⁷⁸ The additional resonances in the spectra of the nominally stoichiometric material LiMn_2O_4 can be assigned by using our hyperfine shift scale (Figure 5) to tetrahedral lithium environments nearby Mn^{4+} ions. These Mn^{4+} ions arise from the substitution of Li^+ in the octahedral (16d) site: For every Li^+ substituted on this site, five $\text{Mn}^{3.5+}$ ions must be oxidized to Mn^{4+} . Additional resonances at lower frequency than the main spinel (520 ppm) resonance were observed for spinels prepared above 850 °C or in inert atmospheres.⁵⁶ These peaks were ascribed to the presence of Mn^{3+} ions in the Li local coordination sphere, caused by the presence of Mn^{2+} ions on the tetrahedral (8a) site of the spinel structure. Now, the substitution of a Mn^{2+} for Li^+ requires that two $\text{Mn}^{3.5+}$ ions are reduced to Mn^{3+} for charge balance.

4.1.1. Cation-Doped Spinel

The Jahn–Teller distortion that occurs on intercalation of LiMn_2O_4 to form $\text{Li}_2\text{Mn}_2\text{O}_4$ is associated with a large change in cell volume.⁶⁶ One possible source of capacity fade in the spinel material has been ascribed to this Jahn–Teller distortion, which can occur (particularly at the surface of the particles) when the oxidation state of the manganese drops below 3.5 during discharge.^{66,79} Doping has been investigated extensively in the spinel system because it represents a method for controlling the oxidation state of the manganese at the end of discharge (of the ca. 4 V plateau).⁶⁹ On the basis of charge balance arguments, substitution of a manganese ion for a dopant cation with charge of $n+$ will result in the oxidation of $(3.5 - n)2$ manganese ions with average oxidation states of 3.5 to Mn^{4+} .

The spectra of the doped materials (Cr^{3+} , Ni^{2+} , Zn^{2+} , Li^+ , Co^{3+} , Al^{3+}) are similar to those seen for the nominally stoichiometric materials, and sets of resonances between 500 and 700 ppm are seen on cation doping^{17,51} in addition to that of the normal spinel environment (at ca. 500 ppm). Again, these resonances are assigned to lithium ions near manganese(IV) cations. The lower intensity of the additional resonances seen on Cr^{3+} substitution, in comparison to Zn^{2+} or Ni^{2+} substitution, is consistent with the oxidation of fewer manganese ions near the dopant ions. For the Li- and Zn-doped spinels, resonances at ca. 2300 ppm were also observed, which are assigned to lithium ions in the octahedral sites of the spinel structure. In the case of Zn doping, it is clear that the preference of Zn^{2+} for the tetrahedral site of the spinel structure forces the lithium onto the octahedral site.

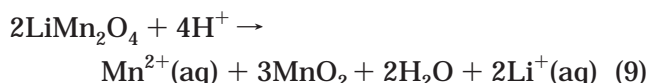
The NMR results indicate that cation doping does not increase the manganese oxidation states of all cations in the whole phase evenly. Instead, the manganese cations near the dopant cations are oxidized, leaving the bulk relatively unperturbed. This is borne out in the mechanism of deintercalation of these systems, which differs noticeably from the deintercalation mechanism of stoichiometric LiMn_2O_4 . Two-phase behavior was observed during charging of stoichiometric LiMn_2O_4 samples synthesized at 650 °C and above.⁸⁰ In contrast, the results for $\text{Li}_{1.05}\text{Mn}_{1.95}\text{O}_4$ (whose potential profile was shown in Figure 10) indicate that the lithium cation is deintercalated from the different local sites sequentially.⁵⁶ Li is deintercalated first from the site containing all $\text{Mn}^{3.5+}$ ions in its local coordination sphere (ca. 500 ppm); this is followed by Li deintercalation from sites nearby progressively more Mn^{4+} . The resonance at 2100–2300 ppm can be seen throughout the whole charging range studied, indicating the lithium in the octahedral sites is not deintercalated. Li is pinned in the tetrahedral sites near these octahedral Li ions and Mn^{4+} ions. We proposed that the presence of excess Li^+ , which serves to pin the tetrahedral Li ions in the lattice, helps to prevent the formation of a series of cation-ordered phases during charging.⁵⁶ Instead $\text{Li}_{1+x}\text{Mn}_{2-x}\text{O}_4$ forms a continuous solid-solution on charging and discharging,⁸¹ improving the stability of this material during extended cycling.

On deintercalation of ca. 25% of the Li ions from the tetrahedral site of $\text{Li}_{1.05}\text{Mn}_{1.95}\text{O}_4$, the additional resonances due to Li in tetrahedral sites near Mn^{4+} ions disappear.⁵⁶ The fine structure returns on cooling the sample to -60 °C. This indicates that the creation of Li-ion vacancies on charging results in a noticeable increase in Li mobility, involving jumps between the different tetrahedral sites.⁵⁶ Verhoeven et al. used 2D ^7Li NMR experiments to study the dynamics of Li in the fully lithiated material $\text{Li}_{1.04}\text{Mn}_{1.96}\text{O}_4$.⁵⁷ Their ^7Li NMR spectra are very similar to our ^6Li spectra of a similar material and also the “stoichiometric” material prepared at 600 °C (Figure 11). At temperatures above room temperature, they detected “cross-peaks” in the 2D exchange spectra between the ^7Li resonances at 500–650 ppm, indicating that motion between different Li sites in the

spinel structure was occurring on a millisecond time scale. This was consistent with the complete collapse of the fine structure at higher temperatures in our earlier work, where it was ascribed to either mobility of Li^+ or mobility of the holes on the manganese ions near the defects in these materials (i.e., the octahedral 16d Li ions¹⁷).⁴⁴ Later variable-temperature NMR results for $\text{LiNi}_{0.1}\text{Mn}_{1.9}\text{O}_4$, where similar phenomena were observed, suggested that Li^+ motion must play a role in the collapse of the fine structure.⁴⁶ By monitoring the change in cross-peak intensity as a function of temperature, Verhoeven et al. extracted an activation energy for the jump process of 0.5 ± 0.1 eV and also an estimate for the difference in energy between Li in the normal tetrahedral site and Li in the site that gives rise to the resonance at ca. 590 ppm of ca. 700 K (or 0.05 eV). However, their assignments of the spectra are very different from ours.⁵⁶ They assigned the two most intense extra resonances at ca. 550 and 590 ppm in Figure 11 (and at slightly higher frequencies in their study) to Li in the 16d (Mn) and 16c sites, respectively. These assignments were made based on the earlier neutron diffraction experiments⁸² but, if correct, suggest that the 16c site is occupied in significant concentrations, even at room temperature. The 16c site is an octahedral site which is empty in LiMn_2O_4 but is occupied on insertion of Li to form $\text{Li}_2\text{Mn}_2\text{O}_4$.⁸³ Given our direct observation of the 16d Li site (at 2300 ppm¹⁷) and that a much larger shift than 590 ppm is predicted for the 16c site, based on our hyperfine shift scale,⁴⁴ we suggest that the motion observed here is due to 8a–8a hops, the measured difference in energy between the two sites (0.05 eV) arising from the effect of the Li incorporation into the octahedral (16d) site and formation of the Mn^{4+} ions nearby the “590 ppm” site. The authors suggest that their activation energy corresponds to that of an 8a–16c jump. Most likely, the 8a–8a jump process does occur via the 16c site, the 16c representing a metastable intermediate state. In this case, the measured activation energy still corresponds to that of a 8a–16c hop; however, it seems unlikely that the 16c site is populated for a significant length of time, as implied by this study.

NMR can be used to follow the changes in the electrode materials following multiple charging cycles to determine why some materials fail and others maintain high capacities for extended cycling times. For example, Tucker et al. performed a series of detailed lithium NMR studies to explore the effect of cation doping on the long-term stability of the spinel materials.^{49,51} They systematically explored a series of proposed failure mechanisms by preparing model electrode materials where structural changes associated with the proposed failure mechanisms were intentionally introduced. The lithium spectra of the model compounds were then compared with spectra of electrodes extracted from cells that had been charged/discharged for varying numbers of cycles. For example, samples were soaked in moisture-contaminated electrolyte, and the spectra of these were compared to the spectra of the cycled materials. Soaking in wet electrolyte resulted in a shift of the spinel peak to 633 ppm and the appearance of a

resonance at 0 ppm due to the SEI (surface electrode interphase). This shift was not observed in the spectra of the cycled materials. This was in contrast to cells cycled at Stony Brook, where a shift to higher frequency was observed on extended cycling,⁸⁰ presumably a consequence of moisture introduced during cell assembly. Both studies ascribed the shift to Mn^{2+} dissolution and the consequent increase in oxidation state of the spinel material which can occur via a reaction such as⁸⁴



Li^+ loss, but without an increase in manganese oxidation state, can also occur due to ion exchange of Li^+ for any H^+ ions in the electrolyte.⁸⁵ Sato et al. showed that the ion-exchange process occurred predominantly on the surface for crystalline spinel samples, the oxidation state of the manganese ions at surface remaining close to 3.5, the average Mn oxidation state of the bulk increasing to 3.9 on treatment with acid.⁸⁶ Pickup et al. used Li NMR to examine the effect of chemical delithiation in sulfuric acid solutions on the spinel material.⁸⁷ A resonance was observed at ca. 950 ppm for delithiated spinel samples $\text{Li}_x\text{Mn}_2\text{O}_4$, $x < 0.3$, which was ascribed to Li in the tetrahedral site in Mn^{4+} -rich domains in the center of the particles. The authors also proposed that these domains resulted from H^+/Li^+ ion-exchange on the surfaces of the particles; the presence of a surface layer of HMn_2O_4 was supported by parallel FTIR studies. The 950 ppm resonance was seen in earlier studies at the top of charge for stoichiometric spinels and following multiple charge–discharge cycles.⁸⁰

An alternative approach for investigating the hydrogen content of cathode materials involves the use of ^2H or ^1H NMR. For example, we showed that ^2H NMR could be used to detect deuterons in samples following chemical or electrochemical reduction.⁸⁸ This approach was used to follow the structural changes that occur on acid leaching of Li_2MnO_3 .⁸⁹ ^2H NMR signals are much easier to detect than ^1H signals because of the much smaller electron–nuclear dipolar couplings involving ^2H due to its smaller γ_{N} . A ^2H NMR signal from $\text{Li}_{1.05}\text{Mn}_{1.95}\text{O}_4$ soaked in $\text{D}_2\text{-SO}_4$ due to ion-exchanged deuterons has been obtained, but no studies following extended cycling have been performed to date.⁹⁰

Finally, NMR has also been used to study other spinel materials that do not contain manganese. For example, the intercalation/deintercalation of lithium titanate spinels such as $\text{Li}_{4/3+x}\text{Ti}_{5/3}\text{O}_4$ ⁹¹ and $\text{Li}_{1.1}\text{Ti}_{1.9}\text{O}_{4+\delta}$ ⁹² have been investigated. These materials may be used as anode materials in combination with cathodes operating at 4 V (vs Li) to produce cells with potentials of ca. 2.5 V.⁹³ These materials are either diamagnetic or metallic,⁹⁴ and unlike the manganates, only very small differences in shifts are seen for Li in the different sites of the spinel structure. Nonetheless, these shift differences are enough to allow the concentrations of the different sites to be quantified and monitored following insertion of Li^{92} or as a function sample preparation method.⁹⁴

4.2. Cr^{3+} - and Ni^{2+} -Substituted Layered Lithium Manganates

Lithium NMR spectroscopy has similarly been applied to investigate the local structure and cycling properties of a number of alternative layered manganese cathode materials. Layered, monoclinic LiMnO_2 is isostructural with LiCoO_2 and has been widely studied as a possible cathode material.^{95,96} Unfortunately, this material transforms on cycling at 3–4 V (vs Li) to the more thermodynamically stable spinel phase.^{97,98} Cation doping has been used to stabilize the layered phase with some success.^{99,100} One series of materials that has generated considerable recent interest includes several cathodes, in particular, containing Ni^{2+} or Cr^{3+} ($\text{Li}[\text{Li}_{0.2}\text{Mn}_{0.4}\text{Cr}_{0.4}]\text{O}_2$ and $\text{Li}[\text{Ni}_{0.5}\text{Mn}_{0.5}]\text{O}_2$) where the charging and discharging cycles involve multiple electron transfers per transition-metal ion.^{6,9,10,101} The manganese remains in the +4 valence state at all times, preventing the instabilities associated with Mn^{3+} (i.e., the layered-to-spinel conversion). High capacities of up to 190–220 mAhg^{-1} have been seen for these materials.

Chromium was shown to cycle reversibly between Cr^{3+} and Cr^{6+} in the mixed Cr–Mn oxide $\text{Li}[\text{Li}_{0.2}\text{Mn}_{0.4}\text{Cr}_{0.4}]\text{O}_2$.^{6,102} Lithium NMR spectroscopy showed that the material contains Li_2MnO_3 -like and Mn^{4+} -doped LiCrO_2 local environments or domains.⁴⁷ Only the Li ions in the Mn^{4+} -doped LiCrO_2 regions of this “nanocomposite” are removed on cycling and largely responsible for the capacity, while the Li_2MnO_3 parts were inactive. The toxicity of Cr^{6+} restricts the use of this cathode material, and subsequent NMR work has focused on solid solutions of $\text{Li}[\text{NiMn}]_{0.5}\text{O}_2$ and Li_2MnO_3 .

Although the widely studied layered material LiNiO_2 functions via the reversible cycling of nickel between oxidation states of 3 and 4, nickel may also be cycled between Ni^{2+} and Ni^{4+} at higher voltages in both layered materials and spinels. For example, the spinel $\text{LiNi}_{0.5}\text{Mn}_{1.5}\text{O}_4$ cycles at ca. 4.8 V, the manganese, present as Mn^{4+} in this material, acting as an inert spectator ion.¹⁰³ The presence of Ni^{2+} (and not Ni^{3+}) in the spinels $\text{LiNi}_x\text{Mn}_{2-x}\text{O}_4$ was clearly demonstrated by NMR.⁴⁶ A similar $\text{Ni}^{2+}/\text{Ni}^{4+}$ process occurs in layered $\text{LiNi}_{0.5}\text{Mn}_{0.5}\text{O}_2$ and its Li-excess versions at a much lower voltage (between ca. 3.7 and 4.6 V).^{9,10,104,105}

^6Li NMR has been used to study the local environments in the Li_2MnO_3 – $\text{Li}(\text{NiMn})_{0.5}\text{O}_2$ solid solutions ($\text{Li}[\text{Ni}_x\text{Mn}_{(2-x)/3}\text{Li}_{(1-2x)/3}]\text{O}_2$). Li resonances due to Li ions in the predominantly Li layers (500–800 ppm) and in the transition-metal layers (1360 and 1560 ppm) can be clearly resolved at frequencies close to those seen for similar environments in Li_2MnO_3 (Figure 12).^{106,107} Surprisingly, even for the $x = 0.5$ end member, Li ions are still observed in the transition-metal layers (circled in Figure 12), indicating that Ni^{2+} – Li^+ exchange between the layers has occurred. The presence of nickel in the Li layers has been confirmed by diffraction experiments.^{104,105} The intensities of the resonances due to Li in the transition-metal layers were used to develop a model for cation ordering and demonstrate that the ordering in these layers was far from random. The Li ions in

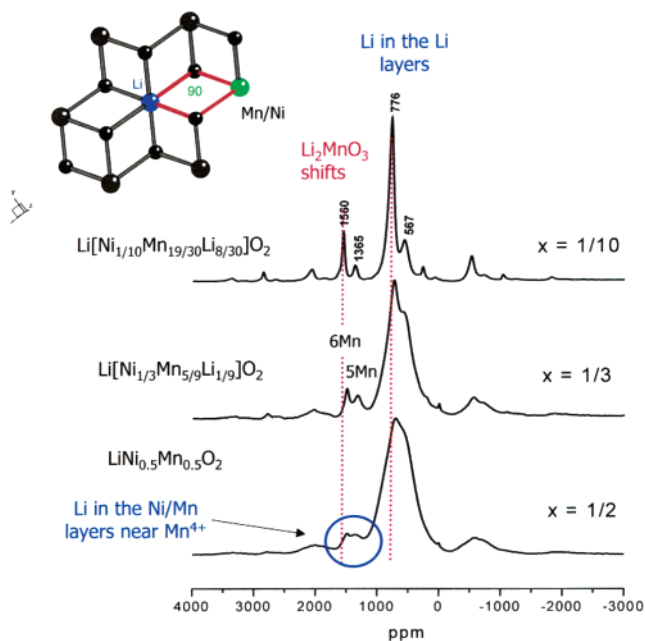


Figure 12. ${}^6\text{Li}$ MAS NMR spectra of $\text{Li}[\text{Li}_{(1-2x)/3}\text{Mn}_{(2-x)/3}\text{Ni}_x]\text{O}_2$, with $x = 1/10$, $1/3$, and $1/2$. The resonances corresponding to local environments $\text{Li}(\text{OMn})_6$ and $\text{Li}(\text{OMn})_4(\text{OLi})_2$ found in Li_2MnO_3 are marked. The $\text{Li}(\text{OMn})_6$ local environment is shown on the right. The frequencies of the major resonances are indicated; asterisks indicate spinning sidebands.

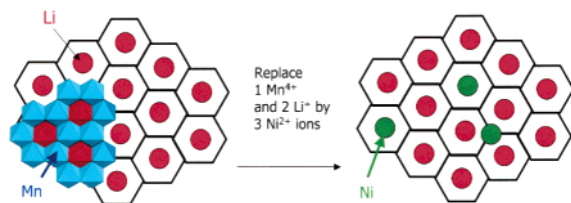


Figure 13. Schematic of the ordering scheme found in Li_2MnO_3 showing the honeycomb structure formed by Li (red circles) and Mn (left-hand side) and the structure derived by replacing two Li and one Mn by three Ni (green circles).

the Ni/Mn layers show a strong preference for substitution in environments near six Mn^{4+} , as found in the end member compound Li_2MnO_3 . A model was proposed that was based on the “honeycomb” ordering of the Mn^{4+} and Li^+ ions in the Mn/Li layer of Li_2MnO_3 , where the Ni^{2+} ions substitute into ordered layers so as to minimize the number of $\text{Li}^+-\text{Ni}^{2+}$ contacts (Figure 13).¹⁰⁷

Studies of these materials following charging and discharging showed that both the Li in the Li layers and in the transition-metal layers participate in the electrochemistry.¹⁰⁶ Even the Li in the Ni/Mn layers can be cycled reversibly at least in the first few cycles.¹⁰⁸ Preliminary results suggest that the Li vacancies created in this process at the top of charge may represent a possible mechanism for creating increased disorder in these materials following extended cycling.

4.3. LiCoO_2 and Related Materials

LiCoO_2 -related cathode materials have been investigated extensively by NMR. The NMR of these systems may be used to follow not only the oxidation

of the Co^{3+} and doped ions, but also changes in the electronic conductivities of these materials. In particular, the NMR spectra are extremely sensitive to semiconductor-to-metal phase transitions.¹⁰⁹ Although low-spin d^6 Co^{3+} ions are nominally diamagnetic, the layered (O3) LiCoO_2 (Figure 1) and the layered O2 polytype show a very weak, temperature-independent (Van-Vleck) paramagnetism,¹¹⁰ which is presumably due to mixing in of higher (paramagnetic) states. The labels “O2” and “O3” for the two structures indicate that the Li environment is octahedral in both but that the stacking sequences of the oxygen layers are ABCB and ABCABC, leading to two and three sets of Co and Li layers in the hexagonal unit cell, respectively.

The ${}^6\text{Li}$ and ${}^7\text{Li}$ spectra of the O3 and O2 LiCoO_2 phases both show a resonance at -0.2 ppm consistent with lithium in an essentially diamagnetic local environment and the presence of low-spin (t_{2g}^6) Co^{3+} ions.^{28,110,111} Shift anisotropies, obtained by analysis of the ${}^7\text{Li}$ and ${}^6\text{Li}$ NMR line shapes, were extremely close to those calculated by using the experimentally determined values for the susceptibility χ_m for both phases. ${}^{59}\text{Co}$ ($I = 7/2$) NMR has also been used to probe the structure of these materials and extract detailed information concerning the coordination environments in these phases.^{110,112} O2 and O3 show quite different ${}^{59}\text{Co}$ MAS NMR spectra, and the ${}^{59}\text{Co}$ ($I = 7/2$) quadrupolar coupling constant (QCC) for the octahedral site in O2 is much larger than that found for the Co site in the O3 material, consistent with the differences in the two structures: the CoO_6 octahedra in the O2 structure share a face and three edges with the LiO_6 octahedra, while they only share (6) edges in the O3 structure.¹¹⁰

NMR spectroscopy has been used to follow the cycling of Li_xCoO_2 .¹⁰⁹ The results indicate that Co^{4+} ions are formed during the initial stages of deintercalation.¹⁰⁹ A broad resonance appears at $x = 0.94$, the shift being ascribed to a Knight shift, due to interaction between the Li nuclei and the conduction electrons in the t_{2g}^* band formed from the overlapping t_{2g} cobalt orbitals (Figure 14). The NMR results suggest that the biphasic region that exists in Li_xCoO_2 from $0.75 \leq x \leq 0.94$ is due to this phase transition. Additional ${}^7\text{Li}$ resonances have been seen for Li-excess nonstoichiometric $\text{Li}_{1+x}\text{CoO}_2$, which have been ascribed to the presence of paramagnetic Co^{2+} ions that are formed in conjunction with oxygen and cobalt vacancies.⁵⁵ Materials synthesized at higher temperatures have also been shown to contain oxygen vacancies. These oxygen vacancies result in the presence of five-coordinate Co^{3+} ions, the NMR results suggesting that these Co^{3+} ions are not diamagnetic but rather present as so-called “intermediate-spin” Co^{3+} defects.¹¹³

Lithium NMR has also been used to investigate the Ni^{3+} doping in LiCoO_2 .²⁸ A series of ${}^7\text{Li}$ NMR resonances were observed, which correspond to local environments formed by Ni^{3+} substitution in the first and second cation coordination spheres surrounding the lithium ions. The resonances can be assigned by using similar arguments as those used to assign the spectra of the manganates. Recent DFT calculations

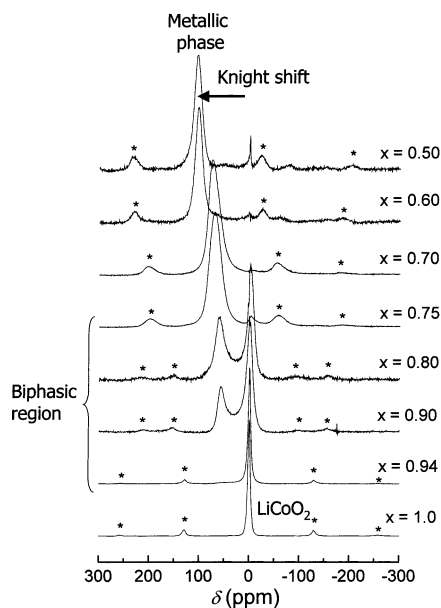


Figure 14. ${}^7\text{Li}$ MAS NMR spectra for Li_xCoO_2 (asterisks indicate spinning sidebands). The spikes at 0 ppm seen in the spectra of $x = 0.50$ and 0.6 are artifacts. The LiCoO_2 local environment and resonance due to the metallic phase are marked. (Reprinted with permission from ref 109. Copyright 1999 Royal Society of Chemistry.)

have shown (in contrast to earlier studies²⁸) that the negative shifts seen in these systems are due to Ni^{3+} ions in the Li first coordination shell (90° interactions), while the positive shifts are due to 180° interactions with half-filled e_g orbitals.⁵² The large positive shifts are caused by the delocalization mechanism involving the partially filled e_g^* orbitals, while the negative shifts are due to the polarization mechanism now involving the filled t_{2g} orbitals (formed from the metal d_{xy} , d_{xz} , and d_{yz} and the oxygen 2p orbitals) (see section 3.1). These new assignments do not significantly alter the conclusions reached in earlier papers. The distributions of the Ni^{3+} ions and the extent of Ni^{3+} substitution were quantified by extracting the intensities of the different resonances, the results demonstrating that the $\text{LiNi}_{1-y}\text{Co}_y\text{O}_2$ phases have a tendency to form cobalt-rich clusters.^{28,29} ${}^7\text{Li}$ NMR spectra of the partially deintercalated material $\text{Li}_x\text{Ni}_{0.3}\text{Co}_{0.7}\text{O}_2$, ($1 < x \leq 0.85$) indicate that the Ni^{3+} ions are oxidized at a lower potential than the Co^{3+} ions, the results suggesting that $\text{Ni}^{3+}/\text{Ni}^{4+}$ electronic hopping occurs in the early stages of charge. However, at $\text{Li}_{0.7}\text{Ni}_{0.3}\text{Co}_{0.7}\text{O}_2$ where in principle all the Ni^{3+} should be oxidized to diamagnetic Ni^{4+} , an NMR signal at ca. 20 ppm is seen. This is not consistent with the presence of only Ni^{4+} and Co^{3+} ions (which are both diamagnetic) and indicates that both Ni^{3+} and Co^{3+} are oxidized in this composition range. Furthermore, the variable-temperature NMR results for this sample suggest that both hopping between both Ni and Co ions occurs ($\text{Ni}^{3+}/\text{Ni}^{4+}$ and $\text{Ni}^{4+} + \text{Co}^{3+} \rightarrow \text{Ni}^{3+} + \text{Co}^{4+}$). Thus, the question as to which ion is being oxidized was suggested to be “irrelevant” in this range. At $x = 0.40$, metallic behavior was seen by NMR (and thermoelectric power measurements) but electronic conductivity measurements showed that the conductivity is still an activated process. The discrepancy was ascribed

to the presence of Ni^{4+} ions, which result in local distortions and prevent full electronic delocalization between Co^{3+} and Co^{4+} ions.²⁹

NMR studies have shown that structural defects such as oxygen vacancies and, to a lesser extent, intermediate-spin Co^{3+} are created upon Mg substitution in LiCoO_2 .¹¹⁴ ${}^7\text{Li}$ resonances with noticeable Knight shifts were seen by NMR, even before Li^+ ion deintercalation, but no evidence for metallic conductivity was seen from the electric properties. This was ascribed to the presence of metallic behavior at the local level in small domains surrounding the doped Mg^{2+} . The domains are presumably too well separated and too small to allow percolation (of the conduction electrons) throughout the solid.¹¹⁴ Doping with other transition metals such as Fe has been also probed by NMR,¹¹⁵ and the electrochemical properties of the “O2 phase” of LiCoO_2 have been investigated in some detail.¹¹⁶

Finally, ${}^{27}\text{Al}$ ($I = 5/2$) and ${}^{59}\text{Co}$ NMR spectroscopy have been used to probe Al^{3+} in Al-doped lithium cobalt oxides and lithium nickel oxides.^{117,118} A ${}^{27}\text{Al}$ chemical shift of 62.5 ppm was observed for the environment $\text{Al}(\text{OC}_6)_6$ for an Al^{3+} ion in the transition-metal layers, surrounded by six Co^{3+} ions. Somewhat surprisingly, this is in the typical chemical shift range expected for tetrahedral environments (ca. 60–80 ppm), but no evidence for occupancy of the tetrahedral site was obtained from X-ray diffraction and IR studies on the same materials.¹¹⁷ Substitution of the Co^{3+} by Al^{3+} in the first cation coordination shell leads to an additive chemical shift decrease of ca. 7 ppm, and the shift of the environment $\text{Al}(\text{OAl})_6$ (20 ppm) seen in spectra of materials with higher Al content is closer to that expected for octahedral Al. The spectra are consistent with a continuous solid solution involving octahedral sites randomly occupied by Al and Co.¹¹⁷ It is possible that the unusual ${}^{27}\text{Al}$ shifts seen for this compound are related to the Van-Vleck susceptibility of this compound.

4.4. Lithium Phosphates

Recently, LiFePO_4 , which adopts the olivine structure, has been widely studied as a possible cheap cathode material.¹² Although the specific capacities of this material and the related NASICON structures are relatively low (typically 100 mAhg^{-1}), these compounds are cheap and open up new avenues for research. ${}^7\text{Li}$ MAS NMR studies of a series of olivines LiMPO_4 with $M = \text{Mn}, \text{Fe}, \text{Ni},$ and Co were carried out by Tucker et al.^{64,119} A single resonance with large spinning sidebands envelope was observed for all the compounds, indicating the presence of one local environment for the lithium cations. In contrast to the lithium manganese oxide spinels, much smaller shifts from -90 to 70 ppm were seen. The difference between the compounds was rationalized by considering the electronic configuration of the transition-metal cation site in C_s symmetry. Interestingly, the smaller shifts observed in these compounds and in the related vanadium-containing NASICONs⁶² is most likely related to the same phenomena that results in the high voltages of these systems (the

$\text{Fe}^{2+}/\text{Fe}^{3+}$ couple is at 2.8–3.5 V in these structures¹²⁰), namely, the so-called inductive effect of the phosphate groups. The covalent P–O bonds of the phosphate groups will presumably increase the ionic character of the Li–O and M–O bonds in these compounds,¹²⁰ reducing the extent of overlap and thus hyperfine interactions in these materials.

4.5. Vanadates

Highly oxidized oxides of vanadium, chromium, niobium, and molybdenum are well known for their ability to intercalate large concentrations of lithium ions on electrochemical reduction.^{121–127} Although many vanadium compounds have limited cycle lives in lithium-ion cells, limiting their commercial use, the vanadium oxides V_2O_5 , V_6O_{13} , and LiV_3O_8 , in particular, are all potential rechargeable 3 V electrode materials and suitable for use in conjunction with polymer electrolytes. These systems have received considerable attention by NMR spectroscopists. In addition to lithium NMR, ^{51}V MAS NMR spectroscopy represents a powerful tool for studying the local environments in these materials, particularly for compounds containing the diamagnetic, d^0 ions V^{5+} . We briefly discuss some of the information that can be obtained from ^{51}V NMR before describing the applications of NMR to these materials.

4.5.1. ^{51}V NMR

The ^{51}V nucleus is quadrupolar (spin 7/2, natural abundance 99.76%), and thus, the spectra can be affected by both the first- and second-order quadrupole interaction, though the second-order broadening is generally not the largest source of line broadening in these materials.¹²⁸ In general, three major anisotropic interactions influence the line shapes seen in the ^{51}V NMR spectra of solid samples: (i) the quadrupolar interaction, (ii) the chemical shift anisotropy (CSA), which can be significant for ^{51}V , and (iii) the dipolar interaction between the ^{51}V nucleus under observation and nearby nuclei or electrons. Analysis of the line shapes of these compounds is typically nontrivial, particularly at moderate or high field strengths, and careful simulation of the spectra is required to extract the various parameters describing the CSA (σ_{11} , σ_{22} , σ_{33}) and quadrupolar tensors. The line shapes of the ^{51}V NMR spectra are strongly influenced by the CSA in high magnetic fields and by the quadrupolar interaction in low magnetic fields, and thus, spectra should be acquired at multiple field strengths to ensure accurate measurements of the various interactions.

Although much of the ^{51}V NMR has been performed on model systems or catalytic materials containing vanadium,^{129,130} compounds such as V_2O_5 or VOPO_4 are used in both the catalysis and lithium battery fields, and many of the results can be used to help elucidate the structures of vanadium-containing cathode materials. ^{51}V NMR spectra are sensitive to changes in the vanadium coordination number and distortions of the vanadium local environments from regular tetrahedra or octahedra.^{131–133} ^{51}V isotropic chemical shifts of between –400 and –800 ppm are seen for vanadium oxides, and unfortunately, unlike

^{27}Al and ^{29}Si NMR,^{134,135} the isotropic chemical shifts for ^{51}V nuclei in vanadates in different coordination environments overlap. The anisotropy of the chemical shift is, however, sensitive to the arrangement of oxygen atoms in the first coordination sphere: Vanadium atoms in distorted octahedral sites are typically associated with CSAs that are nearly axially symmetric and with spans ($\Delta\sigma = \sigma_{11} - \sigma_{33}$) of ca. 600–1400 ppm. For vanadium atoms in distorted tetrahedral sites, a chemical shift tensor with a large asymmetry parameter η (which indicates the deviation from axial symmetry $\eta = (\sigma_{11} - \sigma_{22})/(\sigma_{iso} - \sigma_{33})$, $0 \leq \eta \leq 1$; $\eta = 0$ for an axially symmetric tensor) is obtained along with a span of 400–600 ppm. The span drops to 100–300 ppm for a slightly distorted tetrahedral site. The isotropic chemical shift is sensitive to the type of atoms in the second coordination sphere,^{136–138} providing additional structural information.

As discussed in section 2.2, ^{51}V NMR spectra of V^{IV} compounds with localized d^1 V^{4+} ions are typically “invisible” by NMR when standard MAS NMR methods are used. In contrast, ^{51}V spectra may be detected for metallic V^{4+} samples,¹³⁹ and large shifts are typically observed as a result of the Knight shift. For instance, a large negative Knight shift was observed at –4788 ppm for $\alpha\text{-VO}_2$.¹⁴⁰ ^{51}V resonances for the V^{5+} ions in mixed $\text{V}^{5+}/\text{V}^{4+}$ compounds may, however, be “visible”. A good example is provided by the work of Delmaire et al.,¹⁴¹ who assigned the resonance at –1447 ppm observed in reduced forms of $\text{Bi}_4\text{V}_2\text{O}_{11-\delta}$ to V^{5+} ions near V^{4+} ions, the large shifts resulting from $\text{V}^{5+}-\text{O}-\text{V}^{4+}$ hyperfine interactions. V_2O_5 does not show metallic behavior on partial or complete reduction of V^{5+} to V^{4+} or V^{3+} . Evidence for partial delocalization of spin density has been obtained for some reduced vanadates by using ESR and NMR spectroscopy, but in these systems delocalization results from a hopping mechanism rather than from metallic behavior.^{62,142,143} The main problem associated with the use of ^{51}V NMR to characterize cathode materials is the broadening and/or loss of the signal on reduction, so that it becomes difficult, or impossible, to follow change in the vanadium local environment during lithium intercalation/deintercalation. However, NMR of other nuclei such as ^6Li or ^{31}P can sometimes be performed in parallel to probe these systems.^{144,145}

4.5.2. NMR Studies of Vanadium Oxides

The vanadium oxide, V_2O_5 , shows particular promise as a positive electrode material in polymer batteries. Because of the existence of the short vanadyl bond,¹⁴⁶ it can either be considered as a two-dimensional layered structure comprising VO_5 square pyramids or a 3D structure formed from VO_6 octahedra. The strong anisotropy of the structure accounts for its ability to accommodate lithium. Intercalation to form $\text{Li}_x\text{V}_2\text{O}_5$ at ca. 3.3 V vs Li^0/Li^+ results in two phases, α ($x < 0.1$) and ϵ ($0.35 < x < 0.7$),¹⁴⁷ which differ in their interlayer spacing. $\delta\text{-LiV}_2\text{O}_5$ is formed after the shearing of the layers.¹⁴⁸ For $1 < x < 2$, the δ phase undergoes an irreversible transformation involving considerable reconstruction to form

a γ phase that can cycle between $0 < x < 2$.¹⁴⁹ The intercalation of a third lithium atom into the structure yields the ω phase, which is able to cycle for more than 100 cycles between 3.4 and 1.9 V, yielding a specific energy of 450 Wh/kg.¹⁵⁰

Numerous studies have been performed using ^6Li and/or ^{51}V NMR of chemically and electrochemically intercalated V_2O_5 bronzes,^{60,143,151} different $\text{Li}_x\text{V}_2\text{O}_5$ phases ($0 < x < 2$),^{152,153} and $\text{Li}_x\text{V}_2\text{O}_5$ aerogels with compositions of $1.00 < x < 5.84$.^{62,142} Intercalation of lithium causes distortions resulting in a decrease in the a lattice parameter, an increase in the c parameter (puckering of the V_2O_5 layers¹⁴⁸), and a change in the coordination of the lithium. Different ^7Li MAS NMR resonances are seen for the various lithium sites encountered during electrochemical lithium intercalation: $\alpha\text{-Li}_x\text{V}_2\text{O}_5$ (−16 ppm; trigonal), $\epsilon\text{-Li}_x\text{V}_2\text{O}_5/\epsilon\text{II-Li}_x\text{V}_2\text{O}_5$ (−25/−22 ppm; trigonal), $\delta\text{-Li}_x\text{V}_2\text{O}_5$ (−12 ppm; tetrahedra), $\gamma\text{-Li}_x\text{V}_2\text{O}_5$ phase (5 and 16 ppm; distorted octahedra and tetrahedra respectively), and $\zeta\text{-Li}_x\text{V}_2\text{O}_5$ (10 ppm).¹⁵⁴ The lithium sites in the γ -phase are associated with smaller QCCs, smaller dipolar couplings, and smaller shifts. Sites with low occupancies were more readily seen with ^7Li NMR due to its higher sensitivity, while higher resolution spectra were obtained with ^6Li NMR.

Hirschinger et al.¹⁴³ used NMR to show that the biphasic domain seen on chemical lithiation of V_2O_5 at high temperatures to form lithiated β (^7Li NMR resonance at −27 ppm due to monocapped trigonal prisms) and β' (−31 ppm; tetrahedral site) phases should be extended from $x = 0.33$ to 0.48 (at 600 °C).^{155,156} The unpaired electrons become increasingly delocalized as the lithium content decreases in the β/β' phases, in contrast to the γ phase, where the electrons were localized on specific vanadium sites.

Stallworth et al. showed that the Li sites in V_2O_5 aerogels occupy sites with axial symmetry, consistent with proposed structural models where the intercalated lithium ions are situated at the apical oxygen position between adjacent V_2O_5 layers.^{62,142} New sites are occupied on incorporation of larger amounts of lithium, which are associated with nonbridging oxygens in the equatorial plane of the VO_5 unit. ^{51}V NMR resonances were seen for all the reduced samples, allowing the $\text{V}^{4+}/\text{V}^{5+}$ ratio to be evaluated.

In addition to structural information, ^7Li MAS NMR T_2 relaxation measurements and analysis of ^7Li line shapes have been used to probe the dynamics of the lithium ions.^{13,153} Holland et al.¹³ identified two different species with different mobilities (interfacial Li (longer T_2 , rapid dynamics) and intercalated lithium (shorter T_2 , slower dynamics)) in the electrochemically lithiated V_2O_5 xerogel matrix. Li hopping frequencies were extracted from an analysis of the ^7Li line widths and the appearance of a quadrupolar splitting as the temperature decreased in a related system.¹⁵³

$\text{Li}_{1+x}\text{V}_3\text{O}_8$ has received considerable attention as a cathode material for secondary lithium batteries over the past few years.^{157–162} $\text{Li}_{1+x}\text{V}_3\text{O}_8$ has a layered framework suitable for reversible lithium intercalation processes that can allow up to four Li^+ ions per formula unit to be inserted (i.e., x can vary from 0 to

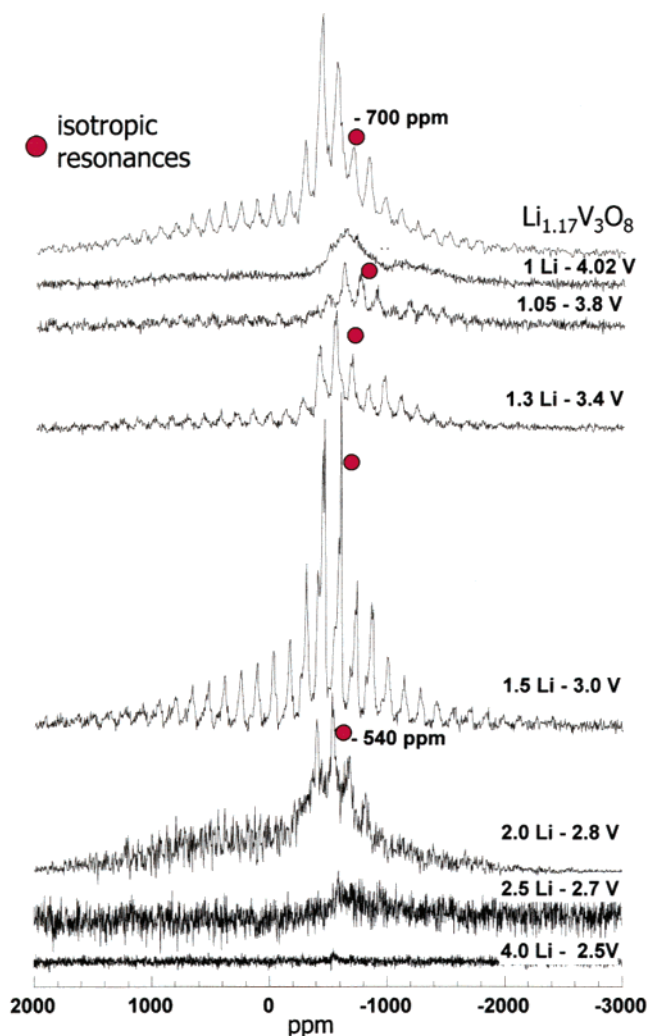


Figure 15. ^{51}V MAS NMR spectra of $\text{Li}_{1+x}\text{V}_3\text{O}_8$ obtained at different stages of the intercalation process ($\nu_r = 13$ kHz), plotted in a quantitative mode. The isotropic resonances are marked with circles.

4). The compound forms a continuous solid solution between 4.2 and 3.0 V and shows two reversible phase transitions at lower potential during cycling. The V_3O_8 layers of LiV_3O_8 are comprised of vanadium in square pyramids (V1), distorted octahedra (V2), and more regular octahedral (V3).¹⁶⁰ Experimental and theoretical studies performed by Benedek et al.,¹⁶¹ Picciotto et al.,¹⁵⁹ and Jouanneau¹⁶² suggested a number of different possible (octahedral and tetrahedral) sites for Li.

Both the ^{51}V and ^7Li NMR spectra show multiple vanadium and lithium local environments for the as-synthesized material ($x = 0.15$), and the spectra cannot be explained by using a simple model¹⁴⁵ based on the number of crystallographically distinct vanadium sites.^{159,161} On Li-ion intercalation, the ^{51}V resonances sharpen and shift to higher frequencies (Figure 15); three sharp resonances along with two broader resonances are clearly resolved for the samples prepared at potentials of 3.4 and 3.0 V ($x = 0.3$ and 0.5, respectively). This behavior is consistent with solid–solution behavior in this potential range and is ascribed to the presence of localized V^{4+} defects at x close to 0 and electron delocalization for $1 > x > 0.05$. Three lithium sites were observed in the ^7Li

NMR spectra for $0 < x < 1$, which are assigned to the octahedral site and two tetrahedral sites between the lithium layers. A phase transition has been seen in the electrochemical data at ca. 2.8 V to form $\text{Li}_2\text{V}_3\text{O}_8$, but no evidence is seen for this transition with structural probes (such as diffraction and transmission electron microscopy). The phase transition results in a dramatic change in the NMR spectra. A noticeable decrease in intensity and resolution of the ^{51}V resonances is seen, which has been ascribed to a first-order electronic transition with charge ordering and the formation of localized V^{4+} and V^{5+} ions. The lithium NMR spectra are similarly consistent with localized paramagnets. Small negative shifts are seen, consistent with the presence of d electrons in the d_{xy} orbitals of the vanadium ions.

Lithium intercalation in V_6O_{13} has been studied by Stallworth et al.⁶⁰ Variable-temperature ^7Li NMR indicated considerable mobility for Li^+ in the intercalated materials. The ^7Li NMR data were compared with ESR spectra and near-edge X-ray absorption fine structure (NEXAFS) data on the same materials, and a correlation between vanadium oxidation state (from NEXAFS data) and NMR shift was observed. The authors explained the shifts in terms of different coupling mechanisms between the V^{4+} and V^{3+} shifts. The shifts were, however, extracted from static NMR experiments, and it is possible that some of the different local environments, typically revealed in a MAS spectrum, were not seen in this study.

4.5.3. Vanadium Phosphates

More recently, lithium vanadium phosphates ($\text{Li}_3\text{V}_2(\text{PO}_4)_3$ and $\text{Li}_3\text{FeV}(\text{PO}_4)_3$,^{163,62} with open NASICON framework structures, have also been studied. Reversible electrochemical lithium deintercalation/reintercalation at a higher potential (in comparison to the $\text{V}^{5+}/\text{V}^{4+}$ couples seen for the oxides) of between 3 and 3.5 V (vs Li^0/Li^+) is seen along with high lithium diffusion rates. VOXO_4 materials ($X = \text{S}, \text{P}, \text{As}$)^{164–167} contain two- or three-dimensional frameworks^{168–170} that can accommodate lithium. They have high theoretical specific capacities (from 135 to 165 mAhg^{-1} , depending on X), reversible Li intercalation occurring at a potential of ca. 4 V for $\beta\text{-VOPO}_4$ ¹⁶⁵ and at 3.5–3.7 V for $\alpha_{\text{II}}\text{-VOPO}_4$.^{166,167}

^{51}V , ^6Li , and ^{31}P MAS NMR spectroscopy have been performed to study the two first electrochemical cycles of $\alpha_{\text{II}}\text{-VOPO}_4$ and $\beta\text{-VOPO}_4$.¹⁴⁴ Lapina et al.¹⁷¹ and Siegel et al.¹⁷² determined both the magnitude and relative orientation of the quadrupole and chemical shift tensors for the α_{I} , α_{II} ($\delta_{\text{iso}} = -755$ ppm), and $\beta\text{-VOPO}_4$ ($\delta_{\text{iso}} = -735$ ppm) phases from ^{51}V NMR data with slightly different results being obtained between the two groups for the α_{II} phase. ^6Li , ^{31}P , and ^{51}V magic angle spinning (MAS) NMR were used to follow the evolution of $\alpha_{\text{II}}\text{-VOPO}_4$ during the two first electrochemical cycles. Lithium intercalation in $\alpha_{\text{II}}\text{-VOPO}_4$, to form $\alpha_{\text{II}}\text{-LiVOPO}_4$, occurs in two voltages on the first reduction, at 3.7 (16% of the total capacity) and 3.5 V (84% of the total capacity), resulting in a ^6Li resonance at 120 ppm (Figure 16) characteristic of $\alpha_{\text{II}}\text{-LiVOPO}_4$. The subsequent lithium deintercalation occurs in three steps, all of them

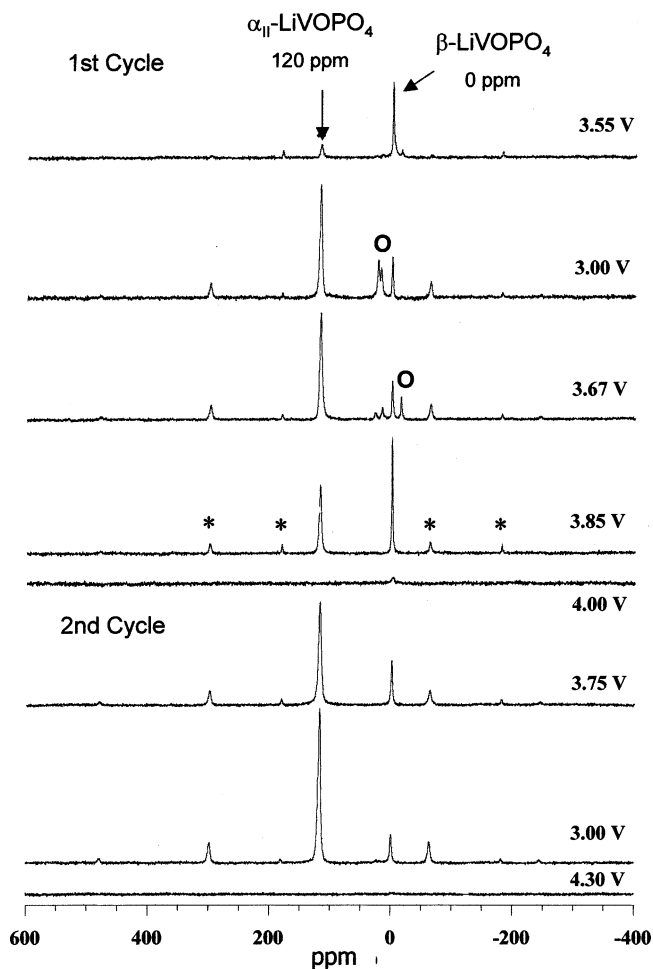


Figure 16. Quantitative ^6Li MAS NMR spectra of $\alpha_{\text{II}}\text{-Li}_x\text{-VOPO}_4$ acquired during the first and second electrochemical cycles at $B_0 = 7.1$ T ($\nu_r = 8.0$ kHz). The shifts of the isotropic resonances are marked next to the peaks. The circles and asterisks indicate extra impurity peaks and sidebands, respectively.

involving the α_{II} phase, at 3.5 (26%), 3.7 (16%), and 3.9 V (58%), while the second lithium intercalation takes place in two steps at 3.9 (75%) and 3.7 V (25% of the total capacity). These changes reflect an electrochemically driven structural rearrangement that occurs upon cycling of $\alpha_{\text{II}}\text{-VOPO}_4$, which leads to a change in the lithium intercalation/deintercalation potential. This transformation was proposed to involve local rearrangements of ions as well as the nucleation and growth of well-defined phases. A ^6Li signal corresponding to the β phase, present as an impurity, is seen even at high potentials (3.75 V) at 0 ppm.

Only the nonlithiated diamagnetic phase may be seen by ^{51}V NMR, lithium intercalation resulting in a dramatic loss of signal, presumably due to the large ^{51}V –electron hyperfine interaction (as discussed in section 2.2), the ^6Li NMR resonance at 120 ppm confirming the presence of V^{4+} ions. Thus, the method cannot be used to follow the lithium intercalation into the different sites in the host structure. The percentage of β phase (12%) present as an impurity could be extracted from the ^{51}V MAS NMR spectrum. The signal corresponding to the β phase disappears at the beginning of the discharge but reappears at the end of the cycle, at high potential (4.0 V), showing that

the α_{II} and β phases cycle independently. The intensity of α_{II} phase decreased as a function of cycle number, suggesting that other paramagnetic phases are formed; this is confirmed by observation of additional resonances in the ^6Li and ^{31}P MAS NMR spectra of the same materials.

No ^{51}V NMR studies have been performed on the rhombohedral form of $\text{Li}_{3-x}\text{V}_2(\text{PO}_4)_3$ due to the localization of electrons on the V^{4+} and V^{3+} ions. ^7Li NMR experiments have however been performed on this system, which suggest that ions on the M(3) sites of the NASICON structure in $\text{Li}_3\text{V}_2(\text{PO}_4)_3$ move onto the M(1) sites on extraction of Li to form $\text{LiV}_2(\text{PO}_4)_3$.⁶² A shift of the isotropic resonance from 85 to 62 ppm on deintercalation of two Li^+ ions is attributed to the change in site geometry and the change in vanadium oxidation state from V^{3+} to V^{4+} . Finally, ^7Li NMR studies performed on the monoclinic form of $\text{Li}_x\text{V}_2(\text{PO}_4)_3$ provide strong evidence for Li and vanadium charge ordering on insertion of lithium, the ordering driving the series of phase transitions seen for this material.¹⁷³

5. Conclusions

NMR represents a powerful method for studying the local structures and electronic properties of cathode materials as a function of state of charge. The research reviewed in this article clearly demonstrates that it is now possible to obtain a wealth of information from the NMR spectra of cathode materials, even in the paramagnetic or metallic state, both prior to and following electrochemical cycling of a battery. The paramagnetic properties of many of these systems, rather than being a complication, can often provide increased resolution of resonances from different local environments. The lithium hyperfine shifts of many systems can be rationalized in terms of the coordination environment for lithium and the numbers and types of unpaired electrons on the nearby paramagnets. In the case of systems whose hyperfine shifts obey a Curie–Weiss Law, it is often possible to predict the magnitude and direction of the shifts by analyzing the connectivity between lithium and nearby paramagnetic ions.

NMR may be used to probe the effect of doping on local structure. For example, NMR studies of the spinel phases show that cation doping results in an increase in the oxidation state of the manganese ions near the cation dopant, while cation doping in LiCoO_2 has a dramatic effect on the electronic structure of the material. NMR may be used to determine the cation ordering and investigate the effect of local structure on the electrochemical properties of the cathode materials. In phosphates and vanadates, additional probes such as ^{51}V and ^{31}P NMR provide additional information concerning local structure and electronic properties. In conclusion, NMR has now been applied to a wide range of cathode materials for lithium-ion batteries and is rapidly becoming an essential characterization tool in this research area.

6. Acknowledgments

Support from the NSF via DMR 9901308 and 0211353 is gratefully acknowledged. Additional sup-

port comes from the Assistant Secretary for Energy Efficiency and Renewable Energy, Office of Freedom-CAR, and Vehicle Technologies of the U.S. Department of Energy via subcontract No. 6517749 with the Lawrence Berkeley National Laboratory. C.P.G. thanks the current and former members of her group (Y. J. Lee, C. Pan, Y. Paik, W. S. Yoon, J. Breger, and M. Jiang) and co-workers B. Meyer and N. Leifer who have contributed to the work described herein. Insightful discussions with D. Carlier, M. Menetrier, and G. Ceder are gratefully acknowledged.

7. References

- (1) Bruce, P. G. *Chem. Commun.* **1997**, 1817.
- (2) Guyomard, D.; Tarascon, J. M. *Solid State Ionics* **1994**, *69*, 222.
- (3) Koksang, R.; Barker, J.; Shi, H.; Saidi, M. Y. *Solid St. Ionics* **1996**, *84*, 1.
- (4) Winter, M.; Besenhard, J. O.; Spahr, M. E.; Novak, P. *Adv. Mater.* **1998**, *10*, 725.
- (5) Tarascon, J.-M.; Armand, M. *Nature* **2001**, *414*, 359.
- (6) Ammundsen, B.; Paulsen, J. *Adv. Mater.* **2001**, *13*, 943.
- (7) Nagaura, T.; Tozawa, K. *Prog. Batteries Solar Cells* **1990**, *9*, 209.
- (8) Dahn, J. R.; von Sacken, U.; Michal, C. A. *Solid State Ionics* **1990**, *44*, 87.
- (9) Ohzuku, T.; Makimura, Y. *Chem. Lett.* **2001**, 744.
- (10) Lu, Z.; MacNeil, D. D.; Dahn, J. R. *Electrochem. Solid State Lett.* **2001**, *4*, A191.
- (11) Thackeray, M. M.; David, W. I. F.; Bruce, P. G.; Goodenough, J. B. *Mater. Res. Bull.* **1983**, *18*, 461.
- (12) Padhi, A. K.; Nanjundaswamy, K. S.; Goodenough, J. B. *J. Electrochem. Soc.* **1997**, *144*, 1188.
- (13) Holland, G. P.; Buttry, D. A.; Yarger, J. L. *Chem. Mater.* **2001**, *14*, 3875.
- (14) Wagemaker, M. M.; Kentgens, A. P. M.; Mulder, F. M. *Nature* **2002**, *418*, 397.
- (15) Gerald, R. E.; Sanchez, J.; Johnson, C. S.; Klinger, R. J.; Rathke, J. W. *J. Phys. Condens. Mater.* **2001**, *13*, 8269.
- (16) Chevallier, F.; Letellier, M.; Morcrette, M.; Tarascon, J.-M.; Frackowiak, E.; Rouzaud, J.-N.; Béguin, F. *Electrochem. Solid-State Lett.* **2003**, *6*, A225.
- (17) Grey, C. P.; Lee, Y. J. *Solid State Sci.* **2003**, *5*, 883.
- (18) Park, S.-H.; Kleinsorge, M.; Grey, C. P.; Parise, J. B. *J. Solid State Chem.* **2002**, *167*, 310.
- (19) Meyer, B.; Leifer, N.; Greenbaum, S.; Grey, C. P. Manuscript in preparation.
- (20) Kittel, C. *Introduction to Solid State Physics*, 6th ed.; John Wiley & Sons: New York, 1986.
- (21) Carrington, A.; McLachlan, A. D. *Introduction to Magnetic Resonance*; Harper and Row: New York, 1967.
- (22) Kohler, F. H. In *Magnetism: Molecules to Materials*; Miller, J. S., Drillon, M., Eds.; Wiley-VCH: New York, 2001.
- (23) Albanese, N. F.; Chasteen, N. D. *J. Phys. Chem.* **1978**, *8*, 910.
- (24) van Willigen, H. *J. Magn. Reson.* **1980**, *39*, 37.
- (25) Atherton, N. M.; Shackleton, J. F. *Mol. Phys.* **1980**, *39*, 1471.
- (26) Bertini, I.; Briganti, F.; Luchinat, C.; Xia, Z. *J. Magn. Reson.* **1992**, *99*, 235.
- (27) Pan, C. M. A. Thesis, State University of New York at Stony Brook, Stony Brook, NY, 2002.
- (28) Marichal, C.; Hirschinger, J.; Granger, P.; Menetrier, M.; Rougier, A.; Delmas, C. *Inorg. Chem.* **1995**, *34*, 1773.
- (29) Carlier, D.; Menetrier, M.; Delmas, C. *J. Mater. Chem.* **2001**, *11*, 594.
- (30) McConnell, H. M. *J. Chem. Phys.* **1957**, 27.
- (31) McConnell, H. M.; Robertson, R. E. *J. Chem. Phys.* **1958**, *29*, 1361.
- (32) Cox, P. A. *Transition Metal Oxides*; Clarendon Press: Oxford, 1995.
- (33) Nayeem, A.; Yesinowski, J. P. *J. Chem. Phys.* **1988**, *89*, 4600.
- (34) Lee, Y. J.; Grey, C. P. *J. Phys. Chem. B* **2002**, *106*, 3576.
- (35) Mehring, M. *Principles of High-Resolution NMR in Solids*; Springer-Verlag: New York, 1983.
- (36) Haeberlen, U. *High-Resolution NMR in Solids*; Academic: New York, 1976.
- (37) Brough, A. R.; Grey, C. P.; Dobson, C. M. *J. Chem. Soc., Chem. Commun.* **1992**, 742.
- (38) Bertini, I.; Luchinat, C.; Parigi, G. *Solution NMR of Paramagnetic Molecules*; Elsevier: Amsterdam, 2001.
- (39) Grey, C. P.; Smith, M. E.; Cheetham, A. K.; Dobson, C. M.; Dupree, R. *J. Am. Chem. Soc.* **1990**, *112*, 4670.
- (40) Goodenough, J. B. *Magnetism and the Chemical Bond*; Interscience: New York, 1963.
- (41) Hatfield, W. E. *Solid State Chemistry Techniques*; Oxford University Press: Oxford, 1987.

- (42) Bloembergen, N. *Physica* **1950**, *16*, 95.
- (43) Brough, A. R.; Grey, C. P.; Dobson, C. M. *J. Am. Chem. Soc.* **1993**, *115*, 7318.
- (44) Lee, Y. J.; Wang, F.; Grey, C. P. *J. Am. Chem. Soc.* **1998**, *120*, 12601.
- (45) Lee, Y. J.; Grey, C. P. *Chem. Mater.* **2000**, *12*, 3871.
- (46) Lee, Y. J.; Eng, C.; Grey, C. P. *J. Electrochem. Soc.* **2001**, *148*, A249.
- (47) Pan, C.; Lee, Y. J.; Ammundsen, B.; Grey, C. P. *Chem. Mater.* **2002**, *14*, 2289.
- (48) Gee, B.; Horne, C. R.; Cairns, E. J.; Reimer, J. A. *J. Phys. Chem. B* **1998**, *102*, 10142.
- (49) Tucker, M. C.; Reimer, J. A.; Cairns, E. J. *Electrochem. Solid State Lett.* **2000**, *3*, 463.
- (50) Lee, Y. J.; Park, S.-H.; Eng, C.; Parise, J. B.; Toby, B. H.; Grey, C. P. *Chem. Mater.* **2002**, *14*, 194.
- (51) Tucker, M. C.; Reimer, J. A.; Cairns, E. J. *J. Electrochem. Soc.* **2001**, *148*, A951.
- (52) Carlier, D.; Ménétrier, M.; Grey, C. P.; Delmas, C.; Ceder, G. *Phys. Rev. B* **2003**, *67*, 174103.
- (53) Burley, J.; Battle, P. D.; Gallon, D. J.; Sloan, J.; Grey, C. P.; Rosseinsky, M. J. *J. Am. Chem. Soc.* **2002**, *124*, 620.
- (54) Greedan, J. E.; Raju, N. P.; Davidson, I. J. *J. Solid State Chem.* **1997**, *128*, 209.
- (55) Levasseur, S.; Menetrier, M.; Suard, E.; Delmas, C. *Solid State Ionics* **2000**, *128*, 11.
- (56) Lee, Y. J.; Grey, C. P. *J. Electrochem. Soc.* **2002**, *149*, A103.
- (57) Verhoeven, V. W. J.; de Schepper, I. M.; Nachtegaal, G.; Kentgens, A. P. M.; Kelder, E. M.; Schoonman, J.; Mulder, F. M. *Phys. Rev. Lett.* **2001**, *86*, 4314.
- (58) Morgan, K. R.; Collier, S.; Burns, G.; Ooi, K. *J. Chem. Soc., Chem. Commun.* **1994**, 1719.
- (59) Rozier, P.; Savariault, J. M.; Galy, J.; Marichal, C.; Hirschinger, J.; Granger, P. *Eur. J. Solid State Inorg. Chem.* **1996**, *33*, 1.
- (60) Stallworth, P. E.; Kostov, S.; denBoer, M. L.; Greenbaum, S. G.; Lampe-Onnerud, C. *J. Appl. Phys.* **1998**, *83*, 1247.
- (61) Stallworth, P. E.; Johnson, F. S.; Greenbaum, S. G.; Passerini, S.; Flowers, J.; Smyrl, W.; Fontanella, J. J. *Solid State Ionics* **2002**, *146*, 43.
- (62) Gaubicher, J.; Wurm, C.; Goward, G.; Masquelier, C.; Nazar, L. *Chem. Mater.* **2000**, *12*, 3240.
- (63) Arrabito, M.; Bodoardo, S.; Penazzi, N.; Panero, S.; Reale, P.; Scrosati, B.; Wang, Y.; Guo, X.; Greenbaum, S. G. *J. Power Sources* **2001**, *97-8*, 478.
- (64) Tucker, M. C.; Doeff, M. M.; Richardson, T. J.; Finones, R.; Reimer, J. A.; Cairns, E. J. *Electrochem. Solid State Lett.* **2002**, *5*, A95.
- (65) Thackeray, M. M.; David, W. I. F.; Bruce, P. G.; Goodenough, J. B. *Mater. Res. Bull.* **1983**, *18*, 461.
- (66) Thackeray, M. M. *Prog. Solid State Chem.* **1997**, *25*, 1.
- (67) Gummow, R. J.; de-Kock, A.; Thackeray, M. M. *Solid State Ionics* **1994**, *69*, 59.
- (68) Liu, W.; Kowal, K.; Farrington, G. C. *J. Electrochem. Soc.* **1998**, *145*, 459.
- (69) Amatucci, G.; Du Pasquier, A.; Blyr, A.; Zheng, T.; Tarascon, J.-M. *Electrochem. Acta* **1999**, *45*, 255.
- (70) Cho, J.; Thackeray, M. M. *J. Electrochem. Soc.* **1999**, *146*, 3577.
- (71) Shao-Horn, Y.; Hackney, S. A.; Kahaian, A. J.; Kepler, K. D.; Skinner, E.; Vaughn, J. T.; Thackeray, M. M. *J. Power Sources* **1999**, *82*, 496.
- (72) Mustarelli, P.; Massarotti, V.; Bini, M.; Capsoni, D. *Phys. Rev. B* **1997**, *55*, 12018.
- (73) de-Kock, A.; Rossouw, M. H.; de-Picciotto, L. A.; Thackeray, M. M.; David, W. I. F.; Ibberson, R. M. *Mater. Res. Bull.* **1990**, *25*, 657.
- (74) Masquelier, C.; Tabuchi, M.; Ado, K.; Kanno, R.; Kobayashi, Y.; Maki, Y.; Nakamura, O.; Goodenough, J. B. *J. Solid State Chem.* **1996**, *123*, 225.
- (75) Xia, Y.; Yoshio, M. *J. Electrochem. Soc.* **1997**, *144*, 4186.
- (76) Xia, Y.; Zhou, Y.; Yoshio, M. *J. Electrochem. Soc.* **1997**, *144*, 2593.
- (77) Gao, Y.; Dahn, J. R. *J. Electrochem. Soc.* **1996**, *143*, 100.
- (78) Paulsen, J. M.; Dahn, J. R. *Chem. Mater.* **1999**, *11*, 3065.
- (79) Yamada, A. *J. Solid State Chem.* **1996**, *122*, 160.
- (80) Lee, Y.; Wang, F.; Mukerjee, S.; McBreen, J.; Grey, C. J. *Electrochem. Soc.* **2000**, *147*, 803.
- (81) Xia, Y.; Yoshio, M. *J. Electrochem. Soc.* **1996**, *143*, 825.
- (82) Berg, H.; Kelder, E. M.; Thomas, J. O. *J. Mater. Chem.* **1999**, *9*, 427.
- (83) David, W. I. F.; Thackeray, M. M.; de-Picciotto, L. A.; Goodenough, J. B. *J. Solid State Chem.* **1987**, *67*, 316.
- (84) Hunter, J. C. *J. Solid State Chem.* **1981**, *39*, 142.
- (85) Ooi, K.; Miyai, Y.; Sakakihara, J. *Langmuir* **1991**, *7*, 1167.
- (86) Sato, K.; Poojary, D. M.; Clearfield, A.; Kohno, M.; Inoue, Y. *J. Solid State Chem.* **1997**, *131*, 84.
- (87) Pickup, D. M.; Simon, D.; Fookan, M.; Krampitz, H.; van Eck, E. R. H.; Kelder, E. M. *J. Mater. Chem.* **2003**, *13*, 963.
- (88) Paik, Y.; Osegovic, J. P.; Wang, F.; Bowden, W.; Grey, C. P. *J. Am. Chem. Soc.* **2001**, *123*, 7564.
- (89) Paik, Y.; Grey, C. P.; Johnson, C. S.; Kim, J.-S.; Thackeray, M. M. *Chem. Mater.* **2002**, *14*, 5109.
- (90) Paik, Y.; Naqvi, N.; Grey, C. P. Unpublished data.
- (91) Ronci, L. F.; Stallworth, P. E.; Alamgir, F.; Schiros, T.; van Sluytman, J.; Guo, X.; Reale, P.; Greenbaum, S.; den Boer, M.; Scrosati, B. *J. Power Sources* **2003**, *119*, 631.
- (92) Krtil, P.; Dedecek, J.; Kostlanova, T.; Brus, J. *Electrochem. Solid State Lett.* **2004**, *7*, A163.
- (93) Ohzuku, T.; Ueda, A.; Yamamoto, N. *J. Electrochem. Soc.* **1995**, *142*, 1431.
- (94) Kartha, J. P.; Tunstall, D. P.; Irvine, J. T. S. *J. Solid State Chem.* **2000**, *152*, 397.
- (95) Armstrong, A. R.; Bruce, P. G. *Nature* **1996**, *381*, 499.
- (96) Capitaine, F.; Gravereau, P.; Delmas, C. *Solid State Ionics* **1996**, *89*, 197.
- (97) Bruce, P. G.; Armstrong, A. R.; Gitzendanner, R. L. *J. Mater. Chem.* **1999**, *9*, 193.
- (98) Shao-Horn, Y.; Hackney, S. A.; Armstrong, A. R.; Bruce, P. G.; Gitzendanner, R. L.; Johnson, C. S.; Thackeray, M. M. *J. Electrochem. Soc.* **1999**, *146*, 2404.
- (99) Wang, H.; Jang, Y.-I.; Chiang, Y.-M. *Electrochem. Solid State Lett.* **1999**, *2*, 490.
- (100) Davidson, I. J.; McMillan, R. S.; Murray, J. J. *J. Power Sources* **1995**, *54*, 205.
- (101) Ammundsen, B.; Paulsen, J. M.; Davidson, I. J.; R. S. Liu, R. S.; Shen, C. H.; Chen, J. M.; Jang, Y. J.; Lee, J. *J. Electrochem. Soc.* **2002**, *179*, A431.
- (102) Balasubramanian, M.; McBreen, J.; Davidson, I. J.; Whitfield, P. S.; Kargina, I. *J. Electrochem. Soc.* **2002**, *149*, A176.
- (103) Gao, Y.; Myrtle, K.; Zhang, M.; Reimers, J. N.; Dahn, J. R. *Phys. Rev. B* **1996**, *54*, 16670-675.
- (104) Lu, Z.; Dahn, J. R. *J. Electrochem. Soc.* **2002**, *149*, A815.
- (105) Lu, Z.; Beaulieu, L. Y.; Donabarger, R. A.; Thomas, C. L.; Dahn, J. R. *J. Electrochem. Soc.* **2002**, *149*, A778.
- (106) Yoon, W. S.; Paik, P.; Yang, X.-Q.; Balasubramanian, M.; McBreen, J.; Grey, C. P. *Electrochem. Solid State Lett.* **2002**, *5*, A263.
- (107) Yoon, W.-S.; Iannopolo, S.; Grey, C. P.; Carlier, D.; Gorman, J.; Reed, J.; Ceder, G. *Electrochem. Solid State Lett.* **2004**, *7*, A167.
- (108) Grey, C. P.; Yoon, W. S.; Reed, J.; Ceder, G. *Electrochem. Solid State Lett.* **2004**, *7*, A290.
- (109) Menetrier, M.; Saadoun, I.; Levasseur, S.; Delmas, C. *J. Mater. Chem.* **1999**, *9*, 1135.
- (110) Siegel, R.; Hirschinger, J.; Carlier, D.; Matar, S.; Menetrier, M.; Delmas, C. *J. Phys. Chem. B* **2001**, *105*, 4166.
- (111) Tucker, M. C.; Reimer, J. A.; Cairns, E. J.; Choi, S.; Manthiram, A. *J. Phys. Chem. B* **2002**, *106*, 2842.
- (112) Peeters, K. M. P. J.; van Bommel, M. J.; Neilen-ten Wolde, P. M. C.; van Hal, H. A. M.; Keur, W. C.; Kentgens, A. P. M. *Solid State Ionics* **1998**, *112*, 41.
- (113) Levasseur, S.; Menetrier, M.; Shao-Horn, Y.; Gautier, L.; Audemer, A.; Demazeau, G.; Largeteau, A.; Delmas, C. *Chem. Mater.* **2003**, *15*, 348.
- (114) Levasseur, S.; Menetrier, M.; Delmas, C. *J. Power Sources* **2002**, *112*, 419.
- (115) Alcantara, G. R.; Jaraba, M.; Lavela, P.; Tirado, J. L. *Chem. Mater.* **2003**, 1210.
- (116) Carlier, D.; Saadoun, I.; Croguennec, L.; Menetrier, M.; Suard, E.; Delmas, C. *Solid State Ionics* **2001**, *144*, 263.
- (117) Gaudin, E.; Taulelle, F.; Stoyanova, R.; Zhecheva, E.; Alcantara, R.; Lavela, P.; Tirado, J. L. *J. Phys. Chem. B* **2001**, *105*, 8081.
- (118) Stoyanova, J. R.; Zhecheva, E.; Kuzmanova, E.; Alcantara, R.; Lavela, P.; Tirado, J. L. *Solid State Ionics* **2000**, *128*, 1.
- (119) Tucker, M. C.; Doeff, M. M.; Richardson, T. J.; Finones, R.; Reimer, J. A.; Cairns, E. J. *J. Am. Chem. Soc.* **2002**, *124*, 3832.
- (120) Padhi, A. K.; Nanjundaswamy, K. S.; Masquelier, C.; Okada, S.; Goodenough, J. B. *J. Electrochem. Soc.* **1997**, *144*, 1609.
- (121) Prasad, S. S. In *Handbook of solid-state batteries and capacitors*; Munshi, M. Z. A., Ed.; World Scientific: Singapore, 1995; p 467.
- (122) DeSilvestro, J.; Haas, O. *J. Electrochem. Soc.* **1990**, *137*, 5C.
- (123) Besenhard, J. O.; Schollhorn, R. *J. Electrochem. Soc.* **1977**, *124*, 968.
- (124) Campanella, L.; Pistoia, G. *J. Electrochem. Soc.* **1971**, *128*, 1905.
- (125) Dickens, P. G.; Reynolds, G. J. *Solid State Ionics* **1981**, *5*, 331.
- (126) Besenhard, J. O.; Heydecke, J.; Fritz, H. P. *Solid State Ionics* **1982**, *6*, 215.
- (127) Julien, C.; Khelifa, A.; Guesdon, J. P.; Gorenstein, A. *Appl. Phys.* **1994**, *A59*, 173.
- (128) Rehder, D. *Bull. Magn. Reson.* **1982**, *4*, 33.
- (129) Mastikhin, V. M.; Lapina, O. B.; Krasilnikov, V. N.; Ivakin, A. A. *React. Kinet. Catal. Lett.* **1984**, *24*, 119.
- (130) Zamarev, K. I.; Mastikhin, V. M. *Colloids Surf.* **1984**, *12*, 401.
- (131) Fotiev, A.; Slobodin, B. V.; Hodos, M. Y. *Vanadates, their Synthesis, Composition and Properties*; Nauka: Moscow (in Russian), 1988.
- (132) Hawthorne, F. G.; Calvo, C. *J. Solid State Chem.* **1977**, *22*, 157.
- (133) Fotiev, A. A.; Ivakin, A. A. *Vanadates of Divalent Metals and their Synthesis*; Sverdlovsk (in Russian), 1970.

- (134) Muller, D.; Gessner, W.; Grimmer, A. R. *Z. Chem.* **1977**, *B12*, 453.
- (135) Klinowski, J. *Prog. NMR Spectrosc.* **1984**, *16*, 237.
- (136) Eckert, H.; Wachs, I. E. *J. Phys. Chem.* **1989**, *93*, 6796.
- (137) Pletnev, R. N.; Lazukova, N. I.; Gubanov, V. A. *Zh. Fiz. Khim.* **1977**, *51*, 2359.
- (138) Gubanov, V. A.; Pletnev, R. N.; Lisson, V. N.; Chirkov, A. K. *Spectrosc. Lett.* **1977**, *10*, 527.
- (139) Umeda, J. I.; Kusumoto, H.; Narita, K. *J. Phys. Soc. Jpn.* **1966**, *21*, 619.
- (140) Skibsted, J.; Nielsen, N. C.; Bildsoe, H.; Jakobsen, H. *Chem. Phys. Lett.* **1992**, *188*(5–6), 405.
- (141) Delmaire, F.; Rigole, M.; Zhilinskaya, E. A.; Aboukais, A.; Hubaut, R.; Mairesse, G. *Phys. Chem. Chem. Phys.* **2000**, *2*, 4477.
- (142) Stallworth, P. E.; Johnson, F. S.; Greenbaum, S. G.; Passerini, S.; Flowers, J.; Smyrl, W. *J. Appl. Phys.* **2002**, *92*(7), 3839.
- (143) Hirschinger, J.; Mongrelet, T.; Marichal, C.; Granger, P.; Savariault, J.-M.; Deramond, E.; Galy, J. *J. Phys. Chem.* **1993**, *97*, 10301.
- (144) Dupré, N.; Gaubicher, J.; Siegel, R.; Brunelli, M.; Hirschinger, J.; Quarton, M. Manuscript in preparation.
- (145) Dupré, N.; Gaubicher, J.; Guyomard, D.; Grey, C. P. *Chem. Mater.* **2004**, *16*, 2725.
- (146) Murphy, D. W.; Christian, P. A.; DiSalvo, G. J.; Waszczak, J. V. *Inorg. Chem.* **1979**, *18*, 2800.
- (147) Whittingham, M. S. *J. Electrochem. Soc.* **1975**, *123*, 315.
- (148) Galy, J. *J. Solid State Chem.* **1992**, *100*, 229.
- (149) Cocciantelli, J. M.; Doumerc, J. P.; Pouchard, M.; Broussely, M.; Labat, J. *J. Power Sources* **1991**, *34*, 103.
- (150) Delmas, C.; Cognac-Auradou, H.; Cocciantelli, J. M.; Menetrier, M.; Doumerc, J. P. *Solid State Ionics* **1994**, *69*, 257.
- (151) Bose, M.; Basu, A. *Solid State Ionics* **1986**, *18–19*, 902.
- (152) Cocciantelli, J. M.; Suh, K. S.; Senegas, J.; Doumerc, J. P.; Pouchard, M. *J. Phys. Chem. Solids* **1992**, *53*, 57.
- (153) Cocciantelli, J. M.; Suh, K. S.; Senegas, J.; Doumerc, J. P.; Soubeyroux, J. L.; Pouchard, M. *J. Phys. Chem. Solids* **1992**, *53*, 51.
- (154) Savariault, J. M.; Deramond, E.; Galy, J.; Mongrelet, T.; Hirschinger, J. *Mol. Cryst. Liq. Cryst.* **1994**, *244*, 367.
- (155) Galy, J.; Hardy, A. *Bull. Soc. Chim. Fr.* **1964**, *451*, 2808.
- (156) Galy, J.; Darriet, J.; Hagenmuller, P. *Rev. Chim. Miner.* **1971**, *8*, 509.
- (157) Bonino, F.; Ottaviani, M.; Scrosati B.; Pistoia, G. *J. Electrochem. Soc.* **1988**, *135*, 12.
- (158) Pistoia, G.; Pasquali, M.; Tocci, M.; Manev, V. Moshchev, R. V. *J. Power Sources* **1985**, *15*, 13.
- (159) de Picciotto, L. A.; Adendorff, K. T.; Liles D. C.; Thackeray, M. M. *Solid State Ionics* **1993**, *62*, 297.
- (160) Wadsley, A. D. *Acta Crystallogr.* **1957**, *10*, 261.
- (161) Benedek, R.; Thackeray, M. M.; Yang, L. H. *Phys. Rev. B* **1999**, *60–9*, 6335.
- (162) Jouanneau, S. These de Doctorat, Universite de Nantes, 2001.
- (163) Nanjundaswamy, K. S.; Padhi, A. K.; Goodenough, J. B.; Okada, S.; Ohtsuka, H.; Arai, H.; Yamaki, J. *Solid State Ionics* **1996**, *92*, 1.
- (164) Gaubicher, J.; Le Mercier, T.; Chabre, Y.; Angenault, J.; Quarton, M. *J. Electrochem. Soc.* **1999**, *146*, 4375–4379.
- (165) Gaubicher, J.; Chabre, Y.; Angenault, J.; Lautié, A.; Quarton, M. *J. Alloys Compd.* **1997**, *262*, 34.
- (166) Dupré, N.; Gaubicher, J.; Le Mercier, T.; Wallez, G.; Quarton, M. *Solid State Ionics* **2001**, *140*, 209.
- (167) Dupré, N.; Gaubicher, J.; Angenault, J.; Wallez, G.; Quarton, M. *J. Power Sources* **2001**, *97*, 532.
- (168) Jordan, B.; Calvo, C. *Can. J. Chem.* **1973**, *51*, 2621.
- (169) Gopal, R.; Calvo, C. *J. Solid State Chem.* **1972**, *5*, 432.
- (170) Tietze, R. *Aust. J. Chem.* **1981**, *34*, 2035.
- (171) Lapina, O. B.; Khabibulin, D. F.; Shubin, A. A.; Bondareva, V. M. *J. Mol. Catal. A* **2000**, *162*, 38.
- (172) Siegel, R.; Dupré, N.; Quarton, M.; Hirschinger, J. Manuscript in preparation.
- (173) Yin, S.-C.; Grondy, H.; Strobel, P.; Huang, H.; Nazar, L. F. *J. Am. Chem. Soc.* **2003**, *125*, 326.

CR020734P

Battery Separators

Pankaj Arora* and Zhengming (John) Zhang

Celgard, LLC, 13800 South Lakes Dr., Charlotte, North Carolina 28273

Received March 30, 2004

Contents

1. Introduction and Scope	4419
2. Battery and Separator Market	4420
3. Separator and Batteries	4421
4. Separator Requirements	4422
5. Separator Types	4422
5.1. Microporous Separators	4422
5.2. Nonwovens	4422
5.3. Ion Exchange Membranes	4423
5.4. Supported Liquid Membranes	4423
5.5. Polymer Electrolyte	4423
5.6. Solid Ion Conductors	4423
6. Separator for Nonaqueous Batteries	4423
6.1. Lithium Ion	4424
6.1.1. Separator Development	4424
6.1.2. Separator Requirements	4427
6.1.3. Separator Properties/Characterization	4429
6.1.4. Effect of Separator on Cell Performance and Safety	4436
6.2. Lithium Polymer	4440
6.3. Lithium-Ion Gel Polymer	4441
6.4. Lithium Primary Systems	4443
6.4.1. Separator Requirements	4443
6.4.2. Chemistries	4444
7. Separator for Aqueous Batteries	4445
7.1. Leclanche (Zinc Carbon)	4446
7.2. Alkaline Zinc MnO ₂	4446
7.3. Lead-Acid Batteries	4447
7.3.1. Flooded Electrolyte Lead Acid	4447
7.3.2. Valve Regulated Lead Acid (VRLA)	4449
7.4. Nickel Systems	4450
7.4.1. Nickel–Cadmium	4450
7.4.2. Nickel–Metal Hydride	4451
7.4.3. Nickel–Hydrogen	4452
7.5. Zinc Systems	4452
7.5.1. Silver–Zinc	4452
7.5.2. Nickel–Zinc	4454
7.5.3. Zinc–Air	4455
7.5.4. Zinc–Bromine	4456
7.6. Redox Flow Batteries	4456
8. Mathematical Modeling of Batteries/Separators	4457
9. Summary	4458
10. Future Directions	4458
11. Acknowledgments	4459
12. References	4459



Pankaj Arora is a Senior Research Engineer at Celgard LLC in Charlotte, NC. He specializes in the design and modeling of electrochemical power sources and is currently working in the Battery Applications Laboratory of Celgard, where he helps guide separator development work for lithium batteries. He has a B.Tech. degree in Electrochemical Engineering from the Central Electrochemical Research Institute in Karaikudi, India, and a Ph.D. degree in Chemical Engineering from the University of South Carolina, Columbia, SC. Pankaj can be reached by email at pankajarora@celgard.com.



Zhengming (John) Zhang is Vice President of New Technology at Celgard LLC in Charlotte, NC. He has been working in Solid State Ionics, Batteries, and Battery Separators since 1984. He has published more than 50 papers and patents and has co-edited a book on battery. He has been an invited speaker for many professional conferences, invited lecturer for United Nations Development Program, and is a Visiting Professor at Xiamen University, Fujian, China. He has a B.S. in Mechanical Engineering from Shanghai University, Shanghai, China, an M.S. in Electrochemistry from Shandong University, Jinan City, China, and a Ph.D. in Materials Chemistry from the University of California at Santa Barbara, Santa Barbara, CA. John can be reached by email at zjzhang@celgard.com.

1. Introduction and Scope

Many advances have been made in battery technology in recent years, both through continued improvement of specific electrochemical systems and through the development and introduction of new

* Corresponding author. E-mail: pankajarora@celgard.com. Telephone: 704 587 8478. Fax: 704 588 7393

battery chemistries. Nevertheless, there is still no one "ideal" battery that gives optimum performance under all operating conditions. Similarly, there is no one separator that can be considered "ideal" for all battery chemistries and geometries.

A separator is a porous membrane placed between electrodes of opposite polarity, permeable to ionic flow but preventing electric contact of the electrodes. A variety of separators have been used in batteries over the years. Starting with cedar shingles and sausage casing, separators have been manufactured from cellulosic papers and cellophane to nonwoven fabrics, foams, ion exchange membranes, and microporous flat sheet membranes made from polymeric materials. As batteries have become more sophisticated, separator function has also become more demanding and complex.

Separators play a key role in all batteries. Their main function is to keep the positive and negative electrodes apart to prevent electrical short circuits and at the same time allow rapid transport of ionic charge carriers that are needed to complete the circuit during the passage of current in an electrochemical cell.^{1,2} They should be very good electronic insulators and have the capability of conducting ions by either intrinsic ionic conductor or by soaking electrolyte. They should minimize any processes that adversely affect the electrochemical energy efficiency of the batteries.

Very little work (relative to research of electrode materials and electrolytes) is directed toward characterizing and developing new separators. Similarly, not much attention has been given to separators in publications reviewing batteries.¹⁻¹⁰ A number of reviews on the on cell fabrication, their performance, and application in real life have appeared in recent years, but none have discussed separators in detail. Recently a few reviews have been published in both English and Japanese which discuss different types of separators for various batteries.¹¹⁻²⁰ A detailed review of lead-acid and lithium-ion (Li-ion) battery separators was published by Boehnstedt¹³ and Spontitz,¹⁴ respectively, in the *Handbook of Battery Materials*. Earlier Kinoshita et al. had done a survey of different types of membranes/separators used in different electrochemical systems, including batteries.¹¹

The majority of the separators currently used in batteries were typically developed as spin-offs of existing technologies. They were usually not developed specifically for those batteries and thus are not completely optimized for systems in which they are used. One positive result of adapting existing technologies is that they are produced in high volume at relatively low cost. The availability of low cost separators is an important consideration in the commercialization of batteries, because the battery industry traditionally operates with thin profit margins and relatively small research budgets.

The purpose of this paper is to describe the various types of separators based on their applications in batteries and their chemical, mechanical and electrochemical properties, with particular emphasis on separators for lithium-ion batteries. The separator

requirements, properties, and characterization techniques are described with respect to lithium-ion batteries. The separators used in other batteries are only discussed briefly. Despite the widespread use of separators, a great need still exists for improving the performance, increasing the life, and reducing the cost of separators. In the following sections, an attempt is made to discuss key issues in various separators with the hope of bringing into focus present and future directions of research and development in separator technologies.

2. Battery and Separator Market

The battery industry has seen enormous growth over the past few years in portable, rechargeable battery packs. The majority of this surge can be attributed to the widespread use of cell phones, personal digital assistants (PDA's), laptop computers, and other wireless electronics. Batteries remained the mainstream source of power for systems ranging from mobile phones and PDA's to electric and hybrid electric vehicles. The world market for batteries was approximately \$41 billion in 2000, which included \$16.2 billion primary and \$24.9 billion secondary cells.²¹

A recent study from Freedonia has predicted aggregate U.S. demand for primary and secondary batteries to climb 5.5% annually through 2007 to \$14 billion. The growth will be driven by strong demand for battery-powered electronic devices like digital cameras and 3G wireless phones, and increasing production of electrical and electronic equipment. The secondary battery demand is expected to outpace the primary battery market gains through 2007 benefiting from strong growth in the use of high-drain portable electronic devices. The lead-acid batteries will account for over half of all rechargeable demand in 2007, although lithium-ion and NiMH batteries will record the strongest growth. Alkaline batteries could remain the dominant type, accounting for more than two thirds of all primary battery sales in 2007.²²

The rechargeable battery (NiCd, NiMH, and lithium-ion) market for 2003 for portable electronics was around \$5.24 billion, around 20% more than 2002. The lithium-ion battery market was around \$3.8 billion (~73%). They are now used in more than 90% of cellphones, camcorders, and portable computers, worldwide, and have also been adopted in power tools recently.²³

The tremendous progress in lithium-ion cells is clearly visible with as much as a 2-fold increase in the volumetric and gravimetric energy density for both 18650 and prismatic cells between 1994 and 2002. In past few years the lithium-ion production has expanded to South Korea (Samsung, LG, etc.) and China (BYD, B&K, Lishen, etc.) from Japan. Several Japanese (Sanyo, Sony, MBI, NEC, etc.) and Korean (LG Chemical) manufacturers have also moved their manufacturing plants to China.²³ Japan, which controlled 94% of the global rechargeable battery market in 2000, has seen its market share drop to about 65% of the global market.²³⁻²⁵ The continued growth in lithium-ion battery market has led to a strong demand for battery separators. All the

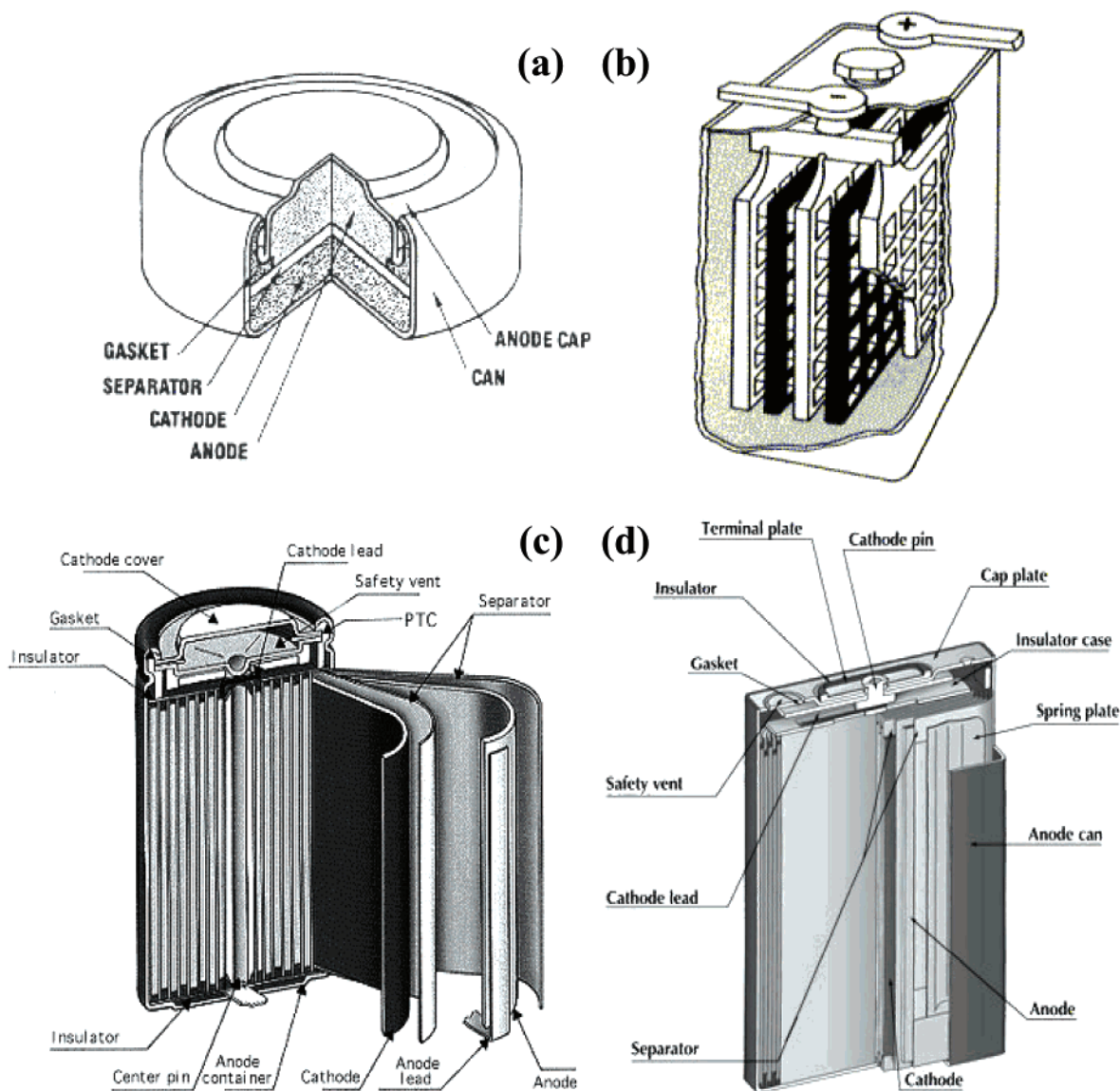


Figure 1. Typical battery configurations: (a) button cell; (b) stack lead-acid; (c) spiral wound cylindrical lithium-ion; (d) spiral wound prismatic lithium-ion.

major separator manufacturers (Celgard, Asahi, and Tonen) have either increased their capacity in 2003 or are planning to increase it in 2004.^{26–28}

There is not too much information available on the battery separator market in the literature. It is estimated that about 30% of the rechargeable lithium battery market or \$1.5 billion is the size of the battery materials or components market. Battery separators for lithium batteries are about a \$330 million market within the total battery components market.^{29,30} Recently, the Freedonia Group has reported that the U.S. demand for battery separators will increase to \$410 million in 2007 from \$237 million in 1977 and \$300 million in 2002, respectively.^{31,32}

3. Separator and Batteries

Batteries are built in many different shapes and configurations—button, flat, prismatic (rectangular), and cylindrical (AA, AAA, C, D, 18650, etc.). The cell components (including separators) are designed to

accommodate a particular cell shape and design. The separators are either stacked between the electrodes or wound together with electrodes to form jellyrolls as shown in Figure 1. Stacked cells are generally held together by pressure from the cell container. The lithium-ion gel polymer stacked cells are prepared by bonding/laminating layers of electrodes and separators together. The separator properties should not change significantly during the bonding process. In some cases, the separators are coated to help in bonding process, thus reducing the interfacial resistance.^{33–35}

In the conventional way of making spirally wound cells, two layers of separators are wound along with the positive and negative electrodes, resulting in a positive/separator/negative/separator configuration. They are wound as tightly as possible to ensure good interfacial contact. This requires the separators to be strong to avoid any contact between the electrodes through the separator. The separator also must not yield and reduce in width, or else the electrodes may contact each other. Once wound, the jellyroll is

inserted into a can, and filled with electrolyte. The separator must be wetted quickly by the electrolyte to reduce the electrolyte filling time. A header is then crimped into the cell to cover the can from top. In some prismatic cells, the jellyroll is pressed at high temperatures and pressures and then inserted into thin prismatic (rectangular) cans. A typical 18650 lithium-ion cell uses around 0.07–0.09 m² of separator, which is approximately 4–5% of the total cell weight.³⁶

4. Separator Requirements

A number of factors must be considered in selecting the best separator for a particular battery and application. The characteristics of each available separator must be weighed against the requirements and one selected that best fulfills these needs. A wide variety of properties are required of separators used in batteries. The considerations that are important and influence the selection of the separator include the following:

- Electronic insulator
- Minimal electrolyte (ionic) resistance
- Mechanical and dimensional stability
- Sufficient physical strength to allow easy handling
- Chemical resistance to degradation by electrolyte, impurities, and electrode reactants and products
- Effective in preventing migration of particles or colloidal or soluble species between the two electrodes
- Readily wetted by electrolyte
- Uniform in thickness and other properties

The order of importance of the various criteria varies, depending on the battery applications. The above list presents a broad spectrum of requirements for separators in batteries. In many applications, a compromise in requirements for the separator must generally be made to optimize performance, safety, cost, etc. For example, batteries that are characterized by small internal resistance and consume little power require separators that are highly porous and thin, but the need for adequate physical strength may require that they be thick.

In addition to the above general requirements each battery type has other requirements essential for good performance and safety. For example, separators in sealed nickel–cadmium (NiCd) and nickel–metal hydride (NiMH) batteries should be highly permeable to gas molecules for overcharge protection, the separator in lithium-ion cells should have a shutdown feature for good safety, separators for alkaline batteries should be flexible enough to be wrapped around the electrodes, and the separator for an SLI (starting, lighting and ignition) battery could also serve as a mechanical-shock cushion.

5. Separator Types

Separators for batteries can be divided into different types, depending on their physical and chemical characteristics. They can be molded, woven, nonwoven, microporous, bonded, papers, or laminates. In recent years, there has been a trend to develop solid and gelled electrolytes that combine the electrolyte and separator into a single component.

In most batteries, the separators are either made of nonwoven fabrics or microporous polymeric films. Batteries that operate near ambient temperatures usually use separators fabricated from organic materials such as cellulosic papers, polymers, and other fabrics, as well as inorganic materials such as asbestos, glass wool, and SiO₂. In alkaline batteries, the separators used are either regenerated cellulose or microporous polymer films. The lithium batteries with organic electrolytes mostly use microporous films.

For the sake of discussion, we have divided the separators into six types—microporous films, nonwovens, ion exchange membranes, supported liquid membranes, solid polymer electrolytes, and solid ion conductors. A brief description of each type of separator and their application in batteries are discussed below.

5.1. Microporous Separators

They are fabricated from a variety of inorganic, organic, and naturally occurring materials and generally contain pores that are greater than 50–100 Å in diameter. Materials such as nonwoven fibers (e.g. nylon, cotton, polyesters, glass), polymer films (e.g. polyethylene (PE), polypropylene (PP), poly(tetrafluoroethylene) (PTFE), poly(vinyl chloride) (PVC)), and naturally occurring substances (e.g. rubber, asbestos, wood) have been used for microporous separators in batteries that operate at ambient and low temperatures (<100 °C). The microporous polyolefins (PP, PE, or laminates of PP and PE) are widely used in lithium based nonaqueous batteries (section 6.1), and filled polyethylene separators in lead-acid batteries (section 7.3), respectively.

5.2. Nonwovens

Nonwovens are textile products that are manufactured directly from fibers. They are defined as a manufactured sheet, web, or matt of directionally or randomly oriented fibers, bonded by friction, and/or cohesion, and/or adhesion excluding paper and products which are woven, tufted, stitchbonded incorporating binding yarns or filaments, or felted by wetmilling whether or not additionally needed. The fibers may be of natural or manmade origin. They may be staple or continuous filaments or maybe formed in situ.³⁷

The macroporous fibrous matrix is either dry laid, meltblown, or wet laid. The wet laid process is very similar to the papermaking process. The fibers are bonded together by chemical or thermal bonding. The meltblown process is a binderless process and there the polymer fiber web is extruded. Typical pore sizes of the fibrous matrix vary from 1 to 100 μm.

Nonwovens are widely utilized as separators for several types of batteries. Lightweight, wet laid nonwovens made from cellulose, poly(vinyl alcohol), and other fibers have achieved considerable success as separators for popular primary alkaline cells of various sizes. The key nonwoven attributes include consistently uniform basis weight, thickness, porosity and resistance to degradation by electrolytes. Nonwovens are also successfully employed as separators in NiCd's.

Table 1. Types of Separators Used in Different Type of Secondary Lithium Batteries

battery system	type of separator	composition
lithium-ion (liquid electrolyte)	microporous	polyolefins (PE, PP, PP/PE/PP)
lithium-ion gel polymer	microporous microporous	PVdF polyolefins (PE, PP, PP/PE/PP) coated with PVdF or other gelling agents
lithium-polymer (e.g. Li-V ₆ O ₁₃)	polymer electrolyte	poly(ethylene oxide) with lithium salt

The materials used in nonwoven fabrics include a single polyolefin, or a combination of polyolefins, such as polyethylene (PE), polypropylene (PP), polyamide (PA), poly(tetrafluoroethylene) (PTFE), polyvinylidene fluoride (PVdF), and poly(vinyl chloride) (PVC). Nonwoven fabrics have not, however, been able to compete with microporous films in lithium-ion cells. This is most probably because of the inadequate pore structure and difficulty in making thin (<25 μm) nonwoven fabrics with acceptable physical properties.

5.3. Ion Exchange Membranes

These membranes are generally fabricated from polymeric materials containing pores with diameters of less than 20 Å. The transport properties of ions in these membranes are characterized by strong interactions between the permeating species and the molecular structure of the polymer. This interaction is due to the presence of ion-exchange groups in the membrane, which allows the membrane to discriminate between permeating or migrating ions by virtue of their specific charge.

Radiation grafted membranes such as Permion manufactured by RAI Research Corporation are ion-exchange membranes. Such membranes are used as battery separators in alkaline batteries. They are made from PE, PP, or Teflon-based films, which have excellent oxidation resistance and superior chemical resistance to alkali. However, they are totally impervious to electrolyte flow, and therefore, they have almost infinite resistance as a separator in this form. By using radiation grafting and cross-linking techniques, however, selected chemical species are grafted as pendant chains to the base structure of the linear polymer without altering the inert backbone. This modification imparts desirable hydrophilic properties to the films without materially impairing their excellent chemical resistance. This paper provides a very limited discussion on ion exchange membranes, as their application in batteries is very limited.

5.4. Supported Liquid Membranes

These types of separators consist of a solid matrix and a liquid phase, which is retained in the microporous structure by capillary forces. To be effective for batteries, the liquid in the microporous separator, which generally contains an organic phase, must be insoluble in the electrolyte, chemically stable, and still provide adequate ionic conductivity. Several types of polymers, such as polypropylene, polysulfone, poly(tetrafluoroethylene), and cellulose acetate, have been used for porous substrates for supported-liquid membranes. The PVdF coated polyolefin-based microporous membranes used in gel-polymer lithium-ion battery fall into this category. Gel polymer

electrolytes/membranes are discussed briefly in section 6.3.

5.5. Polymer Electrolyte

Polymer electrolytes (e.g., poly(ethylene oxide), poly(propylene oxide)) have attracted considerable attention for batteries in recent years. These polymers form complexes with a variety of alkali metal salts to produce ionic conductors that serve as solid electrolytes. Their use in batteries is still limited due to poor electrode/electrolyte interface and poor room temperature ionic conductivity. Because of the rigid structure, they can also serve as the separator. Polymer electrolytes are discussed briefly in section 6.2.

5.6. Solid Ion Conductors

They serve as both separator and electrolyte. These are generally inorganic materials that are impervious barriers to gases and liquids. They allow one or more kinds of ions to migrate through their lattice when a potential gradient or a chemical gradient is present. These types of separators are beyond the scope of this article.

6. Separator for Nonaqueous Batteries

All lithium based batteries use nonaqueous electrolytes because of the reactivity of lithium in aqueous solution and because of the electrolyte's stability at high voltage. The majority of these cells use microporous membranes made of polyolefins. In some cases, nonwovens made of polyolefins are either used alone or with microporous separators. This section will mainly focus on separators used in secondary lithium batteries followed by a brief summary of separators used in lithium primary batteries.

Lithium secondary batteries can be classified into three types, a liquid type battery using liquid electrolytes, a gel type battery using gel electrolytes mixed with polymer and liquid, and a solid type battery using polymer electrolytes. The types of separators used in different types of secondary lithium batteries are shown in Table 1. The liquid lithium-ion cell uses microporous polyolefin separators while the gel polymer lithium-ion cells either use a PVdF separator (e.g. PLION cells) or PVdF coated microporous polyolefin separators. The PLION cells use PVdF loaded with silica and plasticizer as separator. The microporous structure is formed by removing the plasticizer and then filling with liquid electrolyte. They are also characterized as plasticized electrolyte. In solid polymer lithium-ion cells, the solid electrolyte acts as both electrolyte and separator.

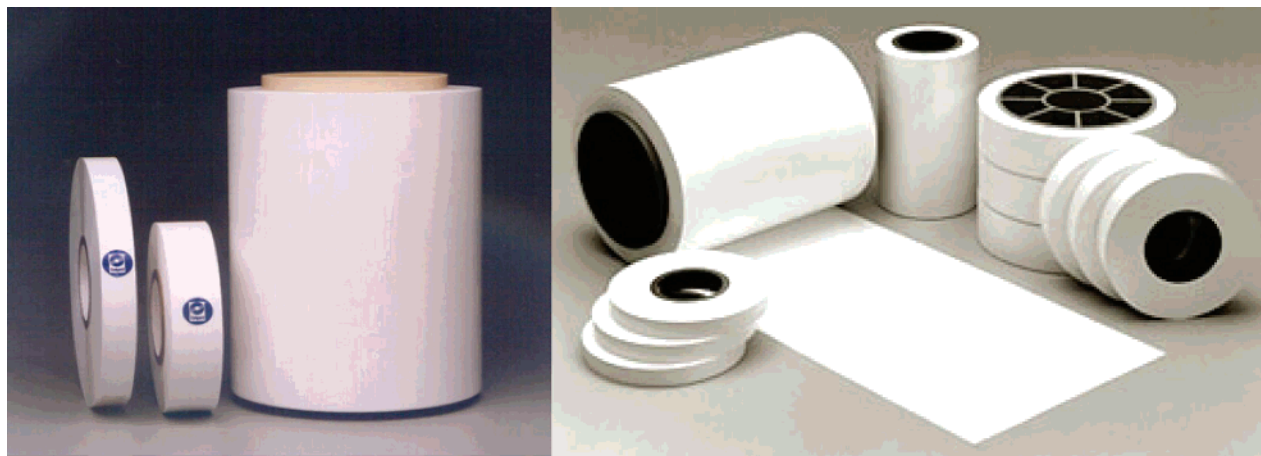


Figure 2. Polyolefin separators used in lithium-ion batteries.

6.1. Lithium Ion

The past decade has seen significant advances in the ambient temperature lithium battery technology. Lithium-ion batteries are the preferred power source for most portable electronics because of their higher energy density, longer cycle life, and higher operational voltage as compared to NiCd and NiMH systems. In 2002, 66% of the total rechargeable battery market for mobile IT and communication devices used lithium-based batteries and the rest used nickel-based batteries.^{38,39}

A typical lithium-ion cell consists of a positive electrode composed of a thin layer of powdered metal oxide (e.g., LiCoO_2) mounted on aluminum foil and a negative electrode formed from a thin layer of powdered graphite, or certain other carbons, mounted on a copper foil. The two electrodes are separated by a porous plastic film soaked typically in LiPF_6 dissolved in a mixture of organic solvents such as ethylene carbonate (EC), ethyl methyl carbonate (EMC), or diethyl carbonate (DEC). In the charge/discharge process, lithium ions are inserted or extracted from the interstitial space between atomic layers within the active materials.

Sony's introduction of the rechargeable lithium-ion battery in the early 1990s precipitated a need for new separators that provided not only good mechanical and electrical properties but also added safety through a thermal shutdown mechanism. Although a variety of separators (e.g., cellulose, nonwoven fabric, etc.) have been used in different type of batteries, various studies on separators for lithium-ion batteries have been pursued in past few years as separators for lithium-ion batteries require different characteristics than separators used in conventional batteries.

A novel microporous separator using polyolefins has been developed and used extensively in lithium-ion batteries since it is difficult for conventional separator materials to satisfy the characteristics required in lithium-ion batteries. In lithium-ion batteries two layers of separators are sandwiched between positive and negative electrodes and then spirally wound together in cylindrical and prismatic configurations. The pores of the separator are filled with ionically conductive liquid electrolyte.

Microporous polyolefin membranes (see Figure 2) in current use are thin ($<30 \mu\text{m}$) and are made of

polyethylene (PE), polypropylene (PP), or laminates⁴⁰ of polyethylene and polypropylene. They are made up of polyolefins materials because they provide excellent mechanical properties, chemical stability and acceptable cost.^{41,42} They have been found to be compatible with the cell chemistry and can be cycled for several hundred cycles without significant degradation in chemical or physical properties.

Commercial membranes offer pore size in the range $0.03\text{--}0.1 \mu\text{m}$, and 30–50% porosity. The low melting point of PE enables their use as a thermal fuse. As the temperature approaches the melting point of the polymer, $135 \text{ }^\circ\text{C}$ for PE and $165 \text{ }^\circ\text{C}$ for PP, porosity is lost. The trilayer material (PP/PE/PP)⁴³ has been developed by Celgard where a PP layer is designed to maintain the integrity of the film, while the low melting point of PE layer is intended to shutdown the cell if an over-temperature condition is reached.¹⁰⁸ Asahi Kasai's flat-film membrane "Hipore" is available in thicknesses ranging from $20 \mu\text{m}$ to several hundred micrometers, and with highly uniform pore sizes ranging from 0.05 to $0.5 \mu\text{m}$.⁴⁴ The major manufacturers of lithium-ion battery separators along with their typical products are listed in Table 2.

In recent years there have been a strong demand for higher capacity lithium-ion cells because of the strong growth in portable electronics. One way to achieve higher capacity is by reducing the thickness of separators. The battery manufacturers have started using 20 and $16 \mu\text{m}$ separators in higher capacity ($>2.0 \text{ A h}$) cylindrical cells, and $9 \mu\text{m}$ separators in lithium-ion gel polymer cells.

Nonwoven materials have also been developed for lithium-ion cells but have not been widely accepted, in part due to the difficulty in fabricating thin materials with good uniformity and high strength.¹⁴ Nonwoven separators have been used in button cells and bobbin cells when thicker separators and low discharge rates are acceptable.

6.1.1. Separator Development

The process for making lithium-ion battery separators can be broadly divided into dry^{45,46} and wet⁴⁷ processes. Both processes usually employ one or more orientation steps to impart porosity and/or increase tensile strength. The dry process involves melting a polyolefin resin, extruding it into a film, thermally

Table 2. Major Manufacturers of Lithium-Ion Battery Separators along with Their Typical Products

manufacturer	structure	composition	process	trade name
Asahi Kasei	single layer	PE	wet	HiPore
Celgard LLC	single layer	PP, PE	dry	Celgard
	multilayer	PP/PE/PP	dry	Celgard
	PVdF coated	PVdF, PP, PE, PP/PE/PP	dry	Celgard
Entek Membranes	single layer	PE	wet	Teklon
Mitsui Chemical	single layer	PE	wet	
Nitto Denko	single layer	PE	wet	
DSM	single layer	PE	wet	Solupur
Tonen	single layer	PE	wet	Setela
Ube Industries	multi layer	PP/PE/PP	dry	U-Pore

Table 3. Manufacturing Process of Typical Microporous Film

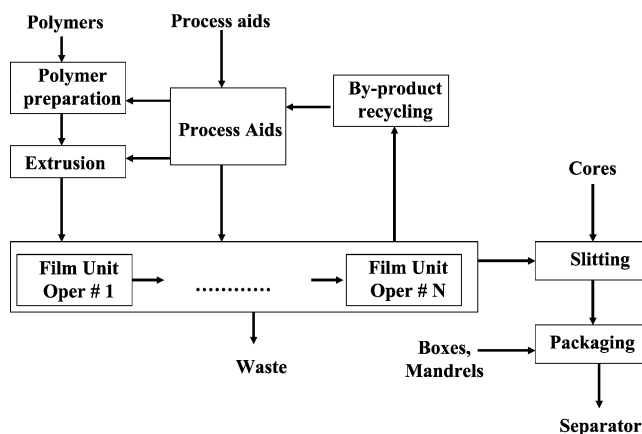
process	mechanism	raw material	properties	typical membranes	manufacturers
dry process	drawing	polymer	simple process anisotropic film	PP, PE, PP/PE/PP	Celgard, Ube
wet process	phase separation	polymer + solvent polymer + solvent + filler	isotropic film large pore size high porosity	PE PE	Asahi, Tonen Asahi

annealing it to increase the size and amount of lamella crystallites, and precisely stretching it to form tightly ordered micropores.^{48–52} In this process, a row lamellar crystal structure is generated in the polymer in the initial extrusion step. This nonporous structure is highly oriented as a result of extrusion and annealing conditions. The films are then stretched to form micropores. This microporous structure is continuous throughout the bulk interior of the membrane.⁵³

Polypropylene and polyethylene microporous films obtained by this method are available from Celgard^{48,50,54,55} and Ube.⁵⁶ The dry process is technologically convenient because no solvents are required. However, only a uniaxial stretching method has been successful to date, and as a result, the pores are slitlike in shape and the mechanical properties of films are anisotropic. The tensile strength in the lateral direction is relatively low.

Wet process (phase inversion process)^{57,58} involves mixing of hydrocarbon liquid or some other low-molecular weight substance generally with a polyolefin resin, heating and melting the mixture, extruding the melt into a sheet, orientating the sheet either in the machine direction (MD) or biaxially, and then extracting the liquid with a volatile solvent.^{45,59} Separators made by the wet process are available from Asahi Kasei,⁶⁰ Tonen,^{61–63} and Mitsui Chemicals⁶⁴ and more recently from Polypore/Membrana and Entek.⁶⁵ The structure and properties of the membranes can be changed by controlling the composition of the solutions and the evaporation or subtractions of solvents in the gelation and solidification processes. The separators made by wet process use ultrahigh-molecular-weight polyethylene (UHMWPE). The use of UHMWPE gives good mechanical properties as well as some degree of melt integrity.

Ihm et al. have given a nice overview of the wet process by preparing a separator with polymer blends of high-density polyethylene (HDPE) and ultrahigh molecular weight polyethylene (UHMWPE).⁵⁸ They showed that the mechanical strength and drawing characteristics are influenced by the content and the molecular weight of the UHMWPE contained in a

**Figure 3.** Generalized process for lithium-ion separator manufacturing.⁶⁶ Each step of the separator manufacturing process has online detection systems to monitor the quality of the separator.

polyolefin blending solution. The manufacturing process of typical microporous film by dry and wet process is compared in Table 3.

A simplified flowchart for separator manufacturing process is shown in Figure 3.⁶⁶ The virgin polymer is prepared and mixed with processing aids (e.g., antioxidants, plasticizer, etc.) and then extruded. The extruded polymer then goes through different steps, which vary from process to process. For the dry process, it can involve film annealing and stretching, while for the wet process, it can involve solvent extraction and stretching. The finished film is then slit into required widths and packed into boxes and shipped to the battery manufacturers. With the advent of thinner separators, the film handling during manufacturing steps has become very important for the final quality of the film. Each step of the separator manufacturing process has online detection systems to monitor the quality of the separators.

Uniaxially oriented films generally have high strength in only one direction, whereas biaxially oriented films are relatively strong in both machine direction (MD) and transverse direction (TD). Although intuitively one might expect biaxially oriented films to be preferred over uniaxially oriented films,

Table 4. Typical Properties of Some Commercial Microporous Membranes

separator/properties	Celgard 2730	Celgard 2400	Celgard 2320	Celgard 2325	Asahi Hipore	Tonen Setela
structure	single layer	single layer	trilayer	trilayer	single layer	single layer
composition	PE	PP	PP/PE/PP	PP/PE/PP	PE	PE
thickness (μm)	20	25	20	25	25	25
gurley (s)	22	24	20	23	21	26
ionic resistivity ^a (Ω cm ²)	2.23	2.55	1.36	1.85	2.66	2.56
porosity (%)	43	40	42	42	40	41
melt temp (°C)	135	165	135/165	135/165	138	137

^a In 1 M LiPF₆ EC:EMC (30:70 by volume).

in practice biaxial orientation provides no performance advantage. In fact, biaxial orientation tends to introduce TD shrinkage. This shrinkage, at elevated temperatures, can allow electrodes to contact each other. The separator must have sufficient strength in the machine direction so that it does not decrease in width or break under the stress of winding. The strength in the transverse direction is not as important as that in the machine direction during the process of making spirally wound batteries. The minimum generally practical requirement for the mechanical strength of the 25-μm separator is 1000 kg/mm².⁵⁸

The typical properties of some commercial microporous membranes are summarized in Table 4. Celgard 2730 and Celgard 2400 are single layer PE and PP separators, respectively, while Celgard 2320 and 2325 are trilayer separators of 20 and 25 μm thickness. Asahi and Tonen separators are single layer PE separators made by the wet process. Basic properties, such as thickness, gurley, porosity, melt temperature, and ionic resistivity are reported in Table 4. These properties are defined in section 6.1.3.

Efforts have been made to find a new route for dry process using biaxial stretching techniques for preparing polypropylene microporous films, which may have submicrometer pore sizes and narrow pore size distributions and high permeability to gases and liquids combined with good mechanical properties. The biaxially stretched polypropylene microporous films (Micpor) were made by using nonporous polypropylene films of high β-crystal content.⁶⁷ The porosity of these films can be as high as 30–40%, with an average pore size of approximately 0.05 μm. The pores on the surface were almost circular in shape compared to slitlike pores observed in uniaxial stretched samples and exhibited high permeability to fluids with good mechanical properties and almost circular pore shape with narrow pore size distribution.^{68–70}

The PP/PE bilayers⁴⁰ and PP/PE/PP trilayer separators were developed by Celgard. Multilayer separators offer advantages by combining the lower melting temperature of PE with the high-temperature strength of PP. Nitto Denko has also patented a single-layer separator made from a blend of PE/PP by the dry stretch process.⁷¹ According to the patent, the separator has microporous regions of PE and PP. On heating in an oven, the impedance of the separator increases near the melting point of PE and the impedance remains high until beyond the melting point of PP. However, battery performance data have not been presented.

Microporous polyethylene separator material composed of a combination of randomly oriented thick and thin fibrils of ultrahigh molecular weight polyethylene (UHMWPE), Solupur, manufactured by DSM Solutech, is also an interesting separator material for lithium-ion batteries. Solupur is fabricated in standard grades with base weights ranging from 7 to 16 g/m² and mean pore size ranging from 0.1 to 2.0 μm and a porosity of 80–90%.⁷² Ooms et al. carried out a study on a series of DSM Solupur materials with different permeability. Rate capability and cycling tests of these materials were compared with commercial available separators in CR2320 type coin cells. Solupur materials showed low tortuosity, high strength and puncture resistance, excellent wettability, and good high rate capability and low-temperature performance because of its high porosity and UHMWPE structure.⁷³

Recently Nitto Denko has developed a battery separator made by a wet process that had high puncture strength and high heat rupture resistance.⁷⁴ They used a polyolefin resin with a high molecular weight rubber as its main component materials and cross-linked through oxidation in air. The melt rupture temperature, as measured by thermomechanical analysis was over 200 °C in this material. They also tried cross-linking ultrahigh molecular weight polyethylene with electron-beam and ultraviolet irradiation, but this had the side effect of causing deterioration in the polyolefin including rupture of the main chains and therefore resulted in reduced strength.

ENTEK Membranes LLC has developed Teklon—a highly porous, ultrahigh molecular weight polyethylene separator for lithium-ion batteries. At the writing of this publication, the separator is available in small quantities. Pekala et al. characterized Celgard, Setela, and Teklon separators in terms of their physical, mechanical, and electrical properties.⁷⁵

Celgard's separators are by far the best-characterized battery separators in the literature as they have been widely used in numerous battery systems. Bierenbam et al.⁴⁵ has described the process, physical and chemical properties, and end-use applications. Fleming and Taskier⁷⁶ described the use of Celgard microporous membranes as battery separators. Hoffman et al.⁷⁷ presented a comparison of PP and PE Celgard microporous materials. Callahan discussed a number of novel uses of Celgard membranes. Callahan and co-workers⁹⁸ also characterized Celgard membranes by SEM image analysis, mercury porosimetry, air permeability, and electrical resistivity, and later they characterized the puncture strength

and temperature/impedance data for Celgard membranes.⁴⁰ Spotnitz et al. reported short-circuit behavior in simulated, spirally wound cells, as well as impedance/temperature behavior and thermomechanical properties.¹⁰⁸ Yu⁷⁸ found that a trilayer structure of PP/PE/PP Celgard microporous membranes provided exceptional puncture strength.

Nonwoven materials such as cellulosic fibers have never been successfully used in lithium batteries. This lack of interest is related to the hygroscopic nature of cellulosic papers and films, their tendency to degrade in contact with lithium metal, and their susceptibility to pinhole formation at thickness of less than 100 μm . For future applications, such as electric vehicles and load leveling systems at electric power plants, cellulosic separators may find a place because of their stability at higher temperatures when compared to polyolefins. They may be laminated with polyolefin separators to provide high-temperature melt integrity.

Asahi Chemical Industry carried out an exploratory investigation to determine the requirements for cellulose based separators for lithium-ion batteries.⁷⁹ In an attempt to obtain an acceptable balance of lithium-ion conductivity, mechanical strength, and resistance to pinhole formation, they fabricated a composite separator (39–85 μm) that consists of fibrilliform cellulosic fibers (diameter 0.5–5.0 μm) embedded in a microporous cellulosic (pore diameter: 10–200 nm) film. The fibers can reduce the possibility of separator meltdown under exposure to heat generated by overcharging or internal short-circuiting. The resistance of these films was equal to or lower than the conventional polyolefin-based microporous separators. The long-term cycling performance was also very comparable.

Pasquier et al.⁸⁰ used paper based separators in flat pouch type lithium-ion batteries and compared the performance with cells made with Celgard type polyolefin based separators. The paper separators had good wetting properties and good mechanical properties but did not provide the shutdown effect essential for large lithium-ion batteries. Their resistance was similar to polyolefin separators, and when all water traces were removed from paper, their cycling performance was similar to that of Celgard separators. The paper-based separators can be used in small flat pouch type cells where high strength and shutdown behavior is not required. For larger spherically wound cells, which require strong separators with a shutdown feature, one can never use paper-based separators.

Recently Degussa announced that they have developed Separion separators for lithium batteries by combining the characteristics of flexible polymeric separators with the advantages of chemical and thermally resistant and hydrophilic ceramic materials. Separion is produced in a continuous coating process. Ceramic materials, e.g., alumina, silica, and/or zirconia are slip coated and hardened onto a support.^{81,82} According to Degussa, Separion separators have an excellent high temperature stability, superior chemical resistance, and good wettability,

especially at low temperatures. They tested the performance and safety behavior of Separion separator in 18650 cells and found the performance to be comparable to that of polyolefin-based separators.⁸³

The potential use of polymeric ion-exchange membranes in the next generation single-ion secondary lithium polymer batteries was shown by Sachan et al.^{84,85} Conductivities exceeding 10^{-4} S/cm with transference numbers of unity were achieved for Nafion converted to the Li^+ salt form.

To obtain a thin (less than 15 μm) separator for lithium batteries, Optodot has taken a different approach of high-speed coating of a metal oxide sol-gel coating on a smooth surface followed by a delamination step to provide the free-standing separator. Using this approach, separator with thicknesses from 6 to 11 μm was made on large-scale production coating equipment.⁸⁶ They found that the sol-gel separators with a thickness in the middle of this range of 8–9 μm have the preferred combination of thinness and strength. The metal oxide sol-gel coating is water-based with no organic solvents present. The coating formulations include a polymer and a surfactant. The polymer provides improved coating rheology, mechanical strength, and other properties. The surfactant provides improved wetting properties on the substrate. The films prepared were around 11 μm thick, with 45% porosity, and were completely wettable in nonaqueous electrolyte and had a melt temperature greater than 180 °C. These films are relatively thin and should help in increasing the capacity but may not be strong enough for tightly wound cells. Moreover, the shutdown temperature of the separator seems to be very high and thus not suitable for lithium-ion batteries.

Gineste et al. carried out the grafting of hydrophilic monomers onto PP or PE separators to improve the wettability of separators used in secondary lithium batteries with a lower content of wetting agents.^{87,88} They used a PP film (Celgard 2505) of 50 μm thickness after irradiating in air by electron beams with a dose ranging from 0.5 to 4 Mrad. The irradiated film was grafted by a monofunctional monomer (acrylic acid, AA), in the presence of difunctional cross-linking agent (diethylene glycol dimethacrylate, DEGDM). The separators start losing mechanical properties, when the grafting ratio is higher than 50%.

6.1.2. Separator Requirements

In lithium-based cells, the essential function of battery separator is to prevent electronic contact, while enabling ionic transport between the positive and negative electrodes. It should be usable on high-speed winding machines and possess good shutdown properties. The most commonly used separators for primary lithium batteries are microporous polypropylene membranes. Microporous polyethylene and laminates of polypropylene and polyethylene are widely used in lithium-ion batteries.⁸⁹ These materials are chemically and electrochemically stable in secondary lithium batteries.

The general requirements⁹⁰ for lithium-ion battery separators are given below.

6.1.2.1. Thickness. The lithium-ion cells used in consumer applications use thin microporous separators (<25 μm). The separators being developed for EV/HEV applications will require thicker ($\sim 40 \mu\text{m}$) separators. The thicker the separator, the greater the mechanical strength and the lower the probability of punctures during cell assembly but the smaller the amount of active materials that can be placed in the can. The thinner separators take up less space and permit the use of longer electrodes. This increased both capacity and, by increasing the interfacial area, rate capability. The thinness also makes it a low resistance separator.

6.1.2.2. Permeability. The separators should not limit the electrical performance of the battery under normal conditions. Typically the presence of separator increases the effective resistivity of the electrolyte by a factor of 6–7. The ratio of the resistivity of the separator filled with electrolyte divided by the resistivity of the electrolyte alone is called MacMullin number. MacMullin numbers are as high as 10–12 have been used in consumer cells.

6.1.2.3. Gurley (Air Permeability). Air permeability is proportional to electrical resistivity, for a given separator morphology. It can be used in place of electrical resistance (ER) measurements once the relationship between gurley and ER is established. The separator should have low gurley values for good electrical performance.

6.1.2.4. Porosity. It is implicit in the permeability requirement; typically lithium-ion battery separators have a porosity of 40%. Control of porosity is very important for battery separators. Specification of percent porosity is commonly an integral part of separator acceptance criteria.

6.1.2.5. Wettability. The separators should wet out quickly and completely in typical battery electrolytes.

6.1.2.6. Electrolyte Absorption & Retention. A separator should be able to absorb and retain electrolyte. Electrolyte absorption is needed for ion transport. The microporous membranes usually do not swell on electrolyte absorption.

6.1.2.7. Chemical Stability. The separators should be stable in the battery for a long period of time. They should be inert to both strong reducing and strong oxidizing conditions and should not degrade or lose mechanical strength or produce impurities, which can interfere with the function of the battery. The separator must be able to withstand the strong oxidizing positive electrode and the corrosive nature of the electrolyte at temperatures as high as 75 °C. The greater the oxidation resistance, the longer the separator will survive in a cell. Polyolefins (e.g., polypropylene, polyethylene) exhibit high resistance to most of the conventional chemicals, good mechanical properties, and a moderate temperature range for application making them ideal polymers for lithium-ion battery separators. Polypropylene separators exhibit better oxidation resistance properties when in contact with the positive electrode in a lithium-ion cell. Thus, the oxidation resistance prop-

erties of trilayer (PP/PE/PP) separators with PP as the outside layer and PE as inner layer are superior.

6.1.2.7. Dimensional Stability. The separator should lay flat and should not curl at the edges when unrolled, as this can greatly complicate cell assembly. The separator should also not shrink when exposed to electrolyte. The cell winding should not affect the porous structure in any adverse way.

6.1.2.8. Puncture Strength. The separators used in wound cells require a high puncture strength to avoid penetration of electrode material through the separator. If particulate material from the electrodes penetrates the separator, an electrical short will result and the battery will be rejected. The separators used in lithium-ion batteries require more strength than the one used in lithium primary batteries. The primary lithium batteries have only one rough electrode, and thus it requires less strength. As empirically observed, for most applications, the puncture strength should be at least 300 g/mil for separators used in lithium-ion cells. Mix penetration strength is a better measure of separator strength in a battery compared to puncture strength.

6.1.2.9. Mix Penetration Strength. The susceptibility of separators to particle penetration is characterized by mix penetration strength.⁴⁹ During the winding of the spiral wrap construction considerable mechanical pressure is applied to the cathode–separator–anode interface. Any loose particle could be forced through the separator and short the cell. The mix penetration strength should be at least 100 kgf/mil for separators used in lithium-ion cells.

6.1.2.10. Thermal Stability. Lithium-ion batteries can be poisoned by water, and so materials going into the cell are typically dried at 80 °C under vacuum. Under these conditions, the separator must not shrink significantly and definitely must not wrinkle. Each battery manufacturer has specific drying procedures. The requirement of less than 5% shrinkage after 60 min at 90 °C (in a vacuum) in both MD and TD direction is a reasonable generalization.

6.1.2.11. Pore Size. A key requirement of separators for lithium batteries is that their pores be small enough to prevent dendritic lithium penetration through them. Membranes with submicrometer pore sizes have proven adequate for lithium batteries.

6.1.2.12. Tensile Strength. The separator is wound with the electrodes under tension. The separator must not elongate significantly under tension in order to avoid contraction of the width. A tensile strength specification is sometimes given, but the key parameter is Young's modulus in the machine direction. Since Young's modulus is difficult to measure, a 2% offset yield is a good measure; less than 2% offset at 1000 psi is acceptable for most winding machines.

6.1.2.13. Skew. Ideally, when a strip of separator is laid out, the separator should be straight and not bow or skew. In practice, however, some skew is often observed. If sufficiently extreme, the skew can cause misalignment between the electrodes and separator. Skew can be measured by laying the separator flat

Table 5. General Requirements for Lithium-ion Battery Separator⁹⁰

parameter	goal
thickness ^{a,b} (μm)	<25
electrical resistance (MacMullin no., ^c dimensionless)	<8
electrical resistance (ohms cm^2)	<2
gurley ^d (s)	$\sim 25/\text{mil}$
pore size ^e (μm)	< 1
porosity (%)	~ 40
puncture strength ^f (g/mil)	>300
mix penetration strength (kgf/mil)	>100
shrinkage ^g (%)	<5% in both MD and TD
tensile strength ^h (%)	<2% offset at 1000 psi
shutdown temp ($^{\circ}\text{C}$)	~ 130
high-temp melt integrity ($^{\circ}\text{C}$)	>150
wettability	complete wet out in typical battery electrolytes
chemical stability	stable in battery for long period of time
dimensional stability	separator should lay flat; be stable in electrolyte
skew (mm/m)	<0.2

^a ASTM D5947-96. Standard Test Methods for Physical Dimensions of Solid Plastics Specimens. ASTM International. ^b ASTM D2103. Standard Specification for Polyethylene Film and Sheeting, ASTM International. ^c Caldwell, D. L.; Poush, K. A. U.S. Patent, 4,464,238, 1984. ^d ASTM D726. Standard Test Methods for Identification of Fibers in Textiles. ASTM International. ^e ASTM E128-99. Standard test method for Maximum Pore Diameter and Permeability of Rigid Porous Filters for Laboratory Use. ASTM International. ^f ASTM D3763. Standard Test Method for High-Speed Puncture Properties of Plastics using Load and Displacement Sensors. ASTM International. ^g ASTM D1204. Standard Test methods for Linear Dimensional Changes of Nonrigid Thermoplastic Sheeting or Film at Elevated Temperatures. ASTM International. ^h ASTM D882. Standard Test Method for Tensile Properties of Thin Plastic Sheeting. ASTM International.

on a table parallel with a straight meter stick. The skew should be less than 0.2 mm/m of separator.

6.1.2.14. Shutdown. Lithium-ion batteries separators provide some margin of protection against short circuit and overcharge in lithium-ion cells. The separators exhibit a large increase in impedance at temperature about 130 $^{\circ}\text{C}$ that effectively stops ionic transport between the electrodes.^{91,92} The greater the mechanical integrity of the separator above 130 $^{\circ}\text{C}$, the greater the margin of safety the separator can provide. If the separator loses mechanical integrity, then the electrodes can come into direct contact, react chemically, and result in thermal runaway. The shutdown behavior of a separator can be characterized by heating the separator (saturated with electrolyte) to high temperatures and simultaneously monitoring the electrical resistance of the separator.^{92,108}

6.1.2.15. High-Temperature Stability. A separator might provide an extra margin of safety if it can prevent the electrodes from contacting one another at high temperatures. Separators with good mechanical integrity at high temperatures can provide a greater margin of safety for lithium-ion cells. Thermal mechanical analysis (TMA) can be used to characterize the high-temperature stability of separators. Utilizing TMA, the separator is held under constant load and the degree of elongation vs. temperature is measured; at the temperature where the separator loses mechanical integrity, the elongation increases dramatically.

6.1.2.16. Electrode Interface. The separator should form a good interface with the electrodes to provide sufficient electrolyte flow.

In addition to the above properties, the separator must be essentially free of any type of defects (pinholes, gels, wrinkles, contaminants, etc.). All of the above properties have to be optimized before a membrane qualifies as a separator for a lithium-ion

battery. The general requirements for lithium-ion battery separators are also summarized in Table 5.

6.1.3. Separator Properties/Characterization

Separators are characterized by structural and functional properties; the former describes what they are and the latter how they perform. The structural properties include chemical (molecular) and microcrystalline nature, thickness, pore size, pore size distribution, porosity, and various chemical and physical properties such as chemical stability, and electrolyte uptake. The functional properties of interest are electrical resistivity, permeability, and transport number. It is useful to characterize separator materials in terms of their structural and functional properties and to establish a correlation of these properties with their performance in batteries. A variety of techniques are used to evaluate separators. Some of these techniques are discussed in this section.

6.1.3.1. Gurley. Separator permeability is usually characterized by air permeability. The gurley number expresses the time required for a specific amount of air to pass through a specific area of separator under a specific pressure. The standard test method is described in ASTM-D726 (B).

The gurley number is used to characterize separators because the measurement is accurate and easy to make, and deviations from specific values are a good indication of problems. Air permeability (gurley) is proportional to electrical resistance (ER), for a given separator morphology.⁹⁸ Gurley can be used in place of ER measurements once the relationship between gurley and ER is established. A lower gurley value means higher porosity, lower tortuosity, and accordingly lower ER.

6.1.3.2. Electrical Resistance. The measurement of separator resistance is very important to the art of battery manufacture because of the influence the

separator has on electrical performance. Electrical resistance is a more comprehensive measure of permeability than the Gurley number, in that the measurement is carried out in the actual electrolyte solution. The ionic resistivity of the porous membrane is essentially the resistivity of the electrolyte that is embedded in the pores of the separator. Typically, a microporous separator, immersed in an electrolyte has an electrical resistivity about 6–7 times that of a comparable volume of electrolyte, which it displaces. It is a function of the membrane's porosity and tortuosity, the resistivity of the electrolyte, the thickness of the membrane, and the extent to which the electrolyte wets the pores of the membrane.⁹³ The electrical resistance of the separator is the true performance indicator of the cell. It describes a predictable voltage loss within the cell during discharge and allows one to estimate rate limitations.

Classical techniques for measuring electrical resistivity of microporous separators have been described by Falk and Salkind⁵ and by Robinson and Walker.⁹⁴ The resistivity of an electrolyte is more accurately determined by ac methods since dc can polarize the electrodes and cause electrolysis of the solution. Modern ac impedance measuring systems allow rapid measurements of cell resistance over a wide range of frequencies from which resistance can be calculated free of capacitance effects. Compared to the dc techniques, the equipment required and the theory necessary to interpret the ac techniques are more complex; however, ac measurements yield information about long-range migration of ions and polarization phenomena occurring within the cell. In an ac measurement, a sinusoidal voltage is applied to a cell, and the sinusoidal current passing through the cell as a result of this perturbation is determined. A four-electrode cell is usually used for resistivity measurements. The outer two electrodes serve to apply a sinusoidal potential, and the resulting current passing through the inner two electrodes is measured. This technique is employed to avoid the complications arising from a nonuniform potential field near the outer two electrodes. An excellent review of experimental techniques for measuring electrical resistivity in aqueous solution is available.^{95,96}

The separator resistance is usually characterized by cutting small pieces of separators from the finished material and then placing them between two blocking electrodes. The separators are completely saturated with the electrolyte. The resistance (Ω) of the separator is measured at a certain frequency by ac impedance techniques. The frequency is chosen so that the separator impedance is equal to the separator resistance. To reduce the measurement error, it is best to do multiple measurements by adding extra layers. The average resistance of single layer is determined from multiple measurements. The specific resistivity, ρ_s (Ω cm), of the separator saturated with electrolyte is given by

$$\rho_s = \frac{R_s A}{l} \quad (1)$$

where R_s is the measured resistance of separator in

Ω , A is the electrode area in cm^2 , and l is the thickness of membrane in cm. Similarly, the specific resistivity of the electrolyte, ρ_e (Ω cm), is given by

$$\rho_e = \frac{R_e A}{l} \quad (2)$$

where R_e is the measured resistance of electrolyte in Ω . The ratio of the resistivity of a separator membrane to that of the electrolyte is called the MacMullin number, N_m , which can be used to predict the influence of the separator on battery performance.⁹⁷

$$N_m = \frac{\rho_s}{\rho_e} = \frac{\tau^2}{\epsilon} \quad (3)$$

where τ is the tortuosity and ϵ is the porosity of the separator. The MacMullin number describes the relative contribution of a separator to cell resistance. It is almost independent of electrolyte used and also factors out the thickness of the material. It assumes that the separator wets completely in the electrolyte used for the test. From eqs 1 and 3, the electrical resistance of a microporous membrane is given by the following^{5,114}

$$R_m = \rho_e \left(\frac{\tau^2 l}{\epsilon A} \right) \quad (4)$$

It has been shown for Celgard membranes that the membrane resistance can be related to the Gurley number by⁹⁸

$$R_m A = \frac{\rho_e}{5 \times 18 \times 10^{-3}} t_{\text{gur}} d \quad (5)$$

where R_m is the membrane resistance (Ω), A is the membrane area (cm^2), ρ_e is the specific electrolyte resistance (Ω cm), t_{gur} is the Gurley number (10 cm^3 air, 2.3 mmHg), d is the pore size, and $5 \times 18 \times 10^{-3}$ is a scaling factor.

The usual procedure for characterizing battery separators is to cut several test samples from the finished material. Thus, only a small portion of the separator is actually examined. Ionov et al. has proposed an alternative technique to measure the resistance of a separator over a large separator area.⁹⁹ In this technique, the separator material is passed through an electrolyte bath between electrical resistance measuring transducers. The set of transducers installed in the bath transverse to the moving sheet of separator material examines the whole surface of the material. If the production process ensures good uniformity in the physicochemical properties of the separator material over the whole surface, the transducer outputs will clearly be close to one another. A nonuniform separator will cause significant deviations from the average value at various sections of the material. In this case, the sections having lower or higher resistance compared with the average value should be regarded as flawed.

6.1.3.3. Porosity. The porosity is important for high permeability and also for providing a reservoir of electrolyte in the cell. Higher and uniform porosity is desirable for unhindered ionic current flow. Non-

uniform porosity leads to nonuniform current density and can further lead to reduced activity of the electrodes. Cell failure can result because during discharge some areas of the electrodes work harder than other.

Porosity of a separator is defined as the ratio of void volume to apparent geometric volume. It is usually calculated (eq 6) from the skeletal density, basis weight, and dimensions of the material and so may not reflect the accessible porosity of the material.

$$\text{porosity (\%)} = \left[1 - \frac{(\text{sample weight}/\text{sample volume})}{\text{polymer density}} \right] \times 100 \quad (6)$$

The standard test method is described in ASTM D-2873. The actual or accessible porosity can also be determined by the weight of liquid (e.g., hexadecane) absorbed in the pores of the separator. In this method, the separator weight is measured before and after dipping in hexadecane solvent, and the porosity is calculated (eq 7) by assuming that volume occupied by hexadecane is equal to the porous volume of the separator.

$$\text{porosity (\%)} = \frac{\text{volume occupied by hexadecane}}{(\text{volume of polymer} + \text{volume occupied by hexadecane})} \times 100 \quad (7)$$

6.1.3.4. Tortuosity. Tortuosity is the ratio of mean effective capillary length to separator thickness. The tortuosity factor, τ of a separator can be expressed by

$$\tau = \frac{l_s}{d} \quad (8)$$

where l_s is the ion path through the separator and d is the thickness of the separating layer.

Tortuosity is a long-range property of a porous medium, which qualitatively describes the average pore conductivity of the solid. It is usual to define τ by electrical conductivity measurements. With knowledge of the specific resistance of the electrolyte and from a measurement of the sample membrane resistance, thickness, area, and porosity, the membrane tortuosity can be calculated from eq 3.

This parameter is widely used to describe the ionic transport by providing information on the effect of pore blockage. A tortuosity factor $\tau = 1$, therefore, describes an ideal porous body with cylindrical and parallel pores, whereas values of $\tau > 1$ refer to more hindered systems. Higher tortuosity is good for dendrite resistance but can lead to higher separator resistance.

6.1.3.5. Pore Size and Pore Size Distribution. For any battery applications, the separator should have uniform pore distribution to avoid performance losses arising from nonuniform current densities. The submicrometer pore dimensions are critical for preventing internal shorts between the anode and the cathode of the lithium-ion cell, particularly since these separators tend to be as thin as 25 μm or less.

This feature will be increasingly important as battery manufacturers continue to increase the cell capacity with thinner separators. The pore structure is usually influenced by polymer composition, and stretching conditions, such as drawing temperature, drawing speed, and draw ratio. In the wet process, the separators produced by the process of drawing after extraction (as claimed by Asahi Chemical and Mitsui Chemical) are found to have much larger pore size (0.24–0.34 μm) and wider pore size distribution than those produced by the process of extraction (0.1–0.13 μm) after drawing (as claimed by Tonen).⁵⁸

The testing of battery separators and control of their pore characteristics are important requirements for proper functioning of batteries. Mercury porosimetry has been historically used to characterize the separators in terms of percentage porosity, mean pore size and pore size distribution.¹⁰⁰ In this method, the size and volume of pores in a material are measured by determining the quantity of mercury, which can be forced into the pores at increasing pressure. Mercury does not wet most materials, and a force must be applied to overcome the surface tension forces opposing entry into the pores.

The hydrophobic (e.g. polyolefins) separators are also characterized with Aquapore (non-mercury porosimetry) technique, where water is used in place of mercury. This is a very useful technique for characterizing polyolefin-based separators used in lithium batteries.¹⁰¹ Porosimetry gives pore volume, surface area, mean pore diameter, and pore size distribution. In a typical experiment, the sample is placed in the instrument and evacuated. As the pressure increase, the quantity of water forced into the pores increases in proportion to the differential pore volume, the size of the pores corresponding to the instantaneous pressure. Thus, increasing the pressure on a membrane having a given pore size distribution results in a unique volume vs pressure or pore diameter curve. The pressure required for intrusion of water into a pore of diameter, D , is given by following equation

$$D = \frac{4\gamma \cos \theta}{p} \quad (9)$$

where D is the diameter of the pore assuming the pore to be cylindrical, p is the differential pressure, γ is the surface tension of the nonwetting liquid, water, and θ is the contact angle of water. The pores generally are not of spherical shape of a constant diameter. They usually vary in their form and size. Thus, statements of any pore diameter are always to be viewed with the above in mind.

Another technique, capillary flow porometry has been developed by Porous Materials Inc.¹⁰² to characterize battery separators.^{103,104} The instrument can measure a number of characteristics of battery separators such as size of the pore at its most constricted part, the largest pore size, pore size distribution, permeability, and envelope surface area.¹⁰⁹

Scanning electron microscopy (SEM) is also used to examine separator morphology. SEM pictures of some commercial membranes are shown in Figures

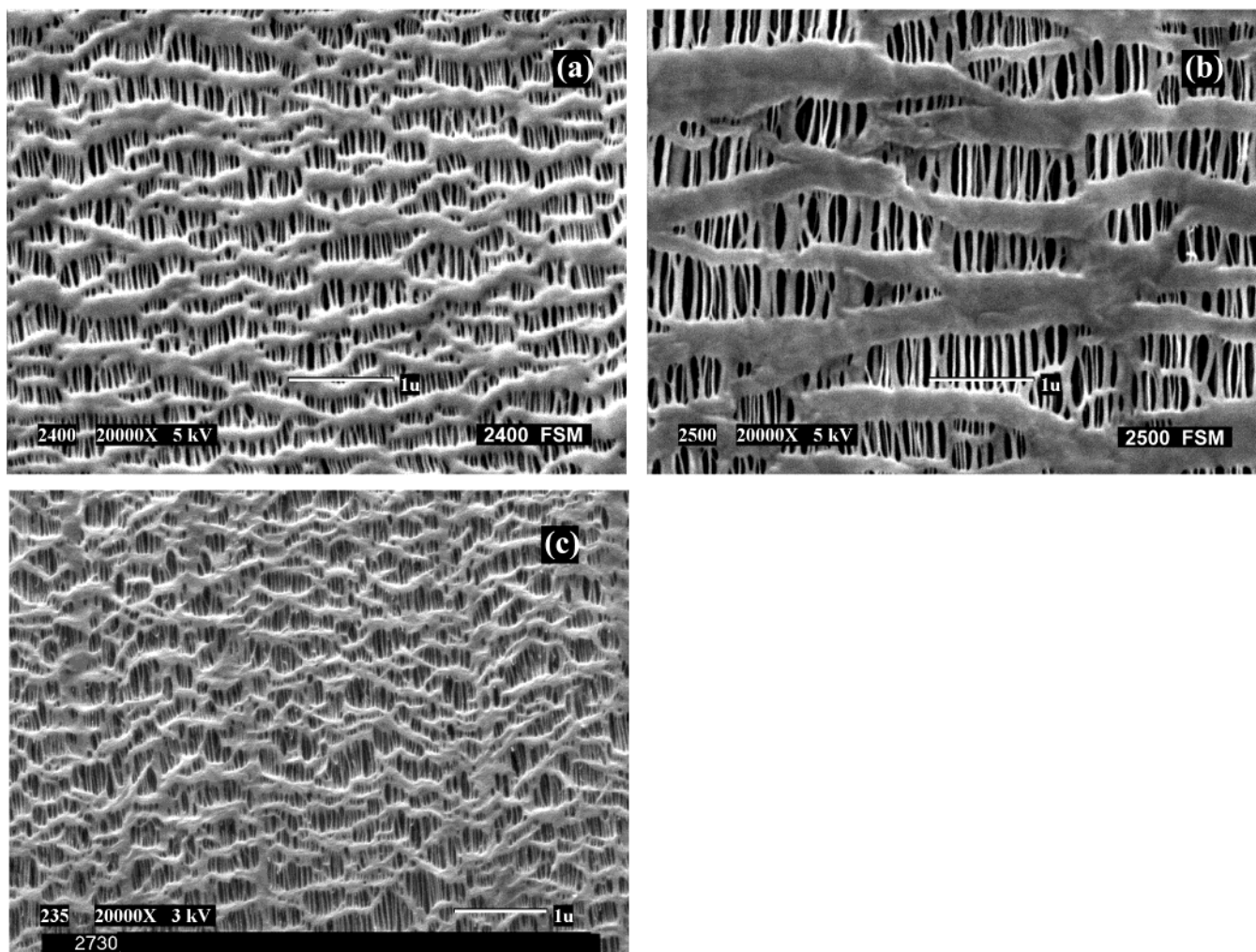


Figure 4. Scanning electron micrographs of the surface of single layer Celgard separators used in lithium batteries: (a) 2400 (PP), (b) 2500 (PP), and (c) 2730 (PE).

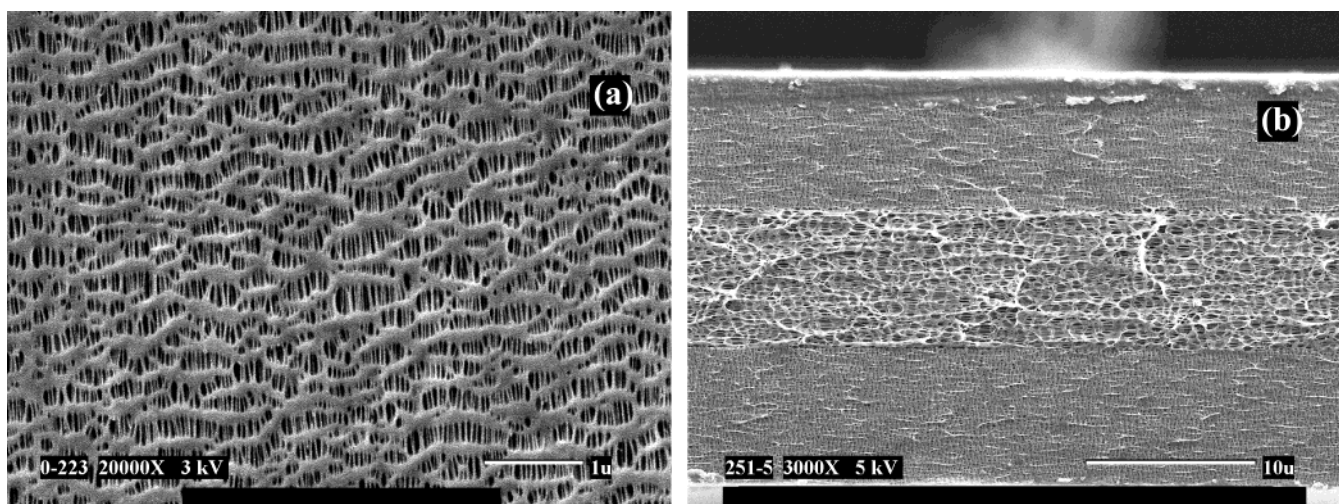


Figure 5. Scanning electron micrographs of Celgard 2325 (PP/PE/PP) separator used in lithium-ion batteries: (a) surface SEM and (b) cross-section SEM.

4–6. The surface SEM of Celgard 2400, 2500, and 2730 are shown in Figure 4. It is clear from the images that the pores are uniformly distributed. Both Celgard 2400 and 2500 are single layer PP separators, but the pore size of Celgard 2500 is substantially larger than Celgard 2400. Thus, it has lower resistance and is more suited for high rate applications.

Figure 5 shows the surface SEM and cross-section SEM of Celgard 2325. The surface SEM only shows the PP pores while the PE pores are visible in the cross-section. It is clear from the image that all three layers are of equal thickness. The SEM of separators made by wet process are shown in Figure 6. The pore structure of all of these membranes is very similar.

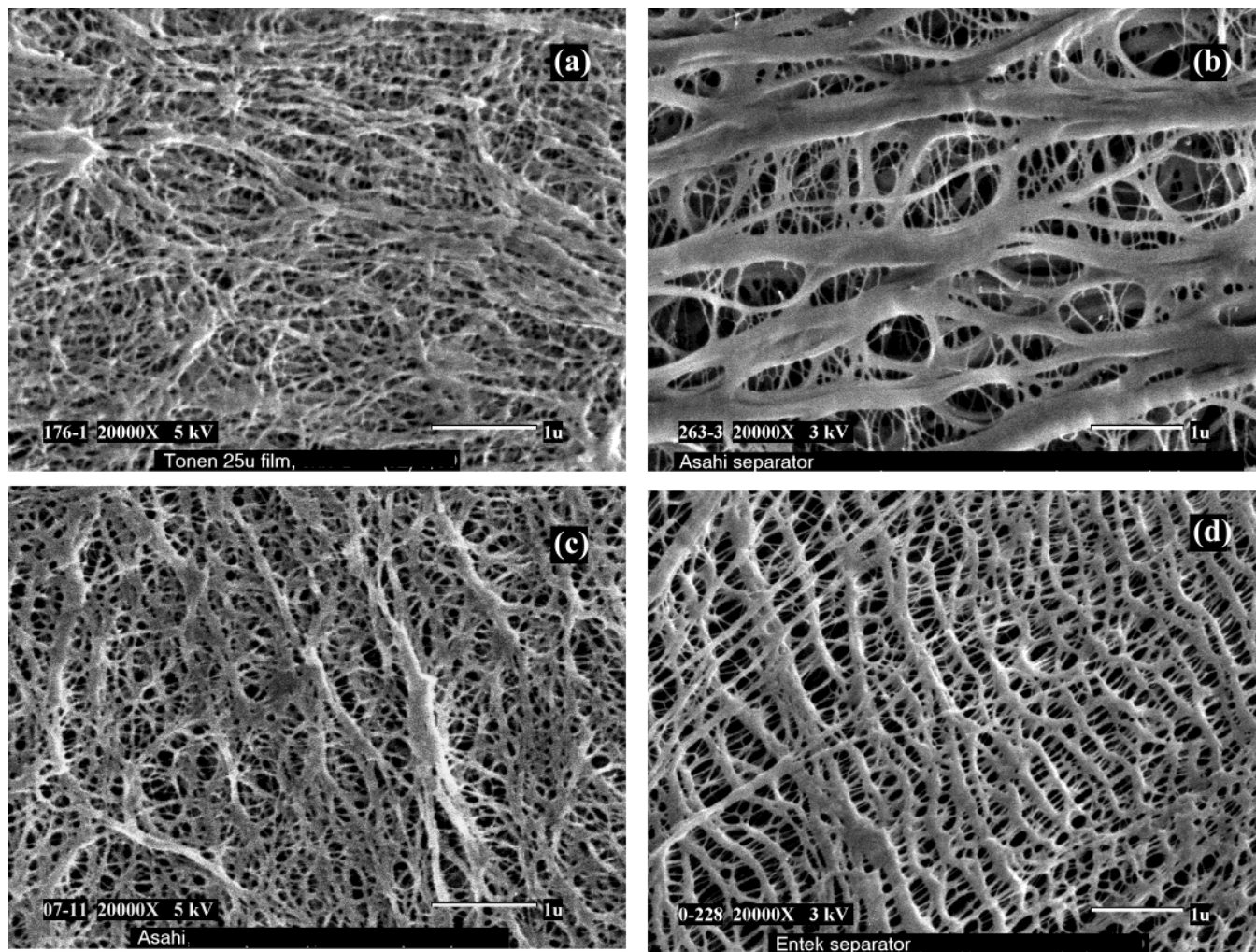


Figure 6. Scanning electron micrographs of separators made by wet process and used in lithium-ion batteries: (a) Setela (Tonen), (b) Hipore-1 (Asahi), (c) Hipore-2 (Asahi), and (d) Teklon (Entek).

Asahi-1 (Figure 6b) separator has significantly larger pores compared to the other membranes.

Image analysis has been used to characterize the pore structure of synthetic membrane materials.¹⁰⁵ The Celgard films have also been characterized by scanning tunneling microscopy, atomic force microscopy, and field emission scanning electron microscopy.^{53,106} The pore size of the Celgard membranes can also be calculated from eq 5, once the MacMullin number and gurley values are known.

6.1.3.6. Puncture Strength. A separator is required to have sufficient physical strength to endure the rigors of cell assembly and day-to-day charge-discharge cycling. Physical strength is required to withstand basic handling, cell blocking/assembly, physical shock, punctures, abrasion, and compression.

The puncture strength (PS) is the weight that must be applied to a needle to force it completely through a separator.^{45,107} It has been used to indicate the tendency of separators to allow short-circuits in a cell that may occur due to holes generated in the separator by the rough surface of an electrode during the battery assembly and charge-discharge cycle. The PS requirement for lithium-ion batteries is higher than lithium-foil batteries, because the separator must contend with two rough surfaces. Commercially

available puncture strength machines made for textiles tend to give meaningless results when testing battery separator membranes. More reproducible results can be obtained with a load frame (such as an Instron Machine). The mix penetration strength is a better measure of mechanical strength for battery separators as it measures the force required to create a short through the separator when electrode mix is pushed through it.

The strength of the separator depends greatly on the materials used and the manufacturing method. The wet-biaxial method simultaneously stretches in the MD and TD directions and thus achieves a material that has tensile modulus and rupture strength in both directions. Both high polymer entanglement and stretching help increase the physical strength of the separator.

6.1.3.7. Mix Penetration Strength. The force required to create a short through a separator due to mix (electrode material) penetration defines mix penetration strength. In this test force (with a $\frac{1}{2}$ in. diameter ball) is applied on the positive electrode/separator/negative electrode sandwich, and the force at which the mix penetrates through the separator and creates an electronic short is called mix penetration force. Mix penetration strength is used to indicate the tendency of separators to allow short-

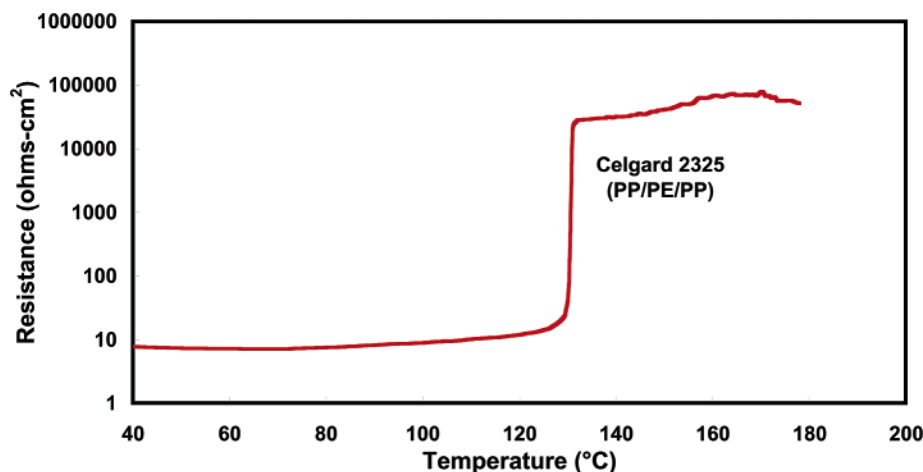


Figure 7. Internal impedance (at 1 kHz) of Celgard 2325 (PP/PE/PP) separator as a function of temperature. Heating rate: 60 °C/min.

circuits during battery assembly. The mix penetration resistance test is more closely related to particle penetration resistance compared to puncture resistance.⁴⁹

6.1.3.8. Tensile Strength. The tensile strength measurements (e.g., Young's modulus, percent offset strength, elongation at break, and stress at break) can be made by utilizing widely known standard procedures. These tests are carried out in both MD and TD directions. The tensile properties are dependent on the manufacturing process. The uniaxially oriented films have high strength in only one direction, whereas biaxially oriented films are more uniformly strong in both MD and TD directions. ASTM test method D88-00, "Standard test method for tensile properties of thin plastic sheeting", is an appropriate test.

The separator should be strong enough to withstand mechanical handling during cell winding and assembly. It should be dimensionally stable and should not neck down during winding. The decrease in width will allow the electrodes to touch each other and create a short. Thus, the tensile property of the separator should be very strong in MD direction compared to TD direction.

6.1.3.9. Shrinkage. Shrinkage test is carried out on both MD and TD directions. In this test, the dimensions of separators are measured and then stored at 90 °C for a fixed time. The shrinkage is then calculated from the change in dimensions as shown in eq 10.

$$\text{shrinkage (\%)} = \frac{L_i - L_f}{L_i} \times 100 \quad (10)$$

where L_i is the initial length and L_f is the final length of separator after high temperature storage. The uniaxially stretched separators tend to shrink in the MD direction only, while the biaxially stretched separators shrink in both MD and TD directions. The shrinkage of separators can also be compared by carrying out the thermal mechanical analysis (TMA) test at a constant load and rate.

6.1.3.10. Shutdown. Separator shutdown is a useful and essential mechanism for limiting temper-

ature and preventing venting in short-circuited cells.¹⁰⁸ It usually takes place close to the melting temperature of the polymer when the pores collapse turning the porous ionically conductive polymer film into a nonporous insulating layer between the electrodes. At this temperature there is a significant increase in cell impedance and passage of current through the cell is restricted. This prevents further electrochemical activity in the cell, thereby shutting the cell down before an explosion can occur.

The ability of the PE based separator to shutdown the battery is determined by its molecular weight, percent crystallinity (density) and process history. Material properties and processing methods might need to be tailored so that the shutdown response is spontaneous and complete. The optimization needs to be done without affecting the mechanical properties of the material in the temperature range of interest. This is easier to do with the trilayer separators manufactured by Celgard since one material is utilized for the shutdown response and another for the mechanical properties. Polyethylene containing separators, in particular trilayer laminates of polypropylene, polyethylene, and polypropylene, appear to have the most attractive properties for preventing thermal runaway in lithium-ion cells.^{109,110} The shutdown temperature of 130 °C is usually enough to control the cell heating and avoid thermal runaway in lithium-ion cells. A lower temperature shutdown will be desirable if it does not affect the separator mechanical properties or high-temperature cell performance in any adverse way.

The shutdown property of separators is measured by measuring the impedance of a separator while the temperature is linearly increased.^{92,108} Figure 7 shows the actual measurement for Celgard 2325 membrane. The heating rate was around 60 °C/min, and the impedance was measured at 1 kHz. The rise in impedance corresponds to a collapse in pore structure due to melting of the separator. A 1000-fold increase in impedance is necessary for the separator to stop thermal runaway in the battery. The drop in impedance corresponds to opening of the separator due to coalescence of the polymer and/or to penetration of the separator by the electrodes; this phenomenon is

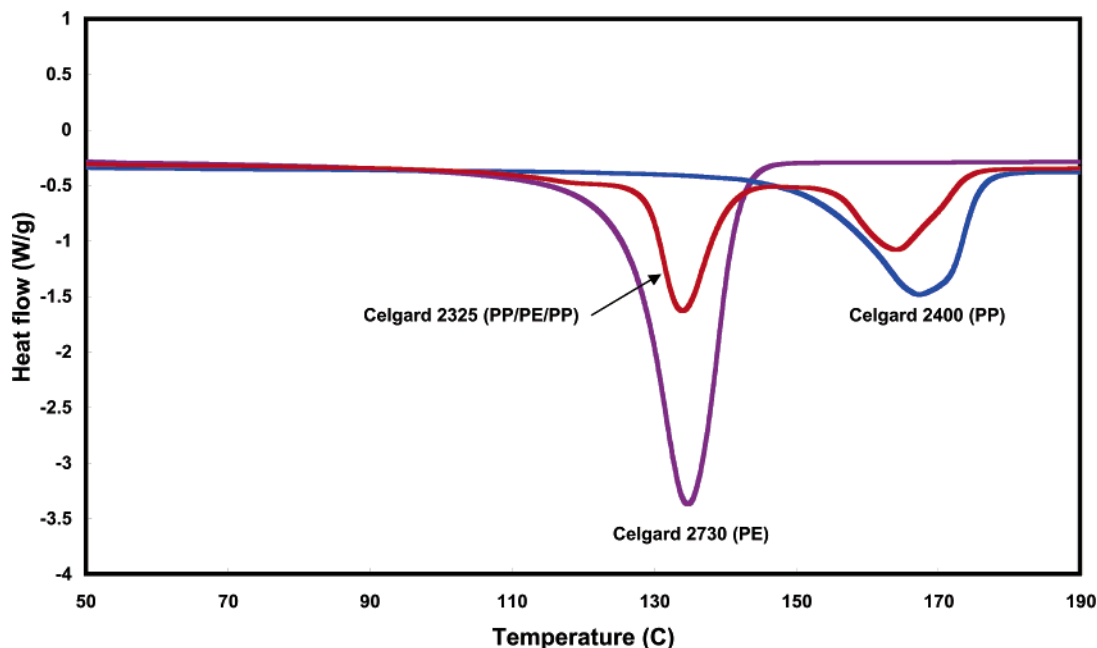


Figure 8. DSC of Celgard 2730 (PE), 2400 (PP), and 2325 (PP/PE/PP).

referred to as a loss in “melt integrity”. This test is fairly reliable in indicating the temperature at which the impedance rises but shows some variability in characterizing the subsequent drop in impedance.

In Figure 7, the shutdown behavior of a multilayer (PP/PE/PP) separator (Celgard 2325) is shown. The impedance rise occurred near the melting point of polyethylene (130 °C) and remained high until such time as the melting point of polypropylene (165 °C) is attained. The shutdown temperature of the separator is governed by the melting point of the separator material. At the melting point the pores in the separator collapse to the form a relatively nonporous film between the anode and the cathode. This was confirmed by DSC as shown in Figure 8. The DSC scan in Figure 8 gives a peak melting temperature of 135 °C for Celgard 2730, 168 °C for Celgard 2400, and 135/165 °C for Celgard 2325. The shutdown behavior of thinner separators (<20 μm) is very similar to thicker separators. The battery manufacturers have been very successful in using the thinner separators without compromising on the shutdown behavior of the separators.

Laman et al. introduced the use of impedance measurements as a function of temperature to characterize shutdown separators.⁹² Using a temperature scan rate of 1 °C/min, they found that the impedance increased several orders of magnitude near the melting point of the separator. They verified the patent claims of Lundquist et al.¹¹¹ that bilayer separators of PE and PP gave a temperature window of high impedance extending approximately between the melting point of the polymers. The concept of using separators consisting of distinct layers, one of which could act as a fuse, was developed by Lundquist et al.^{112,113} Laman’s results have been corroborated by Geiger et al.⁴⁰ and Spotnitz et al.^{108,114} Spotnitz et al. developed a thin layer cell which

allowed temperature scan rates of 5 °C/min and higher and obtained results similar to those of Laman et al.

Prior work related with shutdown separators also involved application of waxes on membranes.^{115,116} In these cases, the wax or low melting polymers were coated on the polyolefin separator. The disadvantage of this technique is that the coating can block the pores of the separator and thus can affect the performance by increasing separator resistance. Moreover, the coating level has to be very high to get complete shutdown.

The shutdown characteristic provides protection from external short-circuit and during cell over-charge. It provides little protection from internal shorts should they occur. Should the electrodes touch each other or become shorted from a dendritic growth of soluble impurity or other dendrite forming soluble material, the separator only helps in avoiding delayed failures. In the case of an instant failure during an internal short circuit, the heating rate is too high and the separator shutdown is not fast enough to control the heating rate.

6.1.3.11. Melt Integrity. The separators used in lithium-ion batteries should have high-temperature melt integrity. The separator should maintain its melt integrity after shutdown so that the electrodes do not touch and create a short. This helps in avoiding the thermal runaway even when the cell is exposed to high temperatures. Thermal mechanical analysis (TMA) is a very good technique to measure the high-temperature melt integrity of separators.

TMA involves measuring the shape change of a separator under load while the temperature is linearly increased. Typically, separators show some shrinkage and then start to elongate and finally break as shown in Figure 9. This test utilizes a small separator samples (about 5–10 mm length (MD) and

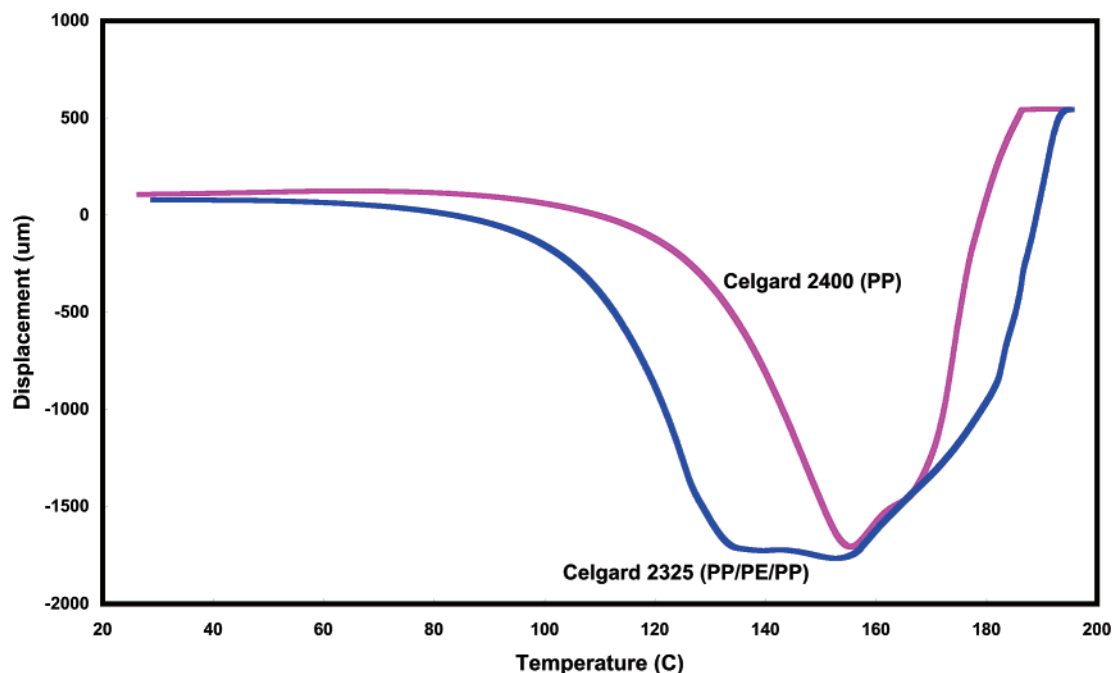


Figure 9. TMA of Celgard 2400 (PP) and 2325 (PP/PE/PP). A constant load (2 g) is applied while the temperature is ramped at 5 °C/min.

Table 6. TMA Data for Typical Celgard Separators

	Celgard 2400	Celgard 2325
shrinkage onset temp (°C)	121	106
deformation temp (°C)	156	135, 154
rupture temp (°C)	183	192

about 5 mm width), which is held in mini-instron type grips. The sample is held with a constant 2 g load while the temperature is ramped at 5 °C/min past the melting point until the tension ruptures the film. Three parameters are reported from TMA test—shrinkage onset temperature, melt temperature, and melt rupture temperature. It has proved to be a more reproducible measure of melt integrity of the separator.¹⁰⁸

Figure 9 shows the TMA data for two different Celgard membranes. The shrinkage onset temperature, deformation temperature, and rupture temperature are summarized in Table 6. The single layer PP membrane (Celgard 2400) showed a higher softening temperature (~121 °C), a deformation temperature around 160 °C, and a very high rupture temperature around 180 °C. The multilayer polypropylene/polyethylene/polypropylene separator (Celgard 2325) combined the low-temperature shutdown property of polyethylene with the high-temperature melt integrity of polypropylene, resulting in a separator with softening (~105 °C) and melt temperature (~135 °C) very similar to that of PE and rupture temperature (~190 °C) very similar to that of PP.

Separators with melt integrity greater than 150 °C are desirable for lithium-ion cells. The trilayer separators with polypropylene on the outside help in maintaining the melt integrity of the separators at higher temperatures compared to single layer PE separators. This is especially important for bigger lithium-ion cells being developed for hybrid and electric vehicles.

6.1.3.12. Wettability and Wetting Speed. Two physical properties of separators, which are important to the operating characteristics of a battery, are electrolyte absorption and electrolyte retention. Any good separator should be able to absorb a significant amount of electrolyte and also retain the absorbed electrolyte when the cell is in operation. These are more important in sealed cells where no free electrolyte is present. A maximum amount of electrolyte in the separator is desirable to achieve minimum cell internal resistance.

The separator wettability can limit the performance of batteries by increasing the separator and cell resistance. Separator wetting speed can be correlated with electrolyte filling time in real cells. The wetting speed is determined by the type of polymer (surface energy), pore size, porosity, and tortuosity of the separators. There is no generally accepted test for separator wettability. However, simply placing a drop of electrolyte on the separator and observing whether the droplet quickly wicks into the separator is a good indication of wettability. The contact angle is also a good measure of wettability.

The uptake of electrolyte by many hydrophobic polymer separators can be enhanced either by wetting agents or ionic-functional groups (e.g. ion-exchange membranes).

6.1.4. Effect of Separator on Cell Performance and Safety

Although the material of a battery separator is inert and does not influence electrical energy storage or output, its physical properties greatly influence the performance and safety of the battery. This is especially true for lithium-ion cells, and thus the battery manufacturers have started paying more attention to separators while designing the cells. The cells are designed in such a way that separators do not limit the performance, but if the separator properties are

Table 7. Safety and Performance Tests for Lithium-Ion Batteries and the Corresponding Important Separator Property and Its Effect on the Cell Performance and/or Safety

cell property	separator property	comments
cell capacity	thickness	cell capacity can be increased by making the separator thinner
cell internal resistance	resistance	separator resistance is a function of thickness, pore size, porosity, and tortuosity
high rate performance	resistance	separator resistance is a function of thickness, pore size, porosity, and tortuosity
fast charging	resistance	low separator resistance will aid in overall faster charging by allowing higher and/or longer constant current charging
high-temp storage	oxidation resistance	oxidation of separators can lead to poor storage performance and reduce performance life
high-temp cycling	oxidation resistance	oxidation of separators can lead to poor cycling performance
self-discharge	weak areas, pinholes	soft shorts during cell formation and testing can lead to internal current leakage
long-term cycling	resistance, shrinkage, pore size	high resistance, high shrinkage and very small pore size can lead to poor cycling performance
overcharge	shutdown behavior; high-temp melt integrity	separator should completely shutdown and then maintain its melt integrity at high temp
external short circuit	shutdown behavior	separator shutdown stops the cells from overheating
hotbox	high-temp melt integrity	separator should be able to keep the two electrodes apart at high temp
nail crush	shutdown (to stop delayed failure)	in the case of internal shorts, the separator may be the only safety device to stop the cell from overheating
bar crush	shutdown (to stop delayed failure)	in the case of internal shorts, the separator may be the only safety device to stop the cell from overheating

not uniform, or if there are other issues, it can affect the performance and safety of cells. This section will focus on the effect of the separator properties on cell performance and safety. Table 7 shows different types of safety and performance tests for lithium-ion batteries and the corresponding important separator property and how it affects performance and/or safety.

To achieve good performance of lithium-ion cells, the separators should have low resistance, low shrinkage and uniform pore structure. The separator with high resistance will perform poorly during high rate discharge and will also increase the cell charging time. Low shrinkage is a very important characteristic for separators, especially for higher capacity cells. These cells are used in high-speed laptop computers, which can experience higher temperatures (~ 70 – 75 °C) under certain conditions.¹¹⁷ This can lead to shrinkage of separators and ultimately higher cell resistance and poor long-term cycling. The shrinkage in TD direction can lead to safety issues because of an internal short between the electrodes. Larger pores can lead to shorts during cell manufacturing or can fail during hipot testing. Larger pores will allow more soft shorts and higher self-discharge, especially during high-temperature storage. Very small pore size can lead to higher resistance and poor cycle life during high-temperature cycling and storage. Thus, the pore size of the separator should be optimized to achieve good strength and performance.

One of the ways to increase cell capacity is by decreasing the thickness of separators. The newer high capacity cells (>2.0 A h) generally use 20 and 16 μm separators as compared to 25 μm separators used in cells with 1.6–1.8 A h capacity. The thinner separators offer lower resistance and help in increasing the capacity. However, they can hold less elec-

trolyte and their mechanical strength is not as high as thicker separators. Thus, appropriate changes should be made in cell design to keep the cell safe. The handling and manufacturing of thinner separators is also a challenge for the separator manufacturers. They are required to maintain the same electrical and mechanical properties and to have better quality for thinner separators. The separator manufacturers have installed better controls and quality standards and have started offering 16- μm separators. A lot of battery experts are of the opinion that the 16- μm is the thinnest they can use and still maintain the stringent performance and safety requirements of lithium-ion cells.

The separators inside the lithium-ion batteries experience extreme oxidizing environment on the side facing the positive electrode and extreme reducing environment on the side facing the negative electrode. The separators should be stable in these conditions during long-term cycling especially at high temperatures. Separators with poor oxidation resistance can lead to poor high-temperature storage performance and poor long-term cycling behavior. The oxidation resistance properties of trilayer (PP/PE/PP) separators with PP as the outside layer and PE as inner layer is superior compared to polyethylene separators. This is because of the better oxidation resistance properties of polypropylene in contact with the positive electrode in a lithium-ion cell.

The products formed by the decomposition of the electrolyte can also block the pores of the separator, leading to increase in cell resistance. The separators with lower resistance also helps in better low temperature performance. At very low temperatures, the resistance of the electrolytes is very high and thus smaller contribution from separator helps in keeping the cell resistance lower.

Zeng et al.¹¹⁸ has shown that small amounts of active lithium metal could be added to a lithium-ion battery via the separator by using vacuum deposition techniques. The lithium films (4–8 μm) were deposited onto a microporous PP film and showed that the lithium electrochemically reacted with either electrode and thus the intrinsic irreversible capacity of the negative electrode was compensated for using volumetrically efficient lithium metal. This may be a novel idea to allow higher capacity designs but is likely impractical and uneconomical due to issues involved with lithium plating on polymer films and handling the resulting films.

The lithium-ion cells have demonstrated power loss when aged and/or cycled at high temperatures. Norin et al.¹¹⁹ demonstrated that the separator is at least partly responsible for the power loss due to the intrinsic increase in its ionic resistance. They showed that impedance increased significantly upon cycling and/or aging of lithium-ion cells at elevated temperatures and that separators accounts for $\sim 15\%$ of the total cell impedance rise. They later reported that the loss in ionic conductivity of the separator was due to blocking of the separator pores with the products formed due to electrolyte decomposition, which was significantly accelerated at elevated temperatures.¹²⁰

The U.S. Department of Transportation (DOT) classifies all lithium-ion batteries as hazardous materials for shipping in the same category as lithium metal primary batteries.¹²¹ It grants exceptions based on the cell capacity and ability of the cells to pass specified tests. There are several groups that regulate, or provide testing, to verify safe operation of lithium-ion cells under abuse conditions. In addition, the UL Laboratories,^{122,123} the International Electrotechnic Commission,¹²⁴ and the United Nations¹²⁵ have developed standardized safety testing procedures. These tests are designed to ensure that cells are safe to ship and are resistant to typical abuse conditions such as internal shorting, overcharge, overdischarge, vibration, shock, and temperature variations that may be encountered in normal transportation environments.

Underwriters Laboratories (UL) requires that consumer batteries pass a number of safety tests (UL 1642¹²⁶ and UL-2054¹²⁷). There are similar recommendations from UN for transport of dangerous goods,¹²⁸ and from the International Electrotechnical Commission (IEC) and Japan Battery Association.¹²⁹ An abnormal increase in cell temperature can occur from internal heating caused by either electrical abuse—overcharge or short circuit—or mechanical abuse—nail penetration or crush. A higher cell temperature could also be a result of external heating. For this reason, battery packs containing lithium-ion cells are designed with safety control circuits that have redundant safety features (PTC, CID, vent, thermal fuse, etc.). Shutdown separators are one of the safety devices inside the cell and act as a last line of defense. The separator shutdown is irreversible, which is fine for polyethylene-based separators, which melt around 130 $^{\circ}\text{C}$.

The impedance of the separator increases by 2–3 orders of magnitude due to an increase in cell

temperature, which results from cell abuse (e.g., short circuit, overcharge). The separator should not only shutdown around 130 $^{\circ}\text{C}$, but it should also maintain its mechanical integrity at higher temperatures, preferably at temperatures. If the separator does not shutdown properly then the cell will continue to heat during an overcharge test and can lead to thermal runaway. The high-temperature melt integrity of separators is also a very important property to keep the cell safe during extended overcharge or during extended exposure to higher temperatures.

Figure 10 shows a typical short-circuit curve for an 18650 lithium-ion cell with shutdown separator, LiCoO_2 positive electrode, and MCMB carbon negative electrode. The cell does not have other safety devices (e.g., CID, PTC), which usually work before separator shutdown. As soon as the cell is short-circuited externally through a very small shunt resistor, the cell starts heating because of the large current drained through the cell. The shutdown of the separator, which occurs around 130 $^{\circ}\text{C}$, stops the cell from heating further. The current decrease is caused by increase of battery internal resistance due to separator shutdown. The separator shutdown helps in avoiding the thermal runaway of the cell.

Cells can be overcharged when the cell voltage is incorrectly detected by the charging control system or when the charger breaks down. When this happens, the lithium ions remaining in the cathode are removed and more lithium ions are inserted into the anode than under standard charging conditions. If the lithium insertion ability of the carbon anode is small, lithium metal in the form of dendrites may be deposited on the carbon and this causes a drastic reduction in thermal stability. At higher charging rates, the heat output increases greatly because the joule heat output is proportional to I^2R . Several exothermic reactions (e.g., reaction between lithium and electrolyte, thermal decomposition of anode and cathode, thermal decomposition of electrolyte, etc.) occur inside the cell as its temperature increases. Separator shutdown happens when the cell temperature reaches the melting point of polyethylene as shown in Figure 11. The CID and PTC of the 18650 cells was removed to test the performance of separator alone. The current decrease is caused by increase of battery internal resistance due to separator shutdown. Once the pores of the separator have closed due to softening, the battery cannot continue to be charged or discharged, and thus thermal runaway is prevented. During continued overcharge, the separator should maintain its shutdown feature and should not allow the cell to heat again. It should also maintain its melt integrity and should not allow the two electrodes to touch each other.

The separator should also not allow any dendrite to penetrate through the separator to avoid internal shorts. During an internal short, the separator is the only safety device that can stop the thermal runaway, if the failure is not instant. If the heating rate is too high, then instant failure will occur which cannot be stopped by separator shutdown. If the heating rate

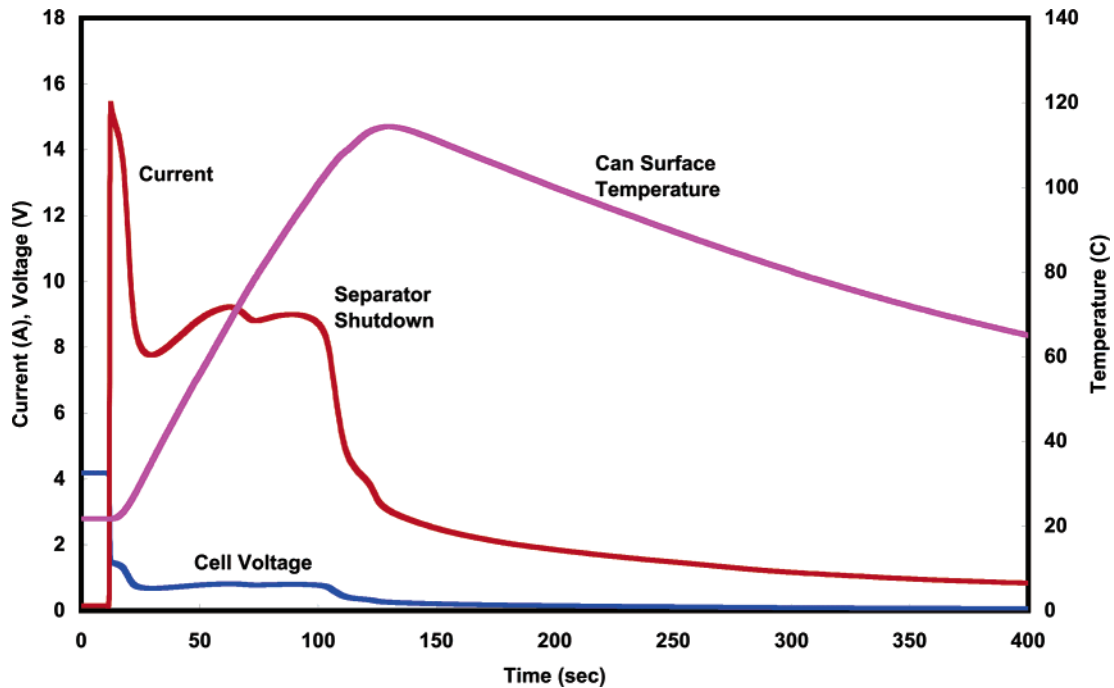


Figure 10. Typical short-circuit behavior of a 18650 lithium-ion cell with shutdown separator and without PTC (positive temperature coefficient) and CID (current interrupt device). This test simulates an external short circuit of a cell.

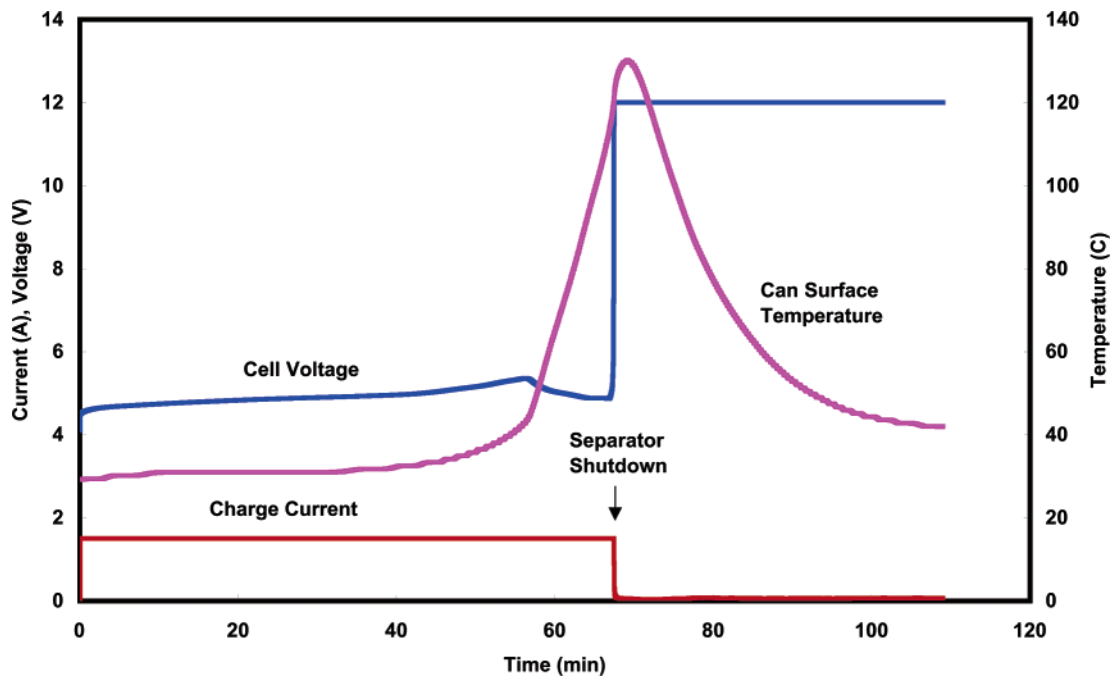


Figure 11. Typical overcharge behavior of a 18650 lithium-ion cell with shutdown separator. The PTC (positive temperature coefficient) and CID (current interrupt device) were removed from the cell header.

is not too high then the separator shutdown can help in controlling the heating rate and stop thermal runaway.

Generally in a nail penetration test, an instantaneous internal short would result the moment the nail is tucked into the battery. Enormous heat is produced from current flow (double layer discharge and electrochemical reactions) in the circuit by the metal nail and electrodes. Contact area varies according to depth of penetration. The shallower the depth, the smaller the contact area and therefore the greater the local current density and heat pro-

duction. Thermal runaway is likely to take place as local heat generation induces electrolyte and electrode materials to decompose. On the other hand, if the battery is fully penetrated, the increased contact area would lower the current density, and consequently all tests would pass the nail penetration test. Internal short-circuit tests are more difficult to pass than the external short-circuit tests described earlier, because contact area between metal nail contact is smaller than the contact area between current collectors, where the current density would therefore be larger.

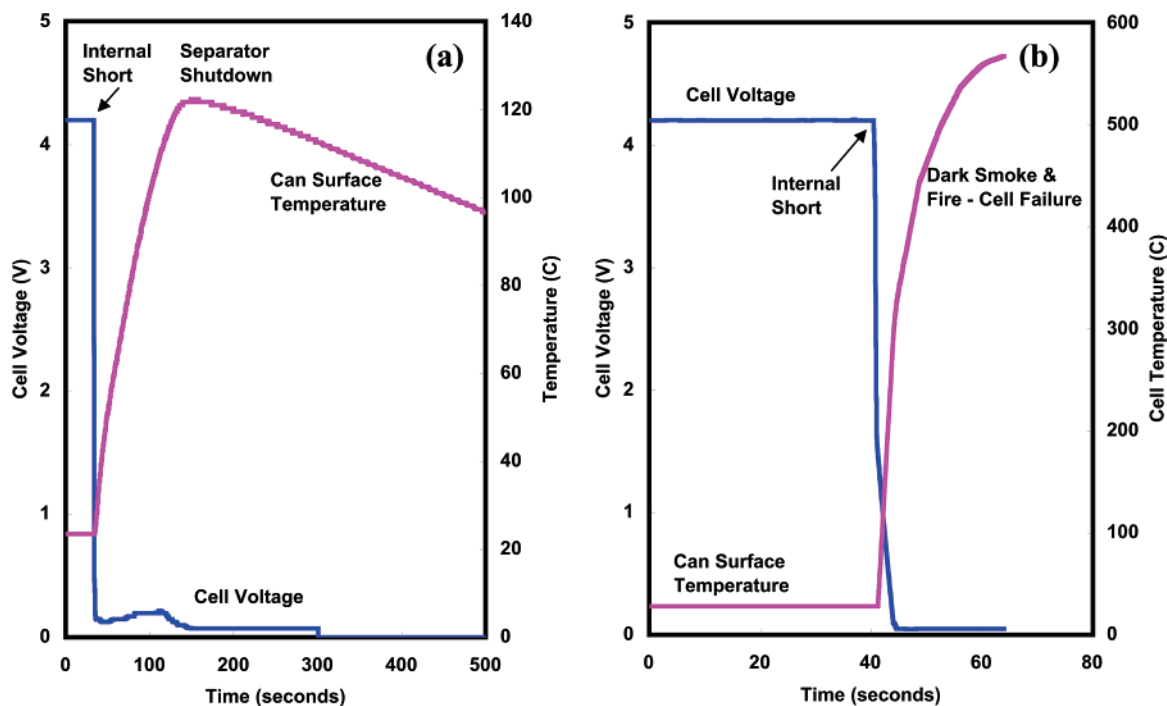


Figure 12. Typical nail penetration behavior of a 18650 lithium-ion cell with shutdown separator. This test simulates internal short circuit of a cell. Key: (a) cell passed nail penetration test; (b) cell failed nail penetration test.

Figure 12 shows the typical nail penetration behavior of a 18650 lithium-ion cell with shutdown separator, LiCoO_2 positive electrode, and MCMC carbon negative electrode. Clearly, there was a voltage drop from 4.2 to 0.0 V, instantaneously, as the nail penetrates through (when an internal short circuit occurs), and the temperature rose. When the heating rate is low, the cell stops heating when the temperature is close to separator shutdown temperature as shown in Figure 12a. If the heating rate is very high, then the cell continues to heat and fails the nail penetration test as shown in Figure 12b. In this case, the separator shutdown is not fast enough to stop cell from thermal runaway. Thus, the separator only helps in avoiding delayed failures in the case of internal short circuit as simulated by nail and bar crush tests. Separators with high-temperature melt integrity and good shutdown feature (to avoid delayed failures) are needed to pass the internal short-circuit test. Thinner separators ($<20 \mu\text{m}$) used in high capacity cells should offer shutdown and high-temperature melt integrity properties similar to those of thicker separators. The decrease in separator strength should be balanced with changes in cell design. The separator properties across the length and width should be very uniform to keep the cell safe during abnormal use.

The mechanism and characteristics of thermal cutoff devices in several prismatic lithium-ion cells was studied by Venugopal¹³⁰ by monitoring the impedance at 1 kHz and the open circuit voltage (OCV) of the cells as a function of temperature. All the cells studied contained PE-based separators with a shutdown temperature between 130 and 135 °C. Within this narrow temperature range, the shutdown separators caused a sharp and irreversible rise in impedance of the cell. Single layer PE separators were effective up to around 145 °C, above which they

demonstrated a meltdown effect. Trilayer separators had meltdown temperatures as high as 160 °C because of the presence of additional layers of higher melting PP. It was found that the separators are not able to shutdown the cell completely. In the case of an overcharged test, the cell could continue to charge at lower currents even after the shutdown event, rendering the cell a potential hazard if not disposed immediately and safely. This usually does not become an issue in commercial cells because the cell manufacturers have addressed this issue by including multiple cutoff devices within a single cell.

Development efforts are under way to displace the use of microporous membranes as battery separators and instead use gel electrolytes or polymer electrolytes. Polymer electrolytes, in particular, promise enhanced safety by eliminating organic volatile solvents. The next two sections are devoted to solid polymer and gel polymer type lithium-ion cells with focus on their separator/electrolyte requirements.

6.2. Lithium Polymer

Because of their high theoretical capacity, lithium polymer batteries have long been identified as a very promising technology to meet the requirements of upcoming applications such as standby power and electric vehicles. Research and development of polymer electrolytes for ambient-temperature rechargeable lithium batteries has always been very active. Rapid progress for the past 2 decades in this field has led to numerous monographs and reviews.^{131–137} These polymers are generally polyethers, poly(ethylene oxide) (PEO), or poly(propylene oxide) (PPO).

Solid polymer electrolytes serve two principal roles in rechargeable lithium batteries. Not only do they function as the traditional electrolyte, i.e., the me-

dium for ionic transport but also they function as the separator which insulates the cathode from the anode. Consequently, the polymer electrolyte must have sufficient mechanical integrity to withstand electrode stack pressure and stresses caused by dimensional changes, which the rechargeable electrodes undergo during charge/discharge cycling.

Lithium polymer electrolytes formed by dissolving a lithium salt LiX (where X is preferably a large soft anion) in poly(ethylene oxide) PEO can find useful application as separators in lithium rechargeable polymer batteries.^{138–140} Thin films must be used due to the relatively high ionic resistivity of these polymers. For example, the lithium-ion conductivity of PEO–Li salt complexes at 100 °C is still only about $1/100$ th the conductivity of a typical aqueous solution.

A polymer electrolyte with acceptable conductivity, mechanical properties and electrochemical stability has yet to be developed and commercialized on a large scale. The main issues which are still to be resolved for a completely successful operation of these materials are the reactivity of their interface with the lithium metal electrode and the decay of their conductivity at temperatures below 70 °C. Croce et al. found an effective approach for reaching both of these goals by dispersing low particle size ceramic powders in the polymer electrolyte bulk.^{141,142} They claimed that this new “nanocomposite polymer electrolytes” had a very stable lithium electrode interface and an enhanced ionic conductivity at low temperature, combined with good mechanical properties. Fan et al.¹⁴³ has also developed a new type of composite electrolyte by dispersing fumed silica into low to moderate molecular weight PEO.

The gel type polymer electrolyte prepared by dispersing ceramic powders (e.g., Al_2O_3) into a matrix formed by a lithium salt solution contained in a poly(acrylonitrile) (PAN) network was reported by Appetecchi et al.¹⁴⁴ These new types of composite gel electrolytes had high ionic conductivity, wide electrochemical stability, and particularly, high chemical integrity even at temperatures above ambient. Kim et al.¹⁴⁵ used a blend of PVdF–HFP and PAN as a matrix polymer to attain high ionic conductivity and good mechanical strength. The PAN can give mechanical integrity and structural rigidity to a porous membrane without inorganic fillers. The high ionic conductivity was due to the high volume of pores and a high affinity of the membrane for electrolyte solution.¹⁴⁶

6.3. Lithium-Ion Gel Polymer

The solid polymer electrolyte approach provides enhanced safety, but the poor ambient temperature conductivity excludes their use for battery applications, which require good ambient temperature performance. In contrast, the liquid lithium-ion technology provides better performance over a wider temperature range, but electrolyte leakage remains a constant risk. Midway between the solid polymer electrolyte and the liquid electrolyte is the “hybrid polymer” electrolyte concept leading to the so-called gel polymer lithium-ion batteries. Gel electrolyte is a two-component system, viz., a polymer matrix

swollen with a liquid electrolyte. The gel polymer electrolyte approach to the lithium-ion technology combines the positive attributes of both the liquid (high ionic conductivity) and solid polymer electrolytes (elimination of leakage problems).

Gel polymer lithium-ion batteries replace the conventional liquid electrolytes with an advanced polymer electrolyte membrane. These cells can be packed in lightweight plastic packages as they do not have any free electrolytes and they can be fabricated in any desired shape and size. They are now increasingly becoming an alternative to liquid-electrolyte lithium-ion batteries, and several battery manufacturers, such as Sanyo, Sony, and Panasonic have started commercial production.^{147,148} Song et al.¹⁴⁹ have recently reviewed the present state of gel-type polymer electrolyte technology for lithium-ion batteries. They focused on four plasticized systems, which have received particular attention from a practical viewpoint, i.e., poly(ethylene oxide) (PEO), poly(acrylonitrile) (PAN),¹⁵⁰ poly(methyl methacrylate) (PMMA),^{151,152} and poly(vinylidene fluoride) (PVdF) based electrolytes.^{153–157}

One particular version of the lithium-ion gel polymer cells, also known as plastic lithium-ion cell (PLION), was developed by Bellcore (now Telcordia Technologies).^{158–160} In this case, Gozdz et al. developed a microporous plasticized PVdF–HFP based polymer electrolyte which served both as separator and electrolyte. In PLION cells, the anode and cathode are laminated onto either side of the gellable membrane. Good adhesion between the electrodes and the membranes is possible because all three sheets contain significant amounts of a PVdF copolymer that can be melted and bonded during the lamination step.

The PVdF–HFP separators used in PLION cells were around 3 mil thick, and had poor mechanical properties. It has been reported that the major source of rate limitation in PLION cells was the separator thickness.¹⁶¹ The rate capability of these cells can be significantly improved by decreasing the separator thickness to that typically used in liquid electrolyte system. Moreover, in the absence of shutdown function, the separator does not contribute to cell safety in any way. Park et al. reported that the HFP content in separators did not have any significant impact on cell performance.¹⁶² The Bellcore process has proven to be an elegant laboratory process but is difficult to implement in large-scale production.

To overcome the poor mechanical properties of polymer and gel polymer type electrolytes, microporous membranes impregnated with gel polymer electrolytes, such as PVdF, PVdF–HFP, and other gelling agents, have been developed as an electrolyte material for lithium batteries.^{163–173} Gel coated and/or gel-filled separators have some characteristics that may be harder to achieve in the separator-free gel electrolytes. For example, they can offer much better protection against internal shorts when compared to gel electrolytes and can therefore help in reducing the overall thickness of the electrolyte layer. In addition the ability of some separators to shutdown

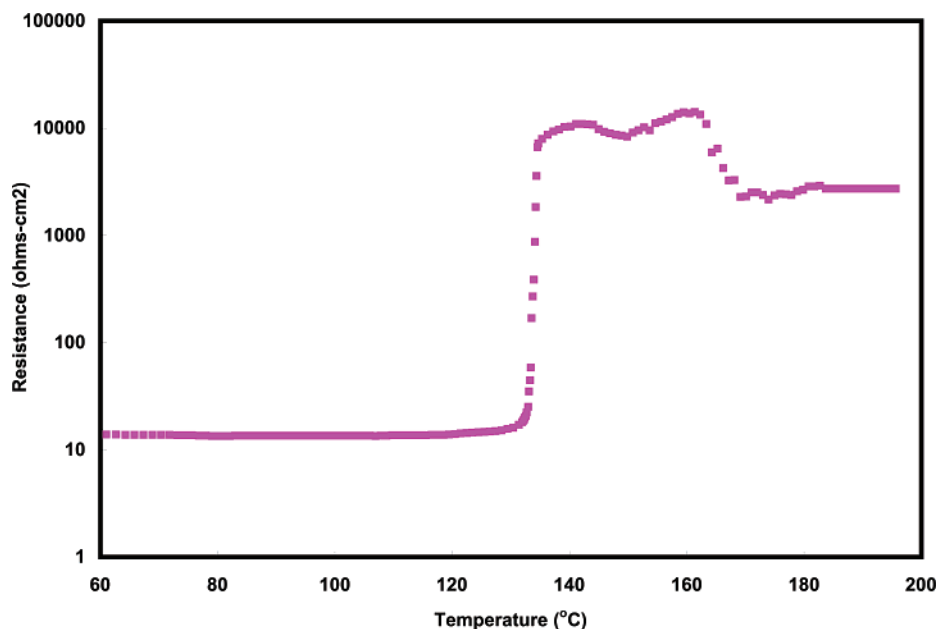


Figure 13. Internal impedance (at 1 kHz) of PVdF coated Celgard trilayer separators as a function of temperature. Heating rate: 60 °C/min.

at a particular temperature allows safe deactivation of the cell under overcharge conditions.

The shutdown behavior of PVdF coated Celgard trilayer membranes is shown in Figure 13. The shutdown is defined by the sharp increase in resistance around 130 °C. The PVdF coating should be porous and should not block the pores to maintain similar ionic conductivity. The scanning electron micrographs of the PVdF coated membrane is shown in Figure 14. The cross section SEM of Celgard 3300 provides visual evidence that the coating is porous and is not blocking the pores of the top PP layer.

Abraham et al.¹⁷⁴ were the first ones to propose saturating commercially available microporous polyolefin separators (e.g., Celgard) with a solution of lithium salt in a photopolymerizable monomer and a nonvolatile electrolyte solvent. The resulting batteries exhibited a low discharge rate capability due to the significant occlusion of the pores with the polymer binder and the low ionic conductivity of this plasticized electrolyte system. Dasgupta and Jacobs^{163,175} patented several variants of the process for the fabrication of bonded-electrode lithium-ion batteries, in which a microporous separator and electrode were coated with a liquid electrolyte solution, such as ethylene-propylenediene (EPDM) copolymer, and then bonded under elevated temperature and pressure conditions. This method required that the whole cell assembling process be carried out under scrupulously anhydrous conditions, which made it very difficult and expensive.

More recent methods proposed by Motorola^{176,177} and Mitsubishi Electric¹⁷⁸ researchers differ in implementation details, but they share a common feature in that a separate adhesive layer (PVdF) is applied to the separator and used to bond the electrode and the separator films, using in the first case the hot, liquid electrolyte as an in situ PVdF plasticizer. Recently, Sony^{179,180} researchers described the use of a thin, liquid electrolyte-plasticized polyacrylonitrile

layer directly applied either to the electrode or the separator surfaces as an effective ion-conductive adhesive. Sanyo^{181,182} investigators, on the other hand, used thermally polymerizable additives to gel, or solidify, liquid electrolyte solutions in a wound, packaged battery.

The ceramic fillers (e.g. Al₂O₃, SiO₂, TiO₂) can greatly influence the characteristics and properties of polymer electrolyte by enhancing the mechanical stability and the conductivity.^{141,183–186} γ -LiAlO₂, Al₂O₃, and MgO were used as fillers by Prosini et al.¹⁸⁷ in a PVdF–HFP polymer matrix to form self-standing, intrinsically porous separators for lithium-ion batteries. The MgO based separators showed the best anode and cathode compatibilities.

Liu et al.¹⁸⁸ has successfully prepared a PVdF–HFP/PE composite gel electrolyte by cast method. They showed that when the PE content was over 23 wt %, the electrical impedance of the composite gel electrolyte increased rapidly by several orders of magnitude, around the melting point of PE. The SEM pictures showed that the PE particles were fused and formed into a continuous film at or near the PE melting point, which cuts off the ion diffusion. This shutdown feature of the composite gel electrolyte can help in preventing the cell runaway under abusive usage. Similarly, poly(ethylene oxide) (PEO) coated separators were prepared by Kim et al.¹⁸⁹ by coating PEO onto a microporous PE separators. The ionic conductivity of PEO coated membranes was higher than the base film. Kim et al. prepared the polymer electrolytes by coating poly(ethylene oxide) (PEO) and poly(ethylene glycol dimethacrylate) (PEGDMA) onto a microporous polyethylene membrane (Asahi Kasei, 25 μ m, 40% porosity).¹⁹⁰ They showed that the relative weight ratio of PEO and PEGDMA coated on to the microporous membrane played a critical role in determining the uptake of electrolyte solution and ionic conductivity.

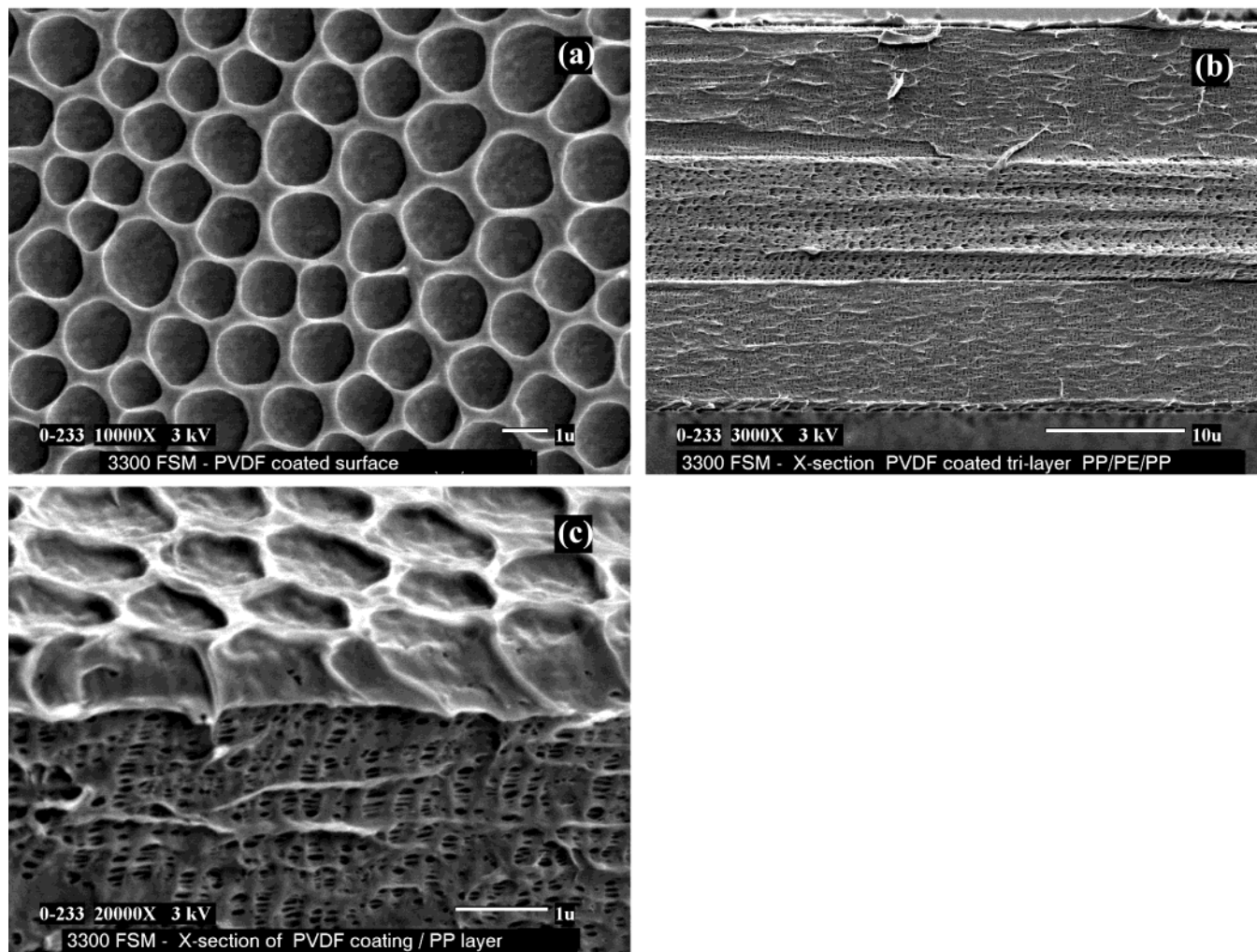


Figure 14. Scanning electron micrographs of Celgard PVdF coated separators used in lithium gel polymer batteries: (a) surface SEM, (b) cross-section SEM of coated trilayer, and (c) cross section of PVdF coating.

6.4. Lithium Primary Systems

Lithium primary batteries, with their outstanding performance and characteristics, are being used in increasing quantities in a variety of applications, including cameras, memory backup circuits, security devices, calculators, watches, etc. They were first used in early 1970s in selected military applications, but since then they have been designed using a number of different chemistries, in a variety of sizes and configurations, and have been used in different consumer applications. They are attractive because of their high voltage, high specific energy, good power density, flat discharge characteristic, good low temperature performance, and superior shelf life.

The term "lithium battery", applies to many different types of chemistries, each using lithium as the anode but differing in cathode material, electrolyte, and chemistry as well as in design and other physical and mechanical features. Lithium primary batteries can be classified into several categories, based on the type of electrolyte (or solvent) and cathode material used—soluble cathode cells (e.g., SO_2 , SOCl_2 , SO_2Cl_2), solid cathode cells (e.g., V_2O_5 , MnO_2 , $(\text{CF})_n$, FeS_x , CuO), and solid electrolyte cells (I_2 (P_2VP)). The Li-I_2 system is unique as the cell reaction product, LiI , forms the separator in situ. In the large cylindrical

size batteries, three chemistries are currently available for consumer applications: Li-MnO_2 , Li-CF_x , and Li-FeS_2 . Li-MnO_2 and Li-CF_x cells are 3 V cells that come in special sizes and are typically used in cameras, safety devices, industrial applications, etc. Li-FeS_2 is a 1.5 V battery that is a drop-in replacement for primary alkaline and C/Zn batteries.

As the separator requirements for most of the above batteries are very similar, they will not be dealt with in detail. In this section, we will generally describe the separator requirements followed by a brief discussion on few selected systems.

6.4.1. Separator Requirements

The requirements for the separator properties are generally lower in lithium primary cells compared to lithium secondary cells. The lack of a charging process helps avoid undesirable electrochemical deposits (e.g., dendrites) as well as the generation of oxidizing substances. The mechanical strength requirements are less severe because the negative electrode is made of lithium foil, which is relatively smooth. Further, the shutdown behavior of separator is not mandatory because the thermal runaway occurs only when the cell temperatures goes beyond 180°C (melting point of lithium). The basic require-

Table 8. Separators and Their Manufacturers for Major Primary Lithium Battery Systems

battery system	type of separator	compositions (manufacturer)
Li/SO ₂	microporous	glass fiber; ^a polypropylene; ^b Tefzel
Li/SOCl ₂	microporous	glass fiber; ^c glass mat or filter paper
Li/MnO ₂	microporous	polypropylene ^d (Celgard); polyethylene (Asahi Kasei)
Li/(CF) _n	microporous	polypropylene ^e
Li/CuO	microporous	nonwoven glass
Li/V ₆ O ₁₃	microporous	polypropylene (Celgard 2400) ^f
Li/V ₂ O ₅	solid-ion conductor	poly(ethylene oxide)–lithium salt ^g
Li/FeS ₂	microporous	polypropylene ^h
Li/CuCl ₂	microporous	polypropylene ⁱ
solid electrolyte (Li–I ₂ (P2VP))	solid ion conductor	Tefzel LiI film (self-healing) ^j

^a Walk, C. R. In *Lithium Batteries*; Gabano, J. P., Ed.; Academic Press: New York, 1983, p 281. ^b Linden, D.; McDonald, B. J. *Power Sources* **1980**, *5*, 35. ^c Klinedinst, K. A. *J. Electrochem. Soc.* **1984**, *131*, 492. ^d Moses, P. R.; Turchan, M. J.; Taylor, A. H.; Mank, R. M. In *Lithium Batteries*; Gabano, J. P., Ed.; Academic Press: New York, 1983, p 333. ^e Morita, A.; Iijima, T.; Fujii, T.; Ogawa, H. *J. Power Sources* **1980**, *5*, 111. ^f Abraham, K. M.; Goldman, J. L.; Holleck, G. L. *Lithium Batteries*; Venkatesetty, H. V., Ed.; The Electrochemical Society, Inc.: Pennington, NJ, 1981; p 271. ^g Armand, M. B. Second International Meeting on Lithium Batteries, Extended Abstracts No. 2, Paris, France. *Solid State Ionics* **1983**, *9/10*, 745. ^h Walk, C. R. In *Lithium Batteries*; Gabano, J. P., Ed.; Academic Press: New York, 1983, p 265. ⁱ Uetani, Y.; Yokoyama, K.; Okamoto, O. J. *Power Sources* **1980**, *5*, 89. ^j Liang, C. C.; Holmes, C. F. J. *Power Sources* **1980**, *5*, 3.

ments are very generic—low electrical resistance, thin, high strength, low shrinkage, relatively small pore size, and no defects. As is true for separators for use in lithium-ion batteries, all the properties of separators for primary lithium batteries should be very uniform.

The most common separator by far used in these cells is the single layer PP separator made by Celgard (Celgard 2400) as shown in Table 8.

6.4.2. Chemistries

The separators used in major lithium primary systems are listed in Table 8. The majority of the lithium primary systems shown in Table 8 use microporous membranes (single layer PP or PE) as separators. Some of the systems are discussed below.

6.4.2.1. Lithium MnO₂. The Li/MnO₂ battery is the most widely used primary lithium battery. It is used in a wide variety of applications such as long-term memory backup, safety and security devices, cameras, many consumer devices, and military electronics. It uses a lithium anode, microporous polypropylene separator impregnated with electrolyte, and MnO₂ cathode. It is available in many configurations (including coin, bobbin, spirally wound cylindrical, and prismatic configurations in multicell batteries) and in designs for low, moderate, and moderately high drain application.

The Li/MnO₂ coin cells use a lithium anode disk, which is separated from the manganese dioxide pellet cathode by a nonwoven polypropylene separator, impregnated with the electrolyte. The bobbin-type design contains a central lithium anode core surrounded by the manganese oxide cathode, separated by a polypropylene separator impregnated with the electrolyte. The bobbin design maximizes the energy density due to the use of thick electrodes and the maximum amount of active materials. In the spirally wound cells, the lithium anode and the cathode are wound together with a microporous polypropylene separator to form the jelly roll. These cells are

designed for high-current pulse applications as well as continuous high-rate operation.

The lithium MnO₂ system has been preferred over lithium CF_x for the primary lithium cell market for its lower cost and essentially equivalent performance for camera (cylindrical cells), watch (coin cells), and memory applications. Dan et al. published results for an AA size rechargeable size cell based on Li/MnO₂ chemistry with energy density of 125–140 W h/kg and 280–315 W h/L. The cell used a polypropylene separator and was able to pass all safety tests (short circuit, overcharge, deep discharge, crush, and nail penetration).¹⁹¹ Ikeda¹⁹² and co-workers reported the development of “long life and high reliability Li/MnO₂ cell for back up” and demonstrated how the microporous structure of Celgard flat sheet membranes reduced self-discharge to provide reliable operation for up to 10 years.

6.4.2.2. Lithium CF_x. The Li/CF_x battery consists of a lithium anode, polycarbon monofluoride cathode, and microporous polypropylene separator saturated with organic electrolyte. These batteries are used as power sources for watches, portable calculators, memory applications, and so on.

6.4.2.3. Lithium Iron Sulfide. Energizer has marketed Li–FeS₂ (L91) AA-size cells since 1990.¹⁹³ These cells usually have a high surface area jellyroll construction, using pyrite (FeS₂) coated onto aluminum foil as the cathode, a polyolefin (polypropylene) microporous separator, and a lithium foil anode. This system is particularly well suited for high drain and constant power applications, where its higher operating voltage extends service time.

6.4.2.4. Lithium SO₂. The lithium SO₂ systems are mainly used in military and some industrial and space applications. This system is particularly known for its capability to handle high current and high power requirements, for its excellent low-temperature performance, and for its long shelf life. They are typically fabricated in cylindrical structure by spirally winding rectangular strips of lithium foil, a microporous polypropylene separator, the cathode electrode, and a second separator layer.

6.4.2.5. Lithium SOCl_2 . The lithium SOCl_2 battery has one of the highest cell voltages (~ 3.6 V) and energy densities of the practical battery systems. These batteries have been fabricated in a variety of sizes and designs, ranging from wafer or coin cells with capacities as low as 400 mA h to cylindrical cells in bobbin and spirally wound electrode structures and to large 10 000 A h prismatic cells. Li/ SOCl_2 bobbin batteries are manufactured in a cylindrical configuration. The anode is made of lithium foil, which is swaged against the inner wall of the can, the separator is made of nonwoven glass fibers, and the cathode is made of Teflon-bonded acetylene black.

6.4.2.6. Lithium TiS_2 . In 1990, W. R Grace & Co developed rechargeable Li– TiS_2 cells with high energy density, and excellent cycle life. To improve the safety, they developed a fusible separator (SafeTsep) for use in both primary and secondary lithium batteries.¹¹² The separator consists of two or more microporous layers with at least one of the layers capable of transforming to a nonporous membrane at a temperature between 100 and 150 °C. The additional layers maintain the dimensional stability of the separator during this transformation.¹¹³

6.4.2.7. Lithium Bromine. Ultrafine porous polymer membranes were prepared by Weininger et al.¹⁹⁴ by adding sodium benzoate or other salts of benzoic acid to the melted polymer in a weight ratio of 70–85 parts of benzoate to 30–15 parts of polymer. The salt does not dissolve in the polymer but forms a dispersion or colloidal suspension. Processing the polymer involved milling on differential rolls with the benzoate salt at 140–160 °C for PE or 170–180 °C for PP. The mixtures are then cooled close to the softening point of the polymer and sheeted into 0.0005 in thick films. The final leaching of the sheets is done in water at 20–55 °C. The salt was generally extracted over a period of 1–16 h. However, leaching is almost complete within 5–10 min. The polymers are also irradiated with high-energy electrons of 20 Mrad at a dose rate of 10 Mrad/min before or after extraction of the salt. This irradiation step is employed to improve the thermal and mechanical properties of the porous polymer. Irradiation after leaching is more effective in strengthening mechanical and thermal properties, but by this treatment, the smallest pores are closed by cross-linking. These membranes are flexible, about 50% porous, have extremely fine pore sizes (40–120 Å), and are used as separators in rechargeable lithium bromine batteries. The lithium bromine system is not a commercial system. A lot of developmental work has gone into developing the system, but it still is not commercialized.

6.4.2.8. Lithium Iron Sulfide (High Temperature). High-temperature molten salt Li–Al/LiCl–KCl/ FeS_x cells are known for their high energy density and superior safety. At one point they were being actively pursued for electric vehicle and pulse-power applications. Historically, boron nitride (BN) cloth or felt has been used as the separator in flooded-electrolyte cells, while MgO pressed-powder plaques have been used in starved-electrolyte cells.

Martino et al. have demonstrated the use of BN felt separators in engineering tests.¹⁹⁵ They have high porosity ($\sim 90\%$), and hence, low ionic resistance, in addition to excellent compatibility with other cell materials at the operating temperature of 470 °C. However, this separator is too expensive and has poor mechanical properties and so cannot prevent electrode shape change during cell operation.¹⁹⁶

MgO, Y_2O_3 , and AlN powder-based separators are substantially less expensive.^{197,198} Cell assembly with such powder separators is simple and amenable to mass production. Although powder separators were shown to maintain their integrity and conform to small dimensional changes of electrodes, their porosity ($\sim 50\%$) is considerably lower than that of BN felt and this drawback can limit their application to stationary load-leveling systems operating at low current densities.¹⁹⁷

Shimizu et al. has developed a low-cost MgO porous particle separator, which possessed both the high porosity ($\sim 85\%$) of the BN felt and the high mechanical resistance of powder separators.¹⁹⁹ The separator was prepared by loosely sintering fine MgO powder with $\text{Mg}(\text{NO}_3)_2$ as the binder. The particles thus formed showed excellent performance as separators in Li–Al/ FeS_x cells.

The state of development of the BN-felt separator is more advanced than that of the MgO powder separator. However, the ceramic powder separator has the potential for lower cost than the felt separator.

7. Separator for Aqueous Batteries

The aqueous batteries use water based electrolytes (e.g., KOH electrolyte for NiCd and NiMH and H_2SO_4 electrolyte for lead acid), which are less resistive than nonaqueous electrolytes. Polyolefin materials are generally suitable for use in the manufacture of separators for these batteries, but they are not inherently wettable by aqueous electrolytes. Such electrolytes are therefore unable to penetrate the pores of a separator formed from such a material, so that ion migration through the pores in solution will not occur without modification. This problem is sometimes overcome by treating the polyolefin material with a surfactant, which allows an aqueous electrolyte to wet the material. However, such surfactant can be removed from the surfaces of the polyolefin material when electrolyte is lost from the device, for example during charging and discharging cycles, and it is not subsequently replaced on the material when the electrolyte is replenished.

This problem has also been more durably addressed by modifying the surface properties of the polyolefin materials used to form polymeric sheets, by graft-copolymerizing to those surfaces a monomeric substance which, after copolymerization, confers hydrophilic properties and, in some cases, ion exchange properties. This technique has been found to be practical when the porous substrate is formed from PE, which has been found to lend itself well to a graft-copolymerization reaction of this kind. However, it has been found that when such a reaction is

attempted using polyolefin materials other than PE, the rate of the grafting reaction is reduced significantly.

Graft polymerization is a convenient method for the modification of the physical and chemical properties of polymer materials and is of particular interest for synthesis of the hydrophilic membranes. Graft copolymerization can be achieved by various methods such as an exposure to ionizing radiation or ultraviolet light and the use of chemical initiators. Ionizing radiation is one of the most promising methods because of its rapid and uniform formation of active sites for initiating grafting throughout the matrix. Under appropriate experimental conditions, modifications of polymer properties can be accomplished not only on the surface but also throughout the polymer.

There have been several reports on radiation grafting of acrylic and methacrylic acid onto various substrates. These include both the direct grafting method and the preirradiation method to synthesize ion-exchange membranes. Two cation exchange membranes modified with the carboxylic acid group for a battery separator were prepared by radiation-induced grafting of acrylic acid (AA) and methacrylic acid (MA) onto a polyethylene film by Choi et al.²⁰⁰ They found that KOH diffusion flux of AA-grafted PE membrane and MA-grafted PE membrane increased with an increase in the degree of grafting. AA-grafted PE membrane had a higher diffusion flux than MA-grafted PE membrane. Electrical resistance of both membranes decreased rapidly with an increase in the degree of grafting up to 120% and then leveled off.

Battery separators having carboxylic acid group were prepared by radiation induced grafting of acrylic acid onto a polyolefin nonwoven fabric (PNF). The PNF comprised approximately 60% polyethylene and 40% polypropylene. It was found that the wetting speed, electrolyte retention, thickness, and ion-exchange capacity increased, whereas the electrical resistance decreased with increasing grafting yield.²⁰¹ The surface characteristics of the separators can also be modified by plasma discharge.

This subsequent section discusses different types of aqueous batteries and the separators used in those batteries. The recent work in the development of new separators for aqueous batteries will also be discussed in detail.

7.1. Leclanche (Zinc Carbon)

Dry cells have been well-known for over 100 years and form the technical basis of today's modern dry cell industry. Zinc carbon cells are the most widely used of all the primary batteries worldwide because of their low cost, availability, and acceptability in various situations. The two major separator types ever used or in use are gelled paste and paper coated with cereal or other gelling agents such as methylcellulose.²⁰² The paste type is dispensed into the zinc can, and the preformed bobbin is inserted, pushing the paste up the can walls between the zinc and the bobbin. A typical paste electrolyte uses zinc chloride, ammonium chloride, water, and starch or flour as the gelling agents. The coated-paper type uses a special paper coated with flour, starch, regenerated cellulose,

or other gelling agent on one or both sides.²⁰³ The paper selected must be of low metallic impurity. A kraft paper separator provides thinner separator spacing, lower internal resistance, and increased active materials volume.²⁰⁴ One of the critical functions of the separator is to keep the zinc can surface properly wetted.

As the paste separator is relatively thick compared with the paper liner, about 10% or more manganese dioxide can be accommodated in a paper-lined cell, resulting in a proportional increase in capacity.²⁰⁵ The pasted separator carbon-zinc cells were phased out more than a decade ago. All the cells made since then are paper-lined constructions.

The performance and capacity advantages of alkaline batteries vs carbon-zinc is resulting in the continuous decline of this battery. The low cost of the carbon zinc cell is a major reason for its continued use. Thus, cost is a major consideration in the development and selection of separators for this system.

7.2. Alkaline Zinc MnO₂

Since its introduction in the early 1960s, the alkaline manganese dioxide (Zn/MnO₂) cell has advanced to a dominant position in the portable battery market. It gets its name from the use of alkaline solutions as electrolyte. Alkaline cells have many acknowledged advantages over zinc-carbon, including a higher energy density, longer shelf life, superior leakage resistance, better performance in both continuous and intermittent duty cycles, and lower internal resistance, which allows them to operate at high discharge rates over a wider temperature range.

In general, alkaline MnO₂ cells use "macroporous" nonwoven separators made from fibrous materials and binders. Various blends of fibers including cellulose, synthetic fiber, such as PVA fiber, nylon rayon, etc. are used in producing this type of separator. Other types such as gelled, inorganic, and radiation-grafted separators have been tried, but they have not gained much practical use. Some of the more advanced nonwoven separators are made by coating fibers made of an acrylonitrile polymer with a surface layer of an acrylic acid which has carboxyl groups, that are then mixed with polypropylene fiber and bound by a PVA fiber. The carboxyl group is partially cross-linked, resulting in swelling, but remains insoluble in the electrolyte. This demonstrates the complexity of today's separators in contrast to earlier separator materials, which were primarily cellulosic.

Techniques commonly used to produce fibrous webs include the wet laid, dry laid carded, and meltblown processes. The wet laid or paper making process is the predominant method for several reasons. The wet laid process, configured properly, allows for the blending of cellulosic and polymeric components. Also, the ability to use short cut length and fine denier fiber provides for consistent blending, uniform formation, and controlled pore structure.¹²

Because of the removal of mercury from the alkaline MnO₂ cell, there has been a re-formulation in the anode paste. Because of this change, these cells

now use a nonwoven laminated to cellophane as the separator to ensure against shorting due to zinc solubility and migration. This can lead to higher separator resistance. The key to success of such a lamination is to use an adhesive (e.g., PVA) that will not interfere with the ionic movement of the electrode. Some manufacturers of the mercury free cells use nonwoven mat of much smaller pore size made possible by the availability of 0.1–0.3 denier man-made fiber. The smaller diameter fiber allows for more uniform web formation at low ream weight and thickness resulting in improved high rate performance. Often a compromise must be struck between wicking rate and average pore size.

The rechargeable Zn–MnO₂ battery is an outgrowth of the primary battery. In these type of batteries, a “microporous” type separator is required to resist dendritic growth more likely to evolve as a result of numerous recharges. Materials like cellophane, grafted membrane, or polymeric films can be used as laminates to absorptive substrates. Another approach providing a similar effect is to coat a fibrous base with a layer of viskose. Both cellophane and viskose materials have remarkable properties in that they are electroporeable when wetted with KOH. To produce the functional laminate, the base nonwoven is designed for wicking and absorbency while the cellophane or membrane provides the short resistance. The adhesive used in laminating the separator must not adversely affect electrical resistance and should not interfere with the electrochemical behavior of the cell. On the basis of sales, the alkaline Zn–MnO₂ market is about 3–4 times larger than the lithium-ion battery market.² As this particular article is mainly focused on separators used in lithium-based batteries, we will not be discussing Zn–MnO₂ separators in more detail.

7.3. Lead-Acid Batteries

It has been a long time since the invention of the lead-acid battery, but it still represents the most important secondary chemical power source—both in number of types and diversity of application. The lead-acid battery has maintained its leading role for so many decades due to its competitive electrical characteristics and price and due to its adaptability to new applications. It is manufactured in a variety of sizes and designs, ranging from less than 1 to over 10 000 A h.²⁰⁶

Lead-acid batteries can be classified into three major types or categories, namely, automotive (SLI), stationary, and motive power (industrial). In addition, there are many special batteries that cannot be easily categorized as either of the above types. As these types of batteries are constructed with different materials and design to meet the requirements of their intended end uses, each requires a particular separator with specific material composition, mechanical design, and physical, chemical, and electrochemical properties that are tailored for the battery and its relevant specific uses. These batteries are generally available in flooded electrolyte or valve regulated (sealed) versions. In this section the types

and properties of separators used for lead-acid batteries are reviewed. The reader is referred to recent reviews published by Boehnstedt^{13,207,208} and others^{209–211} for detailed descriptions of lead-acid separators.

7.3.1. Flooded Electrolyte Lead Acid

Separators currently used in lead-acid batteries can be classified based on their materials of construction into four major types: plastic (PE/silica, PVC/silica, sintered PVC), paper (phenolic resin impregnated cellulose), glass (glass fiber mat), and rubber (hard rubber/silica, flexible rubber/silica, coated rubber/silica) separators. Table 9 shows the different types of separators used in batteries along with their manufacturing process and main features. Glass, paper, and sintered PVC separators can be classified as macroporous separators having an average pore diameter greater than 10 μm while all other separators can be classified as microporous separators having an average pore diameter smaller than 1 μm. All of these separators can be utilized as leaf separators in battery construction. Polyethylene can be used also for enveloped separators around either the positive or the negative plate. The use of “envelope” separators is popular in small, sealed cells, SLI, motive power, and standby batteries to facilitate production and to control lead contamination during manufacturing.

The environment concerns surrounding the lead-acid battery (e.g., the automotive battery) have been increasing in severity in recent years. The improvements and development of the separators have proceeded in accordance with the changes in the specifications for the batteries which were first made with wooden separators (the preferred wood was Oregon cedar as it contained small amounts of lignin that enhanced the performance of lead negative), then progressed through microporous rubber separators, cellulose separators, and synthetic pulp separators (SPG) with glass mats, to PVC separators, and now polyethylene separators have evolved. This sequential change in separator technology has provided continuous improvements in the charge and discharge efficiency of batteries and has given high vehicle-starting capability and reliability. Moreover, short circuits (caused by particles of active material dislodged from the battery plates) are prevented due to the smaller pores and excellent electrochemical oxidation resistance of the PE separator. These features contributed greatly to the improvement in battery life.

Rubber separators have good voltage characteristics, the ability to retard antimony transfer, properties to retard dendrite growth, and good electrochemical compatibility.²¹² Due to the hydrophilic properties of the rubber composition, the separators are highly wettable and renewable for the dry-charging process. Paik et al. showed that ACE-SIL (sulfur cured, hard rubber) separators performed well in industrial stationary or traction batteries, FLEX-SIL (electron-beam-cured, flexible rubber separator) separators are suited for deep-cycling batteries, and MICROPOR-

Table 9. Typical Separators Used in Lead-Acid Battery Systems

separator	class	manufacturing process	properties
wood	paper	cellulosic separators made from cotton linters or craft pulp and generally coated with phenolic resin for acid resistance and strength	comparatively large pore size and relatively high electrical resistance
hard-rubber ²¹³	rubber	made by mixing natural rubber, rehydrated precipitated silica, and sulfur, which is then extruded and calendared, vulcanized under water, and dried	finer pore diameter (0.2 μm average), relatively lower electrical resistance, excellent oxidation resistance, retards antimony transfer
flexible rubber ²¹³	rubber	made by mixing natural rubber, rehydrated precipitated silica, which is then extruded and calendared, irradiated with an ionizing electron beam, and dried	flexible, fine pore structure (0.06 μm average), retards antimony transfer
glass-mat rubber ²¹³	rubber/glass mat	made by mixing a polymeric emulsion, precipitated silica, and rubber, which is then coated on a fiberglass mat and finally cured and dried	finer pore diameter (<0.2 μm average), high porosity, excellent thermal dimensional stability
sintered PVC	plastic	made by sintering PVC powder of a particle size ranging between 10 and 20 μm	medium pore size (10–20 μm), generally good chemical resistance
synthetic PVC	plastic	made from mixture of PVC, silica fine powder, and a solvent, and then extruded, calandered, and extracted	small to medium average pore size and relatively low electrical resistance
synthetic pulp with glass mat	plastic/glass	made from blending PE synthetic pulp, synthetic fiber, and fine silica powder and then heat treated	medium pore size, low electrical resistance, and long service life at high temp; more difficult to process and assemble
polyethylene (PE)	plastic	made from a mixture of UHMW PE powder, fine silica powder and mineral oil, which is extruded as a film, calendered, and made porous by extraction	fine pore size, low electrical resistance, high puncture resistance, and strongly resistant to oxidation
glass fiber mat	glass	deposition on a single sheet, a mixture of fibers dispersed in an aqueous solution	excellent wettability, durable in an acid environment, good resiliency, high temp stability, more difficult to process and assemble

SIL (a coated, glass mat and rubber separator) separators have been found to be good choice for high rate discharging or cranking applications and for various types of gel cells.²¹³ Recently Daramic DC UHMW PE has demonstrated excellent performance in these applications, as well.

Poly(vinyl chloride) (PVC) and polyethylene (PE) separators have been the most commonly used separators in automotive batteries for the last 20 years. Polyethylene separators have a narrow pore size distribution. The PVC separator is built up by sintering PVC powder in general of a particle size ranging between 10 and 20 μm . The decrease of particle size in the sintered product is negligible compared to the particle size of the raw materials. The pores are dispersed homogeneously with a medium size ranging between 10 and 20 μm . Since a PVC separator exclusively consists of PVC, it exhibits advantageously good chemical resistance against acid and alkaline solutions. Unlike PE, PVC is disadvantaged due to its brittleness. The decline in PVC separators in recent years is in part due to their tendency to yield chloride ions from chemical attack.

The battery separator currently used by most flooded cell type lead-acid battery manufacturers are of the microporous PE type. It was invented in the late 1960s by W. R. Grace & Co.²¹⁴ The term

“polyethylene separators” is somewhat misleading, since such a separator consists mainly of agglomerates of precipitated silica, being held within a network of extremely long-chain UHMW PE.²¹⁵ A typical PE separator formulation comprises precipitated silica (~60 wt %), UHMW PE (~20 wt %), and mineral process oil (~15 wt %), as well as some processing aids, like antioxidants and/or proprietary surface tension modifiers.^{216,217}

The microporous PE separator is commercially manufactured by passing the ingredients through a heated extruder, passing the extrudate generated by the extruder through a die and into the nip formed by two heated calendar rolls to form a continuous web, extracting a substantial amount of the processing oil from the web by use of a solvent, drying the extracted web, slitting the web into lanes of predetermined width, and winding the lanes into rolls.²¹⁶

The PE separators have excellent microporous structure for electrolyte flow with minimal lead particle deposits; excellent ductility, strength, and toughness for envelopability and plate puncture resistance; excellent oxidation, chemical and thermal resistance to resist premature deterioration; and good manufacturability with high production efficiency and relatively low raw material cost, which reduces overall manufacturing costs.²¹⁸ The PE pocket sepa-

Table 10. Comparison of Properties of Different Separators Used in Lead-Acid Batteries

property	rubber	cellulose	PVC	PE	glass fiber
year available	1930	1945	1950	1970	1980
electrical resistance	very poor	poor	poor	very good	very good
porosity	sufficient	good	poor	good	very good
battery performance (cold crank)	poor	sufficient	sufficient	very good	very good
maximum pore size	good	poor	sufficient	very good	poor
mean pore diameter	good	poor	poor	very good	poor
purity	good	fair	good	good	good
resistance to shorting	good	poor	poor	very good	poor
corrosion resistance	very good	poor	good	very good	good
oxidation resistance	fair	poor	good	very good	very good
envelopable (sealability)	very poor	very poor	sufficient	very good	very poor
flexibility	brittle	brittle	brittle	excellent	good

ration is in almost all aspects significantly superior to leaf separation. Only PE separators can be enveloped and can develop good sealability. It has low electrical resistance, sufficient porosity, small pore size, and great resistance to both shorting and corrosion. The PE separator, by virtue of its low electrical resistance, generally provides better cold cranking performance. These separators are very flexible and offer excellent oxidation resistance if the residual oil content is controlled and/or proprietary chemical modifiers have been incorporated. A comparison of the properties of different types of separators is given in Table 10.

PE separators have contributed to improved battery specific energy and specific power, increased battery cycle life, and higher temperature operating capabilities. PE separators have gained in popularity and have generally replaced PVC, cellulose, glass fiber, and other conventional separators. The transition to microporous PE envelope separators started in the U.S. in the 1970s, followed by Europe in the 1980s. Today, PE separators have captured almost 100% of the U.S. market and more than 70% of the remaining worldwide automotive markets.²¹⁹

In a flooded cell type lead-acid battery, the battery separator typically has “ribs” or protrusions extending from at least one planar face of the separator. Such ribs are either formed integrally with the backweb of the separator or can be subsequently applied to the backweb as a bead of same or different material as the backweb, or they can be formed by embossing the backweb. The ribs function is to provide proper spacing between the plates and to provide a space wherein free electrolyte resides. The ribs also provides pressure to hold the electrodes in contact with the separator. This reduces the need for precise dimensional control on the cell components. Microporous PE separators typically have a configuration comprising a backweb having a predetermined thickness and a plurality of parallel or patterned ribs spaced apart by a predetermined distance and extending outwardly from one planar surface of the backweb. The ribs extend continuously in a longitudinal direction parallel to the edges of the separator material. The thickness of the backweb and height and spacing of the ribs is specified to the separator manufacturer by the battery manufacturer; based on specifications designed to maximize certain battery characteristics desired by the battery manufacturer. SLI batteries tend to have separators that

are thinner than “industrial” lead-acid batteries used for standby power sources and traction devices.

Endoh²²⁰ has reported that one reason for the occasionally shortened life of batteries assembled with PE pocket separators is the development of internal short circuits at the bottom part of the PE separator due to anodic corrosion causing active material to shed from the positive plates and leak through the separators. He also found that when synthetic pulp (SP) separators with glass mats are used, it is possible not only to restrain the shedding from positive plates but also to protect the separators against intensive oxidation so that no internal short circuits take place. He concluded that the use of SP separators with a glass mat is required to produce long service-life batteries, especially in tropical regions.

Higashi et al.²²¹ carried out endurance test under high-temperature conditions on automotive batteries made with three different types of separators. One group was assembled with PE pocket separators for the negative plates, another with PE pocket separators with glass mats for the positive plates, and a third with leaf-type synthetic pulp separators with glass mats. They concluded that battery assembly with PE pocket separators with a glass mat is an effective way to achieve good endurance (i.e. life extension at high temperature), and leaf-type synthetic pulp separators with glass mats are the best approach for hot climatic conditions.

7.3.2. Valve Regulated Lead Acid (VRLA)

An important development in lead-acid battery technology is the valve regulated lead-acid battery. These batteries operate on the principle of oxygen recombination, using a “starved” or immobilized electrolyte. The oxygen generated at the positive electrode during charge can, in these battery designs, diffuse to the negative electrode, where it can react, in the presence of sulfuric acid, with freshly formed lead. The separator material should provide innumerable gas channels between the plates through which oxygen can migrate from the positive to the negative electrode. These batteries differ from its flooded electrolyte precursor in a number of important ways.²²² They have been manufactured for many years with microfiber glass separators, also called absorptive glass mat (AGM). They are inherently resistant to acid stratification and have the additional important advantage of being essentially

Table 11. Separators and Their Manufacturers for Nickel and Zinc Based Battery Systems

battery system	type of separator	manufacturer and composition
nickel–cadmium	microporous	nylon, Pellon 2505, Polypropylene
nickel–metal hydride	microporous	polypropylene (Scimat, Freudenberg)
nickel–hydrogen	microporous	polymer–inorganic compounds, asbestos, zirconium oxide cloth, Celgard 3501, polypropylene
nickel–zinc	supported liquid membrane, microporous, ion-exchange	polypropylene (Celgard 3400, 3501), PVA
silver–zinc	ion exchange microporous	Permion (RAI); Silvergard (RAI); cross-linked PVA
zinc–HgO	microporous	pellon, cellophane, Celgard 3400
zinc–air	ion-exchange microporous	cellulose, poly(vinyl alcohol), polyolefins, poly(vinyl chloride)
	microporous	PVA cross-linked with dimethylolurea
zinc/bromine	microporous	asbestos, nonwoven/polypropylene laminate
	ion-exchange	polyolefins (Daramic)
		nafion (DuPont)

maintenance free. The separator is a crucial component in determining the useful life of a VRLA cell. While a prime function of the VRLA cell separator is to hold the cell's electrolyte in place, it must also offer characteristics that prevent major failure mechanisms occurring in the cell's positive and negative plates.

The microglass separator, since its discovery by McClelland and Devitt, has been the material of choice for VRLA designs.^{223,224} It is a wet laid nonwoven (glass fiber) "paper" and is manufactured on a paper machine. The type of paper machine used by the manufacturer can influence the separator properties. Three properties—porosity, uniformity, and fiber directionality—are important attributes that can be influenced by the type of fiber used. The glass fiber, which has a zero contact angle with the acid, is durable in the acid environment, and the fine fiber structure also has good resiliency to allow for a sustained pressure against the plate. The microglass separator has a high porosity in the 90–95% range and is very conformable. The separator can adapt to imperfections in the plate surface. The separator also has high-temperature stability. Recent studies have shown that higher levels of fine fiber and higher separator compression provide improved cycle performance in VRLA batteries.^{225–228}

On the other hand, AGM separators offer little control over the oxygen transport rate or the recombination process. The arrival of too much oxygen to the negative plate could result in overheating, hindrance of the battery's ability to recharge, or even a loss of capacity. Furthermore, AGM separators exhibit low puncture resistance.

7.4. Nickel Systems

The nickel-based systems include the flowing systems: nickel–iron (Ni/Fe), nickel–cadmium (NiCd), nickel–metal hydrides (NiMH), nickel–hydrogen (Ni/H₂), and nickel–zinc (Ni/Zn). All nickel systems are based on the use of a nickel oxide active material (undergoing one valence change from charge to discharge or vice versa). The electrodes can be pocket type, sintered type, fibrous type, foam type, pasted type, or plastic roll-bonded type. All systems use an alkaline electrolyte, KOH.

The separators may be simple absorbent material except in Ni/Zn where zinc solubility creates zinc electrode shape change and zinc dendrites, resulting

in shorts. The fundamental cause for zinc electrode shape change is nonuniform current distribution across the electrode surface. This leads to concentration gradients, which in turn give rise to densification and dendrite formation. In the other systems, solubility of the negative materials is minimal, and therefore, failure by shorting is nonexistent or delayed for a large number of cycles. The vented Ni/Fe, Ni/Cd, and Ni/Zn cells are mostly constructed in a prismatic configuration. Systems built in a sealed cylindrical pressurized configuration are NiCd, NiMH, and Ni–H₂. The pressure configuration in the NiCd and NiMH differs from the Ni–H₂. In the former, pressure is used to hold the electrodes and separator in contact. In the latter pressure is the result of storage of a gaseous reactant. The type of separators and their manufacturers for nickel-based systems are listed in Table 11

7.4.1. Nickel–Cadmium

The NiCd secondary battery is the most popular alkaline secondary battery, and it is available in several cell designs and in a wide range of sizes. It is a very reliable, sturdy, long-life battery, which can be operated effectively at relatively high discharge rates and over a wide temperature range.

7.4.1.1. Vented NiCd. The vented NiCd battery is one of the best-known power sources in the commercial and military fields, particularly for aircraft and communication applications. It has excellent high rate and low temperature performance capabilities. It also has a long useful life capability and is both physically and electrochemically rugged.

Early separators used in NiCd cells for space applications consisted of materials as ordinary as Whatman filter paper⁵ and eventually nonwoven nylon felt (Pellon 2505). Pellon 2505 was more stable than cellulosic separators, but it too had stability limitations. In the late 1960s and early 1970s, nonwoven polypropylene saw limited use in NiCd cells. The PP separators were quite useful where sterilization (heating the cell to 135 °C) was required.^{229,230} The major difficulty with nonwoven polypropylene was that it was only marginally wettable, and the amount of electrolyte that can be placed in the cell was limited.

In the early 1980s, Pellon Corporation (now Freudenberg) discontinued the manufacturing of Pellon 2505. This led to the qualification of Pellon

2536 in 1984 as the new separator material for the major portion of NiCd applications in the U.S.^{231,232} Hughes Aircraft took a different approach by evaluating Freudenberg FS2117 (a nonwoven nylon fabric), nonwoven polypropylene impregnated with polybenzimidazole (PBI) and zirconium oxide material (Zircar) impregnated with either PBI or polysulfone (PS).²³³ Their objective was to develop a separator that is chemically stable for a minimum of 10 years and has a better electrolyte retention and gas permeability than the state-of-the-art Pellon 2505 separator. The main purpose of the polymer impregnation of the zirconia material was to improve the mechanical strength of the fabric, which was too fragile for easy handling in the fabrication of the NiCd cells. The purpose of the PBI impregnation of the polypropylene felt was to improve the wettability in the electrolyte. They found that Zircar impregnated with PBI was the best separator for geosynchronous orbit applications while Zircar impregnated with PS was best for low earth orbit applications. The PP impregnated with PBI found to be as good as Pellon 2505 separator in some cell designs but had longer life because of excellent chemical stability and was additionally less expensive than zirconia material.

The separator used in vented NiCd's is a thin, multiple ply combination. It consists of a cloth (woven or felted nylon) that electrically separates the positive and negative plates and an ion-permeable plastic membrane (microporous polypropylene, Celgard 3400, a wettable variant of Celgard 2400) that serves as the gas barrier. This thin gas barrier, which becomes relatively soft when wetted, is frequently placed between two layers of cloth separators and receives significant mechanical support from them. Previously, cellophane has also been used as the gas barrier layer. Studies done by Hill²³⁴ and Feldman and Verville²³⁵ showed superior performance of NiCd batteries with Celgard microporous polypropylene separators as compared to cellophane. The authors attribute this improvement to the better chemical and thermal stability of the polyolefin sheet membrane. The outer nylon separator degrades with use by undergoing hydrolysis in the KOH electrolyte, thus seriously degrading the battery life.²³⁶ It involves a slow hydrolysis reaction followed by fast electrochemical oxidations of the hydrolysis reaction products.

7.4.1.2. Sealed NiCd. In sealed cells, the positive and negative electrodes are wound together in a jelly roll with a separator material between them. The working principle of sealed NiCd batteries is based on internal oxygen consumption. As a prerequisite the separator has to be permeable to gaseous oxygen, which is achieved by separator pores being of a specific minimum size and not all of them being filled with electrolyte at the same time, so as to leave some gas channels. Nonwovens (fleeces) made of polyamide, PE, and PP fibers have proven themselves in these cells. With their porosity they can absorb sufficient electrolyte, and due to their pore size distribution, they can simultaneously bind electrolyte and allow oxygen transfer.

Mechanical strength is an important criterion for sealed NiCd cells, because wound cells (spiral type construction) are manufactured automatically at very high speeds. Melt blown PP fleeces, with their excellent tensile properties, are good for these cells. Frequently two layers of the same or different materials are used, to gain increased protection against shorts. For higher temperature applications (up to about 60 °C) PP fleeces are preferred since they offer better chemical stability, though at lower electrolyte absorption.¹²

The nylon-based separators tend to degrade by undergoing hydrolysis in the KOH electrolyte. The products formed by the hydrolysis reaction are believed to cause a charge imbalance between positive and negative electrodes in a sealed NiCd cell leading to a loss of overcharge protection. The harmful products include carbonates, which accumulate in the electrolyte. The nylon degradation also gives rise to ammonia and hydroxylamine redox couple, which can increase the self-discharge rate. The rate of the hydrolysis of Nylon-66 separator material was approximately one-half of that of the nylon-6 material.²³⁷ It is well-known that in sealed NiCd cells a separator weight loss of 10% is often sufficient to cause internal shorting.²³⁸

7.4.2. Nickel–Metal Hydride

The sealed nickel–metal hydride battery has characteristics very similar to those of the sealed NiCd battery. The main difference is that the NiMH battery uses hydrogen, absorbed in a metal alloy, for the active negative material in place of the cadmium used in the NiCd battery. The NiMH batteries have a higher energy density and are considered more environmentally friendly than the NiCd battery. The sealed NiMH battery, however, does not have the very high rate capability of NiCd battery, and is less tolerant of overcharge.

The self-discharge rate of a Ni/MH battery is generally much higher than that of NiCd battery, especially when conventional nylon separators are used.²³⁹ The presence of oxygen and hydrogen gases cause the polyamide materials to decompose, producing corrosion products which poison the nickel hydroxide, promoting premature oxygen evolution and also forming compounds capable of a redox shuttle between the two electrodes which further increases the rate of self-discharge.²⁴⁰ In the case of the NiMH battery, ammonia and amine participate in the shuttle reaction in the same way that the nitrate ion does in the NiCd battery.

Ikoma et al. carried out a detailed investigation to study the self-discharge mechanism and contribution of separators.²⁴¹ They used nonwoven fabric made of conventional polyamide (PA), PP (with surfactant), and a nonwoven fabric whose main material was sulfonated-PP (hydrophilic) as separators. When nonwoven fabric made of chemically stable sulfonated-PP is used as a separator instead of a conventional polyamide separator, the self-discharge rate of the NiMH battery was strongly depressed, to the same level as that of NiCd battery.^{240,242,243}

Recently Nagarajan et al.²⁴⁴ characterized three different commercial AA cells and compared the

materials and cell performance. They used a differential scanning calorimeter (DSC) to determine the materials used as separators. Toshiba cells contained both polyethylene and polypropylene, while the Sanyo and Matsushita cells separators were identified as nonwoven fabrics fabricated from conventional polyamide. Since the Sanyo and Matsushita cells used the conventional polyamide separator, the self-discharge in these cells was substantially higher due to the shuttle reaction of the ammonia and amine, which expedite self-discharge. They also characterized the commercial cells and determined that separators contribution to the overall weight of the AA cell was around 3%.

Scimat Ltd. has shown that acrylic acid grafted nonwoven polyolefin separators have the ability to absorb chemical impurities, for example ammonia, from the alkaline environments. It has been shown that by using a grafted polyolefin separator, the free ammonia present inside a NiMH cell is trapped by the separator, resulting in a reduction in self-discharge to levels normally associated with NiCd cells.²⁴⁵ In October 2002, Scimat Ltd. announced the launch of the next generation of separators for NiMH and NiCd cells using its second-generation grafting technology.²⁴⁶

The commonly used separator material now is the surface treated polypropylene. The surface treatment helps in making the polypropylene permanently wettable. Surface treatments involve the grafting of a chemical such as acrylic acid to the base fibers to impart wettability and is accomplished using a variety of techniques such as UV or cobalt radiation. Another method of imparting wettability to the polypropylene is a sulfonation treatment where the base fiber material is exposed to fuming sulfuric acid. The separator surface is designed to be made hydrophilic to the electrolyte.

Cheng et al.²⁴⁷ carried out the impedance study on a foam-type NiMH battery with nonwoven PP separator to determine the main causes of early cycle deterioration. Their data indicated that the decrease in the voltage characteristic of the battery was due to drying out of the separator that increases the ohmic resistance of the battery and that decay of the total discharge capacity is due to an inactive surface that increases the charge-transfer of the battery.

7.4.3. Nickel–Hydrogen

Nickel–hydrogen batteries offer long cycle life that exceeds that of other maintenance-free secondary battery systems and accordingly makes it suitable for many space applications. Three types of separator materials have been used for aerospace Ni–H₂ cells—*asbestos* (fuel-cell-grade asbestos paper), *Zircar* (untreated knit ZYK-15 Zircar cloth),²⁴⁸ and *nylon*.^{1,249} In year 2000, Japan supplied over 90% of the nickel–hydrogen battery separators globally.²⁵⁰

Fuel-cell-grade asbestos is a nonwoven fabric with a thickness of 10–15 mil. The asbestos fibers are made into a long roll of nonwoven cloth by a carding or paper-making process. Asbestos is a controversial material with respect to health considerations in addition to potentially being a source of corrosion at

high temperatures. Although asbestos is still in use, there is a trend to replace it with *Zircar* (zirconium oxide cloth). *Zircar* fibrous ceramic separators are available in textile product forms (*Zircar* Products, Inc.). These textiles are composed of zirconium oxide fibers stabilized with approximately 10% yttrium oxide.²⁵¹ These materials offer the extreme temperature and chemical resistance of ceramic zirconia. They are constructed of essentially continuous individual filaments fabricated in flexible textile forms. *Zircar* has the drawback of being expensive and delicate from an assembly perspective. Aerospace cells have shown excellent medium term performances with their nylon separators, but it is known that nylon is weak in terms of its stability over time and its temperature sensitivity.²⁴⁹

Zirfon separator is a new alternative for Ni–H₂ batteries. It is a porous composite separator material composed of a polysulfone matrix and ZrO₂, which is present in a powder form. The manufacturing is based on the film-casting technique. It is very stable in concentrated KOH solutions at elevated temperatures. These films are around 300 μm thick.²⁵² SORAPEC has tested *Zirfon* in Ni–H₂ cells and has indicated that it is one of the best separators.²⁴⁹

7.5. Zinc Systems

Zinc is a nontoxic, relatively inexpensive, and abundant material. It is the most electropositive metal which is fully compatible with aqueous electrolytes. Its low (negative) electrode potential and its high hydrogen overpotential make it a very suitable negative electrode material for use in aqueous electrolytes.²⁵³

Although primary cells with zinc electrodes are widespread, secondary systems based on the same materials still suffer from a short lifetime arising from problems caused by zinc mass redistribution, undesirable changes in zinc morphology, and the influence of zinc ions on the opposite electrodes. Because nickel–zinc and manganese dioxide systems are otherwise suitable for electric vehicle propulsion, an effort to develop a long-lasting secondary storage battery is very desirable. One avenue would be to find a better separator for such systems. A lot of work has been done by different groups in developing new separators for zinc-based secondary systems, but none of them have been very successful in developing long cycle life zinc systems. The type of separators and their manufacturers for zinc-based systems are listed in Table 11.

7.5.1. Silver–Zinc

The first practical silver–zinc battery was developed more than 60 years ago. Since then, primary and secondary silver–zinc batteries have attracted a variety of applications due to their high specific energy, proven reliability and safety, and the highest power output per unit weight and volume of all commercially available batteries. However, they find very limited use in commercial applications, because of their high price and limited cycle life. Development of a battery separator which will improve the performance and life of zinc based alkaline cells has been

and continues to be the focus of concerted efforts in many battery groups, both in industry and academia.

The separator used in silver–zinc cells should be permeable to water and hydroxyl ions, stable in strong alkaline solutions, and not oxidized by the solid silver oxide or dissolved silver ions and should retard the migration of dissolved ions to the anode.²⁰³ A sophisticated separator system is needed to avoid short-circuits resulting from growth of dendrites.⁵ Because of the slight solubility of silver oxides in alkaline electrolyte, little work had been done with zinc/silver oxide cells until 1941 when Andre²⁵⁴ suggested the use of a cellophane barrier. Cellophane prevents migrating silver ions from reaching the anode²⁵⁵ by reducing them to insoluble silver metal. The cellophane is oxidized and destroyed in the process, making it less effective for long-life cells. Cycle life is very limited, even with the best separators known to date.

In general, secondary silver–zinc cells require a minimum of three different separators. The inner separator, or positive interseparator, serves both as electrolyte reservoir and as a barrier to minimize oxidation of the main separator by the highly oxidative silver electrode. This separator is usually made of a relatively inert fiber such as nylon or polypropylene. The outer separator, or negative interseparator also serves as an electrolyte reservoir and can also, ideally, serve to stabilize the zinc electrode and retard zinc penetration of the main separator, thus minimizing the dendrite growth. Improvement in cell life has been reported with improved inorganic negative electrode interseparators utilizing such materials as asbestos and potassium titanate.²⁵⁶ Asbestos helps in preventing or reducing the magnitude of short circuits and also acts as a silver “stopper”, but it is bulky and reacts with silver oxide. It may also contaminate the cell with iron and posts a health risk during fabrication. A potassium titanate mat helps to reduce zinc shape changes as well as the magnitude of short circuits. It is also bulky and more expensive.¹

The primary ion exchange separator remains the key to the life of the secondary silver cell. The cellulose (cellophane, treated cellophane, and fibrous sausage casing) are usually employed in multiple layers as the primary separators for these cells.²⁵⁷ Cellophane has to be specifically treated as battery grade, meaning a very low content of glycerine (or deglycerinated), since glycerine is an organic material that causes fast degradation of the cell performance by weakening the texture of the cellulosic material under the influence of the strong oxidants (silver peroxide and silver monoxide) present in colloidal form.²⁵⁸ Cellophane prevents migrating silver ions from reaching the anode by reducing them to insoluble silver metal.²⁵⁹ The cellophane is oxidized and destroyed in the process, making it less effective for long-life cells. It also physically inhibits the zinc dendrite formation.²⁶⁰ Cellophane film is typically drawn to a thickness of 1 mil, and usually five or six layers are used to wrap the cathode (silver plate) in the cell.²⁶¹

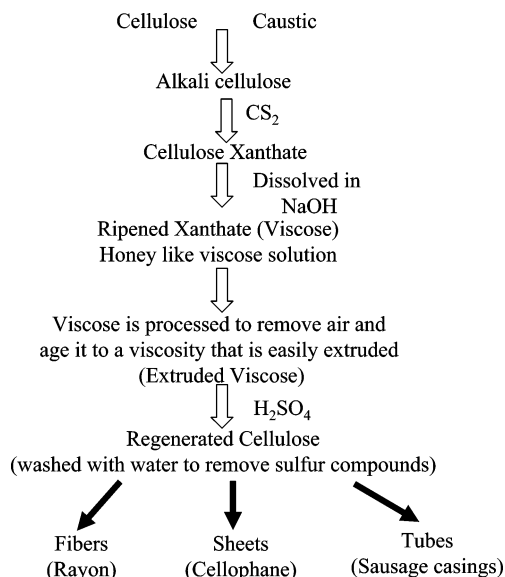


Figure 15. Viscous process for regenerated cellulose.²⁶³

The tendency for cellulose to degrade in alkaline solutions has been addressed by using multiple layers of the separator in the battery. Lewis et al.²⁶² showed that double-ply UCB cellophane films were less subject to dendritic hard shorting by zinc and retained some degree of polymerization “DP” after extended cycling. Another way to minimize cellulose degradation in alkaline solutions has been to keep the KOH concentration high (around 45%). The rate of degradation reaction slows down due to the KOH tying up the water used in the hydrolysis reaction.²⁶³ The silver-treated cellophane gives improved life performance, reduction in rates of silver migration, and promotes a longer performance life, compared to plain cellophane.²⁶⁴ However, cellophane still has significant disadvantages in terms of poor resistance to attack by the alkaline electrolyte and by active materials in the electrodes. These limit the wet life of cells, even when used in multiple layers. Cellophane is also ineffective in preventing shape change, which curtails cycle life.

Thomas Danko has described the manufacturing process and properties of cellulose in detail.²⁶³ The term regenerated cellulose refers to cellulose that has been converted from a solubilized cellulose derivative back into a pure cellulose derivative. The most notable of these processes is the viscous process in which cellulose of fairly high DP can be dissolved and maintained at viscosities that are easy to handle (up to 300000 cps). Figure 15 describes the viscous process in detail.²⁶³ The molecular weight of cellulose is described by the degree of polymerization (DP), which is the number of glucose units in the molecular chain. The final DP is selected based on desired properties and a balance of the regeneration process conditions. Purity of the cellulose plays an important role in the production of regenerated cellulose. The impurities (hemicellulose which is a low DP polysaccharide) in the cellulose reduces the strength of the final film. The properties of the regenerated cellulose can vary depending on the source of wood pulp used (purity) and the regeneration conditions used to

convert the xanthate derivative back in to cellulose. By using a high purity wood pulp, a stronger and less porous film can be made.

For battery separators, regenerated cellulose is placed on the surface of nonwoven so that the nonwoven is available to promote the wicking of the electrolyte. The nonwovens should not allow the penetration of viscose into itself. Suitable nonwovens are made from polypropylene, poly(vinyl alcohol), and hardwood hemps. Regenerated cellulose films are commonly used in alkaline manganese cells, both primary and secondary, in NiCd industrial batteries, as well as in silver–zinc batteries.

A variety of other separators have been proposed and developed to replace or complement the cellulose, such as poly(vinyl alcohol) (PVA),²⁶⁵ radiation-grafted polyethylene,²⁶⁰ microporous polypropylene, inorganic separators,²⁵⁶ and other synthetic polymer membranes. The inorganic separators are stable at higher temperatures ($\sim 150^\circ\text{C}$), and also resist attack by silver oxides and electrolyte, but it leads to higher cell resistance and they are more expensive. Modified polyethylene films are thinner than standard materials leading to higher energy density. They also provide a greater resistance to attachment by silver oxides and electrolyte but are more expensive, more difficult to handle and provide lower resistance to zinc penetration.¹ It requires a coating of the appropriate material(s) to improve the resistance to zinc and silver.

The degradation in mechanical properties of nonwoven battery separator was studied by Danko²⁶⁶ by storing the separators in 40% KOH for long period of time. The test showed that among the nonwovens, the polyamide retained about 93% of its initial tensile strength whereas poly(vinyl alcohol) and cellulosic nonwovens retained only 55% and 35%, respectively. Adding the viscose coating to the nonwovens improved tensile strength retention by 20–25% for the poly(vinyl alcohol) and cellulosic materials. The viscose-coated polyamide retained more than 98% of its initial tensile strength.

Recently Serenyl used a flexible alkaline separator (FAS) in Silver–Zinc cells, which consists of a microporous polyolefin film, with inorganic filler.²⁶⁷ This can be folded around the silver and/or zinc electrodes to form conventional “U” wraps or heat sealed bags. They showed that the FAS was not attacked by the electrolyte and helps in inhibiting the “shape change” of zinc electrode.

Another commonly used alternate separator material is prepared from a radiation graft of methacrylic acid onto a polyethylene membrane such as Permion.²⁵⁹ The graft makes the film wettable and permeable to the electrolyte. The low resistance Permion 2192 barrier membrane is suitable for high-rate KOH cells while higher resistance Permion 2193 is suitable for low rate NaOH cells. Cellophane is still often used in conjunction with the grafted separator as a sacrificial barrier. The lamination of cellophane to either side of the Permion membrane results in a synergistic action for stopping silver migration.²⁶⁸ Lee and co-workers²⁶⁹ reported that Permion extended the service life of Zn/AgO button cells from 2 to up

to as much as 4–5 years. RAI Research Corporation also developed an improved ion-exchange membrane (Silvergard), which has better selectivity toward silver-ion diffusivity than other ion-exchange membranes.

7.5.2. Nickel–Zinc

The nickel–zinc (NiZn) system is attractive as a secondary cell because of its high energy density and low material cost and the low level of potential pollutants contained. The widespread use of nickel–zinc batteries, particularly as electric vehicle power sources, would be strongly enhanced by significantly extending the deep-discharge cycle life beyond the current level of 100–300 cycles.²⁷⁰ Considerable work has been done in the past to develop a suitable separator for nickel– and silver–zinc batteries.^{271,272} An excellent discussion of separator development is contained in a comprehensive review.²⁷³

These cells generally fail because of zinc dendrite shorting or zinc electrode shape changes.²⁷⁴ To mitigate the problem of dendrite growth and subsequent shorting, battery separators should contain submicrometer-size pores, longer pore paths, increased thickness, and multiple layers.²⁷⁵ As these solutions all lead to increased resistance losses in batteries, a compromise in the properties of separators is necessary. The separator can also influence shape change. Separators with rapid mass transfer properties will reduce the electro-osmosis effects and concentration gradients within the battery, thus slowing the rate of shape change. A lot of developmental work has been done on the nickel–zinc system, but it is still not a commercial system.

The most common material used is cellophane, which is a cellulose film, which acts as a membrane and is capable of resisting zinc penetration. The cycle life of cells utilizing this material is severely limited due to the hydrolysis of the cellophane in alkaline solution. Various methods have been tried to stabilize cellulose materials, such as chemical treatment and radiation grafting to other polymers, but none have, as of now proved economically feasible. The most successful zinc migration barrier material yet developed for the nickel–zinc battery is Celgard microporous polypropylene film.¹ It is inherently hydrophobic so it is typically treated with a wetting agent for aqueous applications.

There are two broad classes of separators employed in nickel–zinc batteries; a main separator, which exhibits resistance to dendrite penetration, and an interseparator, which principally acts as an electrolyte reservoir and wicking layer. Both main and interseparator should be resistant to chemical attack by the alkaline electrolyte and resistant to oxidative attack by nascent oxygen, permanently wettable by the electrolyte, flexible, heat sealable, tear resistant, and inexpensive.

The two basic kinds of nickel–zinc main separators are the membranes and the microporous separators. Membrane separators are those in which ionic transport occurs through the interaction of the hydrophilic groups attached to the polymer with the ionic groups in the electrolyte. Ionic transport through mi-

croporous separators, on the other hand, occurs by diffusion through discrete pores. Other than wetting, there is essentially no interaction of this type of main separator with the electrolyte.

An important advantage of the microporous separator is that it has high water and electrolyte permeability leading to less electrode shape change. They can be prepared from chemically inert polymers, and hence have good chemical and oxidation resistance. The disadvantages of the microporous membranes are risk of dendrites shorting through the discrete pores and greater scope for zinc oxide to deposit within the separator pores. Membrane separators should provide greater resistance to zinc dendrite penetration, much lower rates of active material migration away from the negative electrode, and probably no deposition of zinc oxide within the separator. Their main disadvantages are the higher rates of negative electrode shape change resulting from poor mass transfer properties and the greater vulnerability to chemical attack.²⁷⁶

Lundquist²⁷⁶ compared the performance of membrane separators with microporous separators and found that the rate of zinc electrode shape change is greater in batteries with membrane separators although in either case shape change was the primary failure mode. Batteries containing separators with the lowest electrolytic resistivity and highest water permeability gave the longest cycle life. The results favored the use of microporous separators since its superior mass transfer characteristics minimize the rate of shape change.

Studies made by several authors, such as Poa,²⁷⁷ Wagner,²⁷⁸ and Brown,²⁷⁹ have shown significant improvement in the performance of NiZn rechargeable batteries, when microporous polyolefin flat sheet membranes were used as separators. Poa and co-workers examined the diffusion of the OH⁻ electrolyte through candidate separator materials, including microporous polypropylene, Celgard 3501 (Celgard 2500 coated with a proprietary surfactant). The OH⁻ diffusional flow for Celgard 3501 was found to be greater than either the traditional swollen, nonporous cellophane separator used in the battery or a nonporous methacrylic acid grafted and cross-linked polyethylene.²⁷⁷

Krejci et al. studied the transport of zincate ions through modified microporous PP separators (Celgard 3401, Celgard 3501) using polarography and conductometry.²⁸⁰ Celgard 3401 and 3501 were chosen because they are proven to have slow redistribution of zinc material, good mechanical properties, and low electrical resistivity. Soluble Nafion as an ion exchange modifying agent was applied to the PP microporous separators. They studied the influence of Nafion and surfactant (coated on 3401 and 3501) on transport of zinc ions through the membrane. It was found that the zincate ions transport through the membrane was higher for higher conductivity membranes and vice versa. Higher amounts of surfactant and Nafion coating increase both the membrane conductivity and the membrane's ability to allow zinc ions to pass.

Castle Technology Corporation had developed a supported liquid membrane battery separator to prevent zinc dendrite growth and decrease the shape changes on zinc electrode.²⁸¹ These membranes use a highly specific organic transport reagent contained in a microporous membrane support to transport hydroxyl ions while rejecting zincate ions. Several materials (polyvinyl chloride (PVC), PVC copolymer, nylon, nonwoven PP, and microporous PP) were tested, and Celgard 2500 was found to be the best material because of its larger pore size and higher porosity.

The nickel zinc system would be a suitable power source for many portable devices if the cells were tightly sealed and had a prolonged life. In sealed nickel–zinc batteries, oxygen, which is formed on the positive electrode, has to recombine with metallic zinc at the negative electrode. The microporous membrane must have some degree of permeability to oxygen.²⁸² Sato et al. developed a separator which consisted of nylon nonwoven cloth coated with poly(vinyl alcohol) (PVA) containing boric acid. The separator has a high ionic conductivity and is resistant to zincate ion penetration.²⁸³

To address the zinc dendrite problem in nickel–zinc cells, eVionyx claims to have developed a proprietary membrane system that is nonporous, has very high ionic conductivity, is of low cost, and can block zinc dendrite penetration even in high concentrations of KOH.^{284–286} The polymeric membrane has an ionic species contained in a solution phase thereof. The ionic species behaves like a liquid electrolyte, while at the same time the polymer-based solid gel membrane provides a smooth impenetrable surface that allows the exchange of ions for both discharging and charging of the cell.

7.5.3. Zinc–Air

For many applications zinc–air technology offers the highest available energy density of any primary battery system. It also offers a flat discharge voltage, long shelf life, safety and ecological benefits, and low energy cost. Since these cells are open to the ambient atmosphere, a factor limiting universal applications of zinc–air technology is the trade off between long service life and maximum power capability.

The separator materials used in zinc–air batteries should be inert to oxidation, stable in cells at high potentials, chemically inert to KOH at high temperatures, have a fine porous capillary structure to hold the electrolyte in the pores (and limit diffusion of oxygen gas), have a high bubble pressure, and exhibit low electrical resistance. Usually a polypropylene membrane such as treated Celgard 2500 or Celgard 3501 is used as separator in these cells. The function of the separator is to prevent cross mixing of the positive and negative electrolytes but to still allow the transport of ions. Because of its porosity, the cationic compound produced in the anode reaction can easily pass through the separator to cathode that leads to an increased polarization and decreased capacity and battery life. The separator should be able to stop the passage of these cationic compounds to increase the cell life. The commercial Zn–air cells

also use laminated separators (e.g. Celgard 4560 and Celgard 5550), which have a microporous membrane laminated with a nonwoven.

Dewi et al. used a cationic polysulfonium membrane as a separator in a zinc–air cell. They showed that the polysulfonium membranes were highly effective in preventing zinc cation permeation from the anode to the cathode compared to the commercially available PP separators.²⁸⁷

A new polymeric separator membrane has been developed for alkaline electrochemical systems (e.g. metal/air, Zn/Ni, Zn/MnO₂, Zn/HgO etc.) by Schubert et al.^{288,289} It is a water-soluble copolymer of acrylic acid and sodium styrenesulfonate monomers (PAASS). The monomer ratio is varied to manipulate electrolyte absorption and ionic resistivity of the copolymer. Processes have been developed to coat PAASS onto conventional nonwoven separator papers to produce composite membranes. The monomer ratio and the coating weight can be adjusted to balance ionic resistivity and shorting protection to provide adequate overall performance. PAASS coated separators demonstrate good barrier properties to soluble zincate and silver species. Preliminary use of PAASS separator materials in a rechargeable Zn/air system showed a significant improvement in shorting protection over microporous materials such as Celgard 3401.

The primary zinc–air cells have captured the hearing aid market, but the rechargeable zinc–air battery is still in the developmental stage.

7.5.4. Zinc–Bromine

The zinc–bromine battery is an attractive technology for both utility-energy storage and electric-vehicle applications. The technology has been limited in use and not commercialized due to two major drawbacks, the tendency of zinc to form dendrites and the high solubility of bromine in the aqueous zinc bromide electrolytes. Dendritic zinc deposits could easily short circuit the cell, and the high solubility of bromine allows diffusion and direct reaction with the zinc electrode, resulting in self-discharge of the cell.

Various materials have been used as separators in zinc–bromine cells. Ideally a material is needed which allows the transport of zinc and bromide ions but does not allow the transport of aqueous bromine, polybromide ions, or complex phase structures. Ion selective membranes are more efficient at blocking transport than nonselective membranes.²⁹⁰ These membranes, however, are more expensive, less durable, and more difficult to handle than microporous membranes (e.g., Daramic membranes).²⁹¹ The use of ion selective membranes can also produce problems with the balance of water between the positive and negative electrolyte flow loops. Thus, battery developers have only used nonselective microporous materials for the separator.²⁹²

Microporous separators have the advantage of being relatively low-cost and adequately stable in the electrolyte, but unfortunately they contribute to energy-efficiency losses in the battery. Rapid trans-

port of bromine through microporous separators and accumulation of a bromine–oil complex in the separator lead to efficiency losses. Thus, improved separators with lower bromine mass transport and higher electrolytic conductivity would be beneficial for improving the energy efficiency of zinc–bromine batteries.

7.6. Redox Flow Batteries

The redox flow battery (RFB) concept was first proposed by L. H. Thaller at the NASA Lewis Research Center, Cleveland, OH.^{293,294} Since then, it has been investigated as one of the energy storage systems for solar power, nuclear power, load leveling purposes, and electric vehicles.²⁹⁵

The all-vanadium RFB developed by the University of New South Wales has the advantage of a higher electromotive force (1.4 V in a vanadium system compared to 1.1 V in an Fe/Cr system) and a higher energy density compared with other RFB systems.²⁹⁶ It employs V(II)/V(III) and V(IV)/V(V) redox couples in the negative and positive half-cell electrolytes. The ideal membrane for this system should exhibit low permeation rates of the active species to minimize self-discharge and also have low area resistivity to minimize losses in internal energy. Further, the membrane should also exhibit good chemical stability for long cycle life. The energy losses in a V–RFB are partly caused by the undesired transport of vanadium ions of different oxidation states across the membrane, which separates the anolytic from the catholytic solution in the battery system.²⁹⁷

Ion exchange membranes of cation and anion selectivity are usually used as the membrane separators for V–RFB. Commercially available cation selective CMV membrane (Asahi Glass) degrades by the fully charged anolyte,²⁹⁸ but the Nafion membrane (Dupont) does not appear to degrade. However, the current efficiency of the V–RFB using Nafion decreases due to self-discharge of the vanadium ions, which permeated through the membrane.²⁹⁸ Furthermore, the cost of Nafion is exceptionally high. Chlorosulfonated polyolefin membrane shows a good resistivity to oxidation and its resistivity in the RFB, almost equal to Nafion.²⁹⁹ It has also been reported that a cross-linked chlorosulfonated homogeneous membrane formed by accelerated electron radiation at 2.5 Mrad/pass had a longer lifetime than the non cross-linked membrane because of the increase in the chemical stability.^{300,301}

Microporous membranes perform poorly in V–RFB compared to ion exchange membranes due to their poor selectivity. Modification of low cost microporous separators to impart perm-selective properties could lead to significant cost reduction. Chieng et al. developed a composite membrane from Daramic (a microporous separator), treated with Amberlite 400CG (an ion-exchange resin), and cross-linked using divinylbenzene.^{302,303} The separator selectivity was improved by partially blocking or by reducing the pore size or by incorporating some ion exchange capability to the separator. The chemical stability of the membrane was found to be excellent, and the membrane was not susceptible to fouling.³⁰⁴ Sulfonation of the

cross-linked Daramic separators was done to impart some cation-exchange capacity, and it was successful in reducing the amount of water transport across the membrane in V-RBC.³⁰⁵ The scale-up of sulfonation process is both difficult and expensive due to the very corrosive nature of concentrated sulfuric acid. Incorporation of cation-exchange groups using poly(sodium 4-styrenesulfonate) (PSSS) has been studied, and results show that the method reduces the water transport across the membrane. The PSSS treatment step can be easily scaled up.³⁰⁶

Diffusion coefficients of vanadium ions in CMS (Neosepta made by Tokuyama Soda), CMV (Selemion made by Asahi Glass), and CMX (Neosepta made by Tokuyama Soda) cation exchange membranes were determined by measuring the ion-exchange fluxes of the vanadium ions with H_3O^+ ions using a dialysis cell.²⁹⁷ The lowest diffusion coefficients were observed in the CMS membrane for all vanadium ions. CMS membranes were found to be most suitable for V-RFB, as it was expected to prevent cross contamination of vanadium ions.³⁰⁷

One of the most important requirements that must be met is the membrane's ability to prevent excessive transfer of water from one half cell to the other. The preferential transfer of water can be a problem in the vanadium battery as one half-cell (the negative half cell in the case of cation exchange membranes) is flooded and becomes diluted, while the other becomes more concentrated, adversely affecting the overall operation of the cell. Most of the membranes show good initial water transfer properties, but their performance deteriorates with exposure to the vanadium solutions. Sukkar et al.³⁰⁸ evaluated various polyelectrolytes to determine whether they could improve the selectivity and stability of the membranes in the vanadium redox cell solutions. Both the cationic and anionic polyelectrolytes evaluated improved the water transfer properties of the membranes, although upon extended exposure to the vanadium electrolyte the modified membranes did not maintain their improved water transfer properties. The solvent based Nuosperse 657 modified membrane displayed exceptional properties initially but also failed to maintain its performance with extended exposure to the vanadium solutions.

Another system under investigation is the iron/chromium redox flow battery (Fe/Cr RFB) developed by NASA. The performance requirements of the membrane for Fe/Cr RFB are severe. The membrane must readily permit the passage of chloride ions, but should not allow any mixing of the chromium and iron ions. An anionic permselective membrane CDIL-AA5-LC-397, developed by Ionics, Inc., performed well in this system.³⁰⁹ It was prepared by a free radical polymerization of vinylbenzyl chloride and dimethylaminoethyl methacrylate in a 1:1 molar ratio. One major issue with the anionic membranes was its increase in resistance during the time it was exposed to a ferric chloride solution. The resistance increase termed "fouling" is related to the ability of the ferric ion to form ferric chloride complexes, which are not electrically repelled by the anionic membrane. An experiment by Arnold and Assink indicated that

fouling decreased when the degree of cross-linking of the anion-exchange membrane was increased.³¹⁰

Hruska et al.³¹¹ evaluated various microporous materials (Celgard 5511 composed of porous polypropylene and Daramic W0733 composed of porous polyethylene) to reduce the coulombic efficiency loss caused by the oxidation of the iron plate. The chemical resistances of both Celgard and Daramic membranes in iron electrolytes were excellent at $\text{pH} = 0$. Celgard separators with very low resistivity offered some improvement in coulombic efficiency but the Daramic separators gave very high coulombic efficiencies in a laboratory size redox cell. Daramic separators also limited the ferric ion diffusional loss to about 3% for both charge and discharge modes of operation. Two commercial ion exchange membranes were also evaluated in this study: Neosepta ACH-45T (Tokuyama Soda Company Ltd.) and Selemion DMV (Asahi Glass Company Limited). In laboratory cells, the membranes discolored, giving evidence of deterioration, and the resistivity of the membrane increased significantly. The increased resistivity was attributed to FeCl_4^- fouling. Thus, attempts at lowering the polarization by maintaining a pH differential across the cell with commercial anion membranes were unsuccessful because of membrane fouling. In spite of the poor voltaic performance of the membrane, the overall Coulombic efficiency was found to be exceptionally good.

8. Mathematical Modeling of Batteries/Separators

Computer simulations have been used as a tool for understanding and optimizing battery performance since the 1970s.³¹²⁻³¹⁴ Continued progress in computational tools has enabled ever-increasing sophistication in battery modeling and a steady increase in the number of systems to which modeling has been applied. Today it is possible to obtain simulation codes for all of the major rechargeable batteries, some of which are available for free.³¹⁵

The mathematical models of different types of batteries (lead-acid,^{316,317} NiMH,³¹⁸ lithium-ion^{319,320}) have been developed during the past few years.³¹⁵ This has led to a better understanding of those systems. The present models consider only the thickness and porosity of the separators. Not much work has been done in incorporating the effect of physical and chemical properties of separators on the performance and safety of batteries. This is also because the microstructure of separators and their effect on transport properties in batteries are generally known only qualitatively. A thorough understanding of the microstructure of separators would be beneficial for modeling studies and optimization of electrochemical systems. This will help in making the battery model predictions more practical and reliable.

The separator pore structure is usually very complex. It consists of a porous network of interconnected pores, which are filled with liquid electrolyte. A complete description of the pore structure would require a very intricate model. Simulations are only practically possible if the structure is represented by a simplified quasi-continuum involving a few param-

eters. In such an approach, the “effective” electrolytic conductivity, σ_{eff} , is often defined by⁹⁷

$$\sigma_{\text{eff}} = \epsilon^\alpha \sigma_0, \quad \alpha \approx 1.5 \quad (11)$$

where σ_0 is the bulk ionic conductivity of the electrolyte, ϵ is the void volume fraction of separator filled with electrolyte, and α is the Bruggeman exponent. The general applicability of $\alpha \sim 1.5$, appears questionable because separator pores are never of an ideal shape. Fan and White³²¹ chose a α value of 2.5 for separators in NiCd batteries, and Doyle et al.³²² used 3.3 for lithium-ion batteries. Arora et al.³²³ measured the value as 2.4 for PVdF based separators by measuring the separator and electrolyte conductivity at different salt concentrations. Doyle et al. used an even higher Bruggeman exponent of 4.5 for quantifying the ionic conductivity of their plasticized electrolyte membrane.³²²

Patel et al. showed that a Bruggeman exponent of 1.5 is often not valid for real separator materials, which do not have uniform spherical shape.³²⁴ Porous networks based on other morphologies such as oblate (disk-type) ellipsoids or lamellar increase the tortuous path for ionic conductivity and result either in a significant increase of the exponent α , or in a complete deviation from the power law. They showed that spherical or slightly prolate ellipsoidal pores should be preferred for separators, as they lead to higher ionic conductivity separators.

Tye³²⁵ explained that separator tortuosity is a key property determining transient response of a separator and steady-state electrical measurements do not reflect the influence of tortuosity. He recommended that the *distribution of tortuosity* in separators be considered; some pores may have less tortuous paths than others. He showed mathematically that separators with identical average tortuosities and porosities could be distinguished by their unsteady-state behavior if they have different distributions of tortuosity.

Doyle et al.³²² used a mathematical model to examine the effect of separator thickness for the PVdF:HFP gel electrolyte system and found that decreasing separator thickness below 52 μm caused only a minor decrease in ohmic drop across the cell. The voltage drops in the electrodes were much more significant. Mao and White³²⁶ developed a mathematical model for discharge of a Li/TiS₂ cell. Their model predicted that increasing the thickness of the separator from 25 to 100 μm decreased the discharge capacity from 95% to about 90%; further increasing separator thickness to 200 μm reduced discharge capacity to 75%. These theoretical results indicate that conventional separators (25–37 μm thick) do not significantly limit mass transfer of lithium.

The use of electroactive polymers for overcharge protection has been recently reported for lithium-ion batteries.^{327,328} The electroactive polymer incorporated into a battery's separator is an attractive new option for overcharge protection. Thomas et al.³²⁹ developed a mathematical model to explain how electroactive polymers such as polythiophene can be used to provide overcharge protection for lithium-ion

batteries. The model shows that, as the cell potential exceeds the oxidation potential of the polymer, the cell is transformed, over a time scale of a few minutes, from a battery into a resistor, after which a steady-state overcharge condition is attained.

9. Summary

The ideal battery separator would be infinitesimally thin, offer no resistance to ionic transport in electrolytes, provide infinite resistance to electronic conductivity for isolation of electrodes, be highly tortuous to prevent dendritic growths, and be inert to chemical reactions. Unfortunately, in the real world the ideal case does not exist. Real world separators are electronically insulating membranes whose ionic resistivity is brought to the desired range by manipulating the membranes thickness and porosity.

It is clear that no single separator satisfies all the needs of battery designers, and compromises have to be made. It is ultimately the application that decides which separator is most suitable. We hope that this paper will be a useful tool and will help the battery manufacturers in selecting the most appropriate separators for their batteries and respective applications. The information provided is purely technical and does not include other very important parameters, such as cost of production, availability, and long-term stability.

There has been a continued demand for thinner battery separators to increase battery power and capacity. This has been especially true for lithium-ion batteries used in portable electronics. However, it is very important to ensure the continued safety of batteries, and this is where the role of the separator is greatest. Thus, it is essential to optimize all the components of battery to improve the performance while maintaining the safety of these cells. Separator manufacturers should work along with the battery manufacturers to create the next generation of batteries with increased reliability and performance, but always keeping safety in mind.

This paper has attempted to present a comprehensive review of literature on separators used in various batteries. It is evident that a wide variety of separators are available and that they are critical components in batteries. In many cases, the separator is one of the major factors limiting the life and/or performance of batteries. Consequently, development of new improved separators would be very beneficial for the advanced high capacity batteries.

10. Future Directions

Up until more recent history, most of the separators and membranes historically used had not been specifically developed for battery applications. Thus, future research should be aimed at developing separators that are specifically tailored for battery applications. The general objectives of separator research should be as follows: (a) to find new and cost-effective separators, (b) to understand the separator properties in batteries, and (c) to optimize separator properties related to specific cell performance, life,

and safety. One way to achieve some of these goals will be to develop mathematical models that reflect the effects of separator resistance, thickness, pore size, shrinkage, tortuosity, and mechanical strength on the final performance and safety of batteries. The battery separators for tomorrow will demand more than just good insulation and mechanical filtration; they will require unique electrochemical properties.

11. Acknowledgments

The authors would like to acknowledge numerous colleagues and staff members at Celgard, LLC., and Polypore, International, Inc., for their help with the preparation and publication of this paper.

12. References

- Linden, D.; Reddy, T. B. *Handbook of Batteries*, 3rd ed.; McGraw-Hill: New York, 2002.
- Besenhard, J. O. Editor, *Handbook of Battery Materials*; Wiley-VCH: Weinheim, Germany, 1999.
- Berndt, D. *Maintenance Free Batteries*, 3rd ed., Research Studies Press Ltd.: Taunton, Somerset, England, 2003.
- Bode, H. *Lead-Acid Batteries*; John Wiley: New York, 1977.
- Falk, S. U.; Salkind, A. J. *Alkaline Storage Batteries*; John Wiley: New York, 1969.
- Fleischer, A.; Lander, J. J. *Zinc-Silver Oxide Batteries*; John Wiley: New York, 1971.
- Brodd, R. J.; Friend, H. M.; Nardi, J. C., Eds. *Lithium Ion Battery Technology*; ITE-JEC Press: Brunswick, OH, 1995.
- Wakihara, M.; Yamamoto, O., Eds. *Lithium Ion Batteries, Fundamentals and Performance*; Wiley-VCH: New York, 1998.
- Yoshino, A. *Chem. Ind.* **1995**, 146, 870.
- Schalkwijk, W. A. V., Ed. *Advances in Lithium Ion Batteries*; Kluwer Academic: New York, 2002.
- Kinoshita, K.; Yeo, R. *Survey on Separators for Electrochemical Systems*; LBNL: January 1985.
- Benett, J.; Choi, W. M. Developments in small cell separators. In *Proceedings of the 10th Annual Battery Conference on Applications and Advances*; IEEE: New York, 1995; p 265.
- Boehnstedt, W. In *Handbook of Battery Materials*; Besenhard, J. O., Ed.; VCH Wiley: Amsterdam and New York, 1999.
- Spotnitz, R. In *Handbook of Battery Materials*; Besenhard, J. O., Ed.; VCH Wiley: Amsterdam and New York, 1999.
- Shirai, H.; Spotnitz, R. *Lithium Ion Secondary Battery—Materials and Applications*; Yoshio, K, Ed.; Nikkan Kogyo Shin-bun: Tokyo, 1996; p 91 (in Japanese).
- Shirai, H.; Spotnitz, R.; Atsushi, A. *Chem. Ind.* **1997**, 48, 47 (in Japanese).
- Hiroshi, T. In *The Latest Technologies of the New Secondary Battery Material*; Ogumi, Z., Ed.; CMC: Tokyo, 200X; p 99 (in Japanese).
- Hiroshi, T. In *Advanced Technologies for Polymer Battery*; Oyama, N., Ed.; CMC: Tokyo, 200X; p 165 (in Japanese).
- Koichi, K. In *Advanced Technologies for Polymer Battery*; Oyama, N., Ed.; CMC: Tokyo, 200X; p 174. (In Japanese).
- Kiyoshi, K. In *Lithium Secondary Battery Technology for the 21st Century*; Kanamura, K., Ed.; CMC: Tokyo, 200X; p 116.
- Brodd, R. J.; Bullock, K. R.; Leising, R. A.; Midaugh, R. L.; Miller, J. R.; Takeuchi, E. *J. Electrochem. Soc.* **2004**, 151, K1.
- Battery Power Prod. Technol.* **2003**, 7 (May), 15.
- Takeshita, H. Presented at The 21st International Seminar & Exhibit on Primary & Secondary Batteries, Fort Lauderdale, FL, Florida Educational Seminars Inc., March 8, 2004.
- Battery EV Technol.* **2004**, 28 (Jan), 2.
- Pilot, C. The Worldwide Rechargeable Battery Market. Presented at Batteries 2004, 6th ed.; Paris, June 2–4, 2004.
- Celgard LLC <http://www.celgard.com>.
- Celgard completes capacity expansion, Global Sources, <http://www.globalsources.com>, February 04, 2004.
- Asahi Kasei adding battery membrane capacity. *Nikkei Net Interact.* <http://www.nni.nikkei.co.jp/AC/TNKS/Nni20030806D06JFA23.htm>, August 7, 2003.
- Advanced Rechargeable Battery Industry 2001/2002, Nomura Research Institute Limited, 2002.
- About Edison Batteries, Inc., <http://www.optodot.com/sys-tmpl/htmlpage/>.
- Battery and Fuel Cell Components*; The Fredonia Group: 2003.
- Adv. Battery Technol.* **2004**, 40 (Feb), 22.
- Hamano, K.; Yoshida, Y.; Shiota, H.; Shiraga, S.; Aihara, S.; Murai, M.; Inuzuka, T. U.S. Patent 6,664,007, B2, 2003.
- Sun, L.; Chen, G.; Xu, D.; Abe, T. Presented at the 204th Meeting of The Electrochemical Society, 2003; Abstract 423.
- Sun, L. U.S. Patent 2003/0152828A1, 2003.
- Johnson, B. A.; White, R. E. *J. Power Sources* **1998**, 70, 48.
- Hoffman, H. G. *Proceedings of the Tenth Annual Battery Conference on Applications and Advances*; IEEE: New York, 1995; p 253.
- Bradford, S. M. *Battery Power Prod. Technol.* **2004**, (Mar), 17.
- Frost & Sullivan Research World Rechargeable Battery Markets for Mobile IT and Communication Devices (A575–27); 2002.
- Geiger, M.; Callahan, R. W.; Diwiggins, C. F.; Fisher, H. M.; Hoffman, D. K.; Yu, W. C.; Abraham, K. M.; Jillson, M. H.; Nguyen, T. H. Presented at The Eleventh International Seminar on Primary and Secondary Battery Technology and Application, Fort Lauderdale, FL, Florida Educational Seminars Inc., Feb 28–Mar 3, 1994.
- Tanba, H. *Molding Process* **1999**, 11, 759.
- Adachi, A.; Spotnitz, R. M.; et al. *Osaka Chem. Marketing Center* **1997**, 69–80.
- Yu, W. C.; Hux, S. E. U.S. Patent, 5,952,120, 1999.
- Hipore, Asahi Kasai, <http://www.asahi-kasai.co.jp/membrane/english/tradenm/t07.html>.
- Bierenbaum, H. S.; Isaacson, R. B.; Druin, M. L.; Plovan, S. G. *Ind. Eng. Chem. Prod. Res. Dev.* **1974**, 13, 2.
- Jpn. Ind. News* **1996**, 91.
- Kim, S. S.; Lloyd, D. R. *J. Membr. Sci.* **1991**, 64, 13.
- Druin, M. L.; Loft, J. T.; Plovan, S. G. U.S. Patent 3,801,404, 1974.
- Schell, W. J.; Zhang, Z. *The Fourteenth Annual Battery Conference on Applications and Advances, Long Beach, CA*; IEEE: New York, 1999; p 161.
- Isaacson, R. B.; Bierenbaum, H. S. U.S. Patent 3,558,764, 1971.
- Kamei, E.; Shimomura, Y. U.S. Patent 4,563,317, 1986.
- Yu, T. H. Processing and Structure–Property Behavior of Microporous Polyethylene—From Resin to Final Film Ph.D. Dissertation, Virginia Polytechnic Institute and State University, Blacksburg, VA, 1996.
- Sarada, T.; Sawyer, L. C.; Ostler, M. I. *J. Membr. Sci.* **1983**, 15, 97.
- Bierenbaum, H. S.; Daley, L. R.; Zimmerman, D.; Hay, I. L. U.S. Patent, 3,843,761, 1974.
- Hamer, E. A. G. U.S. Patent, 4,620,956, 1986.
- Hiroshi, K.; Tetuo, A.; Akira, K. U.S. Patent 5,691,047, 1997.
- Kesting, R. E. *Synthetic Polymeric Membranes*, 2nd ed.; John Wiley & Sons Inc.: New York, 1985; Chapter 2.
- Ihm, D. W.; Noh, J. G.; Kim, J. Y. *J. Power Sources* **2002**, 109, 388.
- Takita, K.; kono, K.; Takashima, T.; Okamoto, K. U.S. Patent, 5,051,183, 1991.
- Mochiyuki, A.; Jpn. Patent 8064194, 1996.
- Kotaro, T.; Koichi, K.; Tatsuya, T.; Kenkichi, O. U.S. Patent 5,051,183, 1991.
- Koichi, K.; Kotaro, T.; Mamoru, T.; Tatsuya, T. Jpn. Patent 8012799, 1996.
- Norimitsu, K.; Kotaru, T.; Koichi, K.; Hidehiko, F. U.S. Patent 6,153,133, 2000.
- Akinao, H.; Kazuo, Y.; Hitoshi, M. U.S. Patent 6,048,607, 2000.
- Pekala, R. W.; Khavari, M. U.S. Patent 6,586,138, 2003.
- Userguide, FreedomCar Separator Costing Document, February 2003.
- Xu, M.; Hu, S.; Guan, J.; Sun, X.; Wu, W.; Zhu, W.; Zhang, X.; Ma, Z.; Han, Q.; Liu, S. U.S. Patent 5,134,174, 1992.
- Fisher, H. M.; Wensley, C. G. U.S. Patent 6,368,742, 2002.
- Zhu, W.; Zhang, X.; Zhao, C.; Zu, W.; Hou, J.; Xu, M. *Polym. Adv. Technol.* **1996**, 7, 743.
- Sadamitsu, K.; Ikeda, N.; Hoki, Manabu, Nagata, K.; Ogino, K. World Patent Application 02066233A1, 2002.
- Higuchi, H.; Matsushita, K.; Ezoe, M.; Shinomura, T. U.S. Patent 5,385,777, 1995.
- Calis, G. H. M.; Daemen, A. P. M.; Gerrits, N. S. J. A.; Smedinga, J. T. *J. Power Sources* **1997**, 65, 275.
- Ooms, F. G. B.; Kelder, E. M.; Schoonman, J.; Gerrits, N.; Smedinga, J.; Calis, G. *J. Power Sources* **2001**, 97–98, 598.
- Yamamura, Y.; Ooizumi, S.; Yamamoto, K. Separator for rechargeable lithium ion batteries with high puncture strength and high melt rupture temperature. *Nitto Denko Technol. Rep.* (http://www.nitto.com/rd/rd6_1.html), **2001**, 39, 39.
- Pekala, R. W.; Khavari, M.; Dobbie, G.; Lee, D.; Fraser-Bell, G. Presented at the 17th International Seminar & Exhibit on Primary and Secondary Batteries, Fort Lauderdale, FL, Florida Educational Seminars, Inc., March 6–9, 2000.
- Fleming, R.; Taskier, H. *Prog. Batteries Solar Cells* **1990**, 9, 58.
- Hoffman, D.; Fisher, H.; Langford, E.; Diwiggins, C. *Prog. Batteries Solar Cells* **1990**, 9, 48.
- Yu, W. C.; Callahan, R. W.; Diwiggins, C. F.; Fischer, H. M.; Geiger, M. W.; Schell, W. J. Presented at the North America Membrane Society Conference, Breckenridge, CO, 1994.
- Kuribayashi, I. *J. Power Sources* **1996**, 63, 87.

- (80) Pasquier, A. D.; Gozdz, A.; Plitz, I.; Shelburne, J. Presented at the 201st meeting of The Electrochemical Society, Philadelphia, PA, May 12–17, 2002.
- (81) Augustin, S.; Volker, H.; Gerhard, H.; Christian, H. *Desalination* **2002**, *146*, 23.
- (82) <http://www.separion.com>.
- (83) Hying, C. Separion separators for lithium batteries—safety & performance. Presented at Batteries 2004, 6th Ed.; Paris, June 2–4, 2004.
- (84) Sachan, S.; Ray, C. A.; Perusich, S. A. *Polym. Eng. Sci.* **2002**, *42*, 1469.
- (85) Sachan, S.; Perusich, S. Electrochemical Society Meeting, Seattle, 1999.
- (86) Carlson, S. A. *Membr. Sep. Technol. News* **2004**, *22*, 8.
- (87) Abraham, K. M. *Electrochim. Acta* **1993**, *38*, 1233.
- (88) Gineste, J. L.; Pourcell, G. *J. Membr. Sci.* **1995**, *107*, 155.
- (89) Hoffman, D. K.; Abraham, K. M. In *Proceedings of the Fifth International Seminar on Lithium Battery Technology and Applications*; Florida Educational Seminars, Inc.: Deerfield Beach, FL, 1991.
- (90) USABC “Development of low cost separators for lithium-ion batteries”, RFPI 2001.
- (91) Laman, F. C.; Sakutai, Y.; Hirai, T.; Yamaki, J.; Tobishima, S. *Ext. Abstr., 6th Int. Meet. Lithium Batteries* **1992**, 298–300.
- (92) Laman, F. C.; Gee, M. A.; Denovan, J. *J. Electrochem. Soc.* **1993**, *140*, L51.
- (93) Abraham, K. M. *Electrochim. Acta* **1993**, *38*, 1233.
- (94) Robinson, R. G.; Walker, R. L. In *Batteries*; Collins, D. H., Ed.; The MacMillan Company: New York, 1963; p 15.
- (95) Lander, J. J.; Weaver, R. D.; Salkind, A. J.; Kelley, J. J. In *Characteristics of Separators for Alkaline Silver Oxide Zinc Secondary Batteries. Screening Methods*; Cooper, J. E., Fleischer, A., Eds.; NASA Technical Report NAS 5-2860, 1964.
- (96) Kilroy, W. P.; Moynihan, C. T. *J. Electrochem. Soc.* **1978**, *125*, 520.
- (97) MacMullin, R. B.; Muccini, G. A. *AIChE J.* **1956**, *2*, 393.
- (98) Callahan, R. W.; Nguyen, K. V.; McLean, J. G.; Propost, J.; Hoffman, D. K. *Proceedings of the 10th International Seminar on Primary and Secondary Battery Technology and Application*; Florida Educational Seminars, Inc.: Fort Lauderdale, FL, 1993.
- (99) Ionov, V. V.; Isakevitch, V. V.; Katalovsky, E. E.; Chernokoz, A. *J. Power Sources* **1990**, *30*, 321.
- (100) Lowell, S.; Shields, E. *Powder Surface Area and Porosity*, 3rd ed.; Chapman and Hall: New York, 1991.
- (101) PMI Conference 2000 Proceedings, PMI short course, Ithaca, NY, Oct 16–19, 2000.
- (102) Porous Materials Inc. <http://www.pmiapp.com>.
- (103) Jena, A. K.; Gupta, K. M. *J. Power Sources* **1999**, *80*, 46.
- (104) Jena, A. K.; Gupta, K. M. *J. Power Sources* **2001**, *96*, 214.
- (105) Zeman, L.; Denault, L. *J. Membr. Sci.* **1992**, *71*, 221.
- (106) Chen, R. T.; Saw, C. K.; Jamieson, M. G.; Aversa, T. R.; Callahan, R. W. *J. Appl. Polym. Sci.* **1994**, *53*, 471.
- (107) Fujii, T.; Mochizuki, T. U.S. Patent, 5, 759, 678, 1998.
- (108) Spotnitz, R.; Ferebee, M.; Callahan, R. W.; Nguyen, K.; Yu, W. C.; Geiger, M.; Dwiggens, C.; Fischer, H.; Hoffman, D. *Proceedings of the 12th International Seminar on Primary and Secondary Battery Technology and Applications*; Fort Lauderdale, FL, Florida Educational Seminars, Inc.: Fort Lauderdale, FL, 1995.
- (109) Venugopal, G.; Moore, J.; Howard, J.; Pandalwar, S. *J. Power Sources* **1999**, *77*, 34.
- (110) Venugopal, G. The role of plastics in lithium-ion batteries. *Proceedings of the 3rd Annual Conference on Plastics for Portable and Wireless Electronics*; Philadelphia, PA, 1997; p 11.
- (111) Lundquist, J. T.; Lundsager, C. B.; Palmer, N. L.; Troffkin, H. J.; Howard, J. U.S. Patent 4,731,304, 1998.
- (112) Lundquist, J. T.; Lundsager, C. B.; Palmer, N. I.; Troffkin, H. J. U.S. Patent 4,650,730, 1987.
- (113) Zuckerbrod, D.; Giovannoni, R. T.; Grossman, K. R. *Proceedings of the 34th International Power Sources Symposium*; Cherry Hill, NJ, 1990; p 172.
- (114) Spotnitz, R.; Ferebee, M. W. *Meeting Abstracts, The Electrochemical Society Inc., Volume 96–2, Fall Meeting, San Antonio, TX, October 6–11*; The Electrochemical Society: New York, 1996.
- (115) Faust, M. A.; Suchanski, M. R.; Osterhoudt, H. W. U.S. Patent No. 4,741,979, 1988.
- (116) Matthias, U.; Dieter, B.; Heinrich, R.; Thomas, B.; U.S. Patent, 6,511,517, 2003.
- (117) Maleki, H.; Shamsuri, A. K. *J. Power Sources* **2003**, *115*, 131.
- (118) Zeng, S.; Moses, P. R. *J. Power Sources* **2000**, *90*, 39.
- (119) Norin, L.; Kostecki, R.; McLarnon, F. *Electrochem. Solid State Lett.* **2002**, *5*, A67.
- (120) Kostecki, R.; Norin, L.; Song, X.; McLarnon, F. *J. Electrochem. Soc.* **2004**, *151*, A522.
- (121) *Hazardous Materials Regulations*; Code of Federal Regulations, CFR49 173.185.
- (122) UL1640, Lithium Batteries. Underwriters Laboratories, Inc.
- (123) UL2054, Household and Commercial Batteries. Underwriters Laboratories, Inc.
- (124) Secondary Lithium Cells and Batteries for Portable Applications. International Electrotechnic Commission, IEC 61960-1 and IEC 61960-2.
- (125) Recommendations on the Transport of Dangerous Goods, Manual of Tests and Criteria. United Nations: New York, 1999.
- (126) Safety Standard for Lithium Batteries, UL 1642, Underwriters Laboratories Inc, Third Edition, 1995.
- (127) Standard for Household and Commercial Batteries, UL 2054, Underwriter Laboratories, Inc., 1993.
- (128) UN Recommendations on the Transport of Dangerous Goods, December 2000.
- (129) A Guideline for the Safety Evaluation of Secondary Lithium Cells. Japan Battery Association, 1997.
- (130) Venugopal, G. *J. Power Sources* **2001**, *101*, 231.
- (131) Alamgir, M.; Abraham, K. M. In *Lithium Batteries: New Materials, Developments and Perspectives*; Industrial Chemistry Library 5; Pistoia, G., Ed.; Elsevier: New York, 1994; Chapter 3.
- (132) Gray, F. M. *Polymer Electrolytes*; RSC Materials Monograph; The Royal Society of Chemistry: Cambridge, U.K., 1997.
- (133) Fauteux, D.; Massucco, A.; McLin, M.; Van Buren, M.; Shi, J. *Electrochim. Acta* **1995**, *40*, 2185.
- (134) North, M.; Markin, T. L.; Hooper, A.; Tofield, B. C. Second International Meeting on Lithium Batteries, Paris, France, April 25–27, 1984; Extended Abstracts # 19.
- (135) *Chem. Int.* **1982**, (June, No. 3), 14.
- (136) Appetecchi, G. B.; Dautzenberg, G.; Scrosati, B. *J. Electrochem. Soc.* **1996**, *143*, 6.
- (137) Armand, M. *Solid State Ionics* **1983**, *9 & 10*, 745.
- (138) Lightfoot, P.; Mehta, M. A.; Bruce, P. G. *Science* **1993**, *262*, 883.
- (139) Vincent, C. A.; Scrosati, B. *Modern Batteries. An Introduction to Electrochemical Power Sources*; Arnold: London, 1993.
- (140) Appetecchi, G. B.; Passerini, S. *J. Electrochem. Soc.* **2002**, *149*, A891.
- (141) Croce, F.; Appetecchi, G. B.; Persi, L.; Scrosati, B. *Nature (London)* **1998**, *394*, 4496.
- (142) Croce, F.; Persi, L.; Ronci, F.; Scrosati, B. *Solid State Ionics* **2000**, *135*, 47.
- (143) Fan, J.; Fedkiw, P. S. *J. Electrochem. Soc.* **1997**, *144*, 399.
- (144) Appetecchi, G. B.; Romagnoli, P.; Scrosati, B. *Electrochem. Commun.* **2001**, *3*, 281.
- (145) Kim, D. W.; Sun, Y. K. *J. Power Sources* **2001**, *102*, 41.
- (146) Chojnacka, J.; Acosta, J. L.; Morales, E. *J. Power Sources* **2001**, *97–98*, 819.
- (147) Nishi, Y. *Advances in Lithium Ion Batteries*; van Schalkwijk, W., Scrosati, B., Eds.; Kluwer Academic/Plenum Publishers: New York, 2002.
- (148) EE Times.com: <http://www.eet.com/story/OEG19990121S0013>.
- (149) Song, J. Y.; Wang, Y. Y.; Wan, C. C. *J. Power Sources* **1999**, *77*, 183.
- (150) Min, H. S.; Ko, J. M.; Kim, D. W. *J. Power Sources* **2003**, *119–121*, 461.
- (151) Jo, S. I.; Sohn, H. J.; Kang, D. W.; Kim, D. W. *J. Power Sources* **2003**, *119–121*, 478.
- (152) Kim, H. S.; Kum, K. S.; Cho, W. I.; Cho, B. W.; Rhee, H. W. *J. Power Sources* **2003**, *124*, 221.
- (153) Abraham, K. M.; Alamgir, M. *Solid State Ionics* **1994**, *70–71*, 20.
- (154) Schmutz, C.; Tarascon, J. M.; Gozdz, A. S.; Schmutz, C. N.; Warren, P. C.; Shokoohi, F. K. *Proc. Electrochem. Soc.* **1995**, *94* (28), 330.
- (155) Murata, K.; Izuchi, S.; Yoshihisa, Y. *Electrochim. Acta* **2000**, *45*, 1501.
- (156) Jiang, Z.; Carroll, B.; Abraham, K. M. *Electrochim. Acta* **1997**, *42*, 2667.
- (157) Song, J. Y.; Cheng, C. L.; Wang, Y. Y.; Wan, C. C. *J. Electrochem. Soc.* **2002**, *149*, A1230.
- (158) Gozdz, A. S.; Schmutz, C. N.; Tarascon, J. M.; Warren, P. C. U.S. Patent, 5,456,000, 1995.
- (159) Gozdz, A. S.; Tarascon, J. M.; Schmutz, C. N.; Warren, P. C.; Gebizlioglu, O. S.; Shokoohi, F. *Tenth Annual Battery Conference on Advances and Applications, Long Beach, CA, January 10–13*; IEEE: New York, 1995; 301.
- (160) Tarascon, J. M.; Gozdz, A. S.; Schmutz, C. N.; Shokoohi, F. K.; Warren, P. C. *Solid State Ionics* **1996**, *86–88*, 49.
- (161) Pasquier, A. D.; Warren, P. C.; Culver, D.; Gozdz, A. S.; Amatucci, G.; Tarascon, J. M. *Proc. Electrochem. Soc.* **1999**, *99* (24), 360.
- (162) Park, C. K.; Kakirde, A.; Ebner, W.; Manivannan, V.; Chai, C.; Ihm, D. J.; Shim, Y. J. *J. Power Sources* **2001**, *97–98*, 775.
- (163) Dasgupta, S.; Jacobs, J. K. U.S. Patent, 5,437,692, 1995.
- (164) Abraham, K. M.; Alamgir, M.; Hoffman, D. K. *J. Electrochem. Soc.* **1995**, *142*, 683.
- (165) Pandalwar, S. L.; Howard, J. N.; Venugopal, G.; Oliver, M. U.S. Patent, 5,716,421, 1998.
- (166) Gozdz, A. S.; Plitz, I.; Du Pasquier, A.; Zheng, T. *Proceedings of the 200th ECS Meeting, Fall 2001, Phoenix, AZ, 2001*; Vol. 2000–2001, pp 336–351.
- (167) Gozdz, A. S. U.S. Patent 6,328,770, 2001.

- (168) Kim, D. W.; Oh, B.; Park, J. H.; Sun, Y. K. *Solid State Ionics* **2000**, *138*, 41.
- (169) Wang, Y.; Sejdic, J. T.; Steiner, R. *Solid State Ionics*, **2002**, *148*, 443.
- (170) Gozdz, A. S.; Plitz, I.; DuPasquier, A.; Zheng, T. Presented at the 198th Meeting of the Electrochemical Society, Phoenix, AZ, Oct 22–27, 2000.
- (171) Spotnitz, R. M.; Wensley, C. G. U.S. Patent 6,322,923, 2000.
- (172) Fabrice, C.; Bradford, R. WO 02/50929 A2, 2002.
- (173) Jeong, Y. B.; Kim, D. W. *J. Power Sources* **2004**, *128*, 256.
- (174) Abraham, K. M.; Alamgir, M.; Hoffman, D. K. *J. Electrochem. Soc.* **1995**, *142*, 683.
- (175) Dasgupta, S.; Jacobs, J. K. U.S. Patent 5,498,489, 1996.
- (176) Gies, P.; Charles, R. A.; Dieken, J. World Patent 00/13248, 2000.
- (177) Eschbach, F. O.; Oliver, M. U.S. Patent, 5,681,357, 1997.
- (178) Hamano, K.; Shiota, H.; Shiraga, S.; Aihara, S.; Yoshida, Y.; Murai, M.; Inuzuka, T. U.S. Patent, 5,981,107, 1999.
- (179) Akashi, H. U.S. Patent, 5,658,686, 1997.
- (180) Akashi, H. Paper presented at the International Symposium on Polymer Electrolytes, ISPE-5, Uppsala, Sweden, Aug 11–16, 1996.
- (181) Fujii, T. *Proceedings of the 17th International Seminar & Exhibit on Primary and Secondary Batteries*, Florida Educational Seminars, Inc.: Boca Raton, FL, 2000.
- (182) Nakane, I.; Narukawa, S. Presented at Power 2000, The 8th Annual International Conference on Power Requirements for Mobile Computing and Wireless Communications, San Diego, CA, Sept 24–27, 2000.
- (183) Kim, K. M.; Ryu, K. S.; Kang, S. G.; Chang, S. H.; Chung, I. J. *Macromol. Chem. Phys.* **2001**, *202*, 866.
- (184) Kim, K. M.; Park, N. G.; Ryu, K. S.; Chang, S. H. *Polymer* **2002**, *43*, 3951.
- (185) Kim, K. M.; Ko, J. M.; Park, N. G.; Ryu, K. S.; Chang, S. H. *Solid State Ionics* **2003**, *161*, 121.
- (186) Scrosati, B.; Croce, F.; Persi, L. *J. Electrochem. Soc.* **2000**, *147*, 1718.
- (187) Prossini, P. P.; Villano, P.; Carewska, M. *Electrochim. Acta* **2002**, *48*, 227.
- (188) Liu, X.; Kusawake, H.; Kuwajima, S. *J. Power Sources* **2001**, *97–98*, 661.
- (189) Kim, D. W.; Ko, J. M.; Chun, J. H.; Kim, S. H.; Park, J. K. *Electrochem. Commun.* **2001**, *3*, 535.
- (190) Kim, D. W.; Noh, A.; Chun, J. H.; Kim, S. H.; Ko, J. M. *Solid State Ionics* **2001**, *144*, 329.
- (191) Dan, P.; Mengeritski, E.; Geronov, Y.; Aurbach, D.; Weisman, I. *J. Power Sources* **1995**, *54*, 143.
- (192) Ikeda, H.; et al. *Proceedings of the Symposium on Lithium Batteries*; The Electrochemical Society: Pennington, NJ, 1984; Vol. 84, 311.
- (193) Grady, J. P. Presented at the 20th International Seminar and Exhibit on Primary and Secondary Batteries, Fort Lauderdale, Florida, Florida Educational Seminars, Inc., Mar 17–20, 2003.
- (194) Weininger, J. L.; Holub, F. F. *J. Electrochem. Soc.* **1970**, *117*, 340.
- (195) Martino, F. J.; Gay, E. C.; Moore, W. E. *J. Electrochem. Soc.* **1982**, *129*, 2701.
- (196) Swaroop, R. B.; Battles, J. E. *J. Electrochem. Soc.* **1981**, *128*, 1873.
- (197) Mathers, J. P.; Boquist, C. W.; Olszanski, T. W. *J. Electrochem. Soc.* **1978**, *125*, 1913.
- (198) Bandyopadhyay, G.; Swaroop, R. B.; Battles, J. E. *J. Electrochem. Soc.* **1982**, *129*, 2187.
- (199) Shimizu, Y.; Terasaki, M.; Kashihara, S. *J. Power Sources* **1984**, *13*, 235.
- (200) Choi, S. H.; Park, S. Y.; Nho, Y. C. *Radiat. Phys. Chem.* **2000**, *57*, 179.
- (201) Choi, S. H.; Kang, H. J.; Ryu, E. N.; Lee, K. P. *Radiat. Phys. Chem.* **2001**, *60*, 495.
- (202) Navy Primary and Secondary Batteries, Design and Manufacturing Guidelines, Department of the Navy, Sept 1991; p 85.
- (203) Linden, D. *Handbook of Batteries*, 2nd ed.; McGraw-Hill: New York, 1994.
- (204) Vinal, G. *Primary Batteries*; Wiley: New York, 1950.
- (205) Mantell, C. L. *Batteries & Energy Systems*, 2nd ed. McGraw-Hill: New York, 1983.
- (206) Mardegain, S. B. *Battery Power Prod. Technol.* **2003**, (Jan).
- (207) Boehnstedt, W. *J. Power Sources* **1996**, *59*, 45.
- (208) Boehnstedt, W. *J. Power Sources* **2004**, *133*, 59.
- (209) Lander, J. J. *Proceedings of the Symposium on Battery Separators*; The Electrochemical Society: Columbus, OH, 1974; p 4.
- (210) Prout, L. *J. Power Sources* **1993**, *46*, 117.
- (211) Vinal, G. W. *Storage Batteries*; Wiley: New York, 1945.
- (212) Butherus, A. D.; Lindenberger, W. S.; Vaccaro, F. J. *Bell Syst. Technol. J.* **1970**, *1377*.
- (213) Paik, S. L.; Terzaghi, G. *J. Power Sources* **1995**, *53*, 283.
- (214) Kung, J. *J. Power Sources* **1994**, *48*, 129.
- (215) Wang, L. C.; Harvey, M. K.; Stein, H. L.; Scheunemann, U. The Role of UHMW-PE in Microporous PE Separators. *Proceedings of the 12th Annual Battery Conference on Applications & Advances*; IEEE: New York, 1997; p 69.
- (216) Larsen, D. W.; Kehr, C. L. U.S. Patent 3,351,495, 1996.
- (217) Boehnstedt, W. *J. Power Sources* **2001**, *95*, 234.
- (218) Wang, L. C.; Harvey, M. K.; Ng, J. C.; Scheunemann, U. *J. Power Sources* **1998**, *73*, 74.
- (219) Boehnstedt, W. *J. Power Sources* **1996**, *59*, 45.
- (220) Endoh, H. *J. Power Sources* **1996**, *599*, 51.
- (221) Higashi, T.; Endoh, H. *J. Power Sources* **1998**, *73*, 110.
- (222) Rand, D. A. J.; Woods, R.; Dell, R. M. *Batteries for Electric Vehicles*; Research Studies Press: 1998; ISBN 0-86380-205-0.
- (223) McClelland, D. H.; Devitt, J. L. U.S. Patent 3,862,861, 1975.
- (224) Zguris, G. C. *J. Power Sources* **1998**, *73*, 60.
- (225) Zguris, G. C. *J. Power Sources* **1997**, *67*, 307.
- (226) Zguris, G. C. *J. Power Sources* **1996**, *59*, 131.
- (227) Pavlov, D.; Ruvski, S.; Naidenov, V.; Sheytanov, G. *J. Power Sources* **2000**, *85*, 164.
- (228) Ferreira, A. L. *J. Power Sources* **1999**, *78*, 41.
- (229) Britting, A. O. *Proceedings of the 1981 Goddard Space Flight Center Battery Workshop*; NASA Conference Publication 2217; NASA: Washington, DC, 1981; p 327.
- (230) Britting, A. O. *J. Power Sources* **1984**, *12*, 305–316.
- (231) Morrow, G. W. *J. Power Sources* **1987**, *21*, 313.
- (232) Francis, R. W.; Haag, R. L. *J. Power Sources* **1986**, *18*, 147.
- (233) Lim, H. S.; Pickett, D. F. Separator Evaluation in NiCd Cells. *Proceedings of the Intersociety Energy Conversion Engineering*; IEEE: New York, 1990; Vol. 3, p 61.
- (234) Hill, J. M. U.S. Army ERADCOM, Devet-TR-75-F, 1979.
- (235) Feldman, K.; Verville, G. DREO Technical Note, 78-6, 1978.
- (236) Lim, H. S.; Margerum, J. D.; Verzwylvel, S. A.; Lackner, A. M. *Proceedings of the 27th Power Sources Conference, Atlantic City, NJ, June 21–24, 1976*; p 83.
- (237) Lim, H. S.; Margerum, J. D.; Verzwylvel, S. A.; Lackner, A. M.; Knechtli, R. C. *J. Electrochem. Soc.* **1989**, *136*, 605.
- (238) Scott, W. R.; Rusta, D. W. NASA RP 1052, 1979.
- (239) Fetchenko, M. A.; Venkatesan, S.; Ovshinsky, S. *Proceedings of the Symposium on Hydrogen Storage Materials, Batteries & Electrochemistry*; 1992; p 141.
- (240) Wada, M. *Polym. Adv. Technol.* **1994**, *5*, 645.
- (241) Ikoma, M.; Hoshina, Y.; Matsumoto, L.; Iwakura, C. *J. Electrochem. Soc.* **1996**, *143*, 1904–1907.
- (242) Ikoma, M.; Takahashi, O.; Tsuboi, R.; Matsumoto, L. *Denki Kagaku* **1993**, *61*, 997.
- (243) Furukawa, N. *J. Power Sources* **1994**, *51*, 45.
- (244) Nagarajan, G. S.; Van Zee, J. W. *J. Power Sources* **1998**, *70*, 173–180.
- (245) Cook, J. A.; Lancaster, I. M. *Proc. Electrochem. Soc.* **1998**, *98* (15), 55.
- (246) Scimat's latest separators. *Batteries Int.* **2002** (Oct).
- (247) Cheng, S.; Zhang, J.; Liu, H.; Leng, Y.; Yuan, A.; Cao, C. *J. Power Sources* **1998**, *74*, 155–157.
- (248) Hamling, P.; Hamling, B. H. Zirconia Battery Separators—An historical perspective and development update. *Proceedings of the 11th Annual Battery Conference on Applications & Advances*; IEEE: New York, 1996; p 15.
- (249) Vermeiren, P. H.; Adriansens, W.; Moreels, J. P.; Leysen, R. *Int. J. Hydrogen Energy* **1998**, *23*, 5, 321–324.
- (250) *Chem. Business Newsbase* **2001** (July 25).
- (251) <http://www.zircarzirconia.com>.
- (252) Vermeiren, P. H.; Adriansens, W.; Leysen, R. *Int. J. Hydrogen Energy* **1996**, *21*, 8, 679–684.
- (253) Barak, M., Ed. *Electrochemical Power Sources*; Peter Peregrinus: London, 1980.
- (254) Andre, H. *Bull. Soc. Fr. Elect.* **1941**, *6* (1), 132.
- (255) Agostino, V. D.; Lee, J.; Orban, G. In *Grafted Membranes in Zinc-Silver Oxide Batteries*; Fleisher, A., Lander, J. J., Eds.; Wiley: New York, 1971; p 271.
- (256) Charkey, A. *Proc. 26th Annual Power Sources Symp.* **1976**, *87*.
- (257) Karpinski, A. P.; Makovetski, B.; Russell, S. J.; Serenyi, J. R.; Williams, D. C. *J. Power Sources* **1999**, *80*, 53–60.
- (258) Himy, A. *Silver Zinc Battery—Phenomena & Design Principles*, 1st ed.; Vantage Press: New York, 1986.
- (259) Agostino, V. D.; Lee, J.; Orban, G. In *Grafted Membranes in Zinc-Silver Oxide Batteries*; Fleisher, A., Lander, J. J., Eds.; Wiley: New York, 1971; p 271.
- (260) Himy, A. *Silver-Zinc Batteries: Phenomena and Design Principles*, 1st ed.; Vantage Press: New York, 1983; p 31.
- (261) Lewis, H.; Grun, C.; Salkind, A. *J. Power Sources* **1997**, *65*, 29.
- (262) Lewis, H.; Jackson, P.; Salkind, A.; Danko, T.; Bell, R. *J. Power Sources* **2001**, *96*, 128.
- (263) Danko, T. Properties of cellulose separators for alkaline secondary batteries. *Proceedings of the 10th Annual Battery Conference on Applications & Advances*; IEEE: New York, 1995; p 261.
- (264) Lewis, H. L.; Hammersley, V. L.; Wharton, S. P. NSW: evaluation of cellophane separation in model rechargeable silver-zinc cell. Presented at the 38th Power Sources Conference, Cherry Hill, NJ, 1998.

- (265) Lewis, H.; Henderson, S.; Danko, T. Separator composition evaluation in model rechargeable silver zinc cells. *Proceedings of the 16th Annual Battery Conference on Applications & Advances*; IEEE: New York, 2001.
- (266) Danko, T. Strength Properties of Separators in Alkaline Solutions. *Proceedings of the 11th Annual Battery Conference on Applications & Advances*; IEEE: New York, 1996; p 283.
- (267) Serenyl, R. *Proceedings of the 41st Power Sources Conference, Philadelphia, June 14–17, 2004*; 2004; p 465.
- (268) Megahed, E. A.; Davig, D. C. *Power Sources*; Academic: London, 1981; Vol. 8.
- (269) Lee, J.; Agostino, V. D.; Zapisek, S.; Freid, R.; Cannizzaro, J. *Membranes and Ionic and Electronic Conducting Polymers*; Yeager, E. B., Ed.; The Electrochemical Society Inc.: Pennington, NJ, 1983; p 245.
- (270) Drumm, J. J. British Patent 365,125, 1930.
- (271) Kishimoto, T.; Yamane, M.; Bogauchi, T.; Eguchi, Y. U.S. Patent 5,320,916, 1994.
- (272) Kishimoto, T.; Yamane, M.; Bogauchi, T.; Eguchi, Y. U.S. Patent 5,547,779, 1996.
- (273) McLarnon, F. R.; Cairns, E. J. *J. Electrochem. Soc.* **1991**, *138* (Feb).
- (274) McBreen, J.; Cairns, E. J. In *Advances in Electrochemistry & Electrochemical Engineering*; Gerischer, H., Tobias, C. W., Eds.; Wiley: New York, 1978; Vol. 11; pp 273–351.
- (275) Bennon, D. N. A review of membrane separators and Zinc–Nickel oxide battery development. Prepared for Argonne National Laboratory under Contract No. 31-109-38-5455, October 1980.
- (276) Lundquist, J. T. *J. Membr. Sci.* **1983**, *13*, 337.
- (277) Poa, D. S.; Cook, G. M.; Yao, N. P. ANL/OEPM-83–4. National Technical Information Service: 1983.
- (278) Wagner, C. A.; Almerini, A.; Smith, R. L. *Proceedings of the 29th International Power Sources Symposium*; The Electrochemical Society Inc.: Pennington, NJ, 1980.
- (279) Brown, R. A.; Cloyd, J. S. *Proceedings of the 29th International Power Sources Symposium*; The Electrochemical Society Inc.: Pennington, NJ, 1980.
- (280) Krejci, I.; Vanysek, P.; Trojaneck, A. *J. Electrochem. Soc.* **1993**, *140*, 2279.
- (281) *J. Power Sources* **1984**, *11*, 242–243.
- (282) Bugnet, B.; Doniat, D.; Rouget, R. *Proc. 40th Power Sources Conf.* **2002**, *10* (13), 535.
- (283) Sato, Y.; Kanda, M.; Niki, H.; Ueno, M.; Murata, K.; Shirogami, T.; Takamura, T. *J. Power Sources* **1983**, *9*, 147.
- (284) Chen, M.; Tsai, T. U.S. Patent 6,605,391, 2003.
- (285) Chen, M.; Li, L. F.; Tsai, T. U.S. Patent, 6,358,651, 2002.
- (286) Chen, M.; Cao, F.; Liang, L.; Tsai, T.; Faris, S. *Proc. 41st Power Sources Conf.* **2004**, 473.
- (287) Dewi, E. L.; Oyaizu, K.; Nishide, H.; Tsuchida, E. *J. Power Sources* **2003**, *115*, 149–152.
- (288) Schubert, M. A.; Myers, J. P.; Thrasher, G. T. Acrylic Acid–Sodium Styrene Sulfonated Copolymer Separator Coatings for Alkaline Electrolytes. Presented at the 202nd Meeting of the Electrochemical Society, Salt Lake City, UT.
- (289) Schubert, M. A.; Myers, J. P. *Proc. 41st Power Sources Conf.* **2004**, 122.
- (290) Will, F. G. *J. Electrochem. Soc.* **1979**, *126*, 36.
- (291) Bellows, R.; Einstein, H.; Grimes, P.; Kantner, E.; Malachuk, P.; Newby, K.; Tsein, H. Development of a Circulating Zn–Br₂ Battery Phase I. Final Report, Exxon Research and Engineering Company and Sandia National Laboratories, SAND82-7022, Jan 1983.
- (292) Cathro, K. J.; Constable, D. C.; Hoobin, P. M. *J. Power Sources* **1988**, *22*, 29–57.
- (293) Thaller, L. H. U.S. Patent 3,996,064, 1976.
- (294) Jorne, J. *Am. Sci.* **1983**, 71 507.
- (295) Sum, E.; Skyllas-Kazacos, M. *J. Power Sources* **1985**, *15*, 179.
- (296) Skyllas-Kazacos, M.; Grossmith, F. *J. Electrochem. Soc.* **1987**, *134*, 2950.
- (297) Wiedemann, E.; Heintz, A.; Lichtenthaler, R. N. *J. Membr. Sci.* **1998**, *141*, 207.
- (298) Skyllas-Kazacos, M.; Kasherman, D.; Hong, D. R.; Kazacos, M. *J. Power Sources* **1991**, *35*, 399.
- (299) Ohya, H.; Kawahara, T.; Kang, A. S.; Aihara, M.; Negishi, Y. *Denki Kagaku* **1994**, *62*, 863.
- (300) Hwang, G. H.; Ohya, H. *J. Membr. Sci.* **1997**, *132*, 55.
- (301) Hwang, G. J.; Ohya, H. *J. Membr. Sci.* **1996**, *120*, 55.
- (302) Chieng, S. C.; Kazacos, M.; Skyllas-Kazacos, M. *J. Power Sources* **1992**, *39*, 11.
- (303) Chieng, S. C.; Kazacos, M.; Skyllas-Kazacos, M. *J. Membr. Sci.* **1992**, *75*, 81.
- (304) Mohammadi, T.; Skyllas-Kazacos, M. *J. Membr. Sci.* **1995**, *98*, 77.
- (305) Mohammadi, T.; Skyllas-Kazacos, M. *J. Membr. Sci.* **1995**, *107*, 35.
- (306) Mohammadi, T.; Skyllas-Kazacos, M. *J. Power Sources* **1995**, *56*, 91.
- (307) Wiedemann, E.; Heintz, A.; Lichtenthaler, R. N. *J. Membr. Sci.* **1998**, *141*, 215.
- (308) Sukkar, T.; Kazacos, M. S. *J. Membr. Sci.* **2003**, *222*, 249.
- (309) Assink, R. A. *J. Membr. Sci.* **1984**, *17*, 205.
- (310) Arnold, C.; Assink, R. A. *J. Appl. Polym. Sci.* **1984**, *29*, 2318.
- (311) Hruska, L. W.; Savinell, R. F. *J. Electrochem. Soc.* **1981**, *128*, 18.
- (312) Newman, J.; Tiedemann, W. *AIChE J.* **1975**, *21*, 25.
- (313) Newman, J. S. *Electrochemical Systems*, 2nd ed.; Prentice Hall Inc.: Englewood Cliffs, NJ, 1991.
- (314) Vidts, P. D.; White, R. E. *J. Electrochem. Soc.* **1997**, *144*, 1343.
- (315) Ceder, G.; Doyle, M.; Arora, P.; Fuentes, Y. *MRS Bull.* **2002**, *27*, 619.
- (316) Newman, J.; Tiedemann, W. *J. Electrochem. Soc.* **1997**, *144*, 3081.
- (317) Gu, H.; Nguyen, T. V.; White, R. E. *J. Electrochem. Soc.* **1987**, *134*, 2953.
- (318) Vidts, P. D.; Delgado, J.; White, R. E. *J. Electrochem. Soc.* **1995**, *142*, 4006.
- (319) Doyle, M.; Fuller, T. F.; Newman, J. *J. Electrochem. Soc.* **1993**, *140*, 1526.
- (320) Fuller, T. F.; Doyle, M.; Newman, J. *J. Electrochem. Soc.* **1994**, *141*, 1.
- (321) Fan, D.; White, R. E. *J. Electrochem. Soc.* **1991**, *138*, 17.
- (322) Doyle, M.; Newman, J.; Gozdz, A. S.; Schumtz, C. N.; Tarascon, J. M. *J. Electrochem. Soc.* **1996**, *143*, 1890.
- (323) Arora, P.; Doyle, M.; Gozdz, A. S.; White, R. E.; Newman, J. *J. Power Sources* **2000**, *88*, 219.
- (324) Patel, K. K.; Paulsen, J. M.; Desilvestro, J. *J. Power Sources* **2003**, *122*, 144.
- (325) Tye, F. L. *J. Power Sources* **1983**, *9*, 89.
- (326) Mao, Z.; White, R. E. *J. Power Sources* **1993**, *43–44*, 181.
- (327) Denton, F.; Howard, J. N.; Anani, A. A.; Fernandez, J. M. U.S. Patent 6,228,516, 2001.
- (328) Mao, H.; Wainwright, U.S. Patent 6,074,766, 1990.
- (329) Thomas-Alyea, K. E.; Newman, J.; Chen, G.; Richardson, T. J. *J. Electrochem. Soc.* **2004**, *151*, A509.

CR020738U

Three-Dimensional Battery Architectures

Jeffrey W. Long,^{*,†} Bruce Dunn,^{*,‡} Debra R. Rolison,^{*,†} and Henry S. White^{*,§}

Surface Chemistry Branch, Code 6170, Naval Research Laboratory, Washington, DC 20375, Department of Materials Science and Engineering, UCLA, Los Angeles, California 90095, and Department of Chemistry, University of Utah, Salt Lake City, Utah 84112

Received December 4, 2003

Contents

1. Introduction	4463	5. Structural Characterization of 3-D Electrode Architectures	4478
1.1. Drivers for 3-D Power	4463	5.1. Characterization of the Pore–Solid Architecture	4478
1.2. What Do We Mean by 3-D?	4465	5.1.1. Physisorption	4479
2. Quantitative Advantages of 3-D Cell Architectures	4467	5.1.2. Small-Angle Scattering Techniques	4479
2.1. Overview of Length Scales in 3-D Battery Designs	4467	5.1.3. Electron Microscopy	4479
2.2. Quantifying the Advantages of 3-D Architectures	4467	5.1.4. Scanning Probe Microscopy	4480
2.3. Current Distribution in 3-D Batteries	4469	5.2. Corroboration of Electrochemical Processes with Spectroscopic Techniques	4481
2.3.1. Interdigitated Electrode Arrays	4469	6. Fabrication En Route to 3-D Integration of Architectural Components	4483
2.3.2. Plate, Tubule, and Aperiodic 3-D Architectures	4470	6.1. Micromachining	4483
2.4. Overall Design Issues	4470	6.1.1. Carbon MEMS (C-MEMS)	4483
2.5. Cathodes and Anodes Separated by Nanometer-Wide Electrolytes	4470	6.1.2. Micromachining of Silicon Molds	4484
3. Prior Examples of Small Power	4471	6.2. 3-D Fabrication Based on 2-D Structures: Origami	4485
3.1. Scope of Small Power	4471	7. Advances toward Integration of Active Components into a 3-D Battery	4486
3.2. Miniaturizing Microreactors and Fuel Cells	4471	7.1. Present Status	4486
3.2.1. Compact Mixed Reactors	4471	7.2. Electrodeposition of Dielectrics—Separators and Cation-Conductive Electrolytes	4486
3.2.2. Microfabrication Approaches for Small Power	4472	7.3. Hybrid Polymer–Aerogel Nanoarchitectures as Electrochemical Capacitors	4487
3.2.3. Membraneless Opportunities with Laminar Flow in Microfluidic Reactors	4472	7.4. Solid-State Electrical Characterization of Conformal, Ultrathin Polymer Dielectrics	4487
3.2.4. Power in Vivo and Biologically Derived	4472	7.5. Ultrathin Polymer Electrolyte—Leakage Currents	4488
3.3. Thin-Film Batteries	4473	7.6. Last Step: Add an Interpenetrating Anode	4488
3.4. Generating Power from Ambient Sources	4474	7.7. Packaging of 3-D Batteries	4489
3.5. Hybrid Micropower	4474	8. Conclusions	4489
4. Component Design for 3-D Battery Structures	4474	9. Acknowledgments	4489
4.1. Thinking Like Architects	4474	10. References	4489
4.2. Porous Membranes as Structure-Directing Templates	4475		
4.3. Template Synthesis of Ordered Macroporous Solids with Colloidal Crystals	4476		
4.4. Template Synthesis of Mesoporous Solids with Supramolecular Assemblies	4476		
4.5. Hierarchical Designs Based on Templating Strategies	4477		
4.6. Aerogels and Related Nanostructures—Aperiodic Pore–Solid Architectures	4478		

1. Introduction

1.1. Drivers for 3-D Power

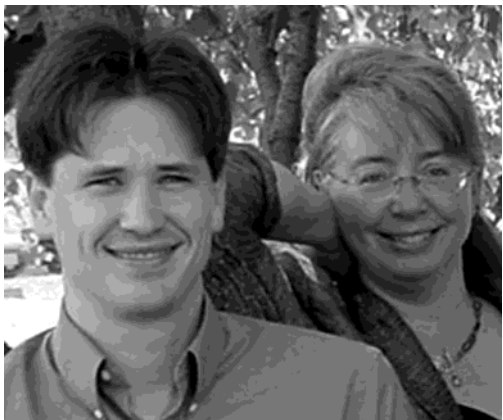
The worldwide thirst for portable consumer electronics in the 1990s had an enormous impact on portable power. Lithium ion batteries, in which lithium ions shuttle between an insertion cathode (e.g., LiCoO₂) and an insertion anode (e.g., carbon), emerged as the power source of choice for the high-performance rechargeable-battery market. The performance advantages were so significant that lithium ion batteries not only replaced Ni–Cd batteries but left the purported successor technology, nickel–metal hydride, in its wake.¹ The thick metal plates of

* To whom correspondence should be addressed. J.W.L.: e-mail, jwlong@ccs.nrl.navy.mil; telephone, (+1)202-404-8697. B.D.: e-mail, bdunn@ucla.edu; telephone, (+1)310-825-1519. D.R.R.: e-mail, rolison@nrl.navy.mil; telephone, (+1)202-767-3617. H.S.W.: e-mail, white@chem.utah.edu; telephone, (+1)810-585-6256.

† Naval Research Laboratory.

‡ UCLA.

§ University of Utah.



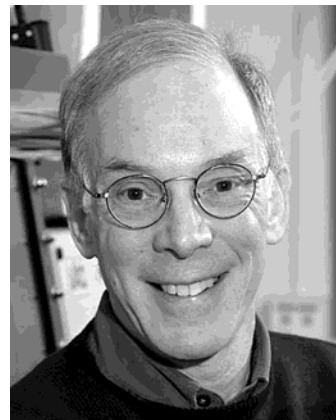
Jeffrey Long (left) was born in Great Falls, Montana in 1970, but he spent most of his early years in Winston-Salem, NC. He received a B.S. in Chemistry with Honors from Wake Forest University in 1992. Working with Prof. Royce Murray, he earned a Ph.D. in Chemistry from the University of North Carolina at Chapel Hill in 1997. His research focuses on nanostructured materials, particularly hybrid nanoarchitectures for applications in sensing, separations, and electrochemical energy storage and conversion.

Debra Rolison (right) was born in Sioux City, Iowa in 1954. She received a B.S. in Chemistry from Florida Atlantic University in 1975 and a Ph.D. in Chemistry from the University of North Carolina at Chapel Hill in 1980 under the direction of Prof. Royce W. Murray. She joined the Naval Research Laboratory as a research chemist in 1980 and currently heads the Advanced Electrochemical Materials section. She is also an Adjunct Professor of Chemistry at the University of Utah. Her research at the NRL focuses on multifunctional nanoarchitectures, with special emphasis on new nanostructured materials for catalytic chemistries, energy storage and conversion, biomolecular composites, porous magnets, and sensors.

traditional batteries gave way to lithium ion cells in which the anode, separator/electrolyte, and cathode were stacked, spiral wound, or folded.² Although the materials in today's batteries differ from those of the displaced technologies and the energy density of the electrochemical cell is decidedly larger, the basic two-dimensional (2-D) character and layer-by-layer construction of the cell remains intact. The next generation of lithium ion-polymer electrolyte batteries will offer improvements in gravimetric and volumetric energy densities (Wh g^{-1} and Wh L^{-1} , respectively), but the same configurations will prevail.³

Another massive market force is expected to develop over the next decade in the area generally known as microelectromechanical systems or MEMS.⁴ This field grew out of the integrated-circuits (IC) industry, and in less than a decade, MEMS devices successfully established high-volume commercial markets for accelerometers and pressure sensors in the automotive industry, ink-jet print heads, and digital micromirrors for image projection. By 2001, the global market for MEMS was nearly \$14 billion.⁵ Developments in the MEMS field seem to be continual, and MEMS devices are beginning to make significant contributions in new arenas, including fluidics, wireless communications, sensors, and optics.⁶⁻⁹ The rapid expansion of MEMS into new areas is due to the development of surface micromachining techniques, which involve photolithographic patterning, deposition, and selective etching of multilayered films to form device structures.¹⁰

There is tacit recognition that power is a vital issue for the continued development of the MEMS device



Bruce Dunn holds the Nippon Sheet Glass Chair in Materials Science & Engineering at UCLA. He received his B.S. at Rutgers University and his M.S. and Ph.D. degrees at UCLA. He was a staff scientist at the General Electric Corporate Research and Development Center before joining the UCLA faculty in 1980. His research interests concern the synthesis of ceramics and inorganic materials and characterization of their electrical, electrochemical, and optical properties. A continuing theme in his research is the use of sol-gel methods to synthesize materials that incorporate specific dopants and are capable of developing unique microstructures and properties. The areas presently being studied in his group include biosensors, intercalation compounds, aerogels, and organic/inorganic hybrid materials.



Henry White was born in Chapel Hill, North Carolina in 1956. He received a B.S. in Chemistry from the University of North Carolina in 1978 and a Ph.D. in Chemistry from the University of Texas at Austin in 1982. He held a postdoctoral appointment at the Massachusetts Institute of Technology from 1983 to 1984 and was on the faculty of the Department of Chemical Engineering and Materials Science at the University of Minnesota from 1984 to 1993. He is currently a Professor of Chemistry at the University of Utah. His research interests include magnetic-field-induced transport, oxide films and corrosion, iontophoretic transdermal drug delivery, and electrochemical phenomena at electrodes of nanometer dimensions.

field. In particular, the issue of how to power MEMS-based sensors and actuators has been largely neglected.¹¹ While a conventional macroscopic power supply could be employed for these devices, the prospect of powering arrays of micromachined sensors and actuators is likely to lead to interconnection problems, cross-talk, noise, and difficulty in controlling the power delivered. In contrast, the complexity of power delivery is reduced if one were to design the power supply to be of the same dimensional scale as the sensors and actuators. Specifically, site-specific power can be realized, and improvements in noise and power efficiency may be achieved.

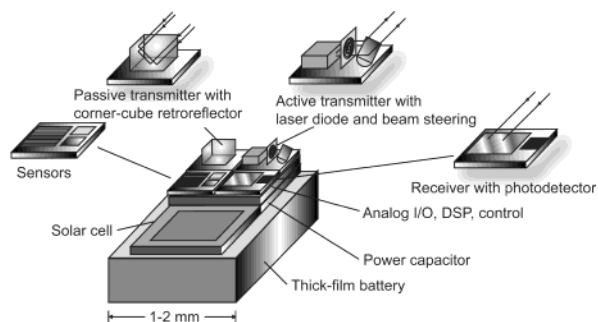


Figure 1. Smart dust mote and its components: Micro-fabricated sensors, optical receiver, signal-processing and control circuitry; the power source consists of a solar cell and a thick-film battery. (Derived with permission from ref 16. Copyright 2001 IEEE)

The power needs for MEMS devices are diverse—and batteries may not be the best choice to provide power to systems based on various types of MEMS drives. For example, magnetic drives operate at less than 1 V, but they require generating hundreds of milliamperes, which becomes a difficult challenge for batteries sized on the subcentimeter scale. The required micro- to nanoampere current levels for electrostatic and piezoelectric MEMS are feasible for batteries, but the tens to hundreds of volts that are needed will present difficulties for batteries with nominal voltages of 3 V. However, there may be a niche for batteries that would be used to power 10–15 V drives.

A more reasonable application for batteries is in the area of MEMS-based sensing. In one particularly exciting direction, batteries supply power to autonomous nodes, with each node containing one or more sensors, along with powering the computation and communication capabilities necessary to relay the findings of each node.¹² One approach, “smart dust”, represents an excellent example where integrated batteries may contribute; the basic device is shown in Figure 1. The device integrates into a single package, MEMS components (sensors, beam steering), optical communication components (optical receiver, semiconductor laser diode), signal-processing and control circuitry, and a power source based on batteries and solar cells, in a volume on the order of a cubic millimeter.

A calculation of the power requirements of the smart dust mote underscores our point that the present generation of batteries cannot effectively power this device. Thin-film batteries are among the most advanced of the lithium battery systems, with a capability to scale down to dimensions on the same order of magnitude as the cubic millimeter of the dust mote.¹³ The energy density for the thin-film system is $\sim 2 \text{ J mm}^{-3}$,¹⁴ which matches or exceeds standard lithium ion systems, such as those that power laptop computers. A key design requirement for the smart dust mote is that the power consumption cannot exceed $10 \mu\text{W}$. If the dust mote uses this power continuously over a day, it will consume $\sim 1 \text{ J}$.

Can a thin-film battery supply the 1 J per day of energy necessary to power a smart dust mote? At first glance, it would appear that there should be no problem; the device consumes 1 J mm^{-3} and the

battery is able to supply 2 J mm^{-3} . The reality, however, is that thin-film batteries are 2-D devices. Such batteries are necessarily thin in order to prevent power losses typically associated with the slow transport of ions, but a practical limitation arises from the fracture of cathode films that get too thick ($> 2 \mu\text{m}$), which leads to low capacity per square millimeter. With a typical device thickness on the order of $15 \mu\text{m}$, a thin-film battery requires a significant amount of area in order to supply 2 J mm^{-3} .

The real question becomes whether a thin-film battery can supply what the smart dust mote requires within the constraints of the areal “footprint” available for the battery on the smart dust mote—1 J of energy over 1 mm^2 of “real estate.” The traditional yardsticks by which battery energy and power are normalized are weight and volume [i.e., gravimetric and volumetric energy (and power) densities]. These metrics are no longer sufficient when one considers portable power for small devices: such devices have limited area available to integrate components into a system. For this reason it is important to establish the effective area of the power source, its footprint, and to normalize the available energy (and/or power) to this area.

The energy per unit area as reported for several lithium thin-film batteries ranges from 0.25 to $\sim 2 \times 10^{-2} \text{ J mm}^{-2}$.¹⁵ Thus, thin-film batteries, despite their excellent energy per unit volume, fall far short of being able to power a smart dust mote for 1 day. If the areal footprint were made 100 times larger (at 1 cm^2), the thin-film approach would be acceptable. The consequences of the 2-D nature of thin-film batteries are easily overlooked. The calculation by Koeneman et al. ignored the 2-D character of thin-film batteries when they concluded that these batteries could carry out some 60 000 actuations of a “smart bearing”.¹¹ When one considers the actual area available for the power source on the device, only about 1200 actuations are possible.

Smart dust motes are not just intriguing lab toys but successfully demonstrated devices.¹⁶ However, because of the inability to obtain scale-appropriate lithium ion batteries, the first devices tested were powered with hearing-aid batteries. The example of the smart dust mote illustrates a critical issue concerning all small power designs and their effective integration on-board the device. To power devices with limited real estate and maintain a small areal footprint, batteries must somehow make good use of thickness. Three-dimensional configurations offer a means to keep transport distances short and yet provide enough material such that the batteries can power MEMS devices for extended periods of time. The detailed calculations discussed in section 2 show that batteries configured as 3-D structures can readily achieve the 1 J mm^{-2} areal footprint required to power the smart dust mote.

1.2. What Do We Mean by 3-D?

Lithium ion batteries use insertion processes for both the positive and negative electrodes, leading to the term “rocking chair” battery.¹ The resulting transport of Li ions between the electrodes, usually

arranged in a parallel-plate configuration, is 1-D in nature. To minimize power losses resulting from slow transport of ions, the thickness of the insertion electrodes, as well as the separation distance between them, is kept as small as possible. This approach may appear counterintuitive in the effort to produce a useful battery, because reducing the thickness of the electrode results in lower energy capacity and shorter operating time. Thus, battery design always trades off between available energy and the ability to release this energy without internal power losses.

In recent years there has been the realization that improved battery performance can be achieved by reconfiguring the electrode materials currently employed in 2-D batteries into 3-D architectures. Some of the envisioned approaches are reviewed in more detail in section 2. The general strategy of this approach is to design cell structures that maximize power and energy density yet maintain short ion transport distances. While many possible architectures can achieve this goal, a defining characteristic of 3-D batteries is that transport between electrodes remains one-dimensional (or nearly so) at the microscopic level, while the electrodes are configured in complex geometries (i.e., nonplanar) in order to increase the energy density of the cell within the footprint area. A 3-D matrix of electrodes (in a periodic array or an aperiodic ensemble) is necessary to meet both the requirements of short transport lengths and large energy capacity. Improvements in energy per unit area and high-rate discharge capabilities are two of the benefits that may be realized for these 3-D cells.

Perhaps the most obvious 3-D design is that consisting of interdigitated electrodes shown in Figure 2a. This prototype configuration is used in modeling studies, the results of which are reviewed in section 2. The anode and cathode consist of arrays of rods separated by a continuous electrolyte phase. The spatial arrangement of the anode and cathode arrays determines the current–potential distribution. Clearly, the short transport distances lead to a much lower interelectrode ohmic resistance as compared to traditional planar battery configurations.

A central feature for the interdigitated configuration is that the arrays need to be periodic. A variation on this approach is to use interdigitated plates rather than rods (Figure 2b), which is analogous to stacking 2-D batteries with parallel connection.

There is no particular reason that the electrolyte must serve as the continuous phase in 3-D battery architectures. Another 3-D design utilizes a concentric arrangement where the rod array is composed of one of the active electrode materials and is then coated by an electrolyte layer. The other electrode material then fills the remaining free volume and serves as the continuous phase, as shown in Figure 2c. As was discussed for the above battery configurations, short transport distances between the insertion electrodes lead to low ohmic resistance. Although a periodic arrangement is shown in Figure 2c, it is not clear at the present time whether this is beneficial or not with respect to the current–potential distribution. Relaxing the periodicity condition may be an

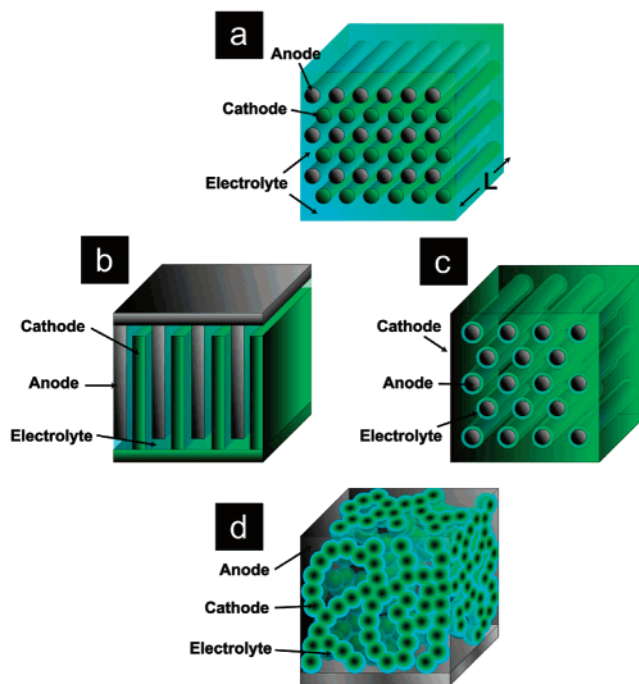


Figure 2. Examples of prospective 3-D architectures for charge-insertion batteries: (a) array of interdigitated cylindrical cathodes and anodes; (b) interdigitated plate array of cathodes and anodes; (c) rod array of cylindrical anodes coated with a thin layer of ion-conducting dielectric (electrolyte) with the remaining free volume filled with the cathode material; (d) aperiodic “sponge” architectures in which the solid network of the sponge serves as the charge-insertion cathode, which is coated with an ultrathin layer of ion-conducting dielectric (electrolyte), and the remaining free volume is filled with an interpenetrating, continuous anode.

important consideration, because prospective synthetic techniques, such as templating through mesoporous membranes, do not necessarily produce periodic arrays.

A completely aperiodic 3-D battery configuration is the “sponge” approach, where the electrolyte layer is formed around a random 3-D network of electrode material (Figure 2d). This design strategy also represents a concentric configuration in that the electrolyte envelops the electrode material while the other electrode material fills the mesoporous and macroporous spaces and surrounds the electrolyte. Short transport-path characteristics between the insertion electrodes are preserved with this arrangement. In contrast to the other 3-D designs, all battery components— anode, cathode, and electrolyte—are continuous throughout the sponge structure.

The above discussion provides the context for 3-D batteries. That is, there are a variety of small power applications, typified by MEMS devices, which the most advanced, 2-D lithium battery systems are unable to satisfy. The inability to provide sufficient power is because of configuration and not because of intrinsic energy density. Three-dimensional designs offer the opportunity to achieve milliwatt-hour energies in cubic millimeter packages and, more importantly, with square millimeter footprints. While such power sources may not influence the enormous commercial markets in cell phones and laptop computers, they are certain to impact emerging markets where

integrated power is required for communication, sensing, and networking.

This paper discusses the prospects for creating 3-D architectures for batteries. We next introduce calculations for the 3-D interdigitated array battery (Figure 2a), which will illustrate the design considerations under which the 3-D configuration leads to better performance than the conventional 2-D one. Other sections then discuss the prior art in small power, followed by the materials, synthetic, and fabrication approaches required to achieve 3-D designs. Finally, we review the present status of the systems most likely to demonstrate true 3-D battery operation.

2. Quantitative Advantages of 3-D Cell Architectures

2.1. Overview of Length Scales in 3-D Battery Designs

The four architectures introduced in Figure 2 have wide-ranging length scales and geometries that are largely dictated by their respective methods of fabrication. These length scales and geometries will determine the performance characteristics of 3-D batteries based on these architectures. Thus, before attempting to quantify some of the advantages (as well as the disadvantages) of 3-D cells, a brief overview is presented of the methods of fabrication currently employed, with emphasis on the resulting geometrical and scale differences. Detailed descriptions of the fabrication procedures are presented in section 4.

At present, only the individual component arrays (i.e., individual cathode or anode arrays) of the periodic interdigitated electrode cell (Figure 2a) have been fabricated using lithographic methods. The results of these limited efforts, however, provide a rough guide to what is possible in battery design within the microlithographic laboratory. Typically, the electrodes are cylindrical rods with diameters ranging from 5 to 100 μm and lengths from 10 to 200 μm . For instance, Madou and co-workers have fabricated an array of cylindrical carbon electrodes with $\sim 10\text{-}\mu\text{m}$ diameter and $\sim 200\text{-}\mu\text{m}$ length.¹⁷ Lithographic fabrication methods also allow other geometries beyond cylinders to be considered (e.g., triangular rods). It is most probable that the use of current lithographic methods will continue to yield structures with lateral dimensions (i.e., electrode diameter and electrode-to-electrode spacing) on the micrometer length scales, with more emphasis placed on increasing the length of the electrode, L , to achieve high aspect ratios. This strategy yields the high areal energy capacity that drives the interest in 3-D designs (vide infra). Other periodic arrays, such as those based on the use of origami to “unfold” an array of lithographically designed cathodes and anodes on a base support¹⁸ and of arrays of plates (Figure 2b), are also envisioned at the micrometer length scale. Smaller lateral dimensions will likely be obtained in the future with advances in lithographic methods.

One disadvantage of all periodic interdigitated electrode cells is that the primary current distribu-

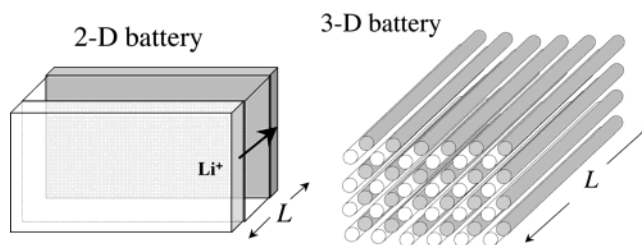


Figure 3. 2-D parallel-plate and 3-D interdigitated-array batteries.

tion is nonuniform.¹⁹ This nonuniformity can be readily recognized by inspection of Figure 2a and realizing that the distance between the anodes and cathodes is variable along the circumference on any individual electrode. A quantitative description of this issue is discussed below.

The concentric tubule arrays and aperiodic continuous sponge architectures are based on *conformal deposition methods*, in which layers of electrolyte and/or electrode materials are sequentially^{20–23} or simultaneously assembled within an array of pores in a membrane (Figure 2c) or in an aperiodic array (Figure 2d). Film deposition methods (see section 7) can yield electrode and electrolyte films of nanometer thicknesses, and in fact, a prototype of the aperiodic architecture has been recently reported.^{20–23} Thus it is possible to envision batteries soon in which the cathode and anode are separated by 10 nm. However, at these distances, the physical structure of the interface must be exceedingly stable to prevent shorting of the electrodes. In addition, electrostatic interactions between the cathode and anode (i.e., “overlapping” double layers) and exceedingly fast transport rates within the separator will undoubtedly influence the current–voltage curves in complex ways that are just now being investigated.²⁴ One key advantage of these 3-D architectures (and unlike the periodic interdigitated array) is that the current density across the electrode surfaces is uniform.

2.2. Quantifying the Advantages of 3-D Architectures

As discussed in section 1, the key advantage associated with the proposed 3-D battery structures is the ability to achieve large areal energy capacities without making sacrifices in power density that may result from slow interfacial kinetics (associated with a small electrode area-to-volume ratio) and/or ohmic potential losses (associated with long transport distances). This argument is now quantitatively demonstrated in the following paragraphs for the 3-D interdigitated electrode array shown in Figure 2a.

To facilitate a demonstration of the advantages of the 3-D architecture, we quantitatively compare metrics related to performance (e.g., areal energy capacity, active surface area) of a conventional 2-D parallel-plate design with the 3-D interdigitated array cell (Figure 3). We assume a thin-film 2-D battery that comprises a 1-cm²-area anode and cathode, each 22.5- μm -thick and separated by a 5- μm -thick electrolyte. The total volume of electrodes and separator is $5 \times 10^{-3} \text{ cm}^3$ (the cell housing is ignored for simplicity, but is expected to be a comparable

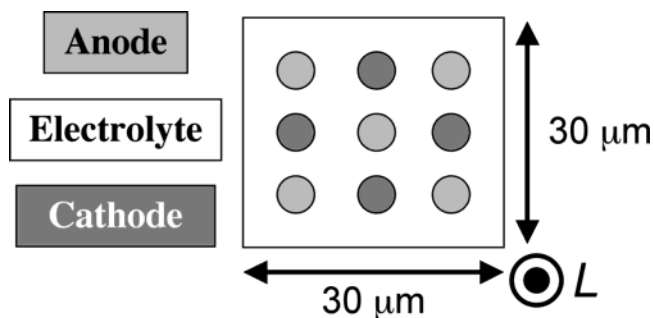


Figure 4. Square array of interdigitated anodes and cathodes.

percentage of the total volume in both 2-D and 3-D designs).

It is relatively straightforward to show that a corresponding 3-D square-array battery (Figure 4) with the same total volume (i.e., $5 \times 10^{-3} \text{ cm}^3$), constructed from $5\text{-}\mu\text{m}$ -radius cathode and anodes that are separated (center to center) by $10 \mu\text{m}$, contains $\sim 39\%$ of the energy capacity of the thin-film design. Clearly, the lower energy capacity is due to a higher percentage of the total volume being occupied by the electrolyte. While the energy capacity of the 3-D design varies with the shape and arrangement of the electrodes, it will always be lower than that of the 2-D design for equal total volumes.

There are several intriguing advantages of the 3-D design that are not reflected in the above numbers. For instance, the active cathode and anode surface areas in the 3-D design are 3.5 cm^2 each, significantly larger than the 2-D design (1 cm^2). This difference favors the 3-D design through a reduction in interfacial kinetic overpotential, which is inversely proportional to the electrode area. In addition, the distance that ions must be transported in discharging the 2-D battery is 350% larger than in the 3-D design. Thus, in principle, the 3-D design is significantly less susceptible to ohmic losses and other transport limitations. To achieve equal transport length scales in the 2-D design (i.e., by decreasing the electrode thickness to $5 \mu\text{m}$) would require a 330% increase in the areal footprint in order to maintain equal cell volume, a significant disadvantage in employing these devices in MEMS and microelectronic applications.

While the above comparison of 2-D and 3-D designs indicates that the 3-D battery has inherently lower energy capacity per total cell volume, in fact, the capacity of the 3-D design can be increased without limit by increasing L , without sacrificing the small areal footprint or high power density. As shown in Figure 5, for the same areal footprint, i.e., 1 cm^2 , the above square array 3-D design with $L = 500 \mu\text{m}$ has a capacity that is 350% larger than the 2-D design. Such a microbattery would contain 222 222 cathodes and 222 222 anodes, with $\sim 35 \text{ cm}^2$ each of active cathode and anode area!

Clearly L cannot be increased without limit, as the ohmic resistance of the electrodes will become sufficiently large to offset the advantages of increased areal capacity. While this problem has not been treated systematically, it is clear that the optimized value of L will be determined by the electronic

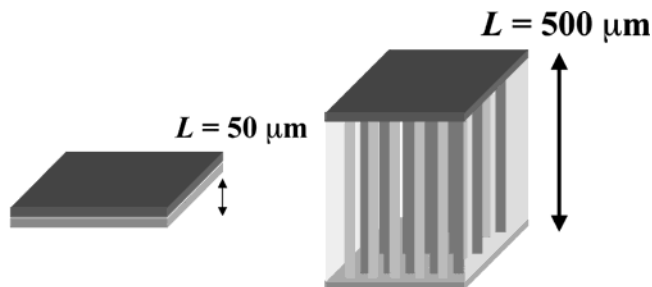


Figure 5. An increase in the height of the interdigitated 3-D battery, L , results in increased areal energy capacity and electrode area, without an increase in transport distances.

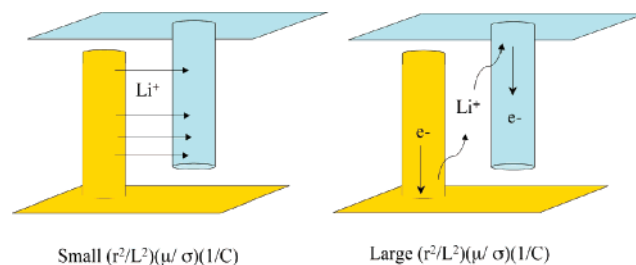


Figure 6. Dependence of electrode utilization on electrode conductivity (σ) and ion diffusivity (D). L and r are the length and radius of the electrodes, respectively.

conductivity of the electrode materials (σ) and the ionic conductivity of the electrodes and electrolyte, in addition to the electrode geometry, as indicated in Figure 6.

The dimensionless number $U = (r^2/L^2)(\mu/\sigma)(1/C)$, where r is the radius of the electrode, μ is ionic mobility of cations (Li^+), and C is the volumetric energy capacity (C/cm^3), is a quantitative measure of uniformity of current across the 3-D electrode surfaces and, thus, whether the electrode material is uniformly utilized during cell charging and discharging. Decreasing U corresponds to a more uniform current distribution along the length of the electrode. This scenario is a desired one, as long as the decrease in U results from high electronic conductivity in the electrodes (i.e., large σ), rather than low ionic conductivity in the electrolyte (i.e., small μ). Increasing U corresponds to a more nonuniform discharge of the electrodes, which may result in underutilization of the electrode materials during rapid discharge, as well as increasing stress along the length of the electrodes. Similarly, $U = (w^2/h^2)(\mu/\sigma)(1/C)$ for a rectangular electrode in the interdigitated plate design (Figure 2b), where w is the electrode thickness and h is the electrode height measured from the base. Clearly, numerical values of U will depend on electrode geometry and materials.

The arguments developed in this section apply to all of the potential 3-D designs shown in Figure 2. In each design, an increase in areal energy capacity can be obtained by simply increasing L , without any loss of power density due to interfacial kinetics or slow ion transport. Similar to the interdigitated array cell, this advantage is eventually limited by the electronic conductivity of the electrode materials.

It is worth noting that the 3-D interdigitated plate design of Figure 2b can be realized by stacking 2-D

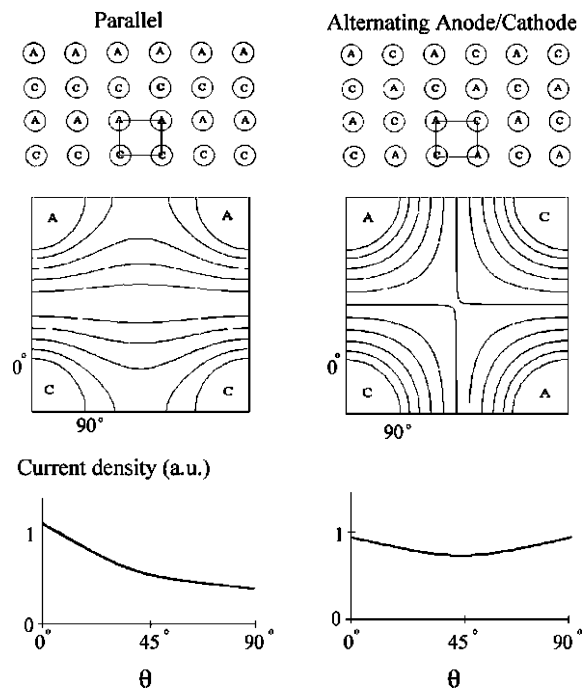


Figure 7. Top panels: Schematic diagram of 3-D cylindrical battery arrays in parallel row (left) and alternating anode/cathode (right) configurations. Middle panels: Isopotential lines between cathode (C) and anode (A) for unit battery cells. Bottom panel: Current densities (in arbitrary units, a.u.) at the electrode surfaces as a function of the angle θ (see middle panel for definition of θ). The area of the cathodes and anodes is equal throughout the diagram. (Reprinted with permission from ref 19. Copyright 2003 Elsevier.)

thin-film batteries. However, to maintain the key advantage of low ohmic potential losses, it is necessary for the thickness of the film electrodes to be greatly reduced. Currently, low-cost manufacturing techniques limit film electrodes to thicknesses greater than about $\sim 20 \mu\text{m}$.

2.3. Current Distribution in 3-D Batteries

2.3.1. Interdigitated Electrode Arrays

All interdigitated electrode arrays suffer from a nonuniform primary current distribution. Figures 7 and 8 show examples of the potential and primary current distributions for representative interdigitated microbattery designs, computed using finite element simulation,²⁵ with the assumption of a uniform electrolyte conductivity. To allow comparison of the current densities between different battery designs, all simulations assume identical values of the voltage between cathode and anode. Current densities are plotted in the same arbitrary units in each figure, allowing direct comparison of the relative power output of different interdigitated geometries. Isopotential lines within the “unit cell” of each interdigitated design are also presented. The lengths of the cathodes and anodes, L , are assumed to be sufficiently long to ignore end effects.¹⁹

Figure 7 illustrates the sensitivity of the current distribution to electrode placement for two similar interdigitated designs. In the parallel row design, alternating rows of cylindrically shaped cathodes and

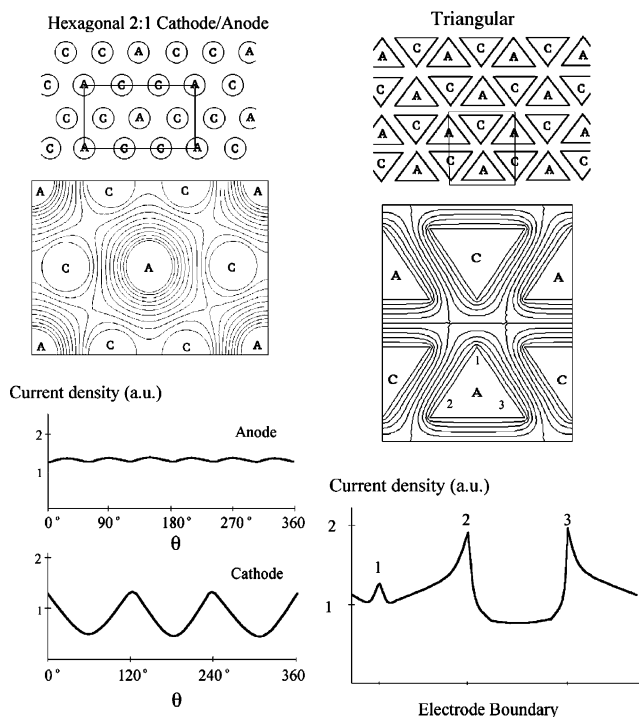


Figure 8. (Top panel, left) Schematic diagram of hexagonal 2:1 cathode/anode battery array. (Top panel, right) Schematic diagram of triangular battery array. (Middle panel) Isopotential lines between cathode (C) and anode (A) for unit battery cell. (Bottom panel) Current density at the cathode and anode surfaces, plotted on the same a.u. scale used in Figure 7. (Reprinted with permission from ref 19. Copyright 2003 Elsevier.)

anodes are placed on a rectangular grid. This arrangement of electrodes results in high current flow between each neighboring cathode/anode pair (i.e., at $\theta = 0^\circ$), with a relatively steep decrease ($\sim 40\%$) in current between adjacent cathodes or anodes ($\theta = 90^\circ$).

A significantly better design based on the rectangular grid is the alternating cathode/anode configuration in which each anode is surrounded by four nearest neighbor cathodes (and vice versa). In this geometry, the higher number of nearest neighbor electrodes of opposite polarity permits a significantly more uniform primary current density at each electrode. However, even in this improved geometry, the current varies by 20% along the electrode circumference, a limitation that may not be tolerable in some cells. The primary current uniformity may be improved by increasing the ratio of the electrode grid spacing to the electrode radius in this cell, but at the sake of reducing power density.

Unlike the conventional battery, a 3-D interdigitated array need not contain equal numbers of anodes and cathodes. Indeed, there may be situations where battery design is optimized by using unequal number densities of cathodes and anodes in order to balance the capacities of the active materials and the kinetics of the charge-transfer reactions. The left-hand side of Figure 8 shows an example of an interdigitated design utilizing twice as many cathodes as anodes. Here, each anode is surrounded by six cathodes, providing a relatively uniform current density on the anode while sacrificing current uniformity at the

cathodes. This design might be useful in a 3-D microbattery where a uniform current density is critical at one electrode (e.g., an insertion electrode).

Modern microlithography allows for the fabrication of essentially any envisioned electrode and cell geometry. Specifically, electrodes need not have the cylindrical shape considered in the previous examples. For example, the close-packed array of triangular cathodes and anodes shown on the right-hand side of Figure 8 would be expected to yield greater cell capacity and increased power. The tradeoff of this design, obviously, is the highly nonuniform primary current. Such a geometry may be appropriate in a situation where the net current is limited by electron-transfer kinetics, and thus the current distribution is uniform across the electrode surface regardless of the electrode geometry.

It is clear that while significant increases in both power and areal energy capacity are obtainable from 3-D interdigitated arrays relative to conventional 2-D batteries, the inherent difficulty in achieving a uniform current distribution may limit some devices. However, interdigitated electrode geometries and configurations not considered above are likely to yield current distributions significantly better than the examples described here.

2.3.2. Plate, Tubule, and Aperiodic 3-D Architectures

The issue of the nonuniform current density is not important for the plate, tubule, and aperiodic architectures shown in Figure 2. The current density in these architectures will be perfectly uniform due to the 1-D nature of transport between anode and cathode. Radial transport occurs in the tubular and aperiodic architecture, while planar transport is operative in the plate architecture (neglecting end effects).

2.4. Overall Design Issues

Modeling the overall current–voltage behavior of 3-D cells is a complex function that depends on many factors (ionic and electronic conductances, interfacial reaction kinetics, charge capacity, etc.). Because of the wide range of possible (and mostly unexplored) architectures, this will be a rich field of study for electrochemical engineers and will likely lead to new design concepts in battery technology. Interdigitated electrode arrays are highly susceptible to stress due to both the nonuniform current density and finite electronic conductivity of the electrodes. Thus, a delicate balance of the geometrical length scales (electrode radius and length, and the spacing between electrodes) and materials properties will be required in optimizing any 3-D battery.

2.5. Cathodes and Anodes Separated by Nanometer-Wide Electrolytes

As noted in section 3.1, the fabrication of cells in which the cathode and anode are separated by a conformal thin-film electrolyte, perhaps a few tens of nanometers in thickness, is on the near horizon. Thus, it is interesting to consider potential phenomena, not normally considered in battery design, that

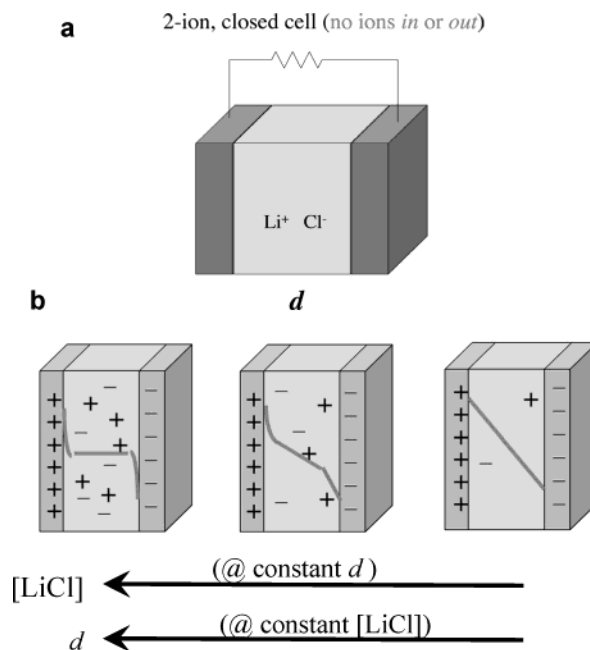


Figure 9. (a) Schematic of a closed cell containing LiCl. The number of ions (Li⁺ and Cl⁻) is assumed to be constant. (b) The dependence of the potential profile across the two-ion cell as a function of the electrolyte thickness, *d*, and ion concentration.

will be operative when the electrodes are placed in such close proximity to one another.

For simplicity, we consider a closed cell such as that shown in Figure 9a, which contains LiCl as the electrolyte. Assuming that the cathode and anode are separated by 10 nm (an experimentally achieved separation distance), it is instructive to first consider any direct physical or chemical interactions between the electrodes. Clearly at 10 nm, electron tunneling between the surfaces will be negligibly slow, the decay length of tunneling being ca. 1 Å.²⁶ Thus, the electrodes are not *electronically* coupled, and normal redox reactions at the cathode and anode are still necessary for battery operation. At shorter distances, e.g., 1 nm, the electrodes would spontaneously discharge via direct tunneling between the cathode and anode, a process equivalent to shorting the battery. Thus, there is a theoretical lower limit on the thickness of the battery separator.

Although the cathode and anode are not in electronic communication at 10 nm, their presence is known to each other through the electrical fields that originate from their respective surface charges. As shown in Figure 9b, the overlap of the electrical double layers is more significant as either the distance between the electrodes, *d*, is reduced or the concentration of the electrolyte is decreased. The role of the electrolyte concentration is quantitatively expressed through the Debye length, κ^{-1} ,²⁶ which can be estimated for a 1:1 electrolyte at room temperature using the expression, κ^{-1} (nm) $\sim 0.3/[LiCl]^{1/2}$, where [LiCl] is the molar concentration (M) of the electrolyte. In essence, κ^{-1} represents how well the electrolyte shields the solution interior from the electrical charge of the electrode surfaces. A 1 M LiCl solution corresponds to $\kappa^{-1} = 0.3$ nm, while a 10 mM solution corresponds to a κ^{-1} of 3 nm. As a rule of thumb, the

electric potential drops to about 5% of its surface value at a distance from the surface of $\sim 3\kappa^{-1}$ (i.e., ~ 9 nm in a 10 mM LiCl solution). Thus, two electrodes separated by 10 nm in a 10 mM LiCl solution will clearly be in *electrostatic* contact through their overlapping double layers.

The consequence of overlapping double layers on battery operation has only been recently considered, and our understanding of this effect is rudimentary.²⁴ The electric fields will almost certainly have an effect on the transport of ions through the electrolyte, as migration will be important in the strong fields of the double layers, which can approach or exceed 10^6 V cm⁻¹. Whether transport of Li⁺ is impeded or enhanced by the field will depend on signs of the electrode charges (determined by the potentials of zero charge, an ill-defined quantity for most battery electrode materials) and whether the battery is being charged or discharged. Modeling of this phenomenon requires a simultaneous consideration of transport (e.g., Nernst–Planck equation), electrostatics (Poisson equation), and statistical thermodynamics (Boltzmann equation), similar to recent modeling of the influence of double-layer structure on transport at individual nanometer-scale electrodes²⁷ and Levich's treatment of the dynamic diffuse layer at macroscopic planar electrodes.²⁸

At small electrode separations, the *number* of ions in the electrolyte between the electrodes is quite small. For instance, the average nearest neighbor distance between cations in 10 mM LiCl solution is ~ 2 nm. Thus, on average, only a few Li⁺ ions are located between cathode and anode at any position on the electrode surfaces, and these few ions carry the current at that surface position. The number of ions is so small in this situation that the battery can be well described as a capacitor, with the separator being a nonionic dielectric material, resulting in a linear potential drop between the electrodes (Figure 9b). In addition, even if migration from the electrical double layers is neglected, the small separation distance between the electrodes will result in enormous diffusional fluxes. If sufficiently high, these fluxes can lead to breakdown of electroneutrality and formation of a space-charge layer in the electrolyte.²⁷ Much effort in the future will be required to explore and quantify these ideas.

3. Prior Examples of Small Power

3.1. Scope of Small Power

The development of small power sources for portable electronics goes well beyond miniaturization of batteries and fuel cells.⁴ Other approaches under development include miniaturizing combustion engines and thermoelectrics and harvesting energy from ambient sources such as vibration and temperature differences. Most of these approaches are directed at consumer products and are not designed to save real estate. Nonetheless, it is apparent that decreasing the size of power sources and moving to micro- and even nanoscale power sources offers a number of opportunities.²⁹

Table 1 lists examples of electron-producing power

Table 1. Types of Electron-Producing Power Sources

electrochemical	thermal/nuclear/ mechanical-to-electric
batteries	thermoelectrics
fuel cells, biofuel cells, semi-fuel cells	pyroelectrics
supercapacitors, ultracapacitors	thermionics
photovoltaics	β -cells (nuclear "solar" cells)
harvesting adventitious energy/fuel	harvesting adventitious energy/work
	radioisotope thermoelectric generators (RTGs)— α - or β -emitting nuclear sources

sources, not all of which are electrochemical. The importance of integrating nanotechnology to improve these power sources has been discussed, especially for portable applications.³⁰ Some of these sources are described in greater detail in this section and emphasize those approaches that have demonstrated power production in centimeter dimensions or smaller sizes. The hybrid micropower supplies discussed at the end of this section begin to address the issue of achieving energy and power capabilities in small footprint areas.

3.2. Miniaturizing Microreactors and Fuel Cells

Miniaturization of electrochemical power sources, in particular batteries and fuel cells, has been described as a critical—but missing—component in transitioning from in-lab capability to the freedom of autonomous devices and systems.^{29,30} In top-down approaches, macroscopic power sources are scaled to the microlevel usually by the use of fabrication methods, often in combination with new materials. Power generation schemes that can themselves be microfabricated are particularly appealing, as they can lead to a one-stop fabrication of device/machine function with an integrated power source.

3.2.1. Compact Mixed Reactors

One miniaturization challenge common to fuel cells and batteries—and of critical relevance in designing microscopically and nanoscopically featured 3-D batteries—is scaling down the phase that separates the anode from the cathode. The separator must prevent direct electronic contact yet permit electrical contact (ion flux) between the active electrodes. Electrodes in rechargeable batteries can undergo morphological changes that compromise the integrity of the whole cell, e.g., by establishing a direct electronic path (hard shorts), such as the metal needles that grow off of a charged–discharged zinc electrode and may pierce the separator (glass, polymer, paper) with potentially pyrophoric consequences (one reason the alkaline cell is a primary, use-once, cell).

Fabrication issues can arise when thinning the separator material or in trying to ensure high-quality, preferably pinhole-free coverage of dimensionally scaled-down anodes and cathodes. One strategy that can be used to avoid fabricating a separator at all, at least in electrolyzers and fuel cells, takes advantage of decades of work in compact mixed

reactors (CMR), where the specificity of electrocatalyzed active electrodes permits intermixing of reactants (or fuel/oxidant).³¹ The catalytic specificity bypasses the need for a physical barrier, as long as the electrodes are electronically isolated. Another engineering design feature of these single-chamber systems is the hydrodynamic flow of the molecular reactants.

In 1990, Dyer applied the CMR concept of hydrodynamic control of mixed reactant flow to a thin-film planar fuel cell.³² The electrical (i.e., ionic) contact between the fuel cell anode and cathode was maintained by diffusion across/through a hydrous aluminum oxide film (≤ 50 -nm-thick) sandwiched between the electrocatalytic electrodes, with the top Pt electrode deposited so as to be sufficiently porous for gases to pass through to the alumina membrane. The specific areal power that was generated with a mixed H_2/O_2 flow was $1\text{--}5\text{ mW cm}^{-2}$ at a cell voltage of 950 mV. By using a lightweight substrate (Kapton) onto which the Pt electrodes and hydrous alumina interlayer were deposited as thin films, a power density of 100 W kg^{-1} was reported. Similar results were obtained upon replacing the hydrous alumina membrane with the proton-exchange polymer membrane Nafion, raising the possibility of fabricating conformal, "open-face" fuel cells on a flexible substrate.

3.2.2. Microfabrication Approaches for Small Power

The nickel–zinc battery provides a good example of how macroscopic power sources can be miniaturized via microfabrication methods. A patterned, side-by-side configuration was fabricated with an electroplated zinc anode and a NiOOH cathode (total cell area of 1 to 5 mm^2).³³ A photosensitive epoxy served as the separator and was also used to define the side walls of the cell. The open-circuit voltage of the cells was 1.7–1.8 V. The energy density reported for these Ni–Zn microbatteries (2 J cm^{-2} at 50 mA discharge) is similar to that available with thin-film batteries, although the performance does not achieve the targeted energy density of 1 J mm^{-2} .¹³ The cells do generate reasonable power levels: at a 1 mA discharge rate, the 2-mm^2 cells generate 1–2 mW. As discussed in section 3.5, the Ni–Zn battery is feasible as the energy-storage component in a hybrid micropower system.

Fuel cells incorporating lithographic methods and masking/deposition/etching protocols have been fabricated on Si wafers and thereby satisfy two critical needs in a standard fuel cell: collection of electrons (current collectors) and controlling the flow field of fuel and oxidant.³⁴ Kelley et al. produced a miniature direct methanol fuel cell (DMFC) with a current–voltage and fuel utilization performance that matched standard-sized DMFCs prepared in-lab.^{35,36} A working volume for the miniature DMFC of 12 mm^3 was reported, with an operational performance of 822 W h kg^{-1} at $70\text{ }^\circ\text{C}$.³⁵

In more recent reports, a thin-film fuel cell sandwiched between two silicon wafers that had been anisotropically etched to form feed holes and channels for the reactants (H_2 and O_2) demonstrated a stable voltage of 0.75 V over 300 h at a current

demand of 100 mA cm^{-2} .³⁷ The electrode footprint, which was smaller than the silicon wafers, was $22.5\text{ mm} \times 22.5\text{ mm}$. The same authors have also adapted silicon micromachining to fabricate a twin fuel-cell stack³⁸ using a previously described flip-flop structure sandwiched between silicon wafers again acting as current collectors and flow distributors.³⁴

Wainwright et al. recently microfabricated a polymer-based fuel cell with on-board hydrogen storage. One of the key goals of this work is to provide independent sizing of power and energy capacity in a passive system requiring no fans, pumps, or external humidification.³⁹ The first performance reported was for a device built on a ceramic substrate (alumina), but devices built on silicon and polymeric substrates are also mentioned. The microfabricated fuel-cell block is coupled to a metal–hydride storage block, printed with inks of $\text{LaAl}_{0.3}\text{Ni}_{4.7}$, which generates hydrogen by desorption when placing a 20 mA load on the fuel cell.³⁹

3.2.3. Membraneless Opportunities with Laminar Flow in Microfluidic Reactors

One way to ease any difficulties that may arise in fabricating a membrane, especially in design configurations that are not planar, is to go membraneless. Recent reports take advantage of the laminar flow innate to microfluidic reactors^{40–42} to develop membraneless fuel cells. The potential of the fuel cell is established at the boundary between parallel (channel) flows of the two fluids customarily compartmentalized in the fuel cell as fuel (anolyte) and oxidant (catholyte). Adapting prior redox fuel cell chemistry using a catholyte of $\text{V}^{\text{V}}/\text{V}^{\text{IV}}$ and an anolyte of $\text{V}^{\text{III}}/\text{V}^{\text{II}}$,⁴³ Ferrigno et al. obtained 35 mA cm^{-2} at 1.1 V (for a power density of 38 mW cm^{-2}) at a linear flow rate of 12.5 cm s^{-1} ,^{44,45} which was comparable to that seen with the standard redox fuel cell reported by Kummer and Oei;⁴³ the fuel utilization was, however, much lower. Luo et al. adapted the enzyme-catalyzed redox that powers biofuel cells to create a membraneless microfluidic fuel cell using a molecular fuel (1,4-dihydrobenzoquinone) and a laccase-catalyzed cathode to reduce molecular oxygen. The maximum power density reported was $80\text{ }\mu\text{A cm}^{-2}$ at 150 mV ($8.3\text{ }\mu\text{W cm}^{-2}$) and a linear flow rate of 1 cm s^{-1} , but the cell could sustain 0.35 V at lower current densities.⁴⁶

3.2.4. Power in Vivo and Biologically Derived

One area in which miniaturization has progressed beyond the size regime of interest to the laptop and cellular telephone industry is to provide in vivo power in biomedical applications.⁴⁷ An implantable defibrillator battery, which must provide pulse power (on demand) with high energy density, was achieved by coupling two smaller batteries (Li/MnO_2 primary battery plus a Li/iodine cell) with a packaged volume on the order of 10 mL.⁴⁸ Such power sources must have low self-discharge rates.

In an effort to use biological energy transduction to miniaturize a biofuel cell for in vivo applications, Heller and co-workers have created membraneless, caseless cells that can function under physiological

conditions.^{49–54} The current collectors are microfibers of carbon that are catalyzed with enzymes to oxidize glucose (via glucose oxidase) and reduce O_2 (laccase or bilirubin oxidase) and wired to their respective carbon current collectors with osmium-based redox polymers. The active area of the most recent miniature biofuel cell is 0.44 mm^2 , and this glucose oxidase/laccase-catalyzed biofuel cell produced 0.78 V in a pH 5 buffer at a power density of $2.68 \mu\text{W mm}^{-2}$.⁵³ The improved cell voltage was obtained by using an osmium redox polymer with a more reducing potential, which lowered the overvoltage necessary to drive the coupled enzyme/cofactor redox to convert the glucose fuel to gluconolactone.

Recently a new hybrid power source has been reported that couples oxidation at a dye-photosensitized nanocrystalline semiconducting SnO_2 photoanode with the enzyme-catalyzed reduction of O_2 .⁵⁵ Although miniaturization has not yet been reported for this new hybrid, the developments already achieved to miniaturize biofuel cells coupled to those being developed for charge-insertion oxides should be technically transferable to this system.

3.3. Thin-Film Batteries

Miniaturization of batteries has been an active area of industrial research because of the need for portable power sources for such items as watches, hearing aids, and cameras. These miniaturization approaches are based, for the most part, on traditional battery manufacturing, and it is only within the past decade that researchers have begun to employ fabrication methods that rely on more advanced material-processing approaches such as vapor deposition and solution processing. Lithium batteries, in particular, have received considerable attention because of their high energy density. Two complementary lithium batteries have emerged: one is based on polymer electrolytes; the other is based on inorganic electrolytes.¹⁵ The former, which is actually a thick-film system, is the basis for commercial products that provide milliwatt-hour of energy. Primary batteries of the type $\text{Li}/\text{Li}_x\text{MnO}_2$, marketed by Panasonic among other companies, are on the order of $0.3\text{--}0.5\text{-mm}$ -thick and offer between 10 and 20 mA h at 3 V. Secondary (i.e., rechargeable) lithium polymer batteries are also being developed.⁵⁶ The polymer electrolyte in most cases is a gel electrolyte formed by polymers and organic solutions of lithium salts or is a plasticized polymer electrolyte.^{2,57,58}

Inorganic electrolytes lend themselves much more readily to thin-film batteries. Over a decade ago, Eveready Battery developed thin-film Li/TiS_2 secondary batteries, which used a sputtered lithium oxysulfide glass as the electrolyte,⁵⁹ while other thin-film batteries using glassy oxides as the electrolyte continue to be developed.¹⁵ The fact that these inorganic electrolytes have low conductivity at room temperature is compensated by the short diffusion length of only a few micrometers. The fabricated batteries are truly thin film as various vapor deposition methods are used to fabricate the cathode and anode as well as the electrolyte. The total thickness of the active components is in the range of $10\text{--}20 \mu\text{m}$; however,

the thickness of the actual battery is on the order of $100 \mu\text{m}$ because of packaging and the critical need to protect the components from moisture.

The thin-film secondary lithium battery system that has progressed the furthest is that developed at the Oak Ridge National Laboratory.¹³ The electrolyte in this case is a lithium phosphorus oxynitride ("Lipon") which is deposited by rf magnetron sputtering, as is the cathode, followed by thermal evaporation of the lithium. A number of different cathode materials, including layered transition metal oxides^{60,61} and vanadium oxides,⁶² have been reported and, for the most part, excellent results have been obtained. The thin-film batteries achieve operating lifetimes of thousands of cycles and routinely operate at current densities above 1 mA cm^{-2} . In tailoring these batteries for integrated circuit (IC) applications, which involve solder reflow at temperatures of $250 \text{ }^\circ\text{C}$, this group developed a lithium-free approach where the anode is formed by electroplating lithium on a copper current collector.⁶³

The research on thin-film batteries has led to considerable understanding of the kinetics and structural changes occurring during lithium insertion and deinsertion in amorphous and nanocrystalline films.¹³ However, the fact remains that these thin-film batteries have limited capacity, because of the thickness of the cathode, while the overall cell resistance can be larger than desired, because of the cathode/electrolyte interface. As a result, cell energies are in the range of $100\text{--}500 \mu\text{W h cm}^{-2}$. As discussed previously, these systems are considerably below the 1 J mm^{-2} values required for powering MEMS devices.

An interesting direction to thin-film battery fabrication is the use of forward-transfer methods based on laser-assisted direct-write processes. This processing method is a soft transfer that minimally affects the materials being laid down, so it is compatible with the transfer of metals, oxides, polymers, and even liquid and gel electrolytes. The variant known as MAPLE-DW (matrix-assisted pulsed-laser evaporation-direct write)⁶⁴ has recently been used to direct-write a lithium ion battery.⁶⁵ The MAPLE-fabricated LiCoO_2 -carbon/carbon microbattery prototype was sealed within trilayer metal-polymer laminate and cycled in air. A typical microbattery with a footprint of $4 \text{ mm} \times 4 \text{ mm}$ (patterns can be written to $10 \mu\text{m}$) has a capacity of $155 \mu\text{A h}$ (at a C/5 rate, where a 1 C rate completely discharges the full capacity of the battery in 1 h) and 100 mA h g^{-1} of LiCoO_2 . Because carbon was included in the transfer ink with the charge-insertion oxide, the electrode could be deposited in thicker layers than a sputter-deposited thin-film battery without creating severe ohmic losses. The resulting prototype approaches the power that other thin-film batteries provide but did so with a footprint smaller than 1 cm^2 . An advantage of such direct-write fabrication is that it can ultimately use the electronics substrate as part of the power-source packaging to save weight in the battery system. Current work is aimed at coupling Li ion microbatteries with energy-harvesting devices (solar cells, RF antennae, etc.) for hybrid power supply applications.

Kushida et al. recognized the limitation of the low capacity of thin-film lithium batteries for IC applications when they demonstrated the operation of arrays of thin-film lithium batteries.⁶⁶ Rather than develop a power generator for an entire chip, this work was directed at providing local power to individual (or a few) VLSI circuits. The battery took the form of a 3×1 array in which three parallel $100\text{-}\mu\text{m}$ -wide stripes of cathode material were crossed by a $200\text{-}\mu\text{m}$ -wide stripe of lithium. A spin-on phosphosilicate glass was used as the separator, while the cathode material (LiMn_2O_4) was deposited by solution processing in a trench etched in the silicon wafer to provide better device definition. The prospect of a battery array is an interesting one, and although the energy per unit area was not very high ($\sim 35\ \mu\text{W h cm}^{-2}$), the concept of supplying localized power at the individual circuit level is intriguing.

3.4. Generating Power from Ambient Sources

One important area of MEMS sensor technology is the development of distributed sensors, some of which are embedded, remote sensors in buildings and other structures. Battery replacement is difficult or impractical in this case and approaches for generating power from ambient sources are being pursued. The most familiar ambient energy source is solar and the use of photovoltaics is widely used. Solar energy, however, is not always available for embedded sensors and for this reason another ambient energy source of interest for powering small devices is the use of mechanical vibration. Beeby and co-workers reported the use of an electromagnetic transducer based on the movement of a magnetic pole with respect to a coil.⁶⁷ This electromechanical power generator uses neodymium iron boride permanent magnets mounted on a spring board inside an inductive coil. As the mass deflects from the vibration, there is a varying amount of magnetic flux passing through the coil. An electromotive force is induced (Faraday's law), the magnitude of which is proportional to the rate of change of the coil position. Shaking the device causes the magnets to vibrate at 322 Hz. The device occupies a volume of $240\ \text{mm}^3$ and generated a maximum useful power of 0.53 mW, corresponding to a $25\text{-}\mu\text{m}$ amplitude at an excitation frequency of 322 Hz.

Another power generator that converts vibrational energy to electrical energy is based on a mass-spring-resonator structure.⁶⁸ Laser micromachined copper springs were fabricated into different patterns to optimize device performance. In this device, generators with a volume of $1\ \text{cm}^3$ were able to produce up to 4.4 V peak-to-peak with maximum root-mean-square power of over $800\ \mu\text{W}$. The vibration required to generate this power had frequencies ranging from 60 to 110 Hz with $200\text{-}\mu\text{m}$ amplitude. The fabricated generator was able to drive an infrared transmitter, and the authors contend that the device is capable of driving low-power integrated circuits.

Another approach to converting vibrations in the environment is the use of an inertial generator based on thick-film piezoelectric materials.⁶⁹ A prototype generator was produced enabling the authors to

establish some operating parameters and fabrication methods. For the most part, these methods are expected to provide low power, as the first devices produced an output of 3 mW.

3.5. Hybrid Micropower

In the use of 3-D batteries to power MEMS devices, the tacit assumption is that the battery serves as the electrochemical power source. That is, the battery directly supplies all the energy for the device. A hybrid power supply is an alternative concept based on combining energy conversion and energy storage.¹¹ In this case, the battery is a component of the power supply rather than the sole power source. The batteries are expected to provide power when the energy conversion device is not working or when additional power is required, i.e., pulse power for communication. The energy conversion device, which obtains energy from ambient sources, is used to power the microsystem and charge the batteries.

Koeneman et al. described a micropower supply that was designed to power a "smart bearing".¹¹ The ambient energy, a rotating shaft, was converted using a wire coil. Energy storage was accomplished using a thin-film lithium battery. Because of the device application, a suitable actuation driver was required to deflect the membrane. Although the device was not built, the analysis established that a hybrid power supply could be integrated with a MEMS device to provide on-board power. One interesting point in the analysis is that the authors did not consider the 2-D nature of the battery and overestimated the number of actuations by 50 times.

A more recent paper considered the use of a hybrid power supply for powering autonomous microsensors.⁷⁰ Such devices are similar to the dust mote pictured in Figure 1 and described in the Introduction. This hybrid power supply combined a solar cell to meet standby requirements and to charge the battery, which was the microfabricated Ni-Zn battery described in section 3.2. The authors also showed that if the battery alone was to serve as the power source, the footprint would be substantially larger, over $12\ \text{cm}^2$. The hybrid device was constructed and some feasibility experiments were carried out, but no actual devices were powered.

4. Component Design for 3-D Battery Structures

4.1. Thinking Like Architects

Jumping out of Flatland⁷¹ to a true third dimension (rather than stacking 2-D elements, which seems to be the microlithography community's perception of 3-D) permits the use of hierarchical designs: nanostructured electrode materials, organized into larger macroscopic features. One of the most critical components of these new battery designs is an initial degree of "nothingness", that is a continuous phase of porosity. This open volume is then available to be filled with a second phase, for example an infiltrated electrolyte or even an opposing electrode structure, forming a true 3-D, intermingled battery assembly. Following IUPAC conventions, pores are identified

by their respective sizes: macropores (>50 nm), mesopores (2–50 nm), and micropores (<2 nm).⁷² Nanopore and nanoporous are not internationally defined terms, so they are an unknown and often misleading class of pores.

Chemical methods are ideally suited to construct textured materials with features of solid and void on the meso- or nanoscale. The chemistry can include such techniques as sol–gel synthesis, chemical vapor deposition (CVD), and electrodeposition, where molecular or ionic precursors are reacted under controlled conditions to assemble the desired solid structures. Combining such techniques with structure-directing templates (porous membranes, colloidal crystals, micelles, etc.) permits the design of hierarchical structures with pore sizes that cover a wide range from mesopores to large macropores. In an alternative to template synthesis, sol–gel methods are used to assemble 3-D networks of nanoscale particles into a monolithic wet gel. With careful processing of these gels to remove the pore-filling fluid, aerogels and related structures are rendered that exhibit aperiodic, through-connected void networks of mesopores and/or macropores.

An extensive research effort is currently underway to produce common battery materials, including carbons and transition-metal oxides, in various meso-structured and nanostructured forms. The basic functional requirements for these new materials are largely the same as for conventional secondary battery electrodes: a combination of electrical conductivity and the ability to undergo reversible ion-insertion reactions. However, the inherent characteristics of nanostructured electrode materials, an extensive electrode/electrolyte interface and facile transport of ions through the void volume, yield superior electrochemical performance relative to conventional battery materials. In practically all of the cases discussed below, electrode materials designed with 3-D nanostructured interfaces exhibit significantly better charge-storage properties, particularly under high rates of charge/discharge, than do conventional forms of the same composition, and in some instances, the nanostructured materials provide unexpectedly high overall capacity due to the defective nature of nanoscale solids.

The following section focuses specifically on those design strategies that produce either monoliths or supported films that may then serve as a solid but textured platform in the first design step toward a 3-D battery architecture.

4.2. Porous Membranes as Structure-Directing Templates

The use of porous membranes as templates for electrode structures was pioneered by Martin and co-workers nearly 20 years ago,⁷³ and this approach has since been extended to include numerous electrode compositions and geometries^{73–78} and applications beyond energy storage, including sensing and separations.⁷⁹ In this approach, chemical and electrochemical routes are used to fill in the cylindrical, uniform, unidirectional pores of a free-standing membrane with electrochemically active materials and

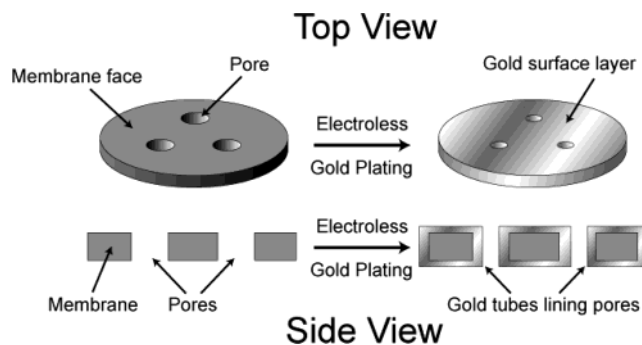


Figure 10. Schematic showing the conversion of a porous membrane into a template in which the pores are filled or coated to form random ensembles or ordered arrays of nanometer- and micrometer-scale cylinders or tubes. (Derived with permission from ref 87. Copyright 1997 Electrochemical Society.)

structures (Figure 10a). The pores in such membranes may be either random, as in “track-etched” polycarbonate, or an ordered array, as in electrochemically prepared alumina membranes. The pores in these membranes can be as small as 10 nm and range upward into the hundreds of nanometers and micrometers.

Various strategies are used to produce electrode structures within the membrane pores, including sol–gel synthesis, CVD, electrodeposition, and electroless deposition. With careful control of the synthetic conditions, the pores are either filled completely or preferentially coated at the pore walls, producing hollow tubes (see Figure 10b). Following infiltration with the desired electrode material, the membrane is subsequently removed under conditions that do not disturb the active material, leaving an array of either solid nanofibers or nanotubes attached to a current collector like the bristles of a brush (Figure 11). In this case there is very limited inter-connectedness between the nanofibers, except at the current collector base.

Using this approach, template-synthesized electrodes have been prepared not only from metals, but from TiO_2 ,⁷⁵ V_2O_5 ,^{80,81} LiMn_2O_4 ,^{82,83} SnO_2 ,^{84–86} TiS_2 ,⁸⁷ carbon,^{88–90} and various conducting polymers.⁹¹ The final templated feature need not consist of a single material or phase. Martin and co-workers prepared striped metal nanorods of gold and platinum,⁹² which was a concept ultimately extended to the preparation of nanoscopic barcodes⁹³ and optical tags.⁹⁴ Recently Dewan and Teeters infiltrated alumina membranes to template a device: a V_2O_5 xerogel–carbon battery using a poly(ethylene oxide)–lithium triflate electrolyte.⁹⁵

Many of the templated electrode ensembles described above function as high-performance battery electrodes in lithium-containing electrolytes.⁷⁶ The fibrous morphology of these templated electrodes reduces the solid-state transport distances for lithium ions participating in the charge-storage reaction. This feature facilitates not only good cyclability but also rapid charging and discharging. For example, template-synthesized SnO_2 electrodes deliver gravimetric capacities that are orders of magnitude higher than a thin-film control electrode when discharged at greater than a 50 C rate. The void spaces between

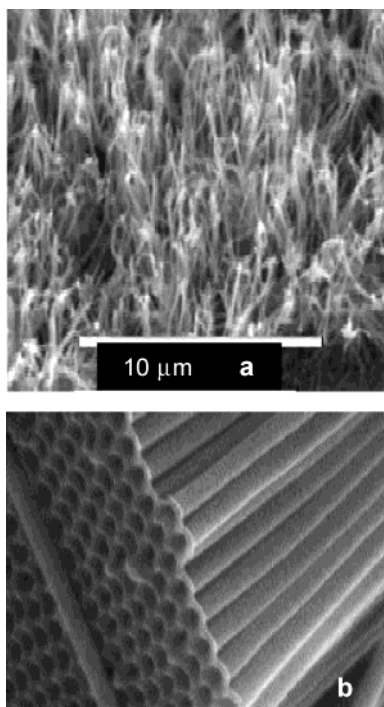


Figure 11. Electron micrographs of membrane-templated electrodes: (a) ensemble of rods (Reprinted with permission from ref 80. Copyright 1999 Electrochemical Society.); (b) array of nanotubes (Reprinted with permission from ref 79. Copyright 2001 American Chemical Society.)

the individual electrode fibers also provide room for expansion during electrode cycling, which is a particular problem for SnO_2 , because a Sn metal phase alloys with electrogenerated Li metal, with accompanying large volume changes.

In a related approach, these same porous alumina membranes serve as a mask through which O_2 plasmas are used to etch underlying carbon films.^{96,97} This etching process produces honeycomb carbon structures that are positive replicas of the alumina-membrane mask. This process has successfully produced honeycomb structures of both diamond⁹⁶ and graphitic carbon,⁹⁷ with pore sizes in the carbon replica around 70 nm.

4.3. Template Synthesis of Ordered Macroporous Solids with Colloidal Crystals

The porous membrane templates described above do exhibit three-dimensionality, but with limited interconnectedness between the discrete tubelike structures. Porous structures with more integrated pore–solid architectures can be designed using templates assembled from discrete solid objects or supramolecular structures. One class of such structures are three-dimensionally ordered macroporous (or 3-DOM) solids,⁹⁸ which are a class of inverse opal structures.⁹⁹ The design of 3-DOM structures is based on the initial formation of a colloidal crystal composed of monodisperse polymer or silica spheres assembled in a close-packed arrangement. The interconnected void spaces of the template, ~ 26 vol % for a face-centered-cubic array, are subsequently infiltrated with the desired material.

Strategies for filling the void space of the colloidal crystal utilize sol–gel chemistry, salt precipitation,

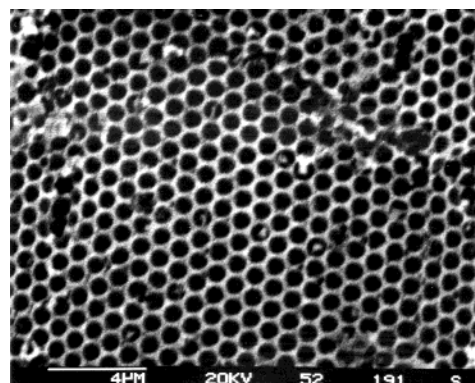


Figure 12. Inverse opal of vanadium oxide ambigel. The pores are formed by packing 1- μm styrene beads and infiltrating a vanadium sol. (Reproduced with permission from ref 100. Copyright 2002 The Royal Society of Chemistry.)

CVD, and electrodeposition, depending on the desired composition. Removal of the colloidal templating spheres renders a negative replica (the inverse opal) structure of the active material, with an interconnected, 3-D array of pores, typically sized in the hundreds of nanometers.

This general procedure for producing macroporous solids has recently been exploited to synthesize electrode architectures that are targeted for lithium battery applications. Sakamoto and Dunn synthesized inverted opal structures of V_2O_5 by infiltrating a colloidal crystal template with a vanadia sol–gel formulation.¹⁰⁰ The resulting macroporous structure is shown in Figure 12. The walls are composed of vanadium oxide ambigel, leading to a hierarchical architecture that demonstrated high capacity for lithium at high discharge rates. Stein and co-workers have expanded this concept further to produce macroporous ordered structures of V_2O_5 , SnO_2 , and LiNiO_2 .^{98,101} Hierarchical electrode structures are generated by this method as well, with the inorganic skeleton of the 3-D ordered macroporous structure composed of fused nanoscale grains of electrode material that are themselves mesoporous. Macroporous carbon structures have also been produced by infiltrating organic precursors into the interstitial void of silica sphere colloidal crystals, followed by carbonization and removal of the silica template.^{102–106}

4.4. Template Synthesis of Mesoporous Solids with Supramolecular Assemblies

These same general templating strategies are extended into the mesopore size regime with the use of self-assembled supramolecular arrays, a topic which has been extensively reviewed elsewhere.^{107–121} In this approach, ionic surfactants or block copolymers are assembled into micellar aggregates or liquid-crystalline phases. With careful tuning of the reaction conditions, these assemblies can be organized into either highly ordered hexagonal, lamellar, or cubic structures, or more disordered wormlike structures. The microscale phase segregation in these systems acts to restrict and direct the growth of an inorganic guest phase, which can be incorporated by various methods. With transcriptive synthesis the

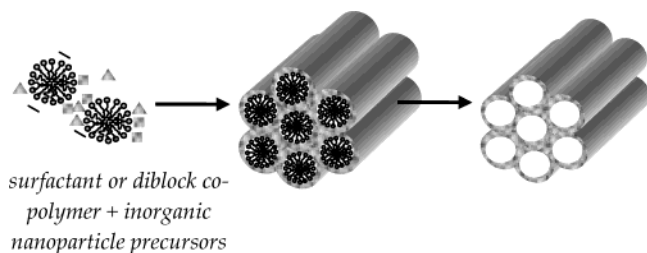


Figure 13. Self-assembled organic template (micellar or liquid crystalline) that directs the assembly of the inorganic phase about the structure-directing organic phase. (Courtesy of Prof. Sarah Tolbert, UCLA.)

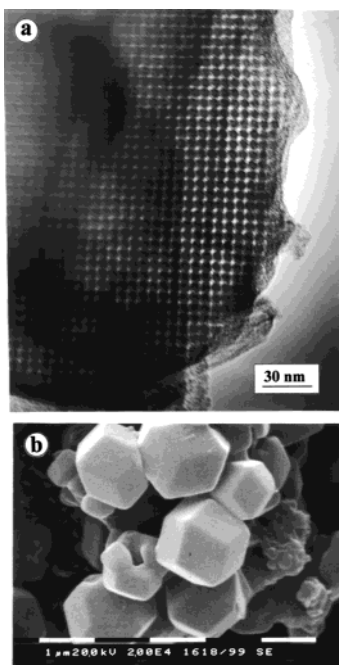


Figure 14. Nanocast carbon. (Reprinted with permission from ref 122. Copyright 1999 American Chemical Society.)

supramolecular assembly is first formed separately followed by infiltration of the guest phase. Synergistic synthesis encompasses the process whereby template self-assembly and inorganic phase synthesis are combined in a cooperative reaction scheme to produce the mesostructured hybrid (Figure 13).

In either the transcriptive or synergistic strategy, removal of the organic template by extraction or calcination renders the inorganic mesoporous structure. For synthetic schemes that are not compatible with the formation of stable template assemblies, an alternative approach is to use a preformed, templated inorganic host, such as mesoporous silica, as a mold to “nanocast” the desired material as an inverse replica of the host, such as that seen in Figure 14.¹²²

In the following section, we restrict our discussion to templated mesoporous solids that are of potential interest as battery electrodes, including many transition-metal oxides and carbon. This slice of the literature still points the interested reader to many articles on the synthesis and physical characterization of relevant mesoporous materials. A much smaller number of electrochemical studies with templated mesoporous electrodes have been published, and these studies in particular will be noted.

The synergistic synthesis method for supramolecular templating was initially developed for silica solids, but this chemistry is being expanded to include a number of transition-metal oxides, including some of interest for electrochemical applications.^{112,123} Among these, mesoporous TiO_2 has been the most widely investigated, primarily due to its potential employment in photovoltaic cells.¹²⁴ Combining liquid-phase titania precursor chemistry and templating strategies has produced mesoporous TiO_2 structures, with both ordered and wormlike pore structures.^{125–133} Grätzel and co-workers have reported on the reversible lithium ion insertion reactions of mesoporous anatase TiO_2 .^{127,134,135} Similar strategies have been used to generate mesoporous WO_3 , an important electrochromic oxide, where the high surface areas and mesoporous pathways facilitate rapid coloration/decoloration responses.^{136,137}

Another route to mesoporous, electrochemically active phases utilizes electrodeposition methods, where the presence of surfactants or a liquid-crystalline phase at the electrode surface directs the formation of the growing film. The templated electrodeposition approach was initially developed by Attard et al. to produce mesoporous platinum films.¹³⁸ This protocol was followed to develop mesoporous tin as a potential anode for Li ion batteries and nickel/nickel oxide electrodes for aqueous-based batteries.^{139,140} Related strategies have also been used to prepare mesoporous V_2O_5 ¹⁴¹ and conducting polyaniline (as nanowire arrays).¹⁴² In addition to driving the electrodeposition process, the electrochemical interface can be controlled to promote the formation of hybrid assemblies of surfactant–inorganic in dilute surfactant solutions en route to forming mesoporous oxide films, as demonstrated by Stucky et al.^{143,144}

Templated mesoporous carbon structures are generally produced by first incorporating organic precursors into the void space of a preformed mesoporous silica or aluminosilicate template, either by liquid infiltration or CVD methods. Following pyrolysis of organic components, the inorganic templates are removed, rendering an inverse carbon replica. This approach was first reported by Ryoo and co-workers¹²² and has subsequently been extensively adapted to generate various mesoporous carbon structures.^{104,145–161} The pore–solid architectures of these carbon solids can be designed on the basis of the choice of inorganic template from among the many available and range from ordered 2-D structures to more disordered 3-D structures. These mesoporous carbons are promising candidates as electrochemical materials in double-layer capacitors. The mesoporous pathways within these electrode structures promote rapid transport of electrolyte ions during cycling, resulting in electrodes that can be charged and discharged rapidly with only minimal loss of capacity.^{150,162–164}

4.5. Hierarchical Designs Based on Templating Strategies

Hierarchical structures with pore–solid features that cover a wide size range within one structure, as seen in Figure 15, are achieved by carefully combin-

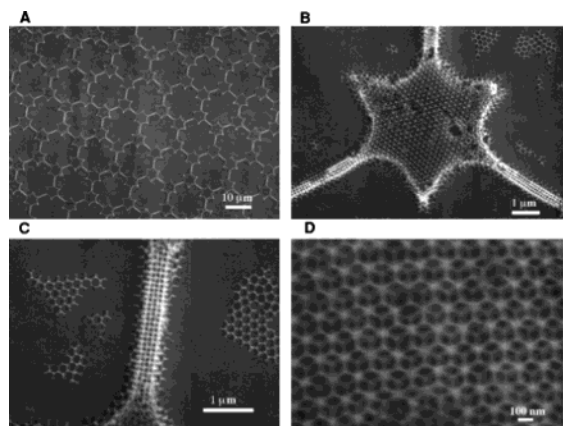


Figure 15. Hierarchical structure formed by combining liquid-phase templating with micromolding. (Reprinted with permission from ref 166. Copyright 1998 American Association for the Advancement of Science.)

ing the liquid-phase templating approaches described above: surfactant templating (up to 10 nm), block copolymer templating (up to 30 nm), and colloidal crystal templating (100 nm–1 μm).^{165,166} This strategy can be used directly to fabricate inorganic structures or indirectly for hierarchical, porous carbon structures that are produced by inverse replication of a corresponding hierarchical inorganic mold.¹⁶¹ These synthetic processes can be further combined with micromolding techniques to create features up to 1 mm.¹⁶⁶

4.6. Aerogels and Related Nanostructures—Aperiodic Pore–Solid Architectures

An ordered porous network is not a prerequisite in designing high-performance 3-D battery structures.¹⁶⁷ Sol–gel methods can be used to synthesize monolithic gels that are composed of a 3-D interconnected network of nanoscale particles, co-continuously intermingled with a phase of fluid-filled pores. The processing of these wet gels to render the dried forms must be carefully controlled so that the highly porous architecture is retained. The direct evaporation of typical pore-filling fluids (high-surface-tension liquids such as water and alcohols) creates capillary forces at the liquid–vapor interface, resulting in pore collapse and a partially densified porous solid known as a xerogel. This structural collapse is avoided if the pore fluid is removed under supercritical conditions where no liquid–vapor interface is ever established. Gels processed by supercritical fluid extraction, usually with CO_2 as the pore fluid, are denoted as aerogels.^{167–170}

In an alternative to supercritical drying, the pore fluids in a wet gel are replaced with a low-surface-tension, nonpolar liquid, such as an alkane, which is then allowed to evaporate under subcritical or ambient-pressure conditions.^{170–172} The resulting solids, denoted as “ambigels” (for ambient-pressure-dried gels),¹⁶⁷ do exhibit a moderate degree of densification but retain a large fraction of pore volume, with pores usually in the mesopore size range.^{173–175} The densification that accompanies ambient-pressure drying provides for more mechanically rugged monolithic

forms than those for comparable aerogels. A fourth scheme of pore-fluid removal utilizes a freeze-drying process to render highly porous “cryogels”.^{176–180}

Aerogels and related structures have the important characteristics of extremely high surface area and a through-connected, aperiodic network of porosity. Additionally, these solids can be cast and molded into a range of shapes and forms or cast as thin films on planar supports. One attribute that seems to set these aperiodic architectures apart from the mesoporous ordered solids, even the nominally 3-D porous ones, is proven performance in rate-critical applications. The rapid and facile flux of molecules through the aerogel architecture avoids the potentially devastating loss of throughput through 1-D channels if a blockage occurs.¹⁸¹ Aerogels have already demonstrated orders of magnitude faster response for sensing, energy storage, and energy conversion than other pore–solid architectures.^{167,181}

Electrically conductive aerogels have been prepared from a range of transition metal oxides, including vanadium oxide,^{172,182–189} manganese oxide,^{173,174,190} molybdenum oxide,^{191–193} and tin oxide.¹⁹⁴ All of these nanostructured oxide forms exhibit improved performance as Li ion insertion electrodes in conventional electrochemical cells.^{167,195} For example, vanadium pentoxide aerogel electrodes accommodate the reversible electrochemical insertion of up to four Li ions per V_2O_5 unit. In addition to higher overall capacities, aerogel electrodes deliver more energy (capacity) under high charge–discharge rates than do conventional materials.

Carbon aerogels are typically derived from the reaction of resorcinol (or related aryl precursors) and formaldehyde, which leads to a polymer gel. The postprocessed polymeric aerogels are then pyrolyzed in inert atmospheres at high temperature to form highly conductive, monolithic carbon structures that retain the characteristics of an aerogel.^{196–198} The synthesis of carbon aerogels offers considerable flexibility as the pore–solid organic architecture can be adjusted by simple changes in the initial reaction conditions of the polymer gel. Through such variations, carbon aerogels can be prepared in either predominantly mesoporous or macroporous forms. Carbon aerogels are being exploited as electrodes for electrochemical capacitors, where the high surface area, through-connected porosity, and electronic conductivity of the aerogel promote rapid charge–discharge reactions.^{199–201} Commercial supercapacitors based on carbon aerogels are available from several companies.

5. Structural Characterization of 3-D Electrode Architectures

5.1. Characterization of the Pore–Solid Architecture

The common feature of the 3-D electrode structures described above is the intimate intermingling of solid and void space, in either ordered or aperiodic arrangements, with textures covering an extensive range of length scales. This section reviews the experimental methods used to characterize the pore

size and structure and to determine the electrochemical properties of the pore–solid nanoarchitectures. The quality and type of pore structure in such an architecture often determines the electrochemical performance of the resulting battery material. For instance, when the pore structure is infiltrated with a liquid electrolyte, interconnected mesopores and macropores provide an open pathway for the diffusion of electrolyte ions that participate in the charge-storage mechanisms. The size and interconnectedness of the pore network will be crucial in achieving true intermingled cathode/electrolyte/anode designs.

From the standpoint of electrochemical performance, micropores (less than 2 nm) are a far less desirable design component for 3-D power. Even when employed in traditional electrochemical cells, the electrode area within a micropore is not fully utilized in energy-storage mechanisms, due to the lower effective electrolyte conductivity within the micropore and sieving effects for larger electrolyte ions.^{202,203} Although templated microporous materials, especially in carbon, have been fabricated and characterized for catalytic and adsorbent applications, we are not including this class of materials for further 3-D design consideration because of the inability to electrify the surface area within micropores on a practical time scale.

5.1.1. Physisorption

Gas adsorption techniques are often used to characterize the pore structure of materials possessing micropores, mesopores, and small macropores.²⁰⁴ Adsorption measurements with probes such as N_2 provide information on accessible surface area and pore volume. In addition, careful analysis of the experimental data also yields information about pore sizes, shapes, and the degree of interconnectedness.²⁰⁵ Various mathematical models can be used to fit the experimental data from adsorption isotherms, yielding pore–size distribution (PSD) plots describing the pore structure in the mesopore and small macropore regime. The generation of PSD plots is critical in the characterization of structured materials with aperiodic pore–solid architectures, such as aerogels and ambigels, where it is difficult to directly image the pore structure with microscopic techniques. In Figure 16, the pore–size distributions are contrasted for birnessite, a Na^+ -templated, sol–gel-derived lamellar polymorph of MnO_2 , expressed in three types of pore–solid nanoarchitectures (xerogel, ambigel, and aerogel). The PSD plots make it clear that the pore structure in xerogels comprises micropores and small mesopores, while the distribution in the aerogel is weighted toward the larger mesopores and macropores. The ambigel lives up to its name with few micropores and macropores and most of its pore volume represented in mesopores sized from 15 to 30 nm.¹⁷⁵ Reporting just the average pore diameter does not begin to capture the richness of the nanoarchitectures: xerogel, 9 nm; ambigel (hexane), 12 nm; ambigel (cyclohexane), 17 nm; and aerogel, 19 nm.

5.1.2. Small-Angle Scattering Techniques

A second approach to pore–structure analysis, small-angle scattering (SAS), probes the heteroge-

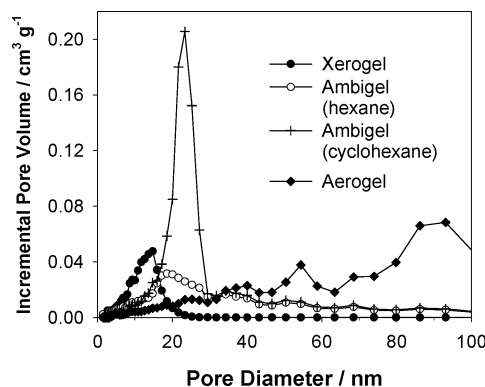


Figure 16. The pore-size distribution for sol–gel-derived birnessite $Na_3MnO_2 \cdot xH_2O$ as processed into three pore–solid nanoarchitectures: xerogel, ambigel, and aerogel. Distributions are derived from N_2 physisorption measurements and calculated on the basis of a cylindrical pore model. (Reprinted with permission from ref 175. Copyright 2001 American Chemical Society.)

neities in electron density within porous architectures.^{204,206} Small-angle scattering measurements extend the range of length scales that can be analyzed, revealing features from micropores to the large macropores that cannot be effectively probed by gas adsorption. Another distinguishing feature of SAS techniques is that both open and isolated pores contribute to the experimentally observed structure. The results of gas adsorption analysis and such SAS techniques as small-angle X-ray scattering (SAXS) can be combined to provide the most thorough characterization of complex pore–solid architectures. A key recent advancement for SAS methods has been the development of the chord-length distribution (CLD) approach, which yields much more accurate characterizations of pore sizes and distributions than with previous SAS approaches.^{207,208}

5.1.3. Electron Microscopy

Electron microscopy techniques are routinely applied to structured nanomaterials to assess the solid morphology for features from tens of micrometers to nanometers in size. Traditional microscopy methods provide useful information in the form of 2-D projection images, but they do not fully describe the 3-D structures discussed in the preceding section. However, the recent advancements in computer-aided electron microscopy techniques do provide 3-D information for structured solids.^{209–212} One such approach based on high-resolution electron microscopy (HREM) was developed by Terasaki, Stucky, Ryoo and others specifically for porous structures exhibiting long-range periodicity on the mesoscale (i.e., templated mesoporous solids).^{212–216} In this method, 2-D projected HREM images of the sample taken at different symmetry orientations are subjected to Fourier transform analysis to determine the crystal structure factors and ultimately to obtain a 3-D representation of the ordered structure. The measurements provide information on the sizes, shapes, and connectivity of the ordered pore structures in such materials as templated mesoporous silica and carbon (see Figure 17). Unfortunately, these methods are not applicable

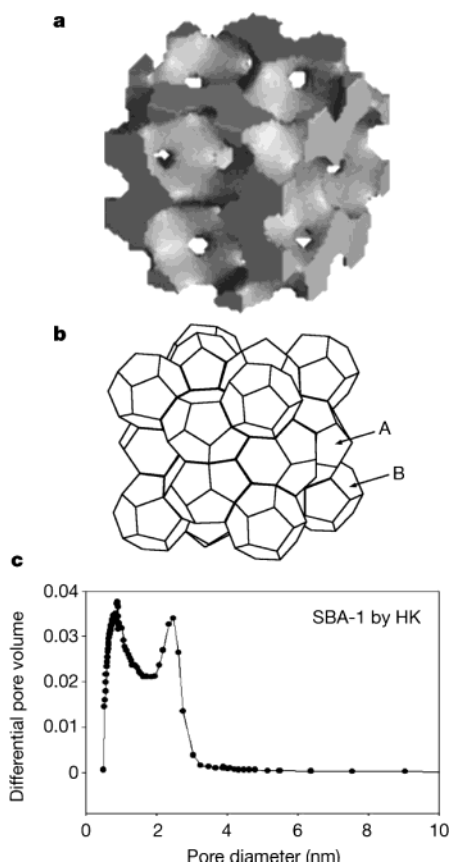


Figure 17. High-resolution electron micrographic determination of cage and bimodal pore structure in the mesoporous silicates SBA-6 and SBA-6: (a) 3-D structure of SBA-6 derived from the electrostatic potential map showing large (A) and small (B) cages with associated large and small pores; (b) schematic of the large and small cages in the SBA family; (c) pore sizes for calcined SBA-1 determined by Horvath–Kawazoe analysis of the argon adsorption isotherm branch. (Reprinted with permission from ref 213. Copyright 2000 Macmillan Magazines, Ltd.)

for materials with irregular or hierarchical pore–solid architectures.

A more general approach to 3-D structure determination is electron tomography, where the 3-D image of a solid (in a thin slice) is reconstructed from a series of 2-D images taken at regular tilt angle intervals.²⁰⁹ Although not yet a common technique for materials science, electron tomography is emerging as a powerful tool for imaging complex solids with features approaching the nanometer scale.²¹⁷ This technique is also more generally applicable to the textured materials described in this review, as it does not rely on any long-range order within the sample.

In addition to providing insights into sample morphology, electron tomography can also be exploited to derive 3-D compositional information. For instance, energy-filtered transmission electron microscopy (EFTEM) or Z-contrast scanning transmission electron microscopy (STEM) can be combined with tomography to provide 3-D elemental mapping capabilities, within some limitations, for light and heavy elements, respectively.²⁰⁹ In the future, electron tomography will be highly beneficial for characterizing the multifunctional architectures that are currently being designed for 3-D power sources.

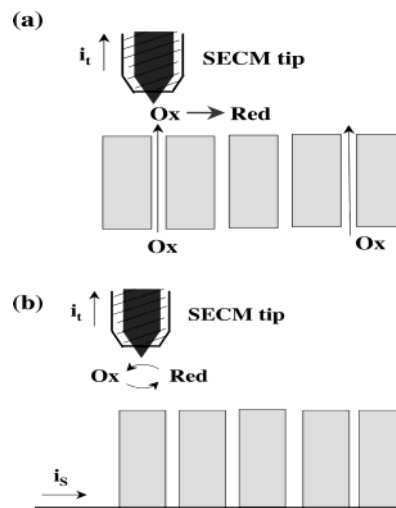


Figure 18. Schematic drawing depicting SECM measurement of (a) molecular transport within a porous material and (b) electrochemical activity on one electrode in a battery array.

5.1.4. Scanning Probe Microscopy

Scanned probe microscopies (SPM) that are capable of measuring either current or electrical potential are promising for in situ characterization of nanoscale energy storage cells. Mass transfer, electrical conductivity, and the electrochemical activity of anode and cathode materials can be directly quantified by these techniques. Two examples of this class of SPM are scanning electrochemical microscopy (SECM) and current-sensing atomic force microscopy (CAFM), both of which are commercially available.

In the SECM measurement (Figure 18), a small microelectrode (typically a metal or carbon electrode) is rastered across the surface of interest, and the current resulting from a Faradaic reaction is measured.^{218–220} The experiment is arranged such that the tip current is proportional to the local concentration of a redox species, which in turn may reflect molecular transport rates within a porous matrix (Figure 18a)²²¹ or the electron-transfer activity at an electrode (Figure 18b).

Quantitative theories of various SECM experiments are well-developed and have been applied in investigations of both electrochemical and nonelectrochemical systems,²²² including, for example, investigations of electro-osmotic flow and transport rates in fuel-cell membranes.²²³ Because one detects molecules that are undergoing random diffusion, the spatial resolution of SECM is not as great as that of scanning tunneling microscopy. However, the nanoscale pore structure in Nafion membranes has been imaged by this technique, demonstrating better than 5-nm spatial resolution.²²⁴ And in contrast to STM or AFM, the SECM signal is very specific to local chemistry, providing a wealth of information about local concentrations of ions and molecules, chemical kinetics, and transport rates.

A complementary microscopy to SECM is CAFM, in which the AFM tip is made of a metal such that current can be measured as the tip is scanned, in contact, across the surface.²²⁵ Conducting-AFM offers the advantage of directly measuring local electrical

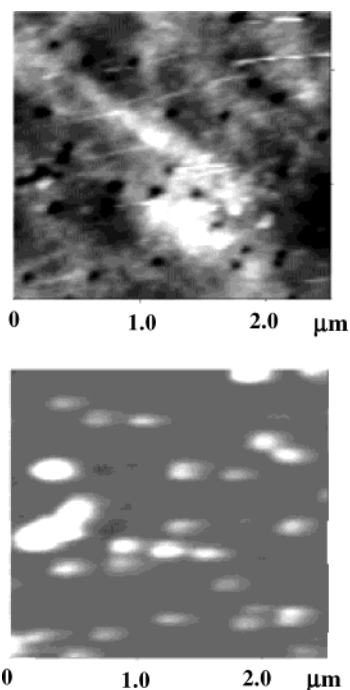


Figure 19. SECM–AFM images of a polycarbonate membrane containing 100-nm-radius pores. (Top) AFM topography image; (Bottom) SECM image of $\text{Ru}(\text{NH}_3)_6^{3+}$ transport in membrane pores. (Reprinted with permission from ref 227. Copyright 2001 American Chemical Society.)

conductivity, which can be inferred only from the SECM measurement. More importantly, both topography and surface electronic conductivity can be measured simultaneously, allowing the experimentalist to correlate structure and reactivity. An example of this is the CAFM imaging of electronic defects in the native oxide on titanium electrodes, which shows that high conductivity is associated with grain boundaries of the underlying metal.²⁵ Additional CAFM studies have focused on the investigation of the electrical properties of electrocatalytic Pt nanoparticles deposited on and in a porous Ti/TiO₂ film.²²⁶

A recent development in SPM technology is the combination of SECM and AFM to produce a hybrid high-resolution microscope that allows simultaneous topographic and electrochemical imaging.²²⁷ Figure 19 shows an example of this measurement in which pore structure and molecular transport of a redox-active molecule ($\text{Ru}(\text{NH}_3)_6^{3+}$) were simultaneously imaged at ~ 1 -nm resolution. Inspection of this image clearly shows a correlation between transport rates and pore structure.

Potential applications of SECM and CAFM in fundamental studies of nanoscale batteries and battery materials are readily envisioned. For instance, a small ion-selective electrode can be used as the SECM tip, providing a means to image and quantify Li^+ distribution and transport rates. A second application is mapping the electrostatic potential distribution between cathode and anode using a well-poised reference electrode as the scanning tip. Conducting-AFM imaging of battery electrode matrices comprising electronically insulating electrolyte and a conducting material would allow rapid visualization of electrical connectivity.

5.2. Corroboration of Electrochemical Processes with Spectroscopic Techniques

Three-dimensional electrode nanoarchitectures exhibit unique structural features, in the guise of amplified surface area and the extensive intermingling of electrode and electrolyte phases over small length scales. The physical consequences of this type of electrode architecture have already been discussed,¹⁶⁷ and the key components include (i) minimized solid-state transport distances; (ii) effective mass transport of necessary electroreactants to the large surface-to-volume electrode; and (iii) magnified surface—and surface defect—character of the electrochemical behavior. This new terrain demands a more deliberate evaluation of the electrochemical properties inherent therein.

Many of the traditional electroanalytical methods can be coupled to spectroscopic measurements, either ex situ or in situ, to elucidate the electronic and structural changes that accompany the electrochemical charge-storage process. The simplest approach takes advantage of the electrochromic properties of the various transition-metal oxides and the changes that occur upon charge insertion and de-insertion. The electrochromic response of thin oxide films supported on conductive, transparent substrates provides an in situ, temporal indicator of electronic state changes that occur during ion-insertion reactions. The power of spectroelectrochemistry arises from the fact that the spectral information, obtained concurrently with the electrochemically driven electronic state changes, decouples from other electrochemical phenomena, such as double-layer capacitance and electrolyte decomposition, which can potentially interfere with the electrochemical-only characterization.²²⁸

Spectroelectrochemical analysis of charge-insertion nanostructured materials already offers important insight into these systems. These methods were recently exploited to characterize the electrochemical processes of nanostructured manganese oxide ambigel and xerogel films.^{175,229} Spectroelectrochemical measurements were used to corroborate electronic state changes with the observed electrochemical response for the insertion of small cations (Li^+ , Mg^{2+}) and the unexpected insertion of a bulky organic cation (tetrabutylammonium). Vanadium pentoxide exhibits two distinct electrochromic features that can be assigned to the $\text{V}^{\text{V}}/\text{V}^{\text{IV}}$ transition at either stoichiometric V_2O_5 sites or V sites adjacent to oxygen vacancy defects.²³⁰ Exploiting this phenomenon, Rhodes et al. were able to assign these different physical environments in the voltammetry for sol-gel-derived V_2O_5 (Figure 20) and to track the relative distributions of these two energetically distinct insertion sites for sol-gel-derived V_2O_5 films as a function of temperature–atmosphere treatments.^{231,232}

For more sophisticated spectroelectrochemical analysis, electrochemical cycling is coupled with X-ray absorption spectroscopy (XAS) methods, which probe electronic and local atomic structures with element specificity.^{233,234} Because XAS techniques are compatible with in situ investigations and do not require long-range structural order for analysis, they are

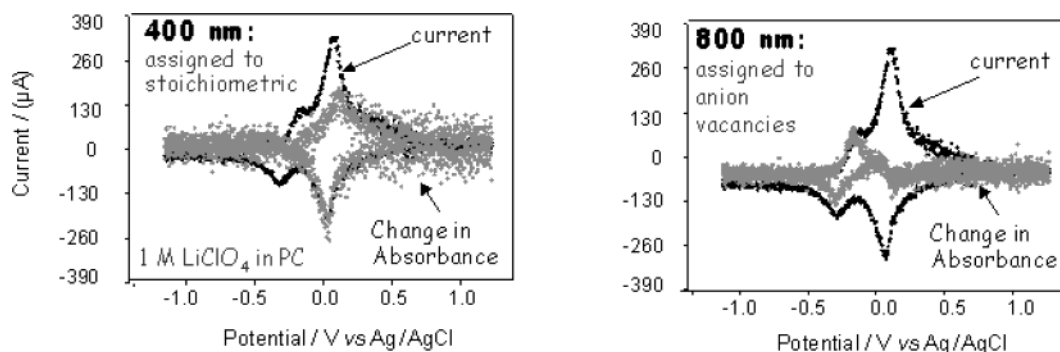


Figure 20. Spectroelectrochemical analysis of thin films of V_2O_5 ambigels supported on conductive glass (indium–tin oxide). The current response is given by the continuous line, and the change in absorbance monitored at 400 and 800 nm as a function of potential (and time) is shown as individual data points. The V_2O_5 ambigel was prepared by gelation of aqueous metavanadate, dried from cyclohexane, and calcined in air at 170 °C. (Printed with permission from ref 232.)

often used to characterize complex battery materials as a function of electrochemical state.^{235–239} Sol–gel-derived V_2O_5 electrodes are prime candidates for XAS analysis due to their disordered, nanoscale nature and exceptional electrochemical properties.^{240–245} As noted earlier, V_2O_5 ambigels and aerogels exhibit anomalously high capacities for Li ion insertion, with insertion of up to four Li per V_2O_5 for electrochemical lithiation and up to six Li per V_2O_5 with chemical lithiation.²⁴⁵ On the basis of the conventional insertion mechanisms, any lithiation beyond $x = 2$ for the formula $Li_xV_2O_5$ should result in the formation of V^{III} sites in the oxide lattice. Passerini et al. reported that for chemically lithiated V_2O_5 , the formal vanadium oxidation state unexpectedly did not go below the V^{IV} state, even with lithiation up to $Li_{5.8}V_2O_5$, suggesting charge delocalization beyond the V sites.²⁴⁵ But Mansour et al. recently described in situ XAS analysis of V_2O_5 aerogels and ambigels, demonstrating that with electrochemical cycling the high degree of Li ion insertion is accompanied by the formation of V^{IV} and subsequently V^{III} sites, when the degree of lithiation surpasses two Li per V_2O_5 .^{243,244}

One concern that might arise in using electronic spectroscopy to quantify highly defective structures is hinted at by results with nanostructured birnessite $Na_0MnO_2 \cdot xH_2O$. The color center in MnO_2 is the Mn^{4+} center, so optical density is lost in the visible spectrum as $Mn(III)$ sites are electrogenerated (see Figure 21). The as-prepared and calcined birnessite ambigel is mixed valent but predominantly $Mn(IV)$, which can be quantitatively assayed by chemical redox titration.^{174,175} The initial visible spectrum, which measures the electronic state of the Mn centers, has a lower absorbance than the material after electro-oxidation, in agreement with the chemically determined mixed-valence state of the initial material. The spectrochemical determination of the $Mn(III)/Mn(IV)$ ratio, however, does not match that obtained by chemical titration and undercounts the amount of $Mn(IV)$. Because of the high surface-to-volume ratio and greater defect nature of these nanostructured materials, we question whether any spectroscopic electronic state measurement truly measures a localized site that remains unaffected by the vacancies that arise in these materials.

Characterizing (experimentally and computationally) and exploiting the nature of defects in charge-

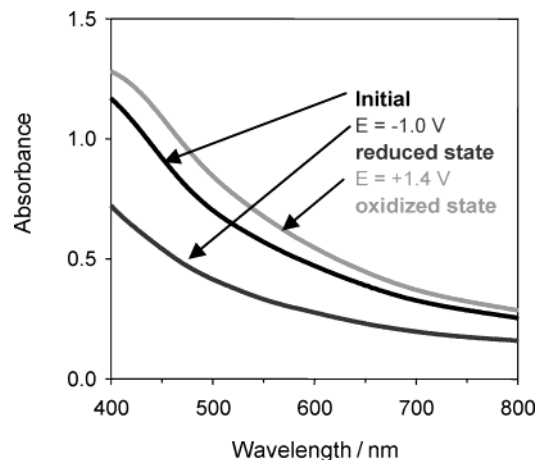


Figure 21. Visible absorption spectra for a 1.6- μm -thick $Na_0MnO_2 \cdot xH_2O$ birnessite ambigel film in 1 M $LiClO_4$ /propylene carbonate as a function of electrode potential. (Reprinted with permission from ref 175. Copyright 2001 American Chemical Society.)

storage materials is a key area of future research in the drive to improve the performance of batteries and ultracapacitors.¹⁶⁷ As discussed above, the aerogel forms of disordered $V_2O_5 \cdot 0.5H_2O$ afford Li-to- V_2O_5 stoichiometries of 4–6,^{183,195} while those for the bulk, crystalline material are 1–2.²⁴⁶ One clue to this impressive improvement in the Li ion capacity of V_2O_5 can be found by inducing deliberate defects in polycrystalline V_2O_5 :²⁴⁷ Creation of proton-stabilized cation-vacancies increases the capacity 23% relative to the $\sim 170 \text{ mA h g}^{-1}$ obtained with the as-received, micrometer-sized polycrystalline V_2O_5 .

While XAS techniques focus on direct characterizations of the host electrode structure, nuclear magnetic resonance (NMR) spectroscopy is used to probe local chemical environments via the interactions of insertion cations that are NMR-active nuclei, for example lithium-6 or -7, within the insertion electrode. As with XAS, NMR techniques are element specific (and nuclear specific) and do not require any long-range structural order in the host material for analysis. Solid-state NMR methods are now routinely employed to characterize the various chemical components of Li ion batteries: metal oxide cathodes, Li ion-conducting electrolytes, and carbonaceous anodes.^{248,249} Coupled to controlled electrochemical insertion/deinsertion of the NMR-active cations, the

chemical shifts of the ^6Li or ^7Li are used to distinguish between chemically distinct ion insertion sites within the host electrode structure, to differentiate electrochemically inactive Li ion sites, and to assess the mobilities of Li ions. Nuclear magnetic resonance studies of battery electrodes have recently been extended to in situ investigations of lithium insertion in carbon electrodes by Chevallier et al.²⁵⁰

6. Fabrication En Route to 3-D Integration of Architectural Components

6.1. Micromachining

The three-dimensional electrode arrays that are the basis for the interdigitated 3-D battery design (Figure 2a) have been fabricated successfully using different micromachining methods. Micromachining has emerged as an indispensable approach for fabricating materials into complex geometries.²⁵¹ These methods evolved from the realm of integrated circuits as researchers developed techniques for deposition, photolithographic patterning, and selective etching, among other processes. Distinctions can be drawn between bulk machining, where three-dimensional features are etched in bulk materials, and surface micromachining, where features are built up, layer-by-layer, on the surface of a substrate. Surface micromachining also involves the use of sacrificial films that are later dissolved to release the free-standing components. In both types of micromachining, photolithography serves as the basis for fabricating three-dimensional features.

Three-dimensional electrode arrays have been fabricated using two very different micromachining methods. One approach, named carbon MEMS or C-MEMS, is based on the pyrolysis of photoresists. The use of photoresist as the precursor material is a key consideration, since photolithography can be used to pattern these materials into appropriate structures. The second approach involves the micromachining of silicon molds that are then filled with electrode material. Construction of both anode and cathode electrode arrays has been demonstrated using these microfabrication methods.

6.1.1. Carbon MEMS (C-MEMS)

The synthesis and electrochemical properties of carbon films prepared from positive photoresist have been reported.^{252–254} The initial direction for this work was the fabrication of carbon interdigitated electrodes. In this work, positive photoresist was spin coated on a silicon substrate, patterned by photolithography, and pyrolyzed to form the carbon electrode. In more recent work, laser excitation has been used to both pyrolyze the film and to write the electrode pattern.²⁵⁵

The influence of pyrolysis conditions on the structure, morphology, electrical properties, and electrochemical behavior has been investigated. Raman spectroscopy shows that characteristic sp^2 carbon bands form from the pyrolysis treatments. The electrochemical properties for a few of the electrode systems have been reported and, for the most part,

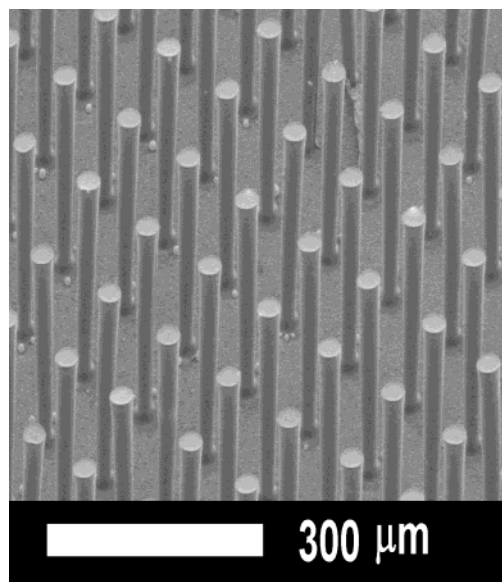


Figure 22. Array of carbon electrodes prepared by the C-MEMS process. The aspect ratio is approximately 20:1. (Courtesy of Prof. Marc Madou, University of California—Irvine.)

these pyrolyzed electrodes behave similarly to those of glassy carbon, a standard carbon electrode used in electrochemical studies. It is evident that good electrochemical responses are obtained for materials pyrolyzed at temperatures above 800 °C, although the best properties seem to occur at pyrolysis temperatures above 1000 °C. Voltammetric measurements show that the electron-transfer kinetics measured for $\text{Fe}(\text{CN})_6^{3-/4-}$ and $\text{Ru}(\text{NH}_3)_6^{3+/2+}$ are comparable to those determined for other carbon films and glassy carbon.²⁵⁴ One interesting difference with glassy carbon is that it is possible to prepare pyrolyzed carbon electrodes with lower oxygen content. The low oxygen content in the carbon film and its smooth surface are believed to be responsible for low capacitance ($8 \mu\text{F}/\text{cm}^2$), a feature that may be important for analytical applications.

Although these first studies were directed at 2-D interdigitated electrodes ($L/d \ll 1$) whose structures are not very useful for the proposed 3-D designs, it is apparent, nonetheless, that this microfabrication approach can be adapted for 3-D array electrodes. The recent work reported by Madou and colleagues demonstrated the types of electrode arrays that constitute the key design element for the interdigitated 3-D battery.¹⁷ By using a process similar to their initial work,²⁵⁴ but with a negative photoresist, carbon arrays with much higher L/d ratios were prepared, as shown in Figure 22.

The results by Madou et al. are especially significant, as they clearly demonstrate the ability to fabricate array electrodes with aspect ratios that are on the order of 20:1. At these aspect ratios, the analytical models indicate that the capacity of 3-D batteries exceeds that of 2-D geometries. Two key questions remain to be answered for C-MEMS: are these electrodes electrochemically reversible to lithium, and what is the resistance of rods with such high aspect ratios?

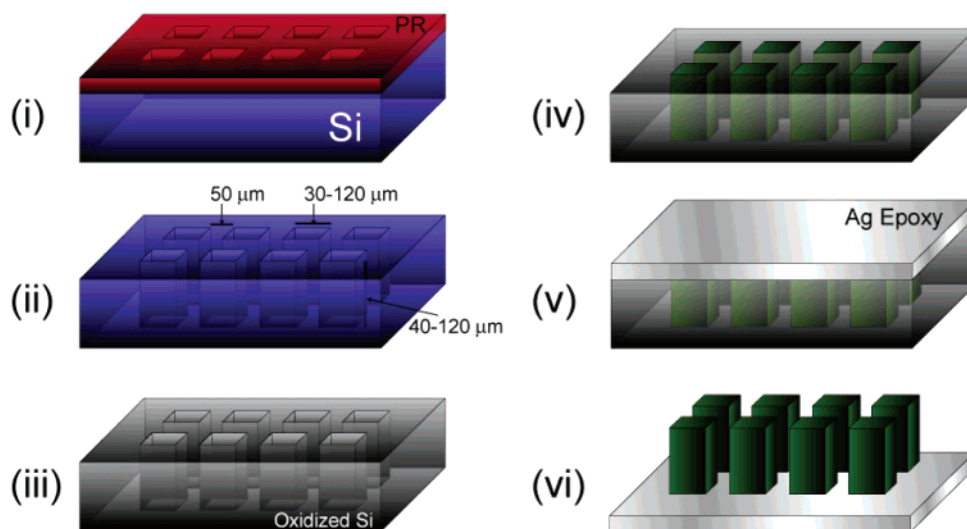


Figure 23. Processing flow for 3-D electrode array fabrication using silicon micromachining with colloidal filling of the electrode material. The six steps are identified as the following: (i) patterned photoresist (PR) on silicon substrate, (ii) PR removal after DRIE micromachining, (iii) insulate silicon mold by oxidation, (iv) colloidal electrode filling material centrifuged into the mold, (v) silver epoxy added to provide mechanical stability and electrical contact, (vi) the electrode flipped over and released from the mold by immersion in a TEOAH solution.

This first question concerning electrochemical properties has been answered in a series of half-cell experiments using the C-MEMS array as the working electrode and lithium as both the counter and reference electrode.²⁵⁶ In these experiments, reversible intercalation of lithium was demonstrated with C-MEMS array electrodes with an aspect ratio as high as 6:1. Voltammetric sweeps indicate that the electrochemical behavior is similar to that of coke electrodes as most of the lithium intercalation occurs below 0.5 V, with a broad deintercalation peak at 0.3 V. Galvanostatic measurements on the C-MEMS arrays show a large irreversible capacity loss on first discharge followed by good cycling properties, which is also consistent with the behavior of coke electrodes. The lithium capacity normalized to the footprint area of the electrode array is 0.125 mA h cm⁻². This value is nearly twice that of an unpatterned pyrolyzed film of SU-8 photoresist.²⁵⁶ The reason for the higher capacity is due to the greater active volume, contributed by the carbon posts, over the footprint area. Gravimetrically, these lithium capacities are within the range of values reported for coke electrodes. However, as discussed in the Introduction, the more relevant parameter to use in characterizing array electrodes is the lithium capacity per unit area of the array footprint.

The second key question—the resistance of carbon rods with high aspect ratios—is just beginning to be addressed. The first measurements made on individual pyrolyzed carbon rods with $L/d = 6$ and a diameter of $\sim 25 \mu\text{m}$ indicated resistance values on the order of 90–100 ohms. These measured values are reasonably consistent with calculated resistances based on the resistivity values reported for pyrolyzed photoresist. Future work that combines experiments with simulations will be able to establish how lithium capacity varies with aspect ratio.

6.1.2. Micromachining of Silicon Molds

A second approach for fabricating electrode arrays has involved micromachining of silicon molds,²⁵⁷ which are filled with electrode material by colloidal processing methods. In contrast to C-MEMS, this fabrication approach is suitable for both anodes and cathodes, as one merely alters the composition of the powders. The process flow for electrode array fabrication is depicted in Figure 23.

The silicon molds are prepared using photolithography and deep-reactive ion etching (DRIE). A 12- μm layer of photoresist is spin-coated onto a silicon wafer and patterned with an array of circles, ranging from 30–120 μm in diameter, 50 μm apart. The UV-exposed sections are dissolved away with developer and 40–120- μm -deep holes in the exposed areas of silicon are created by DRIE. From these dimensions, it was possible to explore the fabrication of electrode arrays of different L/d ratios. The mold is cleaned in a Piranha bath ($\text{H}_2\text{SO}_4/\text{H}_2\text{O}_2$ solution) and a 1 μm thick thermal oxide is grown on the silicon using wet oxidation at 1100 °C. The presence of the oxide layer helps in releasing the infiltrated electrode array.

The second step involves filling the silicon mold with the electrode powders. Several different active electrode powders were investigated including LiCoO_2 , carbon black, single-wall carbon nanotubes (SWNT), and vanadium oxide nanorolls (VONR). The active material is mixed with a binder (polyvinylidene fluoride, PVdF) in order to keep the array intact. The addition of binder is a standard procedure in the fabrication of battery electrodes, as is the addition of carbon black to improve the electronic conductivity of cathodes.¹ The silicon mold was placed in a vial containing a suspension of the electrode powders in ethylene glycol and then centrifuged, during which time the powders filled the silicon mold. The mold was removed from the vial and heated to 200 °C to evaporate the ethylene glycol and melt the PVdF,

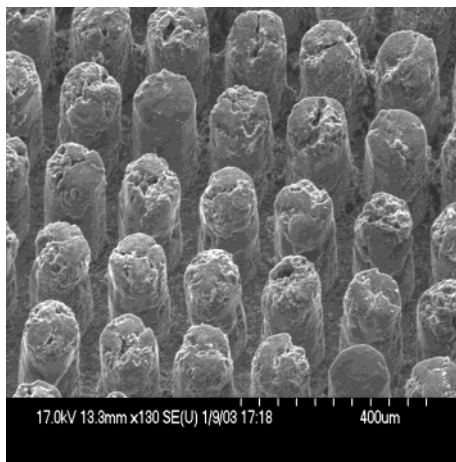


Figure 24. Electrode array prepared by the powder processing method shown in Figure 23. The electrode array structure is intact, although the individual rods contain defects.

thus binding the active electrode powders. Silver epoxy was spread over the back of the mold to maintain the mechanical integrity of the array as well as to provide electrical contact.

The final step in the process is to remove the electrode array from the silicon mold. This releasing function is accomplished by immersing the filled mold in an aqueous solution of tetraethylammonium hydroxide (TEAOH) heated to 80 °C. As the TEAOH begins to dissolve the silicon, the electrode array separates from the mold, usually as an intact piece. An SEM image of an array of vanadium oxide nanorolls is shown in Figure 24. It is evident from this photomicrograph that the fabrication process is far from perfect. The individual rods have defects including pores and cracks, and the arrays occasionally have missing rods.

The electrochemical properties of the micromachined electrode arrays have been determined for several of the electrode materials. In these half-cell experiments, the electrode array served as the working electrode and lithium as the counter and reference electrodes. The first experiments were carried out on carbon arrays composed of powders of Ketjen Black. Reversible intercalation and deintercalation of lithium were obtained, and reversible capacities in the range of 0.4–0.5 mA h cm⁻² were reported.²⁵⁷

Recent results with vanadium oxide nanorolls indicate that array electrodes prepared with these materials exhibit reversible intercalation of lithium and behave in much the same fashion as conventional VONR electrodes. Discharge curves for the first three cycles of a VONR array for $L/d = 3$ and a footprint area of 10 mm² are shown in Figure 25. The plateaus observed in these experiments are consistent with the results we obtained for well-ordered VONR powders.²⁵⁸ Figure 25 shows that the arrays exhibit good cycling properties and the lithium capacity normalized to the footprint area is ~ 1.5 mA h cm⁻². This electrode-area-normalized capacity is about 10 times higher than the value reported for thin-film cathodes.¹³ Once again the higher capacity for the footprint area is due to the greater volume contributed by the VONR posts.

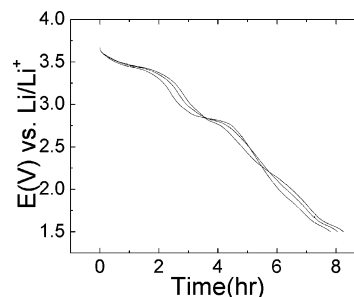


Figure 25. Discharge curves for the first three cycles for an electrode array composed of vanadium oxide nanorolls (see Figure 24). The current was 20 μ A and the footprint for the electrode array was 10 mm².

The micromachining of silicon molds is one key factor that determines the dimensions of the electrode array and, therefore, the energy of the 3-D battery. The use of electrochemical etching in HF to fabricate high-aspect-ratio trenches in silicon was introduced in 1990.²⁵⁹ Several groups have applied this technique in the fabrication of microstructures.²⁶⁰ Recently, Chamran et al. reported the use of this technique for 3-D microbattery fabrication.²⁶¹ The process flow is shown in Figure 26a. High intensity from the illumination source ensures that the electronic hole concentration is sufficiently high to sustain the etching process. The locations of the etched holes are determined by the initiation tips lithographically formed on top of the wafer before the photoelectrochemical etching starts. The narrow dimension concentrates the local electric field and ensures that etching occurs primarily at the tip. The resulting mold has etched holes with L/d ratios > 10 . The importance of high, localized fields for electrochemical micromachining has also been exploited to create precision features below 100 nm by using a sequence of 500-ps pulses.²⁶²

Calculations indicate that 3-D batteries constructed from electrode arrays with the dimensions shown in Figure 26b will be capable of providing over 2 mW h in a 5-mm³ package, an appropriate size and energy for powering MEMS devices. The holes are 5 μ m in diameter by 100- μ m-long and the center-to-center distance between holes is 10 μ m. For such dimensions, it is not known whether the colloidal processing approach described above will be effective, and it may be necessary to develop alternative powder-filling methods.

6.2. 3-D Fabrication Based on 2-D Structures: Origami

Another approach to forming 3-D electrode structures is based on various folding strategies. This "origami" approach was first reported for electronic and optoelectronic systems, as there is great interest in developing three-dimensional electronic networks and microelectronic devices. The folding of both planar²⁶³ and linear²⁶⁴ structures into 3-D configurations has been demonstrated; the adaptation of this work to electrochemical devices is just starting. Shao-Horn et al. reported on the assembly of 3-D electrochemical structures using patterned 2-D electrode sheets.¹⁸ The electrodes were designed to fold at

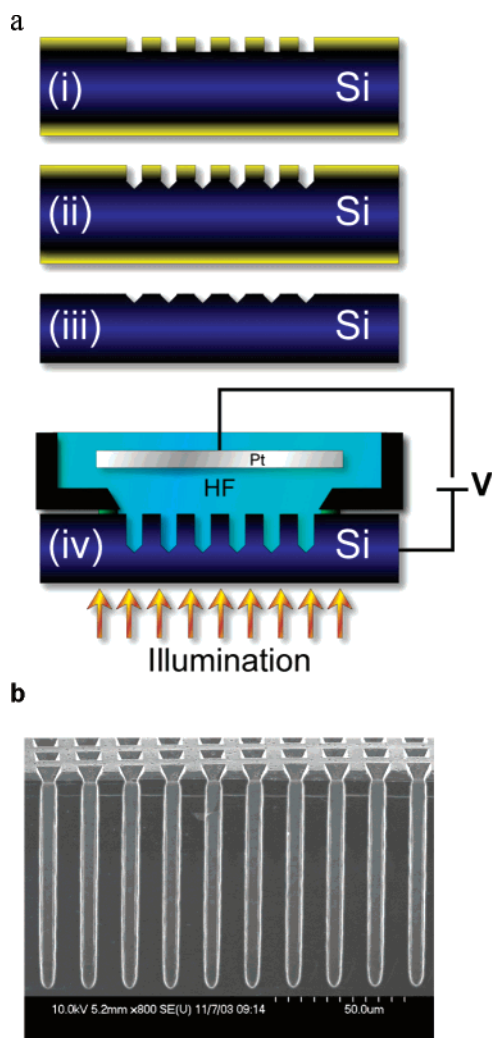


Figure 26. (a) Process flow for the fabrication of high-aspect-ratio holes in silicon as based on photoassisted etching: (i) thermal oxide is grown on n-Si and patterned; (ii) KOH etching through the holes; (iii) removal of oxide; and (iv) photoassisted anodic etching of silicon in HF. (b) Cross-section of silicon etched by the photoassisted process yielding an array of holes of 5- μm diameter by $\sim 100\text{-}\mu\text{m}$ -long; the center-to-center distance between holes is 10 μm .

specific creases based on the application of Lorentz forces. The 3-D structure is then assembled by the sequential folding of the 2-D electrode sheets. This work is clearly at its inception, as current efforts have only been able to achieve limited folding. Efforts are underway to demonstrate a 3-D capacitor structure.

The attractive feature of the origami approach is the prospect of using readily manufacturable 2-D patterning to form the electrochemical components. By proper folding, these 2-D components are then assembled into 3-D structures. The difficulty to date seems to be in the actual folding process. A significant difference between the 3-D electronic structures and the electrochemical structures is that the former rely on capillary forces from molten solder to achieve folding. As the liquid solder tries to minimize surface area, it self-assembles the 1-D or 2-D precursors into a 3-D structure. Upon cooling, the solder serves to provide both electrical connection and mechanical stability to the 3-D electronic network. The solder approach is not viable for electrochemical devices,

because the anode and cathode must be electrically isolated. Nonetheless, the use of capillary force to cause folding is attractive, and it would seem that there is an opportunity to use other materials with more compatible electrical properties. Much of the work done with conducting polymers that serve as actuators under various applied forces may also be adaptable to the origami effort.²⁶⁵

7. Advances toward Integration of Active Components into a 3-D Battery

7.1. Present Status

The construction of an operational, fully 3-D battery has yet to be achieved. However, as the previous sections have shown, on an individual basis, most of the active components for the 3-D designs presented in Figure 2 have been demonstrated successfully. Both anode and cathode array electrodes, the design elements that form the basis of the interdigitated battery (Figure 2a), have been fabricated and their electrochemical properties determined. The next key step is to carefully align these arrays so that interdigitation is achieved. The concentric tubule approach is also well along as carbon honeycomb electrode structures have recently been prepared.⁹⁷ These structures represent the continuous electrode phase (Figure 2c) and can serve as the porous membrane template, instead of alumina, for growing electrode materials.⁷⁴ One critical feature that needs to be resolved is the presence of an electrolyte that separates the two electrodes.

Of all the battery designs, it is the continuous sponge that is furthest along toward integrating components into a 3-D architecture (Figure 2d). This approach involves the design and fabrication of a three-dimensional network from the appropriate nanoscale building blocks, including the use of “nothing” (void space) and deliberate disorder as design components. A recent accomplishment in this area has been the electrodeposition of a conformal electrolyte layer on an aerogel substrate: complete integration of the electrode and electrolyte in a random 3-D network. The last step in the fabrication of this 3-D battery is to integrate an interpenetrating anode.

The importance of developing pinhole-free, electrolyte films of nanometer thickness is potentially useful for all 3-D battery designs. For this reason, most of this section reviews the synthesis and characterization of this ultrathin polymer electrolyte with an emphasis on topics such as leakage currents and dielectric strength, which become critically important at the nanoscale. A few comments concerning the packaging of 3-D batteries are made at the end.

7.2. Electrodeposition of Dielectrics—Separators and Cation-Conductive Electrolytes

One of the key steps en route to a 3-D nanoscopic battery requires fabricating an ultrathin film of a polymer separator/electrolyte over chemically stable, physically rugged, cation-insertion oxide scaffolds, such as supported films of MnOx ambigels.²⁰ In

keeping with our architectural metaphor, the fabrication protocol should be capable of painting the polymer as a conformal, ultrathin coating onto the walls of the battery building without protruding deeply into the rooms (and clogging the continuous porous network). The experiments underway create ultrathin, electronically insulating, cation-permeable films on charge-insertion oxide nanoarchitectures via electropolymerization of aryl monomers. The advantages of electropolymerizing aryl monomers include the ability to self-limit the growth of the electrogenerated polymer, usually by depositing from neutral or basic electrolytes, to yield thin (usually ~ 10 nm thick), poorly electron-conductive polymer layers that conformally coat all electrifiable surface area. Especially appealing in the design of interpenetrating 3-D batteries, electropolymerization provides a fabrication protocol that should be feasible within nanoarchitectures (unlike line-of-sight chemical vapor deposition approaches) and should ensure intimate contact at the electrode–polymer–electrolyte interface.

Such conformal, ultrathin polymer separators must satisfy a range of physical and chemical requirements in order to perform at the level necessary for charge insertion on the nanometer scale. These attributes include (i) highly electronically insulating, preferably $> 10^{-15}$ S cm $^{-1}$; (ii) pinhole-free to prevent electronic shorts between the charge-insertion cathode and the anode; (iii) ionically conducting to the charge-insertion ion (which in some designs may be a cation other than Li $^{+}$), preferably without the need for solvent or plasticizing molecules dissolved or partitioned into the polymer film; (iv) chemically nondegradable and electrochemically stable against Li metal, i.e., over a 3–4 V (vs Li) range; (v) forms a stable interface with metallic lithium, preferably without forming a highly resistive solid-electrolyte interphase layer; and (vi) exhibits a high dielectric strength, preferably $> 10^6$ V cm $^{-1}$.

The use of nanoscale (5–30-nm-thick) solid polymer electrolytes should significantly improve rate capabilities for batteries and other solid-state ionic devices and represents a considerable improvement over current micrometer-thick solid electrolytes used in thin-film batteries.^{13,266} The electro-oxidation of *o*-phenylenediamine in aqueous pH 9 electrolyte onto manganese oxide (MnO $_2$) ambigels produces a conformal polymer film that retains the mesoporosity of the original oxide and is so defect-free over the > 200 m 2 /g nanoscopic MnO $_2$ network that it prevents reductive dissolution of the MnO $_2$ nanoarchitecture upon immersion in aqueous acid.²⁰ Beyond serving as a protective coating, the poly(*o*-phenylenediamine) acts as a selective ion-transport membrane, where proton transport from the external electrolyte through the polymer coating is determined by the electrochemical state of the polymer, a phenomenon known as “electrochemical ion gating”.²⁶⁷

7.3. Hybrid Polymer–Aerogel Nanoarchitectures as Electrochemical Capacitors

The recognition that self-limited arylamine-based polymers could be electrochemically activated in aqueous acids has led to a new class of 3-D hybrid

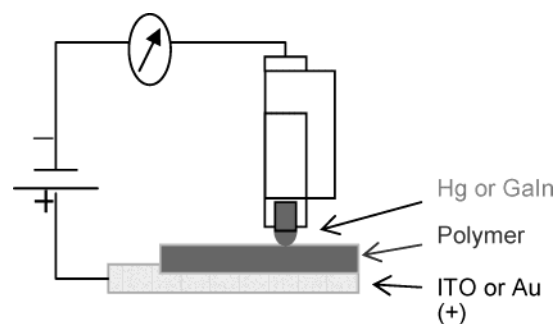


Figure 27. Schematic for solid-state electrical measurements with ultrathin polymer separators electrodeposited onto planar indium–tin oxide (ITO) or Au substrates. The top electrode makes a soft contact with the polymer by slow evaporation of Au or direct contact with a liquid metal (either Hg or GaIn eutectic) using a micrometer-controlled syringe to control the approach to contact. Measurements are made in an argon-filled glovebox to minimize effects of O $_2$ and H $_2$ O.

electrode structures. As mentioned previously, carbon aerogels are attractive electrode structures for electrochemical capacitors, because their open pore structures, high surface areas, and high electronic conductivities facilitate rapid charge–discharge reactions. However, carbon aerogels ultimately have very limited energy densities as electrochemical capacitors, since energy storage occurs primarily by the double-layer capacitance mechanism. This limitation has been addressed recently at the Naval Research Laboratory by the application of conformal, ultrathin poly(*o*-methoxyaniline) (POMA) coatings to conventional carbon aerogel electrodes. Preliminary experiments indicate that the addition of the pseudocapacitance of the POMA coatings increases the volumetric capacitance of the hybrid electrode structure by $\geq 200\%$, even at high rates of charge–discharge.²¹

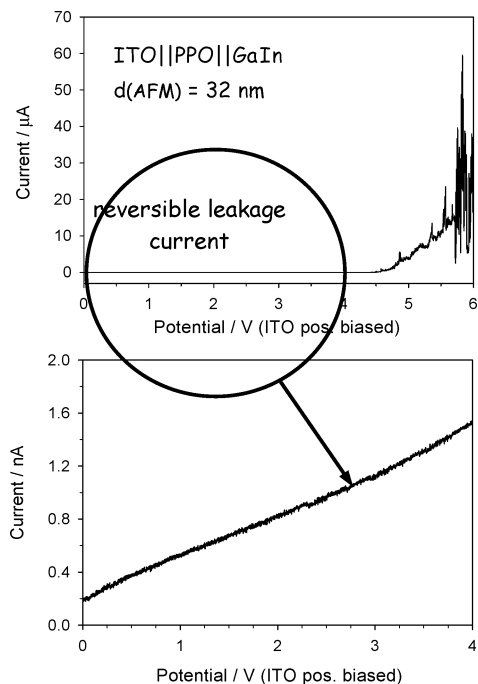
7.4. Solid-State Electrical Characterization of Conformal, Ultrathin Polymer Dielectrics

Although the literature on electrodeposited electroactive and passivating polymers is vast, surprisingly few studies exist on the solid-state electrical properties of such films, with a focus on systems derived from phenolic monomers,^{268,269} and apparently none exist on the use of such films as solid polymer electrolytes. To characterize the nature of ultrathin electrodeposited polymers as dielectrics and electrolytes, solid-state electrical measurements are made by electrodeposition of poly(phenylene oxide) and related polymers onto planar ITO or Au substrates and then using a two-electrode configuration with a soft ohmic contact as the top electrode (see Figure 27).²³ Both dc and ac measurements are taken to determine the electrical and ionic conductivities and the breakdown voltage of the film.

The electronic insulation of these electrodeposited polymer layers must hold to a two-terminal voltage of 4 V if lithium (or lithium ion) anodes are to be used in the 3-D nanobattery. Because the polymers must also be thin, high dielectric strengths are critical. As seen in Table 2, diminishing the thickness of the dielectric to the nanoscale exacts a higher standard in terms of the quality of the dielectric. For example,

Table 2. Required Dielectric Strengths for Nanometer-Thick Dielectrics

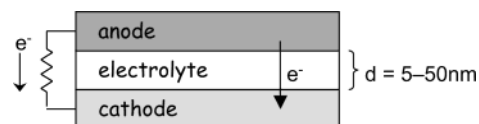
dielectric thickness/nm	field across dielectric at 3 V/(MV cm ⁻¹)
5	6
10	3
20	1.5
50	0.6

**Figure 28.** Solid-state dc electrical measurements of polyphenylene oxide in an ITO||PPO||GaIn sandwich. The thickness of the polymer was measured by tapping-mode atomic force microscopy. (Reprinted with permission from ref 23. Copyright 2004 American Chemical Society.)

placing 3 V across a 10 nm thick dielectric requires a material with a dielectric strength of 3×10^6 V cm⁻¹. Dielectrics do exist with that degree of field strength, e.g., quartz at 7×10^6 V cm⁻¹²⁷⁰ as well as polymers, e.g., poly(2,6-dimethylphenylene oxide) (PDPO) at 2.3×10^6 V cm⁻¹.²⁷¹

With an ITO||PPO||GaIn sandwich and the two-electrode configuration shown in Figure 27, a dielectric strength of $\geq 1.4 \times 10^6$ V cm⁻¹ is obtained for 32-nm-thick electrodeposited poly(phenylene oxide).²³ This value agrees with an estimated dielectric strength derived from previously reported current–voltage electrical data on 180-nm-thick poly(phenylene oxide).²⁶⁸ At voltages <4.5 V dc, the ohmic response in Figure 28 is stable; at applied voltages > 4.5 V dc, the current increases 4 orders of magnitude, from a few nanoamperes to tens of microamperes. Thus, 4.5 V dc is used to calculate an apparent dielectric strength.

The 10 000-fold increased currents at >4.5 V dc are not due to irreversible breakdown of the polymer dielectric, however, because an ohmic response is again obtained when $V_{\text{appl}} < 4.5$ V dc.²³ It appears that a reversible ion or atom migration, derived from the soft contact electrode, may be occurring. This possibility has recently been invoked to explain phenomena reported for certain molecular electronics

**Figure 29.** Schematic of the 1-D transport between an anode and cathode separated by an ultrathin, conformal polymer electrolyte.**Table 3. Self-Discharge Times for a 3-D Nanobattery as a Function of Electrolyte Thickness and Electrical Conductivity**

$\sigma_{\text{elec}}/\text{S cm}^{-1}$	thickness, d/nm	discharge time/h ^a
10^{-9}	5	10^{-5}
10^{-16}	5	10^2
10^{-16}	50	10^3

^a The calculation assumes a cathode structure with 50 μg of MnO_2 , 100 cm² of real electrode surface area, an electrode capacity of 120 mA h g⁻¹, and a 3 V operating voltage. Leakage current is calculated from the equation, $I_{\text{leak}} = V\sigma_{\text{elec}}A/d$, where V is the voltage and A is the electrode area. Discharge time is calculated by dividing capacity by the leakage current.

junctions formed at monomolecular layers between Au contacts.²⁷²

Ions can be introduced into these conformal, ultrathin polymers by exposure to nonaqueous electrolytes. Electrochemical cycling of the MnO_2 ||PPO hybrid in 1 M $\text{LiClO}_4/\text{CH}_3\text{CN}$ shows that Li ions are transported through the ~ 30 -nm-thick polymer film to the underlying metal oxide.²² Spectroelectrochemical measurements verify that the polymer-encapsulated mesoporous MnO_2 nanoarchitecture undergoes the normal cation-insertion reactions with Li ions from the external electrolyte; the charge under the voltammetric curves is comparable with and without the polymer.

7.5. Ultrathin Polymer Electrolyte—Leakage Currents

As discussed in section 2.5, one must be cognizant of the thickness of the dielectric/electrolyte that is sandwiched by the 3-D interpenetrating anode and cathode. Even with highly electronically insulating polymers, nanoscale distances that surpass those necessary to sustain quantum tunneling can lead to leakage currents, arising from small electrical conductivities at such short transport path lengths. For the 1-D transport characteristic of the aperiodic 3-D nanoarchitecture, as shown schematically in Figure 29, and with a dielectric thickness that falls below 0.1 μm , self-discharge can render 3-D nanobatteries useless, as shown in Table 3. The importance of negligible electronic conductivity for the dielectric cannot be overemphasized when the length scales are nanoscopic.

7.6. Last Step: Add an Interpenetrating Anode

Two-thirds of the assembly necessary to form the sponge architecture for a 3-D battery have now been demonstrated. By having a suitable pinhole-free, thin-to-ultrathin polymer barrier formed over the “walls” of the battery architecture, the remaining free volume can be filled with a counter electrode, as described above and depicted schematically in Figure

2d. The resulting architecture will be a solid-state, fully integrated 3-D battery. The use of mesoporous, high surface area aerogels and ambigels as substrates maximizes the interface between the cathode and anode, while the electrodeposited polymer minimizes the separation between the cathode and anode. In contrast to other 3-D designs, this nanostructure collapses to a uniform 2-D current density distribution and more effectively utilizes available volume.

7.7. Packaging of 3-D Batteries

A key issue that must be addressed in order for 3-D batteries to become viable for small power applications is packaging. The need to protect the battery in a volumetrically efficient package design without affecting battery materials or chemistry is a significant challenge. As discussed throughout this paper, MEMS devices represent an appropriate application where 3-D batteries could be well-utilized, and the prospect of developing a conveniently packaged power source, especially one attached to the backside of the device so that the real estate available for the micromachine is not reduced (see Figure 1), would be an attractive direction. It would seem, therefore, that packaging approaches for 3-D batteries should be those that lead to independently packaged components that can be readily integrated into portable power applications.

The packaging of 3-D batteries is likely to extend beyond those designs developed for lithium polymer and thin-film batteries. The packaging protocols developed for integrated circuit technologies appear to be extremely useful, since many of the objectives of IC packaging are identical to those of batteries.²⁵¹ Two approaches which are particularly attractive are the methods developed for single chip packages: chip carriers (ceramic or polymer) and TO (transistor outline) headers. Both approaches lead to hermetic sealing and conveniently interface the component to the "outside world". One advantage with batteries is that the wire bonding requirements for attaching leads is much less demanding than that of integrated circuits. The extensive experience with these approaches and the wide variety of packaging materials available ensure that the vital issue of process compatibility with battery chemistry and materials can be addressed successfully. The resulting packaged device, a "battery chip" designed to provide milliwatt-hour energies in cubic millimeter packages, could be readily integrated on microdevices for portable power.

8. Conclusions

One of the lessons learned in the 1990s was that the enormous need for high-performance portable power is not diminishing. Consumer electronics continues to be a vibrant, worldwide market force, leading to ever-increasing demands for portable power. The inability of lithium ion batteries to fully satisfy consumer electronics has been one of the principal motivations for the dramatic rise in fuel-cell research and development. As the dimensions of devices continue to shrink, the question arises as to

how power sources of comparable scale will be fabricated. The 2-D configurations of traditional batteries may not be effective here, despite their high energy density. Instead, energy conversion and harvesting approaches may be more suitable for powering microdevices, simply because of the ability to provide on-board power. These directions are being actively investigated.

Three-dimensional batteries offer a different approach to the portable power field. In this paper we have presented 3-D designs that emphasize power sources with small areal footprints but do not compromise power and energy density. While this approach may not help solve the power needs for cell phones and laptop computers, it will have a significant impact on current and future generations of microdevices. In particular, distributed sensor networks and wireless communication systems are representative areas where 3-D batteries would be welcomed enthusiastically because the power supplies currently in use are many times the size of the device.

This paper has established some of the design rules for 3-D batteries and the accompanying materials and fabrication strategies. The battery materials field is already beginning to explore 3-D concepts. Hierarchical designs based on nanostructured materials, including the deliberate management of void space, have been organized into larger macroscopic structures and the first results are impressive, with larger gravimetric capacities for lithium and higher discharge rates. It is because of this activity in materials that most of the necessary components for 3-D batteries are already in hand and the demonstration of the first operational 3-D batteries is imminent.

9. Acknowledgments

This work has been made possible by the support of the U. S. Office of Naval Research (ONR) and the Office of the Secretary of Defense through the Multidisciplinary University Research Initiative (MURI) on 3-D Microbatteries (under Grant N00014-01-1-0757). In particular, the authors would like to thank three visionary scientific officers at the ONR who during their various tenures advocated programs to explore electrochemical power from an integrated 3-D perspective: Robert Nowak, Richard Carlin, and Michele Anderson. We also wish to acknowledge the contributions of our insightful and productive colleagues: Christopher Rhodes [ONR-MURI postdoctoral associate (2002–2004)], Michael Doescher [NRC–NRL postdoctoral associate (2002–2005)], Rhonda Stroud (NRL), Christopher Smith, Ryan Hart, George Baure, Fardad Chamran, Jimmy Lim, Chai-Won Kwon, and Tim Yeh. We also appreciate the efforts of our colleagues who provided personal communications and allowed us to include some of their work: Prof. Marc Madou (University of California-Irvine), Prof. Kris Pister (University of California-Berkeley), Prof. C.-J. Kim (UCLA), and Prof. Sarah Tolbert (UCLA).

10. References

- (1) Wakihara, M. *Mater. Sci. Eng. R-Rep.* **2001**, *33*, 109.
- (2) Tarascon, J.-M.; Armand, M. *Nature* **2001**, *414*, 359.

- (3) Sadoway, D. R.; Mayes, A. M. *MRS Bull.* **2002**, *27*, 590.
- (4) Pescovitz, D. *Small Times* **2002**, *2*, 20.
- (5) Mullins, J. *IEEE Spectrum* **2001**, 23.
- (6) Lin, L. Y.; Wu, M. C.; Sawada, R.; Mohr, J. A. *J. Lightwave Technol.* **2003**, *21*, 582.
- (7) Niarchos, D. *Sensors Actuators A-Phys.* **2003**, *106*, 255.
- (8) Tilmans, H. A. C.; De Raedt, W.; Beyne, E. *J. Micromech. Microeng.* **2003**, *13*, S139.
- (9) Hartnagel, H. L.; Rodriguez-Girones, M. *IEICE Trans. Electron.* **2003**, *E86C*, 1911.
- (10) Mehregany, M.; Zorman, C. A. *MRS Bull.* **2001**, *26*, 289.
- (11) Koeneman, P. B.; Busch-Vishniac, I. J.; Wood, K. L. *J. Microelectromech. Sys.* **1997**, *6*, 355.
- (12) Kahn, J. M.; Katz, R. H.; Pister, K. S. J. *J. Commun. Networks* **2000**, *2*, 188.
- (13) Bates, J. B.; Dudney, N. J.; Neudecker, B.; Ueda, A.; Evans, C. D. *Solid State Ionics* **2000**, *135*, 33.
- (14) Note that $1 \text{ W h} = 3600 \text{ J}$, and a 2 J mm^{-3} energy density corresponds to $0.56 \text{ mW h mm}^{-3}$. The MEMS community reports energy units as J, whereas the battery community typically uses W h, and we will use the established conventions for energy units when discussing the work from these respective communities.
- (15) Souquet, J. L.; Duclot, M. *Solid State Ionics* **2002**, *148*, 375.
- (16) Warneke, B.; Last, M.; Liebowitz, B.; Pister, K. S. J. *IEEE Comput. Magazine* **2001**, *34*, 44.
- (17) Wang, C.; Taherabadi, L.; Randhawa, A.; Madou, M.; Kwon, C.-W.; Dunn, B. In *Abstracts of the 204th Meeting of the Electrochemical Society*; Electrochemical Society: Pennington, NJ, 2003; Abstr. #1276.
- (18) Shao-Horn, Y.; Hidrovo, C.; Jurga, S. M.; Smith, H. I.; Barbastathis, G. In *Abstracts of the 204th Meeting of the Electrochemical Society*; Electrochemical Society: Pennington, NJ, 2003; Abstr. #1279.
- (19) Hart, R. W.; White, H. S.; Dunn, B.; Rolison, D. R. *Electrochem. Commun.* **2003**, *5*, 120.
- (20) Long, J. W.; Rhodes, C. P.; Young, A. L.; Rolison, D. R. *Nano Lett.* **2003**, *3*, 1155.
- (21) Long, J. W.; Dening, B. M.; Rolison, D. R. *J. Non-Cryst. Solids* **2004**, in press.
- (22) Rhodes, C. P.; Long, J. W.; Doescher, M. S.; Dening, B. M.; Rolison, D. R. *J. Non-Cryst. Solids* **2004**, in press.
- (23) Rhodes, C. P.; Long, J. W.; Doescher, M. S.; Rolison, D. R. *J. Phys. Chem. B* **2004**, *108*, in press.
- (24) Smith, C. P.; White, H. S. Submitted for publication.
- (25) Boxley, C. J.; White, H. S.; Gardner, C. E.; Macpherson, J. V. *J. Phys. Chem. B* **2003**, *107*, 9677.
- (26) Bard, A. J.; Faulkner, L. R. *Electrochemical Methods*, 2nd ed.; John Wiley: New York, 2001.
- (27) Smith, C. P.; White, H. S. *Anal. Chem.* **1993**, *65*, 3343.
- (28) Levich, V. G. *Physicochemical Hydrodynamics*; Prentice Hall: New York, 1962.
- (29) Curtright, A. E.; Bouwman, P. J.; Wartena, R. C.; Swider-Lyons, K. E. *Int. J. Nanotechnol.* **2004**, *1*, 149.
- (30) *Approaches to Combat Terrorism (ACT): Opportunities for Basic Research, Joint Workshop by The Directorate of the Mathematical and Physical Sciences, NSF and the Intelligence Community*; National Science Foundation (http://www.mitre.org/public/act/10_22_final.pdf), 2003.
- (31) Priestnall, M. A.; Kotzeva, V. P.; Fish, D. J.; Nilsson, E. M. *J. Power Sources* **2002**, *106*, 21.
- (32) Dyer, C. K. *Nature* **1990**, *343*, 547.
- (33) Humble, P. H.; Harb, J. N.; LaFollette, R. *J. Electrochem. Soc.* **2001**, *148*, A1357.
- (34) Lee, S. J.; Chang-Chien, A.; Cha, S. W.; O'Hayre, R.; Park, Y. I.; Saito, Y.; Prinz, F. B. *J. Power Sources* **2002**, *112*, 410.
- (35) Kelley, S. C.; Deluga, G. A.; Smyrl, W. H. *AIChE J.* **2002**, *48*, 1071.
- (36) Kelley, S. C.; Deluga, G. A.; Smyrl, W. H. *Electrochem. Solid-State Lett.* **2000**, *3*, 407.
- (37) Yu, J.; Cheng, P.; Ma, Z.; Yi, B. *J. Power Sources* **2003**, *124*, 40.
- (38) Yu, J.; Cheng, P.; Ma, Z.; Yi, B. *Electrochim. Acta* **2003**, *48*, 1537.
- (39) Wainright, J. S.; Savinell, R. F.; Liu, C. C.; Litt, M. *Electrochim. Acta* **2003**, *48*, 2869.
- (40) Beebe, D. J.; Mensing, G. A.; Walker, G. M. *Annu. Rev. Biomed. Eng.* **2002**, *4*, 261.
- (41) Quake, S. R.; Scherer, A. *Science* **2000**, *290*, 1536.
- (42) Choban, E. R.; Markoski, L. J.; Stoltzfus, J.; Moore, J. S.; Kenis, P. A. *Power Sources Proc.* **2002**, *40*, 317.
- (43) Kummer, J. T.; Oei, D.-G. *J. Appl. Electrochem.* **1985**, *15*, 619.
- (44) Ferrigno, R.; Stroock, A. D.; Clark, T. D.; Mayer, M.; Whitesides, G. M. *J. Am. Chem. Soc.* **2002**, *124*, 12930.
- (45) Ferrigno, R.; Stroock, A. D.; Clark, T. D.; Mayer, M.; Whitesides, G. M. *J. Am. Chem. Soc.* **2003**, *125*, 2014.
- (46) Luo, T.-J. M.; Fei, J.; Lim, K. G.; Palmore, G. T. R. In *Nanotechnology and the Environment*; Karn, B., Masciangioli, T., Colvin, V. L., Alivisatos, A. P., Eds.; American Chemical Society: Washington, DC, 2004; in press.
- (47) Takeuchi, E. S.; Leising, R. A. *MRS Bull.* **2002**, *27*, 624.
- (48) Drews, J.; Wolf, R.; Fehrmann, G.; Staub, R. *J. Power Sources* **1999**, *80*, 107.
- (49) Chen, T.; Barton, S. C.; Binyamin, G.; Gao, Z. Q.; Zhang, Y. C.; Kim, H.-H.; Heller, A. *J. Am. Chem. Soc.* **2001**, *123*, 8630.
- (50) Mano, N.; Heller, A. *J. Electrochem. Soc.* **2003**, *150*, A1136.
- (51) Mano, N.; Mao, F.; Heller, A. *J. Am. Chem. Soc.* **2002**, *124*, 12962.
- (52) Mano, N.; Mao, F.; Heller, A. *J. Am. Chem. Soc.* **2003**, *125*, 6588.
- (53) Mano, N.; Mao, F.; Shin, W.; Chen, T.; Heller, A. *Chem. Commun.* **2003**, 518.
- (54) Kim, H.-H.; Mano, N.; Zhang, X. C.; Heller, A. *J. Electrochem. Soc.* **2003**, *150*, A209.
- (55) de la Garza, L.; Jeong, G.; Liddell, P. A.; Sotomura, T.; Moore, T. A.; Moore, A. L.; Gust, D. *J. Phys. Chem. B* **2003**, *107*, 10252.
- (56) Murata, K.; Izuchi, S.; Yoshihisa, Y. *Electrochim. Acta* **2000**, *45*, 1501.
- (57) Meyer, W. H. *Adv. Mater.* **1998**, *10*, 439.
- (58) Song, J. Y.; Wang, Y. Y.; Wan, C. C. *J. Power Sources* **1999**, *77*, 183.
- (59) Jones, S. D.; Akridge, J. R. *J. Power Sources* **1993**, *44*, 505.
- (60) Neudecker, B. J.; Zuhr, R. A.; Kwak, B. S.; Bates, J. B.; Robertson, J. D. *J. Electrochem. Soc.* **1998**, *145*, 4148.
- (61) Wang, B.; Bates, J. B.; Hart, F. X.; Sales, B. C.; Zuhr, R. A.; Robertson, J. D. *J. Electrochem. Soc.* **1996**, *143*, 3203.
- (62) Bates, J. B.; Dudney, N. J.; Lubben, D. C.; Gruzalski, G. R.; Kwak, B. S.; Yu, X.; Zuhr, R. A. *J. Power Sources* **1995**, *54*, 58.
- (63) Neudecker, B. J.; Dudney, N. J.; Bates, J. B. *J. Electrochem. Soc.* **2000**, *147*, 517.
- (64) Piqué, A.; Chrisey, D. B.; Auyeung, R. C. Y.; Fitz-Gerald, J.; Wu, H. D.; McGill, R. A.; Lakeou, S.; Wu, P. K.; Nguyen, V.; Duignan, M. *Appl. Phys. A* **1999**, *69*, S279.
- (65) Wartena, R.; Curtright, A. E.; Arnold, C. B.; Piqué, A.; Swider-Lyons, K. E. *J. Power Sources* **2004**, *126*, 193.
- (66) Kishida, K.; Kuriyama, K.; Nozaki, T. *Appl. Phys. Lett.* **2002**, *81*, 5066.
- (67) El-hami, M.; Glynne-Jones, P.; White, N. M.; Hill, M.; Beeby, S.; James, E.; Brown, A. D.; Ross, J. N. *Sensors Actuators A* **2001**, *92*, 335.
- (68) Ching, N. N. H.; Wong, H. Y.; Li, W. J.; Leong, P. H. W.; Wen, Z. *Sensors Actuators A* **2002**, *97-98*, 685.
- (69) Glynne-Jones, P.; Beeby, S. P.; White, N. M. *IEEE Proc.-Sci. Meas. Technol.* **2001**, *148*, 68.
- (70) Harb, J. N.; LaFollette, R. M.; Selfridge, R. H.; Howell, L. L. *J. Power Sources* **2002**, *104*, 46.
- (71) Abbott, E. A. *The Annotated Flatland—A Romance of Many Dimensions*; Perseus Publishing: Cambridge, MA, 2002.
- (72) Sing, K. S. W.; Everett, D. H.; Haul, R. A. W.; Moscou, L.; Pierotti, R. A.; Rouquerol, J.; Siemieniowska, T. *Pure Appl. Chem.* **1985**, *57*, 603.
- (73) Penner, R. M.; Martin, C. R. *J. Electrochem. Soc.* **1986**, *133*, 310.
- (74) Martin, C. R. *Chem. Mater.* **1996**, *8*, 1739.
- (75) Lakshmi, B. B.; Patrissi, C. J.; Martin, C. R. *Chem. Mater.* **1997**, *9*, 2544.
- (76) Sides, C. R.; Li, N. C.; Patrissi, C. J.; Scrosati, B.; Martin, C. R. *MRS Bull.* **2002**, *27*, 604.
- (77) Hulteen, J. C.; Martin, C. R. *J. Mater. Chem.* **1997**, *7*, 1075.
- (78) Martin, C. R.; Mitchell, D. T. In *Electroanalytical Chemistry*; Bard, A. J., Rubinstein, I., Eds.; Marcel Dekker: New York, 1999; Vol. 21.
- (79) Rouhi, A. M. *Chem. Eng. News* **2001**, *79*, 29.
- (80) Patrissi, C. J.; Martin, C. R. *J. Electrochem. Soc.* **1999**, *146*, 3176.
- (81) Patrissi, C. J.; Martin, C. R. *J. Electrochem. Soc.* **2001**, *148*, A1247.
- (82) Li, N. C.; Patrissi, C. J.; Che, G. L.; Martin, C. R. *J. Electrochem. Soc.* **2000**, *147*, 2044.
- (83) Nishizawa, M.; Mukai, K.; Kuwabata, S.; Martin, C. R.; Yoneyama, H. *J. Electrochem. Soc.* **1997**, *144*, 1923.
- (84) Li, N. C.; Martin, C. R. *J. Electrochem. Soc.* **2001**, *148*, A164.
- (85) Li, N. C.; Martin, C. R.; Scrosati, B. *Electrochem. Solid-State Lett.* **2000**, *3*, 316.
- (86) Li, N. C.; Martin, C. R.; Scrosati, B. *J. Power Sources* **2001**, *97-8*, 240.
- (87) Che, G.; Jirage, K. B.; Fisher, E. R.; Martin, C. R.; Yoneyama, H. *J. Electrochem. Soc.* **1997**, *144*, 4296.
- (88) Che, G.; Lakshmi, B. B.; Martin, C. R.; Fisher, E. R.; Ruoff, R. S. *Chem. Mater.* **1998**, *10*, 260.
- (89) Che, G. L.; Lakshmi, B. B.; Fisher, E. R.; Martin, C. R. *Nature* **1998**, *393*, 346.
- (90) Che, G. L.; Lakshmi, B. B.; Martin, C. R.; Fisher, E. R. *Langmuir* **1999**, *15*, 750.
- (91) Martin, C. R. *Acc. Chem. Res.* **1995**, *28*, 61.
- (92) Martin, B. R.; Dermody, D. J.; Reiss, B. D.; Fang, M. M.; Lyon, L. A.; Natan, M. J.; Mallouk, T. E. *Adv. Mater.* **1999**, *11*, 1021.
- (93) Nicewarner-Peña, S. R.; Freeman, R. G.; Reiss, B. D.; He, L.; Peña, D. J.; Walton, I. D.; Cromer, R.; Keating, C. D.; Natan, M. J. *Science* **2001**, *294*, 137.
- (94) Keating, C. D.; Natan, M. J. *Adv. Mater.* **2003**, *15*, 451.
- (95) Dewan, C.; Teeters, D. *J. Power Sources* **2003**, *119*, 310.

- (96) Masuda, H.; Watanabe, M.; Yasui, K.; Tryk, D.; Rao, T.; Fujishima, A. *Adv. Mater.* **2000**, *12*, 444.
- (97) Li, N. C.; Mitchell, D. T.; Lee, K. P.; Martin, C. R. *J. Electrochem. Soc.* **2003**, *150*, A979.
- (98) Stein, A.; Schroden, R. C. *Curr. Opin. Solid State Mater. Sci.* **2001**, *5*, 553.
- (99) John, S.; Busch, K. *J. Lightwave Technol.* **1999**, *17*, 1931.
- (100) Sakamoto, J. S.; Dunn, B. *J. Mater. Chem.* **2002**, *12*, 2859.
- (101) Stein, A. *Adv. Mater.* **2003**, *15*, 763.
- (102) Kang, S.; Yu, J. S.; Kruk, M.; Jaroniec, M. *Chem. Commun.* **2002**, 1670.
- (103) Gundiah, G.; Govindaraj, A.; Rao, C. N. R. *MRS Bull.* **2001**, *36*, 1751.
- (104) Yoon, S. B.; Kim, J. Y.; Yu, J.-S. *Chem. Commun.* **2001**, 559.
- (105) Zakhidov, A. A.; Baughman, R. H.; Iqbal, Z.; Cui, C. X.; Khayrullin, I.; Dantas, S. O.; Marti, I.; Ralchenko, V. G. *Science* **1998**, *282*, 897.
- (106) Zakhidov, A. A.; Khayrullin, I. I.; Baughman, R. H.; Iqbal, Z.; Yoshino, K.; Kawagishi, Y.; Tatsuhara, S. *Nanostructured Mater.* **1999**, *12*, 1089.
- (107) Lindén, M.; Schacht, S.; Schüth, F.; Steel, A.; Unger, K. K. *J. Porous Mater.* **1998**, *5*, 177.
- (108) Liu, T. B.; Burger, C.; Chu, B. *Prog. Polym. Sci.* **2003**, *28*, 5.
- (109) Soler-Illia, G. J. d. A. A.; Crepaldi, E. L.; Grosso, D.; Sanchez, C. *Curr. Opin. Coll. Interface Sci.* **2003**, *8*, 109.
- (110) Soler-Illia, G. J. d. A. A.; Sanchez, C.; Lebeau, B.; Patarin, J. *Chem. Rev.* **2002**, *102*, 4093.
- (111) Schüth, F. *Chem. Mater.* **2001**, *13*, 3184.
- (112) Yang, P. D.; Zhao, D. Y.; Margolese, D. I.; Chmelka, B. F.; Stucky, G. D. *Chem. Mater.* **1999**, *11*, 2813.
- (113) Mann, S.; Burkett, S. L.; Davis, S. A.; Fowler, C. E.; Mendelson, N. H.; Sims, S. D.; Walsh, D.; Whilton, N. T. *Chem. Mater.* **1997**, *9*, 2300.
- (114) Palmqvist, A. E. C. *Curr. Opin. Coll. Interface Sci.* **2003**, *8*, 145.
- (115) Gin, D. L.; Gu, W. Q.; Pindzola, B. A.; Zhou, W. J. *Acc. Chem. Res.* **2001**, *34*, 973.
- (116) Lin, H. P.; Mou, C. Y. *Acc. Chem. Res.* **2002**, *35*, 927.
- (117) Patarin, J.; Lebeau, B.; Zana, R. *Curr. Opin. Coll. Interface Sci.* **2002**, *7*, 107.
- (118) Forster, S. In *Colloid Chemistry I; Topics in Current Chemistry*; Antonietti, M., Ed.; Springer: Berlin, 2003; Vol. 226.
- (119) Schüth, F. *Angew. Chem., Int. Ed.* **2003**, *42*, 3604.
- (120) Ying, J. Y.; Mehnert, C. P.; Wong, M. S. *Angew. Chem., Int. Ed.* **1999**, *38*, 56.
- (121) Polarz, S.; Antonietti, M. *Chem. Commun.* **2002**, 2593.
- (122) Ryoo, R.; Joo, S. H.; Jun, S. *J. Phys. Chem. B* **1999**, *103*, 7743.
- (123) Yang, P. D.; Zhao, D. Y.; Margolese, D. I.; Chmelka, B. F.; Stucky, G. D. *Nature* **1998**, *396*, 152.
- (124) Grätzel, M. *J. Sol-Gel Sci. Technol.* **2001**, *22*, 7.
- (125) Wang, Y. D.; Ma, C. L.; Sun, X. D.; Li, H. D. *Appl. Catal. A-Gen.* **2003**, *246*, 161.
- (126) Wang, Y. D.; Ma, C. L.; Sun, X. D.; Li, H. D. *J. Non-Cryst. Solids* **2003**, *319*, 109.
- (127) Kavan, L.; Rathousky, J.; Grätzel, M.; Shklover, V.; Zukal, A. *Microporous Mesoporous Mater.* **2001**, *44*, 653.
- (128) Froba, M.; Muth, O.; Reller, A. *Solid State Ionics* **1997**, *101*, 249.
- (129) Kluson, P.; Kacer, P.; Cajthaml, T.; Kalaji, M. *J. Mater. Chem.* **2001**, *11*, 644.
- (130) Yun, H.-S.; Miyazawa, K.; Zhou, H. S.; Honma, I.; Kuwabara, M. *Adv. Mater.* **2001**, *13*, 1377.
- (131) Yoshitake, H.; Sugihara, T.; Tatsumi, T. *Chem. Mater.* **2002**, *14*, 1023.
- (132) Zheng, J.-Y.; Pang, J.-B.; Qiu, K.-Y.; Wei, Y. *J. Mater. Chem.* **2001**, *11*, 3367.
- (133) Nishimura, S.; Shishido, A.; Abrams, N.; Mallouk, T. E. *Appl. Phys. Lett.* **2002**, *81*, 4532.
- (134) Krtil, P.; Fattakhova, D.; Kavan, L.; Burnside, S.; Grätzel, M. *Solid State Ionics* **2000**, *135*, 101.
- (135) Kavan, L.; Attia, A.; Lenzmann, F.; Elder, S. H.; Grätzel, M. *J. Electrochem. Soc.* **2000**, *147*, 2897.
- (136) Ozkan, E.; Lee, S. H.; Liu, P.; Tracy, C. E.; Tepehan, F. Z.; Pitts, J. R.; Deb, S. K. *Solid State Ionics* **2002**, *149*, 139.
- (137) Cheng, W.; Baudrin, E.; Dunn, B.; Zink, J. I. *J. Mater. Chem.* **2001**, *11*, 92.
- (138) Attard, G. S.; Bartlett, P. N.; Coleman, N. R. B.; Elliott, J. M.; Owen, J. R.; Wang, J. H. *Science* **1997**, *278*, 838.
- (139) Nelson, P. A.; Owen, J. R. *J. Electrochem. Soc.* **2003**, *150*, A1313.
- (140) Nelson, P. A.; Elliott, J. M.; Attard, G. S.; Owen, J. R. *Chem. Mater.* **2002**, *14*, 524.
- (141) Liu, P.; Lee, S. H.; Tracy, C. E.; Yan, Y. F.; Turner, J. A. *Adv. Mater.* **2002**, *14*, 27.
- (142) Huang, L. M.; Wang, Z. B.; Wang, H. T.; Cheng, X. L.; Mitra, A.; Yan, Y. X. *J. Mater. Chem.* **2002**, *12*, 388.
- (143) Baeck, S. H.; Choi, K. S.; Jaramillo, T. F.; Stucky, G. D.; McFarland, E. W. *Adv. Mater.* **2003**, *15*, 1269.
- (144) Choi, K. S.; Lichtenecker, H. C.; Stucky, G. D.; McFarland, E. W. *J. Am. Chem. Soc.* **2002**, *124*, 12402.
- (145) Jun, S.; Joo, S. H.; Ryoo, R.; Kruk, M.; Jaroniec, M.; Liu, Z.; Ohsuna, T.; Terasaki, O. *J. Am. Chem. Soc.* **2000**, *122*, 10712.
- (146) Ryoo, R.; Joo, S. H.; Kruk, M.; Jaroniec, M. *Adv. Mater.* **2001**, *13*, 677.
- (147) Joo, S. H.; Jun, S.; Ryoo, R. *Microporous Mesoporous Mater.* **2001**, *44*, 153.
- (148) Kruk, M.; Jaroniec, M.; Kim, T. W.; Ryoo, R. *Chem. Mater.* **2003**, *15*, 2815.
- (149) Kim, T. W.; Park, I. S.; Ryoo, R. *Angew. Chem., Int. Ed.* **2003**, *42*, 4375.
- (150) Lee, J.; Yoon, S.; Oh, S. M.; Shin, C. H.; Hyeon, T. *Adv. Mater.* **2000**, *12*, 359.
- (151) Fuertes, A. B.; Nevskaja, D. M. *J. Mater. Chem.* **2003**, *13*, 1843.
- (152) Fuertes, A. B.; Nevskaja, D. M. *Microporous Mesoporous Mater.* **2003**, *62*, 177.
- (153) Yu, J. S.; Kang, S.; Yoon, S. B.; Chai, G. *J. Am. Chem. Soc.* **2002**, *124*, 9382.
- (154) Lu, A. H.; Schmidt, W.; Schüth, F. *New Carbon Mater.* **2003**, *18*, 181.
- (155) Lu, A. H.; Schmidt, W.; Spliethoff, B.; Schüth, F. *Adv. Mater.* **2003**, *15*, 1602.
- (156) Yoon, S. B.; Kim, J. Y.; Yu, J.-S. *Chem. Commun.* **2002**, 1536.
- (157) Yang, H. F.; Shi, Q. H.; Liu, X. Y.; Xie, S. H.; Jiang, D. C.; Zhang, F. Q.; Yu, C. Z.; Tu, B.; Zhao, D. Y. *Chem. Commun.* **2002**, 2842.
- (158) Kim, S. S.; Pinnavaia, T. J. *Chem. Commun.* **2001**, 2418.
- (159) Vix-Guterl, C.; Boulard, S.; Parmentier, J.; Werckmann, J.; Patarin, J. *Chem. Lett.* **2002**, 1062.
- (160) Han, B. H.; Zhou, W. Z.; Sayari, A. *J. Am. Chem. Soc.* **2003**, *125*, 3444.
- (161) Taguchi, A.; Smätt, J. H.; Lindén, M. *Adv. Mater.* **2003**, *15*, 1209.
- (162) Yoon, S.; Lee, J. W.; Hyeon, T.; Oh, S. M. *J. Electrochem. Soc.* **2000**, *147*, 2507.
- (163) Lee, J.; Yoon, S.; Hyeon, T.; Oh, S. M.; Kim, K. B. *Chem. Commun.* **1999**, 2177.
- (164) Zhou, H. S.; Zhu, S. M.; Hibino, M.; Honma, I. *J. Power Sources* **2003**, *122*, 219.
- (165) Soten, I.; Ozin, G. A. *Curr. Opin. Coll. Interface Sci.* **1999**, *4*, 325.
- (166) Yang, P. D.; Deng, T.; Zhao, D. Y.; Feng, P. Y.; Pine, D.; Chmelka, B. F.; Whitesides, G. M.; Stucky, G. D. *Science* **1998**, *282*, 2244.
- (167) Rolison, D. R.; Dunn, B. *J. Mater. Chem.* **2001**, *11*, 963.
- (168) Kistler, S. S. *Nature* **1931**, *127*, 741.
- (169) Hüsing, N.; Schubert, U. *Angew. Chem., Int. Ed. Engl.* **1998**, *37*, 23.
- (170) Pierre, A. C.; Pajonk, G. M. *Chem. Rev.* **2002**, *102*, 4243.
- (171) Harreld, J.; Wong, H. P.; Dave, B. C.; Dunn, B.; Nazar, L. F. *J. Non-Cryst. Solids* **1998**, *225*, 319.
- (172) Coustier, F.; Lee, J. M.; Passerini, S.; Smyrl, W. H. *Solid State Ionics* **1999**, *116*, 279.
- (173) Long, J. W.; Swider-Lyons, K. E.; Stroud, R. M.; Rolison, D. R. *Electrochem. Solid-State Lett.* **2000**, *3*, 453.
- (174) Long, J. W.; Stroud, R. M.; Rolison, D. R. *J. Non-Cryst. Solids* **2001**, *285*, 288.
- (175) Long, J. W.; Qadir, L. R.; Stroud, R. M.; Rolison, D. R. *J. Phys. Chem. B* **2001**, *105*, 8712.
- (176) Yamamoto, T.; Nishimura, T.; Suzuki, T.; Tamon, H. *Carbon* **2001**, *39*, 2374.
- (177) Xu, J. J.; Yang, J. S. *Electrochem. Commun.* **2003**, *5*, 230.
- (178) Yang, J. S.; Xu, J. J. *J. Power Sources* **2003**, *122*, 181.
- (179) Tamon, H.; Ishizaka, H.; Yamamoto, T.; Suzuki, T. *Drying Technol.* **2001**, *19*, 313.
- (180) Tamon, H.; Ishizaka, H.; Yamamoto, T.; Suzuki, T. *Carbon* **1999**, *37*, 2049.
- (181) Rolison, D. R. *Science* **2003**, *299*, 1698.
- (182) Passerini, S.; Ressler, J. J.; Le, D. B.; Owens, B. B.; Smyrl, W. H. *Electrochim. Acta* **1999**, *44*, 2209.
- (183) Salloux, K.; Chaput, F.; Wong, H. P.; Dunn, B.; Breiter, M. W. *J. Electrochem. Soc.* **1995**, *142*, L191.
- (184) Zhang, F.; Passerini, S.; Owens, B. B.; Smyrl, W. H. *Electrochem. Solid-State Lett.* **2001**, *4*, A221.
- (185) Chaput, F.; Dunn, B.; Fuqua, P.; Salloux, K. *J. Non-Cryst. Solids* **1995**, *188*, 11.
- (186) Coustier, F.; Passerini, S.; Smyrl, W. H. *J. Electrochem. Soc.* **1998**, *145*, L73.
- (187) Dong, W.; Rolison, D. R.; Dunn, B. *Electrochem. Solid-State Lett.* **2000**, *3*, 457.
- (188) Harreld, J. H.; Dong, W.; Dunn, B. *MRS Bull.* **1998**, *33*, 561.
- (189) Le, D. B.; Passerini, S.; Guo, J.; Ressler, J.; Owens, B. B.; Smyrl, W. H. *J. Electrochem. Soc.* **1996**, *143*, 2099.
- (190) Passerini, S.; Coustier, F.; Giorgetti, M.; Smyrl, W. H. *Electrochem. Solid-State Lett.* **1999**, *2*, 483.
- (191) Dong, W.; Dunn, B. *J. Non-Cryst. Solids* **1998**, *225*, 135.
- (192) Dong, W.; Dunn, B. *J. Mater. Chem.* **1998**, *8*, 665.
- (193) Dong, W.; Mansour, A. N.; Dunn, B. *Solid State Ionics* **2001**, *144*, 31.
- (194) Harreld, J. H.; Sakamoto, J.; Dunn, B. *J. Power Sources* **2003**, *115*, 19.
- (195) Owens, B. B.; Passerini, S.; Smyrl, W. H. *Electrochim. Acta* **1999**, *45*, 215.
- (196) Bock, V.; Emmerling, A.; Fricke, J. *J. Non-Cryst. Solids* **1998**, *225*, 69.

- (197) Schaefer, D. W.; Pekala, R.; Beaucage, G. *J. Non-Cryst. Solids* **1995**, *186*, 159.
- (198) Tamon, H.; Ishizaka, H.; Mikami, M.; Okazaki, M. *Carbon* **1997**, *35*, 791.
- (199) Frackowiak, E.; Beguin, F. *Carbon* **2001**, *39*, 937.
- (200) Li, W. C.; Reichenauer, G.; Fricke, J. *Carbon* **2002**, *40*, 2955.
- (201) Pekala, R. W.; Farmer, J. C.; Alviso, C. T.; Tran, T. D.; Mayer, S. T.; Miller, J. M.; Dunn, B. *J. Non-Cryst. Solids* **1998**, *225*, 74.
- (202) Koresh, J.; Soffer, A. *J. Electrochem. Soc.* **1977**, *124*, 1379.
- (203) Salitra, G.; Soffer, A.; Eliad, L.; Cohen, Y.; Aurbach, D. *J. Electrochem. Soc.* **2000**, *147*, 2486.
- (204) Kaneko, K. *J. Membr. Sci.* **1994**, *96*, 59.
- (205) Webb, P. A.; Orr, C. *Analytical Methods in Fine Particle Technology*; Micromeritics Instrument Corp.: Norcross, GA, 1997.
- (206) Fratzl, P. *J. Appl. Crystallogr.* **2003**, *36*, 397.
- (207) Göltner, C. G.; Smarsly, B.; Berton, B.; Antonietti, M. *Chem. Mater.* **2001**, *13*, 1617.
- (208) Smarsly, B.; Antonietti, M.; Wolff, T. *J. Chem. Phys.* **2002**, *116*, 2618.
- (209) Midgley, P. A.; Weyland, M. *Ultramicroscopy* **2003**, *96*, 413.
- (210) Terasaki, O.; Ohsuna, T.; Liu, Z.; Kaneda, M.; Kamiya, S.; Carlsson, A.; Tsubakiyama, T.; Sakamoto, Y.; Inagaki, S.; Che, S.; Tatsumi, T.; Cambor, M. A.; Ryoo, R.; Zhao, D.; Stucky, G.; Shindo, D.; Hiraga, K. In *Nanoporous Materials III, Studies in Surface Science and Catalysis*; Sayari, A., Jaroniec, M., Eds.; Elsevier: Amsterdam, 2002; Vol. 141.
- (211) de Jong, K. P.; Koster, A. J. *Chem. Phys. Chem.* **2002**, *3*, 776.
- (212) Thomas, J. M.; Terasaki, O.; Gai, P. L.; Zhou, W. Z.; Gonzalez-Cabret, J. *Acc. Chem. Res.* **2001**, *34*, 583.
- (213) Sakamoto, Y. H.; Kaneda, M.; Terasaki, O.; Zhao, D. Y.; Kim, J. M.; Stucky, G.; Shim, H. J.; Ryoo, R. *Nature* **2000**, *408*, 449.
- (214) Sakamoto, Y.; Diaz, I.; Terasaki, O.; Zhao, D. Y.; Pérez-Pariente, J.; Kim, J. M.; Stucky, G. D. *J. Phys. Chem. B* **2002**, *106*, 3118.
- (215) Kaneda, M.; Tsubakiyama, T.; Carlsson, A.; Sakamoto, Y.; Ohsuna, T.; Terasaki, O.; Joo, S. H.; Ryoo, R. *J. Phys. Chem. B* **2002**, *106*, 1256.
- (216) Carlsson, A.; Kaneda, M.; Sakamoto, Y.; Terasaki, O.; Ryoo, R.; Joo, S. H. *J. Electron Microsc.* **1999**, *48*, 795.
- (217) Fernandez, J. J.; Lawrence, A. F.; Roca, J.; Garcia, I.; Ellisman, M. H.; Carazo, J. M. *J. Struct. Biol.* **2002**, *138*, 6.
- (218) Engstrom, R. C. *Anal. Chem.* **1984**, *56*, 890.
- (219) Bard, A. J.; Fan, F.-R. F.; Mirkin, M. V. *Anal. Chem.* **1989**, *61*, 132.
- (220) Bard, A. J.; Fan, F.-R. F.; Mirkin, M. V. In *Electroanalytical Chemistry*; Bard, A. J., Ed.; Marcel Dekker: New York, 1994; Vol. 18.
- (221) Bath, B. D.; White, H. S.; Scott, E. R. *Imaging molecular transport across membranes*; John Wiley: New York, 2001.
- (222) *Scanning Electrochemical Microscopy*; Bard, A. J.; Mirkin, M. V., Eds.; John Wiley: New York, 2001.
- (223) Bath, B. D.; White, H. S.; Scott, E. R. *Anal. Chem.* **2000**, *72*, 433.
- (224) Fan, F.-R. F.; Bard, A. J. *Science* **1995**, *270*, 1849.
- (225) Miki, T.; Yanagi, H. *Langmuir* **1998**, *14*, 3405.
- (226) Macpherson, J. V.; Gueneau de Mussy, J.-P.; Delplancke, J.-L. *Electrochem. Solid-State Lett.* **2001**, *4*, E33.
- (227) Macpherson, J. V.; Jones, C. E.; Barker, A. L.; Unwin, P. R. *Anal. Chem.* **2002**, *74*, 1841.
- (228) Heineman, W. R. *J. Chem. Educ.* **1983**, *60*, 305.
- (229) Long, J. W.; Young, A. L.; Rolison, D. R. *J. Electrochem. Soc.* **2003**, *150*, A1161.
- (230) Talledo, A.; Granqvist, C. G. *J. Appl. Phys.* **1995**, *77*, 4655.
- (231) Rhodes, C. P.; Dong, W.; Long, J. W.; Rolison, D. R. In *Solid State Ionics IV*; Wachsman, E. D., Swider Lyons, K. E., Carolan, M. F., Garzon, F. H., Liu, M., Stetter, J. R., Eds.; Electrochemical Society: Pennington, NJ, 2003; Vol. PV2002-26.
- (232) Dong, W.; Long, J. W.; Rolison, D. R. Unpublished data, 2001, Naval Research Laboratory.
- (233) Parsons, J. G.; Aldrich, M. V.; Gardea-Torresdey, J. L. *Appl. Spec. Rev.* **2002**, *37*, 187.
- (234) de Groot, F. *Chem. Rev.* **2001**, *101*, 1779.
- (235) McBreen, J.; Balasubramanian, M. *JOM-J. Miner. Met. Mater. Soc.* **2002**, *54*, 25.
- (236) Balasubramanian, M.; Sun, X.; Yang, X. Q.; McBreen, J. *J. Power Sources* **2001**, *92*, 1.
- (237) Yoon, W. S.; Grey, C. P.; Balasubramanian, M.; Yang, X. Q.; McBreen, J. *Chem. Mater.* **2003**, *15*, 3161.
- (238) Yoon, W. S.; Kim, N.; Yang, X. Q.; McBreen, J.; Grey, C. P. *J. Power Sources* **2003**, *119*, 649.
- (239) Hwang, B. J.; Tsai, Y. W.; Santhanam, R.; Liu, D. G.; Lee, J. F. *J. Electrochem. Soc.* **2003**, *150*, A335.
- (240) Giorgetti, M.; Berrettoni, M.; Passerini, S.; Smyrl, W. H. *Electrochim. Acta* **2002**, *47*, 3163.
- (241) Giorgetti, M.; Passerini, S.; Smyrl, W. H.; Mukerjee, S.; Yang, X. Q.; McBreen, J. *J. Electrochem. Soc.* **1999**, *146*, 2387.
- (242) Giorgetti, M.; Mukerjee, S.; Passerini, S.; McBreen, J.; Smyrl, W. H. *J. Electrochem. Soc.* **2001**, *148*, A768.
- (243) Mansour, A. N.; Smith, P. H.; Baker, W. M.; Balasubramanian, M.; McBreen, J. *Electrochim. Acta* **2002**, *47*, 3151.
- (244) Mansour, A. N.; Smith, P. H.; Baker, W. M.; Balasubramanian, M.; McBreen, J. *J. Electrochem. Soc.* **2003**, *150*, A403.
- (245) Passerini, S.; Le, D. B.; Smyrl, W. H.; Berrettoni, M.; Tossici, R.; Marassi, R.; Giorgetti, M. *Solid State Ionics* **1997**, *104*, 195.
- (246) Livage, J. *Solid State Ionics* **1996**, *86-88*, 935.
- (247) Swider Lyons, K. E.; Love, C. T.; Rolison, D. R. *Solid State Ionics* **2002**, *152-153*, 99.
- (248) Grey, C. P.; Greenbaum, S. G. *MRS Bull.* **2002**, *27*, 613.
- (249) Grey, C. P.; Lee, Y. J. *Solid State Sci.* **2003**, *5*, 883.
- (250) Chevallier, F.; Letellier, M.; Morcrette, M.; Tarascon, J.-M.; Frackowiak, E.; Rouzaud, J. N.; Beguin, F. *Electrochem. Solid-State Lett.* **2003**, *6*, A225.
- (251) Madou, M. *Fundamentals of Microfabrication*; CRC Press: Baton Rouge, LA, 1997.
- (252) Kim, J.; Song, X.; Kinoshita, K.; Madou, M.; White, B. *J. Electrochem. Soc.* **1998**, *145*, 2314.
- (253) Kostecky, R.; Song, X. Y.; Kinoshita, K. *J. Electrochem. Soc.* **2000**, *147*, 1878.
- (254) Ranganathan, S.; McCreery, R.; Majji, S. M.; Madou, M. *J. Electrochem. Soc.* **2000**, *147*, 277.
- (255) Kostecky, R.; Song, X. Y.; Kinoshita, K. *Electrochem. Solid-State Lett.* **2002**, *5*, E29.
- (256) Wang, C.; Taherabadi, L.; Jia, G.; Madou, M.; Yeh, Y.; Dunn, B. *Electrochem. Solid-State Lett.* **2004**, in press.
- (257) Baure, G.; Kwon, C.-W.; Lee, G. G.; Chamran, F.; Kim, C.-J.; Dunn, B. In *Micropower and Microdevices*; Brandon, E. J., Ryan, A., Harb, J., Ulrich, R., Eds.; Electrochemical Society: Pennington, NJ, 2002; Vol. PV2002-25.
- (258) Sun, D.; Kwon, C.-W.; Baure, G.; Richman, E.; MacLean, J.; Dunn, B.; Tolbert, S. H. Submitted for publication.
- (259) Lehmann, V.; Foll, H. *J. Electrochem. Soc.* **1990**, *137*, 653.
- (260) Foll, H.; Christophersen, M.; Carstensen, J.; Hasse, G. *Mater. Sci. Eng. R-Rep.* **2002**, *39*, 93.
- (261) Chamran, F.; Christophersen, M.; Kim, C.-J. In *Abstracts of the 204th Meeting of the Electrochemical Society*; Electrochemical Society: Pennington, NJ, 2003; Abstr. #1292.
- (262) Kock, M.; Kirchner, V.; Schuster, R. *Electrochim. Acta* **2003**, *48*, 3213.
- (263) Gracias, D. H.; Kavthekar, V.; Love, J. C.; Paul, K. E.; Whitesides, G. M. *Adv. Mater.* **2002**, *14*, 235.
- (264) Whitesides, G. M.; Boncheva, M. *Proc. Natl. Acad. Sci. U.S.A.* **2002**, *99*, 4769.
- (265) Smela, E. *Adv. Mater.* **2003**, *15*, 481.
- (266) Jang, Y. I.; Dudney, N. J.; Blom, D. A.; Allard, L. F. *J. Electrochem. Soc.* **2002**, *149*, A1442.
- (267) Burgmayer, P.; Murray, R. W. *J. Am. Chem. Soc.* **1982**, *104*, 6139.
- (268) Dubois, J.-E.; Tourillon, G.; Pham, M.-C.; Lacase, P.-C. *Thin Solid Films* **1980**, *69*, 141.
- (269) McCarty, R. L.; Thomas, R. E.; Irene, E. A.; Murray, R. W. *J. Electroanal. Chem.* **1990**, *290*, 79.
- (270) Whitehead, S. *Dielectric Breakdown of Solids*; Oxford University Press: Oxford, UK, 1953.
- (271) Adohi, B.; Gosse, J. P.; Gosse, B. *J. Phys. III* **1991**, *1*, 1623.
- (272) Service, R. F. *Science* **2003**, *302*, 556.

CR020740L

Nonaqueous Liquid Electrolytes for Lithium-Based Rechargeable Batteries

Kang Xu

Electrochemistry Branch, Sensor and Electron Devices Directorate, U.S. Army Research Laboratory, Adelphi, Maryland 20783-1197

Received November 3, 2003

Contents

1. Introduction and Scope	4303	8. Novel Electrolyte Systems	4362
1.1. Fundamentals of Battery Electrolytes	4303	8.1. Problems Facing State-of-the-Art Electrolytes	4362
1.2. The Attraction of “Lithium” and Its Challenge	4304	8.2. Functional Electrolytes: Additives	4363
1.3. From “Lithium” to “Lithium Ion”	4305	8.2.1. Bulk Electrolyte: Ion Transport	4364
1.4. Scope of This Review	4306	8.2.2. Anode: SEI Modification	4366
2. Electrolyte Components: History and State of the Art	4306	8.2.3. Cathode: Overcharge Protection	4372
2.1. Solvents	4307	8.3. New Electrolyte Components	4378
2.1.1. Propylene Carbonate (PC)	4308	8.3.1. Nonaqueous Solvents	4378
2.1.2. Ethers	4308	8.3.2. Lithium Salts	4383
2.1.3. Ethylene Carbonate (EC)	4309	8.4. Novel Electrolytes with a Wide Temperature Range	4390
2.1.4. Linear Dialkyl Carbonates	4310	8.4.1. Low-Temperature Performance	4390
2.2. Lithium Salts	4310	8.4.2. High-Temperature Performance	4399
2.2.1. Lithium Perchlorate (LiClO ₄)	4311	8.5. Electrolytes of Low Flammability	4400
2.2.2. Lithium Hexafluoroarsenate (LiAsF ₆)	4312	8.6. Polymer and Polymer Gel Electrolytes	4405
2.2.3. Lithium Tetrafluoroborate (LiBF ₄)	4312	8.6.1. Solid Polymer Electrolyte	4406
2.2.4. Lithium Trifluoromethanesulfonate (LiTf)	4312	8.6.2. Gel Polymer Electrolyte	4408
2.2.5. Lithium Bis(trifluoromethanesulfonyl)imide (LiIm) and Its Derivatives	4313	9. Concluding Remarks	4410
2.2.6. Lithium Hexafluorophosphate (LiPF ₆)	4314	10. Acknowledgments	4410
2.3. Brief Summary	4315	11. References and Notes	4411
3. Liquid Range of Electrolyte Solutions	4315		
4. Ion Transport Properties	4318		
5. Electrochemical Stability: on Inert Electrodes	4322		
5.1. Anion of Lithium Salts	4323		
5.2. Solvents	4325		
6. Electrochemical Stability: on Active Electrodes	4326		
6.1. Passivation on Lithium Anode	4326		
6.2. Electrolyte/Carbonaceous Anode Interface: SEI	4329		
6.2.1. Exfoliation and Irreversible Capacities on a Carbonaceous Anode	4329		
6.2.2. Mechanism of SEI Formation	4331		
6.2.3. Characterization of Surface Chemistry	4337		
6.3. Electrolyte/Cathode Interface	4341		
6.3.1. Passivation Film on a Cathode	4342		
6.3.2. Characterization of Surface Chemistry	4344		
6.3.3. Breakdown of Surface Layer	4346		
6.3.4. Passivation of Current Collector	4347		
6.4. A Few Words on Surface Characterizations	4351		
7. Chemical and Thermal Stability/Safety of Electrolytes	4352		
7.1. Long-Term Stability of Electrolytes at Elevated Temperatures	4352		
7.2. Stability of the SEI or Surface Layer at Elevated Temperatures	4354		
7.3. Thermal Safety of Electrolytes against Abuse	4357		

1. Introduction and Scope

1.1. Fundamentals of Battery Electrolytes

Electrolytes are ubiquitous and indispensable in all electrochemical devices, and their basic function is independent of the much diversified chemistries and applications of these devices. In this sense, the role of electrolytes in electrolytic cells, capacitors, fuel cells, or batteries would remain the same: to serve as the medium for the transfer of charges, which are in the form of ions, between a pair of electrodes. The vast majority of the electrolytes are electrolytic solution-types that consist of salts (also called “electrolyte solutes”) dissolved in solvents, either water (aqueous) or organic molecules (nonaqueous), and are in a liquid state in the service-temperature range. [Although “nonaqueous” has been used overwhelmingly in the literature, “aprotic” would be a more precise term. Either anhydrous ammonia or ethanol qualifies as a “nonaqueous solvent” but is unstable with lithium because of the active protons. Nevertheless, this review will conform to the convention and use “nonaqueous” in place of “aprotic”.]

Because of its physical location in the electrochemical devices, that is, being sandwiched between positive and negative electrodes, the electrolyte is in close interaction with both electrodes; therefore, when new electrode materials come into use, the need for



Kang Xu was born in Chengdu, China, and received his B.S. degree in Chemistry from Southwest Normal University in Chongqing, China, in 1985 and M.S. in Polymer Chemistry from Lanzhou Institute of Chemical Physics, Academy of Sciences, in 1988. After working on polymer electrolyte materials from 1988 to 1992 at Chengdu Institute of Organic Chemistry, Academy of Sciences, he went to Arizona State University and received a Ph.D. degree in Chemistry in 1996 under the tutelage of C. Austen Angell. From 1997 to 2002, he was awarded the National Research Council Research Associate Fellowship and the American Society for Engineer Education Postdoctoral Fellowship, respectively, and he served during the tenures as a guest researcher at U.S. Army Research Laboratory with T. Richard Jow as academic advisor. He was employed by the U.S. Army Research Laboratory in 2002. His research interests concern materials development for electrochemical energy storage applications, which include lithium or lithium ion batteries and electrochemical capacitors. He won R&D Achievement Awards from the Department of the Army in 1999, 2001, and 2002 for his work on electrolyte materials. He authored over 60 research publications and 11 patents and is a member of the Electrochemical Society.

compatible electrolytes usually arises. The interfaces between the electrolyte and the two electrodes often dictate the performance of the devices. In fact, these electrified interfaces have been the focus of interest since the dawn of modern electrochemistry¹ and remain so in the contemporary lithium-based rechargeable battery technologies.

In a battery,² the chemical nature of positive and negative electrodes (also called cathode and anode, respectively, although by a more strict definition, this convention is only correct during discharge) decides the energy output, while the electrolyte, in most situations, defines how fast the energy could be released by controlling the rate of mass flow within the battery. Conceptually, the electrolyte should undergo no net chemical changes during the operation of the battery, and all Faradaic processes are expected to occur within the electrodes. Therefore, in an oversimplified expression, an electrolyte could be viewed as the inert component in the battery, and it must demonstrate stability against both cathode and anode surfaces. This electrochemical stability of the electrolyte, which in actual devices is usually realized in a kinetic (passivation) rather than thermodynamic manner, is of especial importance to rechargeable battery systems, but it is often challenged by the strong oxidizing and reducing nature of the cathode and the anode, respectively. The severity of this challenge is ever increasing with the pursuit of new battery systems with higher energy densities, which drives the exploration of a more oxidizing cathode and a more reducing anode as

candidate electrode materials, and thus constantly requests improvements in electrolyte stability. Ad hoc surface chemistry is often necessary for the kinetic stability of these new electrolyte/electrode interfaces. While the potencies of electrode materials are usually quantified by the redox potential in volts against some certain reference potential,³ the stability of an electrolyte can also be quantified by the range in volts between its oxidative and reductive decomposition limits, which is known as the "electrochemical window". Obviously, the redox potential of both electrode materials must fall within this electrochemical window to enable a rechargeable battery operation.

Certainly, electrochemical stability is only one of the requirements that an electrolyte should meet. A generalized list of these minimal requirements should include the following: (1) It should be a good ionic conductor and electronic insulator, so that ion transport can be facile and self-discharge can be kept to a minimum. (2) It should have a wide electrochemical window, so that electrolyte degradation would not occur within the range of the working potentials of both the cathode and the anode. (3) It should also be inert to other cell components such as cell separators, electrode substrates, and cell packaging materials. (4) It should be robust against various abuses, such as electrical, mechanical, or thermal ones. (5) Its components should be environmentally friendly.

1.2. The Attraction of "Lithium" and Its Challenge

Lithium has long received much attention as a promising anode material. The interest in this alkali metal has arisen from the combination of its two unique properties: (1) it is the most electronegative metal (~ -3.0 V vs SHE), and (2) it is the lightest metal (0.534 g cm⁻³).³ The former confers upon it a negative potential that translates into high cell voltage when matched with certain cathodes, and the latter makes it an anode of high specific capacity (3.86 A h g⁻¹). In the 1950s lithium metal was found to be stable in a number of nonaqueous solvents despite its reactivity,⁴ and this stabilization was attributed to the formation of a passivation film on the lithium surface, which prevents it from having a sustained reaction with electrolytes. Intensified research activities resulted in the commercialization of a series of lithium-based primary cells in the 1960s and 1970s, and the electrolyte solvents ranged from organic (propylene carbonate) to inorganic (thionyl chloride and sulfur dioxide).⁵⁻⁸

The continued efforts to expand lithium chemistry into rechargeable technology, however, encountered severe difficulties in terms of the cycle life and safety.^{9,10} Soon it was realized that the source of the problems was the morphology of the lithium crystals newly deposited from the electrolytes upon recharge.^{11,12} Needlelike lithium crystals (called "dendrite") grow on the anode upon charge and, during the subsequent discharge, become electrically isolated from the substrate due to nonuniform dissolution rates at different sites of the dendrite. The direct victim of such lithium loss is energy density, because excessive lithium has to be used in the cell to make up for the loss.¹³ But more seriously, a hazard could

be caused by such “dead lithium” crystals, which are electrochemically inactive but chemically hyper-reactive due to their high surface area. When dendrite growth pierces the separator and results in an internal short, thermal runaway and explosion ensue.

The work on rechargeable lithium batteries from the 1970s to 1980s overwhelmingly concentrated on the electrolyte formulation, in the hope that proper choices of electrolyte solvents or salts would suppress or even eliminate the dendritic deposition of lithium. Among the numerous electrolyte systems investigated, an ether-based solution developed by an Israeli company seems to have achieved the apex for lithium metal-based rechargeable batteries.¹⁴ A lithium electrode is highly stable in this solution up to 120 °C because of excellent surface passivation,¹⁵ and over 300 depth discharge cycles have been reported.¹⁶ A novel redox mechanism between the salt, LiAsF_6 , and solvent, 1,3-dioxolane, shuts down the cell chemistry at temperatures higher than 125 °C, thus preventing thermal runaway.^{16,17} However, dendrite formation, especially at high charge rates, still results in capacity fade.¹⁸ In 1989 incidents of fire due to lithium rechargeable batteries in the electronic devices, followed by the manufacturer recalls, highlighted the end of general enthusiasm in lithium metal as an anode.¹⁹

1.3. From “Lithium” to “Lithium Ion”

The failure of lithium as an anode due to dendrite formation prompted the search for a way to circumvent the drastic morphological change of the anode during cell cycling. As a result, “host–guest” chemistry was considered. Also known as “intercalation”- or “insertion”-type electrodes, this concept of reversible chemistry had been applied earlier to cathode materials for lithium batteries, as represented by the trail-blazing work of Whittingham^{20,21} and the significant improvements by Goodenough et al. and others.^{22,23} Most of the host materials are transition metal oxides or chalcogenides with stable crystal lattices, and their layer or tunnel structures provide the pathways for guest ions such as the lithium ion to diffuse. By injecting or extracting electrons, the redox reactions occur on the host lattice while mobile guest ions intercalate into or deintercalate from the host matrix to compensate for regional electroneutrality. During the whole intercalation/deintercalation cycle, there are no Faradaic changes in the “guest ion”. If a similar intercalation host could be found and used as an anode material, then a battery employing such intercalation cathodes and anodes would only require the lithium ion to shuttle back and forth between the electrodes without the presence of lithium metal. The nickname “rocking-chair battery” was given to such a device that uses dual intercalation electrodes,²⁴ the working principle of which is schematically depicted in Figure 1, using the example of the state-of-the-art lithium ion chemistry.

The concept of rocking-chair lithium batteries was confirmed experimentally by using lithiated oxides ($\text{Li}_6\text{Fe}_2\text{O}_3$, LiWO_2) as interaction anodes and other oxides (WO_3 , TiS_2 , V_2O_5) as cathodes in nonaqueous

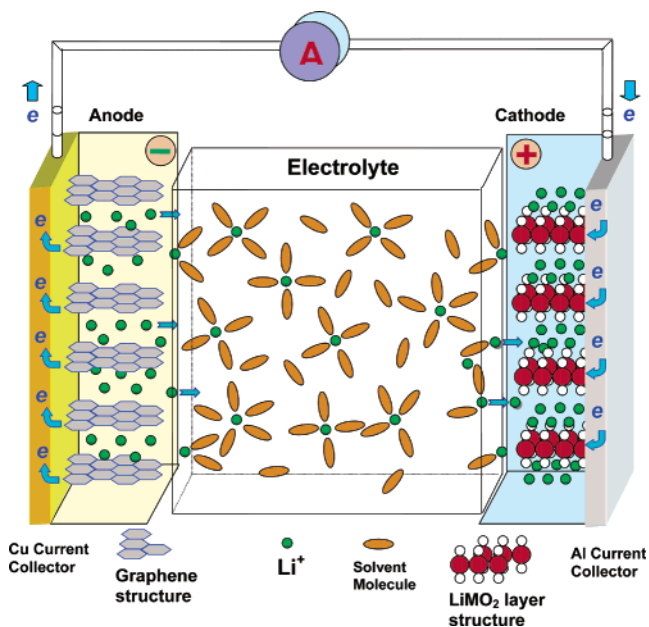


Figure 1. Schematic description of a “(lithium ion) rocking-chair” cell that employs graphitic carbon as anode and transition metal oxide as cathode. The undergoing electrochemical process is lithium ion deintercalation from the graphene structure of the anode and simultaneous intercalation into the layered structure of the metal oxide cathode. For the cell, this process is discharge, since the reaction is spontaneous.

electrolytes.^{25,26} However, the enhanced safety and extended cycle life were not sufficient to offset the penalty in energy density caused by the replacement of lithium metal; hence, these systems were never commercialized.^{27,28}

A breakthrough was made when Japanese researchers exploited an old concept of using carbonaceous materials as anode intercalation host.^{29–31} The term “lithium ion battery” that was introduced by those researchers eventually prevailed and replaced the other aliases such as “rocking-chair”,²⁴ “shuttlecock”,³² or “swing” batteries.³³ In the charged state of these carbonaceous anodes, lithium exists in its ionic rather than metallic state, thus eliminating any possibility of dendrite lithium. The advantage of this new host is highlighted by the low cost of carbon and the high lithium ion activity in the intercalation compound; the latter renders an anode potential close to that of lithium metal and minimizes the energetic penalty. In 1990 both Sony³⁴ and Moli³⁵ announced the commercialization of cells based on petroleum coke and LiCoO_2 , though Sony was generally credited for making this technology a commercial reality. In the same year Dahn and co-workers published their seminal report on the principle of lithium intercalation chemistry with graphitic anodes and the effect of electrolyte solvent in the process.³⁶ In fact, the conclusions drawn therein constitute the foundation for the current lithium ion battery industry:

(1) Electrolyte solvents decompose reductively on the carbonaceous anode, and the decomposition product forms a protective film. When the surface of the anode is covered, the film prevents further decomposition of the electrolyte components. This film is an ionic conductor but an electronic insulator.

(2) This reductive decomposition process occurs only during the first charge and is absent in the following cycles so that the carbonaceous anode can be cycled many times in the electrolyte, yielding stable capacity.

(3) The chemical structure of the electrolyte solvents critically influences the nature of the protective film, and ethylene carbonate was found to be an essential component of the solvents that protects the highly crystalline structure of graphite.

Obviously, the film formed on a carbonaceous anode plays a critical role in enabling a lithium ion device to work reversibly. Presuming that the surface nature of the carbonaceous anode at low potentials is similar to that of lithium metal in nonaqueous electrolytes, Dahn and co-workers adopted a model developed earlier by Peled to describe the passivation on lithium metal³⁷ and named this surface film on carbonaceous anodes a "solid electrolyte interface" (SEI). This term soon became the most frequently used key word in publications concerning lithium ion technology in the following decade. Although it will turn out later that the exact mechanism involved in the formation is far more complicated and remains a controversial topic even today, it has been generally agreed that the electrolyte reduction products are the main components of an SEI and dictate the chemical as well as thermal properties of the electrode.

The decade following Dahn's publication witnessed an explosive growth in lithium ion technology research, and essentially all aspects of lithium ion technology were explored with state-of-the-art techniques, while the main excitement revolved around developing new materials such as carbonaceous anode and metal oxide cathode materials and the electrolyte solvents and salts compatible with them. The result of those intensified efforts was the successful commercialization and the rapid thriving of this youngest battery chemistry. By 2000, the quantity of lithium ion cells manufactured reached ~620 million units with a market value of ~1 billion dollars,³⁸ accounting for more than a 90% share of the rechargeable battery market³⁹ or 63% of total sales in portable batteries. The employment of new materials and novel engineering designs has pushed the cycle life, energy, and power density of this technology to more than 2000 cycles, 160 W h kg⁻¹, and 5000 W kg⁻¹, respectively.⁴⁰ The major driving force of this market remains the so-called "small formula batteries" with capacities smaller than 1 A h; however, industry-size lithium ion cells are increasingly being used in space, military, and other special applications, especially as traction power sources for electric or hybrid electric vehicle (EV/HEV) applications.⁴⁰

1.4. Scope of This Review

Since the inception of lithium ion technology, there have been several reviews summarizing the knowledge accumulated about this new technology from various perspectives, with the latest being in 2003.^{41–48} Because electrolytes interact closely with both cathode and anode materials during the operation, their effect on cell performance has been discussed in

almost every one of these reviews. On the other hand, attention has always been focused on electrode materials, especially the anodes, and electrolytes as an important component of the cell have not been comprehensively treated in any dedicated reviews.

This review intends to fill this deficit by summarizing the progress made during the last 10 years in the research and development of electrolytes for lithium-based batteries. Since lithium ion chemistry is by far the only successfully commercialized rechargeable lithium-based technology, emphasis will be placed on the electrolytes developed for this system. Liquid electrolytes will take the central stage, and the scope of the review will include their ionics, phase diagrams, interfaces with cathode and anode materials, long-term chemical stability in the device, thermal properties and performance at extreme temperatures, and safety characterizations. Whenever an interdisciplinary topic involving both electrolyte and other cell components is encountered (i.e., electrolyte/electrode interface and passivation of electrodes), emphasis will be placed on the role and effect of electrolyte components.

For the convenience of this discussion, a somewhat arbitrary demarcation was drawn between "state-of-the-art" (SOA) and "novel" electrolyte systems, with the former referring to the ones currently used in commercialized lithium ion cells and the latter to the ones improved over the SOA systems but still under development. It should be pointed out that the exact electrolyte compositions in commercialized devices are usually proprietary knowledge, but publications from the affiliated researchers normally disclose sufficient information to reveal the skeletal electrolyte components employed. The distinction made in this review concerning the previously mentioned demarcation is based on such open literature.

This review will focus on the literature published from 1990 to the middle of 2003. Meanwhile, a certain amount of attention will also be allocated to the electrolytes for lithium batteries to avoid omitting the important progress made in these closely related fields. When selecting references, efforts were made to ensure academic quality as well as ready public accessibility. For this reason, patents, various technical reports, and conference/workshop presentations/abstracts were avoided to the extent possible. There were exceptions, though, when there was no alternative reference source. Finally, although comprehensive coverage was attempted, it is essentially impossible to cover every aspect in an exhaustive manner. The choice of the references and the organization of the content reflect the personal view of the author only.

2. Electrolyte Components: History and State of the Art

Most compositions of lithium electrolytes are based on solutions of one or more lithium salts in mixtures of two or more solvents, and single-solvent formulations are very rare, if there are any. The rationale behind this mixed solvent formulation is that the diverse and often contradicting requirements of bat-

Table 1. Organic Carbonates and Esters as Electrolyte Solvents

Solvent	Structure	M. Wt	$T_m/^\circ\text{C}$	$T_b/^\circ\text{C}$	η/cP 25 °C	ϵ 25 °C	Dipole Moment/debye	$T_f/^\circ\text{C}$	d/gcm^{-3} , 25 °C
EC		88	36.4	248	1.90, (40 °C)	89.78	4.61	160	1.321
PC		102	-48.8	242	2.53	64.92	4.81	132	1.200
BC		116	-53	240	3.2	53			
γ BL		86	-43.5	204	1.73	39	4.23	97	1.199
γ VL		100	-31	208	2.0	34	4.29	81	1.057
NMO		101	15	270	2.5	78	4.52	110	1.17
DMC		90	4.6	91	0.59 (20 °C)	3.107	0.76	18	1.063
DEC		118	-74.3 ^a	126	0.75	2.805	0.96	31	0.969
EMC		104	-53	110	0.65	2.958	0.89		1.006
EA		88	-84	77	0.45	6.02		-3	0.902
MB		102	-84	102	0.6			11	0.898
EB		116	-93	120	0.71			19	0.878

^a The mp of DEC recorded in various literature sources (books, papers, commercial catalogs) has been -43°C , which was corrected by a very recent measurement (ref 50e). This widespread error of 30° seems to stem from a single source in 1921, which was then registered by *Beilstein Handbuch* and escaped detection for approximately eight decades.

tery applications can hardly be met by any individual compound, for example, high fluidity versus high dielectric constant; therefore, solvents of very different physical and chemical natures are often used together to perform various functions simultaneously. A mixture of salts, on the other hand, is usually not used, because anion choice is usually limited, and performance advantages or improvements are not readily demonstrated.

Solid polymer and gel polymer electrolytes could be viewed as the special variation of the solution-type electrolyte. In the former, the solvents are polar macromolecules that dissolve salts, while, in the latter, only a small portion of high polymer is employed as the mechanical matrix, which is either soaked with or swollen by essentially the same liquid electrolytes. One exception exists: molten salt (ionic liquid) electrolytes where no solvent is present and the dissociation of opposite ions is solely achieved by the thermal disintegration of the salt lattice (melting). Polymer electrolyte will be reviewed in section 8 ("Novel Electrolyte Systems"), although lithium ion technology based on gel polymer electrolytes has in fact entered the market and accounted for 4% of lithium ion cells manufactured in 2000.³⁸ On the other hand, ionic liquid electrolytes will be omitted, due to both the limited literature concerning this topic and the fact that the application of ionic liquid electrolytes in lithium ion devices remains dubious. Since most of the ionic liquid systems are still in a supercooled state at ambient temperature, it is unlikely that the metastable liquid state could be maintained in an actual electrochemical device, wherein electrode materials would serve as effective nucleation sites for crystallization.

2.1. Solvents

In accordance with the basic requirements for electrolytes, an ideal electrolyte solvent should meet

the following minimal criteria: (1) It should be able to dissolve salts to sufficient concentration. In other words, it should have a high dielectric constant (ϵ). (2) It should be fluid (low viscosity η), so that facile ion transport can occur. (3) It should remain inert to all cell components, especially the charged surfaces of the cathode and the anode, during cell operation. (4) It should remain liquid in a wide temperature range. In other words, its melting point (T_m) should be low and its boiling point (T_b) high. (5) It should also be safe (high flash point T_f), nontoxic, and economical.

For lithium-based batteries, the active nature of the strongly reducing anodes (lithium metal or the highly lithiated carbon) and the strongly oxidizing cathodes (transition metal based oxides) rules out the use of any solvents that have active protons despite their excellent power in solvating salts, because the reduction of such protons and/or the oxidation of the corresponding anions generally occurs within 2.0–4.0 V versus Li,⁴⁹ while the charged potentials of the anode and the cathode in the current rechargeable lithium devices average 0.0–0.2 V and 3.0–4.5 V, respectively. On the other hand, the nonaqueous compounds that qualify as electrolyte solvents must be able to dissolve sufficient amounts of lithium salt; therefore, only those with polar groups such as carbonyl (C=O), nitrile (C≡N), sulfonyl (S=O), and ether-linkage (–O–) merit consideration.

Since the inception of nonaqueous electrolytes, a wide spectrum of polar solvents has been investigated, and the majority of them fall into either one of the following families: organic esters and ethers. The most commonly used solvents from these families, along with their physical properties, are listed in Tables 1 and 2, respectively,⁵⁰ where the melting temperature of diethyl carbonate (DEC) deserves special attention because a significant correction has been made recently.^{50e}

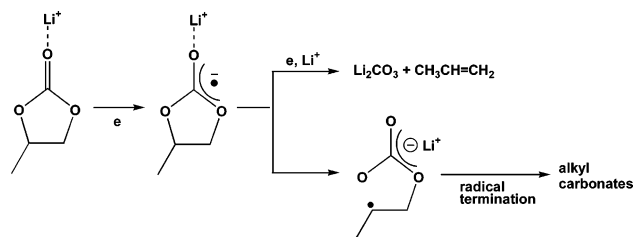
Table 2. Organic Ethers as Electrolyte Solvents

Solvent	Structure	M. Wt	$T_m/^\circ\text{C}$	$T_b/^\circ\text{C}$	η/cP 25 $^\circ\text{C}$	ϵ 25 $^\circ\text{C}$	Dipole Moment/debye	$T_f/^\circ\text{C}$	d/gcm^{-3} , 25 $^\circ\text{C}$
DMM		76	-105	41	0.33	2.7	2.41	-17	0.86
DME		90	-58	84	0.46	7.2	1.15	0	0.86
DEE		118	-74	121				20	0.84
THF		72	-109	66	0.46	7.4	1.7	-17	0.88
2-Me-THF		86	-137	80	0.47	6.2	1.6	-11	0.85
1,3-DL		74	-95	78	0.59	7.1	1.25	1	1.06
4-Me-1,3-DL		88	-125	85	0.60	6.8	1.43	-2	0.983
2-Me-1,3-DL		88			0.54	4.39			

An interesting observation should be made concerning the dependence of the physical properties on molecular cyclicity, since it will have a significant effect on the formulation of electrolytes for lithium ion cells. While all of the ethers, cyclic or acyclic, demonstrate similar moderate dielectric constants (2–7) and low viscosities (0.3–0.6 cP), cyclic and acyclic esters behave like two entirely different kinds of compounds in terms of dielectric constant and viscosity; that is, all cyclic esters are uniformly polar ($\epsilon = 40\text{--}90$) and rather viscous ($\eta = 1.7\text{--}2.0$ cP), and all acyclic esters are weakly polar ($\epsilon = 3\text{--}6$) and fluid ($\eta = 0.4\text{--}0.7$ cP). The origin for the effect of molecular cyclicity on the dielectric constant has been attributed to the intramolecular strain of the cyclic structures that favors the conformation of better alignment of molecular dipoles, while the more flexible and open structure of linear carbonates results in the mutual cancellation of these dipoles.

2.1.1. Propylene Carbonate (PC)

Among these solvents, cyclic diesters of carbonic acid have undoubtedly attracted the main research attention throughout the entire history of lithium batteries, especially in the past decade, when their role in forming an SEI on carbonaceous anodes became recognized. However, the early interest in these compounds arose solely from their high dielectric constant and, hence, their ability to dissolve a wide variety of lithium salts. In 1958, it was observed that lithium could be electrodeposited from a solution of LiClO_4 in PC,⁵¹ and PC became the immediate focus of investigation.^{4,9,10} Its wide liquid range (defined by the difference between T_m and T_b , Table 1), high dielectric constant, and static stability with lithium made it a preferred solvent, and considerable efforts were made to purify it⁵² when a less-than-ideal stripping/plating efficiency ($\leq 85\%$) for lithium was observed during cycling. The capacity of lithium cells with PC electrolytes also fades accordingly.^{4,9,10,54} However, it was soon realized that this poor cycling efficiency was more intrinsic to the electrolyte solvent than contaminant-originated, and the reaction between the PC and the newly deposited lithium particles was thought to be the cause.⁹ More recent studies employing spectroscopic means have confirmed the PC reduction on a newly formed lithium

Scheme 1. Reduction of PC on a Lithium Surface: One-Electron Process

surface, and a one-electron reduction process has been proposed (see Scheme 1).⁵⁵

The overall capacity fading of lithium cells using PC-based electrolytes, however, is a more complicated mechanism, although Scheme 1 plays a part in it. The static stability of PC against a lithium surface had been attributed earlier to the existence of a protective layer,^{37,56} which consists of the decomposition products shown in Scheme 1, and prevents the sustained reaction of PC with lithium.⁵⁵ On the other hand, it was the dynamic reactivity that results in the lithium loss during cycling,⁹ for which the main cause is related to the nonuniform morphological change of the lithium surface rather than chemical corrosion. Figure 2 schematically shows this nonuniformity of the lithium surface during the cycling process, where uneven growth of the electrodeposited lithium crystals results in dendrites that in subsequent discharge processes (lithium dissolution) produce lithium particles that are electrically isolated from the lithium anode. Microscopic studies have confirmed the existence of dendrites (Figure 3) and have attributed their formation to the presence of a passivation film.^{37,57} Serious safety hazards are often caused by the generation of both dendrites and isolated lithium crystals.^{58,59} The former creates internal shorts, and the latter is chemically active with the electrolyte solvents due to their huge surface areas.

2.1.2. Ethers

In view of the poor cycling efficiency and the potential hazards associated with PC, people turned to ethers for improved lithium morphology. In the 1980s, ethers were widely preferred by researchers as an alternative candidate, because of their low

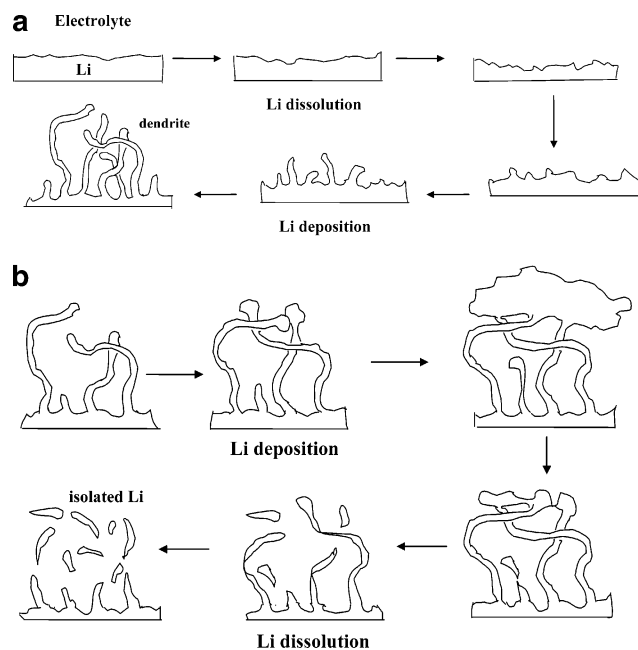


Figure 2. (a) Schematic description for the growth of dendrite crystals on a Li surface. The film consisting of decomposition products as shown in Scheme 1 prevents the growth of large granular crystals but rather promotes the formation of treelike dendrites. (b) Schematic description for the formation of isolated lithium particles from Li dendrites. The uneven dissolution of the dendrites leaves lithium crystals detached from the lithium substrate. The isolated lithium crystals become electrochemically “dead” but chemically reactive due to their high surface area.



Figure 3. Micrograph of a single dendrite lithium grown in PC. (Reproduced with permission from ref 57 (Figure 6a). Copyright 1989 The Electrochemical Society.)

viscosity and resultant high ionic conductivity, but, most of all, the better lithium morphology during cycling.⁶⁰ The cycling efficiency of lithium was reported to be 88% in tetrahydrofuran (THF),^{60–62} an average of 96% in 2-methyltetrahydrofuran (2-Me-THF),^{62–65} 97% in polymethoxy ethers⁶⁶ and dimethoxy propane,⁶⁷ and 98% in diethyl ether,^{62,68} although the safety concern over the high vapor pressure of diethyl ether renders it an impractical candidate. The formation of dendritic lithium seemed to be sufficiently suppressed in these solvents even at high charge rates.⁶² However, efforts to incorporate ether-based electrolytes in lithium cells were still troubled by the poor capacity retention,^{68–70} and prolonged cycling

(>100 cycles) of the cells still produced dendrite deposition,⁷¹ which terminated the cells by creating shorts,⁷² despite the improved lithium morphology observed in the short term.

In addition to the problem with the lithium anode, a new factor contributing to the capacity fade surfaced as the oxidative decomposition of ether-based compounds on the cathode surface.^{61,67,73} Electrochemical studies on these ether-based electrolytes placed the potential for the oxidative breakdown of the ether functionality at relatively low potentials. On a platinum surface, for example, THF was found to be oxidized at 4.0 V vs Li, while PC remained stable up to 5.0 V.⁷⁴ In an actual cell, ethers are more readily decomposed at even lower potentials, because of the highly catalytic surface of cathode materials.⁷⁶ With the application of more potent 4.0 V cathode materials (Li_xMO_2 , M = Mn, Ni, or Co) in lithium or lithium ion cells, the possibility of using ether compounds as solvents or cosolvents diminished.^{75,77} During the 1990s, various ethers were gradually phased out in most of the electrolyte systems under investigation. The failure of ether-based electrolytes served as a perfect example to illustrate that, in a battery, the electrolyte (solvents and salts) must cope with challenges from both the anode and the cathode. On the other hand, the advantage of organic esters, especially cyclic alkyl carbonates, was rediscovered because of their excellent stability against oxidation on cathode surfaces.^{74,78,79}

2.1.3. Ethylene Carbonate (EC)

The interest in alkyl carbonates was renewed with the emergence of the lithium ion “shuttle” concept.^{24–31} Gone with the lithium anode is the difficult issue of lithium morphology; subsequently, the higher anodic stability of PC made it once again a promising candidate. In the first generation of the commercial lithium ion cells, a PC-based electrolyte was used by Sony along with Li_xCoO_2 as the cathode and petroleum coke as the anode.³¹ However, the real renaissance for using alkyl carbonates as lithium electrolyte solvents was not brought about by PC but, quite unexpectedly, by its high melting cousin EC.

Compared with PC, EC has comparable viscosity and slightly higher dielectric constant, which are favorable merits for a solvent candidate (Table 1). In fact, its dielectric constant is even higher than that of the most common electrolyte solvent on the earth: water ($\epsilon \sim 79$).³ However, because of its high melting point ($\sim 36^\circ\text{C}$), it was never favored as an ambient-temperature electrolyte solvent in the early days of lithium battery research: the liquid range of the electrolytes based on it would be too restricted. Its higher melting point than those of other members of the carbonate family (Table 1) is believed to arise from its high molecular symmetry, which renders it a better stabilized crystalline lattice.^{80, 81}

EC was considered as an electrolyte cosolvent for the first time by Elliot in 1964, who noted that, due to the high dielectric constant and low viscosity of EC, the addition of it to electrolyte solutions would favor ion conductivity.⁸² The findings did not attract particular attention from the battery community

until the early 1970s, when Scrosati and Pistoia exploited it to advantages for lithium battery electrolytes. They reported that, owing to the suppression of the melting point by the presence of the solute, a room-temperature melt would form, and extra suppression could be obtained when a small percentage (9%) of PC was added.⁸³ Further investigation found that electrolytes based on EC as compared with PC demonstrated improvements, not only in bulk ion conductivity but also in interfacial properties such as lower polarization on various cathode surfaces.⁸⁴ Following these reports, EC began to appear as an electrolyte cosolvent in a number of new electrolyte systems under investigation, many of which still contained ethers.^{72,73,85–88} However, the first commercialized rechargeable lithium battery used an ether-free composition, an EC/PC mixture, as the electrolyte solvent.^{89,90} Despite the melting-point suppression by the solute and other cosolvents, the higher liquidus temperatures of the electrolyte due to EC remained a factor limiting the low-temperature applications of the lithium cell.

The unique position of EC as a lithium battery electrolyte was established in 1990 when Dahn and co-workers reported the fundamental difference between EC and PC in their effects on the reversibility of lithium ion intercalation/deintercalation with graphitic anodes.³⁶ Despite the seemingly minute difference in molecular structure between the two, EC was found to form an effective protective film (SEI) on a graphitic anode that prevented any sustained electrolyte decomposition on the anode, while this protection could not be realized with PC and the graphene structure eventually disintegrated in a process termed “exfoliation” because of PC cointercalation. The reason for the effectiveness of the SEI has incited a lot of research interest in the past decade but remains an unsolved mystery, although it is generally believed that EC undergoes a reduction process on the carbonaceous anode via a similar path to that shown in Scheme 1. Because of the important role this SEI plays in lithium ion chemistry, the research efforts on this topic will be reviewed in a dedicated section (section 6).

2.1.4. Linear Carbonates

After Sony successfully marketed the first generation lithium ion cells, numerous competitors emerged and a pursuit for higher energy density started. With the energetic advantage of highly crystalline carbon (graphitic) over disordered carbon being recognized, EC became the core and indispensable component of the electrolyte formulation.

During the early 1990s, efforts were made to expand the limited liquid range of EC-based electrolytes by using different cosolvents, including PC,^{91,92} THF and 2-Me-THF,^{73,85–88} diethoxyethane (DEE),^{93,94} and dimethoxyethane (DME).^{45,95–97} None of these cosolvents performed satisfactorily though, because the presence of PC usually caused a large irreversible capacity in the initial cycle of the lithium ion cell,^{36,91,92} while the ethers were found to be unstable against the oxidation catalyzed by the surface of the charged cathode.^{93,94} Thus, it was generally realized that, for

a lithium ion cell that employs graphite as an anode and 4.0 V metal oxide (LiMO_2 , $M = \text{Co}, \text{Ni}$) as a cathode, the electrolyte must have oxidative stability up to ~ 5 V vs Li.^{95–97}

In 1994 a formulation that successfully met such a standard was first described in open literature by Tarascon and Guyomard, who used a linear carbonate, dimethyl carbonate (DMC), as a cosolvent with EC.^{98,99} As it has been pointed out, linear carbonates differ from their cyclic cousins by their low boiling points, low viscosity, and low dielectric constant. They can form homogeneous mixtures with EC at any ratio, and the resultant mixed electrolytes benefit not only from the melting-temperature suppression of EC but also from the low viscosity (higher ion conductivity) of DMC. But what surprises researchers is the wide electrochemical stability window of this mixture electrolyte: it remains stable on a spinel cathode surface up to 5.0 V. Considering that these linear carbonates, in the absence of EC, are readily liable to oxidation on cathode surfaces at ~ 4.0 V vs Li,⁷⁶ the origin for the above improvement in the electrochemical window remains unclear, because the anodic stabilities of the ether-based electrolytes were hardly raised by their mixing with EC^{93,94} or PC.^{95,96} It seems that a synergistic effect is achieved when EC and DMC (or other linear carbonates) are mixed because the merits of each individual solvent are imparted on to the resultant mixture: high anodic stability of EC on cathode surfaces, high solvation power of EC toward lithium salts, and low viscosity of DMC to promote ion transport.

This new formulation of electrolytes based on a mixture of EC with a linear carbonate set the main theme for the state-of-the-art lithium ion electrolytes and was quickly adopted by the researchers and manufacturers.^{97,100–103} Other linear carbonates were also explored, including DEC,^{104–106} ethylmethyl carbonate (EMC),¹⁰⁷ and propylmethyl carbonate (PMC),^{108,109} and no significant differences were found between them and DMC in terms of electrochemical characteristics. The direct impact of this electrolyte innovation is that the first generation carbonaceous anode petroleum coke was soon replaced by graphitic anode materials in essentially all of the lithium ion cells manufactured after 1993. At present, the electrolyte solvents used in the over one billion lithium ion cells manufactured each year are almost exclusively based on the mixture of EC with one or more of these linear carbonates, although each individual manufacture may have its own proprietary electrolyte formulation.

2.2. Lithium Salts

An ideal electrolyte solute for ambient rechargeable lithium batteries should meet the following minimal requirements: (1) It should be able to completely dissolve and dissociate in the nonaqueous media, and the solvated ions (especially lithium cation) should be able to move in the media with high mobility. (2) The anion should be stable against oxidative decomposition at the cathode. (3) The anion should be inert to electrolyte solvents. (4) Both the anion and the cation should remain inert toward the other cell components such as separator, electrode substrate,

Table 3. Lithium Salts as Electrolyte Solutes

Salt	Structure	M. Wt	T _m /°C	T _{decomp.} / °C in solution	Al-corrosion	σ / mScm ⁻¹ (1.0 M, 25 °C)	
						in PC	in EC/DMC
LiBF ₄		93.9	293 (d)	> 100	N	3.4 ^a	4.9 ^c
LiPF ₆		151.9	200 (d)	~ 80 (EC/DMC)	N	5.8 ^a	10.7 ^d
LiAsF ₆		195.9	340	> 100	N	5.7 ^a	11.1 ^c
LiClO ₄		106.4	236	>100	N	5.6 ^a	8.4 ^d
Li Triflate	Li ⁺ CF ₃ SO ₃ ⁻	155.9	>300	>100	Y	1.7 ^a	
Li Imide	Li ⁺ [N(SO ₂ CF ₃) ₂] ⁻	286.9	234 ^b	>100	Y	5.1 ^a	9.0 ^e
Li Beti	Li ⁺ [N(SO ₂ CF ₂ CF ₃) ₂] ⁻				N		

^a Reference 111. ^b Reference 146. ^c Reference 114. ^d Reference 115. ^e Reference 116.

and cell packaging materials. (5) The anion should be nontoxic and remain stable against thermally induced reactions with electrolyte solvents and other cell components.

The available choice of lithium salts for electrolyte application is rather limited when compared to the wide spectrum of aprotic organic compounds that could make possible electrolyte solvents. This difference could be more clearly reflected in a comprehensive report summarizing nonaqueous electrolytes developed for rechargeable lithium cells, in which Dahn and co-workers described over 150 electrolyte solvent compositions that were formulated based on 27 basic solvents but only 5 lithium salts.^{50b}

Because of the small ionic radius of lithium ion, most simple salts of lithium fail to meet the minimum solubility requirement in low dielectric media. Examples are halides, LiX (where X = Cl and F), or the oxides Li₂O. Although solubility in nonaqueous solvents would increase if the anion is replaced by a so-called "soft Lewis base" such as Br⁻, I⁻, S²⁻, or carboxylates (R-CO₂⁻), the improvement is usually realized at the expense of the anodic stability of the salt because these anions are readily oxidized on the charged surfaces of cathode materials at <4.0 V vs Li.

Most of the lithium salts that are qualified for the minimal solubility standard are based on complex anions that are composed of a simple anion core stabilized by a Lewis acid agent. For example, the anion of lithium hexafluorophosphate (LiPF₆) could be viewed as F⁻ complexed by the Lewis acid PF₅. Such anions, also known as anions of superacids, have a structure in which the formal negative charge is well distributed by the strongly electron-withdrawing Lewis acid ligands, and the corresponding complex salts are usually lower melting and better soluble in low dielectric media than their parent salts.

The requirement for chemical inertness further excluded a family of lithium salts that have been widely used in primary lithium batteries: LiAlX₄ (X = halides).¹¹⁰ Since the Lewis acidities of the AlX₃ are so strong, their complexation with the moderate

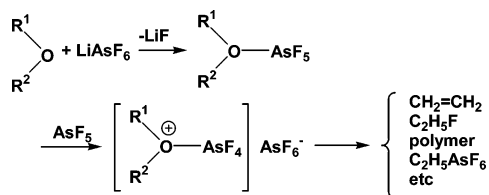
bases such as Cl⁻ does not fully neutralize their activity, and as a result, they would attack most of the nonaqueous solvents, especially ethers. The AlX₄⁻ anions also cause severe corrosion to other cell components such as the separators, usually made of polypropylene, and the insulating sealant, as well as the metallic packaging materials. On the other hand, anions based on milder Lewis acids can remain stable with organic solvents under normal conditions (e.g., ambient temperature) and have been preferentially investigated by researchers. These salts include lithium perchlorate (LiClO₄) and various lithium borates, arsenates, phosphates, and antimonates, LiMX_n (where M = B or As, P, and Sb and n = 4 or 6, respectively). Table 3 lists some examples of these salts along with some basic physical properties,^{50c} including ion conductivity data at room temperature in PC or EC/DMC (1:1), respectively.^{50d,111–116} A brief summary of a few selected lithium salts of significance during the development of lithium cell electrolytes is given below.

2.2.1. Lithium Perchlorate (LiClO₄)

LiClO₄ has been a popular electrolyte solute owing to its satisfactory solubility and high conductivity (~9.0 mS cm⁻¹ in EC/DMC at 20 °C) as well as its high anodic stability (up to 5.1 V on a spinel cathode surface in EC/DMC).⁹⁹ Recent studies found that SEI films formed in LiClO₄ electrolytes, on both lithium and carbonaceous anode surfaces, are of lower impedance than those formed in LiPF₆ or lithium tetrafluoroborate (LiBF₄) electrolytes, because the HF is absent in the former.^{104,117} It is believed that HF, generated as the hydrolysis product of LiPF₆ and LiBF₄ by trace moisture in the electrolyte solvents, reacts with either alkyl carbonate or Li₂CO₃ and forms the highly resistive LiF.^{117,118} Compared with other lithium salts, LiClO₄ also has the merits of being relatively less hygroscopic and is stable to ambient moisture.

However, the high oxidation state of chlorine (VII) in perchlorate makes it a strong oxidant, which readily reacts with most organic species in violent ways under certain conditions such as high temper-

Scheme 2. Reaction between LiAsF₆ and Ether Solvents

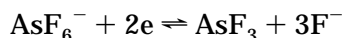


ature and high current charge.^{58,119} Actually, back in the 1970s it had already been realized that LiClO₄ was impractical as an electrolyte solute for industry purposes;¹¹⁹ nevertheless, it is still frequently used as a salt of convenience in various laboratory tests because it is easy to handle and economical.^{43,79,91,94}

2.2.2. Lithium Hexafluoroarsenate (LiAsF₆)

While researchers focused on the morphology of lithium cycling in nonaqueous electrolytes during the late 1970s, it was found that the salt plays an important role beside the solvents, and in general, LiAsF₆ was a superior salt to LiClO₄ as an electrolyte solute for lithium batteries.⁵⁴ For a long period, the combination of LiAsF₆ with various ethers became the most popular system under investigation.^{60,62,68,69,78} On average, lithium cycling efficiencies could reach >95% in these systems,^{54,62,66} although long-term cycling in these electrolytes still promoted the growth of lithium dendrites.⁷¹ Chemical deterioration was also detected, as indicated by the discoloration of the LiAsF₆/2-Me-THF solution with time, and a reaction between LiAsF₆ and the solvent was suspected.^{65,68} A mechanism was proposed based on the Lewis acidity of As(V), which cleaves the ether linkage and produces a series of gaseous and polymeric products (see Scheme 2).⁶⁸

The cathodic stability of the AsF₆⁻ anion was studied on a glassy carbon surface, and a reduction process was found at ~1.15 V vs Li:¹²⁰



The above process was observed only in the initial cycles. Nevertheless, any electrochemical reduction of As(V) would raise concern about the safety of using LiAsF₆ in a commercial battery, because, while arsenate in its high oxidation state (V) is not particularly toxic, As(III) and As(0) species are.^{68,120–122} From the electrochemical point of view, however, the above reduction could be a benefit, especially for lithium ion cells, since an SEI formed on an anode at > 1.0 V vs lithium would be very stable during the operation of a lithium ion cell according to a semi-empirical rule,¹⁰⁶ which will be discussed in more detail in section 6.

Very similar to the case of LiClO₄, an SEI formed from LiAsF₆-based electrolytes, either on a lithium or carbonaceous anode, mainly consists of alkyl carbonates or Li₂CO₃ rather than LiF, as one would expect from the behavior of its close structural brothers LiPF₆ or LiBF₄.^{104,117,118} This can be attributed to the much less labile As–F bond that is resistive to hydrolysis.¹²⁰

The anodic stability of the AsF₆⁻ anion proved to be high. In proper solvents, such as esters rather than ethers, the electrolyte based on this salt can remain stable up to 4.5 V on various cathode surfaces.^{78,99} The combination of cathodic and anodic stability would have made LiAsF₆ a very promising candidate salt for both lithium and lithium ion batteries had the toxicity not been a source of concern. Instead, it was never used in any commercialized cells but is still frequently used in laboratory tests even today.^{14–18,123–125}

2.2.3. Lithium Tetrafluoroborate (LiBF₄)

Like LiAsF₆, LiBF₄ is a salt based on an inorganic superacid anion and has moderate ion conductivity in nonaqueous solvents (Table 3). It was out of favor in the early days of lithium battery research because the ether-based electrolytes containing it were found to result in poor lithium cycling efficiencies, which decayed rapidly with cycle number.^{60,126–128} The reactivity of LiBF₄ with lithium was suspected as discoloration occurred with time or heating.¹²⁸

The researchers who initiated the study on LiBF₄ mentioned the multiple advantages of LiBF₄ as compared with other salts (e.g., less toxicity than LiAsF₆ and higher safety than LiClO₄),¹²⁸ but its moderate ion conductivity has been a major obstacle to its application. More recent studies on its ionic and limiting properties in various nonaqueous systems established that, among the most common anions encountered, BF₄⁻ has the highest mobility, but its dissociation constant is significantly smaller than those of LiAsF₆ and LiPF₆.^{111,129} The unfavorable balance of these two properties results in the moderate ion conductivity.

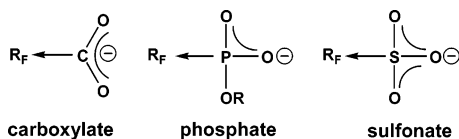
Electrochemically, the BF₄⁻ anion was found to be stable against oxidation on a glassy carbon (GC) surface up to 3.6 V vs a standard calomel electrode (SCE), which translates into ~5.0 V vs lithium.^{130,131} When a distinction is made, this stability limit is somehow lower than those of AsF₆⁻ and PF₆⁻ anions; however, caution must be exercised here, as these data were measured on GC with quaternary ammonium as supporting electrolyte, instead of on a surface of cathode materials. This could result in substantial difference.⁷⁶

The use of LiBF₄ in lithium-based cells has been rare because of its inferior ion conductivity until recently, when the thermal instability of LiPF₆ and the moisture sensitivity became recognized. Attempts to replace LiPF₆ in lithium ion cells have been made, and the cells based on LiBF₄ electrolytes showed improved performance, not only at elevated temperatures up to 50 °C¹³² but, surprisingly, also at low temperatures as well.^{132–135} These observations could bring this salt back to research favor.

2.2.4. Lithium Trifluoromethanesulfonate (LiTf)

Another family of lithium salts is based on the conjugate bases of the organic superacids, where acid strength is increased because of the stabilization of anions by the strongly electron-withdrawing groups, usually perfluorinated alkyls. In these anions, the

delocalization of the formal negative charge is practically realized by a combination of the inductive effect of the electron-withdrawing groups and the conjugated structures:



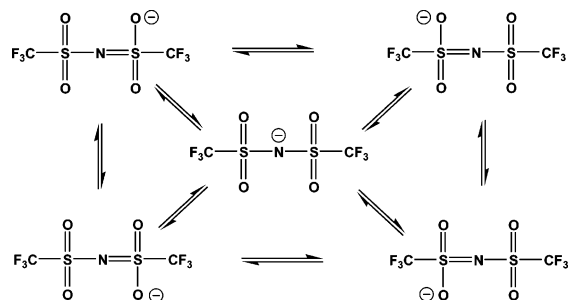
The attempt to use these salts originated from the hope that their dissociation constants would be high even in low dielectric media, and the organic nature of perfluorinated alkyls would always assist the solubility of the salts in nonaqueous solvents. Because of the requirement for electrochemical stability, lithium carboxylates ($\text{R}_\text{F}\text{-CO}_2\text{Li}$, where R_F^- = perfluorinated alkyls) are excluded from consideration, because their oxidation still occurs at ~ 3.5 V vs lithium, which is similar to the cases of their non-fluorinated counterparts.²² Obviously, the electron-withdrawing groups do not stabilize the carboxylate anions sufficiently to alter their oxidative stability.

On the other hand, sulfonate ($-\text{SO}_3\text{Li}$) became the anion of choice because it is highly resistant to oxidation, thermally stable, nontoxic, and insensitive to ambient moisture as compared with LiPF_6 or LiBF_4 .¹²² As the simplest member of this category ($\text{R}_\text{F} = \text{CF}_3$), lithium triflate (LiTf) received extensive research as a candidate for lithium/lithium ion cells. Other similar salts studied include perfluoroethyl sulfonate ($\text{R}_\text{F} = \text{C}_2\text{F}_5$), perfluorobutylsulfonate ($\text{R}_\text{F} = \text{C}_4\text{F}_9$),^{129–131} and the oligomeric versions that are based on polyether linkages.^{136,137}

One major drawback of these sulfonate salts is their poor ion conductivity in nonaqueous solvents as compared with other salts. In fact, among all the salts listed in Table 3, LiTf affords the lowest conducting solution. This is believed to be caused by the combination of its low dissociation constant in low dielectric media^{122,138} and its moderate ion mobility¹²⁹ as compared with those of other salts. Serious ion pairing in LiTf -based electrolytes is expected, especially when solvents of low dielectric constant such as ethers are used.^{111,122}

The stability of the Tf^- anion toward lithium has been studied by both electrochemical and spectroscopic means.¹³⁹ While the surface analysis using X-ray photoelectron spectra (XPS) found only a trace of LiF , in addition to Li_2CO_3 , present on the lithium surface, indicating that this anion was not reactive with lithium, a poor lithium morphology was identified in LiTf -based electrolytes. Electrochemical quartz crystal microbalance (EQCM) detected a very rough surface of the cycled lithium, most likely related to the formation of dendritic lithium. A simultaneous impedance measurement confirmed the poor morphology with ever-increasing interfacial impedance due to the incessant reactions between the rough lithium surface and the electrolyte. This sustained reaction resulted in a thick and resistive SEI film that was not favorable to battery operation. However, in at least one case, LiTf was found to outperform the state-of-the-art solute LiPF_6 , where an atypical

Scheme 3. Resonance States of the Imide (Im) Anion



anode (carbon fiber) was used, and LiTf -based electrolytes in various solvent mixtures (EC/DMC, PC/DMC, or EC/DME) showed better Coulombic efficiency ($\sim 98\%$) and discharge capacity.¹⁴⁰

The anodic stability of the Tf^- anion, as measured on a GC surface, was not found to be particularly high:¹³⁰ inferior to BF_4^- and PF_6^- but better than ClO_4^- . *Ab initio* calculations yielded similar conclusions,¹³¹ and results measured on porous carbon electrodes were consistent with those measured on GC.⁸¹

The real obstacle that eventually eliminated LiTf as a candidate for lithium ion battery application is the serious aluminum corrosion that occurred in LiTf -based electrolytes. Used as the substrate material to carry cathode active material in the cell, Al is constantly subject to high potentials during cell operation and, thus, must maintain inertness against anodic dissolution. However, because of a special interaction between the Tf^- anion and Al, the latter dissolves anodically at ~ 2.7 V and starts to pit at ~ 3.0 V.¹⁴¹ At 4.0 V vs lithium, the normal working potential of a charged cell, the anodic dissolution current is ~ 20 mA/cm² in PC. This high corrosion rate leaves LiTf virtually little possibility of being used as an electrolyte solute for any high voltage cells, either lithium or lithium ion.

2.2.5. Lithium Bis(trifluoromethanesulfonyl)imide (LiIm) and Its Derivatives

In 1984, Foropoulos and DesMarteau reported a new acid based on an imide anion stabilized by two trifluoromethanesulfonyl (triflic) groups.¹⁴² Because of the strong electron-withdrawing nature of the triflic groups and the conjugation between them and the lone electron pair on the nitrogen, the formal negative charge in the anion is well delocalized, as shown by the resonance structures in Scheme 3.

As a result, the acid strength of the proton is approximately equivalent to that of sulfuric acid in nonaqueous media.¹⁴² In view of the excellent miscibility of this anion with organic nonpolar materials, Armand et al. proposed using its lithium salt (later nicknamed "lithium imide", or LiIm) in solid polymer electrolytes, based mainly on oligomeric or macromolecular ethers.¹⁴³ In no time, researchers adopted its use in liquid electrolytes as well, and initial results with the carbonaceous anode materials seemed promising.⁹⁵ The commercialization of this new salt by 3M Corporation in the early 1990s sparked considerable hope that it might replace the poorly

conducting LiTf, the hazardous LiClO₄, the thermally unstable LiBF₄ and LiPF₆, and the toxic LiAsF₆ in lithium battery applications.¹²² Extensive studies of this salt were carried out to determine its ionics in nonaqueous solutions^{111,116,129,130,131,139} and its applications in lithium or lithium ion cells.^{45,96,144,145}

LiIm proved to be safe, thermally stable, and highly conducting: it melts at 236 °C without decomposition (a rarity among lithium salts) and does not decompose until 360 °C.¹⁴⁶ Its ion conductivity in THF is an order of magnitude higher than that of LiTf, although lower than those of LiAsF₆ and LiPF₆,^{111,116,122} and when no Al is used, a lithium ion cell based on a LiNiO₂ cathode and a petroleum coke anode can yield up to 1000 deep discharge cycles with LiIm in an EC/DMC solution.⁴⁵

Ionics studies by Webber and Ue revealed that this salt dissociates very well even in low dielectric solvents, although its large anion size usually results in a higher solution viscosity than those of other salts in a given solvent system. Thus, its good ion conductivity should be the result of a compromise between a high degree of dissociation and low mobility.^{122,129} In this sense, LiIm favors solvents with a low dielectric constant. Electrochemical stability tests were carried out on a GC electrode, and Im⁻ was found to be stable against oxidation in EC/DMC up to 2.5 V vs a Ag⁺/Ag reference, which translates to ~5.0 V vs Li, an oxidation limit lower than those for LiBF₄ and LiPF₆,^{130,131} but still high enough to be practical. The morphology of cycling lithium in LiIm-based electrolytes is apparently superior to that in other salt-based electrolytes.¹³⁹

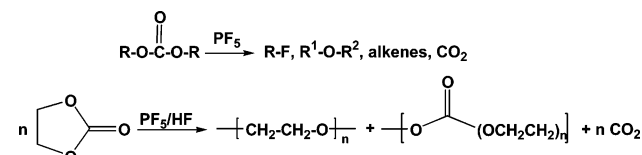
Despite all of these merits, the application of LiIm in lithium ion cells never materialized because it caused severe Al corrosion in electrolytes based on it.¹⁴¹ In situ surface studies using EQCM established a reaction between the Im⁻ anion and the Al substrate in which Al(Im)₃ is produced and adsorbed on the Al surface.¹⁴⁷ Undoubtedly, this corrosion of a key component of the cell by Im⁻ greatly restricts the possible application of LiIm, because the role of Al as a cathode substrate in the lithium-based battery industry is hard to replace, due to its light weight, resistance to oxidation at high potential, excellent processability, and low cost.

Efforts were made to reduce the reactivity of Im⁻ toward Al. Other salts that could passivate Al were used as additives with LiIm, and the results were encouraging.¹⁴⁷ Also, structural modification of the imide anion was made by extending the perfluorinated alkyl chain and was found to be effective, although at the price of lower ion conductivity.^{141,148} Although LiIm has never been used in any commercial lithium ion devices, it remains an interesting salt to be investigated, especially for the polymer-based electrolytes.⁴⁷

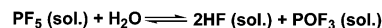
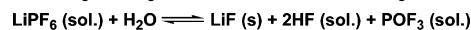
2.2.6. Lithium Hexafluorophosphate (LiPF₆)

Among the numerous salts vying for lithium/lithium ion batteries, LiPF₆ was the obvious winner and was eventually commercialized. The success of LiPF₆ was not achieved by any single outstanding property but, rather, by the combination of a series

Scheme 4. Decomposition of Carbonates by PF₅



Scheme 5. Hydrolysis of LiPF₆ Salts by Moisture



of well-balanced properties with concomitant compromises and restrictions. For example, in the commonly used carbonate solvent mixtures it has a lower conductivity than LiAsF₆ (Table 3),^{99,111,116} a lower dissociation constant than LiIm,¹²⁹ a lower ionic mobility than LiBF₄,¹²⁹ a lower thermal stability than most of the other salts,¹⁴⁹ a lower anodic stability than LiAsF₆ and LiSbF₆,^{130,131} and a lower chemical stability toward ambient moisture than LiClO₄, LiIm, and LiTf. However, none of these other salts could meet all these multifaceted requirements simultaneously as well as LiPF₆ does.

LiPF₆ was proposed as an electrolyte solute for lithium-based batteries in the late 1960s,¹⁴⁹ and soon its chemical and thermal instabilities were known.¹⁵⁰ Even at room temperature, an equilibrium exists:



The generation of the gaseous product, PF₅, drives the equilibrium to the right, and this process is favored by elevated temperatures. In the presence of nonaqueous solvents, the strong Lewis acid PF₅ tends to initiate a series of reactions, such as ring-opening polymerization or cleavage of ether linkages (Schemes 2 and 4).^{68,151,152}

On the other hand, the P–F bond is rather labile toward hydrolysis by even trace amounts of moisture in nonaqueous solvents, producing a series of corrosive products (Scheme 5). Thermal gravimetric analysis (TGA) reveals that, in a dry state, LiPF₆ loses 50% of its weight at >200 °C¹⁴¹ but that, in nonaqueous solutions, the deterioration occurs at substantially lower temperatures, for example, as low as 70 °C.

The sensitivity of LiPF₆ toward ambient moisture, solvents, and high temperature not only restricts its range of applications, especially in nonaqueous batteries, but also causes tremendous difficulty in its preparation and purification.¹⁵⁰ Before the 1990s, most of the commercially available LiPF₆ had high amounts of LiF and HF, and the purity issue became part of the reason the potential of LiPF₆ was not fully realized until recently. The manufacture of high-purity LiPF₆ (HF < 10 ppm) in industrial scale was achieved by Japanese companies in the late 1980s, finally leading to the commercialization of lithium ion technology and the ensuing extensive research.^{86,120,122}

In nonaqueous solvents based on mixed alkyl carbonates, LiPF₆ remains one of the most conducting salts. For example, in EC/DMC (1:1) the conductivity is 10.7 mS cm⁻¹, only fractionally lower than that of

LiAsF₆. According to the ionic studies on the limiting properties in various solvents, this excellent conductivity results from the combination of its ionic mobility and dissociation constant, although in neither category does LiPF₆ stand at the most outstanding position.^{111,129}

Average ion mobility: LiBF₄ > LiClO₄ >
LiPF₆ > LiAsF₆ > LiTf > LiIm

Dissociation constant: LiTf < LiBF₄ < LiClO₄ <
LiPF₆ < LiAsF₆ < LiIm

The reversed order in the above two properties clearly demonstrates the conflicting nature of the requirements and the advantage of the well-balanced properties of LiPF₆.

Electrochemical studies on a GC electrode and various metal oxide-based cathode surfaces confirm that the solution of LiPF₆ in mixed carbonates can effectively resist oxidation up to 5.1 V,^{99,130} thus making it one of the few salts that can actually support the operation of 4.0 V cathode materials. LiPF₆ also effectively passivates an Al substrate at high potentials.^{141,153,154} It is generally accepted that the anion participated in forming a protective film on Al, although there is no consensus as yet concerning the mechanism of the process.^{141,153–156}

The above merits made LiPF₆ the salt of choice when lithium ion technology leaped from concept into product. In 1990, it was used by Sony in the first generation lithium ion cell,¹⁵⁷ and since then, its position in the lithium ion industry has remained unchallenged. Like EC as an indispensable solvent component, LiPF₆ has become the indispensable electrolyte solute for almost all lithium ion devices manufactured in the past decade.

2.3. Brief Summary

After more than a decade of exploration, the skeletal components of the electrolyte for the commercialized lithium ion devices have been identified. Within the various brands of lithium ion cells, the exact electrolyte composition differs from manufacturer to manufacturer, and the formulas remain proprietary information; however, the overwhelming majority of these are apparently based on two indispensable components: EC as the solvent and LiPF₆ as the solute. In most cases, one or more linear carbonates, selected from DMC, DEC, or EMC, are also used as cosolvents to increase the fluidity and reduce the melting point of the electrolyte, thus forming the popular composition consisting of LiPF₆/EC/linear carbonate(s).

However, certain restrictions on battery performance arise from these state-of-the-art electrolytes, for which these two indispensable components are mainly responsible: (1) a low-temperature limit (−20 °C) set by EC due to the high melting point and the high liquidus temperature it confers upon the solvent mixture, and (2) a high-temperature limit (50 °C) set by LiPF₆ due to its reactivity with solvents. As a result, the commercialized lithium ion batteries can

only deliver their rated capacity and power in the temperature range −20 to 50 °C. Below temperatures from −20 to −30 °C, both the capacity utilized and the rate at which it is delivered (power) are decimated. This reduction in performance at low temperatures is usually temporary, and rated capacity can be recovered once the battery is brought back to >20 °C. However, at temperatures higher than 60 °C, the performance deterioration is permanent, because the reactions between the electrolyte solute and solvents are irreversible. Furthermore, the decomposition products of these irreversible processes, which are often gaseous, can lead to hazardous pressure build-up within the batteries.

3. Liquid Range of Electrolyte Solutions

The liquid range of a nonaqueous electrolyte system is defined at the upper limit by the temperature at which one of its components begins to vaporize (also called the bubble temperature, θ_b) and at the lower limit by the temperature at which one of its components begins to crystallize (liquidus temperature, θ_l).¹⁵⁸ Apparently, along with restrictions imposed by other factors, this range could serve as the main basis for estimating the operating limits of lithium-based devices that employ such an electrolyte system. Surprisingly, despite the significance of this issue to practical applications, there have been rather few studies dedicated to the thermophysical properties of the electrolytes, especially considering the large amount of effort spent on studying ion conduction and electrochemical properties.

Tarascon and Guyomard were perhaps the first researchers to try to delineate a temperature range for lithium ion electrolytes.⁹⁹ Following their seminal formulation of new electrolytes based on cyclic and linear carbonates, they measured boiling (bp) and melting points (mp) for LiPF₆/EC/DMC solutions as the function of EC/DMC compositions. They found that the bp of the electrolytes as a function of composition exhibits a monotonic decrease from that of EC (248 °C) to that of DMC (91 °C) with such a severe curvature that, for most of the compositions, it is dominated by the lower boiling component. The same trend was observed in a similar system (PC/DEC) by Ding recently,¹⁵⁸ who made the observation that enhancing the bp for a mixed solvent system by adding a higher boiling component would have little effect because of the previously mentioned dependence. In other words, the upper limit of the liquid range for a binary system is mainly determined by the bp of the lower boiling component. There is sufficient reason to believe that this rule would hold true for ternary or higher order systems.

It must be pointed out that, in the state-of-the-art electrolytes, the actual high-temperature limits for application in cells are usually not set by the upper boundary of the liquid range because other factors might push the limits far lower. For example, the upper boundary of the liquid range is ~90 °C for DMC-, 110 °C for EMC-, and 120 °C for DEC-based electrolytes, all of which are far above the high-temperature limit set by the salt LiPF₆ (70 °C).¹⁵²

Even if LiPF_6 is replaced by more thermally stable salts, the thermal stability of passivation films on both the anode and the cathode would still keep the high-temperature limits lower than 90°C , as do the thermal stability of the separator ($<90^\circ\text{C}$ for polypropylene), the chemical stability of the insulating coatings/sealants used in the cell packaging, and the polymeric binder agents used in both cathode and anode composites.

The lower boundary of the liquid range, on the other hand, does usually serve as the low-temperature limit for the electrolytes. The mp of $\text{LiPF}_6/\text{EC}/\text{DMC}$ was determined as a function of solvent composition by Tarascon and Guyomard, who concluded that $\text{LiPF}_6/\text{EC}/\text{DMC}$ could be used in the solvent compositions between 3:7 and 8:2 at temperatures down to -25°C .⁹⁹ The mp-dependence on solvent composition that was reported in the work, however, does not seem to be rational, since it shows a long plateau at $\sim -10^\circ\text{C}$ in 30–90% DMC after an initial drop from 20°C at 20% DMC,⁹⁹ whereas a typical simple eutectic feature would be expected instead. When a closer comparison is made between the results by Tarascon and Guyomard and the more recent studies by Ding et al.,^{50e,159,160} it becomes obvious that in the former work no distinction was made between the liquidus and solidus temperatures; that is, the mp's at 20% and 90% DMC are liquidus temperatures, while the rest (the plateau section) seem to be solidus temperatures as measured by Ding et al. This confusion could have arisen from the fact that, for the intermediate compositions between 30% and 80% DMC, the liquidus transition usually appears as a broad peak of relatively negligible thermal effect that could evade notice, while the solidus transition usually appears as a sharp and conspicuous peak.

Systematic construction of carbonate mixture phase diagrams was performed by Ding et al.^{50e,159,160} for a series of binary carbonate solvent systems that are frequently used as lithium ion electrolyte solvents. It was found that all of the binary combinations between EC, PC, DMC, EMC, and DEC yield the same basic feature of simple eutectic-type phase diagrams, characterized by the V-shaped liquidus lines intersecting at the eutectic composition with a horizontal solidus line, although the details of each individual diagram vary greatly depending on their mp and cyclicity. Figure 4 shows a collection of such phase diagrams mapped for some EC-based binary solvent systems.

In these phase diagrams, the liquidus line represents the temperature at which one of the components crystallizes, while, below the solidus line, the whole system solidifies. Between the solidus and liquidus lines are the regions where solid and liquid coexist. Since there is no solid phase above the liquidus lines and the liquid is thermodynamically stable, Ding et al. suggested that the liquidus temperatures should be adopted as the lower boundary of the liquid phase, instead of the solidus temperatures.^{159,160} The patterns of these phase diagrams are typical of binary systems in which the two components are mutually soluble in their liquid states but

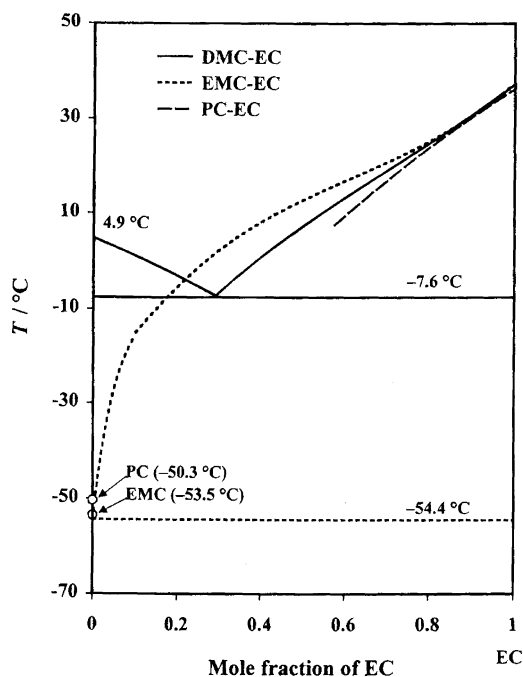


Figure 4. Liquid–solid phase diagrams of EC/DMC, EC/EMC, and PC/EC. (Reproduced with permission from ref 159 (Figure 9). Copyright 2000 The Electrochemical Society.)

insoluble in their solid states; therefore, solid solutions do not form below solidus temperatures, and the binary system exists in the form of a heterogeneous mixture of both solids.

Typically, the liquidus lines of a binary system curve down and intersect with the solidus line at the eutectic point, where a liquid coexists with the solid phases of both components. In this sense, the mixture of two solvents should have an expanded liquid range with a lower melting temperature than that of either solvent individually. As Figure 4 shows, the most popular solvent combination used for lithium ion technology, $\text{LiPF}_6/\text{EC}/\text{DMC}$, has liquidus lines below the mp of either EC or DMC, and the eutectic point lies at -7.6°C with molar fractions of ~ 0.30 EC and ~ 0.70 DMC. This composition corresponds to volume fractions of 0.24 EC and 0.76 DMC or weight fractions of 0.28 EC and 0.71 DMC. Due to the high mp of both EC (36°C) and DMC (4.6°C), this low-temperature limit is rather high and needs improvement if applications in cold environments are to be considered.

A rather counterintuitive conclusion that can be extracted from these phase diagrams, however, is that simply introducing a low-melting component does not necessarily extend the liquid range, as evidenced by the replacement of DMC by the lower melting EMC (-53°C) in an EC-based binary solvent system (Figure 4). The mismatch between the EC and EMC mp's creates a liquidus line that approaches the mp of EC for most of the compositions; therefore, the liquid range toward the low-temperature end actually shrinks as compared with that of the EC/DMC binary system. The replacement of DMC by another low-melting linear carbonate, DEC (-74°C), produces a similar effect.^{23d} It was proposed later that this poor compatibility between EC and linear carbonates

originates from the intrinsic differences found at the molecular level, that is, in the number of structural conformations that was allowed for by their freely rotatable single bonds.¹⁵⁸

The comparison between the phase diagrams has led to the conclusion that the compatibility between different solvents is determined by two factors: (1) molecular structure similarity and (2) melting point proximity.^{50e,158–160} Thus, from the viewpoint of phase diagram study alone, the effort to advance the liquid range toward lower temperature would be far more effective if cyclic–cyclic or linear–linear binary systems were formulated rather than the cyclic–linear combination that is currently used as the state-of-the-art lithium ion electrolytes. Unfortunately, most of the possible formulations under these categories would be vetoed by other considerations such as ion conductivity, electrochemical stability, and SEI formation on electrodes, and the cyclic–linear combination remains the formulation of choice. Viewed from another angle, the low-temperature limit on the device will remain a challenge as long as the high-melting EC remains an indispensable solvent component for the lithium ion electrolytes, because it will dominate the lower boundary of the liquid range no matter what linear cosolvents were used.

The phase diagrams shown in Figure 4 only describe the thermal properties of the binary *solvents*, while in practical applications the *salt solutions* of these solvent mixtures would be of greater interest. Ding et al. studied the effect of salt on the liquidus and solidus line locations at various concentrations up to 1.0 M and concluded that both lines would be depressed on temperature axes by a limited number of degrees.¹⁵⁹ At the salt concentrations investigated, it seems that the basic shape of the phase diagram remains unchanged, while the liquidus and solidus lines parallel those of the corresponding solvents. Thus, one can reliably estimate the phase transition temperatures of an electrolyte to be formed from a solvent with a known phase diagram.

In the actual application of the electrolytes at low temperatures, another thermal property that is closely related to the phase diagram and should not be ignored is the so-called “supercooling” behavior,^{161–163} which occurs when the liquid circumvents crystallization at its mp or liquidus/solidus temperature, usually because the high viscosity of the solvent system at this temperature prevents the timely reorganization of molecules to ordered conformations. As a result, the solvent remains fluid at the temperatures below their thermodynamic freezing point, and this metastable liquid is called a “supercooled liquid”. The supercooled state ends when the glass transition occurs at some lower temperature and turns the system into a disordered (noncrystalline) solid phase. Since supercooling actually delays or even eliminates crystallization of solvent components, the liquid range of the solvent system could be substantially extended from the liquidus down to the glass transition temperature (T_g). This extended range could potentially benefit the operation of the electrolyte at low temperatures, and there are numerous examples in which electrolytes were tested at temperatures far

below their liquidus temperatures without pronounced deterioration.^{164,165}

However, an electrolyte is only kinetically stable below its liquidus line, and the presence of any nucleating agent could trigger the formation of a solid phase. In an electrochemical device, the rough surface of the electrode composite, the fibers of the separator, or the edges of current collectors and tabs can all act as such a nucleating agent; therefore, the extended liquid range of electrolytes by supercooling seems rather unreliable. Ding et al. studied the supercooling behavior of the EC/EMC system and the effect of various carbon particles on its diminution.¹⁶⁶ They found that, in this particular carbonate mixture, only the liquidus temperature could be successfully bypassed at a given cooling rate (10 °C/min), while, at the solidus temperature, binary crystallization occurs with negligible supercooling. Carbon particles effectively diminish the supercooling by providing nucleation seeds and effectively promoting the primary crystallization of EC at or near its liquidus temperature. The effectiveness of these carbon particles lies in the order

MCMB > activated carbon > carbon black

where MCMB stands for mesocarbon microbeads, a popular carbonaceous anode material used in the lithium ion batteries.

On the other hand, the presence of the salt, LiPF₆, assists the occurrence of supercooling by increasing the solution viscosity and by depressing the liquidus temperature. At practical concentrations of LiPF₆ (~1.0 M), even the solidus temperature can be circumvented, since there is no crystallization process observed for LiPF₆/EC/EMC solution down to –120 °C, while the glass transition occurs at –103 °C. In such concentrated solutions, even the presence of MCMB cannot initiate crystallization, and the supercooling is completely suppressed at the cooling rate of 10 °C/min.

Thus, in actual applications, supercooling might well exist when electrolytes are used at low temperatures and result in an extended liquid range. However, it should be emphasized that such an extended range remains fragile, since the supercooling as a kinetically stable behavior is highly conditional and unpredictable during the operation of the device. The diminution or even elimination of supercooling is entirely possible if a slower cooling rate is employed or long-term storage at low temperature is exercised, but almost certainly, any prolonged operation of an electrolyte below the liquidus line would eventually encounter precipitation of solvent components and result in performance deterioration. Therefore, the reliable low-temperature limit should still be set by the liquidus lines as depicted in the phase diagram.

Following the seminal formulation of electrolytes based on carbonates by Tarascon and Guyomard,^{98,99} a lot of effort had been made to modify those binary lithium ion electrolytes. Often, ternary, quaternary, and even higher order solvent systems were proposed, and the difficulty in constructing the phase diagrams for these systems increased dramatically

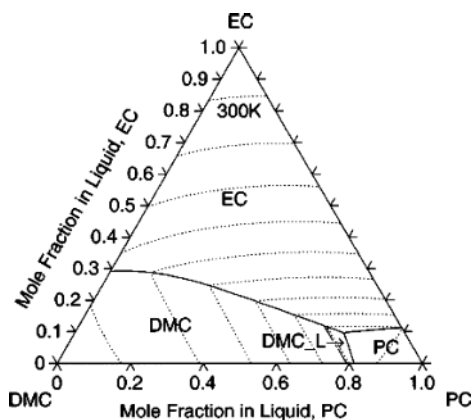


Figure 5. Calculated ternary phase diagram for EC/PC/DMC as expressed in the form of a composition triangle plane. The dotted lines represent the isotherms with 10 K intervals with 300 K marked. (Reproduced with permission from ref 167 (Figure 12). Copyright 2003 The Electrochemical Society.)

due to the amount of experimental work required. Consequently, the possibility of using computer modeling to circumvent the laborious experimental mapping was considered.¹⁶⁷ Because a phase diagram is merely a graphic representation of thermodynamics through minimizations in the free energy of the system under certain constraints, free-energy modeling of individual phases in a multicomponent system should represent the phase boundary through phase equilibrium calculations. Since the electrolyte systems are usually used at constant pressure conditions, the Gibbs free energy is the quantity minimized in calculating phase equilibria, and the computational approach commonly known as the CALPHAD method was used by Liu. The initial attempt seemed to be successful because phase diagrams of unary systems for neat DMC, EC, and PC, and of binary systems of EC/DMC, PC/DMC, and EC/PC were reproduced with satisfactory accuracy when compared with the work of Ding et al. Furthermore, by combining the three binary systems, a ternary phase diagram for EC/PC/DMC was predicted as shown in Figure 5. As one would expect, the eutectic composition was heavily PC-rich because PC was the lowest melting of the three components. Although the eutectic composition as predicted in the ternary phase diagram (0.10 EC/0.15 DMC/0.75 PC) was impractical for cell applications because of PC's destructive effect on most carbonaceous anodes, the effectiveness of PC, when used in smaller amounts (<30%), in improving low-temperature performance had been confirmed.¹⁶⁸ Undoubtedly, continued efforts to predict the thermal properties of ternary or higher order systems should be encouraged for prospective electrolytes, as they would provide useful knowledge for estimating their operating temperature range.

4. Ion Transport Properties

The ability to conduct ions is the basic function of electrolytes, which would determine how fast the energy stored in electrodes can be delivered. In liquid electrolytes, the transport of ions is realized via a two-step process: (1) the solvation and dissociation

of ionic compounds (usually crystalline salts) by polar solvent molecules and (2) the migration of these solvated ions through the solvent media.

During the solvation, the stability of the salt crystal lattice is energetically compensated by the coordination of solvent dipoles with the naked ions (especially cations); therefore, these ions should always migrate with a "solvation sheath" around them, which consists of a certain number of oriented solvent molecules. According to the results obtained from various modeling approaches including ab initio quantum mechanics, the small ionic radius of lithium usually allows no more than four solvent molecules in its solvation sheath.^{129,169–171} Using a new mass spectrum (MS) technique, a more recent determination of the coordination number (CN) for lithium ions seems to support these computational results: among the various solvated lithium ion species, the peaks corresponding to $\text{Li}(\text{sol})_{2-3}^+$ are the most abundant no matter whether the solvent is EC, PC, or γ -butyrolactone (γ BL).^{172,173} This latter experimental observation also revealed the stability of the solvation sheath, which obviously remains intact even during the electrospraying under vacuum and the subsequent ionization process. Therefore, there should be sufficient confidence in the general belief that the composition of solvated lithium ion remains unchanged during its migration in an electrolyte solution.¹ Considering that both cation and anion could be coordinated by solvents, ion conduction actually consists of the oriented movement of ion/solvent complexes of both charges.

Ionic conductivity σ , which quantifies the ion conduction ability, reflects the influence of these two aspects, that is, solvation/dissociation and the subsequent migration, in terms of the free ion number n_i and the ionic mobility μ_i :

$$\sigma = \sum_i n_i \mu_i Z_i e \quad (1)$$

where Z_i is the valence order of ionic species i , and e is the unit charge of electrons. For a single salt solution, the cations and anions are the only two charged species present.¹⁷⁴

Ion conductivity has essentially become the quantity used as the field-trial standard for any prospective electrolytes, because it can be easily measured with simple instrumentation, and the results are highly accurate and reproducible. The methodology and the fundamental principles involved with the measurement have been summarized in a detailed review.¹⁷⁵ On the other hand, no reliable method has been available so far for the exact determination of ion mobility (or a related property, diffusivity D_i) and ionization degree, especially in electrolyte solutions in the concentration ranges of practical interest.¹

The lack of ionic mobility data causes a serious inconvenience when the ion conduction ability of an electrolyte is evaluated, because the measured conductivity is the result of the overall migration of both anions and cations, while for lithium batteries only the portion of the current that was carried by the lithium cation matters. This portion of the current from lithium ion movement, which determines the

rate at which the battery operates, is quantified by the lithium ion transference number (t_{Li}):

$$t_{\text{Li}} = \frac{\mu_{\text{Li}}}{\sum_i \mu_i} \quad (2)$$

There have been numerous efforts aimed at estimating the lithium ion transference numbers in nonaqueous solutions, and the data obtained via different approaches vary appreciably. Nevertheless, it is generally accepted that, in much diluted nonaqueous solutions, lithium ion transference numbers range from 0.20 to 0.40, depending on the properties of salts and solvents.^{1,111,129,138,176–178} In other words, the anions are much more mobile than the lithium ions in nonaqueous electrolytes. The small cation current portion in nonaqueous electrolytes is believed to be caused by the high surface charge density on the cations (especially lithium ion) due to their small ionic radii, so they are much more favorably solvated and must move at slower speed with the solvation sheath, while high populations of anions could remain relatively “naked”. Solvation enthalpy calculations for cations and anions support this argument.^{169,176,178} In typical carbonate solvents, the former range between 20 and 50 kcal mol⁻¹ while the latter are below 10 kcal mol⁻¹.

A lithium ion transference number significantly less than 1 is certainly an undesired property, because the resultant overwhelming anion movement and enrichment near electrode surfaces would cause concentration polarization during battery operation, especially when the local viscosity is high (such as in polymer electrolytes), and extra impedance to the ion transport would occur as a consequence at the interfaces. Fortunately, in liquid electrolytes, this polarization factor is not seriously pronounced.

The unavailability of data on dissociation degree and mobility has thus made ion conductivity an alternative metric that has been universally adopted by the battery research and development community to evaluate the transport ability of electrolytes. However, it should always be remembered that such a metric of convenience is based on an unstated assumption; that is, the increase in the overall conductivity should originate, at least partially, from the improvement in the cation conductivity. Qualitatively, this assumption holds true, since a correlation does usually exist between ion conductivity and power performance in batteries, although quantitatively the distribution of this increase between anions and cations is unknown.

The efforts to improve ion conductivity have revolved around eq 1, that is, aiming at increasing either the salt dissociation degree (n_i) or the ionic mobility (μ_i). Since these two factors are decided simultaneously by the physicochemical natures of the salt and solvents, different approaches involving either of these electrolyte components have been adopted.

For lithium electrolytes, the only variable in salt structure is the anion. In a given nonaqueous solvent system, the dissociation of a lithium salt would be

facilitated if the anion is well stabilized by electron-withdrawing functionalities. Successful examples of such anions include PF₆⁻ or Im⁻, whose lithium salts dissociate readily as compared to those based on the parental anions (LiF and lithium alkylamide, respectively).

On the other hand, the mobility of an ion is known to vary inversely with its solvation radius r_i according to the Stokes–Einstein relation:¹

$$\mu_i = \frac{1}{6\pi\eta r_i} \quad (3)$$

where η is the viscosity of the media. With the cation species fixed, this approach seems to be of little use to increase cation mobility. However, a larger anion with lower anion mobility shows the application of this approach in another way, which results in a higher cation transference number, although the overall conductivity could decrease because of the reduction in the anion contribution. This effect was observed in imide and its derivatives.¹³⁸ The extremity of this approach was represented by the salts with oligomeric or polymeric anions, where t_+ approaches 1.0 but the overall ion conductivities suffer drastically.^{136,137,179–182} Hence, the approach of using large anions to enhance t_{Li} is not widely pursued in liquid electrolytes.

So far, very few attempts at improving ion conductivity have been realized via the salt approach, because the choice of anions suitable for lithium electrolyte solute is limited. Instead, solvent composition tailoring has been the main tool for manipulating electrolyte ion conductivity due to the availability of a vast number of candidate solvents. Considerable knowledge has been accumulated on the correlation between solvent properties and ion conductivity,¹ and the most important are the two bulk properties of the solvents, dielectric constant ϵ and viscosity η , which determine the charge carrier number (n_i) and ion mobility (μ_i), respectively.

In order for a solvated ion to migrate under an electric field, it must be prevented from forming close ion pairs with its counterions by the solvating solvent. The effectiveness of the solvent molecule in shielding the interionic Coulombic attraction is closely related with its dielectric constant. The critical distance for the ion pair formation q is given by eq 4 according to Bjerrum's treatment, with the hypothesis that ion-pair formation occurs if the interionic distance is smaller than q .^{1,183}

$$q = \frac{|z_i z_j| e^2}{8\pi\epsilon_0 \epsilon kT} \quad (4)$$

where z , ϵ_0 , k , and T are the valence orders of ions, the dielectric constant of vacuum, Boltzmann's constant, and temperature, respectively. Apparently, in a solvent with a higher dielectric constant, ions would have a higher probability of staying free at a given salt concentration and ion association would be less likely to occur. Most of these solvents are of high boiling temperature and high viscosity (Table 1).

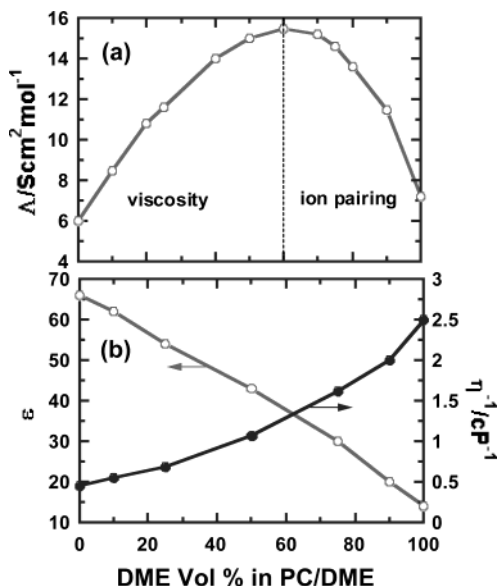


Figure 6. (a) Optimization of ion conductivity in mixed solvents: 1.0 M LiClO₄ in PC/DME. (b) Dependence of dielectric constant (ϵ) and fluidity (η^{-1}) on solvent composition. These plots are reconstructed based on the data reported in refs 187 and 194, respectively.

When solvated ions migrate within the electrolyte, the drag force applied by the surrounding solvent molecules is measured by solvent viscosity η . Thus, in a solvent of lower viscosity, the solvated ions would move more easily in response to an applied electric field, as expressed by the Einstein–Stokes relation (eq 3). Solvents of low viscosity have always been considered the ideal candidates for electrolyte application; however, their actual use was restricted because most of these solvents have low dielectric constants (Tables 1 and 2) and cannot dissociate ions effectively enough to prevent ion pairing.

Since a high dielectric constant and low viscosity usually cannot be integrated into a single solvent,¹⁸⁴ a solvent mixture, usually binary with one of the components selected for ϵ and the other for η , was used to formulate electrolytes for lithium batteries with the hope that a balance between these two properties could be arrived at via such mixing.^{185–187} The concept was rapidly accepted by researchers of the 1980s, usually using cyclic carbonates for their high ϵ and linear or cyclic ethers for their low η .^{72,73,78,87,89,127,188–191} In almost all the cases, ion conductivity in mixed solvents is superior to that in single solvents, as Figure 6a shows for LiClO₄ in PC/DME, and a maximum in conductivity is usually realized in medium compositions.

A series of works by Matsuda et al. composed perhaps the first systematic study to explore the physical foundation for such a mixing effect.^{127,187,193,194} Using PC/DME as a model system, they investigated the dependence of vapor pressure, dielectric constant, and viscosity on solvent composition, and they correlated these variations with ion conduction. It was found that the dielectric constant varied with solvent composition by following an almost linear relation, with slight positive deviations, while viscosity always showed a pronounced negative deviation from what a linear relation would predict (Figure 6b). For such binary solvent systems, approximate quantifications

of the solvent mixing effect on these two properties were given:^{195,196}

$$\epsilon_s = (1 - x_2)\epsilon_1 + x_2\epsilon_2 \quad (5)$$

$$\eta_s = \eta_1^{(1-x_2)}\eta_2^{x_2} \quad (6)$$

where ϵ_s , η_s , ϵ_i , η_i , and x_i are the dielectric constant and viscosity of the mixture or the pure solvent components and the volume fraction of the individual solvent component, respectively.

Either ϵ_s or η_s varies with solvent composition in a monotonic way, and the additive effect of each term seems to be able to account for the manner in which ion conductivity varies with solvent composition. At low DME concentration in the PC/DME system, the mixture has a high dielectric constant, so that the salt dissociates more completely. However, in this region, the high viscosity, which impedes ionic movement, dominates the ion conduction (Figure 6a). With increasing DME content, the dielectric constant remains relatively high, but the system viscosity falls drastically and the solvated ions migrate with higher mobility. As a result, a net increase in ion conductivity is achieved. Further increases in DME content (or low PC content) result in a very low dielectric medium where the effect of ion pair formation outweighs that of low viscosity; thus, ion conductivity drops with the increase in DME content. Therefore, the maximum in ion conductivity versus solvent composition as shown in Figure 6a is actually the result of the compromise between the effects of the dielectric constant and viscosity. Such a compromise illustrates the superiority of mixed solvent versus single solvent electrolytes.

A simple mathematical treatment based on this model successfully reproduced the variation in ion conductivity with solvent composition as observed in experiments on numerous different systems. It also proposed that, in an ideal situation where no ion pair formation is present, the change in ion conductivity should follow a linear relation as predicted by the semiempirical Walden's law:¹⁹⁴

$$\Lambda\eta_s = \text{constant} \quad (7)$$

where Λ is the ion conductivity as normalized against salt concentration (molar conductivity). The Walden product ($\Lambda\eta_s$) can be viewed as an ion conduction metric that is normalized against both the solvent viscosity and the salt concentration (i.e., the free ion number if no ion pairing occurs); therefore, its value serves to the first approximation as a quantification of ion dissociation degree in electrolytes with either a given solvent or a given salt.^{111,122}

Although the above findings came from studies on mixtures of the cyclic carbonate PC with ethers, they remain qualitatively true for mixtures of cyclic and linear carbonates, that is, compositions of the state-of-the-art lithium electrolytes. Most likely, it was the work by Matsuda et al. that delineated the basic guidelines for electrolyte formulation, which eventually led to the formulations by Tarascon and Guyomard using cyclic (high ϵ) and linear (low η) carbonate mixtures.^{93,98,99}

Further analysis of related studies seems to argue that the success of the high- ϵ /low- η combination might not be due to the simple additive effect of these two properties but, rather, a synergistic action of these two variables through a mechanism that involves the solvent's preference for cations in its solvation sheath. During the dissolution process of a certain salt lattice in mixed solvents, the solvation of the ions by a solvent molecule of a higher dielectric constant would be energetically favored over that by a molecule of a lower dielectric constant. Consequently, it would be reasonable to expect that, after equilibrium is established in the solution, the ions would have solvation sheaths that are mainly composed of the high- ϵ solvents. Modeling results using molecular quantum mechanics support this hypothesis by showing that the less favored solvent molecules (low ϵ) actually could be readily replaced by the favored ones.¹⁹⁷ Thus, in the EC/EMC system, the solvation shell should be predominantly composed of EC.¹⁷¹ The most forceful evidence of this comes from the experimental observation, where a new MS technique employing low-energy ionization was applied to electrolytes based on a series of binary compositions, including EC/DEC, EC/DMC, PC/DEC, PC/DMC, γ BL/DEC, and γ BL/DMC. In each of these systems, the overwhelmingly abundant species detected were the solvation complexes of lithium with the cyclic solvents (EC, PC, or γ BL), with coordination numbers between 2 and 3.¹⁷³

This selective solvation of lithium ions by high- ϵ solvent molecules would exclude the solvents of low- η from the solvation sheath and leave the latter as free, noncoordinating solvent molecules. As a result, the media in which the solvated ions migrate are mainly composed of these free solvent molecules, which impart their low- η to benefit the movement of the solvated ions. In this way, a synergistic participation from both high- ϵ and low- η solvents contributes to the optimization of ion conduction.

The implication of such a picture of the solution structure on the microscopic level not only concerns ion transport but also further relates to the electrochemical stability of the electrolytes in lithium ion cells, because these solvent molecules in the solvation sheath, such as EC or PC, migrate with the ions to electrode surfaces and are probably more involved in the oxidative or reductive processes than the noncoordinating, low- η solvent molecules, such as the linear carbonates. This could have a profound impact on the chemical nature of the electrolyte/electrode interfaces (section 6).

Knowing how ion conduction is determined by the interplay between the dielectric constant and viscosity, the dependence of ion conductivity on different variables that are of practical interest can be explained consistently. Extensive studies have been carried out on the effects of salt concentration, solvent composition, and temperature on ion conductivity in different electrolyte systems,^{113,195,196,198,199} among which the most representative is the meticulous work by Ding et al. on a series of binary systems pertinent to the state-of-the-art lithium ion cells.^{195,196} Figure 7 shows the LiPF₆/EC/DMC system as an example

of surface plots based on the close fit of experimental data to a fourth degree trivariant polynomial function:

$$\sigma = f(m, x, T) \quad (8)$$

where σ , m , x , and T are ion conductivity in mS cm⁻¹, salt concentration in mol kg⁻¹, the mole fraction of EC, and temperature in °C, respectively. Figure 7 summarizes the changes in ion conductivity with these variables and exhibits a general trend which has been observed repeatedly for various electrolyte systems. This trend allows the tailoring of salt concentration and solvent composition to maximize ion conductivity at a given temperature for practical interests:

(1) Salt Concentration (m). At low salt concentrations (<1.0 m), the number of free ions increases with salt concentration; consequently, ion conductivity also increases until it peaks at a higher concentration. After this conductivity maximum, any increase in salt concentration results in higher ion aggregation and higher viscosity of the solution, which reduces both the free-ion number and the ionic mobility simultaneously. The location of this maximum conductivity on the salt concentration axes (m_{\max}) is decided by the dielectric constant of the solvents as well as temperature. Generally speaking, a higher dielectric constant would shift the occurrence of ion pairing to higher salt concentrations, while a higher temperature reduces the solution viscosity. The common result of both scenarios is the shift of m_{\max} to higher salt concentrations.

(2) Solvent Composition (x_{EC}). At a given temperature, the solvent composition determines the outcome of the interplay between dielectric constant and viscosity; hence, a similar relation between σ and x_{EC} as shown for the PC/DME system in Figure 6a should be expected, as is indeed the case. However, temperature and salt concentration have such a pronounced effect on this dependence of conductivity on solvent composition that sometimes this relation will appear as monotonic in the given range of solvent compositions.

For example, at a given salt concentration of 1.6 m, solvents with a higher x_{EC} are favored at high temperatures (>50 °C) because the influence of viscosity is less pronounced and σ increases monotonically with x_{EC} . At low temperatures (<10 °C), this relation is reversed because of the predominate role of viscosity. At intermediate temperatures between 20 and 40 °C, σ peaks versus x_{EC} , indicating that at neither high nor low x_{EC} is the compromise between ϵ and η able to optimize ion conduction. Similarly, salt concentration also affects the dependence of conductivity on solvent composition and produces the various shapes in σ - x_{EC} relations shown in Figure 7, including single maximum curves and monotonic increases or decreases at different salt concentrations and temperatures.

(3) Temperature (T). With other variables being the same, ion conductivity increases with temperature monotonically until at very high temperatures the dielectric constant outweighs the viscosity in affecting ion conduction. Such high temperatures,

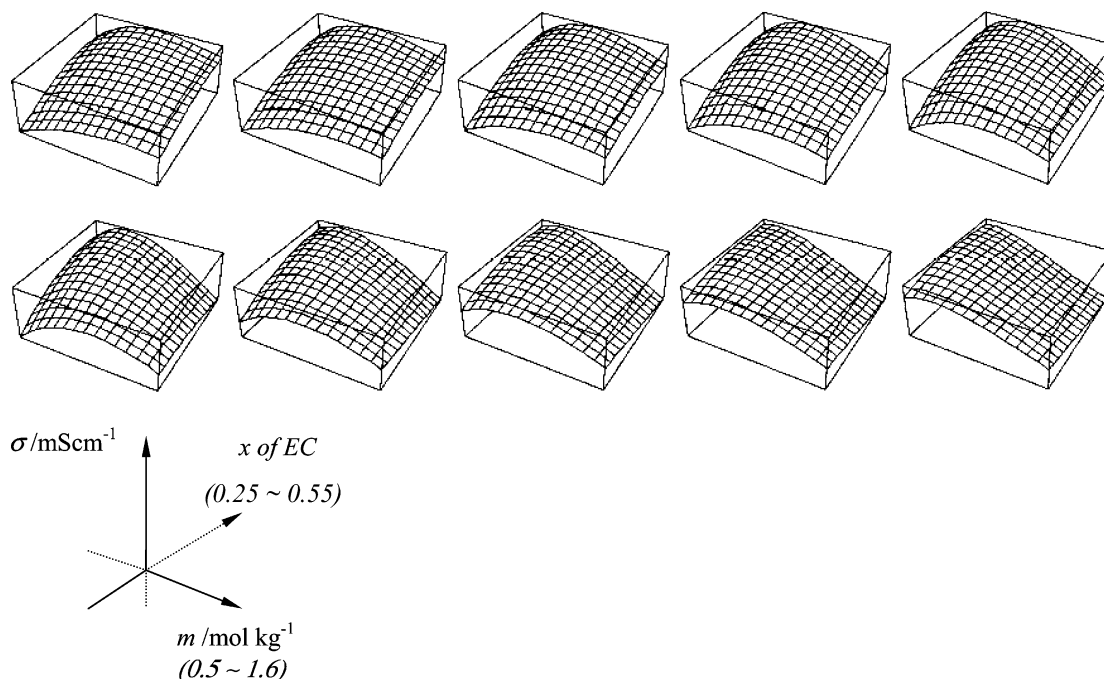


Figure 7. Detailed mapping of the dependence of ion conductivity on salt concentration (m), solvent composition (x), and temperature (T) in a commonly used binary solvent system EC/DMC by surface plots. The orientations, titles, and units of the axes used in the plots are shown in the bottom portion of the figure, and the temperatures for these plots are, in order of their appearance, from 60 to -30 °C in 10 °C increments. The σ ranges for the surface plots are, in order of their appearance, (8.49, 16.7), (7.78, 14.6), (7.03, 12.6), (6.23, 10.6), (5.44, 8.7), (4.63, 7.00), (3.14, 5.47), (1.93, 4.14), (1.04, 3.00), and (0.46, 2.06) mS cm $^{-1}$. (Reproduced with permission from ref 195 (Figure 4). Copyright 2001 The Electrochemical Society.)

however, are usually beyond the range of practical interest.^{195,200} Conversely, ion conductivity at sub-ambient temperatures is predominately determined by the increase in solution viscosity, although the dielectric constant becomes higher simultaneously.

A higher salt concentration accelerates the drop of ion conductivity with decreasing temperature, because it contributes to a higher viscosity. The combined effect of higher viscosity and low temperature is shown by the steeper σ - T curves of higher m . Solvent composition, on the other hand, also has a definite though mild influence on the temperature-dependence of ion conductivity. The surface plots in Figure 7 reveal that the change of conductivity with temperature speeds up as the solvent becomes EC-richer,¹⁹⁵ though different mechanisms involving either predominant ϵ or η at low or high salt concentrations, respectively, are believed to be at work.

To see more clearly the temperature effect on ion conduction, the logarithmic molal conductivity was plotted against the inverse of temperature, and the resultant plots showed apparent non-Arrhenius behavior, which can be nicely fitted to the Vogel–Tamman–Fulcher (VTF) equation:

$$\sigma = AT^{-1/2}e^{-B/R(T-T_0)} \quad (9)$$

where A and B are constants characteristic of the conduction process and T_0 is the vanishing conductivity temperature, which can be determined through fitting. The T_0 values obtained were found to be closely related to the glass transition temperatures of the solution systems, which agreed with the

general knowledge that ion transport in liquids or any noncrystalline polymer media is coupled with solvent media.^{162,163,200}

In summary, these trends in the change of conductivity with m , x_{EC} , and T can be consistently interpreted in terms of the change of ϵ and η with these same variables. Since these factors and their effect on ion conductivity are not unique to the system illustrated, LiPF $_6$ /EC/DMC, these trends should provide general guidance as to how ion conductivities of other electrolyte systems with similar compositions would change with these same variables, and they should constitute a useful database for the understanding of more complex systems, such as ternary or quaternary mixtures.

5. Electrochemical Stability: on Inert Electrodes

The cycle life of a rechargeable battery depends on the long-term reversibility of cell chemistries, and the electrochemical stability of the electrolyte plays a crucial role in maintaining this reversibility. In electrochemistry, there have been numerous techniques developed to measure and quantify the electrochemical stability of electrolyte components, and the most frequently used technique is cyclic voltammetry (CV) in its many variations.^{201,202}

In voltammetric experiments, the oxidative or reductive decompositions of the investigated electrolyte components (solvents or salts) are made to occur on an electrode whose potential is controlled, and the corresponding decomposition current recorded as the function of the potential is used as the criterion for

the stability limits. However, in contrast to the simpler task of measuring ion conduction or determining phase boundaries, the electrochemical decomposition is often a very complicated process, determined not only by thermodynamic factors but, more importantly, also by kinetic factors such as the electrode surface, scan rate, and concentration of the species under study. Therefore, electrochemical stability data for a given substance depend heavily on the conditions under which they are measured and defined, and the electrochemical stability limits as reported in the literature are not always consistent with each other. Depending on the concentration of the target component in the solution under study and the working electrode used, the voltammetry techniques favored by the researchers of the battery community fall into three major categories.

The first approach is the standard voltammetry technique used in conventional analytical electrochemistry.²⁰² Normally the target components are dissolved at much diluted concentrations in a supporting electrolyte, and the electrodes used are made of inert materials such as glassy carbon (GC), nickel (Ni), and noble metals such as gold (Au), silver (Ag), and platinum (Pt). The advantages of this approach include the following: (1) the diffusion pattern of the investigated species is well-defined in the diluted solution so that the redox properties thus determined can be more reliably linked to the thermodynamic properties;²⁰¹ (2) it is possible to study the decomposition behavior of solvents and salts separately so that their contributions to the overall stability of the electrolyte can be distinguished. However, the wide application of this approach is restricted by the availability of supporting electrolytes, which are supposed to be stable in the potential ranges where the target components decompose. In the case of lithium-based electrolytes, the wide electrochemical stability window of the electrolyte solvents and salts makes it hardly possible to find a supporting medium that is more resistant against decomposition. An additional disadvantage of this approach also includes the fact that the surface of the inert electrode, usually nonporous, is very different in catalytic activity from the porous surfaces of the composite electrode materials used in real electrochemical devices. As a consequence, this approach could overestimate the electrochemical stability of the components.⁷⁶

The second approach is an adaptation of the voltammetry technique to the working environment of electrolytes in an operational electrochemical device. Therefore, neat electrolyte solutions are used and the working electrodes are made of active electrode materials that would be used in an actual electrochemical device. The stability limits thus determined should more reliably describe the actual electrochemical behavior of the investigated electrolytes in real life operations, because the possible extension or contraction of the stability window, due to either various passivation processes of the electrode surface by electrolyte components or electrochemical decomposition of these components catalyzed by the electrode surfaces, would have been

reflected.^{75,76,93,94,98,99} However, since neat electrolyte solutions are used as both the targets of study and the supporting electrolyte, the observed stability is the result of the possible contributions from all components, and it is often difficult to distinguish whether the stability limits are set by the solvent or the salt decompositions, especially in the case of anodic (oxidation) limits. Because of the high concentration of electrolytes used, it is also difficult to apply a thermodynamic interpretation to the stability data obtained in this way. Furthermore, the coexistence of the reversible redox processes that may occur simultaneously on these active electrode materials can make the determination of electrochemical stability limits difficult, and frequently even the definition of electrochemical stability becomes ambiguous because of the passivation on active electrodes. The stability data for various lithium ion cell electrolytes determined in this way are therefore still scarce despite their importance.

As a compromise between the above two approaches, the third approach adopts nonactive (inert) materials as working electrodes with neat electrolyte solutions and is the most widely used voltammetry technique for the characterization of electrolytes for batteries, capacitors, and fuel cells. Its advantage is the absence of the reversible redox processes and passivations that occur with active electrode materials, and therefore, a well-defined onset or threshold current can usually be determined. However, there is still a certain arbitrariness involved in this approach in the definition of onset of decomposition, and disparities often occur for a given electrolyte system when reported by different authors.^{50d,75,76,130,131,203} Therefore, caution should be taken when electrochemical stability data from different sources are compared.

This section will discuss the electrochemical stabilities of different solvents and salts used in state-of-the-art electrolytes that were determined with nonactive electrodes (i.e., in the first and the third approaches). When active rather than inert electrodes are used as working surfaces, many complicated processes, including the reversible electrochemical redox chemistries as well as surface passivation, occur simultaneously. These related materials will be dealt with in a dedicated section (section 6).

5.1. Anion of Lithium Salts

Table 4 lists selected electrochemical stability data for various lithium salt anions that are commonly used in lithium-based electrolytes, with the measurement approaches indicated. Although it has been known that the reduction of anions does occur, sometimes at high potentials, the corresponding processes are usually sluggish and a definite potential for such reductions is often hard to determine. The reduction of solvents, occurring simultaneously with that of anions on the electrode, further complicates the interpretation efforts. For this reason, only the anodic stability of salt anions is of interest, while the cathodic limit of the salt in most cases is set by the reduction of its cation (i.e., lithium deposition potential).

Table 4. Anodic Stability of Electrolyte Solutes: Nonactive Electrodes

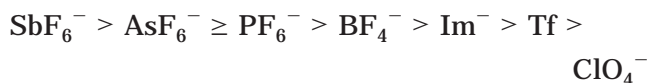
salt	solvent	conc/M	working electrode	E_a^a (V/(mA cm ⁻²))	approach	ref
ClO ₄ ⁻	PC	0.65	GC	6.1 (1.0)	3	130, 131 ^b
	PC		Pt	4.6	3	204
BF ₄ ⁻	PC	0.65	GC	6.6 (1.0)	3	130, 131, 81 ^c
	EC/DMC		AC	4.78	2	
PF ₆ ⁻	THF	0.001	GC	4.4 (0.1)	1	120 ^d
	SL	0.001	GC	4.8 (0.1)	1	120
	PC	0.65	GC	6.8 (1.0)	3	130, 131
	none ^e	none	GC	4.94 (1.0)	3	206
	none	none	Pt	5.00 (1.0)	3	206
	EC/DMC	1.0	AC	4.55	2	81
AsF ₆ ⁻	PC	0.65	GC	6.8 (1.0)	3	130, 131
	none	none	GC	5.05 (1.0)	3	206
	none	none	Pt	5.10 (1.0)	2	206
	EC/DMC	1.0	AC	4.96	3	81
	THF	1.0	GC	4.25 (0.1)	1	120
	THF	0.009	GC		1	120
	SL	0.8	GC	4.69 (0.1)	1	120
	THF	1.0	GC	4.10 (0.1)	1	120
SbF ₆ ⁻	PC	0.65	GC	7.1 (1.0)	3	130, 131
	PC	0.65	GC	6.0 (1.0)	3	130, 131
Tf ⁻	PC	0.10	Pt	5.0 (0.5)	3	207
	EC/DMC	1.0	AC	4.29	2	81
	PC	0.65	GC	6.3 (1.0)	3	130, 131
Bet ⁻	PC	0.1	GC	6.2 (0.5)	3	207
	PC	0.65	GC	6.3 (1.0)	3	130, 131
Im ⁻	PC	0.1	Pt	5.3 (0.5)	3	130, 131
	none	none	GC	5.06 (1.0)	3	206
	none	none	Pt	5.13 (1.0)	3	206
	EC/DMC	1.0	AC	4.33	2	81

^a Anodic limit, potential referred to Li⁺/Li, cutoff current density in parentheses. ^b Scan rate: 5 mV s⁻¹. ^c Activated carbon as working surface. Scan rate: 10 mV s⁻¹. ^d Supporting electrolyte 0.1 M Bu₄NBF₄. Scan rate: 100 mV s⁻¹. ^e The solvent-free condition was realized by using an ionic liquid based on imidazolium cation, at 80 °C. Scan rate: 20 mV s⁻¹.

The most noteworthy observation among the entries of Table 4 is that these anodic stability data are widely diversified depending on the conditions under which they were obtained. For example, the anodic stability limits of PF₆⁻, AsF₆⁻, and SbF₆⁻ determined in THF solutions are obviously lower than those determined in carbonate solutions, and a possible explanation lies in the fact that THF itself is not an oxidation-resistant solvent; therefore, its own decomposition is most likely responsible for these limits.¹²⁰

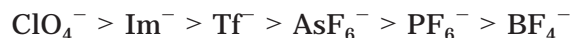
The rather systematic work was performed by Ue et al., who used tetraalkylammonium salts as supporting electrolytes and measured the oxidation potential of a number of anions, most of which were considered promising candidates for lithium-based batteries.^{50d,130,131} Figure 8 shows the linear sweep voltammograms obtained from these solutions with a GC electrode.^{50d} The reduction limits seem to be caused by the decomposition of the ammonium cations, as evidenced by the similar cathodic current response for all of these solutions in Figure 8 and further confirmed by the analysis conducted on the decomposition products.²⁰⁴ On the other hand, the oxidation limits were determined simultaneously by both salt and solvent. For example, the anodic limits were set by the unstable anions (Tf⁻ and ClO₄⁻), whereas solvent PC would be oxidized first if stable anions such as BF₄⁻ and PF₆⁻ are present. By using a more oxidation-resistant solvent, glutaronitrile

(GLN), the stability order of these anionic species was determined as¹³⁰

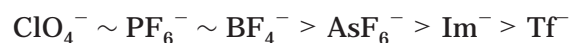


It should be pointed out that the above anodic stability order is highly conditional, since the order had been determined by approach 2 above, where the stability limits are defined as the potential at which the decomposition current density reaches an arbitrary value (1.0 mA cm⁻² in this case). Any change in this criterion could result in a reversal of the order.

The coupling effects of solvent/salt on electrolyte stability can also be observed when mixture solvents are used, and the stability of the electrolyte can be much improved when a stable solvent/salt is selected. For example, the room-temperature breakdown voltage of electrolytes LiX/EC/DEE lies in the order²⁰⁵



However, when a linear carbonate replaces the unstable ether DEE, the order changes into



It is believed that the reactivity of DEE toward Lewis acids, PF₆⁻ and BF₄⁻, contributes to the early decomposition of the electrolytes.

To exclude the solvent's effect on the anodic stability of salt anions, Koch et al. made a series of salts

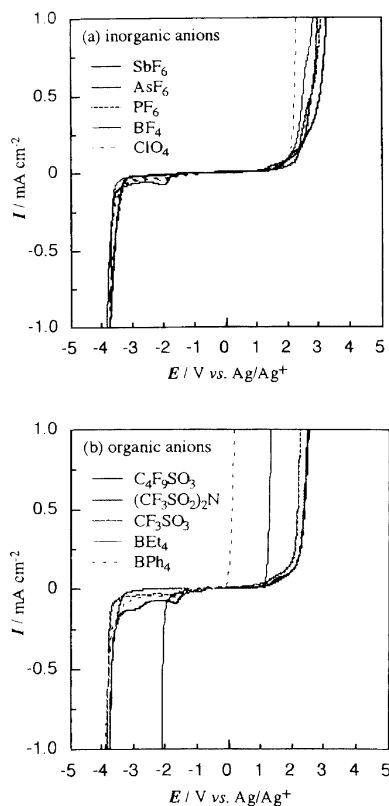


Figure 8. Determination of anodic stability for various anions in PC solution on GC. (Reproduced with permission from ref 130 (Figure 1a and b). Copyright 1997 The Electrochemical Society.)

Scheme 6. Electrochemical Oxidation of the PF_6^- Anion: the Solvents or the Trace Moisture in the Electrolyte Serves as the Proton Source of H-Abstraction



based on a low-melting organic cation and measured the oxidation limits of these solvent-free molten salts on the surfaces of GC, tungsten, and Pt, respectively.²⁰⁶ The “intrinsic anodic stability” measured by them follows an order completely different from the one determined in solvents:



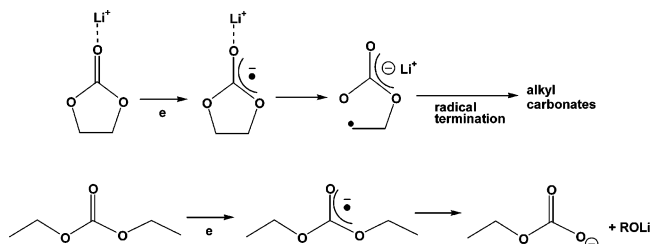
A mechanism was also proposed for the instability of the PF_6^- anion (see Scheme 6).

The above stability order is supported by the results of ab initio calculations, where a correlation has been established between the oxidation limits of these anions and the energy level of their highest occupied molecular orbital (HOMO). However, the gapping discrepancies that exist between “intrinsic” and solution stability limits remain to be explained.

5.2. Solvents

A solvent with an ideal electrochemical stability for a high-energy-density battery purpose should possess high oxidation and low reduction potentials at the same time. Table 5 lists selected electrochemical

Scheme 7. Proposed Single-Electron Mechanism for the Reduction of EC and DEC



stability limits for some nonaqueous solvents commonly used in lithium-based battery research. Despite the inconsistency created by the varying measurement conditions, these data express a general trend that we have discussed in section 2; that is, carbonates and esters are more anodically stable, while ethers are more resistant to cathodic decompositions.

Among cyclic carbonates and esters, EC seems to be more liable toward reduction on nonactive electrodes,^{210–214} which agrees with molecular orbital ab initio calculations of the corresponding radical anions. The difference between EC and PC in reductive reactivity is attributed to the steric effect introduced by the methyl on PC rather than the electronic effect, as supported by the molecular orbital ab initio calculations for the corresponding radical anions.²¹² On the other hand, the reduction of PC seems to be a rather sluggish process, as evidenced by the high background current level distributed in a broad potential range during voltammetric scans. The slow kinetics of PC toward cathodic reduction is correlated with its readiness to intercalate into a graphene structure of carbonaceous anodes and then decompose, causing exfoliation of the latter.²¹⁴

Aurbach and co-workers performed a series of ex situ as well as in situ spectroscopic analyses on the surface of the working electrode upon which the cyclic voltammetry of electrolytes was carried out.^{210–213} On the basis of the functionalities detected in FT-IR, X-ray microanalysis, and nuclear magnetic resonance (NMR) studies, they were able to investigate the mechanisms involved in the reduction process of carbonate solvents and proposed that, upon reduction, these solvents mainly form lithium alkyl carbonates (RCO_3Li), which are sensitive to various contaminants in the electrolyte system. For example, the presence of CO_2 or trace moisture would cause the formation of Li_2CO_3 . This peculiar reduction product has been observed on all occasions when cyclic carbonates are present, and it seems to be independent of the nature of the working electrodes. A single electron mechanism has been shown for PC reduction in Scheme 1, while those of EC and linear carbonates are shown in Scheme 7.²¹⁴

The radical anion is considered to be the common intermediate formed for these carbonate molecules, and its existence in the electrochemical reductions has been confirmed experimentally.¹⁷⁸ As will be revealed later, this mechanism seems to be universal for carbonates, whether on inert or active electrodes, and alkyl carbonates have been widely believed to be a key component in forming a protective interface

Table 5. Electrochemical Stability of Electrolyte Solvents: Nonactive Electrodes

solvent	salt/conc (M)	working electrode	E_a^a	E_c^b	ref	
PC	Et ₄ NBF ₄ /0.65	GC	6.6		130, 131	
	none ^c	Pt	5.0	~1.0	74	
	Bu ₄ NPF ₆	Ni		0.5	212	
	LiClO ₄ /0.1	Au, Pt		1.0–1.2	214	
	LiClO ₄ /0.5	porous Pt	4.0		305	
	LiClO ₄	Pt	4.7		177	
	LiClO ₄	Au	5.5		306	
	LiAsF ₆	Pt	4.8		177	
	EC	Et ₄ NBF ₄ /0.65	GC	6.2		130, 131
		Bu ₄ NPF ₆	Ni		0.9	212
LiClO ₄ /0.1		Au, Pt		1.36	214	
DMC	Et ₄ NBF ₄ /0.65	GC	6.7		130, 131	
	LiClO ₄ /0.1	Au, Pt		1.32	214	
	LiPF ₆ /1.0	GC	6.3		76	
	LiF	GC	5.0		312	
DEC	Et ₄ NBF ₄ /0.65	GC	6.7		130, 131	
	LiClO ₄ /0.1	Au, Pt		1.32	214	
EMC	Et ₄ NBF ₄ /0.65	GC	6.7		130, 131	
	LiPF ₆ /1.0	GC	6.7		76	
γBL	LiAsF ₆ /0.5	Au, Ag		1.25	208	
THF	Et ₄ NBF ₄ /0.65	GC	5.2		130, 131	
	LiClO ₄	Pt	4.2		177	
	LiAsF ₆ /1.0	GC	4.25 (0.1)		214	
	none ^c	Pt	4.0	< -2.0	74	
	LiAsF ₆ /1.0	GC	4.2		64	
	LiAsF ₆	Pt	4.2		177	
	2-Me-THF	LiClO ₄	Pt	4.1		177
		LiAsF ₆ /1.0	GC	4.15 (0.1)		214
LiAsF ₆ /1.0		GC	4.2		64	
LiAsF ₆		Pt	4.1		177	
DME	Et ₄ NBF ₄ /0.65	GC	5.1		130, 131	
	LiClO ₄	Pt	4.5		177	
	LiAsF ₆	Pt	4.5		177	

^{a,b} Anodic and cathodic limits, potential referred to Li⁺/Li. ^c The salt-free condition was realized via an ultramicroelectrode technique.

between active electrodes and electrolytes. In a more general context, since the surface chemistries on both inert and active electrodes have been found to be very similar in most of the nonaqueous electrolytes when these electrodes are polarized to low potentials, the early analytical work, mainly performed by Aurbach and co-workers, should be recognized as the foundation for the later understandings of the SEI on carbonaceous anodes.

6. Electrochemical Stability: on Active Electrodes

The requirement that electrolytes be inert toward both anode and cathode materials is usually realized by the kinetic rather than thermodynamic stability of the former against reductions and oxidations. Given the strong reducing and oxidizing potency of the electrode materials employed in the high-energy-density battery chemistries, the possibility of a thermodynamically stable electrolyte is usually nonexistent, and it is the chemical passivation of these reducing or oxidizing surfaces that ensures the inertness of the bulk electrolytes during cell chemistry.

Passivation is a process where the products from the initial decomposition of electrolyte form a dense, protective film that covers up the pristine surface of the electrode and prevents any sustained decomposition. The electrolyte components that are sacrificed to form such a protective film would have a deter-

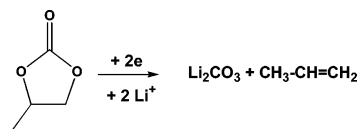
mining influence on the physicochemical nature of the new electrode surface, such as thermal and chemical stability, as well as its impedance to ionic conduction. The occurrence of passivation constitutes the foundation upon which many high-energy-density battery chemistries are built, including lithium-based chemistry. For this reason, the electrolyte/electrode interface has been the focus of research interest for both lithium and lithium ion chemistries.

On the other hand, it should be pointed out that, in addition to the protective effect of passivation, the passivated interface also acts as a barrier to the facile ion transport that occurs between the electrode and electrolyte. More often than not, the bottleneck for the overall battery chemistry is constituted by passivation. Excessive passivation is especially undesired because it reduces the power performance of the cell. For lithium ion cells, this power reduction usually happens on the cathode surface.

6.1. Passivation on Lithium Anode

Almost immediately after lithium metal was found to be stable in nonaqueous electrolytes, researchers suggested that the passivation of the lithium surface by electrolytes is the origin of this unexpected stability, because the reduction potentials of these organic solvents are far above that of lithium.^{4,215–217} Peled was the first author to formally introduce the concept of a protective interface between lithium and elec-

Scheme 8. Proposed Two-Electron Mechanism for the Reduction of PC



trolytes and describe the fundamental physicochemical properties of such an interface.³⁷ He argued that, because of the high electronegativity of lithium, the free contact between it and the electrolyte components never actually exists; instead, the reaction between the lithium electrode and electrolyte components occurs instantaneously, and the solid products from this reaction compose a thin film that grows on the lithium with the reaction. The decomposition could only stop when this film, which is nonconductive to electrons but conductive to ions, covers the whole surface of the lithium and attains a certain thickness. Once formed, the film stays on the lithium surface at all times, and it cannot be completely removed even by the stripping/deposition of lithium. Since this film acts like an electrolyte in its conductive preference, Peled named it the “solid electrolyte interface (or interphase)” (SEI). Considering the low ionic conductivity of solid-state electrolytes, he also proposed that the rate determining step for a redox process on such surfaces would be the diffusion of lithium ions through the SEI,²¹⁸ instead of the electron charge-transfer between electrode and solution species, as was believed before.

Using a parallel capacitor model, Peled and Straze calculated the apparent thickness of the SEI for a series of active metal electrodes, including lithium, calcium, and magnesium, with the equation²¹⁹

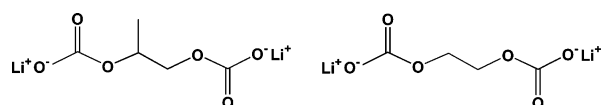
$$L = \frac{\epsilon A}{C\pi(3.6 \times 10^{12})} \quad (10)$$

where A , L , C , and ϵ are the electrode area, the thickness, the capacitance, and the dielectric constant of SEI, respectively. They estimated that the average SEI thickness of lithium in nonaqueous electrolytes is 25–100 Å.^{218,219} Electrons tunneling through the film of this thickness are believed to be minimal.

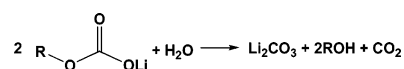
The chemical composition of the SEI is believed to be closely related to the electrolyte composition. For example, in thionyl chloride-based electrolytes, the SEI is proposed to be mainly composed of LiCl,²¹⁸ while it becomes Li₂S₂O₄ in sulfur dioxide-based electrolytes²¹⁸ or Li₂O in ether-based electrolytes.⁵⁶ After performing microscopic observations of lithium surfaces treated with PC-based electrolytes, Dey believed the main component of this interface to be Li₂CO₃, which is the decomposition product of PC through a two-electron mechanism (see Scheme 8).⁵⁶ This conclusion seems to be supported by results from Auger electron spectroscopy (AES) and X-ray photoelectron spectroscopy (XPS).^{220,221} However, more recent studies suggest that the above process might be oversimplified, and the actual process involves a complex competition between a number of reductive reactions of different components.

With surface-sensitive spectroscopic means, Aurbach et al. argued that the main component in the

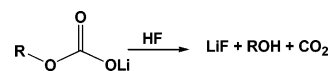
SEI on lithium is not Li₂CO₃ but the lithium salt of alkyl carbonate, and it was most probably formed via a one-electron mechanism followed by radical termination paths as shown in Scheme 1.⁵⁵ This compound has an FT-IR signature at ~1650 cm⁻¹ for the carbonyl stretching, which was confirmed by the characterization of a synthesized authentic sample of a lithium alkyl carbonate, CH₃CH₂CH₂CO₃Li.⁵⁵ Since XPS also detected the decomposition products from lithium salts, which are in the form of simple halides, alkoxides, or oxides, a competition between solvents and salts obviously exists. However, the formation of alkyl carbonate seems to be dominant when EC is present because of the more reactive nature of EC toward cathodic reductions.^{117,209} The formation of lithium alkyl carbonate was also confirmed in an independent diagnosis work, where the reduction products of EC in a supporting electrolyte were hydrolyzed by D₂O and then subject to NMR analysis, which identified ethylene glycol as the main species formed, as indicated by the singlet at $\delta = 3.7$ ppm vs TMS.^{208,212} Thus, Aurbach and co-workers concluded that PC and EC were reduced to the following lithium alkyl dicarbonates, respectively:



Further studies demonstrated that alkyl carbonate is very sensitive to the common contaminants in electrolytes, which is probably the reason that early work identified Li₂CO₃ as the main component in the SEI.¹¹⁸ For example, trace moisture produces Li₂CO₃ when the salt anion is stable (such as ClO₄⁻ or AsF₆⁻):²⁴⁹



However, when the salt anion is susceptible to hydrolysis by trace moisture (such as BF₄⁻ or PF₆⁻), the generated HF eliminates alkyl carbonate as a surface species and only LiF can be observed as the overwhelming species in the SEI:¹¹⁷



Alkyl carbonate is also unstable upon storage on the lithium electrode, probably because of its continuous electrochemical reduction.¹¹⁸ Thus, Aurbach et al. further proposed that the SEI might have a multi-layer structure within which the simple inorganic species such as Li₂CO₃ and Li₂O are more stable and closer to lithium, while alkyl carbonate is more likely to be distributed in the outer layers.^{117,118}

Kanamura et al. carried out detailed XPS studies on lithium electrodes that were either statically treated with or cycled in LiBF₄-based electrolytes.^{222,223} By sputtering the surface of the lithium electrode, they were able to record the depth profile of the related chemical species. Their conclusions are in good agreement with the hypothesis by Aurbach et al.,^{117,118} that is, while alkyl carbonate can be detected

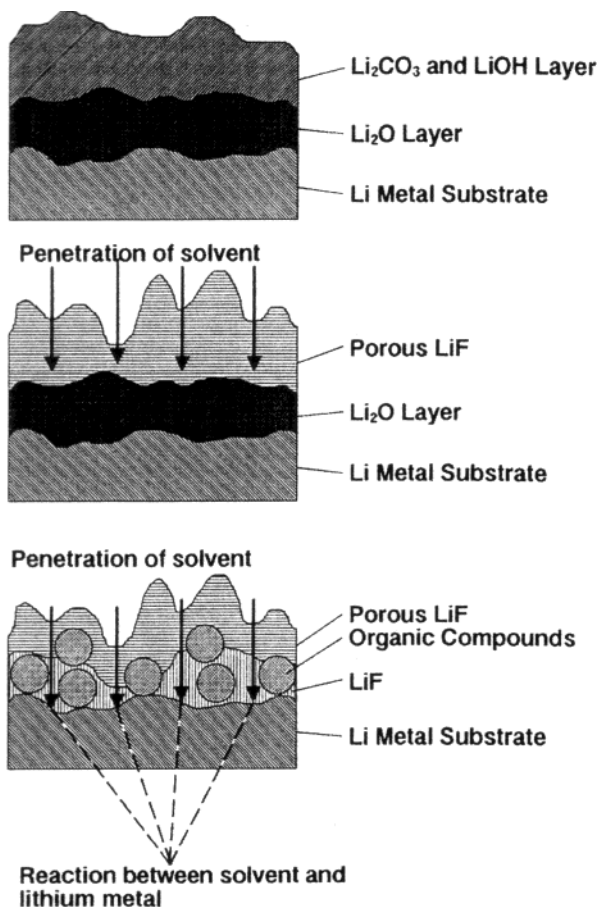


Figure 9. Schematic illustrations of the surface film formed on lithium in nonaqueous electrolytes based on LiBF_4 solutions and the subsequent reactions. (Reproduced with permission from ref 222 (Figure 12). Copyright 1995 The Electrochemical Society.)

in the outlying layer of the SEI, as indicated by its signature binding energy of 289.0 eV at the C 1s region, its abundance rapidly decreases with sputtering time. On the other hand, O 1s spectra clearly reveal the increasing abundance of Li_2O species. LiF exists throughout the SEI and is relatively independent of sputtering, a result of the sensitivity of BF_4^- anion toward trace moisture in electrolytes. Kanamura et al. proposed two possible paths for the formation of LiF : (1) simple acid–base reaction between HF and alkyl carbonate or Li_2CO_3 , or (2) direct reduction of BF_4^- anion by lithium.^{222,223} Additional reactions between the solvents and the lithium electrode also seem possible after the initial formation of the SEI, since the abundance of organic species increases in the inner layer with storage time increases, according to C 1s spectra. These organic species might be some polymeric products that resulted from PC or other carbonates instead of alkyl carbonates alone, as evidenced by the C 1s signal around 286 eV and by an earlier XPS work.²²⁴ This latter process is attributed to the permeation of solvent through the SEI and its subsequent reaction with lithium. The resulting polymeric films, most likely polyether moieties, are embedded with LiF crystals. Figure 9 schematically shows the lithium surface structure and these subsequent reactions of the SEI.²²²

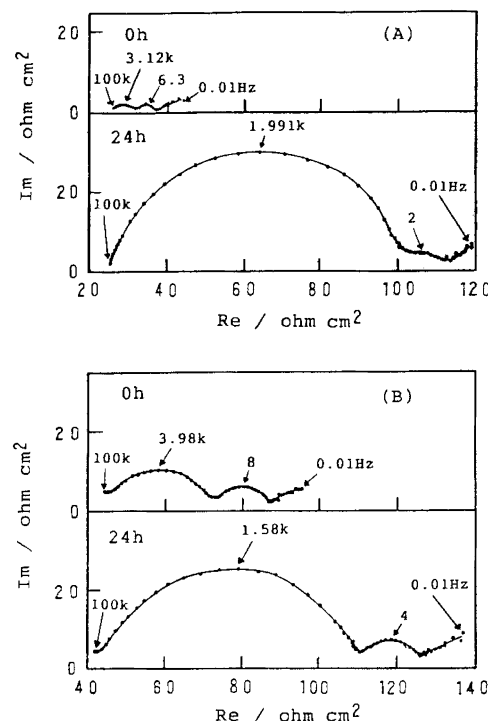


Figure 10. Impedance complex plane (Nyquist plots) of lithium electrode in (A) 1.0 M $\text{LiPF}_6/\text{EC}/\text{PC}$ and (B) 1.0 M $\text{LiClO}_4/\text{EC}/\text{PC}$ at initial time (0.0 h) and after 24 h. Re and Im stand for the real and imaginary parts of the impedance measured, respectively. Frequency was indicated in the figure for selected data points. Note that the first semi-circle corresponds to SEI impedance. (Reproduced with permission from ref 86 (Figure 2). Copyright 1992 The Electrochemical Society.)

Aside from voltammetric techniques, ac impedance is also a powerful tool widely used to study the interfacial properties of lithium in nonaqueous electrolytes. It is one of the few in situ techniques and therefore is often used in combination with voltammetry, known as electrochemical impedance spectroscopy (EIS). As an example, Figure 10 shows the impedance response of a symmetrical cell, lithium|1.0 M LiX in PC/EC |lithium, drawn in the Nyquist plot, where LiX is LiPF_6 or LiClO_4 . Typically, two semi-circles would be observed for such cells at high and medium frequencies, if the time constants for each component are sufficiently separated, along with a spike at the low-frequency end.¹⁷⁵ It is generally accepted that the semicircle at medium frequency corresponds to the ionic migration process in the SEI and the one at lower frequency to the charge-transfer process on lithium, whereas the intercept at the high frequency end with the real axis represents bulk electrolyte resistance. Examination of the interfacial resistance in various electrolyte solutions reveals that the SEI on lithium grows with time of exposure to electrolytes, and the chemical nature of both solvent and salt anion seems to relate closely to the semicircle for the interfacial film.^{86,225–227} For example, the resistance of the SEI that formed in the LiPF_6 -based electrolyte is smaller than the one formed in the LiClO_4 -based electrolyte, and the presence of EC also renders a more conductive SEI on lithium.^{86,225–227} An empirical rule (with frequent exceptions though) might be stated here concerning the resistance of the

SEI: an electrolyte with higher bulk ion conductivity usually results in an SEI of lower impedance, either on a lithium or carbonaceous electrode, as will be discussed in later sections.

As a mass sensor with nanogram sensitivity, a quartz crystal microbalance (QCM) was used in combination with voltammetry by Naoi et al. to monitor the change occurring on the lithium surface during SEI formation.²²⁸ Like EIS, it is one of the few analytical tools that can reveal in situ information on the interfacial process, which includes the change in mass as well as the surface morphology of the lithium electrode. It was found that, during the cycling process, the already-formed SEI was repeatedly destroyed and rebuilt, as indicated by the consistent mass increase with cycle numbers. Among the various combinations of salts and solvents tested, the LiPF₆-based electrolyte seems to have the most rapid reaction kinetics with lithium, since the lithium electrode in it was observed to gain net mass even during the stripping step, suggesting that the reaction kinetics between the fresh lithium surface and the electrolyte is fast enough to compensate for the mass loss caused by the lithium dissolution. On the other hand, the net mass accumulated on lithium is much higher in LiClO₄- and LiTf-based electrolytes than in the LiPF₆-based electrolyte. The conclusion from the above two observations seems to point to a more efficient and protective SEI formed by the LiPF₆-based electrolyte. The author ascribed this result to the trace amount of LiF in the SEI, which is absent in LiClO₄- and LiTf-based electrolytes.¹¹⁸ The measurement of lithium surface roughness also reveals LiPF₆ as the favored salt in electrolytes because it forms a smoother and more uniform SEI, thus minimizing the probability of dendrite growth on a relative scale as compared with the cases of the other salts studied.

The significance of an SEI on lithium stability should be evaluated from two different angles: one is the static stability that relates to standing storage, and the other is the dynamic stability that relates to reversibility. It is the SEI formation on the lithium surface that leaves lithium statically stable in a nonaqueous electrolyte; conversely, the SEI also renders a nonuniform surface morphology for deposited lithium, so that the current density across the surface is unevenly distributed during the lithium stripping/deposition, with the direct consequence being dendrite growth.

The roughness of the SEI depends heavily on the chemical nature of the electrolyte. For example, it was argued that an SEI consisting of LiF/Li₂O would provide a much more uniform current distribution,²²³ while in numerous earlier works it was also observed that trace moisture has a positive effect on the lithium cycling efficiency in nonaqueous electrolytes by assisting in forming a compact and uniform SEI.^{57,229} Nevertheless, the dendrite issue is a major challenge to lithium metal-based chemistry that still remains unresolved. The prospects for this battery technology, still attractive because of its high energy density as compared with the state-of-the-art lithium ion technology, rely on the discovery of a new

electrolyte system that can suppress or even eliminate lithium dendrite formation.

6.2. Electrolyte/Carbonaceous Anode Interface: SEI

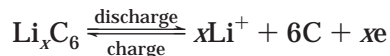
6.2.1. Exfoliation and Irreversible Capacities on a Carbonaceous Anode

It has been known since the mid 1950s that graphite can form intercalation compounds with lithium ions, which are accommodated in the interstitial region between the planar graphene sheets.^{230–232,233} The most lithium-enriched intercalation compound of this family has a stoichiometry of LiC₆, and its chemical reactivity is very similar to that of lithium metal. There have been a number of different chemical approaches to the preparation of these compounds, for example, by direct reactions of graphite with molten lithium at 350 °C,²³² with lithium vapor at >400 °C,²³⁴ or with lithium powder under high pressure,^{235,236} and so forth.

On the other hand, the electrochemical synthesis of these lithium graphite intercalation compounds (Li-GIC) has been proven difficult. In earlier work, it had been found that the most commonly used electrolyte solvent, PC, decomposed reductively on the graphite electrode at a potential of ~0.80 V, and the irreversible process led to the physical disintegration of graphite.²³⁷ The occurrence of this irreversible reduction apparently prohibits any possibility of the lithium ion intercalating into graphite, which should happen at a much lower (and therefore more reductive) potential. The destruction of graphite by PC was repeatedly observed in different electrolytes based on PC, and this disintegrating process of the graphite structure was named “exfoliation”.^{238–243} Besenhard et al. proposed that the exfoliation was caused by the cointercalation of PC molecules with lithium ions into the interplanar structure of the graphite and the subsequent decomposition therein.^{239–242} As a result, the multilayer structure of graphite, which is only held together by weak van de Waals forces, falls apart because of the strain introduced by the gaseous products, believed to be mostly propylene.^{234–237,243}

Realizing that the solvent must be the key to the exfoliation, later researchers explored different polar organic molecules such as dimethyl sulfoxide (DMSO) and DME as candidates to replace PC, in the hope that they would not cointercalate or decompose; but most of these efforts failed to endorse the usefulness of Li-GIC as a negative electrode to replace lithium.^{239–241} In the 1980s, the only successful example of electrochemical intercalation of lithium into graphite was reported by Yazami and Touzain in 1983 with a polymer electrolyte based on poly(ethylene oxide) (PEO).²⁴⁴ As it is essentially impossible for the macromolecular solvent PEO to cointercalate, this electrolyte supported the reversible lithium ion intercalation into and deintercalation from natural graphite. Using electrochemical titration techniques, the potential of the stage I and II Li-GIC was determined to be between 0.50 and 0.20 V vs Li, thus confirming the conceptual feasibility that Li-GIC

could be used as a negative electrode to replace lithium with minimal energetic penalty. Thus, a negative electrode based on the stage I Li-GIC would have the following reversible chemistry:



In the ideal situation of 100% utilization ($x = 1.0$), the capacity corresponding to the above anode half reaction is 372 mA h g^{-1} . However, due to the low ion conductivity of the polymer electrolyte and the high interfacial impedance between it and the graphite electrode, this elegant example of electrochemical preparation of lithiated graphite is of limited practical significance.

Considering the vulnerability of the highly crystalline structure of graphite, some researchers in the late 1980s focused their attention on carbon structure instead of electrolyte formulation. Successes were seen with various amorphous carbon electrodes, including carbon fiber,²⁴⁵ pyrolytic carbons,²⁴⁶ and petroleum coke.²⁴⁷ The insensitivity of these carbonaceous materials to solvent cointercalation seems to be related to their amorphous portion, which has stacking defects that coexist with the tiny crystalline sectors and serve to pin the graphene layers together to suppress the lattice expansion that occurs during the solvent cointercalation. Thus, the indefinite "exfoliation plateau" at 0.80 V is completely absent from these amorphous carbon anodes in PC-based electrolytes,³⁶ and reversible lithium ion intercalation is realized up to $>10^3$ cycles in various nonaqueous electrolytes, although the initial cycles are always accompanied by a portion of irreversible capacity that depends on the nature of the carbon and the composition of the electrolytes.^{36,157} These efforts eventually led to the commercialization of the first generation lithium ion cells.^{29–31,34–35}

However, two penalties, both associated with the energy density, arise from the disordered anode structure: (1) a smaller Coulombic capacity than the theoretical value for LiC_6 and (2) a sloping potential profile during both charging and discharging.^{43,157} The former is caused by the small crystallinity of these amorphous carbons, because it is in the highly ordered graphene sheets where lithium ion could be accommodated, while the latter is caused by a broad distribution of adsorption site energies in the disordered carbons, which leads to a broad potential range within which lithium intercalation occurs.¹²⁵ Figure 11 compares the cycling behavior of an amorphous carbon anode with that of graphite in a half anode cell²⁴⁸ and clearly demonstrates the above two penalties.³⁶ While the latter is certainly disadvantageous because of the unstable cell voltage, the combination of these two results in a much lower energy density that Li-GIC can offer theoretically.

Hence, a dilemma was encountered between energy density and stability for these various forms of carbonaceous materials; that is, as the carbonaceous anode is more graphitic in structure, the degree of lithium ion intercalation may be closer to the ideal ($x = 1.0$), and its potential profile may be closer to that of Li^+/Li and remain relatively flat (therefore

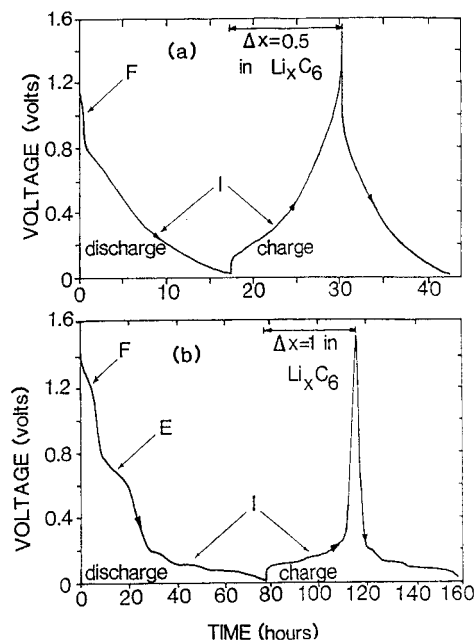


Figure 11. (a) Initial $1\frac{1}{2}$ cycles of a Li/petroleum coke cell. The cell was cycled at a rate of 12.5 h for $\Delta x = 0.5$ in Li_xC_6 . (b) Initial $1\frac{1}{2}$ cycles of a Li/graphite cell. The cell was cycled at a rate of 40 h for $\Delta x = 0.5$ in Li_xC_6 . F denotes the irreversible capacity associated with SEI formation, E the irreversible capacity due to exfoliation, and I the reversible capacity due to lithium intercalation into carbon. 1.0 M LiAsF_6 in EC/PC was used as electrolyte. (Reproduced with permission from ref 36 (Figure 2). Copyright 1990 The Electrochemical Society.)

attractive as an anode candidate), it also becomes more liable to solvent co-intercalation.^{43,96,249,250} It was only after Dahn and co-workers revealed the role of the SEI on the reversibility of carbonaceous electrodes and the effect of EC therein that the energetic advantage of highly graphitic carbonaceous materials regained practical significance for the lithium ion industry.³⁶ As a direct consequence of improvements in electrolyte formulations aided by the knowledge gained in SEI chemistry, amorphous carbonaceous anode materials were gradually phased out from commercial lithium ion technology, starting in the 1990s.³⁸

In retrospect, the significance of Dahn's seminal work lies in two aspects: (1) the fundamental understanding of how carbonaceous materials operate in nonaqueous electrolytes and (2) the more practical side of how the above dilemma concerning energy density and reversibility can be overcome. This knowledge dictates the development of electrolytes for state-of-the-art lithium ion chemistry.

On the fundamental front, Dahn et al. successfully accounted for the irreversible capacity that accompanies all carbonaceous anodes in the first cycling. They observed that the irreversible capacity around 1.2 V follows an almost linear relation with the surface area of the carbonaceous anodes and that this irreversible process is essentially absent in the following cycles.³⁶ Therefore, they speculated that a passivation film that resembles the one formed on lithium electrode in nonaqueous electrolyte^{37,218,219} must also be formed on a carbonaceous electrode via similar electrolyte decompositions, and only because

of the more porous surface of the latter would the capacity associated with the reduction process become noticeable. Once formed, the physicochemical property of this film should be similar to the solid electrolyte model that Peled had proposed for the lithium surface; that is, it is an ionic conductor and an electronic insulator,³⁷ and therefore, the sustained reductive decomposition could be prevented. Hence, the term SEI that Peled had invented for the passivation of lithium electrode was transplanted on the carbonaceous anode materials.

On the practical side, Dahn's work demonstrated that, by altering the electrolyte composition, the exfoliation of graphitic materials could be eliminated, since the chemical nature of the SEI is dictated by electrolyte composition, especially by the solvents. The "magic ingredient" identified in this case is EC, whose structural difference with PC is merely a methyl substituent. As Figure 11 shows, the presence of EC not only prevents the physical disintegration of graphite that occurs at 0.8 V but also supports the reversible intercalation (during the discharge of the half-cell) and deintercalation (during the corresponding charge) of lithium ions at a very low potential, <0.20 V, with Coulombic capacity approximately approaching the theoretical value of LiC_6 . Because PC is present in the electrolyte, a certain degree of graphite exfoliation can still be observed, but obviously EC plays an effective role in suppressing the destruction of the graphite structure. The latter development in electrolyte formulation made by Tarascon and Guyomard effectively suppressed this side reaction to a negligible level,^{44,98,99} although a certain irreversible capacity was always present, accounting for the material supply required by the SEI formation. The irreversible capacity, or the ratio of this capacity to the total reversible capacity (called Coulombic inefficiency), has become one of the parameters for measuring the performance of a certain electrolyte on carbonaceous anodes.

The commercial lithium ion cells on the consumer market nowadays have already undergone a so-called "forming process" at the manufacture sites, during which a stable SEI was formed to ensure that no more irreversible process was left. The Coulombic efficiency of these cells ought to be 100% under the conditions specified for their application. On the other hand, any accidental misuse such as overcharge, high temperature exposure, and mechanic impact might damage the already formed SEI, resulting in more irreversible reactions during charging and consequently a loss from the rated capacity.

6.2.2. Mechanism of SEI Formation

According to Peled's model, the existence of an SEI constitutes the foundation on which lithium ion chemistry could operate reversibly. Therefore, an ideal SEI should meet the following requirements: (1) electron transference number $t_e = 0$ (otherwise, electron tunneling would occur and enable continuous electrolyte decomposition), (2) high ion conductivity so that lithium ions can readily migrate to intercalate into or deintercalate from graphene layers, (3) uniform morphology and chemical composition for ho-

mogeneous current distribution, (4) good adhesion to the carbonaceous anode surface, (5) good mechanical strength and flexibility so that it allows the expansion and contraction of the graphene lattice during the reversible intercalation/deintercalation process, and (6) low solubility in electrolytes so that continuous dissolution of SEI would not occur, resulting in persistent decomposition of electrolyte and consumption of the limited source of lithium from the cathode.

There has been considerable controversy concerning the mechanism of SEI formation on a carbonaceous anode, but it is generally agreed that the initial electrolyte decomposition is responsible and that a competition among a variety of reactions involving the solvent as well as the salt components is also present.

6.2.2.1. Peled's Model: Anode/Electrolyte Interface Film. In their proposal of SEI formation on a carbonaceous electrode in nonaqueous electrolytes, Dahn actually adopted Peled's model for lithium's surface and extended it to carbonaceous electrodes. By this model, a two-dimensional passivation film is established via a surface reaction.

Because of the similar potentials between fully lithiated graphite and lithium metal, it has been suggested that the chemical nature of the SEIs in both cases should be similar.³⁶ On the other hand, it has also been realized that for carbonaceous anodes this formation process is not expected to start until the potential of this anode is cathodically polarized (the discharge process in Figure 11) to a certain level, because the intrinsic potentials of such anode materials are much higher than the reduction potential for most of the solvents and salts. Indeed, this potential polarization process causes one of the most fundamental differences between the SEI on lithium metal and that on a carbonaceous anode. For lithium metal, the SEI forms instantaneously upon its contact with electrolytes, and the reduction of electrolyte components should be indiscriminate to all species possible,^{37,218,219} while, on a carbonaceous anode, the formation of the SEI should be stepwise and preferential reduction of certain electrolyte components is possible.

Endo et al. investigated the reductive decomposition of various electrolytes on graphite anode materials by electron spin resonance (ESR).¹⁷⁸ In all of the electrolyte compositions investigated, which included LiClO_4 , LiBF_4 , and LiPF_6 as salts and PC, DMC, and other esters or ethers as solvents, the solvent-related radical species, which were considered to be the intermediates of reductive decomposition,⁵⁵ were detected only after prolonged cathodic electrolysis. With the aid of molecular orbital calculation, they found that the reduction of salt anion species is very difficult, as indicated by their positive reduction enthalpy and that of free solvent ($\Delta H_r \approx -1 \text{ kcal mol}^{-1}$). However, the coordination of lithium ions with these solvents dramatically reduces the corresponding reduction enthalpy ($\Delta H_r \approx -10^2 \text{ kcal mol}^{-1}$) and renders the reaction thermodynamically favored. In other words, if no kinetic factors were to be considered, the SEI formed on carbonaceous anodes

would predominantly consist of the decomposition products of those solvents in the solvation sheath of lithium ion, which migrates toward the negatively charged anode surface. For state-of-the-art electrolytes, the reduction of cyclic carbonates such as EC and PC should provide the major species to build up the SEI while the participation of linear carbonates should be relatively inconsequential. A similar conclusion was drawn by Wang et al., who employed a high-level density functional theory to investigate the reductive decomposition mechanism for EC molecules in electrolyte solution and found that, while the reduction of a free EC molecule is very unlikely, the coordination of lithium ion to an EC molecule renders the one- or two-electron reduction processes thermodynamically possible in a supermolecular structure such as $\text{Li}^+(\text{EC})_n$ ($n = 1-5$).¹⁷⁰

In view of the possibility that certain electrolyte components could be preferentially reduced on carbonaceous anode, Peled and co-workers explored a means to manipulate the chemical nature of the SEI by deliberately using unstable electrolyte ingredients.¹⁰⁶ They argued that, since these components would be reduced at a higher potential, the SEI would be completed far before solvent cointercalation occurred, and the probability of cointercalation and its following exfoliation could be minimized. EC seems to be such a component due to its reactivity.²¹²⁻²¹⁴ As a measure of the ease with which electrolyte components could be reduced, Peled and co-workers proposed using the vast data bank of the rate constant (k_e) of reduction in aqueous media, and a fair correlation was established between this constant and the SEI formation potential.¹⁰⁶ Thus, k_e could be used as a tool for the selection of electrolyte solvents and salts. According to this model, ideal electrolytes should be formulated with the candidates of $k_e > 10^9 \text{ M}^{-1} \text{ s}^{-1}$. By this standard, AsF_6^- , EC, vinylene carbonate (VC), and CO_2 are favored, while BF_4^- and ClO_4^- are not.

This model conceptually forms the theoretical basis for the later development of electrolyte additives, as evidenced by the success of CO_2 and VC in suppressing the irreversible capacity in the initial cyclings. But so far as major electrolyte components are concerned, this model is not widely applied, since many other properties such as ion conduction and phase diagrams must also be taken into account if the component is present in high concentrations.

6.2.2.2. Besenhard Model: Ternary Graphite Intercalation Compound (GIC). In addition to the indiscriminate versus selective reductions, another fundamental difference between graphite and lithium electrodes is the presence of the interlayer voids of the former that could accommodate both lithium ions and solvent molecules. Therefore, some researchers argued that the reductive decomposition of electrolytes in contact with the former might not be only a simple surface reaction as suggested in Peled's model. Instead, the solvent could cointercalate into graphene layers before they decompose therein, and the passivation film thus formed could penetrate into the structure of graphite.

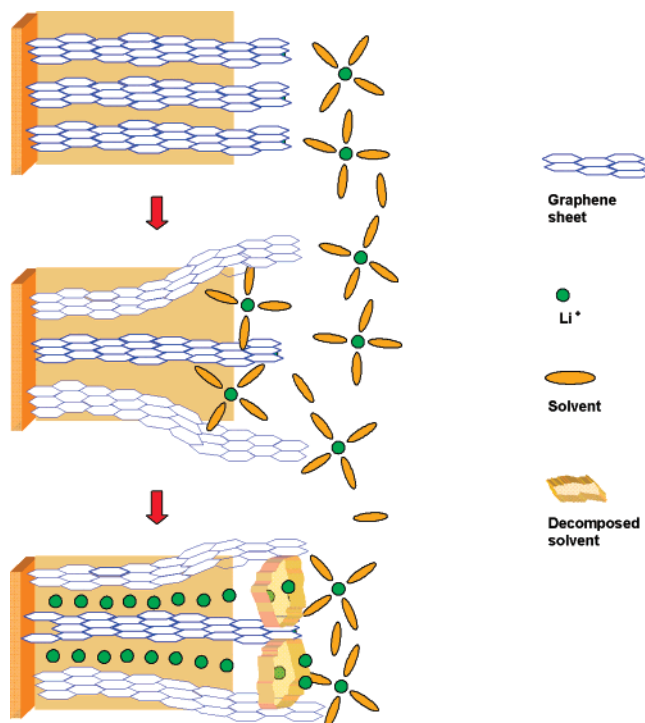


Figure 12. Schematic illustration of the SEI formation mechanism via the decomposition of $\text{Li}(\text{solvent})_x\text{C}_y$. Reconstructed based on ref 251.

The early studies have identified the existence of graphite intercalation compounds with solvent molecules.²³⁹⁻²⁴³ On the basis of the knowledge about these compounds and their reactions, a mechanism for SEI formation was proposed later by Besenhard that involves the initial formation of a ternary GIC [$\text{Li}(\text{solvent})_x\text{C}_y$] and its subsequent decomposition near the edge sites of the graphene planes to form the SEI.²⁵¹ Figure 12 schematically depicts the SEI formation process according to this mechanism. Upon cathodic polarization of the graphite anode, the solvated lithium ion migrates to the negatively charged surface of graphite and is intercalated into graphene layers at $\sim 1.0-0.80 \text{ V}$ before any reduction occurs. The ternary GIC thus formed, for example, $\text{Li}(\text{EC}/\text{DME})_x\text{C}_y$, has a short lifetime and decomposes within the time scale of slow scan CV ($\sim 10^4 \text{ s}$), as indicated by the irreversible peak observed when the scanning rate is low; therefore, according to Besenhard et al., this process might easily be mistaken as an ordinary irreversible reduction of the electrolyte. However, at certain faster scan rates (e.g., 10 mV s^{-1}), part of the solvated ion could still be reversibly removed from graphene interlayer sites.²⁵¹ The reductive decomposition of these cointercalated solvents then renders an SEI that extends from the graphite surface at the edge sites into the interior of the interlayer voids.

The direct evidence that Besenhard et al. presented for the formation of a ternary GIC is the dilatometric measurement of the graphite electrode, which indicates a crystal expansion of 150% at the cointercalation potential.²⁵¹ However, this expansion due to solvent cointercalation was never confirmed on the microscopic level. All of the in situ X-ray diffraction (XRD) measurements conducted by different research-

ers on the cycling graphite failed to offer any evidence that a substantial change in the interlayer distance occurred around the cointercalation potential.^{96,124,252,255} In these experiments, the maximal shift in 2θ of the (002) diffraction peak during graphite cycling, which can reflect the size of the guest species, only corresponds to an expansion of 0.35 Å in the c -axis; hence, bare lithium ions seem to be the only species that can be accommodated.^{252–254} It should be pointed out that the existence of ternary GICs is beyond question, and the doubt here is about whether they could be electrochemically formed under a similar situation in the forming of lithium ion cells.^{256–260} So far, the chemical or electrochemical synthesis of ternary GICs has failed to produce any compositions based on carbonate solvents, despite the success of Ogumi and co-workers with various solvents such as ether or alkylsulfoxide,^{257–260} casting more doubt on the Besenhard model.

In defense of the Besenhard model, Chung et al. argued that the lack of XRD evidence for ternary GICs might be simply due to either their rapid decomposition or the localized presence of them near the graphite edges.²⁵⁵ Since XRD probing of the material is based on the averaged diffraction response of the sample lattice, these wider spacings of the ternary GICs might not be detected as an averaged bulk property.

In situ EQCM studies of graphite in various electrolytes also challenge the formation of ternary GICs with the real-time monitoring of the graphite electrode mass increase during cathodic polarization.¹⁰¹ It was found that, between 0.8 and 0.5 V, where such GICs are supposed to be stable, the mass change per quantity of electricity ($\Delta m/\Delta Q$) was 27–35 g F⁻¹, corresponding well to Li₂CO₃ that has a $\Delta m/\Delta Q$ of 36.9 g F⁻¹. If solvents such as EC ($\Delta m/\Delta Q = 88.07$ g F⁻¹), PC ($\Delta m/\Delta Q = 102.1$ g F⁻¹), or the solvated lithium ion [Li⁺(PC)_{*n*}] ($\Delta m/\Delta Q > 300$ g F⁻¹ assuming a coordination number of 3) cointercalate into the graphene structure, the corresponding mass gain on the graphite anode, which is too conspicuous to miss, should have been well recorded by the quartz crystal sensor.

The thermodynamic stability of a ternary GIC is also questionable. Obviously, between a bare lithium ion and one solvated by molecular dipoles, the intercalation of the former between two giant graphene anions is far more favored thermodynamically than that of the latter. The fully lithiated GIC LiC₆, for example, does not solvate in nonaqueous electrolyte solvents, and the tendency of lithium to prefer binary (i.e., without solvent cointercalation) instead of ternary GICs has also been noticed in the solution syntheses.²⁵⁷

Despite the concerns raised by XRD, EQCM, and thermodynamics, the Besenhard model still received extensive support from various experimental observations as summarized below and soon became the prevalent model used by researchers in the lithium ion battery community.

It had been discovered earlier that when electrolyte solvents decompose reductively on graphite, one of the products is gaseous propylene.²³⁷ Dey et al.

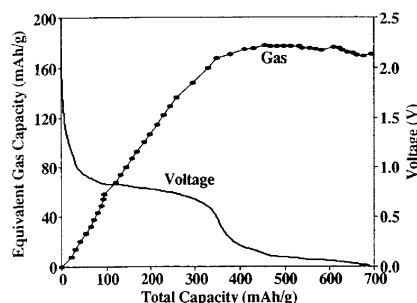
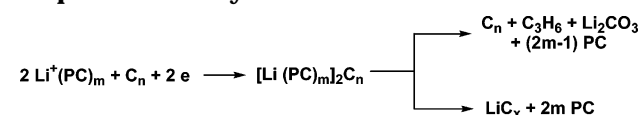
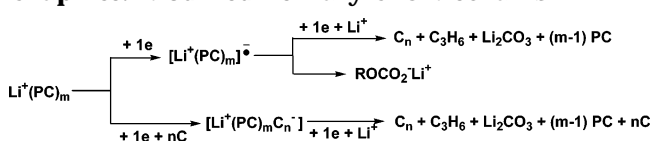


Figure 13. Correlation of gas evolution on a graphite electrode in 1.0 M LiClO₄/PC/EC (50:50) with the irreversible process at 0.80 V during the first discharge. Note the level off of gas volume as soon as reversible lithium ion intercalation starts. (Reproduced with permission from ref 261 (Figure 2). Copyright 1993 The Electrochemical Society).

Scheme 9. Electrochemical Reduction of PC on Graphite: Ternary GIC Mechanism



Scheme 10. Electrochemical Reduction of PC on Graphite: Modified Ternary GIC Mechanism



proposed a surface mechanism involving a two-electron process as shown in Scheme 8. Arakawa and Yamaki quantitatively analyzed the gas volume generated during the electrochemical decomposition of PC on a graphite electrode and found a mismatch between the Coulombic quantity and the equivalents of propylene gas generated, with an efficiency between 50% and 70%, depending on current density.²⁴³ Apparently this result conflicts with Scheme 8, and other reaction processes must also exist simultaneously. Using a kinetic treatment, they suggested a mechanism (see Scheme 9) where a ternary GIC is the intermediate, which underwent two parallel but competitive paths to form either the gaseous product propylene and Li₂CO₃ or lithiated binary GICs. Using this mechanism, Arakawa and Yamaki successfully explained the relation between gas volume rate and time.²⁴³

Following a similar approach, Shu et al. used an EC/PC mixture instead of neat PC as electrolyte solvent, and their analysis of propylene gas volume corroborates the observations of Arakawa and Yamaki.²⁶¹ Furthermore, because EC was present in their electrolyte, the reversible lithium intercalation could occur after a long plateau at ~0.8 V (representing PC decomposition), therefore a correlation between the gas volume and this irreversible process was able to be established, as shown in Figure 13. Considering Aurbach's spectroscopic observations (to be discussed later), a modified mechanism (see Scheme 10) was proposed by Shu et al., wherein a competition exists between the surface reaction leading to radical anions and the formation of ternary

GICs, via the one-electron process in both cases. According to Shu et al., these intermediate species underwent further single-electron reduction and produce Li_2CO_3 and propylene gas, while alkyl carbonates are generated via radical termination as shown in Schemes 1 and 7^{55,214} to become the major ingredients in the surface film.

In separate research, Matsumura et al. performed quantitative analyses of lithium content in graphite electrodes with plasma spectroscopy and correlated the results with the quantities of electricity associated with the reversible and irreversible processes.²⁶² With XPS, they found that after the graphite is delithiated, there is a certain amount of lithium remaining in the graphite that cannot be removed electrochemically. Depth profiles established by sputtering the graphite sample with O_2^+ confirmed that these lithium species are distributed rather evenly in the bulk of the graphite. The author ascribed the existence of these electrochemically nonremovable lithium ions as the result of lithium reaction with active sites on the carbon surface.²⁶² However, there is also the possibility that these lithium signals are from the lithium-containing ingredients in the three-dimensional SEI that exists in the graphite matrix.

Kim and Park investigated the mechanism of lithium ion intercalation in graphite anodes employing solid-state NMR.²⁶³ Their results perhaps offer the most direct evidence in support of Besenhard's GIC model. By adding strongly coordinating additives for lithium ions, 12-crown-4 and 18-crown-6 ethers, into the electrolyte solution, they were able to observe an obvious Knight shift in the ^7Li signals of the graphite powder that was caused by the coordination. Separate ^{13}C NMR tests conducted on the same graphite sample also identified the signals of crown ether as well as carbonate (more likely its decomposition product) in the graphite powder following lithiation. Assuming that the adsorbed additives and solvents on the graphite surface have all been thoroughly removed during the washing procedure that preceded NMR measurements, the above observation should be considered as the first confirmation that solvent molecules indeed are found in the bulk of the graphite, and their cointercalation with lithium ions during the lithiation process would most likely be the path. However, since the author did not present any blank test to prove the effectiveness of the washing procedure, the possibility of surface contamination due to the remnant solvent molecules being trapped in the porous structure of the graphite electrode could not be completely excluded. Nevertheless, solid-state NMR proved to be an effective tool in studying the bulk structure of graphite anodes, and more efforts on SEI mechanisms should be done with this technique.

In situ Raman spectra studies performed on graphite anodes also seem to reveal a cointercalation occurrence that leads to exfoliation. Huang and Frech used solutions of LiClO_4 in EC/EMC and EC/DME as electrolytes and monitored the E_{2g2} band at $\sim 1580\text{ cm}^{-1}$ in the Raman spectra of the graphite that was cycled between 2.0 and 0.07 V.²⁶⁴ Reversible lithium intercalation and deintercalation was indicated by

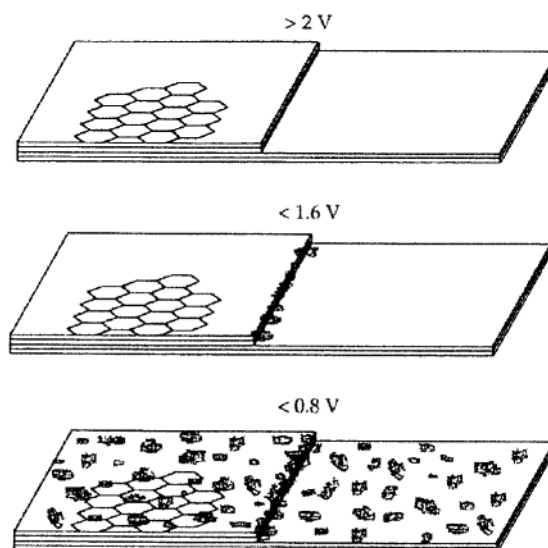


Figure 14. Schematic diagram summarizing the stepwise formation of the SEI on a graphite surface. (Reproduced with permission from ref 266 (Figure 10). Copyright 1997 The Electrochemical Society.)

the corresponding shift of this band in the EC/DMC-based electrolyte. But in the presence of DME, the graphite surface structure was detected to be irreversibly altered in the range between 0.9 and 0.5 V, as indicated by a shoulder on the E_{2g2} band. Since no lithium ion intercalation is supposed to occur in this potential range, the authors attributed the Raman spectral changes to the extensive DME cointercalation. Interestingly enough, a DME-based ternary GIC was indeed electrochemically obtained and identified by Abe and Ogumi and co-workers with XRD.^{257–260} As a matter of fact, the results from this Raman study support the Besenhard model but also cast doubt upon it simultaneously because no such irreversible E_{2g2} band shift had been observed in the EC/DMC electrolytes, although obviously the SEI was formed in that case too.

Various microscopic means were also applied to study the SEI formation process, but the reproducibility of the results is highly dependent on the condition under which the observations were made and the pretreatment history of the samples. Even for the same observation, the interpretations could vary from author to author. For example, with a scanning tunnel microscope (STM), Inaba et al. observed the formation of some "blisters" on the graphite surface during its cathodic polarization and described them as the swelling of the graphene layer due to solvent cointercalation;²⁶⁵ however, Farrington and co-workers, after observing the same phenomenon with an atomic force microscope (AFM), ascribed these island structures to the depositions of the decomposition products from the solvent.²⁶⁶ One common phenomenon that was observed by all of these microscopic experiments is the stepwise formation of the surface species,^{265–269} which appear first near the edge sites of the highly ordered graphite surface at potentials as high as 1.6 V and then grow and cover the whole electrode at potentials below 0.80 V, as shown in Figure 14. Since the intrinsic reduction potentials of the related solvents are much lower

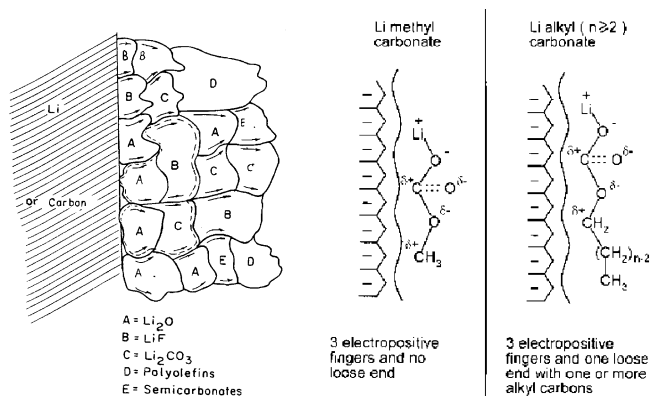


Figure 15. Schematic drawings of various models: (a, left) “mosaic” SEI model by Peled et al. (Reproduced with permission from ref 270 (Figure 1). Copyright 1997 The Electrochemical Society.) (b, right) Surface double layer capacitor model by Ein-Eli (Reproduced with permission from ref 272 (Figure 1). Copyright 1999 The Electrochemical Society.)

(Table 5), the edge-site process at the higher potentials might have been preceded by solvent cointercalation.

Recently, Chung et al. conducted EIS studies on a graphite electrode that had been previously exfoliated in a PC-based electrolyte and then reassembled in an EC-based electrolyte after washing.²⁵⁵ They found that, compared with the fresh graphite electrode or the graphite anode that had been precycled in an EC-based electrolyte, the exfoliated graphite sample exhibited a much higher (>300%) double-layer capacitance, which was roughly proportional to the surface area that was accessible to the electrolyte. On the basis of this observation, Chung et al. postulated that the previous history exfoliation had resulted in a significant rupture of the graphite surface, as confirmed by the STM results obtained by Inaba et al. on the graphite exfoliation process.²⁶⁹ Apparently, between a simple surface reaction model and Besenhard’s model, the latter would more easily account for this surface area increase, because the direct consequence of ternary GIC formation is the creation of new surfaces.

6.2.2.3. Other Models. In addition to Besenhard’s model, the other models were mainly modifications developed from the original Peled’s concept for lithium electrode passivation, with surface reaction as the major process, and emphasis was placed upon the composition and structure of the precipitated film or the interaction between the precipitated products and the bulk electrolyte components.

On the basis of the results from XPS studies by Kanamura and co-workers that the SEI has a multilayered structure,^{222,223} Peled and co-workers modified their lithium electrode passivation model to include carbonaceous anodes and proposed a so-called “mosaic model” to describe the SEI structure on the anode, as Figure 15a shows.²⁷⁰ According to this model, multiple reductive decompositions occur between the negatively charged anode surface and the various electrolyte components simultaneously, depositing a mixture of insoluble products on the anode. This “heteropolymicrophase” SEI consists of many microregions that are of entirely different chemical

natures, ranging from thermodynamically stable anions such as O²⁻, S²⁻, and halides located in the immediate vicinity of the anode surface to partially reduced organic species such as alkyl carbonates and polyolefins located closer to the electrolyte solution. They suggested that, in the SEI of such a structure, the impedance to the intergrain lithium ion transport would be the rate-determining step. Apparently the pattern in which these “mosaic” pieces are arranged is decided by the order in which the electrolyte components are reduced. The reductions are considered to be surface processes, and the structural difference of the anode (lithium or graphite) is considered inconsequential.

In an attempt to explain why a linear methyl alkyl carbonate such as DMC and EMC can form a stable SEI on a graphite surface while ethyl or higher alkyl carbonates such as DEC cannot,^{107,108,271} Ein-Eli proposed another surface model in which the decomposed electrolyte solvents are adhered to the negatively charged graphite anode surface through Coulombic interactions.²⁷² He argued that, during the cathodic polarization of the anode, the decomposition products, in the form of lithium organic salts, would be lined up in a model similar to that of a double-layer capacitor, as Figure 15b shows, and would attach themselves to the existing film via the positively charged lithium ion “head” and the partially positively charged carbons. According to this model, the effectiveness as well as the stability of the SEI would depend on these points of adhesion. The schematic drawing in Figure 15b shows that the decomposition products from methyl alkyl carbonate can form a tight adhesion without “loose ends”, while a loose alkyl tail from DEC or higher alkyl carbonates prevents the formation of a compact film. Like Peled’s original model^{137,218,219} and its modification,²⁷⁰ this model is still based on a two-dimensional surface reaction. It must be pointed out, though, that the graphic representation as shown in Figure 15b might be oversimplified and should only be understood as an empirical rule rather than an accurate picture on the molecular level, considering that the carbonyl bonds in the carbonate molecules have to be distorted out of the sp² plane of the carbonyl carbon to meet the contact points.

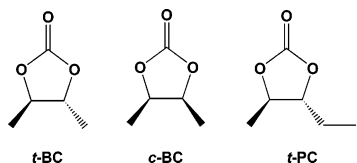
To investigate the failure mechanism of graphite electrodes in nonaqueous electrolytes, Aurbach and co-workers used various electrolyte solvents, salts, and graphite electrodes with varying structures and morphologies and attempted to correlate the SEI effectiveness with these parameters.^{273–275} Their extensive studies led to the conclusions that the failure mechanism is solvent-dependent and exfoliation does not always happen to graphite anodes even if they physically disintegrate. For the reductively stable ether-based solvents (see Table 5), no massive surface film was observed above 0.30 V, and these solvents, coordinating with lithium ions, cointercalated into graphene and caused complete exfoliation of the latter. In this case, the evidence of destroyed crystallinity was obtained by XRD. However, for carbonates that are reductively active, such as EC or PC (Table 5), surface precipitations were observed

at potentials well above that of lithium ion intercalation, which prevented the complete exfoliation of the graphite anode, as indicated by its mainly intact crystallinity.^{255,275} Rather, the physical disintegration in this case could only be caused by the electric isolation of graphite fragments on a macroscopic level, which is the result of both the solvent's chemical nature and the graphite's surface morphology.

On the basis of these conclusions, Aurbach and co-workers proposed a model for SEI formation that makes a compromise between solvent cointercalation (for ether-based solvents) and the surface reaction mechanism (for carbonates). According to the model, the graphite surface in electrolytes based on carbonate solvents including PC was covered with a surface film, and the balance between the kinetics of precipitation of highly cohesive surface films and the kinetics of overall surface reactions producing gaseous products determines whether the graphite is stabilized. In deep crevices that exist on the graphite surface, such gaseous products created sufficient strain and electrically disconnected the graphite fragments. Solvent cointercalation seems less probable with the existence of surface films. Obviously, this model would be able to account for the observed fact that surface area increases after the graphite is cycled in PC-based electrolytes, while the graphene crystal structure remains unchanged on a microscopic scale.²⁵⁵

The drastic difference between EC and PC concerning the stability of the graphite in them, despite their close structural similarity, was ascribed by Aurbach and co-workers to the effect of the methyl group from PC, which intervenes with good adhesion and cohesion of the formed product to the graphite surface,²⁷⁵ in a very similar way, as described by Ein-Eli, to the "alkyl loose tails".²⁷² Thus, the gas evolution kinetics is faster than the buildup of the SEI on the graphite surface, and the electric disconnection and regional disintegration occur, starting at the deep crevices driven by the gas pressure therein.

6.2.2.4. The Mystery of Exfoliation. However, all of the above models that recognize surface reactions as the film formation path were strongly challenged by the results of the comparative studies carried out by Chung et al.^{255,276} To explore the origin of graphite exfoliation, they used a series of model carbonates to study their cointercalation behavior with graphites and found a correlation between the stereo hindrance of the solvent molecules and the behavior of the graphite anodes in the electrolytes based on them. These model carbonates are all structural analogues of PC and include a pair of geometric isomer *trans*- and *cis*-butylene carbonates (*t*-BC and *c*-BC) as well as *trans*-2-pentylene carbonate (*t*-PC):



When the graphite anode was cycled in the electrolytes based on these carbonate solvents, it was found

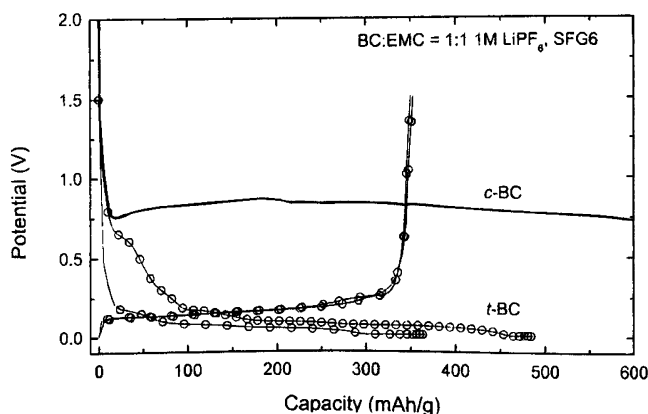
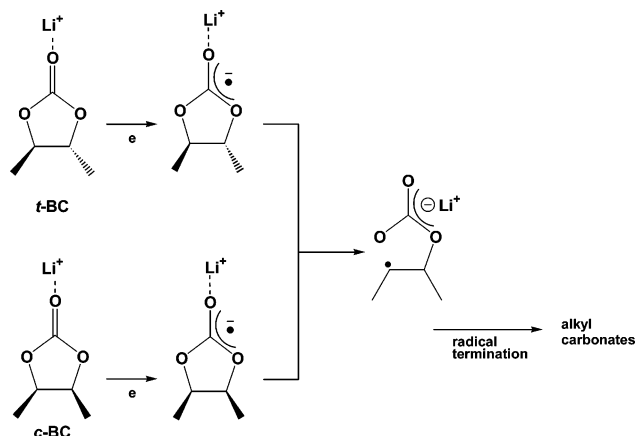


Figure 16. Voltage profiles for the first two lithium intercalation/deintercalation cycles realized on graphite anode in *t*-BC/EMC and *c*-BC/EMC solutions of 1.0 M LiPF₆. (Reproduced with permission from ref 255 (Figure 7). Copyright 2000 The Electrochemical Society.)

Scheme 11. Nondifferentiation of Surface Reactions toward Diastereomers *t*-BC and *c*-BC^a



^a An Identical Radical Anion Was Produced When the Ring-Opening Step Eliminated the Chirality of the Ether Carbon

that reversible lithium intercalation/deintercalation occurred with *t*- but not *c*-BC. The difference between *t*-BC and *c*-BC in terms of the graphite performance is a replica of the difference between EC and PC, as shown in Figure 16. Such different behaviors from geometric isomers *t*-BC and *c*-BC would not be expected if surface reactions dominated the formation of the SEI, as proposed in the models by Peled,^{37,270} Ein-Eli,²⁷² and Aurbach,^{273–275} because the chirality of the carbons would be eliminated once the ring opened to form the radical anion as the predecessor to lithium alkyl carbonates (Scheme 11). Thus, any reasonable model for SEI formation has to involve a mechanism in which the stereo difference between *t*-BC and *c*-BC could be recognized and play a role in determining the physicochemical nature of the resultant SEI. Chung et al. argued that the fundamental concept of the Besenhard model (i.e., the cointercalation of the solvent to form a ternary GIC before any reductive decomposition like the one in Scheme 11) would be able to explain the above stereo effect, since the graphene layer structure would serve as a sub-nanoscale sieve (graphene interlayer distance ~ 0.35 nm) that could tell the difference in the strain introduced by these geometric isomers, as shown in a schematic drawing in Figure 17. Thus, PC and *c*-BC

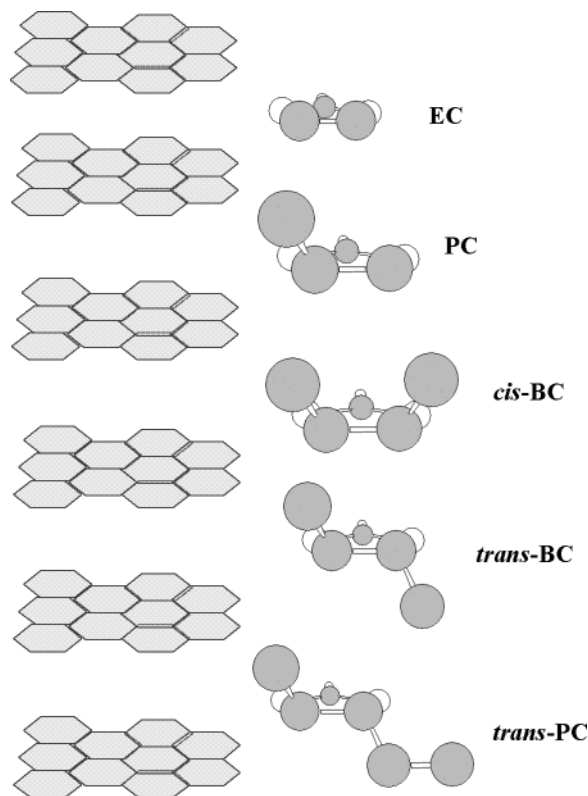


Figure 17. Schematic drawing of the GIC-exfoliation model. Differentiation of the stereo difference among EC, PC, and related carbonates by graphene structure.

have similar stereo hindrances and would exert similar strains into the graphene structure and cause exfoliation, while *t*-BC may experience severe geometric constraints for cointercalation. Hence, it can exhibit a reaction behavior on a graphite surface that is qualitatively different from that of PC.

Again, caution must be taken when using the graphic representation as shown in Figure 17 because such oversimplification might be misleading when a complex process such as the formation of an SEI on graphite is handled. For example, the graphic representation in Figure 17 suggests that cointercalation of solvent occurs without the assistance of lithium ions, while, in actual cointercalation, the solvents that coordinated with lithium ions in the solvation sheath would preferentially cointercalate. With the supermolecular structure of the solvation sheath in consideration, it would be more difficult to predict the effect of diastereomers on cointercalation by the analogue of Figure 17.

On the other hand, with an average solvation number of four, it would be hard to imagine that cointercalation would occur without breaking the solvation structure of the lithium ion, considering the required expansion in the graphite structure to accommodate such a gigantic guest. Most probably, at the edge sites of the graphite where cointercalation occurs, the solvated lithium ion is progressively stripped of its solvation sheath, and the free solvents would then insert into the graphite interior in a close way, as shown by Figure 17.

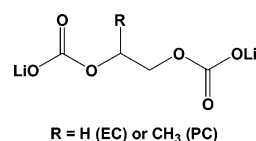
To summarize, various models have been proposed to depict the formation of an SEI on a graphite anode, based on the common knowledge that the reductive

decomposition of electrolyte components leads to the formation of a protective film on the anode. However, these models differ in the mechanism by which the SEI is formed, especially concerning the issue of whether a ternary GIC is formed before the reductive decomposition occurs. Although each of these models can elegantly account for certain experimental observations, the Besenhard model that evolves around solvent cointercalation seems to be supported by the most experimental evidences, despite the fact that the electrochemical formation of a key species of this model, a metastable ternary GIC intermediate, has not been experimentally confirmed. Nevertheless, it is generally agreed nowadays that to a certain extent the solvent cointercalation does occur and is at least a part of the process related to the formation of the SEI. The complete clarification of the above controversy relies on obtaining more experimental evidence at a microscopic level from further studies.

6.2.3. Characterization of Surface Chemistry

Relative to the controversy associated with the mechanism of SEI formation, there is less uncertainty in the knowledge about the chemical composition of the SEI, due mainly to the exhaustive surface spectroscopic studies carried out by Aurbach and co-workers on carbonaceous anodes in various nonaqueous electrolytes, adopting both in situ and ex situ approaches.^{104,108,123,124,249,250} Table 6 lists the chemical compounds as identified by these spectroscopic means and the proposed chemical reactions leading to those species.^{27–284} As it has been pointed out, the solvents, especially the cyclic carbonates, play a more important role in the surface chemistry of the anode than the salt anions.¹⁷⁸

Compared with the surface chemistry of nonactive electrodes^{212–214} or lithium electrode,^{55,117,118,209} similar chemical species were identified despite the differences in the electrode surfaces. A major modification of the previously accepted two-electron reductive pathway as suggested by Dey and Sullivan²³⁷ was proposed by Aurbach and co-workers based on the identification of lithium alkyl carbonate by FT-IR.^{108,124,249} They suggested that the surface reductive process for most carbonate molecules proceeds via a single-electron path leading to the intermediate, as shown in Schemes 1 and 7, and that Li_2CO_3 and alkenes were formed through either the continued reduction of this intermediate or the secondary reaction between it and trace moisture in the system. Specifically, the following structures were assigned to the decomposition products from EC and PC, which supposedly constitute the main composition of the SEI layer:^{102,104,117}



The predecessor of alkyl carbonate, a radical anion, has been experimentally observed by ESR, the life span of which depends on the carbonate structure and ranges from minutes to hours but is independent

of the salt species used.¹⁷⁸ Moreover, this one-electron reduction mechanism does seem to be strongly favored by the fact that the intermediate does not convert to alkenes in 100% yield, reminiscent of the work by and Arakawa and Yamaki²⁴³ and Shu et al.²⁶¹ who have already reported that the generation of gaseous products does not match the electric quantity injected into the anode.

A more quantitative confirmation of alkyl carbonate formation came from transmission electron microscopy (TEM), by which electron diffraction (ED), electron energy loss spectra (EELS), and imaging were conducted on disordered and graphitic carbonaceous anodes cycled in LiClO₄/EC, respectively.²⁸⁰ Although the ED does not identify any crystalline phase other than the hexagonal structured graphite and Li₂CO₃ on the surface (probably suggesting that alkyl carbonates are noncrystalline), the atomic concentration ratio of oxygen and carbon (O/C) as determined by EELS ranges between 1 and 1.5, unequivocally indicating that the proposed alkyl carbonate formed from EC reduction. Interestingly, this O/C ratio was also found to vary with the potential to which the carbonaceous anodes were cathodically polarized: above 0.90 V an O/C ratio = 3.0 was obtained for the presence of Li₂CO₃, while below 0.80 V an O/C ratio = 1.0–1.5 was obtained. Thus, the authors proposed that the SEI was formed in a two-step process: (1) formation of Li₂CO₃ occurs at potentials between 1.0 and 0.80 V, and (2) formation of alkyl carbonates is favored at lower potentials below 0.80 V.

In retrospect, probably a more reasonable explanation could hereby be proposed concerning this potential-dependent reductive decomposition. Combining the observations from Shu et al. about the correlation of gas products with a 0.80 V plateau,²⁶¹ Farrington and co-workers about the deposition of the film onto the surface,²⁶⁶ Aurbach and co-workers about the competition between single- and two-electron reductive paths,^{108,124} and Kanamura et al. about the multilayered structure of the SEI,^{222,223} one can conclude that, at potentials above 0.80 V, where the film has not completely covered the basal surface of graphite, the two-electron process as proposed in Scheme 8 is likely the predominant process because of the good electronic conductivity of the graphite surface, leading to Li₂CO₃ and ethylene; below 0.80 V the single-electron process prevails because of the much slower electron hopping kinetics, leaving the surface with alkyl carbonate depositions and rendering negligible gas evolution simultaneously. Therefore, the potential-dependence of the decomposition compounds as observed in a TEM study by Naji et al.²⁸⁰ is actually the potential-dependence of the competition between one- and two-electron paths, as shown in Schemes 1 and 7.

In addition to FT-IR, XPS experiments performed on a graphite anode that had been cycled in various carbonate-based electrolytes also identified an alkyl carbonate species. Bar-Tow et al. characterized the surface of a highly oriented pyrolytic graphite (HOPG) that had been cycled in LiAsF₆/EC/DEC and found the C 1s signal located at 289 eV,²⁸¹ which had been

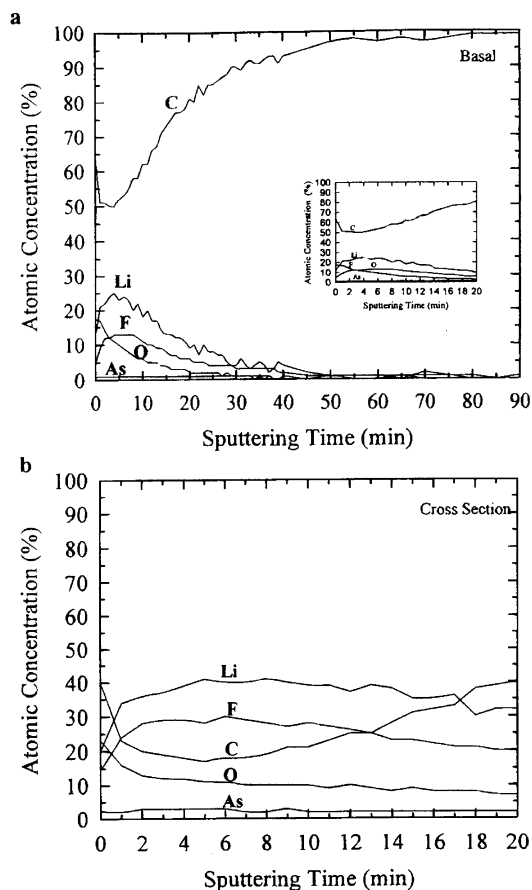


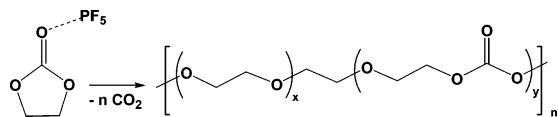
Figure 18. Depth profile of various chemical elements in the SEI formed on HOPG: (a) basal plane and (b) edge section. (Reproduced with permission from ref 281 (Figure 4). Copyright 1999 The Electrochemical Society.)

previously observed on a lithium surface and identified as alkyl carbonates by Kanamura et al.^{222,223,282,283} after referencing with the C 1s signal of Li₂CO₃ at 290.5 eV. Surface sputtering with Ar⁺ reduces the abundance of this species rapidly, suggesting that this species might only be stable on the top layer of the SEI.

Besides lithium alkyl carbonates, XPS also identified a wide variety of decomposition products from other electrolyte components, including polyether moieties as well as the lower valence As species. The depth profile of the SEI established by prolonged sputtering by Ar⁺ reveals the multilayered structure of the SEI, as shown in Figure 18a, in which the organic species such as alkyl carbonate and Li₂CO₃ are present in predominant percentages on the solution side of the SEI while simple inorganic species such as Li₂O or As(0) are more stable on the graphite side of the SEI probably because of the more complete reduction facilitated by faster electron-tunneling kinetics.

Differences in chemical composition were also observed in the SEIs formed on basal planes and edge sites. The former were more enriched with organic species and the latter with inorganic species, especially with the decomposition products that obviously originated from salt anions. The authors thus concluded that, on the basal plane, the major contribution to SEI formation is from solvent reductive

Scheme 12. Formation of Polymeric Species in the SEI



decomposition, whereas, at edge sites, the salt anion decomposition occurs on a larger scale.²⁸¹ This location-dependence of the SEI chemical composition strongly implies that the edge sites of the graphite are the main entrances for lithium ion intercalation.

XPS studies, carried out with LiBF_4 - and LiPF_6 -based electrolytes,²⁷⁷ or with carbonaceous anodes with varying graphitic degrees,¹²⁵ or at different potentials after being fully cycled,¹²⁵ rendered quite similar results, except that the abundance of LiF increased in the SEI because of the higher sensitivity of LiBF_4 and LiPF_6 to moisture. Andersson and Edström observed a large amount of polymeric carbon on the cycled graphite surfaces that was linked with an ether-like oxygen, as evidenced by the signals located between 285.5 and 286.5 eV.²⁷⁷ They attributed the formation of these polymeric species to the ring-opening polymerization of cyclic carbonates initiated by strong Lewis acids such as PF_5 (Scheme 12).

Aside from cyclic carbonates, the decomposition products from linear carbonates were also identified in the forms of either lithium alkyl carbonates or alkoxides, as shown by Scheme 7 and also in Table 6a.^{125,271,279} Relatively, the reduction of linear carbonates was thought to be less consequential as compared to their cyclic counterparts, apparently due to their smaller presence in the solvation sheath of lithium cations.^{170,171}

In accordance with these experimental results, Wang et al. employed density functional theory calculations to comprehensively examine the possible reduction pathways for EC molecules in supermolecular structures $\text{Li}^+(\text{EC})_n$ ($n = 1-5$) and found that, thermodynamically, both one- and two-electron reductive processes are possible.¹⁷⁰ A complete array of the possible reduction products from EC was listed in their paper considering the various competitive pathways, and they concluded that both $(\text{CH}_2\text{OCO}_2\text{-Li})_2$ and $(\text{CH}_2\text{CH}_2\text{OCO}_2\text{Li})_2$ are the leading species in SEI, while minority species such as lithium alkoxide, lithium carbide, and the inorganic Li_2CO_3 coexist.¹⁷⁰

A more recent XPS study by Ross and co-workers challenged the above general conclusion that lithium alkyl carbonates constitute the main composition of the SEI.²⁸⁴ Using ultrahigh vacuum surface analytical methodology, they meticulously examined the reaction between a fully lithiated HOPG and DEC as a function of temperature and found that all carbonate signatures above 289 eV rapidly disappear in the room-temperature range, giving way to Li_2O , although alkyl carbonate as a metastable species did exist in the subambient temperature range briefly. Between 0 and 100 °C, the C/O stoichiometry ratio correspondingly changes from the known 1.6 for DEC to 1.0. Combining these observations, they suggested that oxalate species along with lithium methoxide

were formed in the SEI instead of an alkyl carbonate such as $\text{C}_2\text{H}_5\text{OCO}_2\text{Li}$.^{271,279}

In the FT-IR analysis of an SEI on an anode surface, Ross and co-workers also disagreed with Aurbach and co-workers on the interpretation of the spectra.²⁸⁵ The difference is mainly concentrated on the assignments of two absorption peaks at 838 and 1650 cm^{-1} , respectively, which were ascribed to the bending and stretching of carbonyls in lithium alkyl carbonate.^{55,118} While the former was indeed observed by Ross and co-workers in their spectra, they excluded the possibility of it arising from lithium alkyl carbonate in view of its strong intensity. By comparing the IR spectra of an authentic sample of lithium monoethyl carbonate and propylene oxide, they suggested that the signal might originate from the asymmetric stretching of the O-C-O linkage from an epoxy structure, which was generated from the reductive decomposition of EC via an electrochemical-chemical process that involved the reduction of trace moisture in the electrolyte.²⁸⁵ Considering the low bp of this compound (10.7 °C) and its strong tendency toward ring-opening polymerization by the catalysis of acids or cations, it is very unlikely that it would be a persistent ingredient of the SEI. Perhaps ethylene oxide was only detected as a transient species in the IR studies, which eventually polymerized into an oligoether species. On the other hand, the signature stretching mode of alkyl carbonate at 1650 cm^{-1} was completely absent in IR spectra obtained by these authors.²⁷⁸ By comparison with synthesized spectra based on authentic compound samples, the carbonyl stretching of high intensity was assigned to lithium oxalate ($\text{Li}_2\text{C}_2\text{O}_4$) and succinate ($\text{LiO}_2\text{CCH}_2\text{CH}_2\text{CO}_2\text{Li}$) (Table 6a). While the former was obviously formed from CO_2 through some reductive process, the source for the latter remains unclear. A likely mechanism is the recombination of radicals, which would explain the formation of new C-C bonds. At the same time, the presence of trace moisture complicates the surface chemistries by reacting with lithium alkoxides and renders the SEI with species such as LiOH , CH_3OH , and LiHCO_3 .

Apparently, the above controversy regarding the identification of chemical species in the anode SEI will require further analytical work to resolve.

In addition to chemical compositions, another important aspect about SEI formation that is of practical significance to the forming of lithium ion cells is the potential range in which the above reactions occur leading to the formation of the SEI. Because of the earlier observation of the plateau near 0.80 V^{36,237} and the concurrent gas evolution,^{243,261} it was generally believed that the formation of the SEI occurred at this potential. An in situ analysis using a differential electrochemical mass spectrum (DEMS) performed on graphite as well as other electrode surfaces confirmed the above process by simultaneously recording voltammetry and analyzing the gaseous products from the electrode being cathodically polarized. It was found that hydrogen and ethylene were produced during the first cycle at about 1.50 and 0.80 V, respectively, as indicated by their molecular peaks as well as fragmentation patterns

Table 6. Reductive Decompositions on Carbonaceous Anodes

A. Electrolyte Solvents		
Solvents	Reactions	Refs.
PC, EC:	$\text{PC} + 2\text{e} + 2\text{Li} \longrightarrow \text{Li}_2\text{CO}_3 + \text{H}_3\text{C}-\text{HC}=\text{CH}_2$	237
		55, 104, 125, 249, 250, 274, 277, 281
		262
MF:		249
γ BL:		123
Linear Carbonates:		108, 123, 214, 271, 279
		284
B. Electrolyte Salts and Other Components		
Salt	$\text{LiClO}_4 + \text{ne} + 2\text{n Li} \rightleftharpoons \text{Li}_2\text{O} + \text{LiClO}_3, \text{LiClO}_2 + \text{LiCl}$	249
	$\text{LiAsF}_6 + 2\text{e} + 2\text{Li}^+ \longrightarrow \text{AsF}_3 + 3\text{LiF}$ $\text{AsF}_3 + 2\text{ne} + 2\text{nLi}^+ \longrightarrow \text{Li}_n\text{AsF}_{3-n} + \text{nLi}^+$	120, 249, 250
	$\text{LiPF}_6 + 2\text{e} + 2\text{Li} \longrightarrow \text{PF}_3 + 3\text{LiF}$ $\text{LiPF}_6 \rightleftharpoons \text{LiF} + \text{PF}_5$ $\text{PF}_5 + \text{H}_2\text{O} \longrightarrow 2\text{HF} + \text{POF}_3$ $\text{PF}_5 + 2\text{ne} + 2\text{n Li}^+ \longrightarrow \text{LiPF}_{6-n} + \text{nLiF}$	125, 250, 279
Contaminants	$\text{H}_2\text{O} + \text{e} + \text{Li}^+ \longrightarrow \text{LiOH} + \text{H}_2$	249, 250
	$2\text{CO}_2 + 2\text{e} + 2\text{Li}^+ \longrightarrow \text{Li}_2\text{CO}_3 + \text{CO}$	249, 250
	$\text{O}_2 + 4\text{e} + 4\text{Li}^+ \longrightarrow 2\text{Li}_2\text{O}$	249, 250
Secondary Reactions	$\text{LiMF}_n + \text{H}_2\text{O} \longrightarrow \text{LiM}_x\text{O}_y + \text{nHF} + \text{MO}_2\text{F}$ <p>M = P or B; n = 4, 6</p>	125
		104
		104, 124, 249
	$2\text{CO}_2 + 2\text{e} + 2\text{Li}^+ \longrightarrow 2\text{Li}_2\text{CO}_3 + \text{CO}$ $\text{Li}_2\text{CO}_3 + 2\text{HF} \longrightarrow \text{LiF} + \text{CO}_2 + \text{H}_2\text{O}$	124 104, 124, 277

in the MS.²⁸⁶ No sign of CO or CO₂ had been found, contradicting Schemes 1, 7, and 8. The production of H₂ was ascribed to the reduction of trace moisture

contamination; thus, the SEI formation process seemed to start below ~0.80 V. However, since the MS can only detect gaseous species, another surface

spectroscopic means based on FT-IR was used as a complimentary analysis. It was concluded that, since the salt anion concentration near the electrode decreases rapidly at the same potential as H_2 is formed, the first electrolyte decomposition should occur at potentials near 1.50 V. Microscopic observations on the graphite surface cycling in nonaqueous electrolytes were in agreement with this conclusion; that is, surface deposits were visualized at potentials as high as 2.0–1.50 V near the edge sites, while basal planes would be completely covered at potentials below 0.80 V.^{266,267} The combination of DEMS²⁸⁶ and AFM^{266,267} results perfectly echoed the conclusions drawn by Bar-Tow et al.²⁸¹ that the film at the edge sites was mainly formed by the reductive process of salt anions at higher potentials (~ 1.50 V), while the film on basal planes that is formed at lower potentials (~ 0.80 V) has the contribution mainly from solvent reductions.

A few other studies on the SEI placed the occurrence of SEI formation in lower potential ranges that overlap with those of the lithium intercalation process, that is, below 0.25 V. Using a plasma spectrometer, Matsumura et al. conducted quantitative chemical analyses on the lithium content in carbonaceous anodes that were electrochemically lithiated at different stages and correlated the irreversible lithium content (i.e., the electrochemically irremovable lithium that was consumed to form the SEI and then remained therein) with the cathodic polarization potential.²⁶² Unexpectedly, they found that a rather high portion ($>80\%$) of the lithium was distributed in the potential range 0.50–0.01 V, with a relatively small percentage in the potential range above 0.80 V, where the formation of the SEI was thought to have occurred.

Similar results were obtained by Zhang et al., who analyzed the galvanostatic cycling data of a graphite anode in $LiPF_6/EC/PC/EMC$ and calculated the distribution of irreversibility in the first lithiation process in different potential ranges.²⁸⁷ They found that, of the total 7% irreversible capacity in the first forming cycle, a majority ($\sim 6\%$) was generated within the potential range between 0.25 and 0.04 V, where different stages of LiGIC were formed. The quantitative difference between the results of Zhang et al.²⁸⁷ and Matsumura et al.²⁶² on the irreversible lithium at low potential ranges might be due to the different graphitic degrees of the carbon anode materials that were used in their investigations, but the common observation of these two experiments is that, concurrent with lithium intercalation, some other irreversible processes are also underway. A reasonable explanation would be that SEI formation is not completed above 0.80 V but continued deep within the potential range where lithium ion intercalation proceeds.

The electrochemical impedance analysis carried out in the same study by Zhang et al. seemed to confirm the above speculation with the change in the resistance of the SEI film as a function of the lithiation potential and corresponded well with the irreversible capacity analysis. Figure 19 shows the potential-dependence of the resistance for lithium ions in the

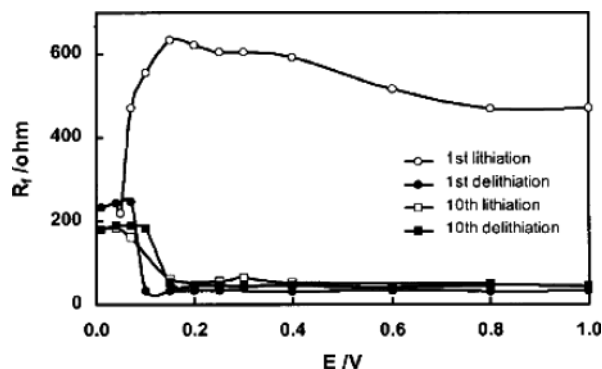


Figure 19. Dependence of the resistance (R_f) of the SEI film on the cell voltage for the lithium/graphite half-cell using $LiPF_6/EC/EMC$ (3:7 wt) as electrolyte. Shown are the data for the 1st and the 10th cycles under galvanostatic conditions with the rate of $0.05 \text{ mA h cm}^{-2}$. (Reproduced with permission from ref 287 (Figure 4). Copyright 2001 The Electrochemical Society.)

SEI film when the graphite anode is repeatedly cycled in $LiPF_6/EC/EMC$ (3:7 wt). In the potential range above 0.25 V, R_f remains relatively stable at a high level, where solvent decomposition is believed to account for half of the irreversible lithium. The SEI film at this stage is incomplete and porous and, hence, unable to shield the graphite surface from further solvent reactions. A drastic decrease in R_f within a narrow range of 0.20–0.04 V, which accounts for more than half of the irreversible capacity, probably represents a process in which the compact and conductive SEI film is formed and starts to protect the graphite surface.²⁸⁷ Thus, the authors proposed that SEI formation on a graphite surface actually goes through two stages: (1) at potentials above 0.25 V, where solvent decomposition leaves a primitive surface deposition that is porous and also electronically conducting, and (2) at potentials below 0.25 V, where an insulating and compact SEI is formed. Once formed, this SEI film is protective of the graphite anode, and a reversible impedance response is expected, as shown by Figure 19 for all of the lithiation/delithiation processes after the first lithiation. The above potential-dependence of SEI resistance was reproducible when $LiPF_6/PC/EC/EMC$ (1:1:3 wt) was used despite the higher irreversible capacity due to the presence of PC.²⁸⁷

The origin of these reductive processes in the lithiation potential range remains unclear, but it does not necessarily involve new components from bulk electrolytes. One possibility is that the radical intermediates, as shown in Schemes 1 and 7, undergo further single-electron reduction, leading to lithium salts with simple anions such as CO_3^{2-} , O_2^- , or F^- ,^{222,223} while reactions between intercalating lithium ions and the active sites of the graphite interior such as hydroxyls or carbene radicals are also possible.²⁶²

6.3. Electrolyte/Cathode Interface

Compared with the research interest in the passivation of anodes, especially materials with carbonaceous origins, there have been relatively few studies dedicated to the understanding of the interface formed between electrolytes and cathode surfaces. A

probable reason might be the stability of these cathode hosts against solvent cointercalation and exfoliation due to the layered structure being held together by Coulombic interactions between oppositely charged slabs composed of metal cations and oxide anions.²⁸⁸ Nevertheless, irreversible decompositions, although oxidative in nature, do occur on cathode surfaces, and the decomposition products very likely form a passivation film that prevents any sustained solvent decomposition. In this sense, the interface between electrolyte and cathode should possess the same physicochemical fundamentals of the SEI on anodes, that is, electronic insulator and lithium ion conductor. A number of authors have used the term “SEI” as well to describe the passivation of cathode surfaces in lithium/lithium ion cells; however, by the currently accepted convention the term is usually reserved for carbonaceous anodes. Instead, a more general reference of “passivation film” or “surface layer” has been used for electrolyte/cathode interfaces.

6.3.1. Passivation Film on a Cathode

The detection of protective films on cathode surfaces has not been as straightforward as that of the SEI on anodes, partially because a native surface film, mainly composed of Li_2CO_3 , already exists on all transition metal oxide cathode materials based on manganese, cobalt, and nickel.^{289–294} This surface component could arise from the precursors used to synthesize these metal oxides or, more likely, from the reaction between the metal oxides and the CO_2 in the atmosphere during the processing of these strongly oxidizing materials.²⁹⁰ Upon contact with electrolytes, this native film is usually eroded by the acidic electrolyte salts currently employed by the lithium ion industry, and to make things more complicated, the active materials are usually involved in the subsequent oxidation of the electrolyte solvents on the exposed cathode surface. Proving the existence of a surface film on the cathodes has been difficult, and spectroscopic identification, which has been proven to be an effective tool in studying the SEI on anodes, often yields ambiguous results.

Goodenough and co-workers were perhaps the earliest authors to suggest that a film exists on the cathode/electrolyte interface.²⁹⁵ In an attempt to simulate the ac impedance responses of an intercalation-type cathode in liquid electrolytes, they discovered that $\text{Li}_{1-x}\text{CoO}_2$ in PC cannot be described as a simple intracomponent lithium ion diffusion; instead, a more complex electrochemical process, including the formation of a surface layer on the electrode due to the oxidation of the electrolyte, must be considered. They proposed an equivalent circuit, shown in Figure 20, for the lithium intercalation process into such cathodes, wherein R_e , R_{sl} and C_{sl} , R_{ct} and C_{ct} , and Z_w represent the bulk resistance of electrolytes, the resistance and capacitance of the surface layer, the resistance and capacitance of the charge-transfer process, and the Warburg impedance, respectively. In such a model, lithium migration has to go through the surface layer because of its serial nature in order for the charge-transfer and further diffusion within

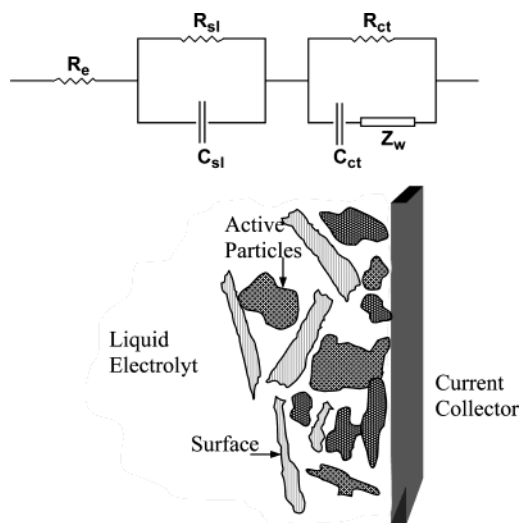


Figure 20. Equivalent circuit based on surface layer formation on cathode materials (a, top) and the electrolyte/cathode interface (b, bottom). (Reconstructed based on ref 295.)

the solid to occur. This equivalent circuit and its numerous variations have become a universally adopted model that simulates the behavior of both anode and cathode in nonaqueous electrolytes.

In formulating new electrolyte compositions that can withstand the high potentials of the cathode materials, Guyomard and Tarascon also realized that oxidative decomposition of electrolyte components occurred on cathode surfaces, and passivation of the surface prevented the bulk electrolytes from further decompositions.^{93,98} Using $\text{LiPF}_6/\text{EC}/\text{DMC}$ and the manganese spinel LiMn_2O_4 , they systematically explored the origin of the oxidative decomposition by quantitatively analyzing the irreversible capacity associated with electrolyte oxidation and established a correlation between it and the surface area of the composite cathode. Thus, they concluded that the oxidative decomposition of electrolytes on cathodes is surface-catalyzed, and very likely the cathode surface would be covered evenly with a surface layer that is composed of the decomposition products.

Almost during the entire 1990s, the main interest of the lithium ion research community was focused on electrolyte/anode interfaces while its cathode counterpart was overlooked until various lithium ion systems, especially those based on manganese spinel cathodes, were found to suffer power loss and capacity fade upon prolonged cycling or storage at elevated temperatures.^{296–302} Preliminary diagnostic studies pointed to electrolyte/cathode interfaces as the source of the degradation, and intensive research has been carried out to address this issue since the late 1990s.

Aurbach et al. studied the interfacial behavior of various cathode materials in $\text{LiAsF}_6/\text{EC}/\text{DMC}$ using EIS and found that, for all of these cathodes, that is, LiNiO_2 , LiCoO_2 , and $\text{Li}_x\text{Mn}_2\text{O}_4$, the impedance spectra obtained reflected several processes in series.²⁹⁰ In other words, the overall lithium ion intercalation in and deintercalation from a variety of LiMO_2 bulk materials included the inevitable step of lithium ion migration through a certain surface layer in a manner very similar to that of the reversible lithium ion

intercalation/deintercalation process on carbonaceous materials.

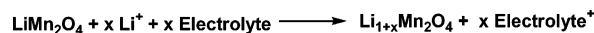
Complementary to the EIS results, wide-line ^7Li NMR research conducted by Greenbaum and co-workers also supported the existence of such a surface layer.²⁹⁹ They reported that the lithiated (discharged) cathode $\text{LiNi}_{0.8}\text{Co}_{0.2}\text{O}_2$ showed two identifiable ^7Li signals with a negligible difference in chemical shift, and these signals were characterized by vastly different spin–lattice relaxation times (T_1). The authors assigned the one with $T_1 < 10$ ms to the intercalated lithium ions in the bulk cathode and the other on the order of seconds to the lithium ions trapped in the surface layer. Corresponding ^{19}F NMR also revealed the existence of a different F other than the binder PVdF; hence, the authors suggested that LiF constitutes the surface layer. However, the double-resonance (^7Li – ^{19}F) measurements that would be sensitive to the presence of LiF were inconclusive.

Visual detection of surface layers on cathodes using microscopy techniques such as SEM seems to be supportive of the existence of LiF as a particulate-type deposition.^{292,294} The current sensing atomic force microscope (CSAFM) technique was used by McLarnon and co-workers to observe the thin-film spinel cathode surface, and a thin, electronically insulating surface layer was detected when the electrode was exposed to either DMC or the mixture EC/DMC. The experiments were carried out at an elevated temperature (70 °C) to simulate the poor storage performance of manganese spinel-based cathodes, and degradation of the cathode in the form of disproportionation and Mn^{2+} dissolution was observed.³⁰⁰ This confirms the previous report by Tarascon and co-workers that the Mn^{2+} dissolution is acid-induced and the electrolyte solute (LiPF_6) is mainly responsible.³⁰¹

The speculation about LiF in the surface layer was supported by McBreen and co-workers, who detected the formation of a surface layer on well-cycled $\text{LiNi}_{0.85}\text{Co}_{0.15}\text{O}_2$ in $\text{LiPF}_6/\text{EC}/\text{DMC}$ with soft X-ray absorption spectroscopy (XAS).³⁰² In the energy region between 500 and 950 eV, the cycled cathode demonstrated major changes at O and F K-edges as compared with the pristine powder or as-prepared cathode samples. By comparing with standard LiF XAS, the authors believed the signals to be arising from the mixture of PVdF (as binder) and LiF on the cathode surface. The source of LiF was believed to be generated by the decomposition of LiPF_6 . Considering that the organic decomposition products are unstable on highly charged cathodes, the authors suggested that the surface layer on the cathode might be composed of a dense coating of LiF. This very resistive surface layer was believed to be responsible for the power loss of the lithium ion cell after prolonged storage.

Aurbach et al. and Andersson et al. also detected the presence of surface layers on cathodes with XPS. The former authors noted that the presence of salts (LiPF_6 and LiAsF_6) played a crucial role in changing the surface state of cathode materials due to their acidic nature, because pure solvents do not change the native surface layer, Li_2CO_3 , when brought into

Scheme 13. Self-Discharge of Spinel Cathode in Electrolyte

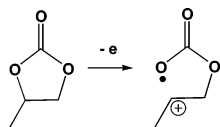


contact with these cathodes.²⁹² They speculated that the hydrolysis products from the salts such as HF, AsF_3 , or AsF_5 reacted with the native surface layer and led to its breakdown. Thus, it is this heavy involvement of salt anion that generates the detected LiF in the surface layer. By correlating with the EIS study, the effect of LiF on cell impedance was confirmed. During prolonged cycling, the surface layer on the cathode seemed to continue to grow; however, the chemical compositions did not experience qualitative changes. Through comparative studies, the latter authors confirmed Aurbach's observation that the pristine Li_2CO_3 surface layer on $\text{LiNi}_{0.80}\text{Co}_{0.20}\text{O}_2$ was changed, as evidenced by a wealth of new chemical components corresponding to the oxidations of both solvents and salt anions, with LiF being the dominant species.^{293,294} In view of the highly oxidative nature of metal oxides, these authors suggested a spontaneous formation process for the new surface layer, in which the direct (hence, nonelectrochemical) redox reactions occur between the active materials of cathode and electrolyte components, leading to the lithiation of the former and the oxidation of the latter (Scheme 13). On a manganese spinel cathode, this spontaneous process was complicated by the coupling of the surface oxidations from electrolyte components with the concomitant Mn_2O_4 disproportionation and Mn^{2+} dissolution.^{293,300} Controversial results from the surface chemistries were obtained.

A few authors argued that the existence of surface layers on cathodes could also be confirmed by the irreversible capacity that only occurs in the first charge process.^{303,304} By correlating this irreversible capacity with cell voltages during the forming process of a LiNiO_2 -based cathode, they concluded that the surface layer was formed via a two-step process: (1) below 3.40 V, where a primitive and resistive film was formed, and (2) between 3.4 and 3.8 V, where a highly conductive film was built up through a further oxidative breakdown of the primitive layer. The EIS study that was carried out simultaneously showed an obvious potential-dependence of the resistance associated with the surface layer (Figure 20), which is characterized by a dramatic drop in the corresponding voltage regions.³⁰³ The possibility of cathode structure reorganization should not be excluded for the irreversible stage between 3.6 and 3.8 V, though, and the authors suggested that probably both electrolyte oxidation and cathode structural transition are responsible.

Similar irreversible processes have been previously observed by Aurbach et al. on LiNiO_2 ²⁹⁰ and Croce et al. on $\text{LiNi}_{0.75}\text{Co}_{0.25}\text{O}_2$ ³⁰⁵ by slow scan cyclic voltammetric (SSCV) measurements. However, in their EIS studies the former authors did not observe any obvious potential-dependence for the resistance associated with the surface layer²⁹⁰ but rather an invariant resistance in the range between 3.6 and 4.2 V. This latter observation is in direct disagreement

Scheme 14. Possible Electrochemical Oxidation Path for PC



with the results of Zhang et al.^{303,304} and Croce et al.,³⁰⁵ where the change of surface-layer resistance with potential is obvious.

Some authors pointed out that the surface layer on the metal oxide cathodes might not be as stable as that on the carbonaceous anode, and the cell power loss and capacity fade are mainly caused by degradation of this electrolyte/cathode interface.²⁹³ Their argument was supported by the increase in impedance with cycling, which very likely suggests a continued growth of surface layers on the cathode.²⁹² There was also one report revealing the complete absence of surface layers on cathodes after prolonged cycling, probably indicating that the electrolyte components or impurities react with the surface layer and leave the cathode surface with the IR-insensitive LiF.²⁹⁸

6.3.2. Characterization of Surface Chemistry

The overwhelming majority of the studies on the oxidative decompositions of solvents and salt anions were carried out on nonactive electrodes.^{74,81,120,130,131,204,206,207,306–308} On the basis of the detection of ring-opening reactions by in situ FT-IR, a mechanism involving a single-electron process producing a radical cation was proposed for carbonate solvents (Scheme 14).³⁰⁷ Subsequent decomposition of the intermediates leads to gaseous as well as solid products, which form a solid film on the electrode. The existence of such radical species during the oxidative decompositions of electrolyte components has been confirmed for a wide variety of electrolytes by ESR, and the surface of a charged cathode (LiCoO₂ at 4.3 V) is identified as the source of its generation, because a parallel blank test with electrolytes in the absence of a cathode produces no radical species.³⁰⁹ The authors depict a picture of delocalized radical cation structures that are coordinated by the neighboring solvent molecules, whose half-life is on the order of minutes depending on the electrolytes. Thus, it is reasonable to believe that Scheme 14 represents the initial oxidative cleavage of the carbonate solvents.

The systematic surface characterization was conducted by Aurbach and co-workers using FT-IR spectroscopy for LiCoO₂, LiNiO₂, and LiMn₂O₄ spinel cathodes.²⁹⁰ After cycling in electrolyte LiAsF₆/EC/DMC between 3.0 and 4.4 V, all of the cathode surfaces were found to be covered with a wealth of new chemical species, while the signals corresponding to the native Li₂CO₃ diminished. Preliminary interpretation of these spectra led the authors to conclude that the species very much resemble the lithium alkyl carbonates observed on various anode surfaces that have been formed, as supported by the signals around 1650 cm⁻¹. With further study, they confirmed that the electrolyte-related species were

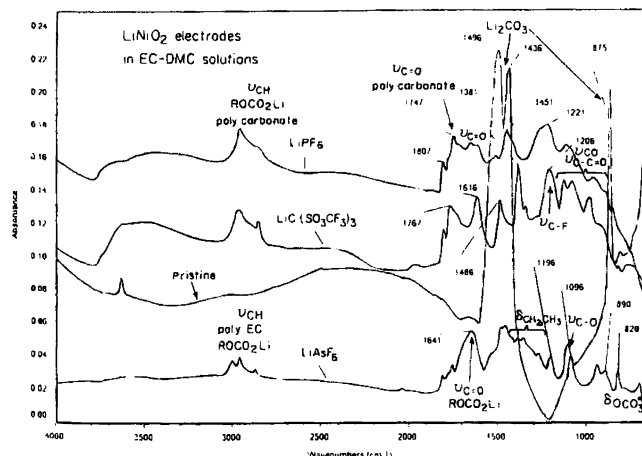
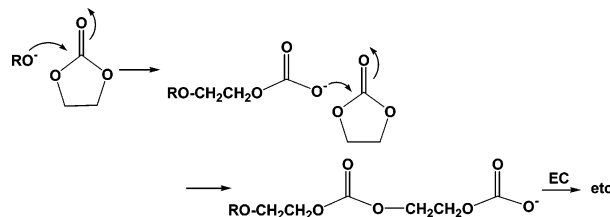
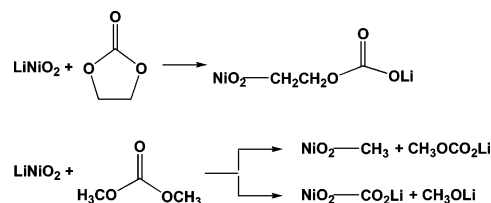


Figure 21. FTIR spectra (diffuse reflectance mode) measured from a pristine LiNiO₂ composite cathode and with a cathode after galvanostatic cycling in Li salt/EC/DMC solutions. (Reproduced with permission from ref 292 (Figure 1). Copyright 2000 The Electrochemical Society.)

Scheme 15. Possible Mechanism for the Formation of Polycarbonates



Scheme 16. Surface Nucleophilic Reactions between LiNiO₂ and Electrolyte Solvents



formed on the cathode surface upon storage or cycling but emphasized that, because of the complicated nature of the surface oxidation processes, it is impossible to obtain an unambiguous picture of the surface chemistry.²⁹² Since the native Li₂CO₃ does not change when in contact with pure (salt-free) solvents, the salt anions obviously played a crucial role in forming these new surface species. Cycling seems to facilitate the surface chemistry, as Figure 21 shows, since a variety of absorptions corresponding to C–H, C=O, and C–O bonds were identified. The carbonyl functionality around 1800–1700 cm⁻¹ was believed to be polycarbonate species, a possible source of which could be the oxidation of EC or the ring-opening polymerization of EC catalyzed by a nucleophilic mechanism (Scheme 15). The nucleophilic initiator RO[•], as evidenced by the absorptions near 1100 cm⁻¹, could be generated on the surface of the cathode because of the possible reactions between the active mass and the solvents (Scheme 16). Meanwhile, the signals around 1650 cm⁻¹ (asymmetric C=O), 1350–1300 cm⁻¹ (symmetric C=O), 1100 cm⁻¹ (C–O), and 850 cm⁻¹ (OCO₂⁻) still suggest species with similar structure to alkyl carbonates. Since the mechanism

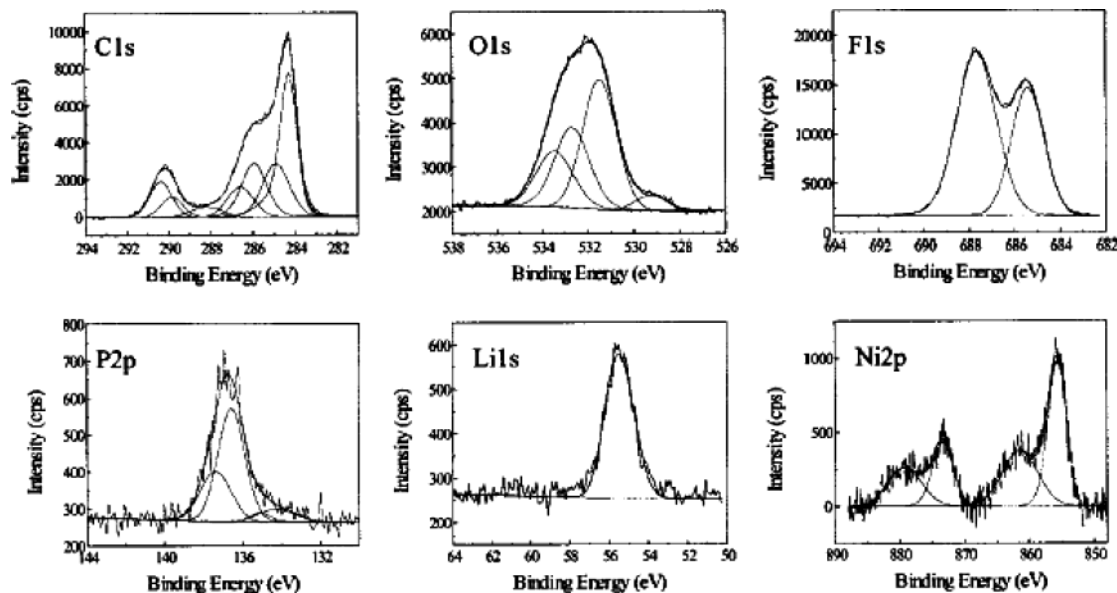


Figure 22. C 1s, O 1s, F 1s, P 2p, Li 1s, and Ni 2p XPS spectra for $\text{LiNi}_{0.8}\text{Co}_{0.2}\text{O}_2$ cycled in $\text{LiPF}_6/\text{EC}/\text{DEC}$. (Reproduced with permission from refs 294 (Figure 6). Copyright 2002 The Electrochemical Society.)

in Scheme 16 involves direct electron transfer from electrolyte solvents to electrode active mass, these reactions are spontaneous and do not require cell charging to initiate.

XPS and energy-dispersive X-ray analysis (EDAX) of the cathode surface chemistry clearly revealed that, in various electrolytes using different salts, the salt anions or the impurities related to them were also heavily involved in the surface layer formation.²⁹² EDAX detected a pronounced increase in the F content of the surface after the cathode was cycled in LiPF_6 or LiAsF_6 solutions, and appreciable amounts of As or P were also present on the surface. The surface chemistries of a cathode cycled in LiAsF_6 solution as detected by XPS correlated well with FT-IR, which confirmed the formation of organic and inorganic carbonates with signals at 285 and 290 eV as well as RO^- . The peak at 294 eV was ascribed to polycarbonate species, in accordance with the peaks around $1800\text{--}1700\text{ cm}^{-1}$ in FT-IR. However, the cathode surface that had been cycled in LiPF_6 solutions lacked the signs of all carbonate or polycarbonate species, and the authors attributed the absence of these carbonyl-containing compounds to the role of HF, which reacts with carbonates and leaves LiF on the surface. This is supported by the F 1s spectra with a strong 685 eV signal, which is smaller for cathode surfaces cycled in LiAsF_6 solution. Further examination of F 1s spectra also points to other F-containing species with P–F and As–F bonds, which are evident in As 3d and P 2p spectra as well. Interestingly, Ni 2p signals of oxidation states for various Ni species were also detected in all of the cathode surfaces that were cycled in either LiPF_6 or LiAsF_6 solutions, as expected from the surface reactions involving LiNiO_2 as a nucleophilic agent (Scheme 16).

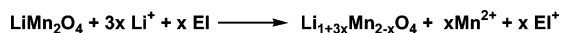
More recent XPS studies were conducted by Andersson et al. on a similar $\text{LiNi}_{0.8}\text{Co}_{0.2}\text{O}_2$ cathode cycled in $\text{LiPF}_6/\text{EC}/\text{DEC}$, and more detailed efforts were made to assign the signature signals for various

surface species.²⁹⁴ Figure 22 lists the XPS spectra generated from the cathode sample after the formation cycle. In C 1s spectra, three new peaks were ascribed to a polymeric moiety (285.1 eV), a carbon in ether linkage (286.8 eV), and a semi-carbonate such as an alkyl carbonate (290.0 eV). The polymeric moiety could be attributed to hydrocarbon species or polymers based on an ether linkage. On the other hand, quantitative analyses through peak deconvolution showed that a majority of the surface lithium content is accounted for by the presence of LiF, LiPF_6 , and Li_2CO_3 , and alkyl carbonates as well as polycarbonates are also likely. The F 1s spectrum corroborates the dominant presence of LiF by the peak at 684.9 eV, while the other F signal arises from the binder PVdF. P 2p spectra could be deconvoluted into a series of contributing components, which should include the oxidation products from LiPF_6 such as Li_xPF_y .

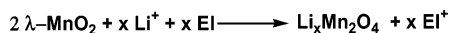
Obviously, the above compounds might result from several possible reactions. Since they did not find the transformation of the metastable alkyl carbonate into Li_2CO_3 upon high-temperature storage, as they had observed on carbonaceous anodes, Andersson et al. challenged the spontaneous reaction mechanism suggested in Scheme 16 and proposed that the carbonate species on cathode surfaces would be polycarbonates instead of simple alkyl carbonates.²⁹⁴ Furthermore, self-discharge that leads to lithiation of the cathode host was observed during storage; hence, the authors argued that a mechanism similar to Scheme 13 would be more likely. Thus, the initiation for EC polymerization would be more likely realized by the electrophilic attack from the Lewis acid, PF_5 , a decomposition product of LiPF_6 , instead of a nucleophilic attack from RO^- . The fact that PF_5 reacts with cyclic carbonates, leading to polymerization of the latter, seems to favor this rationale.²⁹⁸

In a parallel study performed on the spinel cathode LiMn_2O_4 , Eriksson et al. reported both XPS and FT-IR results²⁹³ that conflicted with those by Aurbach

Scheme 17. Mechanism for Electrolyte Oxidation Coupled with Spinel Disproportionation and Mn²⁺ Dissolution



Scheme 18. Mechanism for Electrolyte Oxidation on a Fully Charged Cathode Surface



et al.^{290,292} Besides polymeric species that were most likely polyethers, there was no sign of any carbonate-like species detected when the spinel was cycled in a LiPF₆-based electrolyte, as evidenced by both C 1s and O 1s XPS and FT-IR spectra. F 1s still identified LiF as the major surface species along with partially decomposed products from LiPF₆ as well as the MnF₂ species. When LiPF₆ was replaced by LiBF₄, semi-carbonate moieties began to appear in C 1s; therefore, the authors concluded that HF, which was more abundant in LiPF₆ solutions, removed the initially formed carbonate species. Meanwhile, a wealth of IR absorptions also indicated the formation of polyether structures for which the mechanism of formation from EC or linear carbonates remains unclear.

The formation of surface species on a spinel cathode surface is complicated by the coupling of electrolyte oxidation with the cathode structural disproportionation and the subsequent Mn²⁺ dissolution.^{296,300,310} Combining Scheme 13 with the latter considerations, a modified mechanism was proposed by Eriksson et al. (Scheme 17).²⁹³ This mechanism only seems to apply when the cathode is not fully charged (<4.3 V). Since disproportionation can no longer occur at the fully delithiated potentials (4.3 V) where almost all manganese species are in the Mn⁴⁺ state and λ-MnO₂ exists as the stable lattice, an alternative mechanism was also proposed by the same authors to account for the surface oxidation of electrolytes in this case (Scheme 18). Since similar surface layers have been observed on spinel cathodes in partially and fully charged states, their thickness and chemical composition do not seem to be dependent on the cathode potential, while thickness does increase with both storage time and temperature.

6.3.3. Breakdown of Surface Layer

While the low potential limit an electrolyte faces in lithium ion cells is set by the lithium metal deposition on carbonaceous anodes, the high limit is decided by the breakdown of the surface layer on cathode materials. At potentials above this limit, the protection against electron tunneling is lost and the decomposition of bulk electrolyte components occurs. Because of the limited amount of research carried out on cathode surfaces, there is no microscopic picture available for this breakdown mechanism and it remains unknown whether a global dissolution or physical disintegration of the surface layer is involved or, rather, following a similar mechanism of dielectric capacitor “breakdown”, the surface layer remains largely intact but the high potential of the cathode “burns through” pathways for electron conduction at local sites on the surface.

The knowledge about this decomposition upper limit of potential is significant for practical applica-

tions of the electrolytes in actual lithium ion cells, because a number of factors related to the operation of the cell rely on it, such as the potential limit within which the cell can be cycled, the overcharge margin that a certain electrolyte formulation can provide, and the design and selection of cathode materials. Nevertheless, inadequate studies have been conducted so far on this issue, and most of the studies on the oxidative decomposition of electrolytes were carried out on nonactive electrodes on which the oxidative processes for carbonate-based solvents were generally believed to occur at potentials higher than 4.0 V despite the widely scattered data from the different electrode surfaces, salt species, and cutoff criteria employed in those investigations (Tables 4 and 5). However, considering the vast differences in surface areas as well as surface functionalities between the nonactive electrodes and composite cathode materials, there is sufficient reason to question whether the decomposition limits of electrolytes as determined on these nonactive electrodes would serve as reliable references when cathode composites of higher surface area and hence higher surface catalytic activity are in contact with electrolytes.

The discrepancies in stability limits caused by the differences in the surface areas of working electrodes had been noticed by Guyomard and Tarascon early on.⁹³ The solvent oxidation obviously proceeded with much slower kinetics on Pt electrodes than on composite cathode materials based on spinel manganese oxide. Cattaneo and Ruch³¹¹ and Imhof and Novák³¹² also recognized the importance of using the actual battery electrode materials instead of nonactive electrodes to obtain more relevant decomposition potentials of electrolyte components in lithium ion cells. They used manganese dioxide (MnO₂), LiNiO₂, LiCoO₂, and spinel LiMn₂O₄ as working electrodes, and they investigated the potential of cathode surface layer breakdown, which was found to vary in a pronounced way with each cathode surface: 4.2 V for LiClO₄/PC on MnO₂,³¹¹ 4.2 V for LiIm/PC on LiNiO₂,³¹² and 4.8 V for LiIm/PC on both LiCoO₂ and LiMn₂O₄.³¹² By means of an in situ MS technique, these authors confirmed that the breakdown process was accompanied by the evolution of gas that consisted mainly of CO₂ and other species related to salt anions, an indication of bulk decomposition of electrolyte components that involve both salt and solvent.^{311,312}

A more conspicuous example is the anodic stability of linear carbonate (Figure 23).⁷⁶ While the anodic limits for both DMC and EMC are above 5.0 V on GC, as observed by similar measurements,³¹³ the major decomposition current starts before 4.5 V for both solvents when a composite cathode based on spinel LiMn₂O₄ is used as working electrode.⁷⁶ Apparently, the enormous difference between GC and a composite cathode could not be explained solely by the larger surface area of the latter. It seems more likely that the irreversible oxidative processes were catalyzed by the active mass of the spinel surface, possibly involving spinel lattice disproportionation. Therefore, the stability limits as measured on all of these nonactive and nonporous electrodes can be

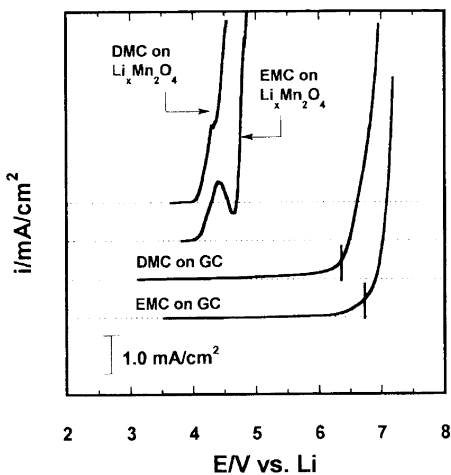


Figure 23. Anodic stability of linear dialkyl carbonates on GC and a composite cathode surface. Electrolytes: 1.0 M LiPF₆ in DMC or EMC, respectively. (Reproduced with permission from ref 76 (Figure 2). Copyright 1999 The Electrochemical Society.)

Table 7. Electrochemical Stability of Electrolyte Solvents: Active Electrodes

electrolyte	working electrode	E_a^a	ref
1.0 M LiClO ₄ /PC/DME (1:1)	LiV ₃ O ₈	4.6	307
1.0 M LiAsF ₆ /PC/DME (1:1)	LiV ₃ O ₈	4.7	307
1.0 M LiClO ₄ /EC/DEE (1:1)	LiMn ₂ O ₄	4.55	93
1.0 M LiIm/EC/DEE (1:1)	LiMn ₂ O ₄	4.4	99
1.0 M LiIm/EC/DME (1:1)	LiMn ₂ O ₄	4.35	99
1.0 M LiPF ₆ /EC/DEE (1:1)	LiMn ₂ O ₄	3.8	93
1.0 M LiBF ₄ /EC/DEE (1:1)	LiMn ₂ O ₄	3.4	99
1.0 M LiClO ₄ /PC	LiMn ₂ O ₄	>5.1	99
1.0 M LiBF ₄ /EC/DMC (2:1)	LiMn ₂ O ₄	>5.1	98
1.0 M LiClO ₄ /EC/DMC (2:1)	LiMn ₂ O ₄	>5.1	99
1.0 M LiPF ₆ /EC/DMC (2:1)	LiMn ₂ O ₄	>5.1	44, 98
1.0 M LiClO ₄ /EMS	LiMn ₂ O ₄	5.8	75, 314
1.0 M LiIm/EMS	LiMn ₂ O ₄	5.8	75, 314
1.0 M LiPF ₆ /EMS	LiMn ₂ O ₄	5.8	314
1.0 M LiPF ₆ /EiBS	LiMn ₂ O ₄	5.8	314
1.0 M LiPF ₆ /DMC	LiMn ₂ O ₄	~4.0	314
1.0 M LiPF ₆ /EMC	LiMn ₂ O ₄	4.5	314
1.0 M LiPF ₆ /FPMS/DMC	LiMn ₂ O ₄	5.55	314
1.0 M LiPF ₆ /FPMS/EMC	LiMn ₂ O ₄	5.55	314
1.0 M LiPF ₆ /EC/PC/DMC (1:1:2)	LiNiVO ₄	>4.9	314

^a Anodic limits, potential referred to Li^{+/}Li.

misleading, and the authentic anodic stability limits of any electrolyte component in an actual lithium ion device can only be evaluated on the surface of the electrode that is used in the device.

Unfortunately, this approach for electrochemical stability determination has not been widely adopted. The few exceptions include the seminal electrolyte work by Guyomard and Tarascon.^{98,99} In the formulation of new electrolytes for lithium ion technology, the spinel composite electrode was used as the standard working surface in all of the voltammetric measurements. The oxidative decomposition limits of the new electrolytes thus determined are summarized in Table 7 along with a handful of stability data that were determined in a similar approach for other electrolyte systems.

Figure 24 shows the result of the voltammetry for EC/DMC- and EC/DEE-based electrolytes. The typical two-step process between 3.9 and 4.3 V corre-

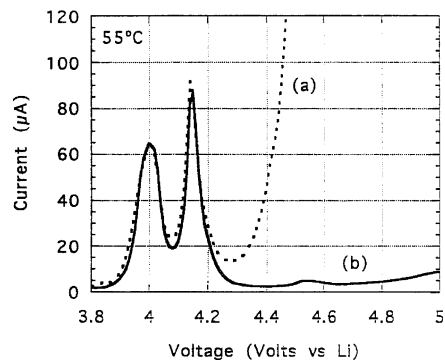


Figure 24. Voltammogram at 55 °C for the electrolytes (a) 1.0 M LiClO₄/EC/DEE and (b) 1.0 M LiPF₆/EC/DMC on spinel cathode LiMn₂O₄. (Reproduced with permission from ref 98 (Figure 1). Copyright 1993 The Electrochemical Society.)

sponds to the delithiation of the spinel structure, which is reversible. The oxidative decomposition of DEE occurs below 4.4 V almost immediately after the delithiation is completed. This proximity to the potential of the cathode electrochemistry leaves little tolerance for overcharge. On the other hand, the EC/DMC-based electrolyte only shows negligible background current before 5.1 V. After 4.3 V, the spinel lattice has actually turned into λ -MnO₂. On the surface of the λ -MnO₂, the low current of the EC/DMC exhibits the extreme stability of this mixed carbonate formulation. As already pointed out in earlier sections, the replacement of ether compounds by linear carbonate results in a significant expansion of the oxidative potential limits by ~0.80 V.

The anodic limit for the electrochemical stability of these carbonate mixtures has been determined to be around 5.5 V in numerous studies.^{314–317} Thus, new electrolyte formulations are needed for any applications requiring >5.0 V potentials. For most of the state-of-the-art cathode materials based on the oxides of Ni, Mn, and Co, however, these carbonate mixtures can provide a sufficiently wide electrochemical stability window such that the reversible lithium ion chemistry with an upper potential limit of 4.30 V is practical.

When the poor anodic stability of DMC or EMC alone on a similar cathode surface is considered,⁷⁶ the role of EC in stabilizing the solvent system becomes obvious. A conclusion that could be extracted from these studies is that the existence of EC not only renders the electrolyte system with superior cathodic stability by forming an effective SEI on the carbonaceous anode but also acts as a key component in forming a surface layer on the cathode surface that is of high breakdown potential. It is for its unique abilities at both electrodes that EC has become an indispensable cosolvent for the electrolyte used in lithium ion cells.

6.3.4. Passivation of Current Collector

Another issue closely related with the anodic stability of electrolytes is the interaction between electrolyte components and the commonly used cathode substrate Al in lithium ion cells.

Al and Cu foils are used as current collectors for cathode and anode materials, respectively, in lithium

ion cells. In a working lithium ion cell that uses liquid electrolytes, the thin coating of active electrode materials is soaked with the liquid electrolytes and the interaction between the electrolyte components and the current collectors strongly affects the performance stability of the cell, especially at the cathode side, where Al is constantly held at high potentials. It has been confirmed by numerous observations that, in well-cycled lithium ion cells, the Al substrate suffers severe pitting-like corrosion at a fully charged state, which leads to a shortened calendar life and fading capacity.^{298,318,319} Because very thin Al foils are used (down to 10 μm) in consideration of the energy density, the pitting could cause complete disintegration and fragmentation in some cases.

Few significant efforts were made on this issue before a new lithium salt (LiIm) was found to cause serious Al corrosion in nonaqueous electrolytes during the early 1990s.¹⁴¹ Only in recent years has an in-depth understanding of this phenomenon been obtained, a direct result from the increased research interest driven by the expectation that this new salt may replace the thermally unstable LiPF_6 .^{153,154,320–323}

Al is thermodynamically unstable, with an oxidation potential at 1.39 V.³ Its stability in various applications comes from the formation of a native passivation film, which is composed of Al_2O_3 or oxyhydroxide and hydroxide.³²⁰ This protective layer, with a thickness of ~ 50 nm,³²² not only stabilizes Al in various nonaqueous electrolytes at high potentials but also renders the Al surface coating-friendly by enabling excellent adhesion of the electrode materials. It has been reported that with the native film intact Al could maintain anodic stability up to 5.0 V even in LiIm-based electrolytes.¹⁴⁷ Similar stability has also been observed with Al pretreated at 480 $^\circ\text{C}$ in air, which remains corrosion-free in $\text{LiClO}_4/\text{EC}/\text{DME}$ up to 4.2 V.¹⁵⁶ However, since mechanical damage of the native film (e.g., accidental abrasion) is often inevitable during electrode processing and cell assembly, the in situ re-forming of a protective surface layer in lithium ion cells depends strongly on the electrolytes.

In comparison with the surface layer chemistry on active cathode materials where both salt anions and solvents are involved, a general perception extracted from various studies is that the salt species has the determining influence on the stabilization of the Al substrate while the role of solvents does not seem to be pronounced, although individual reports have mentioned that EC/DME seems to be more corrosive than PC/DEC.³²¹ Considering the fact that pitting corrosion occurs on Al in the polymer electrolytes LiIm/PEO³²² or LiTf/PEO,³²³ where the reactivity of these macromolecular solvents is negligible at the potentials where the pitting appears, the salt appears to play the dominant role in Al corrosion.

Among the various lithium salts investigated, LiPF_6 , LiAsF_6 , and LiBF_4 were found to effectively passivate and stabilize Al at higher potentials (> 4.2 V) than required by the operation range of common cathode materials based on LiNiO_2 , LiCoO_2 , and LiMn_2O_4 , while LiIm, LiTf, and their derivatives

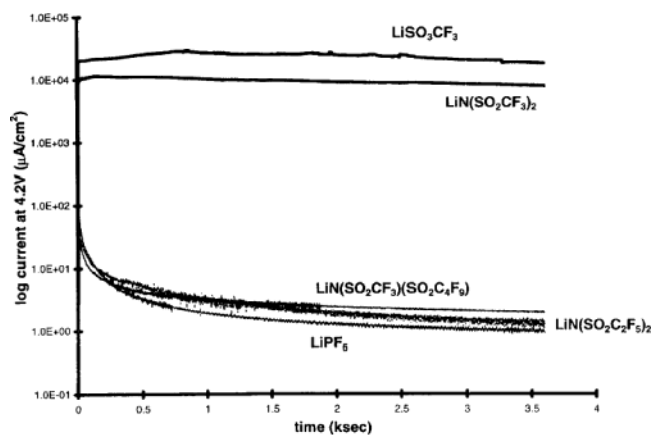
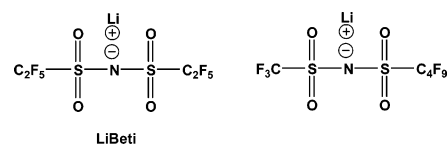


Figure 25. Al corrosion current density at 4.20 V (vs Li^+/Li) in 1.0 M PC solutions of various lithium salts showing a difference between Tf^- , Im^- , and other anions. (Reproduced with permission from ref 141 (Figure 1). Copyright 1997 Elsevier.)

usually caused severe corrosion on the Al surface, as indicated by the high anodic current at potentials as low as 3.0 V.^{141,147,155,156} Figure 25 compares the ability of selected lithium salts to stabilize the Al surface in the electrolytes containing them. The passivating ability of the salt anion does not appear to depend on the solvent used, and in one solvent mixture, EC/DME, the following stability order is established:¹⁵⁶



New synthetic efforts generated a few structural derivatives of LiIm with longer perfluorinated alkyls such as LiBeti and a lithium salt of an asymmetric imide anion, and the stability of Al in the electrolytes based on these salts was found to be much improved when compared with those in electrolytes based on LiIm and LiTf.^{141,148}



Krause et al. thus believed that a correlation existed between anion molecular weight and their protective abilities, although the complete mechanism is not clear.¹⁴¹

A distinctive dissimilarity between the passivation of Al and the formation of an SEI on a graphitic anode is the effectiveness of surface pre-formation: while it has been reported in numerous studies that an SEI formed in one electrolyte can continue to protect the graphite structure when the anode is transferred to another exfoliating electrolyte (such as PC),^{250,255,324} Al that has been pretreated in LiPF_6 - or LiBF_4 -based electrolytes still suffers severe anodic corrosion when switched to LiTf- or LiIm-based electrolytes.^{141,156} This observation provides additional evidence supporting the hypothesis that an oxidative decomposition of anions occurs at the Al surface.¹⁴¹

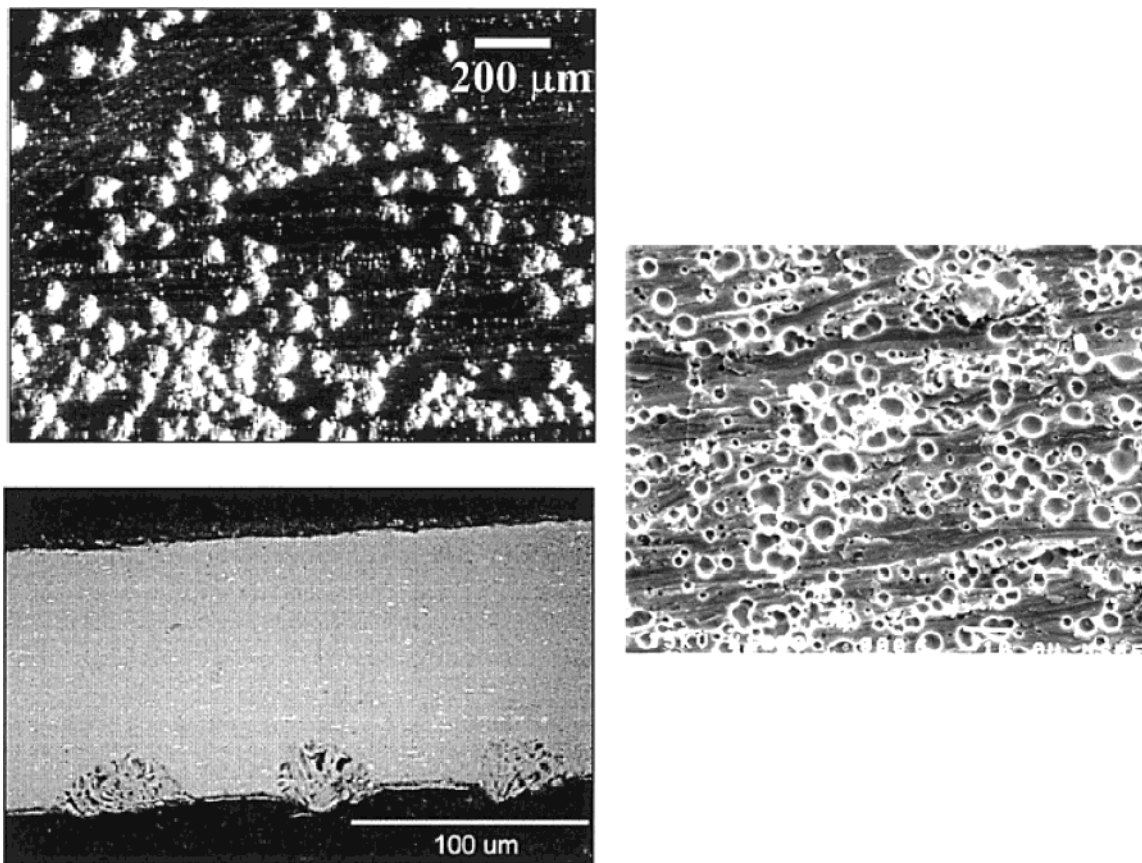
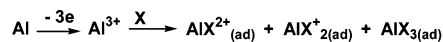


Figure 26. Micrographs of a corroded Al surface in various electrolytes. (a, top left) Micrograph in LiPF₆/EC/DMC electrolyte, after 150 electrical cycles. The light areas are mounds or nodules. (Reproduced with permission from ref 321 (Figure 7). Copyright 1999 The Electrochemical Society.) (b, bottom left) SEI image of the cross-sectional view of the mounds as shown in part a. (Reproduced with permission from ref 321 (Figure 8a). Copyright 1999 The Electrochemical Society.) (c, right) Micrograph in LiIm/PEO after 1 h of galvanostatic polarization at 100 μA cm⁻². (Reproduced with permission from ref 322 (Figure 14). Copyright 1999 The Electrochemical Society.)

Microscopic examination of the aged Al retrieved from well-cycled cells found that, even in electrolytes based on LiPF₆ or LiBF₄, localized pitting occurred on the Al (Figure 26a).^{298,318,319} Closer examination of these corrosion sites under an SEM revealed that what had optically appeared to be a “pit” was actually a “mound” or “nodule” (Figure 26b) where both Al(0) and Al₂O₃ existed, according to XPS analysis.³²¹ Due to the anodic state of the Al during the electric cyclings in these cells, the presence of Al(0) practically suggests that the mounds were somehow electrically isolated from the foil. The authors presented two possible explanations for this situation: (1) corrosion and its associated reaction products undermined the surface of a developed pit and caused the overlying metal to bulge or break away or (2) a soluble Al(III) corrosion product was electrodeposited onto the poorly conductive solid corrosion products during the cathodic process (discharge) so that reduction actually occurred. The fact that the open circuit voltage (OCV) of Al lies between 3.2 and 3.6 V makes the latter reductive step possible in normal battery cyclings.

On the other hand, when the electrolyte salts were LiTf or LiIm, serious corrosions in the form of high-density pits were visible before any extensive cycling was conducted,^{141,322} as shown by Figure 26c, where Al was merely polarized anodically in a LiIm-based electrolyte for a much smaller time scale than that

Scheme 19. Al Corrosion in Nonaqueous Electrolytes



of prolonged cycling in an actual rechargeable cell. The damage to Al in these cases was on a macroscopic scale.

Impedance analyses of the Al under corrosion were conducted via EIS. On the basis of the models previously established for the corrosion of other metals in both aqueous and nonaqueous electrolytes,^{325,326} the corrosion process was proposed as a two-step adsorption/oxidation/desorption process (Scheme 19).^{147,156}

The impedance response with frequency can be closely simulated by the equivalent circuit shown in Figure 27a, where R_e , R_{ct} , C_{dl} , R_{ad} , and C_{ad} represent the resistance or capacitance for the electrolyte solution, charge-transfer, double layer, and adsorbed layer, respectively. An interesting correlation was found between the passivating ability of various anions and the resistances of the two impedance components R_{ct} and R_{ad} , which are high for LiPF₆- and LiBF₄-based electrolytes and low for LiTf- or LiIm-based electrolytes.¹⁵⁶ Using the rationale proposed by the authors, the former component (R_{ct}) is

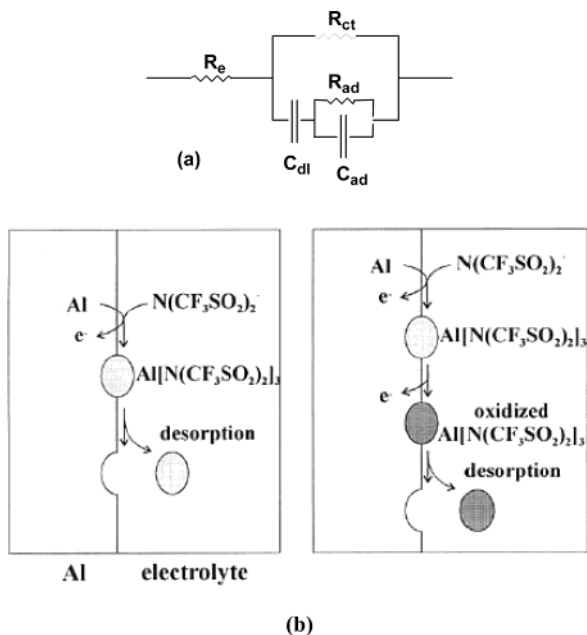


Figure 27. (a) Equivalent circuit used to express the corrosion process of Al. (b) Schematic representation of a possible mechanism for Al corrosion in LiIm-based electrolytes. (Reproduced with permission from ref 147 (Figure 14). Copyright 2000 The Electrochemical Society.)

related to the exchange current (i^0) at the electrolyte/Al surface:

$$R_{ct} = \frac{RT}{nFi^0} \quad (11)$$

while R_{ad} indicates whether an adsorbed (passivation) layer could adhere to the surface of Al. Therefore, the physicochemical nature of the passivation layer is dictated by its chemical composition, which is in turn strongly affected by the anion oxidation chemistry.

Surface chemical characterization of the passivation layer on the Al surface has been performed mainly via XPS, and the interpretation of results generated by various researchers still remains controversial. Because salt anions with active fluorine (LiPF₆, LiAsF₆, and LiBF₄) are able to form stable surface layers on Al and protect it from corrosion, early studies had suggested that fluoride species such as LiF and AlF₃ are crucial to the protection.^{141,153,154} The XPS study by Kanamura et al. seemed to support this speculation, having observed the F 1s signal at 686.5 eV on Al that had been passivated in LiPF₆/PC electrolyte.^{148,327} Thus, they concluded that the surface species on Al after prolonged exposure to the above electrolyte consisted of a mixture of Al₂O₃ and AlF₃.

Krause et al. challenged this assignment of the F 1s signal.¹⁴¹ In their XPS study of Al cycled in electrolytes based on LiIm, LiBeti, and LiPF₆, they also observed this F signal that is typical of metal fluoride, but they believed that LiF instead of AlF₃ would be responsible for it because of the detection of Li and the relative abundance of these two elements. Carbonate species as indicated by both C 1s and O 1s spectra were also present, which may exist in the forms of either Al₂(CO₃)₃ or Li₂CO₃. Thus, the authors postulated that oxidation of solvent also

occurs, probably by an Al⁺-mediation mechanism. According to this mechanism, upon polarization of Al at high potentials, highly reductive intermediates of Al⁺ were generated,^{328,329} and they migrated to the vicinity of the passivation layer/electrolyte interface, where they subsequently reacted with adsorbed anions or solvents. Thus, the reaction kinetics depend on how readily the anions or solvents are adsorbed on the Al surface or surface layer.

The depth profile established by Ar⁺ sputtering detects the distinct difference between the Al surfaces that are aged in various electrolytes, which suggests that a much thicker surface layer is formed in LiIm than in LiPF₆ or LiBeti electrolytes.¹⁴¹ It appears that the high corrosion of Al in a LiIm-based electrolyte stems from a relatively porous and diffuse passivation layer where the high levels of LiF contribute to the disorder and porosity of the otherwise dense and protective Al₂O₃ or carbonate layer. The latter is found in Al surfaces passivated in LiBeti or LiPF₆.¹⁴¹ Combining the above observations, Krause et al. explained the correlation between anion size and the passivating ability by referring to the ability to adsorb on the Al surface. Thus, small anions such as Tf⁻ and Im⁻ tend to adsorb to a high packing density, and their reduction by Al⁺ predominates the surface process, with the product of LiF rendering the film nonprotective. Beti⁻ anions adsorb poorly, and therefore, the reduction of solvent molecules prevails, with the surface layer consisting of a dense protective carbonate species. It must be pointed out that this mechanism remains to be confirmed with more direct evidence of the presence of Al⁺ because the reductive process of solvents at a positively charged cathode does sound very unusual.

On the other hand, an XPS study by Braithwaite et al. on aged Al in LiPF₆/EC/DMC or LiPF₆/PC/DEC identified Li, F, and P as the major surface species, and the authors believed that the signals for these species were not simply from the adsorbed electrolytes because twice as much F was observed on the surface than would be associated with the PF₆⁻ anion.³²¹ The existence of these nonstoichiometric compositions suggested that the oxidative decomposition of the salt anion had occurred. The high binding energy of Li as observed in Li 1s spectra indicates that such Li species exist in a very electron-deficient environment, as one similar to LiF. However, the observed binding energy for F is typical for the -CHF₂ species and distinctively different from that of a metal fluoride. Further attempts to analyze these pit nodules by XPS analysis proved to be inconclusive because of the high inhomogeneity of these areas, which exhibited complex chemistries that varied from nodule to nodule. In general, high concentrations of Li and F as well as Al₂O₃ were confirmed. On the basis of these seemingly conflicting results, the authors concluded that the role of these surface species formed in nonaqueous electrolytes could not be determined, and the protection against corrosion could simply have come from the native passivation film Al₂O₃.

More recently, Kanamura et al. studied the corrosion of an Al electrode that was anodically polarized

at a series of potentials in nonaqueous electrolytes based on LiIm, LiTf, and a new asymmetric imide, $\text{Li}(\text{CF}_3\text{SO}_2)(\text{C}_4\text{F}_9\text{SO}_2)\text{N}$, using both XPS and FT-IR.¹⁴⁸ These spectra confirmed the presence of organic species on the Al surface, and by monitoring the IR signature absorption for the carbonate functionality at 1710 cm^{-1} , they determined that these species appeared at $\sim 3.6\text{ V}$ in LiIm- and LiTf-based electrolytes; however, when using LiPF_6 , LiBF_4 , and LiClO_4 , this absorption was not found till 5.2, 4.4, and 4.6 V,³²⁷ respectively. Hence, they argued that, while Al was well passivated by the native Li_2CO_3 film, such an oxidation by electrochemical means would not occur. In other words, the difference in the effect of the electrolyte components on Al stability is not in how they decompose to form a new protection layer—such as through the familiar mechanism of SEI formation—but in how inert they are to the existing native layer. This inertness depends on the cathode potential, and the occurrence of solvent oxidation is indicative of the breakdown of the native passivation film. Apparently, Tf^- and Im^- anion species are corrosive to the native film, so the breakdown potential of it is much lower in the electrolytes based on these salts. Therefore, it would be reasonable to believe that a reaction occurring between Al_2O_3 and electrolyte solutes at high potentials is responsible for the onset of major corrosion, during which the coordination ability of Im^- and Tf^- anions toward Al^{3+} acts as the driving force that accelerates the anodic dissolution of Al substrate.

Large anion size was also found to favor Al stabilization, since the 1710 cm^{-1} signature did not appear till a potential higher than 5.0 V was reached for the new, asymmetric imide. Unlike the interpretation of Krause et al.,¹⁴¹ Kanamura et al. attributed its inertness to the well-distributed negative charge and the lower probability of these anions forming an ion pair with Al^{3+} .¹⁴⁸

The only in situ and semiquantitative study on Al corrosion was carried out by Yang et al. using EQCM to monitor the mass change of an Al electrode in various electrolytes based on LiIm, LiTf, LiPF_6 , LiBF_4 , and LiClO_4 .¹⁴⁷ The most interesting discovery was that, during the process of corrosion in all of the electrolytes, the mass change of Al was positive (i.e., the Al electrode gained net weight) instead of losing weight, as one would expect from a simple anodic dissolution of Al.

Furthermore, normalization of the weight gain against the corresponding charge quantity offered a semiquantitative method to identify the possible species formed, and in the case of LiBF_4 - and LiPF_6 -based electrolytes, $\Delta m/\Delta Q = 26\text{--}27$ was obtained, suggesting that essentially identical species were adsorbed on Al. Compounds with similar $\Delta m/\Delta Q$ values include AlF_3 ($\Delta m/\Delta Q = 19$) and $\text{Al}_2(\text{CO}_3)_3$ ($\Delta m/\Delta Q = 30$). On the other hand, LiTf- and LiIm-based electrolytes are characterized by very high $\Delta m/\Delta Q$ values. For example, in chronoamperometry stepped from 2.0 to 4.5 V, an Al electrode in LiIm/PC is accompanied by a $\Delta m/\Delta Q = 174$. It appears that the initial oxidation could be due to the formation of an Al compound of large molecular weight such as Al-

$(\text{Im})_3$ ($\Delta m/\Delta Q = 280.2$) or a reaction intermediate of Al^+ or of a solution species,¹⁴¹ but these compounds rapidly desorb from the Al surface, reducing the numerator in $\Delta m/\Delta Q$.

On the basis of the EQCM observations, the authors proposed an adsorption/oxidation/desorption mechanism for the severe pitting corrosion of Al in LiIm- and LiTf-based electrolytes, which is schematically shown in Scheme 19 and Figure 27b.¹⁴⁷ According to this mechanism, Al oxidizes to form adsorbed $\text{Al}(\text{Im})_3$ that eventually desorbs from the surface because these species are soluble in the electrolyte solvents. It is the desorption of these oxidized products that leaves the otherwise smooth Al surface with pits. The possibility also exists that, before desorption occurs, the adsorbed species undergoes further oxidation; however, since the oxidation of Im^- is insignificant below 4.5 V according to studies carried out on nonactive electrodes similar to Al,^{81,130,131,206} it seems unlikely that further oxidation of the adsorbed $\text{Al}(\text{Im})_3$ would occur.

On the other hand, the oxidized products in LiPF_4 and LiBF_4 electrolytes could consist of less soluble species such as AlF_3 and $\text{Al}_2(\text{CO}_3)_3$, as suggested by $\Delta m/\Delta Q = 26\text{--}27$, indicating negligible desorption from the Al surface and therefore less corrosion of the Al substrate.

6.4. A Few Words on Surface Characterizations

Beyond any doubt, the electrode/electrolyte interfaces constitute the foundations for the state-of-the-art lithium ion chemistry and naturally have become the most active research topic during the past decade. However, the characterization of the key attributes of the corresponding surface chemistries proved rather difficult, and significant controversy has been generated. The elusive nature of these interfaces is believed to arise from the sensitivity of the major chemical compounds that originated from the decomposition of electrolyte components.

Hence, the presence of trace impurities, which either pre-exist in pristine electrode and bulk electrolyte or are introduced during the handling of the sample, could profoundly affect the spectroscopic images obtained after or during certain electrochemical experiments. This complication due to the impurities is especially serious when ex situ analytic means were employed, with moisture as the main perpetrator. For cathode/electrolyte interfaces, an additional complication comes from the structural degradation of the active mass, especially when over-delithiation occurs, wherein the decomposition of electrolyte components is so closely entangled with the phase transition of the active mass that differentiation is impossible. In such cases, caution should always be exercised when interpreting the conclusions presented.

On the other hand, when the chemical composition of the surface layer is discussed, distinction should be made regarding the conditions under which such characterizations were carried out and the history of the electrode surface. For example, an electrode surface that was subjected to long-term cycling is certainly different from the surface state of the same

electrode that only experienced the initial forming process. Unfortunately, this distinction was seldom made in the literature. Most work also failed to characterize the pre-existing film on the electrode surface prior to electrochemical studies, and this neglect could lead to significant misinterpretation of the surface chemistry, because organic species could pre-exist on cathode as well as anode surfaces as the result of various contaminations or processing. In this sense, to obtain insightful understanding about the interfacial chemistries in a lithium ion cell, close collaboration is still needed between electrochemical and spectroscopic characterizations.

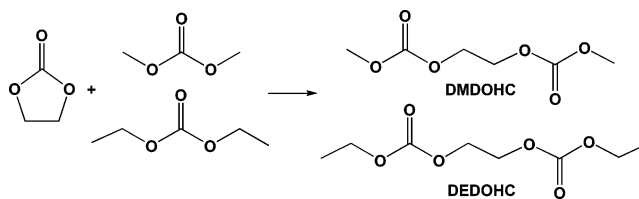
7. Chemical and Thermal Stability/Safety of Electrolytes

7.1. Long-Term Stability of Electrolytes at Elevated Temperatures

In most cases, the electrochemical stability of electrolyte components was studied at room temperature with various galvanostatic or voltammetric experimental techniques that were conducted within a certain time scale, usually $<10^5$ s. The stability thus determined should be considered relatively "transient" where the application in a longer time frame comparable to the cell lifetime is concerned, since the effect of those irreversible reactions of slow kinetics at room temperature, occurring either between the bulk electrolyte components (chemical) or between the electrodes and the electrolytes (electrochemical), cannot be factored in by such time-limited measurements. Only when stability of electrolytes is considered in a longer time frame ($t \sim 10^6$ s or up to months) can the impact of these reactions be visible. As a consequence of the slow irreversible processes, the performances of the lithium cells are often adversely affected, as typically evidenced by the persistent fade in capacity, loss in power rate, and increasing internal pressure within the cell, which can be attributed respectively to the irreversible consumption of the limited lithium ion sources, the depositions of high-impedance products on the electrode surface, and the generation of gaseous products by slow reactions.^{152,277,297,309}

On the other hand, since most of these reactions are thermally activated, their kinetics are accelerated by the rise in temperature in an Arrhenius-like manner. Therefore, within a much shorter time scale, the adverse effect of these reactions could become rather significant during the storage or operation of the cells at elevated temperatures. In this sense, the long-term and the thermal stability of electrolytes can actually be considered as two independent issues that are closely intertwined. The study of temperature effects on electrolyte stability is made necessary by the concerns over the aging of electrolytes in lithium-based devices, which in practical applications are expected to tolerate certain high-temperature environments. The ability of an electrolyte to remain operative at elevated temperatures is especially important for applications that are military/space-related or traction-related (e.g., electric or hybrid electric vehicles). On the other hand, elevated tem-

Scheme 20. Bulk Reaction between Electrolyte Components at Elevated Temperatures

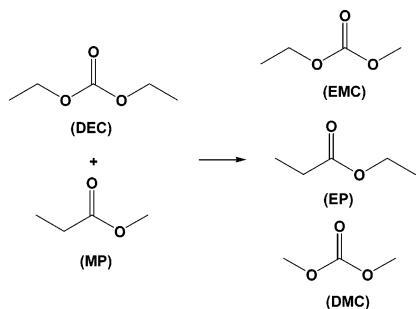


peratures are also often used as an accelerating tool to study the otherwise slow reactions at ambient conditions.

The intrinsic instability of the state-of-the-art electrolyte systems seems to arise mainly from the interaction between the cyclic carbonate and the Lewis acids, HF, PF₅, or PO_xF_y,^{150,330} which are generated by the decomposition or the hydrolysis of LiPF₆ by trace moisture. While typical electrolyte compositions such as LiPF₆/EC/DMC could seem to be indefinitely stable at room temperature in the proper containers,³³¹ Kinoshita and co-workers found that significant decomposition occurred during storage under He atmosphere at 85 °C, as indicated by discoloration, gas production, and solid precipitation.¹⁵² They estimated that at 85 °C the reactions were accelerated 10-fold as compared with the case of room temperature. Chemical analysis conducted on the stored electrolyte solution with a gas chromatograph detected the formation of a series of new species, among which the major component had a higher retention time (thus lower volatility) than EC. Through comparison with an authentic sample, the authors identified this species as dimethyl-2,5-dioxahexane carboxylate (DMDOHC), which was obviously formed from the ring-opening of EC and its subsequent transesterification with DMC (Scheme 20). Electrolytes based on an EC/DEC mixture rendered the corresponding product, DEDOHC, as shown in Scheme 20.^{48a,298} The effect of such a transesterification species on the performance of electrolytes in lithium ion cells has not been described.

Other species with higher retention times were suggested to be the products formed through the coupling of two ring-opened EC or oligoether compounds. On the other hand, the ¹H NMR conducted on the reacted electrolyte showed broad singlet bands of equal intensity at 3.746 and 4.322 ppm vs TMS, which resembled those reported for the poly(ether carbonate) as polymerization products of EC.^{332,333} The authors concluded that the polymerization and the transesterification were possibly initiated by PF₅. To confirm this hypothesis, they introduced newly generated PF₅ gas into the solvent mixture EC/DMC. After 10 h at room temperature, similar reaction patterns were observed by chromatography, with the above mixed carbonate as the major decomposition product, although its abundance was much lower. Minor differences unaccounted for between the two chromatographs were attributed to the presence of Li⁺ as well as the high ambient temperature in the thermal reaction.

By monitoring the change in the ratio of EC/DMC over time, Kinoshita and co-workers also noticed that EC decreased at a more rapid rate than DMC,

Scheme 21. Ester Exchange between Electrolyte Solvents

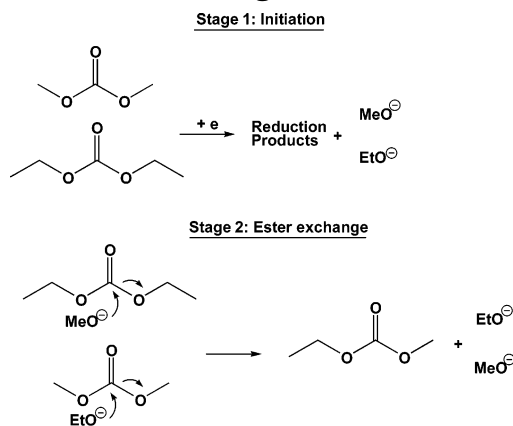
probably because PF_5 preferentially attacks the cyclic structure of EC. This hypothesis is consistent with the well-studied ring-opening polymerization of EC that is usually initiated by cationic species, as shown in Schemes 4, 12, and 15. The polymeric product could be a mixture of oligoether and polycarbonate structures.^{332,333}

Besides salt/solvent interactions, the ester exchange between linear carbonates was also observed during the cycling of the cells. Terasaki et al. were the first to observe that a significant amount of EMC was formed in a solvent mixture of DMC and DEC and proposed a reductively initiated mechanism.³³⁴ Interestingly, a corresponding oxidatively initiated mechanism was suggested by Ohta et al., when they observed that EMC, ethyl propionate, and DMC were generated from the original solvent mixture of DEC and methyl propionate (Scheme 21).³³⁵ In both cases, EC was used as a cosolvent and LiPF_6 as an electrolyte salt, but no identification of any products that involved the participation of these two components was reported, probably because of the slow kinetics at room temperature or the insensitivity of the analytical method used to detect the new products.

Takeuchi et al. thoroughly investigated the ester-exchange reaction between DMC and DEC in the presence of PC and LiPF_6 . By exposing the solvent mixture to individual cell components, including charged electrode materials at different potentials, salts, and acid impurities (HF), and monitoring the generated EMC content by means of a gas chromatograph, they conclusively proved that the ester-exchange process was reductively initiated by the lithiated carbon anode with potentials below 1.50 V and essentially negated the oxidative mechanism proposed by Ohta et al.³³⁶ Since DMC and DEC could also be detected from the original PC/EMC mixture in the presence of the lithiated carbon, the exchange process should be reversible.

In a further effort to identify the active intermediate that initiates the reaction, they tested the effect of a few possible ingredients on the production of EMC based on the knowledge about the chemical composition of the SEI on carbonaceous anodes. These model compounds included Li_2CO_3 , LiOCH_3 , and LiOH , while lithium alkyl carbonate was not tested due to its instability and therefore rare availability.³³⁷ The results unequivocally showed that LiOCH_3 effectively catalyzes the ester exchange.

A two-stage mechanism was proposed by Takeuchi et al. based on these observations, wherein the

Scheme 22. Ester Exchange Reaction Mechanism

generation of alkoxide anions is followed by the addition of them to the carbonyls of linear carbonates (Scheme 22). In other words, the ester-exchange reaction should start concurrently with the formation of the SEI, as shown in Scheme 7. According to the above mechanism, the alkoxide anions, once generated in the first stage, would continue to be produced in a chain reaction manner, and the above ester exchange would continue through the cell cyclings and be independent of the SEI formation. However, the authors found that the extent of the ester-exchange reaction was dependent on the anode surface passivation, and the complete formation of the SEI eventually prevented it. Therefore, a termination process had to exist at some stage, and the authors suggested that a cathode surface in a charged state would serve as such a terminator by quenching (oxidizing) the alkoxide anions. In view of the acidic nature of the electrolytes based on LiPF_6 , neutralization of alkoxide anions by trace acid is another possible termination means.

The absence of EC in the discussions of all these reports^{334–336} is interesting, since one would suspect that, based on the knowledge about EC reactivity, alkoxide could also attack its cyclic structure and cause irreversible reactions.^{152,285,332,333} One possibility would be that, using gas chromatography, the identification of a high-volatility species such as linear carbonate is easy and reliable, while the formation of the polymeric species, which EC would most likely decompose into, is more difficult to detect.

Endo et al. studied the gradual degradation of electrolyte solutions in lithium or lithium ion cells by monitoring the production of active radical species with ESR.³³⁷ To elongate the lifetime of the radicals so that their hyperfine structure could be analyzed, a spin-trapping technique was adopted to stabilize the original radicals generated from the reductive decompositions of electrolyte solvents on the anode surface. In this way, the authors were able to gain an insight into the structure of the radical species. The authors found that, even in the presence of a good, protective SEI, generation of active alkyl radicals, rather than radical anions, continued in the electrolyte and that a chain reaction initiated by cathodic polarization of the electrode was very likely responsible. In other words, once the radicals were produced in the initial cathodic polarization, the

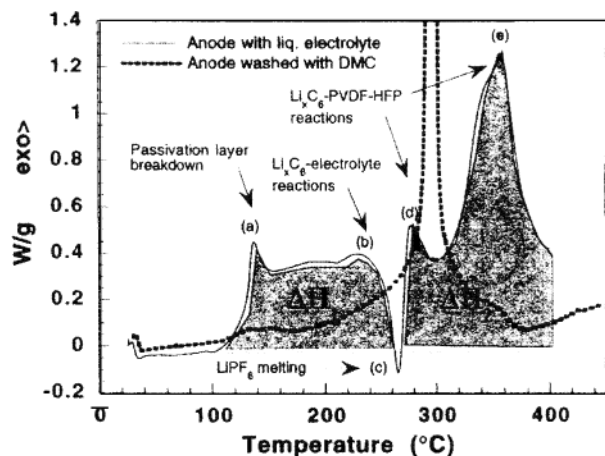


Figure 28. DSC trace of the reactions occurring between a fully lithiated graphitic anode and electrolyte. Anode surfaces both rinsed with DMC and unrinsed were studied. (Reproduced with permission from ref 338 (Figure 1). Copyright 1998 The Electrochemical Society.)

gradual decomposition of electrolyte solvents could occur in the bulk of the solution without involving electrodes. This propagation of radicals inevitably led to the polymerization of solvents. Using liquid chromatography, which is more sensitive to the detection of polymeric species, reductively induced polymerization of ester-based solvents was confirmed.

In the gradual degradation mechanism proposed by those authors, radical anions are first generated during SEI formation through a single-electron process, as proposed by Aurbach et al.,^{108,124,249} and then polymerization proceeded gradually from these radical anions with subsequent and continuous production of more active alkyl radicals. In this sense, even a perfect SEI that insulates any electron transfer through it cannot prevent the continuous degradation of electrolyte solvents.

7.2. Stability of the SEI or Surface Layer at Elevated Temperatures

The presence of a protective SEI or surface layer prevents those irreversible reactions of electrolytes on anode/cathode surfaces that are otherwise favored by thermodynamics. Like the chemical process in the bulk electrolyte, the reactivity of the surface films formed in state-of-the-art electrolytes is negligible at room temperature. However, during long-term storage and cycling, their stability is still under question.

When conducting a differential scanning calorimetry (DSC) study on the stability of carbonaceous anodes in electrolytes, Tarascon and co-workers found that, before the major reaction between lithiated carbon and fluorinated polymers in the cell, there was a transition of smaller thermal effect at 120 °C, marked peak (a) in Figure 28.³³⁸ They ascribed this process to the decomposition of SEI into Li_2CO_3 , based on the previous understanding about the SEI chemical composition and the thermal stability of lithium alkyl carbonates.^{102,117,249,281} Interestingly, those authors noticed that the above transition would disappear if the carbonaceous anode was rinsed in DMC before DSC was performed, while the other major processes remained (Figure 28). Thus,

they concluded that the components of the SEI layer are soluble in DMC.³³⁸ Because of the similar physicochemical properties between various linear carbonate solvents, this dissolution of the SEI might very likely be universal in all state-of-the-art electrolytes.

This corrosion of the SEI by linear carbonate solvents would undoubtedly produce adverse effects on the performance of lithium ion cells. During long-term cycling, the damaged SEI has to be repaired constantly by the same electrochemical reactions that occurred in the initial formation process, which consumes the limited lithium ion source in the cell and increases the impedance at the electrode/electrolyte interface.

A more detailed study on the thermal stability of the SEI on lithiated and delithiated graphitic anodes was carried out by Amatucci and co-workers.³³⁹ By storing the cells at 70 °C for 4 days and then resuming cycling at room temperature, they presented direct evidence that the SEI was damaged at the elevated storage temperature by successfully detecting the reappearance of the irreversible process at 0.75 V, which has been previously determined to be the formation of the SEI by reductive decomposition of the electrolyte. Furthermore, a correlation was also established between the capacity loss after such storages and the rebuilding of the SEI, with the latter being proportional to such factors as the storage temperature, the storage time, and the surface area of the anode. An Arrhenius behavior was actually observed for the dependence of capacity loss on the storage temperature, with an activation energy of 39.8 kJ mol^{-1} .³³⁹

As expected, the state-of-charge (SOC) of the anode also influences this rebuilding process, since the capacity loss due to the storage is much higher for the fully lithiated carbon anode than for the fully delithiated one. This fact was explained by the authors in terms of the reactivity of the carbon surfaces, which are partially exposed because of SEI corrosion, toward electrolyte components. Thus, intercalated lithium ions continuously diffuse from the interior of the graphitic structure through the imperfect SEI coverage and participate in the reaction with electrolyte solvents to re-form the SEI. Under stationary storage, an equilibrium would be reached between the SEI dissolution rate and the lithium ion diffusion rate. However, the net effect would be the irreversible consumption of electrolyte solvents as well as lithium ions.

The long-term deterioration of the SEI at elevated temperatures also was observed by McLarnon and co-workers, who conducted postmortem analyses on the electrodes from consumer lithium ion cells that were stored at various temperatures between 40 and 70 °C for weeks.²⁹⁸ Using the IR absorption at 838 cm^{-1} as the indicator of the SEI component, they quantitatively correlated the stability of the SEI on a carbonaceous anode against storage temperature and SOC. In an extreme situation where the cell was stored at 70 °C with 9% swing of SOC, no remaining SEI was found on the anode surface.

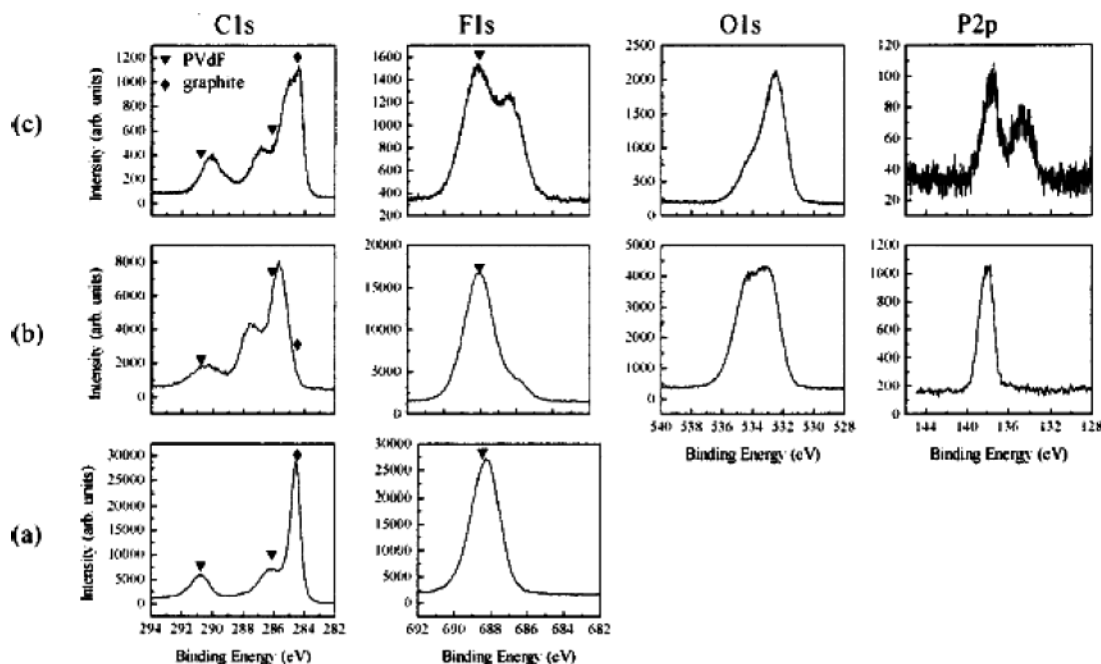
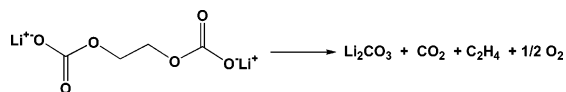


Figure 29. C 1s and O 1s XPS spectra for fresh, precycled, and stored graphite anodes. (Reproduced with permission from ref 294 (Figure 17). Copyright 2002 The Electrochemical Society.)

Scheme 23. Thermal Decomposition of Lithium Alkyl Carbonate in the SEI



Tarascon and co-workers proposed that the SEI on a carbonaceous anode is subject not only to simple dissolution but also to decomposition at elevated temperatures ($>120\text{ }^\circ\text{C}$) into Li_2CO_3 .³³⁸ While the existence of some chemical process was generally agreed upon by various authors, they differed vastly on what the original SEI components had turned into through the process.^{277,278,284,340}

In agreement with Tarascon and co-workers,³³⁸ Dahn and co-workers proposed that the thermal decomposition of the SEI occurred via the transformation of the metastable lithium alkyl carbonate into stable Li_2CO_3 (Scheme 23).^{340–342} This suggestion was supported by Amine and co-workers, who studied the change of surface chemistry on well-cycled carbonaceous anodes with elevated temperature storage by using XPS and observed the conspicuous presence of Li_2CO_3 on the graphite surface that was stored at $70\text{ }^\circ\text{C}$ for prolonged durations ($>$ weeks), as indicated by the C 1s signal at 290.4 eV in Figure 29.²⁹⁴ Additional evidence came from the decreasing ether/alkoxide signal at 287.4 eV in C 1s spectra and 534 eV in O 1s spectra. Furthermore, the elemental carbon signal at 284.5 eV was also clearly visible, indicating that the original SEI layer had been damaged, which left parts of the bulk graphene layers exposed.

However, Li_2CO_3 was not observed by Andersson and Edström in their XPS analysis of the graphitic anode that had been precycled and then stored at $60\text{ }^\circ\text{C}$ for 7 days.²⁷⁷ They found that, during the storage, the original SEI consisting of lithium alkyl carbonate was indeed unstable and disappeared with time, as

indicated by the decreasing C 1s signal at 291 eV (corresponding to ROCO_2Li), but the new species did not seem to be Li_2CO_3 , since the C 1s signal appeared at $290\text{--}290.5\text{ eV}$ instead of at 292 eV . These new species, still of a carbonyl nature, were thought by the authors to be polycarbonate formed from the ring-opening polymerization of EC. The discrepancy between the works of Amine et al. and Edström et al. could have arisen from the difference in the storage duration, which was much longer in the former case.

One common conclusion shared by both groups of researchers was the dramatic increase in LiF content as a result of the storage, which became the major species on the anode surface.^{277,294} Because of the relatively low abundance of alkyl carbonate species in the original SEI and the large amount of LiF after storage, the authors disagreed with Kanamura et al., who attributed the formation of LiF to the reaction of lithium alkyl carbonate or Li_2CO_3 with HF.²⁸² Rather, they suggested that, the direct decomposition of fluorinated salt anions (PF_6^- or BF_4^-) occurred at the elevated temperature and formed LiF through a variety of possible reactions.

A distinct difference between the behaviors of LiBF_4^- and LiPF_6^- -based electrolytes must be pointed out. The recycling after storage at $60\text{--}80\text{ }^\circ\text{C}$ revealed that lithium/graphite half-anode cells with LiBF_4^- -based electrolyte suffered serious capacity loss, while with LiPF_6^- -based electrolyte they maintained stable performance, as Figure 30 shows. A similar trend was found for a graphite anode with a different SOC, and a threshold value ($60\text{ }^\circ\text{C}$) for the storage temperature seemed to exist for this performance degradation. Qualitatively the same surface species were detected by XPS analyses on graphitic anodes that were formed in LiPF_6^- - and LiBF_4^- -based electrolytes; therefore, the above difference could not be explained by chemistries. Andersson et al. speculated that the morphology of the major surface species, LiF, played

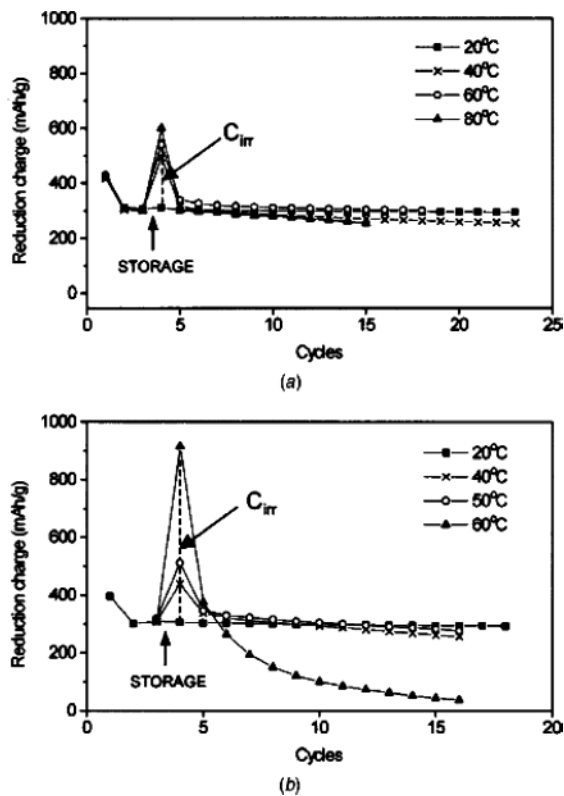


Figure 30. Capacity loss due to storage at elevated temperatures for Li/graphite half-cells. All cells were precycled at room temperature (cycles 1–3) prior to storage at indicated temperatures for 1 week, followed by continued cycling at room temperature. The electrolytes used were EC/DMC (2:1) and (a) 1.0 M LiPF₆ or (b) 1.0 M LiBF₄. The cells were stored in delithiated states. (Reproduced with permission from ref 277 (Figure 2). Copyright 2001 The Electrochemical Society.)

a critical role in defining the surface state of the anode. A highly speculative mechanism was proposed in accordance with this hypothesis in which the LiF formed at 60 °C from a LiBF₄-based electrolyte blocks the intercalation edge sites of the graphitic anode more effectively than the LiPF₆-based counterparts.²⁷⁷

The work by Ross and co-workers on the thermal stability of DEC on a lithiated graphitic anode further challenged the proposal that Li₂CO₃ was formed during the decomposition of the SEI.²⁸⁴ By the well-controlled exposure of the fully lithiated graphite LiC₆ to DEC vapor in a vacuum and gradually heating the electrode, they used XPS to monitor the transformation of the SEI as the function of temperature. From 0 to 110 °C, the major surface species were believed to be oxalate anions as well as alkoxides, while, from 120 to 140 °C, obvious chemical reactions were observed. On the basis of the C/O stoichiometric change, it seemed that organic anions such as oxalate anions were converted into simple inorganic anions. The authors thus proposed that, in the exothermic process that was observed by Tarascon and co-workers in the DSC experiment,³³⁸ the SEI most probably decomposed into simple inorganic species such as Li₂O and CO, instead of Li₂CO₃.²⁸⁴

On a cathode surface, the instability of electrolytes at elevated temperatures is also well studied, and it has been generally established that the continuous

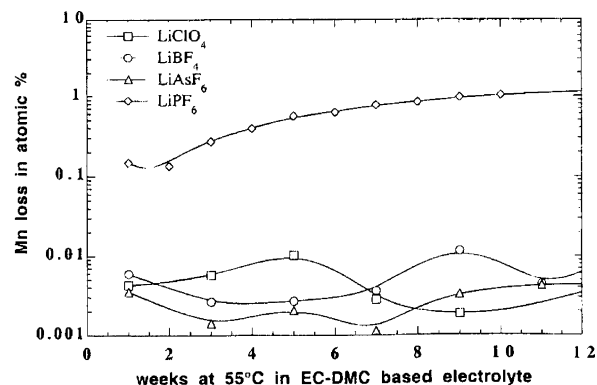


Figure 31. Effect of lithium salt on Mn²⁺ dissolution from Li_{1.05}Mn_{1.95}O₄ stored in EC/DMC (2:1) electrolytes at 55 °C. The Mn²⁺ concentrations in the electrolytes were determined by atomic absorption spectroscopy. (Reproduced with permission from ref 301 (Figure 4). Copyright 1999 The Electrochemical Society.)

decomposition and rebuilding of surface layers are responsible for the fade in capacity and loss in power.^{296,297,343–346}

Using thermogravimetric analysis (TGA), Du Pasquier et al. studied the thermal breakdown of the surface layer on a spinel cathode that was aged in LiPF₆/EC/DMC at 100 °C for 8 h,³⁰¹ and they detected the presence of two distinct weight loss processes at 140 and 500 °C. While assigning the latter to the transformation of spinel into Mn₂O₃, they believed that the former process corresponded to the burning of the organic coating on the cathode surface and the concomitant release of CO₂, similar to the thermal transition that had been observed on the graphitic anode in the same temperature range.³³⁸ Naturally, at room temperature, the above destructive process might only proceed with negligible kinetics.

For a spinel manganese cathode, the decomposition of the SEI is often entangled with the instability of the cathode structure in electrolytes at elevated temperatures, and the participation of electrolyte components in the Mn²⁺ dissolution or the disproportionation of the spinel is already widely accepted.^{293,301,343} The acidic nature of the electrolyte, originated from the moisture-sensitivity of PF₆⁻ or BF₄⁻ anions, is obviously the main cause, since a close correlation has been established by Du Pasquier et al. between the HF content and the Mn²⁺ content in the electrolyte³⁰¹ and LiPF₆ has been identified as the salt species that causes the most severe Mn²⁺ dissolution in state-of-the-art electrolytes^{301,343} (Figure 31), apparently due to its higher tendency to hydrolyze. Elevated temperatures promote this dissolution process in a pronounced way, as Figure 32 shows. The continuous trend in Mn²⁺ concentration implies that the dissolution process is kinetically governed, and there is no threshold temperature at which this process is switched on. However, acceleration does occur above 40 °C.³⁰¹ XRD analyses on the recovered spinel powder stored at 100 °C revealed the formation of a new phase, which the authors identified to be a protonated λ-MnO₂ that is partially inert with respect to electrochemistry. To account for the Mn²⁺ concentration and the formation of a protonated λ-MnO₂ phase, the authors believed that

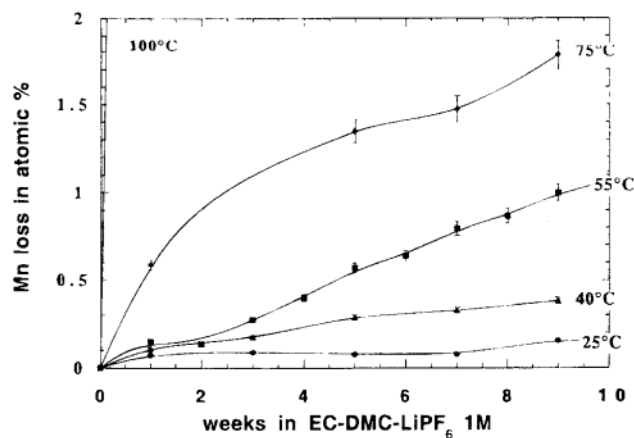
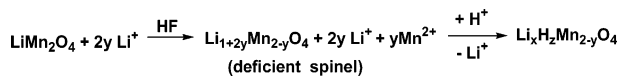


Figure 32. Effect of elevated temperatures on Mn^{2+} dissolution from $\text{Li}_{1.05}\text{Mn}_{1.95}\text{O}_4$ stored in $\text{LiPF}_6/\text{EC}/\text{DMC}$ (2:1). The Mn^{2+} concentrations in the electrolytes were determined by atomic absorption spectroscopy. (Reproduced with permission from ref 301 (Figure 1). Copyright 1999 The Electrochemical Society.)

Scheme 24. Structural Transformation of a Spinel Cathode at Elevated Temperatures Assisted by the Acidic Species in a LiPF_6 -Based Electrolyte



a proton–lithium ion-exchange process occurred instead of simple disproportionation (Scheme 24).³¹⁰ The structural transformation of spinel cathode materials is mainly responsible for the capacity fading of lithium ion cells based on them and LiPF_6 -containing electrolytes. Although other authors differ on the mechanism by which the capacity loss is caused, they generally agree that the acidic nature of the electrolyte plays an influential role.^{296,300,346} Thus, to make the advantages of spinel cathode materials feasible, the acidic nature of the electrolytes has to be mitigated, and the replacement of lithium salts based on anions with labile fluorine such as PF_6^- , BF_4^- , and AsF_6^- seems to be a logical solution.

On the other hand, the adverse effect of HF on capacity seems to be much less significant to other cathode materials based on LiNiO_2 and LiCoO_2 , which exhibit higher stability during storage at elevated temperatures, although an abundance of LiF found on cathode surfaces still indicates the reaction of a salt anion, most probably after its hydrolysis by trace moisture.^{294,302} In the XPS analysis conducted on a $\text{LiNi}_{0.8}\text{Co}_{0.2}\text{O}_2$ cathode that had been stored at various temperatures up to 70 °C, Andersson et al. reported that the surface chemistry did not show any apparent dependence on storage temperature, storage duration, or SOC (i.e., the polycarbonates and various F-containing species in the surface layer remain stable regardless of storage temperature).²⁹⁴ However, quantitative changes in the relative ratio of these species did occur during the storage, and it was believed that a thicker surface layer was formed as a result of longer storage at higher temperature. This conclusion was drawn from the simultaneous increase of C and O species during the storage despite the fact that F species actually decreased at the same

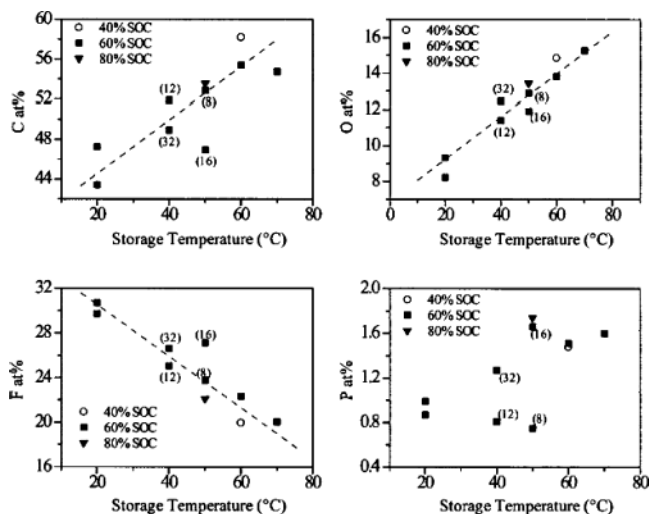


Figure 33. Relative amount (atom %) of surface species C, O, and F on cathode samples as a function of storage temperature. Numbers in parentheses indicate the storage duration in weeks. (Reproduced with permission from ref 294 (Figure 8). Copyright 2002 The Electrochemical Society.)

time, as Figure 33 shows. This unexpected trend in F abundance contradicts the knowledge about the instability of LiPF_6 salt at elevated temperatures as well as the results of LiF content on graphite^{277,294} and spinel materials^{301,343} during similar storage tests. To account for this abnormality, the authors argued that, while it would be impossible for the F content to actually decrease with temperature, the screening of the F 1s signal by an overlaying surface compound that is non-fluorine in nature could occur and would reduce the opportunity for the F 1s electron to escape.²⁹⁴ In other words, the polymeric and inorganic moieties grown on a cathode surface camouflage the increased LiF content.

7.3. Thermal Safety of Electrolytes against Abuse

The catastrophic scenario for the thermal reaction between electrolytes and electrode materials in a lithium-based cell is called “thermal runaway”,^{347–351} whose onset temperature determines the safety limit of lithium-based cells. Thermal runaway occurs when the amplitude of an accidental temperature hike in the cell, usually initiated by local overheating, reaches a certain threshold value, and the heat thus generated can no longer be thermally dissipated but instead triggers a series of exothermic side reactions. Since the rate of heat generation is higher than that of heat dissipation, these exothermic processes proceed under an adiabatic-like condition and the global cell temperature experiences an uncontrollable rise. Figure 34a shows an example of a thermal runaway that was initiated in a well-cycled (25 times) lithium cell by a 140 °C hot box test.³⁴⁸ Once initiated, thermal runaway apparently does not terminate until the reactive agents are completely consumed or, in most cases, the cell ruptures, venting with flames and smoke and sometimes even explodes.^{348,351,352} For lithium or lithium ion batteries of industry sizes (i.e., a capacity of > 10 A h), serious safety hazards would ensue from such a thermal breakdown.

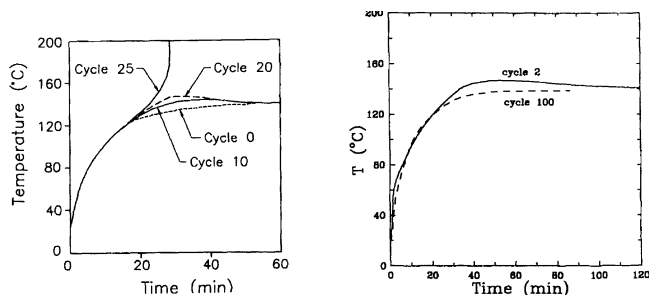


Figure 34. Temperature response of (a, left) cycled lithium (Li/MnO₂) and (b, right) lithium ion (coke/LiCoO₂) cells subjected to a 140 °C hot box test. These cells contain LiAsF₆/EC/PC and LiPF₆/PC/DEC as electrolytes, respectively, and were cycled at room temperature to the indicated cycle numbers. Note that the thermal runaway occurs for a lithium cell that has been cycled 25 times due to the formation of high surface area lithium, while extended cycling actually offers better safety to lithium ion cells (Reproduced with permission from ref 348 (Figures 1 and 4). Copyright 1994 Elsevier.)

The concern over the safety of lithium-based cells drew a great deal of attention after the unsuccessful commercialization of lithium cells.^{353–358} The surface morphology of the well-cycled lithium electrode was believed to be the main source for thermal runaway, because the presence of high surface area dendritic lithium would greatly promote the exothermic reactions between lithium and electrolyte, thus lowering the threshold temperature at which self-heating occurred. As Figure 34a shows, the temperature of the fresh cell (cycle 0) under the same testing condition does not show any temperature overshoot but instead approaches 140 °C in an asymptotical manner, as would be expected from a thermally inert object. Temperature overshoot, a sign of self-heating within the cell, increases monotonically with cycle number until, after 25 cycles, the cell possesses a highly reactive lithium surface and undergoes thermal runaway, as characterized by the dramatic rise in temperature.³⁴⁸ At the time, the role played by cathode materials in the safety of lithium cells seems to be overshadowed by the presence of lithium anodes because of the much higher reactivity of the latter.

The replacement of lithium by carbonaceous anode materials eliminated the highly reactive anode surface as a possible trigger for thermal runaway and led to the successful commercialization of lithium ion technology in the 1990s. However, safety remains an issue, since thermal runaway can be caused by mechanisms other than the formation of lithium dendrites. A general opinion is that the replacement of the metallic lithium by a carbonaceous anode does improve safety, as Figure 34b shows.^{348,351,352,359} In contrast to a metallic lithium anode, a well-cycled carbonaceous anode offers additional self-heat suppression, as evidence by the absence of the temperature overshoot which was originally observed in a fresh cell. For most commercial lithium ion cells, the onset temperature that would trigger a thermal runaway is considered to be >150 °C.^{351,352,360}

According to mathematic modeling and abuse tests, the normal operation for most lithium or lithium ion cells that use nonaqueous electrolytes should not induce sufficient heat to raise the cell temperature

above the onset threshold. Instead, thermal runaway is often caused by various abuses, which could be thermal (overheating), electrical (accidental overcharge, high pulse power extraction), or mechanical (crushing, internal or external short circuit).^{349,351,352} Various techniques have been employed to evaluate the safety of lithium ion cells, including hotbox^{348,360} and accelerating rate calorimetry (ARC)^{348,360,361} as well as abuse tests such as overcharging, shorting, crushing, and nail-penetration.^{351,352} Profound differences in the abuse tolerance were found among the lithium ion cells from various manufacturers despite the common onset temperature of ~160 °C for nearly all these cells. In addition to the cell materials (electrolyte and electrode) that determine the amount of heat generation and the rate of heat release, the cell design and engineering was also found to be of vital importance for abuse tolerance by affecting the efficiency of heat dissipation.^{349,355,360,361} The presence of excess electrolytes can increase the overall thermal conductivity of the cell by 55–70% and eliminate its dependence on OCV but cannot alter the anisotropy of heat flow within the cell. For example, in an electrolyte-filled cathode/separator/anode stack that simulates an actual lithium ion cell, the cross-plane thermal conductivity is ~10 times lower than the in-plane one.³⁶⁰ In agreement with the above results, Leising et al. compared the internal and external temperatures of a prismatic 1500 mA h lithium ion cell during an external short, and they found a difference of 40 °C between the two.³⁵² The consequence of this anisotropy in thermal conductivity is especially serious for the popular spiral-wound cell design because it creates an adiabatic-like environment for any thermal perturbation occurring near the core of the cell and increases the opportunity for thermal runaway.

At elevated temperatures, there are five possible reactions that can occur between the cell components: (1) thermal decomposition of bulk electrolyte; (2) chemical reduction of electrolyte by the anode; (3) chemical oxidation of electrolyte by the cathode; (4) thermal decomposition of the cathode and anode; or (5) melting of the separator and the consequent internal short. To identify which of these contributes the decisive amount of heat that is critical in initiating the thermal runaway, it is necessary to study the thermal responses of these individual components or component couples separately.

The bulk electrolyte components do not seem to be such an initiation, since the thermal decomposition of the salts and the interactions between the salts and the solvents start as low as 70 °C,^{150,152,330,337} and the thermal effect of these reactions is generally negligible as compared with the processes involving the fully charged anode and cathode materials.³⁶¹

In early research efforts, attention was concentrated on carbonaceous anodes because of the earlier experiences with metallic lithium. Dahn and co-workers studied the thermal response of carbonaceous materials in the presence of electrolytes in an adiabatic environment created in a thermal analysis technique known as accelerating rate calorimetry (ARC). By choosing an arbitrary threshold value for

the self-heating rate (SHR) of $0.02\text{ }^{\circ}\text{C min}^{-1}$, they found that, besides the lithiation state of the anode, electrolyte composition had a critical effect on the onset temperature of thermal runaway, with the SHR increasing in the order



While the rationale for the above order remains to be well-understood, the authors speculated that the relative effectiveness and solubility of the SEI as well as the reactivity of these bulk solvents might be responsible.³⁴⁸ Overall, this study showed that the reaction between the electrolyte and the lithiated carbon could trigger thermal runaway, except at much higher onset temperatures than those of lithium electrodes.

In their DSC studies on the SEI of carbonaceous anodes, Du Pasquier et al. identified the exothermic process at $120\text{--}140\text{ }^{\circ}\text{C}$ as the transformation of the alkyl carbonate-dominated SEI into the more stable Li_2CO_3 , and the heat generation associated with this process strongly depended on the surface area of the electrode. The reduction of electrolytes by lithiated carbon occurred between 210 and $230\text{ }^{\circ}\text{C}$, with comparable reaction heat to that of the transformation of an SEI.³³⁸ According to the $140\text{ }^{\circ}\text{C}$ hotbox test that was conducted with a lithium ion cell, it seemed that the breakdown of the SEI could be excluded as the cause for thermal runaway.³⁴⁸ Works by other authors confirmed the occurrence of this SEI transformation process at $>100\text{ }^{\circ}\text{C}$ and the dependence of its heat generation on the carbonaceous anode surface,^{359,362,363} but they disagreed on its role in initiating thermal runaway. For example, Joho et al. systematically measured the heat evolution of various graphitic anodes in the presence of $\text{LiPF}_6/\text{EC}/\text{DMC}$ between 80 and $220\text{ }^{\circ}\text{C}$ and evaluated the possibility that the graphitic anode was the source for thermal runaway in lithium ion cells. On the basis of the overall heat capacity data of the Sony 18650 lithium cell, they estimated that the temperature rise in the cell as the result of heat generation of those processes ranged between 30 and $90\text{ }^{\circ}\text{C}$, depending on the surface area as well as the irreversible capacity of the anode, and concluded that, while the transformation occurred at $>100\text{ }^{\circ}\text{C}$, a temperature hike of this amplitude could place the cell well in the range of thermal runaway onset temperatures between 160 and $180\text{ }^{\circ}\text{C}$; therefore, the thermal decomposition of the SEI and the subsequent reduction of electrolyte components by lithiated carbon could be the source that initiates thermal runaway.³⁵⁹

In their further study on the thermal reaction between carbonaceous anodes and electrolytes, Richard and Dahn improved the ARC technique and miniaturized it for small sample amounts ($<1.0\text{ g}$) while retaining the sensitivity.^{340,341} The self-heating was measured for MCMB in various electrolytes with different initial heating temperatures, and the SHR profile, characterized by a common initial peak, was obtained for nearly all of the tests, as shown in Figure 35. The authors speculated that the SHR profile represented in Figure 35 featured characteristics of three distinct reaction processes. The initial peak,

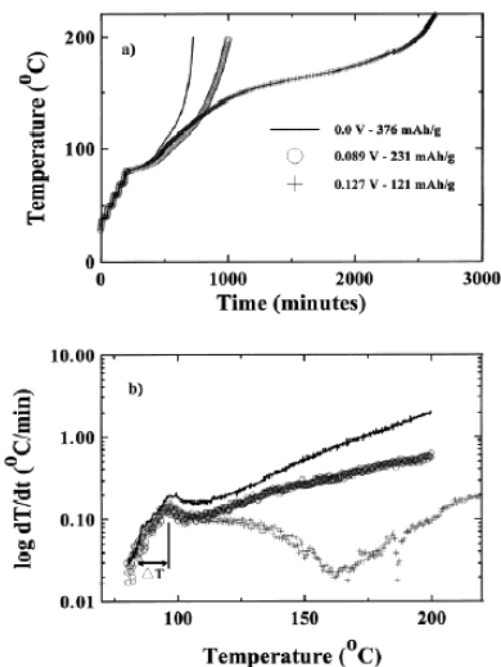


Figure 35. Temperature–time (a) and SHR (b) profiles measured for lithiated MCMB in $\text{LiPF}_6/\text{EC}/\text{DEC}$ (33:67). The MCMB electrodes were lithiated to three compositions: $\text{Li}_{0.75}\text{C}_6$ (0.0 V), $\text{Li}_{0.45}\text{C}_6$ (0.089 V), and $\text{Li}_{0.25}\text{C}_6$ (0.127 V). (Reproduced with permission from ref 340 (Figure 8). Copyright 1999 The Electrochemical Society.)

which appears to be relatively independent of the lithiation degree of the carbonaceous anode, should represent a reaction that proceeds until one of the reactants is depleted. The decomposition of bulk electrolyte does not contribute to the SHR until $190\text{ }^{\circ}\text{C}$; therefore, there must be another exothermic process between 150 and $190\text{ }^{\circ}\text{C}$. During this temperature range, the SHR does depend on the lithiation degree of the anode, with the more lithiated anode generating a higher SHR. XRD analysis confirmed that this process does consume the intercalated lithium in the graphite interior.

On the basis of the above observation, Dahn and co-workers proposed a thermal reaction scheme for the coupling of carbonaceous anodes and electrolytes. The initial peak, which was almost identical for all of the anode samples and independent of lithiation degrees, should arise from the decomposition of the SEI because the amount of SEI chemicals was only proportional to the surface area. This could have been due to the transformation of the metastable lithium alkyl carbonate into the stable Li_2CO_3 . After the depletion of the SEI, a second process between 150 and $190\text{ }^{\circ}\text{C}$ was caused by the reduction of electrolyte components by the lithiated carbon to form a new SEI, and the autocatalyzed reaction proceeded until all of the intercalated lithium was consumed or the thickness of this new SEI was sufficient to suppress further reductions. The corresponding decrease in SHR created the dip in the least lithiated sample in Figure 35. Above $200\text{ }^{\circ}\text{C}$ (beyond the ARC test range as shown in Figure 35), electrolyte decomposition occurred, which was also an exothermic process.

The tests with various electrolytes revealed that both electrolyte salts and solvent compositions affect

the initial SHR below 100 °C, which is of critical importance to the initiation of thermal runaway. For example, using the threshold value of the SHR at 0.02 °C min⁻¹ as the sign of onset, the self-heating for MCMB in LiPF₆/EC/DEC (33:67) starts at 80 °C, whereas it begins at 50 °C in LiBF₄/EC/DEC (50:50) and at 70 °C in LiPF₆/EC/DEC (50:50). The SHR profiles obtained for the MCMB anode in LiBF₄/EC/DEC did not show the initial peak that corresponds to the transformation of the SEI, suggesting that the SEI formed on the carbonaceous anode in LiBF₄-based electrolyte did not contain high amounts of metastable components such as lithium alkyl carbonate, as the SEI formed in LiPF₆- or LiAsF₆-based electrolytes would have. This inference was in agreement with the work by Aurbach et al.,^{104,117} Kana-mura et al.,^{222,223} and Andersson and Edström.²⁷⁷ On the basis of these ARC results, these authors believed that if a lithiated MCMB containing LiPF₆/EC/DEC (33:67) was heated directly to 150 °C, the known threshold for thermal runaway for most commercial lithium ion cells, the anode would self-heat at a rate of 100 °C min⁻¹. Hence, the universal self-heating behavior of a lithiated carbonaceous anode in the presence of electrolytes is very useful for predicting the initial self-heating in a practical lithium ion cell when combined with the overall heat capacity of the cell.³⁴⁰

The seminal work by Maleki et al. in 1999 seemed to provide a direct answer to the question about which of the five possible processes was responsible for the thermal runaway of a lithium ion cell.³⁶¹ Using ARC, they first determined the thermal runaway onset temperature in a lithium ion cell based on LiCoO₂/graphite with LiPF₆/EC/DMC/DEC to be 167 °C. The thermal reaction, however, was found to start at 123 °C and continued to self-heat the system to the above onset temperature. Using DSC and TGA, they further determined the heat evolution as well as the thermal profile for the individual components of the cell in the presence of electrolytes, which included cathode, anode, and anode binder (PVdF).

Thus, the total exothermic heat generation of 697 J g⁻¹ was recorded for the anode-related reactions, which included the major heat generated from anode/binder reactions starting at 210 °C and the anode/electrolyte reactions starting at 125 °C. The breakdown of the SEI on the anode occurred at 120 °C, as characterized by the distinct peak, which followed an endothermic process that was attributed by the authors to the bulk electrolyte decomposition below 100 °C. While the heat effect of the SEI breakdown seemed negligible as compared to those of the cathode/electrolyte and anode/electrolyte reactions, it contributed to the self-heating of the cell. For cathode-related processes, the total exothermic heat generation was 407 J g⁻¹, with the major thermal reaction starting at 167 °C. In other words, although the heats associated with anode-related reactions are higher, the heat from the cathode processes was released at a relatively lower temperature and was more likely responsible for the triggering of thermal runaway.

A comparison was made between the profiles of heat evolution associated with the reactions of the

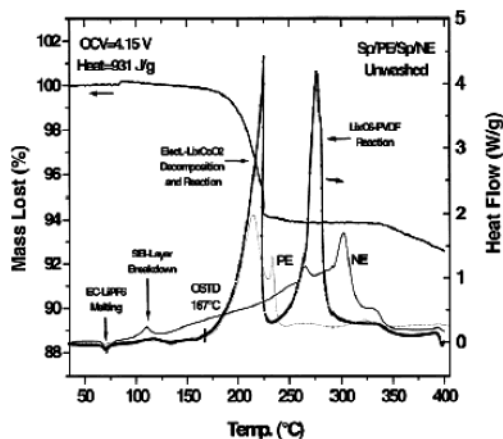
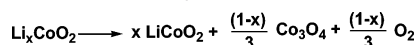
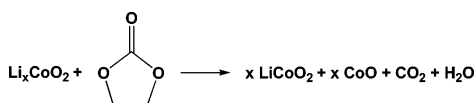


Figure 36. Comparison of DSC and TGA profiles for a cathode (PE), anode (NE), and separator (SP) composite with those of cathode/electrolyte and anode/electrolyte. Note the close match between the DSC/TGA profiles of the stack and the cathode/electrolyte couple. The OCV of the stack is 4.15 V. (Reproduced with permission from ref 361 (Figure 4). Copyright 1999 The Electrochemical Society.)

cathode/electrolyte and the anode/electrolyte, and a close match was identified between the DSC profile of the cathode/electrolyte couple and that of the cell stack, which consisted of cathode/separator/anode in the presence of electrolytes in a simulation of an actual lithium ion cell (Figure 36).³⁶¹ Therefore, the authors concluded that the thermal runaway was mainly caused by the heat generation from the cathode material, which decomposed to release oxygen, and the electrolyte components were oxidized subsequently. While the reaction of the anode/binder occurred at a relatively higher temperature, its substantial heat certainly contributed to the ultimate consequences of the thermal runaway. In a more comprehensive conclusion, the safety of a given lithium ion cell is dominated by the electrolyte reactions with the cathode and with the anode simultaneously.

The thermal decomposition of various cathode materials based on transition metal oxides has been known since the potential of these materials as rechargeable lithium-based batteries became realized, and the decomposition chemistry releasing oxygen has usually been thought to proceed at temperatures above 200 °C.^{362,364–366} Interestingly, Maleki et al. found that the presence of a surface layer on the cathode, which was formed through the decomposition of electrolytes on the cathode during the cycling of the cell, actually promoted the thermal decomposition of the cathodes to occur at a lower temperature with higher heat generation and mass loss. The decomposition of the surface layer served as the thermal trigger for the major oxygen-releasing process.

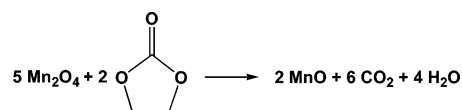
A direct result of the work by Maleki et al. is the gradual shift of safety research from carbonaceous anode to cathode materials. In the following years, Dahn and co-workers used an improved ARC technique to conduct a series of systematic investigations on the reaction between electrolyte and cathode materials based on LiCoO₂^{367–369,371} and spinel LiMn₂O₄.^{368,370} These studies have depicted a clear picture regarding the safety of lithium ion devices.

Scheme 25. Thermal Decomposition of LiCoO_2 in the Absence of Electrolyte**Scheme 26. Thermal Combustion of EC by the Cathode LiCoO_2** 

In a standard electrolyte, $\text{LiPF}_6/\text{EC}/\text{DEC}$, the fully delithiated LiCoO_2 (OCV = 4.2 V) showed the threshold SHR of $0.02 \text{ }^\circ\text{C min}^{-1}$ at $\sim 130 \text{ }^\circ\text{C}$ that eventually led to thermal runaway at $160 \text{ }^\circ\text{C}$. It had been found that the thermal decomposition of LiCoO_2 occurred at a much higher temperature ($> 200 \text{ }^\circ\text{C}$) with oxygen generation (Scheme 25). The existence of Co_3O_4 had been confirmed by XRD analysis conducted on a cathode sample that was heated to $320 \text{ }^\circ\text{C}$. However, MacNeil and Dahn found that the presence of electrolyte solvents catalyzed the decomposition of LiCoO_2 by reacting with the oxygen, thus greatly lowering the onset temperature at which oxygen was released. XRD analysis performed on the cathode after its reaction with EC/DEC showed that, when solvents were present, a new phase "CoO" was generated in addition to Co_3O_4 and the unreacted LiCoO_2 .³⁶⁹ The authors ascribed the formation of this Co(II) species to the reducing power of the organic solvents. In an ideal situation with full combustion of EC, the authors proposed the reaction scheme shown in Scheme 26. As a result, the presence of organic species as fuel not only reduced the onset temperature for the thermal decomposition of LiCoO_2 but also rendered the reaction more exothermic. This solvent effect, that is, lower onset temperature and higher reaction heat for thermal decomposition of cathode materials due to the participation of electrolyte solvents, has actually been observed previously by Maleki et al., who ascribed it to a complex synergistic mechanism among the electrolyte components and LiCoO_2 that catalyzed the reaction between electrolytes and the liberated oxygen.³⁶¹ Undoubtedly, as fuel in the adiabatic system, the presence of organic solvents in the electrolyte increases the chance of thermal disaster for lithium ion cells.

In contrast to that of solvents, the effect of the electrolyte solute, LiPF_6 , on the thermal decomposition of the cathode, LiCoO_2 , was found to be suppression instead of catalyzation.³⁶⁹ The SHR of a partially delithiated cathode was measured in a series of electrolytes with various salt concentrations, and a strong suppression of the self-heating behavior was found as the concentration of LiPF_6 increased above 0.50 M. The mechanistic rationale behind this salt effect is still not well understood, but the authors speculated that the salt decomposition coated the cathode with a protective layer that acted as a combustion retardant. On the basis of these results, the authors recommended a higher salt concentration ($> 1.50 \text{ M}$) for LiCoO_2 -based lithium ion cells is preferred in terms of thermal safety.

Parallel studies carried out on a manganese spinel LiMn_2O_4 -based cathode showed that this cathode

Scheme 27. Thermal Combustion of EC by a Fully Delithiated Spinel Cathode

material could offer improved thermal safety as compared to LiCoO_2 , but the SHR in this case was very sensitive to the relative amount of electrolyte compared to that of the cathode, while the corresponding dependence was not found with $\text{LiCoO}_2/\text{electrolyte}$.³⁶⁸ Thus, only when the electrolyte/cathode ratio was in the vicinity of 1:6, which is close to the actual electrolyte/cathode ratio in lithium ion cells, would the LiMn_2O_4 -based cathode show a lower SHR than LiCoO_2 -based cells, in consistence with the hotbox data.³⁶⁸

Similar to the results obtained on the thermal reaction of LiCoO_2 , the SHR of $\text{Li}_x\text{Mn}_2\text{O}_4$ in the presence of $\text{LiPF}_6/\text{EC}/\text{DEC}$ reached the threshold value of $0.02 \text{ }^\circ\text{C min}^{-1}$ at $\sim 150 \text{ }^\circ\text{C}$, indicating the beginning of exothermic events; then the system gradually self-heated to $275 \text{ }^\circ\text{C}$. In comparative tests, LiMn_2O_4 in the absence of electrolytes showed a detectable thermal event at $\sim 160 \text{ }^\circ\text{C}$ and converted from the λ - MnO_2 structure to β - MnO_2 one, while the oxidation of electrolyte solvent led to MnO with increased exothermic effect. Since MnCO_3 and Mn_2O_3 were also detected by XRD analysis, CO_2 and H_2O were suspected to be the combustion products of the solvents.³⁷⁰ Assuming EC as the fuel to be fully combusted, 1 mol of delithiated spinel material can release 2 mol of oxygen and generate heat that is sufficient to raise the cell temperature over $300 \text{ }^\circ\text{C}$, based on the heats of combustion for EC ($1161.4 \text{ kJ mol}^{-1}$) and DEC (2715 kJ mol^{-1}) (see Scheme 27). In experiments, the actual rise in the ARC sample temperature was only $80 \text{ }^\circ\text{C}$, most probably due to incomplete combustion or depletion of solvent.³⁷⁰

Therefore, the presence of the electrolyte solute, LiPF_6 , added complexity to the thermal decomposition of the LiMn_2O_4 -based cathode. Contrary to the salt effect found with the LiCoO_2 cathode,³⁶⁹ the onset temperature of exothermic activity as represented by $\text{SHR} > 0.02 \text{ }^\circ\text{C min}^{-1}$ decreased as the concentration of LiPF_6 increased.³⁷⁰ Apparently, LiCoO_2 and LiMn_2O_4 have fundamental differences in the way they react with solvent in the presence of salt. It seemed that the salt mainly contributes to an initial thermal instability, which increases with LiPF_6 -concentration.³⁷⁰

Pointing out that the acidic nature of LiPF_6 assists the dissolution of Mn^{2+} into electrolyte solution,^{301,343} the authors speculated that HF in the electrolyte solution efficiently cleans up the spinel surface of MnO ; therefore, the bulk electrolyte solvents can be continuously exposed to the fresh surface of Mn_2O_4 and be oxidized.³⁷⁰ As a result, solvent oxidation would proceed more rapidly as compared with the case of an electrolyte that is less acidic. Therefore, for a spinel manganese-based lithium ion cell, a higher thermal safety would be obtained with lower salt concentration, and the authors suggested 0.5 M as the optimum concentration at which the ion

conductivity and thermal reactivity could be best balanced.³⁷⁰

A recent publication discussing the salt effect on the thermal safety of a LiCoO₂ cathode was entitled with an intriguing but seemingly paradoxical question: "Can an electrolyte for lithium ion batteries be too stable?", which revealed the relative importance of the interfacial stability arising from the passivation efficiency against that of the "intrinsic stability" with respect to the safety of cathode materials in lithium ion cells.³⁷¹ Using an improved DSC technique that enabled the direct analysis of electrolytes containing volatile components, the authors investigated the thermal stability of the LiCoO₂ cathode in the presence of the electrolytes based on LiPF₆, LiIm, and LiBeti. The latter two salts, which were based on an imide anion stabilized by two perfluorinated sulfonyl groups, had been developed in the early 1990s to replace the thermally unstable LiPF₆ and have been reported to be thermally stable till >300 °C.¹⁴⁶

Surprisingly, when the cathode material, LiCoO₂, was in the presence of these "thermally stable" salts, LiIm and LiMe, much higher reactivity was detected than that in the presence of LiPF₆, as indicated by the total absence of any combustion suppression on SHR that had been observed with LiPF₆.³⁷¹ DSC results of LiCoO₂ in the presence of LiIm- or LiBeti-based electrolytes confirmed the above observation, which showed the onset thermal decomposition of LiCoO₂ to be at ~280 °C, whereas in LiPF₆-based electrolytes the same thermal event was much suppressed in terms of heat evolution as the concentration of LiPF₆ increased. In other words, the presence of LiIm and LiBeti did not introduce any increase in the thermal stability of the electrode, while LiPF₆, although believed to be thermally unstable, efficiently suppressed the thermal decomposition of the cathode.

The authors ascribed the above "abnormality" to the passivation of the cathode surface by the reaction products of the electrolyte solvent and salt. Since LiPF₆ readily decomposes organic solvents such as EC through a ring-opening mechanism at relatively low temperatures, the decomposition products, which were believed to consist of a wide variety of compounds, including a PEO-like polymer shown by Schemes 4, 12, and 15, deposited on the cathode surface and formed a protective layer between the highly oxidizing cathode materials and the bulk electrolyte solvents. According to the hypothesis of the authors, this polymeric coating on the cathode particles strongly delayed the thermal combustion of the solvents by hindering the release of oxygen, resulting in a more controlled thermal decomposition of LiCoO₂. On the other hand, similar polymer species were not formed from LiIm- or LiBeti-based electrolytes because of the stability of these salts, and the thermal combustion of electrolyte solvents in the presence of charged cathode materials proceeded unhindered, releasing heat that is sufficient to trigger thermal runaway.

Another well-studied salt, LiBF₄, was also believed to be more thermally and chemically stable than LiPF₆ in terms of its higher tolerance against trace

moisture and lower tendency to react with cyclic carbonates in a manner similar to that shown by Schemes 4, 12, and 15.^{132,133} However, a similar paradoxical conclusion was drawn about the thermal safety of LiCoO₂ in the presence of the electrolyte based on it, whose inability to produce polymeric coatings on the cathode is held responsible.³⁷¹ The above results from Dahn and co-workers suggested that the salts that were traditionally thought to be thermally stable, such as LiBF₄, LiIm, and LiBeti, should not be used in lithium ion cells if the thermal safety is the top concern in the application environment, which includes large size cells working under high-rate discharge, at elevated temperatures or at the risk of mechanic abuses and so forth, and that LiPF₆ remains the electrolyte solute of choice in terms of thermal safety.

8. Novel Electrolyte Systems

8.1. Problems Facing State-of-the-Art Electrolytes

Summarizing the materials reviewed in sections 2–7, one can immediately conclude that the current state-of-the-art electrolyte systems for lithium ion batteries are far from perfect and that, at least in the following four aspects, there is still room for possible improvement. Therefore, research and development efforts are continued in an attempt to reformulate new electrolyte systems or to modify the current state-of-the-art electrolyte systems.

(1) Irreversible Capacity. Because an SEI and surface film form on both the anode and cathode, a certain amount of electrolyte is permanently consumed. As has been shown in section 6, this irreversible process of SEI or surface layer formation is accompanied by the quantitative loss of lithium ions, which are immobilized in the form of insoluble salts such as Li₂O or lithium alkyl carbonate.²⁶² Since most lithium ion cells are built as cathode-limited in order to avoid the occurrence of lithium metal deposition on a carbonaceous anode at the end of charging, this consumption of the limited lithium ion source during the initial cycles results in permanent capacity loss of the cell. Eventually the cell energy density as well as the corresponding cost is compromised because of the irreversible capacities during the initial cycles.

The extent of the irreversible capacity depends on both the anode material and the electrolyte composition. Empirical knowledge indicates that the PC presence, which is well-known for its tendency to cause the exfoliation of the graphene structures, is especially apt to induce such irreversible capacities. On the other hand, reformulation of the electrolyte may lead to significant reduction in the irreversible capacity for given electrode materials.

(2) Temperature Limits. The two indispensable components of the present lithium ion electrolyte systems are LiPF₆ as salt and EC as solvent. Unfortunately, these two components also impart their sensitivity to extreme temperatures to the lithium ion technology, thus imposing temperature limits to the operation of lithium ion cells. In a somewhat oversimplified account, one can hold EC responsible

for the lower, and LiPF_6 for the higher, temperature instabilities.

Thus, at temperatures lower than the liquidus temperature (usually above $-20\text{ }^\circ\text{C}$ for most electrolyte compositions),^{50e,159,160} EC precipitates and drastically reduces the conductivity of lithium ions both in the bulk electrolyte and through the interfacial films in the system. During discharge, this increase of cell impedance at low temperature leads to lower capacity utilization, which is normally recoverable when the temperature rises. However, permanent damage occurs if the cell is being charged at low temperatures because lithium deposition occurs, caused by the high interfacial impedance, and results in irreversible loss of lithium ions. An even worse possibility is the safety hazard if the lithium deposition continues to accumulate on the carbonaceous surface.

At temperatures higher than $60\text{ }^\circ\text{C}$, various decompositions occur among the electrolyte components, electrode materials, and SEI or surface layers, while LiPF_6 acts as a major initiator or catalyst for most of these reactions.^{152,310,332,333} The damage caused by high-temperature operation is permanent. Because gaseous products accumulate, a safety hazard is also likely. Therefore, the specified temperature range for the normal operation of most commercial lithium ion cells is $-20\text{ }^\circ\text{C}$ to $+50\text{ }^\circ\text{C}$. While sufficient for most consumer purposes, the above range severely restricts the applications of lithium ion technology for special areas such as military, space, and vehicle traction uses.

(3) Safety and Hazards. The linear carbonate solvents are highly flammable with flash points usually below $30\text{ }^\circ\text{C}$. When the lithium ion cell is subject to various abuses, thermal runaway occurs and causes safety hazards. Although electrode materials and their state-of-charge play a more important role in deciding the consequences of the hazard, the flammable electrolyte solvents are most certainly responsible for the fire when a lithium ion cell vents. The seriousness of the hazard is proportional to the size of the cell, so flame-retarded or nonflammable lithium ion electrolytes are of special interest for vehicle traction batteries.

(4) Better Ion Transport. In most nonaqueous electrolytes, the ion conductivity is much lower as compared with aqueous solutions, and the part of the current that is carried by the lithium ions is always less than half.¹⁷⁶ Although it has been found that, for actual cell operation, the impedances at the interfaces of anode/electrolyte and cathode/electrolyte weigh far more than the bulk ion conductivity does, there is a semiempirical rule with very few exceptions: the higher the bulk ion conductivity of an electrolyte is, the more conductive the SEI or surface films formed in this electrolyte can be. On the other hand, the improvement in lithium ion transference number is certainly welcome, although its significance in liquid electrolytes might not be as high as in polymer electrolytes.

Since the inception of lithium ion technology, there has been a great deal of research aimed at improving the state-of-the-art electrolyte systems via various

approaches, including the development of new electrolyte solvents and salts and the application of functional additives. This section is dedicated to cover these efforts, most of which, although, have not been adopted in actual lithium ion electrolytes.

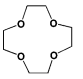
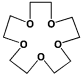
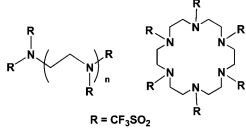
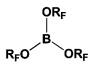
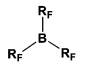
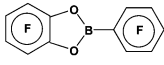
8.2. Functional Electrolytes: Additives

Instead of entirely replacing the major components of the current state-of-the-art electrolyte systems that cause problems, an efficient and economical alternative is to modify certain targeted functions of the electrolytes by incorporating a new component at small concentrations, known as an additive, so that its potential impact on the existing electrolyte can be minimized. In this way, the bulk properties of the electrolyte system can be maintained with the already proven merits such as cost and environmental concerns barely changed, since the presence of the new component in the bulk is negligible. On the other hand, the additive could significantly change the targeted property. This is especially pronounced in terms of interfacial properties because these additives are usually preferentially involved in interfacial redox processes before the main components of the bulk electrolyte are.

The additive approach has been used for lithium batteries to improve the surface morphology of a lithium electrode so that dendrite growth can be avoided.^{10, 372–375} Since the concept of the SEI was proposed by Peled et al.,³⁷ the emphasis has been placed on the reductive decomposition of these additives and the effect of the decomposition products on the physicochemical properties of the SEI. Obviously, when carbonaceous materials replaced lithium metal as anodes, the same line of thought led to the attempts at controlling the SEI chemistry by means of using various additives.³⁷⁶ During the past decade, this approach has been thoroughly studied, the focus of which has been placed at the SEI on the anodes, although additives targeting other cell components have also been developed. However, because of direct commercial interest, most of the work on additives has never been published in technical journals, especially the work that has eventually been accepted for use in commercial lithium ion cells. As an alternative, patent disclosures and conference abstracts did reveal scattered information about this aspect, although fundamental insight is usually unavailable in these forms of literature. In recent years, electrolytes containing additives have been named “functional electrolytes” by some researchers.³⁷⁷

According to the functions targeted, the numerous chemicals tested as electrolyte additives can be tentatively divided into the following three distinct categories: (1) those used for improving the ion conduction properties in the bulk electrolytes; (2) those used for SEI chemistry modifications; and (3) those used for preventing overcharging of the cells. Since the additives designed for the last purpose are usually compounds with oxidation potentials close to the operating potential of the cathode materials, the coverage of additive studies has included essentially

Table 8. Performance-Enhancing Additives for Bulk Properties

Additive Structures	Host Electrolyte System	Remarks	Ref.
 12-crown-4	LiBF ₄ /PEO,	Unhelpful with t_{Li} negative effect on cycle life;	379, 380, 382
 15-crown-5	LiClO ₄ /PC	toxic.	379
 R = CF ₃ SO ₂ aza-ethers	LiCl/THF or LiBr/THF	Low solubility in polar solvents; instability with LiPF ₆ .	384 385
 R _F = perfluoro- or partially fluoro-alkyls, perfluorophenyls etc borates	LiF/DME; CF ₃ CO ₂ Li/DME	Less electrochemically and thermally stable than borane.	386–388
 R _F = perfluoro- or partially fluoro-alkyls, perfluorophenyls etc boranes	LiX/DME (X=F, Cl, Br, I); LiX/PC/EC/DMC; LiF/DMC; CF ₃ CO ₂ Li/DME; C ₂ F ₅ CO ₂ Li/DME	Improves thermal stability of spinel. Improves thermal stability of LiPF ₆ . No negative effect on anode SEI.	313, 386, 387, 389–391
 boronates	LiF/DME; LiF/EC/DMC;	Most significant effect on ion conductivity. Cycling stability on both LiMn ₂ O ₄ and LiNi _{0.8} Co _{0.2} O ₂ .	392

every major component of the lithium ion cell that interacts with the electrolytes.

8.2.1. Bulk Electrolyte: Ion Transport

The ability of crown ether to coordinate with lithium ion has long been recognized, and in terms of the cavity size, 12-crown-4 and 15-crown-5 have been identified as the most efficient ligands for lithium ion.³⁷⁸ The idea of using these cyclic polyether compounds to promote the solvation of lithium salts in nonaqueous electrolytes was actively pursued when rechargeable cells based on lithium metal electrodes were still the commercial objective. It has been found that the presence of both 12-crown-4 and 15-crown-5 can effectively improve the solubility of the lithium salts and increase the ionic conductivity in the resultant electrolytes, especially when the solvents have low dielectric constants.^{379–383} This improvement in bulk ion conductivity is also reflected in the interface properties, as the charge-transfer resistance on the LiCoO₂ cathode is also reported to be reduced because of the presence of 12-crown-4.^{380,382} The electrochemical stability limits are not obviously influenced by crown ethers, but considering their ether-like structure, one should be concerned with their stability on the fully charged cathode surface in the long term. In polymer-based electrolytes, 12-crown-4 was also found to decrease the glass transition temperature of the system.³⁸²

On the other hand, since the increase of ion conductivity is realized through the coordination of lithium ions by crown ether molecules, the lithium

transference number is lowered as a result of its presence. In other words, the addition of crown ethers in nonaqueous electrolytes actually promotes the undesired anion transport. The main barrier for the application of crown ethers in electrolyte, however, is their toxicity. The environmental concern over the processing and disposal of any materials containing these crown ethers makes it impossible for industry to adopt them in large-scale applications.

To develop an additive that selectively coordinates with salt anions and frees lithium ion for conduction, McBreen and co-workers pursued a molecular design and tailor-synthesis approach that yielded several families of novel compounds based on nitrogen or boron centers with strongly electron-withdrawing substituents.

The first family of the so-called anion receptors was aza-ethers that were based on cyclic or linear amides, where the nitrogen core was made electron-deficient by the perfluoroalkylsulfonyl substituents so that these amides would preferentially interact with the electron-rich anions through Coulombic attraction, contrary to how their unsubstituted counterparts would act.^{384,385} Two selected representatives from the aza-ether family are shown in Table 8. When used as additives in solutions of various lithium halides LiX in THF, these novel compounds were found to increase both the solubility and the ion conductivity of these solutions. For example, the ion conductivity of the LiCl/THF solution was 0.0016 mS cm⁻¹, while the LiCl/THF solution with one of the linear aza-ethers containing eight perfluoroalkylsulfonyl substituents ($n = 5$ for the linear aza-ether shown in

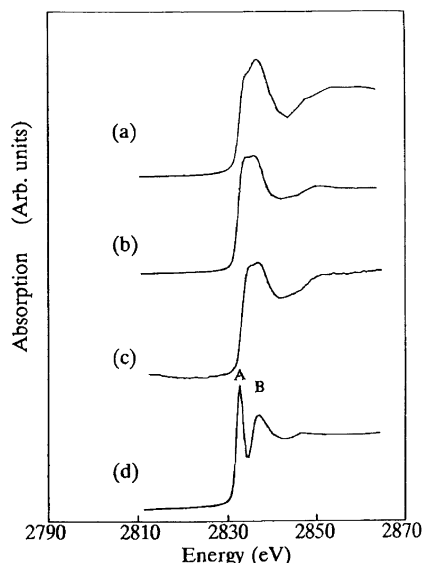


Figure 37. NEXAFS spectra at the K-edge of chloride for (a) LiCl crystal, (b) 0.2 M LiCl/THF, (c) 0.2 M LiCl/THF + 0.1 M aza-ether that does not have electron-withdrawing substituents on N, and (d) 0.2 M LiCl/THF + 0.1 M linear aza-ether with $n = 3$ in Table 8. Note the white line peak split when the electron-withdrawing substituents perfluoromethylsulfonyl are present. (Reproduced with permission from ref 384 (Figure 2). Copyright 1996 The Electrochemical Society.)

Table 8) exhibited an increase of ~ 900 times at 1.4 mS cm^{-1} .³⁸⁴ There was an obvious relationship between the ability of the aza-ether to coordinate the lithium cations and the extent by which ion conductivity was improved, since the latter proportionally increased with both the number of the electron-withdrawing substituents in the molecule and the electron-withdrawing ability of the substituents.^{384,385} For example, tosylsulfonyl, a weaker electron-withdrawing group as compared with perfluoroalkylsulfonyl, proved to be a much less efficient additive.³⁸⁵ On the basis of these dependences, it seemed that these aza-ethers did act as anion receptors in the nonaqueous solutions.

To further confirm that these aza-ethers actually coordinate with the salt anions, the authors used near X-ray absorption fine structure spectroscopy (NEXAFS) to study the coordination symmetry of the chloride anion in LiCl/THF solutions, in the absence or presence of aza-ether additives, and detected that the presence of the additives created a clear split in the Cl K-edge white line peak, as shown in Figure 37, indicative of the interaction between chloride and the electron-deficient nitrogen.³⁸⁴ Further XRD studies conducted on complex crystals grown from the cosolutions of the cyclic aza-ether and lithium halide salts supported the above NEXAFS observations with new Bragg peaks representing a larger d spacing ($\sim 15 \text{ \AA}$) in the crystal. Thus, the authors concluded that these new aza-ethers are indeed anion receptors, whose preference in coordinating ions was an exact opposite to that of the conventional crown ethers. With the addition of these molecules, the ion conductivity and the lithium transference number were enhanced simultaneously, a benefit that has rarely

been achieved thus far in nonaqueous lithium electrolytes.

Unfortunately, these aza-ethers showed limited solubility in the polar solvents that are typically preferred in nonaqueous electrolytes, and the electrochemical stability window of the LiCl-based electrolytes is not sufficient at the 4.0 V operation range required by the current state-of-the-art cathode materials. They were also found to be unstable with LiPF₆.³⁹⁰ Hence, the significance of these aza-ether compounds in practical applications is rather limited, although their synthesis successfully proved that the concept of the anion receptor is achievable by means of substituting an appropriate core atom with strong electron-withdrawing moieties.

In their continued efforts, McBreen and co-workers selected boron, an electron-deficient atom, as the core to build a series of new anion receptors using the same tactics with electron-withdrawing substituents. These new additives can be classified roughly into these three subcategories: borate,^{386–388} borane,^{313,386,387,389–391} and boronate.³⁹² Selected representatives from each category are also listed in Table 8.

Basically, these boron-based anion receptors are much more efficient in coordinating anions, perhaps because of the electron-deficient nature of boron, since most of them can even effectively dissociate LiF up to 1.0 M, which is virtually insoluble in most organic solvents, and yield ion conductivities as high as 6.8 mS cm^{-1} in DME.³¹³ Considering that the electrochemical oxidation potential for F⁻ is $\sim 5.9 \text{ V}$, this new electrolyte does indeed seem attractive in providing a wide electrochemical stability window. On a GC electrode, the electrochemical stability limits were found to be in the range 4.05–5.50 V, usually set by the oxidation of electrolyte solvents,^{388,392} while, on various cathode materials, stable cycling performance was observed with the upper voltage limit as high as 4.30–4.50 V.^{313,387,390} Cycling tests at elevated temperature ($55 \text{ }^\circ\text{C}$) further showed that the electrolytes based on LiF coordinated by these additives were stable when compared with the state-of-the-art electrolytes based on LiPF₆.³⁸⁹ Similar stability was also found on the carbonaceous anode surface, where the authors concluded that the presence of these anion receptors did not interfere with the formation of the SEI film, and the dissolution of the SEI was not detected even after heat treatment that would dissolve LiF salt.³⁹¹

Among the three subcategories, boronate compounds seemed to be the most efficient in coordinating with anions and enhancing lithium ion stability, although the number of electron-withdrawing substituents in boronate is only two. The authors thus inferred that the ability of these anion receptors to capture an anion depends not only on the electron-deficiency of the core atom but perhaps also on the steric hindrance presented by these substituents on the core. With only two substituents, the core of the boronates is obviously more exposed and therefore more easily accessible for an anion. The higher ion conductivity achieved by boronate additive therefore comes from the better balance between the electron-deficiency and steric openness of this compound as

compared with boranes and borates.³⁹² On the other hand, in terms of ion conductivity enhancement, borates and boranes behave similarly,³⁸⁶ though borates show less stability electrochemically and thermally than boranes.³⁸⁷

The solubility of these boron-based additives is also much higher than that of aza-ethers, and their effects on ion conductivity were studied in popular electrolyte solvent mixtures such as PC/EC/DMC³⁸⁷ or EC/DMC.^{388,389,392} Although for the salts such as LiPF₆, which are already well dissociated in these solvent mixtures, the enhancement in ion conductivity by the anion coordination might not be as pronounced as that for lithium halides, there is one advantage for LiPF₆ being used with these additives: the thermally unstable LiPF₆ is effectively stabilized by the presence of tris(pentafluorophenyl)borane (TPFPB), as indicated by the slow scan cyclic voltammetry experiments conducted on a spinel cathode surface after storage at 55 °C for 1 week.³⁹⁰ The authors attributed this stabilization to the coordination of PF₆ anion, which elongated the interatomic distance between Li and F. This hypothesis was supported by the conclusion of a molecular dynamic simulation published earlier, wherein Tasaki and Nakamura postulated that the reactivity of lithium cation and F⁻ would be suppressed by the elongated distance between them if an effective anion coordination was achieved.³⁹³

Since these anion receptors based on boron offer a wide variety of merits, their application seems promising if the cost and toxicology do not constitute any serious barrier for industry-scale productions.

8.2.2. Anode: SEI Modification

Due to the core importance of the SEI formation on carbonaceous anodes, the majority of the research activities on additives thus far aim at controlling the chemistry of the anode/electrolyte interface, although the number of publications related to this topic is rather limited as compared with the actual scale of interest by the industry. Table 9 summarizes the additives that have been described in the open literature. In most cases, the concentration of these interface-targeted additives is expected to be kept at a minimum so that the bulk properties of the electrolytes such as ion conduction and liquid ranges would not be discernibly affected. In other words, for an ideal anode additive, its trace presence should be sufficient to decouple the interfacial from bulk properties. Since there is no official standard available concerning the upper limit on the additive concentration, the current review will use an arbitrary criterion of 10% by weight or volume, above which the added component will be treated as a cosolvent instead of an additive.

With few exceptions, the additives that are intended for the modification of the SEI usually have high reduction potentials, which ensure that these additives are reduced on the anode surface before the bulk electrolyte components are involved. In other words, during the first charging of a lithium ion cell, an SEI with the chemical signature from an additive would have been formed before the potential of the carbonaceous anode reached the onset reduction

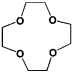
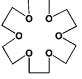
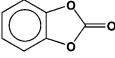
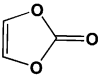
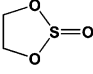
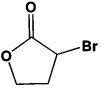
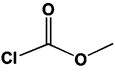
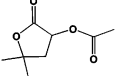
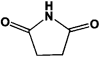
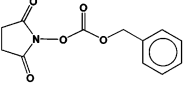
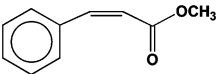
value for bulk electrolyte solvents, especially PC. Naturally, certain requirements have to be met by the decomposition products of the additives, such as insolubility in electrolytes, film compactness, and low impedance to lithium ion transport.

The search for potential SEI additives in the past decade has been carried out mainly on a trial-and-error basis until, recently, a semiempirical rule was developed to facilitate the screening process, which judges the readiness of a certain compound to be reduced on the anode by the energy level of its lowest unoccupied molecular orbital (LUMO).^{377,394} The basis of this rule is the assumption that a molecule with a lower energy level of its LUMO should be a better electron acceptor and, therefore, more reactive on the negatively charged surface of the anode. Sharing the view that interfacial stability originates from the reactivity, this rule is conceptually related to the selecting tool for the SEI-forming electrolyte components as proposed by Peled et al.,¹⁰⁶ despite the fact that the latter was based on a kinetic consideration (exchange current) of the molecule instead of a thermodynamic one (LUMO energy level). Quantum calculations have yielded LUMO energy levels for most of the commonly used electrolyte solvents as well as some of the tested SEI additives, which are compiled in Table 10.^{255,377,394,408} Apparently, the LUMO levels for all aliphatic cyclic carbonates are virtually identical, whereas structural modifications with an aromatic bond, double bond, or substitution of halogen atoms cause large decreases in the LUMO level.²⁵⁵ This trend is in good agreement with the experimental findings, since most of the additives that demonstrated promising performances in electrolytes indeed possess one of the active functionalities. A fairly linear relationship has been established between the LUMO energy level and the reduction potential for these additives.³⁷⁷

The current efforts with SEI additives usually aim at one of these two distinct but closely interrelated goals: (1) to minimize the irreversible capacity needed in the first cycle to form the SEI and (2) to enable the use of PC at higher concentrations in the electrolyte. While the former would generally benefit a lithium ion cell in terms of a more stable SEI, the latter is of special significance to the purpose of adapting the electrolytes based on PC to the highly graphitic anode materials so that the operating temperature can be expanded toward the lower limit without sacrificing energy density.

In the early era of lithium ion cell research, Aurbach et al. noticed that the presence of CO₂ in the electrolyte had pronounced effects on the lithiation behavior of graphitic anodes. A number of electrolytes, which were thought to be incompatible with graphite because they are based on solvents such as methyl formate or THF, delivered much improved performance under 3–6 atm of CO₂.²⁵⁰ They proposed that CO₂ participated in the formation of the SEI by a two-electron process, yielding Li₂CO₃, which assisted in the buildup of the protective surface film.²⁴⁹ However, in PC-based electrolytes, CO₂ presence proved to be ineffective,¹²³ while, in electrolytes based on carbonate mixtures such as EC/DMC, the

Table 9. Anode SEI Additives

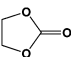
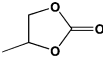
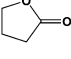
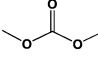
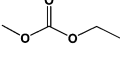
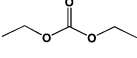
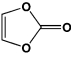
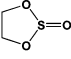
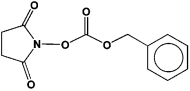
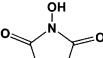
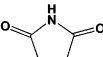
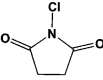
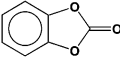
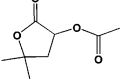
Additive Structures	Host Electrolyte System	Remarks	Ref.
CO₂	LiAsF ₆ /MF LiAsF ₆ /EC/DMC etc.	Non-effective for PC-suppression; internal pressure.	104, 123, 249, 250, 272
SO₂	LiClO ₄ /EC/DME LiAsF ₆ /MF LiAsF ₆ DMC, LiAsF ₆ /PC etc.	Effective for PC-suppression; anodic stability unknown; corrosive; safety hazard.	251 395 396
 12-crown-4	LiAsF ₆ /PC LiClO ₄ /EC/PC	Effective for PC-suppression; preferential solvation of Li ion; high concentration needed; toxic.	250, 261, 397, 398
 18-crown-6	LiClO ₄ /EC/PC	Not as effective as 12-crown-4; high concentration needed; toxic.	261
 catecholic carbonate (CC)	LiPF ₆ /PC/DEC	Effective for PC-suppression; anodically stable.	377, 409
 vinylene carbonate (VC)	LiIm/PC/EC/DMC LiPF ₆ /PC LiPF ₆ /DMC LiAsF ₆ /EC/DMC	Effective for PC-suppression; increases SEI stability at high temp.; anodically stable.	400 401 402 404
 ethylene sulfite (ES)	LiClO ₄ /PC	Effective for PC-suppression; anodically stable.	399
 α-bromo-γ-butyrolactone	LiPF ₆ /PC		410
 methyl chloroformate	LiPF ₆ /PC		410
 2-acetyloxy-4,4-dimethyl-4-butanolide	LiClO ₄ /PC	Preferential solvation of Li ion; Participation in SEI formation.	411
 succinimide	LiPF ₆ /PC/EMC		377
 N-benzyloxycarbonyloxysuccinimide	LiPF ₆ /PC/EMC		377
 methyl cinnamate			48b

effect of CO₂ seemed to be negligible.¹⁰⁴ These efforts could be viewed as the first attempts of modifying the SEI with electrolyte additives.

SO₂, on the other hand, was found to be a much more efficient additive, as its presence at less than

20% effectively suppressed the cointercalation of PC and supported the reversible lithium intercalation/deintercalation of graphitic anodes at low potentials.^{395,396} The reduction potential of SO₂ was found to be at ~2.7 V, far above that corresponding to the

Table 10. LUMO Energy Level and Reduction Potentials of Solvents and Additives

Solvent/Additive	LUMO/eV	Reduction Potential (vs. Li ⁺ /Li)		Refs.
		on GC	on GR	
 EC	1.175 0.97	0.9	0.8	212, 251, 377 255
 PC	1.235 1.02	1.0	0.78	214, 377 255
 γBL	1.049 0.91			377 255
 DMC	1.054	1.32		214, 377
 EMC	1.248 1.17			377 255
 DEC	1.288 1.21	1.32		214, 377 255
 VC	0.10 -0.14	1.4		377 255 214
 ES	0.035 0.03	1.6	1.8~2.1	377, 399 255
 BCSC	0.234	1.52		377
 N-hydroxysuccinimide (HSC)	0.208	1.6		377
 SC	0.186	1.6		377
 N-chlorosuccinimide (CSC)	-0.527	3.2	> 2.5	377
 CC	1.10			377, 409
 2-acetyloxy-4,4-dimethyl-4- butanolide	0.688		1.3~1.1	411

cointercalation/decomposition process of PC.^{251,395,396} Thus, Ein-Eli et al. believed that the SEI formation was initiated by the predominant decomposition of SO₂.^{395,396} On the basis of the FT-IR analysis of the graphitic anode surface, they suggested that, in addition to the solvent decomposition products, lithium

alkyl carbonate, the SEI also contained reduction products originated from SO₂ such as Li₂S and lithium oxysulfur species. An extra merit of SO₂ as an additive in electrolytes is the increase in ion conductivity, which is caused by its high dielectric constant and low viscosity.³⁹⁶ However, the obvious

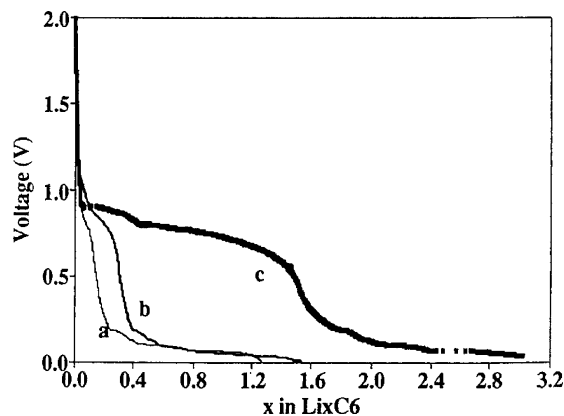


Figure 38. Effect of crown ethers on the irreversible capacity. Voltage profiles of a graphite anode in 1.0 M $\text{LiClO}_4/\text{EC}/\text{PC}$ (1:1) electrolyte containing (a) 1.0 M 12-crown-4, (b) 1.0 M 18-crown-6, and (c) no crown ethers. (Reproduced with permission from ref 261 (Figure 3). Copyright 1993 The Electrochemical Society.)

disadvantages of such an additive are the concerns over corrosion and the environmental and safety hazard issues related to the chemical nature of SO_2 . Its instability on cathode materials has not been well addressed either, since most of the published results were obtained on lithium/graphite half-cells.

Besides CO_2 and SO_2 , other gaseous species such as N_2O were also considered as additives,³⁷⁶ but none of these ideas seemed practical for the lithium ion industry, because the application of such approaches would certainly introduce an additional cost as well as safety concerns for the commercial cells, especially when increased internal pressure due to the gas production during prolonged cycling had already become a persistent problem for the manufacturers of industry-size lithium ion cells.

In the early 1990s, Wilkinson and Dahn realized that, in addition to enhancing ion conductivity, crown ethers could also reduce the irreversible capacity associated with the reduction process at 0.80 V when the electrolyte was based on high concentrations of PC.³⁹⁷ Shu et al. studied the phenomenon by using 12-crown-4 and 18-crown-6 as additives in $\text{LiClO}_4/\text{EC}/\text{PC}$ and established the direct connection between the decrease in gas evolution associated with the 0.80 V irreversible process and the addition of 12-crown-4.³⁹⁸ As Figure 38 shows, the effectiveness of these crown ethers in suppressing the PC cointercalation/decomposition seems to be related to the cavity size,²⁶¹ knowing that 12-crown-4 serves as a better chelating agent for lithium ion than 18-crown-6.³⁷⁸ The authors suggested that, unlike most of the additives that obey the empirical rule of the LUMO energy level, a crown ether might not be chemically involved in the formation of the SEI but rather affect this process indirectly by means of preferential solvation of lithium ions. Thus, the exclusion of PC molecules from the solvation sheath rather than the reductive decomposition of crown ethers is responsible for the reduced irreversible process at 0.80 V.³⁹⁸

Their hypothesis was confirmed by the work of Aurbach and co-workers, who performed detailed FT-IR investigations on the graphitic anode surface that

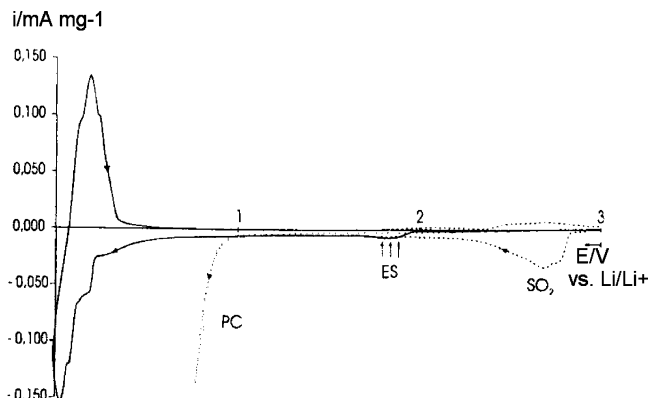


Figure 39. Stabilization of a graphitic anode in 1.0 M LiClO_4/PC electrolyte by 5% ES. For comparison, the voltammograms of a graphitic anode in 1.0 M LiClO_4/PC electrolyte with 10% SO_2 were also shown. (Reproduced with permission from ref 399 (Figure 3). Copyright 1999 The Electrochemical Society.)

was cycled in electrolytes containing 12-crown-4.²⁵⁰ Since the peaks corresponding to the possible reduction products of 12-crown-4 were absent in the spectra, they concluded that the effect of crown ether was not due to its participation in the buildup of the SEI. Instead, the prevention of graphene exfoliation was very likely due to the absence of PC molecules in graphene interlayers, a direct result of its expulsion from the lithium ion solvation sheath. This was even so when the concentration of 12-crown-4 was only one tenth of the salt concentration. The effectiveness of 12-crown-4 in suppressing PC cointercalation/decomposition is further demonstrated by the cycling of the graphitic anode in electrolytes based on neat PC.²⁵⁰ Considering that the main signals collected from the anode surface during the experiment were at $\sim 1661\text{ cm}^{-1}$, which is characteristic of the carbonyl stretching in lithium alkyl carbonate, the authors suggested that PC was forced to be reduced on the surface via a single-electron process. This seemed to be in good agreement with the previous report that only within graphene structures would PC likely undergo reduction via a two-electron process and result in exfoliation.

Despite the highly efficient performance of crown ethers in reducing the irreversible capacity at the anode side, especially when PC-based electrolytes were used, the toxic nature of these compounds still prevented their application in commercial lithium ion cells.

A sulfur analogue of EC, ethylene sulfite (ES), was proposed as an additive for PC-based electrolytes by Winter and co-workers,³⁹⁹ apparently because of its structural similarity to EC and its potential, under reductive conditions, to release SO_2 , a known additive that effectively suppresses PC decomposition.^{395,396} As the voltammetry in Figure 39 shows, ES in only 5% presence successfully eliminated the exfoliation of the graphite anode, whereas 10% SO_2 failed. The irreversible process corresponding to the reduction of ES occurred at $\sim 2.0\text{ V}$, lower than that of SO_2 by $\sim 0.80\text{ V}$; however, the quantity of charge associated was much lower. According to the authors, the above apparent gap between the reduction potentials of ES

and SO_2 actually excluded the self-suggesting assumption that the SEI-forming ability of ES should stem from its tendency to release SO_2 , which in turn participates chemically in the buildup of SEI in a mechanism suggested by Ein-Eli et al.^{395,396} Furthermore, the reduction of SO_2 was reversible, whereas the reduction of ES did not seem to be, as evidenced by the absence of any anodic current in Figure 39.

On the other hand, the attempt to use ES as a bulk solvent proved to be unsuccessful because of the high irreversible capacity caused by the reduction of ES, although it looked like the reversible capacity associated with lithium intercalation was not affected by the irreversible process at 2.0 V. Considering that these results were obtained in an anode half-cell where lithium was the excess material, one should realize that the irreversible reduction of ES would cost the capacity of a full lithium ion cell. Therefore, ES should only be used as an additive at small concentrations.

The anodic stability of the electrolyte was not negatively affected by the presence of ES in LiClO_4/PC , as evidenced by the cyclic voltammetry carried out on the LiMn_2O_4 surface. The onset of major electrolyte decomposition, seemingly contributed by the oxidation of PC, occurs at ~ 4.8 V, which would allow the safe use of most state-of-the-art cathode materials based on LiCoO_2 , LiMn_2O_4 , or LiNiO_2 . The first cycling of the cathode half-cell, $\text{Li}/\text{LiMn}_2\text{O}_4$, was shown in the report, but without the extended cycling of this cell or full lithium ion cells.³⁹⁹

Among the various additives tested, vinylene carbonate (VC) might be the most famous in the lithium ion research and development community, although the number of publications related to it seems to be rather small. Its importance can be evidenced by the number of companies that vied for the patent rights for it.^{400–402}

The reactivity of VC apparently arises from its polymerizable vinyl functionality and its structure of high strain, which is caused by the sp^2 -hybridized carbons on the ring (Tables 9 and 10).⁴⁰³ The small concentration of VC can effectively reduce the irreversible capacity associated with the 0.80 V process in almost any PC-based electrolyte,⁴⁰⁰ and its presence, even in bulk concentrations, does not constitute any instability on the charged surface of either anode or cathode materials. In the latter case, an electrolyte of 1.0 M $\text{LiPF}_6/\text{PC}/\text{VC}$ performed reversibly up to 4.3 V with a LiMn_2O_4 cathode.⁴⁰¹ In a recent report Aurbach and co-workers thoroughly described the effect of VC as additive in electrolytes for lithium ion cells based on the graphitic anode and LiMn_2O_4 or LiNiO_2 cathode, using various techniques including EIS, EQCM, FT-IR, and XPS.⁴⁰⁴ According to the voltammetry results of their work, there was no discernible characteristic reductive process in voltammetry that could be unambiguously assigned to the reduction of VC on the graphitic anode, in sharp contrast to the cases of other additives that showed distinctive reduction processes at high potentials. The only difference between VC-containing and VC-free electrolytes was the much-reduced irreversible capacity at 0.90–0.80 V. This visual absence of the VC

reduction process could be attributed either to the possibility that the passivation of the graphitic anode by the decomposition products was so efficient that the reduction of VC only occurred to a trace extent or to the possibility that the scan rate employed in the experiments (1.0 mV s^{-1}) was too fast for any quasi-equilibrium to be established between the additive VC and the anode surface, the result of which was the total drowning of the VC reduction peak by the main event occurring at the lower potentials. According to a separate voltammetry study carried out on inert electrodes (Au and GC), VC could be reduced irreversibly at 1.4 V.²¹⁴

EIS results indicated that the impedance on a graphite surface was much lower in the presence of VC; however, at elevated temperatures (60°C), it became higher than those of VC-free electrolytes. EQCM using a gold-plated quartz crystal detected that the mass accumulation in VC-containing electrolytes was higher by 50% as compared with the cases of VC-free electrolytes during voltammetric scanning between 3.0 and 0.5 V, indicating that the reactive VC might be profoundly involved in the formation of the SEI. The comparison between the FT-IR spectra collected on both gold mirror and graphite electrodes for VC-free and VC-containing electrolytes further confirmed the participation of VC with characteristic absorptions at $\sim 3000 \text{ cm}^{-1}$, representing the possible existence of polymeric moieties in addition to the alkyl carbonates observed commonly on a graphitic anode that was cycled in carbonate-based solvents.

The surface chemistry of VC on graphite was also semiquantitatively investigated by C 1s and F 1s spectra in XPS analyses,⁴⁰⁴ as shown by Figure 40. Apparently, the presence of VC drastically reduced the content of LiF in the SEI, as indicated by the LiF signal at 685 eV, which only appeared as a shoulder for that of PVdF (anode binder) at 687 eV while it was the predominant species in VC-free electrolyte. On the other hand, the abundance of lithium alkyl carbonate in the SEI as represented by the signal at 289 eV was increased with VC concentration. This improvement of the SEI chemistry with higher lithium alkyl carbonate content and lower LiF content was reflected in the increased stability of a VC-containing electrolyte, which demonstrated a more stable performance in a lithium/graphite anode half-cell at an elevated temperature of 60°C , while the identical cell based on VC-free electrolyte suffered constant capacity loss.⁴⁰⁴

The possible impact of VC on the stability of an electrolyte at a cathode surface was also investigated and no obvious negative effect of VC on either LiNiO_2 (Figure 41) or LiMn_2O_4 was observed at up to 4.2 V. A slight kinetic improvement due to the presence of VC, as indicated by the better resolved peaks and higher current response, was observed in the slow scan voltammetry, as shown in Figure 41.⁴⁰⁴ FT-IR studies on the cycled cathode surface indicated the formation of surface species that were probably oligomeric VC, originating from the cationic polymerization on the delithiated cathode surfaces.

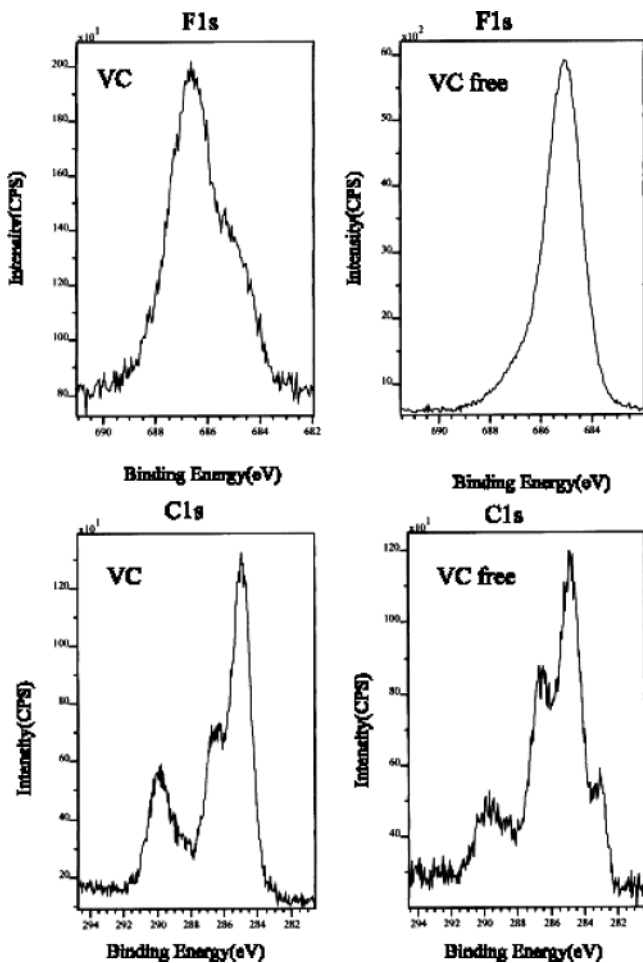


Figure 40. XPS C 1s and F 1s spectra of graphitic anodes cycled in 1.0 M LiAsF₆/EC/DMC electrolyte. 5% VC was used as additive in the left spectra. Note the different scales for the two F 1s spectra. (Reproduced with permission from ref 404 (Figure 10). Copyright 2002 Elsevier.)

In conclusion, many authors believed that VC was a rather effective additive for chemical modification of the anode SEI. It not only reduced the irreversible capacity during the initial charging process of lithium ion cells, but it also improved the stability of the SEI at elevated temperatures. Because of VC participation, the new SEI chemistry contained polymeric species that stemmed from the reductive polymerization of VC, which was characterized by a high content of alkyl carbonate functionalities. Comparative studies of this additive in commercial lithium ion cells proved that VC presence improved cycle life performance.^{405–407}

It should be mentioned that the commercially available VC usually contained a small percentage (<2%) of prohibiters that stabilized the reactive VC from polymerizing upon storage. These compounds were usually radical scavengers such as 2,6-di-*tert*-butyl-*p*-cresol (DBC) or butylated hydroxytoluene (BHT). Recently, reports pointed out that the presence of these prohibiters actually had a negative impact on the anodic stability of VC on various cathode materials, and VC of high purity was of vital importance in obtaining reproducible performance in lithium ion cells.^{404,408}

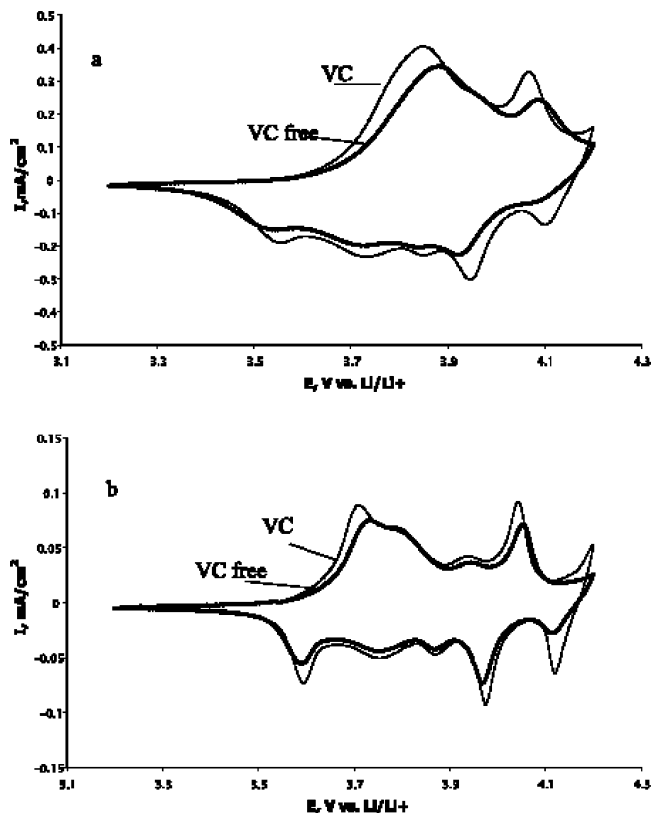


Figure 41. Cyclic voltammograms of a LiNiO₂ cathode in VC-free and VC-containing 1.0 M LiAsF₆/EC/DMC electrolyte at scan rates of (a) 0.50 mV s⁻¹ and (b) 0.1 mV s⁻¹. (Reproduced with permission from ref 404 (Figure 11). Copyright 2002 Elsevier.)

Another highly efficient additive for the anode SEI is catecholate carbonate (CC), reported by Wang et al., which has a benzene ring fused with a functionality structurally similar to EC (Tables 9 and 10).^{377,409} Like VC, in small percentage (~2%), it suppresses the irreversible capacity due to PC decomposition/cointercalation at 0.80 V and supports extended cycling of the graphitic anode in LiPF₆/PC/DEC. A study on the concentration-dependence of this irreversible capacity indicated that the optimum content of CC lies between 0.5% and 2%. The authors postulated that the mechanism through which CC stabilized the graphitic anode against exfoliation by PC should involve the direct participation of CC in the formation of the SEI, since its small concentration does not allow for preferential solvation as crown ether does. They further proposed that in electrolyte solutions CC served as a radical scavenger and quenched PC radical anions so that the continued reduction of PC via a two-electron process was inhibited.

The anodic stability of the electrolyte containing 2% CC was tested on a LiCoO₂ cathode, and no obvious oxidative decomposition was observed. It must be noted, though, that the above conclusion was based on a voltammetry experiment conducted with a relatively high scanning rate (15 mV s⁻¹). The performance test of the electrolyte LiPF₆/PC/DEC with 2% CC in a full lithium ion cell was shown to deliver a slightly fading capacity when cycling between 2.75 and 4.10 V.

The continued efforts in this area in recent years generated a series of reactive compounds as potential candidates, which include halogenated species such as bromo- γ -BL,⁴¹⁰ other γ BL derivatives,⁴¹¹ compounds containing vinyl groups,^{412,413} and compounds that belong to the succinimide family³⁷⁷ (Tables 9 and 10). Most of these additives were reported to be effective in reducing the irreversible capacities in the first charge process, while some also successfully eliminated the cointercalation of PC and avoided the exfoliation of graphitic anodes. Among these works, one interesting mechanistic study was carried out by Matsuo et al., who employed a ¹³C NMR technique to investigate the effect of γ BL derivatives on lithium solvation and found that PC molecule was excluded from the solvation sheath of lithium ions by these additives.⁴¹¹ Thus, these authors suggested that γ BL derivatives might suppress PC decomposition via a mechanism that combines both preferential solvation as crown ethers do and direct chemical participation as most of the other additives do, although the preferential solvation effect would be negligible when the concentration of these additives is far below 1.0 M.

The work on SEI-modification additives is currently carried out throughout the lithium ion research community, and candidates of new structure are being tested in large numbers. As a result, the major lithium ion manufacturers have applied various additives in their electrolyte formulations. However, the lack of information in the open literature makes the in depth and comprehensive review of this new branch of electrolyte chemistry difficult.

8.2.3. Cathode: Overcharge Protection

Unlike the anode-targeted additives discussed in the preceding part, the additives intended for cathode protection have a much longer history than lithium ion technology itself and were originally developed for rechargeable cells based on lithium metal anodes and various 3.0 V class cathode materials.

It has been long recognized that the accidental overcharge of lithium cells would lead to irreversible decomposition of electrolyte components, which is mainly the oxidative decomposition of solvents on a cathode surface and whose reaction heat and gaseous products are responsible for the hazardous thermal runaway. Since the overwhelming majority of the charging protocols are based on cell voltage as the indicator for the end-of-charge, such accidents are especially likely to occur for multicell battery packs in which cells with mismatched capacities are put in series. To avoid the cell degradation or hazards related to overcharging, cells for battery packs must be handpicked to match a nominal capacity or each individual cell within the pack must be regulated externally with electronic devices, such as positive temperature coefficient (PTC) resistors or integrated circuits (IC). However, both remedies add to the manufacturing cost and lead to a lower energy density of the cells.

As an alternative, Abraham and co-workers proposed an electrochemical mechanism built in the electrolyte that is able to shunt the excess charge

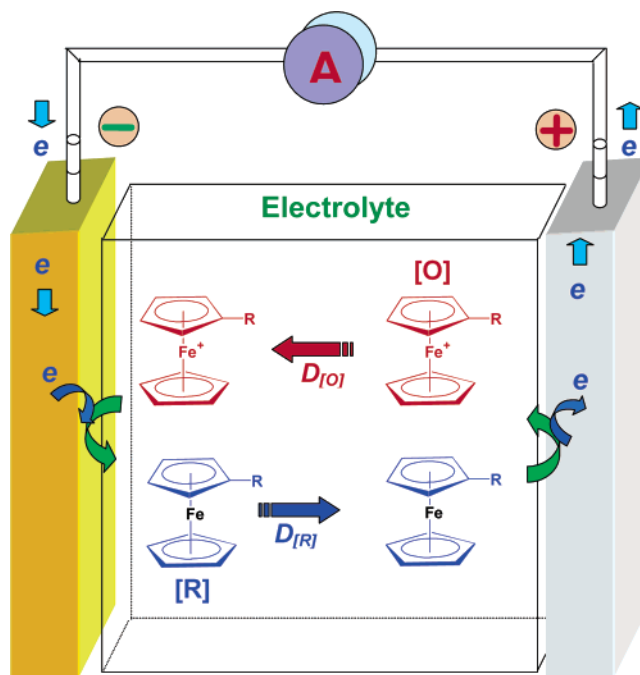


Figure 42. Schematic representation of the shuttling occurring in an overcharged cell that is based on electrolytes containing redox additive as protection.

injected into the cell when overcharge occurs.^{414,415} The mechanism, intended to prevent the oxidative decomposition of electrolyte solvents at the cathode surface, was based on a redox additive that has an oxidation potential slightly lower than that of the electrolyte anodic decomposition and would serve as a current shuttle under the condition of overcharge, as Figure 42 shows. On an overcharged cathode surface, the redox additive would be transformed into its oxidized form [O], which, via diffusion across the cell electrolyte, would be reduced back to its original (reduced) state [R] on the surface of a negatively charged anode. Thus, the reversible nature of the redox couple [R]/[O] would maintain the above cycle of “oxidation–diffusion–reduction–diffusion” indefinitely and hence lock the cathode potential at the oxidation potential of [R] until termination of the charge. Ideally, no permanent damage would be done to the cell capacity during the redox shuttling, since the Faradaic current was only carried by the reversible redox reactions, while, energetically, the excess charge injected would be neither stored in the cathode nor consumed in reversible decompositions but rather dissipated in the form of heat associated with the shuttling current. Therefore, the net result of the above redox shuttling mechanism during overcharging could be viewed as a controlled internal short, and the effectiveness of a certain redox additive could be evaluated in terms of the maximum overcharge current it can shuttle.

Narayanan et al. conducted a theoretical analysis on the cell parameters that determined this maximum shuttling current.⁴¹⁶ By assuming that the mass transport of the redox couple [R]/[O] is mainly realized by means of diffusion—which is reasonable because the low concentration of [R]/[O] at the additive level makes the field-assisted migration negligible—they applied the finite linear diffusion

approximation to gain the diffusion-limited steady-state overcharge current i as

$$i = \frac{nFADC}{l} \frac{\exp\left\{nF\left(\frac{E_c - E_c^0}{RT}\right)\right\}}{1 + \exp\left\{nF\left(\frac{E_c - E_c^0}{RT}\right)\right\}} \quad (12)$$

where F , A , D , l , C , E_c , and E_c^0 are the Faraday constant, electrode area, diffusion coefficient for [R] or [O], interelectrode spacing, total concentration of the additive ([R] + [O]), single electrode potential of the cathode, and formal potential of the redox couple [R]/[O], respectively.

Obviously, when no overcharging exists (i.e., $E_c - E_c^0 \ll 0$), the shuttle current is negligible, while the redox reaction remains not activated.

On the other hand, when overcharge does occur, eq 12 could be much simplified on the condition that $E_c - E_c^0 \gg RT/nF$, and eq 12 is transformed into

$$i = \frac{nFADC}{l} = i_d \quad (13)$$

The applied condition represents a relatively large positive deviation of the single-electrode potential for a cathode from the oxidation potential of the redox couple [R]/[O]. For a single-electron reaction at room temperature, the above criterion for the deviation $E_c - E_c^0$ corresponds to $RT/nF = 0.026$ V, and one would therefore expect the simplification that leads to eq 13 to hold true for most of the overcharge situations encountered in practical applications.

Thus, eq 13 expresses the limiting overcharge current that can be sustained by a particular choice of redox additive and electrochemical conditions, and it suggests that this maximum diffusion current i_d is independent of the cell potential or the formal potential of the redox couple but is solely determined by its concentration and diffusion coefficient in the electrolyte. In the case that the overcharge current becomes too high for the redox couple to shuttle, as would happen when a large terminal voltage is mistakenly set during constant potential charge, any excess current over the maximal limit specified by eq 13 would continue to delithiate the cathode material and cause irreversible decompositions, and safety hazards would eventually be caused by this overflowing charge.

To maximize the current limit that could be shunted by redox additives so that the occurrence of such irreversible processes due to overflowing current could be more efficiently suppressed, the redox additive apparently should be present in the electrolyte at high concentrations, and both its oxidized and reduced forms should be very mobile species. Where the criteria for selecting potential redox additives are concerned, these requirements can be translated into higher solubility in nonaqueous media and lower molecular weight. In addition to solubility and diffusion coefficients, the following requirements should also be met by the potential redox additives: (1) the formal potential of the redox couple [R]/[O] should be lower than the onset potential for major decom-

position of electrolyte solvents but high enough to ensure a full utilization of cathode active mass; (2) the electrochemical reversibility of the redox reactions should not degrade discernibly within the time frame of cell life; (3) the additive should be inert before and after activation by overcharging (i.e., both oxidized and reduced forms of the additive must not react with any electrolyte components).

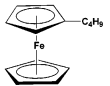
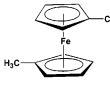
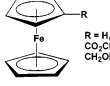
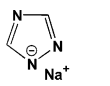
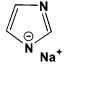
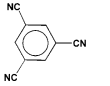
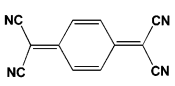
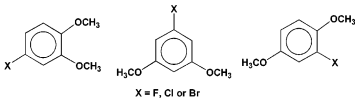
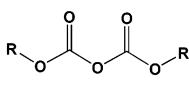
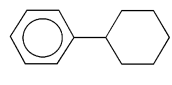
During the past two decades, the redox shuttle mechanism has been influencing researchers as the most promising solution to the challenge of cathode overcharge, and among the limited number of publications, most of the additives were selected based on their redox potentials.

The cathode materials employed for the early lithium-based systems were 3.0 V class oxides or sulfides; thus, the redox potential for the additive should be located in the neighborhood of 3.2–3.5 V. Accordingly, the first generation redox additive proposed by Abraham et al. was based on the iodine/iodide couple,⁴¹⁵ which could be oxidatively activated at the cathode surface at 3.20 V and then reduced at the lithium surface.^{414,415,417–420} For most of the ether-based solvents such as THF or DME that were used at the time, the oxidation potential of iodide or triiodide occurred below that of their major decompositions, while the high diffusion coefficients of both iodine and iodide in these electrolyte systems ($\sim 3 \times 10^{-6}$ cm² s⁻¹) offered rapid kinetics to shuttle the overcharge current. Similarly, bromides were also proposed.^{418–420} However, this class of halide-based additives were deemed impractical due to the volatility and reactivity of their oxidized forms (halogen).

The well-known redox compounds based on the metallocene family, which are much more amicable than halide/halogen couples, were also first investigated by Abraham and co-workers as redox shuttles.^{421,422–426} These organometallic complexes consist of a metal core—usually Fe or Co—coordinated by two cyclopentadienyl ligands, as Table 11 shows, and they are able to undergo reversible redox reactions in the neighborhood of 3.2–3.5 V.⁴²¹ The electron exchange occurs through the change of valence orders of the metal core; however, the formal potential of this redox process not only varies with the metal core but also is sensitive to the substitution on the cyclopentadienyl rings.⁴²⁴ The number as well as the chemical nature of the substituents (electron-donating or -withdrawing) could affect the potential by as much as ± 0.30 V.⁴²⁷ Theoretically, this substitution-sensitivity offers a convenient tool to tailor the redox potential of these metallocenes for various cathode materials.^{422,425}

Abraham et al. tested the performance of an *n*-butyl-substituted ferrocene in a lithium/TiS₂ cell, where LiAsF₆/THF or LiAsF₆/2MeTHF was used as an electrolyte. They found that, under overcharge conditions, the voltage of the cell containing ferrocene as an additive leveled off at 3.25 V, corresponding well to its redox potential of 3.18–3.50 V, while the reference cell without additive was overcharged up to 5.0 V, corresponding to the decomposition of THF.⁴²² No capacity loss was observed in successive cyclings after the overcharge test, thus confirming

Table 11. Cathode Surface Layer Additives: Overcharge Protection

Additive Structures	Host Electrolyte System	Type	E_{onset}/V	Ref.
I/I ₂	LiAsF ₆ /THF	Redox	3.2~3.5	414, 415, 417~420
 <i>n</i>-butylferrocene		Rodox	3.18	421, 422, 423
 1,1'-dimethylferrocene	LiAsF ₆ /EC/2-Me-THF	Rodox	~ 3.0	416
 ferrocene derivatives R = H, Bu, COCH ₃ , COC ₂ H ₅ , CO ₂ CH ₃ , CONH ₂ , CH ₂ N(CH ₃) ₂ , CH ₂ OK, CHO, (CH ₃) ₂ , CH ₂ OCH ₃	LiAsF ₆ /EC/PC	Rodox	3.09~3.55	429
 1,2,4-Triazole, Na salt	LiIm/PEO	Rodox	3.1	431
 imidazole, Na salt	LiIm/PEO	Rodox	2.5	431
 1,3,5-tricyanobenzene (TCB)	LiIm/PEO	Rodox	2.9	431
 tetracyanoquinodimethane (TCNQ)	LiIm/PEO	Rodox	3.5	431
 substituted benzenes X = F, Cl or Br	LiPF ₆ /PC/DMC	Rodox	3.93~4.27	432, 434
 pyrocarbonate		Gas/CID ^a	> 4.0	48b, 440
 cyclohexylbenzene		Gas/CID	> 4.0	48b, 440

CID: current interrupter device activated by internal pressure.

that the additive based on ferrocene had little deleterious effect on the stability of the cell components. These promising results initiated a new round of research activities based on structural modifications on the cyclopentadienyl rings.⁴²⁵⁻⁴²⁹

In a systematical study, Golovin et al. investigated a series of metallocene derivatives in terms of their redox potentials, mass transport properties, and chemical and electrochemical stabilities in both electrochemical test cells and commercial-size AA rechargeable cells.⁴²⁹ Figure 43 shows the complete voltammetric scan of the ferrocene-containing elec-

trolyte on a GC working electrode, where the peaks indicated as O2 and O3 represent the oxidation of cyclopentadienyl rings and electrolyte solvents, respectively, while R2 and R3 stand for the reductive decomposition of electrolyte solvents and the deposition of lithium from solution. Obviously, on the anode side, the limit was set by the lithium deposition, as the reduction of solvents only occurs in the first charging cycle in a lithium-based cell. The anodic limit, on the other hand, was imposed by the O2. The redox potential of the shuttle agent ferrocene was indicated by a pair of closely located peaks [R1]/[O1]

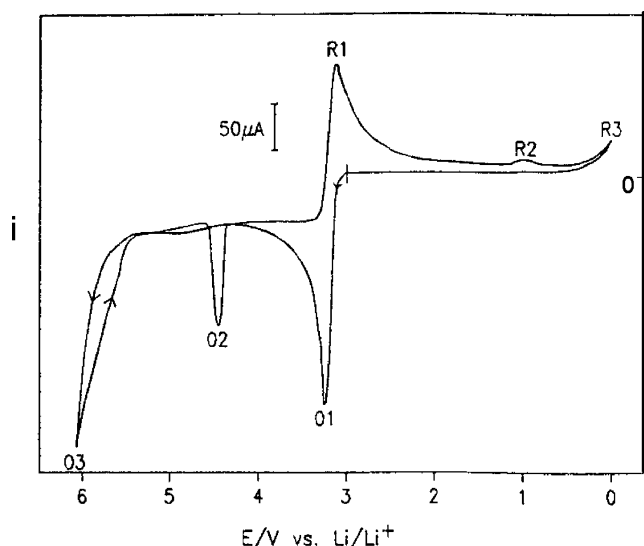


Figure 43. Cyclic voltammograms of 0.08 M ferrocene in 1.0 M LiAsF₆/EC/PC conducted at 20 mV s⁻¹. (Reproduced with permission from ref 429 (Figure 2). Copyright 1992 The Electrochemical Society.)

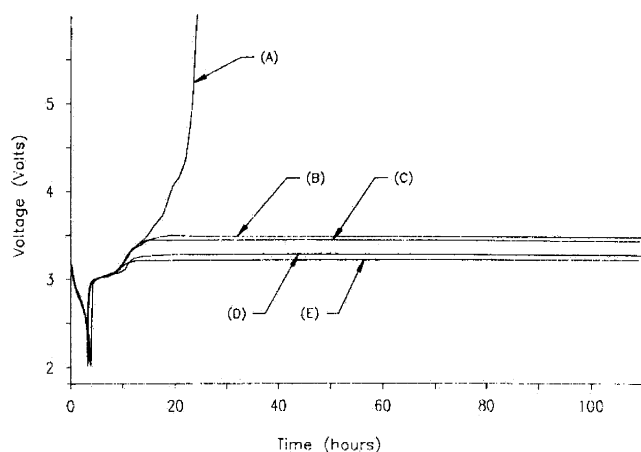


Figure 44. Voltage profile of overcharged Li/Li_xMnO₂ AA cells containing different substituted ferrocenes as redox additives in 1.0 M LiAsF₆/EC/PC: (A) reference; (B) ferrocenyl ketone; (C) dimethylaminomethylferrocene; (D) ferrocene; (E) *n*-butylferrocene. (Reproduced with permission from ref 429 (Figure 6). Copyright 1992 The Electrochemical Society.)

at ~3.25 V, which occurred reversibly. With various substitutions on the cyclopentadienyl rings (Table 11), the redox potential could be adjusted to occur in the range 3.09–3.55 V. For cathode materials based on Li_xMnO₂, whose potential at full charge is 3.50 V, these substituted ferrocenes could make feasible candidates as redox additives, since their redox potentials can be adjusted to be between those of the major oxidative decomposition of electrolytes (>4.0 V) and the cathode full utilization (3.50 V).

The effect of these ferrocene-based additives on overcharge protection is shown in Figure 44, where AA cells based on lithium, Li_xMnO₂, and electrolytes with or without additives were overcharged. In the absence of these redox shuttles (A), the cell voltage continues to rise, indicating the occurrence of major irreversible decompositions within the cell whereas the presence of shuttle agents (B–E) locks the cell potential in the vicinity of their redox potentials

indefinitely. The successive cyclings of these overcharged cells showed that no adverse effect was caused by these ferrocene additives on cycle life. Furthermore, the reversibility of the redox reactions and the long-term stability of them with respect to other cell components were also tested. The authors had observed over a hundred “turnovers” of these ferrocene shuttles in the cell while demonstrating a reversible shuttle effect, and prolonged cyclings of these cells showed excellent cycle life, indicating the good compatibility between ferrocene additives and the bulk electrolytes.

The practical importance of overcharge protection by these ferrocene additives was further confirmed with a battery pack in which cells with mismatched capacity were intentionally connected in series and subjected to overcharge.⁴²⁷ As expected, the added ferrocene acted to prevent the cell with low capacity from being overcharged as the other cell continued to charge. At the end of the charge, all cells had attained essentially the same state-of-charge, and successive discharge and recharge showed excellent cycling characteristics, despite the mismatched capacities in the pack. If no redox additives were used, such mismatch in capacity would result in poor cycle life or even hazards.

The ability of these ferrocenes as carriers for shuttling current through the cell was determined by charging the cell with a constant current at the fully charged state (3.5 V). When the interelectrode spacing was between 25 and 50 μm, the limiting shuttle current of these ferrocenes was found to be as high as 2.0 mA cm⁻².⁴²⁹

One adverse effect of these additives on cell performance seemed to be related to their blocking of ionic paths on the surface of cathode materials, as indicated by the reduced power capabilities in the presence of ferrocenes. Analysis on the concentration changes of ferrocene additives in the electrolyte solutions before and after their exposure to cathode materials established that an adsorption of ferrocene species occurred on the cathode surface, 93% of which would be covered when as low as 0.3 M ferrocenes were present in the electrolyte solution.⁴²⁹ This surface deactivation resulted in the loss of both rate capability and capacity.

Redox shuttles based on aromatic species were also tested. Halpert et al. reported the use of tetracyanoethylene and tetramethylphenylenediamine as shuttle additives to prevent overcharge in TiS₂-based lithium cells and stated that the concept of these built-in overcharge prevention mechanisms was feasible.⁴³⁰ Richardson and Ross investigated a series of substituted aromatic or heterocyclic compounds as redox shuttle additives (Table 11) for polymer electrolytes that operated on a Li₂Mn₄O₉ cathode at elevated temperatures (85 °C).⁴³¹ The redox potentials of these compounds ranged between 2.8 and 3.5 V, and like ferrocene-based additives, they are only suitable for cathode materials of low voltage.

Accompanying the commercialization of lithium ion technology, the emergence of 4.0 V class cathode materials based on spinel, LiCoO₂, and LiNiO₂ presents a more stringent requirement for the selection

of shuttle additives, since few redox couples could undergo reversible turnover at such high potentials near 4.0 V. Among those few were some organometallic complex compounds with Fe, Ru, Ir, or Ce as metal cores and phenanthroline or bipyridine as ligands. Their redox potentials were found to be in the vicinity of 4.0 V, and like ferrocenes, fine adjustment in the redox potential could be realized by varying the chemical nature, number, and relative positions of the substituents on the aromatic rings.⁴³² However, these complexes had very limited solubilities (<50 mM) in nonaqueous media, which, in combination with their large molecular weight and size (hence, low diffusion coefficient), contributed to a low shuttle current limit. Tests in a cathode half-cell using $\text{LiPF}_6/\text{PC}/\text{DMC}$ showed that under overcharge the hike in cell voltage was only delayed, but not locked, at the level of the redox potential, apparently due to the low limiting diffusion current that these organometallic redox additives can carry.⁴³²

Inspired by earlier reports that some substituted aromatic compounds can be reversibly reduced and oxidized in the neighborhood of 4.0 V,⁴³³ Adachi et al. focused their attention on a series of anisole-based compounds, which have two methoxy substituents and one halogen substituent on the benzene ring (Table 11).⁴³² The high solubility of this class of organic compounds in carbonate-based electrolytes makes them a family of more promising candidates than the metal complexes. The cyclic voltammetry of one of those potential redox additives, 4-fluoro-1,2-dimethoxybenzene, was shown in Figure 45a. Of the two electrochemical processes, as represented by the two pairs of peaks located between 4.0 and 4.75 V, the one on the positive side is similar to the characteristic profile of a reversible redox couple as judged by the separation of the anodic and cathodic peaks as well as their shape. Similar behavior was also observed for bromo-substituted counterparts with higher shuttle voltage.

A correlation was found between the reversibility of these redox couples and the relative positions of the two methoxy groups. Among the various anisole compounds investigated, only those with the two methoxy groups at 1,2- (ortho-) and 1,4- (para-) positions showed reversibility at the 4.0 V region, while 1,3- (meta-) counterparts were oxidized irreversibly, as indicated by the absence of the corresponding reduction process in Figure 45b. The authors proposed that the stabilization of the oxidized product by methoxy substituents plays an important role in determining whether the reaction is reversible. Similar to the rationale for the aromatic electrophilic substitution that is familiar to organic chemists, the canonical structures of the possible oxidized states with the largest contribution are used to explain this stabilization effect by substitutes, as shown in Scheme 28.

It was assumed that, during an oxidation of these aromatic moieties, an electron would be removed from the aromatic ring at the location where the electron-donating methoxy is positioned. Whether this oxidation is reversible critically depends on the stability of the produced cationic product. On the

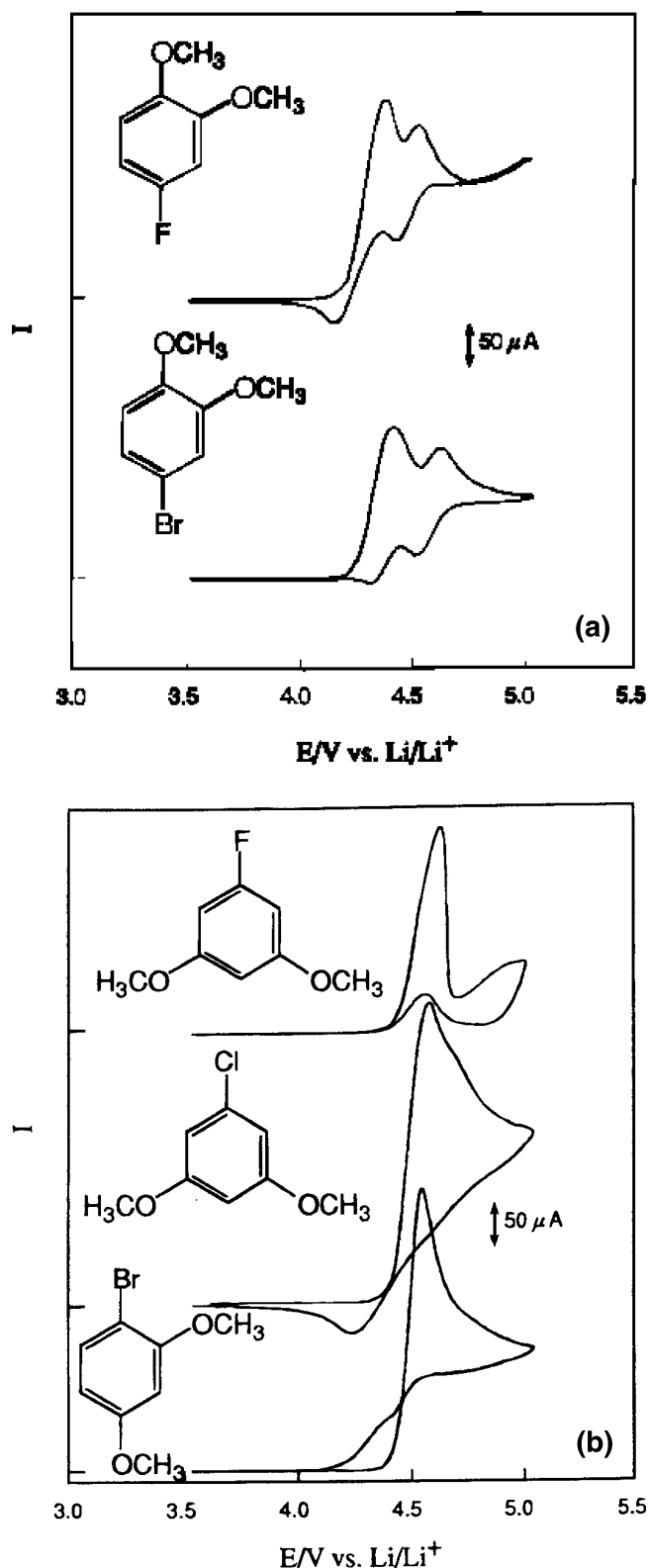
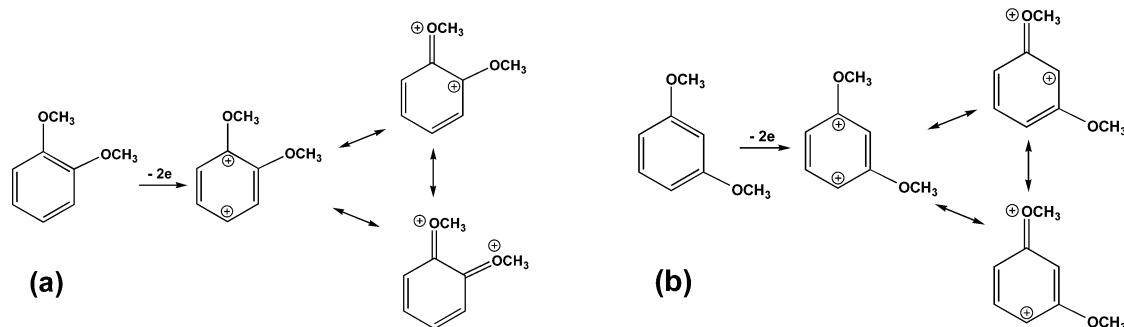


Figure 45. Cyclic voltammetry of (a) 4-halo-1,2-dimethoxybenzenes (Reproduced with permission from ref 432 (Figure 8). Copyright 1999 The Electrochemical Society.) and (b) 1,3-dimethoxybenzenes in $\text{LiPF}_6/\text{PC}/\text{DMC}$ on Pt (Reproduced with permission from ref 432 (Figure 9). Copyright 1999 The Electrochemical Society.)

other hand, the stability of this cationic product relies on the effectiveness of the delocalization of the formal charge. Apparently, the lone pair of electrons on the methoxy oxygen can effectively contribute to this

Scheme 28. Effect of Methoxy Relative Position on the Stabilization of the Oxidized State of Anisole Redox Additives: (a) 1,2-Methoxybenzene, Whose Oxidized Product Was Stabilized by the Neighboring Methoxy; (b) 1,3-Methoxybenzene, in Which the Meta Methoxy Fails To Stabilize the Dianion



delocalization if the methoxy is at either ortho- (Scheme 28a) or para-positions (not shown in Scheme 28), while the methoxy at the meta-position (Scheme 28b) cannot. In this sense, the unstable oxidized product from the meta-substituted compounds would act like an intermediate and readily undergo further side reactions, thus rendering the original oxidation irreversible. The position of the halogen does not seem to be important, as long as the two methoxy groups are either para or ortho to each other; however, its presence is critical, since 1,4-dimethoxybenzene itself shows no reversible redox behavior. Thus, the role of the halogen in affecting the stability of the cationic species remains unclear. Nevertheless, the empirical structure–property relationship discovered by the authors for the anisole family could serve as a useful guideline for the future selection of redox additives.

Overcharge tests were carried out in LiCoO₂ cathode half-cells that contained these additives, and a redox shuttle effect was observed between 4.20 and 4.30 V, close to the redox potentials of these additives. The same shuttling effect was observed even after 2 months of storage for these cells, indicating the stability and redox reversibility of these additives. A closer examination of the capacity retention revealed that 4-bromo-1,2-dimethoxybenzene seemed to have the best shuttle-voltage performance for the 4.0 V lithium cell used.⁴³² The stability of these additives against reductive decomposition was also tested by the authors on metallic lithium as well as on carbonaceous anodes, and no deterioration was detected.

A convincing analysis carried out in this work established a direct connection between the shuttle current and the thermal effect in the cell, and it helps us to understand energetically the mechanism by which redox additives worked as shuttle carriers. As Figure 46 shows, calorimetric measurement was performed on cells that were being overcharged simultaneously, while the voltage profiles and heat flows were plotted together to reveal the correlation. In the reference cell, where no additive was present, there was no heat flow until the very end of the charge, where electrochemical decomposition of the electrolyte solvents and the thermal reaction between cathode and electrolyte would occur. On the other hand, the obvious thermal effect could be detected for the test cell containing 4-bromo-1,2-dimethoxy-

benzene as soon as the cell voltage leveled off because redox shuttling started. This suggests that the current supplied over 4.3 V (or after 60 h) is neither stored in the cathode nor consumed by irreversible decompositions. Rather, the shuttling redox couples convert this part of the current into heat during their repeated movement across the cell. In other words, during the course of shuttling, no work is done by the current to change the state-of-charge in the cathode, and all of the current supplied is dissipated by the diffusion of [O] and [R] species of the redox additive.

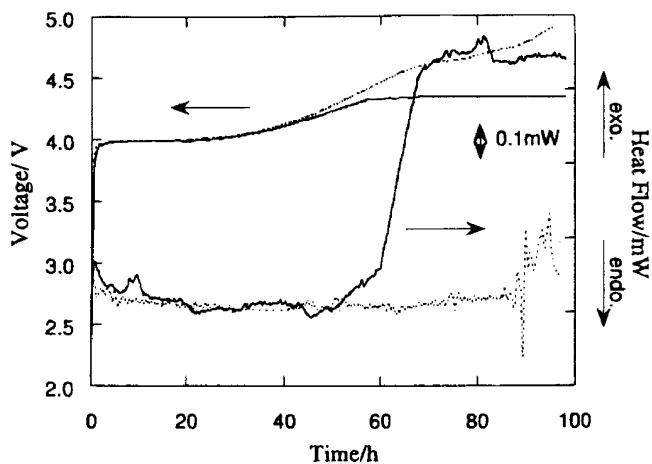


Figure 46. Correlation between the voltage profiles and heat flow of a cell under overcharge: cells with 100 mM 4-bromo-1,2-dimethoxybenzene (solid lines) and reference cell (dashed lines) (Reproduced with permission from ref 432 (Figure 17). Copyright 1999 The Electrochemical Society.)

Following Adachi et al., aromatic compounds with similar functionalities were proposed for polymer electrolytes as redox shuttle additives, which included bipyridyl and biphenyl carbonates and difluoroanisoles.^{48b,434} All these additives could protect the cathode from overcharging in the vicinity of 4.1 V.⁴³⁴

Other less prominent types of additives, also intended for overcharge protection, were termed “shutdown additives” in the battery industry based on their tendency at high potentials to release gas, which in turn would activate a current interrupter device (CID), or to polymerize and block the ion passage in the electrolyte. The former included such

compounds as pyrocarbonates,^{48b} biphenyl,^{48b,435,436} cyclohexylbenzene,^{48b} and phenyl-*tert*-butyl carbonate,⁴³⁷ while the latter include biphenyl and other substituted aromatic compounds.^{438,439} Related publications on these additives have been absent except for patent disclosures and conference presentations. However, according to Yoshino et al., some of these additives have been used in commercial lithium ion cells for several years.^{48b,440} The major difference between these additives and the redox shuttles is that, once activated by the cathode potential, the gassing or polymerizing of these additives terminates the cell permanently, while the operation of redox additives is nondestructive, at least theoretically. Since the redox additives have a maximal current limit defined by their diffusion coefficient and concentration, the presence of the gassing- and polymerizing-type additives would serve as a more reliable line of defense against catastrophic failure from overcharging. Therefore, the integration of multiple additives of different types into a single electrolyte seems to be a feasible approach on the condition that the destructive additives should have higher activation potential.

8.3. New Electrolyte Components

The modification of electrolytes via additives is attractive to industry as an economical approach; however, its impact on electrolyte performance is mainly restricted to tuning interfacial-related properties because of their small concentration in the electrolyte, while other challenges for the state-of-the-art electrolytes such as temperature limits, ion conductivity, and inflammability are still determined by the physical properties of the bulk components. Improvements in these bulk-related properties can only be realized by replacing the bulk components of the electrolytes with new solvents and salts, but such efforts have been met with difficulty, since more often than not the improvement in the individually targeted properties is achieved at the expense of other properties that are also of vital importance to the performance of electrolytes. Such "collateral damage" undermines the significance of the improvements achieved and, in some cases, even renders the entire effort unworthy.

Nevertheless, research activities in this arena continue to be driven by the potential commercial interest that might arise from any possible replacement of the state-of-the-art electrolyte components. Realizing that the probability of success is rather limited with any radical change of the entire electrolyte system, an increasing number of researchers on novel electrolytes are adopting the current state-of-the-art electrolytes as the platforms for innovation and attempting to approach the targeted improvements without serious sacrifices in the well-established merits, which at least should include (1) facile ion transport as characterized by ion conductivities above 5 mS cm^{-1} at room temperature, (2) electrochemical stability on both carbonaceous anode and metal oxide cathode materials in the range 0–5 V, (3) inertness to other cell parts such as packaging materials and anode and cathode current collectors,

(4) wettability toward porous separators as well as electrode materials, (5) relatively low toxicity, and (6) relatively low cost.

This section reviews these research efforts in the past decade on developing new solvents and lithium salts for nonaqueous electrolytes of lithium ion cells, but the cosolvents or additives developed for nonflammable electrolytes, most of which are phosphorus or fluorinated molecules, are not included, since their presence is intended for improvement in safety rather than performance. They will be reviewed in section 8.5.

With few exceptions, these new electrolyte solvents focus on possible improvements in low-temperature performance, while new salts are intended to offer higher thermal stability. This divided directions of pursuit after the targeted improvements is apparently created by the fact that solvent and salt, respectively, impose the upper and lower temperature limits of the current state-of-the-art electrolytes.

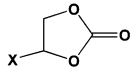
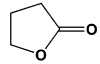
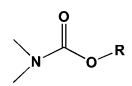
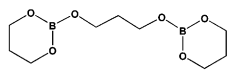
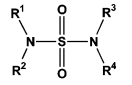
8.3.1. Nonaqueous Solvents

The state-of-the-art electrolytes use mixtures of cyclic and acyclic carbonates as solvents, whose functions are to solvate lithium salts and to facilitate lithium ion transport, respectively. The key cyclic solvent, EC, is also responsible for forming a protective SEI on graphitic anodes and probably a similar surface layer on metal oxide cathodes. However, this indispensable solvent simultaneously sets the narrow range of service temperature for these electrolytes with its high melting point, while its replacement by other low-melting solvents such as its structural analogue PC is often rendered difficult by the requirement for SEI-forming ability. The attempts at solving this dilemma have been directed at the structural modification of either EC or PC so that a balance between low melting point and favorable interfacial chemistry could be reached.

On the other hand, the linear carbonates used in the state-of-the-art electrolytes, DMC, DEC, and EMC, serve as diluents to the high-melting and viscous EC. They have been known to be unsuitable as single solvents because of their inability to solvate lithium salts as well as their instability on the oxidizing surface of cathode materials, while the gassing of lithium ion cells during long-term cycling is also believed to arise from them. However, any possible replacements for linear carbonates to serve as cosolvents with EC or PC should at least possess the major prerequisites of lower viscosity and lower melting point.

Preferably, the new solvents are also expected to possess better stability or ability in interfacial chemistry on both anode and cathode materials so that the new electrolyte formulation can rely less on EC; or they are expected to be less inflammable, as a major shortcoming of the linear carbonates is their low flash points (T_f) (Table 1). In the search for new solvents, fluorination has been adopted as a favorable approach to achieve improvements in these two aspects because the presence of C–F bonds in organic molecules is found to affect interfacial chemistry on carbonaceous anodes in a positive manner,^{441–443} and

Table 12. Novel Nonaqueous Solvents and Their Major Properties

Solvent Structures	Remarks	Ref.
 <p>X = Cl, F, CF₃</p> <p>cyclic carbonates</p>	Halogen-substitution lowers m.p. and improves SEI-formation ability; high self-discharge rate from CIEC; toxicity remains unknown.	446, 447, 449 442, 452 443, 453
 <p>γBL</p>	Unique match with LiBF ₄ .	123, 208, 133, 458–460
<p>H(CH₂)_n C(=O)O(CH₂)_mH</p> <p>n = 0–7 m = 1–4</p> <p>linear esters</p>	Better low-temperature performance.	406, 461–463
<p>X(CF₂)_n C(=O)O(CH₂)_mH</p> <p>n = 1–7 m = 1–2 X = F or H</p> <p>fluorinated esters</p>	Better low-temperature performance; better SEI-formation ability; lower inflammability.	464, 465
<p>R¹ O C(=O) O R²</p> <p>R¹ = CH₃, CH₂CH₃, CH₂CH₂CH₃, CH₂CF₃ R² = CH₂CF₃, CH(CF₃)₂</p> <p>fluorinated carbonates</p>	Better low-temperature performance; better SEI-formation ability; lower inflammability.	466
<p> R = CH₂CF₃, CH(CF₃)₂</p> <p>fluorinated carbamates</p>	Resistive SEI; low capacity.	466
<p>R-O-[(CH₂)_mO]_n-C(F₂)₂-C(FH)X</p> <p>R = alkyl X = F or R_F</p> <p>fluorinated ethers</p>	Improved SEI chemistry; increased safety under thermal abuse.	441
 <p>glycol borate ester (BEG)</p>	Moderate ion conductivity; higher t_{Li} ; good anodic stability on Pt.	467
<p>R¹-S(=O)₂-R²</p> <p>R¹ = Me R² = Et, Pr, iBu, R_F</p> <p>sulfones</p>	High ion conductivity; good anodic stability on cathode materials; alkyl fluorination improves SEI chemistry on graphite.	75, 314
<p> R¹⁻⁴ = alkyls, alkoxyis, alkoxyalkyls</p> <p>sulfamides</p>	Moderate ion conductivity; poor anodic stability on Pt.	468

many organofluorine compounds act as flame-retardants.^{444,445} Table 12 summarizes the novel electrolyte solvents according to their structural cyclicity.

8.3.1.1. Cyclic Solvents. Halogen substitution on the carbonate ring of EC and PC is postulated to serve the dual purpose of lowering melting temperature by breaking the molecular symmetry and improving the SEI-forming ability. Shu et al. used chloroethylene carbonate (CIEC) as a cosolvent for PC and found that an effective and protective SEI could be formed on a graphitic anode, with the

Coulombic efficiency in the first charging cycle comparable to that of the commercial electrolytes for lithium ion cells.^{446,447} The potential plateau at 0.80 V, characteristic of the reductive decomposition of PC, was completely eliminated due to the presence of CIEC, while a new process was observed at 1.70 V. When taking the irreversible capacity in the first cycle as a metric, the optimum concentration of CIEC was determined to be 30 vol %, ⁴⁴⁸ although in a ternary solvent system containing EC, its concentration could be minimized to 5%.⁴⁴⁷ Further electro-

chemical studies confirmed that CIEC forms a compact and uniform SEI on the surface of the graphitic anode that can prevent the cointercalation of PC and the subsequent exfoliation of graphene even in PC-rich electrolytes,^{449,450,451} and the origin of this effective interfacial chemistry seems to be the reductive decomposition of CIEC at 1.70 V, which generates CO₂ as a major intermediate, as indicated by the conspicuous absorption at 2341 cm⁻¹ in in situ FT-IR spectra.⁴⁴⁹ The fate of CO₂ is yet unclear, but a strong possibility is its further reduction into lithium alkyl carbonate as a major component of the new SEI. Since this process occurs at a potential far above that of PC cointercalation, graphitic materials could successfully be used in CIEC/PC mixed solvents. Naturally, such a formulation without EC should offer much better performance at subzero temperatures.

The tests in full lithium ion cells, however, yielded less than satisfactory results.⁴⁴⁷ Despite the stable cell life observed during the test of >800 cycles, only 92% Coulombic efficiency was achieved, as compared with the 98+% Coulombic efficiency for the corresponding anode half-cells. Initial suspicion about the anodic instability of CIEC was excluded, because this less-than-ideal efficiency did not lead to obvious capacity fading, and cyclic voltammetry carried at high potentials up to 4.2 V showed no discernible oxidation of CIEC, suggesting that CIEC is at least as stable as EC on the cathode surface. Therefore, the above loss in charge efficiency should come from the combined presence of both anode and cathode materials. Shu et al. thus proposed a shuttle-like mechanism in which CIEC was reductively cleaved on a carbonaceous anode, yielding the organic products related to alkyl carbonates and LiCl. Since LiCl is weakly soluble in nonaqueous media, chloride would diffuse to the cathode surface and be oxidized into Cl₂. This internal chemical shuttling process between the anode and cathode surfaces consumes charges, and its reversibility accounts for the constantly low Coulombic efficiency during long-term cycling tests. This internal self-discharge mechanism is obviously undesirable and eventually rendered CIEC an impractical cosolvent.

Considering the virtually zero solubility of LiF in nonaqueous media, McMillan et al. synthesized the fluorinated counterpart of CIEC.⁴⁴² As expected, the shuttle phenomenon was eliminated because of the fluorination, as evidenced by the quantitative Coulombic efficiency, while a similar SEI effect was maintained, since FEC/PC mixed solvent can support reversible lithiation/delithiation of the graphitic anode materials. However, capacity was observed to fade by 37% in 200 cycles. Follow-up work on this solvent has been minimal.⁴⁵²

Similar structural modification was also performed on PC. Trifluoropropylene carbonate (TFPC) was synthesized in the hope that a novel electrolyte free of linear carbonates could be formulated with improved safety in the case of fire.^{443,453} Like CIEC and FEC, it is liquid at room temperature with a high flash point (134 °C), but its high viscosity results in slower ion transport within the electrolytes, because the maximum ion conductivity at room temperature

achieved by these cyclic-only electrolytes is 6.6 mS cm⁻¹ (for LiPF₆ in TFPC/EC 1:3) and in neat TFPC it is only ~3.0 mS cm⁻¹. On the other hand, EIS studies carried on anode half-cells found that the CIEC/TFPC couple forms the least resistive SEI film. While the electrochemical behavior of neat TFPC was not described, the cathodic stability of the electrolytes based on mixed solvents, TFPC/CIEC and TFPC/EC, was tested with a graphitic anode, and no reductive processes characteristic of TFPC were visible, in addition to those of CIEC (1.70 V) and EC (0.60 V). Similar to the cases of CIEC and FEC, its presence did prevent PC cointercalation, but the irreversible capacity associated with PC decomposition still accounted for ~132 mA h g⁻¹ of the irreversible capacity in the anode half-cell, which was ~40% of the total charge. Spectroscopic means, including XPS and FT-IR, were used to analyze the SEI chemistry on the anode, and the presence of a C–F bond was identified, indicating the decomposition products of TFPC do constitute part of the SEI. Cycling performance of these electrolytes was tested in anode and cathode half-cells, but no data on full lithium ion cells were shown.⁴⁵³

Among the limited choices of candidates intended to replace cyclic carbonates, γ -butyrolactone (γ BL) seemed to be the most promising and therefore closest to practical application. γ BL has long been considered a possible component for electrolytes in lithium/lithium ion cells due to its moderately high dielectric constant, relatively low viscosity, EC-like structure, and excellent solvating ability.^{454–456} Its reductive behavior has been studied on inert electrode surfaces,^{208,209} lithium surfaces,^{222,457} and graphite surfaces.¹²³ Unfortunately, in the early era of lithium ion technology, Aurbach and co-workers had found that γ BL/LiAsF₆ solution failed to perform satisfactorily in lithium ion cells based on the graphite anode unless under an atmosphere of CO₂, thus diminishing its possible application.¹²³ Detailed mechanistic studies attributed the failure to metallic lithium deposition on the carbonaceous anode surface and the subsequent reaction with γ BL, which was made possible by the high resistance of the SEI formed in γ BL-based electrolytes.¹⁷⁷

The publications related to the use of γ BL as an electrolyte solvent for lithium ion cells have been scarce until recently, when a Japanese group from Toshiba reported the electrolyte based on a solution of LiBF₄ in γ BL/EC mixtures for laminated thin lithium ion cells.^{133,458} This new formulation, when used in combination with a graphitic carbon fiber, exhibited stable cell performance with 94% Coulombic efficiency in the first cycle. Most importantly, it afforded much higher thermal stability than the electrolytes based on LiPF₆ solutions, since storage of the cell at full state-of-charge (4.20 V) at 85 °C only led to negligible capacity loss. The low-temperature performance was also much improved as compared to the cases of state-of-the-art electrolytes, with 88% of the nominal capacity retained at –20 °C at the drain rate of 0.5 C. Since the new formulation is free of linear carbonates, its tolerance against thermal abuse should be superior to that of the current

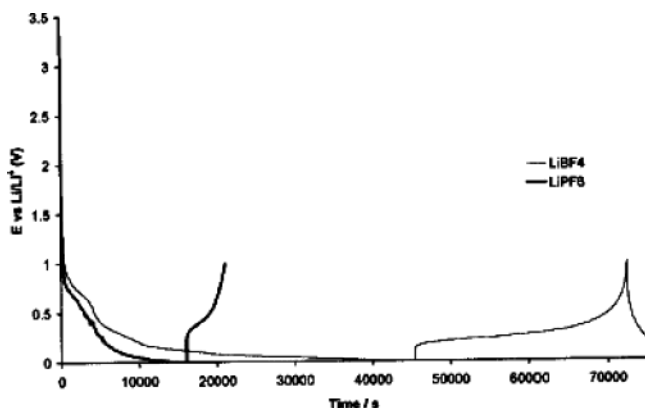
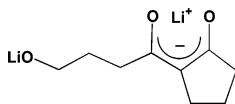


Figure 47. Voltage profile of graphitic anode in LiPF_6 and LiBF_4 solutions in $\gamma\text{BL}/\text{EC}$ (1:1). (Reproduced with permission from ref 460 (Figure 1). Copyright 2003 The Electrochemical Society.)

commercial lithium ion cells. Preliminary results showed that the gassing of this new electrolyte is much less severe, and an independent study employing the in situ DEMS technique confirmed that the dominant participation of γBL in SEI formation reduced the gas evolution by forming a γ -alkoxy- β -keto ester.⁴⁵⁹



The spectroscopic identification of the β -keto ester and the reduction mechanism leading to it have been previously described by Aurbach and co-workers when studying the surface chemistry of γBL -based electrolytes on various electrodes polarized to low potentials.^{123,208,209}

Interestingly, all the above improvements seemed to be unexpectedly achieved from components (LiBF_4 and γBL) that were already tested individually and considered inferior in performance to the commonly used LiPF_6 and various carbonates. According to a more recent publication, this unique match between LiBF_4 and γBL originates from some interactions between the two that are not yet understood.⁴⁶⁰ For example, among the five salts investigated that included LiBF_4 , LiPF_6 , LiAsF_6 , LiIm , and LiClO_4 , only LiBF_4 in $\gamma\text{BL}/\text{EC}$ supported reversible lithium intercalation/deintercalation with capacities close to the theoretical value, as Figure 47 shows. Other salts seemed to suffer from a highly resistive surface film on the graphite surface, which worsened with cycling number. Although extensive characterizations were carried out with techniques such as XRD, SEM, and XPS, the nature of this interaction remains unclear.

8.3.1.2. Linear Solvents. For novel solvents that are intended to replace linear carbonates, the emphasis was placed on such properties as melting temperature, viscosity, and inflammability of the solvents. As Table 12 shows, these solvents can be roughly classified into four groups: (1) linear esters or carbonates,^{406,461–463} (2) fluorinated esters,^{464,465} (3) fluorinated carbonates,⁴⁶⁶ and (4) fluorinated ethers.⁴⁴¹

Like linear carbonates, none of these linear esters were used as single solvents but rather as cosolvents

with cyclic components including EC and PC. Binary, ternary, and even quaternary compositions were formulated with these esters, and improvements of low-temperature performance were described.^{406,461–463} According to Herreyre et al., ternary compositions based on ethyl acetate (EA) and methyl butyrate (MB) demonstrated electrochemical stability up to 4.85 V on the cathode surface at 60 °C, while the compositions containing lower molecular weight methyl acetate (MA) deteriorated.⁴⁰⁶ Similar conclusions were drawn by Smart et al., who investigated a series of linear esters and carbonates as low-temperature electrolyte components and found that a desirable SEI (i.e., less resistive and protective) could only be formed when esters of higher molecular weight were used, although esters of lower molecular weight could afford higher bulk ion conductivity at low temperatures because of their lower viscosities.⁴⁶² Judged on the basis of the reversible capacity in the first charge cycle achieved by a graphite anode in quaternary electrolytes, $\text{LiPF}_6/\text{EC}/\text{DEC}/\text{DMC}/\text{ester}$, the esters with longer alkyl chains were obviously superior to the ones of lower molecular weight:

ethyl propionate (EP, 340.75 mA h g⁻¹) >
ethyl butyrate (EB, 309.46 mA h g⁻¹) >
MA (236.5 mA h g⁻¹) > EA (214.2 mA h g⁻¹)

The above cell performance order is almost the reversal of that for the low-temperature ion conductivity, which clearly shows the decoupling of interfacial properties from bulk properties. Thus, Smart et al. concluded that the nature of the SEI instead of bulk ion conductivity plays the key role when new solvents are selected.

To improve the thermal stability of electrolytes against lithium metal electrodes, various fluorinated organic solvents were tested as electrolyte solvents (Table 12).^{441,464–466} For example, Yamaki et al. introduced a series of partially fluorinated esters in which the fluorination was conducted on the carboxylic acid section and used them as single solvents for electrolytes,⁴⁶⁵ while Smart et al. synthesized a series of partially fluorinated carbonates for similar purposes.⁴⁶⁶ When compared with their nonfluorinated counterparts, the presence of fluorination in these molecules was reported to result in lower melting points, higher anodic stability, increased safety, and favorable SEI-forming characteristics on metallic lithium or graphitic anodes. For fluorinated carbonates a number of electrochemical techniques such as Tafel polarization and micropolarization confirmed that facile kinetics of lithium ion intercalation were made possible because of the new SEI chemistry imparted by those fluorinated solvents. In terms of interfacial resistance and utilized capacity, fluorinated carbonates are generally superior to the fluorinated carbamates studied (Table 12).⁴⁶⁶

8.3.1.3. Other Novel Solvents. In addition to molecules based on carboxylic and carbonic esters, other types of organic polar compounds were also explored as possible solvent candidates but with limited success. Zhang and Angell synthesized a dimeric glycol ester of boric ester (BEG, Table 12) in

the hope that the electron-deficient boron of the molecule would assist in dissociating lithium salts and coordinating with anions.⁴⁶⁷ The solvent, despite its high viscosity, can dissolve various lithium salts to appreciable concentrations, and it exhibited particular stabilization of metallic lithium at elevated temperatures up to 100 °C. With EC as cosolvent, the electrolytic solution of LiClO₄ and LiIm showed moderate ion conductivities on the level of 10⁻³ S cm⁻¹. The anodic stability of the electrolytes based on this borate ester was measured on a Pt electrode, and a wide electrochemical stability window of ~5.8 V was reported. The cathodic stability of the borate ester on graphitic anode material was also confirmed by cycling an MCMB electrode in an electrolyte LiClO₄ in BEG/EC, which yielded stable cycles. Considering the high viscosity of both solvent components used in the study, the above cell test results appear to be promising, but better results could be achieved if conventional diluents such as linear carbonate were used. However, no further work has been reported on this interesting solvent.

Choquette et al. investigated the possibilities of using a series of substituted sulfamides as possible electrolyte solvents (Table 12).⁴⁶⁸ These compounds are polar but viscous liquids at ambient temperature, with viscosities and dielectric constants ranging between 3 and 5 mPa s and 30 and 60, respectively, depending on the alkyl substituents on amide nitrogens. The ion conductivities that could be achieved from the neat solutions of LiIm in these sulfamides are similar to that for BEG, that is, in the vicinity of 10⁻³ S cm⁻¹. Like BEG, it should be suitable as a polar cosolvent used in a mixed solvent system, though the less-than-satisfactory anodic stability of the sulfamide family might become a drawback that prevents their application as electrolyte solvents, because usually the polar components in an electrolyte system are responsible for the stabilization of the cathode material surface. As measured on a GC electrode, the oxidative decomposition of these compounds occurs around 4.3–4.6 V when 100 μA cm⁻² was used as the cutoff criterion, far below that for cyclic carbonate-based solvents.

Another class of organic compounds that could make promising electrolyte solvents for lithium-based rechargeable cells is based on alkyl sulfones. Since most of these compounds are solids with melting points above ambient temperature, interest was rarely invested in them when possible candidates for electrolyte solvents are considered. One exception is the cyclic member, tetramethylene sulfone (also known as sulfolane), whose melting temperature is close to room temperature (27 °C) and whose dielectric constant is close to that of PC (60 at 25 °C). The electrolyte based on the salt solutions of this cyclic sulfone remains liquid till subzero temperatures because of the freezing-depression effect of the solute. Matsuda et al.⁴⁶⁹ and Morita et al.⁴⁷⁰ have individually tested it as a cosolvent for lithium cells, and focus was placed on the lithium cycling efficiencies. Generally decent ion conductivity could be achieved either with sulfolane as a single solvent or with mixed solvents based on it. For example, 15 mS cm⁻¹ at

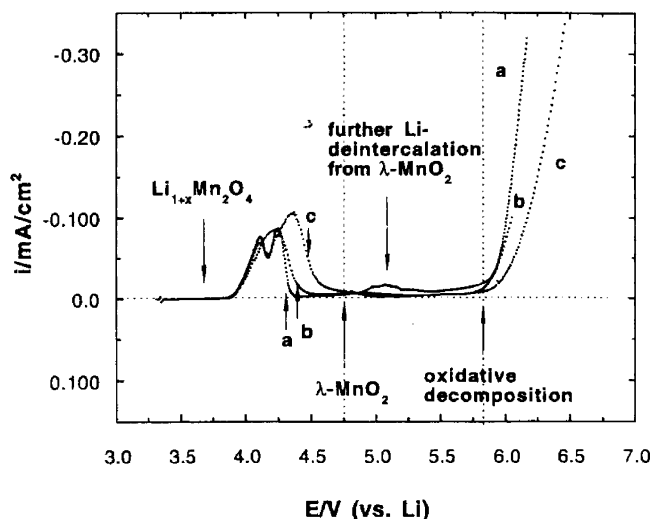


Figure 48. Anodic stability as measured on a spinel Li_{1-x}Mn₂O₄ cathode surface for EMS-based electrolytes: (a) LiIm; (b) LiClO₄; (c) LiTf. In all cases, 1.0 m lithium salt solutions were used, and slow scan voltammetry was conducted at 0.1 mV s⁻¹, with lithium as counter and reference electrodes and spinel Li_{1-x}Mn₂O₄ as working electrode. (Reproduced with permission from ref 75 (Figure 3). Copyright 1998 The Electrochemical Society.)

room temperature has been measured for LiPF₆ in a sulfolane/DME mixture, which should obviously be attributed to the combined effect of the high dielectric constant of sulfolane and the low viscosity of DME. On the other hand, the higher melting temperatures of the linear counterparts of sulfolane excluded them from being considered as room-temperature electrolyte solvents. For example, the lithium cell based on the simplest member of the linear sulfone family, dimethyl sulfone (DMS, mp 110 °C), has to operate at 150 °C, although, surprisingly, high Coulombic efficiency and stable performance could be achieved even at that high temperature.⁴⁷¹

With the introduction of structural asymmetry, Xu and Angell attempted to reduce the lattice energy of the sulfone molecules so that the melting temperature of linear sulfones could be lowered to the level that allowed room-temperature application.⁷⁵ They synthesized five linear sulfones with asymmetric alkyl substituents and found that all of these compounds were liquids or solids that melt in the vicinity of room temperature. They were able to dissolve various lithium salts up to 3.0 M and yield moderate ion conductivity, and the most interesting solvent candidate from the family was the simplest member, ethylmethyl sulfone (EMS), which has an extraordinarily high dielectric constant (95 at 20 °C, as compared with 89 of EC).³¹⁴ When tested on the surface of a spinel-based composite cathode material, this solvent showed an electrochemical stability window of approximately 5.80 V, as Figure 48 shows. This high anodic stability limit, which remains the highest ever known on the surface of a composite cathode material (versus an inert electrode), is significant, since it would allow the various applications of high potential requirements such as a energy storage device with 5.0 V class cathode materials or electrolytic and electroanalytic devices that need an inert supporting medium. The usefulness of this

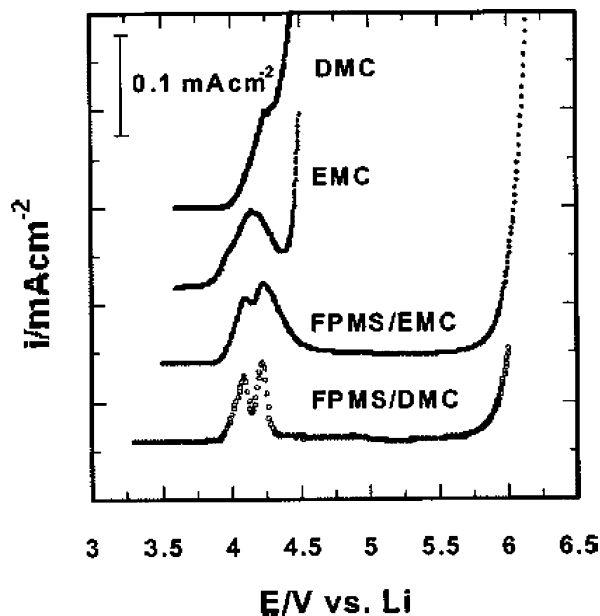


Figure 49. Effect of cosolvent FPMS on the anodic stability of the mixed solvents. Also shown for comparison are the neat linear carbonates. In all cases, 1.0 m LiPF₆ solutions were used, and slow scan voltammetry was conducted at 0.1 mV s⁻¹, with lithium as counter and reference electrodes and spinel Li_xMn₂O₄ as working electrode. (Reproduced with permission from ref 314 (Figure 6). Copyright 2002 The Electrochemical Society.)

anodically stable solvent has been confirmed by the various applications that followed the report of Xu and Angell.^{316,317,472,473} For example, Seel and Dahn have successfully used EMS as the nonaqueous electrolyte for an anion intercalation cell, which enables the otherwise impossible staging of graphene layers with PF₆⁻ anions at 5.60 V;³¹⁶ and the electrolyte based on the same sulfone also supported the complete delithiation of a new cathode material at ~5.4 V.³¹⁷

Unfortunately, EMS cannot form an effective SEI on graphitic anode materials, thus undermining the possibility of its use in lithium ion cells. In their further work, Xu and Angell partially fluorinated the alkyl of an asymmetric linear sulfone, inspired by the reports that fluorinated alkyl could improve the SEI chemistry on a graphitic anode.^{441–443} The fluorinated sulfone, 3,3,3-trifluoropropylmethyl sulfone (FPMS), has a melting point at 56 °C and could only be used as cosolvent with other diluents such as DMC and EMC.³¹⁴ The anodic stability of sulfone compounds seemed to be maintained, despite the presence of fluorination and the mixing with linear carbonates, as evidenced by the oxidative limits at ~5.70 V observed in Figure 49 for the mixed solvents. The SEI-forming ability, however, was indeed improved due to the fluorination, as shown by Figure 50, wherein the electrolytes based on these mixed solvents supported reversible lithium ion intercalation/deintercalation of the graphite anodes. The cycling tests in the longer term confirmed that the surface of a graphitic anode was well protected because close-to-unity Coulombic efficiency was obtained, and the authors suggested that FPMS might be a promising

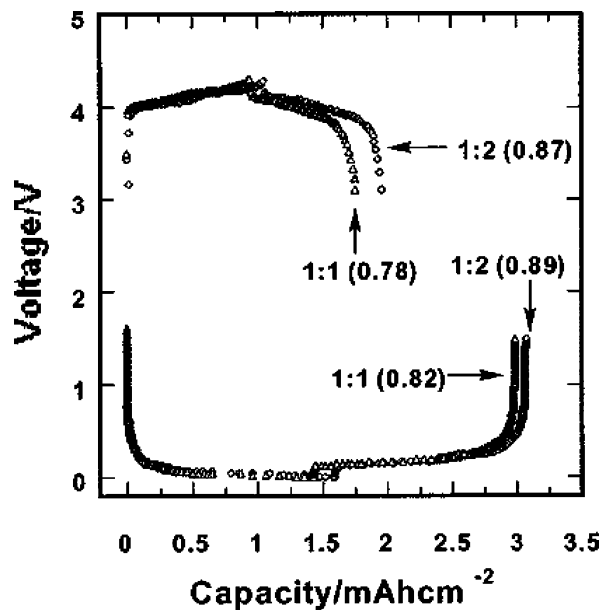


Figure 50. Galvanostatic cycling of anode (Li/graphite) and cathode (Li/Li_xMn₂O₄) half-cells using 1.0 m LiPF₆ in FPMS/EMC 1:1 and 1:2 mixture solvents, respectively. $j = 0.001$ mA cm⁻². (Reproduced with permission from ref 314 (Figure 8). Copyright 2002 The Electrochemical Society.)

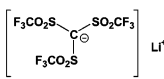
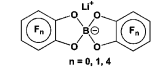
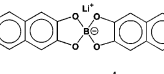
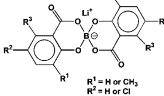
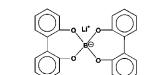
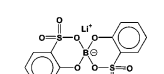
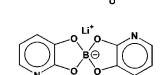
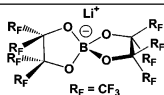
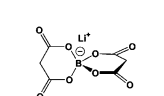
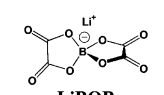
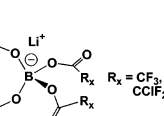
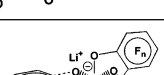
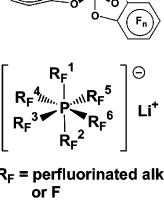
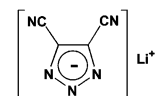
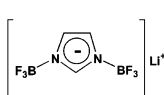
candidate for the lithium ion cell if the manufacturing cost of it could be reduced.

8.3.2. Lithium Salts

The pursuit of new lithium salts has been driven by the thermal instability of the current state-of-the-art lithium salts that were based on perfluorinated anions, and the thermal as well as chemical inertness has been taken as the main metric to evaluate any potential candidates to replace those salts, although, similar to the new solvent efforts, often the improvement in these properties comes at the price of other properties that are equally important for the operation of a lithium ion cell.

8.3.2.1. Lithium Tris(trifluoromethanesulfonyl)methide (LiMe). Following the development of LiIm, Dominey invented a new lithium salt based on a carbanion that is stabilized by three perfluorinated methanesulfonyl groups.⁴⁷⁴ Because of the effective delocalization of the formal charge on the anion, the salt LiMe (Table 13) could be dissolved in various nonaqueous media and showed better ion conductivities than LiIm.¹⁴⁶ Its stability at high temperature is confirmed by TGA studies, which detected no sign of decomposition before 340 °C, while accordingly the electrolyte solution based on the salt remained stable at 100 °C. The electrochemical stability of the salt was studied in THF solution, and the cyclic voltammetry conducted on GC showed major anodic decomposition process at ~4.0 V. Although, on the basis of the previously published data this decomposition seemed to be caused by the solvent THF rather than by the salt anion,^{64,74,177} the authors did not report further electrochemical measurements in other more stable solvents.¹⁴⁶ Initially the salt was reported to be inert toward an Al current collector,^{116,153} but a more detailed study later found that corrosion of Al

Table 13. Novel Lithium Salts and Their Major Properties

Salt	Structure	M. Wt	T _d / °C ^a	E _a / V ^b (solvent -electrode)	σ / mScm ⁻¹ (0.7~1.0 M, 25 ° C/ solvent)	Ref.
LiMe		417.9	340	4.4 (THF-GC) 4.0 (EC/DMC-GC)	7.1 (EC/DMC) 12 (EC/MF/DMC)	116, 146, 474
aromatic Li borates		233.4~ 305.4	250 (n=0)	3.6 (PC-SS ^c , n=0 ^d) 3.7 (PC-Au, n=1) 4.1 (PC-Au, n=4)	0.6 (PC, n=0) 5.6 (EC/DME, n=0) 0.77 (PC, n=1) 11.07 (DME, n=4) 1.22 (PC)	475~477, 481
		334.1	320	3.75 (PC-Pt)	3.84 (PC/DME) 1.39 (PC/EC)	478, 482
		290.0~ 427.7	260 (R ¹⁻³ =Cl) 290 (R ¹⁻³ =H) 310 (R ¹⁻² =Cl) 320 (R ¹ =CH ₃)	4.0 (PC-SS, R ¹⁻³ =H) 4.4 (PC-Pt, R ¹⁻³ =Cl) 4.4 (PC-Pt, R ¹⁻³ =H) 4.3 (PC-Pt, R ¹⁻² =Cl) 4.1 (PC-Pt, R ¹ =CH ₃)		477, 481
		386.1				478, 481
		293.9		4.6 (EC/DMC-Pt)		479
		219.9		3.95 (PC/DMC-Pt)		480
non-aromatic Li borates		681.9	280	5.4 (DME-Pt) 5.0 (PC-Pt)	11.1 (DME)	483
		221.9	245		5.6 (DMSO)	113
		193.9	~300 (d)	4.5 (PC-Pt)	3.1 (PC) 9.0 (DME) 7.5 (EC/DMC)	113, 155, 324, 483~486, 488, 489
		469.9~667.9	100	4.5 (PC-Pt)	8.0 (PC/DMC)	493
chelated Li phosphates		361.9 (n=0) 577.9 (n=4)	150 (n=0)	3.7 (PC-Ni, n=0) 3.95 (EC/DMC-Pt, n=1) 4.3 (EC/DEC-Pt, n=4)	3.89 (EC/THF, n=0) 2.09 (EC/DEC, n=4)	494 (n=0) 495 (n=4)
	Li FAP		451.9~433.9		5.0 (DME-Pt) 5.0 (EC/DMC-Pt)	8.17 (PC/EC/DMC, R ¹⁻² = i-C ₃ F ₇ , R ³⁻⁶ =F) 8.2 (EC/DMC, R ¹⁻³ = C ₂ F ₅ , R ⁴⁻⁶ =F)
Li azolate		124.9				501
Li imidazolid		209.9		4.85 (DMC-Pt)	5.06 (EC/EMC)	502

^a Thermal decomposition temperature determined by TGA. ^b Anodic stability limit determined by cyclic voltammetry. ^c Stainless steel working electrode. ^d Number of fluorine substituents on the aromatic ring.

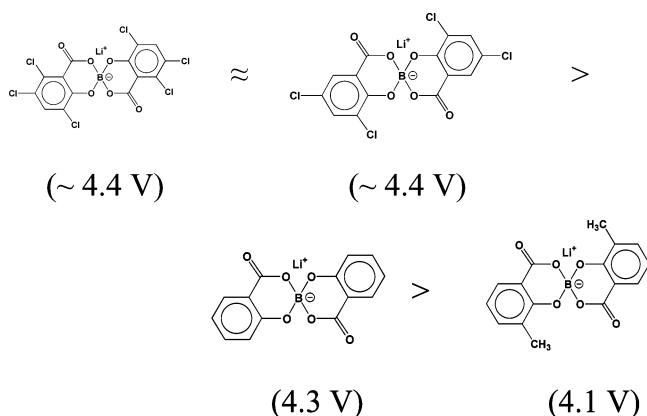
does occur in various LiMe-based electrolytes at potentials above 4.5 V, though somehow it is less severe than that for the case of LiIm.¹⁴⁷ Therefore, its application in high-potential lithium ion cells

seems unlikely because Al is universally adopted as the current collector for the cathode materials.

8.3.2.2. Lithium Borates with Aromatic Ligands. A new class of lithium salts was developed

by Barthel et al. in the mid 1990s based on a borate anion chelated by various aromatic ligands.^{475–480} Table 13 summarizes the representative members from this class along with their selected physical and electrochemical properties. The authors described the synthesis and chemical or physical characterizations of these salts in detail but only provided limited electrochemical data. Generally speaking, this class of salts is rather stable thermally and decomposes only at very high temperatures without melting, although moisture can still decompose them through hydrolysis.⁴⁸¹ The solubilities of most of these salts in nonaqueous media seemed to be dependent on the substitution of aromatic ligands, and moderate to good ion conductivities have been reported, ranging from 0.6 to 11.1 mS cm⁻¹ depending on the solvents used.

The stabilities of these salts against oxidation were studied with cyclic voltammetry on various inert electrodes, and an interesting correlation was established between the number of electron-withdrawing substituents on aromatic rings and the anodic stabilities (i.e., higher oxidation potentials were found for the better stabilized borate anions with more electron-withdrawing groups). This correlation could be well explained by the order of the HOMO energy levels obtained by quantum chemical calculations.^{477,479} Thus, the anodic decomposition potential ranges from 3.6 V for the unsubstituted borate⁴⁷⁵ to 4.60 V for the borate with fluorinated and sulfonated aromatic ligands.⁴⁷⁹ A similar relationship was reported by Sasaki et al., who listed the following order of oxidation potential limits according to the voltammetry results obtained on a Pt electrode, and revealed the obvious dependence of the anodic stability of these anions on the electron density of the aromatic rings.⁴⁸¹



In addition to the above thermodynamic consideration, kinetics also play an important role in determining the anodic stability of these salts. For example, some salts whose decomposition products are polymeric moieties were found to passivate the electrode surface effectively.⁴⁷⁸ Therefore, although the intrinsic oxidation potentials for these anions were not as high (~4.0 V), they showed stability up to 4.50 V in subsequent scans. It should be cautioned here, though, as the passivation was only observed on an inert electrode surface, whether similar passivations would occur on an actual cathode surface

and act to extend the potential range of application for these salts remains to be tested. Al was reported to be stable in the electrolytes based on at least two of these salts.^{479,480}

The cycling test for one of the salts was conducted by Handa et al. in lithium cells using a low-potential cathode material, V₂O₅.⁴⁸² OCV and initial discharging behavior similar to those of other nonaqueous electrolytes were reported, although no data concerning extended performance were given. The key property that would decide whether these salts could be used in lithium ion technology (i.e., the ability of forming a protective SEI on the surface of graphitic materials) has not been reported for any of these salts.

8.3.2.3. Lithium Borates with Nonaromatic Ligands. The presence of aromatic ligands in Barthel's salts was believed to be responsible for the high melting points and basicity of the borate anions, which in turn translate into moderate or poor solubilities and ion conductivities as well as low anodic stabilities. To avoid use of these bulky aromatic substituents, Xu and Angell synthesized a series of borate anions that are chelated by various alkyl-based bidentate ligands, which serve as electron-withdrawing moieties by the presence of fluorine or carbonyl functionalities.^{113,483,484} Table 13 lists the selected members of this aromatic-free borate family. Compared with their aromatic counterparts, these novel salts showed much higher ion conductivity and anodic stability, while maintaining comparable thermal stability. Detailed studies of ionics indicated that these salts could well dissociate in the media of moderate dielectric constants and yield ion conductivities slightly lower than those for state-of-the-art electrolyte solvents.^{485,486} As an example, in EC/DMC solutions of lithium bis(oxalato)borate (LiBOB) and LiPF₆, the ion conductivities are 7.5 and 10 mS cm⁻¹, respectively. For at least one of these salts, the lithium ion transport number seemed to be higher than 0.50 because of the large anions size.^{485,486} The dependence of ion conductivity on salt concentration is also different from the familiar bell-shaped dependences observed for LiPF₆- or LiBF₄-based solutions: the isothermal ion conductivity of these lithium borate solutions remains almost independent of salt concentration in the range 0.5–1.0 M, which could be advantageous for practical applications.

Among these new borates, particular attention should be paid to a salt based on oxalato ligands, which has aroused intense interest recently in the lithium ion research and development community. This salt was invented by Lischka et al.⁴⁸⁷ and independently synthesized and investigated by Xu and Angell, who also gave it the popular name LiBOB. Following these extensive physical characterizations, a rather comprehensive electrochemical evaluation was conducted on this salt by Xu et al.,^{155,324,488,489} who found that the solutions of LiBOB in mixed carbonate solvents met the complete set of stringent requirements for electrolyte solute intended for lithium ion cell applications: (1) it is anodically stable on the surface of composite cathode materials up to 4.3 V, (2) it can form a protective SEI on the

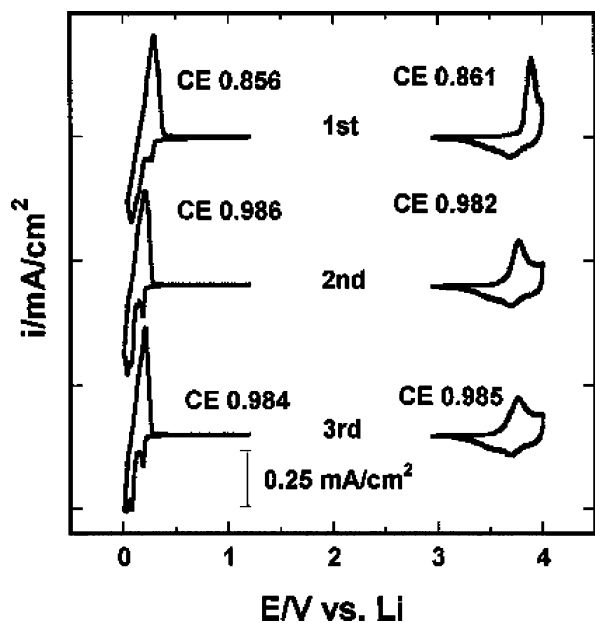


Figure 51. Cathodic and anodic stability of LiBOB-based electrolytes on metal oxide cathode and graphitic anode materials: Slow scan cyclic voltammetry of these electrode materials in LiBOB/EC/EMC electrolyte. The scan number and Coulombic efficiency (CE) for each scan are indicated in the graph. (Reproduced with permission from ref 155 (Figure 2). Copyright 2002 The Electrochemical Society.)

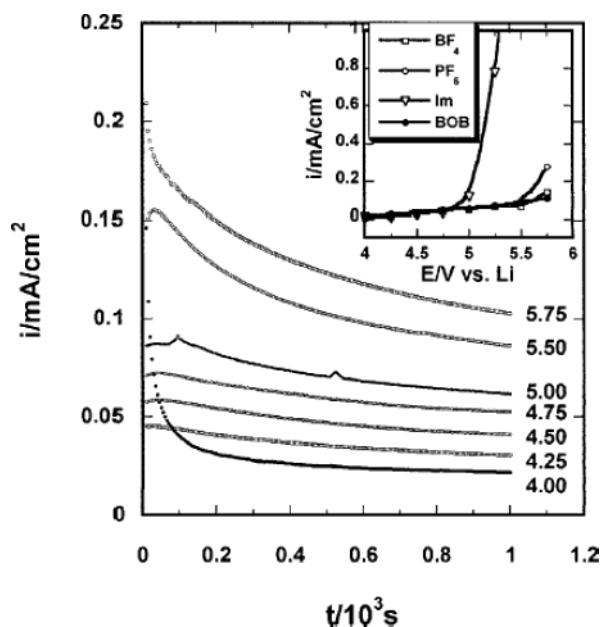


Figure 52. Passivation of Al substrate in LiBOB-based electrolytes: Time-decaying current observed on an Al electrode at various potentials containing 1.0 M LiBOB in EC/EMC. Inset: the dependence of steady-state current density (at $t = 10^3$ s) on applied potential as obtained on an Al electrode in electrolytes based on various salts in the same mixed solvent. (Reproduced with permission from ref 155 (Figure 1). Copyright 2002 The Electrochemical Society.)

surface of graphitic anode materials that supports reversible lithium ion intercalation/deintercalation, and (3) it stabilizes an Al current-collector at high potentials up to 6.0 V. Figures 51 and 52 present a brief summary of these qualifications, by all of which LiBOB showed performances comparable with or

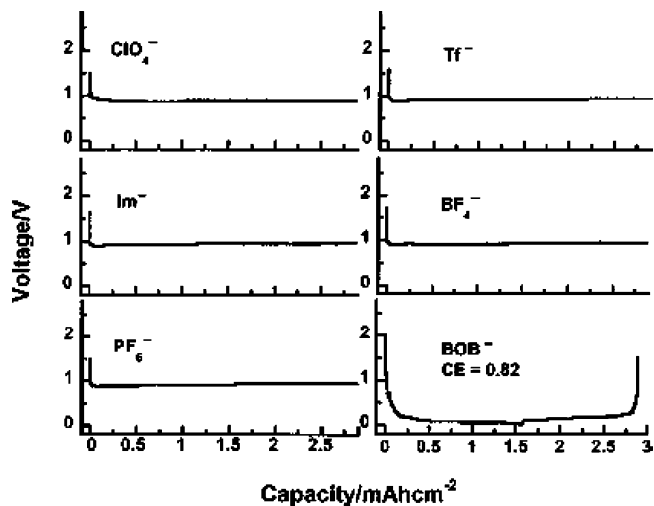


Figure 53. Stabilization of graphite in PC by LiBOB. Voltage profiles of lithium/graphite half-cells containing 1.0 M lithium salts in neat PC as electrolytes. Only for LiBOB/PC was the complete lithiation/delithiation cycle achieved. (Reproduced with permission from ref 324 (Figure 1). Copyright 2002 The Electrochemical Society.)

even superior to those of LiBF_4 , LiClO_4 , and LiPF_6 . Especially, compared with the industry standard, LiPF_6 , this salt also offers the additional advantages of being thermally stable, being economical in terms of manufacturing cost, being more environmentally friendly by decomposing into less corrosive products in the presence of moisture. The combination of these merits has not been found in other novel salts thus far investigated and has certainly made LiBOB a hopeful contender for lithium ion technology applications. The stable performance of LiBOB-based electrolytes was confirmed by the extended cycling of the full lithium ion cells using such electrolytes, where no capacity fading was detected during the operation of ~ 200 cycles.¹⁵⁵

An unexpected but certainly welcomed discovery on LiBOB is its peculiar cathodic chemistry.³²⁴ As has been pointed out in the preceding sections, the cornerstone of lithium ion technology is the formation of a protective SEI on the carbonaceous materials, and the conventional wisdom in this technology is that PC cannot be used in combination with graphitic anode materials because of its strong tendency to cointercalate and exfoliate the graphene structure. Prior to LiBOB, the presence of electrolyte solutes alone has never been able to challenge this wisdom, as Figure 53 shows. As an exception, however, LiBOB in neat PC solution successfully enables the reversible lithium ion intercalation/deintercalation on various graphitic anode materials, with capacity utilization and Coulombic efficiencies comparable with those of the state-of-the-art electrolytes. Considering that similar stabilization of graphene structure in PC was only able to be achieved by molecular additives before, the authors postulated that the BOB anion must have participated in the SEI formation during the initial lithiation process of the graphite, most likely through a single-electron reductive process.³²⁴ The durability of such a protective SEI was put to a stringent test by cycling a full lithium ion cell based on LiBOB/PC or other EC-free formulations as elec-

trolites. As the result, stable capacity and quantitative Coulombic efficiency were obtained for up to 100 cycles, similar to the case of the state-of-art electrolytes.³²⁴ Since these formulations are EC-free, the lower temperature limit that has been plaguing EC-centered electrolytes should be much improved.

Xu et al. emphasized that the significance of the above serendipity lies not only in the fact that PC-rich solvents could be used with graphitic anode materials because of LiBOB but more in the perspective that the unofficial law governing the selection of electrolyte solvents could be revised, and unprecedented flexibility is offered by LiBOB to the reformulating of lithium ion electrolytes, where the displacement of the high-melting-point component EC is no longer restricted by the concern over the stability of the graphitic anode.

In the subsequent investigations, these authors adopted a preformation technique to differentiate the steps for the formation of an effectively protective SEI by LiBOB.⁴⁸⁸ They systematically interrupted the lithiation of a graphite anode in LiBOB/PC at a series of potentials and then tested the survivability of these preformed anodes in LiPF₆/PC, which would have severely exfoliated the graphene structure had there been no protective SEI present. The results confirmed the critical role of BOB anion in the protection of graphitic anodes and, perhaps more importantly, found that an SEI sufficiently effective in protecting graphite against PC cointercalation and exfoliation was not completely formed till ~0.60 V. They thus concluded that a 1.60 V reduction process that was universally observed for all LiBOB-based electrolytes might not have a direct relation with the formation of this effective SEI.⁴⁸⁸

XPS analysis was also conducted by Xu et al. to characterize the surface chemistry of a graphitic anode resulted from LiBOB electrolyte, which yielded an entirely different image of the SEI in terms of the relative abundances of the chemical species, as Figure 54 shows.⁴⁸⁹ With BOB-anion participation, the content of chemical species similar to lithium alkyl carbonate became the major components of the SEI, as evidenced by the prominent peak at ~289 eV. The authors believed that these alkyl carbonate-like species are originated from the oxalate moiety of the BOB anion and are mainly responsible for the effective protection of graphitic anodes. A tentative mechanism was proposed accordingly in Scheme 29.⁴⁸⁹ Qualitatively, the chemical species present in the SEI formed by a LiBOB-based electrolyte seemed to be identical to those formed by LiPF₆ counterparts, since the comparison between the XPS C 1s spectra indicated that essentially the same peak locations for hydrocarbon, ether-containing species, and semi-carbonates were found in both spectra (Figure 54). This fact could suggest that similar active agents originated from the state-of-the art electrolytes are present in the LiBOB-originated SEI, despite the fact that these species are much more populated due to the involvement of BOB anion in SEI formation.

Further studies on LiBOB as a potential replacement for LiPF₆ were carried out by Liu et al., who reported that, due to the absence of HF and the much

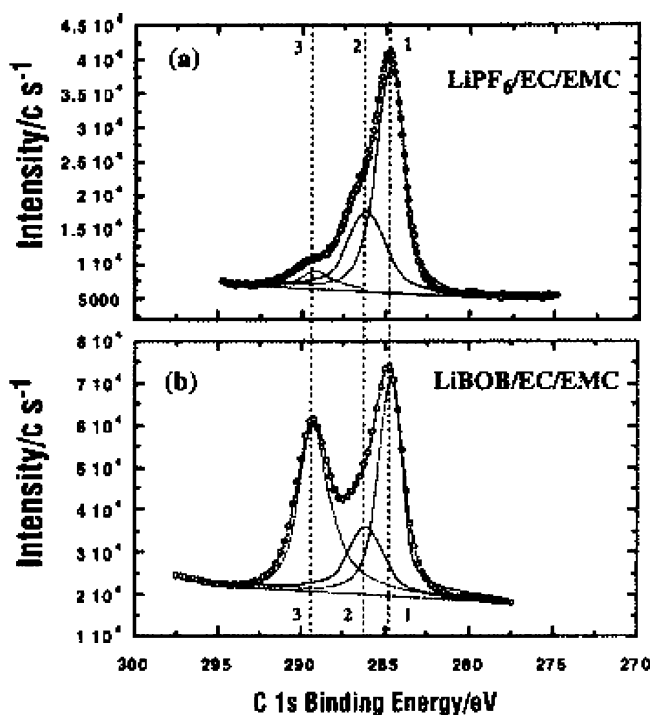
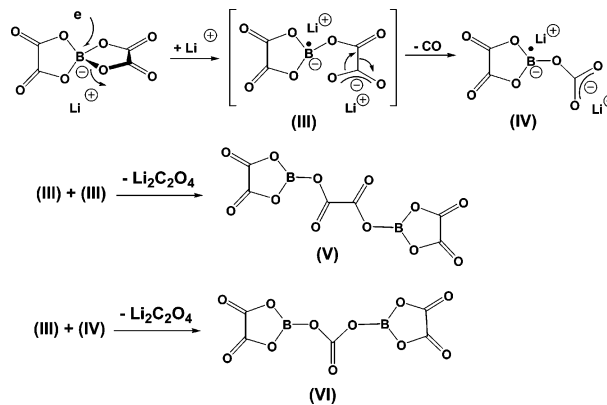


Figure 54. Peculiar surface chemistry of BOB anion on graphitic anode material: XPS C 1s spectra for a graphitic anode surface cycled in LiBOB- and LiPF₆-based electrolytes. The peaks were resolved into three major contributions representing (1) hydrocarbon at 284.5 eV, (2) oligo-ether linkages at 286.5 eV, and (3) lithium alkyl carbonates at 289.37 eV, respectively. (Reproduced with permission from ref 489 (Figure 3). Copyright 2003 The Electrochemical Society.)

Scheme 29. Proposed Mechanism for BOB Reductive Decomposition on a Graphitic Surface at Low Potentials



weakened acidity of the LiBOB electrolyte, cathode materials based on spinel LiMn₂O₄ were well stabilized, and the dissolution of Mn²⁺ species, which had been considered a main cause of the capacity fading of this class of cathode materials, was nearly eliminated.⁴⁹⁰ The thermal safety of LiBOB-based electrolytes against reductive decompositions was also compared with that of the LiPF₆ counterpart by Jiang and Dahn, who concluded that LiBOB is a much safer electrolyte solute as compared with LiPF₆ on a graphitic anode because its exothermic reaction with the fully lithiated MCMB was delayed by 90 °C due to the presence of LiBOB.⁴⁹¹ However, considering the conclusions by Maleki et al.³⁶¹ and especially

MacNeil and Dahn,³⁷¹ whether the LiBOB-based electrolytes are safer against thermal runaway would still depend on their interaction with the cathode materials.

On the basis of the findings on LiBOB performance in nonaqueous solvents and other advances made to improve the low-temperature performance of lithium ion electrolytes, Jow and co-workers proposed that an electrolyte with a much wider temperature range could be formulated using LiBOB alone or in combination with other salts.⁴⁹² The following section (8.4) will be dedicated to this topic.

Another series of lithium borates with nonchelating alkyl ligands were briefly reported by Yamaguchi et al. recently, where perhalogenated carbonyls were used to make the ligands electron-withdrawing.⁴⁹³ Their solubilities in linear carbonates are obviously superior to that of LiBOB, as solutions of these salts could be made in neat DMC or DEC with concentrations higher than 1.0 m. The anodic stabilities of the electrolytes based on these salts were measured on Pt and found to be comparable with those of electrolytes based on LiBOB, while Al substrates were not corroded in these electrolytes at potentials up to 4.8 V. However, the thermal stability of these salts seemed to be inferior to that of the chelated borates with either aromatic or alkyl ligands, although their decomposition temperatures, ranging between 94 and 135 °C, were still higher than that of LiPF₆. Among these salts, the one with the perfluorinated carbonyl ligands was considered to be the best-performing, and the cycling of a graphitic anode half-cell containing a solution of this salt in EC/EMC showed that stable capacity could be obtained during 50 cycles. With the exceptions of the initial cycles, quantitative Coulombic efficiency was observed, indicating this salt is stable against cathodic reductions on graphitic anode materials. However, no data of full lithium ion cells were reported.

8.3.2.4. Lithium Chelatophosphates. If the work of Barthel et al. and Angell et al. on various borate-based salts could be viewed as the structural modification of a perhalogenated borate salt (LiBF₄) that was already used in commercial lithium ion cells, then similar modifications were also carried out on the more popular salt LiPF₆, the industry standard of lithium ion cell electrolytes.

Handa et al. reported the synthesis of a phosphorus equivalent of Barthel's salts in which the hexavalent phosphorus(V) was coordinated by three bidentate ligands, 1,2-benzenediolato-*O,O'*.⁴⁹⁴ Its thermal stability is similar to that of its boron counterparts, and moderate ion conductivity was achieved in nonaqueous media. The authors attributed the less-than-satisfactory ion conduction to the large size of the anions, which increased the viscosity of the resultant electrolyte solutions. The anodic stability limit, as measured by voltammetry on a Ni electrode, was below 3.7 V. A preliminary test of this salt in EC/THF was conducted in a lithium cell using the low potential cathode, V₂O₅, and the authors believed that this salt could be a superior electrolyte solute, judging from the utilized cell capacity that was close to the theoretical value.

On the basis of their previous experiences with lithium borates coordinated by substituted ligands, Barthel and co-workers modified the chelatophosphate anion by placing various numbers of fluorines on the aromatic ligands.⁴⁹⁵ Table 13 lists these modified salts and their major physical properties. As expected, the introduction of the electron-withdrawing fluorines did promote the salt dissociation and reduce the basicity of phosphate anion, resulting in increased ion conductivity and anodic stability. The phosphate with the perfluorinated aromatic ligands showed an anodic decomposition limit of 4.3 V on Pt in EC/DEC solution. So far, these modified lithium phosphates have attracted only academic interest, and their future in lithium ion cell applications remains to be determined by more detailed studies.

8.3.2.5. Lithium Fluoroalkyl Phosphates (LiFAP). Since the P–F bonds in PF₆[−] anion are labile toward the attack of moisture and other nucleophiles such as the organic solvents with high electron-donicity, they are believed to be the source for the instability of the state-of-the-art electrolytes. Recent structural modification of PF₆[−] anion was conducted by Satori et al. via the partial replacement of fluorine substituents with perfluoroalkyls in the hope that chemical as well as thermal stability of the resultant salts (LiFAP) could be improved due to the inert nature of the P–C bonds.^{496,497} Since the new substituents are also strong electron-withdrawing groups, the main merits of LiPF₆, such as good solubility and ion conductivity, are expected to be maintained.

In their patent disclosure, Satori et al. described eight such salts with different perfluorinated alkyls,⁴⁹⁷ the representatives of which are listed in Table 13 along with the main physical and electrochemical properties. Among these salts, the most thoroughly investigated is the lithium salt based on an anion with three pentafluoroethyl groups. Hydrolysis studies confirmed that, due to the replacement of fluorine by the much bulkier perfluorinated alkyls, the sensitivity of the anion toward moisture is much reduced, as evidenced by the almost negligible amount of H₂O consumption during 70 h of storage (Figure 55) and, correspondingly, the negligible HF level in the electrolyte.⁴⁹⁸ The much lower reactivity of LiFAP should be the result of the combined effects of the lower chemical activity of the P–C bond and the spatial hindrance to the attack of H₂O. Ion conductivities of LiFAP in mixed carbonate solvents were slightly lower as compared with LiPF₆, obviously due to the larger anion size; however, comparable anodic stability was observed for LiFAP in the voltammetry scan conducted on a Pt electrode; that is, the major oxidative event occurred at ~5.0 V, although a higher background current level at potentials above 4.0 V was observed. Preliminary cycling tests were conducted in cathode half-cells based on LiMn₂O₄ using LiFAP/EC/DMC as electrolyte, and higher capacity was obtained than with LiPF₆ despite the fact that the capacity of the cells based on both electrolytes faded in a similar manner.

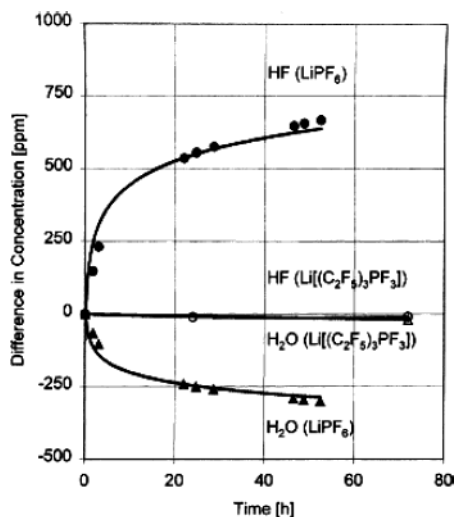


Figure 55. Presence of fluoroalkyls enhancing the anion stability against moisture. Consumption of H_2O and the generation of HF in 1.0 M salt solutions of EC/DMC with added H_2O at 500 ppm (for LiPF_6) and 1000 ppm (for LiFAP), respectively: triangle, H_2O concentration; circle, HF concentration. (Reproduced with permission from ref 498 (Figure 2). Copyright 2001 Elsevier.)

More stringent electrochemical characterizations were carried by Aurbach and co-workers, who comparatively investigated the interfacial properties of the electrolytes based on LiFAP on anode and cathode materials against the benchmark salts LiPF_6 and LiBet through various instrumental means, including voltammetry, EIS, FT-IR, and XPS.^{499,500} They found that, while on both the graphitic anode and the spinel cathode the LiFAP-based electrolyte showed higher capacity utilization and better capacity retention, slower kinetics for lithium ion intercalation/deintercalation were found in both cases. The cause for the slow kinetics seemed to be related to the resistive SEI and surface films on each electrode, which was unexpected because there should have been little LiF present in the SEI, due to the stability of LiFAP, and it was concluded that LiF was mainly responsible for the high-impedance interfaces on either the anode or the cathode with LiPF_6 as the electrolyte solute. FT-IR and XPS indicated that LiFAP-based electrolytes generated higher amounts of lithium alkyl carbonate on the inert electrode (Pt and Au) surfaces that were cathodically polarized to simulate the surface chemistry on a cycled graphitic anode, but these spectroscopic means failed to identify any direct involvement of FAP anion in SEI formation. Nevertheless, it is apparent that in LiFAP-based electrolytes the surface species are mainly reduction products from solvents, while in LiPF_6 -based electrolytes the anion is apparently more involved in the reductive decompositions, as evidenced by the XPS C 1s and F 1s spectra.⁴⁹⁹ The higher stability of LiFAP is shown clearly by Figure 56, wherein two sets of CV were measured for LiFAP- and LiPF_6 -based electrolytes after stabilization of the electrode and after 1 week of cyclings, respectively. In all the voltammetric profiles, four distinct stages of lithium intercalation are visible, but a very significant difference exists between LiFAP and LiPF_6 : nearly identical current responses for LiFAP but an

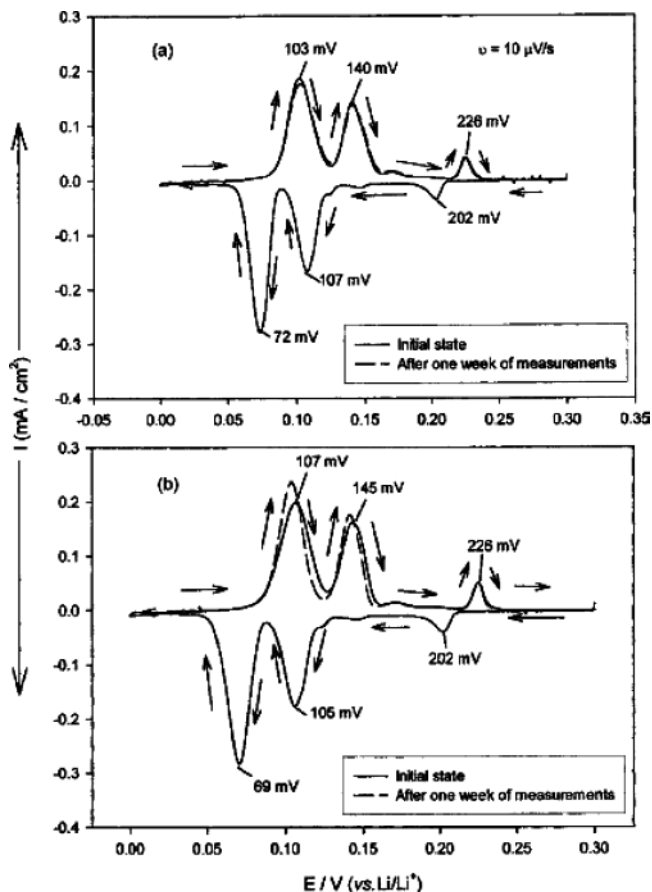


Figure 56. Slow scan ($10 \mu\text{V s}^{-1}$) voltammetry on a graphite working electrode: (a) 1.0 M LiFAP in EC/DEC/DMC; (b) LiPF_6 in EC/DEC/DMC. Solid line: pristine graphite. Dashed line: after 1 week of cycling. (Reproduced with permission from ref 499a (Figure 4). Copyright 2003 The Electrochemical Society.)

obvious gap for LiPF_6 in the anodic section were observed. In other words, there were long-term secondary processes in the LiPF_6 -based electrolyte that affected the electrode kinetics, while the graphitic anode in the LiFAP-based electrolyte was under better protection from such undesirable processes.

Therefore, the authors concluded that, although direct identification was not available through spectroscopic means, the FAP anion must have participated in the formation of surface layers, which served as protection against sustained decompositions on one hand but were also responsible for the high impedance across the interfaces on the other. These robust surface films might exist on both anode and cathode surfaces and consist mainly of lithium alkyl carbonates because of the low level of HF in the solution.

The thermal stability of LiFAP was also studied by Aurbach and co-workers in EC/DEC/DMC solution using ARC. As compared with LiPF_6 , LiFAP delayed the onset thermal decomposition of the electrolyte by $\sim 10^\circ\text{C}$; however, the self-heating became much more severe once the reactions started.⁵⁰⁰ The above ARC was conducted in the absence of electrode materials.

In brief summary, LiFAP as a potential replacement for LiPF_6 would result in a stable performance in lithium ion cells with possibly increased thermal

stability, but the power rate of such cells would probably be inferior to that of the state-of-the-art electrolytes. If the manufacturing cost of producing these perfluorinated anions could be reduced, LiFAP or its derivatives might be a competitive electrolyte solute for lithium ion electrolytes.

8.3.2.6. Lithium Salts Based on Heterocyclic Anions. Lithium salts based on organic anions where the formal charge is delocalized throughout substituted heterocyclic moieties were also reported sporadically, which included, for example, lithium 4,5-dicyano-1,2,3-triazolate⁵⁰¹ and lithium bis(trifluoroborane)imidazolid (LiId).⁵⁰² The former was developed as a salt to be used for polymer electrolytes such as PEO, and no detailed data with respect to electrochemistry were provided, while the latter, which could be viewed as a Lewis acid–base adduct between LiBF₄ and a weak organic base, was intended for lithium ion applications (Table 13).

Because of the organic presence in these anions, the corresponding lithium salts are highly soluble in media of low or medium dielectric constants and could provide ion conductivities comparable to those of LiPF₆. LiId was reported to have high anodic stability as compared with LiPF₆, although the background current of the electrolytes based on it was higher than those for LiPF₆ counterparts at potentials above 4.0 V, as measured by cyclic voltammetry on Pt. The compatibility of this salt with LiNi_{0.8}Co_{0.2}O₂ cathode material was investigated by testing the corresponding half-cells, and performances comparable with or better than those of LiPF₆-based electrolytes were reported. However, in the case of MCMB, it took longer for LiId-based electrolyte to reach full utilization of the capacity, and it was only after ~10 cycles when the difference between LiId and LiPF₆ vanished. A higher irreversible capacity was also associated with LiId in the first cycle, where the Coulombic efficiency was 10.2% versus 6.2% for LiPF₆, suggesting that more charges were consumed in building up an SEI when LiId was the electrolyte solute. On the other hand, the authors argued that this capacity loss was negligible in terms of the total capacity. Considering the presence of B–F bonds in the anion of LiId, its thermal and chemical stability should be similar to that of LiBF₄, and its potential applications to replace LiPF₆ remain to be confirmed by further studies.

8.4. Novel Electrolytes with a Wide Temperature Range

8.4.1. Low-Temperature Performance

Following its rapid rise to dominance in the consumer cell market intended for portable electronics, lithium ion technology was actively considered for special applications such as those in military and space missions.^{503–505} However, the poor performance of the state-of-the-art lithium ion cells at temperatures below –20 °C remained a major obstacle to enabling the normal operations in harsh environments that are frequently encountered in those missions. For example, according to a comprehensive

survey of the commercial lithium ion cells made by major manufacturers in the late 1990s, the power rate and energy density that can be delivered at –40 °C averaged only 1.25% and 5% of those achievable at room temperatures, respectively.⁵⁰⁶ A similar survey conducted a few years later showed that significant progress had been made, where as much as 30% of the rated capacity was deliverable at –40 °C by the best cells tested.⁵⁰⁷ However, the deteriorated performance still plagued the reliable operations of this technology. Despite the sharp differences among the cells from various manufacturers, a common observation concerning their low-temperature behavior is that the major deterioration in performance occurs below –20 °C, while above this threshold temperature at least 80% of the rated capacity is deliverable.^{505,507}

This sharp decline in cell output at subzero temperatures is the combined consequence of the decreased capacity utilization and depressed cell potential at a given drain rate, and the possible causes have been attributed so far, under various conditions, to the retarded ion transport in bulk electrolyte solutions,^{503,508,509,510} the increased resistance of the surface films at either the cathode/electrolyte interface^{506,507} or the anode/electrolyte interface,^{461,504,511} the resistance associated with charge-transfer processes at both cathode and anode interfaces,^{134,135,512} and the retarded diffusion coefficients of lithium ion in lithiated graphite anodes.^{165,513} The efforts by different research teams have targeted those individual electrolyte-related properties to widen the temperature range of service for lithium ion cells.

8.4.1.1. Solvent Approach. Since the high-melting EC constitutes 30–50% of the bulk electrolyte in most of the commercial lithium ion cells, it has been the primary blame for the poor performances of such electrolytes at low temperatures, and its mixing with other lower melting cosolvents has been the most favorable approach so far adopted by the researchers with the aim to develop an electrolyte for subambient applications. As a pioneering attempt to develop a low temperature for lithium ion chemistry, Ein-Eli et al. used methyl formate (MF, mp –99 °C) and reported the ion conductivity at –40 °C for LiMe in EC/MF (1:3) to be 5.4 mS cm^{–1}.¹⁰² The authors concluded that the depression effect of MF rendered the electrolyte liquid at such low temperatures. However, the performance of the anode half-cell was not improved ideally as expected, since only 50% deliverable capacity was achieved at –2 °C, which far exceeded the extent by which the bulk ion conductivity dropped. The possible origin for this discrepancy might arise from the elimination of supercooling at temperatures below –20 °C due to the presence of electrode particles in the anode half-cell, which are absent in conductivity cells, but more likely, it indicates that the bulk ion conductivity may not dictate the performance of the electrolytes in an actual lithium ion device. Since electrolytes based on neat MF failed to form an effective SEI on graphite and the stability of a graphite anode in the above EC/MF mixture solvents was clearly dependent on the EC presence, it appears that reductive decomposition

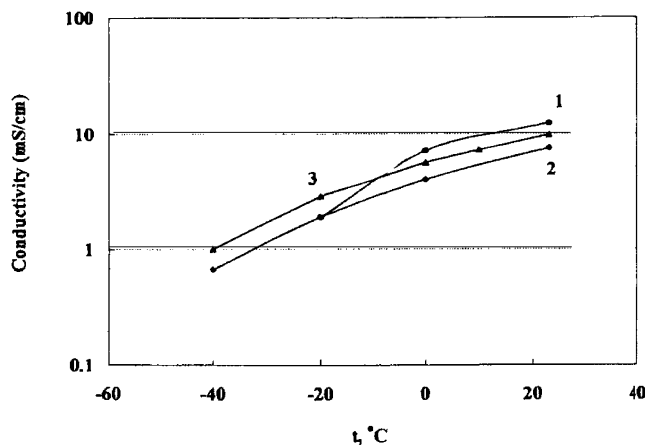


Figure 57. Ion conductivity of electrolytes containing 1.0 M LiPF₆ in (1) EC/DMC (3:7), (2) EC/DEC (3:7), and (3) EC/DMC/DEC (1:1:1). (Reproduced with permission from ref 508 (Figure 1). Copyright 1999 The Electrochemical Society.)

of MF made it an unfavorable candidate despite its low melting temperature.

An important contribution to the search for a low-temperature electrolyte was made by Smart et al. in late 1990s, apparently driven by the needs of NASA for the application of lithium ion devices in space missions.^{461,462,466,508,515} The basic strategy of the team was to minimize the concentration of EC in the ternary or quaternary electrolyte formulations so that a synergistic effect could be reached by the various components based on either linear carbonates or esters. In an ideal scenario of role assignment, less than 30% EC would suffice for the effective solvation of lithium salts and ensure the formation of an effective SEI on electrode surfaces, while the majority components such as the low-melting DEC and the less viscous DMC would confer upon the mixture solvents a low liquidus temperature and facile ion transport at low temperatures. Figure 57 shows this synergistic effect achieved in a ternary electrolyte through the comparison of the temperature-dependence of ion conductivities against the corresponding binary electrolytes.⁵⁰⁸ The discharge characteristics of the cells based on these electrolytes were also compared at $-20\text{ }^{\circ}\text{C}$, as Figure 58 shows. An apparent gap exists among the electrolytes in terms of the delivered cell capacity, although at room temperature all of the electrolyte compositions behave similarly. In an extensive characterization of the irreversible capacity during the initial cycle, the durability and resistance of the SEI, the self-discharge rate, and so forth, the ternary electrolyte was shown to possess a series of intermediary qualities as compared with the binary baselines. The authors believed that it was these well-balanced properties of the ternary composition that made it an excellent candidate for subzero applications.

An important conclusion that these authors drew based on their polarization and EIS studies is that the properties of the SEI film on a graphite anode surface play a far more decisive role in determining the kinetics of the lithiation/delithiation at low temperatures than does the bulk ion conductivity, although it is necessary for the latter to achieve a

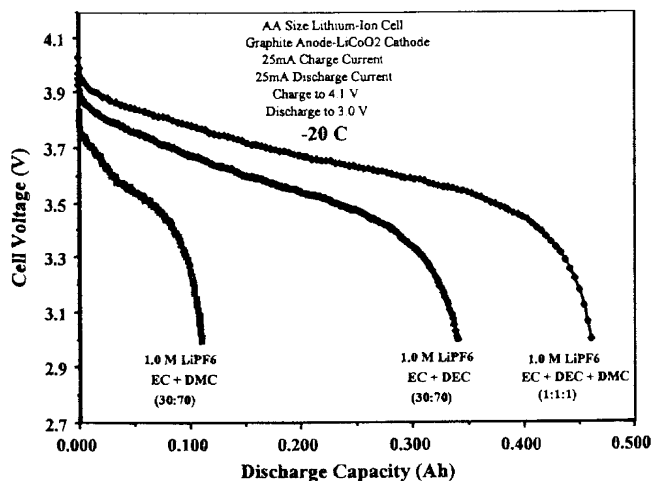


Figure 58. Comparison of the discharge profiles of graphite-based AA-size lithium ion cells at $-20\text{ }^{\circ}\text{C}$ among the various electrolytes. (Reproduced with permission from ref 508 (Figure 7). Copyright 1999 The Electrochemical Society.)

threshold value.^{461,462} In other words, the reformulation of these low-temperature electrolytes has to consider the surface chemistry of the new cosolvents in addition to their positive effects on ion conductivity. This conclusion, now well accepted as a basic guideline, has been confirmed by the numerous examples found later, where the most conductive electrolytes do not necessarily provide the best improvement at low temperatures.^{134,168,511,512}

Following the initial work by Smart et al., similar efforts were reported based on various binary and ternary compositions, such as EC/DMC/EMC (1:1:1),^{503,505,509} EC/DMC/DEC (2:2:1),⁵⁰⁵ EC/EMC (1:3),⁵⁰⁵ EC/DMC/methylpropyl carbonate (MPC) and EC/DMC/isopropyl carbonate (iPC) at a series of varying compositions.⁵¹⁴ Unfortunately, below $-30\text{ }^{\circ}\text{C}$ the above compositions still failed to function well.⁵¹⁵

In view of the limited improvements, Smart et al. sought to use linear alkyl esters, which are lower melting than the common alkyl carbonates by an average of $20\text{--}30\text{ }^{\circ}\text{C}$ (Table 1). On the basis of the experience that MF was incompatible with graphitic anodes, they chose alkyl esters of higher carboxylic acids so that carboxylate connected with an alkyl instead of H as in MF. Thus, acetates such as MA and EA and higher carboxylates such as EP and EB were used to formulate quaternary electrolytes on the basis of the ternary compositions EC/DMC/DEC (T).^{461,462} As expected, due to the introduction of these esters, the ion conductivity was obviously improved, while both anodic and cathodic stability as measured on a Pt surface were negatively affected. In terms of compatibility with a graphite anode, there exists an apparent distinction between the acetates (MA and EA) and the esters of higher carboxylic acids (EP and EB), since the reversible capacities that can be utilized by the electrolytes containing the acetates are much lower, and EP- or EB-based electrolytes yield comparable performances with the ternary baseline. Therefore, the authors speculated that the SEI formed in the presence of low molecular weight esters appeared to be resistive and inadequately protective, whereas, in the presence of esters of

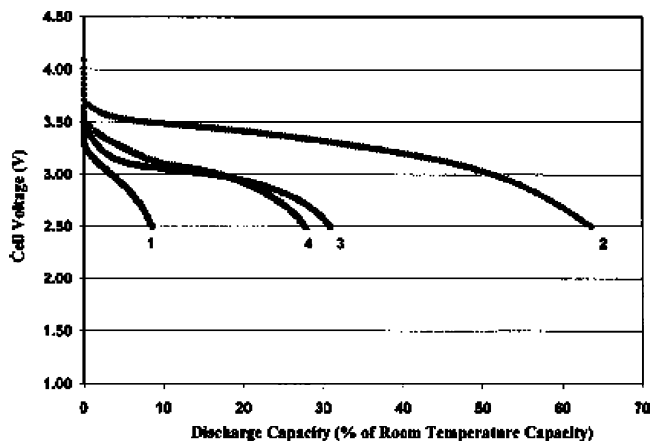


Figure 59. Effect of ester-containing quaternary electrolytes on the discharge capacity of AA-size lithium ion cells (0.4–0.5 A h) at $-40\text{ }^{\circ}\text{C}$ under the drain rate of 25 mA. The electrolytes are (1) 1.0 M $\text{LiPF}_6/\text{EC}/\text{DEC}/\text{DMC}$ (1:1:1), (2) 0.75 M $\text{LiPF}_6/\text{EC}/\text{DEC}/\text{DMC}/\text{MA}$ (1:1:1:1), (3) 0.75 M $\text{LiPF}_6/\text{EC}/\text{DEC}/\text{DMC}/\text{EA}$ (1:1:1:1), and (4) 0.75 M $\text{LiPF}_6/\text{EC}/\text{DMC}/\text{MA}$ (1:1:1). (Reproduced with permission from ref 462 (Figure 12). Copyright 2002 The Electrochemical Society.)

higher molecular weight, the SEI could be formed with more desirable attributes. Combining the observations of Ein-Eli et al.,¹⁰² Smart et al.,^{461,462} and Herreyre et al.,⁴⁰⁶ it could be tentatively concluded that longer alkyl chains in the carboxylic acid section of the esters play a critical role in determining the cathodic stability of this component on a graphite anode. The tests in AA-size full lithium ion cells were only reported for EA- and MA-based quaternary electrolytes, and Figure 59 shows the discharging profiles of these cells at $-40\text{ }^{\circ}\text{C}$. Despite their negative effect on anode capacity utilization at room temperature, MA and EA still improved the capacity significantly.

On the other hand, the presence of these esters in the electrolyte solutions raised concern over the long-term performance at room temperatures, because EIS studies indicated that the resistance associated with the SEI film increased at a much higher rate for ester-based electrolytes as compared with the compositions that were merely based on carbonates. The authors attributed this rising cell impedance to the reactivity of these esters toward the electrode active material, which resulted in the continued growth of the SEI film in the long term and suggested that alkyl esters, especially those of acetic acid, might not be appropriate cosolvents for low-temperature application electrolytes.⁴⁶¹

The work of Herreyre et al., however, took a much more optimistic tone on the use of linear esters EA and MB.⁴⁰⁶ In $\text{LiCoO}_2/\text{graphite}$ cells, the ternary electrolyte compositions such as 1.0 M LiPF_6 in EC/DMC/EA, EC/DMC/MB, and PC/EC/MB were reported to be able to deliver as much as 88–95% of the rated capacity at $-30\text{ }^{\circ}\text{C}$ with a $C/2$ rate or 81–87% at $-40\text{ }^{\circ}\text{C}$, while at room temperature the capacity fading rate (0.05% per cycle for MB and 0.09% per cycle for EA) and capacity retention with high-temperature storage ($60\text{ }^{\circ}\text{C}$, 14 days at full state-of-charge) of these cells were comparable with those of the state-of-the-art electrolytes (0.05% per

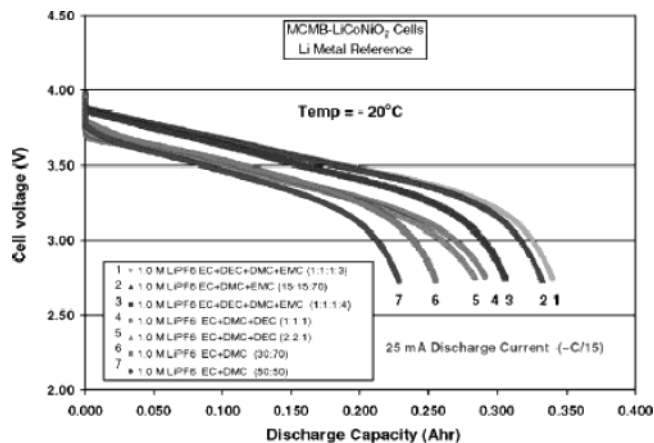


Figure 60. Discharge capacities of $\text{LiNiCoO}_2/\text{MCMB}$ lithium ion cells at $-20\text{ }^{\circ}\text{C}$ with different carbonate-based electrolytes. Cells are charged at room temperature and discharged using a $C/15$ rate. (Reproduced with permission from ref 515 (Figure 4). Copyright 2003 Elsevier.)

cycle). Thus, the authors concluded that these new electrolytes could be used as cosolvents for low-temperature electrolytes. Considering that Smart et al. and Herreyre et al. used entirely different cells as their testing vehicles, the above discrepancy might not be too incomprehensible, since similar discrepancies had been encountered when the trends observed in anode half-cells did not correlate well with that of prototype cells with a different cell design.⁴⁶² It actually indicated the complexity in the operation of lithium ion chemistry, during which various factors including chemistry as well as engineering exert their influences.

Besides the Coulombic capacity, Herreyre et al. also pointed out that the depression in cell voltage at low temperatures could be mitigated by EA and MB as cosolvents because of the reduced resistance in both bulk electrolyte and electrolyte/electrode interfaces. Moreover, they found that this cell voltage depression was also related to the salt concentration; using 1.5 M instead of 1.0 M LiPF_6 in the electrolyte enabled the increase of the cell working range from -30 to $-40\text{ }^{\circ}\text{C}$, as, in most cases, the cell cycling is regulated by a preset cutoff potential.

Out of the belief that the alkyl esters are reactive in a lithium ion cell during the long-term operation, Smart et al. proposed a “carbonate-only” guideline and formulated a series of quaternary compositions consisting of EC/DEC/DMC/EMC, in which the EC concentration remained under 25%.⁵¹⁵ The solution of 1.0 M LiPF_6 in EC/DEC/DMC/EMC (1:1:1:3) was reported to be the best composition, whose ion conductivity at $-40\text{ }^{\circ}\text{C}$ was 1.32 mS cm^{-1} , and its cycling in $\text{LiNiCoO}_2/\text{MCMB}$ lithium ion cells was comparable to that of the baseline electrolyte 1.0 M LiPF_6 in EC/DMC (3:7) or (1:1) at room temperatures. At $-20\text{ }^{\circ}\text{C}$, the superiority of these quaternary electrolytes became pronounced, as compared with the ternary and binary baselines shown in Figure 60.

More importantly, these electrolytes also allowed the lithium ion cells based on them to be charged at low temperatures at reasonable rates, as shown by Figure 61, which had been impossible for most of the lithium ion cells because the high impedance of the

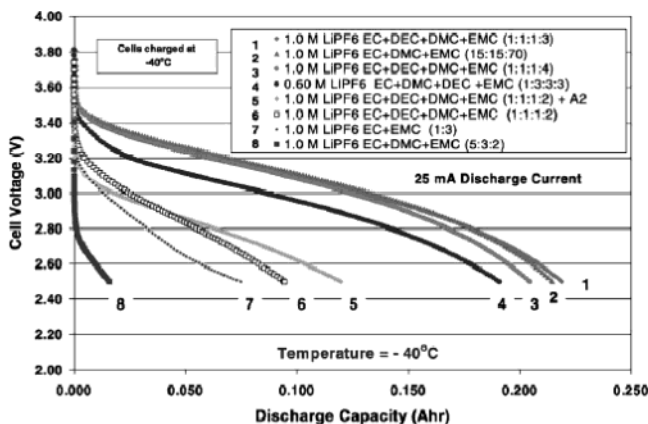


Figure 61. Discharge capacities of LiNiCoO₂/MCMB lithium ion cells at $-40\text{ }^{\circ}\text{C}$ with different carbonate-based electrolytes. Cells are charged at $-40\text{ }^{\circ}\text{C}$ and discharged using a $C/4$ rate. (Reproduced with permission from ref 515 (Figure 6). Copyright 2003 Elsevier.)

cells at a discharged state would result in lithium deposition on a graphite surface due to the high overpotential.⁵¹⁵ Using a three-electrode cell, Smart et al. monitored the potential of the cathode and anode of a LiNiCoO₂/MCMB lithium ion cell during its cycling at $-20\text{ }^{\circ}\text{C}$, and they confirmed that, although the potential of the graphite anode was indeed driven to negative regions in the charge process, no lithium deposition occurred, as evidenced by the absence of a potential plateau at 0.0 V corresponding to lithium stripping in the following discharge process, which had been observed previously in a similar cell using LiPF₆/EC/EMC (1:3) as the electrolyte.¹⁶⁵ They attributed this to the facile kinetics of lithium ions in the bulk electrolyte as well as in the SEI film on the graphite anode. The cycling tests of SAFT prototype lithium ion cells carried out in a wide temperature range between -70 and $40\text{ }^{\circ}\text{C}$ confirmed that the above quaternary composition is an excellent low-temperature electrolyte. As illustrated in Figure 62, when the cell is continuously cycled at $-20\text{ }^{\circ}\text{C}$ using a $C/10$ charge rate and a $C/5$ discharge rate, stable capacity retention can be obtained with 80% of the rated capacity delivered. Using lower rates ($C/15$ charge and $C/10$ discharge), 70% of the rated capacity can be accessed even when cycled at $-40\text{ }^{\circ}\text{C}$.

Fluorinated carbonates were also used by Smart et al. as low-temperature cosolvents (Table 12), in the hope that better low-temperature performances could be imparted by their lower melting points and favorable effects on SEI chemistry.⁴⁶⁶ Cycling tests with anode half-cells showed that, compared with the ternary composition with nonfluorinated carbonates, these fluorinated solvents showed comparable and slightly better capacity utilizations at room temperature or $-20\text{ }^{\circ}\text{C}$, if the cells were charged at room temperature; however, pronounced differences in discharge (delithiation) capacity could be observed if the cells were charged (lithiated) at $-20\text{ }^{\circ}\text{C}$, where one of these solvents, ethyl-2,2,2-trifluoroethyl carbonate (ETFEC), allowed the cell to deliver far superior capacity, as Figure 63 shows. Only 50% of the capacity deliverable at room temperature was

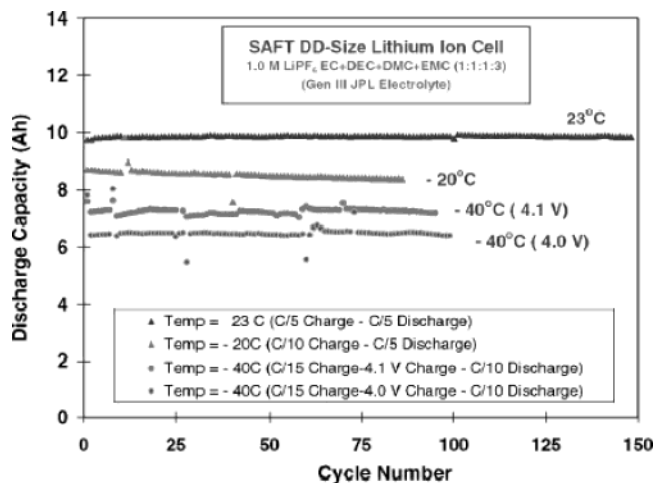


Figure 62. Cycle life performance of SAFT DD-size lithium ion cells containing 1.0 M LiPF₆/EC/DEC/DMC/EMC (1:1:1:3) at various temperatures. Cutoff voltages for low-temperature charge were indicated in the graph. (Reproduced with permission from ref 515 (Figure 11). Copyright 2003 Elsevier.)

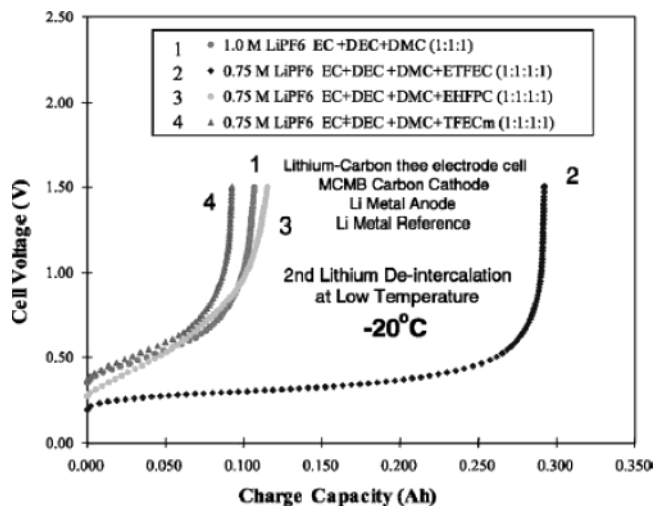


Figure 63. Delithiation capacity of an MCMB anode at $-20\text{ }^{\circ}\text{C}$ in various electrolytes following charge (lithiation) at $-20\text{ }^{\circ}\text{C}$. The drain rate is 50 mA ($\sim C/12$). (Reproduced with permission from ref 466 (Figure 4). Copyright 2003 Elsevier.)

achieved in the best case, however. EIS and polarization studies on the interface between the electrolyte and the graphitic anode showed that these fluorinated cosolvents in general created less resistive surface films and more rapid charge-transfer kinetics when compared with nonfluorinated carbonates, and the difference increased with decreasing temperature. Full lithium ion cells based on LiNi_xCo_{1-x}O₂ and MCMB were also assembled with one of these novel solvents, and good reversibility was observed, although no data on subzero temperature tests were reported.

According to the authors, additional merits of such fluorinated carbonates would include their lower flammability and higher stability against storage at elevated temperatures as compared with their nonfluorinated counterparts; therefore, the incorporation of these novel solvents into the current commercial

lithium ion cells seems promising if the manufacturing costs and environmental requirements do not constitute any obstacle.

In addition to linear carbonates, PC was also considered as a cosolvent that could help to improve the low-temperature performance of the electrolytes, mainly due to its wide liquid range and solvation ability to lithium salts. This latter property seems to be a merit relative to the linear carbonates, whose dielectric constants are generally below 10 and whose displacement of EC usually causes the solubility of lithium salts to decrease in such mixed solvents, especially at low temperatures.

To characterize the effect of PC addition on the related properties of the electrolytes, Zhang et al. carried out a comparative study on PC/EC/EMC (1:1:3) and EC/EMC (3:7).¹⁶⁸ They found that, because of the higher viscosity of PC, the ion conductivity of the former formulation was lower at subzero temperatures, and its declination accelerated with decreasing temperature. Nevertheless, due to the large portion of linear carbonates in the formulation, the compromise in ion conductivity was marginal. Discharge tests in LiNiO₂/graphite lithium ion cells were carried out down to -30 °C, and PC-containing electrolytes was found to outperform the baseline. According to the authors, this improvement could not be attributed to the bulk ion conductivity of the PC-based electrolyte but to the lower cell impedances associated with the films on both cathode and anode surfaces. No cycling tests below -20 °C were described. Considering that PC would induce higher irreversible capacities in the initial cycles and eventually result in lower capacity in cathode-limit lithium ion cells, the use of it as a low-temperature electrolyte cosolvent is possible only if one of the following measures is adopted to suppress the cointercalation and decomposition of PC: (1) the use of SEI-modifying additives, (2) the use of special salts that can help form a more protective SEI (such as LiBOB), or (3) the surface modification of the graphite anode.

8.4.1.2. Salt Approach. Another less expected approach aimed at low-temperature electrolytes was also proposed by Zhang et al., who reported that the replacement of LiPF₆ by LiBF₄ would result in improved discharge capacity of lithium ion cells.^{134,135}

LiBF₄ had been considered an inferior electrolyte solute to LiPF₆ due to its lower ion conductivity in nonaqueous solvents and the less protective SEI formed by these electrolytes, and its application in commercial lithium ion cells seemed to be possible only in the unique solutions containing γ BL. As Figure 64 shows, in the entire temperature range from 60 to -60 °C, LiBF₄ exhibited a lower ion conductivity than LiPF₆ in PC/EC/EMC (1:1:3) solutions,¹³⁴ while a similar trend was found for EC/DMC/DEC solutions as well.¹³⁵ However, all the LiBF₄-containing lithium ion cells obviously outperformed their LiPF₆ counterparts in discharge capacity at temperatures below 0 °C, and as Figure 65 shows, at -40 °C, its PC/EC/EMC solution was still able to deliver up to 86% of the rated capacity, while the LiPF₆ counterpart could only access 72%. These results once again confirmed that ion conductivity in

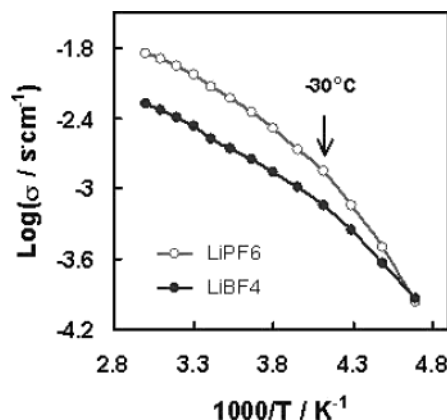


Figure 64. Arrhenius plots of the ion conductivities for the electrolytes composed of 1.0 M lithium salts in PC/EC/EMC (1:1:3). (Reproduced with permission from ref 134 (Figure 1). Copyright 2002 Elsevier.)

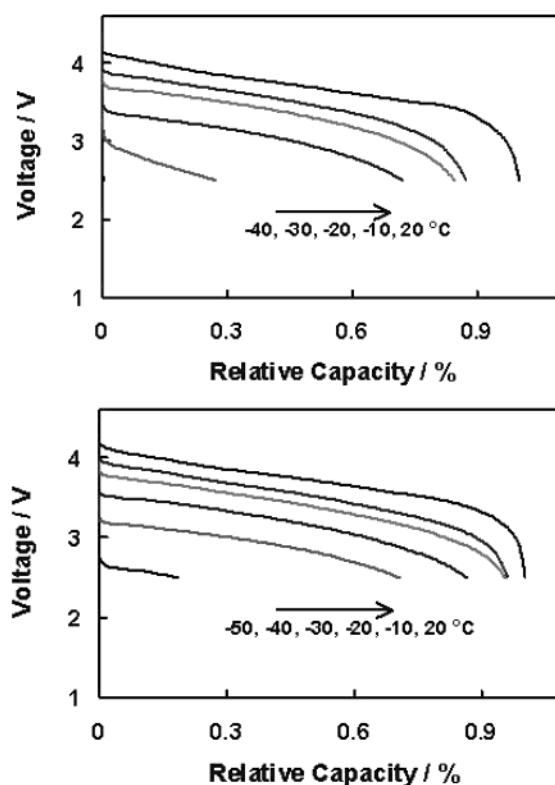


Figure 65. Comparison between the discharge capacities for lithium ion cells at various temperatures. Relative capacity was defined as the ratio of the capacity at the specified temperature to the one obtained at 20 °C: (a, top) LiPF₆/EC/PC/EMC (1:1:3); (b, bottom) LiBF₄/EC/PC/EMC (1:1:3). (Reproduced with permission from ref 134 (Figure 2). Copyright 2002 Elsevier.)

the bulk electrolytes does not dictate low-temperature performance.

By EIS analysis of the corresponding lithium ion cells, Zhang et al. showed that the impact of SEI resistance on total cell impedance was rather negligible, and hence, they attributed the superior low-temperature behavior of LiBF₄-based electrolytes to the lower resistance associated with the so-called "charge-transfer processes", which are usually represented in impedance spectra by the semicircle at the lower frequency region.⁵¹⁶ This suggestion could be viewed as a further extension of the conclusion

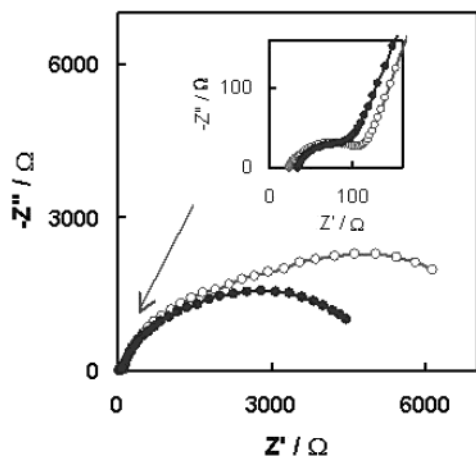


Figure 66. Nyquist plots of the impedance spectra as measured for the fully charged lithium ion cells at $-30\text{ }^{\circ}\text{C}$ in which the inset shows the magnified view of the high-frequency part. Electrolytes are 1.0 m LiPF₆ (hollow) and LiBF₄ (solid) in PC/EC/EMC (1:1:3). Note that the semicircles in the inset are almost invisible in the scale of the whole spectra. (Reproduced with permission from ref 134 (Figure 4). Copyright 2002 Elsevier.)

drawn by Smart et al., who had identified R_{SEI} as the limiting resistance in the lithium cell operation at low temperatures.⁴⁶² In fact, Smart et al. had already realized the effect of R_{ct} on low-temperature behavior, since they also used an effective exchange current density to represent the lithium ion intercalation kinetics. This latter quantity should reflect the overall effect of R_{SEI} and R_{ct} .^{462,508}

Thus, by comparing the impedance spectra of the lithium ion cells, Zhang et al. showed that the resistance corresponding to the charge-transfer process (R_{ct}) dominates the total cell resistance at low temperatures. For example, at $-30\text{ }^{\circ}\text{C}$ (Figure 66), the semicircle and the interception corresponding to R_{f} and R_{b} have to be magnified in the inset to be visible. Considering the huge difference between the magnitudes of R_{b} or R_{f} and R_{ct} , the authors concluded that the poor low-temperature performance of lithium ion cells is caused by the slow kinetics of charge-transfer at these temperatures. The decoupling of the bulk resistance (R_{b} , related to the ion conductivity in the bulk electrolytes) from the charge-transfer process and film resistances (R_{ct} and R_{f} , related to the ion transport in the surface film and the Faradaic process, respectively) can also be clearly seen in Figure 66 (at $-30\text{ }^{\circ}\text{C}$): that is, although the cell based on LiBF₄ has higher R_{b} (the inset), its R_{ct} is much lower than that of the cell with LiPF₆.¹³⁴ Similar observations were also made with EC/DMC/DEC formulations.¹³⁵ It should be noted that, since full lithium ion cells were used in these EIS studies, R_{ct} and R_{f} mentioned above should reflect the combination of these corresponding processes on both anode/electrolyte and cathode/electrolyte interfaces.

In another work unrelated to the low-temperature electrolytes, Mohamedi et al. characterized the spray-deposited thin film of spinel cathode material by means of EIS and studied the correlation between electrolyte composition and the impedance components. Among the three lithium salts investigated, the lowest R_{ct} and R_{f} were obtained in a LiBF₄-based

electrolyte.⁵¹⁷ This observation indirectly corroborated the conclusions of Zhang et al. and seemed to indicate that LiBF₄ possessed certain qualities of an electrolyte solute for low-temperature-oriented applications. In combination with the advances obtained in the solvents approach, further improvement in the performance at extreme temperatures might be a probable perspective.

8.4.1.3. Limiting Factors for Low-Temperature Operation. One controversial topic that has raised wide attention relates to the limiting factors of the low temperature of lithium ion cells. The researchers not only debated about whether the anode or cathode controls the overall low-temperature performance of a full lithium ion cell but also disagree upon the rate-determining steps that govern the low-temperature kinetics of lithium ion intercalation at the graphitic anode.

Due to the contributions from Smart et al.,⁴⁶² the emphasis of low-temperature study on electrolytes has been placed on the anode side, and the SEI film on the graphitic surface has generally been recognized as the most resistive component in the journey of the lithium ions during the cell operation, which must travel across the electrolyte and intercalate into or deintercalate from the bulk graphite structure. This hypothesis was mainly established on the basis of two observations made in the EIS studies of the lithium/graphite half-cells: (1) the resistance corresponding to the surface film component (R_{SEI}) far outweighs the component representing electrolyte bulk resistance, and (2) the steep temperature-dependence of R_{SEI} in the low-temperature ranges below $-20\text{ }^{\circ}\text{C}$ matches the rapid deterioration of the half-cell performance, while the ion conductivities do not suffer any dramatic drop in this range.^{164,168} These two phenomena have been repeatedly observed in various electrolyte systems in which novel cosolvents were added to depress the liquidus temperature and to improve solution transport properties, and complementary evidence was also obtained from various electrochemical polarization techniques.^{466,511,512}

The above hypothesis was questioned by Huang et al., who suggested that the critical factor that limits the anode capacity accessible at the low temperatures is the kinetics of the lithium ion in the bulk carbonaceous anode instead of the surface film.⁵¹³ Their argument was based on the universally observed asymmetric behavior of graphitic anodes toward lithiation and delithiation at low temperatures; that is, while the fully charged graphite can release the intercalated lithium ions at temperatures below $-20\text{ }^{\circ}\text{C}$ with relative readiness, the attempt to lithiate a fully discharged graphite anode at the same temperature is severely hampered by the high resistance at the surface. Considering the electrolyte nature of the SEI, which serves as an electronic insulator but an ionic conductor, the authors pointed out that it should neither behave like a diode that only impedes lithium insertion but allows extraction nor vary in its resistance depending on the state-of-charge of the graphite. Therefore, the above asymmetric behavior should not be attributed to the SEI, whose resistance should

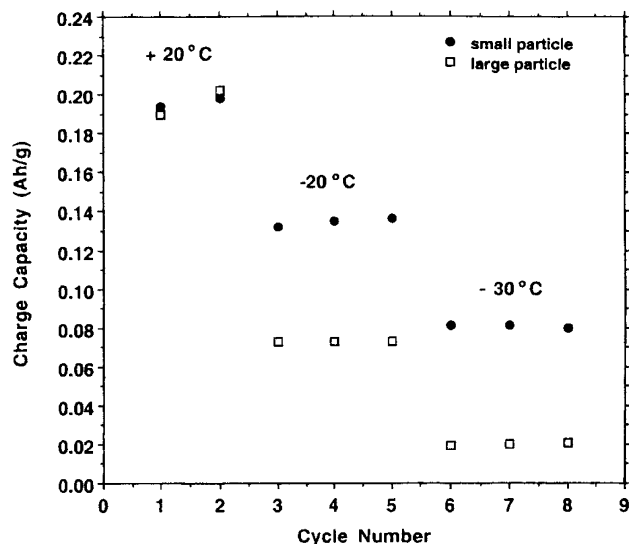


Figure 67. Effect of coke particle size on the charge capacity at various temperatures. (Reproduced with permission from ref 513 (Figure 8). Copyright 2000 The Electrochemical Society.)

be independent of the lithiation degree in the graphite, but rather to the lithium ion diffusion within the carbonaceous anode structure, which has directionality due to the concentration polarization. Thus, the diffusion coefficient of lithium ion within the carbonaceous anode (D_{Li}) would always be higher for lithium deintercalation but lower for intercalation, and the gap between the two processes becomes more prominent as temperature goes down.⁵¹³

To further support their argument that low-temperature lithium ion intercalation is governed by lithium diffusion instead of the SEI, the authors investigated the effect of carbon particle size on its specific capacity by choosing two carbonaceous anodes of the same capacity at room temperature but different particle sizes (6 and 25 μm). They found that, when cycling at temperatures below $-20\text{ }^\circ\text{C}$, the anode with fine particles outperformed the one with coarse particles in the charge capacity, as Figure 67 shows. The authors believed that this particle size effect was consistent with their contention that lithium diffusion is the rate-determining step that limits the low-temperature performance of carbonaceous anodes, because the large diameter of the 25 μm particle would require longer lithium diffusion lengths and, consequently, a lower lithiation degree would be realized in this case, with the assumption that D_{Li} is the same for both anode materials.

Combining the above evidences, Huang et al. further concluded that the improvement in the low-temperature performances of lithium ion cells would eventually rely on the effort to develop anode materials of high lithium diffusion coefficients instead of the electrolytes and SEI that were less resistant.

The conclusion of Huang et al. was supported by Lin et al., who used a three-electrode cell design to monitor the voltage profile of both the anode and cathode in a full lithium ion cell during cycling at low temperatures and found that these cyclings resulted in the deposition of metallic lithium on the

graphite surface and the subsequent permanent capacity loss when an unusual cycling regulation was applied to deal with the reduced capacity accessible at low temperatures.¹⁶⁵ These authors attributed the lithium deposition to the excessive concentration polarization on the graphite surface.

However, more recent work by Wang et al.⁵¹¹ and Zhang et al.⁵¹² seemed to present convincing evidence challenging the suggestion by Huang et al. that electrolyte and the SEI resistances do not affect the low-temperature performance of graphitic anodes. The former authors used the combination of the galvanostatic intermittent titration (GITT) technique and EIS to analyze the individual impedance components that simulate graphite in the quaternary electrolyte composition $\text{LiPF}_6/\text{EC}/\text{PC}/\text{DMC}/\text{EMC}$ (4:1:3:2). Since the reaction resistance as measured by GITT is the sum of the electrolyte bulk resistance, R_{SEI} , R_{ct} , stage transformation, and the resistance that corresponds to lithium diffusion in graphite, it is possible to distinguish the impact of their temperature-dependences on the overall electrode kinetics. They found that, during the low-temperature cyclings, the diffusional resistances were similar during charge and discharge, thus contradicting the hypothesis by Huang et al. that the concentration-dependence of lithium diffusion would result in higher concentration polarization to lithiation than to delithiation. Furthermore, in a quantitative manner, they also found that the magnitude of R_{SEI} makes it the dominating component at the low temperatures when compared with the other impedance components and, hence, concluded that at $-30\text{ }^\circ\text{C}$ the limiting factor for the lithium intercalation is R_{SEI} .

The latter authors used anode and cathode symmetrical cells in EIS analysis in order to simplify the complication that often arises from asymmetrical half-cells so that the contributions from anode/electrolyte and cathode/electrolyte interfaces could be isolated, and consequently, the temperature-dependences of these components could be established. This is an extension of their earlier work, in which the overall impedances of full lithium ion cells were studied and R_{ct} was identified as the controlling factor.^{134,135} As Figure 68 shows, for each of the two interfaces, R_{ct} dominates the overall impedance in the symmetrical cells as in a full lithium ion cell, indicating that, even at room temperature, the electrodic reaction kinetics at both the cathode and anode surfaces dictate the overall lithium ion chemistry. At lower temperature, this determining role of R_{ct} becomes more pronounced, as Figure 69c shows, in which "relative resistance", defined as the ratio of a certain resistance at a specific temperature to that at $20\text{ }^\circ\text{C}$, is used to compare the temperature-dependences of bulk resistance (R_b), surface layer resistance (R_{sl}), and R_{ct} . For the convenience of comparison, the temperature-dependence of the ion conductivity measured for the bulk electrolyte is also included in Figure 69 as a benchmark. Apparently, both R_b and R_{sl} vary with temperature at a similar pace to what ion conductivity adopts, as expected, but a significant deviation was observed in the temperature dependence of R_{ct} below $-10\text{ }^\circ\text{C}$. Thus, one

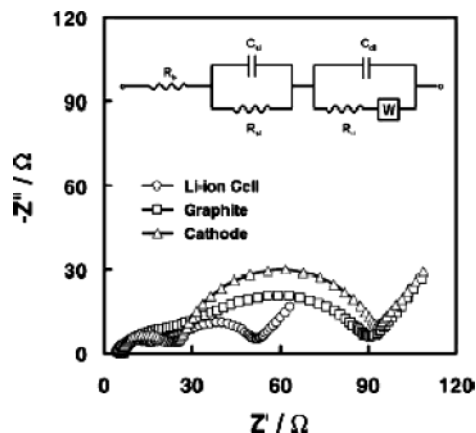


Figure 68. Nyquist plots of a charged lithium ion cell, a lithiated graphite/graphite cell, and a delithiated cathode/cathode symmetrical cell. The inset is an equivalent circuit used for the interpretation of the impedance spectra. (Reproduced with permission from ref 512 (Figure 3). Copyright 2003 Elsevier.)

could conclude that the rate-determining factor that limits the capacity utilization of the graphitic anode as well as the cathode should most likely be R_{ct} .

Perhaps a more important finding by these authors is the “concentration-dependence” of R_{ct} . As Huang et al. has pointed out, R_{SEI} should be independent of state-of-charge,⁵¹³ and the authors proved that R_{SEI} remains relatively constant on both charged and discharged anode and cathode surfaces, as shown by the insets of Figure 70. However, R_{ct} showed a strong dependence on the lithiation degree of both the anode and cathode. Two extreme situations were simulated in Figure 70, which correspond to a fully charged lithium ion cell, wherein the cathode is delithiated and the anode is lithiated, and a fully discharged lithium ion cell, wherein the cathode is lithiated and the anode is delithiated. Apparently, in the former case, R_{ct} on both the anode and cathode is substantially high, indicating a high polarization for the lithiation of the anode and delithiation of the cathode, while the reverse processes for each electrode are much easier in a fully charged lithium ion cell. Hence, these authors proposed that the asymmetrical behavior of lithium ion cells at low temperature most likely originated from the concentration-dependence of R_{ct} instead of the directionality of lithium diffusion within the bulk graphite anode.⁵¹² Since in numerous reports R_{ct} has been shown to be closely related to SEI or surface film properties, although its physical significance remains ambiguous,⁵¹⁶ a fact beyond doubt is that this rate-determining component is under the influence of electrolyte composition, as evidenced by Smart et al.’s success.⁵¹⁵ On the other hand, the suggestion by Huang et al. that the electrolyte and SEI do not control the low-temperature performance of lithium ion cells seems to be challenged in these electrode/electrolyte systems.

It must be noted here that the observation made by Zhang et al. about the dominating magnitude of R_{ct} could be electrode-specific because R_{ct} is not always higher than R_{SEI} in all systems and at all temperatures. At least in the works by Smart et al.^{461,462} and Wang et al.,⁵¹¹ R_{ct} in magnitude is comparable with or even smaller than R_{SEI} . Certainly,

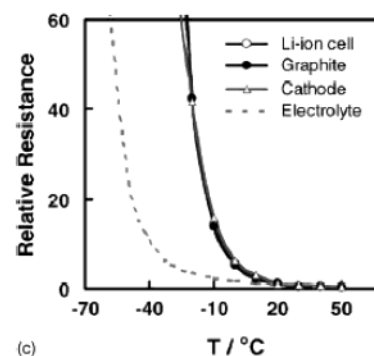
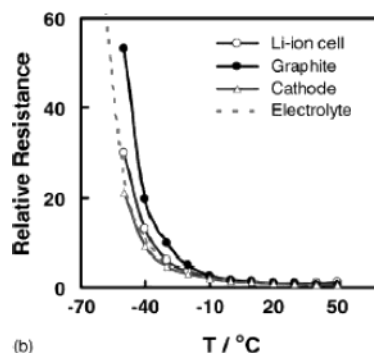
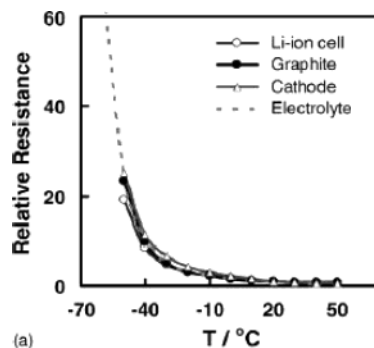


Figure 69. Comparison for temperature-dependence of the relative resistances of a charged lithium ion cell, a lithiated graphite/graphite cell, and a delithiated cathode/cathode cell. The dashed curves show the “relative resistance” of the electrolyte, which was taken as the ratio of the electrolytic conductivity at a specific temperature to the conductivity at 20 °C: (a) R_b ; (b) R_{s1} ; (c) R_{ct} . (Reproduced with permission from ref 512 (Figure 4). Copyright 2003 Elsevier.)

as long as the temperature-dependence and “concentration-dependence” of R_{ct} remain unchanged, the relative magnitude of R_{ct} versus R_{SEI} should not reverse the conclusion by Zhang et al. Nevertheless, in such situations it seems to be necessary to define a new quantity that would more accurately describe the overall kinetics of lithium ion intercalation/deintercalation in the surface film. The interface exchange current derived from various polarization techniques that has been used by Smart et al. could be such a quantity, because both R_{SEI} and R_{ct} are taken into account.

In most of the situations discussed above, the graphite anode was investigated as the single and isolated component, while no or little consideration was given to the other components where simultaneous electrochemical processes occurred. In a full

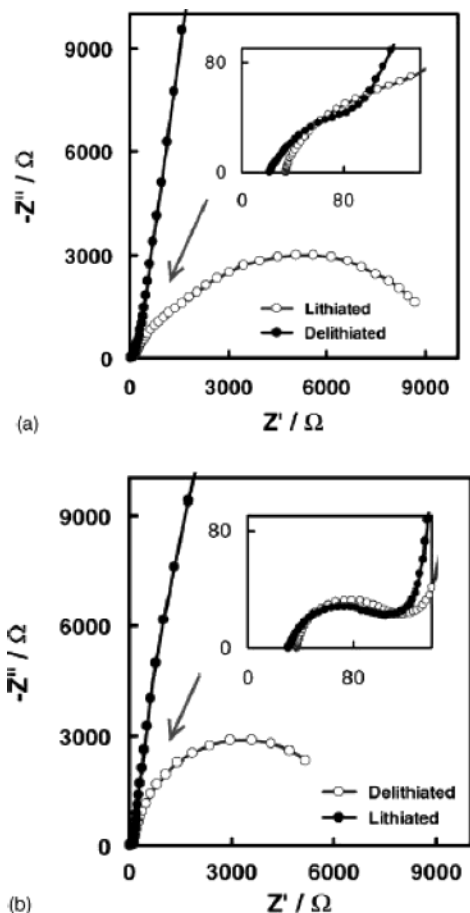


Figure 70. Asymmetrical behavior of R_{ct} toward lithiation and delithiation. Comparison between the Nyquist plots of the anode and cathode symmetrical cells at different states-of-charge: (a) graphite/graphite; (b) cathode/cathode. (Reproduced with permission from ref 512 (Figure 5). Copyright 2003 Elsevier.)

lithium ion cell, which integrates all of those components, including electrolyte, separator, cathode, and anode, the identification of the limiting factor for low-temperature performance becomes more complicated, and conflicting conclusions have been reported from various authors. Clearly, these conclusions are highly conditional and most likely system-specific; therefore, caution should always be taken when interpreting the results of these studies.

Conceptually, besides SEI and charge-transfer resistance in the interfaces as well as lithium diffusion coefficients in the electrodes, the possible limiting factors that might affect the kinetics of lithium ion chemistry could also be electrode surface area and porosity, electrode density and loading, affinity of binder toward electrolyte, and separator porosity and lipophilicity. Any material or engineering flaw could make any of these factors the rate-determining step of the kinetics; hence, it is not strange that different limiting factors have been identified for different lithium ion systems when low-temperature performance was investigated.

Ozawa was perhaps the first author who tried to determine whether the anode or cathode acts as the kinetic bottleneck in a full lithium ion cell, although the purpose at the time was not intended for low-temperature considerations.¹⁵⁷ In interpreting the

Nyquist plots obtained in the EIS analysis of the first generation of Sony 18650 cells, he assigned the larger semicircle at lower frequency to the anode/electrolyte interface and the smaller at medium frequency to the cathode/electrolyte interface on the basis that the diameter of the former relies on the state-of-charge of the anode, while the latter becomes larger in diameter when the surface area of the LiCoO_2 cathode decreases. Thus, he concluded that the charge-transfer process occurring at the anode/electrolyte interface is the slowest step for the whole cell chemistry. However, since the EIS study was conducted on the lithium ion cell without an independent reference electrode, the attempt to separate the contribution from each individual electrode to the overall cell impedance is deemed unreliable. His way of assigning the two semicircles to individual electrodes was also questionable, since it is well accepted that these semicircles correspond to different processes rather than different electrode interfaces.^{134,462} As has been shown in Figure 68, since the time constants for these two electrochemical components, R_{SEI} and R_{ct} , are comparable at anode/electrolyte and cathode/electrolyte interfaces, respectively, the impedance spectra of a full lithium ion could have similar features in which the higher frequency semicircle corresponds to the surface films on both the anode and the cathode, and the other at lower frequency corresponds to the charge-transfer processes occurring at both the anode and the cathode.⁵¹²

By incorporating an independent lithium reference electrode in a commercial lithium ion cell from A&T, Nagasubramanian managed to separate the contributions from the anode and cathode to cell impedance and established their individual temperature profiles.⁵⁰⁶ He found that the increase in cell impedance with decreasing temperature mostly came from the cathode/electrolyte interface, while the contributions from the anode/electrolyte interface or the bulk resistance were negligible. Similar impedance behavior was also observed in commercial cells from Moli and Panasonic.⁵⁰⁶ Thus, he concluded that the interfacial resistance at the cathode, which should include both R_{SEI} and R_{ct} , is mainly responsible for the poor cell performance at low temperatures. This conclusion was supported by Chen et al., who investigated the 18650 lithium ion cell assembled by Polystor using EIS and identified charge-transfer resistance at the $\text{LiNi}_{0.8}\text{Co}_{0.2}\text{O}_2$ cathode/electrolyte interface as the main contributor of overall cell impedance, although the study was only carried out at room temperatures.⁵¹⁸ An indirect evidence for this conclusion came from the XPS studies conducted by Andersson et al. on the cathode and anode surface from the same lithium ion cell, which showed that the surface film on the cathode is much thicker compared with the anode SEI.²⁹⁴

The opposite conclusion was reported by Lin et al.,¹⁶⁵ who used a three-electrode configuration to study the electrode polarization of the MCMC anode and LiCoO_2 cathode under galvanostatic conditions. They found that in all cases the polarization at the MCMC anode surface far outweighs that at the cathode to such an extent that the potential profile

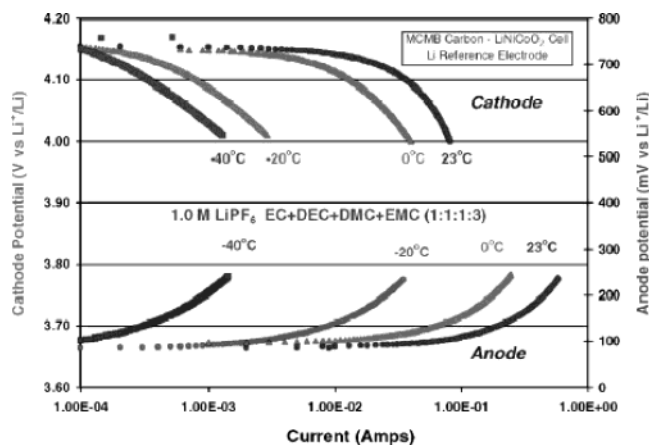


Figure 71. Tafel polarization measurement at different temperatures performed on MCMB and LiNiCoO₂ electrodes in 1.0 M LiPF₆/EC/DEC/DMC/EMC (1:1:1:3). (Reproduced with permission from ref 515 (Figure 8). Copyright 2003 Elsevier.)

of the full lithium ion cell actually mirrors that of the anode. This dominance of anode polarization becomes even more severe at low temperatures, and the logical conclusion should be that the kinetics at the graphitic anode are the rate-determining step.

In a more recent survey of the commercial lithium ion cells, Fan believed that the resistance of the cathode surface layer was the factor limiting the low-temperature performance of the cell chemistry.⁵⁰⁷ Unlike the previous researchers who also believed that the cathode acted as the limiting factor,^{462,506,512} Fan specifically excluded the role of R_{ct} when he made the identification, and his major arguments were based on the summary and interpretation of the previously published data on lithium diffusion coefficients in both the cathode and anode and the fact that the surface area of the cathode is normally only a fraction of the anode. Without data from direct measurement, the above speculation seems to be premature; hence, further experimental confirmation is needed.

With the aim of gaining insight into the kinetics of lithium intercalation/deintercalation of both anodes and cathodes in novel low-temperature electrolytes, Smart et al. carried out the Tafel polarization experiments on MCMB and LiNiCoO₂ electrodes as a function of temperature in a three-electrode cell, and the results are summarized in Figure 71. In the temperature range from ambient to -40 °C, the limiting current densities observed on the anode remained higher than those observed on the cathode. In other words, under the condition of galvanostatic cycling at low temperatures, the cathode would be preferentially polarized and very likely serves as the bottleneck for the kinetics of lithium ion chemistry. As pointed out earlier, these polarization current densities reflect the resistances of both the surface film and charge-transfer on anodes and cathodes, respectively. Interestingly, the temperature-dependences established for the limiting current densities on anodes and cathodes showed that, as temperature decreases, the gap between the polarizations at anode/electrolyte and cathode/electrolyte interfaces rapidly closes (Figure 71), predicting a switch of rate-

determining step in the temperature ranges below -40 °C if other factors such as the precipitation of bulk electrolyte components do not intervene.

The EIS studies using symmetrical cells by Zhang et al. presented a third answer to the question about whether the cathode or the anode is the limiting factor.⁵¹² They showed that the controlling factor for each electrode, R_{ct} , is comparable in magnitude at room temperature for a graphite as well as a LiNiO₂ electrode (Figure 68); and with decreasing temperatures down to -20 °C, these charge-transfer quantities also decline following a matching profile (Figure 69c). Therefore, merely on the basis of the impedance measurement, it would be difficult to tell which interface is rate-determining. Thus, the authors concluded that charge-transfer processes in both the anode and the cathode limit the capacity utilization at subambient temperatures.

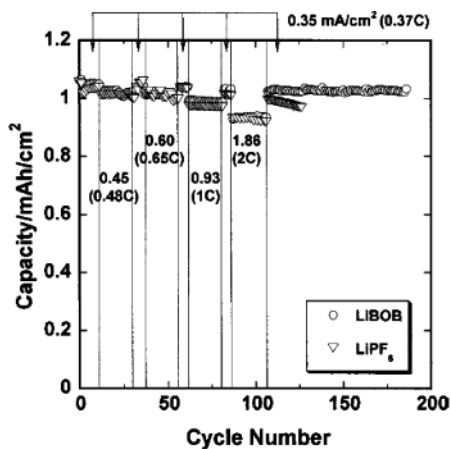
8.4.2. High-Temperature Performance

Compared with the efforts spent on the low-temperature performance, less attention has been paid to the applications of lithium ion technology at elevated temperatures, with perhaps storage stability as the only exception. Cycling tests at temperatures above 50 °C have been rarely reported in the literature, most likely owing to the chemical instability of LiPF₆ in the organic solvents at elevated temperature and the difficulty of replacing it with new lithium salts.

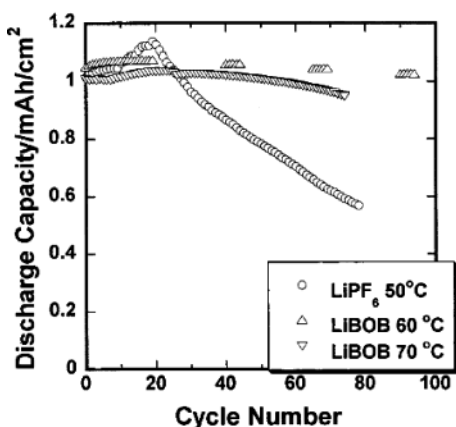
Using the thermally stable salt LiBOB, Xu et al. showed that a full lithium ion cell can operate at temperatures up to 70 °C with limited capacity fading, while LiPF₆-based cells suffer obvious permanent capacity loss, as shown in Figure 72.^{155,492} The authors believed that the chemical stability of BOB anion and the absence of reactive decomposition products such as HF and PF₅ confer upon the electrolyte stable performance at elevated temperatures. Liu et al. also reported the improved cycling performance of lithium ion cells based on the spinel cathode and LiBOB-containing electrolyte at elevated temperatures.⁴⁹⁰ Since Mn²⁺-dissolution caused by the HF from LiPF₆ has resulted in a severe capacity fading problem for spinel-based cathode materials, especially at elevated temperatures, the application of this promising cathode material has been prevented; therefore, the thermal and chemical stability of it in the presence of LiBOB might have special significance.

Another salt that is less sensitive to moisture than LiPF₆, LiBF₄, was also tested as an electrolyte solute intended for high-temperature applications. Zhang et al. reported that electrolytes based on this salt could allow the lithium ion cells to cycle at temperatures up to 70 °C.¹³² Irreversible reactions occurred at temperatures above 80 °C, and the cells lost capacity rapidly, which was accompanied by the rise of cell impedance simultaneously.

As the structurally modified version of LiPF₆, LiFAP has also been reported to be less chemically sensitive due to the partial replacement of fluorine with the more stable perfluorinated alkyls.^{496,497} Aurbach and co-workers investigated the stability of



(a)



(b)

Figure 72. Capacity and capacity retention of the full lithium ion cells based on graphite as anode, LiNiO_2 as cathode, and LiPF_6 or LiBOB in EC/EMC as electrolytes: (a) room temperature; (b) elevated temperatures. (Reproduced with permission from ref 155 (Figure 5). Copyright 2002 The Electrochemical Society.)

the electrolytes based on this salt at elevated temperatures in anode half-cells.^{499a} To ensure the complete formation of the SEI on the graphitic anode, all cells subjected to high-temperature testing were preconditioned by cycling at room temperature. As the inset of Figure 73 shows, the half-cell containing baseline electrolyte with LiPF_6 as salt suffers an immediate capacity loss at 60 °C, while the half-cells based on LiFAP solutions could be cycled at this temperature for 50 times before deterioration happened. Surprisingly, the most stable behavior was demonstrated by the electrolyte based on the mixed salt 0.50 M $\text{LiFAP}/0.50$ M LiPF_6 , which not only delivered stable performance at 60 °C (Figure 73) but also showed higher capacity and lower fading rate even at 80 °C. As a rationale for the mixed salt effect, these authors in their more recent work proposed that some possible bulk reactions occurred between the two salts, one of which is the nucleophilic substitution of the fluorinated alkyl by F^- , forming new P–F bonds and HCF_2CF_3 .^{499b} Since the FAP^- anion in this reaction actually serves as HF -scavenger, it should have a positive effect on both the performance of the Li–graphite electrodes and the thermal behavior of the solutions.

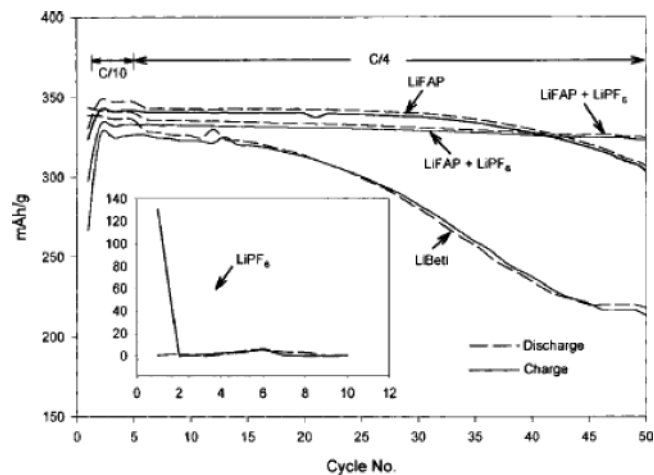


Figure 73. Cycling of graphite anode half-cells at 60 °C after extended cycling at room temperatures. 1.0 M LiFAP , 0.50 M $\text{LiFAP}/0.50$ M LiPF_6 , and 1.0 M LiPF_6 (inset) in EC/DEC/DMC (2:1:2) were used as electrolytes. (Reproduced with permission from ref 499a (Figure 6). Copyright 2003 The Electrochemical Society.)

8.5. Electrolytes of Low Flammability

As diluents of low viscosity for the electrolyte solutions, the linear carbonates or esters were used at high concentrations along with EC, and their high flammability, as indicated by the low flash points (Tables 1 and 2), has imparted the state-of-the-art electrolyte systems with potential fire hazards in the situations of various types of accidents and abuses. Hence, these organic solvents serve as fuel for the various combustion processes, whether in open air when cells are ruptured and accidental sparks ignite their vapors³⁵¹ or under hermetic conditions where overcharge or overheating trigger thermal runaway.^{340,341,360}

The efforts aiming to improve the thermal safety of electrolytes under these abuse conditions have intensified in recent years, partially driven by the more stringent safety requirements for large industry lithium ion cells intended for electric vehicle (EV) or hybrid electric vehicle (HEV) applications. Unlike consumer-size lithium ion cells with capacities below 2 A h, the battery packs for the above applications are usually based on individual cells of 10 A h or higher in capacity, and the dangerous combination of flammable solvents with the highly energetic electrodes in such scaled-up systems would be severely magnified by the amount of materials contained in the cell. For example, a recent test, which was designed as a close simulation of a car accident in real life, showed that violent fire and explosion ensued from the ignition of electrolyte vapors by an externally generated spark when a fully charged lithium ion cell vented.⁵¹⁹

Since any compromise in cell energy density for the sake of safety would be undesired, most of the research efforts were concentrated on the reformulation of the electrolytes by using a flame-retarding additive or cosolvent, with the goal that its presence, kept at a minimum, could result in nonflammability or at least retarded flammability of the whole electrolyte system.

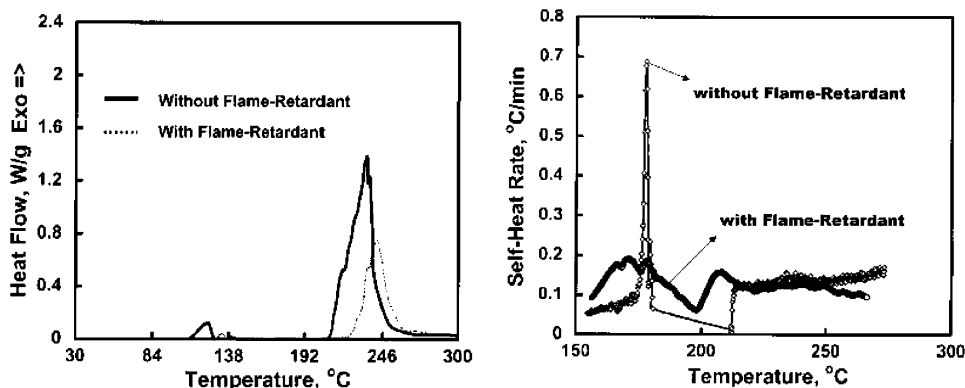


Figure 74. Improved thermal stability of an electrolyte by flame retardant HMPN: (a, left) DSC traces for baseline electrolyte with (1.68%) and without HMPN in the presence of a fully lithiated graphite anode (Reproduced with permission from ref 523 (Figure 5). Copyright 2000 The Electrochemical Society.); (b, right) SHR of baseline electrolyte with (10.0%) and without HMPN in the presence of metallic lithium. (Reproduced with permission from ref 523 (Figure 6). Copyright 2000 The Electrochemical Society.)

The early patent disclosures have claimed the application of a wide spectrum of gas-evolving ingredients and phosphorus-based organic molecules as flame retarding additives in the electrolytes.⁵²⁰ Pyrocarbonates and phosphate esters were typical examples of such compounds. The former have a strong tendency to release CO_2 , which hopefully could serve as both flame suppressant and SEI formation additive, while the latter represent the major candidates that have been well-known to the polymer material and fireproofing industries.^{521,522} The electrochemical properties of these flame retardants in lithium ion environments were not described in these disclosures, but a close correlation was established between the low flammability and low reactivity toward metallic lithium electrodes for some of these compounds. Further research published later confirmed that any reduction of flammability almost always leads to an improvement in thermal stability on a graphitic anode or metal oxide cathode.

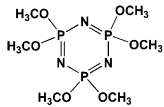
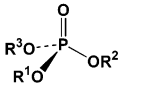
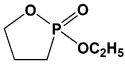
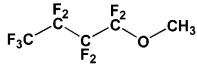
Prakash and co-workers described the first application of a flame retardant additive in an electrolyte solution that has been commonly used for lithium ion technology.⁵²³ By using a substituted cyclic phosphorimide, hexamethoxycyclophosphazene (HMPN), at additive levels ($<10\%$), they investigated the improvement in thermal stability of the baseline electrolyte $\text{LiPF}_6/\text{EC}/\text{DMC}$ by means of DSC and ARC, respectively. As Figure 74a shows, the presence of HMPN at concentrations below 2% resulted in a dramatic reduction in the thermal reactivity of the electrolyte toward the fully lithiated graphite anode, as indicated by the much lower heat generation as well as the much delayed onset temperature of the major exothermic process. The improved stability was also found in the self-heating of the electrolyte under adiabatic conditions in the presence of metallic lithium, as Figure 74b shows. The maximum SHR of the baseline electrolyte at 178 °C was apparently triggered by the melting of lithium (mp 180 °C), which induced a high rate of self-heating at 0.68 °C min^{-1} , while the presence of 10% HMPN effectively suppressed this self-heating process, with a maximum SHR of 0.16 °C min^{-1} at 170 °C. The authors attributed these improvements in thermal stability

to the nonflammability of HMPN with a mechanism of passivating the surface of lithium. Because of its small presence, HMPN does not show any negative impact on the electrochemical stabilities of the baseline electrolyte, as indicated by the cyclic voltammetry experiments as well as the preliminary cycling results in a cathode half-cell based on $\text{LiNi}_{0.8}\text{Co}_{0.2}\text{O}_2$.

Similar improvements in thermal stability were also made with a series of partially fluorinated esters by Yamaki et al.,⁴⁶⁵ who used these fluorinated esters shown in Table 12 as the single solvents for electrolytes intended for the application of rechargeable metallic lithium cells. Compared with their nonfluorinated counterparts, the thermal stability of these electrolytes against both metallic lithium and LiCoO_2 cathode materials was significantly improved, and in both cases, the onset temperatures for the major exothermic reactions were postponed to above 300 °C. The authors believed that the higher stability of the fluorinated esters against metallic lithium was related to their chemical reactivity at room temperature with lithium, the reaction products of which coated the surface of lithium with a thick SEI film that delayed the reaction of the molten lithium at higher temperatures. On the other hand, since the intrinsic decomposition of LiCoO_2 cathode materials occurred at ~ 300 °C, the authors attributed the thermal event observed in the temperature range between 300 and 350 °C to the combination of the individual thermal decompositions of LiCoO_2 and electrolyte. The cycling efficiencies of metallic lithium in those fluorinated esters were also studied, based on which the authors proposed that rechargeable cells using metallic lithium as anode might be practical due to the stabilization effects of those solvents on both the lithium anode and LiCoO_2 cathode. No data were reported on the reduction behavior of those solvents on graphitic anodes; therefore, the application of these novel solvents in lithium ion cells remains to be investigated.

Following the pioneering work by Prakash and co-workers,⁵²³ the researchers of the electrolytes for lithium ion cells started to concentrate their attention on the organophosphorus(V) compounds, and a number of publications since 2001 marked this renewed

Table 14. Flame-Retarding Additives or Solvents

Solvent Structures	$T_m/^\circ\text{C}$	$T_b/^\circ\text{C}$	ϵ (20 $^\circ\text{C}$)	Remarks	Ref.
 <p style="text-align: center;">HMPN</p>	49	> 250		Solid with m.p. at 49 $^\circ\text{C}$; miscible with carbonates; improve thermal stability with graphite or Li (DSC, ARC) at additive level.	523 526
 <p style="text-align: center;">alkyl phosphates</p>	($\text{R}^{1-3}=\text{CH}_3$) -46 ($\text{R}^{1-3}=\text{C}_2\text{H}_5$) -56.4 ($\text{R}^{1-3}=\text{CF}_3$) -19.6 ($\text{R}^{1-2}=\text{CF}_3$, $\text{R}^3=\text{CH}_3$) -22.5 ($\text{R}^1=\text{CF}_3$, $\text{R}^{2-3}=\text{C}_2\text{H}_5$) 210 ($\text{R}^{1-3}=\text{C}_6\text{H}_5$) ($\text{R}^{1-3}=\text{C}_4\text{H}_9$)	197 215 178 203 210	20.7 13 10.5 12 15	Viscous liquids; miscible with carbonates; render nonflammability at 20% if fluorinated; improve SEI stability on anode.	524, 525 526~530 531
 <p style="text-align: center;">EEP</p>				Used as additive with TMP; improves SEI stability on anode.	532
 <p style="text-align: center;">MFE</p>	-135	60		Used with EMC as co-solvent; no flash point; improves thermal stability.	534, 535

interest in nonflammability of electrolytes.^{524–532} The overwhelming choice of these compounds has certainly originated from the in-depth knowledge about the combustion of organic materials accumulated in the polymer industry, where halogenated and organophosphorus compounds have been identified as the most effective flame retardants.^{521,522,533} Traditionally, two major models have been proposed to explain the flame retardation achieved by these compounds: (1) char-formation, which builds up a thermal barrier between the condensed and gaseous phases, and (2) radical-scavenging, by which the chain reaction is inhibited in the gaseous phase due to the radical traps formed by the decomposition products of these additives.⁵³³

Wang et al. seemed to favor the second mechanism when the effectiveness of organophosphate in flame retardation was discussed in their work.⁵²⁴ Using trimethyl phosphate (TMP, $\text{R}^{1-3} = \text{CH}_3$ in Table 14) as the flame retardant additive/cosolvent, they confirmed that when TMP content was higher than a certain threshold value, which depends on the flammability of the baseline solvents, the electrolyte could be rendered nonflammable. On the basis of the previous findings that the radical species containing phosphate have been detected in the MS, they proposed that such radicals act like a trap to scavenge the main active agent for flame propagation, H^\bullet radicals. To estimate the minimum amount (N_{limit}) of TMP needed in any binary electrolyte composition to achieve nonflammability, they even derived an empirical equation:

$$\log N_{\text{limit}} = 2.6 - 9.3 \left[\frac{C_{\text{P}} T_{\text{H}}}{C_{\text{H}} T_{\text{P}}} \right] \quad (14)$$

The unitless quantity in eq 14, $C_{\text{P}} T_{\text{H}}/C_{\text{H}} T_{\text{P}}$, is the so-called “nonflammability index” defined by the authors using the atom content of H or P in the two electrolyte components and their boiling points, respectively. Qualitatively, this equation is of general significance

in that the effectiveness of a certain flame retardant is proportional to the percentage of P in its molecule and inversely to its bp, while, for the baseline components, their flammability is proportional to their bp and inversely to the H content in their molecule. The lower flammability of the electrolyte formulated with TMP was also confirmed to yield higher thermal stability by calorimetry tests, in which the thermal reaction between $\text{LiPF}_6/\text{EC}/\text{DEC}$ and the LiCoO_2 cathode was apparently suppressed due to the presence of 20% TMP.

Unfortunately, TMP was found to be cathodically unstable on a graphitic anode surface, where, in a manner very similar to PC, it cointercalated into the graphene structure at 1.20 V and then decomposed to exfoliate the latter, although its anodic stability did not seem to be a problem. For this reason, TMP has to be used in amounts less than 10% with EC and other carbonates in high concentration in order to achieve decent performance in lithium ion cells. However, capacity fading caused by the increase of cell impedance cast doubt on the application of this flame retardant in a lithium ion cell.⁵²⁴ To avoid the poor cathodic stability of TMP on graphitic anodes, the possibility of using it with other amorphous carbon electrodes was also explored by the authors.⁵²⁵

The above flame retardants, HMPN and TMP, along with another commercially available alkyl phosphate, triethyl phosphate (TEP), were systematically characterized by Xu et al.⁵²⁶ To quantify the flammability of the electrolytes so that the effectiveness of these flame retardants could be compared on a more reliable basis, these authors modified a standard test UL 94 HB, intended for solid polymer samples, and measured the self-extinguishing time (SET) instead of the universally used flame propagation rate.^{520a} Compared with the UL 94 HB, this new quantity is more appropriate for the evaluation of the electrolytes of low flammability, since the electrolytes that are determined to be “retarded” or “nonflammable” by this method all showed zero flame propa-

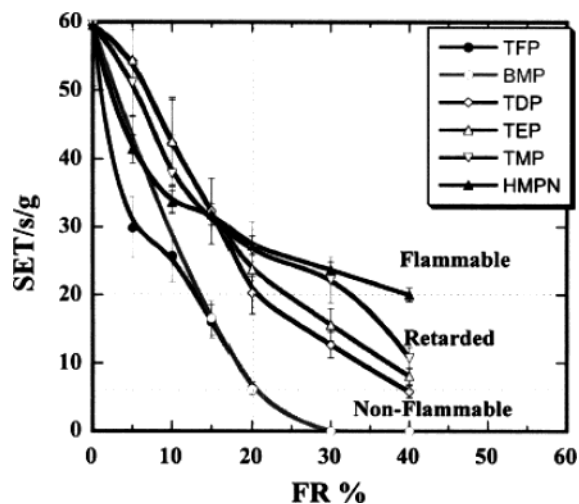
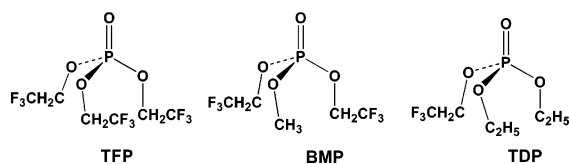


Figure 75. Flammability of the electrolytes containing various phosphorus-based flame retardants (FR). All electrolytes are composed of these flame retardants in 1.0 M $\text{LiPF}_6/\text{EC}/\text{EMC}$. (Reproduced with permission from ref 529 (Figure 1). Copyright 2003 The Electrochemical Society.)

gation rate. Since the SET thus obtained could be normalized against the amount of electrolytes, the reproducibility of flammability data was also improved, and comparison between these different flame retardants was made possible.

Figure 75 shows the dependence of the normalized SET on the concentration of different additives/cosolvents in a baseline electrolyte 1.0 M $\text{LiPF}_6/\text{EC}/\text{EMC}$ (1:1). Apparently, the flammability decreases steadily with the concentration of TMP, TEP, and HMPN, but even in high concentrations, they fail to render the electrolytes completely nonflammable.

In their further work, Xu et al. combined the effects of the two different groups of flame retardants, halogens and phosphates, into one molecule in the hope that the integration would result in the improvement of flame retarding efficiency.^{527–530} For this purpose, they synthesized a series of organophosphates with partially fluorinated alkyls, which included TFP, BMP, and TDP.



A brief summary of their physical properties is provided in Table 14. Their effects on the flammability of the baseline electrolyte are also compared in Figure 75. Apparently, the combination of fluorination with phosphate structure has brought the expected higher efficiency in suppressing burning. For example, with 20% TFP the electrolyte was rendered nonflammable.

While all these phosphate-based cosolvents were shown to be rather stable on various cathode materials, Xu et al. concentrated the evaluation effort on the reduction behavior of these flame retardants at the surface of graphitic anode materials. Figure 76 shows the results obtained with electrolytes containing high concentrations of TMP, TEP, and HMPN.

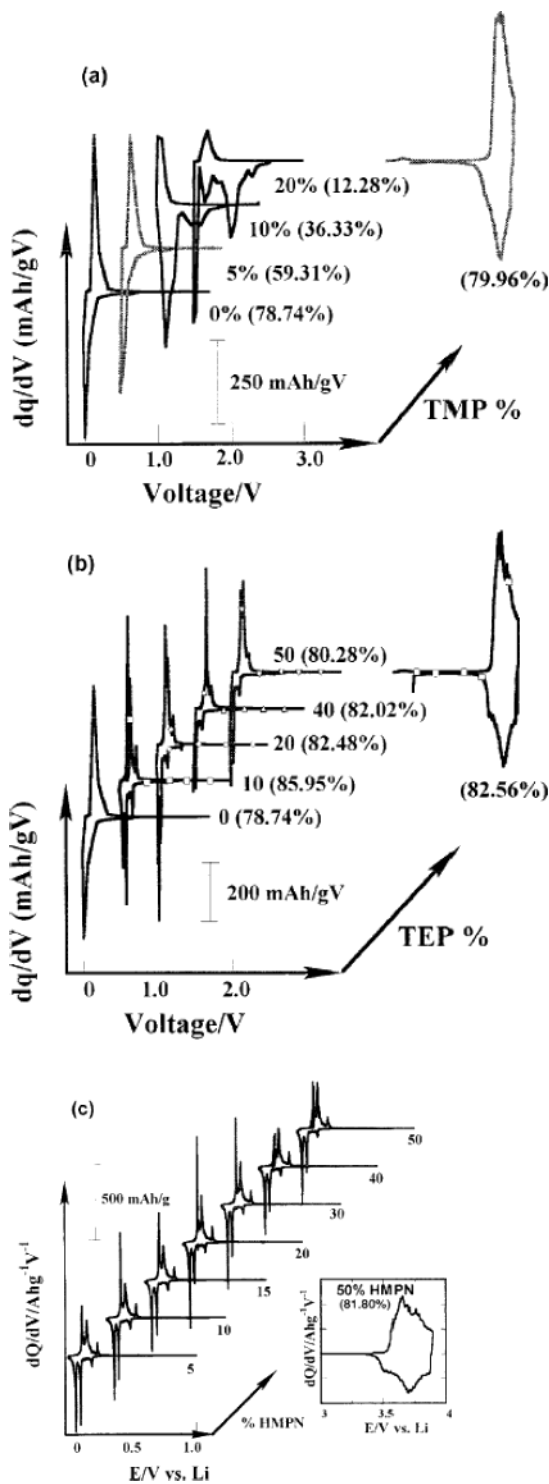


Figure 76. Cathodic stability on graphitic anode: Differential capacity vs voltage plots for anode and cathode half-cells containing different concentrations of (a) TMP, (b) TEP, and (c) HMPN. Only the first cycles are shown. Concentrations are indicated in the graph with the Coulombic efficiency for each cycle in the parentheses. (Reproduced with permission from ref 526 (Figure 2). Copyright 2002 The Electrochemical Society.)

While confirming the results reported by Wang et al. that TMP is cathodically unstable, the authors also showed that longer alkyl substituents (as in TEP) improved cathodic stability, although, in long-term cycling or storage at elevated temperatures, the reductive decomposition of TEP still caused poor cell

performances. Among the three nonfluorinated cosolvents, HMPN was the only exception: its presence up to 40% did not have any negative impact on the cathodic stability of the electrolyte on the graphitic anode. Whether it also participated in the formation of the SEI remained to be investigated.

The fluorinated phosphates, on the other hand, showed generally improved cathodic stability, the extent of which seemed to be proportional to the content of fluorine in the molecule. The stability was further confirmed by the storage test of these electrolytes in a fully charged lithium ion cell at 60 °C. The cycling of the lithium ion cells with these electrolytes containing up to 40% TFP and BMP showed little difference from the baseline electrolyte at room temperature and at moderate drain rate, while the extended cycling up to 300 times delivered stable capacity with negligible fading. Like HMPN, these flame retardants also seemed to be involved in the formation of a more effective SEI on carbonaceous anode materials because higher concentrations of them always resulted in higher capacity retention in the extended cycle life tests.

However, as Figure 77 shows, the presence of TFP did render the lithium ion cells with lower rate capability, although reformulation of the baseline electrolyte with a higher content of the low viscosity solvent could alleviate the loss in rate performance. A similar trend was found with HMPN, which was more viscous than TFP. Studies on ion conductivity and EIS corresponded well with the above findings; that is, the resistances associated with the ion transport in both bulk electrolyte⁵²⁸ and the electrode/electrolyte interfaces⁵³⁰ increased with the presence of these flame retardants. In other words, even with the electrochemically stable TFP and HMPN, the improvement in low flammability has to be realized at the expense of cell performance because the flammability of a system is mainly a bulk property and the reduction of it requires the use of flame retardants in high concentrations. On the other hand, if the stringent standard of "nonflammability" set by Xu et al. is abandoned and thermal stability with respect to electrode materials as measured by DSC or ARC is adopted as the criterion, then these flame retardants could be used at much lower concentrations, that is, as additives instead of cosolvents. This difference has been shown by the work of Wang et al. and Xu et al.

While the consideration of nonflammability and SEI stability favors a high concentration of these organophosphorus compounds in electrolytes, the capacity utilization, rate capabilities, and low-temperature operation require that they be used at minimal concentrations. A compromise would be reached between 15 and 20% TFP or BMP in a binary 1.0 M LiPF₆ in EC/EMC (1:1) system or at higher than 30% in a ternary 1.0 M LiPF₆ in PC/EC/EMC (1:1:3) system. Such electrolytes are completely or at least nearly nonflammable. To further alleviate the above tradeoff, Xu et al. suggested that new cosolvents of higher flame retarding ability should be tailor-made.⁵³⁰

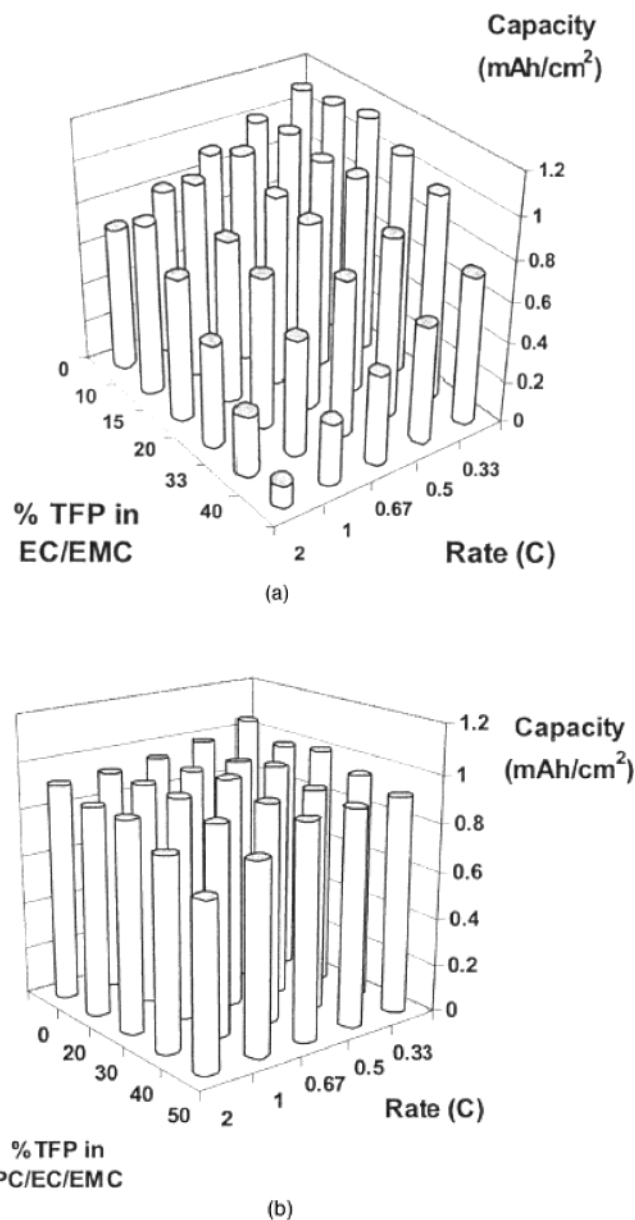


Figure 77. Effect of TFP concentration in different baseline electrolytes on the rate performance of the lithium ion cells: (a) 1.0 m LiPF₆/EC/EMC (1:1); (b) 1.0 m LiPF₆/PC/EC/EMC (3:3:4). (Reproduced with permission from ref 530 (Figure 5). Copyright 2003 The Electrochemical Society.)

Amine and co-workers reported similar organophosphates with larger alkyl (TBP) or aromatic (TPP) substituents, as Table 14 shows.⁵³¹ They adopted an improved UL 94 vertical burning technique to evaluate the efficiency of these flame retardants in the baseline 1.0 M LiPF₆/EC/DEC (1:1) and tried to correlate the flammability of the resultant electrolytes with their thermal stability against a lithiated graphite anode under adiabatic conditions. They found that the flame propagation rate was significantly reduced even with only 1% TPP, while the optimum content of it was 5%. The exothermic reactions of the electrolytes with the fully lithiated graphite were effectively suppressed, as indicated by the lower SHR, lower heat generation, and higher onset temperature, similar to the observations of Prakash et al. and Wang et al. These authors

believed that the char-formation mechanism was responsible for the delayed thermal decomposition.

Like all the phosphates investigated as cosolvents, TBP and TPP showed higher anodic stability, as confirmed by their cycling in lithium ion cells based on a $\text{LiNi}_{0.8}\text{Co}_{0.2}\text{O}_2$ cathode up to 4.2 V, and separate cyclic voltammetry tests also showed that they would not decompose anodically below 5.0 V on an inert working electrode. Little capacity fading was detected during the extended tests of TPP or TBP in full lithium ion cells up to 150 cycles.

In view of the poor cathodic stability of TMP on a graphitic anode, Ota et al. recently described a cyclic phosphate ethylene ethyl phosphate (EEP) (Table 14) to be used with TMP as the additive for the modification of the SEI.⁵³² They found that 5% EEP could render the electrolyte 1.0 M $\text{LiPF}_6/\text{EC}/\text{DEC}/\text{TMP}$ (6:2:2) stable on the graphite surface down to low potentials and support the reversible intercalation/deintercalation of lithium ions, while the electrolyte 1.0 M $\text{LiPF}_6/\text{EC}/\text{DEC}/\text{TMP}$ (6:2:2) without EEP steadily decomposed at 0.40 V in a manner similar to that for PC. The decomposition plateau at a much lower potential as compared with the case of neat TMP solution, as reported by Wang et al.,⁵²⁴ should be attributed to the high EC content used by Ota et al. in their electrolyte composition. The evidence from XPS and FT-IR seemed to confirm that EEP was directly involved in the formation of the SEI, as both spectra detected the signature stretching of P–O bonds that did not exist in EEP-free electrolyte. The authors suggested that EEP underwent a ring-opening decomposition while participating in the surface chemistry on the graphite surface during charge. In temperature-programmed decomposition mass spectra (TPD-MS), such an SEI was shown to be more thermally stable even than the SEI formed by the baseline electrolyte 1.0 M $\text{LiPF}_6/\text{EC}/\text{DEC}$ (1:1): the former decomposes at 125 °C and the latter at 110 °C. The authors summarized that EEP should be a promising additive for lithium ion electrolyte because it showed the simultaneous merits of being flame retardant and an SEI modifier.

Another non-phosphorus cosolvent was recently described as the bulk component for a nonflammable electrolyte by Arai, who used a partially fluorinated ether, methyl nonafluorobutyl ether (MFE), to form a binary mixture solvent with the linear carbonate EMC and reported the complete elimination of the flash point of the electrolyte thus-based (Table 14).^{534,535} The 18650 lithium ion cells using graphite/ LiCoO_2 and 1.0 M $\text{LiBetri}/\text{MFE}/\text{EMC}$ (8:2) delivered the same capacity at low drain rates (0.1 C) as the baseline electrolyte 1.0 M $\text{LiPF}_6/\text{EC}/\text{EMC}$ (3:7) but showed no thermal runaway under the abusive conditions of nail-penetration of an overcharged cell; however, the rate capability of this nonflammable electrolyte is very low. Galvanostatic and EIS studies on the corresponding cathode and anode half-cells identified that the highly resistive anode/electrolyte interface was the source for this problem. With 0.5 M EC and 0.1 M LiPF_6 salt as additives in the MFE-based bulk electrolyte, the polarization was significantly reduced, as shown in Figure 78. The presence

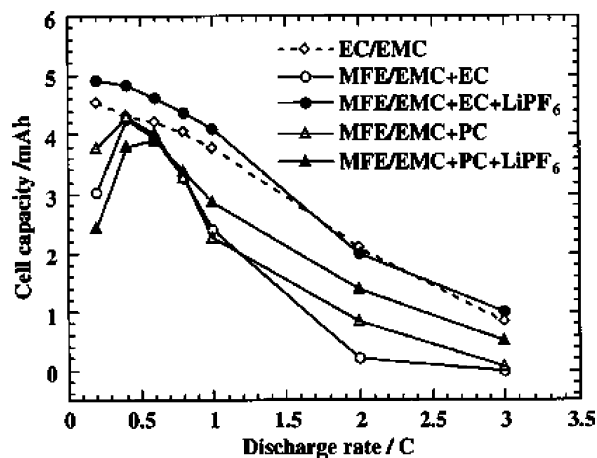


Figure 78. Rate capability of graphite/ LiCoO_2 lithium ion cells using nonflammable MFE-based electrolytes and EC/EMC baseline. (Reproduced with permission from ref 534 (Figure 6). Copyright 2003 The Electrochemical Society.)

of EC and LiPF_6 led to the significant reductions in not only R_{ct} but also R_{SEI} , while XPS and FT-IR confirmed that an increase in the amount of lithium alkyl carbonate was simultaneously observed on the graphite surface. In other words, the newly formulated nonflammable electrolyte based on MFE remained dependent on the use of EC and LiPF_6 . This probably showed from another angle why EC and LiPF_6 are indispensable components in the state-of-the-art electrolytes.

One surprise in Arai's results is perhaps the anodic stability of the ether-based solvent MFE, which remained stable anodically at up to 4.2 V on the LiCoO_2 surface. Considering the numerous previous reports that the ether linkage is oxidatively decomposed near 4.0 V,^{74,75,78,93} one might attribute this additional stability of MFE to the fluorination of the molecule.

The MFE-based nonflammable electrolyte was also tested in lithium ion cells using a spinel cathode.⁵³⁵ The effects of EC and LiPF_6 seemed to be distinguished: while the presence of EC improved the rate capability of these lithium ion cells, longer cycle life with higher capacity retention could only be achieved by further addition of LiPF_6 . On the basis of the above results, the authors believed that MFE-based bulk electrolyte provided a better baseline in terms of safety and nonflammability, although further optimization should be carried out on this new baseline.

8.6. Polymer and Polymer Gel Electrolytes

Polymer electrolytes intended for applications in lithium-based cells could be roughly divided into two major classifications: (1) those based on neat high polymers, which serve as both solvent to dissolve lithium salts and mechanical matrix to support processability,^{536–540} and (2) those based on polymers gelled by conventional electrolyte solutions, wherein the small organic molecules serve as the major solvents, while the low percentage of high polymer, fully swollen by these solvents, acts only to provide dimensional stability.^{541,542} In recent literature the former is usually referred to as solid polymer elec-

trolytes (SPEs), and the latter as gel polymer electrolytes (GPEs). Due to the poor ion conductivities, SPEs remain materials of mere academic interest, with only remote prospects for their applications. On the other hand, GPEs have shown much higher feasibility, and second generation lithium ion cells from the major manufacturers have incorporated these novel electrolytes. Apparently the proximity of GPEs to the conventional nonaqueous electrolytic solutions, in physical chemistry and electrochemistry, is the main reason.

The current section does not intend to comprehensively review SPE and GPE materials, as the preceding sections do to liquid electrolytes, mainly because of the fact that a number of recent reviews have covered this field thoroughly,^{41–48,536–542} the latest of which was published in 2003,^{48b} and also the fact that the most promising systems, that is, GPEs, are similar in many ways to the conventional liquid electrolytes, including their electrochemical stabilities on various electrodes and the corresponding interfacial chemistries. Rather, a more general overview will be given on both systems with little detailed discussion on any individual electrolyte, although exceptions apply to a few selected systems that are of special significance.

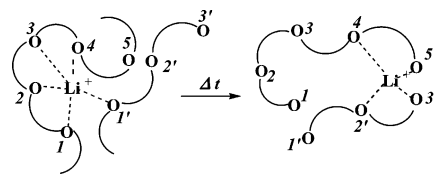
8.6.1. Solid Polymer Electrolyte

While Wright and co-workers were the first group of researchers to discover that the ether-based polymer poly(ethylene oxide) (PEO) was able to dissolve inorganic salts and exhibit ion conduction at room temperature,⁵⁴³ it was the suggestion from Armand et al. that placed these novel materials at the center stage of lithium electrolyte research for more than a decade.⁵⁴⁴ The number of comprehensive reviews on this subject could serve as an indicator of the general enthusiasm for these materials during the period.^{41,47,536–542}

At the time, the targeted device was the rechargeable cell using a metallic lithium anode, and the worldwide interest was mainly stimulated by the following projected advantages that these polymer electrolytes could potentially offer when compared to their liquid counterparts: (1) excellent processability and flexibility that could enable the fabrication of ultrathin lithium cells of various geometric shapes so that high energy and power density could be achieved for versatile applications, (2) higher safety due to the absence of flammable organic solvents and the much lower reactivity of macromolecules toward lithium, (3) the possible prevention of the growth of lithium dendrite crystals upon cycling, and (4) the high dimensional stability that could lead to the elimination of a separator, so further improvement in both energy density and manufacturing cost could be achieved due to the simplified cell configuration and enhanced packing efficiency.

Despite the initial misinterpretation in the ion conduction mechanism, it was soon realized that the ion conduction in PEO and other similar polyether-based media mainly occurred in the amorphous phases. Increasing evidences were obtained that ionic motion in these polymer ion conductors was closely

Scheme 30. Schematic Illustration of Lithium Ion Transport in Polyether Media (Redrawn from Ref 536)



associated with certain local structural relaxations related to the glass transition of the polymer.⁵³⁸ A generally accepted model described a microscopic sequence in which lithium ions were coordinated by the ether oxygen atoms on the segments of a polymeric chain in a similar way to their complexation by crown ethers or other oligoether-based solvents. A continuous segmental rearrangement accompanied by the gradual replacement of the ligands in the solvation sheath of lithium ions, hence, resulted in the long-range net displacement of lithium ions, as Scheme 30 shows.⁵³⁹ Thus, these polymer-salt complexes may exhibit mechanical properties which are similar in most ways to those of true solids due to chain entanglement of the polymer host, while the microscopic environment that a lithium ion sees remains liquidlike and the ion conductivity is “coupled” to the local segmental motion of the polymer. The latter property is often characterized by the glass transition temperature (T_g) of the polymer, which to a great extent determines the mechanical strength and hence processability of a polymer material.

The above coupling between ion transport and mechanical properties has created a perpetual dilemma concerning the prospect of using these polymer ion conductors, since the efforts to improve their ion conductivities—typically between 0.01 and 0.001 mS cm⁻¹ at room temperatures and far short of supporting normal operation in lithium (ion) cells—were always met by sacrificing dimensional stability. Various new host polymers with low T_g were investigated, which included the more flexible polypropylene oxide (PPO) hosts that remain completely amorphous at room temperatures, the siloxane- or phosphazene-based polymers whose low T_g renders the polymer host more flexible and facilitates faster ion conduction, the comb-type polyethers in which ether linkages are attached as side-chains to the backbone so that more flexible segmental motion is possible, the polymer composite electrolytes that have incorporated inorganic additives to eliminate the crystallinity of polyether segments, and so forth. However, almost always before the ion conductivities reach the coveted goal of the “liquidlike” level (i.e., > 1.0 mS cm⁻¹), the mechanical strength of these polymers approaches “liquidlike” state, thus conflicting with the fundamental reason polymer electrolytes are desired. The introduction of chemical cross-linking or the preparation of various interpenetrating networks (IPNs) indeed improves the dimensional stability of polymer electrolytes, but the ion conductivity swings back to levels < 0.01 mS cm⁻¹.

During the two decades following the initial proposal by Armand, essentially little progress was made concerning the actual application of SPEs, where the

poor ion conduction exists as a seemingly insurmountable barrier. Due to the low level ion conductivity, little has been known about the electrochemical stability of these polymer electrolytes on various intercalation-type electrode materials, and even less about their cycling in actual lithium and lithium ion cells. On the basis of a general survey of the most solid polymer electrolyte systems developed so far, an upper limit in ambient-temperature ion conductivity seems to exist at 0.1 mS cm^{-1} for any polymer host whose mechanical strength could afford the formation of a free-standing film.^{538–541} Applications at high temperature seem to be a solution to the poor ion conductivities, but a high rate of degradation often deters the efforts, as indicated by the fading capacities of such cells.

Various attempts have been made to break the coupling of ion transport from the polymeric segmental relaxation. Combining the projected merits of SPEs and superionic glass electrolytes that have been the subject of intensive study in solid-state ionics since the late 1970s, Angell and co-workers proposed an innovative approach of “polymer-in-salt” to bypass the poor ion conductivity of the “salt-in-polymer” SPEs.⁵⁴⁵ In the proposed “ionic rubber”, a polymer material of high molecular weight is used only at additive levels as a sheer provider of mechanical strength and filming processability, whereas the bulk of the electrolytes consist of the highly conductive ionic liquid. Ideally, these materials should have a T_g low enough to remain rubbery at room temperature while preserving the lithium ion conductivities similar to those of the typical ionic liquid systems because most of the ions would be free of coordination with polymer segments due to the small presence of the latter. Unfortunately, although the initial results with simple lithium salts confirmed the conceptual feasibility of the approach, exceeding difficulties were encountered in the attempts to formulate a practical system, which should be based on an ionic liquid or such mixtures that not only have low melting and glass-transition temperatures but also are inert to the polymer additives at these temperatures as well as retain electrochemical stability in a wide potential range.^{546,547}

More recently, Ingram et al.⁵⁴⁸ and Wright et al.⁵⁴⁹ independently tried to develop new polymer hosts with secondary structures similar to that of a liquid crystalline state, so that ion transport could occur with a higher degree of freedom in the highly oriented environments and become at least partially decoupled from the polymer segmental relaxations. Ion conductivities approaching “liquidlike” values have been obtained on the condition that the liquid crystalline state could be maintained.⁵⁴⁹ However, the incorporation of these novel polymer materials in electrochemical devices remains to be tested.

On the other hand, ion conductivity is not the only obstacle that prevents the application of SPEs. In 1994, Anderman published a review highly critical of the prospects for the application of SPEs in electrochemical devices, in which he questioned almost all of the previously projected advantages from the viewpoint of cell design and engineering.⁵⁵⁰

He argued that (1) the flexibility that a polymer electrolyte could offer presents no true advantage to cell design, since the current cell components (i.e., electrodes coated on substrates and a separator based on polyolefin films) already possess sufficient flexibility, and limitations on the geometric shapes of lithium cells do not come from the rigidity of electrolytes but rather from the terminals/connectors as well as economical considerations; (2) the low reactivity of a polymer toward an electrode would very likely be counteracted by the micrometer thickness of such polymer materials, since the chances of an internal short increase significantly (the necessity for thin films arises from the poor ion conductivities of such electrolyte materials and the need to provide sufficient ion flux for the normal cell operation); (3) the safety of polymer electrolyte-based cells would be further challenged by technical difficulties, since it would be almost impossible to manufacture a polymer film of micrometer thickness in large scale and pinhole free; and (4) there would be hardly any improvement in the tolerance against mechanical abuse for the polymer electrolytes, since they do not offer superior mechanical strength to that of the presently used polyolefin separators.

In addition to the criticisms from Anderman, a further challenge to the application of SPEs comes from their interfacial contact with the electrode materials, which presents a far more severe problem to the ion transport than the bulk ion conduction does. In liquid electrolytes, the electrodes are well wetted and soaked, so that the electrode/electrolyte interface is well extended into the porosity structure of the electrode; hence, the ion path is little affected by the tortuosity of the electrode materials. However, the solid nature of the polymer would make it impossible to fill these voids with SPEs that would have been accessible to the liquid electrolytes, even if the polymer film is cast on the electrode surface from a solution. Hence, the actual area of the interface could be close to the geometric area of the electrode, that is, only a fraction of the actual surface area. The high interfacial impedance frequently encountered in the electrochemical characterization of SPEs should originate at least partially from this reduced surface contact between electrode and electrolyte. Since the porous structure is present in both electrodes in a lithium ion cell, the effect of interfacial impedances associated with SPEs would become more pronounced as compared with the case of lithium cells in which only the cathode material is porous.

Even after all the above issues, that is, mechanical strength, ion conductivity, and interfacial resistance, have been resolved, SPEs still have to face the crucial issue of surface chemistry on each electrode if the application is intended for lithium ion technology, and there is no reason to be optimistic about their prospects.

Despite the wide variety of polymer hosts that have been synthesized and tested, the fundamental chemical structures adopted for SPEs remain strictly ether-based and are variations of the original oligo(ethylene oxide) structure, primarily due to the fact that no

other chemical linkages are able to possess sufficient solvation power for inorganic salts while remaining amorphous and flexible at room temperature. The inability of ether-based solvents, such as DME and DEE, to form an effective SEI on carbonaceous anodes has been reported in numerous reports, where porous and highly resistive SEIs originating from these solvents have been described. Moreover, the anodic stability of these ethers on cathode materials does not offer relief, since their oxidative decomposition potentials have been reported to be well below 4.0 V, which falls in the reversible lithiation/delithiation range for most of the metal oxide cathode materials and far below the oxidation limits of ~ 5.5 V set by carbonate-based solvents. Although the reduction in the reactivity of ether linkages could be expected because of the giant molecular size of the polymer solvent, the long-term stability of such polyether materials sandwiched between a graphite anode and a metal oxide cathode does raise concern. This concern is indirectly supported by the fact that, among the few rare publications wherein the cycling behavior of SPEs was tested under either galvanostatic or voltammetric conditions, decent cycle life was obtained only when low-potential cathodes such as V_2O_5 , TiS_2 , or polymeric electroactive materials were used, while the industry standard $LiCoO_2$ or other 4.0 V class cathode materials always rendered poor cycling performances.

In a brief summary, although the studies on SPEs remain of academic interest in the areas of materials science and solid state ionics, their immediate application in any commercial electrochemical devices, especially in the state-of-the-art lithium ion industry, seems to be remote. Considering the multilateral challenges that SPE materials are facing, any isolated breakthrough in an individual property might not be sufficient to justify replacement of the current electrolytes used in lithium ion cells. However, it must be cautioned that the above judgment is strictly based on the *status quo* of lithium ion technology, which could change with the improvement of electrode materials. Hence, one should not draw premature conclusions about the fate of SPEs because, after all, science development is full of unexpected. Recent advances made by Scrosati and co-workers have shed a light of hope on the SPE applications in lithium/lithium ion cells intended for elevated-temperature environments, where the disadvantage of low ion conductivity could be avoided.^{501,551–555}

8.6.2. Gel Polymer Electrolyte

Compared with SPEs, GPEs are much closer to actual applications because they inherited the major properties from the bulk liquid electrolytes, including ion conduction, electrochemical stability on both carbonaceous anode and various metal oxide cathode materials, safety, and tolerance against mechanical and electric abuses. Moreover, since the polymer at additive levels only serves as the skeleton providing dimensional integrity, the ether linkage is no longer the sole choice of building block for its chemical structure, thus eliminating potential concerns over the electrochemical stability that might arise from

the oxidative or reductive degradations of polymer segments in a lithium or lithium ion cell environment. Certainly, the concomitant consequence of the low polymer presence in GPEs is the poorer mechanical strength as compared with the cases of the pure SPEs, and either chemical or physical cross-linking is frequently necessary for the dimensional stability of such gel materials.

The recent advances of GPE materials have been exhaustively covered in two general review articles up to 2000.^{541,542} Especially in the review by Song et al., a rather systematical coverage was given on the most popular GPE systems that were based on PEO, poly(acrylonitrile) (PAN), poly(methyl methacrylate) (PMMA), and poly(vinylidene fluoride) (PVdF), along with an excellent discussion of the fundamental aspects concerning the formation, morphological structure, and physical stability of GPE.⁵⁴¹ Because of the wide variety of polymer and copolymer hosts available in the market, the number of new GPE systems reported in the literature is ever increasing, especially in recent years, while the bulk electrolyte compositions and hence the fundamental electrochemistry associated remain relatively constant. It is not the objective of the current section to review those individual systems in detail.

On the application front, GPE technology has been used by most of the major manufacturers of lithium ion cells following the third generation lithium ion cells of Sony, and an energy density of 180 W h K g^{-1} was reported.² The specific polymer hosts used in commercial lithium ion cells were seldom reported in the open literature for obvious reasons. It should be mentioned here that, in marketing terms, these cells are often confusingly referred to as “polymer lithium ion cells”, giving the wrong impression that solvent-free SPEs are in use.

The only commercial GPE cell that had been described in the open literature was perhaps the Bellcore/Telcordia technology based on a fluorinated polymer, PVdF, from which one could readily sense that the key factor controlling the success of certain polymer hosts in lithium ion cells is no longer material chemistry only, and that more often than not the processing and fabrication of the GPE plays the decisive role.⁵⁵⁶

As pointed out by Song et al.,⁵⁴¹ the significance of the Bellcore technology rested with its technical innovation rather than scientific discovery because PVdF-based polymers as a host for GPE had been investigated by Feuillade et al.⁵⁵⁷ and Tsuchida et al.^{558,559} as early as two decades ago. However, what distinguished Bellcore technology not only from those early studies but more generally from all of the previous research in polymer electrolytes was that the traditional approach of preparing a homogeneous GPE film was abandoned and replaced by a two-step process, in which PVdF–hexafluoropropylene (HFP) copolymer was first processed into a microporous film that could be assembled with cathode and anode films in an ambient atmosphere, and then the whole cell assembly could be activated by liquid electrolytes in a similar manner, where the traditional polyolefin separator was wetted by liquid electrolyte. After

activation, the liquid electrolyte swells the originally microporous film and eventually forms a GPE. Since the only step that must be conducted in a moisture-controlled environment is the electrolyte injection, the advantages of this technology in terms of manufacturing cost and operational ease are apparent.

Perhaps more important than cost is the solution to the crucial problem of interfacial contacts that always plagues homogeneous GPE films prepared from traditional approaches. Since both cathode and anode composite materials are coated on their substrates with the same PVdF–HFP copolymer as the binder, the “in situ gellification” following the electrolyte activation effectively fuses the three cell components into an integrated multilayer wafer without physical boundaries, so that the interfaces between anode and electrolyte or cathode and electrolyte are well extended into the porous structures of these electrodes, with close similarity to the interfaces that a liquid electrolyte would access.

Another important merit of the “in situ gellification”, rarely mentioned by various authors in the literature, is that the limitation on electrolyte composition can be relaxed. In the traditional process of making a GPE, the liquid electrolyte has to be heated with the polymer host to form the gel, during which the thermal instability of the lithium salt (LiPF_6 or LiBF_4) and the volatility of the solvents (DMC, EMC, etc) could possibly cause the resultant GPE to deviate from the desired composition or even to degrade. It is for this reason that in most of the literature on GPE the liquid electrolytes have to be based on LiIm , LiBeti as salts, and EC/PC as solvents. In Bellcore technology, on the contrary, the state-of-the-art electrolytes, the typical of which is $\text{LiPF}_6/\text{EC}/\text{DMC}$, could be used, since gellification occurs only after the cells are assembled.⁵⁵⁶

According to Tarascon and co-workers, the swelling of PVdF–HFP by liquid electrolytes was never complete due to the semicrystalline nature of the copolymer, which tends to microphase-separate after the activation by electrolyte. On the other hand, it is those crystalline domains in the gelled PVdF–HFP that provide mechanical integrity for the resultant GPE.⁵⁵⁶ Thus, a dual phase structure was proposed for the Bellcore GPE by some authors, wherein the amorphous domain swollen by a liquid electrolyte serves as the ion conduction phase, while tiny crystallites act as dimensional stabilizer.

Apparently, the formation of the microporous structure within the PVdF–HFP copolymer was of critical importance to the success of Bellcore technology, and the ion conductivity was proportional to the uptake of the liquid electrolyte. To achieve the desired porosity of PVdF film, Bellcore researchers prepared the initial polymer blend of PVdF with a plasticizer dibutylphthalate (DBP), which was then extracted by low boiling solvents after film formation. Thus, a pore-memory would be left by the voids that were previously occupied by DBP. However, due to the incomplete dissolution of such high-melting DBP during the extraction process, the pore-memory could never be restored at 100% efficiency.^{556,559} Beside the total volume of pores thus created by the plasticizer,

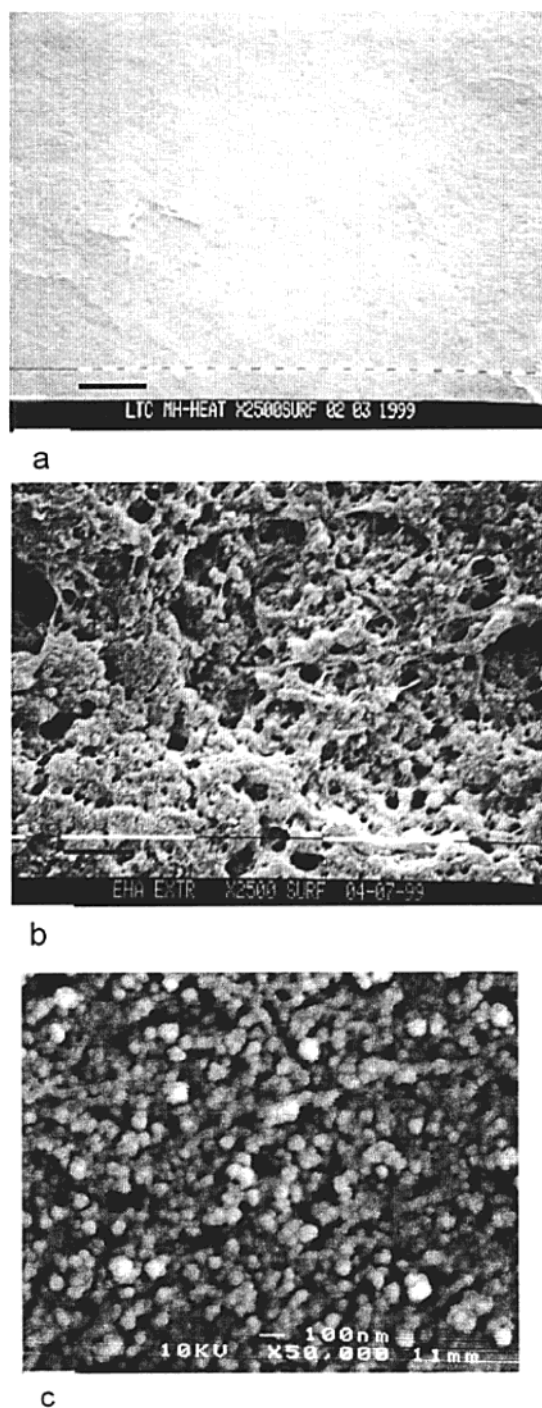


Figure 79. SEM of methanol-extracted separators prepared in the weight ratio of plasticizer/PVdF–HFP/ SiO_2 of 5:3:2. The extracted plasticizer in parts a and c is DBP, and that in part b is an oligomer with molecular weight 450. Note that the scale in parts a and b is 5.0 μm and that in part c is 100 nm. (Reproduced with permission from ref 561 (Figure 2). Copyright 2000 The Electrochemical Society.)

the distribution of pore sizes, their interconnectivity, and the affinity of the inner wall of pores toward liquid electrolytes would all influence the final uptake of electrolytes.^{560,561}

Improvements based on Bellcore technology were reported recently by Wunder and co-workers.^{561,562} Using PEO oligomers instead of DBP, they obtained the PVdF–HFP microporous films with the pore size increased from nanoscale to microscale, as shown in

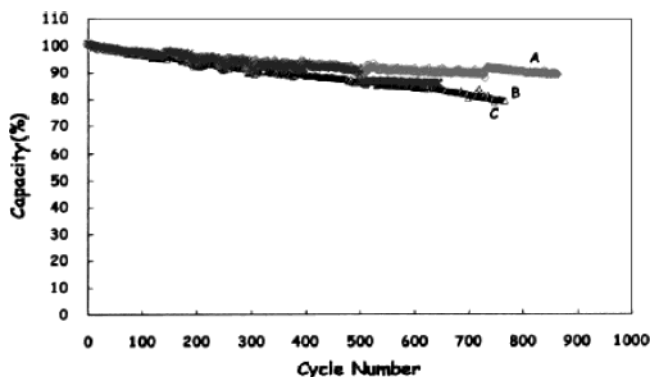


Figure 80. Cycle life of 2 A h cells (A and B) and a 25 A h cell (C) at 100% depth-of-charge at ambient temperature. (Reproduced with permission from ref 563 (Figure 7). Copyright 2001 Elsevier.)

Figure 79. As a result, the ion conductivity rose by $\sim 70\%$ from 0.2 mS cm^{-1} of DBP-extracted GPE to 1.2 mS cm^{-1} of the oligomer-extracted counterpart. The cycling tests in a lithium ion cell based on MCMB/LiCoO₂ showed an improvement in capacity by 40% and in rate capability by 70%. In their further work, Wunder and co-workers used polystyrene (PS) to form a blend with PVdF–HFP copolymer, which, via a “phase-inversion” technique, yielded a microporous film that could possess an ion conductivity as high as 4.0 mS cm^{-1} .⁵⁶² Characterization using various analytic means led the authors to conclude that the presence of PS increases pore volume, wherein the liquid electrolyte forms a highly conductive path, while the swollen PVdF–HFP region is relatively resistive, corresponding to the low ion conductivities found in the GPE based on homogeneous PVdF by previous investigators.^{557–559} At this stage, the demarcation between GPE and the traditional microporous separators based on polyolefin materials becomes quite ambiguous.

The Bellcore GPE technology, bearing the brand name of “plastic lithium ion cells” or “PLion cells”, has been licensed worldwide to various battery manufacturers, and a recent report by Han et al. described the adaptation of it to large lithium ion cells designed as traction power in electric vehicle applications.⁵⁶³ Figure 80 shows the cycle life of such cells at room temperatures, while tests of an improved 28 A h cell carried out between 60 and -20°C yielded 95% and 60% of the rated capacity, respectively. These cells also passed all the safety tests, including external short circuit, high current charge, impact, nail-penetration, and heating, with the exception of overcharge, where the cells became swollen and burst into flames between 105% and 150% of overcharged capacities. Since there is always a concern over the stability of the C–F bond in PVdF polymers with respect to the fully lithiated carbonaceous anode,³³⁸ there is doubt once again about the appropriateness of fluorinated polymers as GPE hosts for lithium-based cell applications. However, it should be kept in mind that the lithium ion cells based on liquid electrolytes behave similarly under the same abusive conditions. A more likely situation is that the reaction of the fluorinated polymers with carbonaceous anodes occurs at much higher temper-

atures so that it is not responsible for the thermal runaway induced by overcharge. According to the investigations by Maleki et al.^{360,361} and Dahn et al.,^{369–371} cathode/electrolyte interaction, instead of anode/electrolyte interaction, should be the main source of the hazard to safe operation.

9. Concluding Remarks

The traditional role of electrolytes in batteries is of less consequence than the electrode materials. While the recent understandings about electrolytes in lithium-based rechargeable cells revealed that the chemical composition of electrolytes profoundly affects the cell performance in many aspects—from lithium cycling efficiency to rate capability, and from capacity retention at various temperatures to tolerance against abuses—the fact remains that the choice of electrolyte components is dictated by the electrode materials in use. Thus, the current state-of-the-art electrolyte systems in lithium ion cells are tailor-made for the specific cell chemistry in which the various electrolyte components yield ad hoc surface chemistries on metal oxide cathodes and especially on graphitic anodes. Radical change in electrolyte composition is not expected to be likely, as long as the cell chemistry remains the reversible shuttling of lithium ions between those metal oxides and graphitic carbons, but innovations will continue to be carried out concerning the rate performance, temperature range of service, safety of scaled-up cells, and “solidification” of the electrolyte.

On the other hand, the emergence of new cell chemistries would call for reformulation of the electrolytes, as has always been the case during the history of lithium battery development. There have been numerous such efforts in seeking more energetic or safer cathode materials, which include the novel 5.0 V class mixed metal oxides and the more recent olivine iron phosphate family, while metallic lithium remains a main attraction as a potential anode considering its tremendous energy density. In the latter case, electrolyte reformulation has been used as a main factor in controlling the undesired formation of dendritic lithium during the long-term cyclings, an example of which is the work of Aurbach et al., who found ad hoc surface chemistry on metallic lithium provided by an ether-based electrolyte similar to that of a carbonaceous anode.^{14,18} Polymer-based electrolytes are also expected to be effective in regulating the surface morphology of metallic lithium. Upon the successful solution of the safety issue of the lithium electrode, the revival of the lithium cell is a possibility, along with new electrolyte formulations that cater to the new cell chemistries.

10. Acknowledgments

The author wants to thank Dr. Wu Xu (Arizona State University) and Ms. Deborah Funk (Army Research Laboratory) for the meticulous and critical reading of the manuscript, and Dr. Vera Zhuang (Lawrence Berkeley National Laboratory) for the invaluable input concerning the spectroscopic characterization of surface chemistry; Dr. Shengshui

Zhang (U.S. Army Research Laboratory) offered assistance in locating numerous literature sources, and the discussions with Dr. Zhang, Dr. Jan Allen (U.S. Army Research Laboratory), and Professor Takeshi Abe (Kyoto University) were helpful to the author. Special acknowledgments should be given to Dr. Richard Jow (U.S. Army Research Laboratory) and Professor C. Austen Angell (Arizona State University) for the encouragement and discussions, and Dr. Wishvender Behl (U.S. Army Research Laboratory) for granting me access to his complete collection of electrochemistry literature.

11. References

- (1) For fundamentals of modern electrochemistry, see: Bockris, J. O'M.; Reddy, A. K. N. *Modern Electrochemistry*, 2nd ed.; Plenum Press: New York, 2000; Vol. 2.
- (2) For elementary readings concerning battery technology and chemistry, see: Linden, D., Ed. *Handbook of Batteries*, 2nd ed.; McGraw-Hill: New York, 1995; 3rd ed.; McGraw-Hill: New York, 2001.
- (3) The redox potentials against the standard hydrogen electrode (SHE) for various reactions, usually called "electrochemical series", are listed in the annually updated *CRC Handbook of Chemistry and Physics*; CRC Press: Boca Raton, FL. On the other hand, unless otherwise indicated, the potential values used in this review are all referred to the Li⁺/Li reference electrode.
- (4) Jasinski, R. *High Energy Batteries*; Plenum Press: New York, 1967.
- (5) Fraioly, A. V.; Barber, W. A.; Feldman, A. M. U.S. Patent 3,551,205, 1970.
- (6) Schneider, A. A.; Moser, J. U.S. Patent 3,674,562, 1972.
- (7) Moser, J. U.S. Patent 3,660,163, 1972.
- (8) Fukuda, M.; Ijima, T. In *Power Sources*; Collins, D. H., Ed.; Academic Press: London, 1975; Vol. 5, p 713.
- (9) Selim, R.; Bro, P. *J. Electrochem. Soc.* **1974**, *121*, 1457.
- (10) Raul, R. D.; Brummer, S. B. *Electrochim. Acta* **1977**, *22*, 75.
- (11) Koch, V. R.; Young, J. H. *J. Electrochem. Soc.* **1978**, *125*, 1371.
- (12) Yoshimatsu, I.; Hirai, T.; Yamaki, J. *J. Electrochem. Soc.* **1988**, *135*, 2422.
- (13) Broadhead, J.; Trumbore, F. A. In *Power Sources*; Collins, D. H., Ed.; Academic Press: London, 1975; Vol. 5, p 661.
- (14) Dan, P.; Mengeritsky, E.; Geronov, Y.; Aurbach, D.; Weissman, I. *J. Power Sources* **1995**, *54*, 143.
- (15) Aurbach, D.; Gofer, Y.; Ben-Zion, M. *J. Power Sources* **1992**, *39*, 163.
- (16) Aurbach, D.; Weissman, I.; Zaban, A.; Ein-Eli, Y.; Mengeritsky, E.; Dan, P. *J. Electrochem. Soc.* **1996**, *143*, 2110.
- (17) Aurbach, D.; Zaban, A.; Ein-Eli, Y.; Weissman, I.; Chusid, O.; Markovski, B.; Levi, M. D.; Levi, E.; Schechter, A.; Granot, E. *J. Power Sources* **1997**, *86*, 91.
- (18) Aurbach, D.; Zinigrad, E.; Teller, H.; Dan, P. *J. Electrochem. Soc.* **2000**, *147*, 1274.
- (19) Dominey, L. A. In *Nonaqueous Electrochemistry*; Aurbach, D., Ed.; Marcel-Dekker: New York, 1999; Chapter 8.
- (20) Whittingham, M. S. *Science* **1976**, *192*, 1126.
- (21) Whittingham, M. S. *Prog. Solid State Chem.* **1978**, *12*, 1.
- (22) (a) Mizushima, K.; Jones, P. C.; Wiseman, P. J.; Goodenough, J. B. *Mater. Res. Bull.* **1980**, *15*, 783. (b) Mizushima, K.; Jones, P. C.; Wiseman, P. J.; Goodenough, J. B. *Solid State Ionics* **1981**, *3/4*, 171.
- (23) Murphy, D. W.; Christian, P. *Science* **1979**, *205*, 651.
- (24) Armand, M. In *Materials for Advanced Batteries*; Murphy, D. W., Broadhead, J., Steele, B. C. H., Eds.; Plenum Press: New York, 1980; p 145.
- (25) Lazzari, M.; Scrosati, B. *J. Electrochem. Soc.* **1980**, *127*, 773.
- (26) Auborn, J.; Barberio, Y. L. *J. Electrochem. Soc.* **1987**, *134*, 638.
- (27) Semkov, K. W.; Sammels, A. F. *J. Electrochem. Soc.* **1987**, *134*, 766.
- (28) Scrosati, B. *J. Electrochem. Soc.* **1992**, *139*, 2776.
- (29) Nagaura, T.; Nagamine, M.; Tanabe, I.; Miyamoto, N. *Prog. Batteries Sol. Cells* **1989**, *8*, 84.
- (30) Nagaura, T.; Ozawa, K. *Prog. Batteries Sol. Cells* **1990**, *9*, 209.
- (31) Nishi, Y.; Azuma, H.; Omaru, A. U.S. Patent 4,959,281, 1990.
- (32) Ohzhku, T.; Ueda, A.; Nagayama, M. *J. Electrochem. Soc.* **1993**, *140*, 1862.
- (33) Bittihn, R.; Herr, R.; Hoge, D. *J. Power Sources* **1993**, *43/44*, 223.
- (34) Nagaura, T. *Proceedings of the 5th International Seminar on Lithium Battery Technology and Applications*, Deerfield Beach, FL, March 5–7, 1990; Florida Educational Seminars, Inc.: Boca Raton, FL.
- (35) Dahn, J. R.; von Sacken, U.; Fong, R. *Extended Abstracts of the 178th Electrochemical Society Meeting*, Seattle, WA, Oct. 14–19, 1990; Abstract No. 42; Electrochemical Society: Pennington, NJ.
- (36) Fong, R.; von Sacken, U.; Dahn, J. R. *J. Electrochem. Soc.* **1990**, *137*, 2009.
- (37) Peled, E. *J. Electrochem. Soc.* **1979**, *126*, 2047.
- (38) Brodd, J. *Extended Abstracts of the 201st Electrochemical Society Meeting*, Philadelphia, PA, May 12–17, 2002; Abstract No. 259; Electrochemical Society: Pennington, NJ.
- (39) Hannon, D. *Purchasing Magazine* **2002**, Feb. 21.
- (40) Broussely, M. *11th International Meeting on Lithium Batteries*, Monterey, CA, June 23–28, 2002; Abstract No. 415; Electrochemical Society: Pennington, NJ.
- (41) Megahed, S.; Scrosati, B. *J. Power Sources* **1994**, *51*, 79.
- (42) Brandt, K. *Solid State Ionics* **1994**, *69*, 173.
- (43) Sawai, K.; Iwakoshi, Y.; Ohzuhu, T. *Solid State Ionics* **1994**, *69*, 273.
- (44) Guyomard, D.; Tarascon, J. M. *Solid State Ionics* **1994**, *69*, 222.
- (45) Ebner, W.; Fouchard, D.; Xie, L. *Solid State Ionics* **1994**, *69*, 238.
- (46) Arora, P.; White, R. E.; Doyle, M. *J. Electrochem. Soc.* **1998**, *145*, 3647.
- (47) Tarascon, J. M.; Armand, M. *Nature* **2001**, *414*, 359.
- (48) (a) Blomgren, G. E. *J. Power Sources* **1999**, *81/82*, 112. (b) Blomgren, G. E. *J. Power Sources* **2003**, *119/121*, 326.
- (49) Fry, A. J. *Synthetic Organic Electrochemistry*, 2nd ed.; John Wiley: London, 1989.
- (50) The physical data were extracted and compiled from the following literature sources: (a) Jang, G. J.; Tomkins, R. P. T. *Nonaqueous Electrolytes Handbook*; Academic Press: New York, 1972; Vol. 1. (b) Dudley, J. T.; Wilkinson, D. P.; Thomas, G.; LeVae, R.; Woo, S.; Blom, H.; Horvath, C.; Juzkow, M. W.; Denis, B.; Juric, P.; Aghakian, P.; Dahn, J. R. *J. Power Sources* **1991**, *35*, 59. (c) *Aldrich Handbook of Fine Chemicals and Laboratory Equipment*; Aldrich Chemical Co.: 2003–2004. (d) Ue, M.; Ida, K.; Mori, S. *J. Electrochem. Soc.* **1994**, *141*, 2989. (e) Ding, M. S.; Xu, K.; Zhang, S.; Jow, T. R. *J. Electrochem. Soc.* **2001**, *148*, A299.
- (51) Harris, W. S. *Electrochemical Studies in Cyclic Esters*. Ph.D. Thesis, University of California, Berkeley, CA, 1958.
- (52) Jasinski, R.; Kirkland, S. *Anal. Chem.* **1967**, *39*, 1663.
- (53) Jasinski, R.; Carroll, S. *Anal. Chem.* **1968**, *40*, 1908.
- (54) Rauh, R. D.; Reise, T. F.; Brummer, S. B. *J. Electrochem. Soc.* **1978**, *125*, 186.
- (55) Aurbach, D.; Daroux, M. L.; Faguy, P. W.; Yeager, E. *J. Electrochem. Soc.* **1987**, *134*, 1611.
- (56) Dey, A. N. *Thin Solid Films* **1977**, *43*, 131.
- (57) Aurbach, D.; Gofer, Y.; Langsam, J. *J. Electrochem. Soc.* **1989**, *136*, 3198.
- (58) Newman, G. H.; Francis, R. W.; Gaines, L. H.; Rao, B. M. *J. Electrochem. Soc.* **1980**, *127*, 2025.
- (59) Rauh, R. D.; Brummer, S. B. *Electrochim. Acta* **1977**, *22*, 85.
- (60) Koch, V. R.; Young, J. H. *J. Electrochem. Soc.* **1978**, *125*, 1371.
- (61) Koch, V. R. *J. Electrochem. Soc.* **1979**, *126*, 181.
- (62) Koch, V. R.; Goldman, J. L.; Mattos, C. J.; Mulvaney, M. *J. Electrochem. Soc.* **1982**, *129*, 1.
- (63) Koch, V. R.; Young, J. H. *Science* **1979**, *204*, 499.
- (64) Goldman, J. L.; Mank, R. M.; Young, J. H.; Koch, V. R.; Young, J. H. *J. Electrochem. Soc.* **1980**, *127*, 1461.
- (65) Desjardins, C. D.; Cadger, T. G.; Salter, R. S.; Donaldson, G.; Casey, E. J. *J. Electrochem. Soc.* **1985**, *132*, 529.
- (66) Foos, J. S.; McVeigh, J. *J. Electrochem. Soc.* **1983**, *130*, 628.
- (67) Foos, J. S.; Stolki, T. J. *J. Electrochem. Soc.* **1988**, *135*, 2769.
- (68) Abraham, K. M.; Goldman, J. L.; Natwig, D. L. *J. Electrochem. Soc.* **1982**, *129*, 2404.
- (69) Dampier, F. W. *J. Electrochem. Soc.* **1981**, *128*, 2501.
- (70) Abraham, K. M.; Pasquariello, D. M.; Martin, F. J. *J. Electrochem. Soc.* **1986**, *133*, 661.
- (71) Yoshimatsu, I.; Hirai, T.; Yamaki, J. *J. Electrochem. Soc.* **1988**, *135*, 2422.
- (72) Abraham, K. M.; Foos, J. S.; Goldman, J. L. *J. Electrochem. Soc.* **1984**, *131*, 2197.
- (73) Geronov, Y.; Puresheva, B.; Moshtev, R. V.; Zlatilova, P.; Kosev, T.; Staynov, Z.; Pistoia, G.; Pasquali, M. *J. Electrochem. Soc.* **1990**, *137*, 3338.
- (74) Campbell, S. A.; Bowes, C.; McMillan, R. S. *J. Electroanal. Chem.* **1990**, *284*, 195.
- (75) Xu, K.; Angell, C. A. *J. Electrochem. Soc.* **1998**, *145*, L70.
- (76) Xu, K.; Ding, S.; Jow, T. R. *J. Electrochem. Soc.* **1999**, *146*, 4172.
- (77) Simon, B.; Boeue, J. P.; Broussely, M. *J. Power Sources* **1993**, *43/44*, 65.
- (78) Plichta, E.; Slane, S.; Uchiyama, M.; Salomon, M.; Chua, D.; Ebner, W. B.; Lin, H. W. *J. Electrochem. Soc.* **1989**, *136*, 1865.
- (79) Uchida, I.; Sato, H. *J. Electrochem. Soc.* **1995**, *142*, L139.
- (80) Angell, C. A.; Choi, Y. *J. Microsc.* **1986**, *141*, 251.
- (81) Xu, K.; Ding, S.; Jow, T. R. *J. Electrochem. Soc.* **2001**, *148*, A267.
- (82) Elliott, W. Report No. 1, Contract NAS 3-6015 (N 65-11518), Sept 1964.

- (83) Pistoia, G.; De Rossi, M.; Scrosati, B. *J. Electrochem. Soc.* **1970**, *117*, 500.
- (84) Pistoia, G. *J. Electrochem. Soc.* **1971**, *118*, 153.
- (85) Subbarao, S.; Shen, D. H.; Deligiannis, F.; Huang, C. K.; Halpert, G. *J. Power Sources* **1990**, *29*, 579.
- (86) Takami, N.; Ohsaki, T.; Inada, K. *J. Electrochem. Soc.* **1992**, *139*, 1849.
- (87) Arakawa, M.; Tobishima, S.; Hirai, T.; Yamaki, J. *J. Electrochem. Soc.* **1986**, *133*, 1527.
- (88) Surampudi, S.; Shen, D. H.; Huang, C. K.; Narayanan, S. R.; Attia, A.; Halpert, G.; Peled, E. *J. Power Sources* **1993**, *43/44*, 21.
- (89) Tobishima, S.; Arakawa, M.; Hirai, T.; Yamaki, J. *J. Power Sources* **1989**, *26*, 449.
- (90) McMillan, R. S.; Juskow, M. W. *J. Electrochem. Soc.* **1991**, *138*, 1556.
- (91) Yamaura, J.; Ozaki, Y.; Morita, A.; Ohta, A. *J. Power Sources* **1993**, *43/44*, 233.
- (92) Zhang, S. S.; Liu, Q. G.; Yang, L. L. *J. Electrochem. Soc.* **1993**, *140*, L107.
- (93) Guyomard, D.; Tarascon, J. M. *J. Electrochem. Soc.* **1992**, *139*, 937.
- (94) Tarascon, J. M.; Guyomard, D.; Baker, G. L. *J. Power Sources* **1993**, *43/44*, 689.
- (95) Dahn, J.; von Sacken, U.; Juskow, M. W.; al-Janaby, H. *J. Electrochem. Soc.* **1991**, *138*, 2207.
- (96) Ohzuku, T.; Iwakoshi, Y.; Sawai, K. *J. Electrochem. Soc.* **1993**, *140*, 2490.
- (97) Huang, S. Y.; Kavan, L.; Exnar, I.; Grätzel, M. *J. Electrochem. Soc.* **1995**, *142*, L142.
- (98) Guyomard, D.; Tarascon, J. M. *J. Electrochem. Soc.* **1993**, *140*, 3071.
- (99) Tarascon, J. M.; Guyomard, D. *Solid State Ionics* **1994**, *69*, 293.
- (100) Zheng, T.; Liu, Y.; Fuller, E. W.; Tseng, S.; von Sacken, U.; Dahn, J. *J. Electrochem. Soc.* **1995**, *142*, 2581.
- (101) Morita, M.; Ichimura, T.; Ishikawa, M.; Matsuda, Y. *J. Electrochem. Soc.* **1996**, *143*, L26.
- (102) Ein-Eli, Y.; Thomas, S. R.; Chadha, R.; Blakley, T. J.; Koch, V. R. *J. Electrochem. Soc.* **1997**, *144*, 823.
- (103) Chu, A. C.; Josefowicz, J. Y.; Farrington, G. C. *J. Electrochem. Soc.* **1997**, *144*, 4161.
- (104) Aurbach, D.; Ein-Eli, Y.; Markovsky, B.; Zaban, A.; Luski, S.; Carmeli, Y.; Yamin, H. *J. Electrochem. Soc.* **1995**, *142*, 2882.
- (105) Koetschau, L.; Richard, M. N.; Dahn, J. R.; Soupart, J. B.; Rousche, J. C. *J. Electrochem. Soc.* **1995**, *142*, 2906.
- (106) Peled, E.; Golodnitsky, D.; Menachem, C.; Bar-Tow, D. *J. Electrochem. Soc.* **1998**, *145*, 3482.
- (107) Ein-Eli, Y.; Thomas, S. R.; Koch, V. R.; Aurbach, D.; Schecheter, A.; Markovsky, B. *J. Electrochem. Soc.* **1996**, *143*, L273.
- (108) Ein-Eli, Y.; McDevitt, S. F.; Aurbach, D.; Markovsky, B.; Schecheter, A. *J. Electrochem. Soc.* **1997**, *144*, L180.
- (109) Sekai, K.; Azuma, H.; Omaru, A.; Fujita, S.; Imoto, H.; Endo, T.; Yamaura, K.; Nishi, Y. *J. Power Sources* **1993**, *43/44*, 241.
- (110) Linden, D. In *Handbook of Batteries*, 2nd ed.; Linden, D., Ed.; McGraw-Hill: New York, 1995; Chapters 14 and 36.
- (111) Ue, M. *J. Electrochem. Soc.* **1995**, *142*, 2577.
- (112) Ravdel, B.; Abraham, K. M.; Gitzendanner, R.; Marsh, C. *Extended Abstracts of the 200th Electrochemical Society Meeting*, San Francisco, CA, Sept 2–7, 2001; Abstract No. 97; Electrochemical Society: Pennington, NJ.
- (113) Xu, W.; Angell, C. A. *Electrochem. Solid State Lett.* **2001**, *4*, E1.
- (114) Hossain, S. *Handbook of Batteries*, 2nd ed.; Linden, D., Ed.; McGraw-Hill: New York, 1995; Chapter 36.
- (115) Schmidt, M.; Heider, U.; Kuehner, A.; Oesten, R.; Jungnitz, M.; Ignat'ev, N.; Sartori, P. *J. Power Sources* **2001**, *97/98*, 557.
- (116) Walker, C. W.; Cox, J. D.; Salomon, M. *J. Electrochem. Soc.* **1996**, *143*, L80.
- (117) Aurbach, D.; Zaban, A.; Schecheter, A.; Ein-Eli, Y.; Zinigrad, E.; Markovsky, B. *J. Electrochem. Soc.* **1995**, *142*, 2873.
- (118) Aurbach, D.; Ein-Ely, Y.; Zaban, A. *J. Electrochem. Soc.* **1994**, *141*, L1.
- (119) Jasinski, R.; Carroll, S. *J. Electrochem. Soc.* **1970**, *117*, 218.
- (120) Nanjundiah, C.; Goldman, J. L.; Dominey, L. A.; Koch, V. R. *J. Electrochem. Soc.* **1988**, *135*, 2914.
- (121) Koch, V. R. *J. Electrochem. Soc.* **1979**, *126*, 181.
- (122) Webber, A. *J. Electrochem. Soc.* **1991**, *138*, 2586.
- (123) Ein-Eli, Y.; Markovsky, B.; Aurbach, D.; Carmeli, Y.; Yamin, H.; Luski, S. *Electrochim. Acta* **1994**, *39*, 2559.
- (124) Aurbach, D.; Ein-Eli, Y. *J. Electrochem. Soc.* **1995**, *142*, 1746.
- (125) Gnanaraj, J. S.; Levi, M. D.; Levi, E.; Salitra, G.; Aurbach, D.; Fischer, J. E.; Claye, A. *J. Electrochem. Soc.* **2001**, *148*, A525.
- (126) Matsuda, Y.; Morita, M.; Takada, K. *J. Electrochem. Soc.* **1984**, *131*, 1991.
- (127) Matsuda, Y.; Morita, M.; Yamashita, T. *J. Electrochem. Soc.* **1984**, *131*, 2821.
- (128) Takata, K.; Morita, M.; Matsuda, Y. *J. Electrochem. Soc.* **1985**, *132*, 126.
- (129) Ue, M. *J. Electrochem. Soc.* **1994**, *141*, 3336.
- (130) Ue, M.; Takeda, M.; Takehara, M.; Mori, S. *J. Electrochem. Soc.* **1997**, *144*, 2684.
- (131) Ue, M.; Murakami, A.; Nakamura, S. *J. Electrochem. Soc.* **2002**, *149*, A1572.
- (132) Zhang, S. S.; Xu, K.; Jow, T. R. *J. Electrochem. Soc.* **2002**, *149*, A586.
- (133) Takami, N.; Ohsaki, T.; Hasebe, H.; Yamamoto, M. *J. Electrochem. Soc.* **2002**, *149*, A9.
- (134) Zhang, S. S.; Xu, K.; Jow, T. R. *Electrochem. Commun.* **2002**, *4*, 928.
- (135) Zhang, S. S.; Xu, K.; Jow, T. R. *J. Solid State Electrochem.* **2003**, *7*, 147.
- (136) Xu, K.; Angell, C. A. *Electrochim. Acta* **1995**, *40*, 2401.
- (137) Ito, K.; Ohno, H. *Electrochim. Acta* **1998**, *43*, 1247.
- (138) Croce, F.; D'Aprano, A.; Nanjundiah, C.; Koch, V. R.; Walker, C.; Salomon, M. *J. Electrochem. Soc.* **1996**, *143*, 154.
- (139) Naoi, K.; Mori, M.; Naruoka, Y.; Lamanna, W. M.; Atanasoski, R. *J. Electrochem. Soc.* **1999**, *146*, 462.
- (140) Ishikawa, M.; Morita, M.; Asao, M.; Matsuda, Y. *J. Electrochem. Soc.* **1994**, *141*, 1105.
- (141) Krause, L. J.; Lamanna, W.; Summerfield, J.; Engle, M.; Korba, G.; Loch, R.; Atanasoski, R. *J. Power Sources* **1997**, *68*, 320.
- (142) Foropoulos, J.; DesMarteau, D. D. *Inorg. Chem.* **1984**, *23*, 3720.
- (143) Armand, M.; Gorecki, W.; Andreani, R. *Proceedings of the 2nd International Meeting on Polymer Electrolytes*; Scrosati, B., Ed.; Elsevier: London, 1989; p 91.
- (144) Xu, K.; Day, N. D.; Angell, C. A. *J. Electrochem. Soc.* **1996**, *143*, L209.
- (145) Wang, X.; Yasukawa, E.; Kasuya, S. *J. Electrochem. Soc.* **2000**, *147*, 2421.
- (146) Dominey, L. A.; Koch, V. R.; Blakley, T. *Electrochim. Acta* **1992**, *37*, 1551.
- (147) Yang, H.; Kwon, K.; Devine, T. M.; Evans, J. W. *J. Electrochem. Soc.* **2000**, *147*, 4399.
- (148) Kanamura, K.; Umegaki, T.; Shiraiishi, S.; Ohashi, M.; Takehara, Z. *J. Electrochem. Soc.* **2002**, *149*, A185.
- (149) Methlie, G. J. U.S. Patent 3,415,687, 1968.
- (150) Wiesboeck, R. A. U.S. Patent 3,654,330, 1972.
- (151) Kawamura, T.; Kimura, A.; Egashira, M.; Okada, S.; Yamaki, J. *J. Power Sources* **2001**, *104*, 260.
- (152) Sloop, S. E.; Pugh, J. K.; Wang, S.; Kerr, J. B.; Kinoshita, K. *Electrochem. Solid-State Lett.* **2001**, *4*, A42.
- (153) Behl, W. K.; Plichta, E. J. *J. Power Sources* **1998**, *72*, 132.
- (154) Behl, W. K.; Plichta, E. J. *J. Power Sources* **2000**, *88*, 192.
- (155) Xu, K.; Zhang, S.; Jow, T. R.; Xu, W.; Angell, C. A. *Electrochem. Solid-State Lett.* **2002**, *4*, A26.
- (156) Zhang, S.; Jow, T. R. *J. Power Sources* **2002**, *109*, 458.
- (157) Ozawa, K. *Solid State Ionics* **1994**, *69*, 212.
- (158) Ding, M. S. *J. Electrochem. Soc.* **2003**, *150*, A455.
- (159) Ding, M. S.; Xu, K.; Jow, T. R. *J. Electrochem. Soc.* **2000**, *147*, 1688.
- (160) Ding, M. S.; Xu, K.; Jow, T. R. *J. Therm. Anal. Calorim.* **2000**, *62*, 177.
- (161) Ding, M. S. *J. Electrochem. Soc.* **2002**, *149*, A1063.
- (162) Angell, C. A. *Science* **1995**, *267*, 1924.
- (163) Angell, C. A. *Chem. Rev.* **2002**, *102*, 2627.
- (164) Plichta, E. J.; Behl, W. K. *Proceedings of the 38th Power Sources Conference*, Cherry Hill, NJ, 1998; p 444.
- (165) Lin, H. P.; Chua, D.; Salomon, M.; Shiao, H. C.; Hendrickson, M.; Plichta, E.; Slane, S. *Electrochem. Solid-State Lett.* **2001**, *4*, A71.
- (166) Ding, S. P.; Xu, K.; Zhang, S. S.; Jow, T. R.; Amine, K.; Henriksen, G. L. *J. Electrochem. Soc.* **1999**, *146*, 3974.
- (167) Liu, Z. K. *J. Electrochem. Soc.* **2003**, *150*, A359.
- (168) Zhang, S. S.; Xu, K.; Allen, J. L.; Jow, T. R. *J. Power Sources* **2002**, *110*, 217.
- (169) Blint, J. R. *J. Electrochem. Soc.* **1995**, *142*, 696.
- (170) Wang, Y.; Nakamura, S.; Ue, M.; Balbuena, P. B. *J. Am. Chem. Soc.* **2001**, *123*, 11708.
- (171) Yanase, S.; Oi, T. *J. Nucl. Sci. Technol.* **2002**, *39*, 1060.
- (172) Fukushima, T.; Matsuda, Y.; Hashimoto, H.; Arakawa, R. *Electrochem. Solid-State Lett.* **2001**, *4*, A127.
- (173) Matsuda, Y.; Fukushima, T.; Hashimoto, H.; Arakawa, R. *J. Electrochem. Soc.* **2002**, *149*, A1045.
- (174) It should be pointed out that the simple summation of the contribution from each individual ionic species comes from the assumption that the Kohlrausch independent ion rule, established for infinitely diluted solutions, still applies in the electrolytes of practical salt concentrations (~1.0 M), which is incorrect due to the intensive interionic couplings in the latter. However, eq 1 remains qualitatively useful (see ref 1).
- (175) For an excellent introductory reading on ac impedance techniques for the purpose of ion conductivity measurement or study of interfacial properties, please see: Linford, R. G. In *Electrochemical Science and Technology of Polymers*, 2nd ed.; Linford, R. G., Ed.; Elsevier Applied Science: London, 1990; p 281.
- (176) Blomgren, G. E. In *Lithium Batteries*; Gabano, J. P., Ed.; Academic Press: London, 1983.
- (177) Tobishima, S.; Okada, T. *Electrochim. Acta* **1985**, *30*, 1715.

- (178) Endo, E.; Ata, M.; Tanaka, K.; Sekai, K. *J. Electrochem. Soc.* **1998**, *145*, 3757.
- (179) Tsuchida, E.; Kobayashi, N.; Ohno, H. *Macromolecules* **1988**, *21*, 96.
- (180) Zhou, G.; Khan, I. M.; Smid, J. *Polym. Commun.* **1989**, *30*, 52.
- (181) Zhang, S. S.; Wan, G. X. *J. Appl. Polym. Sci.* **1993**, *48*, 405.
- (182) Tada, Y.; Sato, M.; Takeno, N.; Nakacho, Y.; Shigehara, K. *Chem. Mater.* **1994**, *6*, 27.
- (183) Robinson, R. A.; Stokes, R. H. *Electrolyte Solutions*; Butterworths: London, 1959; p 392.
- (184) Some organic nitrogen-containing compounds (nitriles, nitroalkyls, amides, etc.) are the rare exceptions to this rule. For example, for acetonitrile, $\epsilon = 36$ and $\eta = 0.3$ cP at room temperature. However, the poor electrochemical stability of these compounds prevented them from being used in batteries.
- (185) Jasinski, R. *Electrochem. Technol.* **1968**, *6*, 28.
- (186) Saito, T.; Ikeda, H.; Matsuda, Y.; Tamura, H. *J. Appl. Electrochem.* **1976**, *6*, 85.
- (187) Matsuda, Y.; Satake, H. *J. Electrochem. Soc.* **1980**, *127*, 877.
- (188) Tobishima, S.; Yamaji, A. *Electrochim. Acta* **1984**, *29*, 267.
- (189) Tobishima, S.; Yamaji, A.; Okada, T. *Electrochim. Acta* **1984**, *29*, 1471.
- (190) Arakawa, M.; Tobishima, S.; Hirai, T.; Yamaki, J. *J. Electrochem. Soc.* **1986**, *133*, 1527.
- (191) Tobishima, S.; Arakawa, M.; Hirai, T.; Yamaki, J. *J. Power Sources* **1987**, *20*, 293.
- (192) Tobishima, S.; Arakawa, M.; Yamaki, J. *Electrochim. Acta* **1990**, *35*, 383.
- (193) Matsuda, Y.; Nakashima, H.; Morita, M.; Takasu, Y. *J. Electrochem. Soc.* **1981**, *128*, 2552.
- (194) Matsuda, Y.; Morita, M.; Kosaka, K. *J. Electrochem. Soc.* **1983**, *130*, 101.
- (195) Ding, M. S.; Xu, K.; Zhang, S. S.; Amine, K.; Henriksen, G. L.; Jow, T. R. *J. Electrochem. Soc.* **2001**, *148*, A1196.
- (196) Ding, M. S.; Jow, T. R. *J. Electrochem. Soc.* **2003**, *150*, A620.
- (197) Blint, R. *J. Electrochem. Soc.* **1997**, *144*, 787.
- (198) Choquette, Y.; Brisard, G.; Parent, M.; Brouillette, D.; Perron, G.; Desnoyers, J. E.; Armand, M.; Gravel, D.; Lougui, N. *J. Electrochem. Soc.* **1998**, *145*, 3500.
- (199) Chen, H. P.; Fergus, J. W.; Jang, B. Z. *J. Electrochem. Soc.* **2000**, *147*, 399.
- (200) Smedley, S. I. *The Interpretation of Ionic Conductivity in Liquids*; Plenum Press: New York, 1980; Chapter 3.
- (201) Evans, D. H.; O'Connell, K. M.; Petersen, R. A.; Kelly, M. J. *J. Chem. Educ.* **1983**, *60*, 290.
- (202) Bard, A. J.; Faulkner, L. R. *Electrochemical Methods—Fundamentals and Applications*, 2nd ed.; John Wiley & Sons: New York, 2000.
- (203) Ue, M.; Murakami, A.; Nakamura, S. *J. Electrochem. Soc.* **2002**, *149*, A1572.
- (204) Eggert, G.; Heitbaum, J. *Electrochim. Acta* **1986**, *31*, 1443.
- (205) Guyomard, D.; Tarascon, J. M. *J. Power Sources* **1995**, *54*, 92.
- (206) Koch, V. R.; Dominey, L. A.; Nanjundiah, C.; Ondrechen, M. J. *J. Electrochem. Soc.* **1996**, *143*, 798.
- (207) Kita, F.; Kawakami, A.; Sonoda, T.; Kobayashi, H. In *New Sealed Rechargeable Batteries and Supercapacitors*; Barnett, B. M., Dowgiallo, E., Halpert, G., Matsuda, Y., Takehara, Z., Eds.; The Electrochemical Society Proceedings Series; Pennington, NJ, 1993; PV 93-23, p 321.
- (208) Aurbach, D.; Gottlieb, H. *Electrochim. Acta* **1989**, *34*, 141.
- (209) Aurbach, D. *J. Electrochem. Soc.* **1989**, *136*, 906.
- (210) Aurbach, D.; Gofer, Y. *J. Electrochem. Soc.* **1991**, *138*, 3529.
- (211) Goren, E.; Chusid, O.; Aurbach, D. *J. Electrochem. Soc.* **1991**, *138*, L6.
- (212) Aurbach, D.; Gofer, Y.; Ben-Zion, M.; Aped, P. *J. Electroanal. Chem.* **1992**, *339*, 451.
- (213) Aurbach, D.; Chusid, O. *J. Electrochem. Soc.* **1993**, *140*, L155.
- (214) Zhang, X.; Kostecki, R.; Richardson, T. J.; Pugh, J. K.; Ross, P. N. *J. Electrochem. Soc.* **2001**, *148*, A1341.
- (215) Tiedemann, W. H.; Bennion, D. N. *J. Electrochem. Soc.* **1973**, *120*, 1624.
- (216) Jorne, J.; Tobias, C. W. *J. Electrochem. Soc.* **1974**, *121*, 994.
- (217) Jorne, J.; Tobias, C. W. *J. Appl. Electrochem.* **1975**, *5*, 279.
- (218) Peled, E. In *Lithium Batteries*; Gabano, J. P., Eds.; Academic Press: London, 1983; p 43.
- (219) Peled, E.; Straze, H. *J. Electrochem. Soc.* **1977**, *124*, 1030.
- (220) Dousek, F. P.; Jansta, J.; Rihaz, J. *J. Electroanal. Chem.* **1973**, *46*, 281.
- (221) Nazri, G.; Muller, R. H. *J. Electrochem. Soc.* **1985**, *132*, 1385.
- (222) Kanamura, K.; Tamura, H.; Shiraiishi, S.; Takehara, Z. *J. Electrochem. Soc.* **1995**, *142*, 340.
- (223) Kanamura, K.; Shiraiishi, S.; Takehara, Z. *J. Electrochem. Soc.* **1996**, *143*, 2187.
- (224) Epelboin, I.; Froment, M.; Garreau, M.; Thevenin, J.; Warin, D. *J. Electrochem. Soc.* **1980**, *127*, 2100.
- (225) Thevenin, J. G.; Muller, R. H. *J. Electrochem. Soc.* **1987**, *134*, 273.
- (226) Gaberšček, M.; Jamnik, J.; Pejovnik, S. *J. Electrochem. Soc.* **1993**, *140*, 308.
- (227) Gaberšček, M.; Pejovnik, S. *J. Electrochem. Soc.* **1999**, *146*, 933.
- (228) Naoi, K.; Mori, M.; Shinagawa, Y. *J. Electrochem. Soc.* **1996**, *143*, 2517.
- (229) Geronov, Y.; Schwager, F.; Muller, R. H. *J. Electrochem. Soc.* **1982**, *129*, 1422.
- (230) Hérol, A. *Bull. Soc. Chim. Fr.* **1955**, *187*, 999.
- (231) Guérard, D.; Hérol, A. *Carbon* **1975**, *13*, 337.
- (232) Billaud, D.; Hérol, A. *Carbon* **1979**, *17*, 183.
- (233) *Graphite Intercalation Compounds*, Vol. I and II; Zabel, H., Solin, S. A., Eds.; Springer-Verlag: New York, 1990 and 1992.
- (234) Bagouin, M.; Guérard, D.; Hérol, A. *C. R. Acad. Sci., Ser. C* **1966**, *262*, 557.
- (235) Guérard, D.; Hérol, A. *C. R. Acad. Sci., Ser. C* **1972**, *275*, 571.
- (236) Avdeev, V. V.; Nalimova, V. A.; Semenenko, K. N. *High-Pressure Res.* **1990**, *6*, 11.
- (237) Dey, A. N.; Sullivan, B. P. *J. Electrochem. Soc.* **1970**, *117*, 222.
- (238) Eichinger, G. *J. Electroanal. Chem.* **1976**, *74*, 183.
- (239) Besenhard, J. O. *Carbon* **1976**, *14*, 111.
- (240) Besenhard, J. O.; Möhwal, H.; Nickl, J. J. *Carbon* **1980**, *18*, 399.
- (241) Besenhard, J. O.; Fritz, H. P. *Angew. Chem., Int. Ed. Engl.* **1983**, *22*, 950.
- (242) Besenhard, J. O.; Fritz, H. P. *J. Electroanal. Chem.* **1974**, *53*, 329.
- (243) Arakawa, M.; Yamaki, J. *J. Electroanal. Chem.* **1987**, *219*, 273.
- (244) Yazami, R.; Touzain, P. *J. Power Sources* **1983**, *9*, 365.
- (245) Yazami, R.; Guérard, D. *Power Sources* **1993**, *43/44*, 39.
- (246) Kanno, R.; Takeda, Y.; Ichikawa, T.; Nakanishi, K.; Yamamoto, O. *J. Power Sources* **1989**, *26*, 535.
- (247) Mohri, M.; Yanagisawa, N.; Tajima, Y.; Tanaka, H.; Mitate, T.; Nakajima, S.; Yoshida, M.; Yoshimoto, Y.; Suzuki, T.; Wada, H. *J. Power Sources* **1989**, *26*, 545.
- (248) The configuration of the "half anode cell" enables the separate evaluation of the anode material alone; thus, it is widely used as a convenient tool. However, it should be kept in mind that the "anode materials" under study are actually "cathode materials" in this half-cell: Li[electrolyte|carbonaceous "anode"]. To make things more confusing, different researchers use both "charge" (referring to this carbonaceous material in an imaginary full lithium ion cell, therefore, conceptually correct) and "discharge" (referring to this half-cell, therefore, operationally correct) to describe the same process of lithiating the carbon electrode in this half-cell. Since there is no standard convention, caution must be taken when electrochemical literature concerning this topic is being studied. This review will use less ambiguous terms such as "lithiation" or "delithiation" for the cycling of anode half-cells.
- (249) Chusid, O.; Ein Ely, Y.; Aurbach, D.; Babai, M.; Carmeli, Y. *J. Power Sources* **1993**, *43/44*, 47.
- (250) Aurbach, D.; Ein-Eli, Y.; Chusid, O.; Carmeli, Y.; Babai, M.; Yamin, H. *J. Electrochem. Soc.* **1994**, *141*, 603.
- (251) Besenhard, J. O.; Winter, M.; Yang, J.; Biberacher, W. *J. Power Sources* **1993**, *54*, 228.
- (252) Dahn, J. R. *Phys. Rev. B* **1991**, *44*, 9170.
- (253) Jiang, Z.; Alamgir, M.; Abraham, K. M. *J. Electrochem. Soc.* **1995**, *142*, 333.
- (254) Aurbach, D.; Levi, M. D.; Levi, E.; Schechter, A. *J. Phys. Chem. B* **1997**, *101*, 2195.
- (255) Chung, G.; Kim, H.; Yu, S.; Jun, S.; Choi, J.; Kim, M. *J. Electrochem. Soc.* **2000**, *147*, 4391.
- (256) Although by the solution method the ternary GICs composed of [Li⁺(solv)-graphite] were indeed synthesized and identified by XRD, the solvents used were mostly ether compounds that have high donicity toward lithium ion. Similar Li GICs with carbonate molecules were never obtained. On the contrary, even via the solution method, binary GICs (i.e., bare lithium ion intercalation without solvent) instead of ternary ones were often preferentially formed in these ether solvents, casting more doubt about the possibility of their formation via lithium ion cells. The large *c*-axis distance measured by XRD for these ternary GICs ranged between 7 and 11 Å and confirmed from another angle that in situ XRD carried out on a graphite anode during its cycling never detected such GICs. See refs 257–260 for the preparation and characterization of various ternary GICs based on ether compounds and lithium ion.
- (257) Mizutani, Y.; Abe, T.; Ikeda, K.; Ihara, E.; Asano, M.; Harada, T.; Inaba, M.; Ogumi, Z. *Carbon* **1997**, *35*, 61.
- (258) Abe, T.; Mizutani, Y.; Tabuchi, T.; Ikeda, K.; Asano, M.; Harada, T.; Inaba, M.; Ogumi, Z. *J. Power Sources* **1997**, *68*, 216.
- (259) Mizutani, Y.; Abe, T.; Inaba, M.; Ogumi, Z. *Synth. Met.* **2002**, *125*, 153.
- (260) Abe, T.; Kawabata, N.; Mizutani, Y.; Inaba, M.; Ogumi, Z. *J. Electrochem. Soc.* **2003**, *150*, A257.
- (261) Shu, Z. X.; McMillan, R. S.; Murray, J. J. *J. Electrochem. Soc.* **1993**, *140*, 922.
- (262) Matsumura, Y.; Wang, S.; Mondori, J. *J. Electrochem. Soc.* **1995**, *142*, 2914.
- (263) Kim, Y.; Park, S. *J. Electrochem. Soc.* **2001**, *148*, A194.
- (264) Huang, W.; Frech, R. *J. Electrochem. Soc.* **1998**, *145*, 765.

- (265) Inaba, M.; Siroma, Z.; Funabiki, A.; Ogumi, Z.; Abe, T.; Mizutani, Y.; Asano, M. *Langmuir* **1996**, *12*, 1535.
- (266) Chu, A. C.; Josefowicz, J. Y.; Farrington, G. C. *J. Electrochem. Soc.* **1997**, *144*, 4161.
- (267) Hirasawa, K. A.; Sato, T.; Asahina, H.; Yamaguchi, S.; Mori, S. *J. Electrochem. Soc.* **1997**, *144*, L81.
- (268) Alliata, D.; KötZ, R.; Novák, P.; Siegenthaler, H. *Electrochem. Commun.* **2000**, *2*, 436.
- (269) Inaba, M.; Siroma, Z.; Kawatate, Y.; Funabiki, A.; Ogumi, Z. *J. Power Sources* **1997**, *68*, 221.
- (270) Peled, E.; Golodnitsky, D.; Ardel, G. *J. Electrochem. Soc.* **1997**, *144*, L208.
- (271) Ein-Eli, Y.; McDewitt, S. F.; Laura, R. *J. Electrochem. Soc.* **1998**, *145*, L1.
- (272) Ein-Eli, Y. *Electrochem. Solid-State Lett.* **1999**, *2*, 212.
- (273) Aurbach, D.; Markovsky, B.; Gamolsky, K.; Levi, E.; Ein-Eli, Y. *Electrochim. Acta* **1999**, *45*, 67.
- (274) Aurbach, D.; Levi, M. D.; Levi, E.; Schechter, A. *J. Phys. Chem. B* **1997**, *101*, 2195.
- (275) Aurbach, D.; Teller, H.; Levi, E. *J. Electrochem. Soc.* **2002**, *149*, A1255.
- (276) Chung, G.; Kim, H.; Jun, S.; Kim, M. *Electrochem. Commun.* **1999**, *1*, 493.
- (277) Andersson, A. M.; Edström, K. *J. Electrochem. Soc.* **2001**, *148*, A1100.
- (278) Zhuang, G.; Ross, P. *Electrochem. Solid-State Lett.* **2003**, *6*, A136.
- (279) Aurbach, D.; Markovsky, B.; Schechter, A.; Ein Eli, Y. *J. Electrochem. Soc.* **1996**, *143*, 3809.
- (280) Naji, A.; Ghanbaja, J.; Humbert, B.; Willmann, P.; Billaud, D. *J. Power Sources* **1996**, *63*, 33.
- (281) Bar-Tow, D.; Peled, E.; Burstein, L. *J. Electrochem. Soc.* **1999**, *146*, 824.
- (282) Kanamura, K.; Tamura, H.; Takehara, Z. *J. Electroanal. Chem.* **1992**, *333*, 127.
- (283) Kanamura, K.; Tamura, H.; Shiraiishi, S.; Takehara, Z. *J. Electroanal. Chem.* **1995**, *394*, 49.
- (284) Lee, C.; Mun, B.; Ross, P. N. *J. Electrochem. Soc.* **2002**, *149*, A1286.
- (285) Zhang, X.; Pugh, J. K.; Ross, P. N. *Electrochem. Solid-State Lett.* **2001**, *4*, A82.
- (286) Imhof, R.; Novák, P. *J. Electrochem. Soc.* **1998**, *145*, 1081.
- (287) Zhang, S.; Ding, M. S.; Xu, K.; Allen, J.; Jow, T. R. *Electrochem. Solid-State Lett.* **2001**, *4*, A206.
- (288) Some metal oxide structures are unstable when over-delithiated, and as a consequence, the crystal lattice collapses to form a new phase that is electrochemically inactive. Examples are the so-called "Jahn-Teller effect" for spinel cathodes and similar behavior for LiNiO₂ and LiCoO₂ materials as well. These irreversible processes are considered to be caused by the intrinsic properties of the crystalline materials instead of electrolytes and are, therefore, beyond the scope of the current review. See ref 46 for a detailed review.
- (289) Mansour, A. *Surf. Sci. Spectrosc.* **1996**, *3*, 279.
- (290) Aurbach, D.; Levi, M. D.; Levi, E.; Teller, H.; Markovsky, B.; Salitra, G.; Heider, U.; Heider, L. *J. Electrochem. Soc.* **1998**, *145*, 3024.
- (291) Aurbach, D. *J. Power Sources* **2000**, *89*, 206.
- (292) Aurbach, D.; Gamolsky, K.; Markovsky, B.; Salitra, G.; Gofer, Y.; Heider, U.; Oesten, R.; Schmidt, M. *J. Electrochem. Soc.* **2000**, *147*, 1322.
- (293) Eriksson, T.; Andersson, A. M.; Bishop, A. G.; Gejke, C.; Gustafsson, T.; Thomas, J. O. *J. Electrochem. Soc.* **2002**, *149*, A69.
- (294) Andersson, A. M.; Abraham, D. P.; Haasch, R.; MacLaren, S.; Liu, J.; Amine, K. *J. Electrochem. Soc.* **2002**, *149*, A1358.
- (295) Thomas, M. G. S. R.; Bruce, P. G.; Goodenough, J. B. *J. Electrochem. Soc.* **1985**, *132*, 1521.
- (296) Jang, D. H.; Shin, Y. J.; Oh, S. M. *J. Electrochem. Soc.* **1996**, *143*, 2204.
- (297) Xia, Y.; Zhou, Y.; Yoshio, M. *J. Electrochem. Soc.* **1997**, *144*, 2593.
- (298) Zhang, X.; Ross, P. N.; Kostecky, R.; Kong, F.; Sloop, S.; Kerr, J. B.; Striebel, K.; Cairns, E. J.; McLarnon, F. *J. Electrochem. Soc.* **2001**, *148*, A463.
- (299) Wang, Y.; Guo, X.; Greenbaum, S.; Liu, J.; Amine, K. *Electrochem. Solid-State Lett.* **2001**, *4*, A68.
- (300) Matsuo, Y.; Kostecky, R.; McLarnon, F. *J. Electrochem. Soc.* **2001**, *148*, A687.
- (301) Du Pasquier, A.; Blyr, A.; Courjal, P.; Larcher, D.; Amatucci, G.; Gérard, B.; Tarascon, J. M. *J. Electrochem. Soc.* **1999**, *146*, 428.
- (302) Balasubramanian, M.; Lee, H. S.; Sun, X.; Yang, X. Q.; Moodenbaugh, A. R.; McBreen, J.; Fischer, D. A.; Fu, Z. *Electrochem. Solid-State Lett.* **2002**, *5*, A22.
- (303) Zhang, S. S.; Xu, K.; Jow, T. R. *Electrochem. Solid-State Lett.* **2002**, *5*, A92.
- (304) Zhang, S. S.; Xu, K.; Jow, T. R. *J. Electrochem. Soc.* **2002**, *149*, A1521.
- (305) Croce, F.; Nobili, F.; Deptula, A.; Lada, W.; Tossici, R.; D'Epifanio, A.; Scrosati, B.; Marassi. *Electrochem. Commun.* **1999**, *1*, 605.
- (306) Rasch, B.; Cattaneo, E.; Novak, P.; Vielstich, W. *Electrochim. Acta* **1991**, *36*, 1397.
- (307) Kanamura, K.; Toriyama, S.; Shiraiishi, S.; Takehara, Z. *J. Electrochem. Soc.* **1995**, *142*, 1383.
- (308) Ossola, F.; Pistoia, G.; Seeber, R.; Ugo, P. *Electrochim. Acta* **1988**, *33*, 47.
- (309) Matsuta, S.; Kato, Y.; Ota, T.; Kurokawa, H.; Yoshimura, S.; Fujitani, S. *J. Electrochem. Soc.* **2001**, *148*, A7.
- (310) Blyr, A.; Sigala, C.; Amatucci, G.; Guyomard, D.; Chabre, Y.; Tarascon, T. M. *J. Electrochem. Soc.* **1998**, *145*, 194.
- (311) Cattaneo, E.; Ruch, J. *J. Power Sources* **1993**, *43/44*, 341.
- (312) Imhof, R.; Novák, P. *J. Electrochem. Soc.* **1999**, *146*, 1702.
- (313) Sun, X.; Lee, H. S.; Lee, S.; Yang, X. Q.; McBreen, J. *Electrochem. Solid-State Lett.* **1998**, *1*, 239.
- (314) Xu, K.; Angell, C. A. *J. Electrochem. Soc.* **2002**, *149*, A920.
- (315) Fey, G. T.; Li, W.; Dahn, J. R. *J. Electrochem. Soc.* **1994**, *141*, 2279.
- (316) Seel, J. A.; Dahn, J. R. *J. Electrochem. Soc.* **2000**, *147*, 892.
- (317) Lu, Z. H.; Dahn, J. R. *J. Electrochem. Soc.* **2001**, *148*, A710.
- (318) Shembel, E. M.; Apostolova, R. D.; Strizhko, A. S.; Belosokhov, A. I.; Naumenko, A. F.; Rozhkov, V. V. *J. Power Sources* **1995**, *54*, 421.
- (319) Zhang, S. S.; Ding, M. S.; Jow, T. R. *J. Power Sources* **2001**, *102*, 16.
- (320) Lopez, S.; Petit, J. P.; Dunlop, H. M.; Butruille, J. R.; Tourillon, G. *J. Electrochem. Soc.* **1998**, *145*, 823.
- (321) Braithwaite, J. W.; Gonzales, A.; Nagasubramanian, G.; Lucero, S. J.; Peebles, D. E.; Ohlhausen, J. A.; Cieslak, W. R. *J. Electrochem. Soc.* **1999**, *146*, 448.
- (322) Chen, Y.; Devine, T. M.; Evans, J. W.; Monteiro, O. R.; Brown, I. G. *J. Electrochem. Soc.* **1999**, *146*, 1310.
- (323) Munshi, M. Z. A.; Gopalienger, R.; Owens, B. B. *Solid State Ionics* **1988**, *27*, 259.
- (324) Xu, K.; Zhang, S.; Poese, B. A.; Jow, T. R. *Electrochem. Solid-State Lett.* **2002**, *5*, A259.
- (325) Diard, J. P.; LeCanut, J. M.; LeGorrec, B.; Montella, C. *Electrochim. Acta* **1998**, *43*, 2469.
- (326) Casparac, R.; Martin, C. R.; Lisac, E. S.; Mandic, Z. *J. Electrochem. Soc.* **2000**, *147*, 991.
- (327) Kanamura, K.; Okagawa, T.; Takehara, Z. *J. Power Sources* **1995**, *57*, 119.
- (328) Atanasoski, R. T.; Law, H. H.; Tobias, C. W. *Electrochim. Acta* **1987**, *32*, 877.
- (329) Atanasoski, R. T.; Serb, J. *J. Chem. Soc.* **1992**, *57*, 935.
- (330) Christe, K. O.; Dixon, D. A.; McLemore, D.; Wilson, W. W.; Sheehy, J. A.; Boatz, J. *J. Fluorine Chem.* **2000**, *101*, 151.
- (331) Polypropylene or stainless steel containers are normally used, but glass containers can be severely corroded by LiPF₆-containing electrolytes, because the formation of gaseous SiF₄ serves as the driving force for the reaction between the fluorinated Lewis acids PF₅ or HF and the main composition of glass Na₂-SiO₃.
- (332) Vogdanis, L.; Heitz, W. *Macromol. Rapid Commun.* **1986**, *7*, 543.
- (333) Vogdanis, L.; Martens, B.; Uchtmann, H.; Hensel, F.; Heitz, W. *Macromol. Chem.* **1990**, *191*, 465.
- (334) Terasaki, M.; Yosjida, H.; Tukamoto, H.; Mizutani, M.; Yamachi, M. *Denki Kagaku* **1993**, *61*, 1417.
- (335) Ohta, A.; Koshina, H.; Okuno, H.; Murai, H. *J. Power Sources* **1995**, *54*, 6.
- (336) Takeuchi, E. S.; Gan, H.; Palazzo, M.; Leising, R. A.; Davis, S. M. *J. Electrochem. Soc.* **1997**, *144*, 1944.
- (337) Endo, E.; Ata, M.; Sekai, K.; Tanaka, K. *J. Electrochem. Soc.* **1999**, *146*, 49.
- (338) Du Pasquier, A.; Disma, F.; Bowmer, T.; Gozdz, A. S.; Amatucci, G.; Tarascon, J. M. *J. Electrochem. Soc.* **1998**, *145*, 472.
- (339) Zheng, T.; Gozdz, A. S.; Amatucci, G. G. *J. Electrochem. Soc.* **1999**, *146*, 4014.
- (340) Richard, M. N.; Dahn, J. R. *J. Electrochem. Soc.* **1999**, *146*, 2068.
- (341) Richard, M. N.; Dahn, J. R. *J. Electrochem. Soc.* **1999**, *146*, 2078.
- (342) MacNeil, D. D.; Larcher, D.; Dahn, J. R. *J. Electrochem. Soc.* **1999**, *146*, 3596.
- (343) Pistoia, G.; Antonini, A.; Rosati, R.; Zane, D. *Electrochim. Acta* **1996**, *41*, 2683.
- (344) Amatucci, G. G.; Schmutz, C. N.; Blyr, A.; Sigala, C.; Gozdz, A. S.; Larcher, D.; Tarascon, J. M. *J. Power Sources* **1997**, *69*, 11.
- (345) Antonini, A.; Bellito, C.; Pasquali, M.; Pistoia, G. *J. Electrochem. Soc.* **1998**, *145*, 2726.
- (346) Tsunekawa, H.; Tanimoto, S.; Marubayashi, R.; Fujita, M.; Kifune, K.; Sano, M. *J. Electrochem. Soc.* **2002**, *149*, A1326.
- (347) Levy, S. C.; Bro, P. *Battery Hazards and Accident Prevention*; Plenum Press: New York, 1994; p 115.
- (348) von Sacken, U.; Nodwell, E.; Sundher, A.; Dahn, J. *Solid State Ionics* **1994**, *69*, 284.
- (349) Chen, Y.; Evans, J. W. *J. Electrochem. Soc.* **1996**, *143*, 2708.
- (350) Song, L.; Evans, J. W. *J. Electrochem. Soc.* **1998**, *145*, 2327.
- (351) Tobishima, S.; Yamaki, J. *J. Power Sources* **1999**, *81/82*, 882.
- (352) Leising, R. A.; Palazzo, M. J.; Takeuchi, E. S.; Takeuchi, K. J. *J. Electrochem. Soc.* **2001**, *148*, A838.
- (353) Hasegawa, K.; Arakawa, Y. *J. Power Sources* **1993**, *43/44*, 523.

- (354) Gee, M. A.; Laman, F. C. *J. Electrochem. Soc.* **1993**, *140*, L53.
- (355) Chen, Y.; Evans, J. W. *J. Electrochem. Soc.* **1994**, *141*, 2947.
- (356) Newman, J.; Tiedemann, W. *J. Electrochem. Soc.* **1995**, *142*, 1054.
- (357) Pals, C. R.; Newman, J. *J. Electrochem. Soc.* **1995**, *142*, 3274.
- (358) Pals, C. R.; Newman, J. *J. Electrochem. Soc.* **1995**, *142*, 3282.
- (359) Joho, F.; Novák, P.; Spahr, M. E. *J. Electrochem. Soc.* **2002**, *149*, A1020.
- (360) Maleki, H.; Al Hallaj, S.; Selman, J. R.; Dinwiddie, R. B.; Wang, H. *J. Electrochem. Soc.* **1999**, *146*, 947.
- (361) Maleki, H.; Deng, G.; Anani, A.; Howard, J. *J. Electrochem. Soc.* **1999**, *146*, 3224.
- (362) Zhang, Z.; Fouchard, D.; Rea, J. R. *J. Power Sources* **1998**, *70*, 16.
- (363) Biensan, P.; Simon, B.; Pérès, J. P.; de Guibert, A.; Broussely, M.; Bodet, J. M.; Perton, F. *J. Power Sources* **1999**, *81/82*, 906.
- (364) Dahn, J. R.; Fuller, E. W.; Obrovac, M.; von Sacken, U. *Solid State Ionics* **1994**, *69*, 265.
- (365) Arai, H.; Okada, S.; Sakurai, Y.; Yamaki, J. *J. Electrochem. Soc.* **1997**, *144*, 3117.
- (366) Schilling, O.; Dahn, J. R. *J. Electrochem. Soc.* **1998**, *145*, 569.
- (367) MacNeil, D. D.; Christensen, L.; Landucci, J.; Paulsen, J. M.; Dahn, J. R. *J. Electrochem. Soc.* **2000**, *147*, 970.
- (368) MacNeil, D. D.; Hatchard, T. D.; Dahn, J. R. *J. Electrochem. Soc.* **2001**, *148*, A663.
- (369) MacNeil, D. D.; Dahn, J. R. *J. Electrochem. Soc.* **2001**, *148*, A1205.
- (370) MacNeil, D. D.; Dahn, J. R. *J. Electrochem. Soc.* **2001**, *148*, A1211.
- (371) MacNeil, D. D.; Dahn, J. R. *J. Electrochem. Soc.* **2003**, *150*, A21.
- (372) Matsuda, Y. *J. Power Sources* **1993**, *43*, 1.
- (373) Hirai, T.; Yoshimatsu, I.; Yamaki, J. *J. Electrochem. Soc.* **1994**, *141*, 2300.
- (374) Kovač, M.; Miličević, S.; Kovač, A.; Pejovnik, S. *J. Electrochem. Soc.* **1995**, *142*, 1390.
- (375) Mogi, R.; Inaba, M.; Jeong, S.; Iriyama, Y.; Abe, T.; Ogumi, Z. *J. Electrochem. Soc.* **2002**, *149*, 2002.
- (376) Besenhard, J. O.; Wagner, M. W.; Winter, M.; Jannakoudakis, A. D.; Jannakoudakis, P. D.; Theodoridou, E. *J. Power Sources* **1993**, *43/44*, 413.
- (377) Gong, J. B.; Tsumura, T.; Nakamura, H.; Yoshio, M.; Yoshitake, H.; Abe, T. *202nd Meeting of the Electrochemical Society*, Salt Lake City, UT, Oct 20–24, 2002; Abstract No. 200; Electrochemical Society: Pennington, NJ.
- (378) Izatt, R. M.; Bradshaw, J. S.; Nielsen, S. A.; Lamb, J. D.; Christensen, J. J. *Chem. Rev.* **1985**, *85*, 271.
- (379) Morita, M.; Hayashida, H.; Matsuda, Y. *J. Electrochem. Soc.* **1987**, *134*, 2107.
- (380) Nagasubramanian, G.; Di Stefano, S. *J. Electrochem. Soc.* **1990**, *137*, 3830.
- (381) Salomom, M. *J. Solution Chem.* **1990**, *19*, 1225.
- (382) Nagasubramanian, G.; Attia, A. I.; Halpert, G. *J. Electrochem. Soc.* **1992**, *139*, 3043.
- (383) Lonergan, M. C.; Ratner, M. A.; Shriver, D. *J. Am. Chem. Soc.* **1995**, *117*, 2344.
- (384) Lee, H. S.; Yang, X. Q.; McBreen, J.; Choi, L. S.; Okamoto, Y. *J. Electrochem. Soc.* **1996**, *143*, 3825.
- (385) Lee, H. S.; Sun, X.; Yang, X. Q.; McBreen, J.; Callahan, J. H.; Choi, L. S. *J. Electrochem. Soc.* **2000**, *146*, 9.
- (386) Lee, H. S.; Yang, X. Q.; Xiang, C. L.; McBreen, J.; Choi, L. S. *J. Electrochem. Soc.* **1998**, *145*, 2813.
- (387) Sun, X.; Lee, H. S.; Yang, X. Q.; McBreen, J. *J. Electrochem. Soc.* **1999**, *146*, 3655.
- (388) Sun, X.; Lee, H. S.; Yang, X. Q.; McBreen, J. *J. Electrochem. Soc.* **2002**, *149*, A355.
- (389) Sun, X.; Lee, H. S.; Yang, X. Q.; McBreen, J. *Electrochem. Solid-State Lett.* **2001**, *4*, A184.
- (390) Sun, X.; Lee, H. S.; Yang, X. Q.; McBreen, J. *Electrochem. Solid-State Lett.* **2002**, *5*, A248.
- (391) Sun, X.; Lee, H. S.; Yang, X. Q.; McBreen, J. *Electrochem. Solid-State Lett.* **2003**, *6*, A43.
- (392) Lee, H. S.; Sun, X.; Yang, X. Q.; McBreen, J. *J. Electrochem. Soc.* **2002**, *149*, A1460.
- (393) Tasaki, K.; Nakamura, S. *J. Electrochem. Soc.* **2001**, *148*, A984.
- (394) Morita, M.; Ishikawa, M.; Matsuda, Y. In *Lithium Ion Batteries: Fundamentals and Performance*; Wakihara, M., Yamamoto, O., Eds.; Wiley-VCH: New York, 1999; p 156.
- (395) Ein-Eli, Y.; Thomas, S. R.; Koch, V. R. *J. Electrochem. Soc.* **1996**, *143*, L195.
- (396) Ein-Eli, Y.; Thomas, S. R.; Koch, V. R. *J. Electrochem. Soc.* **1997**, *144*, 1159.
- (397) Wilkinson, D.; Dahn, J. R. U.S. Patent 5,130,211, 1992.
- (398) Shu, Z. X.; McMillan, R. S.; Murray, J. J. *J. Electrochem. Soc.* **1993**, *140*, L101.
- (399) Wrodnigg, G. H.; Besenhard, J. O.; Winter, M. *J. Electrochem. Soc.* **1999**, *146*, 470.
- (400) Simon, B.; Boeue, J.-P. U.S. Patent 5,626,981, 1997.
- (401) Barker, J.; Gao, F. U.S. Patent 5,712,059, 1998.
- (402) Naruse, Y.; Fujita, S.; Omaru, A. U.S. Patent 5,714,281, 1998.
- (403) Jehoulet, C.; Biensan, P.; Bodet, J. M.; Broussely, M.; Moteau, C.; Tessier-Lescourret, C. In *Batteries for Portable Applications and Electric Vehicles*; Holmes, C. F., Landgrebe, A. R., Eds.; The Electrochemical Society Proceeding Series; Pennington, NJ, 1997; P. V. 97-18, P974.
- (404) Aurbach, D.; Gamolsky, K.; Markovsky, B.; Gofer, Y.; Schmidt, M.; Heider, U. *Electrochim. Acta* **2002**, *47*, 1423.
- (405) Contestabile, M.; Morselli, M.; Paraventi, R.; Neat, R. J. *J. Power Sources* **2003**, *119/121*, 943.
- (406) Herreyre, S.; Huchet, O.; Barousseau, S.; Perton, F.; Bodet, J. M.; Biensan, Ph. *J. Power Sources* **2001**, *97/98*, 576.
- (407) Broussely, M.; Blanchard, P.; Biensan, Ph.; Planchat, J. P.; Nechev, K.; Staniewicz, R. J. *J. Power Sources* **2003**, *119/121*, 859.
- (408) Oesten, R.; Heider, U.; Schmid, M. *Solid State Ionics* **2002**, *148*, 391.
- (409) Wang, C.; Nakamura, H.; Komatsu, H.; Yoshio, M.; Yoshitake, H. *J. Power Sources* **1998**, *74*, 142.
- (410) Najj, A.; Ghanbaja, J.; Willmann, P.; Billaud, D. *Electrochim. Acta* **2000**, *45*, 1893.
- (411) Matsuo, Y.; Fumita, K.; Fukutsuka, T.; Sugie, Y.; Koyama, H.; Inoue, K. *J. Power Sources* **2003**, *119/121*, 373.
- (412) Santer, H. J.; Möller, K.-C.; Ivanco, J.; Ramsey, M. G.; Netzer, F. P.; Yamaguchi, S.; Besenhard, J. O.; Winter, M. *J. Power Sources* **2003**, *119/121*, 368.
- (413) Möller, K.-C.; Santer, H. J.; Kern, W.; Yamaguchi, S.; Besenhard, J. O.; Winter, M. *J. Power Sources* **2003**, *119/121*, 561.
- (414) Holleck, G. L.; Harris, P. B.; Abraham, K. M.; Buzby, J.; Brummer, S. B. Technical Report No. 6, Contract N00014-77-0155; EIC Laboratories: Newton, MA, 1982.
- (415) Abraham, K. M.; Brummer, S. B. In *Lithium Batteries*; Gabano, J., Ed.; Academic Press: New York, 1983.
- (416) Narayanan, S. R.; Surampudi, S.; Attia, A. I.; Bankston, C. P. *J. Electrochem. Soc.* **1991**, *138*, 2224.
- (417) Abraham, K. M.; Pasquariello, D. M.; Willstädt, E. B. *Proceedings of the 33rd International Power Sources Symposium*, Cherry Hill, NJ, June 13–16, 1988; The Electrochemical Society, Inc.: 1988; p 38.
- (418) Behl, W. K.; Chin, D. T. *J. Electrochem. Soc.* **1988**, *135*, 16.
- (419) Behl, W. K.; Chin, D. T. *J. Electrochem. Soc.* **1988**, *135*, 21.
- (420) Behl, W. K. *J. Electrochem. Soc.* **1989**, *136*, 2305.
- (421) Abraham, K. M.; Pasquariello, D. M. U.S. Patent, 4,857,423, 1989.
- (422) Abraham, K. M.; Pasquariello, D. M.; Willstaedt, E. B. *J. Electrochem. Soc.* **1990**, *137*, 1856.
- (423) Abraham, K. M. *Electrochim. Acta* **1993**, *38*, 1233.
- (424) Mason, J. G.; Rosenblum, M. *J. Am. Chem. Soc.* **1960**, *82*, 4206.
- (425) Wilkinson, D. P.; Dudley, J.; Golovin, N. In *Rechargeable Lithium Batteries*; Subbarao, S., Koch, V. R., Owens, B. B., Smyrl, W. H., Eds.; The Electrochemical Society: Pennington, NJ, 1990; PV 90-5, p 77.
- (426) Abraham, K. M. In *Rechargeable Lithium Batteries*; Subbarao, S., Koch, V. R., Owens, B. B., Smyrl, W. H., Eds.; The Electrochemical Society: Pennington, NJ, 1990; PV 90-5, p 1.
- (427) Cabrera, C. R.; Bard, A. J. *J. Electroanal. Chem.* **1989**, *273*, 147.
- (428) Cha, C. S.; Ai, X. P.; Yang, H. X. *J. Power Sources* **1995**, *54*, 255.
- (429) Golovin, M. N.; Wilkinson, D. P.; Dudley, J. T.; Holonko, D.; Woo, S. *J. Electrochem. Soc.* **1992**, *139*, 5.
- (430) Halpert, G.; Surampudi, S.; Shen, D.; Huang, C. K.; Narayanan, S.; Vamos, E.; Perrone, D. *J. Power Sources* **1994**, *47*, 287.
- (431) Richardson, T. J.; Ross, P. N. *J. Electrochem. Soc.* **1996**, *143*, 3992.
- (432) Adachi, M.; Tanaka, K.; Sekai, K. *J. Electrochem. Soc.* **1999**, *146*, 1256.
- (433) Hammerich, O.; Parker, V. D. *Electrochim. Acta* **1973**, *18*, 537.
- (434) Kerr, J. B.; Tian, M. U.S. Patent 6,045,952, 2000.
- (435) Mao, H.; Wainwright, D. S. Canadian Patent 2,205,683, 1997.
- (436) Yoshio, M.; Yoshitake, H.; Abe, K. *204th Meeting of Electrochemical Society*, Orlando, FL, Oct 12–16, 2003; Abstract No. 280.
- (437) Kuboki, T.; Ohsaki, T. U.S. Patent 6,413,679, 2002.
- (438) Reimers, J. N.; Way, B. M. U.S. Patent 6,074,777, 2000.
- (439) Mao, H. Canadian Patent 2,163,187, 1995.
- (440) Yoshino, A. In *Proceedings of the 4th Hawaii Battery Conference*, ARAD Enterprises, Hilo, HI, Jan 8, 2002; ARAD Enterprises: Hilo, HI; p 102.
- (441) Besenhard, J. O.; von Werner, K.; Winter, M. U.S. Patent 5,916,708, 1999.
- (442) McMillan, R.; Sleg, H.; Shu, Z. X.; Wang, W. *J. Power Sources* **1999**, *81/82*, 20.
- (443) Inaba, M.; Kawatate, Y.; Funabiki, A.; Jeong, S. K.; Abe, T.; Ogumi, Z. *Electrochim. Acta* **1999**, *45*, 99.
- (444) Petrella, R. V. In *Flame Retardant Polymeric Materials*; Lewin, M., Atlas, S. M., Pearce, E. M., Eds.; Plenum Publishing: New York, 1978; Vol. 2, p 159.
- (445) Cullis, C. F.; Hirshler, M. M. *The Combustion of Organic Polymers*; Clarendon Press: Oxford, 1981.
- (446) Shu, Z. X.; McMillan, R. S.; Murray, J. J.; Davidson, I. J. *J. Electrochem. Soc.* **1995**, *142*, L161.

- (447) Shu, Z. X.; McMillan, R. S.; Murray, J. J.; Davidson, I. J. *J. Electrochem. Soc.* **1996**, *143*, 2230.
- (448) For this reason CIEC and FEC were treated as cosolvents in this review, instead of as additives as they were in most literature sources.
- (449) Winter, M.; Novák, P. *J. Electrochem. Soc.* **1998**, *145*, L27.
- (450) Najj, A.; Ghanbaja, J.; Willmann, P.; Billaud, D. *J. Power Sources* **1999**, *81/82*, 207.
- (451) Winter, M.; Imhof, R.; Joho, F.; Noák, P. *J. Power Sources* **1999**, *81/82*, 818.
- (452) Nagasubramanian, G. The 1999 Joint International Meeting of the Electrochemical Society, Honolulu, HI, Oct 17–22, 1999; Abstract 334; Electrochemical Society: Pennington, NJ.
- (453) Arai, J.; Katayama, H.; Akahoshi, H. *J. Electrochem. Soc.* **2002**, *149*, A217.
- (454) Salomon, M.; Plichta, E. *J. Electrochim. Acta* **1985**, *30*, 113.
- (455) Chagnes, A.; Carré, B.; Willmann, P.; Lemordant, D. *J. Power Sources* **2002**, *109*, 203.
- (456) Fukushima, T.; Matsuda, Y.; Hashimoto, H.; Arakawa, R. *J. Power Sources* **2002**, *110*, 34.
- (457) Rendek, L. J.; Chottiner, G. S.; Scherson, D. A. *J. Electrochem. Soc.* **2003**, *150*, A326.
- (458) Takami, N.; Sekino, M.; Ohsaki, T.; Kanda, M.; Yamamoto, M. *J. Power Sources* **2001**, *97/98*, 677.
- (459) Lanz, M.; Novák, P. *J. Power Sources* **2001**, *102*, 277.
- (460) Chagnes, A.; Carré, B.; Willmann, P.; Dedryvére, R.; Gonbeau, D.; Lemordant, D. *J. Electrochem. Soc.* **2003**, *150*, A1255.
- (461) Smart, M. C.; Ratnakumar, B. V.; Surampudi, S.; Wang, Y.; Zhang, X.; Greenbaum, S. G.; Hightower, A.; Ahn, C. C.; Fultz, B. *J. Electrochem. Soc.* **1999**, *146*, 3963.
- (462) Smart, M. C.; Ratnakumar, B. V.; Surampudi, S. *J. Electrochem. Soc.* **2002**, *149*, A361.
- (463) Vetter, J.; Novák, P. *J. Power Sources* **2003**, *119/121*, 338.
- (464) Nakajima, T.; Dan, K.; Koh, M. *J. Fluorine Chem.* **1998**, *87*, 221.
- (465) Yamaki, J.-I.; Yamazaki, I.; Egashira, M.; Okada, S. *J. Power Sources* **2001**, *102*, 288.
- (466) Smart, M. C.; Ratnakumar, B. V.; Ryan-Mowrey, V. S.; Surampudi, S.; Prakash, G. K. S.; Hu, J.; Cheung, I. *J. Power Sources* **2003**, *119/121*, 359.
- (467) Zhang, S. S.; Angell, C. A. *J. Electrochem. Soc.* **1996**, *143*, 4047.
- (468) Choquette, Y.; Brisard, G.; Parent, M.; Brouillette, D.; Perron, G.; Desnoyers, J. E.; Armand, M.; Gravel, D.; Slougui, N. *J. Electrochem. Soc.* **1998**, *145*, 3500.
- (469) Matsuda, Y.; Morita, M.; Yamada, K.; Hirai, K. *J. Electrochem. Soc.* **1985**, *132*, 2538.
- (470) Morita, M.; Okada, Y.; Matsuda, Y. *J. Electrochem. Soc.* **1987**, *134*, 2665.
- (471) Bach, S.; Baffier, N.; Pereira-Ramos, J. P.; Messina, R. *J. Power Sources* **1993**, *43/44*, 569.
- (472) Yan, W.; Lerner, M. M. *J. Electrochem. Soc.* **2001**, *148*, D83.
- (473) Park, S. H.; Winnick, J.; Kohl, P. A. *J. Electrochem. Soc.* **2002**, *149*, A1196.
- (474) Dominey, L. A. U.S. Patent, 5,273,840, 1993.
- (475) Barthel, J.; Wühr, M.; Buestrich, R.; Gores, H. J. *J. Electrochem. Soc.* **1995**, *142*, 2527.
- (476) Barthel, J.; Buestrich, R.; Carl, E.; Gores, H. J. *J. Electrochem. Soc.* **1996**, *143*, 3565.
- (477) Barthel, J.; Buestrich, R.; Carl, E.; Gores, H. J. *J. Electrochem. Soc.* **1996**, *143*, 3572.
- (478) Barthel, J.; Buestrich, R.; Gores, H. J.; Schmidt, M.; Wühr, M. *J. Electrochem. Soc.* **1997**, *144*, 3866.
- (479) Barthel, J.; Schmidt, M.; Gores, H. J. *J. Electrochem. Soc.* **1998**, *145*, L17.
- (480) Barthel, J.; Schmidt, M.; Gores, H. J. *J. Electrochem. Soc.* **2000**, *147*, 21.
- (481) Sasaki, Y.; Handa, M.; Kurashima, K.; Tonuma, T.; Usami, K. *J. Electrochem. Soc.* **2001**, *148*, A999.
- (482) Handa, M.; Fukuda, S.; Sasaki, Y.; Usami, K. *J. Electrochem. Soc.* **1997**, *144*, L235.
- (483) Xu, W.; Angell, C. A. *Electrochem. Solid-State Lett.* **2000**, *3*, 366.
- (484) Xu, W.; Angell, C. A. *Solid State Ionics* **2002**, *147*, 295.
- (485) Videa, M.; Xu, W.; Geil, B.; Marzke, R.; Angell, C. A. *J. Electrochem. Soc.* **2001**, *148*, A1352.
- (486) Xu, W.; Shusterman, A.; Videa, M.; Velikov, V.; Marzke, R. L.; Angell, C. A. *J. Electrochem. Soc.* **2003**, *150*, E74.
- (487) Lischka, U.; Wietelmann, U.; Wegner, M. DE 19829030 C1, 1999.
- (488) Xu, K.; Zhang, S.; Jow, T. R. *Electrochem. Solid-State Lett.* **2003**, *6*, A117.
- (489) Xu, K.; Lee, U.; Zhang, S.; Wood, M.; Jow, T. R. *Electrochem. Solid-State Lett.* **2003**, *6*, A144.
- (490) Amine, K.; Liu, J.; Kang, S.; Belharouak, I.; Hyung, Y.; Vissers, D.; Henriksen, G. *J. Power Sources* **2004**, *129*, 14.
- (491) Jiang, J.; Dahn, J. R. *Electrochem. Solid-State Lett.* **2003**, *6*, A180.
- (492) Jow, T. R.; Ding, M. S.; Xu, K.; Zhang, S. S.; Allen, J. L.; Amine, K.; Henriksen, G. L. *J. Power Sources* **2003**, *119/121*, 343.
- (493) Yamaguchi, H.; Takahashi, H.; Kato, M.; Arai, J. *J. Electrochem. Soc.* **2003**, *150*, A312.
- (494) Handa, M.; Suzuki, M.; Suzuki, J.; Kanematsu, H.; Sasaki, Y. *Electrochem. Solid-State Lett.* **1999**, *2*, 60.
- (495) Eberwein, M.; Schmidt, A.; Schmidt, M.; Zabel, M.; Burgemeister, T.; Barthel, J.; Kunz, W.; Gores, H. J. *J. Electrochem. Soc.* **2003**, *150*, A994.
- (496) Sartori, P.; Ignatyev, N. The 194th Meeting of the Electrochemical Society, Boston, MA, Nov 1–6, 1998; Abstract 160.
- (497) Sartori, P.; Ignatyev, N. U.S. Patent 6,210,830, 2001.
- (498) Schmidt, M.; Heider, U.; Kuehner, A.; Oesten, R.; Jungnitz, M.; Ignat'ev, N.; Sartori, P. *J. Power Sources* **2001**, *97/98*, 557.
- (499) (a) Gnanaraj, J. S.; Levi, M. D.; Gofer, Y.; Aurbach, D.; Schmidt, M. *J. Electrochem. Soc.* **2003**, *150*, A445. (b) Gnanaraj, J. S.; Zinigrad, E.; Asraf, L.; Sprecher, M.; Gottlieb, H. E.; Geissler, W.; Schmidt, M.; Aurbach, D. *Electrochem. Commun.* **2003**, *5*, 946.
- (500) Gnanaraj, J. S.; Zinigrad, E.; Levi, M. D.; Aurbach, D.; Schmidt, M. *J. Power Sources* **2003**, *119/121*, 799.
- (501) Egashira, M.; Scrosati, B.; Armand, M.; Béranger, S.; Michot, C. *Electrochem. Solid-State Lett.* **2003**, *6*, A71.
- (502) Barbarich, T. J.; Driscoll, P. F. *Electrochem. Solid-State Lett.* **2003**, *6*, A113.
- (503) Plichta, E. J.; Behl, W. K. *Proceedings of the 38th Power Source Conference*, Cherry Hill, NJ, 1998; p 444.
- (504) Plichta, E. J.; Hendrickson, M.; Thompson, R.; Au, G.; Behl, W. K.; Smart, M. C.; Ratnakumar, B. V.; Surampudi, S. *J. Power Sources* **2001**, *94*, 160.
- (505) Hamlen, R.; Au, G.; Brundage, M.; Hendrickson, M.; Plichta, E.; Slane, S.; Barbarello, J. *J. Power Sources* **2001**, *97/98*, 22.
- (506) Nagasubramanian, G. *J. Appl. Electrochem.* **2001**, *31*, 99.
- (507) Fan, J. *J. Power Sources* **2003**, *117*, 170.
- (508) Smart, M. C.; Ratnakumar, B. V.; Surampudi, S. *J. Electrochem. Soc.* **1999**, *146*, 486.
- (509) Shiao, H. C.; Chua, D.; Lin, H.; Slane, S.; Salomon, M. *J. Power Sources* **2000**, *87*, 167.
- (510) Sawai, K.; Ohzuku, T. *J. Electrochem. Soc.* **2003**, *150*, A674.
- (511) Wang, C.; Appleby, A. J.; Little, F. E. *J. Electrochem. Soc.* **2002**, *149*, A754.
- (512) Zhang, S. S.; Xu, K.; Jow, T. R. *J. Power Sources* **2003**, *115*, 137.
- (513) Huang, C.-K.; Sakamoto, J. S.; Wolfenstine, J.; Surampudi, S. *J. Electrochem. Soc.* **2000**, *147*, 2893.
- (514) Gitzendanner, R.; Ehrlich, G.; Marsh, C.; Marsh, R. The 194th Meeting of the Electrochemical Society, Boston, MA, Nov 1–6, 1998; Abstract 157; Electrochemical Society: Pennington, NJ.
- (515) Smart, M. C.; Ratnakumar, B. V.; Whitcanack, L. D.; Chin, K. B.; Surampudi, S.; Croft, H.; Tice, D.; Staniewicz, R. *J. Power Sources* **2003**, *119/121*, 349.
- (516) The physical significance of the impedance response corresponding to the semicircle at lower frequency has been ambiguous. Conventionally it was assigned to the "charge-transfer" for the electrochemical reactions; hence, conceptually, it should not be influenced by electrolytes due to the presence of the electronically insulating surface films. However, experiences show that it is in fact readily affected by the chemical composition of the electrolytes; therefore, it should involve an interfacial process that is sensitive to the surface film formation. There was a suggestion (see ref 518) that the SEI is a mixed conductor for both ions and electrons, so that the electrons can transport across it to reach the redox reaction sites. This hypothesis is well able to explain why R_{ct} is affected by SEI chemical composition, however, at the risk of overturning the fundamentals of lithium ion chemistry.
- (517) Mohamedi, M.; Takahashi, D.; Itoh, T.; Uchida, I. *Electrochim. Acta* **2002**, *47*, 3483.
- (518) Chen, C. H.; Liu, J.; Amine, K. *J. Power Sources* **2001**, *96*, 321.
- (519) Roth, E. P.; Crafts, C. C.; Doughty, D. H. The 202nd Meeting of the Electrochemical Society, Salt Lake City, UT, Oct 20–24, 2002; Abstract 216.
- (520) (a) Yokoyama, K.; Fujita, S.; Hiwara, A.; Naruse, Y.; Toriida, M.; Omaru, A. U.S. Patent 5,580,684, 1996. (b) Narang, S. C.; Ventura, S. C.; Dougherty, B. J.; Zhao, M.; Smedley, S.; Koolpe, G. U.S. Patent 5,830,600, 1998. (c) Narang, S. C.; Ventura, S. C.; Cox, P. U.S. Patent 6,168,885, 2001.
- (521) Lyons, J. W. *The Chemistry and Uses of Flame Retardants*; John Wiley & Sons: New York, 1970.
- (522) Cullis, C. F.; Hirshler, M. M. *The Combustion of Organic Polymers*; Clarendon Press: Oxford, 1981.
- (523) Lee, C. W.; Venkatachalapathy, R.; Prakash, J. *Electrochem. Solid-State Lett.* **2000**, *3*, 63.
- (524) Wang, X.; Yasukawa, E.; Kasuya, S. *J. Electrochem. Soc.* **2001**, *148*, A1058.
- (525) Wang, X.; Yasukawa, E.; Kasuya, S. *J. Electrochem. Soc.* **2001**, *148*, A1066.
- (526) Xu, K.; Ding, M. S.; Zhang, S.; Allen, J. L.; Jow, T. R. *J. Electrochem. Soc.* **2002**, *149*, A622.
- (527) Xu, K.; Zhang, S.; Allen, J. L.; Jow, T. R. *J. Electrochem. Soc.* **2002**, *149*, A1079.
- (528) Ding, M. S.; Xu, K.; Jow, T. R. *J. Electrochem. Soc.* **2002**, *149*, A1489.

- (529) Xu, K.; Ding, M. S.; Zhang, S.; Allen, J. L.; Jow, T. R. *J. Electrochem. Soc.* **2003**, *150*, A161.
- (530) Xu, K.; Zhang, S.; Allen, J. L.; Jow, T. R. *J. Electrochem. Soc.* **2003**, *150*, A170.
- (531) Hyung, Y. E.; Vissers, D. R.; Amine, K. *J. Power Sources* **2003**, *119/121*, 383.
- (532) Ota, H.; Kominato, A.; Chun, W.-J.; Yasukawa, E.; Kasuya, S. *J. Power Sources* **2003**, *119/121*, 393.
- (533) Granzow, A. *Acc. Chem. Res.* **1978**, *11*, 177.
- (534) Arai, J. *J. Electrochem. Soc.* **2003**, *150*, A219.
- (535) Arai, J. *J. Power Sources* **2003**, *119/121*, 388.
- (536) Ratner, M. A.; Shriver, D. F. *Chem. Rev.* **1988**, *88*, 109.
- (537) Watanabe, M. In *Solid State Ionics: Materials and Applications*; Chowdari, B. V. R., Ed.; World Scientific Publishing Co.: Singapore, 1992; p 149.
- (538) Sanchez, J.-Y. In *Solid State Ionics: Materials and Applications*; Chowdari, B. V. R., Ed.; World Scientific Publishing Co.: 1992; p 159.
- (539) Armand, M. *Solid State Ionics* **1994**, *69*, 309.
- (540) Shriver, D. F.; Bruce, P. G. In *Solid State Electrochemistry*; Bruce, P. G., Ed.; Cambridge University Press: Cambridge, U.K., 1995; p 95.
- (541) Song, J. Y.; Wang, Y. Y.; Wan, C. C. *J. Power Sources* **1999**, *77*, 183.
- (542) Dias, F. B.; Plomp, L.; Veldhuis, J. B. J. *J. Power Sources* **2000**, *88*, 169.
- (543) (a) Fenton, D. E.; Parker, J. M.; Wright, P. V. *Polymer* **1973**, *14*, 589. (b) Wright, P. V. *Br. Polym. J.* **1975**, *7*, 319. (c) Wright, P. V. *J. Polym. Sci., Polym. Phys. Ed.* **1976**, *14*, 955.
- (544) (a) Armand, M. B.; Chabagno, J. M.; Duclot, M. *The 2nd International Conference on Solid Electrolytes*, St. Andrews, Scotland, 1978; Abstract No. 65. (b) Armand, M. B.; Chabagno, J. M.; Duclot, M. In *Fast Ion Transport in Solids*; Duclot, M. J., Vashishta, P., Mundy, J. N., Shenoy, G. K., Eds.; North-Holland, Amsterdam, 1979.
- (545) Angell, C. A.; Liu, C.; Sanchez, E. *Nature* **1993**, *362*, 137.
- (546) Angell, C. A.; Fan, J.; Liu, C.; Lu, Q.; Sanchez, E.; Xu, K. *Solid State Ionics* **1994**, *69*, 343.
- (547) Angell, C. A.; Xu, K.; Zhang, S.-S.; Videa, M. *Solid State Ionics* **1996**, *86/88*, 17.
- (548) Imrie, C. T.; Ingram, M. D.; McHattie, G. S. *J. Phys. Chem. B* **1999**, *103*, 4132.
- (549) Zheng, Y.; Chia, F.; Ungar, G.; Wright, P. V. *Chem. Commun.* **2000**, *16*, 1459.
- (550) Anderman, M. *Solid State Ionics* **1994**, *69*, 336.
- (551) Scrosati, B.; Croce, F.; Persi, L. *J. Electrochem. Soc.* **2000**, *147*, 1718.
- (552) Persi, L.; Croce, F.; Scrosati, B.; Plichta, E.; Hendrickson, M. A. *J. Electrochem. Soc.* **2002**, *149*, A212.
- (553) Pamerio, S.; Satolli, D.; D'Epifano, A.; Scrosati, B. *J. Electrochem. Soc.* **2002**, *149*, A414.
- (554) Aihara, Y.; Appetecchi, G. B.; Scrosati, B. *J. Electrochem. Soc.* **2002**, *149*, A849.
- (555) Appetecchi, G. B.; Aihara, Y.; Scrosati, B. *J. Electrochem. Soc.* **2003**, *150*, A301.
- (556) Tarascon, J.-M.; Gozdz, A. S.; Schmutz, C.; Shokoohi, F.; Warren, P. C. *Solid State Ionics* **1996**, *86/88*, 49.
- (557) Feuillade, G.; Perche, P. *J. Appl. Electrochem.* **1975**, *63*, 5.
- (558) Tsuchida, E.; Ohno, H.; Tsunemi, K. *Electrochim. Acta* **1983**, *28*, 591.
- (559) Tsunemi, K.; Ohno, H.; Tsuchida, E. *Electrochim. Acta* **1983**, *28*, 833.
- (560) Du Pasquier, A.; Zheng, T.; Amatucci, G. G.; Gozdz, A. S. *J. Power Sources* **2001**, *97/98*, 758.
- (561) Wang, H.; Huang, H.; Wunder, S. L. *J. Electrochem. Soc.* **2000**, *147*, 2853.
- (562) Huang, H.; Wunder, S. L. *J. Electrochem. Soc.* **2001**, *148*, A279.
- (563) Han, K. N.; Seo, H. M.; Kim, J. K.; Kim, Y. S.; Shin, D. Y.; Jung, B. H.; Lim, H. S.; Eom, S. W.; Moon, S. I. *J. Power Sources* **2001**, *101*, 196.

CR030203G

State of Understanding of Nafion

Kenneth A. Mauritz* and Robert B. Moore*

Department of Polymer Science, The University of Southern Mississippi, 118 College Drive #10076, Hattiesburg, Mississippi 39406-0001

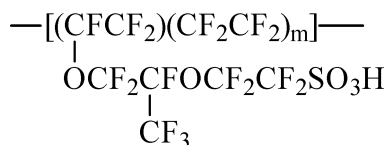
Received July 19, 2004

Contents

1. Introduction	4535
2. Morphological Characterization Using X-rays and Neutrons	4538
2.1. Early Studies of Nafion Morphology	4538
2.2. Scattering from PFSI Solutions and Recast Films	4543
2.3. Evaluation of Nafion Morphology through Studies of Oriented Membranes	4545
2.4. Current Models for the Morphology of Nafion	4548
2.5. The State of Understanding from X-ray and Neutron Investigations	4554
3. Microscopy Studies	4555
4. The Nature of Water, Other Solvents, and Ions in Nafion	4559
5. Mechanical Properties	4575
6. Molecular Simulation of Structure and Properties	4576
7. Conclusions	4581
8. Acknowledgment	4582
9. Literature References	4582

1. Introduction

Nafion ionomers were developed and are produced by the E. I. DuPont Company. These materials are generated by copolymerization of a perfluorinated vinyl ether comonomer with tetrafluoroethylene (TFE), resulting in the chemical structure given below.



Equivalent weight (EW) is the number of grams of dry Nafion per mole of sulfonic acid groups when the material is in the acid form. This is an average EW in the sense that the comonomer sequence distribution (that is usually unknown to the investigator and largely unreported) gives a distribution in m in this formula. EW can be ascertained by acid–base titration, by analysis of atomic sulfur, and by FT-IR spectroscopy. The relationship between EW and m is $\text{EW} = 100m + 446$ so that, for example, the side chains are separated by around 14 CF_2 units in a membrane of 1100 EW.

Common at the time of this writing are Nafion 117 films. The designation “117” refers to a film having 1100 EW and a nominal thickness of 0.007 in., although 115 and 112 films have also been available. Early-reported studies involved 1200 EW samples as well as special experimental varieties, some being rather thin. The equivalent weight is related to the property more often seen in the field of conventional ion exchange resins, namely the ion exchange capacity (IEC), by the equation $\text{IEC} = 1000/\text{EW}$.

The mention of the molecular weight of high equivalent weight ($\text{EW} > 1000 \text{ g}\cdot\text{mol}^{-1}$) Nafion is almost absent in the literature, although the range 10^5 – 10^6 Da has been mentioned. As this polymer does not form true solutions, the common methods of light scattering and gel permeation chromatography cannot be used to determine molecular weight as well as the size and shape of isolated, truly dissolved molecules. Studies of the structure of this polymer in solvent (albeit not a true solution) will be mentioned in the scattering section of this review. It should be noted that Curtin et al. performed size exclusion chromatography determinations of the molecular weight distribution in Nafion aqueous dispersions after they were heated to high temperatures (230, 250, and 270 °C).¹ Before heating, there was a high molecular weight shoulder on a bimodal distribution, due to molecular aggregates, but this shoulder disappeared upon heating, which indicated that the aggregates were disrupted. The peaks for the monomodal distribution for the heated samples were all located at molecular weights slightly higher than $10^5 \text{ g}\cdot\text{mol}^{-1}$. Also, light scattering experiments revealed that the radius of gyration had a linear dependence on the molar mass of the aggregates, which suggests that the particles are in the form of rods or ribbons, or at least some elongated structure.

Nafion ionomers are usually derived from the thermoplastic $-\text{SO}_2\text{F}$ precursor form that can be extruded into sheets of required thickness. Strong interactions between the ionic groups are an obstacle to melt processing. This precursor does not possess the clustered morphology that will be of great concern in this article but does possess Teflon-like crystallinity which persists when the sulfonyl fluoride form is converted to, for example, the K^+ form by reacting it with KOH in water and DMSO. Thereafter, the $-\text{SO}_3\text{H}$ form is achieved by soaking the film in a sufficiently concentrated aqueous acid solution. Extrusion of the sulfonyl fluoride precursor can cause microstructural orientation in the machine direction,

* Address correspondence to either author. Phone: 601-266-5595/4480. Fax: 601-266-5635. E-mail: Kenneth.Mauritz@usm.edu; RBMoore@usm.edu.



Dr. Kenneth A. Mauritz has been a Professor in the School of Polymers and High Performance Materials at the University of Southern Mississippi since 1984. He received a Ph.D. in Macromolecular Science at Case Western Reserve University in 1975. After a postdoctoral assignment at Case Western Reserve, he joined Diamond Shamrock Corporation as a Research Chemist in 1976. There, he began his long and continuous involvement with Nafion materials, mainly in the area of the molecular structure–property characterization and modeling as related to membrane performance optimization in chlor-alkali electrochemical cells for the production of chlorine and caustic. Later, at the University of Southern Mississippi, he produced some of the first inorganic/Nafion nanocomposite materials based on membrane–in situ sol–gel processes for inorganic alkoxides. Mauritz has collaborated with the coauthor of this review, R. B. Moore, in a number of projects involving Nafion materials. He has contributed numerous papers, reviews, and presentations on the topic of Nafion. He has coedited and contributed to the book *Ionomers: Synthesis, Structure, Properties and Applications* and was cochairperson of the 2003 Gordon Research Conference on Ion Containing Polymers. Other research interests include self-assembled, nanostructured organic–inorganic materials via domain-targeted inorganic syntheses in phase separated ionomers, microscopy, spectroscopy, dielectric relaxation/electrical impedance analysis, and the thermal, dynamic mechanical, and diffusion properties of polymers.

and this can be seen in the small-angle X-ray scattering peak that is attributed to the clustered morphology. Moreover, this orientation can affect the swelling and electrical conductance properties (anisotropy) of the ionomer form.

The earliest concerted effort in the research and development of Nafion perfluorosulfonate ionomers was directed toward their use as a permselective membrane separator in electrochemical cells used in the large scale industrial production of NaOH, KOH, and Cl₂. In short, the membrane in this application, in addition to keeping Cl₂ and H₂ gases separated, prevents the unfavorable back migration of hydrated OH[−] ions from the catholyte (concentrated aqueous NaOH or KOH) chamber, while allowing for the transport of hydrated Na⁺ ions from the anolyte chamber in which is aqueous NaCl.

Early experimental versions of Nafion within the context of chlor-alkali cells² consisted of SO₂F precursor forms that were first reacted on only one side with ethylenediamine (EDA) before the conversion of the remainder of the membrane to the sulfonate form took place. The result was a well-defined stratum of sulfonamide cross-links, that were formed upon heating after reaction, that served to reduce swelling at the catholyte interface, which, in turn, reduced OH[−] back migration.^{3–6} However, these EDA-modified membranes proved inadequate in chlor-alkali cells due to the chemical degradation of these cross-links



Dr. Robert B. Moore is currently a Professor in the School of Polymers and High Performance Materials at the University of Southern Mississippi. He received his Ph.D. in Analytical Chemistry from Texas A&M University in 1988 under the direction of Professor Charles R. Martin. His graduate research was focused on the chemical and morphological investigations of perfluorosulfonate ionomers. He then joined the group of Professor Adi Eisenberg at McGill University as a postdoctoral fellow and continued his work on the morphological characteristics of random ionomers using small-angle X-ray scattering methods. In 1991, he joined the faculty in the Department of Polymer Science at the University of Southern Mississippi. His research interests include structure–property relationships in ion-containing polymers, random ionomers, semicrystalline ionomers, ionomer membranes, and blends. A key consideration in this work, which has spanned from 1983 to the present, has involved the link between ionic aggregation and crystallization in semicrystalline ionomers, specifically Nafion. He has presented numerous papers and invited lectures on the topic of morphological manipulations of Nafion through the development of novel processing procedures and blends. He is currently an officer in the Division of Polymer Chemistry of the American Chemical Society and is the cochair of the 2005 Gordon Research Conference on Ion Containing Polymers.

in the harsh chemical environment. The membranes currently used in this application are of a sulfonate/carboxylate bilayer variety.

A lesser number of papers have appeared regarding the carboxylate version of Nafion, and the works of Yeager et al.,^{7,8} Seko et al.,⁹ and Perusich et al.¹⁰ are of special note. Nafion-like carboxylate materials have also been reported.¹¹ These similar materials will not be discussed here, as the exclusive emphasis is on the stronger-acid sulfonated versions because this critical review is within a collection of articles in which perfluorinated ionomers are considered within the context of fuel cells.

The DuPont Nafion materials, both sulfonate and carboxylate varieties, are not entirely unique, as similar perfluorinated ionomers have been developed by others such as the Asahi Chemical Company (commercial name: Aciplex) and the Asahi Glass Company (commercial name: Flemion). The comonomer chemical structures of and further information on these materials are given in the recent review article by Doyle and Rajendran.¹² Now commercially unavailable, but once considered a viable alternative, the Dow Chemical Company developed a somewhat similar perfluorinated ionomer that resembled the sulfonate form of Nafion except that the side chain of the former is shorter and contains one ether oxygen, rather than two ether oxygens, that is, $-\text{O}-\text{CF}_2-\text{CF}_2-\text{SO}_3\text{H}$.^{13,14}

The greatest interest in Nafion in recent years derives from its consideration as a proton conducting

membrane in fuel cells. It is clear that the tuning of these materials for optimum performance requires a detailed knowledge of chemical microstructure and nanoscale morphology. In particular, proton conductivity, water management, relative affinity of methanol and water in direct methanol fuel cells, hydration stability at high temperatures, electro-osmotic drag, and mechanical, thermal, and oxidative stability are important properties that must be controlled in the rational design of these membranes. This is a challenge for Nafion materials in which the possible chemical variations are rather limited. And, of course, all of these objectives must be achieved while maintaining low cost for this perfluorinated ionomer in the vast consumer market as well as in military applications. While a number of alternate polymer membranes, including nonfluorinated types, have been developed, Nafion is still considered the benchmark material against which most results are compared.

With respect to the morphological characterization of Nafion, it is important to note that the wealth of information gathered over the years using a variety of scattering methods is inherently indirect and often limited by the necessity of employing rather simple morphological models that involve specific assumptions of structure. While mentioned frequently throughout this review, the cluster-network model of Gierke et al. deserves special mention (from a historical perspective) as a "starting point" in an introduction to this now-vast topic. This model has endured for many years as a conceptual basis for rationalizing the properties of Nafion membranes, especially ion and water transport and ion permselectivity.^{15–17} It is presumed, based on small-angle X-ray scattering (SAXS) studies and several assumptions, that there are ~ 40 Å -in-diameter clusters of sulfonate-ended perfluoroalkyl ether groups that are organized as inverted micelles and arranged on a lattice. These micelles are connected by proposed pores or channels that are ~ 10 Å in size. These $-\text{SO}_3^-$ -coated channels were invoked to account for intercluster ion hopping of positive charge species but rejection of negative ions, such as OH^- , as in the case of chlor-alkali membrane cells.

A few things should be appreciated concerning this historical model. First, it was based on the limited structure–property information that was available at the time, namely the existence of a single SAXS peak and the behavior of this peak with water swelling as well as the observed selective permeation of Na^+ over OH^- ions in membrane chlor-alkali cells. Wide-angle X-ray diffraction (WAXD) investigations determined limited poly(tetrafluoroethylene) (PTFE)-like crystallinity associated with the perfluorocarbon backbone, although this structural detail was not factored into the Gierke model. In the sense that it does not assemble the phase separated morphology from basic chemical structure as, say, driven by a free energy minimization that incorporates molecular interactions as in a molecular simulation procedure, the model cannot be considered to be predictive but is calibrated to experimental data.

In the years following the introduction of the model of Gierke et al., more extensive structure–property studies have been conducted and, in many reports, alternate morphologies have been proposed. Through the use of state-of-the-art scattering methods, our understanding of the morphology of Nafion is evolving to include a more definitive picture of the nature of ionic aggregation in this polymer. It is a goal of this article to examine these studies, point out the salient features, and identify the elements that are in common.

Also, among the earliest concepts that were set forth regarding microstructure are those of Yeager and Steck, who proposed a three-phase model that was significantly different from that of Gierke et al. based on their studies of the diffusion of various ions.¹⁸ As compared with the model of Gierke et al., the clusters do not have a strict geometrical definition (spherical inverted micelles connected by cylindrical pores) and their geometrical distribution has a lower degree of order. Most importantly, there are transitional interphases between hydrophilic and hydrophilic regions, a concept that is becoming increasingly accepted.

It must be emphasized that this article is not meant to be a listing of the very large number of publications dealing with Nafion. To be sure, the literature since the late 1970s, when the main thrust for the development of these materials was membrane chlor-alkali cell technology improvement and, to a lesser degree, water electrolyzers, has proliferated. It was estimated (DuPont library), based on a coarse literature search that was performed a few years prior to this writing, that there were approximately 33 000 papers, patents, and so forth dealing with Nafion, and the number is growing. In part, to limit the scope of this review, the focus is on selected studies that have addressed the most fundamental aspects of the structure and properties of this polymer. Given this limited goal, the important issues of thermal and electrochemical stability, electro-osmotic drag, methanol crossover, gas permeation, and catalyst incorporation have been omitted, although numerous reports on these topics are found throughout the literature.

Chemical degradation in a fuel cell environment is also an important issue that must be addressed and so will be mentioned briefly here. It is thought that generated peroxide radicals attack polymer end groups having H-containing terminal bonds ($-\text{CF}_2\text{COOH}$) that are formed during processing. H_2O_2 , formed by reactions between oxygen and hydrogen, then decomposes, giving $\cdot\text{OH}$ or $\cdot\text{OOH}$ radicals that attack the H-containing terminal bonds, and this initiates chemical decomposition. Membranes become thinner, and fluoride ions are detected in product water. The reader is directed toward the article by Curtin et al., for the details of this mechanism and characterization of the degradation process.¹

Other reviews of the literature on Nafion and similar perfluorinated ionomers have appeared over the years. The early book (1982) by Eisenberg and Yeager, *Perfluorinated Ionomer Membranes*, remains

a useful series of monographs dealing with early work in the area.¹⁹ Later (1996), Heitner-Wirguin assembled a comprehensive review that contains topics not included in the document presented here.²⁰ Most recent is the compilation of Doyle and Rajendran entitled *Perfluorinated Membranes* that contains an excellent history of the evolution of this material that begins with the discovery of PTFE by Plunkett in 1938.¹²

Also, discussions of a number of applications of Nafion are not included in this document and are, at most, mentioned within the context of a particular study of fundamental properties. A number of these systems are simply proposed rather than in actual commercial applications. Membranes in fuel cells, electrochemical energy storage systems, chlor-alkali cells, water electrolyzers, Donnan dialysis cells, electrochromic devices, and sensors, including ion selective electrodes, and the use of these membranes as a strong acid catalyst can be found in the above-mentioned reviews.

It should be mentioned that, because the microstructure and properties of this ionomer are known to be quite sensitive to history and the details of preparation of samples for analysis, an effort has been made in this article, where possible, to delineate these important parameters in each described study so that the results of different investigations can be meaningfully compared.

Finally, the scope of the discussed literature is not confined to recent contributions but extends back to the 1970s because a number of excellent studies have not been repeated since then and often do not appear on Internet search engines.

2. Morphological Characterization Using X-rays and Neutrons

Over the last 30 years, a wealth of morphological information from numerous scattering and diffraction studies of Nafion has been obtained and reported in an attempt to precisely define the molecular/supramolecular organization of perfluorinated ionomers in a variety of physical states. However, while the quality and quantity of data from state-of-the-art instrumentation, facilities, and methods has increased, a universally accepted morphological model for the solid-state structure of Nafion has yet to be defined. The source of the ongoing debate over the morphology of Nafion stems from the fact that this unique ionomer has a random chemical structure that is capable of organizing in the complex formation of ionic and crystalline domains with a significant distribution in dimensions over a wide range of length scales. Moreover, quantitative morphological information is limited by the fact that Nafion yields only a single, broad scattering maximum attributed to characteristic dimensions within the ionic domains and the diffraction reflections of the PTFE-like crystallites are broad and relatively weak due to low degrees of crystallinity.

Unfortunately, the small-angle scattering techniques used in the investigations of Nafion morphology generally probe but a small region of reciprocal space and Fourier inversion methods of analyzing the

data are of limited use. Thus, the investigator is forced to compare the experimentally determined scattered profiles with that predicted by necessarily simple models that must be *assumed* for the structure. To further complicate matters, very low angle scattering information characteristic of long-range dimensions is convoluted by overlapping signals associated with the spatial distribution of crystallites (i.e., a weak maximum or shoulder often attributed to the long spacing between crystallites) and long-range heterogeneities in electron density associated with the disordered distribution of ionic domains (i.e., a small-angle upturn in intensity commonly observed with ionomers). This morphological complexity precludes the general application of simple two-phase models and thus further limits the useful angular range for precise model comparisons.

In considering the complicating factors associated with extracting detailed morphological information from scattering and diffraction data for Nafion, it is not surprising that a number of morphological models, constituting significantly different structural features, have been proposed and are still the focus of considerable debate. Since the vast majority of the applications of Nafion involve the hydrated or solvent swollen state and current processing methods for membrane formation often involve solvent casting, considerable attention has been devoted to the influence of swelling solvents (specifically water) on the characteristic morphological features of perfluorosulfonate ionomers (PFSIs). As noted above, scattering and diffraction studies of these polymers generally yield limited information; however, many groups have demonstrated success in evaluating the influence of solvent swelling on the scattering profiles for comparison and validation of morphological models. Furthermore, recent detailed studies of the morphological continuum from the dry state through the swollen "gel" state to the "dissolved" (or suspended) state, and *visa versa*, have begun to address important questions related to the organization of ionic and crystalline domains and the impact of solvent-casting on the morphology of perfluorosulfonate ionomers. In this section of the review, the prominent morphological studies of Nafion in a variety of physical states will be reviewed with a historical perspective, including a comparative evaluation of the latest state of the debate over the key morphological models.

2.1. Early Studies of Nafion Morphology

During the 1970s and early 1980s, general concepts and morphological details associated with ionic aggregation in the class of lightly ionized polymers, referred to as ionomers, were actively debated in the literature.^{21,22} The fundamental information from these studies, based in large part on small-angle X-ray scattering (SAXS) studies of dry, polyethylene²³ and polystyrene-based ionomers,^{24,25} formed the foundation for the morphological characterization of Nafion.²⁶ By the late 1970s, experimental evidence for ionic aggregation in Nafion from small-angle scattering data was emerging,²⁷⁻³⁰ and this new information subsequently led to extensions of the prevailing models for the structure of ionomers

to the interpretation of ionic domain morphology in the perfluorosulfonate ionomer systems.

Using SAXS and wide-angle X-ray diffraction (WAXD), Gierke and co-workers^{16,17,31,32} examined and compared the morphological features of Nafion, having a range of equivalent weights, in the unhydrolyzed sulfonyl fluoride precursor form, the hydrolyzed sulfonic acid form, and the neutralized metal sulfonate form. For the unhydrolyzed precursor, a low angle SAXS maximum near $0.5^\circ 2\theta$ and a diffraction peak at $18^\circ 2\theta$ (superimposed on a broad amorphous halo from 10 to $20^\circ 2\theta$) were observed for samples having equivalent weights (EW, the grams of polymer per equivalent of sulfonate groups) ranging from 1100 to 1800 g/equiv. Since these scattering and diffraction peaks were found to increase in intensity with equivalent weight (i.e., with an increase in the statistical length of crystallizable PTFE chain segments between side chains) and were also found to disappear at temperatures near the melting point of PTFE, these features were attributed to crystalline organization within the fluorocarbon matrix. With the hydrolyzed form of Nafion, an additional scattering peak was observed at $\sim 1.6^\circ 2\theta$, corresponding to a Bragg spacing of 3–5 nm, characteristic of a system containing ionic clusters within a semicrystalline matrix. It is important to note here that the term “ionic clusters” (used conventionally in the perfluorosulfonate ionomer literature) generally refers to nano-phase separated, hydrated ionic aggregates, and this term differs from the current definition used for other dry ionomers (e.g., sulfonated polystyrene) to designate regions of closely spaced ionic multiplets.³³

In contrast to the SAXS and WAXD behavior observed for the crystalline features, the ionomer peak was shown to increase in intensity and shift to lower angles with a decrease in equivalent weight. Furthermore, for a given equivalent weight, this peak was found to shift to lower angles and increase in intensity with increasing water content. Based on these findings, and considering the three most prevalent models for the morphology of ionomers at the time, including a model of spherical clusters on a paracrystalline lattice, a core–shell model, and a lamellar model, Gierke and co-workers concluded that the water-swollen morphology of Nafion was best described by a model of ionic clusters that were approximately spherical in shape with an inverted micellar structure.^{17,31} In consideration of the high ionic permselectivity and the requirement of a percolation pathway for ionic transport in Nafion membranes, the spherical ionic clusters were further proposed to be interconnected by narrow channels, constituting a morphology referred to as the cluster-network model,¹⁶ shown in Figure 1.

Based on this new model for the morphology of Nafion, the dimensional variations of the scattering entities with water content were used in simple space-filling calculations to estimate the cluster diameter, the number of sulfonate sites per cluster, and the number of water molecules per cluster.^{16,17} The results of these model calculations showed that, for a given equivalent weight, the cluster diameter,

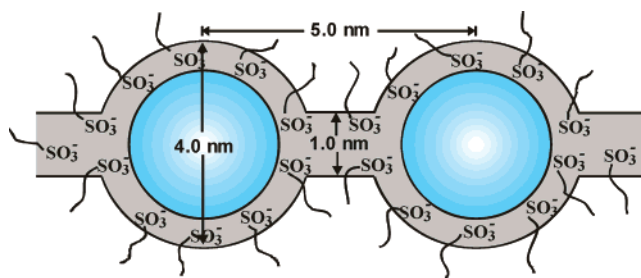


Figure 1. Cluster-network model for the morphology of hydrated Nafion. (Adapted with permission from ref 16. Copyright 1983 Elsevier.)

the exchange sites per cluster, and the number of water molecules per exchange site increased linearly with water content. While the linear relationships were not addressed in this study, the growth of clusters with increasing water content was proposed to occur by a combination of expansion in cluster size and a redistribution of the sulfonate sites to yield fewer clusters in the fully hydrated material.¹⁷ Although this original, yet phenomenological, cluster-network model has received significant acceptance in the literature and has served as the foundation for numerous studies of morphology–property relationships of Nafion, it has also been vigorously debated with respect to alternative morphologies that are also quantitatively consistent with a wide range of scattering results. Specifically, current studies focused on the morphological and dimensional changes that occur with variations in solvent swelling have raised critical questions related to the shape and spatial distribution of the ionic clusters within the semicrystalline matrix of Nafion.

Roche and co-workers used SAXS and small-angle neutron scattering (SANS) to study the morphology of 1200 EW Nafion membranes in the acid and neutralized forms with a range of water contents.^{34,35} In the as-received state, Nafion was found to have three contrast regions (i.e., a three-phase system) in the angular range probed by SAXS and SANS consisting of a crystalline phase, ionic clusters, and an inhomogeneous matrix phase. By quenching the Na^+ form ionomer from 330°C , the sample was rendered amorphous, as confirmed by WAXD, and the low angle scattering maximum, corresponding to a Bragg spacing of ~ 18 nm, was found to disappear. From these results, the 18 nm peak, also observed by Gierke,¹⁷ was attributed to interference between crystalline structures. In considering the lamellar periodicity (i.e., the long spacing) of ~ 100 nm observed in PTFE, the fact that copolymerization is known to decrease the lamellar thickness, and the average spacing of about 1.5 nm between side chains in 1200 EW Nafion, it was concluded either that a nonrandom distribution of side chains exists in some portion of the material or that the side groups were somehow included in the crystalline structure.³⁴

Using contrast matching methods of SANS,³⁵ Nafion was swollen with various mixtures of H_2O and D_2O in order to highlight the scattering features of the water swollen ionic domains. Furthermore, quenched samples were used in these studies to eliminate the scattering features attributed to the crystalline do-

mains. Roche et al. found that these quenched samples exhibited just the ionomer peak at $q \approx 1.2 \text{ nm}^{-1}$ (q is the scattering vector equal to $(4\pi/\lambda) \sin \theta$, where λ is the wavelength of the scattered radiation and θ is half the scattering angle, 2θ) and a low angle upturn in intensity at $q < 0.5 \text{ nm}^{-1}$. In agreement with the behavior expected from a simple, two-phase system (i.e., a hydrophobic phase and a hydrophilic phase), the normalized scattering intensities of the water swollen membranes were found to vary linearly with relative fractions of D_2O in H_2O . This observation indicated that both the zeroth-order scattering at low q -values and the ionomer peak arise from the same scattering length density differences and could be attributed to the same morphological features (i.e., clusters).³⁵ To account for the larger dimensions associated with the zeroth-order scattering, an inhomogeneous distribution of clusters within the fluorocarbon matrix was proposed. Moreover, these results demonstrated that the zeroth-order scattering could not be attributed to impurities, as previously proposed for other ionomer systems.³⁵

In agreement with the work of Gierke et al.,¹⁷ Roche and co-workers found that the intensity of the ionomer peak increased and the position of the scattering maximum shifted to lower angles with increasing water content.³⁴ A Porod analysis of the SAXS data over a wide range of scattering angles also indicated that the majority of water molecules in the swollen ionomer were phase separated with sharp phase boundaries. Despite the close agreement in scattering results between both groups, Roche et al. argued that an interparticle scattering concept associated with Gierke's cluster-network model was unlikely due to the lack of evidence for a required potential giving rise to ordering of a paracrystalline lattice.³⁴ As an alternative, the origin of the ionomer peak was attributed to an intraparticle scattering model for which the scattering maximum corresponded to characteristic distances between structural elements inside the ionic particles.^{34,35} While this intraparticle scattering model was consistent with the morphology proposed for other ionomers, a detailed quantitative analysis in support of this model was not provided.

Fujimura et al. reported the results of detailed SAXS and WAXD experiments in a series of two papers focused on defining the morphological origins of the two scattering maxima³⁶ and evaluating various scattering models for the origin of the ionomer peak.³⁷ Samples characterized in this work included Nafion with a range of equivalent weights (1100 EW through 1500 EW) in the acid, Na^+ , and Cs^+ forms. To further investigate the effect of ionic interactions on the morphology of Nafion,^{17,34} the sulfonate groups of these materials were also chemically derivatized to yield carboxylated and nonionic, sulfonyl chloride analogues to Nafion. In agreement with the previous scattering studies of Nafion, two scattering maxima at $s \approx 0.07$ and 0.3 nm^{-1} (the scattering vector s is defined as $s = (2 \sin \theta)/\lambda$) were observed and attributed to morphological features associated with crystalline and ionic domains, respectively.

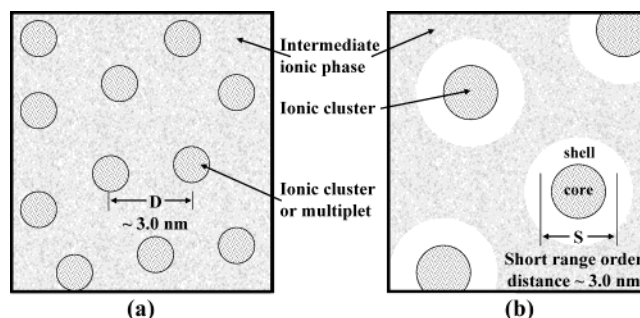


Figure 2. Two morphological models used to describe the origin of the ionic SAXS maximum observed for Nafion: (a) the modified hard-sphere model depicting interparticle scattering and (b) the depleted-zone core-shell model depicting intraparticle scattering. (Adapted with permission from ref 36. Copyright 1981 American Chemical Society.)

In the analysis of the low angle scattering maximum at $s \approx 0.07 \text{ nm}^{-1}$, Fujimura et al. found that the intensity was greatest for the carboxylated and nonionic forms of Nafion, relative to the regular sulfonated ionomer.³⁶ In agreement with the work of Gierke¹⁷ et al., this low angle maximum also increased in intensity with increasing equivalent weight. Similarly, a detailed analysis of the crystallinity in these materials by WAXD indicated that 1100 EW Nafion was 23% and 18–14% crystalline in the nonionic and carboxylated forms, respectively, while it was 12–3% crystalline in the sulfonated forms. With varying equivalent weight from 1100 EW to 1500 EW, the degree of crystallinity increased from 12% to 22%.³⁶ Based on the quantitative correlation of this SAXS and WAXD information and on the behavior observed with uniaxial deformation, the origin of the low angle scattering maximum at $s \approx 0.07 \text{ nm}^{-1}$ was attributed to an average spacing between crystalline lamellar platelets.³⁶

The effect of solvent swelling (with water) on the characteristic dimensions of the ionic clusters associated with the scattering maximum at $s \approx 0.3 \text{ nm}^{-1}$ was also evaluated for 1100 EW Nafion. With the cesium sulfonate form of the ionomer, ionic clusters were shown to exist in the dry state.³⁶ With increasing water content, the cluster dimensions deduced from the scattering maxima were shown to increase.³⁷ Furthermore, over a range of water contents, the microscopic degree of swelling, as determined by SAXS, was found to be much greater than the macroscopic degree of swelling.³⁷ A similar correlation of microscopic versus macroscopic dimensions was observed for Nafion subjected to varying degrees of uniaxial deformation.³⁷ Based on these observations, Fujimura et al. concluded that the scattering behavior of Nafion is best described by an intraparticle core-shell model (Figure 2b) similar to that proposed by MacKnight²³ and co-workers³⁸ rather than an interparticle, two-phase, hard sphere model proposed by Cooper et al.³⁹ (Figure 2a). In this particular core-shell model an ion-rich core is proposed to be surrounded by an ion-poor shell (i.e., a depleted zone)³⁷ that is composed mainly of perfluorocarbon chains. These core-shell particles are dispersed in a matrix of fluorocarbon chains containing nonclustered ions and multiplets, such that the

short-range order distance within the core-shell particle gives rise to the ionic scattering maximum.

While the nonaffine swelling behavior observed by Fujimura et al.³⁷ has been reproduced by many others in subsequent studies and has been the focus of significant debate over the years, it is important to note that the argument against the interparticle hard sphere model relies on the key assumptions that the clusters are uniformly distributed in space and that no redistribution of the ionic groups occurs during swelling. However, the cluster-network model proposed by Gierke¹⁷ clearly allows for cluster reorganization during swelling, and the low angle upturn in scattering intensity observed by Roche et al.³⁵ strongly suggests an inhomogeneous distribution of clusters. With the recognition of the importance of these considerations, Fujimura et al. attempted to quantitatively distinguish the two models by conducting a thorough analysis of the scattering data with the aid of computer simulation.³⁷ For both the core-shell model and the two-phase hard sphere model, quantitative expressions for the variations in the scattering profiles with water uptake were derived from standard scattering theories and fit to the experimental data. Unfortunately, however, this analysis was inconclusive, as both models adequately fit the experimental data and were found to yield similar effects on the variation of the profiles with water uptake and deformation. Moreover, the core-shell model does not give a clear view of long-range structure such as that which might be useful in understanding long-range properties such as molecular transport. In a more recent SAXS investigation, Miura and Yoshida⁴⁰ also supported the core-shell model but suggested (without quantitative support) that some degree of ionic redistribution with swelling in different solvents was possible due to differences in internal stresses within the cluster morphology. Nevertheless, later investigators would challenge this view in favor of the two-phase model.

The organization of crystalline domains in Nafion was further investigated by Starkweather using X-ray diffraction analysis of oriented fiber samples.⁴¹ The unit cell structure derived from the indexed diffraction patterns indicated that the crystallites in Nafion were packed in a hexagonal lattice with true three-dimensional character and cell dimensions roughly equivalent to those of PTFE. Furthermore, the positions of the principal 100, 101, and 002 reflections for the sulfonyl fluoride precursor were essentially unchanged as the polymer was hydrolyzed to the potassium sulfonate form. Peak width measurements, following the Scherrer approach, were used to estimate minimum values for the crystallite size. This analysis suggested that the crystallite size along the *c*-axis was 4.4 nm (or 34 carbon atoms along a planar zigzag conformation), which was noted to be significantly larger than the average of 15 CF₂ groups between side chains in the copolymer.

Based on the fiber diffraction data and the morphological constraints imposed by Geirke's cluster-network model,¹⁷ Starkweather developed a model for the crystalline structure of perfluorosulfonate ionomers.⁴¹ Given a 1 nm wall space between clusters,

this proposed model consisted of a bilayer of hexagonally packed planar zigzag chains with the side chains extending outward on both sides into the clusters. With the assumption that all comonomer units were incorporated in a head-to-tail configuration, this arrangement allowed for all side chains to be on the same side of the planar zigzag chains such that the crystallite thickness could exceed the average separation distance between side chains. While this model provides a simple illustration of the packing of small crystallites between clusters, it was, however, acknowledged to involve "a very efficient use of the polymer's components".⁴¹

One concern for this bilayer model arising from the diffraction data was noted to involve the width of the 100 reflection; the Scherrer analysis indicated that the size of the crystals normal to the chain axis was on the order of 3.9 nm rather than the proposed 1 nm bilayer thickness. In addition, a number of further considerations raise important questions as to the validity of this model. For example, given the recognition that Nafion contains a heterogeneous distribution of clusters³⁵ (i.e., long-range heterogeneities observed in the SAXS profiles at low angles), rather than a homogeneous network of clusters and channels in an ordered paracrystalline lattice,¹⁷ it is not necessary to impose the organization of crystals in the narrow space between nearest neighbor clusters. Furthermore, Nafion is a statistical copolymer that is likely to contain both short and long runs of TFE units between side chains. The longer runs could thus pack into small PTFE-like crystallites in regions somewhat removed from the ionic domains. These crystallites, while few in number, would provide the three-dimensional order required to yield the observed WAXD reflections and the high ΔH_f and T_m values similar to those for PTFE as reported by Starkweather.⁴¹ More recent studies, discussed below, provide strong evidence for this alternative organization of crystallites and clusters in Nafion.

In 1986, Kumar and Pineri published a report focused on the interpretation of small-angle X-ray and neutron scattering data for perfluorosulfonated ionomer membranes in order to elucidate the possible cluster morphology in PFSI membranes.⁴² This detailed study involving model calculations and comparisons of experimental scattering profiles to theoretical fits was placed in context with the morphological models of Nafion, to date. Since the paracrystalline lattice model (i.e., the basis for calculations from the Gierke cluster-network model)¹⁷ was found to be inadequate to explain the observed scattering and swelling data, and the depleted-zone core-shell model relied on questionable assumptions involving the applicability of Bragg's equation in estimating microscopic versus macroscopic swelling and the requirement of a constant number of clusters with swelling,^{36,37} an alternative model involving noninteracting hard spheres was chosen for this analysis. With this model, Kumar and Pineri found that the SAXS ionomer peak could be quantitatively attributed to the interference between clusters, assuming them to be noninteracting hard spheres.⁴² Furthermore, the increase in intensity at very low angles

was accounted for by considering a previously neglected intensity term for scattering from a dense group of particles and/or an intercluster potential arising from Coulombic interactions between clusters.

In contrast to Gierke's model,¹⁷ which predicted a large increase in the number of ions per cluster, with increasing water content, parameters from these model calculations⁴² showed a moderate increase in N_p at low water uptake and a significant decrease in N_p at higher water contents. This behavior was attributed to an increase in elastic forces on the chains that effectively forces some ions out of the existing clusters at high degrees of swelling, thus decreasing the N_p . Since the ions forced out of clusters with swelling are free to form other clusters, the average distance between clusters was argued to be an invalid measure of the microscopic swelling without some account for the change in the total number of clusters. For Nafion of different equivalent weights, Kumar and Pineri also found that the number of ionic sites per cluster, and thus the cluster radius, only moderately decreased with increasing equivalent weight.⁴² This observation, as confirmed by Manley et al.⁴³ in a later study using a similar model analysis, was noted to again show a distinct discrepancy with the results of Gierke, which indicated a sharp decrease in N_p with increasing equivalent weight.

The spatial distribution of clusters in water-swollen Nafion was investigated by Dreyfus and co-workers through SANS experiments.⁴⁴ The shape and intensity of the scattering profiles obtained from samples with water contents ranging from 6 to 26% (by volume) were fit to a local-order model that describes the distribution of spherical, hydrated clusters in a locally ordered structure with four first neighbors located at a well-defined distance embedded in a matrix of completely disordered (gaslike) clusters. Using a radial distribution function for this locally ordered (tetrahedral) structure and a form factor for homogeneous spheres, the following intensity function was derived

$$I(q) = \frac{I(0)}{S(0)} \left(\frac{3(\sin qR - qR \cos R)}{(qR)^3} \right)^2 \left(1 + z \frac{\sin qD}{qD} - z' \frac{3(\sin q\alpha D - q\alpha D \cos q\alpha D)}{(q\alpha D)^3} \right)$$

where $I(0)$ and $S(0)$ are the coherent scattering intensity and an interference term at $q = 0$, respectively; q is the scattering vector, R is the radius of the scattering particle, D is the distance between locally ordered particles, αD is the distance from the origin cluster beyond which a disordered distribution of clusters exists; and z and z' are the number of clusters in the locally ordered structure and the number of clusters in the volume corresponding to the correlation hole between 0 and αD , respectively. The a priori choice of a diamond-like structure led to the refinement of constant values of $\alpha = 1.122$, $z = 4$, and $z' = 4.39$.

With this local-order model,⁴⁴ only two adjustable parameters (D and R) were needed to obtain reason-

able fits over the q -range 0.2 – 2.6 nm^{-1} . Based on the excellent agreement between the theoretical and experimental SANS curves, the authors concluded that both the small-angle upturn and the ionomer peak may be attributed to the existence and spatial distribution of ionic clusters. Using the values of D and R from the model fits (e.g., $D = 3.4 \text{ nm}$ and $R = 1.7 \text{ nm}$ for the fully hydrated membrane), the specific surface area per charge site on the cluster was found to be relatively constant at 73 \AA^2 . In agreement with previous studies that suggested a redistribution of ions between clusters with swelling,¹⁷ the number of charge sites per cluster was calculated using space-filling arguments based on the D values and found to increase from ~ 25 to 45 with increasing hydration. Despite the excellent fits with this local-order model, however, the number of charge sites per cluster, directly calculated from the R values, was unrealistically large. In addition, the fundamental requirement of this model for an attractive potential between neighboring clusters in the formation of the local-order structure is consistent with the suggestion by Kumar and Pineri⁴² that the small-angle upturn could be attributed to such a potential; however, this plausible correlation was not addressed in this analysis.

Lee et al.⁴⁵ utilized a novel combination of small- and wide-angle neutron scattering methods to study local and long-range structure of water in Nafion 117 membranes. Since small-angle scattering methods suffer from an inherent inability to probe a sufficiently large region of reciprocal space, the results of small-angle (low q) and wide-angle (high q) scattering experiments were combined so that direct Fourier mathematical inversions (integral transforms) could be applied to data that were thereby expanded over q -space. Using this method, atom–atom radial distribution functions for the atom pairs associated with water (i.e., H–H and O–H) in the cluster domains of Nafion were calculated to provide real space information. It was stated that Nafion in the Ni^{2+} ion exchanged form was used so that the counterion radial distribution function could be derived, as well, although these results do not appear in the report.

It is important to describe the preparation of these samples, which were annealed at high temperature in dry nitrogen gas and then rapidly quenched in liquid nitrogen.⁴⁵ Because they were thereby rendered amorphous, there was no scattering due to the PTFE-like crystallinity that would complicate the data interpretation. Membranes were boiled in NiCl_2 solutions and then soaked in H_2O , D_2O , and $\text{H}_2\text{O}/\text{D}_2\text{O} = 50:50$ solutions. Due to the elimination of crystallinity from the melt-quench pretreatment, these samples were considerably hydrated at 41 vol %.

The following equation shows the relationship between the partial structure factors, $S_{\alpha\beta}(q)$, and the atom–atom correlation functions, $g_{\alpha\beta}(r)$, that refer to the distance, r , between atoms α and β :

$$S_{\alpha\beta}(q) = 4\pi\rho \int r^2 [g_{\alpha\beta}(r) - 1] \frac{\sin(qr)}{qr} dr$$

ρ is the macroscopic density. This equation was inverted to give $g_{\alpha\beta}(r)$ using the principle of maximum entropy. The total coherent structure factor is a linear combination of all of the partial structure factors where each term is multiplied by the product of the atomic fractions and coherent scattering lengths of the species α and β .

The intramolecular correlations of O–H at $r = 1.00$ Å and of H–H at $r = 1.56$ Å are identical, and the second peaks show small differences, perhaps arising from interactions between water molecules and sulfonate groups, although it would seem that water coordination around Ni^{2+} would have to be considered, as well. From this, the authors concluded that the structure of water in the clusters is essentially that of water in the bulk state.⁴² This would seem reasonable considering that the water uptake of these samples corresponded to an average of 21 H_2O molecules per $-\text{SO}_3^-$ group.

The H–H radial distribution appears in the function $r[g_{\text{HH}}(r) - 1]$ which was plotted versus distance r . The peak observed at low r was associated with the cluster radius. If the clusters are *assumed* to be spherical, this distribution is consistent with a cluster radius of 18.5 Å, which is similar to values based on scattering based estimates from other studies.^{17,42} At higher r , the function shows a mean periodicity of these structures (i.e., cluster center-to-center distance) of 70 Å. This would leave a rather large space between the “surfaces” of adjacent clusters of 33 Å, which seems rather large, especially when compared to that estimated in the model of Gierke et al.,¹⁷ which was only around 10 Å. The analysis ceased to be of an *ab initio* nature when the assumption of spherical clusters was made and the 33 Å space had to be accounted for. The authors explain that these data reflect a continuous network of water structure rather than an array of isolated hydrated clusters for two reasons. (1) 41 vol % of water is considerably above the percolation threshold, and a structure in which water is distributed in spheres of this size and having this center-to-center spacing can only accommodate 8 vol % of water. (2) Because the cluster center-to-center spacing is much larger than the cluster diameter, $g_{\text{HH}}(r)$ would be expected to drop to around zero at about $r = 40$ Å before approaching the asymptote of 1.00 at large r , which it does not. These and other arguments led the authors to invoke the presence of connective water structures and suggested a view consisting of rodlike aqueous regions that intersect at “nodes” (i.e., clusters).⁴⁵ It should be remembered that these data and the derived conclusions refer to the distribution of water—the sole scattering source in these experiments—throughout the Nafion structure and not to the direct structure of Nafion.

2.2. Scattering from PFSI Solutions and Recast Films

In the early 1980s, reports surfaced that detailed procedures for dissolving Nafion membranes in water/alcohol mixtures at elevated temperatures and pressures.^{46,47} Currently, Nafion solutions are available commercially, and these solutions are now used in

commercial processes to uniformly cast thin membranes for fuel cell applications. Since the properties and performance of Nafion membranes are directly related to their complex morphology, and the supermolecular organization of ionic and crystalline domains may be altered by the processing history, it is of great importance to understand the nature of these Nafion solutions and the subsequent evolution of morphological development during the casting process. With this fundamental knowledge, the means to enhance the transport properties and efficiencies of PFSI membranes by controlling and tailoring the morphology for specific applications may be realized.

With the availability of dissolution procedures for Nafion, Aldebert and co-workers used SANS to study the nature and structure of Nafion solutions in water and ethanol.⁴⁸ Similar to the case observed in the scattering results of Nafion membranes, the “solutions” were found to be heterogeneous, yielding a single scattering maximum attributed to interference between nanometer-scale scattering objects that were distributed throughout the total volume of the sample. Moreover, since the separation distance, d , varied systematically with the volume fraction of the ionomer, ϕ_v , the particles were suggested to exhibit electrostatic repulsion similar to that observed for a colloidal suspension of charged particles. Since the experimental plot of $\log d$ versus $\log \phi_v$ varied following the law $d \sim \phi_v^{-0.5}$, the solutions in both water and ethanol were assumed to consist of a dispersion of rodlike particles.^{48,49} In comparing the scattering results to dimensional parameters calculated from three different models (i.e., a three-dimensional fcc lattice, a two-dimensional hexagonal array of rods, and a cubic phase of rods), the authors found that the cubic phase model was most likely. Furthermore, the rodlike particles were suggested to have a compact cylinder structure with the solvent–polymer contact at the surface of the charged “micelle” as opposed to a more open coil model. The center of the rodlike particles was also proposed to contain crystallites of the PTFE backbone segments oriented along the rod axis.⁴⁹

From SAXS results, Rebrov and co-workers also found that Nafion solutions could be characterized as containing colloidal suspensions of anisotropic polymeric particles.⁵⁰ By manually extrapolating the experimental scattering curves to a state of infinite dilution in order to eliminate interparticle interference effects, the form of the scattering particles was suggested to most closely resemble that of flattened disklike particles. While this questionable practice of approximating the scattering profiles at infinite dilution raises concern as to the validity of the chosen form factor, the results are qualitatively consistent with the previous study of Aldebert et al.⁴⁸ in that Nafion “solutions” are not “true” solutions but contain relatively large colloidal aggregates of anisotropic structure with dimensions exceeding 15 nm.

More recently, Loppinet and co-workers have used both SAXS and SANS (with contrast variation methods) to characterize the morphology of dilute PFSI solutions having a volume fraction of polymer less

than 0.5%.^{51,52} The intensity profiles of these dilute solutions were found to decrease as $1/q$ at low q -values in a manner typical of rodlike particles. The scattering profiles in the low q -range were also found to satisfactorily fit the form factor of cylindrical particles having a radius of ~ 2.0 – 2.5 nm. For higher volume fraction solutions, the asymptotic behavior of the scattering profiles was also found to be consistent with that predicted for cylindrical particles. By studying the effect of various solvents, different counterions, and added salt, the formation of the colloidal particles was attributed to aggregation of the neutral part of the ionomer chains. In contrast to the behavior of low molecular weight surfactants, the rodlike shape of the polymeric particles did not show evidence of any phase transitions with changes in concentration, salt, temperature, or the nature of the solvent or counterions. Furthermore, the size of the cylindrical particles was shown to be related to the polymer–solvent interfacial energy. Using SANS contrast variation studies, the particles were found to be dense, indicating that the thickness of the polymer–solvent interface is negligible compared to the cross-sectional size. From the apparently high particle densities calculated from the constant neutron scattering length densities, the authors suggest that the rods contain a crystallinity index of approximately 50%. At relatively high volume fractions (i.e., 5–20%), the cylinders are proposed to be distributed in the solution with the existence of some local order. Space-filling analysis assuming a local order in a hexagonal array yields radius values consistent with the previous determinations.

Since Nafion films possess excellent chemical stability and a high affinity toward large organic cations, Nafion solutions have been widely used in the formation of polymer modified electrodes for a variety of electroanalytical investigations. For many of these applications, it has been assumed that the morphologies, physical properties, and chemical characteristics of the solution-cast PFSI films were identical to those of the as-received membranes. Moore and Martin, however, discovered that this simple assumption was inaccurate.^{53,54} For example, Nafion films cast from ethanol–water solutions at room temperature (i.e., the general method used to produce polymer-modified electrodes), referred to as recast films, were found to be “mud-cracked”, brittle, and soluble at room temperature in a variety of polar organic solvents. In contrast, the as-received Nafion membranes are flexible, tough, and insoluble in virtually all solvents at temperatures below ~ 200 °C. However, through the application of high boiling point solvents in the casting procedure, Moore and Martin demonstrated that the desirable properties of as-received Nafion could be reconstituted in solution-cast films and membranes, referred to as solution-processed films, if the casting temperature exceeded ~ 160 °C.⁵³ This observation suggested that the contrast in properties between the recast and solution-processed films was of a morphological origin and the resulting solid-state structure of the cast films was a function of the macromolecular organization of chains in solution during solvent evaporation.

Using WAXD and SAXS, Moore and Martin found that the as-received and solution-processed films were semicrystalline (having similar degrees of crystallinity), while the recast films were virtually amorphous.^{54,55} The SAXS profiles of the as-received and solution-processed films displayed a distinct ionomer peak at $q = 1.2$ nm⁻¹, attributed to the presence of ionic clusters, and a prominent low angle maximum at $q = 0.5$ nm⁻¹, attributed to the long spacing within well-organized crystalline domains. In contrast, the scattering profile of the recast material displayed only the ionomer peak at $q = 1.2$ nm⁻¹. While all samples possessed ionic clusters, regardless of processing history, the enhancement in crystallinity and physical properties of the solution-processed films was attributed to the ability of the ionomer chains to reorganize from the colloidal aggregate state in solution to a more entangled network in the solid film with added thermal energy and solvation from the high boiling point solvents at elevated casting temperatures. The presence of ionic clusters in the recast films was attributed to the aggregation of ions on the surface of the contacting micelle-like colloidal particles in the absence of solvent. Moreover, the high solubility and “mud-cracked” character of the recast material supported the conclusion that the colloidal morphology observed in solution remained intact in the recast state with little if any chain entanglement or coalescence between particles.

Gebel and co-workers used a similar high temperature casting procedure with high boiling point solvents to prepare reconstructed Nafion membranes.⁵⁶ WAXD and SAXS results from this study indicated that the morphology of the PFSI membranes reconstructed at room temperature (i.e., cast at room temperature with added high boiling point solvent) or at high temperature was different from that of the as-received membrane. In agreement with the results of Moore and Martin,^{53,54} the room temperature cast membranes were essentially noncrystalline, while the high temperature process reestablished significant crystallinity with long-range order.

The morphology of recast Nafion films, processed at room temperature in wet and dry environments, was studied by Scherer and co-workers using WAXD and SAXS.⁵⁷ In agreement with the previous studies, room temperature casting yielded little if any crystallinity in the resulting films.⁵⁴ The films cast under wet environments, however, yielded intense scattering maxima positioned at lower q -values relative to those of the films cast under dry conditions. Based on this behavior, the authors suggested that the number and size of the clusters increased with increasing relative humidity during the casting process. Since previous studies of the morphology of as-received films also show an increase in the intensity of the ionomer peak and a shift to lower q -values with increasing water content, the assertion that relative humidity during casting affects the cluster morphology seems inconclusive within the context of this limited study. Nevertheless, the results of this study and the above investigations strongly support the general suggestion that specific casting procedures may be developed to alter the crystalline and ionic

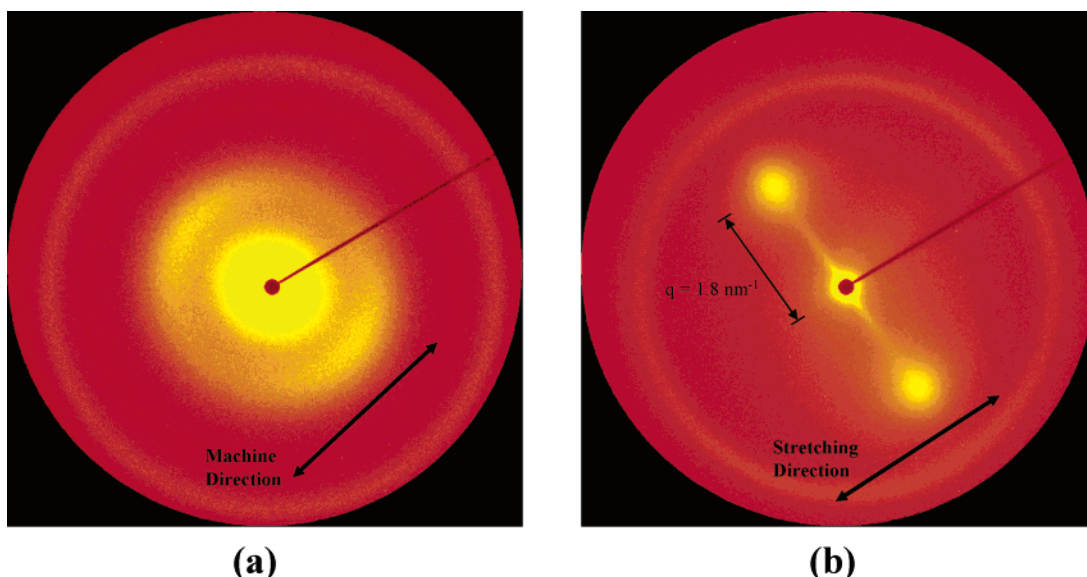


Figure 3. 2-D SAXS scattering patterns of (a) as-received Nafion, showing a slight morphological anisotropy in the ionic domains from the membrane calendaring process, and (b) uniaxially oriented Nafion ($\lambda_b = 5.4$).

cluster morphologies in an attempt to control and tailor the properties of Nafion films and membranes.

2.3. Evaluation of Nafion Morphology through Studies of Oriented Membranes

Given the morphological complexity of Nafion membranes and the limited structural information that can be extracted from the relatively diffuse scattering profiles, the elucidation of detailed morphological models has required the study of controlled morphological manipulations by processes including solvent swelling and mechanical deformation. Over the years, a variety of groups have demonstrated that the application of uniaxial extension provides a particularly useful means of evaluating the size, shape, and spatial distribution of crystallites and ionic domains in Nafion. Moreover, structural information obtained from these studies has been used to differentiate the various morphological models that have been proposed for PFSIs.

Gierke et al. reported the first data showing the effect of tensile drawing on the SAXS profiles of the unhydrolyzed Nafion precursor and that of the hydrolyzed ionomer.¹⁷ For the oriented nonionic precursor, the low angle scattering maximum attributed to a periodicity associated with the organization of PTFE-like crystallites was observed only in the meridional scan, implying a periodicity in the long spacing along the fiber axis. In contrast, SAXS scans of an oriented, hydrolyzed ionomer showed that the ionomer peak was only observed in a scattering direction perpendicular to the draw direction, implying a periodicity normal to the fiber axis.

A similar analysis was conducted by Fujimura et al.³⁷ on cesium-neutralized Nafion with orientations up to $\lambda_b = 1.5$ (where λ_b is the ratio of the final extended length to the initial undrawn length). Over a range of orientations, the ionomer peak was observed to shift to lower angles and decrease in intensity in the meridional (draw) direction, while a shift to higher angles and an increase in intensity

was observed in the equatorial direction. Using the Bragg spacings calculated from the peak maxima, a nonaffine deformation behavior was observed between the microscopic and macroscopic dimensions. This observation led to a conclusion, similar to that proposed to explain solvent swelling behavior, that nonaffine behavior was inconsistent with an interparticle scattering model yet could be accounted for by deformation of a core-shell particle.

More recently, Moore and co-workers found that Nafion membranes, neutralized with tetraalkylammonium ions, could be oriented with high elongation at elevated temperatures (e.g., 200 °C for tetrabutylammonium form Nafion) to yield extremely anisotropic WAXD and SAXS scattering patterns.^{58–60} With uniaxial deformation (ranging up to $\lambda_b = 5.4$) at temperatures above the ionomers' α -relaxation (as determined using dynamic mechanical analysis) followed by cooling to room temperature, the oriented morphology was observed to be stable in the absence of stress. Using a 2-dimensional area detector, the scattering patterns were shown to increase in intensity at azimuthal angles perpendicular to the stretching direction (i.e., equatorial scattering) with a profound decrease in intensity (to the point of disappearance) at angles parallel to the stretching direction (i.e., meridional scattering) with increasing orientation.⁵⁸ At relatively high orientations (greater than ca. $\lambda_b = 2.0$), only equatorial spots at $q = 1.8 \text{ nm}^{-1}$ were observed (Figure 3). In contrast to the earlier studies of oriented membranes containing inorganic ions,^{17,37} the equatorial peak position of the TBA⁺ form membranes remained constant with elongation. A circular integration over all azimuthal angles of the scattering patterns was performed to calculate the relative invariant, Q , for samples having a range of elongations. A significant increase in Q with elongation was attributed to an increase in the extent of ionic aggregation with elongation to yield a matrix with fewer lone ion pairs in the highly oriented membranes.⁵⁸

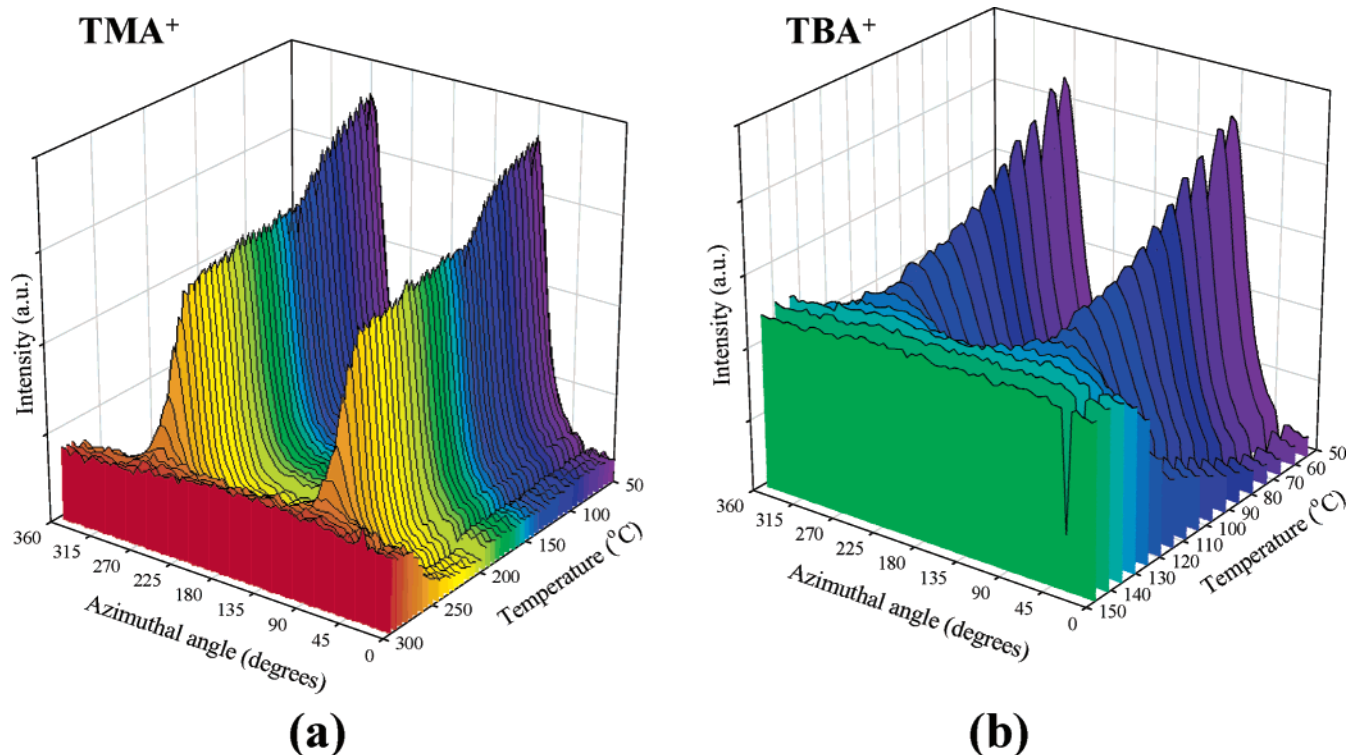


Figure 4. Azimuthally integrated SAXS profiles as a function of temperature for (a) TMA⁺ and (b) TBA⁺ forms of uniaxially oriented Nafion.

The thermal relaxation behavior of oriented Nafion membranes was also evaluated using time-resolved synchrotron SAXS analysis.⁶¹ For oriented membranes neutralized with tetramethyl- (TMA⁺), tetraethyl- (TEA⁺), tetrapropyl- (TPA⁺), and tetrabutylammonium ions (TBA⁺), the anisotropic scattering patterns were found to relax back to isotropic patterns as the samples were heated from 50 to 300 °C (see Figure 4). Moreover, the temperature at which the morphological relaxation occurred tracked with the size of the tetraalkylammonium ions, following the order TBA⁺ < TPA⁺ < TEA⁺ < TMA⁺. This relaxation behavior of the ionic domains was noted to be in excellent agreement with the order of the principle dynamic mechanical relaxations (α -relaxations) for these materials. Thus, the thermal relaxation of the scattering patterns was attributed to the onset of ion-hopping (i.e., the thermally activated process of redistributing ion pairs between aggregates in the electrostatic network in order to relieve local stress on the chain segments). With a weakened electrostatic network for the samples containing large tetrabutylammonium ions, the onset of ion-hopping is activated at lower temperatures, allowing for significant chain mobility and morphological reorganization.

Elliott and co-workers performed a detailed SAXS investigation of the morphology of Nafion membranes that were subjected to uniaxial and biaxial deformation.^{62,63} For as-received membranes, manufactured by Du Pont using an extrusion process, the cluster reflection was shown to exhibit a limited degree of arching in the direction perpendicular to the machine direction. Upon uniaxial extension, this arching was observed to increase in a manner consistent with previous studies. This arching was rationalized on

the basis of an interparticle scattering model and contrasted to the behavior predicted for an intraparticle model.⁶³ With the interparticle scattering model, the arching was explained by an increase in coherence of the intercluster spacings perpendicular to the draw direction, accompanied by a corresponding reduction in coherence in the parallel direction. In contrast, the observed arching with respect to the intraparticle scattering model was noted to be unlikely, since it would require an elliptical deformation of the clusters, as independent scatterers, and an electron density difference between the long and short axes of the elliptically shaped clusters. Using a model-independent maximum entropy method for reconstructing a 2-dimensional electron density map in real space from that corresponding to the scattering data, the intercluster spacings parallel to the draw direction were found to be almost random, while the spacings in the transverse direction were observed to display distinct periodicity.⁶¹ Furthermore, the clusters in the drawn sample were found to be somewhat agglomerated relative to their distribution in the as-received membrane. Based on this finding, the anisotropic shape of the small-angle upturn was attributed to scattering between oriented cluster agglomerates having periodic dimensions significantly larger than the intercluster spacings. For extruded membranes drawn perpendicular to the machine direction (i.e., a sequential biaxial draw), the anisotropic morphology was found to persist, but to an extent much less oriented than that observed for membranes drawn parallel to the machine direction. Relatively isotropic morphologies were obtained only when the membranes were processed with a simultaneous biaxial draw.

In a subsequent communication,⁶² Elliott and co-workers found that uniaxially oriented membranes swollen with ethanol/water mixtures could relax back to an almost isotropic state. In contrast, morphological relaxation was not observed for membranes swollen in water alone. While this relaxation behavior was attributed to the plasticization effect of ethanol on the fluorocarbon matrix of Nafion, no evidence of interaction between ethanol and the fluorocarbon backbone is presented. In light of the previous thermal relaxation studies of Moore and co-workers,⁶¹ an alternative explanation for this solvent induced relaxation may be that ethanol is more effective than water in weakening the electrostatic interactions and mobilizing the side chain elements. Clearly, a more detailed analysis of this phenomenon involving a dynamic mechanical and/or spectroscopic analysis is needed to gain a detailed molecular level understanding of this relaxation process.

Londono et al. reported the results of a synchrotron SAXS study of oriented Nafion membranes.⁶⁴ As the elongation was increased to 150%, meridional scattering of the ionomer peak disappeared while the intensity profile narrowed azimuthally about the equator. At 150% elongation, an equatorial streak, similar to that shown in Figure 3b, was observed and noted to resemble the SAXS pattern of drawn fibers containing a microfibrillar morphology. Using a finely collimated X-ray beam (100 μm) and stacked films, edge-on scattering patterns were obtained for orientations parallel and perpendicular to the stretching direction. The observation of an isotropic scattering pattern from the orientation parallel to the stretching direction confirmed the fibrillar morphology of oriented Nafion. Furthermore, based on this analysis, the authors suggest that the morphology of uniaxially drawn Nafion consists of oriented cylindrical or lamellar domains, rather than spherical clusters. From these scattering results alone, a definitive distinction between cylinders or lamella was not possible. Simultaneous SAXS/WAXD measurements were also collected in-situ during the orientation process. The (100) crystalline reflection of the PTFE-like crystallites was observed to narrow about the equator at a rate of almost double that of the orientation of the ionic domains. While the authors acknowledge the bilayer lamellar model proposed by Starkweather,⁴¹ the SAXS/WAXD results are stated to indicate that lamellar ionic domains may also be present in the amorphous phase. However, if the Starkweather model were strictly considered, such that the crystalline bilayers were intimately linked to the lamellar ionic domains, then the orientation of the ionic and crystalline domains should have tracked together with a one-to-one correlation.

Computational methods combined with a novel approach in the application of scattering physics were recently employed by Barbi et al. in a synchrotron SAXS study of the nanostructure of Nafion as a function of mechanical load.⁶⁵ A new method of multidimensional chord-distribution function (CDF) analysis was used to visualize the multiphase nano-

structure information of Nafion in direct space following established procedures used to study oriented semicrystalline polymers and strained elastomers. Based on the classical ionomer domain model of Gierke¹⁷ (i.e., ionic clusters as inverted micelles interconnected by channels), the deformation behavior of Nafion in the dry state was evaluated over a range of deformations from 0 to 125%. During the deformation, the channels between clusters are proposed to open and widen in the direction of strain and merge with adjacent domains to form slab-shaped domains that align together in the draw direction.⁶⁵ Using contour maps constructed from the CDF analysis, the average domain thickness D_t (i.e., the dimension perpendicular to the draw direction) and the maximum domain height D_h (i.e., along the draw direction) were determined. As the elongation was varied from 50% to 125% (near the break point), the domain thickness decreased from 1.9 to 1.5 nm, while the domain height increased from 3 to 6 nm. From this real space information, and the noted absence of autocorrelation peaks on the meridian, the ionic domains were concluded not to be cylinders. With respect to the polymer matrix, the crystalline domains were shown to be cylindrical in nature and undergo plastic deformation and parallelization upon elongation. At high elongations, the CDF analysis indicated a broad distribution of crystallite sizes with an ultimate inclination of 40° relative to the draw direction.

Recently, van der Heijden et al. have used simultaneous SAXS/WAXD to study the morphological variation in Nafion during the deformation process of uniaxial extension.⁶⁶ Using absolute values of the Hermans orientation factor, the orientations of both the ionomer and crystalline domains were quantitatively compared with respect to the draw ratio. The structural anisotropy at length scales between 0.2 and 4 nm was evaluated based on a ratio, α , of the crystalline to ionomer domain orientation factors. For draw ratios below 200%, α values were observed to be well below 1.0, indicating that the ionomer domains oriented more readily than the crystalline domains. Based on this observation, a simple model involving the deformation of spherical ionic domains into ellipsoidal shaped structures was rejected, since the clusters would not be expected to deform more than their surrounding matrix. Beyond 200% elongation, the α values approached 1.0, indicating that the crystalline and ionic domain orientation was correlated with respect to elongation. This two-stage orientation behavior was thus explained based on a new consideration of Nafion morphology (see below) as a collection of bundled, elongated polymeric aggregates containing relatively extended chain crystals. Upon stretching, two orientation mechanisms were postulated to occur simultaneously: at small draw ratios, the large bundles rotate such that the elongated aggregates in the bundles are more or less correlated in orientation, and at large draw ratios, the alignment of individual elongated aggregates is refined in the draw direction due to sliding and/or disentangling of the aggregates from each other. Further analysis of the crystalline morphology indi-

cated that the degree of crystallinity remained constant as a function of the draw ratio.

2.4. Current Models for the Morphology of Nafion

Since the early studies of Nafion morphology, numerous investigators have attempted to reconcile a wealth of structural information with observed properties (specifically, transport properties) in order to develop a well-defined morphological model for perfluorosulfonate ionomers. As noted in the studies above, the complicating factors associated with this endeavor include the random chemical structure of the copolymer, the complexity of co-organized crystalline and ionic domains, vast morphological variations with solvent swelling, the relatively low degree of crystallinity, and the diffuse, heterogeneous nature of the morphology that leads to a wide range of domain dimensions. While the majority of morphological information about Nafion has originated from small-angle scattering and wide-angle X-ray diffraction experiments, the simple fact remains that this polymer yields very little characteristic detail in the dimensions probed by these methods. Thus, the quest for a universally accepted model continues with a spirited debate in the current literature.

The principle scattering models for the morphology of Nafion that have been proposed to date include a cluster-network model proposed by Gierke et al.¹⁶ (Figure 1), a modified (depleted-zone) core-shell model proposed by Fujimura et al.^{36,37} (Figure 2b), a local-order model first proposed by Dreyfus et al.,^{44,67–69} a lamellar model proposed by Litt,⁷⁰ a sandwich-like model proposed by Haubold et al.,⁷¹ and a rodlike model proposed by Rubatat et al.⁷² Central to each of these models is the recognition that the ionic groups aggregate in the perfluorinated polymer matrix to form a network of clusters that allow for significant swelling by polar solvents and efficient ionic transport through these nanometer-scale domains. These models do, however, differ significantly in the geometry and spatial distribution of the ionic clusters. While the complications associated with modeling the spatial distribution of ions within a semicrystalline matrix are often either ignored or simply eliminated through various thermal treatments, the experimental evidence of PTFE-like crystals in Nafion is undeniable. Thus, the validity of a given model in *completely* describing the morphology of Nafion requires a reasonable account for the existence of crystallites in the presence of a pervasive ionic network.

The original cluster-network model proposed by Gierke et al.^{16,17,31,32} (also referred to as the cluster-channel model) has been the most widely referenced model in the history of perfluorosulfonate ionomers. Despite the very large number of papers and reports that have strictly relied on this model to explain a wide variety of physical properties and other characteristics of Nafion, this model was never meant to be a definitive description of the actual morphology of Nafion, and the authors recognized that further experimental work would be required to completely define the nature of ionic clustering in these ionomers.¹⁷ For example, the paracrystalline, cubic lattice

of close-packed spheres was only chosen to describe the spatial distribution of inverted micelle clusters for the convenience of simple space-filling calculations. The cluster dimensions obtained from these calculations were consistent with other experimental information (e.g., from TEM analysis); however, the observed spatial distribution of clusters was not, by any means, paracrystalline. Furthermore, the existence of 1 nm channels connecting the clusters was proposed in order to reconcile the highly permselective transport properties of Nafion containing inverted micelles.^{16,31} With channels, a network of clusters could exist with a percolation pathway through the membrane; however, no direct experimental evidence has ever revealed the existence of channels in these polymers. On the other hand, this cluster-network model was the first to attribute the SAXS maximum in Nafion to an interparticle origin, and it offered the possibility of slight morphological reorganization during solvent swelling.¹⁷ Both of these considerations have prevailed through the test of time and are currently featured in the modern understanding of this polymer.

In a manner following the scattering studies of other ionomeric systems, the intraparticle, modified core-shell model of Fujimura et al.³⁷ lost popularity through the late 1980s and has since been more or less discounted as a reasonable model for the morphology of Nafion. Recent SANS analysis of water-swollen Nafion was performed by Gebel and Lambard with a quantitative comparison of the core-shell models to other interparticle scattering models.⁶⁷ Using the depleted-zone core-shell model of Fujimura,³⁷ the theoretical profiles showed a poor fit to the experimental data, and the dimensional and contrast values extracted from the best fits were found to be unrealistic. Furthermore, the existence of isolated ion pairs constituting the matrix in the depleted-zone core-shell model was noted to be highly questionable in swollen membranes and confirmed to be improbable by ESR measurements.⁷³

In considering the ionomer peak observed for Nafion to be of an interparticle origin, a more quantitative approach to extracting detailed structural information from the scattering data involved the application of a modified hard sphere model.⁵² In the work of Kumar and Pineri⁴² (discussed above), the SAXS peak was accounted for quantitatively (in both position and intensity) as arising from the interference between clusters, assuming them to be noninteracting hard spheres. With calculations based on the modified hard sphere model,^{24,25} the theoretical peak value of the relative intensity invariant over an intermediate q -range was found to be within 15% of the experimentally observed intensity invariant for samples having different equivalent weights, different cationic forms, and different water contents. Recently, Orfino and Holdcroft used the modified hard sphere model to determine the characteristic dimensions associated with the ionic clusters in dry and hydrated Nafion.⁷⁴ With reasonable fits to the experimental scattering profiles, their model calculations indicated that the number density of clusters decreased from 3.2×10^{19} to 9.7×10^{18} clusters/cm³

upon hydration, while the cluster size increased from a radius of 1.12 to 2.05 nm. Although this observation is in agreement with the morphological reorganization proposed in the cluster-channel model of Gierke,¹⁷ a comparison of the model parameters determined for the radius of the ionic core and the radius of closest approach to the size of a single, hydrated ionic group led the authors to the conclusion that clusters could be simply bridged by single ionic sites rather than organized ionic channels.⁷⁴

The local-order model, first applied by Dreyfus et al. (see above),⁴⁴ is another interparticle scattering model used to define the spatial distribution of spherically shaped ionic clusters in Nafion. More recently, Gebel and Lambard demonstrated that the local-order model provided a better fit to SAXS and SANS profiles of hydrated Nafion than those of the depleted-zone core-shell and modified hard sphere models over the range of scattering vectors between 0.3 and 2.0 nm⁻¹.⁶⁷ At larger q -values, the deviation between the model fit and experimental data was attributed to the fact that the model assumes monodisperse clusters having a homogeneous electron density. While additional terms allowing for polydispersity in dimensions were noted to yield improvement in the model fits, the added adjustable parameters were deemed undesirable. Using a Debye-Bueche model to fit the small-angle upturn (i.e., a method found successful for other ionomer systems), heterogeneities having a correlation length on the order of 8 nm were found to best reproduce the excess intensity at low q -values. Although this dimension was noted to be surprisingly small for "large-scale" heterogeneities, the excellent agreement with the size of the correlation-hole in the radial distribution function of the local-order model was acknowledged. To extract further information from the scattering at low angles, an ultras-small-angle USAXS camera was used to significantly extend the low q -range.⁶⁴ While this analysis yielded correlation lengths for large-scale density fluctuations in excess of 300 nm, no detailed description of the morphological origin of these heterogeneities was offered, and their existence in contrast to the assumed "gaslike" order of the local-order model was not reconciled.

Gebel and Moore⁶⁸ also applied the local-order model to the SAXS and SANS study of a series of short-side-chain perfluorosulfonate ionomers, ranging in equivalent weights from 635 to 1269 g/equiv. These PFSIs differ from Nafion in the structure of their side chain, which contains only one ether linkage and two CF₂ units separating the sulfonate group from the perfluorinated backbone. Moore and Martin⁵⁵ reported the first SAXS and WAXD characterization of these new PFSIs, showing that these polymers possessed a morphology similar to that of Nafion, having both crystalline and ionic domain structures that varied with equivalent weight and water content. Subsequently, Gebel and Moore quantitatively analyzed this initial SAXS data in combination with new SANS data using the local-order model.⁶⁸ In agreement with the findings for Nafion,^{44,67} the local-order model was found to satisfactorily reproduce the scattering profiles for the short-side-chain ma-

terials, having intermediate equivalent weights. For the short-side-chain PFSIs having high equivalent weights, the model fits were found to deviate significantly from the experimental profiles. This observation was attributed to the relatively high crystallinity of the blocky ionomers;⁵⁵ long runs of PTFE units in the high equivalent weight ionomers yielded an intense crystalline peak at low q -values that influenced the observed position of the ionomer peak. Deviations observed for the low EW ionomer were attributed to the very large water uptake (~80 wt %) as a result of the absence of crystallinity.⁵⁵ For this system (i.e., the 635 EW ionomer), the highly swollen morphology was suggested to be more appropriately described as a polymer-in-water system.⁶⁸ Thus, based on recent studies of PFSI solutions and the reasonable fit of the scattering profile to the form factor of cylinders, the morphology of the swollen 635 EW system was proposed to resemble a connected network of rods,^{51,52} as opposed to a locally ordered distribution of spherical clusters. This new concept for the morphology of PFSIs will be discussed in more detail below.

Through consideration of the morphological and dimensional changes that had been observed in SAXS analyses of Nafion during swelling and deswelling experiments, Litt⁷⁰ proposed a reevaluation of Nafion morphology that could provide a simpler rationalization of the literature than the current interparticle models based on spherical clusters.^{17,37,44} The principal concern addressed by this proposal was that a major reorganization of the ionic domains is required to explain the fact that the observed Bragg dimensions from the ionomer peak varied almost linearly with water content as opposed to the 1/3-power dependence expected for isotropic (affine) swelling of spherical structures. Furthermore, since the swelling/deswelling behavior is observed to be reversible, the extent of morphological reorganization required with the cluster-network model was argued to induce nonrecoverable plastic flow. Using the SAXS data of Gierke et al.¹⁷ over a limited range of water contents, Litt showed that the d spacings are proportional to the volume of absorbed water.⁷⁰ Based on this observation, a lamellar model consistent with the bilayer structure suggested by Starkweather⁴¹ was proposed for the morphology of Nafion. In this model, the ionic domains are defined as hydrophilic "micelle" layers separated by thin, lamellar PTFE-like crystallites. As water absorbs between the lamella and separates them, then the increase in d spacing between ionic domains is expected to be proportional to the volume fraction of water in the polymer and the swelling behavior should be completely reversible, thus eliminating the requirement of morphological reorganization.

While the lamellar model proposed by Litt⁷⁰ provides a convenient and simple explanation for the swelling behavior of Nafion, an important morphological feature observed in the SAXS and SANS profiles of PFSIs, namely the low angle maximum attributed to the crystalline, interlamellar long spacing, is ignored in this analysis. In studies of short-side-chain PFSIs, Gebel and Moore⁶⁸ found that the

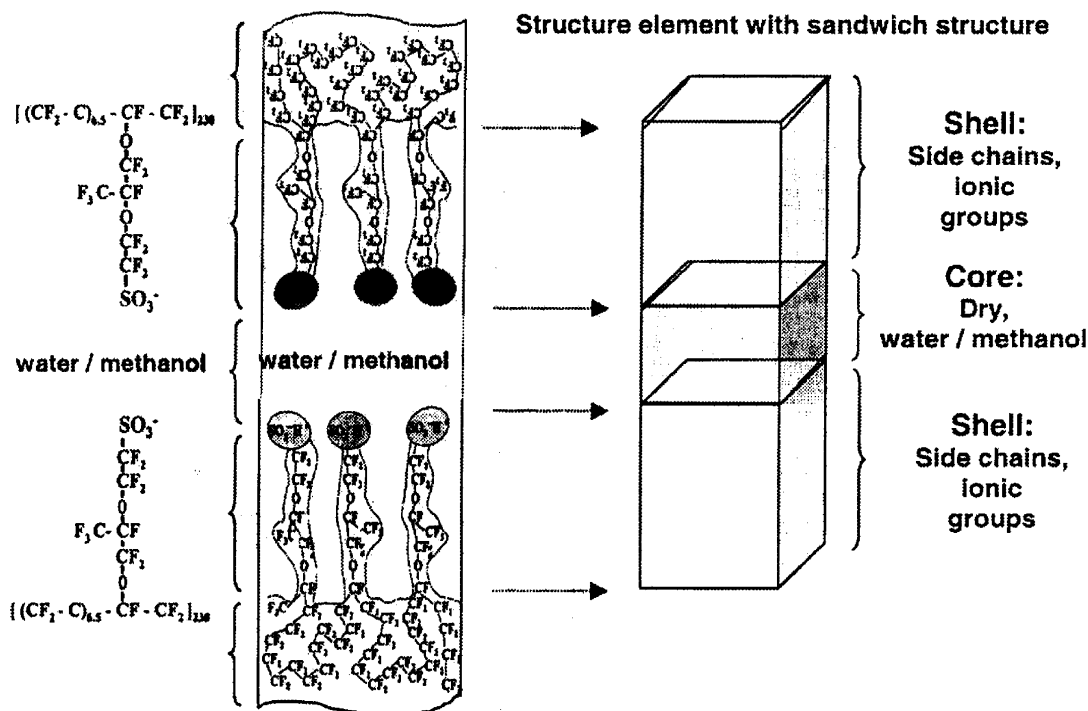


Figure 5. Sandwich-like structural element proposed for the morphological organization of Nafion. (Reprinted with permission from ref 71. Copyright 2001 Elsevier.)

swelling behavior of the ionic domains in these PFSIs is identical to that observed for Nafion; however, the interlamellar spacings shift with water content in a manner significantly different from that of the intercluster spacings. This observation was also confirmed by Young et al. through SANS studies of Nafion swollen with a variety of polar organic solvents.⁷⁵ Since the lamellar model essentially stipulates a parallel shift for the two maxima attributed to a lamellar structure of the ionic domains imposed by the semicrystalline character of the polymer, the observation of dissimilar shifts indicates that the lamellar model is an oversimplification in the global description of the morphology of Nafion. In an attempt to reconcile the dissimilar shifts with the constraints of the lamellar model, Young et al.⁷⁵ have proposed a preferential partitioning of solvents into regions of the structure that do not give rise to the ionic scattering maxima (presumably domains of amorphous fluorocarbon chains between crystallites). Nevertheless, this consideration implies that at least a portion of the crystallites in Nafion are separated by nonionic regions, which is different from the case of the crystallites that impose the lamellar ionic structure as explicitly dictated by the lamellar model. To date, no such morphology has been observed for Nafion.

A variation of the lamellar model was recently proposed by Haubold et al.,⁷¹ in which synchrotron SAXS studies were performed on acid form Nafion 117 samples. The molecular weight of these samples was reported to be $250\,000\text{ g}\cdot\text{mol}^{-1}$, and the experiments were conducted on dry samples in air and samples equilibrated with water, methanol, and a range of water/methanol mixtures using an in situ flow cell. The most fundamental result of this study is that the data show the usual ionomer peak at $q = 1.4\text{ nm}^{-1}$, which gives a Bragg spacing of $d = 2\pi/q \approx$

4.0 nm , in harmony with the results of all other SAXS investigations. The scattering cross section data was fitted to a layered model whose basic structure element (i.e., the scattering particle) is a “sandwich” (Figure 5). The outer portion of this sandwich (the “shell”) consists of the side chains, including the sulfonic acid groups, and the inner liquid portion (the “core”) consists of the water/methanol molecules. To provide channels that serve as conduction pathways for protons through the membrane, these structural elements were proposed to be juxtaposed in a linear fashion so that the liquid core regions are contiguous.

The structure factor chosen for this “sandwich” model is that of a rectangular parallelepiped whose dimensions are those of the monodisperse sandwich particles with an overall random orientation.⁷¹ A least-squares fit of the model scattering cross section to the experimental data yielded the dimensions of the core thickness, c , the combined thickness of the two shells, s , as well as the lateral dimensions a and b . Also issuing from the fit were the electron density contrasts for the core and shell regions. From the model fits, the basic structure element was shown to have lateral dimensions a and b between the values of 1.5 and 4.5 nm, and the total thickness of the sandwich, $c + s$, was about 6.0 nm. Fitted values of s , c , a , and b , were also plotted versus the volume percent of methanol in water, which showed that c decreased while s increased with increasing percent methanol. The molecular interpretation of this observation was that as the methanol composition increased from 0 to 100%, the spacing between $-\text{SO}_3\text{H}$ groups on the two different shells (the region in which the solution is located) decreased from approximately 2.7 to 1.3 nm, while the shells ($s/2$) extended from approximately 1.7 to 2.5 nm. The latter result implies a change in conformation and/or packing of side chains and main chains; however,

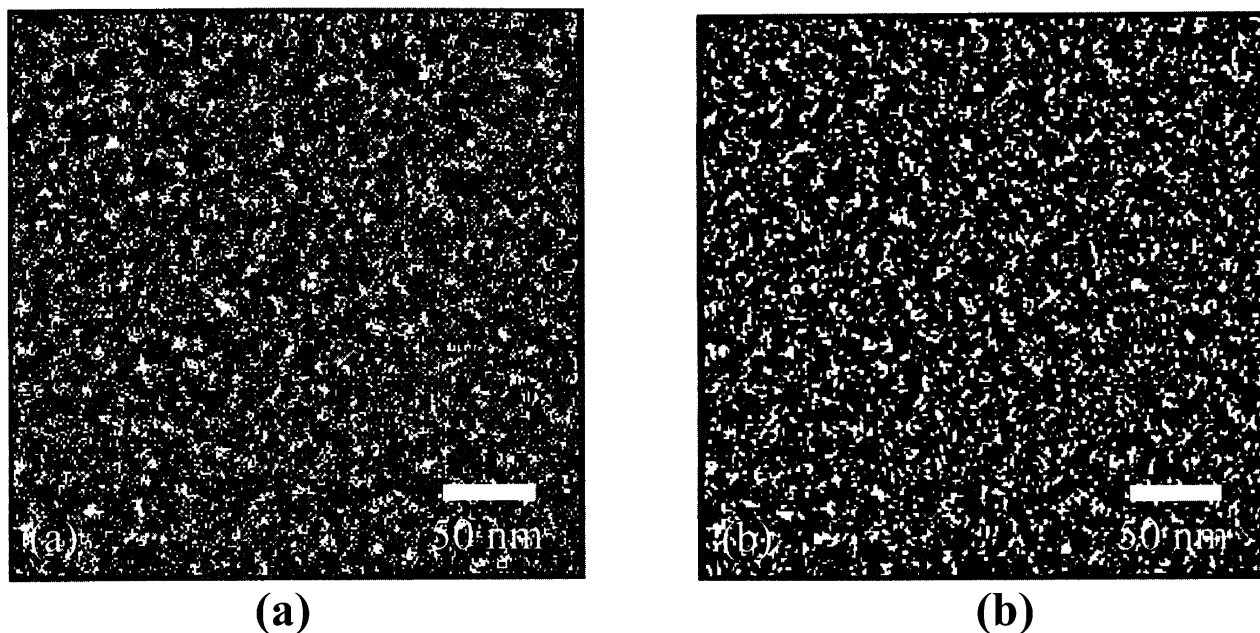


Figure 6. MaxEnt reconstruction of SAXS data from as-received Nafion equilibrated under (a) ambient humidity and (b) 100% RH. (Reprinted with permission from ref 63. Copyright 2000 American Chemical Society.)

the scattering contrast (relative to the average electron density throughout the membrane) for the shell versus percent methanol was found to be relatively constant. Thus, the authors concluded that methanol “leaves the side chains nearly unaffected”, although the meaning of this in consideration of the extension of the side chains is unclear. While this sandwich model was presented within the context of direct methanol fuel cell membranes, it does not offer a complete, unambiguous 3-dimensional pattern of hydrophobic/hydrophilic organization, but rather of local structure. Nor is there any information regarding rearrangement of the main chains, sections of which are known to organize into limited crystalline regions.

A methodological improvement in the analysis of SAXS data of Nafion has recently provided a new perspective on the spatial distribution of clusters in PFSIs. Elliott et al.⁶² have reported SAXS studies of water-swollen Nafion 115 in the acid form and various cation forms in which the membrane water content was quantitatively adjusted using an environmental sample holder with controlled humidity. The radially integrated SAXS profiles show the usual cluster reflection that moves to lower scattering angle with increasing humidity as well as the usual small-angle upturn at low scattering vector magnitudes. From the behavior of the cluster peak position (d -spacing) versus volume fraction of absorbed water, it was concluded that cation exchange does not affect the hydrated morphology. In direct contradiction to both the lamellar morphology, as suggested by Litt,⁷⁰ and other models based on individual three-dimensional clusters (i.e., noninteracting hard spheres),⁴² it was further noted that d was neither directly proportional to the water volume fraction nor proportional to the cube root of this quantity.

Using a novel, model-independent maximum entropy method to interpret the SAXS data, Elliott et al.⁶³ presented a self-consistent morphological para-

digm for PFSIs, which was capable of reconciling the microscopic and macroscopic swelling behavior of these materials. The maximum entropy (MaxEnt) method was used in this analysis to determine the most statistically probable structure for Nafion from the experimental SAXS data. Through this analysis, 2-dimensional SAXS patterns (in reciprocal space) were transformed to generate real space, two-dimensional projections of electron density distributions within a representative volume of the membrane. The technique of spatial filtering was also used to highlight particular features of the electron density maps with respect to different features of the underlying SAXS patterns in discrete scattering vector ranges. Specifically, a low pass filter was applied to mask the cluster reflection, while a high pass filter was used to mask the small-angle upturn prior to applying the maximum entropy data manipulation.

Interpretation of the MaxEnt electron density maps, termed “reconstructions”, led to the conclusion that the most statistically probable scattering model for Nafion is of an ion clustered morphology with a hierarchical scale of structures.⁶³ Figure 6 shows a maximum entropy reconstruction of SAXS data for Nafion H⁺ under ambient humidity and 100% RH. The clusters in these “images” are the white spots and are often seen as agglomerated (clusters of clusters), and more so for the 100% RH case. With an increase in water uptake, the MaxEnt reconstructions showed that the average cluster separation increases with a concurrent decrease in the cluster number density. An important fact is that the “microscopic swelling”, defined in terms of the Bragg spacing for the cluster reflection, does not transform in an affine manner with the macroscopic swelling. Particularly, the relative intercluster expansion is greater than that of the bulk sample dimensions. This behavior was explained as a consequence of the

decrease in the number density of clusters with swelling.

The distribution of clusters observed in the MaxEnt reconstructions was also shown to be nonuniform, suggesting an agglomeration or clustering of clusters.⁶³ By applying a low pass filter (to highlight long-range structure), this agglomeration was linked to the small-angle upturn observed in the SAXS profiles. With confirmation from the MaxEnt analysis of oriented samples (see above), the small-angle upturn was concluded to be produced by the independent scattering from cluster agglomerates yet fundamentally caused by ionic aggregation. Thus, the principal scattering features of Nafion (i.e., the small-angle upturn and the ionomer peak) were noted to be produced by two distinct scattering mechanisms operating on different size scales.

The evolution of PFSI structure from the dry state through the water-swollen state to solution was studied by Gebel using small-angle scattering methods.⁷⁶ With respect to recent studies suggesting that PFSI solutions contain rodlike structures,^{51,52} the aim of this investigation was to gain an understanding of the morphological changes that occur as the ionomer is converted from the highly swollen state to solution during the dissolution process, and *visa versa* during the solution-casting process. Using a high temperature swelling process, water-swollen membranes with water volume fractions ranging from $\phi_w = 0.3$ to 0.93 were obtained. Similarly, homogeneous, aqueous solutions with concentrations up to a polymer volume fraction $\phi_p = 0.12$ were prepared, allowing for an overlap in polymer volume fraction between the solution and swollen membrane states. For the water-swollen membranes, the scattering profiles showed the prominent shift of the ionomer peak to lower q -values with increasing water content, in agreement with previous studies. A plot of the microscopic degree of swelling (defined as the increase in the Bragg distance of the ionomer peak maximum relative to the Bragg distance extrapolated for the dry membrane) versus the macroscopic linear expansion over the large range of water contents revealed a significant change in swelling behavior (i.e., a change in slope) at a linear expansion of 30%. In a double logarithmic plot of the Bragg distance versus the polymer volume fraction, ϕ_p , the change in slope was found to occur at $\phi_p = 0.5$. For low water contents, the slope of this plot was equal to -1.33 , while, at high water contents ($\phi_p < 0.5$), the slope dropped to -0.5 . This behavior was thus attributed to an inversion from a water-in-polymer state at low water contents to a polymer-in-water state at high water contents. The asymptotic behavior of the scattering curves for the water-swollen membranes was also evaluated following the Porod law in order to extract values for the specific surface (i.e., σ , equal to the area of the polymer–water interface per polar headgroup) of the scattering particles. For all samples, the asymptotic behavior was the same, and the average Porod limit yielded a specific surface value of $\sigma = 55 \text{ \AA}^2$. This observation, in agreement with other studies involving a low range of water contents, confirmed the strong significance of this parameter

in defining the structure of swollen membranes and further supports the conclusion that considerable structural reorganization occurs during the swelling process in order to keep constant the specific surface with increasing cluster size.

The slope of -0.5 in the double logarithmic plot of the Bragg distance versus the polymer volume fraction for the highly swollen membranes was noted to be consistent with a dilution of rodlike polymer aggregates.^{51,52} Furthermore, the small-angle scattering profiles of Nafion solutions and the highly swollen membranes were virtually superimposable in the q -range from 0.7 to 2.0 nm^{-1} , suggesting that the local structure on the scale of a few nanometers was identical. Since previous studies of these solutions provided strong evidence for the existence of rodlike aggregates,^{51,52} this observation led to the conclusion that the morphology of highly swollen membranes could be considered as a network of rodlike polymer particles. The deviation of the scattering curves at small angles ($q < 0.7 \text{ nm}^{-1}$) was attributed to the presence of nodes in the network structure and to large scale heterogeneities. It is important to note that this connected network of rodlike structures connected by nodes was proposed earlier by Lee et al.⁴⁵ to explain their SANS data probing the local water structure in Nafion.

Based on the results of this scattering analysis of Nafion over a wide range of water contents, combined with energetic considerations, Gebel proposed a conceptual description for the swelling and dissolution process shown schematically in Figure 7.⁷⁶ In this qualitative model, the dry membrane is considered to contain isolated, spherical ionic clusters with diameters of $\sim 1.5 \text{ nm}$ and a center-to-center separation distance of $\sim 2.7 \text{ nm}$. With the absorption of water, the clusters swell to hold pools of water surrounded by ionic groups at the polymer–water interface in order to minimize the interfacial energy. As the water content increases to between $\phi_w = 0.3$ and 0.5, structural reorganization occurs to keep constant the specific surface area, and the onset of percolation is achieved by the formation of connecting cylinders of water between the swollen, spherical clusters. At ϕ_w values greater than 0.5, an inversion of the structure occurs such that the structure resembles a connected network of rods. Finally, as the membrane “dissolves” into solution, the rodlike structures separate to yield a colloidal dispersion of isolated rods. While this model offered a plausible mechanism for the evolution in structure from the widely accepted concept of isolated clusters for membranes containing relatively low water contents to rodlike structures in solution, no thermodynamic justification for the phase inversion process at $\phi_w = 0.5$ was offered. Moreover, the fact that the scattering profiles near this phase inversion point did not show a significant change in contour is difficult to rationalize.

To further probe the phase behavior of hydrated Nafion, Rollet et al.⁷⁷ used a contrast matching method in the SANS analysis of Nafion membranes neutralized with tetramethylammonium ions. With 12 hydrogen atoms per counterion, the $\text{N}(\text{CH}_3)_4^+$ ions

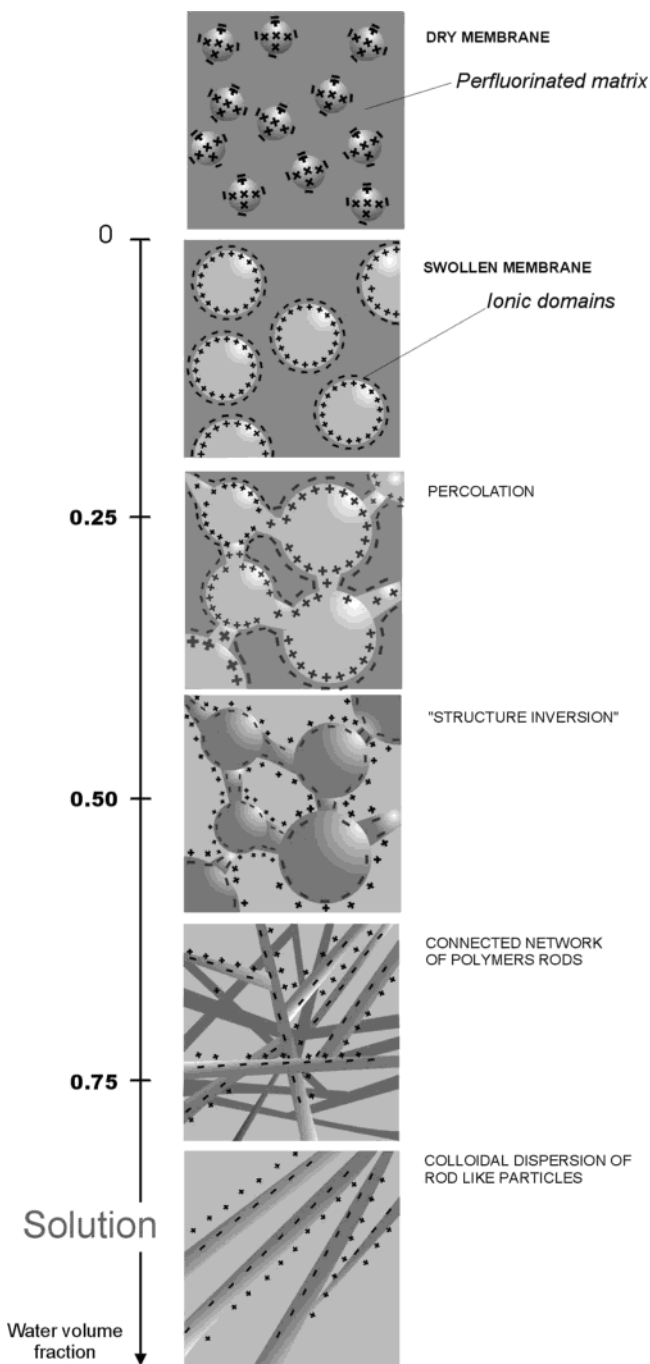


Figure 7. Conceptual model for the morphological reorganization and continuity of the ionic domains in Nafion as the dry membrane is swollen with water to the state of complete dissolution. (Reprinted with permission from ref 76. Copyright 2000 Elsevier.)

were found to be excellent neutron scatterers that provided a third source of scattering contrast, thereby acting as a useful morphological probe at the interface between the water and polymer domains. By varying the water composition with a range of H₂O/D₂O mixtures, the contrast profile of the scattering domains was evaluated to gain a new insight into the structure of Nafion. The relative magnitudes of scattering features in the SANS profiles were shown to vary systematically with the H₂O/D₂O composition, indicating that the N(CH₃)₄⁺ ions were condensed in a thin layer with the sulfonate groups at the interface between the hydrophobic polymer parts and the

water domains. Through the assumption of spherical aggregates and the recognition that no structural change occurs when H₂O is replaced by D₂O, the structure factor contribution to the scattered intensity was eliminated by dividing the SANS profiles obtained with various H₂O/D₂O mixtures by the intensity profile for Nafion in pure water.⁷⁷ The resulting normalized profiles were shown to present a clear minimum near $q = 1.5 \text{ nm}^{-1}$ that shifted toward smaller q -values as the composition of D₂O decreased. In considering the form factor for spherical core-shell particles, the two opposing geometries (i.e., a water core surrounded by a counterion shell or a polymer core surrounded by a counterion shell) were used to simulate SANS curves comparable to the experimental data. While the general shape of the curves for both simulations resembled the experimental data and showed a clear minimum near $q = 1.5 \text{ nm}^{-1}$, only the "polymer core surrounded by a counterion shell" geometry matched the shift of this minimum toward smaller q -values. Thus, based on this analysis, the authors concluded that the morphology of hydrated Nafion is best described as polymer aggregates surrounded by water.⁷⁷ Although an attempt was made to model both spherical and elongated particles using a similar approach, the authors acknowledged that a conclusive distinction between these shapes was not possible given the limited q -range of the experimental data.

In a second paper, Rubatat and co-workers⁷² used a combination of small-angle X-ray and neutron scattering techniques, including USAXS, to probe characteristic dimensions in hydrated Nafion over the range from 1 to 1000 nm. Through a combination of the USAXS and SAXS data, the entire scattering curve of Nafion was presented to show the extended small-angle upturn attributed to long-range heterogeneities in electron density, the low angle maximum attributed to supralamellar dimensions of the crystalline domains, and the ionomer peak attributed to intercluster interferences. In addition, double logarithmic plots of the scattering data $I(q)$ versus q showed two regimes of linear intensity decay; at low angles, the data followed a q^{-1} power law, while, at high angles, the intensity decay followed the expected q^{-4} power law indicative of a sharp interface for the scattering particles. The q^{-1} regime was noted to fit the behavior expected for scattering from rodlike particles over the range of wave vectors from $2\pi/L$ to $2\pi/D$, where L and D are the rod length and diameter, respectively. Based on the observed span of scattering vector in this regime, the rodlike particles were estimated to have dimensions of $D \approx 6 \text{ nm}$ and $L \geq 100 \text{ nm}$.

Scattering data over the extended range of q -space were also collected from Nafion samples containing a wide range of water contents ($\phi_w = 0.05\text{--}0.84$).⁶⁹ While systematic shifts in the intensities and positions of the structure maxima (i.e., the crystalline and ionomer peaks) were observed and consistent with those found by others, the general shapes of the scattering profiles for all samples were quite similar. This observation supported the assumption that the swelling process simply involves a dilution of the



Figure 8. Schematic representation of an entangled network of elongated rodlike aggregates in Nafion. Long-range heterogeneities arising from bundles of locally ordered aggregates are proposed to give rise to the low angle increase in scattered intensity. (Reprinted with permission from the original author.)

scattering entities rather than inducing a strong structural reorganization of the cluster morphology, as suggested earlier by Gebel.⁷⁶ In plotting the characteristic (Bragg) distances, $2\pi/q^*$, corresponding to the two structure maxima, versus the polymer volume fraction, two microscopic swelling regimes were observed, in agreement with that found by Gebel.⁷⁶ For high ϕ_p , the swelling process was observed to follow a power law close to ϕ^{-1} , in agreement with the results of Fujimura^{36,37} and Litt.⁷⁰ For low ϕ_p (below $\phi_p = 0.6$), the swelling process was observed to change to a power law close to $\phi^{-0.5}$, suggesting a dilution of cylindrical shaped particles. To reconcile the shift in swelling behavior observed at $\phi_p \approx 0.6$ with the suggested rodlike morphology of the scattering particles, the authors proposed that the aggregates are more ribbonlike than rodlike, with a cross-sectional thickness and width close to 2 and 8 nm, respectively.⁷² At low water contents, the ribbons are considered to pack face-to-face in a manner that allows for an initial dilution law with an exponent of -1 . However, at high water contents (low ϕ_p), where the distance between aggregates is greater than 8 nm, the orientation distribution around the long axis becomes isotropic in a manner that allows the aggregates to be considered as cylinders with a dilution law following an exponent of -0.5 .

Therefore, in the context of a morphology considered to be fundamentally characterized by the presence of elongated aggregates, the authors propose that the intermediate q -range provides information related to the size, shape, and spatial distribution of the aggregates, while the very small q -range (i.e., the small-angle upturn) may be attributed to larger bundles of aggregates (see Figure 8) with a long-range heterogeneous distribution.⁷² Between these regions in q -space lies information related to the distribution of crystallites in Nafion. Unfortunately, the degree of crystallinity in Nafion is low (e.g., 8–12 wt %³⁶), and thus, little conclusive information about

this morphological feature has been extracted from these scattering studies. As noted in this study, the swelling behavior observed for this scattering feature is surprisingly large (i.e., increases in interdomain distances from 10 to 100 nm with increasing water content) relative to that expected for expansion of interlamellar dimensions. Clearly, additional investigations of this morphological feature are warranted in order to more fully understand the origin of this scattering maximum. If the crystalline domains are contained within the rodlike aggregates, as previously proposed,⁴⁹ then the interlamellar dimensions should track with a corresponding increase in the rod length. On the other hand, the interlamellar correlations may be of an interaggregate origin, and the dimensions should thus track with some function of the interaggregate spacing. To date, this question remains to be answered.

2.5. The State of Understanding from X-ray and Neutron Investigations

Over the period of about two decades, numerous models have been proposed for the morphology of Nafion based on information gathered from small-angle scattering and wide-angle diffraction studies. While these distinctly different models have varied significantly in quantitative and qualitative detail, many have weathered the test of time and remain the focus of debate in the current literature. In all these studies, one fact remains constant; the morphology of Nafion is complex. Fortunately, state-of-the-art scattering methods and data analysis techniques are providing a wealth of new morphological information that may be correlated with other morphological and physical property studies to bring forward a deeper understanding of the complex nature of Nafion.

In reviewing the evolution of information that has been reported from these morphological studies, it should be recognized that each of the principal models for the morphology of Nafion, while distinct in their conceptual design, contains relevant aspects of structure that collectively facilitate a more global understanding of the molecular organization of perfluorosulfonate ionomers. By recognizing the specific perspective by which a particular model was developed, a number of interesting disparities between the different models may be reconciled. For example, a relatively new rodlike model has been recently modified to include the possibility of ribbonlike aggregates that may assemble locally,⁷² at low water contents, in a lamellar fashion. By narrowing the perspective to a limited range of water contents, suddenly the rodlike and lamellar models are in agreement. In a similar fashion, the excellent mechanical integrity of swollen Nafion membranes may be attributed to entanglements of the proposed elongated polymeric aggregates in the solid state. At these entanglement or crossover points, local nodes may exist⁷⁶ such that, at moderate water contents, the swollen nodes may appear as isolated clusters. This perspective reconciles the rodlike and cluster-network models.

The morphological information and interpretations currently reported for Nafion still support the concept

of a connected network of ionic domains through which polar solvents and ionic species permeate. The principal focus of these important investigations continues to be aimed at understanding the structural nature of the ionic domains, such as the size, shape, and spatial distributions of the clusters. One consensus that appears to be developing in the current literature is that the ionic domains in hydrated Nafion possess some degree of anisotropy in shape and heterogeneity in their spatial distribution. In contrast to a regularly ordered morphology, this general conception of a more irregular, heterogeneous structure is consistent with the random chemical structure of PFSIs. As we learn more about the organization of these ionic domains, however, the simple concept of "ionic clusters" in these materials becomes more convoluted. Although the ions clearly cluster as a result of the nanoscale phase separation between polar and nonpolar constituents of the copolymer, the notion of discrete ionic clusters or contiguous ionic domains depends on the perspective of the method used to probe the morphology and the chemical composition of the membrane (e.g., the state of hydration). Nevertheless, the current models and their detailed methods of structural analysis now constitute useful tools that may be applied to precise evaluations of morphology–property relationships in these benchmark materials. Moreover, these tools may be used to characterize trends in controlled morphological manipulations of PFSIs through various processing procedures (e.g., solution-casting, thermal treatments, mechanical deformation, etc.) that may prove to enhance the membrane properties over those of as-received Nafion.

The nature of the crystalline component in Nafion has received much less attention than that of the ionic domains, and thus, the relevance of this morphological feature to the technologically important properties of the membranes is still unclear. Since the initial studies of Nafion morphology, the crystalline component has been recognized as an important structural feature and often considered as a necessary component that provides mechanical integrity and a barrier to solvent swelling. With respect to current models, however, the crystallites may be considered to exist within elongated polymeric aggregates or as critical structures that impose the organization of the ionic domains. In the rodlike models, the crystallites may play a minor role to that of entanglements in affecting the mechanical behavior of the swollen membranes. On the other hand, the lamellar model suggests that the crystallites are the principal factor in limiting ionic domain swelling. Clearly, further work is required to resolve this important issue. In addition, as Nafion is the benchmark in studies of many new membrane materials for fuel cell applications, the role of crystallinity (if needed at all) in affecting desirable membrane properties must be addressed.

3. Microscopy Studies

Microscopic studies, regardless of the method of producing images, have an advantage in being able to provide a direct visualization of the sizes, shapes,

and geometrical distribution of ionic clusters, crystallites, and the continuous perfluorinated matrix. The usual problems regarding sample thickness and provision of sufficient electron density contrast, as well as possible artifacts, are present. The SAXS and SANS methods of structural inquiry have advantages that are specific to the nature of the underlying wave–particle interactions. On the other hand, the results are usually prejudiced by the need to assume a particular model, which must necessarily be simple so that the most basic geometrical parameters can be extracted.

Ceynowa performed electron microscopic studies of 60–80 nm thick microtomed Nafion 125 membranes that were converted, for the purpose of affecting electron density contrast, to the Pb^{2+} form, and all of the excess cations and co-ions were removed.⁷⁸ It is the heavy metal that provides electron density contrast between the phase in which it resides and the surrounding phase. These membranes were then exposed to ethanol and 1,2-epoxypropane, although these solvents would not have remained in the samples under the vacuum in the microscope column. The micrographs consisted of uniformly distributed "points" that were presumed to be ion clusters that were 3–6 nm in diameter.

Fujimura et al., in addition to their SAXS studies, performed TEM investigations of thin sections of 100 EW Nafion in the cesium ion form.³⁷ The important details of sample preparation were not provided in this paper, although it is likely that the samples were sectioned from membranes rather than being films cast from solution. The heavy Cs^+ counterion associated with the sulfonate groups provides electron density contrast so as to highlight the cluster regions. It should be appreciated that these samples were only ~60 nm thin, so that, in principle, if the characteristic intercluster spacing is ~4 nm, there will be only ~15 clusters to span the thickness of this sample. A micrograph of this sample shows isolated particles that are, on average, a few nanometers in diameter.

Xue et al. also performed TEM investigations of Nafion 117 morphology.⁷⁹ Solution-cast films, of thicknesses in the range 50–100 nm and stained by RuO_4 , showed good contrast. It was explained how this staining agent would be selectively incorporated in the side chain domains, notwithstanding the fact that none of the usual unsaturated $\text{C}=\text{C}$ bonds for staining reactions exist in these regions. FTIR and X-ray fluorescence analyses showed that this was the case based on the fact that residual water, which would be found in the most hydrophilic regions, was oxidized to give RuO_2 . Therefore, the observed features would likely be clusters. Three phases were observed on the basis of white, gray, and dark regions in micrographs: Spherical clusters, in the diameter range 25–50 Å, were surrounded by interfaces and were uniformly dispersed throughout an organic matrix across the field of view. While the concept was earlier advanced by Yeager et al.,¹⁸ Xue et al. claimed to be the first to view three phases in Nafion using the TEM technique.

Rieberer and Norian investigated unstained microtomed Nafion 117 samples using TEM.⁸⁰ The thinner edges of the 50 nm thick sections of the K⁺ form were used so as to probe regions having thickness on the order of 10 nm. Other samples consisted of films cast from ethanol solutions. The solution-cast samples were exchanged to the Cs⁺ form to affect good electron density contrast. In both cases, steps were taken to minimize beam damage to these thin sections, as explained in the paper. TEM images of the Cs⁺ form samples showed clusters having sizes in the range 1–5 nm, the average of which is around the value of intercluster Bragg spacings that was derived from SAXS studies. Bright regions, due to phase contrast fringes, were said to be nonionic channel areas representing a third phase of the system. The microtomed samples showed the same features as those that were solution-cast. These studies included X-ray energy dispersive spectroscopy (EDS) and energy loss spectrometry (EELS) microanalyses of elemental composition. In particular, the Cs-to-S mole ratio was found to be close to unity, showing essentially complete ion exchange so that all of the sulfonate groups are accounted for in the clusters seen on the micrographs.

Porat et al. performed TEM (zero-loss bright field) studies of very thin Nafion films that were cast from ethanol/water solutions, and some of the conclusions are as follows.⁸¹ It was suggested that the backbone had a planar zigzag conformation in large orthorhombic crystallites as in polyethylene, in contrast with the helical conformation found in poly(tetrafluoroethylene). This is an interesting result, although there are no other studies that support this view. Sulfur imaging indicated the presence of sulfonate clusters that are 5 nm in size.

Lehmani et al. studied the surface morphology of dry and hydrated acid form Nafion membranes using atomic force microscopy (AFM) in tapping mode.⁸² The digital images were also analyzed for surface roughness. The results for “cleaned” samples that were dried under vacuum at 80 °C show “supernodular aggregates” of spherical domains having diameters of ~45 nm. These domains, that appear rather distinct on the images, are of a size scale that is greater than the Bragg spacings derived from the SAXS profiles of these materials. It is unclear as to whether these features are strictly a surface phenomenon and/or the result of sample preparation. The surfaces probed were the actual membrane surfaces rather than those of a fresh surface of a film cross-section that was produced by cutting or freeze fracture. Thus, the observed structures may not be representative of the membrane interior.

On a finer level, spherical grains that have an average diameter of 11 Å are seen. A section analysis, which consisted of a plot of image contrast intensity versus distance, indicated that there is a mean periodicity of around 49 Å, which is close to the values of the SAXS Bragg spacing usually associated with intercluster distances. This, as well as other microscopic studies, favors the model of phase separation as opposed to the core–shell model as applied to the interpretation of scattering data. The hydrated

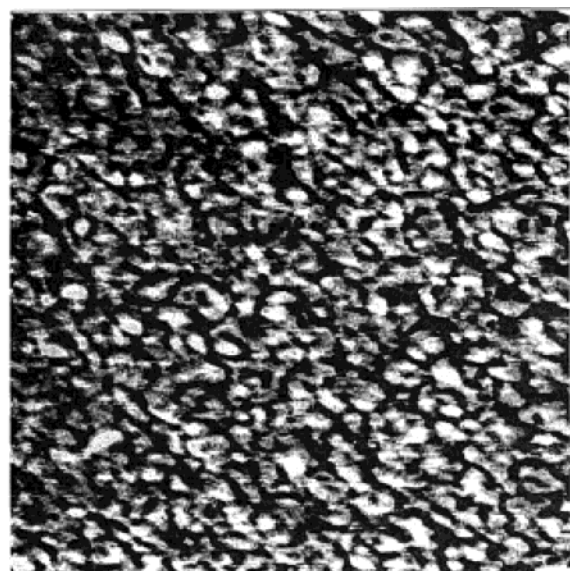
sample was prepared by placing a drop of water on it, and the AFM apparatus was kept in a constant humidity chamber. The supernodular structure was preserved, and the surface was less rough than that of the dry sample.

McLean et al. used AFM to elucidate the surface and near-surface ionic domain and semicrystalline morphologies of Nafion 117 in the K⁺ form, as well as Surlyn and sulfonated poly(styrene-*co*-ethylene/butylene-*co*-styrene) (Kraton) ionomers to which comparisons were made.⁸³ In AFM, the tapping mode phase generates image contrast on the basis of small regions being hard versus soft or, in a general sense, sharp viscoelastic gradients. Similar to the method of dynamic mechanical analysis, but on a smaller scale of interrogation, the phase angle that is plotted in two dimensions across the surface refers to the lag between the oscillatory motion of the cantilever to which a probe tip is attached and the oscillating input signal to the piezoelectric drive for the cantilever.

The stiff regions observed in the studies of McLean et al. were assigned to fluorocarbon crystalline domains, the size of which was around 10 nm. The crystalline packing was referred to as lamellae which are not organized into stacks, as is the case for the Surlyn ionomers that were studied. An interesting outcome of the “normal” tapping studies was the discovery of a very thin (~5 Å) fluorine-rich layer over the surface in which the contrasted soft regions are amorphous.

Other experiments involved lower oscillation amplitude tapping on the same sample after a normal tapping experiment was conducted over the surface. The authors suggested that attractive tip interactions with ionic domains dominate the phase signal under these conditions so as to produce greater contrast in the sense of phase difference. In this way, the ionic domains are seen more clearly. The low amplitude experiments revealed ionic domains of size 4–5 nm, which is in agreement with the results of earlier TEM experiments.^{37,81} The ionic domains, appearing as irregularly shaped, were not resolved to a degree to which distinct boundaries and interphase as well as amorphous regions could be seen because these features overlapped and artifacts of the AFM method relating to feature edges must be considered. No long-ranged patterned organization of the clusters was seen, which is in agreement with the observation of a well-studied broad, single SAXS peak attributed to polar–nonpolar phase separation in these materials.

Images were also obtained for Nafion K⁺ samples that were soaked in deionized water using low oscillation energy so as to sense hydrated ionic clusters. An ambient humidity conditioned (control) sample exhibited 4–10 nm in diameter clumps of multiple (unresolvable) ionic domains. Upon exposure to water, the ionic features became enlarged in a way that they were elongated and appear somewhat as channels having a width of 7–15 nm, as seen in Figure 9. While Figure 9 might offer a view of contiguous hydration pathways, the morphology particularly is that of the K⁺ ionic form so that caution must be exercised in applying this information in rationalizing the proton conductance and other prop-



A



B

Figure 9. Low oscillation energy tapping mode phase images of a K^+ form Nafion 117 membrane. In part A, sample was exposed to ambient, room temperature humidity (ionic species are in the light regions). In part B, sample was exposed to deionized water. The images are $300\text{ nm} \times 300\text{ nm}$, and the phase range is $0\text{--}80^\circ$. (Reprinted with permission from ref 83. Copyright 2000 American Chemical Society.)

erties of sulfonic acid form Nafion within the context of PEM fuel cells.

In addition to providing a “direct” visualization of ionic clusters, the discovery of the thin fluorine-rich layer may have important implications with regard to the liquid/vapor sorption of these materials. To be sure, the nature of this layer would depend on the specific liquid or vapor environment contacting the membrane surface. In particular, the molecular polarity of the environment and its influence on surface tension would be involved. The difference between the liquid water versus saturated water vapor sorption was mentioned in this report. Also, the contact angle experiments of Zawodzinski et al.

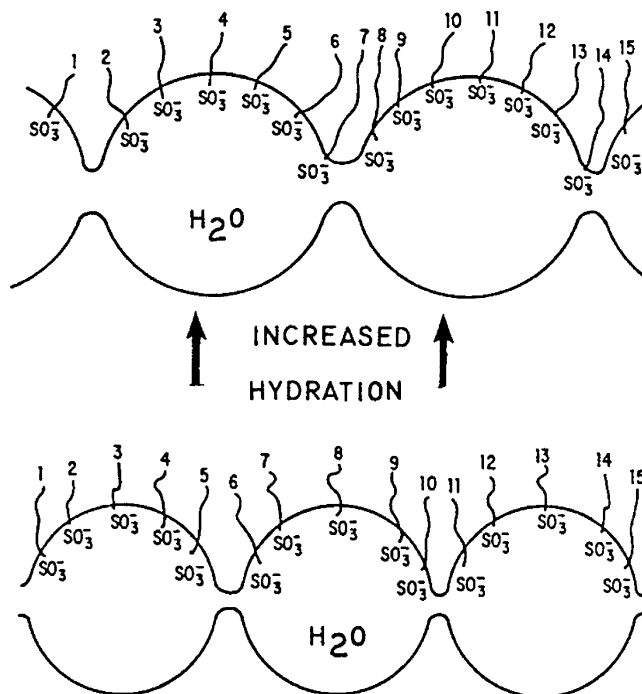


Figure 10. Evolution of a smaller number of larger clusters with increased hydration of Nafion ionomers, according to Gierke, Munn, and Wilson. (Reprinted with permission ref 17. Copyright 1981 Wiley.)

suggest that the surface of Nafion is of very high fluorocarbon composition.⁸⁴ This phenomenon, which has been known for some time, is referred to as “Schroeder’s Paradox”.^{85,86}

McLean et al. offer interesting comments that have implications regarding molecular transport. It was mentioned that polar–nonpolar interfacial tension would restrict the formation of high surface/volume narrow channels and drive the system to larger ionic domain dimensions. In fact, a simple model calculation by Gierke et al. implied that increasing hydration would cause a smaller number of larger clusters, that is, cluster coalescence,¹⁷ and the morphology of the water soaked K^+ form sample seen in Figure 10 supports this idea. Presumably this occurs by individual ion-hopping events or cluster coalescence, or a combination of both. From a thermodynamic perspective, this process might be viewed as a continuous and spontaneous minimization of the overall hydrophilic–hydrophobic interfacial free energy by decreasing the cluster surface/volume ratio. To be sure, the concept of “interface”, in the usual continuum sense, becomes blurred at this fine ultrastructural level and the “roughness” of the hydrated phase has been discussed by a number of authors.

It was also mentioned by McLean et al. that ions and polar solvent molecules must necessarily diffuse across thin amorphous fluorocarbon or interfacial regions between swollen polar domains. However, all of this does not require the need for channels with diameters of 10 \AA that are coated with SO_3^- groups for long-range transport. In any case, a simple consideration of the steric volume of SO_3^- groups in relation to the size of these channels leads to the conclusion that more than one group would have difficulty fitting into this very small volume. Related

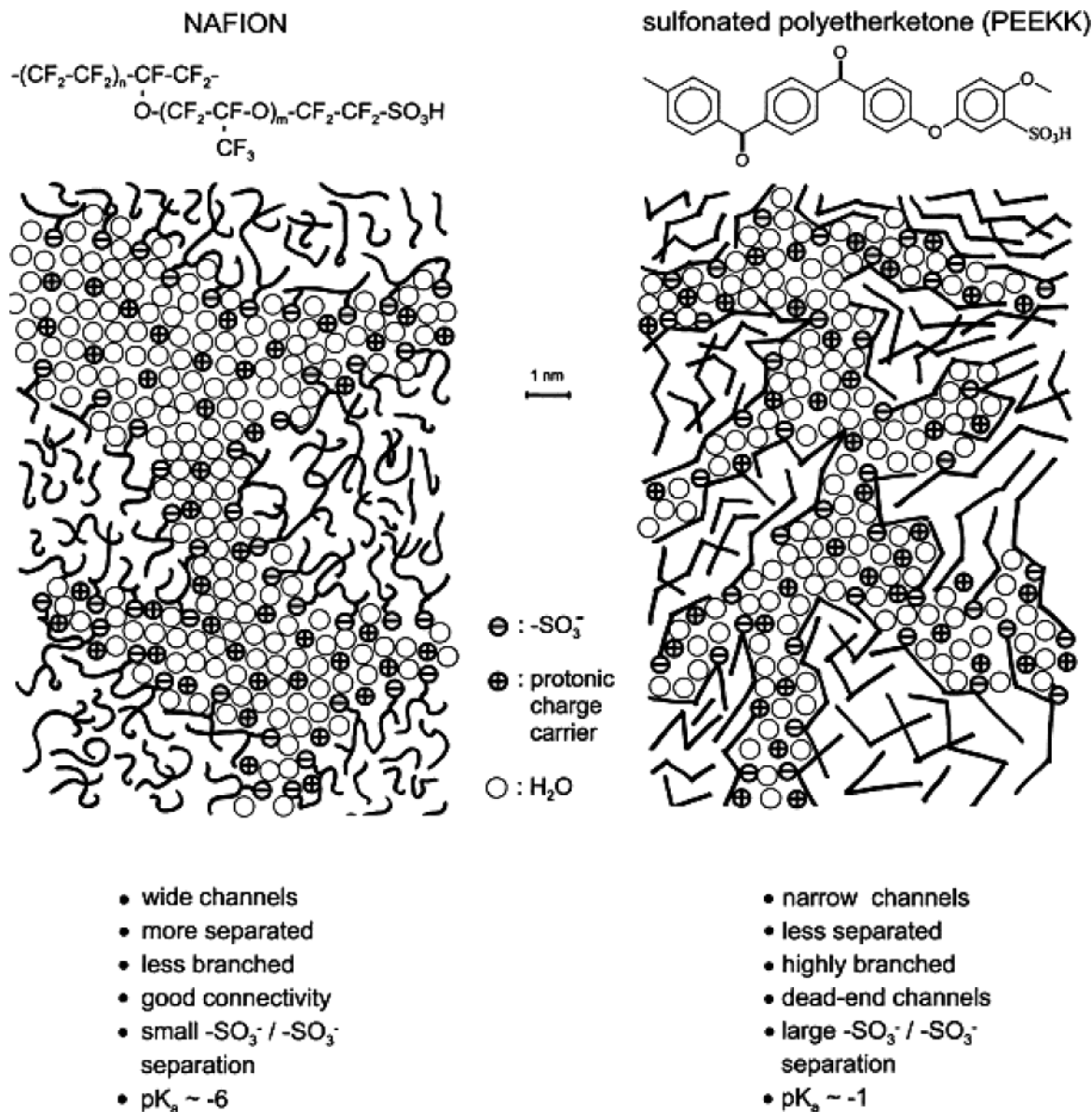


Figure 11. Stylized view of Kreuer of the nanoscopic hydrated structures of Nafion and sulfonated polyetherketone. (Reprinted with permission from ref 91. Copyright 2003 Elsevier.)

to this discussion is the conclusion of Tovbin,⁸⁷ which was based on the X-ray scattering results of Ozerin et al.,⁸⁸ that the channels through the perfluorocarbon regions are around 50% wider than those proposed by Gierke et al.

As mentioned earlier, Orfino and Holdcroft performed SAXS studies of acid form Nafion 117 samples that were in the dry and wet (19% of total swollen weight) states.⁷⁴ One of the conclusions was that, upon hydration, the number of ionic clusters decreases while their size increased, which also supports the concept of the evolution of a smaller number of larger clusters, as advanced by Gierke et al. and later factored into the equilibrium swelling model of Mauritz and Rogers that will be described later.⁸⁹ An important goal of this study was to determine the nature of the ubiquitous “ionic channels”. In a wet membrane, 89% of the ionic sites were calculated as residing in the cores whose average diameter was 4.10 nm. There are 74 SO_3H groups per cluster, and the average length of channels between adjacent

clusters was found to be between 0.30 and 0.88 nm. Owing to these very small channel lengths, it was concluded that the cores can be connected by only a single ionic site so that the concept of a pore has no meaning on this scale.

James et al. also performed AFM tapping mode phase investigations of Nafion 115 membranes while the samples were in an environmental chamber of controlled humidity.⁹⁰ The data from their experiments were presented in a somewhat different fashion from that usually seen in the literature. Rather than mapping the phase angle ψ , $\sin \psi$, which is directly proportional to the energy loss, was mapped. This energy loss is due to either viscoelastic or tip adhesion effects. An increased viscoelastic energy change would involve local material softening due to water incorporation. An adhesion energy change would involve enhanced attraction between the tip probe and inserted water structures. The authors argued that, at the frequency of the cantilever, the viscoelastic effect would be negligible and the adhe-

sive mechanism predominates. Their studies indicated that while the number of clusters decreased, the size of the average cluster increased with increasing humidity, which, again, is reinforced by the conclusions of others as discussed throughout this section. The images showed clusters with sizes in the range 5–30 nm. The sizes at the upper end of this range are considerably greater than those proposed on the basis of SAXS studies, and these large features were attributed to aggregates of clusters of size 3–5 nm. The larger structures were rationalized as cluster agglomerates, as also proposed by Elliott et al. as a result of their SAXS studies.⁶³ These AFM studies also detected features that are the consequence of extrusion of the precursor form.

Kreuer discusses the structure of Nafion as compared to the structure of lower cost, thermally stable, oxidation resistant, sulfonated poly(ether ketone) membranes within the context of fuel cells.⁹¹ While it is not intended to discuss the latter nonperfluorinated materials here, Kreuer's review contains a good summary of the state of knowledge of Nafion up to the time of his writing. The nanoscopic view, depicted in Figure 11, is described as an arrangement of low dimensional polymeric objects (which might be called clusters), the spaces between which are filled with water (channels). This picture is based on the SAXS studies of Gebel.⁷⁶

However, Kreuer states that SAXS information, by itself, cannot resolve the question of whether this model is more appropriate than the inverse micelle model of Gierke et al., that, in a general sense, would possess more morphological order than that reflected in the SAXS scattering profiles.¹⁷ Regardless of issues regarding the interpretation of SAXS data, it is worth noting that the nanoscale morphology seen in Figure 11 is rather similar to that seen in the AFM images of McLean et al.⁸³ The concept of water as being an extended second phase is reasonable considering the low degree of morphological order. In summary, compared with poly(ether ketone), Nafion has wide versus narrow water channels, the hydration pockets are more separated, the percolated hydration structure is less branched with good connectivity, and there are no dead end channels; there is less hydrophobic–hydrophilic interface, and the inter-sulfonate group separation is less. These differences in morphology between the two membranes were explained as being the consequence of having a less hydrophobic backbone, sulfonic acid groups that are less acidic than those attached to a perfluorocarbon structure, and a reduced flexibility of the backbone for the case of sulfonated poly(ether ketone).

4. The Nature of Water, Other Solvents, and Ions in Nafion

In 1972, when the main thrust for these then-new materials was the development of efficient polymer membranes for chlor-alkali cells, the E. I. du Pont Co. reported much information, mostly in the form of product literature, in the form of empirical equations regarding the water mass and volume uptake of sulfonate form Nafion as a function of EW (in the range 1000–1400), some alkali metal counterion

forms, and the molarity (0–14 M) of aqueous electrolyte solutions in which the films were equilibrated.⁹² At that time, it was already understood that the properties of these materials were very sensitive to swelling history so that these equations applied for the “standard pretreatment” of boiling in pure water for 30 min. Information was also presented on water absorption at room temperature versus the temperature of initial equilibration (uptake decreases with increasing initialization temperature), as well as percent swelling in organic solvents, as well as mixed solvents, at room temperature. Compared with the conventional sulfonated cross-linked polystyrene ion exchange membranes, Nafion swells to a greater extent in a number of organic solvents than it does in water. This information was useful in estimating dimensional changes which were reduced by fabric reinforcement in chlor-alkali electrochemical cells. While the general trends described by these equations will hold for current grades of extruded Nafion films, their use in an absolute sense might be questioned and should especially be avoided for solution-cast membranes, especially those of low EW.

Yeo investigated the swelling of Nafion sulfonate membranes in the acid as well as alkali counterion forms, in a number of hydrogen bonding solvents.^{93,94} Percent mass uptake versus solvent solubility parameter (δ) curves appeared to have two maxima and therefore dual cohesive energy densities, each of which was said to correspond to a distinct morphological feature. It was suggested that the peak at low δ corresponds to interactions with the tetrafluoroethylene regions, while the peak at high δ reflects more polar solvent molecules that would prefer to interact with the ionic regions.

Gebel et al. also performed swelling studies of Nafion 117 membranes.⁹⁵ They measured sample expansion along three directions—along and perpendicular to the machine direction, as well as along the thickness direction—after equilibration in the given solvent and also calculated the actual number of solvent molecules per SO_3^- group at swelling equilibrium. It was concluded that the Gutmann donor number of the solvent, which is related to cation solvation energy and has units of $\text{kcal}\cdot\text{mol}^{-1}$, is a parameter that is more important than the solvent solubility parameter. Nor did the data correlate well with solvent dielectric constant or interfacial surface tension. Moreover, a plot of expansion versus solubility parameter was seen to not be in harmony with the dual cohesive energy density concept of Yeo, as the data of Gebel et al. appeared rather scattered. In the view of Gebel et al., at the time of their writing, the solvent was considered to be exclusively contained in the clusters.

Duplessix et al. used water vapor pressure isotherm (i.e., water uptake vs external relative humidity) data combined with simultaneous isotherm differential microcalorimeter analysis to determine the average heat of absorption per water molecule for 1200 EW acid form samples.²⁹ Hysteresis was seen between sorption and subsequent desorption curves at 25 °C, and nonzero water content remained at zero relative humidity, indicating the presence of tightly

bound water. Average heat of water absorption versus water content curves showed that the former remains at a constant value of around $-12 \text{ kcal}\cdot\text{mol}^{-1}$ up to an uptake that corresponds to about 5 H_2O molecules per SO_3H group, where the negative sign of this energy indicates exothermicity. It was a significant fact that this binding energy, which must be associated with water of hydration, is the same for samples dried at room temperature as it is for samples dried at 220°C . At higher water uptakes that cause polymer swelling, this energy continuously decreases to a value that is around $4 \text{ kcal}\cdot\text{mol}^{-1}$, which is approximately the strength of a hydrogen bond in liquid water. The decrease in energy occurs at a lower content for the sample dried at 220°C , which implies a polymer structural rearrangement with change in pretreatment.

Rodmacq et al. (same CENG group) applied the same analyses to the Na^+ - and Fe^{2+} -neutralized forms, the latter of which permits the use of Mossbauer spectroscopy.³⁰ The vapor pressure isotherms at room temperature for both ion forms were seen to be similar. Heat of absorption versus water content plots for the Fe^{2+} salts dried at room temperature indicate that the energy of absorption of the first few water molecules is $13 \text{ kcal}\cdot\text{mol}^{-1}$ (essentially the same as that for the acid form), and this somewhat constant energy then drops at higher water contents. The low water content value is lower at $10 \text{ kcal}\cdot\text{mol}^{-1}$ for the Na^+ form although no reason was offered to account for this difference. It must be said that the results of these Mossbauer studies, as well as the results of other similar studies of Nafion, have more to say about the state of Fe in this environment than about the morphology of the host polymer.

Zawodzinski et al. determined the water uptake of acid form Nafion 117 at 30°C in experiments that equilibrated membrane samples in a sealed relative humidity environment that was controlled by LiCl solutions of known tabulated water activity or equilibrium partial pressure p/p_0 .⁹⁶ Vapor pressure isotherm curves were determined by measuring mass uptake, expressed in terms of number of moles of H_2O per mole of SO_3H groups = λ versus p/p_0 . The plot showed a somewhat small increase in λ with increasing p/p_0 until an uptake of around 6 $\text{H}_2\text{O}/\text{SO}_3\text{H}$ was reached, after which the increase was considerably greater. The results can be interpreted in terms of a condition of tightly bound, SO_3H -associated water in the initial stage and the evolution of more loosely bound water in the latter stage. These results are in essential harmony with those of the similar studies of Duplessix et al. for the acid form.²⁹ Zawodzinski et al. also compared the water uptake of membranes exposed to saturated water vapor with the uptake resulting from contact with liquid water and discovered that the former was less than the latter.⁹⁷ This is the case despite the fact that water activity in both cases is, on the basis of macroscopic thermodynamics, theoretically equal to 1.00. This was discussed in the above section on Microscopy Studies in relation to the paper of McLean et al., in which the existence of a thin fluorine-rich layer was discovered in their AFM investigations.⁸³ In theory, while such a hydrophilic

water barrier would influence the rate of water uptake, the equilibrium water uptake, which was reported by Zawodzinski and others, should not be affected in this way. Clearly, more research is required regarding this phenomenon and its influence on properties.

Later, Hinatsu et al. studied the uptake of water, from the liquid and vapor states at various temperatures, in acid form Nafion 117 and 125, and Aciplex and Flemion membranes, although the latter two similar products will not be discussed here.⁹⁸ These studies were motivated by a concern over the deleterious effects, involving either overly dry or overly wet membranes, on electrical conductivity within the context of polymer electrolyte fuel cells and polymer electrolyte water electrolyzers.

The membranes used in these studies had undergone a rather rigorous cleaning procedure. The liquid uptake studies were performed by simple, careful weight uptake experiments over the range $25\text{--}130^\circ\text{C}$. All water vapor uptake versus relative humidity isotherm studies were conducted at 80°C using a thermostated glass apparatus involving a water vapor reservoir, a quartz spring attached to a sample basket for mass uptake, and a pressure gauge.

The results of the water equilibrium uptake studies that were conducted at room temperature (25°C), for samples that were predried in a vacuum at 25 , 80 , and 105°C for various times, are as follows. Upon immersion in distilled water, the samples that were dried at room temperature attained and maintained the same uptake versus predrying time. On the other hand, the water contents of the samples that were dried at 80 and 105°C underwent a rapid decrease versus drying time, with the greatest decrease for the highest temperature. This behavior was interpreted in a general way as open microstructures caused by the formation of large, hydrated ion clusters upon swelling and "pore" shrinkage and reorientation of the side chains upon drying, the latter of which is reversed upon reexposure to water at elevated temperatures. Perhaps another way of stating this would be to say that the structures have been "annealed". In the usual sense, this involves improved molecular packing, that is, a decrease in free volume that is encouraged by thermal kinetic energy by heating. Thus, the sample dried at 105°C would have been in a state closer to a true equilibrium condition of optimal main and side chain packing and therefore exhibited the least water uptake.

Cleaned membranes that were dried at 80°C were referred to as the "N" (normal) form, and those dried at 105°C , as the "S" (shrunken) form. Membranes prepared by preboiling were referred to as the "E", or expanded, form. These symbols are mentioned here because they were used in other reports to refer to membranes prepared under similar respective conditions.

Liquid water uptake versus temperature curves were established over the temperature range $25\text{--}130^\circ\text{C}$ for Nafion that was vacuum-dried at the above two temperatures (S and N forms) as well as for a sample that was preboiled in water for 2 h (E form). Uptake increased with increasing immersion tem-

perature for both forms over the entire temperature range, with the N form value being greater than that of the S form at a given temperature, but the preboiled sample uptake was constant up to 100 °C. The lower uptakes for the S form can be attributed to a condition of more densely packed main chains and side chains affected during predrying. However, at immersion temperatures higher than 100–110 °C, the uptake for the different forms becomes the same, and this “transition” temperature range was said to correspond to the glass transition of acid form Nafion, as this relaxation was reported and termed in the early paper of Yeo and Eisenberg.⁹⁹ The conclusion is that, after the passage of the membrane through this transition, its thermal history was erased.

The water uptake isotherm curves of Hinatsu et al., at 80 °C, for very well dried membranes, were reflective of initial hydration of sulfonic acid groups for the slow curve rise region at low RH, followed by swelling during the high rise region. These authors suggested that the difference in uptake for the liquid versus vapor phase is more complex, involving an additional, condensation process on the interior pore walls (a “pore”, presumably was intended to be a cluster) in the latter, whereas sorption from the liquid phase is “direct”. On the other hand, it might be argued that hydrogen bonds must be broken in the liquid phase before sorption occurs whereas isolated water molecules can be sorbed from the vapor phase without this requirement. In any case, the cause of the differences between the sorption of saturated water vapor and liquid water (both having a theoretical water activity of 1.00) does not seem to be entirely understood at present.

The authors also mention the interesting result that uptake from water vapor at 80 °C was less than that at lower temperatures, as reported by others, and that this difference was not due to the predrying procedure.¹⁰⁰ It was suggested that water would condense on the membrane surface with more difficulty at the higher temperature and that this would retard sorption. This situation is of obvious significance with regard to humidified membranes in fuel cells. Also, as seen in other studies, the water uptake increases with decreasing EW.

Futerko and Hsing presented a thermodynamic model for water vapor uptake in perfluorosulfonic acid membranes.¹⁰¹ The following expression was used for the membrane–internal water activity, a_1 , which was borrowed from the standard Flory–Huggins theory of concentrated polymer solutions:¹⁰²

$$a_1 = (1 - \phi_2) \exp[(1 - 1/r)\phi_2 + \chi\phi_2^2]$$

ϕ_2 is the polymer volume fraction, χ is the polymer–solvent (water) interaction parameter, and r is the polymer equivalent unit/mole of water volume ratio that is calculated on the basis of the densities of dry polymer and water as well as the EW and molecular weight of water. $\phi_2 = r/(r + \lambda)$, where λ is the number of water molecules per sulfonic acid group.

A number of concerns can be raised over the use of this simplistic equation that was derived for

concentrated polymer solutions which, at best, can be applied to amorphous polymers with randomly distributed solvent molecules rather than systems having two phases of very different chemical compositions—in this case, a sharp contrast between strongly hydrophobic and strongly hydrophilic regions. Moreover, the strong interactions among water molecules, ion exchange groups, ether groups in the side chains, and the hydrophobic backbone in a phase separated system cannot be represented by the single quantity χ that, additionally, was originally intended to account for weak interactions.

The Flory–Huggins equation was modified to account for “proton-transfer complexes” of the sort $\text{SO}_3^- \cdots \text{H}_3\text{O}^+$. In short, a fraction of the water content was viewed as being strongly bound in these complexes, and this reduces the effective water concentration in the membrane. One might view the water molecules bound to these complexes as not being osmotically active, as would be “free” or mobile water. This reasonable concept was based on the IR studies of Zecchina et al.^{103,104} If the fraction of SO_3H groups that exist in these complexes is λ_c , then ϕ_2 increases to the effective value of $(r + \lambda_c)/(r + \lambda)$. Then, the constant for the equilibrium $\text{SO}_3\text{H} + \text{H}_2\text{O} \leftrightarrow \text{SO}_3^- \cdots \text{H}_3\text{O}^+$ was given by $K = \lambda_c / [(1 - \lambda_c)a_1]$.

The simultaneous solution of the equations for a_1 , ϕ_2 , and K will yield an a_1 versus λ curve if all the underlying parameters were known. To this end, Futerko and Hsing fitted the numerical solutions of these simultaneous equations to the experimental points on the above-discussed water vapor uptake isotherms of Hinatsu et al.⁹⁸ This determined the best fit values of χ and K . χ was first assumed to be constant, and in improved calculations, χ was assumed to have a linear dependence on ϕ_2 , which slightly improved the results in terms of estimated data fitting errors. The authors also describe methods for deriving the temperature dependences of χ and K using the experimental data of other workers.

The authors discuss Schroeder’s paradox, referred to elsewhere in this review, and the fact that liquid water uptake increases but saturated water uptake decreases with temperature. And, at low temperature, the water uptake by membranes in contact with saturated vapor is greater than that by membranes in contact with liquid water, which suggests a fundamental difference in membrane microstructure for the two situations. An energy level diagram of thermodynamic states versus temperature was proposed, based on this Flory–Huggins-based model.

By their nature, and in contrast with microscopic and scattering techniques that are used to elucidate long-ranged structure, spectroscopic methods interrogate short-range structure such as interactions between fixed ions in side chains and counterions, main chain conformations and conformational dynamics, and the fundamental hopping events of water molecules. The most common methods involve infrared (mid-IR and to a much lesser extent near- and far-IR) and solid-state NMR spectroscopies, although other approaches, such as molecular probes, have been utilized.

The long-ranged transport of ions, hydrated protons, water, and other solvent molecules through Nafion depends on the morphology on the dimensional scale interrogated by SAXS, SANS, TEM, and AFM methods. This is the scale at which critical issues involving the size of, shape of, and spacing between the ionic domains are important. To formulate a realistic transport model, detailed knowledge of the long-range spatial organization of these domains, the manner in which regions of concentrated hydration structures are incorporated in these domains, and the contiguous interdomain water structure is essential. These aspects must be understood in order to account for the obstacles to migration and how these obstacles form a percolation topology that is expressed in measured ionic conductivities, diffusion coefficients, and other transport parameters. While these *geometrical* considerations are important, it is also important to understand the nature of fundamental interactions experienced by these migrating species with functional groups on the polymer. In particular, different ion exchange groups will cause different degrees of swelling as well as different Coulombic and hydrogen bonding interactions with counterions and solvents. These interactions, that are operative on the scale of less than ~ 10 Å, are appropriately studied by spectroscopic means.

In an early study, Mauritz et al. investigated anion–cation interactions within Nafion sulfonate membranes versus degree of hydration using FTIR/ATR and solid state NMR (SSNMR) spectroscopies. An understanding of the dynamic ionic–hydrate molecular structures within and between the sulfonate clusters is essential for a fundamental understanding of the action of these membranes in ion transport. This information can be directly related to the equilibrium water swelling that, in turn, influences molecular migration.

This FTIR spectroscopic study was aimed at monitoring the effects of monovalent alkali counterion type (Li^+ , Na^+ , K^+ , Rb^+) and degree of hydration upon the vibrational state of the fixed sulfonate groups in 1100 EW membranes in which the cation/sulfonate ratio was 1:1.¹⁰⁵ The location and width of the peak for the $-\text{SO}_3^-$ symmetric stretching vibration are sensitive to these variables due to an induced polarization of S–O dipoles in the sulfonate group by the electrostatic field of the adjacent cation. This peak wavenumber, ν_s , is relatively independent of water content and cation type at high degrees of hydration but shifts to higher values and broadens as the water content decreases. These changes were interpreted in terms of increased sulfonate–cation Coulombic interactions as water is removed. The relative population of solvent-separated ions decreases as the fraction of contact ion pairs increases. The shift is largest for Li^+ , which has the greatest hydration number and highest surface charge density. Smaller shifts are observed for the Na^+ and K^+ forms, and none are observed for Rb^+ , which hydrates poorly, if at all, and has a low surface charge density.

Caution should be applied in interpreting ATR spectra because this is a surface technique that only interrogates structure within a distance of a few

microns beneath the surface. Moreover, thin, transparent solution-cast films may not have the same morphology as those of extruded sheets.

SSNMR studies based on ^7Li , ^{23}Na , and ^{133}Cs nuclei for 1100 EW samples whose sulfonate groups were exchanged with these cations (no excess counterions or co-ions being present) were conducted versus water content.^{106,107} The spectra reflect the influence of the immediate chemical environment about these cations that have spins greater than $1/2$ and, therefore, possess quadrupole moments. It is the interaction of these quadrupole moments with local electric field gradients that influences the chemical shift (δ) and line width of the observed resonance. In this case, the electric field is mainly due to $-\text{SO}_3^-$ anions as shielded by water molecules.

For ^{23}Na a plot of δ versus $\text{H}_2\text{O}/\text{Na}^+$ mole ratio = r is essentially flat at high water contents until r is lowered to where there are less than ~ 6 H_2O molecules per $\text{SO}_3^- \text{Na}^+$ ion pair. At higher water contents, most $-\text{SO}_3^- \text{Na}^+$ pairs are separated by liquidlike water molecules, but since the hydration number of Na^+ is 4, a considerable population of cations must exist in contact ion pairs for $r < 6$. In fact, δ greatly increases when r decreases from 6, providing evidence for contact ion pairs. On the average, there are not enough water molecules present to form complete hydration shells that would provide electrostatic shielding around the Na^+ ions. Contact ion pairing was discussed many years ago to rationalize the decrease in ionic mobility in simple electrolytes with increasing concentration.¹⁰⁸ The FTIR and SSNMR spectroscopic results presented here also are in harmony with a four-state model of ionic–hydrate association–dissociation equilibrium between bound and unbound cations in simple electrolyte solutions, as proposed by Eigen et al.^{109,110} The broadening of the symmetric SO_3^- FTIR peak upon membrane drying is considered as evidence of a multistage association–dissociation equilibrium subject to restrictions imposed by the polymer host. A molecular based model for ion conductivity in Nafion would have to incorporate this mechanism.

The chemical shift and line width observed for each water content were taken as weighted averages of the values in the free and bound states, and from two equations expressing these averages, P_b and P_f , the mole fractions of bound and free Na^+ ions, respectively, were extracted. P_b significantly increases as the approximate hydration number that might be expected for a $\text{SO}_3^- \text{Na}^+$ pair is approached from the direction of considerable hydration.

The ^{23}Na NMR parameters of Nafion are not greatly affected by changing EW in the range of water content where valid comparisons are possible,¹¹¹ and this reflects the short-ranged nature of these dynamic ionic–hydrate structures.

The behaviors of the ^7Li and ^{133}Cs resonances for membranes incorporating these counterions are qualitatively similar to that for the samples incorporating the ^{23}Na probe. δ for the Cs^+ form undergoes a significant shift at the lowest water content, which is reasonable considering the low hydration capacity of this large cation.

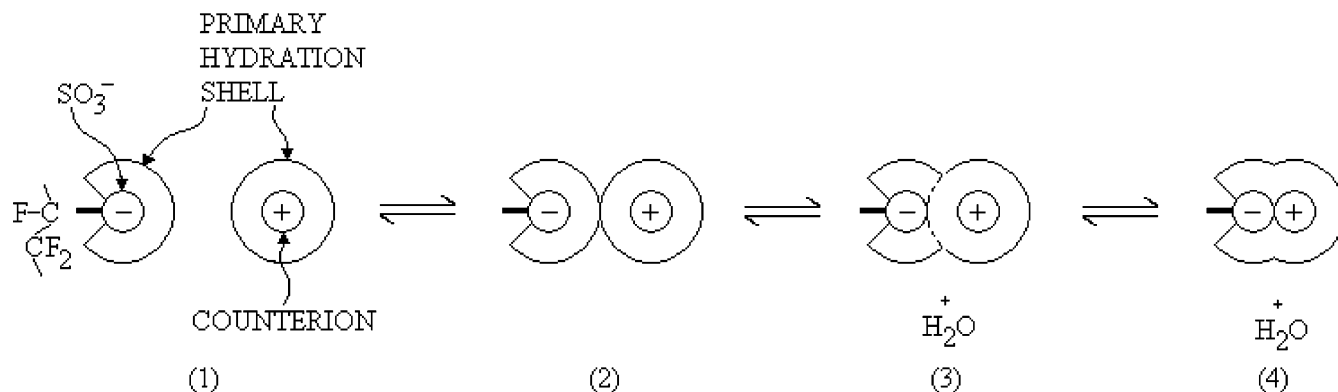


Figure 12. Four state model of the hydration-mediated counterion–side chain association–dissociation equilibrium, of Mauritz. (Reprinted with permission from ref 107. Copyright 1982 American Chemical Society.)

The interpretation of these SSNMR results is in agreement with that issuing from the FTIR studies of the same systems, as discussed earlier.

Mauritz et al., motivated by these experimental results, developed a statistical mechanical, water content and cation-dependent model for the counterion dissociation equilibrium as pictured in Figure 12. This model was then utilized in a molecular based theory of thermodynamic water activity, a_w , for the hydrated clusters, which were treated as micro-solutions. a_w determines osmotic pressure, which, in turn, controls membrane swelling subject to the counteractive forces posed by the deformed polymer chains. The reader is directed to the original paper for the concepts and theoretical ingredients.¹⁰⁷

Another noteworthy early IR spectroscopic study of Nafion (125 and 152) membranes, in the acid as well as various counterion forms, was that of Heitner-Wirguin, who assigned a number of characteristic bands and compared the spectra to those of sulfonated polyethylene (Redcat) membranes.¹¹²

Falk et al. conducted early FTIR studies of the structure of water in this ionomer, and the papers of these investigators serve as an excellent resource for the various band assignments, as tabulated in the book edited by Eisenberg and Yeager.¹⁹ The results of these studies were significant on a quantitative basis, in part, due to their careful control of water content by a vapor equilibrium technique that allowed for reproducibility as well as precise determination of the $\text{H}_2\text{O}/\text{SO}_3^-$ ratio.¹¹³

Falk inspected the fundamental bands of the HDO isotope of water in Na^+ form Nafion (125 and 142) sulfonate membranes. The bands of HDO are simpler and lend themselves to less ambiguous interpretation than the bands of H_2O or D_2O , as either the D–O or H–O stretching band can be studied in isolation for low and high D/H ratios, respectively. At low water contents (1.6 $\text{H}_2\text{O}/\text{SO}_3^-$ mol/mol), both the O–H and O–D stretching bands occur as doublets (3660, 3520 cm^{-1} and 2695, 2588 cm^{-1} , respectively), and at higher frequencies than those of HDO in liquid water. The conclusion was that O–H groups in water molecules exist in two different molecular environments at low water contents. In particular, the low frequency component was associated with hydrogen bonded O–H groups, while that at high frequency reflected non-hydrogen bonded O–H groups, perhaps

belonging to H_2O molecules at the hydrophobic–hydrophilic interface.

Falk, based on his FTIR studies of H_2O -, D_2O -, and HDO-containing Nafion, also rationalized that hydrated clusters either were much smaller than those proposed by Gierke et al.¹⁷ or possessed a shape that deviated greatly from sphericity such that fluorocarbon structural fragments intrude into cluster regions. In retrospect, this early view is more commensurate with recent visualizations based on subsequent experimental structural evidence, especially the structures displayed in pictures by Kreuer.⁹¹ Despite the considerable hydration capacity of Nafion, hydrogen bonding between water molecules in maximally hydrated samples is considerably less extensive than that in liquid water. This situation might be rationalized in terms of a high surface-to-volume ratio (S/V) for clusters of this size as well as the fact that when H_2O molecules are confined in such small spaces, a large relative population must reside at hydrophobic–hydrophilic interfaces, especially if the interfaces are irregular.

The idea of convoluted or rough interfaces is in contrast with the view of Rollet et al., who concluded that the ionic domains are spherical (In fact, this was an assumption in a local-order model.) and that interfaces between hydrophobic and hydrophilic phases are sharp, although this situation changes when the temperature is greater than 60 °C.¹¹⁴ This conclusion is based on the results of SANS investigations of Nafion 117 membranes as a function of temperature, nature and charge of the counterion, concentration of electrolyte solutions in which the membranes were equilibrated, and membrane pretreatment.¹¹⁴ These particular conclusions were based on an analysis of scattering data in the Porod region where the intensity scales as q^{-4} . These authors offer the general conclusion that the nanostructure of Nafion is governed by interfacial phenomena.

Spectra at higher water contents indicated an increasing relative population of water molecules in O–H \cdots O hydrogen bonds, and the shift of the low wavenumber O–H stretching component to lower frequencies reflected increasing strength of the hydrogen bonds. The fact that the peak wavenumber of the high frequency component was constant is harmonious with the notion that these groups have O–H \cdots - $-\text{CF}_2$ juxtapositions. At least qualitatively, the

ratio of the integrated absorbances under the O—H—CF₂ and O—H···O peaks should yield information on the geometry of the aqueous domains in terms of surface-to-volume. For a water uptake corresponding to 2 H₂O molecules per SO₃⁻ group, 24% of OH groups do not participate in hydrogen bonds. For high water contents, however, the peaks were not able to be resolved.

Kujawski et al. used FTIR/ATR spectroscopy to study side chain interactions with the alkali counterion series in Nafion 117 membranes that were equilibrated in water, ethanol, and 2-propanol.¹¹⁵ These results were compared against the spectra of a membrane consisting of an interpenetrating network of polyethylene and sulfonated poly(styrene-*co*-divinylbenzene) (PESS). The behavior of the symmetric stretching band of the sulfonate group of Nafion showed that, for dry membranes, the smaller the counterion radius, the stronger is the ion pair interaction, as earlier noted by Lowry and Mauritz¹⁰⁵ and Falk et al.¹¹⁶ In the Li⁺ form equilibrated in pure 2-propanol, ν_s was affected in a fashion similar to that caused by pure water. On the other hand, this band was unaffected by the alcohol in the PESS membrane, meaning that the SO₃⁻Li⁺ ion pairs were not dissociated in this hydrocarbon system. The implication is that Li⁺ cations were solvated by 2-propanol molecules in Nafion but not in PESS and the strong alcohol affinity of the perfluorinated ionomer was due to the greater acid strength of the SO₃H groups. For water-isopropanol mixtures, ν_s was noted to be constant over the composition range. This was interpreted to mean that the strengths of hydrogen bonding of the alcohol and water molecules with the sulfonate group are practically identical. However, the membrane internal composition of the binary solution may not be the same as that of the external solution in which the membrane was equilibrated, and partition coefficients were not determined.

Cable et al. similarly studied the influence of hydrophobic as well as hydrophilic counterions on characteristic vibrations of the sulfonate and the two perfluoroether groups in the side chains of Nafion 117 membranes using FTIR/ATR spectroscopy.¹¹⁷ The symmetric SO₃⁻ stretching band for dry Na⁺ form membranes shifted to higher wavenumbers with increase in degree of neutralization by this cation but, in contrast, shifted to lower wavenumbers with increasing neutralization with tetrabutylammonium cations (TBA⁺). The latter behavior was attributed to diminished polarization of the SO₃⁻ groups by the hydrophobic TBA⁺ cations that have a low surface charge density as opposed to the influence of the stronger electrostatic fields posed by the smaller Na⁺ counterions that have a larger surface charge density.

Cable et al. also noted two distinct bands in the region 1000–950 cm⁻¹, in which resides the absorption envelope for the symmetric C—O—C stretching vibration. This spectral feature was earlier observed by Heitner-Wirguin¹¹² as well as Lowry and Mauritz.¹⁰⁵ Heitner-Wirguin noted a small shift in this band when the Na⁺ counterion is replaced by transition metal counterions. The spectra of Lowry and Mauritz for dry Li⁺, Na⁺, K⁺, and Rb⁺ forms

show the low wavenumber component as a shoulder at ~970 cm⁻¹ on the dominant peak at ~980 cm⁻¹. The ~970 cm⁻¹ peak becomes more prominent and better resolved with hydration, particularly for the Li⁺ and Na⁺ forms, and the evolution of this low wavenumber component with increasing degree of hydration is especially evident for the Li⁺ form. These facts were taken to suggest that parts of the perfluoroether side chains penetrate the ionic clusters rather than forming a neat inverted micelle as depicted in the Gierke model. A closer inspection of the spectra in this region shows a fainter shoulder on this absorption envelope at 995 cm⁻¹, which was verified by Falk and later seen by Cable et al., although the origin of this peak has not been addressed.¹¹⁸

Cable et al. observed that the low wavenumber component (965 cm⁻¹) increased in wavenumber with increase in degree of Na⁺-neutralization of dry samples and that this shift correlates with the increasing peak wavenumber shift of the symmetric stretching vibration in SO₃⁻ groups. On the other hand, the high wavenumber component (980 cm⁻¹) does not shift with either counterion type or hydration. The general view is that a portion of the ether groups in the side chains are strongly influenced by the state of ion pair association while the ether groups near the backbone are shielded from these interactions. In addition to consideration of through-space Coulombic field perturbations on the C—O—C vibration, through-bond inductive effects, that is, vibrational coupling within the span of a few bonds from a polarized SO₃⁻ group, should also be considered as a mechanism. These conclusions are supported by the fact that the FTIR spectrum of a corresponding sulfonyl fluoride Nafion precursor film, that did not have cluster morphology, exhibited only a single ether band at ~980 cm⁻¹.

The frequency of the symmetric stretch does not vary with degree of neutralization for hydrated membranes, which was attributed to the shielding of sulfonate anions from the electrostatic field of the Na⁺ ions.

Risen et al. investigated cation–anion interactions using far IR spectroscopy (50–300 cm⁻¹) to study Nafion sulfonate membranes that were neutralized by cations in the series Na⁺, K⁺, Rb⁺, and Cs⁺ and the series Mg²⁺, Ca²⁺, Sr²⁺, and Ba²⁺, as well as the acid form.¹¹⁹ The spectra in this region for hydrated samples show a broad but well-defined band below 300 cm⁻¹ that is not present for the acid form. For both the monovalent alkali and divalent alkaline earth series, the band monotonically shifts to lower frequencies, f , such that $f \propto M^{-1/2}$, where M is the cation mass, and the slope of the line is greater for the divalent series. These facts identify this band with harmonic oscillations of the cations in the force field of the fixed SO₃⁻ anions. Moreover, the force constant is essentially the same for each ion in the monovalent series and, likewise, the force constant is essentially the same for each ion in the divalent series. Based on the slopes of these lines and harmonic oscillator theory, the force constants for the members of the monovalent cation series are less than those of the divalent cation series. This fact

reflects stronger cation–anion Coulombic interactions owing to the greater charge of the divalent ions.

Interestingly, this “ion motion band” is not influenced by water as seen in dehydration studies. While sample preparation details were given in this report, the exact water contents of these samples were not stated; rather, samples were referred to as “dry”, “partially dry”, or “hydrated”. While far IR spectroscopy has not been exploited in the study of Nafion, it is clear that information regarding cation–anion binding and vibrational frequencies would be of great importance in understanding and modeling ion-hopping kinetics, using activated rate theory.

Another study involving cation–sulfonate interactions in Nafion (1200 EW) is that of Yeager, who investigated the property of equilibrium ion exchange selectivity at 25 °C.¹²⁰ The results of this study are relevant with regard to the use of this ionomer as a chromatographic medium or as a membrane through which more than one cation is simultaneously transported. The degree of H⁺ exchange in the acid form was determined for mono- and divalent cations and expressed in terms of ion exchange selectivity coefficients, $K_{H^+M^+}$, and $K_{H^+M^{2+}}$, respectively, that involve the equivalent ionic fraction of the given ion, M⁺, in the ionomer, the external solution molarity, and the cation activity coefficient. One result is that, for the alkali metal series Li⁺, Na⁺, K⁺, Rb⁺, Cs⁺, as well as Ag⁺, and Tl⁺, there is a larger spread in $K_{H^+M^+}$ values than that seen for conventional cross-linked sulfonated polystyrene ion exchange resins. The spread for the alkaline earth series is smaller than that for the alkali metals. In both cases, selectivity decreased with increasing membrane hydration. Also, it was seen that exchange of alkali metal cations from anhydrous methanol solutions was very similar to that for the aqueous solutions.

Yeager suggests that the major factor involved in the ion exchange selectivity of Nafion is the positive entropy change associated with the replacement of H⁺ with the metal ion, which is accompanied by water release and polymer contraction.

Barnes studied the nature of water in Nafion 117 membranes in various alkali metal cation forms using near-IR (NIR) spectroscopy.¹²¹ Advantages of the use of this spectral range (in this case, over the wavelengths 1100–2500 nm) are that there are no obscuring CF₂ overtone bands and that band shifts due to hydrogen bonding are greater than the characteristic bands that are seen in the mid-IR range. The NIR water bands of interest are the combination bands 1890 nm (type I: non-hydrogen bonded water) and 1920 nm (type II: hydrogen bonded water with bond angles around 110°), as discussed by Luck.¹²²

Both type I and type II water forms were detected, and the I/II mole ratio was rather constant at 1:2.2 for the Na⁺ form having the low H₂O/SO₃[−] mole ratios of 0.06, 0.5, and 1.2. These numbers were derived from the areas under the two deconvoluted peaks. The ratio of type I to II water molecules decreases in the order for the series Na⁺ > K⁺ > Rb⁺ > Cs⁺, which is reasonable considering that the cation hydration number decreases in this order and shows the structure-breaking action of cations with

high surface charge density. The somewhat linear plot of type I water versus square of the cation radius was taken to suggest that water molecules are not only distributed around cation–anion associations, but a fraction resides close to the perfluorinated backbone, as earlier suggested by Falk et al.¹²³ and Yeager et al.¹²⁴ In fact, The NIR spectrum of PTFE homopolymer showed that type I water is the only form found in this matrix.

The molecular mobility of water in Nafion was investigated using NMR spectroscopy, by Starkweather and Chang,¹²⁵ Boyle et al.,¹²⁶ and Bunce et al.¹²⁷ The overall conclusion of these studies was that water possessed less mobility than that of liquid water and that there were cooperative motions among the molecules and strong interactions with the ion exchange groups.

Sivashinsky and Tanny, in an early paper, used ¹H NMR to study water in Nafion 125 that had been boiled and then converted to the Na⁺ form by soaking in aqueous NaCl.¹²⁸ The water content was such that H₂O/SO₃[−] was 16:1 (mol/mol), which corresponds to a condition where there are a considerable number of water molecules in excess of those that would be tightly bound in hydration shells around the ions. It is unclear in this document as to whether excess electrolyte was leached from these samples, but it is a reasonable assumption. The theoretical model of Bloembergen, Purcell, and Pound for the temperature dependence of relaxation processes for water adsorbed on a surface was seen to fit their data.¹²⁹ From the minimum in a T_1 (spin–lattice relaxation time) versus reciprocal temperature plot at ~250 K, a correlation time ($\tau_c = 1.7 \times 10^{-9}$ s) was extracted that was 2 orders of magnitude larger than that for supercooled water, but 4 orders of magnitude shorter than that for ice at the same temperature.¹³⁰ This was taken to imply that the structure of water that is mobile at ~250 K is more akin to that of a supercooled liquid or what might be thought of as a glass. Also, free induction decay studies versus temperature did not reflect freezing in the sense of a first-order phase transition. A conclusion based on the T_1/T_2 value at the T_1 minimum was that water molecules existed in a number of environmental states. Coupled with heat of fusion data obtained from DSC experiments, it was concluded that the presence of small “pores” and interaction between the water and the matrix were the most important structure-determining factors.

Boyle et al. also performed ¹⁹F NMR investigations of the fluorocarbon backbone in 1100 and 1500 EW acid form samples in the hydrated state in the temperature range −120 to 160 °C.¹³¹ No effort was made in sample preparation to remove impurities from these samples, which can be problematic. The interpretations of the results for 1100 EW are as follows. T_2 data for a low degree of hydration (7%) showed that the backbone motions are considerably slower than those in the SO₂F precursor form in the high temperature region, which was said to reflect constraints posed by ion clustering, as there are no clusters in the precursor form. For a water content of 25%, there is greater motion in the temperature

range in which these motions are activated, and this was ascribed to a plasticizing effect of the water, presumably in terms of weakening electrostatic interactions in the clusters. The T_2 behavior for the 1500 EW samples up to +120 °C shows greater mobility than that for the 1100 EW sample that had comparable water content. In essence, the explanation for this was that there are fewer clusters in the 1500 EW sample that would constrain matrix motion.

Pineri et al. correlated the results of DSC, NMR, ESR, water sorption isotherms, and dynamic mechanical analyses of hydrated acid form Nafion 120 membranes that had undergone temperature cycling.¹³² They concluded that water sorption properties have a strong dependence on temperature. Desorption occurs during cooling from room temperature for contents greater than around 8 wt %, and this is followed by freezing. Also, the water vapor pressure decreases during this cooling to establish a new thermodynamic equilibrium. Desorption was seen to take place above what was then termed the “glass transition of the ionic phase” (~220 K) during the heating of a liquid nitrogen cooled sample that had 15 wt % water. Earlier, Starkweather and Chang similarly referred to a “glass transition of the aqueous domains” based on dynamic mechanical and dielectric relaxation experiments, as well as proton NMR spectroscopy.¹²⁵ After this desorption event (from the “ionic phase”), the water was said to freeze, as evidenced by a DSC exothermic peak, and this also results in an increase in elastic modulus. An endothermic peak was said to correspond to a frozen-to-mobile transformation in the hydration microstructure, and the fractions of desorbable and non-desorbable water were calculated as a function of water content. Pineri et al. were in disagreement with the conclusions of Sivashinsky and Tanny¹²⁸ in that the former believed that their DSC peaks reflected a first-order transition having to do with the sorption or desorption of water into or out of the ionic phase but disregarded the idea of a pore-size effect. Characteristic water desorption times and changes in the number of mobile protons were determined at different temperatures using proton NMR spectroscopy. It should be cautioned that these results have significance within the context of the particular manner in which these samples were prepared. For example, the membranes were not boiled, as usual, as part of an initialization process.

Yoshida and Miura also studied the nature of water, in terms of freezing and non-freezing fractions, in 1100 EW samples in the Li^+ , Na^+ , K^+ , NH_4^+ , and alkylammonium counterion forms, using DSC.¹³³ The degree of neutralization of the sulfonic acid groups for all the cations was around 90%, and the measurements were performed on samples of various water contents over the temperature range 100–50 K. For example, cooling curves starting at 310 K (37 °C), at the rate of 10 K/min, for the Li^+ form, showed exothermic peaks—first-order transitions—whose magnitudes were enhanced, and the peak temperatures increased with increasing water content. The peak widths decreased in this order of cation type but were not as narrow as that of pure water. These peaks,

beneath the freezing temperature of pure bulk water, were said to be due to water crystallizing in the membrane. Heating curves showed a single endothermic peak at around 270 K (−3 °C) that was attributed to water melting. These peaks shifted to lower temperature, broadened, and became more asymmetric with decreasing water content. It is reasonable that smaller “ice” crystals that would exist at lower water content on this dimensional scale would have lower crystallization and melting temperatures for the usual surface/volume considerations, as discussed in crystallization theory.

These investigators classified the incorporated water molecules into three categories: nonfreezing, freezing bound, and free water. The freezing bound water peak at the lowest temperature was distinct, but the peaks for nonfreezing and free water were difficult to separate and the combined area under them was simply treated as being due to “free water”. The heat of fusion of pure water and the areas under the exothermic peaks were used to calculate relative free versus freezing bound water content, and the total amount of freezing water was estimated from the area under the single melting endotherm peak. In plots of the amounts of the three types of water with increasing total water content, it is seen that a threshold must be exceeded before freezing water can exist.

Nonfreezing water molecules were considered to exist in hydration shells around the given cation. Presumably, mobility restrictions placed on ion-contacting water molecules, posed by the strong electric fields, prevent these water molecules from crystalline packing, as in the so-called “structure-breaking” effect in simple aqueous electrolytes. The amounts of nonfreezing and freezing bound water decreased with decreasing “hydration radius”. While not explicitly defined in this paper, “hydration radius” apparently refers to the radius of the bare cation plus the thickness of a well-defined hydration shell, as this quantity was said to decrease in the order $\text{K}^+ < \text{Na}^+ < \text{Li}^+$ and the hydration numbers decrease in this order.

This is another study that illustrates that the ensemble of water molecules can be partitioned into different classes. The state of a water molecule depends on whether it is directly interacting with a cation—and is a function of cation type—and on the total water content, which, when low, will not provide for enough molecules to form distinct crystallites.

The properties of Nafion at freezing temperatures can be quite relevant, for example, within the context of fuel cells in vehicles with regard to cold-starting, as well as the degradation of membrane/electrode assemblies due to the freezing of in situ water.

Miura and Yoshida also investigated the changes in the microstructure of 1100 EW Nafion sulfonate membranes, in alkali, ammonium, and alkylammonium cation forms, that were induced by swelling in ethanol using DSC, dynamic mechanical analysis (DMA), SAXS, and electron probe microanalysis (EPMA).¹³⁴ These studies were performed within the context of liquid pervaporation membranes that could potentially be used to separate ethanol from water

in azeotropic mixtures. The treatment consisted of drying membranes from a water-swollen state and an ethanol-swollen state. The membranes were swollen for 1 week in these liquids at 296 K, after which they were dried under vacuum at room temperature for 1 week.

The DMA results showed a large difference between the relaxations of the water-treated and EtOH-treated membranes for some of the cation types (and only slight differences for the others). It should be cautioned that the assignment of the $\tan \delta$ peaks in this paper should be reconsidered in the light of the more recent studies of Moore et al.¹³⁵ It was suggested that these viscoelastic changes reflected a condition where ionic clusters undergo rearrangement by swelling in EtOH, and it was deduced, based on their SAXS analysis, that, when Na^+ and ammonium were the counterions, the sizes of the ion clusters in the EtOH-treated-dried membranes (SAXS Bragg spacing of 2.8 nm) were smaller than those in the water-treated-dried membranes (SAXS Bragg spacing of 3.3 nm). EPMA sulfur mappings on the surfaces of a Na^+ form membrane showed dots about 100 nm in size that were attributed to aggregates of clusters, although the images are not of such a quality as to ascertain the structure of these units. A digital image analysis provided information on the number density, size, and shape distribution of these cluster aggregates. The results of this analysis were that the number of cluster aggregates in the EtOH-dried sample was less than that for the water-dried sample and that the dispersion of cluster aggregates was more homogeneous with EtOH treatment. These authors speak of the relaxation of stresses that are frozen in during membrane processing, as caused by the incorporation of EtOH, and this is said to be responsible for the changes in structure and properties.

MacMillan et al. studied the dynamics of water molecules in Nafion 117 using ^1H , ^2H , and ^{19}F NMR spectroscopy.¹³⁶ Special care was taken to remove impurities from samples, including paramagnetic contaminants as well as oligomers and precursor fragments, which often does not occur in sample preparation.^{137,138} A transition in relaxation behavior at a characteristic temperature T_t was observed. T_t is defined as the temperature at which the slopes of the T_1 (spin–lattice), T_2 (spin–spin), and $T_{1\rho}$ (rotating frame spin–lattice) relaxation times versus $1000/T$ curves undergo a sharp change. For a hydration level of 15.9%, T_t is approximately -10 °C. T_t shifts to higher values with decreasing degree of hydration. Sorbed water molecules behave much as in the bulk and are not greatly modified by their polymer environment. The activation energy is small, which reflects high rotational mobility with low hydrogen bond density for $T > T_t$. It is worthy to note that Escoubes and Pineri reported an endothermic peak seen in the microcalorimetric studies of Nafion having 15% water at around -15 °C, which is close to T_t .¹³⁹

^{19}F T_1 and T_2 values indicate that the polymer relaxation is unaffected by the presence or absence of water. These results differ from the NMR results

of Boyle et al., which indicated increased mobility with hydration.¹³¹

It was suggested that there is a range of temperatures over which SO_3H groups go from being fully dissociated to being fully associated upon cooling, and this temperature range depends on the properties of the water at a given degree of hydration.

For T below this range, a large population of protons appears to be in a solidlike environment and contribute to the T_2 and $T_{1\rho}$ relaxation.¹⁴⁰ The motional correlation time, τ_c , was assumed to have an Arrhenius dependence on T . On T_2 and $T_{1\rho}$ versus $1000/T$ plots, a change in slope was associated with the onset of acid group reassociation. The activation energies for molecular reorientation were rather large, to the extent that up to four hydrogen bonds must be broken to affect this motion. This suggested a highly ordered supercooled fluid of hydrogen bonded water, although the molecular mobility of water in this system is much greater than that in ice. The belief was expressed that water forms complex cage-like structures, or clathrates, of a number of molecules. τ_c at 253 K monotonically decreased from 6.6×10^{-7} to 6.5×10^{-12} s as the average number of H_2O molecules per SO_3H group increased from 1.1 to 11.6, which would indicate greater rotational mobility. It was concluded that supercooling occurs at much lower temperatures than those for water that resides in regular shaped pores,¹⁴¹ and this was attributed to irregularly shaped clusters within Nafion, a concept that was perhaps earliest expressed by Falk.^{113,118} This picture is somewhat different from that of Yoshida and Miura, who spoke of water crystallizing in the usual sense. It must be remembered that their results were for cation exchanged, rather than acid form, samples, and protons from the acid groups can be directly incorporated into the water molecule structure, whereas cations interact with water molecules by forming hydration shells.¹³³ MacMillan et al. considered that the high surface/volume aspect of water clusters inhibits the formation of ice. A simple model that relates correlation time to pore radius showed that the cluster surface varies as $r^{2.5}$ rather than r^2 , which means that the surface/volume is greater than that on the basis of a solid sphere, hence, the term “fuzzy sphere”.

It will be recalled that Sivashinsky and Tanny also favored the idea of supercooled water whose structure is influenced by being in pores as opposed to the idea of freezing water.¹²⁸ While the NMR experiments of Sivashinsky and Tanny were performed on the Na^+ form, τ_c at ~ 250 K was 1.7×10^{-9} s, which is in the midrange of those obtained by MacMillan et al. for different water contents. It is difficult to imagine water as forming ice in the usual bulk sense in these confined spaces having high surface/volume.

Cation–sulfonate interactions, as well as proton mobility, are also expressed in the electrical conductance behavior of these membranes. Many studies of this property have been reported, and there is no attempt in this review to cite and describe them all. Rather, a few notable examples are chosen. Most testing is done using alternating current of low voltage to avoid complications in the form of chemical

changes at membrane–electrode interfaces that might occur with direct current.

Cahan and Wainright showed that there is an inherent problem with two electrode cells in that membrane/blocking electrode interfacial impedance interferes with the measurement of the bulk impedance at low frequencies and that use of the four electrode system eliminates this problem.¹⁴² In the absence of this interfacial effect, conductivity is independent of frequency from the dc range up to at least 10^5 Hz. These conclusions were reinforced by the impedance studies of Fontanella et al. in which the electrodes were of both large and small area in a two-electrode configuration.¹⁴³ Thus, the four electrode configuration is generally preferred, although the measured values reflect conductivity along the plane of the membrane rather than along the more relevant thickness direction. There is also the issue of conductivity anisotropy in the plane of the membrane that is generated by melt extrusion of films. A study by Gardner et al. demonstrated that this is in fact the case.¹⁴⁴ There is also the question as to whether the in-plane conductivity is the same as that along the perpendicular direction.

Environmental control that fixes a known concentration of solvent in the membrane under test is also important. The reader is encouraged to consult the review, and references therein, of conductivity measurement techniques by Doyle and Rajendran.¹²

Gavach et al. studied the high frequency electrical resistance of Nafion 117 membranes in various monovalent counterion forms using an ac impedance analyzer. For low water contents, the resistance was seen to increase to very high values as the water content decreased, which can be attributed at least in part to ion pair formation as oppositely charged ions become increasingly less separated by water molecules. The alkaline cation series follows a trend opposite to that for the ion mobilities in pure water.¹⁴⁵ Later Gavach et al. performed this analysis for various counterion forms as a function of water content.¹⁴⁶ Curves for specific conductivity versus number of moles of water molecules per SO_3^- group exhibited an overall organized trend of upward displacement in the following order for the cation forms: $\text{Al}^{3+} < \text{Mg}^{2+} < \text{Mn}^{2+} < \text{Ca}^{2+} < \text{K}^+ < \text{Na}^+ < \text{Li}^+ < \text{H}^+$. There is a clear correlation with cation valence.

For a given cation at relatively high degree of hydration, there is a simple monotonic line, in some cases with slight curvature, on the Z' versus Z'' diagram, and this corresponds to a pure resistance, not strongly linked to morphology, in a situation where ions can readily hop between clusters in this swollen state. But, when the degree of hydration is lowered, there is, in addition, a semicircle that develops, and this is suggested to be due to a capacitive effect owing to an accumulation of ions on each side of intercluster channels that have been significantly narrowed. While not stated in this article, the semicircle can be considered to reflect a form of fluctuating interfacial polarization with a characteristic relaxation time during which cooperative charge motions accumulate and dissipate during

half of the period of electric field oscillation. The effects of percolation and ion pairing are significant at lower hydration levels.

Using a simple electrostatic interaction-based model factored into reaction rate theory, the energy barrier for ion hopping was related to the cation hydration radius. The conductance versus water content behavior was suggested to involve (1) a change in the rate constant for the elementary ion transfer event and (2) a change in the membrane microstructure that affects conduction pathways.

Earlier, Gavach et al. studied the “superselectivity” of Nafion 125 sulfonate membranes in contact with aqueous NaCl solutions using the methods of zero-current membrane potential, electrolyte desorption kinetics into pure water, co-ion and counterion self-diffusion fluxes, co-ion fluxes under a constant current, and membrane electrical conductance.¹⁴⁷ “Superselectivity” refers to a condition where anion transport is very small relative to cation transport. The exclusion of the anions in these systems is much greater than that as predicted by simple Donnan equilibrium theory that involves the equality of chemical potentials of cations and anions across the membrane–electrolyte interface as well as the principle of electroneutrality. The results showed the importance of membrane swelling; there is a loss of superselectivity, in that there is a decrease in the counterion/co-ion mobility, with greater swelling.

The situation for hydrated Nafion in the acid form, or as containing aqueous acids or strong bases, is more complex because protons and “defect protons” (i.e., OH^- ions), migrate according to a somewhat different mechanism. Proton transfer in either case occurs throughout and between clusters of hydrogen bonded water molecules to a degree that depends on the relative water content.

While it is beyond the scope of this review to elucidate details of the current views of proton transport across hydrogen bonds in aqueous systems, the reader is referred to the paper by Eikerling et al.¹⁴⁸ These authors describe the three main options as follows: (1) An excess proton can be a part of an H_3O^+ ion in which all of the three protons are equivalent. (2) The proton is placed between the two water molecules in the hydrogen bond in an H_5O_2^+ grouping, in the view of Zundel.¹⁴⁹ (3) The proton is a part of an Eigen H_9O_4^+ cluster comprised of an H_3O^+ ion and three H_2O molecules strongly attached to each of the three protons of the H_3O^+ species.¹⁵⁰

Eikerling, in this paper, presents a phenomenological model for proton conductivity and mobility in a hydrated Nafion channel and incorporated this model into a statistical model of a multichannel structure consisting of hydrophobic regions throughout which are water-filled channels (pores). A shortcoming of this model is that polymer structure is not factored into the calculations. Mechanisms for proton transport along the negatively charged surface and “bulk” of a pore are factored in. The surface mechanism has a higher activation energy but a higher concentration of charge carriers, and the balance between surface and bulk effects depends on the surface density of SO_3^- groups and pore size. The model accounts for

the effect of proton localization sites, dependent on EW, and pore water content and overall swelling. Theoretical estimates of the membrane conductivity agree with experimental data. In another paper, Eikerling and Kornyshev describe a theoretical treatment of activated proton transfer in a single pore with sulfonated groups on the surface.¹⁵¹

Aldebert et al. studied the room temperature conductance of 1100 EW Nafion membranes using a method that also measured the swelling due to a contacting liquid.¹⁵² The membranes tested were in the H⁺ as well as Li⁺, Na⁺, and Rb⁺ forms, and the solvents used were water, ethanol (EtOH), *N*-methylformamide (NMF), and propylene carbonate (PC). Prior to use, the membranes were boiled in nitric acid, washed with distilled water, and dried. The conductance, measured versus time from the onset of swelling, showed plots in which there was an abrupt rise so that a hold-up time, t_0 , could be extracted by extrapolating the fast rise portion of the curve back to zero conductance on the time axis. This is similar to the time lag method for measuring gas diffusion coefficients in membranes.¹⁵³ Ultimately, the curves approached asymptotic behavior. Cation diffusion coefficients were derived using the equation $x^2 = 8Dt_0$, where x is the thickness of the membrane before swelling. D for membranes contacting water was seen to decrease with increasing counterion radius and with the Guttmann donor number of the solvent. This can be accounted for in the usual sense by the fact that larger cations solvate less and so become less mobile. D for the H⁺ form ($1.08 \times 10^{-6} \text{ cm}^2 \cdot \text{s}^{-1}$) was close to the value for pure water ($0.83 \times 10^{-6} \text{ cm}^2 \cdot \text{s}^{-1}$), and this was taken to mean that protons are highly "solvated". D for the Li⁺ form decreased in the following order for the solvents: H₂O > EtOH > NMF > PC. This can be rationalized in terms of the relative affinity of these solvents for the cation. Because D is defined within the context of early-time data—that is, before the conductance reaches an asymptote—it might be questioned as to whether D for the cation forms truly represents a value representative of a membrane in equilibrium with the solvent because diffusion coefficients in swollen systems can be reduced by plasticization effects.

Cappadonia et al. studied the electrical conductivity of acid form Nafion 117 membranes using an impedance analyzer as a function of temperature and water content over the range 0–29.8 g of H₂O/100 g of Nafion.^{154,155} It was seen that there is a high temperature regime over which the activation energy is low and decreases with increasing water content. In a low temperature range, the activation energy is higher and also monotonically decreases with increasing water content. The temperature for this conductance discontinuity occurs at around 260 K for water contents greater than 8 g of H₂O/100 g of Nafion. It was expressed that the most probable cause for this transition was freezing water. This idea was said to be reinforced by the DSC results of Chen et al., who noted an endothermic peak in Nafion samples, having comparable water content, beginning at ~253 K.¹⁵⁶ The freezing point depression, as

in other studies, was attributed to water having to crystallize in very confined spaces.

Fontanella and co-workers studied the effect of high pressure variation on the conductivity as well as the ¹H, ²H, and ¹⁷O NMR spectra of acid form Nafion117 membranes that were exposed to various humidities.¹⁵⁷ Variation of pressure allows for a determination of activation volume, ΔV , presumably associated with ionic and molecular motions. Conductivities (σ) were obtained from complex electrical impedance diagrams and sample geometry, and ΔV was determined from the slope of linear isothermal $\ln \sigma$ versus p graphs based on the equation $\Delta V = -kT[d \ln \sigma/dp]_T$, where p is the applied pressure. At room temperature, ΔV was found to be $2.9 \text{ cm}^3 \cdot \text{mol}^{-1}$ for a sample conditioned "in atmosphere" and was $6.9 \text{ cm}^3 \cdot \text{mol}^{-1}$ for a sample that was conditioned in 25% relative humidity, where the latter contained the lesser amount of water.

Activation volumes were derived from pressure dependent NMR experiments using the equation $\Delta V = -kT[d \ln T_1/dp]_T$, where T_1 is the spin–lattice relaxation time. ΔV values for the ¹H and ²H NMR experiments were close to each other as well as to the values based on conductivity. These results imply that the electrical transport is correlated with water molecule rotation. There is a trend of increasing ΔV with decreasing water content.

Paddison et al. performed high frequency (f) dielectric relaxation studies, in the Gigahertz range, of hydrated Nafion 117 for the purpose of understanding fundamental mechanisms, for example, water molecule rotation and other possible processes that are involved in charge transport.¹⁵⁸ Pure, bulk, liquid water is known to exhibit a distinct dielectric relaxation in the range 10–100 GHz in the form of an ϵ'' versus f peak and a sharp drop in the real part of the dielectric permittivity at high f .¹⁵⁹ A network analyzer was used for data acquisition, and measurements were taken in reflection mode.

Not surprisingly, ϵ' and ϵ'' increased with increasing water content, but especially when the water content reached 6 and 13 H₂O/SO₃H (mol/mol). This, by the usual argument, may reflect a situation where, at these hydration levels, there are water molecules beyond those that are ion-bound that are free to rotate and therefore increase the overall polarizability. There appear to be no peaks that rise above the considerable noise in the loss spectra, as seen in the spectra for pure water. The low f behavior of the ϵ'' versus f curves exhibits a $1/\omega$ ($\omega = 2\pi f$) dependence, so that specific conductivity values could be extracted in the usual way. These conductivities compare favorably with those obtained by Zawodzinski et al.¹⁶⁰

Alberti et al. investigated the influence of relative humidity on proton conductivity and the thermal stability of Nafion 117 and compared their results with data they obtained for sulfonated poly(ether ether ketone) membranes over the broad, high temperature range 80–160 °C and RHs from 35 to 100%.¹⁶¹ The authors constructed a special cell used in conjunction with an impedance analyzer for this purpose. Data were collected at high temperatures within the context of reducing Pt catalyst CO poison-

ing in direct methanol fuel cells at higher temperatures as well as the accompanying problem of membrane dehydration.

Nafion exhibited better proton conductance, especially at low RH, but the differences diminish or even vanish with increasing RH and increasing temperature. An interesting finding is that when RH is held constant, the conductivity remains constant over the temperature range 80–160 °C. It was suggested that the conductivity increase that would be “expected” (presumably, on the basis of faster proton hopping kinetics in the absence of a matrix)—but not seen—with increasing temperature is counteracted by a membrane microstructure change that reduces the mobility and/or concentration of the charge carriers, and an increase in polymer crystallinity was offered as a possible cause.

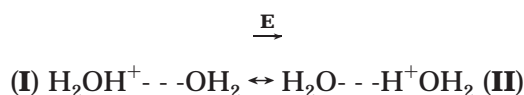
Alberti et al. also describe experiments dealing with reversibility during heating–cooling cycles at constant RH, as well as membrane swelling and chemical degradation, and the reader is referred to this report for the various interesting details.

Proton transfer in hydrogen bonds, referred as the Grotthuss mechanism in older treatises on reaction rate theory,¹⁶² and H₂O molecule rotational motion as well as the structural reorganization and diffusion within extended hydration structures are important fundamental molecular events within the context of membrane applications that depend on proton conductance. Membranes in H₂–O₂ fuel cells are of great current interest in this regard. These molecular events also underlie the function of membranes in the arena of membranes in chlor-alkali electrolytic cells,¹⁶³ water electrolyzers for the production of H₂,¹⁶⁴ and membranes used in Donnan dialysis processes that are used to strip metal ions, such as those of copper and nickel, from electroplating waste solutions.¹⁶⁵ Yeager and Gronowski provide a good listing of such applications, a number of which involve Nafion.¹⁶⁶ Related to this is the strong acidity of Nafion in the protonated form and its use as a solid substrate in organic synthesis as a superacid catalyst.^{167–169}

Of particular relevance (and often overlooked in the polymer community) is the work of Zundel et al., who conducted fundamental studies of the relationship between H⁺ conductivity and the IR spectra of aqueous acidic media, including cross-linked sulfonated polystyrene (SPSA) in the acid form versus degree of hydration.^{170,171} There is an IR spectral feature in the form of a continuous superposition of absorbance that begins in the region of O–H stretching for H₂O (~3500 cm⁻¹) and extends to lower wavenumbers, which is referred to as “continuous absorption”. In acids this continuum is caused by the rapid fluctuation of protons (rate ~ 10¹⁴ s⁻¹) due to a combination of their tunneling and barrier hopping in the hydrogen bond of H₅O₂⁺ groupings. Interaction between hydrogen bonds of different groupings via proton dispersion forces causes this continuum of vibrational energy levels owing to a distribution of distances between, and orientations of, hydrogen bonds in the network. The hydrogen bonds in these groupings are very polarizable, being 1–2 orders of

magnitude larger than the usual electronic polarizabilities. Thus, the state of these bonds is very sensitive to their environment, and the presence of ions can induce considerable polarization that suppresses continuous absorption. H₅O₂⁺ groupings are linked via H bridges with other H₂O molecules or with –SO₃⁻ acceptor groups. Protons are transferred over larger distances when these groupings shift within the extended hydration network by thermal rearrangement, and the rate-determining step of H⁺ migration is this structural diffusion.

Eigen addressed this topic in earlier literature¹⁷² although structural diffusion, according to Zundel, is more complex than the simple rotation of H₃O⁺ to affect favorable bond orientation for H⁺ transfer to a neighboring H₂O molecule. The large polarizability of hydrogen bonds in H₅O₂⁺ groupings was said to account for the high H⁺ conductivity of hydrated SPSA membranes as well as other acidic systems.¹⁷³ In the absence of an electric field, **E**, there is a dynamic equilibrium between two proton boundary structures, but when **E** is present, the weight of boundary structure II is increased because the hydrogen bond is easily polarized. Furthermore, the



proton can rapidly transfer within H₃O⁺ to one of the outer H atoms in boundary structure II (H⁺OH₂ → HOHH⁺) and another H⁺ transfer can take place with a third adjacent H₂O molecule and thermal rearrangement causes H₅O₂⁺ groupings to become redefined. This is the essence of so-called “structural diffusion”. Because H⁺ motions are coupled and these groupings exist within a more extended hydration environment, proton conductivity is in fact a cooperative process¹⁷⁴ that is sensitive to structuring influences within the supportive medium. In the case of –SO₃⁻–H⁺OH₂ groupings in SPSA, the time-averaged position of H⁺ is biased toward the water molecule at low degrees of hydration,¹⁷⁵ and if H₂O/SO₃H ≥ 2, excess protons will shift from acid–water H bonds to H bonds between H₂O molecules and the IR continuous absorption and H⁺ conductivity become great.

Ostrowska and Narebska noted an infrared continuous absorption in hydrated acid form Nafion 120 membranes that began at 3400 cm⁻¹ and extended toward low wavenumbers.¹⁷⁶ This feature was not present in dry membranes and, based on the work of Zundel et al., was proposed to be due to the existence of H₅O₂⁺ and H₉O₄⁺ groups, in which there are easily polarizable hydrogen bonds. This paper by Ostrowska and Narebska is also useful, as it contains a number of band assignments for Nafion.

Mauritz and Gray analyzed the IR continuous absorption of hydrated Na⁺OH⁻ and K⁺OH⁻-imbibed Nafion sulfonate membranes for the purpose of correlating this phenomenon to the current efficiency (cation transference number) of chlor-alkali electrochemical cells.¹⁷⁷ In this case, the similar issue of OH⁻ (“defect proton”) conductivity is important. A distinct continuous absorption appeared in the spec-

tra, as seen for membranes equilibrated in different high concentrations of aqueous Na^+OH^- and K^+OH^- . The continuous absorption arises from easily polarized hydrogen bonds in H_3O_2^- groupings and reflects the mobility and concentration of OH^- ions as influenced by the electrostatic fields about K^+ ions. This view was reinforced by the fact that the continuous absorption versus $[\text{OH}^-]$ profile correlated inversely with the experimental current efficiency versus $[\text{OH}^-]$ profile. Also seen in the spectra was a shoulder on the high wavenumber side of the main O–H stretching peak which is the signature of non-hydrogen bonded OH groups.

A more recent view of proton transport is that of Kreuer, who, compared with the Zundel-based view, describes the process on different structural scales within phase separated morphologies. The smallest scale is molecular, which involves intermolecular proton transfer and the breaking and re-forming of hydrogen bonds. When the water content becomes low, the relative population of hydrogen bonds decreases so that proton conductance diminishes in a way that the elementary mechanism becomes that of the diffusion of hydrated protons, the so-called "vehicle mechanism".^{178,179}

The next level is concerned with transport within "channels" as depicted in Figure 11. The condition in these regions is described in terms of charge distributions as deriving from solutions of the Poisson–Boltzmann (P–B) equation. This P–B approach can be questioned for a number of reasons, the first of which is that the equation is rooted in macroscopic-continuum-based electrostatic theory. In spaces that are only somewhat greater than 1 nm in width, there is molecular granularity rather than the required continuum and the dielectric constant is a ubiquitous parameter although approximate treatments can be made. Moreover, the imposition of a simple geometry for the channels for the purpose of solving the P–B equation ignores the complexity of the regions that are, in fact, ill-defined and most likely of complex shapes.

The highest level, at structural scales > 10 nm, is that over which long-range transport takes place and diffusion depends on the degree of connectivity of the water pockets, which involves the concept of percolation. The observed decrease in water permeation with decreasing water volume fraction is more pronounced in sulfonated poly(ether ketone) than in Nafion, owing to differences in the state of percolation.¹⁸⁰ Proton conductivity decreases in the same order, as well.

Another important property of Nafion is that of water diffusion. A number of studies of this property have appeared in the literature, and some notable examples are as follows.

Yeo and Eisenberg investigated the diffusion of water in Nafion by sorption from the contacting liquid into dry samples and measuring weight uptake versus time over the temperature range 0–99 °C.¹⁸¹ The resultant diffusion coefficients (D) increased from about 10^{-6} to 10^{-5} cm^2/s with increasing temperature, and the activation energy was determined to be 4.5 kcal/mol.

Takamatsu et al. studied the diffusion of water into the acid as well as mono-, di-, and trivalent salt forms of 1155 and 1200 EW samples.¹⁸² The gravimetric uptakes of membranes immersed in distilled liquid water versus time were determined. Three approximate diffusion formulas were applied to the data, and all yielded essentially the same result. The $\log D$ versus $1/T$ plots, over the range 20–81 °C, yielded activation energies of 4.9 and 13.0 kcal/mol for the acid and K^+ forms, respectively. Diffusion coefficients of various mineral cations that permeated from aqueous electrolytes were considerably smaller than that of water. Also, $\log D$ was seen to be proportional to the quantity q/a , where q is the charge of the cation and a is the center-to-center distance between the cation and fixed anion in a contact ion pair.

Yeager and Steck derived diffusion coefficients for water in totally hydrated Nafion120 membranes that were exchanged with alkali metal cations, using a radiotracer technique.¹⁸ At 25 °C, D for the Na^+ form was 2.65×10^{-6} cm^2/s and the values for the K^+ and Cs^+ forms were somewhat smaller, which would seem to reflect the lower maximal degree of hydration of these forms.

Yeager et al.,¹⁸³ again based on radiotracer studies of the self-diffusion of different ions ($^{22}\text{Na}^+$, Cs^+ , $^{36}\text{Cl}^-$, $^{35}\text{SO}_4^-$, $^{125}\text{I}^-$) in 1150 and 1200 EW Nafion membranes that were in contact with dilute and concentrated electrolytes, were the first to introduce the concept of mixed interphase regions of intermediate polarity. In dilute solution, room temperature studies,¹⁸⁴ Cs^+ and I^- ions were rationalized as having more tortuous diffusion pathways than Na^+ ions and water molecules. For concentrated solutions at 80 °C, Cl^- and SO_4^{2-} ion diffusion coefficients are smaller than those for Na^+ ions, and D for Cl^- ions is greater than that for the SO_4^- anions.

In this conceptual (nonmathematical) model there is the view of hydrophobic semicrystalline perfluorocarbon regions and irregular-shaped aggregates of fixed ions. Small cations and water molecules reside mainly in the ion cluster centers and diffuse along different pathways than those for large cations having low hydration energies and anions which were thought to preferentially migrate through an intermediate phase containing a few water molecules and a few side chains. The high diffusion rates and low tortuosity of Na^+ ions and water molecules are explained by the nonspherical shapes of the clusters.

This view stands in contrast to the condition of having well-defined spherical clusters and sharp phase boundaries as depicted in the model of Gierke et al.

Millet determined self-diffusion coefficients for Na^+ and Cs^+ ions in hydrated 1200 EW membranes using conductivity measurements and the Einstein equation, $D_+ = u_+ kT$, where u_+ is the absolute mobility of the given cation.¹⁸⁵ u_+ can be derived from the equivalent conductivity according to $\Lambda = \sigma_+/C_+ = Fu_+$, where σ_+ is the specific conductivity, C_+ is the cation concentration (calculated on the basis of the dry membrane density, EW, and the water content), and F is the Faraday constant. The values of D_+ determined via these conductivity measurements

were compared with those determined by the radio-tracer technique of Yeager et al.^{186–188} to test the validity of the Einstein equation for this system. The water contents of these membranes corresponded to H₂O/SO₃⁻ mole ratios in the range 6.6–11.3 for the Cs⁺ form and 11.9–18.4 for the Na⁺ form at 25 and 40 °C. The results showed that the *D*₊ values compared well with those of Yeager et al.

Zawodzinski et al. determined ¹H diffusion coefficients, *D*, in Nafion 117 having water contents over a range corresponding to H₂O/SO₃H = 2–14 mol/mol using pulsed field gradient spin-echo ¹H NMR spectroscopy.¹⁸⁹ This study was conducted within the context of understanding the nature of water as well as water concentration profiles and water management in fuel cell membranes. *D* was extracted from the NMR data using the following equation:

$$\ln \left[\frac{A(g)}{A(0)} \right] = -\gamma^2 D g^2 \delta^2 \left(\Delta - \frac{\delta}{3} \right)$$

A(*g*) is the signal intensity observed with an applied gradient *g*, *A*(0) is the intensity in the absence of an applied gradient, γ is the nuclear gyromagnetic ratio, and δ and Δ are time intervals of the pulsed field gradient spin-echo sequence.

D, measured in this way, ranged from 0.6×10^{-6} to 5.8×10^{-6} cm²/s over this range of water content in increasing order.

While *D* issuing from these experiments is not strictly the diffusion coefficient of water per se, but rather that of ¹H throughout the ensemble of environments in the hydration microstructure, these authors rationalized that it could in fact be identified with *D* at both high and low water contents. It should be appreciated that self-diffusion coefficients measured in this way reflect fundamental hopping events on a molecular scale.

Later, Jones, Inglefield, and co-workers performed fundamental solid-state NMR studies of acid form 1100 EW Nafion. Pulse field gradient NMR experiments interrogated the translational motions of water, ethanol, and fluorocarbon components in their systems.¹⁹⁰ ¹⁹F spin diffusion studies yielded important information on the size of the backbone (CF₂)_{*x*} and perfluoroalkyl ether regions in the hydrated and dry conditions.¹⁹¹ Static (nonspinning) ¹⁹F studies indicated the location of molecular penetrants within the nanophase-separated morphology. The reader is referred to the original paper for the explanations of this method, model assumptions, and so forth. One basic assumption is that the side chains form a distinct domain separate from a distinct domain consisting of the perfluorinated polymer backbone. The interpretation of the results is as follows. The spin diffusion results indicated domains in dry and solvent-swollen samples that are in the nanometer range, and this is commensurate with pendant group aggregation, which is in harmony with the structural view issuing from SAXS experiments on the same material. Although the NMR information does not provide information regarding the shape of the aggregates, interfaces are detected. The signature of an interface is graphical curvature that precedes the linear section of magnetization change versus square

root of time plots for spin diffusion. The spin diffusion results support the idea that the side chain phase is continuous with little tortuosity, which accounts for the rapid long-range transport of water and lower alcohols.

¹²⁹Xe gas, under pressure, was used by Jones, Inglefield, and co-workers as a probe of morphology based on the fact that its spectrum is sensitive to local molecular environment. Domains that are involved in penetrant uptake and diffusion can be inferred. The studies showed two overlapping resonances, one being assigned to an amorphous perfluoroethylene environment and the second to side chain domains. The latter regions are more heterogeneous, owing to the considerable line width.

Morphology based on chemical environment can be probed using ¹⁹F NMR spectroscopy because the chemical shifts of F atoms in the side chains are considerably separated from those in the backbone. Conformational dynamics as affected by domain-selective solvent incorporation are reflected in the widths of static ¹⁹F peaks. These conformational motions, in turn, can influence the migration of solvent penetrants.

Spin diffusion between the backbone and side chain resonances can be used to study domain size. For dry Nafion the side chain domains were found to be of the size 3.8 nm and these domains had a periodicity of around 10 nm. The first number is around that commonly associated with the diameter of a spherical cluster based on microscopic and scattering studies. The 10 nm spacing remains to be assigned to a structural feature. It is noted that the AFM studies of McClean et al.,⁸³ described earlier, identify fluorocarbon crystalline domains of size ~10 nm for the K⁺ form, and whether the coincidence of this number with the periodicity deduced by Meresi et al.¹⁹¹ is significant or fortuitous remains to be shown. Upon addition of 20 wt % water, domain size increases to 6.5 nm, but the periodicity is essentially unchanged. An ethanol uptake of 20 wt % causes a greater morphological rearrangement, giving a domain size of 11 nm and a periodicity of 19 nm. The repeat length is calculated using spin diffusion plots (linear extrapolation to zero magnetization on magnetization vs time plots). Static ¹⁹F line shapes showed that ethanol selectively plasticizes the side chain group domains.

NMR is the most fundamental *molecular-specific* probe of diffusion. Polymer motions and the spectroscopic signature of a given nucleus can be unambiguously related to a particular morphological domain. The size and time scale of the experiments are such that the fundamental hopping events of diffusing molecules can be sampled.

Plots of *D* versus water volume fraction¹⁹⁰ show that the concentration dependence of *D* is in fact described well by the Fujita free volume equation.¹⁹⁰ This was surprising considering that the underpinning of this equation simply involves available free volume for molecular hopping. The interpretation is that water molecules plasticize the perfluoroalkyl ether side chain domains and this increases *D* with increasing water content. *D* for water varied from

10^{-4} to 10^{-7} cm²/s, and these values are similar to those determined by Zawodzinski et al., as discussed above. Moreover, D for water versus temperature followed WLF behavior, which is also linked to free volume theory. D for ethanol was comparable to that for water although the concentration dependence was stronger and the free volume concept was not found to apply. This can be related to the fact that ¹⁹F spin diffusion and line shape analyses indicated larger morphological changes upon addition of ethanol as compared to water and greater plasticization of the side chain domains.

Sodaye et al. attempted to probe the free volume in various monovalent and divalent counterion forms of Nafion 117 that were swollen in water and alcohol using positron annihilation lifetime spectroscopy (PALS).¹⁹² The underlying concept is that free volume on the molecular level can influence polymer chain conformation and chain dynamics, which will affect transport and mechanical properties. While other techniques, such as gas diffusion, can indirectly interrogate materials for free volume, PALS is currently the only direct probe on an atomistic level. The details of this method will be omitted here, and it will simply be mentioned that the spectroscopic data are fitted to a quantum mechanical model that assumes spherical holes, of radius R , that are meant to represent free volume. The assumption of spherical holes is a limitation considering that the free space between polymer chains must not only be of complex geometry but must also be contiguous rather than existing in isolated discrete pockets of a dynamic nature. In short, there was seen to be a very small monotonic increase in R from 3.49 to 3.55 Å in proceeding from the H⁺ to Cs⁺ form. The free volume fraction was determined to be essentially unchanged across the range of alkali cations. The significance of these results can be questioned, given that the range of solvent swelling as well as solvent and ion diffusivity varies significantly over this range. Also, the difference in R between the water- and ethanol-swollen H⁺ forms (3.49 vs 3.67 Å) is somewhat insignificant. Thus, it must be concluded that these PALS experiments have not yielded information that correlates strongly with these critical properties of water-swollen Nafion, and this may be due in part to the overly simplistic model that was applied to the data.

A controversial model for the structure of Nafion is that which proposes a lamellar morphology, due to Litt.⁷⁰ Litt makes a number of arguments to support this model, but the most direct evidence consists of plots of the Bragg spacing, d , associated with clusters, versus water content, as seen in Figure 13. The plot comes from the paper by Gierke et al.,¹⁷ although this d versus water content behavior was also observed by Fujimura et al.³⁷ Litt points out that a lamellar structure would swell in only one dimension, which accounts for the linear d versus water content graphs. Swelling, on the microscopic level, occurs by having water incorporating between the lamellae, thereby pushing them farther apart. The bilayer structure presented by Starkweather⁴¹ is in fact commensurate with the model of Litt.

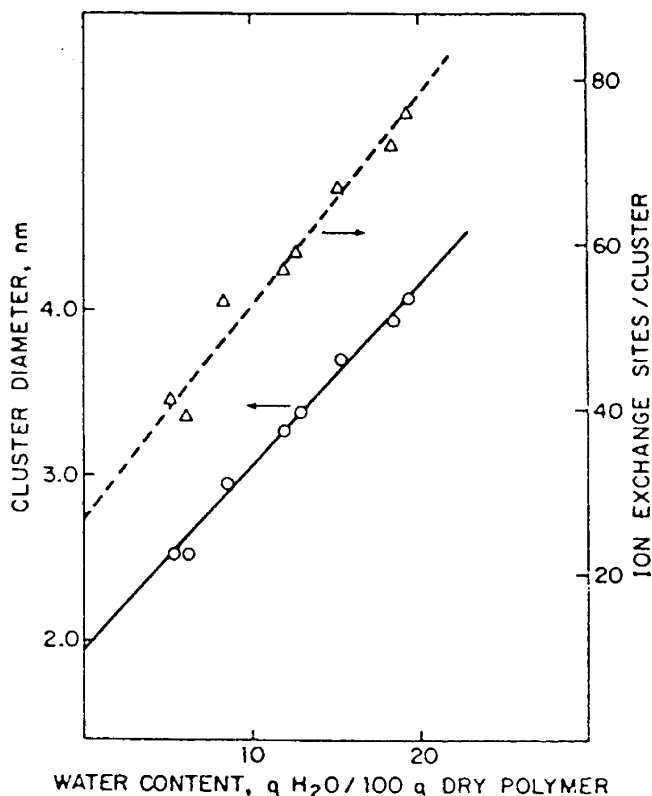


Figure 13. Dependence of cluster diameter and number of SO₃⁻ groups per cluster on water content in 1200 EW Nafion according to Gierke, Munn, and Wilson. (Reprinted with permission from ref 17. Copyright 1981 Wiley.)

Also, in support of the Litt model, Plate and Shibaev observed that hydrated membranes behave in a fashion as brushlike polymers. This suggested to these authors that Nafion has a multilayer structure such that water forms aggregates in lamellar domains,¹⁹³ and this view was said to be supported by the results of the neutron diffraction and Mossbauer spectroscopic experiments of Timashev.¹⁹⁴

This structural view can be compared with that of Gebel et al., who conducted SAXS and SANS studies of water-swollen (around 10–90 polymer volume percent) Nafion 117 in different cation forms.¹⁹⁵ The picture emerging from their studies consists of the aggregation of ionomer chains into elongated bundles which can be in the form of cylinders at high water content (2-D swelling) or ribbons (1-D lamellar swelling). Gebel et al. make the statement that “for high (polymer) volume fraction...the dilution process is similar to those of a lamellar structure...” These bundles have diameters that are ~40 Å, have lengths greater than 1000 Å, and are surrounded by “electrolyte”. This is an extension of the view of elongated aggregates in dilute perfluorosulfonate ionomer solutions. As noted earlier, in the scattering section of this review, Nafion does not form true solutions in the sense of having individual polymer chains freely intermixed with the solvent molecules.

Another spectroscopic method that has been used to study the multiphase structure of Nafion uses photophysical probes. This is well explained in a paper by Kalyanasundaram and Thomas, and references therein.¹⁹⁶ These authors studied the perturbations of the five predominant vibronic band intensi-

ties in fluorescence spectra of pyrene (Py), an aromatic chromophore, in a broad variety of organic solvents whose molecules have different dipole moments, as well as in micelles. The ratio of the intensity of peak 3 to peak 1 (I_3/I_1) decreases with increasing environmental polarity, and this ratio was the highest for perfluorinated saturated hydrocarbons.

Lee and Meisel incorporated Py, at levels of 10^{-3} M or more, into 1200 EW acid form samples that were swollen with water and with *tert*-butyl alcohol.¹⁹⁷ It was concluded based on the I_3/I_1 value for water swollen samples that the Py molecules were located in the water clusters and were most likely near fluorocarbon–water interfaces. It was also concluded, based on both absorption and emission spectra, that the probes had strong interactions with the SO_3^- groups that were exchanged with Ag^+ and Pb^{2+} cations in the case of water containing samples. Likewise, the pyrene molecules were rationalized as being surrounded by *tert*-butanol molecules in that case. However, excimer formation (due to the presence of adjacent pyrene molecules) in the *tert*-butyl alcohol system suggested the loss of cluster morphology.

Szentirmay et al. studied the microchemical environments of Nafion 117 in the acid and Na^+ forms using Py and $\text{Ru}(\text{bpy})_3^{2+}$ probes in fully hydrated ($\sim 40\%$) samples in various cation forms.¹⁹⁸ $\text{Ru}(\text{bpy})_3^{2+}$ emission spectra cannot be interpreted in terms of environmental polarity in as straightforward a fashion as in the case of Py, but blue shifts can reflect this aspect. One of the results of this study was that the microenvironment polarities were such that I_3/I_1 values for Py are between those for fluorocarbon and aqueous environments, and this conclusion was strengthened by the results of $\text{Ru}(\text{bpy})_3^{2+}$ probe studies, as well as the similar conclusion of Lee and Meisel. Another conclusion that was reached was that the SO_3^- clusters are chemically heterogeneous, an idea that was in line with the view of Yeager and Steck, who spoke of mixed interfacial regions.¹⁸

Robertson and Yeager used Py and $\text{Ru}(\text{bpy})_3$ probes for the purpose of locating the locations of Cs^+ and I^- ions in the nanophase-separated morphology.¹⁹⁹ It is known that these probes take residence in the intermediate polarity hydrophobic–hydrophilic interfacial regions. The studies concluded that Cs^+ ions were located in the aqueous regions, but I^- ions were in the interfacial regions.

It is perhaps a shortcoming of mobile probes that one must deduce where it is located based, for example, on the measured value of I_3/I_1 in the case of Py, and this presupposes that the basic features of the morphology are already known. One could not assign the probe location as being cluster domains if such domains had not been known to exist beforehand. Furthermore, the issue of whether large probe molecules perturb their molecular surroundings is the subject of debate. It would seem that the greatest benefit derives from establishing a semiquantitative degree of polarity of the phase in which the average Py molecule resides.

It is important to know whether complete ion exchange has been affected in a given sample, that

is, whether all of the sulfonic acid groups have been neutralized by the chosen cations of charge $+z$ e, as ion content can affect swelling, mechanical, and other properties. Young et al. determined the extent of ion exchange in Nafion 117 membranes in the K^+ , Cs^+ , Mg^{2+} , Ca^{2+} , Co^{2+} , Zn^{2+} , Cu^{2+} , Al^{3+} , and Fe^{3+} forms using cold-neutron-capture prompt γ neutron activation analysis (PGAA).²⁰⁰ PGAA is particularly suited for evaluation of chemical composition, being sensitive to trace ions and hydrogen, and is a nondestructive technique. In short, the nuclei of many elements in a sample placed in a neutron beam absorb neutrons and become an isotope of higher mass number in an excited state. Then, prompt γ rays are emitted by de-excitation of the compound nuclei and measured via a high resolution γ ray detector and the data appear as peaks on counts versus energy spectra, each element having a characteristic peak.

Four forms of membrane pretreatments were used, and the reader is referred to this report for the details of each. The as-received sample was seen to have K^+ contaminant, perhaps being a residue from conversion from the SO_2F form using KOH, but the samples that were pretreated using mineral acids were completely converted to the SO_3H form and the K^+ contaminant was removed in the process. The resultant acid forms were soaked in dilute (0.01 M) and concentrated (2 M) metal chloride salt solutions, and excess electrolyte was leached out of the latter by refluxing in DI/DS water. The peak intensity for a given atom was normalized to the peak intensity of sulfur, so that the average counterion/ SO_3 (mole/mole) ratio could be ascertained. In short, 94–100% of the SO_3H groups can be exchanged and conversions are slightly lower for the monovalent cations. This might be due to the lower hydration numbers, especially for the Cs^+ cation, and no data were reported for Li^+ and Na^+ ions that have greater hydration numbers. Also, it was shown that the excess chloride salts are in fact leached out of the membrane by refluxing with DI/DS water.

Other experiments were performed to affect partial ion exchange by soaking membranes in 0.01 M electrolytes in which the mole ratio of cation-to-sulfonate group was 1:2, 1:1, and 2:1. It was found that an external electrolyte concentration of 0.01 M was not high enough to totally convert all of the sulfonated groups to the desired cation form. An excess of 2:1 was found to be necessary for this purpose.

Increasing z increased the degree of exchange, as more than one sulfonate group can interact with a single cation.

These experiments are of significant value, as many studies have been reported in which complete ion exchange was assumed to take place but not verified.

As mentioned, this review is focused primarily on a survey of the vast literature dealing with the structure and properties of Nafion in the sulfonic acid and cation exchanged sulfonate forms. The literature on the carboxylate version is sparse and currently of lesser interest, as its application seems to be limited to membranes in chlor-alkali cells, and since it is a

less-strong acid than SO_3H , is not of interest in the arena of fuel cell membranes. It should be mentioned, however, that the carboxylate form is considerably more acidic than analogous hydrocarbon ion exchange resins. In this regard, the work of Yeager et al. in comparing cation and water self-diffusion coefficients, found by a radiotracer method, for the sulfonated and carboxylate forms of 1200 EW, is of importance.¹²⁴ In short, it was found that when the membranes are in contact with 0.10 M aqueous solutions of sodium and cesium chloride containing the ^{22}Na and ^{137}Cs isotopes in each respective case, cation diffusion proceeds faster in the carboxylate form, although this form has the lower water uptake. Yeager et al. also investigated and compared the sorption and transport properties of these two forms in concentrated aqueous NaCl and NaOH solution environments, and the differences were rationalized in terms of ion pairing.²⁰¹ The apparent $\text{p}K_{\text{a}}$ of the carboxylate form was determined to be 1.9, which is rather low and due to the electron withdrawing effect of fluorine atom substitution. Consequently, the carboxylic acid form can be totally neutralized in alkali electrolyte solutions.

The in-depth FTIR investigations, of Perusich, of the methyl ester ($-\text{CO}_2\text{CH}_3$), carboxylic acid, and potassium carboxylate forms should also be mentioned.²⁰² In addition to constructing a useful extensive tabulation of band assignments for these as well as the sulfonate materials, Perusich established quantitative expressions that allow for the computation of equivalent weight and acid content using the 555 cm^{-1} C–F and 982 cm^{-1} C–O–C ether bands, based on thin film absorbance measurements. This information is very useful for the accurate, reproducible, and rapid compositional measurements of this polymer. Also, the time evolution of bands during the conversion from the methyl ester to acid forms was reported.

5. Mechanical Properties

The mechanical properties of Nafion materials have not been of the most critical importance, as in the case of commercial thermoplastics or composite materials that are expected to be load-bearing. Rather, the primary focus has been on transport properties. To be sure, the mechanical integrity of membranes as mounted in cells, and under the perturbation of pressure gradients, swelling-dehydration cycles, mechanical creep, extreme temperatures, and the onset of brittleness and tear resistance, is important and must be taken into consideration.

The E. I. DuPont Co. presented empirical equations for the tensile strength, elongation at yield, and tensile modulus as a function of cation type, water content, and equivalent weight in the range $1000 \leq \text{EW} \leq 1400$ and at temperatures in the range $0 \leq T \leq 85\text{ }^\circ\text{C}$.²⁰³ These equations were shown in early product literature, as well.

Aside from this, the literature on the subject has largely been concerned with dynamic mechanical properties where experiments have been performed to gather data consisting of loss tangent ($\tan \delta$) and storage tensile modulus (E'). Rather than being

related to mechanical properties under considerable deformations within an application context, this information was used to identify thermomechanical transitions that were assigned to morphological features in the microphase separated morphology. The following is a historical presentation of these investigations.

In an early study, Yeo and Eisenberg noted a transition, labeled α , for the acid form ($\text{EW} = 1365\text{ g mol}^{-1}$) at around $110\text{ }^\circ\text{C}$ ($\tan \delta$ maximum).²⁰⁴ This relaxation was initially considered as the glass transition of the nonionic phase because, in these limited studies, water was seen to have only a minor effect on the magnitude or position of this peak. A β peak for the same dry acid form was seen at around $20\text{ }^\circ\text{C}$, which shifted to lower temperature with increasing water content, and this was discussed in terms of a glass transition of the polar regions. A γ peak at around $-100\text{ }^\circ\text{C}$ was mentioned as being of the same origin as in PTFE, that is, due to short-range molecular motions in the tetrafluoroethylene phase.

Later, Kyu and Eisenberg discussed dynamic mechanical relaxations for the same acid form of Nafion and re-examined their earlier interpretations.²⁰⁵ The γ relaxation retained its original interpretation. However, the α peak, having the greatest intensity, was reassigned as the glass transition of the polar regions because it had by then come to be seen as sensitive to ion type, degree of neutralization, and water content. The β peak was reassigned as the glass transition of the Nafion matrix.

Tant et al. reported a dynamic mechanical transition of around $100\text{ }^\circ\text{C}$ (maximum in G'') for acid form Nafion having 1140 EW.²⁰⁶ Since this transition also appeared for the sulfonyl fluoride precursor, but at a much lower temperature ($\sim 0\text{ }^\circ\text{C}$), they concluded that it involved main chain motions that are restricted by the conversion to the acid form. These motions were further restricted by the conversion to the Na^+ sulfonate form owing to strong ionic associations between the side chains. In contrast with the work of Kyu and Eisenberg, no transition appeared at $0\text{ }^\circ\text{C}$ in addition to that at $100\text{ }^\circ\text{C}$. While the equivalent weights of the samples utilized by Eisenberg and Kyu and Tant et al. were not quite the same, the notable difference in matrix T_{g} assignment is cause for confusion.

Miura and Yoshida²⁰⁷ noted a dynamic mechanical $\tan \delta$ peak at $120\text{ }^\circ\text{C}$ at 1 Hz, labeled α , for “dry” 1100 EW acid form Nafion. These investigators assigned this transition to motions within the polar clusters because it was sensitive to cation type.

Cable and Moore performed DMA (dynamic mechanical analysis) studies of various Nafion membranes including the acid form.²⁰⁸ A $\tan \delta$ peak with maximum at $110\text{ }^\circ\text{C}$, referred to as “ T_{g} ”, was seen, and there is a suggestion of a shoulder on the low temperature side that might arise from another mechanism. As this membrane was dried at only $60\text{ }^\circ\text{C}$, the possibility of residual water incorporation exists. Moore and Cable concluded that the α relaxation was due to chain motions within and/or near the ion-rich domains and that the β relaxation was

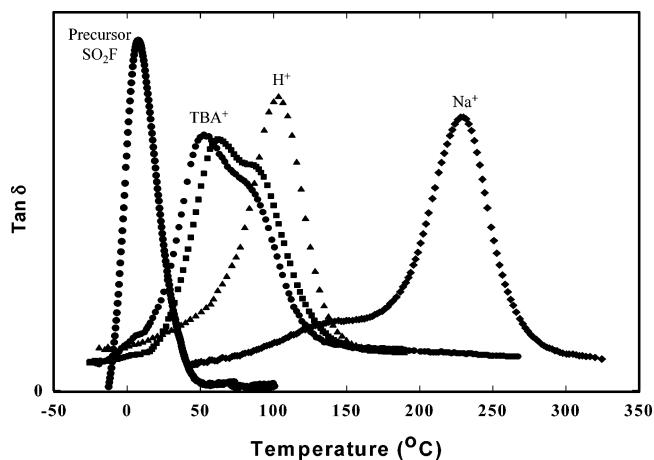


Figure 14. Dynamic mechanical data plotted as $\tan \delta$ versus temperature for Nafion in various forms.

due to chain motions of amorphous fluorocarbon units well removed from the ionic aggregates, that is, the matrix.¹³⁵ These investigators referred to chain motions within an electrostatic network rather than viewing the polar and fluorocarbon components as being isolated, discrete domains. This is in harmony with the view of Kyu and Eisenberg, who stated that "...whatever happens in one of the phases would be expected to have a strong effect on the other phase because of the intimate contact between the phases coupled with their small size." Mauritz and Young adopted this view in their DMA studies of Nafion/[organically modified silicate] nanocomposites.²⁰⁹

The effect of counterion type and size on the dynamic mechanical properties of Nafion has been studied recently by Moore and co-workers^{135,208} using a variety of organic, alkylammonium ions in comparison to the more conventional alkali metal ions. Figure 14 compares the $\tan \delta$ versus temperature plots of the Nafion precursor (i.e., the nonionic, sulfonyl fluoride form) to those of the ionomer in the H^+ , Na^+ , and tetrabutylammonium ion (TBA^+) forms. In the absence of electrostatic interactions, the sulfonyl fluoride precursor displays a single α relaxation near 0 °C. As a result of this low temperature relaxation, the precursor may be easily melt-processed into thin films for later membrane applications. However, once the polymer is converted to the sodium sulfonate form (by hydrolysis and subsequent neutralization), the ionomer yields a profound shift in the α relaxation to a temperature near 250 °C. Note that this form of the ionomer is no longer melt-processible due to strong Coulombic interactions that yield a dynamic electrostatic network (i.e., a physically cross-linked system) that persists to temperatures well above the melting point of the PTFE-like crystallites. In addition to the dominant α relaxation, a weak shoulder near 150 °C is observed and assigned to the β relaxation, in agreement with the work of Eisenberg.²¹⁰ For Nafion in the acid form, the α and β relaxations are observed at temperatures ~ 100 °C lower than that for the sodium sulfonate form of the ionomer. This shift to lower temperatures has been attributed to a reduction in the strength of the interactions between the SO_3H groups (i.e., comparably weak hydrogen bond interactions) relative to

the strong dipole–dipole interactions between the SO_3^-Na^+ groups.²⁰⁸

To further investigate the molecular origins of the α and β relaxations in Nafion, Moore and co-workers utilized a series of alkylammonium ions to systematically alter the dynamic mechanical response of the ionomer with respect to the strength of electrostatic interactions. When Nafion is neutralized to contain large tetrabutylammonium ions, the α and β relaxations are observed to shift to temperatures even below that of the acid form of the ionomer, as shown in Figure 14. Moreover, the magnitude of the β relaxation is seen to increase significantly to a level comparable to that of the α relaxation. This behavior was attributed to a weakening of the electrostatic interactions and a plasticization effect of the large organic counterions.²¹¹ Using a series of alkylammonium ions, from tetramethylammonium (TMA^+) to tetradecylammonium (TDecA^+), the α and β relaxations were found to shift monotonically over a range of temperatures from near that observed for the sodium form of the ionomer (i.e., with the small TMA^+ form) to near that of the α relaxation of the sulfonyl fluoride precursor (i.e., for the large TDecA^+ form). In addition, the magnitude of the β relaxation was observed to increase with counterion size to a point where it becomes the dominant relaxation for counterions larger than tetrahexylammonium. Based on these results and recent correlations of this DMA data with studies of molecular dynamics and morphological relaxations observed using variable temperature SS NMR and SAXS experiments,^{212, 213} the α relaxation is attributed to the onset of long-range mobility of both the main and side chains as a result of a destabilization of the electrostatic network (i.e., through the activation of a *dynamic* network involving significant ion-hopping processes). In contrast, the β relaxation is associated with the onset of segmental motions of chains within the framework of a *static* network of physically cross-linked chains.²¹⁴

6. Molecular Simulation of Structure and Properties

Mauritz summarized a number of molecular models of ionomer structure, including those pertaining to Nafion, that had had been formulated up to 1996.²¹⁵ Within the context of the title of this review, it should be appreciated that the results contribute to the "state of understanding" only if they are verifiable by careful experimentation. To be sure, theoretical predictions are welcome in the design of experiments and pointing the way toward useful applications.

The cluster-network model of Gierke et al. has already been discussed in the Introduction as being the first realistic model for rationalizing a number of properties of Nafion membranes.

Hsu, Barkley, and Meakin addressed the percolation aspect of hydrated clusters in relation to insulator-to-conductor transitions.²¹⁶ As the concentration of clusters on a hypothetical grid, that is, a three-dimensional lattice, increases, "islands" of clusters will grow in size and become interconnected. Eventu-

ally, a threshold volume fraction, C_0 , is reached where the pathways span the macroscopic dimensions of the grid—the percolation channels—and long-ranged ionic conduction is possible. The conductivity, σ , near and above C_0 obeys the following power law.

$$\sigma = \sigma_0(C - C_0)^n$$

This is a general equation that can be applied to any material that can support charge percolation. C_0 not only depends on dimensionality but also the manner in which the two components (one insulating, the other conducting) are dispersed, and the factor $(C - C_0)^n$ involves topological connectivity. The prefactor σ_0 depends on the particular conduction mechanism that operates within and between two adjacent clusters and involves interactions among ions, water molecules, and the ionomer. It is the one factor that involves the chemical identity of the system. This equation was tested by experimental measurements of σ for membranes of different equivalent weights and containing various uptakes of aqueous sodium hydroxide.

In short, C_0 was found to be 0.10, which is less than the value for a completely random system—which implies that the clusters were not randomly dispersed. A log–log plot of σ versus $C - C_0$ was found to be linear where n , the slope of the line, was 1.5, which in fact is in the established theoretical range of 1.3–1.7.

Of course, this equation and its theoretical underpinnings does not constitute a model as such and certainly does not address the structural specifics of Nafion, so that it is of no predictive value, as experimental data must be collected beforehand. On the other hand, the results of this study clearly elucidate the percolative nature of the ensemble of contiguous ion-conductive clusters. Since the time of this study, the notion of extended water structures or aggregated clusters has been reinforced to a degree by the morphological studies mentioned above.

In a related experimental study, Cirkel and Okada compared mechanical and electrical percolation that developed during the gelation of 3:1 (v/v) 2-propanol/water “solutions” of Nafion 117 in the acid and Na^+ forms.²¹⁷ Attention should be paid to the particular manner in which these samples were prepared, as different conditions may yield different results. Also, caution should be applied in comparing these results with those of percolation studies using preformed films, such as that of Hsu et al.²¹⁶

In relatively dilute solutions, Nafion is said to exist in the form of rodlike aggregates of practically the same size^{49,51} that are in equilibrium with loose ionomers⁷³ such that at higher concentrations the aggregates dominate.²¹⁸ The reader should consult the more recent papers of Gebel et al., cited earlier, for a more detailed view of Nafion “solutions”.

The relative viscosity η_r and storage modulus G' were determined by Cirkel and Okada in experiments using a rheometer in oscillatory rotational mode and Couette sample geometry as a function of Nafion volume fraction, φ , and angular frequency, ω , for the acid and sodium forms at 25 °C. Parallel experiments

were performed with an electrical impedance analyzer that measured conductivity, σ , vs ω for different φ values for an applied sinusoidal field.

The rheological properties change behavior, relative to more dilute solutions, above $\varphi = 0.2$, where non-Newtonian behavior is then exhibited. The power law dependence of η on φ is in harmony with the Zimm rather than the Rouse model, which suggests that hydrodynamic interactions between these polymers, in a mean field sense, are important. Electrical properties also begin to deviate for Nafion solutions above $\varphi = 0.2$, and mechanical percolation is essentially the same for the sodium and acid forms.

An interesting conclusion is that, as opposed to the Na^+ form, there is no electrical percolation threshold for the proton form, although conductive clusters must grow with increasing polymer volume fraction in both cases. In short, no clusters that span macroscopic dimensions form at a critical volume threshold for the acid form. These results are interpreted in two sketches, each having connected polymer strands above the percolation threshold so that there is mechanical percolation in either case. In one picture (Na^+ form), the sulfonate groups are evenly spaced so that electrical percolation exists, but for the acid form, these groups are more closely spaced in aggregates so as to cause voids along electrical pathways. It would need to be explained how, upon drying, the acid form gel evolves to form highly proton conducting membranes.

The concepts and techniques discussed by Cirkel and Okada are relevant with a view toward modifying the structure of solution cast Nafion membranes by manipulating counterion type, solvent, temperature, and other variables.

Hsu and Berzins used effective medium theories to model transport and elastic properties of these ionomers, with a view toward their composite nature, and compared this approach to that of percolation theory.²¹⁹

Hsu and Gierke presented an elastic theory for the clustering of ions in hydrated Nafion.³¹ This model presumes the existence of clusters and is unconcerned with the process of how clusters are actually created. Rather, it was intended to determine the equilibrium diameters of hydrated clusters given this assumed morphology. The equilibrium hydrated cluster diameter results from a minimization of a free energy composed of an elastic term and the non-specific interactions: $\text{SO}_3^- - \text{CF}_2$, $\text{SO}_3^- - \text{SO}_3^-$, $\text{H}_2\text{O} - \text{H}_2\text{O}$, H_2O at cluster surfaces, H_2O in the second layer from the cluster/hydrophobic surfaces, and H_2O in the bulk state. A severe limitation of this model is that it is semiphenomenological and therefore of little predictive value. This is so because prior knowledge of the dependence of the tensile modulus upon counterion type, water content, EW, and the diameter of an average dry cluster determined from SAXS studies, as well as the details of the experimental water vapor pressure sorption isotherm, is required in the calculations.

Mauritz and Rogers constructed a water vapor sorption isotherm model for ionomers with inherently clustered morphologies, as applied to Nafion mono-

valent cation–sulfonate forms.²²⁰ While it requires that all water molecules and fixed ions reside in clusters—a limitation—the theory provides for the variance of the average number of fixed ions in a cluster versus water content. The predicted quantities are the average number of sorbed water molecules per ionized side chain, n , the cluster radius extension ratio, λ , and the volume fraction of the cluster phase when the ionomer is equilibrated in either pure water or water vapor of relative humidity x . The driving force for cluster expansion is the osmotic pressure posed by visualized “ionic micro-solutions” within clusters, Π . Π was derived from a molecular theory of membrane–internal water activity that reflects (1) the hydration numbers of the ion exchange group and counterion, (2) the relative free versus bound water population, and (3) the sulfonate–counterion association–dissociation equilibrium, which depends on water content. Factor 3 was accounted for using a two or four state statistical mechanical model, involving hydration and ion pair energies, that was based on the earlier FTIR and solid-state NMR studies of Mauritz et al., of these materials.^{105,107} Π is resisted by a polymer contractile pressure, P , that is a function of a modulus, E , and λ , and equilibrium is considered as a condition where $\Pi = P$. A constitutive equation for λ versus n was assumed that allows for the evolution of a smaller number of larger clusters, as earlier described by Gierke et al.¹⁷

One of the limitations of this model is that the confinement of water molecules within clusters precludes its use within the context of water transport simulation because cluster-connective hydration structure is absent. Furthermore, water activity and contractile modulus are macroscopic based concepts whose application at the nanoscopic level is dubious. P is represented by a function borrowed from macroscopic elastic theory that contains E , and there is no microstructure-specific model for the resistance to deformation that can be applied to Nafion so that one is forced to use experimental tensile moduli by default.

Verbrugge and Hill presented a “macrohomogeneous” model for the transport of ions and solvent through ion exchange membranes using the Nernst–Planck equation.²²¹ No molecular mechanisms were factored into this model. These investigators did not feel that nanoscopic cavities that were connected by smaller charged pores existed, owing to the high radiotracer-based diffusion coefficients measured for bisulfate ions in Nafion 117 membranes, but they preferred a tortuous hydrophilic network phase of pores having diameters ~ 6 nm.²²² Pintauro and Verbrugge reported a model that calculated partition coefficients for a pore containing an electrolyte on the basis of adsorption onto the surfaces of pores that contain the fixed charge species.²²³ Bontha and Pintauro then applied this model to Nafion 117 membranes by treating them as arrays of parallel cylindrical pores.²²⁴ The Nafion model calculations accounted for electrostatic interactions between the pore surfaces and counterions, coions, and solvent molecules, as well as counterion/coion solvation free

energies. In this sense, the model was molecular-specific, but the use of the Poisson–Boltzmann equation to calculate the electrostatic potential in a pore can be questioned because this equation is based on the theory of macroscopic electrostatics but the pores are on the dimensional scale of atomic “granularity”. This model also has the feature of computing the dielectric constant as a function of radial distance in the cylindrical pore. The result indicated that water molecules are basically frozen in place near the pore wall due to the alignment of dipoles by the electric field, while near the cylindrical pore axis the water molecules exist in a state similar to bulk water. The reader is encouraged to compare these results with the results of Paul and Paddison, referred to later in this review, who also calculated pore permittivity versus radial distance in cylindrical pores using a more rigorous atomistic model. Despite the differences in the two approaches, the essential results are the same.

Eikerling et al. presented a random network and effective medium theory-based model of charge transport in “porous polymers”.²²⁵ The model adopts the view of clusters as being inverted micelles with connecting channels, much as in the Gierke model. There are three elementary types of bonds that are meant to represent conductances between bulklike water filled “blue (b) pores” and dry “red (r) pores”. The terminology is somewhat confusing, as a “pore” is meant to be a cluster and clusters are connected by “channels”. The pores have no chemical identity or structure other than having—or not having—excess water in the amount w . Both pore types contain water that is tightly bound by solvation of SO_3^- groups at the “inner pore surfaces”, and it is the excess water that can percolate when w is sufficiently high. There are “bonds” of random probabilities that connect the pores, and they are represented by elements consisting of three electrical resistors in series (i.e., pore–bond–pore), and the three conductivities add in the usual reciprocal fashion. These elements are linked to form an equivalent electrical circuit over the entire statistical ensemble. Kirchoff equations of simple electrical theory for this random network are solved in an approximate fashion by considering a single bond as being embedded in an effective medium of surrounding bonds. This is a site percolation problem in which the variable is x , the fraction of blue pores, and, as such, addresses the connectivity of the pore-channel network. The probabilities of b–b, r–r, and b–r bonds are given by x^2 , $(1 - x)^2$, and $2x(1 - x)$, respectively.

This model, when applied to Nafion as a function of water content, indicated a so-called quasi-percolation effect, which was “verified” by electrical impedance measurements. “Quasi-percolation” refers to the fact that the percolation threshold calculated using the single bond effective medium approximation (namely, $x_c = 0.58$, or 58% blue pore content) is quite larger than that issuing from a more accurate computer simulation. This number does not compare well with the threshold volume fraction calculated by Barkely and Meakin using their percolation approach, namely 0.10, which is less than the value for

a completely random system, which implies that the clusters are not randomly dispersed.²¹⁶

It should also be mentioned that capacitors were then added in parallel with the resistors in equivalent circuit elements because the frequency-dependent experimental electrical impedance data had a component that was 90° out of phase with the resistor.

The many details of this theory are omitted here. Nothing dealing with chemical groups and the forces that drive the morphology of ionomers is factored into this model, which limits its use in predicting fuel cell membrane performance. Moreover, it seems impossible to relate the quasi-percolation threshold to the real structure. Nonetheless, the view of conductance from the perspective of percolation is very appropriate.

Paddison and Zawodzinski performed fundamental calculations aimed at ascertaining side chain conformation.²²⁶ This fragment of the secondary structure is related to tertiary structure, that is, morphology, as it would determine, in large degree, how the side chains pack in micellar structures 40–50 Å in size. Packing, in turn, is related to hydration microstructure and the transport of ions and protons throughout these ionomers assuming that realistic hydration energetics are included in the calculations. These studies were conducted within the context of proton conducting membranes. The authors mentioned a particular need to establish a molecular basis for understanding electro-osmotic drag, that is, water transport as coupled with proton transport.

Self-consistent field, *ab initio* molecular orbital computations were performed on small molecules, namely $F_3C-O-CF_3$, to simulate the ether groups, and CF_3SO_3H , to simulate the ion exchange group at the end of the side chain. The energetics of a single H_2O molecule in the vicinity of these model compounds was determined to establish the water affinity of the ether and sulfonate groups. This water content is not high enough so as to cause swelling, and the single molecule is intended to be but a probe of its environment.

The calculations determined that the ether group was stiff and hydrophobic, but the SO_3^- group was strongly hydrophilic and flexible. However, the conclusion of ether group hydrophobicity may not be in harmony with the FTIR spectroscopic evidence of Lowry and Mauritz¹⁰⁵ as well as that of Moore et al.¹¹⁷ It was earlier mentioned that the band characteristic of this group has two components, at 965 and 980 cm^{-1} , for each of the two C–O–C groups in the side chain. By comparison, there is only one band in this region for the Dow short-side-chain membrane that only has one ether group. The band for the ether group closest to the sulfonate groups (965 cm^{-1}) shifts with water content, indicating either hydrogen bonding interactions with water molecules, through-bond inductive effects caused by proton dissociation in the SO_3H groups, or a combination of both. The ether group closest to the backbone, however, would seem to be shielded from water molecules. This result is also commensurate with the suggestion of Falk et al., based on their FTIR studies, referred to earlier, in

that the hydrophilic–hydrophobic interface is not sharp.

Using a molecular dynamics simulation (MM2) with no water molecules present, the side chain was predicted to be in a folded conformation at a temperature of 300 K. The C–O–C group was stiff, but the SO_3^- group, flexible. The folded conformation may simply be due to the artificial condition that the long side chain was isolated and not interacting with other side chains, and a curling of the unsolvated side chain having two ether oxygens would seem to be commensurate with minimizing interatomic energies. Discrete H_2O molecules should be packed around the side chains, rather than utilizing a dielectric continuum model of a solution environment to render the calculations realistic for a swollen state. A more realistic simulation would also involve more than one side chain.

Paddison, in later work, added more water molecules (up to 6) to the minimum energy side chain structure.²²⁷ Information relating to acid dissociation and local proton dynamics was obtained. One result of the calculations is that after the first hydration shell around the sulfonic acid group is complete, there is more effective shielding of the proton from the anion by the water molecules. Paddison stressed that this model, in which water molecules are clustered around a single sulfonate group, must be extended to include neighboring sulfonate groups so that proton transfer between them can be properly modeled.

Information extracted from the calculations for single acid molecule clusters was used, along with experimental information derived from SAXS measurements,^{17,228,229} in a water and proton transport model using a nonequilibrium statistical mechanical framework.^{230–232} Diffusion coefficients were calculated for Nafion 117 in cases where the number of water molecules per sulfonate group was 6, 13, and 22.5. More specifically, this model computes a “corrected” friction coefficient for the transport of H_3^+O in a hydrated pore/channel of cylindrical geometry. The diffusion coefficient is derived using the friction coefficient in the Einstein equation. Not accounted for, as mentioned by Paddison et al., is the contribution to mobility by proton hopping between water molecules, that is, the Grotthuss mechanism. The dielectric constant of water was assumed to be that of the bulk state, although Paul and Paddison presented a statistical mechanical model that determines the permittivity of water in hydrated polymer electrolyte membrane pores of cylindrical shape.²³³ Other assumptions of geometry and theoretical-computational details are beyond the scope of this review, and the reader is directed to the cited papers. The results of these computations were in agreement with diffusion coefficients obtained from pulsed field gradient NMR diffusion measurements.

Later, Paul and Paddison presented a statistical mechanical model that was used to calculate the dielectric permittivity in the water domains, that is, the pores, of Nafion.²³⁴ For computational purposes, a pore was taken as being of cylindrical geometry. The main prediction is that in a fully hydrated

membrane there is a central region within the pores where the water is similar to that in the bulk (i.e., has a dielectric constant ~ 80), but as one proceeds toward the pore walls, the water is increasingly more bound. This is essentially the same result predicted by Bontha and Pintauro using a different, less fundamental, modeling approach, as described earlier in this review.²²⁴

Niemark et al. investigated solvation and transport in Na^+ form Nafion using molecular simulations.^{235,236} Molecular mechanics energy optimizations of oligomers of 10 monomer units in a vacuum, as well as smaller oligomers that were solvated by water, methanol, and a water–methanol mixture, were performed using a potential force field based on electron density calculations, simulations of vapor–liquid equilibrium of lower perfluoroalkanes and ethers, and the thermodynamic properties of aqueous sodium sulfate solutions. The vacuum calculations yielded two conformations of the fluorocarbon skeleton, depending on the initial conformation in which the chain was placed before the simulation: either stretched for the initial all-trans conformation or highly folded and spiral-like for a randomly bent chain. When solvated, the oligomers, of smaller length, were more folded in water as compared to methanol and the side chain was stiff. H_2O and MeOH molecules formed hydrogen bonds with the oxygen atoms in the fixed SO_3^- anions, and these bonds have a lifetime considerably longer than the time scales required for rotational motions in the bulk. Water molecules could weakly hydrogen bond to the ether oxygen closest to the ion exchange group. For hydrated membranes having K^+ counterions, water did not form a continuous subphase, but isolated domains having less than 100 water molecules were predicted. It might be argued that a larger, more realistic ensemble of molecules and polymer molecular fragments would be required in a simulation to render this result credible, which is mentioned by Niemark. The statement is also made that it is not necessary to have a continuous hydrophilic phase in order to calculate water diffusion coefficients comparable to experimental values.

Khalatur et al. performed more aggressive molecular simulations of the structure of hydrated Nafion using integral equation theory.²³⁷ The details of the underlying theory, approximations, nature of force fields, computational algorithms, and so forth, are beyond the scope of this review and so will be omitted here. Semiempirical molecular orbital self-consistent field–rotational isomeric state calculations were performed in order to determine the equilibrium, energy-minimized conformations of fragments of the chain as well as “complexes” having a single water molecule probe. The polymer PRISM integral equation theory was used to calculate density–density intermolecular pair-correlation functions that reflect averaged particle density as a function of distance from any particle and determine the relation between the chemical structures of macromolecules and pair potentials and intermolecular correlation. While being essentially “atomistic”, the modeled structures had a measure of coarse-graining in that small

chemical groups were lumped together into effective spherical interactive force centers.

The calculations depicted a minimum energy conformation of an isolated side chain that is only slightly twisted, which was rationalized as being favorable with regard to the ability of water molecules to access the SO_3H groups. This structure was noted as being similar to the curled-up conformation determined by Paddison and Zawodzinski.²²⁶ Khalatur et al. also note that their energy-minimized side chain structure is rather different from that suggested by Litt in his lamellar model.⁷⁰

Another result is that water molecules preferentially reside at the terminus of the side chain (i.e., at the sulfonate group), which is not surprising, but also that the ether groups in the side chains are hydrophobic, which may be questioned by some investigators, as earlier noted in this review.

The addition of a small amount of water intensifies the drive for SO_3H group aggregation. Water, as predicted, is in a well-ordered state on local and mesoscopic scales, as evidenced by the NMR data of McMillan et al.,²³⁸ and is thought to exist in cagelike structures similar to clathrates. The water content in these calculations is above and below that corresponding to 4 H_2O molecules per SO_3H group, although it is unclear as to whether enough water molecules are present to allow for liquidlike water. Nor is it clear as to how many polymer chains are used in the calculations. In any case, the results reinforce the view of irregularly shaped cluster surfaces, or “fuzzy spheres” having a high surface area/volume aspect. This view is basically that of Falk¹¹³ and later Kreuer.⁹¹ These irregular or rough surfaces are amenable to the formation of water channels along which charge transport can take place.

None of the models address the question of how the main chains are packed, and details of crystallinity are neither factored into nor predicted by mathematical models of the structure and properties of Nafion. Chains packed in crystalline arrays are usually considered to be rigid within the context of certain properties; for example, with regard to diffusion, crystallites are viewed as impenetrable obstacles. ^{19}F NMR studies indicate otherwise. Molecular motions that do not significantly alter symmetry can in fact occur in polymer crystals. It would seem, for example, that the response of the Nafion structure to applied stress would depend on the flexibility of the polymer backbone, a certain fraction of which is incorporated in crystalline regions. On the other hand, Starkweather showed that the crystallinity and swelling of Nafion are not correlated.

At first thought, it might be considered that the steric restrictions posed by the large fluorine atoms would cause conformational rigidity due to restricted bond rotations. Hsu, however, showed that the conformations of the TFE chains in the crystalline regions in Nafion are in fact dynamic in that they can undergo helix reversals; that is, the handedness of the helix is easily reversed.²³⁹ These helix reversals are also seen in PTFE.²⁴⁰ This disorder phenomenon causes considerable conformational entropy and is

involved in the overall thermodynamics of the system. The principal IR spectroscopic signature of a helix reversal in PTFE is a very temperature-sensitive peak doublet in the range 600–700 cm^{-1} .²⁴¹ Temperature-dependent IR studies, conducted in the range –30 to 110 °C, showed an activation energy of only 1 $\text{kcal}\cdot\text{mol}^{-1}$. The overall conclusion is that fluoropolymer chains are rather flexible in the sense of torsion.

Jang et al. conducted full atomistic molecular dynamics simulations on two fictitious Nafion-like extreme chemical microstructures. One structure was an 80 unit chain consisting of a single block of 10 consecutive perfluorosulfonic vinyl ether (PSVE) units that were placed at the end of a single block of 70 TFE units. The other structure, referred to as “dispersed”, was also a chain of 80 monomer units in which single PSVE units were placed between blocks of 7 TFE units.²⁴² The total systems in either case consisted of four chains, and there were 15 water molecules per sulfonic acid group so that the total number of atoms in the simulations was 4568. The fundamental inter- and intramolecular interactions consisted of van der Waals, electrostatic, bond stretching, bond angle bending, and torsional bond rotation energetics.

These structures are fictional in the sense that these sequences do not correspond to the actual statistical polymerization based on the comonomer reactivity ratio, although it was said that the results have significance with respect to Nafion structural optimization and guidance in the search for Nafion replacements. Also, the non-insignificant degree of crystallinity of Nafion was not accounted for in the model.

The reader is referred to this paper for the details of the structure “annealing procedure”, equation of motion integration, and so forth.

While most of the conclusions are intuitive (e.g., predicted phase segregation), the results regarding interfaces are noteworthy. These regions were predicted to be heterogeneous in the sense of hydrophobic and hydrophilic patches. A hydrophilic patch consists of overlapping hydration shells about sulfonate groups while a hydrophobic patch consists of water-contacting perfluorocarbon groups. The calculations indicated that the interfaces are heterogeneous, much as suggested by Yeager some time ago, and that the diblock system has larger patches, that is, a greater degree of segregation, both ideas of which are intuitive.

While the computational-limited number of atoms is appreciated, the use of only four relatively short chains raises questions regarding the predicted morphologies. In principle, the sample space in these calculations is not large enough to generate an ensemble of periodic or quasi-periodic hydrophobic–hydrophilic phase components that would be sampled by high resolution TEM, AFM, or scattering techniques that reveal long-range structure.

Finally, simulations of the mean-squared displacement versus time for water and hydronium molecules were performed. The diffusion of water at this degree of hydration was seen to be greater for the more

segregated (diblock) structure. However, the diffusion of hydronium was determined to be insensitive to monomer sequence. It was pointed out that protons in these simulations are only allowed to move by the “vehicular” mechanism, that is, by translation as a part of an overall H_3O^+ molecule, whereas, in reality, protons can hop between adjacent water molecules via a combination of activated rate and tunneling processes.

Tanimura and Matsuoka calculated energy barriers for proton transfers in the small model compound associations ($[\text{CF}_3\text{SO}_3/\text{H}^+/\text{SO}_3\text{CF}_3]^{-1}$ and $[\text{CF}_3\text{SO}_3/\text{H}^+/\text{H}_2\text{O}/\text{SO}_3\text{CF}_3]^{-1}$) using an ab initio density functional quantum calculation method.²⁴³ Curves for energy versus distance between H^+ and an oxygen atom on an adjacent SO_3^- group in a sulfonate–sulfonate pair, while the distance between the two S atoms was held constant, were generated. The value of the energy barrier in the presence of one water molecule, of 2.1 $\text{kcal}\cdot\text{mol}^{-1}$, is close to the experimental value of 2.3 $\text{kcal}\cdot\text{mol}^{-1}$ for an 1100 EW Nafion membrane in which there are 18.2 mol of water per mole of SO_3^- sites. Of course, these calculations involve very local proton hopping events in the absence of perturbations posed by other water molecules and the phase separated polymer structure as well as molecular dynamics.

At the time of this writing, it must be conceded that there have been no fundamental principles-based mathematical model for Nafion that has predicted significantly new phenomena or caused property improvements in a significant way. Models that capture the essence of percolation behavior ignore chemical identity. The more ab initio methods that do embrace chemical structure are limited by the number of molecular fragments that the computer can accommodate. Other models are semiempirical in nature, which limits their predictive flexibility. Nonetheless, the diversity of these interesting approaches offers structural perspectives that can serve as guides toward further experimental inquiry.

7. Conclusions

A comprehensive review of the state of understanding of the fundamental structure and properties of Nafion perfluorosulfonate materials, at the time of this writing, has been presented based on recent as well as historical literature that either survived the test of time or influenced further research trends. Since the greatest interest in Nafion in recent years derives from its consideration as a proton conducting membrane in fuel cells, research has been largely driven by this critical application. Through the collective information acquired from the detailed works of many research groups and institutions, a broader understanding of this technologically important material has emerged. Although many of these contributions have exposed a significant number of critical relationships between structure (both chemical and morphological) and the unique properties of Nafion, it is widely accepted that much more remains to be learned.

While most long-range structure interrogations via SAXS and SANS methods have had to assume

structure factor models, and microscopic methods have been limited by resolution limits, a theme that has persisted is that the morphology of Nafion is quite complex and at least of a three-phase nature. There is no long-range patterned organization of hydrophilic clusters in a hydrophobic and semi-crystalline perfluorocarbon phase. Hydrophilic–hydrophobic interfaces are not discrete phase discontinuities, but the evidence suggests them to be “rough” or “fuzzy”. The evolution of morphological models for this complex polymer has involved many distinct conceptual designs; however, the relevant aspects of structure in these models have shown several important unifying perspectives, depending on ion and water content and the specific range of dimensions probed by the varying methods of analysis. With the inevitable improvements in techniques and methods of morphological characterization, a much more detailed representation of the true structure of perfluorosulfonate ionomers will be realized.

Water in sufficiently hydrated samples is an extended phase, and the clusters can be anisotropic and are contiguous to form percolation pathways, although the exact nature of interdomain water structure remains under debate. The more local, that is, molecular, organization of water, cation–sulfonate interactions and associations, and cation hydration and mobility have been investigated using spectroscopic, thermal analyses, sorption isotherm, and electrical conductivity studies. Water has been classified in terms of freezing versus nonfreezing or tightly bound around ions versus free or liquidlike, and the degree of hydrogen bonding in water clusters has been well-characterized. This information has been, and will be, valuable in the interpretation of water, ion, and proton transport data issuing from diffusion and electrical conductivity studies.

The long- and short-ranged motions in the backbone and side chains in Nafion, that have appeared as variously assigned transitions in dynamic mechanical studies, have only recently been probed on a molecular level using methods of high resolution NMR spectroscopy. This valuable information concerning chain dynamics is only just now emerging to yield important insight into the origins of mechanical relaxations of perfluorosulfonate ionomers in a variety of physical states.

The static mechanical properties of Nafion, while not the primary concern, save for the requirement of membrane integrity in electrochemical cells, have been investigated as a function of equivalent weight, counterion type, and solvent uptake. Undoubtedly, these properties are also a function of morphology, yet little specific information on this topic exists to date. While the number of primary chemical structure variations of Nafion sulfonate materials is very limited, morphology and, therefore, properties can, however, be manipulated by sample prehistory variables such as temperature and temperature cycles, swelling in different solvents, orientation, and solution and melt preprocessing schemes. With new methods of membrane preparation and the drive toward thinner membranes for improved transport properties, the need for critical morphology-mechan-

ical property relationships will become an important future consideration.

As noted in the Molecular Simulation of Structure and Properties section, there have been no fundamental principle-based mathematical models for Nafion that have predicted new phenomena or caused property improvements in a significant way. This is due to a number of limitations inherent in one or the other of the various schemes. These shortcomings include an inability to sufficiently account for chemical identity, an inability to simulate and predict the long-range structure as would be probed by SAXS or TEM, and the failure to simulate structure over different hierarchy levels. Certainly, advances in this important research front will emerge and be combined with advances in experimentally derived information to yield a much deeper state of understanding of Nafion.

8. Acknowledgment

The authors wish to acknowledge support for this work provided by the MRSEC Program of the National Science Foundation under Award Number DMR-0213883. Original SAXS data presented in this article were obtained through research carried out at the National Synchrotron Light Source, Brookhaven National Laboratory, which is supported by the U.S. Department of Energy, Division of Materials Sciences and Division of Chemical Sciences, under Contract No. DE-AC02-98CH10886. Finally, the authors want to recognize the invaluable assistance of Laura Fosselman in the preparation of this document.

9. Literature References

- (1) Curtin, D. E.; Lousenberg, R. D.; Henry, T. J.; Tangeman, P. C.; Tisack, M. E. *J. Power Sources* **2004**, *131*, 41.
- (2) Hora, C. J.; Maloney, D. E. *Electrochem. Soc. Ext. Abstr.* **1977**, *77* (2), 1145.
- (3) Grot, W. G. U.S. Patents 3,969,285 (1976), 4,026,783 (1977), 4,030,988 (1977).
- (4) Burkhardt, S. K.; Maloney, D. E. U.S. Patent 4,168,216 (1979).
- (5) Covitch, M. J.; Lowry, S. R.; Gray, C. L.; Blackford, B. In *Polymeric Separation Media*; Cooper, A. R., Ed.; Plenum: New York, 1982; p 257.
- (6) Yeager, H. L.; Kipling, B.; Dotson, R. L. *J. Electrochem. Soc.* **1980**, *127* (2), 303.
- (7) Robertson, M. A. F. Ph.D. Thesis, University of Calgary, 1994.
- (8) Robertson, M. A. F.; Yeager, H. L. *Macromolecules* **1996**, *29*, 5166.
- (9) Seko, M.; Ogawa, S.; Kimoto, K. In *Perfluorinated Ionomer Membranes*; Eisenberg, A., Yeager, H. L., Eds.; ACS Symposium Series No. 180; American Chemical Society: Washington, DC, 1982; Chapter 15, p 365.
- (10) (a) Doyle, M.; Lewittes, M. E.; Roelofs, M. G.; Perusich, S. A. *J. Phys. Chem. B* **2001**, *105*, 9387. (b) Doyle, M. E.; Lewittes, M. E.; Roelofs, M. G.; Perusich, S. A.; Lowrey, R. E. *J. Membr. Sci.* **2001**, *184*, 257. (c) Perusich, S. A. *Macromolecules* **2000**, *33*, 3431. (d) Perusich, S. A.; McBrearty, M. *Polym. Eng. Sci.* **2000**, *40*, 214. (e) McBrearty, M.; Perusich, S. A. *Polym. Eng. Sci.* **2000**, *40*, 201. (f) Perusich, S. A.; Avakian, P.; Keating, M. Y. *Macromolecules* **1993**, *26*, 4756.
- (11) (a) Hashimoto, T.; Fujimura, M.; Kawai, H. p 217. (b) Seko, M.; Ogawa, S.; Kimoto, K. p 365. (c) Sata, T.; Onoue, Y. p 411. (d) Ukihashi, H.; Yamabe, M. p 427. In *Perfluorinated Ionomer Membranes*; Eisenberg, A., Yeager, H. L., Eds.; ACS Symposium Series No. 180; American Chemical Society: Washington, DC, 1982.
- (12) Doyle, M.; Rajendran, G. *Handbook of Fuel Cells Fundamentals, Technology and Applications*; John Wiley & Sons: Chichester, U.K., 2003; Vol. 3, Part 3, Chapter 30, p 351.
- (13) Tant, M. R.; Darst, K. P.; Lee, K. D.; Martin, C. W. In *Multiphase Polymers: Blends and Ionomers*; Utracki, L. A., Weiss, R. A., Eds.; ACS Symposium Series No. 395; American Chemical Society: Washington, DC, 1989; Chapter 15, p 370.

- (14) Xu, G. *Polymer* **1993**, *25*, 397.
- (15) Gierke, T. D.; Hsu, W. Y. In *Perfluorinated Ionomer Membranes*; Eisenberg, A., Yeager, H. L., Eds.; ACS Symposium Series No. 180; American Chemical Society: Washington, DC, 1982; Chapter 13, p 283.
- (16) Hsu, W. Y.; Gierke, T. D. *J. Membr. Sci.* **1983**, *13*, 307.
- (17) Gierke, T. D.; Munn, G. E.; Wilson, F. C. *J. Polym. Sci., Polym. Phys.* **1981**, *19*, 1687.
- (18) Yeager, H. L.; Steck, A. J. *Electrochem. Soc.* **1981**, *128*, 1880.
- (19) Eisenberg, A.; Yeager, H. L. *Perfluorinated Ionomer Membranes*; ACS Symposium Series 180; American Chemical Society: Washington, DC, 1982.
- (20) Heitner-Wirguin, C. *J. Membr. Sci.* **1996**, *120*, 1.
- (21) Holliday, L. *Ionic Polymer*; Applied Science Publishers: London, 1975.
- (22) Eisenberg, A.; King, M. *Ion Containing Polymers in Polymer Physics*; Academic: New York, 1977; Vol. 2.
- (23) MacKnight, W. J.; Taggart, W. P.; Stein, R. S. *J. Polym. Sci., Polym. Symp.* **1974**, *45*, 113.
- (24) Yarusso, D. J.; Cooper, S. L. *Macromolecules* **1983**, *16*, 1871.
- (25) Yarusso, D. J.; Cooper, S. L. *Polymer* **1985**, *26*, 371.
- (26) *Perfluorinated Ionomer Membranes*; Eisenberg, A., Yeager, H. L., Eds.; ACS Symposium Series No. 180; American Chemical Society: Washington, DC, 1982.
- (27) Gierke, T. D. *152nd Meeting of the Electrochemical Society, Ext. Abstr.*; **1977**, *124*, 319C.
- (28) Pineri, M.; Duplessix, R.; Gauthier, S.; Eisenberg, A. In *Ions in Polymers*; Eisenberg, A., Ed.; ACS Symposium Series No. 187; American Chemical Society: Washington, DC, 1980; p 283.
- (29) Duplessix, R.; Escoubes, M.; Rodmacq, B.; Volino, F.; Roche, E.; Eisenberg, A.; Pineri, M. In *Water in Polymers*; Rowland, S. P., Ed.; ACS Symposium Series No. 127; American Chemical Society: Washington, DC, 1980; p 469.
- (30) Rodmacq, B.; Coey, J. M.; Escoubes, M.; Roche, E.; Duplessix, R.; Eisenberg, A.; Pineri, M. In *Water in Polymers*; Rowland, S. P., Ed.; ACS Symposium Series No. 127; American Chemical Society: Washington, DC, 1980; p 487.
- (31) Hsu, W. Y.; Gierke, T. D. *Macromolecules* **1982**, *15*, 101.
- (32) Gierke, T. D.; Munn, G. E.; Wilson, F. C. In *Perfluorinated Ionomer Membranes*; Eisenberg, A., Yeager, H. L., Eds.; ACS Symposium Series No. 180; American Chemical Society: Washington, DC, 1982; p 195.
- (33) Eisenberg, A.; Hird, B.; Moore, R. B. *Macromolecules* **1990**, *23*, 4098.
- (34) Roche, E. J.; Pineri, M.; Duplessix, R.; Levelut, A. M. *J. Polym. Sci., Polym. Phys. Ed.* **1981**, *19*, 1.
- (35) Roche, E. J.; Pineri, M.; Duplessix, R. *J. Polym. Sci., Polym. Phys. Ed.* **1982**, *20*, 107.
- (36) Fujimura, M.; Hashimoto, T.; Kawai, H. *Macromolecules* **1981**, *14*, 1309.
- (37) Fujimura, M.; Hashimoto, R.; Kawai, H. *Macromolecules* **1982**, *15*, 136.
- (38) Roche, E. J.; Stein, R. S.; Russell, T. P.; MacKnight, W. J. *J. Polym. Sci., Polym. Phys. Ed.* **1980**, *18*, 1497.
- (39) Marx, C. L.; Caulfield, D. F.; Cooper, S. J. *Macromolecules* **2000**, *33*, 6541.
- (40) Miura, Y.; Yoshida, H. *Tokyo Metrop. Univ.* **1990**, *40*, 4349.
- (41) Starkweather, H. W., Jr. *Macromolecules* **1982**, *15*, 320.
- (42) Kumar, S.; Pineri, M. *J. Mol. Sci., Part B: Polym. Phys.* **1986**, *24*, 1767.
- (43) Manley, D. S.; Williamson, D. L.; Noble, R. D.; Koval, C. A. *Chem. Mater.* **1996**, *8*, 2595.
- (44) Dreyfus, B.; Gebel, G.; Aldebert, P.; Pineri, M.; Escoubes, M.; Thomas, M. *J. Phys. (Paris)* **1990**, *51*, 1341.
- (45) Lee, E. M.; Thomas, R. K.; Burgess, A. N.; Barnes, D. J.; Soper, A. K.; Rennie, A. R. *Macromolecules* **1992**, *25*, 3106.
- (46) Grot, W. G.; Chadds, F. European Patent 0,066,369, 1982.
- (47) Martin, C. R.; Rhoades, T. A.; Fergusson, J. A. *Anal. Chem.* **1982**, *54*, 1639.
- (48) Aldebert, P.; Dreyfus, B.; Pineri, M. *Macromolecules* **1986**, *19*, 2651.
- (49) Aldebert, P.; Dreyfus, B.; Gebel, G.; Nakamura, N.; Pineri, M.; Volino, F. *J. Phys. (Paris)* **1988**, *49*, 2101.
- (50) Rebrov, A. V.; Ozerin, A. N.; Svergun, D. I.; Bobrova, L. P.; Bakeyev, N. F. *Polym. Sci. U. S. S. R.* **1990**, *32*, 1515.
- (51) Loppinet, B.; Gebel, G.; Williams, C. E. *J. Phys. Chem. B* **1997**, *101*, 1884.
- (52) Loppinet, B.; Gebel, G. *Langmuir* **1998**, *14*, 1977.
- (53) Moore, R. B.; Martin, C. R. *Anal. Chem.* **1986**, *58*, 2569.
- (54) Moore, R. B.; Martin, C. R. *Macromolecules* **1988**, *21*, 1334.
- (55) Moore, R. B.; Martin, C. R. *Macromolecules* **1989**, *22*, 3594.
- (56) Gebel, G.; Aldebert, P.; Pineri, M. *Macromolecules* **1987**, *20*, 1425.
- (57) Halim, J.; Scherer, G. G.; Stamm, M. *Macromol. Chem. Phys.* **1994**, *195*, 3783.
- (58) Cable, K. M.; Mauritz, K. A.; Moore, R. B. *Polym. Prepr.* **1994**, *35* (1), 421.
- (59) Cable, K. M.; Mauritz, K. A.; Moore, R. B. *Polym. Prepr.* **1994**, *35* (2), 854.
- (60) Cable, K. M.; Mauritz, K. A.; Moore, R. B. *Chem. Mater.* **1995**, *7*, 1601.
- (61) Landis, F. A.; Moore, R. B.; Page, K. A.; Han, C. C. *Polym. Mater.: Sci. Eng.* **2002**, *87*, 121.
- (62) Elliott, J. A.; Hanna, S.; Elliott, A. M. S.; Cooley, G. E. *Polymer* **2001**, *42*, 2551.
- (63) Elliott, J. A.; Hanna, S.; Elliott, A. M. S.; Cooley, G. E. *Macromolecules* **2000**, *33*, 4161.
- (64) Londono, J. D.; Davidson, R. V.; Mazur, S. *Polym. Mater. Sci. Eng.* **2001**, *85*, 23.
- (65) Barbi, V.; Funari, S. S.; Gehrke, R.; Scharnagl, N.; Stribeck, N. *Polymer* **2003**, *44*, 4853.
- (66) Van der Heijden, P. C.; Rubatat, L.; Diat, O. *Macromolecules*, in press.
- (67) Gebel, G.; Lambard, J. *Macromolecules* **1997**, *30*, 7914.
- (68) Gebel, G.; Moore, R. B. *Macromolecules* **2000**, *33*, 4850.
- (69) Rollet, A.-L.; Gebel, G.; Simonin, J.-P.; Turq, P. *J. Polym. Sci., Part B: Polym. Phys.* **2001**, *39*, 548.
- (70) Litt, M. H. *Polym. Prepr.* **1997**, *38*, 80.
- (71) Haubold, H.-G.; Vad, T.; Jungbluth, H.; Hiller, P. *Electrochim. Acta* **2001**, *46*, 1559.
- (72) Rubatat, L.; Rollet, A.-L.; Gebel, G.; Diat, O. *Macromolecules* **2002**, *35*, 4050.
- (73) Szajdzinska-Pietek, E.; Schlick, S.; Plonka, A. *Langmuir* **1994**, *10*, 1101.
- (74) Orfino, F. P.; Holdcroft, S. *J. New Mater. Electrochem. Syst.* **2000**, *3*, 287.
- (75) Young, S. K.; Trevino, S. F.; Beck Tan, N. C. *J. Polym. Sci., Part B: Polym. Phys.* **2002**, *40*, 387.
- (76) Gebel, G. *Polymer* **2000**, *41*, 5829.
- (77) Rollet, A.-L.; Diat, O.; Gebel, G. *J. Phys. Chem. B* **2002**, *21*, 3033.
- (78) Ceynowa, J. *Polymer* **1978**, *19*, 73.
- (79) Xue, T.; Trent, J. S.; Osseo-Asare, K. *J. Membr. Sci.* **1989**, *45*, 261.
- (80) Rieberer, S.; Norian, K. H. *Ultramicroscopy* **1992**, *41*, 225.
- (81) Porat, Z.; Fryer, J. R.; Huxham, M.; Rubinstein, I. *J. Phys. Chem.* **1995**, *99*, 4667.
- (82) Lehmani, A.; Durand-Vidal, S.; Turq, P. *J. Appl. Polym. Sci.* **1998**, *68*, 503.
- (83) McLean, R. S.; Doyle, M.; Sauer, B. B. *Macromolecules* **2000**, *33*, 6541.
- (84) Zawodzinski, T. A.; Gottesfeld, S.; Shoichet, S.; McCarthy, T. J. *J. Appl. Electrochem.* **1993**, *23*, 86.
- (85) Schroeder, P. *Z. Phys. Chem. (Munich)* **1993**, *45*, 57.
- (86) Zawodzinski, T. A.; Derouin, C.; Radzinski, S.; Sherman, R. J.; Smith, V. T.; Springer, T. E.; Gottesfeld, S. *J. Electrochem. Soc.* **1993**, *140*, 1041.
- (87) Tovbin, Y. K. *Zh. Fiz. Khim.* **1988**, *72*, 55.
- (88) Ozerin, A. N.; Rebrov, A. V.; Yakunin, A. N.; Bessonova, N. P.; Dreiman, N. A.; Sokolov, N. F.; Bakeev, L. F. *Vysokomol. Soedin., Ser. A* **1986**, *28*, 2303.
- (89) Mauritz, K. A.; Rogers, C. E. *Macromolecules* **1985**, *18*, 483.
- (90) James, P. J.; McMaster, T. J.; Newton, J. M.; Miles, M. J. *Polymer* **2000**, *41*, 4223.
- (91) Kreuer, K. D. *Handbook of Fuel Cells—Fundamentals, Technology and Applications*; Vielstich, W., Lamm, A., Gasteiger, H. A., Eds.; John Wiley & Sons Ltd: Chichester, U.K., 2003; Vol. 3, Part 3.
- (92) Grot, W. G. F.; Munn, G. E.; Walmsley, P. N. Presented at the 141st National Meeting of the Electrochemical Society, Houston, TX, 1972.
- (93) Yeo, R. S. *Polymer* **1980**, *21*, 432.
- (94) Yeo, R. S. *J. Appl. Polym. Sci.* **1986**, *32*, 5733.
- (95) Gebel, G.; Aldebert, P.; Pineri, M. *Polymer* **1993**, *34*, 333.
- (96) Zawodzinski, T. A.; Neeman, M.; Sillerud, L. O.; Gottesfeld, S. *J. Phys. Chem.* **1991**, *95*, 6040.
- (97) Zawodzinski, T. A.; Derouin, C.; Radzinsky, S.; Sherman, R. J.; Smith, V. T.; Springer, T. E.; Gottesfeld, S. *J. Electrochem. Soc.* **1993**, *140*, 1041.
- (98) Hinatsu, J. T.; Mizuhata, M.; Takenaka, H. *J. Electrochem. Soc.* **1994**, *141* (6), 1493.
- (99) Yeo, S.; Eisenberg, A. *J. Appl. Polym. Sci.* **1977**, *21*, 875.
- (100) Zawodzinski, T. A.; Davey, J.; Springer, T.; Gottesfeld, S. *Electrochem. Soc. Ext. Abstr.* **1992**, *Vol. 92-2*, Abstract No. 94, p 149.
- (101) Futerko, P.; Hsing, I.-M. *J. Electrochem. Soc.* **1999**, *146* (6), 2049.
- (102) Flory, P. J. *Principles of Polymer Chemistry*; Cornell University Press: Ithaca, NY, 1953; pp 495–540.
- (103) Buzzoni, R.; Bordiga, G.; Ricchiardi, G.; Spoto, G.; Zecchina, A. *J. Phys. Chem.* **1995**, *99*, 11937.
- (104) Zecchina, A.; Geobaldo, G.; Spoto, G.; Bordiga, G.; Ricchiardi, G.; Buzzoni, R.; Patrini, G. *J. Phys. Chem.* **1996**, *100*, 16584.
- (105) Lowry, S. R.; Mauritz, K. A. *J. Am. Chem. Soc.* **1980**, *102*, 4665.
- (106) Komoroski, R. A.; Mauritz, K. A. *J. Am. Chem. Soc.* **1978**, *100*, 7487.
- (107) Komoroski, R. A.; Mauritz, K. A. In *Perfluorinated Ionomer Membranes*; Eisenberg, A., Yeager, H. L., Eds.; ACS Symposium Series 180; American Chemical Society: Washington, DC, 1982; p 113.

- (108) Robinson, R. A.; Stokes, R. H. *Electrolyte Solutions*, 2nd ed.; Dover: Mineola, NY, 2002; Chapter 14.
- (109) Diebler, H.; Eigen, M. *Z. Phys. Chem. (Muenchen)* **1959**, *20*, 299.
- (110) Eigen, M.; Tamm, K. *Z. Elektrochem.* **1962**, *66*, 93, 107.
- (111) Komoroski, R. A. *Adv. Chem. Ser.* **1980**, *187*, 155.
- (112) Heitner-Wirguin, C. *Polymer* **1979**, *20*, 371.
- (113) Falk, M. *Can. J. Chem.* **1980**, *58*, 1495.
- (114) Rollet, A.-L.; Gebel, G.; Simonin, J.-P.; Turq, P. *J. Polym. Sci., Part B: Polym. Phys.* **2001**, *39*, 548.
- (115) Kujawski, W.; Nguyen, Q. T.; Neel, J. *J. Appl. Polym. Sci.* **1992**, *44*, 951.
- (116) Quezado, S.; Kwak, J. C. T.; Falk, M. *Can. J. Chem.* **1984**, *62*, 958.
- (117) Cable, K. M.; Mauritz, K. A.; Moore, R. B. *J. Polym. Sci., Part B: Polym. Phys.* **1995**, *33*, 1065.
- (118) Falk, M. In *Perfluorinated Ionomer Membranes*; Eisenberg, A., Yeager, H. L., Eds.; ACS Symposium Series 180; American Chemical Society: Washington, DC, 1982; p 139.
- (119) Peluso, S. L.; Tsatsas, A. T.; Risen, W. M. *Spectral Studies of Ions in Perfluorocarbonsulfonate (Nafion) Ionomers*; Office of Naval Research Technical Report No. TR-79-01, 1971.
- (120) Yeager, H. L. In *Perfluorinated Ionomer Membranes*; Eisenberg, A., Yeager, H. L., Eds.; ACS Symposium Series 180; American Chemical Society: Washington, DC, 1982; p 25.
- (121) Barnes, D. J. In *Structure and Properties of Ionomers*; Pineri, M., Eisenberg, A., Eds.; D. Reidel Publ. Co.: Dordrecht, 1987; p 501.
- (122) Luck, W. A. P. In *Synthetic Membrane Processes*; Belfort, G., Ed.; Academic Press: New York, 1984; p 21.
- (123) Quezado, S.; Kwak, J. C. T.; Falk, M. *Can. J. Chem.* **1984**, *62*, 958.
- (124) Yeager, H. L.; Twardowski, Z.; Clarke, L. M. *J. Electrochem. Soc.* **1982**, *129* (2), 324.
- (125) Starkweather, H. W.; Chang, J. J. *Macromolecules* **1982**, *15*, 752.
- (126) Boyle, N. G.; McBrierty, V. J.; Douglass, D. C. *Macromolecules* **1983**, *16*, 75.
- (127) Bunce, N. J.; Sondheimer, S. J.; Fyfe, C. A. *Macromolecules* **1986**, *19*, 333.
- (128) Sivashinsky, N.; Tanny, G. B. *J. Appl. Polym. Sci.* **1981**, *26*, 2625.
- (129) Bloembergen, N.; Purcell, E. M.; Pound, R. V. *Phys. Rev.* **1948**, *73*, 679.
- (130) Resing, H. A. *Adv. Relaxation Proc.* **1967-8**, *1*, 109.
- (131) Boyle, N.; McBrierty, V. J.; Eisenberg, A. *Macromolecules* **1983**, *16*, 80.
- (132) Pineri, M.; Volino, F.; Escoubes, M. *J. Polym. Sci., Polym. Phys. Ed.* **1985**, *23*, 2009.
- (133) Yoshida, H.; Miura, Y. *J. Membr. Sci.* **1992**, *68*, 1.
- (134) Miura, Y.; Yoshida, H. *Mem. Fac. Technol., Tokyo Metropol. Univ.* **1990**, *40*, 4349.
- (135) Moore, R. B.; Cable, K. M. *Polym. Prepr. (Am. Chem. Soc., Div. Polym. Chem.)* **1997**, *38* (1), 272.
- (136) MacMillan, B.; Sharp, A. R.; Armstrong, R. L. *Polymer* **1999**, *40*, 2471.
- (137) Martin, C. R.; Rhoades, T. A.; Ferguson, J. A. *Anal. Chem.* **1982**, *54*, 1639.
- (138) Rieke, P. C.; Vanderborgh, N. E. *J. Membr. Sci.* **1987**, *32*, 313.
- (139) Escoubes, M.; Pineri, M. In *Perfluorinated Ionomer Membranes*; Eisenberg, A., Yeager, H. L., Eds.; ACS Symposium Series 180; American Chemical Society: Washington, DC, 1982; p 9.
- (140) MacMillan, B.; Sharp, A. R.; Armstrong, R. L. *Polymer* **1999**, *40*, 2481.
- (141) Angell, C. A. In *Water, a Comprehensive Treatise*; Franks, F., Ed.; Plenum: New York, 1982; Vol. 7.
- (142) Cahan, B. D.; Wainright, J. S. *J. Electrochem. Soc.* **1993**, *140*, L185.
- (143) Fontanella, J. J.; McLin, M. G.; Wintersgill, M. C.; Calame, J. P.; Greenbaum, S. G. *Solid State Ionics* **1993**, *66*, 1.
- (144) Gardner, C. L.; Anantaraman, A. V. *J. Electroanal. Chem.* **1998**, *449*, 209.
- (145) Gavach, C.; Pamboutzoglou, N.; Nedyalkov, N.; Pourcelly, G. *J. Membr. Sci.* **1989**, *45*, 37.
- (146) Pourcelly, G.; Oikonomou, A.; Gavach, C. *J. Electroanal. Chem.* **1990**, *287*, 43.
- (147) Lindheimer, A.; Molenat, J.; Gavach, C. *J. Electroanal. Chem.* **1987**, *216*, 71.
- (148) Eikerling, M.; Kornyshev, A. A.; Kuznetsov, A. M.; Ulstrup, J.; Walbran, S. *J. Phys. Chem. B* **2001**, *105*, 3636.
- (149) Zundel, G.; Metzger, H. *Z. Phys. Chem.* **1968**, *58*, 225.
- (150) Wicke, E.; Eigen, M.; Ackermann, T. *Z. Phys. Chem.* **1954**, *1*, 340.
- (151) Eikerling, M.; Kornyshev, A. A. *J. Electroanal. Chem.* **2001**, *502*, 1.
- (152) Aldebert, P.; Guglieme, M.; Pineri, M. *Polym. J.* **1991**, *23* (5), 399.
- (153) Helfferich, F. *Ion Exchange*; McGraw-Hill: New York, 1962; p 351.
- (154) Cappadonia, M.; Erning, J. W.; Stimming, U. *J. Electroanal. Chem.* **1994**, *376*, 189.
- (155) Cappadonia, M.; Erning, J. W.; Niake, S. M.; Stimming, U. *Solid State Ionics* **1995**, *77*, 65.
- (156) Chen, R. S.; Jayakody, S. G.; Greenbaum, S. G.; Pak, Y. S.; Xu, G.; McLin, M. G.; Fontanella, J. *J. Electrochem. Soc.* **1993**, *140*, 889.
- (157) Chen, R. S.; Stallworth, P. E.; Greenbaum, S. G.; Fontanella, J. J.; Wintersgill, M. C. *Electrochim. Acta* **1995**, *40* (3), 309.
- (158) Paddison, S. J.; Reagor, D. W.; Zawodzinski, T. A. *J. Electroanal. Chem.* **1998**, *459*, 91.
- (159) Ellison, W. J.; Lamkaouchi, K.; Moreau, J.-M. *J. Mol. Liq.* **1996**, *68*, 171.
- (160) Zawodzinski, T. A.; Neeman, M.; Sillerud, L. D.; Gottesfeld, S. *J. Phys. Chem.* **1991**, *95*, 6040.
- (161) Alberti, G.; Casciola, M.; Massinelli, L.; Bauer, B. *J. Membr. Sci.* **2001**, *185*, 73.
- (162) Glasstone, S.; Laidler, K. J.; Eyring, H. *The Theory of Rate Processes*; McGraw-Hill: New York, 1941; pp 550 and 573.
- (163) Mauritz, K. A. Morphological Theories. In *Ionomers: Synthesis, Structure, Properties and Applications*; Tant, M. R., Mauritz, K. A., Wilkes, G. L., Eds.; Blackie Academic & Professional: London, 1997.
- (164) Yeo, Y. S. In *Perfluorinated Ionomer Membranes*; Eisenberg, A., Yeager, H. L., Eds.; ACS Symposium Series No. 180; American Chemical Society: Washington, DC, 1982; p 453.
- (165) Kipling, B. In *Perfluorinated Ionomer Membranes*; Eisenberg, A., Yeager, H. L., Eds.; ACS Symposium Series No. 180; American Chemical Society: Washington, DC, 1982; p 475.
- (166) Yeager, H. L.; Gronowski, A. A. In *Ionomers: Synthesis, Structure, Properties and Applications*; Tant, M. R., Mauritz, K. A., Wilkes, G. L., Eds.; Blackie Academic & Professional: London, 1997; p 333.
- (167) Olah, G. A.; Dyer, P. S.; Prakash, G. K. S. *Synthesis* **1980**, *7*, 513.
- (168) Sondheimer, S. J.; Bunce, N. J.; Fyfe, C. A. *J. Macromol. Sci., Rev. Macromol. Chem. Phys.* **1986**, *C26* (3), 353.
- (169) Ferry, L. L. *J. Macromol. Sci., Chem.* **1990**, *A27* (8), 1095.
- (170) Zundel, G. *Hydration and Intermolecular Interaction*; Academic Press: New York, 1969.
- (171) Zundel, G. In *The Hydrogen Bond, Recent Developments in Theory and Experiments*; Schuster, P., Zundel, G., Sandorfy, C., Eds.; North Holland: Amsterdam, 1976; Vol. II, Chapter 15, p 683.
- (172) Eigen, M. *Angew. Chem.* **1963**, *75*, 489.
- (173) Zundel, G. *J. Membr. Sci.* **1982**, *11*, 249.
- (174) Interactions and Structures of Ionic Solvates—Infrared Results. Zundel, G.; Fritsch, J. In *Physics of Ionic Solvation*; Dogonadze, R. R., Kalman, E., Kornyshev, A. A., Ulstrup, J., Eds.; Elsevier: Amsterdam, 1984.
- (175) Leuchs, M.; Zundel, G. *J. Chem. Soc., Faraday Trans 2* **1978**, *74*, 2256.
- (176) Ostrowska, J.; Narebska, A. *Colloid Polym. Sci.* **1983**, *261*, 93.
- (177) Mauritz, K. A.; Gray, C. L. *Macromolecules* **1983**, *16*, 1279.
- (178) Kreuer, K. D. *Chem. Mater.* **1998**, *8*, 610.
- (179) Kreuer, K. D.; Rabenau, A.; Weppner, W. *Angew. Chem., Int. Ed. Engl.* **1982**, *21*, 208.
- (180) Kreuer, K. D. *J. Membr. Sci.* **2001**, *185*, 29.
- (181) Yeo, S. C.; Eisenberg, A. *J. Appl. Polym. Sci.* **1977**, *21*, 875.
- (182) Takamatsu, T.; Hashiyama, M.; Eisenberg, A. *J. Appl. Polym. Sci.* **1979**, *24*, 2199.
- (183) Yeager, H. L. In *Structure and Properties of Ionomers*; NATO ASI Series C; D. Reidel: Dordrecht, 1987; Vol. 198, p 377.
- (184) Yeager, H. L. In *Perfluorinated Ionomer Membranes*; Eisenberg, A., Yeager, H. L., Eds.; ACS Symposium Series No. 180; American Chemical Society: Washington, DC, 1982; p 42.
- (185) Millet, P. *J. Membr. Sci.* **1990**, *50*, 325.
- (186) Lopez, M.; Kipling, B.; Yeager, H. L. *Anal. Chem.* **1977**, *49*, 629.
- (187) Yeager, H. L.; Steck, A. *Anal. Chem.* **1979**, *51*, 862.
- (188) Yeager, H. L.; Kipling, B. *J. Phys. Chem.* **1979**, *83*, 1836.
- (189) Zawodzinski, T. A.; Neeman, M.; Sillerud, L. O.; Gottesfeld, S. *J. Phys. Chem.* **1991**, *95*, 6040.
- (190) Gong, X.; Bandis, A.; Tao, A.; Meresi, G.; Inglefield, P. T.; Jones, A. A.; Wen, W.-Y. *Polymer* **2001**, *42*, 6485.
- (191) Meresi, G.; Wang, Y.; Bandis, A.; Inglefield, P. T.; Jones, A. A.; Wen, W.-Y. *Polymer* **2001**, *42*, 6153.
- (192) Sodaye, H. S.; Pujari, P. K.; Goswami, A.; Manohar, S. B. *J. Polym. Sci., Part B: Polym. Phys.* **1997**, *35*, 771.
- (193) Plate, N. A.; Shibaev, V. P. *Brush-like Polymers and Liquid Crystals*; Khimija: Moscow, 1980; p 304 (Russ. transl.).
- (194) Timashev, S. F. *Physical Chemistry of Membrane Processes*; Khimija: Moscow, 1988; p 237 (Russ. transl.).
- (195) Rubatat, L.; Rollet, A. L.; Gebel, G.; Diat, O. *Macromolecules* **2002**, *35*, 4050.
- (196) Kalyanasundaram, K.; Thomas, J. K. *J. Am. Chem. Soc.* **1977**, *99* (7), 2039.
- (197) Lee, P. C.; Meisel, D. *Photochem. Photobiol.* **1985**, *41*, 21.
- (198) Szentirmay, M. N.; Prieto, N. E.; Martin, C. R. *J. Phys. Chem.* **1985**, *89*, 3017.
- (199) Robertson, M. A. F.; Yeager, H. L. *Macromolecules* **1996**, *29*, 5155.

- (200) Young, S. K.; Trevino, S. F.; Beck Tan, N. C.; Paul, R. L. Army Research Laboratory Report ARL-TR-2679, March 2002.
- (201) Twardowski, Z.; Yeager, H. L.; O'Dell, B. *J. Electrochem. Soc.* **1982**, *129* (2), 328.
- (202) Perusich, S. A. *Macromolecules* **2000**, *33*, 3431.
- (203) Grot, W. G. F.; Munn, G. E.; Walmsley, P. N. Presented at the Electrochemical Society Meeting, Houston, TX, May 7–11, 1972; paper no. 154.
- (204) Yeo, S. C.; Eisenberg, A. *J. Appl. Polym. Sci.* **1977**, *21*, 875.
- (205) Kyu, T.; Eisenberg, A. In *Perfluorinated Ionomer Membranes*; Eisenberg, A., Yeager, H. L., Eds.; American Chemical Society Symposium Series 180; American Chemical Society: Washington, DC, 1982; Chapter 6, p 79.
- (206) Tant, M. R.; Darst, K. P.; Lee, K. D.; Martin, C. W. In *Multiphase Polymers: Blends and Ionomers*; Utracki, L. A., Weiss, R. A., Eds.; American Chemical Society Symposium Series 395; American Chemical Society: Washington, DC, 1989; Chapter 15, p 370.
- (207) Miura, Y.; Yoshida, H. *Thermochim. Acta* **1990**, *163*, 161.
- (208) Cable, K. M. Tailoring Morphology-Property Relationships in Perfluorosulfonate Ionomers. Ph.D. Dissertation, University of Southern Mississippi, 1996.
- (209) Young, S. K.; Mauritz, K. A. *J. Polym. Sci., Part B: Polym. Phys.* **2001**, *39* (12), 1282.
- (210) Kyu, T.; Hashiyama, M.; Eisenberg, A. *Can. J. Chem.* **1983**, *61*, 680. Also cross reference #195 (version 7/6/04).
- (211) Moore, R. B.; Cable, K. M.; Croley, T. L. *J. Membr. Sci.* **1992**, *75*, 7.
- (212) Page, K. A.; Moore, R. B. *Polym. Prepr. (Am. Chem. Soc., Div. Polym. Chem.)* **2003**, *44* (1), 1144.
- (213) Landis, F. A.; Moore, R. B.; Page, K. A.; Han, C. C. *Polym. Mater. Sci. Eng. (Am. Chem. Soc., Div. Polym. Mater. Sci. Eng.)* **2002**, *87*, 121.
- (214) Page, K. A.; Cable, C. A.; Moore, R. B. Manuscript in preparation.
- (215) Mauritz, K. A. In *Ionomers: Synthesis, Structure, Properties and Applications*; Tant, M. R., Mauritz, K. A., Wilkes, G. L., Eds.; Blackie Academic & Professional: London, 1997; p 95.
- (216) Hsu, W. Y.; Barkley, J. R.; Meakin, P. *Macromolecules* **1980**, *13*, 198.
- (217) Cirkel, P. A.; Okada, T. *Macromolecules* **2000**, *33*, 4921.
- (218) Cirkel, P. A.; Okada, T.; Kinigasa, S. *Macromolecules* **1999**, *32*, 5321.
- (219) Hsu, W. Y.; Berzins, T. *J. Polym. Sci., Polym. Phys. Ed.* **1985**, *23*, 933.
- (220) Mauritz, K. A.; Rogers, C. E. *Macromolecules* **1985**, *18*, 483.
- (221) Verbrugge, M. W.; Hill, R. F. *J. Electrochem. Soc.* **1990**, *137*, 886.
- (222) Verbrugge, M. W.; Hill, R. F. *J. Electrochem. Soc.* **1990**, *137*, 893.
- (223) Pintauro, P. N.; Verbrugge, M. W. *J. Membr. Sci.* **1989**, *44*, 197.
- (224) Bontha, J. R.; Pintauro, P. N. *Chem. Eng. Sci.* **1994**, *49*, 3835.
- (225) Eikerling, M.; Kornyshev, A. A.; Stimming, U. *J. Phys. Chem. B* **1997**, *101*, 10807.
- (226) Paddison, S. J.; Zawodzinski, T. A. *Solid State Ionics* **1998**, *113–115*, 333.
- (227) Paddison, S. J. *Handb. Fuel Cells—Fundam., Technol. Appl.* **2003**, *3* (3), 396.
- (228) Kreuer, K. D. *J. Membr. Sci.* **2001**, *185*, 29.
- (229) Ise, M. Ph.D. Thesis, University of Stuttgart, 2000.
- (230) Paddison, S. J.; Paul, R.; Zawodzinski, T. A. In *Proton Conducting Membrane Fuel Cells II*; Gottesfeld, S., Fuller, T. F., Eds.; Electrochemical Society Proceedings Series; Electrochemical Society: Pennington, NJ, 1999; Vol. 98-27, p 106.
- (231) Paddison, S. J.; Paul, R.; Zawodzinski, T. A. *J. Electrochem. Soc.* **2000**, *147*, 617.
- (232) Paddison, S. J.; Paul, R.; Zawodzinski, T. A. *J. Chem. Phys.* **2001**, *115*, 7753.
- (233) Paul, R.; Paddison, S. J. *J. Chem. Phys.* **2001**, *115* (16), 7762.
- (234) Paul, R.; Paddison, S. J. *Solid State Ionics* **2004**, *168*, 245.
- (235) Vishnyakov, A.; Niemark, A. V. *J. Phys. Chem. B* **2000**, *104*, 4471.
- (236) Vishnyakov, A.; Niemark, A. V. U. S. Army NSC Report: Modeling of Microstructure and Water Vapor Sorption and Transfer in Permselective Membranes, 2000.
- (237) Khalatur, P. G.; Talitskikh, S. K.; Khokhlov, A. R. *Macromol. Theory Simulat.* **2002**, *11*, 566.
- (238) MacMillan, B.; Sharp, A. R.; Armstrong, R. L. *Polymer* **1999**, *40*, 2481.
- (239) Hsu, W. Y. *Macromolecules* **1983**, *16*, 745.
- (240) Matsushige, K.; Enoshita, R.; Ide, T.; Yamanchi, N.; Taki, S.; Takemura, T. *Jpn. J. Appl. Phys.* **1977**, *16*, 681.
- (241) Rosser, R. W.; Schrag, J. L.; Ferry, J. D.; Greaser, M. *Macromolecules* **1977**, *10*, 978.
- (242) Jang, S. S.; Molinero, V.; Cagin, T.; Goddard, W. A. *J. Phys. Chem. B* **2004**, *108*, 3149.
- (243) Tanimura, S.; Matsuoka, T. *J. Polym. Sci., Part B: Polym. Phys.* **2004**, *42*, 1905.

CR0207123

